PROCEEDINGS BOOK OF THE 9th

ADVANCED ENGINEERING DAYS

9-10 July 2024 / TABRIZ, IRAN

International Engineering Symposium



Congress Chairman

PROF. DR. MURAT YAKAR

http://aed.mersin.edu.tr/





ISBN: 978-625-8101-87-4

ADVANCED ENGINEERING DAYS

The proceedings of the
9th Advanced Engineering Days







Editor-in-Chief

Prof. Dr. Murat YAKAR

Editors

Prof. Dr. Khalil Valizadeh KAMRAN

Res. Asst. Aydın ALPTEKİN

ISBN: 978-625-8101-87-4

Tabriz, 2024

HONOR BOARD

Ali Hamza PEHLİVAN – Governor of Mersin Province
Prof. Dr. Erol YAŞAR – Rector of Mersin University
Prof. Dr. Safar NASROLLAHZADEH, Rector of University of Tabriz
Prof. Dr. Orhan AYDIN – Rector of Tarsus University
Prof. Dr. Ömer ARIÖZ – Rector of Toros University

SCIENCE BOARD

Prof. Dr. Murat YAKAR (Mersin University)
Prof. Dr. İlker Fatih KARA (Mersin University)
Prof. Dr. Mehmet Cihan AYDIN (Bitlis Eren University)
Prof. Dr. Ali Rıza SÖĞÜT (Konya Technical University)
Prof. Dr. Şükrü DURSUN (Konya Technical University)
Prof. Dr. Fatmir BASHOLLI (Albanian University, Albania)
Prof. Dr. Donato ABRUZZESE (Roma "Tor Vergata" University, Italy)
Prof. Dr. Edmönd Höxha (Albania University, Titana Albania)
Prof. Dr. Hysen Mankolli (University of Maryland College Park, USA)
Prof. Dr. Erdem KOCADAĞISTAN (Erzurum Atatürk University)
Prof. Dr. Sailesh Iyer (Rai University, India)
Prof. Dr. Khalil Valizadeh KAMRAN (University of Tabriz, IRAN)
Prof. Dr. Spase Shumka (Albania Agriculture University, Albania)
Prof. Dr. Mehmet Cihan AYDIN (Bitlis Eren University)
Prof. Dr. S. Kazem Alavipanah, University of Tehran
Prof. Dr. Manouchehr Farajzadeh, Tarbiat Modares University
Prof. Dr. Hamid Reza Ghafarian Malamiri, Yazd University
Prof. Dr. Seyed Ali Almodaresi, Islamic Azad University of Yazd branch
Prof. Dr. Hossein Nazmfar, University of Mohaghegh Ardabili
Prof. Dr. Orhan Gündüz, İzmir institute of technology, Turkey
Assoc. Prof. Dr. Hossein Aghighi, Shahid Beheshti University
Assoc. Prof. Dr. Ali Shamsoddini, Tarbiat Modarres University
Assoc. Prof. Dr. Ara Toomanian, University of Tehran
Assoc. Prof. Dr. Alireza Gharagozlou, Shahid Beheshti University
Assoc. Prof. Dr. Najmeh Neysani Samany, University of Tehran
Assoc. Prof. Dr. Sayyad Asghari Saraskanroud, University of Mohaghegh Ardabili
Assoc. Prof. Dr. Hossein Vahidi, Ferdowsi University of Mashhad
Assoc. Prof. Dr. Ali Tahaei, Kharazmi University
Assoc. Prof. Dr. Masoud Minaei, Ferdowsi University of Mashhad
Assoc. Prof. Dr. Shirn Mohammadkhan, University of Tehran
Assoc. Prof. Dr. Arif Oğuz ALTUNEL (Kastamonu University)
Assoc. Prof. Dr. Furkan AYAZ (Mersin University)
Assoc. Prof. Dr. Erdinç AVAROĞLU (Mersin University)
Assoc. Prof. Dr. Nida NAYCI (Mersin University)
Assoc. Prof. Dr. Musa ÇIBUK (Bitlis Eren University)
Assoc. Prof. Dr. Ümit BUDAK (Bitlis Eren University)
Assoc. Prof. Dr. Beyhan KOCADAĞISTAN (Erzurum Atatürk University)
Assoc. Prof. Dr. Barış BULDUM (Mersin University)
Assoc. Prof. Dr. İskender ÖZKUL (Mersin University)
Assoc. Prof. Dr. Şenay GÜNGÖR (Nevşehir Hacı Bektaş Veli University)
Assoc. Prof. Dr. Lyudmyla Symochko (Uzhhorod National University, Ukraine)
Assoc. Prof. Dr. Davron Aslonqulovich Juraev (University of Economy and Pedagogy) Uzbekistan
Assoc. Prof. Dr. Gordana Kaplan, Eskisehir Technical University, Turkey
Assoc. Prof. Dr. Babak Vaheddoust, Bursa Technical University, Turkey
Assoc. Prof. Dr. A. Can Zulfikar, Istanbul Technical University, Turkey
Assoc. Prof. Dr. Saeed Samadianfard, University of Tabriz
Assoc. Prof. Dr. Hossein Soltani-Jigheh, Azarbaijan Shahid Madani University
Assist. Prof. Dr. Mohammadali Maysami, University of Tabriz
Assist. Prof. Dr. Kambiz Falsafian, University of Tabriz
Asst. Prof. Dr. Mehmet Rida Tur (Batman University)

Asst. Prof. Dr. Rana Valizadeh Kamran, Azarbaijan Shahid Madani University
Asst. Prof. Dr. Omid Rafieyan, Islamic Azad University of Tabriz branch
Asst. Prof. Dr. Mohammad Ebriahim Ramezni, Islamic Azad University of Tabriz branch
Asst. Prof. Dr. Navid Hooshangi, University of Arak
Asst. Prof. Dr. Abuzar Nasiri, University of Firoozabad
Asst. Prof. Dr. Samira Abushova, Azerbaijan National Academy of Science, Azerbaijan
Dr. Hakan DOĞAN (Turkish State Meteorological Service)
Dr. Cihan YALÇIN (Ministry of Industry and Technology)

ORGANIZING BOARD

Prof. Dr. Murat YAKAR (Mersin University)
Prof. Dr. Jalal Shiri, Vice Chancellorship for Research and Technology (University of Tabriz)
Prof. Dr. Khalil Valizadeh Kamran, Head of organizing committee (University of Tabriz)
Prof. Dr. Cengiz ALYILMAZ (Uludağ University)
Prof. Dr. Semra ALYILMAZ (Uludağ University)
Prof. Dr. Şükrü DURSUN (Konya Technical University)
Prof. Dr. Mehmet Cihan AYDIN (Bitlis Eren University)
Prof. Dr. Erdem KOCADAĞISTAN (Erzurum Atatürk University)
Prof. Dr. Saeid Shojaei, Director of International & Academic Cooperation Directorate (University of Tabriz)
Prof. Dr. Abolfazl Ghanbari (University of Tabriz)
Prof. Dr. Reza Tarinejad (University of Tabriz)
Prof. Dr. Ataallah Nadiri (University of Tabriz)
Prof. Dr. Hossein Navid (University of Tabriz)
Assoc. Prof. Dr. Hashem Rostamzadeh, Head of Faculty of Planning and Environmental Sciences (University of Tabriz)
Assoc. Prof. Bakhtiar Feizizadeh (University of Tabriz)
Assoc. Prof. Dr. Iraj Teymouri (University of Tabriz)
Assoc. Prof Dr. Hossein Karimzadeh (University of Tabriz)
Assoc. Prof Dr. Mohsen Aghayari (University of Tabriz)
Assoc. Prof Dr. Seyed Jamaleddin Peighambardoust (University of Tabriz)
Assoc. Prof. Dr. Beyhan KOCADAĞISTAN (Erzurum Atatürk University)
Assoc. Prof. Dr. Ali ULVİ (Mersin University)
Asst. Prof. Dr. Sadra Karimzadeh, Head of scientific committee (University of Tabriz)
Asst. Prof Dr. Amir Aminzadeh Ghavifekr (University of Tabriz)
Asst. Prof. Dr. Vahdettin DEMİR (KTO Karatay University)
Asst. Prof. Dr. Esra URAY (KTO Karatay University)
Dr. Hakan DOĞAN (Turkish State Meteorological Service)
Dr. Behnam Khorrami (University of Tabriz)
Lect. Atilla KARABACAK (Mersin University)
Lect. Şafak FİDAN (Mersin University)
Res. Asst. Aydın ALPTEKİN (Mersin University)
Res. Asst. Abdurahman Yasin YİĞİT (Mersin University)
Res. Asst. İrem YAKAR (Istanbul Technical University)
Eng. Engin KANUN (Mersin University)
Eng. Mücahit Emre ORUÇ (Mersin University)
Eng. Seda Nur Gamze HAMAL (Mersin University)

Iran Time, UTC +3:30

Dr. S. Mohammad-Reza S. Noorani

09.00-10.40	Session 1: Mechanical Engineering Tuesday Room 1
	Creating micro-scale mixing by controlled diffusion Tuhid Pashaee Golmarz, Saleh Khorasani
	Simulation of the failure in an aluminum alloy using a comprehensive damage model Ali Zahedi
	Experimental Investigation of Nozzle Diameter Effect on Tensile Strength of PLA Material in FDM Processes Farid Gholipour, MohammadReza Shabgard, Mohammad Baraheni, Mojtaba Farhudian
	Dynamic response of a curved composite beam under moving mass Hadi Teymouri, Ghadir Ahmadi Jeyed, Hasan Biglari, Nazli Sami
	Free vibrations of functionally graded sheets using HSNDT Hadi Teymouri, Kaveh Karimkhani, Erfan Rahmatzadeh, Hasan Biglari
	Deformation analysis of elastic plate under static extended loading by FEM Arya Gholami, Hadi Teymouri, Amirreza Nikmard, Aidin Badiee, Hasan Biglari
	Numerical analysis of composite beams with piezoelectric actuators Rasa Rahimi Behbood, Hadi Teymouri, Hasan Biglari, Taraneh Sheidaei
	Finite element analysis of tensile testing for Carbon fiber Epoxy composite plate Amir Javadzadeh Khoei, Mohammad Reza Khoshravan Azar
	Characterization of fracture behavior of the aluminum alloy 6061 using an uncoupled fracture criterion Ali Zahedi
	Two-phase numerical simulation of an inkjet nozzle using the level-set method Paniz Rezazadeh Azar, Sajad Rezazadeh, Maziar Javadi, Mirmahdi SeyedValilu

Dr. S. Mohammad-Reza S. Noorani

10.50-12.30	Session 2: Mechanical Engineering Tuesday Room 1
	Thermo-economic evaluation and comprehensive analysis of a power generation system based on flame-assisted fuel cells and supercritical carbon dioxide cycle Amirreza Javaherian, Samar Fazlollahi, Seyed Mohammad Seyed Mahmoudi, Faramarz Talati
	Finite Element Analysis of CFRP and GFRP Compressed Natural Gas Maryam Ranjbar, Mohammad Reza Khoshravan Azar
	Skin Imaging methodology to improve analysis of geometric deviation Elnaz Ghanbary Kalajahi, Mehran Mahboubkhah, Ahmad Barari
	Modeling, resizing and optimization of HEV for FTP driving cycle Reza Yasoubi, Erfan Rahmatzadeh
	The numerical simulation of fluid-structure interaction by phase-field method Hanieh Abbasi, Sajad Rezazadeh
	Numerical simulation of compact heat exchanger with dynamic moving walls Maziar Javadi, Sajad Rezazadeh, Paniz Rezazadehazar, MirMahdi Seyyedvalilu
	Numerical study of heat transfer on the surface of the cone Ghazaleh Babazadeh Asbagh, Faramarz Talati
	Numerical investigation of the effect of different parameters in preventing the emission of polluting gasses in a room using air curtains Ghazaleh Babazadeh Asbagh, Moharram Jafari, Faramarz Ranjbar
	Exergetic and thermoeconomic analysis of biogas motorized cogeneration systems used in wastewater treatment plant Adnan Berber, Oğuzhan Dağcı
	Estimation of critical rotary velocity of stepped shaft using Dunkerley and FE methods Ahmad Balande, Hasan Biglari, Hadi Teymouri

Dr. S. Mohammad-Reza S. Noorani

12.40- 14.10	Session 3: Mechanical Engineering Tuesday Room 1
	LCCP and TEWI Evaluation for Various Refrigerants Used in Refrigerated Display Cabinets Melis Öder, Adnan Berber
	Effects of burial depth in the behavior of buried pipelines subjected to traffic load Arsalan Amanollahi-Asl, Hasan Biglari
	Simulation and analysis of fracture toughness and crack propagation in a composite sheet based on multi-scale modeling method Ghadir Ahmadi Jeyed, Hasan Biglari
	Obtaining the buckling capacity of composite pipe under axial load and external pressure Arsalan Nojavan Kohnehshahri, Hasan Biglari
	Fluid flow and heat transfer of water-based nanofluids in plate-fin heat sink Ali Rahbar, Hamidreza Toloueinasab, Amirreza Javaherian, Mohsen Zeinali, Moharram Jafari
	Numerical investigation of pressure drop and heat transfer using nanofluids in microchannels Milad Rezaei, Ali Rahbar, Hamidreza Toloueinasab, Amirreza Javaherian, Moharram Jafari
	Natural frequency analysis of a plate strengthened in dry and underwater conditions in the presence of added mass effects Ghadir Ahmadi Jeyed, Mohammad Gandomkar, Hasan Biglari
	Enhancing Vehicle Stability and Yaw Performance Using Sliding Mode Control Based on Nonlinear Model Amirreza Mirzajani, Mohammad Ali Hamed, Sevda Rezazadeh Movahhed
	Influence of Soil Characteristics on the Performance of Buried Pipelines under Traffic Load Arsalan Amanollahi-Asl, Hasan Biglari
	A computational fluid dynamics simulation on a marine engine turbocharger to enhance the output power Amirreza Javaherian, Reza Mahmoodi, Peyman Rahmani

Prof. Dr. A. Khorshiddoust

14.20-15.50	Session 4: Environmental Engineering Tuesday Room 1
	Remote Sensing and Hydrometeorological Analysis of River Delta Dynamics: A Case Study of the Kur River Delta Turkan Mamishova
	The effect of solar radiation on O^3 pollution concentration in urban areas, case of Tehran, Iran. Iraj Teimuri, Mohammad Nemati, Sajjad Moshiri, Ayat Khaleel Dhiab Gharibawy
	Prediction of water quality indices utilizing easily accessible elements: A case study of Qatur River Milad Sharafi, Javad Behmanesh, Vahid Rezaverdinejad, Saeed Samadianfard
	Where are the most qualified parks located? A case study of city of Tabriz Elmira Davatgar Khorsand, Akbar Rahimi
	Enhancing water treatment efficiency: a study on coagulant dosage prediction in water treatment plant Milad Sharafi
	Evaluation of urban environmental quality in District 4 of Tabriz metropolis using CRITIC model Hassan Mahmoudzadeh
	Evaluation of quantile mapping and linear scaling bias correction methods for NASA-IMERG historical monthly precipitation data Ahmad Abu Arra, Eyüp Şişman
	Iranian Gardens as Nature-based Solutions to Improve Thermal Comfort Arman Rastkhadiv, Akbar Rahimi
	AQI-based box model using GIS and remote sensing over Kirkuk city, Iraq Huda Jamal Jumaah, Khalil Valizadeh Kamran

Prof. Dr. Ali Mohammad Khorshiddoust

16.00-17.20	Session 5: Environmental Engineering Tuesday Room 1
	Hospital site selection using AHP-based GIS in Tikrit City, Iraq Mohammed Hashım Ameen, Hafssa Ali Abdullah, Huda Jamal Jumaah, Eapak Qasim Hasan
	Application of remote sensing methods and tools in detecting pollution in the Caspian Sea and their impact on the water surface temperature of the Azerbaijan Ismayil Zeynalov, Ulker Mahmudova, Rena Ahmedova, Aybeniz Ahmedova, Almaz Rustamova
	Spatiotemporal Dynamic Simulation of Carbon Storage and Sequestration in response to Land Use/Land Cover Changes Bahman Veisi Nabikandi, Farzin Shahbazi, Ahmad Hami
	An Integrated Model-Data Fusion Approach to Measuring the Habitat's Quality and Degradation in Marivan County Bahman Veisi Nabikandi, Khalil Valizadeh Kamran, Ahmad Hami
	Assessing Cultural Ecosystem Services of Urban Agriculture: Analysis of Small-Scale using Smart-PLS Software Arman Rastkhadiv, Bahman Veisi Nabikandi
	Spatial Analysis of photosynthesis function in reducing air temperature in Tehran parks Ali Tymoori, Saeed Jahanbakhsh Asl, Ali Mohammad Khorshiddoust
	The Study of Water Pollution Caused by Wastewater Entering Mehranrud River in Tabriz Mohammadreza Jafarnezhad, Sara Jafari Behtash, Ali Mohammad Khorshiddoust
	The Impact of Geotourism on Sustainable Development in Mountainous Areas: A Case Study of Kamtal National Park Seyed Asadollah Hejazi, Mahdi Javadi

Prof. Dr. Ali Mohammad Khorshiddoust

17.30-18.50	Session 6: Environmental Engineering Tuesday Room 1
	Geotourism in Kandovan Village: A Stunning Blend of Natural Wonders and Rock Architecture Seyed Asadollah Hejazi, Mahdi Javadi
	Spatial-temporal patterns of Nitrogen Oxides (〖No〗_x) with Sentinel-5 satellite imagery (Kurdistan Region of Iraq) Nader Habibzadeh, Dara Hashem Ahmad
	Analysis of environmental pollution caused by the movement of dust particles Peyman Yariyan, Bakhtiar Feizizadeh, Khalil Valizadeh Kamran
	Evaluation of the environmental effects of Sungun copper mine using the DPSIR framework Mohsen Aghayari Hir, Nahid Rahimzadeh
	An Analysis on smallness index of residential parcels of the urban fabric in Tabriz city Fereidoun Babaei Aghdam, Alireza Omidpour, Murat Yakar
	Estimation and comparison of evaporation losses from the dam reservoir using intelligent gene expression programming model and empirical methods: A case study of Sattarkhan Ahar Dam Vahdat Ahmadifar, Reza Delirhasannia, Tima Mohammadzadeh

Dr. L. Naghipour

09.00-10.40	Session 7: Geomatics Engineering Tuesday Room 2
	Down-scaling of MODIS land Cover product using Landsat images to detect changes in Google Earth Engine Mostafa Mahdavifard, Samaneh Bagheri, Sadra Karimzadeh, Khalil Valizadeh Kamran
	Geospatial arbitrations with Landsat and Sentinel images in evaluating temperature variations over the New Delhi region of India Jagadish Kumar Mogaraju
	Hydrological analysis for disaster management in Şanlıurfa region Berra Nur Önay, Halil İbrahim Şenol
	Road extraction with high-resolution UAV images using deep learning algorithms Halil İbrahim Şenol
	Assessment of green space changes using NDVI index via Google Earth Engine and ArcGIS platforms: A case study of Isfahan, Ahvaz, and Maragheh Cities, Iran Paria Ali Mohammadi, Iraj Teymuri
	Graph neural networks in determining the road network Nurettin Sinanoğlu, Elif Sertel
	A Geospatial Approach to Vegetation Monitoring: Multi-Indices Analysis with Landsat 8 via Google Earth Engine Emre Akturk
	Harnessing Solar Energy: Mapping the Potential and Performance of Middle Eastern Countries Meysam Hasanzadeh, Khalil Valizadeh Kamran
	Assessing the riskiness of the factors affecting the desirability of natural hazard crisis management (Earthquake) in the high-rise (Baghmisheh town, Tabriz metropolis) Khalil Valizadeh Kamran, Sadra Karimzadeh, Behdad Fouladbanjeh, Babak Nouri

Dr. M. Jeihouni

10.50-12.30	Session 8: Geomatics Engineering Tuesday Room 2
	Local climate zone classification using deep learning and remote sensing data Melike Nicancı Sinanoğlu, Şinasi Kaya
	Monitoring post-earthquake debris removal process with multi-temporal Sentinel 2 satellite imagery: The case of Antakya Ugur Alganci, Dursun Zafer Seker
	Enhancing Warehouse Efficiency Through Geographic Information Systems Onur Yurekli, Muhammed Enes Atik
	Emergency and Terminated Evacuation of Supermarket Warehouse Using Indoor Navigation by Dijkstra's Algorithm Deniz Doga Isik, Şaziye Özge Atik
	Comparing the accuracy of extracting surface features from Landsat and UAV imagery Mohammad Saleh Chavoshi, Hassan Emami
	Identifying the Available Lands for Solar Energy Farms Using GIS Spatial Analysis: Case Study, Kirkuk City and its Suburbs Ghadah Hasan Mohammedfatih, Khalil Valizadeh Kamran, Qayssar Mahmood Ajaj, Aboolfazl Ghanbari
	A Satellite-based Monitoring for Air Pollution in Urban Areas (Case Study: Tabriz City) Arash Rahmani Zadeh, Hassan Emami, Shahla Taghizadeh Sofiani
	Monitoring and Forecasting of Spatiotemporal Expansion Pattern of Tabriz Metropolis during in a period of 30 years Hassan Emami, Rahman Zarei, Saleh Fasihi
	Evaluation of Integration and Accessibility Metrics for Metropolitan Metro Lines Esra Gizem Ugur, Zaide Duran, Dursun Zafer Seker
	Understanding the Relationship Between Seismic Events and Atmospheric Conditions, A Case Study of Antakya Abdullah Sukkar, Ugur Alganci, Dursun Zafer Seker
	Comparative study of urban development in Tabriz and Mersin Fereidoun Babaei Aghdam, Shiva Sattarzadeh Salehi, Murat Yakar

Dr. L. Naghipour

12.40-14.10	Session 9: Geomatics Engineering Tuesday Room 2
	Fire-risk assessment with Dong model based on anthropogenic and natural factors (study area: Arasbaran forest) Sajjad Moshiri, Ahmad Nikdel Monavvar, Khalil Valizadeh Kamran, Omid Rafieyan
	Comparative Analysis of 3D Models Generated by Close Range Photogrammetry and Smartphone-Based LiDAR Sensor Koray Aksu, Esra Günaydın, Zaide Duran
	Hyperspectral classification of minerals using K-means and PLS-DA models Ahmad Nikdel Monavvar, Sajjad Moshiri, Seyed Hossein Faghih, Iraj Teymouri, Sadra Karimzadeh
	Optimal Spatial Distribution of Mosques in The City of Hillah / Iraq Using Evolutionary Algorithms and Geographic Information Systems Abolfazl Ghanbari, Falih Hassan Ali
	Evaluation of the relationship between the ecological spatial inequality with the parameters of urban heat islands, population and green space of Tabriz metropolis Mir Ali Seyed Mosaffayi, Saeed Ahmadian, Sajjad Moshiri
	Evaluation of the Impact of Air Pollution Parameters on Land Surface Temperature of the Metropolis of Tabriz. Saeed Ahmadian, Mir Ali Seyed Mosaffayi
	Assessing of spatio-temporal changes of Normalized Impervious Surface index (case study: metropolis of Tabriz) Mahdiyeh Shokati Sefidan, Ahmad Nikdel Monavvar, Sajjad Moshiri, Khalil Valizadeh Kamran, Iraj Teymouri, Fereydoun Babaei Aghdam

Dr. Mehrdad Jeihouni

14.20- 15.50	Session 10: Geomatics Engineering Tuesday Room 2
	Evaluating Land Surface Temperature Variations around Fault Lines and Their Correlation with Groundwater Levels Using Remote Sensing Fatemeh Sedghi, Khalil Valizadeh Kamran
	Exploring Spectral Reflectance and Classification of Wheat, Barley and Alfalfa Crops Using Hyperspectral Imaging Fatemeh Sedghi, Sadra Karimzadeh
	Monitoring surface water area changes of Najaf Sea in Iraq using RS and GIS for sustainable development Abolfazl Ghanbari, Huda Jamal Jumaah
	Sustainable ecological development planning (case study: County of Tabriz) Hamed Panahdar, Shahram Roostaei, Ahmad Nikdel Monavvar, Sajjad Moshiri
	Investigating the influence of atmospheric parameters on Aerosol optical depth in Iran Sajedeh Morady Par
	Hyperspectral remote sensing in environmental studies Mehrdad Jeihouni
	Remote sensing applications in agriculture Mehrdad Jeihouni
	Smart agriculture Mehrdad Jeihouni

Dr. B. Khorrami

16.00-17.30	Session 11: Geomatics Engineering Tuesday Room 2
	Surface soil moisture Retrieval using Sentinel-1 SAR data models Dubois in Ardabil Plain Maryam Sadeghi, Sadra Karimzadeh, Khalil Valizadeh Kamran
	Exploring the Potential of U-Net Architectures for Classifying Different Maize Genotypes Using Multispectral UAV Imagery Ismail Colkesen, Umut Gunes Sefercik, Taskin Kavzoglu, Mustafacan Saygi, Muhammed Yusuf Ozturk, Osman Yavuz Altuntas, Mertcan Nazar, Ilyas Aydin, HasanTonbul
	Monitoring Land Cover Changes by Satellite Images Using Deep Learning Neural Network Models in Tehran with a Sustainable Development Approach Mahdi Farhangi, Gholamreza Fallahi, Alireza Gharagozlou
	Virtual Field Practice Education for Total Station Bashar Helal, Veli İlçi, Kaan Bati
	Engineering approaches to reduce seismic vulnerability based on spatial analysis Peyman Yariyan, Sadra Karimzadeh, Mahyat Shafapourtehrany
	Precise digital twin production by UAV and TLS data fusion Umut Gunes Sefercik, Muhammed Madak, Mertcan Nazar
	Creation of Coefficient of Friction Maps of Flood Areas with Remote Sensing Technique Yunus Tektaş, Nizar Polat
	Transformer Based Land Use and Land Cover Segmentation Cengiz Avcı, Elif Sertel
	Investigation of real estate sales to foreigners in Turkey based province and year Nuri Erdem
	An integrated GIS and location-based service approach applied to geomarkting and customer behavior mapping in Tabriz Bakhtiar Feizizadeh

Dr. B. Khorrami

17.40-19.20	Session 12: Geomatics Engineering Tuesday Room 2
	3D Documentation of an Archaeological Cave in Şuayip City, Şanlıurfa Nizar Polat
	Production of agricultural cadastre map using object-oriented processing of UAV images of Tabriz farms Abulfazl Ghanbari, Habil Khorrami, Mostafa Musapour
	Impact of Different Image Acquisition Modes on the Multispectral UAV-Based NDVI Maps İlyas Aydın, Umut Gunes Sefercik
	Thermal Analysis of Building Facades Using UAV Emine Beyza Dörtbudak, Nizar Polat
	Quantifying Land Surface Temperature through Multispectral Landsat-9 Satellite Images Mohammadali Abbasi, Mahdi Hasanlou, Saeid Homayoni
	The effect of ground control point distribution in the improving of UAV corridor mapping accuracy Mobina Ahmadi Asoor, Alireza Afary, Ebadat Ghanbari Parmehr
	Automated Insulator Defect Detection in UAV images for Power Line Monitoring using YOLO-v8 Model Reza Rahimi Nejadbougar, Ebadat Ghanbari Parmehr, Alireza Afary, Samira Mavaddati
	Detection of stress in rice fields using satellite images and plant spectral indices Sara Amani, Ebadat Ghanbari Parmehr, Alireza Afari, Narjes Mahmoody-Vanolya
	Accuracy analysis of strawberry field detection using different machine learning algorithms and vegetation indices on the Google Earth Engine Ceren Akgül, Füsun Balık Şanlı, Osman Salih Yılmaz

Dr. S. Samadianfard

09.00-10.40	Session 13: Agricultural and Biosystems Engineering Wednesday Room 1
	Smart Agriculture: Leveraging Information Technology and Human Expertise for Sustainable Farming Adel Taheri Hajivand, Kimia Shirini, Sina Samadi Ghareveran
	LSTM Deep Learning for Acoustical Sorting of Jujube Fruits Sayed Javad Sajadi
	A Review of Artificial Intelligence Optimization Algorithms in Scheduling Problems with Constrained Resources in Mechanization Adel Taheri Hajivand, Kimia Shirini, Mehran Salehi, Ali Meshkini
	Investigation of pigment extraction from dry and wet microalgae Leila Nadaei, Hanieh Shokrkar
	Exploring Green Chili Pepper Recognition in Dense Foliage Greenhouses Using Deep Learning Segmentation Algorithms for Robotic Harvesting Hossein Akhtari, Hossein Navid, Javad Robati, Nayer Etminan Far, Ali Gaffarnejad
	Intelligent Seed Type Detection for Seed Drills Using Logistic Regression and Infrared Sensors Ali Ghaffarnezhad, Hossein Navid, Hadi Karimi
	Investigation of daily reference evapotranspiration modeling with up to three meteorological parameters at Bandar Abbas station Parastoo Amirzehni, Saeed Samadianfard, AmirHossein Nazemi, AliAshraf Sadradini
	Design and Implementation of an Unmanned Agricultural Machine for Automated Driving and Spraying Emirhan Kaya, Hasan Dilmaç, Veli İlçi
	Estimating daily reference evapotranspiration using remote sensing parameters by implementing Extreme Learning Machine optimized by Quantum-Inspired Algorithm Parastoo Amirzehni, Saeed Samadianfard, AmirHossein Nazemi, AliAshraf Sadradini

Dr. M.A. Maysami

10.50- 12.30	Session 14: Agricultural and Biosystems Engineering Wednesday Room 1
	Estimating reference evapotranspiration in an arid region using a MODIS sensor and machine learning algorithms Hamed Talebi, Saeed Samadianfard, Hatice Çıtakoğlu
	Artificial Intelligence (AI) in Agricultural Mechanization: A Mini Review Reza Kheyri
	A novel deep learning-based method for Potato Leaf Disease Classification Kimia shirini, Adel Taheri Hajivand,Sina Samadi Ghareveran
	Assessing the Impact of Climate Change on Evaporation in Maragheh Region Using Time Series Models Vahdat Ahmadifar, Reza Delirhasannia, Tima Mohammadzadeh
	Estimation of fractional vegetation cover dynamics based on remote sensing in Shabestar, Iran Aylar Mohammadi, Abolfazl Majnooni Heris, Reza Hassanpour
	Empirical Bayesian Kriging for Soil Available Phosphorus Mapping Shahla Rahmani Siyalarz, Ali Keshavarzi, Fuat Kaya
	Comparison of geospatial based interpolation techniques for spatial distribution of Soil Organic Carbon (SOC) Ali Keshavarzi, Koyel Sur, Fuat Kaya, Shahla Rahmani Siyalarz
	Prediction of potato leaf disease severity using deep learning regression Sayed Javad Sajadi, Fakhtak Taliei

Dr. M. Razavifar

12.40-14.00	Session 15: Chemical Engineering Wednesday Room 1
	Effect of Thermal Pre-Treatment of gamma-Alumina and Ceria-Zirconia on Three-Way Catalyst Performance Hossein Sheikh, Yousef Zaynali
	Humidification Modeling in a Wetted Wall Tower Saghar Babaei, Kamran Keynejad, Hedayat Azizpour, Mohammad Mahdi Heydari, Sara Mansouri
	Modeling of Ultrasonic Reactor and Investigation of Pressure Distribution Sara Mansouri, Kamran Keynejad, Hedayat Azizpour, Mohammad Mahdi Heydari, Saghar Babaei
	Optimization of effective parameters on catalytic performance in zone-coated three-way catalyst using Taguchi method Tal'at Moeini, Yousef Zaynali
	Investigating the amount carotenoid extraction using chemical methods from microalgae Leila Nadaei, Hanieh Shokrkar
	Using Tween solvent to extract chlorophyll and carotenoids from Chlorella vulgaris Leila Nadaei, Hanieh Shokrkar
	A Facile Synthesis Method of Bis (Ethanolammonium) Hexahydroxoplatinum (IV) Solution for Platinum Supported Catalysts Faezeh Farrokhpey, Yousef Zaynali
	Boosting the photocatalytic activity of ZnCo2O4 spinel via anchoring on graphene nanoplatelets for removing the ciprofloxacin antibiotic Shadi Ebrahimi, Mohammad Mehdi Heydari, Azadeh Ebrahimian Pirbazari, Reza Zarghami, Fatemeh Esmaeili Khalil Saraei

Dr. M. Razavifar

14.10-15.30	Session 16: Chemical Engineering Wednesday Room 1
	Study the effect of morphology and structure of CeO2/TiO2 and CeO2/ZrO2 heterostructures on the degradation efficiency of tetracycline Mohammad Moradi, Mohammad Mehdi Heydari, Azadeh Ebrahimian Pirbazari, Fatemeh Esmaeili Khalil Saraei
	Modeling a Recuperator to Investigate Velocity Distribution and Pressure Drop by Varying the Cross-Section Geometry of its Pipes Erfan Farsijani, Kamran Keynejad, Hedayat Azizpour, Zahra Nasrollahi
	Removal of hydroquinone from aqueous solution using novel Fe-Mg bimetallic oxide: synthesis, characterization and isotherm modeling Hesam Malekzadeh, Mohammad Zabihi, Morteza Faghihi
	Study of pH effect on the degradation of naproxen in aqueous solution using MnO2 photocatalyst Seyed Taha Hosseini Koohi, Zahra Nasrollahi, Kamran Keynejad
	Modeling of Fluid Flow and Heat Transfer Inside Fin-and-Tube Heat Exchanger with Hexagonal Cross-Section of Tubes Reza Ghafuri, Zahra Nasrollahi, Hedayat Azizpour, Kamran Keynejad
	Complete photocatalytic removal of Ciprofloxacin using NiAl2O4 spinel grafted on graphene nanosheets Elnaz Pazdar
	The Deposition-precipitation of Plasmonic Ag/Ag3PO4 Nanoparticles on ZnS Micro/nanospheres for Photocatalytic Treatment of Methyl Orange and Tetracycline Artificial Effluents Sogand Rajaei Farid, Mohammad Amin Habibi, Azadeh Ebrahimian Pirbazari, Fatemeh Esmaeili Khalil Saraei
	Factors Affecting the Electrolysis of Sodium Chloride by a Membrane Electrochemical Cell for the Production of Sodium Hydroxide in an Environmentally Friendly Method Mohammad Amin Habibi, Sogand Rajaei Farid, Kamran Keynejad, Hedayat Azizpour
	Adsorption study of methyl orange dye removal from aqueous solutions by using a novel polymeric MOF nanosorbent Niloofar Razmi, Mohammad Zabihi, Sirous Ebrahimi

Dr. A. A. Ghavifekr

15.40-17.10	Session 17: Electrical and Electronics Engineering Wednesday Room 1
	Robust Position Control of AC Servo Motor Using Sliding Mode Control (SMC) Optimized by Grey Wolf Optimization (GWO) Algorithm Navid Salahshoor, Mahmood Moghadasian
	Optimized H-Infinity Controller for Torque Control of PMSM Using Grasshopper Optimization Algorithm (GOA) Mehran Khalaj Afshar, Mahmood Moqhadasian
	Analysis of Different Distribution Configuration for Optimal Photovoltaic Integration: A Case Study Klajdi Kamberi, Donard Shaliu, Marialis Çelo, Bajram Leka
	Designing PID Controller for Speed Control of Autonomous Vehicle by Utilizing Improved Grey Wolf Optimization Algorithm Arman Nagizadeh, Amir A.Ghavifekr, Ayta Mollazadeh
	Enhancing Distribution Network Resilience by Integration Renewable Energy Sources and Energy Storage Sina Roudnil, Kasra Shafiei, Saeid Ghassem Zadeh
	sEMG based Hand Gesture Recognition via Simple Feature Extraction and LSTM Model Ramin Soleimani, Saeed Meshgini, Mohammad Reza Sayyed Noorani
	IMU-based Movement Control of Robotic Manipulators – Aided by CoppeliaSim Alireza Ashrafi Majd, Mohammad Reza Sayyed Noorani
	Forecasting Survival Rate from ICU Data Based On LightGBM Mahmood Seyyedzadeh, Alireza Tajdid, Ali Firouzi Abriz, Kashish Rai
	Implementation and Optimization of PID Controller Using HHO Algorithm for DC Encoder Motor in Autonomous Guided Vehicles (AGV) Mohammad Javad Saeidi, Mahmoud Moqadasian

Dr. A. A. Ghavifekr

17.20-19.00	Session 18: Electrical and Electronics Engineering Wednesday Room 1
	Optimal Design of 1 MW Grid-Connected Solar Power Plant for increasing Solar Radiation by using PVsyst Software Amirreza Samadi Bonab, Parisa Shirinabadi, Kazem Zare, Sina Asadian, Khadim Moin Siddiqui, Neel Kamal
	EEG-Based Classification of Mental Stress Induced by Arithmetic Task Morteza Jafari Malali, Sepideh Zolfaghari, Aysel Davar
	A Third-Order Quadrature Sinusoidal Oscillator Using Operational Amplifiers Mohammad Rashtian, Mahdi Shabani, Houman Farsadpour
	Design and Characterization of a Discrete Curvature-Compensated Bandgap Voltage Mohammad Rashtian, Houman Farsadpour, Mahdi Shabani, Ali Karimi
	Transformer-BiGRU: Hybrid Deep Model for Wind Power Prediction Elman Ghazaei, Amir A. Ghavifekr, Paolo Visconti
	GenTradeCast: A Precise Forecasting Predictive Model in Peer-to-Peer Energy Trading Markets–A Dataset Case Study of Germany Ashkan Safari, Amir A. Ghavifekr
	Application of Quantum Neural Networks for Robotic Motion Control Ashkan Safari, Amir A. Ghavifekr, Hossein B. Jond, Roberto De Fazio, Mina Salim, Khadim Moin Siddiqui, Neel Kamal, Ajay Kumar
	New organ design for humans: electrical generating neural network inspired by eel Arya Gholipoor Hanizi, Sina Asadian
	Optimal Sizing of a Grid Connected Microgrid Using Firefly Algorithm Sina Asadian, Ali Firouzi Abriz, Arash Faramarzi
	Estimation of elbow joint angle based on single channel electromyography signal of selected arm muscle, using machine learning methods Ayla Ahmadi, Babak Rezaee Afshar
	Design of Adaptive PID Controller for Lower Limb Exoskeleton Robot Based on Hybrid Model of Genetic Algorithm and Improved Black Hole Optimization Amir Ata Nikjoo, Mohanna Arefnezhad
	Neuromusculoskeletal Modeling of Elbow Flexion/Extension – Aided by OpenSim MohammadReza Sayyed Noorani, Farhad Farkhondeh Tale Navi, Kimiya Khojand

19.10- 21.30	Session 19: Mix Wednesday Room 1
	Radar study of mudflow formation mechanisms on the territory of Azerbaijan Said Safarov, Elnur Safarov
	Investigating LULC Change Impacts on Surface UHI Using RS Data case study: Kerman city Amin Raisi Moghadam, Khalil Valizadeh Kamran
	The role of innovative food packaging in food quality and safety Samin Adineh
	Numerical Study on the Solidification Process in Conical Shell and Tube Latent Heat Energy Storage Tanks Amirhossein Gholamzadeh, Ardalan Shafiei Ghazani
	A Comparative Study on the Performance of LQG/LTR and Optimized SMIT Controllers in Tracking Control of Flying-Wing UAVs Sevda Rezazadeh Movahhed, Mohammad Ali Hamed
	Output Feedback Control Using Enhanced SMIT Controller Based on Sliding Mode Observer for Longitudinal Control of Rudderless Flying-Wing UAVs Sevda Rezazadeh Movahhed, Mohammad Ali Hamed
	Engineering an efficient hemostatic fabric by modifying regenerated cellulose Nastaran Alipour, Roya Salehi
	Preparation of mineral distribution map using Hyperion images: A case study of Northwest of Kerman Province Hossein Fekrat, Vahid Kakapor, Maryam Sadeghi, Khalil Valizadeh Kamran, Hassan Emami
	Synthesis and in situ oxidation of copper nanoparticles by glow discharge plasma on liquid Nazila Mahmoudian, Fatemeh Baharlounezhad, Mohammad Ali Mohammadi, Mohadeseh Mousavi, Ali Soltani Vala
	Investigating the physical properties of carbon nanotubes modified by plasma method Mohaddeseh Mousavi, Fatemeh Baharlounezhad, Mohammad Ali Mohammadi, Nazila Mahmoudian
	The plasma synthesis and treatment of tungsten oxide nanoparticles Fatemeh Baharlounezhad, Mohammad Ali Mohammadi
	Adapting cities to climate change Mahmoud Asoude Khyal , Nasser Mashganbari, Ali Hamedi, Hassan Mahmoodzadeh
	Water resource management and the effects of reducing rainfall in cities Ali Hamedi, Mahmoud Asoude Khyal, Hassan Mahmoodzadeh, Reza Mahdinia
	The effects of urban management on green space: solutions and challenges: A case study of Tabriz city Mahmoud Asoude Khyal, Nasser Mashganbari, Ali Hamedi, Hassan Mahmoodzadeh
	Narrative review of enzymatic oil refining Afsaneh Ahansaz
	Facile synthesis of Mn-doped carbon aerogel composite cathode for electrochemical oxidation of Cefepim drug waste from contaminated water Tala Babaei, Mahmoud Zarei, Paria Rostamzadeh, Hannaneh Mortaghi Ghasemi
	Thermofluidic analysis of backward facing step Couette-Poiseuille flow with symmetric corrugations and upper moving wall Hamidreza Toloueinasab, Ramin Abdollahi, Ali Rahbar, Seyed Esmail Razavi

Dr. A. Hosseini Baghanam

09.00- 11.50	Session 20: Civil Engineering Wednesday Room 2
	Estimation of control points of the surface model obtained by unmanned aerial vehicle with artificial neural network Ali Kavak, Halil Kısacıkoğlu, Vahdettin Demir, Aydın Alptekin, Murat Yakar
	The Importance of Determining Value-Based Land Shares: Business Center Application Muhammed Emin Işık, Nuri Erdem
	Development of Porous Asphalt Pavement using Recycled Surface Dressed Pavement Material (RSM) Ibrahim Sheikh Ibrahim, Hassan Shuaibu Abdulrahman
	Statistical evaluation of theoretical and nonparametric approaches to Standardized Precipitation Index Ahmad Abu Arra, Eyüp Şişman
	Suspended sediment dynamics in the semiarid Mediterranean environment: A case study of the Ksob basin, Algeria Fouad Sakhraoui, Ahmad Abu Arra, Mahmoud Hasbaia, Eyüp Şişman
	Assessment of drought using a probabilistic standardized index Burak Kızılöz, Gizem Aylin Şahin
	Environmental sustainability in line with urban infrastructure development with focus on sustainable development Mahdi Jalili Marand, Sheyda Sarikhan Kheljan
	Effect of Groundwater Level Change on Retaining Wall Design İhsan Yaman, Abdülkadir Özcan, Esra Uray
	Literature Review of Artificial Intelligence and Geostatistical Analyses in Geotechnical Engineering Hatice Beyza Urgancı, Burak Bilir, Esra Uray, Vahdettin Demir
	Improvement Effect of Artificial Puzolan Waste Material and Cement Additive on Crushed Stone Ground and Taguchi Method Mehmet Hilmi Tutumlu, Esra Uray
	An analysis on the distributional justice of medical centers in the 2nd district of Tabriz metropolis Rogayeh Sharafi, Mahmoud Asoude Khyal, Ali Hamedi, Hassan Mahmoodzadeh
	Hydroclimatic Trend Analysis of Gorgan Coastal Region, Iran Vahid Azimi, Hirsa Taherimashhadi
	Hydrodynamic Analysis of Lake Urmia: Effects of Causeway and Water Levels on Flow Patterns Mehran Dadashzadeh, Alireza Mojtahedi, Javad Parsa
	Investigation of damping properties on the wavelet-based damage detection in steel beam under noise effect: A numerical study Farhad Jedari Zare Zadeh, Mehran Dadashzadeh
	Unraveling topological features of complex networks Leyla Naghipour, Khalil Valizadeh Kamran, Mohammad Taghi Aalami, Vahid Nourani
	Forecasting of Beyşehir Lake Levels with Artificial Neural Networks and Levenberg Training Algorithm Beyza Değişli, Vahdettin Demir
	Evaluating the Effect of Monopile Diameter on the Static Deformation Response Using Finite Element Method Özgür Lütfi Ertuğrul, Fatma Dülger Canoğulları
	Investigation of Loading Frequency Effects on the Dynamic Lateral Load- Displacement Curves of Monopiles Özgür Lütfi Ertuğrul, Fatma Dülger Canoğulları

Dr. Feizizadeh

12.00-13.50	Session 21: Remote sensing of Disasters/GeoAI Wednesday room 2
	Evaluation of GPM and TRMM Precipitation Data versus Observational data in Lake Urmia Basin Fatemeh Hosseinpour Asl, Saeed Jahanbakhsh Asl, Hashem Rostamzadeh
	Pollution Study of Hajilar Chai Basin in East Azerbaijan Province, Iran Ali Mohammad Khorshiddoust, Ali Asghar Azad, Azadeh Mirzaahmadi
	Investigating the texture of region 5 of Tabriz city with emphasis on earthquake vulnerability Shiva Sattarzadeh Salehi, Firouz Jafari
	Analysis of Urban Planning policies in earthquake-affected areas and lessons from the cities of Kahramanmaraş and Hatay in Türkiye Fereidoun Babaei Aghdam, Shiva Sattarzadeh Salehi, Murat Yakar, Aydin Alptekin
	Engineering analysis of multidimensional vulnerability due to earthquake occurrence Peyman Yariyan, Abolfazl Ghanbari, Mohammadreza Karami
	Accuracy assessment of captured land-covered maps in urban fringes, (cases from Tabriz, Iran and Mersin, Turkiye) Fereidoun Babaei Aghdam, Shiva Sattarzadeh Salehi, Murat Yakar, Khalil Valizadeh Kamran
	A review of GIS application in urban green landscapes Mohammad Khezrollah, Zanyar Samadi Todar, Khalil Valizadeh Kamran
	Evaluating the performance of remote sensing to monitor the severity of drought through the comparison of three drought severity indicators (NDDI, NDWI and NDVI) in the Karkheh basin Vahid Kakapor, Hossein Fekrat, Maryam Sadeghi, Khalil Valizadeh Kamran, Maryam Bayati Khatibi
	Comparing the efficiency of Object-Based fuzzy operators in extraction of urban built-up area of Tabriz metropolis Mostafa Mousapour, Bakhtiar Feizizadeh
	Identification of Sunflowers (Helianthus annuus L.) from Multi-Temporal UAV Orthomosaics Using Deep Learning Models Esra Yildirim, Ismail Colkesen, Umut Gunes Sefercik
	Assessment of Urban Green Space Using UAV-Based Green Leaf Index: A Case Study of Harran University Osmanbey Campus Nizar Polat, Seyma Akca

14.00-16.20	Session 22: Mix Wednesday Room 2
	Ensuring information security in teaching students Asrorov Oybek Asror Ogli
	The effectiveness of hybrid automobiles and the reduction of urban pollution. Case study Ledia Bozo , Asllan Hajderi , Rrezart Bozo
	Mapping potential risk factors of cultural monument sites at the middle and upper part of River Vjosa in the accelerated climate change circumstances Laura Shumka
	Skin Imaging methodology to improve analysis of geometric deviation Elnaz Ghanbary, Mehran Mahboubkhah, Ahmad Barari
	A case survey of dietary intake for assessing diet diversity score among vulnerable groups of society Estela Pinderi, Joana Vogli, Marinela Leka
	The impact of the magnetic field on the reduction of pollution from vehicles, Case study Asllan Hajderi, Ledia Bozo
	Acoustic pollution in industrial environments Fatmir Basholli, Aydin Alptekin
	Simulation based on historical data and expectations for tsunamis in the Adriatic and Ionian seas Fatmir Basholli, Adisa Daberdini, Rrapo Ormeni
	Reconstruction of the historical building based on archaeological excavations and studies Khojiakbar Egamberdiyev, Noila Xidirova, Asilbek Shukurov, Jakhongir Davronov, Jonibek Xolmurodov
	Methodology for teaching computer science using information and communication technologies Madina Makhkamova, Noila Xidirova, Sadokat Kamolova
	Modeling the stability indicator taking into account the bending deformation of the freight car body Anzhelika Shvets, Leontii Muradıan, Angela Shvets
	Length-weight relationships of the Twait shad - *Alosa falax* (Lacepède, 1803) from the South western Adriatic coast of Albania Nertila Muçollari, Spase Shumka
	Energy production and income of 5 kW solar power plant in Boukan, Iran Khadijeh Mirza

	Study of the influence of different car types on the wear indicators of the “wheel-rail” couple Angela Shvets
	Energy Piles Design Parameters Optimization by using Fuzzy Logic Çetin Önder İncekara
	Aluminum Forging Technology, Applications and Analysis Sait Gül, Esat Erdinç Önel, Hüseyin Tat
	Modeling of Fluid Flow and Heat Transfer Inside Fin-and-Tube Heat Exchanger with Pentagonal Cross-Section of Tubes Reza Ghafuri, Zahra Nasrollahi, Hedayat Azizpour, Kamran Keynejad
	Innovative Intelligent Methods in Integer Programming Javad Nematian, Khadijeh Daneshfar, Neda Shahmohammadi

Dr. B. Khorrami

16.30-17.30	Session 23: Mechatronics Engineering Wednesday Room 2
	Designing a Flexible Interface Mechanism to Convert an Industrial Gripper into a System Suitable for Medical Applications Leila EffatiAghdam, Hamidreza Arefi, Seyed Mohammadreza Akrami, Reza Abdollahi
	Simulation, trajectory design and motion control of robotic hand with sensing force control Ali Korehpaz Saeid, Reza Abdollahi, Seyed Mohammadreza Akrami, Melika Fahmi
	Influence of new advanced split injection strategy on emissions and performance of a dual-fuel RCCI engine Seyed Ali Sadri Jahanshahi, Amirreza Javaherian, Mortaza Yari
	Smooth Path Planning for Autonomous Mobile Robots: Integration of Improved A-Star with Artificial Potential Field Method Amir Amjadi, Samira Kharratian, Seyed Mohammadreza Akrami, Yousef Seyfari
	Neuromusculoskeletal Modeling of Elbow Flexion/Extension – Aided by OpenSim MohammadReza Sayyed Noorani, Farhad Farkhondeh Tale Navi, Kimiya Khojand

Dr. Aghdasi Alamdari

17.40-19.00	Session 24: Computer Engineering Wednesday Room 2
	Separation of active zones of electromyographic signals Kudratjon Zohirov, Sardor Boykobilov, Mamadiyor Sattorov
	Comparative Analysis of Machine Learning and Deep Learning Models for Multilingual Multitarget Stance Detection Muhammad Ebrahim Ahmadi, Monireh Hosseini
	Offensive Context detection in social network using graph neural net Minou Kouh Soltani
	Enhancing VM Migration in Clouds with Heuristic-based Granular Computing Seyyed Meysam Rozehkhani, Farnaz Mahan
	Honeypot-Based Detection of Advanced Persistent Threats: A New Methodology Maryam Mohammadzad, Jaber Karimpour
	Transfer learning-based face mask detection Salar Mokhtari Laleh, Seyed Mahdi Abdi Oskouei, Mohammad Sarhangzadeh
	Strategic Monitoring and Proactive Measures for Mitigating Network-Level Threats and Malware in Albania Klorenta Pashaj, Eralda Gjika, Vilma Tomco
	Person Identification in Healthcare Applications Using Binary Chimp Optimization-based EEG Channel Selection Shabnam Oskouei, Saeed Meshgini, Hadi S. Aghdasi

19.10-20.10	Session 25: Cultural Heritage Wednesday Room 2
	Investigation of Stone Deterioration in Gaziantep Yüzükçü Inn İlhami Ay, Murat Dal, Şefika Ergin
	Investigation of Stone Deterioration in Gaziantep Lala Mustafa Pasha Inn İlhami Ay, Murat Dal, Şefika Ergin
	Investigation of Stone Deterioration in Gaziantep Tabakhane Bridge İlhami Ay, Şefika Ergin, Murat Dal
	Investigation of Stone Deterioration in Gaziantep Balıklı Masjid İlhami Ay, Şefika Ergin, Murat Dal
	Investigation of Stone Deterioration in Gaziantep Köseç Ahmet Ağa Fountain İlhami Ay, Şefika Ergin, Murat Dal

20.20-21.10	Session 26: Energy Engineering Wednesday Room 2
	Data-driven Energy Management of H-MGs using Fuzzy Reinforcement Learning Azam Salari, Mahdi Zeinali, Mousa Marzband
	Wind Energy Potential of Turkey Seçkin Tekin, Emine Banu Burkut, Murat Dal
	Focus on solar energy in architecture and design Emine Banu Burkut, Seçkin Tekin, Murat Dal

Dr. B. Khorrami

21.20- 22.20	Session 27: Geology Science and Engineering Wednesday Room 2
	Impact of industrial use on nitrogen dioxide air pollutant distribution (case example: Tabriz, Iran) Paria Ali Mohammadi, Iraj Teymuri
	Statistical Analysis and Machine Learning Applications of radiolarite-hosted manganese mineralization in Taşdemir (Kahramanmaraş, Türkiye) Cihan Yalçin
	Utilizing International Experiences in the Revitalization of Lake Urmia Seyyed Asadullah Hijazi, Saye Habibzadeh
	Identification and classification of karst landforms based on Cvijic, Waltham, Fookes, Komatina and Herak models (Case study: Travertine springs of Badab Soort) Shahram Roostaei, Bahareh Akbari
	Investigation of land use change effects on water quality of Tabriz plain Zahra Sedghi, Ata Allah Nadiri
	Monitoring the impacts of investment in the tourism sector on land use changes in the Hir City using the Change Detection Technique Mohsen Aghayari Hir, Sahar Ahmadzadeh Naghadeh, Milad Manzelati
	Integrated Assessment of Forest Fire Vulnerability: A Multi-dimensional Approach Elnaz Nejatiyanpour, Omid Ghorbanzadeh, Josef Strobl, Khalil Gholamnia, Rasoul Yousefpour, Mahmoud Daneshvar Kakhki, Hamid Amirnejad, Mahmouh Sabouhi Sabouni
	Ground deformation monitoring in Hatay Airport using GACOS-corrected StaMPS PSI Mahmut Gorken, Umut Gunes Sefercik, Mertcan Nazar
	Türkiye cracked the code in topographic earth representation Arif Oguz Altunel, Samet Doğan
	Mapping Wetlands Using Sentinel-2 Satellite Imagery and Auxiliary Data with Google Earth Engine Zelalem Getachew Ayalke, Aziz Şişman
	Enhancement of Zirconium Oxide-Based Graphite Electrode through Mechanochemical Methods for Electrochemical Applications Mary Gojeh, Ishaya Sugbeh Alhassan, Manasseh Tachia Bwankwot, Jonah Rebeccah Aji, Habiba Kakangi Dalhatu, Solomon Ogobuto

22.30-24.10	Session 28: Mix Wednesday Room 2
	Photogrammetric recording of epigraphic documentation Cengiz Alyılmaz
	The importance of academic field work in social sciences Semra Alyılmaz, Cengiz Alyılmaz
	Building interior modeling with Wearable Mobile LIDAR Atilla Karabacak, Murat Yakar
	3D Modeling with Wearable Mobile LIDAR and Mezitli Stone Bridge example Atilla Karabacak, Murat Yakar
	3D Modeling of Mersin University Vocational School of Technical Sciences with Wearable Mobile LIDAR Atilla Karabacak, Murat Yakar
	Investigation of natural factors affecting landslide formation Aydın Alptekin, Murat Yakar

Content	Page
Creating micro-scale mixing by controlled diffusion Tuhid Pashaee Golmarz, Saleh Khorasani	1-4
Simulation of the failure in an aluminum alloy using a comprehensive damage model Ali Zahedi	5-7
Experimental investigation of nozzle diameter effect on tensile strength of PLA material in FDM processes Farid Gholipour, MohammadReza Shabgard, Mohammad Baraheni, Mojtaba Farhoudian	8-10
Dynamic response of a curved composite beam under moving mass Hadi Teymouri, Ghadir Ahmadi Jeyed, Hasan Biglari, Nazli Sami	11-14
Free vibrations of functionally graded sheets using HSNDT Hadi Teymouri, Kaveh Karimkhani, Erfan Rahmatzadeh, Hasan Biglari	15-18
Deformation analysis of elastic plate under static extended loading by FEM Arya Gholami, Hadi Teymouri, Amirreza Nikmard, Aidin Badiee, Hasan Biglari	19-21
Numerical analysis of composite beams with piezoelectric actuators Rasa Rahimi Behbood, Hadi Teymouri, Hasan Biglari, Taraneh Sheidaei	22-24
Finite element analysis of tensile testing for carbon fiber epoxy composite plate Amir Javadzadeh Khoei, Mohammad Reza Khoshravan Azar	25-27
Characterization of fracture behavior of the aluminum alloy 6061 using an uncoupled fracture criterion Ali Zahedi	28-30
Two-phase numerical simulation of an inkjet nozzle using the level-set method Paniz Rezazadeh Azar, Sajad Rezazadeh, Maziar Javadi, MirMahdi Seyyed Valilu	31-33
Thermo-economic evaluation and comprehensive analysis of a power generation system based on flame-assisted fuel cells and supercritical carbon dioxide cycle Amirreza Javaherian, Samar Fazlollahi, Seyed Mohammad Seyed Mahmoudi, Faramarz Talati	34-36
Finite element analysis of CFRP and GFRP compressed natural gas Maryam Ranjbar, Mohammad Reza Khoshravan Azar	37-39
Skin imaging methodology to improve analysis of geometric deviation Elnaz Ghanbary, Mehran Mahboubkhah, Ahmad Barari	40-42
Modeling, resizing and optimization of HEV for FTP driving cycle Reza Yasoubi, Erfan Rahmatzadeh	43-45
The numerical simulation of fluid-structure interaction by phase-field method Hanieh Abbasi, Sajad Rezazadeh	46-48
Numerical simulation of compact heat exchanger with dynamic moving walls Maziar Javadi, Sajad Rezazadeh, Paniz Rezazadeh Azar, MirMahdi Seyyed Valilu	49-51
Numerical study of heat transfer on the surface of the cone Ghazaleh Babazadeh Asbagh , Faramarz Talati	52-54
Numerical investigation of the effect of different parameters in preventing the emission of polluting gasses in a room using air curtains Ghazaleh Babazadeh Asbagh, Moharram Jafari, Faramarz Ranjbar	55-57
Exergetic and thermoeconomic analysis of biogas motorized cogeneration systems used in wastewater treatment plant Adnan Berber, Oguzhan Dağcı	58-60
Estimation of critical rotary velocity of stepped shaft using Dunkerley and FE methods Ahmad Balande , Hasan Biglari, Hadi Teymouri	61-63
LCCP and TEWI evaluation for various refrigerants used in refrigerated display cabinets Adnan Berber, Melis Öder	64-67

Effects of burial depth in the behavior of buried pipelines subjected to traffic load 68-71
Arsalan Amanollahi-Asl, Hasan Biglari

Simulation and analysis of fracture toughness and crack propagation in a composite sheet based on multi-scale modeling method 72-76
Ghadir Ahmadi Jeyed, Hasan Biglari

Obtaining the buckling capacity of composite pipe under axial load and external pressure 77-79
Arsalan Nojavan Kohnehshahri, Hasan Biglari

Fluid flow and heat transfer of water-based nanofluids in plate-fin heat sink 80-82
Ali Rahbar, Hamidreza Toloueinasab, Amirreza Javaherian, Mohsen Zeinali, Moharram Jafari

Numerical investigation of pressure drop and heat transfer using nanofluids in microchannels 83-85
Milad Rezaei, Ali Rahbar, Hamidreza Toloueinasab, Amirreza Javaherian , Moharram Jafari

Natural frequency analysis of a plate strengthened in dry and underwater conditions in the presence of added mass effects 86-89
Ghadir Ahmadi Jeyed, Mohammad Gandomkar, Hasan Biglari

Enhancing vehicle stability and yaw performance using sliding mode control based on nonlinear model 90-93
Amirreza Mirzajani, Sevda Rezazadeh Movahhed, Mohammad Ali Hamed

Influence of soil characteristics on the performance of buried pipelines under traffic load 94-97
Arsalan Amanollahi-Asl, Hasan Biglari

A computational fluid dynamics simulation on a marine engine turbocharger to enhance the output power 98-100
Amirreza Javaherian, Reza Mahmoodi, Peyman Rahmani

Remote sensing and hydrometeorological analysis of River Delta dynamics: A case study of the Kur River Delta 101-104
Turkan Mamishova

The effect of solar radiation on O^3 pollution concentration in urban areas, case of Tehran, Iran 105-108
Iraj Teimuri, Mohammad Nemati, Sajjad Moshiri, Ayat Khaleel Dhiab Gharibawy

Prediction of water quality indices utilizing easily accessible elements: A case study of Qatur River 109-112
Milad Sharafi, Javad Behmanesh, Vahid Rezaverdinejad, Saeed Samadianfard

Where are the most qualified parks located? A case study of city of Tabriz 113-115
Elmira Davatgar Khorsand, Akbar Rahimi

Enhancing water treatment efficiency: a study on coagulant dosage prediction in water treatment plant 116-119
Milad Sharafi

Evaluation of urban environmental quality in District 4 of Tabriz metropolis using CRITIC model 120-136
Hassan Mahmoudzadeh

Evaluation of quantile mapping and linear scaling bias correction methods for NASA-IMERG historical monthly precipitation data 137-140
Ahmad Abu Arra, Eyüp Şişman

Iranian gardens as nature-based solutions to improve thermal comfort 141-143
Arman Rastkhadiv, Akbar Rahimi

AQI-based box model using GIS and remote sensing over Kirkuk city, Iraq 144-146
Huda Jamal Jumaah, Khalil Valizadeh Kamran

Hospital site selection using AHP-based GIS in Tikrit City, Iraq 147-149
Mohammed Hashim Ameen, Hafssa Ali Abdullah, Huda Jamal Jumaah , Eapak Qasim Hasan

Application of remote sensing methods and tools in detecting pollution in the Caspian Sea and their impact on the water surface temperature of the Azerbaijan 150-152
Ismayil Zeynalov, Ulker Mahmudova, Rena Ahmedova, Aybeniz Ahmedova, Almaz Rustamova

Spatiotemporal dynamic simulation of carbon storage and sequestration in response to land use/land cover changes 153-156
Bahman Veisi Nabikandi, Farzin Shahbazi, Ahmad Hami

An integrated model-data fusion approach to measuring the habitat's quality and degradation in Marivan County 157-160
Bahman Veisi Nabikandi, Khalil Valizadeh Kamran, Ahmad Hami

Assessing cultural ecosystem services of urban agriculture: Analysis of small-scale using Smart-PLS software 161-164
Arman Rastkhadiv, Bahman Veisi Nabikandi

Spatial analysis of photosynthesis function in reducing air temperature in Tehran parks 165-173
Ali Teymoori , Saeed Jahanbakhsh Asl, Ali Mohammad Khorshiddoust

The Study of Water Pollution Caused by Wastewater Entering Mehranrud River in Tabriz 174-180
Mohammadreza Jafarnezhad, Sara Jafari Behtash, Ali Mohammad Khorshiddoust

The impact of geotourism on sustainable development in mountainous areas: A case study of Kamtal National Park 181-183
Seyed Asadollah Hejazi, Mahdi Javadi

Geotourism in Kandovan Village: A stunning blend of natural wonders and rock architecture 184-186
Seyed Asadollah Hejazi, Mahdi Javadi

Spatial-temporal patterns of Nitrogen Oxides (No_x) with Sentinel-5 satellite imagery (Kurdistan Region of Iraq) 187-190
Nader Habibzadeh, Dara Hashem Ahmad

Analysis of environmental pollution caused by the movement of dust particles 191-195
Peyman Yariyan, Bakhtiar Feizizadeh, Khalil Valizadeh Kamran

Evaluation of the environmental effects of Sungun copper mine using the DPSIR framework 196-202
Mohsen Aghayari Hir, Nahid Rahimzadeh

An analysis on smallness index of residential parcels of the urban fabric in Tabriz city 203-205
Fereidoun Babaei Aghdam, Alireza Omidpour, Murat Yakar

Estimation and comparison of evaporation losses from the dam reservoir using intelligent gene expression programming model and empirical methods: A case study of Sattarkhan Ahar Dam 206-211
Vahdat Ahmadifar, Reza Delirhasannia, Tima Mohammadzadeh

Down-scaling of MODIS land Cover product using Landsat images to detection changes in Google Earth Engine 212-215
Mostafa Mahdavifard, Samaneh Bagheri, Sadra Karimzadeh, Khalil Valizadeh Kamran

Geospatial arbitrations with Landsat and Sentinel images in evaluating temperature variations over the New Delhi region of India 216-221
Jagadish Kumar Mogaraju

Hydrological analysis for disaster management in Şanlıurfa region 222-225
Berra Nur Önay, Halil İbrahim Şenol

Road extraction with high-resolution UAV images using deep learning algorithms 226-228
Halil İbrahim Şenol

Assessment of green space changes using NDVI index via Google Earth Engine and ArcGIS platforms: A case study of Isfahan, Ahvaz, and Maragheh Cities, Iran 229-231
Paria Ali Mohammadi, Iraj Teymuri

Graph neural networks in determining the road network 232-234
Nurettin Sinanoğlu, Elif Sertel

A geospatial approach to vegetation monitoring: Multi-indices analysis with Landsat 8 via Google Earth Engine 235-237
Emre Aktürk

Harnessing solar energy: Mapping the potential and performance of Middle Eastern Countries 238-240
Meysam Hasanzadeh, Khalil Valizadeh Kamran

Assessing the riskiness of the factors affecting the desirability of natural hazard crisis management (Earthquake) in the high-rise (Baghmisheh town, Tabriz Metropolis) 241-245
Khalil Valizadeh Kamran, Sadra Karimzadeh, Behdad fuladpanjeh, Babak Nouri

Local climate zone classification using deep learning and remote sensing data 246-248
Melike Nicancı Sinanoğlu, Şinasi Kaya

Monitoring post-earthquake debris removal process with multi-temporal Sentinel 2 satellite imagery: The case of Antakya 249-251
Ugur Alganci, Dursun Zafer Seker

Enhancing warehouse efficiency through geographic information systems 252-254
Onur Yurekli, Muhammed Enes Atik

Emergency and terminated evacuation of supermarket warehouse using indoor navigation by Dijkstra's Algorithm 255-258
Deniz Doğa Işık, Şaziye Özge Atik

Comparing the accuracy of extracting surface features from Landsat and UAV imagery 259-262
Mohammad Saleh Chavoshi, Hassan Emami

Identifying the available lands for solar energy farms using GIS spatial analysis: A case study, Kirkuk City and its suburbs 263-266
Ghadah Hasan Mohammedfatih, Khalil Valizadeh Kamran, Qayssar Mahmood Ajaj , Aboolfazl Ghanbari

A satellite-based monitoring for air pollution in urban areas: A case study of Tabriz City 267-270
Arash RahmaniZadeh, Hassan Emami, Shahla Taghizadeh Sofiani

Monitoring and forecasting of spatiotemporal expansion pattern of Tabriz Metropolis during in a period of 30 years 271-274
Hassan Emami, Rahman Zarei, Saleh Fasihi

Evaluation of integration and accessibility metrics for metropolitan metro lines 275-277
Esra Gizem Ugur, Zaide Duran, Dursun Zafer Seker

Understanding the relationship between seismic events and atmospheric conditions: A case study of Antakya 278-280
Abdullah Sukkar, Ugur Alganci, Dursun Zafer Seker

Comparative study of urban development of Tabriz, Iran and Mersin, Turkiye 281-285
Fereidoun Babaei Aghdam, Shiva Sattarzadeh Salehi, Murat Yakar

Fire-risk assessment with Dong model based on anthropogenic and natural factors: A case study of Arasbaran Forest 286-294
Sajjad Moshiri, Ahmad Nikdel Monavvar, Khalil Valizadeh Kamran, Omid Rafieyan

Comparative analysis of 3D models generated by close range photogrammetry and smartphone-based LiDAR sensor 295-297
Koray Aksu, Esra Günaydın, Zaide Duran

Hyperspectral classification of minerals using K-means and PLS-DA models 298-300
Ahmad Nikdel Monavvar, Sajjad Moshiri, Seyed Hossein Faghih, Iraj Teymouri, Sadra Karimzadeh

Optimal Spatial Distribution of Mosques in The City of Hillah / Iraq Using Evolutionary Algorithms and Geographic Information Systems 301-303
Abolfazl Ghanbari, Falih Hassan Ali

Evaluation of the relationship between the ecological spatial inequality with the parameters of urban heat islands, population and green space of Tabriz metropolis 304-308
Mir Ali Seyed Mosaffayi, Saeed Ahmadian, Sajjad Moshiri

Evaluation of the Impact of Air Pollution Parameters on Land Surface Temperature of the Metropolis of Tabriz 309-311
Saeed Ahmadian, Mir Ali Seyed Mosaffayi

Assessing of spatio-temporal changes of Normalized Impervious Surface index (case study: metropolis of Tabriz) 312-316
Mahdiyeh Shokati Sefidan, Ahmad Nikdel Monavvar, Sajjad Moshiri, Khalil Valizadeh Kamran, Iraj Teymouri, Fereydoun Babaei Aghdam

Evaluating Land Surface Temperature Variations around Fault Lines and Their Correlation with Groundwater Levels Using Remote Sensing 317-319
Fatemeh Sedghi, Khalil Valizadeh Kamran

Exploring Spectral Reflectance and Classification of Wheat, Barley and Alfalfa Crops Using Hyperspectral Imaging 320-322
Fatemeh Sedghi, Sadra Karimzadeh

Monitoring surface water area changes of Najaf Sea in Iraq using RS and GIS for sustainable development 323-325
Abolfazl Ghanbari, Huda Jamal Jumaah

Sustainable ecological development planning (case study: County of Tabriz) 326-328
Hamed Panahdar, Shahram Roostaei, Ahmad Nikdel Monavvar, Sajjad Moshiri

Investigating the influence of atmospheric parameters on Aerosol optical depth in Iran 329-334
Sajedeh Morady Par

Hyperspectral remote sensing in environmental studies 335-337
Mehrdad Jeihouni

Remote sensing applications in agriculture 338-340
Mehrdad Jeihouni

Smart agriculture 341-343
Mehrdad Jeihouni

Surface soil moisture Retrieval using Sentinel-1 SAR data models Dubois in Ardabil Plain 344-348
Maryam Sadeghi, Sadra Karimzadeh, Khalil Valizadeh Kamran

Exploring the Potential of U-Net Architectures for Classifying Different Maize Genotypes Using Multispectral UAV Imagery 349-352
Ismail Colkesen, Umut Gunes Sefercik, Taskin Kavzoglu, Mustafacan Saygi, Muhammed Yusuf Ozturk, Osman Yavuz Altuntas, Mertcan Nazar, Ilyas Aydin, HasanTonbul

Monitoring Land Cover Changes by Satellite Images Using Deep Learning Neural Network Models in Tehran with a Sustainable Development Approach 353-355
Mahdi Farhangi, Gholamreza Fallahi, Alireza Gharagozlou

Virtual Field Practice Education for Total Station 356-358
Bashar Helal, Veli İlçi, Kaan Bati

Engineering approaches to reduce seismic vulnerability based on spatial analysis 359-364
Peyman Yariyan, Sadra Karimzadeh, Mahyat Shafapourtehrany

Precise digital twin production by UAV and TLS data fusion 365-368
Umut Gunes Sefercik, Muhammed Madak, Mertcan Nazar

Creation of Coefficient of Friction Maps of Flood Areas with Remote Sensing Technique 369-372
Yunus Tektaş, Nizar Polat

Transformer Based Land Use and Land Cover Segmentation 373-376
Cengiz Avcı, Elif Sertel

Investigation of real estate sales to foreigners in Turkey based province and year 377-379
Nuri Erdem

An integrated GIS and location-based service approach applied to geomarketing and customer behavior mapping in Tabriz 380-385
Bakhtiar Feizizadeh

3D Documentation of an Archaeological Cave in Şuayip City, Şanlıurfa 386-389
Nizar Polat

Production of agricultural cadastre map using object-oriented processing of UAV images of Tabriz farms 390-393
Abulfazl Ghanbari, Habil Khorrami, Mostafa Musapour

Impact of Different Image Acquisition Modes on the Multispectral UAV-Based NDVI Maps 394-396
Ilyas Aydın, Umut Gunes Sefercik

Thermal Analysis of Building Facades Using UAV 397-400
Emine Beyza Dörtbudak, Nizar Polat

Quantifying Land Surface Temperature through Multispectral Landsat-9 Satellite Images 401-404
Mohammadali Abbasi, Mahdi Hasanlou, Saeid Homayoni

The effect of ground control point distribution in the improving of UAV corridor mapping accuracy 405-407
Mobina Ahmadi Asoor, Alireza Afary, Ebadat Ghanbari Parmehr

Automated Insulator Defect Detection in UAV images for Power Line Monitoring using YOLO-v8 Model 408-410
Reza Rahimi Nejadbougar, Ebadat Ghanbari Parmehr, Alireza Afary, Samira Mavaddati

Detection of stress in rice fields using satellite images and plant spectral indices 411-415
Sara Amani, Ebadat Ghanbari Parmehr, Alireza Afari, Narjes Mahmoody-Vanolya

Accuracy analysis of strawberry field detection using different machine learning algorithms and vegetation indices on the Google Earth Engine 416-418
Ceren Akgül, Füsun Balık Şanlı, Osman Salih Yılmaz

Smart Agriculture: Leveraging Information Technology and Human Expertise for Sustainable Farming 419-421
Adel Taheri Hajivand, Kimia Shirini, Sina Samadi Ghareveran

LSTM Deep Learning for Acoustical Sorting of Jujube Fruits 422-424
Sayed Javad Sajadi

A Review of Artificial Intelligence Optimization Algorithms in Scheduling Problems with Constrained Resources in Mechanization 425-428
Adel Taheri Hajivand, Kimia Shirini, Mehran Salehi, Ali Meshkini

Investigation of pigment extraction from dry and wet microalgae 429-431
Leila Nadaei, Hanieh Shokrkar

Exploring Green Chili Pepper Recognition in Dense Foliage Greenhouses Using Deep Learning Segmentation Algorithms for Robotic Harvesting 432-434
Hossein Akhtari, Hossein Navid, Javad Robati, Nayer Etminan Far, Ali Gaffarnejad

Intelligent Seed Type Detection for Seed Drills Using Logistic Regression and Infrared Sensors 435-437
Ali Ghaffarnezhad, Hossein Navid, Hadi Karimi

Investigation of daily reference evapotranspiration modeling with up to three meteorological parameters at Bandar Abbas station 438-440
Parastoo Amirzehni, Saeed Samadianfard, AmirHossein Nazemi, AliAshraf Sadradini

Design and Implementation of an Unmanned Agricultural Machine for Automated Driving and Spraying 441-444
Emirhan Kaya, Hasan Dilmaç, Veli İlçi

Estimating daily reference evapotranspiration using remote sensing parameters by implementing Extreme Learning Machine optimized by Quantum-Inspired Algorithm 445-447
Parastoo Amirzehni, Saeed Samadianfard, AmirHossein Nazemi, AliAshraf Sadradini

Estimating reference evapotranspiration in an arid region using a MODIS sensor and machine learning algorithms 448-451
Hamed Talebi, Saeed Samadianfard, Hatice Çıtakoğlu

Artificial Intelligence (AI) in Agricultural Mechanization: A Mini Review 452-461
Reza Kheyri

A novel deep learning-based method for potato leaf disease classification 462-464
Kimia Shirini, Adel Taheri Hajivand, Sina Samadi Ghareveran

Assessing the Impact of Climate Change on Evaporation in Maragheh Region Using Time Series Models 465-469
Vahdat Ahmadifar, Reza Delirhasannia, Tima Mohammadzadeh

Estimation of fractional vegetation cover dynamics based on remote sensing in Shabestar, Iran 470-472
Aylar Mohammadi, Abolfazl Majnooni Heris, Reza Hassanpour

Empirical Bayesian Kriging for Soil Available Phosphorus Mapping 473-475
Shahla Rahmani Siyalarz, Ali Keshavarzi, Fuat Kaya

Comparison of geospatial based interpolation techniques for spatial distribution of Soil Organic Carbon (SOC) 476-479
Ali Keshavarzi, Koyel Sur, Fuat Kaya, Shahla Rahmani Siyalarz

Prediction of potato leaf disease severity using deep learning regression 480-482
Sayed Javad Sajadi, Fakhtak Taliei

Effect of Thermal Pre-Treatment of g-Alumina and Ceria-Zirconia on Three-Way Catalyst Performance 483-485
Hossein Sheikh, Yousef Zaynali

Humidification modeling in a wetted wall tower 486-488
Saghar Babaei, Kamran Keynejad, Hedayat Azizpour, Mohammad Mahdi Heydari, Sara Mansouri

Ultrasonic reactor modeling and investigation of pressure distribution 489-492
Sara Mansouri, Kamran Keynejad, Hedayat Azizpour, Mohammad Mahdi Heydari, Saghar Babaei

Optimization of effective parameters on catalytic performance in zone-coated three-way catalyst using Taguchi method 493-495
Tal'at Moeini, Yousef Zaynali

Investigating the amount carotenoid extraction using chemical methods from microalgae 496-498
Leila Nadaei, Hanieh Shokrkar

Using Tween solvent to extract chlorophyll and carotenoids from *Chlorella vulgaris* 499-501
Leila Nadaei, Hanieh Shokrkar

A Facile Synthesis Method of Bis (Ethanolammonium) Hexahydroxoplatinum (IV) Solution for Platinum Supported Catalysts 502-505
Faezeh Farrokhpey, Yousef Zaynali

Boosting the photocatalytic activity of $ZnCo_2O_4$ spinel via anchoring on graphene nanoplatelets for removing the ciprofloxacin antibiotic 506-508
Shadi Ebrahimi, Mohammad Mehdi Heydari, Azadeh Ebrahimian Pirbazari, Reza Zarghami, Fatemeh Esmaeili Khalil Saraei

Study the effect of morphology and structure of CeO_2/TiO_2 and CeO_2/ZrO_2 heterostructures on the degradation efficiency of tetracycline 509-511
Mohammad Moradi, Mohammad Mehdi Heydari, Azadeh Ebrahimian Pirbazari, Fatemeh Esmaeili Khalil Saraei

Modeling a Recuperator to Investigate Velocity Distribution and Pressure Drop by Varying the Cross-Section Geometry of its Pipes 512-514
Erfan Farsijani, Kamran Keynejad, Hedayat Azizpour, Zahra Nasrollahi

Removal of hydroquinone from aqueous solution using novel Fe-Mg bimetallic oxide: synthesis, characterization and isotherm modeling 515-517
Hesam Malekzadeh, Mohammad Zabihi, Morteza Faghihi

Study of pH effect on the degradation of naproxen in aqueous solution using MnO_2 photocatalyst 518-520
Seyed Taha Hosseini Koohi, Zahra Nasrollahi, Kamran Keynejad

Modeling of fluid flow and heat transfer inside fin and tube heat exchanger with pentagonal cross section of tubes 521-524
Reza Ghafuri, Zahra Nasrollahi, Hedayat Azizpour, Kamran Keynejad

Complete photocatalytic removal of Ciprofloxacin using $NiAl_2O_4$ spinel grafted on graphene nanosheets 525-527
Elnaz Pazdar, Shadi Ebrahimi, Mohammad Mehdi Heydari, Azadeh Ebrahimian Pirbazari, Fatemeh Esmaeili Khalil Saraei

The deposition-precipitation of plasmonic Ag/Ag_3PO_4 nanoparticles on ZnS Micro/nanospheres for photocatalytic treatment of methyl orange and tetracycline artificial effluents 528-531
Sogand Rajaei Farid, Mohammad Amin Habibi, Azadeh Ebrahimian Pirbazari, Fatemeh Esmaeili Khalil Saraei

Factors affecting the electrolysis of sodium chloride by a membrane electrochemical cell for the production of sodium hydroxide in an environmentally friendly method 532-534
Mohammad Amin Habibi, Sogand Rajaei Farid, Kamran Keynejad, Hedayat Azizpour

Adsorption study of methyl orange dye removal from aqueous solutions by using a novel polymeric MOF nanosorbent 535-537
Niloofar Razmi, Mohammad Zabihi, Sirous Ebrahimi

Robust Position Control of AC Servo Motor Using Sliding Mode Control (SMC) Optimized by Grey Wolf Optimization (GWO) Algorithm 538-541
Navid Salahshoor, Mahmood Moghadasian

Optimized H-Infinity Controller for Torque Control of PMSM Using Grasshopper Optimization Algorithm (GOA) 542-545
Mehran Khalaj Afshar, Mahmood Moqhadasian

Analysis of Different Distribution Configuration for Optimal Photovoltaic Integration: A Case Study 546-548
Klajdi Kamberi, Donard Shaliu, Marialis Çelo, Bajram Leka

Designing PID Controller for Speed Control of Autonomous Vehicle by Utilizing Improved Grey Wolf Optimization Algorithm 549-552
Arman Nagizadeh, Amir A. Ghavifekr, Ayta Mollazadeh

Enhancing Distribution Network Resilience by Integration Renewable Energy Sources and Energy Storage 553-556
Sina Roudnil, Kasra Shafiei, Saeid Ghassem Zadeh

sEMG based Hand Gesture Recognition via Simple Feature Extraction and LSTM Model 557-560
Ramin Soleimani, Saeed Meshgini, Mohammad Reza Sayyed Noorani

IMU-based Movement Control of Robotic Manipulators – Aided by CoppeliaSim 561-564
Alireza Ashrafi Majd, Mohammad Reza Sayyed Noorani

Forecasting Survival Rate from ICU Data Based on LightGBM 565-568
Mahmood Seyyedzadeh, Alireza Tajdid, Ali Firouzi Abriz, Kashish Rai

Implementation and Optimization of PID Controller Using HHO Algorithm for DC Encoder Motor in Autonomous Guided Vehicles (AGV) 569-572
Mohammad Javad Saeidi, Mahmoud Moqadasian

Optimal Design of 1 MW Grid-Connected Solar Power Plant for increasing Solar Radiation by using PVsyst Software 573-576
Amirreza Samadi Bonab, Parisa Shirinabadi, Kazem Zare, Sina Asadian, Khadim Moin Siddiqui, Neel Kamal

EEG-Based Classification of Mental Stress Induced by Arithmetic Task 577-580
Morteza Jafari Malali, Sepideh Zolfaghari, Aysel Davar

A Third-Order Quadrature Sinusoidal Oscillator Using Operational Amplifiers 581-583
Mohammad Rashtian, Mahdi Shabani, Houman Farsadpour

Design and Characterization of a Discrete Curvature-Compensated Bandgap Voltage Reference 584-586
Mohammad Rashtian, Houman Farsadpour, Mahdi Shabani, Ali Karimi

Transformer-BiGRU: Hybrid Deep Model for Wind Power Prediction 587-589
Elman Ghazaei, Amir A. Ghavifekr, Paolo Visconti

GenTradeCast: A Precise Forecasting Predictive Model in Peer-to-Peer Energy Trading Markets–A Dataset Case Study of Germany 590-593
Ashkan Safari, Amir A. Ghavifekr

Application of Quantum Neural Networks for Robotic Motion Control 594-597
Ashkan Safari, Amir A. Ghavifekr, Hossein B. Jond, Roberto De Fazio, Mina Salim, Khadim Moin Siddiqui, Neel Kamal, Ajay Kumar

New organ design for humans: **electrical generating neural network inspired by eel** 598-600
Arya Gholipoor Hanizi, Sina Asadian

Optimal Sizing of a Grid Connected Microgrid Using Firefly Algorithm 601-604
Sina Asadian, Ali Firouzi Abriz, Arash Faramarzi

Estimation of elbow joint angle based on single channel electromyography signal of selected arm muscle, using machine learning methods 605-611
Ayla Ahmadi, Babak Rezaee Afshar

Design of Adaptive PID Controller for Lower Limb Exoskeleton Robot Based on Hybrid Model of Genetic Algorithm and Improved Black Hole Optimization 612-615
Amir Ata Nikjoo, Mohanna Arefnezhad

Neuromusculoskeletal Modeling of Elbow Flexion/Extension – Aided by OpenSim 616-619
Mohammad Reza Sayyed Noorani, Farhad Farkhondeh Tale Navi, Kimiya Khojand

Radar study of mudflow formation mechanisms on the territory of Azerbaijan 620-623
Said Safarov, Elnur Safarov

Investigating LULC Change Impacts on Surface UHI Using RS Data case study: Kerman City 624-627
Amin Raisi Moghadam, Khalil Valizadeh Kamran

The role of innovative food packaging in food quality and safety 628-631
Samin Adineh

Numerical Study on the Solidification Process in Conical Shell and Tube Latent Heat Energy Storage Tanks 632-635
A. Gholamzadeh, A. Shafiei Ghazani

A Comparative Study on the Performance of LQG/LTR and Optimized SMIT Controllers in Tracking Control of Flying-Wing UAVs 636-638
Sevda Rezazadeh Movahhed, Mohammad Ali Hamed

Output Feedback Control Using Enhanced SMIT Controller Based on Sliding Mode Observer for Longitudinal Control of Rudderless Flying-Wing UAVs 639-641
Sevda Rezazadeh Movahhed, Mohammad Ali Hamed

Engineering an efficient hemostatic fabric by modifying regenerated cellulose 642-644
Nastaran Alipour, Roya Salehi

Preparation of mineral distribution map using Hyperion images: A case study of Northwest of Kerman Province 645-648
Hossein Fekrat, Vahid Kakapor, Maryam Sadeghi, Khalil Valizadeh Kamran, Hassan Emami

Synthesis and in situ oxidation of copper nanoparticles by glow discharge plasma on liquid 649-651
Nazila Mahmoudian, Fatemeh Baharlounezhad, Mohammad Ali Mohammadi, Mohaddeseh Mousavi, Ali Soltani Vala

Investigating the physical properties of carbon nanotubes modified by plasma method 652-654
Mohaddeseh Mousavi, Fatemeh Baharlounezhad, Mohammad Ali Mohammadi, Nazila Mahmoudian

The plasma synthesis and treatment of tungsten oxide nanoparticles 655-657
Fatemeh Baharlounezhad, Mohammad Ali Mohammadi

Adapting cities to climate change 658-660
Mahmoud Asoude Khyal, Nasser Mashganbari, Ali Hamedi, Hassan Mahmoodzadeh

Water resource management and the effects of reducing rainfall in cities 661-663
Ali Hamedi, Mahmoud Asoude Khyal, Hassan Mahmoodzadeh, Reza Mahdinia

The effects of urban management on green space: solutions and challenges: A case study of Tabriz city 664-666
Rogayeh Sharafi, Mahmoud Asoude Khyal, Ali Hamedi, Hassan Mahmoodzadeh

Narrative review of enzymatic oil refining 667-669
Afsaneh Ahansaz

Facile synthesis of Mn-doped carbon aerogel composite cathode for electrochemical oxidation of Cefepim drug waste from contaminated water 670-672
Tala Babaei, Mahmoud Zarei, Paria Rostamzadeh, Hannaneh Mortaghi Ghasemi

Thermofluidic analysis of backward facing step Couette-Poiseuille flow with symmetric corrugations and upper moving wall 673-675
Hamidreza Toloueinasab, Ramin Abdollahi, Ali Rahbar, Seyed Esmail Razavi

Estimation of control points of the surface model obtained by unmanned aerial vehicle with artificial neural network 676-679
Ali Kavak, Halil Kısacıkoğlu, Vahdettin Demir, Aydın Alptekin, Murat Yakar

The importance of determining value-based land shares: Business center application 680-682
Muhammed Emin Işık, Nuri Erdem

Development of Porous Asphalt Pavement using Recycled Surface Dressed Pavement Materials (RSM) 683-685
Ibrahim Sheikh Ibrahim[1], Hassan Shuaibu Abdulrahman

Statistical evaluation of theoretical and nonparametric approaches to Standardized Precipitation Index 686-689
Ahmad Abu Arra, Eyüp Şişman

Suspended sediment dynamics in the semiarid Mediterranean environment: A case study of the Ksob basin, Algeria 690-693
Fouad Sakhraoui, Ahmad Abu Arra, Mahmoud Hasbaia, Eyüp Şişman

Assessment of drought using a probabilistic standardized index 694-696
Burak, Kızılöz, Gizem Aylin Şahin

Environmental sustainability in line with urban infrastructure development with focus on sustainable development 697-699
Mahdi Jalili Marand, Sheyda Sarikhan Kheljan

Effect of groundwater level change on retaining wall design 700-702
İhsan Yaman, Abdülkadir Özcan, Esra Uray

Literature Review of Artificial Intelligence and Geostatistical Analyses in Geotechnical Engineering 703-705
Hatice Beyza Urgancı, Burak Bilir, Esra Uray, Vahdettin Demir

Improvement Effect of Artificial Pozzolan Waste Material and Cement Additive on Crushed Stone Ground and Taguchi Method 706-708
Mehmet Hilmi Tutumlu, Esra Uray

An analysis on the distributional justice of medical centers in the 2nd district of Tabriz metropolis 709-711
Rogayeh Sharafi, Mahmoud Asoude Khyal, Ali Hamedi, Hassan Mahmoodzadeh

Hydroclimatic Trend Analysis of Gorgan Coastal Region, Iran 712-716
Vahid Azimi, Hirsa Taherimashhadi

Hydrodynamic Analysis of Lake Urmia: Effects of Causeway and Water Levels on Flow Patterns 717-720
Mehran Dadashzadeh, Alireza Mojtahedi, Javad Parsa

Investigation of damping properties on the wavelet-based damage detection in steel beam under noise effect: A numerical study 721-723
Farhad Jedari Zare Zadeh, Mehran Dadashzadeh

Unraveling topological features of complex networks 724-726
Leyla Naghipour, Khalil Valizadeh Kamran, Mohammad Taghi Aalami, Vahid Nourani

Forecasting of Beyşehir Lake Levels with Artificial Neural Networks and Levenberg Training Algorithm 727-731
Beyza Değişli, Vahdettin Demir

Evaluating the Effect of Monopile Diameter on the Static Deformation Response Using Finite Element Method 732-734
Özgür Lütfi Ertuğrul, Fatma Dülger Canoğulları

Investigation of Loading Frequency Effects on the Dynamic Lateral Load- Displacement Curves of Monopiles 735-737
Özgür Lütfi Ertuğrul, Fatma Dülger Canoğulları

Evaluation of GPM and TRMM Precipitation Data versus Observational data in Lake Urmia Basin 738-741
Fatemeh Hosseinpour Asl, Saeed Jahanbakhsh Asl, Hashem Rostamzadeh

Pollution Study of Hajilar Chai Basin in East Azerbaijan Province, Iran 742-747
Ali Mohammad Khorshiddoust, Ali Asghar Azad, Azadeh Mirzaahmadi

Investigating the texture of region 5 of Tabriz city with emphasis on earthquake vulnerability 748-751
Shiva Sattarzadeh Salehi, Firouz Jafari

Analysis of Urban Planning policies in earthquake-affected areas and lessons from the cities of Kahramanmaraş and Hatay in Türkiye 752-756
Fereidoun Babaei Aghdam, Shiva Sattarzadeh Salehi, Murat Yakar, Aydin Alptekin

Engineering analysis of multidimensional vulnerability due to earthquake occurrence 757-760
Peyman Yariyan, Abolfazl Ghanbari, Mohammadreza Karami

Accuracy assessment of captured land-covered maps in urban fringes, (cases from Tabriz, Iran and Mersin, Turkiye) 761-765
Fereidoun Babaei Aghdam, Shiva Sattarzadeh Salehi, Murat Yakar, Khalil Valizadeh Kamran

A review of GIS application in urban green landscapes 766-771
Mohammad Khezrollah, Zanyar Samadi Todar, Khalil Valizadeh Kamran

Evaluating the performance of remote sensing to monitor the severity of drought through the comparison of three drought severity indicators (NDDI, NDWI and NDVI) in the Karkheh basin 772-777
Vahid Kakapor, Hossein Fekrat, Maryam Sadeghi, Khalil Valizadeh Kamran, Maryam Bayati Khatibi

Comparing the efficiency of Object-Based fuzzy operators in extraction of urban built-up area of Tabriz metropolis 778-781
Mostafa Mousapour, Bakhtiar Feizizadeh

Identification of Sunflowers (*Helianthus annuus* L.) from Multi-Temporal UAV Orthomosaics Using Deep Learning Models 782-785
Esra Yildirim, Ismail Colkesen, Umut Gunes Sefercik

Assessment of Urban Green Space Using UAV-Based Green Leaf Index: A Case Study of Harran University Osmanbey Campus 786-789
Nizar Polat, Seyma Akca

Ensuring information security in teaching students 790-791
Asrorov Oybek Asror ogli

The effectiveness of hybrid automobiles and the reduction of urban pollution: A case study 792-795
Ledia Bozo, Asllan Hajderi, Rrezart Bozo

Mapping potential risk factors of cultural monument sites at the middle and upper part of River Vjosa in the accelerated climate change circumstances 796-798
Laura Shumka

Skin Imaging methodology to improve analysis of geometric deviation 799-801
Elnaz Ghanbary, Mehran Mahboubkhah, Ahmad Barari

A case survey of dietary intake for assessing diet diversity score among vulnerable groups of society 802-804
Estela Pinderi, Joana Vogli, Marinela Leka

The impact of the magnetic field on the reduction of pollution from vehicles: A case study 805-808
Asllan Hajderi, Ledia Bozo

Acoustic pollution in industrial environments 809-811
Fatmir Basholli, Aydın Alptekin

Simulation based on historical data and expectations for tsunamis in the Adriatic and Ionian seas 812-814
Fatmir Basholli, Adisa Daberdini, Rrapo Ormeni

Reconstruction of the historical building based on archaeological excavations and studies 815-817
Khojiakbar Egamberdiyev, Noila Xidirova, Asilbek Shukurov, Jakhongir Davronov, Jonibek Xolmurodov

Methodology for teaching computer science using information and communication technologies 818-820
Madina Makhkamova, Noila Xidirova, Sadokat Kamolova

Modeling the stability indicator taking into account the bending deformation of the freight car body 821-823
Anzhelika Shvets, Leontii Muradian, Angela Shvets

Length-weight relationships of the Twait shad - *Alosa falax* (Lacepède, 1803) from the South western Adriatic coast of Albania 824-826
Nertila Muçollari, Spase Shumka

Energy production and income of 5 kW solar power plant in Boukan, Iran 827-829
Khadijeh Mirza

Study of the influence of different car types on the wear indicators of the "wheel-rail" couple 830-832
Angela Shvets

Energy piles design parameters optimization by using fuzzy logic 833-836
Çetin Önder İncekara

Aluminum Forging Technology, Applications and Analysis 837-840
Sait Gül, Esat Erdinç Önel, Hüseyin Tat

Modeling of fluid flow and heat transfer inside fin and tube heat exchanger with pentagonal cross section of tubes 841-844
Reza Ghafuri, Zahra Nasrollahi, Hedayat Azizpour, Kamran Keynejad

Innovative intelligent methods in integer programming 845-847
Javad Nematian, Khadijeh Daneshfar, Neda Shah Mohammadi

Designing a Flexible Interface Mechanism to Convert an Industrial Gripper into a System Suitable for Medical Applications 848-855
Leila Effati Aghdam, Hamidreza Arefi, Seyed Mohammadreza Akrami, Reza Abdollahi

Simulation, trajectory design and motion control of robotic hand with sensing force control 856-865
Ali Korehpaz Saeid, Reza Abdollahi, Seyed Mohammadreza Akrami, Melika Fahmi

Influence of new advanced split injection strategy on emissions and performance of a dual-fuel RCCI engine 866-868
Seyed Ali Sadri Jahanshahi, Amirreza Javaherian, Mortaza Yari

Smooth Path Planning for Autonomous Mobile Robots: Integration of Improved A-Star with Artificial Potential Field Method 869-872
Amir Amjadi, Samira Kharratian, Seyed Mohammadreza Akrami, Yousef Seyfari

Neuromusculoskeletal Modeling of Elbow Flexion/Extension – Aided by OpenSim 873-876
Mohammad Reza Sayyed Noorani, Farhad Farkhondeh Tale Navi, Kimiya Khojand

Separation of active zones of electromyographic signals 877-879
Kudratjon Zohirov, Sardor Boykobilov, Mamadiyor Sattorov

Comparative Analysis of Machine Learning and Deep Learning Models for Multilingual Multitarget Stance Detection 880-887
Muhammad Ebrahim Ahmadi, Monireh Hosseini

Offensive Context detection in social network using graph neural net 888-890
Minou Kouh Soltani

Enhancing VM Migration in Clouds with Heuristic-based Granular Computing 891-893
Seyyed Meysam Rozehkhani, Farnaz Mahan

Honeypot-Based Detection of Advanced Persistent Threats: A New Methodology 894-896
Maryam Mohammadzad, Jaber Karimpour

Face Mask Detection System by Transformer Learning Model 897-900
Salar Mokhtari Laleh, Seyed Mahdi Abdi Oskouei, Mohammad Sarhangzadeh

Strategic Monitoring and Proactive Measures for Mitigating Network-Level Threats and Malware in Albania 901-903
Klorenta Pashaj, Eralda Gjika, Vilma Tomco

Person Identification in Healthcare Applications Using Binary Chimp Optimization-based EEG Channel Selection 904-907
Shabnam Oskouei, Saeed Meshgini, Hadi S. Aghdasi

Investigation of Stone Deterioration in Gaziantep Yüzükçü Inn 908-911
İlhami Ay, Murat Dal, Şefika Ergin

Investigation of Stone Deterioration in Gaziantep Lala Mustafa Pasha Inn 912-915
İlhami Ay, Murat Dal, Şefika Ergin

Investigation of Stone Deterioration in Gaziantep Tabakhane Bridge 916-918
İlhami Ay, Şefika Ergin, Murat Dal

Investigation of Stone Deterioration in Gaziantep Balıklı Masjid 919-922
İlhami Ay, Şefika Ergin, Murat Dal

Investigation of Stone Deterioration in Gaziantep Köseç Ahmet Ağa Fountain 923-926
İlhami Ay, Şefika Ergin, Murat Dal

Data-driven Energy Management of H-MGs using Fuzzy Reinforcement Learning 927-929
Azam Salari, Mahdi Zeinali, Mousa Marzband

Wind Energy Potential of Türkiye 930-933
Seçkin Tekin, Emine Banu Burkut, Murat Dal

Focus on solar energy in architecture and design 934-936
Emine Banu Burkut, Murat Dal, Seçkin Tekin

Impact of industrial use on nitrogen dioxide air pollutant distribution (case example: Tabriz, Iran) 937-940
Paria Ali Mohammadi, Iraj Teymuri

Statistical Analysis and Machine Learning Applications of radiolarite-hosted manganese mineralization in Taşdemir (Kahramanmaraş, Türkiye) 941-943
Cihan Yalçın, Yusuf Uras, Tekin Akkütük

Utilizing International Experiences in the Revitalization of Lake Urmia 944-947
Seyyed Asadullah Hijazi, Saye Habibzadeh

Identification and classification of karst landforms based on Cvijic, Waltham, Fookes, Komatina and Herak models (Case study: Travertine springs of Badab Soort) 948-950
Shahram Roostaei, Bahareh Akbari

Investigation of land use change effects on water quality of Tabriz plain 951-953
Zahra Sedghi, Ata Allah Nadiri

Monitoring the impacts of investment in the tourism sector on land use changes in the Hir City using the Change Detection Technique 954-964
Mohsen Aghayari Hir, Sahar Ahmadzadeh Naghadeh, Milad Manzelati

Integrated Assessment of Forest Fire Vulnerability: A Multi-dimensional Approach 965-967
Elnaz Nejatiyanpour, Omid Ghorbanzadeh, Josef Strobl, Khalil Gholamnia, Rasoul Yousefpour, Mahmoud Daneshvar Kakhki, Hamid Amirnejad, Mahmoud Sabouhi Sabouni

Ground deformation monitoring in Hatay Airport using GACOS-corrected StaMPS PSI 968-971
Mahmut Gorken, Umut Gunes Sefercik, Mertcan Nazar

Türkiye cracked the code in topographic earth representation 972-974
Arif Oguz Altunel, Samet Doğan

Mapping Wetlands Using Sentinel-2 Satellite Imagery and Auxiliary Data with Google Earth Engine 975-978
Zelalem Getachew Ayalke, Aziz Şişman

Enhancement of Zirconium Oxide-Based Graphite Electrode through Mechanochemical Methods for Electrochemical Applications 979-981
Mary Gojeh, Ishaya Sugbeh Alhassan, Manasseh Tachia Bwankwot, Jonah Rebeccah Aji, Habiba Kakangi Dalhatu, Solomon Ogobuto

Photogrammetric recording of epigraphic documentation 982-984
Cengiz Alyılmaz

The importance of academic field work in social sciences 985-987
Semra Alyılmaz, Cengiz Alyılmaz

Building interior modeling with wearable mobile LIDAR 988-991
Atilla Karabacak, Murat Yakar

3D Modeling with Wearable Mobile LIDAR and Mezitli Stone Bridge example 992-994
Atilla Karabacak, Murat Yakar

3D Modeling of Mersin University Vocational School of Technical Sciences with Wearable Mobile LIDAR 995-998
Atilla Karabacak, Murat Yakar

Investigation of natural factors affecting landslide formation 999-1001
Aydın Alptekin, Murat Yakar

Advanced Engineering Days

aed.mersin.edu.tr

Creating micro-scale mixing by controlled diffusion

Tuhid Pashaee Golmarz *[1] **Saleh Khorasani** [2]

[1]*University of Tabriz, Faculty of Mechanical Engineering, Iran, tuhid.pashaeee@tabrizu.ac.ir*
[2]*Urmia University, Department of Mechanical Engineering, Iran, khorasani.saleh@yahoo.com*

Cite this study: Pashaee Golmarz, T., & Khorasani, S. (2024). Creating micro-scale mixing by controlled diffusion. Advanced Engineering Days, 9, 1-4.

Keywords
Mixing
Micro dimension
Diffusion
CFD

Abstract

The present work is a numerical and three-dimensional simulation of an H-shaped passive micromixer. The flow inside the channels is considered a creeping flow. An unorganized grid is used and modeling is done for three different geometries with three different diffusion coefficients. The results show that case 1 has better results than the others. In addition, the results indicate that a better result is obtained by increasing the diffusion coefficient.

Introduction

Creating micro-scale mixing by controlled diffusion is a fascinating concept that has significant applications in various fields, including chemistry, biology, and engineering. By manipulating the diffusion processes, scientists and researchers can effectively mix small volumes of fluids at a micro-scale level. This precise control over mixing is crucial in many applications, such as chemical reactions, drug synthesis, and lab-on-a-chip technologies [1]. One approach involves designing microfluidic devices with specific channel geometries, surface properties, and flow rates to enhance diffusion and induce mixing. Another method utilizes external factors like electric fields or acoustic waves to influence the movement and mixing of particles or molecules. These techniques not only enable efficient and rapid mixing but also offer the advantage of reduced sample volumes, decreased reaction times, and improved reaction yields. The ability to create micro-scale mixing by controlled diffusion opens up new possibilities for advancements in various scientific disciplines and holds great potential for future innovation [2].

Passive micromixers operate primarily based on flow modification through certain channel design features, without requiring any external energy input. The primary goals of these unique microchannel design elements are to repeatedly split and recombine the flow [3-5], introduce fluid rotation [6], establish micro-vortices [7-8], and induce chaotic mixing [9]. Many researchers have presented excellent works in this field, including the work of Fan et al. [10]. They discussed the use of diffusion as a key mechanism for molecular mixing in microfluidic devices. It explained how the small length scale of microchannels allowed for precise control and prediction of flow streams. In another work, Horiuchi and Morizane [11] discussed the mixing processes in a micro-mixer using diffusion. They described how two liquids were gradually mixed by diffusion when injected into the micro-mixer, and the diffusion distance was proportional to the square root of the diffusion time.

In the present work, the passive micromixer is simulated using two separate U-shaped channels in three dimensions, and the effect of the diffusion coefficient and the geometry of the channels on the mixing quality is investigated.

Material and Method

An H-shaped microfluidic device for controlled mixing via diffusion is treated in this model. For a predetermined amount of time, the apparatus brings two distinct laminar streams into contact. The contact surface is well-defined, and the number of species that diffuse from one stream to the other may be managed by adjusting the flow rate. Since the geometry effect is also examined in this work, Figure 1 shows the examined cases and different sizes. The value of "**a**" shown in the figure is studied for three values of 5, 10, and 20 micrometers.

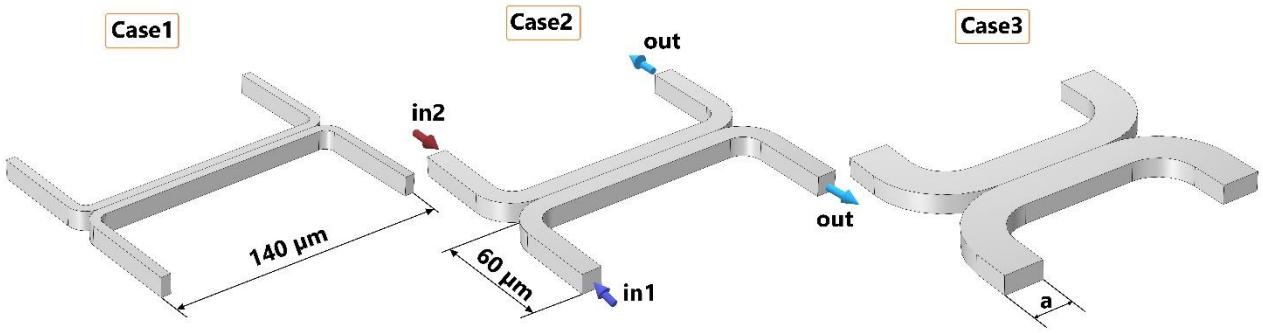


Figure 1. Different geometries studied in the present work and their geometric dimensions

To prevent uncontrollably convective mixing, the design attempts to preserve a laminar flow field when the two streams, 1 and 2, are combined. Only diffusion should be used to move species between streams 1 and 2 such that species with low diffusion coefficients remain in their streams. At the inlet, the flow rate is roughly 0.1 mm/s. The Creeping Flow interface can be used in situations when the Reynolds number is much less than 1, as in this simulation it is 0.001. The incompressible Stokes equations remain when the convective term in the Navier-Stokes equations is removed:

$$\nabla.\left(-pI + \mu(\nabla u + (\nabla u)^T)\right) = 0$$
$$\nabla.u = 0 \quad (1)$$

Species are mixed in the device at comparatively lower quantities than in the solvent—in this case, water. This indicates that the diffusive transport may be described by Fick's law and that the solute molecules exclusively interact with water molecules. Consequently, the solute's mass-balance equation is as follows:

$$-\nabla.(-D\nabla c + cu) = 0 \quad (2)$$

where D is the diffusion coefficient of the solute (m^2/s) and c is its concentration (mol/m^3).

Since mixing quality is the most important parameter in this work, this quantity is studied and calculated as follows:

$$\text{Mixing Quality} = \left|1 - \frac{(c - c0/2)_{out}}{(c - c0/2)_{in}}\right| * 100 \quad (3)$$

Results

Since the current approach involves numerical simulation, the independence from the grid must be verified first. The output mixing quality in case 2 and the diffusion coefficient of 5e-11 m2/s were extracted in this work using 4 distinct cell numbers.

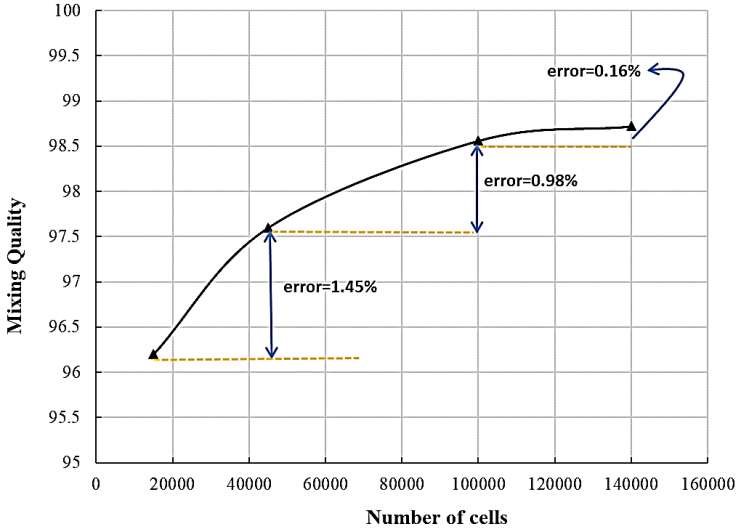


Figure 2. Grid independence diagram for four different cell numbers

In light of Figure 2 and the extremely tiny and advantageous error in the quantity of 100,000 cells, the same quantity is thought to be necessary to carry out the remaining work. All three models under investigation have their output concentration displayed in Figure 3. Also shown in Figure 4 is the mixing quality graph for each of the three models.

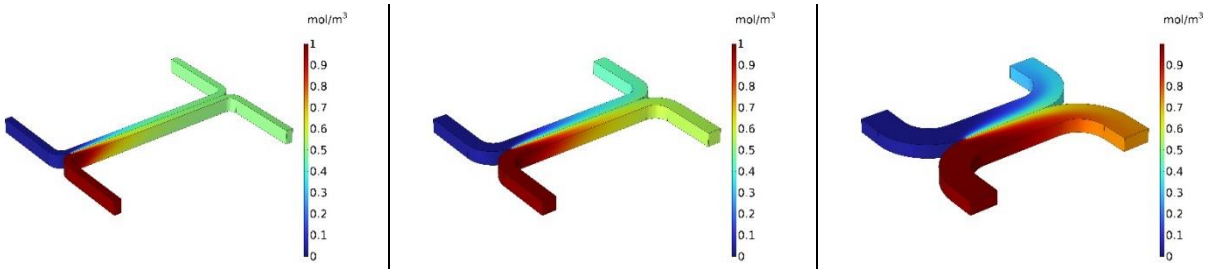


Figure 3. Concentration contour for all three simulated models

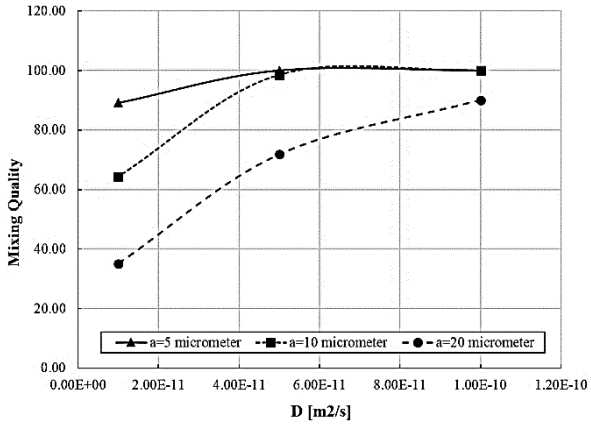


Figure 4. Mixing quality for all three models simulated in the present work

Discussion

It can be seen in Figure 3 that cases 1 and 2 have better results than case 3, and of course, Figure 4 proves that case 1 also works better than case 2. Also, this graph shows that by increasing the diffusion coefficient, a better result is obtained.

Conclusion

This study is a three-dimensional numerical simulation of a passive micromixer in the H-shape. It is thought that the flow within the canals is creeping. Three distinct geometries with three different diffusion coefficients are modeled using an unstructured grid. The outcomes demonstrate that case 1 performs better than the others. Furthermore, the data show that raising the diffusion coefficient yields superior results.

References

1. Pashaee Golmarz, T., & Hakimollahi, M. (2023). Drug delivery system evaluation based on microsimulation technique. 5th International Congress On Engineering, Technology and Innovation, Darmstadt University, Germany.
2. Maadi, M., & Pashaee Golmarz, T. (2014). Investigation of mixing and simulation of an electroosmotic micromixer. Journal of Mechanical Science and Technology, 28, 3223-3230.
3. Afzal, A., & Kim, K. (2012). Passive split and recombination micromixer with convergent divergent walls. Chem. Eng. J. 203,182–192.
4. Juraeva, M., & Kang, D.J. (2020). Mixing performance of a cross-channel split-and recombine micro-mixer combined with mixing cell, Micromachines, 11 (7) 685.
5. Ansari, M.A., Kim, K.-Y. (2010). Mixing performance of unbalanced split and recombine micomixers with circular and rhombic sub-channels. Chem. Eng. J. 162 (2),760–767.
6. Lee, S.W., & Lee, S.S. (2008). Rotation effect in split and recombination micromixing, Sensors Actuators B 129 (1), 364–371.
7. Ansari, M.A., Kim, K.-Y., & Kim, S.M. (2018). Numerical and experimental study on mixing performances of simple and vortex micro t-mixers, Micromachines 9 (5), 204.

8. Tripathi, E., Patowari, P.K., & Pati, S. (2021). Numerical investigation of mixing performance in spiral micromixers based on dean flows and chaotic advection, Chem. Eng. Process.-Process Intensif. 169, 108609.
9. Yuan, S., Zhou, M., Peng, T., Li, Q., & Jiang, F. (2022). An investigation of chaotic mixing behavior in a planar microfluidic mixer, Phys. Fluids 34 (3), 032007.
10. Fan, J., Li, Sh., Wu, Z., & Chen, Z. (2019). Diffusion and mixing in microfluidic devices. Microfluidics for Pharmaceutical Applications, 79-100.
11. Horiuchi, T., & Morizane, y. (2017). Visualization of diffusion mixing in a micro-mixer with flow paths fabricated by photolithography. Material Technologies and Applications to Optics, Structures, Components, and Sub-Systems III, 1037206.

Advanced Engineering Days

aed.mersin.edu.tr

Simulation of the failure in an aluminum alloy using a comprehensive damage model

Ali Zahedi

University of Mohaghegh Ardabili, Faculty of Engineering, Iran, azahedi@uma.ac.ir

Cite this study: Zahedi, A. (2024). Simulation of the failure in an aluminum alloy using comprehensive damage model. Advanced Engineering Days, 9, 5-7

Keywords
Ductile fracture
Shear fracture
Necking
Finite element
Forming

Abstract

The accurate description of plastic behavior and failure characteristics of sheet metals are crucial to obtaining reliable results through the simulation of different forming processes. This research aims to provide a comprehensive tool to predict failure initiation in the sheet metal industry. To do so, according to the different failure mechanisms, three distinct criteria are applied to cover necking instability, ductile fracture, and shear fracture of aluminum alloy EN AW-7108 T6. This method is based on the macroscopic view of the stresses and strains which makes it more practical. Using the available experimental data and ABAQUS finite element tool, calibration of the material parameters of the fracture models was performed via a numerical-experimental hybrid approach. The feasibility and efficiency of the provided material model were examined on the typical three-point bending of a double chamber extrusion component made from the same aluminum alloy. A comparison between the force-displacement response of the simulation results with experiment data indicates acceptable accuracy.

Introduction

In order to reduce the weight of automotive components various aluminum alloys as well as high-strength steels are being introduced. In comparison with traditional steels, these materials typically expose lower ductility that may lead to damage and fracture in a hostile loading condition. There exist two main damage mechanisms (1) ductile fracture and (2) shear fracture. However, necking occurrence in sheet metal components is usually prior to the failure and is considered as an instability initiation point.

Recently researchers have been keen on developing fracture criteria to cover the broad loading conditions. Considering the three stages of nucleation, growth, and coalescence of voids in the ductile damage initiation, Lou et al. [1] presented a fracture criterion and applied it to predict the ductile fracture. Habibi et al. [2] applied various fracture criteria to evaluate their failure prediction capability in the forming of high-strength steels. They showed that despite the accuracy of fracture models in the prediction of fracture initiation, each criterion needs different calibration tests. Rahmaan et al. [3] investigated the effect of different stress states on the fracture behavior of high-strength aluminum alloys. They calibrated a generalized fracture model through different tensile experiments and constructed the fracture locus.

In some metal forming processes like as traditional deep drawing, the ratio of the surface strains is approximately constant. In this process forming limit diagrams (FLDs) is a reliable tool to predict the safe/unsafe zone of forming [4]. However, when the complexity of the loading condition arose, for example in the multi-stage forming of parts in the automotive industry, the non-linear strain paths during the forming process undermined the effectiveness of the FLD. Basak and Panda [5] investigated the applicability of the fracture criteria in the complex forming processes. They reported a reasonable accuracy in the determination of the fracture strains through simulation.

In the literature of the work, usually, a single failure model has been considered. This research aims to engage the main three failure mechanisms in the simulation of the forming processes.

Material and Method

The explicit solver of the ABAQUS 6.14 was used to simulate the occurring of damage phenomenon in the aluminum alloy EN AW-7108 T6. As a typical test, three-point bending was designed according to Figure 1.

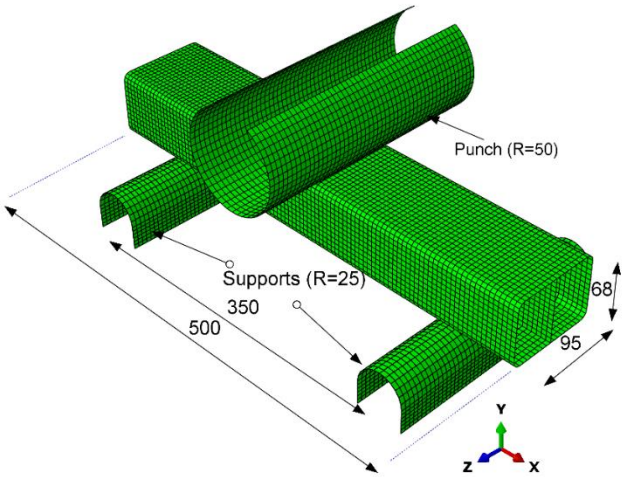


Figure 1. The constructed finite element model of the three-point bending test (dimensions are in mm)

In order to define the ductile damage initiation criterion Equation (1) was used to calculate the equivalent plastic strain at fracture [6]:

$$\bar{\epsilon}_D^{pl} = \frac{\epsilon_T^+ \sinh[k(\eta^- - \eta)] + \epsilon_T^- \sinh[k(\eta - \eta^+)]}{\sinh[k(\eta^- - \eta^+)]} \quad (1)$$

Where k is a material constant. $\epsilon_T^+, \epsilon_T^-$ related to the $\bar{\epsilon}_D^{pl}$ for the equi-biaxial compression and equi-biaxial tension deformation state. Beside η^+, η^- are indicating stress triaxiality with the values of $+{}^2/_3$ and $-{}^2/_3$ in equi-biaxial compression and equi-biaxial tension deformation state, respectively. So three distinct experiments are required to calibrate the ductile fracture criterion. Hooputra [6] utilized the Erichsen test ($\eta = +{}^2/_3$), the plane strain state test ($\eta = +{}^1/_{\sqrt{3}}$) and the uniaxial tension test ($\eta = +{}^1/_3$). Obtained values for the studied aluminum alloy are summarized in Table 1.

Table 1. Ductile fracture constants according to Hooputra experiments [6]

Constants	Quasi-static	Dynamic ($\dot{\epsilon} = 250\ s^{-1}$)
ϵ_T^+	0.26	0.44
ϵ_T^-	193.0	1494.0
k	5.277	8.6304

The equivalent plastic strains in shear damage was also taken as Equation (2):

$$\bar{\epsilon}_S^{pl} = \frac{\epsilon_S^+ \sinh[c(\theta_S - \theta_S^-)] + \epsilon_S^- \sinh[c(\theta_S^+ - \theta_S)]}{\sinh[f(\theta_S^+ - \theta_S^-)]} \quad (2)$$

Where $\theta_S = (1 - \kappa_S\eta)/\phi$ in which κ_S is a material constant and $\phi = {}^{\tau_{max}}/_{\sigma_{eq}}$. In addition, θ_S^+, θ_S^- are the values of θ_S in the η^+, η^- boundaries, respectively. Accordingly, $(\epsilon_S^+, \epsilon_S^-, c, \kappa_S)$ four constants need to be calibrated. Hooputra used tensile specimens with a groove to determine the constants. In order to create different deformation states, multiple groove angle to the loading direction was tested. The calibrated constant through the experiments on the aluminum alloy is provided in Table 2.

Table 2. Shear fracture constants according to Hooputra experiments [6]

Constants	Quasi-static	Dynamic ($\dot{\epsilon} = 250\ s^{-1}$)
ϵ_S^+	0.26	0.35
ϵ_S^-	4.16	1.2
c	4.04	2.05
κ_S	0.3	0.3

Results

The final deformed shape of the simulation is presented in Figure 2-(a). good qualitative agreement can be observed between experimental observations in Figure 2-(b) and simulation final deformation output.

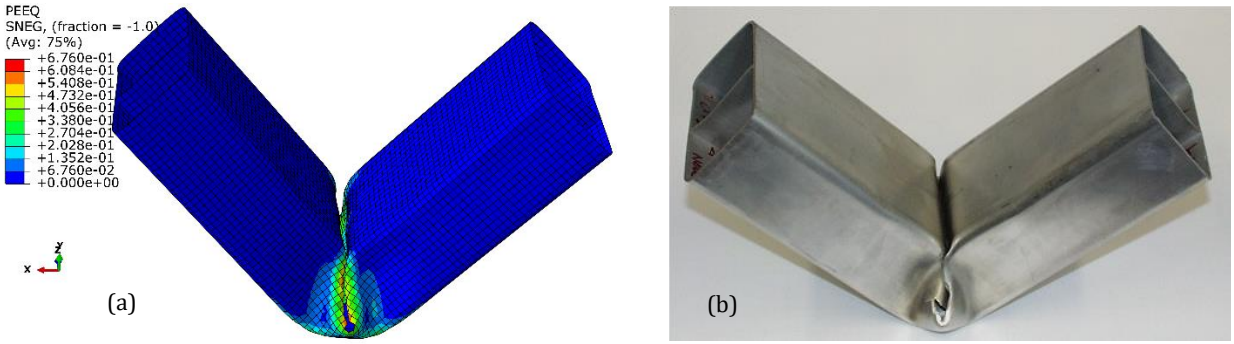


Figure 2. The comparison of the final deformed shaped (a) the simulation (b) the experiment [6]

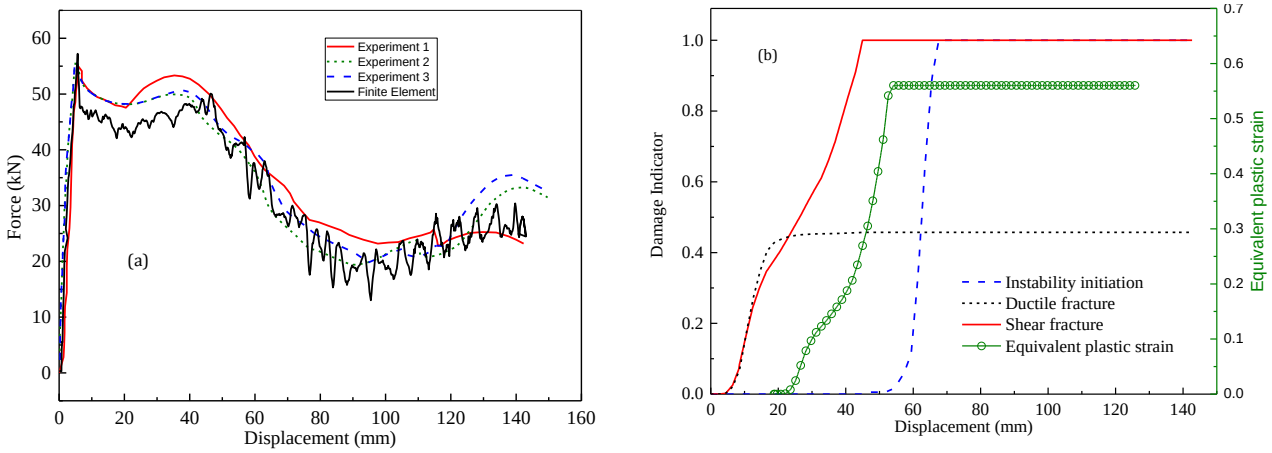


Figure 3. (a) The force-displacement response from the three-point bending test (b) the evolution of different damage indicators and plastic strain of the critical element

Discussion

According to Figure 3-(a), the force-displacement curve of the punch stroke is compared with three experiments conducted separately in [6]. Again, there is a very good match between real test results and simulation which validates the precision of the material model. Figure 3-(b) depicts the progression of damage of three introduced failure scenarios for the firstly deleted element in FE model. After reaching the critical value for each criterion, the load carrying capacity of the element changes to zero and is removed from the model. In addition, the history of equivalent plastic strain of the respective element is plotted

Conclusion

Considering three different failure mechanisms, a finite element model was constructed which led to very close results in comparison with experiments. The presented approach could be used in the simulation of various sheet metal forming processes or in the crash problems.

References

1. Lou, Y., Huh, H., Lim, S., & Pack, K. (2012). New ductile fracture criterion for prediction of fracture forming limit diagrams of sheet metals. International Journal of Solids and Structures, 49(25), 3605-3615.
2. Habibi, N., Ramazani, A., Sundararaghavan, V., & Prahl, U. (2018). Failure predictions of DP600 steel sheets using various uncoupled fracture criteria. Engineering Fracture Mechanics, 190, 367-381.
3. Rahmaan, T., Butcher, C., Kim, S., & Worswick, M. J. (2022). Characterization and prediction of fracture in 6000- and 7000-series aluminum alloy sheet under various stress states. Thin-Walled Structures, 173, 108958.
4. Hosford, W. F., & Caddell, R. M. (2011). Metal forming: mechanics and metallurgy. Cambridge university press.
5. Basak, S., & Panda, S. K. (2023). Use of uncoupled ductile damage models for fracture forming limit prediction during two-stage forming of aluminum sheet material. Journal of Manufacturing Processes, 97, 185-199.
6. Hooputra, H., Gese, H., Dell, H., & Werner, H. (2004). A comprehensive failure model for crashworthiness simulation of aluminium extrusions. International Journal of Crashworthiness, 9(5), 449-464.

Advanced Engineering Days

aed.mersin.edu.tr

Experimental investigation of nozzle diameter effect on tensile strength of PLA material in FDM processes

Farid Gholipour [*1], MohammadReza Shabgard [1], Mohammad Baraheni [2], Mojtaba Farhoudian [1]

[1] *University of Tabriz, Faculty of Mechanical Engineering, Iran, faridd.gholiipour@gmail.com, mrshabgard@tabrizu.ac.ir, mojtaba.farhoodiyan@gmail.com*
[2] *Arak University, Faculty of Mechanical Engineering, Iran, mbaraheni@arakut.ac.ir*

Cite this study: Gholipour, F., Shabgard, M., Baraheni, M., & Farhoudian, M. (2024). Experimental investigation of nozzle diameter effect on tensile strength of PLA material in FDM processes. Advanced Engineering Days, 9, 8-10

Keywords
Additive manufacturing
3D printing
Nozzle diameter
Tensile strength

Abstract

The fused deposition modeling (FDM) process is the most widely used additive manufacturing and 3D printing method. One of the most important challenges of the FDM process is the strong dependence of mechanical and physical properties on printing parameters. The purpose of this research is to investigate the effect of the basic printing parameter of nozzle diameter (at two diameters of 0.4 and 0.6 mm) with nozzle temperatures of 200 degrees Celsius on tensile strength. Examining the results of the tensile strength of the samples showed that Increasing the diameter of the nozzle diameter from 0.4 to 0.6 mm in both printing temperatures improved the printability and reduced microholes. The highest tensile strength corresponds to the nozzle of 0.6 mm (36.8 MPa) and the lowest tensile strength corresponds to the nozzle of 0.4 mm (30.3 MPa) at the temperature of 200 degrees Celsius. Also, the scanning electron microscope images of the fracture surface of the printed samples showed that all the printed samples have micro-holes at the interface between the layers, and removing these micro-holes is inevitable due to the nature of FDM 3D printing.

Introduction

The revolutionary process of 3D printing is characterized by its layer-by-layer construction, setting it apart from traditional manufacturing techniques. This additive manufacturing approach, exemplified by material extrusion (FDM), enables the creation of intricate three-dimensional objects by depositing thermoplastic filaments layer upon layer. Fused Deposition Modeling (FDM) stands out for its simplicity and cost-effectiveness in fabricating complex parts, making it a cornerstone in modern manufacturing. [1-2]

Afrose investigated the effect of fabrication orientation on tensile strength and fatigue properties of PLAfilament and It was concluded that the tensile strength reached the maximum in the direction of 0° constructions, but the fatigue life reached the maximum in the direction of 45° constructions at all wheel loading levels. [3]

In Kiendl's research, it was shown that by changing the pattern and direction of printing for PLA material, it is possible to control the mechanical properties and determine the failure mechanism. They showed that the anisotropy (difference of mechanical properties in different directions) is much less for the crossed state, and by increasing the angle of the print filaments compared to the angle of application of force, more favorable mechanical properties can be achieved. [4]

Akhundi showed that increasing the temperature of the nozzle improves the quality of the printed layers, and the results of their mechanical tests showed that poly lactic acid printed at the highest temperature has the highest mechanical properties. They used five nozzle temperatures of 210, 220, 230, 240, and 250°C. [5]

Material and Method

In this research, poly lactic acid filament with standard diameter of 1.75 mm, glass to rubber transition temperature of 70°C and melting temperature of 175°C was used. PLA filament is the most common type of filament in industries and is used to make a wide range of artifacts. The unique features of this filament make it usable in any type of 3D printer, from beginner to professional. In this research, the nozzle diameter parameter as a variable parameter and its effect on mechanical properties and tensile strength have been investigated. In Table 1, the fixed parameters of printing are presented. The selection ranges have been chosen based on the proposal of the manufacturer of PLA filament so that the minimum melting temperature is 180 degrees Celsius and the maximum is 230 degrees Celsius.

Table 1. Fixed print parameters

Print parameter	Range	Unit
Plate temperature	60	°C
Layer thickness	0.2	mm
Print speed	30	m/s
Filling density	100	%
Print pattern	linear	-
Nozzle temperature	190	°C

The sample design is drawn according to the ASTM-D638 tensile test standard in CATIA software for printing in a 3D printer, and the printer used is the Creality Ender 3V3 model & made in China. In Figure 1, the printed samples are shown according to the input parameters.



Figure 1. The printed samples before, during and after the tensile strength test

In order to check the reproducibility of the results, the uniaxial tensile test has been repeated at least three times for each sample. The tensile test was carried out at ambient temperature with a displacement rate of 1 mm/min and the test continued until the complete rupture of the samples. After the tensile test, the results were extracted as displacement force curves and finally the results were converted into strain stress.

In addition, for investigating the microstructure, printability and fracture mechanism of printed samples of poly lactic acid, scanning electron microscope imaging of the fracture surface was used.

Results

In figure 2, the engineering stress-strain and extracted values of final tensile strength and elongation for PLA printed with a linear pattern and nozzle temperature of 200 °C are presented at two printing diameter of 0.4 and 0.6 mm.

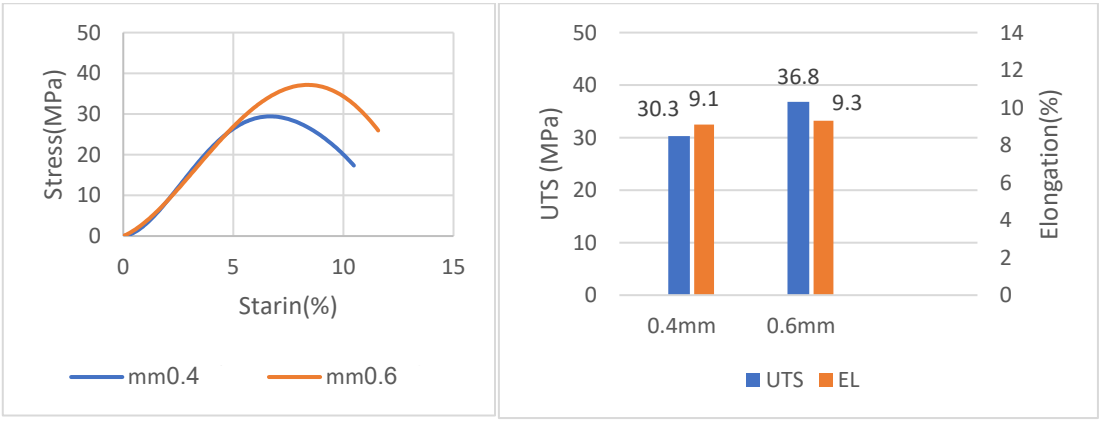


Figure 2. Engineering stress-strain and extracted values of final tensile strength and elongation

Discussion

Based on figure 2, it can be seen that the final tensile strength value for the sample with a nozzle diameter of 0.6 mm is higher and equal to 36.8 MPa. As can be seen, the elongation changes for these two samples also have an upward trend, and the highest elongation value was obtained for the sample printed at 0.6 mm, which is equal to 9.3%, and the lowest value is also 9.1% for the sample printed at 0.4 mm.

Nozzle diameter is one of the basic parameters of FDM printing, because it directly affects the properties of melt rheology, polymer melt flow and feeding system. Increasing the diameter of the nozzle causes better bonding and adhesion in the background and better fluidity in the arrangement of layers. As can be seen in the SEM images in Figure 3, the density of micro pores at the interface of the layers decreases with increasing diameter, which causes an increase in tensile strength.

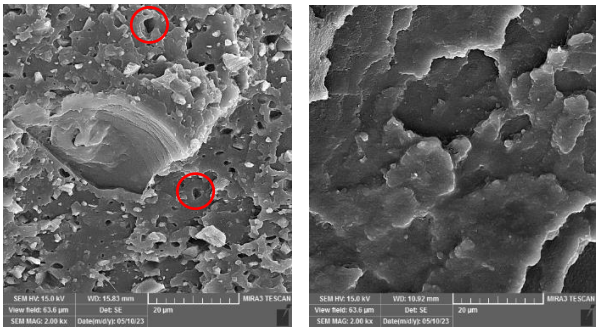


Figure 3. SEM images taken for a temperature of 200 °C with 1000x magnification. from left to right:0.4 ,0.6mm

Conclusion

In this research, the mechanical properties, microstructure and printability of PLA samples considering the basic parameter of FDM printing, diameter were investigated. The diameter parameter was considered at two different levels for printing PLA samples. The diameter of 0.4 and 0.6 mm were the input parameters of printing. In addition, all the samples were printed with a linear pattern. After the successful printing of the samples, the mechanical properties and printability were checked using uniaxial tensile test and scanning electron microscope, and the following results were obtained as the most prominent achievements:

1. An increase in the diameter of the nozzle causes better bond and adhesion in the background and better fluidity in the arrangement of layers and an increase in relative density by reducing air pores.
2. The increase in the diameter of the nozzle causes a decrease in the number of thermal cycles during printing, a decrease in the complexity and the layered opening of the printed part due to the thermal cycle (heating and cooling), which increases the tensile strength.
3. The scanning electron microscope images of the fracture surface of the printed PLA samples showed that all the printed samples have micro holes at the interface between the layers and removing these micro holes is inevitable due to the nature of FDM 3D printing.

References

1. Gaynor AT, Meisel NA, Williams CB, Guest JK. Multiple-Material "Topology Optimization of Compliant Mechanisms Created Via PolyJet Three-Dimensional Printing". J Manuf Sci Eng Trans ASME 2014;136.
2. Mohamed OA, Masood SH, Bhowmik JL.(2015) "Optimization of fused deposition modeling process parameters: a review of current research and future prospects". Adv Manuf;3:42–53
3. Afrose MF, Masood SH, Iovenitti P, Nikzad M, Sbarski I. (2016) "Effects of part build orientations on fatigue behaviour of FDM-processed PLA material.". Prog Addit Manuf; part 1:21–8.
4. Kiendl J, Gao C. (2020) "Controlling toughness and strength of FDM 3D-printed PLA components through the raster layup." Compos Part B Eng
5. Akhoundi B, Nabipour M, Hajami F, Shakoori D. (2020). An experimental study of nozzle tempreture and Heat Treatment (Annealing) Effects on Mechanical Properties of High- Temperature Polylactic Acid in Fused Deposition Modeling. Polym Eng Sci

Advanced Engineering Days

aed.mersin.edu.tr

Dynamic response of a curved composite beam under moving mass

Hadi Teymouri [*1], Ghadir Ahmadi Jeyed [1], Hasan Biglari [1], Nazli Sami [1]

[1] *University of Tabriz, Department of Mechanical Engineering, Iran, hteymouri@tabrizu.ac.ir, ghadir.ahmadi@tabrizu.ac.ir, hbiglari@tabrizu.ac.ir, nazliwsamiw@gmail.com*

Cite this study: Teymouri, H., Jeyed, G. A., Biglari, H., & Sami, N. (2024). Dynamic response of a curved composite beam under moving mass. Advanced Engineering Days, 9, 11-14

Keywords
Composite Beam
Dynamic Response
Navier Method
Moving Mass

Abstract

The current study endeavors to explore the dynamic behavior of a composite curved beam under the influence of a moving mass loading. The dynamic response of a curved beam subjected to a moving mass is a critical factor to consider when designing components such as bridges, railway rails, and fabrication processes. The dynamic deflection of the composite curved beam subjected to moving mass loading was determined by utilizing the first-order theory of shear and Hamilton's principle to derive differential equations with partial derivatives that govern the problem in the domains of space and time. These equations were then converted to ordinary differential equations in the time domain via Navier's method and finally solved using Newmark's method of differential equations in the time domain. The validation of the beam under the moving mass was conducted using a flat beam, and the obtained results exhibited a high degree of concurrence with the references that were reviewed. The factors that influence dynamic behavior have also been examined. The results indicate that the spectrum of oscillations for layering $[45.-45.-45.45]$ and $[0.90.90.0]$ is at its maximum and minimum values, respectively.

Introduction

Understanding the response of an investigated structure to dynamic forces over time is possible through the dynamic behavior of the structure. Numerous structures are subject to mechanical stress, and one of the most significant obstacles in device development is the vibration caused by vehicle motion on structures like railroads, bridges, and roadways.

Yang et al. [1] used the analytical solution to determine the dynamic response of a horizontally curved beam under a vertical and horizontally moving load. They considered both a single moving load and a set of equally spaced moving loads. Meher et al. [2] utilized Green's function to examine the dynamic response of the beam to a moving mass. Using Green's function, the equations of motion for the Euler-Bernoulli beam under a constant-velocity concentrated mass were formulated in matrix form. Utilizing the Euler-Bernoulli theory, Lin and Lee [3] examined the instability and vibration of a moving concentrated mass along a curved beam under various boundary conditions.

On the other hand, numerous engineering disciplines—including mechanics, civil engineering, and aerospace-apply composite structures owing to their minimal weight and high strength. The dynamic behavior of a sandwich beam featuring a porous core and composite surfaces under moving mass was examined and investigated by Bigleri et al. [4]. The dynamic response of a layered composite beam to a constant-velocity oscillating mass was investigated by Jafari et al. [5].

Limited research has been conducted regarding the dynamic behavior of composite curved beams when subjected to moving mass loading. This research endeavors to address this deficiency in the context of composite curved beams.

Material and Method

Figure 1 illustrates the layered composite curved beam, characterized by a constant width b and thickness h, which is subject to a moving mass. R and θ represent the radius of curvature and arc angle of the beam, respectively. On the middle surface of the beam, the three coordinates x, y, and z are denoted to indicate the longitudinal, transverse, and thickness directions, respectively. u and w represent displacements in the x and z orientations, respectively, while ∅ denotes the rotational motion of the beam's cross-section about its axis. The first-order shear theory has been used to obtain the differential equations governing the beam [6].

$$\begin{aligned} u(x,z,t) &= u_0(x,t) + z\phi(x,t) \\ w(x,z,t) &= w_0(x,t) \end{aligned} \tag{1}$$

where u_0 and w_0 represent, respectively, the x and y displacements of the middle surface.

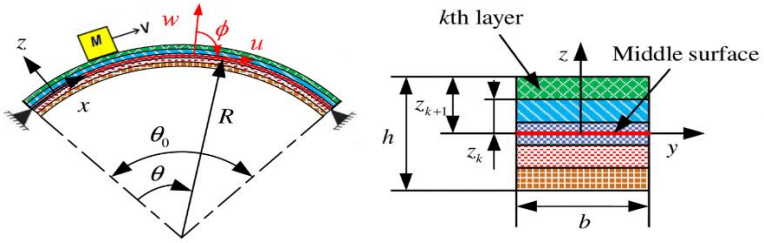


Figure 1. Schematic of curved composite beam

$$\begin{aligned} &\begin{Bmatrix} \sigma_\theta \\ \tau_{\theta z} \end{Bmatrix}_k = \begin{bmatrix} E_x^k & 0 \\ 0 & \bar{Q}_{55}^k \end{bmatrix} \begin{Bmatrix} \varepsilon_\theta \\ \gamma_{\theta z} \end{Bmatrix}_k, \quad \frac{1}{E_x^k} = \frac{\cos^4(\alpha^k)}{E_{11}} + \left(\frac{1}{G_{12}} - \frac{2\upsilon_{12}}{E_{11}}\right)\cos^2(\alpha^k)\sin^2(\alpha^k) + \frac{\sin^4(\alpha^k)}{E_{22}} \\ &\bar{Q}_{55}^k = G_{13}\cos^2(\alpha^k) + G_{23}\sin^2(\alpha^k) \end{aligned} \tag{2}$$

The angle at which the fibers of the kth layer intersect the x-axis, denoted as α^k. E_{11} and E_{22} represent the modulus of elasticity and perpendicular direction, respectively, of the composite material in relation to the fibers. G_{12}, G_{13}, and G_{23} represent the shear modulus, while υ_{12} denotes Poisson's coefficient. Hamilton's law establishes the following fundamental differential equations ():

$$\delta\int_{t_1}^{t_2}(T + W_M - U)\,\mathrm{dt} = 0 \Rightarrow \begin{cases} \delta T = \int_V \rho_i(\dot{u}\delta\dot{u} + \dot{w}\delta\dot{w})dV + M\dfrac{V^2}{R} + \left[\int_0^{\theta_0} M\left(V^2 w_0'' + 2V\dot{w}_0' + \ddot{w}_0\right)\right]\delta w_0\delta_D(R\theta - Vt)R\mathrm{d\theta dt} \\ \delta U = \dfrac{1}{2}\int_0^{\theta_0}\int_{-\frac{h}{2}}^{\frac{h}{2}} b\left[\sigma_\theta\delta\varepsilon_\theta + \sigma_{\theta z}\delta\gamma_{\theta z}\right](1 + \dfrac{z}{R})R\mathrm{dzd\theta} \\ \delta W_M = \int_0^{\theta_0} Mg\cos\left(\dfrac{\theta_0}{2} - \theta\right)\delta_D(R\theta - Vt)\delta w_0 R\mathrm{d\theta dt} + \int_0^{\theta_0} Mg\sin\left(\dfrac{\theta_0}{2} - \theta\right)\delta_D(R\theta - Vt)\delta u_0 R\mathrm{d\theta dt} \end{cases} \tag{3}$$

The strain energy, kinetic energy, and external work energy of the forces applied to the structure are denoted by U, T, and W, respectively, in the relationship above. The normal and shear strains are denoted by ε_θ and $\gamma_{\theta z}$. Navier's method is employed to convert the simplified equations into time domain ordinary differential equations, which are subsequently delineated.

$$u_0(\theta,t) = \sum_{i=1}^{N} u_i(t)\cos\left(\frac{i\pi R\theta}{L}\right), w_0(\theta,t) = \sum_{i=1}^{N} w_i(t)\sin\left(\frac{i\pi R\theta}{L}\right), \phi(\theta,t) = \sum_{i=1}^{N}\phi_i(t)\cos\left(\frac{i\pi R\theta}{L}\right) \tag{4}$$

The result of simplification is the general form shown below.

$$[\mathbf{M}]\{\ddot{\mathbf{X}}\} + [\mathbf{C}]\{\dot{\mathbf{X}}\} + [\mathbf{K}]\{\mathbf{X}\} = \{\mathbf{F}\} \tag{5}$$

Total damping matrix, stiffness matrix, and mass matrix, respectively, are denoted by $[c]$, $[K]$, and $[M]$ in the preceding equation. The equation (5) is solved by Newmark's method.

Results

Following a verification of the work's accuracy against previous publications, we proceed to analyze the parameters of the sheet under consideration in this section. The following are the geometric and mechanical properties of the composite curved beam:

$$L = 1m, \quad h = 0.05m, \quad b = 0.025m$$

$$E_{11} = 200\,Gpa, \quad E_{22} = 8.96\,Gpa, \quad \upsilon_{12} = 0.3, \quad G_{13} = 7.1\,Gpa, \quad \rho = 1580\,\frac{kg}{m^3}$$

Figure 2 illustrates a comparison between the dynamic rise of a single-layer smooth beam and the results of the investigation [7] in order to verify the precision of the results pertaining to the dynamic response of the curved composite beam under the influence of a moving mass. It should also be noted that a radius of one is required to transform a curved beam into a straight beam, specifically a large curved beam. Figure 2 illustrates that the current findings exhibit an obvious similarity to those of prior research.

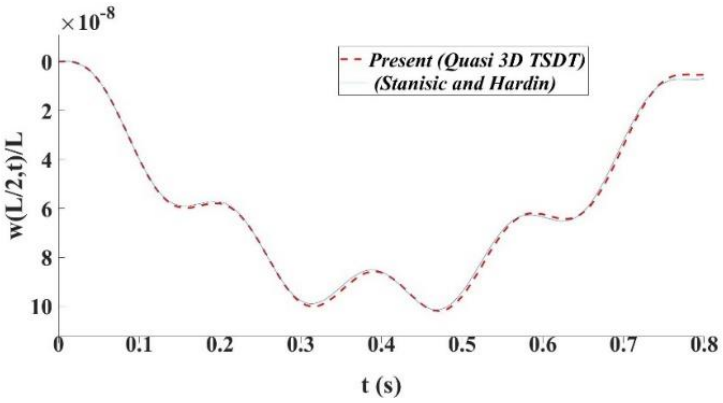


Figure2. Comparative analysis of the dynamic response of a curved composite beam subjected to a moving mass with the works cited in [7]

The impact of various layers on the dynamic response of the composite curved beam is illustrated in Figure 3. The range of forced fluctuations of the system is illustrated in Figure 3, with the maximum and lowest values corresponding to layering [45. −45. −45. 45] and 0.90.90.0], respectively. Modifying the arrangement of fibers directly impacts the composite beam's stiffness and, in turn, its deflection.

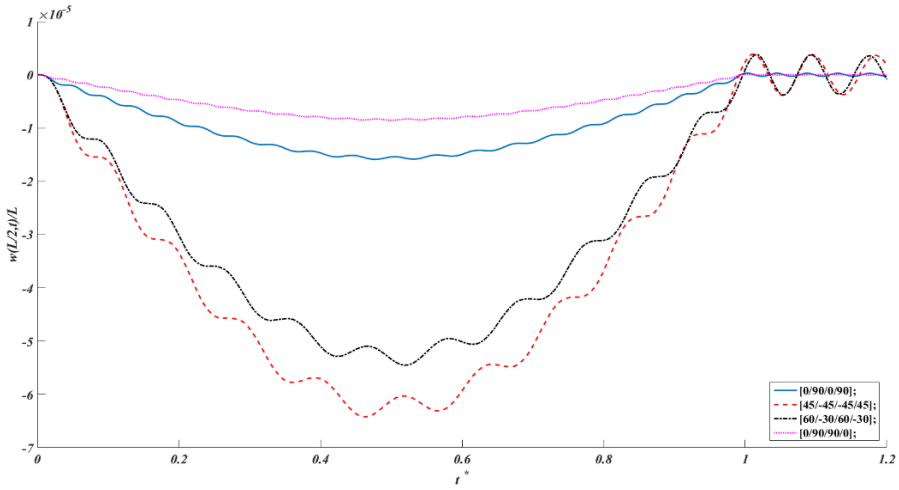


Figure3. The effect of different layers on the dynamic response of a composite curved beam under moving mass

Conclusion

The current investigation focused on the dynamic analysis of a composite curved beam subjected to a moving mass. The present analysis incorporated the beam's displacement field according to the principles of first order

shear theory. By applying Hamilton's principle, the equations governing the dynamic response of the system were derived. Considering the boundary conditions of simple supports on both sides of the composite curved beam, Navier's analytical method in the space domain and Newmark's numerical solution in the time domain were employed to solve differential governing equations utilizing partial derivatives. The results indicate that the spectrum of oscillations for layering [45. −45. −45. 45] and [0.90.90.0] is at its maximum and minimum values, respectively.

References

1. Yang, Y. B., Wu, C. M., & Yau, J. D. (2001). Dynamic response of a horizontally curved beam subjected to vertical and horizontal moving loads. Journal of Sound and Vibration. 242(3), 519–537.
2. Meher, S., Parida, S., & Behera, R. K. (2020). On the Response of a Beam Structure to a Moving Mass Using Green's Function. in Advances in Applied Mechanical Engineering: Select Proceedings of ICAMER. 455–463.
3. Lin, S. M., & Lee, K. W. (2016). Instability and vibration of a vehicle moving on curved beams with different boundary conditions.Mechanics of Advanced Materials and Structures. 23(4), 375–384.
4. Biglari, H., Teymouri, H.,& Shokouhi, A. (2024) Dynamic Response of Sandwich Beam with Flexible Porous Core Under Moving Mass. Mechanics of Composite Materials, pp. 1–20, 2024.
5. Jafari-Talookolaei, R. A., Kargarnovin, M. H., & Ahmadian, M. T. (2012). On the dynamic response of a delaminated composite beam under the motion of an oscillating mass. Journal of Composite Materials. 46(22), 2863–2877.
6. Shao, D., Hu, S. , Wang, Q., & Pang, F. (2016). A unified analysis for the transient response of composite laminated curved beam with arbitrary lamination schemes and general boundary restraints. Composite Structures. 154, 507–526.
7. Stanišić, M. M., & Hardin, J. C. (1969). On the response of beams to an arbitrary number of concentrated moving masses. Journal of the Franklin Institute. 287(2), 115–123.

Advanced Engineering Days

aed.mersin.edu.tr

Free vibrations of functionally graded sheets using HSNDT

Hadi Teymouri *[1], Kaveh Karimkhani [1], Erfan Rahmatzadeh [1], Hasan Biglari [1]

[1]University of Tabriz, Department of Mechanical Engineering, Iran, hteymouri@tabrizu.ac.ir, kave.ka95@gmail.com, erfan.rahmatzadeh.1@gmail.com, hbiglari@tabrizu.ac.ir

Cite this study: Teymouri, H., Karimkhani, K., Rahmatzadeh, E., & Biglari, H. (2024). Free vibrations of functionally graded sheets using HSNDT. Advanced Engineering Days, 9, 15-18

Keywords
Free Vibration
FGM
Navier Method
High-order shear and normal deformation theory

Abstract

High-order shear and normal deformation theories (HSNDT) were applied to conduct a free vibration analysis of the sheet composed of functionally graded materials for this article. The rectangular, straightforward support conditions sheet is the subject of discussion. The system's governing equations are acquired through the utilization of the energy method. Navier's analytical method in the space domain was employed to solve the obtained equations of motion, which are complex differential equations containing partial derivatives. Comparisons with previously provided answers for specific scenarios are provided to verify the accuracy of the acquired results. The investigation and comparison of the natural frequencies of the rectangular sheet for various metal and ceramic combinations distinguishes this article from others containing similar content.

Introduction

In recent years, engineering science disciplines have focused on the analysis and investigation of sheets composed of functionally graded materials. This is due to the remarkable properties that these materials demonstrate when exposed to challenging working conditions, particularly in the context of various types of engineering structures. The advantage of functionally graded materials is that their mechanical properties alter in tandem with the change in properties in a gradual and seamless manner. This enables them to retain their stiffness while circumventing prevalent challenges that affect alternative composite materials, including discontinuity. Additionally, stress diagrams and inadequate resistance to thermal disturbances at the interfaces between layers should be avoided [1].

Zhao et al. presented an analysis of the free vibrations of a FGM sheet utilizing the Kp-Ritz element method within this particular context [2]. For static and dynamic analysis as well as buckling in sandwich sheets with isogeometric geometry and functionally graded isotropic materials, Thai et al. introduced a generalized shear theory. Their theory is founded on the classical framework of sheet mechanics [3].Matsunaga [4] conducted a discussion and analysis of the natural frequency and deformation of shallow casings constructed from FGM materials. Jin et al. [5] present a novel, exact three-dimensional solution for the free vibrations of functionally graded rectangular plates of arbitrary thickness while maintaining general boundary conditions.

This study presents a free vibration analysis of a sheet made up of functionally graded materials through the application of high-order shear and normal deformation theories. This article is unique in that it conducts an examination and comparison of the natural frequencies of the rectangular sheet across different combinations of metals and ceramics.

Material and Method

A sheet with dimensions a and b and a thickness of h is regarded as illustrated in Figure 1. As previously stated, the shell is composed of a functionally graded material in which a heterogeneous combination of metal and ceramic exists between its upper and lower surfaces, with the former consisting entirely of metal and the latter of ceramic. The displacement field in the sheet may be mathematically represented as follows [6]:

$$u_1(x,y,z) = u(x,y) + g(z)\frac{\partial w(x,y)}{\partial x} + f(z)\psi_1(x,y),$$
$$u_2(x,y,z) = v(x,y) + g(z)\frac{\partial w(x,y)}{\partial y} + f(z)\psi_2(x,y), \quad (1)$$
$$u_3(x,y,z) = w(x,y), \quad f(z) = z - \frac{4z^3}{3h^2},\ g(z) = f(z) - z,$$

Consequently, u1, u2, and u3 denote the displacements in the x, y, and z dimensions, u, v, and w denote the corresponding displacements on the shell's midpoint (z=0), and ψ1 and ψ2 symbolize the rotation about the shell, respectively. x and y axes are presented.

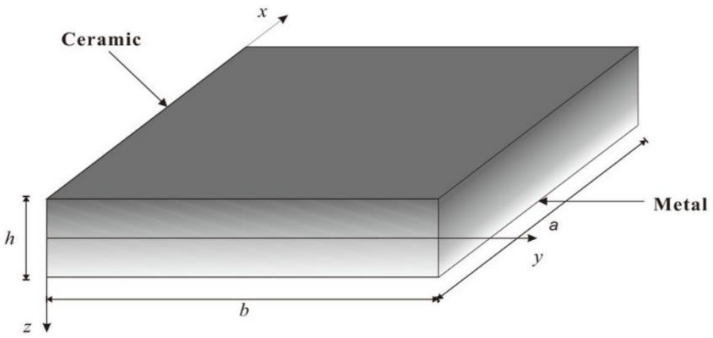


Figure 1. Schematic of FGM sheet

Hooke's law states that the relationship between stress and strain components for an isotropic structure is as follows [7]:

$$\begin{Bmatrix}\sigma_{11}\\ \sigma_{22}\\ \sigma_{23}\\ \sigma_{13}\\ \sigma_{12}\end{Bmatrix} = \begin{bmatrix} C_{11}(z) & C_{12}(z) & 0 & 0 & 0\\ C_{12}(z) & C_{22}(z) & 0 & 0 & 0\\ 0 & 0 & C_{44}(z) & 0 & 0\\ 0 & 0 & 0 & C_{55}(z) & 0\\ 0 & 0 & 0 & 0 & C_{66}(z)\end{bmatrix}\begin{Bmatrix}\varepsilon_{11}\\ \varepsilon_{22}\\ \gamma_{23}\\ \gamma_{13}\\ \gamma_{12}\end{Bmatrix}, \quad (2)$$

$$C_{11}(z) = C_{22}(z) = \frac{E(z)}{1-\nu^2(z)},\quad C_{12}(z) = \nu(z)C_{11}(z), C_{44}(z) = C_{55}(z) = C_{66}(z) = G(z) = \frac{E(z)}{2\left[1+\nu(z)\right]},$$

The governing equations and boundary conditions that describe the dynamic behavior of a structure can be obtained from the subsequent relationship, in accordance with Hamilton's principle [8]:

$$\int_{t_1}^{t_2}(\delta T - \delta U)\,dt = 0, \quad (3)$$

T and *U* represent the kinetic and strain energies, respectively, in the preceding relationship. After deriving the equations, the following Navier's method solution for a sheet with basic roller supports can be considered:

$$u(x,y,t) = \sum_{n=1}^{\infty}\sum_{m=1}^{\infty} U_{mn}\exp(i\omega t)\cos(c_m x)\sin(c_n y), v(x,y,t) = \sum_{n=1}^{\infty}\sum_{m=1}^{\infty} V_{mn}\exp(i\omega t)\sin(c_m x)\cos(c_n y), \quad (4)$$
$$w(x,y,t) = \sum_{n=1}^{\infty}\sum_{m=1}^{\infty} W_{mn}\exp(i\omega t)\sin(c_m x)\sin(c_n y), \psi_1(x,y,t) = \sum_{n=1}^{\infty}\sum_{m=1}^{\infty} X_{mn}\exp(i\omega t)\cos(c_m x)\sin(c_n y),$$
$$\psi_2(x,y,t) = \sum_{n=1}^{\infty}\sum_{m=1}^{\infty} Y_{mn}\exp(i\omega t)\sin(c_m x)\cos(c_n y), \quad c_m = \frac{m\pi}{a}, \quad c_n = \frac{n\pi}{b}$$

The symbol ω denotes the natural frequency of the sheet in the aforementioned relationship.

Obtaining the natural frequencies of the sheet in question is possible by solving the subsequent matrix form that results from substituting the aforementioned relationships into the extracted equations.

$$[K]\{s\} = \omega^2 [M]\{s\} \quad (5)$$

Total displacement, stiffness matrix, and mass matrix, respectively, are denoted by $\{s\}$, $[K]$, and $[M]$ in the preceding equation.

Results

Following a verification of the work's accuracy against previous publications, we proceed to analyze the parameters of the sheet under consideration in this section. The sheet possesses the geometric properties a=1m, b/a=2, and h/a=0.05. A consideration can be given to a variety of alternatives when combining metals and ceramics, as indicated by their respective mechanical properties in Tables 1 and 2.

Table 1. Mechanical properties of several metal samples

		E (GPa)	ν	ρ (kg/m3)	E/ρ (GPa.m3/kg)
Aluminum	Al	70	0.3	2707	0.0259
Titanium Alloy	Ti-6Al-4V	105.7	0.298	4429	0.0239
Stainless steel	SUS304	207.78	0.3177	8166	0.0254

Table 2. Mechanical properties of several ceramics samples

		E (GPa)	ν	ρ (kg/m3)	E/ρ (GPa.m3/kg)
Alumina	Al2O3	380	0.3	3800	0.1000
Zirconia	ZrO2	151	0.3	3000	0.0503
Silicon nitride	Si3N4	322.27	0.24	2370	0.1360

The comparison between the values of natural frequencies for a known value of profile power in four distinct vibration modes presented in Table 3 and the findings of Zhao et al.'s article [2] reveals a clear and substantial concurrence.

Table 3. Dimensionless natural frequency ($\Lambda_{mn} = \omega_{mn}\sqrt{\frac{\rho_c}{E_c}}$) validation using the paper by Zhao et al. [2]

		(m,n)=(1,1)	(m,n)=(1,2)	(m,n)=(2,1)	(m,n)=(2,2)
q=0.5	Presented analysis	3.9385	9.4073	9.4073	14.451
	Zhao et al.	3.8947	9.3645	9.3645	14.365

In regards to combinations of metals and ceramics, nine modes can be evaluated. The numbers of these nine modes appear in Table 4.

Table 4. Different combinations of metal and ceramics

Case Num	1	2	3	4	5	6	7	8	9
Metal	Al	Al	Al	Ti-6Al-4V	Ti-6Al-4V	Ti-6Al-4V	SUS304	SUS304	SUS304
Ceramic	Al2O3	ZrO2	Si3N4	Al2O3	ZrO2	Si3N4	Al2O3	ZrO2	Si3N4

The natural frequencies of the rectangular sheet for various metal and ceramic combinations are presented in Table 5. Based on the data presented in the table, it is evident that the alloy steel and zirconia emit the lowest natural frequencies, while aluminum and silicon nitride produce the highest natural frequencies.

Table 4. Natural frequencies (Hz) of rectangular sheet for different combinations of metal and ceramic

Case number	(m,n)=(1,1)	(m,n)=(1,2)	(m,n)=(2,1)	(m,n)=(2,2)
1	204.9982	326.9365	688.1414	807.0518
2	173.5113	276.6614	581.9593	682.3837
3	212.9191	339.5506	714.5794	838.0158
4	194.8021	310.6195	653.4544	766.2411
5	164.3295	262.0303	551.2378	646.3814
6	197.9074	315.5749	663.9031	778.5022
7	187.1215	298.3439	627.4544	735.6862
8	158.3206	252.4957	531.4647	623.3029
9	186.1080	296.7602	624.3188	732.0833

Conclusion

By applying the theories of high-order shear and normal deformation, the current study examined the effects of unconstrained vibration on a sheet composed of functionally graded materials. The equations of the system were derived by applying Hamilton's principle. The analytical method of Navier was applied in the space domain to solve partial differential governing equations while considering the boundary conditions of simple supports. Aluminum and silicon nitride generate the highest natural frequencies, whereas alloy steel and zirconia emit the lowest natural frequencies in this study.

References

1. Reddy, J. (2000). Analysis of functionally graded plates. International Journal for Numerical Methods in Engineering, 47 (1-3), 663–684.
2. Zhao, X., Lee, Y. Y., & Liew, K. M. (2009). Free vibration analysis of functionally graded plates using the element-free kp-Ritz method. Journal of Sound and Vibration. 319 (3-5), 918–939.
3. Thai, C. H., Kulasegaram, S., Tran, L. V., & Nguyen-Xuan, H. (2014) Generalized shear deformation theory for functionally graded isotropic and sandwich plates based on isogeometric approach. Computers and Structures. 141, 94–112.
4. Matsunaga, H. (2008). Free vibration and stability of functionally graded shallow shells according to a 2D higher-order deformation theory. Composite Structures. 84(2), 132–146.
5. Jin, G., Su, Z., Shi, S., Ye, T., & Gao, S. (2014). Three-dimensional exact solution for the free vibration of arbitrarily thick functionally graded rectangular plates with general boundary conditions. Composite Structures. 108, 565–577.
6. Sayyad, A. S., and Ghugal, Y. M. (2019). Static and free vibration analysis of laminated composite and sandwich spherical shells using a generalized higher-order shell theory. Composite Structures. 219, ,129–146.
7. Reddy, J. N. (2003). Mechanics of laminated composite plates and shells: theory and analysis. CRC press.
8. Biglari, H., Teymouri, H.,& Shokouhi, A. (2024) Dynamic Response of Sandwich Beam with Flexible Porous Core Under Moving Mass. Mechanics of Composite Materials, pp. 1–20, 2024.

Advanced Engineering Days

aed.mersin.edu.tr

Deformation analysis of elastic plate under static extended loading by FEM

Arya Gholami [1], Hadi Teymouri [*1], Amirreza Nikmard [1], Aidin Badiee [1] , Hasan Biglari [1]

[1]University of Tabriz, Department of Mechanical Engineering, Iran, aryagh515@gmail.com, hteymouri@tabrizu.ac.ir, amrreza.nikmard82@gmail.com, aidinbadiee@gmail.com, hbiglari@tabrizu.ac.ir

Cite this study: Gholami, A., Teymouri, H., Nikmard, A., Badiee, A., & Biglari, H. (2024). Deformation analysis of elastic plate under static extended loading by FEM. Advanced Engineering Days, 9, 19-21

Keywords
Static loading
FEM
Plate's deformation
Articulated supports
Girder supports

Abstract

Given the extensive use of sheets and shells in numerous industries today, such as shipbuilding, automotive, oil, gas, and petrochemical (particularly in oil and gas transmission pipes), it is essential and indispensable to investigate the probability of failure and damage through the study of their deformation under specific loads. Sheets and shells are used extensively in these many industries. This work investigates rectangular sheets, considering arrangements with two articulated supports and two girder supports under extensive static loading. An evaluation and analysis of the results are carried out by means of the finite element technique. Validation was carried out with the help of the Abaqus program in order to ensure that the desired results were achieved.

Introduction

Principal components of aerospace structures, such as fuselages, missiles, bulkheads, helicopter blades, and control surfaces, are composed of plates and casings. A comprehensive approach to the analysis of plate and shell structures is imperative due to the diverse array of applications, geometries, and materials that comprise them. This requires the implementation of pertinent theories and methodologies [1].

Huang et al. [2] examined a finite deformation approximation solution for an elastic circular plate with the assumption of uniform membrane strain and the von Kármán equations. Using the differential quadrature element method, Liu et al. [3] examined the static solution of three-dimensional elasticity equations concerning thick rectangular laminated composite plates. He et al. [4] solved the problem of bimodular functionally graded thin plates subjected to significant deformation by utilizing the variational method and numerical simulation technique. By means of numerical analysis and experimental validation, Aune et al. [5] examine the inelastic behavior of thin steel and aluminum plates subjected to airblast loading. Biglari et al. [6] investigate the dynamic response and time history of the impact force of the sandwich plate with the auxetic core under low-velocity impact by using high-order shear and normal deformation theory (HSNDT). The purpose of this investigation is to examine the impact force acting on the plates.

In this research, rectangular sheets are evaluated after being subjected to substantial static loads. The study takes into consideration setups that include two articulated supports and two girder supports. The method of finite elements is used in order to carry out an assessment and analysis of the outcomes.

Material and Method

Following the completion of the computations, the unknown values for the nodes are derived by using the finite element technique. In order to determine the values of these parameters inside the elements, we need to make use of a polynomial that is appropriate for the circumstances related to the issue. For the purpose of this article, the following polynomial expression will be used [1]:

$$w(x,y) = \alpha_1 + \alpha_2 x + \alpha_3 y + \alpha_4 x^2 + \alpha_5 xy + \alpha_6 y^2 + \alpha_7 x^3 + \alpha_8 x^2 y + \alpha_9 xy^2 + \alpha_{10} y^3 + \alpha_{11} x^3 y + \alpha_{12} xy^3 \quad (1)$$

The values of x and y are expressed in this expression using the local coordinate system of the element, as illustrated in Figure 1.

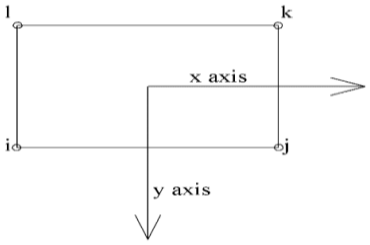


Figure 1. Schematic of a 2D element

The symbol [di] is used to represent the displacement matrix associated with node i. This matrix is defined by the subsequent relationship [1]:

$$[d_i] = [w_i, (\beta_x)_i, (\beta_y)_i]^T \quad (2)$$

β_x and β_y represent the x and y-direction slopes of the plane, respectively. The definition of the stiffness matrix for each element is as follows:

$$[K]^e = \int\int_A [B]^T [D][B] dxdy \quad (3)$$

$[K]$, $[B]$, and $[D]$, represent the stiffness matrix, strain-displacement matrix, and stiffness matrix, respectively, in the aforementioned relationship. Furthermore, the force matrix is defined as follows for each element:

$$[F]^e = \int\int_A [N]^T \, p(x, y) dxdy \quad (3)$$

The variables $[N]$ and $P(x.y)$ represent the order of the interpolation matrix and the loading type, respectively, in the relationship described above.

The stiffness matrix of the entire system is required in order to solve the problem's general equations. The rigidity matrices of the elements are assembled directly to produce this matrix. The force matrices of the elements are similarly utilized to construct the force matrix of the entire system. Equation 4 is ultimatey defined by employing the matrix data.

$$[K][d] = [F] \quad (4)$$

Preceding this, we have:

$$[d] = [K]^{-1}[F] = [d_1, d_2, d_3, ..., d_{(n+1)2}]^T \quad (5)$$

Results

With two hinged and two articulated supports, the aforementioned sheet is subjected to a substantial $140 \frac{N}{m^2}$. Specifications for sheets are detailed in Table 1.

Table 1. Mechanical properties of plate

ν	E (GPa)	l(m)	b(m)	t(m)
0.3	210	3	2	0.025

The vertical displacement and slope graphs of the nodes situated in the middle web of the sheet are depicted in two graphs (2) and (3). As illustrated in Figure 2, the node in the middle experiences the greatest displacement, while the nodes at the sheet's edges, situated at its extremities, exhibit the smallest displacement. Additionally, Figure 3 demonstrates that the slope of the sheet attains its minimum value in the middle, which is zero. In the vertical direction, it is evident that the zero value is also present at the sheet's margins.

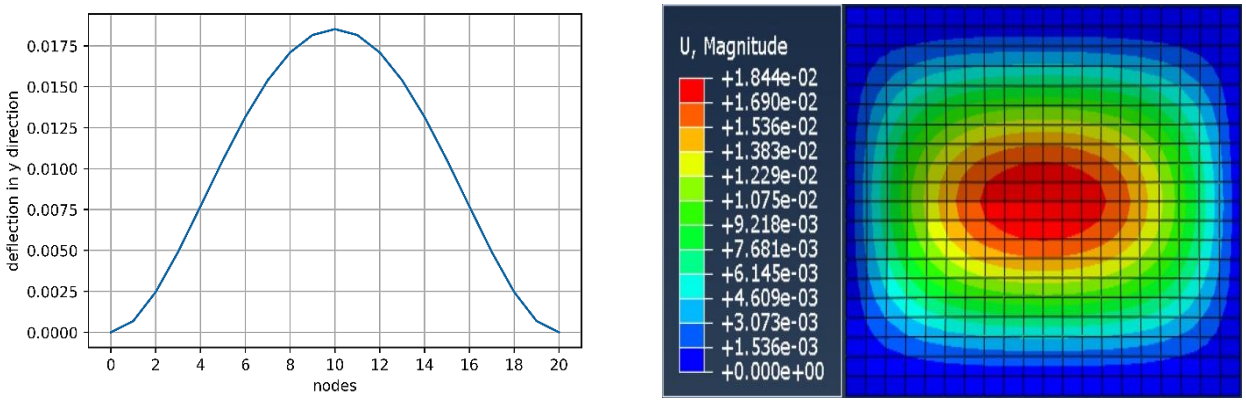


Figure 2. Vertical displacement of nodes in the sheet under extensive static loading

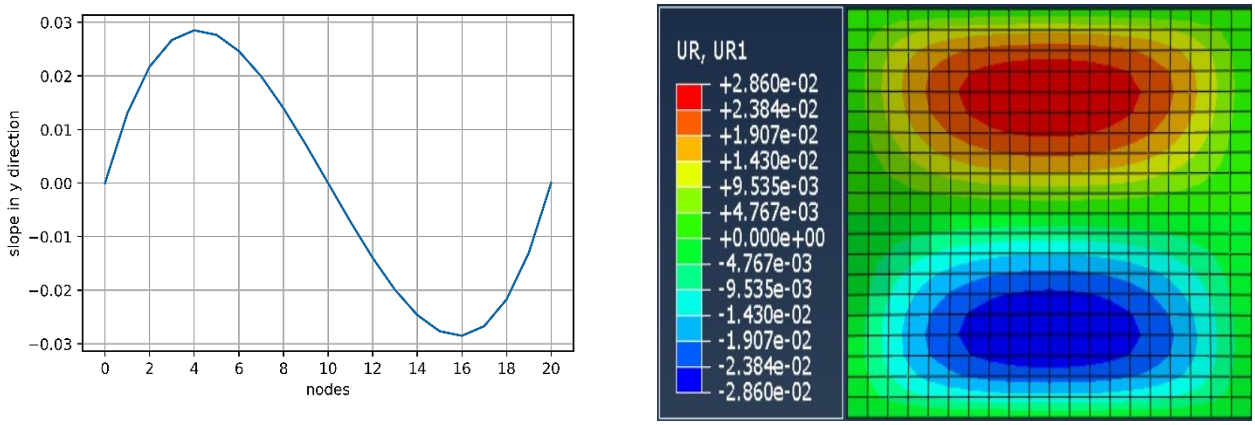


Figure 3. Vertical slope of nodes in the sheet under extensive static loading

Conclusion

The current research investigates rectangular sheets that have been exposed to significant static loads. The study takes into consideration configurations that include two articulated supports and two girder supports at the same time. The method of finite elements is used in order to carry out an assessment and analysis of the outcomes. The intended outcomes were verified through the implementation of validation using the Abaqus software. The significant finding of this article is that the minimum displacement occurs in the end nodes situated at the sheet's margins, while the maximum displacement is associated with the intermediate node.

References

1. Hughes, T. J. R. (1986). Finite Element Methods for Plates and Shell Structures. Element Technology.
2. Huang, X., Wang, M. , Feng, Y., Wang, X., & Qiu, X. (2023). Finite deformation analysis of the elastic circular plates under pressure loading. Thin-Walled Structures. 188, 110864.
3. Liu, F. L. (2000). Static analysis of thick rectangular laminated plates: three-dimensional elasticity solutions via differential quadrature element method. International Journal of Solids and Structures. 37(51), 7671–7688.
4. He, X. T., Wang, X. G., Pang, B., Ai, J. C., & Sun, J.-Y. (2023). Variational Solution and Numerical Simulation of Bimodular Functionally Graded Thin Circular Plates under Large Deformation. *Mathematics*. 11(14), 1-23.
5. Aune, V., Valsamos, G., Casadei, F., Larcher, M., Langseth, M., & Børvik, T. (2017). Numerical study on the structural response of blast-loaded thin aluminium and steel plates. International Journal of Impact Engineering. 99, 131–144.
6. Biglari, H., Teymouri, H., & Foroutan, M. (2024). Application of Auxetic Core to Improve Dynamic Response of Sandwich Panels Under Low-Velocity Impact. *Arabian Journal for Science and Engineering.*

Advanced Engineering Days

aed.mersin.edu.tr

Numerical analysis of composite beams with piezoelectric actuators

Rasa Rahimi Behbood [*1], Hadi Teymouri [1], Hasan Biglari [1] , Taraneh Sheidaei [1]

[1] University of Tabriz, Department of Mechanical Engineering, Iran, rasarahimibehbood@gmail.com, hteymouri@tabrizu.ac.ir, hbiglari@tabrizu.ac.ir, taranehsheidaei@gmail.com

Cite this study: Behbood, R. R., Temouri, H., Biglari, H., & Sheidaei, T. (2024). Numerical analysis of composite beams with piezoelectric actuators. Advanced Engineering Days, 9, 22-24

Keywords
Piezoelectric
Finite Element Method
Composite
Shear mode

Abstract

A significant amount of interest has been generated in the incorporation of piezoelectric actuators into composite beams as a result of the potential uses that they may have in the areas of vibration reduction and structural control. This research aims to conduct a numerical study that examines the behavior of composite beams enhanced with piezoelectric actuators. Additionally, the validity of the suggested models and the practicality of utilizing shear-mode actuators in smart beams are explored and explained. For the computations presented in this paper, the finite element method was utilized. The validation of the present results was conducted with other articles prior to the acquisition in order to check their accuracy. According to the study, deflection is greatest when the layups' orientation is -45/45/PZT/45/-45.

Introduction

For the last 5 decades, the use of piezoelectric components as electromechanical transducers in sensors as well as in actuator applications has been continuously increasing. More recently, piezoelectrics have been among the most suitable materials for extending the structural capabilities beyond those of purely passive load-carrying ones [1]. When a material has the potential to perform both sensing and actuating tasks, it is called a smart material [2]. Piezoelectric materials are often used in smart structures because they can be easily controlled by an applied voltage and are relatively easy to model [3]. Flexible beams incorporating piezoelectric elements are used in many applications, such as precision positioning, noise and vibration sensing, and cancellation, and generate deflection in beams [4].

Sun and Zhang [5] gestured at the idea of exploiting the shear mode to create transverse deflection in sandwich beams. They formulated an analytical model of a sandwich beam with a shear piezoelectric actuator that occupies the entire core. Moreover, they have shown that shear-mode actuators can offer many advantages over extension-mode actuators. Benjedou et al. [6] approached modeling a finite-element sandwich beam with shear and extension piezoelectric elements, which employed the displacement field of Zhang and Sun [5].

This work uses numerical methods to explore composite beams using piezoelectric actuators. Also discussed are the models' validity and the practicalities of using shear-mode actuators in smart beams.

Material and Method

A composite beam with piezoelectric actuator is considered as Figure 1. In this work PZT-5H is used as core actuator and Graphite epoxy as composite material with these properties:

PZT-5H properties:

$Q_{11} = 126\ [GPa], Q_{12} = 84.1\ [GPa], Q_{13} = 79.5\ [GPa]$

$Q_{22} = 117\ [GPa], Q_{23} = 84.1\ [GPa], Q_{33} = 126\ [GPa]$

$Q_{44} = 23\ [GPa], Q_{55} = 23.25\ [GPa], Q_{66} = 23\ [GPa]$

$d_{31} = d_{32} = -274.8 \times 10^{-12}\ [mV^{-1}], d_{15} = d_{24} = 739.13 \times 10^{-12}\ [mV^{-1}], d_{33} = 590 \times 10^{-12}\ [mV^{-1}]$

Graphite-Epoxy (Engineering constants):

$$E_1 = 200\ [GPa], E_2 = E_3 = 10\ [GPa], G_{12} = G_{13} = 6\ [GPa], G_{23} = 5\ [GPa], \nu_{12} = \nu_{13} = \nu_{23} = 0.25$$

Applied voltage is: V = 10 v

Considered geometry for the 3D-beam is: t_piezo = 2 mm, t_composite = 1 mm, L = 10 cm

According to the Hooke's law stress-strain relations between composite and PZT element with third axis(through thickness-axis) poling direction can be expressed as above:

$$\begin{Bmatrix}\sigma_{xx}\\ \sigma_{yy}\\ \sigma_{zz}\\ \sigma_{xz}\\ \sigma_{yz}\\ \sigma_{xy}\end{Bmatrix} = \begin{bmatrix}Q_{11} & Q_{12} & Q_{13} & 0 & 0 & 0\\ Q_{12} & Q_{22} & Q_{13} & 0 & 0 & 0\\ Q_{13} & Q_{13} & Q_{33} & 0 & 0 & 0\\ 0 & 0 & 0 & Q_{55} & 0 & 0\\ 0 & 0 & 0 & 0 & Q_{55} & 0\\ 0 & 0 & 0 & 0 & 0 & Q_{66}\end{bmatrix}\begin{Bmatrix}\varepsilon_{xx}\\ \varepsilon_{yy}\\ \varepsilon_{zz}\\ \gamma_{xz}\\ \gamma_{yz}\\ \gamma_{xy}\end{Bmatrix} - \begin{bmatrix}0 & 0 & d_{31}\\ 0 & 0 & d_{31}\\ 0 & 0 & d_{33}\\ 0 & d_{15} & 0\\ d_{15} & 0 & 0\\ 0 & 0 & 0\end{bmatrix}\begin{Bmatrix}E_x\\ E_y\\ E_z\end{Bmatrix} \quad (1)$$

where σ_{ij}, ε_{ij} and Q_{ij} are the components of the reduced stress tensor, reduced strain tensor and stiffness matrix, respectively; d_{31} and ; d_{15} are the piezoelectric extension and shear coefficients, respectively; and E_{ij} is the electric field applied across the thickness of an extension-mode actuator and a shear-mode actuator, respectively.

These equations was applied to calculate transverse deflection of the beam in ABAQUS software.

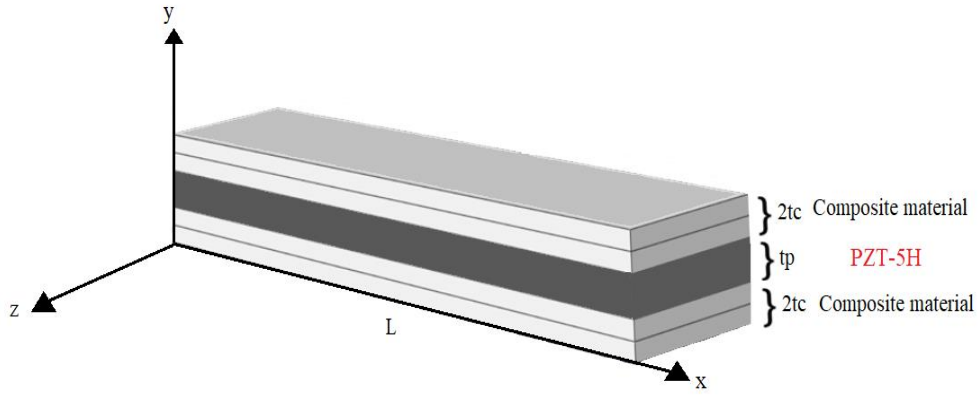


Figure 1. Schematic of smart beam

Results

In this work Finite Element Method was applied for calculations, its important to say that mesh of the beam got converged on 9750 cubic elements and results are extracted with this amount of elements. Figure 2 illustrates a comparison between the present study and Khedir results [7]. A comparison of the transverse deflection of various construction orientations under the C-C boundry condition is illustrated in Figure 3. When the orientation of the layups is -45/45/PZT/45/-45, the deflection is greater, as shown in this figure.

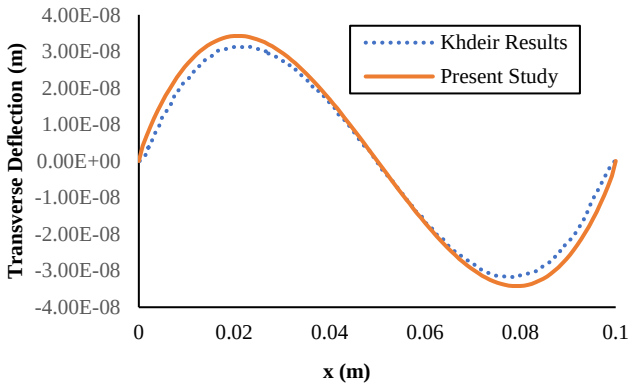


Figure 2. Comparing transverse deflection of present study and Khdeir results

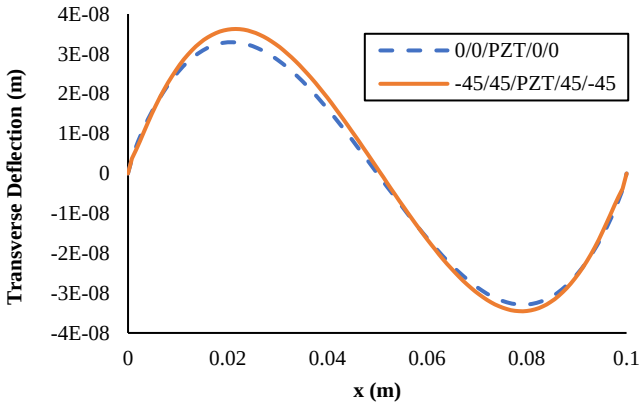


Figure 3. Comparing transverse deflection of different layup orientations in C-C boundry condition

Conclusion

The objective of this investigation is to investigate the behavior of composite beams that have been enhanced with piezoelectric actuators through a numerical study. Furthermore, this study investigates and elucidates the efficacy of employing shear-mode actuators in smart beams. The present investigation utilized the Finite Element Method to analyze the spurious effects of fabrication orientation in composite materials. Furthermore, the accuracy of the results was enhanced through the application of three-dimensional relations. Based on the findings of the research, layups with an orientation of -45/45/PZT/45/-45 exhibit greater deflection value, and in certain circumstances, this can be advantageous when aiming for greater deflection.

References

1. Cinefra, M., Valvano, S., & Carrera, E. (2015). A layer-wise MITC9 finite element for the free-vibration analysis of plates with piezo-patches. International of Journal of Smart and Nano Materials. 6(2), 85–104.
2. Newnham, R. E., & Ruschau, G. R. (1991). Smart electroceramics. Journal of the American Ceramic Society. 74(3), 463–480.
3. Lee, C.K. (1987). Piezoelectric laminates for torsional and bending modal control: theory and experiment. Cornell University.
4. Khdeir, A. A., & Aldraihem, O. J. (2001). Deflection analysis of beams with extension and shear piezoelectric patches using discontinuity functions. Smart Matrials and Structures. 10(2), 212.
5. Sun, C. T., & Zhang, X. D. (1995). Use of thickness-shear mode in adaptive sandwich structures. Smart Matrials and Structures. 4(3), 202.
6. Benjeddou, A., Trindade, M. A. & Ohayon, R. (1999). New shear actuated smart structure beam finite element. AIAA Journal.37(3), 378–383.
7. Aldraihem, O. J., & Khdeir, A. A. (2000). Smart beams with extension and thickness-shear piezoelectric actuators. Smart Matrials and Structures. 9(1), 1–9.

Advanced Engineering Days

aed.mersin.edu.tr

Finite element analysis of tensile testing for carbon fiber epoxy composite plate

Amir Javadzadeh Khoei *[1], **Mohammad Reza Khoshravan Azar** [1]

[1]*University of Tabriz, Department of Mechanical Engineering, Iran, amirjavadzadeh1401@ms.tabrizu.ac.ir, rkhosh@tabrizu.ac.ir*

Cite this study: Khoei, A. J., & Azar, M. R. K. (2024). Finite element analysis of tensile testing for carbon fiber epoxy composite plate. Advanced Engineering Days, 9, 25-27

Keywords
Tensile test
Failure criterion
CFRP
Finite element method
Abaqus

Abstract

Tensile testing is vital for assessing the mechanical properties of carbon fiber-reinforced polymer composites due to their widespread use in various industries. While ASTM D3039/D3039M standardizes the testing procedure, it can be resource-intensive and may not fully capture complex stress and strain distributions. Finite element analysis (FEA) is proposed as a computational approach to simulate and analyze composite behavior. This study aims to create a comprehensive FEA model using software like Abaqus to simulate the ASTM D3039/D3039M standard for carbon fiber epoxy composite plates. It will examine how sample geometry and changes in composite parts affect stress, strain distribution, and failure mechanisms, aiming to enhance the understanding of CFRP mechanical behavior and improve design and manufacturing processes.

Introduction

Composite materials, particularly carbon fiber reinforced polymer (CFRP) composites, have gained widespread adoption in various industries due to their exceptional strength-to-weight ratio and tailorable properties. Among these materials' most fundamental characterization tests is the tensile test, which determines critical mechanical properties such as tensile strength, elastic modulus, and Poisson's ratio. Accurately determining these properties is crucial for the reliable design and analysis of composite structures. experimental tensile testing, as outlined in standards such as ASTM D3039/D3039M [1], provides a direct means of characterizing the tensile response of composite materials.

In this study, a finite element model is developed to simulate the tensile testing of a carbon fiber epoxy composite plate using a commercial FEA software package. The model incorporates the material properties and layup configuration of the composite, as well as the geometry and boundary conditions of the tensile test specimen. The objectives of this work are to (1) validate the finite element model by comparing its predictions with experimental results from the literature, (2) investigate the influence of various parameters (e.g., fiber orientation, stacking sequence) on the tensile response, and (3) analyze the stress and strain distributions within the specimen during tensile loading.

Material and Method

The elastic properties, layer strengths, and Intralaminar fracture toughness of the composite material mentioned are as follows in Table 1.

Table 1. Mechanical properties of a typical unidirectional laminate [2]

Items	Elastic properties		Ply strengths		Intralaminar fracture toughnesses	
1	E_{11} (GPa)	100	X_t (MPa)	2000	G_f^t (kJ/m^2)	100
2	E_{22} (GPa)	8.11	X_c (MPa)	1000	G_f^c (kJ/m^2)	25
3	$G_{12} = G_{13}$ (GPa)	4.65	Y_t (MPa)	100	G_m^t (kJ/m^2)	2
4	G_{23} (GPa)	5.00	Y_C (MPa)	160	G_m^c (kJ/m^2)	2
5	$\nu_{12} = \nu_{13}$	0.3	S_{12} (MPa)	140	G_s (kJ/m^2)	2
6	ν_{23}	0.4	-	-	-	-

Stacking sequences and fiber orientations

The stacking sequence of the laminates is affecting the behavior of composite materials laminates. For instance, the strength, stiffness, fatigue failure, and energy absorption of laminate change when the stacking sequences of

the laminates change [3]. The composite laminate considered in this study consists of unidirectional (UD) carbon fiber/epoxy prepreg plies. The properties of the carbon fibers and epoxy matrix are the same as those in Table 1. The UD lamina properties are calculated using the standard rule of mixtures and the inverse rule of mixtures [4].

Finite Element Model The composite plate has a stacking sequence of $[0, 0, 90, 0, 0]_S$ with five layers arranged symmetrically about the mid-plane, and $[0, 0, 0, 0, 90, 0]_S$ stacking sequence at the bottom and top of the plate with a steel material at the outer layers. The dimensions of the plate are 250 mm × 25 mm × 1 at the middle part and 250 mm × 25 mm × 3 at the bottom and top parts of the plate.

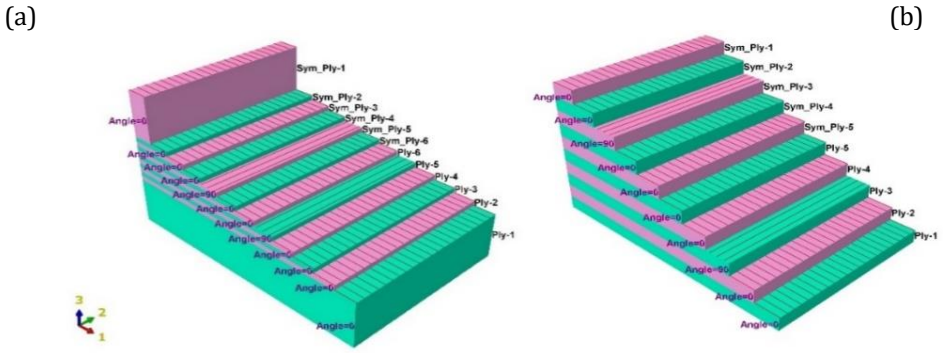


Figure 1. Composite layup (output by Abaqus software), (a) Upper and lower parts, (b) middle part.

The boundary conditions are applied to simulate the gripping of the specimen in the tensile testing machine, similar to the previous model. One end of the specimen is fixed, while the other end is subjected to a prescribed displacement of 20 mm.

Results and Discussion

Based on the provided document, the focus is on the standard test method for determining the in-plane tensile properties of Epoxy matrix composite materials reinforced by high-modulus fibers. This paper outlines the Stress-Strain diagram of the plate while it is under tensile testing, and investigates the Tsai-Wu and Tsai-Hill failure criterion measurements. It also discusses the displacement of the middle of the plate that undergoes fracture during the test.

Figure 2 (a) indicates that the material has a distinct yield point, characterized by the peak stress level before the slight drop. This peak is followed by a decrease in stress, signifying that the material has begun to undergo plastic deformation. After the initial drop, the material exhibits strain hardening, where the stress required to continue deforming the material increases again, albeit not to the initial peak level. The fluctuations in stress levels after the yield point may be caused by different phenomena such as necking, where the cross-sectional area of the material specimen decreases, or by the testing setup and material characteristics.

Eventually, the stress levels out, suggesting that the material has reached a state of work hardening or is undergoing uniform plastic deformation across its length.

The diagram shows that the maximum tension obtained is 1890.91 MPa Considering the change of the layup of the plate from [0,0,0,0,0]s to [0,0,90,0,0]s, it can be seen that the expected stress for the composite plate decreased from 2000 MPa, and It reached a logical number of 1890.91, which indicates that the tolerable force has declined by changing the layup in the direction of stretching the plate.

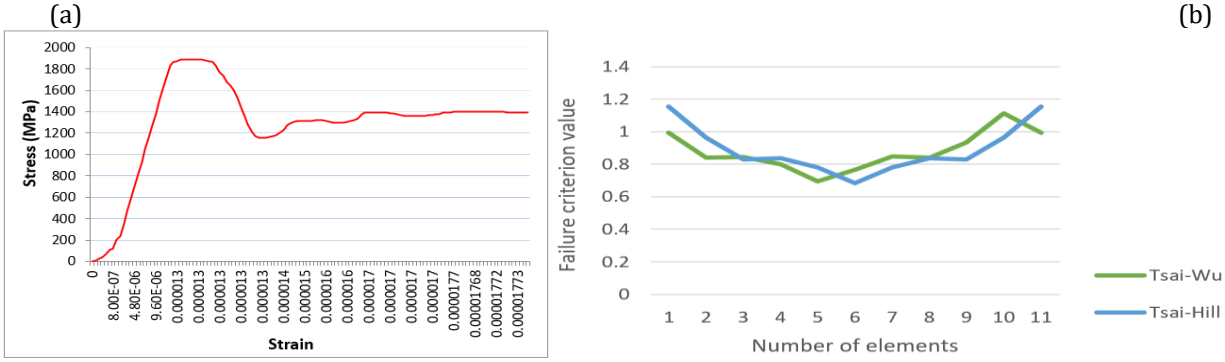


Figure 2. (a) Stress-Strain diagram of the CFRP plate, (b) Comparison of Hill's and Wu's failure criteria for the center elements of the middle plane.

The Tsai–Wu failure criterion is widely used in the design and failure analysis of composite structures due to its simple form and high prediction accuracy [5]. The Tsai–Hill criterion was formulated by referring to distortional energy [6-7] and is thus an interactive criterion that takes into account the effect of the in-plane shear stress. The condition for failure is given by the following inequality:

$$(\frac{\sigma_{11}}{X})^2 - \frac{\sigma_{11}\,\sigma_{22}}{X^2} + (\frac{\sigma_{22}}{Y})^2 + (\frac{\tau_{12}}{S^L})^2 \geq 1 \qquad (1)$$

where the failure parameters X and Y depend on the considered quadrant of the coordinate plane, being $X = X^T$ or $X = X^C$ if $\sigma_{11} \geq 0$ or $\sigma_{11} < 0$, respectively, and $Y = Y^T$ or $Y = Y^C$ if $\sigma_{22} \geq 0$ or $\sigma_{22} < 0$, in the same order. Tsai–Hill FI is given by the expression in Eq [8].

Upon analyzing Figure 2 (b), it is evident that both failure criteria follow a somewhat similar pattern as the number of elements increases. However, they are not identical. Some key observations include:

Both criteria values dip around the 3rd element and peak around the 9th element, indicating that the properties or behavior of the elements at these specific positions might influence the failure criterion value.

Tsai-Wu appears to have a slightly higher value than Tsai-Hill for most elements, except for the 3rd, where Tsai-Hill exceeds Tsai-Wu, and the 10th element, where they are almost equal.

A notable increase in both criteria values from the 8th to the 9th element suggests a significant change in the failure characteristics.

The lowest values for both criteria appear to be at the 3rd element, which may indicate a point of lower failure risk, depending on the context.

Conclusion

The paper indicates that the stacking sequence of the composite laminate significantly affects its mechanical behavior, with changes in layup leading to variations in stress and strain distributions and ultimately influencing the material's failure mechanisms. The study compares two failure criteria, Tsai-Wu and Tsai-Hill, finding that while they follow a similar pattern, Tsai-Wu generally yields higher values, except at certain elements. This suggests that the choice of failure criterion can impact the prediction of material failure in composite structures. and also provides detailed mechanical properties of the composite material, including elastic properties, layer strengths, and intralaminar fracture toughness. The stress-strain diagram of the plate under tensile testing shows a distinct yield point, followed by plastic deformation and strain hardening, which are characteristic of the material's behavior under tensile loading.

In conclusion, the study contributes to a better understanding of the mechanical behavior of CFRP composites under tensile loading. It offers insights that can be used to optimize composite materials' design and manufacturing processes, ultimately improving their performance and reliability.

References:

1. ASTM D3039/D3039M-14, "Standard Test Method for Tensile Properties of Polymer Matrix Composite Materials," ASTM International, West Conshohocken, PA, 2014.
2. Yokoyama, N., Donadon, M. V., & De Almeida, S. F. M. (2010). A numerical study on the impact resistance of composite shells using an energy based failure model. Composite Structures, 93(1), 142–152. https://doi.org/10.1016/j.compstruct.2010.06.006
3. Bezzie, Y. M., Paramasivam, V., Tilahun, S., & Selvaraj, S. K. (2021). A review on failure mechanisms and analysis of multidirectional laminates. Materials Today: Proceedings, 46, 7380-7388.
4. Daniel, I. M., & Ishai, O. (2006). Engineering mechanics of composite materials (Vol. 3). New York: Oxford university press.
5. Chen, X., Sun, X., Chen, P., Wang, B., Gu, J., Wang, W., Chai, Y., & Zhao, Y. (2021). Rationalized improvement of Tsai–Wu failure criterion considering different failure modes of composite materials. Composite Structures, 256, 113120. https://doi.org/10.1016/j.compstruct.2020.113120.
6. Hill, R. (1965). Theory of mechanical properties of fibre-strengthened materials—III. Self-consistent model. Journal of the Mechanics and Physics of Solids, 13(4), 189-198.
7. Tsai, S. W. (1968). Strength theories of filamentary structure. Fundamental aspects of fiber reinforced plastic composites.
8. Nali, P., & Carrera, E. (2012). A numerical assessment on two-dimensional failure criteria for composite layered structures. Composites Part B: Engineering, 43(2), 280-289.

Advanced Engineering Days

aed.mersin.edu.tr

Characterization of fracture behavior of the aluminum alloy 6061 using an uncoupled fracture criterion

Ali Zahedi*

University of Mohaghegh Ardabili, Faculty of Engineering, Iran, azahedi@uma.ac.ir

Cite this study: Zahedi, A. (2024). Characterization of fracture behavior in aluminum alloy 6061 using an uncoupled fracture. Advanced Engineering Days, 9, 28-30

Keywords
Fracture
Stress triaxiality
Finite element
Characterization

Abstract

The fracture behavior of the metals is one of the most intriguing and challenging areas of the material characters. In this research, a newly developed fracture criterion is used to investigate the fracture behavior of 6061 aluminum alloy. The utilized model is associated with the micro mechanisms of void nucleation, void growth, and evolution of void coalescence. In addition, a new term called secondary voids band and rotation of voids effect are considered in the model. So, a series of uniaxial tension tests on the different designed geometries are conducted to cover a broad range of stress triaxiality and Lode parameters. The parallel simulations in ABAQUS explicit solver were performed to apply the fracture model through VUSDFLD subroutine on the tests. So, the material constants are derived with regard to the force-displacement response of specimens in the tests. The comparison of the final outputs with experiments indicates the reliability and applicability of the results on the real-forming processes.

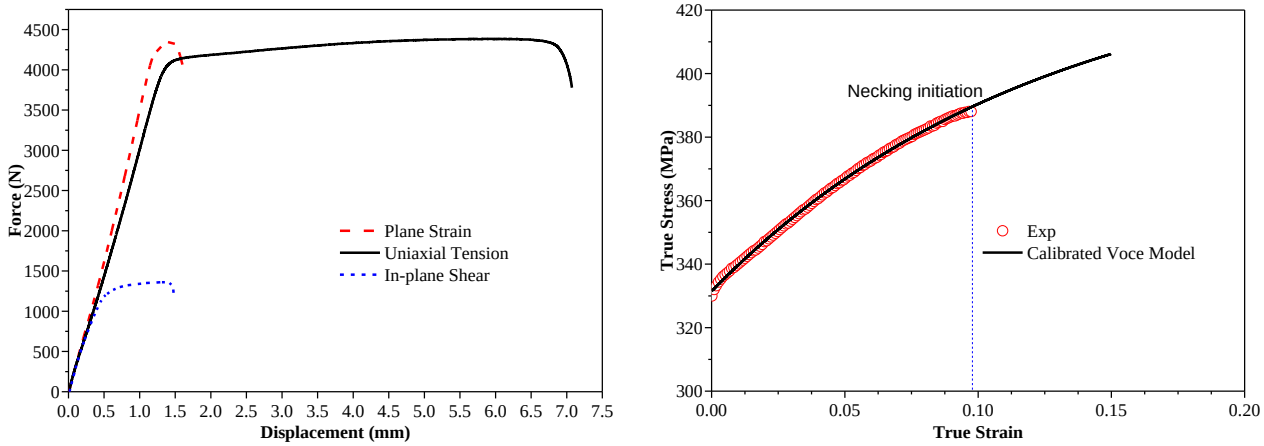
Introduction

Today's new demands and also the increasing rate of industrial growth led to the manufacturing of novel materials and alloys. In the meantime, identifying the properties of the materials and adapting them to new conditions is of indisputable importance. Ductile fracture behavior is a well-known property of metals that not only plays a key role in the design of a product but also affects its function and durability. From the macroscopic point of view, decreasing the strength and stiffness of a metallic material indicates fracture initiation. Microscopically, such a failure is observed in three stages void nucleation, void growth, and their coalescence. Valuable research has been fulfilled to correlate the fracture phenomenon with the applied stresses and strains [1]. Fracture prediction tools lay in various categories, while in one of the prevalent ones, there exist two types of ductile fracture criteria: coupled, and uncoupled ductile fracture criteria. In a coupled ductile fracture model, the weakening of a material is considered in the damage formulations while in the latter one, the fracture instant is predicted. Coupled criteria are suitable in investigations while the history of loading is of importance; Zahedi [2] studied damage initiation and propagation in the incremental forming through a coupled damage criterion.

Bao and Wierzbicki [3] investigated the effect of stress triaxiality on the fracture strain. They constructed the Al2024 fracture locus and reported a nonlinear relation. Considering a broad range of stress triaxiality, Lou et al. [4,5]presented multiple ductile fracture criteria. Thereafter, Bai and Wierzbicki [6] modified the well-known Mohr-Coulomb criterion to describe ductile fracture of metal. The modified Mohr-Coulomb (MMC) fracture locus was found to be a good approximation of the experimental data points of Al 2024. More recently, Quach et al. [7] proposed a ductile fracture model in which all of the influencing parameters on the fracture initiation in metals are considered. The aim of this research is to investigate the fracture behavior of the Al 6061 using newly developed fracture criteria of Quach. In this regard, a series of experimental and numerical tests have been conducted.

Material and Method

The plastic response of the Al6061 was extracted through uniaxial tensile tests according to the ASTM08 standard which is presented in Figure 1. According to the plastic behavior of the sheet metal, the Voce hardening model is fitted to the experimental data and resulted in the form of $\bar{\sigma} = 331.5 + 106.5(1 - e^{-8.07\bar{\varepsilon}_p})$. According to Figure 2, in addition to the standard geometry Figure 2-(a), two other geometries were utilized to induce different stress states and provide sufficient data to calibrate the fracture model.



(a) (b)

Figure 1. (a) The force-displacement curves of experimental tests, (b) The plastic behavior of the Al6061 sheet in the standard uniaxial tension tests with the calibrated Voce hardening model.

In order to define the ductile fracture initiation criterion Equation (1) was applied via VUSDFLD subroutine in the ABAQUS explicit solver to calculate the equivalent plastic strain at fracture [7]. The C3D8R element was used in the simulations and according to the experiments, a quasi-static displacement was considered.

$$\bar{\varepsilon}_f = \frac{C_1}{\left(\frac{\sigma_1}{\bar{\sigma}} + \frac{\tau_{max}}{\bar{\sigma}}\right)^{C_2}\left[\left(3 + \sqrt{3}C_3\right)\frac{\tau_{max}}{\bar{\sigma}} - C_3\right]} \quad (1)$$

Where C_1, C_2 and C_3 are material constants. From the macroscopic point of view, the effect of maximum tension stress and maximum shear stress is considered. On the other side, the role of stress triaxiality $(\eta)$and either Lode parameter (μ) in the fracture initiation could be investigated here. So, applying the existing relation between stress tensor arrays and (η, μ), the damage value is calculated via $D = \int_0^{\bar{\varepsilon}_f} \frac{1}{\varepsilon_f(\eta,\mu)} d\varepsilon$. in the damage code, $D = 0$ is considered for the intact condition of an element and, $D = 1$ for the loss of load-carrying capacity of it.

Results

Utilized specimens in experimental tests are illustrated in Figure 2. Different cut-outs in specimens induced various stress states. So, using the least mean square method and based on the force-displacement response of experiments, the material constants in the developed fracture model are calibrated and provided in Table 1. The initiation frame of the finite element simulations is also depicted in Figure 2. With the aid of the fracture model, the necking and fracture initiation locations were predicted in good agreement with the experimental results. The contour plots of equivalent plastic strain in the specimens are presented in Figure 2.

Table 1. Ductile fracture constants according.

Constants	C_1	C_2	C_3
	2.81	1.80	3.1

Discussion

Stress triaxiality and Lode parameters influence void shape and size in the void growth stage of the fracture phenomenon. Three regimes of low, medium, and high stress triaxiality are implemented in the tests. The internal necking mode is caused by the maximum principal stress, while the shear localization mode is caused by the shear linking of voids along the direction of the maximum shear stress.

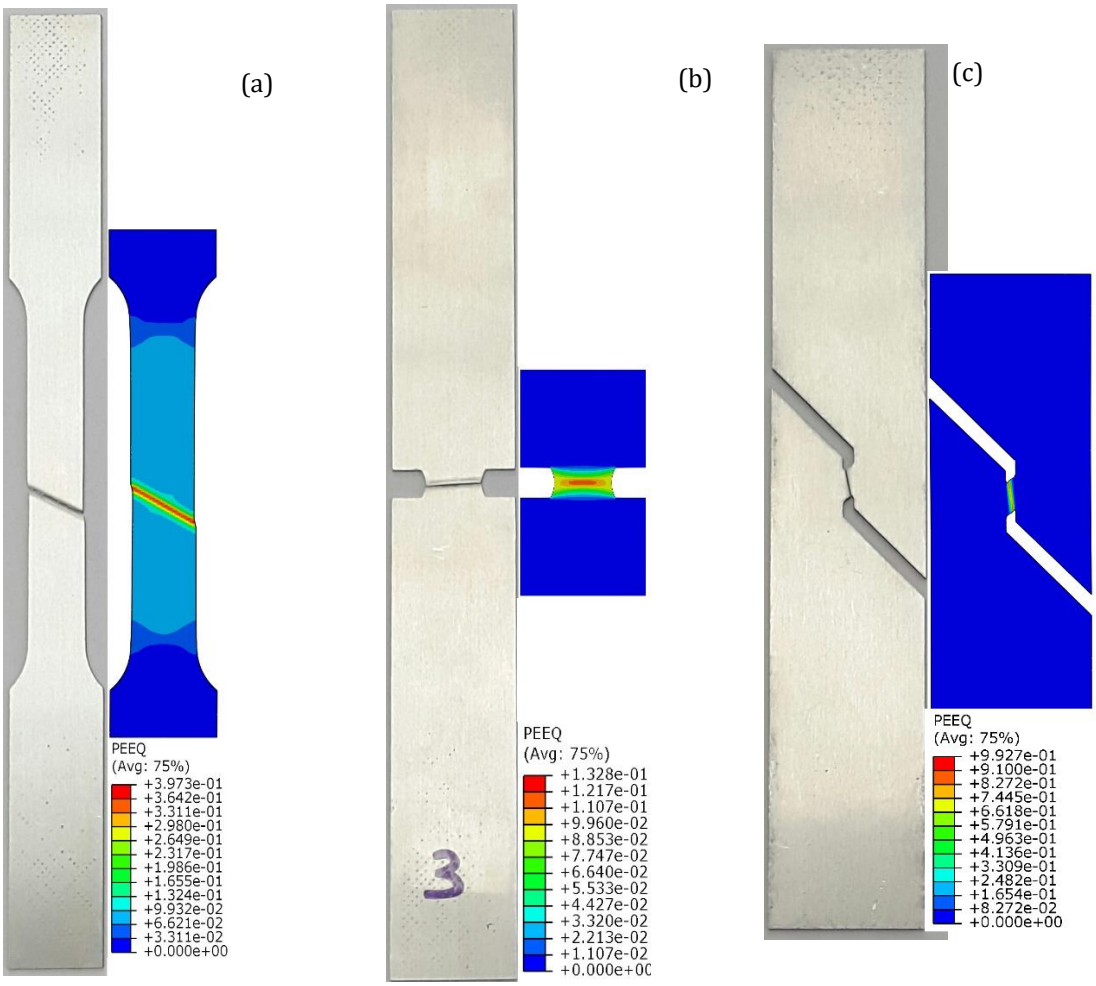


Figure 2. The specimens used in tension experiments and FE evaluations; (a) uniaxial, (b) plane strain, and (c) in-plane shear.

Conclusion

A new uncoupled fracture criterion was calibrated for the Aluminum alloy 6061. The obtained results enlighten the role of different mechanisms in fracture initiation of the 6061 aluminum alloys. Besides, the calibrated material constants including the plastic and fracture behavior of the sheet metal can be applied in the investigation of different sheet metal forming processes.

References

1. Bai Y., Wierzbicki T. (2008) A new model of metal plasticity and fracture with pressure and Lode dependence. International Journal of Plasticity, 24, 1071–96.
2. Zahedi Dizajyekan, A. (2023). Investigation of Fracture Mechanism in Single Point Incremental Forming of AA5052 Aluminum Alloy Using the Bao-Wierzbicki Damage Model. *Journal Of Applied and Computational Sciences in Mechanics*, *35*(4), 63-76.
3. Bao Y., Wierzbicki T. (2005) On the cut-off value of negative triaxiality for fracture. Engineering Fracture Mechanics, 72:1049–69.
4. Lou Y., Yoon J.W., Huh H. (2014) Modeling of shear ductile fracture considering a changeable cut-off value for stress triaxiality. International Journal of Plasticity, 54:56–80.
5. Lou Y., Huh H., Lim S., Pack K. (2012) New ductile fracture criterion for prediction of fracture forming limit diagrams of sheet metals. International Journal of Solids and Structures, 49:3605–15.
6. Bai Y., Wierzbicki T. (2010) Application of extended Mohr-Coulomb criterion to ductile fracture. International Journal of Fracture, 161:1–20.
7. Quach H., Kim J.J., Nguyen D.T., Kim Y.S. (2020) Uncoupled ductile fracture criterion considering secondary void band behaviors for failure prediction in sheet metal forming. International Journal of Mechanical Science, 169, 105297.

Advanced Engineering Days

aed.mersin.edu.tr

Two-phase numerical simulation of an inkjet nozzle using the level-set method

Paniz Rezazadeh Azar[1], Sajad Rezazadeh *[1], Maziar Javadi [1] MirMahdi Seyyed Valilu [1]

[1]Faculty of Renewable Energies, Department of Mechanical Engineering, Urmia University of Technology Urmia, Iran, panizrezazadehazar@gmail.com, sor.mems@gmail.com, zaniajavadi@gmail.com, mahdivalilu@gmail.com

Cite this study: Azar, P. R., Rezazadeh, S., Javadi, M., & Valilu, M. S. (2024). Two-phase numerical simulation of an inkjet nozzle using the level-set method. Advanced Engineering Days, 9, 31-33

Keywords
Inkjet
Level-set
Nozzle
Fluid
Comsol

Abstract

A 3D numerical simulation was done by the finite element method and specifically Comsol software. Considering that the mentioned model is two-phase, the main challenge in this case has been the validation of the data obtained from the software with the data available in the technical literature. Finally, this numerical work was done by selecting the level-set method to simulate the two-phase flow and the relevant results were presented. To validate the present numerical work, the results related to the mass of the ink drop produced during the time have been calculated and compared with the data available in the technical literature, and the comparison of the numerical results obtained with the data available in the technical literature shows a very good match. The results are It is worth mentioning that the independence of the results from the number of networks has also been investigated. Due to the low velocity and consequently the Reynolds number, the fluid flow regime is slow and incompressible, the flow is unsteady. The fluid is the Newtonian agent, and the solution of the energy equation is omitted. The size and speed of the dropped drop can be calculated and affected, and the effect of geometry, fluid properties, etc. can be studied. All simulations have been done using COMSOL Multiphysics 6.1 software.

Introduction

The foundation of inkjet technology lies in the precise deposition of small fluid droplets onto a surface, typically a piece of paper. Designers explore various parameters to understand printer characteristics, such as altering the geometry and type of inkjet to produce droplets of different volumes. The speed and resolution of the resulting images serve as fundamental metrics for printer performance. The velocity of ink ejected through the nozzle significantly influences the size and velocity of the droplets sprayed. Developing simulation models to comprehend fluid flow is crucial for optimizing printer functionality. These printers find applications in diagnostics, analysis, and drug research [1]. Evaluating ink properties via traditional screen imaging methods poses challenges. Computational fluid dynamics (CFD) offers an alternative by allowing the examination of ink droplet flow dynamics. Both Newtonian and non-Newtonian inks have been developed for this purpose [2,3]. Researchers such as Messerschmitt [4] and Xu and Willenbacher [5] utilized high-speed video imaging technologies to study the ink separation process into droplets, identifying three main regions: the pre-injection zone, the attachment zone up to detachment, and the ink spreading and settling zone. Yang and Liu [6] conducted experiments at varying velocities to assess ink adhesiveness and found that ink maintained higher adhesiveness at higher velocities.

This study employs numerical analysis to examine the weight of ink droplets. Specifically, the main goal is to simulate the beginning of the ink drop formation process inside the inkjet nozzle using the two-phase modeling method (level-set method). After passing through the nozzle and being separated, the ink drop continues its path inside the channel until it reaches the outlet. Providing the contour of velocity and concentration at different times to analyze the volume and mass of the drop provides the user with a suitable way to predict the movement of ink in real printing devices.

Model Description and Method

Figure 1 shows the studied inkjet geometry. Because of its symmetry, a two-dimensional axial-symmetry model can be used. Initially, the space between the inlet and the nozzle is filled with ink. Additional ink is injected through

the inlet within 10 microseconds, causing the ink to flow out of the nozzle. When the injection stops, a single drop of ink separates and continues until it reaches the target.

The level set method is a practical method for modeling the movement of the interface of two fluids in a two-phase fluid. When the level adjustment function φ is equal to 0.5, it represents the boundary or two-phase interface, where φ is equal to 0, it represents the air-fluid, and when it is equal to 1, it represents the ink fluid. In a transition layer close to the boundary, φ changes slowly from 0 to 1. The boundary moves with the fluid flow velocity, u, in the boundary region. The following equation describes the movement of the level adjustment function, continuity, and momentum equations respectively:

$$\frac{\partial \varphi}{\partial t} + u.\nabla\varphi + y\left[\left(\nabla.\left(\varphi(1-\varphi)\frac{\nabla\varphi}{|\nabla\varphi|}\right)\right) - \varepsilon\nabla.\nabla\varphi\right] = 0 \quad (1)$$

$$(\nabla.u) = 0 \quad (2)$$

$$\rho\left(\frac{\partial u}{\partial t} + u.\nabla u\right) - \nabla.\left(\mu(\nabla u + \nabla u^T)\right) + \nabla p = F_{st} \quad (3)$$

The model simplifications are based on the following assumptions:

- Negligible heat generation within the product.
- The fluid is assumed to be both incompressible and laminar.
- Gravity effects are considered during inkjet operation.
- Consistent air and ink thermophysical properties are assumed throughout the analysis.

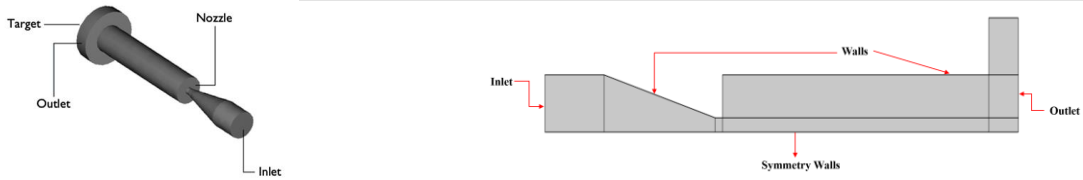


Figure 1. 3D model (left) and 2D view and boundary conditions (right) of inject geometry

To validate the present numerical work, the results related to the mass of the ink drop produced over time were calculated and compared with the data available in the technical literature [7] and it has been done via Comsol software, which is presented in Figure 2. As can be seen in the figure, at t=0 [s], the mass of the drop is zero, which is completely justified from a scientific point of view, because at this time no drop has been formed at all. With time, the mass of the droplet increases, and after approximately 1 second, its mass remains constant and only moves in the direction of the nozzle until it reaches its end. Moreover, the comparison of the obtained numerical results with the data available in the technical literature shows a very good agreement of the results. It is worth mentioning that the independence of the results from the number of grids was also examined and finally the number of 8500 elements was selected from very fine, fine, medium, and coarse elements. Figure 3 also illustrates the velocity of droplet movement at different times.

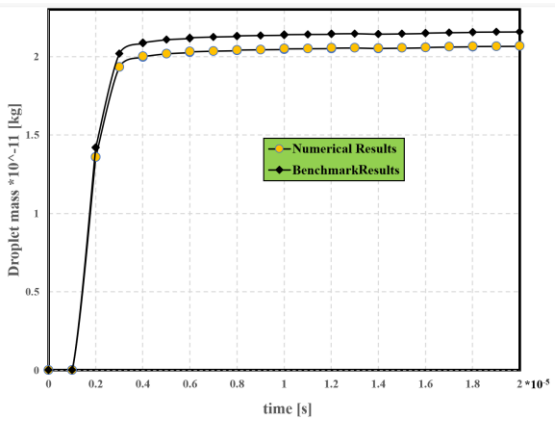


Figure 2. Validation of data extracted for droplet mass against [7]

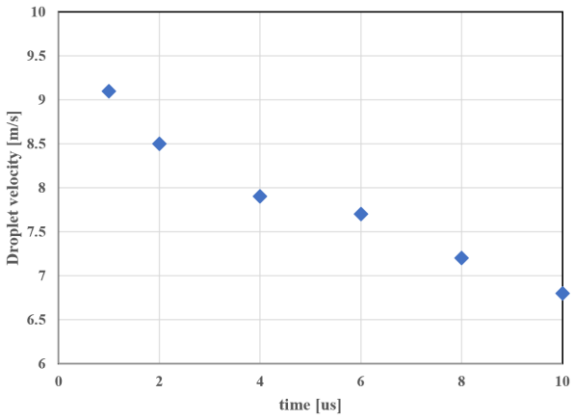


Figure 3. Droplet velocity over time

Results

Figure 4 shows the contours of velocity distribution and volume fraction. At the zero moment, no droplet is formed, but over time, the droplet is injected into the chamber from the nozzle and flows with a certain velocity

and concentration. Next, the ink droplet moves towards the target part, and due to gravity, its velocity is reduced and a trail is formed behind it, until it finally reaches the target section and is ready to be used.

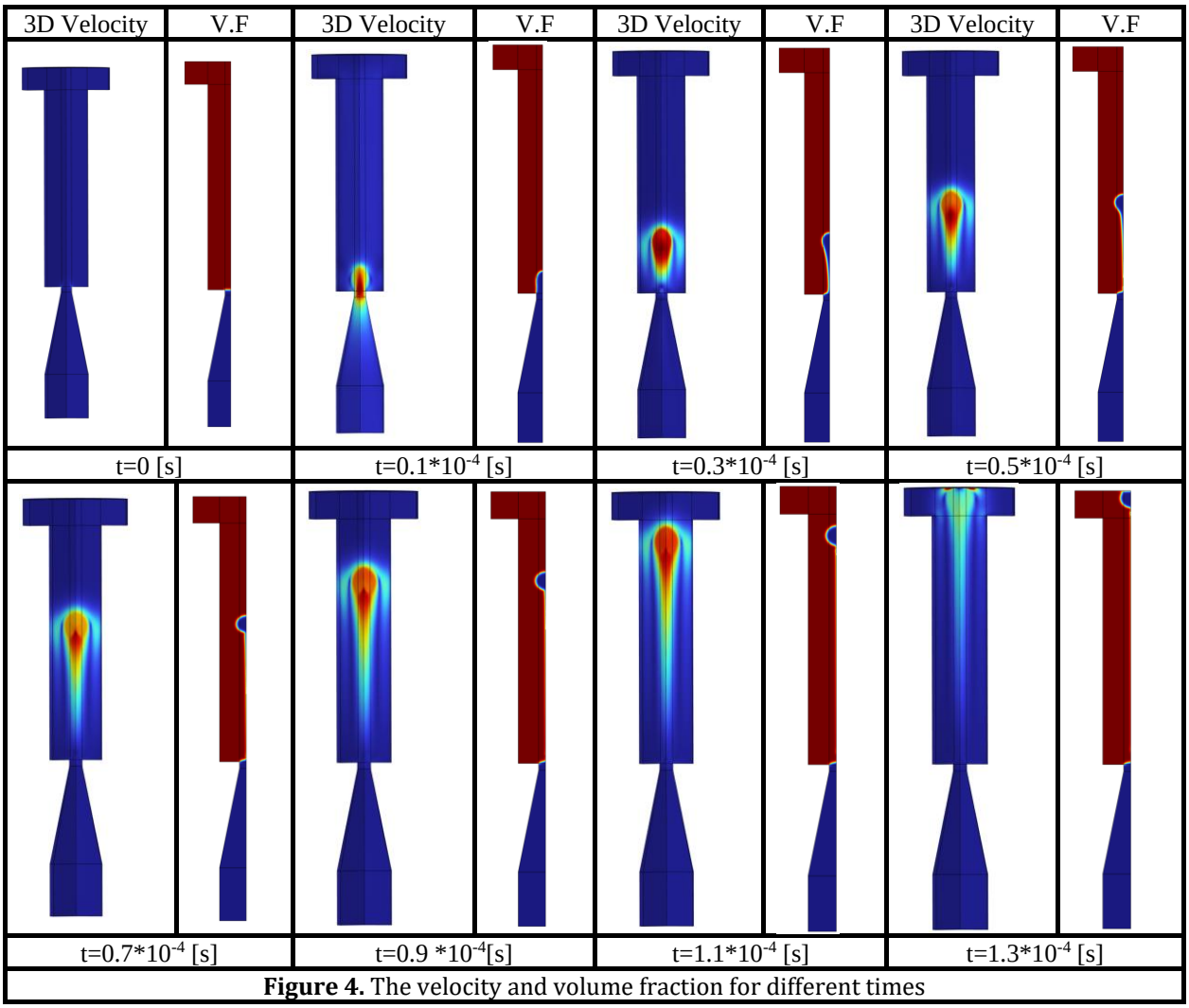


Figure 4. The velocity and volume fraction for different times

Conclusion

The process of forming an ink drop inside the nozzle of the device is one of the two-phase processes that is simulated in this article by the level adjustment method. Over time, the drop is injected into the nozzle and moves as a trailing drop in the direction of the channel, and its speed gradually decreases. However, according to the law of conservation of mass, the volume of the drop remains constant.

References

1. Stanley, O., & James A, S. (1988). Fronts Propagating with Curvature Dependent Speed: Algorithms Based on Hamilton-Jacobi Formulations. Journal of computational physics, 79, 12-49.
2. Osher, StanlyJ.;Fedkiw,RonaldP “Leve-lSetMethod sand Dynamic” .(2002).
3. James A, S. (1999). Level Set Methods and Fast Marching Methods: Evolving Interfaces in Computational Geometry”, Fluid Mechanics, Computer Vision, and Materials Science.
4. Messerschmitt E. (1982). Rheological Considerations for Screen Printing Inks. Screen Print, 72 (10), 62-65.
5. Xu C, Willenbacher N. (2018). How Rheological Properties Affect Fine-Line Screen Printing of Pastes: A Combined Rheological and High-Speed Video Imaging Study. Journal of Coating Technology and Research. 15 (6), 1401–1412.
6. Yang, Y., & Liub, F. (2011). Study on the Relationships between Offset Ink Tack Value and Its Viscosity, the Separation Velocity. Advanced Materials Research, 332-334,1704- .2011 ,1708
7. Tofan, T., Kruggel-Emden, H., Turla, V., & Jasevičius, R. (2021). Numerical Modeling of the Motion and Interaction of a Droplet of an Inkjet Printing Process with a Flat Surface. Applied Science. 11(2),527.

Advanced Engineering Days

aed.mersin.edu.tr

Thermo-economic evaluation and comprehensive analysis of a power generation system based on flame-assisted fuel cells and supercritical carbon dioxide cycle

Amirreza Javaherian [*1], Samar Fazlollahi [2], Seyed Mohammad Seyed Mahmoudi [1], Faramarz Talati [1]

[1] *University of Tabriz, Department of Mechanical Engineering, Iran, a_javaherian@tabrizu.ac.ir, s_mahmoudi@tabrizu.ac.ir, talati@tabrizu.ac.ir*
[2] *University of Tabriz, Department of Agricultural Engineering, Iran, samar.fazlollahi@gmail.com*

Cite this study: Javaherian, A., Fazlollahi, S., Seyed Mahmoudi, S. M., & Talati, F. (2024). Thermo-economic evaluation and comprehensive analysis of a power generation system based on flame-assisted fuel cells and supercritical carbon dioxide cycle. Advanced Engineering Days, 9, 34-36

Keywords
Flame-assisted fuel cells
Super-critical carbon dioxide
Thermodynamic analysis
Comprehensive study

Abstract

The present research aims to model flame-assisted solid oxide fuel cells plant integrated with a supercritical carbon dioxide cycle, analyzing their energy, exergy, and thermo-economic performances using EES software. By applying the first and second laws of thermodynamics, the cost formation process for exergy flows through thermo-economic analysis is described. The case study results reveal that the net output power of the system is 2.33 MW. A parametric study investigates key functional variables of the system components, including the effects of current density and fuel utilization factor of the fuel cells for the equivalence ratio of 2 of the fuel-rich combustion chamber. Results show that increasing the current density causes to initially increasing the net output power and then decreasing. A similar trend is observed in the exergy efficiency as the fuel utilization factor increases. Additionally, the study finds that increasing the fuel utilization factor reduces total net power. Rising the current density and fuel utilization factor both result in reduction in actual voltage. However, while increasing the current density leads to decrease in the unit exergy cost of the electricity, and increase in fuel utilization factor leads to increase in the unit exergy cost of the electricity.

Introduction

Renewable energies have become a vital alternative to fossil fuels, advancing due to their sustainability and less water consumption in power generation systems. Among these technologies, fuel cells have emerged as a leading solution. Recently, environmentally friendly Solid Oxide Fuel Cells (SOFCs) have gained significant attention for their exceptional high electrical efficiency, low sensitivity to carbon monoxide, and high operating temperatures, making them an excellent option for cogeneration and multigeneration applications [1]. The use of hydrogen fuel in SOFCs is an emerging technology that directly converts the chemical energy of the fuel into electrical energy through electrochemical reactions. However, hydrogen fuel is not always readily available and is typically produced by reforming hydrocarbon fuels. This process converts the fuel into syngas, which consists of carbon monoxide and hydrogen, and can be used in fuel cells [2]. EES software is a versatile tool for engineers, facilitating the efficient solving of complex thermodynamic problems and, with its extensive database and user-friendly interface, simplifies analysis and enables parametric studies and is utilized for the present research's analyses.

Schöffer et al. [3] investigated hybrid systems combining SOFCs and supercritical carbon dioxide cycles. They found that gas recirculation at the cathode increases system efficiency and reduces heat exchanger size, while optimizing pinch points decreases heat exchanger network size. However, two-stage compression in the carbon dioxide cycle only marginally improves thermal efficiency compared to conventional cycles, making cathode gas recirculation a more thermodynamically favorable design aspect for minimizing heat exchanger requirements. Mojaver et al. [4] studied how to improve a system that produces both heat and electricity. They used an integrated power generation system including SOFCs, supercritical CO_2 Brayton cycles, and Rankine cycles. They examined

the key functional indicators of the system, i.e., output power, fuel and hot water usage, and efficiency. They found that increasing the fuel utilization in the system reduces the output power and increases hot water consumption. Additionally, optimizing the system reduced fuel and hot water utilization while maintaining high output power. They determined that at the system's optimal operating condition, the system can achieve 10.02% electrical efficiency, 3169 g/s of hot water consumption, and 302 kg/MWh of carbon dioxide emission index.

In this study, a novel configuration for the solid oxide fuel cells is introduced and besides the case analysis of the system focusing on key performance indicators, parametric study is also conducted to examine the impact of these variables.

Material and Method

The schematic diagram of the proposed power generation system is depicted in Figure 1.

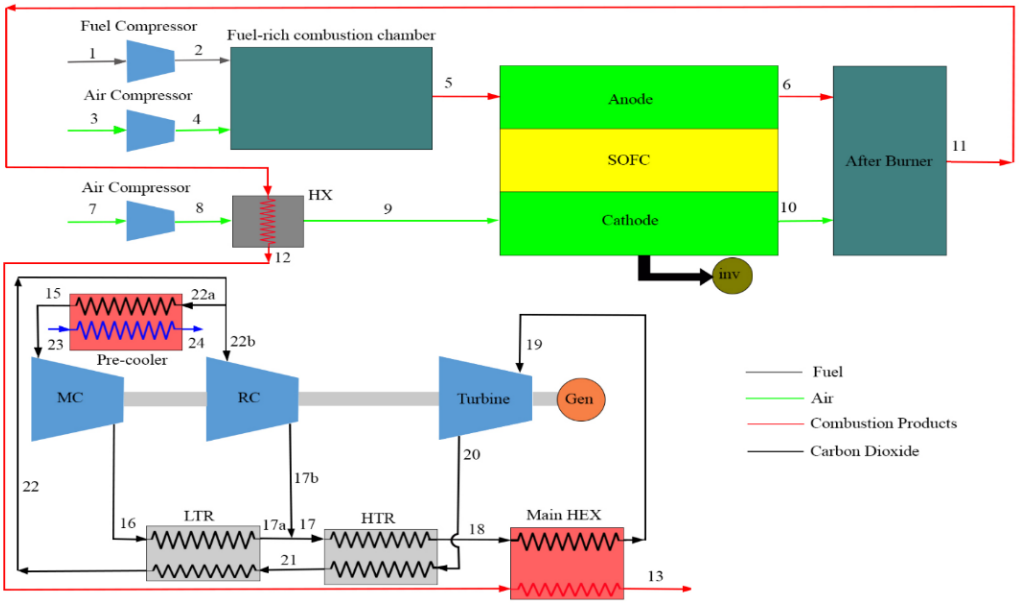


Figure 1. Schematic of the studied flame-assisted SOFCs integrated with supercritical CO_2 cycle

Methane (CH_4) fuel and air enter compressors at atmospheric pressure and temperature to reach the operating pressure of the combustion chamber. After compression, the fuel and air flow to the fuel-rich combustion chamber where the pre-reforming reaction starts. Chemical reactions provide the operating temperature of the combustion products required in the SOFC, which then exit and enter the anode. Meanwhile, another air stream goes to the third compressor for combustion and acquires the operating temperature from a heat exchanger that receives heat from the afterburner exhaust gases. This air stream provides the oxygen needed in the cathode and enters the cathode from stream 7. The inlet gases on the anode side undergo an electrochemical reaction with the inlet air stream from the cathode side. After participating in the reaction, these gases exit through streams 6 and 10. For improving fuel cell performance and increasing thermal efficiency, unutilized synthetic gases from the fuel cell are reacted with the outlet air in the cathode section of the afterburner chamber. The resulting combustion products are then expelled from the combustion chamber.

Due to ohmic resistance, species concentration, and activation energy, the electric potential difference of the solid oxide fuel cell decreases from its ideal state. Therefore, the net voltage produced is equal to the ideal voltage minus the sum of the voltage losses [5].

$$V_{Actual} = V_N - [V_{act} + V_{conc} + V_{ohm}] \quad (1)$$

where, V_{act} represents the voltage drop due to the activation energy, V_{conc} represents the voltage drop due to species concentration, and V_{ohm} represents the voltage losses due to the electrical resistance of the anode, cathode, and electrolyte.

The power generated by the fuel cell stack can be calculated using the following equation [5]:

$$W_{SOFC,DC} = N_{FC} A_a J V_{Actual} \quad (2)$$

In the above equation, N_{FC} shows the number of fuel cells, A_a represents active cross-sectional area of the fuel cell, and J represents the current density.

In order to recover the waste heat of the exhaust gases of the SOFC system, a recompression supercritical carbon dioxide cycle is utilized as the downstream cycle, as shown in Figure 1. The proposed system also generates electrical power and can lead to enhanced performance of the entire plant from energy and exergy viewpoints.

Results

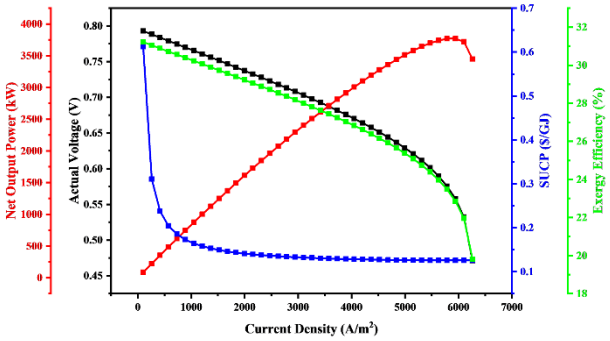


Figure 2. Effect of current density on the actual voltage of the fuel cell, net output power, exergy efficiency, and the unit exergy cost of electricity.

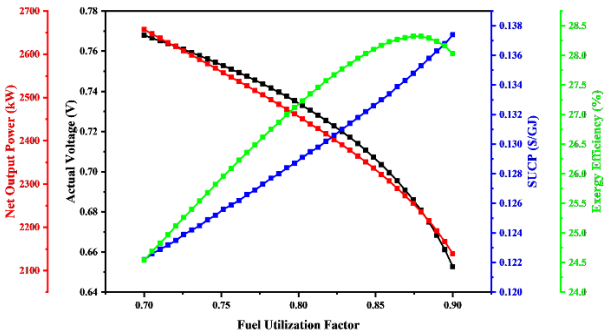


Figure 3. Effect of fuel utilization factor on the actual voltage of the fuel cell, net output power, exergy efficiency, and the unit exergy cost of electricity.

Discussion

The variations in the actual voltage of the fuel cell, net output power, exergy efficiency, and the unit exergy cost of electricity are analyzed against the current density, which are shown in Figure 2. Considering the voltage drops due to activation, concentration, and ohmic losses, as the current density increases, the actual voltage decreases. The net output power initially increases and then decreases. Additionally, the current density is inversely related to the exergy efficiency and unit exergy cost of electricity.

The mentioned parameters, are also studied relative to the fuel utilization factor. As the fuel utilization factor rises, both the electrical voltage and the net output power diminish, while the unit exergy cost of the electricity escalates. Moreover, the exergy efficiency first increases with an increase in the fuel utilization factor but subsequently decreases. This trend can also be observed in Figure 3.

Conclusion

The study reveals how current density and fuel utilization factor affect system's performance. Increasing the current density reduces fuel cell voltage and exergy efficiency, with net output power first increasing and then decreasing, while costs show an inverse trend. Moreover, Higher fuel utilization results in decreased voltages and net power, alongside a rise in the unit exergy cost of electricity. Notably, exergy efficiency initially rises before subsequently declining.

References

1. Calise, F., d'Accadia, M. D., Palombo, A., & Vanoli, L. (2006). Simulation and exergy analysis of a hybrid solid oxide fuel cell (SOFC)–gas turbine system. Energy, 31(15), 3278-3299.
2. O'hayre, R., Cha, S. W., Colella, W., & Prinz, F. B. (2016). Fuel cell fundamentals. John Wiley & Sons.
3. Schöffer, S. I., Klein, S. A., Aravind, P. V., & Pecnik, R. (2021). A solid oxide fuel cell-supercritical carbon dioxide Brayton cycle hybrid system. Applied Energy, 283, 115748.
4. Mojaver, P., Abbasalizadeh, M., Khalilarya, S., & Chitsaz, A. (2020). Co-generation of electricity and heating using a SOFC-ScCO2 Brayton cycle-ORC integrated plant: investigation and multi-objective optimization. International Journal of Hydrogen Energy, 45(51), 27713-27729.
5. Sadeghi, M., Chitsaz, A., Mahmoudi, S. M. S., & Rosen, M. A. (2015). Thermoeconomic optimization using an evolutionary algorithm of a trigeneration system driven by a solid oxide fuel cell. Energy, 89, 191-204.

Advanced Engineering Days

aed.mersin.edu.tr

Finite element analysis of CFRP and GFRP compressed natural gas

Maryam Ranjbar [*1], **Mohammad Reza Khoshravan Azar** [2]

[1]*University of Tabriz, Faculty of Aerospace Engineering, Iran, ma.ranjbar134@gmail.com*
[2]*University of Tabriz, Faculty of Mechanical Engineering, rkhosh@tabrizu.ac.ir*

Cite this study: Ranjbar, M., & Azar, M. R. K. (2024). Finite element analysis of CFRP and GFRP compressed natural gas. Advanced Engineering Days, 9, 37-39

Keywords
CNG
Finite element method
Composite materials
Abaqus

Abstract

The design and safety of CNG tanks is very important due to their increasing use in cars. In the finite element method, metal and composite CNG tanks were analysis with the help of Abaqus software, and the results were validated. In this study, mechanical properties of composite materials carbon fiber reinforced polymer (CFRP) and glass fiber reinforced polymer (GFRP), the thickness and laminate stacking sequence of the CNG tank layers and the load are considered as input and the stress and strain value as output. In addition to being light, composite tanks have more resistance to internal pressures, in this study, a reduction in stress under working pressure of 43%, 41%, 56%, and 27% has been achieved in CFRP and GFRP with [±50] and [0,±50] fiber orientations, respectively.

Introduction

Compressed Natural Gas (CNG) is used as a good alternative in land transportation in many countries. The manufacturing of CNG fuel tanks requires strict adherence to safety standards and stringent production licensing due to the potential for serious damage (Kashyzadeh, 2021). Initially, CNG fuel tanks were made of metal; however, the adoption of composite materials has brought about several advantages, including lightweight construction, high stiffness, excellent corrosion resistance, and extended lifetime(Roy & Tsai, 1988). Sulaiman et al. utilized Abaqus software to perform finite element analysis of a composite tank under internal pressure, specifically investigating the influence of twist angle. Their findings were compared with experimental results, showing good agreement between them (Sulaiman, Borazjani, & Tang, 2013). Rafiee and Torabi predicted the internal pressure of composite tanks while considering production uncertainties (Rafiee & Torabi, 2018).

Material and Method

For the study of composite CNG tanks, the primary method for theoretical analysis involves using the finite element method for stress and strain analysis. As shown in Figure *1*, the CNG tank is modeled in Abaqus software, adhering to the standard dimensions specified in reference (Seyedi, 2019). According to the working load mentioned in the same reference, the inner surface of the tank experiences hydrostatic pressures of 27.5 MPa and 41.3 MPa.

Initially, a simulation was performed on a metal CNG tank with the characteristics outlined in Table 1. Various mesh configurations were employed, and the model was thoroughly analyzed. Figure 2 illustrates the acceptable mesh convergence in the tank, achieved with 27,081 elements. To assess the von Mises stress results in comparison to the reference data (Seyedi, 2019), as show as Figure 3 the simulation error was found to be 2%, affirming the accuracy of the chosen methodology. Next the composite materials of CFRP and GFRP mentioned Table *2* consists of 24 layers, the thickness of each layer is 1 mm, and the[±θ] and [0,±θ] orientations of the fibers is theta between 30 to 60.

Table 1. Material properties of 34CrMo4

Property	Value	Property	Value	Property	Value
E/*GPa*	210	ρ /kg/m^3	7850	ν	0.3

Source:(Seyedi, 2019)

Table 2. Material properties of composites

Property	Value		Property	Value	
	CFRP[1]	GFRP[2]		CFRP[1]	GFRP[2]
E_1 /GPa	125.90	41.29	X_T /MPa	2000	884.5
E_2=E_3 /GPa	11.30	4.21	X_C /MPa	1100	837.17
G_{12} = G_{13} /GPa	5.43	3.16	Y_T = Z_T /MPa	80	37.38
G_{23} /GPa	3.98	3.0	Y_C = C z /MPa	280	145
$\nu_{12} = \nu_{13}$	0.30	0.31	S_{12} = S_{13} /MPa	120	44.765
ν_{23}	0.42	0.42	S_{23} /MPa	120	50.88

Source:(Tie, Zhang, Hou, & Li, 2020)[1], (Xudong, Qijian, & Chen, 2018)[2]

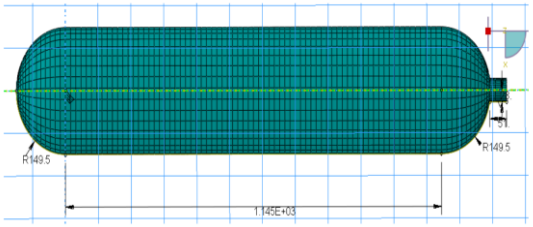


Figure 1. Geometry of CNG tank

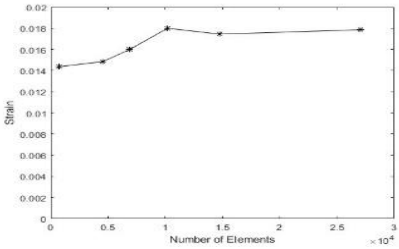


Figure 2.Mesh convergence



(a1) (a2) (b1) (b2)

Figure 3. Von Mises Stress for metal CNG tanks 41.3 MPa (a1)this paper (a2)reference (Seyedi, 2019), 27.5MPa (b1) this paper (b2) reference (Seyedi, 2019)

Results

In this study, stress and strain between composite materials GFRP and CFRP and metallic materials were compared. In the Figure 4, σ_{11} was compared for the [±θ] orientations of the fibers. The results indicate an increase in the strength of the CFRP composite tank compared to the metallic tank. It is evident from this diagram that fiber orientation also plays a significant role in stress tolerance of the tanks, with fibers oriented at [±50] providing higher resistance, while at [±30], GFRP performs weaker than metalic. In Figure 5, ε_{11} were compared, showing that the performance of CFRP is better than both metal and GFRP. With changes in fiber orientation, as show in Figure 6, composite materials, except for GFRP, exhibit better performance at angles of [0,±30] and [0,±40]. Similar to the stress arrangement, ε_{11} of CFRP and metal perform better than GFRP composite material, as shown in Figure 7.

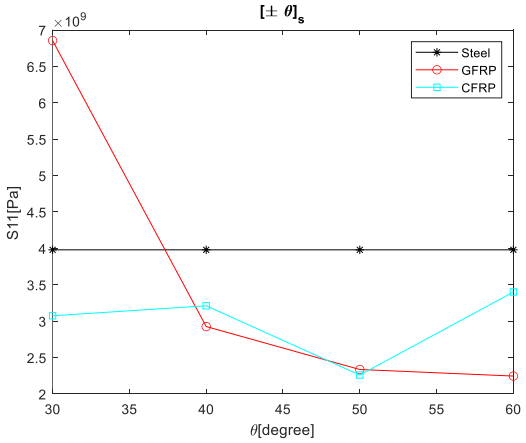


Figure 4. Stress in different fibers angles (degree)

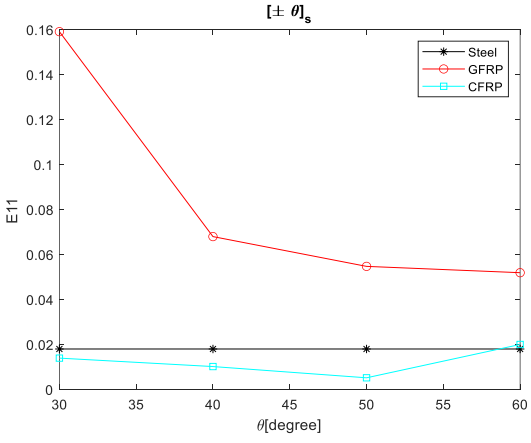


Figure 5. Starin in different fibers angles (degree)

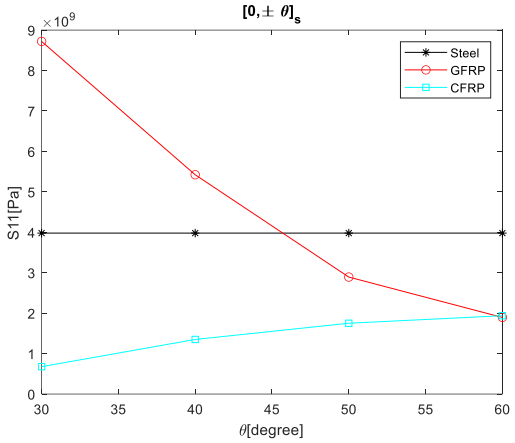


Figure 6. Stress in different fibers angles (degree)

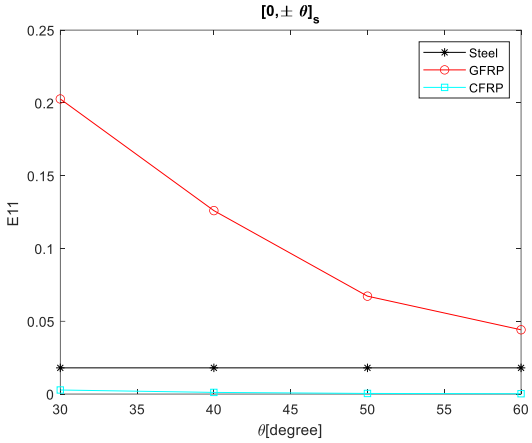


Figure 7. Strain in different fibers angles (degree)

Conclusion

Composite materials, in addition to their weight advantage, can increase the design safety factor of tanks if placed in the proper arrangement [±θ]. This will make CNG tanks safer under pressure compared to steel tanks.

References

1. Kashyzadeh, K. R. a. R. K., Seyed Saeid and Omidi Bidgoli, Mostafa and Petrů, Michal and Amiri Asfarjani, Alireza. (2021). An Optimum Fatigue Design of Polymer Composite Compressed Natural Gas Tank Using Hybrid Finite Element-Response Surface Methods. Polymers, 13(4), 483. Retrieved from https://www.mdpi.com/2073-4360/13/4/483
2. Rafiee, R., & Torabi, M. A. (2018). Stochastic prediction of burst pressure in composite pressure vessels. Composite Structures, 185, 573-583. doi:https://doi.org/10.1016/j.compstruct.2017.11.068
3. Roy, A. K., & Tsai, S. W. (1988). Design of Thick Composite Cylinders. Journal of Pressure Vessel Technology, 110(3), 255-262. doi:10.1115/1.3265597
4. Seyedi, S. M. (2019). Numerical, Experimental and Optimization of
5. Composite Tanks with Non-Metallic Primer (CNG
6. Fourth Type). (Master). University of Eyvanakey, Iran.
7. Sulaiman, S., Borazjani, S., & Tang, S. H. (2013). Finite element analysis of filament-wound composite pressure vessel under internal pressure. IOP Conference Series: Materials Science and Engineering, 50(1), 012061. doi:10.1088/1757-899X/50/1/012061
8. Tie, Y., Zhang, Q., Hou, Y., & Li, C. (2020). Impact damage assessment in orthotropic CFRP laminates using nonlinear Lamb wave: Experimental and numerical investigations. Composite Structures, 236, 111869.
9. Xudong, Z., Qijian, W., & Chen, W. (2018). Experimental and numerical study of GFRP-reinforced steel tube under axial impact loads. International Journal of Impact Engineering, 122, 23-37.

Advanced Engineering Days

aed.mersin.edu.tr

Skin imaging methodology to improve analysis of geometric deviation

Elnaz Ghanbary [*1], Mehran Mahboubkhah [1], Ahmad Barari [2]

[1]*University of Tabriz, Department of Mechanical Engineering, Iran, Elghanbaryk@gmail.com, Mahboobkhah@tabrizu.ac.ir*
[2]*University of Ontario Institute of Technology, Department of Mechanical and Manufacturing Engineering, Canada, Ahmad.barari@uoit.ca*

Cite this study: Ghanbary, E., Mahboubkhah, M., & Barari, A. (2024). Advancing geometric deviation analysis with Skin Imaging methodology. Advanced Engineering Days, 9, 40-42

Keywords
Geometric Deviation
Skin Model Shapes
Digital Twin
Machine Vision Inspection
Point Cloud

Abstract

Geometric variation are inherent in manufactured surfaces due to manufacturing error and measurement uncertainty. The nominal surface model defined by the designer is ideal geometry. The need for non-ideal geometry is addressed by the Geometric Product Specification (GPS) standard, which introduces the concept of Skin Model to detail the geometric deviations of the surface. Despite its importance, few methodologies exist for skin model generation. A skin model is a continuous surface that consists of an infinite set of points. Coordinate Metrology provides real information about the surface geometry in the form of a finite set of discrete data points. 'Skin Imaging' methodology, as a new approach of skin model, provides an enriched continuous two-dimensional (2D) representation of the geometric deviation of three-dimensional (3D) surface, processed from discrete data points. Skin Image illustrates the actual geometric deviation of the manufactured surface from the ideal geometry via intensity variation of its pixels. This paper examines geometric deviations in three planar case studies using Skin Imaging, showcasing this methodology's effectiveness in providing a detailed model of the actual manufactured surface and aiding in the smart assessment of geometric deviations.

Introduction

Detailed Deviation Zone Evaluation (DZE) is the pinnacle of Coordinate Metrology, providing a model of the actual manufactured surface from a discrete, unorganized point cloud, enabling estimation of deviations at non-measured locations. This model is particularly required for establishing a closed-loop of manufacturing and inspection processes, an online manufacturing error detection and correction cycle [1-3] , and the precise assessment of design tolerances and assembly accuracy [4-6].

The most important approach to generate DZE of the surface is introduced in GPS standard (ISO 22432) [7] as Skin Model. Skin Model is non-ideal geometrical model of the surface which can be generated at the early stage of the product lifecycle, or during the manufacturing process based on the results of Coordinate Metrology [8]. Anwer et al. [9] investigated the fundamentals of the skin model at a conceptual, geometric and computational level. Schleich et al. [10] declared that the skin model can be used in various applications of manufacturing and inspection. The finite element method was used by Lalehpour and Barari [11] to generate the Skin Model.

The concept of *Skin Imaging* methodology has been recently introduced in [12], presenting a novel approach of skin model. It was thoroughly discussed on planar and non-planar surfaces such as Non-Uniform Rational B-Spline (NURBS). While Skin Model is a detailed, continuous 3D digital twin of the surface, Skin Image is 2D digital twin that captures the *actual* geometric deviation of surface through its pixels' intensity variations. Its fundamentals are further discussed in [2] with its extension to cylindrical and spherical industrial case studies. Skin Imaging efficiently converts unorganized, discrete 3D PC into grayscale 2D image, simplifying neighbor searches and enabling the use of image processing for the smart inspection of geometric deviations. In the current paper, Skin Imaging is employed to evaluate and analyze the geometric deviation of three planar case studies.

Material and Method

PCs deviation calculation - Acquiring PCs of the inspected planar surface, the ideal surface is fitted to PC by Principal Coordinate Analysis (PCA) [12]. X_{PCA} and Y_{PCA} in "Figure 1" are the coordinates of the image-point on the fitted plane, and Z_{PCA} is the deviation of the measured point from the fitted plane.

Skin Image generation - The $(X\text{-}Y)_{PCA}$ plane is divided to obtain the cells of the image's matrix. Deviation of the measured points are used to define the value of each cell such that if a cell contains an image-point (black points in "Figure 1"), its Z_{PCA} is considered as the value of that cell. Cell values without image-points (red cell in "Figure 1") are interpolated from the surrounding points P'_1, P'_2 and P'_3. The variations of cells' values represent the geometric variation of the surface. Matrix values are mapped to the 0-255 integer range to display the Skin Image.

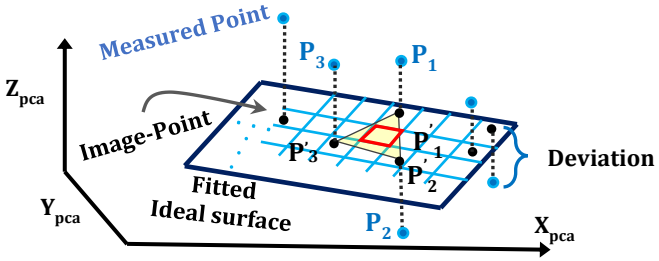


Figure 1. Skin Image generation procedure

Results

Case study 1- flat surface: "Figure 2" shows a ground aluminum workpiece. This is a flat surface with low deviation and all its PC have similar deviations (average deviation is 0.005mm). Therefore, its skin image shows low intensity variation and as illustrated by the image histogram all its pixels have dark intensity.

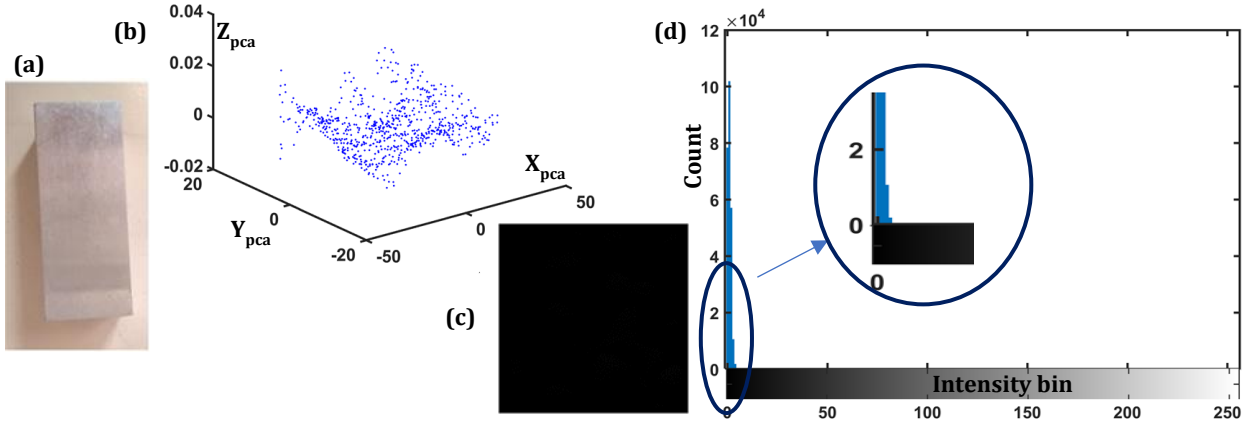


Figure 2. Case study 1(a) Flat surface, (b) PC, (c) Skin Image, (d) Histogram of the Skin Image

Case study 2 - surface with general defect: "Figure 3" shows a curved surface that most of its measured PC have considerable deviation. This will result in bright corresponding pixels for them in skin image. As illustrated in the histogram, the image includes most of the intensity bins in considerable counts, since the fact that general defect occurs continuously on the surface from a maximum deviation to minimum deviation and/or vice versa.

Case study 3 - "Figure 4" displays a ground surface with local defects. The defects appeared in bright intensity in the image due to the high deviation of their PC. The more deviated the defect is, the brighter the corresponding pixels are. Since the deviations of the points are almost similar and just the defected parts have considerable deviations, the number of the histogram's bin with considerable counts is lower compared with the case study 2.

Discussion

Analyzing the Skin Image, deviation zone evaluation can be done with full-grown image processing techniques. According to Table 1. and histograms of the skin images, the inspected surface is flat if the maximum intensity in the image is considerably low (such as for the first case study is 5); this means that the pixels are almost in a similar value and the PCs are in a similar deviation from the ideal surface. The average intensity is low, as well. The histogram of the skin image with a wide shape represents the surface with general defect, while the compressed histogram shows that there are some local anomalies. Besides, the average intensity of the image belonging to case study 2, as the general defected surface, is considerably higher than case study 3, as the locally defected surface.

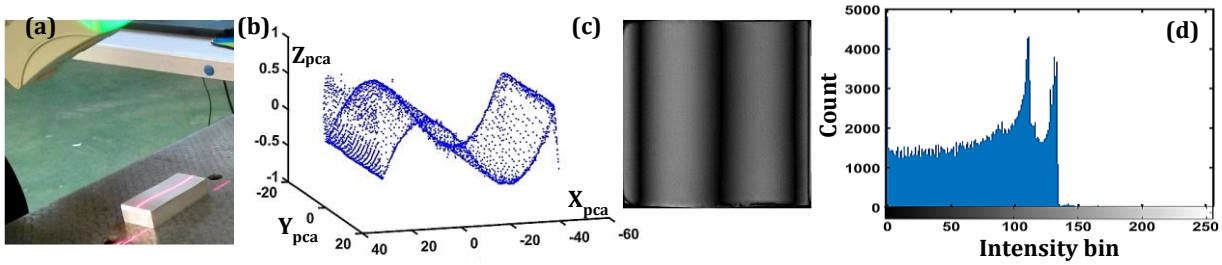


Figure 3. Case study 2; (a) surface with general defect, (b) PC, (c) Skin Image, (d) Histogram of the Skin Image

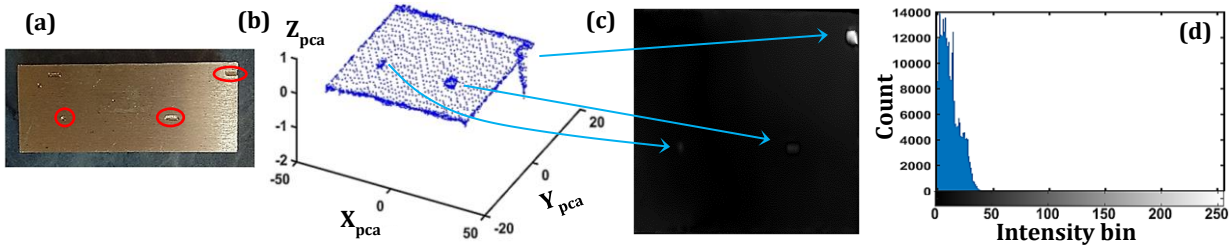


Figure 4. Case study 3; (a) surface with local defects, (b) PC, (c) Skin Image, (d) Histogram of the Skin Image

Table 1. Skin Image information for the case studies

Case Studies	Number of PC	Average deviation of PC	Image Maximum intensity	Image Average intensity
1	2029	0.005	5	1.024
2	3947	0.303	253	75
3	2451	0.084	255	11.88

Conclusion

Skin image, as the new paradigm of the Skin Model, is a 2D digital twin of the inspected surface, such that intensity variation of its pixels is proportional to geometric deviation of the surface. The efficiency of this method was demonstrated by analyzing DZE of three planar case studies.

References

1. Berry, C., & Barari, A. (2019). Cyber-Physical System Utilizing Work-Piece Memory in Digital Manufacturing. IFAC-PapersOnLine, 52(10), 201-206.
2. Ghanbary Kalajahi, E., Mahboubkhah, M., & Barari, A. (2023). Skin Imaging: A Digital Twin for Geometric Deviations on Manufactured Surfaces. Applied Sciences, 13(23), 12971.
3. Barari, A., & Pop-Iliev, R. (2009). Reducing rigidity by implementing closed-loop engineering in adaptable design and manufacturing systems. Journal of Manufacturing Systems, 28(2-3), 47-54.
4. Shen, T.-H., & Lu, C. (2023). Assembly accuracy analysis of cylindrical parts based on skin model shapes considering form deviations and local surface deformations. Precision Engineering, 80, 256-273.
5. Shen, T., & Lu, C. (2023). An Approach of Assembly Deviation Analysis based on Jacobian Model and Skin Model Shapes. 1557-1562.
6. Zhao, G., Li, J., Zhang, B., Zhang, P., Wang, H., & Xiao, W. (2022). An Aero-Engine Assembly Deviation Analysis Method Based on Skin Model Shapes. 78-89.
7. STANDARD, I. I. (2011). Geometrical product specifications (GPS) — General concepts - Part 1: Model for geometrical specification and verification (ISO 22432:2011(E)) General concepts —Part 1: Model for geometrical specification and verification.
8. Zhang, M., Anwer, N., Stockinger, A., Mathieu, L., & Wartzack, S. (2013). Discrete shape modeling for skin model representation. Proceedings of the Institution of Mechanical Engineers, Part B: Journal of Engineering Manufacture, 227(5), 672-680.
9. Anwer, N., Schleich, B., Mathieu, L., & Wartzack, S. (2014). From solid modelling to skin model shapes: Shifting paradigms in computer-aided tolerancing. CIRP Annals, 63(1), 137-140.
10. Schleich, B., Anwer, N., Mathieu, L., & Wartzack, S. (2014). Skin Model Shapes: A new paradigm shift for geometric variations modelling in mechanical engineering. Computer-Aided Design, 50, 1-15.
11. Lalehpour, A., & Barari, A. (2017). Developing skin model in coordinate metrology using a finite element method. Measurement, 109, 149-159.
12. Ghanbary Kalajahi, E., Mahboubkhah, M., & Barari, A. (2023). On detailed deviation zone evaluation of scanned surfaces for automatic detection of defected regions. Measurement, 221, 113462.

Advanced Engineering Days

aed.mersin.edu.tr

Modeling, resizing and optimization of HEV for FTP driving cycle

Reza Yasoubi[1], Erfan Rahmatzadeh [2]

[1] *Iran University of Science and Technology, Department of Automotive Engineering, Iran, reza_yasoubi@auto,iust.ac.ir*
[2] *University of Tabriz, Department of Mechanical Engineering, Iran, erfan.rahmatzadeh.1@gmail.com*

Cite this study: Yasoubi, R., & Rahmatzadeh, E. (2024). Modeling, resizing and optimization of HEV for FTP driving cycle. Advanced Engineering Days, 9, 43-45

Keywords
Hybrid electric vehicle
Optimization
ADVISOR
Series-parallel hybrid
Sizing

Abstract

When contrasting conventional vehicles with hybrid electric vehicles, the latter notably excels in both fuel economy and emission reduction. Optimizing the size of powertrain components and adjusting control system parameters is recommended to enhance HEV efficiency in these aspects and ensure customer satisfaction with the vehicle's driving dynamics. Determining the optimal design for a hybrid vehicle poses a complex challenge, necessitating exploration of various methodologies to achieve an optimal solution. This research aims to determine the optimal design that maximizes performance across metrics including fuel economy, emissions, and acceleration. Optimization focuses on engine power (ICE), battery module, electric motor power (EM), generator, final drive ratio, and overall drag coefficient. Utilizing four different sizes for each component, a total of four thousand ninety-six designs are analyzed using the Simulink tool within ADVISOR for FTP driving cycles. The results show an increase in fuel economy by almost 7% and a decrease in fuel emissions by about 8%. The final drive ratio and number of battery modules have an inverse relationship with pollutant production, while the generator's maximum power has a direct relationship and greater impact.

Introduction

Nowadays, due to issues such as industrial waste and factory garbage, excessive usage of fossil fuels, destroying of green spaces, we face a noticeable increase in global warming and air pollution. According to researches, one of the biggest sources of energy consumption and environmental pollution worldwide is vehicles, with the automotive industry using over 49% of the world's oil reserves [1]. Therefore, we must look for solutions that reduce the production of pollutants while still using vehicles; one of the proposed and focused solutions is the use of hybrid vehicles. Hybrid vehicles are a combination of internal combustion and electric vehicles. By optimizing the combination of their individual components, we can achieve maximum vehicle performance while producing less pollution and fuel consumption.

There is a lot of research on the parametric optimization of powertrain components. To give examples of some studies similar to this one, we can mention that the study conducted in [2] by Gao and S.K. Porandla used 4 optimization techniques for a Chevrolet Lumina in a parallel Mid-Size Sedan and in to meet EcoCAR Mobility standards, Two Engines, four electric motors, plus two battery packs were explored as [3] he aim of the development and so on.

In this research, with a 15% tolerance on initial values of selected parameters (engine power, battery module count, electric motor power, generator power, car drag coefficient, and final gear ratio), finally we conducted 16 optimal combinations of components presented in Table 2. This proves an approximate 15% improvement compared to [4].

Material and Method

In this paper, ADVISOR software [5],[6] is used to optimize the Toyota Prius which has a series-parallel configuration [7], with the default model components values 1.5L engine that generates 43kw, a Nickel Metal Hydride battery with 40 modules, and a 31kw permanent magnet motor, these values are from ADVISOR itself. It is the real component value of the second generation of TOYOTA Prius [8]. These seven components were selected

to optimize (Engine, Battery, Electric motor, Generator, Vehicle overall drag coefficient, and Final drive ratio) by changing their size in (Federal Test Procedure (FTP) driving cycle to examine the vehicle performance, fuel economy, and emissions especially. The fuel economy of the Toyota Prius in ADVISOR is 46.9 mpg and the emissions are HC 0.872, CO 0.99, and NOx 0.218 (gram/mile) for The Federal Test Procedure (FTP) driving cycle as shown in the figure 1.

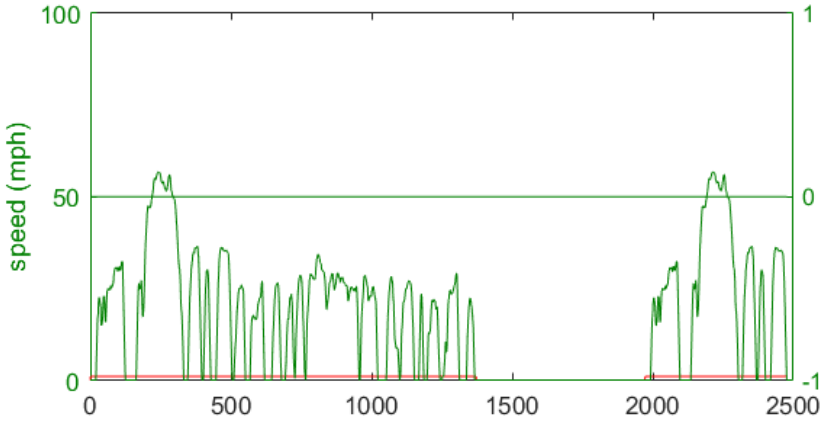


Figure 1. FTP driving cycle [1]

Results

The experiment involved adjusting the sizes of components within a 15% range from their initial values as shown in Table 1. Four different sizes were tested for each component, resulting in a total of 4096 designs being evaluated. The objective was to identify designs that outperformed the default results. During the FTP driving cycle, 4096 unique values are employed for every powertrain component. This enables a comprehensive evaluation of performance and fuel efficiency.

Table 1. Calculated component values selected

Parameters	Engine power (KW)	Battery module	Motor power (KW)	Final drive ratio	Generator power (KW)	Vehicle drag coefficient
Default	43	40	31	3.93	15	0.3
1	49	46	35	4.5	17	0.32
2	46	43	33	4.25	16	0.31
3	41	37	29	3.68	14	0.29
4	39	34	27	3.4	13	0.28

As a result, by comparing all 4096 component size values, the most efficient and acceptable results were gathered in Table 2. Comparison of HEV before opt, and HEV after optimization for the desired driving cycle using ADVISOR is shown in Table 3.

Table 2. The optimum vehicle design for FTP driving cycle

Parameters	Engine power (KW)	Battery module	Motor power (KW)	Final drive ratio	Generator power (KW)	Vehicle drag coefficient	Fuel consumption	Max. speed	Acceleration time 0-60 mph in s	HC	CO	NOx
Default	43	40	31	3.93	15	0.3	46.9	101.5	15.3	0.872	0.99	0.218
1	41	46	35	4.5	17	0.29	48	13.8	88.5	0.822	0.947	0.214
2	41	46	35	4.5	17	0.28	48.1	13.8	88.5	0.821	0.946	0.214
3	41	46	35	4.5	16	0.29	48	13.8	88.5	0.822	0.947	0.214
4	41	46	35	4.5	16	0.28	48.1	13.8	88.5	0.821	0.946	0.214
5	39	46	35	4.5	17	0.29	49.3	14.3	88.6	0.774	0.905	0.211
6	39	46	35	4.5	17	0.28	49	14.3	88.6	0.782	0.916	0.212
7	39	46	33	4.5	17	0.32	48.7	14.4	88.6	0.775	0.91	0.214
8	39	46	33	4.5	17	0.29	48.8	14.4	88.6	0.776	0.906	0.212
9	41	46	35	4.5	17	0.29	48	13.8	88.5	0.822	0.947	0.214
10	41	46	35	4.5	17	0.28	48.1	13.8	88.5	0.821	0.946	0.214
11	41	46	35	4.5	16	0.29	48	13.8	88.5	0.822	0.947	0.214
12	41	46	35	4.5	16	0.28	48.1	13.8	88.5	0.821	0.946	0.214
13	39	46	35	4.5	17	0.29	49.3	14.3	88.6	0.774	0.905	0.211
14	39	46	35	4.5	17	0.28	49	14.3	88.6	0.782	0.916	0.212
15	39	46	33	4.5	17	0.32	48.7	14.4	88.6	0.775	0.91	0.214
16	39	46	33	4.5	17	0.29	48.8	14.4	88.6	0.776	0.906	0.212

Table 3. FTP driving cycle results

Constraint	HEV bef. opt.	HEV aft. opt.
Fuel Eco. (mpg)	46.9	48
HC (gr/mile)	0.872	0.822
CO (gr/mile)	0.99	0.947
NOx (gr/mile)	0.218	0.214
0-60 mph (s)	15.3	13.8
Max Accel. (m/s2)	3.413	4.36
Max speed (m/s)	45.37	39.6

In examining possible scenarios, we reached two excellent results, both of which were obtained through simulation, showing more than 10% improvement compared to the actual optimized version of the car in [9]. This can be referred to as a better performance with less money. We can also some choices with little difference with optimized design in this study based on our aim.

Conclusion

This paper highlights the significance of hybrid electric vehicles and their impact on the environment. It also compares conventional vehicles [10-12] to hybrid electric vehicles, utilizing numerous optimization algorithms to enhance HEV performance. Specifically, the paper focuses on enhancing the TOYOTA PRIUS (HEV) with series-parallel architecture using ADVISOR software. The ANOVA analysis technique is employed to analyze the size of the internal combustion engine (ICE), battery, electric motor (EM), and generator, aiming to boost fuel efficiency and reduce emissions. Results show that with little effort you can reach more than 7% optimization before and after optimization.

In the future, there is potential to optimize additional components in HEV related to control strategy and battery such as high SOC, and low SOC. Furthermore, exploring different optimization algorithms like the DIRECT algorithm, Simulated Annealing, and Genetic Algorithm could be beneficial. Additionally, experimenting with other types of vehicles and software such as PSAT or MATLAB/Simulink for optimization purposes can be considered.

References

1. Ding, N.P., Krishnamachar & Lie, Tek Tjing., *The electric vehicle: A review.* International Journal of Electric and Hybrid Vehicles. 9. 49., 2017.
2. Gao, W.P., S.K.. *Design Optimization of a Parallel Hybrid Electric Powertrain.* 2005.
3. Jianning Zhao, A.S., *Design and Control Co-Optimization for Hybrid Powertrains: Development of Dedicated Optimal Energy Management Strategy,.* IFAC-PapersOnLine,, 2016. **49**(11).
4. Mohr, S.W., Jianliang & Ellem, G. & Ward, James & Giurco, Damien., *Projection of world fossil fuels by country. Fuel.* 2015.
5. Muta, K., M. Yamazaki, and J. Tokieda, *Development of new-generation hybrid system THS II-Drastic improvement of power performance and fuel economy*. 2004, SAE Technical Paper.
6. Horie, T. *Development aims of the new CIVIC hybrid and achieved performance*. in *Proc. SAE Hybrid Vehicle Technologies Symp.* 2006.
7. Owen, N., O.R. Inderwildi, and D.A. King, *The status of conventional world oil reserves—Hype or cause for concern?* Energy Policy, 2010. **38**: p. 4743-4749.
8. Varun, M. and C. Kumar, *Problems in electric vehicles.* Int. J. Appl. Res. Mech. Eng, 2012. **2**(1): p. 63-73.
9. Ahmed, A., A. Thakan, and S. Pradhan, *Modeling and optimization of HEV for FTP driving cycle.* AIP Conference Proceedings, 2024. **2962**(1).
10. Tran, M.-K., et al., *Design of a hybrid electric vehicle powertrain for performance optimization considering various powertrain components and configurations.* Vehicles, 2020. **3**(1): p. 20-32.
11. Tran, M.-K., et al., *Design of a Hybrid Electric Vehicle Powertrain for Performance Optimization Considering Various Powertrain Components and Configurations.* Vehicles, 2021. **3**(1): p. 20-32.
12. Bitsche, O. and G. Gutmann, *Systems for hybrid cars.* Journal of power sources, 2004. **127**(1-2): p. 8-15.

Advanced Engineering Days

aed.mersin.edu.tr

The numerical simulation of fluid-structure interaction by phase-field method

Hanieh Abbasi[1], Sajad Rezazadeh [*1]

[1] Urmia University of Technology, Faculty of Renewable Energies, Department of Mechanical Engineering, Urmia, Iran.
Hanieh.abasi@yahoo.com, Sor.mems@gmail.com

Cite this study: Abbasi, H., & Rezazadeh, S. (2024). The numerical simulation of fluid-structure interaction by phase-field method. Advanced Engineering Days, 9, 46-48

Keywords
FSI
2-way interaction
Sloshing
COMSOL Multiphysics
Phase field

Abstract

Fluid-structure interaction (FSI) occurs when a flexible structure such as a baffle is in contact with the flow and the flow forces lead to a change in its displacement. When a tank is partially filled with fluid, the free surface of the fluid moves and consequently hits the tank. To minimize the effects of this phenomenon, anti-slip elements such as baffles are used against the sudden movement of the fluid. In the present work, it is shown how a heavier fluid such as water can create a movement in the baffle and change the fluid flow pattern. Also, the effect of baffle thickness and Young's modulus parameters on the pressure and velocity of fluid has been investigated. The obtained results illustrated that the thickness changes affect the studied parameters more than Young's modulus. When the fluid hits the baffle, the pressure distribution diagram experiences vital fluctuations, and after that, in the subsequent times of slashing, due to the return of the fluid and the presence of the vortex behind the baffle, negative pressure was observed in this diagram. Finally, the extracted data for the elastic beam have been validated against the published data.

Introduction

Fluid-structure interaction refers to a state where a fluid flow interacts with the body of a solid structure; Applying heat or pressure load by a fluid to a solid body changes the flow forces, and this change in the flow forces in turn leads to a change in the displacement of the structure, in such systems it is not possible to focus only on the structure and the surrounding flow Ignore it or focus on the flow and ignore the structure, these two should be considered together. One of the common cases of two-way FSI is the slashing phenomenon; In this phenomenon, when the tank partially filled with fluid is exposed to permanent or transient external forces, the free surface of the liquid moves and hits the walls of the tank and exchanges forces with the walls of the tank; Here, the movement of the free surface of the liquid inside the container due to external stimulation is very complicated, which is why the analytical solutions are limited to simple geometries such as cylindrical, rectangular and spherical tanks. To minimize slashing, anti-slip elements such as baffles can be introduced to resist fluid movement. Kandasamy et al. [1] presented an analysis of the effectiveness of different baffle designs in limiting fluid slippage in semi-full tanks of trucks, Craig and Kingsley [2] developed a method that uses a baffle design technique to optimize design variables. Offers.

In the context of the deterrent effect of different baffles on the sloshing phenomenon, in the article of Yamin Gan et al [3], horizontal baffles, vertical baffles, and T-shaped baffles were investigated in sloshing tanks; and also the position, dimensions, and depth of the baffle, presented and discussed;

It is known that the shape of the baffle has a non-negligible role in the deflection of the tank; In the case that the tank is under a horizontal harmonic excitation, the vertical baffle is a more effective method to reduce the deviation range, while in the case of the horizontal baffle, when the tank is under roll excitation, the method is more effective; Although the T-shaped baffle has the best suppression effect on tank tilting under horizontal excitation, it has a limited suppression effect under roller excitation and will complicate the drooping phenomenon when the baffle height is changed.[4]

In the present research, the water dropping in a rectangular cube tank with a flexible baffle has been studied; In this research, it is shown how a heavier fluid can create movement in an obstacle and change the fluid flow; In

this model, the Lagrangian-Eulerian technique (ALE) is used to model the interaction between the structure and the fluid as well as the phase field.

At first, there is a heavier liquid like water in the left area and air also fills the rest of the computational space; When the water is released and reaches the baffle, the baffle begins to bend due to the inertial force of the heavy fluid and moves away from its original position; In the following, we obtained numerical results by changing some parameters of the baffle and checking the pressure and velocity of the fluid passing through it.

Material and Method

The geometry of the model consists of a small container with a thin baffle in the middle; This container is 30 mm long, 5 mm wide, and 10 mm high. The top of the flexible baffle is fixed on the container and it hangs freely inside the container. This baffle is 9 mm high, 4 mm wide and 0.3 mm deep. A primary dam from water is released and when it reaches the baffle, it moves away from its initial position; Displaced air naturally enters the container on the opposite side of the baffle, if the baffle was the size of the container, water could not penetrate to the right side. The following assumptions are currently considered. The fluid flow is unsteady, Newtonian fluids with constant properties, the energy equation is neglected, the solid body is assumed to be elastic, and the fluid flow is slow and incompressible. Considering that the present model has not been worked in another article or thesis for validation, the data of the work of Fallah et al. [5] were used, in which an internal flow of air around a two-dimensional cylinder including an elastic blade passes; The mentioned work has been validated by the data extracted from the results of the work of Srinkans[6], Turk and Heron[7], in the form of data such as average drag cofficient ($\overline{C_D}$), Strouhal number (St) and average Nusselt number ($\overline{NU}$) has been achieved.

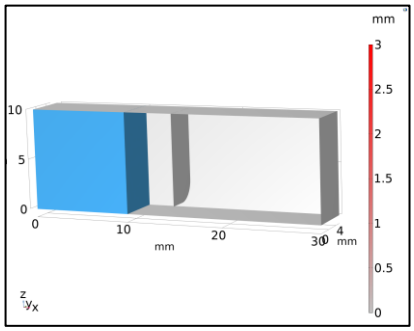


Figure 1. The initial density of the liquid inside the container.

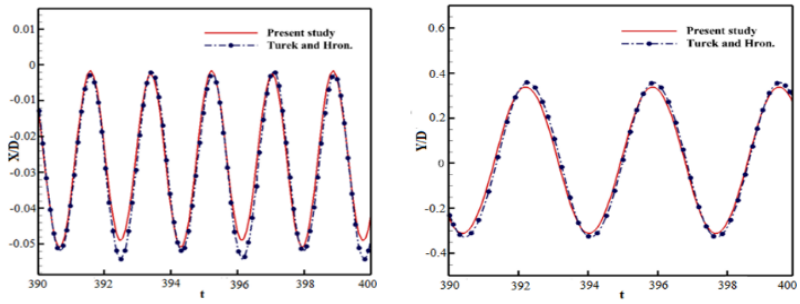


Figure 2. The time history of the tip displacement of the splitting beam in (a) x and (b) y direction is shown.

Governing equations

In current work, the Phase field model has been used for two-phase interface movement simulation. This method presents better results compared to the other methods such as level-set.

Equations of fluid properties

Continuity: $\rho\nabla.u = 0$ (1)

Momentum: $\rho(u.\nabla)u = \nabla.[-pI + \mu(\nabla u.(\nabla u)^T)] + F + \rho g$ (2)

Phase field equation

$\nabla GI.\nabla GI + \sigma_w GI\nabla.\nabla GI = (1 + 2\sigma_w)GI$ (3)

Results

The changes in pressure and velocity in specific time intervals have been investigated for the baffle with a thickness of 0.3 and Young's modulus of 2 MPa as illustrated in Figure 3. The figure on the left represents the initial position of the fluid and the second figure shows the pressure contour, we can see that this contour represents the hydrostatic pressure in the fluid, which has increased with increasing depth according to the relationship P = ρgh (darker color of the contour indicates an increase in pressure). The next figure presents the velocity contour in 5 different sections due to the smallness of the analytical geometry and the effects of slashing, the changes in velocity and its maximum value do not follow the rules and have negligible changes, and the last figure shows the pressure distribution along the dashed line. It is under the obstacle at the position (x=2, y=2, z=0.75).

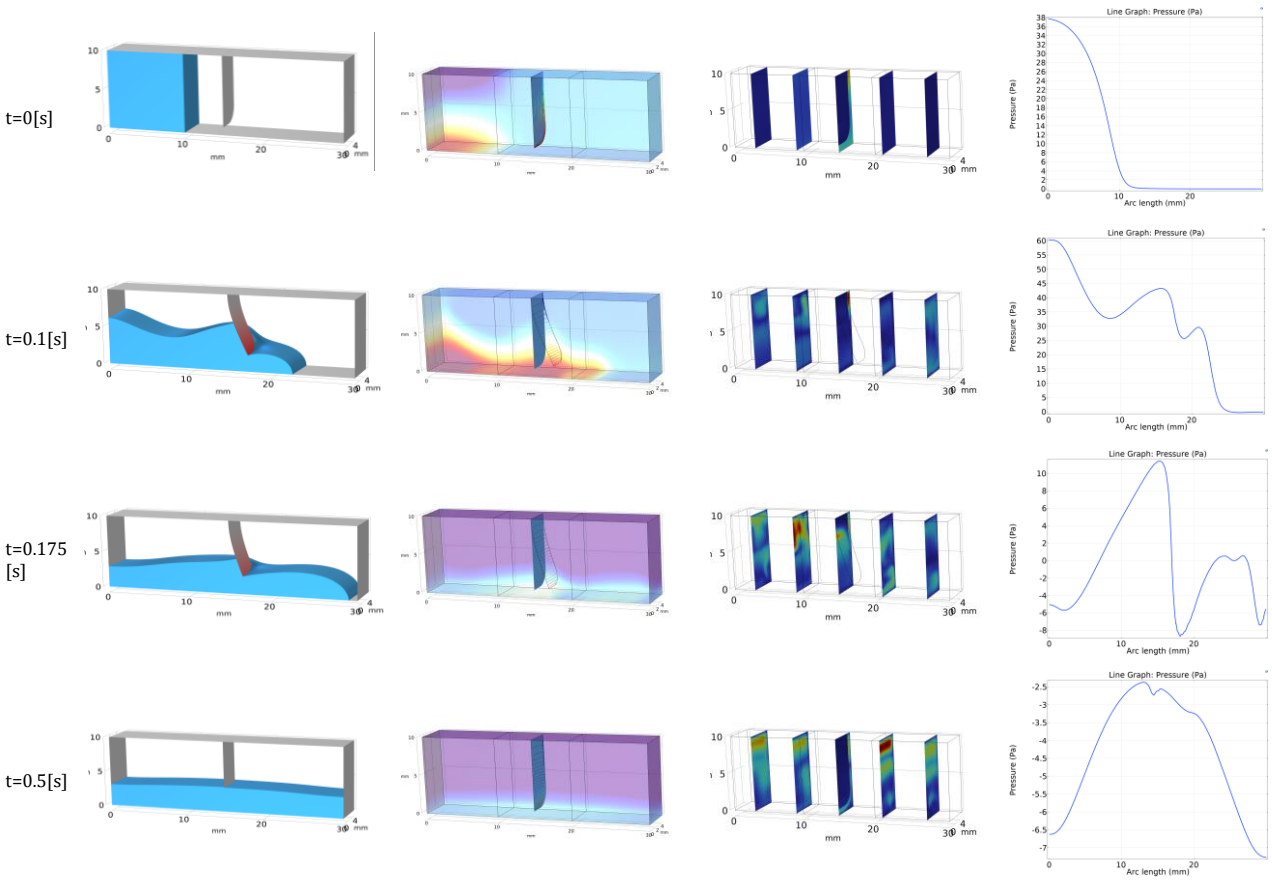


Figure 3. Changes in pressure and velocity in certain time intervals

Conclusion

In this study, we simulated the tank containing a water and elastic baffle that interaction with each other. When we let the water flow, the elastic baffle starts deforming according to water slashing. Accordingly, the pressure and velocity fields experience important changes over time. We concluded that this baffle plays an important role and can conserve the tank from sudden movement of water and fatigue.

References

1. Kandasamy, T., & Rakheja, S., and Ahmed, A. K. W. (2010). An Analysis of Baffles Designs for Limiting Fluid Slosh in Partly Filled Tank Trucks, Open Transport. J. *volume 4*. pp. 23–32. 10.2174/1874447801004010023
2. Craig, K. J., & Kingsley, T. (2007). Design Optimization of Containers for Sloshing and Impact, Struct. Multidisc. Optim, pp. 33.71
3. Yamin Guan,. & Caihong Yang. (2020). Numerical investigation on the effect of baffles on liquid sloshing in 3D rectangular tanks based on nonlinear boundary element method. *International Journal of Naval Architecture and Ocean Engineering Maune.volume12*. pp. 399-413https://doi.org/10.1016/j.ijnaoe.2020.04.002
4. Javanshir,Alireza.(2013). Numerical investigation of three-dimensional slashing in a liquid-containing tank. Master's thesis. Mashhad Ferdowsi University
5. Abbasnejad fallah,davoud., & Rezazadeh,Sajad.,& Rad,Mohammad.and Jalili,Habib.(2022). Numerical investigation of heat transfer and mixing process phenomena inside a channel containing a triangular bluff body and elastic micro-beam: gap spacing and geometric characteristic effects. *Volume 26*.10.1007/s10404-022-02527-1
6. Srikanth S, Dhiman A, Bijjam SJIJoTS (2010). Confined flow and heat transfer across a triangular cylinder in a channel. Int J Thermal Sci 49:2191–2200. https://doi.org/10.1016/j.ijthermalsci.2010.06.010
7. Turek S, Hron J (2006) Proposal for numerical benchmarks for fluid- structure interaction between an elastic object and laminar incompressible flow. Fluid-structure interaction. Lecture notes in computational science and engineering, vol 53. Springer, Berlin, Heidelberg. https://doi.org/10.1007/3-540-34596-5_15

Advanced Engineering Days

aed.mersin.edu.tr

Numerical simulation of compact heat exchanger with dynamic moving walls

Maziar Javadi [1], Sajad Rezazadeh *[1], Paniz Rezazadeh Azar [1] MirMahdi Seyyed Valilu [1]

[1] *Urmia University of Technology, Faculty of Renewable Energies, Department of Mechanical Engineering, Urmia, Iran, zaniajavadi@gmail.com, sor.mems@gmail.com, panizrezazadehazar@gmail.com, mahdivalilu@gmail.com*

Cite this study: Javadi, M., Rezazadeh, S., Azar, P. R., & Valilu, M. S. (2024). Numerical simulation of compact heat exchanger with dynamic moving walls. Advanced Engineering Days, 9, 49-51

Keywords
Heat
Fluid flow
Static and dynamic
Exchanger

Abstract

The present work deals with the numerical investigation of the effect of the presence of a dynamic wall on the thermal performance of the compact heat exchanger. We aim to improve the heat transfer rate in small-scale heat exchangers and also to reduce the pressure drop by using a dynamic wall with an oscillating waveform. This type of deformation in the wall of the channel in which the fluid flows causes better mixing and reduces the possibility of the formation of thick thermal boundary layers. Hence, the heat transfer between the walls and the fluid increases. In addition, the oscillation of the wall and the occurrence of deformation in it in the form of a wave creates a pumping effect similar to a peristaltic pump, which compensates for the pressure drop caused by friction.

Introduction

There are different types of compact heat exchangers available, including plate heat exchangers, shell and tube heat exchangers, and finned tube heat exchangers. Each type has its unique design features and advantages depending on the specific application requirements. overall, compact heat exchangers offer numerous benefits such as improved thermal performance, reduced energy consumption, smaller footprint, lower maintenance costs, and increased operational flexibility. These advantages make them a preferred choice for many industries where space constraints and efficiency are crucial factors. Figure 1 shows the use of a compact heat exchanger geometry.

Compact heat exchangers play a crucial role in the heating systems of buildings by efficiently transferring heat from one fluid to another. These heat exchangers are designed to maximize the surface area for heat exchange while minimizing the volume and weight of the unit, making them particularly suitable for various heating applications in buildings. Figure 2 demonstrates the geometry of the heat flux in a static configuration with a flat upper wall. Water is heated as it flows from the inlet to the outlet due to a heat flux at the bottom side of the heat sink. The delivered heat rate at the bottom boundary is set to 125 W. The upper wall undergoes dynamic deformation, assuming a sinusoidal waveform. Pressure remains constant at the inlet, while the outlet remains thermally insulated with no applied pressure. The dynamic wall is also thermally insulated, and both walls consistently adhere to a no-slip condition. The ambient temperature is maintained at a constant value of T = 27°C. Copper is a highly effective conductor of heat, and copper plates are commonly used in various applications where efficient heat transfer is crucial such as heat exchangers [1-4].

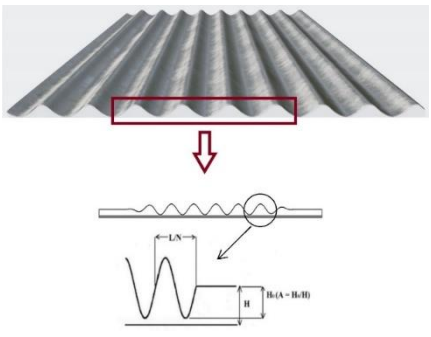


Figure 1. use of a compact heat exchanger in the heating system of a residential building

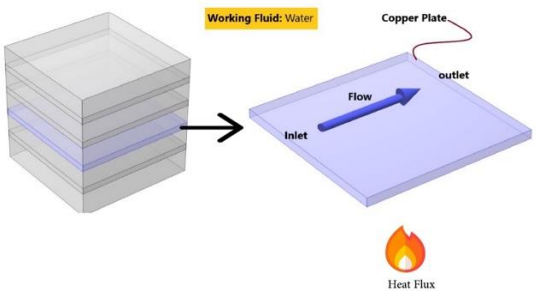


Figure 2. the geometry of the heat flux in a static configuration with a flat upper wall

Material and Method

In this study, we utilize the continuity, Navier-Stokes, and energy equations to conduct a numerical solution for the water domain, employing the boundary conditions detailed in Table 1. The density is represented as a function of temperature, and we apply the Boussinesq approximation, resulting in the equations provided in (1), (2), and (3).

$$div\left(\rho\vec{V}\right)=0 \tag{1}$$

$$div\left(\rho\vec{V}\vec{V}\right)=-gradP+\nabla.\left(\mu\nabla\vec{V}\right) \tag{2}$$

$$div\left(\rho\vec{V}C_pT\right)=div\left(kgradT\right) \tag{3}$$

We have established solutions for both static and dynamic scenarios. The solution from the static case serves as the initial value for addressing the dynamic case. The equation that governs the displacement of the sinusoidal moving wall involves two smoothing functions, denoted as "flc2hs," with dual arguments. These functions are applied to eliminate the initial flow effects.

To achieve a transient oscillating configuration, the upper wall of the dynamic wall heat exchanger is intentionally deformed. The displacement of the upper wall, denoted as "u," is defined by:

$$u=AYf_X(X)sin\left(2\pi\left(-tf+X\frac{N}{L}\right)\right)f_t(t) \tag{4}$$

Where:

$$f_t(t)=flc2hs\left(t-\frac{1}{f},\frac{1}{f}\right) \tag{5}$$

The overall heat transfer coefficient of the heat exchanger is defined as:

$$h=\frac{q}{\bar{T}_w-\bar{T}_f} \tag{6}$$

The following assumptions have been considered to model the problem:

- The flow is incompressible and at the same time laminar due to the low velocity of the fluid flow.
- To facilitate the solution of the problem, first the condition is a steady state and then it turns into the real state i.e. unsteady state.

The boundary conditions to solve both the static and dynamic cases are illustrated as follows. Also figure 3 shows the boundary condition schematically (Inlet: P=50 [Pa] and T=T0=27 [°C], Outlet: P=0 [Pa] and $\frac{\partial T}{\partial x}=0$, Bottom wall:

u=v=0 (no-slip condition) and q=125 [W], Top wall:u=v=0 (no-slip condition) and $\frac{\partial T}{\partial y}=0$):

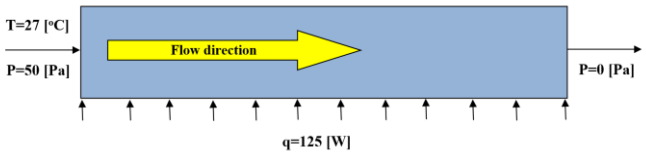


Figure 3: the boundary conditions of the proposed model

Results

The governing equations and related initial and boundary conditions that are specified mathematically by equations (1) to (6) are solved numerically by the finite element method. In transient conditions, we employ the Arbitrary Lagrangian-Eulerian (ALE) method, which becomes necessary when the wall undergoes deformation, leading to domain changes that require a mesh capable of free movement, compatible with the ALE approach. In the transient case, we choose a time step of $1/f/20$, and the solution is computed over some time of $50/f$ to achieve the desired results. To study the mesh independence in the current work, six different finite element meshes, are employed.

To ensure the precision and reliability of the current numerical simulation in addressing analogous problems, a rigorous validation process was executed. This involved a meticulous comparison of the mass flow rates obtained in our study with those derived from a preceding investigation conducted by Leal et al. [19]. The mass flow rate, measured in $kg.m^{-2}s^{-1}$, was calculated by dividing the mass flow rate presented in our current study by the flow

area, considering various relative amplitude values expressed as percentages. The results generated by our present computational model were then meticulously compared with those obtained by Leal et al. [19]. Remarkably, a close alignment between the two datasets was observed, as illustrated in Fig. 6. This congruence serves as compelling evidence affirming the validity of the current numerical methodology, attesting to its applicability in solving similar problem domains. Figure 7 shows the temperature distribution diagram versus time when A=0.9, F=50 [Hz], and H= 1 [mm]. The figure illustrates that at t=0.1 [s], there are extreme temperature fluctuations and these are also evident at t=0.2 and 0.3 [s], but it can be clearly stated that from t=0.5 [s] to t=1 [s], the temperature changes are almost identical.

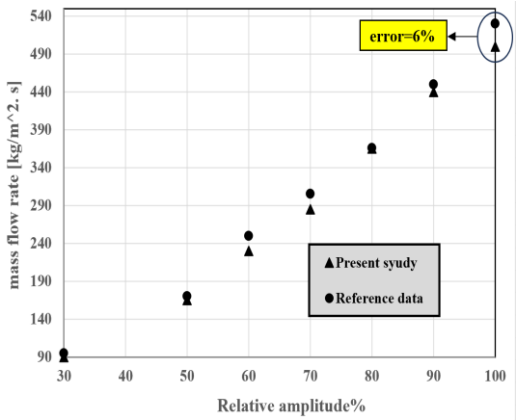


Figure 6. The validation of numerical results with reference data

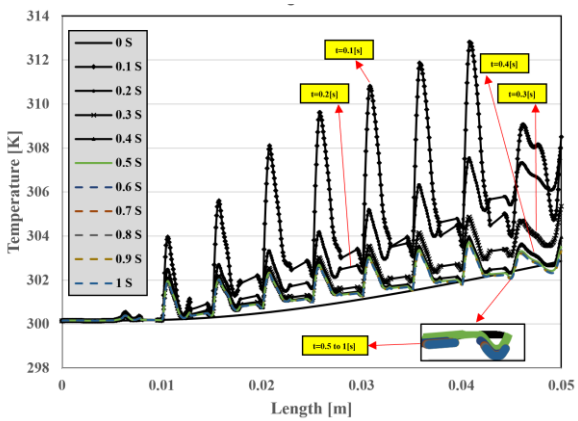


Figure 7. The temperature distribution diagram versus time when A=0.9, F=50 [Hz], and H= 1 [mm]

Conclusion

This study presents a numerical investigation of two-dimensional laminar flow and heat transfer inside a channel with static and dynamic wall boundaries. The FEM has been used to solve the unsteady governing equations. It has been concluded that there are extreme temperature fluctuations and these are also evident at t=0.2 and 0.3 [s], but it can be clearly stated that from t=0.5 [s] to t=1 [s], the temperature changes are almost identical.

References

[1] Ahamed S, Uddin MM. Estimating uncertainty of earthquake rupture using Bayesian neural network. Physics Stat. 2019. Retrieved from: arXiv.org.
[2] Uddin MM. Finite Difference Analysis of Stress Distribution Around an Elliptical Hole in a Plate Subjected to Axial Loading. International Journal of Modern Developments in Engineering and Science. 2023;2(4):1-4.
[3] Uddin MM. Studying the Scratching Behavior of Nb/Nbc Nanolaminate Using Molecular Dynamics Atomistic Simulations. Northern Illinois University. ProQuest Dissertations Publishing; 2020.
[4] Léal L, Topin F, Lavieille P, Tadrist L, Miscevic M. Simultaneous integration, control and enhancement of both fluid flow and heat transfer in small scale heat exchangers: A numerical study. International Communication of Heat and Mass Transfer. 2013;49:36- 40.

Advanced Engineering Days

aed.mersin.edu.tr

Numerical study of heat transfer on the surface of the cone

Ghazaleh Babazadeh Asbagh *[1], **Faramarz Talati**[1]

[1] *University of Tabriz, Faculty of Mechanical Engineering, Department of Mechanical Engineering, The Islamic Repablic of Iran, ghazalebabazadeasbgh1400@ms.tabrizu.ac.ir, talati@tabrizu.ac.ir*

Cite this study: Babazadeh Asbagh, Gh., & Talati, F. (2024). Numerical study of the bulk temperature heat transfer and the temperature contour on the surface of the cone. Advanced Engineering Days, 9, 52-54

Keywords
Constant heat flux
Constant temperature
Heat transfer converging
Diverging cone

Abstract

In this study, the rate of heat transfer on the outer surface of a cone was numerically calculated. The objective was to determine the bulk temperature under two boundary conditions: constant temperature and constant heat flux. A cone was chosen and examined in four different scenarios using air as the working fluid and aluminum as the cone material. The flow regime in this problem was turbulent, and the two-equation k-ε realizable EWT model were used for analysis. The flow rate was kept constant in all cases. The scenarios included constant temperature and constant heat flux for flows from the large diameter to the small diameter and vise versa. It is expected that under constant temperature conditions, the bulk temperature graph will exhibit an exponential trend, whereas under constant heat flux conditions, the graph will be linear.This research provides insights into the thermal behavior of converging and diverging nozzles under different boundary conditions, contributing to the optimization of their design and performance.

Introduction

Heat transfer and methods for calculating the convective heat transfer coefficient in converging and diverging nozzles have been of significant interest to researchers and remain critically important across various applications [1]. The extensive utilization of nozzles includes applications in rockets [2], air removal from condensers, various turbines such as steam and water turbines, and jet engines.

Another vital application of nozzles and diffusers is examining fluid pressure drop and convective heat transfer rates in channels [3]. In 1987, Hartnett et al. studied boundary layer heat transfer from a rotating cone or disk to fluids with Prandtl numbers ranging from 0.001 to infinity under conditions of constant temperature and uniform heat flux. They provided a highly accurate heat transfer correlation equation applicable to all Prandtl numbers [4].

In this study, computational fluid dynamics (CFD) using Ansys Fluent [5] is utilized to perform three-dimensional simulations. The simulations consider constant temperature and constant heat flux boundary conditions for converging and diverging nozzles (nozzle and diffuser) at identical flow rates. Initially, heat transfer and temperature contours on the outer surface are calculated and compared. The ultimate goal is to derive and compare the bulk temperature profiles for the two specified boundary conditions.

Materials and Method

Figure 1 depicts the model under investigation in this study, which comprises a hollow cone with air as the working fluid. Table 1 presents the specifics of this cone, with all parameters held constant. During the simulation, two cases were investigated. In case 1, the flow direction was from top to bottom, with the flow entering from the larger diameter section and exiting from the smaller diameter section.

Subsequently, in case 2, the flow direction was reversed, with the flow entering from the smaller diameter section and exiting from the larger diameter section. In the fist scenario, the hollow cone functions as a nozzle, while in the second case, it works as a diffuser. It is crucial to highlight that the flow rate remains constant at 3.4 kg/s, resulting in varying inlet velocities for the fluid in both the nozzle and diffuser conditions. The boundary

conditions that define the problem depicted in Figure 1. In condition A, the wall in both the nozzle and diffuser states is kept at constant temperature (1000k), while in condition B, the wall is subjected to a constant heat flux (500 W/m^2).

In order to maintain uniform flow rates throughout the project, and given the variable diameters of the inlet in both the nozzle and diffuser states, different inlet velocities are considered for the nozzle and diffuser conditions.

Since flow rate is constant the velocity at inlet and outlet sections are different.

Furthermore, in the first case, the inlet fluid temperature is 1500 K with an outlet temperature of 2000 K. In contrast, in the second case, the inlet fluid temperature is 900 K with an outlet temperature of 1000 K.

Table 1. Simulated cone data

Items	Value
D_1	100 (mm)
D_2	50 (mm)
H	500 (mm)

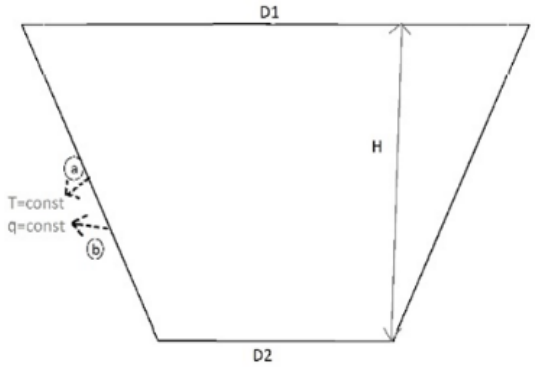


Figure 1. Schematic of the cone investigated in this study

Results

The first case corresponds to the investigation of a nozzle where the fluid enters at D1 and exits at D2. In this case scenario A is considered where the wall is maintained at a constant temperature. Figure 2(a) illustrates the temperature diagram, showing an exponential increase in temperature until it reaches a constant value.

Figure 2(b) shows the bulk temperature profile under condition B, where the wall of the nozzle is subjected to a constant heat flux. This reveals a linear increase in temperature until it stabilizes at a constant value.

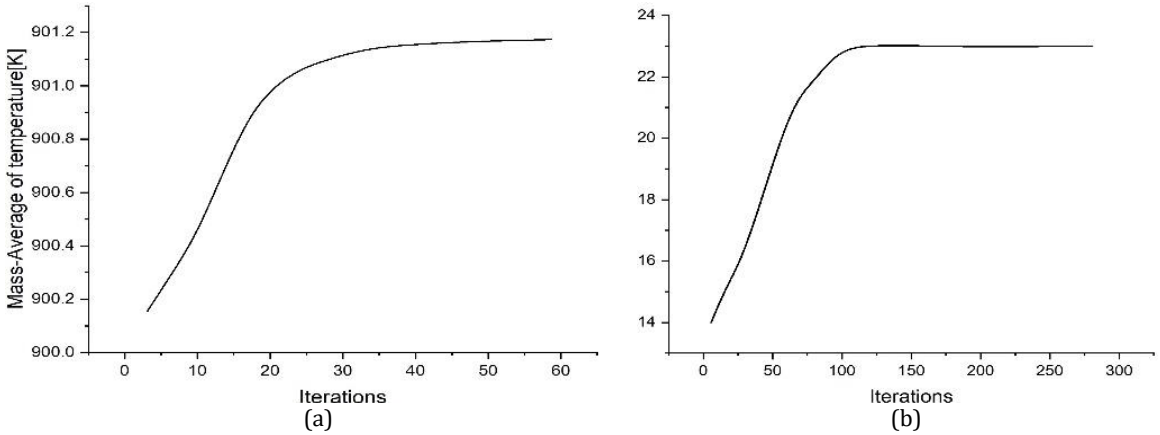
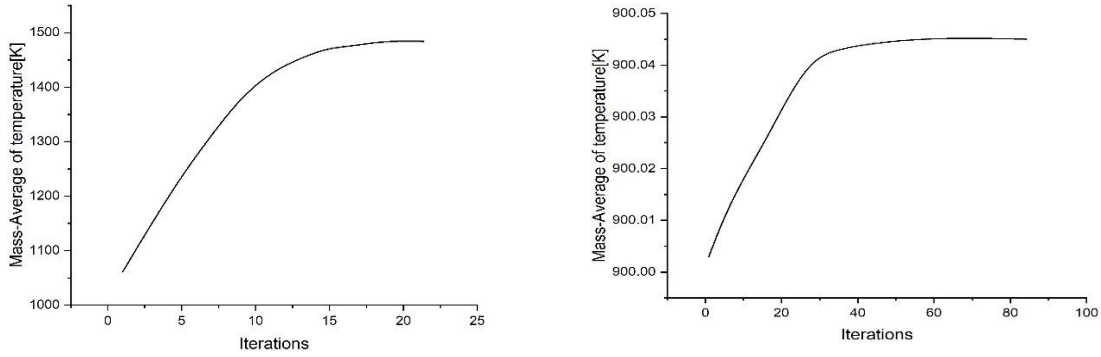


Figure 2. Nozzle: (a) bulk temperature profile under constant temperature condition, (b) bulk temperature profile under constant heat flux condition

The second case involves examining a diffuser where the fluid enters at D2 and exits at D1. Firstly, in scenario A, the wall is maintained at a constant temperature. Figure 3(a) depicts the bulk temperature profile under this condition, displaying an exponential increase in temperature until it stabilizes at a constant value.

Figure 3(b) illustrates the bulk temperature profile under a constant heat flux boundary condition. The temperature increases linearly until it reaches a stable, constant value.



(a) (b)

Figure 3. Diffuser: (a) bulk temperature profile under constant temperature condition, (b) bulk temperature profile under constant heat flux condition

Discussion

In this study, the thermal behavior of a hollow cone with air as the working fluid was investigated under different boundary conditions.

The results indicate that the temperature distribution varies significantly depending on whether the wall temperature is held constant or subjected to a constant heat flux. Specifically, in the nozzle configuration, where the fluid enters from a larger diameter and exits from a smaller one, the highest temperatures are observed on the cone wall due to the influence of the wall temperature.

Conversely, in the diffuser configuration, where the fluid enters from a smaller diameter and exits from a larger one, the temperature distribution is influenced by both the fluid and wall temperatures, leading to variations in heat transfer along the cone's surface. These findings underscore the importance of considering boundary conditions in analyzing heat transfer phenomena in such geometries.

Conclusion

This study aimed to estimate the rate of heat transfer and the temperature contour on the outer surface of a cone, as well as to determine the bulk temperature under two boundary conditions: constant temperature and constant heat flux. The significance of heat transfer in cones necessitates this investigation.

The temperature contours and bulk temperature graphs for both the nozzle and diffuser were calculated and analyzed under the specified boundary conditions. It was observed that, for the constant temperature boundary condition, both in the nozzle and diffuser, the bulk temperature graph exhibited an exponential trend. In accordance with the constant heat flux boundary condition, the temperature exhibited a linear increase in both the nozzle and diffuser.

These findings underscore the significance of accounting for boundary conditions in the analysis of heat transfer phenomena in conical geometries.

References

1. Razmjooei, M., & Saboohi, Z. (2019). Review of methods for calculating convective heat transfer coefficient in combustion chambers and convergent-divergent nozzles. Technology in Aerospace Engineering, 2(3), 10.
2. Carlson, D. J., & Huglond, R. F. (2013). Particle drag and heat transfer in rocket nozzles. Vol.2, No.11, May 7.
3. Zhu, J., Dou, R., Hu, Y., Zhang, S., & Wang, X. (2020). Heat transfer of multi-slot nozzles air jet impingement with different Reynolds numbers. December 24.
4. Hartnett, J. P., & Minkowycz, W. J. (1987). Heat transfer from a rotating cone or disk to fluids of any Prandtl number. Vol.14, No.3.
5. Dehghani, M. A. (Translator). (n.d.). Numerical simulation with Fluent software. Naghoos Publications.

Advanced Engineering Days

aed.mersin.edu.tr

Numerical investigation of the effect of different parameters in preventing the emission of polluting gasses in a room using air curtains

Ghazaleh Babazadeh Asbagh*[1], Moharram Jafari[1], Faramarz Ranjbar[1]

[1] *University of Tabriz, Faculty of Mechanical Engineering, Department of Mechanical Engineering, The Islamic Repablic of Iran, ghazalebabazadeasbgh1400@ms.tabrizu.ac.ir, mjafari@tabrizu.ac.ir, s.ranjbar@tabrizu.ac.ir*

Cite this study: Babazadeh Asbagh, G., & Jafari, M., & Ranjbar,F. (2024). Numerical investigation of the effect of different parameters in preventing the emission of polluting gasses in a room using air curtains. Advanced Engineering Days, 9, 55-57

Keywords
Air curtain
Emission of polluting gas
Turbulence
Free and wall jet

Abstract

In recent years, air curtains have been increasingly utilized across various industries and applications. These systems introduce high-speed airflow into the environment, creating a barrier that effectively blocks insects, dust, suspended particles, pollutants, and heat transfer from entering the designated area. This study investigates two types of air curtain jets—free jets and wall jets—within an environment equipped with an air curtain designed to contain the dispersion of pollutant gas. A range of parameters is examined, including varying jet widths and different angles of wall jet deployment across various lengths. The investigation is conducted under three distinct pressure conditions. The primary objective is to determine the minimum velocity threshold required for the air curtain jet, which is crucial for efficiently reducing the dispersion of pollutant gas, while optimizing energy consumption during air curtain operation.By adjusting the air curtain jet, it is possible to reduce energy consumption while maintaining the air curtain's effectiveness. The validation of this research is performed numerically using ANSYS Fluent software.

Introduction

The first air curtain, patented by Theophilus van Kannel in 1888 (1), was conceived as a device to hinder the infiltration of air into buildings. Van Kannel's primary objective was to mitigate the ingress of cold air and pollutants. Air curtains are widely used for creating air barriers in various contexts. They find extensive applications in preventing the spread of pollutants such as carbon dioxide during fires in buildings (2), tunnels (3), and underground metros (4). Moreover, air curtains are utilized for dust control in mines (5) and factories (6). In 2021, Khayrullina et al. (7) conducted a numerical investigation focusing on two types of jets, free and wall jets, for the first time without considering angle, temperature, or changes in air outlet velocity. They achieved the creation of a wall jet followed by a free jet solely by placing a wall with varying lengths at the air discharge region. Their study aimed air curtains play a crucial role in modern architecture and industry, providing versatile solutions for environmental control challenges.

Inspired by khayrullina et al.(7), this study delves into the examination of two types of jets—free jets and wall jets – within a room equipped with an air curtain aimed at containing pollutant gas (Co_2) dispersion. This investigation encompasses various parameter including different jet widths, diverse wall jet angles along different lengths, while pollutant gas (Co_2) emission occurs under three distinct pressure conditions.Additionally, the study focuses on isothermal conditions without recirculation.The objective is to identify the minimum velocity threshold of the air curtain jet, crucial for effective prevention of pollutant gas (Co_2) dispersion, thereby optimizing energy consumption during air curtain operation.

Material and Method

The simulation system conducted in this study, as depicted in Figure 1, consists of a room with an air curtain system to prevent the spread of pollutant gas (Co_2).

Two general cases are considered for this study:

Case 1: The air curtain jet is simulated as a free jet, with jet widths (b) of 0.1, 0.2, and 0.4 m.

Case 2: A wall is placed, causing the air curtain jet to transition from a free jet to a wall jet. The width of the air curtain outlet jet in Case 2 is set at 0.2 and 0.4 m, with lengths of 0.5, 1, and 2 m for the wall.

Additionally, for each wall length, angles of -5°, 0°, +5°, +10°, and +15° are considered, where negative indicates bending to the right and positive indicates bending to the left .

In this simulation, the pollutant gas (Co_2) is released from the left side of the air curtain at pressures of 0.5, 1.5, and 2.5 Pa.The main objective of this study is to determine the minimum velocity of the air curtain jet under all conditions, with a simultaneous aim to reduce energy consumption. This ensures if individuals standing or sitting at a specified distance from the right side of the room can breathe oxygen effectively.

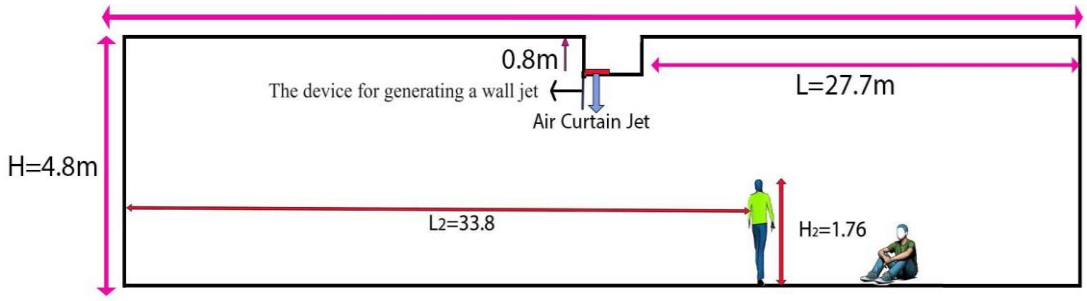


Figure 1. Geometry of the study room

The boundary conditions employed in this study contain of velocity conditions at the discharge nozzle, where various velocities are considered, accompanied by a 5% turbulence intensity. All solid surfaces are treated as zero-thickness walls, modeled as no-slip walls. Pressure conditions of 0.5, 1.5, and 2.5 Pa, alongside zero gauge pressure, are applied to the right side of the geometry, while a pressure outlet condition is applied to the left side, with a 5% turbulence intensity in both cases. All simulations are conducted under isothermal conditions. The simulations were conducted using ANSYS Fluent R2 2021, solving the two-dimensional RANS equations with the SST k-omega model. The SIMPLEC algorithm, consistent with prior research, was employed for pressure-velocity coupling, with second-order pressure interpolation. Additionally, simulations were performed under steady-state conditions.

Results

In Figure 2, the contour plot illustrates the distribution of pollutant gas mass fraction under specific conditions, where the air curtain jet is configured as a wall jet with a wall angle of +5°. The wall length measures 1 m, and the air curtain jet width is set to 0.4 m. This depiction demonstrates the efficacy of the air curtain in impeding the dispersion of the pollutant gas within the defined parameters. Figure 3 complements this observation by presenting the velocity contour in the same configuration.

Under the specified scenario with a pollutant gas pressure of 0.5 Pa, it is determined that the optimal velocity required to effectively prevent the spread of the pollutant gas is 3.4 m/s. Through a comprehensive analysis of various influencing factors, it is conceivable to achieve a reduction in both velocity and energy consumption while maintaining efficient pollutant control. This insight holds significance for the optimization and enhancement of air curtain jet systems in indoor environments, contributing to improved indoor air quality management practices.

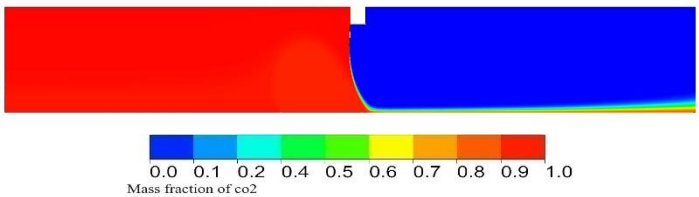


Figure2. Pollutant gas mass fraction contour in a wall jet case configuration with a wall angle of +5° degrees, a wall length of 1 m, and a jet width of 0.4 m.

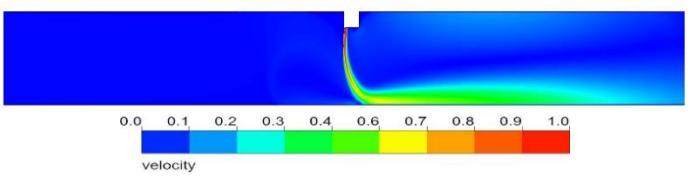


Figure3. Velocity contour in a wall jet case configuration with a wall angle of +5° degrees, a wall length of 1 m, and a jet width of 0.4 m.

Discussion

By analyzing the contours, significant effects of both the width of the jet and the length of the wall in the wall jet case on the performance of the air curtain in preventing the dispersion of pollutant gas in a confined room can be discerned. Additionally, the influence of the wall angle in the second case is not as pronounced, suggesting it may be disregarded.

For future investigations, it is recommended to install two air curtains, one above and precisely beneath it, to thoroughly examine the impact of various factors on the performance of the air curtains.

Conclusion

In this section, a comprehensive analysis of the data and contours has been conducted to examine the overall results. Initially, in the case of free jets, it is observed that increasing the width of the jet outlet of the air curtain leads to a decrease in the optimal velocity of the air curtain jet. This positive effect is accompanied by an increase in the inlet pressure of the pollutant gas (Co_2) into the room, and increasing the width of the jet contributes to improving the performance of the air curtain in reducing the spread of the pollutant gas (Co_2).

By comparing the data obtained from free jets and wall jets, it is concluded that wall jets perform better than free jets. Wall jets work at more optimal velocities and also contribute to improving the efficiency of the air curtain.

A comparison of the optimal velocities of different wall jets reveals that the 2-meter wall length of the wall jet has the lowest optimal velocity.

Furthermore, an increase in the inlet pressure of the pollutant gas (CO_2) in the 2-meter wall length of the wall jet case with a jet width of 0.4 meters results in the lowest optimal velocity, thereby demonstrating effective control of the pollutant gas (CO_2).

In conclusion, the 2-meter wall jet with a jet width of 0.4 meters exhibits the lowest optimal velocities among all experiments.

Furthermore, the results of the mass fraction charts of pollutant gas (CO_2) against non-dimensional height indicate that in various conditions, if a person is on the right side of the room (whether sitting or standing), the pollutant gas (CO_2) has no significant effect on the person.

Additionally, another conclusion shows that the wall angle in wall jet conditions does not have much influence on the optimal velocity and efficiency of the air curtain, and the wall angle can be disregarded.

References

1. Van Kannel, T. (1888). U.S. Patent No. 387,571. Washington, DC: U.S. Patent and Trademark Office.
2. Felis, F., Pavageau, M., Elicer-Cortés, J. C., & Dassonville, T. (2010). Simultaneous measurements of temperature and velocity fluctuations in a double stream-twin jet air curtain for heat confinement in case of tunnel fire. International Communications in Heat and Mass Transfer, 37(9), 1191-1196.
3. Yoo, Y.-H., Shin, H.-J., Kim, H.-G., Lee, C.-W., & Qui, T. (2018). Experiment study on enhancing performance of the air curtain in subsea tunnels. Journal of Mining and Earth Sciences, 59(3), 44-49.
4. Juraeva, M., Lee, J.-H., & Song, D.-J. (2011). A computational analysis of the train-wind to identify the best position for the air-curtain installation. Journal of Wind Engineering and Industrial Aerodynamics, 99(5), 554-559.
5. Wang, Y., Jiang, Z., Chen, J., Chen, J., & Wang, M. (2019). Study of high-pressure air curtain and combined dedusting of gas water spray in multilevel ore pass based on CFD-DEM. Advanced Powder Technology, 30(9), 1789-1804.
6. Wang, J., Huo, Q., Zhang, T., Liu, F., Wang, S., Ma, Z., & Jiang, S. (2021). Performance evaluation for a coupled push--pull ventilation and air curtain system to restrict pollutant dispersion in a factory building. Journal of Building Engineering, 43, 103164.
7. Khayrullina, A., Blocken, B., Magalhaes de Almeida, M. O., van Hooff, T., & van Heijst, G. (2021). Impact of a wall downstream of an air curtain nozzle on air curtain separation efficiency. Building and Environment, 197, 107873.

Advanced Engineering Days

aed.mersin.edu.tr

Exergetic and thermoeconomic analysis of biogas motorized cogeneration systems used in wastewater treatment plant

Adnan Berber *[1], **Oguzhan Dağcı** [1]

[1] *University of Selcuk, Faculty of Technology, Department of Mechanical Engineering, Türkiye, aberber@selcuk.edu.tr, 208171001004@lisansustu.selcuk.edu.tr*

Cite this study: Berber A., & Dağcı O. (2024). Exergetic and thermoeconomic analysis of biogas motorized cogeneration systems used in wastewater treatment plant. Advanced Engineering Days, 9, 58-60

Keywords
Biogas
Cogeneration
Exergy
Exergoeconomic Analysis

Abstract

In this study, the exergetic analysis of a biogas powered gas engine cogeneration system is presented. The cogeneration system has been introduced and the system components have been examined in detail. Depending on the flow chart of the facility, the temperature, pressure and mass flow rates of each point were taken instantly via scada and on-site measurements. With these features, the enthalpies, entropies, energy and exergies of each point were calculated numerically with the help of the EES (Engineering Equation Solver) package program. According to the calculated values, the exergy efficiency of the cogeneration system was found to be 39%. It has been seen that the component with the highest exergy efficiency of the system was the hydraulic separator with 87% efficiency, the least efficient component was the sludge exchanger with 25.2% efficiency. For every 1 kWh of electricity produced by the gas engine, 0.484 m^3 of biogas with 64% methane content is consumed. Exergoeconomic analysis is based on the specific cost method (SPECO).

Introduction

The progress of society and the increase in people's living standards, there has been a significant increase in the demand for heat and electricity. This increase in demand has led to significant fossil fuel consumption. As a result, there has been an increase in greenhouse gas emissions and ecological damage [1]. To address these climate issues, countries around the world have implemented renewable energy substitution plans to encourage the use of renewable resources [2]. The use of cogeneration technologies is an extremely important aspect of the modern heat and energy production market. In each of the presented cases, the modification of the simplest system with the infrastructure that allows obtaining cogeneration conditions leads to the improvement of the cycle operating parameters [3].

In this study, Konya WWTP with a daily capacity of 200,000 m^3 was examined. The facility was introduced in general, and then the components in the system were examined. Exergetic and exergoeconomic analyzes were performed for real operating conditions. The analysis results were evaluated in terms of cost and efficiency and it was aimed to improve the overall performance of the system.

Material and Method

In this study, Konya Water and Sewerage Enterprise (KOSKİ) biogas fed gas engine cogeneration system is used to convert biogas into energy. The system consists of pumps, digesters, heat exchangers, gas motors, blowers, gas balloons, desulphurization unit, boilers and other related equipment (Figure 1).

Biogas produced by stabilizing the wastewater treatment plant sludge within the same facility is used as fuel in the system. The content of biogas produced in the WWTP is given in Table 1.

The biogas coming out of the digester comes to the desulfurization unit. Biogas with Sulphur removal via spraying system and stored in balloon which capacity is 4000 m^3. In line with its use, it is sent to gas engines through blowers and burned. As a result of this combustion, electricity is produced by gas engines, each with a capacity of 834 KW. Waste heat is also used thanks to flue gas exchangers. This system is called cogeneration

system, which means combined power. The heating system obtained from the cogeneration system and supported by boilers when necessary is used in the sludge heating process. In this process, called the mesophilic process, the sludge is tried to be kept stable at approximately 35 °C by means of heat exchangers [5]. The mesophilic process continues in this way.

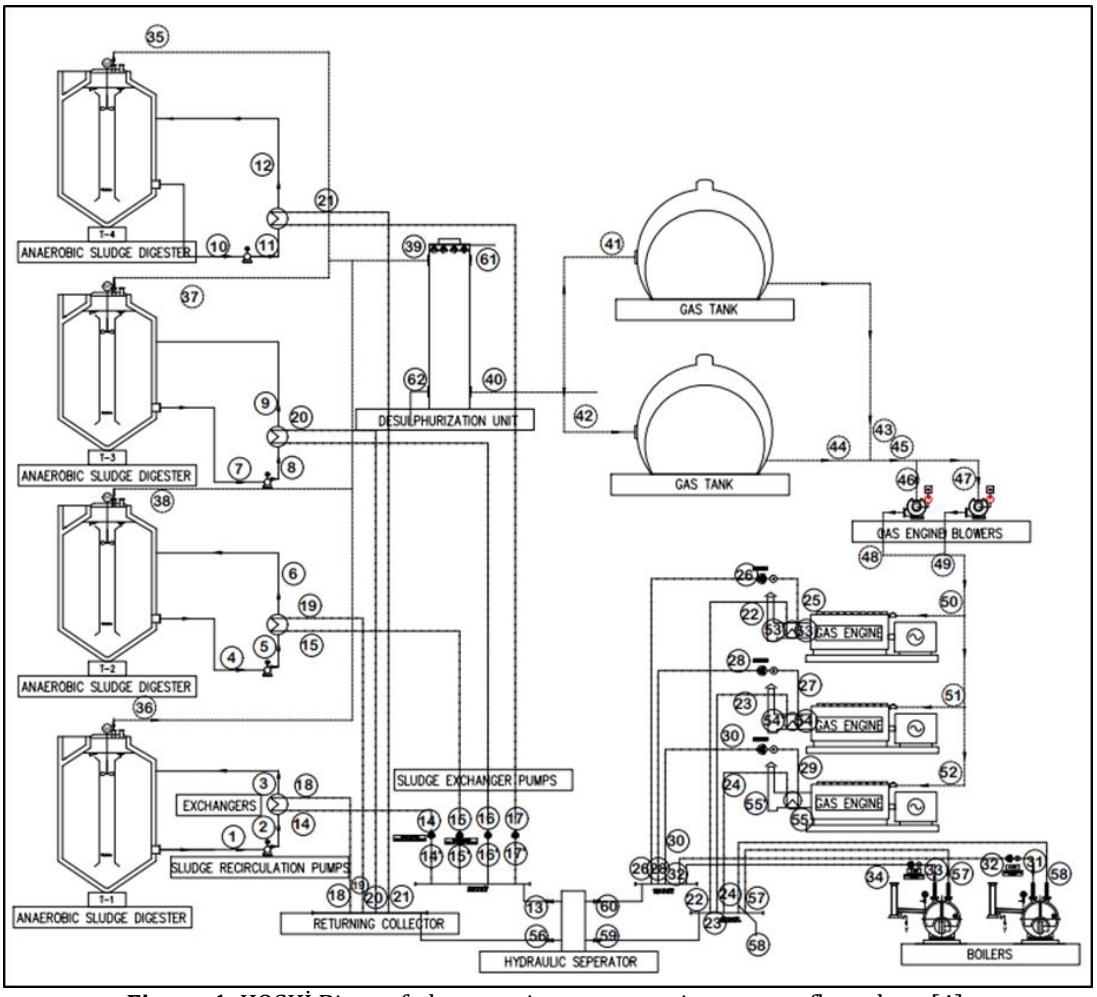


Figure 1. KOSKİ Biogas fed gas engine cogeneration system flow chart [4].

Table 1. The content of biogas produced in the wastewater treatment plant[a]

Contents	Volumetric value (%)
CH_4	64,0
CO_2	35,0
N_2	0,35
H_2	0,20
H_2S (2500-3000 ppm)	0,45
LHV (kJ/kg)	18.892
HHV (kJ/kg)	21.265

[a] These values were taken from experimental measurements of KOSKİ wastewater treatment plant.

Results

The exergy efficiency of the gas engine is approximately 39%. The 61% percentage of the total exergy, entering the gas engine cogeneration system, is destroyed. Irreversible combustion process, heat losses and friction are the main factors that cause exergy destruction in the gas engine. Sludge recirculation pump and hot water The exergy efficiencies of the feed pump were found to be 46% and 36.4%, respectively. The efficiency of the exhaust gas heat transfer exchanger pump was found to be 43.6%. The exergy efficiency of the balance vessel, which serves to

balance the pressure difference and temperature tolerance on the flow and return lines, was found to be 87%. Exergy destruction in the heat exchanger units in the system is caused by the high temperature difference between the two fluids mixed together.

The exergetic efficiency of the sludge exchanger was found to be 25.2%. The reason why the efficiency of the exchanger is lower than the efficiency of the balance tank is that the exergy destruction between two immiscible fluids is greater. The exergetic efficiencies of boiler and gas engine blowers were found to be 57% and 48%, respectively. Although the boiler is a 2-pass hot water boiler, higher efficiency is obtained from 3-pass boilers.

Discussion

If improvements are to be made in an established system, some improvements should be made to increase efficiency. Although the exergy loss in the gas engine and heat boiler is high, the exergoeconomic factor parameter is quite low compared to other equipment. An improvement to increase the performance of these equipment will not only increase the investment cost, but will also positively affect the system performance. Since the sludge exchanger, which has a relatively low efficiency value, has a high exergoeconomic factor, the improvement to be made here will not provide the cost-effective performance we want. As can be seen, exergoeconomic factors and exergy loss parameters give us ideas for making improvements on the system.

Conclusion

In this study, the exergy efficiency of a biogas-fed gas engine cogeneration system using biogas produced in Konya KOSKI wastewater treatment plant as fuel was calculated using real operating data. For every 1 kWh of electricity produced by a gas engine, 0.484 m of 64% methane content is produced biogas is consumed. The total exergy of the fuel and air entering the gas engine was found to be 2843.2 kW. 834 kW of the exergy is converted into electricity. While the component with the highest exergy efficiency of the system was the hydraulic separator with 87% efficiency, the component with the lowest efficiency was the sludge exchanger with 25.2% efficiency. The equipment with the highest Levelized Cost Value is the gas engine with a value of 6.2437 and the lowest one is hot water feeding pump which is 0.0180. When we examine it in terms of relative cost difference, it is seen that the lowest value is the hydraulic separator with 0.1527, and the highest value is the sludge exchanger with 3.595.

As a result, the designer's priority is to increase the efficiency of the system by evaluating the results of exergoeconomic performance measures. In cases where increasing the exergy efficiency of the system is more important than the cost, the components that have the most impact on the increase in system efficiency, that is, the components with the highest variable value, should be improved. In cases where cost is more important, emphasis should be placed on improving components that require minimum investment and minimizing exergy destruction per unit improvement cost.

References

1. M.A. Vaziri Rad, A. Kasaeian, X. Niu, K. Zhang, O. Mahian, (2023). Excess electricity problem in off-grid hybrid renewable energy systems: a comprehensive review from challenges to prevalent solutions, Renew. Energy 212 (2023) 538–560,
2. S.D. Agyeman, B. Lin, (2022). Nonrenewable and renewable energy substitution, and low–carbon energy transition: evidence from North African countries, Renew. Energy 194 (2022) 378–395,
3. Swiątkowski T. (2022) An innovative conversion of a district heating water-tube boiler for cogeneration of electricity and heat, Results in Engineering Volume 13, March 2022, 100350
4. KOSKI scada systems.
5. METCALF, Eddy. Inc. (2003). Wastewater engineering: treatment and reuse. New Y: Metcalf & Eddy, 2003.

Advanced Engineering Days

aed.mersin.edu.tr

Estimation of critical rotary velocity of stepped shaft using Dunkerley and FE methods

Ahmad Balande [1], Hasan Biglari [1], Hadi Teymouri [1]

[1] University of Tabriz, Department of Mechanical Engineering, Iran, ahmadbalande.13@gmail.com, hbiglari@tabrizu.ac.ir, hteymouri@tabrizu.ac.ir

Cite this study: Balande, A., Biglari, H., & Temouri, H. (2024). Estimation of critical rotary velocity of stepped shaft using Dunkerley and FE methods. Advanced Engineering Days, 9, 61-63

Keywords
Natural Frequencies
FEM
Euler-Bernoulli beam
Dunkerley and Rayleigh equation

Abstract

This investigation involves the determination of the critical rotary velocity of stepped shafts. Stepped shafts are employed to convert reciprocating motion (from pistons) into rotational motion in crankshafts. Additionally, they regulate valve timing and guarantee proper combustion in camshafts. In industrial apparatus, such as compressors and pumps Stepped shafts are essential for the reduction of vibrations and the preservation of alignment. The theory of Euler-Bernoulli beam with Dunkerley and Rayleigh equations was applied to a stepped shaft, and the degree of correspondence between the theory and the Finite Element Method (FEM), which was simulated in ABAQUS, was investigated by varying the various parameters. In this article, the innovation is the presentation of the acceptable error rate ranges for normal shaft formulations to be used in stepped shafts.

Introduction

Stepped shafts are essential components in a variety of industries because they can accommodate varying levels of tension and enable precision alignment and load distribution. Its applications include the automotive industry, industrial machinery, and robotics. The primary applications of stepped shafts are the crankshaft and camshaft, which are engine components that are classified as automotive industry. In contrast to the latter, which is intended to regulate valve timing and guarantee proper combustion, they are employed to convert reciprocating motion (originating from pistons) into rotational motion. Regarding engine components, transmission systems are another excellent illustration of how torque is transferred between ratios through the use of stepped shafts in both manual and automatic transmissions. It would be negligent to neglect to mention that the shafts in question are essential components of mechanized limbs and joint mechanisms. Their varying diameters enable precise movement, sustain varying loads, and facilitate a variety of bearing sizes.

Yue et al. [1] have contrasted the accuracy of the natural frequencies' results after modeling a conventional stepped shaft using various methodologies. Bose et al. [2] employed ANSYS software to conduct a three-dimensional FEM analysis to investigate the natural harmonics of a functionally graded rotor system. The flexural vibration of Timoshenko beams was modeled by Abolbashari et al. [3] as a sequence of interconnected distributed and aggregated elements. The distributed lumped modeling technique is employed to determine the natural frequencies of a homogeneous beam with a variety of boundary conditions.

This study presents the modal analysis of a stepped shaft using FEM in ABAQUS and the Dunkerley equation for the Euler-Bernoulli beam as a theoretical approach. This article distinctively represents the notion of exploiting the equations of a normal shaft for a stepped shaft by the Dunkerley equation. Specifically considering the cohesion of the discriminate parameters in stepped shafts using normal shaft formulas, theoretically and via FEM. Not to mention the significance of a low error rate between them in the ranges that they would present a good efficiency, so that can be used vice versa for the stepped one.

Material and Method

A stepped shaft is composed of two normal shafts with dimensions of L and d, which are constants of 35 cm and 3 cm, respectively, and the other one with dimensions of l and D. Xi is the parameter that it will be swept, which is the distance from the start of the shaft to the middle of the shaft with a wider diameter (D) that is

illustrated in Figure 1. A steel material with a density (ρ) of 7800, a Young modulus (E) of 210 GPa, and a Poisson's ratio (ν) of 0.28 has been utilized in this paper [4]:

$$\omega_g = \left(\frac{\pi}{L}\right)^2 \sqrt{\frac{EI}{m}} \tag{1}$$

$$\frac{1}{\omega^2} = \frac{1}{\omega_g^2} + \frac{1}{\omega_1^2} + \frac{1}{\omega_2^2} + \frac{1}{\omega_3^2} + \cdots = m_1\delta_{11} + m_2\delta_{22} + m_3\delta_{33} + \cdots \;\&\; \delta_{ij} = \frac{b_j x_i}{6EIL}(L^2 - b_j^2 - x_i^2) \tag{2}$$

ω_g represents the natural frequency of a Euler-Bernoulli beam (L*d shaft) calculated from formula (1) also regarded as Rayleigh equation. Formula (2) is the Dunkerley equation that ω represents natural frequency of stepped shaft. m is mass per length of the shafts with I being the moment of inertia of L length shaft. δ_{ij} denotes the deflection of shaft in point i with the applied unit load at point j. Figure 1 shows the schematic of stepped shaft.

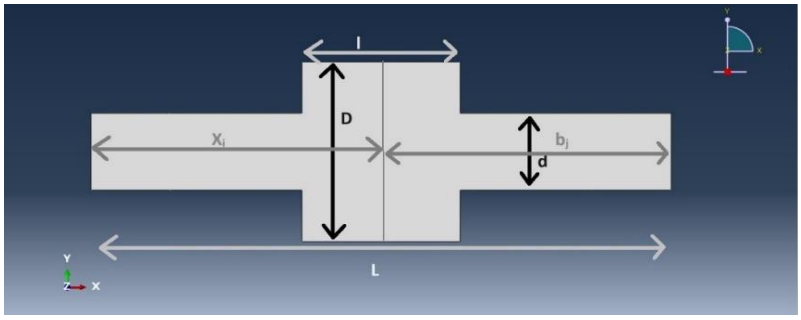


Figure 1. Schematic of Stepped Shaft

FEM has been used in ABAQUS for simulation. 3 boundary conditions were applied with the first one being that the linear motion in x axis direction was locked. 2nd and 3rd conditions are depicted in the figures 2 & 3.

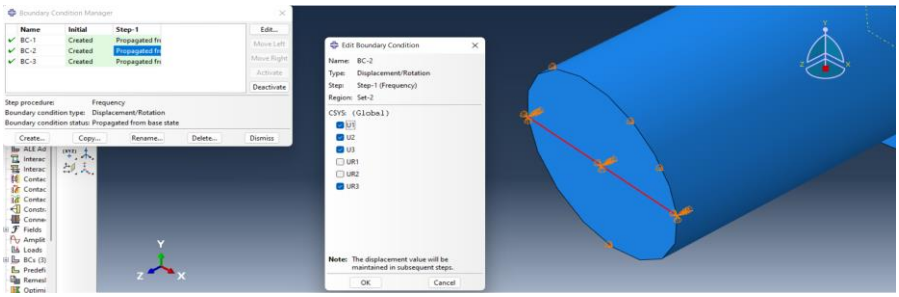


Figure 2. Schematic of 2nd boundary condition

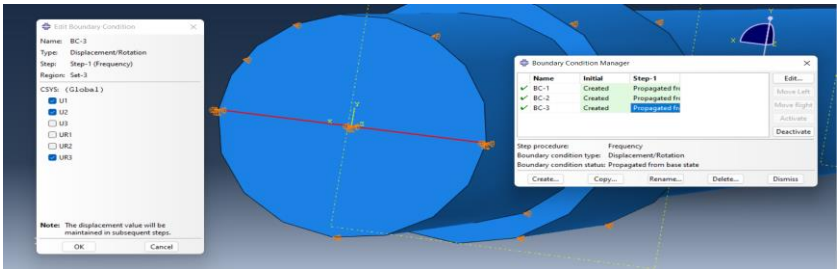


Figure 3. Schematic of 3rd boundary condition

It is also worth noting that the Tet element shape was used to mesh the entire part.

Results

In order to validate formula (1) for the normal shaft and ensure the reliability of the Finite Element Method (FEM) simulation, a manual evaluation of the formula was compared to the real-time simulation results. This comparison was conducted to ensure an error of less than 5%. Table 1 presents a comparative analysis between the FEM and theoretical results for different D/d ratios. Similarly, Table 2 and Table 3 show comparative analyses between the FEM and theoretical results for different x_i/L ratios and l/L ratios, respectively.

Table 1. A Comparison between FEM and theory results for different D/d ratio with these assumptions: $\frac{x_i}{l} = 0.5 \; and \frac{l}{L} = 0.1$

	$\frac{D}{d}$	$\left(\frac{\omega}{\omega_g}\right)_{FEM}$	$\left(\frac{\omega}{\omega_g}\right)_{th}$
1	1.1	1.01	0.98
2	1.2	1.00	0.96
3	1.33	0.99	0.926

Table 2. A Comparison between FEM and theory results for different x_i/L ratio with these assumptions: $\frac{D}{d} = 1.2 \; and \frac{l}{L} = 0.1$

	$\frac{x_i}{L}$	$\left(\frac{\omega}{\omega_g}\right)_{FEM}$	$\left(\frac{\omega}{\omega_g}\right)_{th}$
1	0.1	1.00	0.99
2	0.2	1.02	0.98
3	0.3	1.00	0.97
4	0.5	1.00	0.95
5	0.57	1.00	0.96

Table 3. A Comparison between FEM and theory results for different l/L ratio with these assumptions: $\frac{D}{d} = 1.2 \; and \frac{x_i}{L} = 0.5$

	$\frac{l}{L}$	$\left(\frac{\omega}{\omega_g}\right)_{FEM}$	$\left(\frac{\omega}{\omega_g}\right)_{th}$
1	0.1	1.01	0.96
2	0.25	1.04	0.90
3	0.5	1.12	0.82
4	0.75	1.18	0.76

Conclusion

The current study examined the effects of various parameters on the natural frequencies of a stepped shaft by implementing the theories of the Euler-Bernoulli beam and the Dunkerley equation. Regarding equation (2), in order to use it for a stepped shaft, the condition of l/L<0.1 must be satisfied. This is the primary reason why, in Table 3, as the indicated ratio increases beyond the threshold, the error rate between the Finite Element Method (FEM) and the theoretical results increases drastically. The source of this error stems from the increase in the value of l, which consequently leads to an increase in the value of D, resulting in a strengthening of the stiffness (EI). Excluding the results presented in Table 3, the maximum error rate across the remaining tables is 5.5%. In conclusion, this paper provides the acceptable ranges of error rates for the normal shaft formulas to be utilized in the analysis of stepped shafts.

References

1. Yue, L., Guojun, Y., Suyuan, Y. (2013). A comparison of the finite element modeling methods for the natural frequencies' computation of stepped shaft
2. Bose, A., Sathujoda, P. (2019). Natural frequency analysis of a functionally graded rotor system using three-dimensional finite element method
3. Abolbashari, M., Farshidianfar, A., Soheili, S. (2009). Flexural vibration of propeller shafts using distributed lumped modeling technique
4. Mechanical Engineering Design book, Shigley. (Eleventh Edition)

Advanced Engineering Days

aed.mersin.edu.tr

LCCP and TEWI evaluation for various refrigerants used in refrigerated display cabinets

Adnan Berber *[1], **Melis Öder** [1]

[1] *University of Selcuk, Faculty of Technology, Department of Mechanical Engineering, Konya, Türkiye, aberber@selcuk.edu.tr, melisoder19@gmail.com*

Cite this study: Berber A. & Öder M. (2024). LCCP and TEWI evaluation for various refrigerants used in refrigerated display cabinets. Advanced Engineering Days, 9, 64-67

Keywords
RDC
LCCP
TEWI
Refrigeration

Abstract

Refrigerated display cabinets (RDCs) play an important role in the cold chain and provide storage at specific temperature ranges for chilled and frozen foods. Due to the high global warming potential value of the refrigerants used in RDCS, they have a high impact on global warming. Therefore, it is important to use environmentally friendly refrigerants in RDCs. In this study, Life Cycle Climate Performance (LCCP) and Total Equivalent Warming Impact (TEWI) analyses were conducted to assess the environmental impacts of R404A, R410A, R134A, R1234yf and R290 refrigerants used in RDCs in supermarket environments. According to the LCCP analysis, R404A, R410A, R134A and R1234yf refrigerants emit %40,61, %34,03, %27,63 and %13,3 more carbon emissions at RDCs, respectively, compared to R290 refrigerant. TEWI analysis shows that R404A emit %45,96, R410A emit %39,10, R134A emit %32,22 and R1234yf emit %16 more carbon emissions, respectively, than R290 refrigerant in RDCs.

Introduction

Refrigerated display cabinets (RDC's) are crucial for preserving and showcasing food products but consume significant energy, contributing to 60% of supermarket energy use [1]. They primarily use hydrofluorocarbon (HFC) refrigerants with high Global Warming Potential (GWP), contributing to 15% of total energy consumption and 1% of global CO_2 emissions [2]. Despite regulations promoting low-GWP alternatives like hydrofluoroolefins (HFOs) and hydrocarbons (HCs), concerns over flammability limit HC adoption [3]. Methods like Total Equivalent Warming Impact (TEWI) and Life Cycle Climate Performance (LCCP) assess RDC's environmental impacts, focusing on direct GHG emissions and energy use efficiency [4].

Within the scope of this study, it is aimed to contribute to the literature by performing LCCP and TEWI analysis of R404A, R410A, R134A, R1234yf and R290 refrigerants.

Material and Method

RDCs are known to work on the principle of mechanical vapor compression refrigeration cycle. The mechanical vapor compression refrigeration cycle is given in figure 1.

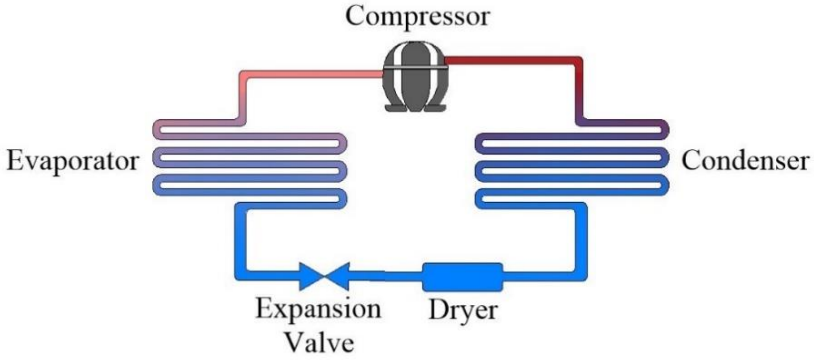


Figure 1. Mechanical vapor compression refrigeration cycle

In a mechanical vapor compression refrigeration cycle, the gas phase refrigerant at high pressure and temperature in the compressor enters the condenser where a change of state takes place. The refrigerant at low temperature and pressure, which passes into the liquid phase, enters the evaporator by reducing its pressure to the evaporator inlet pressure level at the expansion valve. The refrigerant coming to the evaporator passes from the liquid phase to the gas phase by drawing heat from the environment. At this time, as a result of the event occurring in the evaporator, cooling occurs and cold air is sent over the products. The refrigerant in the gas phase comes to the compressor and the cycle is thus completed.

GWP values of refrigerants are extremely important in terms of global warming. GWP values of the refrigerants used in the study are given in Table 1.

Table 1. GWP value table for refrigerants

Refrigerants	GWP
R404A	3922
R410A	2088
R134A	1430
R1234yf	4
R290	3

LCCP analysis is found with the help of the following equation [5].

LCCP = Direct Emissions + Indirect Emissions (1)

Direct Emissions take into account refrigerant leakage over the lifetime of the chiller and are calculated by [5].

Direct Emissions = C × (L × ALR × EOL) × (GWP + Adp. GWP) (2)

Indirect Emissions are expressed as in the equation below [5].

Indirect Emissions = $L \times AEC \times EM + \sum(m \times MM) + \sum(MR \times RM) + C \times (1 + L \times ALR) \times RFM + C \times (1 - EOL) \times RFD$ (3)

TEWI analysis is calculated with the following formula [6]

TEWI = Direct Emissions + Indirect Emissions (4)

Direct emissions can be calculated with the help of the following equation [6].

Direct Emissions = C x (L x ALR + EOL) x GWP (5)

In order to calculate indirect emissions, the following equation is used [6].

Indirect Emissions = AEC x EM x L (6)

Results

LCCP analysis results are given in Figure 2. According to the LCCP analysis results, the LCCP value of R290, a natural and environmentally friendly refrigerant used in RDCs, is 42008,02 $kgCO_{2e}$, while the LCCP values of the other refrigerants are 70729,62 $kgCO_{2e}$, R410A refrigerant 63676,8 $kgCO_{2e}$, R134A refrigerant 58047,47 $kgCO_{2e}$, R1234yf refrigerant 48451,25 $kgCO_{2e}$. Considering these results, it is determined that R290 refrigerant emits less carbon emissions than other refrigerants.

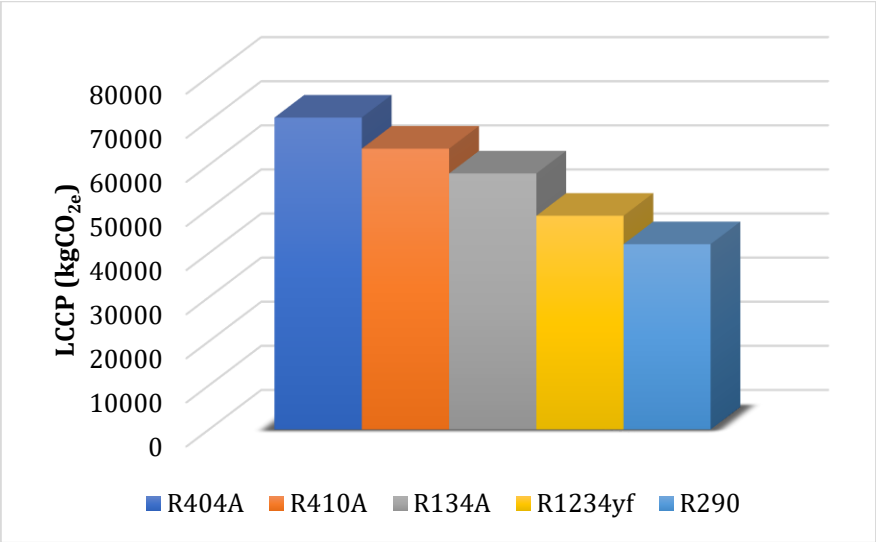


Figure 2. LCCP analysis results

TEWI analysis results are given in Figure 3. According to the analysis results, the TEWI value of R290 refrigerant, a natural and environmentally friendly refrigerant used in RDCs, is 33727,71 $kgCO_{2e}$, TEWI values of other refrigerants are 62416,26 $kgCO_{2e}$ for R404A refrigerant, 55378,32 $kgCO_{2e}$ for R410A refrigerant, 49758,50 $kgCO_{2e}$ for R134A refrigerant, 40153,04 $kgCO_{2e}$ for R1234yf refrigerant. According to these results, it is determined that the TEWI value of R290 refrigerant is lower. This is because the ODP and GWP values of R290 refrigerant are lower than other refrigerants.

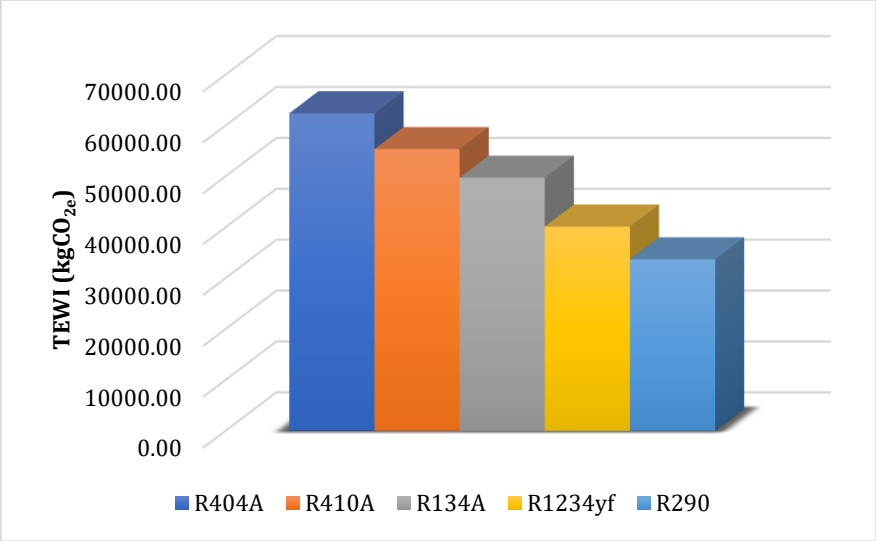


Table 3. TEWI analysis results

Conclusion

Within the scope of this study, LCCP and TEWI analyses were carried out to examine the thermodynamic and environmental impacts of R410A and R290 refrigerants used in RDCs. As a result of these analyzes, the following results were obtained.

- The LCCP analysis for assessing environmental impacts takes into account total greenhouse gas emissions from the production of refrigerants to their disposal. R290 refrigerant has a LCCP value of %40,61 less than R404A, %34,03 less than R410A, %27,63 less than R134A, %13,3 less than R1234yf and R290 is the least environmentally harmful refrigerant among them.
- TEWI analysis evaluates the global warming potential of fluids by considering direct and indirect emissions. TEWI values of R290 refrigerant were %45,96 lower than R404A, %39,10 lower than R410A, %32,22 lower than R134A and %16 lower than R1234yf.

References

1. Rivers, N. Management of energy usage in a supermarket refrigeration systems. in The Institute of Refrigeration. 2005.
2. Tassou, S. A., Ge, Y., Hadawey, A., & Marriott, D. (2011). Energy consumption and conservation in food retailing. Applied Thermal Engineering, 31(2-3), 147-156.
3. James, S. and C. James, The food cold-chain and climate change. Food Research International, 2010. 43(7): p. 1944-1956.
4. Li, G., Comprehensive investigation of transport refrigeration life cycle climate performance. Sustainable Energy Technologies and Assessments, 2017. 21, 33-49.
5. Lee, H., et al., LCCP evaluation on various vapor compression cycle options and low GWP refrigerants. International Journal of Refrigeration, 2016. 70: p. 128-137.
6. Andrade, A., Zapata-Mina, J., & Restrepo, A. (2024). Exergy and environmental assessment of R-290 as a substitute of R-410A of room air conditioner variable type based on LCCP and TEWI approaches. *Results in Engineering*, *21*, 101806.

Advanced Engineering Days

aed.mersin.edu.tr

Effects of burial depth in the behavior of buried pipelines subjected to traffic load

Arsalan Amanollahi-Asl [*1], **Hasan Biglari** [2]

[1]*University of Tabriz, Department of Mechanical Engineering, Iran, arsalan.amanollahi@gmail.com, hbiglari@tabrizu.ac.ir*

Cite this study: Amanollahi-Asl, A., & Biglari, H. (2024). Effects of burial depth in the behavior of buried pipelines subjected to traffic load. Advanced Engineering Days, 9, 68-71

Keywords
Buried pipe
Burial depth
Traffic load
Soil settlement
FEM

Abstract

The behavior of buried pipelines under traffic load is a crucial aspect to consider in ensuring the safe and efficient operation of pipeline systems. One significant factor that influences the response of buried pipelines is the burial depth. This study investigates the effects of burial depth on the behavior of buried steel pipelines subjected to traffic load. The burial depth of pipelines plays a critical role in determining their structural integrity and response to external loads. A numerical model was developed using Abaqus for this study. The pipeline is treated as a deformable, flexible shell element with uniform material properties. An elasto-plastic analysis based on the Mohr-Coulomb theory was performed to account for the mechanical properties of the soil. To validate the findings presented in this article, a comparison was made between the obtained results and those of reference work. The results indicate that different burial depths significantly influence the behavior of the pipelines, including the magnitude and distribution of stress and deflection of pipeline, but the amount of soil settlement remains approximately constant.

Introduction

Buried pipes experience loads from the surrounding soil, whether they are placed in tunnels, or buried under highways, railways, or airports. Live loads, which are commonly referred to as surface loads, pertain to static or quasi-static forces exerted on the surface of the ground as a result of ground transportation traffic. The distribution of stresses in a semi-infinite elastic medium due to a point load applied at its surface was initially calculated by the French mathematician Boussinesq. However, this solution assumes an elastic, homogeneous, and isotropic medium, which does not accurately represent the soil characteristics [1].

Lee [2] has conducted a comprehensive investigation using finite element analysis (FEA) methods to examine various aspects related to the failure of flexible buried steel pipes subjected to earthquake loads. In the study by Khademi Zahedi et al. [3], the effectiveness of polyethylene repair patches for defective pipelines was investigated. Finite element analysis was conducted to calculate the maximum stress values, providing insights into the patches' performance. Alzabeebee et al. [4] studied the response of buried pipes to the UK standard traffic load. The soil pressure estimation method used in the UK for calculating the effects of traffic loads on buried pipes relies on a simplified equation derived from the Boussinesq solution.

Understanding the effects of burial depth on the behavior of buried pipelines subjected to traffic load is crucial for ensuring the long-term reliability and sustainability of underground pipeline systems.

Material and Method

The operational range of water pressure in pipelines falls within the range of approximately 276 kPa (40 psi) to 414 kPa (60 psi). Hence, to investigate the critical condition of buried pipelines, the maximum water pressure of 414 kPa will be utilized in this study [2].

To examine the failure characteristics of buried pipelines resulting from traffic load, a specific study was conducted on a relatively large-diameter steel pipeline used for water supply. The analysis performed in this study focused on the elastic, perfectly plastic, and isotropic behavior of the pipeline, as outlined in “Table 1” shown below [2,5,6]:

Table 1. Material properties of pipeline

Terms	Density (kg/m^3)	Young's modulus (MPa)	Poisson's ratio	Yield strength (MPa)	Tensile strength (MPa)
Value	7850	210.7×10^3	0.3	490	690 to 840

To conduct the study on steel pipelines used as water supply lifelines, the size of the pipeline was determined based on the specifications outlined in BS EN 10224:2002. The largest diameter steel pipeline was selected, with a wall thickness of 20 mm and an outer diameter of 1524 mm [7]. For the finite element analysis, a pipeline length of 100 meters was chosen [2].

To investigate the interaction between soil and buried structures under traffic load, the study focused on cohesive saturated soil. The mechanical properties of the soil were analyzed using the elasto-plastic approach based on the Mohr-Coulomb theory. "Table 2" provides the characteristics and properties of the soil [2]:

Table 2. Material properties of soil

Type of soil	Density (kg/m^3)	Young's modulus (MPa)	Poisson's ratio	Cohesive strength (C - kPa)	Friction angle (ϕ - deg)	Dilation angle (ψ - deg)
Cohesive saturated soil	2000	48	0.45	252	29	2

The pressure on the pipe from a surface traffic live load depends on factors such as vehicle weight, tire pressure and size, vehicle speed, and some other factors. Typically, the H20 highway loading is used for design purposes. The wheel loadings for H20 trucks are determined according to the standards set by the American Association of State Highway and Transportation Officials (AASHTO). Based on AASHTO standards, the wheel loading for H20 trucks is calculated based on "Figure1". The traffic load magnitude resulting from H20 truck loading was chosen to be 544,780 Pa [3].

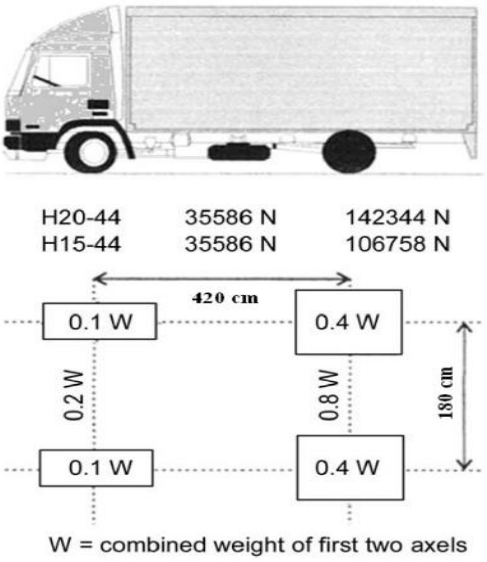


Figure 1. Traffic loading, H20 truck

C3D20R elements were chosen to simulate the behavior of soil. For modeling the pipe, S8R element, a three-dimensional reduced shell continuum element with eight nodes, was selected. The selection of second-order elements over first-order elements is based on their superior accuracy. The stress and strain operator of first-order elements only accounts for constant volumetric stress and strain throughout the entire element. In contrast, second-order elements offer a more accurate solution by incorporating stress and strain operators between two edge stress and strain operators [2].

Results

To validate the findings of this paper, a comparison is made with the findings of Lee [2] which focused on a similar topic. The reference model used in the comparison involves a soil-pipe block subjected to live load pressure, internal pipe pressure, and soil weight load (dead load). The results, as shown in "Figure 2", demonstrate the excellent accuracy of the proposed model. This comparison reinforces the reliability of the findings presented in this paper.

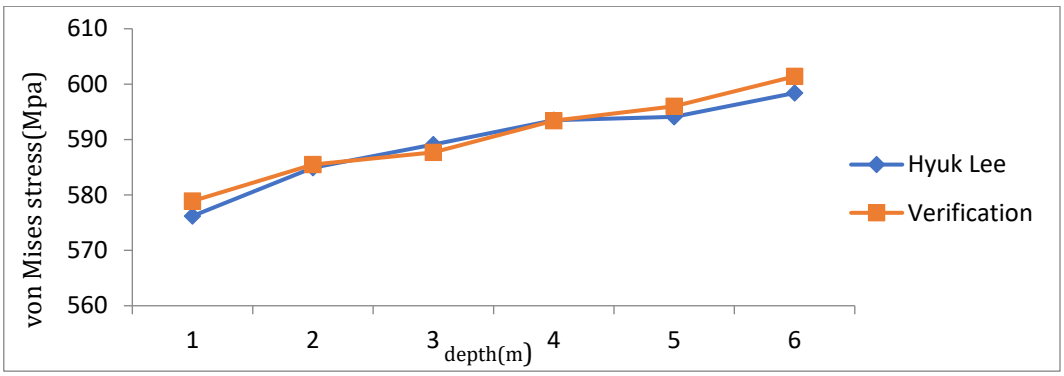


Figure 2. Comparative analysis of maximum von Mises stress with Hyuk Lee's research [1]

As illustrated in "Figure 3", there is a direct correlation between the buried pipe depth and the magnitude of stress, indicating that as the burial depth of the pipe increases, the amount of stress also increases. Furthermore, as the depth of the buried pipeline increases, "Figure 4" illustrates a decrease in pipe displacement. "Figure 5" demonstrates that there is no significant change in the amount of soil settlement with varying burial depths of the pipe. In other words, the soil settlement remains independent of the depth at which the pipe is buried.

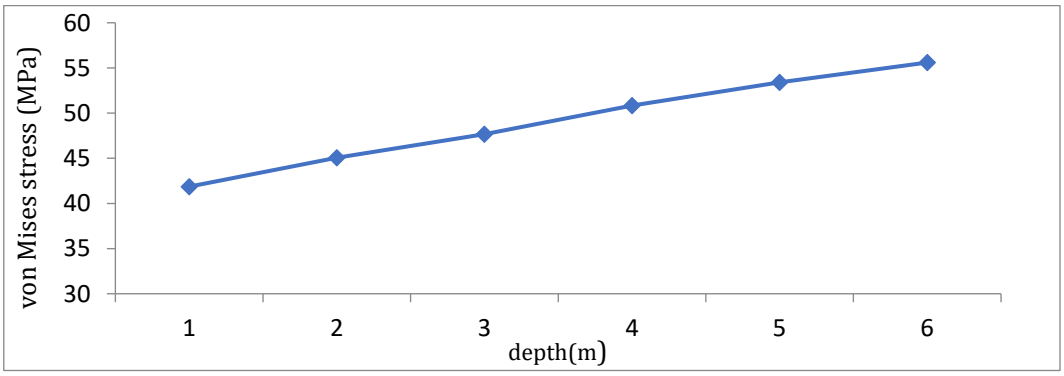


Figure 3. Maximum stress of buried pipeline

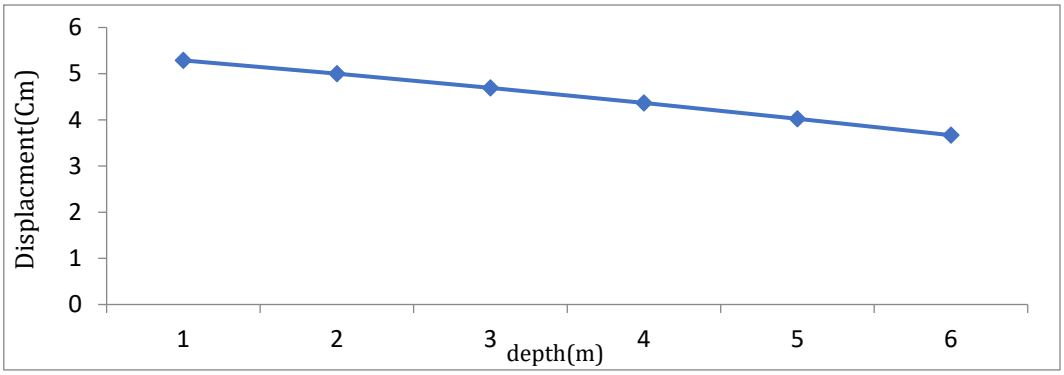


Figure 4. Maximum settlement of buried pipeline

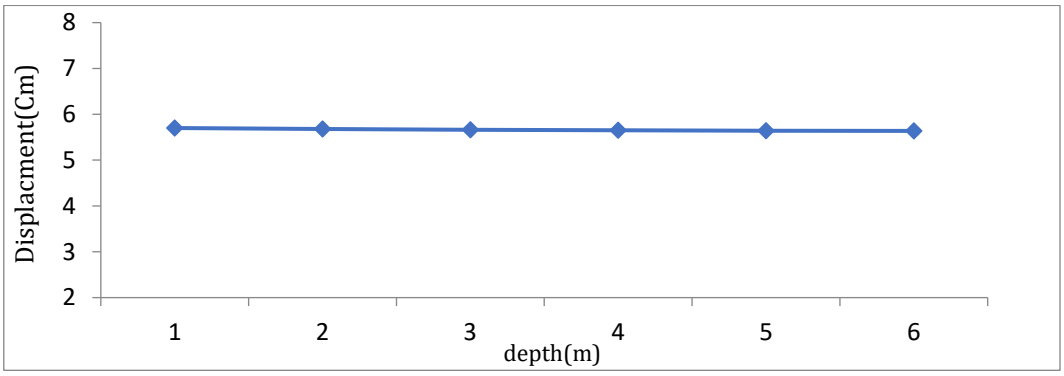


Figure 5. Maximum settlement of soil

Conclusion

The study revealed that burial depth plays a crucial role in determining the structural response and integrity of buried pipelines. The analysis of stress distribution, demonstrated that different burial depths significantly influence the behavior of the pipelines. Additionally, it was found that the choice of burial depth affects the magnitude and distribution of stress and displacement in the pipelines. However, the amount of soil settlement was found to be independent of the burial depth. These findings emphasize the importance of considering burial depth as a key design parameter for optimizing the performance and durability of buried pipelines under traffic load. The outcomes of this study can contribute to more accurate design guidelines, improved maintenance strategies, and enhanced reliability of underground pipeline systems. Further research in this field could focus on investigating additional factors that may interact with burial depth to further enhance the understanding of buried pipeline behavior.

References

1. Mosler, A. P. (1990). Buried pipe design, New York, NY (USA) McGraw Hill Book Co.
2. Lee, H. (2010). Finite element analysis of a buried pipeline. Master's thesis, The University of Manchester, Manchester, UK, Retrieved from https://www.escholar.manchester.ac.uk/jrul/item/?pid=uk-ac-man-scw:97322
3. Khademi-Zahedi, R., & Shishesaz, M. (2019). Application of a finite element method to stress distribution in buried patch repaired polyethylene gas pipes. *Underground Space*, *4*(1), 48-58.
4. Alzabeebee, S., Chapman, D., Jefferson, I., & Faramarzi, A. (2017). The response of buried pipes to UK standard traffic loading. *Proceedings of the institution of civil engineers-geotechnical engineering*, *170*(1), 38-50.
5. BSI. (2002b) Seamless steel tubes for pressure purpose - Technical delievery conditions - Part 2: Non-alloy and alloy tubes with specified elevated temperature properties. IN CEN (Ed. *BS EN 10216-2:2002.* London, BSI.
6. Liu, P. F., Zheng, J. Y., Zhang, B. J., & Shi, P. (2010). Failure analysis of natural gas buried X65 steel pipeline under deflection load using finite element method. *Materials & Design*, *31*(3), 1384-1391.
7. BSI. (2002a) Nonalloy steel tubes and fittings for the conveyance of water and other aqueous liquid - Technical delivery conditions. IN CEN (Ed. *BS 10224:2002).* London, BSI.

Advanced Engineering Days

aed.mersin.edu.tr

Simulation and analysis of fracture toughness and crack propagation in a composite sheet based on multi-scale modeling method

Ghadir Ahmadi Jeyed [*1], Hasan Biglari [1]

[1]*University of Tabriz, Department of Mechanical Engineering, Iran, Ghadir.ahmadi@tabrizu.ac.ir, hbiglari@tabrizu.ac.ir*

Cite this study: Jeyed, G. A., & Biglari, H. (2024). Simulation and analysis of fracture toughness and crack propagation in a composite sheet based on multi-scale modeling method. Advanced Engineering Days, 9, 72-76

Keywords
Composite
Multiscale
RVE mode
Fracture toughness
Crack propagation
XFEM

Abstract

The representative volume element (RVE) is a potential method for modeling the fracture behavior of nanocomposites. To compute the effective material properties of heterogeneous materials, homogenization procedures are applied to a smaller, statistically representative sample of materials called RVE. RVE is essential for predicting the macroscopic response of composite materials because it captures the diversity and complexity of the microstructure. It also makes it possible to employ microscopic qualities to generate valuable macroscopic properties for composite material design and manufacturing. This study presents the extended finite element method (XFEM) in nanocomposites for fracture behavior modeling and crack growth analysis. It also introduces the idea of composite and the multiscale approach of RVE representative element volume.

Introduction

To analyze crack propagation in the Abaqus software, three methods are available: VCCT, Cohesive Element, and XFEM. The VCCT method requires knowledge of the crack growth plane and the presence of an initial crack in the structure. When using the XFEM method to investigate crack growth, the potential area where the crack may propagate needs to be determined. On the other hand, the adhesive element method analyzes crack growth by incorporating a layer of adhesive element or considering adhesive properties in all areas where crack formation and progression are possible. Each of these methods has been developed based on its own operational logic and underlying idea, resulting in specific applications for each [1]. The concept of the Representative Volume Element (RVE) involves selecting a representative section of a composite material that captures its essential microstructural features. This RVE serves as a computational domain for analyzing the mechanical response of the composite. By applying appropriate boundary conditions and constitutive models, the RVE analysis enables the investigation of composite behavior under various loading conditions. The Extended Finite Element Method (XFEM) is a numerical technique that extends the capabilities of traditional finite element analysis to model cracks, defects, and other material discontinuities. XFEM provides a powerful tool for accurately capturing the complex behavior of composite materials, including crack initiation, propagation, and interactions with the microstructure. The enrichment functions used in XFEM allow for the representation of crack behavior without the need for explicit meshing around the crack, resulting in improved computational efficiency and accuracy [2-4].

Incorporating multiscale and micromechanical models within the RVE and XFEM framework further enhances the predictive capabilities of composite material simulations. Multiscale modeling techniques bridge the gap between microstructural features, such as fiber-matrix interactions, and macroscopic behaviors, enabling the investigation of the influence of microstructural parameters on the overall mechanical properties of the composite. Micromechanical models, such as the Mori-Tanaka method or the Voigt-Reuss-Hill approach, provide a means to estimate the effective properties of the composite based on the properties of its constituents and their spatial distribution [5-6].

The purpose of this article is to study fracture toughness and crack growth using the finite element method at both macro and micro scales. The Abaqus software plugin is employed to model the micro viewpoint, utilizing the Representative Volume Element (RVE) model. Additionally, the mechanical properties of the fiber, matrix, and interface are taken into consideration.

Calculation of composite stiffness and Stress intensity factor (SIF)

One of the most well-known micromechanical models for calculating one-way composite stiffness utilizing the aspect ratio effect is the Halpin Tsai model, which covers all kinds of reinforcement geometries[7].

$$\frac{E}{E_m} = \frac{1 + \xi\eta\varphi_f}{1 - \eta\varphi_f} \tag{1}$$

$$\eta = \frac{\frac{E_f}{E_m} - 1}{\frac{E_f}{E_m} + \xi} \tag{2}$$

When unidirectional fillers are parallel to the loading direction:

$$\xi = \frac{2W}{t} \tag{3}$$

When one-way fillers are perpendicular to the loading direction, ξ=2 .W is the length or width of the filler plate and t is the thickness of the filler plate. ξ is the shape factor, which depends on the filler geometry and loading direction. Note that (w/t) is the aspect ratio of the filler plate.

The stress intensity factor before the crack tip was calculated for a modified version of the sample using the following equations[5].

$$K_I = \frac{P_c\sqrt{\pi a}}{wt} f_1\left(\frac{a}{w}\right) \tag{4}$$

$$K_{II} = \frac{P_c\sqrt{\pi a}}{wt} f_2\left(\frac{a}{w}\right) \tag{5}$$

where P_c is at the critical load at failure, α is the loading angle, w is the specimen length, t is the specimen thickness, and a is the crack length. In turn, K_I and K_{II} are obtained using the geometric coefficients $f_1\left(\frac{a}{w}\right)$ and $f_2(\frac{a}{w})$, respectively, which are obtained through finite element analysis of the Arcan sample. Also, the rate of energy release for isotropic materials with edge cracks can be calculated from the following relations[5]:

$$G_I = \frac{{K_I}^2}{E},\ G_{II} = \frac{{K_{II}}^2}{E} \quad \text{(Plane stress)} \tag{6}$$

$$G_I = \frac{(1-\nu^2){K_I}^2}{E},\ G_{II} = \frac{(1-\nu^2){K_{II}}^2}{E} \quad \text{(Plane strain)} \tag{7}$$

Simulation of stress intensity factor and crack propagation based on XFEM

The material parameters of the glass fiber, epoxy matrix, and fiber/matrix interface, as well as the composite glass/epoxy, are shown in tables 1 and 2, respectively[2].

Table 1. Material parameters of the glass fiber, epoxy matrix and fiber/matrix interface

E_f (Gpa)	E_m (Gpa)	E_i (Gpa)	ν_f	ν_m	ν_i	ρ_f (g/cm^3)	ρ_m (g/cm^3)	ρ_i (g/cm^3)	$G_{Ic.m}$ (N/mm)	$G_{Ic,i}$ (N/mm)	σ_m (Mpa)	σ_i (Mpa)
73.1	3.45	30	0.22	0.35	0.20	2.4	1.06	1.0	1.2	0.8	100	80

Table 2. Elastic parameters of GFRP laminate single layer [2]

E_{11} (Gpa)	$E_{22} = E_{33}$ (Gpa)	$G_{12}=G_{13}$ (Gpa)	G_{23} (Gpa)	$\nu_{12}=\nu_{13}$	ν_{23}
24.5	6.694	2.73	2.96	0.23	0.28

Crack propagation in homogeneous and isotropic materials is described and simulated from a macromechanical point of view in order to compute fracture toughness. The following are the steps for simulating crack propagation and fracture toughness in composite materials with Abaqus software with macro and micro models:

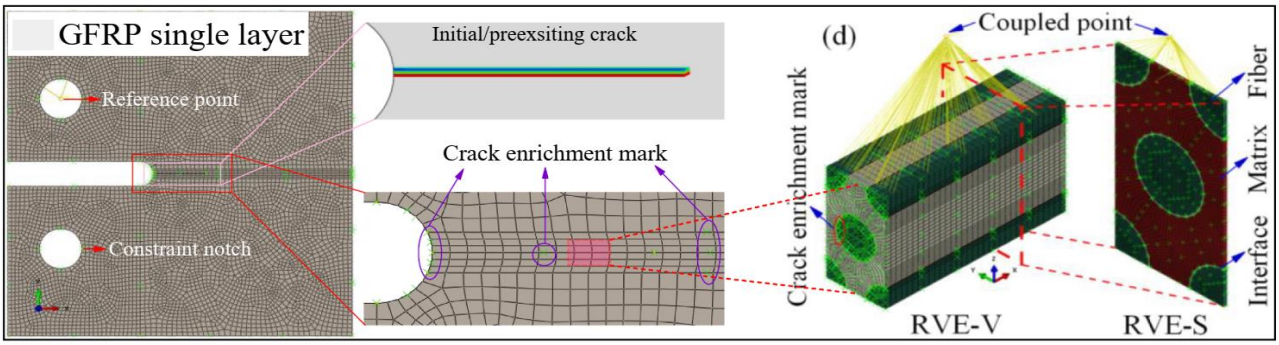


Figure 1. Schematics of the boundary, loading on the models and finite element mesh using the XFEM based on RVE model [2]

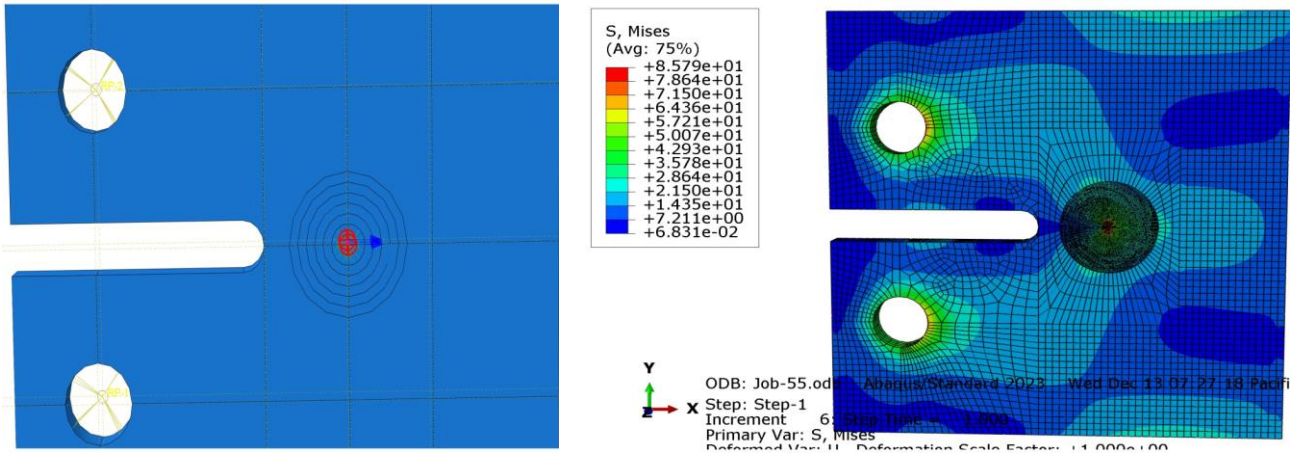


Figure 2. Modeling the stress intensity factor using J-integral method of carbon/epoxy composite with K_I =14.59

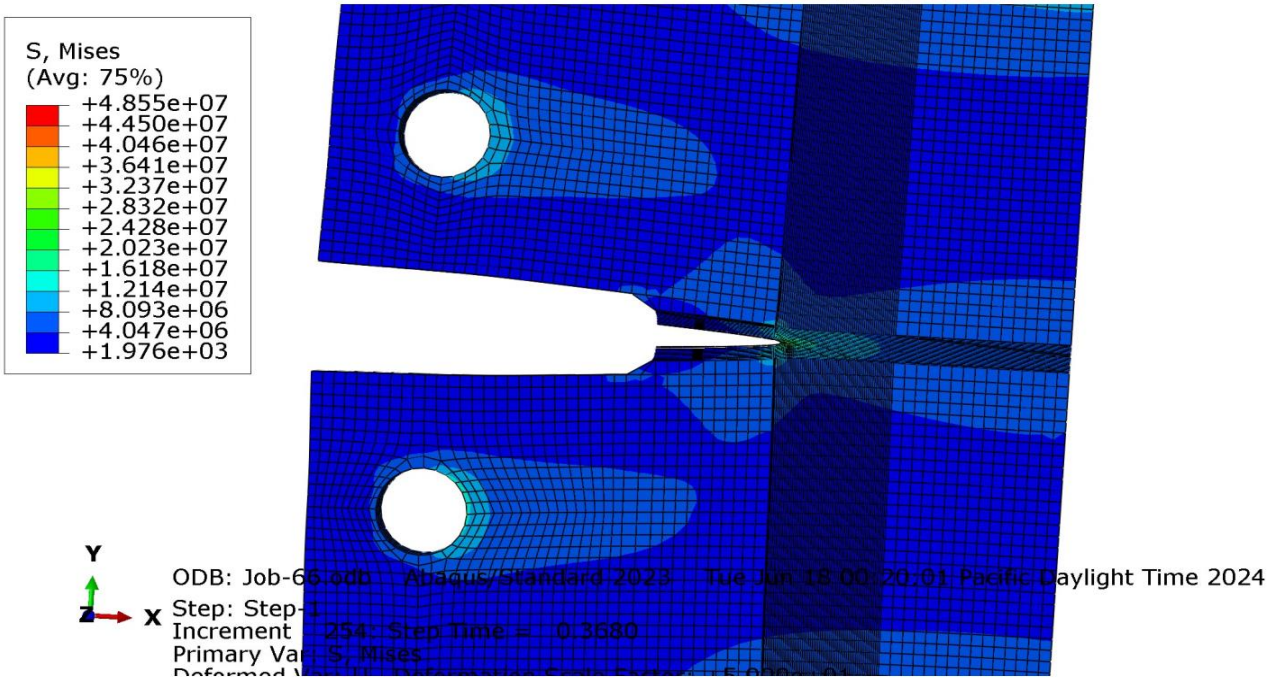


Figure 3. Crack propagation simulation based on XFEM model

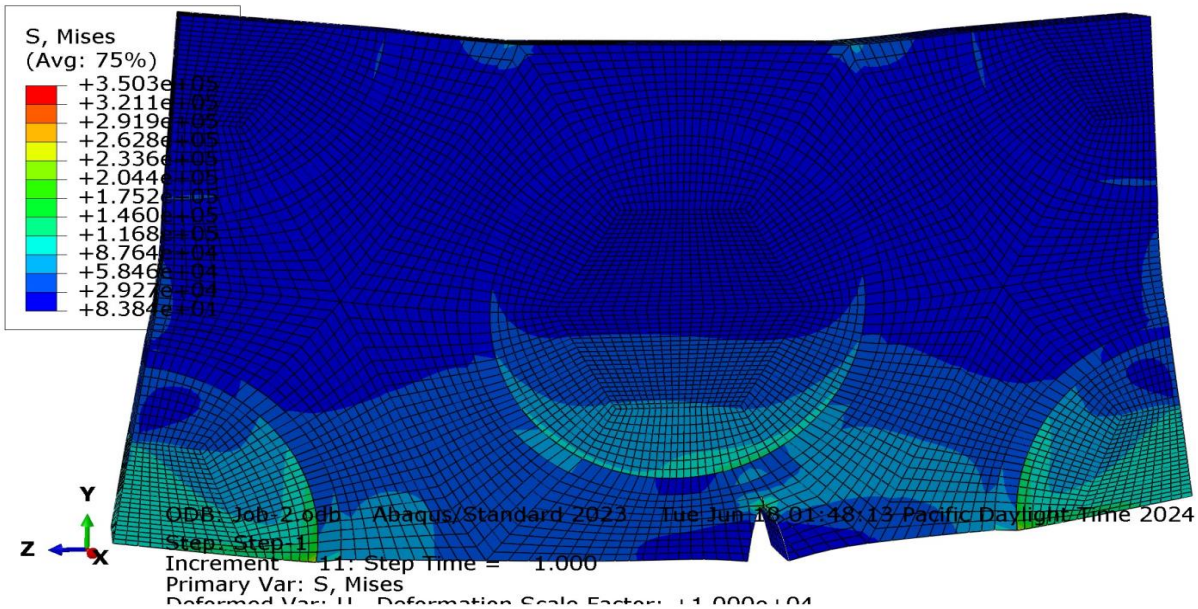


Figure 4. Simulation of crack growth with the XFEM method for the representative volume element model (RVE)

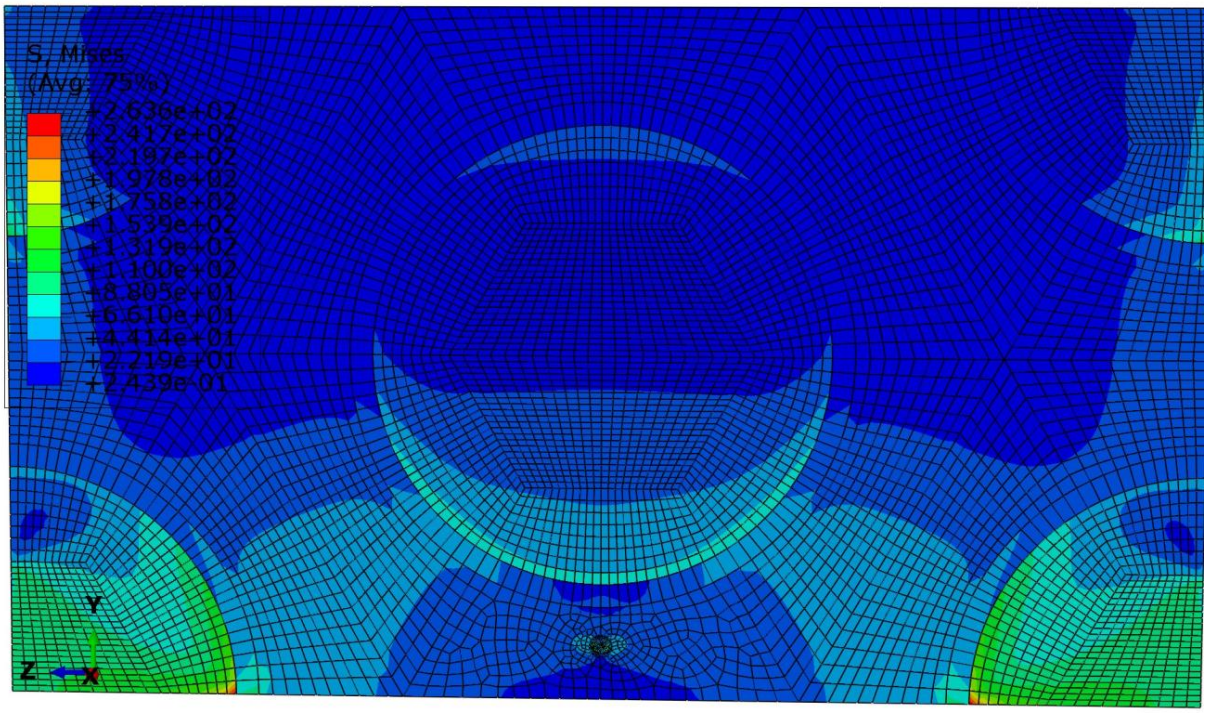


Figure 5. The stress intensity coefficient for the representative volume element (RVE) with the value of K_I=1.53

Conclusion

The Representative Volume Element (RVE) is a crucial concept in the analysis of composite materials. It serves as a computational domain that captures the essential microstructural features of the material. The size of the RVE is a critical consideration. It should be large enough to contain sufficient information about the microstructure, ensuring it is representative of the material's characteristics. The Extended Finite Element Method (XFEM) offers several advantages over traditional finite element methods when dealing with cracks and their propagation in materials .

For the purpose of RVE modeling in this article, the Abaqus software plugin was utilized. Abaqus provides a comprehensive and widely-used platform for finite element analysis, including the implementation of XFEM capabilities. By using Abaqus and incorporating the RVE + XFEM approach, the authors were able to investigate the behavior of cracks within composite materials and study the influence of microstructural features on crack propagation. The results obtained from the simulations demonstrated that the crack propagation was influenced

by the graded interface properties between the matrix and the fiber. As the crack approached the fiber, the interface's properties hindered further crack progression. This behavior can be attributed to the mechanical properties of the fiber and the graded nature of the interface, effectively impeding the crack's advancement. These findings highlight the significance of considering the microstructural details and the interaction between the constituents when analyzing crack propagation in composite materials.

Reference

1. Yu, Z., Zhang, J., Shen, J. and Chen, H., 2021. Simulation of crack propagation behavior of nuclear graphite by using XFEM, VCCT and CZM methods. Nuclear Materials and Energy, 29, p.101063.
2. Zhao, Changfang, Rui Ren, Jianlin Zhong, Kheng Lim Goh, Kebin Zhang, Zhengdong Zhang, and Guigao Le. "Intralaminar crack propagation of glass fiber reinforced composite laminate." In *Structures*, vol. 41, pp. 787-803. Elsevier, 2022.
3. Naghdinasab, Mohsen, Amin Farrokhabadi, and Hamidreza Madadi. "A numerical method to evaluate the material properties degradation in composite RVEs due to fiber-matrix debonding and induced matrix cracking." *Finite Elements in Analysis and Design* 146 (2018): 84-95.
4. Zamanian, M., Ashenai Ghasemi, F. and Mortezaei, M., 2021. Interphase characterization and modeling of tensile modulus in epoxy/silica nanocomposites. *Journal of Applied Polymer Science*, *138*(5), p.49755.
5. Chong, A.C., et al., Fracture toughness and fatigue crack propagation rate of short fiber reinforced epoxy composites for analogue cortical bone. Journal of biomechanical engineering, 2007. 129(4): p. 487-493
6. Farrokhabadi, A., Madadi, H., Naghdinasab, M., Rafie, A., Taghizadeh, S.A. and Herráez, M., 2022. Micromechanical investigation of cross-ply carbon composite laminates with glass microtubes using CZM and XFEM. *Mechanics of Advanced Materials and Structures*, *29*(26), pp.5624-5636.
7. Zamanian, Milad, Faramarz Ashenai Ghasemi, and Mehrzad Mortezaei. "An efficient nanoscale representative volume element simulation including graded interphase for tensile behavior of epoxy/silica nanocomposites." *Journal of Applied Polymer Science* 138, no. 45 (2021): 51332.

Advanced Engineering Days

aed.mersin.edu.tr

Obtaining the buckling capacity of composite pipe under axial load and external pressure

Arsalan Nojavan Kohnehshahri [*1], **Hasan Biglari** [1]

[1] *University of Tabriz, Department of Mechanical Engineering, Iran, arsalan.nojavan.k@gmail.com, hbiglari@tabrizu.ac.ir*

Cite this study: Nojavan Kohnehshahri, A., & Biglari, H. (2024). Analysis of composite pipe under axial loading. Advanced Engineering Days, 9, 77-79

Keywords
Composite pipe
Composite
buckling capacity
FEM
ABAQUS

Abstract

The purpose of this research is to evaluate the buckling capacity of composite pipe under combined axial load and external pressure. Determining the buckling capacity of composite pipes under combined axial load and external pressure is a critical aspect in structural engineering, especially in industries such as oil and gas. This study investigates the interaction between axial load and external pressure on the buckling behavior of composite pipes through finite element analysis. Composite pipes are widely used in industries due to their favorable strength-to-weight ratio and corrosion resistance. Understanding the buckling characteristics of these pipes is essential to ensure their structural health and safety in various industries. This study uses simulation to investigate the buckling behavior of composite pipe under different loading conditions. The purpose of this study is to help design and optimize composite pipe systems by providing insight into the behavior of composite pipes under different loading conditions. In this research, valuable guidance is provided for the development of composite pipes with the ability to withstand axial load and efficient external pressure to give.

Introduction

Composite pipes are used in various industries due to their distinct properties and benefits. Their use can be mentioned in oil and gas transmission lines.[1] They are also used to transport corrosive fluids. [2-3] One of the main advantages of composite pipes is their excellent resistance to weight ratio, which makes them lighter and more economical than traditional metal pipes. In addition, composite pipes are resistant to corrosion and are suitable for use in challenging environments where metal pipes may degrade over time. Analysis of composite pipes under different loadings is an important research area in materials engineering and structural mechanics. Understanding the behavior of these pipes under different loads and obtaining the buckling capacity is very important to ensure their structural integrity and effectiveness in different uses. Axial loading and external pressure can lead to complex stress distributions and deformation patterns in composite material. This study seeks to investigate the buckling capacity of composite pipes to combined loading using analytical methods and simulations. The results of this analysis will help to develop more efficient and reliable designs for composite pipes in a wide range of industrial applications.

Material and Method

In this study, a composite pipe with a length of 5000 mm and a radius of 2000 mm has been analyzed. This composite pipe consists of 8 layers, the thickness of each layer is 0.5 mm. The layering of this pipe is symmetrical and the layering is according to formula $[\pm 70]_{2S}$. Fibers have fiber orientation angles of positive 70 degrees and negative 70 degrees.

In "Figure 1" it shows the location of the layers, the direction angles of the fibers and the way of loading on the pipe. The material of the pipe is CFRP. “Table 1” shows materials properties such as elasticity modulus, shear modulus and Poisson's ratio.

This pipe has been analyzed using the FEM method.[4] For the analysis of this pipe, the boundary conditions are considered as$(u_{1\&2} = u_{R1\&R2\&R3} = 0, u_3 = open)$. Axial force and external pressure are applied to the pip.

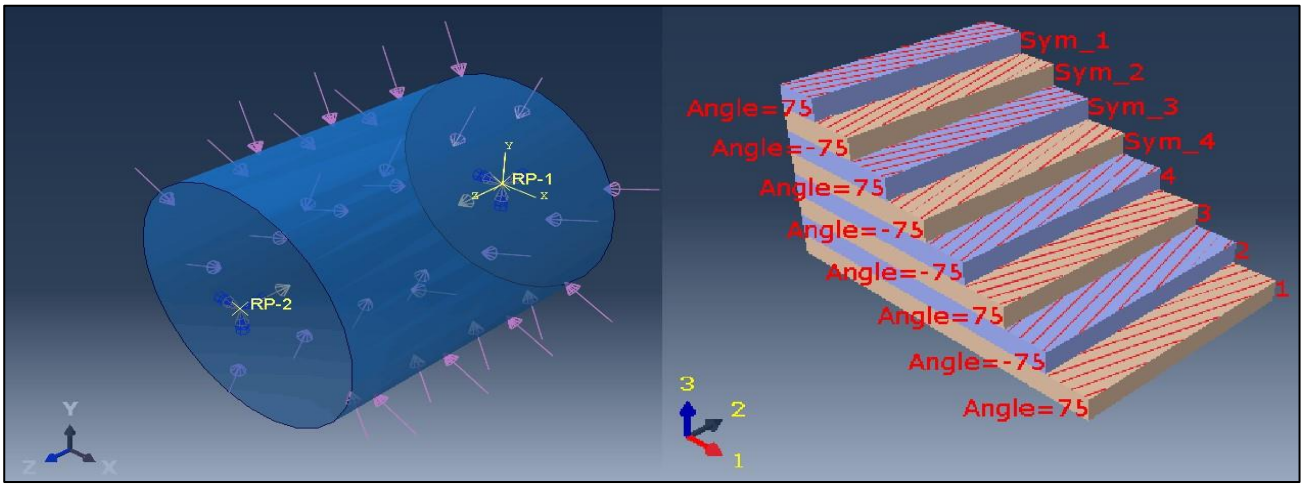


Figure 1. Layering placement, fiber direction angles and the way of loading on the pipe

Table 1. Materials properties

Items	Value
E_1	13600 Pa
E_2	8200 Pa
E_3	8200 Pa
G_{12}	5500 Pa
G_{13}	5500 Pa
G_{23}	3310 Pa
ϑ_{12}	0.3
ϑ_{13}	0.3
ϑ_{23}	0.4

Results

The buckling capacity values of the composite pipe are obtained for certain values of axial load (axial load is applied compressively and equally from both sides to the pipe) and external pressure. "Figure 2"shows the analyzed pipe, which shows the deformation of the composite as a result of the application of axial force and external pressure. The values obtained for the buckling capacity of the pipe in the first case, in which the value of the external pressure force is assumed to be constant, and the buckling capacity of the pipe is calculated for different axial forces, which are shown in "Table 2". In the second case, the value of the axial force is assumed constant and the buckling capacity of the pipe has been calculated for different external pressures, which is shown in the table "Table 3".

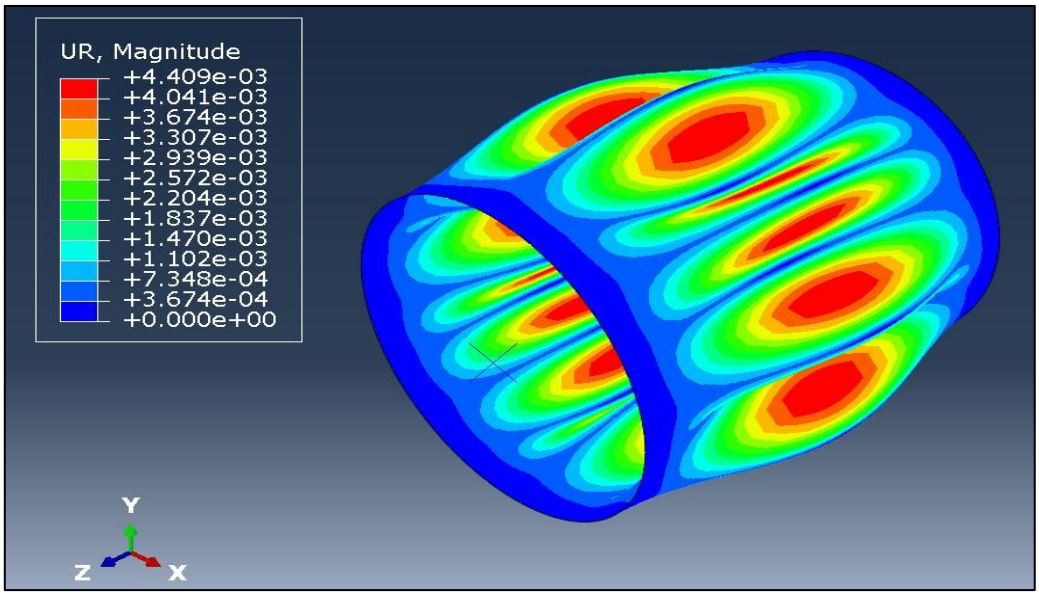


Figure 2. Deformation of the composite pipe as a result of the application of axial force and external pressure

Table 2. The obtained values for the buckling capacity of the pipe in the first case

Buckling capacity (pressure) (MPa)	Force (KN)
1.499×10^{-3}	1.5
1.199×10^{-3}	6
1.199×10^{-3}	12

Table 3. The obtained values for the buckling capacity of the pipe in the second case

Buckling capacity (Force) (KN)	Pressure (MPa)
3.998×10^{-4}	3
9.995×10^{-5}	12
4.997×10^{-5}	24

Discussion

In this research, the capacity of the composite pipe has been calculated for two cases. From two cases, it can be concluded that with increasing external pressure or increasing axial force, the buckling capacity of composite pipe decreases. The results of this study shed light on the behavior of composite pipes under different loading conditions and provide valuable insight for the design of pipes that can effectively withstand axial load and external pressure. The simulation done in this research has helped to understand the basic principles governing the buckling behavior of composite pipes. This study has been able to predict the buckling capacity of pipes by considering material properties, geometrical characteristics and loading conditions. With this study, the structural performance and safety of composite pipes can be increased in various industrial applications.

References

1. Taheri-Behrooz, F., Esmaeel, R. A., & Taheri, F. (2012). Response of perforated composite tubes subjected to axial compressive loading. Thin-Walled Structures, 50(1), 174-181.
2. Yang, C. (2000). Design and analysis of composite pipe joints under tensile loading. Journal of Composite Materials, 34(4), 332-349.
3. Prabhakar, M. M., Rajini, N., Ayrilmis, N., Mayandi, K., Siengchin, S., Senthilkumar, K., ... & Ismail, S. O. (2019). An overview of burst, buckling, durability and corrosion analysis of lightweight FRP composite pipes and their applicability. Composite Structures, 230, 111419.
4. Das, R. R., & Baishya, N. (2016). Failure analysis of bonded composite pipe joints subjected to internal pressure and axial loading. Procedia Engineering, 144, 1047-1054.

Advanced Engineering Days

aed.mersin.edu.tr

Fluid flow and heat transfer of water-based nanofluids in plate-fin heat sink

Ali Rahbar *[1], Hamidreza Toloueinasab [1], Amirreza Javaherian [1] Mohsen Zeinali [1], Moharram Jafari [1]

[1] *University of Tabriz, Department of Mechanical Engineering, Iran, ali.rahbar98 @ms.tabrizu.ac.ir, hr_tolouienasab@tabrizu.ac.ir, a_javaherian@tabrizu.ac.ir, m.zeinali@tabrizu.ac.ir, mjafari@tabrizu.ac.ir*

Cite this study: Rahbar, A., Toloueinasab, H., Javaherian, A., Zeinali, M., Jafari, M. (2024). Fluid flow and heat transfer of water-based nanofluids in plate-fin heat sink. Advanced Engineering Days, 9, 80-82.

Keywords
Heat sink
Heat transfer
Nanofluid
Electronic device cooling
Ansys Fluent

Abstract

In this study, the fluid flow and heat transfer characteristics of turbulent nanofluids flow in plate-fin heat sink are studied. Using the K-Ɛ turbulence model, the characteristics of the fluid flow through the plate-fin heat sink are described and simulated using Ansys Fluent software. A constant heat flux boundary condition is applied on the base plate of heat sink and all the other surfaces of the heat sink are insulated. Four different kinds of nanofluids are utilized as working fluids which are SiO_2, Al_2O_3, ZnO, and CuO dispersed in distilled water as a base fluid. Volume fractions of 2% and a distinctive nanoparticle diameter of 60 nm were employed. Results indicate that nanofluids can improve the performance of the heat sink. Viscosity has an important role in the pressure drop in the heat sink. Also, the improvement in the thermal transportation of nanofluids increases the convective heat transfer coefficient.

Introduction

Nowadays, with the increasing usage of electronic components, as well as reducing the size of these components and increasing their computing power, the need to use different cooling methods is felt more than ever. Some of these methods are available such as jet impingement cooling [1,2], pool boiling [3], two-phase flow in microchannel [4,5], etc.

Nanofluid flow can be utilized as one of the passive techniques for improving heat transfer due to its higher thermal conductivity compared to pure fluid [6,7]. Recently, Nanofluid flow and heat transfer have been studied by several authors. Sheikholeslami et. al., [7] studied the effect of a mutable magnetic field on nanofluid forced convective heat transfer. Mohammed et al. [8] numerically studied the fluid flow and heat transfer characteristics of various nanofluids with various volume fractions in different MCHS shapes. It was found that the heat transfer coefficient increased by increasing the nanoparticles concentration. The finite Volume Method (FVM) on large scale is being used for simulating nanofluid flow heat transfer [9].

The current study examines 3D turbulent forced convective flow in Plate-Fin Heat Exchanger (PFHS) using different nanofluids in water-based fluid. The single-phase method was adopted, moreover the Nusselt number for turbulent forced convective in PFHS was investigated to show the effect of nanofluids on the system parameters.

Material and Method

Figure 1 shows 3D model geometry and the model of PFHS used for numerical analysis. Also, the geometric parameters of PFHS are listed in Table 1.

In this study, two types of Fluids (air, water) and four types of nanofluids (AL_2O_3-Water, CuO-Water, SiO_2-water, ZnO-water) with volume fractions of 0.02 and 60 nm diameter are analyzed. Inlet fluid temperature is 294°K, and the material of heat sinks is aluminum with thermal conductivity of 202 W/mK, Fluid velocity values through passages of the heat sink are 6.5, 8.0, 10.0, and 12.2 m/s, respectively. The base of the PFHS was heated uniformly with heat loads of 10 W,100 W [10], and the heat flux of 100W/cm^2 [11]. The PFHS performance, the governing

mass, momentum, and energy equations were written with assumptions such as three-dimensional, turbulent, incompressible, and steady flow [10]. Also, the Buoyancy effect and radiation heat transfer effects are negligible.

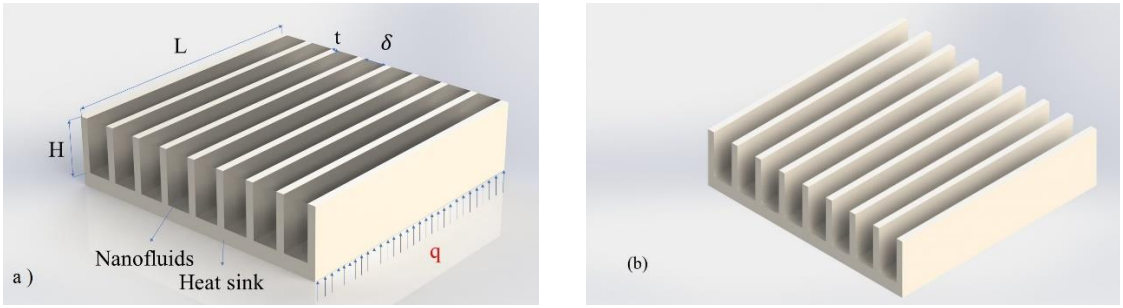


Figure 1. (a): Schematic diagrams of plate fin heat sink (b): 3D model geometry [10]

Table 1. Geometrical parameters of heat sink [10]

Fin length, L (mm)	Fin height, H (mm)	Fin number, N	Fin thickness, t (mm)
51	10	9	1.5

The continuity, momentum, and energy equations are calculated from Eqs. (1)-(6).

Continuity equation [10]:

$$\frac{\partial}{\partial x_j}(\rho \bar{u}_i) = 0 \tag{1}$$

Momentum equations [10]:

$$\frac{\partial}{\partial x_j}\left(\rho \bar{u}_j \bar{u}_i\right) = -\frac{\partial \bar{P}}{\partial x_i} + \frac{\partial}{\partial x_j}\left(\mu \frac{\partial \bar{u}_i}{\partial x_j} + \tau_{ij}\right) \tag{2}$$

Where τ_{ij} is the Reynolds stress term given by [10]:

$$\tau_{ij} = \mu_t \left(\frac{\partial \bar{u}_i}{\partial x_j} + \frac{\partial \bar{u}_j}{\partial x_i}\right) - \frac{2}{3}\rho \delta_{ij} k \tag{3}$$

Where μ_t is turbulent viscosity and $k = \frac{1}{2}\left(\overline{u'^2} + \overline{v'^2} + \overline{w'^2}\right)$ is the turbulent kinetic energy. Eq. (3) introduces two unknowns (μ_t and k), which require two equations for closure. For high Reynolds number flows the turbulent viscosity can be represented as [10]:

$$\mu_t = \rho \mathcal{C}_\mu \frac{k^2}{\varepsilon} \tag{4}$$

where $\mathcal{C}_\mu$ is a constant and ε is the dissipation rate of energy. The closure equations used to evaluate the turbulent viscosity and energy dissipation rate take the form [10]:

$$\frac{\partial}{\partial x_j}\left(\rho \bar{u}_j k\right) = \frac{\partial}{\partial x_j}\left[\left(\mu + \frac{\mu_t}{\sigma_k}\right)\frac{\partial k}{\partial x}\right] + \mu_t \left(\frac{\partial \bar{u}_i}{\partial x_j} + \frac{\partial \bar{u}_j}{\partial x_i}\right)\cdot \frac{\partial \bar{u}_i}{\partial x_j} - \rho\varepsilon \tag{5}$$

$$\frac{\partial}{\partial x_j}\left(\rho \bar{u}_j \varepsilon\right) = \frac{\partial}{\partial x_j}\left[\left(\mu + \frac{\mu_t}{\sigma_\varepsilon}\right)\frac{\partial \varepsilon}{\partial x}\right] + \mathcal{C}_1 \frac{\varepsilon}{k}\mu_t \left(\frac{\partial \bar{u}_i}{\partial x_j} + \frac{\partial \bar{u}_j}{\partial x_i}\right)\cdot \frac{\partial \bar{u}_i}{\partial x_j} - \mathcal{C}_2 \rho \frac{\varepsilon^2}{k} \tag{6}$$

For the k– ε model, the constant terms take the values [10]:

$$\mathcal{C}_\mu = 0.09\,,\ \mathcal{C}_1 = 1.44\,,\ \mathcal{C}_2 = 1.92\,,\ \sigma_k = 1.0\,,\ \sigma_\varepsilon = 1.3 \tag{7}$$

$$\rho_f C_{p.f}\left(u\frac{\partial T_f}{\partial x} + v\frac{\partial T_f}{\partial y} + w\frac{\partial T_f}{\partial z}\right) = k_f\left(\frac{\partial^2 T_f}{\partial x^2} + \frac{\partial^2 T_f}{\partial y^2} + \frac{\partial^2 T_f}{\partial z^2}\right) \tag{8}$$

The energy equation for the Fluid flow [12]:

The energy equation for the solid domain [12]:

$$k_s\left(\frac{\partial^2 T_s}{\partial x^2} + \frac{\partial^2 T_s}{\partial y^2} + \frac{\partial^2 T_s}{\partial z^2}\right) = 0 \tag{9}$$

Results

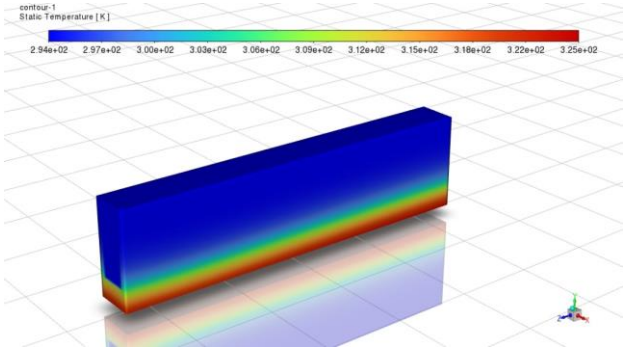


Figure 2. Water flow which is used as coolant fluid

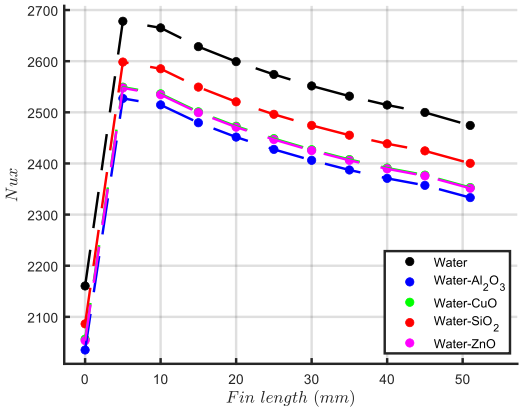


Figure 3. Local Nusselt number values along the channel according to maximum velocity for different nanofluids

Discussion

Figure 2 shows the temperature contour of the water flow, which is used as the cooling fluid. As it can be seen, the temperature distribution is uniform. Figure 3 shows the local Nusselt number by different fin length, the minimum local Nusselt number for each nanofluid obtained at length of 0 mm, and the maximum local Nusselt number observed at length of 5 mm. Al_2O_3 has a minimum local Nusselt number and water has a maximum local Nusselt number, also all local Nusselt numbers are converged along the fin length.

Conclusion

In this work, the cooling performance of water and nanofluids at Ø= 2%, of (Al_2O_3-CuO-SiO_2-ZnO) in an electronic chip is investigated numerically using ANSYS–Fluent. It can be concluded that water may be replaced with CuO nanofluid and ZnO nanofluid as a coolant in electronic cooling systems. Viscosity has an important role in the pressure drop in the heat sink. Also, the improvement in the thermal transportation of nanofluids increases the convective heat transfer coefficient.

References

1. Y.M. Chung, K.H. Luo, Unsteady heat transfer analysis of an impinging jet, J.Heat Transfer (2002), https://doi.org/10.1115/1.1469522.
2. K. Nishino, M. Samada, K. Kasuya, K. Torii, Turbulence statistics in the stagnation region of an axisymmetric impinging jet flow, Int. J. Heat Fluid Flow (1996), https://doi.org/10.1016/0142-727X(96)00040-9.
3. M. Arik, A. Bar-Cohen, Pool boiling of perfluorocarbon mixtures on silicon surfaces, Int. J. Heat Mass Transfer (2010), https://doi.org/10.1016/j.ijheatmasstransfer.2010.06.034.
4. Honda, H. and J. Wei, Enhanced boiling heat transfer from electronic components by use of surface microstructures. Experimental Thermal and Fluid Science, 2004. 28(2-3): p. 159-169.
5. S. Lin, K. Sefiane, J.R.E. Christy, Prospects of confined flow boiling in thermal management of microsystems, Appl. Therm. Eng. (2002), https://doi.org/10.1016/S1359-4311(01)00124-7.
6. M. Sheikholeslami, M.T. Mustafa, D.D. Ganji, Effect of Lorentz forces on forced-convection nanofluid flow over a stretched surface, Particuology 26 (2016) 108–113.
7. M. Sheikholeslami, M.M. Rashidi, D.D. Ganji, Numerical investigation of magnetic nanofluid forced convective heat transfer in existence of variable magnetic field using two phase model, J. Mol. Liq. 212 (2015) 117–126.
8. H.A. Mohammed, P. Gunnasegaran, N. Shuaib, Influence of various base nanofluids and substrate materials on heat transfer in trapezoidal microchannel heat sinks, Int. Commun. Heat Mass Transf. 38 (2011) 194–201.
9. A. Vatani, H.A. Mohammed, Turbulent nanofluid flow over periodic rib-grooved channels, Eng. Appl. Comput. Fluid Mech. 7 (2013) 369–381.
10. Yu, X., et al., Development of a plate-pin fin heat sink and its performance comparisons with a plate fin heat sink. Applied thermal engineering, 2005. 25(2-3): p. 173-182.
11. Abdollahi, A., et al., Fluid flow and heat transfer of nanofluids in microchannel heat sink with V-type inlet/outlet arrangement. Alexandria Engineering Journal, 2017. 56(1): p. 161-170.
12. S.E. Ghasemi, A.A. Ranjbar, M.J. Hosseini, Experimental and numerical investigation of circular minichannel heat sinks with various hydraulic diameter for electronic cooling application, Microelectron. Reliab. (2017).

Advanced Engineering Days

aed.mersin.edu.tr

Numerical investigation of pressure drop and heat transfer using nanofluids in microchannels

Milad Rezaei *[1], Ali Rahbar [1], Hamidreza Toloueinasab [1], Amirreza Javaherian [1], Moharram Jafari [1]

[1] *University of Tabriz, Department of Mechanical Engineering, Iran, Milad.rezaei98@ms.tabrizu.ac.ir, ali.rahbar98 @ms.tabrizu.ac.ir, hr_tolouienasab@tabrizu.ac.ir, a_javaherian@tabrizu.ac.ir, mjafari@tabrizu.ac.ir*

Cite this study: Rezaei, M., Rahbar, A., Toloueinasab, H., Javaherian, A., Jafari, M. (2024). Numerical investigation of pressure drop and heat transfer using nanofluids in microchannels. Advanced Engineering Days, 9, 83-85

Keywords
Microchannel
Nanofluid
Pressure drop
Heat transfer

Abstract

In this study, the displacement heat transfer of the incompressible flow in the quiescent state in the rectangular microchannel is investigated in three dimensions using the numerical method in the Ansys-Fluent software. The obtained results show that the use of nanofluids compared to water fluid due to their high thermal conductivity improve the heat transfer in the microchannel. Also, the comparison of Nusselt number values shows that nanofluids have a higher Nusselt number value than the water base fluid. As a result, the heat transfer rate is higher. Furthermore, Fe_3O_4 nanofluid has the highest heat transfer among the studied nanofluids.

Introduction

Improving the efficiency of cooling systems is one of the most important concerns of industries such as electronic systems, heat exchangers, etc., with the advancement of technology in electronic systems in small sizes with high processing speed and scales less than Hundred nanometers, fast and massive operation at very high speed (several GHz), using motors with high power and high heat load have become very important. Therefore, using advanced and optimal cooling systems is inevitable. Common methods to increase heat transfer include increasing the surface area and adding solid metal particles to the base fluid. Optimizing heat transfer systems is usually done by increasing their surface by surfaces such as fins and microchannels. With the advancement of technology in order to make channels with micro dimensions, it has become acceptable to use microchannel as an exchanger. Microchannel is a device that is used to control the temperature of electronic components with high heat flux, which compression and increasing the ratio of surface to volume of heat transfer, high thermal efficiency and low weight are among its advantages and characteristics. These advantages are of particular importance in electronic industries for high heat transfer. Another method of increasing heat transfer is the use of solid metal particles in the base fluid, which by mixing nanometer-sized particles (nanoparticles) with a low volume percentage with the base fluid, creates a fluid with relatively new physical properties, which is called nanofluid.
In a numerical study, Zhao, C. and T. Lu [1] considered the nanoparticle size and the number of channels in microchannel heat transfer and their introduced method. The obtained results show that according to the increase in the number of channels and decrease in effective thermal conductivity, the Nusselt number increases. On the other hand, Toh, K., X. Chen, and J. Chai [2] investigated fluid flow and heat transfer in a microchannel with constant heat flux. The results showed that at lower Reynolds numbers, the water temperature increases.

In this study, the displacement heat transfer of the incompressible flow in the quiescent state in the rectangular microchannel is investigated in three dimensions using the numerical method in the Ansys-Fluent software.

Material and Method

The geometric dimensions of the Microchannel are given according to Table 1 and Fig. 1. The assumption is that a heat flux is generated at the bottom plate of the heat sink to simulate a condition of a CPU chip that conducts

heat to the heat exchanger next to it. As shown in Fig. 1c, there are 11 channels (marked with a number from left side to right side) designed inside the heat sink when looking from the cross-sectional view [3].

Table 1. Geometric dimensions [3]

Width (W_{hs})	Length (L_{hs})	Height (Hhs)	W_{ch}	L_{ch}	H_{ch}
6.2 mm	18 mm	0.5 mm	200 μm	10 mm	400 μm

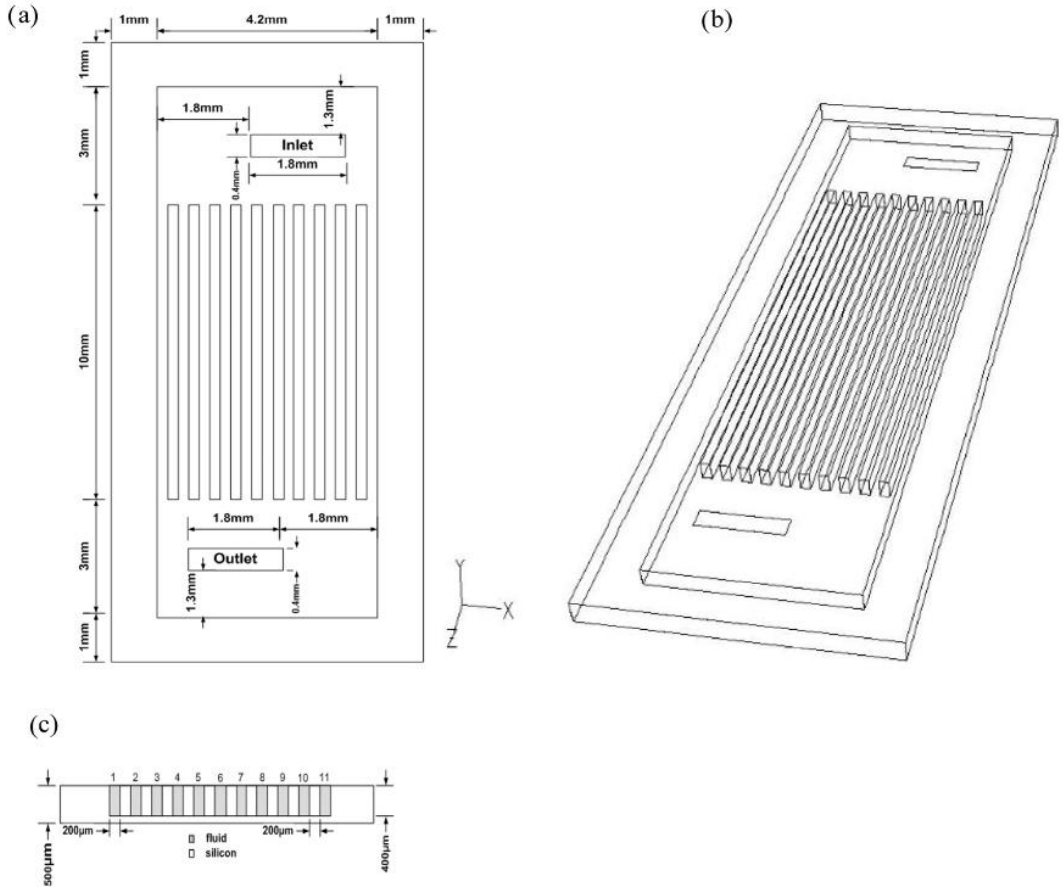


Figure 1. (a) Top view of the MCHS (Z-X plan), **(b)** Schematic diagram of V-typed inlet/outlet arrangement, **(c)** dimensions of the MCHS (X-Y plan) [3]

The material of the MCHS is of silicon. The flow enters from the inlet and is collected at the outlet vertically. The flow entering the test section is thermally and hydrodynamically fully developed.
The continuity equation for laminar and incompressible flow is as follows:

$$\frac{\partial \mathrm{u}}{\partial \mathrm{x}} + \frac{\partial \mathrm{v}}{\partial \mathrm{y}} + \frac{\partial \mathrm{w}}{\partial \mathrm{z}} = 0 \tag{1}$$

The momentum conservation equation (Navier-Stokes) is given in the form of the following relations. The final form of these equations is shown below in the three directions y, x and z respectively.

$$\rho_f \left(u\frac{\partial u}{\partial x} + v\frac{\partial u}{\partial y} + w\frac{\partial u}{\partial z}\right) = -\frac{\partial_\rho}{\partial_x} + \mu_f \left(\frac{\partial^2 u}{\partial x^2} + \frac{\partial^2 u}{\partial y^2} + \frac{\partial^2 u}{\partial z^2}\right) \tag{2}$$

$$\rho_f \left(u\frac{\partial v}{\partial x} + v\frac{\partial v}{\partial y} + w\frac{\partial v}{\partial z}\right) = -\frac{\partial_\rho}{\partial_y} + \mu_f \left(\frac{\partial^2 v}{\partial x^2} + \frac{\partial^2 v}{\partial y^2} + \frac{\partial^2 v}{\partial z^2}\right) \tag{3}$$

$$\rho_f \left(u\frac{\partial w}{\partial x} + v\frac{\partial w}{\partial y} + w\frac{\partial w}{\partial z}\right) = -\frac{\partial_\rho}{\partial_z} + \mu_f \left(\frac{\partial^2 w}{\partial x^2} + \frac{\partial^2 w}{\partial y^2} + \frac{\partial^2 w}{\partial z^2}\right) \tag{4}$$

The energy equation for fluid flow is as follows:

$$\rho_f C_{pf} \left(u\frac{\partial T_f}{\partial x} + v\frac{\partial T_f}{\partial y} + w\frac{\partial T_f}{\partial z}\right) = k_f \left(\frac{\partial^2 T_f}{\partial x^2} + \frac{\partial^2 T_f}{\partial y^2} + \frac{\partial^2 T_f}{\partial z^2}\right) \tag{5}$$

The energy equation for the solid region is obtained from the following expression:

$$k_s \left(\frac{\partial^2 T_s}{\partial x^2} + \frac{\partial^2 T_s}{\partial y^2} + \frac{\partial^2 T_s}{\partial z^2}\right) = 0 \quad (6)$$

Results

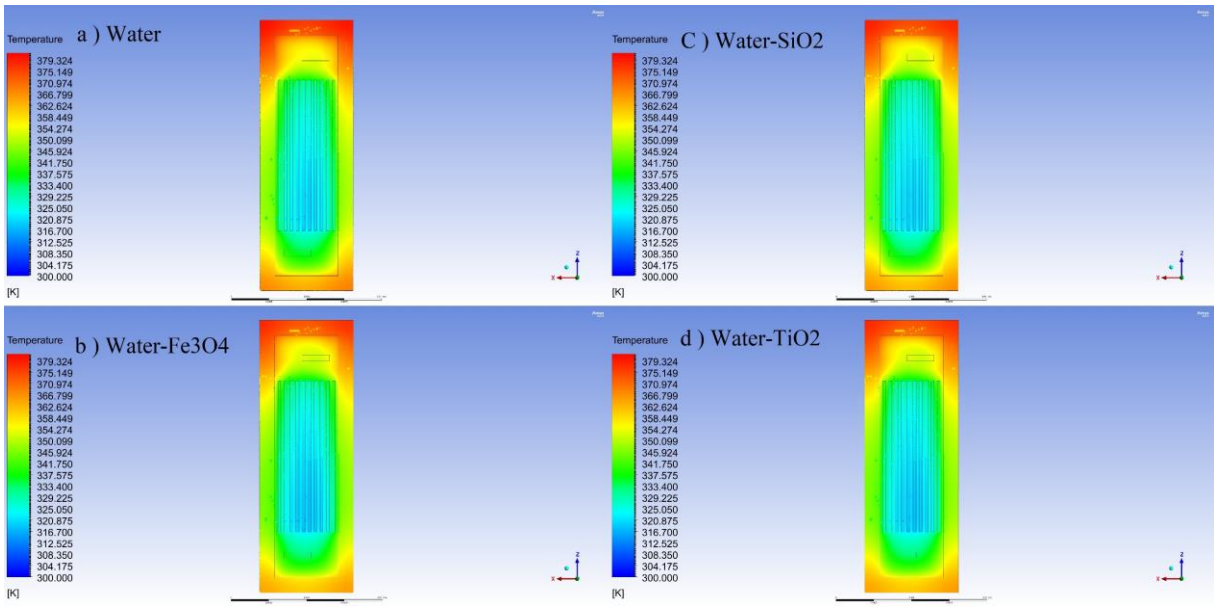


Figure 2. The Temperature contours for different nanofluids at Re = 1333: **a)** Water, **b)** Water-Fe3O4, **c)** Water-SiO2, **d)** Water-TiO2

Discussion

As a result of the water fluid flowing in the channels embedded in the microchannels, it can be seen that temperature changes occurred and there is a slight temperature difference in the water fluid and SiO_2 nanofluid in the channels. Fe_3O_4 nanofluid has the maximum pressure drop on the microchannel. The reason for this is having the highest density compared to other nanofluids. Fe_3O_4 nanofluid has the maximum value of Nu number among other nanofluids.

Conclusion

According to the investigation carried out in this research, the following general conclusions can be considered:

I. As a result of the water fluid flowing in the channels embedded in the microchannels, it can be seen that temperature changes occurred and there is a slight temperature difference in the water fluid and SiO_2 nanofluid in the channels.
II. Fe_3O_4 nanofluid has the maximum pressure drop on the microchannel. The reason for this is having the highest density compared to other nanofluids.
III. Fe_3O_4 nanofluid has the maximum value of Nu number among other nanofluids.
IV. The amount of heat transfer in Fe_3O_4 nanofluid is higher than other nanofluids, because the thermal conductivity of Fe_3O_4 nanoparticle is higher than the other two nanoparticles TiO_2 and SiO_2.
V. The data indicate that the pressure drop of nanofluids is high compared to water fluid.
VI. The amount of heat transfer increases with the increase of Re number in all four fluids, and the highest value of Nu number is for Fe_3O_4 nanofluid and the lowest for water fluid and SiO_2 nanofluid.

References

1. Zhao, C. and T. Lu, Analysis of microchannel heat sinks for electronics cooling. International Journal of Heat and Mass Transfer, 2002. 45(24): p. 4857-4869.
2. Toh, K., X. Chen, and J. Chai, Numerical computation of fluid flow and heat transfer in microchannels. International Journal of Heat and Mass Transfer, 2002. 45(26): p. 5133-5141.
3. Abdollahi, A., et al., Fluid flow and heat transfer of nanofluids in microchannel heat sink with V-type inlet/outlet arrangement. Alexandria Engineering Journal, 2017. 56(1): p. 161-170.

Advanced Engineering Days

aed.mersin.edu.tr

Natural frequency analysis of a plate strengthened in dry and underwater conditions in the presence of added mass effects

Ghadir Ahmadi Jeyed [*1], Mohammad Gandomkar [2], Hasan Biglari [1]

[1]*University of Tabriz, Department of Mechanical Engineering, Iran, Ghadir.Ahmadi@tabrizu.ac.ir, hbiglari@tabrizu.ac.ir*
[3]Malek Ashtar University of Technology, *Department of Mechanical Engineering, Iran,* mgd_gandomkar@mut-es.ac.ir

Cite this study: Jeyed, G. A., Gandomkar, M., & Biglari, H. (2024). Natural frequency analysis of a plate strengthened in dry and underwater conditions in the presence of added mass effects. Advanced Engineering Days, 9, 86-89

Keywords
Natural frequency fluid
Acoustics
Added mass
FEM analysis
Submersion

Abstract

Modal analysis is essential for obtaining natural frequencies and mode shapes in marine structure engineering design. If the structure's excitation frequency approaches its natural frequency, it becomes unstable. The natural frequencies of a structure are lower in water than they are in vacuum, so finding a way to reduce the natural frequencies of structures under water, as well as the effect and calculation of the added mass, is an important issue. The natural frequency changes of a reinforced sheet in air and in water were investigated in this article using the acoustic properties of water fluid. For this purpose, ABAQUS software was used to investigate the effects of added mass in various vibration modes. It has been demonstrated that in higher modes and frequencies, the effect of the surrounding fluid is reduced, as is its added mass.

Introduction

The inertia that a body adds to a system when it moves through fluid is known as added mass, or virtual mass. When compared to structures in air or a vacuum, this effect can cause the natural frequencies of submerged structures to decrease. This is due to the fact that increasing a structure's mass lowers its velocity, which lowers its frequency. When the structure is surrounded by rigid walls or is near a rigid surface, the effect is more noticeable [1]. The added mass for fully submerged hulls is usually constant, but when a hull is close to the water's surface, it can vary significantly. Natural frequency analysis plays a crucial role in structural engineering by determining the dynamic characteristics of a system. When studying the natural frequencies of a reinforced plate, it becomes necessary to account for various factors such as different environmental conditions (dry and underwater) and the impact of added mass. In dry conditions, the natural frequencies of a reinforced plate are primarily influenced by factors like material properties, geometry, and boundary conditions. The plate's stiffness and mass distribution are significant contributors to its natural frequencies. Analytical techniques like the Rayleigh method or finite element analysis (FEA) can be utilized to compute these frequencies. In underwater conditions, additional considerations come into play [2]. The presence of water alters the dynamic behavior of the reinforced plate due to effects like added mass, hydrodynamic pressure, and fluid-structure interaction. These effects can significantly impact the natural frequencies of the plate. The added mass effect occurs because the water surrounding the plate adds mass to the system, effectively increasing its inertia. Consequently, the natural frequencies decrease compared to the dry condition. The magnitude of the added mass effect is dependent on factors such as the plate's geometry, water density, and the volume of fluid displaced by the plate. To incorporate the added mass effects, one approach is to modify the mass matrix within the FEA formulation [3]. This adjustment takes into account the added mass contribution resulting from the interaction between the fluid and the plate. Additionally, it is important to consider the hydrodynamic pressure acting on the plate's surfaces, as it can affect the natural frequencies. Analyzing the natural frequencies of a reinforced plate under the influence of added mass effects and underwater conditions is a complex task. It often necessitates advanced numerical methods such as computational fluid dynamics (CFD) combined with structural analysis. In conclusion, a comprehensive natural frequency analysis of a reinforced plate in dry and underwater conditions requires consideration of factors such as material properties, geometry, boundary conditions, added mass

effects, hydrodynamic pressure, and fluid-structure interaction. The specific methodology and software tools employed may vary depending on the problem's complexity and the desired level of accuracy [4].

The frequency of the plate strengthened without water and in presence of water:

Frequency of reinforced plate without water to calculate the frequency here, we use the Rayleigh method. As we know, in Rayleigh method we have [5]:

$$U_{max} = K_{max} \tag{1}$$

By considering the damping in the following form that satisfies the four-sided boundary conditions, the frequency is obtained [5,6]:

$$\omega_{air} = \frac{22.79}{a^2}\sqrt{\frac{1}{\rho}[D_x + D_y(\frac{a}{b})^4 + \frac{2}{3}H(\frac{a}{b})^2]} \tag{2}$$

$$\omega_{fluid} = \frac{22.79}{a^2}\sqrt{\frac{m}{\rho(m+m_a)}[D_x + D_y(\frac{a}{b})^4 + \frac{2}{3}H(\frac{a}{b})^2]} \tag{3}$$

Frequency analysis of the plate strengthened in dry conditions and under water

Studying the vibration behavior of marine structures, along with hydromechanical design, is one of the most important aspects of structure design. The local or general vibration of the structure's body in the presence of water is diametrically opposed to the vibration of the body in the absence of water and the presence of air. Because when the structure comes into contact with water, two additional phenomena occur: mass and damping, causing a change in the structure's natural frequency. The calculation of the natural frequency of structures serves this purpose; if the structure's frequency is close to its natural frequency, the structure will be aggravated and destroyed, and the importance of obtaining the natural frequency is determined here. The structure's natural frequency is higher in air than in water because the added mass factor is added to the structure's mass in water, causing the frequency to decrease [6-7]. In general, the natural frequencies of a structure in water are lower than those in God, owing to the effect of added mass in water. Figure 1 depicts the schematic of the reinforced sheet, while Tables 1 and 2 show the dimensions of the sheet and reinforced material, respectively.

Table 1. Specifications of plate strengthened dimensions

s (mm)	a (mm)	b (mm)	c (mm)	h (mm)	l (mm)
50	300	300	4	4	20

Table 2. Mechanical properties plate strengthened [3]

$\rho(kg/m^3)$	E(Gpa)	G(Gpa)	ν
7800	208	70	0.49

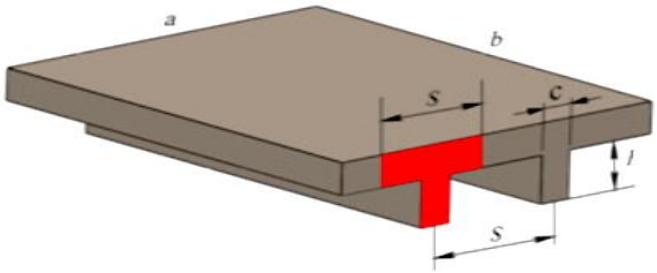


Figure 1. Specifications of plate strengthened dimensions

Table 3 shows the bulk modulus (B =), fluid density (sea water), and fluid type characteristics for the acoustic analysis.

Table 3. Fluid specifications

$\rho(kg/m^3)$	B(Pa)
1025	2.7×10^9

Table 3 shows theρ is density of seawater, and B is representing the fluid's bulk modulus. The Verification section, which is one of the Help sections of the ABAQUS software, presents a significant number of solved issues in numerous domains and compares these problems to known theories. It demonstrates the correctness of ABAQUS software in the realm of acoustic difficulties[7]. The C3D10 element was utilized to simulate the modeling sheet. It is a continuous, three-dimensional, first-order element with decreased integration points. This article presents the numerical findings of the natural frequency in air and immersed in water using the acoustic method under the boundary conditions of four free sides. The first and second modes are displayed. In the instance of water vibration, the view of the surrounding outside water has been removed as a result of mode observation, but it has had an impact on calculations. Figures 2 show the findings of the natural frequency analysis in air for the first and second modes.

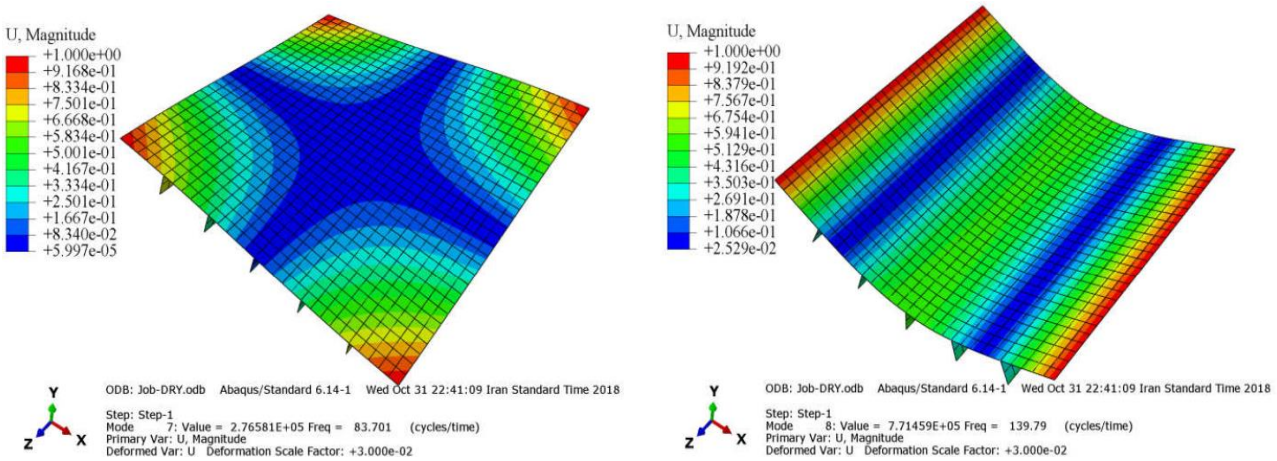


Figure 2. Frequency analysis of the first and second mode of 83.701 and 139.79 in air respectively

To simulate the sheet and the surrounding water environment, the C3D10 and AC3D4 elements were employed, which are continuous, three-dimensional, first-class elements with fewer integration points. The meshing takes the form of a structure, and the sheet meshing is the same size in and out of water. It should be noted that in order to determine the size of the element, the network was refined in numerous steps and convergence was tested. For the fluid model surrounding the structure, the fluid's dimensions should be increased until the increase in volume does not affect the structure's frequencies and the frequencies found in different fluid dimensions converge and achieve stable solutions. Figure 3 shows the findings of the modal analysis.

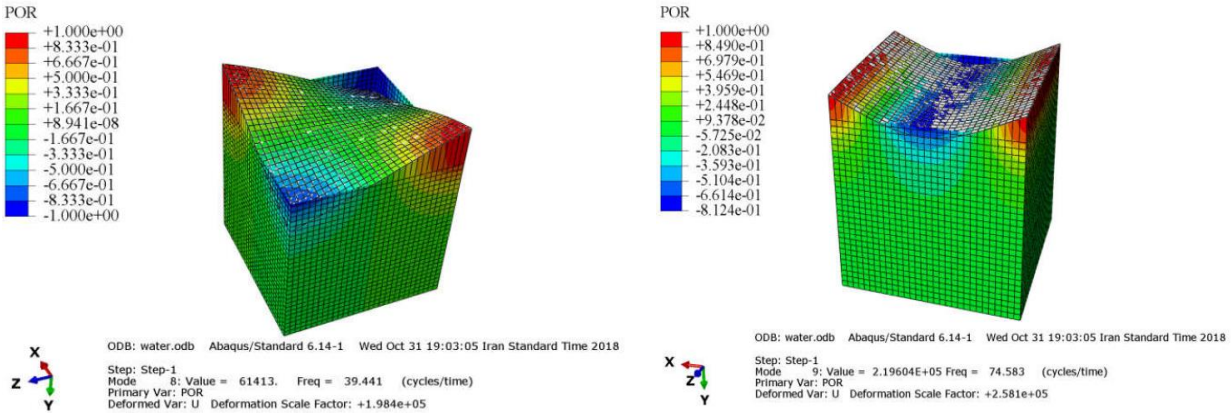
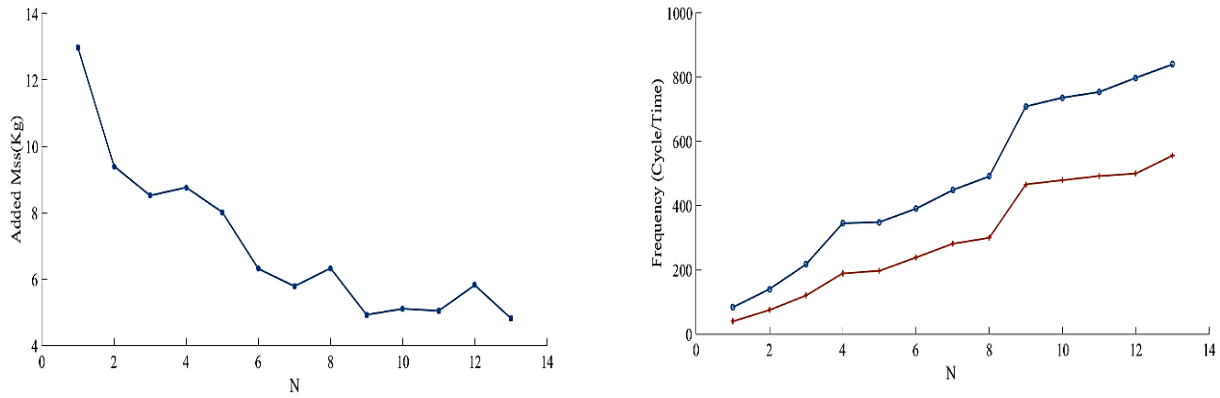


Figure 3. Frequency analysis of the first and second mode of 39.441 and 74.583 in water respectively

The shape of structural modes in air and water is found to be the same for all samples, implying that altering the fluid medium has no effect on the shape of the structural modes. As we know, the extra mass floating in the fluid is proportional to the frequency in the fluid and vacuum, as follows. where m represents the floating mass and fluid contributed mass to the structure, as well as the structure's frequency in the fluid and in vacuum. The strengthened sheet's mass in air is approximately 3.75 kg. The mass formula for determining the extra mass is provided in equation 4 [8]:

$$\frac{\omega_f}{\omega_v} = \sqrt{\frac{m}{m_a + m}} \tag{4}$$



(a) **(b)**

Figure 4 . (a) Diagram of added mass in terms of mode and (b) frequency in vacuum and water

Conclusion

This article examines the modes of the structure, the shape of the modes derived from the submerged vibration, and the lack of influence of the fluid environment on the modes' shape. The modes were found to be identical to those obtained from the vibration of the same structure in the air. The fluid's dimensions are analyzed for the fluid model around the structure until the volume increases without changing the structure's frequencies, at which point the frequencies obtained in the fluid's various dimensions converge and approach stable solutions. The fluid's dimensions are approximately four times larger than the underwater device's dimensions.

When the reinforced sheet comes in contact with water, its natural frequency is lower than when it is in the air. This difference in frequency can be attributed to the combined effects of water damping and the increased mass parameter. The analysis's findings demonstrate that the fluid environment and damping qualities have a significant impact on the sheet's vibration behavior, and that these factors must be taken into account when calculating and analyzing free vibration and figuring out the natural frequencies of the structure in contact with the fluid.

Reference

[1] Zienkiewicz, O. Co. "Coupled vibrations of a structure submerged in a compressible fluid." In Proc. of Symposium on Finite Element Techniques held at the University of Stuttgart. 1969.

[2] Min, Cheon-hong, Han-il Park, Jang-ho Yoo, and Hyun-gi Jung. "An Experimental Study on High-Frequency Vibration Analysis of a Circular Cylindrical Shell in Contact with Water." In The Twenty-first International Offshore and Polar Engineering Conference. International Society of Offshore and Polar Engineers, 2011.

[3] Rezvani, Seyed Saed, and Mehdi Saeed Kiasat. "Analytical and experimental investigation on the free vibration of a floating composite sandwich plate having viscoelastic core." Archives of Civil and Mechanical Engineering 18, no. 4 (2018): 1241-1258.

[4] Robinson, N. J., and S. C. Palmer. "A modal analysis of a rectangular plate floating on an incompressible liquid." Journal of sound and vibration 142, no. 3 (1990): 453-460.

[5]Kundu, P.K; “Fluid mechanic”, Academic Press Inc, 1990.

[6]Chakraverty,S; “vibration of plates”,Taylor and Francis group Boca Raton London New York, 2008.

[7] ABAQUS 6.14 Documentation, 2017.

[8] Liang, Cho-Chung, Ching-Chao Liao, Yuh-Shiou Tai, and Wen-Hao Lai. "The free vibration analysis of submerged cantilever plates." Ocean Engineering 28, no. 9 (2001): 1225-1245.

Advanced Engineering Days

aed.mersin.edu.tr

Enhancing vehicle stability and yaw performance using sliding mode control based on nonlinear model

Amirreza Mirzajani *[1], **Sevda Rezazadeh Movahhed** [1], **Mohammad Ali Hamed** [1]

[1]*University of Tabriz, Department of Mechanical Engineering, Iran, amirrezamirzajani1@gmail.com, sevda.rezazadeh@tabrizu.ac.ir, ma.hamed@tabrizu.ac.ir*

Cite this study: Mirzajani, A., Rezazadeh Movahhed, S., Hamed, M., (2024). Enhancing vehicle stability and yaw performance using sliding mode control based on nonlinear model. Advanced Engineering Days, 9, 90-93

Keywords
Vehicle stability
Sliding Mode Control
Yaw Rate Control
Lateral Stability

Abstract

This paper investigates the control problem of vehicle lateral stability and yaw rate using a nonlinear two-degree-of-freedom (2-DOF) dynamic model, employing the sliding mode control (SMC) method. The proposed control strategy aims to enhance vehicle stability and performance under various driving conditions by addressing the complexities of nonlinear dynamics. Through detailed simulations, the effectiveness of the SMC approach is demonstrated. The results indicate significant improvements in lateral stability and yaw rate control, and accurate path tracking. The findings suggest that the SMC method offers a robust solution for advanced vehicle stability control systems, with promising potential for real-world applications.

Introduction

In modern automotive engineering field, vehicle stability and safety have significant importance. For this purpose, many researchers have focused on designing a robust control structure for ensuring desired stability and performance in vehicle dynamics. For example, Canale and colleagues [1,2] conducted two separate studies on investigating the yaw rate control through the application of vertical torque control at constant vehicle speed. They implemented a second-order sliding mode algorithm to develop a robust controller.

This paper explores a nonlinear 2-DOF model for controlling lateral stability and yaw rate using sliding mode control (SMC). Vehicle stability control systems are critical for maintaining trajectory and preventing accidents. SMC, known for its robustness against nonlinearities, is a suitable control approach in this regard. The simulation results demonstrate the effectiveness of the designed closed-loop system in terms of increasing system stability and output performance.

Material and Method

In this section, in order to analyze vehicle motion and design the proposed control structure, a nonlinear 2-DOF bicycle dynamic model is first presented. This model, commonly used in vehicle dynamics, provides a simple yet effective representation of the vehicle's behavior, especially in lateral motion. The 2-DOF bicycle vehicle model used to describe the vehicle lateral dynamics and yaw motion is shown in Figure 1 [3]. The Eqs. (1,2) represent the vehicle dynamic equations as follows [4]:

$$\dot{V}_y = \frac{1}{m}\left[2F_{yf}\cos\delta + 2F_{xf}\sin\delta + 2F_{yr}\right] \tag{1}$$

$$\dot{r} = \frac{1}{I_z}\left[-2F_{yr}l_r + \left(2F_{xf}\sin\delta + 2F_{yr}\cos\delta\right)l_f\right] \tag{2}$$

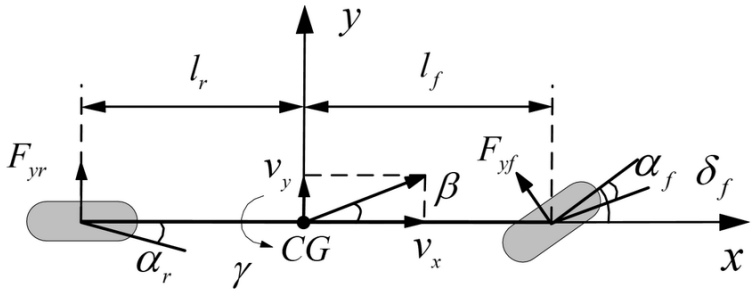


Figure 1. 2-DOF bicycle model [3]

where F_{xf} and F_{yf} , F_{yr} denote the longitudinal and lateral forces, respectively. δ is the steering input angle. V_y and r represent the lateral velocity and yaw rate correspondingly. Also, l_f and l_r are the distance from the center of mass to the front axle and the rear axle, respectively.

Additionally, to precisely model the active forces on the wheels, the Dugoff tire dynamic model is implemented. This model is well-known for its ability to account for the complex interactions between tires and the road surface [5]. The vehicle trajectory (X,Y) is also obtained from the following equations:

$$\dot{X} = V_x \cos\psi - V_y \sin\psi \qquad (5)$$
$$\dot{Y} = V_x \sin\psi + V_y \cos\psi$$

where ψ is yaw angle, and V_x demonstrates longitudinal velocity. The necessary parameters for dynamic modeling of the vehicle are listed in Table 1.

Table 1. The basic parameters for vehicle dynamic modeling

Parameters	symbols	value
m	Mass	1030 kg
I_z	Yaw moment of inertia	1080 Kg.m^2
l_f	Distance from the center of mass to the front axle	1 m
l_r	Distance from the center of mass to the rear axle	1.5 m
C_σ	Longitudinal stiffness of tires	30,000 N/rad
C_α	Lateral stiffness of tires	50,000 N/rad
μ	Friction Coefficient	0.8
C_f	Cornering stiffness of front tire	30,000 N/rad
C_r	Cornering stiffness of rear tire	30,000 N/rad

In the next step, a sliding mode control (SMC) approach is employed in order to enhance the stability of the vehicle. SMC is chosen due to its robust nature and effectiveness in handling system uncertainties and disturbances. By defining the sliding surface based on system tracking error, the controller tries to maintain the system on the specified trajectory. The controller aims to drive the angular velocity tracking error to zero, which means minimizing the difference between the actual angular velocity (r) and the desired value (r_d). The desired angular velocity is obtained according to Eq. 6 [6].

$$r_d = \frac{V_x}{\left(l_f + l_r\right) + k_{us} V_x^2}\delta \qquad (6)$$

k_{us} represents the understeer coefficient which is calculated from Eq. (7).

$$k_{us} = \frac{m\left(l_f C_f - l_r C_r\right)}{\left(l_f + l_r\right) C_f C_r} \qquad (7)$$

where C_f and C_r are the cornering stiffness of front and rear tires. By considering the sliding surface $S = r - r_d$, the control input is determined as follows:

$$u_c = -\frac{1}{I_{zn}} M_{zn} - \rho sign(S) \tag{8}$$

where M_{zn} and I_{zn} represent the nominal torque and nominal moment of inertia, respectively. Ultimately, the dynamic Equation (2) will be rewritten by applying the control signal as follows:

$$\dot{r} = \frac{1}{I_z} M_z + u_c \tag{9}$$
$$M_z = -2F_{yr} l_r + \left(2F_{xf} \sin\delta + 2F_{yr} \cos\delta\right) l_f$$

Results and Discussion

Through simulations, three key results illustrating the proposed control system performance are obtained. Figures (2,3) represent lateral velocity and yaw rate, respectively. Fig. (4) shows the trajectory of the dynamic system response with and without control action. The simulation results indicate that the proposed method significantly enhances vehicle stability. Specifically, the presented figures demonstrate that the SMC method achieves reduced lateral velocity and yaw rate, ensuring that the vehicle maintains a steady lateral movement. Moreover, the method ensures a reasonable trajectory path, indicating that the vehicle follows the desired path accurately.

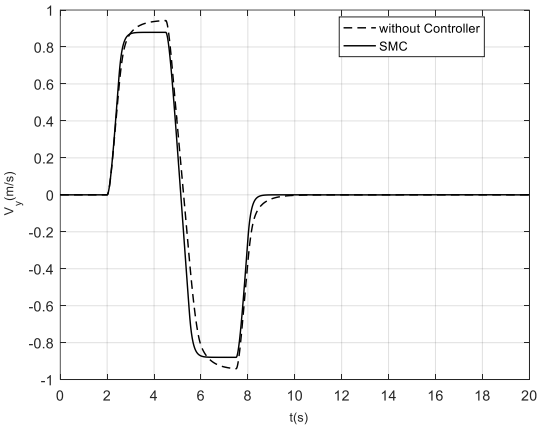


Figure 2. Lateral velocity (m/s)

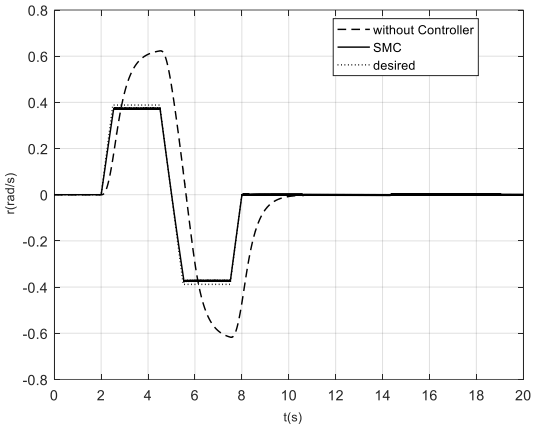


Figure 3. Yaw rate (rad/s)

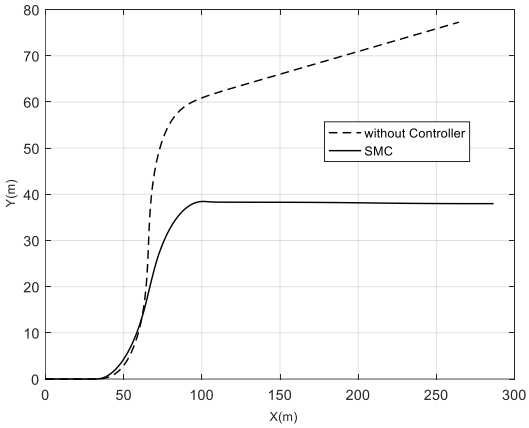


Figure 4. Trajectory in $(X-Y)$ plane (m)

Conclusion

In this study, the control problem of vehicle lateral stability and yaw rate is addressed using a nonlinear 2-DOF dynamic model, which employs the sliding mode control (SMC) method. The simulation results indicate that the SMC method significantly enhances vehicle stability. Specifically, the presented figures demonstrate reduced lateral velocity, well-controlled yaw rate, and reasonable trajectory path. Overall, this method shows great potential for practical implementation in advanced vehicle stability control systems.

References

1. Canale, M., Fagiano, L., Milanese, M., & Borodani, P. (2006). Robust vehicle yaw control using active differential and internal model control techniques. 2006 American control conference.
2. Canale, M., Fagiano, L., Ferrara, A., & Vecchio, C. (2008). Vehicle yaw control via second-order sliding-mode technique. IEEE Transactions on Industrial Electronics, 55(11), 3908-3916.
3. Hu, C., Wang, Z., Taghavifar, H., Na, J., Qin, Y., Guo, J., & Wei, C. (2019). MME-EKF-based path-tracking control of autonomous vehicles considering input saturation. IEEE Transactions on Vehicular Technology, 68(6), 5246-5259.
4. Jazar, R. N. (2008). Vehicle dynamics (Vol. 1): Springer.
5. Bian, M., Chen, L., Luo, Y., & Li, K. (2014). *A dynamic model for tire/road friction estimation under combined longitudinal/lateral slip situation* (0148-7191). Retrieved from
6. Shtessel, Y., Edwards, C., Fridman, L., & Levant, A. (2014). Sliding mode control and observation (Vol. 10): Springer.

Advanced Engineering Days

aed.mersin.edu.tr

Influence of soil characteristics on the performance of buried pipelines under traffic load

Arsalan Amanollahi-Asl [*1], Hasan Biglari [1]

[1]*University of Tabriz, Department of Mechanical Engineering, Iran, arsalan.amanollahi@gmail.com, hbiglari@tabrizu.ac.ir*

Cite this study: Amanollahi-Asl, A., & Biglari, H. (2024). Influence of soil characteristics on the performance of buried pipelines under traffic load. Advanced Engineering Days, 9, 94-97

Keywords
Buried pipe
Soil Characteristics
Traffic load
Soil settlement
FEM

Abstract

The behavior of buried pipes under traffic loading is significantly affected by the properties of the surrounding soil. This study aims to investigate the impact of various soil properties on the behavior of pipelines subjected to vehicular loads. By employing advanced numerical modeling techniques using Abaqus, various soil types, including cohesive and sandy soils, are simulated under both saturated and unsaturated conditions. A Mohr-Coulomb theory-based elasto-plastic analysis is performed to reflect the mechanical properties of the soil, and the pipeline is modeled as a deformable, flexible shell element. The findings of this study have been verified through comparison with reference results, ensuring their accuracy and reliability. The study involved obtaining and comparing the maximum stress, pipe displacement, and settlement values for different soil conditions. The results emphasize a significant difference between cohesive and sandy soils under both saturated and unsaturated conditions.

Introduction

In the design of a buried piping system, it is crucial to take into account multiple factors. However, it is essential not to neglect the properties of the pipe material or the characteristics of the soil surrounding the pipe in any design. During the design process, soil parameters such as soil type, density, and moisture content are typically considered. Among these, soil stiffness plays a crucial role in determining the performance of the pipe-soil system. Past observations have indicated that a greater soil density leads to a higher soil stiffness. Consequently, soil density is often given significant consideration in the design of piping systems [1].

Zhan et al. [2] analyzed how variations in filling material type (soil type) and pipe burial depth affect the load exerted on PVC pipes. Huang et al. [3] created a three-dimensional finite element model to examine how buried steel pipes behave mechanically when subjected to different loads. Their model accounted for the interaction between soil layers, pavement structures, and buried steel pipes. By applying this model, they were able to accurately calculate the mechanical reactions of the buried pipes under various loads.

The objective of this study is to investigate the effects of soil properties on the behavior of buried pipelines subjected to traffic loads. By examining the interplay between soil characteristics and the response of pipelines, valuable insights can be gained regarding the mechanisms governing the interaction between pipelines and soil.

Material and Method

In this study, the maximum water pressure of 414 kPa (60 psi) is used to investigate critical conditions in buried pipelines. This value is within the operational range of water pressure typically observed in pipelines, which ranges from approximately 276 kPa (40 psi) to 414 kPa (60 psi) [4].

The analysis focused on the elastic, perfectly plastic, and isotropic behavior of a relatively large-diameter steel pipeline used for water supply, as outlined in "Table 1" below [4,5,6]:

Table 1. Material properties of pipeline

Terms	Density (kg/m3)	Young's modulus (MPa)	Poisson's ratio	Yield strength (MPa)	Tensile strength (MPa)
Value	7850	210.7×10^3	0.3	490	690 to 840

The study utilized the H20 highway loading specification, which is commonly employed for design purposes. The wheel load magnitudes for H20 design trucks are determined following with standards established by the American Association of State Highway and Transportation Officials. The traffic load magnitude employed in this study, corresponding to the H20 truck loading scenario, was 544,780 Pa [7].

To model the pipeline, this study used a large-diameter steel pipeline under BS EN 10224:2002. The chosen pipeline measured 1524 mm in outer diameter and 20 mm in wall thickness [8]. A 100-meter-long pipeline was modeled for the finite element study.

The mechanical properties of different soils were analyzed through an elasto-plastic approach based on the Mohr-Coulomb theory. The investigation considered two representative soil types and examined the impact of soil moisture content by evaluating characteristic elastic property values for both unsaturated and saturated soil conditions. The characteristics and properties of soils are presented in "Table 2" [4].

Table 2. Material properties of soil

Type of soil	Density (kg/m^3)	Young's modulus (MPa)	Poisson's ratio	Cohesive strength (C - kPa)	Friction angle (ϕ - deg)	Dilation angle (ψ - deg)
Moist sandy soil	1850	24	0.2	17	40	2
Saturated sandy soil	2160	96	0.25	17	40	2
Moist cohesive soil	1700	19	0.25	252	29	2
Saturated cohesive soil	2000	48	0.45	252	29	2

The behavior of soil was simulated using C3D20R elements, while the pipe was modeled using S8R elements, a three-dimensional reduced shell continuum element with eight nodes. The preference for second-order elements over first-order elements is due to their higher accuracy [4].

Results

The results of this study are compared with those of Lee [2], who examined a related subject, to verify our findings. The outcomes, which are displayed in "Table 3," reveal how accurate the suggested model is.

Table 3. Comparative analysis of maximum stress of buried pipeline with Hyuk Lee's research

	Burial depth	1	2	3	4	5	6
Maximum stress of buried pipeline(Mpa)	Hyuk Lee	578.9	585.5	587.7	593.4	596	601.4
	validation	576.2	584.9	589.1	593.5	594.1	598.4

The stress of a pipeline buried in sandy soil is higher than that of cohesive soil, as illustrated in "Figure 1". The reason for this discrepancy is that sandy soil has a higher density than cohesive soil. The weight on top of the pipe is increased by the soil's higher density. Consequently, the pipe experiences a notable rise in stress. Additionally, when comparing the saturated and moist conditions, it is observed that the saturated state exhibits a much lower stress level than the unsaturated condition.

"Figure 2" illustrates that the pipe's displacement is greatest in moist cohesive soil and lowest in saturated cohesive soil. In comparison to the unsaturated state, there is less pipe settlement in the saturated state. It was determined that the pipe's displacement amount reduces as soil saturation rises.

According to "Figure 3", soil settlement is less in saturated conditions compared to moist conditions. The greatest soil settlement occurs in moist cohesive soil, while the least occurs in saturated cohesive soil. In unsaturated conditions, cohesive soil settles more than sandy soil; however, in saturated conditions, the opposite is true.

Conclusion

This study demonstrates that soil properties significantly impact the behavior of buried pipelines subjected to traffic loads. Through comprehensive numerical modeling, we observed that various soil characteristics, including type, stiffness, cohesion, and moisture content, influence the deformation and stress distribution in pipelines. The obtained results show that Saturated soils experience less soil settlement compared to unsaturated (moist) soils. Additionally, the maximum stress experienced by the buried pipeline in saturated soils

is significantly lower than in moist soils and The amount of pipe displacement is reduced in saturated soil conditions compared to moist soil conditions. These insights highlight the necessity of considering soil properties in the design and maintenance of buried pipeline systems to ensure their structural integrity and longevity under traffic-induced stresses. By accounting for these factors, engineers can develop a more resilient pipeline infrastructure capable of withstanding the complex interactions between soil and traffic loads.

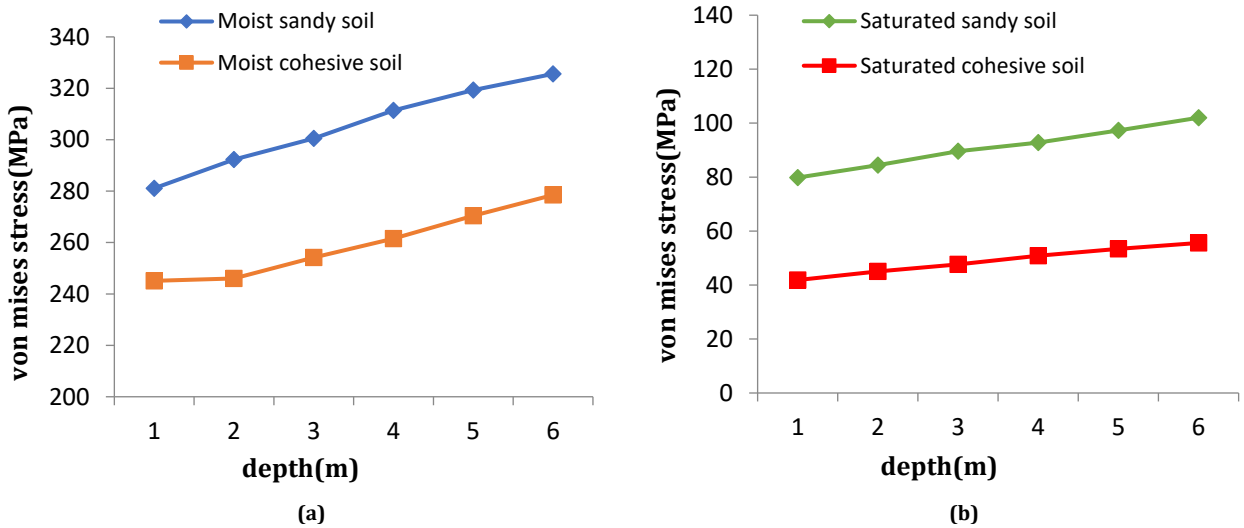


Figure 1. Maximum stress of buried pipeline: (a) Moist soils, (b) Saturated soils

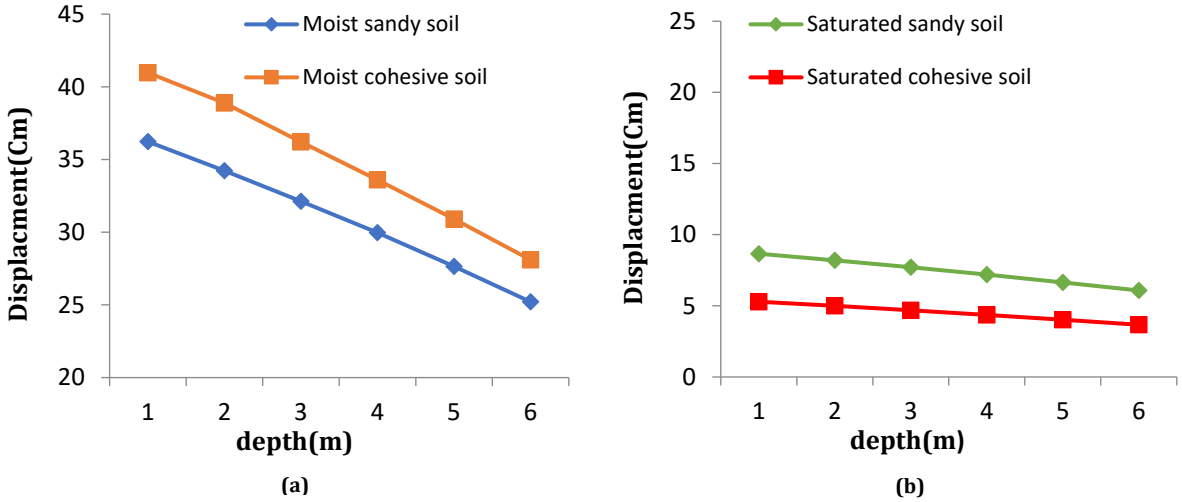


Figure 2. Maximum settlement of buried pipeline: (a) Moist soils, (b) Saturated soils

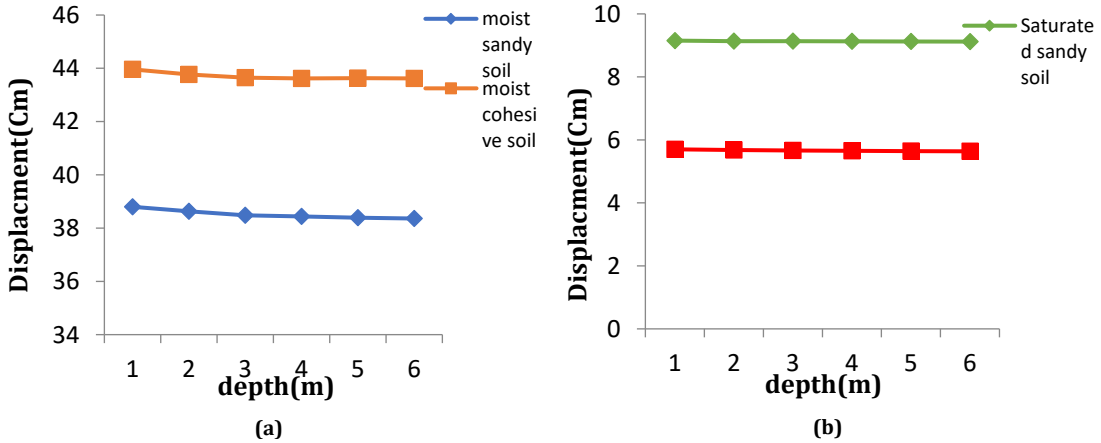


Figure 3. Maximum settlement of soil: (a) Moist soils, (b) Saturated soils

References

1. Mosler, A. P. (1990). Buried pipe design, New York, NY (USA) McGraw Hill Book Co.
2. Zhan, C., & Rajani, B. (1997). Load transfer analyses of buried pipe in different backfills. Journal of transportation engineering, 123(6), 447-453.
3. Huang, C., Chen, J., & Sun, Y. (2022). Mechanical simulation and calculation methodology of buried steel pipes under multiple loads. *Case Studies in Construction Materials*, *17*, e01662.
4. Lee, H. (2010). Finite element analysis of a buried pipeline. Master's thesis, The University of Manchester, Manchester, UK, Retrieved from https://www.escholar.manchester.ac.uk/jrul/item/?pid=uk-ac-man-scw:97322
5. BSI. (2002b) Seamless steel tubes for pressure purpose - Technical delievery conditions - Part 2: Non-alloy and alloy tubes with specified elevated temperature properties. IN CEN (Ed. *BS EN 10216-2:2002.* London, BSI.
6. Liu, P. F., Zheng, J. Y., Zhang, B. J., & Shi, P. (2010). Failure analysis of natural gas buried X65 steel pipeline under deflection load using finite element method. *Materials & Design*, *31*(3), 1384-1391.
7. Khademi-Zahedi, R., & Shishesaz, M. (2019). Application of a finite element method to stress distribution in buried patch repaired polyethylene gas pipes. Underground Space, 4(1), 48-58.
8. BSI. (2002a) Nonalloy steel tubes and fittings for the conveyance of water and other aqueous liquid - Technical delivery conditions. IN CEN (Ed. *BS 10224:2002).* London, BSI.

Advanced Engineering Days

aed.mersin.edu.tr

A computational fluid dynamics simulation on a marine engine turbocharger to enhance the output power

Amirreza Javaherian*[1], Reza Mahmoodi [2], Peyman Rahmani [1]

[1]University of Tabriz, Department of Mechanical Engineering, Iran, a_javaherian@tabrizu.ac.ir, rahmanipeyman1373@gmail.com
[2] Islamic Azad University, Tabriz Branch, Department of Mechanical Engineering, Iran, stu.r.mahmoodi@iaut.ac.ir

Cite this study: Javaherian, A., Mahmoodi, R., & Rahmani, P. (2024). A computational fluid dynamics simulation on a marine engine turbocharger to increase the output power. Advanced Engineering Days, 9, 98-100

Keywords
Turbocharger
Marine Diesel Engine
Turbocharger Matching
Performance Improvement

Abstract

In this research, a comprehensive study on the selection and adaptation of turbochargers for a marine diesel engine with 1300 horsepower is presented. This process involves a detailed analysis of engine specifications, operating conditions, and performance requirements to determine the most suitable turbocharger options for the engine. The results obtained from the analysis of the ventilation system for the 1300 hp engine reveal that EFR 91S74, S300SX-E 91S75 and GT42 turbochargers show superior performance characteristics in compatibility with the engine. Also, in order to increase the output power of the engine by 200 hp, the S300SX-R 88X77, EFR (92X79), S400SX-E 96X75 and GTX 4508 turbochargers are the proper options. This research provides an in-depth understanding of the turbocharger selection and matching process for marine diesel engines and clarifies critical considerations and methods for optimizing engine performance. Also, the considered turbocharger of the proposed engine has been evaluated from the perspective of computational fluid dynamics for different engine speeds.

Introduction

Marine diesel engines are internal combustion engines specifically designed for use in marine environments. These engines are commonly used to power various types of watercraft, including ships, boats, and submarines. These engines are known for their strength, reliability and efficiency, and these factors have made them a popular choice for marine propulsion. One of the key advantages of marine diesel engines is their high output torque, which makes them suitable for powering large and heavy ships.

Considering that the diesel engine is an important part of marine vessels, the optimal design of the propulsion system is important. The vital factors in the design of marine diesel engines are [1]: Optimum adjustment of the engine with the floating propeller, optimizing auxiliary systems required for engine operation (lubricating oil, fuel, cooling system, etc.), preventing harmful and damaging vibrations, generating auxiliary power in marine vessels, and optimal thermal recovery of engine combustion products. Several improvements have been proposed to increase the energy efficiency of large marine engines, including the use of materials with high temperature resistance, utilization of waste heat from exhaust gases, and improvement of the thermodynamic cycle of the engine [2-5]. Meanwhile, the turbocharging system is very important; Because the use of this system leads to an increase in engine power while improving fuel consumption and relatively low costs [6].

The research of Mizitras et al. [7], emphasizing the vital role of the turbocharger in providing the air required for the engine combustion process, introduced a new method for matching and selecting a single intake system with a two-stroke marine engine. The proposed method consisted of three steps. In the first step, the engine performance was estimated and compressor family databases were developed using a zero-dimensional single-engine cylinder model and a parametric compressor tool, respectively. The second stage included checking the compatibility of the compressor and engine maps and identifying the compressor maps that meet the specified requirements. The third phase consisted of turbine matching and selection of the optimal compressor and turbine to minimize specific engine fuel consumption for a selected propeller curve. The results showed that the developed

method can identify a suitable turbocharger that has the potential to improve engine fuel consumption by 2-4%. In general, this research presented a comprehensive method for choosing a turbocharger and matching it with a two-stroke marine engine with a focus on improving fuel consumption and engine efficiency.

In this study, we conduct a thorough analysis of a marine diesel engine's turbocharger, identifying critical parameters that influence the matching process. Subsequently, to boost the engine's output power by 200 horsepower, we carefully select turbochargers that align with the new engine characteristics. Additionally, we explore geometric modifications to the existing turbocharger to ensure optimal compatibility with the enhanced engine's operational requirements.

Material and Method

In the first step of matching the turbocharger with the proposed marine diesel engine, the mass flow rate of the air consumed by the engine must be calculated. The mass flow rate of air utilized by the engine is dependent on the produced power, the ratio of air to fuel and the brake specific fuel consumption.

$$W_f = \frac{Power \times BSFC}{60} \tag{1}$$

$$W_a = \frac{Power \times A/F \times BSFC}{60} \tag{2}$$

where the quantities BSFC and A/F represent the brake specific fuel consumption and air-fuel ratio, respectively.

In the next step, the absolute pressure of the air inside the manifold must be calculated according to the equation of the ideal gas state and from the following relation:

$$MAP = \frac{W_a \times R \times (460 + T_m)}{VE \times \frac{N}{2} \times V_d} \tag{3}$$

In the above equation, MAP is the absolute pressure of the manifold (in psia) required to provide engine power, W_a is the air flow rate of the engine (in lbm/min), R is the global gas constant, T_m represents the inlet air temperature of the manifold (in °F), VE is volumetric efficiency, N is engine speed in rpm, and V_d is engine displacement (in in^3). Based on the above relation, we can write:

$$V_d = \frac{W_a \times R \times (460 + T_m)}{VE \times \frac{N}{2} \times MAP_{req}} \tag{4}$$

In Table 1, the main operational specifications of the 1300 hp diesel engine are presented.

Table 1. Main operational specifications of the 1300 hp diesel engine

Engine rpm	Inlet air pressure (kPa)	Air manifold guage pressure (kPa)	Brake specific fuel consumption (gr/kWh)
1750	86.32	40	240.4
2250	86.32	130	227
2550	86.32	170	231.5
2800	86.32	230	257

Results

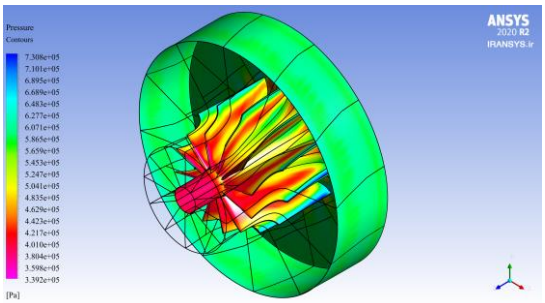


Figure 1. Pressure contours of the turbine of 1300 hp engine turbocharger

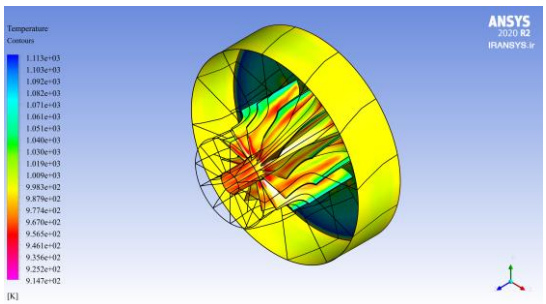


Figure 2. Temperature contours of the turbine of 1300 hp engine turbocharger

Discussion

By considering the engine operational conditions, a set of turbochargers were examined to match the engine specifications and for 1300 hp engine, EFR 91S74, S300SX-E 91S75 and GT42 turbochargers showed superior performance characteristics in compatibility with the engine. Also, for the 1500 hp engine, S300SX-R 88X77, EFR (92X79), S400SX-E 96X75 and GTX 4508 turbochargers were the best options. Also, using computational fluid dynamics tools, an analysis was performed on the turbochargers and the results, including pressure and temperature distribution contours are represented in Figures 2 and 3, respectively.

Conclusion

Our investigation focused on selecting turbochargers for typical marine diesel engines. After analyzing the ventilation system of a 1300 hp engine, we identified three proper-performing turbochargers: EFR 91S74, S300SX-E 91S75, and GT42. These models demonstrated superior compatibility with the engine. Additionally, we explored options for power enhancement, including the evaluation of S300SX-R 88X77, EFR (92X79), S400SX-E 96X75, and GTX 4508 turbochargers. These modifications could led to a substantial 200 hp increase in the output power of the engine. Furthermore, To assess the impact of geometric changes on the basic turbocharger to enhance the output power, we employed computational fluid dynamics simulations. Our research contributes valuable insights to turbocharger optimization in marine propulsion systems.

References

1. Mollenhauer, K., & Tschöke, H. (Eds.). (2010). Handbook of diesel engines (Vol. 1). Berlin: Springer.
2. Kyrtatos, A., Spahni, M., Hensel, S., Züger, R., & Sudwoj, G. (2016, June). The development of the modern low-speed two-stroke marine diesel engine. In International Council on Combustion Engines (CIMAC) Congress, paper (No. 120).
3. Pierce, D., Haynes, A., Hughes, J., Graves, R., Maziasz, P., Muralidharan, G., ... & Daniel, C. (2019). High temperature materials for heavy duty diesel engines: Historical and future trends. Progress in Materials Science, 103, 109-179.
4. Singh, D. V., & Pedersen, E. (2016). A review of waste heat recovery technologies for maritime applications. Energy conversion and management, 111, 315-328.
5. Zhao, J. (2017). Research and application of over-expansion cycle (Atkinson and Miller) engines–A review. Applied Energy, 185, 300-319.
6. Aghaali, H., & Ångström, H. E. (2015). A review of turbocompounding as a waste heat recovery system for internal combustion engines. Renewable and sustainable energy reviews, 49, 813-824.
7. Mizythras, P., Boulougouris, E., & Theotokatos, G. (2019). A methodology for single turbocharger-marine engine matching.

Advanced Engineering Days

aed.mersin.edu.tr

Remote sensing and hydrometeorological analysis of River Delta dynamics: A case study of the Kur River Delta

Turkan Mamishova

Baku State University, Azerbaijan, turkan.memishova@gmail.com

Cite this study: Mamishova, T. (2024). Remote sensing and hydrometeorological analysis of River Delta dynamics: A case study of the Kur River Delta. Advanced Engineering Days, 9, 101-104.

Keywords
Coastal infrastructure
Geospatial analysis
Coastal erosion
Risk assessment
Climate change adaptation

Abstract

This study delves into the intricate interplay of factors influencing the fluctuations in the water level of the Caspian Sea, focusing primarily on climate variations, seismic activities, and coastal processes. Employing high-resolution satellite imagery and data gathered from terrestrial hydrometeorological stations, the research unveils the profound impact of sea level changes on the geomorphological features of the coastal zone, particularly emphasizing the Kura River delta. The findings of this investigation serve as a cornerstone for the development of economically efficient strategies in the construction of coastal zone infrastructure. Furthermore, they provide invaluable insights into the formulation of adaptation measures necessary to mitigate the effects of Caspian Sea level fluctuations. By comprehensively understanding the multifaceted dynamics at play, stakeholders can better prepare and implement measures to safeguard coastal communities and vital infrastructure against the challenges posed by the ever-changing Caspian Sea environment.

Introduction

In general, river deltas are highly dynamic and sensitive environments exposed to a wide range of natural and man-made influences. Since the Caspian Sea has no access to the ocean, its level changes are irregular and cover a wide range.The level changes cause the geomorphological structure of the Kurin delta to be very dynamic, as well as the Volga river delta. Therefore, solving issues such as infrastructure planning, land cover and land use efficiency improvement, settlement expansion, ecosystem protection and development in the Kura River delta creates the need for a comprehensive study of the geomorphological changes occurring in the river and coastal zone. In addition, due to recent mistakes in the management of water use of the Kura river, the water of the river has reached its drying limit, and the construction of dams in Ana and Bala Kura to prevent this is a factor that has an important impact on the geomorphological structure of the delta. The management of the Kura River and the coastal zone, which is subject to such intensive effects, requires continuous and high-precision monitoring of the geomorphological dynamics of the delta, which is difficult to achieve only with traditional topographical measurements .

Material and Method

In this study, high-resolution satellite images such as Tasseled Cap Transformation (Brightness, Greenness, Moisture) and DSAS (Digital Coastal Analysis System) were used to determine delta area dynamics, coastal zone and shoreline variability, their impact areas, and quantitative indicators of geomorphological processes. processed by semi-automated methods.

Kura delta it consists entirely of accumulative coastal forms [1]. Determining the geographical position of the coastline by remote sensing is not limited by weather, surface, sea conditions or geographic environment, and it has the capability of fast, flexible and continuous monitoring [2]. Using satellite imagery, and several factors present difficulties: changes in sea level, movement of the coastline due to swell and subsidence, presence of waves, and the presence of wats and wetlands along the coast that act as part of the water itself. is misclassified by showing [3] In this work, atmospheric and geometric correction operations were performed on satellite images in advance to determine the automatic position of the coastline using ArcGis and ENVI software. Landsat 1985-

2020 as a database for delineating coastlines in research 5 , Landsat 8 and Sentinel 2 satellite images were used. Detecting delta progradation over 35 years from 1985 to 2020 with a five-year interval Modified Normalized Difference Water Index (MNDWI), Normalized Difference Vegetation Index (NDVI) and Tasseled Cap Transformation (TCT) method for application has been done. Although NDVI is set to assess the density and condition of vegetation, it even allows to separate 2 other classes, i.e. water and bare land [4].

In the next step , the TCT method, widely and successfully used in remote sensing, was applied to clearly distinguish the "soil-water cover" [5]. However, TCT coefficients are sensor-dependent, and specific coefficients have been calculated based on reflectance data from Landsat and Sentinel 2 satellites [6]. After this analysis, the position of the coastline (geographical coordinates) was determined with higher accuracy and its fluctuations were determined accordingly . The satellite image processed by this method is given in Figure 1.



Figure 1. Geographical position of the coastline in 1985-2020

Results

As it can be seen, during the period 1985-2020, the coastline moved both towards the sea and towards the land. Using ArcGis tools, transects (perpendicular lines) were calculated every 300 m to measure shoreline displacements. Thus, when looking at the comparison every five years, the coastline in the area of 1985-1990 was 244.7 m on average, during 1990-1995 it was 472.5 m landward, in 1995-2000 it was 155.5 m, in 2000- It moved 10.5 m during 2005, 303.1 m during 2005-2010, 263.6 m during 2010-2015, and 67.1 m on average during 2015-2020 . Above , from 1985 to 2000, it can be observed that the coastline moved towards the sea . During these years, on average, the coastline has moved 11.9 m towards the sea. The result of calculations for the years 1985 and 2020 alone shows that the coastline has moved seaward by an average of 345.5 m (Figure 2).

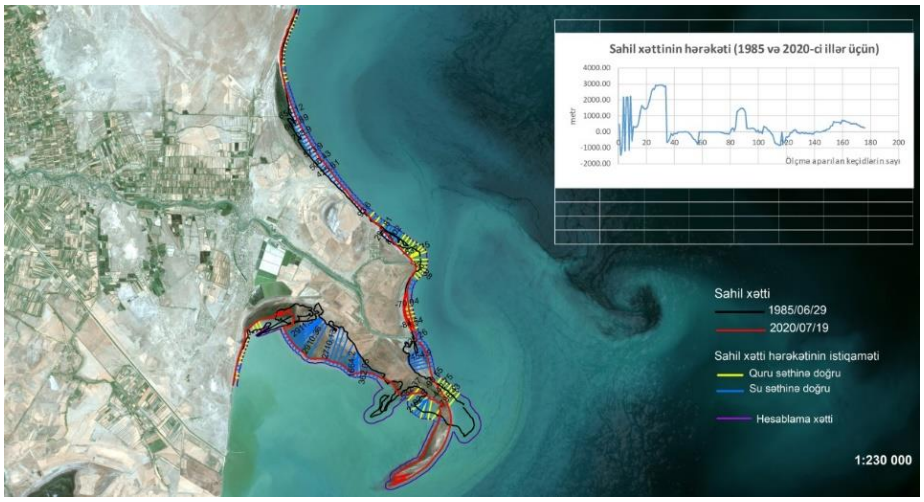


Figure 2 . Coastline erosion in 1985 and 2020

In parallel, the evolution of the delta for the considered years was studied and area changes were calculated . Thus, from 1985 to 1995, the rise of the Caspian Sea level by 1.37 m resulted in an average decrease of 31.18 km 2 of area in the Kura River delta , and a decrease of 1.39 m from 1995 to 2000 resulted in an increase in area of 16.9 km^2 was observed.

Discussion

In Figure 4, it is possible to see that the fluctuation of the level of the Caspian Sea affects the changes occurring in the delta area (Figure 6). In recent years, the minimum sea level in the Caspian Sea was recorded in 1977 at -29 m. Since 1978, the sea level has risen and was recorded at -26.66 m in 1995, after which the sea level decreased by 50 cm in 1998 and then remained practically constant until 2003 and then in 2005. 30 until cm increased to the level of -26.8 m. Since 2005, the level has decreased by 8-10 cm per year with very small fluctuations.

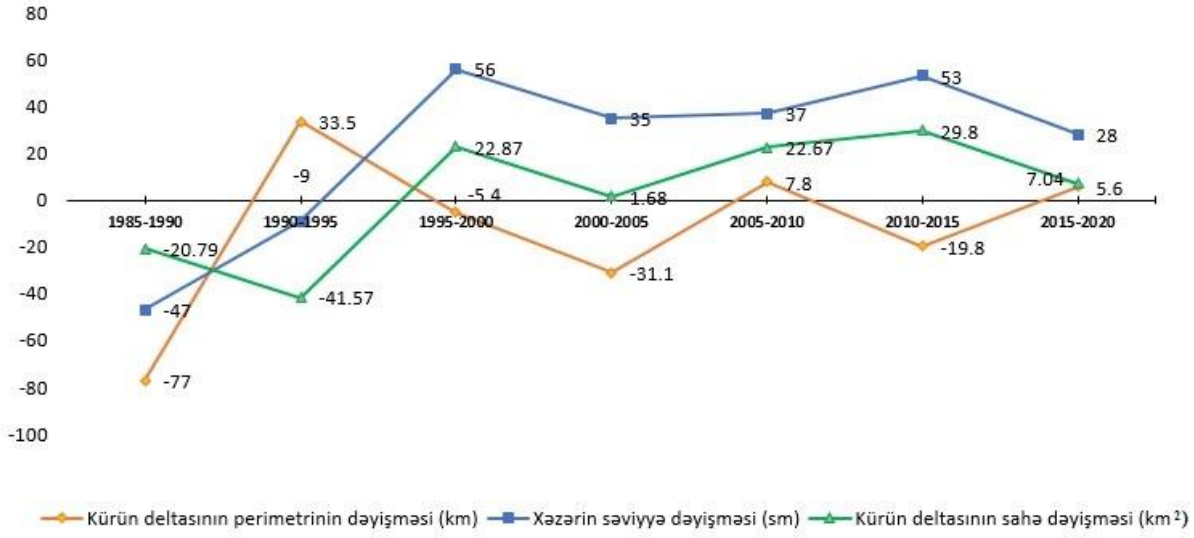


Figure 4. Relationship between Caspian Sea level changes and the area and perimeter of the Kura delta

In 2020, the Caspian Sea reached its reference level of -28 meters. This historical event was observed for the 3rd time since 1837, when instrumental measurements began (Figure 4). Let's note "About the legal status of the Caspian Sea" In the Convention, the term "Normal outlet line" which is the annual mean coastline at minus 28.0 meters is taken as the basis for the distribution of water between Caspian littoral countries. For this reason, it is important to accurately calculate the geographic coordinates of the coastline at the reference level by processing high-resolution satellite images with appropriate software.The result. According to most researchers, the main factor that causes fluctuations in the level of the Caspian Sea is climate. Although river flows, precipitation, and evaporation caused by the climate are accepted as the main indicators, the sharp level changes that began in 1977 and continue to this day cannot be explained by these factors alone. The studies conducted in the direction of studying the relationship between fluctuations in the level of the Caspian Sea and seismic processes have revealed that it plays a partial role in this process. In other words, even insignificant displacements of the edge of the South Caspian plate due to seismic events are believed to cause serious fluctuations in sea level both during the preparation of earthquakes and after their occurrence. The research conducted in this work shows that there is an important correlation between the number of earthquakes and level fluctuations and the importance of conducting deeper research in this direction.

Conclusion

The study found that the erosion (mainly due to subduction) and marine accumulation processes in the coastal zone of the Kura delta are closely related to the change in the level of the Caspian Sea. The rise of the level of the Caspian Sea (1977–1996) led to the intensification of the erosion processes (correlation coefficient: 0.82), and the weakening of the accumulation processes. The stabilization and lowering of the sea level (1996-2019) led to the slowing down of subduction processes and the strengthening of accumulation processes (correlation coefficient: -0.46).

The processing of high-resolution satellite images, as well as the processing and analysis of data from terrestrial hydrometeorological stations, revealed that sea level changes have a serious effect on the geomorphological indicators of the coastal zone, including the Kura River delta. The researches conducted in this direction are important from the point of view of economically efficient construction of the infrastructure of the coastal zone against the background of level fluctuations of the Caspian Sea.

References

1. Shirinov N.Sh., Valiyev XA, and Aliyev YG: Nature and ecology of the shores of the Caspian Sea. Elm Baku-1998,
2. Mamishova TT Due to the drop in the level of the Caspian Sea evaluation of the geomorphological properties of the coastal region based on the processing of satellite images . Intercontinental Geoinformation Days, 2022 p.266-269
3. Markham BL, Barker JL Landsat MSS and TM post calibration dynamic ranges, exoatmospheric reflectance's and at-satellite temperature: EOSAT. Landsat Technical Notes 1986; 1: pp. 3-8.
4. Frazier PS, Page KJ Water body detection and delineation with Landsat TM data. Photogrammetric Engineering and Remote Sensing 2000; 66 (12): p. 1461-1467.
5. Yamamoto KH, Finn MP. Approximating tasselled cap values to evaluate brightness, greenness, and wetness for the Advanced Land Imager (ALI): US Geological Survey Scientific Investigations Report 2012–5057, p.9.
6. Gardashov RH, Mamishova TT. Study of the dynamics of the coastal zone of the Caspian sea based on satellite image processing. XI All-Russian conference with international participation "Contemporary problems of optics of natural waters" (ONW'2021) Sankt-Petersburg- 2021, c 187-193

Advanced Engineering Days

aed.mersin.edu.tr

The effect of solar radiation on O^3 pollution concentration in urban areas, case of Tehran, Iran

Iraj Teimuri*[1], Mohammad Nemati [1], Sajjad Moshiri [2], Ayat Khaleel Dhiab Gharibawy [2]

[1]*University of Tabriz, Department of Urban and Regional Planning, Iran, Iraj-teymuri@tabrizu.ac.ir, mo.nemati@tabrizu.ac.ir*
[2]*University of Tabriz, Department of Remote Sensing & GIS, Iran, sajjadmoshiri@gmail.com, ayatkhaleeldhiab123@gmail.com*

Cite this study: Teimuri, I., & Nemati, M., & Moshiri, S., & Garibavi, A. K. D. (2024). The effect of solar radiation on O^3 pollution concentration in urban areas, case of Tehran, Iran. Advanced Engineering Days, 9, 105-108

Keywords
Solar radiation
Ozon
Landuse
Tehran

Abstract

Solar radiation, acting as a catalyst, transforms nitrogen oxides in the presence of organic compounds into ozone. The concentration of this pollutant in urban areas is influenced by factors such as land use, open spaces, asphalt surfaces, and solar radiation intensity. This study investigates the relationship between solar radiation and ozone concentration in Tehran. Data from Sentinel-5 satellite products (for ozone concentration) and MODIS products (for solar radiation) were analyzed using Zonal Analysis and Pearson correlation tests. The findings reveal that the highest ozone concentration occurs in agricultural, industrial, workshop, transportation, and warehousing land uses. Additionally, a positive correlation (with a coefficient of 0.76) exists between solar radiation and ozone concentration in Tehran, Iran.

Introduction

Among the consequences of using fossil fuels in cities is producing various pollutants. One of these pollutants, which is a result of incomplete combustion in vehicles, is the NOx group of pollutants. The reaction of nitrogen oxides (NOx gases) and volatile organic compounds (VOCs) in the presence of sunlight (photochemical reaction) leads to the production of ozone gas at the city level. Maximum ozone concentrations occur in the afternoon and are generally considered a summer pollutant. Exposure to ozone causes multiple respiratory problems such as asthma attacks, decreased lung function, and lung diseases. The concentration of this pollutant at the urban level can be related to various factors such as urban land use, open spaces, asphalt surfaces, and the intensity of solar radiation. Among the factors affecting the distribution of ozone concentration in the city, the purpose of this study is to investigate the relationship between the intensity of solar radiation and ozone concentration.

In this regard, (1) presented evidence for a positive correlation between solar radiation and ozone formation in the troposphere during daylight hours. This finding emphasizes the role of sunlight in driving ozone production near the Earth's surface. In Baghdad, Iraq investigate the seasonal variations in ozone concentration within the stratosphere and its connection to solar radiation patterns. This broadened the scope by demonstrating the impact of solar radiation on ozone levels at higher altitudes (2). Also, (3), explored how alterations in solar radiation intensity, specifically due to cloud cover, can influence tropospheric ozone levels. This highlights the importance of considering atmospheric conditions alongside solar radiation when examining ozone concentration.

Material and Method

Average ozone concentration from Sentinel-5P (4) in summer for the period 2019 to 2023 obtained in Google Earth Engine. This dataset provides offline high-resolution imagery of total column ozone concentrations. Also, MCD18A1.061 Surface Radiation Daily/3-Hour (5) was used for Solar Radiation during the same period. The MCD18C2 Version 6.1 is a Moderate Resolution Imaging Spectroradiometer (MODIS) Terra and Aqua combined Photosynthetically Active Radiation (PAR) gridded Level 3 product produced daily at 0.05 degree (5,600 meters

at the equator) resolution with estimates of PAR every 3 hours. The information layer related to the land use of Tehran city was also prepared from the master plan of this city.

Pearson's correlation and Least Square Regression test were used for data analysis. At first, the data image system related to solar radiation and ozone concentration and urban land use layer was selected for all data in UTM, Zone 39 with wgs1984 computational ellipse. Then, using the land use layer, the Zonal function was executed on the data of solar radiation and ozone separately. The output of the tables shows the average concentration of ozone and solar radiation in the land uses of Tehran (Table 1) Finally, the tables are entered into Excel, and in There Pearson's correlation test and regression line equation were calculated.

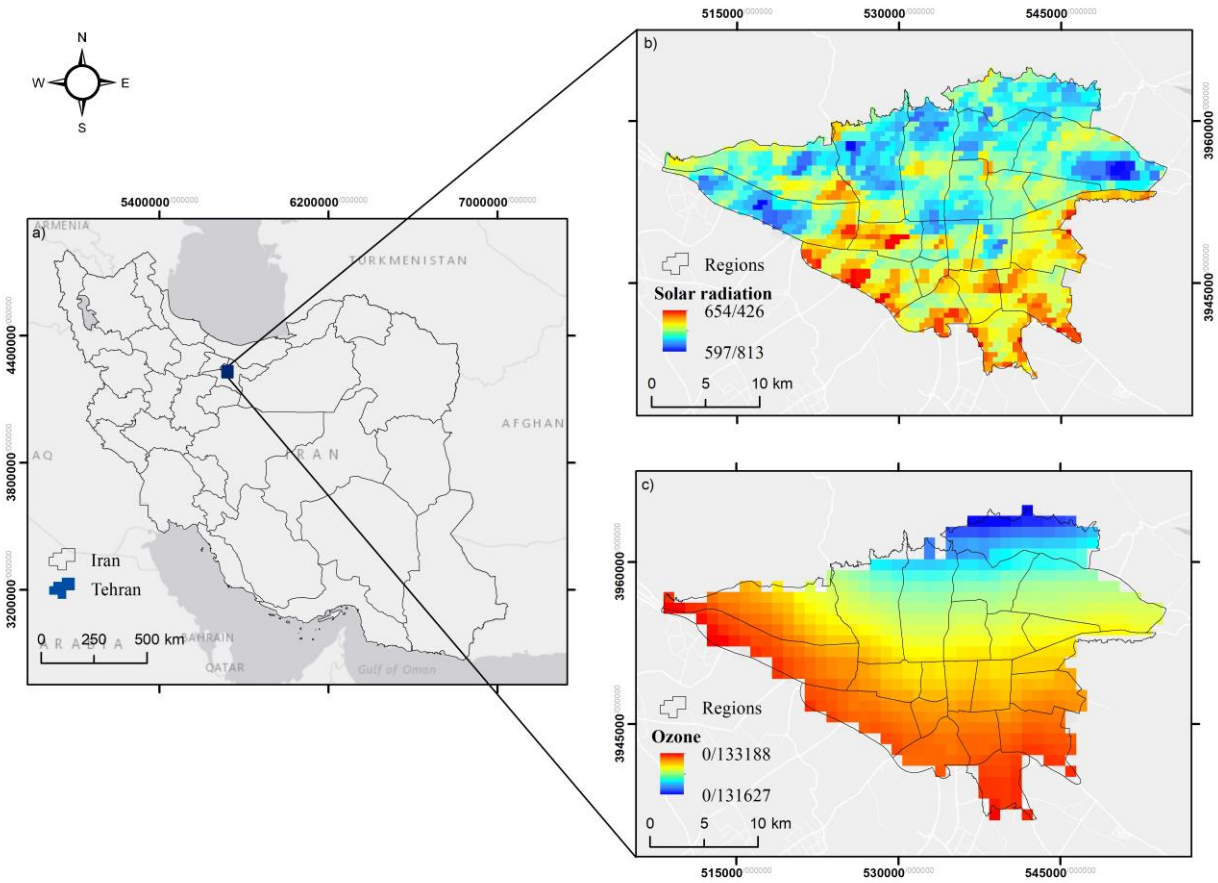


Figure 1. Geographic location of the study area: a) Iran, b) Solar radiation in Tehran, c) Ozone in Tehran.

Tehran, the capital of the Islamic Republic of Iran (IRI), is situated in the northern part of the country and has a population of approximately 8.7 million people. During the day, this number can increase to over 12.5 million due to daily commuters from nearby cities for work or study (6). Ranking as the 19th largest city in the world by population, Tehran encompasses 349 neighborhoods over an area of about 620 km^2. The city's topography and meteorological conditions significantly contribute to its poor air quality. Located at altitudes ranging from 1050 to 1800 meters above sea level and encircled by the Alborz Mountain Range, the polluted air often becomes trapped within the city.

Results

According to the results, the highest observed ozone is 0.1329 mol/m^2 and the lowest is 0.1324 mol/m^2. Also, the highest solar radiation in Tehran is 633.50 W/m^2 and the lowest observed amount is 615.78 W/m^2 (Table 1).

The research findings from the Zonal function indicate that the highest average solar radiation and ozone concentration are observed for agricultural, transportation, warehousing, workshop, and industrial purposes. Additionally, according to Figure 1, the highest solar radiation is observed in the southern and southwestern regions of Tehran. Similarly, the highest ozone concentration is also observed in the southern urban areas, forming a belt from southeast to south and southwest of Tehran. The results of the Pearson correlation test and least squares error also show that the correlation coefficient obtained between solar radiation and ozone concentration is 0.76, indicating a strong association between solar radiation and ozone. The regression equation fitted for solar radiation data with ozone concentration is shown in Figure 2.

Table 1. Solar radiation and O^3 concentration mean in land uses

Landuse	Solar radiation (W/m^2)	O^3 (mol/m^2)
Agriculture	633/50	0/1329
Transportation and storage	630/76	0/1328
Green space	625/52	0/1327
Industrial	625/15	0/1329
Urban infrastructure	622/35	0/1327
Military	622/28	0/1327
Barren land	622/03	0/1326
Residential	620/37	0/1326
Commercial	618/61	0/1327
Non-Categorical	615/78	0/1324

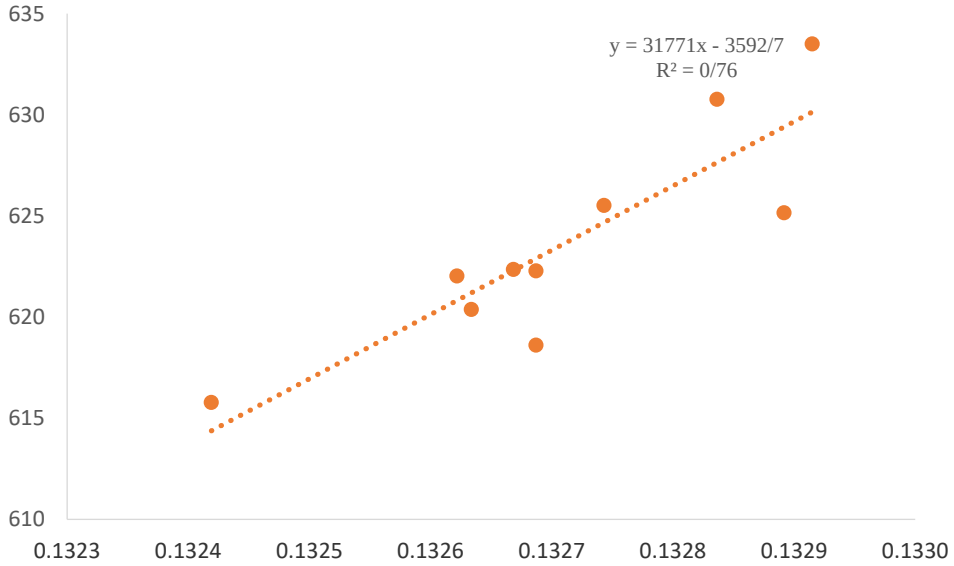


Figure 2. Correlation between solar radiation and O^3 concentration.

Discussion

As previously mentioned, the reaction of nitrogen oxides (NOx) and volatile organic compounds (VOCs) in the presence of sunlight (photocatalytic reaction) leads to the production of ozone gas in urban areas. In this study, the solar radiation layer was considered as the photocatalytic agent in the hypothetical environment. According to the findings of the Pearson correlation test, the research demonstrated a strong positive correlation between solar radiation intensity and ozone concentration at the city level. The correlation coefficient, as shown in Figure 2, was 0.76. However, other factors, potentially acting as catalysts in this reaction, were beyond the scope of the present study. These findings align with previous research by Jasaitis et al. (2016) and Wang et al. (2022), which also emphasized the positive correlation between solar radiation and ozone formation during daylight hours. Given the significant role and importance of various land uses in ozone formation at the city level, future research should further investigate and explore these factors.

Conclusion

The reaction of nitrogen oxides (NOx) and volatile organic compounds (VOCs) in the presence of sunlight (photocatalytic reaction) leads to the production of ozone gas in urban areas. Therefore, this study aimed to investigate the relationship between solar radiation and ozone concentration in Tehran. To achieve this, data from the MODIS and Sentinel-5 satellites were used to create raster layers of solar radiation and ozone concentration for the 5 years from 2019 to 2023 during the summer. Data extraction for solar radiation intensity and ozone concentration was performed using Google Earth Engine, followed by analysis in ArcGIS and Excel. The research findings demonstrated a positive and significant correlation (correlation coefficient of 0.76) between solar radiation intensity and ozone concentration in Tehran. However, other factors may also contribute to ozone pollution levels in different urban areas, warranting further research in this field.

References

1. Jasaitis D, Vasiliauskienė V, Chadyšienė R, Pečiulienė M. Surface Ozone Concentration and Its Relationship with UV Radiation, Meteorological Parameters and Radon on the Eastern Coast of the Baltic Sea. Atmosphere. 2016; 7(2):27. https://doi.org/10.3390/atmos7020027.
2. Ghalib, Wedyan & Al-Taai, Osama & Abbood, Zainab. (2020). The Influence of Solar Radiation on Ozone Column Weight over Baghdad City. IOP Conference Series: Materials Science and Engineering. 928. 10.1088/1757-899X/928/7/072089.
3. Wang D , Wang J , Yang Y , Jia W , Jiang X , Wang Y. (2022). Impact of meteorological conditions on tropospheric ozone and associated with parameterization methods for quantitative assessment and monitoring. Frontiers in Environmental Science. Vol. 10. DOI=10.3389/fenvs.2022.981104
4. Google Earth Engine. Accessed via: https://developers.google.com/earth-engine/datasets/catalog/COPERNICUS_S5P_OFFL_L3_O3.
5. Google Earth Engine. Accessed via: https://developers.google.com/earth-engine/datasets/catalog/MODIS_061_MCD18A1.
6. Hosseini, V., Shahbazi, H., 2016. Urban air pollution in Iran. Iran. Stud. 49 (6), 1029–1046. https://doi.org/10.1080/00210862.2016.1241587.

Advanced Engineering Days

aed.mersin.edu.tr

Prediction of water quality indices utilizing easily accessible elements: A case study of Qatur River

Milad Sharafi [*1], Javad Behmanesh [1], Vahid Rezaverdinejad [1], Saeed Samadianfard [2]

[1] *Urmia University, Department of Water Engineering, Iran, st_m.sharafi@urmia.ac.ir, j.behmanesh@urmia.ac.ir, v.verdinejad@urmia.ac.ir*
[2] *University of Tabriz, Department of Water Engineering, Iran, s.samadian@tabrizu.ac.ir*

Cite this study: Sharafi, M., Behmanesh, J., Rezaverdinejad, V., & Samadianfard, S. (2024). Prediction of water quality parameters utilizing readily available elements: A case study of Qatur River. Advanced Engineering Days, 9, 109-112

Keywords
Hydrology
Data mining
Water quality
Machine learning
Sodium absorption ratio

Abstract

In the field of irrigation, water quality plays an effective role in determining its compatibility with soil and different crops. However, the measurement of sodium absorption ratio (SAR) and electrical conductivity (EC) parameters are associated with various challenges such as cost and time-consuming, calibration error, and maintenance problems. Accordingly, this research was conducted to predict SAR and EC parameters utilizing easily accessible parameters including sulfate and chloride in Qatur River located in the northwest of Iran from 1993 to 2019. The utilized models included random forest (RF) combined with genetic algorithm (GA). The analysis of the findings derived from this research demonstrated that the RF-GA-3 model had the best performance in the Qatur River station with RMSE=0.809 (meq/lit) and 0.146 (dS/m) respectively for SAR and EC parameters. Also, the evaluation of the utilized parameters indicated that chloride has a significant role in the prediction accuracy of SAR and EC parameters, and if sulfate is not measured, it can be used as a promising alternative. The information obtained from this research will serve as a comprehensive guide for researchers on water quality monitoring for irrigation purposes.

Introduction

Rivers are the primary source of surface water supply in the world and furnish the quantity of water required for different sectors [1]. The quantity and quality of river water have been significantly diminished in current years due to reasons such as population growth [2], disregard for environmental concerns [3], and excessive consumption of surface water resources [4]. Among the main issues associated with the utilization of low-quality water in agriculture is the rise in salinity and sodium levels in the soil [5]. Considering the important role of salt and sodium in irrigation water, the measurement of electrical conductivity (EC) and sodium absorption ratio (SAR) is very important, however, their experimental measurement is often time-consuming and requires spending a lot of money. As a result, the use of alternative methods such as intelligent models have become very important due to saving time and money [6].

In research, Melesse et al. [7] forecasted the salinity of the Babol River, Iran, utilizing RF and M5P models combined with incremental regression (AR), random subspace (RS), and random committee (RC) algorithms during the period 1980-2016. The evaluation of this research indicated that the AR-M5P model with a correlation coefficient of 0.99 had higher accuracy than other models. In research, Salarijazi and Ghorbani [8] estimated the EC of the river for Zarin Gol and Ramian stations located in the north of Iran using an improved simple regression model. The evaluation of the findings of this investigation demonstrated that the combination of logarithmic transformation and linear model led to the creation of the best combination among different combinations. In a study, Ubah et al. [9] predicted water quality parameters of Ele River Nnewi, Anambra State using an artificial neural network. The parameters used included pH, TDS, EC, and sodium (Na), which were predicted over one year. The evaluation of the outcomes revealed that the artificial neural network model with a coefficient of

determination of about 0.9 had a satisfactory accuracy for all parameters and the usage of this model was recommended for further studies in Anambra state.

The use of methods that provide real-time water quality parameters in rivers with high accuracy is becoming more important. Therefore, predicting these parameters using easily available elements saves time and money. The current research was carried out to accurately predict EC and SAR parameters in the Qatur River located in the Aras River catchment, using random forest (RF) and random forest models combined with a genetic algorithm (GA). Finally, the models will be evaluated using different evaluation criteria.

Material and Method

In recent years, the quality of the Aras River has potentially decreased due to factors such as intense agricultural activities and waste from fruit juice factories [10], and the need to monitor water quality has become more important than in the past. Therefore, to monitor the water quality, the condition of the Qatur River in the right branch of the Aras River has been investigated. Qatur River is a river in eastern Turkey and northwestern Iran, which originates from the of Sarai district in eastern Turkey and finally joins the Aras River near the city of Julfa, Iran. Figure 1 indicates the geographical location of the investigated station.

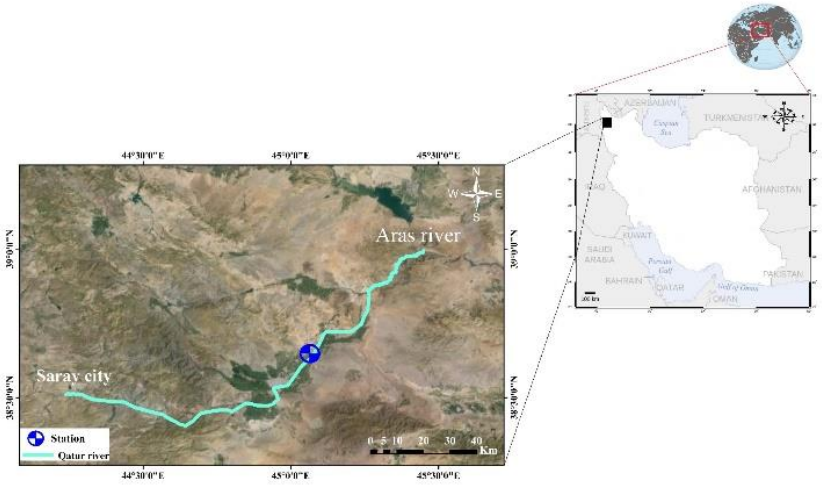


Figure 1. The location of the studied station

Random forest (RF)

The random forest algorithm is a potent ensemble learning algorithm widely used for diverse tasks such as regression, classification, and unsupervised learning. It was presented by Breiman and is known for its superior performance [11]. The algorithm performs by making a collection of DTs, where individual tree is trained on a various subset of the unique training data [12]. Random forest is known for its robustness against noise and overfitting, making it appropriate for solving intricate and non-linear problems in various domains, including hydrological engineering [13].

Genetic algorithm (GA)

Genetic algorithms (GAs) are a type of non-deterministic models that are inspired by Darwinian theory [14]. Unlike other optimization methods, GAs do not require the calculation of partial derivatives or deal with mixed-integer problems [15]. Instead, GAs focus on evaluating the objective function. One of the advantages of GA is that they search for solutions from multiple starting points, rather than just one. This helps to reduce the risk of getting stuck in a local optimum [16]. GAs use probabilistic transition rules to guide the search process, ensuring a diverse exploration of the solution space [17].

In this research, three different scenarios have been utilized to evaluate the role of input parameters on SAR and EC parameters, and the order of the considered scenarios was based on the Pearson correlation coefficient. Table 1 also indicates the scenarios utilized to evaluate the role of input parameters.

Table 1. The input combinations of the studied models.

Scenario	Input		Output
1	SO_4		SAR-EC
2	Cl		SAR-EC
3	SO_4	Cl	SAR-EC

Results

In this research, three scenarios of predictor variables including Cl and SO_4 were considered as inputs to the models (Table 1). Table 2 shows the results of the models utilized in the test period based on correlation coefficient (R) and root mean square error (RMSE) criteria for Qatur River station.

The evaluation of the studied models of the SAR parameter prediction indicated that the RF-GA-3 model with criteria R = 0.983 and RMSE = 0.809 (meq/lit) has had the best performance compared to other models. For the EC parameter, the results also indicated that the RF-GA-3 model with criteria R = 0.995 and RMSE = 0.146 (dS/m) has the highest accuracy. The results are in agreement with the results of Hassan et al. [18] who predicted water quality parameters utilizing classification algorithms and indicated that the MLR model with an accuracy of 99.83% is known as a valuable model in EC parameter prediction.

Table 2. The evaluation results of the models used in Qatur River station.

Parameter	SAR (meq/lit)		EC (dS/m)	
Scenario	R	RMSE (meq/lit)	R	RMSE (dS/m)
RF-1	0.862	2.348	0.876	0.813
RF-2	0.969	1.078	0.989	0.219
RF-3	0.977	0.923	0.992	0.215
RF-GA-1	0.896	1.927	0.918	0.598
RF-GA-2	0.977	0.939	0.99	0.213
RF-GA-3	0.983	0.809	0.995	0.146

Figure 2 indicates the scatter plots for the best scenario in each model for predicting SAR at the Qatur River station. The comparison of the coefficient of determination in all four models indicates that the RF-GA-3 model with a coefficient of determination of 0.9655 performed better than other scenarios. After the RF-GA model, the RF-3 model also has a higher correlation value than other scenarios with a coefficient of determination of 0.955.

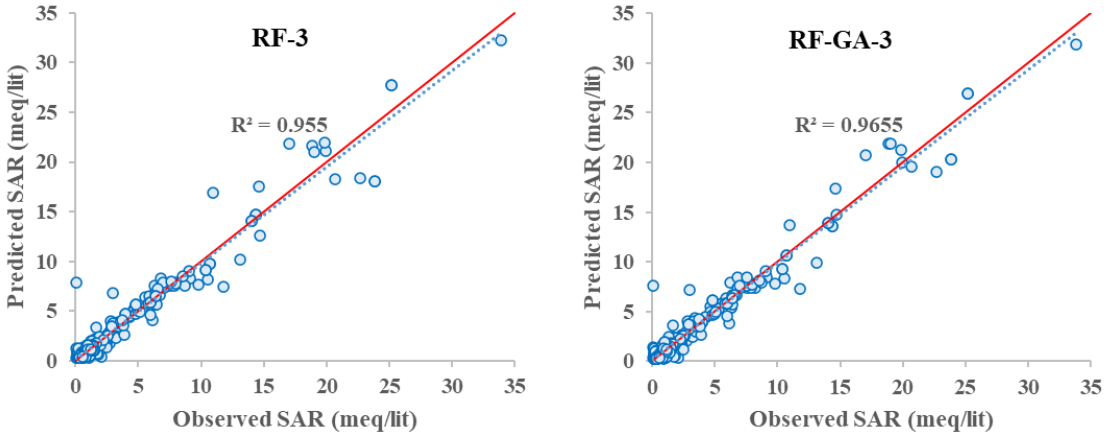


Figure 2. Scatter plots of the best scenario for predicting the SAR parameter at Qatur River station.

Discussion

Comparing the results of this research with previous research indicates the high accuracy of the utilized models. For example, in research, Gorgij et al. [19] predicted the SAR of irrigation water in the Urmia Lake basin, Iran, using the long-term short-term memory (LSTM) method. The evaluation of the results of this study indicated that the LSTM model with R = 0.89 had acceptable results for predicting SAR in the Urmia Lake basin. However, the maximum correlation coefficient was 0.983 in the Qatur River station in the present study, respectively. In another study, Aldrees et al. [20] predicted water quality parameters in Pakistan utilizing different machine-learning techniques. The evaluation of the results of this investigation indicated that the DT-Adaboost model with R=0.91 had suitable accuracy for predicting EC. On the other hand, the maximum correlation coefficient in the Qatur River station in the present investigation was 0.995.

Conclusion

Measuring SAR and EC parameters in addition to being expensive, faces various challenges. Therefore, this investigation has been carried out to predict SAR and EC parameters utilizing easily accessible parameters

including sulfate and chloride in the Qatur River station. The utilized models include RF and RF-GA, which were evaluated utilizing different evaluation criteria. The evaluation of the outcomes of this examination indicated that the RF-GA-3 model with R = 0.983, and 0.995, respectively, for SAR and EC parameters had the highest accuracy in the Qatur River station. The evaluation of the results of the models indicated that the RF-GA hybrid model can predict SAR and EC parameters as a reliable tool. The utilized hybrid models have a significant potential to help farmers and managers of irrigation systems in making more efficient decisions because the accurate prediction of SAR and EC parameters will lead to a correct understanding of the quality of the water used and the correct operation of the systems.

References

1. Giri, S. (2021). Water quality prospective in Twenty First Century: Status of water quality in major river basins, contemporary strategies and impediments: A review. Environmental Pollution, 271(19), 116-128.
2. Fida, M., P. Li, Y. Wang, S.K. Alam, & A. Nsabimana. (2023). Water contamination and human health risks in Pakistan: a review. Exposure and Health, 15(3), 619-639.
3. Sarker, B., K.N. Keya, F.I. Mahir, K.M. Nahiun, S. Shahida, & R.A. Khan. (2021). Surface and ground water pollution: Causes and effects of urbanization and industrialization in South Asia. Scientific Review, 7(3), 32-41.
4. Mousazadeh, M., B. Paital, Z. Naghdali, Z. Mortezania, M. Hashemi, E. Karamati Niaragh, M. Aghababaei, M. Ghorbankhani, E. Lichtfouse, & M. Sillanpää. (2021). Positive environmental effects of the coronavirus 2020 episode: a review. Environment, Development and Sustainability, 23(1), 12738-12760.
5. Pincay, J.M.C. & M.F.P. Cantos. (2024). Analysis of Soil Salinization as an Environmental Issue in Latin America. Journal of Ecological Engineering, 25(1), 146-152.
6. Woźniak, M., J. Szczotka, A. Sikora, & A. Zielonka. (2024). Fuzzy logic type-2 intelligent moisture control system. Expert Systems with Applications, 238(5), 121-134.
7. Melesse, A.M., K. Khosravi, J.P. Tiefenbacher, S. Heddam, S. Kim, A. Mosavi, & B.T. Pham. (2020). River water salinity prediction using hybrid machine learning models. Water, 12(10), 2951-2964.
8. Salarijazi, M. & K. Ghorbani. (2019). Improvement of the simple regression model for river'EC estimation. Arabian Journal of Geosciences, 12(1), 1-14.
9. Ubah, J., L. Orakwe, K. Ogbu, J. Awu, I. Ahaneku, & E. Chukwuma. (2021). Forecasting water quality parameters using artificial neural network for irrigation purposes. Scientific Reports, 11(1), 24438-24451.
10. Nasehi, F., A. Hassani, M. Monavvari, A. Karbassi, & N. Khorasani. (2013). Evaluating the metallic pollution of riverine water and sediments: a case study of Aras River. Environmental Monitoring and Assessment, 185(13), 197-203.
11. Breiman, L. (2001). Random forests. Machine learning, 45(4), 5-32.
12. Biau, G. & E. Scornet. (2016). A random forest guided tour. Test, 25(1), 197-227.
13. Arshad, A., A. Mirchi, J. Vilcaez, M.U. Akbar, & K. Madani. (2024). Reconstructing high-resolution groundwater level data using a hybrid random forest model to quantify distributed groundwater changes in the Indus Basin. Journal of Hydrology, 628(12), 130-145.
14. Hüe, X., *Genetic algorithms for optimization*. 1997, Citeseer.
15. McKinney, D.C. & M.D. Lin. (1994). Genetic algorithm solution of groundwater management models. Water Resources Research, 30(6), 1897-1906.
16. Albadr, M.A., S. Tiun, M. Ayob, & F. Al-Dhief. (2020). Genetic algorithm based on natural selection theory for optimization problems. Symmetry, 12(11), 1758-1771.
17. Costa-Carrapiço, I., R. Raslan, & J.N. González. (2020). A systematic review of genetic algorithm-based multi-objective optimisation for building retrofitting strategies towards energy efficiency. Energy and Buildings, 210(12), 109-124.
18. Hassan, M., M. Hassan, L. Akter, M. Rahman, S. Zaman, H. Khan, N. Jahan, R.N. Smrity, J. Farhana, & M. Raihan. (2021). Efficient prediction of water quality index (WQI) using machine learning algorithms. Human-Centric Intelligent Systems, 1(3), 86-97.
19. Gorgij, A.D., G. Askari, A. Taghipour, M. Jami, & M. Mirfardi. (2023). Spatiotemporal forecasting of the groundwater quality for irrigation purposes, using deep learning method: long short-term memory (LSTM). Agricultural Water Management, 277(2), 108-119.
20. Aldrees, A., H.H. Awan, M.F. Javed, & A.M. Mohamed. (2022). Prediction of water quality indexes with ensemble learners: Bagging and Boosting. Process Safety and Environmental Protection, 168(1), 344-361.

Advanced Engineering Days

aed.mersin.edu.tr

Where are the most qualified parks located? A case study of city of Tabriz

Elmira Davatgar Khorsand*[1], Akbar Rahimi [2]

[1]*University of Tabriz, Landscape Architecture, Iran, elmiradavatgar@gmail.com*
[2] *University of Tabriz, Faculty of Planning and Environmental Science, Urban and Regional Planning department, Iran, akbar.rahimi@gmail.com*

Cite this study: Davatgar Khorsand, E., & Rahimi, A. (2024). Where are the most qualified parks located? A case study of city of Tabriz. Advanced Engineering Days, 9, 113-115

Keywords
Parks
Quality
Tabriz
ARC GIS
Green space

Abstract

Green space services are essential for attaining a sustainable city. Today, the importance of green spaces in the lives of city dwellers is clear to everyone and urban green areas must be accessible and usable for all groups of people in the city. The present study evaluates the quality of urban parks in different areas of Tabriz city, focusing on accessibility, physical infrastructure, security, and cultural factors. The required information for this study has been collected by questionnaires that distributed randomly in different areas of Tabriz city. Finally collected information have analyzed by ARC GIS software based on Getis Ord Gi and the Moran index. The results show significant differences between the quality of parks in upper and lower socio-economic areas of city. In the rich neighborhoods, parks are much more qualified in compared to poor areas.

Introduction

Rapid urbanization has led to large urban populations. Modeling has predicted that, most of this increase will occur in existing metropolises or new cities (Rahimi et al., 2023). Green spaces as a unique part of urban areas, are essential for sustainable development. In addition to their importance in ecosystem services and maintaining environment (such as reducing the effect of urban heat islands, improving air quality, etc.), they have a significant role on the quality of life of urban society and the health of residents in issues such as increasing physical activity opportunities, reducing stress levels, improving mental and physical health, increasing the value of property and commercial activity (Wolch et al., 2014; Breuste & Rahimi, 2015). Therefore, urban parks must be usable by all groups of people all over the city (Rahimi et al., 2023; Breuste & Rahimi, 2015).

Unfortunately, green inequalities are apparent in all locations and on all scales (Mashhoodi, 2021). Most researchers believe that planning to create suitable and qualified green infrastructure for the well-being of all residents is essential all over the city and it should be so regardless of ethnicity, race, gender, and socio-economic conditions (Rahimi et al., 2023). This will not be achieved without considering justice. Spatial justice is one of the most important kinds of justice that is related to urban issues and acts as a bridge between environmental balance and social equities (Rahimi et al., 2023). Now in this study we want to know if there is spatial justice in terms of the quality of parks in Tabriz city or not? Due to importance of this issue, all the parks in all neighborhoods of this city have been evaluated.

Material and Method

The city of Tabriz is selected as case study in this research. Tabriz is one of the largest metropolises in Iran. It is located in the center of East Azerbaijan province. This city is historically important due to the strategic location on the Silk Road route. Nowadays, Tabriz has a total area of 244.91 km2. Tabriz's green space per capita is much lower than national and international standards and according to studies, it is equal to 1.69 square meters per capita (Rahimi et al., 2023). So, we can understand that, this city has experienced ecological damages over the years (Dadashpoor et al., 2019; Breuste & Rahimi, 2015). Nowadays only 2.7 % (6.78 Km^2) of the city's area is dedicated to city parks (Official master plan of Tabriz, 2016). Furthermore, the growth in size and population of the city has led to tremendous economic and social changes due to extensive changes in land use and sociocultural conditions (Rahimi et al., 2023;

Dadashpoor et al., 2019; Breuste & Rahimi, 2015). According to Rahimi et al (2023), the city of Tabriz has divided to 3 socio- economic areas as high, medium, and low classes (Figure 1).

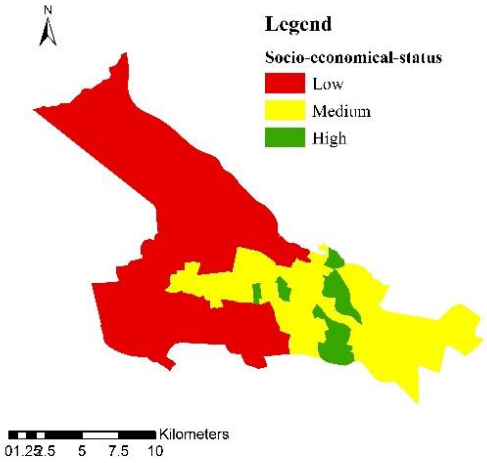


Figure 1. Socio-economic divisions of Tabriz city (Rahimi et al., 2023).

In this study, after determining the classification of Tabriz city, indicators affecting the quality of urban parks were extracted in the form of 4 indicators of accessibility, security, cultural and physical conditions, and questions were designed to measure them in the form of a Likert scale questionnaire. According to Cochran's formula, 384 questionnaires were distributed randomly throughout the city of Tabriz. Finally collected information regarding the quality of the parks of Tabriz was insert into the ARC GIS software and analyzed by hot spot and Moran index. By adding the map of socio-economic conditions of Tabriz city to the specific results of questionnaires, the quality of parks in different neighborhoods of Tabriz city can be visible.

Results

Results are presented regarding the condition of the urban parks quality, considering the socio-economic conditions. This includes results for the four sets of indicators considered: accessibility, security, cultural and physical conditions. Figure 2 shows the distribution of the park's quality all over Tabriz according to citizens' reports and the Getis-Ord Gi analysis. A greater quality is observed in higher socio-economic areas. As we move away from the eastern affluent districts, conditions gradually change from very suitable to suitable, moderate, and unsuitable. Figures 3 and Table 1 present the results of Moran's index analysis. Spatial correlation and cluster distribution in park quality were observed. Results show a significant difference in the use of urban parks between the eastern (which mainly include districts with high socio-economic conditions) and the western (mainly consisting of low socio-economic districts) parts of the city. There is no significant spatial correlation between the conditions of park quality in other parts of the city.

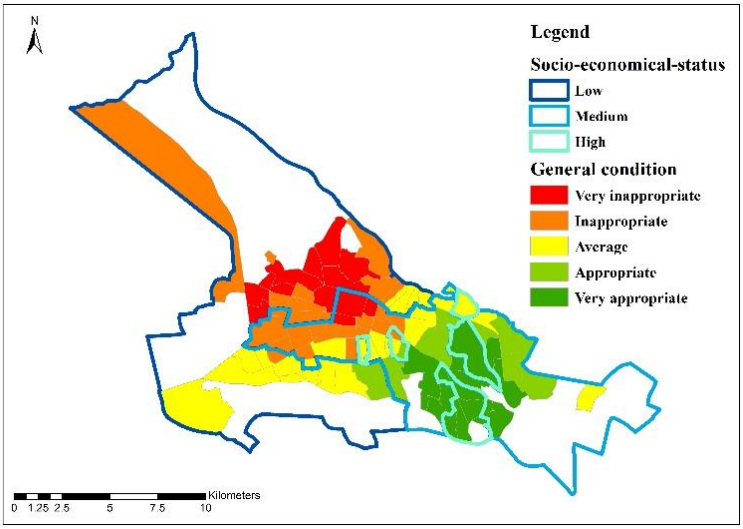


Figure 2. Hot spot analyzes about the quality of parks all over the city of Tabriz.

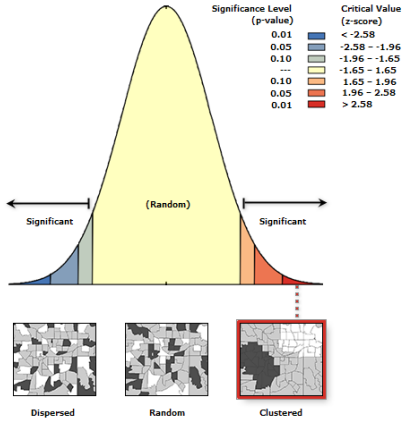


Figure 3. Moran's index analyzes about the quality of parks all over the city of Tabriz.

Table 1. Global Moran's I summary

Moran's index	0.098955
Expected index	-0.002326
Variance	0.000707
Z-score	3.809910
p-value	0.000139

Discussion

According to the results, very favorable and favorable park quality is visible in the eastern parts of the city. This corresponds to areas with middle and high socio-economic conditions and their surroundings. These areas are modern and new districts of the city. They have been built according to the current planning regulations and consider the needs of today's urban dwellers. Versus modern areas, the western and northern parts of Tabriz city are self-organized and Socio-economically disadvantaged areas (Dadashpoor et al., 2019). Hot spot analyze map shows low quality parks are located in these areas. According to Pugalis (2009), the quality of the urban environment is the result of the city's economic growth. Breuste and Rahimi (2015) reported better accessibility to green spaces in areas with high socio-economic status than in poorer areas.

Conclusion

The purpose of this study was to investigate the condition and desirability of park quality in the city of Tabriz (Iran), with socio-economic perspective. Results indicate there is a significant spatial injustice between quality of urban green spaces in different socio-economic areas. Although these results are specific to the city of Tabriz, according to the conditions, the results can be generalized to many cities in Iran and other countries that have similar or close social and cultural conditions to Iran. The findings of this research can be a reference for managers, planners, and designers to evaluate the strengths and weaknesses of past performance. In order to improve urban green infrastructure.

References

1. Breuste, J., & Rahimi, A. (2015). Many public urban parks, but who profits from them? The example of Tabriz, Iran. Ecological Processes, 4 (6): (2015).
2. Dadashpoor, H., Azizi, P., & Moghadasi, M. (2019). Analyzing spatial patterns, driving forces and predicting future growth scenarios for supporting sustainable urban growth: Evidence from Tabriz metropolitan area, Iran. Sustainable Cities and Society, Sustainable Cities, and Society, 47 (2019) 101502.
3. Mashhoodi, B. (2021). Environmental justice and surface temperature: Income, ethnic, gender, and age inequalities. Sustainable Cities and Society, 68. 102810. doi:10.1016/j.scs.2021.102810
4. Pugalis, L, (2009), The culture and economics of urban public space design: Public and professional perceptions, Urban Design International, 14 (4): 215–230.
5. Rahimi, A., Davatgar Khorsand, E., Breuste, J., & Karimzadeh, H. (2023). Gender Justice in Green Space Use in Relation to Different Socio-Economic Conditions in Tabriz, Ira. Sustainable Cities and Society, 99 (2023) 104973. https://doi.org/10.1016/j.scs.2023.104973
6. Wolch, JR., Byrne, J., & Newell, J P. (2014). Urban green space, public health, and environmental justice: The challenge of making cities 'just green enough', Landscape and Urban Planning, 125: 234–244.

Advanced Engineering Days

aed.mersin.edu.tr

Enhancing water treatment efficiency: a study on coagulant dosage prediction in water treatment plant

Milad Sharafi[*1]

[1]*Urmia University, Department of Water Engineering, Iran, st_m.sharafi@urmia.ac.ir*

Cite this study: Sharafi, M. (2024). Enhancing water treatment efficiency: a study on coagulant dosage prediction in water treatment plant. Advanced Engineering Days, 8, 116-119

Keywords
Coagulant Dosage
Water Quality
Environmental Impact
Wilmott's Index

Abstract

Accurate prediction of coagulant dosage is important for keeping water quality standards and public health protection, surpassing traditional jar tests in precision, efficiency, and adaptability. This precision guarantees the effective removal of pollutants and consistent water quality results, and by reducing the usage of chemicals, minimizes waste generation and reduces the environmental impact of the treatment process. Hence, the current investigation was conducted to precisely predict the coagulant dosage in Iran's Nahand water treatment plant. This was achieved by employing a support vector machine (SVM), stochastic gradient descent (SGD), and support vector machine combined with stochastic gradient descent (SVM-SGD). Consequently, various parameters such as water temperature, electrical conductivity, discharge, hydrogen potential, initial chloride, and nephelometric turbidity unit were examined across six scenarios to identify the optimal input combination based on five criteria. The findings revealed that SVM, SGD, and SVM-SGD exhibited accuracy levels with Wilmott's index of agreement of 0.63, 0.67, and 0.91, respectively, and were deemed reliable for predicting coagulant dosages. The consequences of this research hold considerable value as serve as a beneficial resource for water treatment plant operators, leading to cost and time savings in the coagulation process.

Introduction

Determining the coagulant dosage is a multidimensional and complex process, involving non-linear dynamics and different variables [1]. It goes beyond mere considerations of raw water properties like turbidity, pH, and temperature. The intricacy also arises from external variables like rapid mixing, the hydraulic qualities of the coagulation reservoir, and the current environmental conditions [2]. Conducting a jar test, as one of the common methods of coagulant dose determination, poses challenges due to the scale disparity between the test and full-scale treatment operations [3]. The small-scale setup of the jar test may not accurately mirror the intricate dynamics of larger treatment systems. Variables like mixing strength, settling time, and fluctuations in water quality can introduce intricacies in establishing the best coagulant quantity [4]. Nevertheless, these are just some of the constraints of the jar trial for computing coagulant quantity in water treatment facilities.

Information obtained from treatment systems has recently been scrutinized using intelligent methodologies to clarify the connection between input factors and the optimal coagulant quantity as the resultant outcome [6]. Zhang et al. [7] conducted a research study where they assessed the efficacy of Support Vector Machine (SVM) and K-Nearest Neighbors (KNN) models in predicting coagulant dose. The study findings indicated that both models exhibited comparable accuracy levels in coagulant dose prediction and were evenly matched in terms of performance. Narges, Ghorban [2] conducted a study assessing the effectiveness of the Artificial Neural Network Fuzzy Inference System (ANFIS) in forecasting the doses of alum and polyaluminum chloride coagulants. The outcomes revealed that the suggested model accurately predicted the amounts of these coagulants, yielding correlation coefficients of 0.85 for alum and 0.84 for polyaluminum chloride. Ghasemi et al. [8] compared the efficacy of ANFIS, SVR, and artificial neural network (ANN) models in forecasting coagulant dosage. The findings revealed that the ANN model, boasting a remarkable coefficient of determination of 0.94, outperformed the other models employed in the study. Lin et al. [9] conducted an investigation focusing on the utilization of deep learning techniques for the prediction of coagulant levels in water treatment. This investigation highlighted a substantial enhancement in projection accuracy through the deployment of deep learning algorithms, which demonstrate the adaptability of these methodologies in projecting water treatment procedures.

This study aimed to predict the coagulant dosage (CD) as accurately as possible in the Nahand water treatment plant located in the northwest of Iran and use the support vector machine (SVM) combined with stochastic gradient descent (SGD) during 2021-2022. Nahand water treatment plant with a capacity of 1200 lit/s and despite supplying a significant part of the sanitary water of Tabriz city, due to high turbidity in the Nahand dam water (especially during floods) it disrupts the water purification process, which causes a pressure drop in most areas of Tabriz city. Consequently, providing an efficient and reliable model for predicting the coagulant dosage has played an essential role in the water quality of this treatment plant, which will save time and cost.

Material and Method

Study area

In this examination, the parameters of water temperature (Temp), electrical conductivity (EC), discharge (Q), hydrogen potential (pH), initial chloride (Init Cl), and nephelometric turbidity unit (NTU) recorded in Nahand water treatment plant, Iran, from 2021 to 2022, used to predict the daily amount of ferric chloride ($FeCl_3$) using SVM, SGD and SVM-SGD models. Nahand water treatment plant has coordinated 38° 05′ N and 46° 23′ W and an altitude of 1655 m, which is located 1.5 km from the northern part of Tabriz metropolitan. Also, the location of the Nahand dam and water treatment plant station is shown in Fig. 1. The data used in the present investigation were also obtained from the regional water company of East Azerbaijan province.

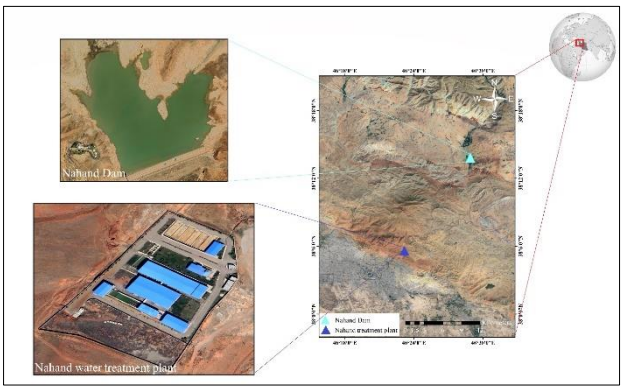


Figure 1. Study area location

Support Vector Machine (SVM)

Support Vector Machine (SVM) is a powerful supervised learning algorithm used for classification and regression tasks. It works by finding the optimal hyperplane that best separates different classes in the feature space [10]. SVM is effective in high-dimensional spaces and is versatile due to its ability to handle both linear and non-linear data [11]. By maximizing the margin between classes, SVM aims to improve generalization and reduce overfitting [12]. SVM's robustness and versatility make it a popular choice in various applications, including image classification, text categorization, and bioinformatics.

Stochastic Gradient Descent (SGD)

Stochastic Gradient Descent (SGD) is a fundamental optimization algorithm widely used in training machine learning models [13]. It is particularly useful when dealing with large datasets due to its efficiency in processing data in small batches [14]. The key idea behind SGD is to update the model's parameters iteratively by computing the gradient of the loss function concerning a single training example or a mini-batch of examples. By updating the parameters based on stochastic gradients, SGD introduces randomness into the optimization process, which can help escape local minima and reach the global minimum more efficiently [15].
In this research, three different scenarios have been utilized to evaluate the role of input parameters on CD parameter, and the order of the considered scenarios was based on the Pearson correlation coefficient. Table 1 also indicates the scenarios utilized to evaluate the role of input parameters.

Table 1. The input combinations of the studied models.

Scenario	Input parameters						Output
1	Init Cl	Q					CD
2	Init Cl	Q	EC	Temp			CD
3	Init Cl	Q	EC	Temp	pH	NTU	CD

Results

In the present research, the prediction of the coagulant dosage in the Nahand Water Treatment Plant for the period of 2021 to 2022 has been made. This parameter is predicted using SVM, SGD and SVM-SGD models. In addition, three different scenarios have been utilized to investigate the impact of parameters. At the same time, the performance of the models was evaluated using the correlation coefficient (R), root mean square error (RMSE), normalized root mean square error (NRMSE), and Willmott's index of agreement (WI).

The evaluation results of the models utilizing different scenarios are given in Table 2. A comparison of all models indicated that the third scenario of the SVM-SGD model with R=0.9, RMSE=4.39 (mg/lit), NRMSE=0.07, and WI=0.91 had the highest accuracy compared to other models. After the SVM-SGD model, the third scenario of the SGD model with R=0.88, RMSE=6.73 (mg/lit), NRMSE=0.11, and WI=0.67 has performed better than other scenarios. Also, among the different scenarios of the SVM model, the last scenario showed better performance with R=0.85, RMSE=6.94 (mg/lit), NRMSE=0.11, and WI=0.63. The results of this study agree with the results of Achite et al. [16], who predicted coagulant dosage in the Sidi Yacoub treatment plant using a random forest (RF) model combined with a genetic algorithm (GA) and showed that the proposed model with WI = 0.98 has high accuracy in prediction.

Table 2. The evaluation results of the models

Model	Evaluation criteria			
	R	RMSE (mg/lit)	NRMSE	WI
SVM-1	0.52	8.74	0.14	0.18
SVM-2	0.71	8.15	0.13	0.36
SVM-3	0.85	6.94	0.11	0.63
SGD-1	0.55	8.20	0.13	0.65
SGD-2	0.58	7.46	0.12	0.69
SGD-3	0.88	6.73	0.11	0.67
SVM-SGD-1	0.61	8.01	0.13	0.43
SVM-SGD-2	0.76	7.42	0.12	0.58
SVM-SGD-3	0.90	4.39	0.07	0.91

Figure 2 shows the violin and lollipop plots for all three scenarios. According to two plots, the third scenario of all models has higher accuracy than other scenarios.

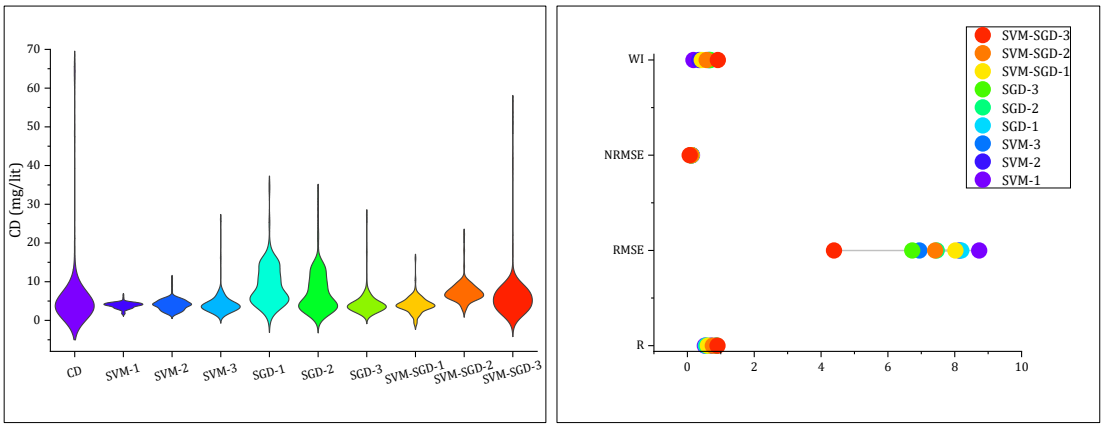


Figure 2. Violin and lollipop plots.

Discussion

Examining the outcomes of this investigation exhibited that the use of SVM-SGD model is superior to traditional methods, which often rely on manual and heuristic settings and may lead to non-optimal dose decisions, and these combined models Increased the accuracy of coagulant dosage prediction. SVM-SGD can continuously learn and adapt based on real-time data, leading to more precise dosage recommendations and improved treatment outcomes. Finally, one of the limitations of this study is the lack of access to other water quality parameters, and the use of more parameters to evaluate their impact is suggested for future studies.

Conclusion

This investigation aimed to precisely predict the coagulant dosage in the Nahand water treatment plant by utilizing SVM, SGD, and SVM-SGD models across three different scenarios. The analysis of the findings of this research indicated that the combined SVM-SGD model significantly increased the prediction accuracy of the

standalone SVM and SGD models by achieving WI = 0.91. The utilization of combined algorithms is advised as a valuable instrument for future investigations, while the enhancement of algorithms can contribute to the refinement of modeling accuracy.

References

1. Iwuozor, K.O. (2019). Prospects and challenges of using coagulation-flocculation method in the treatment of effluents. Advanced Journal of Chemistry-Section A, 2(2), 105–127.
2. Narges, S., A. Ghorban, K. Hassan, & K. Mohammad. (2021). Prediction of the optimal dosage of coagulants in water treatment plants through developing models based on artificial neural network fuzzy inference system (ANFIS). Journal of Environmental Health Science and Engineering, 19(1), 1543–1553.
3. Achite, M., S. Farzin, N. Elshaboury, M. Valikhan Anaraki, M. Amamra, & A.K. Toubal. (2024). Modeling the optimal dosage of coagulants in water treatment plants using various machine learning models. Environment, Development and Sustainability, 26(2), 3395–3421.
4. Wang, K.-J., P.-S. Wang, & H.-P. Nguyen. (2021). A data-driven optimization model for coagulant dosage decision in industrial wastewater treatment. Computers & Chemical Engineering, 152(14), 107–121.
5. Kim, J., C. Hua, K. Kim, S. Lin, G. Oh, M.-H. Park, & S. Kang. (2024). Optimizing coagulant dosage using deep learning models with large-scale data. Chemosphere, 350(2), 140–157.
6. Benalia, A., L. Atime, O. Baatache, A. Khalfaoui, A.F. Ghomrani, K. Derbal, A. Pizzi, A. Panico, E.M. Bouchareb, & R. Bouchareb. (2024). Removal of lead in water by coagulation flocculation process using Cactus-based natural coagulant: optimization and modeling by response surface methodology (RSM). Environmental Monitoring and Assessment, 196(3), 1–23.
7. Zhang, K., G. Achari, H. Li, A. Zargar, & R. Sadiq. (2013). Machine learning approaches to predict coagulant dosage in water treatment plants. International Journal of System Assurance Engineering and Management, 4(1), 205–214.
8. Ghasemi, M., M. Hasani Zonoozi, N. Rezania, & M. Saadatpour. (2022). Predicting coagulation–flocculation process for turbidity removal from water using graphene oxide: a comparative study on ANN, SVR, ANFIS, and RSM models. Environmental Science and Pollution Research, 29(48), 72839–72852.
9. Lin, S., J. Kim, C. Hua, S. Kang, & M.-H. Park. (2023). Comparing artificial and deep neural network models for prediction of coagulant amount and settled water turbidity: Lessons learned from big data in water treatment operations. Journal of Water Process Engineering, 54, 103–117.
10. Cervantes, J., F. Garcia-Lamont, L. Rodríguez-Mazahua, & A. Lopez. (2020). A comprehensive survey on support vector machine classification: Applications, challenges and trends. Neurocomputing, 408, 189-215.
11. Khan, S.N., S.U. Khan, H. Aznaoui, C.B. Şahin, & Ö.B. Dinler. (2023). Generalization of linear and non-linear support vector machine in multiple fields: a review. Computer Science and Information Technologies, 4(3), 226-239.
12. Tanveer, M., T. Rajani, R. Rastogi, Y.-H. Shao, & M. Ganaie. (2022). Comprehensive review on twin support vector machines. Annals of Operations Research, 1-46.
13. Tian, Y., Y. Zhang, & H. Zhang. (2023). Recent advances in stochastic gradient descent in deep learning. Mathematics, 11(3), 682.
14. Song, S., K. Chaudhuri, & A.D. Sarwate. *Stochastic gradient descent with differentially private updates*. in *2013 IEEE global conference on signal and information processing*. 2013. IEEE.
15. Johnson, T., P. Agrawal, H. Gu, & C. Guestrin. *AdaScale SGD: A user-friendly algorithm for distributed training*. in *International Conference on Machine Learning*. 2020. PMLR.
16. Achite, M., S. Samadianfard, N. Elshaboury, & M. Sharafi. (2023). Modeling and optimization of coagulant dosage in water treatment plants using hybridized random forest model with genetic algorithm optimization. Environment, Development and Sustainability, 25(10), 11189–11207.

Advanced Engineering Days

aed.mersin.edu.tr

Evaluation of urban environmental quality in District 4 of Tabriz metropolis using CRITIC model

Hassan Mahmoudzadeh*

University of Tabriz, Department of Urban and Regional Planning, Iran, mahmoudzadeh@tabrizu.ac.ir

Cite this study: Mahmoudzadeh, H. (2024). Evaluation of urban environmental quality in District 4 of Tabriz metropolis using CRITIC model. Advanced Engineering Days, 9, 120-136

Keywords
Urban environment quality
Spatial Modeling
Comparative approach
CRITIC model
District 4
Tabriz

Abstract

In the urban environment, the quality refers to the capacity that provides and fulfill the material and spiritual needs of inhabitants. In order to improve the quality of urban life and standard of living for their citizens, planners and managers strive to raise Urban Environmental Quality. The objective of this study is to evaluate the quality of urban environment through the spatial analysis of a multi-criteria decision-making method (MCDM) utilizing the CRITIC model. This research is conducted in district 4 of the Tabriz Metropolis Municipality. In order to determine the quality of an urban environment, air pollution, vegetation coverage, land surface temperature, production of waste, population density, noise pollution, health care per capita, green spaces per capita, recreational spaces per capita, and distance from fault lines are used. After evaluating and producing environmental quality maps in district 4, 10 indicators were tested for significance and a comparative evaluation of sub-districts was conducted in order to determine which sub-districts was in better condition based on a statistical analysis of the T-test results. In accordance with the CRITIC model, there are significant differences between averages of waste production, population density, noise pollution, distance from fault lines, Land Surface Temperature, Normalized difference vegetation index, and distance from fault lines between the sub-districts. It appears that recreational space, air pollution, health care per capita, and green space per capita are not meaningfully different on averages. The preparation of environmental quality maps reveals the importance of meaningful indicators at the neighborhood level in the district 4. In all sub-districts by strengthening the continuity of the landscape through the development of ecological corridors and an increase in per capita can contribute to the improvement of the quality of the urban environment.

Introduction

Urban populations surpassed rural populations for the first time in 2007 and have been growing modestly ever since, and they will comprise almost two-thirds of the world's population by 2050[1]. Since urbanization has become a global trend, many urban regions have expanded physically and have replaced natural surfaces with impervious manmade surfaces[2, 3]. It has decreased evapotranspiration, polluted the environment, and increased energy demand[4-6]. With the growth of urban populations and the expansion of infrastructure-based economies, there is an increasing need for land to accommodate the growing infrastructure[7, 8]. There are many pressing concerns facing planners and municipal authorities in the nation today, including economic and social development, poverty alleviation, promoting and sustaining income and employment opportunities, and building democratic and harmonious societies[9-11]. Emissions from industrial sources, congestion in transportation, and pollution are just a few examples of environmental concerns[12-14]. It should be noted that the urban environment throughout Iran is deteriorating, which threatens the future of the cities, particularly large urban centers[15, 16]. Rapid population and economic growth will negatively impact the environment regardless of whether cities are or are not at their ecological carrying capacity[17-19]. As a consequence of urbanization, a

number of environmental issues have been exacerbated, including loss of natural vegetation, loss of wetlands, open spaces, and wildlife habitats, changes in local and regional climate, and an increase in water, electricity, and infrastructure demand[20-24]. It is essential to have timely information on the temporal and geographic patterns of urban environmental quality in order to develop new policies that support environmental sustainability and smart growth[12].

It is necessary to conduct assessments of urban environmental quality in order to plan and manage urban areas more effectively[25]. UEQ is an index which summarizes a city's environmental, social, and economic characteristics[26]. The concept of UEQ encompasses indicators that relate to physical, social, spatial, and economic dimensions[13, 27, 28]. In addition to urban planning, infrastructure services, economic implications, policy making, and social science research, UEQ might impact a wide range of governmental domains[29, 30]. A useful tool for measuring urban environmental quality is to construct an Urban Environmental Quality Index (UEQI)[31]. In order to gain a better understanding of environmental threats and vulnerabilities, this index may be applied to other locations. In addition, city administrative units may be able to determine which interventions should be prioritized in regions that are experiencing significant environmental, social, and economic issues by recognizing the multiple dimensions of urban environments.

Urban overpopulation has induced particular socio-economic changes as well as unequal access to urban resources. These factors are without doubt significant contributors to the quality of life in urban settings. As a multidisciplinary concept, urban quality of life (UQoL) addresses economic, social, political, environmental, physical, and psychological aspects of a city[32].A major determinant of UQoL is urban environmental quality (UEQ)[33, 34]. In terms of UEQ, it can be characterized as multidisciplinary and complex, with spatial and temporal variations[31]. Therefore, it has proven to be an effective tool for studying and planning urban environments in a multidimensional manner[35]. There are other bio-geochemical processes in urban environments that can result in a variety of pollution-related problems across a range of ecological scales (such as air pollution, noise pollution, and climate change)[36, 37]. In other words, urban environmental quality is an assessment of a city's suitability for human habitation[38]. Urban environments have been studied extensively, but most have explored UEQ in relation to changes in variables at local and small scales[34, 39, 40]. A seasonal change in urban environments seems to be another effective factor to consider when assessing dynamism and change [41-44]. The latest studies incorporate socio-economic data into UEQ calculations[45-47]. UEQ analysis has also been conducted using geohazard potential [48, 49]. Even though UEQ is a spatial-temporal index for urban management and planning, there are several examples of spatial models being implemented without regard to time. For modeling and mapping UEQs, most studies utilize principal component analysis (PCA) and weighted layer overlays in GIS. It was reported by [50],[51], [52],[53] and [54] For spatial mapping and analysis of environmental issues in urbanized areas, different experimental methods, geostatistics, and change detection techniques were proposed. It is common practice to use multicriteria decision analysis (MCDA) methods in environmental planning, since it provides a broader outlook on a problem [55-59]. when human intervention in processing and evaluation of variables is not necessary, CRITIC is an effective method in assessing Urban Environmental Quality. This method is an objective method for determining the weight of criteria that involves the intensity of conflict and incompatibility between the components of a decision problem [60]. It is common for decision makers to perform multivariate analysis based on their experience, knowledge, and understanding, so their subjective point of view affects the weight of the criteria. As the number of criteria increases, the possibility of human error increases, which raises concerns about the reliability of the results [61]. A numerical valuation approach is used in the CRITIC method to overcome such problems, which eliminates the need for personal judgments. By using CRITIC model, this study attempts to model UEQ for district 4 of Tabriz by comparing parameters related to physical environment, built-up area, and natural hazards (i.e. 2 and 4). We deliberately chose district 4 that run west-to-east, because it closely reflect the city's environmental conditions. As one of the largest cities in Iran with a population of 1.7 million [62], Tabriz suffers from severe environmental conditions [63-65], the continuation of which will, no doubt, cause severe consequences within the next few years.

Material and Method

Study area

The study area includes district 4 of Tabriz including, with a population of 315,183 and a territorial span of 2529 ha (Fig. 1). Environmental, demography, economic, institutional, and land-use characteristics have been taken into consideration when selecting the district 4 that represent the greater urban area of Tabriz [66].

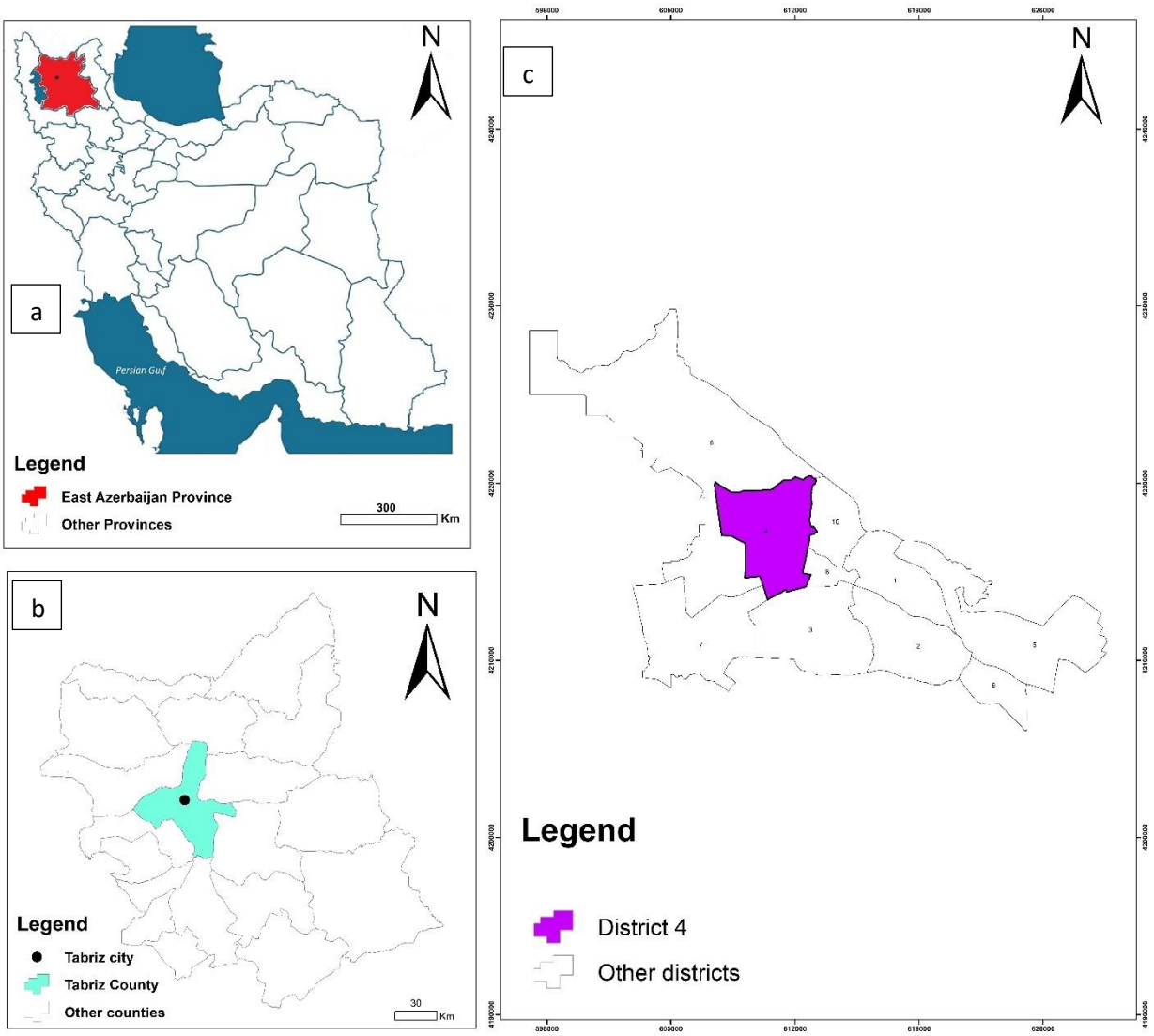


Figure 1. The study area is district 4 from west to center of Tabriz (c), Tabriz (b) is located in the East Azerbaijan province of Iran (a).

Methodology

Figure 2 illustrates the steps involved in Urban Environment Quality calculation: extraction of Urban Environment Quality indicators, preparation of GIS layers, Standardization, Urban Environment Quality mapping, and Comparative comparison.

Measurement of UEQ by developing indicators

Cities have a physical environment domain that contains indicators related to natural characteristics (air pollution, vegetation cover, and Land Surface temperature) whereas the built-up domain contains indicators related to construction (production of waste, population density, noise pollution, health care per capita, green space per capita, recreational space per capita) and natural hazards (distance from Fault). Based on these categories, UEQ modeling can be conducted for the major domains of the city (Table1).

Industrialized and densely populated districts often have higher levels of air pollution[48] and is largely caused by traffic, resulting in adverse health effects on respiratory systems[76]. The effects of air-land interactions are reflected in surface parameters such as LST[77, 78]. In urban districts, temperatures tend to be higher than in their surrounding areas, which contributes to energy consumption, greenhouse gas emissions, a rise in heat-related diseases, and poor water quality[79-81]. The distance to a fault is the most important and rated model in evaluating earthquake vulnerability[82].

The generation of municipal solid waste (MSW) is an inevitable consequence of human activity[83]. A majority of urban MSW comes from settlements, businesses, and small industries[84]. Mixed with MSW, these wastes pose a health threat as well as a possible environmental threat[85].In addition, it threatens the groundwater resources

and soil[86]. Pollutants from solid wastes negatively affect soil physico-chemical properties, resulting in low vegetation production[87].

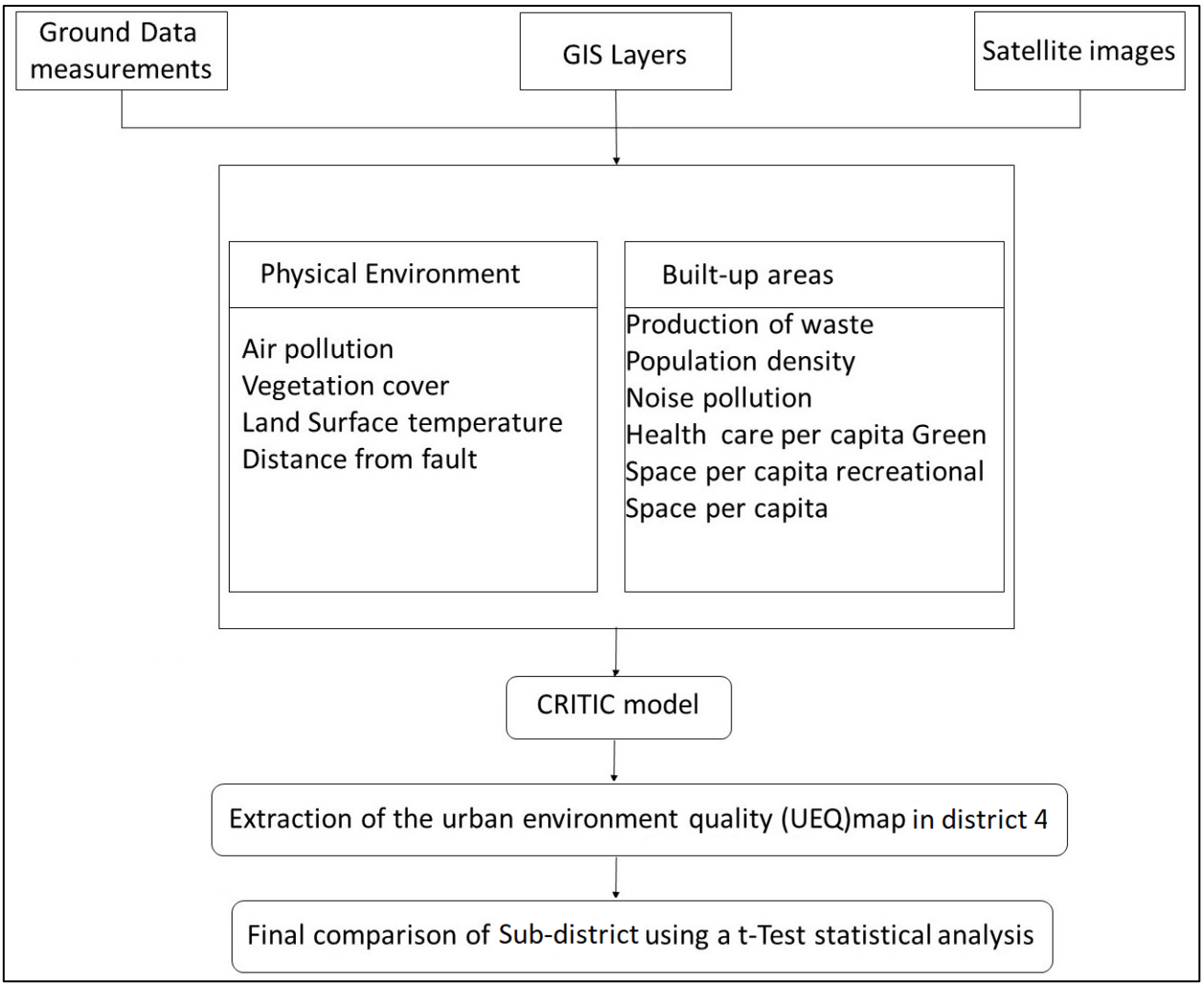


Figure 2. Step by step procedure for spatial UEQ modeling.

Domain	*Indicator*	*Equation*	*Equation elements*	*Data source*	*Reference*
Physical environment	Air Quality Index(AQI)	$AQIap = \frac{AQI_{uc} - AQI_{lc}}{BP_{uc} - AQI_{lc}}(C_{ap} - BP_{lc}) + AQI_{lc}$	AQI_{ap} is the index for given air pollutant (ap); AQI_{uc} and AQI_{lc} are the values corresponding to upper and lower of each breakpoint category (BP), respectively; C_{ap} is the concentration of each air pollutant; BP_{uc} and BP_{lc} are, respectively, the upper and lower concentrations of air pollutants at each breakpoint category.	Tabriz air quality measurement stations	[67]
	Normalized Difference Vegetation Index (NDVI)	$NDVI = \frac{R_{Nir} - R_r}{R_{Ni} + R_r}$	*RNir* and *Rr* are, respectively, the spectral reflectance of Landsat-8 OLI bands 5 and 4.	Landsat 8	[68]
	Land Surface temperature	$Ts = \frac{1}{C10}\{a(1 - C10 - D10) + [b(1 - C10 - D10) + C10 + D10]T10 - D10\,Ta\}$	*Ts* is LST; *T10* is brightness temperature of Landsat 8 band 10; *Ta* is mean atmospheric temperature; *a* and *b* are the constants used to approximate the derivative of the Planck radiance function for the TIRS band 10, *C10* and *D10* are the internal parameters for the Mono-Window algorithm	Landsat 8	[69]
	Distance from Fault line	$Deuc = (\sum_{i=1}^{p}(xi - yi)2)^{1/2}$	If x and y are two points in the p component,The	Digitizing the fault line from the geological	[70]

			Euclidean distance between these two can be calculated.	map and applying the Euclidean distance function	
built-up Environment	Production of waste	Wp=pop× ADWPP	Production of waste equlals Average daily waste production per person(ADWPP) multiplied by the population	Census data	[71]
	Population density	$\text{Popdensity} = \frac{P_i}{A_i}$	Popdensity is population density per pixel, p_i is population in pixel, A_i is area (hectare).	Census data	[34]
	Noise pollution	NdB=10log10×(P2P1)	Ndb is the ratio of the two-power expressed in deciBels, dB P2 is the output power level P1 is the input power level. Sounds above 85 dB are harmful.	Definition of 200 x 200-meter grid and maximum sound measurement in district 4 with the Light Weight Noise Meter GM1357 Digital Handy Sound Level Meter for Sound Quality Control	[72]
	Health care space per capita(m)	$H_{pc}=\frac{HA_i}{P_i}$	Health care space per capita is the division of HA_i (m^2) to population.	Census data	[73]
	Recreational space per capita	$H_{pc}=\frac{RSA_i}{P_i}$	Recreational space per capita is the division of RSA_i (m^2) to population.	Census data	[74]
	Green space per capita	$GS_{pc}=\frac{GSA_i}{P_i}$	Green space per capita is the division of GSA_i (m^2) to population.	Census data	[75]

By absorbing pollutants and releasing oxygen, urban green space (UGS) provide numerous benefits to urban residents[88-90], assist in maintaining the city's natural urban environment by providing clean air, water, and soil[90, 91]. Another parameter of interest is population density, or the number of people per unit area[92], which has an impact on the physico-chemical properties of soils and dust, including metal concentrations and speciations[93]. Noise pollution is also a major contributor to environmental pollution that poses a threat to the health of humans and living things[94], it causes aggression, petulance, and lack of concentration, as well as hearing loss and mental disorders[95]. Health care coverage on a per capita basis at the neighborhood level improves access to the health system for citizens and improves the quality of urban environments by reducing travel for therapeutic purposes[96]. Urban green space per capita is considered to be the most important quantitative indicator of urban green infrastructure[97]. UGS per capita should be at least 9 m2 and 50 m2 for good urban environmental quality, according to the World Health Organization[98]. It is common for urban residents to interact with the natural environment as part of recreational activities[99]. As part of UEQ assessments, recreation encourages physical activity and active lifestyles, potentially reducing health risk factors such as obesity and cardiovascular disease[100]. Moreover, recreational activities promote social interaction, empower individuals, and foster social cohesion[74]. Urban expansion and high-quality development require an assessment of geotechnical seismic vulnerability in districts with seismic activity [101]. Indicators for UEQ calculation have been derived from GIS data, satellite images, and ground data. In accordance with the spatial resolution of Landsat data, a 30-meter pixel size was selected for the selected data sets.

In order to conduct a literature review, the most influential variables from various land sources, official statistics, remote sensing techniques and geographic information systems were collected and analyzed. Since citizens have access to water in the same manner as before purified water was used for domestic purposes, water quality was not considered in the model. A significant part of the urban transportation index is based on the absence of an efficient public transportation system in Tabriz, which reflects in the AQI index the reliance on personal vehicles as a means of transportation. The author acknowledge that more indicators could have been examined, but I have still assessed and quantified the most significant and influential indicators.

Criteria importance through intercriteria correlation (CRITIC)

When using multi-attribute decision making (MADM), multiple options are examined and the best option is selected based on a variety of factors[102]. The evaluation of UEQ and the selection of the optimal option of neighborhoods is a typical, critical, and highly influential MADM problem[103]. A key element in MADM is attribute weights, which have a major influence on the results of the decision-making process[104]. For determining attribute weights, numerous approaches have been utilized[60].CRITIC is a common objective approach to measuring criteria importance by correlating them with other criteria[105]. As part of the CRITIC method, the contrast intensity and contradictory nature of the assessment criteria are considered[106]. The CRITIC method

relies solely on the decision matrix for determining the relative importance of indicators[107]. In this method, the weights are determined based on the contrast intensity and conflict evaluation of the decision problem. Additionally, human intervention is not required for the evaluation process[108]. The steps of the method can be described as follows:

i. The decision matrix is normalized using the following equation:

$$a_{ij}^{+} = \frac{a_{ij} - a_j^{worst}}{a_j^{best} - a_j^{worst}} \quad (1)$$

where *a+ ij* denotes the normalized value of the *i*th design on the *j*th response.
ii. The following multiplicative aggregation equation is used to determine the amount of information contained in the *j*th response:

$$C_j = \sigma_j \sum_{k=1}^{n} (1 - r_{jk}) \quad (2)$$

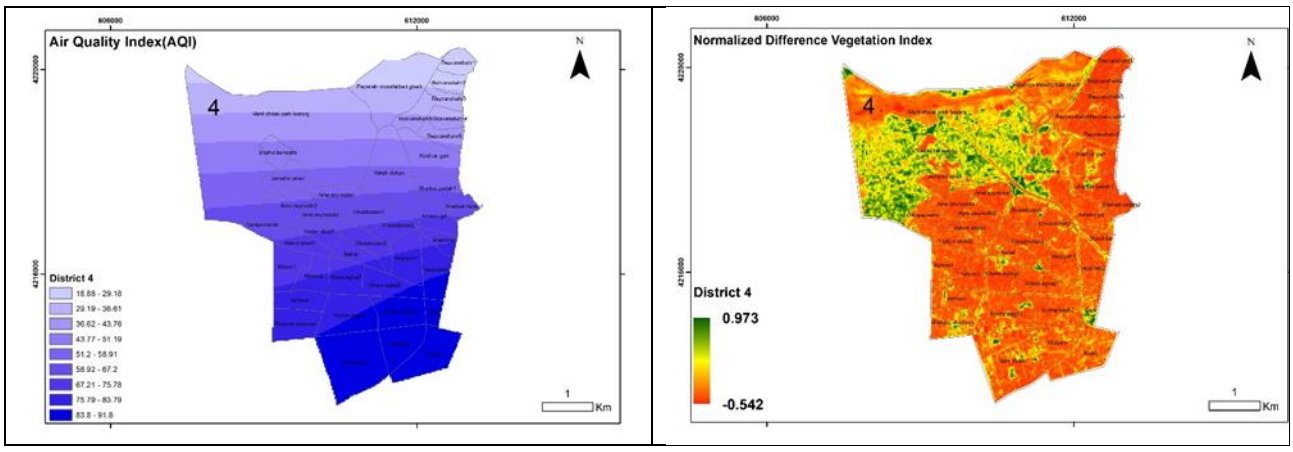
where _*j* denotes the standard deviation of the *j*th response and *rjk* represents the correlation coefficient between two different responses.
iii. The objective weights (*w*j) are determined by using the following equation:

$$w_j = \frac{C_j}{\sum_{k=1}^{m} C_k} \quad (3)$$

As a result, this method assigns a high value of weights to those responses with high standard deviation and low correlation with other responses[109].

Results

A comparison map of indicators for calculating UEQ in district 4 is shown in figure 2. There is a significant concentration of Normalized Difference Vegetation Index (NDVI) in the northern part of district 4. In district 4, LST shows higher values in the southern and northern parts, and decreases with the increase in greenery areas in the middle areas. Population density determines the waste production index, which is increased in district 4 in the south to the center. Based on a population density index, district 4 has a higher population density than other districts, and the eastern parts are more populous than the western parts. This has some effect on environmental quality. In district 4, the airport and small industries and production workshops contribute to high noise pollution. Health care space per capita index is more concentrated in the central neighborhoods. District 4 has a lot of green space, the value decreases rapidly in the other neighborhoods as we move away from the north. Recreational space per capita on a local scale in district 4 lacks this index severely, but the northern areas are more capable of improving it. District 4 has the highest safety index due to its distance from fault lines, but its infrastructure is in need of significant maintenance to ensure continued safety (Fig 3).



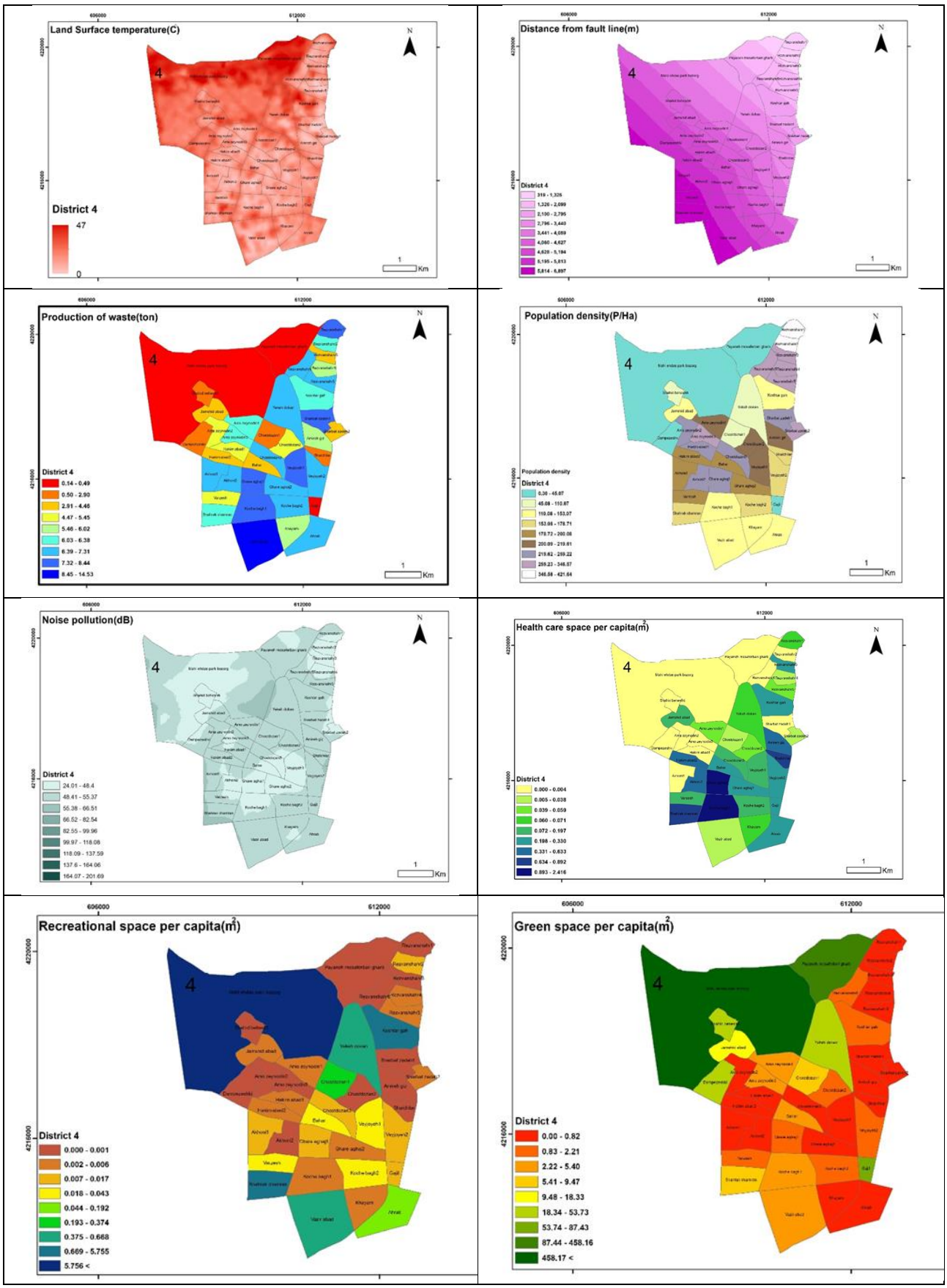
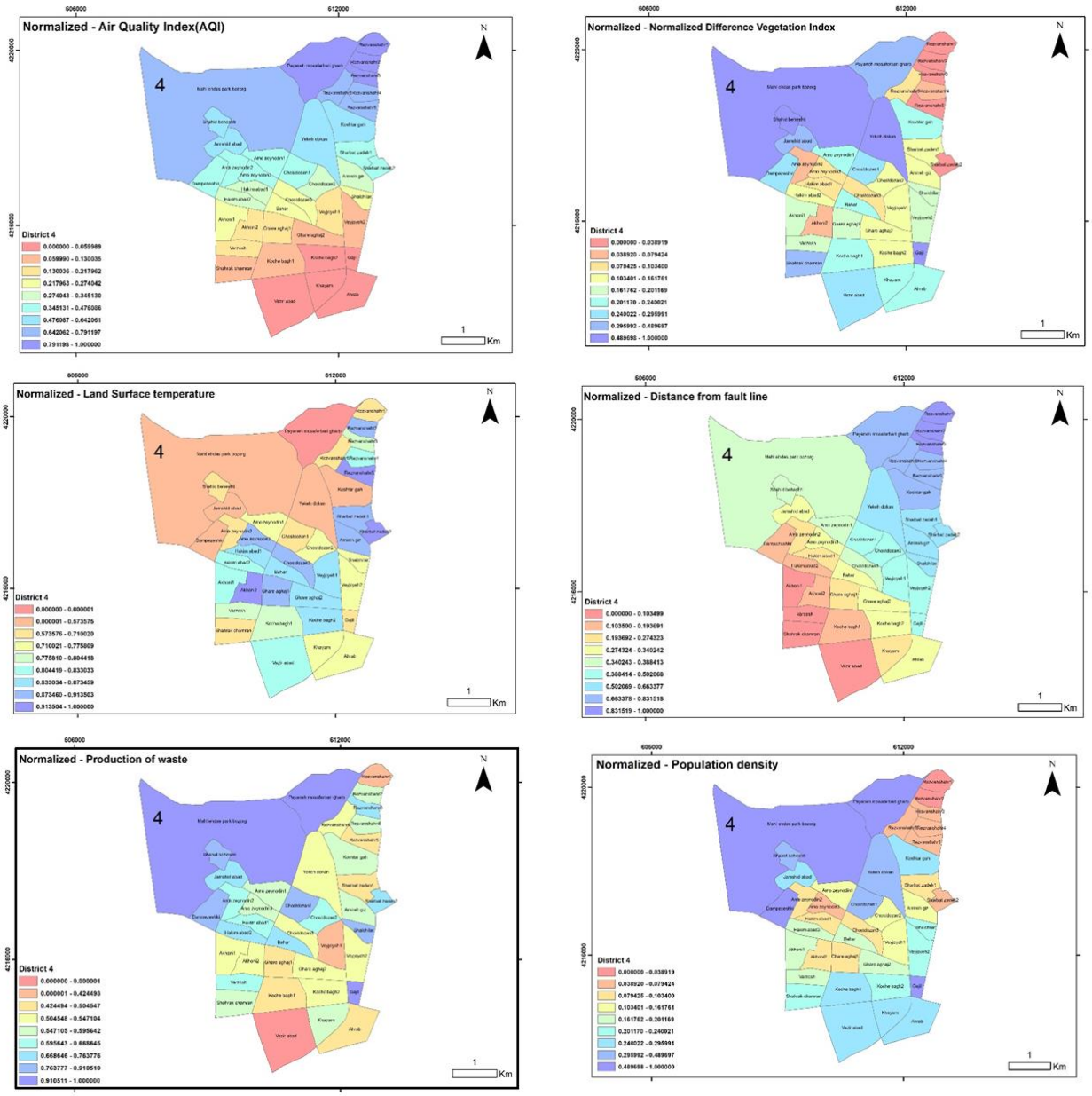


Figure 3. Indicators for calculation of UEQ in district 4. (a). Air Quality Index (AQI), (b). Normalized Difference Vegetation Index (NDVI), (c). Land Surface temperature(c°), (d). Distance from fault line(m), (e). Production of waste(ton), (f). Population density, (g). Noise pollution(dB), (h). Health care space per capita(m^2), (i). Recreational space per capita(m^2), (j) Green space per capita(m^2).

Spatial analysis of UEQ

Using the methods described in table 1, the maps prepared by the methods described in figure 2 for district 4 reveals that the investigated variables differ in terms of average, minimum and maximum parameters, which indicates that this question requires a comparative assessment from a perspective of environmental quality. According to CRITIC model implementation procedure, the environmental quality map is generated in two steps. First, ten indicators are prepared and normalized (Fig 5) and then a correlation matrix is calculated between them (Table 2).



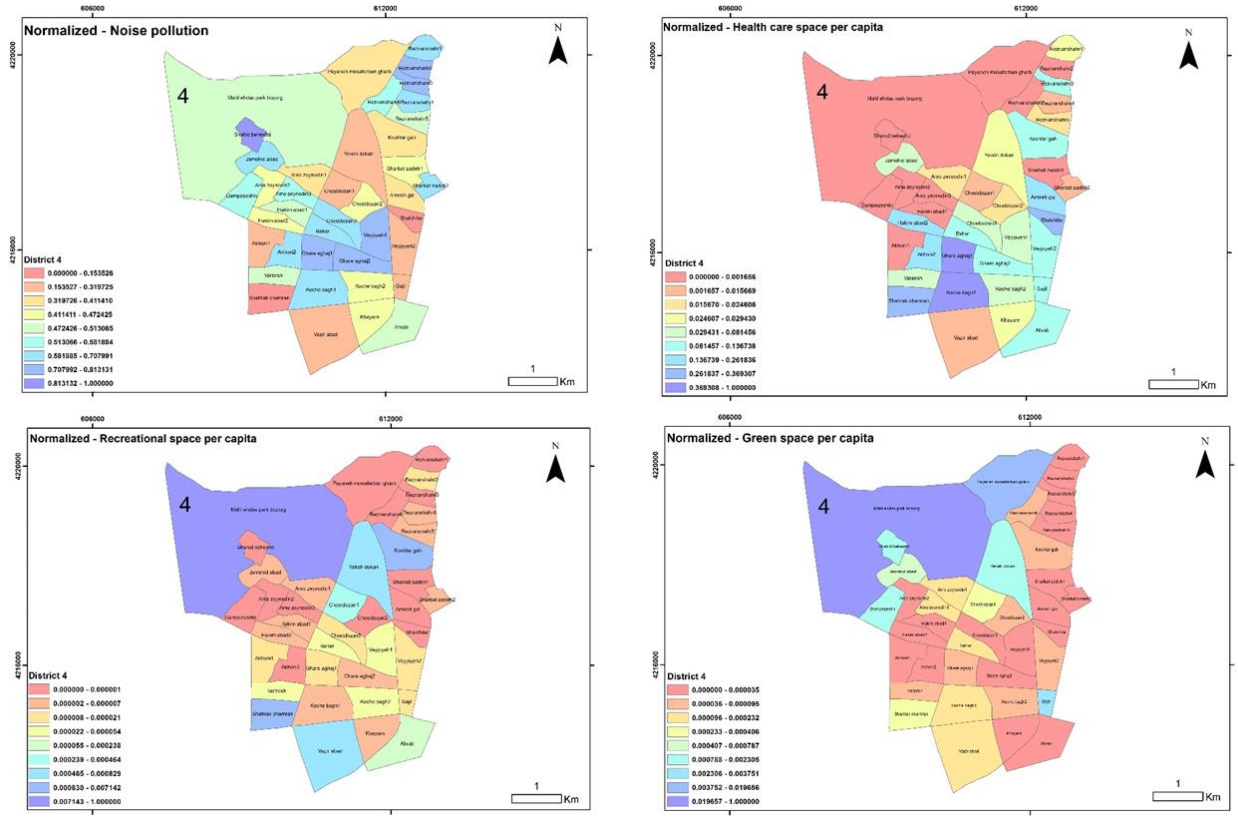


Figure 4. Maps of the normalized variables for the districts of 4**,** (**a**). Air Quality Index (AQI), (**b**). Normalized Difference Vegetation Index (NDVI), (**c**). Land Surface temperature(c◦), (**d**). Distance from fault line(m), (**e**). Production of waste(ton), (**f**). Population density, (**g**). Noise pollution(dB), (**h**). Health care space per capita(m^2), (**i**). Recreational space per capita(m^2), (**j**) Green space per capita(m^2).

Table.2. The final statistical results of layers in the district 4

Variable	Mean	Standard deviation	Mean× Standard deviation	Weight
Air Quality Index(AQI)	8.391	.278	2.331050	**0.129**
Normalized Difference Vegetation Index (NDVI)	7.739	.234	1.814732	**0.101**
Land Surface temperature	11.671	.184	2.152613	**0.119**
Distance from Fault line	9.003	.257	2.313669	**0.128**
Production of waste	7.667	.183	1.403799	**0.078**
Population density	8.793	.228	2.005782	**0.111**
Noise pollution	8.723	.205	1.788578	**0.099**
Health care space per capita	9.709	.205	1.994613	**0.110**
Recreational space per capita	7.124	.158	1.126075	**0.062**
Green space per capita	7.105	.158	1.122752	**0.062**

Second, using the contrast matrix generated by subtracting one from the correlation, I have determined the final weights separately for each variable in the district 4 by multiplying the average of each variable in its standard deviation and dividing this answer by its sum (Table 2).

Weighted linear combinations of urban environmental quality maps have been generated for districts 4 using standardized layers and associated weights obtained through the CRITIC model based on following equations (Fig.5) (Equations 4).

UEQ^{1}_{D4}= 0.129AQI[2]+ 0.099NP[3]+ 0.119LST[4]+ 0.101NDVI[5]+ 0.111PD[6]+ 0.078POW[7]+ 0.062RSPC[8]+ 0.110HCSPC[9]+ 0.062GSPC[10]+ 0.128DFFL[11] …..(4)

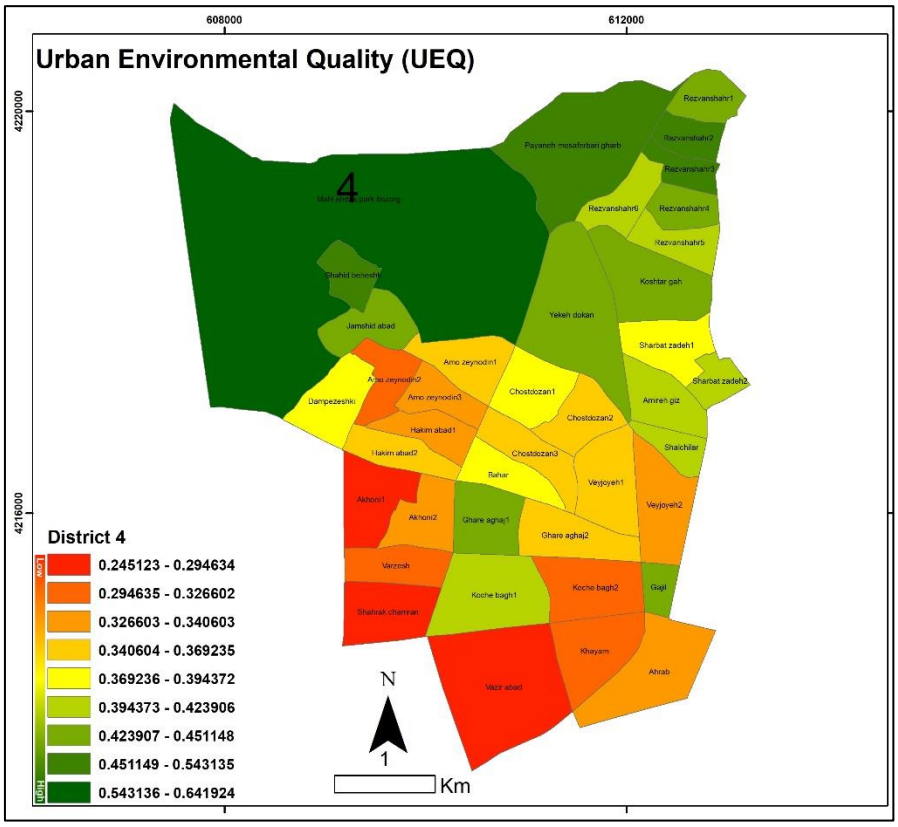


Figure. 5. *UEQ map of district 4 using a weighted linear combination of variables based on the CRITIC model.*

According to the comparison of the final urban environment map in sub-district level(fig.5), there is a significant difference in the quality of the urban environment between different neighborhoods within the district 4. The final map of UEQ in district 4 shows that, there are several neighborhoods in district 4 that offer better environmental conditions than other districts in the area, including Mahale Ehdas Park Bozorg, Rezvanshahr, Qara-Aghaj and Gajil (adjacent to Golestan Park).

Model Evaluation by implementation of the statistical T Test

When comparing the average of a group with a default value, the T test is used to determine whether there is a significant difference. An independent-samples t test is used to determine whether there are significant differences in averages between groups organized separately from each other in sub-independent groups [110]. According to Table 4, the results for independently selected groups, district 4, show that six of ten indicators are significantly different in the sub districts (Table.4).

Table. 4. Independent Samples Test results to determine significant differences between averages

Independent Samples Test

[1] Urban Environmental Quality

[2] Air Quality Index(AQI)

[3] Noise pollution(NP)

[4] Land Surface temperature(lst)

[5] Normalized Difference Vegetation Index(NDVI)

[6] Population density(PD)

[7] Production of waste(POW)

[8] Recreational space per capita(RSPC)

[9] Health care space per capita(HCPC)

[10] Green space per capita(GSPC)

[11] Distance from Fault line(DFFL)

		Levene's Test for Equality of Variances		t-test for Equality of Means						
		F	Sig.	**t**	df	Sig. (2-tailed)	Mean Difference	Std. Error Difference	95% Confidence Interval of the Difference	
									Lower	Upper
AQI (Air Quality Index)	Equal variances **not** assumed	18.56	0.00	-0.76	57.01	0.45	-2.56	3.35	-9.26	4.15
Normalized Difference Vegetation Index (NDVI)	Equal variances assumed	0.24	0.62	-0.91	72.00	0.37	-0.02	0.02	-0.05	0.02
Land Surface Temperature (LST)	Equal variances assumed	0.43	0.51	-3.12	72.00	0.00	-1.97	0.63	-3.23	-0.71
Distance from fault	Equal variances **not** assumed	26.16	0.00	11.31	49.76	0.00	2843.65	251.40	2338.64	3348.66
Waste production	Equal variances assumed	1.74	0.19	3.87	72.00	0.00	2.08	0.54	1.01	3.14
Population density	Equal variances assumed	3.92	0.051	4.26	72	0.00	83.54	19.57	44.52	122.57
Sound Intensity Index	Equal variances assumed	2.43	0.12	-27.16	72.00	0.00	-15.31	0.56	-16.44	-14.19
Health center space pc	Equal variances **not** assumed	10.22	0.002	-1.40	33.57	0.17	-1.19	0.85	-2.92	0.53
Recreational space pc	Equal variances assumed	0.31	0.58	0.25	72.00	0.81	6.14	24.98	-43.65	55.93
Green space pc	Equal variances assumed	1.50	0.22	0.61	72.00	0.54	400.32	656.53	-908.44	1709.08

It is evident that the averages of the sub-districts differ significantly with respect to waste production, population density, sound intensity, proximity to fault lines, land surface temperature, and vegetation difference index, but there are no significant differences between the other indicators.

Consequently, the indicators' direct and indirect contributions to achieving the environmental quality map are summarized as follows. The four indicators sound intensity, distance from fault line, land surface temperature, and normalized difference vegetation index provide high quality in northern sub-districts in comparison to two indicators waste production and population density southern sub-districts. Therefore, a comparative comparison of subdistricts indicates that northern sub-district are environmentally superior.

Discussion

In the urban environment quality map for district 4, it was determined that the Bozorg Park in the northwest, Qara Aghaj in the center, and Gajil in the east have shown significantly better environmental conditions as a result of the abundance of green areas and vacant land. As a result of the proximity to industrial and petrochemical land uses in district 4, high population densities, and destruction of green space, the western neighborhoods of district 4 have poor environmental quality, and the disruption of natural landscapes directly impacts air quality, green space availability, land surface temperature, and noise pollution.

Even though the average difference among sub-districts of district 4 is not significant, the air quality index for southern areas of district 4 is lower than northern areas, primarily due to the high population density, the high use of cars, and proximity to worn-out tissues. In order to improve the quality of the environment, public

transportation can be improved and diesel usage at Tabriz Power Plant can be limited during colder months. There are ways to reduce the land surface temperature in district 4, including increasing parks and green space levels, as well as prioritizing sensitive age groups (children and the elderly) in deficient neighborhoods.
NDVI measures the greenness of an environment. By adding green spaces and green roofs to vertical surfaces, the UEQ of the environment can be increased.
District 4 should consider expanding green corridors in order to enhance the quality of their UEQ, since green space is distributed in a centralized manner in northern areas. A direct relationship exists between population density and waste production, and these indicators are higher in northern of district 4 as compared southern areas. For these indicators to improve in district 4, it appears necessary to implement solutions such as separating the source from the trash, eliminating plastic bags, and promoting municipal tax deductions. One of the most expensive and time-consuming variables in this study was sound pollution, which has an inverse relationship with green space and population density, and it peaks during the early morning and evening hours.
The most important findings of the research can be summarized as follows:
There is a North-South decrease in Urban Environment Quality (UEQ) in district 4 of Tabriz as a result of a spatial modeling study.
UEQ conditions are better in northern areas of district 4.
Six of ten indicators are significantly different among the two neighborhoods, according to the T-test analysis of the models' inputs.
In terms of UEQ, green areas rank highest while commercial and high-density residential land uses are at the bottom.
It is considered an efficient way to improve the quality of the environment in district 4 to implement fixed sound intensity recording systems. This is along with expanding public transportation to reduce the use of personal vehicles. The diversity of variables in this study is consistent with similar studies that use both natural and human indicators [31, 41, 111]. Most researchers use multivariate analysis methods as the basis for quantitatively evaluating environmental quality[34, 39, 112, 113]. This research has benefited from the efficiency of this method along with statistical analysis.

Conclusion

According to the United Nations Sustainable Development Agenda for the third millennium, sustainable development for cities and communities is an important objective. A comparative approach and MCDM tools were used to examine the UEQ in district 4 of Tabriz metropolis. In order to analyze the urban environmental quality, 10 main variables include Health center space pc, Recreational space pc, Population density, AQI, Sound Intensity Index, Distance from fault, LST, NDVI was identified. In order to map research variables quantitatively, satellite images were used for NDVI index, sound intensity was measured with the Light Weight Noise Meter GM1357 Digital Handy Sound Level Meter for Sound Quality Control, air pollution data was collected from Tabriz air quality measurement stations, and population statistical block data of district 4 was used to prepare per capita and distance variables. The CRITIC model uses correlation and standard deviation to avoid the use of subjective judgment in order to produce a more realistic map of urban environmental quality. In future studies, the author propose applying multi-temporal satellite images and landscape metrics to examine land use changes and ecological connectivity condition on UEQ. There is no doubt that the rapid urbanization trend in Tabriz metropolis especially in 4 district will be responsible for the development of building lands and shrinking of green and ecological lands, resulting in the downward trend in the UEQ index. Ecological space (farms, green spaces, and water bodies) and unoccupied lands in the district 4 was considered as potential elements for raising UEQ conditions in the district 4. The diversity of variables in this study is consistent with similar studies that use both natural and human indicators. Most researchers use multivariate analysis methods as the basis for quantitatively evaluating environmental quality. This research has benefited from the efficiency of this method along with statistical analysis. Following are some practical recommendations for improving the UEQ in distric 4 based on the obtained scores:
Enhancing and reviving damaged natural areas to increase their balanced distribution within the ecological network while protecting the remaining green areas.
Increasing artificial green areas will facilitate the establishment of a balanced distribution.
Enhance the size of green areas by establishing large green areas in order to reduce the effects of urban heat islands.
To reduce earthquake vulnerability, upcoming urban development should be directed towards the south.
It is important to mix land use and adopt the policy of creating multi-core urban centers in order to reduce personal travel.
Utilizing smart growth and infill development strategies to promote urban renewal through the activation of deteriorated textures.
Encourage the culture of waste segregation at the source in order to reduce the volume of municipal solid waste.

Instead of increasing sales density and altering land use in an arbitrary manner, sustainable sources of income should be considered.

References

1. Rode, P., *Trends and challenges: global urbanisation and urban mobility.* Megacity mobility culture, 2013: p. 3-21.
2. Liu, Z., C. He, Y. Zhou, and J. Wu, *How much of the world's land has been urbanized, really? A hierarchical framework for avoiding confusion.* Landscape Ecology, 2014. **29**(5): p. 763-771.
3. Yang, K., et al., *A time-series analysis of urbanization-induced impervious surface area extent in the Dianchi Lake watershed from 1988–2017.* International Journal of Remote Sensing, 2019. **40**(2): p. 573-592.
4. Pata, U.K., M. Aydin, and I. Haouas, *Are natural resources abundance and human development a solution for environmental pressure? Evidence from top ten countries with the largest ecological footprint.* Resources policy, 2021. **70**: p. 101923.
5. Qiu, G.-y., et al., *Effects of evapotranspiration on mitigation of urban temperature by vegetation and urban agriculture.* Journal of Integrative Agriculture, 2013. **12**(8): p. 1307-1315.
6. Zhang, X., et al., *Linking urbanization and air quality together: A review and a perspective on the future sustainable urban development.* Journal of Cleaner Production, 2022: p. 130988.
7. Artmann, M., et al., *How smart growth and green infrastructure can mutually support each other—A conceptual framework for compact and green cities.* Ecological Indicators, 2019. **96**: p. 10-22.
8. Mell, I., *Global green infrastructure: lessons for successful policy-making, investment and management*. 2016: Routledge.
9. Colantonio, A., *Urban social sustainability themes and assessment methods.* Proceedings of the Institution of Civil Engineers-Urban Design and Planning, 2010. **163**(2): p. 79-88.
10. Dominelli, L. and H.-b. Ku, *Green social work and its implications for social development in China.* China Journal of Social Work, 2017. **10**(1): p. 3-22.
11. Roseland, M., *Sustainable community development: integrating environmental, economic, and social objectives.* Progress in planning, 2000. **54**(2): p. 73-132.
12. Afrin, T. and N. Yodo, *A survey of road traffic congestion measures towards a sustainable and resilient transportation system.* Sustainability, 2020. **12**(11): p. 4660.
13. Liang, L., Z. Wang, and J. Li, *The effect of urbanization on environmental pollution in rapidly developing urban agglomerations.* Journal of cleaner production, 2019. **237**: p. 117649.
14. Srivastava, R.K., et al., *Controlling NOx emission from industrial sources.* Environmental progress, 2005. **24**(2): p. 181-197.
15. Atash, F., *The deterioration of urban environments in developing countries: Mitigating the air pollution crisis in Tehran, Iran.* Cities, 2007. **24**(6): p. 399-409.
16. Jowkar, H., S. Ostrowski, M. Tahbaz, and P. Zahler, *The conservation of biodiversity in Iran: threats, challenges and hopes.* Iranian Studies, 2016. **49**(6): p. 1065-1077.
17. Destek, M.A. and A. Sinha, *Renewable, non-renewable energy consumption, economic growth, trade openness and ecological footprint: Evidence from organisation for economic Co-operation and development countries.* Journal of cleaner production, 2020. **242**: p. 118537.
18. Pham, N.M., T.L.D. Huynh, and M.A. Nasir, *Environmental consequences of population, affluence and technological progress for European countries: A Malthusian view.* Journal of environmental management, 2020. **260**: p. 110143.
19. Rees, W. and M. Wackernagel, *Urban ecological footprints: why cities cannot be sustainable—and why they are a key to sustainability.* Urban ecology: an international perspective on the interaction between humans and nature, 2008: p. 537-555.
20. Austin, G., *Green infrastructure for landscape planning: integrating human and natural systems*. 2014: Routledge.
21. Hollis, G., *Environmental impacts of development on wetlands in arid and semi-arid lands.* Hydrological Sciences Journal, 1990. **35**(4): p. 411-428.
22. McPhearson, T., D. Maddox, B. Gunther, and D. Bragdon, *Local assessment of New York City: Biodiversity, green space, and ecosystem services.* Urbanization, Biodiversity and Ecosystem Services: Challenges and Opportunities: A Global Assessment, 2013: p. 355-383.
23. Nagendra, H., H. Sudhira, M. Katti, and M. Schewenius, *Sub-regional assessment of India: effects of urbanization on land use, biodiversity and ecosystem services.* Urbanization, biodiversity and ecosystem services: challenges and opportunities: a global assessment, 2013: p. 65-74.
24. Stefanakis, A.I., *The role of constructed wetlands as green infrastructure for sustainable urban water management.* Sustainability, 2019. **11**(24): p. 6981.

25. Molina, L.T., E. Velasco, A. Retama, and M. Zavala, *Experience from integrated air quality management in the Mexico City Metropolitan Area and Singapore.* Atmosphere, 2019. **10**(9): p. 512.
26. Gunawan, O., R.P. Armitage, and P. James, *An Urban Environmental Quality index for Salford, Greater Manchester: A disaggregated approach.* 2012.
27. Moradi, B., et al., *A Scenario-Based Spatial Multi-Criteria Decision-Making System for Urban Environment Quality Assessment: Case Study of Tehran.* Land, 2023. **12**(9): p. 1659.
28. Roy, S., et al., *Evaluating urban environment quality (UEQ) for Class-I Indian city: an integrated RS-GIS based exploratory spatial analysis.* Geocarto International, 2022: p. 2153932.
29. Bateman, I.J., et al., *Bringing ecosystem services into economic decision-making: land use in the United Kingdom.* science, 2013. **341**(6141): p. 45-50.
30. Burton, I., et al., *From impacts assessment to adaptation priorities: the shaping of adaptation policy.* Climate policy, 2002. **2**(2-3): p. 145-159.
31. Musse, M.A., D.A. Barona, and L.M.S. Rodriguez, *Urban environmental quality assessment using remote sensing and census data.* International journal of applied earth observation and geoinformation, 2018. **71**: p. 95-108.
32. Nadrian, H., et al., *Exploring the dimensions of urban quality of life associated with urban traffic jam: The development and validation of an instrument.* Journal of Transport & Health, 2022. **26**: p. 101463.
33. Nichol, J. and M.S. Wong, *Mapping urban environmental quality using satellite data and multiple parameters.* Environment and Planning B: Planning and Design, 2009. **36**(1): p. 170-185.
34. Liang, B. and Q. Weng, *Assessing urban environmental quality change of Indianapolis, United States, by the remote sensing and GIS integration.* IEEE Journal of Selected Topics in Applied Earth Observations and Remote Sensing, 2010. **4**(1): p. 43-55.
35. Wentz, E.A., et al., *Six fundamental aspects for conceptualizing multidimensional urban form: A spatial mapping perspective.* Landscape and Urban Planning, 2018. **179**: p. 55-62.
36. DiMento, J.F., *1. Worldwide Environmental Quality and the Role of Law*, in *The Global Environment and International Law*. 2021, University of Texas Press. p. 1-12.
37. Meju, M.A., *Geoelectrical investigation of old/abandoned, covered landfill sites in urban areas: model development with a genetic diagnosis approach.* Journal of Applied geophysics, 2000. **44**(2-3): p. 115-150.
38. Van Kamp, I., K. Leidelmeijer, G. Marsman, and A. De Hollander, *Urban environmental quality and human well-being: Towards a conceptual framework and demarcation of concepts; a literature study.* Landscape and urban planning, 2003. **65**(1-2): p. 5-18.
39. Liu, Y., et al., *Assessing the urban environmental quality of mountainous cities: A case study in Chongqing, China.* Ecological Indicators, 2017. **81**: p. 132-145.
40. Redo, D.J., T.M. Aide, and M.L. Clark, *The relative importance of socioeconomic and environmental variables in explaining land change in Bolivia, 2001–2010.* Annals of the Association of American Geographers, 2012. **102**(4): p. 778-807.
41. Assaye, R., K. Suryabhagavan, M. Balakrishnan, and S. Hameed, *Geo-spatial approach for urban green space and environmental quality assessment: a case study in Addis Ababa City.* Journal of Geographic Information System, 2017. **9**(2): p. 191-206.
42. Faisal, K. and A. Shaker, *An investigation of GIS overlay and PCA techniques for urban environmental quality assessment: a case study in Toronto, Ontario, Canada.* Sustainability, 2017. **9**(3): p. 380.
43. Gonzalez-Trevizo, M., et al., *Research trends on environmental, energy and vulnerability impacts of Urban Heat Islands: An overview.* Energy and Buildings, 2021. **246**: p. 111051.
44. Shi, H., et al., *Urban Heat Island and its regional impacts using remotely sensed thermal data—A review of recent developments and methodology.* Land, 2021. **10**(8): p. 867.
45. Baba, H. and Y. Asami, *Regional differences in the socio-economic and built-environment factors of vacant house ratio as a key indicator for spatial urban shrinkage.* Urban and Regional Planning Review, 2017. **4**: p. 251-267.
46. Li, J., J. Gong, J.-M. Guldmann, and J. Yang, *Assessment of urban ecological quality and spatial heterogeneity based on remote sensing: a case study of the rapid urbanization of Wuhan City.* Remote Sensing, 2021. **13**(21): p. 4440.
47. Roy, S., et al., *Evaluating urban environment quality (UEQ) for Class-I Indian city: An integrated RS-GIS based exploratory spatial analysis.* Geocarto International, 2022(just-accepted): p. 2153932.
48. Lu, C., et al., *Evaluation and planning of urban geological and ecological environment quality.* Arabian Journal of Geosciences, 2021. **14**(2): p. 1-8.
49. Sousa, J.J., et al., *Geohazards Monitoring and Assessment Using Multi-Source Earth Observation Techniques.* Remote Sensing, 2021. **13**(21): p. 4269.
50. Schneider, A., *Monitoring land cover change in urban and peri-urban areas using dense time stacks of Landsat satellite data and a data mining approach.* Remote Sensing of Environment, 2012. **124**: p. 689-704.

51. Fonseka, H., et al., *Urbanization and its impacts on land surface temperature in Colombo metropolitan area, Sri Lanka, from 1988 to 2016.* Remote Sensing, 2019. **11**(8): p. 957.
52. Pope, R. and J. Wu, *Characterizing air pollution patterns on multiple time scales in urban areas: A landscape ecological approach.* Urban Ecosystems, 2014. **17**(3): p. 855-874.
53. Núñez-Alonso, D., L.V. Pérez-Arribas, S. Manzoor, and J.O. Cáceres, *Statistical tools for air pollution assessment: multivariate and spatial analysis studies in the Madrid region.* Journal of analytical methods in chemistry, 2019. **2019**.
54. Gruenhagen, L. and C. Juergens, *Multitemporal Change Detection Analysis in an Urbanized Environment Based upon Sentinel-1 Data.* Remote Sensing, 2022. **14**(4): p. 1043.
55. Ghosh, S., N.D. Chatterjee, and S. Dinda, *Urban ecological security assessment and forecasting using integrated DEMATEL-ANP and CA-Markov models: A case study on Kolkata Metropolitan Area, India.* Sustainable Cities and Society, 2021. **68**: p. 102773.
56. Matthies, M., C. Giupponi, and B. Ostendorf, *Environmental decision support systems: Current issues, methods and tools*. 2007, Elsevier. p. 123-127.
57. Moss, R.H., et al., *The next generation of scenarios for climate change research and assessment.* Nature, 2010. **463**(7282): p. 747-756.
58. Velasquez, M. and P.T. Hester, *An analysis of multi-criteria decision making methods.* International journal of operations research, 2013. **10**(2): p. 56-66.
59. Wanderer, T. and S. Herle, *Creating a spatial multi-criteria decision support system for energy related integrated environmental impact assessment.* Environmental Impact Assessment Review, 2015. **52**: p. 2-8.
60. Şahin, M., *A comprehensive analysis of weighting and multicriteria methods in the context of sustainable energy.* International Journal of Environmental Science and Technology, 2021. **18**(6): p. 1591-1616.
61. Tzeng, G.-H. and J.-J. Huang, *Multiple attribute decision making: methods and applications*. 2011: CRC press.
62. Center, I.S., *Detailed Results of the Census of Population and Housing of the Year*. 2016.
63. Moosavi, M. *An introduction to environmental challenges of life in slum settlements of Tabriz*. in *2011 2nd International Conference on Humanities, Historical and Social Sciences*. 2011.
64. Taheri, M., M. Gholamalifard, M.J. Ghazizade, and S. Rahimoghli, *Environmental impact assessment of municipal solid waste disposal site in Tabriz, Iran using rapid impact assessment matrix.* Impact Assessment and Project Appraisal, 2014. **32**(2): p. 162-169.
65. Ouria, M. and A.T. de Almeida, *How to decarbonize developing cities by 2050: a case from Tabriz-Iran.* Renewable Energy, 2021. **178**: p. 620-638.
66. Dadashpoor, H., P. Azizi, and M. Moghadasi, *Analyzing spatial patterns, driving forces and predicting future growth scenarios for supporting sustainable urban growth: Evidence from Tabriz metropolitan area, Iran.* Sustainable Cities and Society, 2019. **47**: p. 101502.
67. Bishoi, B., A. Prakash, and V. Jain, *A comparative study of air quality index based on factor analysis and US-EPA methods for an urban environment.* Aerosol and Air Quality Research, 2009. **9**(1): p. 1-17.
68. Fung, T. and W. Siu, *Environmental quality and its changes, an analysis using NDVI.* International Journal of Remote Sensing, 2000. **21**(5): p. 1011-1024.
69. Mudede, M.F., S.W. Newete, K. Abutaleb, and N. Nkongolo, *Monitoring the urban environment quality in the city of Johannesburg using remote sensing data.* Journal of African Earth Sciences, 2020. **171**: p. 103969.
70. Haghighi Fard, S.M. and N. Doratli, *Evaluation of Resilience in Historic Urban Areas by Combining Multi-Criteria Decision-Making System and GIS, with Sustainability and Regeneration Approach: The Case Study of Tehran (IRAN).* Sustainability, 2022. **14**(5): p. 2495.
71. Bahauddin, K. and M. Uddin, *Prospect of solid waste situation and an approach of Environmental Management Measure (EMM) model for sustainable solid waste management: case study of Dhaka city.* Journal of Environmental Science and Natural Resources, 2012. **5**(1): p. 99-111.
72. Chiarini, B., A. D'Agostino, E. Marzano, and A. Regoli, *The perception of air pollution and noise in urban environments: A subjective indicator across European countries.* Journal of environmental management, 2020. **263**: p. 110272.
73. Takano, T. and K. Nakamura, *An analysis of health levels and various indicators of urban environments for Healthy Cities projects.* Journal of Epidemiology & Community Health, 2001. **55**(4): p. 263-270.
74. Donnelly, P. and J.J. Coakley, *The role of recreation in promoting social inclusion*. 2002: Laidlaw Foundation Toronto.
75. De la Barrera, F., S. Reyes-Paecke, and E. Banzhaf, *Indicators for green spaces in contrasting urban settings.* Ecological indicators, 2016. **62**: p. 212-219.
76. Laumbach, R.J. and H.M. Kipen, *Respiratory health effects of air pollution: update on biomass smoke and traffic pollution.* Journal of allergy and clinical immunology, 2012. **129**(1): p. 3-11.

77. Dihkan, M., F. Karsli, A. Guneroglu, and N. Guneroglu, *Evaluation of surface urban heat island (SUHI) effect on coastal zone: The case of Istanbul Megacity.* Ocean & Coastal Management, 2015. **118**: p. 309-316.
78. Khandelwal, S., R. Goyal, N. Kaul, and A. Mathew, *Assessment of land surface temperature variation due to change in elevation of area surrounding Jaipur, India.* The Egyptian Journal of Remote Sensing and Space Science, 2018. **21**(1): p. 87-94.
79. Haines, A., R.S. Kovats, D. Campbell-Lendrum, and C. Corvalán, *Climate change and human health: impacts, vulnerability, and mitigation.* The Lancet, 2006. **367**(9528): p. 2101-2109.
80. Dodman, D., *Urban form, greenhouse gas emissions and climate vulnerability*, in *Population dynamics and climate change*. 2009, UNFPA-IIED London, UK. p. 64-79.
81. Alcoforado, M.J. and H. Andrade, *Global warming and the urban heat island*, in *Urban ecology*. 2008, Springer. p. 249-262.
82. Alizadeh, M., et al., *Earthquake vulnerability assessment for urban areas using an ann and hybrid swot-qspm model.* Remote Sensing, 2021. **13**(22): p. 4519.
83. Periathamby, A. *Municipal waste management*. in *Waste*. 2011. Elsevier.
84. Kumar, S., et al., *Assessment of the status of municipal solid waste management in metro cities, state capitals, class I cities, and class II towns in India: An insight.* Waste management, 2009. **29**(2): p. 883-895.
85. Ferronato, N. and V. Torretta, *Waste mismanagement in developing countries: A review of global issues.* International journal of environmental research and public health, 2019. **16**(6): p. 1060.
86. Anilkumar, A., D. Sukumaran, and S.G.T. Vincent, *Effect of municipal solid waste leachate on ground water quality of Thiruvananthapuram District, Kerala, India.* Applied Ecology and Environmental Sciences, 2015. **3**(5): p. 151-157.
87. Singh, S., N.J. Raju, W. Gossel, and P. Wycisk, *Assessment of pollution potential of leachate from the municipal solid waste disposal site and its impact on groundwater quality, Varanasi environs, India.* Arabian Journal of Geosciences, 2016. **9**(2): p. 1-12.
88. Rao, P. and K. Puntambekar, *Evaluating the Urban Green Space benefits and functions at macro, meso and micro level: case of Bhopal City.* B BR, 2011. **377**: p. 31.16.
89. Gonzales, L. and D. Magnaye, *Challenges to the Multi-Functional Uses and Multifarious Benefits of Urban Green Spaces: Basis of Urban Biodiversity Planning and Management in the City of Manila, Philippines.* International Journal of Environmental Science & Sustainable Development, 2016. **1**(1).
90. ThiLoi, D., P.A. Tuan, and K. Gupta, *Development of an index for assessment of urban green Spacesat city level.* International Journal of Remote Sensing Applications, 2015. **5**(1): p. 78.
91. Anguluri, R. and P. Narayanan, *Role of green space in urban planning: Outlook towards smart cities.* Urban Forestry & Urban Greening, 2017. **25**: p. 58-65.
92. Chen, J., B. Wang, S. Huang, and M. Song, *The influence of increased population density in China on air pollution.* Science of the Total Environment, 2020. **735**: p. 139456.
93. Acosta, J., et al., *Influence of population density on the concentration and speciation of metals in the soil and street dust from urban areas.* Chemosphere, 2015. **134**: p. 328-337.
94. Floroian, L., A. Lungu, and M. Badea, *Study on the Effect of Noise Pollution on Public Health.* Bulletin of the Transilvania University of Brasov. Series VI: Medical Sciences, 2022: p. 1-8.
95. Jariwala, H.J., H.S. Syed, M.J. Pandya, and Y.M. Gajera, *Noise pollution & human health: a review.* Indoor Built Environ, 2017: p. 1-4.
96. Rydin, Y., et al., *Shaping cities for health: complexity and the planning of urban environments in the 21st century.* The lancet, 2012. **379**(9831): p. 2079-2108.
97. Badiu, D.L., et al., *Is urban green space per capita a valuable target to achieve cities' sustainability goals? Romania as a case study.* Ecological Indicators, 2016. **70**: p. 53-66.
98. Planning, W.U., *Environment and Health: From Evidence to Policy Action—Meeting Report.* World Health Organization, 2010. **119**.
99. Soga, M. and K.J. Gaston, *Extinction of experience: the loss of human–nature interactions.* Frontiers in Ecology and the Environment, 2016. **14**(2): p. 94-101.
100. Sallis, J.F., M.F. Floyd, D.A. Rodríguez, and B.E. Saelens, *Role of built environments in physical activity, obesity, and cardiovascular disease.* Circulation, 2012. **125**(5): p. 729-737.
101. Bahadori, H., A. Hasheminezhad, and A. Karimi, *Development of an integrated model for seismic vulnerability assessment of residential buildings: Application to Mahabad City, Iran.* Journal of Building Engineering, 2017. **12**: p. 118-131.
102. Drobne, S. and A. Lisec, *Multi-attribute decision analysis in GIS: weighted linear combination and ordered weighted averaging.* Informatica, 2009. **33**(4).
103. Nesticò, A., R. Passaro, G. Maselli, and P. Somma, *Multi-criteria methods for the optimal localization of urban green areas.* Journal of Cleaner Production, 2022. **374**: p. 133690.
104. Dahooie, J.H., et al., *A novel dynamic credit risk evaluation method using data envelopment analysis with common weights and combination of multi-attribute decision-making methods.* Computers & operations research, 2021. **129**: p. 105223.

105. Piasecki, M. and K. Kostyrko, *Development of weighting scheme for indoor air quality model using a multi-attribute decision making method.* Energies, 2020. **13**(12): p. 3120.
106. Krishnan, A.R., M.M. Kasim, R. Hamid, and M.F. Ghazali, *A modified CRITIC method to estimate the objective weights of decision criteria.* Symmetry, 2021. **13**(6): p. 973.
107. Žižović, M., B. Miljković, and D. Marinković, *Objective methods for determining criteria weight coefficients: A modification of the CRITIC method.* Decision Making: Applications in Management and Engineering, 2020. **3**(2): p. 149-161.
108. Zafar, S., Z. Alamgir, and M. Rehman, *An effective blockchain evaluation system based on entropy-CRITIC weight method and MCDM techniques.* Peer-to-Peer Networking and Applications, 2021. **14**(5): p. 3110-3123.
109. Diakoulaki, D., G. Mavrotas, and L. Papayannakis, *Determining objective weights in multiple criteria problems: The critic method.* Computers & Operations Research, 1995. **22**(7): p. 763-770.
110. George, D. and P. Mallery, *IBM SPSS statistics 26 step by step: A simple guide and reference*. 2019: Routledge.
111. Krishnan, V.S. and C.M. Firoz, *Regional urban environmental quality assessment and spatial analysis.* Journal of urban management, 2020. **9**(2): p. 191-204.
112. Shao, Q., et al., *Developing a sustainable urban-environmental quality evaluation system in China based on a hybrid model.* International journal of environmental research and public health, 2019. **16**(8): p. 1434.
113. Javanbakht, M., et al., Spatial-temporal analysis of urban environmental quality of Tehran, Iran. Ecological Indicators, 2021. 120: p. 106901.

Advanced Engineering Days

aed.mersin.edu.tr

Evaluation of quantile mapping and linear scaling bias correction methods for NASA-IMERG historical monthly precipitation data

Ahmad Abu Arra[*1, 2], **Eyüp Şişman** [1, 3]

[1]*Yildiz Technical University, Department of Civil Engineering, Istanbul, Türkiye, ahmad.arra@std.yildiz.edu.tr; esisman@yildiz.edu.tr*
[2]*An-Najah National University, Department of Civil Engineering, Nablus, Palestine, s11419527@stu.najah.edu*
[3]*Istanbul Medipol University, School of Engineering and Natural Sciences, Department of Civil Engineering, Istanbul, Türkiye, esisman@medipol.edu.tr*

Cite this study: Abu Arra, A., & Şişman, E. (2024). Evaluation of quantile mapping and linear scaling bias correction methods for NASA-IMERG historical monthly precipitation data. Advanced Engineering Days, 9, 137-140

Keywords
Quantile Mapping
Linear Scaling
NASA
IMERG
Monthly precipitation

Abstract

Accurate precipitation data is crucial for effective water resources management, especially in regions experiencing climate change. This study aims to evaluate the effectiveness of IMERG (NASA) monthly precipitation data by applying Quantile Mapping (QM) and Linear Scaling (LS) bias correction methods. The uncorrected and corrected IMERG data were compared against observed in-situ data to assess improvements achieved through bias correction. Various statistical metrics, including correlation coefficient (CC), mean square error (MSE), root mean square error (RMSE), mean bias error (MBE), and percent bias (PB), were used for the comparison. The Antalya station in Türkiye, spanning from 2010 – 2022, was used as an application. The obtained results indicate that while the direct use of IMERG data showed a strong correlation with observed data (R^2 = 0.805, CC = 0.897), the MSE and RMSE were relatively high (1675.226 and 40.930, respectively). The LS method improved bias-related metrics significantly, reducing the MBE to 0.0 and PB to 0.0%, though it had minimal impact on other metrics such as CC and MSE. Similarly, the QM method showed slight improvements in R^2 and CC, with significant reductions in MBE (0.219) and PB (-0.32%). Despite these enhancement, overall accuracy metrics exhibited limited changes, indicating that these methods primarily address biases. By ensuring access to more accurate precipitation, water resources managers can make better-informed decisions, significantly impacting water availability, distribution, and sustainability.

Introduction

Accurate and reliable precipitation data are essential for various hydrological and climatological studies [1]. Satellite-based precipitation products, such as the Integrated Multi-satellite Retrievals for GPM (IMERG) from NASA, offer a valuable source of data, particularly in regions challenging data availability problems. However, satellite precipitation estimates often contain biases that can limit their utility [2]. To improve the accuracy of satellite-derived precipitation data, bias correction methods such as Quantile Mapping (QM) and Linear Scaling (LS) are commonly applied [3, 4]. These methods adjust the satellite data to better match observed in-situ measurements, thereby enhancing their reliability for hydrological applications.

This study aims to evaluate the effectiveness of the IMERG monthly precipitation data by applying QM and LS bias correction methods. The corrected satellite data are then compared against observed in-situ data to assess the improvements achieved through bias correction. The comparison procedure will be done using different statistical metrics, such as correlation coefficient, Root Mean Square Error (RMSE), and Percent Bias (PB). This study used monthly precipitation data from the Antalya station in Antalya, Türkiye, for the period between 2010 and 2022 as an application. The selection of this station provides a comprehensive record for evaluating the effectiveness of the bias correction methods applied to the IMERG data. Also, this research aims to provide insights into the performance of these correction methods and their potential impact on the accuracy of precipitation estimates, ultimately contributing to better water resource management and planning.

Material and Method

Data collection

For this study, monthly precipitation data from NASA's IMERG product and observed in-situ data from the Antalya meteorological station spanning from 2010 to 2022 were collected from the Turkish State Meteorological Service. The selected station provides a comprehensive record of observed precipitation, serving as a reliable benchmark for evaluating the satellite data. The monthly average precipitation for IMEG data is 2.36 mm, while for observed data, it is 2.26 mm. The IMERG data, known for its high spatial and temporal resolution, was obtained from the NASA database, ensuring consistency and coverage for the study period.

Linear scaling

LS is a simpler method that adjusts the mean of the satellite data to match the mean of the observed data. This method involves calculating a scaling factor based on the ratio of the mean observed precipitation to the mean satellite precipitation. The IMERG data is then multiplied by this scaling factor to correct for biases in the overall precipitation amounts [2].

Quantile mapping

QM involves mapping the cumulative distribution functions (CDFs) of the satellite and observed data. This method adjusts the satellite data by aligning its quantiles with those of the observed data, effectively correcting for biases across the entire distribution. The QM process includes fitting a CDF to the IMERG data and another to the observed data, followed by transforming the IMERG data based on these fitted CDFs [3].

Statistical metrics

This research evaluates the effectiveness of the IMERG monthly precipitation data by applying QM and LS bias correction methods. The evaluation and comparison process includes different statistical metrics such as the coefficient of determination (R^2), Pearson's Correlation Coefficient (CC), Mean Squared Error (MSE), Root Mean Squared Error (RMSE), Mean Absolute Error (MAE), Mean Bias Error (MBE), and Percent Bias (PB). These metrics provide a comprehensive assessment of the corrected data's performance, highlighting the reduction in biases and improvements in data accuracy. By employing these metrics, the study ensures a robust analysis of the bias correction methods, facilitating a detailed comparison and validation against observed in-situ data.

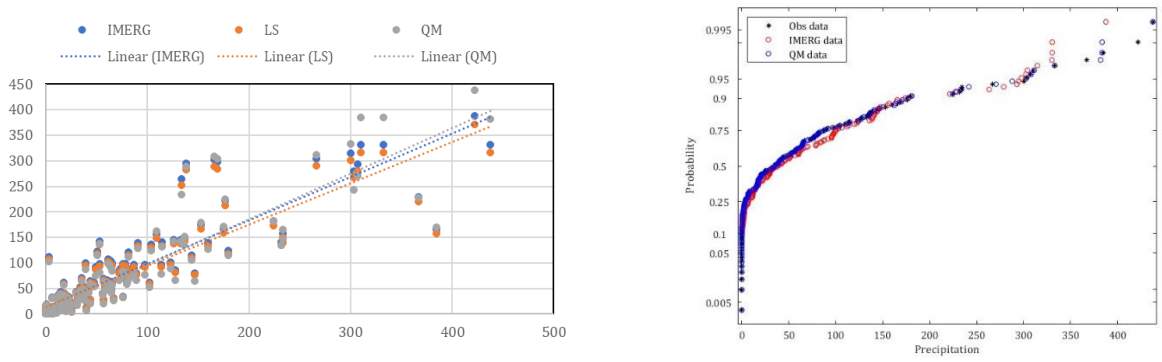
Results

The comparison of monthly IMERG data without correction and after bias correction with observed data at Antalya station from 2010 to 2022, as depicted in the scatter plot (Figure 1 and Table 1), reveals interesting insights regarding the effectiveness of bias correction methods. When IMERG data was used directly, it showed a strong correlation with observed data, with an R^2 value of 0.805 and a CC of 0.897. However, the MSE and RMSE were relatively high at 1675.226 and 40.930, respectively, indicating significant discrepancies in absolute terms. The MAE was 22.637, and the MBE was -3.251, suggesting a slight underestimation by the IMERG data. The percent bias (PB) was 4.748%, reflecting a small systematic bias.

Applying the Linear Scaling (LS) bias correction method to the IMERG data resulted in minimal improvements in the correlation metrics, with the R^2 and CC remaining unchanged at 0.805 and 0.897, respectively (Figure 1 and Table 1). The MSE and RMSE showed slight reductions to 1644.178 and 40.548, respectively, and the MAE improved marginally to 22.073. Importantly, the LS method completely eliminated the mean bias error, bringing it to 0.000, and consequently, the percent bias was also corrected to 0.000% (Figure 1 and Table 1). The Quantile Mapping (QM) method provided a similar pattern of results, with an R^2 value of 0.814 and a CC of 0.902, indicating a slight improvement over both raw IMERG and LS-corrected data. The MSE and RMSE further decreased to 1637.653 and 40.468, respectively. While the MAE slightly increased to 22.547, the MBE improved to 0.219, and the PB corrected to -0.320%, showing the effectiveness of QM in reducing systematic bias (Figure 1 and Table 1). Despite these improvements in bias-related metrics, the overall accuracy metrics like R^2, CC, MSE, RMSE, and MAE showed minimal changes, suggesting that while bias correction methods effectively address systematic bias, they may have a limited impact on the overall accuracy of the dataset.

Table 1. Statistical metrics comparing the observed monthly precipitation data with IMERG data without any BC method, IMERG data with LS BC method, and IMERG data with QM BC method at Antalya station.

	R^2	CC	MSE	RMSE	MAE	MBE	PB (%)
Observed vs IMERG	0.805	0.897	1675.23	40.93	22.64	-3.25	4.75
Observed vs LS	0.805	0.897	1644.18	40.55	22.07	0.00	0.00
Observed vs QM	0.814	0.902	1637.65	40.47	22.55	0.22	-0.32



a) b)

Figure 1. a) Scatter plot comparing IMERG, LS, and QM corrected precipitation data against observed values, b) Probabilities for observed data, IMERG data, and IMERG data with QM BC method.

Discussion

LS and QM are prominent bias correction methods that can be effectively applied to both historical and future climate data. Historical applications of these methods are well-documented, as seen in numerous studies, such as in the article by Yang et al. [5]. These methods are crucial in addressing the systematic biases inherent in datasets like NASA's IMERG, which, despite its high reliability and extensive use in various studies and applications [6], still exhibits biases that necessitate correction. The efficacy of LS and QM in reducing MBE and PB is evident from the results, which show significant improvements in these metrics. However, the lack of improvement in other statistical metrics like CC, MSE, and RMSE can be attributed to the fundamental design of these methods, which focus primarily on bias adjustment rather than overall accuracy enhancement.

In the context of water resources management, the importance of accurate and bias-corrected precipitation data cannot be overstated. Accurate data is essential for effective planning, management, and decision-making in water resources, particularly in the face of climate variability and change [6, 7]. Bias correction methods like LS and QM play a pivotal role in ensuring that the data used for these purposes is as accurate and reliable as possible. While these methods excel in addressing systematic biases, it is essential to continue exploring and developing complementary techniques that can enhance overall data accuracy. This holistic approach will ensure that water resource managers have access to the best possible information, enabling them to make informed decisions that can significantly impact water availability, distribution, and sustainability in both the short and long term.

Conclusion

In conclusion, the study showed the application of LS and QM as effective bias correction methods for improving the accuracy of precipitation data from NASA's IMERG dataset at the Antalya station, Antalya, Türkiye. While these methods significantly reduced MBE and PB, they did not show improvements in other metrics such as CC, MSE, and RMSE. This outcome highlights the specialized nature of LS and QM in addressing systematic biases rather than enhancing overall data accuracy. The findings underscore the importance of bias correction in the context of water resources management, where accurate precipitation data is vital for informed decision-making and sustainable resource planning. The successful application at the Antalya station suggests the potential for broader implementation of these methods in different climatic regions and datasets, thereby improving the reliability of hydrological forecasts and climate models.

References

1. Fowler, H. J., Blenkinsop, S., & Tebaldi, C. (2007). Linking climate change modelling to impacts studies: recent advances in downscaling techniques for hydrological modelling. International Journal of Climatology: A Journal of the Royal Meteorological Society, 27(12), 1547-1578
2. Zhu, G., Liu, Y., Wang, L., Sang, L., Zhao, K., Zhang, Z., ... & Qiu, D. (2023). The isotopes of precipitation have climate change signal in arid Central Asia. Global and Planetary Change, 225, 104103.
3. Boé, J., Terray, L., Habets, F., & Martin, E. (2007). Statistical and dynamical downscaling of the Seine basin climate for hydro-meteorological studies. International Journal of Climatology: A Journal of the Royal Meteorological Society, 27(12), 1643-1655.
4. Lenderink, G., Buishand, A., & Van Deursen, W. (2007). Estimates of future discharges of the river Rhine using two scenario methodologies: direct versus delta approach. Hydrology and Earth System Sciences, 11(3), 1145-1159.

5. Yang, M., Ni, Q., Diao, X., & Xiong, Q. (2024). Comparative analysis of bias correction methods for IMERG V06 precipitation products: case study in Guangxi, China. Remote Sensing Letters, 15(3), 192-202.
6. Teutschbein, C., & Seibert, J. (2012). Bias correction of regional climate model simulations for hydrological climate-change impact studies: Review and evaluation of different methods. Journal of hydrology, 456, 12-29.
7. Fang, G. H., Yang, J., Chen, Y. N., & Zammit, C. (2015). Comparing bias correction methods in downscaling meteorological variables for a hydrologic impact study in an arid area in China. Hydrology and Earth System Sciences, 19(6), 2547-2559.

Advanced Engineering Days

aed.mersin.edu.tr

Iranian gardens as nature-based solutions to improve thermal comfort

Arman Rastkhadiv*[1], Akbar Rahimi[2]

[1] *Tabriz University, Department of Landscape Architecture, Iran, armanrastkhadiv@gmail.com*
[2] *Tabriz University, Department of Urban and Reginal Planning, Iran, Akbar.rahimi@gmail.com*

Cite this study: Rastkhadiv, A., & Rahimi, A. (2024). Iranian gardens as nature-based solutions to improve thermal comfort. Advanced Engineering Days, 9, 141-143

Keywords
Nature-Based Solutions
Ecosystem Services
Microclimate
El-Goli Garden

Abstract

Urban gardens significantly contribute to human health and well-being by providing ecosystem services such as microclimate regulation, thermal comfort, carbon sequestration, and water purification. Recognized as nature-based solutions (NBS), these spaces offer cost-effective, sustainable approaches to urban adaptability and resilience, addressing social, environmental, and economic challenges. Iranian gardens, renowned for their artistic and architectural value, exemplify the use of NBS to create improved microclimates in arid regions. Historically, these gardens served multiple purposes, including recreation, cultural events, and environmental regulation. This study examines the El-Goli Garden in Tabriz, Iran, focusing on elements like water features, dense vegetation, and strategic landscape design that enhance thermal comfort. The research highlights how integrating traditional Iranian garden practices into modern urban planning can foster sustainable, resilient cities. The findings advocate for leveraging these nature-based solutions to reduce energy consumption, improve environmental quality, and enhance urban livability in the face of global climate change.

Introduction

Urban green spaces and urban gardens can have a significant impact on human health and well-being, with the primary benefits stemming from contact with nature and the ecosystem services provided by such spaces contributing to healthier living [1,2]. Therefore, recognizing the importance of urban gardens as a nature-based solution (NBS) for public health and well-being is crucial [3]. Nature-based solutions were first introduced in 2008 in relation to ecosystem services [4]. These solutions, inspired by nature, offer cost-effective approaches to enhancing urban adaptability and resilience while simultaneously delivering human and ecological benefits, thus aiding communities in addressing social, environmental, and economic challenges sustainably [5]. NBS can provide a wide range of beneficial ecosystem services to the urban environment, such as microclimate regulation, thermal comfort, carbon sequestration, water purification, food provision, and more [6].

Iranian gardens serve as valuable examples of art and architecture, promoting Iranian Garden design in other regions, particularly in Islamic territories [7]. Iranian Gardens, exemplifying some of the most distinguished styles of garden design in the world [8], have been employed by Iranian architects for thousands of years to moderate the local climate [9]. In historical periods, due to the lack of urban facilities, Iranian kings used these gardens for multiple purposes, addressing recreational needs as well as cultural, economic, productive, habitat, and environmental regulatory requirements [10]. Iran's hot and dry climate has always valued lush and green gardens as cool, serene places for comfort, pleasure, and recreation [11]. Given Iran's arid region, the Iranian Garden's primary objective is to create improved microclimates for its inhabitants [12]. Thus, the Iranian Garden provides thermal comfort by creating shade, favorable breezes, and cool air resulting from the combination of water and vegetation [13]. Therefore, the aim of this research is to examine Iranian Gardens as nature-based solutions for enhancing thermal comfort. The case study of this research is the El-Goli Garden in Tabriz. Accordingly, the characteristics and elements that contribute to thermal comfort as one of the ecosystem services of the El-Goli Garden will be examined and discussed.

Material and Method

This study employs a descriptive-analytical research method to investigate the elements contributing to thermal comfort in Iranian gardens, both natural and artificial. The research aims to identify these elements and

analyze their impact on thermal comfort, emphasizing their role as nature-based solutions in urban spaces. The study begins with a comprehensive literature review to establish a theoretical framework, focusing on the principles of thermal comfort and the specific characteristics of Iranian gardens. Data collection involves both field observations and archival research. Field observations are conducted in El-Golli Garden, where natural elements (such as vegetation, water bodies, and topography) and artificial components (such as architecture, materials, and shading structures) are systematically documented.

Results and Discussions

The study of Iranian gardens reveals a multifaceted approach to enhancing thermal comfort through various natural and architectural elements. Key features such as water elements, vegetation, landscape design, and structural layouts collectively contribute to creating a comfortable microclimate. These findings align with established principles of landscape architecture and urban planning, demonstrating the efficacy of traditional practices in modern contexts. Water Elements Water features, including ponds, streams, and fountains, play a crucial role in the thermal regulation of Iranian gardens. These elements facilitate evaporative cooling, a process that significantly lowers ambient temperatures and increases humidity levels. According to [14], the evaporation of water absorbs heat from the surrounding air, creating a cooler microclimate. This effect is particularly beneficial in arid regions where Iranian gardens are typically found, providing a natural method for mitigating heat stress. Vegetation Dense plantings of trees, shrubs, and groundcover are integral to the cooling effects observed in Iranian gardens. Vegetation provides shade, which directly reduces the heat load on the garden surface and lowers surrounding air temperatures. Moreover, the process of evapotranspiration—where plants release water vapor—further contributes to cooling. Studies have shown that urban green spaces with significant vegetation can reduce temperatures by several degrees, enhancing thermal comfort for visitors (15). Landscape Design The strategic design of garden landscapes, including terracing and elevation changes, is pivotal in optimizing airflow and enhancing natural ventilation. Terraces and varied elevations can direct and amplify breezes, facilitating the movement of cooler air throughout the garden. Research indicates that well-planned landscape designs can improve air circulation, reduce stagnant hot air pockets, and promote a more uniform distribution of cooler air. Orientation and placement the orientation and placement of garden elements are meticulously planned to maximize natural ventilation. By aligning pathways, seating areas, and structures with prevailing wind directions, gardens can harness breezes to enhance cooling (16). This approach not only improves thermal comfort but also reduces the reliance on artificial cooling methods. Strategic orientation can significantly enhance the efficacy of passive cooling techniques in outdoor spaces. Pathways and Gathering Spots The thoughtful layout of pathways, seating areas, and gathering spots ensures that visitors can find comfortable places to rest and socialize. Well-designed circulation patterns facilitate airflow and provide access to shaded areas, contributing to overall comfort. Research suggests that the spatial organization of outdoor environments can influence thermal perception and user satisfaction, highlighting the importance of design in enhancing thermal comfort. Enclosures and Microclimate Iranian gardens are typically enclosed by walls, creating a sense of privacy and protection. These enclosures help to create a microclimate within the garden by reducing wind speed and maintaining cooler temperatures. The walls act as barriers that mitigate the effects of external climatic conditions, preserving the internal microclimate. Also enclosed gardens can maintain more stable and cooler temperatures compared to open spaces, providing a more comfortable environment for users. Figure 1 and Table 1 show the most important key features of Eel-Goli Garden in terms of thermal comfort.

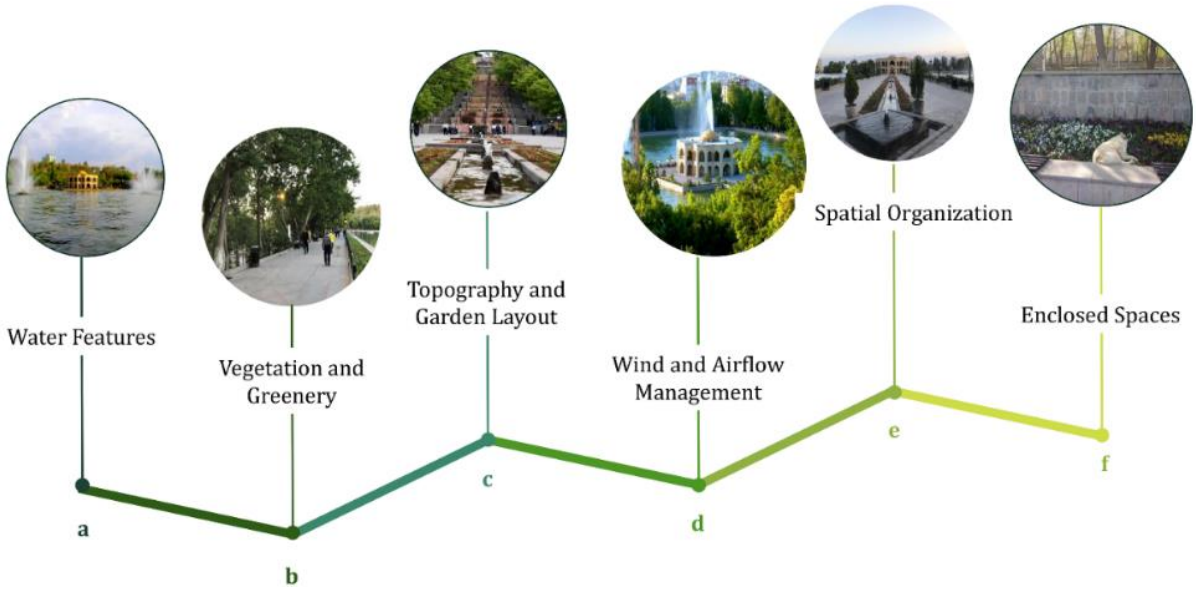


Figure 1. Key features of El-Goli Garden as a nature-based solution

Table 1. Characteristics and elements that contribute to thermal comfort in EL-Goli Garden

Items	Feature keys	Definition
a	Water Features	Elements such as ponds, streams, and fountains cool the air through evaporation and create a microclimate that lowers temperatures and increases humidity, improving thermal comfort.
b	Vegetation and Greenery	Dense plantings of trees, shrubs, and groundcover provide shade, reduce ambient temperatures, and enhance evapotranspiration, contributing significantly to cooling effects.
c	Topography and Garden Layout	The strategic design of garden landscapes, including terracing and elevation changes, can optimize airflow and enhance natural ventilation, promoting cooler environments.
d	Wind and Airflow Management	The orientation and placement of garden elements are designed to facilitate natural ventilation, using breezes to cool the space and increase thermal comfort
e	Spatial Organization	The thoughtful layout of pathways, seating areas, and gathering spots ensures that visitors can find comfortable places to rest and socialize. Well-designed circulation patterns also facilitate airflow and access to shaded areas
f	Enclosed Spaces	Iranian gardens are typically enclosed by walls, creating a sense of privacy and protection. These enclosures help to create a microclimate within the garden by reducing wind speed and maintaining cooler temperatures

Conclusion

The integration of key features in Iranian gardens, such as water elements, dense vegetation, strategic landscape design, and thoughtful spatial organization, exemplifies nature-based solutions that enhance thermal comfort. These gardens create microclimates, optimize airflow, and provide shade, significantly improving the thermal environment. Traditional design principles of Iranian gardens offer valuable strategies for sustainable urban planning and landscape architecture, addressing climate adaptation and urban resilience. These practices reduce energy consumption, improve environmental quality, and increase well-being, preserving cultural heritage while contributing to resilient, sustainable, and livable cities. The research highlights the relevance of traditional landscape practices in modern contexts, advocating their integration into urban design to create healthier and more comfortable environments.

References

[1] Genter, C., Roberts, A., Richardson, J., & Sheaff, M. (2015). The contribution of allotment gardening to health and wellbeing: A systematic review of the literature. British Journal of Occupational Therapy, 78(10), 593-605.
[2] Khani, S., Rastkhadiv, A., & Abdollahi, A. (2023). Vandalism in Urban Parks; An analysis on demographic characteristics and the intention and behavior of Vandals in Marivan City. *Journal of Social Problems of Iran*, *14*(2), 165-200.
[3] Cabral, I., Keim, J., Engelmann, R., Kraemer, R., Siebert, J., Bonn, A., 2017. Ecosystem services of allotment and community gardens: A Leipzig, Germany case study. Urban Forestry & Urban Greening 23, 44- 53.
[4] The World Bank. 2008. Biodiversity, Climate Change and Adaptation: Nature-Based Solutions from the World Bank Portfolio, 112. Washington, DC: The International Bank for Reconstruction and Development / The World Bank.
[5] Dumitru, A., & Wendling, L. (2021). *Evaluating the impact of nature-based solutions: Appendix of methods*. European Commission.
[6] Langergraber, G., Pucher, B., Simperler, L., Kisser, J., Katsou, E., Buehler, D., ... & Atanasova, N. (2020). Implementing nature-based solutions for creating a resourceful circular city. *Blue-Green Systems*, *2*(1), 173-185.
[7] Motedayen, H. (2011). Causes of appearance of Iran's historical gardens. The Monthly Scientific Journal of Bagh-e Nazar, 7(15), 51-62.
[8] Elyasi Gorji F, M Rezaee, Elyasi Gorji A. 2014. Influence of Iranian Garden as Urban Green Spaces on Promotion of Social Interactions Citizens; Case Study: Garden Chehel Sotun (Mellat Park) of Behshahr City, Iran. J. Civil Eng. Urban., 4 (S): 41-47.
[9] Fadaie, H., & Mofidi Shemirani, S. M. (2014). The Parameters of Sustainable Landscape in Iranian Garden Design. In *Advanced Materials Research* (Vol. 935, pp. 320-322). Trans Tech Publications Ltd.
[10] Farzin, S., Khalilnezhad, S. M. R., Moradzadeh Mirzaei, S., & Zarei, A. (2020). Investigation on recognition of the type of multifunctional landscape in Iranian Garden (Case study: Akbariyeh World Heritage Garden). *Manzar, the Scientific Journal of landscape*, *12*(52), 6-17.
[11] Motedayen, H. (2011). Causes of appearance of Iran's historical gardens. The Monthly Scientific Journal of Bagh-e Nazar, 7(15), 51-62.
[12] Haidari, R., & Fekete, A. (2015). The compositional role of water in Iranian Gardens. *Transsylvania Nostra*, *9*(2).
[13] Rezaei, M., & Shahcheraghi, A. (2021). Effect of Planting System of Iranian Garden on Thermal Comfort of Open Spaces; Case Study: Jahan Nama Shiraz Garden. *Naqshejahan-Basic studies and New Technologies of Architecture and Planning*, *11*(3), 1-15.
[14] Mostofa, T., & Manteghi, G. (2020). Influential factors of water body to enhance the urban cooling islands (Ucis): A review. International Transaction Journal of Engineering, Management, & Applied Sciences & Technologies, 11(2), 1-12.
[15] Karimi, A., Sanaieian, H., Farhadi, H., & Norouzian-Maleki, S. (2020). Evaluation of the thermal indices and thermal comfort improvement by different vegetation species and materials in a medium-sized urban park. Energy Reports, 6, 1670-1684.
[16] Abdallah, A. S. H., & Mahmoud, R. M. A. (2022). Urban morphology as an adaptation strategy to improve outdoor thermal comfort in urban residential community of new assiut city, Egypt. Sustainable Cities and Society, 78, 103648.

Advanced Engineering Days

aed.mersin.edu.tr

AQI-based box model using GIS and remote sensing over Kirkuk city, Iraq

Huda Jamal Jumaah [1,*2], Khalil Valizadeh Kamran [1]

[1]Tabriz University, Faculty of Planning and Environmental Science, Remote Sensing and Geographical Information System (GIS) Department, Iran, valizadeh@tabrizu.ac.ir
*[*2]Northern Technical University, Technical Engineering College of Kirkuk, Environment and Pollution Engineering Department, Iraq, huda80@ntu.edu.iq*

Cite this study: Jumaah, H. J., & Kamran, K. V. (2024). AQI-based box model using GIS and remote sensing over Kirkuk city, Iraq. Advanced Engineering Days, 9, 144-146

Keywords
Box model
AQI
$PM_{2.5}$
PM_{10}
Geospatial map

Abstract

Currently, air pollution has become one of the most important risks facing us because of its negative health effects. This study aims to evaluate air pollution in the city of Kirkuk, as the city is considered at the forefront of Iraqi cities in terms of air pollution. Two types of data were used as trained and tested data. Geospatial distribution maps were created based on trained data. A box model was used to measure the concentrations of pollutants in terms of Particulate Matter ($PM_{2.5}$ and PM_{10}). The Air Quality Index AQI then was calculated from the concentrations deduced from the model of each pollutant based on some parameters such as wind speed and length of the box. The model was validated by training and testing data resulting in high accuracies ranging between (75% and 85%) for model performance by trained data, and (91% and 95%) for model evaluation by testing data. Pollutants' geospatial maps proved the bad air distribution in the city which was evaluated as unhealthy in most entire city. AQI-based box model outcomes ranged from (173-180) and were out of standards and evaluated as Unhealthy air. Effective measures must be taken by competent authorities to reduce this pollution.

Introduction

Various cities have air pollution levels, that are at an alarming point, primarily due to the remarkable economic growth since such growth demands big-scale developments, hence its monitoring and prediction is as important as to assess the risks being caused [1]. Air pollution dispersion models constitute an essential element of the air quality management system [2-4]. Simply, the models require two types of data inputs, for example, data on the source or sources emitting pollutants, as well as information on wind velocity and turbulence. This is followed by a model simulation of pollutant transport and dispersion, as well as, perhaps, the pollutant's chemical and physical change and removal processes [5]. The concentration of pollutants depends on many external factors. Firstly, how height is the atmospheric boundary layer affects the dispersion of pollutants [6]. Dispersion models of air together with GIS software proved to be the most popular in airborne contaminants research. Modules are applicable by Python which can be linked to GIS [7]. Consequences of the model are the concentration of air pollutants for a certain period, for specific receptor locations [8]. The air dispersion box model aims to be a simulated atmosphere environment on which a computational framework is built [9].

In this study, we use geospatial mapping of air particulates such as ($PM_{2.5}$ and PM_{10}) for AQI evaluations based on the box model. This model is a sophisticated model that provides a more nuanced picture, as it allow for the integration of multiple factors including the atmospheric conditions, the terrain features and the pollutant characteristics therefore, they can accurately predict the behavior of pollutants in local scenarios. The box model presents one of the most vital components in modern air quality control and also environmental protection.

Material and Method

The data and methods applied in this study are shown in Figure 1. Trained data in terms of $PM_{2.5}$, PM_{10}, and wind speed (u) have been used for geospatial mapping by a minimum curvature spline technique.

The data used represent the average daily data of one season in 2023. An air dispersion box model was developed based on the length of a box and the height of pollutant dispersion. The equation used for calculating $PM_{2.5}$ and PM_{10} concentrations (C) through the box was [10];

$$C = b + \frac{QL}{uH} \qquad (1)$$

where b is the background concentrations, Q is the emission rate, L is the box length, u is the wind speed, and H is the dispersion height. While the equation used for AQI calculation was [11]:

$$AQI = \frac{I_{high} - I_{low}}{C_{high} - C_{low}} (C - C_{low}) + I_{low} \qquad (2)$$

where, I_{low} is the breakpoint of the index equivalent to the lowest breakpoint of pollutant C_{low}, I_{high} is the breakpoint of the index equivalent to the highest breakpoint of pollutant C_{high}, and C is the calculated concentration by box model.

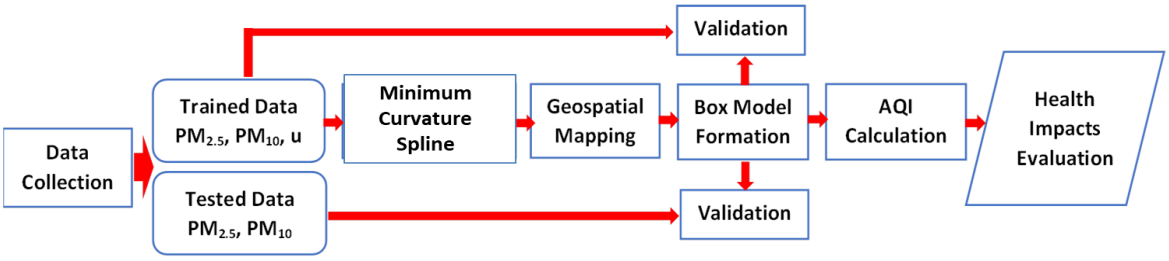


Figure 1. The study methodology.

Results

Geospatial maps of trained data are shown in Figure 2. Besides, the validation of box model performance and model evaluation also have been shown in Figure 3.

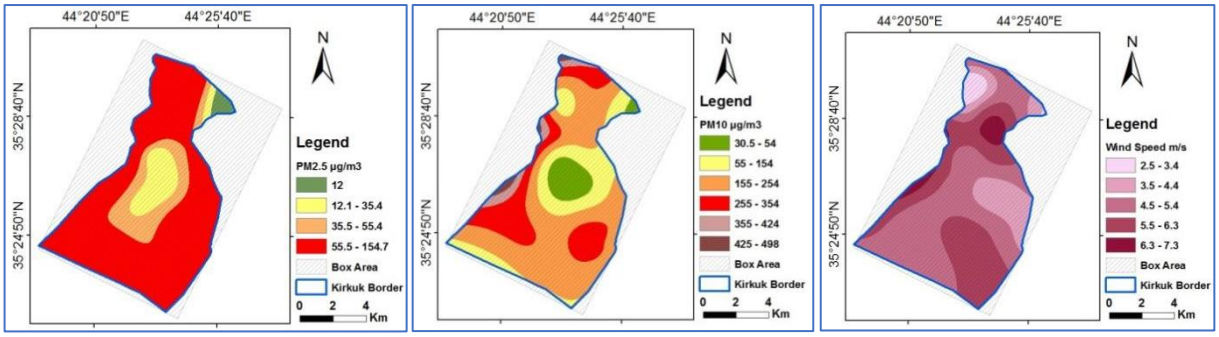


Figure 2. Geospatial resultant maps of trained data.

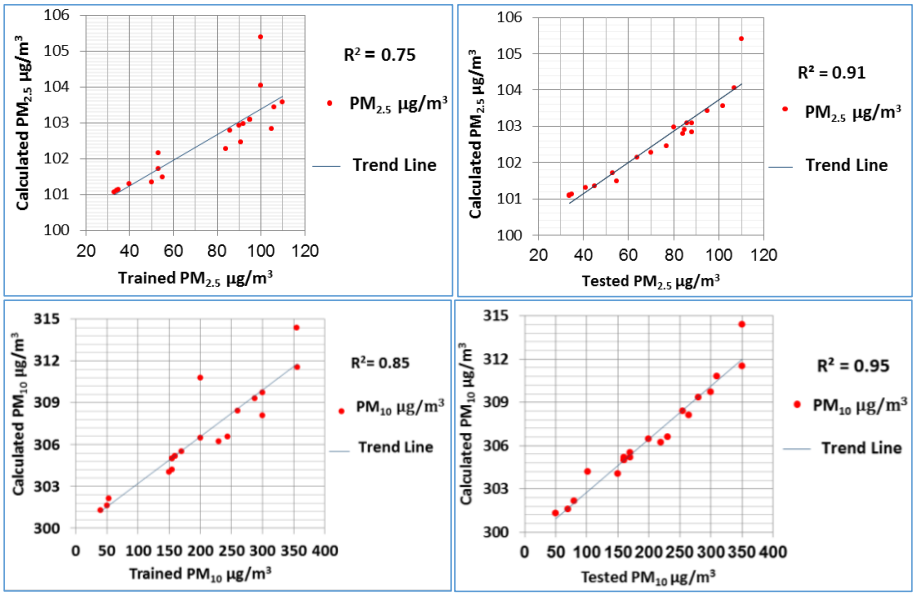


Figure 3. Trained and tested data validation.

Based on Figure 2 the $PM_{2.5}$ geospatial levels ranged between (12 and 154.7) μg/m^3. While the PM_{10} geospatial levels ranged between (30.5 and 498) μg/m^3. The wind speed was between (2.5 and 7.3)m/s. Box model results of $PM_{2.5}$ and PM_{10} concentrations ranged between (101.1 and 105.4) μg/m^3, and (301.3 and 314.4) μg/m^3 respectively. The model was validated with trained data as model performance, and validated with tested data as model evaluation. The resultant coefficients of determination R^2 were determined as 0.75 and 0.85 as model performance, while model evaluation R^2 resulted in 0.91 and 0.95 for $PM_{2.5}$ and PM_{10} respectively. The final calculated AQI-based box models of $PM_{2.5}$ and PM_{10} ranged as (175-177), and (173-180)respectively.

Discussion

According to [11-12] the air can be evaluated as unhealthy air type for sensitive groups of the public and generally unhealthy. PM2.5 distribution map shows unhealthy air in the city except in the center and some parts of the northeast ranged as moderate to unhealthy for sensitive public. Some little parts were distinguished as good air type in the northeast with a value of 12 μg/m3. PM10 distribution map shows good to hazardous values of air pollution. The entire city can be evaluated as unhealthy for the sensitive public. It is very important to have a better understanding of these pollutants as pollution in the air because these are the most harmful to health. AQI-based box model results were also evaluated as unhealthy. Commonly, gained values of AQI cause negative effects on some members of the public but indeed can cause serious health effects to sensitive groups of people.

Conclusion

The study concluded the bad air quality in Kirkuk city where the calculated AQI-based box model evaluated as Unhealthy air and the geospatial maps results proved the same. The developed models were in positive trends which means that increasing the background concentration will increase the calculated values by the models and vice versa. Some recommendations in this state can be applied to eliminate or decrease air pollution effects for example; adopting renewable energy sources, reducing Industrial emissions, enforcing standards of emissions, promoting more green spaces in the city, regular air monitoring, and awareness of the public of the health risk associated air pollution.

References

1. Zhang, J., & Ding, W. (2017). Prediction of air pollutants concentration based on an extreme learning machine: The case of Hong Kong. International Journal of Environmental Research and Public Health, 14(2), 1–19.
2. Juda-Rezler, K. (2010). New challenges in air quality and climate modeling. Archives of Environmental Protection, 3-28.
3. Jumaah HJ, Mansor S, Pradhan B, Adam SN (2018). UAV-Based PM2.5 Monitoring for Small-Scale Urban Areas. International Journal of Geoinformatics 14(4): 61-69.
4. Jumaah, H. J., Ameen, M. H., Kalantar, B., Rizeei, H. M., & Jumaah, S. J. (2019). Air quality index prediction using IDW geostatistical technique and OLS-based GIS technique in Kuala Lumpur, Malaysia. Geomatics, Natural Hazards and Risk, 10(1), 2185-2199.
5. Tiwary, A., & Williams, I. (2018). Air pollution: measurement, modelling and mitigation. Crc Press.
6. Giovannini, L., Ferrero, E., Karl, T., Rotach, M. W., Staquet, C., Trini Castelli, S., & Zardi, D. (2020). Atmospheric pollutant dispersion over complex terrain: Challenges and needs for improving air quality measurements and modeling. Atmosphere, 11(6), 646.
7. Ajaj, Q. M., Shafri, H. Z. M., Wayayok, A., & Ramli, M. F. (2023). Assessing the Impact of Kirkuk Cement Plant Emissions on Land cover by Modelling Gaussian Plume with Python and QGIS. The Egyptian Journal of Remote Sensing and Space Science, 26(1), 1-16.
8. Liang, Y., Jiang, F., Xu, D., Fu, L., Xu, C., Huang, G., & Lin, B. (2024). Construction of a novel mathematical model for predicting pesticide release in soil and its application in rice pest control. Journal of Cleaner Production, 436, 140646.
9. Liang, M., Chao, Y., Tu, Y., & Xu, T. (2023). Vehicle pollutant dispersion in the urban atmospheric environment: A review of mechanism, modeling, and application. Atmosphere, 14(2), 279.
10. Ruangkawsakun, J., & Thepanondh, S. (2014). Air assimilative capacity for sulfur dioxide and nitrogen dioxide: case study the Eastern Region of Thailand. International Journal of Environmental Science and Development, 5(2), 187.
11. Al-jarakh, T. E., Hussein, O. A., Al-azzawi, A. K., & Mosleh, M. F. (2021, June). Design and implementation of IoT based environment pollution monitoring system: A case study of Iraq. In IOP Conference Series: Materials Science and Engineering (Vol. 1105, No. 1, p. 012037). IOP Publishing.
12. Jumaah, H. J., Ameen, M. H., Mahmood, S., & Jumaah, S. J. (2023). Study of air contamination in Iraq using remotely sensed Data and GIS. Geocarto International, 38(1), 2178518.

Advanced Engineering Days

aed.mersin.edu.tr

Hospital site selection using AHP-based GIS in Tikrit City, Iraq

Mohammed Hashim Ameen [1], Hafssa Ali Abdullah [2], Huda Jamal Jumaah [*3], Eapak Qasim Hasan [4]

[1]*Tikrit University, Department of Environmental Engineering, Engineering College, Iraq, Mohammed.hashim@tu.edu.iq*
[2]*Tikrit University, Department of Civil Engineering, Engineering College, Iraq, hafssa.abdullah@tu.edu.iq*
[3*]*Northern Technical University, Department of Environment and Pollution Engineering, Technical Engineering College-Kirkuk, Iraq, huda80@ntu.edu.iq*
[4]*Ministry of Health, Kirkuk Health Directorate, Iraq, eapakqasim@gmail.com*

Cite this study: Ameen, M. H., Hafssa, A. A., Jumaah, H. J., & Eapak, Q. H. (2024). Hospital site selection using AHP-based GIS in Tikrit City, Iraq. Advanced Engineering Days, 9, 147-149

Keywords
Hospital site selection
GIS
AHP
MCA
land suitability

Abstract

There is a high demand for new hospitals in the Tikrit City Governorate due to the growing homogeneity of the population. But since it impacts both construction and management choosing the right hospital locations is essential for infrastructure development. Numerous factors including contamination proximity to existing healthcare facilities financial constraints societal impacts and transitory effects must be taken into account before this expansion is approved. In order to determine and evaluate the ideal sites for new hospital construction and services this study makes use of the Analytic Hierarchy Process (AHP) and the Geographic Information System (GIS). There are two phases to the method: first a detailed evaluation of the city lands suitability for building a hospital is conducted considering factors like proximity to major roads railroads landfills current hospitals and bodies of water as well as the need to avoid residential areas as a constraint. The hospital site location selection process for Tikrit City, GIS-based Multi-Criteria Analysis (MCA), requires studies of several factors that have different weights. Because of its centralized manner of hospital site selection for new institutions, this approach is beneficial to the researchers, policymakers in the city, as well as hospital administrators who have to make decisions.

Introduction

New hospital construction is compulsory as there is an increase in the demand for healthcare facilities caused by the growing urban populations [1]. Such linkage factors as pollution levels, distance to healthcare facilities, finances, as well as social convenience and time constraints are often important considerations during the construction of these critical-for-human-life structures. The urgency for the new hospitals is critically high since the large number of patients seek medical assistance in the developing countries like Tikrit [2-3]. Choosing the right site for a new hospital may reduce the risk of future delays and difficulties associated with it [4]. However, selecting the right site makes it possible for government officials to better prioritize healthcare resources and link health services with the economic and social needs of the community people. It resolves the health disparities that exist in urban areas and remote areas. In addition, it reduces emergency response time and eventually increases the quality of life of the people [5-6]. In Tikrit, rather than being distributed uniformly over the city, medical resources show a big gap which leads to a lack of access and inferiority in healthcare services [7-8]. Now, the city of Tikrit includes six existing districts, however, only three primary hospitals are functional out of which one is under construction in the south of the city. The hospitals inability to cover eastern and western regions does demonstrate the still existing lack of healthcare system development [9].

Therefore, with the existing conditions in mind, this research study's main objective is to figure out the top locations for new hospitals in Tikrit, Iraq with GIS approach which is AHP-based. This involves: (1) evaluating hospital criteria and location determinants, (2) designing maps of area availability & suitability for hospital sites, and (3) utilizing GIS to select the appropriate sites for hospital construction in Tikrit.

Material and Method

Figure 1 displays the methodology that was used for this paper. This study uses two major criteria: distance and land use, with the AHP multi-criteria method establishing their weights for suitability. Table 1 provides the final sub-criteria weights.

The most suitable areas for building a hospital in Tikrit City were determined using a multi-criteria decision-making approach and GIS [10-11].

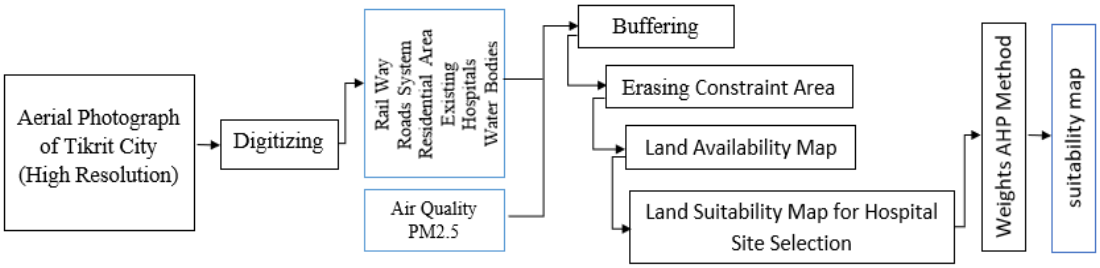


Figure 1. Flowchart of methodology.

Table 1. Final weights of sub-criteria

Main – Criteria	Sub - Criteria	Weight
Land-use	Government	0.310546265
	Agriculture	0.155273133
Airquality_PM2.5	39-45	0.149367915
	46-52	0.082382304
	43-58	0.04539025
Distance from residential	1km	0.086810581
	2km	0.047879463
	3km	0.02638019
Slope	1-3%	0.063979933
	3-6%	0.031989967
Sum		1

Results

Figure 2 displays the multi-criteria method for determining land availability for Tikrit's existing hospital. Figure 3 depicts the geographical appropriateness for selecting existing hospitals in Tikrit City.

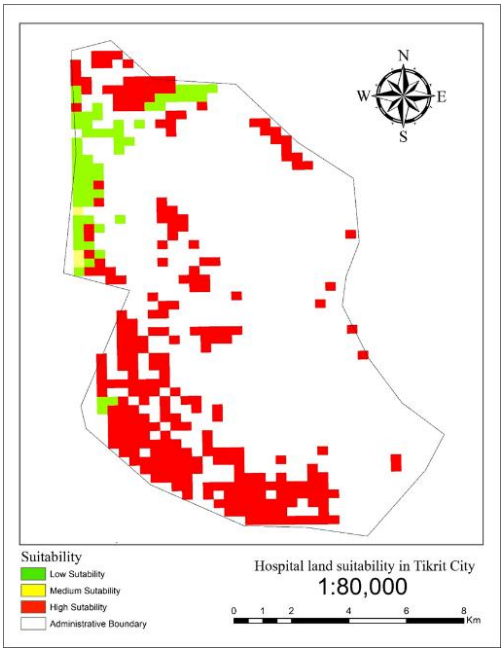


Figure 2. Hospital Land Suitability in Tikrit City



Figure 3. Hospital Land Availability in Tikrit City

Land use categories such as residential areas, water bodies, highways, railroads, existing hospitals, public areas, agricultural, and government locations were among the several layers that were prepared. Roads and railroads were digitized as lines, and polygons for residential, agricultural, bare land, and water bodies were created using digitization. Each hospital was given its own map.

Discussion

Based on Figure 2 it excludes limited places. The city core is mostly residential, with the surrounding areas declared unfit for construction. Buffer zones surrounding small towns, major roads, railways, and bodies of water have also been restricted. This produces four land availability criteria: residential areas, railways, water bodies, and existing hospitals. Suitability is divided into three categories, from low to high. Where the high suitable sites are located in the southern parts, north-west parts, and northern parts of Tikrit City. The medium suitable sites are located in the western parts. The low suitable sites are located in the north-west part of Tikrit City.

While in Figure 3, six factors were utilized to determine land availability and suitability. Finally, it has been shown that a major advantage of AHP is that it can be very useful in creating maps of optimal hospital locations by way of site selection using this procedure.

Conclusion

This study provided criteria for selecting new hospital locations in Tikrit, taking into account the city's urbanization and the necessity for contemporary healthcare facilities. Using GIS-based Multi-Criteria Analysis (MCA), we discovered characteristics such as land use and cover to help guide hospital building. Because of urban space constraints, the AHP technique identified excellent places, including numerous acceptable lands outside the city. Despite the fact that some sites are non-governmental, they can nevertheless be used to build hospitals. Overall, MCA using GIS has been effective in precisely mapping viable hospital sites, assisting decision-makers in developing Tikrit's healthcare infrastructure.

References

1. Alshihab, S., Mohamed Ibrahim, M. I., Hadi, M. A., Syed, A., Arabi, A., Al-Qahtani, A., … Al-Zaidan, M. (2024). Evaluation of warfarin management in primary health care centers in Qatar: A retrospective cross-sectional analysis of the national dataset. Current Problems in Cardiology, 49(4), 102427. doi:10.1016/j.cpcardiol.2024.102427
2. Ameen, M. H., Jumaah, H. J., Kalantar, B., Ueda, N., Halin, A. A., Tais, A. S., & Jumaah, S. J. (2021). Evaluation of PM2.5 particulate matter and noise pollution in tikrit university based on GIS and statistical modeling. Sustainability (Switzerland), 13(17). doi:10.3390/su13179571
3. Jumaah, H. J., Ameen, M. H., Mahmood, S., & Jumaah, S. J. (2023). Study of air contamination in Iraq using remotely sensed Data and GIS. Geocarto International, 38(1), 2178518.
4. Avtar, R., Tripathi, S., Aggarwal, A. K., & Kumar, P. (2019). Population-urbanization-energy nexus: A review. Resources, 8(3), 1–21. doi:10.3390/resources8030136
5. Babalola, M. A. (2018). Application of GIS-based multi-criteria decision technique in exploration of suitable site options for anaerobic digestion of food and biodegradable waste in Oita City, Japan. Environments - MDPI, 5(7), 1–16. doi:10.3390/environments5070077
6. Komalasari, R. (2024). Empowering Informed Healthcare Choices in Rural Areas: SIKDA, a Novel Model for Enhancing Patient Access to Reliable Consumer Health Information. In Emerging Engineering Technologies and Industrial Applications (pp. 148–172). IGI Global.
7. Migdadi, Y. K. A. A., & Omari, A. A. (2019). Identifying the best practices in green operations strategy of hospitals. Benchmarking, 26(4), 1106–1131. doi:10.1108/BIJ-09-2017-0242
8. Prabhune, A., Srihari, V. R., Bidrohi, A. B., Reddy, A., & Mallawaram, A. (2024). Enhancing Accessibility to Primary Healthcare Centres through the Development and Validation of a Machine Learning-based Gravity Model: Strengthening Public Health Coverage. In 2024 International Conference on Intelligent and Innovative Technologies in Computing, Electrical and Electronics (IITCEE) (pp. 1–7). IEEE.
9. Rajsfus, B. F., Mohana-Borges, R., & Allonso, D. (2023). Diabetogenic viruses: linking viruses to diabetes mellitus. Heliyon, 9(4), e15021. doi:10.1016/j.heliyon.2023.e15021
10. Samir M. Al-Balas Hindya O. Al-Maqableh, S. A., & Odeibat, A. M. (2024). Quality status: A SERVQUAL approach to evaluate the effect of the quality of healthcare services on patient satisfaction in Jordan. International Journal of Healthcare Management, 0(0), 1–17. doi:10.1080/20479700.2024.2310375
11. Shareef, M. A., Ameen, M. H., & Ajaj, Q. M. (2020). Change detection and gis-based fuzzy ahp to evaluate the degradation and reclamation land of tikrit city, Iraq. Geodesy and Cartography (Vilnius), 46(4). doi:10.3846/gac.2020.11616

Advanced Engineering Days

aed.mersin.edu.tr

Application of remote sensing methods and tools in detecting pollution in the Caspian Sea and their impact on the water surface temperature of the Azerbaijan

Ismayil Zeynalov [*1], Ulker Mahmudova [1], Rena Ahmedova [1], Aybeniz Ahmedova [1], Almaz Rustamova [1]

[1]*Institute of Geography, Caspian Sea Department, Azerbaijan, ismayil_zeynalov@outlook.com, ulker570920@gmail.com, rena.ahmedova.67@mail.ru, aybenizahmedovageoph@gmail.com, almazrustamova2@gmail.com*

Cite this study: Zeynalov, I., Mahmudova, U., Ahmadova, R., Ahmadova, A., & Rustamova, A. (2024). Application of remote sensing methods and tools in detecting pollution in the Caspian Sea and their impact on the water surface temperature of the Azerbaijan. Advanced Engineering Days, 9, 150-152

Keywords
Caspian Sea
Water surface temperature
Remote sensing
Oil film
Pollution

Abstract

When oil tanker accidents or ruptures in underwater pipelines occur, oil is distributed on the sea surface in the thinnest monomolecular layer. This contributes to climate change through formation conditions as the water surface temperature changes and the deterioration of coastal ecosystems. Therefore, remote sensing methods are needed to detect such contaminants. To date, there are several ways to detect oil contamination on water using remote sensing methods. One of them is satellite surveillance. Satellites photograph the surface of seas and oceans and identify areas of oil pollution by changes in water color or visible traces of pollution. Another method is the use of unmanned aerial vehicles (drones) with certain equipment to detect pollution on the water surface. There is also the technology of using bioindicators - special microorganisms or algae that react to the presence of oil contaminants in water and change their behavior or appearance. Effective detection and assessment of oil contamination on water using remote sensing methods allows to quickly respond to emergency situations and prevent negative consequences for the marine ecosystem and living organisms. In order to identify these phenomena, data gathered by NOAA satellites and the AVHRR pathfinder instrument (Advanced Very High Resolution Radiometer) installed on board are utilized. Additionally, the underlying patterns of the atmosphere-ocean system are revealed through the examination of the average annual fluctuations observed over a significant duration.

Introduction

Surface oil pollution of the Caspian Sea is often caused by natural causes, namely by seepages from oil and natural gas fields on the sea bottom. From the late 19th century, Azerbaijan pioneered the development of shelf and offshore oil fields, and it was the first country to suffer from surface pollution. The Caspian Sea pertains to the world largest oil bearing regions. Total oil reserves of the Caspian Sea region are estimated at above 250 billion barrels[1], which puts it in second place after the Middle East. The main sources of the Caspian Sea surface pollution are considered to be offshore oil production as well as the natural oil seeps at sea bottom. According to some estimations[2], about one million tons of oil is annually leaked to the Caspian Sea [1].

Oil pollutions in the seawater derive mainly from the following sources: a) Daily extraction and transportation of oil in the Sea, b) Oil tankers accidents, and c) Oils spillage from the oil tankers. But, oil pollution in the Caspian Sea more resulted from hydrocarbon leakage from natural bed than from the oil leakage of ships [2].

When oil is exposed to broadband ultraviolet radiation from the sun, or some artificial source, it reflects and absorbs the incident radiation. In the case of oil slicks on the ocean, the reflectance contrast between oil, arid sea water is significant due to the fact that oil has a higher reflectance than sea water in the near ultraviolet region. When oil is exposed to broadband ultraviolet radiation from the sun, or some artificial source, it reflects and

absorbs the incident radiation. In the case of oil slicks on the ocean, the reflectance contrast between oil, arid seawater is significant due to the fact that oil has ‘a higher reflectance than sea water in the near ultraviolet region [3].

Nowadays oil pollution as well as heavy metals and chlorinated hydrocarbons is one of the most widespread and toxic kinds of pollution of marine environment, oil films on the sea surface being able to change mass transfer and energy exchange processes at the air-sea interface.

Information about the temporal variability of the surface temperature is required to study biological communities, ice regime, evaporation amount, heat balance, climate conditions of the adjacent sea area etc. The temperature change during the month, depending on season and meteorological conditions, in different areas of the sea goes in different ways. This work considers the temporal structures of the surface temperature. This makes it possible to compile maps of temperature fields both on the basis of individual contact measurements, and from satellite remote sensing data [4].

Material and Method

Oil product spills and oil films look the same on satellite optical information as areas of high content of organic suspensions. That is, their spectrum in the visible region of reflected and scattered solar radiation is identical to the spectrum of organic suspensions. Currently, they can be identified only by indirect signs. Oil spills extinguish the high-frequency component of wind waves, which manifests itself in a weakening of the signal recorded on the satellite in the visible, near and middle IR ranges.

The radiation coefficient of petroleum products in the medium and far infrared ranges is less than that of water, which leads to a decrease in the radiation temperature of the surface of the water area by 0.2-2K compared with clean water. It should be noted that such a decrease in radiation temperature is not always noticeable on satellite data, since the weakening of wind mixing in oil slicks leads to increased surface warming. Even overheating of the film is possible compared to the surrounding agitated water surface [5].

Thus, due to the inability to formalize the separation of the contributions of chlorophyll and petroleum products to the albedo of the sea, in this work, the term "maps of the indicator of the content of organic suspensions" (A_{org}) was adopted for maps of the albedo of the sea calculated according to the satellite data [6].

In connection with the above, the decoding of oil product spills based on measurements of the equipment installed on satellites is advisory, predictive, and authorial in nature.

The decryption of oil films on the surface of marine areas is also carried out according to the third predictor – the field of roughness of the water surface when analyzing data from radar observations from ERS and RADARSAT.

Spots unmotivated by atmospheric influences and shallow water with low values of the signal reflected by the sea on radar images obtained from these satellites are interpreted as oil films [7].

Due to the high spatial resolution (25 m) and almost all-weather conditions (i.e., the ability to probe in cloudy conditions and in the absence of sunlight), it is sometimes possible to "catch" even such a local source of pollution as, for example, a ship.

Long-term practice has shown that regular operational monitoring of significant water areas is currently possible only on the basis of digital information from the high-resolution scanning radiometer of the NOAA satellite (since 2002 and with the TERRA satellite), since data from only this satellite operating in the "open sky" mode is available for operational use and there are appropriate proven processing techniques.

The main role is played by the radiation temperature of the underlying surface, estimated from measurement data at wavelengths of 11 and 12 μm [8].

Results

The main systematic data from the Global Hydro meteorological Network's ground stations and satellite monitoring can be received through the National Oceanic and Atmospheric Administration's (NOAA) server network [9].

The change in temperature during the month, depending on the time of year and meteorological conditions, occurs differently in different areas of the sea. In this paper, the time structures of the surface temperature are considered. Knowledge of such a structure makes it possible to construct maps of the temperature field both on the basis of individual contact and satellite remote measurements [10].

Discussion

The study we conducted confirmed the validity of the suggested methodological approach and the fundamental principles for organizing experimental satellite monitoring of organic suspended matter in the surface waters of the Caspian Sea and sea surface temperature fields:

- utilizing specific characteristics enables the identification of areas with high concentrations of organic suspended matter, including oil slicks, in surface waters;

- the incorporation of an algorithm accounting for atmospheric effects helps mitigate geographic limitations stemming from shallow waters and meteorological constraints resulting from aerosol interference, thereby enhancing the interpretation of satellite spectrozonal data;
- the selection of NOAA satellites as the primary platform for continuous monitoring of sea surface conditions, along with Terra and ERS satellites for intermittent assessments under specific circumstances, is deemed the most feasible approach in dire situ.

Conclusion

The conducted research has validated the accuracy of the proposed methodological approach and key principles for organizing experimental satellite monitoring of organic suspensions in the surface waters of the Caspian Sea and the temperature patterns of the sea surface:

- By analyzing key indirect indicators, it is feasible to identify regions with high concentrations of organic suspensions, including oil slicks, in surface waters.
- Implementation of an algorithm to account for atmospheric interference aids in mitigating geographical limitations arising from shallow waters and meteorological constraints resulting from aerosol interference, thereby enhancing the interpretation of satellite spectral data.
- The selection of the NOAA satellite system for continuous monitoring of the sea surface and Terra, alongside utilizing ERS platforms for crisis scenarios, is the most suitable option given the current circumstances.

References

1. https://www.researchgate.net/publication/297759776_Multi-Sensor_Satellite_Survey_of_the_Surface_Oil_Pollution_in_the_Caspian_Sea
2. Nejat, S.A., Hermidas Bavand, D., &Farshchi, P. (2018). Environmental challenges in the Caspian Sea and International responsibility of its littoral states. Caspian J. Environ. Sci., Vol. 16 No. 2, pp. 97-110
3. Catoe, C., &McLean, J. (1979). A Multispectral. Look at Oil Pollution Detection Monitoring and Law Enforcement. N80-12622 (NASA) 25 p HC A02/MF A01 CSCL 13B Unclas G3/45 414, 77.
4. Anikiev, V. V., Mishukov, V. F., &Moiseevsky, G. N. & Tkalin, A. V. (1988). The Effect of Oil Films on Water Evaporation and Oxygen Content in Sea Water. Geo Journal Vol. 16, No. 1, First Pacific Symposium on Marine Sciences, pp. 19-24 (6 pages) Published By: Springer.
5. Zeynalov, I., &Makhmudova, U. (2021). The role of satellite observation systems data while researching the water surface temperature of the Caspian Sea. Proceedings of Scientific conference on climate change in the Caspian Sea region, pp. 101-105
6. Abakarov, M.I., et al. (1982) The study of the main factors affecting the surface temperature of reservoirs when measured by remote means. – The first All-Union conference Biosphere and Climate based on space research data. Abstracts of the reports. – Baku, Elm Publishing House, pp.80-82.
7. Grishin, G.A., &Lebedev, N.E. (1990). The use of IR satellite data in ocean and atmospheric monitoring: status and problems. - Exploration of the Earth from space, issue 6, pp.97-104.
8. Kneizys, F.X., et. al. (1980). Atmospheric Transmittance / Radiance: Computer code LOUTRAN-5. AFGL-TR-80-0067. - Air Force Geophysics Laboratory, p. 233
9. Zeynalov, I., &Achmedova, R., (2023). Impact of climate change on the assessment of the content of the indicator organic suspended matter and sea surface temperature of the Caspian Sea. 7th Intercontinental Geoinformation Days (IGD), 7, 127-130
10. Zeynalov, I., Akhmedova, R., Akhmedova, A., & Rustamova, A. (2024). Analysis of the sea surface temperature (SST) of the Caspian Sea from NOAA satellites. Advanced Remote Sensing, 4(1), 1–10.

Advanced Engineering Days

aed.mersin.edu.tr

Spatiotemporal dynamic simulation of carbon storage and sequestration in response to land use/land cover changes

Bahman Veisi Nabikandi [*1], Farzin Shahbazi [2], Ahmad Hami [1]

[1]*University of Tabriz, Landscape Architecture Department, Faculty of Agriculture, Iran, bahmanveisi19@gmail.com, hami@tabrizu.ac.ir*
[2]*University of Tabriz, Soil Science Department, Faculty of Agriculture, Iran, shahbazi@tabrizu.ac.ir*

Cite this study: Veisi Nabikandi, B., Shahbazi, F & Hami, A. (2024). Spatiotemporal dynamic simulation of carbon storage and sequestration in response to land use/land cover changes. Advanced Engineering Days, 9, 153-156

Keywords
LULC
Carbon Storage
Carbon Sequestration
InVEST Model
Karaj City

Abstract

The spatiotemporal patterns of ecosystem carbon storage and sequestration in metropolitan regions are expected to be significantly impacted by land use/land cover (LULC) change. The impact of LULC changes on ecosystem services has not been widely addressed for the future. The State-of-the-Art of this investigation is to introduce the crucial role of novel technology i.e., InVEST model and remotely-sensed data to monitor the impact of LULC changes on distribution of carbon storage and sequestration in Karaj City, Iran. Therefore, remote sensing (RS), geographic information systems (GIS), and change trajectories were employed by the matter. The results showed that the built-up land increased by 180.40 km^2 from 2013 to 2023 as a consequence of urban expansion. It was also found that pasture and tree cover respectively decreased by 62.27 km^2 and 8.32 km^2 at the same era. Simultaneously, carbon storage in the study region decreased by 191,501.72 Mg. This research opens an avenue for further investigation to understand the carbon storage and sequestration as affected by LULC.

Introduction

Addressing the urgent issue of global warming is of the utmost significance in the contemporary era. A critical component of climate change mitigation is the enhancement of carbon sequestration's ability to mitigate the effects of global warming [1]. Carbon sequestration is essential to the ecosystem, as it captures carbon dioxide (CO_2) from the atmosphere through carbon cycling. This process, in turn, helps regulate the Earth's climate by reducing atmospheric CO_2 concentrations and releasing oxygen. Changes in land use/land cover (LULC) are one of the primary drivers of carbon sequestration. In recent years, there has been a significant increase in the pursuit of a more comprehensive understanding of the variations in carbon sequestration that are influenced by LULC change [2]. Researchers have been combining a variety of land use prediction models with models such as InVEST to investigate and forecast future carbon sequestration [1]. This has facilitated our understanding of the significance of these ecosystem services.

Mapping LULC change using conventional classifiers is significantly less effective and requires a significant amount of time. Machine learning algorithms have been extensively employed in the extraction of information from remote sensing (RS) and object recognition in recent years as a result of their robust adaptive and self-learning parallel information processing capabilities [3]. At present, cloud computing systems are widely used to monitor changes in a specific region's LULC. In 2010, Google introduced and hosted Google Earth Engine (GEE), a cloud-based spatial analytics platform that is accessible to all geospatial data associated with a variety of satellites and boasts a high level of accuracy. LULC administration and changes in vegetation, soil, and water bodies are among the many applications for which RS has recently become increasingly significant [4].

Despite some research examining the impact of changes in LULC on carbon sequestration in various parts of the world, the research on Iran's spacy Karaj City is still scanty, as no studies have been conducted for assessment of carbon sequestration due to LULC alteration. Therefore, the present study aims to identify the potential impact of LULC on carbon storage and sequestration in Karaj City, Iran for the years 2013 and 2023. The primary objectives of the research are as follows: The first objective is to identify the change in LULC by processing Landsat 8 data using GEE. (ii) Use the InVEST model to assess the potential impact of LULC on carbon sequestration.

Material and Method

Study area

Karaj, the capital of Alborz Province, is situated between north latitude 35˚ 31´ and 36˚ 12´ N and east longitude 50˚ 11´ and 51˚ 29´ E. Its average elevation is approximately 1300m above mean sea level (Figure 1). The annual average precipitation is 261mm, and the climate is semi-arid and chilly. Karaj's metropolis covers 858 km^2. Karaj is the fourth-largest metropolis in Iran [5]. The primary factors that influenced the selection of this region for this research were the diversity of land use and LULC changes that were influenced by population growth and urbanization.

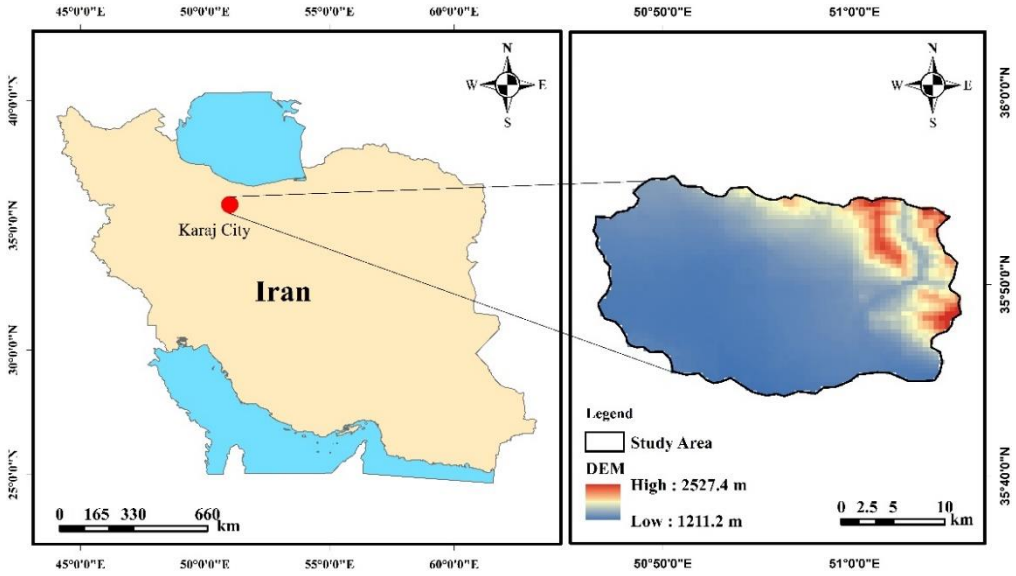


Figure 1. Geographical location and elevation of the study area

Land Use/Land Cover preparing

GEE, a cloud-based platform, has revolutionized RS by enabling access to satellite imagery and other spatial data, serving as one of these instruments [6]. Landsat-8 (OLI) satellite images with a spatial resolution of 30m were employed in this investigation from 2013 to 2023. The GEE platform's command-line code was employed exclusively to classify cloud-free images. The images were spatially filtered using the study area's shape file and time data. In order to more effectively identify ecological environments, this investigation assessed data for all periods of a single season (summer). In a supervised manner, nearly 500 samples were collected annually to classify six categories: built-up, tree cover, cropland, pasture, barren, and water body. The Random Forest (RF) classifier algorithm was used in the GEE algorithm database's supervised classification process to get the land use classes listed above. The RF algorithm has numerous benefits for the classification of terrestrial image data, including the ability to prevent errors such as data noise and excessive cutting. In addition, this algorithm is more effective in larger dimensions and has a higher degree of accuracy than other methods [7].

InVEST Carbon Model

The InVEST 3.14.1 modelling suite, developed by the Natural Capital Project and Stanford University, is a comprehensive tool for estimating and valuing ecosystem services through standalone but linkable models. It provides specific information on the amount of carbon stored in different ecosystem types, which is crucial for environmental management and decision-making [8]. The model requires a raster-based land cover map and data identifying the carbon storage capability in carbon pools for each land cover class. Carbon sequestration involves analyzing the carbon concentration in at least one of the four primary carbon reservoirs: aboveground biomass, soil organic matter, belowground biomass, and dead organic matter. Aboveground biomass includes live plant components above the ground; belowground biomass contains living root systems; and soil organic matter is the largest terrestrial carbon store [9]. Carbon storage and sequestration represent a stock estimation model, and GIS analysis, data organization, and visualization were conducted using ArcGIS 10.8.

Results

The classification results (Figure 2) show that the most dominant category in the study area is built-up (155.10 km^2), followed by pasture (117.27 km^2), cropland (90.29 km^2), barren (54.11 km^2), tree cover (41.93 km^2) and

water body (5.45 km²). From the perspective of changing trends in LULC types during 2013–2023, it was observed that tree cover, pasture, and water body exhibited a continuous and significant decline over the past two decades, while built-up areas, cropland, and barren areas experienced a particularly pronounced increase. Specifically, the region was dominated by built-up and cropland areas with 180.40 and 103.86 km² of LULC in 2023, followed by barren (91.20 km²), pasture (55 km²), tree cover (33.61 km²), and water body (0.08 km²).

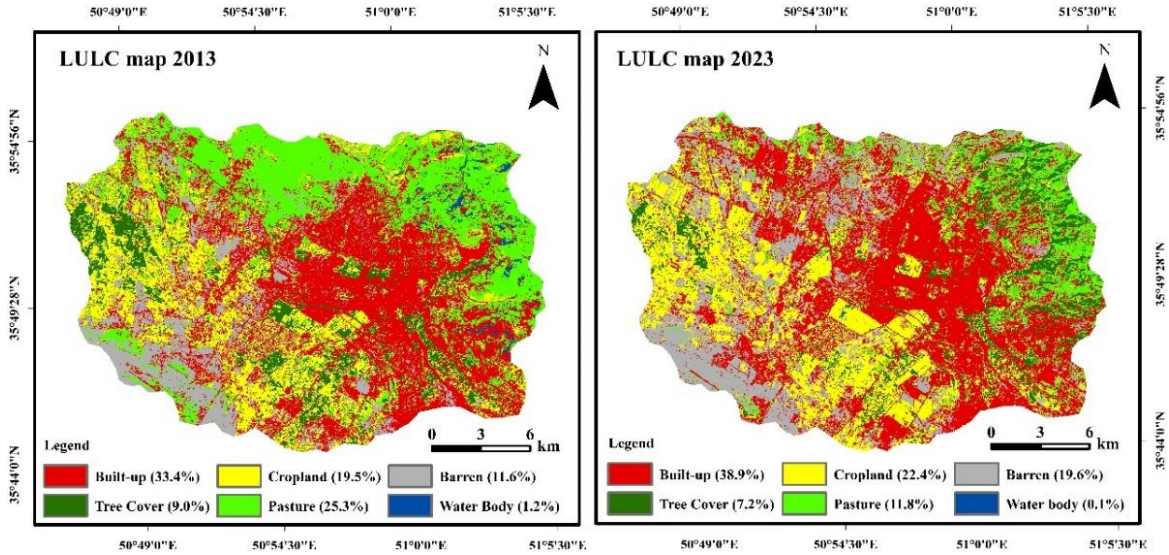


Figure 2. Spatial distribution characteristics of LULC in the study area

The next step was to calculate the total carbon storage throughout the study area based on the LULC map using the InVEST model for the years 2013 and 2023, as well as the carbon sequestration map during this period, which is shown in Figure 3. Based on this figure, in 2013, the central parts of the study area, where dense urban fabric and built-up areas are located, have the lowest amount of carbon storage. While the south and western parts of the study area store more carbon due to the presence of trees and agriculture. The above model estimates that the total carbon content stored in the studied area in 2013 will be around 1,320,866 Mg. Due to changes in tree cover and urbanization, this amount is expected to reach 1,129,365 Mg in 2023.

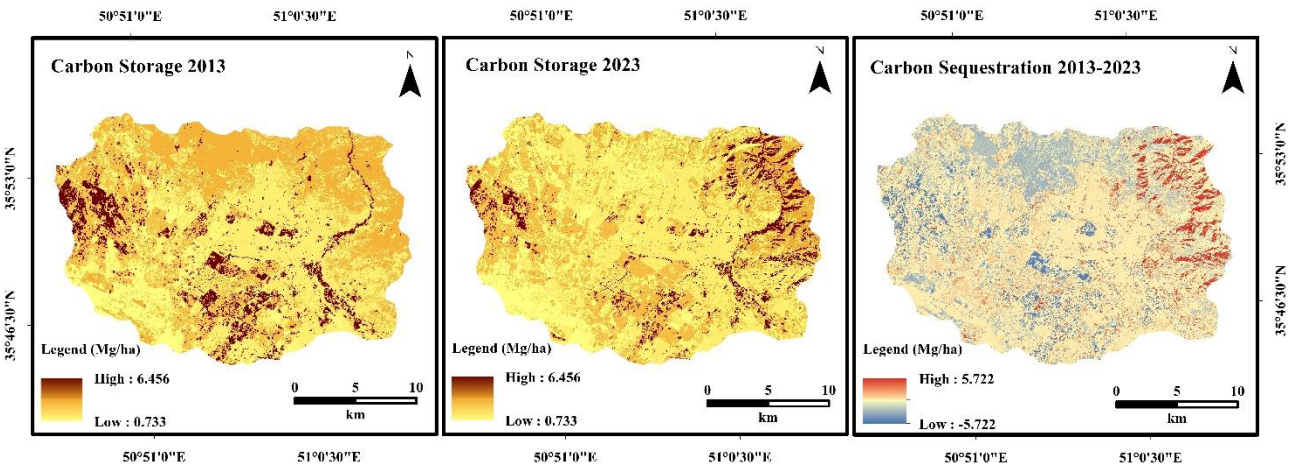


Figure 3. Total Carbon in the year 2013, 2023 and Carbon Sequestered during 2013-2023

Discussion

In recent decades, LULC changes affected by the expansion of urbanization and the increase of human activities have been abundantly reported [10,11]. This challenge is more pronounced in developing countries like Iran, particularly in large cities like Karaj City [12]. This research revealed a trend of expansion of built uses and reduction of ecological spaces, which was also mentioned by Rezaei et al. (2023) [13]. Several studies in China [14], India [15], and Iran [16] have investigated the impact of LULC changes on carbon storage and sequestration. In general, it has been observed that the reduction of natural and ecological spaces reduces carbon absorption capacity and causes less carbon deposition.

Conclusion

This study focuses on how carbon storage and sequestration change over spatiotemporal dynamics in Karaj City's LULC. It does this by using remotely sensed data to connect LULC change and the InVEST model. According to the obtained results, carbon content has decreased dramatically over 2013–2023. Urbanization was identified as the main factor in reducing sequestration across the study area. Furthermore, a significant reduction in carbon sequestration capacity was found due to the loss of ecological spaces such as tree covers, pastures, and cropland. To overcome this, effective land use management strategies are required to minimize the environmental impacts of human activities on carbon sequestration capacity. This research emphasizes the important role of RS in monitoring LULC changes in areas with limited data. Finally, our research reveals a deeper understanding of the links between LULC induced by environmental restoration programs and carbon storage changes. It was concluded that some land use policies, i.e., maintaining green and natural infrastructure and controlling urban development, can reduce the adverse effects of LULC changes on carbon sequestration.

References

1. Wang, Y., Li, M., & Jin, G. (2024). Exploring the optimization of spatial patterns for carbon sequestration services based on multi-scenario land use/cover changes in the changchun-Jilin-Tumen region, China. Journal of Cleaner Production, 438, 140788.
2. Liang, X., Guan, Q., Clarke, K. C., Liu, S., Wang, B., & Yao, Y. (2021). Understanding the drivers of sustainable land expansion using a patch-generating land use simulation (PLUS) model: A case study in Wuhan, China. Computers, Environment and Urban Systems, 85, 101569.
3. Chen, C., Yang, X., Jiang, S., & Liu, Z. (2023). Mapping and spatiotemporal dynamics of land-use and land-cover change based on the Google Earth Engine cloud platform from Landsat imagery: A case study of Zhoushan Island, China. Heliyon, 9(9).
4. Jodhani, K. H., Gupta, N., Parmar, A. D., Bhavsar, J. D., Patel, H., Patel, D., ... & jee Omar, P. (2024). Synergizing google earth engine and earth observations for potential impact of land use/land cover on air quality. Results in Engineering, 22, 102039.
5. Azimi-Yancheshmeh, R., Moeinaddini, M., Feiznia, S., Riyahi-Bakhtiari, A., Savabieasfahani, M., van Hullebusch, E. D., & Lajayer, B. A. (2021). Seasonal and spatial variations in atmospheric PM2. 5-bound PAHs in Karaj city, Iran: Sources, distributions, and health risks. Sustainable Cities and Society, 72, 103020.
6. Patel, A., Vyas, D., Chaudhari, N., Patel, R., Patel, K., & Mehta, D. (2024). Novel approach for the LULC change detection using GIS & Google Earth Engine through spatiotemporal analysis to evaluate the urbanization growth of Ahmedabad city. Results in Engineering, 21, 101788.
7. Teluguntla, P., Thenkabail, P. S., Oliphant, A., Xiong, J., Gumma, M. K., Congalton, R. G., ... & Huete, A. (2018). A 30-m landsat-derived cropland extent product of Australia and China using random forest machine learning algorithm on Google Earth Engine cloud computing platform. ISPRS journal of photogrammetry and remote sensing, 144, 325-340.
8. Grafius, D. R., Corstanje, R., Warren, P. H., Evans, K. L., Hancock, S., & Harris, J. A. (2016). The impact of land use/land cover scale on modelling urban ecosystem services. Landscape Ecology, 31, 1509-1522.
9. Rachid, L., Elmostafa, A., Mehdi, M., & Hassan, R. (2024). Assessing Carbon Storage and Sequestration Benefits of Urban Greening in Nador City, Morocco, Utilizing GIS and the InVEST Model. Sustainable Futures, 100171.
10. Latue, P. C., & Rakuasa, H. (2023). Analysis of land cover change due to urban growth in Central Ternate District, Ternate City using Cellular Automata-Markov chain. Journal of Applied Geospatial Information, 7(1), 722-728.
11. Gaur, S., & Singh, R. (2023). A comprehensive review on land use/land cover (LULC) change modeling for urban development: current status and future prospects. Sustainability, 15(2), 903.
12. Zarandian, A., Mohammadyari, F., Mirsanjari, M. M., & Visockiene, J. S. (2023). Scenario modeling to predict changes in land use/cover using Land Change Modeler and InVEST model: a case study of Karaj Metropolis, Iran. Environmental monitoring and assessment, 195(2), 273.
13. Rezaei, H., Pourebrahim, S., & Karimadini, M. (2023). Development of an Integrated Model Based on Cellular Automata and Markov Chain to Predict Land Use/Cover Changes (Case Study: Karaj City). Journal of Range & Watershed Management, 75(4).
14. Shi, X., Wu, L., Zheng, Y., Zhang, X., Wang, Y., Chen, Q., ... & Nie, T. (2024). Dynamic Estimation of Mangrove Carbon Storage in Hainan Island Based on the InVEST-PLUS Model. Forests, 15(5), 750.
15. Babbar, D., Areendran, G., Sahana, M., Sarma, K., Raj, K., & Sivadas, A. (2021). Assessment and prediction of carbon sequestration using Markov chain and InVEST model in Sariska Tiger Reserve, India. Journal of Cleaner Production, 278, 123333.
16. Adelisardou, F., Zhao, W., Chow, R., Mederly, P., Minkina, T., & Schou, J. S. (2021). Spatiotemporal change detection of carbon storage and sequestration in an arid ecosystem by integrating Google Earth Engine and InVEST (the Jiroft plain, Iran). International Journal of Environmental Science and Technology, 1-16.

Advanced Engineering Days

aed.mersin.edu.tr

An integrated model-data fusion approach to measuring the habitat's quality and degradation in Marivan County

Bahman Veisi Nabikandi [*1], **Khalil Valizadeh Kamran** [2], **Ahmad Hami** [1]

[1]*University of Tabriz, Landscape Architecture Department, Iran, bahmanveisi19@gmail.com, hami@tabrizu.ac.ir*
[2]*University of Tabriz, Remote Sensing and GIS Department, Iran, valizadeh@tabrizu.ac.ir*

Cite this study: Veisi Nabikandi, B., Valizadeh Kamran, K., & Hami, A. (2024). An integrated model-data fusion approach to measuring the habitat's quality and degradation in Marivan County. Advanced Engineering Days, 9, 157-160

Keywords
Habitat Quality
Habitat Degradation
InVEST Model
Sentinel-2
Marivan County

Abstract

Land use patterns have a large impact on biodiversity in ecosystems. As a proxy for biodiversity research, measuring habitat quality and habitat degradation will provide a scientific foundation for ecological protection and land resource management, especially in ecologically fragile regions. Based on land-use data (Sentinel-2 MSI) covering 2023 from the Marivan County of Kurdistan Province, Iran, this paper selected the habitat quality module of the InVEST model to examine the quality and degradation of habitat. The results showed that the region's habitat quality mean index was 0.08, while the area of habitat degradation was 0.20, demonstrating the area's susceptibility to habitat loss. This study has the potential to enhance our comprehension of the present condition of quality and habitat degradation, which has significant consequences for the preservation of biodiversity, the protection of ecological security, and achieving the goal of ecological sustainability.

Introduction

In recent decades, rapid economic development has accelerated urbanization, resulting in significant land use changes. Urban sprawl, in particular, has led to the degradation of natural habitats, causing habitat fragmentation and degradation [1]. Consequently, habitat quality has emerged as a critical concern in the field of biological diversity [2]. Habitat quality is the ability of the ecosystem to provide suitable living conditions for individuals and populations [3]. Today, human activity has caused damage to many ecological lands, including forests, grasslands, and lakes, which were originally part of natural ecosystems. Overexploitation has led to serious environmental consequences, such as soil erosion, habitat degradation, and a drastic decline in biodiversity [1]. To address these challenges, it is essential to assess habitat quality and analyze the factors influencing its evolution [2,3].

Currently, approaches for assessing habitat quality may be divided into two categories: assessment index systems and ecological models. Several studies have developed complete assessment index systems to measure the habitat quality of individuals and populations based on important factors acquired from field research [4]. The assessment index system approach is very accurate; however, conducting field investigations requires significant human and financial resources. Thus, it is only appropriate for doing research on a limited geographic scale. Advances in remote sensing technology have facilitated the emergence of studies on habitat quality and biodiversity on a broad geographical scale and over a long period of time [3]. The InVEST model could be used to examine the correlation between threat sources and land use types, as well as the influence of different ecosystem types on habitat quality. This model has gained significant popularity due to its benefits of effortless data collection, exceptional accuracy, and robust spatial expression capability [3,5]. This research used the InVEST model to measure the quality and degradation of habitats.

Material and Method

Study Area

Marivan City is situated at 31°35°N latitude and 46°10°E longitude, located in the western region of the Kurdistan province in Iran [6] (Figure 1-a & b). The land use and land cover map of Marivan County was derived

from the ESA Sentinel-2 imagery at 10-meter resolution. This map, available through Esri Land Cover, provides a comprehensive view of the county's surface characteristics for the year 2023. The study area is classified into seven distinct classes: water, trees, flooded vegetation, crops, built area, bare ground, and rangeland (Figure 1-c).

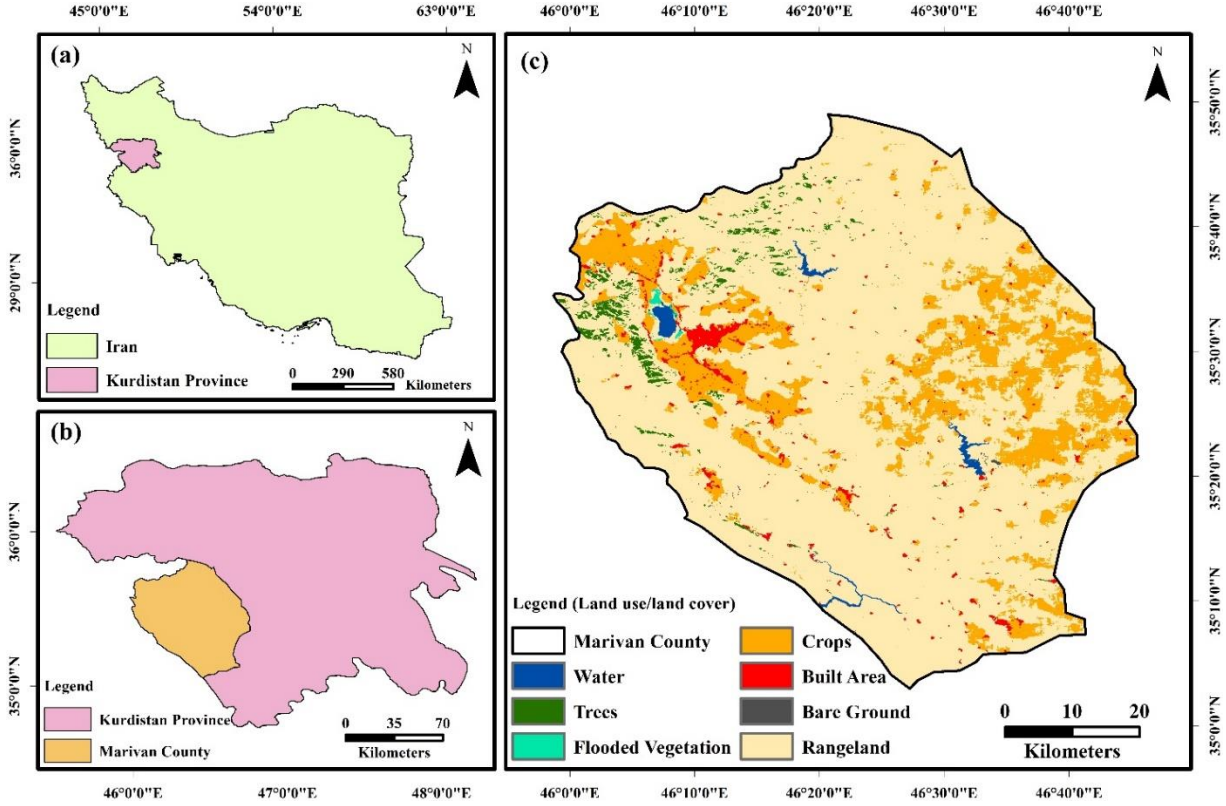


Figure 1. The map illustrates the studied area in Iran (a), Kurdistan province (b), and the land use and land cover of Marivan county (c).

InVEST Habitat Quality model

The InVEST habitat quality model is often used in urban ecology due to its low data requirements and its ability to enhance spatial visualization. The model Measure the level of habitat degradation and the habitat quality index by looking at threat factors, how sensitive different types of habitats are to these factors, and how well the environment fits the species [7]. According to this theory, habitat loss is exacerbated by both threat sensitivity and threat proximity. Briefly, an increase in human activities leads to a decrease in regional biodiversity, worse habitat quality, a greater level of habitat loss, and a more unstable ecosystem [1]. This study examined two land uses, namely agricultural land and built-up regions, as potential sources of hazards due to high levels of human activity. This investigation utilizes data (Table 1) from Rahimi et al. (2023), which pertains to the entirety of Iran [8] and user guide InVEST model [9].

Table 1. Sensitivity of habitat types to each threat factor

Land cover	Habitat suitability	Sensitivity		
		Built Area	Crops	Roads
Water	0.9	0.9	0.6	0.4
Trees	1	1	0.6	0.8
Flooded Vegetation	1	1	0.9	0.5
Crops	0.4	0.8	0.3	0.6
Built Area	0	0	0	0
Bare Ground	0.2	0.3	0.1	0.3
Rangeland	0.6	0.6	0.4	0.4

Results

The quality and degree of habitat degradation in Marivan City in 2023 were determined using remotely sensed data (Sentinel-2), as well as the factors required in the InVEST model (Figure 2). The findings show that the areas with high habitat value in the city are primarily distributed in forest and mountain areas, where habitat threat factors such as built-up areas, crops, and roads are less prevalent (Figure 2-a). The highest value for habitat quality is 0.86, which is related to the southern and northern green areas (Figure 2-a). These areas primarily consist of mountain forest covers that have experienced minimal impact from man-made factors. However, this area's average habitat quality is 0.08, indicating low biodiversity and habitat quality.

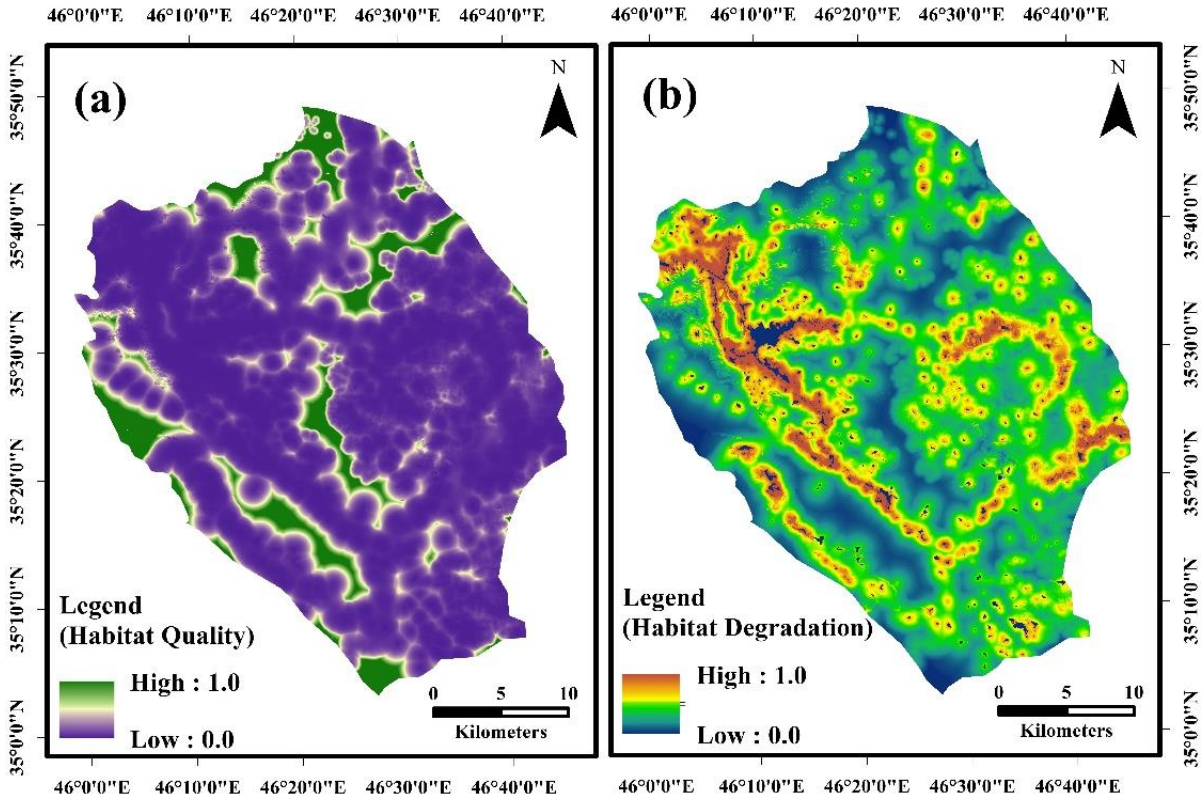


Figure 2. Habitat quality map (a), and Habitat degradation map (b) in the study.

Figure 3-b shows the map of habitat degradation for this year in the range between zero and about 0.82, which generally indicates a high degree of habitat degradation in some places. Because built-up areas are not considered habitat, they do not undergo degradation. However, the areas closest to the threat factors have experienced the most habitat degradation. Accordingly, the areas adjacent to Marivan city and agricultural lands (brown areas in Figure 3-b) contain more habitat degradation than other places. The average degradation for this area was 0.20, which is attributed to the extent of man-made factors throughout the area.

Discussion

Analyzing habitat quality and biodiversity is crucial for regional land use planning and the establishment of environmentally viable communities. The nature of land use and land cover are directly related to the landscape pattern, and this link impacts the structure of regional ecosystems [10]. Habitat quality is compromised by several factors, including roadways, metropolitan areas, agricultural fields, and other similar threats all compromise habitat quality. The InVEST-HQ model assumes that all of these hazards have a cumulative effect [11]. This model may be used to assess and compare the relative effects of threats, with the aim of identifying the risks that have the most significant influence on biodiversity within a given urban ecological environment under investigation. The research evaluated the risks to habitat quality in Marivan County using the InVEST-HQ model established by Sharp et al. (2019) [9]. The findings on threats to habitat quality and the sensitivity analysis for Marivan County were consistent with the research conducted by Ansari et al. (2023) [8].

Conclusion

The goal of this study is to use an integrated model-data fusion approach (remotely sensed data and the InVEST model) to measure how good the habitat is and how much it is being damaged in Marivan County, which is in

Kurdistan Province, Iran. The results of this research indicate that the study area is affected by human activities and has low habitat quality. The reduction of ecological spaces, such as trees and rangelands, coincides with the expansion of human-made spaces, such as built-up areas and crops, in the region. The average habitat quality index for the year 2023 is approximately 0.08, and the degree of degradation is close to 0.20, according to the obtained results. To overcome this situation, effective land management strategies are required to minimize the environmental impacts of human activities on habitat capacity. This research emphasizes the crucial role of remote sensing in monitoring habitat quality and degradation for both short-term and long-term scenarios.

References

1. Tang, J., Zhou, L., Dang, X., Hu, F., Yuan, B., Yuan, Z., & Wei, L. (2023). Impacts and predictions of urban expansion on habitat quality in the densely populated areas: A case study of the Yellow River Basin, China. Ecological Indicators, 151, 110320.
2. Wang, Q., & Wang, H. (2023). Evaluation for the spatiotemporal patterns of ecological vulnerability and habitat quality: implications for supporting habitat conservation and healthy sustainable development. Environmental geochemistry and health, 45(5), 2117-2147.
3. Chen, S., & Liu, X. (2024). Spatio-temporal variations of habitat quality and its driving factors in the Yangtze River Delta region of China. Global Ecology and Conservation, e02978.
4. Xiao, P., Zhou, Y., Li, M., & Xu, J. (2023). Spatiotemporal patterns of habitat quality and its topographic gradient effects of Hubei Province based on the InVEST model. Environment, Development and Sustainability, 25(7), 6419-6448.
5. Zhao, B., Li, S., & Liu, Z. (2022). Multi-scenario simulation and prediction of regional habitat quality based on a system dynamic and patch-generating land-use simulation coupling model—a case study of Jilin Province. Sustainability, 14(9), 5303.
6. Khani, S., Rastkhadiv, A., & Abdollahi, A. (2023). Vandalism in Urban Parks; An analysis on demographic characteristics and the intention and behavior of Vandals in Marivan City. Journal of Social Problems of Iran, 14(2), 165-200.
7. Lei, J., Chen, Y., Li, L., Chen, Z., Chen, X., Wu, T., & Li, Y. (2022). Spatiotemporal change of habitat quality in Hainan Island of China based on changes in land use. Ecological Indicators, 145, 109707.
8. Ansari, A., Ghorbanpour, M., Kazemi, A., & Kariman, K. (2023). Ecological assessment of Iran's terrestrial biomes for wildlife conservation. Scientific Reports, 13(1), 17761.
9. Sharp, R., Douglass, J., Wolny, S., Arkema, K., … & Wyatt, K. (2020). InVEST 3.8.7., User's Guide. The Natural Capital Project, Standford University, University of Minnesota, The Nature Conservancy, and World Wildlife Fund: Standford, CA, USA.
10. Meng, R., Cai, J., Xin, H., Meng, Z., Dang, X., & Han, Y. (2023). Spatio-temporal changes in land use and habitat quality of Hobq desert along the Yellow River section. International Journal of Environmental Research and Public Health, 20(4), 3599.
11. Chen, H., Yan, W., Li, Z., Wende, W., & Xiao, S. (2024). A framework for integrating ecosystem service provision and connectivity in ecological spatial networks: A case study of the Shanghai metropolitan area. Sustainable Cities and Society, 100, 105018.

Advanced Engineering Days

aed.mersin.edu.tr

Assessing cultural ecosystem services of urban agriculture: Analysis of small-scale using Smart-PLS software

Arman Rastkhadiv [*1], **Bahman Veisi Nabikandi** [1]

[1]*University of Tabriz, Landscape Architecture Department, Iran, armanrastkhadiv@gmail.com, bahmanveisi19@gmail.com*

Cite this study: Rastkhadiv, A., & Veisi Nabikandi, B. (2024). Assessing cultural ecosystem services of urban agriculture: Analysis of small-scale using Smart-PLS software. Advanced Engineering Days, 9, 161-164

Keywords
Cultural Ecosystem Services
Urban Agriculture
Smart-PLS
Hokmabad

Abstract

The rapid expansion of urbanization has created many challenges for the well-being of citizens and the sustainability of urban communities. Modern urban green infrastructure, including urban agriculture (UA), introduces Cultural Ecosystem Services (CES) as an ideal solution to address these challenges. However, only a few studies have explored the evaluation of cultural ecosystem services (CES) in relation to urban agriculture (UA). Therefore, this study examined the CES offered in Tabriz's Hokmabad region. We used 300 questionnaires to survey the people of Tabriz, following the Mitra and Lankford methods. The results showed that CES and UA have a significant relationship. The most influential variables were ecotourism and recreation, social relations, and sense of place.

Introduction

Urban Agriculture (UA) has gained significant attention over the past two decades, with various forms such as urban allotment gardens and rooftop farming becoming increasingly prevalent. These spaces serve multiple purposes and provide a range of Ecosystem Services (ES) to urban communities [1]. Among these services, Cultural Ecosystem Services (CES) play a crucial role in enhancing the well-being and quality of life of city dwellers. CES encompasses the non-material benefits that people derive from their interactions with nature [2]. These services include aesthetic enjoyment, recreational opportunities, and spiritual or cultural connections. Urban micro-farms, whether located on rooftops or at ground level, contribute to these cultural services in unique ways [3].

Despite the growing interest in UA and its associated services, there remains a gap in our understanding of the specific cultural contributions made by urban micro-farms. While users generally perceive and appreciate these services, empirical studies on this topic are limited [1]. To address this gap, researchers have developed a methodology for evaluating CES provided by urban micro-farms. The goal of this study is to shed light on the cultural benefits of small-scale UA and explore how Smart-PLS software can aid in assessing these services. By examining a set of UA in Hokmabad, Tabriz, researchers aim to provide valuable insights into the role of UA in enhancing cultural well-being within cities. In summary, this research contributes to our understanding of the CES delivered by urban micro-farms and highlights the importance of considering these services in urban planning and policy-making.

Material and Method

Study area description

The study area is Hokmabad, an urban agricultural district located in Tabriz city, which is situated in the northwest of Iran. Tabriz is the capital of East Azerbaijan Province and is the fourth biggest city in Iran (Figure 1). It is positioned at a height of 1,350 m at the confluence of the Quri River and Aji River [4].

This study examined the CES offered in Tabriz's Hokmabad region. This research used 300 questionnaires to survey the people of Tabriz, following the Mitra and Lankford methods. Multivariate analysis was used to analyze the data. It analysis is a robust and highly appropriate tool for analyzing data in behavioral and social sciences research. Structural Equation Modeling (SEM) and Covariance-based Structural Equation Modeling (CB-SEM) are

two prominent techniques used to analyze complex and multivariate data, with SEM using the variance methodology. Their main characteristic is the ability to analyze numerous independent and dependent variables at the same time. This methodology includes statistical techniques such as factor analysis, regression, and route analysis. The researcher is able to construct numerous associations at the same time, which is why it is called a multiple regression model. The aims of structural equation Modeling, as outlined by [5], are as follows: 1) The structural model is used to represent the relationships between independent (exogenous) and dependent (endogenous) variables. 2) The measurement model is used to represent latent variables. 3) The measurement errors of observable and dependent variables are accounted for in the model. 4) Hypotheses derived from the literature are tested using data through path analysis.

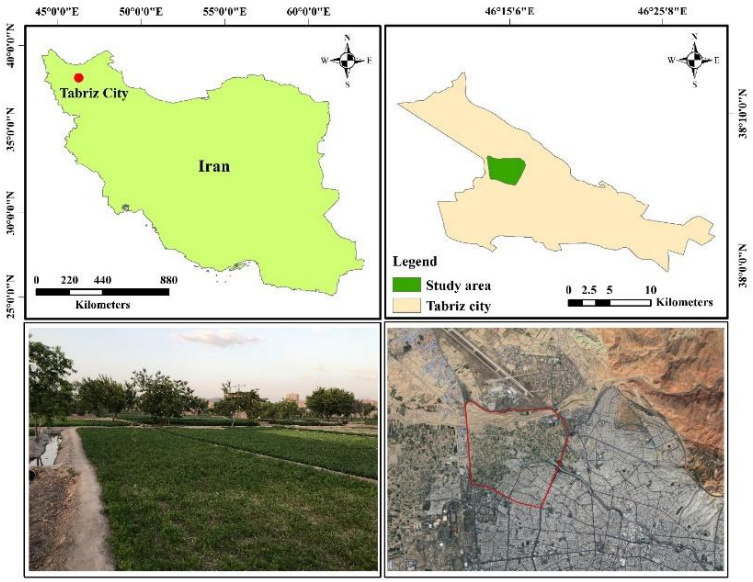


Figure 1. The study area's geographical location

Smart-PLS software is a widely used tool for structural equation modeling (SEM) with a partial least squares (PLS) technique, effective for small sample sizes and non-normally distributed data. It is particularly suitable for evaluating CES due to its ability to model complex relationships and handle measurement errors. The method's strengths include sufficient predictive capability, the ability to manage complex models with multiple variables, and appropriateness for developing new theoretical models. We used Smart-PLS in this research to analyze data, revealing latent variables with limited indicators and capturing multifaceted CES such as recreational, aesthetic value, social relations, sense of place, and other variables related to CES in UA.

Results and discussion

The study used Smart-PLS software to evaluate the reliability and validity of research variables using Composite Reliability (CR), rho-A, average variance extracted (AVE) and Cronbach's Alpha (α) tests. Each of these items should be equal to or greater than 0.7, 0.7, 0.5, and 0.7, respectively. Therefore, this research confirmed the reliability and validity of all the variables of CES in UA in the Hokmabad region (Figure 2).

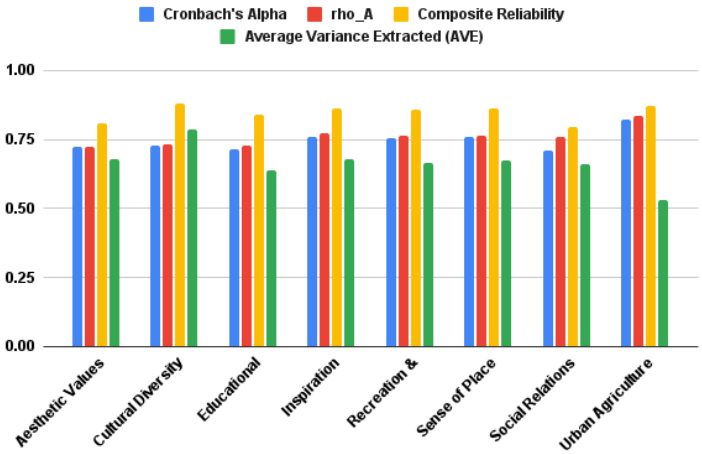


Figure 2. Construct validity and reliability

Path coefficients in linear regression are standardized betas that indicate direct or inverse relationships between latent variables. Positive coefficients indicate direct relationships, while negative coefficients indicate inverse relationships [6]. The magnitude of these coefficients reflects the strength of the relationship, typically ranging between -1 and 1. The significance of path coefficients depends on their magnitude and the beta coefficient's sign. If the obtained value exceeds the required statistic at the chosen confidence level, the relationship or hypothesis is confirmed. At significance levels of 90%, 95%, and 99%, this value is compared with the minimal t-statistics of 1.64, 1.96, and 2.58, respectively, as stated by [7] and [8].

Diagram 3, which displays the path coefficients (the degree of influence of CES variables on UA, indicates a direct and significant relationship between the provided CES and UA in the Hokmabad region of Tabriz City. Meanwhile, Figure 3 reveals that the most influential variables are recreation and ecotourism, social relations, and sense of place, with path coefficients of 0.204, 0.198, and 0.189, respectively. Their t-statistics, at the 99% confidence level, are 4.321, 4.006, and 2.934, respectively (figure 4).

The R^2 Value is a crucial measure in evaluating latent variables in structural models using the Partial Least Squares (PLS) approach. In this study, the R^2 Value for the dependent variable "urban agriculture" is 0.817, indicating that the independent variables (cultural ecosystem services) explain 81.7% of the dependent variable's variation, indicating high research structural model quality (figure 4).

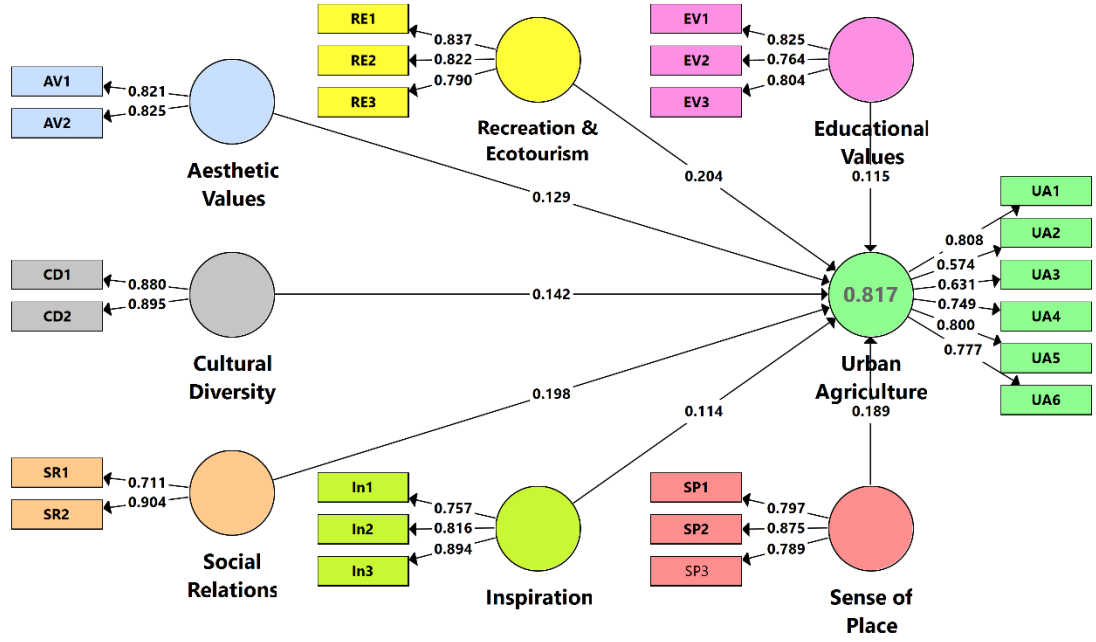


Figure 3. Path coefficients and Coefficient of Determination (R^2)

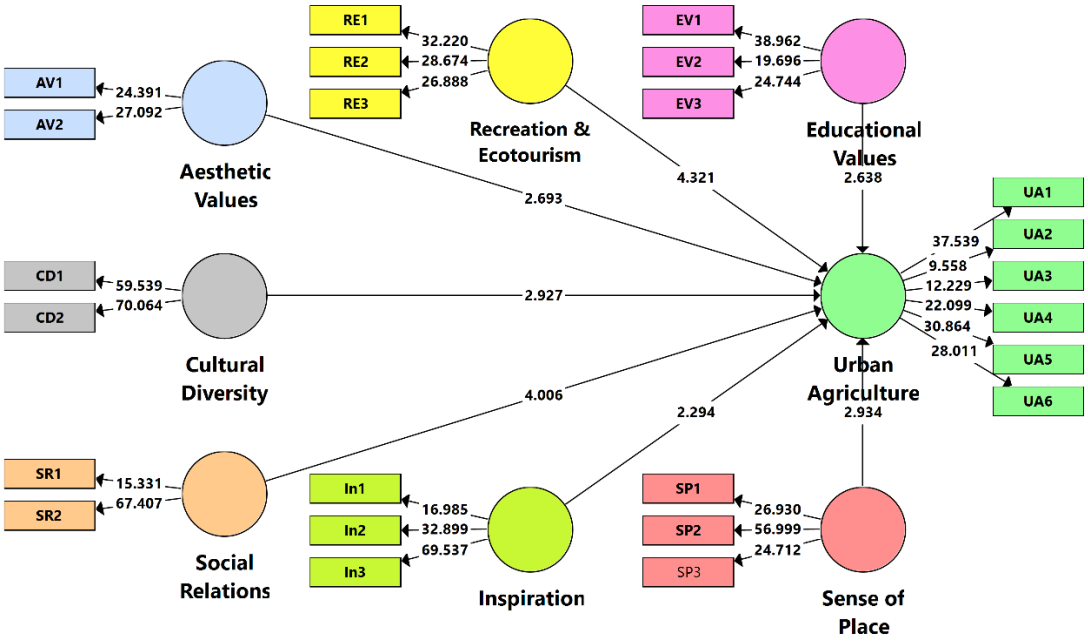


Figure 4. T-statistics of research variables

Diagram 3, which displays the path coefficients (the degree of influence of CES variables on UA), indicates a direct and significant relationship between the provided CES and UA in the Hokmabad region of Tabriz City. The most influential variables are recreation and ecotourism, social relations, and sense of place, with path coefficients of 0.204, 0.198, and 0.189, respectively. Their t-statistics, at the 99% confidence level, are 4.321, 4.006, and 2.934, respectively (Figure 4). These findings align with previous scientific research that demonstrated the relationship between UA and variables such as recreation and ecotourism, social relations, and sense of place. For instance, [9] highlighted how UA can provide recreational spaces and promote ecotourism within urban environments, underscoring the multifunctional benefits of integrating agriculture into urban land use planning. Similarly, [10] showed that urban community gardens foster social interactions, strengthen community ties, and enhance social capital among participants, thereby establishing a direct relationship between UA and social relations. Moreover, [11] emphasized how community gardens and UA contribute to a sense of place by connecting people to their environment and fostering a sense of stewardship and belonging. These previous studies corroborate the current findings, reinforcing the significance of CES in enhancing UA.

Conclusion

This research investigated the impact of CES on UA in the Hokmabad region of Tabriz City using the partial least squares method with Smart-PLS software. SmartPLS software is unique for evaluating CES due to its robust capability in handling complex structural equation modeling. It allows researchers to effectively assess and quantify the direct and indirect relationships between various CES variables and UA, providing comprehensive insights into their influence. This software's precision and reliability make it an invaluable tool for exploring the multifaceted contributions of CES to urban environments. The study revealed a direct and significant relationship between CES and UA, with recreation and ecotourism, social relations, and sense of place being the most influential variables. This study emphasizes the importance of integrating CES into urban planning and policy-making to improve urban residents' well-being and quality of life. Policymakers should incorporate UA into city planning to provide cultural benefits such as recreation, social interaction, and a sense of place. Supporting UA projects can strengthen community ties and improve public health. Additionally, integrating UA into educational programs can foster environmental stewardship. Providing financial incentives and incorporating UA into sustainability goals can further enhance cities' livability and sustainability.

References

1. Giacchè, G., Consalès, J. N., Grard, B. J., Daniel, A. C., & Chenu, C. (2021). Toward an evaluation of cultural ecosystem services delivered by urban micro-farms. Sustainability, 13(4), 1716.
2. Gai, S., Fu, J., Rong, X., & Dai, L. (2022). Users' views on cultural ecosystem services of urban parks: An importance-performance analysis of a case in Beijing, China. Anthropocene, 37, 100323.
3. Sen, S., & Guchhait, S. K. (2021). Urban green space in India: Perception of cultural ecosystem services and psychology of situatedness and connectedness. Ecological Indicators, 123, 107338.
4. Rahimi, A., & Nobar, Z. (2023). The impact of planting scenarios on agricultural productivity and thermal comfort in urban agriculture land (case study: Tabriz, Iran). Frontiers in Ecology and Evolution, 11, 1048092.
5. Kirschkamp, A. (2008). A Contingency-Based View of Chief Executive Officers' Early Warning Behavior. Gabler edition Wissenschaft.
6. Khani, S., Rastkhadiv, A., & Abdollahi, A. (2023). Vandalism in Urban Parks; An analysis on demographic characteristics and the intention and behavior of Vandals in Marivan City. Journal of Social Problems of Iran, 14(2), 165-200.
7. Hair Jr, J. F., Hult, G. T. M., Ringle, C. M., Sarstedt, M., Danks, N. P., Ray, S., ... & Ray, S. (2021). An introduction to structural equation modeling. Partial least squares structural equation modeling (PLS-SEM) using R: a workbook, 1-29.
8. Henseler, J., Ringle, C. M., & Sinkovics, R. R. (2009). The use of partial least squares path modeling in international marketing. In New challenges to international marketing (Vol. 20, pp. 277-319). Emerald Group Publishing Limited.
9. Lovell, S. T. (2010). Multifunctional urban agriculture for sustainable land use planning in the United States. Sustainability, 2(8), 2499-2522.
10. Teig, E., Amulya, J., Bardwell, L., Buchenau, M., Marshall, J. A., & Litt, J. S. (2009). Collective efficacy in Denver, Colorado: Strengthening neighborhoods and health through community gardens. Health & place, 15(4), 1115-1122.
11. Krasny, M. E., & Tidball, K. G. (2017). Community gardens as contexts for science, stewardship, and civic action learning. Urban horticulture: ecology, landscape, and agriculture, 267.

Advanced Engineering Days

aed.mersin.edu.tr

Spatial analysis of photosynthesis function in reducing air temperature in Tehran parks

Ali Teymoori [*1], Saeed Jahanbakhsh Asl [2], Ali Mohammad Khorshiddoust [2]

[1]*Faculty of Planning and Environmental Sciences, the University of Tabriz, Iran, ali_sedegh@yahoo.com*
[2] *University of Tabriz, Department of Climatology, Faculty of Planning and Environmental Sciences, , Tabriz, Iran, s_jahan@tabrizu.ac.ir, khorshid@tabrizu.ac.ir*

Cite this study: Teymoori, A., Asl, S. J., & Khorshiddoust, A. M. (2024). Spatial analysis of photosynthesis function in reducing air temperature in Tehran parks. Advanced Engineering Days, 9, 165-173

Keywords
Photosynthesis
Carbon dioxide
Blue light wavelength
Red light wavelength
Tehran

Abstract

Recognizing and evaluating the process of photosynthesis is an important part of calculating the temperature balance of regions. From a climatic perspective, several factors affect the air temperature of the regions, the most important of which are sunlight, and greenhouse molecules CO_2 and $H2_O$ participating in the photosynthesis process. The study of the role of photosynthesis on air temperature is one of the manifestations of climate issues. Photosynthesis is one of the factors affecting the temperature of air near the surface of the ground and its spatial distribution. The aim of this study was to analyze the spatial role of photosynthesis in reducing carbon dioxide and air temperature near the ground surface. For this purpose, two satellite and field databases were used. In the field method, night and day carbon dioxide data from Parks, daytime temperatures, as well as morphometric data, were used to describe the role of photosynthesis on near-surface temperatures and the intensity of the heat island. The role of the photosynthesis process was explained in combined methods using satellite remote sensing techniques and software, statistical-mathematical methods and the laws of radiation physics. According to extracted maps, in green landuse, the absorption intensity of the blue light wavelength showed good adaptation to the absorption intensity of the red light wavelength, which indicates the role of the photosynthesis process in carbon capture, significant temperature reduction and difference in the microclimate conditions of green and non-green users. According to Wien's law, the maximum wavelength of radiation as a climate variable; in parks was more than in adjacent residential areas. Based on the test results (A-D), the best probability distribution function for 22-year average temperature data near the surface of residential areas nearby the parks was also estimated.

Introduction

Lal studies (2002) showed that from 1980 to 1955, about 18 percent of the land's carbon reserves were degraded and sublimated by mis-management. The amount of soil organic carbon deposits is directly related to how habitat resources are used, so that research by Feiza et al (2008) showed that soil organic carbon sequestration is directly related to the quality of management of three soil axes, biomass and plant remains. As a result of the increase in fossil fuel consumption and the change in forest and highland land use, the concentration of carbon dioxide in the atmosphere increased from 250 ppm in 1850 to 420 ppm in 2021 which according to estimates; will lead to an increase in the average global temperature between 1.5 and 2 T°C for the next 20 years (IPCC, 2021). Modeling Iran's climate future in the period from 2025 to 2049 also shows an increase of at least 1.1 and a maximum of 2.75 T°C in temperature throughout Iran (Waghefi et al., 2019). Several studies have reported that following the increase in temperature, the rate of decomposition and waste of organic carbon in the soil increases, which in turn increases the rate of carbon dioxide emissions and exacerbates biosphere warming (Barančíková et al, 2010; Francaviglia et al, 2013 and Muñoz-Rojas et al, 2017). Concerns about the negative effects of urbanization on the environment of cities have increasingly increased the importance of

urban planning and construction, especially in densely populated cities (Young et al., 2023). High urban heat leads to increased energy consumption and pollutant concentrations and decreased environmental quality and levels of indoor and outdoor comfort and human health. Air pollution is one of the causes of the city's heat island, which has been increasing in large cities in recent years due to its high population density (Arvin, 2018). Along with heat island research, there has been also a lot of research on cool islands that emphasize on the reduction of heat islands with effective landscape planning, and their results have shown that urban forest parks can create the effect of cool urban islands (Wang et al, 2009). Land use change and urban use formation play an important role in climate change and regional air quality; changes in urban surfaces change the dynamic and thermal characteristics of surfaces (Liao, 2015). According to the carbon dioxide emission scenarios released by the IPCC, the concentration of carbon dioxide can increase from the current level of 300 ppm to 800 ppm by the end of the 21st century (Van vuuren et al., 2011). Increasing the concentration of carbon dioxide causes a change in global temperature, rainfall patterns and solar radiation, and thus a change in agricultural productivity (Lobell et al., 2011). Climate change also affects the hydrological cycle and changes the temporal-spatial distribution of water resources that are closely related to the availability of irrigation water and crop growth (Piao et al., 2010). Climate models predict an increase in intensity and abundance of extreme weather events, partly attributed to changes in human emissions, land use, and land cover (Christidis et al., 2011; Das et al., 2011; Newman et al., 2015; Reidmiller et al., 2017). Heat islands are one of the environmental hazards of megacities and mother cities, and various factors such as increased carbon dioxide concentrations can affect their intensity. But these impacts are of greater importance in arid and semi-arid regions of underdeveloped or developing countries. Especially if these areas are not at a high level in terms of ecological development, they will be more sensitive to the increased intensity of these islands. Accordingly, Tehran province on the one hand is classified as a dry and semi-arid climate zone, which is part of the developing regions, and on the other hand, expansion without urban planning, migration, non-compliance with urban planning and architecture laws, inefficient use of natural resources, especially energy (fossil fuels), water and land resources are very vulnerable to the intensity and abundance of heat islands. In addition to facing increased concentrations of atmospheric pollutants daily, Tehran is becoming one of the unplanned cities in terms of horizontal and vertical expansion of the region. The attention to urban spaces and the application of policies that relieve the people of cities from problems such as despair and despair and cause communication with urban spaces and the environment are among the most important tasks of urban institutions (Wright, 2000). Tehran, as the capital of the country, with its own culture and industry, has caused air pollution and replaced vegetation with buildings. Figure (1) shows five temperature floors in the city of Tehran.

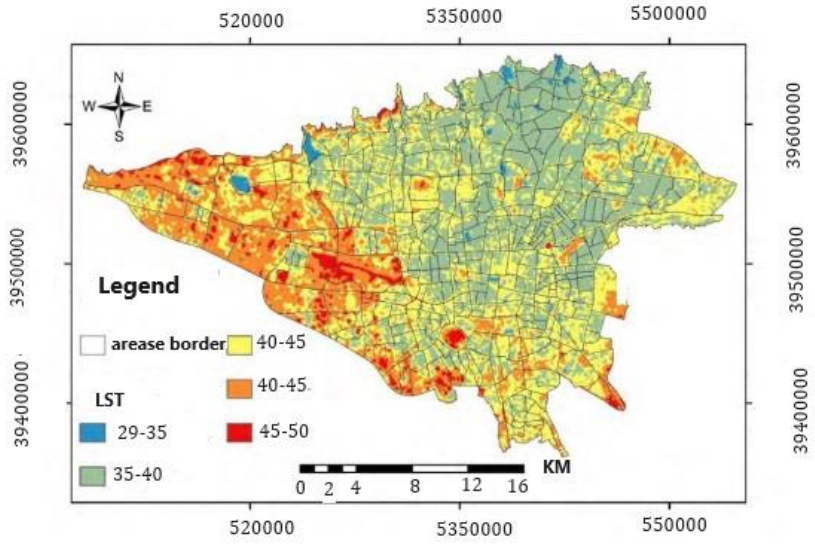


Figure 1. Map of the land surface temperature of Tehran (Mortazavi Asl, 2022)

According to the Figure, the northern parts of the city are often the coolest areas of the city, which increases the heat island area as we move towards the center and South, and reduces the area of the heat islands. The most important factors affecting the per capita emissions of carbon dioxide gas are energy consumption (energy intensity), per capita income, population and urbanization rate. In Tehran, in addition to the high level of factors mentioned, the lack of compliance with environmental laws and regulations by industrial companies, factories and so on has also increased the number of polluting days per year in terms of air quality indicators. One way to do that is to have an unauthorized carbon dioxide concentration crisis and its effects, such as heat islands, diseases, and so on. It plays a key role in the process of photosynthesis and increases the ambient temperature of land surface by absorbing infrared rays. By expanding green applications, the effects of the unauthorized concentration of carbon dioxide gas can be reduced and the ecological balance in the study area by creating a

descending branch of the Kuznets Environmental Curve (KES). In order to understand the role of photosynthesis in reducing the heat islands of Tehran, domestic and foreign studies related to the subject were first studied. Almost none of the researchers have used photosynthesis quality indicators, field methods, and carbon dioxide-dependent calculations in their studies.

Material and Method

Tehran province is limited to Mazandaran Province with a space area of 13,692 km^2 from the north, Qom province from the South, Qazvin province from the west and Semnan province from the east.

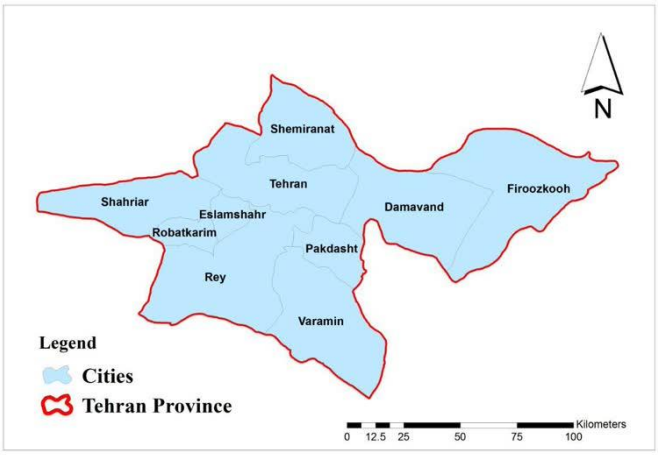


Figure 2. Map of the area of Tehran province

The current study uses two satellite and field databases. Field data include data from the GM8802 carbon dioxide gauge of the Bentec brand, daily temperature data from the digital thermometer, and morphometric data from urban geometry of selected regions. Satellite data was also composed of landsat8, MODIS (Terra and aqua), ASTER, Sentinel 5, and climate data from the University of Idaho during 2000-2023. One of the most important factors affecting the temperature of air near the land surface is the process of photosynthesis. Other factors affecting the intensity of the urban heat island and the temperature near the land surface include wind speed, wind direction, air humidity, cloud cover, aerosol particles, city geometry, vehicles, fossil fuels, area height, Euclidean distance from the city center and concentrations of gas pollutants: CO_2; CO; O_3; SO_2; NO_2 and NO. Selection of study parks with appropriate spatial distribution at the city level; due to differences in species diversity, height, physiographic shape and area, relative humidity, biomass volume, and wind speed (due to variation in species height).The concentration of pollutants and aerosol particles has been done, which eliminates the effect of these factors as interfering variables on the intensity of heat islands (air temperature near the land surface) and highlights the effect of the photosynthesis process. Field and combined methods have been used to achieve research objectives. Data collected by field method include: 1- carbon dioxide data and air temperature with the help of carbon dioxide gm8802 model of the Bentec brand 2 - morphometric data and urban geometry. Morphometric analysis is a good tool for examining the effect of urban structure changes on the heat island. In this method, urban geometry data including the height of the building and the width of the street of the study areas are harvested in a field and then the intensity of the heat islands is calculated. The next step was to predict the intensity of heat islands in the study areas using the Markov Monte Carlo chain in the Matlab software with the photosynthesis process impact approach.

Results

First, the data normality was examined to find the difference between day and night CO_2 in parks using the Kolmogorov-Smirnov and Shapiro Wilk tests, and then using the coupled t test, the difference between the two averages was assessed with a 99% confidence level. Table 1 shows the results of this test.

Table1. Statistical indicators of the paired t test parks

sig	Meaningful level	Average		Standard deviation of the mean		Standard error average	
0.000	.01	Night CO_2	Day CO_2	Night CO_2	Day CO_2	Night CO_2	Day CO_2
		529.48	501.81	68.09	60.95	8.79	7.86

According to Table 1, the probability of a 99% difference between the daily and night averages of carbon dioxide in urban parks is confirmed. The same was used to test the homogeneity of the variance of two CO_2 groups daily in parks and adjacent residential areas. Table 2 shows the results of this test.

Table 2. Independent Levene and t test

	Levene's test		Independent t test		
	F	sig	t	df	sig
Homogeneous variance	.71	.790	-2.140	118	0.34
Heterogeneous variance			-2.140	117.87	.34

According to the results of Table 2, the amount of the Levene's test is greater than the permissible error level, i.e. 0.01, so it is equal to the 99% probability of the daily CO_2 concentration variance of parks and residential areas. Table 3 shows the results of the Independent t-test.

Table 3. Some statistical indicators of nearby parks and residential areas

Average		Standard deviation of the mean		Standard error average	
Residential daily CO_2	CO_2 daily park	Residential daily CO_2	CO_2 daily park	Residential daily CO_2	CO_2 daily park
526.03	501.81	63.02	60.95	8.13	7.86

Based on the information in Tables 2 and 3 with a 99% confidence level, the daily carbon dioxide levels of parks and residential areas were calculated as equivalent to (501.88±7.87) and (526.033±8.13) ppm respectively. Statistically, the numerical difference between the two expressions is not significant, so the process of photosynthesis of parks has not been able to reduce the negative effect of daily CO_2-boosting factors in Tehran. To examine the difference or similarity of the Daily O_2 data of parks and adjacent residential areas, the default normality of the data was first examined and confirmed, then the two groups were examined using the lone variance homogeneity test. Tables 4 and 5 show some statistical indicators and test results, respectively, of nearby parks and residential areas.

Table 4. Some statistical indicators of nearby parks and residential areas

	Average oxygen (by percentage)	Standard deviation	Standard error average
Park	20.66	.088	.011
Residential	20.64	.079	.01

Table 5. Levene's test and T independent test O_2 Parks and adjacent residential areas

	Levene's test		Independent t test		
	F	sig	t	df	sig
Variance homogeneity	0.938	0.335	1.089	118	0.278
Variance heterogeneity			1.089	116.62	0.278

According to Tables 4 and 5 with a 99% O_2 confidence level, the parks and adjacent residential areas are equivalent to (20.66 ± .011) and (20.64±.01) percent respectively. Statistically, the numerical difference between the two expressions is not significant, so the process of photosynthesis of parks has not been able to reduce the negative effect of daily O_2 reduction factors in Tehran. To examine the differences or similarities in the daily O_2 data of parks and adjacent main streets, one of the complementary methods is to examine the effect of photosynthesis on temperatures near the land surface. Tables 6 and 7 show some statistical indicators and test results, respectively, of the parks and adjacent main street.

Table 6. Some statistical indicators parks and adjacent main street

	Average oxygen (by percentage)	Standard deviation	Standard error average
Park	20.66	0.088	0.011
Main Street	20.36	0.077	0.0099

Table 7. Levene's test T independent test O_2 Parks and adjacent main street

	Levene's test		Independent t test		
	F	sig	t	df	sig
Homogeneous variance	1.996	.16	119.51	118	0/00
Heterogeneous variance			119.51	115.87	0/00

The results showed that with a 99% probability of daily oxygen concentration differences the parks and adjacent main street are approved. According to this, The Daily O_2 of the parks and the adjacent main street is equivalent to (20.66 ± .011) and (20.36±.009) respectively. Statistically, the numerical difference between the two expressions is significant, so according to the results of the previous tables, it can be said that the main factor in controlling the concentration of oxygen and carbon dioxide molecules in Tehran was caused by vehicles, and the photosynthesis process has not been able to compete with this factor to reduce the effect of vehicles on reducing the concentration of O_2 and CO_2 in Tehran. After extracting and analyzing the corresponding chronological data of CO_2 and air temperature, the linear function (1) best demonstrated the relationship between the variables studied. The general form of this equation is as follows:

$$Y = -0.0172 * T + 25.01 \quad :(1)$$

In this equation, T is the air temperature in Celsius and Y is the CO_2 concentration in ppm. This equation shows greater accuracy for data measured in open spaces and temperatures greater than zero degrees Celsius. The variance analysis Table 8 was used to evaluate the power of this model.

Table 8. Model variance analysis

Determination coefficient	F-test	Average squares	Total squares	Degree of freedom	Origin of changes
R^2 = .9767		MSR= 3.822	SSR= 3.828	k-1	Regression
R_{Adjust} = .9766	7.171	MSE= .5329	SSE= 91.12	N-k	Error
			SST= 94.94	N-1	Total

Since the ratio of the mean squares has a statistical distribution of F, it is observed that the calculated value F is larger than the value in the Fisher table; therefore, the model has been able to accommodate the change in air temperature caused by the increase in CO_2 concentration. On the other hand, due to the negligible difference between the determination coefficient and the adjusted determination coefficient, high accuracy of the model can be confirmed.

Urban geometry and intensity of heat islands

With the help of the numerical-theoretical Oke،s model, the intensity of the heat islands is calculated when the number of residential floors is between 3 and 22 floors and the width of the crossings is 8, 12, 14 or 20 meters and corresponds to the geometric conditions of the city of Tehran. Table 9 shows the results of the calculations performed with the help of relationship 2

$$\Delta T_{u-r} = 7.45 + 3.97 Ln(\frac{H}{W}) \quad :(2)$$

In this function: H/(W) shows the ratio between the average height of the building to the average width of the building. Based on the calculations:

- Taking into account the width of the 8-meter crossing, increasing the number of floors from 3 to 15 floors increases the intensity of the heat island by 7.11 T°C.
- By applying a fixed width of 14 meters, increasing the number of floors from 3 to 15 floors; the intensity of the heat island increases by 6.2T°C.
- By applying a width of 20 meters, as the number of floors increases from 3 to 15 floors, the intensity of the heat island increases by 5.25T°C.
- Taking into account the number of floors, the widening of the crossings from 8 meters to 20 meters, on average, reduces 3.31 degrees Celsius from the intensity of the heat island.

The results of the Monte Carlo simulation, repeating 100,000 times (N=100,000), showed that at least two heat islands are likely to occur in two urban areas every day, with a probability of 0.4767 percent. Based on the results of Table 10, it can be concluded that in the near future, new urban areas with vertical expansion will host these islands and their effects every day.

The following were compared with the help of the triple tests of Anderson-Darling (A-D), Chi-Square and Kolmogorov-Smirnov (K-S) near the surface of parks and residential areas, and the best density distribution was extracted. Another parameter affecting the intensity of the heat islands is the area of urban green space. Figure 3 map shows the green user area of Tehran province.

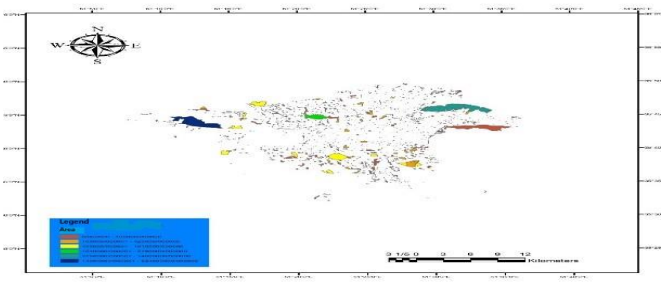


Figure 3. Area of Tehran parks

Based on the calculations performed in ArcMap software, the ratio of the area of the city parks to the total area of the 22 districts was calculated to be approximately .1 percent. According to the results, the increase in the number of building floors from 3 to 15 floors has increased the average temperature of 7.18T°C near the land surface, while the difference in the air temperature of parks compared to adjacent residential areas was calculated at only 0.994T°C; on the other hand, the results well show the multiplication of the standard beta coefficient of pollutants produced by motor vehicles and factories in the increase in the air temperature of the city.

Examination of the land surface temperature in relation to the quality of photosynthesis

This section evaluates the intensity of blue and red light absorption in parks, residential areas and other users to show the effect of photosynthesis on lowering temperatures near the surface. Each of the following maps averages at least 5,000 daily images (between 10 and 16 hours) of the Landsat 9 satellite study band with the help of Google Earth Engine, during the growing season, i.e. for the months of mid-March to the end of May, in conditions where the percentage of cloud cover in the sky is less than 15 percent. Figure 4 shows the intensity of red light absorption (band 4 of the Landsat 9 satellite) in various applications in Tehran.

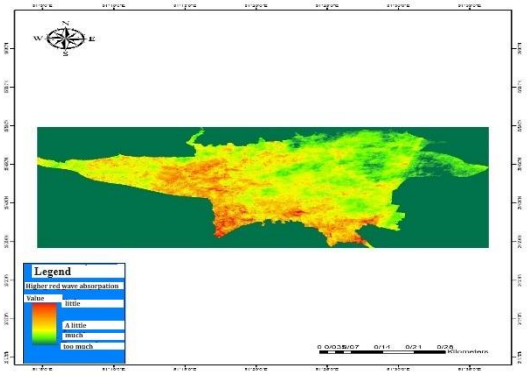


Figure 4. The intensity of the red light absorption in Tehran is based on the band4 of the Landsat 9 satellite.

As the maps show, the intensity of absorption of red light bands (.64-.67 micrometers) and blue light bands (.45-.51 micrometers) in urban and forest parks account for the highest amount and dense industrial or residential centers, the lowest amount, which means converting energy from photons of these two bands into photosynthetic products and preventing its conversion to tangible heat, and thus reducing the temperature near the surface of the Earth in green applications and expressing the role of photosynthesis is in the reduction of air temperature. Figure 5 shows the intensity of blue light absorption in the 22 districts of Tehran during the blue light wave.

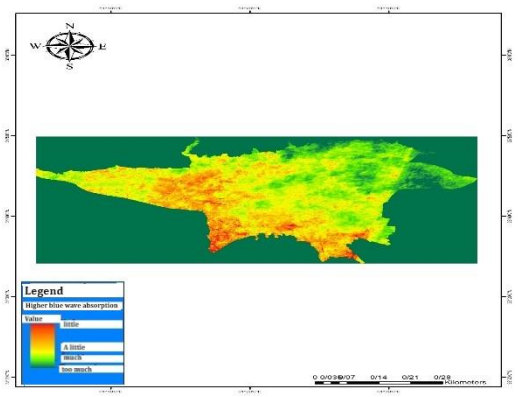


Figure 5. The intensity of the Tehran City's light absorption based on the BAND2 of the Landsat 9 satellite

As map 5 shows, the absorption intensity of the blue light wavelength is a good adaptation to the absorption intensity of the red light wavelength. Map 4 shows that the concept of the role of the photosynthesis process in absorbing these two wavelengths in carbon capture and tangible temperature reduction can be inferred. The same is true for calculating the normalized physical metamorphoses of NDVI, brightness temperature, and emissivity coefficient; the 2023 images of the parks and their adjacent residential areas were taken from the 13th ASTER satellite runway in the Google Earth Engine System for the growing season (the months of May to the end of August).

Discussion

Morphometric analysis is a good tool for examining the effect of urban structure changes on the heat island. Using the Anderson-Darling (A-D), Chi-Square and Kolmogorov-Smirnov (K-S) best fit line tests in Easy Fit software, the 22-year average temperature near the ground surface of the growing season (months of mid-March to the end of spring) of the study parks and adjacent residential areas calculated through the Aster meter in the Google Earth Engine System; with 61 statistical distribution of brass and thus the difference in the effect of parks (photosynthesis) and urban geometry the temperature of the residential neighborhoods was determined. The Oke·s model is one of the most successful models presented in the field of simulating the maximum intensity of the urban Night Heat Island based on the landscape ratio parameter in urban canyons**.** In general, increasing the number of layers relative to the width of the crossings increases the intensity of the heat islands by approximately 2.38 times. Accordingly, it can be said that in Tehran, the nesting of heat islands is expanding in newly established residential areas. Fig. (6) confirms the results of Table 10 well.

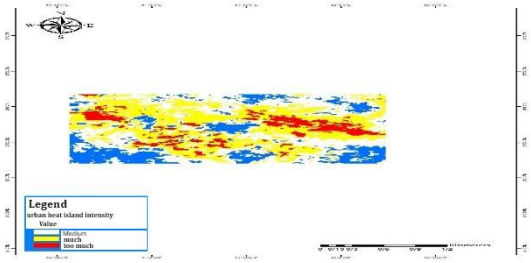


Figure 6 . Map of trends in night heat islands between 2000 and 2023 based on Moody's data (Teymoori et al., 2023)

The map was based on an average of 1,005 images recalled between 2000 and 2023. According to this map, the trend of changes in the night thermal Islands is expanding from the city center to the surrounding cities and settlements. Given the density of residential structures and the concentration of pollutants in urban centers relative to the surrounding area and the impact of these factors on the intensity of heat islands, other factors may have caused these islands to move from the center to the surrounding area. Accuracy in the results of Table 10 indicates the effect of the height of residential structures as one of these factors in the displacement of the city's heat islands. Given the negative effects of the occurrence of heat islands and the effect of urban geometry and the process of photosynthesis on its intensity and weakness, the importance of investigating the likelihood of these islands occurring in urban areas is essential. One of the most efficient and useful techniques for simulating statistical and semi-statistical processes is Monte Carlo simulation. Statistical testing is a means of making a little decision about one or more processes. According to the results, the area of one percent of the green space allocated to the city cannot play an effective role in reducing the heat generated by towers, industries and cars, so we should look for solutions such as increasing green space, using green fuels, preventing the vertical

expansion of the city and so on. It was. Based on "Le Chatelier's principle" principle, in order to examine the effect of the type of use on the temperature near the surface of the Earth, the course of changes in the concentration of carbon monoxide variables, water vapor density, nitrogen dioxide, sulfur dioxide, ozone, water vapor pressure and wind speed in the twelve landuse specified using the LCZ algorithm has been studied and examined in the provinces of Tehran and Alborz Based on this principle, in order to examine the effect of the type of use on the temperature near the surface of the Earth, the course of changes in the concentration of carbon monoxide variables, water vapor density, nitrogen dioxide, sulfur dioxide, ozone, water vapor pressure and wind speed in the twelve lannduse specified using the LCZ algorithm has been studied and examined in the provinces of Tehran and Alborz. Evapotranspiration is an important element of the hydrological cycle that plays an important role in agricultural studies, Water Resources, architectural climate, urban and Regional Planning, and so on ... It does. The results of the present study suggest that real sweating evaporation as one of the products of the photosynthesis process did not have a significant effect on the temperature of 10 meters above the ground compared to other variables under study. Based on the results, the variables studied in some landuse have shown a greater effect on the surface temperature of the Earth, for example, carbon monoxide in industrial landuse has played an important role in increasing the surface temperature of the Earth. This molecule directly and indirectly in areas with a grassy background, forest cover and dense trees has caused a decrease in temperature near the surface of the Earth, one of the reasons of which can be its conversion into a carbon dioxide molecule and participation in the photosynthesis process. Also, the type of landuse has influenced temperature changes near the surface of the Earth. Due to the interaction of variables, their direct and indirect effect on surface temperature has varied. The wind has affected the speed and type of chemical reactions between atmospheric pollutants and climate variables by changing their concentrations, causing changes in the temperature of the Earth's surface, which is why its direct and indirect effects have been different and interesting.

Conclusion

In the present study, the role of the process of photosynthesis of parks and green spaces in Tehran on the reduction of heat islands and temperatures near the surface of the Earth was studied and analyzed spatially. In general, the methods used indicate the lack of significant impact of the green space photosynthesis process on the reduction of heat islands in Tehran, due to the increasing and multiplying effect of factors such as: vertical development of the city; new construction and mass production of greenhouse gases such as CO_2. It was caused by vehicles and factories against the positive but small effects of the photosynthesis process due to the very small percentage of green spaces and city parks. According to the extracted maps, in green landuse, the absorption intensity of the blue light wavelength is a good adaptation to the absorption intensity of the red light wavelength, which shows that this is not true in non-green landuse, from which the concept of the role of the photosynthesis process in the absorption of these two wavelengths in carbon capture and tangible temperature reduction, and thus the microclimate difference(climate variables) of green and non-green applications can be inferred. Also, according to the Wien's displacement law, the maximum wavelength of radiation as a climate variable in parks has varied more than in adjacent residential areas. Based on the results, for each user, the probability density function can be specified and the temperature near the surface of the earth can be calculated at any time. The results of this study were consistent with the research conducted by other domestic and foreign researchers. According to these results, the small per capita percentage of urban green space, unconventional construction with a vertical development approach, industries and cars are the most important causes of the rise of the heat islands of Tehran.

References

1. Barančíková, G., Halas, J., Guttekova, M., Makovnikova, J., Novakova, M., Skalský, R., & Tarasovičová, Z. (2010). Application of RothC model to predict soil organic carbon stock on agricultural soils of Slovakia. Soil and Water Research, 5, 1-9.
2. Christidis, N., Stott, P. A., & Brown, S. J. (2011). The role of human activity in the ecent warming of extremely warm daytime temperatures. Journal of Climate, 24(7), 1922- 930. https://doi.org/10.1175/2011JCLI4150.1.
3. Feiza, V., Feizien, D., Jankauskas, B. and Jankauskien, G., (2008). The impact of soil management on surface runoff, soil organic matter content and soil hydrological properties on the undulating landscape of Western Lithuania, 95, 3-21.
4. IPCC. (2021). "Climate Change Impacts, the Physical Science Basis".
5. Lal, R., 2002. Soil carbon dynamics in cropland and rangeland. Journal of Environment Pollution, 116,353–362.
6. Liao, J.; T. Wang, Z. Jiang, B. Zhuang, M. Xie, C. Yin, X. Wang, J. Zhu, Y. Fu and Y. Zhang. (2015). WRF/Chem modeling of the impacts of urban expansion on regional climate and air pollutants in Yangtze River Delta, China. Atmospheric Environment, 106: 204-214.
7. Lobell, D. B., Schlenker, W., & Costa-Roberts, J. (2011). Climate trends and global crop production since 1980. Science, 333(6042), 616-620. https://doi.org/10.1126/science.1204531

8. Piao, S., Ciais, P., Huang, Y., Shen, Z., Peng, S., Li, J., Zhou, L., Liu, H., Ma, Y., Ding, Y., Friedlingstein, P., Liu, C., Tan, K., Yu, Y., Zhang, T., Fang, J. (2010). The impacts of climate change on water resources and agriculture in China. Nature 467 (7311), 43–51. https://doi.org/10.1038/nature09364.
9. Vaghefi SA, Kaykhaii M, Jhanbakhshi F, Sheikholeslami J, Ahmadi A, Yang H, Abbaspour K. 2019. The future of extreme climate in Iran. Future. 9 (1): 1 - 11.
10. Wang, X.; F. Chen, Z. Wu, M. Zhang, M. Tewari, A. Guenther and C. Wiedinmyer. (2009). Impacts of weather conditions modified by urban expansion on surface ozone: Comparison between the Pearl River Delta and Yangtze River Delta regions. Advances in Atmospheric Sciences.
11. Wright, F, L (2000), Brodacre city: A new community plan, in: City Reader (Legate, R,T and Stout, F Eds), Rouledge, London and New York. Yuan, F., and Bauer, M.E (2007). Comparison of impervious surface area and normalized difference vegetation index as indicators of surface urban heat island effects in Landsat imagery. Remote Sensing of environment 106, 375-386.
12. Yang, Y., Luo, Y., He, S., Dou, M., Wang, R., Zhang, T., Zhang, J. & Wang, F. (2023). Exploring the effect of industrial structure on urban heat island effect with infrared observations. *Infrared Physics & Technology.* https://doi.org/10.1016/j.infrared.2023.104615.
13. Young, Y., Luo, Y., He, S., Dou, M., Wang, R., Zhang, T., Zhang, J. & Wang, F. (2023). Exploring the effect of industrial structure on urban heat island effect with infrared observations. *Infrared Physics & Technology.* https://doi.org/10.1016/j.infrared.2023.104615.

Advanced Engineering Days

aed.mersin.edu.tr

The Study of Water Pollution Caused by Wastewater Entering Mehranrud River in Tabriz

Mohammadreza Jafarnezhad[*1], Sara Jafari Behtash[2], Ali Mohammad Khorshiddoust [3]

[1] *the University of Tabriz, Civil Engineering Department, Iran, madza.efro.me@gmail.com*
[2] *the University of Tabriz, Civil Engineering Department, Iran, s.behtash1402@ms.tabrizu.ac.ir*
[3] *the University of Tabriz, Climatology Department, Iran, khorshid@tabrizu.ac.ir*

Cite this study: Jafarnezhad, M., Jafari Behtash, S., and Mohammad Khorshiddoust, A. (2024). The Study of Water Pollution Caused by Wastewater Entering Mehranrud River in Tabriz. Advanced Engineering Days, 9, 174-180

Keywords
Water Quality
Quality Indicators
River Pollution Index
Mehranrud River

Abstract

Given the importance of environmental issues, preventing water sources from becoming polluted is crucial. This study aims to examine the water pollution of the Mehranrud River in Tabriz and determine the type and amount of potential pollutants in the river water caused by the mixing of urban wastewater and industrial effluents. Additionally, the geographic location of the river, which passes through urban areas, can endanger human health and the environment. Samples were taken from five stations along the river and necessary tests were conducted. The test results were compared with Iran's Water Quality Standard (1053) and the EPA standard, and the data were analyzed using statistical methods. Based on the samples collected and their comparison with Iran's water quality and the EPA standards, a noticeable decline in water quality is observed. The data results indicate that the presence of certain points with industrial and urban effluents has caused a significant drop in the water quality of this river.

Introduction

Nowadays, environmental issues have become one of the world's most significant problems, which can be seen in the decline of river water quality (4). Given that some rivers, like those passing through cities such as Tabriz and Isfahan, are polluted by industrial or urban waste, these pollutants have led to changes in riverbank ecosystems and deeper urban issues. Mehranrud is a 25-km-long river that flows through the city of Tabriz, originating from the Sahand Mountains. The main problem is that several sewage outlets discharge into the river at the study site. In previous years, measures were taken to improve the river, such as preventing urban wastewater from entering the river and constructing small dams to collect water and give the appearance of a fuller river. However, these measures were only temporarily effective. Currently, with wastewater and surface runoff from Tabriz flowing into it and warmer temperatures, the stench has not diminished; it has, in fact, increased, causing distress to residents and posing a threat to public health. Regarding the flow of sewage and surface water from Tabriz into Mehranrud, it is noted that nearly 450 liters of sewage enter the river every second. So far, 80 sewage entry points into Mehranrud have been identified, with most of the sewage originating from Marzdaran suburb and some industries located in the eastern part of the city. The objective of this study was to determine the type and amount of potential pollutants in the river water caused by the mixing of urban wastewater and industrial effluents.

Material and Method

Study Area

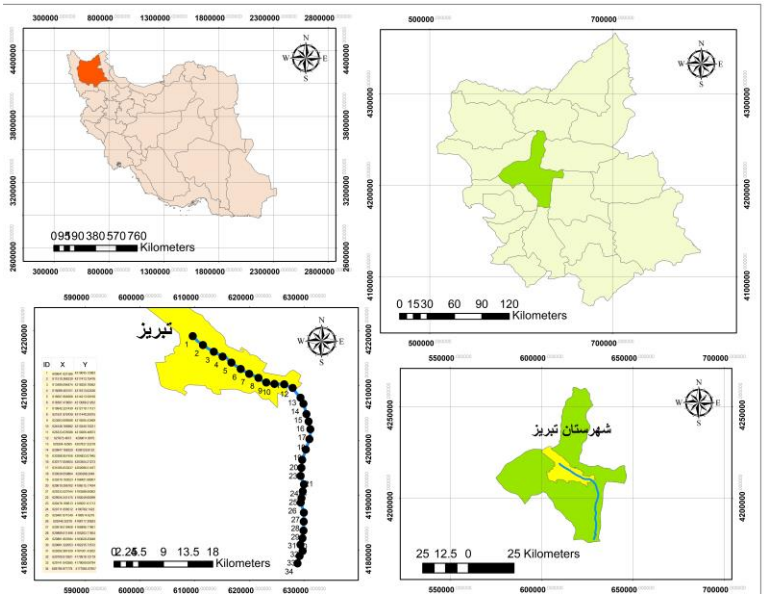


Figure 1. Geographic Location of the Study Area

The study area is located in northwestern Iran, in East Azerbaijan Province and. The Mehranrud River is one of the rivers within the Lake Urmia basin. The study area spans geographically from app Tabriz approximately 38.03 to 38.07 degrees east longitude and 46.39 to 46.31 degrees north latitude.

In Figures 2 and 3, the exact sampling locations are identified using Google Earth. The sampling intervals from locations 1 to 4 are approximately 15 minutes apart, and from location 5, about 2 hours apart, respectively.



Figure 2. Sampling Locations 1 to 4 (Google Earth Map)



Figure 3. Sampling Location 5 on Google Earth Map

Sampling Methodology

The study started in the fall of 2022, selecting five sampling locations. The first station was located at Basij Square, continuing along the river past the Khalat Pushan Tower, and ending at a water passage upstream from Sangy Bridge (above the Abarasan). The aim of the water sampling was to conduct microbiological, chemical, and physical analyses. The results were then compared against Iran's water quality (1053) and EPA standards.
To obtain valuable information, water samples from the river were analyzed to ensure they represented the source material. The typical volume of water for laboratory analysis from rivers is usually between 1 to 3 liters. To ensure accurate dissolved oxygen measurements, care was taken to prevent atmospheric oxygen from entering the water samples. For physical and chemical tests, turbid water was avoided, and suitable samples were transferred to bottles after the suspended materials settled. Given that water quality can vary with depth and width, it is best to sample at multiple points.
Due to the critical nature of the sampling process and to prevent any alteration of water quality parameters because of contaminated hands, we adhered to standard water sampling protocols. This involved opening the sterilized bottle cap without hand contact, holding the bottle neck, submerging it below the water surface, rotating the bottle so its neck was gently upwards, filling it, and then sealing it. The samples were then sent to the Central Laboratory of the University of Tabriz for analysis. Each sample was labeled with location, date, time, and the name of the sampling team. Laboratory tests commenced a day after sampling. To control microbial growth, samples were stored at 4°C in a refrigerator, with a one-day interval between sampling and testing.
In Figure 4, the pollution status of the river and its bank is clearly visible; the impacts of urban pollution have imposed an unsightly appearance on the river.



Figure 4. Riverbank near Basij Square (Sampling Location 3)

Water Quality Index Calculation

The water quality of the Mehranrud River in Tabriz was evaluated and classified using the $IRWQI_{SC}$ index. In the $IRWQI_{SC}$ index, (W_i) denotes the weight of the parameter and (I_i) denotes the quality value of the parameters, which include 11 physical, chemical, and biological parameters. For the calculation of this index, based on the curves and the value of each parameter in this study, equations 1 and 2 were used:

$$IRWQI_{SC} = \left[\prod_{i=1}^{n} I_i^{W_i}\right] \quad (1)$$

$$\gamma = \sum_{i=1}^{n} W_i \quad (2)$$

line	parameter	method	specifications	Measurement accuracy
1	DO	4500	HACH-HQ D40	0.01 mg/L
2	Fecal coliform	3759	Ensure plus	-
3	PH	4500	HACH-HQ D40	-
4	BOD	52210	BD600	0.01 mg/L
5	COD	52210	5220	0.01 mg/L
6	Temperature	2550	HACH-HQ D40	0.1 $°C$
7	PO_4	4500 PO_4	UV/Vis JENWAY 6705	0.01 mg/L
8	NO_3	4500 NO_3	UV/Vis JENWAY 6705	0.01 mg/L
9	NH_4^+	4500 NH_4^+	UV/Vis JENWAY 6705	0.01 mg/L
10	Turbidity	2130	2100 HACH N	0.1 NTU
11	TDS	2340	HACH-HQ D40	0.1 mg/L
12	EC	2510	HACH-HQ D40	$\mu S/cm$

Table 2. Values and Description of $IRWQI_{SC}$ Quality Index (9)

Index range	Description	The color related to the numerical value of index
less than 15	Very bad	Purple
15.9-29	Bad	Red
30.9-44	Relatively bad	Orange
45-55	Average	Yellow
55-70	Good enough	Green
70-85	Good	Blue green blue
More than 85	Very well	Blue

Statistical Data Analysis

In this study, Excel software was used for statistical data analysis and to check for normality. To compare the impact of spatial and temporal conditions of sampling stations on the water quality parameters of the Mehranrud River, a one-way analysis of variance (One-Way ANOVA) was used. Additionally, mean comparisons were performed using Duncan's test at the 0.05 significance level. In the cluster analysis method, data grouping is based on the distance between them, so that samples with less distance from each other are placed in the same group. The main goal of cluster analysis is to create classes and groups where the intra-group diversity and dispersion are less than the inter-group dispersion and scattering. The steps of grouping sampling stations using cluster analysis include preparing the raw data matrix, determining the factor load of each station using factor analysis, merging groups using the Ward method (minimum variance method), and finally grouping and drawing the dendrogram. At the beginning of the clustering process, there are as many clusters as observations, and in the final stage, the data were divided into fewer clusters. Two stations were considered to belong to the same group providing that the measured water quality parameters were sufficiently close to each other.

Results

As mentioned before, the samples collected were transferred to the Central Laboratory of the University of Tabriz for testing. The obtained results were compared with the water quality standards for environmental protection (aquatic ecosystems). Standards 1053 and EPA were used for this comparison. Table 1 presents all the tested data obtained from the samples. In this table, various parameters of the samples were examined, and the standard limit for each parameter according to the mentioned standards was provided.

Table 3. Comparison of Water Sample Parameters with Standards 1053 and EPA

parameter	Unit	Station1	Station2	Station3	Station4	Station5	Standard1053	Standard EPA
PH	-	7.2	7.1	7.1	7.2	8.2	6.5-9	6.5-8.5
EC	µS	869	899	908	930	921	1000	2000
Turbidity	NTU	560	580	580	595	590	5	5
TDS	mg/Lit	31.4	22	20.3	24.3	8.2	1500	500
Alkalinity	ppm CaCO3	270	270	280	280	220	-	-
Hardness	ppm CaCO3	301.8	314.5	313.9	319.5	323.3	500	100
Magnesium	ppm CaCO3	21.7	23	23	23.5	24.8	30	150
Calcium	ppm CaCO3	85	87.9	87.7	89.1	92.1	300	75
Sodium	mg/Lit	91.2	96.7	96.1	97	92	400	200
Potassium	mg/Lit	17.3	17.1	17.4	17.4	12.1	-	12
Chloride	mg/Lit	136.5	111.4	111.6	165.3	103.5	250	-
Sulphate	mg/Lit	149.5	177.9	152.2	162.3	236.5	400	200
Ammonia	mg/Lit	4.5	3.4	4.1	4	5.9	1.5	-
Nitrite	mg/Lit	12.9	0.2>	0.2>	11.4	1.4	3	0.1
Nitrate	mg/Lit	1.2	1.2	1.2	1.3	6.3	50	45
Fluoride	mg/Lit	0.28	0	1.5	1.8	0.26	0.5-1.5	1.5
Phosphate	mg/Lit	0.2>	0.2>	0.2>	0.84	0.2	-	0.3

Discussion

Nitrate Pollution

One of the most significant problems in the drinking water of major cities today is the excessive increase in nitrate levels. Nitrates are colorless and tasteless and cannot be detected in drinking water without chemical testing. Methods for nitrate removal include dilution, ion exchange, reverse osmosis, and distillation. Common sources of nitrates include fertilizers, municipal sewage and sludge, nitrogen fixation from the atmosphere by bacteria, and lightning.

Ammonia

Ammonia (NH3) is a colorless gas composed of nitrogen and hydrogen with a pungent odor. ammonia is highly dangerous and corrosive. Inhalation of low concentrations causes coughing and respiratory irritation, while high concentrations can cause severe damage to the respiratory tract. Inhalation of ammonia can also lead to excessive fatigue.

Water Hardness

Water hardness essentially refers to its capacity to precipitate soap.. Soap is primarily precipitated by calcium and magnesium, Calcium and magnesium are present in large quantities in natural waters, so water hardness is mainly measured based on these two elements. According to the classification of water hardness and the laboratory results obtained, the sample under study falls into the category of very hard water. In drinking water, it can cause indigestion and kidney diseases, as well as internal infections.

Electrical Conductivity

The electrical conductivity of water indicates the amount of dissolved salts. The best method for identifying water and wastewater samples is to measure electrical conductivity, as the anions and cations in wastewater are more abundant than in water.

Nitrites

Nitrites are significant due to their ability to cause methemo-globinemia in humans. The maximum allowable nitrite concentration in water is 3 ppm.

Phosphates

Phosphates exist in nature in three forms: orthophosphates, polyphosphates (or condensed phosphates), and organic phosphates, . Orthophosphates used in agriculture as fertilizers can enter surface waters through soil runoff during floods, precipitation, or snowmelt. The phosphate level in the sample from station 4 is significantly higher than the permissible limit.

Fluoride in Water

Fluoride is an element found abundantly in volcanic regions and in minor quantities in some surface water sources, and in high concentrations in groundwater sources.

Currently, there are three methods for removing excess fluoride from water sources: chemical precipitation, ion exchange, and reverse osmosis.

Sulfates in Water

Sulfates are compounds of sulfur and oxygen and are found as part of natural minerals in some soils and rocks. The maximum allowable sulfate concentration in water is 400 mg/L. The highest sulfate concentration in samples was found at station five, amounting to 236.5 mg/L.

Ammonia Removal from Wastewater

Nitrification is the most common method for the biological removal of ammonia in wastewater. Bacteria decompose ammonia, eventually releasing nitrogen gas into the atmosphere, thereby reducing ammonia levels in the effluent.

In lagoons, wastewater is treated through a combination of physical, biological, and chemical processes. Many treatment stages occur naturally, but some systems use aeration devices to add oxygen to the wastewater. Aeration increases treatment efficiency, thus requiring less land area.

The pH level in nitrification lagoons should typically be between 7.5 and 8.0. The pH of most municipal wastewater naturally falls within this range, but industrial wastewater may vary, so this level must be controlled. The standard temperature range for nitrification ponds should be between 82 and 97 degrees Fahrenheit. Without adequate mixing, sludge volume will undoubtedly increase. Ideally, the sludge depth should remain below 2 feet.

Nitrifying bacteria (BOD reducers) are easily destroyed by heavy metals. Ensure that your effluent contains no toxins that could kill beneficial bacteria.

Table 4. Comparison of Water Sample Parameters with Industrial Water Standards

Items	Station 1	Station 2	Station 3	Station 4	Station 5	Group I	Group II	Group III
PH	7.2	7.1	7.1	7.2	8.2	9-6	9-6	9-6
EC	869	899	908	930	921	<1000	≤2000	>2000
Alkalinity	270	270	280	280	220	<150	≤500	>500
TDS	31.4	22	20.3	24.3	8.2	<50	≤100	>100

Conclusion

The most polluted sampling points are Station 1 and Station 4 in terms of chloride, phosphate, and nitrite levels. The high data values in some points are due to the presence of immediate effluents in the sampled areas. When samples were taken from downstream, the effluent present in the water had dispersed, resulting in a more homogeneous solution. Therefore, the effluent concentration is higher at the upstream station, leading to greater pollution. As this pollution moves downstream, it disperses in the water, making it appear less concentrated. Considering the samples compared to the Iranian water quality standards, it is necessary to treat suspended solids, nitrite, ammonia, calcium hardness, and magnesium hardness to reduce damage and diseases caused by these pollutants to the environment and humans. In addition to these considerations, industrial standards must also be referenced. According to the comparisons made, the alkalinity level falls into Group II, while the electrical conductivity and dissolved solids fall into Group I. If used industrially, further treatment is required. By implementing step-by-step treatments and injecting neutralizing agents that are environmentally friendly, and placing materials at appropriate points in the river where pollution levels are high compared to the standards, these substances can dissolve over time and remove harmful materials from the water through chemical reactions. It is important to ensure that these reactions do not cause a sudden increase in water temperature (thermal pollution).

References

1. Aazami J., Sari A. E., Abdoli A., Sohrabi H., and Van den Brink P.J. Assessment of ecological quality of the Tajan River in Iran using a multimetric macroinvertebrate index and species traits. Environmental Management. 2015;56(1):260-69.

2. Alizadeh M. Water Pollution; an Expertimental Approach. Tehran: MojesabzGreen Wave; 2003 (in Persian).
3. APHA/AWWA/WEF. Standard Methods for the Examination of Water and Wastewater. 22nd ed. Washington DC: American Public Health Association; 2012.
4. Gholizadeh M., and Heydari O. Evaluation of Gorganrood Gorganrud river water quality based on surface water quality indicators in Gonbad Kavous. ijhe IJHE 2020; 13 (1) :33-48
5. Hashemi S., Farzampour T., Ramezani S., Khoshroo G. Guidelines for calculating Iran Water Quality Index. Tehran: Department of Environment;.
6. Khair Soltan Ahmadi, R.; Nazarnejad H., Asadzadeh F.,Analytical evaluation of water quality along the Mahabadchai river with Iran's surface water quality index. 2022.
7. Ouyang Y. Evaluation of river water quality monitoring stations by principal component analysis. Water Research. 2005;39(12):2621-35.
8. Samantray P., Mishra B.K., Panda C.R., Rout S.P. Assessment of water quality index in mahanadi Mahanadi and atharabanki Atharabanki rivers and Taldanda Canal in Paradip Area, India. Journal of Human Ecology. 2009;26(3):153- 61.
9. Zamani A., Mahmoudi R., Fathi E., Biati S., and Ghorbani Dastaki P. Investigating the water quality of Beheshtabad river using Liou pollution index and principal component analysis. Water and Soil, 2019, 33.3: 405-417.

Advanced Engineering Days

aed.mersin.edu.tr

The impact of geotourism on sustainable development in mountainous areas: A case study of Kamtal National Park

Seyed Asadollah Hejazi [1], Mahdi Javadi [*1]

[1]*University of Tabriz, Geomorphology, Iran, s.hejazi@tabrizu.ac.ir, iran.tabriz.mj@gmail.com*

Cite this study: Hejazi, S. A., & Javadi, M. (2024). The impact of geotourism on sustainable development in mountainous areas: A case study of Kamtal National Park. Advanced Engineering Days, 9, 181-183

Keywords
Geotourism
Sustainable development
Mountainous areas
Kamtal National Park

Abstract

Geotourism is recognized as a critical driver of sustainable development in mountainous regions worldwide. This article investigates the impact of geotourism on sustainable development, focusing on Kamtal National Park as a descriptive case study. Geotourism, emphasizing geological and natural attractions, plays a pivotal role in environmental conservation, community engagement, and economic growth in mountainous areas. Using field methods exclusively, this study assesses the geotouristic potentials of Kamtal National Park and highlights its significance in promoting sustainable tourism practices. The findings underscore the integration of geotourism into regional development strategies as a key approach to achieving sustainable goals. By examining Kamtal National Park descriptively, this research explores how geotourism effectively contributes to sustainable development in mountainous regions, offering a model for similar areas globally.

Introduction

Mountainous regions, as one of the world's richest natural resources, have always attracted the attention of tourists and researchers alike. These areas are popular destinations for travelers interested in experiencing culture and nature due to their natural beauty, biodiversity, and various tourist attractions. Geotourism is one of the tools developed to optimize the exploitation of these potentials by tourists and to protect them.

Geotourism, as a specific type of tourism based on geological attractions, has evolved from an educational and awareness-raising tool about geological processes and features to a demand-driven opportunity for economic and social development in mountainous regions. Given the importance of geotourism in economic and social interactions, examining its impacts on sustainable development in mountainous areas is essential.

This article investigates the impact of geotourism on sustainable development, focusing on Kamtal National Park as a descriptive case study. This study uses a field approach to assess the geotouristic potentials of this area and highlight its role in promoting sustainable tourism practices.

This introduction includes an introduction to the topic, its significance, the research objective, and the structure of the article, helping the reader to better understand the content of the article.

Material and Method

Kamtal National Park, covering an area of 70 square kilometers, is located in the northern part of East Azerbaijan Province, Iran, extending to the international border with the Republic of Armenia. This area is recognized as the Kiyamaki Wildlife Sanctuary and experiences mountainous climatic conditions, with warm summers being particularly popular.

This study employed field methods and a case study approach. Key stages included reviewing relevant park documents, direct observations in the area, and interviewing relevant individuals such as park managers, guides, and tourists.

Data collection involved gathering geographical, statistical, and geological information about the region, including geographical maps, geological data, and statistics on visitor numbers and types of tourist activities.

Data were analyzed using statistical methods and content analysis in this study. Analyses included comparative examination of different geotourism potentials within Kamtal National Park and assessing the impacts of geotourism on sustainable development in the region.

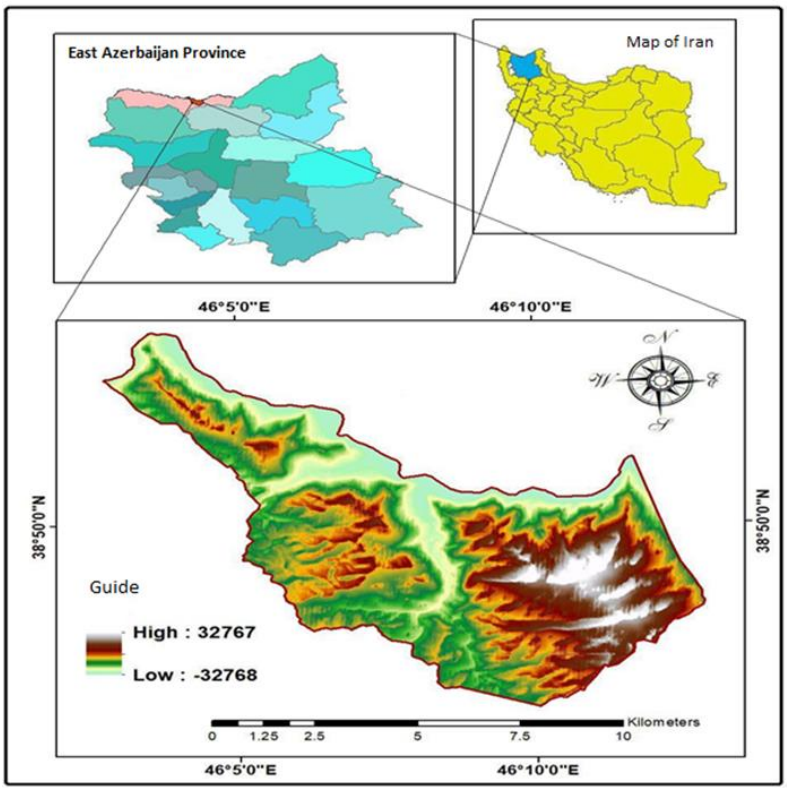


Figure 1. Kental National Park location map

Limitations of this research encompassed time constraints, resource limitations, and challenging weather and terrain conditions, which may have impacted the accuracy and comprehensiveness of the results.

Discussion

The importance of maintaining a balance between tourism development and environmental preservation is emphasized. Effective utilization of natural resources, proper tourism management, and strengthening local community engagement are highlighted as fundamental factors for achieving sustainable development in mountainous regions.

Conclusion

This study examined the impact of geotourism on the sustainable development of mountainous regions, focusing on the case study of Komata National Park. The findings demonstrate that tourism significantly contributes to local economic and social development. Increased local income, job opportunities, and the enhancement of tourism infrastructure are among the benefits observed.

Furthermore, geotourism plays a crucial role in the conservation and sustainable management of natural resources in mountainous areas. Measures such as temporary traffic management, educating tourists on environmental conservation, and promoting local culture are essential for maintaining the balance between tourism development and environmental preservation.

Based on the study's findings, it is recommended to implement more precise management plans to attract tourists, preserve natural resources, and strengthen community ties. Additionally, further research in this field is suggested to better understand the effects of geotourism and improve policy and management strategies.

In conclusion, this research indicates that geotourism can effectively contribute to the sustainable development of mountainous regions, provided that appropriate management and coordination among various stakeholders are ensured.

References

1. Butler, R. W. (1993). Tourism, environment, and sustainable development. *Environmental Conservation, 20*(3), 201-209.

2. Hejazi, S. A., & Javadi, M. (2020). *Geotourism potentials of Komata National Park*. Tabriz: Fadia Publications.

3. Javadi, M. (2019). *The impact of geotourism on sustainable development in mountainous regions: A case study of Komata National Park* (Master's thesis). University of Tabriz, Iran.

4. Ma, L., & Hassink, R. (2013). Tourism and regional economic resilience: A dynamic general equilibrium analysis. *Annals of Tourism Research, 43*, 551-571.

5. United Nations Environment Programme. (2005). *Making tourism more sustainable: A guide for policy makers*.

6. World Tourism Organization. (2020). *Global guidelines to restart tourism*.

Advanced Engineering Days

aed.mersin.edu.tr

Geotourism in Kandovan Village: A stunning blend of natural wonders and rock architecture

Seyed Asadollah Hejazi [1], Mahdi Javadi [*1]

[1]*University of Tabriz, Geomorphology, Iran, s.hejazi@tabrizu.ac.ir, iran.tabriz.mj@gmail.com*

Cite this study: Hejazi, S. A., & Javadi, M. (2024). Geotourism in Kandovan Village: A stunning blend of natural wonders and rock architecture. Advanced Engineering Days, 9, 184-186

Keywords
Geotourism
Kandovan Village
Natural attractions
Sustainable tourism

Abstract

This article explores the geotourism attractions in Kandovan Village, East Azerbaijan Province. Kandovan is one of Iran's unique regions renowned for its distinctive rock-hewn houses and breathtaking natural landscapes including mountains, springs, and valleys. The area is recognized for its volcanic geology and rich mineral springs, offering visitors a unique experience of nature and indigenous culture. Kandovan is acknowledged as a sustainable tourism destination prioritizing the preservation of natural beauty and promotion of indigenous culture and traditions. Sustainable tourism promotion in this area not only creates economic opportunities for the local community but also contributes to environmental conservation and cultural values. This article delves into the positive impacts of geotourism on the local economy, cultural values, and environmental conservation efforts in Kandovan, while proposing strategies for sustainable development of these activities. The article provides a detailed description of geotourism attractions such as Kandovan's mountains, mineral springs, and their cultural and economic impacts. Additionally, it examines the valuable historical and volcanic geological roles in attracting tourists. The sustainability and conservation of these resources are highlighted as necessary challenges and opportunities for the future of tourism in this region.

Introduction

Kandovan Village, located in East Azerbaijan Province, is one of Iran's unique regions that naturally attracts tourists with its distinctive architecture of rock-hewn houses and rich natural landscapes including mountains, springs, and valleys. This area has gained attention as a sustainable tourism destination due to its rich mineral water sources and volcanic geology.

The development of geotourism in Kandovan not only attracts tourists but also contributes to the preservation and development of the region's indigenous culture and traditions. Given Kandovan's high natural and cultural potential, promoting sustainable tourism can significantly aid in environmental conservation and cultural values.

The main objective of this article is to comprehensively examine the attractions and impacts of geotourism in Kandovan. Focusing on natural attractions, rock architecture, and the economic, social, cultural, and environmental impacts of these activities, the article aims to underscore the importance of conserving natural resources and promoting sustainable tourism in Kandovan.

The article is divided into several main sections including geographical and geological overview of Kandovan, history and rock architecture, geotourism attractions, economic and cultural impacts, and finally recommendations for sustainable development of geotourism in the region.

Material and Method

To conduct this study, initial information about the geography of the Kandovan region was gathered, including natural features such as topography, distribution of groundwater and surface water, and the development of mineral water resources from various sources. Additionally, information on existing tourism facilities, including natural and cultural attractions, was examined.

Data collected from various sources, including local reports, maps, and geographical information, were meticulously analyzed. Topographical analysis was specifically conducted to investigate the geographical relationships of geotourism attractions and their impact on tourist attraction.



Figure 1. Photo of Kandavan Village

The study was descriptive and analytical in nature. The research methodology involved case studies and interviews with local residents to gather their perspectives on the impacts of geotourism on local communities, local economy, and environmental conservation.

Modern geographical tools were employed for data collection in this study. The use of GIS (Geographic Information System) and GPS aided in more accurate analysis and visualization of geographical information of the region.

Various statistical methods were used to analyze the collected data. Regression analysis was employed to examine the relationship between geotourism attractions and tourist attraction, and statistical tests were used for validating the results.

This study acknowledged limitations such as restricted access to some data sources and cultural and linguistic differences in data collection, which may have potentially influenced the final outcomes.

This "Materials and Methods" section provides readers with an explanation of how information and data were collected for this study and the methods used for analysis and interpretation

Discussion

Discussion of this study is based on the results obtained from previous research and collected data. In this section, various impacts of geotourism on the sustainable development of Kandovan have been investigated.

One significant aspect of geotourism's impact in Kandovan is its economic effects. With the influx of tourists and the development of tourism facilities, employment opportunities for local youth have increased, and financial income has been generated for various social strata. These initiatives have stimulated local economic growth and contributed to the sustainable development of the region.

Furthermore, geotourism contributes to the preservation and enhancement of local culture and traditions. Given Kandovan's cultural and historical attractions, tourists become acquainted with local traditions and culture, enhancing cultural and social connections and aiding in the preservation of indigenous values.

The influx of tourists into Kandovan also raises environmental issues. Preserving natural resources such as water, air, and agricultural lands against the negative impacts of tourism poses a significant challenge. However, with appropriate strategies and policies, sustainable tourism development in Kandovan can be addressed, preserving the area as a sustainable tourism destination.

The findings of this research are consistent with previous studies on geotourism and sustainable development, demonstrating that promoting sustainable tourism can significantly contribute to the economic, cultural, and environmental enhancement of the region.

Based on the results obtained, recommendations for the sustainable development of geotourism in Kandovan have been proposed. These recommendations include improving tourism facilities, environmental conservation, and enhancing local collaborations to promote sustainable tourism.

Overall, the discussion in this article illustrates that geotourism in Kandovan can serve as a crucial strategy for sustainable economic, cultural, and environmental development in the region.

This discussion explains to the readers how the findings of your study on geotourism in Kandovan can impact the sustainable development of the region and suggests how it can contribute to improving the economic, social, cultural, and environmental conditions of the area.

Conclusion

Based on the analyses and collected data, this study demonstrates that geotourism in Kandovan village, East Azerbaijan province, not only serves as a tourist activity but also plays a crucial role as a significant tool for regional sustainable development. The study examines the positive impacts of geotourism on the local economy, revealing that the influx of tourists into Kandovan has led to increased employment opportunities, improved economic livelihoods, and enhanced local infrastructure.

Furthermore, the study explores the positive cultural and social effects of geotourism on the local community, including the preservation of local culture and traditions, the reinforcement of cultural identity, and the promotion of positive interactions between the local community and tourists. Additionally, the study suggests that with sustainable tourism development and optimal natural resource management, environmental conservation and the preservation of regional natural resources can be achieved.

Therefore, it is recommended to develop comprehensive programs and effective strategies to promote sustainable tourism in Kandovan. These strategies should include improving tourism facilities, providing education and awareness to the local community, and enhancing international collaborations to attract tourists. These initiatives will contribute to achieving sustainable development and enhancing the quality of life for the people in the region.

References

1. Hejazi, S. A., & Javadi, M. (2020). *Geotourism potentials of Komata National Park*. Tabriz: Fadia Publications.
2. Javadi, M. (2019). *The impact of geotourism on sustainable development in mountainous regions: A case study of Komata National Park* (Master's thesis). University of Tabriz, Iran.
3. United Nations World Tourism Organization (UNWTO). (2023). *Global Report on Tourism and Culture*. Retrieved from https://www.unwto.org/global-report-on-tourism-and-culture
4. World Tourism Organization (WTO). (2022). *Tourism and Sustainable Development Goals*. Retrieved from https://www.unwto.org/tourism-sustainable-development-goals
5. Saarinen, J. (2006). Traditions of Sustainability in Tourism Studies. *Annals of Tourism Research, 33*(4), 1121-1140. https://doi.org/10.1016/j.annals.2006.03.007
6. Gössling, S., & Hall, C. M. (2006). Tourism and Global Environmental Change: Ecological, Social, Economic and Political Interrelationships. Routledge.

Advanced Engineering Days

aed.mersin.edu.tr

Spatial-temporal patterns of Nitrogen Oxides (No_x) with Sentinel-5 satellite imagery (Kurdistan Region of Iraq)

Nader Habibzadeh*[1], Dara Hashem Ahmad [2]

[1]*Departmenet of Environmental Science, Tabriz branch, Islamic Azad University, habibzadeh@iaut.ac.ir*
[2]*Departmenet of Environmental Science, Tabriz branch, Islamic Azad University, dara_hashim@yahoo.com*

Cite this study: Habibzadeh, N., & Hashem Ahmad, D. (2024). Spatial-temporal patterns of Nitrogen Oxides (No_x) with Sentinel-5 satellite imagery (Kurdistan Region of Iraq). Advanced Engineering Days, 9, 187-190

Keywords
Air pollutants
Nitrogen oxides
Sentinel-5
Iraq
Kurdistan

Abstract

Air pollution, a significant issue in urban areas, has far-reaching impacts on both human health and the global climate. The use of satellite sensors to measure air pollutants is a widely adopted approach. In this study, we analyzed temporal and spatial changes in nitrogen dioxide (*NO2*) level using data from the TROPOMI sensor on the Sentinel-5 satellite in the Kurdistan region of Iraq. The findings revealed a gradual increase in the density of tropospheric *NO2* over the study period, with the highest and lowest concentrations recorded at 107.70 and 65.22 micromoles per square meter in July 2023 and March 2020, respectively. Notably, the outbreak of the COVID-19 pandemic in 2020 led to a temporary decrease in *NO2* level. The study also identified areas with high *NO2* concentrations, particularly in regions with heavy traffic and industrial activities. These results underscore the need for effective management strategies to control air pollution, especially in urban centers with high traffic volumes and industrial operations, such as Erbil city, and to reduce reliance on fossil fuels. Our findings highlight the pressing issue of air quality deterioration, which has been exacerbated by urban expansion, increased vehicular traffic, and industrialization in the Kurdistan region of Iraq.

Introduction

Air pollution, a significant issue in urban areas, not only has negative impacts on human health while also being important for altering the Earth's climate. The high consumption of energy related to the burning of fossil fuels (Rawlins & Meetham, 1954) and road transportation (Olmo et al., 2011) are among the primary factors contributing to health problems at local, regional, and global levels. The most significant atmospheric pollutants encompass a variety of compounds, including carbon dioxide, sulfur dioxide, carbon monoxide, nitrogen oxides, ozone, methane, unstable organic carbons, chlorofluorocarbons, and suspended particles or aerosols (Saxena & Naik, 2019).. Among these pollutants, nitrogen oxides are considered one of the most important and toxic gases (Park, Shin, Lee, & Lee, 2021). Human activities, particularly the burning of fossil fuels at high temperatures, lead to the annual production of millions of tons of nitrogen dioxide and nitrogen oxides. Satellite remote sensing has become an effective tool for studying atmospheric pollutants due to its ability to provide comprehensive spatial coverage and temporal resolution (Zhou, Zhang, Xue, Li, & Wang, 2023). Satellite remote sensing is revolutionizing the way air pollution is monitored and tracked, challenging the traditional methods. Recent advancements in this field are rapidly reducing uncertainties in measurements, making it a powerful tool for understanding and addressing air quality issues (Anenberg et al., 2020). People from Iraq and the Kurdistan region of Iraq frequently express concerns about the poor air quality in the region, and air pollution has been linked to an increase in cancer cases (Zana, Dedar, Gábor, & Kinga, 2023; Zanist, 2022), with reports of a 20% increase in cancer cases in Basra Province over three years and a doubling of cancer cases in the Kurdistan region of Iraq between 2020 and the present year (Baban, 2023). The Kurdistan region of Iraq is characterized by a significant presence of industrial towns and refineries, which have a substantial impact on air quality. For

instance, oil refineries and metal smelters near the cities of Erbil and Kirkuk are identified as major sources of polluting gases, contributing to air pollution problems (Ahmed, Aziz, Karim, & Hussein, 2022).

In this study we aimed at monitoring the spatial and temporal patterns of NO_X in the Kurdistan region of Iraq using TROPOMI sensor images from the Sentinel-5 satellite in the period of 2018 to 2023. We would address if the concentration of NO_x in the Kurdistan region of Iraq has increased in recent years. Additionally, we were interested to the utilization of Sentinel-5 satellite images to differentiate various zones in the Kurdistan region of Iraq based on the prevalence of NO_x pollution.

Material and Method

Study area:

The Kurdistan region of Iraq is an autonomous region located in the northern part of Iraq, bordering Kurdistan of Iran from the east, Kurdistan of Turkish from the north, and Kurdistan of Syrian from the west. The region is officially governed by the Kurdistan Regional Government that has legal jurisdiction over three provinces, Erbil, Duhok, and Sulaymaniyah (Figure 1).

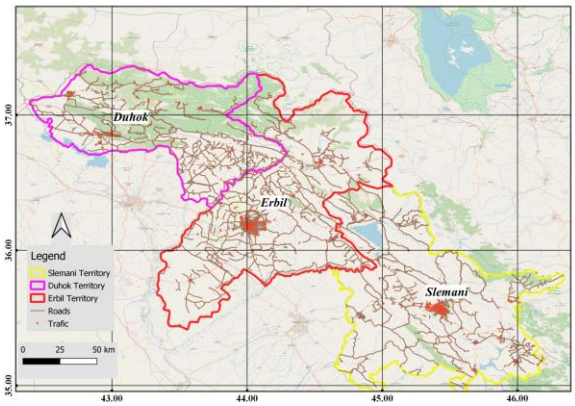


Figure 1 Erbil, Dohuk, and Sulaimaniyah areas of the Kurdistan region of Iraq. Settlements, industrial areas, and vegetation cover are shown with black, red, and green polygons, respectively.

We used Google Earth Engine (GEE) to extract the required data to address spatio-temporal changes of NO_x concentrations using Sentinel-5 data. Earth Engine's filtering and visualization tools were applied to select the desired time range and region. Then, Earth Engine's reducer functions were used to calculate the mean value of NO2 concentrations for the selected region and time range. We export the calculated data in CSV format to analyze it further and visualize it in R environment.

Results

Temporal trends of nitrogen dioxide (NO2)

The temporal changes of nitrogen dioxide (NO2) in the Kurdistan region of Iraq, from the summer of 2018 to March of 2023 were investigated using data from the Sentinel-5 satellite. The study revealed that the highest and lowest mean atmospheric column NO2 during this period were 107.70 and 65.22 micromol per square meter, respectively, occurring on July 2023 and March 2020 (Figure 2). Although, the general trend showed a gradual increase in NO2 density from 2018 to 2023, a lowest amount observed in 2020 with a 79.23 micromol per square meter (Figure 3). Notably, higher NO2 concentrations were observed during warmer periods (July-September) compared to colder periods (January-February) (Figure 4).

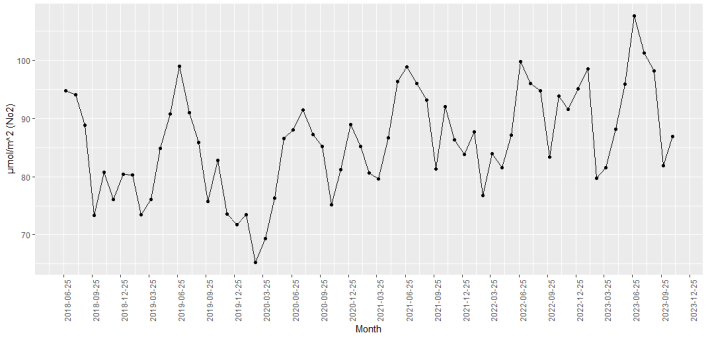


Figure 2 Monthly variations of mean atmospheric column of nitrogen dioxide (NO2) in the Kurdistan Region of Iraq: A Sentinel-5 satellite-derived analysis spanning from fall 2018 to March 2023

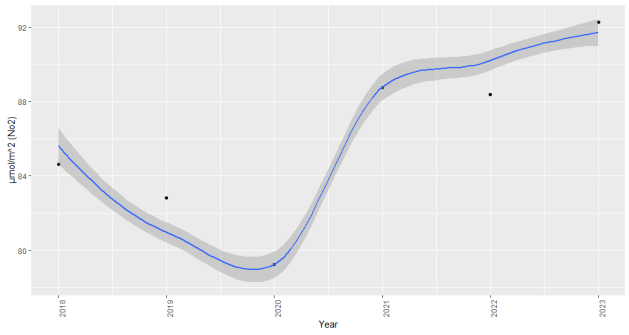


Figure 3 Anuual variations of mean atmospheric column of nitrogen dioxide (NO2) in the Kurdistan Region of Iraq: A Sentinel-5 satellite-derived analysis spanning from fall 2018 to March 2023

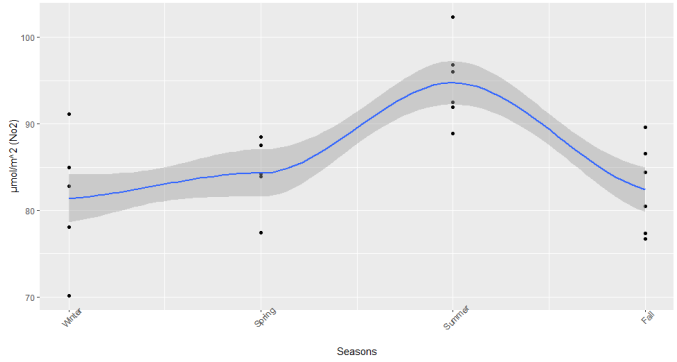


Figure 4 Seasonal variations of mean atmospheric column of nitrogen dioxide (NO2) in the Kurdistan Region of Iraq: A Sentinel-5 satellite-derived analysis spanning from fall 2018 to March 2023

Spatial changes of nitrogen dioxide (NO2)

Based on the data of Sentinel-5 satellite, the spatial changes of NO2 in the Kurdistan region of Iraq were analyzed in different seasons of different years. The results showed that the highest concentration of NO2 was observed in the area of Erbil (Hawler), while the territory of Slemani (Sulaymaniyah) and Duhok cities also showed high concentrations of this gas in smaller parts in some seasons compared to their surroundings. Figure 5 illustrates the spatial distribution of nitrogen dioxide (NO2) concentrations across the study area for the seasons of 2023.

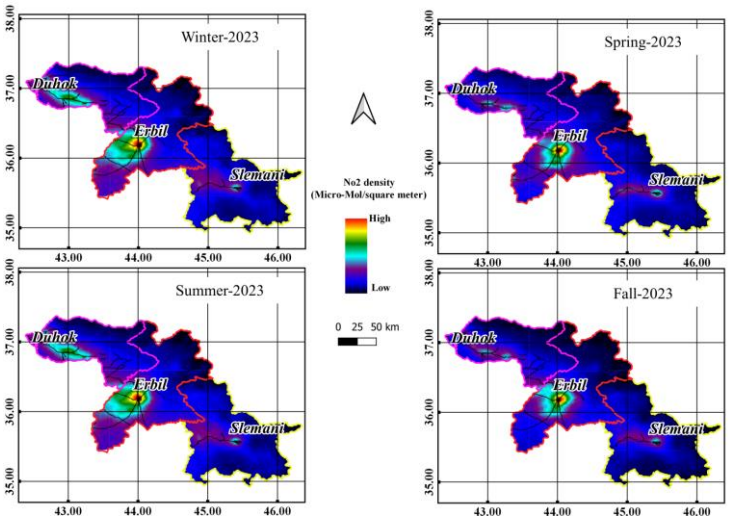


Figure 5 Spatial variations of mean atmospheric column of nitrogen dioxide (NO2) in the Kurdistan Region of Iraq in different seasons of 2023

Discussion

Several factors can be attributed to the high concentration of NO2 in Erbil city. Firstly, the presence of numerous industries, residential areas, and high traffic load contribute to the emission of atmospheric pollutants. Secondly, the low density of vegetation in the area further exacerbates this issue (Figure 1). Specifically, the presence of oil refineries, metal smelters, traffic, and garbage incinerators, including those from a hospital, are identified as the main sources of these emissions (Nematollahi et al., 2022). In the analysis of

annual changes in the column density of tropospheric nitrogen dioxide from 2018 to 2023, the impact of COVID-19-related restrictions in 2020 is prominently observed, similar to other regions globally. These restrictions led to a reduction in urban road traffic volume, particularly in high population density areas, which are major contributors to fossil fuel combustion and, consequently, the concentration of polluting gases, notably nitrogen dioxide (Zhao et al., 2022). Several studies have documented a significant decrease in nitrogen dioxide (NO2) levels during the COVID-19 lockdown period, attributed to reduced traffic and industrial activities. For instance, a study analyzing the impact of lockdown measures on NO2 changes in Central Asian countries found a notable decrease in tropospheric NO2 concentration during the lockdown period (Zhang, Liu, Liu, Hao, & Zhang, 2022). Similarly, global fine-scale changes in ambient NO2 during COVID-19 lockdowns, as observed by the TROPOMI satellite, demonstrated substantial reductions in NO2 concentrations in various cities, emphasizing the impact of reduced traffic on air quality (Zhang et al., 2022).The study's findings indicate that the seasonal peak of No2 gas occurs during the hot months of year (July to September), which contradicts the results of other studies that suggest the higher concentration of this gas ocuuers during the cooler months of year due to the low intensity of sunlight (Shariepour & Aliakbari Bidokhti, 2014). The trend of monthly changes in nitrogen dioxide gas in the study area shows less pollution of the troposphere layer at the end of the winter season, while the air pollution becomes more severe at the beginning of the autumn season.

Conclusion

The research was conducted to perform a temporal-spatial monitoring of NO2 pollution in the Kurdistan region of Iraq using Sentinel-5 satellite data over a 56-month period from 2018 to 2023. The findings revealed a correlation between high NO2 concentrations and urban areas with intense traffic and industrial operations. The study suggests the implementation of management measures to address the increasing NO2 levels, particularly in urban traffic and the reduction of fossil fuel consumption, with a focus on Erbil city.

References

Ahmed, K. O., Aziz, S. Q., Karim, P. H., & Hussein, T. A. (2022). Contemporary trends toward environmental issues in the Kurdistan Region of Iraq. *Prace i Studia Geograficzne*, 109–130. https://doi.org/10.48128/pisg/2021-67.1-07

Anenberg, S. C., Bindl, M., Brauer, M., Castillo, J. J., Cavalieri, S., Duncan, B. N., … West, J. J. (2020). Using Satellites to Track Indicators of Global Air Pollution and Climate Change Impacts: Lessons Learned From a NASA-Supported Science-Stakeholder Collaborative. *GeoHealth*, *4*(7). https://doi.org/10.1029/2020GH000270

Baban, M. (2023). Climate Change in the Kurdistan Region and Iraq; Carbon Dioxide Emission and Air Quality. Retrieved December 17, 2023, from https://rudawrc.net/en/article/climate-change-in-the-kurdistan-region-and-iraq-carbon-dioxide-emission-and-air-quality-2023-09-18

Nematollahi, M. J., Rastegari Mehr, M., Shakeri, A., Amjadian, K., Ebrahimi, P., & Pirouei, M. (2022). Polycyclic aromatic hydrocarbons (PAHs) in soils around oil refineries; Case study: Erbil and Kirkuk refineries, Iraq- A modelling approach. *Journal of Environmental Health Science and Engineering*, *20*(2), 699–716. https://doi.org/10.1007/s40201-022-00809-y

Olmo, N. R. S., Saldiva, P. H. do N., Braga, A. L. F., Lin, C. A., Santos, U. de P., & Pereirai, L. A. A. (2011). A review of low-level air pollution and adverse effects on human health: Implications for epidemiological studies and public policy. *Clinics*, *66*(4), 681–690. https://doi.org/10.1590/S1807-59322011000400025

Park, J., Shin, M., Lee, J., & Lee, J. (2021). Estimating the effectiveness of vehicle emission regulations for reducing NOx from light-duty vehicles in Korea using on-road measurements. *Science of the Total Environment*, *767*, 144250. https://doi.org/10.1016/j.scitotenv.2020.144250

Rawlins, F. I. G., & Meetham, A. R. (1954). Atmospheric Pollution: Its Origins and Prevention. In *Studies in Conservation* (Vol. 1). Amsterdam, The Netherlands: Elsevier. https://doi.org/10.2307/1504980

Saxena, P., & Naik, V. (2019). *Air pollution: sources, impacts and controls* (P. Saxena & V. Naik, Eds.). UK: CAB International. https://doi.org/10.1079/9781786393890.0000

Shariepour, Z., & Aliakbari Bidokhti, A. (2014). An investigation on the status of troposphere No2 over Iran during 2004 to 2012. *Journal of Environmental Studies*, *40*(1). Retrieved from [In Persian]

Zana, F. Al, Dedar, S., Gábor, P., & Kinga, K. (2023). Assessment of air quality and consequent in Erbil, Iraqi Kurdistan region based GEE, GIS, and remote sensing techniques. *E3S Web of Conferences*.

Zanist, H.-A. (2022). Air pollution in Kurdistan Region of Iraq: A review. *Sriwijaya Journal of Environment*, *6*(3), 127–136. https://doi.org/http://dx.doi.org/10.22135/sje.2021.6.3

Zhang, Z., Liu, Y., Liu, H., Hao, A., & Zhang, Z. (2022). The impact of lockdown on nitrogen dioxide (NO2) over Central Asian countries during the COVID-19 pandemic. *Environmental Science and Pollution Research*, *29*(13), 18923–18931. https://doi.org/10.1007/s11356-021-17140-y

Zhao, X., Fioletov, V., Alwarda, R., Su, Y., Griffin, D., Weaver, D., … Lee, S. C. (2022). Tropospheric and Surface Nitrogen Dioxide Changes in the Greater Toronto Area during the First Two Years of the COVID-19 Pandemic. *Remote Sensing*, *14*(7), 1625. https://doi.org/10.3390/rs14071625

Zhou, B., Zhang, S., Xue, R., Li, J., & Wang, S. (2023). A review of Space-Air-Ground integrated remote sensing techniques for atmospheric monitoring. *Journal of Environmental Sciences*, *123*, 3–14. https://doi.org/10.1016/j.jes.2021.12.008

Advanced Engineering Days

aed.mersin.edu.tr

Analysis of environmental pollution caused by the movement of dust particles

Peyman Yariyan *[1], **Bakhtiar Feizizadeh** [1], **Khalil Valizadeh Kamran** [1]

[1]*University of Tabriz, Department of Remote sensing and GIS, Iran, p.yariyan@tabrizu.ac.ir,* Feizizadeh@tabriz.ac.ir, valizadeh@tabrizu.ac.ir

Cite this study: Yariyan, P., Feizizadeh, B., & Kamran, K. V. (2024). Analysis of environmental pollution caused by the movement of dust particles. Advanced Engineering Days, 9, 191-195

Keywords
Environmental pollution
Dust sources
Deep learning
GIS
Iran

Abstract

Dust storms pose significant risks to humans and the environment. For this reason, it is necessary to highlight the vulnerable areas by examining the correlation between the identified dust sources and various Geo-environmental factors. Hence, in this study, a comparative analysis of four hybrid deep learning models was performed for mapping sensitivity to dust sources. The findings of our study provide the effectiveness of deep learning models in the analysis of sensitivity to dust sources and applicable approaches for timely decision-making and environmental risk reduction initiatives.

1. Introduction

The results of new studies indicate the dangers of dust for human health [6]. Dust is one of the atmospheric phenomena that also harm the environment [12]. As far as, breathing air contaminated with dust can cause problems such as heart failure, breathing problems, irregular heartbeat, skin sensitivity and vision loss [5, 7, 13]. Dust or fine dust is a mass of small solid particles of soil and sometimes smoke, etc., in which suspended soil particles are known as the main component of air pollution and can be carried by wind over long distances [14]. Hence, due to the expansion of areas with dust potential due to ecological changes [9], drying up of lakes [2], reduction of vegetation [1], etc.; in Central Asia, in order to reduce dust storms and prevent financial and human losses, it is considered necessary to evaluate the places of origin and distribution of dust [10]. Looking at the research literature in this field, it can be seen that most researchers have focused on the spatial distribution in a small area by tracking the earth observation and one-dimensional chemical [3, 4, 8, 11]. As a result, the aim of this study is to complete the cycle of investigating the expansion of areas with dust potential with a more comprehensive and multifaceted view in order to reduce the resulting environmental risks.

2. Material and Method

2.1 Data and study area

The Urmia lake basin with an area of 51353 km^2 is introduced as the study area in this research (Figure 1). Due to the high concentration of salts, especially chlorine and sodium, the water of Lake Urmia is not suitable for farming and the life of fishes and a large number of aquatic species. Therefore, in the last few years, due to the lowering of the water level and the increase in the drying process of the lake, the production of dust and Small grains of salt have caused many environmental hazards.

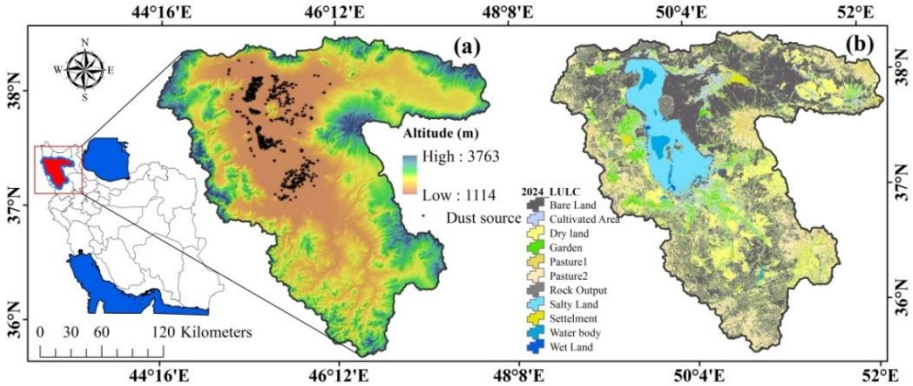


Figure 1. Location of the study area (a: The catchment area of Lake Urmia, b: Land use in 2024)

2.2 Methodology

The process of conducting the research is fully implemented and operational in 4 stages. According to the main goal of the research based on a multifaceted look at the factors affecting the spread of dust, firstly two sets of dependent and independent variables including recorded dust points and 16 factors: Soil depth, Texture, Salinity, Soil moisture, alkaline soil (PH), Sunny hours, Evaporation, Temperature, Humidity, Rainfall, Wind speed, Land use/Land cover (LU/LC), Normalized difference vegetation index (NDVI), Lithology, Elevation and Slope were selected and prepared. In the second stage, multi-linear analysis and Pearson correlation between factors were performed to ensure the independent effect of each. After that, modeling with new hybrid deep learning models was implemented as one of the innovations of the present study, using two datasets. The final stage was to evaluate the performance of each of the models in order to predict and prepare a map of sensitivity to dust sources in the study area.

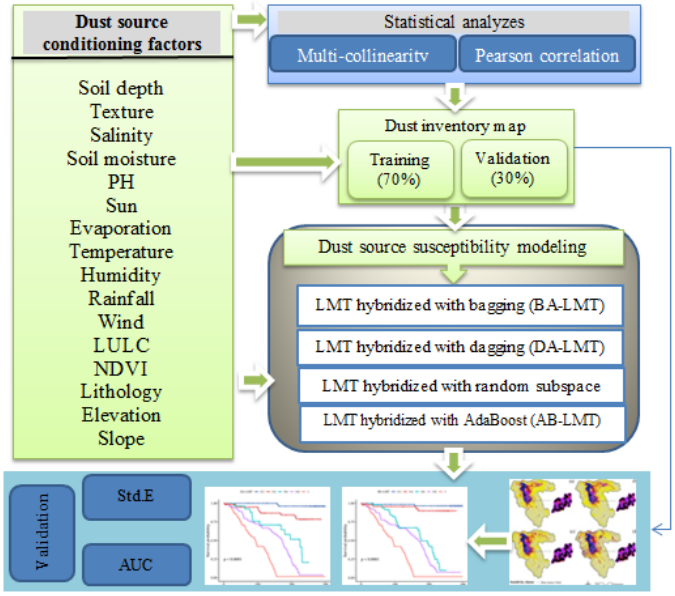


Figure 2. Methodological diagram of the study

3. Results and discussion

3.1 Spatial correlation of factors

Pearson's correlation was used to investigate the spatial correlation between dust driving factors (Figure 3). Values between +1 and -1 indicate the best fit and values above 0 indicate positive correlation. The values show the existence of a positive and independent relationship between each of the factors. So that, all factors can be used in modeling to predict dust sensitivity.

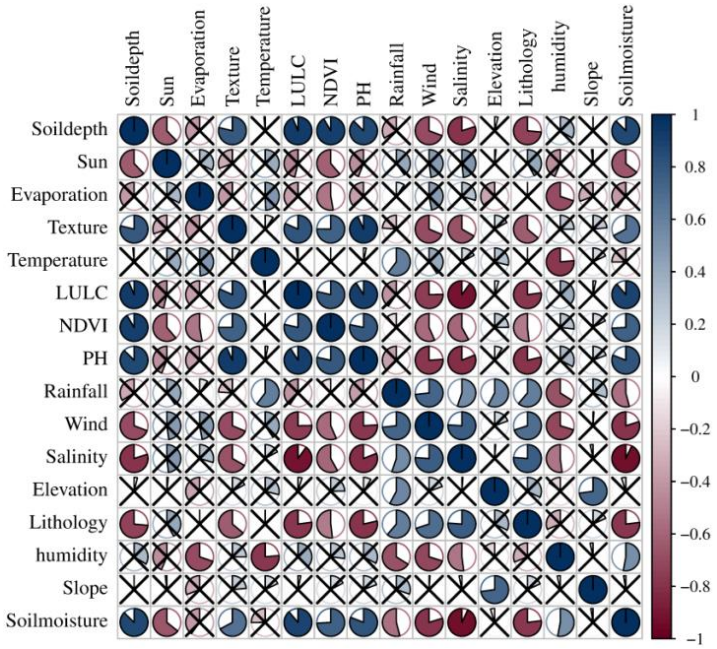


Figure 3. Pearson spatial correlation of factors

Also, multi-linear analysis was used to test the second stage of the independent effect of the factors (Figure 4). Based on the standard (VIF values less than 5 and TOL values above 0.1), the highest VIF for Soil depth was 4.89 and the lowest TOL was 0.204.

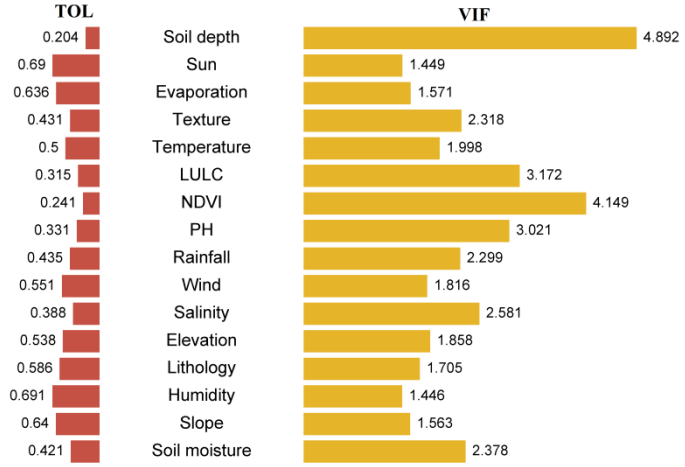


Figure 4. Multi-linear analysis of factors

3.2 Spatial modeling of dust sensitivity

Spatial modeling of sensitivity mapping to dust source and airborne particles caused by the drying of Lake Urmia was done with four models; LMT hybridized with dagging (DA-LMT), LMT hybridized with random subspace (RS-LMT), LMT hybridized with bagging (BA-LMT) and LMT hybridized with AdaBoost (AB-LMT) (Figure 5). The spatial maps of each model were classified based on 5 dust sensitivity classes, very low, low, moderate, high and very high. For the DA-LMT model, the sensitivity values are very low, low, moderate, high and very high, respectively 45%, 36%, 6%, 7% and 6%. These values with significant similarity in RS-LMT model are 44%, 37%, 7%, 7%, and 5%, respectively. However, in the BA-LMT and AB-LMT combined models, with a slight difference, we observe higher values in the high and very high classes. So that in the BA-LMT model, the value for the very low class is 47%, low 33%, moderate 8%, high 7% and very high 6%. After that, these values in the AB-LMT model are 55%, 21%, 5%, 10% and 9%, respectively. The sensitivity maps produced by four combined deep learning models indicate the high potential of dust sources in the middle parts of Lake Urmia, the northern and northeastern parts of the catchment area of Lake Urmia.

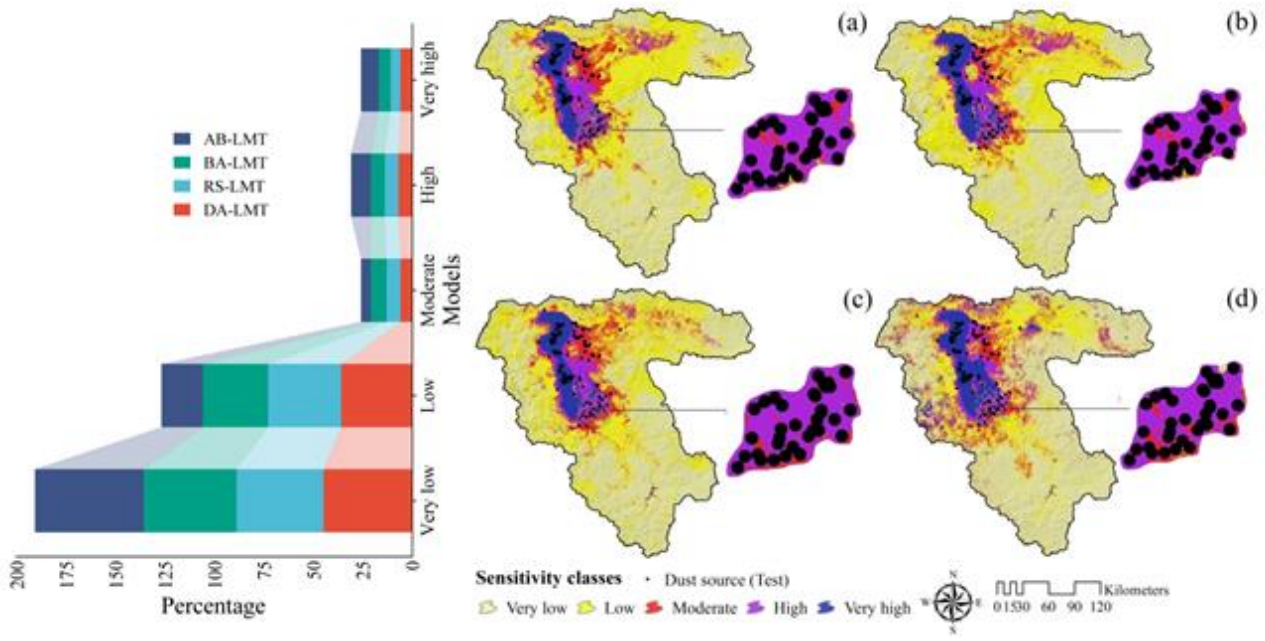


Figure 5. Dust sensitivity of Urmia lake basin, (a) LMT hybridized with dagging (DA-LMT), (b) LMT hybridized with random subspace (RS-LMT), (c) LMT hybridized with bagging (BA-LMT) and (d) LMT hybridized with AdaBoost (AB-LMT)

3.1 Performance assessment of models

The validation and evaluation of the performance of the combined models was calculated by the Area under the ROC Curve index and the error value (Table 1). So that DA-LMT model with AUC= 0.944 and error value 0.013 had the best performance. Although other models also have good performance with AUC value above 0.8.

Table 1. Area under the curve for models

Models	AUC	Std.Error	Asymptotic 95% Confidence Interval	
			Lower Bound	Upper Bound
DA-LMT	0.944	0.013	0.918	0.969
RS-LMT	0.933	0.015	0.904	0.961
BA-LMT	0.935	0.014	0.908	0.963
AB-LMT	0.898	0.018	0.862	0.934

The prediction rate of the models was also evaluated with 300 test samples (Figure 6). The values of the samples were 0 (non-occurrence) and 1 (occurrence). So that the maps of each model are classified with a value between 0 and 1 in five sensitivity ranges of 0.2, 0.4, 0.6, 0.8 and 1. For the DA-LMT model, compared to 300 validation samples with values of 0 or 1 in the spectrum of 0, the number of 60 samples in the values of 0.2, 60 samples in the value of 0.4, 17 samples in the value of 0.6, 11 samples in the value 0.8 and predicted the number of 2 samples in the value of 1. On the other hand, out of 150 samples with a value of 1, 123 samples were classified in the values of 0.8 and 1, which shows the high accuracy of its prediction.

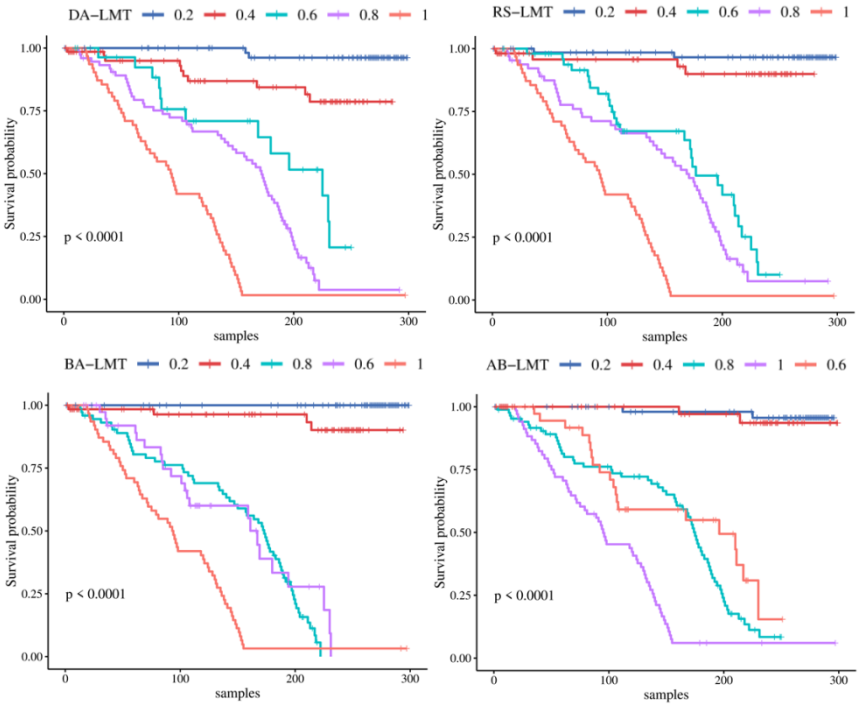


Figure 6. Evaluating the predictive performance of deep learning models

4. Conclusion

Due to the drying up of Lake Urmia and the reduction of vegetation in the region, the catchment area of this lake is among the areas that suffer the most from the consequences of dust transfer. Hence, there is an urgent need to assess the vulnerability caused by dust sources using a multifaceted, comprehensive approach and new techniques. According to this, with the aim of identifying sensitive and vulnerable areas due to dust transfer and evaluating the performance of four combined deep learning models, the focus of this study has been on the catchment area of Lake Urmia. In addition, understanding the influence of multiple driving factors in increasing the density and spread of dust in this region, which is characterized by the approach of complex spatial relations, is significant as one of the innovations of this study. Research findings indicate that DA-LMT hybrid model has a stronger performance compared to other hybrid models. Although the accuracy and performance of other models are also significant and acceptable based on high AUC values. Overall, the process used in this study introduces a complete and unique package that helps manage environmental risks, citizen health, etc. in areas with potential dust sources.

References

1. Al-Taei, A. I., Alesheikh, A. A., & Boloorani, A. D. (2024). Evaluating the effects of land use/land cover change on the emergence of hazardous dust sources in the Tigris-Euphrates Basin. Spatial Information Research, 1-14.
2. Boloorani, A. D., Soleimani, M., Papi, R., Nasiri, N., Samany, N. N., Mirzaei, S., & Al-Hemoud, A. (2024). Assessing the role of drought in dust storm formation in the Tigris and Euphrates basin. Science of The Total Environment, 171193.
3. Cao, Y., Xiao, Y., Wang, Z.-P., Li, Q.-W., Shu, C.-M., Jiang, X.-R., & Wu, S.-L. (2024). Recent progress and perspectives on coal dust sources, transport, hazards, and controls in underground mines. Process Safety and Environmental Protection.
4. Fattahi Masrour, P., & Rezazadeh, M. (2022). Spatio-Temporal Distribution of Various Types of Dust Events in the Middle East during the Period 1996-2015. Journal of the Earth and Space Physics, 47(4).
5. Henning, R. J. (2024). Particulate matter air pollution is a significant risk factor for cardiovascular disease. Current Problems in Cardiology, 49(1), 102094.
6. Lwin, K. S., Tobias, A., Chua, P. L., Yuan, L., Thawonmas, R., Ith, S., . . . Roqué, M. (2023). Effects of desert dust and sandstorms on human health: a scoping review. Geohealth, 7(3), e2022GH000728.
7. Lyles, M. B. (2024). Biological, chemical, and environmental threats of toxic desert dust to military personnel. In Environmental Geochemistry (pp. 697-721): Elsevier.
8. Mohajeri, S. H., Eydi, Z., & Mirshafiei, S. R. (2024). Mapping the distribution and temporal trends of dust storm sources in the Middle East using satellite data. Natural Hazards, 120(1), 389-407.
9. Mousavi, H., Panahi, D. M., & Kalantari, Z. (2024). Dust and climate interactions in the Middle East: Spatio-temporal analysis of aerosol optical depth and climatic variables. Science of The Total Environment, 927, 172176.
10. Ostad-Ali-Askari, K. (2024). Assessment of Dust Event By RS, GIS, MODIS and Statistical Methods Among Satellite Images. GIS, MODIS and Statistical Methods Among Satellite Images (May 12, 2024).
11. Soleimani, A., Toolabi, A., Mansour, S. N., Abdolahnejad, A., Akther, T., Fouladi-Fard, R., . . . Mohammadi, A. (2024). Health risk assessment and spatial trend of metals in settled dust of surrounding areas of Lake Urmia, NW Iran. International Journal of Environmental Analytical Chemistry, 104(5), 1172-1185.
12. Song, L., Bi, X., Zhang, Z., Li, L., Dai, Q., Zhang, W., . . . Feng, Y. (2022). Impact of sand and dust storms on the atmospheric environment and its source in Tianjin-China. Science of The Total Environment, 825, 153980.
13. Tong, D. Q., Gill, T. E., Sprigg, W. A., Van Pelt, R. S., Baklanov, A. A., Barker, B. M., . . . Gaston, C. J. (2023). Health and safety effects of airborne soil dust in the Americas and beyond. Reviews of Geophysics, 61(2), e2021RG000763.
14. Yariyan, P., Amiri, M., Saffariha, M., Avand, M., Ghiasi, S. S., & Tiefenbacher, J. P. (2022). Spatial analysis of environmental factors influencing dust sources in the east of Iran using a new active-learning approach. Geocarto International, 37(26), 11929-11954.

Advanced Engineering Days

aed.mersin.edu.tr

Evaluation of the environmental effects of Sungun copper mine using the DPSIR framework

Mohsen Aghayari Hir*[1], Nahid Rahimzadeh [1]

[1]*University of Tabriz, Faculty of planning and environmental sciences, Iran, aghayarihir@gmail.com, nahidrahimzadeh81@gmail.com*

Cite this study: Aghayari Hir, M. & Rahimzadeh, N. (2024). Evaluation of the environmental effects of Sungun copper mine using the DPSIR framework, Advanced Engineering Days, 9, 196-202

Keywords
Environmental effects
Environmental assessment
DPSIR framework
Sungun copper Mine

Abstract

The DPSIR (Drivers, Pressures, Situations, Impacts and Responses) framework is a method aimed at assessing the current state of the environment and involves a process starting with "driving forces" then moving through "pressures" to "states" and "impacts". Finally, it leads to "responses". In mineral extraction in the villages around Sungun copper, the research results show that the main drivers in this area are the variety of mines with (Wi = 3.875), industrial and commercial activities with (Wi = 3.260). Toxic and heavy substances are caused by mining activity (Wi = 4.011), forest destruction (Wi = 3.899) and loss of agricultural land (Wi = 3.625) as a pressure. The current situation has had the most negative impact on the landscape and ecology of the region with (Wi=3.055) and has had the most positive impact on job opportunities in the region (Wi=3.345). There are no positive improvements has been made in the environment and reducing the negative impacts of mining. In order to improve the environmental quality and reduce the environmental effects of mining, monitoring and increasing community participation, have the highest consensus score (Wi=0.750). Active participation of local authorities has little consensus weight due to weak feasibility (Wi = 3.375).

Introduction

Human activities put a lot of pressure on the environment, and quantifying third stress is a complicated task. It is of great importance to use mechanisms that help guide public decisions towards ensuring social welfare while understanding and identifying the causal interactions of society and the environment. In this sense, the theoretical framework of; driver, pressures, state, impact and responses (DPSIR) model is an instrument to demonstrated the complex structure of environmental problems resulted by interactive processes between society and the environment (7- 23). The DPSIR framework was developed in the late 1990s by the Organization for Economic Co-operation and Development as a tool for structuring and organizing indicators. The origin of this framework is due to the integration of two conflicting fields of study - ecology and economy. Short-term economic rationality and ecological cycles that ensure the renewal of nature and sustainable development do not always coincide (13-21). This theoretical framework has been used by several international reference organizations such as the Organization for Economic Co-operation and Development (OECD), the United Nations Environment and the Environmental Protection Agency (EPA) to integrate economic and environmental dimensions (18). This framework is based on previous environmental frameworks such as PSR (9) and DSR was developed and adopted as a conceptual framework by the European Environment Agency (EEA) (4). Then in 1999, the DPSIR model was promoted to show the cause-and-effect relationship between environmental and human systems and was introduced in a report by Smeets and Weterings (1999) (19) to help policy makers understand the meaning of information in indicator reports. Drivers, which may be social, economic or environmental developments, exert pressure on a particular environment. As a result of these pressures, the state of the environment changes and leads to impacts (social, economic or environmental) that may turn into a social reaction. The response may give feedback to Driver, pressures, situations, or impacts. This model is used to show socio-economic and

environmental problems caused by the development of agricultural activities, water ecosystem destruction and pollution caused by various activities, changes caused by mining activities and determining cause and effect relationships (1, 2).

In this research, the DPSIR framework has been used to explain the cause-and-effect relationship between the Sungun mine and its effects on the environment and surrounding villages. Because one of the major problems in the study area is various pollutions caused by mining and mineral processing. In this study, different indicators have been considered for each of the 5 dimensions of the DPSIR framework, and it has been tried that these indicators show well the different issues that the villages around Sungun copper mine are involved with.

In the future, based on this framework, the management agency will be helped to identify the causes, environmental status and conditions and the ability to cope environmental problems caused by mining activities, as well as to identify shortcomings and provides suitable solutions for sustainable extraction from mines.

Material and Method

Varzaqan Sungun Copper Mine are in geographical coordinates, 46° 37’ to 46° 45’ east longitude and 38° 38’ to 38° 44’ north latitude in northwest of Iran, East Azerbaijan Province. It is located in the ruined village of Sungun (due to mineral resources) It is located in a dense residential area that includes 17 inhabited villages at a distance of 10 kilometers from the mine (Figure 1). The mine is located on a global copper belt in a mountainous area with an average elevation of 2000 meters above sea level. The definitive and extractable reserves of this deposit are 796 and 388 million tons with a grade of 0. 61% copper (4).

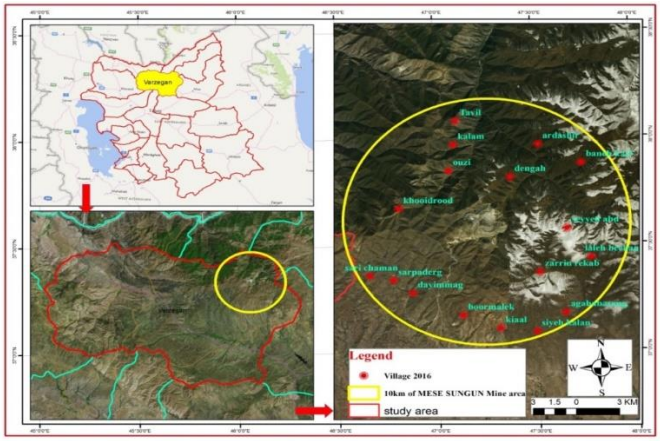


Figure 1. Location of the Sungun Copper Mine

In addition to copper, the mine contains molybdenum, gold, silver and other important elements in the form of associated metals. Mine area and its surroundings are covered with agricultural land, grassland and forest. The most important and valuable habitat around (Arasbaran Protected Area) is located in the vicinity of it. Given that the mine is situated near the villages, its activities in the rural areas have had adverse effects. It has devastated agricultural lands and their natural areas. As a result, it has evacuated some villages in recent years. In addition to the destruction and evacuating of villages, mining activities have disrupted the landscape, erosion, and sedimentation, contaminating water, air, and soil. Arsenic, cobalt, mercury and nickel also enter the environment through this mine, causing pollution and destruction of the environment, especially surrounding plants, leaving much of the area free of vegetation. As a result, water and wind erosion have added to the problems in the region (1, 15, 14, 16, 17).

In this study, the DPSIR framework was used to identify, analyze and evaluate environmental issues related to mineral exploitation in Sungun copper through the sequence of environmental changes. Also, the DPSIR framework was applied to identify the cause, effects and pressures resulting from the exploitation of Sungun copper mine and to analyze and evaluate the environmental issues related to it through the sequence of environmental changes. (D) The driving force and needs that can be economic or social. (P) Are the consequences of driving forces that can be positive or negative. In most studies, the main focus is on the negative aspects of the environment. (S) The change in the state of the environment is due to pressure. (I) the positive or negative change in the state of the environment changes due to mining activities, which occurs in social, economic or environmental dimensions. (R) Are adaptive responses to minimize the negative impacts of mining on the environment (Figure 2).

Five DPSIR indicators are designed in Table 1, each of which is rated on a 5-point Likert scale (level 1: very low; level 5: very high). Based on a 5-point Likert scale, questionnaires were constructed and processed according to descriptive statistics as follows:

Mean value (wMean) is defined as the integral of a continuous function of one or more variables over a given range divided by the measure of the range. In this research wMean is the mean of the overall agreement. (wMean) for 5-point Likert scale is calculated as follows:

(1) $wMean = \sum_{i=1}^{5} X_i P_i(X_i)$

The result of the (wMean) was labeled according to the Likert scale in Table 1.

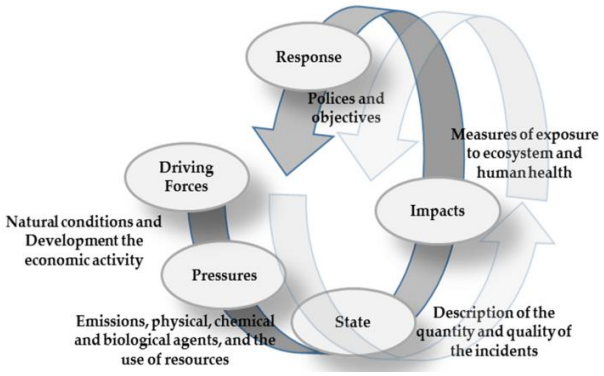


Figure 2. DPSIR framework: continuous feedback process (22)

Table 1: Number of scales

Scale	Numbers
Very low	1.000-1.499
low	1.500-2.499
Medium	2.500-3.499
High	3.500-4.499
Very high	4.500-5000

- Standard deviation (eStD) for Likert scale is calculated as follows:

(3) $$wStD = \sqrt{\sum_{i=1}^{5} \frac{(X_i - wMean)^2}{N}}$$

Consensus (CnS) is defined as the agreement of individuals in a group on an issue. (CnS) for a 5-point Likert scale is calculated as follows (19):

(4) $$CnS\ (X) = 1 + \sum_{i=1}^{5} P_i(X_i) log_2(1 - \frac{|X_i - wMean|}{d_x})$$

Where X is the response, n is the number of the categories in an ordinal scale, xi is the degree of agreement in categori i, Pi is the probability of the occurrence of xi; dx=X -X is the width of categories on the measurement scale, and wMean is the mean of the overall agreement (20).

Results

Driving forces

Through the evaluation of the answers of the villages near the mine, it was determined that the variety of mineral resources with 3.875 and commercial industry with 3.260 are the most driving forces in the study area. Other factors such as population growth, employment and agricultural development were the next driving forces. Agricultural development received the highest consensus with 0.75, which was followed by employment and unemployment at 0.727 and population growth at 0.711. It had a low consensus value. Indicators with high standard deviation have lower consensus values than others.

Table 2. The value of driving forces of environmental effect in the villages of the study area

		Selection probability in Likert scale							
No	**Indicator**	**1**	**2**	**3**	**4**	**5**	**wM**	**wStD**	**CnS**
1	The population growth and immigration	0.073	0.515	0.305	0.023	0.05	2.238	0.530	0.711
2	Employment and unemployment	0.175	0.451	0.341	0	0.025	2.245	0.570	0.727
3	Urbanization	0.200	0.370	0.340	0.070	0.000	2.275	0.545	0.685
4	Industrial and commercial activities	0.050	0.024	0.275	0.500	0.100	3.260	0.538	0.693
5	Agricultural development	0.200	0.400	0.375	0.023	0.000	2.225	0.570	0.753
6	Diversification of mineral resources	0.100	0.220	0.151	0.370	0.150	3.865	0.505	0.508

Pressures

The main pressure caused by mining in Sungun copper was the release of toxic and heavy metals with mean value of 4.011, followed by forest degradation, loss of agricultural land, and dust. In general, these were the indicators that had a high consensus in this consultation. According to table 3, the consensus values (CnS) of the indices vary from 0.570 to 0.665.

Environmental pressures from overuse of resources as well as loss of forest area and agricultural production land were major problems in the local area. However, the greatest environmental pressure on mining activities was the release of heavy metals and wastes from mining and processing in mines. Table 3 shows that the release of toxic and heavy metals was calculated with the highest average of 4.011, followed by forest destruction (3.899) and loss of agricultural land (3.620).

Table 3. The value of driving forces of environmental effect in the villages of the study area

		Selection probability in Likert scale							
No	Indicator	1	2	3	4	5	wM	wStD	CnS
1	Reduction of forest area	0.074	0.035	0.3	0.53	0.15	3.899	0.544	0.663
2	Destruction of agricultural land	0.17	0.135	0.330	0.4	0.1	3.620	0.501	0.586
3	Evacuation of the village and destruction of residential areas	0.100	0.335	0.330	0.125	0.128	2.890	0.505	0.580
4	Reduction of metal mineral resources	0.151	0.285	0.265	0.155	0.150	2.875	0.505	0.517
5	Reduction of non-metal mineral resources	0.075	0.175	0.275	0.225	0.252	3.400	0.520	0.513
6	Heavy and toxic metals	0.100	0.052	0.000	0.428	0.420	4.011	0.618	0.570
7	Wastewater	0.049	0.070	0.300	0.350	0.226	3.580	0.546	0.607
8	Dust	0.023	0.074	0.170	0.427	0.300	3.455	0.593	0.665

States

The villages near the mine have been strongly affected by the pressures caused by mining, of which the air quality and water quality are 3.520 and 3.125, respectively. The average scores of soil quality, loss of biodiversity, environmental incidents, etc. were low in villages near the mine and these indicators showed a low consensus between 0.465 and 0.598, but in villages far from the mine, this value differs (Table 4).

Statistical results of the questionnaire showed that the mining activities did not have a great impact on the general environment of the study area, however, due to the large number of mining activities, the possibility of geological hazards such as landslides in the mine site, etc. in the study area when increasing mining activities, a lot in the future.

Table 4. The value of driving forces of environmental effect in the villages of the study area

		Selection probability in Likert scale							
No	Soil quality	0.165	0.4	0.365	0.020	0.015	2.327	0.550	0.690
1	Water quality	0.1	0.165	0.315	0.2	0.2	3.125	0.500	0.535
2	Air quality	0.050	0.220	0.150	0.435	0.150	3.520	0.525	0.565
3	Biodiversity decline	0.170	0.335	0.320	0.125	0.050	2.555	0.520	0.601
4	Landslide of bench face, waste dump	0.100	0.300	0.328	0.270	0.100	3.070	0.500	0.590
5	Other environmental incident	0.270	0.360	0.170	0.200	0.000	2.400	0.550	0.598
6	Diseases caused by mining activities (noise pollution. exhaust gas. Digestive diseases. skin…)	0.200	0.235	0.220	0.200	0.160	2.870	0.500	0.465
7	Soil quality	0.165	0.4	0.365	0.020	0.015	2.327	0.550	0.690
8	Water quality	0.1	0.165	0.315	0.2	0.2	3.125	0.500	0.535

Impacts

Mining activities can change the environment in a positive and negative way. The positive effects of these activities include improving the social and economic conditions of the society, such as employment opportunities, increasing income, and the source of revenue for the state budget, which is shown by a mean of 3.015 and 3.345, respectively, while the high consensus is 308.00 respectively. Also, the negative effects of these activities on ecological landscapes and infrastructures such as roads, public infrastructures were also with a mean of 3.055 and 3.0785.

However, there is an average consensus on the negative impact of mining on infrastructure, human health, and the landscape of the region. However, no positive impact has been recorded on the development of sources of income for local budgets, nor on improving the quality of life. The best positive impact of mining activities has been employment opportunities and improvement of living standards in some villages.

Table 5. Value of impacts on socio-economic development in the study area

		Selection probability in Likert scale							
No	Indicator	1	2	3	4	5	wM	wStD	CnS
1	Employment opportunity and income	0.028	0.170	0.370	0.3	0.135	3.345	0.513	0.643
2	Increase in source of revenues for the state budget	0.025	0.265	0.420	0.220	0.05	3.015	0.500	0.727
3	Social and economic improvements	0.170	0.320	0.325	0.165	0.000	2.500	0.535	0.637
4	Impact on the propert of the people	0.175	0.305	0.370	0.070	0.065	2.570	0.520	0.597
5	Impact on infrastructure	0.205	0.125	0.265	0.200	0.205	3.078	0.500	0.460
6	Impact on landscape, ecology	0.120	0.255	0.245	0.200	0.170	3.055	0.505	0.500
7	Impact on human health	0.270	0.355	0.125	0.055	0.070	1.920	0.638	0.615

Responses

To minimize the negative effects of the mine, some answers have been suggested, and among the answers, most of the positive answers were given to pollution regulation and environmental quality monitoring with an average value of 3.450. And advanced technological change was highly regarded with an average score of 3.170, as indicated by a consensus value of 0.700. The lowest level of acceptance has been given to the response of institutional measures and social policies.

According to Table 6, solutions to ensure environmental sustainability, including monitoring and increasing community participation, have the highest consensus score (0.750). Solutions related to technological innovations or policies and laws required for the active participation of local authorities and mining and processing companies were not given much attention due to the weakness of feasibility.

Table 6. Value of responses in the study area

		Selection probability in Likert scale							
No	Indicator	1	2	3	4	5	wM	wStD	CnS
1	Environmental rehabilitation and restoration	0.25	0.40	0.125	0.15	0.065	2.140	0.580	0.606
2	Treatment Technologies	0.2	0.270	0.25	0.3	0.020	2.570	0.512	0.565
3	Advanced mining technologies	0.115	0.125	0.340	0.255	0.140	3.170	0.511	0.558
4	Pollution and environmental quality monitoring	0.075	0.115	0.270	0.365	0.155	3.450	0.525	0.573
5	Measure on development planning	0. 178	0.225	0.375	0.100	0.100	2.675	0.513	0.554
6	Measure on development planning	0.175	0.425	0.300	0.050	0.050	2.375	0.547	0.645
7	Environmental education and communication	0.050	0.250	0.525	0.175	0.000	2.825	0.504	0.751
8	An increase on community participation	0.000	0.175	0.325	0.450	0.050	3.375	0.517	0.750

Discussion

Based on the DPSIR framework model, in this paper, a multiple evaluation index system for mine evaluation is built and it shows the chain feedback mechanism as one of the mine indicators accurately. According to the results of the research, the main driving factor in the study area is the presence of mining, which is in line with the researches of (24-25).According to the results of this research, the main pressure of the mine is the release of toxic metals, which is contrary to the results of the paper (23-25) that in this study, the main pressure of mining is the destruction of agricultural and forest lands, and is the same as the results of (8).The most important influencing factors in the current state of the environment is air pollution, which is similar to the research of (2). The positive impact of the mine on the growth of employment in the study area, which is in line with the research (11), and its negative impact is the change of the landscape, which is the same with the research (9).

Conclusion

The results show that the effects of mining activities on the environment in the surrounding villages are evaluated as follows based on the opinions of people living near the mine:

The driving forces for mineral exploitation in the study area are the diversity of mineral resources with 3.875 and the commercial industry with 3.250 are the most driving forces in the study area. The greatest pressure that mining has put on the study area, which is the release of toxic and heavy metals was calculated with the highest average of 4.011, followed by forest destruction (3.899) and loss of agricultural land (3.620) they got. The least impact on the soil is the new exploitation technology does not use toxic chemicals, so mining activities do not significantly affect the quality of soil and water. When the state of the environment changes positively and negatively due to mining activities, these changes include positive and negative changes, the positive impact included employment opportunities with an average of 3.325, followed by income (Wi=3.325) and increasing the government budget (Wi=3000). The negative effects are the destruction of ecological landscape (Wi = 3.050) and

infrastructure (Wi = 3.075). Innovative technology solutions, such as new technologies (Wi = 3.175), pollution and monitoring of environmental quality (Wi = 3.400) are more important. Communication measures to increase community participation in the study area were also highly evaluated by the villagers (Wi = 3.375).

References

1. Aghayari Hir, M., Rahimzadeh, N. (2016). Presenting a conceptual model for assessing environmental sustainability in rural areas around Sungun copper mine based on the DPSIR framework. The 4th Conference on Environmental Planning and Management. Tehran.
2. Castro Lima, J.A.M.; Labanowski, J.; Bastos, M.C.; Zanella, R.; Prestes, O.; Damian, M.L.; Granado, E.; Tiecher, T.; Zafar, M.; & Troian, A. (2020). Modern agriculture transfers many pesticides molecules to watercourses: A case study of a representative rural catchment of southern Brazil. Environ. Sci. Pollut. Res. 2020, 27, 10581–10598.
3. Chen, J., Jiskani, I.M., & Jinliang, C. (2020). Evaluation and future framework of green mine construction in China based on the DPSIR model. Sustain Environ Res 30, 13. doi.org/10.1186/s42834-020-00054-8
4. Ehsani, M., & Unesi, M. (2014). Investigation of environmental crises of acid mine drainage for reduction of water pollution and destruction of rangeland soils. Paper presented at the 7th National on Range and Range management of Iran, Tehran.
5. Gabrielsen, P., & Bosch, P. (2003). Environmental Indicators: Typology and Overview; Technical Report n 25; European Environment Agency: Copenhagen, Denmark, 1–19. doi.org/arXiv:1802.04810v3
6. Karataş, L., Alptekin, A., & Yakar, M. (2022). Mardin historical Kuyumcular (Jewelers) Bazaar restoration evaluation. Advanced Engineering Days (AED), 5, 15-17.
7. Lewison, R.L., Rudd, M.A., Al-Hayek, W., Baldwin, C., Beger, M., Lieske, S. N., Jones, C., Satumanatpan, S., Junchompoo, C., & Hines, E. (2016). How the DPSIR framework can be used for structuring problems and facilitating empirical research in coastal systems. Environ. Sci. Policy, 56, 110–119.
8. Maune, D. F. (2001). Digital elevation model technologies and applications: The DEM user manual. The American Society for Photogrammetry and Remote Sensing. ISBN:1-57083-064-9
9. Nguyen Thi, H. (2016). The status and solutions for environmental protection for mineral exploitation at Tan Thanh district, Ba Ria - Vung Tau province. Unpublished master's thesis. Hanoi University of Mining and Geology, 109pp
10. Naveedh Ahmed, S., Hung Anh, L., & Schneider. P (2020). A DPSIR Assessment on Ecosystem Services Challenges in the Mekong Delta, Vietnam: Coping with the Impacts of Sand Mining, Sustainability 12, no. 22: 9323. https://doi.org/10.3390/su12229323
11. OECD. (1993). Core Set of indicators for Environmental Performance Reviews; A Synthesis Report by the Group on the State of the Environment; OECD Publishing: Paris, France, 1–37.
12. Oenoto, M., Leach, A.W., Kell, L. T., & Mumford, J (2023). Extending the driver-pressure-state-impact-response causal chain framework to include human activities, welfare and management. Collect. Vol. Sci. ICCAT, 80(7): 117-130
13. Philippi, A., Jr., Tucci, C.E.M., Hogan, D.J., & Navegantes, R. (2000). Interdisciplinaridade em Ciências Ambientais; Signus: São Paulo, Brazil, 320.
14. Rasouli, A., Moradi, A., Saman, M., & Sadeghi, A (2016). Spatio-temporal assessment and prediction of the effects of the Sungun copper mine on surrounding land cover / land use changes using remote sensing data and the LCM model. Paper presented at the 3th National Geomatics Conference, Islamic Azad university, Tehran, Iran.
15. Rashidinejad. F. (2002). Environmental Impact Assessment of Sungun Copper Project. Retrieved from
16. Salmasi, R. (2007). Investigating the Impacts of Sungun Copper Mine on the Environment. Paper presented at the Proceedings of the 01st Conference of Environmental Geology and Medicine, Shahid Beheshti University, Tehran. Iran.
17. Samii, A., Aghazadeh, W., & Khodadadi, A. (2007). Environmental Impact Assessment of Sungun Copper Mine. Paper presented at the 26th Symposium of Geosciences. Ministry of Industries and Mines, Tehran. Iran.
18. Schulze, I., & Colby, M.A. (1995). A Conceptual Framework to Support Development and Use of Environmental Information in Decision-Making; European Environment Agency: Washington, DC, USA, 1995, p. 51.
19. Smeets, E., & Weterings, R. (1999). Environmental indicators: typology and overview. Technical Report No. 25, pp. 1–20.
20. Tastle W. J. & Wierman M. J. (2007). Consensus and dissention: A measure of ordinal dispersion. International Journal of Approximate Reasoning 45, 531-545
21. Thi Cuc, N., Phuong, N., Phi, N., & Thi Mai Hoa, P. (2018). Application of DPSIR framework to access environmental impact of white limestone mining and processing in Luc Yen, Yen Bai province.
22. Troian, A, Conill Gomez, M., Tiecher, T., Berbel, J., & Gutierrez-Martin, C. (2021). The drivers-pressures-state-impact-response model to structure cause effect relationships between agriculture and aquatic ecosystems. Sustainability.

23. Yakar, M., Yılmaz, H. M., & Mutluoglu, O. (2014). Performance of photogrammetric and terrestrial laser scanning methods in volume computing of excavation and filling areas. Arabian Journal for Science and Engineering, 39, 387-394.
24. Yang, W., Mengge, X., Wang, Y., Long, T., Deng, S., Deng, B & Fang. N (2023). Evaluation of Enterprise Green Mine Construction Based on DPSIR Model. International Journal of Environmental Research and Public Health 20, no. 6: 4932. doi.org/10.3390/ijerph20064932
25. Zhang, Y., & Wang, Z. (2019). Research on Characteristics and Sustainable Development of Mineral Resources in China. IOP Conf. Ser. Earth Environ. Sci, 300, 022155.

Advanced Engineering Days

aed.mersin.edu.tr

An analysis on smallness index of residential parcels of the urban fabric in Tabriz city

Fereidoun Babaei Aghdam [*1], Alireza Omidpour [1], Murat Yakar [2]

[1]*University of Tabriz, Urban and Regional planning, Iran, F.babayi.ag@gmail.com, alirezaomidpor@gmail.com*
[2]*University of Mersin, Department of Geomatics Engineering, Türkiye, myakar@mersin.ed.tr*

Cite this study: Babaei Aghdam, F., Omidpour, A., & Yakar, M. (2024). An Analysis on smallness index of residential parcels of the urban fabric in Tabriz city. Advanced Engineering Days, 9, 203-205

Keywords
Smallness
Urban fabric
Tabriz city
Residential parcels

Abstract

Smallness of residential parcels in the urban context is one of the most important and widely used issues in the field of urban design, and this issue is mainly seen in worn-out city contexts. The purpose of this research is to identify and analyze the elegance index of residential plots in the urban context of Tabriz city. This research is applied-developmental in terms of purpose and descriptive-analytical in terms of method, and spatial statistical analysis has been used in the research. Arc Gis and Google Earth software were used in this research. The total number of residential plots in Tabriz city is 255,825, of which 200,885 plots with an area of less than 200 square meters have been identified and information about their area has been collected. The analysis of the hotspot index clearly shows the difference in the density of the residential plots between the north and the south with other areas of Tabriz city. In general, according to the results obtained from the research, the fine-grained areas of Tabriz city are mainly in historical contexts and worn-out contexts or informal settlements.

Introduction

The fineness of the pieces in the fabric of the cities is mainly seen in worn and historical fabrics. The fineness of the fabric of Tabriz is one of the distinctive features of this city. The characteristics of Tabriz's historical context are dense streets, old markets, traditional architecture and worn-out context. The worn-out fabric is the whole or part of the urban space whose biological system has been disrupted and inefficient both in terms of its construction and the functioning of its vital components (1).One of the most important problems of urban contexts is the problem of deterioration, which is more noticeable in the historical and old areas of cities.(2) Based on this definition, three indicators of small size (blocks with more than 11% of their plaques have an area of less than 211 square meters), instability (blocks with more than 11% of its buildings are unstable and lack structural system) and impenetrability. Blocks in which more than 11% of the roads are less than a meter in width are considered as criteria for determining the range of worn-out urban fabrics, and parts of the city that include all three indicators are known as worn-out fabrics (3).

Tabriz metropolis, as one of the important cities of the country, has housed a large population throughout history, especially in the last two centuries, due to its important political and economic position. For this reason, today, a large part of the fabric of this city is worn out and problematic (4). The aim of this research is to analyze the fineness index of Tabriz metropolis using It is GIS. Multiple functions (GIS) make it possible to identify the worn - out tissues of the city in appropriate ways. acted better and improved the quality of city management (5). The urban development of Tabriz in recent decades has been formed in fine-grained contexts due to the increasing population. The texture of the city represents the granularity of physical spaces, the communication network and access methods, how to distribute activities and finally the formation and expansion of the city throughout history. (6, 7,8) Generally, every urban texture consists of two main parts 1: body (form) 2: function (role) The combination of body and function shows patterns in terms of wear and tear. Parts of urban tissues whose physical and functional qualities have been reduced and disturbed are worn tissue. It is called wear and tear of the tissue and

its internal elements either due to the age or the lack of development and technical monitoring of the formation of that tissue (9). Dilapidated urban contexts are dilapidated neighborhoods in the urban space that have their own social, economic and cultural issues and complications (10).

Material and Method

The basis of these studies is based on field studies and using the data obtained from the shape file of the comprehensive plan of Tabriz metropolis in 2015 and the required layers, including the limits and coordinates of the parts based on the latest update, and to modify the parts, field visits and Google Earth images are used. has been taken In this research, according to the theoretical foundations, the fineness of the parts in the urban context will be discussed in relation to the worn-out contexts; Then, relying on the principles, standards and concepts raised in the theoretical framework, the fineness index of the parts, which is one of the physical indicators of worn-out urban tissues, was identified and analyzed in the desired range in Google earth and Arc GIS software, and the results were obtained. Reliable quantitative and qualitative information was provided.

Results

Table 1. Analysis of the index of urban smallness in residential uses

Row	Plot area	Number	The intensity of fineness	Total area in hectares	Percent
1	40 <	8691	very intense	25/1	1/12
2	40 – 80	55583	intense	291/44	12/96
3	80 – 120	53541	medium	602/96	26/81
4	120 – 160	42414	weak	595/77	26/49
5	160 – 200	40656	Very weak	733/53	32/62
Total		200885		2248.8	100

Hot spot analysis index

This index is a spatial analysis method that is used to identify patterns or areas that have non-random accumulation of events or events. This analysis is used as an important tool in the field of spatial data analysis and environmental resource management and urban development. Based on this, in Figure 2, the size of residential plots in Tabriz city is shown in 5 spectrums for identification and evaluation.

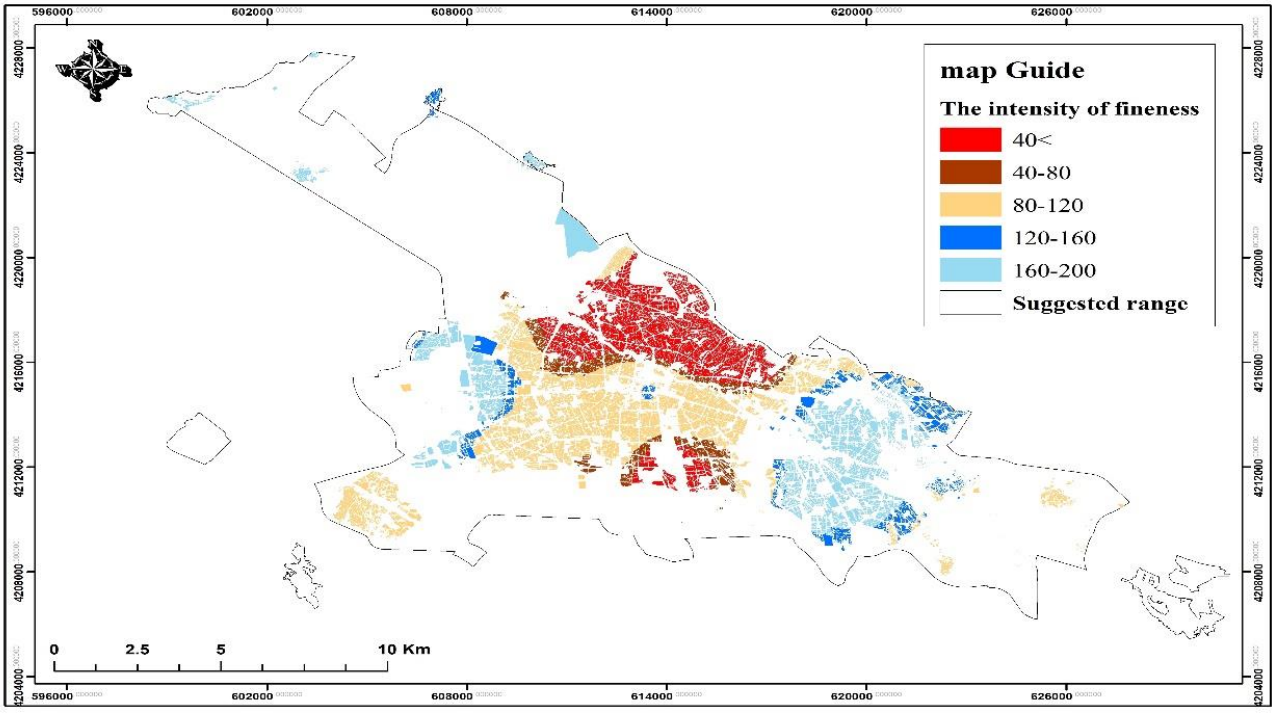


Figure 2. Fine-grained map based on hot spot analysis index of residential areas of Tabriz (source: authors)

Figure 2 shows the intensity of the smallness of the residential parts of Tabriz city. According to this map, the northern areas of Tabriz and parts of the southern part of the city have the most extreme amount of fine grain,

which unplanned and non-observance of construction standards has caused problems for the residents. And the middle parts have medium density and the lowest intensity of density in the residential parts of the west, including Khavaran town and the west of Tabriz city.

Discussion

Granulation index is a relative thing, because the rules of urban planning are different according to the structure of different countries. For example, the quorum of residential land area in most Iranian metropolises is about 200 square meters, while in other countries the issue is completely different. The issue of being small has a significant relationship with the type of use, which means that plates below 200 square meters are common in important uses such as commercial in cities around the world. Based on residential use, a clear example is the determining role of plot area.

Conclusion

The smallness of residential land has a significant impact on urban development and the quality of life of citizens. In this way, the smallness of the urban fabric can intensify traffic and transportation within the city. Dilapidated urban textures are the result of the formation of important and historical parts of the city without the process of urban development. According to this research, in the city of Tabriz, the elegance of the residential plots is 12.1%, the extreme elegance in the northern parts of the city and parts of the south that are more related to important and historical textures is 12.96%. severe, 26.81%. The average percentage of 26.49 and 32.62 is weak and very weak, respectively, in terms of the smallness of residential plots. In order to reduce and prevent issues and problems related to the elegance of residential plots in the city, basic measures must be taken in the field of urban planning and urban management, and all capacities and facilities can be used to improve the work.

References

1. Babaei Aghdam, F., Kamlifar, Z., & Kamlifar, M. (2015). extraction Indicator Hi ID Texture worn out Y urban With Use From System Geographic information (study Case: Tabriz Region 4). Zagros Landscape Geography and Urban Planning Quarterly, 28(8), 19-38
2. Tupchi Sani, A. (2010). Sustainable Urban Regeeration a New Approach to Intervention in Deteriorated Urban Fabric (Implementation Guideline). Mahmood Mohammadi, University Art Esfahan, group Urban
3. Sarai, M., & Mohrekesh, Sh. (2015). Evaluation of the wear and tear of neighborhoods in three cities of Isfahan and participation of residents in the organizing process. Scientific-Research Quarterly of Space Research (Geography), 3, 63-84
4. Haeri, M. (2007). If the city administration knows. Iranshahr, 9-10, 0-0
5. Sarvar, R., Mirzazadeh, R., Soltanzadeh, A., & Sobhani, N. (2016-17). Assess the physical characteristics and problems of Urban Distressed Areas, Case Study: City Oshnavieh. Researches Biannual Journal of Urban Ecology, 2, 39-54
6. Ashtakhari Astehbanati, M., Azhdari, P., & Dehghani, H. (2023). micro-density index map to identify and pay attention to the construction and improvement of worn-out urban fabric (case study of Goyim town, Shiraz Municipality). 17th National Conference on Geography and Environment, Shirvan.
7. Salehi, S. S., & Jafari, F. (2024). Evaluation of the worn texture of the region 4 in Tabriz, Iran, with an emphasis on increasing populatability. Advanced Engineering Science, 4, 25-34.
8. Salehi, S. S., & Jafari, F. (2023). Increasing the efficiency of worn-out urban fabric areas with an emphasis on the segmentation of buildings in the 4th district of Tabriz in Iran. Advanced Engineering Days (AED), 8, 121-124.
9. Chapin, S. (1979). Urban Land Use Planning, New York
10. Loosum, R. (1996). Urban conservation policy and the preservation of historical and cultural heritage: The case of Singapore. Cities, 6, 399-409

Advanced Engineering Days

aed.mersin.edu.tr

Estimation and comparison of evaporation losses from the dam reservoir using intelligent gene expression programming model and empirical methods: A case study of Sattarkhan Ahar Dam

Vahdat Ahmadifar[1], Reza Delirhasannia [*2], Tima Mohammadzadeh [2]

[1]University of Tabriz, Department of Water Engineering and Science, Iran, vahdatahmadifar@yahoo.com, delearhasannia@yahoo.com
[2]Building Art Learner, Ahar Educational Office, Iran, amirabbasahmadifar@gmail.com

Cite this study: Ahmadifar, V., Delirhasannia, R & Mohammadzadeh, T. (2024). Estimation and comparison of evaporation losses from the dam reservoir using intelligent gene expression programming model and empirical methods: A case study of Sattarkhan Ahar Dam. Advanced Engineering Days, 9, 206-211

Keywords
Evaporation losses
Gene expression programming
Empirical equations
Dam reservoir

Abstract

Measuring the amount of evaporation from the free surface of water is one of the important parameters in water resources management. In this research, the gene expression programming (GEP) model was used as an intelligent method to estimate evaporation from the free water surface of Sattarkhan Ahar dam reservoir. The results showed that the best GEP model with a correlation coefficient of 0.862 and a root mean square error of less than 1.438 mm is able to model the amount of evaporation from the free surface of water. Also, the rate of evaporation from the free surface of water was estimated using different empirical equations. The obtained results showed that Meier's equation with correlation coefficient of 0.813 and root mean square error less than 1.913 mm is more accurate than other empirical methods for estimating evaporation from the free surface of water in Sattarkhan Ahar dam. The comparison of empirical equations and GEP method shows that although the correlation coefficient of both methods has a small differences, but the GEP method has less root mean square error than the empirical method and by presenting clear relationships, it is simpler, more understandable.

Introduction

Water shortage is one of the most important and biggest challenges of the current century. On the other hand, the process of evaporation from the free surface of water in lakes, water reservoirs, soil surface and plants are one of the important parameters of water loss in meteorology and hydrology [8]. In dry areas that have limited rainfall, these losses have a significant contribution to the water balance of lakes and reservoirs and can cause a drop in the water level [13,14]. Evaporation pan is a common method for calculating evaporation from the surface of lakes and water reservoirs, as well as measuring evaporation-transpiration of plants [7]. Using the pan method to calculate evaporation is difficult due to factors such as the absence of an evaporation measurement station, lack of regular and correct data collection. In addition to the pan method, it is possible to estimate the amount of evaporation by using meteorological data in the form of empirical equations or equations with a theoretical basis [14]. Brun and Hesch reported that Meyer's empirical method is the most appropriate method to study the evaporation process in Canada due to its simplicity and lack of radiation data [3]. Sattari et al. investigated different empirical relationships of estimation of the free water level for Alaviyan Maragheh dam reservoir, and the accuracy of Meyer's empirical model was reported to be higher than other models in estimating evaporation from the reservoir level of the dam [12]. The use of smart methods in various sciences has been significantly developed in recent years. Considering the ability of these models to solve problems related to mathematical modeling, the attention of researchers in the field of water engineering, especially the modeling of evaporation from reservoirs of dams and lakes, has been drawn to their application. Casey et al used artificial neural network (ANN) models,

development of adaptive neural-fuzzy inference model (ANFIS) and GEP to predict the water level of Iznik Lake in western Türkiye [4]. The results of this research showed the high performance of the GEP model compared to the two used models. Sattari et al. compared the empirical methods with the M5 tree model in the estimation of evaporation loss from the reservoir of Alaviyan Maragheh dam [15]. The results obtained from this research showed the better performance of the M5 model. Tabari and Malekpour Shahraki used intelligent methods to predict the water level of the Amir Kabir Karaj dam reservoir, and finally introduced the supervised (hybrid) neural network model (SICM-ANN) as the most suitable method [11]. Among the various smart methods, the Gene Expression Programming (GEP) method, in addition to being widely used, has performed well in the field of water engineering research [1, 4, 16]. In this research, in the first stage, the prediction of evaporation rate from the free surface of Sattarkhan Dam reservoir water was modeled using GEP smart model in 8 different scenarios, and in the continuation of this research, the evaporation values from the free surface water reservoir of the dam were calculated by empirical methods. In the next stage of this research, in order to evaluate the performance of each method, the results of evaporation estimation were compared with the observed values of evaporation from the pan, and finally, the appropriate model was introduced to estimate the amount of evaporation loss from the reservoir of this dam.

Material and Method

Area specifications and used data

Sattarkhan dam is located 15 km from the center of Ahar city and 120 km from the center of East Azerbaijan province in the Ahar Chai watershed and on the same river. Star Khan Dam is located at 53° 46° East Longitude and 28° 38° North Latitude and 1500 meters above sea surface level (Figure 1). In this research, climatic data, including maximum daily temperature, minimum daily temperature, average daily temperature, relative humidity, wind speed at a height of two meters, and solstice hour related to the evapotranspiration station of Sattarkhan Ahar Dam were used. To model the period, three-year data (1397-1400) has been used in the form of six months between April and September of each year. In this research, various combinations of meteorological parameters affecting evaporation from the free surface of water were defined as inputs to the GEP smart model. Also, evaporation from the free surface of water for the studied area was estimated using existing empirical relationships. The summary of the statistical characteristics of the data used in this research can be seen in Table 1.

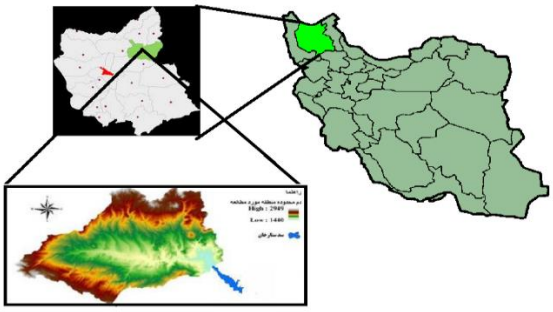


Figure1. Geographical location of Sattarkhan dam

Table 1. Summary of statistical data for study area

Climatology Parameters	Statistical properties			
	Max	Min	Mean	SD
Mean temperature (C)	33.7	2.6	20.3	5.9
Minimum temperature (C)	29.4	-3	12.9	6.5
Maximum temperature (C)	38.2	3.9	27.6	6.8
Relative humidity (%)	86.1	15.2	44.6	17.4
Sunshine hours (hr)	14.2	0	10.3	2.8
Wind speed (km/hr)	12.8	1.9	3.9	1.4
Evaporation amount of the pan (mm)	26.2	0	9.1	4.7

Evaporation losses measurement using evaporation pan

Evaporation pans measure evaporation values directly, the standard pans for doing this are: a) class A pan (American standard), b) English standard pan and c) Russian standard pan. The most famous type of pan used in

hydrology studies in Iran is class A evaporation pan. By using the statistics related to the decrease of water depth inside the evaporation pan in any given period of time, it is possible to estimate the amount of evaporation from the water surface of lakes and reservoirs of dams using the equation 1.

$$E = K \times ET_{pan} \qquad (1)$$

Where, E is Evaporation from the water free surface in reservoirs or lakes in mm/d, K is a constant and dimensionless coefficient, which is considered averagely 0.7 for class A pan and ET_{pan} is evaporation from the pan in mm/d (Safavi, 2014).

In this research, the empirical equations of Mayer, Marciano, Shahtin and Hefner were used to estimate the amount of evaporation from the free surface of water [15].

Gene Expression Programming (GEP)

GEP was invented by Ferreira [5]. In this program, linear and simple chromosomes with a fixed length similar to those used in the genetic algorithm are combined with branch structures of different sizes and shapes similar to the tree diagram in genetic programming. During reproduction, only the slightly modified genome is passed on to the next generation, thus eliminating the need for relatively heavy structures to replicate and mutate (Ferreira, 2001). In this study, GeneXproTools 4.0 software was used to model evaporation from the free surface of water. The operator functions and the fitting function as well as other settings related to the software were selected based on the suggestions made in previous studies [1]. In this research, the data was divided into two parts, training and testing, and in all scenarios, 66% of the data was allocated to training. The performance of the models used in this research has been evaluated based on the calculation of the root mean square error (RMSE) and the correlation coefficient R. The formulas for calculating the above two statistics are given in the equations 2 and 3.

$$R = \left(\frac{\sum_{i=1}^{N} (X_i - \overline{X})(Y_i - \overline{Y})}{\sqrt{\sum_{i=1}^{N} (X_i - \overline{X})^2 * \sum_{i=1}^{N} (Y_i - \overline{Y})^2}} \right) \qquad (2)$$

$$RMSE = \sqrt{\frac{\sum_{i=1}^{N} (Y_i - X_i)^2}{N}} \qquad (3)$$

In these equations x_i is the observed value in the i-th time step, y_i is the estimated value in the i-th time step, N is the number of time steps and X is mean observed value.

Results

Estimation of evaporation from the water free surface with GEP model

In the GEP smart model method, evaporation from the pan on a daily basis was entered as the target variable and the values of the month of the year, maximum temperature, minimum temperature, relative humidity, wind speed and sunshine hours were entered into the model as independent variables. According to the effect of the parameters used in calculating the amount of evaporation from the free surface of water, 8 scenarios were defined. Scenarios that have a higher accuracy in predicting the amount of evaporation from the free surface of water and at the same time use the minimum number of parameters in its modeling, can be more important than other scenarios in the application of the used intelligent model [15]. Table 2 shows the results obtained from the GEP model in the defined scenarios. The obtained results show that scenario number one with six input parameters is the most accurate (R=0.862-RMSE=1.438mm/day). One of the most important points that is important in examining the performance of the scenarios is the results obtained in scenario number 8, which has an acceptable accuracy with the input parameters of solar hours and month number, and compared to scenarios such as 3, 4 and 5, which have more input parameters for the model. They need to show better performance. Figure 2 shows the scatter diagram of evaporation values measured and modeled by GEP method in 8 different scenarios.

Table 2. Results of model performance using GEP in the different scenarios

scenario	Input parameters	R	RMSE (mm)
1	Month number, Maximum temperature, Minimum temperature, Relative humidity, Sunshine hours, Wind speed	0.862	1.438
2	Month number, Maximum temperature, Minimum temperature, Relative humidity, sunshine hours	0.847	1.521
3	Minimum temperature, Relative humidity, Sunshine hours	0.797	1.802
4	Month, Maximum temperature, Minimum temperature, Relative humidity	0.795	1.799
5	Relative humidity, Sunshine hours	0.645	2.450
6	Month number, Relative humidity, Wind speed	0.842	1.487
7	Minimum temperature, Relative humidity	0.829	1.780
8	Month number, Sunshine hours	0.811	1.856

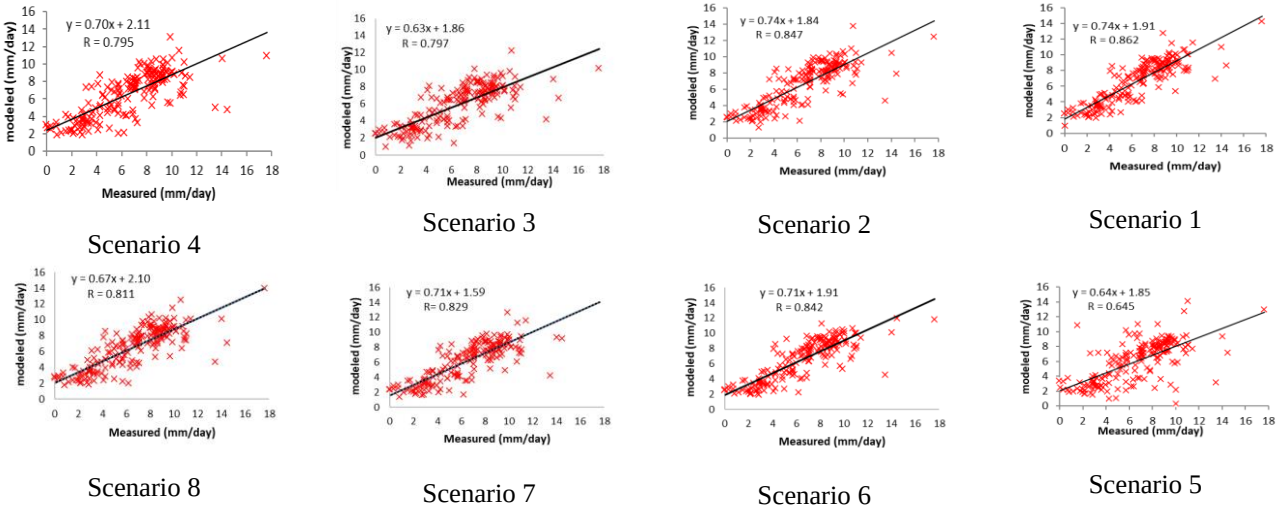


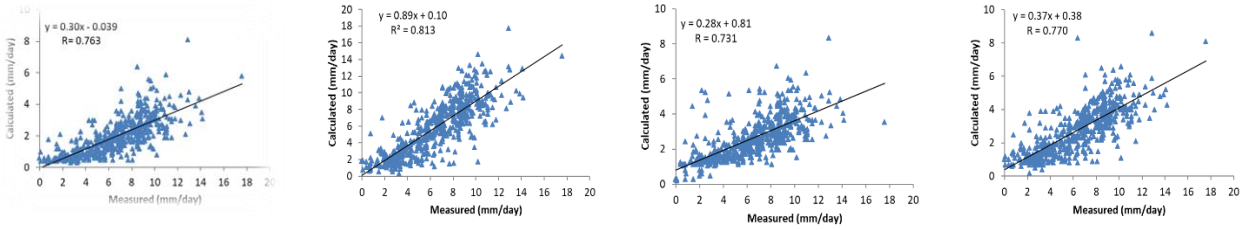
Figure 2. Scatter plots of measured evaporation values and GEP model outputs in the different scenarios

Estimation of evaporation from the water free surface using empirical equations

In order to evaluate the performance of empirical methods in estimating the amount of evaporation from the free surface of water, its values for Sattarkhan Dam were calculated using empirical relations and compared with the values of evaporation from the case pan, the results of which can be seen in Table 3. The obtained results show that Meier's relation (R=0.813 - RMSE=1.845 mm/d) has a better performance than other empirical methods in estimating evaporation from the free water surface of Sattarkhan Ahar Dam reservoir. Figure 3 shows the scatter diagram between evaporation from the pan and empirical equations.

Table 3. The outputs of empirical methods performance

Number	Method Name	R	RMSE (mm)
1	Meyer	0.813	1.913
2	Marciano	0.763	5.022
3	Shahtin	0.770	4.120
3	Hefner	0.731	4.451



Marciano Meyer Hefner Shahtin

Figure 3. Scatter plots of measured pan evaporation values and empirical equations

Discussion

In this research, 8 scenarios were created by combining different climatic parameters as input to the model. The models provided by intelligent GEP method in scenarios 1 and 8 were proposed for the reasons of high accuracy and use of few climatic parameters to estimate evaporation losses from the free surface of water in the study area and similar climates. Examining the performance of different research scenarios shows that the parameters of minimum temperature, maximum temperature and sunny hours have relatively high relative importance in estimating evaporation from the studied area compared to other parameters. Irmak et al. introduced the effect of wind speed, lack of saturated vapor pressure and relative humidity as highly important parameters in estimating evaporation [7].

Conclusion

Examining the performance of empirical relationships also shows that the accuracy of Meyer's relationship in estimating evaporation from the free surface of water is more than other empirical relationships. Yazdani et al. introduced Ivanov's relation for the Amol region [17], Bron and Hesch [3] and Sattari et al [14, 15]. These results show the different effects of different parameters in estimating evaporation from regions with different climates. Comparing the performance of empirical methods with the GEP model showed that although the correlation between the values of evaporation from the pan and calculated by the empirical relations is relatively equal to the correlation of some scenarios, but the empirical relations mean square error is more, which indicates the superiority of the GEP model in estimating the evaporation from Free water level in the study area.

References

1. Ahmadifar, V., Delirhasannia, R., Nazemi, A. H., Sadraddini, A. A. (2015). Modeling drop size emitted from irrigation impact sprinklers using Gene Expression Programing and multiple linear and nonlinear regression methods. Journal of Applied Biological Sciences. 9(2), 50-57.
2. Ahmadifar, V., Delirhasannia, R. Sadraddini, A. A. (2022.) Comparative analysis of 15 major reference evapotranspiration models based on weighing lysimeter measurements for two different grass species grown in three soil textures. Irrig. Drain. 71 (3), 648-664.
3. Burn, D. H. and Hesch, N. M. (2007). Trends in evaporation for the Canadian Prairies. J Hydrology 336: 61– 73.
4. Buyukyildiz, M, Tezel G, Yilmaz, V. (2014). Estimation of the change in lake water level by artificial intelligence methods. Water Resources Management, 28(13), 4747-4763.
5. Ferreira, C. (2001). Gene expression programming: a new adaptive algorithm for solving problems. Comp. Sys, 13(2), 87-129.
6. Ikebuchi, S., Seki, M. and Ohtoh, A. (1988). Evaporation from Lake Biwa. J Hydrol., 102, 427-449.
7. Irmak, S., Haman, D., Jones, J. W. (2002). Evaluations of class A pan coefficient for estimating reference evapotranspiration in a humid location. Journal Irrigation and Drainage Engineering. ASCE., 128 (3), 153–159.
8. Genanu, M., Alamirew, T., Senay, G., Gebremichael, M. (2017). Remote Sensing Based Estimation of Evapo-Transpiration Using Selected Algorithms: The Case of Wonji Shoa Sugar Cane Estate, Ethiopia, Journal of Environment and Earth science, 7(1), 46-59.
9. Karami, F., Bayati Khatibi, M. (2019). The Modeling of Soil Erosion and Prioritizing Sediment Production in Sattarkhan Dam Basin Using MUSLE and SWAT Models. Hydro geomorphology, 6(18), 115-137.
10. Kisi, O., Shiri, J., Nikoofar., B. (2012). Forecasting daily lake levels using artificial intelligence approaches. Computers and Geosciences, 41,1 69-180.
11. Mohammad Rezapour Tabari, M., Malekpour Shahraki. M. M. (2019). Reservoir Water Level Prediction Using Supervised Intelligent Committee Machine Method, Case Study: Karaj Amirkabir Dam, Iran-Water Resources Research, 14(5), 14-26.

12. Safavi, H.R. (2014). Engineering Hydrology, Arkan Danesh, Fourth edition (Isfahan), P:724.
13. Sammen S.S., Mohamed T.A., Ghazali A.H., El-Shafie A., Sidek L.M. (2017). Generalized regression neural network for prediction of peak outflow from dam breach. Water Resources Management 31(1), 549- 562.
14. Sattari, M.T., Ahmadifar, V., Delirhasannia, R., Apaydin, H. (2021). Estimation of the pan evaporation coefficient in cold and dry climate conditions via the M regression tree model. Atmósfera, 34(3), 289-300.
15. Sattari, M.T., Ahmadifar, V., Pashapour Kholf Ansar, R. (2014). M5 tree model based modeling of evaporation losses in Eleviyan reservoir and comparison with empirical equations. Journal of irrigation and water engineering., 17, 107-121.
16. Shiri, J., Zounemat-Kermani, M., Kisi, O. Mohsenzadeh Karimi., S., (2020). Comprehensive assessment of 12 soft computing approaches for modeling reference evapotranspiration in humid locations. Meteorol. Appl. 27 (1), e1841.
17. Yazdani, V., Ghahraman, B., Davari, K. (2011). Determining the best empirical method for estimating water surface evaporation based on sensitivity analysis in paddy rice field in Amol and comparing them with Artificial Neutral Network. Iranian Water Research Journal, 2(7), 47.

Advanced Engineering Days

aed.mersin.edu.tr

Down-scaling of MODIS land Cover product using Landsat images to detection changes in Google Earth Engine

Mostafa Mahdavifard [1,2], Samaneh Bagheri [1,2*], Sadra Karimzadeh [1,2] Khalil Valizadeh Kamran [1,2]

[1]*University of Tabriz, Department of Remote Sensing and GIS, Tabriz, Iran*
[2]*Remote Sensing Laboratory, University of Tabriz, Iran,*
mostafamahdavi842@gmail.com, samanehbagheri99@gmail.com, sa.karimzadeh@tabrizu.ac.ir, valizadeh@tabrizu.ac.ir

Cite this study: Mahdavifard, M., Bagheri, S., Karimzadeh, S., & Valizadeh Kamran, K. (2024). Down-scaling of MODIS land Cover product using Landsat images to detect changes in Google Earth Engine study. Advanced Engineering Days, 9, 212-215

Keywords
Down Scaling
Land Cover
MODIS
Landsat
Google Earth Engine

Abstract

Land cover and land use is one of the basic and complex issues in the changes of the world. The aim of the current study is to downscaling the MODIS land cover product with poor spatial resolution to the medium spatial resolution of Landsat (7, 8) 30 meters of Tabriz city in the online processing system of Google Earth Engine. The results show that the downscaled land coverage of MODIS in 2001, 2010 and 2019 is equal to the overall accuracy of 90.6, 93.02 and 87.5 respectively. Many changes from 2001 to 2010 are related to the change of cropland use to the urban, which has not been observed in 2019, and the reason for this is the creation of farms for cropland. In general, the downscaled MODIS products, including the land surface temperature product and the NDVI product, are recommended for sharpening and increasing its spatial resolution for urban and even provincial and basin levels.

Introduction

Land use and land cover (LULC) are fundamental topics in global change research, serving as the basis for human survival and development (Song et al, 2018). Changes in land use at various scales have significant impacts on land cover, which is crucial for research on global climate change, ecological environment monitoring, and related fields (Coppin et al, 2004). Change detection involves identifying differences in the state of an object or phenomenon over time, providing an accurate reflection of changes that occur over an extended period (Singh, 1989). The timely and precise detection of changes in global land use/cover is closely linked to various aspects of global change, facilitating a better understanding of the relationship between humans and natural phenomena and better resource management and utilization (Zhang et al, 2022; Saha et al ,2022; Yang et al ,2022; Siddik et al 2022.

Remote sensing (RS) is the primary means of LUCD (Sobhani et al, 2021). Remote sensing technologies provide a reliable source of urban land cover/land use data collection (Sheikhghaderi and et al., 2023). Generally Remote sensing (RS) has many advantages such as good timing synchronization, extensive coverage, and long-term observations (Aghazadeh et al., 2023). In this regard, there are various methods, the most widely used of which are downscaling methods. Downscaling is any procedure to infer high-resolution information from low-resolution variables. This technique is based on dynamical or statistical approaches commonly used in several disciplines, especially meteorology, climatology and remote sensing.

The purpose of this study is to downscaling the 500-meter land cover product of Modis using 30-meter Landsat images and finally prepare a map of land cover changes with the downscaling product. This study addresses the innovative approach of MODIS land use products with Landsat imagery for change detection in the Google Earth engine. Using the strengths of this remote sensing dataset, researchers can gain a deeper understanding of land use changes and provide more detailed analyses.

Study area

The city of Tabriz is considered as the capital of Eastern Azerbaijan province and one of the most populous cities in Iran. The population of this city in 1332 is one million 443 thousand 33 people). The city of Tabriz is

located at an approximate height of 1343 meters above sea level at 22 degrees and 14 minutes east, and 31 degrees and 2 minutes north latitude (Figure 1).

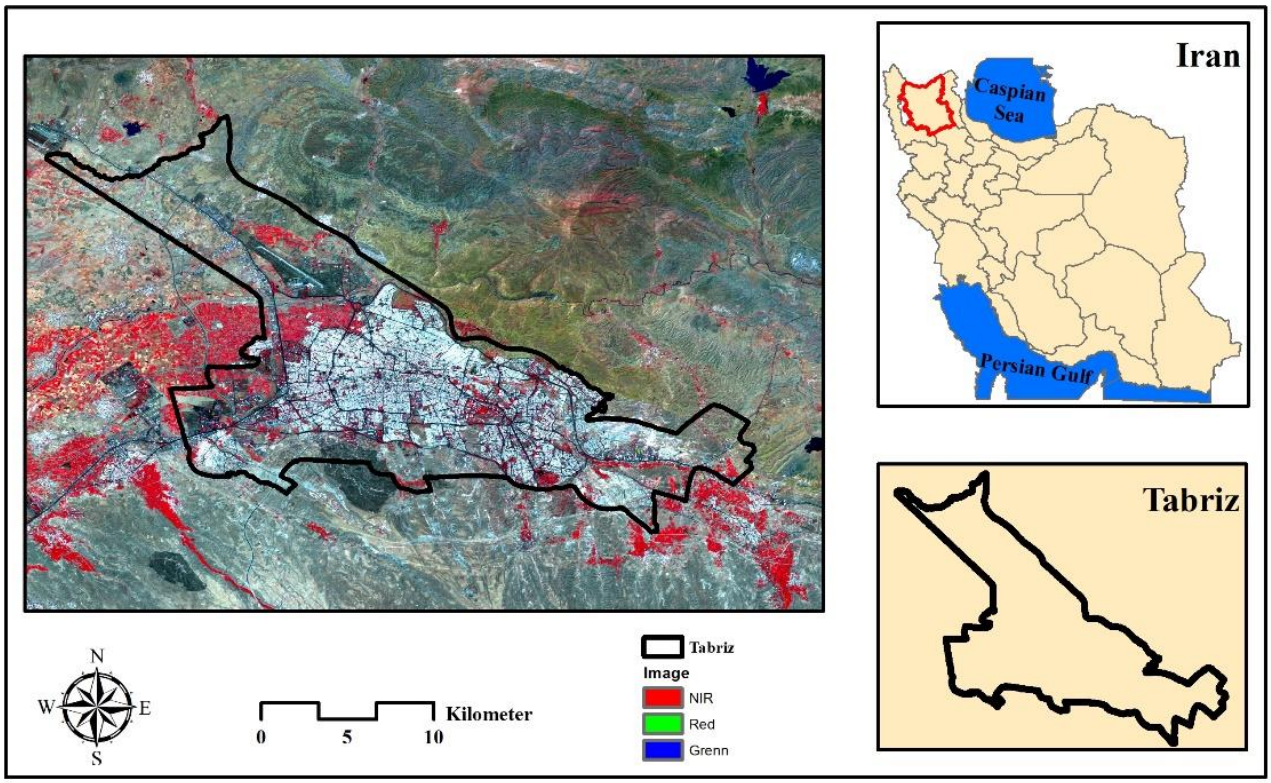


Figure 1. Location of the study area

Material and Method

In this study, the data of the land cover product of MODIS MCD12Q1.061 MODIS Land Cover Yearly Global 500m with a spatial resolution of 500 meters and Landsat images of 30 meters were used for downscaling. In other words, MODIS land cover product and Landsat images of 2001, 2010 and 2019 in Google Earth Engine were used. In order to down scaling the MODIS land use product, one-year Landsat time series images with less than 10% cloud cover were first selected, and then NDBI, NDWI and NDVI indices were calculated and combined to create a median image. In the next step, level 2 of the land use product was used, and finally, the MODIS product and Landsat images were combined and a land cover map was produced with the Random Forest (RF) classification algorithm.

Results

Figure 2 shows the maps produced by downscaling the land cover product of 500 meters of MODIS to 30 meters of Landsat. Initial MODIS land use classification provided an overview of land cover with coarse spatial resolution, while the integration of Landsat images facilitated the refinement of land use information at a finer scale.

Downscaling of MODIS land cover products using Landsat images for change detection in the Google earth engine yielded promising results. Figure 3 shows the changes in land use during the 20-year period. Temporal analysis showed significant changes in land cover during the study period (2001-2019). These changes include the reduction of agricultural land and the increase of urban areas. Table 1 shows the area of land cover changes.

Accuracy evaluation for 2001, overall accuracy 90.6% and kappa coefficient 0.87%, for 2010 overall accuracy 93.02% and kappa coefficient 0.90%, and for 2019 overall accuracy 87.5% and kappa coefficient showed 0.83%. Which confirms the reliability of the down-scale product for detecting changes in land use patterns. Visualizations further illustrated the detected changes and provided valuable insights into the dynamic nature of the landscape at higher spatial resolution.

Table 1. The area of MODIS downscaling land cover

Land Cover	2001 (Km^2)	2010 (Km^2)	2019 (Km^2)
Grassland	71.09	68.67	62.31
Cropland	29.33	24.54	36.22
Urban	90.54	101.10	105.14
Non-Vegetation	62.41	59.07	49.71

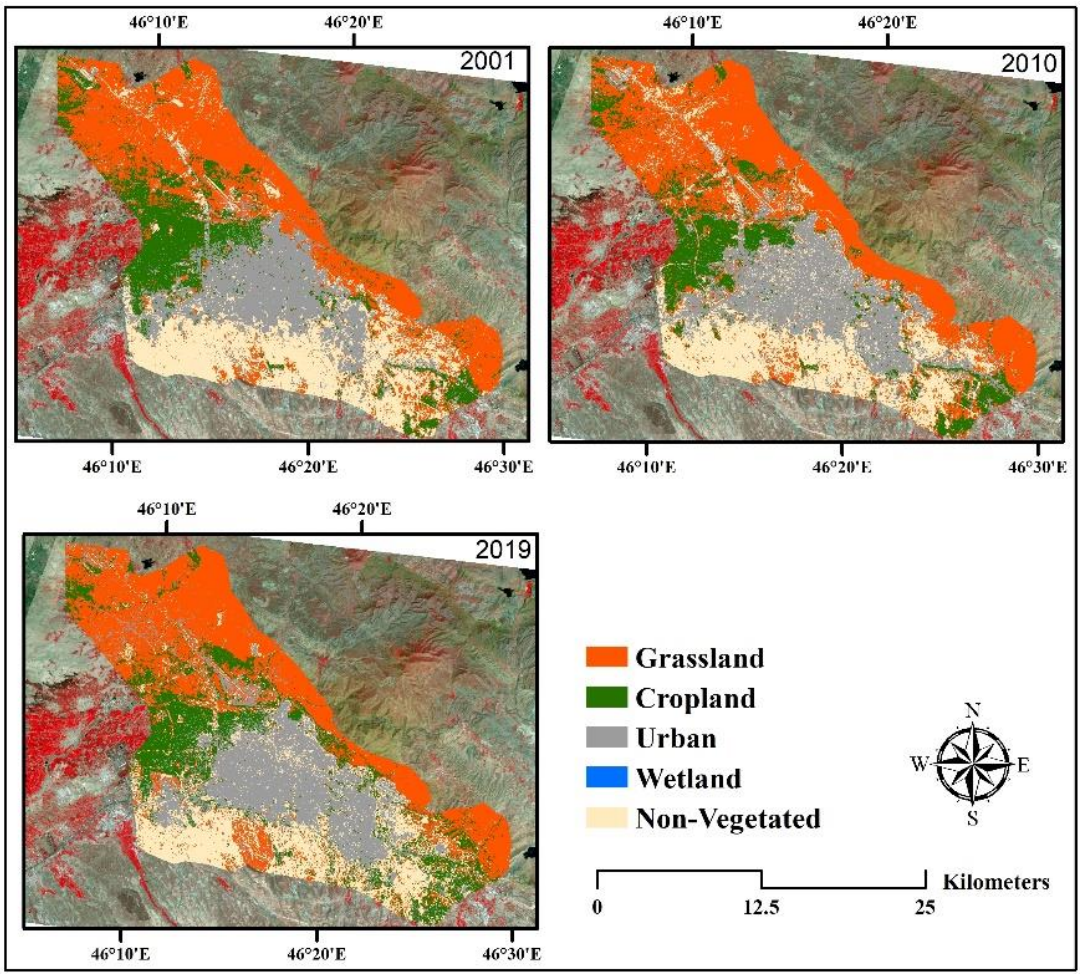


Figure 2. Downscaling map of land cover for study years

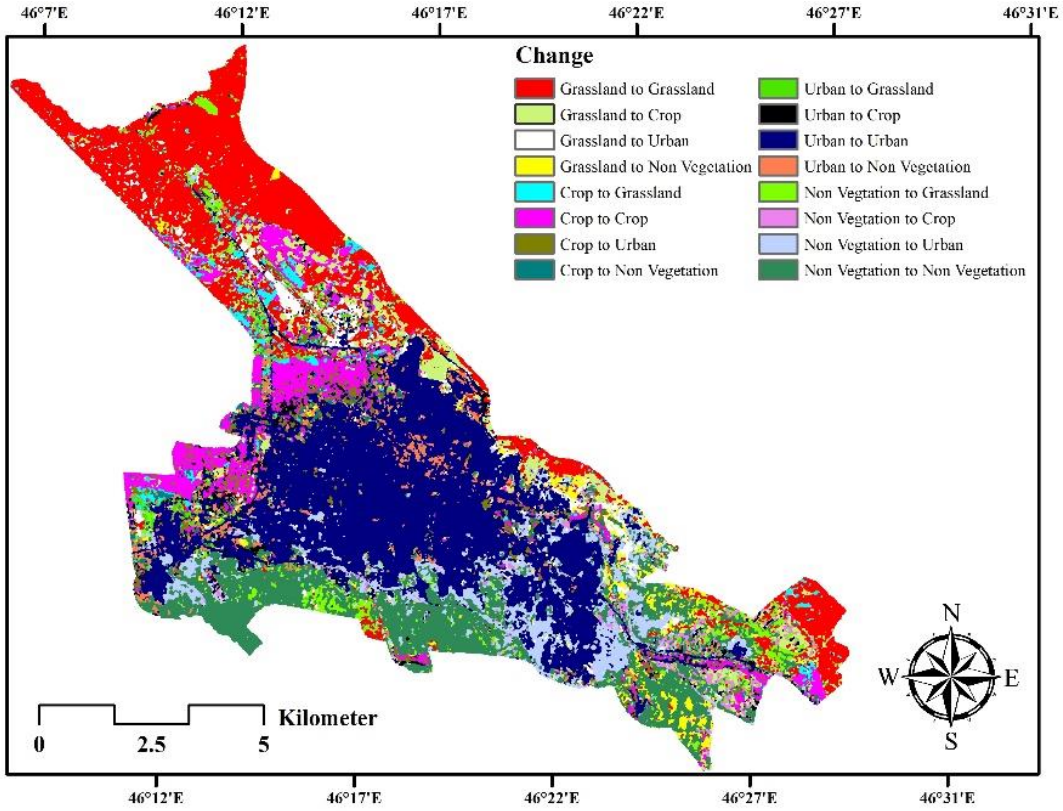


Figure 3. Map of land cover change to change

Discussion

The results emphasize the effectiveness of downscaling MODIS land use products using Landsat images on the Google Earth Engine platform for change detection. The improved spatial resolution achieved through Landsat integration increases the ability to capture land cover changes, which is essential for monitoring dynamic landscapes. The temporal changes observed between 2001 and 2019 show the suitability of this approach for evaluating seasonal changes and long-term trends. The results show a decrease in agricultural land and an increase in urban built-up areas. The accuracy evaluation results confirm the reliability of the downscaled product, and prove the reliability of this method for detecting changes. The computational efficiency of Google Earth Engine facilitates scalability and reproducibility, making this method a valuable tool for researchers and practitioners involved in land use monitoring and environmental management.

Conclusion

In conclusion, the downscaling of MODIS land cover products using Landsat images within Google Earth Engine represents a promising methodology for unraveling the complexities of land use dynamics. This integrated approach contributes to a more comprehensive and accurate assessment of changes in the Earth's surface, offering valuable insights for sustainable land management and decision-making. As remote sensing technologies continue to evolve, the synergistic use of global and high-resolution datasets holds immense potential for advancing our understanding of the ever-changing landscape.

References

1. Aghazadeh, F., Bageri, S., Garajeh, M. K., Ghasemi, M., Mahmodi, S., Khodadadi, E., & Feizizadeh, B. (2023). Spatial-temporal analysis of day-night time SUHI and its relationship between urban land use, NDVI, and air pollutants in Tehran metropolis. *Applied Geomatics*, 1-22.
2. Hedayat Sheikhghaderi, S., Mahdavifard, M., Mohammadi, A., & Alavipanah, S. K. (2023). Performance evaluation of spectral indices and classification algorithms for built-up area extraction using PRISMA hyperspectral images. *Intercontinental Geoinformation Days*, *7*, 37-40..
3. Peng, J., Loew, A., Merlin, O., & Verhoest, N. E. (2017). A review of spatial downscaling of satellite remotely sensed soil moisture. *Reviews of Geophysics*, *55*(2), 341-366.
4. Ribalaygua, J., Torres, L., Pórtoles, J., Monjo, R., Gaitán, E., & Pino, M. R. (2013). Description and validation of a two-step analogue/regression downscaling method. *Theoretical and Applied Climatology*, *114*, 253-269.
5. Saha, M., Kafy, A. A., Bakshi, A., Almulhim, A. I., Rahaman, Z. A., Al Rakib, A., ... & Rathi, R. (2022). Modelling microscale impacts assessment of urban expansion on seasonal surface urban heat island intensity using neural network algorithms. *Energy and Buildings*, *275*, 112452.
6. Siddik, M. S., Tulip, S. S., Rahman, A., Islam, M. N., Haghighi, A. T., & Mustafa, S. M. T. (2022). The impact of land use and land cover change on groundwater recharge in northwestern Bangladesh. *Journal of Environmental Management*, *315*, 115130.
7. Singh, P., Kikon, N., & Verma, P. (2017). Impact of land use change and urbanization on urban heat island in Lucknow city, Central India. A remote sensing based estimate. *Sustainable cities and society*, *32*, 100-114.
8. Sobhani, P., Esmaeilzadeh, H., & Mostafavi, H. (2021). Simulation and impact assessment of future land use and land cover changes in two protected areas in Tehran, Iran. *Sustainable Cities and Society*, *75*, 103296.
9. Yang, K., Hou, H., Li, Y., Chen, Y., Wang, L., Wang, P., & Hu, T. (2022). Future urban waterlogging simulation based on LULC forecast model: A case study in Haining City, China. *Sustainable Cities and Society*, *87*, 104167.

Advanced Engineering Days

aed.mersin.edu.tr

Geospatial arbitrations with Landsat and Sentinel images in evaluating temperature variations over the New Delhi region of India

Jagadish Kumar Mogaraju[*1]

[1]*International Union for Conservation of Nature, Commission on Ecosystem Management, Agro-ecosystems, India, jagadishmogaraju@gmail.com*

Cite this study: Mogaraju, J. K. (2024). Geospatial arbitrations with Landsat and Sentinel images in evaluating temperature variations over the New Delhi region of India. Advanced Engineering Days, 9, 216-221

Keywords
Temperature
Climate change
Landsat
Sentinel
Cloud

Abstract

This work reports that thermal variations can be studied using free and open-source datasets and online web-based platforms. We find a clear indication that temperature deviations were high during the 2000-2012 period over the study area. We find that cloud thresholds of 0%, <25%, <50%, <75%, and <100% applied over satellite images influence our interpretation of temperature disparities. Normalized difference vegetation index is used to find the vegetation spread across the study area, and we find that the quantum of vegetation changed from 2019 to 2024, confirming that temperature and vegetation variations are associated. We conclude that Sentinel-2A and Landsat 8-9 images can be accessed and used with limited efforts to portray the climate situation of a region.

Introduction

Climate change effects are unraveling worldwide with vital indicators specifying anthropogenic intrusions into the environmental or natural landscape [1–3]. Temperature is a significant cue that is not so hard to comprehend by anyone as its effect is far and wide, with imminent repercussions in some places and close to immediate aftermaths in several places [4–8]. Though we find climate as an average of weather events over a longer time scale, it will be too late to react after comprehending the climate label of a specific location [9–12]. Satellite images are saturating our needs to manage natural resources and climate monitoring effectively [13–17]. Knowing the weather at any location has become a reality, and access requirements to temperature and precipitation-related datasets have evolved into a minimal process [18–20]. Landsat 8-9 and Sentinel-2 datasets help comprehend the temperature disparities over diverse locations [21–25]. The temperature anomalies over urban areas are evident and attributed to numerous factors, including population ingress and unsustainable anthropogenic developmental activities [26–28]. Several online platforms can provide data and plots free of cost, which is very helpful in knowing the temperature burden on humans and vice versa [29]. The present study aims to close the gaps in utilizing satellite images to comprehend the temperature variations for 2019 to 2023 with reference to 1961 to 1990.

Material and Method

The datasets and plots required for this study were obtained from EO browser applications of sentinel-hub (for both sentinel-2 and Landsat 8-9 images), https://www.meteoblue.com/, and https://yotka.org/meteo-hist. The images used in this study are from the period 2019-2023. The images were processed and analyzed for temperature differences and cloud cover, and the number of images was reported. Temperature information from images for each year from 2019 to 2023 was compared with the temperature values of 1961-1990. World Meteorological Organization recommends the 1961-1990 period as ideal for comparing climate change, i.e., changes in temperature in this case [30,31]. The study area in 2019 and 2024 is given in Figure 1, and the datasets and outputs provided in this study are given in Figure 2. The study area is New Delhi, spread across 77°E (Long) of the prime meridian and 28°N latitude.

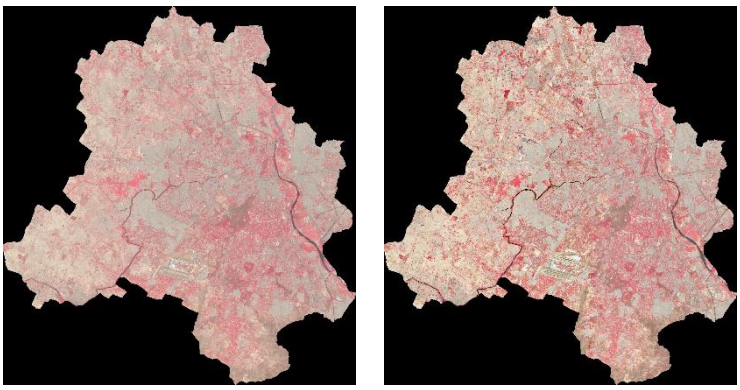


Figure 1. Study area in 2019 (Left) and 2024 (Right): Sentinel-2 Level-2A

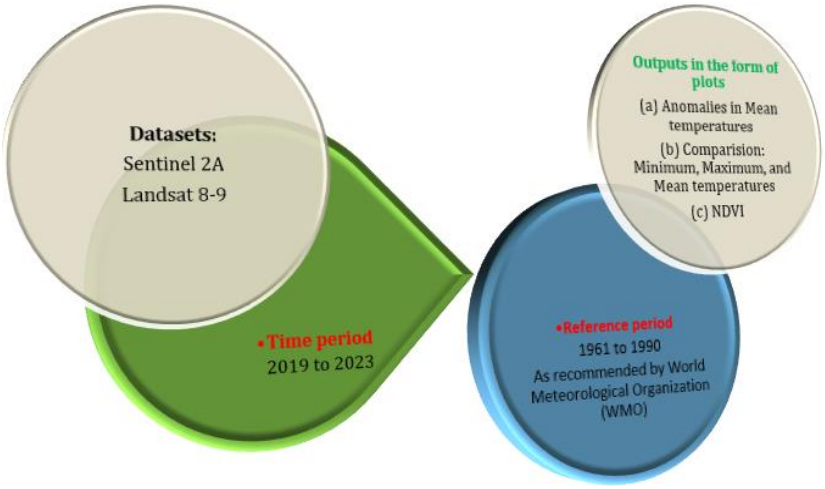


Figure 2. Datasets and outputs

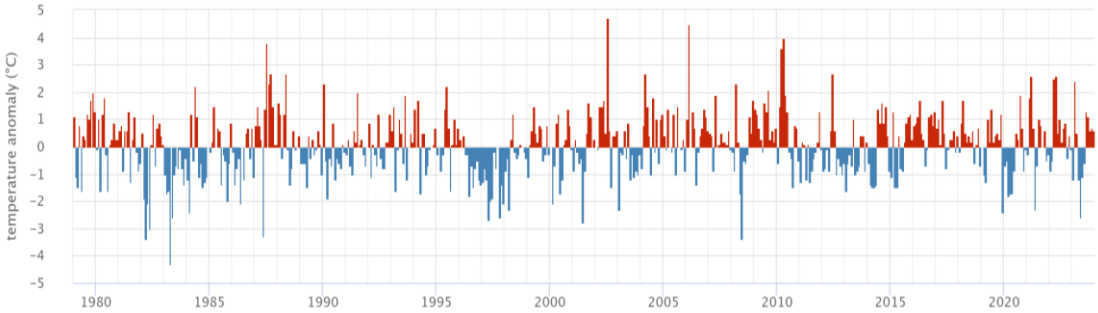


Figure 3. Mean temperature anomalies (1979 to 2024)

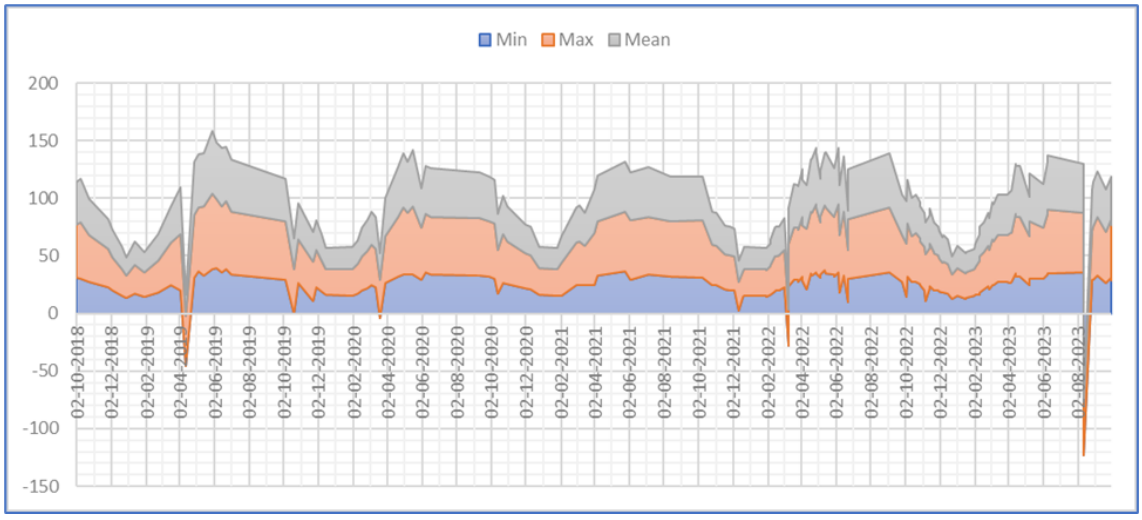


Figure 4. Minimum, Maximum, and Mean temperatures: Cloud (0%) (Landsat 8-9 L2-THERMAL: 156 images)

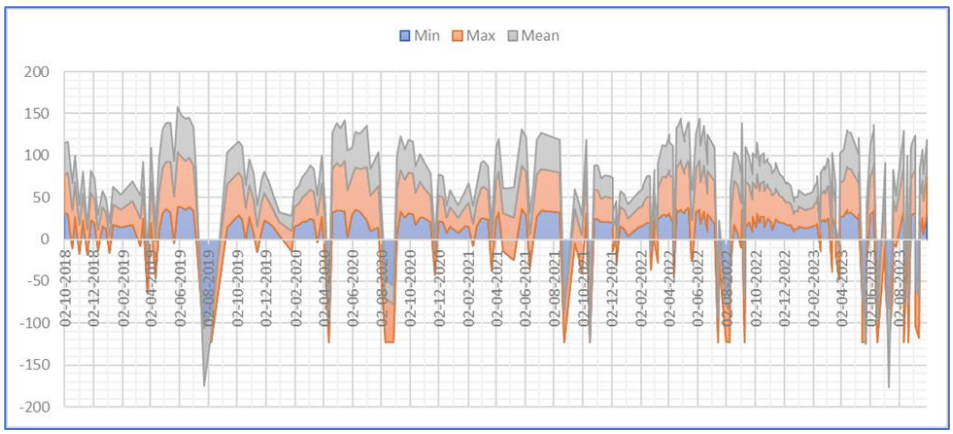


Figure 5. Minimum, Maximum, and Mean temperatures: Cloud (<25%) (Landsat 8-9 L2-THERMAL: 251 images)

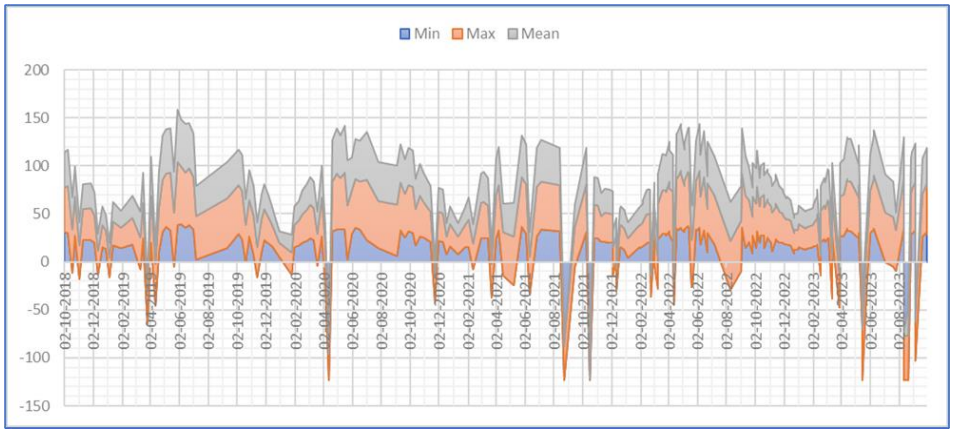


Figure 6. Minimum, Maximum, and Mean temperatures: Cloud (<50%) (Landsat 8-9 L2-THERMAL: 223 images)

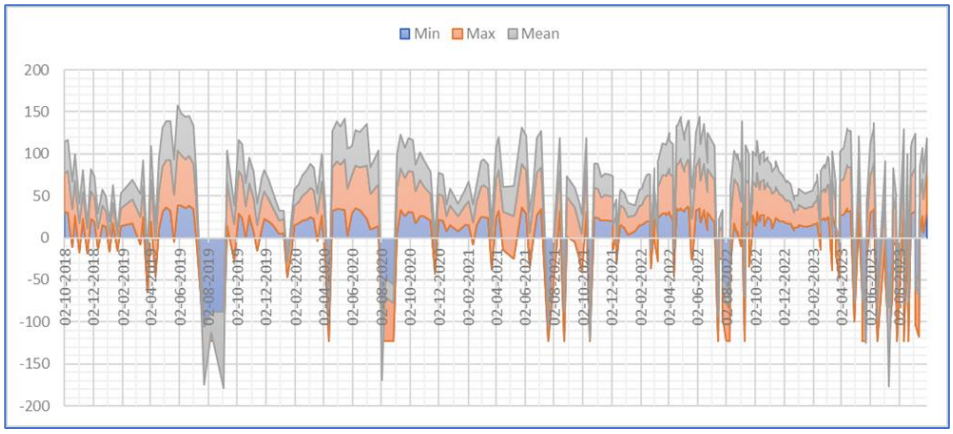


Figure 7. Minimum, Maximum, and Mean temperatures: Cloud (<75%) (Landsat 8-9 L2-THERMAL: 267 images)

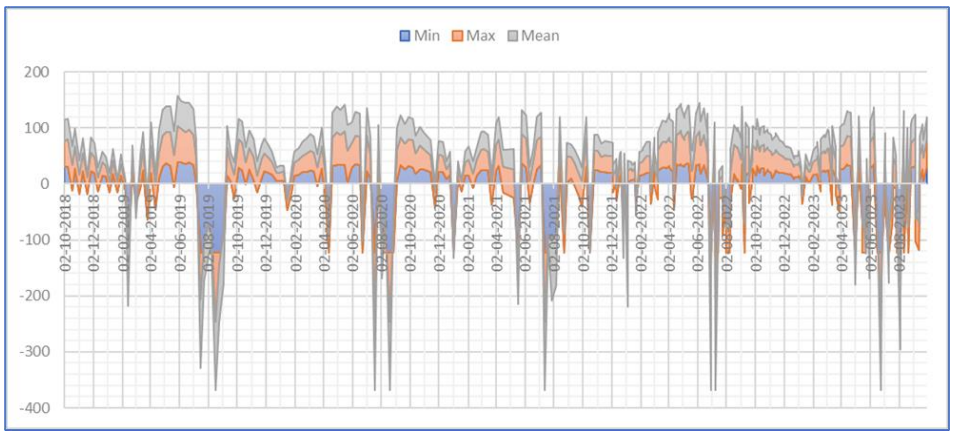


Figure 8. Minimum, Maximum, and Mean temperatures: Cloud (<100%) (Landsat 8-9 L2-THERMAL: 306 images)

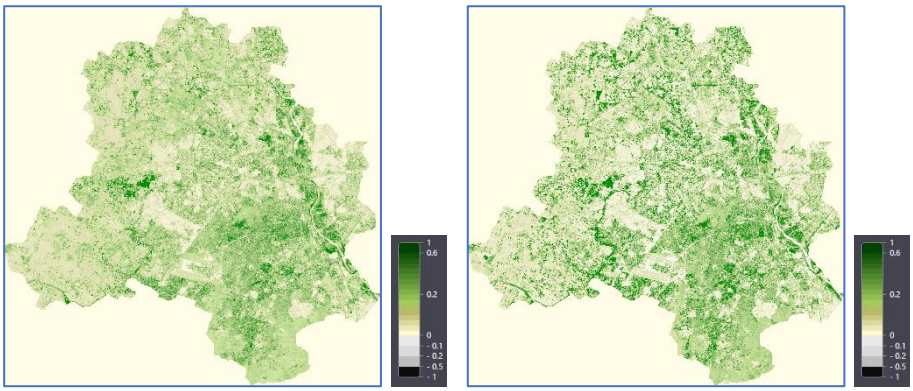


Figure 9. NDVI 2019 (Left) and 2024 (Right): Sentinel-2 Level-2A

Results

The results are given from Figure 3 to Figure 9. We find a clear distinction in the temperature anomalies that peaked during 2000-2012. There were dominant deviations between 2003-2004, 2006-2007, and 2010-2012 (Figure 3). From 2020, the deviations are greater than +2 compared to the mean temperature. We also observed how images with cloud cover influenced interpretation (cumulative). The minimum, maximum, and mean temperature (M3T) were extracted from Landsat 8-9 images (Thermal). Sudden decreases (approximate) in M3T were observed during 02-04-2019 and 02-08-2023 when cloud cover was 0% (Figure 4). When cloud cover threshold is set to < 25%, sudden decreases (approximate) in M3T was observed during 02-08-2019, 02-02-2020, 02-08-2020, 02-08-2021, 02-10-20221, 02-08-2022, 02-06-2023 (Figure 5). Similarly, when the cloud cover threshold is set at <50%, we find six instances of a sudden decrease in M3T (Figure 6). When the cloud cover threshold is set <75%, we find sixteen instances of a sudden decline in M3T (Figure 7). When the cloud cover threshold is set <100%, we find nine instances of a sudden decline in M3T (Figure 8). We opine that the cloud cover threshold may influence our interpretation of temperature deviations, and it should be factored into when analyzing thermal variations across a region of interest. The normalized difference vegetation index or NDVI of the study area during 2019 and 2024 is given in Figure 9. We find a clear vegetation reduction in the study area based on the NDVI values and visual interpretation.

Discussion

This work originated from the common knowledge that temperature generates diverse burdens on humans and other species around them. We set a premise that satellite images can influence our understanding of the actual climate situation over an area. Contingent upon the study premise, we identified the following that may be worth discussing. Sentinel-2 Level-2A and Landsat 8-9 images are free of cost through online platforms. They can be used to study the climate situation of any region of interest (if datasets for that particular date are available). We also find that NDVI plays a crucial role in finding the correlation between temperature deviations and anthropogenic developmental activities on a large scale. We observed that the period from 2000 to 2012 is crucial in defining the climate of the study area. Dominant deviations (continuous) were observed in 2020, signifying this study's importance, considering 2019 to 2023. Cloud cover threshold-based standardization of satellite interpretation is essential when defining thermal variations.

Conclusion

We conclude that urban growth and anthropogenic intrusions over and under natural landscapes might influence the local temperatures and that the thermal variations can be studied using satellite images. We found temperature deviations from normal when we compared our results to those of the reference period (1961-1990).

References

1. Rai, P. K. (2022). Environmental Degradation by Invasive Alien Plants in the Anthropocene: Challenges and Prospects for Sustainable Restoration. *Anthropocene Science*, *1*(1), 5–28. https://doi.org/10.1007/s44177-021-00004-y
2. AghaKouchak, A., Mirchi, A., Madani, K., Di Baldassarre, G., Nazemi, A., Alborzi, A., Anjileli, H., Azarderakhsh, M., Chiang, F., Hassanzadeh, E., Huning, L. S., Mallakpour, I., Martinez, A., Mazdiyasni, O., Moftakhari, H., Norouzi, H., Sadegh, M., Sadeqi, D., Van Loon, A. F., & Wanders, N. (2021). Anthropogenic Drought: Definition, Challenges, and Opportunities. *Reviews of Geophysics*, *59*(2), e2019RG000683. https://doi.org/10.1029/2019RG000683

3. Youssef, Y. M., Gemail, K. S., Atia, H. M., & Mahdy, M. (2024). Insight into land cover dynamics and water challenges under anthropogenic and climatic changes in the eastern Nile Delta: Inference from remote sensing and GIS data. *Science of The Total Environment*, *913*, 169690. https://doi.org/10.1016/j.scitotenv.2023.169690
4. Sorensen, C. J., Salas, R. N., Rublee, C., Hill, K., Bartlett, E. S., Charlton, P., Dyamond, C., Fockele, C., Harper, R., Barot, S., Calvello-Hynes, E., Hess, J., & Lemery, J. (2020). Clinical Implications of Climate Change on US Emergency Medicine: Challenges and Opportunities. *Annals of Emergency Medicine*, *76*(2), 168–178. https://doi.org/10.1016/j.annemergmed.2020.03.010
5. Weilnhammer, V., Schmid, J., Mittermeier, I., Schreiber, F., Jiang, L., Pastuhovic, V., Herr, C., & Heinze, S. (2021). Extreme weather events in europe and their health consequences – A systematic review. *International Journal of Hygiene and Environmental Health*, *233*, 113688. https://doi.org/10.1016/j.ijheh.2021.113688
6. Merz, B., Kuhlicke, C., Kunz, M., Pittore, M., Babeyko, A., Bresch, D. N., Domeisen, D. I. V., Feser, F., Koszalka, I., Kreibich, H., Pantillon, F., Parolai, S., Pinto, J. G., Punge, H. J., Rivalta, E., Schröter, K., Strehlow, K., Weisse, R., & Wurpts, A. (2020). Impact Forecasting to Support Emergency Management of Natural Hazards. *Reviews of Geophysics*, *58*(4), e2020RG000704. https://doi.org/10.1029/2020RG000704
7. Jay, O., Capon, A., Berry, P., Broderick, C., Dear, R. de, Havenith, G., Honda, Y., Kovats, R. S., Ma, W., Malik, A., Morris, N. B., Nybo, L., Seneviratne, S. I., Vanos, J., & Ebi, K. L. (2021). Reducing the health effects of hot weather and heat extremes: From personal cooling strategies to green cities. *The Lancet*, *398*(10301), 709–724. https://doi.org/10.1016/S0140-6736(21)01209-5
8. Kenny, G. P., Notley, S. R., Flouris, A. D., & Grundstein, A. (2020). Climate Change and Heat Exposure: Impact on Health in Occupational and General Populations. In W. M. Adams & J. F. Jardine (Eds.), *Exertional Heat Illness: A Clinical and Evidence-Based Guide* (pp. 225–261). Springer International Publishing. https://doi.org/10.1007/978-3-030-27805-2_12
9. Bruine de Bruin, W., Rabinovich, L., Weber, K., Babboni, M., Dean, M., & Ignon, L. (2021). Public understanding of climate change terminology. *Climatic Change*, *167*(3), 37. https://doi.org/10.1007/s10584-021-03183-0
10. Lloyd, E. A., & Shepherd, T. G. (2020). Environmental catastrophes, climate change, and attribution. *Annals of the New York Academy of Sciences*, *1469*(1), 105–124. https://doi.org/10.1111/nyas.14308
11. Marschütz, B., Bremer, S., Runhaar, H., Hegger, D., Mees, H., Vervoort, J., & Wardekker, A. (2020). Local narratives of change as an entry point for building urban climate resilience. *Climate Risk Management*, *28*, 100223. https://doi.org/10.1016/j.crm.2020.100223
12. Winkelmann, R., Donges, J. F., Smith, E. K., Milkoreit, M., Eder, C., Heitzig, J., Katsanidou, A., Wiedermann, M., Wunderling, N., & Lenton, T. M. (2022). Social tipping processes towards climate action: A conceptual framework. *Ecological Economics*, *192*, 107242. https://doi.org/10.1016/j.ecolecon.2021.107242
13. Kumar, S., Meena, R. S., Sheoran, S., Jangir, C. K., Jhariya, M. K., Banerjee, A., & Raj, A. (2022). Chapter 5—Remote sensing for agriculture and resource management. In M. K. Jhariya, R. S. Meena, A. Banerjee, & S. N. Meena (Eds.), *Natural Resources Conservation and Advances for Sustainability* (pp. 91–135). Elsevier. https://doi.org/10.1016/B978-0-12-822976-7.00012-0
14. Singh, R., Biswakarma, P., Joshi, V., Joshi, S., & Chaudhary, A. (2023). Spatiotemporal change analysis of land use/land cover in NCT of Delhi, India using geospatial technology. *Proceedings of the Indian National Science Academy*, *89*(1), 189–200. https://doi.org/10.1007/s43538-023-00152-2
15. Panwar, H., & Dhote, M. (2022). Degraded Land Management in Urban Areas: The Case of Biodiversity Parks in Delhi. In *Sustainable Urbanism in Developing Countries*. CRC Press.
16. AbdelRahman, M. A. E. (2023). An overview of land degradation, desertification and sustainable land management using GIS and remote sensing applications. *Rendiconti Lincei. Scienze Fisiche e Naturali*, *34*(3), 767–808. https://doi.org/10.1007/s12210-023-01155-3
17. Paul, S., Saxena, K. G., Nagendra, H., & Lele, N. (2021). Tracing land use and land cover change in peri-urban Delhi, India, over 1973–2017 period. *Environmental Monitoring and Assessment*, *193*(2), 52. https://doi.org/10.1007/s10661-020-08841-x
18. Shrivastava, V. K., Shrivastava, A., Sharma, N., Mohanty, S. N., & Pattanaik, C. R. (2023). Deep learning model for temperature prediction: A case study in New Delhi. *Journal of Forecasting*, *42*(6), 1445–1460. https://doi.org/10.1002/for.2966
19. Dash, S. K., Saraswat, V., Panda, S. K., & Pattnayak, K. C. (2022). Temperature extremes and their future projections in selected Indian cities along with their meteorological subdivisions and temperature homogeneous zones. *Urban Climate*, *41*, 101057. https://doi.org/10.1016/j.uclim.2021.101057
20. Sen Roy, S., Sharma, P., Sen, B., Sathi Devi, K., Sunitha Devi, S., Gopal, N. K., Kumar, N., Mishra, K., Katyar, S., Singh, S. P., Balakrishnan, S., Singh, C., Srivastava, K., Lotus, S., Paul, S., Singh, B., Gupta, J. P., Bandopadhyay, S., Das, G., … Mohapatra, M. (2021). A new paradigm for short-range forecasting of severe weather over the Indian region. *Meteorology and Atmospheric Physics*, *133*(4), 989–1008. https://doi.org/10.1007/s00703-021-00788-z
21. Kimothi, S., Thapliyal, A., Gehlot, A., Aledaily, A. N., gupta, A., Bilandi, N., Singh, R., Kumar Malik, P., & Vaseem Akram, S. (2023). Spatio-temporal fluctuations analysis of land surface temperature (LST) using Remote Sensing data (LANDSAT TM5/8) and multifractal technique to characterize the urban heat Islands (UHIs). *Sustainable Energy Technologies and Assessments*, *55*, 102956. https://doi.org/10.1016/j.seta.2022.102956

22. Shrestha, B., Ahmad, S., & Stephen, H. (2021). Fusion of Sentinel-1 and Sentinel-2 data in mapping the impervious surfaces at city scale. *Environmental Monitoring and Assessment*, *193*(9), 556. https://doi.org/10.1007/s10661-021-09321-6
23. Vohra, R., Kumar, A., & Rongali, G. (2024). Multi-scale extraction and spatial analysis of growth pattern changes in urban water bodies using sentinel-2 MSI imagery: A study in the central part of India. *Stochastic Environmental Research and Risk Assessment*, *38*(6), 2397–2423. https://doi.org/10.1007/s00477-024-02686-3
24. Das, N., Bhattacharjee, R., Choubey, A., Agnihotri, A. K., Ohri, A., & Gaur, S. (2022). Analysis of the Spatio-Temporal Variation of the Thermal Pattern of River Ganges in Proximity to Varanasi, India. *Journal of the Indian Society of Remote Sensing*, *50*(6), 1119–1134. https://doi.org/10.1007/s12524-022-01514-x
25. Tamrakar, Y., & Sharma, S. (2024). A Review of Spatial Analysis Techniques Used for LULC Change Detection Over Delhi NCR in the Past Two Decades. In S. Ghosh, M. Kumari, & V. N. Mishra (Eds.), *Geospatial Technology to Support Communities and Policy: Pathways to Resiliency* (pp. 263–287). Springer Nature Switzerland. https://doi.org/10.1007/978-3-031-52561-2_15
26. Islam, Md. M., Shahin, Md., Miraj, Md., Ghosh, S., Islam, Md. N., & Islam, I. (2021). Climate Change Impacts and Mitigation Approach: Coastal Landscape, Transport, and Health Aspects. In Md. N. Islam & A. van Amstel (Eds.), *Bangladesh II: Climate Change Impacts, Mitigation and Adaptation in Developing Countries* (pp. 41–101). Springer International Publishing. https://doi.org/10.1007/978-3-030-71950-0_2
27. Debnath, S., Sarkar, U. K., Kumari, S., Karnatak, G., Puthiyottil, M., Das, B. K., Das, A., Ghosh, B. D., & Roy, A. (2024). Exploring the vulnerability of the coastal wetlands of India to the changing climate and their adaptation strategies. *International Journal of Biometeorology*, *68*(4), 749–760. https://doi.org/10.1007/s00484-024-02620-w
28. Vinod Kumar, T. M., Mohammed Firoz, C., Bimal, P., Harikumar, P. S., & Sankaran, P. (2020). Smart Water Management for Smart Kozhikode Metropolitan Area. In T. M. Vinod Kumar (Ed.), *Smart Environment for Smart Cities* (pp. 241–306). Springer. https://doi.org/10.1007/978-981-13-6822-6_7
29. Berrang-Ford, L., Sietsma, A. J., Callaghan, M., Minx, J. C., Scheelbeek, P. F. D., Haddaway, N. R., Haines, A., & Dangour, A. D. (2021). Systematic mapping of global research on climate and health: A machine learning review. *The Lancet Planetary Health*, *5*(8), e514–e525. https://doi.org/10.1016/S2542-5196(21)00179-0
30. Raheja, L., Wadalkar, R., Chaudhuri, R. R., & Pandit, A. (2024). Surface wind speed trends for the period of 1981–2020 and their implication for a highly urbanised semi-arid Delhi–NCR and surrounding areas. *Journal of Earth System Science*, *133*(2), 112. https://doi.org/10.1007/s12040-024-02322-2
31. Garg, P. K., Shukla, A., Yousuf, B., & Garg, S. (2022). Temperature and precipitation changes over the glaciated parts of Indian Himalayan Region during 1901–2016. *Environmental Monitoring and Assessment*, *194*(2), 84. https://doi.org/10.1007/s10661-021-09689-5

Advanced Engineering Days

aed.mersin.edu.tr

Hydrological analysis for disaster management in Şanlıurfa region

Berra Nur Önay*[1], Halil İbrahim Şenol [1]

[1]*Harran University, Department of Geomatics Engineering, Türkiye, berra34onay@gmail.com, hsenol@harran.edu.tr*

Cite this study: Önay, B., N., & Şenol, H., İ. (2024). Hydrological analysis for disaster management in Şanlıurfa region. Advanced Engineering Days, 9, 222-225

Keywords
Hydrology
GIS
Slope
Aspect
Disaster Management

Abstract

The hydrological analysis of the Şanlıurfa region, as presented in this study, employs SRTM DEM data within an ArcGIS environment to develop a comprehensive understanding of the area's water dynamics for disaster management purposes. By processing DEM data to generate detailed streamlines and topographical maps, including slope and aspect maps, this research offers vital insights into the region's susceptibility to flooding, erosion, and other water-related challenges. These findings not only enhance our understanding of Şanlıurfa's hydrological characteristics but also provide a foundation for further studies in disaster management, water resource management, and sustainable agricultural practices. The methodology showcases the importance of integrating advanced GIS technologies with hydrological data for precise water flow modeling and terrain analysis, emphasizing the potential for such analytical approaches to improve resilience against water-related disasters and inform sustainable land use and water resource management in semi-arid regions.

Introduction

Floods and droughts are among the water-related disasters that cause important environmental problems in Şanlıurfa, a region with a deep history and great agricultural wealth, in the context of southeastern Turkey [1]. On the other hand, floods, which are usually caused by abrupt heavy rains or overflows due to a breach and collapse of the Euphrates and Tigris Rivers, would cause damage to infrastructure, housing, and agricultural lands, in addition to uprooting communities and thus disrupting the very basis of their livelihoods.

The main objectives of disaster management in this context are twofold: to assess and reduce the risk of three major water-related disasters such as floods, droughts and landslides [2]. It would therefore identify patterns of precipitation, river flow, groundwater levels and other data related to hydrology with the aim of making very reliable predictions on the occurrence and impact of such events.

In fact, all the theories and models that exist and that pertain to the field of hydrological analysis and disaster management would contribute to the methodologies towards developing a deeper understanding of the impacts related to water disasters. [Advanced simulation models, such as the Hydrological Simulation Program-Fortran (HSPF) [4] and the Soil and Water Assessment Tool (SWAT) [5, 6], form the basis for an in-depth understanding of watershed behavior and can be used to simulate impacts on water resources for various land use and climate scenarios. Geographic Information Systems (GIS), integrated with remote sensing technologies, have further enhanced the capabilities of hydrological studies and disaster risk management, providing even greater detail for the mapping and analysis of water-related risks [7].

These may be some of the contributions expected from hydrological studies and beyond for disaster management practices in the region. This study has shown the way, which could be replicated in different settings, towards a more resilient and sustainable approach to water resources management and risk reduction of climate-related disasters.

Material and Method

Study Area

Şanlıurfa, in southeastern Turkey, occupies a special position due to the hydrological importance of the area it dominates in relation to the Fertile Crescent of the Mesopotamian Plain, between the historically famous Tigris

and Euphrates Rivers. The hydrology of this area is central to agricultural productivity, while more generally, it really underpins the sustainability of this ecosystem and region for environmental and socio-economic development. The waters of the rivers maintain biodiversity, support the population with domestic and industrial water needs, and support crops of different types and varieties.

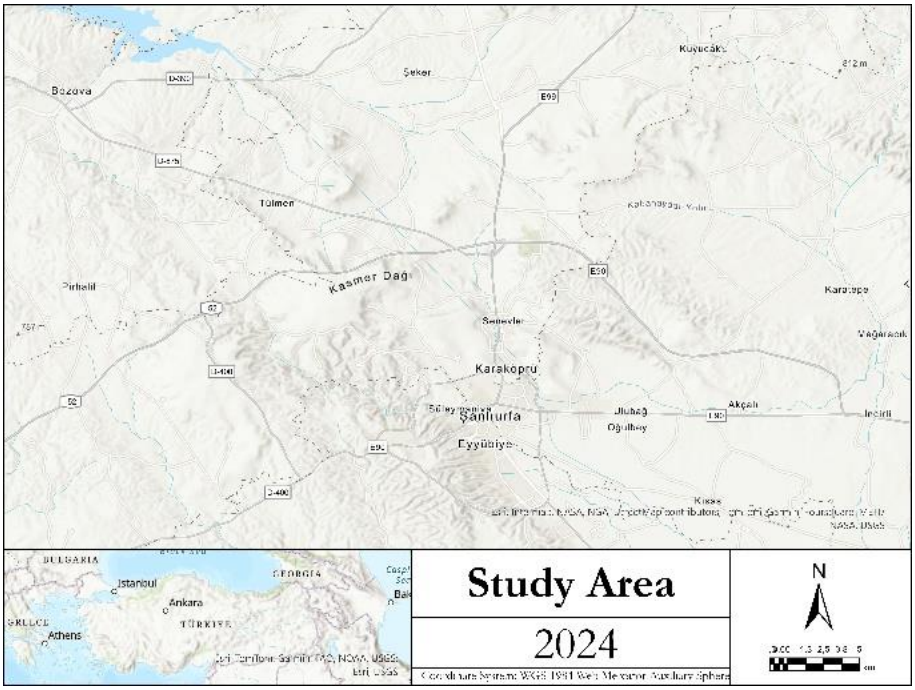


Figure 1. Study Area

Method

The processing of the SRTM DEM data consisted of the first stage of our methodology within ArcGIS Pro to create streamlines. This was done mainly through hydrological modeling functions that would perform the movement of water over the terrain from which the concentration channels are derived for the creation of streamflow. The input criteria for the software used to carry out this exercise are therefore streamlines, delusion and flow patterns necessary for flood risk management and water resources management and are called to delineate a drainage network for this entire region.

We then focused on creating slope and aspect maps from the DEM data. The slope map was derived from the DTM to quantify the steepness of the terrain. In hydrological analysis, it plays a greater role because the surface slope has a huge influence on both the rate and volume of surface runoff, thus directly affecting erosion rates and the ability to transport sediment. On the other hand, the aspect map shows which direction the slopes face, which is important for understanding microclimatic variations and their impact on local hydrology.

In this research, ArcGIS Pro's advanced spatial analysis tools were used in each of the hydrologic models to help improve the accuracy and reliability of each model. Thus, interfacing SRTM data with the dynamic capabilities of ArcGIS Pro will enable detailed mapping of the hydrological characteristics of Şanlıurfa through the various features mentioned above. The results of this work, especially the streamline, slope and aspect maps, will be considered as basic and will be the basis for further hydrological assessment in the field of disaster and management planning.

Results

The hydrological analysis of the Şanlıurfa region, utilizing SRTM DEM data within an ArcGIS environment, yielded significant findings crucial for understanding the area's water dynamics and potential disaster management strategies. After filling gaps in the DEM data and establishing flow directions, the analysis proceeded to delineate the entry and exit points of water lines, leading to the creation of accurate streamlines. These streamlines (Figure 2) provide a detailed visualization of water flow patterns across the terrain, serving as an essential tool for identifying areas at risk of flooding and for planning water resource management and conservation efforts.

Furthermore, the generation of slope and aspect maps from the DEM data offered deeper insights into the topographical features of the region. These maps (Figure 3) are instrumental in assessing the land's susceptibility to erosion, water accumulation, and potential flash flood scenarios. The slope map reveals the terrain's steepness, crucial for understanding runoff patterns and erosion risk. In contrast, the aspect map highlights the directional orientation of slopes, influencing microclimate conditions, vegetation patterns, and snowmelt runoff behaviors.

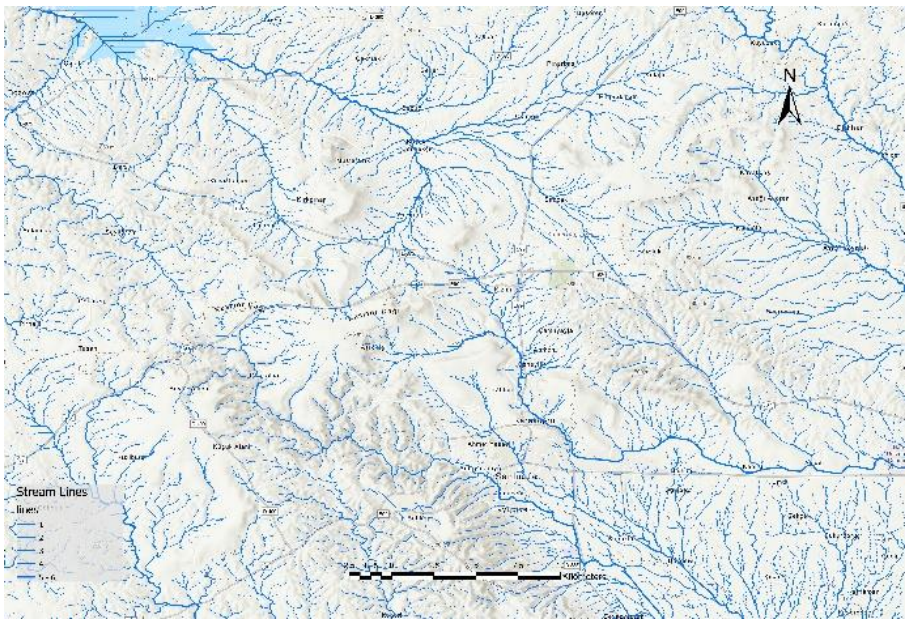


Figure 2. Streamlines of the area

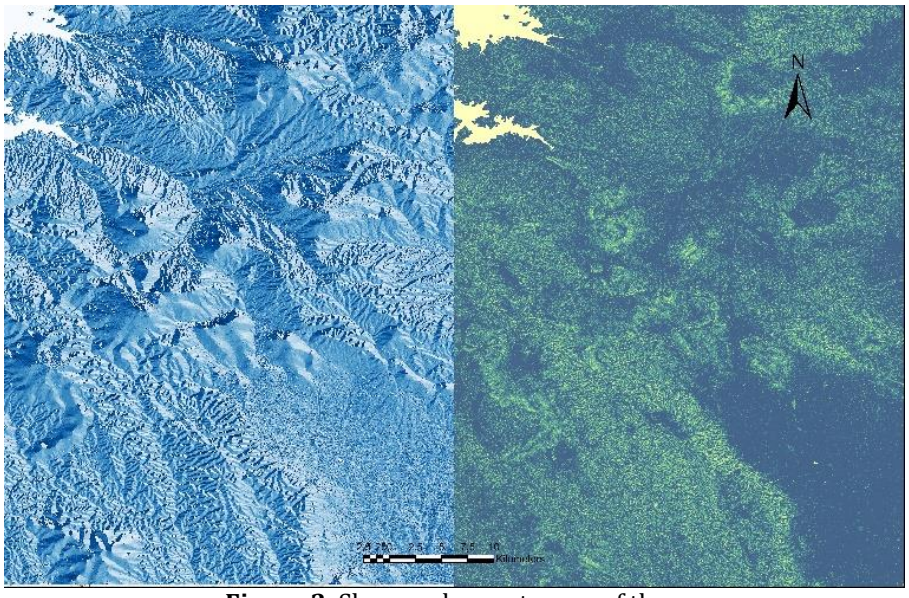


Figure 3. Slope and aspect maps of the area

Together, these outcomes not only enhance our comprehension of the hydrological characteristics of Şanlıurfa but also establish a foundational base for further research and application in flash flood analysis, disaster management planning, and sustainable water resource management in the region. This detailed mapping and analysis underscore the potential of integrating SRTM DEM data with GIS technology to address hydrological challenges and improve disaster management practices in vulnerable areas.

Conclusion

The hydrological analysis of Şanlıurfa, utilizing SRTM DEM data within an ArcGIS Pro environment, provides essential insights into effective water management and disaster risk reduction strategies. The generated streamlines and topographical maps (slope and aspect) offer a comprehensive understanding of the region's hydrological dynamics, highlighting areas susceptible to flooding and erosion. This methodology underscores the value of integrating advanced GIS technologies with hydrological data for precise water flow modeling and terrain analysis. The findings not only facilitate targeted disaster management planning in Şanlıurfa but also serve as a model for similar semi-arid regions facing water-related challenges. Future research could further refine these strategies by incorporating additional environmental variables, showcasing the potential of such analytical approaches in enhancing resilience against water-related disasters and informing sustainable land use and water resource management practices.

References

1. Keskiner, A. D., Cetin, M., & Nagano, T. (2019). Mapping spatio-temporal tendencies of climate types in Geographic Information Systems (GIS) media: A case study in Şanlıurfa and its environs. Mustafa Kemal Üniversitesi Tarım Bilimleri Dergisi, 24, 232-240.
2. Yang, T. H., & Liu, W. C. (2020). A general overview of the risk-reduction strategies for floods and droughts. Sustainability, 12(7), 2687.
3. Gull, S., & Shah, S. R. (2020). Watershed models for assessment of hydrological behavior of the catchments: a comparative study. Water Practice & Technology, 15(2), 261-281.
4. Dey, P. (2021). Sensitivity and uncertainty analysis in hydrological modeling: A case study of South Chickamauga Creek watershed using BASINS/HSPF.
5. Fiseha, B. M., Setegn, S. G., Melesse, A. M., Volpi, E., & Fiori, A. (2013). Hydrological analysis of the Upper Tiber River Basin, Central Italy: a watershed modelling approach. Hydrological processes, 27(16), 2339-2351.
6. Ficklin, D. L., Luo, Y., & Zhang, M. (2013). Watershed modelling of hydrology and water quality in the Sacramento River watershed, California. Hydrological processes, 27(2), 236-250.
7. Singh, P., Gupta, A., & Singh, M. (2014). Hydrological inferences from watershed analysis for water resource management using remote sensing and GIS techniques. The Egyptian Journal of Remote Sensing and Space Science, 17(2), 111-121.

Advanced Engineering Days

aed.mersin.edu.tr

Road extraction with high-resolution UAV images using deep learning algorithms

Halil İbrahim Şenol[*1]

[1]*Harran University, Department of Geomatics Engineering, Türkiye, hsenol@harran.edu.tr*

Cite this study: Şenol, H. İ. (2024). Road extraction with high-resolution UAV images using deep learning algorithms. Advanced Engineering Days, 9, 226-228

Keywords
Road extraction
GIS
Deep learning
UAV
Very high resolution

Abstract

Obtaining continuous data on unplanned urbanization regions is important in terms of making precise plans for future studies in these regions. An unplanned urbanization area was selected and road extraction was performed using very high-resolution Unmanned Aerial Vehicle (UAV) images. In this direction, Sat2Graph deep learning model was used with the Object Detection tool included in the deep learning package published by ArcGIS Pro software and road extraction was performed with very high-resolution UAV image. This will ensure that data updates made through volunteerism are carried out faster and more accurately. Recall, F1 score, precision ratio/uncertainty accuracy, and average producer accuracy of products automatically extracted with the algorithm were determined as 0.816, 0.827, 0.838, and 0.792.

Introduction

Environmental monitoring has been one of the most important development issues in recent years. The studies conducted in this direction have mainly examined the changes in the earth and their impact on the urban and environmental scale. Therefore, the monitoring of urban development remains an important step in the creation of smart cities. In this direction, the use of high resolution unmanned aerial vehicles (UAV) and aerial photography has gained importance [1]. Until now, satellite imagery has generally been used to monitor urban development [2], but with the availability of UAVs in recent years, these processes have started to be carried out with more sensitive data [3]. Although it has become easier to obtain sensitive data with the development of data collection methods, there has been data confusion in the resulting products. Therefore, it has become a necessity to extract meaningful results from the data obtained from the UAV images. Although this manual extraction process has evolved over time with semi-automatic methods, object detection from dense data has become fully automatic with deep learning algorithms in recent years.

Object detection with deep learning on high-resolution images is one of the most important research topics in recent years. The choice of the method used is certainly important, but it is also important to use high-resolution data to prove the effectiveness of the method. While such studies use high-resolution aerial photographs [4], similar studies are carried out with high-resolution satellite images [5, 6]. The choice of data selection depends on the application. While the use of commercial software for object detection is common, the use of deep learning algorithms has become a common practice in recent years [7, 8].

In this study, road extraction was performed using the object detection method using a high-resolution UAV image of Mersin, Turkey and the Sat2Graph deep learning algorithm. The aim of the study is to demonstrate that road extraction can be performed accurately from very high resolution UAV images using deep learning.

Material and Method

Study Area

This study was conducted in a neighborhood in Mersin, Turkey, where I obtained high-resolution UAV imagery (Figure 1). Importantly, the selected region is an important example of unplanned urbanization and draws attention to the need for urban transformation. Due to the unplanned urbanization characteristics of the study area, it is also a notable region for measuring the performance of the deep learning algorithm used for road extraction.

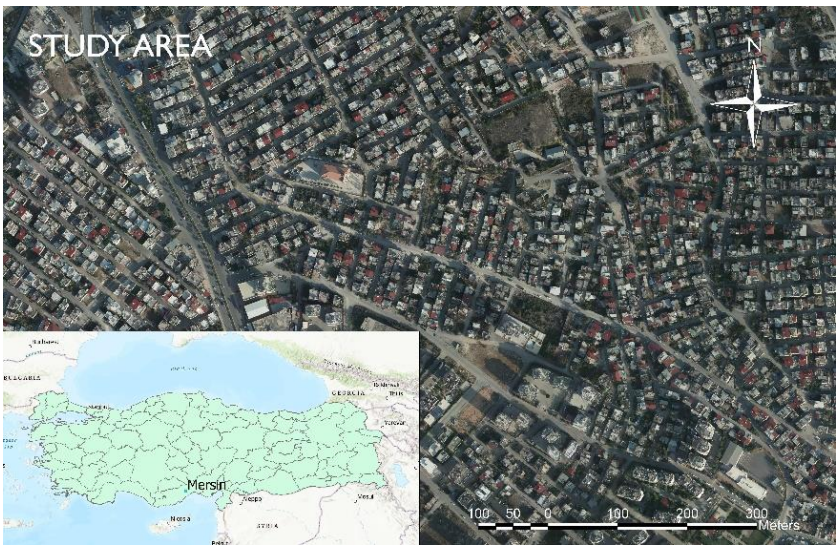


Figure 1. Study Area

Method

This study used the Sat2Graph deep learning method developed by He et al. [9]. The deep learning toolbox published by ArcGIS Pro developers was used to apply this method.

Sat2Graph is a new approach that can encode a road network graph into a 3D tensor. This graph is called GraphTensor Encoding (GTE) and has been developed using a non-repetitive neural network model to convert the input image directly into the road network. G = {V, E} is a road network covering an area of W meters by H meters, where V are vertices and E are edges. GraphTensor Encoding uses Wλ x Hλ x (1 + 3Dmax) to encode the graph, where λ is the spatial resolution that limits the encoded graph and Dmax is the maximum edge that can be encoded [9]. This method combines the advantages of segmentation and graph-based approaches and provides a more effective result.

It is currently used to evaluate the accuracy of various object detection algorithms, including Recall, F1 Score, Precision Ratio/Uncertainty Accuracy (UAcc), Producer Accuracy (Pacc), and manual detection. To evaluate the correct identification ability of our above accuracy evaluation method, the following definitions must be made.

Results

In this study, road extraction from the high-resolution image was performed using the object detection method of the newly developed deep learning tool of Esri ArcGIS Pro. This tool uses the Sat2Graph algorithm and a pre-trained deep learning package. Detailed information about this tool is available from Esri. Since the region used for this study is an area of intense unplanned urbanization, it is important to obtain results in such a region where the distinguishability of roads is low. Figure 2 shows the area where the path inference is performed and the results.

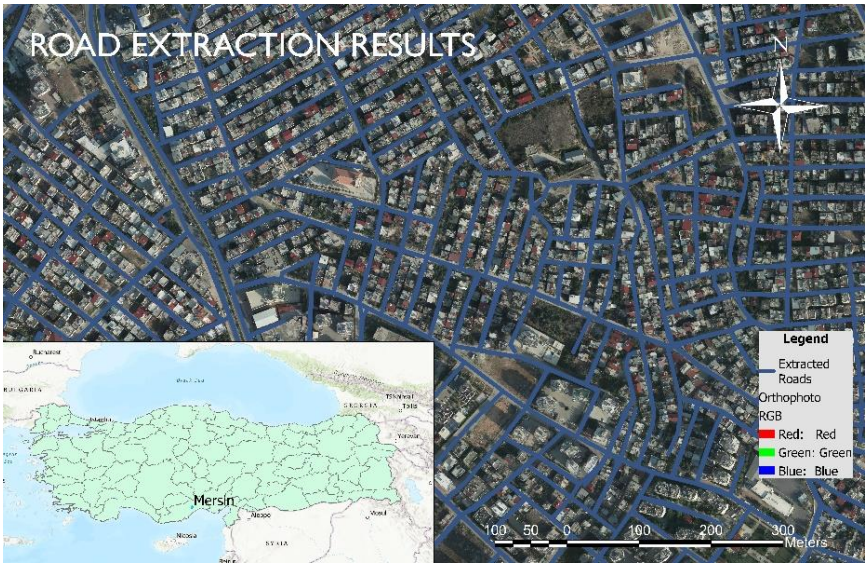


Figure 2. Road extraction results

To reveal the results of road extraction, the ground truth values and the paths obtained by deep learning were compared and accuracy analysis was performed (Table 1). As shown in Figure 4, the data were compared and the results are shown in Table 1.

Table 1. Road extraction results for the very high-resolution UAV images using Sat2Graph

	Total	TP	FP	FN	Recall	F1 Score	Precision (UAcc)	Pacc
Sat2Graph	427	301	58	68	0.816	0.827	0.838	0.792

Conclusion

This study was conducted in three phases. Obtain a very high resolution orthomosaic with a resolution of 7 cm/pix by acquiring and processing the UAV data. Path inference using the Sat2Graph deep learning algorithm in ArcGIS Pro. As a result of the study, the recall, F1 score, UAcc, and Pacc average accuracy of products automatically extracted by the algorithm were determined to be 0.816, 0.827, 0.838, and 0.792. Although the obtained data contain various topological errors, this can be considered normal since the study area is located in an unplanned urbanization zone. However, future studies will be conducted to automatically remove the topological errors. Comparisons can be made by adding more object detection deep learning algorithms in future studies. By making these comparisons with different data, a result can be obtained by choosing the right algorithms for the different data used.

References

1. Biçici, S., & Zeybek, M. (2021). Effectiveness of Training Sample and Features for Random Forest on Road Extraction from Unmanned Aerial Vehicle-Based Point Cloud. Transportation Research Record, 2675(12), 401–418. https://doi.org/10.1177/03611981211029645
2. Yiğit, A. Y., & Uysal, M. (2021). Yüksek Çözünürlüklü İnsansız Hava Aracı (İHA) Görüntülerinden Karayolların Tespiti. Bitlis Eren Üniversitesi Fen Bilimleri Dergisi, 10(3), 1040-1054.
3. Yiğit, A. Y., & Uysal, M. (2020). Automatic road detection from orthophoto images. Mersin Photogrammetry Journal, 2(1), 10-17.
4. Şenol, H. İ., Yiğit, A. Y., Kaya, Y. & Ulvi, A. (2021). İHA ve yersel fotogrametrik veri füzyonu ile kültürel mirasın 3 boyutlu (3B) modelleme uygulaması: Kanlıdivane Örneği. Türkiye Fotogrametri Dergisi, 3(1), 29-36.
5. Yiğit, A. Y., Kaya, Y., & Şenol, H. İ. (2022). Monitoring the change of Turkey's tourism city Antalya's Konyaaltı shoreline with multi-source satellite and meteorological data. Applied Geomatics, 14(2), 223-236.
6. Şenol, H. İ., Kaya, Y., Yiğit, A. Y., & Yakar, M. (2023). Extraction and geospatial analysis of the Hersek Lagoon shoreline with Sentinel-2 satellite data. Survey Review, 1-16.
7. Abdollahi, A., Pradhan, B., Shukla, N., Chakraborty, S., & Alamri, A. (2020). Deep learning approaches applied to remote sensing datasets for road extraction: A state-of-the-art review. Remote Sensing, 12(9), 1444.
8. Xu, Y., Xie, Z., Feng, Y., & Chen, Z. (2018). Road extraction from high-resolution remote sensing imagery using deep learning. Remote Sensing, 10(9), 1461.
9. He, S., Bastani, F., Jagwani, S., Alizadeh, M., Balakrishnan, H., Chawla, S., & Sadeghi, M. A. (2020). Sat2graph: Road graph extraction through graph-tensor encoding. In European Conference on Computer Vision (pp. 51-67). Springer, Cham.

Advanced Engineering Days

aed.mersin.edu.tr

Assessment of green space changes using NDVI index via Google Earth Engine and ArcGIS platforms: A case study of Isfahan, Ahvaz, and Maragheh Cities, Iran

Paria Ali Mohammadi *[1], Iraj Teymuri [1]

[1] Tabriz University, Faculty of planning and Environmental Science, Iran, pariaa.mohammadi@gmail.com, iraj-teymuri@tabrizu.ac.ir

Cite this study: Ali Mohammadi, P., & Teymouri, I. (2024). Assessment of green space changes using NDVI index via Google Earth Engine and ArcGIS platforms: A case study of Isfahan, Ahvaz, and Maragheh Cities, Iran. Advanced Engineering Days, 9, 229-231

Keywords
Green spaces
Google Earth Engine
NDVI Index

Abstract

Spatial changes in green spaces related to the cities of Maragheh, Ahvaz, and Isfahan have been examined using Landsat 8 satellite images. These images are part of Collection 2 data, which is processed for analytical studies such as assessing changes in green spaces or geological applications. In this article, the NDVI is utilized to compare green space changes among the mentioned cities. For the result the density of urban green spaces in all cities of Maragheh, Ahvaz, and Isfahan has decreased over time, with the density of other spaces increasing. These changes in Maragheh and Ahvaz between the years 2010-2016 have been significant and noticeable, while in Isfahan, they have been gradual and less perceptible. This indicates uncontrolled construction in the cities of Maragheh and Ahvaz and more oversight over construction in the city of Isfahan. Among the most significant consequences of this change are endangering the physical and mental health of individuals, reducing recreational and rest areas for citizens, increasing environmental pollution, increasing heat temperatures, and creating heat islands, resulting in a decline in the quality of individual and social life.

Introduction

It is well established that urban green areas provide a wide range of social, aesthetic, environmental and economic benefits (Caspersen, Konijnendijk, & Olafsson, 2006, p. 7)

Green space: An urban green space is directly used for active or passive recreation; or indirectly used by virtue of its positive influence on the urban environment, serving the diverse needs of citizens and thus offering a good quality of life in cities. It can assume different characteristics, e.g. parks, gardens, squares, cemeteries and allotment gardens as well as woodlands and areas for nature and landscape conservation. Urban green is the sum of all green spaces combined to make up the urban green fabric or system (Costa, Erjavec, & Mathey, 2008).

Benefits of green spaces: the benefits of woodland and trees can differ widely between cities and towns due their different environmental and socio-cultural background. The recreational and aesthetic benefits are traditionally important especially in the Nordic countries, whereas the protective and climatic uses of vegetation are more emphasized. Furthermore, while the use of trees to shelter from strong winds is an important issue in some parts, shading is a more important concern in hot climates. In practice, management of the urban forest is a challenging task not only because of harsh growing conditions but also because of various, often conflicting, demands and goals. Therefore, this paragraph will also address geographical and socio-cultural differences in benefits and uses between various regions (Tyrväinen, Pauleit, Seeland, & Vries, 2005, p. 82).

Landsat – 8: Landsat 8 (previously named the Landsat Data Continuity Mission) is a joint NASA/U.S. (NASA's earth observing system project science office, 2019). Landsat's Global Survey Mission is to establish and execute a data acquisition strategy that ensures repetitive acquisition of observations over the Earth's land mass, coastal boundaries, and coral reefs, supporting work in agriculture, geology, forestry, education, mapping, emergency response and disaster relief, as well as providing a long-term record of natural and human-induced changes to the Earth (European space agency, 2024).

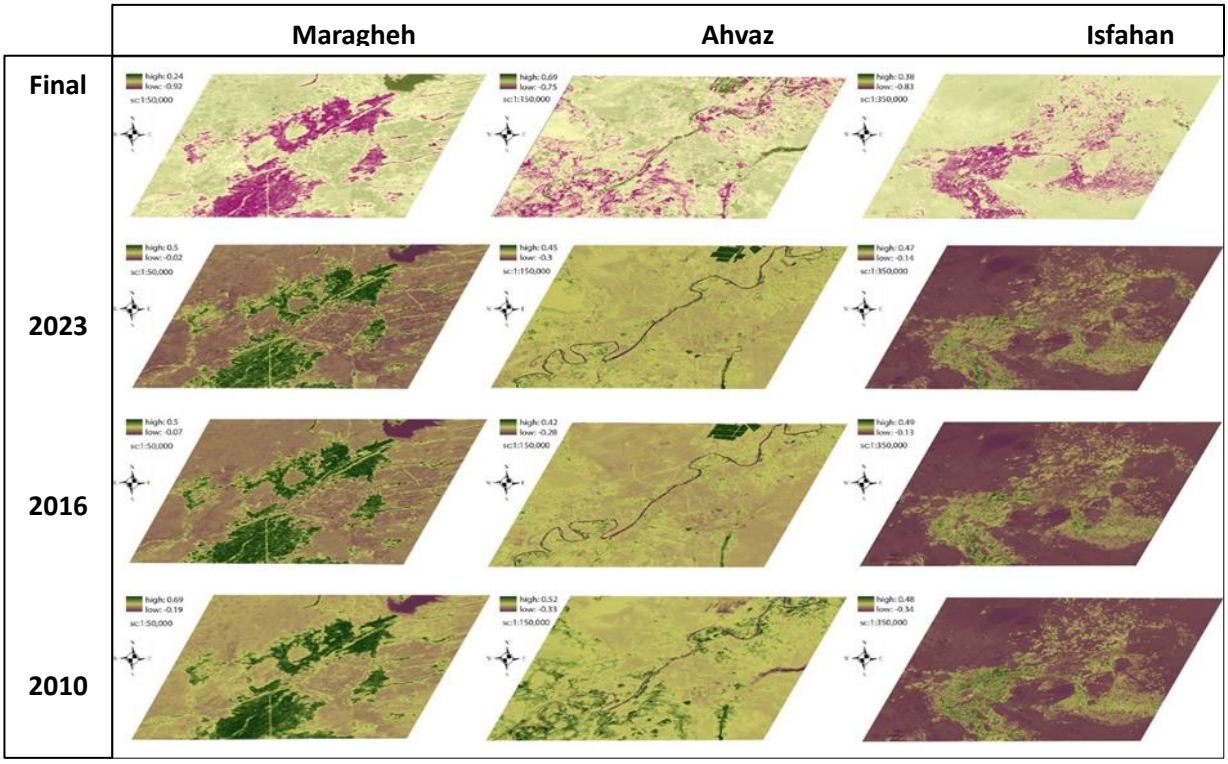
Normalized difference vegetation (NDVI) index: The Normalized Difference Vegetation Index (NDVI) is used on a wide range for many purposes such as monitoring drought. The NDVI helps recompense the inconstant conditions of illumination, surface slope, and other (Lillesand, Kiefer, & Chipman, 2004).

Table 1. Benefits and uses of urban forests, trees and green spaces

Social benefits	Recreation opportunities, improvements of home and work environments, impacts on physical and mental health. Cultural and historical values of green areas.
Aesthetic and architect	Landscape variation through different colors, textures, forms and densities of plants. Growth of trees, seasonal dynamics and experiencing nature. Defining open space, framing and screening views, landscaping buildings
Climate and physical benefits	Cooling, wind control, impacts on urban climate through temperature and humidity control. Air pollution reduction, sound control, glare and reflection on reduction, flood prevention and erosion control
Ecological benefits	Biotopes for flora and fauna in urban environment
Economic benefits	Value of market-priced benefits (timber, berries, mushrooms. ect.), increased property values, tourism

Material and Method

Spatial changes in green spaces related to the cities of Maragheh, Ahvaz, and Isfahan have been examined using Landsat 8 satellite images. These images are part of Collection 2 data, which is processed for analytical studies such as assessing changes in green spaces or geological applications. In this article, the NDVI is utilized to compare green space changes among the mentioned cities, derived from Landsat 8 satellite data from Collection 2. The NDVI is calculated from reflectance measurements in the red and near infrared (NIR) portion of the spectrum (Govaerts & Verhulst, 2010): $\text{NDVI} = \frac{R_{NIR} - R_{RED}}{R_{NIR} + R_{RED}}$



Picture 1. NDVI indexes of Maragheh, Ahvaz, Isfahan cities in 2010, 2016, and 2023

NDVI values range from +1.0 to -1.0. Areas of sand, rock, bare or snow show quite low NDVI values, usually 0.1 or less. Sparse vegetation such as grassland and shrubs or aging green cover has moderate NDVI values corresponding to the 0.2 to 0.5 range. High NDVI values in the range of 0.6 to 0.9 occur in tropical forests and areas with dense vegetation (USGS, science for a changing world, 2018).

For this purpose, the NDVI index of the cities of Maragheh, Ahvaz, and Isfahan has been calculated as three case study cities chosen based on population and area, respectively small, medium, and large, for the years 2010, 2016, and 2023. Finally, using GIS software and the raster calculator command, the NDVI indices have been subtracted from each other in the order of nearest to oldest (2023-2016-2010). The final maps are visible in the first row.

Results

As evident in the above maps, the density of urban green spaces in all cities of Maragheh, Ahvaz, and Isfahan has decreased over time, with the density of other spaces increasing. These changes in Maragheh and Ahvaz

between the years 2010-2016 have been significant and noticeable, while in Isfahan, they have been gradual and less perceptible. This indicates uncontrolled construction in the cities of Maragheh and Ahvaz and more oversight over construction in the city of Isfahan.

Discussion

In the Assessment of urban green space distribution within the scope of european green deal using NDVI Indice; case of Nicosia / Cyprus, the urban green space distribution was determined, and the city's compliance with the European Green Deal was evaluated. The classification data showed that open green areas have a nonhomogeneous distribution throughout the city, and the amount of green space per capita is approximately 200 m^2. According to the classification results of Northern Nicosia, a surface area of 475 km^2, the amount of green space is calculated as 16m^2, constituting 2.97%. Thus, it has been concluded that open green regions are denser in certain parts of the city than others and do not have a homogeneous distribution that can serve the whole town (Eyileten, Esandağli, & Selim, 2022).

The research of Analysis of urban green space changes; case study: region 2 of Tehran investigates the effects of urbanization and urban development on green spaces in region 2 of Tehran quantitatively during two time periods, 1989 and 2002, using aerial image interpretation and Geographic Information System (GIS). According to the analyses conducted, natural green spaces have experienced a significant decrease, while artificial green spaces have shown a considerable increase. It is worth mentioning that the majority of land use changes and reduction in desired levels have occurred in the northern half of the region. Concerning the sub-regions of the area, Zone 8 exhibits the highest reduction in green space coverage, while Zone 6 shows the least reduction (Hashemi, Kafi, Hashemi, & Khan Sefid, 2009).

Conclusion

As mentioned earlier, the density and area of urban green spaces have decreased over time, with little attention paid to their standard per capita. They have been replaced by other built-up uses and road networks. Among the most significant consequences of this change are endangering the physical and mental health of individuals, reducing recreational and rest areas for citizens, increasing environmental pollution, increasing heat temperatures, and creating heat islands, resulting in a decline in the quality of individual and social life.

References

1. Caspersen, O. H., Konijnendijk, C. C., & Olafsson, A. S. (2006). Green space planning and land use: An assessment of urban regional and green structure planning in greater Copenhagen. Geografisk tidsskrift - Danish journal of geography, 106(2), 7-20.
2. Costa, C. S., Erjavec, I. S., & Mathey, J. (2008). Green spaces – a key resoureces for urban sustaiability. the greenkeys approach for developing green spaces. Urbani izziv, 19(2), 198-211.
3. European space agency. (2024, 04 05). Retrieved from https://earth.esa.int/eogateway/missions/landsat-8/objectives
4. Eyileten, B., Esandağli, Ç., & Selim, S. (2022). Assessment of urban green space distribution within the scope of european green deal using NDVI indice; case of Nicosia / Cyprus. Architectural sciences and applications, 7(2), 615-623.
5. Govaerts, B., & Verhulst, N. (2010). The normalized difference vegetation index (NDVI) greenseeker handheld sensor: toward the integrated evaluation of crop management. 2010: Cimmyt.
6. Hashemi, E., Kafi, M., Hashemi, M., & Khan Sefid, M. (2009). Analysis of urban green space changes; case study: region 2 of tehran. Environmental science, 6(3), 73-86.
7. Lillesand, T. M., Kiefer, R. W., & Chipman, J. W. (2004). Remote sensing and image interpretation (5th ed.). New York: John Wiley.
8. NASA's earth observing system project science office. (2019, 10 22). Retrieved from https://eospso.nasa.gov/missions/landsat-8
9. Tyrväinen, L., Pauleit, S., Seeland, K., & Vries, S. d. (2005). Benefits and Uses of Urban Forests and Trees. Berlin: A reference book. Springer.
10. USGS, science for a changing world. (2018, 11 27). Retrieved 04 16, 2024, from https://www.usgs.gov/special-topics/remote-sensing-phenology/science/ndvi-foundation-remote-sensing-phenology

Advanced Engineering Days

aed.mersin.edu.tr

Graph neural networks in determining the road network

Nurettin Sinanoğlu [*1], **Elif Sertel** [1]

[1]*Istanbul Technical University, Communication Systems Department, Türkiye, sinanoglun20@itu.edu.tr, sertele@itu.edu.tr*

Cite this study: Sinanoğlu, N., & Sertel, E. (2024). Graph neural networks in determining the road network. Advanced Engineering Days, 9, 232-234

Keywords
Transformers
Vector Mapping
Graph Learning
Road Network Detection
Remote Sensing

Abstract

Up-to-date and precise road network information is essential for applications like the effective navigation of autonomous vehicles and accessible route determination during disaster response. The automated detection of road network graphs has strong potential to increase the speed and accuracy of these applications, reducing the need for human interaction and ensuring prompt and reliable decision-making in critical scenarios. This study proposes a novel approach that utilizes transformer architecture and imitation learning techniques to automatically detect the road network graphs in very high-resolution aerial images. Unlike traditional methods, our proposed approach iteratively refines the extraction process, particularly excelling in accurately delineating complex intersections. We integrate imitation learning techniques, enabling the model to learn from expert demonstrations and refine its performance over time, leading to improved results in road graph detection.

Introduction

Road mapping techniques currently in use can be divided into two categories: segmentation-based and graph-based methods. Segmentation-based methods [1, 2, 3] achieve commendable pixel-level results but often struggle with maintaining topology correctness. On the other hand, graph-based approaches directly detect road network graphs but encounter challenges in optimization and end-to-end training. Our proposed MTnet directly extracts vertex coordinates, allowing it to deal with more complex cases and deliver. Graph-based methods for road network graph detection [2-5] differ significantly from segmentation-based approaches as they directly produce the graph structure. RoadTracer [2] played a pivotal role in iterative graph generation, leveraging groundtruth initial vertices for initialization. Certain tasks akin to identifying road networks include identifying road boundaries [6], lane lines [7], lanes, and curbs [13]. Although these studies are not directly focused on road network detection, their objectives bear resemblance to ours, and they offer insightful ideas and techniques. Although enhancing topology performance, RoadTracer encountered difficulties at road intersections due to its fixed step length. This limitation was addressed by [2], which replaced direction prediction with heatmap prediction, dynamically adjusting the step length. Despite showcasing superior performance, the post-processing of the heatmap impeded end-to-end optimization. Furthermore, it struggled to distinguish closely located vertices. In contrast to iterative methods, Sat2Graph [13] adopted a direct prediction approach, generating a high-dimensional tensor encoding the road network graph from aerial images. However, it grappled with challenges related to isomorphic encoding, making training supervision complex.

Material and Method

MTnet takes a large RGB aerial image IA 4096×4096 as input. To facilitate iterative graph generation, the agent's past trajectory is recorded in the G graph. Given the size of the input image, MTnet cuts a region of interest (ROI) < R3×L×L L was chosen as 256 in our experiment. The most important reason for this is to limit the dataset allocated to models and patches with low parameter numbers. A ResNet[8] convolutional neural network (CNN) extracts deep feature from the ROI, denoted as FI. The Feature Paradigm Network, along with FI-based segmentation heads, estimates binary segmentation maps S (representing road segment distribution) and I (representing road intersections and broken road endpoints distribution). To capture historical trajectory

information, G is cropped similarly to the ROI, and the cropped G is rasterized to H in R1 x L x L for subsequent stitching. Another CNN network using S, I, and H as input produces the feature tensor FH. The ultimate feature tensor F, which encompasses all essential information for the transformer, is derived through the fusion of the two feature tensors.

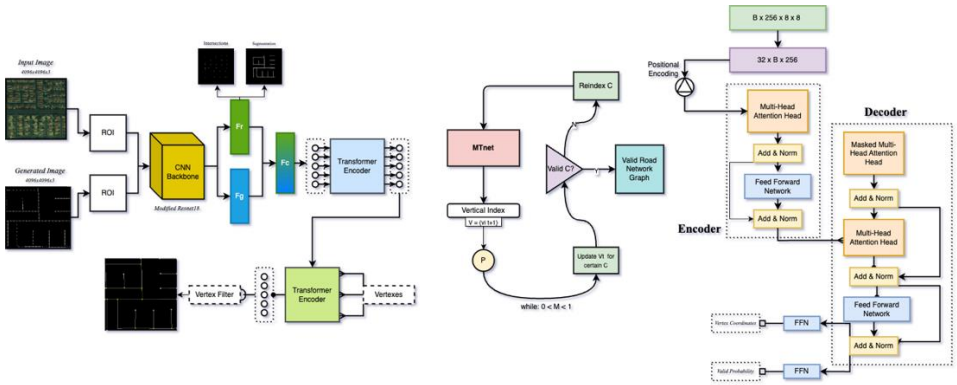


Figure 1. The first image from the left in the figure explains the working mechanism of MTnet. The figure on the right explains the transformer structure.

We utilize the average path length similarity (APLS) metric. The APLS metric assesses the likeness between the actual graph G ∗ and the forecasted graph Gˆ. It selects numerous pairs of vertices from each graph and evaluates the variance in the shortest distance between these pairs as shown in "Figure 1" illustration of the transformer architecture in MTnet B stands for batch size, while N denotes the count of vertex queries within the CNN feature tensor F serves as input, and the transformer divides the feature tensor of size B × 256 × 8 × 8 is divided into a sequence of length 32 in our experiment each containing B × 256 - size tensors. The input tensors are processed by the transformer encoder, generating a sequence of feature tensors as output, maintaining the input's shape. By leveraging the encoder output and vertex queries, the transformer decoder forecasts N vertices {vi t+1} N i=1, accompanied by the corresponding validity probabilities pi t+1 for each vertex vi t+1. Vertices with pi t+1 exceeding a certain threshold are deemed valid, thus influencing graph updates. Before applying Vision Transformer to image segmentation and keypoints detection, it is crucial to prepare the input data appropriately. Images are resized 256x256 to ensure uniform processing. Commonly, resizing is performed to make images compatible with the model's input requirements. Each image entering the model is divided into smaller patches of size 256. The initial step involves converting the image data into a format suitable for processing by Vision Transformer. The image data is tokenized, breaking it down into smaller units or tokens. Tokenization helps in representing the spatial information of the image in a format understandable by the Transformer. The obtained tokens are then embedded into vectors. Embedding is a crucial step where the spatial features of the image are transformed into numerical vectors.

Results

The resulting training set consists of approximately 10K patched samples from diverse aerial images, with 1K samples allocated for validation. The crop size of the Region of Interest (ROI) is set to 256 pixels, L = 256 to balance efficiency. Training labels are generated with τ set to 40 pixels and τ ′ set to 20 pixels. Transformers employ 10 input vertexes (|Q| = N = 10). MTnet is trained with a learning rate of 10−4 and a decay rate of 10−5 over 100 steps. Performance evaluation on the validation set is conducted at the conclusion of each epoch.

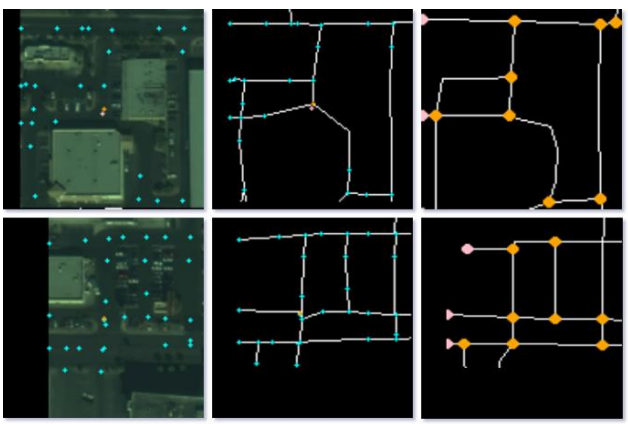


Figure 2. The first image from the left in the figure explains the working mechanism of MTnet. The figure on the right explains the transformer structure.

Discussion

MTnet, an innovative iterative approach designed for the automatic detection of network graphs from aerial images. When given an image as input, MTnet has the capability to directly produce the road network graph, complete with vectors and intersections. The process begins with MTnet predicting sets of potential initial vertors. Subsequently, it step by step constructs the road network graph is traversed, vertex by vertex,
commencing from each of the potential initial vertices. One notable feature of MTnet is its ability to handle complex intersection points that involve an arbitrary number of connected road segments. This capability is facilitated by the use of transformers and deep queries in the model. To assess the performance of MTnet, we conducted evaluations on open available dataset.

Conclusion

The results demonstrated that MTnet achieved Demonstrating cutting-edge performance across a range of evaluation metrics, encompassing pixel-level, intersection-level, and topology-level measurements, including the APLS metric. The superiority of our approach was evident in the experimental results. Looking ahead, we plan to enhance MTnet by incorporating more powerful backbone networks and refining new training methods. Additionally, we aim to adapt MTnet for use in other graph detection tasks, such as build center detection.

References

1. Z. Zhang, Q. Liu, and Y. Wang (2018). Road Extraction by Deep Residual Unet, IEEE Geoscience and Remote Sensing Letters, vol. 15, no. 5, (pp. 749–753), May 2018, doi: 10.1109/LGRS.2018.2802944.
2. F. Bastani, S. He, S. Abbar, M. Alizadeh, H. Balakrishnan, S. Chawla, S. Madden, and D. DeWitt (2018). Roadtracer: Automatic extraction of road networks from aerial images, in Proceedings of the IEEE Conference on Computer Vision and Pattern Recognition, 2018, (pp. 4720–4728).
3. M. Ranzato, S. Chopra, M. Auli, and W. Zaremba (2015). Sequence level training with recurrent neural networks, arXiv preprint arXiv:1511.06732.
4. J. Wang, K. Sun, T. Cheng, B. Jiang, C. Deng, Y. Zhao, D. Liu, Y. Mu, M. Tan, X. Wang et al. (2019). Deep high-resolution representation learning for visual recognition, IEEE transactions on pattern analysis and machine intelligence, vol. 43, no. 10, pp. 3349–3364, 2020. D. Belli and T. Kipf, Image-conditioned graph generation for road network extraction, NeurIPS 2019 workshop on Graph Representation Learning.
5. J. Liang, N. Homayounfar, W.-C. Ma, S. Wang, and R. Urtasun (2019). Convolutional recurrent network for road boundary extraction, in Proceedings of the IEEE Conference on Computer Vision and Pattern Recognition, 2019, (pp. 9512–9521).
6. Z. Xu, Y. Liu, L. Gan, X. Hu, Y. Sun, L. Wang, and M. Liu (2021). csboundary: City-scale road-boundary detection in aerial images for high-definition maps," arXiv preprint arXiv:2111.06020.
7. X. Yang, X. Li, Y. Ye, R. Y. Lau, X. Zhang, and X. Huang (2022). Road detection and centerline extraction via deep recurrent convolutional neural network u-net, IEEE Transactions on Geoscience and Remote Sensing, vol. 57, no. 9, pp. 7209–7220, 2019. S. He and H. Balakrishnan, Lane-level street map extraction from aerial imagery, in Proceedings of the IEEE/CVF Winter Conference on Applications of Computer Vision, 2022, (pp. 2080–2089).
8. Z. Xu, Y. Sun, and M. Liu (2021). icurb: Imitation learning-based detection of road curbs using aerial images for autonomous driving, IEEE Robotics and Automation Letters, vol. 6, no. 2, (pp. 1097–1104).
9. S. Gao, M.-M. Cheng, K. Zhao, X.-Y. Zhang, M.-H. Yang, and P. H. Torr (2019). Res2net: A new multi-scale backbone architecture, IEEE transactions on pattern analysis and machine intelligence.
10. Zhenhua Xu, Yuxuan Liu, Lu Gan, Yuxiang S., Xinyu W., Ming L., Lujia W. (2022). RNGDet: Road Network Graph Detection by Transformer in Aerial Images, arXiv:2202.07824v2 [cs.CV] 26 Jun 2022.
11. Y.-Q. Tan, S.-H. Gao, X.-Y. Li, M.-M. Cheng, and B. Ren, (2020). Vecroad: Point-based iterative graph exploration for road graphs extraction, in Proceedings of the IEEE/CVF Conference on Computer Vision and Pattern Recognition, 2020, (pp. 8910–8918).
12. Y. Xu, W. Xu, D. Cheung, and Z. Tu, (2021). Line segment detection using transformers without edges, in Proceedings of the IEEE/CVF Conference on Computer Vision and Pattern Recognition, 2021, pp. 4257–4266.
13. S. He, F. Bastani, S. Jagwani, M. Alizadeh, H. Balakrishnan, S. Chawla, M. M. Elshrif, S. Madden, and M. A. Sadeghi, (2020). Sat2graph: road graph extraction through graph-tensor encoding, in Computer Vision–ECCV 2020: 16th European Conference, Glasgow, UK, August 23–28, 2020, Proceedings, Part XXIV 16. Springer, 2020, (pp. 51–67).

Advanced Engineering Days

aed.mersin.edu.tr

A geospatial approach to vegetation monitoring: Multi-indices analysis with Landsat 8 via Google Earth Engine

Emre Aktürk[*1]

[1]*Kastamonu University, Department of Forestry, Türkiye, eakturk@kastamonu.edu.tr*

Cite this study: Akturk, E. (2024). A geospatial approach to vegetation monitoring: Multi-indices analysis with Landsat 8 via Google Earth Engine. Advanced Engineering Days, 9, 235-237

Keywords
GEE
Vegetation Indices
Landsat
NDVI
Cloud GIS

Abstract

This study aimed to streamline the production, visualization, and export of 25 different vegetation indices (VIs) using Landsat 8 imagery via Google Earth Engine (GEE). Leveraging GEE's cloud-based platform, the developed algorithm allows users to define their region of interest (ROI), select a date range, and effortlessly compute and visualize a set of VIs. The algorithm uses the 'simpleComposite' function to generate optimal composite images for the desired time period while minimizing atmospheric interference. The easy-to-use interface enables fast decision-making and immediate access to results, reducing time, labor, and computational costs. Future enhancements include extending the algorithm to older Landsat missions (4-5 and 7) and integrating newer data sets such as Landsat 9 and Sentinel-2 for higher spatial resolution. Future modules for time series analysis will provide deeper insight into vegetation dynamics. Overall, this framework provides a comprehensive, scalable solution for vegetation monitoring that adapts to evolving satellite datasets and user needs, representing a significant advancement in remote sensing and environmental analysis.

Introduction

Since the launch of the first Earth monitoring satellite in 1972, there has been a concerted effort to improve the understanding of the relationship between the radiometric response of satellite sensors and vegetation cover [1]. This body of research has particularly emphasized the effectiveness of the red and near-infrared spectral bands for analyzing vegetation characteristics. The utility of remote sensing at this point extends to various fields, including environmental monitoring, biodiversity conservation, and agriculture, by providing vital data on vegetation health and dynamics [2].

Vegetation remote sensing primarily involves the detection of electromagnetic wave reflectance from plant canopies using passive sensors. This reflectance varies with plant species, water content within plant tissues, and other inherent plant characteristics [3]. These variations are influenced by the chemical and morphological properties of the plant surfaces, especially the leaves and other photosynthetic organs [4]. The spectral data used in vegetation analysis span several bands: from the ultraviolet light spectrum (10 to 380 nm), through the visible light spectrum-including blue (450-495 nm), green (495-570 nm), and red (620-750 nm)-to the near and mid-infrared bands (850-1700 nm) [1].

Spectral vegetation indices (VIs) are critical satellite-derived metrics widely used in environmental studies. These indices facilitate monitoring phenological changes, land cover, and land cover transitions, contributing to natural resource management and sustainable development efforts [5-7]. The standardized calculation of VIs across different spatial and temporal scales makes them versatile tools in remote sensing. They provide consistent data across different biomes, land conditions, and soil types, providing reliable measurements of the Earth's surface. In addition, the simplicity of these indices allows for integration across different sensor systems, improving the continuity of essential datasets essential for long-term land surface modeling and climate change analysis [8].

In the field of remote sensing and geographic information systems (GIS), the production of VIs derived from spectral bands has historically been time-consuming, especially for large-scale studies at national, continental, or global scales. However, speeding up advances in remote sensing and GIS technologies have significantly

accelerated the generation of these datasets. This study uses Google Earth Engine (GEE), a cloud-based GIS platform, to facilitate the rapid and efficient VIs production for small to large scales. Within GEE, the necessary coding was implemented to allow users to quickly generate, visualize, and download 25 vegetation indices tailored to their specific study areas. This approach not only improves the accessibility and usability of VIs but also supports their application across platforms, enriching the potential for comprehensive environmental analysis and research.

Material and Method

Since the study is designed for global-scale production and analysis, it does not focus on a specific study area. Instead, users are empowered to define their regions of interest (ROI) according to their own preferences. For this purpose, the study used the Global Administrative Unit Layers (GAUL) dataset, produced by the Food and Agriculture Organization of the United Nations (FAO)[9], which provides administrative boundaries on a global scale within the GEE library. Users can use this dataset to outline their desired work areas based on national or provincial boundaries. Once the code is executed, the 'ROI Selection' section of the user interface panel allows for seamless selection of the region of interest at various levels. Once selected, the selected area is highlighted in red on the GEE map interface, providing a clear visual representation of the study area (Figure 1).

Once the ROI has been determined, users must select the date range for which they wish to generate VIs. At this stage, the algorithm uses Landsat 8 Collection 2 Tier 1 and Real-Time data, representing scaled, calibrated at-sensor radiance values (DN values). A composite image is generated by selecting the optimal pixels least affected by atmospheric conditions from all available images within the specified date range. The 'simpleComposite' algorithm in GEE manages this process [10]. After this, users can click the 'Load & Monitor RGB Landsat Imagery' tab to view the Landsat 8 composite image. This will display the best Landsat 8 composite for the specified date range in the map interface, allowing users to inspect the imagery for potential cloud, snow, or fog interference.

After obtaining the desired Landsat 8 composite image, the next step is to select from the 25 VIs generated using different satellite imagery spectral band combinations. Once a specific VI, such as Normalized Difference Vegetation Index (NDVI), Enhanced Vegetation Index (EVI), or Soil Adjusted Vegetation Index (SAVI), is selected, it can be calculated and visualized within the ROI boundaries on the map interface. Users also have the flexibility to customize the visualization of the selected index within GEE. To export the generated index, users can click the "Export Selected Vegetation Index to Drive" button located at the bottom of the panel. This action sends the raster data of the selected VI in .tif format directly to the user's Google Drive account. Users can further edit and analyze the data from GEE or other GIS platforms.

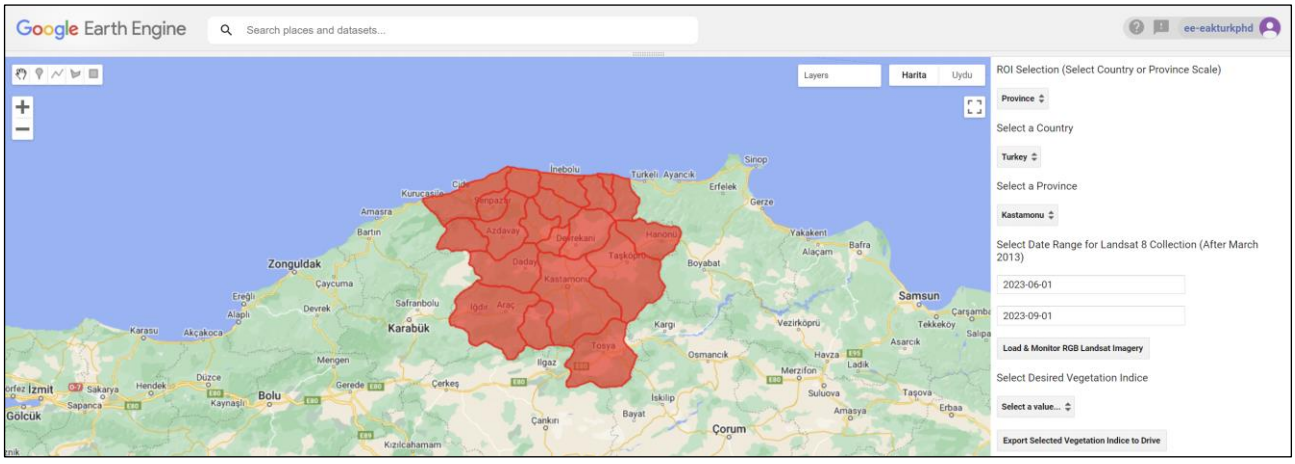


Figure 1. GEE interface for calculating, modifying, and exporting VIs.

Discussion

The algorithm developed within GEE provides a highly efficient, user-friendly approach to VI analysis by significantly reducing the time, effort, and computational requirements associated with traditional image processing. Without this automated approach, users must manually download Landsat 8 imagery, which requires significant disk space and computing power. Further processing steps, including compositing, calculating indices, and exporting results, would require specialized software and a high-performance computer, increasing cost and complexity. By allowing users to directly define their region of interest, select a date range, and calculate any of 25 VIs within the GEE environment, this solution eliminates the need for local storage and processing, streamlining the workflow and enabling rapid analysis across scales.

In addition, easy visualization and export capabilities through the user interface panel facilitate quick decision-making and immediate access to results. Users can visualize their selected indices within the region of interest

with just a few clicks and export the data in a ready-to-use format for further analysis on GEE or other GIS platforms. This automated approach increases productivity and reduces labor and storage costs, providing a comprehensive solution for vegetation monitoring.

Although the current implementation focuses exclusively on Landsat 8 imagery, the algorithm can be extended to include historical data from older Landsat missions, such as Landsat 4-5 and 7. In addition, future updates will include Landsat 9 data to provide continuity and consistency in long-term vegetation analysis. There are also plans to incorporate Sentinel-2 imagery, which provides better spatial resolution than Landsat, to improve the granularity of vegetation monitoring. In addition, efforts are underway to develop modules allowing users to perform time-series analyses of vegetation indices, providing deeper insight into vegetation dynamics and phenological changes.

Conclusion

This study presents a comprehensive solution for vegetation monitoring using Google Earth Engine. The proposed algorithm significantly simplifies and accelerates the analysis process by automating the production, visualization, and export of 25 different vegetation indices. It eliminates the need for extensive data storage and high-performance computing, making vegetation monitoring more accessible and cost-effective. Future updates will ensure compatibility with older Landsat missions and newer datasets such as Landsat 9 and Sentinel-2, expanding the applicability and utility of the algorithm. In addition, upcoming modules that enable time-series analysis will provide users with deeper insights into vegetation dynamics. Ultimately, this approach provides a flexible and scalable framework that can be adapted to evolving satellite datasets and user needs, marking a significant advancement in remote sensing and environmental monitoring.

References

1. Rouse Jr, J. W., Haas, R. H., Schell, J. A., & Deering, D. W. (1973). Monitoring the vernal advancement and retrogradation (green wave effect) of natural vegetation (No. NASA-CR-132982).
2. Bannari, A., Morin, D., Bonn, F., & Huete, A. (1995). A review of vegetation indices. Remote sensing reviews, 13(1-2), 95-120.
3. Liu, C., Sun, P. S., & Liu, S. R. (2016). A review of plant spectral reflectance response to water physiological changes. Chinese Journal of Plant Ecology, 40(1), 80.
4. Zhang, C., & Kovacs, J. M. (2012). The application of small unmanned aerial systems for precision agriculture: a review. Precision agriculture, 13, 693-712.
5. Huete, A. R. (2012). Vegetation indices, remote sensing and forest monitoring. Geography Compass, 6(9), 513-532.
6. Yang, X., Smith, A. M., & Hill, M. J. (2017). Updating the grassland vegetation inventory using change vector analysis and functionally-based vegetation indices. Canadian Journal of Remote Sensing, 43(1), 62-78.
7. Miura, T., Yoshioka, H., Fujiwara, K., & Yamamoto, H. (2008). Inter-comparison of ASTER and MODIS surface reflectance and vegetation index products for synergistic applications to natural resource monitoring. Sensors, 8(4), 2480-2499.
8. Zhao, W., Yu, X., Jiao, C., Xu, C., Liu, Y., & Wu, G. (2021). Increased association between climate change and vegetation index variation promotes the coupling of dominant factors and vegetation growth. Science of the Total Environment, 767, 144669.
9. FAO, GAUL. (2015). Accessed at: https://data.apps.fao.org/map/catalog/static/search?keyword=HiH_boundaries.
10. Li, J., Ma, J., & Ye, X. (2022). A Batch Pixel-Based Algorithm to Composite Landsat Time Series Images. Remote Sensing, 14(17), 4252.

Advanced Engineering Days

aed.mersin.edu.tr

Harnessing solar energy: Mapping the potential and performance of Middle Eastern Countries

Meysam Hasanzadeh *[1], **Khalil Valizadeh Kamran** [1]

[1]*University of Tabriz, Department of Remote Sensing and GIS, Iran, meysam.hasanzadeh@yahoo.com, valizadeh@tabrizu.ac.ir*

Cite this study: Hasanzadeh, M., & Valizadeh Kamran, KH. (2024). Harnessing solar energy: Mapping the potential and performance of Middle Eastern Countries. Advanced Engineering Days, 9, 238-240

Keywords
Renewable Energy
Solar Photovoltaic
MCDA
GIS
Satellite Imagery

Abstract

This study examines the solar energy potential of 12 Middle Eastern countries and evaluates their performance in harnessing this renewable resource. Environmental concerns, such as rising energy consumption and global warming, underscore the urgency to prioritize sustainable energy solutions like solar power. The research employs a comprehensive approach, utilizing geographic information systems, satellite imagery, and multi-criteria decision-making to identify optimal areas for solar power plant development. Factors considered include solar radiation levels, topography, and land use suitability. By comparing each country's installed solar capacity to its population and available suitable land, the study calculates a performance index (PI) to assess their comparative performance. The findings reveal that while the Middle East has significant solar potential, the current installed capacity remains low. Lebanon emerges as the top performer, while Iraq, Syria, Yemen, Iran, and Kuwait exhibit suboptimal outcomes. These insights can inform policy decisions, investment strategies, and technological advancements to accelerate the adoption of solar energy and reduce reliance on non-renewable sources across the region.

Introduction

Environmental pollution and global warming are pressing issues that pose a significant threat to our planet. The Energy Information Administration (EIA) projects a staggering 50% increase in energy consumption from 2018 to 2050. This statistic emphasizes the urgent need to prioritize renewable energy sources and reduce our dependence on fossil fuels [1-2]. The Middle Eastern countries, in particular, have immense potential for the development of solar power plants. Currently, out of the 223 countries worldwide, the Middle East, consisting of 12 countries, accounts for only 0.78% (30,478 megawatts) of the total installed capacity of 3,869,705 megawatts. However, when it comes to solar power plants, this figure increases to approximately 1% according to the International Renewable Energy Agency (IRENA) data in 2024.

To identify suitable areas for constructing solar power plants, various methodologies can be employed. Multi-criteria decision-making methods and geographic information systems (GIS) can be utilized to assess different criteria. These techniques enable the identification of areas with high solar potential and minimal environmental impact [3]. By comparing the percentage of viable areas for solar power plant installation in each country with their installed capacity, it becomes possible to evaluate the performance of individual nations in harnessing solar energy. Such research provides valuable insights that can be leveraged by organizations and governments within these countries to enhance their efforts in promoting the construction of solar power plants. The findings can inform policy decisions, investment strategies, and technological advancements to accelerate the adoption of solar energy and further reduce reliance on non-renewable energy sources.

Material and Method

The study aimed to assess the installed capacity of countries in relation to their population and availability of suitable land for power plant construction. It used statistics published by the International Renewable Energy Agency (IRENA) to calculate the installed capacity per capita as a measure of performance. However, this approach didn't consider each country's potential, prompting a more comprehensive analysis.

The study focused on 12 Middle Eastern countries: Bahrain, Iran, Iraq, Jordan, Kuwait, Lebanon, Oman, Qatar, Saudi Arabia, Syria, United Arab Emirates, and Yemen. It collected data on various criteria, with the global horizontal radiation index (GHI) being a key factor. Adequate sunlight exposure is crucial for optimal solar module performance. Areas with insufficient radiation (less than 3.56 kWh/m2) were excluded based on reports from the National Renewable Energy Laboratory (NREL) [4,5,6,7]. Higher altitudes receive more sunlight, while lower altitudes experience reduced light intensity due to increased atmospheric density. Constructing power plants at higher altitudes becomes less cost-effective due to higher construction and power transmission costs. The study obtained digital elevation model (DEM) from NASA EARTH DATA and selected pixels between 0 and 2000 meters above sea level. A slope map was generated to identify areas with slopes between 0 and 10 degrees, considering that steeper slopes increase construction costs and feasibility challenges [8,9,10]. The land use map, acquired from the ESRI organization, identified Bare Ground and Rangeland as suitable for power plant construction [11].

The study processed images related to the criteria and resampled all maps to a resolution of 30 meters. The Boolean method was used to overlay the maps, resulting in the identification of areas that met all the specified conditions. These areas were then designated as the final map for the study.

Results

Extensive research has been conducted to identify optimal locations for the establishment of solar power plants. This particular study stands out due to its comprehensive scope, encompassing the expansive Middle East region and involving 12 countries. Its objective extends beyond site selection alone. The primary aim is to assess the status of these 12 countries in terms of their installed capacity per capita to their existing potential. The resulting map highlights the suitable areas, with figure 1B illustrating the percentage of the designated area compared to each country's total land area. By dividing the installed capacity of each country by its population, the study also calculates the installed capacity per capita, which is presented in figure 1A. To assess the performance of the 12 studied countries and facilitate comparative analysis, a performance index (PI) was defined. The PI was calculated by dividing the installed capacity per capita of each country by the percentage of the available suitable area (Figure 1C). This metric provides a standardized measure to evaluate and compare the performance of the countries under examination.

PI= installed capacity per capita/ suitable area percentage

The Performance Index (PI, Figure 1C) provides a comprehensive assessment of the performance levels attained by each country. Based on the prevailing geographical expanse and population demographic, the data indicates that Lebanon has demonstrated the most favorable performance. Conversely, the nations of Iraq, Syria, Yemen, Iran, and Kuwait have exhibited suboptimal outcomes, necessitating a concerted effort and increased investment in this particular domain.

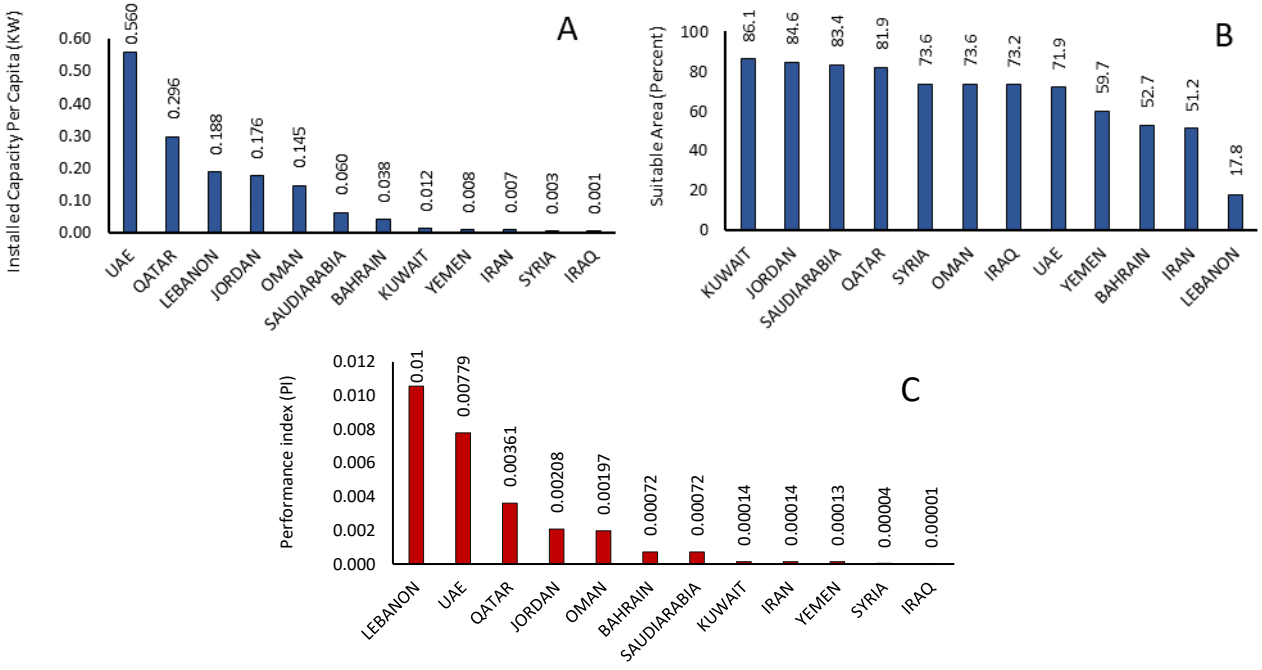


Figure 1. Solar plant installed capacity per capita (A) suitable area percentage for solar plant (B) Performance Index (C)

Discussion

The criteria and methodologies employed in this particular study may vary depending on factors such as the geographical location, environmental conditions, climate patterns, geomorphology, economic factors, infrastructural considerations, and the specific objectives of the study. Through the utilization of multi-criteria decision-making techniques, the criteria can be assigned weights and subsequently overlaid [1, 12, 13, 14, 15]. Given the large scale of the present research, it was constrained to the examination of four criteria. The Boolean method was employed to overlay the map, as it was solely necessary to determine the total area of suitable regions, resulting in a final production map indicating states as either 0 or 1.

Conclusion

This comprehensive study provides valuable insights into the solar energy landscape of the Middle East. By assessing installed capacity, population, and available suitable land, the research offers a nuanced understanding of the performance levels attained by the 12 countries examined. The findings reveal a significant disparity between the region's immense solar potential and the current low installed capacity. While countries like Lebanon and UAE have demonstrated favorable outcomes, others such as Iraq, Syria, Yemen, Iran, and Kuwait exhibit suboptimal performance. These disparities underscore the need for targeted interventions, policy reforms, and increased investment to harness the abundant solar resources in the Middle East. The insights gained can inform strategic decision-making, guide policy development, and catalyze technological advancements to accelerate the transition towards a more sustainable energy future in the region.

References

1. Albraheem, L., & Alabdulkarim, L. (2021). Geospatial analysis of solar energy in riyadh using a GIS-AHP-based technique. ISPRS International Journal of Geo-Information, 10(5), 291. https://doi.org/10.3390/ijgi10050291
2. U. S. (2021). Energy Information Administration. https://www.eia.gov/todayinenergy/detail.php?id=41433/
3. Hasanzadeh, M., Valizadeh Kamran, KH., Feizizadeh, B., & Hassanzadeh Mollabashi, S. (2024). GIS based spatial decision-making approach for solar energy site selection, Ardabil, Iran. International Journal of Engineering and Geosciences, 9(1), 115-130.
4. Abdelrazek, M. (2017). GIS Approach to Find Suitable Locations for Installing Renewable Energy Production Units in Sinai Peninsula, Egypt. [Master's thesis, University of Salzburg].
5. Martins, F. R., Pereira, E. B., & Abreu, S. L. (2007). Satellite-derived solar resource maps for Brazil under SWERA project. Solar Energy, 81(4), 517-528. https://doi.org/10.1016/j.solener.2006.07.009
6. Amillo, A. G., Huld, T., & Müller, R. (2014). A new database of global and direct solar radiation using the eastern meteosat satellite, models and validation. Remote sensing, 6(9), 8165-8189. https://doi.org/10.3390/rs6098165
7. Huld, T. (2017). PVMAPS: Software tools and data for the estimation of solar radiation and photovoltaic module performance over large geographical areas. Solar Energy, 142, 171-181. https://doi.org/10.1016/j.solener.2016.12.014
8. Nebey, A. H., Taye, B. Z., & Workineh, T. G. (2020). Site Suitability Analysis of Solar PV Power Generation in South Gondar, Amhara Region. Journal of Energy, 3519257. https://doi.org/10.1155/2020/3519257
9. Al Garni, H. Z., & Awasthi, A. (2017). Solar PV power plant site selection using a GIS-AHP based approach with application in Saudi Arabia. Applied Energy, 206, 1225-1240. https://doi.org/10.1016/j.apenergy.2017.10.024
10. Tahri, M., Hakdaoui, M., & Maanan, M. (2015). The evaluation of solar farm locations applying Geographic Information System and Multi-Criteria Decision-Making methods: Case study in southern Morocco. Renewable and sustainable energy reviews, 51, 1354-1362. https://doi.org/10.1016/j.rser.2015.07.054
11. https://livingatlas.arcgis.com/landcover
12. Gašparović, I., & Gašparović, M. (2019). Determining optimal solar power plant locations based on remote sensing and GIS methods: A case study from Croatia. Remote Sensing, 11(12), 1481. https://doi.org/10.3390/rs11121481
13. Munkhbat, U., & Choi, Y. (2021). GIS-based site suitability analysis for solar power systems in Mongolia. Applied Sciences, 11(9), 3748. https://doi.org/10.3390/app11093748
14. Alhammad, A., Sun, Q., & Tao, Y. (2022). Optimal solar plant site identification using GIS and remote sensing: framework and case study. Energies, 15(1), 312.
15. Senkal, E., Kaplan, G., & Avdan, U. (2021). Accuracy assessment of digital surface models from unmanned aerial vehicles' imagery on archaeological sites. International Journal of Engineering and Geosciences, 6(2), 81-89. https://doi.org/10.26833/ijeg.696001

Advanced Engineering Days

aed.mersin.edu.tr

Assessing the riskiness of the factors affecting the desirability of natural hazard crisis management (Earthquake) in the high-rise (Baghmisheh town, Tabriz Metropolis)

Khalil Valizadeh Kamran*[1], Sadra Karimzadeh [1], Behdad fuladpanjeh [1], Babak Nouri [1]

[1]University of Tabriz, Remote Sensing and GIS, Iran, Valizadeh@tabrizu.ac.ir, sa.karimzadeh@tabrizu.ac.ir, Behdadfu@gmail.com, surveying2020@gmail.com

Cite this study: Valizadeh Kamran, Kh., & Karimzadeh, S., & Fuladpanjeh, B., & Nouri, B., (2024). Assessing the riskiness of the factors affecting the desirability of natural hazard crisis management (Earthquake) in the high-rise (Baghmisheh town, Tabriz Metropolis), 9, 241-245

Keywords
Natural hazards
Earthquake
Crisis
High-rise construction
Tabriz city

Abstract

The city of Tabriz is considered as the largest population center in the northwest of Iran, and at the same time, it is one of the most seismic cities in the country against the risk of earthquakes. The north fault of Tabriz, which was once far from the city limits of Tabriz. Currently, due to the expansion of high-rise construction and settlement on its territory, it passes through newly built and under-construction settlements. The persistence of natural hazards and the vulnerability of the metropolis of Tabriz has caused these hazards to turn into crises with great losses every year. In this research, the damages caused by the earthquake in the high-rise construction in Baghmisheh were studied. Therefore, first the raw information layers were prepared and then the required layers such as: land use layer of Baghmisheh settlement, construction layers layer, road layer, demographic layers layer, fault layer were prepared, then in the Arc Gis software environment, they were converted into were mapped. Also, AHP technique was used to estimate the relative importance of each criteria. Based on the importance of each criterion, a map of vulnerability and valuation of each was prepared. Then, by analyzing and overlapping the spatial information and calculating the scores and importance of each of the above layers, the final vulnerability map was produced.

Introduction

Natural hazards are an inseparable part of human environment that knows no borders, it affects a small area to a continent and even the whole world and leaves a lot of damage. Due to its vastness, climatic diversity and geographical and geological conditions, our country suffers a lot of losses and damages from natural hazards every year (Ahmadi and Manochehri, 2019). What is important is planning before a crisis occurs, which is one of the important issues facing urban managers today, especially in the field of crisis management, and one of the basic and important tasks of urban and district planners in this field is the allocation of land to Various urban uses are related to the role and function of the city, the urban economy, and also the mutual influence of the uses on each other (Jafarzadeh and Valizadeh, 2017). Earthquake is considered as one of the most important natural disasters and the biggest possible source of damages and injuries from a natural hazard (Pourahmad et al., 2017) and it happens every year all over the world, although it cannot be accurately predicted. he nosed but in order to reduce its damage, remote sensing images and deep learning methods can be used to identify damaged areas and help reduce damages and provide relief; Therefore, the needs of societies for remote sensing have increased. Recent advances in remote sensing and image analysis technologies meet the above needs and lead to a faster and more efficient understanding of earthquake-affected areas (Karimzadeh and Ghasemi, 2002). Most of the researches carried out in relation to the reduction of damage caused by earthquakes have been around the axis and construction methods of building units to increase the building's resistance against earthquakes, and issues such as high-rise construction, density and consolidation of parts have not been addressed. The city of Tabriz is one of the important big cities of Iran, which is in the zone with very high risk in earthquake risk zoning (Alizadeh, 2015). The city of Tabriz is facing obstacles such as high altitude, steep slopes and the possibility of instability of the slopes for physical development in various directions. Also, in relation to the type of land and determining the intensity of earthquake waves, the comparison of geological maps shows that the areas of expansion of young

alluvium in the current area of the city in the direction of the development of the city towards the west and east have a double risk of earthquake in relation to the type It is the earth. The rapid increase in the city's population, which is mainly located in high-risk areas, increases the loss of life resulting from a possible earthquake. Historical earthquakes confirm that the city of Tabriz and localities such as Baghmisheh have a high seismic potential due to their proximity to the Tabriz fault. In the 20th century, no destructive earthquake has occurred in this area, but considering the frequency of earthquakes in Tabriz, we should expect strong earthquakes in this area.

Material and Method

The area studied in this research is specifically Baghmisheh town located in Panj Shahri area, Tabriz metropolis. In the north-eastern side of Tabriz city, the newly founded town of Baghmisheh has been established. This town has been expanded on the great fault of Tabriz, and a lot of loading has been done on it, which is considered one of the areas with a relative risk of earthquakes in Tabriz.

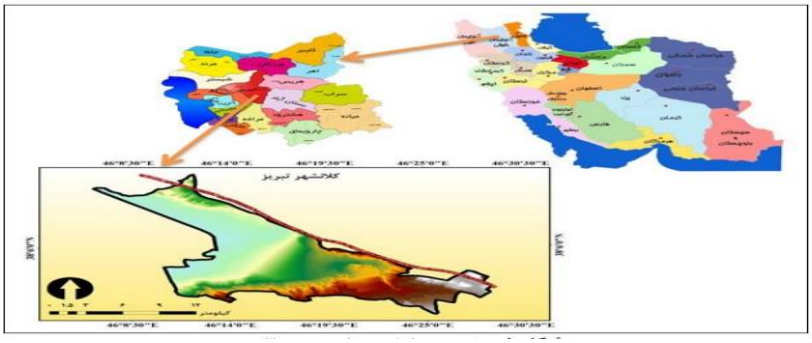


Figure 1. Geographical location of the study area

Data analysis

Land use: In addition to residential uses, there are other uses in the city that are vitally important in the discussion of how to control the crisis caused by the earthquake and reduce its adverse effects (Kazminia and Parisi, 2016). It is for this reason that in these situations, the importance of the building is raised. Based on the importance of each user, they were divided into three groups with high importance or risk, medium importance and less importance.

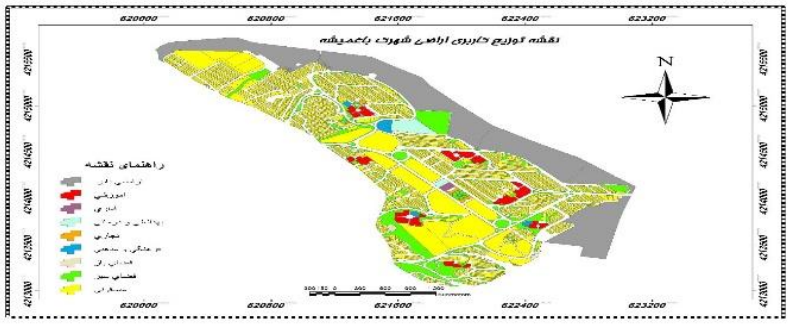


Figure 2. Land use map of Baghmisheh town

According to the level of riskiness of the uses during the earthquake, the uses were valued, and the high-risk uses were assigned a lower value.



Figure 3. User vulnerability map

Number of floors: The number of building floors is a very important indicator in relation to the ratio of the width of the passages and the height of the walls of the buildings; Because with the increase in the number of building floors, the possibility of closing the roads due to the falling debris of high-rise buildings increases and causes disruption in the rescue operation. Based on this, the floors with lower height have medium vulnerability and high value. 3-story buildings have a value of 5 and have a higher risk than their previous floors, 4 and 5 floors have a lower value because they have a higher risk and the largest number of floors in this town are included in these 4-story buildings. Classes 6 and 7 have the highest level of risk and also have the lowest valuation.



Figure 4. Vulnerability map of building floors

Population density: Population density is one of the important indicators of urban life. This index becomes important in the discussion of earthquakes when it is mentioned in vulnerable parts. Here, the population density layer was divided into five classes, which include class 1 from 0 to 150 people, class 2 from 150 to 400 people, class 3 from 400 to 800 people, class 4 from 800 to 1200 and class 5 from 1200 to 1800 people.



Figure 5. Population class map of Baghmisheh town

According to the results of hierarchical analysis, class 1 has the highest value because the level of vulnerability is lower in low density. Class 2 has a value of 7 and is placed in medium vulnerability. Class 3, which has the largest population category and has a value equal to 5, includes high vulnerability. Class 4, which has a value of 3 and includes very high vulnerability. Class 5 has the highest rate and is also the most vulnerable and therefore the least valuable. which is produced from the result of this map of vulnerable areas or classes of Jemit.

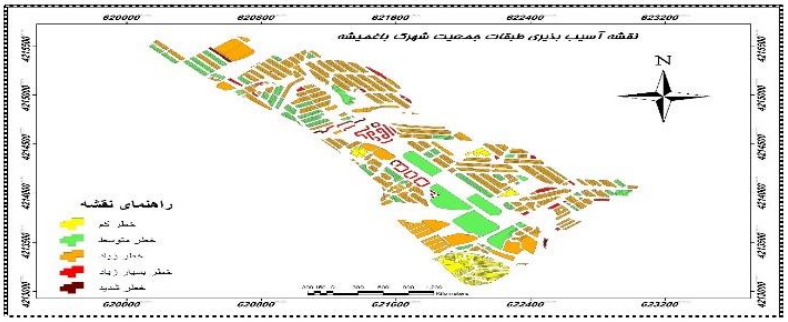


Figure 6. Population vulnerability map

Land slope: In this study, the land slope is divided into four classes based on degree: Class 1 slope between 0 and 4.5 degrees, Class 2 slope between 5.4 and 12 degrees, Class 3 slope between 12 and 21.6 degrees and Class 4 slope between 21 and 39.4 degrees. Based on the degree of slope, the slope map was produced, and based on the degree of vulnerability, the vulnerability map was prepared based on the slope.

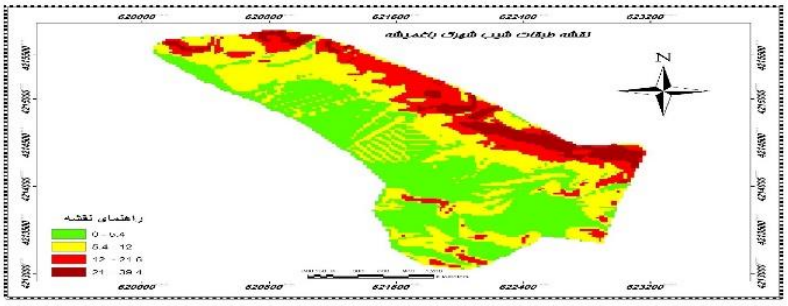


Figure 7. Slope map of Baghmisheh town

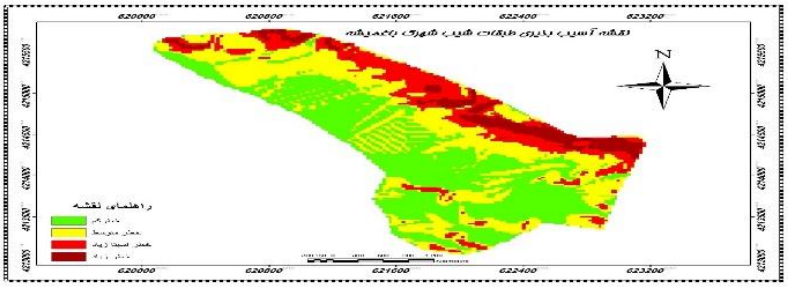


Figure 8. Slope vulnerability map

Finally, by calculating the points and the importance of each of the above layers, the final vulnerability map was produced, which shows the vulnerable areas in 3 classes, the first class or no tar was assigned to the areas that did not have any construction. The class with less risk can be seen in the map in most parts of the town, but the class of high risk areas according to the map can be seen in densely populated areas as well as dense residential areas in terms of population and mostly in areas with a number of 4-story building units.



Figure 9. Final vulnerability map

Results

Considering the risk of rupture in the city of Tabriz, the rupture in the city limits and its impact on the city areas, in the event of a large earthquake, total casualties and extensive damages are predicted in the city, but it is necessary to make a decision in the direction of urban security and implementation. The correctness of the urban development rules in the blue phase made Baghmisheh town of Tabriz to be investigated in this research. In this research, indicators such as slope, building floors, population density, land use, etc. of Baghmisheh town of Tabriz were investigated. To determine the acceptable damage of building parts, only its physical quality is not enough, and building and population densities and roads also have an undeniable effect on this. The existence of a layer of narrow passages blocks the access to the crisis in times of crisis for rescue teams. In terms of the quality index of all layers, the lifespan is between 0-15 years, which I cannot provide completely and comprehensively in this field. Also, there are not many materials and construction materials in this town, and because of the new construction, a strong database is needed for comprehensive and complete studies by the organizations below. It is obvious and clear that with the use of modern technology and knowledge in the field of retrofitting, as well as the requirement and implementation of the engineering and up-to-date regulations by the people and those involved in the construction field, it is possible to reduce the amount of casualties and damages of future earthquakes in each. A place and also this town. The study of materials and materials used in construction and compliance with the principles of urban planning requires more and specialized investigation in the field of the type and method of

using materials that are discussed in the construction of buildings and structures. Despite the fault in the north of Tabriz, with all the security measures, this town is still defenseless against earthquakes. According to the fault map of Tabriz and the failure to respect the proper boundaries of the fault, not only this town but the whole city and even the surrounding area will be defenseless against the activity of this fault. Because this fault is both strong and active, and a huge mass of people surround the fault, which despite all faith-building measures, if it happens, it will result in huge losses and casualties, and the residents must be forced. Building retrofitting standards to reduce the use of earthquakes and standard building construction with a percentage of safety.

References

1. Ahmadi, Abdul Majid, & Manouchehri, Soran. (2019). Assessment of the situation and analysis of factors affecting the desirability of natural hazard crisis management in Qaenat city. Spatial Planning, (2) 10, 23-56.
2. Pourahmad, Ahmed, Ziyari, Karamatullah, & Sadeghi, Alireza. (2017). Spatial analysis of physical resilience components of worn-out urban tissues against earthquakes (case study: District 10 of Tehran Municipality). Spatial Planning (1), 111-130.
3. Alizadeh, Mehdi, (2016), evaluation of the vulnerability of urban infrastructures of Kohdasht with a passive defense approach, master's thesis, supervisor Amanpour, Saeed, Shahid Chamran University of Ahvaz, Department of Geography and Urban Planning.
4. Kazminia, Abdolreza, Maimandi Parisi, Sediqah (2016). Vulnerability zoning of Kerman city buildings against earthquakes using GIS. Promotional Scientific Journal of Mapping and Geospatial Information Engineering, Volume 8, Number 3, 31-47.
5. Karimzadeh, Sadra and Ghasemi, Mohammad, 1402, Assessment of damage to buildings after the Kaheran Marash earthquake in Turkey (year 2023) using radar images with multi-temporal artificial aperture and deep learning, Tabriz International Conference on Investment Opportunities.
6. Jafarzadeh, Jafar, & Valizadeh Kamran, Khalil. (2017). Locating the military barracks in Ardabil city with a passive defense approach (using the combination of remote sensing, GIS and multi-criteria decision making methods). Scientific and Research Quarterly of Research and Urban Planning 9(32), 41-52.

Advanced Engineering Days

aed.mersin.edu.tr

Local climate zone classification using deep learning and remote sensing data

Melike Nicancı Sinanoğlu*[1], Şinasi Kaya [2]

[1]*Istanbul Technical University, Communication Systems Department, Türkiye, nicanci21@itu.edu.tr*
[2]*Istanbul Technical University, Geomatics Engineering Department, Türkiye, kayasina@itu.edu.tr*

Cite this study: Nicancı Sinanoğlu, M., & Kaya, Ş. (2024). Local climate zone classification using deep learning and remote sensing data. 9th Advanced Engineering Days, 9, 246-248

Keywords
Remote Sensing
Local Climate Zones
LCZ Classification
Deep Learning
Instance Segmentation
YOLOv8

Abstract

Local climate zones play an important role in understanding microclimates in urban areas, contributing to urban planning, environmental sustainability and human comfort. Istanbul, a city connecting the European and Asian continents, creates microclimate diversity in city areas with the influence of different land use models. The concept of Urban Heat Island (UHI) arises when urban areas have different temperatures with neighboring rural areas. The lack of a universally accepted definition of the concept of urban and rural areas has created difficulties in the evaluation of this concept. In response to this situation, a standardized Local Climate Zone (LCZ) classification system for urban temperature observations was created. In this study, 47 Istanbul satellite images taken from Google Earth were labeled according to the LCZ classification system, data pre-processing and data augmentation were applied, and the obtained results were subjected to a total of 121 labeled image model training. In conclusion, it contributes to the field of urban climate studies by providing a robust and scalable approach to LCZ classification using advanced deep learning techniques. The results can form the basis for urban planning, environmental sustainability and informed decision-making in the context of Istanbul's urban environment.

Introduction

The burgeoning urban population and the concurrent ecological threats pose formidable challenges to cities grappling with the repercussions of rapid urbanization [1]. This pressure manifests as increased demand for resources, strained infrastructure, and heightened ecological vulnerabilities. The need to balance urban development with environmental sustainability becomes imperative as cities navigate the complexities arising from the interplay of urban expansion, population growth, and ecological considerations.

The 20th century witnessed a rapid surge in urbanization, marked by exponential urban population growth, industrialization, overall population expansion, and densification. This phenomenon has led to a substantial transformation of natural landscapes into artificial surfaces, buildings, and roads, causing significant alterations in urban space and climate [2-3]. The Urban Heat Island (UHI) effect, where the temperature within a city surpasses that of adjacent rural areas [4], is exacerbated by the swift urbanization and changes in land cover [5]. The Urban Heat Island (UHI) effect stands out as a prominent environmental concern arising from the process of urbanization [6]. However, the lack of universally accepted definitions for urban and rural areas complicates the straightforward classification of sites. This ambiguity in urban-rural categorization poses a significant challenge to accurately assessing UHI intensity. The absence of standardized criteria hampers the ability to unequivocally label a location as urban or rural, thereby constraining the scope and precision of UHI research.

In the realm of Urban Heat Island (UHI) studies, the Local Climate Zone (LCZ) scheme has emerged as a pivotal classification system, providing a standardized framework for global urban temperature observations. Stewart and Oke [7] introduced the LCZ concept to objectively classify urban and rural land covers, considering the developmental impact on local temperatures. The LCZ scheme, a recently developed classification system, not only facilitates UHI investigations but also sets a standard for understanding urban temperature dynamics worldwide. The increasing adoption of deep learning methodologies has further enhanced the potential for LCZ mapping.

This paper explores the application of deep learning techniques for LCZ classification, aiming to contribute to the evolving landscape of UHI studies and urban climate research. The following sections delve into the methodology, experimental setup, results, and discussions, providing insights into the effectiveness and potential of deep learning in LCZ mapping.

Material and Method

Our study focuses on the dynamic and culturally rich city of Istanbul, a unique metropolis spanning two continents (Europe and Asia). The city contains various structures that need to be examined in terms of the diversity of LCZ classes. Google Earth was used to create the dataset for Local Climate Zone (LCZ) classification. With its global coverage, high-resolution images, temporal analysis capabilities and cost-effectiveness, Google Earth provides an infrastructure suitable for creating datasets for LCZ classification.

A dataset consisting of 47 images was created for LCZ classification. The resolution of each image in Google Earth is 1024x768 pixels. The dataset contains 17 different LCZ labels, where each image is meticulously labeled. Since the standard image size after labeling is 640x640 pixels, the data was preprocessed and resized in this study. Three different data augmentation methods were used: clockwise, counterclockwise, and upside down, rotating 90 degrees, rotating within ±15 degrees, and degrees of saturation varying between ±20 degrees. The reason for using these is that smaller points can be detected by preventing excessive learning during training.

In the study, the YOLOv8 model, the newest and latest technology that can be used in object detection, image classification and sample segmentation tasks, was used. The YOLO (You Only Look Once) architecture has proven to be a robust and effective framework for object detection tasks. There are some preliminary preparations required for model training with Yolo. Some of these preparations include labeling images and creating a data set. When the created data set is ready for use, some parameters need to be determined to optimize the performance of the model. These factors play a very important role in determining the effectiveness, speed and accuracy of the model. It is important to carefully fine-tune and experiment with these configurations to maximize performance. Although some parameters come as Default, some are specifically determined according to the model. Specifically specified model parameters are Period, Patience, Batch and Image size. Epoch refers to all transitions made through the data set during training. Adjusting this value affects both the training time and the performance of the model. Epoch 150 was chosen here because at this point the performance of the model no longer varies significantly. Patience helps prevent overfitting by stopping training when the model's performance reaches a plateau. The patience value is given as 100 by default, but since the data set is not large, 50 was selected. The batch size for training determines the number of images processed before updating the model's internal parameters. 16 groups are sufficient for GPU memory usage. All images were selected at size 640 to eliminate computational complexity and increase model accuracy. There are various metrics used to measure the performance of the model. These metrics include Box (P, R, mAP50, mAP50-95) and Mask (P, R, mAP50, mAP50-95). Result Box (P, R, mAP50, mAP50-95) respectively; 0.263, 0.341, 0.317, 0.219 and Mask (P, R, mAP50, mAP50-95), respectively; 0.254,0.318,0.404,0.305 are expressed as decimal numbers.

Results

As a result of modeling with Yolov8 architecture using the Istanbul Google Earth images dataset, the Local Climate Zone (LCZ) classification model was developed. The confusion matrix results of the dataset used for this modeling. The model was trained on 47 satellite images, and the results indicate high accuracy in classifying LCZ A and LCZ G. However, further training is needed, especially for distinguishing LCZ1-2-3 in urban areas where it appears challenging.

In particular, LCZ B and LCZ C exhibit some points of confusion in the classification. Additionally, distinguishing between LCZ E and LCZ 8 poses a challenge and shows overlaps with other confused classes. Upon reviewing the results, it is evident that additional visual support is required for the LCZ model training. The current model may benefit from more focused training on LCZ1-2-3 differentiation in urban settings, as well as addressing the confusion points between LCZ B and LCZ C. Furthermore, efforts should be directed towards refining the model's ability to distinguish between LCZ E and LCZ 8.

The resulting images classified by the model are shown in ``Figure 1''. The expressions 1-9 and A-G in these images are abbreviated expressions for the LCZ classes, Structure Types LCZ 1-9 and Land Cover Types LCZ A-G. The percentage expressions stated in the images are an estimate of which LCZ class the marked region belongs to. In some regions, there may be different LCZ classification predictions for the same region on the model due to visual interpretation difficulties arising from various LCZ classes within the region. When the regions where different predictions are made are examined, it is clear that two predictions can be made even in visual interpretation. In order to get a definitive result here, it can be clarified by knowing the region and using other images of the region.

Discussion

In examining the result visuals in ``Figure 1'', it is evident that labeled images with low prediction probabilities often reveal accurate predictions upon closer inspection. Despite low predicted probabilities, the model demonstrates a consistent ability to make correct predictions. However, areas of confusion highlight the need for a more visually and qualitatively prepared dataset, particularly in regions where LCZ classification is challenging.

The analysis suggests that low prediction probabilities alone may not be indicative of inaccurate classifications, and a more nuanced understanding of the model's performance is necessary. Visual inspection of these challenging areas indicates that the model, even with low predicted probabilities, tends to provide accurate LCZ classifications. To address areas of confusion and further enhance the model's performance, the use of a more carefully curated and high-quality dataset is recommended. A dataset that captures the intricacies of LCZ features in challenging scenarios can contribute to achieving high-accuracy LCZ classifications without the need for exhaustive manual inspection.

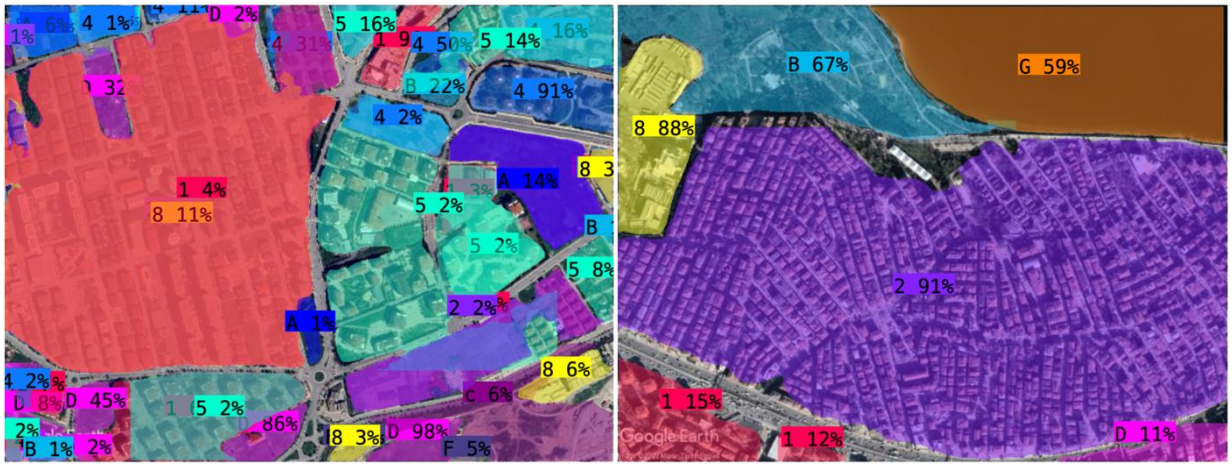


Figure 1. Istanbul city images labeled with LCZ classes using the trained model

Conclusion

In conclusion, although the model demonstrates overall effectiveness, improvements can be made by increasing the dataset quality, especially in areas prone to confusion. Knowing the region and creating a classification model in smaller areas can also contribute to improvement. While creating a model, in addition to satellite images, street images of the region can be examined to contribute to the interpretation. The findings underline the importance of dataset optimization in achieving reliable and accurate LCZ classification results. It is seen as a clear conclusion that a good modeling result can be achieved with a good data set and LCZ classification can be done faster and more accurately.

References

1. Alsaaideh, B. & Tateishi, R. & Phong, D. & Hoan, N. & Al-Hanbali, A. & Xiulian, B. (2017). New urban map of Eurasia using MODIS and multi-source geospatial data. Geo-spatial Information Science. 20. 29-38. 10.1080/10095020.2017.1288418.
2. Taha, H. (1997). Urban climates and heat islands: Albedo, evapotranspiration, and anthropogenic heat. Energy Build. 25, 99–103.
3. Zhao, L. & Lee, X. & Smith, R. & Oleson, K. (2014). Strong contribution of local background climate to urban heat islands. Nature. 511. 216-9. 10.1038/nature13462.
4. Memon, R.A., Leung, D.Y., Chunho, L. (2008). A review on the generation, determination and mitigation of urban heat island. J. Environ. Sci., 20, 120–128.
5. Ruiz, A. & Correa, E. (2015). Adaptive model for outdoor thermal comfort assessment in an Oasis city of arid climate. Building and Environment. 85. 10.1016/j.buildenv.2014.11.018.
6. Yang, C. & Zhan, Q. & Gao, S. & Liu, H. (2020). Characterizing the spatial and temporal variation of the land surface temperature hotspots in Wuhan from a local scale. Geo-spatial Information Science. 10.1080/10095020.2020.1834882.
7. Stewart, I.D. & Oke, T. (2012). Local Climate Zones for Urban Temperature Studies. Bulletin of the American Meteorological Society. 93. 1879-1900. 10.1175/BAMS-D-11-00019.1.

Advanced Engineering Days

aed.mersin.edu.tr

Monitoring post-earthquake debris removal process with multi-temporal Sentinel 2 satellite imagery: The case of Antakya

Ugur Alganci*[1], Dursun Zafer Seker [1]

[1]*Istanbul Technical University, Department of Geomatics Engineering, Türkiye, alganci@itu.edu.tr, seker@itu.edu.tr*

Cite this study: Algancı, U., & Şeker, D. Z. (2024). Monitoring post-earthquake debris removal process with multi-temporal Sentinel 2 satellite imagery: The case of Antakya. Advanced Engineering Days, 9, 249-251

Keywords
Earthquake
Debris removal
Sentinel 2
Multitemporal
Classification

Abstract

One of the important stages of disaster management is the recovery process. For the earthquake case, this process involves reconstruction of the infrastructure facilities and restoration of services such as education, health and transportation. In long term, all these processes require the region to be cleared from debris. This study presents a practical method for debris removal monitoring using multitemporal Sentinel 2 satellite images for the 1-year period after Turkey-Syria earthquakes that occurred in 6 February 2023. The methodology is based on image differentiation and K-means unsupervised binary classification for periodic monitoring. Classification results provided that debris removal process continued in the whole observation period and adopted methodology can achieve accuracy and F1 – score metrics over 80%.

Introduction

Natural disasters harm millions of people worldwide every year. Effective disaster management practices can help prevent or mitigate the impact of disasters like earthquakes. At this point, effective monitoring is crucial for assessing urban damage during disaster management actions [1]. Remote sensing satellites play an important role in earthquake mapping since they provide high-resolution images and geospatial data that help analyze and monitor earthquake-induced changes and damages. This information is essential for disaster response and recovery efforts, enabling timely and targeted assistance to impacted regions. Previous researches used very high resolution (VHR) optical or SAR satellite images for the assessment of damage after the earthquake mainly with a change detection approach as summarized in [1-3].

Debris removal monitoring is another important action in the recovery process after earthquakes where remote sensing can play an important role. Satellite images allow for the precise identification and mapping of debris-covered areas, as well as the assessment of the scale of destruction and the long-term efficacy of debris clearing. Furthermore, constant satellite monitoring aids in assessing the efficacy of debris removal strategies, allowing for a faster and more coordinated recovery process in disaster-affected areas [4].

This study presents a practical and efficient methodology to monitor the debris removal process with use of Sentinel 2 satellite images by a combination of image differentiating and classification.

Material and Method

The Turkey-Syria earthquakes that occurred in 6 February 2023 was chosen as a case study. Antakya region, which was affected by two earthquakes of magnitude 7.8 mw and 7.7 mw on the same day and has a maximum Mercalli index of XII (extreme), is selected as the study area. The study area is located inside the Antakya district of Hatay province, in the south-east of Turkey. Borders are dictated by the main transportation routes, which are D817 on the north and west and D420 on the east and south (Figure 1). Antakya is Hatay province's largest district by population and second in terms of area. The history of civilization in the district dates back to 5000-4000 BS. The Amik Plain, which extends to the northeast of the city and is located in the heart of the Hatay depression area, is covered in a thick layer of alluvial soil with a very high agricultural potential and is also the province's largest land plain. The Asi River is passing from the center of region.

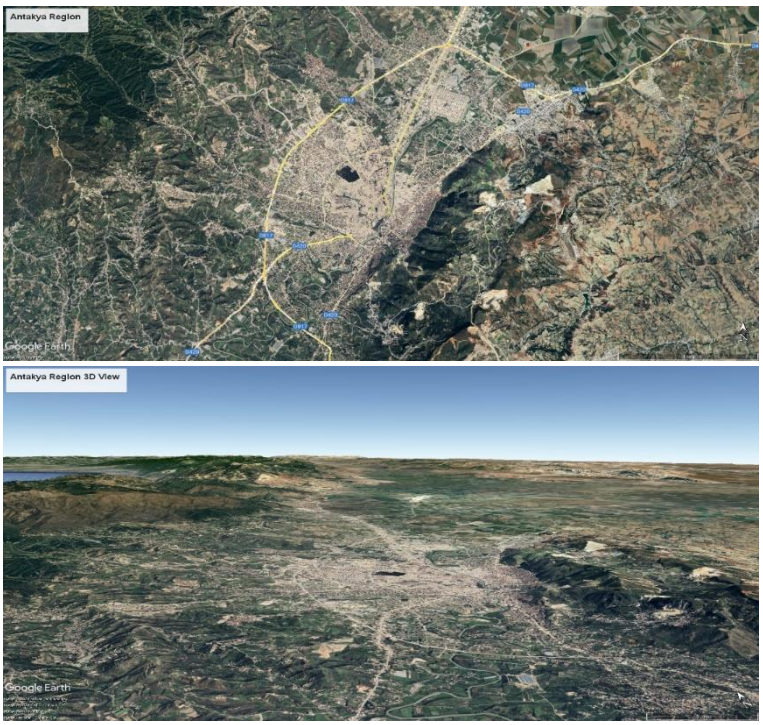


Figure 1. The 2D (top) and 3D (bottom) view of the study region (Google Earth)

The Sentinel 2B images belonging to the study region was used for this study. The image dates were selected as T1: 25.01.2023 (last cloud-free image before earthquakes), T2: 15.04.2023, T3: 24.07.2023, and T4: 29.02.2024. After earthquake image dates were chosen based on the availability of VHR images in Google Earth. These images were obtained in Level 2A processing level, which includes the geometric and atmospheric corrections in addition to radiometric calibration, thus suitable for multi-temporal analysis and classification purposes.

The Sen2Res plugin of SNAP program is used to super resolve the 20 m resolution bands since Bands 2, 3, 4, and 8 have a spatial resolution of 10 m, whereas Bands 5, 6, 7, 8A, 11 and 12 have a spatial resolution of 20 m [5]. Then, all images were clipped to the study region borders. In the next step, bi temporal difference images were produced by subtracting the each after - earthquake image from the reference before image (Figure 2a).

Then an unsupervised classification was performed for each difference image (T1-T2, T1-T3 and T1-T4) with K-Means Clustering algorithm inside SNAP. The cluster number was set to "10", the iteration number was set to "50", the random seed was set to "default". All available difference bands (10 bands) were used in classification. Then the clusters were merged to obtain binary classes that are "debris removed" and "other". Accuracy evaluation was performed with randomly selected control points and verified by Google Earth platform for each date. The most common metrics that are Accuracy and F1-Score was calculated from confusion matrix.

Results

The visual of T1 -T4 period classification result is provided as a sample in Figure 2b. According to accuracy analysis all classification results provided accuracy and F1 – scores over 80%, which indicates an efficient and reliable monitoring of debris removal (Table 1). Areal calculations from classification maps showed that shows that the debris removal process is spread over a period of up to a year expressed by areal increment in debris removed class.

Table 1. Accuracy evaluation results for debris removal monitoring.

Period / Metric	Accuracy	F1 Score
T1 – T2	0.84	0.80
T1 – T3	0.92	0.88
T1 – T4	0.86	0.84

Table 2. Areal values for removed debris through periods.

Period)	Area (Ha)
T1 – T2	898.72
T1 – T3	1,069.06
T1 – T4	1,744.17

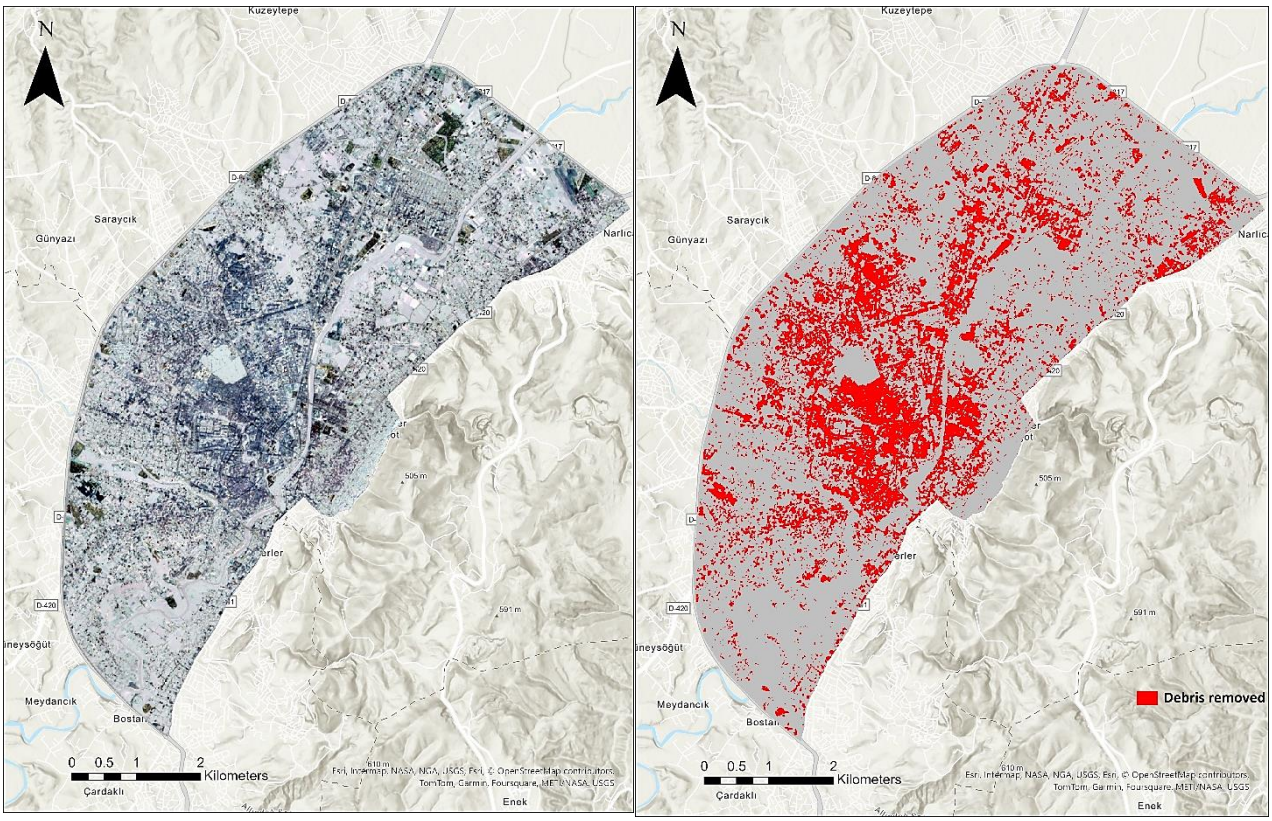


Figure 2. (a)The RGB view of the difference image (T1-T4), (b) binary classification result (T1 – T4)

Discussion

The results of the study revealed that debris removal processes in severely damaged areas can be monitored on a regional scale using medium-high resolution satellite imagery that provides sufficient temporal resolution. The approach is simple, fast and effective. Higher spatial resolution imagery will be required for building-scale assessment.

Conclusion

In this study, a practical method using multi-temporal Sentinel 2 satellite imagery is presented for monitoring the debris removal processes in Antakya district of Hatay province, which was severely damaged by the earthquakes that occurred on February 6, 2023. The methodology, based on image differencing and unsupervised classification processes for different time intervals, demonstrates that debris removal processes can be observed continuously. According to the accuracy assessment results, debris removed regions can be identified with over 80% accuracy and F1-Score for each period.

References

1. Mansouri, B., & Hamednia, Y. (2015). A soft computing method for damage mapping using VHR optical satellite imagery. IEEE Journal of Selected Topics in Applied Earth Observations and Remote Sensing, 8(10),4935-4941.
2. Romaniello, V., Piscini, A., Bignami, C., Anniballe, R., & Stramondo, S. (2017). Earthquake damage mapping by using remotely sensed data: the Haiti case study," Journal of Applied Remote Sensing, 11(1), 016042
3. Dong, L., & Shan, J. (2013) A comprehensive review of earthquake-induced building damage detection with remote sensing techniques. ISPRS Journal of Photogrammetry and Remote Sensing, 84, 85-99.
4. Bekkaye, J. H., & Jafari, N. H. (2024). Application and comparison of remote sensing techniques for data-driven disaster debris quantification. International Journal of Remote Sensing, 45(8), 2808–2831.
5. Brodu, N. (2017). Super-resolving multiresolution images with band-independent geometry of multispectral pixels. IEEE Transactions on Geoscience and Remote Sensing, 55(8), 4610-4617.

Advanced Engineering Days

aed.mersin.edu.tr

Enhancing warehouse efficiency through geographic information systems

Onur Yurekli [1], Muhammed Enes Atik [1]

[1]*Istanbul Technical University, Geomatics Engineering Department, Türkiye, yurekli15@itu.edu.tr, atikm@itu.edu.tr*

Cite this study: Yurekli, O., & Atik, M. E. (2024). Enhancing warehouse efficiency through geographic information systems. Advanced Engineering Days, 9, 252-254

Keywords
GIS
Warehouse
Optimization
Slotting
Route

Abstract

This paper explores the application of Geographic Information Systems (GIS) in achieving warehouse optimization. GIS enables the examination of spatial data to enhance the efficiency of storage and logistics activities. Warehouse optimization primarily targets the optimization of routes and the arrangement of slots. Route optimization maximizes the efficiency of shipment planning, whereas slotting optimization arranges product placement in the warehouse to speed up procedures and lower expenses. This study aims to examine the function of GIS in optimizing routes and slots, present practical instances of its application, and analyze the benefits it provides. GIS implementation in warehouse management streamlines strategic decision-making, enhancing logistics procedures and overall efficiency.

Introduction

In the present era, the significance of logistics and supply chain management cannot be overstated in terms of attaining a competitive edge and enhancing operational efficiency. Efficient warehouse management is a crucial aspect of this process, and when handled adeptly, it lowers expenses and improves the quality of service. Geographic Information Systems (GIS) are becoming increasingly valuable for enhancing efficiency in storage and distribution systems. GIS offers advanced geographic analysis and data visualization tools that enhance crucial warehouse operations, including route and slotting optimization. Route optimization is the act of planning transportation procedures most efficiently. In contrast, slotting optimization involves organizing the positioning of products within the warehouse to reduce processing times and improve labor efficiency. Integrating GIS into warehouse information systems enhances material management positions, refines material data management, and reduces material storage costs. This ultimately enhances warehouse utilization rates and promotes collaboration among various parties in the supply chain [1].

This study examines the utilization of Geographic Information Systems (GIS) in optimizing warehouses. The document delineates the essential data prerequisites, elucidates the advantages of employing genetic algorithms for optimization, and provides comparative evaluations of non-optimized and optimized scenarios. The optimizations' findings are reported using statistical language, emphasizing the efficiency increases attained through these techniques.

Material and Method

Data

This study employed a range of data types to optimize warehouse operations, such as product information, shelf information, product location, orders, and picking lists. The product information comprises product identifiers and characteristics. Shelf information pertains to the storage capabilities and current levels of occupancy of the shelves. Product location data precisely indicates the precise placements of products inside the warehouse layout. Order data comprises both customer requirements and specific order information. Picking lists provide a clear indication of the products that require picking. The analysis will utilize this data.

Genetic Algorithm

Genetic algorithms are essential for improving the effectiveness of warehouse optimization systems by enhancing space usage, logistical operations, and overall performance. Studies have demonstrated that the

integration of genetic algorithms with other optimization techniques such as Bayesian algorithms results in improved cargo space layout, storage strategies, and decreased energy consumption in warehouses. [2,3,4].

The Genetic Algorithm (GA) is an optimization technique that draws inspiration from the process of biological evolution. The process begins by generating a population with random initial values, then assessing each solution's quality based on their fitness ratings. Genetic operators, including selection, crossover, and mutation, are used to combine high-fitness solutions and generate new solutions. This iterative process continues until the optimal solution is discovered, rendering it highly efficient for resolving intricate problems.

Route Optimization

Currently, the most effective methods for optimizing warehouse management routes entail using sophisticated algorithms and technology. Studies indicate that algorithms such as Dijkstra, Floyd-Warshall, Bellman-Ford, ant colony optimization, genetic algorithms, and genetic algorithms paired with fishbone layout designs are successful in optimizing routes for robots and Automated Guided Vehicles (AGVs) in warehouses. [5,6,7].

Slotting Optimization

Optimal slotting in warehouse operations is achieved by employing mathematical programming models to optimally allocate storage spots [8]. Genetic algorithms are essential for improving product placement and order-picking routes, significantly reducing order-picking times [9].

Results

The route drawn in red represents the order picking list collected by an employee and is 160.57 meters long. The route drawn in green represents the optimized version of this route and is 132.54 meters long. The efficiency gained through this optimization is 17.51% (Figure 1).

The heatmaps in the graphic depict the impact of slotting optimization on warehouse efficiency. The figure on the left represents the non-optimized condition, where areas highlighted in red show higher activity concentrations. These red areas suggest inefficiencies and congestion in the paths used for product retrieval. The optimal condition (green line) displays a more equitable activity distribution with diminished red patches. This suggests enhanced workflow and decreased travel lengths within the warehouse. This modification improves the overall operational efficiency and efficacy of product picking and storage processes (Figure 1).

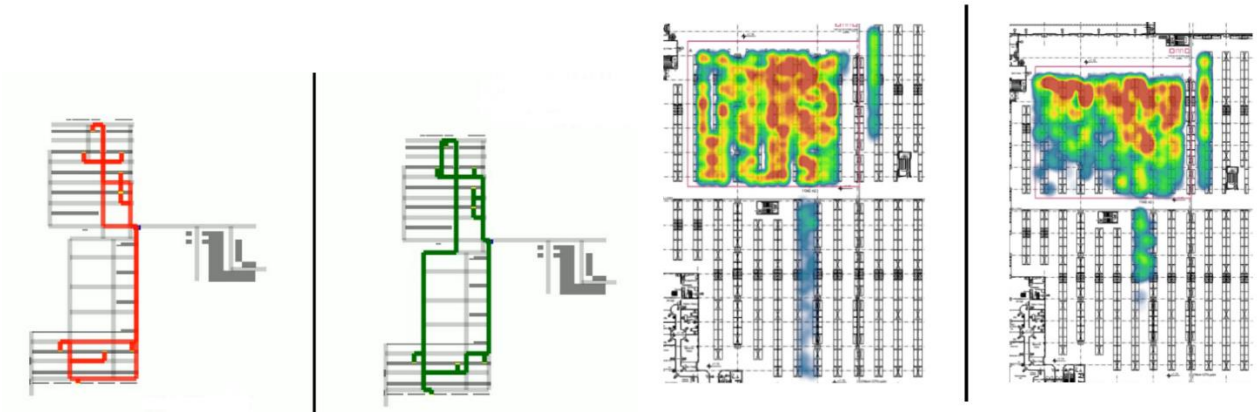


Figure 1. The result of route and slotting optimization. Result of route optimization (right) and heat map for slotting optimization (left).

The analysis of the optimization techniques yielded significant results. The number of locations visited per work order ranged from 1 to 161, with a total of 21,020 work orders examined. As a result of the optimizations, a total distance savings of 1,973.08 kilometers was achieved. Compared to the non-optimized work order visits, a 23.3% increase in efficiency was observed. The results presented in the Table 1 were obtained following the application of optimization techniques.

Table 1. Impact of route planning and slotting optimization techniques on warehouse efficiency

Order Number	Number Orders	Saving (km)	Productivity (%)
100-161	130	25.28	27.2
60-99	2390	345.57	21.8
30-59	5188	599.94	22.6
10-29	6573	764.93	28.7
1-9	6739	237.35	16.2

Conclusion

This work has shown the application of Geographic Information Systems (GIS) and genetic algorithms in warehouse optimization. The investigations demonstrated that utilizing route and slotting optimization applications substantially enhances the efficiency of warehouse operations. The findings emphasize that applying GIS and genetic algorithms can effectively improve the overall performance of logistics operations by aiding strategic decision-making in warehouse management. Subsequent studies should investigate the suitability of these optimization methods in diverse warehouse settings and various logistical situations more thoroughly. Particular focus might be placed on the administration of extensive data collection, immediate real-time data analysis, and swift adjustment to fluctuating demand. Furthermore, it is possible to assess the effects of these applications in other industries through a comparative analysis, and it is also possible to examine the long-term results of incorporating these approaches. These studies will help formulate methods to enhance the application of warehouse optimization on a larger scale and with greater effectiveness.

References

1. Mehdi, Asgari, Siahboomy., Hadi, Sarvari., Daniel, W., Chan., Hala, Nassereddine., Zhen, Chen. (2021). A multi-criteria optimization study for locating industrial warehouses with the integration of BIM and GIS data. Architectural Engineering and Design Management, 17:478-495. doi: 10.1080/17452007.2021.1881880
2. Markowski, T., & Bilski, P. (2021, July 5). Optimization of Autonomous Agent Routes in Logistics Warehouse. International Journal of Electronics and Telecommunications, 559–564. https://doi.org/10.24425/ijet.2021.137846
3. Li, Y., Shi, X., Diao, H., Zhang, M., & Wu, Y. (2021, March 22). Optimization of warehouse management based on artificial intelligence technology. Journal of Intelligent & Fuzzy Systems, 1–8. https://doi.org/10.3233/jifs-189843
4. Wanying, Z., Xiaoqing, W., Ruofei, M., lin, D., & Jianchen, Z. (2021, June 1). Route Optimization of AGVs with an Improved Fishbone Warehouse Layout. IOP Conference Series: Earth and Environmental Science, 791(1), 012047. https://doi.org/10.1088/1755-1315/791/1/012047
5. Babar, M. M., Syed, A. J., Asim, S., Khan, A. R., & Hai, M. A. (2022, December 14). Development of an Algorithm based on the Optimization of space, time and resources of the warehouse using Genetic Algorithms. 2022 3rd International Conference on Innovations in Computer Science & Software Engineering (ICONICS). https://doi.org/10.1109/iconics56716.2022.10100591
6. Chen, J., Kang, S., & Cao, L. (2023, May 8). Bayesian optimization genetic algorithm based on automated stereo warehouse space optimization. https://doi.org/10.21203/rs.3.rs-2886577/v1
7. Ha, W. Y., Cho, K. Y., & Han, C. S. (2022, February 5). Application of Genetic Algorithms to Optimize the Storage Location of Products in Military Logistics. Journal of the Korea Institute of Military Science and Technology, 25(1), 108–116. https://doi.org/10.9766/kimst.2022.25.1.108
8. Viveros, P., González, K., Mena, R., Kristjanpoller, F., & Robledo, J. (2021, January 20). Slotting Optimization Model for a Warehouse with Divisible First-Level Accommodation Locations. Applied Sciences, 11(3), 936. https://doi.org/10.3390/app11030936
9. Kordos, M., Boryczko, J., Blachnik, M., & Golak, S. (2020, July 13). Optimization of Warehouse Operations with Genetic Algorithms. Applied Sciences, 10(14), 4817. https://doi.org/10.3390/app10144817

Advanced Engineering Days

aed.mersin.edu.tr

Emergency and terminated evacuation of supermarket warehouse using indoor navigation by Dijkstra's Algorithm

Deniz Doğa Işık*[1], Şaziye Özge Atik [1]

[1]*Istanbul Technical University, Department of Geomatics Engineering, Türkiye, isikd16@itu.edu.tr; donmezsaz@itu.edu.tr*

Cite this study: Işık, D. D., & Atik, Ş. Ö. (2024). Emergency and terminated evacuation of supermarket warehouse using indoor navigation by Dijkstra's Algorithm. Advanced Engineering Days, 9, 255-258

Keywords
GIS
Indoor Mapping
Warehouse Solutions
Cost Analysis
Spatial Information

Abstract

Indoor navigation maps are taking firm steps towards becoming one of the most effective facilitators that the internet age has brought to humanity. In this progression, its main areas of use stand out in megastructures such as warehouses, which accommodate many places and people that serve more than one purpose. Today, thanks to the widespread use of Internet of Things (IoT) and ease of use by the end user, indoor navigation solutions have gained an important place in warehouse optimization. Moreover, earthquake safety has become a very prominent topic in our country, especially after the February 6 Maraş earthquakes. Living and working in earthquake-safe buildings should be seen as a fundamental right for all humanity. At this point, the emergency evacuation of a supermarket warehouse, which has been determined to be earthquake unsafe, should be re-planned beyond the standard procedure. It will be one of the best examples of indoor navigation solutions for evacuating the warehouse and ensuring the safety of employees in this emergency scenario through Geographic Information Systems (GIS) using 2D floor plans. GIS supports the shortest path by considering minimum cost, furthermore related parameters and queries provides the safest route in the working environment.

Introduction

Humanity's pursuit of continuous and easy processes has significantly influenced the development of technology, particularly in indoor and outdoor navigation systems. While Global Navigation Satellite Systems (GNSS) aid in outdoor navigation, indoor navigation solutions are needed for large spaces like warehouses, where location determination can be challenging. Although indoor navigation is used in warehouse operations, privatization studies are still ongoing. In an emergency scenario, the setup should vary based on the warehouse structure and product content. This study aimed to determine the fastest and most reliable evacuation scenarios for earthquake-resistant products from a supermarket warehouse using 2D floor plans and GIS. Cost analysis was conducted based on network analysis and logistics hardware capacity, and the minimum evacuation time was considered an interpretable issue.

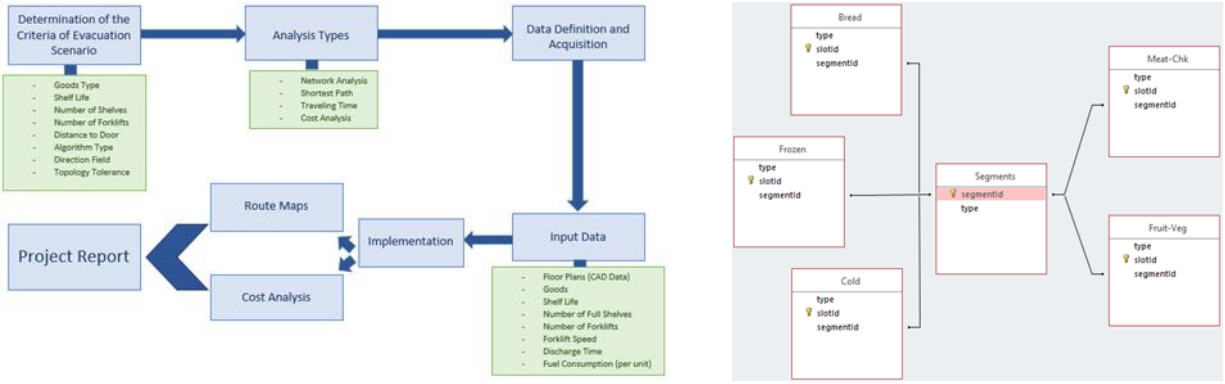


Figure 1. Flowchart of the study (Right), and Entity Table (Left)

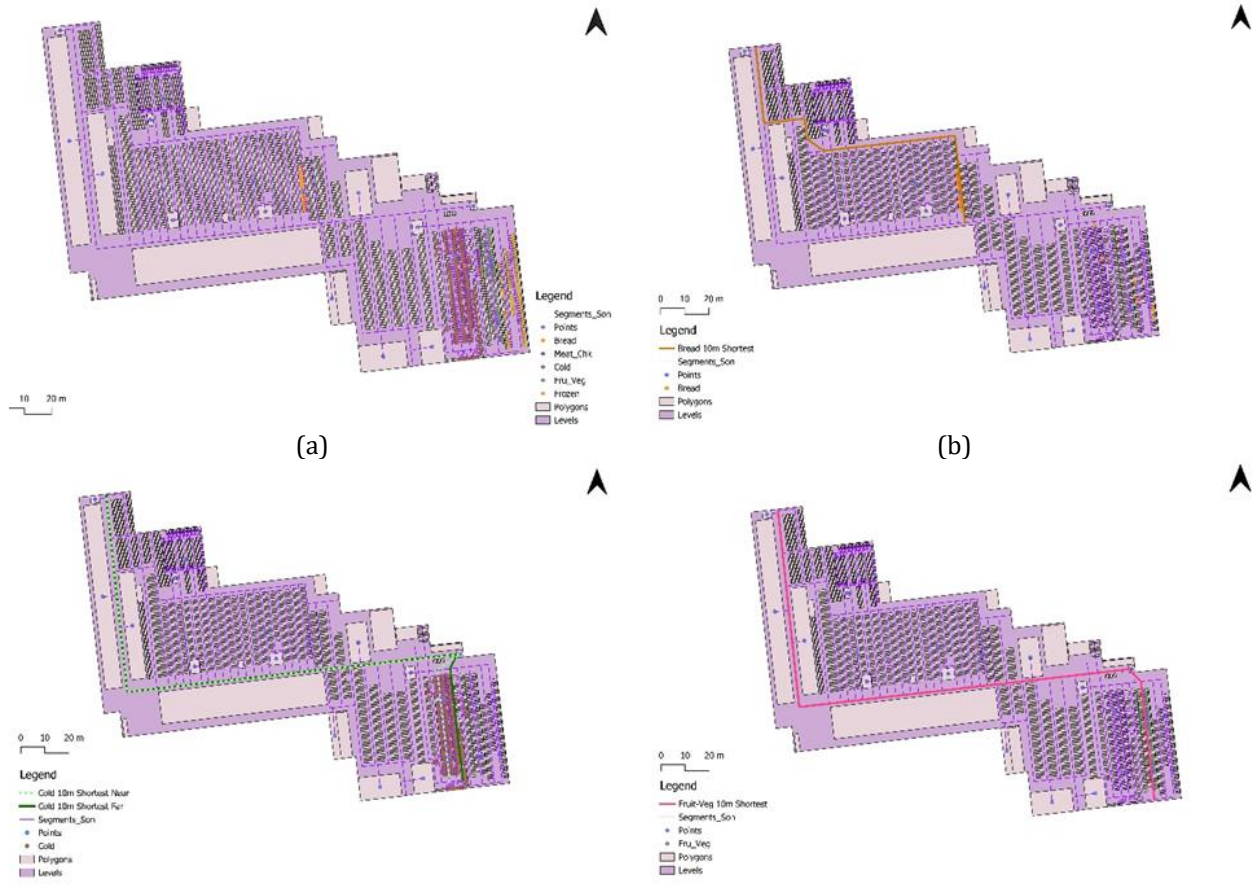
Material and Method

The study used 2D floor plans of a supermarket warehouse in Istanbul, incorporating data from CAD format and the TUREF TM30 Projected Coordinate System. The TM30 coordinate system was chosen for its suitability for the city's dynamics. No terrestrial measurement data was used, and CAD data was deemed sufficient for the thesis. The floor plans were obtained through digitization and customized layers were used to represent the entire warehouse content. The points layer indicated entry and exit points, product wrapping areas, doors, and shelves. Bread, Cold, Frozen, Fru-Veg and Meat-Chk layers represent goods types which need to be evacuated firstly., The Segments layer represented corridors, and the Levels layer represented walkways. The Polygons layer delimited shelves and certain regions, ensuring high accuracy and consistency in operations. The study aimed to design an emergency evacuation scenario for fast-moving consumer goods.

The study focuses on the efficiently evacuating of fast-moving consumer goods in supermarket warehouses using QR codes which is the cheapest and easiest solution (1). The logistics of these products can be directed to the exit by employees in the shortest and most cost-effective way. The TSP (Traveling Salesman Problem) was used in conjunction with Djikstra'a Algorithm to solve the problem. The application is based on defining stops as graphs through nodes and connecting them with edges to create routes. In establishing these connections, data must be associated with each other and topological classifications must be made since a spatial relationship is mentioned here. Topology enables objects in the database to recognize objects around them and to be positioned geometrically. While defining the spatial relationships of linear data such as connectivity and path, the properties of adjacency and containment are used (2). The data is defined with point and line classes, and polygons are considered to ensure distance and cost accuracy. The algorithm determines the closest point and prepares the route for each next stop based on the shortest distance. Algorithm's mathematical solution is based on two formulas in Equation 1 (3). In the equation, D: a cluster of nodes, K: a cluster of edges, G: Graph.

$$D = \{d_0, d_1, d_2, \ldots, d_{n-1}, d_n\}, \quad K = \{k_0, k_1, k_2, \ldots, k_{n-1}, k_n\}, \quad G = \{D, K\} \qquad [1]$$

After understanding this algorithm, network analyzes were created for each product group based on the shortest distance construct. Depending on the placement of the product group in the warehouse, the optimal route to be drawn to the goods exit door was created by evaluating the travel speed and topology tolerance. The important thing here is to make it possible to evacuate the maximum number of products in the shortest time and via the safest route as (a) (b) (c) (d) (e) in Figure 2.



(a) (b)

(c) (d)



(e) (f)

Figure 2. (a)2D Floor Plan (b)Bread Shortest Path Analysis (c)Cold Shortest Path Analysis (d)Fru-Veg Shortest Path Analysis (e)Frozen Shortest Path Analysis (f)Meat-Chk Shortest Path Analysis

Results

As a result of all analyses, considering the obtained routes, the criteria to be considered in the evacuation of the warehouse were evaluated for time, travel distance, logistics hardware and goods stock. As a result of this evaluation, a table and chart (Figure 3) emerged as seen below. This table also shows that when considering the products that need to be evacuated with minimum time schedule from this warehouse.

Although it is thought that the variability of cost results will be low due to the close travel times, the effect of the amount of stocked goods on the result can be clearly seen in the table. In the calculation, the discharge time of a shelf (5 min) multiplies is multiplied with by the forklift number and adds added with (Travel Distance/5 km-h).

Table 1. Cost calculation of the route

Routes	Travel Distance (m)	Shelves	Forklift Number	Time (min.s)	Cost
Frozen_Near	275.1	10	1	53.3	53.3
Frozen_Far	288.2	58	3	103.6	310.8
Fruit-Veg	275.1	38	2	103.3	206.6
Cold_Near	273.3	113	3	278.2	834.6
Cold_Far	273.3	113	3	278.2	834.6
Meat-Chk	245.6	12	1	62.9	62.9
Bread	188.0	15	1	77.3	77.3

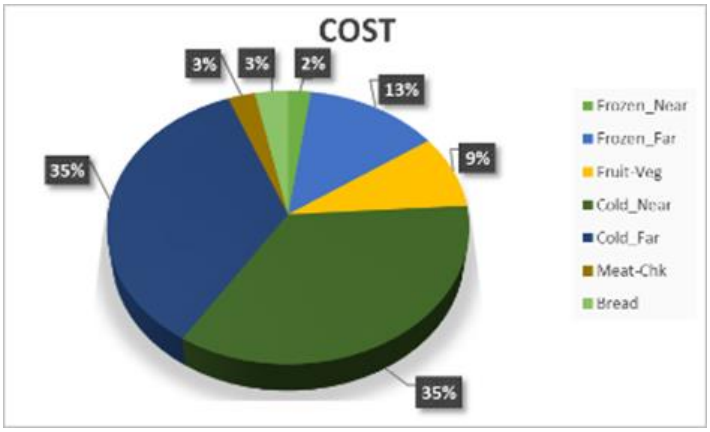


Figure 3. Cost distribution of the routes

Discussion

In cases where the logistics equipment capacity cannot be changed, when the analysis results obtained from the algorithm are supported by facility management data, it is seen that time and cost trigger each other differently than the location-based evaluation process. In this case, the necessity of studies on the development of industrial routing systems with new approaches in which facility management data will be included while creating the algorithm emerges.

Conclusion

The question mentioned in the discussion section needs to be answered in order to reach a conclusion on how warehouse optimization solutions using indoor navigation can go beyond the alternatives offered by current research and use. It is inevitable that any solution to be produced for the "shortest path" will be subject to limitations in algorithms and guidance in this regard, as the place will face the lack of openness to alternatives in emergency situations. For solutions where security is a priority, the information produced in the GIS environment must be used effectively in settlement, architecture and logistics.

References

1. Nikander, J., Järvi, J., Usman, M., & Virrantaus, K. (2013). Indoor and outdoor mobile navigation by using a combination of floor plans and street maps. Progress in Location-Based Services, 233-249.
2. Kuru, G.N. (2019). İstanbul'da Afet Sonrasi Toplanma Ve Barınma Alanlarinin Erişebilirliği, Istanbul Technical University Graduate School
3. Bayzan, Ş. (2005). Araç Rotalarinin En Kısa Yol Algoritmaları Kullanilarak Belirlenmesi Ve .NET Ortaminda Simülasyonu, Pamukkale University, The Graduate School of Natural and Applied Sciences

Advanced Engineering Days

aed.mersin.edu.tr

Comparing the accuracy of extracting surface features from Landsat and UAV imagery

Mohammad Saleh Chavoshi*[1], Hassan Emami[2]

[1]Department of Geomatics, School of Marand Engineering, University of Tabriz, Tabriz, Iran. Smschavoshi2002@gmail.com
[2]Department of Geomatics, School of Marand Engineering, University of Tabriz, Tabriz, Iran. *h_emami@Tabrizu.ac.ir*

Cite this study: Chavoshi, M., & Emami, H. (2024). Comparing the accuracy of extracting surface features from Landsat and UAV imagery. Advanced Engineering Days, 9, 259-262

Keywords
UAV images
Landsat
Vegetation index
Index of residential areas
residential areas

Abstract

The purpose of the present paper is to compare the accuracy of extracting surface features such as vegetation and residential areas (buildings) using UAV and satellite images. Remote sensing based on UAV and satellite images has a good capability and ability to prepare different thematic maps, such as vegetation and residential areas in urban areas. To this end, UAV imagery was first converted into point clouds, which were then used to remove residential areas and vegetation. In the following stage, vegetation was extracted using the NDVI vegetation index from Landsat 8 satellite images, and residential areas were extracted using the BU (Built Up) index. The results revealed that employing UAV data instead of Landsat satellite imagery increased the accuracy of maps obtained by 56% and vegetation by 88%, respectively.

Introduction

Satellite image classification is critical in a variety of applications, including urban planning, environmental monitoring, and land use assessment [1]. Accurate classification of satellite imagery is essential role in numerous fields, including urban management, environmental planning, precision agriculture, and natural resource monitoring [2; 3]. Satellites operate at higher altitudes, providing a broader field of view and covering a larger region. Drones, on the other hand, provide greater resolution because they fly at lower altitudes, resulting in more information in the end. Drones, unlike manned aircraft or satellite imaging, may fly at considerably lower altitudes, allowing for far quicker, less expensive, and independent data production regardless of atmospheric conditions such as cloud cover[4]. When classifying satellite images with modest spatial resolution, such as Landsat, it is difficult to distinguish between plant species and to identify the area covered by weeds. Accurate satellite image classification is critical in a variety of applications, including urban management, environmental planning, precision agriculture, and natural resource monitoring. Accurate data and statistics may be extremely crucial for effectively managing agricultural land areas [5]. Furthermore, reliable, classified information on a range of crops is important for managing agricultural land areas and determining the net national product [6; 7]. Traditional methods for estimating crop area and classifying tree cultivars relied solely on land observation and were extremely expensive, time-consuming, and not broadly applicable. Experts employed remote sensing data to determine the kind and intensity of cultivation for each crop, providing appropriate information to decision-makers [8]. Satellite and UAV data reduces not just human error, but it may also impact numerous agricultural projects, lowering costs and time. Because satellites are designed with a balance of spatial, temporal, and spectral separation power [9], most satellites cannot bring images together with high spatial, temporal, and spectral resolution at the same time, which is a significant limitation in the use of satellite images. Nowadays, as science progresses, images from above captured by UAVs are becoming more accessible. The major benefits of UAV images over satellite images are the determination of the imaging time, high spatial resolution, and no limitations on meteorological circumstances (cloud cover, etc.)[10]. However, collecting large-scale UAV imagery is frequently costly and time-consuming [6]. Remote sensing using unmanned aerial vehicles (UAV) and imagery from satellites has a high potential and aptitude to create various themed maps, such as vegetation and residential regions in urban areas [11; 12]. The objectives of this article are to examine and compare the accuracy of extracting surface features such as vegetation and residential areas (buildings) from UAV and satellite images.

Material and Method

Study area and data set

The research region, which is approximately 679629 square kilometers in size, is located in the center of Switzerland, from latitude 47 degrees and 03 minutes to 47 degrees and 04 minutes north, and from longitude 8 degrees and 24

minutes to 8 degrees and 25 minutes east. Figure 1 displays the research region's area. Table 1 summarizes the data for this study.

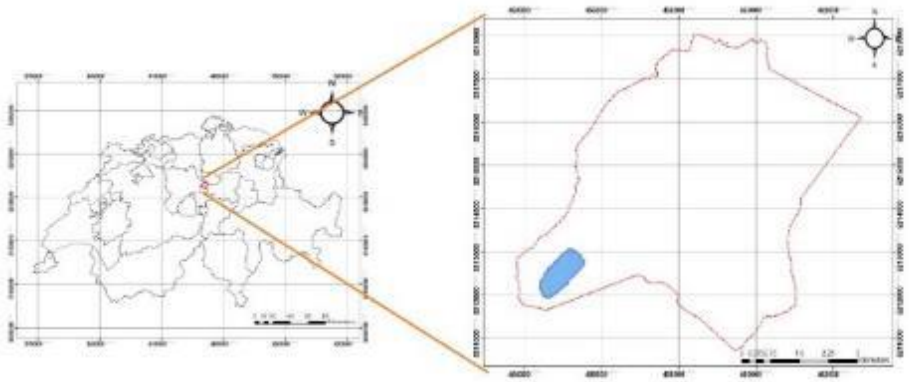


Figure 1. Study area

Table 1. Research data

Data	Data specification
Satellite Images	Landsat 8 satellite data With 195 passes and 27 rows as of 2021
UAV	279 Photos

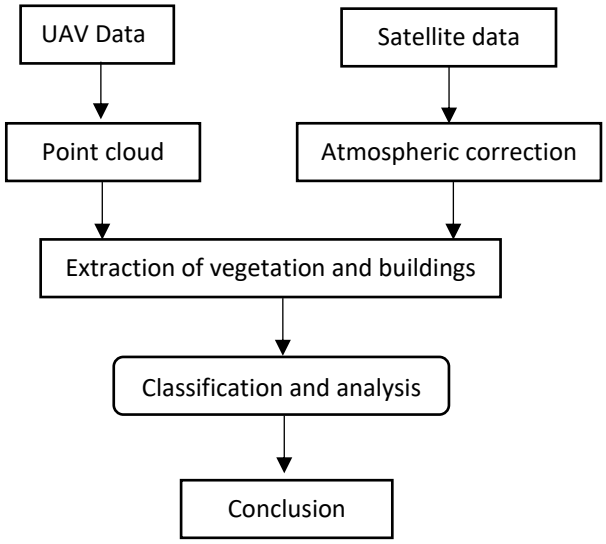


Figure 2. The steps of conducting research

This study was carried out in five steps, as seen in Figure 2. The first stage is to gather drone data and satellite imagery. The second phase involves generating point clouds from drone data and extracting vegetation and structures. In the third stage, we examine the collected data and draw conclusions. In the fourth stage, we apply atmospheric correction to the downloaded images from satellites (Landsat 8). In the sixth stage, we extract vegetation and buildings from Landsat 8 imagery.

Results and discussion

According to Figure 2, a point cloud was generated from the UAV data and we extracted buildings and vegetation from the point cloud. The result is shown in Figures 3 and 4.

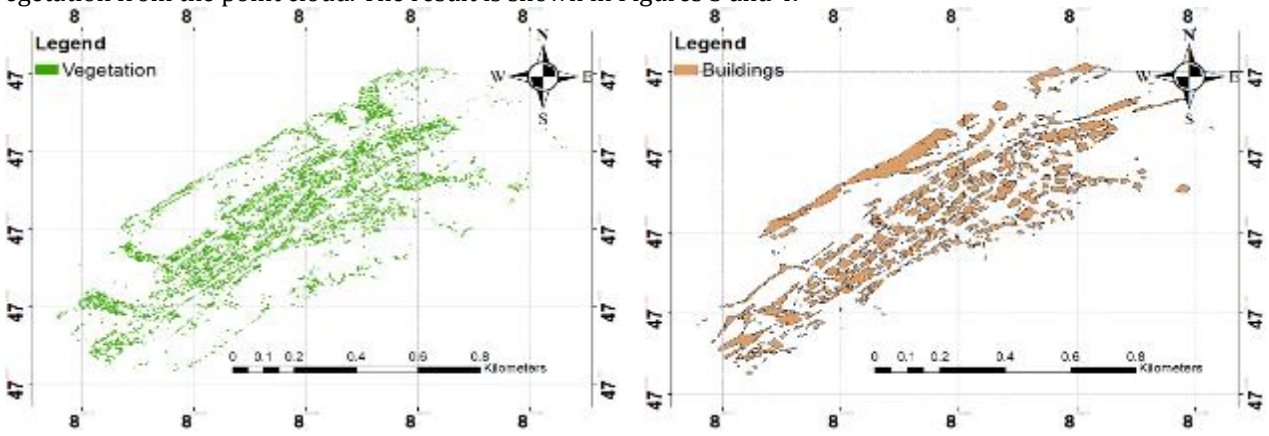


Figure 3. Surface features extracted from UAV images (a) Vegetation and, (b) Buildings

Landsat 8 satellite data was analyzed for vegetation cover and buildings using the NDVI and BU indices. The index formulas are as follows: Figure 4 demonstrates the outcomes of calculating and applying the indices.

NDVI=(NIR-RED) / (NIR+RED). (1)

NDBI=(SWIR1-NIR) / (SWIR1+NIR). (2)

BU (Built Up)=NDBI-NDVI. (3)

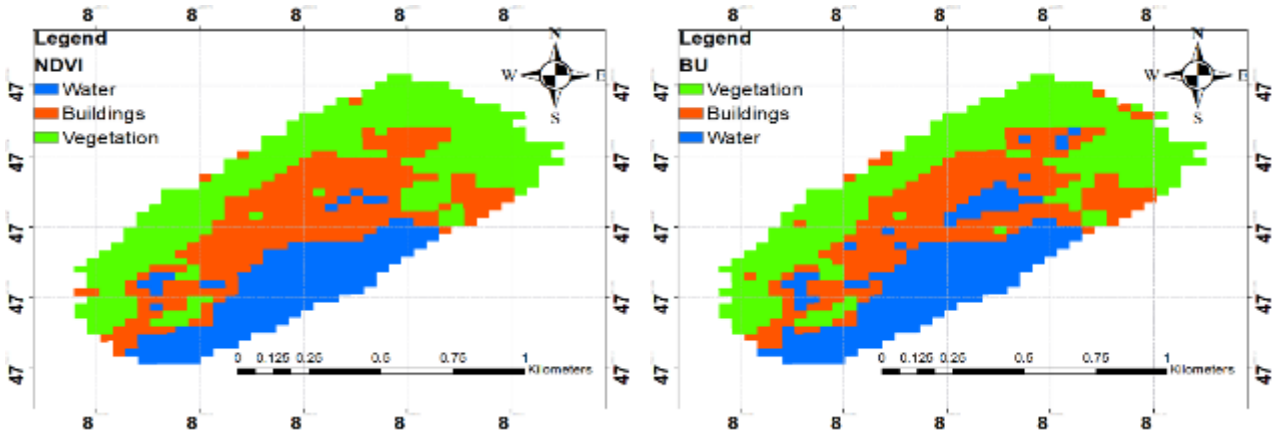


Figure 4. Surface features extracted from Landsat 8 data (a) Vegetation and, (b) Buildings

Figure 5 compares the vegetation from Landsat and UAV imagery.

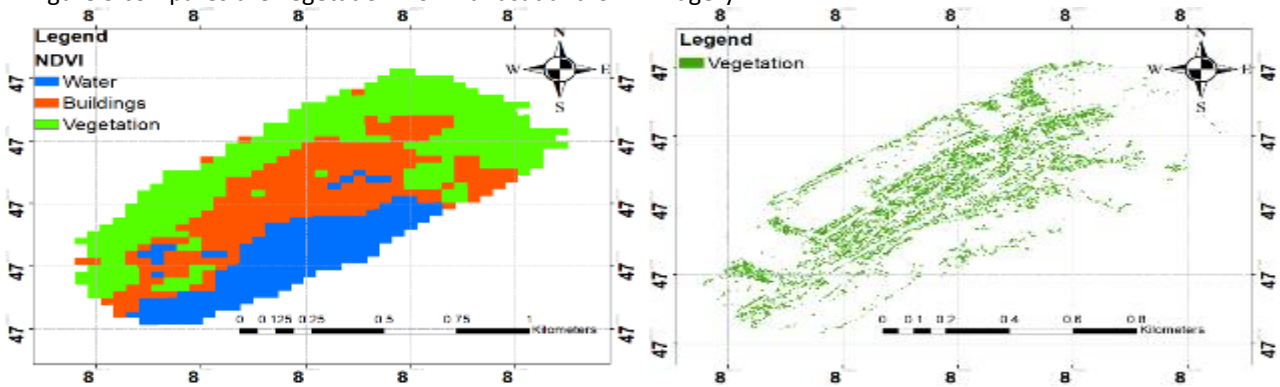


Figure 5. comparison vegetation extracted from UAV and Landsat 8 data (a) Landsat and, (b) UAV data

In addition, figure 6 illustrates compares the buildings from Landsat and UAV imagery.

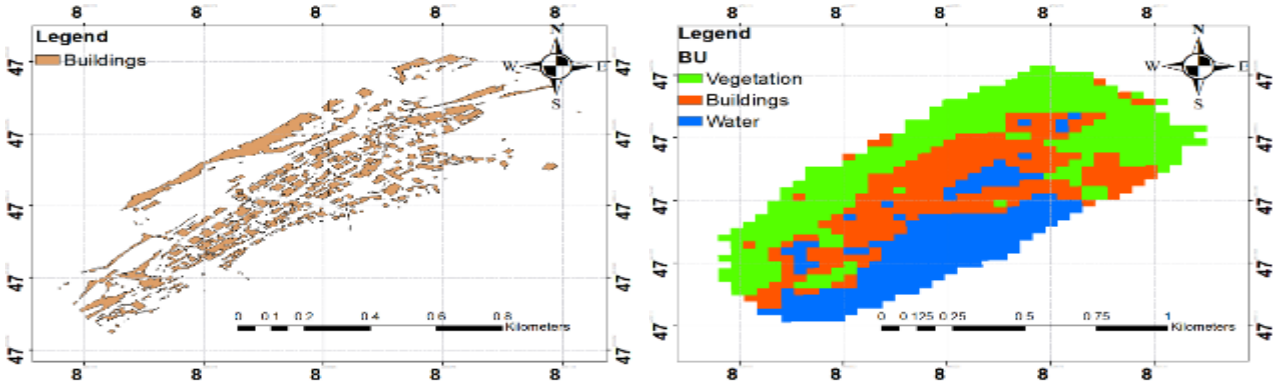


Figure 6. Comparison buildings extracted from UAV and Landsat 8 data, (a) UAV and, (b) Landsat data

.Using satellite data, the area of greenery was 488,700 square kilometers, whereas the area of buildings was 234,900 square kilometers. The number of UAV data points for vegetation was 41,305, whereas the area for buildings was 101,532 square kilometers. Using the orthomosaic data generated from UAV data, it was determined that UAV data is more accurate than satellite data. The results revealed that employing UAV data instead of Landsat satellite imagery increased the accuracy of maps obtained by 56% and vegetation by 88%, respectively.

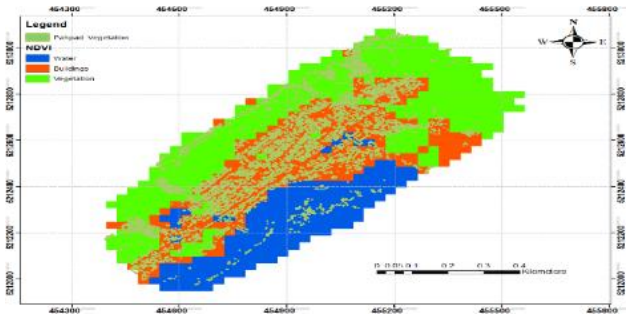


Figure 7. Overlay of UAV and Landsat images for vegetation

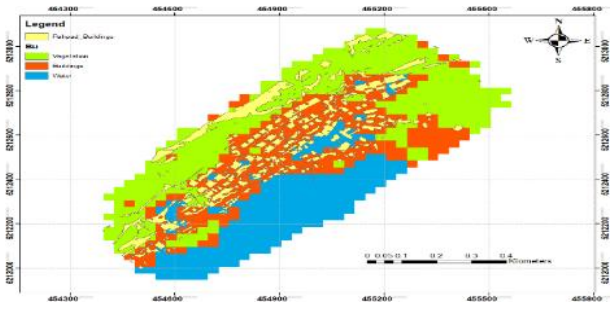


Figure 8. Overlay of UAV and Landsat images for Buildings

Conclusion

Remote sensing using UAVs and imagery from satellites has a high capability and capacity to create various themed maps, such as vegetation and residential regions in urban areas. The objectives of the present paper are to examine and compare the accuracy of extracting surface features such as vegetation and residential areas (buildings) from UAV and satellite imagery. To this end, first point clouds were generated from UAV images, then residential areas and vegetation were extracted from the point clouds. In the following stage, vegetation was extracted using the NDVI vegetation index from Landsat 8 satellite imagery, and residential areas were extracted using the BU (Built Up) index. Satellite and drone imagery were utilized to document vegetation and buildings in the center of Switzerland. Vegetation and buildings were retrieved first from UAV images, followed by satellite Landsat images. Using the orthomosaic imagery created from the region and comparing the two result images, it was determined that UAV images are more accurate than Landsat images. The area of vegetation and buildings in UAV captures is 41,305 and 101,532 square kilometers, whereas Landsat images are 488,700 and 234,900 square kilometers. The results showed that using UAV data instead of Landsat satellite imagery improved map accuracy by 56% and vegetation by 88%.

References

[1] Arabi Aliabad, F., Ghafarian Malamiri, H., Sarsangi, A., Sekertekin, A., & Ghaderpour, E. (2023). Identifying and Monitoring Gardens in Urban Areas Using Aerial and Satellite Imagery. *Remote Sensing, 15*(16), 4053. doi:https://doi.org/10.3390/rs15164053

[2] Meinel, G., Neubert, M., & Reder, J. (2001). The potential use of very high resolution satellite data for urban areas—First experiences with IKONOS data, their classification and application in urban planning and environmental monitoring. *Regensburger Geographische Schriften, 35*, 196-205.

[3] Park, G., Park, K., Song, B., & Lee, H. (2022). Analyzing impact of types of UAV-derived images on the object-based classification of land cover in an urban area. *Drones, 6*(3), 71. doi: https://doi.org/10.3390/drones6030071

[4] Tmušić, G., Manfreda, S., Aasen, H., James, M. R., Gonçalves, G., Ben-Dor, E., . . . Mészáros, J. (2020). Current practices in UAS-based environmental monitoring. *Remote Sensing, 12*(6), 1001. doi: https://doi.org/10.3390/rs12061001

[5] Ambika, A. K., Wardlow, B., & Mishra, V. (2016). Remotely sensed high resolution irrigated area mapping in India for 2000 to 2015. *Scientific data, 3*(1), 1-14. doi:https://doi.org/10.1038/sdata.2016.118

[6] Malamiri, H. R. G., Aliabad, F. A., Shojaei, S., Morad, M., & Band, S. S. (2021). A study on the use of UAV images to improve the separation accuracy of agricultural land areas. *Computers and Electronics in Agriculture, 184*, 106079. doi:https://doi.org/10.1016/j.compag.2021.106079

[7] Chen, M., Zhang, R., Jia, M., Cheng, L., Zhao, C., Li, H., & Wang, Z. (2024). Accurate and Rapid Extraction of Aquatic Vegetation in the China Side of the Amur River Basin Based on Landsat Imagery. *Remote Sensing, 16*(4), 654. doi:https://doi.org/10.3390/rs16040654

[8] Bégué, A., Arvor, D., Bellon, B., Betbeder, J., De Abelleyra, D., PD Ferraz, R., . . . R. Verón, S. (2018). Remote sensing and cropping practices: A review. *Remote Sensing, 10*(1), 99. doi:https://doi.org/10.3390/rs10010099

[9] Emelyanova, I. V., McVicar, T. R., Van Niel, T. G., Li, L. T., & Van Dijk, A. I. (2013). Assessing the accuracy of blending Landsat–MODIS surface reflectances in two landscapes with contrasting spatial and temporal dynamics: A framework for algorithm selection. *Remote Sensing of Environment, 133*, 193-209. doi:https://doi.org/10.1016/j.rse.2013.02.007

[10] Alvarez-Vanhard, E., Corpetti, T., & Houet, T. (2021). UAV & satellite synergies for optical remote sensing applications: A literature review. *Science of remote sensing, 3*, 100019. doi:https://doi.org/10.1016/j.srs.2021.100019

[11] Šiljeg, A., Panđa, L., Domazetović, F., Marić, I., Gašparović, M., Borisov, M., & Milošević, R. (2022). Comparative assessment of pixel and object-based approaches for mapping of olive tree crowns based on UAV multispectral imagery. *Remote Sensing, 14*(3), 757. doi:https://doi.org/10.3390/rs14030757

[12] Liu, Z., Wu, Y., Zhang, X., Li, M., Liu, C., Li, W., . . . Luo, H. (2023). Comparison of variable extraction methods using surface field data and its key influencing factors: A case study on aboveground biomass of Pinus densata forest using the original bands and vegetation indices of Landsat 8. *Ecological Indicators, 157*, 111307. doi:https://doi.org/10.1016/j.ecolind.2023.111307

Advanced Engineering Days

aed.mersin.edu.tr

Identifying the available lands for solar energy farms using GIS spatial analysis: A case study, Kirkuk City and its suburbs

Ghadah Hasan Mohammedfatih [*1], Khalil Valizadeh Kamran [1], Qayssar Mahmood Ajaj [2], Aboolfazl Ghanbari [1]

[1]*University of Tabriz, Department of Remote Sensing and GIS, Iran, & Northern Technical University, Department of Surveying Technologies Engineering, Iraq, ghada66@ntu.edu.iq, valizadeh@tabrizu.ac.ir, a_ghanbari@tabrizu.ac.ir*
[2]*Northern Technical University,* Department of Surveying Technologies Engineering, Iraq, *qayssarrsgis@gmail.com*

Cite this study: Mohammedfatih, G. H., Valizadeh Kamran, K., Ajaj, Q. M., & Ghanbari A. (2024). Identifying the available lands for solar energy farms using GIS spatial analysis: A case study, Kirkuk City and its suburbs. Advanced Engineering Days, 9, 263-266

Keywords
GIS
Spatial Analysis
Solar Energy
Land Availability

Abstract

With the increasing demand for renewable energy, identifying the available areas for installing solar farms is necessary to profit from natural energy and solar radiation. This study aims to use influential factors to analyze by finding undesirable areas for installing solar cells and thus finding available spaces for installing solar cells in the city of Kirkuk and its neighboring districts. Water bodies, land cover, the road network, and electrical power transmission lines are considered among the most important factors used in this study, which are treated using data management and spatial analysis in Geographic Information Systems (GIS). The results indicate that 46.035 % of the area of the study area, which 1915.71 km^2 could be available land for installing solar farms. These areas are distributed throughout all the districts surrounding the city of Kirkuk, and are more prevalent in the Shwan District, northeast of the city, in addition to Laylan District, southeast of the city. It must be noted that the available spaces for installing solar cell farms must be subject to another analysis using one of the methods of weighting the criteria to find the most suitable places for installing cells within the available areas.

Introduction

Renewable energy is considered the main source of sustainable energy, which most industrialized countries in the world seek to rely on instead of fossil fuels in order to promote sustainable development (Alhammad et al. 2022). One of the primary issues facing Iraq is the lack of electricity production, which can be attributed to a variety of reasons such as transmission lines being vulnerable to terrorist sabotage (Tichý 2019), insufficient infrastructure, and rapid urbanization coupled with a slowdown in the construction of new power plants (Mills and Salman 2020). Choosing sites for establishing solar farms using GIS is very important because it provides many large areas in a short time with low cost (Günen 2021). Data management in GIS is critical for integrating and eliminating the different factors involved in determining available land for solar energy farms (Noorollahi, Yousefi, and Mohammadi 2016). Spatial analysis based GIS is an important to assess and identify the availability lands for solar energy farms and other optimal locations projects (Yousefi, Hafeznia, and Yousefi-Sahzabi 2018). The main objective of this study is to determine the available lands to set up the farms of solar energy over Kirkuk City and adjacent districts.

Material and Method

Study area

Kirkuk City is located in north of Iraq and 286 km from the capital (Baghdad). The geographical location of Kirkuk City at longitude 44° 00′E to 44° 50′ E and latitude 35 ° 13′ N to 36 ° 29′ N with a total area of 96.79 km2 (Ajaj et al. 2018). It has boundaries with Erbil Governorate from the north, Salah al-Din Governorate from the south west. Nineveh Governorate from the north west, and Sulaimanya Governorate from the north east. The study

area including Kirkuk City and all surrounding districts which are Shwan, Alton Kupri, Dibbis, Yaychi, Taza, Laylan, and Kara Hingir. The city of Kirkuk has a semi-arid climate characterized by hot, dry summers and cold, rainy winters (Saeed, Al-Khafaji, and Mahmood Al-Faraj 2021). The terrain is characterized by its diversity, as the city extends over a flat plain surrounded by hills and low mountains. The spacious plain and moderate terrain are an important factor in determining various land uses, including agriculture and the development of renewable energy projects such as solar farms.

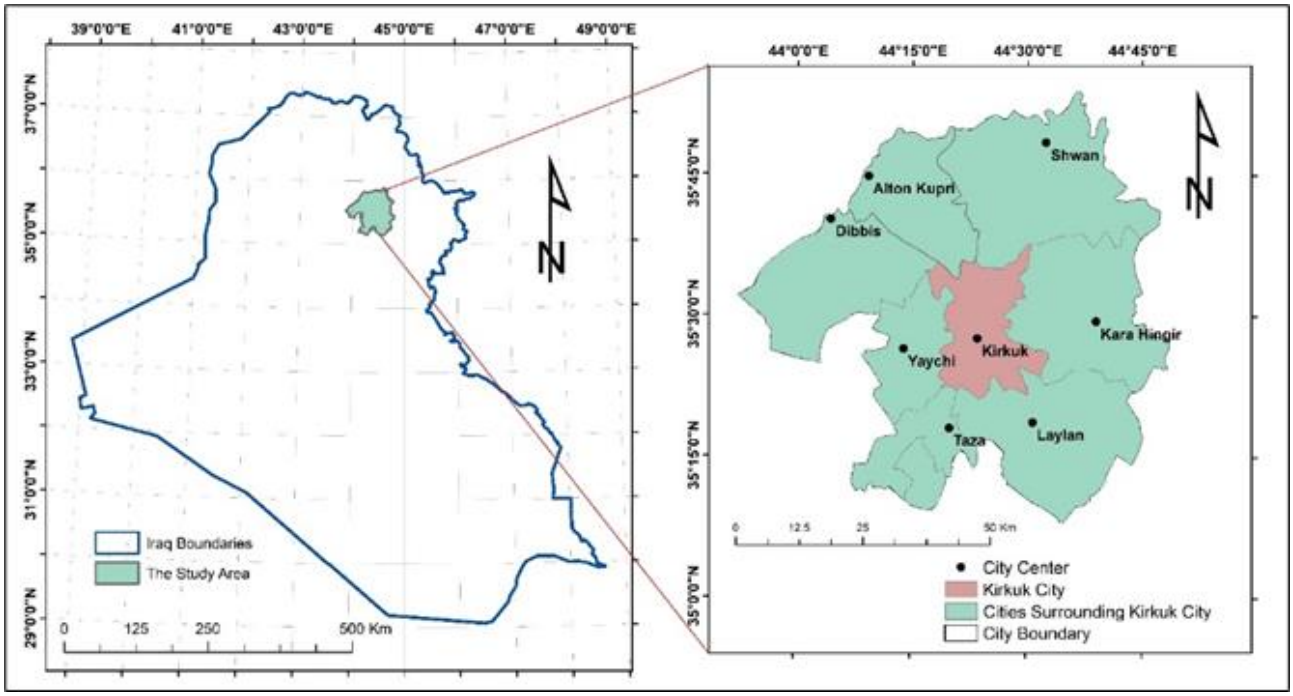


Figure 1. Study area (Kirkuk City and surrounding districts)

Land availability Factors

To identify available lands for installing solar energy farms in Kirkuk city and surrounding districts, several factors are used to ensure the best possible land use while taking into account environmental and infrastructural aspects. These factors include the main roads, bodies of water, electrical power transmission lines, and urban areas. The main road network is a vital factor in determining suitable locations for solar farms to ensure ease of access and maintenance (Alhammad et al. 2022). Bodies of water include rivers, streams and lakes, which are important for maintaining biodiversity and providing water resources (Cantonati et al. 2020). Electrical power transmission lines play an important role in delivering electricity generated from solar farms to the public grid (Imdadullah et al. 2021).

Urban areas include cities, villages, and residential areas from which an appropriate distance must be maintained to avoid interference with the daily life activities of residents. Data on the road network and electrical power transmission lines were obtained from the Kirkuk Urban Planning Department. While the Likelihood Classification Method was used to analyze Landsat satellite images to extract information about urban areas and water bodies. The classification method allows accurate identification of different areas based on the spectral characteristics of the images, which helps in accurately analyzing the available land areas (Phiri and Morgenroth 2017).

Constrain and filtering

The process of integrating and erasing various factors from the study area using data management and spatial analysis in GIS involves systematic steps to identify available locations for installing solar farms. This process begins with collecting data from reliable data (road network and electrical power transmission lines), as well as urban areas and bodies of water. This data is integrated into a GIS system, where it is transformed into geographic layers that can be spatially analyzed. Exclusion criteria are specified for unsuitable areas, such as excluding land within specified distances from roads, bodies of water, electric power transmission lines, and urban areas. Spatial analysis and data management tools are used to determine the remaining valid areas after applying exclusion factors. Solar farms must be located at least 100 m away from main roads, 300 m away from bodies of water and 100 m away from electrical power transmission lines.

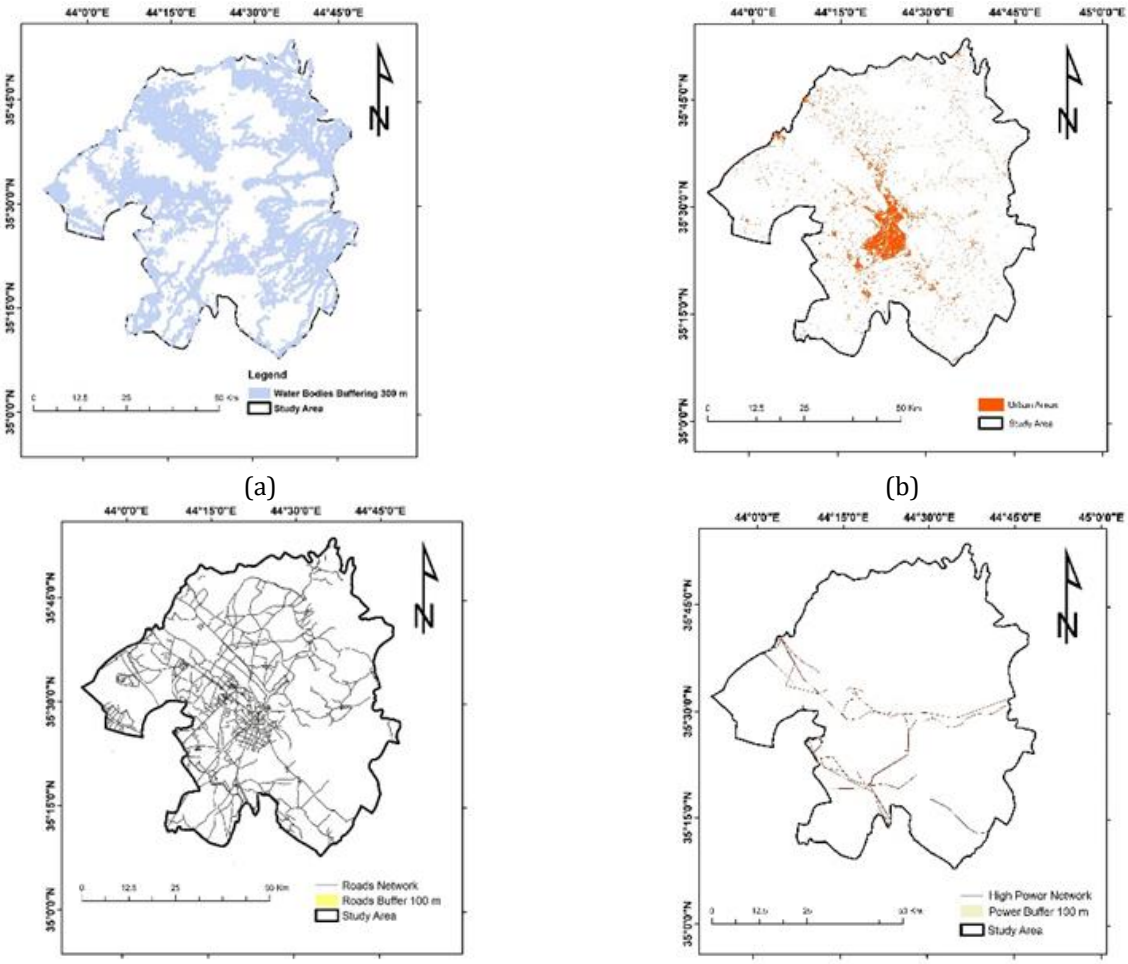


Figure 2: Solar energy farms factors (a) water bodies, (b) land cover, (c) electrical power lines, and (d) roads network

Results

Figure 3 a states the available lands for setting out the solar energy farms at Kirkuk City and its surrounding districts. The available lands are represented by lime dust color and they distributed in most parts of study area, but in large areas in Shwan and Laylan districts. The total area of available lands is 1915.035 km^2 which represent about 46.035 % from whole study area. The constrain areas is illustrates in figure 3 b and represented by magenta color. The total area of forbidden is about 4161.42 km^2.

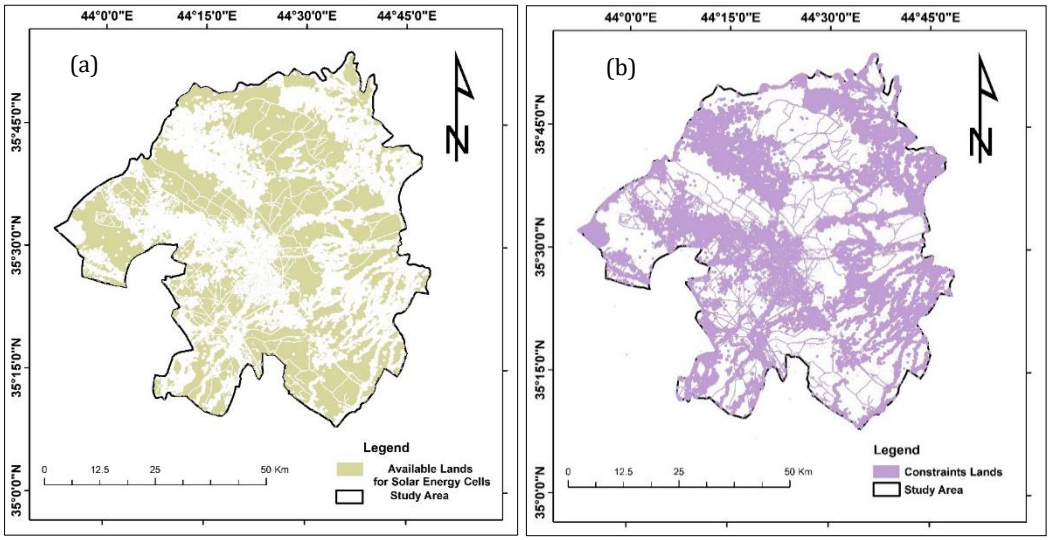


Figure 4. Available lands for solar energy farms over Kirkuk City and the surrounding districts

Discussion

The total area of land available for installing solar farms is considered large areas, most of which can be utilized, and which are determined later by decision-making methods. It must be noted that solar radiation in the region is in high quantities, especially during the summer and spring seasons, which is why it is advisable not to neglect it and to benefit from it to support electrical energy in the region. In addition, this study area is located in the northeast of Kirkuk Governorate, meaning that studies can be conducted on the rest of the governorate's areas, which have large areas.

Conclusion

The outcomes of this study demonstrate the importance of using geographic information systems in determining optimal locations for setting solar energy farms in the city of Kirkuk and its surrounding districts. By integrating data from multiple sources and analyzing it using spatial analysis tools, we were able to identify available land based on specific criteria such as proximity to the main road network, bodies of water, electric power transmission lines, and urban areas. The results showed that there are large areas that meet the specified standards, which provides great opportunities for developing solar energy projects in the region with 46.035 % of the study area. This process not only ensured optimal use of the available land but also preserved the surrounding environment and infrastructure. This study supports the importance of integrated data management and the use of advanced GIS technologies in urban planning and environmental sustainability, and emphasizes the necessity of continuing to update data and improve analysis methods to ensure the maximum possible benefit from our natural resources.

References

1. Ajaj, Qayssar Mahmood et al. 2018. "GIS Based Spatial Modeling to Mapping and Estimation Relative Risk of Different Diseases Using Inverse Distance Weighting (IDW) Interpolation Algorithm and Evidential Belief Function (EBF) (Case Study: Minor Part of Kirkuk City, Iraq)." *International Journal of Engineering and Technology(UAE)* 7(4): 185–91.
2. Alhammad, Abdulaziz, Qian Sun, Yaguang Tao, and and Yaguang Tao Abdulaziz Alhammad, Qian Sun. 2022. "Optimal Solar Plant Site Identification Using GIS and Remote." *Energies, MDPI* 15(1): 312. https://www.mdpi.com/1996-1073/15/1/312/htm%0Ahttps://www.mdpi.com/1996-1073/15/1/312.
3. Cantonati, Marco et al. 2020. "Characteristics, Main Impacts, and Stewardship of Natural and Artificial Freshwater Environments: Consequences for Biodiversity Conservation." *Water (Switzerland)* 12(1).
4. Günen, Mehmet Akif. 2021. "A Comprehensive Framework Based on GIS-AHP for the Installation of Solar PV Farms in Kahramanmaraş, Turkey." *Renewable Energy* 178: 212–25.
5. Imdadullah, Basem Alamri, Md Alamgir Hossain, and M. S. Jamil Asghar. 2021. "Electric Power Network Interconnection: A Review on Current Status, Future Prospects and Research Direction." *Electronics (Switzerland)* 10(17): 1–29.
6. Mills, Robin, and Maryam Salman. 2020. Al-Bayan Center for Planning and Studies *Powering Iraq: Challenges Facing the Electricity Sector in Iraq*.
7. Noorollahi, Younes, Hossein Yousefi, and Mohammad Mohammadi. 2016. "Multi-Criteria Decision Support System for Wind Farm Site Selection Using GIS." *Sustainable Energy Technologies and Assessments* 13: 38–50. http://dx.doi.org/10.1016/j.seta.2015.11.007.
8. Phiri, Darius, and Justin Morgenroth. 2017. "Developments in Landsat Land Cover Classification Methods: A Review." *Remote Sensing* 9(9).
9. Saeed, Fouad H., Mahmoud S. Al-Khafaji, and Furat A. Mahmood Al-Faraj. 2021. "Sensitivity of Irrigation Water Requirement to Climate Change in Arid and Semi-Arid Regions towards Sustainable Management of Water Resources." *Sustainability (Switzerland)* 13(24).
10. Tichý, Lukáš. 2019. "Energy Infrastructure as a Target of Terrorist Attacks from the Islamic State in Iraq and Syria." *International Journal of Critical Infrastructure Protection* 25(November 2017): 1–13.
11. Yousefi, Hossein, Hamed Hafeznia, and Amin Yousefi-Sahzabi. 2018. "Spatial Site Selection for Solar Power Plants Using a Gis-Based Boolean-Fuzzy Logic Model: A Case Study of Markazi Province, Iran." *Energies* 11(7).

Advanced Engineering Days

aed.mersin.edu.tr

A satellite-based monitoring for air pollution in urban areas: A case study of Tabriz City

Arash RahmaniZadeh*[1], Hassan Emami [2], Shahla Taghizadeh Sofiani [3]

[1]*University of Tabriz, Department of Surveying, IRAN, arahmanizadeh@Tabrizu.ac.ir*
[2]*University of Tabriz, Department of Surveying, IRAN, h_emami@Tabrizu.ac.ir*
[3]*Tabriz University of Medical Sciences, Tabriz Health Center, IRAN, sh.taghizade@gmail.com*

Cite this study: Rahmanizadeh, A., Emami, H., & Taghizadeh Sofiani, S. (2024). A satellite-based monitoring for air pollution in urban areas: A case study of Tabriz City. Advanced Engineering Days, 9, 267-270

Keywords
Air Pollution
Sentinel-5P images
TROPOMI sensor
Tabriz city
Atmospheric pollution

Abstract

Air pollution and its consequences for human health are among the world's greatest issues today. Iran, a developing country, is not immune to this issue. In this investigation, Sentinel-5 imagery from satellites were used to conduct a comprehensive monitoring of some of the most critical air pollutants in the Tabriz city from 2019 to 2023. These pollutants included nitrogen dioxide, sulfur dioxide, carbon monoxide, and suspended particles. In this study, level 3 imagery obtained using the Google Earth engine were employed. Furthermore, the validity of the monitoring results was assessed using ground pollutant recording stations. The findings of this evaluation reveal that the values monitored using Sentinel-5 satellite imagery are 64% to 87% 30-days period associated with the values monitored by ground stations. As a result, Sentinel-5 satellite images have great potential for use in macro-management studies aimed at reducing air pollution.

Introduction

Air pollution is broadly described as any chemical, physical, or biological agent that affects the natural structure of the atmosphere. Pollutants of primary concern for public health include PM2.5 (particulate matter with a diameter smaller than 2.5 μm), CO, ozone (O3), NO2, and SO2. Chronic exposure to air pollution kills more people worldwide than HIV/AIDS, malaria, and tuberculosis combined, and more than an order of magnitude higher than all types of violence [1]. Air pollution is the third most common cause of death globally [2]. Air pollution might thus be characterized as a global "pandemic" that needs to be monitored and handled. Remote sensing (RS) and cloud computing technologies enable us to do so. Air pollution is regarded as one of the planet's most serious concerns, contributing significantly to global climate change and early death around the world. The World Health Organization estimates that air pollution causes approximately 4.7 million excess deaths globally each year [2], with estimates ranging from 3 to 10 million depending on disease categories and exposure-response function [3; 4]. Exposure to NO2 may cause 4 million new instances of pediatric asthma each year [5]. According to studies, anthropogenic emissions account for more than 70% of the worldwide health burden caused by air pollution [4; 6]. The primary anthropogenic sources of air pollution are factories, motor vehicles, electricity generation, agricultural operations, and domestic combustion, but non-anthropogenic sources include desert dust, forest fires, and even volcanoes. The growing industrialization of the human population is causing severe strain on air quality in cities around the world [7] . To properly map and monitor air quality, it is necessary to investigate the concentrations of various contaminants in the air [8]. Ground-based sensors provide point data on the concentrations of various gaseous pollutants and greenhouse gases at specific locations [9; 10]. However, for extensive investigation, ground-collected gaseous concentration values are frequently interpolated[11]. The interpolated values produce extremely average findings, which represent a trade-off in terms of precision for research conducted over wide areas [12]. High temporal resolution Remote sensing-based air pollution monitoring and mapping can provide highly precise and near-real-time observations of pollutant concentrations in the atmosphere [8]. The TROPOMI sensor's less than one-day repeat pass provides great temporal resolution for near-real-time mapping and monitoring of air pollutant concentrations [13]. The TROPOMI was created for applications in three key areas: air quality, stratospheric ozone layer, and global climate change consequences [14]. This research explores and analyzes Sentinel-5P gridded air pollution data. In this work, Sentinel-5 satellite imagery was used to conduct comprehensive monitoring of some of the most critical air pollutants in Tabriz city from 2019 to 2023. These pollutants included nitrogen dioxide, sulfur dioxide, carbon monoxide, and suspended

particles. In this study, level 3 photos obtained using the Google Earth engine were employed. Furthermore, the validity of the monitoring findings was assessed using ground pollutant recording stations.

Material and Method

Study area and dataset

Tabriz, a city in northwest Iran, is being studied for air pollution monitoring using Sentinel-5 satellite imagery. Figure 1 illustrates the location of the research region on a map of Iran. The concentrations of nitrogen dioxide, sulfur dioxide, carbon monoxide, and suspended particles in Tabriz were tracked from 2019 to 2023.

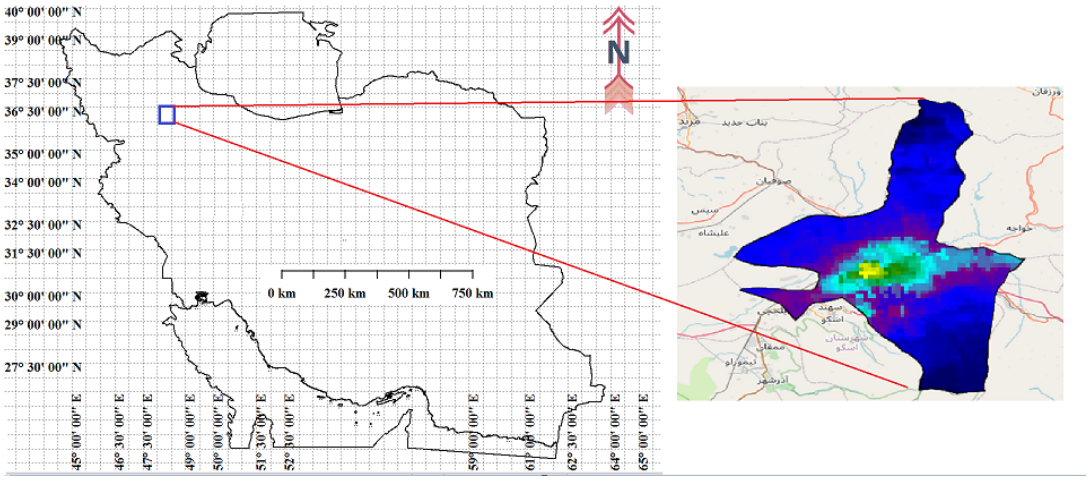


Figure 1. Location of the study area

The European Space Agency established the Sentinel-5 Precursor (Sentinel-5P), an Earth observation satellite. The satellite carries a single payload: the TROPOMI-sensor, a nadir-looking imaging spectrometer. The sensor monitors air pollution by measuring electromagnetic spectrum wavelengths ranging from UV (270–320 nm) to SWIR (2305–2385 nm)[15].

Results and Discussion

Nitrogen dioxide is considered one of the most significant air pollutants. You stated that human activities, particularly the use of fossil fuels, emit millions of tons of nitrogen dioxide each year [16]. The high concentration of carbon dioxide and nitrogen has a deleterious impact on the human respiratory system, worsening the condition of asthmatic patients, particularly youngsters. Figure 2 illustrates an example of the particle size distribution of air pollutants and their yearly minimum-maximum for the city of Tabriz during a five-year period (2019-2023).

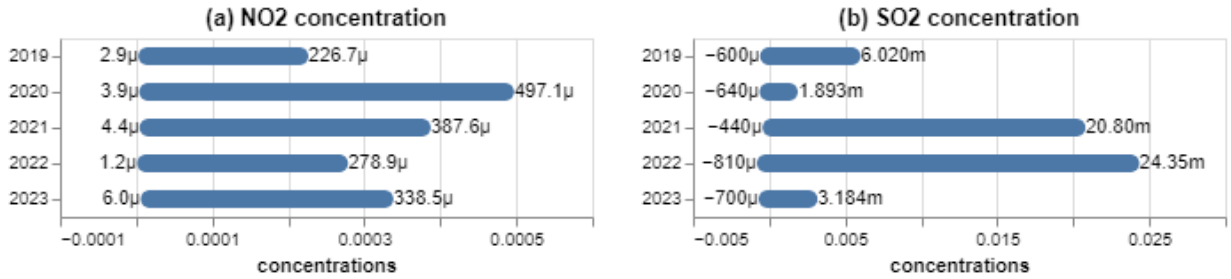


Figure 2. An example of the annual minimum and maximum amount of air pollutants (a) NO2 concentration, (b) SO2 concentration, in the city of Tabriz

The most significant sources of sulfur dioxide gas emissions are thermal power plants and diesel fuel. Figure (b) illustrates that diesel fuel was at its highest in 2021 and 2022, and in the remaining years when natural gas was utilized instead of diesel fuel, this pollution was for example, it would have dropped considerably by 2023. Volcanoes and numerous industrial activities create sulfur dioxide (So2). In addition, humans create more than 80% of sulfur oxides when they burn fossil fuels from fixed polluting sources[17]. Following the yearly analysis of Tabriz's air pollution parameters, we looked at the monthly average of these pollutants. Figure 3 illustrates an example of the comparison of monthly mean for 2019 to 2023 of air pollutants for the city of Tabriz during a five-year period (2019-2023). The results show that in the first and second months of the year, which coincide with

the cold season of Tabriz city, pollution factors have reached their maximum, which includes the use of fuel oil in thermal power plants, indicating that instead of natural gas, fuel oil or polluting fuels are used in these power plants. (NO2), (SO2), and other air pollutants were monitored by both ground stations, and suspended particulate matter pollutants were measured using data from the Crisis Management Headquarters' ground station (concentration of PM10 pollutants). To compare the results of ground and satellite monitoring, the linear correlation coefficient was calculated, and the results are shown in Table 1.

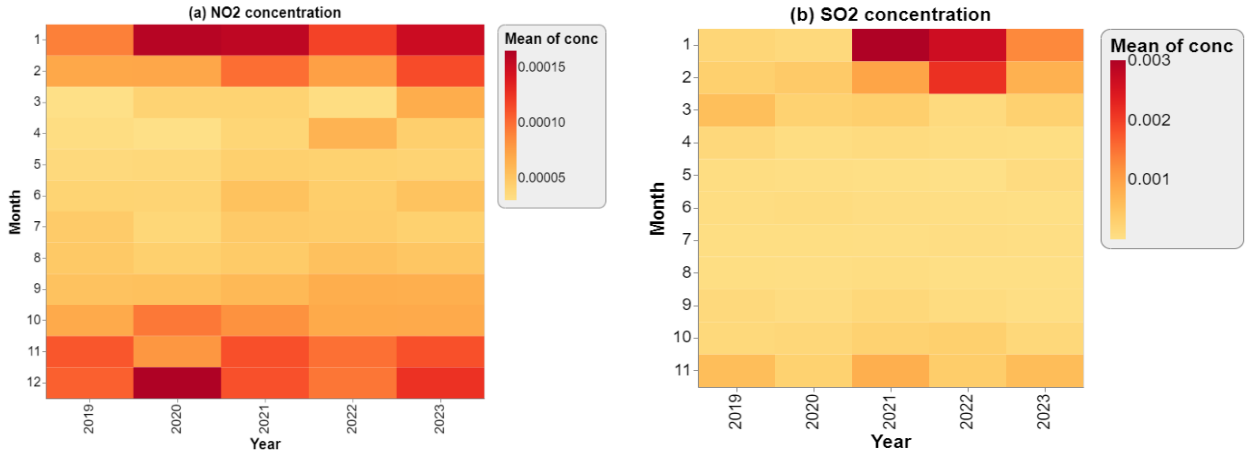


Figure 3. An example of the comparison of monthly mean for 2019 to 2023, (a) NO_2 concentration, (b) SO_2 concentration, in the city of Tabriz

Table 1. Maximum of the 30-day period normalized linear correlation coefficient between ground observations and Sentinel-5 satellite imagery

Pollutant	NO_2	SO_2	O_3	CO	Aerosols
Correlation Coefficient %	87	66	64	87	64

This study examines the importance of satellite RS in air quality monitoring. The findings support the accuracy of the monitoring conducted with Sentinel-5 satellite images. The correlation coefficient values suggest that the data derived from the Sentinel-5 satellite imagery have acceptable dependability; hence, it is possible to the method is used to continuously monitor and regulate air quality in the country. With the emergence of powerful cloud computing systems, such as the Google Earth engine, its free services may be leveraged for heavy processing. On the other hand, because of the low density and often-unsuitable placement of air quality monitoring ground stations, the use of free Sentinel-5 imagery can be useful in monitoring changes in pollutant concentrations throughout the nation.

Conclusion

Air pollution is regarded as one of the most serious problems in Iran today, and it also plays a significant influence in the country's climate change. Factors such as growing populations and the consequent increase in automobile ownership, as well as the presence of different (and often aging) businesses and corresponding energy consumption in Iran, have all contributed to an increase in pollution in many of the country's cities. As a result, precise monitoring of air pollutants with spatial resolution is required, as well as time to establish how to disperse them and propose solutions for managers at the provincial and national levels. The utilization of RS-based techniques and technologies is critical because of the nature of continuous temporal and geographical data creation. The Sentinel-5 satellite and its probe (TROPOMI) are highly capable of recording and monitoring a wide range of rare gases and suspended particles. This study analyzed the capabilities of the TROPOMI (Sentinel-5 satellite) to monitor air pollution, as well as the pattern of changes in various pollutants in Tabriz city during the previous five years. The level of five pollutants, nitrogen dioxide, sulfur dioxide, carbon monoxide, ozone, and suspended particles (aerosols), have been monitored in Tabriz, a big and industrial city, between 2019 and 2023. The monitoring results show that the city of Tabriz is polluted in the months of 1, 2 and 12 AD, which correspond with the cold months of January, February, and December. Thermal power plants in the area and other enterprises that utilize alternative fuels instead of natural gas create the diesel fuel. This is the highest level of pollution recorded in any year from 2019 to 2023. To assess the accuracy of Sentinel-5 satellite image monitoring, pollution recording ground stations in Tabriz were employed. There is 64% to 87% 30-days period connection between satellite picture and ground data. Therefore, Sentinel-5 satellite images may be used to reliably monitor the country's air and apply the results in discussions about controlling and lowering air pollution in the country.

References

[1] Lelieveld, J., Pozzer, A., Pöschl, U., Fnais, M., Haines, A., & Münzel, T. (2020). Loss of life expectancy from air pollution compared to other risk factors: a worldwide perspective. Cardiovascular research, 116(11), 1910-1917. doi: https://doi.org/10.1093/cvr/cvaa025

[2] Murray, C. J., Aravkin, A. Y., Zheng, P., Abbafati, C., Abbas, K. M., Abbasi-Kangevari, M., . . . Abdollahpour, I. (2020). Global burden of 87 risk factors in 204 countries and territories, 1990–2019: a systematic analysis for the Global Burden of Disease Study 2019. The lancet, 396(10258), 1223-1249. https://doi.org/10.1029/2008JD011235

[3] Burnett, R., Chen, H., Szyszkowicz, M., Fann, N., Hubbell, B., Pope III, C. A., . . . Weichenthal, S. (2018). Global estimates of mortality associated with long-term exposure to outdoor fine particulate matter. Proceedings of the National Academy of Sciences, 115(38), 9592-9597. doi:https://doi.org/10.1073/pnas.1803222115

[4] Chowdhury, S., Pozzer, A., Haines, A., Klingmueller, K., Münzel, T., Paasonen, P., . . . Lelieveld, J. (2022). Global health burden of ambient PM2. 5 and the contribution of anthropogenic black carbon and organic aerosols. Environment International, 159, 107020. doi:https:// doi.org/10.1016/j.envint.2021.107020

[5] Achakulwisut, P., Brauer, M., Hystad, P., & Anenberg, S. C. (2019). Global, national, and urban burdens of paediatric asthma incidence attributable to ambient NO2 pollution: estimates from global datasets. The Lancet Planetary Health, 3(4), e166-e178. doi: https://doi.org/10.1016/S2542-5196(19)30046-4

[6] Lelieveld, J., Klingmüller, K., Pozzer, A., Burnett, R., Haines, A., & Ramanathan, V. (2019). Effects of fossil fuel and total anthropogenic emission removal on public health and climate. Proceedings of the National Academy of Sciences, 116(15), 7192-7197. doi:https://doi.org/10.1073/pnas.1819989116

[7] Molina, M. J., & Molina, L. T. (2004). Megacities and atmospheric pollution. Journal of the Air & Waste Management Association, 54(6), 644-680. doi:doi: 10.1080/10473289.2004.10470936

[8] Kelly, F., & Fussell, J. (2011). Air pollution and airway disease. Clinical & Experimental Allergy, 41(8), 1059-1071. doi:doi: https://doi.org/10.1111/j.1365-2222.2011.03776.x

[9] Mayer, H. (1999). Air pollution in cities. Atmospheric environment, 33(24-25), 4029-4037. doi:doi: https://doi.org/10.1016/S1352- 2310(99)00144-2

[10] Wang, M., Arshed, N., Munir, M., Rasool, S. F., & Lin, W. (2021). Investigation of the STIRPAT model of environmental quality: a case of nonlinear quantile panel data analysis. Environment, development and sustainability, 23, 12217-12232. doi:doi: 10.1007/s10668-020-01165-3.

[11] Asha, P., Natrayan, L., Geetha, B., Beulah, J. R., Sumathy, R., Varalakshmi, G., & Neelakandan, S. (2022). IoT enabled environmental toxicology for air pollution monitoring using AI techniques. Environmental research, 205, 112574. doi:doi: https://doi.org/10.1016/j.envres.2021.112574

[12] Ye, Z., Yang, J., Zhong, N., Tu, X., Jia, J., & Wang, J. (2020). Tackling environmental challenges in pollution controls using artificial intelligence: A review. Science of the Total Environment, 699, 134279. doi:doi: https://doi.org/10.1016/j.scitotenv.2019.134279.

[13] Baqer, N. S., Mohammed, H. A., Albahri, A., Zaidan, A., Al-Qaysi, Z., & Albahri, O. (2022). Development of the Internet of Things sensory technology for ensuring proper indoor air quality in hospital facilities: Taxonomy analysis, challenges, motivations, open issues and recommended solution. Measurement, 192, 110920. doi:doi: https://doi.org/10.1016/j.measurement.2022.110920.

[14] Pisoni, E., Farina, M., Carnevale, C., & Piroddi, L. (2009). Forecasting peak air pollution levels using NARX models. Engineering Applications of Artificial Intelligence, 22(4-5), 593-602. doi:doi: https://doi.org/10.1016/j.engappai.2009.04.002

[15] Garane, K., Koukouli, M.-E., Verhoelst, T., Lerot, C., Heue, K.-P., Fioletov, V., . . . Dehn, A. (2019). TROPOMI/S5P total ozone column data: global ground-based validation and consistency with other satellite missions. Atmospheric Measurement Techniques, 12(10), 5263-5287. doi:https://doi.org/10.5194/amt-12-5263-2019

[16] Wang, Y., Liu, P., Schwartz, J., Castro, E., Wang, W., Chang, H., . . . Shi, L. (2023). Disparities in ambient nitrogen dioxide pollution in the United States. Proceedings of the National Academy of Sciences, 120(16), e2208450120. doi:https://doi.org/10.1073/pnas.2208450120

[17] Pattantyus, A. K., Businger, S., & Howell, S. G. (2018). Review of sulfur dioxide to sulfate aerosol chemistry at Kīlauea Volcano, Hawai ‘i. Atmospheric environment, 185, 262-271. doi:https://doi.org/10.1016/j.atmosenv.2018.04.055

Advanced Engineering Days

aed.mersin.edu.tr

Monitoring and forecasting of spatiotemporal expansion pattern of Tabriz Metropolis during in a period of 30 years

Hassan Emami [*1], Rahman Zarei [2], Saleh Fasihi [3]

[1]*University of Tabriz, Department of Surveying, IRAN, h_emami@Tabrizu.ac.ir*
[2]*Remote sensing, Engineering Department of Khatam Al-Anbia Camp, Tabriz, Iran, rahman.zarei61@gmail.com*
[3] *University of Tabriz, Remote sensing and Geographical Information System, Tabriz, Iran, salehfasihi57@gmail.com*

Cite this study: Emami, H., Zarei, R. & Fasihi.S (2024). Monitoring and forecasting of spatiotemporal expansion pattern of Tabriz Metropolis during in a period of 30 years. Advanced Engineering Days, 9, 271-274

Keywords
Urban Development
Landsat
Shannon Entropy
Holden Index
Tabriz city

Abstract

The study analyzed the spatial and temporal expansion patterns of Tabriz Metropolis over a 30-year period. The Shannon model showed a dense physical expansion in 1989, with a maximum value of 2.3025. In 2010, the city's entropy value was 2.0846, indicating urban sprawl. This process was repeated in subsequent years, resulting in more scattered and less dense physical expansion. The results suggest that the city's expansion has become more scattered and less dense over the years. Furthermore, the findings of using Heldren's model to examine Tabriz's urban growth pattern show that the city's urban growth trend has changed over the previous several decades. As a result, based on the coefficients and values derived from each model, it is possible to infer that the suggested hypothesis: Tabriz city's physical expansion throughout the periods (1368 to 1398) while deviating from its development pattern. It has been verified that the city followed the trend of urban spread.

Introduction

Today, the rise of urbanization and the tendency toward urbanism as population increases have resulted in the dimensions and diversity of city development patterns[1]. The physical expansion of the city is caused by the fast increase in urban population in all nations of the globe, particularly emerging countries[2]. The physical development of a city is a dynamic and continuous process in which the physical limits of the city and its physical space expand horizontally and vertically in terms of quantity and quality, and if this process is rapid and unplanned, it results in balanced physical development. Urbanization is not effective [3]. Many approaches have been developed to identify changes in land cover and land usage among various groups. Some of these techniques include comparing the output of image classification algorithms and various methods of revealing changes, such as image difference, principal component analysis, vegetation index difference method, regression method, and vector analysis method [4; 5; 6]. Furthermore, several studies have been undertaken to investigate the physical growth of the city and its varied implications on environmental, economic, and social issues[3; 7; 8] . Other research on land use changes and urban growth has employed a variety of mathematical and statistical models, including the Markov chain model and an automated network for prediction and simulation. The variables influencing urban expansion may be classified into five categories, as follows: (i) environmental variables that can be eliminated, as well as layers that limit urban growth. (ii) Local characteristics, which in some land-use categories are impacted by other land-uses, such as new residential areas that typically develop near existing residential districts. (iii) geographical characteristics of cities, such as distance from urban centers and accessibility; (iv) land use zoning status, as determined by urban planning rules. v) Individual preferences, socioeconomic growth, and political systems, such as population expansion and the central business district. As a result, the purpose of this study is to investigate the extent of Tabriz's physical expansion, identify lands converted to urban use, determine the main growth directions, and examine the city's growth pattern between 1989 and 2019 using satellite images, change detection algorithms, and regional statistics. The impact of this expansion on other usage has been assessed. Another purpose of this study is to identify appropriate options for the city's future expansion based on the findings. This study, in addition to analyzing quantitative factors and indicators affecting Tabriz city's unbalanced growth over a 30-year period, extracts urban uses using the object-oriented classification

method, combines and studies the city's physical-spatial development, as well as the indicators Shannon and Heldren entropy [9; 10].

Material and Method

Study area and dataset

Tabriz, Iran's largest metropolis in the northwest, covers around 131 square kilometers and is located at 23, 46, 11, 46 east longitude and 9, 38, 1, 38 north latitude, with an average height of 1340 meters. This study employed statistical data such as population and housing statistics, as well as spatial data such as Landsat 5, 7, and 8 satellite images, a digital land model, and land usage. This study also employed a time series of Landsat satellite pictures (row 33, pass 168) from 1368 to 1398 at three-year intervals.

Results and Discussion

We studied and identified changing and unchanged areas throughout this period (1989–2019) using differential models, as shown in Figure 1.

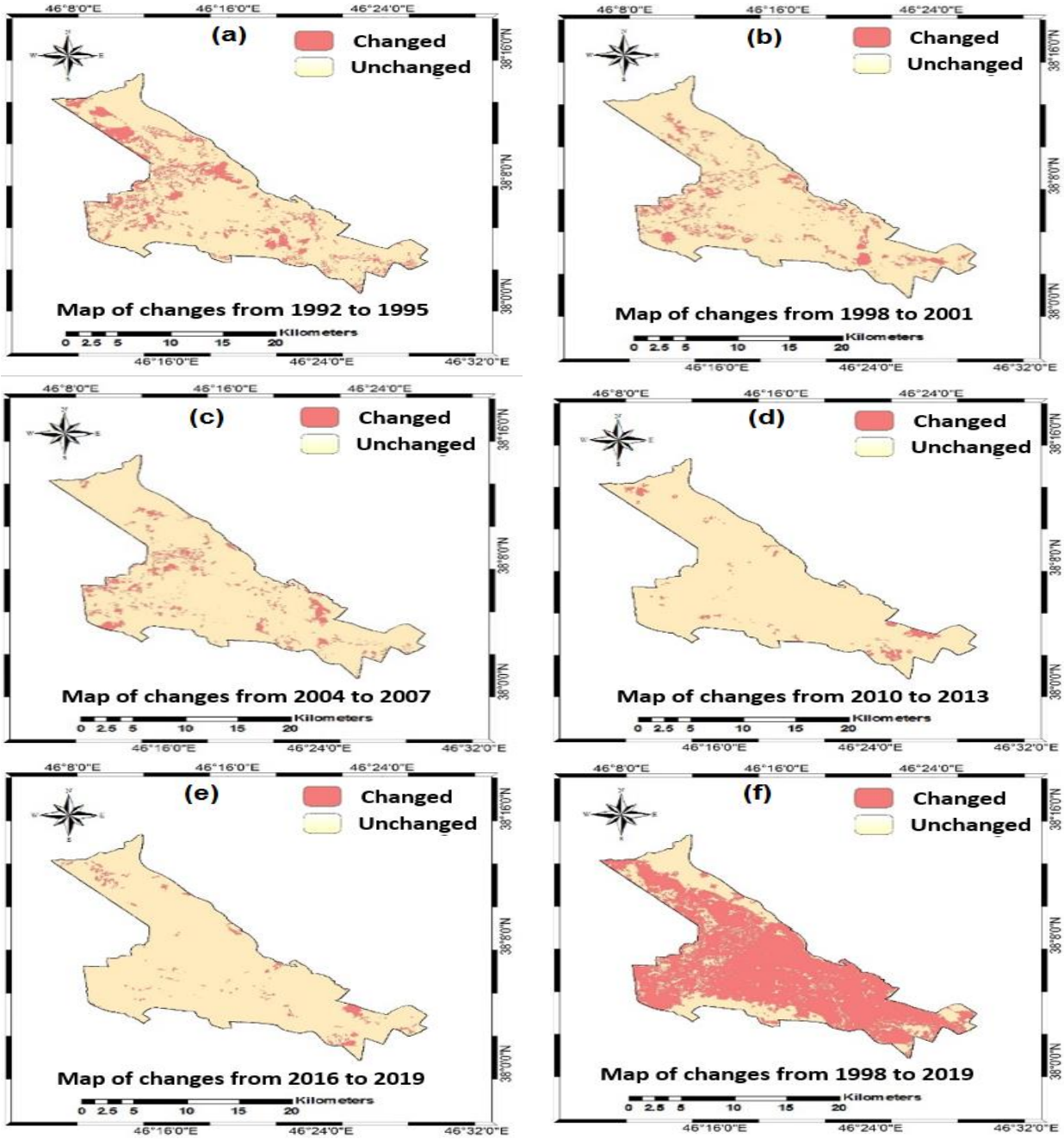


Figure 1. Map of land use changes in Tabriz city in a period of 30 years

As can be observed, more than 90% of Tabriz's lands have changed during the last 30 years, with the majority of the changes taking place around the city. Analyze the trend of city expansion. Shannon's entropy model and Heldren's model were used to study urban growth patterns. For this reason, man-made applications were first identified, and models were then developed using these maps. Figure 2 is one example of these maps.

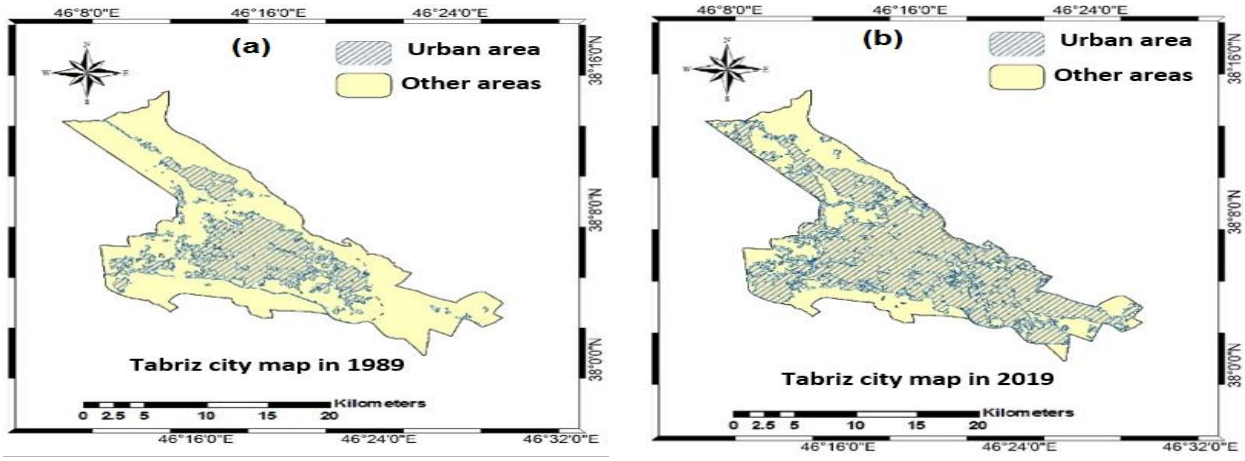


Figure 2. Examples of urban area maps in Tabriz city.

According to the Shannon model, the value of the Shannon coefficient in 1989 was 1.8149, with a maximum value of 2.3025; nevertheless, the relative Shannon coefficient in this year was 0.7882. It is quite far from its maximum, which is (1); therefore, it is possible to conclude that the city's physical expansion this year has been highly dense. This pattern persisted virtually until 1998. As a result, the city has continued its practically focused expansion from the preceding decade. In 2001, the estimated entropy value for Tabriz metropolis was computed as 2.0846, while the highest value was 2.3025. On the other hand, the value of the relative coefficient is 0.90537. As a result, the obtained coefficient indicates the phenomenon of urban sprawl. This trend has been repeated in the following years, so that the absolute and relative coefficients are getting closer and closer to their maximum value, so the entropy coefficients obtained during the periods from 2001 to 2019 show that recently, the physical expansion of the city has become more. Overall, the entropy model findings demonstrate that throughout the analyzed time periods, the numerical value of the coefficient is always larger than the average (0.5). As a result, the phenomenon of urban sprawl has occurred in the Tabriz metropolis; Shannon's irregularity coefficient achieved its maximum level of dispersion in 2019, and both absolute and relative coefficients have risen. In addition, the results of examining the urban growth pattern of Tabriz with Heldren's model indicate that the urban growth process of Tabriz has had different patterns in the last few decades. Thus, in the first period (1989–1998), (2001–2007), and from 2010–2013, horizontal and spiral growth had more weight in the growth pattern of Tabriz city, and in the periods (1998–2001), (2007–2010), and (2013–2019), the factors of population growth and density increase had more weight in the urban growth pattern. The Heldren index in the long term (1989–2019) also shows that the factors of population growth and density increase had more weight in the urban growth pattern. Therefore, from examining the physical pattern of Tabriz city with urban form measurement models, it can be concluded that the physical-spatial growth pattern of Tabriz city is a type of urban dispersion pattern, and this factor has a very important role in the unstable development of Tabriz city and has negative consequences. It has created scattered growth for the city of Tabriz. Therefore, according to the coefficients and values obtained from each of the models, it is possible to conclude that the proposed hypothesis is that the physical growth of the city of Tabriz during the period (1989–2019) while not conforming to the development pattern It has been verified that the city followed the urban sprawl trend.

Conclusion

The process of growth and development of Tabriz metropolis in recent years, with the creation and development of settlements as well as the development of military and government agencies, has extended to the outside and surrounding empty lands, where countless residential units have been added over time. The models utilized in the investigation of the physical-spatial development process yielded the following results: a) the models and methodologies utilized in this study are consistent with the physical-spatial evolution of the Tabriz metropolis from 1989 to 2019. Based on the information and values acquired from Shannon's entropy model results, it can be concluded that Tabriz metropolis grew in a dispersed, horizontal, and non-dense way over the study period. And, as the findings of Heldren's model demonstrate and according to the calculations that have been checked on the population at the beginning and end of the era in Tabriz, as well as the extent and development of the city from the beginning and end of the period. The findings reveal that Tabriz's population has been the

primary driver of physical expansion in the city. The Heldren index over the long period (1989–2019) likewise demonstrates that the elements of population growth and density rise had more weight in the urban growth pattern. As a result of examining the physical pattern of Tabriz city using urban form measurement models, it is possible to conclude that the physical-spatial growth pattern of Tabriz city is a type of urban dispersion pattern and that this factor plays a significant role in Tabriz city's unstable development and has negative consequences. It has caused fragmented expansion for the city of Tabriz. Therefore, according to the coefficients and values derived from each of the models, it is possible to infer from the suggested hypothesis that: the physical expansion of the city of Tabriz throughout the period (1989–2019) while not adhering to the development pattern It has been verified that the city followed the urban sprawl trend.

References

[1] Bagheri, B., & Soltani, A. (2023). The spatio-temporal dynamics of urban growth and population in metropolitan regions of Iran. Habitat International, 136, 102797.

[2] Silveira, J. J., Espíndola, A. L., & Penna, T. (2006). Agent-based model to rural–urban migration analysis. Physica A: Statistical Mechanics and its Applications, 364, 445-456.

[3] Nazarnia, N., Schwick, C., & Jaeger, J. A. (2016). Accelerated urban sprawl in Montreal, Quebec City, and Zurich: Investigating the differences using time series 1951–2011. Ecological indicators, 60, 1229-1251.

[4] Arsanjani, J. J., Helbich, M., Kainz, W., & Boloorani, A. D. (2013). Integration of logistic regression, Markov chain and cellular automata models to simulate urban expansion. International Journal of Applied Earth Observation and Geoinformation, 21, 265-275.

[5] George, J., Baby, L., Arickal, A., Vattoly, J. D., & Use, L. (2016). Land use/land cover mapping with change detection analysis of Aluva Taluk using remote sensing and GIS. International Journal of Science, Engineering and Technology, 4(2), 383-389.

[6] Selvaraj, R., & Nagarajan, S. (2022). Change detection techniques for a remote sensing application: An overview. Cognitive Systems and Signal Processing in Image Processing, 129-143.

[7] Sidhu, N., Rishi, M. S., & Singh, R. (2016). Spatio-temporal study of the distribution of land use and land cover change pattern in Chandigarh, India using remote sensing and GIS techniques. Paper presented at the Geostatistical and Geospatial Approaches for the Characterization of Natural Resources in the Environment: Challenges, Processes and Strategies.

[8] Bibri, S. E., Krogstie, J., & Kärrholm, M. (2020). Compact city planning and development: Emerging practices and strategies for achieving the goals of sustainability. Developments in the built environment, 4, 100021.

[9] Ebrahimzadeh, I., & Rafiei, G. (2009). An Analysis on the Physical Spatial Pattern of Marvdasht Township by Shannon and Heldren Entropy Models, Offering its Utilized Future Expansion Pattern.

[10] Mehrabi, M., & Rafieian, M. (2023). Quantitative analysis of the physical development pattern in Yazd city. Journal of Iranian Architecture & Urbanism (JIAU), 14(2), 233-246.

Advanced Engineering Days

aed.mersin.edu.tr

Evaluation of integration and accessibility metrics for metropolitan metro lines

Esra Gizem Ugur [*1], **Zaide Duran** [2], **Dursun Zafer Seker** [2]

[1]*Istanbul Technical University, Geographic Information Technologies, Türkiye, ugure15@itu.edu.tr*
[2]*Istanbul Technical University, Geomatics Engineering, Türkiye, duranza@itu.edu.tr, seker@itu.edu.tr*

Cite this study: Ugur, E. G., Duran, Z., & Seker, D. Z. (2024). Evaluation of integration and accessibility metrics for metropolitan metro lines. Advanced Engineering Days, 9, 275-277

Keywords
Public Transportation
PTAL Index
Transport Accessibility
GIS

Abstract

Public transportation accessibility is a crucial criterion in urban planning as it affects urban sustainability, spatial justice, air pollution, and quality of life. This study aims to measure the integration and accessibility levels between the metropolitan metro line stations and other public transportation stops. To achieve this, a method was developed using PTAL index criteria, measuring spatial accessibility. Secondly, four stations along a metro line in Istanbul were chosen, and a service area analysis was conducted using GIS software for walking distances of 5, 10, and 15 minutes. The developed method called S_{PTAL} for all public transportation stops within a 15-minute walking distance was calculated, and based on this value, the M_{PTAL} value for the metro stations was determined. Thereby integration and accessibility levels of four stations are established. Open-source data such as the locations of rail systems, Metrobus, bus stops, roads, and operating hours of public transport vehicles were used in the study. The spatial distribution of routes and stops, the reliability of the transportation mode (RM), and the average waiting time at stops (AWT) directly impact integration and accessibility.

Introduction

As the population in cities grows, urban spaces are expanding, resulting in an increased need for urban transportation and spatial accessibility. It is necessary to integrate and enhance the accessibility of public transportation modes within cities. An integrated and accessible public transportation system reduces the number of private vehicles in traffic and decreases air pollution from fossil fuel usage. In consequence, urban sustainability and quality of life improve, social exclusion decreases due to enhanced spatial accessibility, and spatial justice is enhanced. Therefore, several indices have been developed to measure accessibility to public transportation. These indices include PTAI, PTAL, and SI [1]. PTAL is the most widely used index [2]. The London, Delhi, and New South Wales governments utilize the PTAL index to measure accessibility to public transportation and develop projects accordingly. While the components of the PTAL index may vary depending on the application, they generally include different modes of transportation, mode reliability, walking distance to points of interest (POI), and average waiting time at stops [3-4]. According to the PTAL methodology used to evaluate London's transport connectivity, SAP (public transport stops) and POIs are first determined. Assuming a walking speed of 4.8 km/h, the walking distance (WT) from POI to SAP is calculated for each route. The average wait time (AWT) in SAP is calculated by adding the planned wait time and the reliability factor in minutes. Total access time (TAT) to SAP is calculated by adding WT and AWT. Assuming there is no walking time from the SAP to the destination point, the TAT (EDF) frequency is calculated. The accessibility index (AI) value is calculated based on the EDF values. The AI value is found according to the determined PTAL value ranges [4].

The study developed a method by adapting the PTAL index to measure the integration and accessibility between the identified stops along a metro line in Istanbul and other public transportation vehicles within a 15-minute walking distance.

Material and Method

In the study, the parameters of the PTAL index, used to calculate the level of accessibility to points of interest (POIs) via public transportation, were adapted and applied to a metro line in Istanbul and surrounding public

transportation stops. This allowed for measuring the accessibility and integration levels of the metro stops with public transportation. The PTAL index is calculated based on four key parameters: walking distance from the stop to the POI, the number of transportation modes around the POI, transportation mode reliability, and waiting time at the stop [3-4]. When adapting this index for the research, the POIs were considered as the metro stations and the surrounding stops were regarded as the public transportation stops around the metro station.

Road data for the study was obtained from Istanbul Earthquake Science Board Studies of Istanbul Metropolitan Municipality (İBB), transportation stop data from OpenStreetMap (OSM), and the number of buses passing a stop in half an hour and the average waiting time for vehicles were acquired from the timetable panel on Google Maps.

The topological validation of road data was conducted using ArcGIS Pro software. As a result of the topological check, overlapping road segments were identified as tunnels or bridges, and these errors were disregarded. The stop data retrieved from OpenStreetMap (OSM) was classified into bus, metro, and Metrobus stops. If the classified metro stops did not intersect with road data, they were aligned with the nearest road segment. Subsequently, service area analysis was performed using ArcGIS Pro to calculate 5, 10, and 15-minute walking distances towards the metro stations defined as destination points. The slope was not considered during the service analysis. In "Assessing Transport Connectivity in London", the average walking speed was determined as 4.8 km/h (Mayor of London, 2015). The 5, 10, and 15-minute distances were calculated as 400, 800, and 1200 meters, respectively, based on an average walking speed of 4.8 km/h.

The stops were divided into two classes: those with a dedicated lane for themselves, including Metrobus and rail systems, and bus stops. The S_{PTAL} values for the stops were measured individually. To calculate the S_{PTAL} value, three basic parameters that are average waiting time at the stop (AWT), mode reliability (RM), and distance to the metro station (DFS) were scored and then summed with each other shown in Eq. (1).

$$S_{PTAL} = AWT + RM + DFS \tag{1}$$

When calculating the average waiting time at the stop (AWT), the total number of vehicles passing the respective stop during any 30 minutes between 09:00 and 17:00 is determined. The total time (TT) of 30 minutes is divided by the total number of vehicles (TNV), resulting in the average waiting time at the stop (AWT) calculated as in Eq. (2).

$$AWT = \frac{TT}{TNV} \tag{2}$$

The values that M_{PTAL} parameters can get vary depending on whether it is a bus (BS), metrobus (MB), or rail system stop (RS), the distance from the metro stations, and the waiting time at the transportation stop.

Table 1. Values that M_{PTAL} parameters can get

Values	AWT	RM	DFS	DMT
4	0-5 min.	-	-	-
3	>5-10 min.	-	0-400 mt	RS, MB, BS
2	>10-15 min.	RS, MB	>400-800 mt	MB, BS / RS, BS
1	>15 min.	BS	>800-1200 mt	BS

The M_{PTAL} value, which determines the level of accessibility and integration of the metro stations with other public transportation modes is calculated as shown in Eq. 3. This value is obtained by summing the average of the S_{PTAL} values that are assigned at stops, and the number of different transportation modes (DMT) within a 1200-meter walking distance to the metro station.

$$M_{PTAL} = \frac{\Sigma(S_{PTAL})}{TNS} + DMT \tag{3}$$

M_{PTAL} value can range from a minimum of 4 to a maximum of 12. The closer the M_{PTAL} value is to 12, the higher the accessibility and integration of the stop.

Results

In this study, four metro stations named as Yıldız, Fulya, Mecidiyeköy and Çağlayan were examined. The resulting map is shown in Figure 1.

The calculated M_{PTAL} values for the four metro stations are presented in Table 2.

When a scale is created with equal intervals since the M_{PTAL} value can range from a maximum of 12 to a minimum of 4, M_{PTAL} values equal to or lower than 6.6 can be classified as poor, those between 6.7 and 9.3 as moderate, and those between 9.4 and 12 as good. According to this classification, the Yıldız, Çağlayan, and Fulya metro stations fall into the moderate category, while the Mecidiyeköy metro station is in the good category.

Table 2. M_{PTAL} values of the selected metro stations

Metro Stations	DMT	TNS	$\Sigma(S_{PTAL})$	M_{PTAL}
Yıldız	1	18	106	6.9
Fulya	3	25	154	9.2
Mecidiyeköy	3	28	189	9.8
Çağlayan	2	28	171	8.1

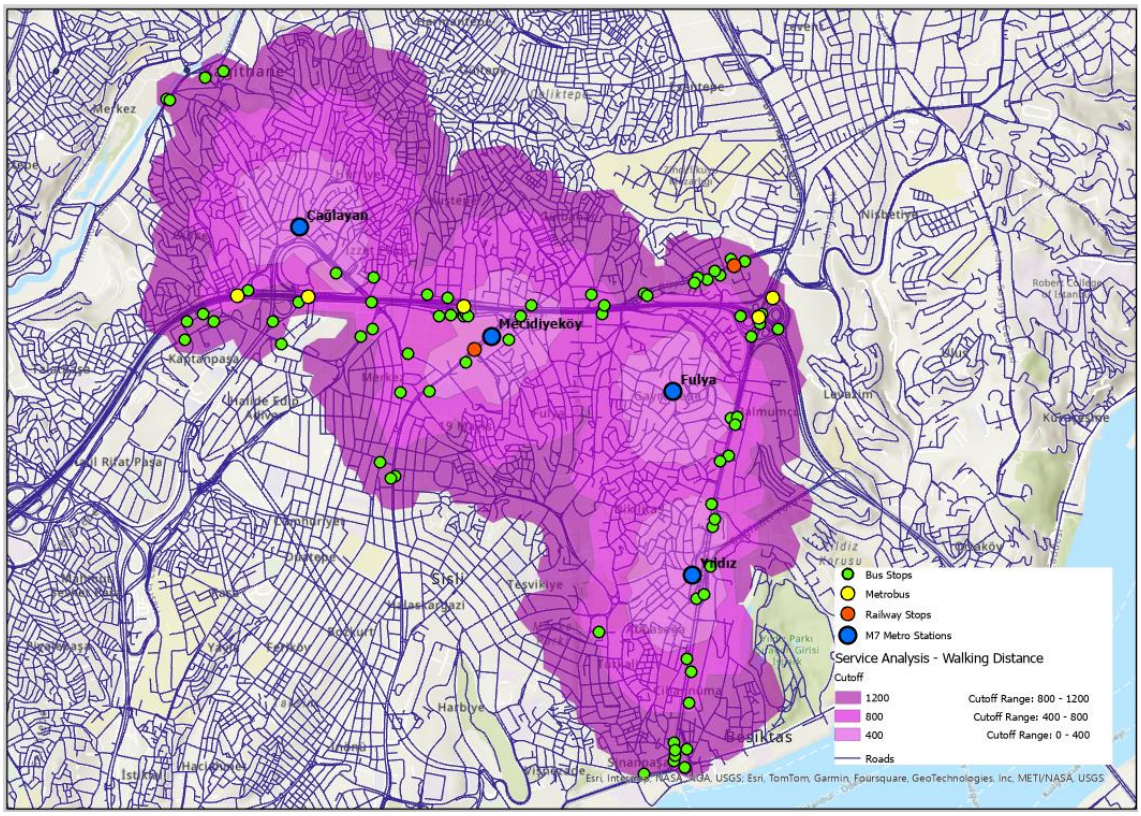


Figure 1. Service analysis for the metro stations and overlapped data in GIS

Discussion

The locations of public transportation stops and the departure times of buses, which are components of the calculation, were obtained from open data sources and assumed to be accurate. The quality of the data affects the accuracy of the calculations since open data sources were utilized in this method. The accuracy of the calculations could be influenced as the average waiting time at the stop was calculated for any half-hour period between 09:00 and 17:00. Additionally, the spatial distribution of roads and stops, as well as the distance from the metro stations (DFS), directly affects the M_{PTAL} value.

Conclusion

By adopting the PTAL index, the developed method provides general information about the integration and accessibility of the relevant station with other public transportation stops, utilizing open data sources and eliminating the need for fieldwork. Furthermore, it has not been found that the PTAL index has not been used to measure the accessibility and integration between public transportation stops in the literature. Thus, the research method, which combines transportation planning with GIS, is distinctive.

References

1. Saghapour, T. Moridpour, S. Thompson, R.G. (2016). Public transport accessibility in metropolitan areas: A new approach incorporating population density, 54 (2016), pp. 273-284.
2. Yang, R. Liu, Y. Liu, Y. Liu, H. Gan, W. (2019). Comprehensive public transport service accessibility index - A new approach based on degree centrality and gravity model. Sustainability, 11 (5634).
3. NIUA. (2021). Study on Public Transport Accessibility Levels (PTAL) in Delhi. https://online.dda.org.in/mpd2041dda/_layouts/MPD2041FINALSUGGESTION/Final_Project_Report.pdf.
4. Mayor of London. (2015). Assessing transport connectivity in London. Transport for London. https://content.tfl.gov.uk/connectivity-assessment-guide.pdf.

Advanced Engineering Days

aed.mersin.edu.tr

Understanding the relationship between seismic events and atmospheric conditions: A case study of Antakya

Abdullah Sukkar [*1], Ugur Alganci [2], Dursun Zafer Seker [2]

[1]*Istanbul Technical University, Graduate School, Geomatics Engineering PhD Program, Türkiye, sukkar20@itu.edu.tr*
[2]*Istanbul Technical University, Department of Geomatics Engineering, Türkiye, alganci@itu.edu.tr, seker@itu.edu.tr*

Cite this study: Sukkar, A., Alganci, U. & Seker, D. Z. (2024). Understanding the relationship between seismic events and atmospheric conditions: A case study of Antakya. Advanced Engineering Days, 9, 278-280

Keywords
Earthquake
Atmospheric parameters
Air Quality
GEE
Air Pollution

Abstract

On February 6th, 2023, Türkiye faced two strong earthquakes with magnitudes of 7.5 and 7.8, resulting in significant destruction that impacted humans, societies, and the environment. This study focused on establishing a relationship between earthquakes and air quality by analyzing remotely sensed atmospheric data to understand the complex interaction of atmospheric dynamics and the impacts of these earthquakes. The analysis includes extracting and examining components such as Aerosol, SO_2, NO_2, CO, and CH_4.

Introduction

On February 6th, 2023, a 7.8-magnitude earthquake struck Türkiye and Syria, followed by numerous aftershocks and a second 7.6-magnitude earthquake, causing extensive devastation. Current estimates report over 50,000 deaths and more than 100,000 injuries. The earthquakes have led to widespread destruction of homes and infrastructure and significant health consequences for the affected populations [1].

The relationship between seismic activities and air quality is complex and influenced by multiple factors. Harmful air pollutants such as nitrogen oxides (NOx), sulfur dioxide (SO_2), volatile organic compounds (VOCs), dioxins, and polycyclic aromatic hydrocarbons (PAHs) pose significant risks to human health [2]. Earthquakes not only cause immediate physical damage but also lead to broader consequences, including ecosystem disruptions and the contamination of air, water, and soil [3]. Studies indicate that earthquakes can affect pollution levels due to the dust released from collapsing structures [4]. This dust can degrade air quality and pose health hazards to those exposed. Strategic measures have been suggested to address and reduce these pollution risks related to earthquakes [5].

In earthquake-prone regions like Türkiye, developing strategies for reducing air pollution risks linked to seismic events is vital. Studies underscore the need for effective measures to prevent and manage air pollution after earthquakes to protect public health [5]. Earthquakes can significantly impact air quality, as evidenced in Adiyaman City, where debris removal after an earthquake resulted in elevated particulate matter pollution [3].

The 2023 Türkiye-Syria earthquake had a significant environmental impact, particularly concerning air pollution and dust particle release. The seismic activity caused considerable damage to various infrastructures, buildings, and industrial sites, emitting harmful pollutants and particulate matter into the air. The collapse of structures and damage to industries released a variety of hazardous substances, including (VOCs), (SO_2), (NO_x), and particulate matter (PM2.5 and PM10). These pollutants posed immediate health risks, exacerbating respiratory and cardiovascular diseases, and had long-term effects on air quality and regional climate patterns. In this context, this study investigates the changes in air quality levels in Hatay province, Türkiye's worst-hit region. Based on data from the Sentinel-5P TROPOMI Satellite Sensor, air pollutants such as UV aerosol index, SO_2, NO_2, CO, and CH_4 were analyzed on a monthly scale for the months before (January), during (February), and after (March) the earthquake. These months were then compared to the average of the same months from 2019 to 2022.

Material and Method

Hatay province was selected as a study area for this study (Figure 1). Hatay is the most affected region by the Türkiye-Syria earthquake in 2023. Hatay is located in the southern part of the Türkiye, specifically along the

Mediterranean coast. It shares borders with Syria to the south and east. The cosmopolitan capital, Antakya, which was destroyed by the earthquake, is situated on the banks of the Orontes River and is encompassed by mountains.

The Sentinel-5P TROPOMI satellite sensor is a crucial tool for various environmental monitoring applications. TROPOMI, launched as part of the Copernicus Sentinel 5 Precursor (S-5P) satellite, provides high-resolution data on atmospheric composition, including trace gases like sulfur dioxide (SO_2), carbon monoxide (CO), nitrogen dioxide (NO_2), and methane (CH_4) [6-7]. The dataset was downloaded and analyzed using the Google Earth Engine (GEE) platform for the study area.

We compared the monthly measurements of certain air pollutants, including Aerosol, SO_2, NO_2, CO, and CH_4, for February (the month of the earthquake) and March (post-earthquake) with the average measurements from February and March of 2019 to 2022. This analysis was conducted to assess how the earthquake impacted air quality in Hatay.



Figure 1. Geographical location and of the study area.

Results

The monthly measurements of pollutants—Aerosol, SO_2, NO_2, CO, and CH_4—for February and March 2023 were compared with the averages from 2019 to 2022. The results, which are spatially represented in Figure 2, show significant variations. Aerosol and CH_4 levels significantly increased in February and March 2023 compared to the average levels. NO_2 levels in February 2023 were close to the average, followed by a slight decrease in March. CO levels decreased slightly in February and more markedly in March compared to the average. SO_2 levels in both February and March 2023 were similar to previous averages.

Discussions

Aerosol refers to tiny particles suspended in the air. These particles can be either natural, such as dust, sea salt, or volcanic ash, or caused by human activities, such as smoke from fires and industrial pollution. Aerosols can influence climate by absorbing or reflecting sunlight and affecting cloud formation. Additionally, they can impact human health by entering the respiratory system. The UV Aerosol Index results indicate that the earthquake triggered significant aerosol emissions into the atmosphere. Comparing the average monthly measurements from 2019 to 2022 with those of the corresponding months in 2023 reveals a marked increase in aerosol levels coinciding with the earthquake. This trend is attributed to the collapse of numerous buildings caused by the earthquake and the subsequent rubble removal efforts, which lasted several months.

CO is mainly generated from the incomplete combustion of fossil fuels and biomass, such as car exhaust, industrial pollutants, and wildfires. CO binds to hemoglobin in the blood, which diminishes the transportation of oxygen to organs and tissues. This leads to the development of cardiovascular disorders and neurological repercussions. While it is possible that the earthquake led to immediate releases of carbon monoxide and dioxide, the data show a decrease in monthly CO levels compared to the 2019-2022 averages.

This reduction may be linked to a downturn in human and industrial activities in the region. Similarly, nitrogen levels fell post-earthquake, where NO_2 is produced when fuel is burned in cars and industrial activities, including power generation.

SO_2 is released into the atmosphere by volcanic eruptions, the combustion of fossil fuels by power plants and industrial facilities, and specific industrial activities. It is responsible for acid rain, which has detrimental effects on ecosystems, soil, and water bodies. SO_2 levels slightly dropped in February relative to previous years' averages. Then, they showed close to the average rates in March.

CH_4 is produced through natural processes, such as degradation in wetlands and human activities, including agriculture (particularly from the digestive processes of ruminant animals), landfills, and coal, oil, and natural gas extraction and transportation. CH_4 is a powerful greenhouse gas contributing to global warming and climate change. Significantly, CH_4 levels have escalated in the entire earthquake region since February. While earthquakes can cause methane emissions, the high mortality rate may also significantly contribute to this increase

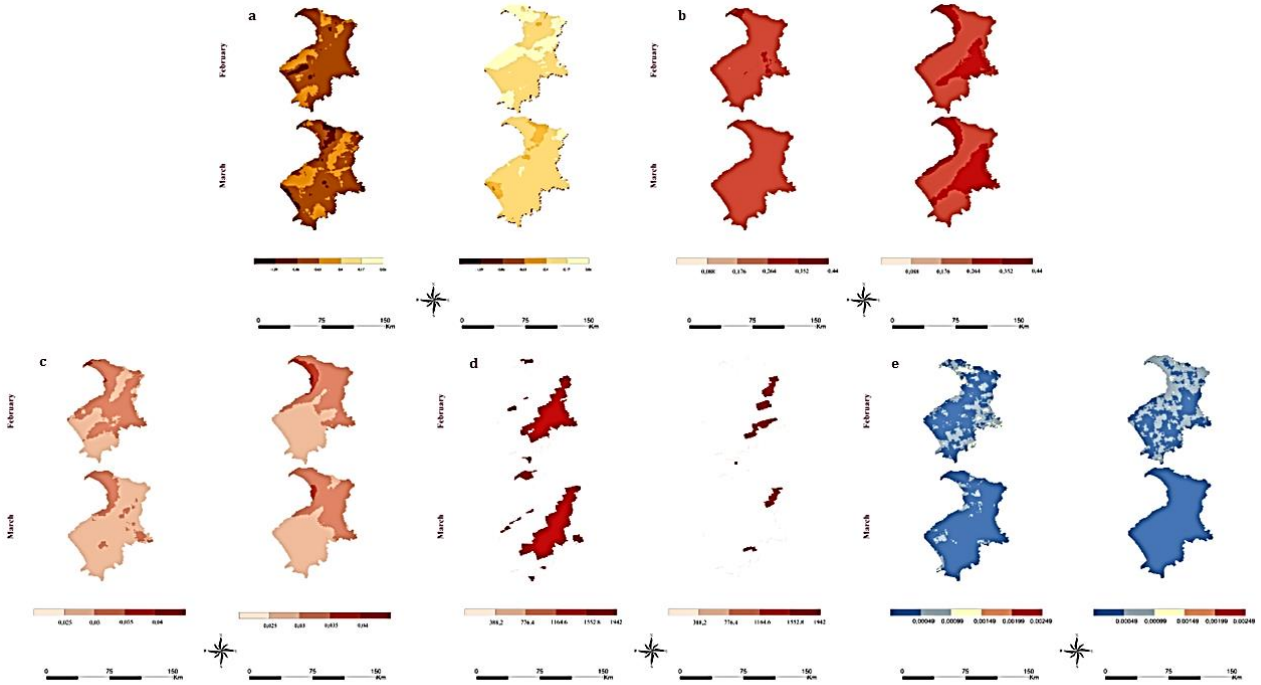


Figure 2. Comparison between the monthly measurements of certain air pollutants, including Aerosol (a), CO (b), NO_2 (c), CH_4 (d), and SO_2 (e), for February (the month of the earthquake) and March (post-earthquake) with the average measurements from February and March of 2019 to 2022.

Conclusions

The recent earthquakes in Türkiye and Syria have caused great loss of life and property, environmental problems, and health problems. In this study, we investigated how the air pollutants have been affected by the earthquake, where the levels of particular pollutants have increased and others have decreased due to declining of human and industrial activities.

References

1. Ahmed, S. K., Chandran, D., Hussein, S., Sv, P., Chakraborty, S., Islam, M. R., & Dhama, K. (2023). Environmental Health Risks After the 2023 Turkey-Syria Earthquake and Salient Mitigating Strategies: A Critical Appraisal. Environmental Health Insights., 17. https://doi.org/10.1177/11786302231200865
2. Manisalidis, I., Stavropoulou, E., Stavropoulos, A., & Bezirtzoglou, E. (2020). Environmental and Health Impacts of Air Pollution: A Review. Frontiers in Public Health, 8. https://doi.org/10.3389/fpubh.2020.00014
3. Vural, E. (2024). Assessment of Particle Matter Pollution during Post-Earthquake Debris Removal in Adiyaman City. Revue Internationale De Géomatique, 33(1), 37–50. https://doi.org/10.32604/rig.2024.047908
4. Somervell, E. R., & Aberkane, T. (2014). The Effects of On-Going Seismic Activity on Air Quality in Canterbury, New Zealand. the Open Atmospheric Science Journal, 8(1), 1–6. https://doi.org/10.2174/1874282301408010001
5. Zanoletti, A., & Bontempi, E. (2024). The impacts of earthquakes on air pollution and strategies for mitigation: a case study of Turkey. Environmental Science and Pollution Research International. https://doi.org/10.1007/s11356-024-32592-8
6. Levelt, P. F., Zweers, D. C. S., Aben, I., Bauwens, M., Borsdorff, T., De Smedt, I., Eskes, H. J., Lerot, C., Loyola, D. G., Romahn, F., Stavrakou, T., Theys, N., Van Roozendael, M., Veefkind, J. P., & Verhoelst, T. (2022). Air quality impacts of COVID-19 lockdown measures detected from space using high spatial resolution observations of multiple trace gases from Sentinel-5P/TROPOMI. Atmospheric Chemistry and Physics, 22(15), 10319–10351. https://doi.org/10.5194/acp-22-10319-2022
7. Cho, Y., Kim, J., Go, S., Kim, M., Lim, H., & Torres, O. (2021). Retrieval of Aerosol Optical Properties over East Asia from TROPOMI using GEMS Aerosol Algorithm https://doi.org/10.5194/egusphere-egu21-6841

Advanced Engineering Days

aed.mersin.edu.tr

Comparative study of urban development of Tabriz, Iran and Mersin, Turkiye

Fereidoun Babaei Aghdam [*1], **Shiva Sattarzadeh Salehi** [1], **Murat Yakar** [2]

[1]*University of Tabriz, Urban and Regional Planning, Iran, F.babayi.ag@gmail.com, sattarzadeh423@gmail.com*
[2]*Mersin University, Department of Geomatics engineering, Türkiye, myakar@mersin.edu.tr*

Cite this study: Babaei Aghdam, F., Salehi, S. S. & Yakar, M. (2024). Comparative study of urban development of Tabriz, Iran and Mersin, Turkiye. Advanced Engineering Days, 9, 281-285

Keywords
Urban development
Mersin
Tabriz
Slum industries
Urban Sprawl

Abstract

Urban development refers to the process of planning, designing, constructing, and managing urban areas to accommodate population growth and improve the quality of life for residents. Therefore, the present study aims to compare the urban development of Ciflik Koy, Mersin, and Andisheh, Tabriz. Descriptive and analytical research methods have been used to collect information from Google Earth satellite images for the years (2023-2009) and documentary and library studies. The results showed that the city of Tabriz has led to industrial and residential slums due to non-observance of the quorum of separation, width of roads, non-observance of safety plans in industrial uses, irregular texture, incompatibility of the city of Tabriz. This is the result of very poor monitoring and control and has led to the destruction of agricultural lands. However, due to the high population growth, the city of Mersin has also destroyed agricultural land, of which Ciflik Koy is a clear example. According to the new construction laws in Turkey, officials and institutions are more involved in complex and high-rise constructions. They put more emphasis on green space per capita and have stronger supervision and control in this field than Tabriz, which has led to an obvious difference in the texture and morphology of the cities.

Introduction

Urbanization has been one of the prominent phenomena of the twentieth century, with profound and extensive impacts on human societies. With the increasing urban population, urban development has become one of the most important challenges facing planners and policymakers worldwide (1). Comparative study of urban development is an approach that can help to better understand the processes, challenges and solutions of urban development in different regions, which deals with the systematic comparison of similarities and differences among cities or urban processes (2,3). also, this approach provides the possibility of learning from successful or unsuccessful experiences of other cities and can help identify the best methods and patterns of urban development. Through comparative analysis, planners and policymakers can benefit from lessons learned in other areas and adopt more suitable solutions for their urban issues (4). By analyzing and comparing different cases, planners and policy makers can benefit from the experiences of other regions and find better solutions for their urban problems (5). These studies also help to better understand the complexities and diversity of urban experiences at the global level (6). With the increasing trend of urbanization in many countries, the importance of focusing on sustainable urban development and preserving urban environment is of special significance (7). Comparative review can help identify successful solutions in the field of sustainable urban development and proper resource management (8,9). Therefore, the current research intends to deal with the nature of development in the cities of Tabriz and Mersin in the last 14 years in order to reach the differences in the principles and rules of urban planning in the two cities.

Material and Method

In this research, descriptive and analytical research methods have been used to collect information from Google Earth and Esri satellite images for the years (2023-2009) and documentary and library studies. The main purpose of this research is to evaluate the nature of urban development and examine the principles and criteria of urban

construction in the metropolitan areas of Mersin and Tabriz as a case study. first of all, the images of land cover in the last 14 years are reviewed using the reference land method in ArcGIS 10.8 software, and then the desired criteria in the construction field and geometric order of parts in each city are compared and evaluated. It should be noted that due to the extent of the cities studied in this research, one area from each city was selected on a case-by-case basis to carry out investigations.

Study Area

Tabriz is a city in the Central District of Tabriz County, in the East Azerbaijan province of northwestern Iran. It is the sixth-most-populous city in Iran (9,10). The metropolis of Tabriz is located in the northwestern corner of the country along the Tehran-Bazargan international axis that connects Iran to Europe. Mersin is the second case of this research which is a large city and port on the Mediterranean coast of southern Turkiye. Mersin lies on the western side of Cukurova, a geographical, economic, and cultural region of Turkey. It is an important hub for Turkey's economy, with Turkiye's largest seaport being located here (8). As urbanization continues eastward, a larger metropolitan region combining Mersin with Tarsus and Adana (the Adana-Mersin Metropolitan Area) is in the making with more than 3.3 million inhabitants “Figure 1”. Tabriz, located in northwestern Iran, and Mersin, situated on the Mediterranean coast of Turkey, are two cities with distinct urban development trajectories. A comparative study of their growth and planning can provide valuable insights into the factors shaping urban landscapes. It should be noted that in the current research, Ciflik Koy neighborhood in Mersin and Andisheh in Tabriz city are used as case examples.

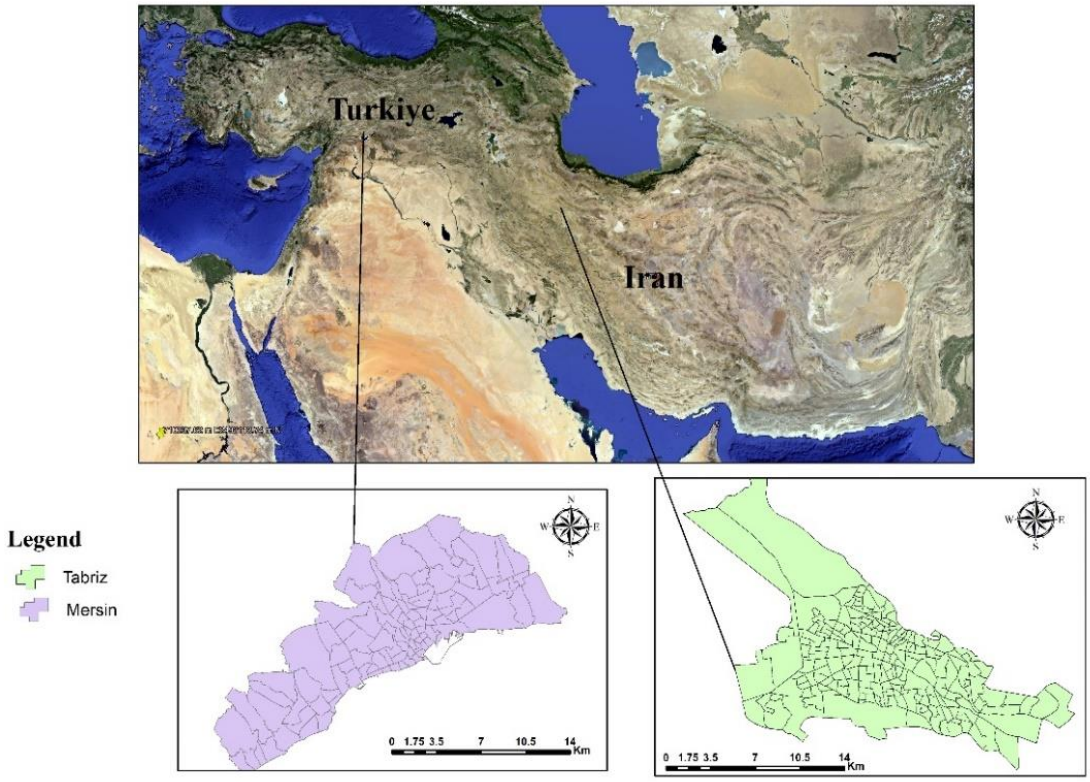


Figure 1. geographical location of the study areas

Results

Urban development is a dynamic and multidimensional process that encompasses physical growth, demographic changes, economic changes, and changes in social and cultural structure. This process is undertaken to enhance the quality of life for citizens and achieve sustainable urban development. Mersin, located in Türkiye, is a major city known for its significant role as an agricultural center. However, the rapid urbanization and uncontrolled construction in the region pose a severe threat to its fertile lands and gardens. Agriculture is crucial for ensuring food security and environmental sustainability. The potential loss of these lands could lead to reduced agricultural production, greater reliance on food imports, and the loss of biodiversity, all of which could have serious consequences. In recent years, the city of Mersin has witnessed the rapid growth of population and urbanization, which has led to the destruction of many fertile agricultural lands and natural vegetation around the city. In addition, reports indicate that illegal construction activities have also increased in restricted and sensitive areas such as beaches and rivers. However, in its urban planning, Mersin Municipality emphasizes to create and

develop green spaces and public gardens in order to preserve the environment and sustainable life. This municipality is also trying to prevent urban sprawl and save land by building new high-rises. These measures may not be enough. Protecting remaining agricultural land, preventing illegal activities, and increasing green spaces in residential areas require more careful planning and implementation by local authorities "Figure 2".

In the newly built areas of Mersin, such as Ciflik Koy, residential plots are designed according to modern urban planning standards and have regular geometric shapes such as rectangles or squares. The passages are also designed in grid and checkered form. But in the old context of the city, the residential parts have irregular and organic shapes, which are caused by the historical and gradual growth of the city and the limit of land separation is determined based on the rules and regulations of urban planning. These limits include the minimum land area, front width, land depth, etc., which must be observed when dividing the land. The purpose of these rules is to create order and organization in urban construction.

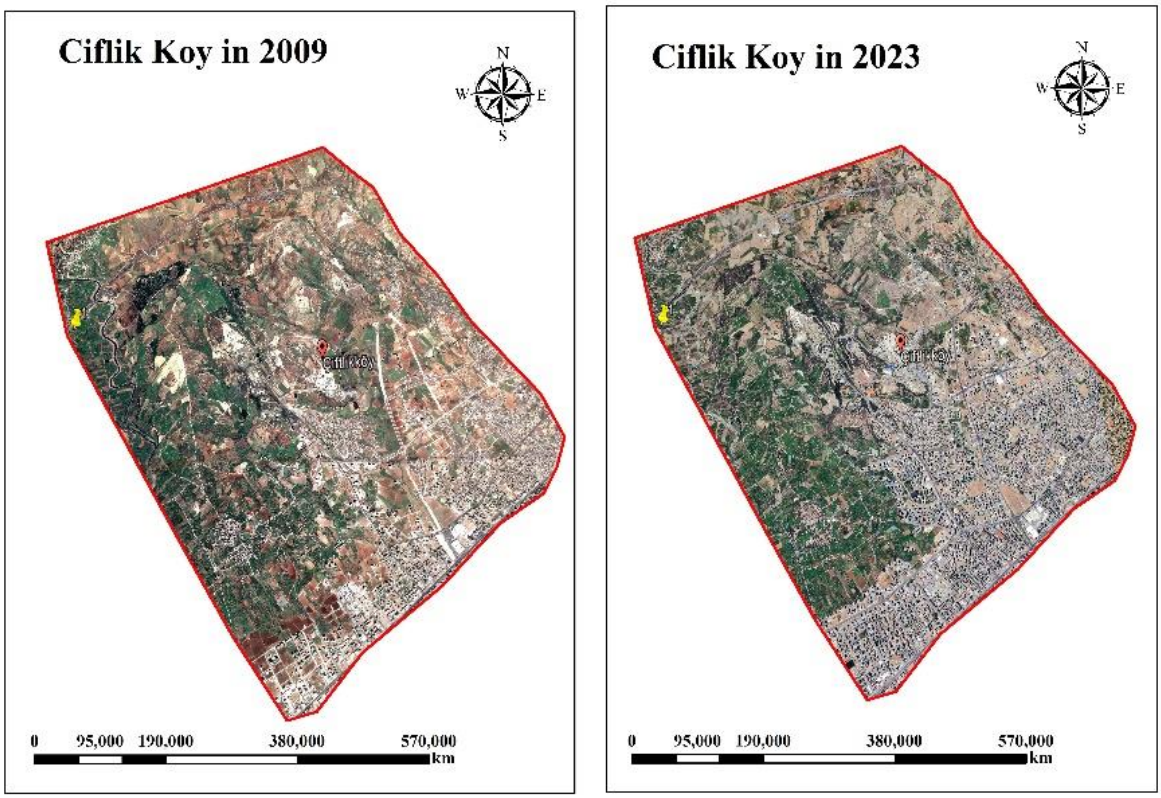


Figure 2. Urban development of Ciflik Koy in 2009 to 2023

Non-implementation of building laws in Tabriz, non-observance of the principles of construction, quorum of segregation especially in industrial uses, and non-creation of safety plans compatible with roads can lead to the destruction of agricultural lands. Construction problems in the city of Tabriz, such as the incompatibility of uses with each other, non-observance of safety design and preparation opinions in industrial constructions, as well as inappropriate width of roads are among the wide problems that due to weak supervision and control, construction Unprincipled is prevalent. Unfortunately, the lack of supervision and control in Tabriz city has led to the destruction of agricultural lands and unprincipled construction. This issue has happened due to the lack of proper implementation of construction laws and weakness in supervision and control. These problems can lead to loss of natural resources and decrease in environmental quality. It seems that there is a need to strengthen the supervision and control and more accurate implementation of existing laws in the field of construction and use of agricultural land in order to solve these problems "Figure 3".

Andisheh town was originally designed for the establishment of light industries, but today it is known as the residence of many rural migrants and low-income workers. Providing cheap housing along with industrial complexes has turned this area into the center of industrial slums. Extensive marginalization in thought has resulted in numerous social and environmental problems. On the one hand, low-income households living in these areas struggle with economic problems and lack of urban services; on the other hand, existing small industries, which often lack environmental standards, have aggravated air pollution and noise pollution in this area. To solve this problem, Tabriz city authorities have tried to help solve the problem by moving and settling marginal residents in new housing units. However, these measures are only a temporary solution and require a review of national and provincial laws and policies to prevent the regrowth of industrial slums.

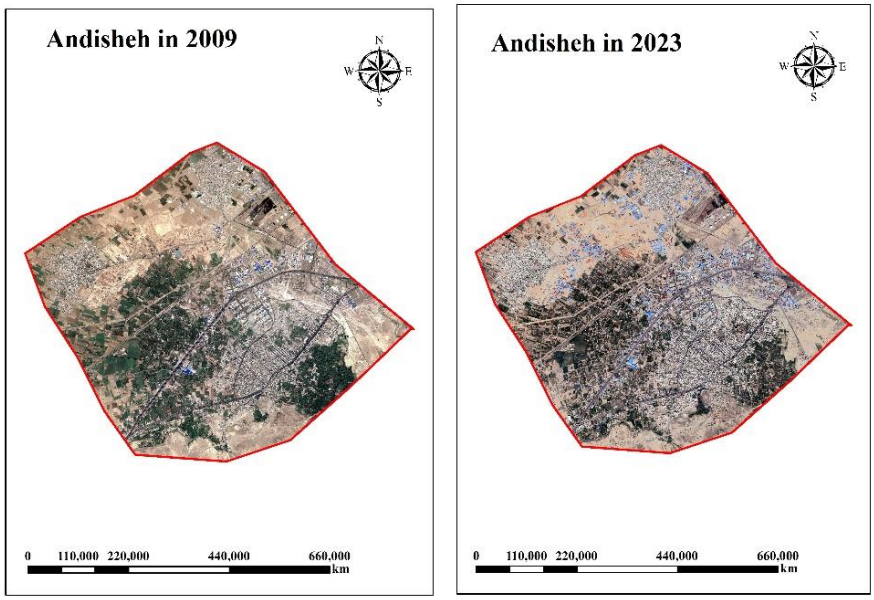


Figure 3. Urban development of Andisheh in 2009 to 2023

Discussion

In Türkiye, urban planning laws and regulations are created centrally by the Ministry of Environment, Urban Development and Climate Change. This ministry is responsible for developing comprehensive urban plans and supervising their implementation. Also, construction control laws are implemented by local municipalities. On the other hand, in Iran, the decision-making and control system in the field of urban planning is decentralized. The Ministry of Roads and Urban Development is responsible for developing general rules and regulations, but municipalities and city councils in each province and city have the main role in planning and controlling construction. This sometimes causes a lack of coordination and differences in urban development procedures in different regions. Considering these differences, it seems that due to the existence of a centralized and coordinated urban planning system in Turkey, monitoring and controlling constructions and observing the principles and rules of urban planning in a city like Mersin is better and more accurate than Tabriz.

Conclusion

The process of urban development faces challenges such as population growth, lack of housing, traffic, environmental pollution, and social and economic inequalities. To deal with these challenges, it is necessary to carry out urban planning with a sustainable development approach and considering economic, social and environmental aspects. Tabriz and Mersin, despite their unique historical and geographical backgrounds, face similar urban development challenges including rapid population growth, informal settlements, and the need to balance economic progress with environmental sustainability. A comparative analysis of these two cities can provide insights into different urban planning approaches, the influence of historical and cultural factors, and the strategies used to tackle common challenges. This examination can offer valuable contributions to the wider conversation on urban development, particularly in the context of developing countries.

Based on the surveys conducted over the past 14 years, the city of Tabriz has led to industrial and residential slums due to non-observance of the quorum of separation, width of roads, lack of safety plans in industrial uses, irregular texture, incompatibility of uses with each other. This is the result of very weak monitoring and control and has led to the destruction of agricultural lands. However, due to the high population growth, the city of Mersin has also destroyed agricultural land, of which Ciflik Koy is a clear example. According to the new construction laws in Turkey, officials and institutions are more concerned with complex construction and high-rise construction. They have more emphasis on green space per capita and have stronger supervision and control in this field than Tabriz, which has led to a clear difference in the texture and morphology of the cities.

References

1. Girroudi, M., Sarwar, R., & Navabakhsh, M. (2018). Comparative comparison of the green city in the urban planning system of Germany and Iran (case study - Berlin and Tehran metropolises). Scientific and Research Quarterly of New Approaches in Human Geography, 10(4), 75-88.

2. James A. Kushner (2003). Comparative Urban Planning Law. An Introduction to Urban Land Development Law in the United States through the Lens of Comparing the Experience of Other Nations.
3. Jokar Sarhengi, A. (2012). A comparative evaluation of the location selection and development of the urban centers of Mazandaran province with an ecological approach. Geography and Development, 23.
4. Tauri, T (2020). Comparative Urbanism, Oxford Bibliographies.
5. Jalalian, Z., Daghi, P. & Karimi (2015). Analysis of urban creep and land use changes (comparative studies of Urmia and Isfahan cities). Physical Development Planning, 2(4), 73-98.
6. Robinson, J. (2022). Introduction: Generating concepts of 'the urban'through comparative practice. Urban Studies, 59(8), 1521-1535.
7. Qadiri, M., Mamsani, & Sogol. (2015). Comparative analysis of sustainable development indicators of Bushehr city with urban areas of the country. Applied Research Journal of Geographical Sciences, 14(35), 49-72.
8. Salehi, S. S., & Jafari, F. (2023). Spatial distribution of public services and facilities in the Sahand new city of Iran. Intercontinental Geoinformation Days, 7, 168-171.
9. Salehi, S. S., & Jafari, F. (2024). An analysis of population distribution and urban public services in the new city of Sahand, Iran. Advanced Land Management, 4(1), 11-25.

Advanced Engineering Days

aed.mersin.edu.tr

Fire-risk assessment with Dong model based on anthropogenic and natural factors: A case study of Arasbaran Forest

Sajjad Moshiri[1], Ahmad Nikdel Monavvar[1] Khalil Valizadeh Kamran[1*], Omid Rafieyan[2]

[1]University of Tabriz, REMOTE SENSING&GIS Department, IRAN, Sajjadmoshiri@gmail.com , ahmadnikdel21@gmail.com , valizadeh@tabrizu.ac.ir
[2]Tabriz Islamic Azad University, Environmental Engineering Department, IRAN, o_rafieyan@yahoo.cam

Cite this study: Moshiri, S, Nikdel, M. A, Valizadeh, K. K., & Rafieyan, O (2024). Fire-risk assessment with Dong model based on anthropogenic and natural factors: A case study of Arasbaran Forest. Advanced Engineering Days, 9, 286-294

Keywords
Fire-risk,
Dong model,
anthropogenic factors,
natural factors,
Arasbaran forest

Abstract

According to statistics published by GWIS, hundreds of fires occur in different regions of Iran every year. Arasbaran forest are one of the rare forest ecosystems and are considered among the 103 biosphere regions of the world, which are unique in terms of special ecological conditions in terms of fauna and flora diversity, and frequent fires in Arasbaran region are one of the important factors of disturbance in this forest ecosystem. Therefore, in order to take preventive measures to reduce the occurrence of forest fires and also to manage this crisis optimally and quickly when it occurs, it is necessary to prepare a map of the areas affected by forest and rangeland fires during the past years, and to identify fire-risk areas in the rangeland and forests of Arasbaran. For this purpose, the application of remote sensing technologies and geographic information system have a positive performance and have proven their efficiency. In this study, the effective factors in fire-risk in two categories, anthropogenic factors: forest type, rangeland type, vegetation density, slope, aspect, elevation, distance from road, distance from cropland, distance from settlement and natural factors: solar radiation, standardized vegetation index (vegetation vigor), vegetation condition index, enhanced vegetation index, temperature- vegetation-moisture dry index, forest type, rangeland type and forest density were extracted as Dong models input and fire-risk modeling was done. According to the results of modeling of anthropogenic factors, the eastern half of the region is among the areas sensitive to fire-risk, which is consistent with the density of the villages in the region. Also, according to modeling, the fire-risk with natural origin is often in the southeast, southwest, and northwest of the region.

Introduction

One of the environmental factors that can affect the forest ecosystem is fire (1). The fire-risk exposure is determined by a complex set of natural and anthropogenic factors (2). wildfires are spreading all over the world, which is one of the main issues and concerns not only from the environmental, but also from the economic, social and security point of view (3,4,5). From the ecological point of view, the development of plant communities affects soil nutrients and biodiversity and causes plant succession (6,7).

According to the statistical information published by GWIS[1], hundreds of fires occur in different regions of Iran every year. Arasbaran forest are one of the rare forest ecosystems and are considered among the 103 biosphere regions of the world, which are unique in terms of special ecological conditions in terms of fauna and flora diversity, and frequent fires in Arasbaran region are one of the important factors of disturbance in this forest ecosystem.

[1] Global Wildfire Information System

Therefore, to take preventive measures to reduce the occurrence of forest fires and to manage this crisis optimally and quickly when it occurs, it is necessary to prepare a map of areas affected by forest fires and rangeland during the past years, and to identify fire-sensitive areas in the rangeland and forests of Arasbaran.

To achieve the above goals; Satellite data provide opportunities for qualitative analysis of forest and other ecosystems at spatial, technological, and spatial scales, and provide the necessary information and tools to create a fire susceptibility map through identification, classification, and fire-risk mapping (8).

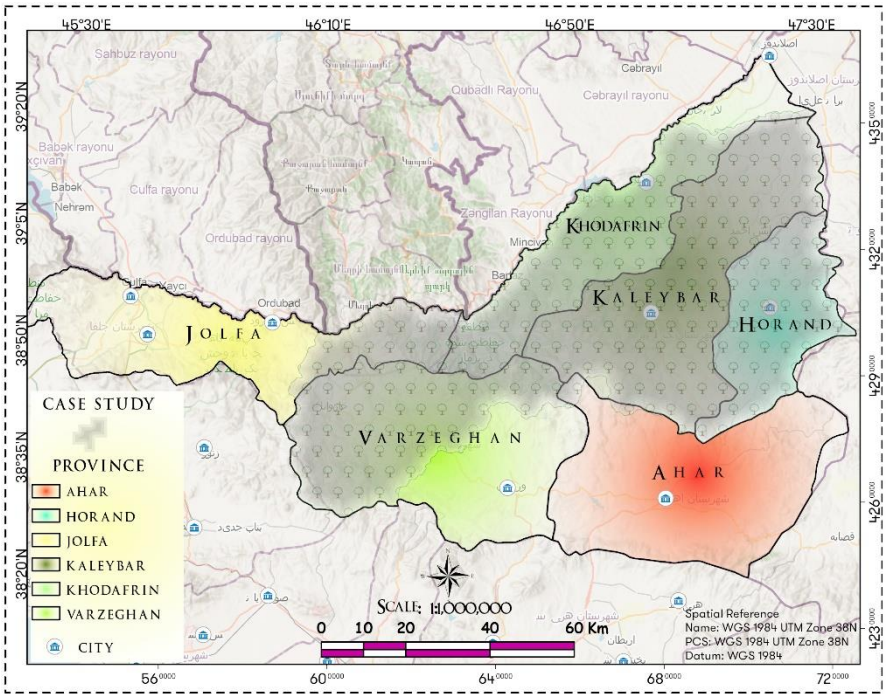
An important challenge in remote sensing studies is the huge volume of satellite images, especially in studies that require downloading multiple and large time series data and heavy processing due to the multitude of parameters required for studies related to forest fires. This problem is well solved by Google Earth Engine (GEE). GEE is a web-based system that, by providing a database of strong satellite images and simple commands, has provided the possibility of all kinds of remote sensing processes without downloading each image that used (9). This system enables users to perform calculations on a large amount of data (from a spatial resolution of 10 meters to several kilometers) without the need for high-powered systems. Based on this, the aim of the current research is to evaluate the fire-risk with Dong modeling in Arasbaran forest.

Material and Method

In this research, the factors: forest type, rangeland type, vegetation density, slope, elevation, distance from road, distance from crop land, distance from settlement, Standardized Vegetation Index (vegetation vigor, SVI), Vegetation Condition Index (VCI), Enhanced Vegetation Index (EVI) and Temperature- Vegetation-Moisture Dry Index (TVMDI), solar radiation and aspect in two groups of anthropogenic and natural factors were extracted for modeling fire-risk for a 9-year period through Landsat-8 images in GEE environment. Then, after standardizing the factors according to Dong model, fire-risk modeling was done. In the following, the fire occurrence points during the past 9 years based on the data of the Natural Resources Organization and the burned area extracted from the RdNBR[2] spectral index through Landsat-8 images in the GEE environment were overlayed with the output of the Dong model and were used as validation of the Dong output.

study area

Arasbaran or Qara Dagh is a vast mountainous area in the north of East Azarbaijan province in the northwest of Iran. In 1976, UNESCO[3] registered 72,460 hectares of land in this area as a biosphere reserve. Arasbaran, Dizmar National Park, Protected Area, parts of Kantal National Park and Kiamaki Wildlife Sanctuary are located within the area. The altitude of the study area ranges from 187 meters in the northeast of the region to 3254 meters in the Kantal peak in the west of the region. Also, the most important river is Aras in the northern border of the region. Selenchai, Kaleibarchai, Sitenchai, Ilganchai, MardanQomchai and Hajilarchai rivers flow into Aras River from east to west respectively (10).



[2] Relative differenced Normalized Burn Ratio

[3] United Nations Educational, Scientific and Cultural Organization

Figure 1. study area

Results

Preparing the factors and modeling the fire-risk

Because various factors that have an impact on the occurrence of fire are used to prepare a fire-risk map, in this research, after examining various models, the Dong model was used to prepare a fire-risk map (11). The mentioned model is calculated to model anthropogenic factors according to the following equation:

(equation,1**)** $$Rc = 7(Vtf + Vtr + Vd) + 5(S+A+E) + 3(Dr + Df + Ds)$$

where Rc is the numerical index of fire-risk, Vtf is the forest vegetation type, Vtr is the rangeland vegetation, Vd is the vegetation density, S is the slope, A is the aspect, E is the elevation, Dr is the distance from road, Df is the distance from croplands, Ds is distance from settlement areas. In addition, the integers (coefficients) indicate the weight of each factor (extra layer weight). At the bottom, research factors can be seen in two categories, anthropogenic and natural.

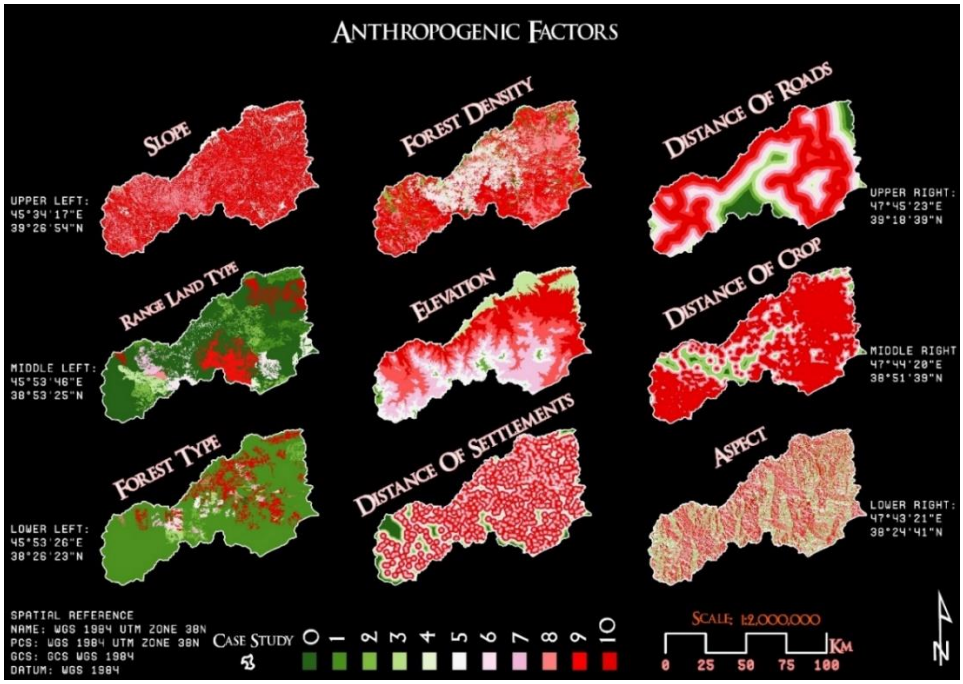


Figure 2. Normalized maps of anthropogenic factors of Dong model

In the next step, to reach the conclusion that how many fires in Arasbaran can have a natural origin and that if the fires in Arasbaran are caused by natural factors, which areas will be more exposed to these types of fires, this time, only natural factors according to Dong's method were modeled. For this purpose, maps of solar radiation (SR), Standardized Vegetation Index (vegetation vigor, SVI), Vegetation Condition Index (VCI), Enhanced Vegetation Index (EVI), forest type (vtf), rangeland type (vtr) and a new drought index called Temperature-Vegetation-Moisture Dry index (TVMDI) were used.

In explaining this index, it should be mentioned that soil moisture (SM) can be used as a direct index of dryness, Land Surface Temperature (LST) and vegetation condition are indirectly related to SM and thus affect the degree of dryness. Each of these three factors has been used separately to evaluate dryness. However, a combination of these three factors was not used for estimation (12). Dong's model based on natural factors is obtained from the following equation:

(equation.2)

$$DNFRM^{4} = 5*(TVMDI+Solar\ Radiation) + 3*(Forest\ Type+RangeLand\ Type+Forest\ Density+VCI+SVI)$$

Table 1. formula of the indices used in the production of fire-risk maps based on natural factors

ID	Index	Relationship	Reference
1	NDVI	$NDVI = (R_{NIR} - R_{Red})/(R_{NIR} + R_{Red})$	(13)
2	LST	$L_\lambda = M_L \times Q_{cal} + A_L - O_i$	(14)

[4] Dong Natural Fire-Risk Model

		$BT = \frac{K_2}{ln[(K_1/L_\lambda)+1]} - 273.15$ $T_s = \frac{BT}{\{1+[(\lambda BT/\rho)ln\varepsilon_\lambda]\}}$	
3	VCI	VCI= (NDVI – NDVI min) (NDVI max– NDVI min)	(15)
4	TVMDI	$PVI = \frac{\rho nir - 1.163\rho red - 0.017}{\sqrt{1+1.163^2}}$ $SM = \frac{\rho nir + 0.86\rho red - 0.082}{\sqrt{1+0.86^2}}$ $TVMDI = \sqrt{LST^2 + SM^2 + (\frac{\sqrt{3}}{3} - PVI^2)}$	(12)
5	SVI	$EVI = \frac{(2.5*\rho nir - \rho red)}{\rho nir + 6*\rho red - 7.5*\rho blue + 1}$ $SVI = \frac{EVI - EVI_{mean}}{EVI_{STD}}$	(16)

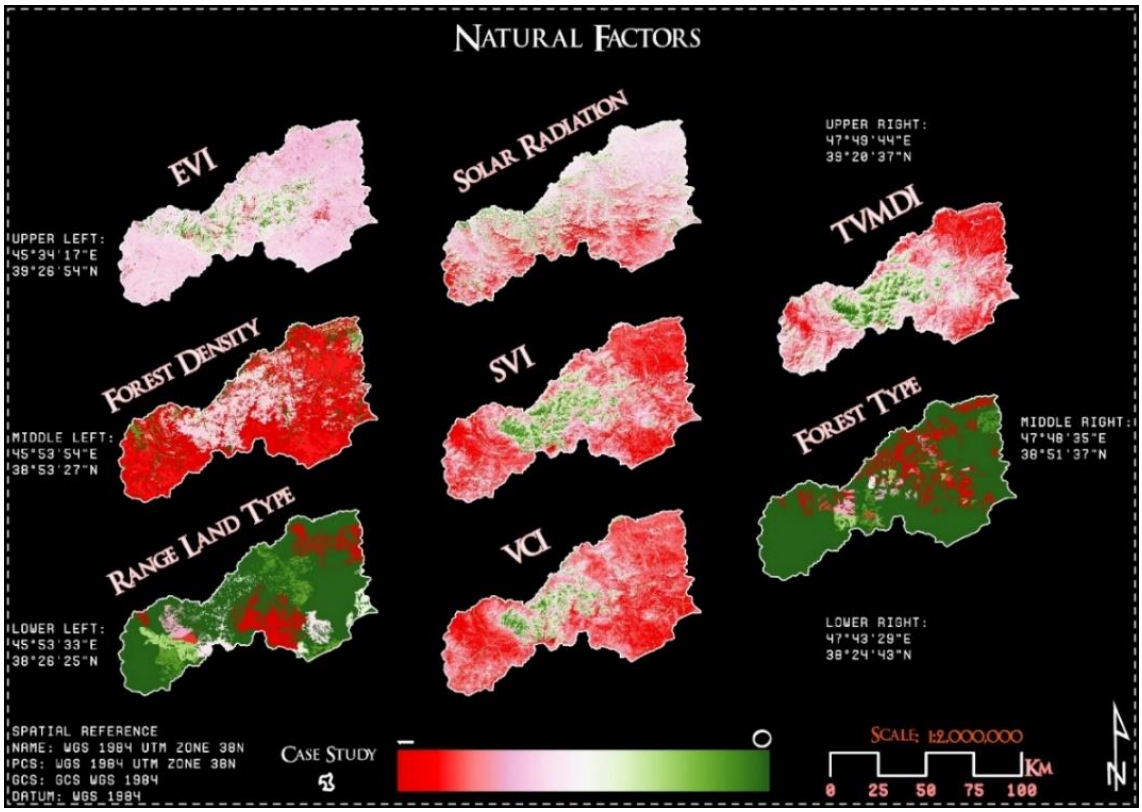


Figure 3. Normalized maps of natural factors of Dong model

In the figure below, the spatial distribution of land cover in the study area, points and burned area obtained from Landsat-8 images and the Natural Resources Organization can be seen. Based on the mentioned map, the land cover of the study area is classified into three groups: forest, rangeland and other land cover. Based on this, 54% are rangeland, 22% are forest areas and 24% are other land cover. On the other hand, according to the Landsat-8 images, 48% of the burned area have occurred in rangeland, 34% in forest areas, and 18% in other land cover. Also, the fire points from Natural Resources organization showed that 55% of the fires are distributed in rangeland, 34% in forest areas and 11% in other land cover.

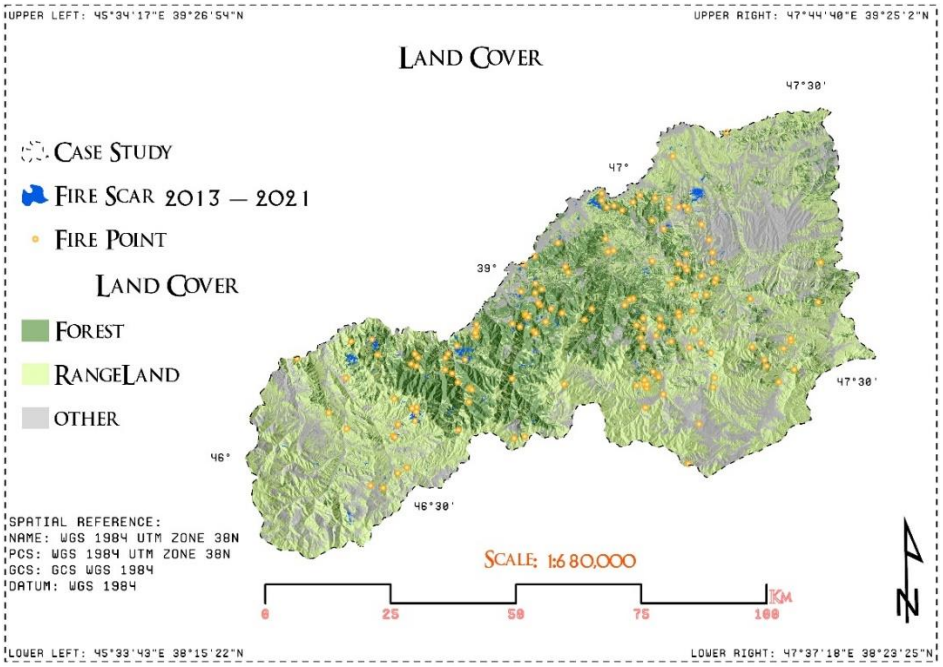


Figure 4. land cover of study area

Preparation of the final fire-risk map

The result of applying Dong's model to anthropogenic and natural factors to prepare a fire-risk map is as shown below. As previously explained, the maps of vegetation type, vegetation density, slope, aspect, elevation, distance from road, distance from crop land, distance from settlement areas were combined in the form of Dong model. And somehow, in addition to the physiographic and ecological parameters, it also emphasizes the anthropogenic factors of fire-risk. Based on this, the eastern half of the region is among the fire-risk areas, which is consistent with the density of the villages in the region. The comparison of the areas affected by fire in the last 9 years (blue polygons) with the below fire-risk map shows that many polygons of the areas that have caught fire in the last 9 years are in high fire-risk sensitive areas (red areas). Areas such as NojehMehr and Mardanqom in the east of the region, as well as the western half of the region between the village of MezhemKaleibar and Khodaafarin, are high fire-risk areas. In addition, almost no area affected by fire is in the green area of the map (low fire-risk). This is a proof of the correctness of the map of fire-risk and the current method can be used in other similar areas.

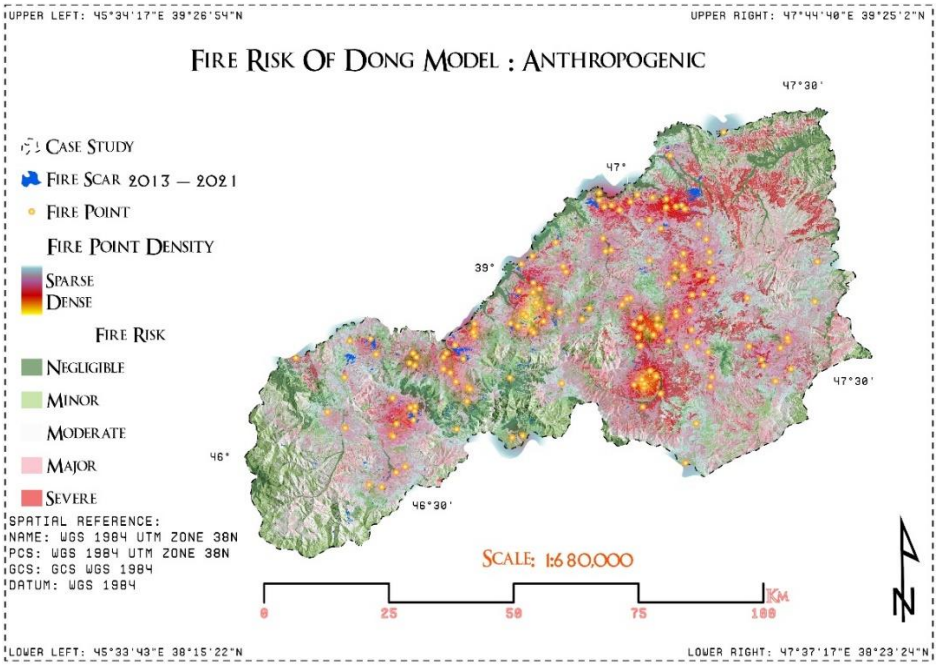


Figure 5. Fire-risk map according to Dong model based on anthropogenic factors

As mentioned in the methodology section, to reach the conclusion that if Arasbaran fires are caused by natural factors, which areas will be more exposed to this type of fires, only natural factors were modeled by Dong model. For this purpose, maps of solar radiation, standardized vegetation index, vegetation condition index, enhanced vegetation index and temperature- vegetation-moisture dry index were used. The result is shown in the figure below. As it can be seen, the centers that are sensitive to fires of natural origin are mostly in the southeast (around Kharwana), southwest (Kaleibar to Ahar) and northwest of the region (AbishAhmad) and it does not have much compatibility with the areas affected by fires in the last 9 years (blue polygons). And this point is another proof of the anthropogenic origin of Arasbaran fires in the past years.

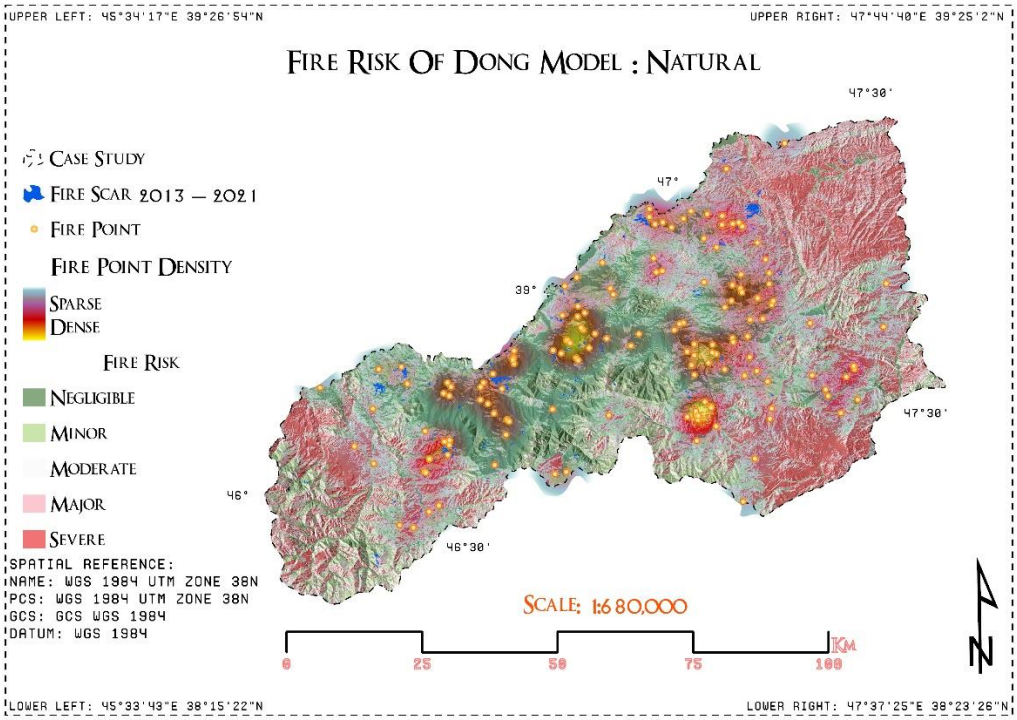


Figure 6. Fire-risk map according to Dong model based on natural factors

Discussion

In this research, it was done to evaluate the fire-risk in Arasbaran forest (Qara Dagh) using Dong modeling. For this purpose, the effective factors in the occurrence of fire were identified and prepared after conducting library studies in two categories, anthropogenic and natural. Using the model that developed by (11), fire-risk modeling was done based on anthropogenic factors. According to the obtained results, the Middle Eastern regions are among the fire-risk regions, which is consistent with the density of the villages in the region.

The comparison of the areas affected by fire in the last 9 years with the fire-risk map shows that many polygons of the areas that have caught fire in the last 9 years are in areas sensitive to high fire-risk. In the following, according to the effect of natural factors on the occurrence of fire, the Dong model was calculated again using natural factors. According to the results, the fire-risk with natural origin is mostly in the south-east and west of the region, and it does not have much compatibility with the areas affected by fire in the last 9 years, and this point is another reason for the anthropogenic origin of Arasbaran fires in the past years.

According to the land cover chart, 54% of the area includes rangeland, 22% forest and 24% other existing uses. In this way, based on the results of the overlapping of the fire zones obtained from the Landsat-8 images with the land cover of the region, 48% occurred in rangeland, 34% in forest areas and 18% in other land cover. Also, the burned points obtained from the Natural Resources Organization show that 55% of fires occur in rangeland, 34% in forest areas and 11% in other land covers.

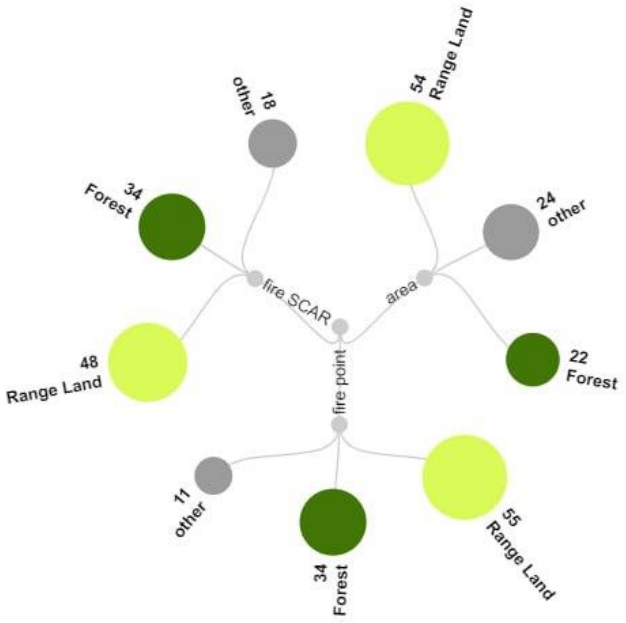


Figure 7. percent of Land cover, Natural Resources Organizations points and landsat-8 areas of fire in the study area

In order to reveal the spatial distribution of fire scar obtained from Landsat-8 images and on the land cover of the region, the map obtained from the Dong model based on anthropogenic factors was overlapped with the point layer of the Natural Resources Organization. According to the results, in the rangeland cover, 24.49% of the points are in the class with major fire-risk, 1.36% are in the negligible class. In forest cover, 10.02% is in the minor class and 0.68% is in the negligible class. For other covers, 4.8% in the moderate class and 1.36% in the major class are distributed. Overlapping the Dong model of anthropogenic factors with fire areas obtained from Landsat-8 images provide the following results: 13.63% of points are in the class with moderate fire-risk and 2.63% are in the negligible class in rangeland cover. In forest cover, 8.93% is in the major class and 2.77% is in the negligible class. For other land covers, 5.47% were distributed in the moderate class and 1.66% in the sever fire-risk class.

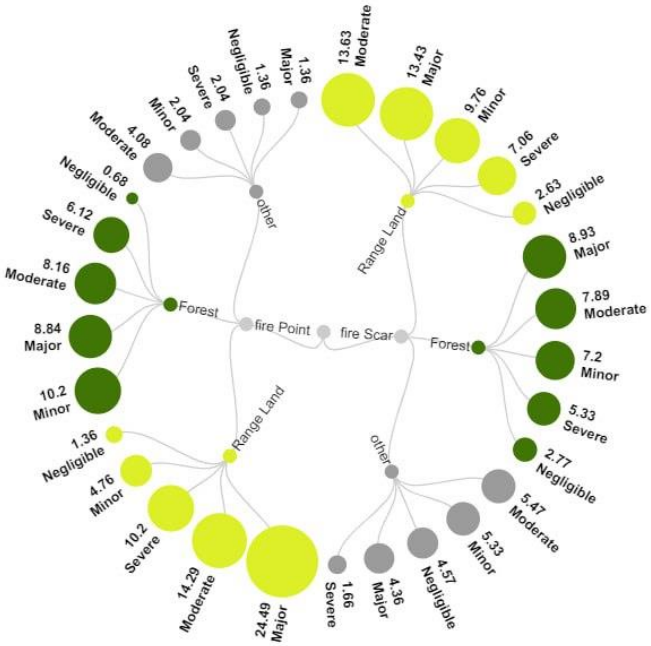


Figure 8. Percent of overlapping of land use with fire-risk classification based on anthropogenic dong model

The results of overlapping the Dong model based on natural factors with the layer of points of the Natural Resources Organization showed that, in the rangeland cover, 18.37% of the points are in the class with moderate fire-risk, and 0.68% are in the negligible class. In forest cover, 14.29% is in the minor class and 0.68% is in the

sever class. For other covers, 6.12% is distributed in the major class and 0% in the negligible class. Overlapping natural factors of Dong's model with burned area obtained from Landsat-8 images yielded the following results: 14.02% of the points are in the class with major fire-risk and 4.23% are in the class with negligible rangeland cover. In forest cover, 9.03% is in the moderate class and 3.04% is in the sever class. For other covers, 5.07% was distributed in the moderate class and 1.11% in the class with negligible fire-risk.

Finally, it can be concluded that anthropogenic factors have the greatest impact in the fires of Arasbaran forest, and preparing short-term, medium-term and long-term plans and participation of the local people in the area regarding prevention, quick reporting, and cooperation in firefighting are very necessary and effective.

According to the results obtained from the calculation of the Dong model for Arasbaran region, the results show the confirmation of the positive performance of the mentioned model. Also, the results of this research are consistent with the findings of (17).

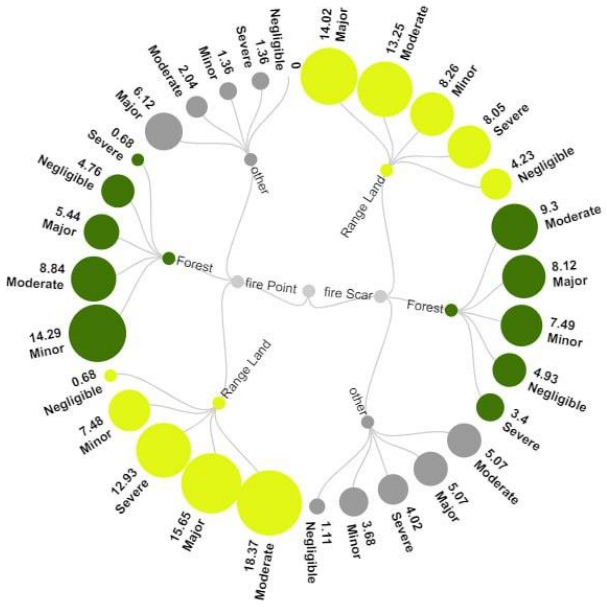


Figure 9. Percent of overlapping of land cover with fire-risk classification based on natural dong model

Conclusion

Arasbaran or Qara Dagh is a vast mountainous area in the north of East Azarbaijan province in the northwest of Iran. In 1976, UNESCO registered 72,460 hectares of land in this area as a biosphere reserve. Therefore, to take preventive measures to reduce the occurrence of forest fire-risk and to manage this crisis quickly and optimally, it is necessary to identify the sensitive area to fire-risk in the rangeland and forest areas of Arasbaran.

To prepare the fire-risk map, maps of vegetation type, vegetation density, slope, aspect, elevation, distance from road, distance from crop land, distance from settlement areas were combined in the form of Dong model, and in addition to physiographic and ecological parameters, it emphasizes the anthropogenic factors of fire-risk.

Based on this, the eastern half of the region is among the fire-risk areas, which is consistent with the density of the villages in the region. The comparison of the areas affected by fire in the last 9 years, with the following fire-risk map, shows that many polygons of the areas that have caught fire in the last 9 years are in high fire -risk areas. In addition, almost no area affected by fire is in the green area of the map (low risk of fire). This issue is a proof of the correctness of the fire-risk map.

To reach the conclusion that if Arasbaran fires are caused by natural factors, which areas will be more exposed to this type of fires, only natural factors were modeled by Dong's method. For this purpose, maps of solar radiation, standardized vegetation index, vegetation condition index, enhanced vegetation index and moisture-temperature- vegetation dry index were used. The hot spots of natural origin are mostly in the south-east and west of the region and do not correspond much with the areas affected by fires in the last 9 years, and this point is another reason for the anthropogenic origin of Arasbaran fires in the past years.

Also, to verify the output of the Dong model, 114 fire points are located based on the data of the Natural Resources organization, 22 points (19%) are located inside the fire-risk zones extracted from the Dong model, and 59 points (52%) are located at 100 meters. and 96 points (84%) were located at 200 meters from the fire polygons, which indicated a good agreement between these two fire-risk maps.

The current research showed the high potential of satellite images and especially the extraordinary ability and facilities of the Google Earth Engine (GEE) system in providing a huge amount of remote sensing data and information, advanced analysis and processing on them for the preparation of fire occurrence maps. The lack of accurate and correct spatial data is one of the limitations and shortcomings of most studies in our country, and

the current region is no exception. Therefore, creating an integrated and large-scale spatial database (Geodatabase) using new RS&GIS technologies and using GEE capabilities in combination with field information is one of the necessities of targeting and modernizing natural resources studies, especially in valuable and sensitive areas such as Arasbaran.

References

1. Barnes, B. V., Zak, D. R., Denton, S. R., & Spurr, S. H. (1998). Landscape assessment: Remote sensing of severity, the normalized burn ratio; and ground measure of severity, the composite burn index. Forest Ecology.
2. Alistair M.S. Smith, Crystal A. Kolden, Travis B. Paveglio, Mark A. Cochrane, David MJS Bowman, Max A. Moritz, Andrew D. Kliskey, Lilian Alessa, Andrew T. Hudak, Chad M. Hoffman, James A. Lutz, Lloyd P. Queen, Scott J. Goetz, Philip E. Higuera, Luigi Boschetti, Mike Flannigan, Kara M. Yedinak, Adam C. Watts, Eva K. Strand, Jan W. van Wagtendonk, John W. Anderson, Brian J. Stocks, John T. Abatzoglou,(2016) The Science of Firescapes: Achieving Fire-Resilient Communities, *BioScience*, Volume 66, Issue 2, 01, Pages 130–146,https://doi.org/10.1093/biosci/biv182.
3. Banazountas, M; Kallidromitou, D; Kassamenos, P; Passes, N, (2006). A decision support system for managing forest fire casualties. Journal of Environmental Management. 1-7.
4. Meguela, S; Huescal, M; Gonzalez, F, (2010). MODIS reflectance and active fire data for burn mapping and assessment at regional level. Ecological Modeling. 67-74.
5. Somashekar, R.K., Ravikumar, P., Mohan Kumar, C.N., Prakash, K.L., and Nagaraja, B.C. (2009) Burnt area mapping of Bandipur National Park, India using IRS 1C/1D LISS III data. Journal of the Indian Society of Remote Sensing, 37(1):37-50.
6. Roy, P, (2003). Forest fire and degradation assessment using satellite remote sensing and Geographic Information System. Satellite Remote Sensing and GIS Application in Agricultural Meteorology. 361- 400.
7. Bajocco, S; Rosalti, L; Ricotta, C, (2009). Knowing fire incidence through fuel phenology. A remotely sensed approach. Ecol. Model. 59- 66.
8. Dong, X; Shao, G; Li-min, D; Zhang, H; Lei, T, (2006). Mapping forest fire-risk zones with spatial data and principal component analysis. Sciences china: Series E Technological Sciences. I140- 149.
9. Gorelick, N., Hancher, M., Dixon, M., Ilyushchenko, S., Thau, D., & Moore, R. (2017). Google Earth Engine: Planetary-scale geospatial analysis for everyone. Remote Sensing of Environment.
10. Moshiri, S, Kamran K. V, Rafieyan, O, Monavvar, N.A & Ramazani, Me (2023). Evaluation of the quality of climate time series maps extracted from GEE (case study: Arasbaran region - Iran). Intercontinental Geoinformation Days (IGD), 7, page numbers, Peshawar, Pakistan.
11. Dong, X., Li-min, D., Guo-fan, S. et al (2005). Forest fire risk zone mapping from satellite images and GIS for Baihe Forestry Bureau, Jilin, China. *Journal of Forestry Research* 16, 169–174. https://doi.org/10.1007/BF02856809
12. Amani, M., Salehi, B., Mahdavi, S., Masjedi, A. and Dehnavi, S. (2017). Temperature-Vegetation-soil Moisture Dryness Index (TVMDI). Remote Sensing of Environment. 197:1-14.
13. Drisya, J. and Roshni, T., (2018). Spatiotemporal variability of soil moisture and drought estimation using a distributed hydrological model. In Integrating Disaster Science and Management, 451-460. Elsevier.
14. Avdan, U. and Jovanovska, G., (2016). Algorithm for automated mapping of land surface temperature using LANDSAT 8 satellite data. Journal of Sensors, 2016, 1–8.
15. Kogan, F. N. (1995). Droughts of the late 1980s in the United States as derived from NOAA polar-orbiting satellite data. Bulletin of the American Meteorological Society, 76(5):655–668.
16. Veneros, J. E. and García, L. (2022).Application of the Standardized Vegetation Index (Svi)and Google Earth Engine (Gee)for Drought Management in Peru. Tropical and Subtropical Agroecosystems,25(1):1–13.
17. Erten, E., Kurgun, V., & Musaoglu, N. (2004, July). Forest fire risk zone mapping from satellite imagery and GIS: a case study. In *XXth Congress of the International Society for Photogrammetry and Remote Sensing, Istanbul, Turkey* (pp. 222-230).
18. Global Wildfire Information System (GWIS), https://gwis.jrc.ec.europa.eu.

Advanced Engineering Days

aed.mersin.edu.tr

Comparative analysis of 3D models generated by close range photogrammetry and smartphone-based LiDAR sensor

Koray Aksu*[1], Esra Günaydın [1], Zaide Duran [1]

[1]*Istanbul Technical University, Geomatics Engineering, Türkiye, koray.aksu@itu.edu.tr, esgunaydin@itu.edu.tr, duranza@itu.edu.tr*

Cite this study: Aksu, K., Günaydın, E., & Duran, Z. (2024). Comparative analysis of 3D models generated by close range photogrammetry and smartphone-based LiDAR sensor. Advanced Engineering Days, 9, 295-297

Keywords
Smartphone
Photogrammetry
LiDAR
Point Cloud
3D Model

Abstract

Close-range photogrammetry is a practical and effective method for creating accurate three-dimensional models of objects. The development of built-in sensors, such as cameras or Light Detection and Ranging (LiDAR) in tablets and smartphones, has significantly broadened their usage capacities. Parameters, including the object's surface properties, environmental conditions (such as lighting), object details, and distance between the object and sensor, are critical factors to consider to ensure the generated model's quality. This study investigates the accuracy of photogrammetric products generated by close range photogrammetry and smartphone-based LiDAR for four distinct objects with varying characteristics and details. The three-dimensional models were created using data acquired from the camera and LiDAR sensor of an Apple iPhone 14 Pro. Additionally, the performance of a Structure from Motion (SfM)-based open-source software was compared with that of SfM-based commercial software in generating models from images. Although the results vary slightly depending on object features, the model obtained from open-source software indicated a good performance and was very close to the commercial software results. The LiDAR sensor of the smartphone was quite successful in modeling objects with fine details.

Introduction

In recent times, advancements in optical systems, Light Detection and Ranging (LiDAR) technologies, and the incorporation of smartphones equipped with these sensors have resulted in the widespread adoption of smartphone-based three-dimensional (3D) modeling across diverse stakeholders. Employing smartphones for close-range photogrammetry can achieve millimeter accuracy, provided that specific conditions, such as consideration of camera-to-object distances [1]. One of the studies examined the performance of depth sensors in Android and Apple devices in various urban environments. The study concluded that achievable accuracies range from approximately 1 to 3 cm, indicating that mobile devices are valuable tools for scanning objects and urban environments [2]. Another study evaluated the effectiveness and limitations of mobile phone-based Structure from Motion (SfM) photogrammetry monitoring rapid soil erosion processes. Additionally, the accuracy of the SfM photogrammetry was assessed in comparison with a terrestrial laser scanner, yielding similar results for 80% of the erosion channel length [3]. In a study aimed at evaluating the performance of the iPad Pro mobile device in modeling objects with diverse detail features and sizes, the study found that the device's performance on objects with the finest details, sculptures, architectural interiors, and building facades was evaluated by comparing it with reference models obtained from laser scanning and point measurements. The study revealed that up to 50% of points of small objects with complex geometries obtained with iPad LiDAR were unaligned with reference models [4]. Hence, a study focused on collecting tree inventory data using smartphone. It evaluated the performance of a smartphone-based photogrammetric method and compared it with manual measurements, resulting in R^2 and RMSE values of 0.95 and 2.71 cm, respectively [5].

The main purpose of this study is to investigate the accuracy of 3D models of small-scale objects with various details generated by close-range photogrammetry and LiDAR measurements. Besides, the study aims to evaluate and compare the effectiveness of open-source and commercial software solutions. In order to determine the accuracy of models, length measurements were made precisely on the objects by calipers.

Data and Methodology

The study demonstrates a comprehensive approach to 3D modeling, creating models with varying surface roughness and colors. The methodology combines close-range photogrammetry and smartphone-based LiDAR sensor, and importantly, utilizes both commercial and open-source software. The study progresses through data collection, pre-processing, 3D modeling, and accuracy assessment. The workflow of the study is presented in Figure 1.

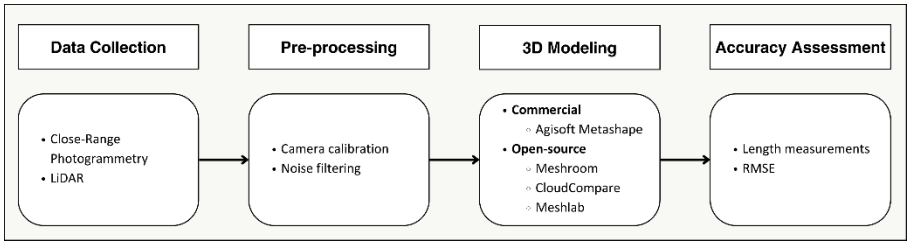


Figure 1. Workflow

The SfM method employs multiple overlapped images for feature extraction and 3D reconstruction algorithms instead of relying on a single stereo pair. It reconstructs camera pose and scene geometry by automatically identifying matching features across multiple images [6]. The two-modeling software used in this study is Agisoft Metashape, one of the well-known SfM-based commercial software [7], and the open-source SfM-based AliceVision Meshroom environment [8]. Another technology, laser scanner devices using LiDAR principles, are widely used for accurate object measurements. LiDAR sensors are segmented according to airborne and ground-based platforms and integrated into mobile phones today. Besides, LiDAR systems acquire highly accurate 3D point data suitable for mapping, modeling, and quantitative surveys, thus serving as essential devices in research and environmental fields [9]. Considering these specifications, it is pertinent to include that the study, aimed at 3D modeling of different objects, explores the efficacy of the LiDAR sensor alongside close-range photogrammetry.

The four small-sized objects whose 3D models will be generated within the study are a candle holder, a cat figurine, an airplane model, and a miner figurine, respectively. From this section onwards, these objects are referred to as Object 1, Object 2, Object 3, and Object 4. The images of the objects were taken using an Apple iPhone 14 Pro.

Results

Length measurements obtained from the models (using Agisoft Metashape, Meshroom, and LiDAR) and measurements obtained by calipers to evaluate the accuracy of the models are presented in Table 1.

Table 1. Length values from 3D Models and hand measurements

Method	Object 1 M1 | M2 | M3 (cm)	Object 2 M1 | M2 | M3 (cm)	Object 3 M1 | M2 | M3 (cm)	Object 4 M1 | M2 | M3 (cm)
Agisoft Metashape	10.29 | 6.52 | 1.19	13.87 | 11.52 | 2.80	21.52 | 14.57 | 2.40	20.66 | 15.82 | 8.29
Meshroom	10.15 | 6.41 | 1.23	14.31 | 11.79 | 2.84	21.52 | 14.54 | 2.63	20.96 | 15.88 | 8.32
LiDAR	12.34 | 6.62 | 1.20	14.34 | 11.67 | 2.81	21.73 | 14.69 | 2.49	20.41 | 15.59 | 8.31
Caliper	11.82 | 7.16 | 1.15	13.56 | 11.64 | 2.90	21.77 | 14.54 | 2.50	20.64 | 15.85 | 8.26

Root mean squared error (RMSE) values of length measurements taken on the models compared to those obtained with a caliper are presented in Table 2. Upon review of the findings, it was noted that the SfM method yielded similar results in modeling Object 1, which is smaller and more geometrically complex than the other objects. However, LiDAR demonstrated higher accuracy for Object 1. Similarly, LiDAR has more precise results for Object 3, which has a simpler geometric structure. For Object 2 and Object 4, the results obtained with the SfM method and commercial software were superior. The 3D models generated with three different method is shown in Figure 2.

Table 2. RMSE values of 3D models comparing with caliper measurements (cm)

Object	Agisoft Metashape	Meshroom	LiDAR
Object 1	1.28	1.44	0.64
Object 2	0.31	0.55	0.52
Object 3	0.22	0.22	0.12
Object 4	0.05	0.24	0.31

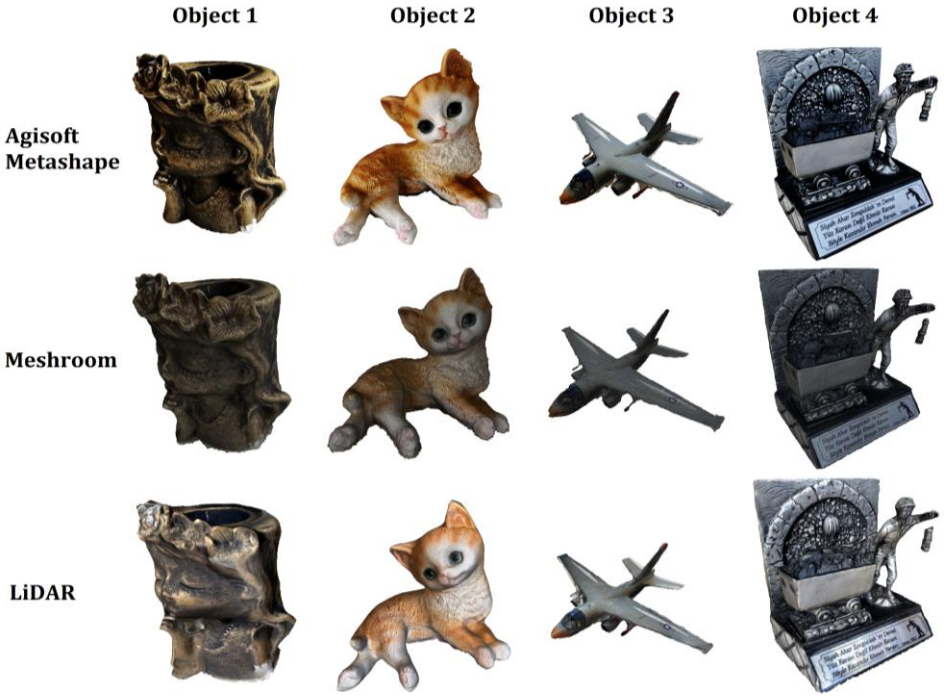


Figure 2. 3D Models

Conclusion

In conclusion, the study demonstrated that using open-source software and smartphone-based LiDAR for object modeling can yield similar accuracy to that achieved with commercial software. This approach represents a cost-effective method for generating 3D models and provides valuable insights for further research.

References

1. Barbero-García, I., Cabrelles, M., Lerma, J. L., & Marqués-Mateu, Á. (2018). Smartphone-based close-range photogrammetric assessment of spherical objects. *The Photogrammetric Record*, 33(162), 283-299.
2. Costantino, D., Vozza, G., Pepe, M., & Alfio, V. S. (2022). Smartphone lidar technologies for surveying and reality modelling in urban scenarios: evaluation methods, performance, and challenges. *Applied System Innovation*, 5(4), 63.
3. Rodríguez, R. F., Ponte, M., Bento, R., & Cardoso, R. (2022). Potential of mobile application based on structure from motion (SfM) photogrammetry to monitor slope fast erosion by runoff water. *Catena*, 216, 106359.
4. Łabędź, P., Skabek, K., Ozimek, P., Rola, D., Ozimek, A., & Ostrowska, K. (2022). Accuracy verification of surface models of architectural objects from the iPad LiDAR in the context of photogrammetry methods. *Sensors*, 22(21), 8504.
5. Ahamed, A., Foye, J., Poudel, S., Trieschman, E., & Fike, J. (2023). Measuring tree diameter with photogrammetry using mobile phone cameras. *Forests*, 14(10), 2027.
6. Westoby, M. J., Brasington, J., Glasser, N. F., Hambrey, M. J., & Reynolds, J. M. (2012). 'Structure-from-Motion'photogrammetry: A low-cost, effective tool for geoscience applications. *Geomorphology*, 179, 300-314.
7. Zeybek, M., & Biçici, S. (2021). 3D dense reconstruction of road surface from UAV images and comparison of SfM based software performance. *Turkish Journal of Remote Sensing and GIS*, 2(2), 96-105.
8. Griwodz, C., Gasparini, S., Calvet, L., Gurdjos, P., Castan, F., Maujean, B., ... & Lanthony, Y. (2021, June). AliceVision Meshroom: An open-source 3D reconstruction pipeline. *In Proceedings of the 12th ACM multimedia systems conference* (pp. 241-247).
9. Saba, N. (2021). Accuracy Assessment of Horizontal Measurements from LiDAR Available in Mobile Phones. *International Journal of Engineering Research & Technology (IJERT)*, 10(11), 126-135.

Advanced Engineering Days

aed.mersin.edu.tr

Hyperspectral classification of minerals using K-means and PLS-DA models

Ahmad Nikdel Monavvar[1], Sajjad Moshiri [1], Seyed Hossein Faghih [2], Iraj Teymouri [3], Sadra Karimzadeh*[1]

[1] University of Tabriz, Department of Remote Sensing and GIS, Iran, ahmadnikdel21@gmail.com , Sajjadmoshiri@gmail.com , Sadra.karimzadeh@gmail.com
[2] University of Tabriz, Geomorphological laboratory, Iran
[3]Department of Urban and Regional Planning, University of Tabriz, Iran, iraj-teymuri@tabrizu.ac.ir

Cite this study: Nikdel, Monavvar, A., Moshiri, S., Faghih, S. H., Teymouri, I., & Karimzadeh, S. (2024). Hyperspectral classification of minerals using K-means and PLS-DA. Advanced Engineering Days, 9, 298-300

Keywords
Hyperspectral
K-means
PLS-DA
Minerals

Abstract

In this study, sampling of barite, trachyandesite, and trachyte minerals was conducted using the HYSPIM spectrometer in a laboratory spectroscopy environment. Following the preparation of the sampling environment, the HYSPIM spectrometer was employed for sample collection. Initially, preliminary settings such as referencing, focusing, and spectrometer camera height were adjusted. Subsequently, spectroscopy of the minerals was carried out in a darkened laboratory environment. The K-means clustering and Partial least squares-discriminant analysis (PLS-DA) are carried out for the hyperspectral samples.

Introduction

Spectroscopy technology, with its capability for use in both laboratory and field environments, has numerous applications across various sciences, including geology, environmental science, and the food industry. This technology can be utilized in spectral ranges from 400 to 2500 micrometers. The physics of visible/near-infrared (VNIR), shortwave infrared (SWIR), and longwave infrared (LWIR) spectroscopy is well understood. Key spectral features in these ranges enable the identification of various materials using laboratory and field spectroscopy, including minerals, vegetation, synthetic materials, snow and ice, and water (Kruse, 2012).

Rocks, as natural materials, have been utilized in various ways by different civilizations. Over the years, stones or minerals have been chosen and used not only to meet specific structural requirements (e.g., beams, columns, arches, walls, etc.) but also to satisfy particular aesthetic needs (Bonifazi et al., 2005). From another perspective, identifying different minerals can enhance valuable mineral explorations, which, beyond economic benefits, also offer substantial advantages in terms of employment and other related aspects. Therefore, spectroscopy technologies are used as an alternative method for geological multispectral mapping (Huynh et al., 2021). Spectral analysis and hyperspectral imaging systems can produce geological maps with high efficiency and accuracy, especially for estimating the abundance of desired materials. Based on the aforementioned aspects of spectroscopy technology and its applications, the objective of the present study is to evaluate the applications of the spectroscopic device for identifying minerals in the spectral range of 400-950 nanometers.

Material and Method

Sampling of barite, trachyandesite, and trachyte minerals was conducted using the HYSPIM spectrometer. Initially, preliminary settings such as referencing (using a white reference), focusing (using a focus cardboard), and spectrometer camera height were adjusted. Subsequently, spectroscopy of the minerals was carried out in a darkened laboratory environment. The sampling outputs were then prepared in the spectroscopy software "Visualizationer" in both .mat and .cube formats. The HyperTools.3 toolbox (Amigo et al., 2015) is used for further analyses. As a first step in preprocessing, the samples were smoothed in a 7x2 window, and the background of the

image was manually removed using a masking tool. The final image was thus prepared for the specified processing tasks, including K-means classification analysis and PLS-DA algorithm modeling of the samples (Figure 1).

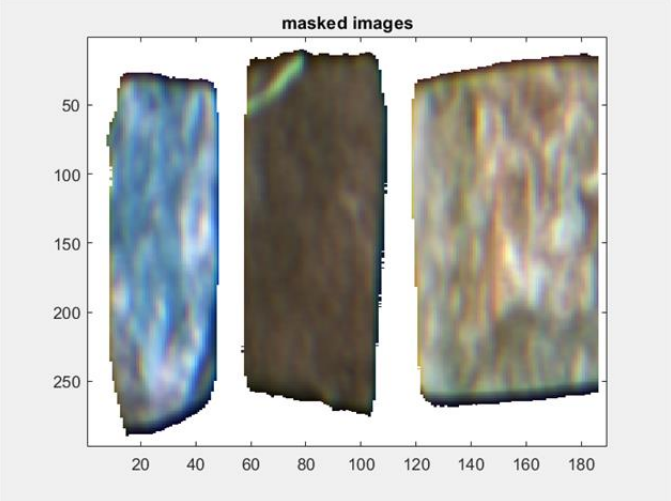


Figure 1. Masked images of the minerals: trachyte (left), trachyandesite (middle) and barite (right).

K-means is an unsupervised learning algorithm used for clustering data into a predefined number of groups (k). The algorithm works by initializing k centroids, then iteratively assigning each data point to the nearest centroid and recalculating the centroids as the mean of the points in each cluster. This process continues until the assignments no longer change significantly. K-means is used to find patterns and groupings in data without prior knowledge of the labels. Alternatively, PLS-DA is a supervised learning technique that combines features of Partial Least Squares (PLS) regression and Linear Discriminant Analysis (LDA). It is used for classification tasks where the goal is to find a linear regression model that can discriminate between different classes. PLS-DA works by projecting the predictor variables into a new space that maximizes the covariance between the predictors and the response variable (class labels), thus enhancing the separation between classes. This method is particularly useful when dealing with high-dimensional data with multicollinearity.

Results

From the K-means clustering, images were classified by inputting them as data and selecting three clusters. As shown in the final output (Figure 2), the surface features of the minerals, such as roughness, smoothness, and the presence of veins, were identified. According to Figure 2, the middle mineral has a smooth surface with a vein in the upper part. In other samples, surface grooves and the unevenness of the minerals can be observed in the lower parts.

Based on the input samples, PLS-DA modeling was performed in three classes. As shown in Figure 3 and Figure 4, the minerals were separated into three distinct classes. The scatter plot of the model output clearly and accurately depicts the samples of the three classes. Additionally, according to the color spectrum of the minerals, the lighter minerals have higher reflectance, while the darker minerals have lower reflectance.

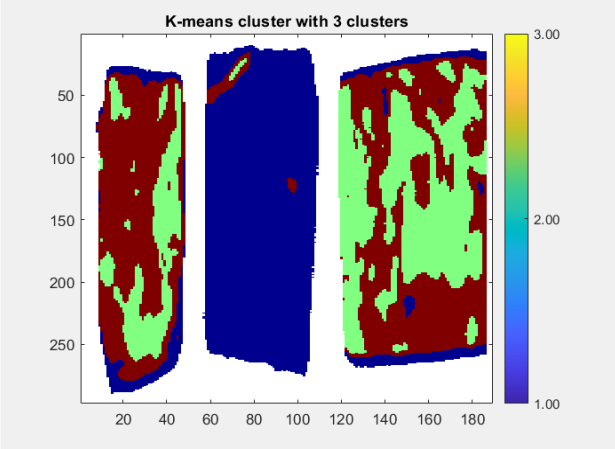


Figure 2. K-means clustering of the three mineral samples. trachyte (left), trachyandesite (middle) and barite (right).

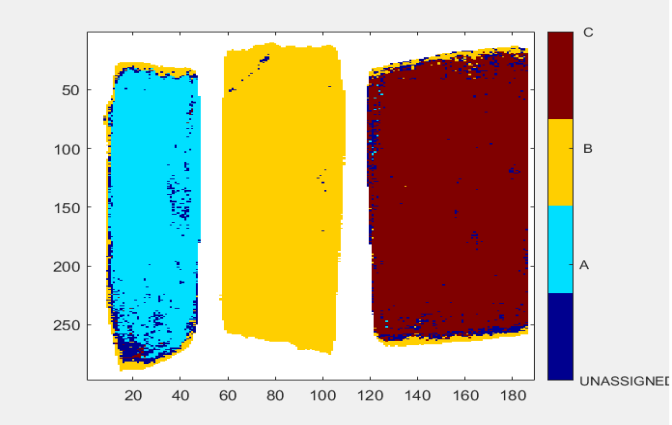


Figure 3. PLS-DA supervised classification of the three mineral samples. trachyte (left), trachyandesite (middle) and barite (right).

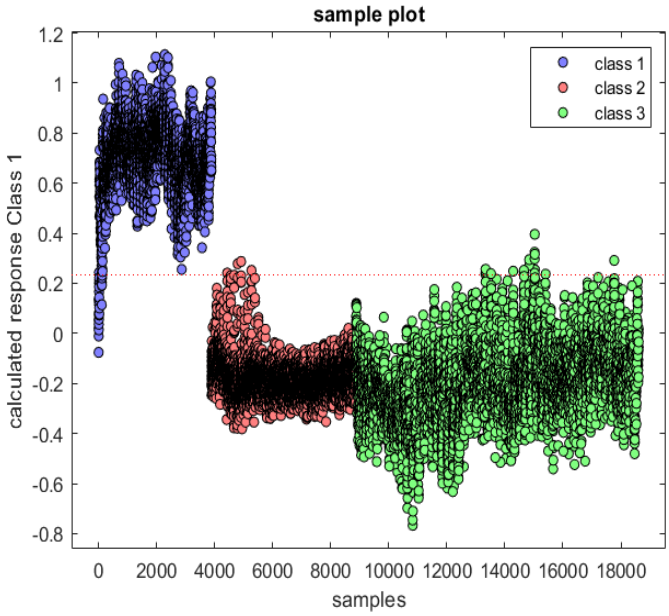


Figure 4. Scatter plots of the discriminated samples.

Conclusion

Hyperspectral classification both remote sensing-based and laboratory-based applications are growing in the recent years. Here, we showed the feasibility of mineral classification using a hyperspectral imager. Both superviased and unsupervised techniques show that differentiating of characteristics of the minerals such as barite, trachyandesite, and trachyte are possible.

References

1. Kruse, F. A. (2012). Mapping surface mineralogy using imaging spectrometry, Geomorphology, 137(1), pp. 41-56.
2. Bonifazi, G, Serranti, S, & Menesatti, P. (2005). Hyperspectral imaging-based techniques in ornamental stone characterization. In Optical Sensors and Sensing Systems for Natural Resources and Food Safety and Quality Vol. 5996, pp. 203-214.
3. Huynh, H.H; Yu, J; Wang, L; Kim, N.H; Lee, B.H; Koh, S.-M; Cho, S; Pham, T.H. (2021). Integrative 3D Geological Modeling Derived from SWIR Hyperspectral Imaging Techniques and UAV-Based 3D Model for Carbonate Rocks. Remote Sens., 13, 3037. https://doi.org/ 10.3390/rs13153037.
4. Amigo, J. M., Babamoradi, H., & Elcoroaristizabal, S. (2015). Hyperspectral image analysis. A tutorial. Analytica chimica acta, 896, 34–51. https://doi.org/10.1016/j.aca.2015.09.030.

Advanced Engineering Days

aed.mersin.edu.tr

Optimal Spatial Distribution of Mosques in The City of Hillah / Iraq Using Evolutionary Algorithms and Geographic Information Systems.

Abolfazl Ghanbari [*1], **Falih Hassan Ali** [1]

[1] *University of Tabriz, Faculty of Planning and Environmental Sciences, Tabriz, Iran, a_ghanbari@tabrizu.ac.ir, falihhassan99@gmail.com*

Cite this study: Ghanbari, A., & Ali, F.H. (2024). Optimal Spatial Distribution Of Mosques In The City Of Hillah / Iraq Using Evolutionary Algorithms And Geographic Information Systems. Advanced Engineering Days, 9, 301-303

Keywords
Evolutionary Algorithms
Spatial Distribution
Mosques
GIS
GA, ABC ,ACO, PSO

Abstract

This report presents some new methods to assess the status and suggest the optimum distribution of mosques in Hillah city / Iraq, and detection of imbalances to identify deficiencies in the distribution and develop proposals and make the appropriate recommendations. Different optimization techniques were used to find close-to-optimal solutions that regarded as one of the approaches of modern artificial intelligence. Therefore, we described a framework of four different optimal algorithms technique (Genetic algorithm (GA), Artificial Bee colony (ABC), Ant colony algorithm (ACO) and particle swarm optimization (PSO)) to solve certain spatial decision problems encountered in geographical information system (GIS). Intelligent search algorithms have the potential to enhance the efficiency of spatial search processes. This report illustrates how these algorithms, when integrated with Geographical Information Systems (GIS), can effectively address spatial decision problems, particularly in optimizing the selection of facility sites.

Introduction

Due to the great importance that the services sector occupies in civil and rural societies, many humanities, applied, planning and geography sciences have attached great importance to it, in line with the capacity and diversity of these services. The importance of studying mosques in Islamic societies comes in the priority of services provided to the population because of the great influence and effect of the mosque in the hearts of Muslims. A follower of the Islamic city at the present time finds the status of the mosque preserved and that the mosques were the central elements around which services gathered.

With the development of contemporary cities in terms of origin and growth, and the development of the elements involved in planning the contemporary city, the planning standards for the mosques differed in terms of geographical distribution and association, and it became difficult to maintain the centralization of the mosque due to the large size of the cities and the need to be near the residential neighbourhoods as a service with a small scope very. This makes the mosques one of the important services that must be planned for their distribution in residential communities, in order to ensure access to them on foot and in the shortest possible time. As planning to distribute it is an important and determining factor for the efficiency of this service and its ability to meet the requirements of the residents of the city.

With the development of science and technology, our daily lives were determined by what computers decide and it takes their decisions in implementation of the algorithms. Algorithms are increasingly used to make decisions about us, or with us - and without realizing it often, they are the minds of computers, smartphones, and the Internet of Things. Facebook updates, police predictions and location search are realistic examples of employing algorithms in our daily lives and usually requires the use of optimization tools.

The utilization of evolutionary algorithms can be highly effective in addressing numerous spatial decision problems. By integrating artificial intelligence and GIS, optimal solutions for a wide range of geographical issues can be identified. This report aims to showcase that spatial search problems, which encompass multiple objectives and constraints, can be effectively tackled by leveraging algorithms and GIS tools.

Material and Method

To achieve the objectives of the report, the descriptive-analytical approach that based on quantitative, analytical and statistical methods and cartographic representation, was used to highlight the spatial characteristics of the sites of mosques in the city of Hillah. Different algorithms have been applied to the solution of distribution problem where these algorithms were employed in dealing with all parameters properly.
There are some sequential steps that will be adopted during this work as follows;

1. Collect the data from various sources such as: maps, tables, charts, satellite images, text data, and some field data.
2. Processing the data by converting it into digital form so that it can be dealt with, categorized, coded, analysed, and stored.
3. Project sites of mosques on the map of the study area.
4. Building a geographical database for the sites of mosques in the study area.
5. Applying the spatial analysis methodology to the sites of the mosques in the study area, by performing the appropriate algorithm tests in a MATLAB program.
6. Presentation, analysis and interpretation of the results.

There are three main candidates' parameters that have been adopted to choose the best location which are:

1. Residential density.
2. Proximity to transportation.
3. Current geographical distribution of the mosques
   According to the data collected, the number of mosques registered was approximately 79 mosques according to the data of the year 2018. In order to show its geographical distribution according to the residential neighbourhoods, Table (1) and Figure (4) were created.

ID	Neighbourhood	No. of Mosques	Population	ID	Neighbourhood	No. of Mosques	Population
1	Alqisbat Alqadima	8	15254	11	Nadir	2	15047
2	Maranih	3	27457	12	Alsiyahiu	6	39124
3	Al'amam	10	24840	13	Alkhasrawia	4	13245
4	Alzawir	1	19450	14	Hayi Babil	1	15045
5	Muhayazim	5	41057	15	Waradiya	2	9415
6	Alakrimyn	6	37457	16	Aljinsia	1	9514
7	Almuhandisin	3	27810	17	Hayi Aljazayir	2	11201
8	Aleaskari	7	32101	18	Albukrliu	6	35014
9	Aljamiea	4	18403	19	Albu Hamir	4	24011
10	Almurtadaa	4	11240				

Table (1) The numerical distribution of population and mosques for each of the neighbourhoods of the Hilla

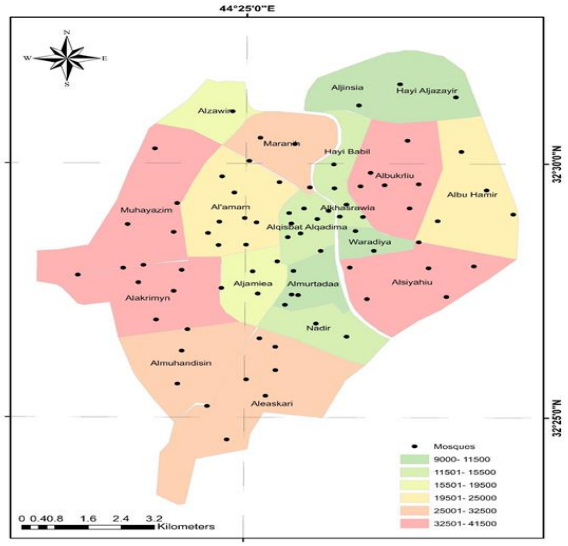


Figure (1) The spatial distribution mosques and the population for each of the neighbourhoods of the Hilla

Results

As a result of previous scenarios and spatial analysis of mosques obtained, this led to several results. Depending on the three determinants that have been put into implementation of the algorithms which are (i. Population ii. Transportation iii. The area served.).
The mosques in the study area at the level of residential neighbourhoods are built regularly according to planning indicators. The average centre of mosques is located in the approximately city centre because it represents the centre of attraction for distributions and it is of natural distribution according to what appeared from the study of the standard distance.

Discussion

In complex situations, the intelligent optimization algorithms can yield highly satisfactory results for optimal location search. This method has been tested by solving a spatial search problem which is to allocate new mosques locations according to the population and transportation constraints derived from a GIS. Taking advantage of natural selection mechanics makes the GA algorithm extremely efficient. The suggested approach can be applied as a planning tool to address location search issues with multiple objectives. Its potential applications include the optimal placement of different public facilities, such as healthcare facilities, educational institutions, open spaces, and emergency services. Notably, the model is implemented in continuous space to enhance accuracy. GAs provide significant advantages for global optimization, eliminating the need for intensive computations. It is also well-suited for problems with a high number of parameters. GAs also have the benefit of not requiring particular programs in order to find the best answer. By appropriately designing chromosomes, the suggested GA approach has the advantage of handling the combined impacts of all parameters collectively.

Conclusion

The ABC algorithm considers how adopting larger connectivity patterns can improve the site placements while solving the spatial problem in a vector-based GIS. The modified ABC model performs relatively similarly to the ACO algorithm, but having a substantially reduced computing cost and solution time, according to the experimental results. The findings further show that ABC can provide very consistent results across various simulations and that switching the movement orientation from forward to backward does not significantly alter the optimization results.

Similarly, combining ACO with GIS is crucial for solving real-world site selection. The only benefits of using ACO are its straightforward model and quick computation performance. it can generate results like ABC but without needing as much time for calculations. Comparisons show that, in contrast to the GA approach, the ACO method is less prone to trap in suboptimal solutions.

In this work, the PSO algorithm was employed to address the challenge of selecting optimal sites for new mosques. The fitness function, which plays a crucial role in PSO by guiding velocity and direction updates, was a key area of focus. The optimal parameters for the PSO algorithm were discussed. Comparative analysis of the PSO, GA, ABC, and ACO algorithms revealed that the PSO algorithm exhibits superior stability and speed. However, the genetic algorithm was more comprehensive in terms of population density and coverage.

References

1. Du, G, Chen, X & Li, X 2006, 'Spatial optimal search based on particle swarm optimization', ACTA GEOGRAPHICA SINICA-CHINESE EDITION-, vol. 61, no. 12, p. 1290.
2. Jayanth, J, Koliwad, S & Kumar, TA 2015, 'Classification of remote sensed data using Artificial Bee Colony algorithm', The Egyptian Journal of Remote Sensing and Space Science, vol. 18, no. 1, pp. 119-26.
3. Karaboga, D & Ozturk, C 2011, 'A novel clustering approach: Artificial Bee Colony (ABC) algorithm', Applied soft computing, vol. 11, no. 1, pp. 652-7.
4. Li, X & Yeh, AGO 2005, 'Integration of genetic algorithms and GIS for optimal location search', International Journal of Geographical Information Science, vol. 19, no. 5, pp. 581-601.
5. Li, X, He, J & Liu, X 2009, 'Intelligent GIS for solving high-dimensional site selection problems using ant colony optimization techniques', International Journal of Geographical Information Science, vol. 23, no. 4, pp. 399-416.
6. Liao, Y, Chen, W, Wu, K, Li, D, Liu, X, Geng, G, Su, Z & Zheng, Z 2017, 'A site selection method of DNS using the particle swarm optimization algorithm', Transactions in GIS, vol. 21, no. 5, pp. 969-83.
7. Mirjalili, S 2019, 'Genetic algorithm', in Evolutionary algorithms and neural networks, Springer, pp. 43-55.
8. Noskova, E, Ulyantsev, V, Koepfli, K-P, O'Brien, SJ & Dobrynin, P 2020, 'GADMA: Genetic algorithm for inferring demographic history of multiple populations from allele frequency spectrum data', GigaScience, vol. 9, no. 3, p. giaa005

Advanced Engineering Days

aed.mersin.edu.tr

Evaluation of the relationship between the ecological spatial inequality with the parameters of urban heat islands, population and green space of Tabriz metropolis

Mir Ali Seyed Mosaffayi*[1], Saeed Ahmadian [2], Sajjad Moshiri [3]

[1]*University of Tabriz, Department of Urban and Regional Planning, Iran, alimossafa1998@gmail.com*
[2]*University of Tabriz, Department of Urban and Regional Planning, Iran, saeedahmadian911@gmail.com*
[3]*Universityof Tabriz, Department of Remote Sensing and GIS, Iran, Sajjadmoshiri@gmail.com*

Cite this study: Seyed Mosaffayi, M. A, Ahmadian, S. & Moshiri, S. (2024). Evaluation of the relationship between the ecological spatial inequality with the parameters of urban heat islands, population and green space of Tabriz metropolis. Advanced Engineering Days, 9, 304-308

Keywords
Spatial Inequality
Critic method
MGWR
Tabriz metropolis

Abstract

Nowadays, it is predicted that by 2050, about 64% of the population of developing countries will live in urban areas. The purpose of this research is to evaluate the relationship between the ecological spatial inequality with the parameter of urban heat islands, population and green space of Tabriz metropolis. In this research, the ecological spatial inequality was weighted using height, vegetation and land surface temperature parameters and using the Critic weighting method, and then the relationship between spatial inequality and the parameters of urban heat islands, population and green space was analyzed using the MGWR model. Is. The results show that region 3 of Tabriz metropolis has the highest percentage in terms of inequality, and also the parameters of population, green space on regions 5 and 9, and the parameter of urban heat islands also have the greatest impact on region 6 of Tabriz metropolis.

Introduction

The urban population has increased from 30% in 1950 to 65% in 2019 (World Bank, 2020) and is expected to reach 66% in 2050 (Yang et al, 2021). In other words, it is predicted that by 2050, about 64% of the population of developing countries and 86% of the population of developed countries will live in urban areas (Geng et al, 2019). This process of increasing urbanization has brought many consequences in the world, the main consequences of which are poverty, deprivation and all kinds of spatial inequalities. Spatial inequality is one of the biggest challenges in developing countries and is a big obstacle to achieving sustainable urban development (Padda & Hamed, 2018).

Investigating spatial inequality in different geographical areas has been the focus of planners and politicians in different periods. The existence of inequality and its different dimensions are important signs of underdevelopment (Johnson, 1970). Spatial inequality means the unequal distribution of opportunities, facilities and power in space (Minot, 2006), spatial inequality can include inequalities between cities and villages, small and large cities, deprived and underprivileged areas, etc. (Yansouri, 2015). Spatial inequality is also measured based on certain criteria, and the status of spatial inequalities may be different based on each index (Stillwell, 2010). The purpose of this research is to evaluate the relationship between the ecological spatial inequality with the parameters of thermal islands, population and green space of Tabriz metropolis.

Material and Method

The purpose of the current research is to evaluate the relationship between the ecological spatial inequality with the parameters of urban heat islands, population and Green space of Tabriz metropolis. Ecological spatial inequality has been weighted using the height, vegetation and land surface temperature parameters and using the Critic weighting method, and then the relationship between the spatial inequality and the parameters of urban heat islands, population and green space has been analyzed using the MGWR model. The outputs of these results in the Arc GIS pro software are spatial analysis based on the 10 regions of Tabriz metropolis.

Study Area

The metropolis of Tabriz is the capital of East Azerbaijan Province in the northwestern of Iran. This city with an area of about 25056 hectares is located in an area with geographical coordinates of 38 degrees north latitude and 46 degrees east longitude. The metropolis of Tabriz generally consists of 10 different areas, which have been selected as the study area in this research (Figure 1).

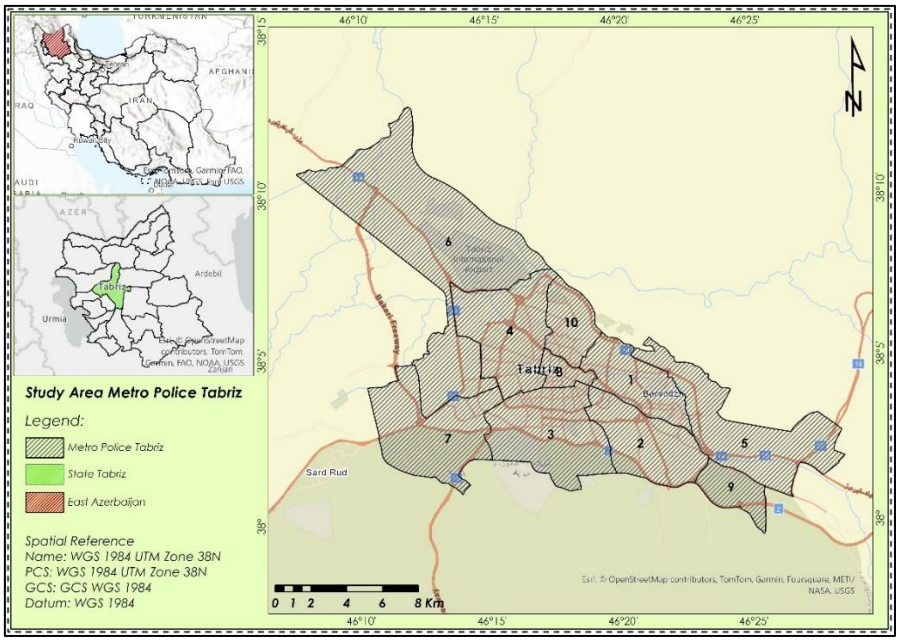


Figure 1. The study area

Results

The ecological spatial inequality consists of three parameters of LST, NDVI and Elevations (Figure 2).

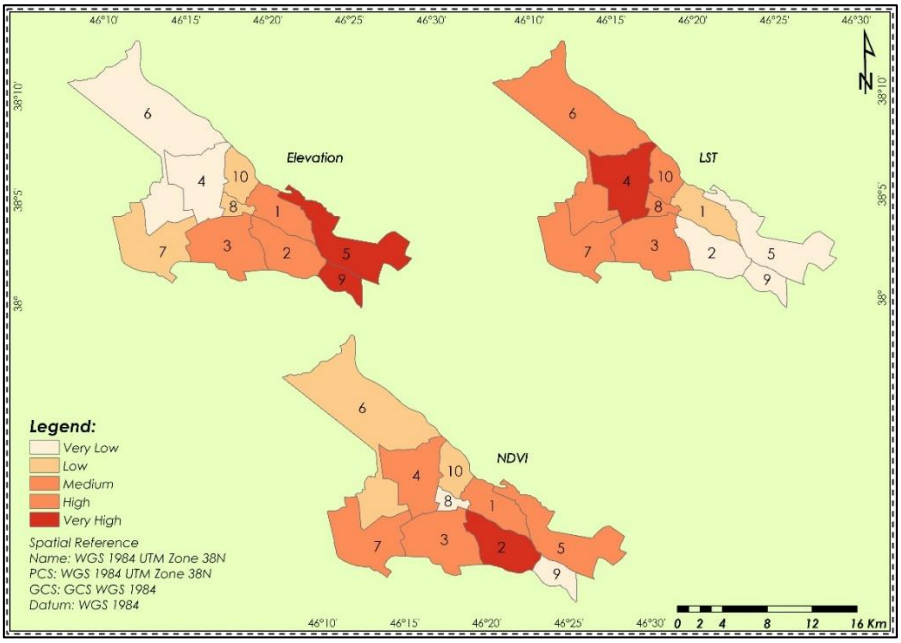


Figure 2. Parameters of Ecological Spatial Inequality

Determining criteria weights: The critical weighting method analyzes data based on the amount of interference and conflict between factors and criteria (Equation 1).

Equation1. $$cjk = \sum_{k=1}^{m}(1 - rjk)$$

In this method, for each of the evaluation criteria, a range of changes in the measured values and among the options are expressed in a format in the membership function. These parameters show the degree of difference of the corresponding criterion values. To calculate the standard deviation of the studied factors and criteria, a

symmetric matrix with dimensions of m*m is created. which includes the correlation coefficients between the formed vectors. The weight of each criterion is also shown in (Table 1):

Table 1. Weight of Parameters

Items	Parameters	Weight
a	Elevation	0.37
b	LST	0.42
c	NDVI	0.22

After extracting the weights, the criteria were overlaid using the SAW method and the resulting map of the superimposition results is shown in (Figure 3).

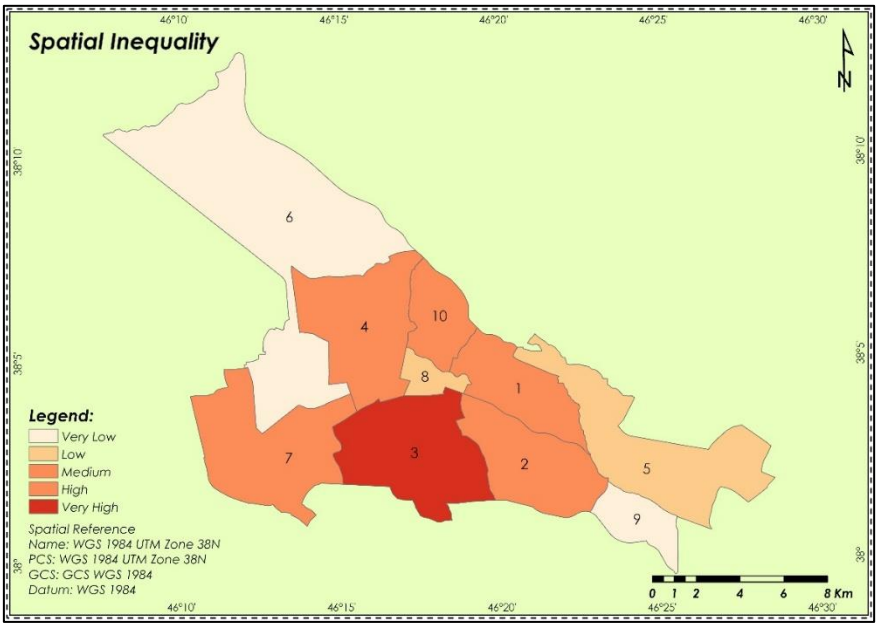


Figure 3. Spatial Ecological Inequality Status

According to the figure.3 ecological spatial disparity is higher in the 3rd region of Tabriz metropolis than in other regions. Then, the relationship between the ecological spatial inequality with the parameters of heat islands, population and green space has been investigated using the MGWR model, and the R^2 value or the effect of each parameter on the ecological spatial inequality is given in (Table 2).

Table 2. R^2 Value of Urban Heat Island Parameters, Population, and Green Space

Items	Parameters	R^2
a	Urban heat Islands	0.01
b	Population	0.2
c	Green Space	0.04

In addition, the status of each parameter of urban heat islands, population, and green space is shown in (Figure 4), and the degree of impact of each of these parameters on ecological spatial inequality, broken down by region, is illustrated in (Figure 5).

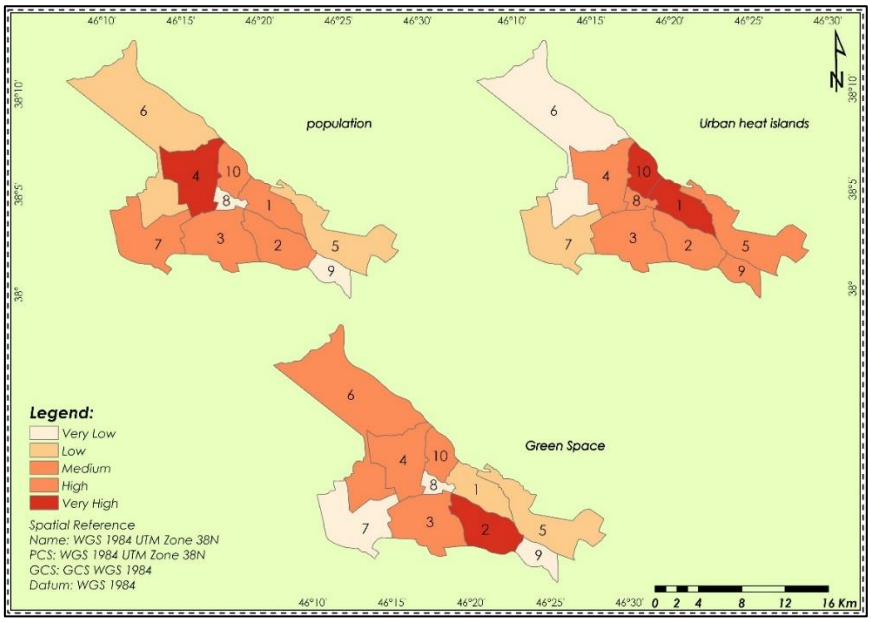


Figure 4. parameter of urban heat islands, population, and green space

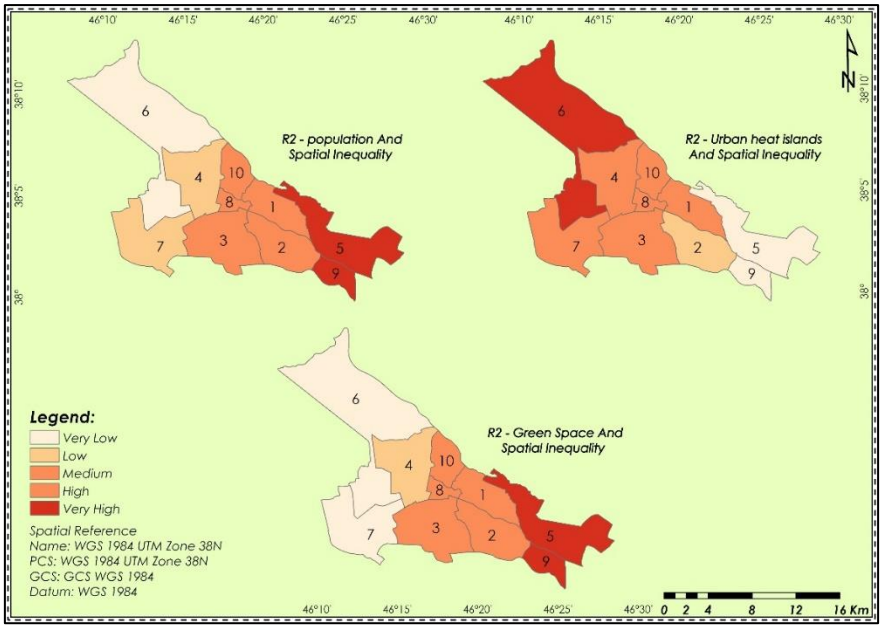


Figure 5. The Impact of Each Parameter on Spatial Ecological Inequality

Discussion

Given the significance of spatial inequality in various global cities, this study evaluates the relationship between ecological spatial inequality and the parameters of urban heat islands, population, and green spaces in different areas of Tabriz. The findings align with previous studies, including those by Seyed Mosaffayi et al. (2024), Qiu et al. (2022), and Kuekcuoglu (2023).

Conclusion

The purpose of this research is to evaluate the relationship between the ecological spatial inequality with the parameters of thermal islands, population and green space of Tabriz metropolis. The relationship between the parameters and spatial ecological inequality was determined that population and green space parameter with R^2, 0.2 and 0.04 have the most impact on areas 5 and 9 of Tabriz metropolis, urban thermal islands parameter also have the most impact on Tabriz region 6 with R^2 0.01 Lays.

References

1. World Bank. (2022). World Bank database. https://data.worldbank.org.cn/. Accessed 13 May 2020.
2. Yang, C. Xia, R., Li, Q., Liu, H., Shi, T., & Wu, G. (2021). Comparing hillside urbanizations of Beijing-Tianjin-Hebei, Yangtze River Delta and Guangdong–Hong Kong–Macau greater Bay area urban agglomerations in China. International Journal of Applied Earth Observation and Geoinformation, 102, 102460.
3. Geng, Y., Fujita T., Bleischwitz R., Chiu A., & Sarkis J. (2019). Accelerating the Transition to Equitable, Sustainable, and Livable Cities: Toward Post-Fossil Carbon Societies. Journal of Cleaner Production, 118020.
4. Padda, I. U. H., & Hameed A. (2018). Estimating multidimensional poverty levels in rural Pakistan: A contribution to sustainable development policies. Journal of Cleaner Production, 197, 435–442.
5. Johnson, EAJ. (1970). The organization of space in developing countries. Cambridge: Harvard University Press.
6. Yasouri, M. (2015). Environmental justice: A way to achieve national sustainable development. Tehran: Center for Islamic Model Development.
7. Still well, J. et al. (2010). Spatial and Social Disparities. In: J. Stillwell et al. (eds.), Spatial and Social Disparities: Understanding Population Trends and Processes.
8. Minot, N., & Baulch B. (2006). Poverty Mapping with aggregate census data: what is the loss in precision? In: Kochendörfer-Lucius G., & Pleskovic B. (eds.), Spatial Disparities and Development Policy. The World Bank.
9. Kuekcuoglu, M. (2023). Analysis of energy justice in natural gas distribution with Multiscale Geographically Weighted Regression (MGWR). Energy Reports, 9, 325-337.
10. Qio, N., Cheng J., & Zhang T. (2022). Spatial disparity and structural inequality in disability patterns across Tianjin Municipality: A multiple deprivation perspective. Habitat International, 130, 102685.
11. Seyed Mosaffayi M.A., Asghari Zamani A., & Teymuri I. (2024). Evaluation of the impact of climate ecology and environmental parameters on urban livability (study area: 10 districts of Tabriz metropolis). Journal of Economic Geography Research, 1403, 1-16.

Advanced Engineering Days

aed.mersin.edu.tr

Evaluation of the Impact of Air Pollution Parameters on Land Surface Temperature of the Metropolis of Tabriz

Saeed Ahmadian [1], Mir Ali Seyed Mosaffayi [*1]

[1]University of Tabriz, Department of Urban and Regional Planning, Iran, saeedahmadian911@gmail.com, alimossafa1998@gmail.com

Cite this study: Ahmadian, S., et al, (2024). Evaluation of the Impact of Air Pollution Parameters on Land Surface Temperature of the Metropolis of Tabriz. Advanced Engineering Days, 9, 309-311

Keywords
Air Pollution
Land Surface Temperature
GWR
Metro Police of Tabriz

Abstract

Many cities around the world suffer from environmental problems, loss of green spaces, increased traffic volume, and excessive energy consumption. Among these, one of the major environmental challenges facing metropolitan areas is the phenomenon of air pollution. The main objective of this research is to evaluate the impact of air pollution parameters on the land surface temperature of the metro police of Tabriz. The effect of air pollution parameters (nitrogen dioxide, sulfur dioxide, and carbon dioxide) and land surface temperature was investigated using the Geographical Weighted Regression (GWR) model. After analysis, it was found that the nitrogen dioxide parameter with an R^2 value of 0.14 had the most impact on regions 5 and 9, the carbon dioxide parameter with an R^2 value of 0.16 had the most impact on region 6, and the sulfur dioxide parameter with an R^2 value of 0.01 had the most impact on regions 6 and 7 of the Metro Police of Tabriz.

Introduction

Nowadays, in many cities, the increase in urban population has led to environmental issues, loss of green spaces, increased traffic volume, excessive energy consumption, and ultimately a decrease in quality of life (Shakarami & Rahnama, 2023). Among these, one of the major environmental challenges facing metropolitan areas is the phenomenon of air pollution. Many cities around the world are facing the challenge of severe particulate pollution from industrial pollutants, and this issue has affected all aspects of urban life (Zhao et al., 2022). The growing trend of air pollution and its harmful effects on human health have been one of the major environmental challenges in recent decades (Xie et al., 2018). According to the latest statistics from the World Health Organization, more than 8 million people worldwide die annually due to exposure to outdoor air pollutants (WHO, 2023). In fact, urban planning in the past has ignored air pollution and technology, while many cities around the world suffer from air pollution (Barwise & Kumar, 2020).

Material and Method

The main objective of this research is to assess the impact of air pollution parameters on the land surface temperature of the metropolitan city of Tabriz. The investigation of the impact of air pollution parameters nitrogen dioxide (No2), sulfur dioxide (So2), and carbon dioxide (Co) and land surface temperature (LST) has been conducted using the Geographical Weighted Regression (GWR) model. The analysis outputs and related maps have also been analyzed in the ArcGIS Pro software.

Study Area

The metro police of Tabriz are the largest metropolis in Iran, located in the northwest region and the center of East Azerbaijan province. The average elevation of this city from sea level is determined to be 1460 meters. According to the latest divisions, the metropolitan city of Tabriz is divided into 10 districts, which have been selected as the study area in this research (Figure 1).

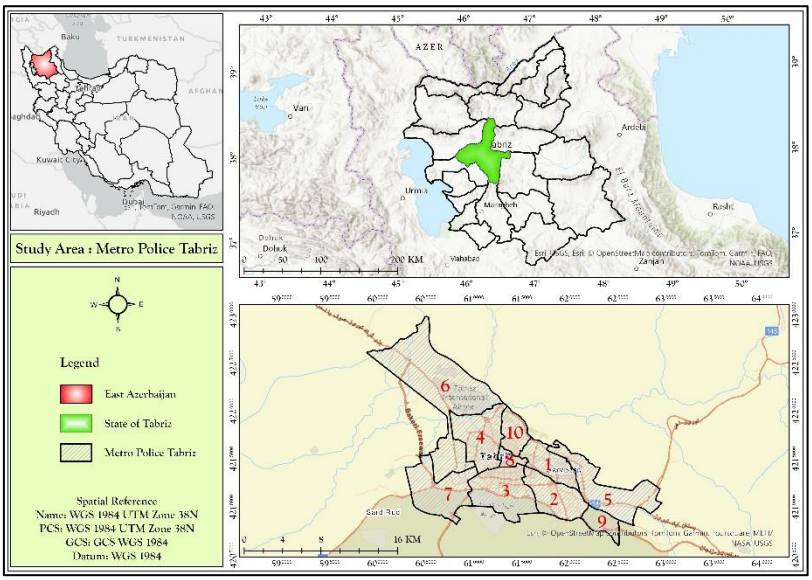


Figure 1. The study area

Results

In this research, first the parameters of nitrogen dioxide gas (No2), sulfur dioxide gas (So2), and carbon dioxide gas (Co), were extracted from the air quality monitoring station data across the metropolitan city of Tabriz, and the land surface temperature was extracted from Terra Climate satellite images (Figure 2).

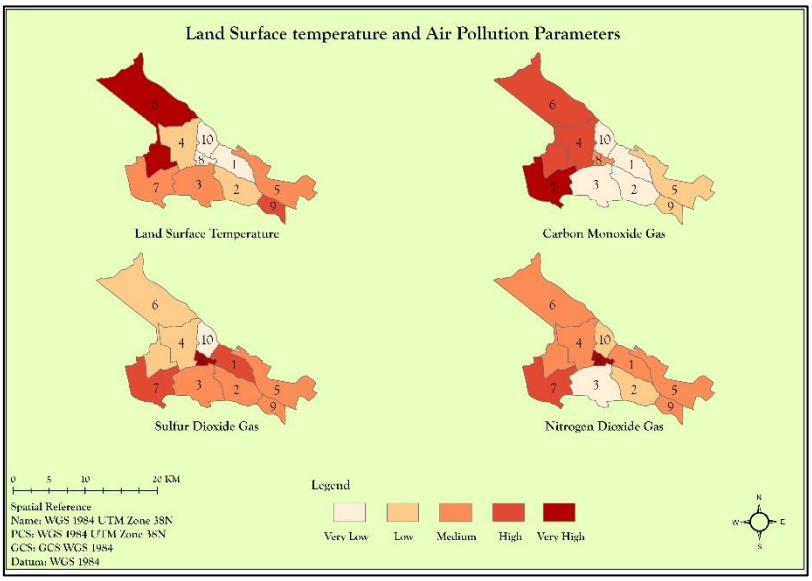


Figure 2. Land Surface Temperature and Air Pollution Parameters

Then, the relationship between the land surface temperature index as an independent variable and the parameters of nitrogen dioxide (No2), sulfur dioxide (So2), and carbon dioxide (Co) as dependent variables was analyzed using the Geographical Weighted Regression (GWR) model. The R^2 values for each of these parameters are shown in (Table 1), and the impact of the parameters on land surface temperature is presented in (Figure 3).

Table 1. R^2 Value of Nitrogen dioxide, Sulfur dioxide, Carbon monoxide

Items	Parameters	R^2
a	Nitrogen dioxide	0.14
b	Sulfur dioxide	0.16
c	Carbon monoxide	0.01

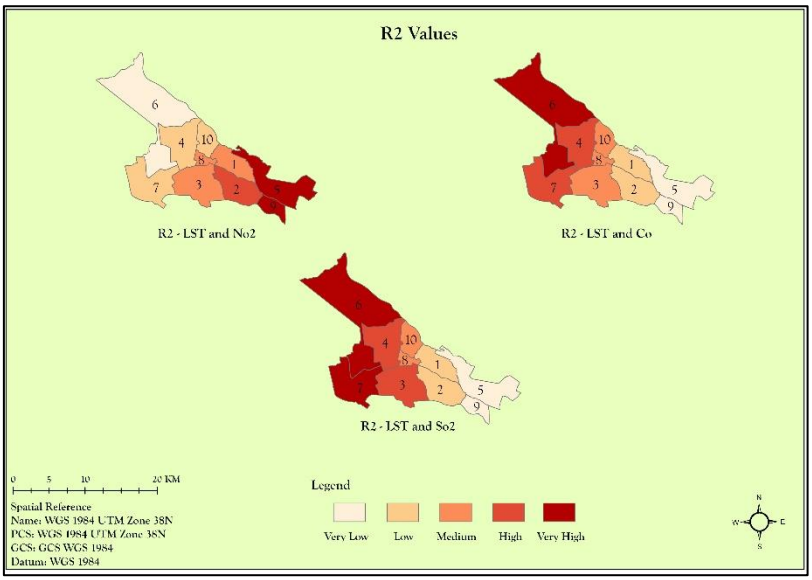


Figure 3. R^2 Values of Nitrogen dioxide, Sulfur dioxide, Carbon monoxide

According to the above figure, the nitrogen dioxide parameter with an R^2 value of 0.14 had the most impact on regions 5 and 9, the carbon dioxide parameter with an R^2 value of 0.16 had the most impact on region 6, and the sulfur dioxide parameter with an R^2 value of 0.01 had the most impact on regions 6 and 7 of the metro police of Tabriz.

Discussion

Considering the importance of air pollution in different cities around the world, the present study evaluated the impact of air pollution parameters on the land surface temperature of the metro police city of Tabriz. Accordingly, the results obtained from this research are consistent with and in line with the findings of other studies, including (Suthar et al., 2024) and (Fan et al., 2018).

Conclusion

The aim of this research was to evaluate the impact of air pollution parameters on the land surface temperature of the metro police of Tabriz. After analyzing the relationships, it was found that the nitrogen dioxide parameter with an R^2 value of 0.14 had the most impact on regions 5 and 9, the carbon dioxide parameter with an R^2 value of 0.16 had the most impact on region 6, and the sulfur dioxide parameter with an R^2 value of 0.01 had the most impact on regions 6 and 7 of the metro police of Tabriz.

References

1. Shakarami, K. & Rahnama, M. R. (2023). Spatial analysis of the impacts of the urban form on the energy consumption of Karaj over the Covid-19 era (2019-2022). Energy and Buildings, 113568.
2. Zhao, X., Zhou, W., Wu, T., & Han, L. (2022). The impacts of urban structure on PM2. 5 pollutions depend on city size and location. Environmental Pollution, 292, 118302.
3. Xie, X., Weng, Y., & Cai, W. (2018). Cobenefits of CO2 mitigation for NOX emission reduction: A research based on the DICE model. Sustainability, 1.1109.
4. Barwise, Y. & Kumar, P. (2020). Designing vegetation barriers for urban air pollution abatement: A practical review for appropriate plant species selection. Npj Climate and Atmospheric Science, 3(1), 12.
5. Fan, J., Wu, L., &, Zhang, F., Cai, H., Wang, X., Lu, X., Xiang, Y. (2018). Evaluating the effect of air pollution on global and diffuse solar radiation prediction using support vector machine modeling based on sunshine duration and air temperature. Renewable and Sustainable Energy Reviews, V (94), pp 732-747.
6. Suthar, G., Kaul, N., &, Khandelwal, S., Singh, S. (2024). Spatiotemporal variation of air pollutants and their relationship with land surface temperature in Bengaluru, India. Remote Sensing Applications: Society and Environment, V (53), 2024, 101830.
7. WHO, (2023). Accessed March 16, 2023.

Advanced Engineering Days

aed.mersin.edu.tr

Assessing of spatio-temporal changes of Normalized Impervious Surface index (case study: metropolis of Tabriz)

Mahdiyeh Shokati Sefidan[1], Ahmad Nikdel Monavvar[1], Sajjad Moshiri[1], Khalil Valizadeh Kamran[*1], Iraj Teymouri[2], Fereydoun Babaei Aghdam[2]

[1]Department of Remote Sensing and GIS, University of Tabriz, Iran, M.shokati16@yahoo.com , ahmadnikdel21@gmail.com, Sajjadmoshiri@gmail.com , valizadeh@tabrizu.ac.ir
[2]Department of Urban and Regional Planning, University of Tabriz, Iran, iraj-teymuri@tabrizu.ac.ir , fbabaei@tabrizu.ac.ir

Cite this study: Shokati, S.M., Monavvar, A. N., Moshiri, S., Kamran, K. V., Teymouri, I., & Aghdam, F. B. (2024). *Assessing of spatio-temporal changes of Normalized Impervious Surface Index) case study: metropolis of Tabriz).* Advanced Engineering Days, 9, 312-316

Keywords
Normalized Impervious Surface Index
Spatio-temporal changes
Physical development
Remote sensing
Metropolis of Tabriz

Abstract

Impervious urban surfaces are defined as any man-made material that water cannot penetrate. It is useful in applications such as optimal using of land, in studies related to land use changes and classification of satellite images, estimation of residential population, evaluation of the urban environment, especially in relation to water quality, urban runoff investigation, investigation of heat islands and its relationship with land cover. In this research, Landsat-8 images were prepared for the period of 2013 and 2023, then the impervious surface index was calculated for metropolis of Tabriz.
According to the results in 2013, 22894 hectares of Tabriz are among pervious surfaces and 7370 hectares of its area are among impervious surfaces. These values for 2023 are respectively 22298 hectares as pervious surfaces and 7966 hectares as impervious surfaces. In other words, the changes caused by the physical development of metropolis of Tabriz in 10-years period are around two percent.

Introduction

The increasing speed of urbanization has more than 50% of the world's population to live in urban areas (1,2). This has led to the physical development of the city in all countries of the world, including developing countries (3). The significance of such increasing urbanization has been creating problems such as health weakening (4), social pressure (5) and Environmental destruction (6). IN other hand, the physical development of cities leads to land use changes (7) and impervious surfaces in cities (8).

Impervious urban surfaces are defined as any man-made material that water cannot penetrate (9). impervious surfaces as an important factor in many studies related to the city and the environment, including in applications such as optimal using of land, in studies related to land use changes and classification of satellite images (10), residential population estimation (11), evaluation of the urban environment, especially in relation to water quality (12), investigation of urban runoff, investigation of heat islands and its relationship with land cover (13) is useful.

In addition, remote sensing technology takes a wide range of applications in urban planning and management due to different spatial, temporal and spectral features with active and passive sensors. also, due to the option of multi-temporal or time series changes for different years, the importance of this technology becomes more interesting. GEE is a web-based system that, by providing a strong database of satellite images and simple commands, has provided the possibility of all kinds of remote sensing processes without downloading every image (14). This system allows users to perform their calculations on a large amount of data (from 10 meters spatial resolution to several kilometers) without to need for high-powered systems. Thus, the goal of the present research is to evaluate the Spatio-Temporal changes of the urban Normalized Impervious Surfaces Index (NISI) in the metropolis of Tabriz by using satellite images in the environment of GEE and ArcGIS.

Material and Method

The data used in this research includes images that extracted from the Landsat-8 satellite for 2013 and 2023 of metropolis of Tabriz, which were processed in the GEE. After preparing the images, the urban Impervious Surfaces Index has been calculated by (equation.1) for metropolis of Tabriz. Then, after calculation of the index, the number of changes for 2013 and 2023 was extracted in the Excel and ArcGIS environments.

Equation1.

$$NISI=\frac{(B_{blue}+B_{green}+B_{red})-B_{NIR}}{(B_{blue}+B_{green}+B_{red})+B_{NIR}}$$

where the B_{blue}, B_{green}, B_{red}, and B_{NIR} values of the Landsat-8 data were set as 492.4 nm (band 2), 559.8 nm (band 3), 664.6 nm (band 4), and 832.8 nm (band 5), respectively. The NISI distinguishes impervious surface from non-impervious surface pixels according to the difference in the pixel gray scale after spectral band calculation (15).

Study Area

metropolis of Tabriz, the capital of East Azarbaijan province, is located at 38 degrees 88 minutes north latitude and 46 degrees 15 minutes east longitude. Tabriz is limited by the Sahand mountain from the south and Aun Ibn Ali mountain from the northwest. This city is one of the 10 metropolises of Iran and the largest metropolis in the northwest. Its population in 2015 is estimated to be 1,558,693.

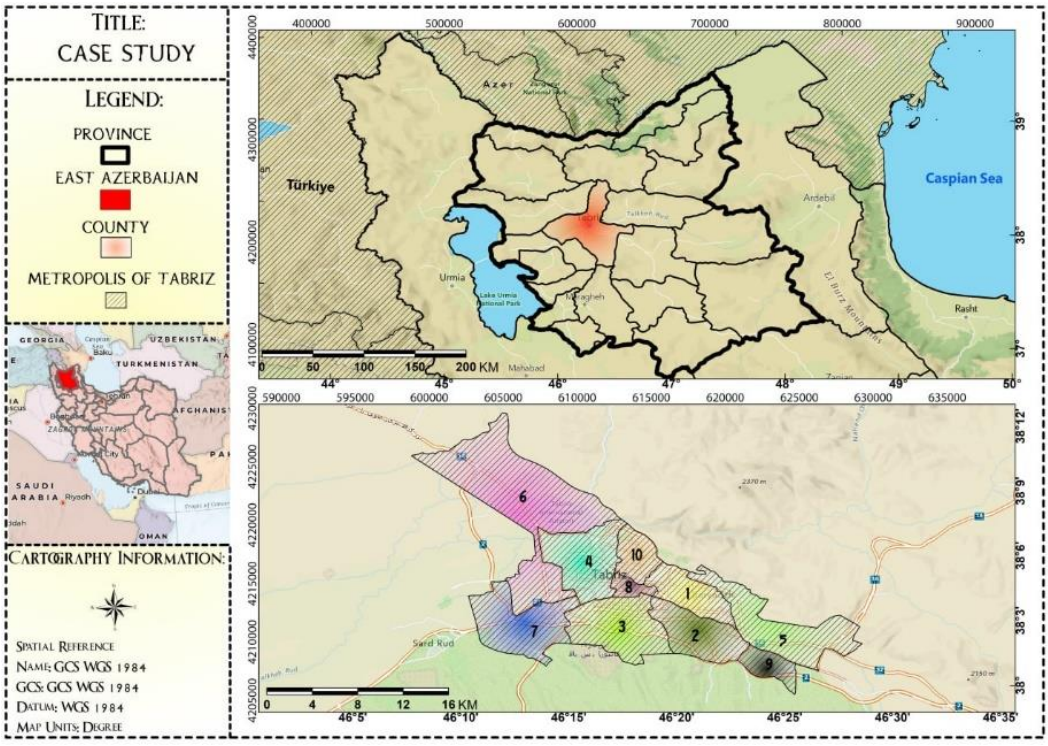


Figure 1. Case of Study

Results

In the present research, the urban Impervious surface Index was calculated for the metropolis of Tabriz. For this purpose, in order to evaluate the spatio-temporal changes of the mentioned index, Landsat-8 images for 2013 and 2023 were prepared in the GEE environment and the index was calculated in the ArcGIS environment. In the first step, the average results of index for the district of metropolis of Tabriz were prepared, then the index values were classified by determining the optimum threshold based on the histogram of the final image into two groups of urban areas (Impervious surfaces) and non-urban areas (pervious surfaces). So value above 0.35 shows urban areas and a value lower than that was considered as non-urban areas.

According to results, the average of index for the district of Tabriz metropolis (Fig.2) is as follow:

district 8 with a value of 0.33, district 10 with a value of 0.32, district 3 with a value of 0.31 and district 9 with a value of 0.30 respectively have the highest average value of the index for 2013. For 2023, districts 8 with a value of 0.33, district 3 with a value of 0.31, district 10 with a value of 0.31 and district 9 with a value of 0.30 obtained the highest average values . The spatial changes of the developed areas can be seen in (figure.2).

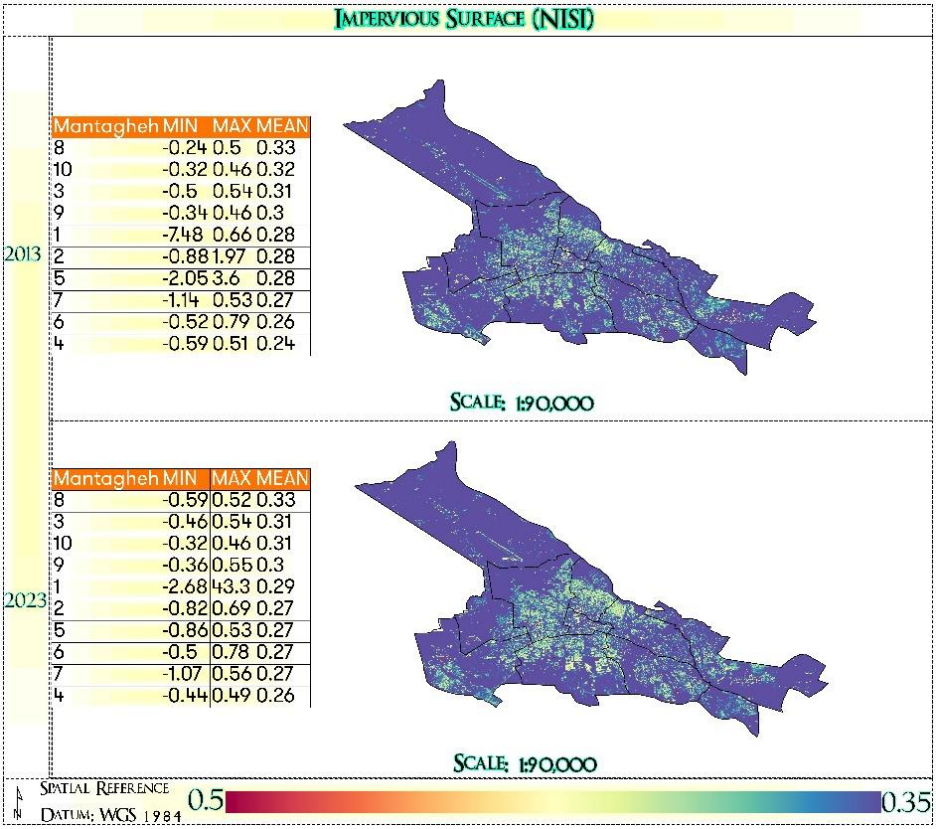


Figure 2. Average value of index in districts

The results of the index were prepared for 2013 and 2023 in terms of percentage and area of changes. According to the results of thresholding the index (table.1), it shows the presence of noticeable changes for the period of 2013 and 2023 in metropolis of Tabriz. So, in 2013, 22894 hectares of Tabriz are among pervious surfaces and 7370 hectares of its area are among impervious surfaces. These values for 2023 are respectively 22298 hectares as pervious surfaces and 7966 hectares as impervious surfaces. In other words, the changes caused by the physical development of Tabriz in a period of 10 years is about two percent. According to the (figure.3), the most changes caused by urban physical development have happened in the central, northern and eastern parts of Tabriz.

Table 1. Quantitative values of index

CLASS		Area (Hectare)	Area (%)	TIME
1	nun-urban	22894	75.64	2013
2	urban	7370	24.35	
1	nun-urban	22298	73.67	2023
2	urban	7966	26.32	

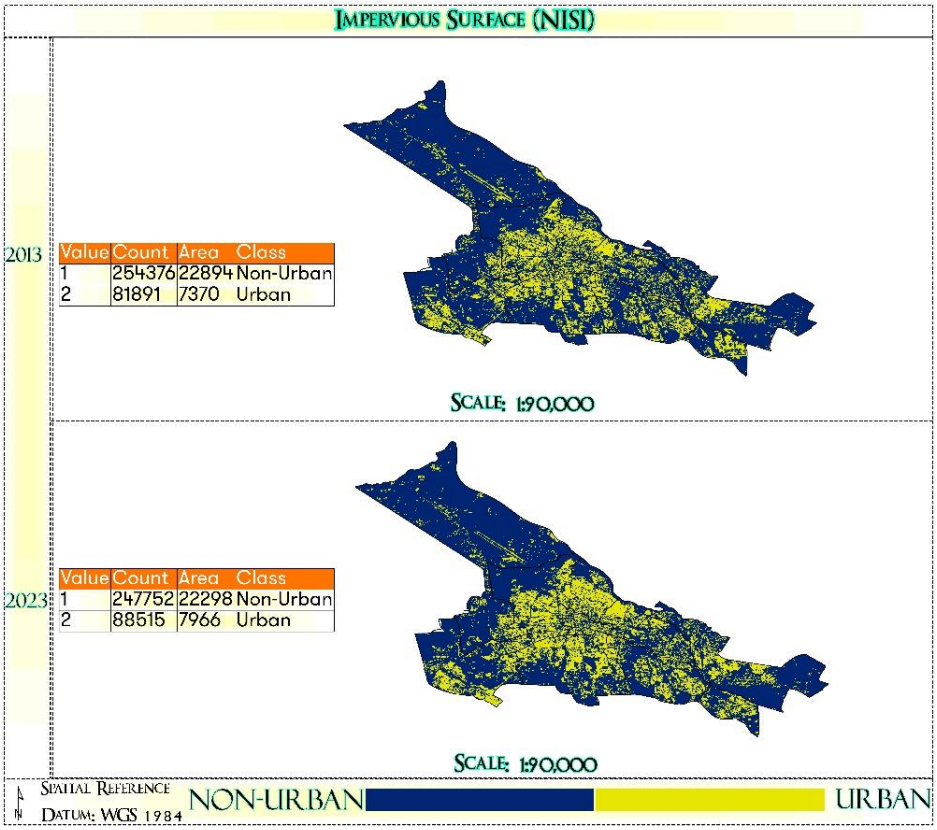


Figure 3. Spatial distribution of index in the study area

Conclusion

Impervious urban surfaces are defined as any man-made material that water cannot penetrate in it. Impervious surfaces are an important factor in many studies related to the city and the environment, including in applications such as optimum land use, in studies related to land use changes and satellite images classification, etc. In the present research, the Impervious index in metropolis of Tabriz was calculated. According to the results, district 8 with a value of 0.33, district 10 with a value of 0.32, district 3 with a value of 0.31 and district 9 with a value of 0.30 respectively have the highest average value of the index for 2013. For 2023, districts 8 with a value of 0.33, district 3 with a value of 0.31, district 10 with a value of 0.31 and district 9 with a value of 0.30 obtained the highest average values. Also, the results of thresholding the index in 2013, 22894 hectares of Tabriz are among pervious surfaces and 7370 hectares of its area are among impervious surfaces. These values for 2023 are respectively 22298 hectares as pervious surfaces and 7966 hectares as impervious surfaces. The results show the physical development of Tabriz is in the central, northern and eastern of city. In other words, this index can be used as an effective index in modeling the physical development of cities. One of the limitations of the present research is the lack of availability of images with a high spatial resolution, which has a significant impact on the results, so the Landsat images used in this research, due to the spatial resolution of 30 meters, do not have a very favorable ability in Impervious Surface Index calculation in urban studies.

References

1. Seto, K.C.; Güneralp, B.; Hutyra, L.R.(2012) Global forecasts of urban expansion to 2030 and direct impacts on biodiversity and carbon pools. Proc. Natl. Acad. Sci. USA, 109, 16083–16088.
2. Wu, J. (2014) Urban ecology and sustainability: The state-of-the-science and future directions. Landsc. Urban Plan., 125, 209–221.
3. Silveira, J. J., Espíndola, A. L., & Penna, T. J. P. (2006) Agent-based model to rural urban migration analysis. Physica A: Statistical Mechanics and its Applications, 364, 445-456.

4. Liu, Y, M. Dijst, J. Faber, S. Geertman, and C. Cui. (2017) Healthy Urban Living: Residential Environment and Health of Older Adults in Shanghai. Health & Place 47:80–89.
5. Graafland, J, and H. Smid. (2017) Reconsidering the Relevance of Social License Pressure and Government Regulation for Environmental Performance of European Smes. Journal of Cleaner Production, 141: 967–977.
6. Adams, S., and E.K.M. Klobodu. (2017) Urbanization, Democracy, Bureaucratic Quality, and Environmental Degradation. Journal of Policy Modeling 39: 1035–1051.
7. Amoateng, P., Cobbinah, P.B., Adade, K.O. (2013) Managing physical development in peri-urban areas of Kumasi, Ghana: A case of Abuakwa. Journal of Urban and Environmental Engineering. 7, 1, 96-109.
8. 38. Poelmans, L. Van Rompaey, A., (2009) Detecting And Modelling Spatial Patterns Of Urban Sprawl In Highly Fragmented Areas: A Case Study In The Flanders– Brussels Region. Landscape And Urban Planning, 93, 10-19.
9. 19. Lu, D., Moran, E., Hetrick, S. (2011) Detection of impervious surface change with multitemporal Landsat images in an urban–rural frontier, ISPRS Journal of Photogrammetry and Remote Sensing, 66, 298–306.
10. 25. Wu, C. (2004) Normalized spectral mixture analysis for monitoring urban composition usingETM+ imagery,Remote Sensing of Environment, 93, 480–492.
11. 17. Lu, D., &Weng, Q. Li, G. (2006) Residential population estimation using remote sensing derived impervious surface approach,International Journal of Remote Sensing, 27(16), 3553-3570.
12. 14. Hurd, J,.Civco, D.L. (2004) Temporal characterization of impervious surfaces for the State of Connecticut, ASPRS Annual Conference Proceedings, Denver, Colorado.
13. 10. Arnold, C. L., Gibbons, C. J. (1996) Impervious surface coverage: The emergence of a key environmental indicator. Journal of the American Planning Association, 62, 243–258.
14. Gorelick, N., Hancher, M., Dixon, M., Ilyushchenko, S., Thau, D., & Moore, R. (2017) Google Earth Engine: Planetary-scale geospatial analysis for everyone. Remote Sensing of Environment.
15. Su, S.; Tian, J.; Dong, X.; Tian, Q.; Wang, N.; Xi, Y. (2022) An Impervious Surface Spectral Index on Multispectral Imagery Using Visible and Near-Infrared Bands. Remote Sensing, 14, 3391.

Advanced Engineering Days

aed.mersin.edu.tr

Evaluating Land Surface Temperature Variations around Fault Lines and Their Correlation with Groundwater Levels Using Remote Sensing

Fatemeh Sedghi[1], Khalil Valizadeh Kamran[*1]

[1] *University of Tabriz, Department of Remote Sensing & GIS, Iran, fatemeh.sedghi@tabrizu.ac.ir, valizadeh@tabrizu.ac.ir*

Cite this study: Sedghi, F., & Valizadeh Kamran, K. H. (2024). Evaluating Land Surface Temperature Variations around Fault Lines and Their Correlation with Groundwater Levels Using Remote Sensing. Advanced Engineering Days, 9, 317-319

Keywords

Fault Lines
Groundwater Level
Land Surface Temperature
Landsat-8

Abstract

Remote sensing observations of land surface temperature (LST) and its relationship with various surface phenomena have recently attracted significant research interest. LST is influenced by various factors, one of which is its strong correlation with groundwater levels. In areas near fault lines, the rise of groundwater along these faults leads to a decrease in LST. In this study, LST data was utilized to identify fault lines. Variations in LST were analyzed using Landsat-8 imagery for the Tabriz city region. The results indicated that LST variations differ across various land cover types, and a sharp decrease in LST was recorded along the fault lines. Additionally, the LST decrease along the fault lines various depending on different land use and cover types.

Introduction

Remote sensing is efficient tool for environmental monitoring, capable of observing temporal and spatial changes in various surface parameters across large regional scales and different time intervals. Land surface temperature (LST) as a key remote sensing parameter, varies due to multiple factors and has diverse applications in studying geothermal energy [1], assessing surface energy balance [2], monitoring soil moisture [3], earthquake prediction [4], and etc.

LST has a high correlation with groundwater levels, with areas of higher groundwater levels exhibiting lower surface temperatures [5]. Groundwater flows to higher levels through fractures and fault lines [6], causing the water table to rise in fractured areas, which leads to a decrease in LST in these regions.

In this study, LST variations were analyzed using Landsat-8 observations to identify fractures and fault lines within the study area. The LST changes across different land use/cover types and areas surrounding fault lines were evaluated.

Material and Method

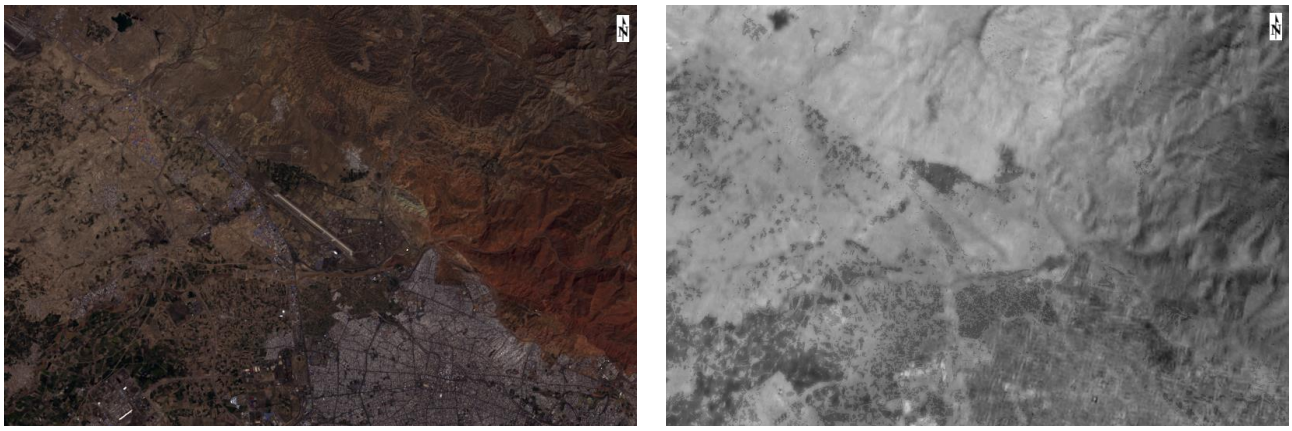
In this study, the variations in land surface temperature (LST) around fault lines in the city of Tabriz were evaluated. For this purpose, LST data were calculated using Landsat-8 imagery for the study area. To assess the relationship between LST variations and fault lines, a shapefile map of the existing fault lines in the area was prepared.

LST data were calculated using the Landsat-8 imagery over the study area, employing the Split Window Algorithm in MATLAB. To analyze LST variations across different land covers, the LST changes were compared

with a land use/cover map. For assessing LST variations in areas around fault lines, the fault line map was overlaid on the satellite image in Arc GIS, and LST profiles perpendicular to the fault line direction were analyzed.

Results

Land surface temperature (LST) data for the study area were calculated using Landsat-8 imagery (Figure 1). The obtained LST data accurately depicted variations in land surface temperature across different land use/covers. Areas with vegetation and water bodies exhibited lower surface temperatures, while urban and bare soil areas exhibited higher surface temperatures.



(a) **(b)**

Figure 1: Landsat-8 RGB image (a) and Land Surface Temperature data (b) of study area

Additionally, evaluation of LST profiles along fault lines revealed a sudden decrease in land surface temperature, indicating higher groundwater levels in these areas. Figure 2 illustrates the profile of LST variations around fault lines. The obtained profile illustrates the variations in land surface temperature across different land covers. At the point where the fault line intersects the profile, there is a sudden decrease in LST. The profile plotted after crossing the fault line, includes LST changes in agricultural area, where due to vegetation has lower surface temperatures. This decrease in land surface temperature occurs along all fault lines. In areas with different land cover types, other factors such as soil moisture, vegetation and various land cover, influence the land surface temperature.

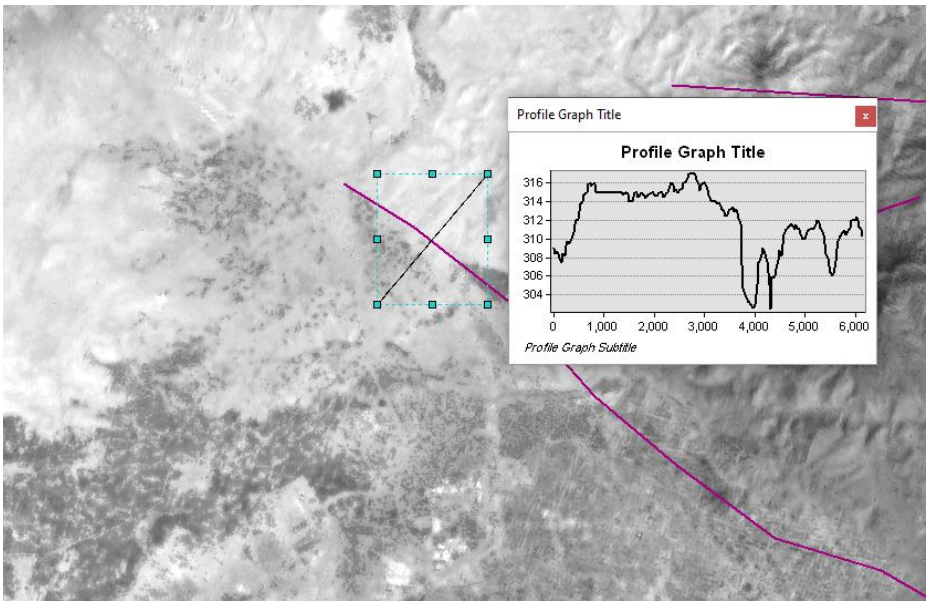


Figure 2: Land Surface Temprature profile across fault line and different land cover.

Discussion

In this study, variations in land surface temperature (LST) across different land covers were evaluated using remote sensing data. The results indicated that LST is influenced by various factors and different land use/land cover types.

The assessment of LST variations around fault lines, revealed a significant decrease in land surface temperature along the fault lines. This incident is due to the rise of groundwater levels along fault lines and fractures.

Therefore, by assessing changes in land surface temperature, various surface phenomena including fractures and faults, can be identified and monitored.

Conclusion

Overall, the findings of this study highlight the utility of remote sensing, particularly LST data from Landsat-8 imagery, in studying surface phenomena. The ability to detect changes in land surface temperature provides valuable insights into the dynamics of the Earth's surface and can aid in the identification and monitoring of geological features such as faults and fractures.

References

1. Gemitzi, A., Dalampakis, P., & Falalakis, G. (2021). Detecting geothermal anomalies using Landsat 8 thermal infrared remotely sensed data. *International Journal of Applied Earth Observation and Geoinformation*, *96*, 102283.
2. Chen, X., Su, Z., Ma, Y., Trigo, I., & Gentine, P. (2021). Remote sensing of global daily evapotranspiration based on a surface energy balance method and reanalysis data. *Journal of Geophysical Research: Atmospheres*, *126*(16), e2020JD032873.
3. Le, M. S., & Liou, Y. A. (2021). Temperature-soil moisture dryness index for remote sensing of surface soil moisture assessment. *IEEE Geoscience and Remote Sensing Letters*, *19*, 1-5.
4. Zhao, X., Pan, S., Sun, Z., Guo, H., Zhang, L., & Feng, K. (2021). Advances of satellite remote sensing technology in earthquake prediction. *Natural Hazards Review*, *22*(1), 03120001.
5. Malik, M. S., Shukla, J. P., & Mishra, S. (2021). Effect of groundwater level on soil moisture, soil temperature and surface temperature. *Journal of the Indian Society of Remote Sensing*, *49*, 2143-2161.
6. Haneberg, W. C. (1995). Steady state groundwater flow across idealized faults. *Water Resources Research*, *31*(7), 1815-1820.

Advanced Engineering Days

aed.mersin.edu.tr

Exploring Spectral Reflectance and Classification of Wheat, Barley and Alfalfa Crops Using Hyperspectral Imaging

Fatemeh Sedghi[1], Sadra Karimzadeh[* 1]

[1] *University of Tabriz, Department of Remote Sensing & GIS, Iran, fatemeh.sedghi@tabrizu.ac.irsa, karimzadeh@tabrizu.ac.ir*

Cite this study: Sedghi, F., & Karimzadeh, S. (2024). Exploring Spectral Reflectance and Classification of Wheat, Barley and Alfalfa Crops Using Hyperspectral Imaging and Remote Sensing Imagery. Advanced Engineering Days, 9, 320-322

Keywords

Hyper Spectral Imaging
Precision agriculture
Wheat
Barley
Alfalfa

Abstract

Recent developments in hyperspectral remote sensing technologies enable acquisition of image with high spectral resolution, which is typical to the laboratory or in situ reflectance measurements. Identifying the spectral behavior of different materials and their differences is important for developing classification methods. In this study, the reflectance spectra of wheat, barley and alfalfa crops were evaluated using hyperspectral imaging. Various preprocessing techniques were applied to remove noise, minimize background effects, and examine the spectral sign of each crop, used for the crop classification. The results indicated that wheat and barley exhibited similar spectral behaviors during the initial growth stage, while alfalfa showed lower reflectance compared to wheat and barley in the 400 to 950 nm wavelength range. The SVM model was used to classify these plant species and effectively distinguished alfalfa from wheat and barley.

Introduction

Remote sensing is a useful tool for monitoring spatiotemporal variations of crop morphological and physiological status and supporting activities in precision agriculture. The current suite of high-resolution hyperspectral remote sensing systems enables precise discrimination and mapping of agricultural crops. In comparison with multispectral imaging, hyperspectral imaging is a more advanced technique that is capable of acquiring a detailed spectral response of target features [1].

Reflectance spectra measured in the field and laboratory have been successfully used to map various surface features, including mineral mapping [2-3], soil classification [4], and studying the unique spectral reflectance patterns of certain vegetation species [5].

The existence of a significant spectral relationship between field and image reflectance spectra can provide numerous applications such as rapid estimation of cultivated area, monitoring endangered or commercial tree species, describing biodiversity, and monitoring changes in species composition over time [6]. In a study using hyperspectral imaging, a specific spectral library for vegetation classification was established [5].

The aim of this study was to evaluate the spectral reflectance of wheat, barley, and alfalfa during the first growth season. Hyperspectral imaging was conducted on prepared samples of the three crops in a laboratory setting. Data processing and generation of spectral signatures for the samples were performed by Hyper-tools software.

Material and Method

To examine the spectral behavior of the three crops—wheat, barley, and alfalfa—using hyperspectral imaging, plant samples of all three crops were utilized during the first growth season. The spectral behavior of the crops was imaged in a laboratory setting using a hyperspectral spectrometer, capturing the spectral behavior of the samples in the 400 to 950 nm wavelength range across 581 spectral bands.

The data processing in this study was conducted using Hyper Tools software. Initially, the spectral behavior of each crop was examined, and the spectral signature of each sample was identified within the 400 to 950 nm wavelength range. In the data preprocessing step, for spectral preprocessing, noise reduction was achieved using the smoothing method with a window size of 7 and a polynomial degree of 2. In the Masking section, background masking was performed by selecting the appropriate wavelength range using the Wavelength Selection method.

The output of the preprocessing step was used as input for the model calibration in the Classification stage. After noise and background effects were removed, in the sample processing and crop classification step, methods such as Correlation/SAM, PCA, and K-means were evaluated. Additionally, sample classification was performed using the SVM model.

Results

The spectral reflectance of the three samples—wheat, barley, and alfalfa—was analyzed using Hyper Tools software. Figure 1 shows the spectral reflectance of the three samples, with the imaged samples from right to left being wheat, alfalfa, and barley, respectively. The evaluation results indicated that the wheat and barley samples exhibited similar spectral behavior, while the alfalfa sample recorded lower reflectance across all bands compared to the wheat and barley samples.

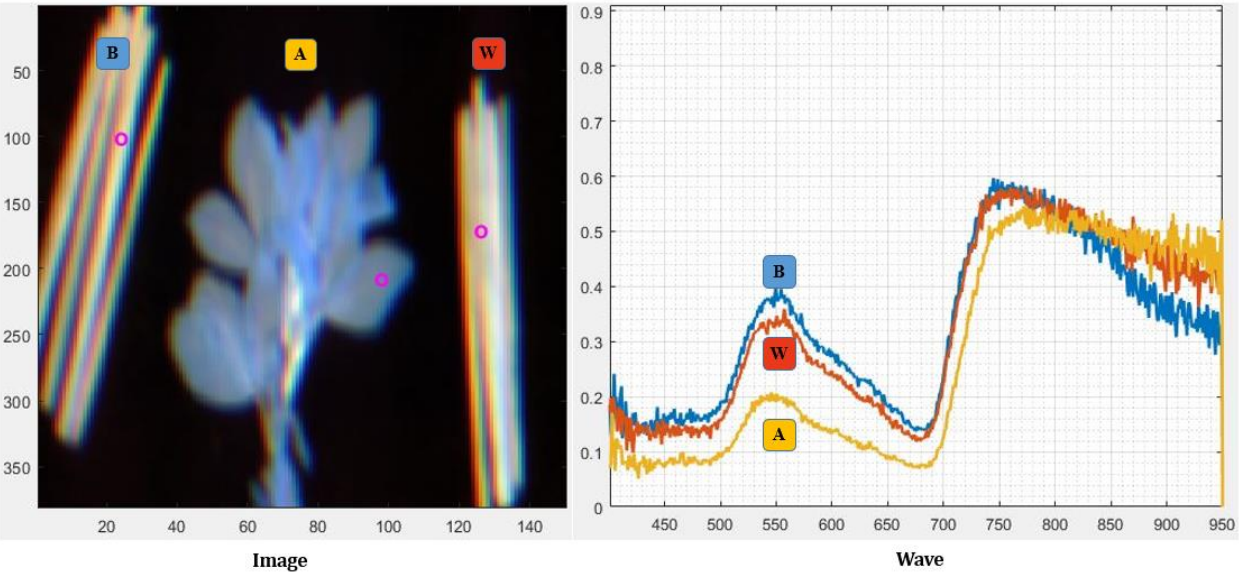


Figure 1: Spectral Reflectance of Alfalfa (A), Wheat (W) and Barley (B) crops.

In the processing step, the spectral reflectance of samples was examined using Correlation/SAM, PCA, and K-means clustering methods. The results from all three methods indicated that the spectral samples of wheat and barley showed a high correlation with each other, making it impractical to classify the image into three distinct classes. Consequently, in the image classification section using the SVM method, the classification was performed into two classes, considering wheat and barley as a single class. Figure 2 shows the results of the SVM

classification method for the two classes: alfalfa and barley-wheat. The results indicated that the spectral reflectance differences for alfalfa effectively distinguished this crop from the other two samples. The edges of the wheat and barley samples recorded different spectral reflectance due to unevenness of sample surfaces during reflectance measurement and were mistakenly classified into the alfalfa class. Additionally, the evaluations revealed that a part of the alfalfa stem exhibited spectral reflectance similar to the wheat and barley samples and was also classified into the wheat-barley plant species class.

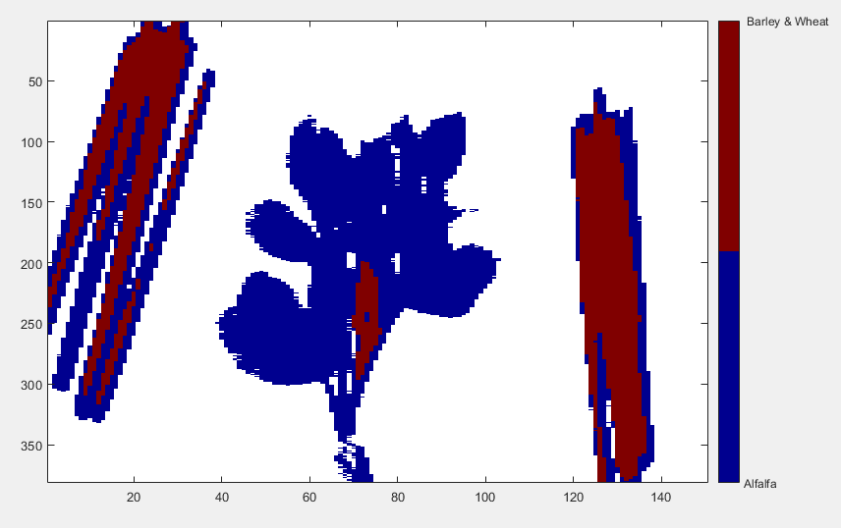


Figure 2: SVM classification result for Alfalfa and Barley/Wheat classes

Conclusion

In this study, the spectral behavior of three plant crops—wheat, barley, and alfalfa—was evaluated using hyperspectral imaging. The investigation of the spectral behavior of the crop samples revealed that wheat and barley exhibited similar spectral behaviors, whereas alfalfa was spectrally distinguishable from the other two species. Additionally, the results of the SVM classification method were able to accurately distinguish the alfalfa species from wheat and barley with high accuracy. The result indicated that hyperspectral imaging can be utilized to analyze the spectral behavior of plant crops, and the resulting data can be applied in the spatiotemporal monitoring of crops and precision agriculture.

References

1. Lu, B., Dao, P. D., Liu, J., He, Y., & Shang, J. (2020). Recent advances of hyperspectral imaging technology and applications in agriculture. *Remote Sensing*, *12*(16), 2659.
2. Kokaly, R. F., King, T. V., & Livo, K. E. (2008). *Airborne hyperspectral survey of Afghanistan 2007: flight line planning and HyMAP data collection* (pp. 1-14). Reston, VA, USA: US Geological Survey.
3. Swayze, G. A., Kokaly, R. F., Higgins, C. T., Clinkenbeard, J. P., Clark, R. N., Lowers, H. A., & Sutley, S. J. (2009). Mapping potentially asbestos-bearing rocks using imaging spectroscopy. *Geology*, *37*(8), 763-766.
4. Brown, D. J. (2007). Using a global VNIR soil-spectral library for local soil characterization and landscape modeling in a 2nd-order Uganda watershed. *Geoderma*, *140*(4), 444-453.
5. Zomer, R. J., Trabucco, A., & Ustin, S. L. (2009). Building spectral libraries for wetlands land cover classification and hyperspectral remote sensing. *Journal of environmental management*, *90*(7), 2170-2177.
6. Nidamanuri, R. R., & Zbell, B. (2011). Use of field reflectance data for crop mapping using airborne hyperspectral image. *ISPRS Journal of photogrammetry and remote sensing*, *66*(5), 683-691.

Advanced Engineering Days

aed.mersin.edu.tr

Monitoring surface water area changes of Najaf Sea in Iraq using RS and GIS for sustainable development

Abolfazl Ghanbari*[1], Huda Jamal Jumaah [2]

*[1]Tabriz University, Iran, a_ghanbari@tabrizu.ac.ir
[2]Northern Technical University, Technical Engineering College of Kirkuk, Environment and Pollution Engineering Department, Iraq, huda80@ntu.edu.iq

Cite this study: Ghanbari, A., & Jumaah, H. J. (2024). Monitoring surface water area changes of Najaf Sea in Iraq using RS and GIS for sustainable development. Advanced Engineering Days, 9, 323-325

Keywords
Surface area
RS
GIS
SVM
NDWI

Abstract

Najaf Sea is a significant water body found in Najaf City in Iraq and plays an essential role in triggering numerous ecological balances and human beings' living standards. The objectives of this study are to determine the changes that Najaf Sea was exposed to during a specific period of time from 2017 to 2024 by using Sentinel-2 satellite images and classifying them with classification methods based on Geographic Information Systems GIS and the use of Artificial Intelligence, where the Normalized Difference Water Index NDWI and Support Vector Machine SVM method was used for classifications based on Sentinel-2 images of the years 2017, 2020, 2022, and 2024. As for the results of the study, it revealed various changes over the years of the study, represented by a decrease in the surface area of sea water in the year 2017, where it was noted through the classification that the lowest area recorded was 213.11 km^2, followed by an increase in 2020, where the highest area was recorded at 302.16 km^2. In subsequent years, it was noted that the surface area of the water decreased from the previous area, but the lake maintained an area with a slight increase from 2022 to 2024.

Introduction

For the various management and sustainable developments aimed at water bodies, it is important to be able to identify changes in the Surface Area [1-2]. the Najaf Sea is one of the important water resources in the country and plays a very essential role in agriculture, the consumption of water and irrigation demands [3]. However, over the course of the decades the square kilometers of the Najaf Sea has has been altered through a variety of causes which are connected to climates and other natural occurrences as well as human activities and approaches to water resource management [4]. Hence there is an implication that Remote Sensing RS and GIS techniques can be used to analyze the temporal characteristics and changes of the water bodies on the earth surface [5]. These technologies provided many significant information, which have been useful in the mappings of change in spatial and temporal information on water resource that is relevant in water resource management and planning [1]. RS allows obtaining detailed imagery and information, which is at large and hard-to-access intervals to control water bodies, such as the Najaf Sea, at large intervals [3]. Using GIS tools are significant in spatial analysis where permits integrating, visualizing, and interpreting remotely sensed images [5]. RS and GIS applications in water scarcity and environmental stress areas are mostly used for surface water changes detection [2-4]. These technologies, are very significant in determining the amount of water bodies are available, and monitoring changes over time, and determine the changes causes[4]. Applying integration of RS and GIS to formulate long-term water management adaptations is beneficial in reducing the fluctuations effects of water and enhance the areas social and economic status [6].
In the recent past, the alterations of the Najaf sea on its surface area have elicited quite a lot of concern. The research designed with the intent of covering a broad understanding of the changes in the surface area of the Najaf Sea and the various causes associated with those changes and their effects using RS techniques and GIS in a time-frame (2017-2024).

Material and Method

Sentinel-2 images of four specific years were downloaded from the Sentinel hub. The images were in high resolution and low cloud cover less than 0.1%. The images represented the years (2017, 2020, 2022, and 2024).

Two classification methods (NDWI, and SVM) were applied for change detection on the surface water area of the sea. The data acquired for this study are shown in Table 1.

Table 1. Sentinel-2 images properties

Image Type	Aquestion Date	Cloud Cover	Resolution	Coordinate system
Sentinel-2 L2A	27/05/2024	0%	High	WGS 84
Sentinel-2 L2A	14/11/2022	0.1%	High	WGS 84
Sentinel-2 L2A	14/12/2020	0%	High	WGS 84
Sentinel-2 L2A	30/11/2017	0%	High	WGS 84

The used NDWI equation in this study can be written as [1-2]:

$$NDWI = (B03 - B08)/(B03 + B08) \quad (1)$$

where, B03 represents band three, and B08 represents band eight.

For a spectral response made up of an explanation of the class item (y_i) is represented by (x_i) the a vector for the r training cases, the SVM equation can be written as [1,7]:

$$f(x) = sign\left(\sum_i^r \propto_i y_i k(x, x_i) + b\right) \quad (2)$$

where $\propto_i$(i = 1, ..., r) represents Lagrange multipliers, $k(x, x_i)$ represents the kernel's item, and b represents the hyperplane space of starting point.

Results

NDWI maps of surface water area changes of Najaf Sea are shown in Figure 1. Besides, the SVM map of surface water area changes of Najaf Sea are shown in Figure 2.

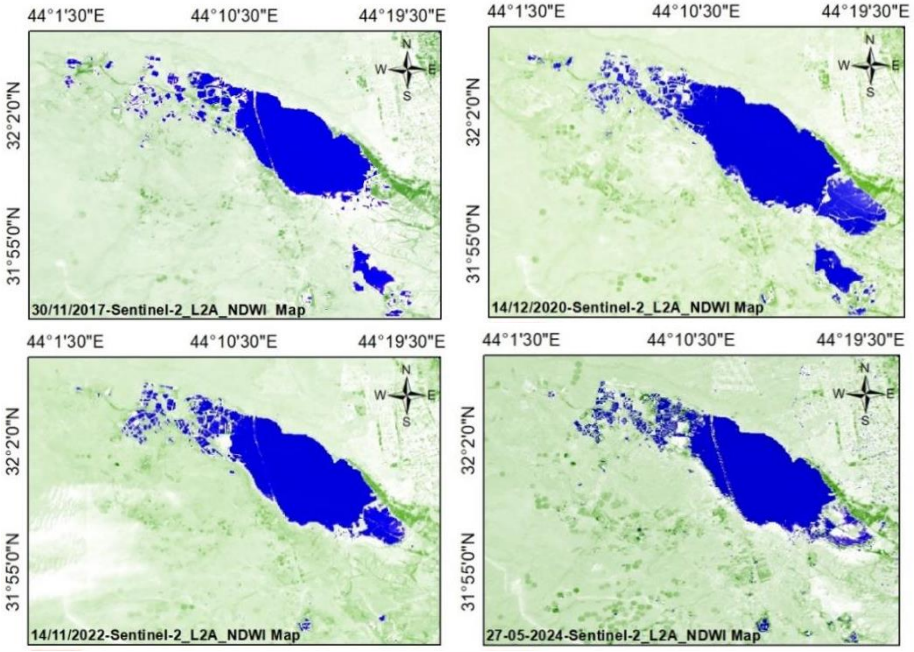


Figure 1. NDWI maps of surface water area changes of Najaf Sea.

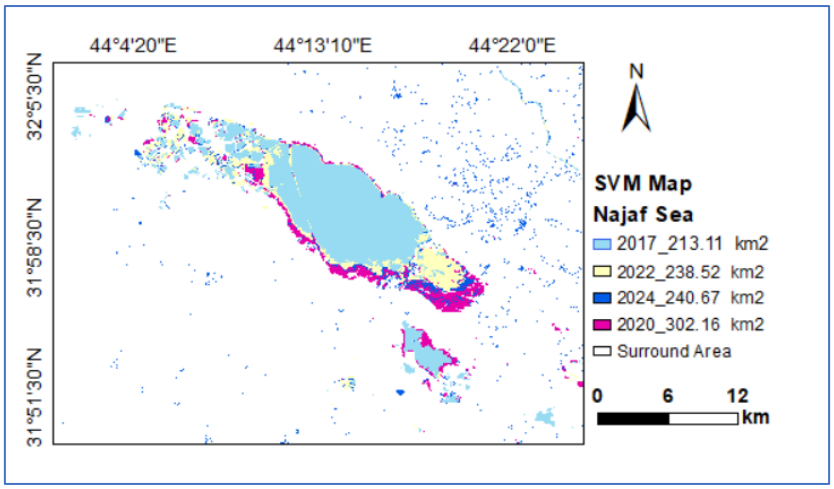


Figure 2. SVM map of surface water area changes of Najaf Sea.

Based on Figure 1 the NDWI maps of surface water area changes of Najaf Sea, it easily can see the variation in the surface area of the sea visually. The maximum changes occurred in the southern-east part of the sea. In 2017 the lowest area are shown on the map while the highest area is shown in 2020. In 2022, and 2024 the surface water area is shown to decrease from 2020. From 2022 to 2024 the sea kept its surface area with a slight increase. In Figure 2, SVM map of surface water area changes of Najaf Sea. The waterbody surface area has been calculated by SVM in each year and compared as shown in the map. During the period of the current study, the smallest surface area of the seawater was in 2017, which amounted to 213.11 km^2. The area increased to 302.16 km^2 in the year 2020, but this rate decreased in the year 2022 to reach 238.52 km^2. While, in 2024, which was represented by heavy rains during this year, the lake retained the previous area with a slight increase, as the surface area reached about 240.67 km^2.

Discussion

Based on the observation of surface water area changes detected by using RS and GIS, the attempt to measure the fluctuation of an area of the Najaf Sea successfully indicates that the sustainability of this precious water resource can be analyzed. Based on [8] Iraq faced a rainfall lack in 2017, while in 2018 rainfall has been increased until 2021, this shows the effect of rainfall on the sea water surface change during the study period. Besides rising temperatures and climate change which caused rainfall lack and increased evaporation, the construction of dams has reduced the water inflow into the sea, and agricultural demand significantly affected decreasing the seawater.

Addressing these problems involves applying an integrated and holistic approach through better management of water through management of the resource through agriculture, enhanced regulation, and cooperation throughout the region to achieve better water use. It is as important to comprehend the change in managing water resources in the region as it is to approach other environmental and development issues in Iraq.

Conclusion

This study examines the variations in the surface area of the Najaf Sea during the years 2017 to 2024 by using the selected Sentinel-2 images, NDWI, and GIS-based SVM. As for the results of the changes, it is possible to observe considerable fluctuations in the area of the sea, starting at around 213.11 km^2 in 2017 to the highest area in 2020 with 302.16 km^2, and consequent variations where the area in 2024 was 240.67 km^2.

The anterior part of this short-term fluctuation is attributed to environmental changes including drought and precipitation. This lowering trend needs the development of enhanced water resource management and the practices of sustainable water utilization. Therefore, it is essential to draw the attention of government and lawmakers to the dynamic changes taking place in the Najaf Sea, with the ultimate goal of taking measures to protect this water body as well as sustainable development of those ecosystems that are directly dependent on it.

References

1. Jumaah, H. J., Ameen, M. H., Mohamed, G. H., & Ajaj, Q. M. (2022). Monitoring and evaluation Al-Razzaza lake changes in Iraq using GIS and remote sensing technology. The Egyptian Journal of Remote Sensing and Space Science, 25(1), 313-321.
2. Jumaah, H. J., Ameen, M. H., & Kalantar, B. (2023). Surface water changes and water depletion of Lake Hamrin, Eastern Iraq, using Sentinel-2 images and geographic information systems. Advances in Environmental and Engineering Research, 4(1), 1-11.
3. Wdaah, E. R., & Nori, A. F. Detection of Land Cover Change in the Sea of Najaf/Iraq for the Period (2005-2022) using Remote Sensing Techniques. International Journal of Advanced Multidisciplinary Research and Studies, 3(2), 1201-1206.
4. Azzawi, J. H., & Abdulameer, I. M. A. (2022, August). Environmental monitoring of water area in the Najaf Sea, Iraq during 1990-2020 using remote sensing data. In AIP Conference Proceedings (Vol. 2437, No. 1). AIP Publishing.
5. Kalantar, B., Ameen, M. H., Jumaah, H. J., Jumaah, S. J., & Halin, A. A. (2020). Zab River (IRAQ) sinuosity and meandering analysis based on the remote sensing data. The International Archives of the Photogrammetry, Remote Sensing and Spatial Information Sciences, 43, 91-95.
6. Nagaraj, R., & Kumar, L. S. (2024). Extraction of Surface Water Bodies using Optical Remote Sensing Images: A Review. Earth Science Informatics, 1-64.
7. Jumaah, H. J., Kalantar, B., Ueda, N., Sani, O. S., Ajaj, Q. M., & Jumaah, S. J. (2021, July). The Effect of war on land use dynamics in Mosul Iraq using remote sensing and GIS techniques. In 2021 IEEE International Geoscience and Remote Sensing Symposium IGARSS (pp. 6476-6479). IEEE.
8. Hadi, A. M., Mohammed, A. K., Jumaah, H. J., Ameen, M. H., Kalantar, B., Rizeei, H. M., & Al-Sharify, Z. T. A. (2022). GIS-based rainfall analysis using remotely sensed data in Kirkuk Province, Iraq: Rainfall analysis. Tikrit Journal of Engineering Sciences, 29(4), 48-55.

Advanced Engineering Days

aed.mersin.edu.tr

Sustainable ecological development planning (case study: County of Tabriz)

Hamed panahdar[1], Shahram Roostaei[*1], Ahmad Nikdel Monavvar[2], Sajjad Moshiri[2]

[1]*Department of Geomorphology, University of Tabriz, Iran, hamed.panahdar@gmail.com, roostaei@tabrizu.ac.ir*
[2]*Department of Remote Sensing and GIS, University of Tabriz, Iran, ahmadnikdel21@gmail.com, Sajjadmoshiri@gmail.com*

Cite this study: Panahdar, H., Roostaei, S., Monavvar, A. N. (2024). *Sustainable ecological development planning (case study: County of Tabriz)*. Advanced Engineering Days, 9, 326-328

Keywords
Land use planning,
Sustainable ecological development,
Factor Analysis,
Weighted Sum,
County of Tabriz.

Abstract

Land use planning and sustainable urban development in the modern areas emphasize essential to balance urbanization, environmental protection, and improving quality of life. Cities performance as sustainable and knowledge-based communities, contributing to social and economic development while protecting resources. For this reason, the purpose of this research is sustainable ecological development planning of Tabriz County. The current method in this research is based on weighted sum modeling. According to the results, it was determined that the sustainable ecological development of Tabriz County is more suitable in the western and eastern areas compared to other regions. Furthermore, according to weighs of ecological factors, it was revealed that the LST factor has the most important impact on the development of Tabriz County, while the DEM and NDVI factors are ranked next.

Introduction

Land use planning and sustainable urban development in the modern areas emphasize essential to balance urbanization, environmental protection, and improving quality of life. Cities performance as sustainable and knowledge-based communities, contributing to social and economic development while protecting resources (Schewenius, 2020). However, illogical urban development leads to increased social and environmental costs and disturbs sustainable development processes, requiring a review of traditional planning paradigms and adopting a comprehensive ecological approach for sustainable urban development (Wang et al., 2020) that considers ecological principles and adopts a harmonious relationship between humans and the environment. Furthermore, cities take an important role in greenhouse gas emissions and climate change, and urban development can contribute to the urban heat island, which has negative impacts on public health (Kattel et al., 2015). Nevertheless, nowadays cities are striving to review their strategies for urban sustainable planning, carefully considering their local and original characteristics, by the main goal of improve quality of life through optimal and efficient application of available resources (wang et al., 2022). Iran, as a quickly urbanize developing country, is experiencing irregular and faster urban development. To control this trend and move towards sustainable development, it is suggested to apply land-use planning principles and detailed urban development plans.

Material and Method

The purpose of this study is to investigate ecological development in county of Tabriz by using LST, NDVI, and DEM factors. Data analysis was achieved by ArcGIS and SPSS environments. Factor analysis was used to extract the weights of factors in the SPSS environment (Oskouee Aras et al., 2024). Then, the layers were standardized in the ArcGIS environment by the Fuzzy membership method with linear function for standardization, and in conclusion, the final map was obtained by overlaying the weighted layers through the Weighted Sum technique.

Study Area

Metropolis of Tabriz, the capital of East Azarbaijan province, is located at 38 degrees 88 minutes north latitude and 46 degrees 15 minutes east longitude. Tabriz is limited by the Sahand mountain from the south and Aun Ibn

Ali mountain from the northwest. This city is one of the 10 metropolises of Iran and the largest metropolis in the northwest. Its population in 2015 is estimated to be 1,558,693.

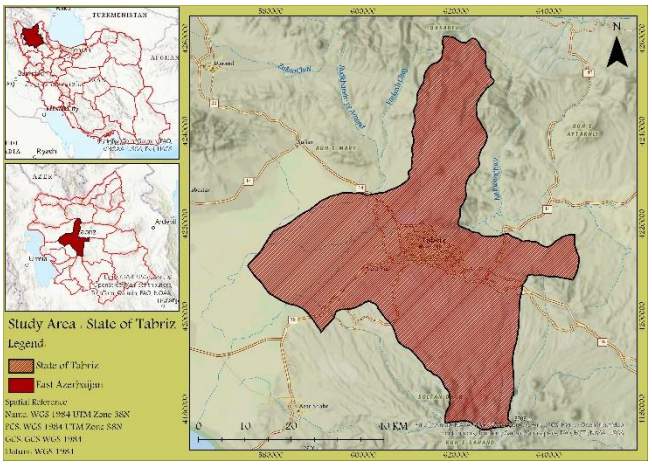


Figure 1. Study Area

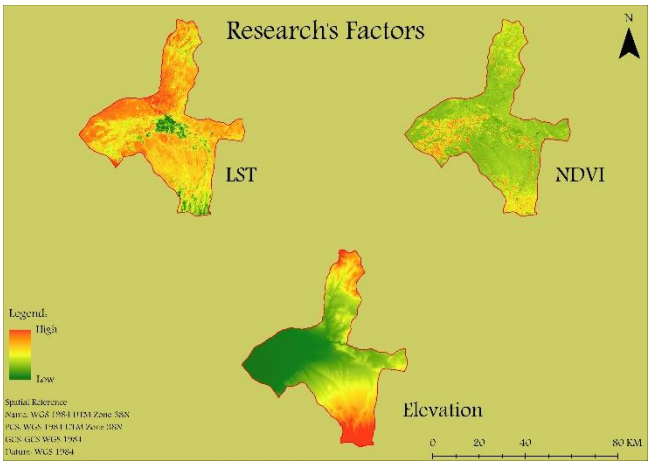


Figure 2. Reasearch Factors

Results

The purpose of the current research is to evaluate the areas prone to Sustainable ecological development in Tabriz metropolis. For this purpose, factors NDVI, LST and DEM were prepared from Satellite images. Then factor analysis was used to extract the weights of the factors. Finally, in order to modeling the sustainable ecological development of area, the weighted sum function was used.

The results of KMO by 0.545 value (Table.1) show the significance of the suitability of the sample size. In this analysis, the minimum factor loading accepted for the items was determined to be 0.4, and the varimax rotation method was used to rotate the factors. according to result of factor analysis the weights of NDVI= 0.354, LST=0.661 and DEM= 0.487 was obtained.

Table 1. KMO and Bartlett's Test

Kaiser-Meyer-Olkin Measure of Sampling Adequacy.		.542
Bartlett's Test of Sphericity	Approx. Chi-Square	51.700
	df	3
	Sig.	.000

The Sustainable ecological development factors were prepared by satellite images, then the layers were overlayed. So, the value of factors was scaled based on fuzzy function. Finally, the weights obtained from factor analysis were used to weight each of the factors, and the final map for sustainable ecological development was obtained by overlaying the layers.

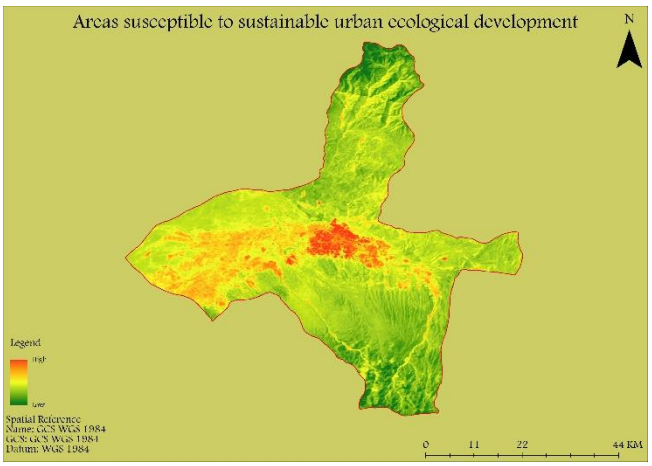


Figure 3. Urban Sustainable Ecological Development Areas Based on the weighted sum

The western areas and parts of the eastern of county of Tabriz are suitable for sustainable ecological development, that portrayed in red shades. These areas show favorable environments, including higher NDVI, lower LST, and suitable DEM, this makes these areas ideal for planning and future development.

Conversely, the southern and northern areas, represented by green, are less suitable for sustainable ecological development. These regions face challenges such as higher land surface temperatures, lower vegetation cover, or unsuitable elevation environments, which, in the absence of suitable planning, can create serious threats to sustainable urban development and the environment.

Conclusion

According to the importance of sustainable ecological development, in the current study, the ecological development planning of Tabriz County has been noted using factors such as NDVI, LST, and DEM. Based on this, the results obtained from this research are in line and consistent with the findings of other studies, such, Zhang et al. (2024) and Nie et al. (2022).

Results

The purpose of this research is the sustainable ecological development planning of Tabriz County via LST, NDVI, and Elevation factors. After analysis, it was determined that the ecological development of Tabriz is more suitable in the western and eastern areas compared to other regions. Furthermore, according to weighs of ecological factors, it was revealed that the LST factor has the most important impact on the development of Tabriz County, while the DEM and NDVI factors are ranked next.

References

1. Kattel, G.R.; Elkadi, H.; Meikle, H. (2015) Developing a complementary framework for urban ecology. Urban For. Urban Green. 12, 498–508.
2. Maune, D. F. (2001). Digital elevation model technologies and applications: The DEM user manual. The American Society for Photogrammetry and Remote Sensing. ISBN:1-57083-064-9
3. Oskouee, A., Nikdel, M, A, Babaei, F., & Teymuri, I. (2024). Spatial analysis of the physical quality of housing in formal and informal settlements (case study: Zone 1 of Tabriz metropolis). Application of remote sensing and GIS in environmental sciences. 3, 38-62.
4. Schewenius, M.; McPhearson, T.; Elmqvist, T. (2020). Opportunities for Increasing Resilience and Sustainability of Urban Social-Ecological Systems: Insights from the URBES and the Cities and Biodiversity Outlook Projects. AMBIO, 43, 434–444
5. Wang, B., Han, Shan., Ao, Yibin., & Liao, Fangwei. (2020). Evaluation and Factor Analysis for Urban Resilience: A Case Study of Chengdu–Chongqing Urban Agglomeration. Buildings Journal, 1-20.
6. Wang, Y., Jiang, Z., Zhing, L. (2022). Sponge City Policy and Sustainable City Development: The Case of Shenzhen. frontiers in environmental science, 1-5.
7. Yang, P., Zhang, X., Hua, L. (2023). Analysis of Urban Ecological Quality Spatial Patterns and Influencing Factors Based on Remote Sensing Ecological Indices and Multi-Scale Geographically Weighted Regression. sustainability Journal. 15, 1-18.
8. Zhang, W., Yuan, Q., Cai, H. (2024). Unravelling regional development through the production-living-ecological perspective: Assessing heterogeneity and expert insights. Urban Climate. 55, 43-51.

Advanced Engineering Days

aed.mersin.edu.tr

Investigating the influence of atmospheric parameters on Aerosol optical depth in Iran

Sajedeh Morady Par*[1]

[1] *Tabriz University, Faculty of Planning and Environmental Sciences, Tabriz, Sajedeh.Morady@tabrizu.ac.ir*

Cite this study: Morady Par, S. (2024). Investigating the influence of atmospheric parameters on Aerosol optical depth in Iran. Advanced Engineering Days, 9, 329-334

Keywords
AOD
meteorology
MODIS
MERRA-2 Reanalysis
AIRS

Abstract

The objectives of this research are to analyze the effect of meteorological factors including: Relative Humidity at Surface, Cloud Fraction, Sea level pressure, Tropopause Pressure, and Omega at 500 hpa, on AOD in Iran. In this work, Terra satellite images and MODIS sensor were used to obtain the monthly AOD values from 2013 to 2022. Meteorological Parameters were extracted from MERRA-2 Reanalysis and AIRS images. In order to investigate the effect of the studied meteorological parameters on the distribution of AOD index, non-linear multiple regression (MNLR) and linear regression were used. Climatology stations of Iran have been used to perform regression methods and for these station points, data related to the studied parameters were extracted using ArcGIS. This work showed that meteorological parameters have a larger proportion of the AOD changes. According to the result of MNLR, 74.75% of variation in Y (AOD index) can be explained by the regression model. Based on the results obtained from both non-linear and linear regression models, and in accordance with the distribution maps of the studied parameters, in the studied time period (2013-2022), the meteorological parameter of cloud fraction has had the most important contribution to the changes in AOD. The omega parameter at the level of 500 hpa was identified as the least effective meteorological parameter on the distribution of AOD. The only difference between the results of the models is the position of the second and third parameters affecting the distribution of AOD. According to the linear model, the second influencing parameter is tropopause pressure and the third influencing parameter is relative humidity. But the non-linear model shows the opposite results in this case

Introduction

With rapid industrialization and urbanization, aerosol particulates and air quality problems caused by them has aroused wider concerns in many areas [26]. Aerosol from anthropogenic pollution can cause serious impacts on atmospheric environment and human health by carrying hazardous materials [25] .AOD is the most important physical parameter for characterizing aerosols, and also one of the dominating factors for evaluating regional atmospheric contamination and climatic effect [9].

In the past years, many researches have been done about aerosol optical depth (AOD) and the trend of it [1, 3, 4, 6, 12, 15, 17, 18, 20, 25]. Researchers have paid special attention to the effect of atmospheric and climatic factors on distribution or concentration of aerosols using the AOD index [7, 13, 14, 16, 23, 26]

The objectives of this research are to analyze the effect of meteorological factors including: Relative Humidity at Surface, Cloud Fraction, Sea level pressure, Tropopause Pressure, Omega at 500 hpa, on AOD. In AOD-related studies, some of the meteorological parameters which mentioned in this work, are analyzed for first time in Iran territory in this paper. In this research, the analysis of the parameters is in the form of average values. The study period is from 2013 to 2022. We need to expand our knowledge about aerosols, especially in this semi-arid region. Iran has been affected by dust storms for decades. Therefore by knowing the weather conditions which can create or aggravate these dusty conditions, and using indices such as AOD index and remote sensing maps, climate planners and city managers can plan better and easier.

Material and Method

In this research, Terra satellite images and MODIS sensor were used to obtain the monthly AOD values. MODIS product includes two distinct retrieval algorithms: the dark target (DT) over dark surfaces (ocean,

vegetated areas) and the deep blue (DB) over dark and bright land surfaces [8]. We have used Deep Blue, Land-only product in present work. DB AODs are at three wavelengths of 0.412, 0.47, and 0.66 μm over land [11].

MODIS AOD products have the advantages of high retrieval accuracy, long time series, and good spatial coverage, which have been validated by a large number of international scholars to have significant application value in aerosol research [24].

To investigate the influence of meteorological parameters including: Relative Humidity at Surface, Cloud Fraction, Sea level pressure (SLP), Tropopause Pressure (TPP), Omega at 500 hpa, on AOD index, non-linear multiple regression (MNLR) and linear regression have been used in this study. The main advantages of nonlinear models are parsimony, interpretability, and prediction [2].

Iranian climatology stations have been used to perform regression methods. The data related to the studied parameters were extracted using "Extract Values to Points" in the ArcGIS software. This method extracts the cell values of a raster based on a set of point features and records the values in the attribute table of an output feature class.

SLP and Omega values have been extracted from MERRA-2 Reanalysis satellite images. MERRA-2 is the updated reanalysis dataset provided by the Global Modeling and Assimilation Office (GMAO) of NASA [22]. Values of other meteorological parameters using AIRS sensor products were obtained. The AIRS was launched on the Aqua satellite on May 4, 2002 [5]. The AIRS orbit covers almost the entire globe twice a day [21]. The AIRS dataset includes many monthly mean geophysical parameters, in addition to surface temperature. AIRS monthly mean products are produced on a global 1° latitude by 1° longitude spatial grid with no spatial gap [19]. The analysis of the parameters is in the form of average monthly values and study period is from 2013 to 2022.

The data used in this research along with their specifications are given in Table 1.

Table 1. Data used in this work

Items	Meteorological Parameters	Unit	Source	Temporal Resolution
1	Aerosol Optical Depth 550 nm (Deep Blue, Land-only) (MOD08_M3 v6.1)	_	MODIS-Terra	Monthly
2	Relative Humidity at Surface (Daytime/Ascending, AIRS-only) (AIRS3STM v006)	percent	AIRS	Monthly
3	Cloud Fraction (Daytime/Ascending, AIRS-only) (AIRS3STM v006)	_	AIRS	Monthly
4	Sea level pressure (M2IMNPANA v5.12.4)	hpa	MERRA-2 Reanalysis	Monthly
5	Tropopause Pressure (Daytime/Ascending, AIRS-only) (AIRS3STM v006)	hpa	AIRS	Monthly
6	Omega at 500 hpa (M2TMNXSLV v5.12.4)	Pa s-1	MERRA-2 Reanalysis	Monthly

Source: You can find the source of data through this link: https://giovanni.gsfc.nasa.gov/

Results

AOD distribution and meteorological parameters (2013-2022)

At first, maps of the average values of the studied parameters were prepared for the study period of 2013-2022. According to the Figure 1 and the average distribution maps of the studied parameters in the study period, the distribution of the maximum aerosol optical depth index values in Iran corresponds to the southern, eastern and central regions of Iran. The maximum value of this index is 0.5 and the minimum value is 0.1. Minimum AOD values are located in the northwest and also corresponding to the Zagros mountain range. The distribution map of the cloud fraction parameter shows that the distribution of the maximum and minimum values of this parameter is opposite to the distribution of the aerosol index over Iran.

The distribution map of relative humidity shows the conformity of the distribution of this parameter with the distribution of cloud fraction. The average value of the maximum relative humidity during the study period is equal to 71.78% and the minimum value is equal to 14.5%. The sea level pressure distribution map shows the maximum values (equal to 1018 hpa) in the northern regions of Iran and the minimum values (1007hpa) in the coastal areas of the south of the country and also corresponding to the deserts of Kavir and Lut. Based on the

tropopause pressure map, clearly, the maximum areas are distributed in the northern half, northwest and northeast, and the average values are distributed in the central line of the country and the minimum values are distributed in the southern half of Iran. The distribution map of Omega or upward movements shows the presence of negative values in mountainous areas and positive values in other areas.

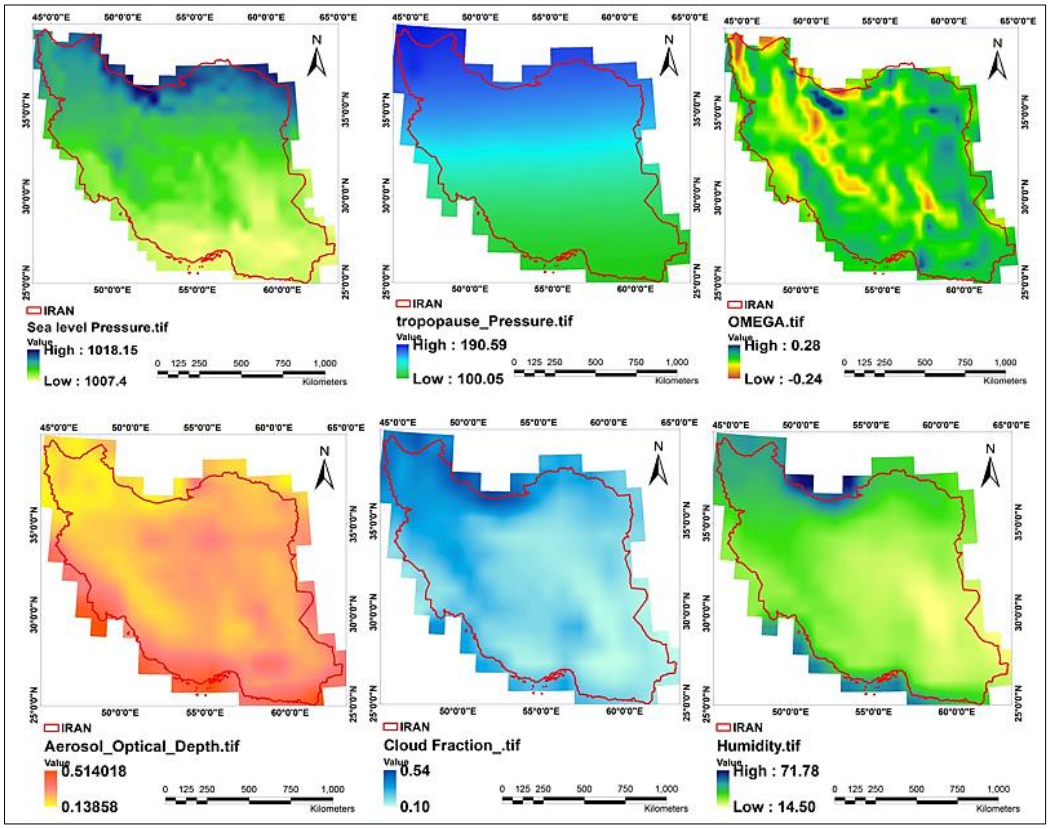


Figure 1. Maps of the average values of the studied parameters

Non-linear multiple regression (MNLR) and linear regression

Independent variables in non-linear multiple regression are: X1: Cloud Fraction X2: Humidity X3: Omega X4: SLP X5: TPP. By using quadratic nonlinear multiple regression model to analyze the impact of meteorological factors on the distribution of AOD index, the following results were obtained (Figure 2 , Figure 3 and Figure 4)

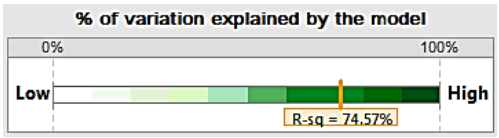


Figure 2. Maps of the average values of the studied parameters

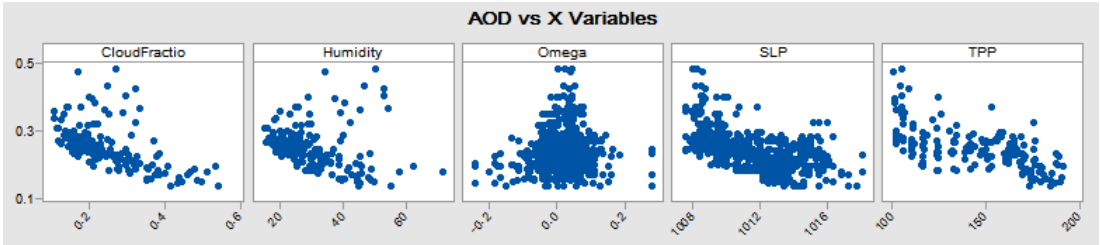


Figure 3. Relationship between X and Y variables

According to Figure 2, 74.75% of variation in Y (AOD index) can be explained by the regression model. The high R-sq value shows the regression model fits the data well. The relationship between cloud fraction, relative humidity, SLP and TPP with AOD is a negative correlation (Figure 3).

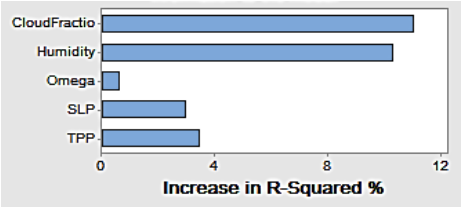


Figure 4. Incremental Impact of X Variables

According to the Figure 4, Long bars represent Xs that contribute the most new information to the model. Based on this figure, and according to the result of the nonlinear regression model, respectively the parameters of cloud fraction, relative humidity, tropopause pressure, sea level pressure and omega have the greatest effect on the AOD index.

The following equation can be used to predict AOD_value for specific values of the X variables, or find the settings for the X variables that correspond to a desired value or range of values for AOD_value.

Final Model Equation

$$AOD = -884 - 70.3\,X1 + 1.1083\,X2 - 47.92\,X3 + 1.834\,X4 - 0.6710\,X5 + 1.575\,X1^2 + 0.000091\,X2^2 - 0.3204\,X3^2 - 0.000949\,X4^2 - 0.000041\,X5^2 - 0.01779\,X1X2 + 0.613\,X1X3 + 0.0688\,X1X4 - 0.002167\,X1X5 - 0.01007\,X2X3 - 0.001092\,X2X4 + 0.04783\,X3X4 - 0.002333\,X3X5 + 0.000676\,X4X5$$

By running the linear regression model between AOD index and each of the variables, similar results were obtained with the non-linear method. The coefficient of determination shows how many percent of the changes in the dependent variable are explained by the independent variables. According Figure 5 and Table 2, and based on the adjusted coefficient of determination, the cloud fraction predictor variable explains 49.4% of the changes in the dependent variable. The predictor variable of relative humidity explains 27.1% of the changes in the dependent variable. Tropopause pressure predictor variable explains 34.1%, sea level pressure predictor variable 27%, and omega predictor variable explains 1.9% of the changes in AOD dependent variable.

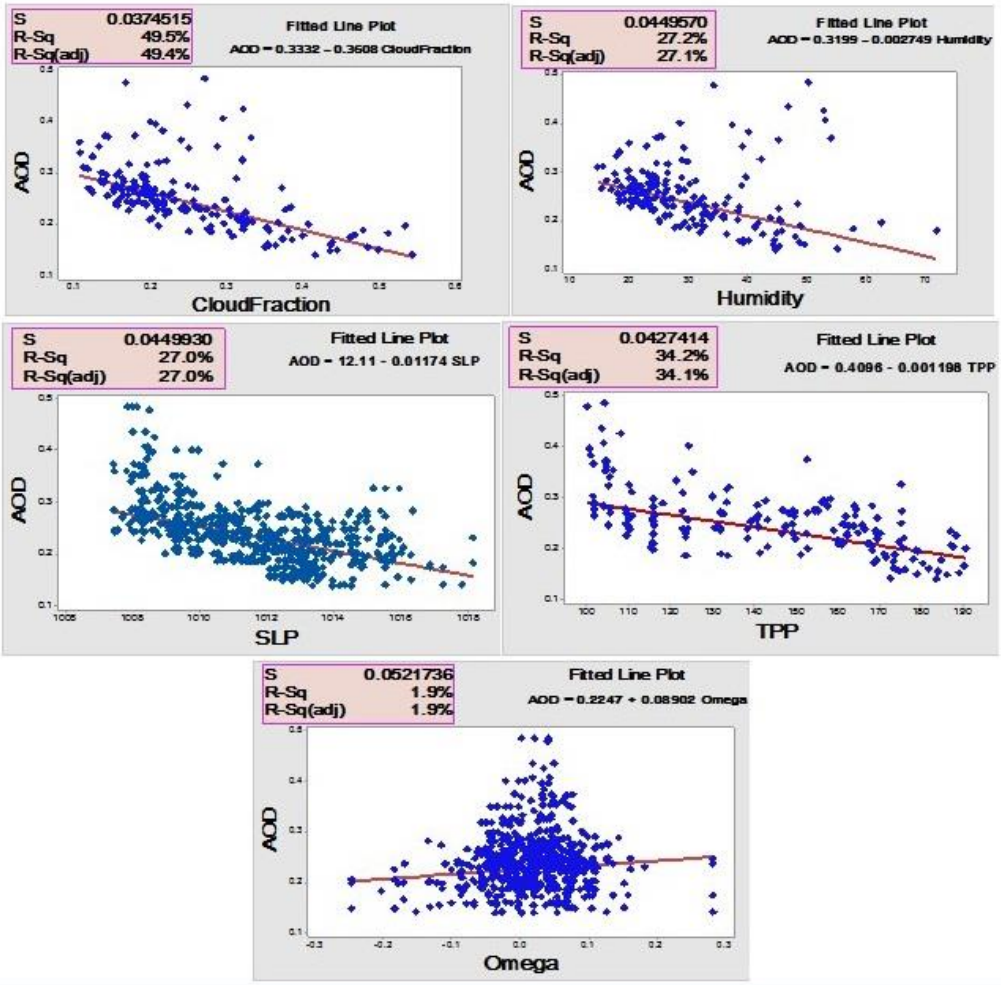


Figure 5. Fitted Line Plots: AOD values versus Cloud Fraction, Humidity, Omega, SLP, and TPP

Table 2. Linear regression model results

AOd			
parameters	**R_Sq**	**R_Sq(adj)**	**Equation for estimating the value of the dependent variable**
Relative Humidity	27.2%	27.1%	AOD_value = 0.3199 - 0.002749 Humidity_value
Cloud Fraction	49.5%	49.4%	AOD_value = 0.3332 - 0.3608 CloudFraction_value
Sea level pressure(SLP)	27%	27%	AOD_value = 12.11 - 0.01174 SLP_value
Tropopause Pressure(TPP)	34.2%	34.1%	AOD_value = 0.4096 - 0.001198 tropopause_value
Omega	1.9%	1.9%	AOD_value = 0.2247 + 0.08902 Omega value

Discussion

Based on the results obtained from both non-linear and linear regression models, and in accordance with the distribution maps of the studied parameters, in the studied time period (2013-2022), the meteorological parameter of cloud fraction has had the most important contribution to the changes in AOD. The only difference between the results of the models is the position of the second and third parameters affecting the distribution of AOD. According to the linear model, the second influencing parameter is tropopause pressure and the third influencing parameter is relative humidity. But the non-linear model shows the opposite results in this case. But other parameters are the same in terms of the amount and importance of influence in both models. The omega parameter at the level of 500 hpa was identified as the least effective meteorological parameter on the distribution of AOD in this research.

Conclusion

This work showed that meteorological parameters have a larger proportion of the AOD changes. This result is consistent with the results of other researches [4]. The parameters studied in this research had not been studied in Iran in relation to AOD index. Unlike the results of other researches that consider the effect of humidity more important, in this research the parameter of cloud fraction has played a more important role than other parameters, especially humidity, in explaining the changes in AOD index. It is suggested that the comprehensive investigation of the effect of the meteorological variables that have been investigated in other researches, together with the parameters studied in this research, should be analyzed to reveal the most influential climatic and meteorological factors in the distribution and change of AOD in the land of Iran.

References

1. Alpert, P., Shvainshtein, O., & Kishcha, P. (2012). AOD trends over megacities based on space monitoring using MODIS and MISR.
2. Archontoulis, S. V., & Miguez, F. E. (2015). Nonlinear regression models and applications in agricultural research. Agronomy Journal, 107(2), 786-798.
3. Arkian, F., & Nicholson, S. E. (2018). Long-term variations of aerosol optical depth and aerosol radiative forcing over Iran based on satellite and AERONET data. Environmental monitoring and assessment, 190, 1-15.
4. Che, H., Gui, K., Xia, X., Wang, Y., Holben, B. N., Goloub, P., ... & Zhang, X. (2019). Large contribution of meteorological factors to inter-decadal changes in regional aerosol optical depth. Atmospheric Chemistry and Physics, 19(16), 10497-10523.
5. Chen, C., Ma, P., Chen, L., Zhang, Y., Zhou, C., Zhao, Sh., Zhang, L., Wang, Zh., 2022, Nitrous Oxide Profile Retrievals from Atmospheric Infrared Sounder and Validation, Atmosphere, 13(4), 619.
6. Dadashi-Roudbari, A., & Ahmadi, M. (2020). Evaluating temporal and spatial variability and trend of aerosol optical depth (550 nm) over Iran using data from MODIS on board the Terra and Aqua satellites. Arabian Journal of Geosciences, 13, 1-23.
7. de Leeuw, G., Kang, H., Fan, C., Li, Z., Fang, C., & Zhang, Y. (2023). Meteorological and anthropogenic contributions to changes in the Aerosol Optical Depth (AOD) over China during the last decade. Atmospheric Environment, 301, 119676.

8. Garrigues, S., Chimot, J., Ades, M., Inness, A., Flemming, J., Kipling, Z ... & Agusti-Panareda, A. (2022). Monitoring multiple satellite aerosol optical depth (AOD) products within the Copernicus Atmosphere Monitoring Service (CAMS) data assimilation system. Atmospheric Chemistry and Physics, 22(22), 14657-14692.
9. Gu, X., Bao, F., Cheng, T., Chen, H., Wang, Y., & Guo, H. (2018). The impacts of regional transport and meteorological factors on aerosol optical depth over Beijing, 1980–2014. Scientific Reports, 8(1), 5113.
10. Hossein Hamzeh, N., Kaskaoutis, D. G., Rashki, A., & Mohammadpour, K. (2021). Long-term variability of dust events in southwestern Iran and its relationship with the drought. Atmosphere, 12(10), 1350.
11. Kim, M. H., Kim, S. W., & Omar, A. H. (2020). Dust lidar ratios retrieved from the CALIOP measurements using the MODIS AOD as a constraint. Remote Sensing, 12(2), 251.
12. Kotrike, T., Pratap, D., & Keesara, V. R. (2021). Validation and trend analysis of satellite-based AOD data over southern India. Aerosol Science and Engineering, 5, 32-43.
13. Li, J., Ge, X., He, Q., & Abbas, A. (2021). Aerosol optical depth (AOD): spatial and temporal variations and association with meteorological covariates in Taklimakan desert, China. PeerJ, 9, e10542.
14. Meng, H., Bai, G., & Wang, L. (2024). Analysis of the spatial and temporal distribution characteristics of AOD in typical industrial cities in northwest China and the influence of meteorological factors. Atmospheric Pollution Research, 15(1), 101957.
15. Pozzer, A., De Meij, A., Yoon, J., Tost, H., Georgoulias, A. K., & Astitha, M. (2015). AOD trends during 2001–2010 from observations and model simulations. Atmospheric Chemistry and Physics, 15(10), 5521-5535.
16. Qi, L., Zheng, H., Ding, D., Ye, D., & Wang, S. (2022). Effects of meteorology changes on inter-annual variations of aerosol optical depth and surface PM2. 5 in China—Implications for PM2. 5 remote sensing. Remote Sensing, 14(12), 2762.
17. Shaheen, A., Wu, R., & Aldabash, M. (2020). Long-term AOD trend assessment over the Eastern Mediterranean region: A comparative study including a new merged aerosol product. Atmospheric Environment, 238, 117736.
18. Srivastava, A., & Saran, S. (2017). Comprehensive study on AOD trends over the Indian subcontinent: a statistical approach. International Journal of Remote Sensing, 38(18), 5127-5149.
19. Susskind, J., Schmidt, G. A., Lee, J. N., & Iredell, L., (2019), Recent global warming as confirmed by AIRS, Environmental Research Letters, 14(4), 044030.
20. Wang, P., Ning, S., Dai, J., Sun, J., Lv, M., Song, Q., ... & Yu, D. (2017). Trends and variability in aerosol optical depth over North China from MODIS C6 aerosol products during 2001–2016. Atmosphere, 8(11), 223.
21. Warner, J. X., Wei, Z., Strow, L. L., Dickerson, R. R., & Nowak, J. B. (2016). The global tropospheric ammonia distribution as seen in the 13-year AIRS measurement record, Atmospheric Chemistry and Physics, 16(8), PP. 5467-5479.
22. Yousefi, R., Wang, F., Ge, Q., Lelieveld, J., & Shaheen, A. (2021). Aerosol trends during the dusty season over Iran. Remote Sensing, 13(6), 1045.
23. Yousefi, R., Wang, F., Ge, Q., Shaheen, A., & Kaskaoutis, D. G. (2023). Analysis of the winter AOD trends over Iran from 2000 to 2020 and associated meteorological effects. Remote Sensing, 15(4), 905.
24. Zhang, Z., Zhang, M., Bilal, M., Su, B., Zhang, C., & Guo, L. (2020). Comparison of MODIS-and CALIPSO-derived temporal aerosol optical depth over Yellow River Basin (China) from 2007 to 2015. Earth Systems and Environment, 4, 535-550.
25. Zheng, C., Zhao, C., Zhu, Y., Wang, Y., Shi, X., Wu, X., ... & Qiu, Y. (2017). Analysis of influential factors for the relationship between PM 2.5 and AOD in Beijing. Atmospheric Chemistry and Physics, 17(21), 13473-13489.
26. Zheng, Y., Wang, X., Zhang, X., & Hu, G. (2022). Multi-spatiotemporal patterns of aerosol optical depth and influencing factors during 2000–2020 from two spatial perspectives: The entire Yellow River Basin region and its urban agglomerations. *International Journal of Applied Earth Observation and Geoformation*, *106*, 102643.

Advanced Engineering Days

aed.mersin.edu.tr

Hyperspectral remote sensing in environmental studies

Mehrdad Jeihouni *[1]

[1] *University of Tabriz, Department of Remote Sensing and GIS, Iran, jeihouni@tabrizu.ac.ir*

Cite this study: Jeihouni, M. (2024). Hyperspectral remote sensing in environmental studies. Advanced Engineering Days, 9, 335-337

Keywords
Crop Biomass
Heavy Metals
LULC Classification
Forest
Wetland

Abstract

Hyperspectral remote sensing revolutionized environmental monitoring by capturing hundreds of narrow spectral bands. This unlocks a wealth of information about Earth's complex systems, from vegetation health to mineral composition. This study highlighted the role of hyperspectral data in environmental studies such as narrow band vegetation indices, crop biomass and yield, heavy metals effects on vegetation, LULC classification, forest management, and wetland vegetation. Hyperspectral remote sensing offers a paradigm shift in environmental research by enabling the acquisition of highly detailed complex spectral information. This study posits that hyperspectral remote sensing holds the potential to unlock a more nuanced understanding of the intricacies inherent within complex environmental systems.

Introduction

The Earth's environment is a complex and dynamic system facing unprecedented challenges due to climate change, anthropogenic activities, and population growth. Effective monitoring and assessment of these environmental resources are crucial for sustainable management and informed decision-making. Remote sensing (RS) has emerged as a powerful tool for gathering timely and spatially-explicit data across various environmental domains.

Among RS techniques, hyperspectral remote sensing stands out for its unparalleled ability to capture detailed spectral information, offering a unique perspective for environmental studies. Unlike traditional multispectral sensors that capture a limited number of broad spectral bands, hyperspectral sensors record hundreds to thousands of contiguous narrow spectral bands across the electromagnetic spectrum (e.g., 400–2500 nm) [1]. This vast amount of spectral information allows for the identification and characterization of unique spectral signatures of various materials present on the Earth's surface. By analyzing these signatures, researchers gain insights into the composition, health, and stress conditions of environmental features like vegetation, soil, water bodies, and minerals.

Hyperspectral data acquisition can be achieved from various platforms, including satellites, airplanes, and unmanned aerial vehicles (UAVs) [2]. Each platform offers advantages and limitations in terms of spatial resolution, spectral range, and revisit frequency. Satellite-borne hyperspectral sensors typically cover large areas but have lower spatial resolution, while UAV-mounted hyperspectral sensors offer higher spatial resolution but capture data over smaller areas.

The frontiers of hyperspectral remote sensing are continuously expanding, offering a powerful tool for understanding and managing our planet's intricate systems. As sensor technology advances, spatial resolution improves, and data processing algorithms become more sophisticated, hyperspectral remote sensing can unveil Earth's secrets with ever-increasing detail, shaping a future of sustainable environmental management and resource utilization. Accordingly, in the last decade hyperspectral remote sensing has been widely used for various applications [1]. This paper will discuss the important applications of hyperspectral remote sensing in environmental studies.

Narrow Band Vegetation Indices

Hyperspectral means narrowband spectral data [3]. Hyperspectral remote sensing, with its vast array of narrow spectral bands, unlocks a new frontier for precision agriculture and empowers the development of Narrow-Band Vegetation Indices (NBVIs). These targeted indices offer superior sensitivity to plant stress compared to broad-band indices derived from multispectral data. The use of hyperspectral images makes it possible to improve the indices by the correction of soil background effects [4]. NBVIs have been developed for different applications [5, 6]. Spectral bands from 550- 800 nm are broadly used to develop vegetation indices of nitrogen and chlorophyll content [7, 8].

Crop Biomass and Yield

Accurate and timely crop biomass and yield estimations are crucial for optimizing agricultural practices and ensuring global food security. Traditional methods of estimating yield and biomass with field measurements are destructive, time-consuming and difficult but hyperspectral remote sensing technology can be used to directly estimate biomass and yield [9]. The detailed information captured by hyperspectral remote sensing allows for the analysis of plant physiological processes reflected in spectral signatures. These signatures are influenced by key parameters like leaf area index (LAI), chlorophyll content, and water stress, all directly related to crop biomass and eventual yield.

Heavy Metals Effects on Vegetation

Heavy metal contamination poses a significant threat to environmental health, impacting soil fertility, water quality, and ultimately, human health. Vegetation often serves as the first point of contact for these contaminants, accumulating heavy metals like lead, cadmium, and arsenic in their tissues [10]. However, traditional methods for detecting heavy metal stress in vegetation are often time-consuming, destructive, and limited in spatial coverage. Hyperspectral remote sensing emerges as a powerful tool for non-invasive and spatially explicit assessment of heavy metal effects on vegetation health. The core principle of detecting heavy metal effects relies on analyzing specific spectral regions sensitive to plant health as regions correspond to pigments and water content. Heavy metal stress can disrupt pigment production and alter water content within plant tissues, resulting in deviations in reflectance at these sensitive spectral bands. The movement of the spectral features in the red edge area is a factor. When plants are healthy and producing more chlorophyll, the red edge tends to shift toward the right to longer wavelengths (increase in the absorption trough at 680 nm). When a plant is stressed by excessive heavy metals in the soil, the spectra tend to shift toward the left and shorter wavelengths. Stress also tends to produce an increase in reflectance at the 680 nm.

Land Use/Cover Classification

Land use/land cover (LULC) patterns are crucial variables of the Earth's system that are intimately connected with environmental monitoring, resource management, and urban planning [11]. The high accuracy of LULC classification with hyperspectral remote sensing is due to its rich spectral information. Different LC types, such as forests, grasslands, urban areas, and agricultural fields, possess unique spectral signatures. These signatures reflect the inherent properties of the materials present on the Earth's surface, influenced by factors like vegetation type, soil composition, and human-made structures. The hyperspectral remote sensing classification process can utilizes spectral libraries [12]. Reference libraries containing spectral signatures of known land cover types. By comparing the each pixel's spectrum with these libraries, the most likely land cover class can be identified.

Forest Management

About 30% of the land surface of the Earth is covered by forests [13]. Forests play a crucial role in maintaining ecological balance, mitigating climate change, and providing essential resources. Effective forest management requires detailed information on species composition, health status, and biomass distribution. Hyperspectral remote sensing data provides unique "fingerprints" for various forest components, including different tree species, vegetation health indicators, and understory composition [14]. By analyzing these spectral signatures, researchers and forest managers gain insights into the intricate structure and health of forest ecosystems.

Wetland Vegetation

Wetlands, with their diverse vegetation communities, play a key role in upholding ecological equilibrium, filtering pollutants, and regulating water flow. Monitoring and characterizing wetland vegetation is essential for effective conservation and management. Spectral signature for various wetland plant species, allows to

distinguish them based on their specific pigment composition and physiological characteristics. By meticulously analyzing these spectral signatures, a comprehensive understanding of wetland vegetation composition and health can be achieved. Hyperspectral remote sensing can be used for mapping mangrove forests, baldcypress forests, bottomland hardwood forests, invasive plants, marsh wetlands [15].

Conclusion

This study comprehensively investigates the applications of hyperspectral remote sensing in environmental studies. It highlighted the role of hyperspectral data in various research fields such as narrow band vegetation indices, crop biomass and yield, heavy metals effects on vegetation, LULC classification, forest management, and wetland vegetation. Looking ahead, hyperspectral remote sensing has the potential to revolutionize environmental studies in these fields by capturing complex spectral details. It enables researchers and land managers to gain a deeper understanding of ever-changing environment and facilitate informed decision-making toward sustainable land use practices and environmental protection. From the present study, it can be concluded that hyperspectral remote sensing holds the key to unlocking a deeper understanding of complex environmental systems.

References

1. Thenkabail, P. S., Lyon, J. G., & Huete, A. (Eds.). (2018). Fundamentals, sensor systems, spectral libraries, and data mining for vegetation. CRC Press.
2. Ortenberg, F. (2018). Hyperspectral sensor characteristics: Airborne, spaceborne, hand-held, and truck-mounted; integration of hyperspectral data with Lidar. In Fundamentals, Sensor Systems, Spectral Libraries, and Data Mining for Vegetation (pp. 41-69). CRC Press.
3. Yao, H., Huang, Y., Tang, L., Tian, L., Bhatnagar, D., & Cleveland, T. E. (2018). Using hyperspectral data in precision farming applications. In Advanced Applications in Remote Sensing of Agricultural Crops and Natural Vegetation (pp. 3-35). CRC Press.
4. Gong, P., Pu, R., Biging, G. S., & Larrieu, M. R. (2003). Estimation of forest leaf area index using vegetation indices derived from Hyperion hyperspectral data. IEEE transactions on geoscience and remote sensing, 41(6), 1355-1362.
5. Mulla, D. J. (2013). Twenty five years of remote sensing in precision agriculture: Key advances and remaining knowledge gaps. Biosystems engineering, 114(4), 358-371.
6. Thenkabail, P. S., Lyon, J. G., & Huete, A. (Eds.). (2019). Advanced Applications in Remote Sensing of Agricultural Crops and Natural Vegetation. CRC Press.
7. Li, J., Zhang, J., Tao, C., Zhao, D., & Gang, C. (2018). Hyperspectral Narrowbands and Their Indices in Study of Nitrogen Content of Cotton Crops. In Advanced Applications in Remote Sensing of Agricultural Crops and Natural Vegetation (pp. 37-48). CRC Press.
8. Haboudane, D., Miller, J. R., Tremblay, N., Zarco-Tejada, P. J., & Dextraze, L. (2002). Integrated narrow-band vegetation indices for prediction of crop chlorophyll content for application to precision agriculture. Remote sensing of environment, 81(2-3), 416-426.
9. Marshall, M., Aneece, I., Foley, D., Xueliang, C., & Biggs, T. (2018). Crop water productivity estimation with hyperspectral remote sensing. In Advanced Applications in Remote Sensing of Agricultural Crops and Natural Vegetation (pp. 79-96). CRC Press.
10. Slonecker, E. T. (2018). Analysis of the effects of heavy metals on vegetation hyperspectral reflectance properties. In Advanced Applications in Remote Sensing of Agricultural Crops and Natural Vegetation (pp. 49-66). CRC Press.
11. Chatziantoniou, A., Petropoulos, G. P., & Psomiadis, E. (2017). Co-Orbital Sentinel 1 and 2 for LULC mapping with emphasis on wetlands in a mediterranean setting based on machine learning. Remote Sensing, 9(12), 1259.
12. Pandey, P. C., Manevski, K., Srivastava, P. K., & Petropoulos, G. P. (2018). The Use of Hyperspectral Earth Observation Data for Land Use/Cover ClassificationPresent Status, Challenges, and Future Outlook. In Advanced Applications in Remote Sensing of Agricultural Crops and Natural Vegetation (pp. 147-173). CRC Press.
13. FAO. (2016). Global Forest Resources Assessment 2015. How are the World's Forests Changing? 2nd ed. FAO Forestry paper, 45pp, FAO, Rome. Available online at: http://www.fao.org/3/a-i4793e.pdf. Visited Jun 2024.
14. Thomas, V. (2018). Hyperspectral remote sensing for forest management. In Advanced Applications in Remote Sensing of Agricultural Crops and Natural Vegetation (pp. 175-195). CRC Press.
15. Ramsey, E., & Rangoonwala, A. (2018). Hyperspectral remote sensing of wetland vegetation. In Advanced Applications in Remote Sensing of Agricultural Crops and Natural Vegetation (pp. 219-245). CRC Press.

Advanced Engineering Days

aed.mersin.edu.tr

Remote sensing applications in agriculture

Mehrdad Jeihouni[*1]

[1] *University of Tabriz, Department of Remote Sensing and GIS, Iran, jeihouni@tabrizu.ac.ir*

Cite this study: Jeihouni, M. (2024). Remote sensing applications in agriculture. Advanced Engineering Days, 9, 338-340

Keywords
Precision Agriculture
Digital Soil Mapping
Crop Stress
Crop Yield Modeling
Crop Mapping

Abstract

In recent years there is a strong need to monitor the state of agriculture on the earth, with various spatio-temporal resolutions. Real-time monitoring is an essential requirement for sustainable global agricultural production. Remote sensing is revolutionizing agriculture by providing and analyzing data collected from satellites, and drones. This study provides a brief review of remote sensing applications in agricultural studies and discuss how spectral, thermal, radar, and hyper-spectral remotely sensed data can play a role in various agricultural fields such as precision agriculture, digital soil mapping, soil characteristics, crop stress, crop identification, crop yield, agricultural land use and crop monitoring.

Introduction

Given the global challenges facing agriculture, there is a need for effective monitoring of crop growth and status across diverse locations and environmental contexts, with different time scales, and for multiple purposes. Real-time monitoring is an essential requirement for sustainable global agricultural production to meet the needs of a 10 billion population by 2050[1]. Here, the critical role of Remote sensing science is highlighted. Remote sensing is a developing technology that is used in various fields such as agriculture. Remote sensing acts as our eyes in the sky, providing a wealth of information about Earth. Satellites, airplanes, and even drones collect data by detecting and measuring the electromagnetic radiation emitted from the planet's surface. By analyzing these signals, scientists can map and monitor everything from land cover changes and forest health to soil moisture and mineral composition. Remote sensing plays a vital role in various fields, from tracking deforestation and monitoring natural disasters to understanding climate change and managing agricultural resources.

Remote sensing is revolutionizing agriculture by providing farmers with a bird's-eye view of their fields. By analyzing data collected from satellites, drones, and airplanes, farmers can monitor crop health in near/real-time, identifying issues like nutrient deficiencies, pests, and water stress. This allows for targeted interventions, optimizing resource use like water and fertilizer, and ultimately leading to increased yields and improved crop quality. Therefore, remote sensing is a key tool for sustainable agriculture, promoting practices that minimize environmental impact while ensuring food security for a growing global population. In this paper important applications of remote sensing in agricultural studies will be discussed.

Precision Agriculture

Precision agriculture integrates Geographic Information Systems (GIS), Global Positioning Systems (GPS) and Remote Sensing (RS) technologies for optimal farm management and increasing productivity [2]. Access to high spatial, spectral, and temporal resolution satellite images has led to the widespread use of remote sensing in various fields of precision agriculture, such as crop monitoring, irrigation management, disease and pest management, weed management, and yield prediction [3, 4, 5]. On the other hand, in recent years, the employing unmanned aerial vehicles (UAVs) have played a prominent role in precision agriculture due to their lower cost and the ability to provide high spatial resolution images (centimeter).

Soil salinity

Soil salinity, the salt content in the soil, is a major environmental hazard. Soil salinity changes the spectral behavior of soil in spectral and microwave regions of the electromagnetic spectrum [6]. Therefore, spectral and active multi-temporal radar remote sensing is significantly useful in identifying the spatio-temporal changes of soil salinity. Therefore, by using satellite images and a limited number of soil samples, digital maps of soil salinity can be prepared at the lowest cost in the shortest time.

Soil moisture

Soil moisture is a key agricultural indicator. However, current soil moisture monitoring infrastructures are point-based, costly and inadequate at large scale [7]. Optical, thermal and microwave remote sensing can be used for soil moisture monitoring [8]. In this regards, the use of different remote sensing sensors makes it possible to prepare soil moisture maps in a large area with a time- and cost-effective approach.

Soil organic matter

Soil organic matter plays a key role in the carbon cycle. The effect of soil organic matter on electromagnetic radiation in the VNIR-SWIR region has been widely reported [9]. Accordingly, spectral remote sensing images can be used to study and monitor soil organic matter in large scales. Moreover, carbon sequestration in the soil can be monitored using remote sensing techniques.

Soil texture

Soil texture is spatially variable and controls most of the soil properties and affects agricultural production and yield. Therefore, describing its variability through space and generating soil texture map has an important role in soil management and sustainable agriculture [10]. Spectral remote sensing has a huge capacity to be used in soil texture studies due to various sensors with different spatial resolutions.

Soil mapping

Soil maps are essential for decision makers and are widely used as central information for environmental and hydrological modeling, agricultural management, nature conservation, and land use planning/management. On the other hand, in recent decade, the need to improve the accuracy and spatial resolution of soil maps has increased. In general, the achievement of sustainable agriculture is required by obtaining reliable and accurate high resolution soil maps for analysis of spatial changes of various parameters and identifying their spatial patterns. Accordingly, the prominent role of remote sensing in this field is highlighted as the most important provider of covariates for accurate soil mapping [11].

Crop stress

Remote sensing techniques require less cost and labor than field surveys for various applications in agriculture. Crop stress is a physiological response of plants when the availability of water [12] or plant nutrients is reduced. Accordingly, when the plant is out of its natural state, changes in its appearance and spectral response appear. These changes can be studied by remote sensing in the range of 400 to 2500 nm of the electromagnetic spectrum.

Crop identification

Spatial monitoring of agricultural production needs updated information on the spatial distribution of crops and the total cultivated area. This emphasizes the development of accurate and efficient methods for mapping and monitoring the distribution of crop types (crop mapping) and agricultural lands [13]. In this regard, by using remote sensing satellites images with different spatial, spectral and temporal resolutions, it is possible to determine the crop type and the cultivated area from local to national or global scale in the shortest time according to time and phenological cycle of plants.

Crop yield modeling and estimation

Monitoring the crop condition and yield estimates at different scales is of particular interest to decision makers in the agricultural sector and critical for economic development of any country [14]. Collecting crop yield information from field interview and crop cutting at regional and province is time-consuming and expensive [15]. Remotely sensed satellite data provided a near-real time data to assess crop yield modeling and estimation

by various vegetation indexes obtained from passive and active sensors. Remote sensing can estimate and model crop yield with the lowest cost in the shortest time from county to national scales.

Agricultural land use and crop monitoring

Regional, national and international land planners and policy makers are looking for land use monitoring information. One of the simplest applications of remote sensing for agricultural purposes is the generating agro-ecological landscape maps [16]. The capacity to monitor changes is achieved by repeating the process of land use mapping at specific time intervals during a period. Besides the high importance of land use maps, is an easy process, but what makes the role of remote sensing in agriculture colorful is the mapping crop practice. Crop mapping and monitoring is a new research line that can achieve high accuracy by using satellite-based hyper-spectral and radar data.

Conclusion

This study presents an overview of remote sensing applications in agriculture. It was shown how spectral, thermal, radar, and hyper-spectral remotely sensed data can play a role in various agricultural fields such as precision agriculture, soil characteristics, digital soil mapping, crop stress, crop identification, crop yield, agricultural land use and crop monitoring. Various remote sensing data are now available at multiple scales (from Km to Cm) enabling the deepening of fundamental knowledge in agriculture and food security.

References

1. Weiss, M., Jacob, F., & Duveiller, G. (2020). Remote sensing for agricultural applications: A meta-review. Remote sensing of environment, 236, 111402.
2. Brisco, B., Brown, R. J., Hirose, T., McNairn, H., & Staenz, K. (1998). Precision agriculture and the role of remote sensing: a review. Canadian Journal of Remote Sensing, 24(3), 315-327.
3. Sishodia, R. P., Ray, R. L., & Singh, S. K. (2020). Applications of remote sensing in precision agriculture: A review. Remote sensing, 12(19), 3136.
4. Pradipta, A., Soupios, P., Kourgialas, N., Doula, M., Dokou, Z., Makkawi, M., ... & Yassin, M. (2022). Remote sensing, geophysics, and modeling to support precision agriculture—Part 2: Irrigation management. Water, 14(7), 1157.Maune, D. F. (2001). Digital elevation model technologies and applications: The DEM user manual. The American Society for Photogrammetry and Remote Sensing. ISBN:1-57083-064-9
5. Peng, Y., Li, Y., Dai, C., Fang, S., Gong, Y., Wu, X., ... & Liu, K. (2019). Remote prediction of yield based on LAI estimation in oilseed rape under different planting methods and nitrogen fertilizer applications. Agricultural and forest meteorology, 271, 116-125.
6. Metternicht, G. I., & Zinck, J. A. (2003). Remote sensing of soil salinity: potentials and constraints. Remote sensing of Environment, 85(1), 1-20.
7. Ford, T. W., & Quiring, S. M. (2019). Comparison of contemporary in situ, model, and satellite remote sensing soil moisture with a focus on drought monitoring. Water Resources Research, 55(2), 1565-1582.
8. Wang, L., & Qu, J. J. (2009). Satellite remote sensing applications for surface soil moisture monitoring: A review. Frontiers of Earth Science in China, 3, 237-247.
9. Angelopoulou, T., Tziolas, N., Balafoutis, A., Zalidis, G., & Bochtis, D. (2019). Remote sensing techniques for soil organic carbon estimation: A review. Remote Sensing, 11(6), 676.
10. Jeihouni, M., Alavipanah, S. K., Toomanian, A., & Jafarzadeh, A. A. (2020). Soil texture fractions modeling and mapping using LS-SVR algorithm. Desert, 25(2), 147-154.
11. Jeihouni, M., Alavipanah, S. K., Toomanian, A., & Jafarzadeh, A. A. (2020). Digital mapping of soil moisture retention properties using solely satellite-based data and data mining techniques. Journal of hydrology, 585, 124786.
12. Virnodkar, S. S., Pachghare, V. K., Patil, V. C., & Jha, S. K. (2020). Remote sensing and machine learning for crop water stress determination in various crops: a critical review. Precision Agriculture, 21(5), 1121-1155.
13. Löw, F., & Duveiller, G. (2014). Defining the spatial resolution requirements for crop identification using optical remote sensing. Remote Sensing, 6(9), 9034-9063.
14. Prasad, A. K., Chai, L., Singh, R. P., & Kafatos, M. (2006). Crop yield estimation model for Iowa using remote sensing and surface parameters. International Journal of Applied earth observation and geoinformation, 8(1), 26-33.
15. Doraiswamy, P. C., Moulin, S., Cook, P. W., & Stern, A. (2003). Crop yield assessment from remote sensing. Photogrammetric engineering & remote sensing, 69(6), 665-674.
16. Weiss, M., Jacob, F., & Duveiller, G. (2020). Remote sensing for agricultural applications: A meta-review. Remote sensing of environment, 236, 111402.

Advanced Engineering Days

aed.mersin.edu.tr

Smart agriculture

Mehrdad Jeihouni[*1]

[1]*University of Tabriz, Department of Remote Sensing and GIS, Iran, jeihouni@tabrizu.ac.ir*

Cite this study: Jeihouni, M. (2024). Smart agriculture. Advanced Engineering Days, 9, 341-343

Keywords
Remote Sensing
Spectroradiometers
Sensor Network
Artificial Intelligence
Internet of Things

Abstract

The agricultural sector faces a multitude of challenges in the 21st century. Population growth demands increased food production, while resource scarcity and environmental concerns necessitate sustainable practices. In this regards, smart agriculture, enabled by advanced technologies, offers a promising solution. It should feed a growing population with limited resources while minimizing environmental impact. Smart agriculture uses modern technologies such as sensor network, hyperspectral remote sensing, drones, machine learning, artificial intelligence (AI), the Internet of Things (IoT), robotics, and big data analytics to increase the quality and quantity of crop production. Smart agriculture is a green method, since it minimizes the use of pesticides and fertilizers in agricultural products. This study provides a brief review of smart agriculture fundamentals and its components such as data collection technologies, remote sensing and drone, sensor network, AI and IoT.

Introduction

The burgeoning human population necessitates a paradigm shift in agricultural practices. Traditional agriculture fails to produce high-quality crops due to the lack of advanced technologies, tools, timely information about crops' status and smart management systems [1]. This compels the agriculture industry to embrace innovative practices for optimal and sustainable food production. Two well-known approaches as precision agriculture and smart agriculture have emerged, each leveraging technology to revolutionize farming. However, they differ in their core focus and the depth of technological integration. In this research, our emphasis is on smart agriculture

Limitation of available agricultural land, water scarcity, and climate change lead to the development of smart agriculture. Smart agriculture, has emerged as a powerful solution for optimizing food production and ensuring global food security by employs a fusion of advanced technologies and data-driven algorithms. Employing smart technologies in agriculture, leads to an increase in food security [2]. Smart agriculture uses modern technologies such as sensors, drones, machine learning (ML), artificial intelligence (AI), the Internet of Things (IoT), robotics, big data analytics, etc. to increase the quality and quantity of crop production [3]. These technologies allow monitoring the crop diagnosis, production, fertilization, and other vulnerabilities. Smart agriculture has many benefits for farmers and the environment, it increase crop yield, reduce resource consumption, improve farm management and enhance sustainability.

Smart agriculture is known as a green approach [4], because it diminishes the ecological footprint of traditional farming [5]. Smart irrigation and minimal use of pesticides and fertilizers in agricultural products lead to sustainable agriculture and environmental protection. The components of smart agriculture are presented in Figure 1. This paper will discuss some of the important components of smart agriculture.

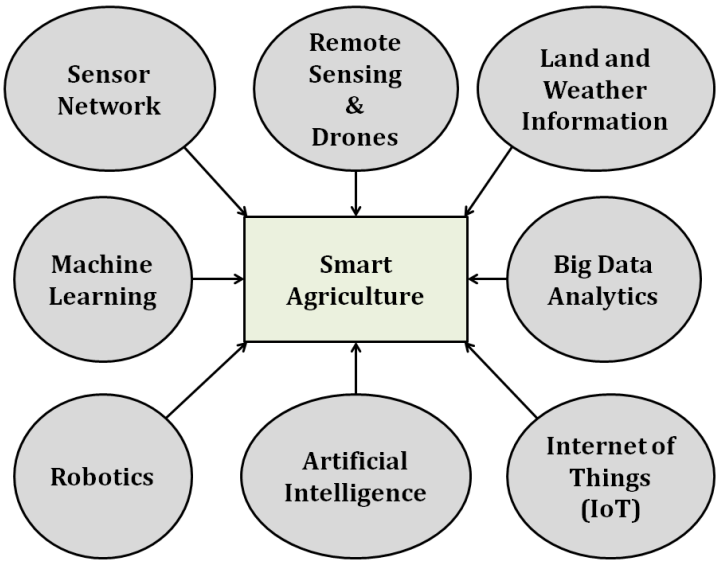


Figure 1. Components of smart agriculture

Data collection technologies

Data forms the backbone of smart agriculture. In smart agriculture, the collected data from sensors, drones, etc. plays a significant role. In fact, meteorological, environmental conditions data can warn farmers against pests and diseases. Farmers can also use the collected data for crop protection and fertilization, resulting in higher yield with minimum environmental impact [6].

Remote sensing and drones

Remote sensing technologies are transforming agricultural practices by providing high-resolution, multispectral data for precision and smart farming. By analyzing data collected from aerial/satellite-based hyperspectral sensors, and field spectroradiometers, scientists and farmers can assess crop health, growth patterns, and environmental stressors. Spectral signatures, unique to different plant species and soil types, allow for the identification of nutrient deficiencies, pest infestations, and water stress. This real-time monitoring empowers data-driven decision making, enabling targeted interventions to optimize fertilizer and water use, minimize crop losses, and ultimately enhance agricultural productivity and sustainability. Drones with spectral and thermal sensors are used as a cheap and fast solution for various purposes such as imaging, plant health monitoring, plant stress, plant diseases, pest management, etc [7]. Moreover, drones are widely used for aerial pesticides, herbicides, fertilizers and foliar spraying application in smart agriculture [8]. This can help to reduce waste and protect the environment.

Sensor network

Smart agriculture requires a network of sensors for data collection [9]. This network acts as the nervous system of a smart agriculture. These sensors are deployed everywhere to collect different types of data such as soil moisture, soil properties, soil temperature, leaf greenness and moisture, precipitation, solar radiation, wind direction, evapotranspiration, etc. in real time [6]. Collecting this crucial information allow farmers to make informed decisions for optimal yield and resource management. For instance, by providing point data at a field-specific level, sensor networks enable farmers to implement precision agriculture practices. Resources like water, fertilizer, and pesticides can be applied only where and when needed, minimizing waste and maximizing efficiency. Sensor networks with probes placed strategically within the soil profile can measure soil moisture content, pH, temperature [10], nutrient levels (nitrogen, phosphorus, potassium, etc.), soil pH, electrical conductivity and organic matter content. This data enables informed decisions regarding irrigation and fertilization practices.

Artificial intelligence

Artificial intelligence (AI) is a branch of computer science focused on intelligent machines. In recent years, the use of artificial intelligence in the agricultural sector has grown significantly [11]. AI with its ability to learn from vast datasets and make intelligent decisions is rapidly transforming smart agriculture domain by enabling powerful data analysis and automation capabilities. AI encompasses a range of techniques such as machine and

deep learning algorithms that enable machines to simulate human intelligence. In smart agriculture, AI algorithms are trained on diverse datasets to perform various tasks, and they learn from vast datasets to make intelligent decisions. Therefore, AI is rapidly transforming agricultural sector.

AI can determine the best crop type and the most suitable time to plant seeds by examining the seasonal sun, weather, wind and rain that affect crop planting cycles [11]. Moreover, AI systems with aid of sensor network can constantly monitor the soil nutrients and compare them with time series data that produced the maximum yields on the specific crop. AI can use datasets to examine the environmental consequences of applying doses and types of fertilizers to find the dose with minimum harmful effect and maximum production. This is how AI helps the agricultural industry to become more environmentally friendly.

Internet of things

The Internet of Things (IoT), a network of interconnected devices collecting and exchanging data, plays a pivotal role in agricultural practice transformation. The concept of IoT is the interaction between all kinds of things or physical objects using the internet connection. The IoT provides the communication infrastructure to connect sensors, vehicles, mobile devices through the Internet [12]. Therefore, farmers can connect to their farms from almost anywhere and anytime employing IoT-enabled technologies [13] and control physical objects of the farm.

Conclusion

This research explores the concept of smart agriculture, explaining its significance, core principles, and the technologies that make it possible. The study highlights how advanced technologies such as sensors, hyperspectral remote sensing, drones, ML, AI, and IoT can revolutionize farming practices. These technologies allow monitoring the crop diagnosis, production, fertilization, aerial pesticides, herbicides, fertilizers and foliar spraying and other vulnerabilities. Smart agriculture has many benefits for farmers and the environment, it increase crop yield, reduce resource consumption, improve farm management and enhance sustainability. Smart agriculture promotes sustainable food production practices and ensures a future of abundance and environmental responsibility. As technology continues to evolve and challenges are addressed, smart agriculture holds immense potential to reshape the global food system for the benefit of generations to come.

References

1. Sarvaiya, J. P., Chaudhari, A. P., & Verma, J. P. (2022). Monitoring agricultural essentials. In Application of Machine Learning in Agriculture (pp. 29-46). Academic Press.
2. Divya, N., Deepthi, S., Kumaar, G. S., & Manoharan, S. (2022). Modeling techniques used in smart agriculture. In Application of Machine Learning in Agriculture (pp. 159-172). Academic Press.
3. Jararweh, Y., Fatima, S., Jarrah, M., & AlZu'bi, S. (2023). Smart and sustainable agriculture: Fundamentals, enabling technologies, and future directions. Computers and Electrical Engineering, 110, 108799.
4. Walter, A., Finger, R., Huber, R., & Buchmann, N. (2017). Smart farming is key to developing sustainable agriculture. Proceedings of the National Academy of Sciences, 114(24), 6148-6150.
5. Boursianis, A. D., Papadopoulou, M. S., Diamantoulakis, P., Liopa-Tsakalidi, A., Barouchas, P., Salahas, G., ... & Goudos, S. K. (2022). Internet of things (IoT) and agricultural unmanned aerial vehicles (UAVs) in smart farming: A comprehensive review. Internet of Things, 18, 100187.
6. Issad, H. A., Aoudjit, R., & Rodrigues, J. J. (2019). A comprehensive review of Data Mining techniques in smart agriculture. Engineering in Agriculture, Environment and Food, 12(4), 511-525.
7. Moradi, S., Bokani, A., & Hassan, J. (2022, November). UAV-based smart agriculture: A review of UAV sensing and applications. In 2022 32nd International Telecommunication Networks and Applications Conference (ITNAC) (pp. 181-184). IEEE.
8. Maddikunta, P. K. R., Hakak, S., Alazab, M., Bhattacharya, S., Gadekallu, T. R., Khan, W. Z., & Pham, Q. V. (2021). Unmanned aerial vehicles in smart agriculture: Applications, requirements, and challenges. IEEE Sensors Journal, 21(16), 17608-17619.
9. Curiac, D. I. (2016). Towards wireless sensor, actuator and robot networks: Conceptual framework, challenges and perspectives. Journal of Network and Computer Applications, 63, 14-23.
10. Thakur, D., Kumar, Y., Kumar, A., & Singh, P. K. (2019). Applicability of wireless sensor networks in precision agriculture: A review. Wireless Personal Communications, 107, 471-512.
11. Javaid, M., Haleem, A., Khan, I. H., & Suman, R. (2023). Understanding the potential applications of Artificial Intelligence in Agriculture Sector. Advanced Agrochem, 2(1), 15-30.
12. Zhang, L., Dabipi, I. K., & Brown Jr, W. L. (2018). Internet of Things applications for agriculture. Internet of things A to Z: technologies and applications, 507-528.
13. Sinha, B. B., & Dhanalakshmi, R. (2022). Recent advancements and challenges of Internet of Things in smart agriculture: A survey. Future Generation Computer Systems, 126, 169-184.

Advanced Engineering Days

aed.mersin.edu.tr

Surface soil moisture Retrieval using Sentinel-1 SAR data models Dubois in Ardabil Plain

Maryam Sadeghi [*1], **Sadra Karimzadeh** [1], **Khalil Valizadeh Kamran** [1]

[1] *University Tabriz, Faculty of Planning and Environmental Science, Department of Remote Sensing and Geographic Information System, Tabriz, Iran., sadegi.maryam92@gmail.com, sadra.karimzadeh@gmail.com, valizadeh@tabrizu.ac.ir*

Cite this study: Sadeghi, M., Karimzadeh, S., & Valizadeh Kamran, K. (2024). Surface soil moisture Retrieval using Sentinel-1 SAR data models Dubois in Ardabil Plain. Advanced Engineering Days, 9, 344-348

Keywords
Soil moisture
Surface roughness
Dubois Model
Ardabil Plain
SENTINEL-1

Abstract

In this study, the Modified Dubois Model semi-empirical model with Topp's model is used to retrieve soil moisture. It involves retrieving the backscattering coefficient from SENTINEL-1 datasets to derive the surface roughness and soil moisture conditions. Firstly, In the Ardabil Plain region, The extracted backscattering for band c sentinel images in 2023/11/06 calculated surface roughness for VV and VH with linear regression. For the Sentinel image on November 6, 2023, as well as from the Sentinel 2 image, the areas with an area >=0.4 were masked from the backscattering image. The performance of the models is evaluated based on field measurements, and the mentioned backscattering model, dobus, is performed for vv and VH with root mean square error (RMSE) of 0.56 and 0.55 dB and mean surface height roughness of .45 cm and 0.002 cm, respectively. The Dubois model estimated relative soil moisture from the backscatter values (σ°) of VV and VH polarizations. The key findings demonstrated that VV polarization obtained higher accuracy in soil moisture recovery. Also, the results of The Top Dubois SSM model is derived from the model that was estimated to have a correlation of 0.64 with SSM in situ, a coefficient of determination of 0.45, and a root mean square error (RMSE) of 0.56.

Introduction

Soil surface moisture is one of the influential elements in hydrology and agriculture. It is an effective parameter as a management Application in agriculture, ecology, hydrology, meteorology, climatology, drought, and flood forecasting on the ground (1). Soil moisture retrieval is often provided on a point-based because surface moisture retrieval over large areas is often time-consuming and difficult due to temporal and spatial variations. Therefore, it is very important to retrieve the surface moisture of the soil at different levels (2). One of the ways that potentially can be achieved using Remote sensing images technologies (2). Currently, because of open access to high resolution and revisit time C-band, the Sentinel-1 constellation is considered the most useful image in soil moisture estimation (1). empirical models, semi-empirical, and theoretical have been proposed to solve these problems (3-5) for the estimation of SSM over bare soil or sparsely vegetated surfaces. surface roughness and Relative soil permittivity can be retrieved from the intensity of radar backscatter by employing various empirical, semi-empirical, and theoretical models (6-12). the Dubois model has the advantage of working even on the sparsely vegetated surface as well as barren land. (11-13) found that soil moisture predicted by the Dubois model is Better performance than the Integral Equation Model (IEM) or Oh models.

Material and Method

Study area

The study area (15) is Ardabil plain, with an approximate area of 1097.23 km2, is an inter-mountain plain located in northwestern Iran with geographical coordinates of 38°5' to 38°27' N and 48°9' to 48°37' E (Fig. 1). The study area has been under conventional tillage system and the sampling sites had arable lands use (16). The

general groundwater flows from other directions into the north–west of the plain48. More than 85% of exploited groundwater is used for agricultural activities, 14% is used for drinking purposes and 1% for industrial use. The climate of the study area is cold and semi-arid (17).

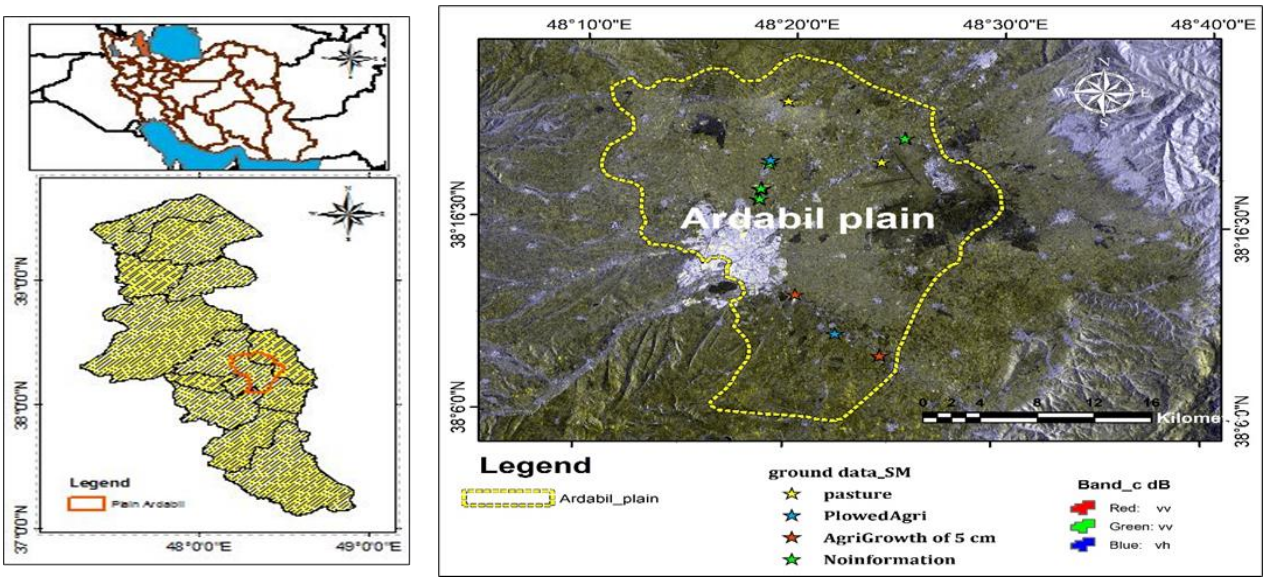


Figure 1. The location is Plain Ardabil in Iran. In-situ SSM measurements were taken (N = 21 samples) over agricultural land including plowed agricultural land, agricultural land with 5 cm of growth, and pasture. This information is overlaid on the image with RGB combinations (VV, HV) from November 6th, 2023.

Satellite data and Method

In this study, we utilized interferometric wide-swath (IW) mode images of SLC and Sentinel-2 for 2023/11/06. SLC in dual-polarization modes (VV and VH) to retrieve soil moisture with a pixel size of 10 m × 10 m. Typically, the level-1 SLC product information indicates the in situ measurements of soil moisture for vertical–vertical (VV) and vertical–horizontal (VH). Sentinel-2B data are available at a spatial resolution of 10 m × 10 m, and it was used to derive an NDVI map over the study area (8). The moisture of the topsoil (depth 0 to 5 cm) was measured by the drying soil moisture method. Sampling was performed on 06/11/2023 when the satellite passed through the area. In situ measurements include 21 samples on bare soil, pasture, and agricultural fields (Baghdadi et al., 2012). Also, the coordinates of the sampling points were taken by GPS. Sentinel Application Platform (SNAP V.9.0.8) software was used for preprocessing Sentinel-1A images. It includes standard procedures such as data import, orbit file application, radiometric calibration, multiview, speckle filter, geometric ground correction, and data conversion (linear to dB) (8). A semi-empirical model has been derived by Dubois (7). the expressions of σ◦VV and σ◦ VH of the modified Dubois model by Baghdadi et al (9,1) are given by Equations (1) and (2):

$$\sigma^{\circ}_{VV} = 10^{-2.37}(\cos^3\theta/\sin^3\theta)\, 10^{0.046\varepsilon\tan\theta}\,(ks\sin\theta)^{1.1}\,\Lambda^{0.7} \quad (1)$$

$$\sigma^{\circ}_{VH} = 10^{-2.75}(\cos^{1.5}\theta/\sin^5\theta)\, 10^{0.028\varepsilon\tan\theta}\,(ks\sin\theta)^{1.4}\,\Lambda^{0.7} \quad (2)$$

where θ is the incidence angle, s is the soil surface roughness (cm), λ is the SAR wavelength (5.6 cm), and k is (2π/λ). The θ and λ are related to the sensor parameters, while and s are the target parameters which are usually unknown θ and expressed in radians in Equations (1) and (2) show that the sensitivity of the radar signal to the soil moisture in decibel scale is dB in VH and VV polarization for an incidence angle of 36◦ (SAR incidence angle in this study 34-38) θ is the incidence angle, ϵ is the real part of the dielectric constant or the relative soil permittivity, and S is the soil surface roughness that indicates the variation in vertical height on the ground (18, 19). k=(2π/λ) is the wave number and λ is the wavelength of the radar. Equation (2) has been inverted to the following formula (7,20). Albeit initially, the model was developed for quad-polarized data for retrieving SSM, but the modified Dubois model allowed to retrieval of SSM using the dual-polarized SAR data like Sentinel–1A. As per the modified Dubois model," can be calculated using Equation (3) using VV and VH polarizations.

$$\varepsilon = \frac{Log(\sigma^{\circ}vv) - Log(AC)}{B} \quad (3)$$

where A = 10-2.37(cos3θ/sin3θ), B = 0.04tanθ, and C=(ks×sinθ)1.1λ0.7. The incidence angle was considered consistent at 38.5 (i.e., middle incidence angle of 30.8-46.0°), wavelength (λ) is 5.3 cm, and the unknown component soil surface roughness "s" was assigned (21,8) as VV 0.44 (0.93-1.03cm) and VH 0.0014 (0.0009-1.93cm).

Results

Here, cross the same polarization VV and ratio of VHwhit using the field measured samples Homosan was used to calculate the root surface roughness of the average surface height with a linear regression model by plotting Vane VH (22). RMS height was correlated to derive surface roughness models VV -0.75 and VH 0.14 and the coefficient of determination was 0.56 and 0.019 estimated at 0.2 and 0.58, respectively. Results of the regression analysis are given in Fig (2).

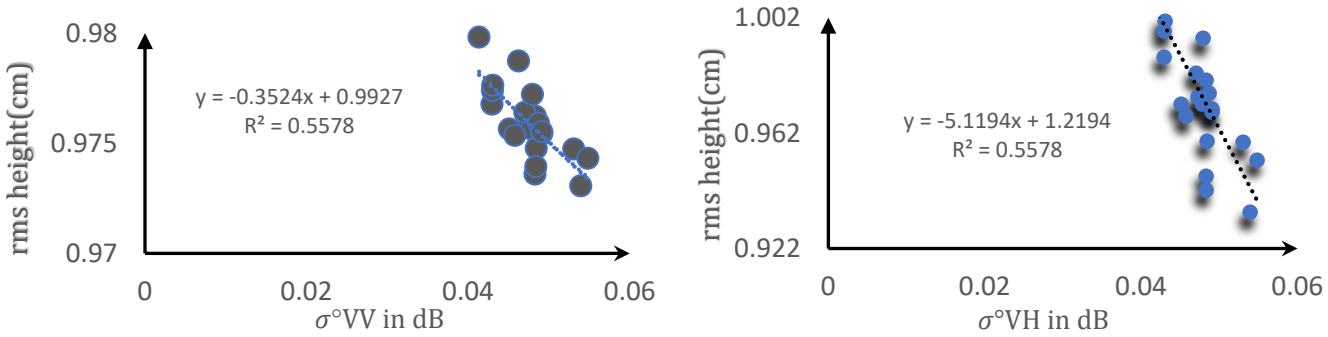


Figure 2. Variation of S σ°VH and S σ°VV with surface roughness (rms height).

Next, the relationship between σ0 values extracted from synthetic aperture radar (SAR) images for soil moisture estimation was obtained using the modified calibrated integral equation of the Dubois model in VV and VH polarizations for November 6, 2023. polarizations soil moisture effect can increased by incorporating VH polarization which is mainly responsible for the backscattering from vegetation biomass. (23, 24). But in this study, due to the fact that in the autumn season, barren and plowed land, pasture and some samples of agricultural fields were measured at the beginning of growth (0-5 cm); The result of backscattering VV obtained high accuracy in soil moisture estimation (Fi g. 3) The NDVI map obtained from Sentinel 2, most of the land coverage areas are between zero and 0.2 valus, which shows the bareness of the studied area Fig (4). In this study, NDVI greater than 0.4 was masked on the backscater obtained from the Sentinel-1 image and then used to calculate so the radar distribution for VV and VH Fig (5).

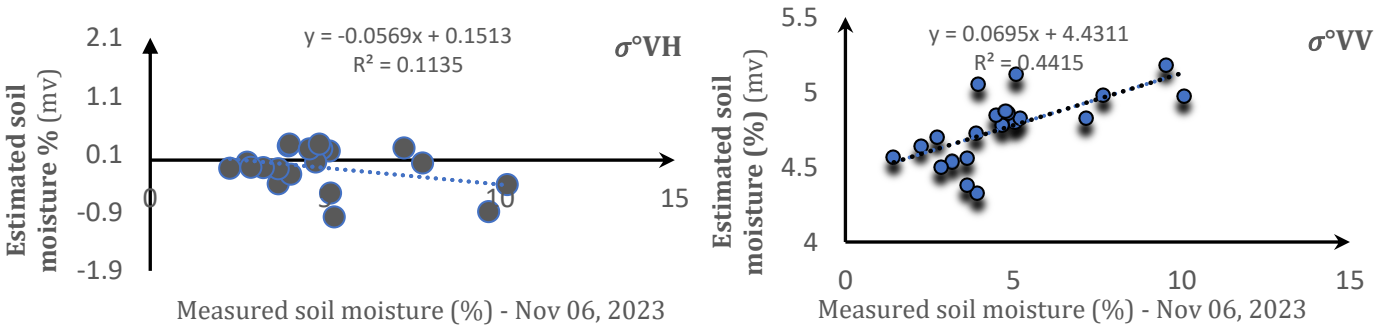


Figure 3. Least squares regression line between in situ measured SSM(normalize) and Topp's model Dubois(mv. %) for VV and VH and satellite derived soil moisture (n= 21) for a Novamber 06, 2023

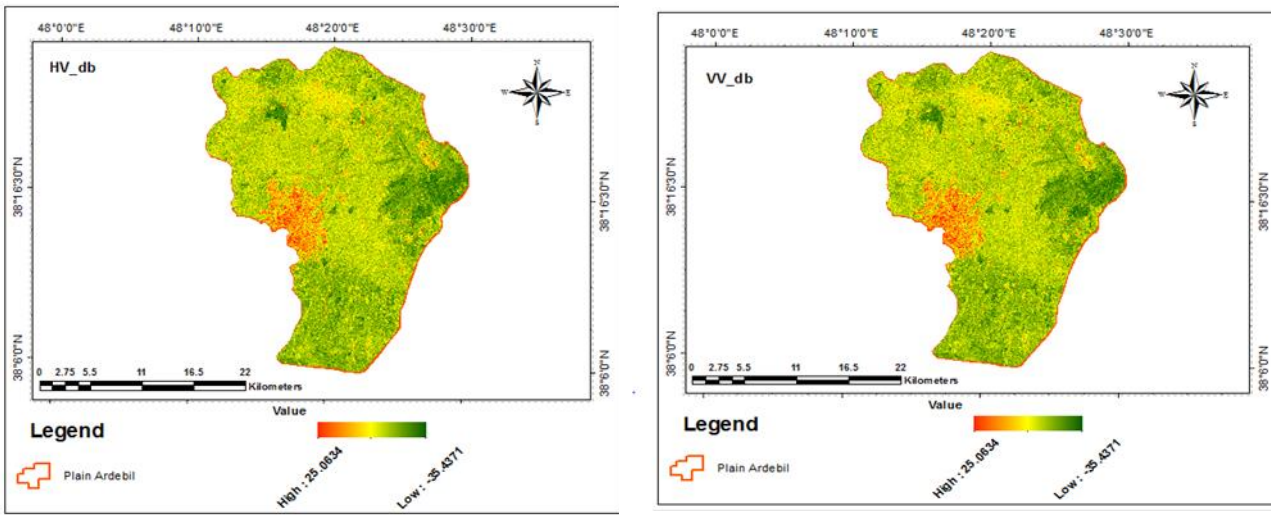


Figure 5. Spatial distribution of estimated SSM (m3/m3) from C-band of Sentinel-1. Pixels shown in white correspond to the region where the NDVI mask was applied (>=0.4).

Discussion

The present study has deployed VV polarization of the C-band of Sentinel-1A to retrieve the spatial pattern of SSM over bare soil and Plowed agricultural land Wet agricultural land (05 cm) and pasture On 06th November 2023. fields. Statistical analysis of the backscattering coefficients for VV was better than VH polarizations. for surface roughness evaluation from the Sentinel-1 images, we obtained sVV and sVH in the height value of the correlate. which strongly suggests that the depolarization ratio defined by sVH, sVV is a good indicator (22) of surface roughness derived from multi-polarized SAR data Retrieval soil moisture was retrieved from the modified Dubois model approach along with Topp's model (Eq. 4). Their accuracy was evaluated with the ground-measured soil moisture data (n=21) collected from different agricultural sites. The valid regions were estimated for the modified Dubois model using suitable NDVI criteria when NDVI ≤ 0.4.

Conclusion

In this study, models presented more accurate results in VV polarization. The obtained results led to the conclusion that the Top Dubois model in VV ratio to the VH polarization in Ardabil plain performs with satisfying accuracy. The results of this study that VV polarization was less affected by vegetation and thus captured SM changes more effectively than VH. It is consistent with the study (25). Several studies have demonstrated that VH polarization is more sensitive to vegetation dynamics and volume scattering than VV polarization, which is responsive to both surface and volume scatterings with direct contributions from the ground (26).

References

1. Mirsoleimani, H. R., Sahebi, M. R., Baghdadi, N., & El Hajj, M. (2019). Bare soil surface moisture retrieval from sentinel-1 SAR data based on the calibrated IEM and dubois models using neural networks. Sensors, 19(14), 3209.
2. Şekertekin, A., Marangoz, A. M., & Abdikan, S. (2018). Soil moisture mapping using Sentinel-1A synthetic aperture radar data. International Journal of Environment and Geoinformatics, 5(2), 178-188.
3. Saux-Picart. S., (2009)."Water and energy budgets simulation over the AMMA-Niger super-site spatially constrained with remote sensing data," J. Hydrol., vol. 375, no. 1/2, pp. 287–295.
4. Blöschl, G. (2019)."Twenty-three unsolved problems in hydrology (UPH)–A community perspective," Hydrological Sci. J., vol. 64, no. 10, pp. 1141–1158.
5. Yang, H., Song, J., Teng, Y., Song, X., Zeng, P., & Jia, J. (2023). Coupling model-driven and data-driven methods for estimating soil moisture over bare surfaces with Sentinel-1A dual-polarized data. IEEE Journal of Selected Topics in Applied Earth Observations and Remote Sensing.
6. Oh, Y., Sarabandi, S., & Ulaby, F. T. (1992). "An empirical model and an inversion technique for radar scattering from bare soil surfaces," IEEE Trans. Geosci. Remote Sens., vol. 30, no. 2, pp. 370–381.
7. Dubois, P. C., Van Zyl, J., & Engman, T. (1995). Measuring soil moisture with imaging radars. *IEEE transactions on geoscience and remote sensing*, *33*(4), 915-926.
8. Munda, S., Gartia, R., & Dash, S. R. (2023). Exploring Agricultural Disparities in Western Odisha: A Comprehensive Study Based on Composite Index Scores. Current Agriculture Research Journal, 11(3).

9. Baghdadi, N., Cresson, R., El Hajj, M., Ludwig, R., & La Jeunesse, I. (2012). Estimation of soil parameters over bare agriculture areas from C-band polarimetric SAR data using neural networks. *Hydrology and Earth System Sciences*, *16*(6), 1607-1621.
10. Dabrowska-Zielinska, K., Musial, J., Malinska, A., Budzynska, M., Gurdak, R., Kiryla, W., ... & Grzybowski, P. (2018). Soil moisture in the Biebrza Wetlands retrieved from Sentinel-1 imagery. *Remote Sensing*, *10*(12), 1979.
11. Thanabalan, P., Kankara, R. S., & Prabhu, K. (2022). Sentinel-1 Synthetic Aperture Radar (SAR) characteristics on shoreline demarcation and change assessment along Mandaikadu, south-west coast of India for the year 2018–2019. *Journal of Coastal Conservation*, *26*(2), 9.
12. Neusch, T., & Sties, M. (1999). Application of the Dubois-model using experimental synthetic aperture radar data for the determination of soil moisture and surface roughness. ISPRS journal of photogrammetry and remote sensing, 54(4), 273-278.
13. Sikdar, M., & Cumming, I. (2004, September). A modified empirical model for soil moisture estimation in vegetated areas using SAR data. In *IGARSS 2004. 2004 IEEE International Geoscience and Remote Sensing Symposium* (Vol. 2, pp. 803-806). IEEE.
14. Neusch, T., & Sties, M. (1999). Application of the Dubois-model using experimental synthetic aperture radar data for the determination of soil moisture and surface roughness. *ISPRS journal of photogrammetry and remote sensing*, *54*(4), 273-278.
15. Valizadeh Kamran, Kh., Sadeghi,M & Hejazi, S.A. (2021). Modeling Land Changes forest Using by LCM in Fandoqhlo Forest Area (Ardabil), Journal of Civil and Environmental Engineering Volume (2021), Issue 1 (spring) 04 November 2020; Accepted: 15 May 2021.
16. Asghari Saraskanroud, S., Snafdiari, Fariba., Darabad,F., Melanuri, E, & Safari, S. (1401). Survey of soil surface moisture in Ardabil city using Landsat 8 and Centile 1 satellite data, thematic axes: computer application in water and soil issues, Protection of water and soil resources (scientific-research). Volume 11, Number 4 - Serial Number 44, July 1401, Page 89-103. DOI. 10.30495/WSRCJ.2022.20006.
17. Ulaby FT, Batlivala PP, Dobson MC (1978) Microwave backscatterdependence on surface roughness, soil moisture, and soil texture: part I-bare soil. IEEE Trans Geosci Electron 16:286–295. https://doi.org/10.1109/TGE.1978.294586
18. Jackson TJ (1993) Measuring surface soil moisture using passive microwave remote sensing. Hydrol Process 7:139–152. https:// doi.org/10.1002/hyp.3360070205
19. Minacapilli, M., Iovino, M., & D'Urso, G. (2006, August). Crop and irrigation water management using high resolution remote sensing and agrohydrological models. In *AIP Conference Proceedings* (Vol. 852, No. 1, pp. 99-106). American Institute of Physics.
20. Gharechelou, S., Tateishi, R., Sri Sumantyo, J. T., & Johnson, B. A. (2021). Soil moisture retrieval using polarimetric SAR data and experimental observations in an arid environment. ISPRS International Journal of Geo-Information, 10(10), 711.
21. Srivastava, M., Begovic, E., Chapman, J., Putnam, N. H., Hellsten, U., Kawashima, T., ... & Rokhsar, D. S. (2008). The Trichoplax genome and the nature of placozoans. *Nature*, *454*(7207), 955-960.
22. Beaudoin, B. C. (1994). Lower-crustal deformation during terrane dispersion along strike-slip faults. *Tectonophysics*, *232*(1-4), 257-266.
23. Ogollah, K., Rucha, K., Aroni, J., & Gichiri, N. (2019). ASSESSMENT REPORT OF THE SOCIO-ECONOMIC IMPACT OF THE OPERATIONALIZATION OF THE MOMBASA-NAIROBI STANDARD GAUGE RAILWAY ON PORT CITY MOMBASA. *Nairobi: School of Business, University of Nairobi*.
24. Zhang, Z., Liu, F., Han, E. H., Xu, L., & Uzoma, P. C. (2019). Effects of Al2O3 on the microstructures and corrosion behavior of low-pressure cold gas sprayed Al 2024-Al2O3 composite coatings on AA 2024-T3 substrate. Surface and Coatings Technology, 370, 53-68.
25. Ghafari, M., Hall, M., Golubchik, T., Ayoubkhani, D., House, T., MacIntyre-Cockett, G., ... & Lythgoe, K. (2024). Prevalence of persistent SARS-CoV-2 in a large community surveillance study. *Nature*, 1-8.

Advanced Engineering Days

aed.mersin.edu.tr

Exploring the Potential of U-Net Architectures for Classifying Different Maize Genotypes Using Multispectral UAV Imagery

Ismail Colkesen*[1], Umut Gunes Sefercik[1], Taskin Kavzoglu[1], Mustafacan Saygi[2], Muhammed Yusuf Ozturk[1], Osman Yavuz Altuntas[1], Mertcan Nazar[1], Ilyas Aydin[1], HasanTonbul[1]

[1]*Gebze Technical University, Engineering Faculty, Department of Geomatics Engineering, Türkiye, icolkesen@gtu.edu.tr*
[2]*Gebze Technical University, Institute of Earth and Marine Sciences, Türkiye, msaygi@gtu.edu.tr*

Cite this study: Colkesen, I., Sefercik, U.G., Kavzoglu, T., Saygi, M., Ozturk, M.Y., Altuntas, O.Y., Nazar, M., Aydin, I. & Tonbul, H. (2024). Exploring the Potential of U-Net Architectures for Classifying Different Maize Genotypes Using Multispectral UAV Imagery. Advanced Engineering Days, 9, 349-352

Keywords
Deep Learning
Maize
Digital Agriculture
UAV
UNet

Abstract

The increasing demand for digital agriculture necessitates agricultural productivity and environmental sustainability advancements. Unmanned Aerial Vehicle (UAV)-based remote sensing technologies offer valuable insights for enhancing crop yields and optimizing resource use compared to traditional ground-based data collection methods. Processing these data sets with deep learning algorithms enables the extraction of precise and highly accurate information about the status of agricultural products during the growing stage. This study employs U-Net, a deep learning architecture based on convolutional neural networks, and Attention Residual U-Net (ARU-Net), which integrates attention gates and residual blocks, to classify 12 maize genotypes from multispectral UAV images. The results demonstrate that the crop map produced with ARU-Net outperforms the classical U-Net in all metrics based on the accuracy assessment. Specifically, in the test dataset comparison, the crop map produced with ARU-Net achieved an F-Score above 90% for all classes, while the U-Net model classified ten maize genotypes with an F-Score of 90% or higher.

Introduction

With a current population of more than 8 billion people, the world's population is expected to exceed 10 billion in about 25 years with a rapidly growing population, necessitating a 70% increase in food supply [1]. Despite this situation, due to the limited cultivated area, the yield obtained from limited cultivated areas must be increased [2]. At this point, intelligent agriculture applications, primarily based on autonomous systems that utilize advanced sensors and artificial intelligence techniques, are vital to increasing agricultural productivity. Using up-to-date equipment such as Unmanned Aerial Vehicle (UAV) technologies in digital agriculture applications provides significant advantages in managing and continuously monitoring limited resources [3]. In this way, it is possible to increase agricultural productivity and sustainability at lower costs, with less labour and, indirectly, less time loss. Additionally, artificial intelligence techniques have successfully extracted precise and highly accurate data from large data sets obtained from UAV systems, an essential tool for the success of agricultural activities and increasing productivity [4]. In recent years, there has been a growing academic interest in smart agriculture applications, mainly focusing on integrating UAV-based data collection technologies and artificial intelligence [5-8]. For example, crop yield prediction with a mean absolute error of 5.51% was achieved by integrating Convolution Neural Network (CNN) and Long-Short Term Memory deep learning architectures from multi-temporal RGB UAV images [9]. In another study, food crop identification was performed from UAV-derived RGB imagery with an average F-Score of 86% using the VGG16 deep learning model [10]. The primary objective of the study is to investigate the effectiveness and potential use of U-shaped deep learning architectures (i.e. U-Net and Attention Residual U-Net) in mapping 12 maize genotypes having similar spectral characteristics using multispectral UAV imagery, which is different from the problems of mapping different crop types frequently encountered in the literature.

Study Area and Dataset

The study area is situated in the field where agricultural activities are conducted by the Sakarya Maize Research Institute in the Arifiye district of Sakarya province, located in northwestern Turkey (Figure 1). In the study area, 12 parcels, each approximately 500m^2 (25m x 20m) and totaling approximately 6900m^2, were designated as test areas for cultivating 12 different maize genotypes. The main dataset used in the study is the orthomosaic acquired on August 24, 2023 from a DJI Phantom 4 UAV equipped with a five-band multispectral camera (Red, Green, Blue, Red edge and Near Infrared). Aerial photographs were acquired at a flight altitude of 50 m with 80% forward and 60% side overlap and orthomosaics were produced using Agisoft Metashape Professional with a Ground Sampling Distance of 2.7 cm and 16-bit resolution. In addition, the pixel differences between the Digital Surface Model and the Digital Terrain Model produced by the DJI Phantom 4 v2 RGB UAV were used to calculate the plant heights called the Canopy Height Model (CHM).

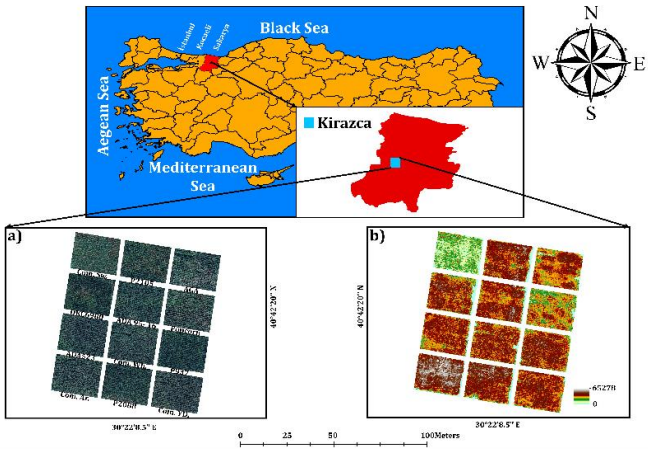


Figure 1. The location of the study area.

Methodology

Within the scope of the study, classical U-Net architecture and the Attention Residual U-Net (ARU-Net) model, an integrated version of residual blocks and attention mechanism, were used to classify 12 different maize genotypes in the study area. The U-Net deep learning model consists of two parts, the encoder and the decoder, and a U-shaped structure [11]. The encoder part aims to extract different features in the image using the classical CNN architecture (Falk et al., 2019). Within this research framework, there are 5-layer groups in total in the encoder part in structures. 3 x 3 convolution layers, batch normalization, Rectified Linear Units (ReLU) activation function, and finally, 2 x 2 maximum pooling layers are used in these layer groups. The pooling layer reduces the size of the feature map. Therefore, 2 x 2 upsampling is added to the second part as a decoder of the U-Net model. The symmetric expansion path provides precise localization through transposed convolutions [12]. The second part of the network consists of upsampling and concatenation followed by typical convolution operations. In the final layer, a 1 x 1 convolution reduces the feature map to the required number of channels to produce the result image. ARU-Net is an end-to-end segmentation network that simultaneously integrates attention mechanisms and residual blocks into the classic U-Net architecture. Attention gates gradually suppress feature responses in irrelevant background regions without the need to clip the region of interest across networks [13]. The residual blocks increase the information flow within the network by overcoming the vanishing gradient problem encountered in deep CNN architectures [14]. Thus, it facilitates information dissemination through rich skip connections within the network, resulting in superior performance with fewer parameters [15].

Results

In addition to the spectral bands derived from the multispectral image for distinguishing between different maize genotypes, the input datasets also included the five components obtained through principal component analysis and canopy height model (CHM) data. Subsequently, artificial data augmentation techniques (90°, 180°, and 270° clockwise rotation) were applied to increase the size of the limited data set for classifying maize genotypes while preserving spectral structure. The resulting dataset was partitioned into 126 x 126 dimensions to develop patch-based deep learning models. Finally, a one-dimensional zero padding was applied to prevent potential errors during the mosaicking of prediction patches, resulting in patches of 128 x 128 dimensions. Consequently, 6916 patches of 128 x 128 dimensions were generated, and the dataset was randomly divided into training (70%), validation (20%), and test (10%) datasets. Python programming language and PyTorch deep learning framework were utilized to construct the U-shaped deep learning models. The models were trained on a high-capacity workstation in the inventory of Gebze Technical University Advanced Remote Sensing Technology Laboratory (ARTLAB). Both models were trained under identical conditions to ensure objective comparisons between models, including a 128 x 128 input size, 100 epochs, 64 batch size, 0.9 momentum, and 0.001 learning rate. Furthermore,

the Adam optimizer was employed for model optimization, while the categorical cross-entropy loss function was selected as the loss function. The best epoch for model prediction was determined based on the minimum validation loss values observed during model training. In the normalized loss graphs obtained from the training phase of the models, no overfitting was observed, and the loss values showed a decreasing trend (Figure 2). The analysis performed by considering the loss graphs showed that the ARU-Net model experienced the minimum loss at the 65th epoch and the U-Net model experienced the minimum loss at the 75th epoch.

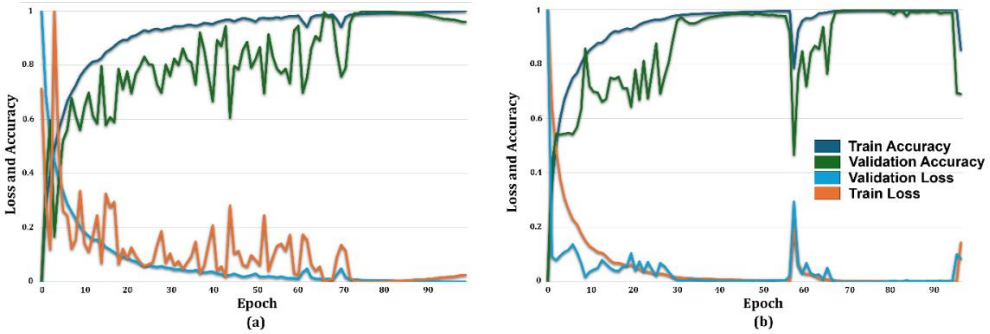


Figure 2. Normalized loss graphs and accuracy values obtained during the training of the models. U-Net (a), and ARU-Net (b).

In the assessment of the performance of the deep learning models, precision, recall, F-Score, Intersection over Union (IoU), Cohen's Kappa coefficient, Dice coefficient, and overall accuracy metrics, which are commonly used in deep learning applications, were calculated for both models (Table 1). Through performance evaluation conducted using a test dataset comprising 692 patches, the ARU-Net (97.06%) model exhibits superior performance to the U-Net (95.69%) model across overall accuracy. On the other hand, the evaluation based on the mean IoU metric shows the highest difference (approximately 4%) between the two models. According to the other accuracy assessment metrics, the difference between the two models is approximately 2%.

Table 1. Accuracy assessment results for U-Net and ARU-Net.

Metrics / Model	U-Net	ARU-Net
Recall	92.51%	94.89%
Precision	93.24%	94.92%
F-Score	92.84%	94.87%
Mean IoU	86.78%	90.36%
Cohen's Kappa	93.30%	95.80%
Dice	95.52%	97.18%
Overall Accuracy	95.69%	97.06%

The results of both models were also compared using the class-based F-Score metric in the direction of the crop maps obtained as a result of classification. Similar to the accuracy assessment metrics, ARU-Net outperformed the U-Net model in classifying all maize genotypes. In the crop map obtained using the ARU-Net model, all maize genotypes were classified with an accuracy of over 90%. In the crop map created using the U-Net model, ten classes were classified with an accuracy score of 90% and above. The lowest F-Score metric obtained from both models was in the Composite White (Com. Wh.) genotype (Figure 3). The highest accuracy score was obtained in the genotype P937 in the U-Net (96.47%) model, while Composite Sweet (Com. Sw.) was obtained in the ARU-Net (97.59%) model.

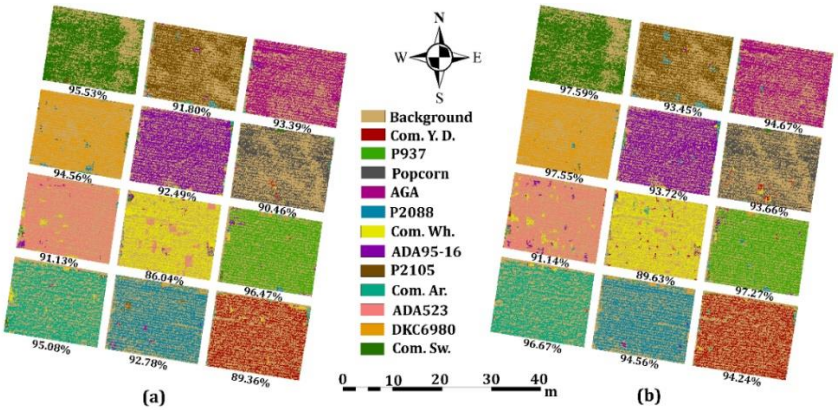


Figure 3. Results of the classified maize genotypes. U-Net (a), and ARU-Net (b).

Conclusion

The study's main objective is to compare the performance of the classical U-Net model and the up-to-date ARU-Net model, an enhanced U-Net integrating attention gate and residual blocks, in classifying 12 maize genotypes from UAV images. The results showed that the ARU-Net model outperformed the U-Net model in terms of average F-Score metric with a difference of 2.03% and better class-based F-Score metric values for the classification of all maize genotypes. Qualitative and quantitative evaluations, based on the most used accuracy assessment metrics and visual interpretation, demonstrate the effectiveness and feasibility of using the ARU-Net model to classify maize genotypes from UAV-derived imagery. While the obtained results show that the classification performance with the U-Net-based ARU-Net model is superior to the classical U-Net model, it should be compared with models built using different deep learning models with deeper network structure and 3D CNN in future studies.

Acknowledgment

This study was supported by the Scientific and Technological Research Council of Turkey (TUBITAK) under Grant Number 121Y392. The authors thank to TUBITAK for their supports. Special thanks to the Ministry of Agriculture and Forestry Sakarya Maize Research Institute for their valuable contributions to the project

References

1. Hunter, M. C., Smith, R. G., Schipanski, M. E., Atwood, L. W., & Mortensen, D. A. (2017). Agriculture in 2050: recalibrating targets for sustainable intensification. Bioscience, 67(4), 386-391.
2. Moradi, S., Bokani, A., & Hassan, J. (2022). UAV-based smart agriculture: A review of UAV sensing and applications. In 2022 32nd International Telecommunication Networks and Applications Conference (ITNAC) (pp. 181-184). IEEE.
3. Food and Agriculture Organization (FAO). Digital Agriculture. Available online: http://www.fao.org/digital-agriculture/en/ (available on 27 May 2024).
4. Hassler, S. C., & Baysal-Gurel, F. (2019). Unmanned aircraft system (UAS) technology and applications in agriculture. Agronomy, 9(10), 618.
5. Ampatzidis, Y., Partel, V., & Costa, L. (2020). Agroview: Cloud-based application to process, analyze and visualize UAV-collected data for precision agriculture applications utilizing artificial intelligence. Computers and Electronics in Agriculture, 174, 105457.
6. Malek, S., Bazi, Y., Alajlan, N., AlHichri, H., & Melgani, F. (2014). Efficient framework for palm tree detection in UAV images. IEEE Journal of Selected Topics in Applied Earth Observations and Remote Sensing, 7(12), 4692-4703.
7. Kussul, N., Lavreniuk, M., Skakun, S., & Shelestov, A. (2017). Deep learning classification of land cover and crop types using remote sensing data. IEEE Geoscience and Remote Sensing Letters, 14(5), 778-782.
8. Cruz, A. C., Luvisi, A., De Bellis, L., & Ampatzidis, Y. (2017). X-FIDO: An effective application for detecting olive quick decline syndrome with deep learning and data fusion. Frontiers in plant science, 8, 289333.
9. Nevavuori, P., Narra, N., Linna, P., & Lipping, T. (2020). Crop yield prediction using multitemporal UAV data and spatio-temporal deep learning models. Remote Sensing, 12(23), 4000.
10. Chew, R., Rineer, J., Beach, R., O'Neil, M., Ujeneza, N., Lapidus, D., ... & Temple, D. S. (2020). Deep neural networks and transfer learning for food crop identification in UAV images. Drones, 4(1), 7.
11. Ronneberger, O., Fischer, P., & Brox, T. (2015). U-net: Convolutional networks for biomedical image segmentation. In Medical image computing and computer-assisted intervention–MICCAI 2015: 18th international conference, Munich, Germany, October 5-9, 2015, proceedings, part III 18 (pp. 234-241). Springer International Publishing.
12. Siddique, N., Paheding, S., Elkin, C. P., & Devabhaktuni, V. (2021). U-net and its variants for medical image segmentation: A review of theory and applications. Ieee Access, 9, 82031-82057.
13. Oktay, O., Schlemper, J., Folgoc, L. L., Lee, M., Heinrich, M., Misawa, K., ... & Rueckert, D. (2018). Attention u-net: Learning where to look for the pancreas. arXiv preprint arXiv:1804.03999.
14. Yu, L., Chen, H., Dou, Q., Qin, J., & Heng, P. A. (2016). Automated melanoma recognition in dermoscopy images via very deep residual networks. IEEE transactions on medical imaging, 36(4), 994-1004.
15. Zhang, Z., Liu, Q., & Wang, Y. (2018). Road extraction by deep residual u-net. IEEE Geoscience and Remote Sensing Letters, 15(5), 749-753.

Advanced Engineering Days

aed.mersin.edu.tr

Monitoring Land Cover Changes by Satellite Images Using Deep Learning Neural Network Models in Tehran with a Sustainable Development Approach

Mahdi Farhangi*[1], Gholamreza Fallahi [1], Alireza Gharagozlou [1]

[1]*Shahid Beheshti University, Faculty of civil, water and environmental engineering, Iran, ma.farhangi@mail.sbu.ac.ir; g_fallahi@sbu.ac.ir; a_gharagozlo@sbu.ac.ir*

Cite this study: Farhangi, M., Fallahi, G., & Gharagozlou, A. (2024). Monitoring Land Cover Changes by Satellite Images Using Deep Learning Neural Network Models in Tehran with a Sustainable Development Approach. Advanced Engineering Days, 9, 353-355

Keywords
Land Cover Classification
Neural Networks
Deep Learning
Change Detection
Sustainable urban development

Abstract

This study investigates the changes in vegetation cover and surface water resources in Tehran from 2015 to 2024 using Sentinel-2 satellite imagery and neural networks. The main objective of this research is to evaluate and analyze the changes in vegetation cover and water resources over the specified period and to produce high-accuracy land use maps. Sentinel-2 satellite data were classified using a neural network algorithm with three hidden layers and 100 epochs. The classification accuracy was assessed using maps prepared by operators in three different areas of Tehran, and the average accuracy for all 22 districts of Tehran was calculated. The results of this study show a 47.49% increase in the vegetation cover area, while the area covered by water has experienced multiple fluctuations over the study period. This research demonstrates the high accuracy of land use and land cover classification and environmental change monitoring using advanced deep learning methods and satellite imagery, which can provide valuable insights for managerial decision-making and planning at the city and provincial levels.

Introduction

Cities, as dynamic environments, require continuous and precise monitoring for optimal management of their natural resources. In this regard, vegetation cover and water resources are vital factors in preserving environmental balance and meeting human and environmental needs(Wang, Zhang, Gao, & Shi, 2024). Given the increasing urbanization and environmental pressures, accurate and continuous monitoring of vegetation cover and water resources in urban areas is of utmost importance.

Satellite images with high resolution and extensive coverage are recognized as effective tools for monitoring and investigating environmental changes(Viana, Girão, & Rocha, 2019). The use of Sentinel-2 satellites images, with high spatial accuracy and short repeat cycles, provides a suitable opportunity for studying changes in vegetation cover and surface water resources. On the other hand, deep learning methods, particularly neural networks, are known for their strong capabilities in analyzing satellite images and classifying their data(Parelius, 2023).

Assessing changes in vegetation cover and surface water in Tehran, as Iran's capital and one of the largest cities in the Middle East, is highly important and necessary. Considering Tehran's urgent need for accurate and continuous monitoring of its vegetation cover and surface water resources, this study, utilizing Sentinel-2 satellite images and deep learning techniques, was conducted. Research efforts like this can assist policy makers in making better decisions regarding natural resources management and in maintaining environmental balance and enhancing citizens' quality of life(Vali, Comai, & Matteucci, 2020). Furthermore, a sustainable development approach ensures monitoring and management practices promote long-term ecological balance and resource conservation.

Monitoring and managing natural resources using satellite images and deep learning techniques have attracted considerable attention in recent years. Numerous studies in this field demonstrate the capabilities and advantages of these methods in analyzing and classifying environmental data(Khelifi & Mignotte, 2020).

Material and Method

This research focuses on enhancing accuracy and precision in image classification to monitor and identify land use changes in two categories: vegetation cover and surface water cover, using satellite images and a deep learning algorithm based on neural networks.

In this study, a multi-method approach was employed for data collection and analysis. First, high-precision satellite images from the Sentinel-2 satellite for the summer season, covering the period from 2015 to 2024, were collected within a particular period of time annually. These images provide extensive information about the study area, including vegetation cover, water, urban structures, and other elements.

As shown in Table 1, the process undertaken in this research to examine and assess land use changes was carried out in three steps.

Table 1. Process of conducting the study

Step 1	Step 2	Step 3
• Collect Sentinel-2 Images • Apply Geometric and Radiometric Corrections • Create False-color Composite	• Neural Network Classification for Three Tehran Areas • Operator Mapping for Vegetation and Water • Assess Classification Accuracy	• Deep Learning Classification for All 22 Tehran Districts • Map Vegetation and Water Cover • Extract Info for Evaluation and Decision-Making

The study area is the city of Tehran, covering 629.372 hectares (in the WGS84 coordinate system) with geographic coordinates 51°5' to 51°37' E and 35°34' to 35°50' N.

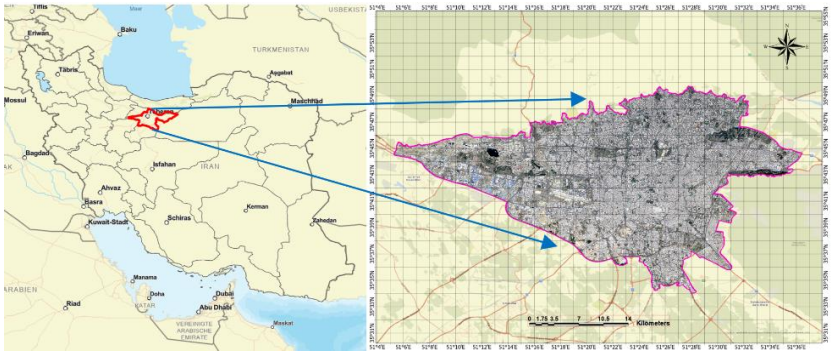


Figure 1. Case study (City of Tehran)

This study uses Sentinel-2 satellite images, part of the European Union's Copernicus Programme, developed in collaboration with the European Space Agency (ESA). These satellites are used for monitoring the environment such as agricultural areas, forestry, natural reserves, water management and disaster control. The study uses a false-color composite containing near-infrared, green, and blue bands with a spatial resolution of 10 meters.

To evaluate the classification accuracy, three sample areas from Tehran City (Districts 3, 16, and 22) were selected as reference areas. The accuracy assessment in these three regions utilized indices such as overall accuracy, kappa coefficient, produce accuracy and user accuracy.

Results

The Table 2 displays the results of accuracy assessment for classifying three regions.

Table 2. Classification Results of Sample Regions

Land Use	Metric (percent)	District 3	District 16	District 22
Vegetation Cover	Overall Accuracy	74.11	76.54	75.74
	Kappa Coefficient	67.35	68.74	68.01
	Producer's Accuracy	99.85	99.96	99.93
	User's Accuracy	74.98	75.97	76.84
Water Cover	Overall Accuracy	74.09	75.23	74.36
	Kappa Coefficient	67.13	66.98	67.35
	Producer's Accuracy	96.99	98.14	97.54
	User's Accuracy	72.31	74.24	73.82

After classifying the regions and adjusting the parameters of the deep neural network, all areas of Tehran city were classified using a network with 4 hidden layers and 100 iterations. Then vegetation and water coverage maps were prepared from 2015 to 2024, and useful information was extracted from them. The results obtained are presented in Figure 2.



Figure 2. Area of Vegetation and Water Coverage in Tehran left to right respectively

The data analysis indicates that over the 10-year period, vegetation cover in Tehran, especially in the years 2023 and 2024, has increased substantially. This increase may be attributed to sustainable urban development and environmental rehabilitation. On the other hand, surface water coverage has exhibited significant fluctuations, which could be influenced by factors such as weather changes and water resource management.

Discussion

The results of this study indicate significant changes in land cover in Tehran from 2015 to 2024. These changes demonstrate the effectiveness of deep learning neural network models in environmental monitoring. The 47.49% increase in vegetation cover indicates the success of sustainable urban development initiatives and policies in Tehran. Fluctuations in surface water coverage also underscore the importance of the complexity of interactions between urban development, weather changes, and irrigation management practices. The use of Sentinel-2 satellite imagery and deep learning algorithms can be effectively employed in monitoring and classifying land cover changes.

Conclusion

The present study demonstrates the effectiveness of deep learning neural networks and Sentinel-2 satellite imagery in monitoring land cover changes in Tehran. The significant increase in vegetation cover and fluctuations in surface water coverage indicate the impacts of sustainable urban development and environmental management. The high classification accuracy suggests that deep learning methods have great potential in producing land cover maps with acceptable accuracy. Incorporating a sustainable development approach ensures that urban planning and environmental management address immediate challenges while promoting long-term ecological co-existence. These findings underscore the importance of adaptive practices to sustain increased vegetation cover and manage water resources. These results underscore the importance of continued investment in green infrastructure and adaptive water management strategies for sustainable urban development. Overall, this study highlights the crucial role of advanced remote sensing and deep learning techniques in improving the understanding and management of urban environmental issues.

References

1. Khelifi, L., & Mignotte, M. (2020). Deep Learning for Change Detection in Remote Sensing Images: Comprehensive Review and Meta-Analysis. *IEEE Access*.
2. Parelius, E. J. (2023). A Review of Deep-Learning Methods for Change Detection in Multispectral Remote Sensing Images. *Remote Sensing*, 15(8), 2092.
3. Vali, A., Comai, S., & Matteucci, M. (2020). Deep Learning for Land Use and Land Cover Classification Based on Hyperspectral and Multispectral Earth Observation Data: A Review. *Remote Sensing*, 12(15), 2495.
4. Viana, C. M., Girão, I., & Rocha, J. (2019). Long-term satellite image time-series for land use/land cover change detection using refined open source data in a rural region. *Remote Sensing*.
5. Wang, L., Zhang, M., Gao, X., & Shi, W. (2024). Advances and Challenges in Deep Learning-Based Change Detection for Remote Sensing Images: A Review through Various Learning Paradigms. *Remote Sensing*.

Advanced Engineering Days

aed.mersin.edu.tr

Virtual Field Practice Education for Total Station

Bashar Helal[1], Veli İlçi[*1], Kaan Bati[2]

[1]*Ondokuz Mayis University, Department of Geomatics Engineering, Turkiye, Basharhlal1996@gmail.com, veli.ilci@omu.edu.tr*
[2]*Haceetepe University, Department of Mathematics and Science Education, Turkiye, kaanbati@hacettepe.edu.tr*

Cite this study: Helal, B., İlçi, V. & Bati, K (2024). Virtual Field Practice Education for Total Station. Advanced Engineering Days, 9, 356-358

Keywords
Virtual Education
Geomatics Engineering
Surveying
Total Station
3D Modeling

Abstract

The main aim of this study is to teach the usage areas, usage purposes, basic measurement principles, and measurement strategies of the total station instrument in a virtual environment. For this purpose, the total station device and related equipment, such as tripod, prism, and telescopic pole, were designed in 3D in a virtual environment by reality. Web programming was chosen to program the virtual environment and simulation process due to its advantages of accessibility, interactivity, performance, and ease of development. Three basic web programming languages and a library were utilized collaboratively during the developed web program process. Javascript programming language is used for mathematical operations and programming methods. HyperText Markup Language (HTML) was used to structure and present the content of the web page. Cascading Style Sheets (CSS) is utilized to describe the presentation of a document written in HTML. Three.js library was used to create and display 3D computer graphics. Fundamental quantities such as angle and distance concepts that can be observed with the total station are included in the model, aiming to improve users' real-time usage practices and to enable them to understand these variables.

Introduction

With rapidly developing technology, crucial changes in our daily lives can be observed in many areas, such as social needs, tools, and ways of accessing information. The field of education has to keep up with these changes in both traditional and e-learning processes (Abdul Halim & Abdul Rasam, 2021). E-learning is still in development and needs to be extensively improved compared to conventional learning (Jia et al., 2022). While pursuing this change sometimes requires updating the information taught and educational materials, greater technology integration is required in applied sciences.

Geomatics is a field of study concerned with investigating, monitoring, and analyzing natural and built environments from metric and thematic perspectives (Botto, Federici, Ferrando, Gagliolo, & Sguerso, 2023). Intensive indoor and outdoor laboratory components are essential requirements for teaching the Geomatics discipline (Abd-Elrahman et al., 2023). These lab directives are conducted in pre-lab preparation, actual data collection, and post-lab computations stages (Abd-Elrahman et al., 2023). During this process, both the devices used and education-training techniques should be updated by technological developments. Geomatics education should apply flexible curricula to deal with the necessity of technological changes (Çoruhlu et al., 2023). To provide the education required by the age, curriculum design, and course delivery must be innovative and adaptable (Çoruhlu et al., 2023). To adapt the newest technologies emerging in this field to the profession, it is necessary to examine the products and prepare the required documents in real or virtual environments (Çoruhlu et al., 2023).

The main aim of this study is to teach the usage areas, usage purposes, basic measurement principles, and measurement strategies of the total station instrument in a virtual environment. For this purpose, the total station device and related equipment, such as tripod, prism, and telescopic pole, were designed in 3D in a virtual environment by reality. Also, benchmark points are added to understand the reference point concepts. In addition, fundamental quantities such as angle and distance concepts that can be observed with the total station are included in the model, aiming to improve users' real-time usage practices and to enable them to understand these variables. Thanks to this virtual environment, students can learn measurement variables of total station and improve theoretical and practical knowledge about total station without going out into the field. In addition, nine

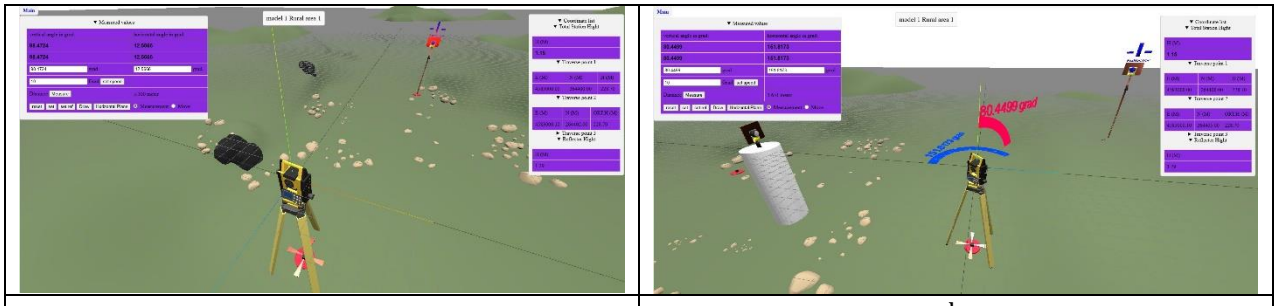
different virtual environments, such as rural and urban areas, are prepared to enable users to develop their practical knowledge about measurement strategies in various environments. Within this virtual environment, the user can freely navigate, change the position of the instruments, conduct the measurements, and see the related observation values and coordinates.

Material and Method

This study aims to give the necessary knowledge and practice about the total station to the students and surveyors by using virtual programming. Web programming was chosen to program the virtual environment and simulation process due to its advantages of accessibility, interactivity, performance, and ease of development. Three basic web programming languages and a library were used collaboratively during the developed web program process. Javascript programming language is used for mathematical operations and programming methods. HyperText Markup Language (HTML) was used to structure and present the content of the web page. Cascading Style Sheets (CSS) is used to describe the presentation of a document written in HTML. Three.js library was used to create and display 3D computer graphics.

The produced virtual tool is mainly focused the understanding the principles of angle and distance measurement of a total station. To achieve this aim, the total station and related equipment, such as tripod, prism, pillar, and telescopic pole, were modeled in the 3D virtual environment. To reflect the real scenario, all these devices are designed as movable.

In the move mode user can settle the total station and the reflectors at the desired positions. When the settlement of the devices is completed, the user can switch to the measurement mode. In the measurement mode, the user can set the horizontal angle to the desired reflector. In this case, it will be seen that the total station device rotates on the horizontal and vertical axes. Simultaneously, vertical and horizontal axis values are seen on the screen. Moreover, the measured horizontal and vertical axis values in grad and the slope distance in meters are given in the above-left drop-down menu. In the above-right drop-down menu, the height of the total station, the height of the reflectors, and the coordinates (in easting, northing, and orthometric height) of the traverse points are given (Figure 1).

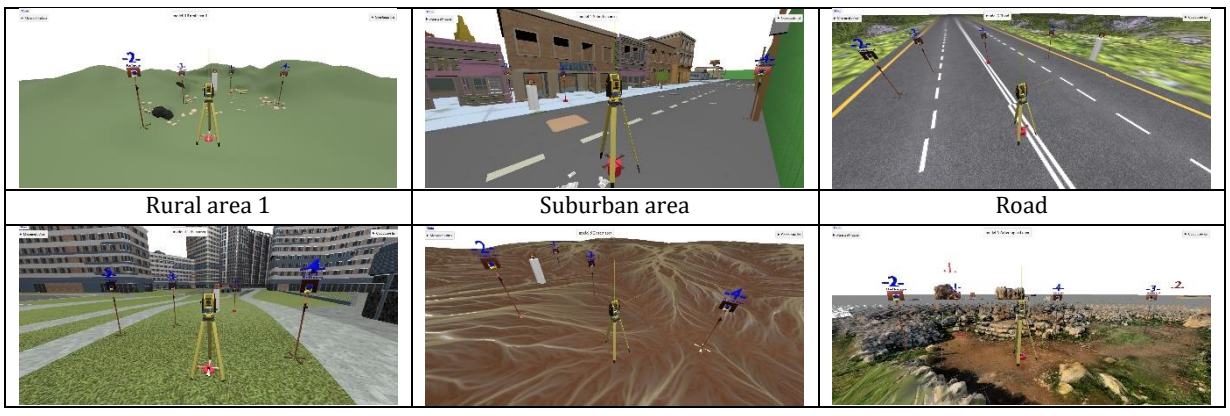


a | b

Figure 1. Measured values in the drop-down menus (a: Axis and b: horizontal and vertical angles)

Different application areas in field studies may require different measurement strategies. To carry this situation to the virtual education environment, 9 different 3D models were used: 2 rural areas, a suburban area, an urban area, a desert area, an archaeological area, a road, a highway, and a building. These models were downloaded from the Sketchfab website which gives opportunity to the users many kinds of 3D environments (Sketchfab, 2024).

After the choice of the desired environment, the user can design the device settlements and start the measurement as explained above. The sample representations of the nine environments are seen in Figure 2.



Rural area 1 | Suburban area | Road

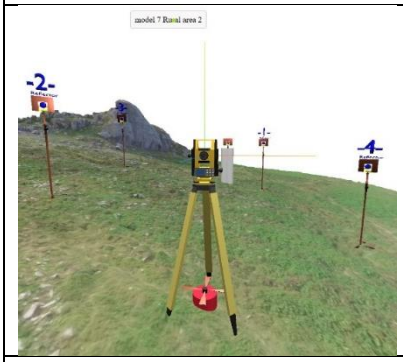
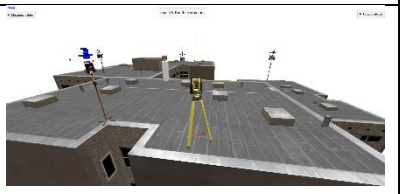
Urban area	Desert area	Arkeological area
		
Rural area 2	Highway	Building structure

Figure 2. The nine different measurement scenarios

Conclusion

Thanks to today's technological opportunities, virtual education has become applicable today. Virtual education can offer an important alternative, especially in educational fields where field studies are frequently used, such as geomatics engineering. In addition, when weather conditions are not suitable or face-to-face education is prevented due to the pandemic, virtual tools will be able to provide alternative education opportunities and ensure that education is not interrupted. In this study, a study was developed for total station training, which is one of the basic devices in survey engineering. In this study, which includes the total station device and related equipment developed in a virtual environment;

- Axes of the device,
- Coordinate concept,
- Ellipsoidal and orthometric height,
- Horizontal and vertical angle concepts,
- Slope and horizontal distance concepts,
- Location and measurement strategies in different environments,

It is intended to be taught. Thus, an alternative training opportunity was provided in cases where field studies were disrupted. In the future study, the contribution of this tool to different student groups in learning the total station device will be investigated and the results will be shared.

References

Abd-Elrahman, A., Atwill, C., Gonzalez, A., Hernandez, K., Barry, D., & Abd-Elrahman, Z. (2023). Virtual Reality (VR) Assisted Geomatics lab Development. *International Archives of the Photogrammetry, Remote Sensing and Spatial Information Sciences - ISPRS Archives*, *48*(1/W2-2023), 933–938. https://doi.org/10.5194/isprs-archives-XLVIII-1-W2-2023-933-2023

Abdul Halim, D., & Abdul Rasam, A. R. (2021). Education 4.0 in cartography: an integrated e-learning materials portal for cartography and digital mapping course. *Proceedings of the ICA*, *4*(December), 1–8. https://doi.org/10.5194/ica-proc-4-1-2021

Botto, M., Federici, B., Ferrando, I., Gagliolo, S., & Sguerso, D. (2023). Innovations in geomatics teaching during the COVID-19 emergency. *Applied Geomatics*, *15*(3), 551–564. https://doi.org/10.1007/s12518-022-00416-4

Çoruhlu, Y. E., Nas, S. E., Uzun, B., Yıldız, O., Şahin, F., Terzi, F., & Çelik, M. Ö. (2023). Development of Guide Material for the Education of Cultural Immovable Heritage Management for Bachelor Students of Geomatics Engineering. *Geomatics and Environmental Engineering*, *17*(4), 77–100. https://doi.org/10.7494/geom.2023.17.4.77

Jia, Z., Zhu, Y., Cao, Y., Dong, M., Zhang, L., & Zhou, X. (2022). GEOMATICS VOCATIONAL EDUCATION in CHINA: CURRENT SITUATION and RECENT DEVELOPMENTS. *International Archives of the Photogrammetry, Remote Sensing and Spatial Information Sciences - ISPRS Archives*, *43*(B5-2022), 9–14. https://doi.org/10.5194/isprs-Archives-XLIII-B5-2022-9-2022

Sketchfab. (2024). Sketchfab. Retrieved from https://sketchfab.com/

Advanced Engineering Days

aed.mersin.edu.tr

Engineering approaches to reduce seismic vulnerability based on spatial analysis

Peyman Yariyan [*1], Sadra Karimzadeh [2], Mahyat Shafapourtehrany [3]

[1]*University of Tabriz, Department of Remote sensing and GIS, Iran, p.yariyan@tabrizu.ac.ir*
[2]*University of Tabriz, Department of Remote sensing and GIS, Iran, sa.karimzadeh@tabrizu.ac.ir*
[3]*University of Bogazici, Department of Geodesy, Turkey, mahyat.shafapour@boun.edu.tr*

Cite this study: Yariyan, P., Karimzadeh, S., & Shafapourtehrany, M. (2024). Engineering approaches to reduce seismic vulnerability based on spatial analysis. Advanced Engineering Days, 9, 359-364

Keywords
Seismic vulnerability
Spatial modeling
Machine learning
GIS
Turkey

Abstract

The main goal of this research is to identify and engineer the relationship between crisis management and earthquake risk management in order to reduce seismic vulnerability in Istanbul, Turkey. Seismic vulnerability prediction maps based on Random Forest (RF), Gradient Boosting Machine (GBM), Naïve Bayes (NB) and Decision Tree (DT) learning models and two sets of independent and dependent factors were prepared. The results indicate the effectiveness of group learning techniques in the development of reliable spatial modeling for seismic vulnerability prediction.

1. Introduction

Natural hazards are one of the most important dangerous phenomena for human settlements [14]. In the meantime, earthquake is considered one of the most destructive natural phenomena, which is one of the most well-known natural disasters in the world due to the wide scope of action, the frequency of occurrences, as well as the extent and severity [8]. The bitter experiences of the past show that the threat of earthquakes in urban areas is expanding globally [10]. Hence, the vulnerability of metropolises and high-density residential areas against earthquakes has a significant relationship with the reaction and behavior of humans, proper urban management and damage reduction planning [13]. Although it is impossible to prevent the occurrence of earthquakes unlike other natural disasters, however, necessary preparations before the event help to make cities less vulnerable [3]. Most of the studies regarding the assessment of seismic vulnerability in cities have been one-dimensional and a limited number of factors have been involved [2, 4, 5, 6]. While human actions, environmental, physical, structural, social, etc. conditions are effective in urban vulnerability [1, 11, 12]. The purpose of this research, is to engineer a multifaceted approach regarding providing a clear situation of the type and extent of seismic vulnerability in the metropolis of Istanbul in Turkey. This approach is based on the use of 12 Structural, Earthly, Social and Physical factors and preparing a training database with the k-means clustering method and seismic vulnerability modeling with machine learning models.

2. Material and Method

2.1 Data and study area

The metropolis of Istanbul, as the capital of Turkey, is located in the geographical position of 28° 00'E to 29° 55'E latitude and 40° 50'N to 41° 30'N longitude (Figure 1). As a tourist city that has higher economic aspects than other Turkish cities, Istanbul has been recognized as the most populous city in Turkey in 2018. Its approximate population is 15 million and the area of Istanbul is 5460 km^2. Considering the existence of 1,500 buildings with a density of 20 floors and above, and demographic studies in 2015 that show the use of non-standard construction materials in 90% of residential buildings in Istanbul, which the occurrence earthquake, human and economic losses will be irreparable

Certainly, potential risks will be minimized through a vulnerability approach [9]. Effective factors in a phenomenon can be both aggravating and can reduce its intensity. Undoubtedly, neither the magnitude of the earthquake nor the intensity of the earthquake can be the only factors affecting the seismic vulnerability. Rather, several factors go hand in hand and determine the severity or reduction of vulnerability. Map of factors used in this study based on 4 main criteria Structural, Earthly, Social and Physical and 12 sub criteria Residential building density, Commercial building density, Building height density, Building density, Distance to fault,

Altitude, Population density, Elderly density, Distance to Fire stations, Distance to Road main, Distance to Hospital and Distance to Fuel stations were prepared using analytical tools in Arc GIS software (Figure 2).

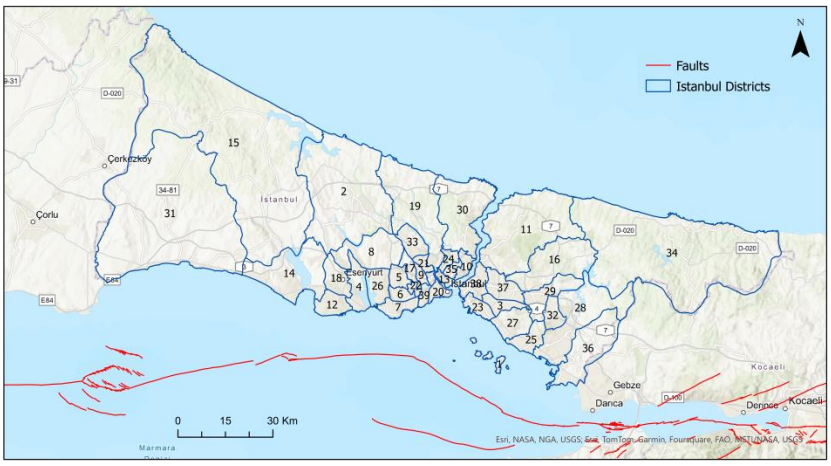


Figure 1. Geographical location of Istanbul metropolis

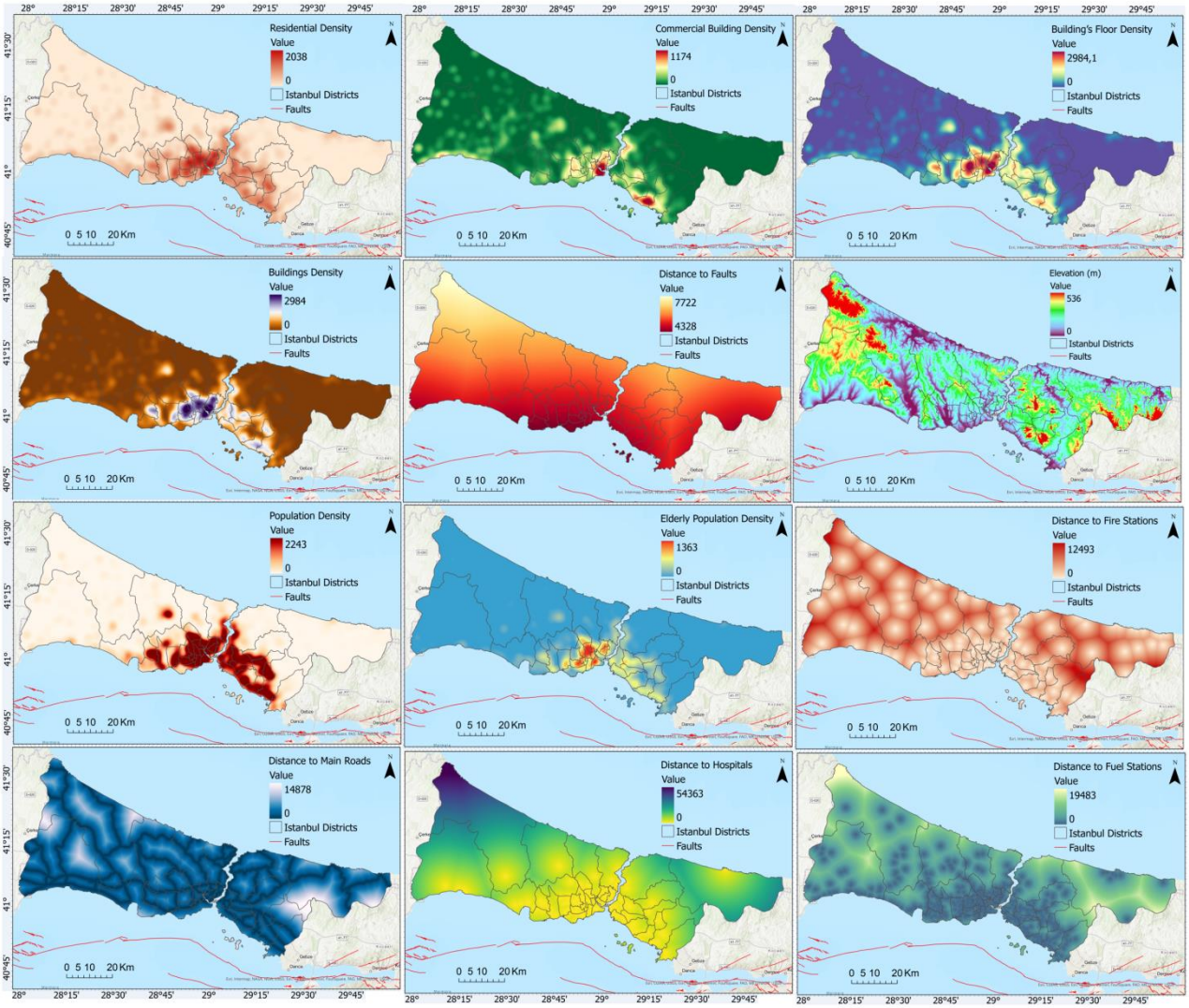


Figure 2. Map of conditional factors affecting the seismic vulnerability of Istanbul

2.2 Research engineering

The research processes are summarized as 4 stages (Figure 3). Selection of effective factors, determination of importance of factors, classification and preparation of clustering model map, preparation of educational database [7], spatial modeling of seismic vulnerability based on four learning models, Random Forest (RF),

Gradient Boosting Machine (GBM), Naïve Bayes (NB) and Decision Tree (DT) and validating the predictive performance of the models are the main steps.

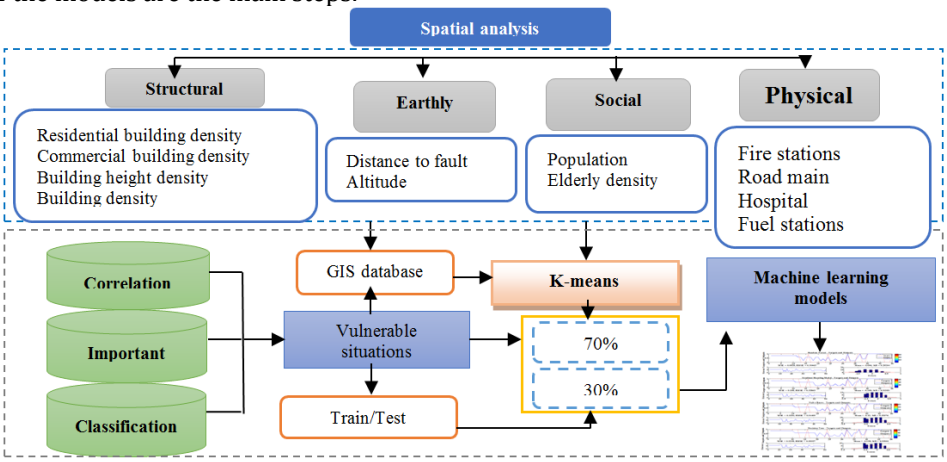


Figure 3. Research methodology

3. Results and discussion

3.1 Important of factors

Determining the importance of each of the factors in order to compare with seismic vulnerability prediction maps and proper planning to reduce the effects of that factor is essential. Hence, the importance of the factors used in this study was calculated based on Gain Ratio (Figure 4). Residential building density with a value of 0.165 was the most important factor in spatial modeling of seismic vulnerability. Also, the layer of main roads was the least important with a value of 0.016.

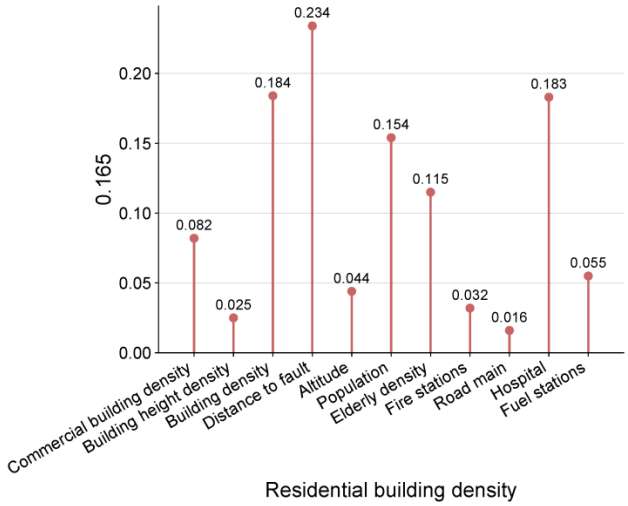


Figure 4. The importance of conditioning factors

3.2 Prediction of seismic vulnerability

Predictive models are tools for predicting future outcomes using data modeling. In summary, seismic vulnerability prediction modeling in this study was done using machine learning with a data mining approach to predict and guess possible future results with the help of existing data. Predictive models are tools for predicting future outcomes using data modeling. In summary, seismic vulnerability prediction modeling in this study was done using machine learning with a data mining approach to predict and guess possible future results with the help of existing data (Figure 5). As mentioned, due to the lack of sufficient recorded records of the damaged places in Istanbul, k-means clustering method was used to prepare the training and testing database through the integration of the classified map of the factors. Urban vulnerability inventory map includes 300 samples (occurrence and non-occurrence) and two sets of training and testing.

Spatial analysis of vulnerability maps shows a similar and significant relationship regarding the vulnerability of the southern parts and around the main river bifurcation of Istanbul, i.e. areas 3, 5, 6, 7, 9, 13, 17, 18, 21, 22, 23, 24, 26, 27, 32, 35, and 37. Examining and comparing the resulting maps with the map of factors shows the proximity of vulnerable areas to the fault line, i.e. marginal areas. The high density of buildings and population in vulnerable areas is also another reason. While the green belt, that is, with low vulnerability, is located from the southwest to the northeast.

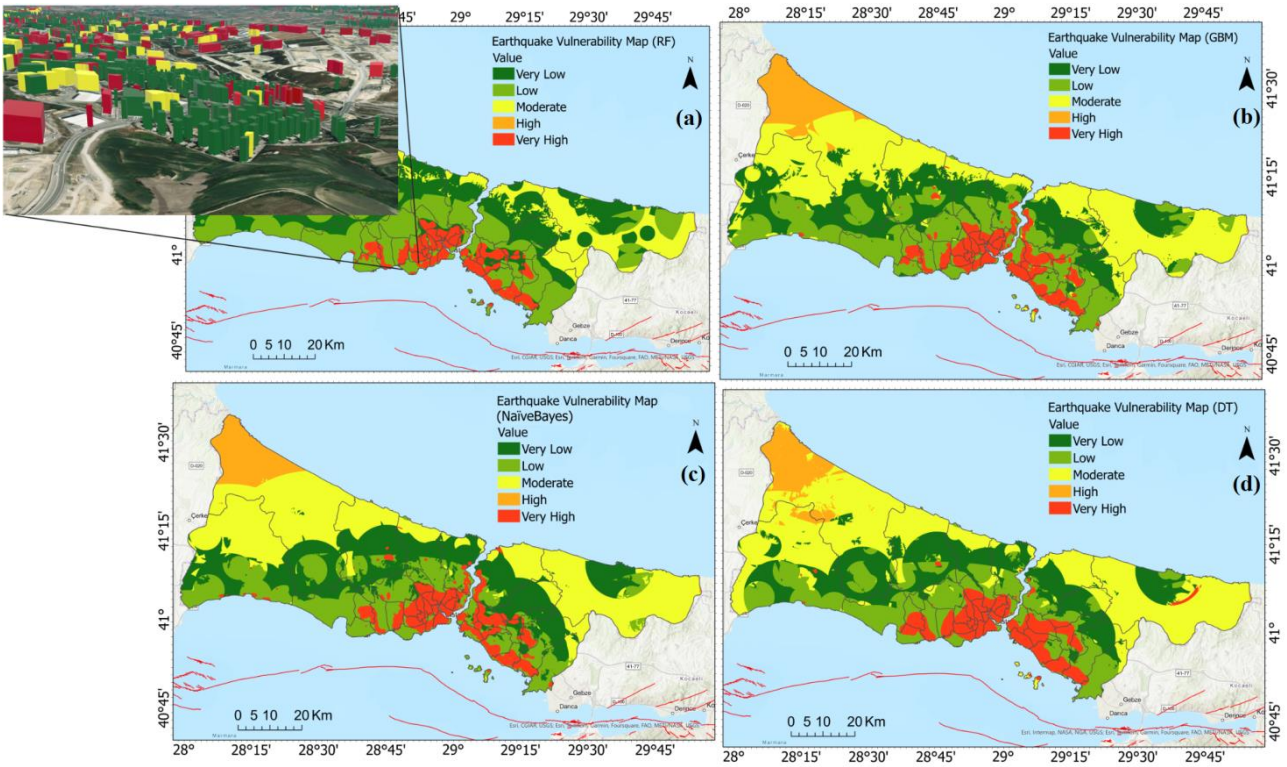


Figure 5. Seismic vulnerability status of Istanbul metropolis based on prediction models, (a) RF, (b) GBM, (c) NB and (d) DT

3.3 Performance validation of models

In order to evaluate the performance of each of the forecasting models regarding the estimation of seismic vulnerability, two measures of Root Mean Square Error (RMSE) and Area under the ROC Curve (AUC) were used to validate the models. RMSE and MSE index for RF model was 0.3 and 0.09, respectively, the lowest error value. After that, in the GBM model, the values are RMSE = 0.32 and MSE = 0.1. The highest error value is observed in the Decision Tree model with RMSE = 0.35 and MSE = 0.12 (Figure 6).

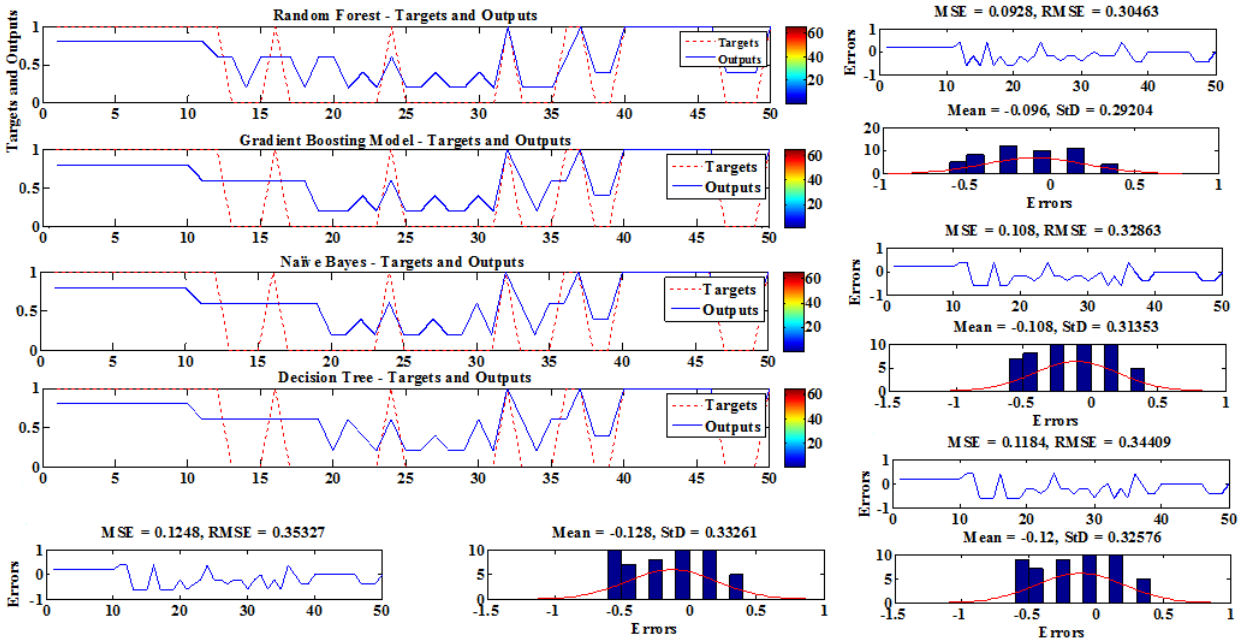


Figure 6. Evaluating the predictive performance of deep learning models

The AUC values calculated for the models also have a significant relationship with the RMSE and MSE values (Figure 7). So that, the best performance based on the AUC index for RF, GBM, NB and DT models with the values

of 0.98, 0.97, 0.964 and 0.96 corresponds to the order of the error value of the models. In other words, the model with the lowest error has the highest AUC value and the best performance in predicting seismic vulnerability.

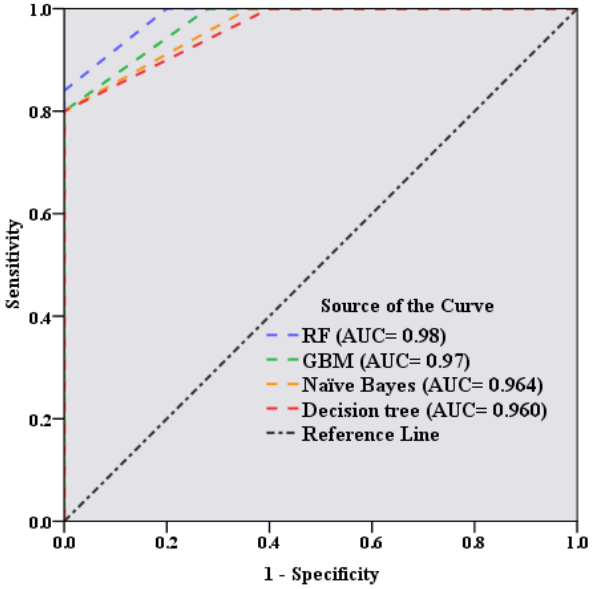


Figure 7. Comparison of prediction performance of learning models based on AUC values

4. Conclusion

Unpleasant experiences of earthquake occurrences and damages in Turkey have caused it to be introduced as one of the most earthquake-prone countries. A study has been conducted with a new approach to describe the seismic vulnerability situation, which includes all the urban areas of Istanbul. Based on the vulnerability data prepared by the clustering model and 12 conditioning factors effective on earthquake vulnerability in Istanbul city, four machine learning models, namely RF, GBM, NB and DT, were used to prepare a seismic vulnerability prediction map. The results of the study showed the following:

(1) In machine learning models, there are significant similarities in the obtained results, which show the high power of the new strategy of building a training database. For this reason, the AUC values calculated for the models indicated high prediction accuracy and relatively minor differences.

(2) The RF model performed best with AUC=0.98. In addition, in areas with high vulnerability, this model had a better prediction with success and a low amount of error. Although the prediction maps produced by other machine learning models were highly accurate.

This study focuses on presenting a new approach regarding the construction of training and testing samples (occurrence and non-occurrence) and provides a precise strategy for researchers when there is no training and testing database.

References

1. El-Maissi, A. M., Argyroudis, S. A., Kassem, M. M., & Nazri, F. M. (2023). Integrated seismic vulnerability assessment of road network in complex built environment toward more resilient cities. Sustainable Cities and Society, 89, 104363.
2. Elyasi, N., Kim, E., & Yeum, C. M. (2024). A machine-learning-based seismic vulnerability assessment approach for low-rise RC buildings. Journal of Earthquake Engineering, 28(3), 760-776.
3. Hagenlocher, M., Renaud, F. G., Haas, S., & Sebesvari, Z. (2018). Vulnerability and risk of deltaic social-ecological systems exposed to multiple hazards. Science of the total environment, 631, 71-80.
4. Kassem, M. M., Nazri, F. M., Farsangi, E. N., & Tan, C. G. (2021). Comparative seismic RISK assessment of existing RC buildings using seismic vulnerability index approach. Paper presented at the Structures.
5. Li, S.-Q., & Gardoni, P. (2024). Seismic loss assessment for regional building portfolios considering empirical seismic vulnerability functions. Bulletin of Earthquake Engineering, 22(2), 487-517.
6. Mosoarca, M., Onescu, I., Onescu, E., & Anastasiadis, A. (2020). Seismic vulnerability assessment methodology for historic masonry buildings in the near-field areas. Engineering Failure Analysis, 115, 104662.
7. Shafapourtehrany, M., Yariyan, P., Özener, H., Pradhan, B., & Shabani, F. (2022). Evaluating the application of K-mean clustering in Earthquake vulnerability mapping of Istanbul, Turkey. International Journal of Disaster Risk Reduction, 79, 103154.

8. Silva, R. F., Marques, R., & Zêzere, J. L. (2024). Spatial distribution, temporal trends and impact of landslides on São Miguel Island from 1900 to 2020 based on an analysis of the Azores historical natural hazards database. Natural Hazards, 120(3), 2617-2638.
9. Singhal, A., & Jha, S. K. (2021). Can the approach of vulnerability assessment facilitate identification of suitable adaptation models for risk reduction? International Journal of Disaster Risk Reduction, 63, 102469.
10. Vitorino, H., Khiali, V., & Rodrigues, H. (2024). Post-earthquake fire risk and loss assessment in urban areas. Innovative Infrastructure Solutions, 9(1), 26.
11. Xofi, M., Domingues, J. C., Santos, P. P., Pereira, S., Oliveira, S. C., Reis, E., . . . Ferreira, T. M. (2022). Exposure and physical vulnerability indicators to assess seismic risk in urban areas: a step towards a multi-hazard risk analysis. Geomatics, Natural Hazards and Risk, 13(1), 1154-1177.
12. Yakar, M., Kamran, K. V., Alptekin, A., Kuşak, L., Unel, F. B., & Yariyan, P. (2024). An Innovative Fusion of New Smile Random Forest and Fuzzy Analysis for Comprehensive Seismic hazard Assessment: A Case Study in Mersin, Türkiye.
13. Yariyan, P., Ali Abbaspour, R., Chehreghan, A., Karami, M., & Cerda, A. (2022). GIS-based seismic vulnerability mapping: a comparison of artificial neural networks hybrid models. Geocarto International, 37(15), 4312-4335.
14. Yariyan, P., Zabihi, H., Wolf, I. D., Karami, M., & Amiriyan, S. (2020). Earthquake risk assessment using an integrated Fuzzy Analytic Hierarchy Process with Artificial Neural Networks based on GIS: A case study of Sanandaj in Iran. International Journal of Disaster Risk Reduction, 50, 101705.

Advanced Engineering Days

aed.mersin.edu.tr

Precise digital twin production by UAV and TLS data fusion

Umut Gunes Sefercik [1], Muhammed Madak*[1], Mertcan Nazar [1]

[1]Gebze Technical University, Department of Geomatics Engineering, Türkiye, sefercik@gtu.edu.tr, m.madak2020@gtu.edu.tr, mnazar@gtu.edu.tr

Cite this study: Sefercik, U. G., Madak, M., & Nazar, M. (2024). Precise digital twin production by UAV and TLS data fusion. Advanced Engineering Days, 9, 365-368

Keywords
Fusion
TLS
UAV
Point cloud
3D model

Abstract

The recent developments have prompted the adoption of diverse methods and technologies in the generation of geospatial information. Furthermore, the growing interest in the digital twin concept and the demand for more realistic three-dimensional (3D) models of objects have contributed to an increased familiarity with 3D modeling research. In this context, unmanned aerial vehicles (UAVs) with their advantage of high-resolution data acquisition and low cost, and terrestrial laser scanners (TLS) with their capability to offer high accuracy and high precision 3D point clouds, were highly utilized. However, both systems are subject to inherent limitations. These include challenges in acquiring data from obstructed objects using UAV technology and difficulty in obtaining information from the upper parts of objects using TLS technology. In this study, an accurate and precise 3D textured mesh model of a railway underpass area was generated through the fusion of UAV and TLS point clouds. The fusion was achieved by aligning the TLS point cloud with the UAV point cloud, with a mean root mean square error (RMSE) of 3.8 cm. The results indicated that the fusion of UAV and TLS point clouds significantly enhanced the 3D modeling performance, particularly in the obstructed sections of the railway underpass, where the UAV point cloud exhibited erroneous geometry.

Introduction

The advent of recent developments has facilitated the utilization of diverse techniques and technologies in the generation of geospatial information from objects. In addition, increased familiarity with the concept of the digital twin and the demand for more realistic and detailed three-dimensional (3D) models of real-world structures for various purposes has stimulated interest in 3D modeling. In this context, the preceding two decades have demonstrated that unmanned aerial vehicle (UAV) technology is a highly preferred tool in numerous studies due to the benefits it offers, including the ability to acquire high-resolution data at a low cost and with minimal labor input, and the capacity to reconstruct objects in high-level-of-detail [1-2]. In addition to UAV technology, terrestrial laser scanners (TLS) are also highly regarded for their ability to generate robust 3D data in the form of high-accuracy and high-precision 3D point clouds [3]. Nevertheless, both techniques have specific drawbacks in 3D reconstruction. UAVs operate based on passive remote sensing which presents difficulties in obtaining information from obstructed objects [4-5]. Conversely, the difficulty in obtaining information from the upper parts of objects and the high operational cost in large areas appear to be some of the drawbacks of TLS [6]. In light of the aforementioned drawbacks, several studies have adopted the fusion of UAV and TLS point clouds as a means of generating more accurate and precise 3D models [7-9]. In this study, an accurate and precise 3D textured mesh model of a railway underpass area was generated through a fusion of point clouds acquired from UAV and TLS surveys. Furthermore, the textured mesh model generated from the UAV and TLS fusion point cloud was compared with the textured mesh model generated using only the UAV point cloud to evaluate whether the 3D modeling performance had been enhanced. Finally, the drawbacks of each method were examined taking into account their respective benefits and the impact of object geometry on the performance of the applied techniques.

Material and Method

During the data acquisition process, aerial photographs were captured using a DJI Phantom 4 Pro V2.0 UAV equipped with a 20-megapixel complementary metal-oxide-semiconductor (CMOS) sensor. TLS point clouds were

acquired via scans conducted by a Leica RTC360 3D laser scanner. The specifications of the utilized equipment are presented in Table 1.

Table 1. The specifications of the utilized equipment

DJI Phantom 4 Pro V2.0 UAV		**Leica RTC360 3D Laser Scanner**	
Weight	1375 g	Type	High-speed, pulse-based, high dynamic time of flight, Laser class 1
Max speed	S-mode: 20 m/s A-mode: 16 m/s P-mode: 14 m/s	Weight	5350 g
Max flight time	Approx. 30 min	Scanning speed	Up to 2,000,000 points/s
Satellite positioning systems	GPS/GLONASS	Scanning accuracy	3/6/12 mm @ 10 m (selectable by user)
Camera sensor	1-inch CMOS 20-megapixel	Camera system	3-camera system (36-megapixel each) capturing 432-megapixel raw image for calibrated 360° x 300° spherical image
Image size	5472×3648 (3:2)	Field of view	360° (horizontal)/300° (vertical)
Gimbal range	-90° to +30° (Pitch)	Range	0.5 m-130 m
Hover accuracy range	Vertical: ±0.1 m (with vision positioning) ±0.5 m (with GPS positioning) Horizontal: ±0.3 m (with vision positioning) ±1.5 m (with GPS positioning)	Accuracy	Angular accuracy 18” Range accuracy 1.0 mm + 10 ppm 3D point accuracy 1.9 mm @ 10 m 2.9 mm @ 20 m 5.3 mm @ 40 m

The aerial photographs were acquired from an altitude of 80 m with an average ground sampling distance (GSD) of 2.20 cm. To conduct the TLS surveys, six scans were carried out in addition to capturing spherical images with the integrated camera system, which contains three 36-megapixel cameras, for point cloud colorization. The UAV point cloud was generated in the Structure from Motion (SfM) based software Agisoft Metashape Professional 2.0.1. The orientation of the aerial photos was carried out with the help of previously established and measured ground control points (GCP) and the geometric accuracy was calculated as a root mean square error (RMSE) of 1.51 cm. The next step was to generate the UAV point cloud from the tie points in high quality option, and noisy parts were manually filtered. During the TLS survey, the point clouds were automatically pre-aligned by the video-enhanced inertial unit using real-time tracking of scanner movement between each setup based on the Visual Inertial System (VIS) [10]. However, to improve the accuracy of the alignment, the point clouds were registered using the cloud-to-cloud method with an RMSE of 6 mm in Leica Cyclone 2021.1.0. Subsequently, the fusion process was conducted by aligning the TLS point cloud with the UAV point cloud. This was accomplished by selecting four well-distributed tie points with known coordinates, which were visible in both point clouds, with a mean RMSE of 3.8 cm. Finally, in Agisoft Metashape Professional a 3D textured mesh model was generated from the fusion point cloud.

Results and Discussion

The resulting UAV and TLS point clouds are shown in Figure 1.

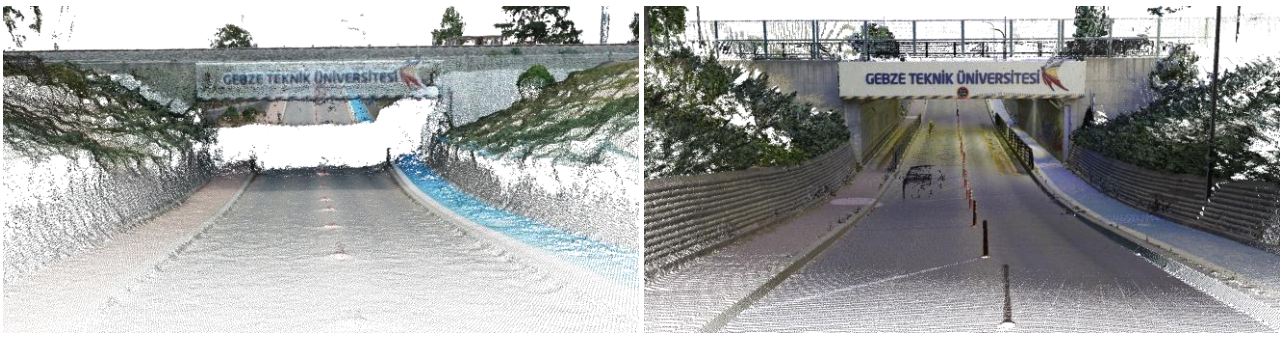


Figure 1. Generated UAV (left) and TLS (right) point clouds in true colors

The total number of points for the UAV and TLS point clouds was approximately 13 million and 60 million, respectively. In contrast to the UAV counterpart, the point cloud derived from the TLS data was of higher density

and had fewer noisy points. In addition, the number of points included in the UAV point cloud is insufficient, particularly in the area of the railway underpass, and there are significant discrepancies between points. Potential contributory factors to this include the flying altitude, camera viewing angle, and object geometry. 3D textured mesh models generated exclusively from the UAV point cloud and the UAV and TLS fusion point cloud are displayed in Figure 2.

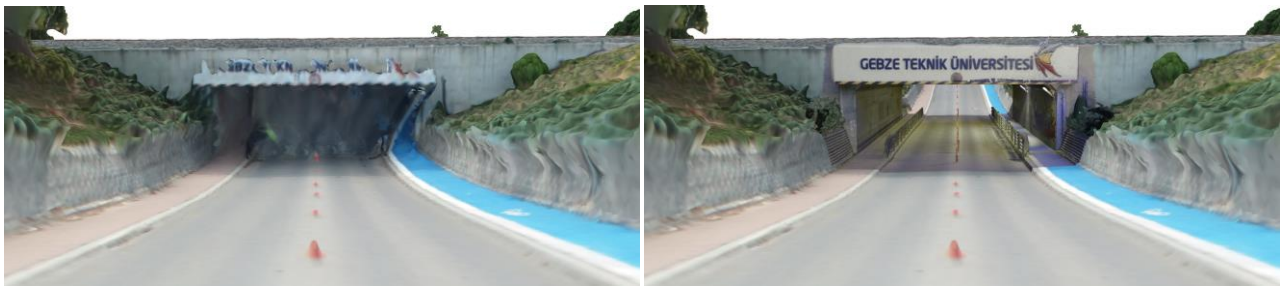


Figure 2. 3D textured mesh models generated exclusively from the UAV point cloud (left) and the UAV and TLS fusion point cloud (right)

The 3D textured mesh model generated from the UAV point cloud displayed a railway underpass and some vertical objects in incorrect geometry. The insufficient number of points in the railway underpass results in a clear manifestation of interpolation error. The 3D modeling performance in covered areas and vertically long objects was relatively low when the 3D textured mesh was generated from the UAV point cloud. However, the performance was significantly improved when the 3D textured mesh was generated from the UAV and TLS fusion point cloud.

Conclusion

In conclusion, the demand for more realistic and accurate 3D models of objects is increasing. Furthermore, a variety of technologies are employed in conjunction with one another to generate 3D meshes with a high level of detail. This study examines the potential for enhancing the performance of 3D textured mesh model generation through the fusion of UAV and TLS point clouds. It compares the effectiveness of this approach with that of the UAV technique alone. Upon analysis of the results, it can be concluded that the performance of 3D modeling was significantly enhanced in the covered railway underpass area and in vertically long objects. In addition, the shortcomings of the UAV point cloud in 3D modeling have been substantially addressed by the fusion with the TLS point cloud.

References

1. Püschel, H., Sauerbier, M., & Eisenbeiss, H. (2008). A 3D model of castle Landenberg (CH) from combined photogrammetric processing of terrestrial and UAV based images. International Archives of the Photogrammetry, Remote Sensing and Spatial Information Sciences, 37(B6b), 93-98.
2. Herrero, M. J., Pérez-Fortes, A. P., Escavy, J. I., Insua-Arévalo, J. M., De la Horra, R., López-Acevedo, F., & Trigos, L. (2022). 3D model generated from UAV photogrammetry and semi-automated rock mass characterization. Computers & Geosciences, 163, 105121.
3. Chen, Z., Zhang, W., Huang, R., Dong, Z., Chen, C., Jiang, L., & Wang, H. (2022). 3D model-based terrestrial laser scanning (TLS) observation network planning for large-scale building facades. Automation in Construction, 144, 104594.
4. Nazar, M., & Sefercik, U. G. (2023). Game development in Unity game engine using optical UAV data. Intercontinental Geoinformation Days, 6, 13-16.
5. Sefercik, U. G., Aydın, I., & Nazar, M. (2023). Quality enhancement in digital twin production of complex architectures with integrated use of terrestrial and aerial images. Advanced Engineering Days (AED), 7, 63-65.
6. Lingua, A., Noardo, F., Spanò, A., Sanna, S., & Matrone, F. (2017). 3D model generation using oblique images acquired by UAV. The International Archives of the Photogrammetry, Remote Sensing and Spatial Information Sciences, 42, 107-115.
7. Mat Adnan, A., Darwin, N., Ariff, M. F. M., Majid, Z., & Idris, K. M. (2019). Integration Between Unmanned Aerial Vehicle and Terrestrial Laser Scanner in Producing 3d Model. The International Archives of the Photogrammetry, Remote Sensing and Spatial Information Sciences, 42, 391-398.
8. Valenti, R., & Paternò, E. (2019). A comparison between TLS and UAV technologies for historical investigation. The International Archives of the Photogrammetry, Remote Sensing and Spatial Information Sciences, 42, 739-745.

9. Panagiotidis, D., Abdollahnejad, A., & Slavík, M. (2022). 3D point cloud fusion from UAV and TLS to assess temperate managed forest structures. International Journal of Applied Earth Observation and Geoinformation, 112, 102917.
10. https://leica-geosystems.com/products/laser-scanners/scanners/leica-rtc360/

Advanced Engineering Days

aed.mersin.edu.tr

Creation of Coefficient of Friction Maps of Flood Areas with Remote Sensing Technique

Yunus Tektaş*[1], Nizar Polat [2]

[1] *Dicle University, Department of Map and Cadastre, Turkey, yunus.tektas@dicle.edu.tr*
[2] *Harran University, Department of Geomatics Engineering, Turkey, nizarpolat@harran.edu.tr*

Cite this study: Tektaş, Y., & Nizar, P. (2024). Creation of Coefficient of Friction Maps of Flood Areas with Remote Sensing Technique. Advanced Engineering Days, 9, 369-372

Keywords
Remote sensing
Coefficient of friction
Flood

Abstract

Floods, one of the most important natural disasters in the world, cause significant loss of life and property. Due to these material and moral losses, the importance of flood events is increasing day by day. In order to minimise the loss of life and property by taking measures against floods, it is important to prepare flood hazard and flood risk maps of the floods that may occur before the floods occur. Hydraulic models are widely used to obtain these maps. HEC-RAS, FLO-2D, MİKE, SOBEK etc. 1 dimensional and / or 2 dimensional hydraulic modelling can be done with programmes. In these hydraulic modelling, the spread of water changes depending on the velocity of the water. One of the most important factors affecting the velocity of water is the roughness of the ground. When determining the roughness of the ground, methods such as the DSİ modified hive method are used for the stream bed, while land use maps are required to determine the roughness of flood areas outside the stream bed. One of the most effective techniques in creating these land use maps is remote sensing in terms of time, cost and convenience. As a result of controlled classification with remote sensing technique, high precision land use status maps can be obtained. Within the scope of this study, the land use status map of the flooding area of the Tigris River, which passes through the historical hevsel garden on the edge of the centre of Diyarbakır and approximately 27 km of the Tigris River, was applied by controlled classification and accuracy analysis on the images of SENTINEL-2 and LANDSAT-9 satellites. With the accuracy analysis, it was determined that the SENTINEL-2 satellite image was the best overall accuracy result with 95.0668% with the spectral angle map algorithm.

Introduction

Flooding is one of the significant natural disasters that can cause substantial loss of life and property. This occurs when the water transmission capacity in the river bed decreases for various reasons, or there is more water in the river bed than it can transmit, leading to water overflowing its banks [1]. Although flooding is a natural phenomenon, its severity and frequency are increasing due to continuous human interventions in nature. Effective flood management and mitigation require a comprehensive understanding and accurate mapping of affected areas. One critical aspect of flood management is understanding the coefficient of friction (CoF) in these regions, as it influences water flow dynamics, sediment transport, and infrastructure stability. Traditional methods for measuring CoF are often time-consuming, labor-intensive, and limited in spatial coverage. However, advancements in remote sensing technologies offer new opportunities to generate friction coefficient maps efficiently and accurately. This study aims to develop a methodology for creating CoF maps of flood-prone areas using remote sensing techniques.

Remote sensing is the technique of recording and analyzing the incoming energy without physical contact with the earth and its resources. It is divided into two classes according to the type of sensor: passive and active sensing. In passive sensing, the energy source is the Sun, whereas in active sensing, the energy source is the satellite [2]. Remote sensing provides a cost-effective and scalable approach to gather extensive spatial data over large and inaccessible areas. By integrating satellite imagery, aerial photography, and advanced sensor technologies, remote sensing can offer high-resolution data on land surface characteristics. Various studies have

demonstrated the utility of remote sensing in hydrology and flood management. For instance, recent research highlights the application of satellite-based synthetic aperture radar (SAR) in mapping flood extents and monitoring changes in water bodies [3][4]. Additionally, LiDAR (Light Detection and Ranging) and multispectral imagery have been successfully used to analyze topographical features and soil moisture content, which are crucial for estimating surface friction properties [5][6].

In order to minimize the loss of life and property by taking measures against floods, it is important to prepare flood hazard and flood risk maps before floods occur. Hydraulic models are widely used to obtain these maps, with roughness values selected according to land use. One of the most effective techniques in creating land use maps is remote sensing, in terms of time, cost, and convenience. High precision land use status maps can be obtained through controlled classification with remote sensing techniques. Within the scope of this study, controlled classification was performed on the images of SENTINEL-2 and LANDSAT-9 satellites. The land use status map of the flood area, approximately 27 km of the Tigris River passing through the historical Hevsel Gardens on the edge of Diyarbakır's center, was produced from the SENTINEL-2 satellite image with high general accuracy. This study will leverage these capabilities of remote sensing to develop CoF maps for flood-prone areas, integrating multispectral satellite data, SAR imagery, and ground truth measurements to calibrate and validate the friction models. Advanced image processing techniques and machine learning algorithms will be employed to analyze the data and generate accurate CoF maps, providing valuable insights for flood risk assessment, infrastructure planning, and emergency response strategies.

Material and Method

The study area is the approximately 27 km long section of the Tigris River in the Tigris-Euphrates Basin No. 21, passing through the Diyarbakır city center (Figure 1) [7].

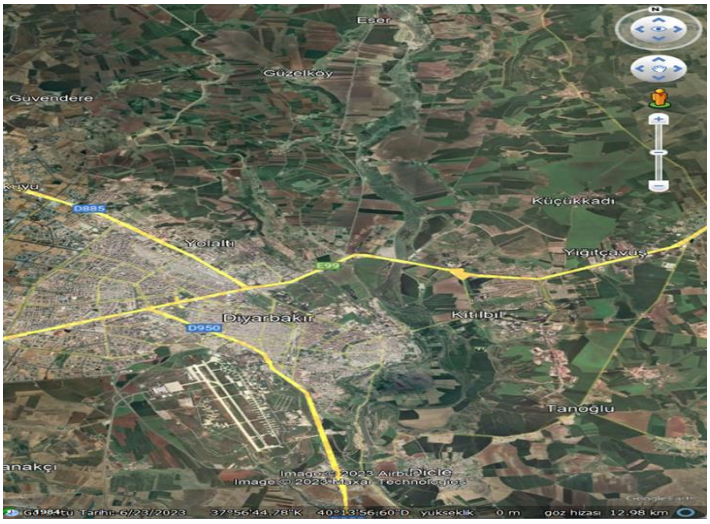


Figure 1. Study area Diyarbakır centre and Tigris River.

In this study, LANDSAT-9 [8] and SENTINEL-2 [9] satellite images were downloaded. Controlled classification and accuracy analysis were performed on these satellite images using the QGIS program. The satellite image with the best accuracy analysis was converted into a raster-based thematic map for flood hydraulic modeling.

On both satellite images, 40 subclass training areas were selected, categorized into four main classes: agricultural land, wooded area, structures, and water. Based on these training areas, controlled classifications were made according to maximum probability, minimum distance, and spectral angle map algorithms.

Accuracy analysis was performed to determine the best algorithm for the controlled classification of both satellite images. For the accuracy analysis, 20 subclass test areas were selected for the four main classes: agricultural land, wooded area, structures, and water. Test areas were selected to ensure they did not coincide with the training areas.

Roughness n values are 0.05 for agricultural lands, 0.08 for wooded areas, 0.06 for building areas, and 0.025 for areas with water bodies [10].

Results

Controlled classifications were performed on satellite images according to maximum probability, minimum distance and spectral angle map algorithms. As a result of the controlled classification, a base land use status map was created to assign the roughness value of the land.

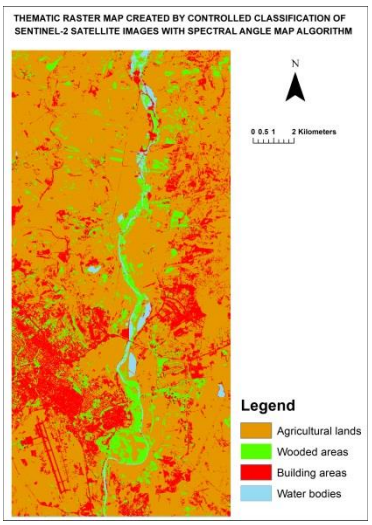


Figure 2. Thematic raster map resulting from controlled classification of SENTINEL-2 satellite imagery.

Accuracy analyses were performed on the land use status maps produced by controlled classification. The general accuracy results of controlled classification with various algorithms are given in Table 1.

Table 1. Accuracy analysis results

Algorithms	SENTINEL-2 Overall Accuracy [%]	LANDSAT-9 Overall Accuracy [%]
Maximum probability	94.1712	74.0325
Minimum distance	78.2264	61.2451
Spectral angle map	95.0668	75.6029

Discussion

This study evaluated the sensitivity of LANDSAT-9 and SENTINEL-2 satellite images in controlled classification and assessed the accuracy of different algorithms. The aim was to determine if remote sensing-derived land use maps can be used for roughness values in flood hydraulic modeling. The highest accuracy was achieved with SENTINEL-2 images, using the spectral angle map algorithm, with a 95.07% accuracy. This result highlights the superior performance of SENTINEL-2 in producing reliable land use maps for hydraulic modeling.

The findings demonstrate that high-resolution satellite imagery and advanced classification algorithms can effectively generate accurate land use maps. These maps can reliably determine roughness values in flood models, enhancing flood simulation and risk assessment accuracy. Integrating these maps into hydraulic models can improve flood prediction and management strategies. In conclusion, SENTINEL-2 imagery and the spectral angle map algorithm are effective for creating accurate land use maps, supporting better flood risk management.

Conclusion

This study demonstrated the effectiveness of using high-resolution satellite imagery, particularly SENTINEL-2, and advanced classification algorithms for generating accurate land use maps. The spectral angle map algorithm, applied to SENTINEL-2 images, achieved the highest accuracy, making it a valuable tool for creating base maps for roughness values in flood hydraulic modeling.The integration of remote sensing techniques into flood risk assessment provides a cost-effective and scalable solution for capturing detailed land surface information. The accurate land use maps produced through these methods enhance the precision of hydraulic models, leading to better flood prediction, management, and mitigation strategies.

In conclusion, the application of SENTINEL-2 satellite imagery and the spectral angle map algorithm in this study has proven to be a reliable approach for improving flood hydraulic modeling. This methodology offers significant potential for advancing flood risk management and reducing the adverse impacts of flooding through more informed and effective decision-making.

References

1. Sargin, A. H. (2013). Coğrafi Bilgi Sistemleri İle Taşkın Riski Ön Değerlendirmesi. Ankara: CBS Şube Müdürlüğü.
2. Wikipedia. (2023). “Uzaktan Algılama”. Accessed: December 27, 2023. https://tr.wikipedia.org/wiki/Uzaktan_alg%C4%B1lama

3. Mason, D. C., Speck, R., Devereux, B., Schumann, G. J. P., Neal, J. C., & Bates, P. D. (2016). Flood detection in urban areas using TerraSAR-X. *IEEE Transactions on Geoscience and Remote Sensing, 54*(2), 882-894.
4. Schumann, G. J. P., & Moller, D. K. (2015). Microwave remote sensing of flood inundation. *Physics and Chemistry of the Earth, Parts A/B/C, 83-84*, 84-95.
5. Jones, C. N., Hankin, B., Wheater, H. S., & Nichols, R. (2020). LiDAR-based surface roughness analysis for flood modelling. *Hydrological Processes, 34*(3), 587-602.
6. Zhu, Z., Woodcock, C. E., Rogan, J., & Kellndorfer, J. (2018). Assessment of spectral, polarimetric, temporal, and spatial dimensions for urban and peri-urban land cover classification using Landsat data. *Remote Sensing of Environment, 211*, 115-128.
7. Google Earth, (2023) Diyarbakır merkez ve Dicle nehri, 23 Haziran 2023 Tarihine Ait Görüntü.
8. Earthexplorer, (2023). "USGS". Accessed: October 30, 2023. https://earthexplorer.usgs.gov/
9. Dataspace, (2023). "COPERNICUS". Accessed: October 29, 2023. https://dataspace.copernicus.eu/
10. Chow, V. T., (1959). Open Channel Hydraulic. McGraw-Hill. 1-728, New York.

Advanced Engineering Days

aed.mersin.edu.tr

Transformer Based Land Use and Land Cover Segmentation

Cengiz Avcı*[1], Elif Sertel [2]

[1]*Istanbul Technical University, Graduate School, Satellite Communication and Remote Sensing, Turkey, avcice16@itu.edu.tr*
[2]*Istanbul Technical University, Geomatics Engineering Department, Sarıyer, İstanbul 34469, Turkey, sertele@itu.edu.tr*

Cite this study: Avci, C., & Sertel, E. (2024). Transformer Based Land Use and Land Cover Segmentation. Advanced Engineering Days, 9, 373-376

Keywords
Transformers
Remote Sensing
Deep Learning
Computer Vision
Semantic Segmentation

Abstract

This study investigates the application of deep learning models for multi-class semantic segmentation of land cover features. Traditionally, machine learning methods struggle with very high resolution image data due to their lack of speed and performance limitations on complex tasks. Convolutional Neural Networks have surpassed traditional methods in accuracy and efficiency. However, the advancement of transformer-based models has further improved performance. We explored and compared the performance of CNN models such as Unet, Unet++, and Deeplabv3+ and transformer-based and vision transformer models SegFormer and Vision Transformer (ViT). We conducted experiments on the very high resolution and manually labelled Landcover.ai dataset, which is ideal for testing semantic segmentation models. We implemented the models on Kaggle's P100 graphical processor units. The SegFormer model achieved the best performance with an overall Intersection over Union (IoU) score of 88.78%. This result surpasses the original Landcover.ai article's proposed CNN-based Deeplabv3+ model's results, which achieved an IoU score of 85.56%. The findings of this study show that transformer models, supported by cloud GPU services, offer significant advancements in land cover classification in Remote Sensing domain.

Introduction

Nowadays, with advancements in aerospace technology, the availability of very high resolution (VHR) remote sensing imagery from satellites, drones, and other imaging platforms has significantly increased. This extensive remote sensing data is now used in computer vision studies such as classification, object detection and image segmentation. Semantic segmentation is a specialized sub-branch of segmentation, that aims to assign a semantic label to each pixel in an image, a process that is crucial for understanding and analysing land use and land cover patterns [1]. However, as image resolutions and sizes have increased, these traditional approaches have proven inefficient, primarily due to challenges related to training time and performance. Deep learning-based segmentation of VHR satellite images is a significant task that provides valuable information for land use/land cover (LU/LC) mapping. The segmentation task becomes more challenging with the increasing number and complexity of LU/LC classes [2].

Deep learning models have gained popularity due to their ability to process large amounts of high-resolution image data rapidly and enable high quality results. Moreover, deep learning methods enable high-resolution results in limited time with multiple processing using backpropagation algorithms [3]. Among these models, Convolutional Neural Networks (CNNs) have become particularly prominent in the field of remote sensing for land use and land cover segmentation. Despite their success, transformer-based models have recently surpassed CNNs in performance for computer vision tasks such as semantic segmentation [4].

Material and Method

In this research, we used Landcoverai dataset that includes 41 orthophoto tiles in Poland. Every tile has about 5 km square. Images have 0,5-meter spatial resolution with 4200 x 4700 pixel sizes. Dataset covers 216.27 km

square area. [5]. This dataset was labeled into five main classes: buildings, woodlands, water, roads and background. The original samples are divided into patches of 512x512 pixels for both masks and images. The dataset was divided into training, validation and testing splits containing 7479, 1602, 1602 patches, respectively.

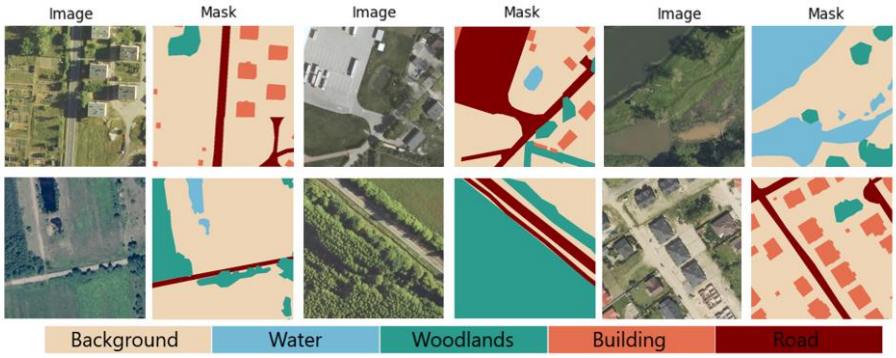


Figure 1. Sample patches and corresponding masks from train set after Preprocessing steps.

Qubvel's Segmentation Library for PyTorch was utilized to implement the CNN models Unet [6], Unet++ [7], and DeepLabv3+ [8], all pretrained on the ImageNet-1k dataset [6]Transformer models, including SegFormer [9] and Vision Transformer [10], were deployed from the Hugging Face model zoo.

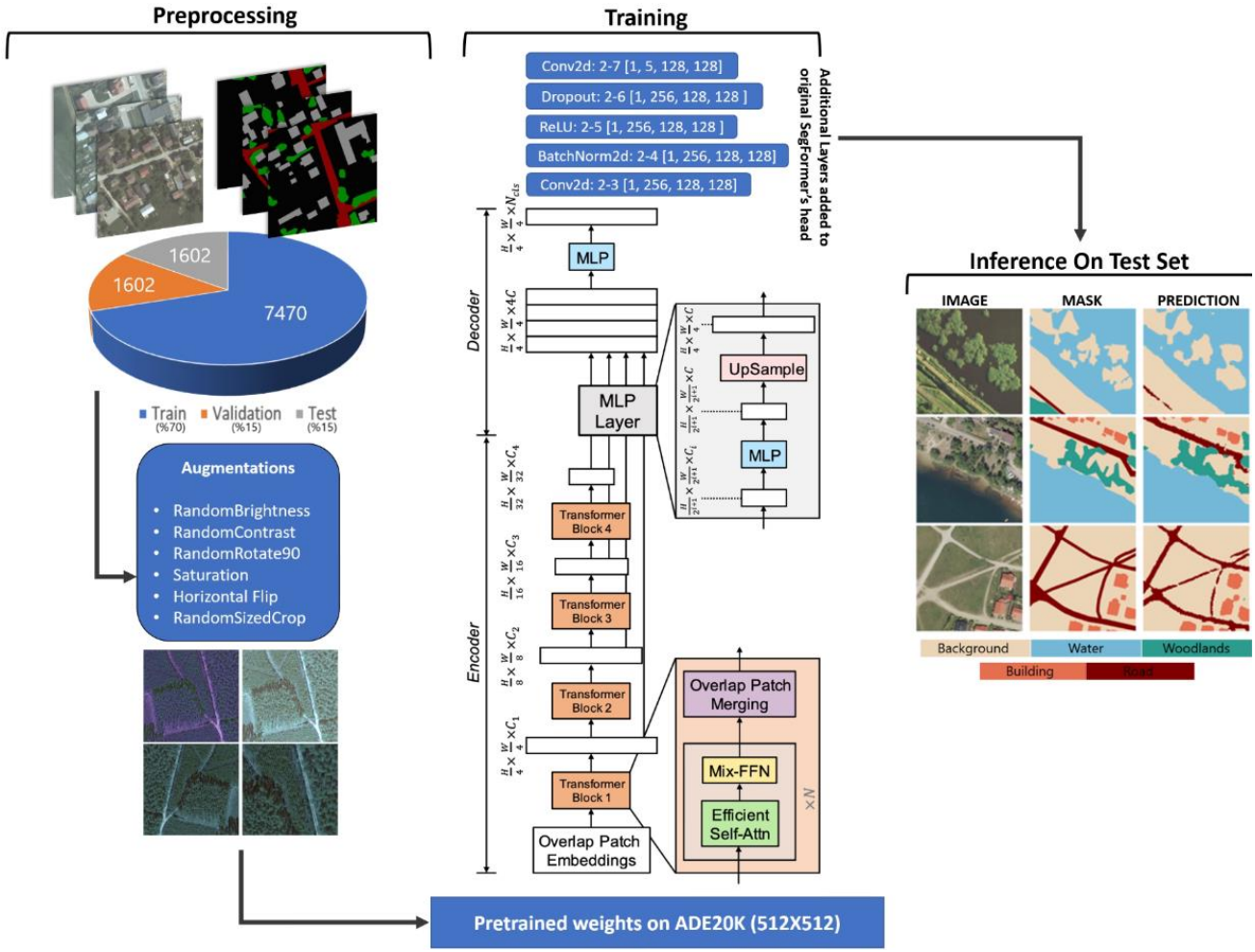


Figure 2. Overall workflow of the study with the extended architecture of SegFormer model [9]

For our proposed model we enhanced the SegFormer architecture by adding several layers at the end (Figure 2). A Conv2d layer increased the feature channels to 256, enabling complex feature learning. BatchNorm2d stabilized training, while ReLU introduced non-linearity.

Dropout was used to prevent overfitting. Finally, another Conv2d layer reduced the feature channels to the desired number of 5 output classes. These additions improved the model's accuracy and robustness in semantic segmentation. Higher batch sizes, when possible, provided more accurate results and reduced training time by

decreasing iteration steps per epoch. All experiments were conducted over 40 epochs with a learning rate of 0.0001, utilizing a learning rate reduction on plateau to optimize model learning efficiently. In our initial experiments, we employed the Dice loss function. However, due to the class imbalance in the dataset, some classes showed poor prediction results. To overcome this problem, we implemented another loss function that incorporates both the Jaccard and Dice losses [11]. Additionally, we utilized the AdamW optimizer to enhance the training [12].

Results and Discussions

To evaluate the performance of the experiments in this research, we used common metrics. These metrics include F1 score, and Intersection over Union (IoU) scores, which collectively assess the models' performance.

Table 1. F1 and IoU Scores Obtained from the Experiments

Model	Encoder	Paramaters	Batch-Size	F1	IoU	Epoch&Time
Deeplabv3+	Resnet50	58+23M	16	91.14	83,42	40/4h14m
Deeplabv3+	Resnext-50	58+22M	16	90.93	82.87	40/4h8m
Unet	Resnet50	31+23M	16	91.41	84,12	40/3h56m
Unet	Resnext-50	31+22M	16	91.31	83,86	40/3h52m
Unet	Resnest200e	31+68M	4	91.23	83,66	40/16h12m
Unet++	Resnet50	60+23M	8	90.54	81,86	40/8h11m
Unet++	Resnext-50	60+22M	8	90.34	81,34	40/8h6m
Segformer	Mit-b0	3,37M	32	93,19	88,78	150/8h29m
ViT	Base-patch16	86M	32	91,93	85,87	150/8h22m
ViT	Base-patch16	86M	64	92,21	86,22	150/4h24m

Best F1 score and IoU obtained with the SegFormer with Mit-b0 base encoder respectively 93,19 and 88,78 in 150 epochs (Table 1) with the approximately 8 hours training time on P-100 graphic processing unit provided by Kaggle. This result surpasses the original Landcoverai article's proposed CNN-based Deeplabv3+ model's results that achieved 85.56% in intersection of union (IoU) score [5].

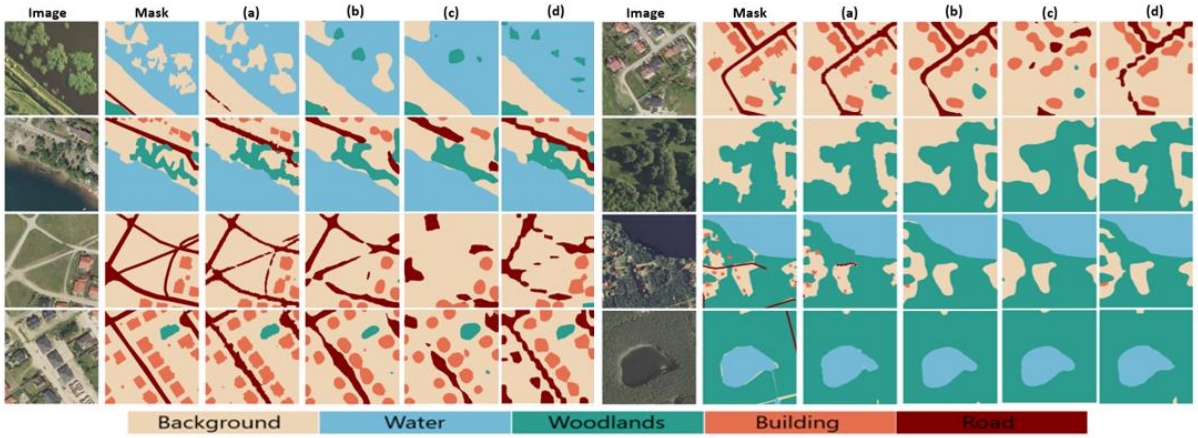


Figure 3. Image, Mask and Predictions for (a) SegFormer, (b) Resnet50-DV3+, (c) Resnext50-DV3+, (d) ViT

In Figure 3, SegFormer model shows superior visual prediction success compared to other models, particularly excelling in the road class, which underscores its overall better performance.

Conclusion

The study examines state-of-the-art deep learning models for multi-class landcover segmentation. Through extensive experimentation on high-resolution images from the Landcover.ai dataset, our study demonstrates the superior performance of transformer-based models over traditional convolutional neural networks (CNNs). Specifically, the SegFormer model achieved an Intersection over Union (IoU) score of 88.78%, surpassing the ViT and other CNN-based models. These findings highlight the significant advancements transformer models bring to remote sensing and LU/LC segmentation. All experiments were conducted on Kaggle's powerful Cloud GPU service, which played a crucial role in achieving high efficiency in processing the high-resolution image data. The achieved result sets a new benchmark for the Landcover.ai dataset and efficiency in semantic segmentation tasks.

References

1. Mo, Y., Wu, Y., Yang, X., Liu, F., & Liao, Y. (2022). Review the state-of-the-art technologies of semantic segmentation based on deep learning. *Neurocomputing*, *493*, 626-646..
2. Sertel, E., Ekim, B., Ettehadi Osgouei, P., & Kabadayi, M. E. (2022). Land use and land cover mapping using deep learning based segmentation approaches and vhr worldview-3 images. *Remote Sensing*, *14*(18), 4558.
3. LeCun, Y., Bengio, Y., & Hinton, G. (2015). Deep learning. *nature*, *521*(7553), 436-444.
4. Han, K., Wang, Y., Chen, H., Chen, X., Guo, J., Liu, Z., ... & Tao, D. (2022). A survey on vision transformer. *IEEE transactions on pattern analysis and machine intelligence*, *45*(1), 87-110.
5. Boguszewski, A., Batorski, D., Ziemba-Jankowska, N., Dziedzic, T., & Zambrzycka, A. (2021). LandCover. ai: Dataset for automatic mapping of buildings, woodlands, water and roads from aerial imagery. In *Proceedings of the IEEE/CVF Conference on Computer Vision and Pattern Recognition* (pp. 1102-1110).
6. Ronneberger, O., Fischer, P., & Brox, T. (2015, October). U-net: Convolutional networks for biomedical image segmentation. In International Conference on Medical image computing and computer-assisted intervention (pp. 234-241). Springer, Cham.
7. Zhou, Z., Rahman Siddiquee, M. M., Tajbakhsh, N., & Liang, J. (2018). Unet++: A nested u-net architecture for medical image segmentation. In *Deep Learning in Medical Image Analysis and Multimodal Learning for Clinical Decision Support: 4th International Workshop, DLMIA 2018, and 8th International Workshop, ML-CDS 2018, Held in Conjunction with MICCAI 2018, Granada, Spain, September 20, 2018, Proceedings 4* (pp. 3-11). Springer International Publishing.
8. Chen, L. C., Zhu, Y., Papandreou, G., Schroff, F., & Adam, H. (2018). Encoder-decoder with atrous separable convolution for semantic image segmentation. In Proceedings of the European conference on computer vision (ECCV) (pp. 801-818)
9. Xie, E., Wang, W., Yu, Z., Anandkumar, A., Alvarez, J. M., & Luo, P. (2021). SegFormer: Simple and efficient design for semantic segmentation with transformers. *Advances in neural information processing systems*, *34*, 12077-12090.
10. Dosovitskiy, A., Beyer, L., Kolesnikov, A., Weissenborn, D., Zhai, X., Unterthiner, T., ... & Houlsby, N. (2020). An image is worth 16x16 words: Transformers for image recognition at scale. arXiv preprint arXiv:2010.11929.
11. Eelbode, T., Bertels, J., Berman, M., Vandermeulen, D., Maes, F., Bisschops, R., & Blaschko, M. B. (2020). Optimization for medical image segmentation: theory and practice when evaluating with dice score or jaccard index. *IEEE transactions on medical imaging*, *39*(11), 3679-3690.
12. Yao, Z., Gholami, A., Shen, S., Mustafa, M., Keutzer, K., & Mahoney, M. (2021, May). Adahessian: An adaptive second order optimizer for machine learning. In *proceedings of the AAAI conference on artificial intelligence* (Vol. 35, No. 12, pp. 10665-10673).

Advanced Engineering Days

aed.mersin.edu.tr

Investigation of real estate sales to foreigners in Turkey based province and year

Nuri Erdem[*1]

[1] *Osmaniye Korkut Ata University, Department of Geomatics Engineering, Türkiye, nurierdem@osmaniye.edu.tr*

Cite this study: Erdem, N. (2024). Investigation of real estate sales to foreigners in Turkey by province and year. Advanced Engineering Days, 9, 377-379

Keywords
Foreign Citizens,
Real Estate Acquisition,
House Sales to Foreigners,
Property

Abstract

The acquisition of immovable property by foreigners living in a country has been one of the most important issues faced by the governments of the country throughout history, many legislative changes have been made and extensive regulations have been made. In this study, province-based density analyses of sales to foreigners in Turkey have been carried out by using TUIK data, and density maps have been created according to the factors determining the province preference and foreign country ratios. In addition, the way in which the acquisition of real estate by foreigners in Turkey has been followed in the historical process, the studies, legal regulations and changes have been examined, and the socio-economic and cultural effects of the activities of foreigners in this process have been investigated.

Introduction

In international law, each state is free to determine which rights may or may not be enjoyed by foreigners in its territory. Each state has determined various systems and principles of implementation in its country based on the authority granted to it by international law regarding the acquisition of immovable property by foreigners (1).

Since each state has a different historical background, socio-economic structure, geographical and cultural characteristics, the property regime it applies is also different. Some states consider foreigners and their own citizens similar and allow foreigners to freely acquire immovable property, while others recognize this right but subject it to various limitations, and some do not allow foreigners to acquire immovable property at all. In Turkey, since 1850, the rights granted to foreigners and especially the right to acquire immovable property have been an important subject of debate. During the Republican period, this issue was not on the agenda for a long time, but with the Economic Measures of 24 January 1980 and especially with the legal regulations made for open economic growth, it became a subject of intense debate (2).

Material and Method

Within the scope of the study, literature on the sale of immovable property to foreigners in Turkey has been reviewed and the current and previous legislative amendments have been analyzed. Provincial and year-based density maps have been created. Within the scope of legal frameworks, the study analyses which factors are more dominant in-house sales to foreigners and the cities most preferred by foreigners.

The parameters used in the study were obtained from TURKSTAT (Turkish Statistical Institute) data covering 81 provinces in Turkey (3). Firstly, the data were organized as files in Excel and associated with the province map of Turkey. Layers were created and the parameters to be used were added on these layers. Year-based thematic maps were created using the classification feature. Again, it was detailed with tables and graphs using the Excel programmer.

In 2013, Sakarya had the lowest number of house sales to foreigners with 103 units and Antalya had the highest number of house sales with 5548 units. Important factors affecting house sales in Antalya are the size of the house, its location in a high-income neighborhood, its sea view, its indoor car park and its proximity to the sea. Antalya, where job opportunities are mostly concentrated in the tourism sector, also had a significant impact on house sales. Antalya was followed by Istanbul with 395 house sales, Sakarya with 26 house sales, Muğla with 116 house sales and Aydın with 103 house sales (Figure 1).

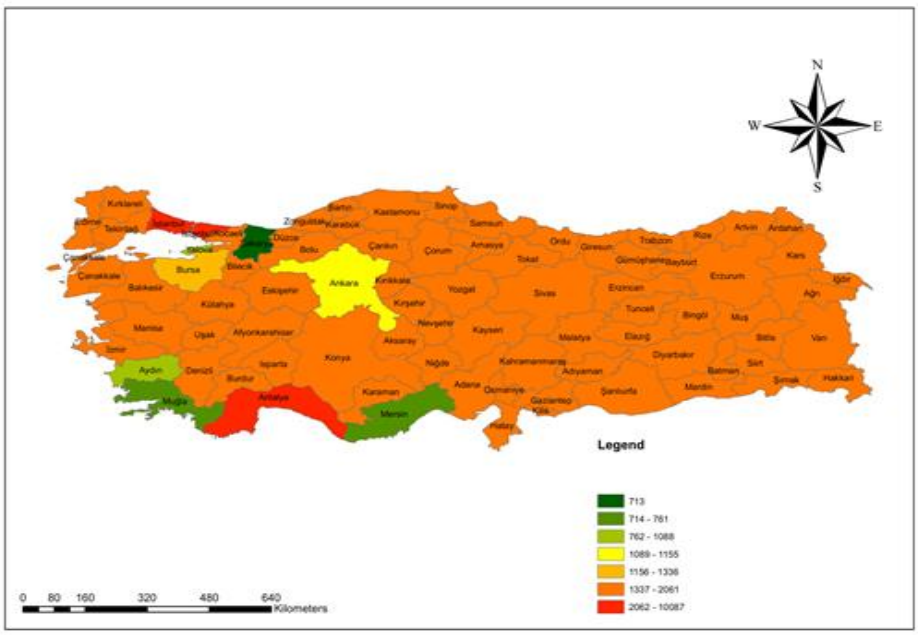


Figure 1. Provinces in Turkey where houses sold to foreigners between 2013 and 2021.

The share of sales to foreigners in total sales is 2.5 per cent. Although this rate indicates a small share, it plays an important role in the housing sector in the provinces where it is located. As a matter of fact, despite the country's housing market, where there has been a price decrease due to the decrease in the demand of domestic consumers, this situation has been less noticeable, especially in the preferred provinces (4).

When the annual growth rates of total house sales in Turkey and house sales to foreigners are compared for the period between 2013 and 2021, it is seen that while there was an increase in the range of approximately 0.7-10 per cent before, sales to foreigners increased at higher rates except for the decline in 2016. In sales to foreigners, where the lowest rate of increase was 20%, the highest rate was 56% in 2014, while an increase of 37% was recorded in 2018 (Figure 2). On the other hand, housing sales to foreigners, which were around 1.5% of total sales on average, had a share of 2.5% in 2018 (5).

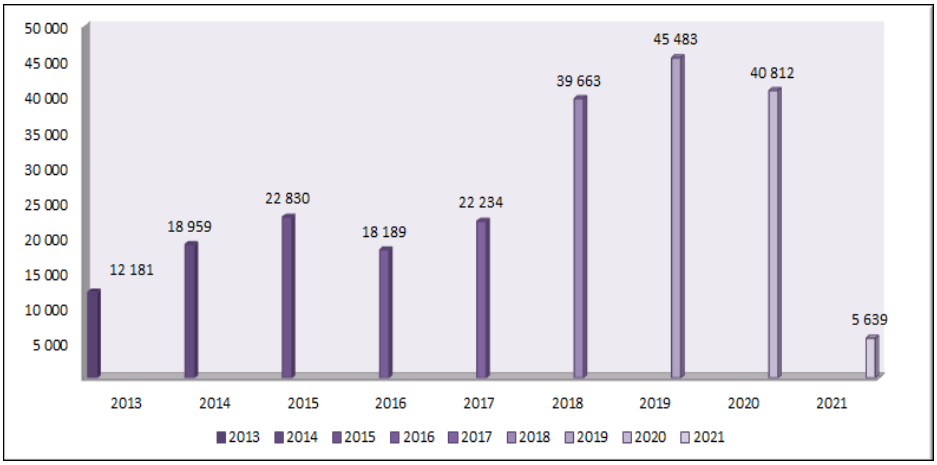


Figure 2. Number of houses sold to foreigners in Turkey between 2013 and 2021

In addition to the decline in foreign investor interest and foreign trade volume due to the impact of the COVID-19 pandemic, the significant contraction in domestic demand and the significant increase in the money supply in Turkey, especially through loans, as well as domestic investors turning to foreign currency, accelerated the depreciation of the TL against foreign currencies. Although this situation had a negative impact on the total number of house sales, it led to an increase in sales to foreigners.

In addition to the variables listed below, which nationalities constitute the predominant demand in housing sales to foreigners, which gained momentum as a result of the legal regulations made between 2012-2018 and the depreciating Turkish Lira after 2017, and which provinces will add color to the study are other topics that will add color to the study.

In housing sales to foreigners according to nationalities, it is observed that Iraqis, who have been attracting attention for years, have not left the summit and have been constantly increasing the number of sales in the total over the years.

It is observed that sales increased mostly in the summer season, while German, British and Swedish sales lagged behind the above-mentioned countries in the years under review. In other words, while the share of European countries in the weight of foreign house sales has decreased in recent years, the share of Middle Eastern countries has increased.

Results and Discussion

In 2013, Antalya was the province where the highest number of foreign nationals bought a house, while Istanbul was the first in 2015 and 2016. Again, according to these data, it is understood that provinces with suitable conditions for sea and summer tourism are more preferred, whereas Trabzon has become the province where a significant increase was experienced in 2014 with a different nature tourism location. Bursa and Sakarya provinces, on the other hand, are subject to immovable property acquisitions as provinces traditionally preferred by cognates or relatives. It can be argued that Ankara and Istanbul are preferred especially for business and investment purposes (6).

House sales to foreigners increased by 20.4% in 2015 compared to the previous year. In 2015, Istanbul ranked first with 7,493 houses and Antalya ranked second with 6,072 houses. Antalya was followed by Bursa with 1,501 houses and Yalova with 1,425 houses. Due to the high quality of life, industry, industry and intensive business opportunities etc. in Istanbul, it has become a preferred city for the acquisition of real estate. At this point, in parallel with the increase in the demand for real estate, the lack of sufficient land has caused the values to increase.

The fact that the houses are generally located on the seafront, view and visibility are the most important factors that increase their prices. In addition, the fact that Istanbul is rich in terms of historical and cultural heritage is also an important parameter in the preference of houses.

Conclusion

In today's world where communication and transportation facilities have increased, people can now easily travel to different countries for holiday or business purposes. It is common to settle temporarily or completely in order to live in the travelled countries. In addition, immovable property purchases for investment purposes are also realized. Due to the natural beauties, historical and cultural richness of our country and its geopolitical position, it attracts great interest of foreigners. With favorable living conditions and economic attractiveness, the activity in the sale of housing to foreigners has been increasing in recent years.

In this process from the past to the present, the acquisition of real estate by foreigners has been on the agenda in every period. Many regulations were made but cancelled by the Constitutional Court. Thanks to the radical changes made in the Reciprocity Law No. 6302 enacted in 2012, foreigners were able to acquire immovable property.

There are many factors in the increase in demand for housing sales to foreigners. In this context, there has been a demand for a metropolitan city close to the seaside and preferably for tourism investments. It can be stated that investors of Arab origin have also led to some mobilization especially in Bursa and Yalova. Since 2013, it has been observed that Istanbul and Antalya provinces have come to the forefront in the provincial preferences of foreigners. Law No. 6302 led to a significant increase in housing sales to foreigners. The main factors in the acquisition of real estate for investment purposes in Turkey are economic, labor force, young population, presence of natural resources, being a strategic bridge country, geopolitical location, climate, historical and cultural tourist attractions.

References

1. Sürer, D., (2008). Türkiye'de Yabancıların Taşınmaz Edinmesi, Marmara Ünv. Yüksek Lisans Tezi.
2. Tanrıvermiş, H., & Apaydın, A. (2013). Türkiye'de Yabancıların Taşınmaz Edinimi ve Etkilerinin Değerlendirilmesi, TÜBİTAK-KAMAG 110G020 KODLU Proje
3. https://www.tuik.gov.tr/
4. Özuğurlu, S. B., & Yılmaz, M. K. (2010). Yabancılara Toprak Satışı: Tarihsel Eğilimler. Memleket Siyaset Yönetim, 5(12), 102-119.
5. Sezgin Şat, A. (2018), İnşaat sektörü, Türkiye İş Bankası İktisadi Araştırmalar Bölümü, Şubat, 1-53
6. Davarcıoğlu Özaktaş, F. (2019). Yabancılara Konut Satışı Ve Reel Efektif Döviz Kuru: Türkiye Örneği Ampirik Çalışma. Ekonomik ve Sosyal Araştırmalar Dergisi, 15(1), 131-147.
7. Candan H., & Oktay E. Yabancıların Türkiye'de Taşınmaz Edinimin Turizm Sektörü Üzerine Etkisi, Yıl 2017, Cilt 6, Sayı 4, Sayfalar 639 – 661

Advanced Engineering Days

aed.mersin.edu.tr

An integrated GIS and location-based service approach applied to geomarkting and customer behavior mapping in Tabriz

Bakhtiar Feizizadeh[*1]

[1]*University of Tabriz, Department of Remote Sensing and GIS, Tabriz, Iran, Feizizadeh@tabrizu.ac.ir*

Cite this study: Feizizadeh, B. (2024). An integrated GIS and location-based service approach applied to geomarkting and customer behavior mapping in Tabriz. Advanced Engineering Days, 9, 380-385

Keywords
Urban restaurant
Geomarketing
CyberGIS
services area mapping

Abstract

This research aimed to analysis delivery services, customer satisfaction, and restaurant sales information of urban restaurants (URs) in Tabriz. For this goal, we analyzed the online food order data of URs sales and food delivery reports for 1050 out of the city's 1250 official restaurants. We collected and analyzed data on the restaurant locations, the number of food orders for each restaurant, and the number of customers and their locations for the year 2021using GIS methods. This was complemented with data on demography, land characteristics, and urban road traffic through a GIS multi-criteria decision analysis. Our results revealed the dynamics of the service areas, the spatial pattern of customer satisfaction. In addition, we evaluated the future extension potential of the service area of each URs. The results indicate that an optimized spatial distribution of the URs together with efficient quality in services can contribute to sustainable urban development. We found a variety of inherent spatial patterns that can be exploited for improving location-based services as well as benefiting the quality of life of citizens and reducing environmental impact.

Introduction

'Geomarketing' can be understood as an approach that leverages GIS and GIScience capabilities. Geomarketing builds on GIS-enabled location-based services and can be implemented for marketing communication, pricing, market segmentation, and geographical targeting. By considering the past and present spatial demographic dataset, GIS-based spatiotemporal analysis can be used to develop an efficient Geomarketing model for a variety of applications, such as business development, sustainability assessment, and customer satisfaction, as well as identifying the local markets and their structure based on the location-based capabilities of GIScience (Touzani and Van Buskirk, 2016). GIS can be used to visualize the outcomes of data mining on maps to reveal spatiotemporal patterns that enable authorities to recognize correlations between market potential and consumer behavior characteristics (Yarosh, 2019). Geomarketing approaches can be applied to marketing if the market is considered in terms of spatial aspects and not just as the statistical behavior of individuals (Libório et al., 2020). GIS applications have been employed in various businesses to generate spatial business models to evaluate the customers and competitors not only from the financial viewpoint but also in terms of spatial patterns and behaviors (Grin, 2020). Geomarketing techniques can be used to support the identification of optimal new places in facility allocations (e.g., opening new factories, shops, restaurants, or expanding a chain of cafes). In this approach, the socio-economic data, spatial data, demographic information such as age and gender, and the required data of the considered goal are evaluated to determine optimal places as part of the concept of smart cities (Dušek et al., 2019; Sharifi et al., 2021).

This study was made possible by the high data availability due to the popularity of smartphones and location-based services in Iranian cities. Location-based applications and programs have greatly gained in popularity in many societies, including Iran. A popular application is to enable food orders from home, both for take away and for delivery. The search data from Google shows how searches have changed over the course of a year after the outbreak of the pandemic. The number of food orders and food deliveries increased significantly. In addition, search interest for 'food delivery'-related questions increased by 100% (Google, 2021). The restaurant industry partially reacted to this situation, and some restaurants even developed new business cases. Restaurant managers and stakeholders need to focus more than ever on spatial marketing capabilities and the importance of location in

their decisions (Li and Hecht, 2021). Therefore, our research aimed to identify restaurant operators' perceptions and associated behavioral or management strategy changes to their services in Tabriz city using integrated cyber GIS and spatial analysis methods.

Material and Method

Case study and dataset

The study area is Tabriz city, which is one of the largest cities in Iran, with about 1.8 million inhabitants (Iranian Census Centre, 2016). Located in the northwest of the country (Figure 1), it is one of the most modern metropolitans in Iran. Historically, Tabriz has been an important trade center on the silk road for decades. Nowadays, it is nationally significant as an industrial, economic, cultural, political, commercial, and educational center (Rezaei et al., 2020). We used a variety of datasets to achieve our research objectives. According to a recent report of the Municipality of Tabriz (2021), there are approximately 1250 restaurants in the city. Our evaluation shows that almost 75 - 85 % of these restaurants are offering online services such as 'take out' and 'food delivery'. Thus, based on the data available from Google Maps and Google Earth, as well as widely known online food order applications in Iran, including Snap Food, Diba Food, Reyhoon, Gwarinpa, and Changal, a total of 1050 restaurants were identified and selected to be analyzed in this study. We obtained data on the location of URs, the number of food orders for each restaurant, and the customer addresses from these applications for the year 2020 and evaluated them using CyberGIS techniques. To analyze the spatial correlation of the restaurants with urban indicators, we also considered the population density, land use, and road traffic data. Therefore, the latest census data, the urban land use map at a scale of 1/2000, and monthly traffic data were gathered from the Municipality of Tabriz. The land value and property data were also obtained from the tax department of Tabriz for the year 2020 as a GIS dataset.

Methodology

In this research, we employed an integrated GIS data-driven approach and spatiotemporal assessment using CyberGIS and GIS spatial decision-support systems for modelling the impacts of COVID-19 on urban restaurants. We used an ensemble approach of marketing science and decision-making in a management sptial and location based geographic components. GIS models can be used to integrate data from various sources with a georeferenced database to perform various and complicated analyzes (Fan and Collischonn, 2014; Dolzhenko, 2017). GIS is, therefore, suitable for the accurate spatial analysis needed for this type of market analysis (Fan and Collischonn, 2014; Mangini et al., 2017; Peñarubia-Zaragoza et al., 2019). In the present study, aside from the functionality assessment of urban restaurants, we also evaluated and identified appropriate areas for new restaurants in the city of Tabriz.

Functionality assessment and customer satisfaction

One of the major objectives of this research was to analyze the efficiency and functionality of urban restaurants during the COVID-19 pandemic. The obtained data show that, as a result of several waves of home quarantine and the associated limitation of restaurants to 'take out' services, the number of take away and delivery orders using various apps has increased significantly during the COVID-19 pandemic. We prepared the input data for spatial pattern analysis and collected the customer satisfaction rates of all restaurants from Google Maps/Earth and food order apps, including Snap Food, Diba Food, Reyhoon, Gwarinpa and Changal. These satisfaction records include information on the food quality, prices, and delivery satisfaction and allow the customers to rank each restaurant from 1 (min) to 5 (max) scores. Based on the individual ranks, each restaurant receives a specific overall score between 1 and 5 based on customer satisfaction. In addition, these applications also record the after-sales feedback of customers as text messages. We collected all the ranking data and text messages and added them as attribute data for the urban restaurants.

Service area and allocation

Facility location optimization includes the selection of a subset of candidate sites and allocating demand to chosen locations (North and Miller, 2017). Optimization modeling techniques have been developed to address a wide variety of location-allocation problems (Laporte et al, 2015). In order to allocate services in a geographical area, it is necessary to evaluate the demand and supply of the services. As mentioned, the food order apps store individual transactions, including the address and identity of the customers for food delivery. We obtained the food order data for each restaurant along with the customers' addresses (without identity information) for the year 2020. We calculated the shortest distance and the shortest possible time for customers to reach an UR and, likewise, the shortest and fastest route for a delivery person to reach customers. Then, service areas for each UR

could be computed based on ranges of both distance and time required for the in-time delivery of food to customers. In addition, the location of customers extracted from population density and the number of food orders recorded by apps as customer location dataset (96735 points) were used as the demand while the locations of the analyzed restaurants (1050 points) served as the supply of service information. Accordingly, we employed the ESRI Network Analyst extension and Service Allocation tools to compute the customers' access to the restaurants. According to the time factor (mean time is 15 minutes) and distance, 90.92% of customers (94735 points) had access to existing services.

Using road traffic data and associated analyzes to measure the required time and distance of travel has already been addressed by earlier research. The previous studies have mostly been based on the fields of health issues and care services (Maleki, 2020, Oluoch et al., 2020), car accidents (Naboureh et al., 2019; Farhangi et al., 2020; Feizizadeh et al., 2021), or fire station allocation and crisis management (Aktaş et al., 2013; Akaya et al., 2020). Furthermore, the use of GIS is increasingly commonly used to determine the spatial accessibility of services based on the distance or travel time from residence to the site of service (Cinnamon et al., 2008). In this study, the time required to overcome the distance between the customer's location and the restaurants were computed and included in the URs service area and Geomarketing assessment. In addition to the time and distance factors, traffic is one of the most critical factors for delivery personnel (Amaguaya and Hernández, 2020). Therefore, we used the data received from the traffic police of Tabriz (TPT, 2021), and evaluated the traffic along the delivery routes under consideration of the appropriate timeframe for food delivery to customers and the shortest distance between the restaurant and the customer. The appropriate time to deliver food to customers varies between 10 and 20 minutes depending on the type of ordered food (fast food versus traditional food). Therefore, the appropriate time was considered to be an average of 15 minutes. The shortest distance in terms of time was also determined based on the data related to the speed limit on the streets determined by the traffic police of Tabriz. We used the ESRI Network Analyst tool to determine the optimal path for the delivery personnel.

Results

The following figures and tables present the main results of the study. Figure 1 shows the overall satisfaction as experienced by customers in the urban restaurants of Tabriz. Figure 2 shows the computed service areas for restaurants based on the number of food delivery reports. Figures 3 show the service areas for urban restaurants based on the customer locations and number of deliveries for each UR.

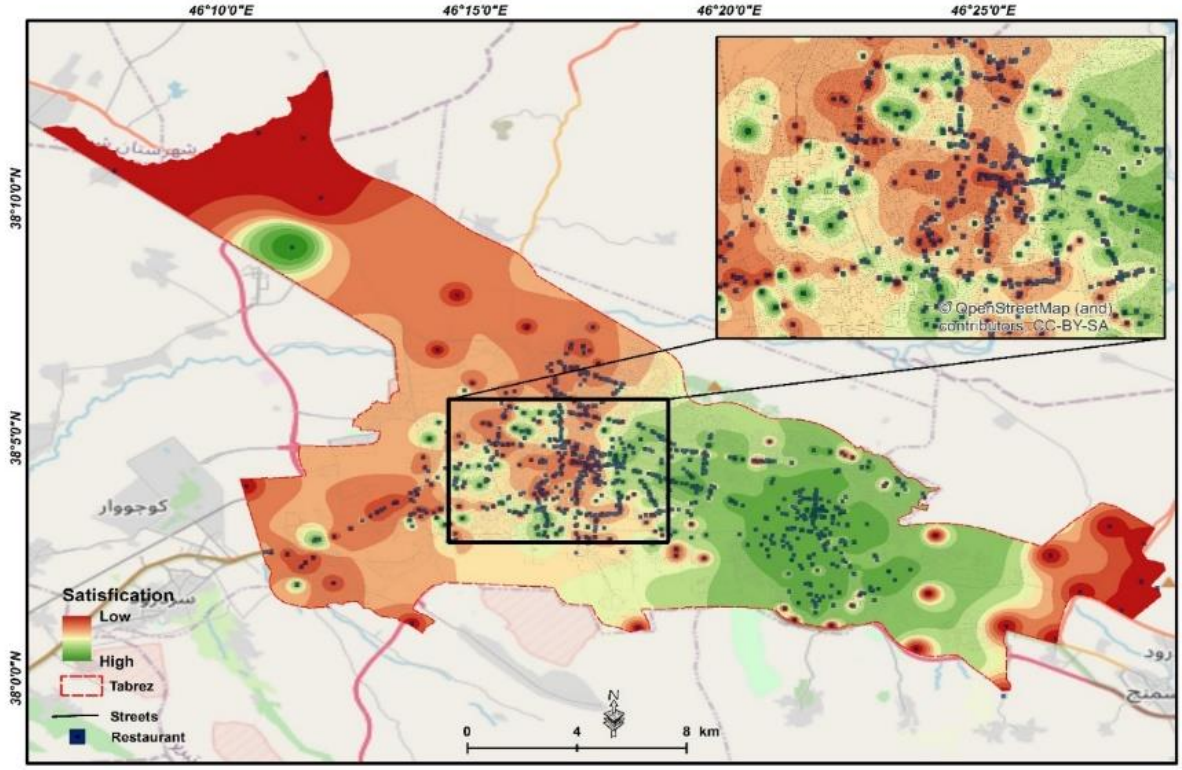


Fig 1. Customer satisfaction as reported in the food delivery reports

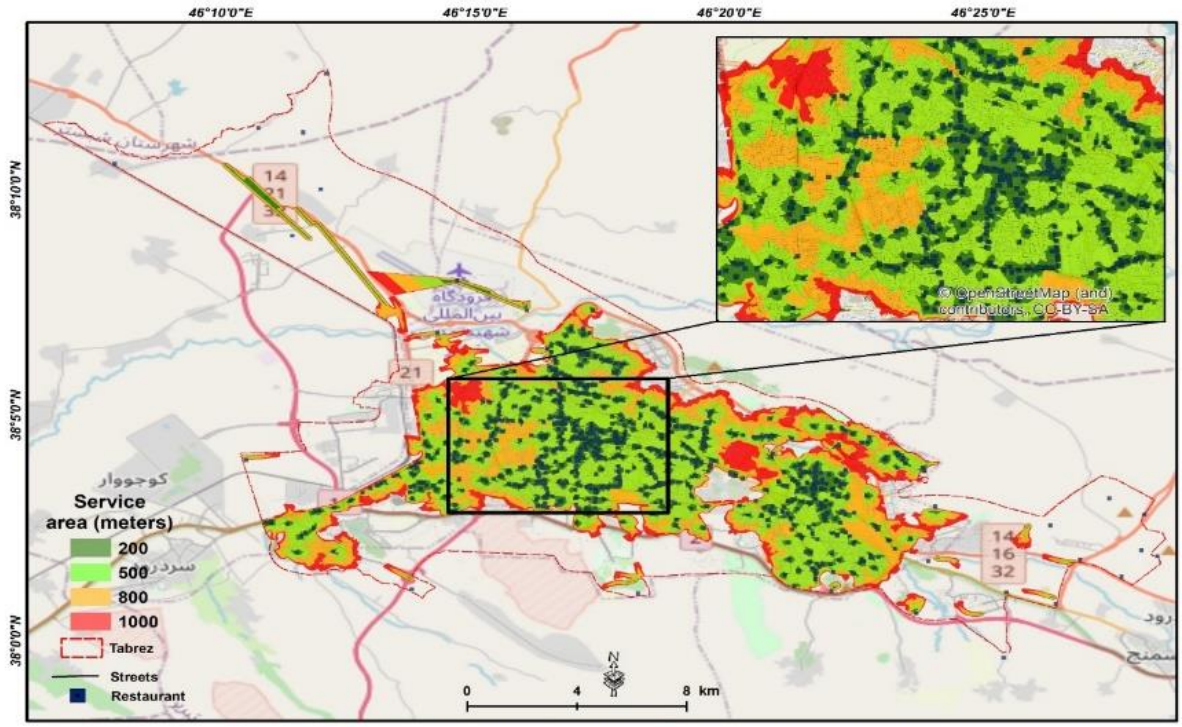


Fig 2. Computed service areas for the URs

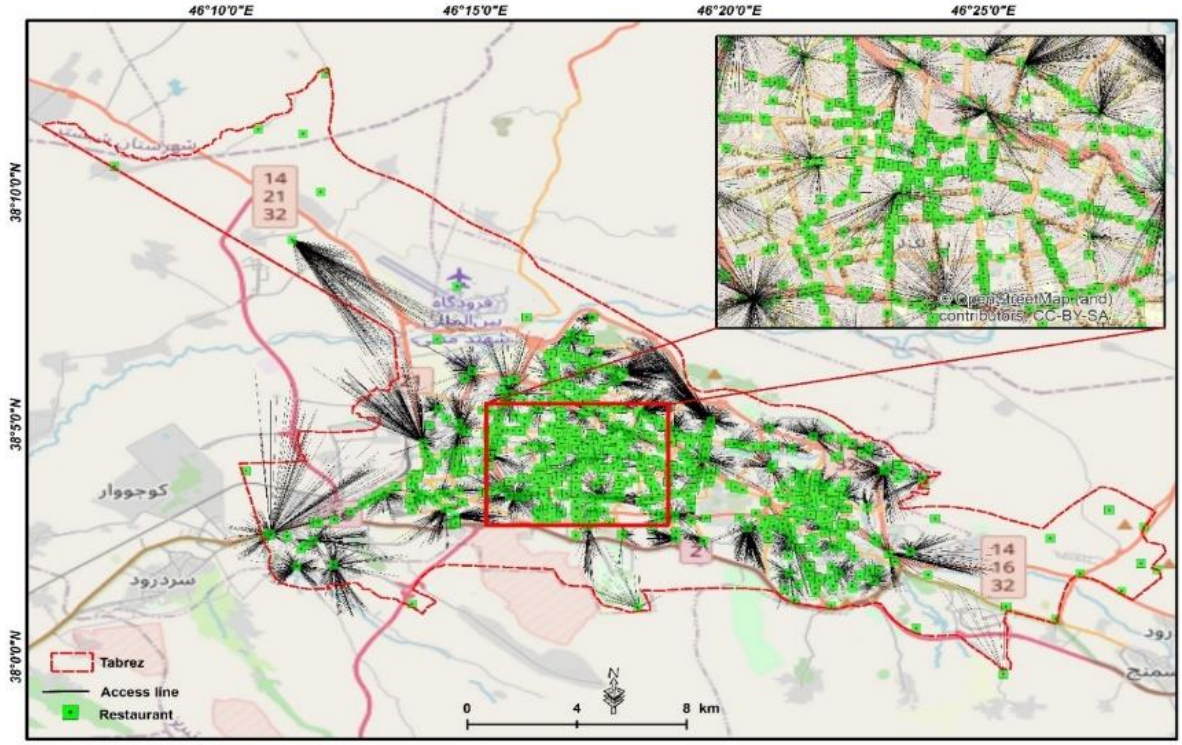


Fig 3. Service allocation results based on the food order delivery and the location of UR customers

Discussion and conclusion

The main objective of this study was to analyze the situation of the restaurant industry and the customer behavior in Tabriz city. The GIS-based analyses for service allocation were carried out using a time interval of 10 to 20 minutes, a service area of 500 to 1100 meters, and were based on data from 1050 restaurants. Our results indicated that 90.92% of the people has access to the restaurant services in the city. Results of URs service area assessment show that the URs in central and eastern areas had far reaching service areas that included their neighborhood and extended to other sub-towns in Tabriz. This shows the functionality of these URs. In the central

areas, with a high population density, tourism, and commercial and administrative services, the number of URs in these areas increased. The Geomarketing analyses revealed that the most significant spatial criteria for the UR suitability assessment were customer satisfaction, delivery service performance, service area, and road traffic, together with education and employment level. We observed different inherent spatial patterns in Tabriz city in terms of the URs functionality and their services for the citizens. There was a significant spatial correlation between the quality-of-life indicators, population density, and the functionality of urban restaurants. The best-known brands and high-quality restaurants are mostly located in wealthy areas with large services areas and high levels of customer satisfaction. As Goodchild predicted in 2010, the positioning technologies build the basis for "knowing where everything is, at all times and the role of the citizen" (Goodchild, 2010 P:13). However, this development was accelerated, where the GIS / location-based service industry grew from a demand to supporting citizens during the home quarantine. We were able to re-establish the importance of GIScience methodologies and methods for location-based marketing of restaurants. In addition, this research underpinned the importance of inherent spatial patterns in urban environments for location-based services and for the benefit of the quality of life of the citizens.

References

1. Aktaş, E., Özaydın, Ö., Bozkaya, B., Ülengin, F., Önsel, Ş., 2013 Optimizing fire station locations for the Istanbul metropolitan municipality. Interfaces, 43(3), 240-255.
2. Akay, A. E., Erdoganm N., Dogan, A., İnanç, T. A. Ş., 2020 Assessment of firefighting teams by using GIS based network analysis method. Turkish Journal of Forest Science, 4(2), 424-435.
3. Amaguaya, F. R. O., Hernández, J. R. H., 2020 Improvement of Public Transport Routes with ArcGIS Network Analyst. Case Study: Urban Center of Milagro, Ecuador. In International Conference on Applied Human Factors and Ergonomics (31-36). Springer, Cham.
4. Cinnamon, J., Schuurman, N., Crooks, V. A., 2008 A method to determine spatial access to specialized palliative care services using GIS. BMC Health Services Research, 8(1), 1-11.
5. Dušek, R., Štumpf, P., Vojtko, V. 2019 Geomarketing: Tool for consumer spending estimation in the Czech tourism & hospitality market. Global Business & Finance Review (GBFR), 24(1), 14-26.
6. Dolzhenko, R. A. 2017 Approaches to geomarketing via office locations serving individuals and legal entities in a commercial bank. Biznes-informatika Business Informatics, (3), 41-55.
7. Fan, F. M., Collischonn, W. 2014 Integração do modelo MGB-IPH com sistema de informação geográfica. Revista Brasileira de Recursos Hídricos, 19(1), 243-254.
8. Feizizadeh, B.,Omrazadeh, D., Ronag, Z., Sharifi, A., Blaschke, T., Lakes, T. 2021. A scenario-based approach for urban water management in the context of the COVID-19 pandemic and a case study for the Tabriz metropolitan area, Iran, Sciences of Total Environment, doi.org/10.1016/j.scitotenv.2021.148272.
9. Farhangi, F., Sadeghi-Niaraki, A., Nahvi, A., Razavi-Termeh, S. V. 2020 Spatial modeling of accidents risk caused by driver drowsiness with data mining algorithms. Geocarto International, doi.org/10.1080/10106049.2020.1831626.
10. Grin, P. 2020 Utilization of machine learning algorithms to support retail chain store location decisions.
11. Google Shopurfood, 2020 Unveiling top Google searches about restaurants & dine-in in 2020, https://www.shopurfood.com/blogs/unveiling-top-google-searches-about-restaurants-dine-in-in-2020.
12. Ghorbanzadeh, O., Feizizadeh, B., Blaschke, T. 2018 Multi-criteria risk evaluation by integrating an analytical network process approach into GIS-based sensitivity and uncertainty analyses. Geomatics, Natural Hazards and Risk, 9(1), 127-151.
13. Iranian Census Centre, 2016 population density and statistics, https://www.amar.org.ir/ .
14. Libório, M.P., Martinuci, O., Laudares,S., Lyrio. R.M., Machado, M., Bernardes, P., Ekel, P. 2020 Measuring Intra-Urban Inequality with Structural Equation Modeling: A Theory-Grounded Indicator, Sustanbility, 12, 8610; doi:10.3390/su12208610.
15. Laporte, G., Nickel, S., da Gama, F.S. 2015 Location Science, Springer.
16. Li, H., Hecht, B. 2021., 3 Stars on Yelp, 4 Stars on Google Maps: A Cross-Platform Examination of Restaurant Ratings. Proceedings of the ACM on Human-Computer Interaction, 4(CSCW3), 1-25.
17. Mangini, E. R., Rossini, F. H. B., Santos, A., Urdan, A. T. 2017 Analysis de geomarkting, Revista Brasileira de Gestão e Desenvolvimento Regional, 13(2).
18. Naboureh, A., Feizizadeh, B., Naboureh, A., Bian, J., Blaschke, T., Ghorbanzadeh, O., Moharrami, M. 2019 Traffic accident spatial simulation modeling for planning of road emergency services. ISPRS International Journal of Geo-Information, 8(9), 371.
19. North, J., Miller, F. L. 2017 Facility location using GIS enriched demographic and lifestyle data for a traveling entertainment troupe in Bavaria, Germany. Decision Support Systems, 99, 30-36.
20. Oluoch, F., Ayodo, G., Owino, F., Okuto, E. 2020 The Cost Implications of Reaching Universal Coverage of Maternity Health Services in Siaya County, Western Kenya.

21. Peñarubia-Zaragoza, M. P., Simancas-Cruz, M., Forgione-Martín, G. 2019 Application of geomarketing to coastal tourism areas. Tourism & Management Studies, 15(4), 7-16.
22. Rezaei, N., Najjari, R., Nezhadfard, A., Mohammadzadeh, R. 2020 Spatial analysis on the recreation of wool retail spaces in Iranian markets (case study: Tabriz Grand Bazaar). Property Management.
23. Sharifi, A., Allam, Z., Feizizadeh, B., Ghamari, H., 2021 Three Decades of Research on Smart Cities: Mapping Knowledge Structure and Trends, Sustainability, 13(13), 7140: doi.org/10.3390/su13137140.
24. Touzani, S., Van Buskirk, R. 2016 Estimating sales and sales market share from sales rank data for consumer appliances. Physica A: Statistical Mechanics and its Applications, 451, 266-276.
25. Yarosh, O. 2019 Digital geomarketing methods for analyzing the development of the economy of modern urban space. In IOP Conference Series: Materials Science and Engineering (Vol. 497, No. 1, p. 012102). IOP Publishing.

Advanced Engineering Days

aed.mersin.edu.tr

3D Documentation of an Archaeological Cave in Şuayip City, Şanlıurfa

Nizar Polat[*1]

[1]*Harran University, Geomatics Engineering Department, Türkiye, nizarpolat@gmail.com*

Cite this study: Polat, N. (2024). 3D Documentation of an Archaeological Cave in Şuayip City, Şanlıurfa. Advanced Engineering Days, 9, 386-389

Keywords
Phoyogrammetry
3D Modelling
Şuayip City
Cave

Abstract

This study focuses on the 3D modeling and documentation of a multi-room archaeologically significant cave located in Şuayip, Şanlıurfa. Utilizing terrestrial photogrammetry, the research aims to create a detailed digital representation of the cave's interior. Challenges such as muddy and swampy floors and inadequate lighting conditions limited full access and the number of photographs taken. Despite these obstacles, the 3D model successfully captured the cave's general condition, wall structures, and spatial layout. The model provides valuable insights into the cave's historical usage and construction techniques, serving as a crucial tool for archaeological research and preservation efforts. Future work will enhance data capture techniques to improve model accuracy and detail.

Introduction

The documentation and preservation of historical artifacts and structures are pivotal in the field of archaeology, serving as a bridge between the past and present. Terrestrial photogrammetry, a technique that involves capturing and processing a series of photographs to create detailed three-dimensional models, has emerged as a vital tool in this domain [1]. This method, particularly when combined with Structure from Motion (SfM) algorithms, allows for the accurate reconstruction of complex surfaces and intricate details of archaeological sites [2]. One of the significant applications of terrestrial photogrammetry is the documentation of archaeologically significant carved stone caves. These caves, often featuring multi-room layouts and intricate carvings, present unique challenges in terms of documentation due to their complex geometries and the inaccessibility of certain areas. The ability to create detailed 3D models and plans of these spaces not only aids in preservation efforts but also facilitates further study and analysis without the need for repeated physical interventions, which can be damaging [3].

The importance of generating accurate plans of archaeologically carved stone cave rooms cannot be overstated. Such plans are crucial for understanding the spatial organization and usage of these historical sites. They provide insights into the construction techniques and cultural practices of the period in which they were created. Additionally, detailed documentation aids in the conservation and restoration processes, ensuring that any interventions are informed and minimally invasive [4][5][6]. The application of Structure from Motion (SfM) in this context allows for the automated construction of 3D models from 2D images taken at different angles. SfM utilizes advanced computer vision techniques to identify and match key points across multiple images, reconstructing the geometry and spatial relationships of the subject [2]. This approach is particularly advantageous in the archaeological documentation of caves, as it can handle the irregular and non-uniform surfaces typical of such environments [1].

The advantages of using terrestrial photogrammetry for documenting historical artifacts and structures are manifold. It offers high precision and accuracy, is non-invasive, and provides a permanent digital record that can be used for various analytical purposes. Moreover, the generated 3D models can be easily shared and disseminated, facilitating collaborative research and public engagement [7][8][9]. The resulting documentation

will serve not only as a record for preservation but also as a foundational tool for further archaeological analysis and research [10][11][12][13]. In this study, we aim to apply these advanced documentation techniques to the historical multi-room cave located in Şuayip, Şanlıurfa. By capturing and processing detailed images of the cave, we will produce a comprehensive 3D point cloud model. This model will enable us to generate accurate settlement plans and sections of the cave at various levels, providing invaluable insights into its spatial organization and construction methods.

Material and Method

Study area

Şuayip City, a historically significant city located in the province of Şanlıurfa in southeastern Turkey, holds a rich cultural and archaeological heritage. Situated within a region known for its ancient civilizations and historical landmarks, Şuayip is renowned for its well-preserved archaeological sites and architectural remnants that date back to various historical periods. The city is particularly notable for its extensive network of rock-carved caves and multi-room subterranean structures, which provide valuable insights into the architectural and engineering practices of the past. These caves, often used for both residential and ceremonial purposes, reflect the intricate craftsmanship and sophisticated construction techniques employed by the inhabitants. This rich historical backdrop enhances the significance of Şuayip's archaeological sites, offering a deeper understanding of the region's historical and cultural evolution

Photogrammetric Process

Photogrammetry is the science of obtaining reliable information about the properties of surfaces and objects without physical contact and measuring and interpreting this information [14][15][16]. Photogrammetry is used in many fields, primarily archaeology, architecture, and medicine [17]. Terrestrial photogrammetry is generally applicable at object-camera distances ranging from a few meters to 200 meters. By taking overlapping and interconnected photographs from different focal points of the target object, it is possible to determine local or global coordinates related to the object and its surface, produce a dense point cloud, and create three-dimensional modeling. The documentation of significant artifacts, especially archaeological sites, historical, and cultural structures, is crucial for their preservation in a digital environment and for their accurate representation in digital form. Terrestrial photogrammetry is sufficient for modeling small structures; however, for larger historical structures such as buildings and minarets, terrestrial photogrammetry alone is inadequate.

Result and Discussion

The cave, modeled in 3D during this study, presented significant challenges due to its muddy and swampy floor, which hindered full entry. Additionally, inadequate lighting conditions limited the number of photographs taken. Despite these obstacles, the 3D model successfully captured the general condition and layout of the cave (Figure 1).

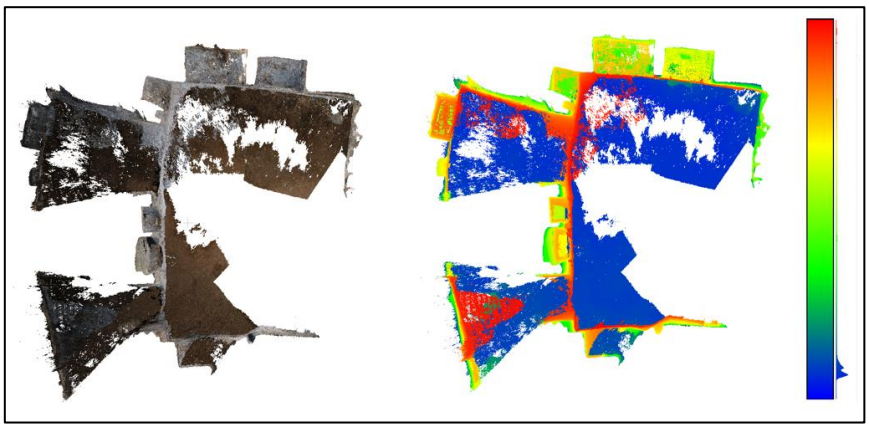


Figure 1. Top view of the cave.

There are numerous analytical possibilities provided by the 3D model. When viewed from the top, the model offers valuable information about the cave's general condition, wall structures, and extensions (Figure 2).

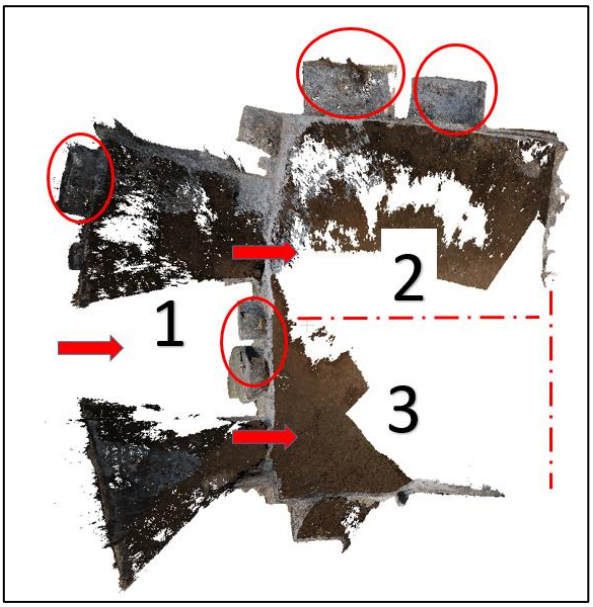


Figure 2. Extensions and layout of the cave.

Figure 2 reveals that the cave consists of two distinct rooms. Two separate doors behind the first room provide access to the other rooms. Arrows indicate the entrances to these rooms. The walls feature protrusions that appear to serve as shelves, which were intricately carved into the rock. This detailed modeling provides insights into the cave's functional aspects and spatial organization. The cross-sections further elucidate the layout and internal structure of the cave (Figure 3).

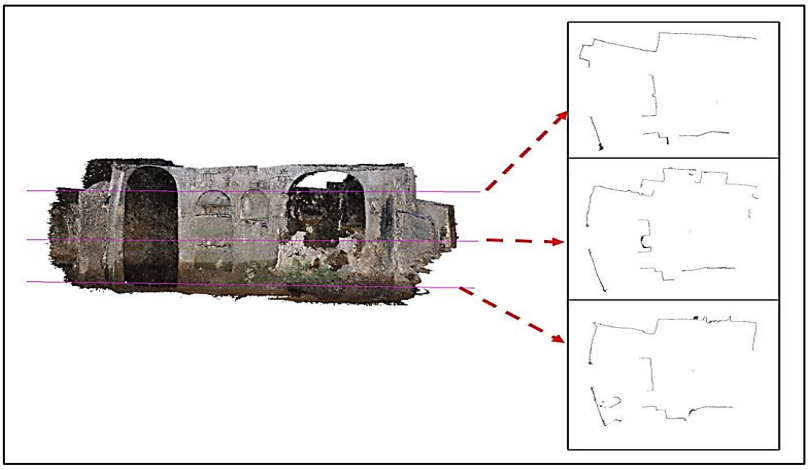


Figure 3. Cross-sections of the cave.

The detailed 3D model allows for comprehensive analysis, including volumetric assessments and spatial relationships within the cave. By examining the top view and cross-sections, one can infer the cave's original use and modifications over time. The presence of carved shelves suggests the cave might have served as a storage or living space, with well-defined areas for different functions. The model's accuracy in depicting the walls and extensions aids in understanding the construction techniques used by the original inhabitants. These insights are crucial for archaeological studies, as they provide a basis for reconstructing historical contexts and daily life within the cave.

Conclusion

The 3D model created in this study provides a valuable representation of the cave's structure and condition, despite the limitations encountered. The ability to analyze the cave's layout, wall structures, and extensions offers significant insights into its historical usage. This model serves as a foundational tool for further archaeological research and preservation efforts. This 3D modeling approach, despite the challenges faced, demonstrates the potential for detailed documentation of archaeological sites that are otherwise difficult to access. Future studies can benefit from improved lighting and floor stabilization techniques to capture data that are more comprehensive.

References

1. Remondino, F., & El-Hakim, S. (2006). Image-based 3D Modelling: A Review. The Photogrammetric Record, 21(115), 269-291.
2. Westoby, M. J., Brasington, J., Glasser, N. F., Hambrey, M. J., & Reynolds, J. M. (2012). "Structure-from-Motion" photogrammetry: A low-cost, effective tool for geoscience applications. Geomorphology, 179, 300-314.
3. Gruen, A. (2012). Development and Status of Image Matching in Photogrammetry. The Photogrammetric Record, 27(137), 36-57.
4. Green, S., Bevan, A., & Shapland, M. (2014). A comparative assessment of structure from motion methods for archaeological research. Journal of Archaeological Science, 46, 173-181.
5. Cowley, D. C., & Stichelbaut, B. (2012). Historic aerial photographic archives for European archaeology. European Journal of Archaeology, 15(2), 217-236.
6. Grussenmeyer, P., & Yasmine, J. (2004). Photogrammetry for the preparation of archaeological excavation. A 3D restitution according to modern and archive images of Beaufort Castle landscape (Lebanon). In XXth Congress of the International Society for Photogrammetry and Remote Sensing (ISPRS) (pp. 809-814).
7. Agisoft LLC. (2020). Agisoft Metashape User Manual: Professional Edition, Version 1.6. Retrieved from https://www.agisoft.com/pdf/metashape-pro_1_6_en.pdf
8. Lerma, J. L., Navarro, S., Cabrelles, M., & Villaverde, V. (2010). Terrestrial laser scanning and close-range photogrammetry for 3D archaeological documentation: The Upper Palaeolithic Cave of Parpalló as a case study. Journal of Archaeological Science, 37(3), 499-507.
9. Hullo, J. F., Grussenmeyer, P., & Farès, S. (2010). Photogrammetry and dense stereo matching approach applied to the documentation of the cultural heritage site of Kilwa (Saudi Arabia). In Actes of 22nd CIPA Symposium, October 11-15, 2009, Kyoto, Japan (pp. 11-15).
10. Doneus, M., Verhoeven, G., Fera, M., Briese, C., Kucera, M., & Neubauer, W. (2011). From deposit to point cloud: A study of low-cost computer vision approaches for the straightforward documentation of archaeological excavations. Geoinformatics, 6(3), 203-212.
11. Sapirstein, P. (2016). Accurate measurement with photogrammetry at large sites. Journal of Archaeological Science, 66, 137-145.
12. Remondino, F., & Cowley, D. (2011). 3D recording for cultural heritage. In Remote Sensing for Archaeological Heritage Management, D. Cowley (ed.), Proc. EAC Symposium (pp. 107-116).
13. Kersten, T. P., & Lindstaedt, M. (2012). Image-based low-cost systems for automatic 3D recording and modelling of archaeological finds and objects. In International Archives of the Photogrammetry, Remote Sensing and Spatial Information Sciences, XXXIX-B5 (pp. 399-404).
14. Öksüz M, Yıldırım Ç, Sağlam Ö, Karaarslan Y, Görmüş K & Kutoğlu Ş H (2011). Zonguldak Kozlu Bölgesi'nin Su Baskınlarına Yönelik Risk Araştırması. TMMOB Harita ve Kadastro Mühendisleri Odası 13. Türkiye Harita Bilimsel ve Teknik Kurultayı. Ankara
15. Yiğit A Y & Uysal M (2020). Automatic Road Detection from Orthophoto Images. Mersin Photogrammetry Journal, 2(1), 10-17.
16. Alptekin A & Yakar M (2020). Mersin Akyar Falezi'nin 3B modeli. Türkiye Lidar Dergisi, 2(1), 5-9.
17. Yiğit A Y, Orhan O & Ulvi A (2020). Investigation of The Rainwater Harvesting Potential at The Mersin University, Turkey. Mersin Photogrammetry Journal, 2(2), 64-75.

Advanced Engineering Days

aed.mersin.edu.tr

Production of agricultural cadastre map using object-oriented processing of UAV images of Tabriz farms

Abulfazl Ghanbari*[1], Habil Khorrami [2], Mostafa Musapour [3]

[1] *Tabriz University, Department of GIS & RS, Iran, a_ghanbari@tabrizu.ac.ir*
[2] *Researcher of ACECR, Iran, Habilkhorrami@yahoo.com*
[3] *Tabriz University, Department of GIS & RS, Iran, Mostafa427@gmail.com*

Cite this study: Ghanbari, A., Khorrami, H., & Musapour, M. (2024). Production of agricultural cadastre map using object-oriented processing of UAV images of Tabriz farms. Advanced Engineering Days, 9, 390-393

Keywords
Agricultural cadastre
Remote sensing
GIS
UAV images
Tabriz

Abstract

Today, remote sensing images are known as the newest and most up-to-date studies for preparing maps and land uses. These images are of great importance in order to provide timely studies, variety of shapes, digitality and the possibility of processing in the preparation of land maps. Therefore, in the corners of the world, these images are used to prepare land maps. If the preparation of agricultural cadastre map using traditional and land methods requires spending a lot of money and time. In this regard, the use of UAV images with high resolution in the world and Iran to prepare maps has been seriously considered. Therefore, in this research, it has been tried to prepare an agricultural cadastre map using UAV images as an example. The studied area is Tabriz city, which was saved in TIFF format after performing geometric corrections and cutting the area in ENVI software. Icognition software was used for segmentation and classification. To carry out this process, after choosing the appropriate scale, aspect ratio and compression ratio, image objects were produced using the segmentation operation. Finally, by using ArcGIS pro software, the intended image for agricultural lands was digitized and cartography was done to obtain the final maps. Using the appropriate image segmentation method to separate agricultural lands provides acceptable results. and realizes the creation of agricultural cadastre maps, according to the experiences gained in the production of such maps over many years, finally, using the visual digitization method is the most suitable method if the proposed UAV images are correctly and geometrically corrected. It seems and the results show higher accuracy than other methods.

Introduction

Remote sensing images have special capabilities in the study of the earth's surface and its constituent factors due to its spectral diversity, preparation of repeated coverages, and cheapness. These data are stored digitally and can be used directly by computer systems. [8] Remote sensing images are known as the newest and most up-to-date information in the preparation of maps and land uses. These images are timely, diverse, digital and processable and are of great importance in the preparation of land maps. The use of high-resolution images, including UAV images, has been seriously considered in Iran for map preparation. [2-4]

Agricultural cadastre is a comprehensive system for registering, classifying and managing information related to agricultural properties. This system includes information such as location, size, ownership, type of use, legal status and value of each piece of agricultural land. Agricultural cadastre is a valuable tool for planning and managing natural resources, facilitating investment in the agricultural sector, ensuring the security of land ownership and preventing land grabbing. [1-3]

The spatial resolution of the sensor specifies the minimum distance between two objects on the ground that can be distinguished separately from each other on the satellite image. This quantity is proportional to the ground

size of each image pixel. For example, each pixel of the image of the IKONOS measuring product in Panchromatic mode is equivalent to an area equal to 1 x 1 square meter on the ground.[1]

Machine learning is one of the main tools of digitization in the fourth industrial revolution. This method allows systems to learn and improve automatically without having to be explicitly programmed to do so. Machine learning has become an important tool for researchers to analyze data and predict reliable and accurate results. This method is divided into two main groups: supervised learning and unsupervised learning. [10]

In this research, with the help of drone images, the study of the agricultural land of Qaramalek, which is one of the western neighborhoods of Tabriz city. This neighborhood is bounded from the east by Kargar Boulevard and Shahid Heydari Street and is adjacent to the neighborhoods of Railway, Shahrak Beheshti, Tabriz Industrial, and Khanh Sazi. The geographic coordinates of Karamelk vary precisely due to the size of this area and its division into different parts. However, the approximate geographical coordinates of Qaramalek can be mentioned as latitude 38.06 to 38.12 degrees north and longitude 46.18 to 46.24 degrees east [6-9].

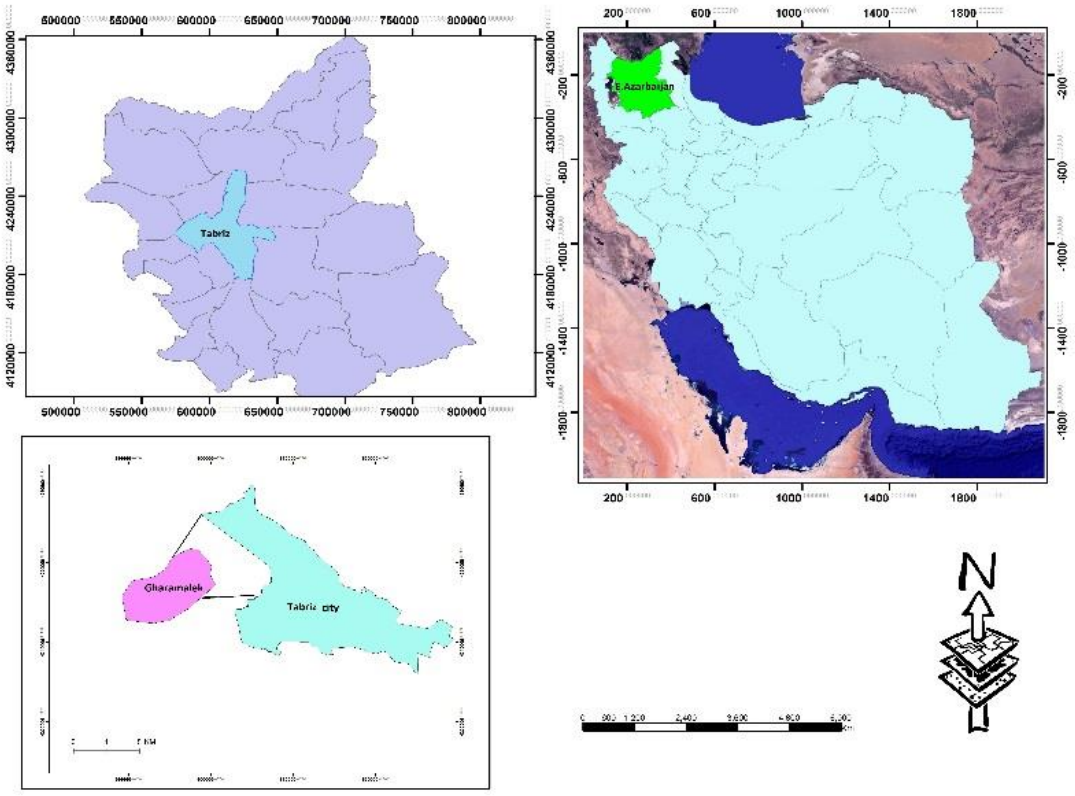


Figure 1. Map of the study area (Source: Authors)

Material and Method

The research method of the current research is descriptive-quantitative and the type of research is applied and the method of collecting data and information is documentary and field. The UAV images used in this research were purchased from the site for 2022 in the area of agricultural land in Qaramalek, Tabriz. The primary and raw data of all gauges have different geometric errors. [5-8] Although the satellite images are subjected to preliminary corrections after receiving them from the satellite at the ground station, they still have errors such as the displacement error caused by the position and elevation, and the UAV images also contain this type of error. Before the data were analyzed and additional geometric corrections were applied and the coordinates were matched to a standard basis. [2]

In this research, Tabriz urban cadastre map 550/1 has been used for geometric correction. Due to the fact that the buildings of Qaramalek village are visible in the UAV image, the corners of several buildings were considered as control points. Geometric correction was done in Envi software environment and the output image was saved in TIFF format. Icognition software was used for segmentation and classification. To carry out this process, first the TIFF format image was defined as a project in Icognition software. To achieve optimal segmentation, the segmentation operation was performed with different scales, shape coefficients and compression coefficients. Therefore, after choosing the appropriate scale, aspect ratio and compression ratio, image objects were produced using the segmentation operation. Finally, by using ArcGIS pro software, the intended image for agricultural lands was digitized and cartography was done to obtain the final maps.

After loading the UAV image, in order to apply radiometric correction of the image and also with the aim of matching the value of the gray levels of the image with the value of the real pixels of ground reflection, the gray levels were converted to radiance and then converted to ground reflection coefficients using atmospheric correction. Radiometric Calibration tool was used for radiometric correction and flash model was used for atmospheric correction in ENVI software environment, Icognition software was used for image classification based on machine learning algorithms based on object oriented processing. . The image of the studied area, which was pre-processed and saved in TIFF format, was called in the environment of this software and saved as a project. In order to produce visual objects, segmentation operations were carried out in different scales, shape coefficients and compression ratios to reach the most appropriate segmentation mode. In this step, the multiple resolution segmentation method was used to segment the image. The most suitable segment included scale 120, shape factor 0.8 and compression factor 0.2. Because in scales higher than 120, the construction of the visual object was not done correctly, so that several distinct complications were placed in one piece, and in scales less than 120, in some cases, one complication was placed in several pieces. took Figures 2 and 5 show the main image of the studied area at a scale of 120 and the average image objects resulting from optimal segmentation.

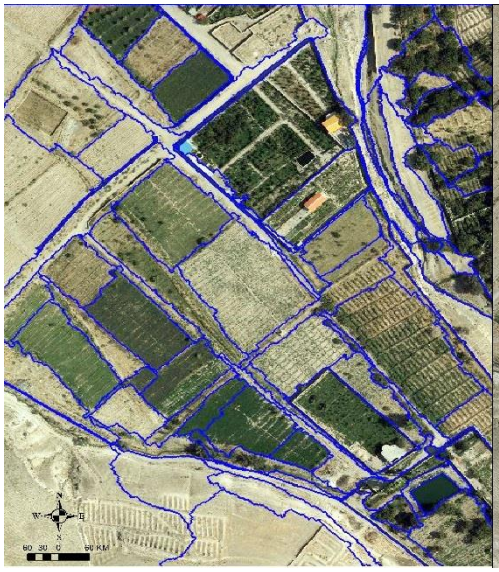


Figure 2. No segmentation

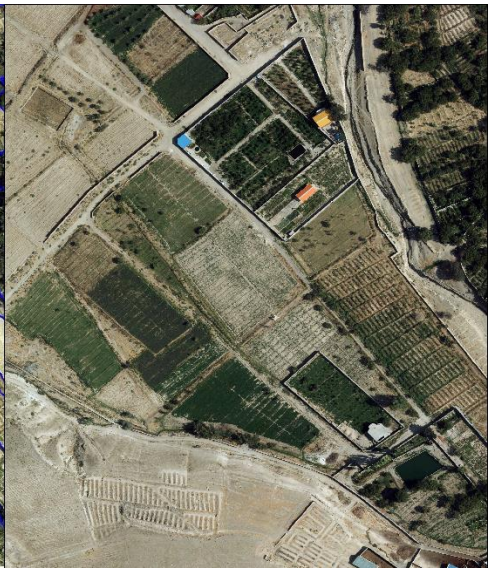


Figure 3. Segmentation in scale 120



Figure 4. Production of visual objects

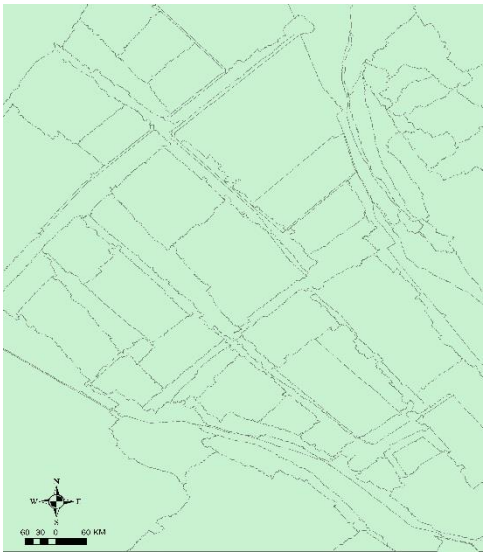


Figure 5. Segmentation in polygon mode

Results

After performing the steps of geometric correction and ground referencing, highlighting the image and applying the Sharp image detection filter, we prepared the agricultural cadastre map. After extracting the segmented image as a polygon file and converting the polygon into a line, digitizing the agricultural land, its agricultural cadastre map was prepared from the drone image of the region. Digitizing the image was done in the Arc GIS software environment. You can see an example of the digitized map in Figure 6 and 7.

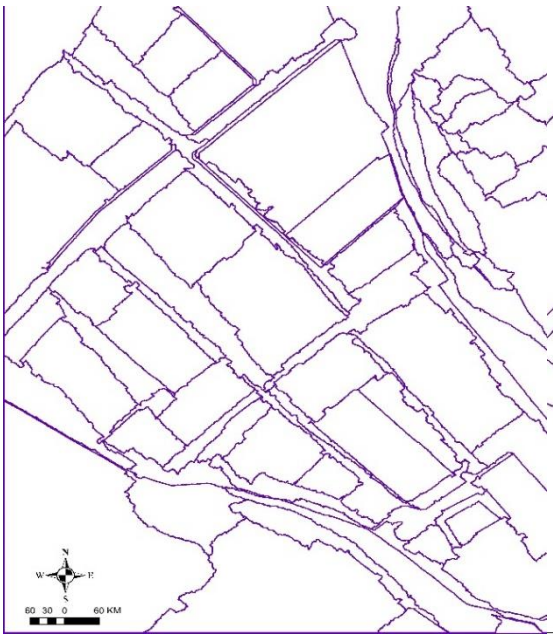


Figure 6. Polygon to line conversion map



Figure 7. Cadastre map produced

Conclusion

As mentioned in the above sections, the preparation of agricultural cadastre map using remote sensing images with high spatial resolution, in addition to the speed of preparation of agricultural cadastre maps, also has acceptable accuracy. which will ultimately save time and money. If we want higher accuracy, we can use UAV images and Quickbird and eye Geo satellite images. To ensure the accuracy of the prepared map, you can randomly control the different locations of the prepared map. and finally, after carrying out the cartographic corrections, it was entered into the agricultural cadastre system. It is also necessary to mention that before digitizing the laws related to the agricultural cadastre, as well as the customary laws of farmers' divisions, so that the agricultural cadastre map in terms of quantity and the quality should be highly accurate.

References

1. M. Chandra Ves. K. Gosh, Alavi Panah, Seyyed Kazem, Ledni, Muslim, 2013, Remote Sensing and Geographical Information System, Tehran University Press.Alptekin, A., & Yakar, M. (2020). Determination of pond volume with using an unmanned aerial vehicle. Mersin Photogrammetry Journal, 2(2), 59-63.
2. Pour Kamal, Mohammad, An Introduction to Cadastre Recognition and Its Applications, First Edition, Publications of Tehran Geographical Information Center, Summer 2017.
3. Mubasheri, Mohammad Reza, Fundamentals of Physics in Remote Sensing and Satellite Technology, Khwaja Nasiruddin Tousi University of Technology Publications, first edition, June 1381.
4. Ghanbari, Abolfazl, Musapour, Mustafa, Khorrmi Hossein Hajlou, Habil, & Anuri, Hossein. (2024). Comparing the efficiency of machine learning classifiers in extracting the physical development area of Hamedan city by using of Object-Based Images Analysis of satellite images.. Scientific-research quarterly journal of geographical information "Sephehr". doi: 10.22131/sepehr.2024.2012503.3024.
5. Masoumi, Ezra, Faizizadeh, Bakhtiar, & Valizadeh Kamran, Khalil. (2022). Providing appropriate parameters in the identification and extraction of buildings and urban features using object-oriented processing techniques of aerial images. Geography and Planning, 26(80), 315-303. doi: 10.22034/gp.2020.41630.2696.
6. Alwedyan, S. (2022). Monitoring Urban Growth and Land Use Change Detection with Gis Techniques In Irbid City, Jordan. International Review for Spatial Planning and Sustainable Development, 11, 253-275. https://doi.org/10.14246/irspsd.11. _2531.
7. Mousavi, Seyyed Mohammad, and colleagues. (2018). The application of object-oriented image processing in the preparation of cadastral maps of agricultural lands. Journal of Mapping Sciences and Techniques, 23(2), 123-134.
8. Lillesand, T., Kiefer, R. J., & Chipman, J. W. (2015). Remote sensing and image interpretation. John Wiley & Sons.
9. Rezaei, Majid, et al. (2016). The application of unmanned aerial imaging and object-oriented image processing in the preparation of cadastral maps of agricultural lands. Journal of Agricultural Sciences and Techniques, 20(3), 523-534.
10. Zarco-Gutiérrez, D., & Lamb, J. W. (2016). Automated land-use and land-cover classification using object-based image analysis and airborne LiDAR data: A case study in the Colombian Andes. Remote Sensing, 8(5), 442

Advanced Engineering Days

aed.mersin.edu.tr

Impact of Different Image Acquisition Modes on the Multispectral UAV-Based NDVI Maps

Ilyas Aydın*[1], Umut Gunes Sefercik[1]

[1] *Gebze Technical University, Department of Geomatics Engineering, Kocaeli, Turkey, ilyasaydin@gtu.edu.tr/ sefercik@gtu.edu.tr*

Cite this study: Aydın, I., & Sefercik, U. G. (2024). Impact of Different Image Acquisition Modes on the Multispectral UAV-Based NDVI Maps. Advanced Engineering Days, 9, 394-396.

Keywords
Coherence
Hover-and-capture
In-motion capturing
Multispectral UAV
NDVI Map
Orthomosaic

Abstract

The numerous advantages such as high geometric and radiometric accuracy and low cost provided UAV as a highly demanded alternative technology for mapping purposes. Integration of multispectral (MS) cameras and RTK positioning capabilities are two of the main factors that arise the preference of UAVs. The quality of the UAV products firstly depends on the quality of real-time collected images. In UAV flights, several parameters have to be determined correctly to provide high-quality imaging. This study aims to demonstrate the effect of image-capturing modes on the UAV NDVI maps. Accordingly, two different MS orthomosaics were produced employing equal time interval (in-motion) and hover-and-capture modes. Using the orthomosaics, two different NDVI maps were generated and the coherency was validated by visual and statistical approaches. The analyses were performed for building, road and vegetation classes separately. The results indicate a difference between NDVI maps of in-motion and hover-and-capture flight modes ±0.079 as RMSE and STD, and ±0.041 as NMAD. While, roofs of the buildings and roads are highly coherent, noticeable differences of ±0.3 were observed on some trees and the boundaries of the objects. The causes of the results were discussed.

Introduction

The high spatial resolution, low cost, user-friendly interfaces, and practical usage capabilities have made unmanned aerial vehicles (UAV) a highly demanded alternative remote sensing technology. Particularly multispectral (MS) UAVs are widely used in many scientific applications within the scope of precision agriculture and forestry, thanks to their wide wavelength sensing capabilities [1-4]. However, real-time images captured by MS UAVs in motion can be affected by various factors such as imaging geometry, exposure and blur. These disruptive effects have a direct impact on the quality of the final UAV products [5]. In many studies in the literature, it is mentioned that hover-and-capture mode is preferred in order to prevent the motion blur effect caused by in-motion imaging [6-8]. However, in this mode, UAV hovers at every photo shooting point that's why the flight time is quite long and this problem cannot be solved with current battery technologies. In UAV-based operations covering extensive areas such as agricultural zones, it's crucial to optimize flight time to strike the right balance considering cost, technical equipment, and time constraints. To address this issue, it's essential to evaluate the efficiency of alternative flight modes, and there hasn't been much analysis of the geometric and radiometric performance of MS UAVs in different flight modes in the literature. In this context, in-motion and hover-and-capture flight modes were employed for MS UAV image acquisition and the coherence between generated orthomosaics and NDVI maps was validated by visual and statistical point and model-based approaches.

Study Area and Materials

The study area, encompassing approximately 6 hectares, is situated in the northern part of the Gebze Technical University Campus, located in the Gebze district of Kocaeli province, Turkey (Figure 1). The study area features a diverse landscape includes natural green spaces with various tree and plant species, alongside man-made elements such as buildings and roads. Aerial photos were captured using a DJI Phantom 4 MS UAV, which is equipped with an FC6360 camera featuring six imaging bands: RGB composite, blue, green, red, red edge, and near-

infrared. Additionally, this UAV is equipped with a real-time kinematic (RTK) GNSS receiver. For the positional accuracy control of photogrammetric products such as MS orthomosaics produced from aerial photos, three polycarbonate control points (CPs) were installed in the study area, paying attention to radial distribution. The 3D coordinate measurements of all CPs were meticulously conducted utilizing the precise CHC i80 GNSS receiver. Furthermore, prior to the flight, MS images of the MAPIR V2 calibration target were captured for radiometric calibration of all bands during the subsequent image processing phase.

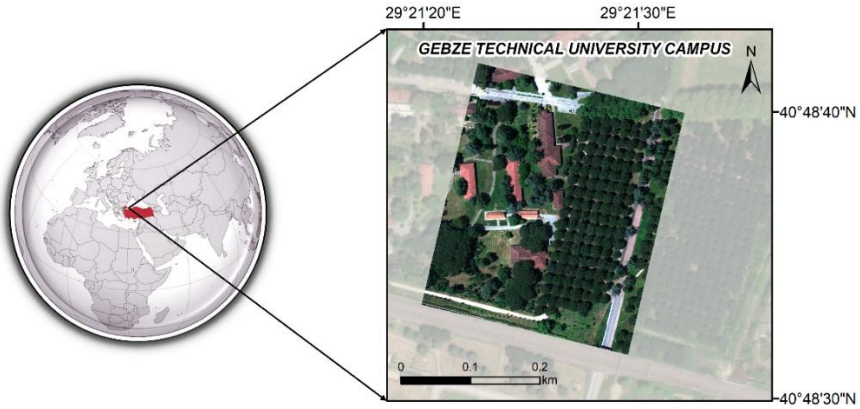


Figure 1. Study area

Methodology

The first step of the methodology was the reconnaissance of the study area and the establishment of CPs. This was followed by image acquisition with two different flight modes, and finally, visual and statistical analysis of the final outputs produced from these images. Flight parameters were set, and automated flights were performed with DJI Ground Station Pro software. Image acquisition was performed in two different flight modes: "capture equal time interval" and "hover-and-capture", with a ground sampling distance (GSD) of 5.5 cm at an altitude of 110 m above ground level. The first flight was conducted in hover-and-capture mode, in which the UAV remains stationary at each image capture point, reducing the blur effect caused by UAV movement and wind-induced shaking. This mode supports UAV stabilization during image acquisition, minimizing deviation from nadir direction. To record the highest reflection values using MS UAV, camera orientation was set to 90°. In the second flight, which covered the same area, the UAV utilized in-motion capturing with an equal time interval mode, taking images every 2.5 sec. All images were radiometrically calibrated using the Structure-from-Motion (SfM)-based software Agisoft Metashape Pro. These calibrated images were then processed in the same software following the photogrammetric workflow, and a five-band orthomosaic was produced in the WGS 84 UTM Zone 35N coordinate system with a resolution of 6 cm. The same workflow was applied for the images acquired with both flight modes and then NDVI maps were produced by calculating the NDVI index from the MS orthomosaics. With the help of model and point-based analyses performed with NDVI maps, the coherence of the data produced from both sources was analyzed.

Results and Conclusion

The geometric accuracy of the generated orthomosaics was controlled by employing three independent control points (ICP) and the root mean square errors (RMSE) were calculated as approximately ±1 cm for both. In model-based spectral coherence analyses of NDVI maps derived from two different flight modes, RMSE, standard deviation (STD), and normalized median absolute deviation (NMAD) metrics were used. The analyses revealed that RMSE and STD of the differences between NDVI maps are both ±0.079, and the NMAD is ±0.041 (Note that NDVI range is ±1) (Figure 2).

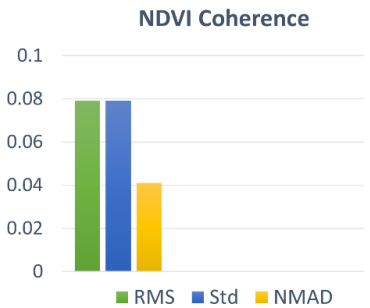


Figure 2. Differences between NDVI maps as RMSE, STD, and NMAD

Figure 3 shows the orthomosaics, NDVI maps and the NDVI differential map representing the difference between two NDVI maps produced from the images taken in-motion and hover-and-capture modes. When the NDVI differential map is analyzed, it is seen that the roofs of the buildings and roads are highly coherent. In contrast, a significant difference of ±0.3 has been identified in the tree boundaries and insides as well as in the boundaries of the buildings (Figure 3c). The change in shadow size, the motion-induced blur effect inherent in the flight modes, or the noisy points are the main reasons for the differences in the NDVI maps. Also, the effect of different point clouds generated from different image acquisition modes in the interpolation, crucial process for the generation of raster orthomosaics may cause the considerable differences on NDVI maps.

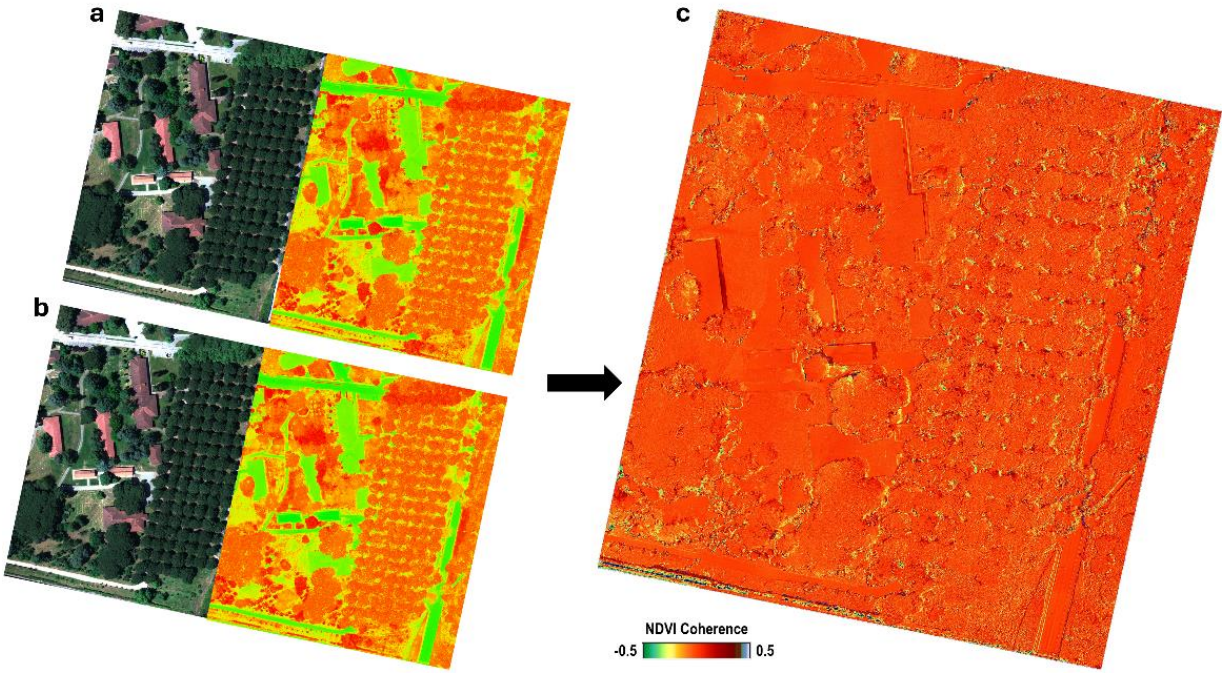


Figure 3. (a) In-motion mode orthomosaic and NDVI map, (b) hover-and-capture mode orthomosaic and NDVI map, (c) NDVI differential map

Overall, in the study, regional differences were determined in the photogrammetric products generated with aerial images from two different flight modes. The results demonstrated that the choice of flight mode impacts the final products, and this factor should be considered according to the specific objectives of UAV studies.

References

1. Johansen, K., Raharjo, T., & McCabe, M. F. (2018). Using multi-spectral UAV imagery to extract tree crop structural properties and assess pruning effects. Remote Sensing, 10(6), 854.
2. Sona, G., Passoni, D., Pinto, L., Pagliari, D., Masseroni, D., Ortuani, B., & Facchi, A. (2016). UAV multispectral survey to map soil and crop for precision farming applications. The international archives of the photogrammetry, remote sensing and spatial information sciences, 41, 1023-1029.
3. Devia, C. A., Rojas, J. P., Petro, E., Martinez, C., Mondragon, I. F., Patiño, D., ... & Colorado, J. (2019). High-throughput biomass estimation in rice crops using UAV multispectral imagery. Journal of Intelligent & Robotic Systems, 96, 573-589.
4. Sefercik, U. G., Kavzoglu, T., Colkesen, I., Nazar, M., Ozturk, M. Y., Adali, S., Dinc, S. (2023). 3D positioning accuracy and land cover classification performance of multispectral RTK UAVs. International Journal of Engineering and Geosciences, 8(2):119-128.
5. Sefercik, U. G., Nazar, M. (2023). Consistency Analysis of RTK and Non-RTK UAV DSMs in Vegetated Areas. IEEE Journal of Selected Topics in Applied Earth Observations and Remote Sensing, 16: 5759-5768.
6. Lam, O. H. Y., Dogotari, M., Prüm, M., Vithlani, H. N., Roers, C., Melville, B., ... & Becker, R. (2021). An open source workflow for weed mapping in native grassland using unmanned aerial vehicle: Using Rumex obtusifolius as a case study. European Journal of Remote Sensing, 54(sup1), 71-88.
7. Bomantara, Y. A., Mustafa, H., Bartholomeus, H., & Kooistra, L. (2023). Detection of Artificial Seed-like Objects from UAV Imagery. Remote Sensing, 15(6), 1637.
8. Genze, N., Wirth, M., Schreiner, C., Ajekwe, R., Grieb, M., & Grimm, D. G. (2023). Improved weed segmentation in UAV imagery of sorghum fields with a combined deblurring segmentation model. Plant Methods, 19(1), 87.

Advanced Engineering Days

aed.mersin.edu.tr

Thermal Analysis of Building Facades Using UAV

Emine Beyza Dörtbudak*[1], Nizar Polat [2]

[1]*Harran University, Department of Geomatics Engineering, Türkiye, beyzadbk@gmail.com, nizarpolat@harran.edu.tr*

Cite this study: Dörtbudak, E. B., & Polat, N. (2024). Thermal Analysis of Building Facades Using UAV. Advanced Engineering Days, 9, 397-400.

Keywords
Thermal
UAV
SfM
Thermal Performance
Orthophoto

Abstract

This study explores the detection and analysis of thermal anomalies in the facades of the Engineering Faculty at Harran University using UAV-mounted thermal cameras. Utilizing a DJI Mavic 3T UAV, high-resolution thermal images were captured and processed to create detailed thermal orthophotos. The data acquisition involved systematic flight planning to ensure comprehensive coverage and optimal environmental conditions. Agisoft Metashape software was employed to generate orthophotos through the structure from motion (SfM) technique, providing accurate georeferencing of the thermal data. Visual inspection of these orthophotos allowed for the identification of cold and hot anomalies, indicative of thermal bridges, insulation failures, and moisture ingress. The findings were validated through cross-referencing with architectural plans and on-site inspections. This methodology demonstrates the effectiveness of UAV-based thermal imaging in assessing building thermal performance, offering significant potential for improving energy efficiency and building maintenance practices.

Introduction

The detection and analysis of thermal anomalies in building facades is crucial for building maintenance and energy efficiency. Using Unmanned Aerial Vehicles (UAVs) equipped with thermal cameras has proven to be a powerful tool for this purpose. By capturing thermal orthophotos of building facades, it is possible to visually interpret and identify areas with cold and hot anomalies, which can indicate issues such as thermal bridging, insulation failures, or moisture ingress. Thermal anomalies significantly impact the energy performance of buildings. Identifying these anomalies allows for targeted interventions that can improve energy efficiency, reduce energy costs, and enhance occupant comfort. Traditional thermal inspections with handheld infrared cameras are time-consuming and limited in scope. In contrast, UAV-mounted thermal cameras offer a more efficient and comprehensive approach, enabling the inspection of large areas and hard-to-reach places with relative ease [1].

UAVs provide a stable platform for thermal cameras, allowing for high-resolution thermal imagery and detailed thermal orthophotos. Studies have shown that UAV-based thermal imaging is effective in detecting various issues, including thermal bridges, air leaks, and moisture accumulation [2]. Capturing thermal data from multiple angles and heights enhances the accuracy and reliability of the analysis. Several factors influence the effectiveness of thermal imaging using UAVs. Environmental conditions, such as ambient temperature, sunlight, and wind, can affect the accuracy of thermal readings. Therefore, it is essential to conduct thermal imaging under optimal conditions, typically during early morning or late evening when the temperature difference between the building interior and exterior is greatest. Additionally, the quality of the thermal camera, including its resolution and sensitivity, is critical for detecting subtle temperature variations [3].

One significant advantage of UAV-based thermal imaging is the ability to create comprehensive thermal orthophotos of building facades. These orthophotos provide a visual representation of the thermal condition of the entire building surface, allowing for easy identification of areas with thermal anomalies. Cold anomalies often indicate areas where heat is escaping from the building, such as through thermal bridges or poorly insulated

sections. Conversely, hot anomalies may suggest areas where external heat is penetrating the building, potentially due to compromised insulation or other defects [4]. Recent advancements in UAV technology and thermal imaging have further enhanced this approach. High-resolution thermal cameras, improved UAV stability, and advanced image processing software enable the generation of detailed and accurate thermal orthophotos, making UAV-based thermal imaging a practical and valuable tool for building inspections and energy audits [5].

Despite the benefits, UAV-based thermal imaging faces challenges. Regulatory constraints, such as restrictions on UAV flights in certain areas, can limit the scope of inspections. Additionally, interpreting thermal images requires expertise and experience to accurately identify and assess thermal anomalies. Combining UAV-based thermal imaging with professional knowledge ensures reliable and actionable insights [6]. Integrating thermal imaging data with Building Information Models (BIM) can further enhance the utility of the collected data. BIM integration provides a comprehensive view of the building's thermal performance, facilitating better planning and decision-making for maintenance and energy efficiency improvements [7].

In conclusion, UAV-mounted thermal cameras for detecting and analyzing thermal anomalies in building facades offer a promising and efficient approach to building maintenance and energy efficiency. Capturing and interpreting thermal orthophotos can identify and address issues related to thermal performance, leading to improved energy efficiency and occupant comfort. As technology advances, UAV-based thermal imaging is likely to become an integral part of building inspection and energy management practices.

Material and Method

This study employs a systematic approach to detect and analyze thermal anomalies in the facades of the Engineering Faculty at Harran University using UAV-mounted thermal cameras (Figure 1). For data acquisition, a DJI Mavic 3T UAV equipped with a high-resolution thermal camera was utilized. The UAV, equipped with a GPS receiver, ensured accurate geotagging of each image. Detailed flight plans were created to cover the building facades comprehensively, with flights conducted during early morning or late evening to maximize temperature contrast between the building interior and exterior [8]. Consistent flight altitude and speed were maintained, capturing thermal images at a resolution of 640x512 pixels. Multiple flight passes were conducted at varying angles for thorough coverage, and each image was geotagged with GPS coordinates.



Figure 1. The facade of the building where the study was conducted

Captured thermal images were processed using Agisoft Metashape, a software based on the structure from motion (SfM) technique [9]. This software created high-resolution thermal orthophotos by stitching individual images into a comprehensive mosaic. The SfM technique effectively generated detailed 3D models from overlapping images, providing a robust basis for analysis. Thermal orthophotos were georeferenced using GPS data from the UAV flights, ensuring accurate location mapping of detected anomalies. Georeferenced thermal orthophotos were visually inspected to identify significant temperature variations. Cold anomalies indicated heat loss through thermal bridges or poor insulation, while hot anomalies suggested external heat penetration [10]. Identified anomalies were documented, noting their precise location, temperature difference, and potential causes. Images were annotated to highlight areas of interest, with detailed descriptions explaining the thermal behavior observed.

Findings from thermal images were cross-referenced with architectural plans and on-site inspections of the Engineering Faculty building to validate detected anomalies, ensuring accuracy and reliability of the analysis [11]. This structured methodology aimed to provide a comprehensive assessment of the thermal performance of the Engineering Faculty building at Harran University. UAV-mounted thermal cameras and advanced image processing techniques enabled detailed and efficient evaluation, facilitating targeted interventions for improving energy efficiency and building maintenance.

Results

Anomalies are clearly visible on the façade, which was thermally photographed within the scope of the study. These anomalies were analyzed in 4 main sections (Figure 2). Within the scope of the study, the anomaly and their causes were emphasized, not the absolute temperature values.

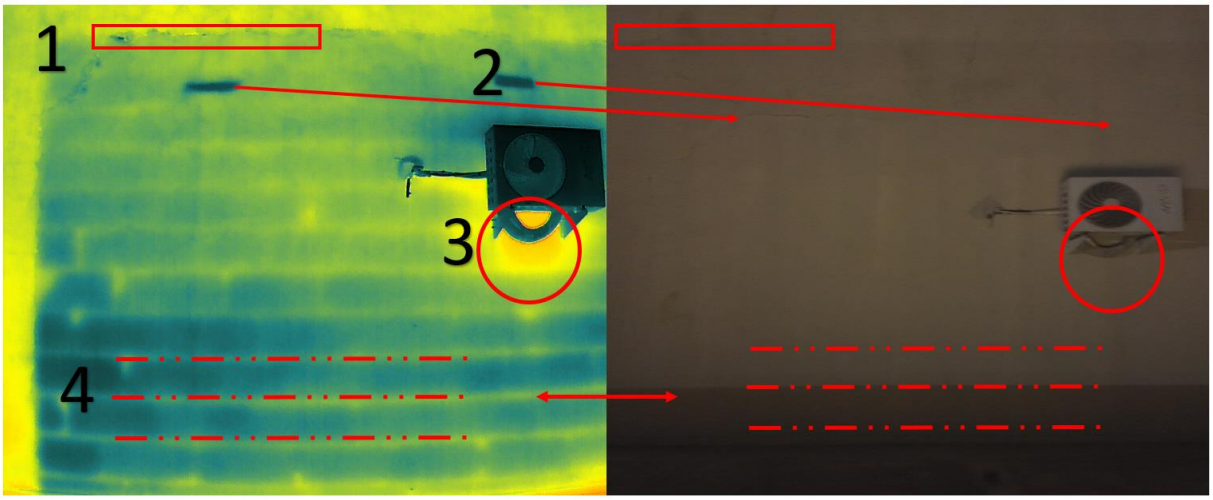


Figure 2. Thermal anomalies on the facade

The part marked with the number 1 in Figure 2 can be expressed as the part where the crack and the paint spilled due to this. When these regions are examined, it is seen that the cracks are cooler. The part marked with number 2 is seen as another cold anomaly. What is interesting here is that there are no cracks or paint flaking on the plaster. Its smooth rectangular shape suggests that it may be an in-wall installation. Anomaly number 3 is seen behind the air conditioner motor. It seems to be warmer, probably due to the relatively low air contact and the effect of the air conditioner motor. Anomaly number 4 is the most interesting part. Under the plaster, the individual elements from which the wall is constructed (the wall or the wall) exhibit different temperatures and become apparent even under the plaster.

Conclusion

This study successfully identified and analyzed thermal anomalies in the facades of the Engineering Faculty at Harran University using UAV-mounted thermal cameras. The captured thermal images revealed several significant anomalies, categorized into four main sections. These included areas with visible cracks and paint spillage, likely causing cooler regions, and a smooth rectangular cold anomaly, potentially indicating an in-wall installation. Additionally, warmer anomalies were observed behind the air conditioner motor, likely due to reduced air contact and the motor's heat. The most intriguing anomaly revealed temperature variations under the plaster, highlighting the individual construction elements of the wall. These findings demonstrate the efficacy of UAV-based thermal imaging in detecting structural and thermal irregularities, providing valuable insights for targeted building maintenance and energy efficiency improvements.

References

1. Rakha, T., & Gorodetsky, A. (2018). Review of Unmanned Aerial System (UAS) applications in the built environment: Towards automated building inspection procedures using drones. Automation in Construction, 93, 252-264.
2. Krawczyk, J. M., Mazur, A. M., Sasin, T., & Stokłosa, A. W. (2015). Infrared Building Inspection with Unmanned Aerial Vehicles. Transactions of the Institute of Aviation, 3(240), 32-48.
3. Kim, H., Lamichhane, N., Kim, C., & Shrestha, R. (2023). Innovations in Building Diagnostics and Condition Monitoring: A Comprehensive Review of Infrared Thermography Applications. Buildings, 13(11), 2829.
4. Barahona, B., Buck, R., Okaya, O., & Schuetz, P. (2021). Detection of thermal anomalies on building façades using infrared thermography and supervised learning. Journal of Physics: Conference Series, 2042(1), 012013.
5. Weber, I., Jenal, A., Kneer, C., & Bongartz, J. (2015). PANTIR - A Dual Camera Setup for Precise Georeferencing and Mosaicing of Thermal Aerial Images. ISPRS Archives, XL-3/W2, 269-2015.
6. Connected Places Catapult. (2022). Heat loss monitoring and control using drones. Retrieved from https://cp.catapult.org.uk/opportunities/

7. Dlesk, A., & Vach, K. (2019). POINT CLOUD GENERATION OF A BUILDING FROM CLOSE RANGE THERMAL IMAGES. ISPRS Archives, XLII-5-W2, 29-2019.
8. Lagüela, S., Diaz-Vilarino, L., Roca, D., & Armesto, J. (2014). Aerial oblique thermographic imagery for the generation of building 3D models to complement Geographic Information Systems. Proc. of QIRT'14.
9. Lowe, D.G., 2004. Distinctive Image Features from ScaleInvariant Keypoints. International Journal of Computer Vision, 60, 2, pp. 91-110.
10. Lagüela, S., Díaz– Vilariño, L., Roca, D., & Lorenzo, H. (2015). Aerial thermography from low-cost UAV for the generation of thermographic digital terrain models. Opto-Electronics Review, 23(1), 78-84.
11. Sirmacek, B., Hoegner, L., & Stilla, U. (2011). An automatic system to detect thermal leakages and damages on building facade using thermal images. IEEE Xplore, 1-4.

Advanced Engineering Days

aed.mersin.edu.tr

Quantifying Land Surface Temperature through Multispectral Landsat-9 Satellite Images

Mohammadali Abbasi[1], Mahdi Hasanlou [*2], Saeid Homayoni [3]

[1]*School of Surveying and Geospatial Engineering, College of Engineering, University of Tehran, Tehran, Iran, mh.abbasi7899@ut.ac.ir*
[2] *School of Surveying and Geospatial Engineering, College of Engineering, University of Tehran, Tehran, Iran, hasanlou@ut.ac.ir*
[3]*Centre Eau Terre Environnement, Institute National de la Recherche Scientifique, Québec, QC G1K 9A9, Canada, saeid.homayouni@ete.inrs.ca*

Cite this study: Abbasi, M., Hasanlou, M., & Homayoni, S. (2024). Quantifying Land Surface Temperature through Multispectral Landsat-9 Satellite Images. Advanced Engineering Days, 9, 401-404.

Keywords
Land surface temperature
Landsat-9
Random Forest
Gradient Boosting
Regression

Abstract

Land surface temperature is one of the most important physical parameters studied in the modeling of earth surface processes. This study aims to estimate the earth's surface temperature from Landsat-9 satellite images using GBoost (GB) and Random Forest (RF) regression methods. In this study, earth surface temperature data was collected simultaneously with the passage of the satellite. Ground measurements along with corrected values of spectral bands and different spectral indices were used as different features for training and testing these methods. The optimal features were optimized using the Recursive Feature Elimination (RFE) feature selection method and the hyperparameters were optimized using the grid search method. To improve accuracy, outlier data identification and removal methods such as the 3-sigma test and box plot method were used. The results show that both methods had similar performance with RMSE equal to 1.24, and the RMSE was reduced by removing outlier data. The Box plot method performed better than the 3-sigma method in removing outlier data, and the RMSE in the GB and RF methods reached 0.89 and 0.77, respectively.

Introduction

Land surface temperature (LST) is one of the most important physical parameters studied in the modeling of earth surface processes and is used in urban heat island monitoring, forest fire detection, weather forecasting, and land cover change tracking. Technological advances, especially in remote sensing using satellite thermal bands, have improved the measurement of LST and provide a better alternative to traditional methods. Remote sensing provides extensive, repeatable, and diverse data and enables accurate temporal and spatial analysis of Earth phenomena. Advanced algorithms, such as artificial neural networks and regression methods, have been developed to estimate LST for specific locations and climates accurately.

MacLean and Ayrets in 1985, presented a model for estimating soil temperature at different depths using multivariate linear regression(Maclean & Ayres, 1985). Rahimi khoob *et al*. in 2013, evaluated three models for estimating the maximum daily air temperature in the Urmia Lake catchment and found that the nonlinear multivariate regression model performed best with RMSE equal to 1.57 and an average absolute error of 3.1(Rahimi Khoob et al., 2005). Yazdani *et al.* in 2013, compared regression methods and neural networks using daily meteorological data from three stations (Mashhad, Sabzevar, Shiraz) and concluded that neural network has higher accuracy(Yazdani et al., 2012). Jouybari Moghadam *et al.* in 2014, evaluated the multilayer perceptron neural network using Landsat-8 satellite images and simulation data, and the results of this evaluation showed that the RMSE error is equal to 1.73 degrees Kelvin(Joybari Moghadam et al., 2015).

This study aims to estimate the land surface temperature in two studied sites located in the cities of Karaj and Mashhad using Landsat-9 satellite images and artificial intelligence methods based on regression methods such as the GBoost Regression method and random forest algorithm. In this study, for training and testing as well as validating different base regression algorithms, ground data collected in the target areas have been used. In regression methods, in addition to spectrally corrected values of different bands of Landsat-9 satellite and various spectral indices, the data collected in the studied areas were used and the Recursive Feature Elimination (RFE) feature selection method and the optimization of the required parameters of each algorithm using the method Grid search has been done. Also, to improve the performance of the algorithms, the outlier data were removed with two 3-sigma test methods and the Box plot method.

Material and Method

In this research, to train and test artificial intelligence networks and regression based on ground data, surface temperature is needed, and for this reason, due to the satellite transit time, there was a need to collect ground data. Ground data on soil temperature were collected at two different stations in Karaj and Mashhad cities. Machine learning methods have made great progress in various fields of remote sensing in recent years, including climate and weather changes, and in the field of artificial intelligence and machine learning, regression methods are used to model and predict temperature changes. Due to the complexity and non-linearity of climate data in surface temperature estimation, more complex regression methods such as random forest and gradient boosting perform better.

Random forest is a supervised machine learning algorithm used for regression and classification problems. This algorithm works by creating a set of decision trees, each constructed with random features. In regression problems, each tree accesses a random subset of the training samples and predicts the target values and the final predicted value is the average of all tree estimates. Also, the random forest can determine the importance of each input feature. Adjustable parameters include the number of trees (n-estimator) and the number of features in each search (max features), which are optimized using the network search method.

Boosting is a method of turning weak learners into strong learners. In this method, each new model corrects the errors of the previous models, and each new tree is built according to the modified version of the original dataset. In Boosting, trees are created sequentially and each new tree is designed to reduce the errors of the previous tree. Each tree learns from the residual errors of the previous trees and updates them, so the next tree learns from the updated version of the errors and the model performance gradually improves.

A three-step optimization process has been considered to increase the accuracy of prediction models and select the best features of satellite images to estimate the earth's surface temperature. First, the RFE feature selection algorithm has been used to select the best variables and reduce the data volume. Then, the optimization and selection of the best parameters for the regression methods were done with the grid search method. Finally, by using the 3-sigma test and box plot, the outlier data that have led to the reduction of network accuracy were removed. The goal of optimization in all stages is to reduce RMSE and increase R-squared to improve the accuracy of forecasting models.

Recursive feature elimination (RFE) is a feature selection method in machine learning that aims to identify and preserve the most relevant features and remove less important features. This method starts by training the model on all features, then evaluates the importance of each feature and removes the least important feature. This process is repeated until a certain number of features are reached or further removal degrades the performance of the model. This method increases the accuracy of feature selection by considering the impact of each feature on the performance of the model(Awad & Fraihat, 2023).

Grid search is a method to identify the optimal hyperparameters of the model. Unlike parameters, hyperparameters cannot be determined from training data. In this method, the model is created and evaluated for each combination of hyperparameters, and the model that has the highest accuracy is selected as the best model. Grid search automates the process of trial and error and is especially used in machine learning to find the optimal hyperparameters that give the most accuracy to the model(LaValle et al., 2004).

In regression analysis, identifying and removing outliers is important to increase model accuracy and reliability, as these outliers can disproportionately affect parameter estimates and lead to biased results. Two common methods for detecting outliers are the 3-sigma rule and the box plot method. Based on the normal distribution, the 3-sigma rule identifies outliers as points that are more than three standard deviations from the mean. The boxplot method, which is robust to non-normal distributions, uses the interquartile range (IQR) to identify outliers. By reducing the influence of outliers, these methods contribute to more accurate and reliable regression models and improve model performance.

Results

The evaluation results of two random forest and GBoost methods show that by applying the RFE feature selection method and grid search to optimize hyperparameters, both methods had similar performance with RMSE equal to 1.24. To improve accuracy and reduce RMSE, outlier data detection and removal methods such as the 3-sigma rule and Box plot method were used. The box plot method performed better than the 3-sigma test in removing outlier data. The performance of the proposed methods was evaluated using the two criteria of determination coefficient R^2 and RMSE, and the results of the mentioned methods are presented in Table 1, which shows the appropriate accuracy of both methods for estimating the temperature of the earth's surface. The effect of removing outlier data was also confirmed by examining the scatter plot of the output of the methods and is presented in Figure 1.

Table 1. Evaluation results of the proposed methods.

Accuracy evaluation criteria	GBoost			Random Forest		
	No outlier data removal	3-sigma test	Box plot	No outlier data removal	3-sigma test	Box plot
R-squared	98.91	99.40	99.46	98.92	99.40	99.60
RMSE	1.24	0.93	0.89	1.24	0.93	0.77

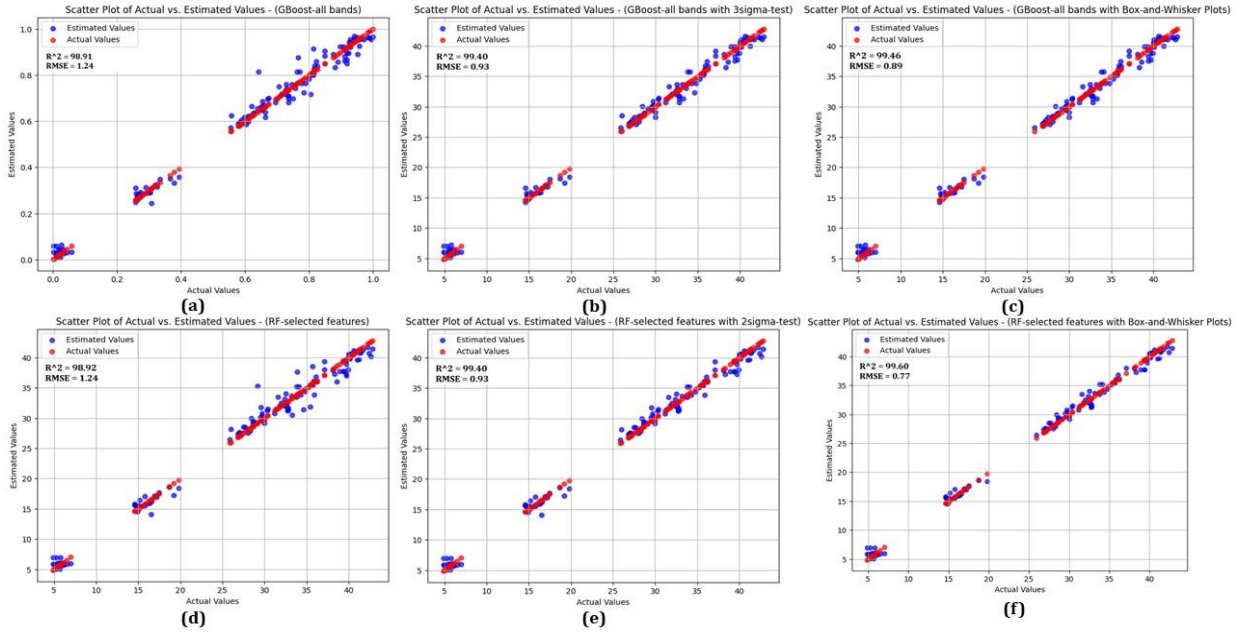


Figure 1. Scatter plots show the two GBoost regression methods (a-c) and random forest (d-f). (a) GBoost scatterplot without removing outliers, (b) removing outliers in GBoost with the 3-sigma test method, (c) removing outliers in GBoost with the boxplot method, (d) scatterplot of the random forest without removing outliers, (e) Removal of outlier data in the random forest with 3 sigma test method, and (f) Removal of outlier data in the random forest with box plot method.

Discussion

Estimating land surface temperature using regression methods and satellite images through bands and spectral indices is a promising approach that combines multispectral data with advanced regression models to increase accuracy. Bands and spectral indices provide important information. Challenges such as high vegetation density and weather conditions can affect the results. Future research could focus on integrating additional data sources and advanced machine learning techniques to further improve robustness and accuracy.

Conclusion

The purpose of this study is to estimate the land surface temperature using two methods random forest regression and gradient boosting. Both methods with optimization through feature removal and grid search have RMSE equal to 1.24. Using the outlier data removal method with a box plot was more effective than the 3 sigma test. Both methods had acceptable accuracy and removing outliers had a positive effect on their performance. As a result, the random forest algorithm and GBoost, combined with feature selection and outlier data management, are suitable for land surface temperature estimation.

References

1. Awad, M., & Fraihat, S. (2023). Recursive Feature Elimination with Cross-Validation with Decision Tree: Feature Selection Method for Machine Learning-Based Intrusion Detection Systems. *Journal of Sensor and Actuator Networks*, *12*(5). https://doi.org/10.3390/jsan12050067
2. Joybari Moghadam, Y., Akhundzadeh, M., & and Sarajian, M. (2014). Estimation of land surface temperature from Landsat-8 satellite images using multilayer perceptron neural network. *National Geomatics Conference*, *August*. https://sid.ir/paper/892043/fa
3. LaValle, S. M., Branicky, M. S., & Lindemann, S. R. (2004). On the relationship between classical grid search and probabilistic roadmaps. *International Journal of Robotics Research*, *23*(7–8), 673–692.

https://doi.org/10.1177/0278364904045481
4. Maclean, S. F., & Ayres, M. P. (1985). Estimation of soil temperature from climatic variables at Barrow, Alaska, USA. *Arctic & Alpine Research*, *17*(4), 425–432. https://doi.org/10.2307/1550867
5. Rahimi Khoob, A., Kochzadeh, M., Mohammadvali Samani, J., & and Sharifi, F. (1384). (2005). Estimating maximum daily temperature using NOAA satellite jmages: case study in Oroomieh lake basin. *Pajouhesh & Sazandegi No 68 Pp: 84-90*, 84–90. https://sid.ir/paper/19811/fa
6. Yazdani, V., Ghahreman, B., Farahi, G., & And Nori, hadise. (2011). (2012). Modeling soil depth temperature by using meteorological parameters. *J. of Water and Soil Conservation, Vol. 19(4), 2013*. https://sid.ir/paper/156329/fa

Advanced Engineering Days

aed.mersin.edu.tr

The effect of ground control point distribution in the improving of UAV corridor mapping accuracy

Mobina Ahmadi Asoor, Alireza Afary*, Ebadat Ghanbari Parmehr

[1]*Babol Noshirvani University of Technology, Faculty of Civil Engineering, Dept. of Geomatics Engineering, Babol, Iran. m.ahmadiasoor@gmail.com, afary@nit.ac.ir, parmehr@nit.ac.ir*

Cite this study: Ahmadi Asoor, M., Afary, A., & Ghanbary Parmehr, E. (2024). The effect of ground control point distribution in the improving of UAV corridor mapping accuracy. Advanced Engineering Days, 9, 405-407

Keywords
Corridor Mapping
UAV Photogrammetry
Ground Control Point
Checkpoint
Flight line

Abstract

Despite the advancements in UAV photogrammetry, challenges still exist in this field. One of these challenges is corridor mapping using UAVs. The significant differences in length and width within the corridor areas ultimately affecting triangulation accuracy and 3D modeling quality. Proper ground control point distribution significantly influences these items. In this research, ground control points with different distributions were examined on two corridors, one with a length of 2.5 kilometers and another with 5 kilometers that captured in a single flight line and no Geotagging. The evaluation is based on the root mean square error of both planimetric and altimetric errors in checkpoints.

Introduction

Ground control points are essential for creating topographic maps with the desired accuracy and precision using UAVs[1]. However, acquiring ground control points can be costly and time-consuming. Researchers are working to develop methods that achieve accuracy, reliability, and confidence in map production without relying heavily on these points or using minimal control points and checkpoints. Consequently, understanding the impact of the number and distribution of ground control points on the achieved accuracy of triangulation and the resulting point cloud in the UAV photogrammetry is crucial [1, 2].

Despite the research, achieving an optimal distribution is one of the most challenging and debated topics in UAV photogrammetry. The diversity of topography in each region leads to varying distributions and quantities of control points, resulting in different levels of accuracy.

One practical application for UAVs is corridor mapping in linear projects, such as road construction, coastal line monitoring, railway construction, and monitoring and reconstruction of power, gas, and water transmission lines. Given the significant difference in length compared to width within corridor areas, the distribution and quantity of control points in these regions are of great importance. Skarlatos et al., investigated the number of control points and distributions in five scenarios, finding that the vertical error was twice the horizontal error due to the longitudinal geometry of the project [3]. Height and planimetric accuracy were better when the control points and checkpoints were evenly spaced [4]. In another study[5], researchers evaluated the impact of control point number, distribution, and flight altitude on the triangulation accuracy in three corridor photogrammetry projects. The best results were obtained when the control points were distributed uniformly along the corridor, and the oblique images were used for processing.

In [6], Ferrer-González et al., used 47 control points along a 525 m corridor in four flight lines. Increasing the number of control points and checkpoints consistently improved triangulation accuracy. Heidari et al., [7] evaluated the control points distribution and optimal imaging modes for producing outputs (point cloud, 3D model, and map) in a project with six flight lines. While the presence of vertical images improved the photogrammetric product accuracy, systematic and non-systematic errors persisted, and the necessity of having at least one control point at the project was emphasized.

Considering the research and studies, one of the most influential factors affecting the accuracy of triangulation in corridor and non-corridor areas is the distribution of control points. In UAV photogrammetry, images are typically captured in multiple flight lines with high overlap. However, in certain areas such as valleys, it may not be feasible to capture images in various flight lines. Additionally, sometimes many images are captured due to

[1] Unmanned Aerial Vehicle

obstacles (such as vegetation) or communication loss between UAV and GPS, resulting in geotagging issues. In such cases, re-imaging the area incurs significant costs. The remaining solution for achieving high triangulation accuracy involves having ground control points with appropriate distribution. The primary goal of this research is to achieve high triangulation accuracy using images without geotags and those captured in a single flight line.

Material and Method

The study area for corridor mapping in this article is two area of the Telar River, Ghaemshahr, Mazandaran, Iran. The first area is located at the geographical coordinates 664445.09m N, 4033691.72m E (in UTM-Z39N). It has 2.5-kilometer-long and 130-meter-wide. The second area is located at the (665766.48m N, 4029258.11m E) and has a 5-kilometer-long and 130-meter-wide (in UTM-Z39N). In the 2.5-kilometer area, 103 images and in the 5-kilometer area, 279 images were captured using a DJI Phantom 4 Pro UAV. The studied areas include rivers, agricultural lands, hills and urban features (Figure 1).

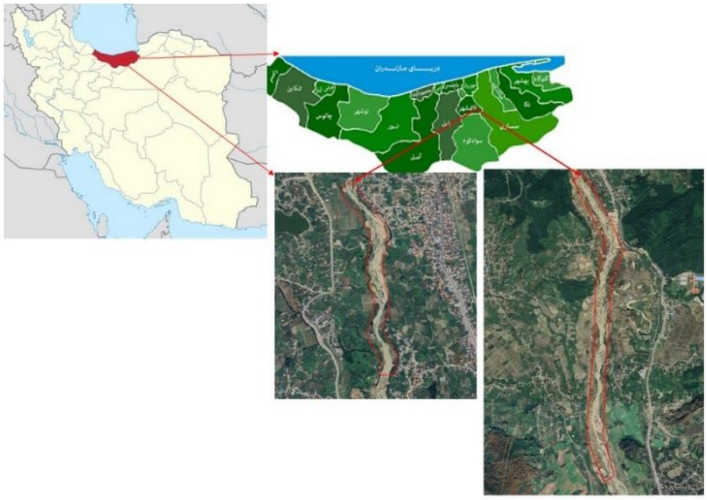


Figure 1. Study areas (Talar River)

Two scenarios were considered for each corridor area under study:

First scenario: In this scenario, as shown in Figure 2, for each study area, two ground control points (represented in red) were placed at the beginning, two more were placed at the end of the corridor and two others were placed within each area. Also, for the accuracy assessment, four checkpoints were placed within each area (represented in green).



Figure 2. a. First scenario for 2.5 km Corridor with 6 ground control points and 4 checkpoints
b. First scenario for 5 km Corridor with 6 ground control points and 4 checkpoints

Second scenario: In this scenario, as shown in Figure 3, eight ground control points (represented in red) used for each study area: two ground control points were placed at the beginning and end of each area (as in the first scenario), two more were placed at the middle and two others were placed within each area. Also, for the accuracy assessment, two checkpoints (represented in green) were placed within each area.



Figure 3. a. First scenario for 2.5 km Corridor with 8 ground control points and 2 checkpoints
b. First scenario for 5 km Corridor with 8 ground control points and 2 checkpoints

Results and Discussion

The purpose of using different distributions of control points is to find an appropriate distribution that leads to an accurate triangulation. The evaluation criterion for triangulation accuracy is the changes resulting from control point distribution that can be calculated using checkpoints. In photogrammetry, checkpoints are Altimetric and Planimetric Points used only for the assessment of the absolute accuracy of triangulation computations.

The results of photogrammetric triangulation conducted in a 2.5-kilometer corridor are presented in Table 1. In the first scenario, the total error was 0.45 meters, with altimetric error of 0.44 meters and planimetric error of 0.10 meters. This is bigger than the error values from second scenario, which included a total error of 0.30 meters, an altimetric error of 0.29 meters, and a planimetric error of 0.10 meters.

Table 1. Error in the checkpoints in the first area for both scenarios (2.5 km Corridor)

Items	Total Error (m)	XY Error (m)	Z Error (m)	N Error (m)	E Error (m)
First Scenario	0.45	0.10	0.44	0.04	0.09
Second Scenario	0.30	0.10	0.29	0.07	0.07

The results of photogrammetric triangulation in the 5-kilometer corridor area are presented in Table 2. In the second scenario, the total error was 0.93 meters, with an altimetric error of 0.91 meters and planimetric error of 0.18 meters. Again, the results in the second scenario are better than the first scenario, which had a total error of 2.29 meters, an altimetric error of 2.26 meters, and planimetric error of 0.36 meters. Considering Tables 1 and 2, in the corridor areas, due to the elongated nature of one dimension of area compared to the other, the altimetric error tends to be greater than the planimetric error.

Table 2. Error in the checkpoints in the second area for both scenarios (5 km Corridor)

Items	Total Error (m)	XY Error (m)	Z Error (m)	N Error (m)	E Error (m)
First Scenario	2.29	0.36	2.26	0.34	0.14
Second Scenario	0.93	0.18	0.91	0.16	0.08

Conclusions

The object of this research is to investigate the accuracy of triangulation when using non-geotagged images captured by a UAV and taken in a single flight line. In this scenario, adjusting the distribution of control points along the corridor becomes a suitable solution for improving both height and planimetric accuracy. To achieve this, two different distributions of control points were processed for two corridors, one with a length of 2.5 kilometers and another with 5 kilometers. For both areas, improved accuracy was achieved when additional control points were placed not only at the corridor's endpoints but also in its center.

These findings highlight the importance of strategically placing ground control points for accurate photogrammetric computations, especially when dealing with non-geotagged images captured in a single flight line. This research showed, that for corridors, additional control points should be measured not only at their endpoints but also in the center of the corridor.

References

1. Abbaspour, m., m. Azar, Khoshlahjeh, and m. Varshosaz, *Impact of the number and position of ground control points in the accuracy obtained for the UAV photogrammetry based prepared.* 2018.
2. Martínez-Carricondo, P., et al., *Assessment of UAV-photogrammetric mapping accuracy based on variation of ground control points.* International journal of applied earth observation and geoinformation, 2018. **72**: p. 1-10.
3. Skarlatos, D., et al., *Accuracy assessment of minimum control points for UAV photography and georeferencing*. First International Conference on Remote Sensing and Geoinformation of Environment. Vol. 8795. 2013: SPIE.
4. Zhou, Y., et al., *GNSS-assisted accurate corridor mapping with small UAV*, in *RFIAP & CFPT 2018*. 2018: Paris, France.
5. Jaud, M., et al., *Suggestions to limit geometric distortions in the reconstruction of linear coastal landforms by SfM photogrammetry with PhotoScan® and MicMac® for UAV surveys with restricted GCPs pattern.* Drones, 2018. **3**(1): p. 2.
6. Ferrer-González, E., et al., *UAV photogrammetry accuracy assessment for corridor mapping based on the number and distribution of ground control points.* Remote Sensing, 2020. **12**(15): p. 2447.
7. Heidarimozaffar, M., R. Zerafatyjamal, and H.T. Khorasani, *Accuracy and Precision of Producing Topographic Maps in Linear Projects by UAV Photogrammetric Method.* 2023. **31**(124): p. 21-38.

Advanced Engineering Days

aed.mersin.edu.tr

Automated Insulator Defect Detection in UAV images for Power Line Monitoring using YOLO-v8 Model

Reza Rahimi Nejadbougar[1], Ebadat Ghanbari Parmehr[1*], Alireza Afary[1], Samira Mavaddati[2]

[1]Babol Noshirvani University of Technology, Dept. of Geomatics Engineering, Babol, Iran, samanrahimi.act@stu.nit.ir, parmehr@nit.ac.ir, afary@nit.ac.ir,
[2]Mazandaran University, Dept. of Electronics, Babolsar, Iran, s.mavaddati@umz.ac.ir

Cite this study: Nejadbougar, R. R., Parmehr, E. G., Afary, A., & Mavaddati, S. (2024). Automated Insulator Defect Detection in UAV images for Power Line Monitoring using YOLO-v8 Model. Advanced Engineering Days, 9, 408-410

Keywords
UAV
Insulator
Deep learning
Yolo-V8

Abstract

This paper proposes a novel power transmission line monitoring method using unmanned aerial vehicles (UAVs) and YOLO-v8, a deep-learning object detection model. Traditional methods for detecting insulator defects, crucial for maintaining grid stability, are time-consuming and prone to human error. This challenge is addressed by leveraging the speed and accuracy of YOLO-v8 to automatically identify potential hazards in aerial images captured by UAVs. The YOLO-v8 model efficiently detected various insulator defects, including Damages and Flashover, by applying bounding boxes to relevant image regions. The trained model achieved a high overall accuracy of 94% (MAP50) on the dataset, with individual class accuracies reaching 97% (Healthy), 99% (Damage), and 85% (Flashover). Furthermore, data augmentation techniques further enhanced the classification accuracy to 98.6%.

Introduction

Power transmission lines are vital for the proper functioning of power systems and human safety. Defects of insulators such as Damages and Flashover over time cause unfortunate risks. Diagnosing these defects is traditionally done by human inspectors, which is a time-consuming, costly, and error-prone process. The use of deep learning and artificial neural networks can significantly improve this process.

Monitoring the insulator defects of power lines is very important because these defects can lead to extensive blackouts and serious risks. The use of deep learning models such as YOLO-v8 enables accurate and fast identification and classification of these defects using aerial images taken by UAVs. This method is an important step towards improving the stability and security of the power network because of its high speed and accuracy.

A new method for insulation fault detection using an improved YOLO-v7 and multi-UAV cooperation system is presented and a multi-UAV collaboration platform and YOLO-v7-C3C2-GAM are improved [1]. The results showed that this method significantly increased transmission line fault detection accuracy and efficiency. A high-voltage network monitoring method using the YOLO-v8s algorithm and UAV aerial images detected defects in insulators and bird's nests and increased the detection accuracy to 92% [2]. Also, monitoring the insulation loss was carried out using the improved YOLO-v4 model and UAV aerial images [3]. This method gives a detection accuracy of 93.81% and a speed of 53 frames per second, and the accuracy increased to 97.26% by pre-processing the images.

In this paper, an approach based on the YOLO-V8 model is proposed to find insulator defects in the power network to accelerate the timely monitoring of these defects. All types of insulator defects have been targeted using aerial images collected by UAVs. By applying the bounding box in the YOLO-V8 format to the images containing the insulator, the classes to be monitored are defined and given to the YOLO model for training. Figure 1, shows an example of images with a bounding box.

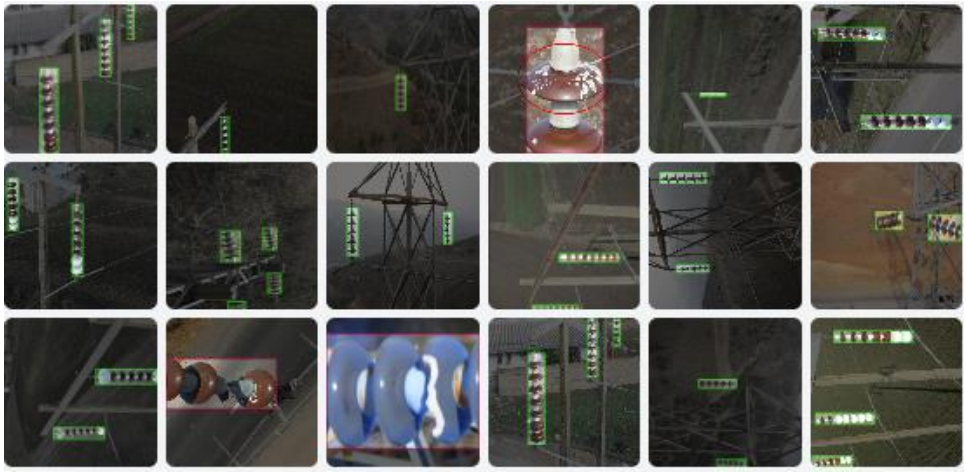


Figure 1. Example of database images with bounding box

Material and Method

The Yolo-V8 model was released by Ultralytics and has various tasks. The YOLO-v8 algorithm consists of three parts: backbone, neck, and head. The backbone extracts features from the image, merges their necks, and predicts the head, objects, and their classes in the image using bounding boxes and class probabilities [4].

This algorithm is utilized to identify the insulator defects. After collecting the data by UAV and labeling the images with the bounding boxes of the Yolo format, pre-processing of the images and data augmentation have been done to achieve higher accuracy. By applying pre-processing and redundancy on the existing data, the Yolo model is called and trained using the UltraLytics library for custom dataset training.

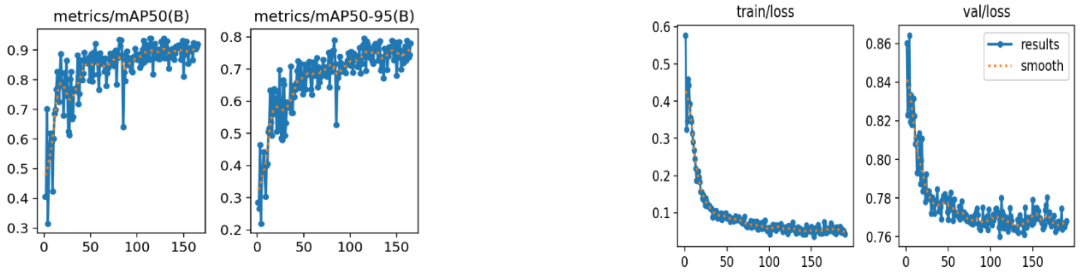
To determine the hyperparameters of the model, these parameters were determined according to the size of the dataset, and the best parameters were experimentally used to increase the accuracy and speed of the model. The hyperparameters of the Yolo model for training the model to achieve insulator defects in aerial images can be seen in Table 1.

Table 1. Yolo model parameters and model input

Model	Input size	Kernel size	Stride	Optimizer	Batch size	Learning rate	Number of images
Yolo-v8 n	640×640	3×3	2	Adam w[1]	32	0.001	1848
Yolo-v8Cls	640×640	3×3	2	Adam w	32	0.001	3601

Results

The results of this study show that the Yolo model can identify and classify insulator defects with optimal accuracy and speed by considering different classes. The accuracy of the model (MAP50) on the dataset and by evaluating the accuracy of the training reached 94% in all images, which includes the accuracy of 97% in the Healthy classes, 99% in the Damage class, and 85% in the insulator Flashover class. Also, in the classification task with augmented images, the accuracy of the YOLO-V8 model reached 98.6%. The following curves (a. object detection and b. classification) show how to train and evaluate the model and the accuracy in identifying targets Figure 2.



(a) (b)

Figure 2. a) The Accuracy and validation progress plot along with the mAP plot, and b) The convergence plot in the training and validation using the yolov8-cls deep model.

The final results after training the YOLO V8 model with object recognition and classification tasks with a customized dataset are as presented in Table 2.

[1] Adaptive Moment with Weight decay

Table 2. The accuracy results of the Yolo model with accuracy evaluation

class	mAP	Top1_acc	Evaluate (Detect)	Evaluate (Classify)
Healthy	97%	98.6%	97%	94.2%
Flashover	85%	98.6%	85%	96.6%
Damaged	99%	98.6%	99%	91.9%

During the prediction of the model with the test dataset and the best weights of the training model, the accuracy of the YOLO model in the detection and classification of the unseen images, to determine the type of insulator defect in the classification task was an average of 91.9% in the class of insulator Damage by 11 images and 96.6% in Insulator Flashover class by 45 images achieved.

Discussion

The proposed method using YOLO-v8 and UAVs demonstrates promising results for automatic insulator defect detection in power transmission lines. The model achieved high accuracy in both identifying anomalies and classifying specific defect types. Compared to traditional manual inspection methods, this approach offers significant advantages in terms of speed, efficiency, and safety. However, some limitations need to be addressed for real-world deployment. Factors such as varying weather conditions and complex backgrounds in aerial imagery can potentially affect detection accuracy. Further research is needed to improve the model's robustness under diverse environmental conditions. Additionally, integrating the system with automated repair or notification protocols could further enhance its practicality for real-time power grid maintenance. Also access to datasets in a high number of monitored classes will lead to a significant impact on the accuracy of detecting power line defects by UAVs.

Conclusion

This study proposed a novel, automated system for power line monitoring using UAVs and YOLO-v8 for insulator defect detection. The YOLO-v8 model achieved high accuracy (94% overall) with strong performance across different defect types. Compared to manual methods, this approach offers significant advantages in speed, efficiency, and safety due to UAV data collection and automated analysis. However, future research is needed to improve robustness under varying weather conditions. Additionally, integrating automated repair protocols and expanding the training dataset for broader defect coverage is crucial for real-world deployment. By addressing these limitations, the proposed solution will improve power line monitoring, leading to a more reliable and safer power network.

References

1. Chang, R.; Zhou, S.; Zhang, Y.; Zhang, N.; Zhou, C.; Li, M. Research on Insulator Defect Detection Based on ImprovedYOLOv7 and Multi-UAV Cooperative System. Coatings **2023**,13, 880. https://doi.org/10.3390/coatings 13050880.
2. Qiang, H.; Tao, Z.; Ye, B.; Yang, R.; Xu, W. Transmission Line Fault Detection and Classification Based on Improved YOLOv8s.Electronics**2023**,12,4537.https://doi.org/10.3390/electronics12214537.
3. qiu, Z.; Zhu, X.; Liao, C; Shi, D.; Qu, W. Detection of Transmission Line Insulator Defects Based on an Improved LightweightYOLOv4Model.ApplSci.**2022**,12,1207.https://doi.org/10.3390/app12031207.
4. Hussain, M. YOLO-v1 toYOLO-v8, the Rise of YOLO and Its Complementary Nature toward Digital Manufacturing and Industrial Defect Detection. Machines 2023, 11,677. https://doi.org/10.3390/machines11070677.

Advanced Engineering Days

aed.mersin.edu.tr

Detection of stress in rice fields using satellite images and plant spectral indices

Sara Amani[1], Ebadat Ghanbari Parmehr*[1], Alireza Afari[1], Narjes Mahmoody-Vanolya[2]

[1] Babol Noshirvani University of Technology, Dept. of Geomatics Engineering, Babol, Iran
[2] University of Tehran, Dept. of Remote Sensing and GIS, Tehran, Iran,
Sarahamani1998@gmail.com, parmehr@nit.ac.ir, afary@nit.ac.ir, mahmoodi.narjes.v@ut.ac.ir

Cite this study: Amani, S., Ghanbari Parmehr, E., Afari, A., & Mahmoody-Vanolya, N. (2024). Detection of stress in rice fields using satellite images and plant spectral indices. Advanced Engineering Days, 9, 411-415

Keywords
Sentinel-2 satellite
Spectral indices
Stress
Rice

Abstract

Satellite images can be used to predict and monitor the performance of many agricultural products because of their availability, vast coverage, and ability to obtain images in a variety of spatial, spectral, and temporal resolutions. Rice plants, due to their high nutritional content and special growth conditions, should be studied at various periods of planting until harvest to maximize use. In this study, photos from the Sentinel-2 satellite and the calculation of several spectral indices in MATLAB software were used to assess rice plant performance and detect field stress. These indices are classified into two types: visible bands and combination indices with both visible and invisible bands. The results showed that the Chlorophyll Index Green (GCI) indicator has the highest accuracy and contrast, and the Visible-band Difference Vegetation Index (VDVI) indicator has the lowest accuracy and contrast in predicting stress in a rice field.

Introduction

The ever-increasing growth of the earth's population and the provision of healthy food for mankind is one of the challenges of today's humans [1,2]. Recent research shows that the growth of agricultural production has decreased significantly. For example, the cultivation of cereal crops, one of the most important sources of human nutrition, has reduced to only about 1% per year, much lower than the population growth rate in the world [3]. As one of the most important grains, rice constitutes the main food of almost half of the world's population. The rice plant is always exposed to many damages and stresses due to high consumption of water, environmental problems, and fertilizer consumption [4]. For this reason, it is necessary to study this plant's performance during different growth stages to prevent damage and stress in rice fields [5]. Today, various remote sensing satellites with the possibility of preparing time series images can be used to investigate and monitor different stages of plant growth. These images with suitable spatial and temporal resolutions provide the possibility of controlling the growth and development of plants, optimal use of agricultural inputs, diagnosis of diseases, and the presence of various plant stresses [6].

In recent years, much research has been conducted in the field of investigating plant performance and diagnosing stress in fields using remote sensing methods. For example, a study aimed to create an indicator model for salt stress detection based on the analysis of different factors of possible rice lines. Finally, an index was developed through a combination of factor analysis, stress tolerance index (STI), and path analysis, which can distinguish tolerant and non-tolerant species [7]. In another research, MODIS satellite data time series, Enhanced Vegetation Index (EVI), and Normalized Difference Fraction Index (NDFI) indices have been used to investigate temperature stress. In conclusion, this study showed that crop phenology obtained from remote sensing data can be used to monitor agricultural systems and complement ground observations. Phenology derived from satellite data allows for a more accurate understanding of how rice agriculture responds to changes in climate conditions [8]. In another research, Etiolation Area (EA) and Etiolation Degree (ED) indices have performed better than other indices applied in the research, in detecting different levels of nitrogen stress by analyzing the dynamic characteristics of rice leaves [9]. In another study, by using aerial hyperspectral images taken during the growth

period of beetroot and spectral indices Normalized Difference Vegetation Index (NDVI), Water Index (WI), The Structure Insensitive Pigment Index (SIPI) and Simple Ratio Pigment Index R430/R680 (SRPI), the stress caused by the presence of two biological factors, Heterodera Schachtii and Rhizoctonia Solani, was investigated. As a result, the stress caused by the Rhizoctonia agent was well recognized by the supervised classification method [10].

The investigation of the research history shows that the use of satellite images and plant spectral indices in evaluating the performance of agricultural products and diagnosing types of stress can be used as an efficient and effective method. This research aims to investigate and compare the performance of different vegetation indices in diagnosing the stress of rice fields using Sentinel-2 satellite images. The innovation of this research is the use and comparison of the performance of two different groups of fractional indices in determining the amount of stress by using visible and invisible bands, as well as comparing the contrast of the anomaly display of the stress of each of these indices.

Material and Method

Study Area

In this research, the Goldasht paddy field research station with 50 hectares of paddy fields, between Babol and Amol cities and geographically located at 52.5° east longitude and 36.4° north latitude, has been used as the study area.

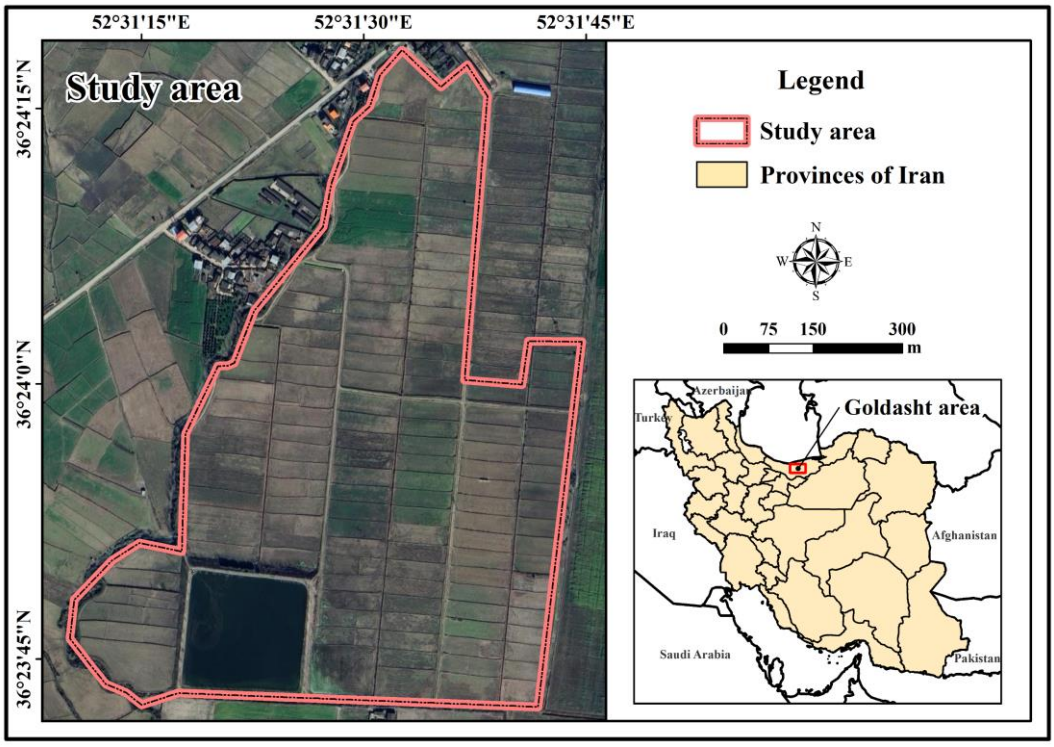


Figure 1. Study area.

Images and data

The Sentinel-2 satellite was developed by the European Union and was launched in 2015. The images of this satellite are multi-spectral with 13 bands in the range of visible, near-infrared, and short-wave infrared. Also, these images have a regular global coverage of the earth's surface, reviewing an area at a time interval of 5 days. [11]. In this research, the images of this satellite have been used to apply the spectral indicator to the studied area. Relevant images were obtained from the Google Earth Engine system. These images were taken according to the time frame of planting, cultivating, and harvesting of rice on 2023.04.19, 2023.07.11, and 2023.08.12.

Spectral indices

Spectral indices are the combination of spectral bands of satellite images that are combined and combined through mathematical operators. These indices are a simple mathematical operation that is applied to two or more bands of the satellite image, as a result of applying these indices, new information is obtained from the images and highlights a special feature of the plant [12]. Today, several indicators have been developed [13] The performance of some of them has been investigated in this research (Table 1). These indicators have been applied using different

bands of Sentinel-2 satellite images in the period between the planting and harvesting of rice plants in the target area and the results have been evaluated. Finally, the results of the indicators have been evaluated using the real data of the stress range (Table 4).

Table 1. Spectral indices.

Indicator	Abbreviation	formula	Reference
Chlorophyll Index Green	GCI	$\left(\frac{\text{NIR}}{\text{GREEN}}\right) - 1$	[15]
Enhanced Normalized Difference Vegetation Index	ENDVI	$\frac{(NIR + GREEN) - (2 \times BLUE)}{(NIR + GREEN) + (2 \times BLUE)}$	[16]
Green Normalized Difference Vegetation Index	GNDVI	$\frac{\text{NIR} - \text{GREEN}}{\text{NIR} + \text{GREEN}}$	[17]
Green Soil Adjusted Vegetation Index	GSAVI	$\frac{\text{NIR} - \text{GREEN}}{\text{NIR} + \text{GREEN} + \text{L}} \times (\text{L} + 1)$	[18]
Visible-band difference vegetation index	VARI	$\frac{\text{GREEN} - \text{RED}}{\text{GREEN} + \text{RED} + \text{BLUE}}$	[19]
Visible-band difference vegetation index	VDVI	$\frac{(\text{GREEN} - \text{RED}) + (\text{GREEN} - \text{BLUE})}{(2 \times \text{GREEN}) + \text{RED} + \text{BLUE}}$	[20]
Green, red ratio index	GRRI	$\frac{\text{GREEN}}{\text{RED}}$	[21]

Results and Discussion

Tables (2) and (3) show the results of the indices applied to the satellite images of rice land in three periods of planting, growing, and harvesting. According to the performance of the indicators and the results of their application, the lowest output value of the indicators represents the range of stress that has been well demonstrated due to the effect on the growth process of the plant. As mentioned earlier, in this research, two different groups of indicators have been used to diagnose stress, which includes: the first group is indicators that use a combination of visible and invisible bands to diagnose stress, and the second group is indicators that have only used visible bands. In the image related to the time of planting when the ground is still full of water, the output of the indicators shows almost the same pattern and due to the low level of greenness, they have the lowest amount of values in the whole field. The left and bottom of the images include a small part of the water well, which is shown in all indicators with visible and invisible combined bands with minimum values (dark red or brown color), and in all indicators with visible bands with maximum values (green color). This performance in indicators with a visible band is the first weakness of this category of indicators compared to indicators with a combined visible and invisible band. As observed, the indices with visible and invisible combined bands show the values of lack of greenness in the study area at the time of planting due to waterlogged land, the border between lands that have cover It is not a plant, and the part of the water well is displayed correctly and with good contrast, but the indicators with the visible band have a good display contrast and the values are not completely correct. In the picture related to time, which includes different stages of rice plant growth, again the performance of two indicator groups is different from each other. The high values of all the indices in this picture (green ranges with values close to one) show the range with vegetation cover. But as shown in Table (2), the indices that used the combination of visible and invisible bands, created a stress range well and with more accurate values and higher contrast in the entire set of rice fields (red, orange, and yellow areas), have shown; While the indicators that only used visible bands have shown less power in identifying areas with tension, and the only improvement in the performance of this category of indicators in this period is the display of water wells with lower values (Table 3). The presence of tension in different parts of the fields can be due to lack of water, lack of proper distribution of fertilizer, and lack of nutrients in the soil, which has caused a decrease in the growth rate of the rice plant and is mainly shown with yellow spots in the output of the indicators. Is. In the harvest stage, like the time of planting, due to the lack of vegetation and the low level of greenness, the indicator values in both groups are at their lowest levels. In these images, the areas with tension are shown in yellow, orange, and red colors with low values.

The performance of the indicators during the harvesting stage was evaluated using actual stress locations (14), and the results are shown in Table (4). According to this table, it can be concluded that indicators with visible and invisible combined bands provide a better representation of stress. Among the indices with visible and invisible bands, the GCI indicator with 96% accuracy has the highest level of accuracy compared to other indices in predicting stress in the field. ENDVI (67.07 percent) and GSAVI (37.42 percent) indices are also in the next ranks with a high percentage of detection. Among the indicators with a visible band, the GRRI indicator has shown a better performance in showing stress, but due to the water well being shown at the time of planting with high values (green color), high accuracy cannot be considered for this indicator.

Table 2. The results of indicators with visible and invisible bands.

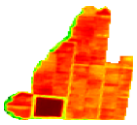
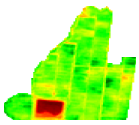
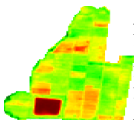
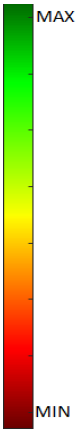
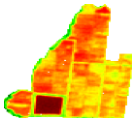
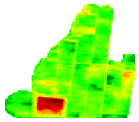
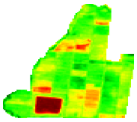
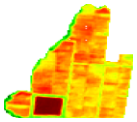
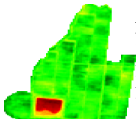
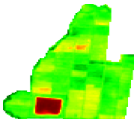
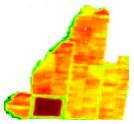
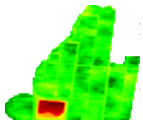
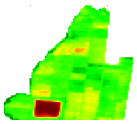
Indicator	The time frame of taking Sentinel-2 satellite images of rice field			color bar
	planting	cultivating	harvesting	
GCI				
ENDVI				
GNDVI				
GSAVI				

Table 3. The results of indices with visible bands.

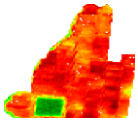
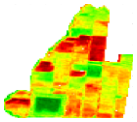
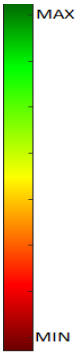
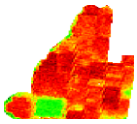
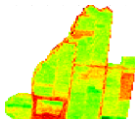
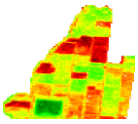
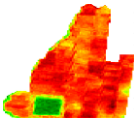
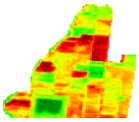
Indicator	The time frame of taking Sentinel-2 satellite images of rice field			color bar
	planting	cultivating	harvesting	
VARI				
VDVI				
GRRI				

Table 4. The percentage of stress ranges identified in each *i*ndicator.

Indicators	GCI	ENDVI	GRRI	GSAVI	GNDVI	VARI	VDVI
Detection percentage	96	67.07	39.1	37.4	36.16	26.1	130

Conclusion

In this research, various spectral indices have been used to identify the stress of the rice field. The results of the performance evaluation of the indicators showed that among the indicators used, the indicators that use the combination of visible and invisible bands have higher accuracy and contrast in predicting tense areas. Considering the importance of the agricultural sector and the impact of various stress factors on production products, it is suggested to use different artificial intelligence methods and machine learning algorithms to detect and monitor various types of stress in rice plants in future research. Also, experts and engineers in the agricultural sector can include different remote sensing methods in the plant care program. The specialized efficiency of the indices mentioned in this research in diagnosing types of biotic and abiotic stresses can also be investigated in future research.

References

1. Khaliq, A., Comba, L., Biglia, A., Ricauda Aimonino, D., Chiaberge, M., & Gay, P. (2019). Comparison of satellite and UAV-based multispectral imagery for vineyard variability assessment. Remote Sensing, 11(4), 436.

2. Eidi, asma, KAZEMIYEH, FATEMEH, Zarifian, Shapour, & Mirloo, Sohrab. (2020). Analysis of Precision Agricultural Problems from the Viewpoint of Agricultural Jihad Experts in Urmia. Journal of Agricultural Science and Sustainable Production, 30(1), 211-223.
3. Hemathilake, D., & Gunathilake, D, (2022). Agricultural productivity and food supply to meet increased demands, in Future Foods. Elsevier, pp. 539-553.
4. Chauhan, B.S., Jabran, K., & Mahajan, G. (2017). Rice production worldwide. Springer, Vol 247.
5. Gold, K.M., (2021). Plant disease sensing: studying plant-pathogen interactions at scale. Msystems, 6(6), pp. 228-21.
6. Loveimi, N., Akram, A., Bagheri, N., & Hajiahmad, A. (2022). Evaluation of Several Spectral Indices for Estimation of Canola Yield using Sentinel-2 Sensor Images. JOURNAL OF AGRICULTURAL MACHINERY, 11(2 (22)), 447-464.
7. Anshori, M. F., Purwoko, B. S., Dewi, I. S., Suwarno, W. B., & Ardie, S. W. (2022). Salinity tolerance selection of doubled-haploid rice lines based on selection index and factor analysis. AIMS Agriculture & Food, 7(3).
8. Wang, H., Ghosh, A., Linquist, B. A., & Hijmans, R. J. (2020). Satellite-based observations reveal effects of weather variation on rice phenology. Remote Sensing, 12(9), 1522.
9. Sun, Y., Zhu, S., Yang, X., Weston, M. V., Wang, K., Shen, Z., ... & Chen, L. (2018). Nitrogen diagnosis based on dynamic characteristics of rice leaf image. Plos one, 13(4), e0196298.
10. Hillnhütter, C., Mahlein, A. K., Sikora, R. A., & Oerke, E. C. (2011). Remote sensing to detect plant stress induced by Heterodera schachtii and Rhizoctonia solani in sugar beet fields. Field Crops Research, 122(1), 70-77.
11. Rapinel, S., Mony, C., Lecoq, L., Clément, B., Thomas, A., & Hubert-Moy, L. (2019). Evaluation of Sentinel-2 time-series for mapping floodplain grassland plant communities. Remote sensing of environment, 223, 115-129.
12. Huete, A., Didan, K., Miura, T., Rodriguez, E. P., Gao, X., & Ferreira, L. G. (2002). Overview of the radiometric and biophysical performance of the MODIS vegetation indices. Remote sensing of environment, 83(1-2), 195-213.
13. DataBase, (2023). "A database for remote sensing indices". Available from: https://www.indexdatabase.de/.
14. Moghaddam, M. K., Samadzadegan, F., Noorollahi, Y., Sharifi, M. A., & Itoi, R. (2014). Spatial analysis and multi-criteria decision making for regional-scale geothermal favorability map. Geothermics, 50, 189-201.
15. Gitelson, A. A., Gritz, Y., & Merzlyak, M. N. (2003). Relationships between leaf chlorophyll content and spectral reflectance and algorithms for non-destructive chlorophyll assessment in higher plant leaves. Journal of plant physiology, 160(3), 271-282.
16. ENDVI. 2019. "Drone Aerial Mapping and Survey". Available from: http://www.aeroeye.com.au/.
17. Clevers, J. G. P. W. (1989). Application of a weighted infrared-red vegetation index for estimating leaf area index by correcting for soil moisture. Remote Sensing of Environment, 29(1), 25-37.
18. Crippen, R. E. (1990). Calculating the vegetation index faster. Remote sensing of Environment, 34(1), 71-73.
19. Gitelson, A. A., Kaufman, Y. J., Stark, R., & Rundquist, D. (2002). Novel algorithms for remote estimation of vegetation fraction. Remote sensing of Environment, 80(1), 76-87.
20. Xiaoqin, W., Miaomiao, W., Shaoqiang, W., & Yundong, W. (2015). Extraction of vegetation information from visible unmanned aerial vehicle images. Transactions of the Chinese Society of Agricultural Engineering, 31(5).
21. Gamon, J. A., & Surfus, J. S. (1999). Assessing leaf pigment content and activity with a reflectometer. The New Phytologist, 143(1), 105-117.

Advanced Engineering Days

aed.mersin.edu.tr

Accuracy analysis of strawberry field detection using different machine learning algorithms and vegetation indices on the Google Earth Engine

Ceren Akgül*[1], Füsun Balık Şanlı [2], Osman Salih Yılmaz [3]

[1]*Yildiz Technical University, Department of Geomatic Engineering, Türkiye, ceren.akgul@std.yildiz.edu.tr*
[2] *Yildiz Technical University, Department of Geomatic Engineering, Türkiye, fbalik@yildiz.edu.tr*
[3]*Manisa Celal Bayar University, Demirci Vocational School, Türkiye, osmansalih.yilmaz@cbu.edu.tr*

Cite this study: Akgül, C., Şanlı, F. B., & Yılmaz, O. S. (2024). Accuracy analysis of strawberry field detection using different machine learning algorithms and vegetation indices on the Google Earth Engine. Advanced Engineering Days, 9, 416-418

Keywords
Google Earth Engine
Strawberry
Koprubasi
Machine Learning Algorithm
Vegetation Index

Abstract

In this study, the aim was to detect cultivated strawberry fields using remote sensing (RS) technologies in the Koprubasi district of Manisa, where commercial strawberry farming is intensive. Machine learning algorithms, spectral bands, and vegetation indices were utilized to find the best combinations for accurate results. Six classes were identified as forests, barren lands, strawberry fields, water surfaces, other agricultural areas, and urban areas, based on land cover and use. These classes were classified using Sentinel-2 images on Google Earth Engine (GEE) platform. CART, RF, SVM, Naive Bayes and KNN algorithms were employed spectral vegetation indices such as NDVI, EVI, ReNDVI, and SAVI. The accuracy was validated with Google Earth Pro images, and validation metrics such as Overall Accuracy (OA) and kappa statistics were calculated. The best result was obtained with the RGB+ NIR+ NDVI band combination using the SVM algorithm. The OA and kappa values were 88.90% and 0.757, respectively. This study serves as a guide for detecting strawberry fields and demonstrates the effective use of RS technologies in agricultural applications.

Introduction

The need for food rises as the world's population grows, placing stress on the agricultural sector and escalating agricultural production operations. Determining production areas and classifying goods are crucial for assessing agricultural production activities in terms of national food security, managing agricultural resources, and evaluating environmental functions [1]. Classification is typically used to determine land use using satellite photography. The procedure of classifying images with distinct spectral components involves first identifying and matching similar features among the pixels that make up the basic unit of the image, then rating the matched pixels within the same attribute group [2]. Crop mapping from satellite images has been performed using many classification methods. In recent years, machine learning algorithms have appeared as more accurate alternatives, particularly for large dimensional and complex data [3]. Specifically, it has been observed that non-parametric machine learning classifiers, like Support Vector Machine (SVM), Random Forest (RF), and Classification and Regression Trees (CART) produce remarkably accurate classification results from remotely sensed images [4]. Six types were defined in this study based on the land cover and use of the area as forest, barren, strawberry fields, water, other agricultural areas, and urban areas. Classification processes were carried out using Sentinel-2 images on the Google Earth Engine (GEE) platform to define these land use/cover classes. GEE is a remote sensing platform that offers numerous spatial analysis capabilities using JavaScript and Python programming languages. Many advanced machine learning algorithms for classification such as, RF, Naïve Bayes (NAIV), CART, and SVM are available in GEE platform [5]. Apart from the standard spectral bands, spectral vegetation indices such as the Normalized Difference Vegetation Index (NDVI), Enhanced Vegetation Index (EVI), Renormalized Difference Vegetation Index (ReNDVI), and Soil Adjusted Vegetation Index (SAVI) were employed, utilizing CART, RF, SVM, NAIV, and KNN algorithms. The overall accuracy (OA) and kappa statistics were computed for the verification

metrics in order to confirm the accuracy of this study using high-resolution Google Earth Pro images in addition to the satellite image utilized.

Material and Method

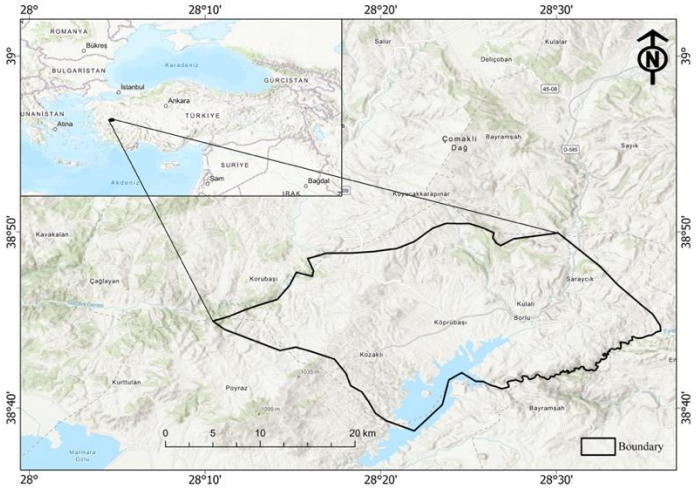


Figure 1 *Koprubasi location map*

The study focuses on the Koprubasi district, which is located inland in southwest Anatolia and eastern Manisa, Türkiye, north of the Gediz River. The district, which has approximately 27,500 hectares, has ideal geographic and climatic conditions for agriculture, especially for cultivating olives, grapes, and strawberries. Sentinel-2 (MSI) Level 2A satellite images, dated 07/07/2019, were used in this study. In the first stage of the study, an image collection was created, and a cloud filter and mask were applied to the created collection. The NDVI, ReNDVI, SAVI, and EVI vegetation indices were calculated and added as bands to the created collection in the second stage. In the third stage, classification was performed using the SVM, RF, KNN, NAIV, and CART algorithms. In the fourth stage, 1,000 random points were generated, and the accuracy of the resulting classification maps was assessed by calculating overall accuracy (OA) and the kappa statistic.

Table 1. Used classification algorithms for seven different senarios

RF	SVM	CART	NAIV	KNN
RGB+NIR	RGB+NIR	RGB+NIR	RGB+NIR	RGB+NIR
RGB+NIR+REDGE	RGB+NIR+REDGE	RGB+NIR+REDGE	RGB+NIR+REDGE	RGB+NIR+REDGE
RGB+NIR+NDVI	RGB+NIR+NDVI	RGB+NIR+NDVI	RGB+NIR+NDVI	RGB+NIR+NDVI
RGB+NIR+EVI	RGB+NIR+EVI	RGB+NIR+EVI	RGB+NIR+EVI	RGB+NIR+EVI
RGB+NIR+ReNDVI	RGB+NIR+ReNDVI	RGB+NIR+ReNDVI	RGB+NIR+ReNDVI	RGB+NIR+ReNDVI
RGB+NIR+SAVI	RGB+NIR+SAVI	RGB+NIR+SAVI	RGB+NIR+SAVI	RGB+NIR+SAVI
RGB+NIR+REDGE +NDVI+RNDVI+EVI+ SAVI	RGB+NIR+REDGE +NDVI+RNDVI+EVI+ SAVI	RGB+NIR+REDGE +NDVI+RNDVI+EVI+ SAVI	RGB+NIR+REDGE +NDVI+RNDVI+EVI+ SAVI	RGB+NIR+REDGE +NDVI+RNDVI+EVI+ SAVI

Results

This study evaluates and compares the performance of various band combinations and machine learning algorithms to detect strawberry fields. Based on the band combinations and machine learning methods employed in the research, the SVM algorithm with the combination of RGB+NIR+NDVI bands produced the most successful results. The kappa statistic and OA values of the study were 0.827 and 88.70determinedively. On the other hand, the lowest accuracy was determined with the combination of RGB+NIR+REDGE+NDVI+RNDVI+EVI+SAVI using NAIVE algorithm, with an OA value of 54.70 and a kappa statistic of 0.357.

Table 2. Overall accuracy and kappa statistics values

Band Combination	Machine Learning Algorithm									
	CART		RF		SVM		NAÏVE		KNN	
	OA (%)	KAPPA	OA (%)	KAPPA	OA (%)	KAPPA	OA (%)	KAPPA	OA (%)	KAPPA
RGB+NIR	76.90	0.660	77.49	0.669	83.90	0.757	74.50	0.588	79.26	0.691
RGB+NIR+REDGE	69.50	0.565	75.20	0.641	83.90	0.758	60.36	0.433	80.00	0.701
RGB+NIR+NDVI	72.50	0.608	77.30	0.668	88.70	0.827	73.50	0.575	79.26	0.691
RGB+NIR+EVI	72.40	0.602	73.70	0.624	85.05	0.772	70.70	0.597	79.26	0.691
RGB+NIR+ReNDVI	73.50	0.622	76.70	0.662	86.20	0.790	73.80	0.582	79.26	0.691
RGB+NIR+SAVI	74.70	0.637	71.37	0.563	83.20	0.749	74.80	0.598	79.26	0.691
RGB+NIR+REDGE+ NDVI+RNDVI+EVI+ SAVI	66.60	0.544	72.70	0.620	83.90	0.757	54.70	0.357	80.00	0.701

Conclusion

This work highlights the efficient implementation of machine learning algorithms, vegetation indices, and remote sensing technologies in agricultural applications, and it acts as a guide for the identification of strawberry fields. This study presents GEE is an efficient and advantageous platform for classifying land use/cover to identify the cultivated areas.

References

1. M. C. Arslanoğlu ve Y. Şimşek, Application Of Machine Learning Algorithms Using Optical Satellite Images For Crop Classification In Google Earth Engine, *Proccedings of International Congress and Workshop on Agricultural Structures and Irrigation,* , Diyarbakır, Turkiye, 12- 15 May, 2022, .
2. O. S. YILMAZ, F. GÜLGEN, R. GÜNGÖR ve F. KADI, Investigation of Land Use Change with Remote Sensing Techniques, The Case of Köprübaşı District, *Journal of Geomatics,* cilt 3, no. (3), pp. 233-241, 2018.
3. H. S. E. Imanni, A. E. Harti, M. Hssaisoune, A. Velastegui-Montoya, A. Elbouzidi, M. Addi, L. E. Iysaouy ve J. E. Hachimi, Rapid and Automated Approach for Early Crop Mapping Using Sentinel-1 and Sentinel-2 on Google Earth Engine; A Case of a Highly Heterogeneous and Fragmented Agricultural Region, 2022.
4. P. Karakuş, Object Based Classification in Google Earth Engine Combining SNIC and Machine Learning Methods (Case Study: Lake Köyceğiz), *Turkish Journal of Remote Sensing and GIS,* cilt 5, no. 1, pp. 125-137, 2024.
5. Neetu ve S. S. Ray, Exploring Machine Learning Classification Algorithms For Crop Classification Using Sentinel 2 Data, *ISPRS-GEOGLAM-ISRS Joint Int. Workshop on "Earth Observations for Agricultural Monitoring", 18–20 February 2019,* , New Delhi, India, 2019.

Advanced Engineering Days

aed.mersin.edu.tr

Smart Agriculture: Leveraging Information Technology and Human Expertise for Sustainable Farming

Adel Taheri Hajivand*[1], Kimia Shirini [1], Sina Samadi Ghareveran [1]

[1]*University of Tabriz , Biosystem Department, Iran,a.taheri@tabrizu.ac.ir, k.shirini@tabrizu.ac.ir, s.samadi@tabrizu.ac.ir*

Cite this study: Hajivand, A. T.,Shirini, K., & Ghareveran, S. S. (2024). Smart Agriculture: Leveraging Information Technology and Human Expertise for Sustainable Farming. Advanced Engineering Days, 9, 419-421

Keywords
Agriculture system
Mission planning
Multifactor system
Multi-objective
Optimization

Abstract

Smart agriculture using information technology and human agricultural experience has been proposed in order to increase productivity with the lowest cost and prevent the need for traditional agriculture. The precision agriculture system, by using technologies such as GIS, GPS, RS and DSS, improves agricultural operations at a specific time and place and uses environmental data to analyze and create a precise action plan for agricultural machinery. In this paper, a mission planning approach for precision agriculture system is investigated. This approach allows agricultural machinery to perform complex missions with collaboration and automation. Due to environmental changes and resource limitations, the precision agriculture system has dynamic characteristics, and in the face of these changes, it must adjust its program and reassign goals to agricultural machinery.

Introduction

The results consist of different mission planning strategies. For example, a computer consists of two computing units U and Uz. These two computing units have the following limitations:

- The ability to calculate U and Uz is the same.
- The maximum number of tasks loaded by a calculation unit.
- In one unit of time, U is able to do two tasks and Uz is able to do one task.
- The cost of executing each task is the same.

Now the computer receives two missions A and B. These two missions must be executed in two time units. Before performing the missions, the separated tasks of these two missions and the relationship between each one are shown in Figure 1:

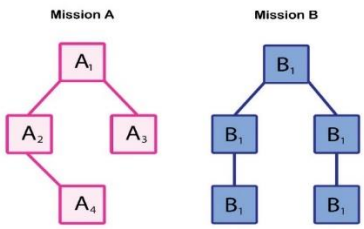


Figure 1. The decomposed tasks of Mission A and B

Mission A is divided into several tasks A1, A2, A3, A4. The same goes for mission B. Assuming that there are four tasks at time t-0 and five tasks at time t-1. Meanwhile, each task has the same complexity. The execution of each task requires two resources. If two related tasks are assigned to different computing units, it costs an additional communication resource. Two possible programs for assigning tasks are shown in Figure 2.

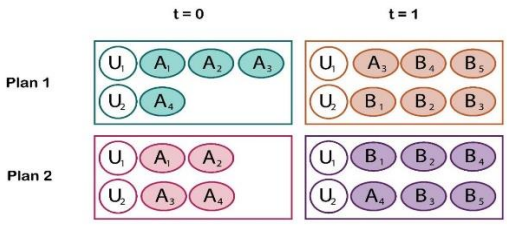


Figure 2. Two possible plans of tasks assignments

As shown in Figure 2, in the first schedule, unit U is fully loaded with three tasks at t0. Meanwhile, U2 receives an A4 assignment. When 1 equals 1, U2 has completed its assigned task and is ready to load the other three tasks.

A multi-agent system is a computer system that consists of several delegated or semi-delegated intelligent agents in a specific environment. With communication and interaction between intelligent agents, this system is able to solve more complex problems that a single agent cannot solve. Due to its high efficiency, this technology has been used in various fields including industry, military, finance, agriculture, etc. Zhong Johan and Liu Chenqing presented a multi-agent framework for large power systems. This framework enables the power system to deal with complexity, uncertainty, real-time information and computations and avoid catastrophic events. The power system with this multifactorial framework quickly adapts to the complex changes of the system and is able to process a large amount of data.

An Hongui et al. have developed a multi-agent simulation model that focuses on interactions in a virtual battlefield and provides details of the dynamics of tactical warfare. Meanwhile, Ying Weir and his team research multi-agent systems in financial business applications, presenting an ontology-based approach to developing smart applications without low-level programming details. Christian Grovermann et al. have developed a new multi-agent system based on mathematical programming, evaluating strategies to reduce the use of harmful pesticides and introducing smart policies for sustainable agriculture in Thailand, which can reduce the use of hazardous pesticides by 34% without adversely affecting income. They have acquired a farm. In summary, multifactorial systems are effective in various fields and have outstanding performance and application, including precision agriculture.

The multi-objective optimization problem (MOP) has become one of the most important topics in the field of optimization. In this domain, it is impossible to simultaneously optimize all the objective functions in an MOP, because the conflict between the objective functions always exists. MOP solution is performed by balancing the advantage of each objective function in order to achieve global optimization.

In the field of smart agriculture, researchers have investigated MOP issues and have achieved many achievements. These applications include multi-objective numerical solutions for pest control in soybean fields, optimization of irrigated and rainfed fields, and the FarmDESIGN model for evaluating farm performance in terms of productivity, economics, and environment.

The precision agriculture system is founded on four main aspects: multi-agent system, agent coalition, multi-objective optimization and task allocation. Despite significant progress in these areas, challenges still exist. These problems include the lack of standards for implementing multi-agent systems, privacy issues, authentication of shared information, and the risk of differential commands. Agent coalition challenges include resource allocation and benefit distribution. Dealing with multi-objective optimization requires evolutionary algorithms to manage conflicting objectives. Allocation of tasks should take into account the dynamic nature of precision agriculture and avoid repetitive calculations when reassigning tasks. Other issues include obtaining environmental information and agent communication.

Material and Method

The multi-objective optimization problem (MOP) in the field of mathematical computing tries to optimize several objective functions with conflicts between them simultaneously in a time interval. This mathematical model is usually formulated in a special way.

$$\min_{X \in D} \{ f_1(X), f_2(X), ..., f_n(X) \}$$

In the above model, the optimization goals are specified as fi(X), f(x),..., fn(X) and the unequal and equal constraints are gi(x) and h;(x), respectively.

Interferences between objectives cause us not to reach optimal values simultaneously, because optimizing one objective may greatly reduce the effect of other objectives. In MOP, each objective must have some concessions to help obtain the best global solution for the entire system. A minimum objective vector and an ideal objective vector are used to limit the Pareto effect. The minimum objective vector is as follows:

$$Z_i^{nad} = \sup_{x \in X} f_i(x) Foralli = 1, ..., k$$

And the ideal target vector is as follows:

$$Z_i^{ideal} = \inf_{x \in X} f_i(x) Foralli = 1, \ldots, k$$

The minimal and ideal objective vectors determine the upper and lower bounds for the values of the Pareto optimal solution, respectively. Therefore, the Pareto optimal solution is not a specific value, but a numerical interval.The cost objective function is one of the most important functions that should be considered. When agricultural machinery performs missions, it needs to consume fuel or batteries. At the same time, agricultural machinery will have some mechanical losses due to equipment wear. In addition, the value of the agricultural machine itself must be considered, since it is not completely safe during the mission. Damage to agricultural machinery is possible, for example, a drone accidentally hits a bird and then crashes, or an unmanned aerial vehicle goes into a canal. The value of an agricultural machine is determined by the value of its equipment such as sensors, cameras, actuators, etc. The cost objective function is defined as follows:

$$C(X) = \sum_{i=1}^{M} \zeta_i + \rho_i * v_i$$

The overall objective function is the ultimate criterion for mission planning. This function includes objective utility function and objective cost function. The overall objective function is defined as E(X).

$$E(X) = \alpha * B(X) + \beta * C(X)$$

Researchers have used two main methods to solve the multi-objective problem. The first method converts multiple objectives into one objective by optimizing linear objectives. But this solution has little accuracy in dynamic and large-scale situations. The second method benefits from computational intelligence with genetic algorithms and crowd optimization. These two algorithms are analyzed in this article.

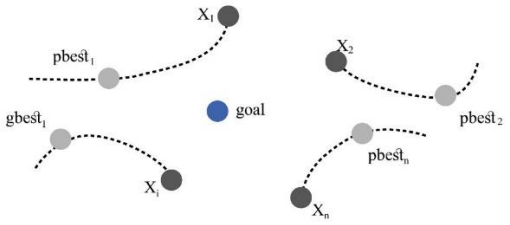


Figure 3. The movement trajectory of the particles

Results

The purpose of the simulation is to carry out a pesticide application task within the precision farming framework. To accomplish this job collaboratively, a coalition of many UAVs is expected to form. The chosen UAVs must spray the herbicide in certain areas as part of the mission. Meanwhile, the kinds and amounts of pesticide used may vary depending on the locality.

Criteria / Solution	Total flying distance	Latest arrival time
Pareto optimal solution	4261.90	51.61
Alternative solution 1	6182.23	65.35
Alternative solution 2	4534.65	63.47

Figure 4. The movement trajectory of the particles results

Conclusion

This work primarily examines the precision farming system's mission planning technique and suggests the implementation's specific steps. Task assignment, agent coalition, multi-objective optimization, and multi-agent systems are the main state-of-the-arts in the precision farming system. The Python platform is used to verify the simulation of the suggested mission planning method.

References

1. Shaikh, T. A., Rasool, T., & Lone, F. R. (2022). Towards leveraging the role of machine learning and artificial intelligence in precision agriculture and smart farming. *Computers and Electronics in Agriculture*, *198*, 107119.
2. Aithal, S., & Aithal, P. S. (2024). Information Communication and Computation Technologies (ICCT) for Agricultural and Environmental Information Systems for Society 5.0. *International Journal of Applied Engineering and Management Letters (IJAEML)*, *8*(1), 67-100.
3. Büyüközkan, G., & Uztürk, D. (2024). Integrated design framework for smart agriculture: Bridging the gap between digitalization and sustainability. *Journal of Cleaner Production*, 141572.

Advanced Engineering Days

aed.mersin.edu.tr

LSTM Deep Learning for Acoustical Sorting of Jujube Fruits

Sayed Javad Sajadi[*1]

[1] *Gonbad Kavous University, Department of Plant Production, Iran, sajadi@gonbad.ac.ir*

Cite this study: Sajadi, S. J. (2024). LSTM Deep Learning for Acoustical Sorting of Jujube Fruits. Advanced Engineering Days, 9, 422-424

Keywords
LSTM
Sorting
Signal Processing
Jujube
STFT

Abstract

This study proposes a novel method for jujube fruit sorting using acoustic analysis. The approach deployed Long Short-Term Memory (LSTM) deep learning to classify jujubes based on their impact sound signals. This technique improves sorting accuracy and efficiency compared to traditional visual inspection. The research demonstrates that the proposed method effectively classifies jujubes based on acoustic properties. The feature extraction identifies informative features, boosting performance beyond conventional machine learning models. Moreover, LSTM deep learning further enhances classification accuracy and robustness. These findings suggest that LSTM deep learning offers a promising avenue for jujube acoustical sorting. This method has the potential to achieve high accuracy and efficiency in fruit quality classification, impacting the jujube industry significantly. The research contributes to the development of intelligent sorting systems and provides a valuable framework for future studies in agricultural product sorting.

Introduction

This paper proposes a new, non-destructive method for sorting jujube fruits by size based on sound analysis. It builds on the success of acoustic techniques for grading other fruits, aiming to overcome the limitations of traditional labour-intensive sorting methods. Jujube fruits change texture as they ripen, which demonstrably affects their acoustic properties and makes them suitable for classification using sound analysis.

The proposed method captures the sound produced when a jujube fruit impacts a surface, followed by feature extraction and deep learning classification [1-4]. This paper mainly focuses on Long Short-Term Memory (LSTM) networks, a type of deep learning that recognizes patterns in sequential data like sound waves. Additionally, it investigates using feature extraction techniques to identify the most informative parts of the sound signal for optimal classification accuracy.

Material and Method

A dataset of 1776 jujubes from the 2022 harvest near Birjand City, Iran, was used. The jujubes were categorized by size (small, medium, large, extra large) following Iranian national standards. A custom-designed system captured the acoustic signature of each jujube by recording the sound generated as the fruit dropped onto a metal plate. The captured audio signals were then digitized for further analysis.

Analyzing both time and frequency is necessary for complex sounds like jujube impacts. This paper uses Short-Time Fourier Transform (STFT) to explore the sound in small segments. By doing this, STFT reveals how the frequency content of the sound changes over time, capturing the nuances that more straightforward methods might miss. In addition to STFT, this research also defines Instantaneous Frequency (IF) and Spectral Entropy (SE) to capture the characteristics of the jujube impact sounds. IF essentially represents the average frequency at any given moment in the sound, and SE tells us how the sound's energy is distributed across different frequencies. By calculating these features (STFT, IF, and SE), we can effectively capture the characteristics of the jujube impact sounds for accurate size classification.

This paper leverages Long Short-Term Memory (LSTM) networks, a recurrent neural network (RNN) type, for jujube fruit size classification based on acoustic features. Unlike standard neural networks, LSTMs excel at

handling sequential data like sound waves. Traditional neural networks have limitations in retaining information from earlier data points. LSTMs address this challenge by incorporating forget, input, and output gates. These gates enable the network to selectively remember or discard information pertinent to the current classification task. This selective memory mechanism makes LSTMs adept at analyzing sequential data, where the entire sequence, not just isolated elements, contributes to the classification [5,6]. The LSTM network receives features extracted from the jujube fruit impact sound using Short-Time Fourier Transform (STFT) in this method. These features serve as the input to the LSTM, which then processes the information and outputs a classification corresponding to the jujube fruit size.

The machine learning model's performance is evaluated using a confusion matrix for a multiclass classification problem. True Positive (TP), False Positive (FP), False Negative (FN), and True Negative (TN) are defined as correct samples, incorrectly classified samples, not incorrectly classified samples, and not correctly classified samples, respectively. The performance metrics used are Accuracy, Sensitivity (Recall), Specificity, Precision, F1-Score, MCC, and Kappa.

Results

The optimized LSTM hyperparameters, including the initial learning rate, number of hidden units, batch size, LSTM depth, and threshold, were selected using the Bayesian Optimization (BO) algorithm. The initial range and corresponding optimized values are illustrated in Table 1.

Table 1. The optimized LSTM hyperparameters were selected using the Bayesian Optimization (BO) algorithm.

LSTM Hyperparameter	Type	Transformation	Range	Optimized Value by BO
Initial Learning Rate	Continuous	log	[0.001, 0.1]	0.0025
Number of hidden Units	Discrete	none	[50, 200]	91
Batch Size	Continuous	none	[32, 12]	127.4607
LSTM Depth	Discrete	none	[1, 3]	1
Threshold	Discrete	none	{150, 200, 250}	250

Using acoustic features, the Long Short-Term Memory (LSTM) model achieved exceptional performance in jujube fruit size classification. The model exhibited near-perfect accuracy (0.9816) on the test dataset, demonstrating robust generalization to unseen data. Furthermore, the LSTM model achieved high precision, sensitivity, F1-score, Matthews Correlation Coefficient (MCC), and Kappa values across all jujube fruit size categories. These metrics collectively indicate the model's ability to accurately classify fruits while minimizing errors, such as false positives and negatives. While some variation in performance was observed across datasets of different sizes, the LSTM model consistently demonstrated promise for jujube fruit size classification using acoustic analysis. These findings suggest that LSTM networks hold significant potential for practical applications in automated jujube fruit sorting based on sound signatures.

Table 1. Performance of the LSTM-BO Deep Learning Model

Evaluation Metric	Total Classes		Individual Classes							
			Train Dataset				Test Dataset			
	Train Dataset	Test Dataset	small	medium	large	Extra large	small	medium	large	Extra large
Accuracy	1.0000	0.9816	1.0000	1.0000	1.0000	1.0000	1.0000	0.9545	1.0000	0.9759
Sensitivity	1.0000	0.9826	1.0000	1.0000	1.0000	1.0000	1.0000	0.9545	1.0000	0.9759
Specificity	1.0000	0.9939	1.0000	1.0000	1.0000	1.0000	0.9836	1.0000	0.9921	1.0000
Precision	1.0000	0.9817	1.0000	1.0000	1.0000	1.0000	0.9535	1.0000	0.9733	1.0000
F1-Score	1.0000	0.9818	1.0000	1.0000	1.0000	1.0000	0.9762	0.9767	0.9865	0.9878
MCC	1.0000	0.9760	1.0000	1.0000	1.0000	1.0000	0.9684	0.9689	0.9827	0.9838
Kappa	1.0000	0.9509	0.4571	0.5153	0.4985	0.5291	0.4888	0.4767	0.5478	0.4990

The confusion matrix of the LSTM deep learning model is shown in Figure 1. The LSTM model performs well classifying large, medium, and small Jujube fruits, as indicated by the high values along the diagonal from the top-left to bottom-right. The model incorrectly predicts two extra-large fruits (as large) and four medium fruits (as small). These misclassifications highlight areas where the model may benefit from further refinement to improve its accuracy in distinguishing between specific fruit sizes, especially when the differences in features are subtle.

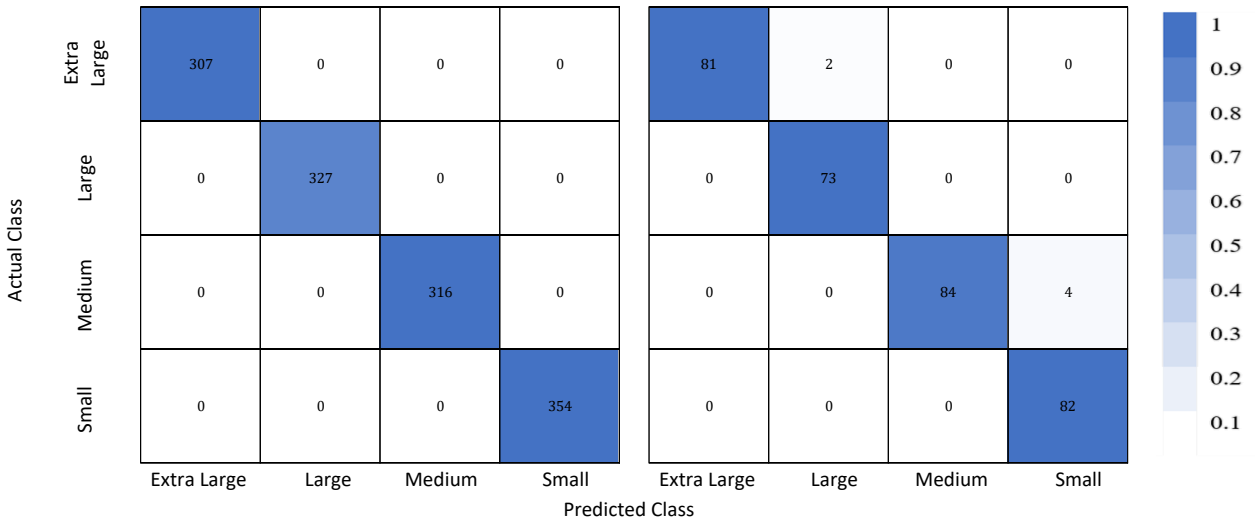


Figure 1. Confusion matrix of the LSTM model over the train (left) and test(right) datasets

Discussion

This study shed light on the promising performance of the LSTM-BO deep learning model in the acoustical sorting of Jujube fruits. These results validate the LSTM model's efficacy and emphasize the significance of hyperparameter optimization in elevating model performance and enhancing its generalization capabilities in intricate classification tasks. Utilizing the confusion matrix for the LSTM-BO model further proves invaluable in evaluating the model's classification performance. The study underscores the importance of synergy between feature selection methods, optimization algorithms, and ML models in achieving optimal classification outcomes and enhancing accuracy, precision, and F1-Score in Jujube nut acoustical classification tasks.

Conclusion

In conclusion, this research contributes significantly to the advancement of acoustic classification in agricultural settings. The study underscores the critical role of methodical model design and optimization in achieving superior classification outcomes. The findings provide valuable insights into the impact of hybrid FS approaches on machine learning model performance, particularly in enhancing accuracy, precision, and overall classification efficacy for intricate sorting tasks. By emphasizing the importance of strategic model design and optimization, this research lays the groundwork for future studies seeking to optimize classification performance in acoustic sorting applications, ultimately propelling advancements in agricultural technology and precision sorting methodologies.

References

1. Hosseinpour-Zarnaq, M., Omid, M., Taheri-Garavand, A., & Mahmoudi, A. (2022). Acoustic signal-based deep learning approach for smart sorting of pistachio nuts. Postharvest Biology and Technology, 185, 111778.
2. Yang, X., Guo, M., Lyu, Q., & Ma, M. (2021). Detection and classification of damaged wheat kernels based on progressive neural architecture search. Biosystems Engineering, 208, 176–185.
3. Guo, M., Ma, Y., Yang, X., & Mankin, R. W. (2019). Detection of damaged wheat kernels using an impact acoustic signal processing technique based on Gaussian modelling and an improved extreme learning machine algorithm. Biosystems Engineering, 184, 37–44.
4. Kurtulmuş, F., Öztüfekçi, S., & Kavdır, İ. (2018). Classification of chestnuts according to moisture levels using impact sound analysis and machine learning. Journal of Food Measurement and Characterization, *12*(4), 2819–2834.
5. Yu, Y., Si, X., Hu, C., & Zhang, J. (2019). A Review of Recurrent Neural Networks: LSTM Cells and Network Architectures. Neural Computation*, 31(7)*, 1235–1270.
6. Sherstinsky, A. (2020). Fundamentals of Recurrent Neural Network (RNN) and Long Short-Term Memory (LSTM) network. Physica D: Nonlinear Phenomena, *404*, 132306.

Advanced Engineering Days

aed.mersin.edu.tr

A Review of Artificial Intelligence Optimization Algorithms in Scheduling Problems with Constrained Resources in Mechanization

Adel Taheri Hajivand*[1], Kimia Shirini [2], Mehran Salehi [3] Ali Meshkini [4]

[1]*University of Tabriz, Agricultural Engineering, Iran,*
[2]*University of Tabriz, Electrical and Computer Engineering, Iran,*
[3]*University of Tabriz, Agricultural Engineering, Iran, salehi@gmail.com*
[4]*University of Tabriz, Agricultural Engineering, Iran, meshkiniali17@gmail.com*

Cite this study: Hajivand, A. T., Shirini, K., Salehi, M., & Meshkini, A. (2024). A Review of Artificial Intelligence Optimization Algorithms in Scheduling Problems with Constrained Resources in Mechanization. Advanced Engineering Days, 9, 425-428

Keywords
Scheduling
Operations
Mechanization
Limited resources
Intelligent algorithms

Abstract

In this paper, research on the topic of project scheduling with resources is classified according to Specified issues and limitations. Each classified area is examined separately, and special emphasis is given to trends in recent research. Papers that include resources and objectives for time/cost are discussed in detail as they present models that represent real-world problems. In agricultural mechanization projects, it is necessary and essential that the operations and activities of the project are carried out in a certain order in a certain and short period of time. Otherwise, the costs of not performing the operation on time will arise, considering the importance of the time index in order to reduce said costs and reduce delays during the work of project scheduling techniques and study, work, especially network models. They are used to accurately check the work method and reduce the amount of work and, as a result, reduce the time to do the work, and they are a suitable solution for the scientific and principled planning of projects and cost reduction. In this article, an overview of the work done in the field of agricultural project scheduling considering resource limitations has been discussed.

Introduction

Planning mechanized agricultural operations is of particular importance. One of the important limiting factors is the need to carry out basic operations such as tillage, planting bed preparation, etc. in limited and sometimes short periods of time. Also, depending on the conditions of each region and the type of product and the type of agricultural system, there is a suitable period of time and a suitable order for the use of machines and the execution of operations for each of the stages of the production process. It will cause the costs of not performing operations on time and a drop in product performance. In order to reduce the above costs, scientific and principled planning of mechanization projects is a suitable solution. In various industries, the techniques of project management science are used for successful and satisfactory planning. In the agricultural sector, in order to succeed in work and achieve the predetermined goals of the mechanized production system with the minimum possible cost and time and maximum product quality, correct and scientific management of projects is necessary and essential (Abdi et al. 2013). The ability and capabilities of distribution estimation algorithms have been used in this research as an efficient tool in planning agricultural mechanization projects.

In this research, the scheduling problems of the project with limited resources (RCPSP) for agricultural and industrial activities have been investigated. An important and different point in agricultural projects compared to civil and industrial projects is the importance of the date of carrying out activities compared to the time of carrying them out. Therefore, in agricultural projects, earlier completion of a project is considered an advantage if it is on time. Do not violate the activities. Because the main goal in agricultural mechanization projects is to increase profits by reducing the costs of untimely operations.

The purpose of this article is to present a comprehensive model focusing on the studies of the last decade and an overview of the methods and algorithms used to solve the RCPSP problem.

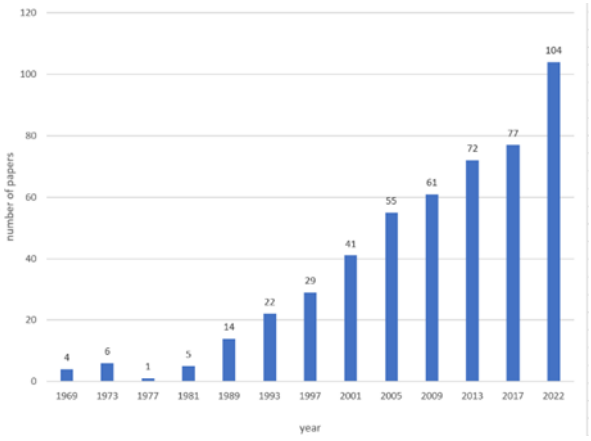


Figure 1. The number of works and studies done on the RCPSP problem.

Material and Method

In this part, we will examine the existing works in agricultural mechanization using the presented algorithms.

In a research example of planning cultural projects, making a movie, holding an international seminar (1994), how to use Garrett's method to model the planning and scheduling of research-industrial projects was investigated. Their purpose is to express Garrett's abilities in modeling planning and scheduling and analysis of industrial research projects and also to explain how to use this method for modeling and planning one of the research projects in the Engineering Research Center of Jihad Sazandeghi was. In their research, they explain that research is the main pillar and foundation of the development of human societies, the studies show that today's industrial and advanced societies are those societies that were not so progressive a few decades ago, which with proper planning and capital They have adopted a reasonable and correct method in the matter of research. Therefore, the limitations in the planning research projects of such projects are of special importance. One of the most important limitations of research projects is the limitation of time and financial resources. Due to the fact that investing in such projects does not have a short-term return, there is not much desire to make large investments in these fields. The presence of such additional restrictions in research projects increases the necessity of planning and controlling these projects equals. The formation of the project in a period of less than 290 days, that is, 270, 270 and 265, respectively, was 19.149980. The results of the 199-table method showed that the amount of the project was reduced by 26,693,330 Rials in 365 days.

Manjari et al. (2013) also used the PERT network method to schedule the construction of a mechanized greenhouse in Khuzestan province and concluded the effectiveness of network models in project scheduling. Dardi (1999) examined how to use the PERT method for modeling and planning industrial research projects. After the implementation of PERT networks for the construction of turbine blades in the Agricultural Jihad Research Center, he states that the PERT network model, in addition to its high flexibility, provides the possibility of presenting a more realistic model of the problem and a better representation of the relationships required in the project. has brought. So that it is possible to plan, machines, equipment and budgeting of the project with more confidence and accuracy.

Abdi (2012) with the aim of investigating the possibility of using network techniques for the scheduling of agricultural mechanization projects in the Tabriz plain, to plan and schedule mechanization projects using GERT networks, he paid for the scheduling of several crops, including alfalfa, wheat, and barley. and rapeseed using network techniques, the results of his research showed that the network method has the ability to plan and schedule agricultural mechanization projects, and network models are a very powerful tool or technique for modeling. planning, scheduling, control and analysis of agricultural mechanization projects.

Judge (2011) planned the mechanization project of wheat and grain corn with the help of PERT networks and concluded that the resulting network model provides a clear vision for the project manager to make timely decisions in the implementation phase. According to the project planning, it has progressed and can produce the product in a mechanized and high-efficiency manner at the desired time.

The resource-constrained project scheduling problem (RCPSP) was first proposed in 1963 by Kelly. So far, many researches have been done in relation to this issue, so that the variety of methods until today is more than the various research techniques in operations, especially linear planning for the timing of harvesting operations and sometimes planting operations. Planning and control techniques, projects, especially remote networks, have not been used much in this field. In Iran, except for limited cases, no research has been done with the use of

network techniques in mechanization projects. Piritgar (2007) should mention that the use of network techniques in industry has expanded greatly, and most of the available cases in the review of sources are from industry (quoted from Abdi et al., 2008)

Abdi (2008) studied the planning and scheduling of agricultural mechanization projects using grid networks in the Tabriz plain. His goal in this research is to investigate the possibility of using Garret networks for scheduling agricultural mechanization projects. He has carried out the timing of several products, including wheat alfalfa, barley and rapeseed, using network techniques. He has reached the following results after conducting the research. Sadri and Sekaki (2013) introduce Garret networks as an efficient and appropriate tool for planning mineral exploration projects because there are many activities in front of us in a mineral exploration project. These activities should be defined according to what stage of exploration we are in and what our goals are. Since exploration projects require a lot of money, having a correct and accurate schedule can be effective in reducing exploration costs. Considering the nature of the activities in such projects, Garrett networks are a suitable method for their planning and scheduling.

At the onset of the RCPSP study, there were no sample sets available for evaluating the performance of proposed algorithms, and most researchers validated the problem using generated data. Due to the large number of proposed features and the lack of sample sets for solving problems, this practice continues to be used in recent research.

Kolisch & Sprecher (1997) proposed a Project Scheduling Problem library (PSPLib) for studying RCPSP [98]. Subsequently, many studies have utilized this data. Additionally, several works have been conducted on real-world examples, demonstrating the importance of this issue in the industrial sector. The first and most well-known set of samples is the Multi-Project Scheduling Problem Library (MPSPLIb) introduced by Homberger (2007) specifically for decentralized RCPSP with local resources [99]. Later, Homberger (2012) expanded this library [36] by adding 60 new samples that show differences in terms of project access to local resources. MPSPLIb provides the possibility of online evaluation of proposed solutions and offers various objective functions. A benchmark set named the Resource-Constrained Multi-Project Scheduling Problem Library (RCMPSPLIB) was created by Perez and Posada.

Results

This paper provides a review of methods for solving the RCPSP, a known NP-hard problem. Agricultural scheduling projects consist of operations and activities that need to be executed in a certain sequence and within a specified time frame. If these operations and activities are not performed on time, it can lead to significant losses in both quantity and quality of the product, thereby incurring substantial unseen costs to the farmer or agricultural unit. Furthermore, agricultural operations require the use of resources which are typically limited. If these resources are not allocated efficiently, the likelihood of activities being delayed increases. In order to reduce the costs of such delays, these projects require planning, scheduling, and scientific and logical management of time and resources. This has become a standard issue in project scheduling, attracting numerous researchers who have used various scheduling methods, including precise, heuristic, and metaheuristic approaches. Consequently, various methods have been developed to address the issue of resource-constrained project scheduling.

Discussion

Approximate algorithms have been most frequently used for solving RCPSP-related problems, with genetic algorithms being among the most common. In none of the existing works has there been any competition between objectives in the multi-objective setting; they have merely addressed the problem by assigning weights to objectives using the weighted sum method. Therefore, future works could focus on creating competition between objectives and employing multi-objective metaheuristic algorithms to solve this problem.

Conclusion

This paper provides an overview of the methods and research published to date. It examines objectives and approaches for solving project scheduling problems, considering some existing works in the field of agriculture, and also addresses the related data. The paper offers an analysis of the problem in terms of objective functions, proposed solution methods, and data. The past decade has seen significant growth in the study of resource-constrained project scheduling. Various objective functions have been explored, including time, resources, and multi-objective functions. Time and resource-based objective functions have been the most studied, particularly with goals of minimizing project duration, average project delay, and total project cost being the most common.

References

1. Adhau ,S., M.L. Mittal, and A. Mittal. 2012. A multi-agent system for distributed multi-project scheduling:An auction-based negotiation approach. Engineering Applications of Artificial Intelligence, 25(8):1738-1751.

2. Adhau ,S., M.L. Mittal, and A. Mittal. 2022. Stochastic resource-constrained multi-project scheduling problem. International Journal of Production Research, 60(4):1411-1423.
3. Araujo,J.A., et al. 2020. Strong bounds for resource constrained project scheduling: Preprocessing and cutting planes. Computers & Operations Research,82: 104-113.
4. Boctor, F.F.1994. An adaptation of the simulated annealing algorithm for solving resource-constrained project scheduling problems,94: 87-104.
5. Chen, H., et al. 2019. Research on priority rules for the stochastic resource constrained multi-project scheduling problem with new project arrival. Computers & Industrial Engineering, 137:106-117
6. Chen, P.-H. and S.M. Shahandashti. 2009. Hybrid of genetic algorithm and simulated annealing for multiple project scheduling with multiple resource constraints. Automation in Construction,18(4):434-443.
7. Chen, T. and C. Ju.2015. Comparative analysis of swarm intelligence and heuristic priority rules for solving multi-project scheduling problem. International journal of computing science and mathematics, 6(6):581-599.
8. Demeulemeester E, HerroelenW.2002. Project Scheduling:A Research Kluwer Academic Publishers, Boston.
9. Dumond, J. and V.A. Mabert.1992. Evaluating project scheduling and due date assignment procedures: an experimental analysis. Management Science,34(1):101-108
10. Dumond, J. 1992. In a multi-resource environment, how much is enough? Jornal of production research, 30(2):395-410.
11. Elbeltagi E. 2009. Project Scheduling in Construction Project Management. Mansoura university,75-89.
12. Glover, F.1989. Tabu search—part I. ORSA Journal on computing,1(3): 190-206.
13. Gutjahr, W.J., et al. 2008. Competence-driven project portfolio selection, scheduling and staff assignment. Central European Journal of Operations Research,16(3):281-306.
14. Karaboga, D. 2005. An idea based on honey bee swarm for numerical optimization, Technical report-tr06, Erciyes university, engineering faculty, computer.
15. Kim, K.W., M. Gen, and G. Yamazaki. 2003.Hybrid genetic algorithm with fuzzy logic for resource-constrained project scheduling. Applied soft computing,2(3):174-188.
16. Kim, S.O. and M.J. Schniederjans. 1989.Heuristic framework for the resource constrained multi-project scheduling problem. Computers & operations research,16(6):541-556.
17. Lee, J-.K. and Y.-D. Kim. 1996. Search heuristics for resource constrained project scheduling. Journal of the Operational Research Society,47(5):678-689.
18. Linyi, D. and L. Yan.2007. A particle swarm optimization for resource-constrained multi-project scheduling problem.International Conference on Computational Intelligence and Security.
19. Liu, D. and Z. Xu, A. 2020. Multi-PR Heuristic for Distributed Multi-Project Scheduling With Uncertain Duration. IEE Access, 8:227780-227792.
20. Liu, M., M. Shan, and J. Wu. 2014. Multiple R&D projects scheduling optimization with improved particle swarm algorithm. The Scientific World Journal.
21. Lo, S.-T., et al. 2008. Multiprocessor system scheduling with precedence and resource constraints using an enhanced ant colony system. Expert Systems with Applications, 34(3):2071-2081.
22. Lova, A., C. Maroto, and P. Tormos A multicriteria heuristic method to improve resource allocation in multiproject scheduling. European journal of operational research, 127(2): 408-424.
23. Merkle, D., M. Middendorf, and H. Schmeck. 2002. Ant colony optimization for resource-constrained project scheduling. IEEE transactions on evolutionary computation,6(4):333-346.
24. Olisch, R. and C. Heimerl.2012. An efficient metaheuristic for integrated scheduling and staffing IT projects based on a generalized minimum cost flow network. Naval Research Logistics (NRL), 59(2):111-127.
25. Rokou, E., M. Dermitzakis ,and K. Kirytopoulos.2014. Multi-project flexible resource profiles project scheduling with Ant Colony Optimization. IEEE International Conference on Industrial Engineering and Engineering Management.
26. Rostami, M. and M. Bagherpour. 2020. A lagrangian relaxation algorithm for facility location of resource-constrained decentralized multi-project scheduling problems. Operational Research,20(2): 857-897.
27. Shirini, K., Taherihajivand, A., Samadi Qharehvern,. 2023. A review of algorithms for solving the project scheduling problem with resource-constrained considering agricultural problems. Agricultural Mechanization, 8(1), 1-14. doi: 10.22034/jam.2023.55751.1227

Advanced Engineering Days

aed.mersin.edu.tr

Investigation of pigment extraction from dry and wet microalgae

Leila Nadaei[1], Hanieh Shokrkar[2*]

[1]Sahand University of Technology, Biotechnology-Environment, Faculty of Chemical Engineering, Tabriz, Iran
leila.nedaiy.76@gmail.com, h_shokrkar@sut.ac.ir

Cite this study: Nadaei, L., & Shokrkar, H. (2024). Investigation of pigment extraction from dry and wet microalgae. Advanced Engineering Days, 9, 429-431

Keywords
Chlorophyll
Microalgae
Dry
Wet
Solvent

Abstract

Microalgae are very important due to the high production of antioxidants, carotenoids, and some other growth properties. In this research, the production and extraction of chlorophyll from mixed microalgae has been done. According to several researches conducted about the production and extraction of chlorophyll from pure algae culture, as well as very few studies about mixed algae, mixed algae cultures have been used in this research. The use of pure cultivation leads to costs of sterilization, maintenance, and the cultivation process, and causes investment and operational costs to rise. Therefore, the use of mixed cultivation significantly reduces production costs. According to the results obtained from comparing the extraction efficiency of total chlorophyll from dry and wet algae by metanol solvent (at ambient temperature and neutral pH), it shows that the extraction rate of chlorophyll a, b, by metanol solvent from wet algae is respectively: 21. 83%, 78.12%, and for dry algae it is 61.34%, 57.19%.

1. Introduction

A pigment is a molecule that has a specific color and can absorb light at different wavelengths depending on the color. Microalgae, in addition to chlorophyll, which is the main effective pigment in the process of photosynthesis, can produce other types of pigments such as carotenoids. Chlorophyll was first identified by Joseph Benaime Conto and Pierre Joseph Pelletier in 1817 [1] and the presence of magnesium in chlorophyll was discovered in 1906 [2]. The function of chlorophyll in plants is to absorb light. Since food webs in every type of ecosystem, from terrestrial to marine, begin with photosynthesis, chlorophyll can be considered the basis for all life on Earth [3]. There are more than 1100 known carotenoids. Carotenoids are used not only as a colorant but also as antioxidant compounds in the food, cosmetics, and pharmaceutical industries [4]. The structure of carotenoids enables biological abilities including photosynthesis, light protection, plant coloring, and cell signaling [5].

In the last few decades, extensive research has been started on the possibility of chlorophyll and carotenoid production from algae, which is easy due to the high efficiency of photosynthesis, growth speed, the possibility of cultivation all year round, and easy downstream processes [7]. It has been widely investigated that some microalgae can grow and produce high amounts of pigments in various limitations such as light, salt, and nitrogen.

Among the methods of separation of these compounds, we can refer to chromatographic methods, solvents, surface absorption, ultrasonic waves, and supercritical fluids. In this research, after microalgae cultivation and harvesting, the process of extracting chlorophyll and carotenoid from microalgae is done using solvent. The main advantage of this type of mining is cost reduction in terms of infrastructure and operational procedures. On the other hand, due to heat treatment, it often requires a large amount of organic solvent, or even a long time [1]. Extraction performed with organic solvents occurs when the solvent is absorbed into the cell wall and causes rupture, thereby exposing the cell contents for extraction. Complete extraction can take a long time and better yields can usually be obtained by stirring or mixing [8]. According to several researches conducted about the production and extraction of chlorophyll and carotenoid from pure algae culture, as well as very few studies about mixed algae, mixed algae cultures have been used in this research. The use of pure cultivation leads to costs of sterilization, maintenance and the cultivation process, and causes investment and operational costs to rise. Therefore, the use of mixed cultivation significantly reduces production costs [9]. Also, by using mixed cultures, since there is no need to disinfect the culture environment, it will be easier to control and operate the

process and make the process economically justifiable. According to research [9] that was conducted to produce pigment from algae, the cost of using mixed algae cultivation is almost half of the cost of pure algae cultivation. Therefore, this study aims to compare dry and wet algae.

2. Materials and methods

2. 1 Cultivation of microalgae

First, mixed and indigenous species of microalgae were collected from the water of the El Guli pool in Tabriz City, East Azerbaijan province. Then the first microalgae cultivation operation was carried out in a 500 ml Erlenmeyer flask with stirring. After the growth of microalgae in Erlenmeyer, it was used with a volume of 12 liters and a working volume of 10 liters for the main cultivation of microalgae in a polycarbonate flat plate photobioreactor. Exposure was done with fluorescent lamps with a light intensity of 260 μ mol m^{-2} s^{-1} and a photometer was used to measure the light intensity. The operating conditions of the photobioreactor were aerated at ambient temperature, pH equal to 7, with a flow rate equal to 8 liters per minute per liter with concentrations of 1.25, 0.8, 0.2, 0.1, 0.1, and 0.1 g/l, respectively.

2.2 Analysis of pigments

In this research, the total amount of pigments was measured by the spectrophotometric method. To measure the content of chlorophyll a, b, first, a volume of 2 mL was taken from the desired sample and centrifuged for 5 min at 4000 rpm and the supernatant was discarded. Then, after washing twice with distilled water and discarding the supernatant, the sample obtained from the centrifuge was re-vortexed. In the next step, the resulting solution was centrifuged for 5 minutes at 4000 rpm. When the resulting precipitate became white, the absorbance of the supernatant liquid was measured and recorded at two wavelengths of 646 and 663 nm. Since the precipitate is not completely bleached, the volume of solvent should be added until the precipitate is completely white. Tween 85% was used to adjust the spectrophotometer. Finally, the chlorophyll content was calculated from the following equation [10].

$$Chla = 16.72\ A_{663} - 9.16\ A_{646} \quad (1)$$

$$Chlb = 34.09\ A_{646} - 15.28\ A_{663} \quad (2)$$

2.3 Investigation of chlorophyll and carotenoid extraction from dry and wet algae

After the completion of microalgae growth and harvesting, metanol solvent was used to compare the efficiency of total chlorophyll extraction from dry and wet algae. Of course, it should be noted that this experiment was performed without stirring, at ambient temperature and pH equal to 7, and the amount of pigment production was recorded at 20, 30, 60, 75, and 90 min. All experiments of this research have been repeated twice.

3. Discussion and results

3. 1 Selection of dry or wet algae to extract chlorophyll

The results of chlorophyll and carotenoid extraction for both types (dry and wet algae) in conditions without stirring, at ambient temperature, and at neutral pH are presented in the graphs of Figure (1). The extraction efficiency of chlorophyll b, a, with the help of methanol solvent from wet algae in 90 minutes has the efficiency of 83.21%, 78.12%, respectively, and for dry algae, it is 61.34%, 19.19% respectively 57% and 53.27%. Few studies have compared the extraction of chlorophyll from dry and wet algae. In the study of Martelli et al [3], the drying of *Isochrysus galbana* algae was investigated by the oven, sunlight, freezing and spraying methods, and wet algae. The results showed that drying reduces the efficiency of total chlorophyll extraction compared to extraction with wet algae [8]. Also, studies show that temperature leads to pigment degradation [10]. The lower yield after the drying process can be explained by the additional drying step leading to the destruction of chlorophyll [12]. Wet algae not only have higher extraction efficiency but also can reduce operating costs by eliminating the drying step. Wet biomass improves extraction by swelling the cell, also facilitating cell wall lysis, and allowing the solvent to access the internal cell contents [13].

The problem with the extraction process with wet algae is the increase in the cost of handling and storage [9]. Because wet algae will disappear in a week at room temperature. Wet algae should be used immediately or kept at a temperature below -20˚C [14]. Therefore, due to conducting numerous tests over a long period and the harsh conditions of keeping wet algae, dry algae has been used to check the extraction rate of pigments.

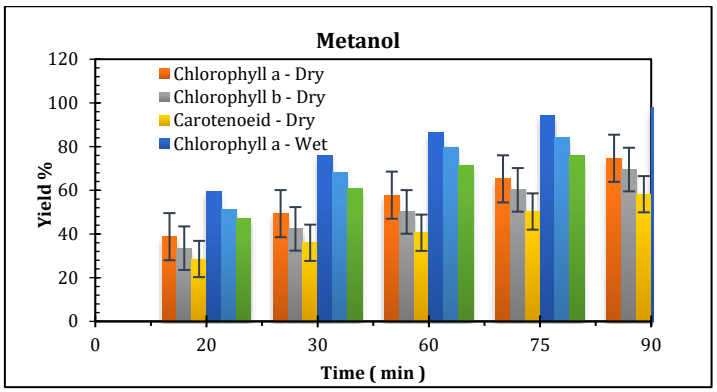


Figure 1. Comparison of extraction efficiency of chlorophyll a, b from dry and wet algae using solvent metanol (without stirring, ambient temperature, and neutral pH).

4. Conclusion

In this research, to produce and extract total chlorophyll, mixed species of microalgae were used. After harvesting and drying microalgae, the pigment extraction process from dry and wet microalgae was investigated. The obtained results show that the amount of extraction of chlorophyll a, b, by methanol solvent from wet algae with the efficiency of 83.21%, 78.12%, respectively compared to dry algae with the efficiency of 61.34%, 19 57% are more. Wet algae not only have higher extraction efficiency but also can reduce operating costs by eliminating the drying step. Wet biomass improves extraction by swelling the cell, also facilitating cell wall lysis, and allowing the solvent to access the internal cell contents. The problem of the extraction process with wet algae is the increase in the cost of handling and storage. Therefore, researchers prefer dry algae for analysis.

References

1. Jeffrey, S. W. (1968). Quantitative thin-layer chromatography of chlorophylls and carotenoids from marine algae. *Biochimica et Biophysica Acta (BBA)-Bioenergetics*, *162*(2), 271-285.
2. Jiménez, C., Cossío, B. R., Rivard, C. J., Berl, T., & Capasso, J. M. (2007). Cell division in the unicellular microalga Dunaliella viridis depends on the phosphorylation of extracellular signal-regulated kinases (ERKs). *Journal of Experimental Botany*, *58*(5), 1001-1011.
3. Martelli, K. S., Chew, K. W., Ooi, C. W., Ong, H. C., Ling, T. C., & Show, P. L. (2019). Extraction of natural astaxanthin from Haematococcus pluvialis using a liquid biphasic flotation system. *Bioresource Technology*, *290*, 121794.
4. Nedaei, L., & Shokrkar, H. (2022). A Review on the Extraction of Chlorophyll and Carotenoids from Microalgae. Iranian Chemical Engineering Journal, 21(123), 45-58.
5. Nedaei, L., & Shokrkar, H. (2022). A review of the effects of different stresses on antioxidant production by Dunaliella algae. Iranian Chemical Engineering Journal.
6. Nedaei, L., and Shokrkar, H. (2023) The effect of the cultivation environment on the productivity of pigment and algae biomass. The fifth National Conference on Environmental Engineering and Management, Qaemshahr.
7. Nedaei, L., and Shokrkar, H. (2023) A review on the effect of different stresses to increase biofuel production from microalgae. 8th clean energy conference, Babol.
8. Panis, G., & Carreon, J. R. (2016). Commercial astaxanthin production derived by green alga Haematococcus pluvialis: A microalgae process model and a techno-economic assessment all through the production line. *Algal research*, *18*, 175-190.
9. Riley, J. P., & Wilson, T. R. S. (2017). The use of thin-layer chromatography for the separation and identification of phytoplankton pigments. *Journal of the Marine Biological Association of the United Kingdom*, *45*(3), 583-591.
10. Nedaei, L., and Shokrkar, H. (2023) Increasing the sustainable growth of algae for biofuel production. 8th clean energy conference, Babol.
11. Panis, G., & Carreon, J. R. (2016). Commercial astaxanthin production derived by green alga Haematococcus pluvialis: A microalgae process model and a techno-economic assessment all through the production line. Algal research, 18, 175-190.
12. Shokrkar, H., & Nedaei, L. (2023). Investigating the effect of solvent type on chlorophyll and carotenoid extraction from dry and wet microalgae. Iranian Chemical Engineering Journal.
13. Shokrkar, H., & Nedaei, L. (2023). Chlorophyll and carotenoid extraction from mixed microalgae; experimental and kinetic study. Biomass Conversion and Biorefinery, 1-13.

Advanced Engineering Days

aed.mersin.edu.tr

Exploring Green Chili Pepper Recognition in Dense Foliage Greenhouses Using Deep Learning Segmentation Algorithms for Robotic Harvesting

Hossein Akhtari [1], Hossein Navid [*1], Javad Robati [2], Nayer Etminan Far [1], Ali Gaffarnejad [1]

[1] *University of Tabriz, Department of Bio system Engineering, Tabriz, Iran, h.akhtari@tabrizu.ac.ir, navid@tabrizu.ac.ir, a.ghaffarnezhad@tabrizu.ac.ir, n.etminanfar@tabrizu.ac.ir*

[2] *University of Maragheh, Department of Bio system Engineering, Maragheh, Iran, javad_rebati2000@ yahoo.com*

Cite this study: Akhtari, H., Navid, H., Robati, J., Far, N. E., & Gaffarnejad, A. (2024). Exploring Green Chili Pepper Recognition in Dense Foliage Greenhouses Using Deep Learning Segmentation Algorithms for Robotic Harvesting. Advanced Engineering Days, 9, 432-434

Keywords

Precision Agriculture
Pepper Recognition
Computer Vision
Deep Learning

Abstract

Based on the fast and high demand of people for food in the near future, the mechanization of harvesting agriculture products will be necessary. Given that green pepper is one of the most widely consumed products of the people, it is also cultivated in greenhouses and needs to be harvested with high speed and accuracy. Therefore, identifying and locating the pepper product is of great importance. Segmentation of the product in the image with the help of computer vision and deep learning algorithms will help significantly in distinguishing it from the surrounding environment of the greenhouse (leaves and branches, etc.). Accurate pepper recognition enables the potential for robot-assisted harvesting. Popularly used in computer vision tasks, YOLOv5 and YOLOv8 deep learning segmentation algorithms are the techniques that can greatly aid in the identification of pepper in an overlapping leaf canopy greenhouse. Yolov5 large with 90% precision and 0.02 seconds speed on GPU, was able to show significant results in the recognition of chili peppers. The performance demonstrated by Yolov5 suggests its potential utility in robotic harvesting applications, particularly in environments with dense foliage such as greenhouses.

Introduction

Robotic harvesting and precise detection of peppers are crucial in modern agriculture due to labor shortages and the need for efficiency [1, 2]. Computer vision techniques, especially deep learning-based models, revolutionize agricultural practices by enabling precise monitoring of crops, including green chilies. Despite challenges like diverse shapes and occlusions, these techniques show promise in enhancing efficiency and sustainability in agriculture [3, 4]. A plethora of research endeavors has been dedicated to developing robust segmentation algorithms for peppers, leveraging state-of-the-art deep learning architectures. Chen et al. (2020) proposed a novel positioning approach based on instance segmentation using a monocular RGB camera, achieving competitive results in accurately positioning sweet pepper crops [5].

Moreover, advancements in convolutional neural network (CNN) architectures have contributed to the development of more efficient and accurate segmentation models. Ren et al. (2021) utilized transfer learning with a fine-tuned VGG16 model for the classification of pepper quality, demonstrating improved anticipation performance and faster convergence rates [6]. The NSGA-II-based pruning algorithm was employed to optimize a YOLOv5l model for green pepper detection, resulting in a 73.9% reduction in model parameters and a 59.0% increase in detection speed [7]. Furthermore, Zhang et al. (2023) proposed an improved YOLOv8 algorithm with a modified C2F module for segmenting agricultural pests and diseases, achieving higher accuracy and versatility [8].

Motivated by the need for more accurate and efficient segmentation techniques for green chilies, this article aims to provide a comprehensive comparative analysis of the YOLOv5 and YOLOv8 models for green chili segmentation and recognition. Building upon previous research findings, the aim is to evaluate the performance of these models in identification green chilies in diverse and complex agricultural settings. Through this comparative analysis, we aim to identify the strengths and limitations of each model and provide insights for future research directions in the field of agricultural products segmentation.

Material and Method

The experimental greenhouse was situated in an agricultural research center on the eastern outskirts of Tabriz, Iran (37°58'33"N 46°33'13"E). The dataset comprised 1000 images of hydroponically cultivated greenhouse peppers. Various images were captured from varying angles and distances, aiming to provide diverse data for training of networks. The peppers were concealed by leaves and other foreign objects, posing a challenge to the detection process. The acquired images were partitioned into training, testing, and evaluation sets at ratios of 80%, 20%, and 10%, respectively. Drawing from the widespread success of the popular YOLO model [9] across various fields, attempts were made to utilize its latest iteration for segmenting and identifying peppers. Therefore, all images were annotated, followed by training and evaluating both the fifth and eighth versions of the YOLO network. It's important to note that the models underwent training via transfer learning.

The YOLO model typically comprises four components: backbone, neck, head, and Non-Maximum Suppression (NMS), each serving a distinct purpose. YOLOv5's backbone is Darknet 53, a CNN architecture emphasizing feature extraction with small filter windows and residual connections. YOLOv8, the newest version of the object detection model, brings improvements with a fresh neural network architecture. It includes Feature Pyramid Network (FPN) and Path Aggregation Network (PAN), along with a streamlined labeling tool for easier annotation. YOLOv8's backbone relies on Cross-Stage Partial connections (CSP), enhancing information flow between various network components [10].

For an equitable comparison, the training of mentioned models was conducted with default hyperparameters of each version. Additionally, the models were trained 30 epochs with a batch size of 8. After conducting numerous trials and consideration of the density of foliage in images, the decision was made to train both models on a large size. In cluttered or complex images, larger models excel at accurately identifying and locating objects amidst background noise or overlapping elements. The performance of trained models was assessed based on segmentation criteria relevant to both speed and accuracy.

Results

To assess the coordination between the model's predictions and the actual targets during training, the segmentation error of both training and validation data was measured in each epoch. Figure 1 depicts the diagram for each model.

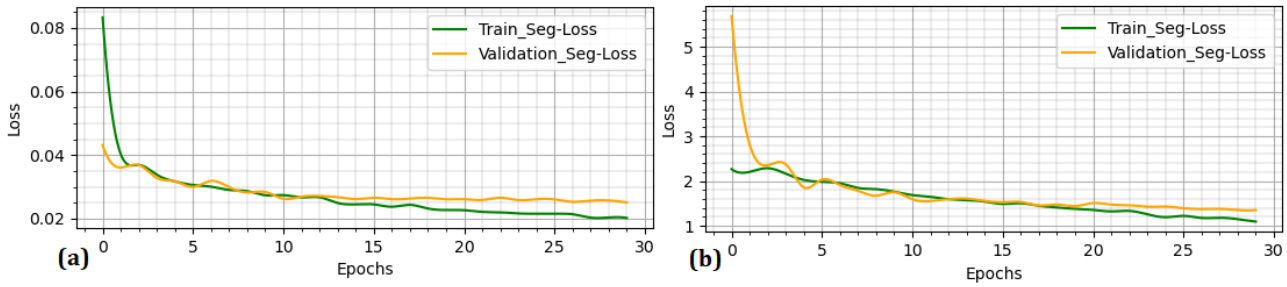


Figure 1. Train and Validation loss of (a) Yolov5 and (b) Yolov8

Table 1 also presents the findings concerning the precision, recall and speed of models for chili pepper test images segmentation. The speed of segmentation for the test images underwent analysis using both the Graphic Processing Unit (GPU) and the Central Processing Unit (CPU). GPU was an NVIDIA QUADRO RTX 4000 card, using the CUDA® parallel programming platform. The CPU included two graphic cores known as Intel HD Graphics 4400 and AMD Radeon HD 8750M.

Table 1. Results of chili pepper segmentation precision, recall, and speed

Items	Yolov5l	Yolov8l
Precision	90%	87%
Recall	77%	76%
Speed (GPU)	0.02s	0.027s
Speed (CPU)	2.32s	2.8s

The performance of the trained models in chili pepper identification was visually compared and evaluated. Multiple images from the test dataset were utilized for this assessment. Figure 2 illustrates an instance of chili pepper identification and segmentation by the two models presented.



Figure 2. Performance of models in image segmentation

Discussion

A lower error value in the training and validation phases of the YOLOv5 model indicates the closeness of its predictions to the real target values and effective convergence of the optimization process. Furthermore, the training and evaluation error values of both models indicated that Adaptive Moment Estimation with Weight Decay (AdamW) [11] in version 8 exhibited inferior performance when contrasted with Stochastic Gradient Descent (SGD) [12] in version 5.

Despite the close proximity of accuracy and speed between the two models, the predictions showed that the performance of YOLOv5 was better than its version 8. The cause of this problem can be the type of architecture and most importantly the training hyperparameters. It can be said that YOLOv8 architecture might not have been as effective for the specific task of green chili pepper recognition in dense foliage greenhouses compared to the architecture used in version 5.

Conclusion

The findings across all three phases of training, evaluation, and testing indicate that YOLOv5 demonstrates effective performance for the targeted task of recognizing green chili peppers in dense foliage greenhouses. The performance demonstrated by YOLOv5 suggests its potential utility in robotic harvesting applications, particularly in environments with dense foliage such as greenhouses.

References

1. Giang, T.T.H. and Y.-J. Ryoo, *Pruning points detection of sweet pepper plants using 3D point clouds and semantic segmentation neural network.* Sensors, 2023. **23**(8): p. 4040.
2. Paul, A., H. Nagar, and R. Machavaram. *Utilizing Fine-Tuned YOLOv8 Deep Learning Model for Greenhouse Capsicum Detection and Growth Stage Determination*. in *2023 7th International Conference on I-SMAC (IoT in Social, Mobile, Analytics and Cloud)(I-SMAC)*. 2023. IEEE.
3. Li, X., et al., *Fast and accurate green pepper detection in complex backgrounds via an improved Yolov4-tiny model.* Computers and Electronics in Agriculture, 2021. **191**: p. 106503.
4. Zhu, W., et al., *Segmentation and recognition of filed sweet pepper based on improved self-attention convolutional neural networks.* Multimedia Systems, 2023. **29**(1): p. 223-234.
5. Chen, C., et al., *Monocular positioning of sweet peppers: An instance segmentation approach for harvest robots.* Biosystems Engineering, 2020. **196**: p. 15-28.
6. Ren, R., et al., *Research on pepper external quality detection based on transfer learning integrated with convolutional neural network.* Sensors, 2021. **21**(16): p. 5305.
7. Nan, Y., et al., *Faster and accurate green pepper detection using NSGA-II-based pruned YOLOv5l in the field environment.* Computers and Electronics in Agriculture, 2023. **205**: p. 107563.
8. Zhang, L., et al., *DCF-Yolov8: An Improved Algorithm for Aggregating Low-Level Features to Detect Agricultural Pests and Diseases.* Agronomy, 2023. **13**(8): p. 2012.
9. Redmon, J., et al. *You only look once: Unified, real-time object detection*. in *Proceedings of the IEEE conference on computer vision and pattern recognition*. 2016.
10. Reis, D., et al., *Real-time flying object detection with YOLOv8.* arXiv preprint arXiv:2305.09972, 2023.
11. Loshchilov, I. and F. Hutter, *Decoupled weight decay regularization.* arXiv preprint arXiv:1711.05101, 2017.
12. Ruder, S., *An overview of gradient descent optimization algorithms.* arXiv preprint arXiv:1609.04747, 2016.

Advanced Engineering Days

aed.mersin.edu.tr

Intelligent Seed Type Detection for Seed Drills Using Logistic Regression and Infrared Sensors

Ali Ghaffarnezhad*[1], Hossein Navid*[2], Hadi Karimi [3]

[1]*University of Tabriz, Department of Biosystems Engineering, Iran, A.ghaffarnezhad@tabrizu.ac.ir*
[2]*University of Tabriz, Department of Biosystems Engineering, Iran, Navid@tabrizu.ac.ir*
[3]*Kerman Agricultural and Natural Resources Research and Education Center, Agricultural Engineering Research Department, Kerman, Iran, H_karimi@areeo.ac.ir*

Cite this study: Ghaffarnezhad, A., Navid, H., & Karimi, H. (2024). Intelligent Seed Type Detection for Seed Drills Using Logistic Regression and Infrared Sensors. Advanced Engineering Days, 9, 435-437

Keywords
Seed type detection
Seed drill
Logistic regression
Classification
Seed sensor

Abstract

This study addresses the critical need for accurate seed type detection in seed drills to enhance crop planting efficiency and food security. Disruptions in seed flow within seed drill tubes can lead to unseeded areas and reduced production, emphasizing the importance of continuous monitoring systems. Various sensors have been developed, but none effectively detect seed types. Building upon previous work, this study presents an intelligent seed type detection method using logistic regression modeling and infrared sensors. The algorithm was tested with wheat, barley, alfalfa, and chickpea seeds, achieving high accuracy in seed classification. Logistic regression, coupled with infrared sensor data, effectively differentiated between wheat and barley seeds. Results demonstrated exceptional accuracy, with occasional misclassifications in barley detection, which can be addressed through the implementation of a confidence variable. Overall, the developed algorithm offers a promising solution for real-time seed type identification in seed drills, contributing to improved precision agriculture practices and food security.

Introduction

Cereals have been a vital food source for humans for generations, making the uniformity, quantity, and quality of wheat and grain planting crucial for food security. Seed drills are used for cereal cultivation, and any issues with these machines can significantly impact crop yields. Disruptions in seed flow within seed drill tubes—caused by factors such as seed depletion in the hopper, malfunctioning seed distribution mechanisms, or blockages—result in unseeded areas in fields and reduced production [1]. Calibrating seed drills is time-consuming and requires regular reassessment. For precision agriculture, it is essential to monitor which parts of the land are cultivated and in what quantity. The lack of visibility of seed flow and distribution for operators highlights the need for continuous seed flow monitoring systems within seed tubes to effectively address these challenges. In recent years, various sensors and algorithms have been developed to monitor seed flow within seed tubes. These sensors include microwave [2], piezoelectric, capacitive [3], laser [4], fiber, solar cell, Light Dependent Resistor (LDR), machine vision, and infrared sensors. However, none of these sensors detect the type of seed being planted.

Accurate monitoring of the planting process requires identifying the type of seed being planted. This identification is critical for choosing the correct regression model to accurately estimate the instantaneous planting rate. Traditionally, users manually input the seed type via the display interface of seed tube monitoring sensors. This enables the sensor to monitor the planting process based on a model specific to the seed type being used. In this study, building on the sensor developed by [5], an algorithm has been devised to automatically identify seeds being planted by seed drills.

Material and Method

In this study, we developed an intelligent seed type detection method using logistic regression modeling. The algorithm was tested with a seed drill unit and various seeds, including wheat, barley, alfalfa, and chickpea. The seed drill unit's metering mechanism featured a fluted roller type, a sliding valve beneath the hopper, and an adjustable flap.

The logistic regression modeling used 15 high-level variables, which were derived from the output of the infrared receiver through detection algorithm transformations [5]. Table 1 lists these variables used in the multivariate linear regression. For the logistic regression, 700 data points were used to classify the four seed types, with 80% allocated for model training and the remaining 20% for evaluation. Additionally, the model was tested for each seed type on a seed drill test platform at four different forward speeds.

Table 1. Variables utilized for the seed type detection

symbol	High-level variable
A	average of the second quartile of 'ones' count per passage in a thousand passes
B	average of the second quartile of 'scans' count per passage in a thousand passes
C	average of 'ones' count per passage in a thousand passes
D	average of 'scans' count per passage in a thousand passes
E	The number of individual passes in a thousand passes
F	The number of dual passes in a thousand passes
G	The number of triple passes in a thousand passes
H	The number of quadruple passes in a thousand passes
I	The number of quintuple passes in a thousand passes
J	The number of sextuple passes in a thousand passes
K	The number of septuple passes in a thousand passes
L	The number of octuple passes in a thousand passes
M	The number of nonuple passes in a thousand passes
N	The number of decuple passes in a thousand passes
O	The average time interval between passages in a thousand passes

Results and discussion

Through investigations conducted on the variables listed in Table 1, it was determined that it is feasible to identify the seeds. Figure 1 illustrates the fluctuations of variable A for four types of seeds: alfalfa, wheat, barley, and chickpeas.

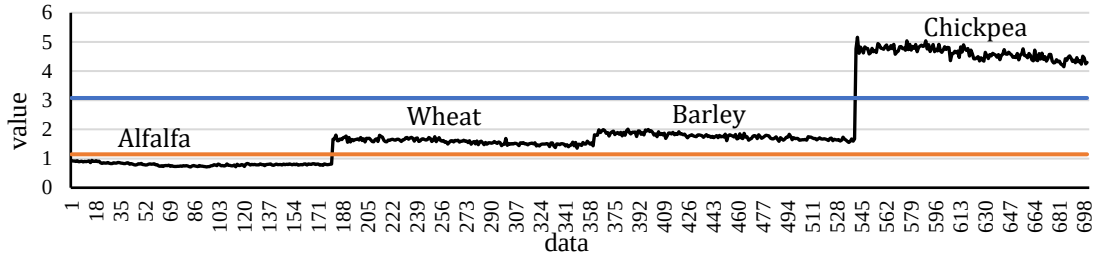


Figure 1. Variable value of A for alfalfa, wheat, barley and chickpea seeds

According to Figure 1, it is apparent that alfalfa and chickpea seeds can be effectively distinguished from other seeds using a single threshold line parallel to the horizontal axis. Thus, a threshold value of 3.0772 was selected for variable A to differentiate chickpea seeds from other types. This value was determined by averaging the highest values of variable A for wheat and barley seeds with the lowest value for chickpea seeds. Consequently, if the value of variable A exceeded 3.0772, the passing seed was identified as a chickpea seed. Similarly, a threshold value of 1.1451 was established for variable A to distinguish alfalfa seeds from other types. This threshold was determined by averaging the highest value of variable A for alfalfa seeds with the lowest values for wheat and barley seeds. If the value of this variable fell below 1.1451, the passing seed was identified as an alfalfa seed. Through this method, the identification of these two seeds is achieved without the need for logistic regression and using minimal processing power.

As depicted in Figure 1, it is evident that distinguishing between wheat and barley seeds solely using a linear threshold is not feasible. Therefore, logistic regression was employed to differentiate between these two types of seeds. For this classification task, 180 data points each for wheat and barley were utilized, with 20% of these data selected for test purposes. The discrimination accuracy achieved with a threshold of 0.5 was 0.986. According to the confusion matrix in Table 2, the logistic regression model correctly identified all wheat seeds and accurately

classified barley seeds in all but one instance, demonstrating the model's exceptional accuracy in seed type differentiation. Table 3 displays the coefficients and variables employed in the logistic regression analysis.

Table 2. Confusion matrix for wheat and barley seeds classification

	Predicted wheat	Predicted barley
Actual wheat	37	0
Actual barley	1	34

Table 3. Variables and coefficients used in logistic regression for distinguishing wheat and barley seeds.

Variable	A	C	D	E	F	G	H	I	J	Intercept	Accuracy
Coefficient	1.928	3.474	1.592	0.516	-0.480	-0.355	-0.675	-0.201	-0.184	-0.253	0.986

Each of the four studied seeds underwent testing and classification across three or four repetitions, with each repetition involving a hundred detections using the developed seed separation algorithm. The results of the classification accuracy for each seed are depicted in Table 4. As shown, the algorithm achieved high accuracy across all seeds, with only occasional misclassifications in barley detection. To address this issue, a confidence variable can be implemented. This variable operates by tracking the seeds detected during sowing and recording the frequency of detections for each seed. The seed with the highest number of detections is then identified as the seed being planted. Over time, as more seeds are detected during planting, the algorithm gains greater confidence in identifying the planted seed.

Table 4. Accuracy of the seed type identification algorithm for the tested seeds.

	Alfalfa			Wheat				Barley				Chickpea		
Rate (g/s)	0.6	1.1	1.8	5	6.9	8.8	10.4	4.5	5.3	6.1	7	5.5	9.2	13
Precision	1	1	1	1	1	1	1	0.98	1	0.99	1	1	1	1

The algorithm devised to differentiate these four seed types was constructed using the cross-sectional area and dimensions of the tested seeds. It is anticipated that the sensor and algorithm may encounter challenges and make errors when distinguishing between different varieties of seeds, such as wheat and barley.

Conclusion

This study presents an innovative approach to seed type detection in seed drills using logistic regression and infrared sensors. By leveraging high-level variables derived from infrared sensor data, the developed algorithm demonstrates promising capabilities in accurately identifying wheat, barley, alfalfa, and chickpea seeds. The method showed high accuracy in distinguishing between seed types, particularly with logistic regression achieving exceptional performance in differentiating wheat from barley seeds. Additionally, the algorithm's ability to adapt to varying forward speeds further enhances its practical applicability in agricultural settings. Despite occasional challenges in barley detection, the proposed confidence variable offers a potential solution to improve overall accuracy over time. Overall, this research contributes to advancing precision agriculture by providing a reliable and efficient means of seed type identification, ultimately optimizing crop planting processes and promoting food security.

References

1. Peng, F., Li, X., Fan, Y., Liao, W., Zhang, W., & Zhang, Z. (2023). Precision Seeding Monitoring System for Cooperative Operation of Multicast Lines. Paper presented at the CCF National Conference of Computer Applications.
2. Xie, C., Yang, L., Zhang, D., Cui, T., Zhang, K., He, X., & Du, Z. (2022). Design of smart seed sensor based on microwave detection method and signal calculation model. Computers and Electronics in Agriculture, 199, 107178.
3. Xu, L., Hu, B., Li, J., Ren, L., Guo, M., Mao, Z., . . . Sun, S. (2023). An efficient seeding state monitoring system of a pneumatic dibbler based on an interdigital capacitive sensor. Computers and Electronics in Agriculture, 209, 107856.
4. Zagainov, N., Kostyuchenkov, N., Huang, Y. X., Sugirbay, A., & Xian, J. (2023). Line laser based sensor for real-time seed counting and seed miss detection for precision planter. Optics & Laser Technology, 167, 109742.
5. Ghaffarnezhad, A., Navid, H., & Karimi, H. (2022). A new algorithm for detecting and measuring seed flow in the seed drills. Paper presented at the 14th National Congress of Mechanical Engineering of Biosystems and Mechanization of Iran, Kermanshah, Iran.

Advanced Engineering Days

aed.mersin.edu.tr

Investigation of daily reference evapotranspiration modeling with up to three meteorological parameters at Bandar Abbas station

Parastoo Amirzehni [*1], Saeed Samadianfard [1], AmirHossein Nazemi [1], AliAshraf Sadradini [1]

[1] *University of Tabriz, Department of Water Engineering, Iran, p.amirzehni@tabrizu.ac.ir, s.samadian@tabrizu.ac.ir, nazemi@tabrizu.ac.ir, sadraddini@tabrizu.ac.ir*

Cite this study: Amirzehni, P., Samadianfard, S., Nazemi, A., & Sadraddini, A. (2024). Investigation of daily reference evapotranspiration modeling with up to three meteorological parameters at Bandar Abbas station. Advanced Engineering Days, 9, 438-440

Keywords
SVM
Hyperband SVR
ET_0

Abstract

The estimation of reference evapotranspiration (ET_0) is very important in water management and the lack of meteorological data in all regions has made it necessary to develop methods with the least input to estimate this parameter. So, In this research, meteorological data from Bandar Abbas station with arid climate in Hormozgan-Iran from 2001 to 2022 were used. Daily ET_0 was calculated using the FAO56-PM equation and was considered as observational data. Using three parameters of maximum and minimum temperature and sunny hours, scenarios were defined. Then daily ET_0 was estimated using SVM and Hyperband SVR models, and the results were compared with statistical indices. According to the results, although the Hyperband SVR model is more optimal, model SVR-3 (R^2=0.813, RMSE=0.828 mm/day, NRMSE=0.149, MAE=0.595 mm/day, NSE=0.183, and WI=0.948) was determined to be the best model for estimating daily ET_0 using three meteorological parameters.

Introduction

In recent years, Artificial intelligence (AI) models were employed for estimating reference evapotranspiration (ET_0) with limited meteorological parameters. Researchers in a study evaluated the accuracy of four machine learning (ML) models and thirteen experimental methods calibrated to estimate ET_0 in arid and semi-arid regions. They concluded average temperature, wind speed, and sunshine hours contribute significantly to the accuracy of ML models. Consequently, these ML models can serve as an alternative to the FAO56-PM method for estimating ET0. Notably, SVM achieved high accuracy even with a limited number of variables [1]. So, the goal of the current study is evaluating the capabilities of Hyperband SVR at estimating ET_0 at arid climate and investigating the impact of the mentioned method in decreasing the estimation errors.

Material and Method

This research was done using meteorological data from the Bandar Abbas station with arid climate, located in Hormozgan province, Iran from 2001 to 2022. This station is located at latitude 27.21 and longitude 56.37; its height is 9.8 meters above sea level (Figure 1). 80% of the data was considered for training and 20% for model testing.

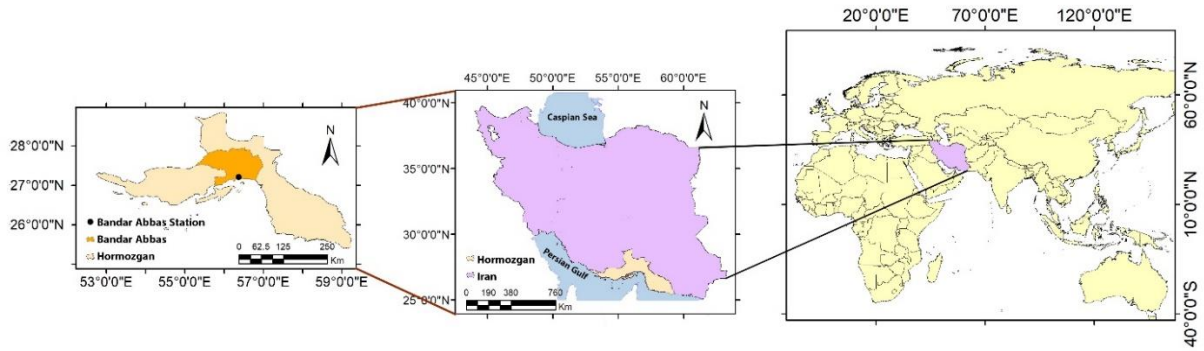


Figure 1. Location of the investigated station

Since ET_0 estimation is a very complex hydrological process, the Support Vector Machine (SVM) proposed by Kurtz and Vapnik [2] has been widely used. This is due to its implementation in solving very complex problems by mapping inputs to features through kernel function transformation. In the current study, the SVM method, and Hyperband SVR were used to ET_0 modeling. Hyperband SVR have been optimized by changing the kernel parameters. ET_0 was calculated using the standard FAO56-Penman-Monteith method and considered observational data.

The highest correlation (R) with ET_0 related to parameters of maximum temperature (Tmax), minimum temperature (Tmin), and sunny hours (sshn) were 0.9, 0.7, and 0.5 respectively. Considering the correlation of parameters with ET_0, scenarios for ET_0 modeling were determined, which have at least 3 parameters listed in Table 1.

Table 1. Defined scenarios

Scenario	Tmax	Tmin	sshn
SVR-1	*		
SVR-2	*	*	
SVR-3	*	*	*
H-SVR-1	*		
H-SVR-2	*	*	
H-SVR-3	*	*	*

The performance of each Scenario was evaluated using standard statistical metrics: the R^2, root mean square error (RMSE), normalized Root Mean Squared Error (NRMSE), mean absolute error (MAE), Nash Sutcliffe efficiency (NSE), and Wilmot coefficient (WI). The value of R^2, serves as an indicator to evaluate the relationship between the predicted and observed values. Other statistical indicators quantify the bias between the predicted value and the observed value, and all indicators range is 0 to 1. A higher R^2, NSE, and WI along with a lower MAE, RMSE, and NRMSE signifies a more accurate prediction.

Results

The results of the statistical indicators of the scenarios are given in Table 2. According to Table 2, it can be seen that the highest R^2 of 0.816 is related to the H-SVR-3 scenario and the lowest is 0.767 related to SVR-1.

Table 2. Statistical results of the models

Scenario	R^2	RMSE (mm/day)	NRMSE	MAE (mm/day)	NSE	WI
SVR-1	0.767	0.924	0.167	0.705	0.767	0.934
SVR-2	0.768	0.922	0.166	0.691	0.768	0.935
SVR-3	0.813	0.828	0.149	0.595	0.813	0.948
H-SVR-1	0.770	0.919	0.166	0.707	0.770	0.933
H-SVR-2	0.775	0.909	0.164	0.691	0.775	0.934
H-SVR-3	0.816	0.821	0.148	0.591	0.816	0.949

The violin-box diagram of the implemented models is shown in Figure 2. A violin plot depicts distributions of numeric data for groups using density curves. The width of each curve corresponds with the approximate frequency of data points in each region. The box diagram also displays the minimum, first quartile, median, third quartile, and maximum statistical values. According to Figure 2, it can be seen that in the estimated models, the maximum evaporation is lower than the observed values and most of the data scatter in each model is around the first and third quadrants.

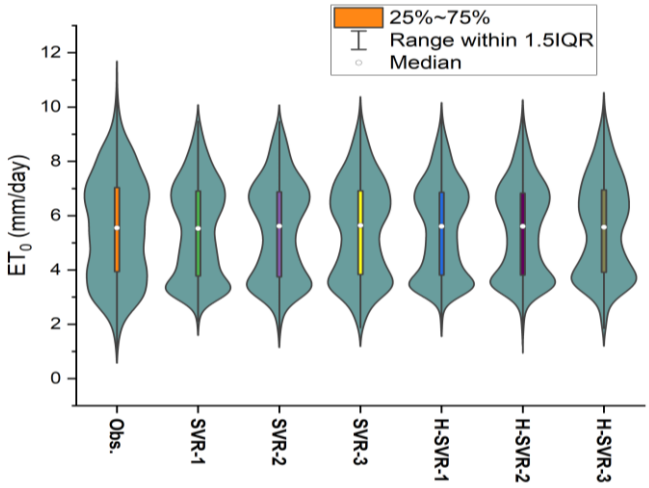


Figure 2. Violin-box plot of models

Additionally, Figure 3 shows the Taylor diagram to compare the performance of the models. The model closer to the reference will be a better model. According to Figure 3, it can be seen that model SVR-3 is close to the reference square and is a better model. Also, the performance of model SVR-2 is very close to model H-SVR-3.

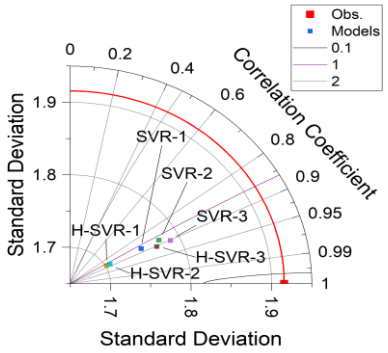


Figure 3. Taylor plot of models

Discussion

The violin-box diagram in Figure 2 shows that the distribution of data in each category is reduced around the median values, and also the median and quartile of all sets are similar to the observed ET_0 values. According to the Taylor diagram in Figure 3, the performance of models H-SVR-1 and H-SVR-2 is very close to each other, that is, instead of using two parameters, only the maximum temperature was used in method H-SVR. Moreover, SVR-2 and H-SVR-3 also have similar and accurate outputs. Finally, according to the correlation and errors (R^2=0.816, RMSE=0.821), model H-SVR-3 performed better, but the SVR-3 (R^2=0.813, RMSE=0.828) is closer to the observed values. The statistical results showed that the optimization of SVR model increased the amount of R^2 by about 0.004 and also reduced the RMSE by about 0.008 mm/day. In a study, researchers used to estimate ET_0 calculated with PM using limited meteorological variables as input, and comparing it. They concluded that AI models performed better than their counterpart methods for ET_0 estimation. The artificial neural network using temperature, solar radiation, and relative humidity as input variables performed best, with the correlation coefficient (r) ranging from 0.992 to 0.998, mean absolute error (MAE) ranging from 0.07 to 0.16 mm/day, and root mean square error (RMSE) ranging from 0.12 to 0.25 mm/day [3]. The difference in the results of this research with the current research can be due to the different input parameters of the models.

Conclusion

Lack of meteorological data is one of the serious challenges in water management and ET_0 estimation in most regions of the world. In this research, daily ET_0 was modeled using three meteorological parameters (Tmax, Tmin, and sshn) by SVR, and Hyperband SVR model. According to the results and the Taylor diagram, although Hyperband SVR improved the output by optimizing the functions and reduced the error, scenario SVR-3 also had an acceptable output and the best model was selected (R^2=0.813, RMSE=0.828 mm/day, NRMSE=0.149, MAE=0.595 mm/day, NSE=0.183, and WI=0.948).

References

1. Amani, S., Shafizadeh-Moghadam, H., & Morid, S. (2024). Utilizing Machine Learning Models with Limited Meteorological Data as Alternatives for the FAO-56PM Model in Estimating Reference Evapotranspiration. Water Resources Management, 38(6), 1921–1942.
2. Cortes, C., Vapnik, V. (1995). Support-vector networks. Machine Learning, 20, 273–297.
3. Fang, S., Lin, Y., Chang, S., Chang, Y., Tsai, B., & Kuo, B. (2024). Using Artificial Intelligence Algorithms to Estimate and Short-Term Forecast the Daily Reference Evapotranspiration with Limited Meteorological Variables. Agriculture, 14(4), 510.

Advanced Engineering Days

aed.mersin.edu.tr

Design and Implementation of an Unmanned Agricultural Machine for Automated Driving and Spraying

Emirhan Kaya [1], Hasan Dilmaç [1], Veli İlçi [*1]

[1]Ondokuz Mayis University, Department of Geomatic Engineering, Turkiye, emrhnky0@gmail.com, hasan.dilmac@omu.edu.tr, veli.ilci@omu.edu.tr

Cite this study: Kaya, E., Dilmaç, H., & İlçi, V. (2024). Design and Implementation of an Unmanned Agricultural Machine for Automated Driving and Spraying. Advanced Engineering Days, 9, 441-444

Keywords
Precision agriculture
Autonomous robots
Unmanned vehicles
Automated spraying
Navigation

Abstract

In our world, which has approximately 27 million square kilometers of arable land, the rapid increase in population causes the emergence of nutrition problems. Meeting the nutritional needs of limited agricultural areas depends on sustainable and efficient agricultural production. Today, while traditional agricultural practices are having difficulty meeting product needs, precision agriculture technologies, which integrate robotics and machine systems considered the future of agriculture, are trying to meet this need. In this study, an Unmanned Ground Agricultural Vehicle (UGAV) was developed for small agricultural enterprises. The developed UGAV consists of four main systems: motion and power, control, navigation and spraying. With the integrated operation of these systems, the UGAV can move autonomously or manually on the desired route in the agricultural field and can spray liquid fertilizer and pesticides at the desired coordinates thanks to the developed software. In addition, the width and height of the UGAV can be adjusted according to the height, structure and planting method of the crops on the field, and thus, efficient spraying can be carried out on different plant species and at different development stages of these crops.

Introduction

According to the reports of the United Nations, the world population, which is currently 7.3 billion, is expected to increase to 8.5 billion in 2030, 9.7 billion in 2050 and 10.4 billion in 2100 [1]. Factors such as population growth, increase in average life expectancy and wars increase the need for food day by day [2]. This growing need pressures agricultural enterprises to produce more [3]. However, meeting the increasing need in limited agricultural areas will be possible by integrating developing technologies into agricultural production. While innovative technologies offer more dynamic processes by improving production methods, developments in robotics and automation systems also contribute to innovative agricultural practices [4].

With the decrease in agricultural areas, the use of fertilizers and pesticides is increasing to meet the increasing nutritional needs and productivity. However, intensive and unconscious use of these substances harms human health and nature. Today's agricultural spraying methods for fertilizers and pesticides can be conducted by human resources, tractors, unmanned aerial vehicles (UAVs) and unmanned ground vehicles (UGVs). Although manual spraying by human power is a standard method, it has crucial shortcomings, such as unequal fertilizer and pesticide distribution and possible adverse effects of these materials on health [5]. In spraying with tractors, more energy is consumed due to high fuel consumption, and some areas, such as high-sloping fields, cannot be reached [6]. In addition, due to the size of the tractor, significant damage to the crops can occur during spraying.

In this study, an Unmanned Ground Agricultural Vehicle (UGAV) that can effectively perform autonomous spraying of fertilizer and pesticide without risking human health was designed. This vehicle, which aims to provide a low-cost solution, especially to small agricultural enterprises, has the ability to spray various products according to different growth periods, thanks to its adjustable body width and height. In addition, it can follow the determined route with high accuracy by providing precise location and direction information and thus can carry out spraying with minimum loss and maximum homogeneity.

Material and Method

The difficulties and limitations encountered in current spraying methods make innovative approaches necessary in designing and using agricultural robotic tools. This situation reveals the need to discover and develop

new methods to make spraying applications more efficient, safe and environmentally friendly. An ideal solution can be provided by tools that can overcome all these challenges and increase the efficiency, safety and sustainability of the agricultural industry.

In order to meet the requirements mentioned above, a UGAV was developed in a project [7] that was supported by Ondokuz Mayıs University (Project no: OMU PYO.MUH.1906.22.002). The UGAV can achieve its tasks by integrating four fundamental systems: motion and power, control, navigation and spraying systems. Schematic representations of these systems are given in Figure 1a.

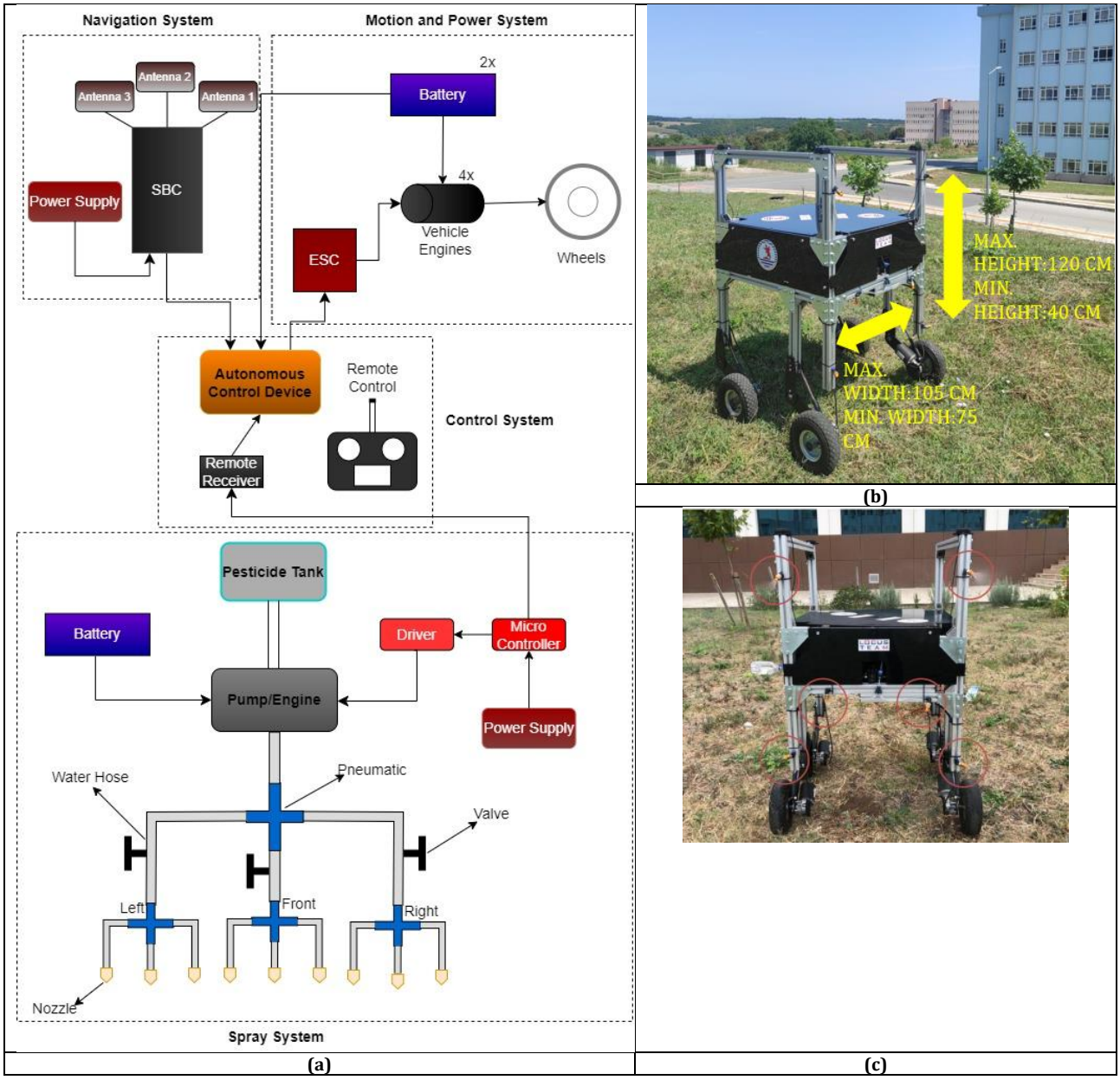


Figure 1. a. Schematic representation of the four systems on UGAV; b. Adjustable height and width of UGAV; c. Spraying with UGAV

The ***Motion and Power System*** *of* UGAV consists of four wheels, four motors connected to each wheel and an independently designed suspension system to ensure terrain adaptability. A design with adjustable dimensions has been adopted for spraying operations to adapt UGAV to various agricultural fields and plants. The vehicle must be lightweight as well as durable. For this reason, aluminium sigma profile material was preferred when producing the body of the UGAV. The designed body allows the width to be adjusted from 75 cm to 105 cm and the height from 40 cm to 120 cm (Figure 1b). This feature is essential to provide the flexibility needed for a customizable and efficient farming application. The power system of the UGAV receives the energy required for all other systems to operate effectively from two LiPo batteries.

Pixhawk Orange Cube controller was used in the ***Control System*** to manage the movement and sensors of the UGAV. Pixhawk Orange Cube is used to control the precise movement of the vehicle's operating position and

direction information received from the navigation system. The route plan is determined using the Mission Planner software, and this route information is transmitted to the control card via telemetry. The vehicle has two different control modes: autonomous and manual. In autonomous mode, it moves autonomously along the specified route. The manual control mode is designed to intervene immediately during autonomous driving. As a result, the Pixhawk Orange Cube controller and integrated systems enable effective management and control of UGAV. This integrated control system plays a vital role in increasing efficiency and precision in agricultural practices.

The SimpleRTK2B-SBC [8], a customizable and programmable dual-band GPS/GNSS RTK Single Board Computer, is used as a ***Navigation System*** in the UGAV. SimpleRTK2B-SBC provides precise location and direction information at a centimeter level. This development board has a GNSS receiver integrated with ZED-F9 modules and the capability to support multiple GNSS system satellites. Using three antennas, precise position, direction and GNSS-based Attitude and Heading Reference System (AHRS) information is obtained. With SimpleRTK2B-SBC, the positions of all three antennas from fixed reference networks can be determined with cm-level accuracy. The microSD reader on the SimpleRTK2B-SBC card enables real-time data recording. This feature allows the data collected by the vehicle during fieldwork to be recorded and analyzed later.

A ***Spraying System*** is a mechanism designed to provide precise and effective spraying applications to specified targets. These systems generally consist of a reservoir, an engine, and a series of optionally adjustable nozzles. The engine distributes the liquid from the tank to different parts of the system and sprays the fertilizers and pesticides to the desired places through nozzles. Additionally, the system is equipped with pneumatics and valves, enabling precise and controlled drug delivery by regulating the drug's flow rate, pressure and spray direction. A software developed for the spraying system was loaded onto the Arduino UNO card. By integrating Arduino UNO and control card, autonomous operation of the spraying system with the UGAV has been ensured. In extreme cases, it is possible to control the system manually via the remote control. The spraying process is triggered when the waypoint determined and selected in the Mission Planner is reached. The system detects this situation and starts spraying (Figure 1c). When the mission is completed, the system automatically stops. However, in unexpected cases, users can give direct commands to the system via the remote control. This feature provides a security measure for extraordinary situations and offers users manual control.

The spraying process takes place by transmitting the medicine from the reservoir to the spraying systems with the help of an engine and through hoses. Pneumatic technology is used to direct hoses into individual channels. The spray systems on the vehicle are controlled through valves located on the left, right and front. These valves control drug delivery, ensuring it is carried out precisely. Since the vehicle is still in the prototype stage, a 5-litre reservoir was used as a representative. The tests show that this reservoir can be emptied entirely within 3.15 minutes due to spraying with six nozzles, and thus, an area of 225 m^2 can be successfully sprayed. Due to the vehicle's higher carrying capacity (approximately 50-60 litres), the reservoir can be expanded depending on demand and need. This allows the vehicle to be used effectively in larger agricultural areas.

Conclusion

In this project, an autonomous ground agricultural vehicle (UGAV) was developed to meet small agricultural enterprises' fertilizer and pesticide spraying needs. The developed vehicle offers the following features:

- The body structure of the vehicle, made of lightweight and durable aluminium profile material, has a structure that can be adjusted in width and height. In this way, spraying different products from the desired height at different times is possible.
- The vehicle can be moved in both autonomous and manual modes. This feature provides ease of application to the user in any condition.
- High-accuracy location information was obtained using a three-antenna GNSS system. In this way, the developed vehicle can easily carry out precise spraying of fertilizer and pesticide.

As a result, it has been determined that the position and direction sensitivity obtained using a three-antenna GNSS set will be helpful for unmanned agricultural vehicles. It is observed that significant savings in labour and consumption of fertilizer and pesticide can be achieved by spraying operations using the produced UGAV.

References

1. United Nations. (2022). World Population Prospects 2022: Summary of Results.
2. Şahin, H. (2022). Dijital Tarım, Tarım 4.0, Akılı Tarım, Robotik Uygulamalar ve Otonom Sistemler. Journal of Agricultural Machinery Science, 18(2), 68-83.
3. Güzey, A., Akıncı, M. M., & Altan, Ş. (2020). Otonom Kara ve Hava Araçları ile Akıllı Tarım: Hasat Optimizasyonu Üzerine Bir Uygulama. Ankara Hacı Bayram Veli Üniversitesi İktisadi ve İdari Bilimler Fakültesi Dergisi, 207-220. https://doi.org/https://doi.org/10.26745/ahbvuibfd.706304

4. Çirkin, E., & Özdağoğlu, A. (2021). Endüstri 4.0 Bünyesindeki Otonom Robotların Sürdürülebilirlik Perspektifleri Açısından Değerlendirilmesi. Erciyes Akademi, 35(4), 1534-1553. https://doi.org/10.48070/erciyesakademi.997049
5. İnan, M., & Karci, A. (2021). Tarımda Ağaç İlaçlamanın Drone'larla Yapılmasında Yeni bir Yöntemin Geliştirilmesi ve Uygulanması. Anatolian Journal of Computer Sciences, 6(2), 72-89.
6. Özkan, A., & Dilay, Y. (2020). Karaman İlinde Tarımsal Üretimde Traktör ve Tarım Makineleri Kaynaklı Kazaların Değerlendirilmesi. Tarım Makinaları Bilimi Dergisi/Journal of Agricultural Machinery Science, 16(1), 32-39. http://dergipark.org.tr/tr/pub/tarmak
7. İlçi, V., Dilmaç, H., Uçarlı, A. C., Doğan, B., Başaran, A., & Kaya, E. (2023). Otonom Kara Aracı İle Tarım Arazilerinin İlaçlanması Ve Gübrelenmesi. PYO.MUH.1908.22.078
8. ArduSimple. (2024). ArduSimpleRTK2B-SBC. https://www.ardusimple.com/product/simplertk2b-sbc-development-kit/

Advanced Engineering Days

aed.mersin.edu.tr

Estimating daily reference evapotranspiration using remote sensing parameters by implementing Extreme Learning Machine optimized by Quantum-Inspired Algorithm

Parastoo Amirzehni [*1], Saeed Samadianfard [1], AmirHossein Nazemi [1], AliAshraf Sadradini [1]

[1] *University of Tabriz, Department of Water Engineering, Iran, p.amirzehni@tabrizu.ac.ir, s.samadian@tabrizu.ac.ir, nazemi@tabrizu.ac.ir, sadraddini@tabrizu.ac.ir*

Cite this study: Amirzehni, P., Samadianfard, S., Nazemi, A., & Sadraddini, A. (2024). Estimating daily reference evapotranspiration using remote sensing parameters by implementing Extreme Learning Machine optimized by Quantum-Inspired Algorithm. Advanced Engineering Days, 9, 445-447

Keywords
ET_0
LAI
LST
NDVI
Remote sensing

Abstract

Accurate and timely estimation of reference evapotranspiration (ET_0) is essential for multiple agricultural applications, including irrigation scheduling, predicting crop yields, and forecasting drought conditions. The lack of stations in all areas is an obstacle to accurate management, on the other hand, remote sensing data as a valuable resource can fill this gap. This paper aims to estimate ET_0 with limited remote sensing parameters. So, meteorological data from Yazd station with an arid climate in Yazd-Iran during 2001 to 2022 were used to calculate daily ET_0 by the FAO56-PM equation and considered as observational data. 8-day data of land surface temperature (LST) day/night and 16-day data of vegetation indices (LAI and NDVI) were interpolated with the cubic spline function and converted into daily data. Daily ET_0 values were estimated using LST day/night, LAI, and NDVI parameters with extreme learning machine (ELM) and hybrid Quantum-Inspired Algorithms-Extreme learning machine (QIS-ELM) models. The results of statistical indices showed that the best model was QAI-ELM-4 (R2=0.454, NRMSE=0.125, MAE=0.713 mm/day, MAPE=10.69, MBE=0.013 mm/day, and WI=0.791) using four remote sensing parameters.

Introduction

Due to the reference evapotranspiration (ET_0) having complex and dynamic processes, it is challenging to estimate it using empirical equations and to do so, high-quality, site-appropriate data are required. Therefore, a simplified model must be developed to estimate ET_0 with high precision by using fewer data. Adopted machine learning algorithms (ML) are a powerful tool for predicting ET_0 in lower time scales, with their application it is possible to obtain prediction models with very high accuracy. In research using the input of different meteorological parameters, they used several different optimized machine learning models and concluded the ELM method outperformed the other models and was thus recommended for ET_0 estimation at all timescales [2]. So, in the current research, only remote sensing parameters have been used to estimate ET_0 By implementation of ELM and QIS-ELM methods.

Material and Method

In this research, daily ET_0 was calculated using the standard FAO56-Penman-Monteith method by meteorological data from the Yazd station with arid climate, located in Yazd province, Iran from 2001 to 2022. This station is located at latitude 31.90 and longitude 54.29, and its height is 1230 meters above sea level (Figure 1) and considered observational data. Considering that satellite images of MODIS are not daily, the data of LST have 8-day intervals and the data of vegetation indicators have 16-day intervals, they were interpolated using the cubic spline function and converted into daily data. New modeling methods are directed towards soft computing, and in order to reach a model with higher speed, better generalization, and less human intervention, an extreme learning machine (ELM) model was developed in the 2000s [1]. Next, ELM model was improved using Quantum-Inspired Algorithms (QIS), which was implemented as Quantum-Inspired Algorithms-Extreme learning machine (QIS-ELM). It should be mention that 80% of the data was considered for training and 20% for model testing.

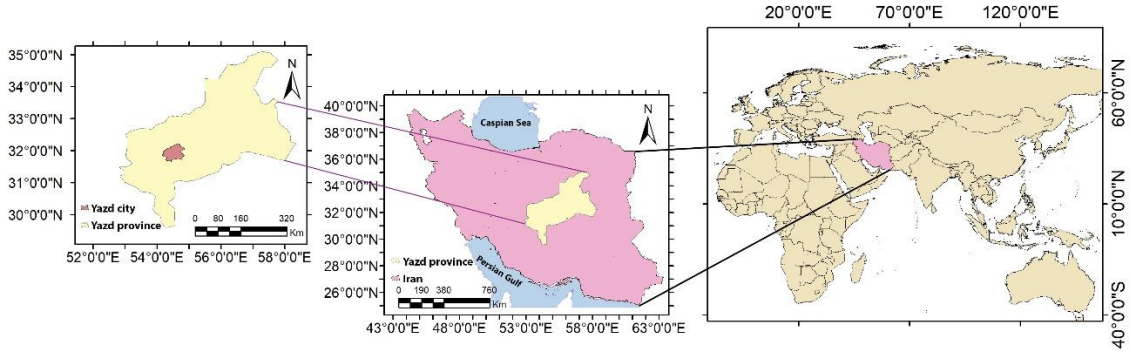


Figure 1. Location of the investigated area

The correlation (R) with ET_0 related to Land Surface Temperature in Day (LST-D), Land Surface Temperature in Night (LST-N), Normalized Difference Vegetation Index (NDVI) and Leaf Area Index (LAI) were 0.61, 0.59, 0.14, and -0.05 respectively. The scenarios are defined according to the degree of correlation of the parameters with ET_0, listed in Table 1.

Table 1. Defined scenarios

Scenario	LST-D	LST-N	NDVI	LAI
1	*			
2	*	*		
3	*	*	*	
4	*	*	*	*

The performance of each Scenario was evaluated using standard statistical metrics: the R^2, Normalized Root Mean Squared Error (NRMSE), Mean Absolute Error (MAE), Mean Absolute Percentage Error (MAPE), Mean Bias Error (MBE), and Wilmot coefficient (WI). The value of R^2, serves as an indicator to evaluate the relationship between the predicted and observed values. Other statistical indicators quantify the bias between the predicted value and the observed value. A higher R^2, and WI along with a lower MAE, NRMSE, MAPE, and MBE signifies a more accurate prediction, and all indicators range is 0 to 1.

Results

The results of the statistical indicators of the scenarios are given in Table 2, and it can be seen that the lowest NRMSE of 0.125 is related to the QIS-ELM-4 and the highest is 0.144 related to ELM-1. Also, the lowest MAPE is 10.69 related to the QIS-ELM-4 and the highest is 12.16 related to the ELM-1.

Table 2. Statistical results of the models

Scenario	R^2	NRMSE	MAE (mm/day)	MAPE	MBE (mm/day)	WI
ELM-1	0.276	0.144	0.803	12.16	0.039	0.718
ELM-2	0.304	0.141	0.794	11.91	0.013	0.746
ELM-3	0.383	0.133	0.755	11.25	0.010	0.778
ELM-4	0.422	0.129	0.730	10.88	0.017	0.793
QIS-ELM-1	0.410	0.130	0.748	11.33	0.030	0.756
QIS-ELM-2	0.418	0.129	0.744	11.23	0.024	0.762
QIS-ELM-3	0.398	0.131	0.736	11.03	0.015	0.772
QIS-ELM-4	0.454	0.125	0.713	10.69	0.013	0.791

The Ridgline plot of the models is given in Figure 2, which shows the distribution of a numeric value for each Scenario. The width of each curve corresponds with the approximate frequency of data points in each region. According to Figure 2, it can be seen that in the estimated models, the concentration and density of the estimated values is around 8 mm/day.

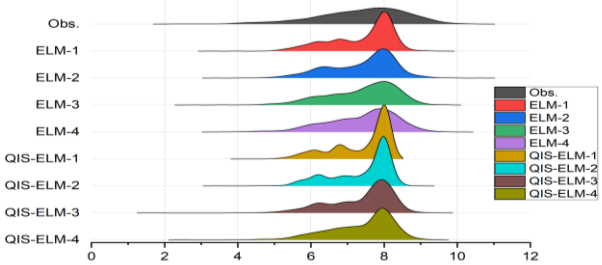


Figure 2. Ridgline plot of models

Additionally, Figure 3 shows the scatter plot to compare the two top scenarios performance. In scatter plot the model distribution closer to the 1:1 line will be a better model. According to Figure 3, it can be seen that ELM-4 (blue) R^2 is 0.434, and in QIS-ELM-4 (red) R^2 is 0.455 which indicates closer to the reference data.

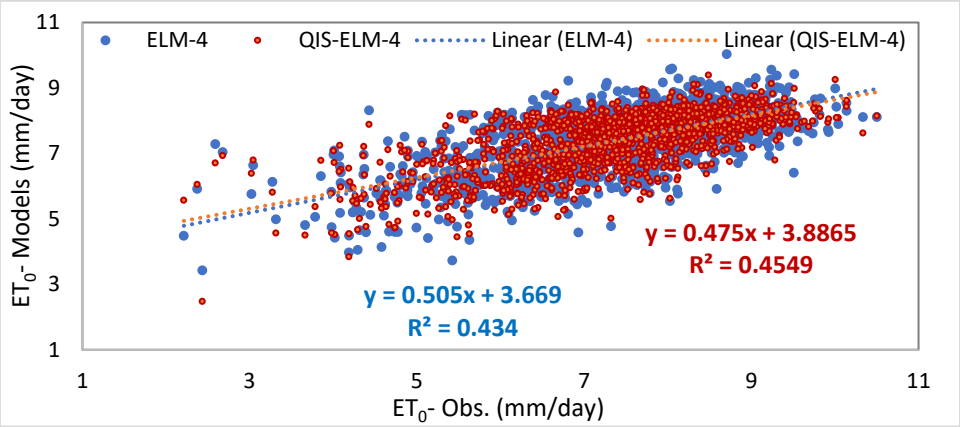


Figure 3. scatter plot of the top scenarios

According to Table 2, it can be seen that ELM has R^2 of 0.422 in the best case. By improving the model in QIS-ELM, the R^2 increased to 454. So, the optimization of the model has caused an increase of about 0.032. Also, the errors of QIS-ELM models are lower than ELM models. Machine learning models were investigated in modeling ET_0 using various input combinations. The results compared to the FAO56-Penman-Monteith data it was observed that machine learning models yielded more accurate estimates across all timescales. ELM method performs MAE 0.6 to 1.03 and RMSE ranging 0.63 to 1.2 mm/day [2]. The difference in the results is due to the difference in the input parameters of the models. In another study, researchers compared four machine learning (ML) models, extreme learning machine (ELM), genetic programming (GP), random forest (RF), and support vector regression (SVR), for estimating daily ET_0 with different limited climatic data as inputs in New Mexico, the results showed that SVR and ELM were the best ML models for all input scenarios in the analyzed climate zones, showing the best stability in testing [3].

Conclusion

In many areas, due to the lack of weather stations, there is not enough data to estimate ET_0, and water management faces a serious challenge. Using remote sensing information can be a suitable alternative in these areas. In this research, the problem of time intervals (8-day LST data and 16-day vegetation index data) was solved using cubic spline remote sensing, and the data of several days were converted into daily data by interpolation. Four remote sensing parameters including LST-D, LST-n, NDVI, and LAI under different scenarios were used as inputs of ELM and QIS-ELM models to estimate ET_0. The scenarios were executed with the input of 1 to 4 parameters. According to the results, QIS improved the output by optimizing the functions, and reduced the errors. The best model was QAI-ELM-4 (R2=0.454, NRMSE=0.125 mm/day, MAE=0.713, MAPE=10.69 mm/day, MBE=0.013, and WI=0.791).

References

1. Huang, G., Zhu, Q., & Siew, C. (2024). Extreme learning machine: Theory and applications. Neurocomputing, 70(1-3), 489-501.
2. Kiraga, S., Peters, R.T., Molaei, B., Evett, S.R., & Marek, G. (2024). Reference Evapotranspiration Estimation Using Genetic Algorithm-Optimized Machine Learning Models and Standardized Penman–Monteith Equation in a Highly Advective Environment. Water, 16(1),12.
3. Mokari, E., DuBois, D., Samani, Z., Mohebzadeh, H., & Djaman, K. (2022) Estimation of daily reference evapotranspiration with limited climatic data using machine learning approaches across different climate zones in New Mexico. Theoretical and Applied Climatology. 147, 575–587.

Advanced Engineering Days

aed.mersin.edu.tr

Estimating reference evapotranspiration in an arid region using a MODIS sensor and machine learning algorithms

Hamed Talebi*[1], Saeed Samadianfard [1], Hatice Çıtakoğlu [2]

[1] *University of Tabriz, Department of Water Science and Engineering, Iran, hamedtalebi99@gmail.com, samadianfard@gmail.com*

[2] *University of Erciyes, Department of Civil Engineering, Türkiye, hcitakoglu@erciyes.edu.tr*

Cite this study: Talebi, H., Samadianfard, S., & Çıtakoğlu, H. (2024). Estimating reference evapotranspiration in an arid region using a MODIS sensor and machine learning algorithms. Advanced Engineering Days, 9, 448-451

Keywords
Evapotranspiration
Machine learning
Remote sensing
MODIS
Land surface temperature

Abstract

Agricultural water management and irrigation planning depend on accurate estimation of reference evapotranspiration (ET0). By using satellite images, it is possible to compensate for the lack of weather information in areas without meteorological stations. Therefore, we have implemented the random forest (RF) and multi-layer perceptron (MLP) algorithms in this study to estimate the monthly ET0 at Ahvaz station (dry climate) using parameters extracted from MODIS sensor images. Then the estimated values of monthly ET0 and calculated monthly ET0 were compared with the FAO-Penman-Monteith equation. Based on the data of satellite images collected from 2005 to 2023, a database was created. During the development of the above models, 75% was used for the model training phase and 25% for the model testing phase. The input variables consisted of land surface temperature (LST) and evapotranspiration index (ET). Results showed that the MLP-1 model with only one LST input parameter had the best accuracy for monthly ET0 estimation in Ahvaz station (R2=0.973, RMSE=0.387, and NS=0.928). Finally, by examining the results of both models, it was found that the MLP model has better accuracy than the RF model in all scenarios.

Introduction

Precise estimation of reference evapotranspiration (ET0) is crucial in water management in the agricultural sector, particularly for arid areas. ET0 is a crucial factor in the water and energy cycles, serving as a significant connection between ecological and hydrological processes. Consequently, precisely estimating ET0 is a significant concern for comprehending the water cycle in soil-plant-atmosphere continuum systems. Conventional approaches for estimating ET0 generally depend on physical principles, but they have several drawbacks when it comes to accurately estimating ET0 in situations where climatic information like sun radiation, wind speed, and air temperature are unavailable. In recent times, advancements in artificial intelligence (AI) techniques and the improvement in the precision of estimation outcomes have heightened the need for these methods across many domains. Artificial intelligence approaches based on machine learning (ML) have been effectively utilized by the natural sciences, particularly hydrology, to estimate intricate and nonlinear processes. As a result, techniques like ML have gained popularity in estimating and predicting ET0. Tabari et al. (2013) employed a multilayer perceptron (MLP) network to calculate ET0 in a semi-arid climate. Their findings demonstrated that the MLP model outperformed other models when utilizing all meteorological inputs [1]. These numbers showed that the MLP model was better at predicting ET0 than the experimental models. Numerous studies have concentrated on estimating ET0 using meteorological station data. However, in regions where there are no meteorological stations, the traditional techniques of estimating ET0 using ground data will not be effective. In such cases, remote sensing (RS) information offers the opportunity to bridge this gap. In such circumstances, satellite images are the optimal and economical approach for assessing ET0 in large regions. The principal sources of satellite images are Landsat, the Moderate Resolution Imaging Spectroradiometer (MODIS), and the Global Land Surface Satellite (GLASS) [2-3]. The objective of this research is to calculate the monthly ET0 in arid climate by utilizing the parameters derived

from the MODIS sensor. Additionally, the accuracy of machine learning methods in estimating the monthly ET0 will be evaluated [2].

Material and Method

The current study used Ahvaz station as its agro-climatic site. Table 1 provides the climatic and locational attributes of the stated station. Figure 1 also exhibits the location maps of the stations under investigation. Ahvaz was defined as having a dry climate according to De marten's classification technique.

Table 1. Characteristics of the studied station

Station	latitude	Longitude	Height (m)	Climate
Ahvaz	31.3442°	48.7442°	22.5	Arid

In this research, the random forest (RF) and multi-layer perceptron (MLP) algorithms were utilized to estimate the monthly ET0 at Ahvaz station. The input parameters were chosen from the MODIS sensor spanning from 2005 to 2023. The training phase utilized 70% of the data, while the test phase utilized the remaining 30%. The parameters employed encompass land surface temperature (LST) and evapotranspiration index (ET). To assess the correctness of the input parameters and models, the estimated monthly ET0 was compared with the monthly ET0 calculated using the FAO-Penman-Monteth equation.

$$ET_0 = \frac{0.408\Delta(R_n - G) + \gamma \frac{900}{T_{min} + 273} U_2(e_s - e_a)}{\Delta + \gamma(1 + 0.34U_2)} \quad \text{Eq.1}$$

Where ET_0 is the reference evapotranspiration (mm d^{-1}), Δ is the slope of the saturation vapor pressure curve (kPa $°C^{-1}$) at the daily mean air temperature (°C), Rn and G are the net solar radiation and soil heat flux density (MJ m^{-2} d^{-1}), γ is the psychrometric constant (kPa $°C^{-1}$), T is the daily mean temperature (°C), U_2 is the mean wind speed (ms^{-1}), e_s is the saturation vapor pressure (kPa), and e_a is the actual vapor pressure (kPa) [3].

LST & ET MODIS

The MOD16A2 Version 6.1 Evapotranspiration product is an 8-day composite product with a 500 m pixel resolution. It uses the Penman-Monteith equation for data collection, incorporating daily meteorological reanalysis data and MODIS remotely sensed data. The MOD11A1 V6.1 product provides daily land surface temperature and emissivity values in a 1200 x 1200 km grid. The temperature value is derived from the MOD11_L2 swath product. Above 30 degrees latitude, some pixels may have multiple observations, with the pixel value being the average of all qualifying observations [3-4].

RF & MLP

Breiman (2001) was the first to propose the RF algorithm. RF is a machine learning algorithm that is based on decision trees. RF can be applied to both classification and regression tasks due to its simplicity and versatility. A decision tree is fitted to various subsets of training data. The advantage of RF is that it can estimate the importance of each input variable. The RF algorithm utilizes many input variables that may contribute to estimation.
Neural networks (NNs) are widely used machine learning models, leveraging the human brain's architecture to solve complex problems. ANNs consist of three layers: the input layer, one or more hidden layers, and the output layer. These layers are interconnected through neurons, with hidden layers assigned weights based on their connections to input variables. ANNs employ supervised and unsupervised learning processes, with supervised learning comparing anticipated output with known output to gain knowledge, and unsupervised learning not requiring relevant output knowledge. Multilayer Perceptron (MLP) is the most commonly used type of ANN for supervised learning, modeling complex nonlinear processes like drought. MLP is a type of Feedforward Neural Network (FFNN) with one or more hidden layers, and data transmission occurs exclusively in the forward direction [3]. In the current study, four performance indexes, including the coefficient of determination (R^2), the root mean square error (RMSE), and Nash–Sutcliffe efficiency (NS), are utilized to measure the model's accuracy [3].

Results

This study utilized three scenarios for both the RF and MLP models to estimate the monthly ET0 at Ahvaz station. These scenarios were based on remote sensing parameters obtained from MADIS. 1: The first scenario exclusively utilizes the LST index; 2: The second scenario solely relies on the ET index; and 3: The third scenario incorporates both the LST and ET parameters. Table 2 illustrates the accuracy of the MLP and RF models for estimating monthly ET0 at Ahvaz station. For the RF model, the R^2, RMSE, and NS values in the testing phase were

0.816-0.964, 0.424-0.838, and 0.662-0.914respectively. For the MLP model, the R^2, RMSE, and NS values in the testing phase were 0.902-0.973, 0.387-0.770, and 0.715- 0.928 respectively.

Discussion

Based on the results obtained, it was determined that scenario 3 (RF-3), which incorporates LST and ET, provides the most accurate estimation of monthly ET_0 using the RF model (R^2=0.964, RMSE=0.424, and NS=0.914). On the other hand, scenario 2 (RF-2) (R^2=0.816, RMSE=0.838, and NS=0.662), which only includes MODIS ET, exhibits the weakest performance. In the estimation of monthly ET0 with the MLP model, it was found that the best and worst scenarios are MLP-1 (R^2=0.973, RMSE=0.387, and NS=0.928) and MLP-2 (R^2=0.902, RMSE=0.770, and NS=0.715), respectively. Finally, by examining the results of both models, it was found that the MLP model has better accuracy than the RF model in all scenarios. Figure 1 displays the time series graph and scatter plot for the test phase of both RF and MLP models under the optimal scenario.

Table 2. Statistical results for Ahvaz station based on RF and MLP models

Model	R^2	RMSE (mm.momth^{-1})	NS
RF-1	0.955	0.457	0.899
RF-2	0.816	0.838	0.662
RF-3	0.964	0.424	0.914
MLP-1	0.973	0.387	0.928
MLP-2	0.902	0.770	0.715
MLP-3	0.968	0.410	0.919

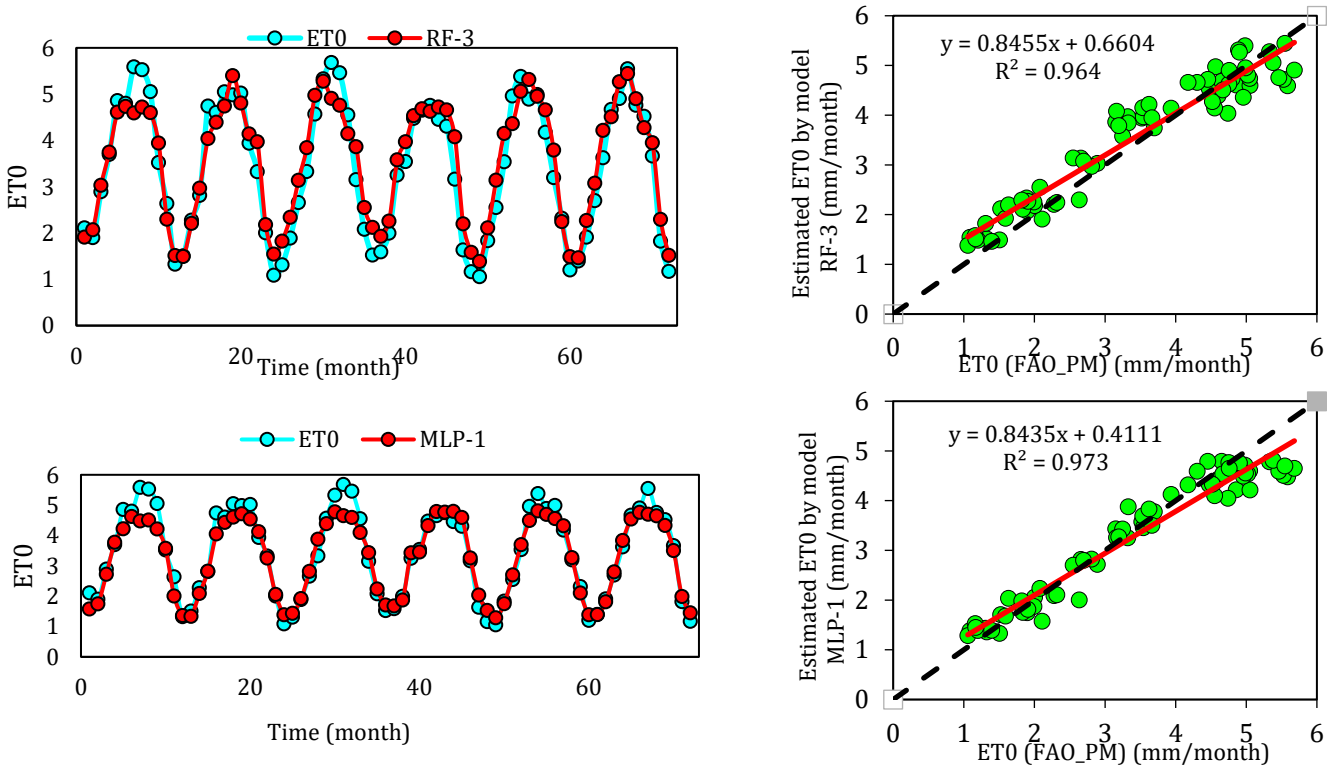


Figure 1. Scatter plots of the observed and estimated ET0 monthly values with RF and MLP models in Ahvaz station.

Conclusion

This study aimed to assess the accuracy of monthly ET0 estimation in an arid climate by utilizing remote sensing parameters obtained from MODIS sensors and machine learning models, specifically random forest (RF) and multi-layer perceptron (MLP) algorithms. The parameters employed encompass land surface temperature (LST) and evapotranspiration index (ET). The estimated monthly ET0 values were compared with the calculated monthly ET0 values using the FAO-Penman-Monteith equation. The RF model achieved R2, RMSE, and NS values of 0.964-0.816, 0.838-0.424, and 0.914-0.662 respectively during the testing phase. The MLP model achieved R2, RMSE, and NS values of 0.973-0.902, 0.770-0.387, and 0.928-0.715 respectively during the testing phase. The findings indicated that the MLP-1 model, which only incorporates one LST input parameter, demonstrated the highest level of accuracy in estimating monthly ET0. The model achieved an R2 value of 0.973, an RMSE value of 0.387, and an NS value of 0.928, signifying its superior performance. In the semi-arid region of Turkey, Yurtseven

and Serengil (2021) investigated the accuracy of the MLP, Support Vector Machine (SVM), RF, and Multiple Linear Regression (MLR) models for estimating ET0. They found that MLP and SVM models performed significantly better in semi-arid regions than other models, which is similar to our findings. To enhance the precision of the findings, it is advisable to employ hybrid machine learning models for estimating monthly ET0 in further research.

References

1. Tabari, H., & Hosseinzadeh Talaee, P. (2013). Multilayer perceptron for reference evapotranspiration estimation in a semiarid region. Neural Computing and Applications, 23(2), 341-348.
2. SUTARİYA, S., ANKUR, H., & TİWARİ, M. (2022). Development of Modeler for Automated Mapping of Land Surface Temperature Using GIS and LANDSAT-8 Satellite Imagery. International Journal of Environment and Geoinformatics, 9(2), 54-59.
3. Talebi, H., Samadianfard, S. & Kamran, K.V. (2023). Investigating the roles of different extracted parameters from satellite images in improving the accuracy of daily reference evapotranspiration estimation. Appl Water Sci 13, 59.
4. Yurtseven, I., & Serengil, Y. (2021). Comparison of different empirical methods and data-driven models for estimating reference evapotranspiration in semi-arid Central Anatolian Region of Turkey. Arabian Journal of Geosciences, 14(19), 1-28.

Advanced Engineering Days

aed.mersin.edu.tr

Artificial Intelligence (AI) in Agricultural Mechanization: A Mini Review

Reza Kheyri[*1]

[1]*University of Tabriz, Department of Biosystems engineering, Iran, Reza.kheiri@tabrizu.ac.ir*

Cite this study: Kheyri, R. (2024). Artificial Intelligence (AI) in Agricultural Mechanization: A Mini Review. Advanced Engineering Days, 9, 452-461

Keywords
Agricultural mechanization
Artificial Intelligence (AI)
Precision agriculture
Productivity
Food security

Abstract

The world population is increasing and demands for food subsequently. Agriculture is in the forefront to respond in this matter. To have sustainable food production, traditional agriculture should be changed. Mechanization is looking for new technologies to improve productivity in agricultural activities. Artificial Intelligence (AI) is the technology that its applications in agricultural mechanization were surveyed. Five major sectors were organized. They include agricultural machinery, irrigation systems, Unmanned Aerial Vehicles (UAVs), agricultural robots, and animal agriculture. This paper surveyed 74 articles from different databases to gather the relevant data. The published articles were found by considering the defined sectors as keywords. Assessing the reported results revealed that AI has numerous applications in agriculture. Each sector uses AI for different purposes and the employment rate is variable in regard to countries. Two UAVs and agricultural robots are the sectors, which have employed AI technology significantly. By using AI in machines and devices, the labor rate has decreased and precision enhanced. These two factors improve productivity and keep down production costs. Moreover, this paper disclosed tends to AI technology has increased and every year the number of farmers who want to have it on their farms went up. To conclude, this mini review determined that employing AI in agricultural mechanization provides AI-based machines and devices, which do the tasks rapidly and precisely. In this case, the traditional manners in agriculture are replaced with practical methods, which can manage the farms and produce agricultural products with the least workforce and cost.

Introduction

In many countries throughout the world, rapid urbanization, an increase in population, and economic development have increased the demands for food. It is part of the issue, but not the entire one, as the world population is growing, which has increased food waste. The United Nations FAO (Food and Agriculture Organization) states that the world population would increase by another 2 billion in 2050 while the additional land area under cultivation will only account to 4% at that time (Dharmaraj & Vijayanand, 2018). According to the 'Agriculture in 2050 Project', the world population will reach about 10 billion by 2050. Consequently, food production will require a 70% boost (Hunter et al., 2017). Agriculture is the bedrock of sustainability of any economy (Arun, 2017). In the past, agricultural activities were limited to food and crop production (Fan et al., 2012). Nevertheless, in the last two decades, it has evolved to processing, production, marketing, and distribution of crops and livestock products. The main concept of Artificial Intelligence (AI) in agriculture is its flexibility, high performance, accuracy, and cost-effectiveness (Eli-Chukwu, 2019). AI technology may be used to decrease the impact on natural ecosystems and improve worker safety, which would ultimately keep food prices low and ensure that the food production will keep pace with the increasing population (Eli-Chukwu, 2019). The field of AI with its rigorous learning capabilities have become a key technique for solving different agriculture related problems (Bannerjee et al., 2018). The application of computers in agriculture was first reported in 1983 (Baker et al., 1983). Although AI presents immense opportunities in agriculture application, there still prevails a deficiency in familiarity with advanced high tech machine learning solutions in farms around the world (Dharmaraj & Vijayanand, 2018). AI from improved data and understanding come improved predictions, enabling more optimal decisions about how to manage farm systems and stimulating the development of decision support and recommender systems (Smith, 2018). The traditional methods that were used by the farmers were not sufficient

to fulfill the requirements. AI in agriculture has brought an agriculture revolution (Talaviya et al., 2020). A direct application of AI or machine intelligence across the farming sector could act to be an epitome of shift in how farming is practiced today (Khandelwal & Chavhan, 2019). The major issue of AI is the numerous applications of this in agriculture, such as irrigation, weeding, and spraying with different sensors or other ways implanted in robots and drones. These technologies limit the use of water, pesticides, and herbicides, preserve soil fertility and help in the effective use of labor, resulting in increased output and quality (Sharma et al., 2023). The farmers to improve their farming skills and to update them as pre-disaster recovery for smart agri-food use AI. Furthermore, it will provide general and specific information about international markets relating to their crops (Junaid et al., 2021). AI is also helpful in reducing the waste that is derived from agricultural activities. Recent statistics indicate that 2.01 billion tonnes of municipal solid waste (MSW) were generated in 2016, which is projected to increase to 3.40 billion tonnes by 2050 (a Waste, 2018).

Agricultural mechanization is directly related to food production and many activities are done by this to respond the demands. Numerous activities have been done over decades. Nevertheless, there have always been gaps that have remained unfilled. In light of the significance of the problem, efforts focus on innovative technologies and/or methods. The emerging AI techniques are sought to be well-suited for application in agriculture (de Souza Melaré et al., 2017). AI is the study and application of computer systems and programs that can simulate human characteristics, including problem solving, learning, perception, understanding, reasoning, and awareness of situations. AI models, including fuzzy logic (FL), expert systems, genetic algorithms (GA), and artificial neural networks (ANN), can solve complicated mapping problems and forecast outcomes. (Yetilmezsoy et al., 2011). Any AI model or domain has a distinct purpose. These systems are efficient at handling complex processes and qualitative characteristics due to their clear linguistic syntax. (Yetilmezsoy et al., 2011). Machine learning and ANN are the most widely applied methods in studies related to automation in agriculture (Jha et al., 2019). AI is going to be able to investigate and assess particular processes in order to decrease and/or stop agricultural waste pollution due to its advancement. Moreover, AI has been extensively used in environmental engineering to address issues with air pollution, water and wastewater treatment modeling, ground water contamination, soil remediation simulation, and SWM strategy planning. (Yetilmezsoy et al., 2011).

This paper aims to survey articles and reported results about AI usages in agricultural mechanization. AI is widely used in agriculture in numerous activities. It is clear that there is a need to review articles that combine all research work conducted on AI applications in the different fields of agriculture. For this reason, this study was done to provide a mini review of AI in agricultural mechanization. This study also includes challenges and limitations facing the implementation of AI in agriculture, as well as AI-based activities' weaknesses.

Material and Method

Some specific fields in agriculture are being developed which are complementary to the food production chain. To realize the AI applications in these fields, the published articles were reviewed and analyzed. Digital technology advancements have brought about dramatic improvements in agriculture by enabling smart systems that can see, operate, and monitor a variety of farm operations in real-time with an intelligence comparable to that of human experts. AI in the development of smart farm machinery, irrigation systems, weed and pest control, fertilizer application, greenhouse cultivation, storage structures, drones for plant protection, crop health monitoring, etc. is being employed (Subeesh & Mehta, 2021). Mechanization converted agricultural activities that require days of human and animal labor draft into a few hours of activities. Mechanization is in the first stage in many developing countries. However, the attempts are expanded to drag other technologies into this area. An AI-powered ecosystem has tremendous potential to make farming practice more controlled and precise by introducing smarter applications (Subeesh & Mehta, 2021). To have clear information, the findings from reviews are organized in the following categories.

AI in agricultural machinery

To carry out a variety of agricultural tasks, modern farmers employ a number of machines and equipment. Farm mechanization has tremendous potential for maximizing farmer labor and increasing crop yields. Tractors are regarded as the most important and unique farm power among them. Tractors are without a doubt a crucial component of farm mechanization and continuously contribute to the daily increase in agricultural output. The tractor-implement system's performance monitoring is an essential component of the agricultural mechanization system. Many indexes on agricultural machines have an intensive potential to be automatized. The third agricultural revolution, often known as the "Green Revolution," began in the 1930s and lasted until the 1960s. During this period, advances in agricultural machinery and the use of pesticides and mineral fertilizers to improve crops were developed (Bochtis et al., 2018). The fourth agricultural revolution occurred during the past two decades, in which there was a significant development in information communication technology (ICT) and AI (Said Mohamed et al., 2021). AI can help operators with running these machines productively and precisely. We can confirm the use of the machinery and calculate the operational costs by measuring the work area of agricultural machines. To develop agriculture, an automatic solution that calculates the work area precisely using

smart technologies and algorithms is essential. AI that records the movement of agricultural machinery and uses it to measure the precise work area of its use (Waleed et al., 2020). The use of the machinery and calculating the operational costs can be confirmed by measuring the work area of agricultural machines. When the task is done consistently throughout the field, the AI algorithms perform well at computing the areas of regular and irregular shapes. Nevertheless, when the field is not evenly covered or when machinery is only utilized at the boundaries, its precision decreases. The use of AI techniques surely reduces the chances of making errors as well as a great help in making critical decisions (Murase, 2000). AI techniques for monitoring the health of agricultural vehicles which can be economically utilized on smartphones instead of expensive Internet of Things (IoT) sensors (Gupta et al., 2020). Big agricultural companies are on the train of developing autonomous tractors, and have integrated many systems such as the machine sync systems, AutoTrack vision, and the AutoTrac row sense system (Burnett et al., 2019). These systems provide remote equipment control for farmers, resulting in increased productivity and precision. Even with autonomous farming vehicles, humans still need to continue to keep monitoring their performance and identify issues with their many attachments. Recent advancements in the In-build display tutorial can result in minimizing the downtime and increasing productivity on large scale farming operations (Gupta et al., 2020).The role of an IT-based smartphone computing system, which consists of expensive sensors and related signal processing equipment, for continual indications of component condition and alarms is quite limited and usual. (Ganguly et al., 2017). It belongs to vibration monitoring, acoustics analysis, oil analysis, tribology, thermography, process parameter monitoring, visual inspections of battery, fuel, air filter clog, engine temperature and other nondestructive testing techniques (Gupta et al., 2019). By going through the results, it becomes understandable that AI plies an undeniable role in agricultural mechanization. To raise productivity in agriculture, this technology is one of the priorities and many countries try to employ it gradually. Nonetheless, there is a need to do experiments and disclose ambiguities to define it as a reliable technology.

AI in irrigation systems

Agriculture is completely related to water sources. As there are shortages in water sources, utilizing new and precise methods is vital. To this aim, AI is suggested. This technology focuses on the new approaches regarding smart farming (SF). The smart irrigation system includes sensors for monitoring water level, irrigation efficiency, climate, etc. Smart irrigation is based on smart controllers and sensors as well as some mathematical relations (Said Mohamed et al., 2021). Developing the agricultural industry with new technology is a major concern for enhancing the country's economy (Mohamed et al., 2016). The application of AI and IoT in cyber-physical farm management is the foundation of smart agricultural technology (Bacco et al., 2019). Precision agriculture's primary goal is to increase spatial management strategies in order to both prevent pesticide and fertilizer overuse and boost crop yield (Amato et al., 2015). Since it determines the irrigation schedule, the estimation of reference evapotranspiration (ETo) is one of the crucial crop irrigation parameters (Cruz-Blanco et al., 2014). The most popular model for predicting evapotranspiration is the Penman-Monteith (PM) model, although it requires a lot of data to get reliable ET estimations (Shitu et al., 2018). Due to GIS's integration with AI, GPS, remote sensing, and other technologies, a substantial amount of water that would otherwise be required for irrigation could be saved (Mohd et al., 2014). An AI-based irrigation system's ability to visualize the outcomes and provide real-time information is one of its most important features. One of the new emerging layers of the AI system is the smart sensor in the industry of agriculture. The smart sensor in the field of agriculture is a need for countries which are having a water scarcity, as well as growing countries that take irrigation to the next level with the help of technology (Divya & Chinnaiyan, 2019). This device is also one of the kinds that is exclusively made to monitor the plants, to yield the better crops, and help in the conservation of the water. A smart platform that manages the components of an automatic precision irrigation system determines the amount of water to be supplied in each cell of the field by integrating geographic, meteorological and soil data, as well as the vegetation map obtained from an aerial survey and the technical specifications of the irrigation machine (Aleotti et al., 2018). This technology improves the fertility of the soil and optimizes the used water, also helping in improving productivity, quality, and efficient manpower (Anil Chougule & Mashalkar, 2022). The most simple system for AI-based irrigation consists of a moisture sensor, a pump, and a microcontroller. A soil moisture sensor measures the soil's moisture content and uses a microcontroller to initiate a pump when the soil's moisture content drops below a predetermined level (Biswas et al., 2021). An AI-based system can give enough information on crop yields early on, and the smart irrigation management system that goes with it can help farmers use resources like water and energy efficiently (Sinwar et al., 2020). The surveyed findings about AI-based irrigation systems explicitly explained its framework. Approaches to this technology are positive and increasing. To have a sustainable agriculture in the future, it is essential to change the traditional irrigation systems and develop new methods that are more productive, as well as IoT and AI.

AI in Unmanned Aerial Vehicles (UAV)

In agriculture, Unmanned Aerial Vehicles (UAVs) are quickly replacing satellites and other aircraft. UAVs were originally intended for military use for surveillance. Whereas satellites and aircraft need high altitudes, cloud penetration, and other characteristics to permit clear photography, UAVs can get high-quality photographs at affordable costs. UAVs operate at lower altitudes, making it easier for them to capture precise photographs. The number of UAVs employed in agriculture is rising rapidly. They can accomplish a number of tasks, including livestock applications, irrigation, weed detection, harvesting, and spraying of agricultural pests (Said Mohamed et al., 2021). For agricultural applications, regularized smart-farming solutions are being considered, including the use of UAVs. The agricultural UAVs are highly capable, and their use has expanded across all areas of agriculture, including pesticide and fertilizer spraying, seed sowing, and growth assessment and mapping (Kim et al., 2019). UAVs have significantly reduced working hours, resulting in increased stability, measurement accuracy, and productivity. UAVs are not only less expensive than most other agricultural machines, they are also easily operated. Moreover, their applications have contributed to the expansion of many areas of agriculture; including, insecticide and fertilizer prospecting and spraying, seed planting, weed recognition, fertility assessment, mapping, and crop forecasting (Sharma, 2021). Like other industries, the agricultural sector has sought innovation by utilizing convergence technologies. UAVs have proven to be highly utilized throughout the agriculture sector. However, agricultural UAVs face numerous technical limitations, such as battery efficiency, low flight time, communication distance, and payload (von Bueren et al., 2015), (Torun, 2000). There are two primary types of UAV platforms: fixed- and rotary-wing. A fixed-wing UAV is similar in appearance to an airplane. It flies via thrust and aerodynamic lifting force. A fixed-wing UAV is typically larger than a rotary-wing model and is used mainly for spraying and photography over a wide range (Li & Yang, 2012). Rotary-wing UAVs can be classified into helicopter and multi-rotor types. They are widely used for spraying and aerial photography (Bernard & Kondak, 2009). Multi-rotor models are named based on the numbers of rotors they possess, such as 'quadcopter,' meaning four rotors (Gómez-Candón et al., 2014).

Octocopters, helicopter types, and fixed-wing types have the largest payload capacities (9.5 kg) and are mainly used for spraying (Dai et al., 2017). Hexacopters and quadcopters are more compact and have a payload capacity of only 1.25–2.6 kg. They are used for reconnaissance and mapping (Özaslan et al., 2016). Fixed- and rotary-wing UAVs have the largest payload (23 kg), followed by the helicopter-type (22 kg) (Kim et al., 2019). These UAVs are equipped with other systems as well as the Global Navigation Satellite System (GNSS) to control them remotely. Nowadays, agricultural UAVs operate in a variety of settings and carry out a wide range of duties. The need for them is growing, and they are utilized in fields, orchards, and rice paddies. The 2D or 3D maps taken by UAVs from agricultural land can provide valuable data. For example, the area of the farmland, soil conditions, and status of the crops can be used to model enhancements and efficiencies (Torres-Sánchez et al., 2014).

There are many advantages to using UAVs in agriculture:

- UAVs can typically land on the edge of cultivated land and do not require a navigation station or specialized airport. In spraying activities, this additionally reduces the no-load flight rate.
- Quick maneuverability is a characteristic shared by rotary wing aircraft, but fixed wing aircraft are also capable of a short turning radius, a quick rate of ascent, and strong performance at extremely low altitudes.
- They are suitable for working in rough terrain and small plots with high efficiency.
- They exhibit lower operational costs due to their reduced flight crew requirements, low labor intensity, and simple maintenance in comparison to traditional manned aircrafts (Del Cerro et al., 2021).

Drone usage in agriculture is increasing for all of these reasons. Therefore, developing AI usages in agricultural activities can guarantee sustainable agriculture in the future.

AI in Agricultural Robots

Many of the younger generations have distanced themselves from agricultural activities due to a lack of knowledge, experience, and challenges related to agriculture. This will surely create concerns about the production of food in the future and its requirements. But new technologies could change traditional agriculture and these days a lot of work is being done by young scientists and engineers to make agriculture simple, smart, economical, productive, time-efficient, sustainable, and contribute to a wealthy and healthy society. Ground and aerial robots combined with AI techniques have the potential to tackle the rising food, fiber, and fuel demands of the rapidly growing population that is slated to be around 10 billion by the year 2050 (Pitla et al., 2020). Robotics has become at the forefront of technological innovation due to increasing demands for productivity, the elimination of tedious tasks, and safety for both the environment and the operator. The same holds true with agricultural robots, which are able to make farming safer, easier, and more profitable for farmers while also producing products of greater quality that have less of a detrimental impact on the environment (Fountas et al., 2022). Combining agricultural robots with digital agriculture techniques is thought to be a useful way to monitor large areas in order to evaluate crop conditions, manage crop inputs more precisely in rows, allow for efficient

harvesting in specialty crops, assess high yielding and resource-efficient crop varieties of research plots, and manage livestock more effectively (Chen, 2018). The demand for automation in the rapidly evolving agricultural equipment industry is moving towards the deployment of large autonomous vehicles. With the continual increase in engine power and the size of manned equipment, there is concern associated with removing the human operator from the field environment-safety and liability. Liability of large autonomous machinery is a driving factor for thinking small. In the event of a malfunction or collision, small Unmanned Ground Vehicles (UGVs) could cause less damage compared to an UGV with a high gross vehicle weight. The concept of replacing conventional large agricultural machines with multiple small-to-medium-sized UGVs is feasible given the advances in autonomous technologies (Blackmore et al., 2004).

One of the most labor-intensive and exhausting agricultural tasks is weeding, which can be done in two ways: mechanically (with blades, fire, etc.) or by spraying chemicals on the plants and weeds. The robotization of these processes enabled mechanical weeding and spot spraying to become widely accepted. The second one being the more challenging as it requires the recognition of the crop in order not to damage it (Fountas et al., 2022). The robotic system requires a visual system in order to identify and distinguish between weeds and crops. Therefore, most weeding robots are equipped with a vision sensor (Champ et al., 2020). Besides the hardware component, software, and specifically AI, plays a crucially important role, as robotic weeding systems need to recognize objects of interest prior to executing any task (Zhang et al., 2012). Summing up, weed detection is a task where vision-based perception and AI systems perform more than adequately in combination.

One of the most vital tasks growers do is crop scouting, which is occasionally disregarded because it frequently goes hand in hand with other duties like weeding, spraying, etc. Depending on the trait under investigation, different visual technologies are employed. Common devices used are color cameras (Yamasaki et al., 2022). Various sensors measuring plant light reflectance, such as IR radiometers and OptRX sensors, and stereo cameras (Fernández-Novales et al., 2021). As long as the sensors are factory calibrated, the measurements they provide could be used in real time. To conclude, these systems have excessive potential regarding crop scouting as most of the attributes related to plant health and status can be visually detected in visible, NIR, and IR regions (Fountas et al., 2022).

Phenotyping, Disease/Insect/Deficiency Detection are other aspects that AI is capable of playing a role in. Numerous robotic phenotyping technologies are available to precisely measure many traits. Machine vision holds the ability to totally automate phenotyping because most plant traits may be measured only through visual information. Existing solutions have already been to detect disease and insects to the fullest the available AI algorithms such as Neural Networks (Durmuş et al., 2017). As not all obstructed symptoms can be identified in the visible spectrum, most of them use color cameras; however, some systems use extra vision sensors, such as RGB-D and spectral cameras, to improve detection rates and accuracy (Karpyshev et al., 2021). The AI-based devices have considerable potential to utilize in phenotyping, disease, insect, and deficiency applications. By employing these devices, the precision rate increases and required costs goes down.

Applying sprays is the conventional method used in agriculture to combat harvest losses. During a crop season, a farmer's primary spraying tasks include controlling weeds, managing pests, and preventing diseases in order to preserve the majority of the harvested crop.

Conventional spraying methods have been shown to be extremely detrimental to the environment because of their consistent application technique. At the moment, the spraying rate is independent of the stage of plant growth and the presence of disease or weeds (Fountas et al., 2022). The problems that most researchers are focusing on are spraying based on disease detection and plant and weed presence (Zaidner & Shapiro, 2016). Additionally, some researchers are trying to optimize the robot's operation by calculating the optimal air assistance for maximum penetration based on the plant volume (Malneršič et al., 2016). The findings are quite encouraging since, under highly favorable circumstances for one of the trials, spraying regulation by a robot has been shown to be so effective that chemical reduction can be decreased by up to 95% (Berge et al., 2012).

Agricultural robotic harvesting has received increased attention to tackle the harvesting problems (Lv et al., 2019). The vision system is the most essential part of a robotic harvester, since it gives the harvesting components important details about the fruit that they detect. The majority (94%) of the methodologies are based on the color information derived from an RGB camera. For fruit detection, image processing based on color indexes is the most applied method in research papers (SepúLveda et al., 2020). Researchers often use non-linear operations like gamma-correction or blurring and morphological operations, among others (Gai et al., 2021), but also use transformations to alternative color spaces (Hayashi et al., 2014) to have better control of the lightness dimension.

AI in Animal Agriculture

Robots or automated systems currently are used in the dairy industry include Automated Milking System (AMS), feeding systems, teat sprayers, calf feeders, and hoofbaths. In order to solve the problems related to the animal industry, a preemptive future response strategy is needed to cope with climate change, improve productivity, improve animal welfare, improve animal food nutritional quality, and prevent animal diseases (Lee, 2022). Recent developments in AI, computer vision, and remote sensing have assisted in the development of

innovative livestock biometrics technologies that extract important physiological data related to animal welfare (Dunshea et al., 2022). Recent innovations in digital technology have made it possible to potentially automate and integrate various methods for assessing animal welfare. These methods include sensor networks with IoT connectivity, remote sensing, computer vision, and AI for agricultural and human-based applications (Morota et al., 2018). For example, to assess the body temperature of cattle continuously, an invasive method for dairy cows by implanting a Radio Frequency Identification (RFID) biosensor on the lower part of the ears is used (Chung et al., 2020). In addition, contactless methods to assess skin temperature, HR and RR of dairy cows using remote sensing cameras and computer vision analysis are employed (Jorquera-Chavez et al., 2019). Using AI technology to improve animal feeding has become an essential approach in maximizing the effectiveness of animal feeding. To implement intelligent animal feeding programs to improve the effect of animal feeding, it has become a mainstream measure to predict the metabolic energy through AI technology, and then provide a reference for animal feed proportioning design (Wang et al., 2023). The process of predicting an animal's metabolic energy using AI in order to help in the proportioning of animal feed is known as intelligent metabolic energy prediction. AMS, often known as robotic dairy farms, are the outcome of utilizing the newest robotics technology to boost milk production via automation and enhanced efficiency (Hostiou et al., 2017). Implementation of AI in dairy farms will require minimal technological additions, automated gates, and cooling systems. A useful application of AI that makes use of comprehensive data from a robotic dairy farm to help small and medium-sized dairy farms become more competitive in a global market that is becoming more and more demanding (Fuentes et al., 2020). The emerging technologies of biometric identification are extensively applied for recognition via skin impression, face features, or eye retina patterns. Animals are currently the subject of biometric recognition technology applications. Muzzle pattern detection of cattle has shown amazing results. Nowadays, they are being used to muzzle pattern image scanning for biometric identification. Animal recognition via muzzle pattern image for different applications has been proliferating gradually (Ahmad et al., 2023). AI has helped develop new and emerging technologies for livestock biometrics to extract key physiological parameters associated with animal welfare (Dunshea et al., 2022). These applications are the most intended uses of AI in animal agriculture. However, they may be developed in regard to the needs for more productivity and precision in different countries. In conclusion, the dependency between AI and animal agriculture is going to increase in the near future.

Results and Discution

To realize the AI applications in agricultural mechanization, many articles and reports from various sources were surveyed. Five major categories were organized. These fundamental sectors in agriculture are agricultural machinery, irrigation systems, Unmanned Aerial Vehicles (UAV), agricultural robots, and animal agriculture. By surveying, it was found that the numbers related to AI in agriculture have been increased specifically in recent decades. Responding to the demands for food by improving productivity was the main reason to utilize AI in agriculture more and more. However, other reasons, as well as precision agriculture, environment protection, real-time detection, decreasing in costs, increasing productivity, predicting and preventing, diagnosing, etc. exist for this aim. In general, all farmers know exactly that the traditional methods for producing any product on farms are not satisfying, while the new technologies are capable of doing a lot of tasks rapidly and accurately. Moreover, to compete with opponents across the world, they should change their strategies.

AI in agricultural machinery wants to decrease the dependency on labor. To this aim, many companies equip their products with computer devices, where these devices can control and monitor any machine such as a person. Employing AI-based devices in agricultural machines is for improving productivity and following the food production rate. It is clear that machines are the fundamental needs in agriculture and mechanization is directly dependent on machines. Automated processes in agricultural activities, which use the least human labor, are the main purpose of AI in agricultural machines. The reviewed articles determined the over growth in the number of reports in recent decades about AI in agricultural machinery. Calculating the operational costs, measuring the work area, monitoring the health of the agricultural vehicles, diagnosing the problems with various attached equipment, minimizing the downtime, increasing productivity, and precision agriculture are the most important goals for developing AI in agricultural machinery by companies and farmers.

Irrigation systems are the second major section in agriculture that necessarily should be improved in regard to water resource protection. The crop yield completely interdepends irrigation systems. AI in these systems provides so much productivity and, in this case, the water waste ratio reduces. The surveyed results disclosed the main purpose of expanding AI-based technologies or devices in agricultural irrigation systems is smart or precision irrigation. AI follows these approaches in irrigation; providing real-time information, smart irrigation is a need for countries which are having a water scarcity, monitoring the plants to yield the better crops, and helps in the conservation of the water. Furthermore, determining the amount of water to be supplied in each cell of the field by integrating geographic, meteorological and soil data, improving the fertility of the soil and optimizing the used water, and improving the judicious use of essential resources such as water and energy for agriculture.

The number of UAVs employed in agriculture is rising rapidly. This paper reveled UAVs' quiddity and applications by surveying reports randomly from various databases. Harvesting, seedling, weed detection,

irrigation, spraying of agricultural pests, livestock applications are their predominant usages in agriculture. Regularizing smart-farming is considered with the use of UAVs. Significantly reduced working hours, increased stability, measurement accuracy, and productivity are the highlighted benefits of UAVs in agriculture. These intelligent machines are not only less expensive than most other agricultural machines, but they are also easy to operate. Technical limitations such as battery efficiency, low flight time, communication distance, and payload are UAVs' weaknesses. Fixed- and rotary-wing are two types of UAVs. Farmers can get useful information which derives from 2D or 3D maps of an agricultural field made by UAVs.

Many efforts are being made to improve agriculture's efficiency, economy, productivity, time management, sustainability, and ability to support a wealthy and healthy society. Robotics is at the forefront of technological progress because of the needs for increased productivity, the elimination of boring labor, and environmental and operator safety. Agricultural robots with digital agriculture techniques re a useful way to monitor large areas. Spraying chemicals and mechanically destroying are two major methods for weeding. The Robotization does both mechanical weeding and spot spraying. To recognize and distinguish crops from weeds, a vision system is required for the robotic systems. AI makes this crucial task as robotic weeding systems need to recognize. Crop scouting is the task that robots in agriculture do by contributing with AI. IR radiometers, OptRX sensors, and stereo cameras have excessive potential in regard to crop scouting. Phenotyping, Disease/Insect/Deficiency Detection are other aspects that AI plays a role in. Machine vision holds the ability to totally automate phenotyping. Color and thermal cameras as well as RGB-D sensors are the AI-based devices that have considerable potential to be utilized in phenotyping, disease, insect, and deficiency applications. A robotic harvester is the vision system that provides critical information about the fruit detected as required by the harvesting components. An RGB camera detects fruit color and often non-linear operations like gamma-correction or blurring and morphological operations were used together with it.

AMS, feeding systems, teat sprayers, calf feeders, hoofbaths are the activities which can be done by AI-based systems. AMS related to robotics increases milk yield. Livestock biometrics to extract key physiological parameters associated with animal welfare is the most important use of AI in animal agriculture. Assessing the body temperature is an example of this usage. Muzzle pattern image scanning is the most well known system for biometric identification. It is applied for recognition via skin impression, face features, or eye retina patterns. To improve the effect of animal feeding, AI technology has become a necessary measure. Measuring the metabolic energy through AI technology provides a reference for animal feed proportioning design.

AI has become a pioneer technology in agriculture and there are numerous purposes for using it. However, improving productivity and following that, reaching food security is the all users' intention. In the assessed sectors, it was shown the advantages outweigh the disadvantages. Anyhow, reliability tests should be done to define it as a standard technology. In addition, educational courses are essential for operators before starting to work with AI-based machines and devices. Encouraging farmers to change their traditional methods in the way to produce agricultural products, when it is possible that they can have a replacement which is not more expensive than the previous systems. For this reason, companies must consider the costs when designing AI-based appliances.

Conclusion

In conclusion, during this mini review, AI applications in agricultural mechanization were surveyed. It determined the main purpose of employing AI in agricultural mechanization is responding to food demands or, in other words, reaching for food security. The published articles in different databases were reviewed to gather data. For categorizing the agricultural activities, five sectors were organized. They include agricultural machinery, irrigation systems, Unmanned Aerial Vehicles (UAV), agricultural robots, and animal agriculture. Each sector uses AI in different ways and this rate is variable regarding countries. The reported results showed two UAVs and agricultural robots are the sectors which have employed AI technology significantly. Precision agriculture is an achievement that is presented in these sectors with AI help. Moreover, this paper disclosed tends to this technology are increasing and every year the number of farmers which want to have it in their farms is going up. Generally, the findings demonstrate that with the increasing world population, the needs for food steeply increase. To cope with this unavoidable growth, the traditional agriculture should be changed. Mechanization is the process that is responsible for improving productivity in agriculture. This sector is looking for any technologies to do its task perfectly. In recent decades, it has focused on AI. By using AI in machines and devices, the labor rate has decreased and precision enhanced. These two factors led to improved productivity and decreased production costs. Finally, it has been proven to make food security traditional manners must be replaced with new techniques.

References

A Waste, W. (2018). 2.0: A Global Snapshot of Solid Waste Management to 2050. *Urban Development. Available online: https://elibrary. worldbank. org/doi/pdf/10.1596/978-1-4648-1329-0 (accessed on 26 May 2021)*.

Ahmad, M., Abbas, S., Fatima, A., Ghazal, T. M., Alharbi, M., Khan, M. A., & Elmitwally, N. S. (2023). AI-Driven livestock identification and insurance management system. *Egyptian Informatics Journal*, *24*(3), 100390. https://doi.org/https://doi.org/10.1016/j.eij.2023.100390

Aleotti, J., Amoretti, M., Nicoli, A., & Caselli, S. (2018, 13-15 Sept. 2018). A Smart Precision-Agriculture Platform for Linear Irrigation Systems. 2018 26th International Conference on Software, Telecommunications and Computer Networks (SoftCOM),

Amato, F., Havel, J., Gad, A.-A., & El-Zeiny, A. M. (2015). Remotely Sensed Soil Data Analysis Using Artificial Neural Networks: A Case Study of El-Fayoum Depression, Egypt. *ISPRS International Journal of Geo-Information*, *4*(2), 677-696.

Anil Chougule, M., & Mashalkar, A. S. (2022). Chapter Ten - A comprehensive review of agriculture irrigation using artificial intelligence for crop production. In K. Kumar, G. Kakandikar, & J. P. Davim (Eds.), *Computational Intelligence in Manufacturing* (pp. 187-200). Woodhead Publishing. https://doi.org/https://doi.org/10.1016/B978-0-323-91854-1.00002-9

Arun, B. (2017). Indian agriculture-status, importance and role in Indian economy. *Journal for Studies in Management and Planning*, *3*(12), 212-213.

Bacco, M., Barsocchi, P., Ferro, E., Gotta, A., & Ruggeri, M. (2019). The Digitisation of Agriculture: a Survey of Research Activities on Smart Farming. *Array*, *3-4*, 100009. https://doi.org/https://doi.org/10.1016/j.array.2019.100009

Baker, D. N., Lambert, J. R., & McKinion, J. M. (1983). GOSSYM: a simulator of cotton crop growth and yield.

Bannerjee, G., Sarkar, U., Das, S., & Ghosh, I. (2018). Artificial intelligence in agriculture: A literature survey. *International Journal of Scientific Research in Computer Science Applications and Management Studies*, *7*(3), 1-6.

Berge, T. W., Goldberg, S., Kaspersen, K., & Netland, J. (2012). Towards machine vision based site-specific weed management in cereals. *Computers and Electronics in Agriculture*, *81*, 79-86. https://doi.org/https://doi.org/10.1016/j.compag.2011.11.004

Bernard, M., & Kondak, K. (2009). Generic slung load transportation system using small size helicopters. 2009 IEEE International Conference on Robotics and Automation,

Biswas, S., Sharma, L. K., Ranjan, R., Saha, S., Chakraborty, A., & Banerjee, J. S. (2021). Chapter 20 - Smart farming and water saving-based intelligent irrigation system implementation using the Internet of Things. In S. Bhattacharyya, P. Dutta, D. Samanta, A. Mukherjee, & I. Pan (Eds.), *Recent Trends in Computational Intelligence Enabled Research* (pp. 339-354). Academic Press. https://doi.org/https://doi.org/10.1016/B978-0-12-822844-9.00043-8

Blackmore, B., Fountas, S., Vougioukas, S., Tang, L., Sørensen, C., & Jørgensen, R. (2004). A method to define agricultural robot behaviours. Automation Technology for Off-Road Equipment Proceedings of the 2004 Conference,

Bochtis, D., Sorensen, C. A. G., & Kateris, D. (2018). *Operations management in agriculture*. Academic Press.

Burnett, K., Samavi, S., Waslander, S., Barfoot, T., & Schoellig, A. (2019). autotrack: A lightweight object detection and tracking system for the sae autodrive challenge. 2019 16th Conference on Computer and Robot Vision (CRV),

Champ, J., Mora-Fallas, A., Goëau, H., Mata-Montero, E., Bonnet, P., & Joly, A. (2020). Instance segmentation for the fine detection of crop and weed plants by precision agricultural robots. *Applications in plant sciences*, *8*(7), e11373.

Chen, G. (2018). *Advances in agricultural machinery and technologies*. CRC Press.

Chung, H., Li, J., Kim, Y., Van Os, J. M. C., Brounts, S. H., & Choi, C. Y. (2020). Using implantable biosensors and wearable scanners to monitor dairy cattle's core body temperature in real-time. *Computers and Electronics in Agriculture*, *174*, 105453. https://doi.org/https://doi.org/10.1016/j.compag.2020.105453

Cruz-Blanco, M., Lorite, I. J., & Santos, C. (2014). An innovative remote sensing based reference evapotranspiration method to support irrigation water management under semi-arid conditions. *Agricultural Water Management*, *131*, 135-145. https://doi.org/https://doi.org/10.1016/j.agwat.2013.09.017

Dai, B., He, Y., Gu, F., Yang, L., Han, J., & Xu, W. (2017, 5-8 Dec. 2017). A vision-based autonomous aerial spray system for precision agriculture. 2017 IEEE International Conference on Robotics and Biomimetics (ROBIO),

de Souza Melaré, A. V., González, S. M., Faceli, K., & Casadei, V. (2017). Technologies and decision support systems to aid solid-waste management: a systematic review. *Waste management*, *59*, 567-584.

del Cerro, J., Cruz Ulloa, C., Barrientos, A., & de León Rivas, J. (2021). Unmanned Aerial Vehicles in Agriculture: A Survey. *Agronomy*, *11*(2).

Dharmaraj, V., & Vijayanand, C. (2018). Artificial intelligence (AI) in agriculture. *International Journal of Current Microbiology and Applied Sciences*, *7*(12), 2122-2128.

Divya, R., & Chinnaiyan, R. (2019, 2019//). Reliable AI-Based Smart Sensors for Managing Irrigation Resources in Agriculture—A Review. International Conference on Computer Networks and Communication Technologies, Singapore.

Dunshea, F. R., Fuentes, S., Gonzalez Viejo, C., & Tongson, E. (2022). The livestock farming digital transformation: implementation of new and emerging technologies using artificial intelligence. *Animal Health Research Reviews*, *23*(1), 59-71. https://doi.org/10.1017/S1466252321000177

Durmuş, H., Güneş, E. O., & Kırcı, M. (2017). Disease detection on the leaves of the tomato plants by using deep learning. 2017 6th International conference on agro-geoinformatics,

Eli-Chukwu, N. C. (2019). Applications of artificial intelligence in agriculture: A review. *Engineering, Technology & Applied Science Research*, *9*(4).

Fan, M., Shen, J., Yuan, L., Jiang, R., Chen, X., Davies, W. J., & Zhang, F. (2012). Improving crop productivity and resource use efficiency to ensure food security and environmental quality in China. *Journal of experimental botany*, *63*(1), 13-24.

Fernández-Novales, J., Saiz-Rubio, V., Barrio, I., Rovira-Más, F., Cuenca-Cuenca, A., Santos Alves, F., Valente, J., Tardaguila, J., & Diago, M. P. (2021). Monitoring and mapping vineyard water status using non-invasive technologies by a ground robot. *Remote Sensing*, *13*(14), 2830.

Fountas, S., Malounas, I., Athanasakos, L., Avgoustakis, I., & Espejo-Garcia, B. (2022). AI-Assisted Vision for Agricultural Robots. *AgriEngineering*, *4*(3), 674-694.

Fuentes, S., Gonzalez Viejo, C., Cullen, B., Tongson, E., Chauhan, S. S., & Dunshea, F. R. (2020). Artificial Intelligence Applied to a Robotic Dairy Farm to Model Milk Productivity and Quality based on Cow Data and Daily Environmental Parameters. *Sensors*, *20*(10).

Gai, J., Xiang, L., & Tang, L. (2021). Using a depth camera for crop row detection and mapping for under-canopy navigation of agricultural robotic vehicle. *Computers and Electronics in Agriculture*, *188*, 106301.

Ganguly, K., Gulati, A., & von Braun, J. (2017). Innovations spearheading the next transformations in India's agriculture.

Gómez-Candón, D., De Castro, A., & López-Granados, F. (2014). Assessing the accuracy of mosaics from unmanned aerial vehicle (UAV) imagery for precision agriculture purposes in wheat. *Precision Agriculture*, *15*, 44-56.

Gupta, N., Khosravy, M., Patel, N., Dey, N., Gupta, S., Darbari, H., & Crespo, R. G. (2020). Economic data analytic AI technique on IoT edge devices for health monitoring of agriculture machines. *Applied Intelligence*, *50*(11), 3990-4016. https://doi.org/10.1007/s10489-020-01744-x

Gupta, S., Khosravy, M., Gupta, N., & DARBARI, H. (2019). In-field failure assessment of tractor hydraulic system operation viapseudospectrum of acoustic measurements. *Turkish Journal of Electrical Engineering and Computer Sciences*, *27*(4), 2718-2729.

Hayashi, S., Yamamoto, S., Saito, S., Ochiai, Y., Kamata, J., Kurita, M., & Yamamoto, K. (2014). Field operation of a movable strawberry-harvesting robot using a travel platform. *Japan Agricultural Research Quarterly: JARQ*, *48*(3), 307-316.

Hostiou, N., Fagon, J., Chauvat, S., Turlot, A., Kling, F., Boivin, X., & Allain, C. (2017). Impact of precision livestock farming on work and human-animal interactions on dairy farms. A review. *Bioscience, Biotechnology and Biochemistry*, *21*, 1-8.

Hunter, M. C., Smith, R. G., Schipanski, M. E., Atwood, L. W., & Mortensen, D. A. (2017). Agriculture in 2050: recalibrating targets for sustainable intensification. *Bioscience*, *67*(4), 386-391.

Jha, K., Doshi, A., Patel, P., & Shah, M. (2019). A comprehensive review on automation in agriculture using artificial intelligence. *Artificial Intelligence in Agriculture*, *2*, 1-12.

Jorquera-Chavez, M., Fuentes, S., Dunshea, F. R., Warner, R. D., Poblete, T., & Jongman, E. C. (2019). Modelling and Validation of Computer Vision Techniques to Assess Heart Rate, Eye Temperature, Ear-Base Temperature and Respiration Rate in Cattle. *Animals*, *9*(12).

Junaid, M., Shaikh, A., Hassan, M. U., Alghamdi, A., Rajab, K., Al Reshan, M. S., & Alkinani, M. (2021). Smart agriculture cloud using AI based techniques. *Energies*, *14*(16), 5129.

Karpyshev, P., Ilin, V., Kalinov, I., Petrovsky, A., & Tsetserukou, D. (2021). Autonomous mobile robot for apple plant disease detection based on cnn and multi-spectral vision system. 2021 IEEE/SICE international symposium on system integration (SII),

Khandelwal, P. M., & Chavhan, H. (2019). Artificial intelligence in agriculture: An emerging era of research. *Research Gate Publication*.

Kim, J., Kim, S., Ju, C., & Son, H. I. (2019). Unmanned Aerial Vehicles in Agriculture: A Review of Perspective of Platform, Control, and Applications. *IEEE Access*, *7*, 105100-105115. https://doi.org/10.1109/ACCESS.2019.2932119

Lee, A. J. (2022). The Smart Ways of Adoption IoT and AI for Sustainable Animal Agriculture.

Li, X., & Yang, L. (2012). Design and implementation of UAV intelligent aerial photography system. 2012 4th International Conference on Intelligent Human-Machine Systems and Cybernetics,

Lv, J., Wang, Y., Xu, L., Gu, Y., Zou, L., Yang, B., & Ma, Z. (2019). A method to obtain the near-large fruit from apple image in orchard for single-arm apple harvesting robot. *Scientia Horticulturae*, *257*, 108758. https://doi.org/https://doi.org/10.1016/j.scienta.2019.108758

Malneršič, A., Dular, M., Širok, B., Oberti, R., & Hočevar, M. (2016). Close-range air-assisted precision spot-spraying for robotic applications: Aerodynamics and spray coverage analysis. *Biosystems Engineering*, *146*, 216-226. https://doi.org/https://doi.org/10.1016/j.biosystemseng.2016.01.001

Mohamed, E. S., Ali, A. M., El Shirbeny, M. A., Abd El Razek, A. A., & Savin, I. Y. (2016). Near infrared spectroscopy techniques for soil contamination assessment in the Nile Delta. *Eurasian Soil Science*, *49*(6), 632-639. https://doi.org/10.1134/S1064229316060065

Mohd, M. M., Soom, M., Amin, M., Kamal, R., & Wayayok, A. (2014). Application of web geospatial decision support system for Tanjung Karang rice precision irrigation water management. International Conference on Agriculture, Food and Environmental Engineering (ICAFEE'2014) Jan,

Morota, G., Ventura, R. V., Silva, F. F., Koyama, M., & Fernando, S. C. (2018). BIG DATA ANALYTICS AND PRECISION ANIMAL AGRICULTURE SYMPOSIUM: Machine learning and data mining advance predictive big data analysis in precision animal agriculture1. *Journal of Animal Science*, *96*(4), 1540-1550. https://doi.org/10.1093/jas/sky014

Murase, H. (2000). Artificial intelligence in agriculture. *Computers and Electronics in Agriculture*, *29*(1/2).

Özaslan, T., Mohta, K., Keller, J., Mulgaonkar, Y., Taylor, C. J., Kumar, V., Wozencraft, J. M., & Hood, T. (2016). Towards fully autonomous visual inspection of dark featureless dam penstocks using MAVs. 2016 IEEE/RSJ International Conference on Intelligent Robots and Systems (IROS),

Pitla, S., Bajwa, S., Bhusal, S., Brumm, T., Brown-Brandl, T. M., Buckmaster, D. R., Condotta, I., Fulton, J., Janzen, T. J., & Karkee, M. (2020). Ground and aerial robots for agricultural production: Opportunities and challenges.

Said Mohamed, E., Belal, A. A., Kotb Abd-Elmabod, S., El-Shirbeny, M. A., Gad, A., & Zahran, M. B. (2021). Smart farming for improving agricultural management. *The Egyptian Journal of Remote Sensing and Space Science*, *24*(3, Part 2), 971-981. https://doi.org/https://doi.org/10.1016/j.ejrs.2021.08.007

SepúLveda, D., Fernández, R., Navas, E., Armada, M., & González-De-Santos, P. (2020). Robotic Aubergine Harvesting Using Dual-Arm Manipulation. *IEEE Access*, *8*, 121889-121904. https://doi.org/10.1109/ACCESS.2020.3006919

Sharma, R. (2021). Review on Application of Drone Systems in Precision Agriculture. *Journal of Advanced Research in Electronics Engineering and Technology*, *7*(2), 5-7.

Sharma, S., Verma, K., & Hardaha, P. (2023). Implementation of artificial intelligence in agriculture. *Journal of Computational and Cognitive Engineering*, *2*(2), 155-162.

Shitu, A., Tadda, M., & Danhassan, A. (2018). Irrigation water management using smart control systems: a review. *Bayero Journal of Engineering and Technology*, *13*(2), 1-12.

Sinwar, D., Dhaka, V. S., Sharma, M. K., & Rani, G. (2020). AI-Based Yield Prediction and Smart Irrigation. In P. K. Pattnaik, R. Kumar, & S. Pal (Eds.), *Internet of Things and Analytics for Agriculture, Volume 2* (pp. 155-180). Springer Singapore. https://doi.org/10.1007/978-981-15-0663-5_8

Smith, M. J. (2018). Getting value from artificial intelligence in agriculture. *Animal Production Science*, *60*(1), 46-54.

Subeesh, A., & Mehta, C. R. (2021). Automation and digitization of agriculture using artificial intelligence and internet of things. *Artificial Intelligence in Agriculture*, *5*, 278-291. https://doi.org/https://doi.org/10.1016/j.aiia.2021.11.004

Talaviya, T., Shah, D., Patel, N., Yagnik, H., & Shah, M. (2020). Implementation of artificial intelligence in agriculture for optimisation of irrigation and application of pesticides and herbicides. *Artificial Intelligence in Agriculture*, *4*, 58-73.

Torres-Sánchez, J., Peña, J. M., de Castro, A. I., & López-Granados, F. (2014). Multi-temporal mapping of the vegetation fraction in early-season wheat fields using images from UAV. *Computers and Electronics in Agriculture*, *103*, 104-113.

Torun, E. (2000). UAV Requirements and design consideration. *Turkish Land Forces Command Ankara (Turkey)*.

von Bueren, S. K., Burkart, A., Hueni, A., Rascher, U., Tuohy, M. P., & Yule, I. J. (2015). Deploying four optical UAV-based sensors over grassland: challenges and limitations. *Biogeosciences*, *12*(1), 163-175. https://doi.org/10.5194/bg-12-163-2015

Waleed, M., Um, T.-W., Kamal, T., Khan, A., & Iqbal, A. (2020). Determining the precise work area of agriculture machinery using internet of things and artificial intelligence. *Applied Sciences*, *10*(10), 3365.

Wang, H., Liu, J., Dong, Z., Song, J., & Zhu, Z. (2023). Artificial intelligence-based metabolic energy prediction model for animal feed proportioning optimization. *Italian Journal of Animal Science*, *22*(1), 942-952. https://doi.org/10.1080/1828051X.2023.2236132

Yamasaki, Y., Morie, M., & Noguchi, N. (2022). Development of a high-accuracy autonomous sensing system for a field scouting robot. *Computers and Electronics in Agriculture*, *193*, 106630.

Yetilmezsoy, K., Ozkaya, B., & Cakmakci, M. (2011). Artificial intelligence-based prediction models for environmental engineering. *Neural Network World*, *21*(3).

Zaidner, G., & Shapiro, A. (2016). A novel data fusion algorithm for low-cost localisation and navigation of autonomous vineyard sprayer robots. *Biosystems Engineering*, *146*, 133-148.

Zhang, C., Huang, X., Liu, W., Zhang, Y., Li, N., Zhang, J., & Li, W. (2012). Information acquisition method for mechanical intra-row weeding robot. *Transactions of the Chinese Society of Agricultural Engineering*, *28*(9), 142-146.

Advanced Engineering Days

aed.mersin.edu.tr

A novel deep learning-based method for potato leaf disease classification

Kimia Shirini [1], Adel Taheri Hajivand *[2], Sina Samadi Ghareveran [1]

[1]*University of Tabriz, Department of Electrical and Computer Engineering, Iran, k.shirini@tabrizu.ac.ir*
[2] *University of Tabriz, Department of Agriculture Engineering, Iran, a.taheri@tabrizu.ac.ir*

Cite this study: Shirini, K., Hajivand, A. T., & Ghareveran, S. S. (2024). A novel deep learning-based method for potato leaf disease classification. Advanced Engineering Days, 9, 462-464

Keywords
Potato Leaf Diseases
Disease Management
Rapid Diagnosis
Deep Learning
Classification
Accuracy

Abstract

Potato disease management plays a crucial role in ensuring optimal crop output. However, the current process of diagnosing and classifying potato leaf diseases is time-consuming and labor-intensive. To address these challenges, this paper proposes an accurate and automated technique for fast detection and classification. Leveraging machine learning and deep learning algorithms, our approach extends beyond the binary classification of existing models by categorizing potato leaves into three classes: Potato Late Blight (PLB), Potato Early Blight (PEB), and Potato Healthy (PH). Our proposed model is trained using the "Plant Village" dataset, which includes images of Early Blight (EB), Late Blight (LB), and Healthy potato leaves. To enhance classification accuracy, we introduce an improved deep learning algorithm with an additional transition layer known as the Efficient Model. This novel approach demonstrates robustness in handling severely skewed training data, mitigating overfitting issues. Experimental results indicate a remarkable performance with an accuracy of 97% on the testing set, surpassing existing models for potato leaf disease detection and classification. Our research presents a significant contribution to the field, offering a comprehensive technique for effectively addressing and reporting on two prevalent potato leaf diseases.

Introduction

Agriculture plays a crucial role in the economic development of any nation. The production of potato crops has significantly contributed to the growth of many devel-oped economies. Field security is a fundamental concern faced by nations worldwide, particularly in developing countries where malnutrition issues are directly linked to agricultural stability [1]. Moreover, potatoes hold significant importance in Pakistan as the fourth-largest crop in terms of production. Recent statistics reveal that potatoes are cultivated across 170,300 hectares, resulting in an overall production of 4 million metric tons [2].

The graph depicting yearly per capita consumption also indicates an upward trend. Consequently, farmers must prioritize the successful growth of potato harvests due to their crucial role as a key component of the economy. Potatoes have emerged as a staple food source capable of meeting the growing demands for quantity and quality. The agriculture industry faces significant challenges in ensuring food security and enhancing nutrition. Potatoes are rich in essential nutri-ents, particularly potassium, magnesium, and vitamins C and B6 [3].

Potatoes rank as the fourth most consumed vegetable crop globally and are a popular staple food in In-donesia. The agricultural sector, including potato production, has experienced rapid growth in the country during this decade. With an annual output of approximately 850,000 tons, potatoes are cultivated across an area of around 60,000 hectares. Indonesia has emerged as the leading potato producer in Southeast Asia, thanks to a yearly in-crease in planting and production areas of approximately 10%. However, various dis-eases can adversely affect potato plants, both pre- and post-harvest, posing a challenge to their cultivation [4]. Illnesses during the growing phase of agricultural products can have a detrimental impact on both the quantity and quality of the yield. It can result in harvest failure or premature harvesting. Many of these issues arise due to inaccurate disease diagnosis and delayed detection of diseases in potato plants. Swift and accurate disease diagnosis is crucial to effectively managing and mitigating the impact of dis-eases on potato cultivation.

Material and Method

Deep Learning has emerged as a powerful tool for various perception tasks, rang-ing from image understanding to voice recognition and robotic exploration [5]. In this study, an implementation of the Convolutional Neural Network (CNN) concept for image recognition is proposed for identifying illnesses in potato leaves. A robust framework is being developed, with a focus on accurate identification and characteri-zation of plant leaf diseases that heavily rely on extracting deep and high-dimensional features. The mining of distinctive characteristics that differentiate images and enable their classification into different classes is excellently performed by deep learning models. Leveraging this capability, a modified model architecture is utilized by our method to effectively identify potato leaf diseases.

Artificial neural network, inspired by the human brain, tries to develop information processing. Each neuron in this network is a processing resource and solves different problems along with other processing elements [6]. In this structure, numerous nodes are parallel to each other with the purpose of overall processing of activities. This data structure is placed in a communication network with different situations, and this network is used by humans for teaching and learning. A neural network usually has an input layer, an output layer, and hidden layers, which are used to improve the performance of the neural network in pattern recognition.

We used three different methods to detect weeds: Decision Tree (DT), Convolutional Neural Network (CNN) and Support Vector Machine (SVM). In the following, we will examine each of these methods in more detail and then conclude why the CNN method performed better [7].

A decision tree is a simple and interpretable machine learning algorithm that works by dividing data into different groups based on their characteristics. The main advantage of this method is its simplicity and speed of implementation. However, the decision tree suffers from a tendency to overfitting and sensitivity to noise in the data, in complex cases and with a lot of data. This method is very suitable for simple problems with little data, but it is not accurate enough to detect weeds that may contain complex features and multiple variables [8].

Support vector machine is one of the powerful algorithms in classification that divides data into two different groups by creating an optimal decision boundary (hyperplane). This method works well especially in high dimension and complex problems. SVM can optimize classification by using different kernels to transform data into higher dimensional spaces. However, this method requires precise setting of the parameters, and if not set correctly, it may not have the desired accuracy. In addition, the computational time of SVM can be high compared to other methods.

A convolutional neural network is a special type of deep neural network that is particularly successful in image processing and complex pattern recognition. This method can extract important and complex features of images by using convolution layers and dense layers. CNN has a high ability to recognize the details of images, and therefore it is very suitable for detecting weeds that require the recognition of delicate and complex patterns. Another advantage of CNN is the ability to learn features automatically from data, without the need for manual feature extraction.

Results

We used three different methods to detect weeds: Decision Tree (DT), Convolutional Neural Network (CNN) and Support Vector Machine (SVM). In this comparison, the CNN method showed a significantly better performance than the other two methods.

The decision tree method was able to provide acceptable results due to its simple and understandable structure, but in more complex cases, its accuracy decreased. The support vector machine method was also able to perform well by using its strong capabilities in data classification, but its results were not reliable enough.

On the other hand, the convolutional neural network method showed the best performance due to its high ability to identify complex patterns and features in images. This method was able to detect weeds with high accuracy and in terms of processing time and accuracy, it performed much better than the other two methods. In general, the use of CNN method is suggested as an efficient and accurate method for weed detection.

Table 1. compare of the different methods

Method	Accuracy
Decision tree	88.9
SVM	89.1
CNN	93.1

Discussion

The use of different machine learning techniques for weed detection has received much attention due to its high importance in modern agriculture and reducing the need to use chemicals. In this study, the three main methods of Decision Tree (DT), Support Vector Machine (SVM) and Convolutional Neural Network (CNN) were investigated and compared for this purpose.

Conclusion

In comparison of these three methods, the convolutional neural network (CNN) has performed better than the decision tree and support vector machine due to its high ability to extract complex features and its high accuracy. This method was able to detect weeds with high accuracy and in terms of processing time and accuracy, it performed much better than the other two methods. In general, the use of CNN method is suggested as an efficient and accurate method for weed detection. This paper should have at most 3 pages.

References

Bacco, M.; Berton, A.; Ferro, E.; Claudio, G.; Alberto, G.; Stefania, M.; Fabio, P.; Massimiliano, R. Giuseppe, V.; Alberto, Z. Smart farming: Opportunities, challenges and technology enablers. In Proceedings of the 2018 IoT Vertical and Topical Summit on Agriculture—Tuscany (IOT Tuscany), Tuscany, Italy, 8–9 May 2018; pp. 1–6.

García-Magariño, I.; Lacuesta, R.; Lloret, J. ABS-SmartComAgri: An agent-based simulator of smart communication protocols in wireless sensor networks for debugging in precision agriculture. Sensors 2018, 18, 998.

Gubbi, J.; Buyya, R.; Marusic, S.; Palaniswami, M. Internet of Things (IoT): A vision, architectural elements, and future directions. Future Gener. Comput. Syst. 2013, 29, 1645–1660.

Patrício, D.I.; Rieder, R. Computer vision and artificial intelligence in precision agriculture for grain crops: A systematic review. Comput. Electron. Agric. 2018, 153, 69–81.

shirini, K., Taherihajivand, A., & samadi Gharehveran, S. (2023). A review of algorithms for solving the project scheduling problem with resource-constrained considering agricultural problems. *Agricultural Mechanization*, *8*(1), 1-14. doi: 10.22034/jam.2023.55751.1227

Taheri hajivand, A., Shirini, K., & Samadi Gharehveran, S. (2024). Balancing Time and Cost in Resource-Constrained Project Scheduling Using Meta-Heuristic Approach. *Journal of Agricultural Machinery*, *14*(2), 215-234. doi: 10.22067/jam.2023.81735.1157

Taherihajivand, A., shirini, K., & samadi Gharehveran, S. (2024). Weed detection in fields using convolutional neural network based on deep learning. *Agricultural Engineering*, *47*(1), 129-142. doi: 10.22055/agen.2024.45327.1688

Zamora-Izquierdo, M.A.; Santa, J.; Martínez, J.A.; Martínez, V.; Skarmeta, A.F. Smart farming IoT platform based on edge and cloud computing. Biosyst. Eng. 2019, 177, 4–17.

Advanced Engineering Days

aed.mersin.edu.tr

Assessing the Impact of Climate Change on Evaporation in Maragheh Region Using Time Series Models

Vahdat Ahmadifar[1], Reza Delirhasannia [*2], Tima Mohammadzadeh [3]

[1]*University of Tabriz, Department of Water Engineering and Science, Iran, vahdatahmadifar@yahoo.com*
[2*1]*University of Tabriz, Department of Water Engineering and Science, Iran, delearhasannia@yahoo.com*
[3]*Building Art Learner, Ahar Educational Office, Iran, amirabbasahmadifar@gmail.com*

Cite this study: Ahmadifar, V., Delirhasannia, R., & Mohammadzadeh, T. (2024). Assessing the Impact of Climate Change on Evaporation in Maragheh Region Using Time Series Models. Advanced Engineering Days, 9, 465-469

Keywords
Climate change
Evaporation
Modeling
Time series

Abstract

In this study, the time series models were used to investigate the effects of climate change on the evaporation and to forecast its values. For this purpose, the daily evaporation data was obtained from the East Azarbaijan Meteorological Head Office for 21 years for the Maragheh Synoptic Station and was prepared as monthly data for use in modeling with time series. After evaluating the accuracy and examining the different models of the SARIMA model time series, with the highest accuracy, the appropriate model was selected. The trend testing on the time series data showed that the evaporation rate at the station was rising and in the coming years, the average evaporation intensity would increase by 26.5 mm per year. The accuracy evaluation of the results indicates that the average square of squares is 19.6 mm/month.

Introduction

The impact of climate change on hydrology is an important issue that cannot be ignored. Studies show that world temperatures are on the rise and the hydrological cycle of precipitation, evaporation, runoff and surface currents are directly interacting with this issue [2,3,6]. Transpiration after rainfall is the most important part of the hydrological cycle. According to scientific reports, the average air temperature has increased by about 0.6 ° C over the past century, and since temperature rise is the most important factor in increasing evaporation, it is expected to increase the temperature increased evaporation values. Transpiration and enable the atmosphere to move more amounts of steam [1]. One of the common methods for calculating evaporation from the surface of the lakes, water tanks, free water levels as well as estimating the evaporation of plants is the use of evaporation pan. The use of evaporation as a simple, low -cost method has been rumored with easy access to the data needed and ease of use for areas with different environmental conditions [5]. The evaporation pan is used in various types, but the use of two types of Class A and Colorado, and in Iran, the use of Class A pan is more common [5]. Due to the complexity and lack of knowledge of physical processes in climatic models such as evaporation, the manufacture of statistical models and expanding them to express these processes, the researchers have attracted the attention of the researchers [8-10]. Ahmadifar et al. [1], using the Minitab statistical software, predicted the trend of maximum temperature changes in northwestern Iran, indicating an increase in temperature in the coming years. According to the results of the studies and the importance of modeling and examining the average evaporation process, especially with time series methods, in the present study investigating the effect of climate change on evaporation and modeling of evaporation values from Maragheh city on monthly scale using time series models were performed.

Material and Method

Study Area

Maragheh county is located in the southwest of East Azarbaijan province with 2186 km^2 area. Maragheh geographically occupied 4.62% of East Azarbaijan province area. The average elevation of this region is 1477 m above the free seas surface level. Figure 1 shows the location of the study area.



Figure 1. The location of studied area in East Azarbaijan province and Iran map

The type of pan used in these stations is class A. The data used in the East Azarbaijan Meteorological Office were produced from 2001 to 2022. Basic data is daily and according to the research goals, these values were prepared on a monthly format.

Time Series Modeling

In order to model with the benefits of time series, first of all, the necessary and sufficient pre-conditions must be done on the data. Time series are static or non-static. The evaluation of situation of the series data is one of the most important stages in this field. Where, if the data is not static, the data should be transform to static and prepared for modeling [4]. The Mini-TAB software (Ver. 17) was used to model and predict time series of evaporation from pan. Consequently, 80% of data was applied for modeling and 20% for validation [1].

Results

The chart of the time series of evaporation from the pan was plotted as in Figure 2. As can be seen, all charts have seasonal character. Using the trend test, it has been found that the amount of monthly evaporation has been increasing for many years. Along 21 years, the evaporation rate increases by 26.5 mm.

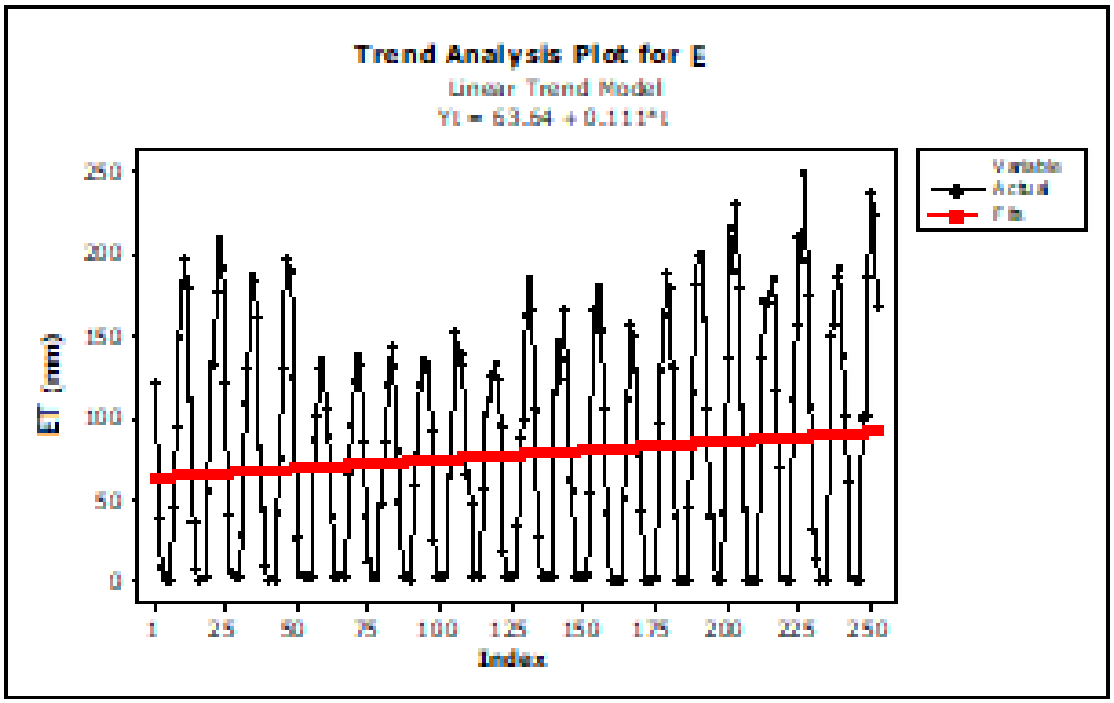


Figure 2. Times series diagram of pan evaporation

Considering the 12 th order difference due to the seasonal nature of the data, the differential series of ACF and PACF charts were plotted in accordance with Figure 3. It was observed that in ACF chart there is a correlation between data in the first and second time delays. As it can be seen, there is a high correlation between data in a timely delay of 12. In the PACF diagram, there is also a correlation in data at the first time delay.

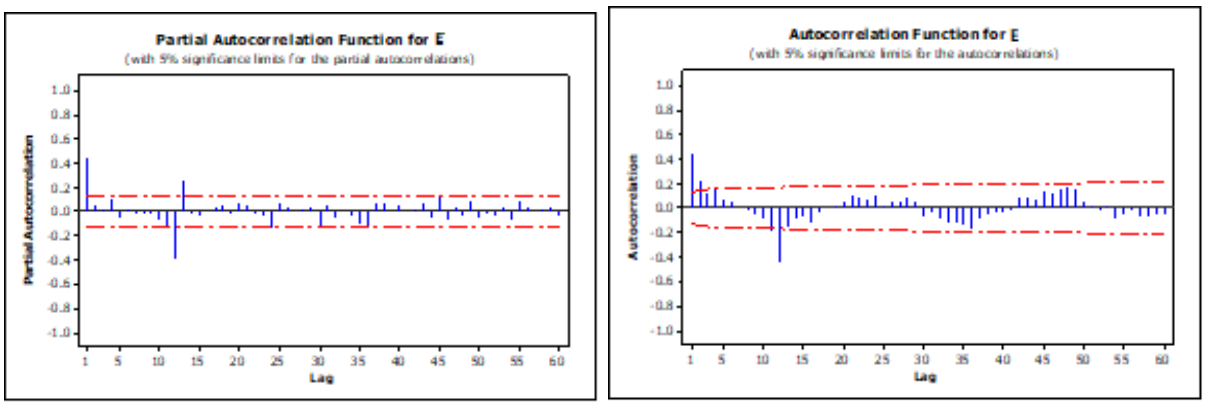


Figure 3. Differential ACF and PACF diagrams

The seasonal model of the SARIMA(p,d,q)(P,D,Q)ω was used for the series modeling. After fitting several models for the Maragheh station's time series, the SARIMA(2,0,1)(1,0,1)12 was finally identified as suitable model. The P-Value statistics of the model parameters were less than 0.05, it is indicating that these parameters are statistically significant. The residuals of the model were used to verify the selected model. Therefore, the ACF and PACF charts were plotted to investigate the independence of the residuals as well as the normal probability plan chart in Figure 4, all of which confirm the model correctness.

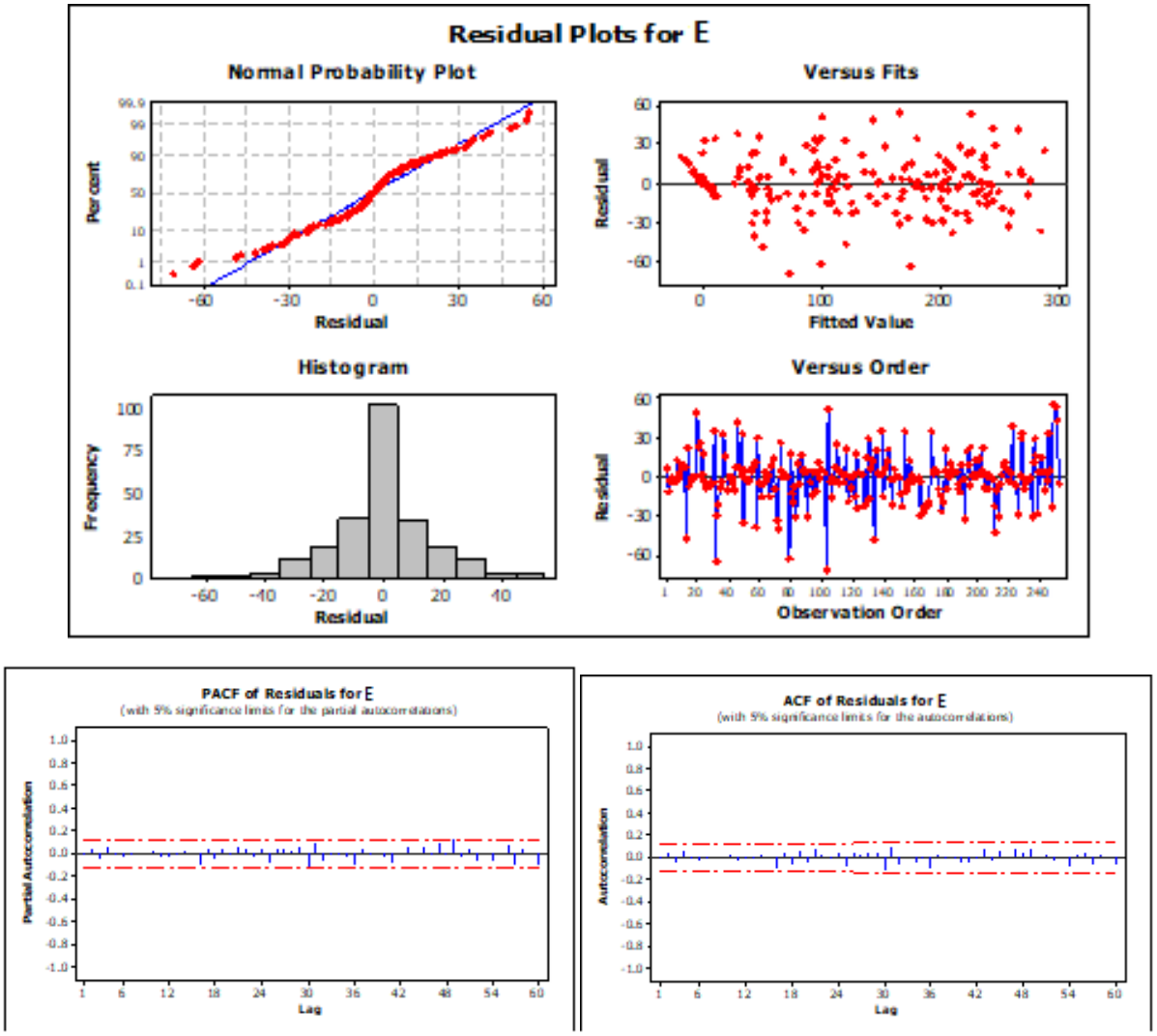


Figure 4. ACF and PACF diagrams and normal probability plot of residuals

In order to better understanding the model similarity with the observational data, Figure 5 was prepared. This figure shows that the given model has satisfied similarity with actual data.

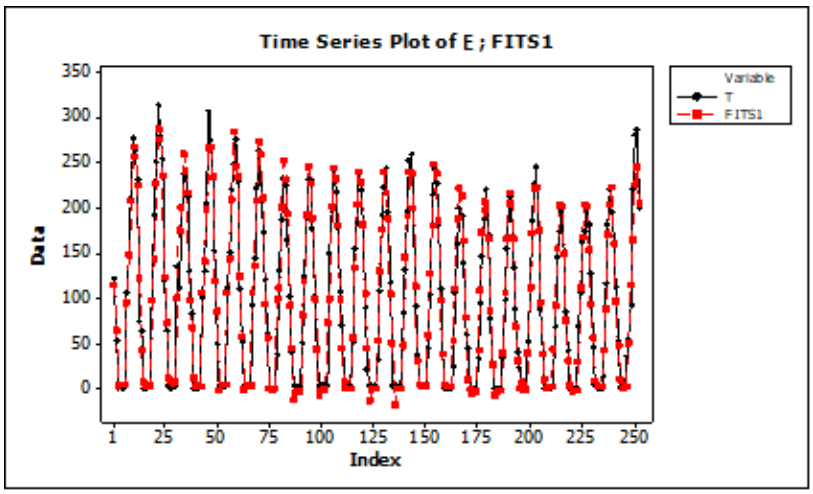


Figure 5. Comparison diagram between model outputs and observations

The results of the fitness in time series models for monthly evaporation data in studied station are presented in Table 1.

Table 1. Accuracy evaluation of time series model for monthly evaporation data

Station	Model	R2	RMSE (mm)
Maragheh	SARIMA(2,0,1)(1,0,1)12	94.1	19.6

The predicted values for up-coming years are also illustrated in Table 2.

Table 2. Predicted evaporation amounts for following years

	Maragheh monthly evaporation (mm)				
Month	2023	2024	2025	2026	2027
January	2.85	2.85	2.85	2.85	2.85
February	2.64	2.64	2.64	2.64	2.64
March	9.83	9.83	9.83	9.83	9.83
April	83.24	83.28	83.28	83.29	83.29
May	167.4	167.43	167.44	167.44	167.45
June	228.37	228.39	228.4	228.42	228.43
July	265.99	266.01	266.02	266.04	266.05
August	283.71	283.73	283.75	283.76	283.78
September	229.92	229.93	229.94	229.95	229.97
October	164.1	164.11	164.12	164.13	164.14
November	99.04	99.04	99.05	99.05	99.06
December	23.52	23.52	23.52	23.52	23.52

Discussion and Conclusion

In this study, time series models were used to predict the effects of climate change on evaporation in Maragheh region. The results showed that the change in evaporation rate in this area was increasing. It was also concluded that the SARIMA model (2,0,1)(1,0,1)12 model is more suitable among applied time series models. This model has good accuracy in predicting evaporation with an average error value of 19.6 mm/month.

References

1. Ahmadifar, V., Delirhasannia, R., Samadianfard, S., Mohammadzadeh, T. (2024). Investigation of trend and prediction of maximum mean temperature in northwest iran using time series models. Water and Soil Science, 34(1), 55-73. (in Persian with English abstract).
2. Molina-Navarro E, Trolle D, Martínez-Pérez S, Sastre-Merlín, A. and Jeppesen, E. (2014). Hydrological and water quality impact assessment of a Mediterranean limno-reservoir under climate change and land use management scenarios. Journal of Hydrology, 509, 354-366.
3. Narsimlu B, Gosain AK and Chahar B.R. (2013). Assesment of future climate change impacts on water resources of Upper Sind River basin India using SWAT model. Water resource manage 27, 3647-3662.
4. Niroumand H. A. (2010). Time Series Analysis. Translated from Cryer, J. D. (1986). Ferdowsi University of Mashhad Pub. 4th edition. Mashhad. 417p. (in Persian with English abstract)

5. Sattari, M T., Ahmadifar, V., Delirhasannia, R., Apaydin, H. (2021). Estimation of the pan evaporation coefficient in cold and dry climate conditions via the M regression tree model. Atmósfera, 34(3), 289-300.
6. Sunyer MA, Madsen H and Ang P.H. (2012). A comparison of different regional climate models and statistical downscaling methods for extreme rainfall estimation under climate change. Atmospheric Research, 103, 119–128.
7. Tabari H and Willems P. (2018). Seasonally varying footprint of climate change on precipitation in the Middle East. Scientific reports, 8, 4435.
8. Veisipour H., Masompour J., Sahne B and yosefi Y. (2010). Analysis of precipitation and temperature trend and forecasting by time series models (Case Study of Kermanshah city). Journal of Geography 3, 63-77. (in Persian with English abstract)
9. Zhou S., Yuan J., Song Z., Tang J and Kang L. (2013). Wind signal Forecasting based on system identification toolbox of MATLAB. Intelligent System Design and Engineering Applications, 1614-1617.
10. Zolfaghari H., Masoompouy Samakosh J and Chahwari S. (2018). Estimating the Growing Degree Days in the Northwest of Iran based on Climate Change Models. Scientific Journals Management System, 49, 221-240. (in Persian with English abstract).

Advanced Engineering Days

aed.mersin.edu.tr

Estimation of fractional vegetation cover dynamics based on remote sensing in Shabestar, Iran

Aylar Mohammadi[1], Abolfazl Majnooni Heris [2], Reza Hassanpour [3]

[1] University of Tabriz Department of Water Engineering, Iran, Aylarmhmd79@gmail.com
[2] University of Tabriz Department of Water Engineering, Iran, majnooni@tabrizu.ac.ir
[3] Research Department of Soil and Water, East Azerbaijan Agricultural and Natural Resources Research and Education Center, Agricultural Research, Education and Extension Organization (AREEO), Tabriz, Iran, r.hassanpour@areeo.ac.ir"

Cite this study: Mohammadi, A., Majnooni Heris, A., & Hassanpour, R. (2024). Estimation of fractional vegetation cover dynamics based on remote sensing in Shabestar, Iran. Advanced Engineering Days, 9, 470-472

Keywords
Fractional vegetation
Coverage
Remote Sensing
Sentinel-2
Shabestar

Abstract

Evaluating FVC is crucial to understanding agricultural land productivity. Accurate and long-term estimation of FVC over extensive areas is essential for various research purposes such as crop yield estimation, earth system science, and sustainable development. With the further development of remote sensing technology, we can now monitor vegetation dynamics long-term and over large areas. Fractional vegetation cover (FVC) is an important ecological parameter that reflects vegetation diversity and biological cover. In this study, we analyzed the fluctuations variations of FVC from 2020 to 2023 Sentinel-2 satellite images were used to estimate FVC values for the years studied.

Introduction

Fractional vegetation cover (FVC) is the amount of an area covered by vegetation, including trees, shrubs, and grasses [1]. Assessing FVC is important for understanding agricultural land productivity. Accurate and long-term estimation of FVC over large areas is essential for various research purposes such as crop yield estimation, earth system science, and sustainable development. There are different methods for measuring fractional vegetation cover, including remote sensing techniques such as satellite imagery and aerial photography. In general, vegetation monitoring through remote sensing involves creating a relationship between vegetation and indicators or using spatial data mining technology [2]. FVC is used by numerous experts to understand the drivers and principles of spatial changes [3]. Fractional Vegetation Cover was determined using Landsat data, specifically the SAVI and NDVI measurements [4]. Some researchers used supervised classification and CIELAB color space threshold classification to extract FVC. They found that the extraction result in CIELAB color space was consistent with the actual value of FVC [5]. The aim of this study is to analyze the spatial and temporal changes in vegetation cover using data from the Sentinel-2 satellite between 2020 and 2023.

Material and Method

The Shabestar Plain covers an area of 1254.7 square kilometers and is located in the western part of East Azerbaijan, in the eastern basin of Lake Urmia. It is considered one of the most important agricultural centers in the province. The Shabestar study area is located in the Lake Urmia catchment area and is of great importance for the country “Figure 1”.

The analysis used Sentinel-2 satellite imagery to examine vegetation trends. Data and satellite images from 2020 to 2023, corresponding to the middle of the growing season, were selected. The biophysical processor in the SNAP software, designed to process Sentinel series satellite images, was used to extract FVC. QGIS software has also been used to create vegetation maps.

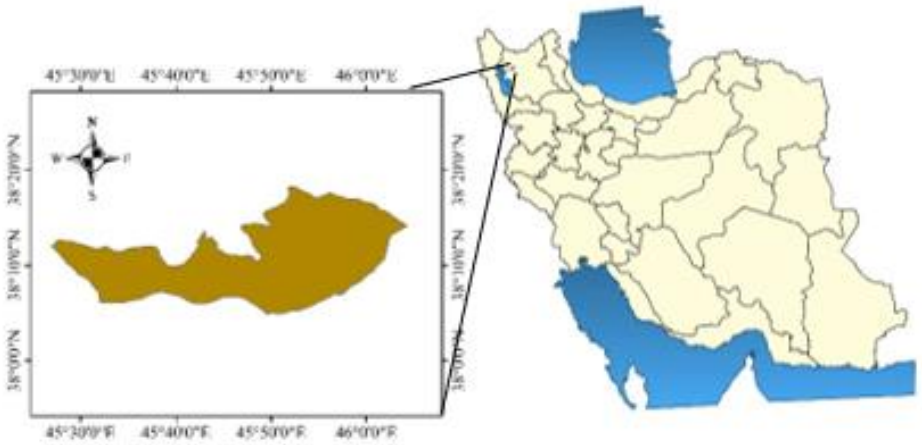


Figure 1. Geographical location of the study area

Results

Annual changes in FVC were plotted a 4-year period (Figure 2). The FVC value was observed to initially decrease over two years but eventually increase in 2023. In general, it can be concluded that the FVC value has increased.

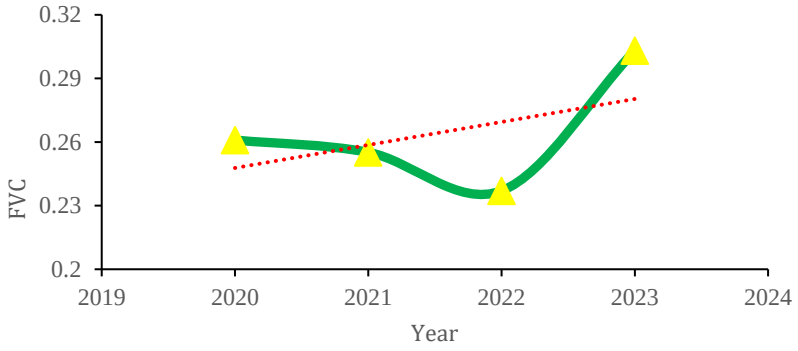


Figure 2. Trend dynamics of FVC determined through sentinel-2 from 2020 to 2023.

Spatial analysis of FVC

Fractional vegetation cover values were created for different parts of the Shabestar Plain and classified into three different classes: less than 0.3, 0.3-0.6, and more than 0.6. These are showen in "Figure 3".

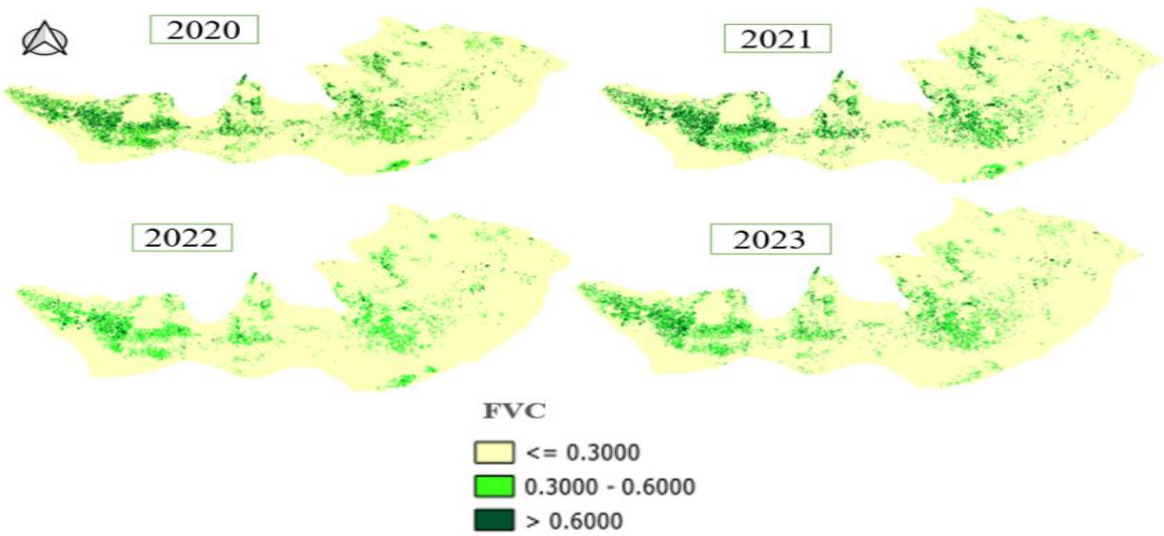


Figure 3. Trend dynamics of FVC determined through sentinel-2 from 2020 to 2023.

Discussion

The average FVC index over the study period was 0.26. The highest and lowest values were 0.303 in 2023 and 0.237 in 2022, respectively. In 2022 and 2021, the FVC value was below average. Throughout the study period, FVC distribution in residential and barren areas was generally low due to human activities. Researches show that vegetation cover in the southwest region is over 60% in the first two years and between 30 and 60% in the following two years. This variation may be related to the specific crop type and timing of harvest. It is possible that in certain years, such as 2022, spring crops were grown in these areas and harvested around the time the photos were taken, or that there was no green cover in the fields at the time of observation.

Conclusion

Evaluating FVC is crucial to understanding agricultural land productivity. Accurate and long-term estimation over FVC in extensive areas is essential for various research purposes such as crop yield estimation, earth system science, and sustainable development. With the further development of remote sensing technology, we can now monitor vegetation dynamics long-term and over large areas. In this study, we used the Sentinel-2 satellite on cloudless days to estimate changes in vegetation cover in the Shabestar Plain during the middle of the growing season. The results suggest that there is an overall increasing trend in FVC changes over the studied years, with an average vegetation cover of 0.264 during this period. According to the maps prepared for FVC, pixels with minimal vegetation can be found in residential and barren areas. However, the vegetation cover in agricultural areas is weak in some years, which may be because the crops had already been harvested at the time the images were taken or had recently been grown as a second crop.

References

1. Xie, Q., Dash, J., Huete, A., Jiang, A., Yin, G., Ding, Y., ... & Huang, W. (2019). Retrieval of crop biophysical parameters from Sentinel-2 remote sensing imagery. *International Journal of Applied Earth Observation and Geoinformation*, *80*, 187-195.
2. Hanan, N. P., Prince, S. D., & Hiernaux, P. H. (1991). Spectral modelling of multicomponent landscapes in the Sahel. *International Journal of Remote Sensing*, *12*(6), 1243-4258.Karataş, L., Alptekin, A., & Yakar, M. (2022). Mardin historical Kuyumcular (Jewelers) Bazaar restoration evaluation. Advanced Engineering Days (AED), 5, 15-17.
3. Cao, Q., Yu, D., Georgescu, M., Han, Z., & Wu, J. (2015). Impacts of land use and land cover change on regional climate: A case study in the agro-pastoral transitional zone of China. *Environmental Research Letters*, *10*(12), 124025.
4. Buyantuyev, A., Wu, J., & Gries, C. (2007). Estimating vegetation cover in an urban environment based on Landsat ETM+ imagery: a case study in Phoenix, USA. *International Journal of Remote Sensing*, *28*(2), 269-291.
5. Zhao, J., Xie, D., Mu, X., Liu, Y., & Yan, G. (2012, July). Accuracy evaluation of the ground-based fractional vegetation cover measurement by using simulated images. In *2012 IEEE International Geoscience and Remote Sensing Symposium* (pp. 3347-3350). Ieee.

Advanced Engineering Days

aed.mersin.edu.tr

Empirical Bayesian Kriging for Soil Available Phosphorus Mapping

Shahla Rahmani Siyalarz [1], Ali Keshavarzi [*1], Fuat Kaya [2]

[1] *University of Tehran, Department of Soil Science, Karaj, Iran, shahla.rahmani@ut.ac.ir, alikeshavarzi@ut.ac.ir*
[2] *Isparta University of Applied Sciences, Department of Soil Science and Plant Nutrition, Çünür, Türkiye, fuatkaya@isparta.edu.tr*

Cite this study: Rahmani Siyalarz, Sh., Keshavarzi, A., & Kaya, F. (2024). Empirical Bayesian Kriging for Soil Available Phosphorus Mapping. Advanced Engineering Days, 9, 473-475

Keywords
Available phosphorus
EBK
Interpolation
Neyshabur

Abstract

Accurate information on the spatial variability of soil nutrients is crucial for sustainable soil management practices, such as the application of fertilizers based on actual needs. This study focused on mapping the spatial distribution of available soil phosphorus in agricultural lands located in Neyshabur, Khorasan-e-Razavi Province, Iran. A total of 150 surface soil samples were collected from a depth of 0-20 cm. After air-drying, crushing, and sieving through a 2-millimeter sieve, standard laboratory methods were used to determine the available phosphorus (P) content in the soil. Empirical Bayesian Kriging (EBK) was employed to create a spatial distribution map of available soil phosphorus. The results revealed that available phosphorus content ranged from 2.4 to 47.6 mg/kg, with an average of 10.53 mg/kg. Notably, over 76% of the agricultural land in the region falls within the phosphorus deficiency range. Given the vital role of phosphorus in food security, this map is a valuable tool for informed fertilizer recommendations. In areas where the phosphorus content is below the optimum level for plants, more precise fertilizer application strategies should be developed. Strategies such as the addition of organic matter and phosphorus-containing fertilizers can be implemented to address phosphorus deficiencies and promote sustainable agricultural practices in Neyshabur. This study highlights the effectiveness of the Empirical Bayesian Kriging (EBK) method for zoning the spatial distribution of phosphorus in the region. EBK is a valuable tool for identifying areas with nutrient deficiencies, allowing targeted interventions and improved soil management.

Introduction

One of the most important natural resources utilized by humans is soil, as it is a valuable resource for agricultural activities, natural resources, socio-economic development, and human survival [10]. Inappropriate use of inputs without considering the spatial changes of these elements in the soil not only has negative effects on crop yield and production, but also leads to adverse environmental consequences such as pollution and groundwater contamination [1]. Phosphorus is the second most essential element for plant growth and plays a key role in plant development, which has received attention from various agricultural and environmental perspectives. Soil phosphorus is considered one of the most important limiting nutrient elements for agricultural production in many parts of the world [8]. In precision agriculture, soil fertility maps are the basis for soil fertilizer recommendations, monitoring of nutritional changes, and are one of the most important tools for predicting nutrient deficiency or toxicity in the soil [5]. Given that determining the spatial patterns of soil properties is crucial for improving resource management and estimating soil characteristics in unsampled locations, the use of geostatistical estimators can increase the accuracy of calculations today [9]. Empirical Bayesian Kriging (EBK) is a geostatistical method that, unlike other kriging methods, does not require manual adjustment of parameters and selection of different models to achieve better results. The calculated standard error in this method is more accurate than other kriging methods. The higher accuracy of this method compared to other geostatistical methods for small and variable data sets is another advantage, although the simulated variograms must be modeled with

precision [4-7]. Previous studies have used the Empirical Bayesian Kriging (EBK) method to map environmental variables and reported that this method has high efficiency [4-7]. The aim of this study is to use the Empirical Bayesian Kriging (EBK) method to map the spatial distribution of available soil phosphorus in a portion of the agricultural lands of Neyshabur, located in the Khorasan-e-Razavi province of Iran.

Material and Method

This research was conducted within an 85 km² study area located in the semi-arid Neyshabur plain, situated in the Khorasan-e-Razavi province of northeastern Iran. Elevation at the site ranged from 1197 to 1316 m, with an average annual rainfall of 233.7 mm and the mean temperature of 14.5°C. Rainfed and irrigated agriculture were the predominant land uses, with winter wheat being the primary crop cultivated; however, barley and citrus were also grown, though to a lesser extent, within the study area. The dominant soil types in the Neyshabur plain are Aridisols and Entisols, which typically exhibit relatively high amounts of calcium carbonate and low soil organic carbon (SOC) content in their uppermost layers. A systematic grid sampling approach was employed, and then 150 surface soil samples were randomly collected (0–20 cm depth). Prior to analysis, the collected samples were air-dried and sieved to < 2 mm. Standard laboratory procedures were then utilized to determine the available soil phosphorus (P) content. In this study, the spatial distribution map of soil available phosphorus was generated using the Geostatistical Analyst tool in ArcGIS 10.5 software, applying the Empirical Bayesian method. Descriptive statistical analyses including minimum, maximum, mean, skewness, kurtosis, and standard deviation were performed to identify the statistical distribution of the data using IBM SPSS Statistics 27 software.

Results

The descriptive statistics of the measured available phosphorus are shown in Table 1. The statistics indicate that the available phosphorus in the study area ranges from 2.4 to 47.6 mg/kg, with a mean of 10.53 mg/kg. The skewness and kurtosis values suggest that the data distribution is within the normal range. Given the standard deviation of 7.8, it can be stated that the data dispersion is not very high, meaning that most of the available phosphorus values in the samples are relatively close to the mean of 10.53.

Table 1. Descriptive statistics of the soil available phosphorus data

Variable	Minimum	Maximum	Mean	Skewness	Kurtosis	Std
P (mg/kg)	2.4	47.6	10.5	0.2	0.4	7.8

The available phosphorus values were measured and presented for 150 soil samples. Figure 1 shows the spatial distribution map of soil available phosphorus generated using the Empirical Bayesian method within the study area.

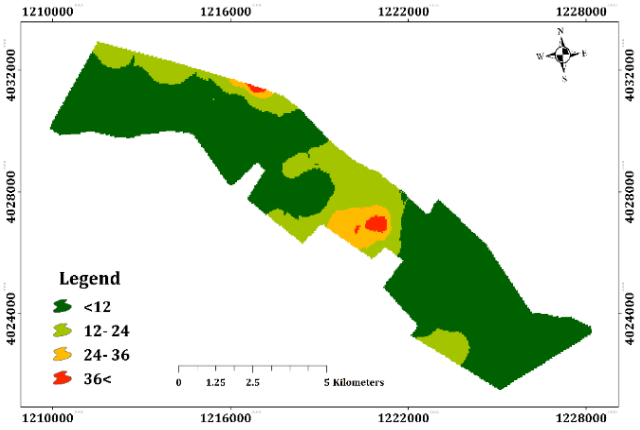


Figure 1. Mapping of soil available phosphorus using Empirical Bayesian Kriging

Plants typically show a positive response to phosphorus-containing fertilizers when available soil phosphorus falls below 12 mg/kg [2]. To map the spatial distribution of available soil phosphorus, four general ranges were used: deficient (less than 12 mg/kg), slightly deficient (12-24 mg/kg), optimal (24-36 mg/kg), and excess (greater than 36 mg/kg) [3]. The Empirical Bayesian Kriging (EBK) map of available soil phosphorus (RMSE = 6.677) in

Figure 1 reveals that most of the studied soils have available phosphorus concentrations below the critical level of 12 mg/kg. Overall, approximately 76.6% of the land area falls within the deficient category (less than 12 mg/kg), while 17.3% falls within the slightly deficient range (12-24 mg/kg). Only a small fraction of the land area falls within the optimal (2.7%, 24-36 mg/kg) or excess (3.4%, greater than 36 mg/kg) categories.

Discussion

The distribution of phosphorus concentration was approximately uniform in all directions, except for two small hot spots observed in the north and center of the study area. Given that a large portion of the study area is within the deficient range for available phosphorus (less than 12 mg/kg), it appears that the application of phosphate fertilizers in the agricultural lands of this region has not been based on soil testing. If this trend continues, it will limit agricultural productivity. Phosphorus is the second most important limiting factor for agricultural production in most regions of the world, including Iran, after nitrogen. Therefore, fertilizer recommendations in this region should be carried out with greater care to prevent the numerous negative consequences of phosphorus deficiency. A previous study on the status of major nutrients in some lands of Guilan province reported that a considerable number of the studied lands had concentrations lower than the critical level, which can significantly impact crop yields [6]. Additionally, a study on the spatial mapping of soil contamination by heavy metals in Esfarayen, North Khorasan province, showed that the empirical Bayesian kriging method, with a lower RMSE compared to other kriging methods, can be a more suitable approach for the spatial zoning of soil nutrients [7].

Conclusion

The results of this research evaluating the available soil phosphorus, based on the prepared map, showed that a high percentage of the land in the region is in a suboptimal nutritional condition for phosphorus. Given that a large part of the available phosphorus in Iran's calcareous soils quickly precipitates and becomes unavailable to plants, it is recommended that methods such as adding organic matter and applying phosphorus-containing fertilizers be quickly adopted in the lands of this region. Considering the significant role of this element in the food security of the community, and based on the obtained map, it is recommended that the application of phosphorus fertilizers be scientifically increased in areas where the amount of phosphorus is less than the optimal level for plants, based on soil testing.

References

1. Ghojehpour, E., Jalali, V., Jafari, A., & Mahmoodabadi, M. (2023). Feasibility of using Copula function in predicting soil available phosphorus and potassium. Agricultural Engineering, 45(4), 377-390.
2. karimi Amirkiasar, M., Kvoosi, M., & Shokri Vahed, H. (2013) . Laboratory and field evaluation some of extraction method to determine phosphorous availability and critical levels in some of paddy soils in Guilan. M.Sc. Thesis, Soil Science, Islamic Azad University, Karaj, Iran, 32 (1), 123-134.
3. Khazaie, E., Bostani, A. A., & Davatgar, N. (2017). Geostatic and GIS evaluation of spatial variability of nitrogen, phosphorus, potassium, and cation exchange capacity in agro-industrial land of Sharif Abad in Qazvin. Iranian Journal of Soil Research, 31(2), 195-213.
4. Mirzaei, R., & Sakizadeh, M. (2016). Comparison of interpolation methods for the estimation of groundwater contamination in Andimeshk-Shush Plain, Southwest of Iran. Environmental Science and Pollution Research, 23, 2758-2769.
5. Roshani, G., & Gharanjiki, A. (2015). Digital mapping of soil fertility for agricultural service centers of Golestan province using Kriging method. Agricultural Engineering, 37(2), 87-99.
6. Shokri Vahed, H., Davatgar, N., Kavoosi, M., Babazadeh jafari, Sh., Rezaee, L., & Shakouri, M. (2022). Overview of the Status of Macro Elements, Salinity, and Organic Carbon in Some Paddy Lands of Gilan Province. Iranian Journal of Soil Research , 36(2), 193-208.
7. Teymourzade, S., Mirzaei, R., & Mohammadi, M. (2019). Application of Empirical Bayesian Kriging to Map Soil Contamination by Heavy Metals (Case study: Esfarayen city). Scientific and Research Electronic Journals ,21(7), 89-105.
8. Wang, Y. P., Law, R. M., & Pak, B. (2010). A global model of carbon, nitrogen and phosphorus cycles for the terrestrial biosphere. Biogeosciences, 7(7), 2261-2282.
9. Wang, Y., Zhang, X., & Huang, C. (2009). Spatial variability of soil total nitrogen and soil total phosphorus under different land uses in a small watershed on the Loess Plateau, China. Geoderma, 150(1-2), 141-149.
10. Yin, C., Zhao, W., & Pereira, P. (2022). Soil conservation service underpins sustainable development goals. Global Ecology and Conservation, 33, e01974.

Advanced Engineering Days

aed.mersin.edu.tr

Comparison of geospatial based interpolation techniques for spatial distribution of Soil Organic Carbon (SOC)

Ali Keshavarzi [*1], Koyel Sur [2], Fuat Kaya [3], Shahla Rahmani Siyalarz [1]

[1] *University of Tehran, Department of Soil Science, Karaj, Iran, alikeshavarzi@ut.ac.ir, shahla.rahmani@ut.ac.ir*
[2] *Punjab Remote Sensing Centre, Ludhiana, Punjab, India, koyelsur3@gmail.com*
[3] *Isparta University of Applied Sciences, Department of Soil Science and Plant Nutrition, Çünür, Türkiye, fuatkaya@isparta.edu.tr*

Cite this study: Keshavarzi, A., Sur, K., Kaya, F., & Rahmani Siyalarz, Sh. (2024). Comparison of geospatial based interpolation techniques for spatial distribution of soil organic carbon (SOC). Advanced Engineering Days, 9, 476-479

Keywords
Soil Organic Carbon
Interpolation
Geostatistics
GIS
Iran

Abstract

Research on soil organic carbon (SOC) has gained popularity in recent times due to its influence on maintaining sustainable development goals. Interpolation techniques like Kriging, IDW, Nearest Neighbor, and Spline are valuable tools for assessing the spatial distribution of SOC. Traditional soil surveys are often time-consuming and not cost-effective. Therefore, geospatial techniques powered by mathematical and statistical interpolation techniques can help derive SOC from a smaller number of samples collected during the survey. This study compared the four mentioned interpolation techniques to create a continuous gridded surface layer. Based on the accuracy assessment, Kriging emerged as the most effective method due to its ability to compute weights based on both spatial location and semivariograms.

Introduction

Soil is an important natural resource composed of both organic and inorganic constituents, exhibiting different physical and chemical variations across locations [1]. Among these properties, soil organic matter (SOM) is particularly important. It plays a vital role in controlling soil fertility, ecosystem services, climate, and the water cycle [2]. Food security is therefore directly linked to SOM [3], and SOM also indirectly supports many other sustainable development goals [4]. Consequently, obtaining SOM maps is crucial for land degradation assessment, as they provide highly informative data. However, estimating soil components on-site is a very laborious procedure. It requires significant manpower and is not cost-effective. Therefore, reliable and low-cost methods for optimizing soil properties are essential. The increasing popularity of Geographic Information Systems (GIS) coupled with machine learning offers solutions for the challenges of soil organic carbon (SOC) assessment. These solutions involve reducing the number of field samples required across a selected region and utilizing various statistical and geostatistical approaches to estimate SOC's spatial variability [5]. Traditional statistical techniques faced difficulties in spatially allocating soil properties at unsampled locations. However, with the advent of GIS techniques, assessing spatial variability has become easier [6]. Geostatistics can effectively handle the spatial allocation of measured SOM variability and its inconsistencies, while also reducing field execution costs. Therefore, the main objective of this study is to evaluate the potential capabilities of different interpolation techniques, such as Kriging, Inverse Distance Weighting (IDW), Nearest Neighbor, and Spline-based interpolation, for predicting the spatial distribution of SOC.

Material and Method

Site description

This research was conducted within an 85 km^2 study area located in the semi-arid Neyshabur plain, situated in the Khorasan-e-Razavi province of northeastern Iran. Elevation at the site ranged from 1197 to 1316 m, with an average annual rainfall of 233.7 mm and the mean temperature of 14.5°C. Rainfed and irrigated agriculture were the predominant land uses, with winter wheat being the primary crop cultivated; however, barley and citrus were

also grown, though to a lesser extent, within the study area. The dominant soil types in the Neyshabur plain are Aridisols and Entisols, which typically exhibit relatively high amounts of calcium carbonate and low soil organic carbon (SOC) content in their uppermost layers. A systematic grid sampling approach was employed, and then 165 surface soil samples were randomly collected (0–20 cm depth). Prior to analysis, the collected samples were air-dried and sieved to < 2 mm. Standard laboratory procedures were then utilized to determine the soil organic carbon (SOC) content.

Geospatial techniques used in the study

(1) Kriging Method: Kriging is a geostatistical approach that utilizes a variogram, formed by the spatial distribution of data, instead of the actual values themselves. Weights are calculated based on the spatial data points and their original influence, allowing this method to reduce bias towards the input values [7]; (2) Inverse Distance Weighting (IDW) Method: This technique assigns weights to interpolating points based on the inverse of their distance from the interpolation point. Since these are independent data points, they only influence the interpolated points around their periphery [8]; (3) Nearest Neighborhood Method: The nearest neighborhood method is a deterministic approach that finds the closest subset of input samples to a query point. It then applies weights to these samples based on their proportionate areas [9]; (4) Spline Method: Spline interpolation utilizes thin-plate smoothing splines with tension to calculate a two-dimensional minimum curvature surface. The specific spline curve used in this method is referenced from Mitas and Mitasova [10].

Results

The four interpolation techniques mentioned earlier (Kriging, Inverse Distance Weighting (IDW), Nearest Neighbor, and Spline) were chosen due to their popularity and established performance in soil science. Here's a comparison of the range of variability in SOC (Soil Organic Carbon) estimated by each technique: Kriging: 0.39 to 1.90, Inverse Distance Weighting (IDW): 0.32 to 2.14, Nearest Neighbor: 0.33 to 2.14, Spline Interpolation: 0.01 to 2.29. Following the interpolation of the surface, the results were compared to ground data points. Kriging exhibited the lowest Root Mean Square Error (RMSE) of approximately 0.13, while the other techniques had considerably higher values exceeding 0.3.

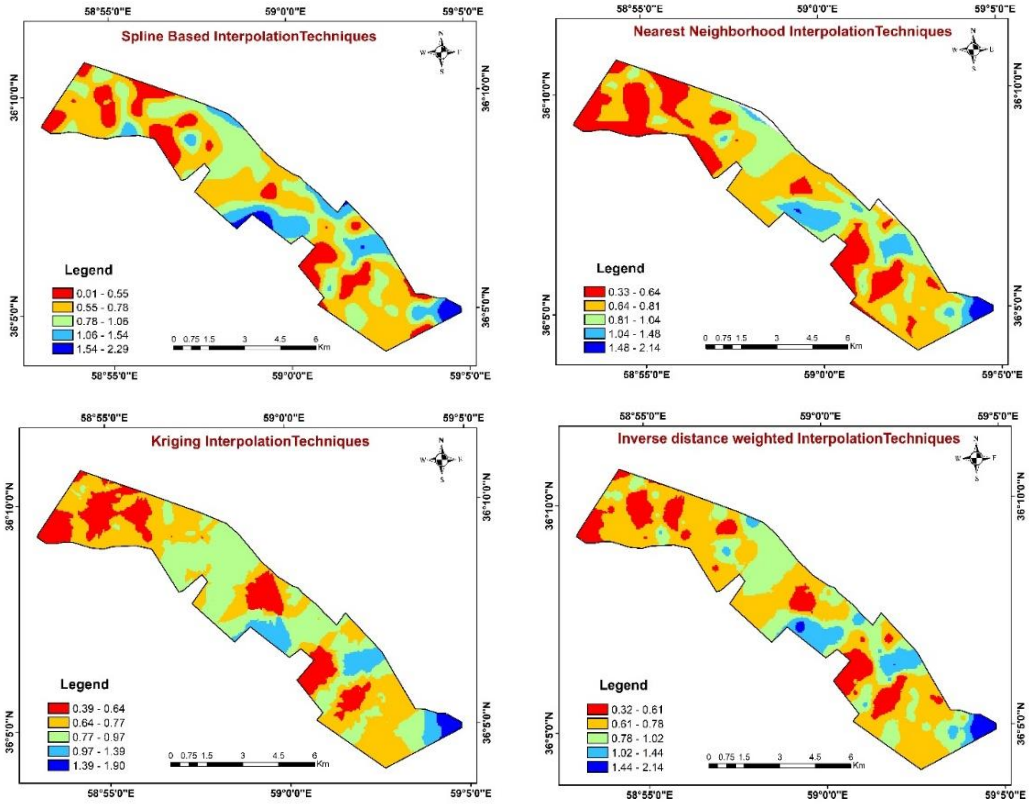


Figure 1: SOC after applying four different interpolation techniques

Discussion

The comparison of interpolation techniques for estimating Soil Organic Carbon (SOC) reveals significant differences in their performance and range of variability. Kriging emerged as the most accurate method, demonstrating the lowest Root Mean Square Error (RMSE) of approximately 0.13 when compared to ground data points. This superior performance can be attributed to Kriging's ability to account for spatial autocorrelation and provide a measure of prediction uncertainty, making it particularly well-suited for soil science applications. In contrast, Inverse Distance Weighting (IDW), Nearest Neighbor, and Spline interpolation techniques exhibited considerably higher RMSE values, exceeding 0.3. This indicates that these methods may introduce more errors in SOC estimation compared to Kriging. However, it's important to note that each method has its own strengths and limitations. For instance, IDW and Nearest Neighbor are simpler to implement and computationally less intensive, which can be advantageous in certain scenarios. The range of variability in SOC estimates also differed among the interpolation techniques. Spline interpolation showed the widest range (0.01 to 2.29), potentially overestimating the variability in SOC content. Kriging, on the other hand, produced a narrower and more conservative range (0.39 to 1.90), which may better reflect the actual variability in SOC across the study area. IDW and Nearest Neighbor methods yielded similar ranges (0.32 to 2.14 and 0.33 to 2.14, respectively), falling between Kriging and Spline in terms of estimated variability. These differences highlight the importance of carefully selecting an interpolation method based on the specific characteristics of the data and the study objectives [11].

Conclusion

This study compared the effectiveness of four interpolation techniques (Kriging, Inverse Distance Weighting (IDW), Nearest Neighbor, and Spline) for mapping the spatial distribution of soil organic carbon (SOC) across a semi-arid region in northeastern Iran. The evaluation revealed Kriging as the most accurate method, achieving the lowest Root Mean Square Error (RMSE) of 0.13 compared to significantly higher errors in the other techniques. This superiority of Kriging stems from its unique ability to incorporate spatial autocorrelation, represented by the variogram, into the interpolation process. This allows Kriging to assign weights to data points based on both their distance and spatial dependence, leading to a more realistic representation of the underlying spatial variability of SOC. The findings of this study highlight the valuable role of geostatistical techniques like Kriging in optimizing soil property assessments. By reducing the number of required field samples and providing accurate spatial maps, Kriging offers a cost-effective and efficient approach for monitoring SOC content and supporting sustainable land management practices. These maps can be instrumental in pinpointing areas with low SOC levels, enabling targeted interventions such as organic matter amendments to improve soil fertility and enhance food security in the region. Furthermore, the ability to map SOC variations can contribute to achieving broader sustainable development goals linked to soil health and ecosystem services.

References

1. Jandl, R., Rodeghiero, M., Martinez, C., Cotrufo, M. F., Bampa, F., Van Wesemael, B., ... & Miglietta, F. (2014). Current status, uncertainty and future needs in soil organic carbon monitoring. Science of the total environment, 468, 376-383.
2. Xie, S., Li, Y., Wang, X., Liu, Z., Ma, K., & Ding, L. (2021). Research on estimation models of the spectral characteristics of soil organic matter based on the soil particle size. Spectrochimica Acta Part A: Molecular and Biomolecular Spectroscopy, 260, 119963.
3. Cotrufo, M. F., & Lavallee, J. M. (2022). Soil organic matter formation, persistence, and functioning: A synthesis of current understanding to inform its conservation and regeneration. Advances in agronomy, 172, 1-66.
4. Lorenz, K., Lal, R., & Ehlers, K. (2019). Soil organic carbon stock as an indicator for monitoring land and soil degradation in relation to U nited N ations' S ustainable D evelopment G oals. Land Degradation & Development, 30(7), 824-838.
5. Paul, O. O., Sekhon, B. S., & Sharma, S. (2019). Spatial variability and simulation of soil organic carbon under different land use systems: geostatistical approach. Agroforestry systems, 93, 1389-1398.
6. Bhunia, G. S., Shit, P. K., & Maiti, R. (2018). Comparison of GIS-based interpolation methods for spatial distribution of soil organic carbon (SOC). Journal of the Saudi Society of Agricultural Sciences, 17(2), 114-126.
7. Arun, P. V. (2013). A comparative analysis of different DEM interpolation methods. The Egyptian journal of remote sensing and space science, 16(2), 133-139.
8. Robinson, T. P., & Metternicht, G. (2006). Testing the performance of spatial interpolation techniques for mapping soil properties. Computers and electronics in agriculture, 50(2), 97-108.

9. Sibson, R. (1981). A brief description of natural neighbour interpolation. Interpreting multivariate data, 21-36.
10. Mitášová, H., & Mitáš, L. (1993). Interpolation by regularized spline with tension: I. Theory and implementation. Mathematical geology, 25, 641-655.
11. Wu, Y. H., & Hung, M. C. (2016). Comparison of spatial interpolation techniques using visualization and quantitative assessment. Applications of spatial statistics, 17-34.

Advanced Engineering Days

aed.mersin.edu.tr

Prediction of potato leaf disease severity using deep learning regression

Sayed Javad Sajadi*[1], Fakhtak Taliei [1]

[1] *Gonbad Kavous University, Department of Plant Production, Iran, sajadi@gonbad.ac.ir, taliei@gonbad.ac.ir*

Cite this study: Sajadi, S. J., & Taliei, F. (2024). Prediction of potato leaf disease severity using deep learning regression. Advanced Engineering Days, 9, 480-482

Keywords
Deep Learning Regression
Potato Leaf Blight
Precision Agriculture
Automated Disease Diagnosis

Abstract

This study presents a deep-learning regression model for automated predicting potato leaf blight severity utilizing digital images. The model's effectiveness was meticulously evaluated against independent test datasets and benchmarked against established machine learning models such as Support Vector Machine (SVM) regression, Random Forest (RF) regression, and even expert scoring by agricultural professionals. The deep learning model demonstrably achieved superior predictive accuracy, attaining a Mean Squared Error (MSE) of 0.45, Root Mean Square Error (RMSE) of 0.67, and Coefficient of Determination (R^2) of 0.89, surpassing all baseline models and methods employed. These findings underscore the substantial potential of deep learning in automating and significantly improving the precision of plant disease diagnosis. This enhanced capability is paramount for the timely and effective implementation of disease management strategies within the agricultural sector. While the model exhibits promising results, the study acknowledges limitations such as dependence on the quality and breadth of the training data, as well as challenges associated with generalizability to previously unseen scenarios. By offering a valuable tool that empowers data-driven decision-making and bolsters the implementation of sustainable agricultural practices, this study contributes significantly to advancing precision agriculture.

Introduction

Potato crops face a significant threat from leaf diseases such as late blight and early blight, caused by the fungi *Phytophthora infestans* and *Alternaria solani*. These diseases can devastate potato crops, leading to substantial economic losses due to reduced yield and compromised quality. In extreme cases, late blight can cause complete crop failure under favourable conditions for the fungus. The disease rapidly destroys foliage, which can occur within a few days in wet weather. While generally less aggressive, early blight can also significantly reduce yields, particularly when potato plants are stressed by factors like drought or nutrient deficiencies [1]

Accurate and early detection of these diseases is paramount for several reasons. Timely intervention upon detection can prevent the spread of the disease to other plants or fields. Additionally, accurate detection ensures that pesticides are only used when necessary, reducing overall chemical use. This targeted approach benefits the environment and lowers production costs for farmers.

Deep learning models, particularly convolutional neural networks (CNNs), have emerged as powerful tools for achieving these goals [1,2]. These models have demonstrated high accuracy rates, with some studies reporting up to 99% success rates. Deep learning can significantly improve the speed and reliability of disease diagnosis, allowing for timely and effective disease management. Furthermore, deep learning for disease prediction not only aids in rapid disease identification but also supports the development of precision agriculture systems. These systems empower farmers to make informed decisions, ultimately protecting the health and productivity of potato crops.

This study aims to develop and evaluate a deep-learning regression model using digital images for accurate disease severity prediction. The model's performance will be rigorously assessed using established metrics like mean squared error (MSE), root mean square error (RMSE), and coefficient of determination (R^2).

Material and Method

This study used a dataset encompassing 1,000 potato leaf images, ensuring sufficient visual diversity for the deep-learning model to effectively learn and identify disease characteristics. An additional 1,000 images of healthy leaves were incorporated to facilitate accurate disease classification. Each image was meticulously annotated with disease information and a severity score ranging from 0 (healthy) to 9 (severe infection).

Data augmentation techniques enhanced the model's robustness and mitigated overfitting. These techniques involved random rotations, flips, zooming, and colour adjustments, effectively simulating various lighting conditions and image orientations encountered in real-world scenarios. The dataset was partitioned for training, validation, and testing purposes, following a 70/15/15 per cent split. Before commencing the training process, all images underwent preprocessing to establish consistency. This crucial step involved normalizing pixel values and resizing the images to conform to the specific input size requirements of the deep learning model. These preprocessing steps are essential for preparing the images for optimal analysis by the model.

Convolutional Neural Networks (CNNs) have established themselves as a highly effective approach for image processing and feature learning tasks. Given these strengths, a CNN architecture was chosen for the disease severity prediction. The selected architecture incorporates an input layer, convolutional layers, activation functions, pooling layers, fully connected layers, dropout layers, and an output layer. The input layer receives the preprocessed potato leaf images, typically in a fixed size, such as 256x256x3 for colour images. Subsequent convolutional layers are responsible for extracting features from the images. Each layer employs learnable filters to capture disease-relevant patterns, such as edges, textures, and complex shapes. To introduce non-linearity and enable the model to learn more intricate relationships, non-linear activation functions like ReLU (Rectified Linear Unit) are implemented following each convolutional layer. Pooling layers then reduce the spatial dimensionality of the features, leading to a decrease in the number of network parameters and computations. This reduction helps to mitigate overfitting. Normalization techniques are strategically employed to standardize layer inputs, accelerating training and enhancing overall model performance [3-6].

Fully connected layers perform high-level reasoning within the neural network following the convolutional and pooling layers. These layers connect each neuron to all activations in the preceding layer, smoothing the feature maps. Dropout layers are strategically placed to prevent overfitting by randomly setting a portion of the input units to zero during training. Finally, the output layer consists of a single neuron with a linear activation function responsible for generating a continuous value representing the predicted disease severity score.

Results

The results assess the model's generalization capabilities on a separate test set containing 300 potato leaf images not encountered during training. The evaluation employed established metrics like Mean Squared Error (MSE), Root Mean Square Error (RMSE), and Coefficient of Determination (R^2) to quantify the model's effectiveness in predicting disease severity scores. The model achieved a commendable performance on the test set, reflected by an MSE of 0.45, RMSE of 0.67, and R^2 of 0.89. When estimating disease severity scores, these metrics translate to high prediction accuracy with a relatively low error rate. Furthermore, a visual comparison of predicted versus actual scores demonstrated the model's proficiency in identifying mild to moderate disease symptoms. It effectively distinguished severely diseased leaves from healthy or minimally affected ones. However, a slight underestimation of scores was observed for both extremes – severely diseased leaves and those with minimal or no damage. The deep learning regression model outperformed traditional machine learning models utilized as baselines, including Support Vector Machine (SVM) regression and Random Forest (RF) regression. SVM achieved an MSE of 1.20, RMSE of 1.10, and R^2 of 0.70, while RF regression attained an MSE of 0.90, RMSE of 0.95, and R^2 of 0.75.

Table 1. The performance of the deep learning regression model on a test dataset

Model	Mean Squared Error (MSE)	Root Mean Squared Error (RMSE)	Coefficient of Determination (R^2)	Notes
CNN Deep Learning	0.45	0.67	0.89	The CNN-based model with optimized architecture for image regression tasks.
Neural Network	0.85	0.92	0.78	A neural network with one hidden layer
Gaussian Process Regression	0.95	0.97	0.76	Non-parametric, probabilistic regression
Support Vector Machine (SVM)	1.20	1.10	0.70	Traditional ML model using a linear kernel and hyperparameter tuning.
Random Forest (RF)	0.90	0.95	0.75	Ensemble ML model with multiple decision trees and averaging for predictions.

Discussion

A deep-learning regression model was developed to evaluate potato leaf disease severity from digital images. This model demonstrated promising capabilities, achieving high accuracy in predicting disease severity scores. The convolutional neural network (CNN) architecture employed by the model allows it to extract intricate features from the images, potentially surpassing human detection of subtle disease indicators. Additionally, the model exhibits transfer learning potential. A pre-trained network on a large dataset can be adapted for this specific task, leveraging existing knowledge and reducing extensive training time. Furthermore, the model's scalability allows it to handle larger datasets and more complex disease-scoring tasks, making it suitable for real-world agricultural applications. The model's rapid image processing and analysis capabilities present a significant opportunity for automation in disease diagnosis, potentially leading to more streamlined crop management practices.

However, the model's performance is contingent upon the quality and variety of training data. Underrepresenting disease types or severities within the training data can lead to biased predictions. While the model performed well on the test set, its generalizability to entirely unseen data, such as data from different geographical locations or potato varieties, requires further investigation. Due to their complexity, deep learning models are susceptible to overfitting, where the model performs exceptionally well on training data but poorly on new information. Mitigation techniques were employed to address this risk; however, continued monitoring is crucial to ensure generalizability. Additionally, the inherent complexity of deep learning models makes it challenging to understand the reasoning behind specific predictions. Finally, training deep learning models necessitates significant computational resources, potentially limiting accessibility for some potential users, particularly in resource-constrained settings.

Conclusion

This deep-learning regression model significantly advances potato leaf disease diagnosis. Its accuracy, feature learning, and scalability strengths make it a valuable tool for agricultural professionals. However, addressing the limitations identified through continued research and development is essential to fully realize its potential for crop management and disease control strategies.

Future research endeavours can address the limitations by collecting a more comprehensive data set encompassing a wider range of disease types, severity levels, and environmental conditions. Furthermore, domain adaptation techniques can improve the model's generalizability for diverse regions and potato varieties. Investigating model simplification strategies can help mitigate the risk of overfitting while maintaining high prediction accuracy. Additionally, developing methods to enhance interpretability, such as feature visualization or model explanation tools, would be beneficial. Finally, optimizing the model for reduced computational demands can broaden its accessibility for deployment in various settings.

References

1. Agarwal, M., Sinha, A., Gupta, S. Kr., Mishra, D., & Mishra, R. (2020). Potato Crop Disease Classification Using Convolutional Neural Network. In A. K. Somani, R. S. Shekhawat, A. Mundra, S. Srivastava, & V. K. Verma (Eds.), Smart Systems and IoT: Innovations in Computing (141), 391–400.
2. Anim-Ayeko, A. O., Schillaci, C., & Lipani, A. (2023). Automatic blight disease detection in potato (Solanum tuberosum L.) and tomato (Solanum lycopersicum, L. 1753) plants using deep learning. Smart Agricultural Technology, 4, 100178.
3. Arshaghi, A., Ashourian, M., & Ghabeli, L. (2023). Potato diseases detection and classification using deep learning methods. Multimedia Tools and Applications, 82(4), 5725–5742.
4. Asif, M. K. R., Rahman, M. A., & Hena, M. H. (2020). CNN based disease detection approach on potato leaves. 2020 3rd International Conference on Intelligent Sustainable Systems (ICISS), 428–432.
5. Barman, U., Sahu, D., Barman, G. G., & Das, J. (2020). Comparative assessment of deep learning to detect the leaf diseases of potato based on data augmentation. 2020 International Conference on Computational Performance Evaluation (ComPE), 682–687.
6. Chen, W., Chen, J., Zeb, A., Yang, S., & Zhang, D. (2022). Mobile convolution neural network for the recognition of potato leaf disease images. Multimedia Tools and Applications, 81(15), 20797–20816.

Advanced Engineering Days

aed.mersin.edu.tr

Effect of Thermal Pre-Treatment of γ-Alumina and Ceria-Zirconia on Three-Way Catalyst Performance

Hossein Sheikh[1], Yousef Zaynali *[2]

[1]Ayegh Khodro Toos Company, Catalyst Department, Mashhad, hosseinsheiikh@gmail.com
[2]University of Mohaghegh Ardabili, Chemical Engineering, Ardabil, y.zaynali@uma.ac.ir

Cite this study: Sheikh, H., & Zaynali, Y. (2024). Effect of Thermal Pre-Treatment of g-Alumina and Ceria-Zirconia on Three-Way Catalyst Performance. Advanced Engineering Days, 9, 483-485.

Keywords
Three-way catalyst
Aging
Thermal pre-treatment
Ceria-zirconia
Alumina

Abstract

During the aging process of automotive catalysts, their effectiveness declines over time, leading to the inefficient use of resources. Developing durable and efficient catalysts requires a comprehensive understanding of catalyst aging mechanisms. This study focuses on investigating the light-off changes that occur during thermally pre-treated oxidized supports of active metals. Various commercial Alumina and Ceria-zirconia (CZ) precursors that underwent different thermal pre-treatments were analyzed to establish relationships between surface area reduction and vehicle catalyst performance. The synthesized PtPdRh/CeZrO2/Al2O3 catalysts were then evaluated by performance test. Overall, the study sheds light on the impact of support material's thermal pre-treatment on catalyst performance.

Introduction

Automobile exhaust emissions are a major global pollution source, affecting the environment and public health. Three-way catalysts (TWCs) have been pivotal in controlling automotive emissions since the late 20th century. Catalyst manufacturers focus on improving reactant access by depositing catalytic components on carriers. TWCs face challenging chemical environments due to exothermic reactions, leading to extensive development efforts.

Inorganic support materials like alumina and ceria-zirconia mixed oxide are commonly used as catalyst carriers, providing various pore sizes for reactant interaction. High temperatures, exceeding 1000°C, can deactivate catalysts, prompting studies on aging-induced deactivation in TWCs.

Alumina is valued for its high-temperature durability and surface area, yet transforms at temperatures over 950°C (Lindqvist, 2014). Ceria, often combined with alumina in TWCs, enhances performance through oxygen storage capacity and noble metal catalyst stabilization(Alikin, Denisov, & Vedyagin, 2019). Zirconium in ceria improves oxygen storage and thermal stability, addressing challenges like maintaining the surface area, preventing sintering, and sustaining oxygen storage (Chen, Cheng, Seo, Schwank, & McCabe, 2015).

The interaction between active metals and oxide supports is critical, with carrier properties influencing this interaction. Excessive palladium loading can lead to deactivation, while rhodium diffusion into alumina can render it ineffective (Rood, Eslava, Manigrasso, & Bannister, 2020).

Factors like sintering, agglomeration, and support properties influence TWC performance, with ongoing research seeking to understand the role of support surface area in deactivation compared to phenomena like platinum-group metal agglomeration and oxygen mobility.

Material and Method

The γ-alumina powders (LA1, LA2) and Ceria-Zirconia (CZ1, CZ2) procured from Sasol and Sinocera Co. in industrial quality for this research. Additionally, Hexahydroxo Platinate (IV) monoethanolamine solution (18.55%), Palladium (II) Nitrate Solution (20.06%), and Rhodium (III) Nitrate Solution (9.73%) were obtained from BASF Co. in industrial grade from Germany. Other chemical substances like Boehmite, Barium acetate, Lanthanum (III) nitrate, Zirconium (IV) oxynitrate, and Nickel (II) nitrate were sourced from Fluka, Aldrich, and Merck companies in analytical grade.

Certain varieties of alumina and CZ, such as LA1, LA2, CZ1, and CZ2, underwent thermal treatment in an electric furnace at temperatures of 550, 750, 850, 950, and 1000°C with a temperature increase rate of 5°C/min for 8 hours at atmospheric environment to modify surface characteristics and phase morphology. Subsequently, catalyst slurries were formulated using TPT (thermally pre_treated) materials and labeled with Two or Three-Part designations: the initial segment indicates the support type, the following part specifies the TPT temperature and the final segment denotes whether the samples were freshly prepared or aged. For example, LA03-950-A signifies LA03 subjected to thermal processing at 950°C with subsequent aging.

Twenty-one variations of PtPdRh/CeZrO2/Al2O3 model catalysts were created using the incipient wetness impregnation technique, employing different TPT supports. The general process for all the synthesized catalysts involved immersing Alumina, Ceria-Zirconia, Boehmite, Barium acetate, Lanthanum nitrate, zirconium oxynitrate, Nickel nitrate in a solution containing Hexahydroxo Platinate (IV) monoethanolamine solution, Palladium (II) Nitrate Solution, and Rhodium (III) Nitrate Solution at room temperature overnight.

In this research, Cordierite monoliths with a cell density of 600 cells per square inch, an outer diameter of 1 in., and a length of 2 in. were utilized. The coating process begins with deep coating and, Subsequently, the monolith is removed from the slurry using pressurized air to clean its blocked channels from excess coating material. Once adequately coated, the monolith is dried. If the loading amount is suitable, the monoliths are dried at 150˚C for 1 hour and then subjected to calcination at 550˚C for 3 hours. The final product is weighed, and any weight change on a dry basis is recorded, aiding in the calculation of noble metal loading.

The prepared catalysts undergo an aging process in a wet air stream (1:10 water: air, v/v). The wet stream is flowed at a volumetric rate of 40 ml/min through a tubular quartz reactor with a diameter of 22 mm, where the monolithic catalyst sample is positioned. The tubular quartz reactor, placed in furnace itself, is oriented vertically with the flow moving from top to bottom. Temperature monitoring occurs directly above the catalyst within the reactor, guiding the temperature control process. The catalysts are aged at 1000°C for 8 hours, with the tubular furnace heating up at a rate of 5°C/min. Once the aging is completed, the wet air flow is halted, and the reactor naturally cools down.

The catalytic performance was evaluated in a stainless-steel reactor where all gas lines directed the mixed reactants to be heated in a furnace, with temperature monitored using a thermocouple. The gas composition included [NO] at 800 ppm, [C3H6] at 110 ppm, [CO2] at 14 vol%, [O2] at 0.57 vol%, [CO] at 0.9 vol%, and N2 as the carrier gas, with a total flow rate of 20000 ml min-1. The gas hourly space velocity (GHSV) of the combined gas mixture was maintained at 25000 h^{-1}. The temperature was incrementally raised and lowered at 20°C/min until reaching the temperature of 50% conversion; T_{50} better called light-off temperature. Downstream, the gas effluents were cooled and analyzed using a gas analyzer model AVL DiTEST 1000.

Results and discussion

The performance of the catalysts in terms of T_{50} values for NO, C_3H_6, and CO conversion is depicted in Figure 1. The pretreatment of Alumina and Ceria-Zirconia at temperatures of 550, 850, 950, and 1000°C has no significant effect on the catalysts' performance, even as the Alumina undergoes a phase change from γ to α. Examination of the aged catalysts reveals no substantial differences in their light-off performance, with similar trends observed in the T_{50} values for CO, HC and, NO conversion.

Conclusion

In summary, our research investigated the effects of sintering and thermal treatment on three-way catalyst performance. Theoretical analysis indicates that sintering can reduce pore accessibility, hindering reactant diffusion and potentially limiting chemical reactions. It may also result in the entrapment of catalytic components, leading to catalyst deactivation. However, our practical observations demonstrated that the temperature of the thermal treatment applied to the alumina support did not significantly impact the overall efficacy of the catalysts in terms of exhaust gas conversion. Additionally, assessments on aged catalyst samples supported these findings, showing no notable variations in T50 values. This implies that while surface area plays a role, factors like particle size, platinum-group metal distribution, and phenomena such as sintering may have a more pronounced influence on CO, HC, and NO conversion rates. Therefore, optimizing catalyst performance necessitates a thorough understanding and consideration of these elements. Further investigation and experimentation are vital to deepen our comprehension of how the catalyst behaves under diverse aging conditions and to identify potential factors that could affect its effectiveness.

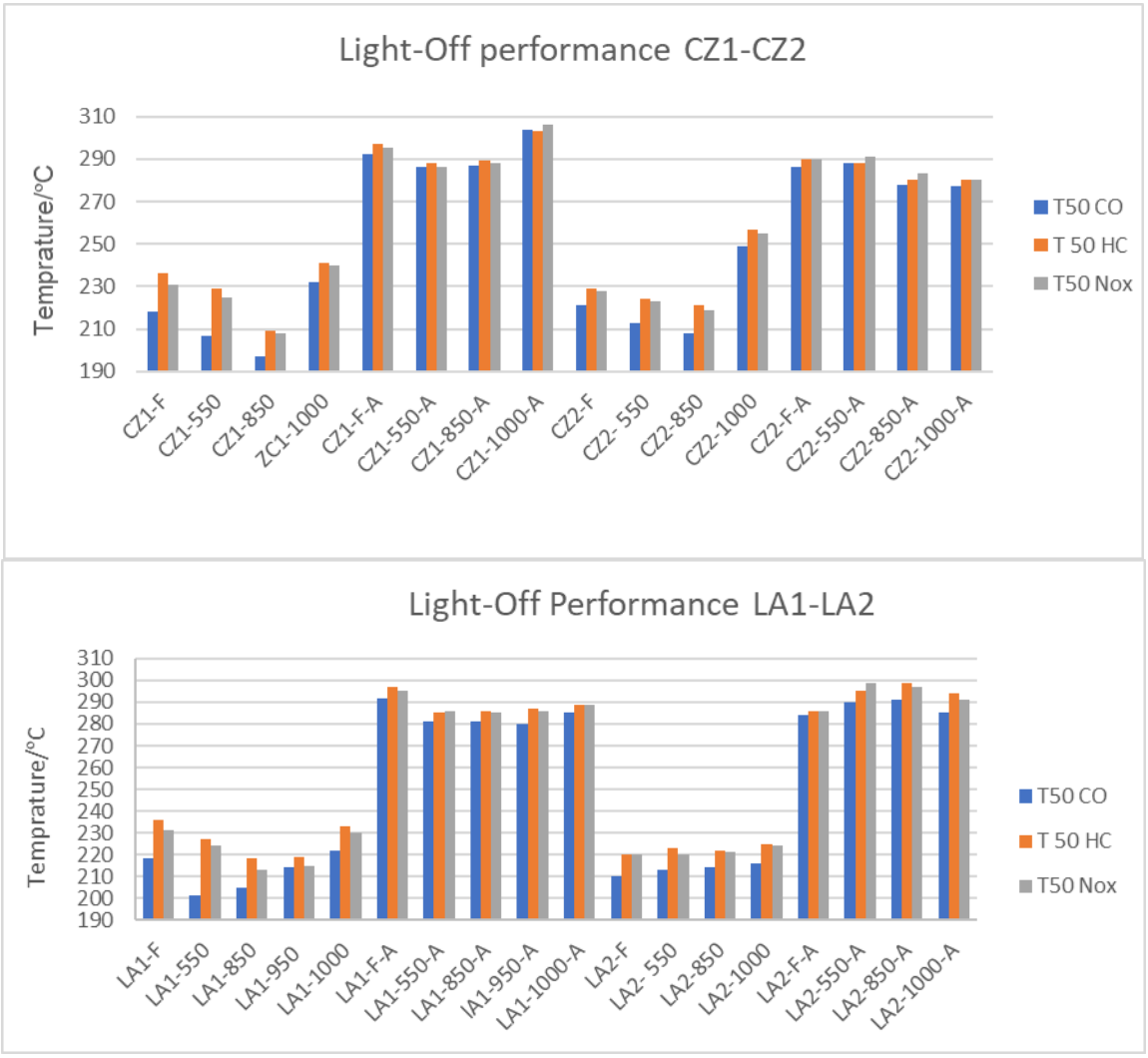


Figure 1. Light-off performance of prepared catalyst.

References

Alikin, E. A., Denisov, S. P., & Vedyagin, A. A. (2019). Partial regeneration of model TWC after high-temperature aging on engine bench. *Topics in Catalysis, 62*(1), 324-330.

Chen, X., Cheng, Y., Seo, C. Y., Schwank, J. W., & McCabe, R. W. (2015). Aging, re-dispersion, and catalytic oxidation characteristics of model Pd/Al2O3 automotive three-way catalysts. *Applied Catalysis B: Environmental, 163*, 499-509.

Lindqvist, S. (2014). Characterization of automotive catalyst ageing.

Rood, S., Eslava, S., Manigrasso, A., & Bannister, C. (2020). Recent advances in gasoline three-way catalyst formulation: A review. *Proceedings of the Institution of Mechanical Engineers, Part D: Journal of Automobile Engineering, 234*(4), 936-949.

Advanced Engineering Days

aed.mersin.edu.tr

Humidification modeling in a wetted wall tower

Saghar Babaei [1], Kamran Keynejad [*1], Hedayat Azizpour [2] Mohammad Mahdi Heydari [1], Sara Mansouri [1]

[1]*University of Tehran, college of Engineering, Fouman Faculty of Engineering, Iran, sagharbabaei98@gmail.com, kamran.keynejad@ut.ac.ir, M.m.heydari77@ut.ac.ir, saramns1999@gmail.com*
[2]*University of Tehran, School of Chemical Engineering, College of Engineering, Iran, h.azizpour@ut.ac.ir*

Cite this study: Babaei, S., Keynejad, K., Azizpour, H., Heydari, S. H., & Mansouri, S. (2024). Modeling a humidification in a wetted wall tower. Advanced Engineering Days, 9, 486-488

Keywords
Humidification
Dehumidification
Wetted wall tower
Mathematical Modeling

Abstract

In this research, we first investigated desalination methods and types of humidification-dehumidification processes. Then, we explained the concept of a wetted-wall tower and discussed modeling it for desalination, humidification, and dehumidification operations. Finally, we studied the effects of diameter, height, and temperature changes to achieve the highest relative humidity. The results showed that a wetted-wall tower can be used to produce drinking water under conditions close to ambient. Increasing the relative humidity to approximately 85% makes this possible.

Introduction

Humidification is a crucial process in various industrial applications, such as air conditioning, food processing, and chemical engineering. Wetted wall towers are commonly used for humidification due to their simplicity and effectiveness. Modeling the humidification process in a wetted wall tower is essential for optimizing the design and operation of these systems. COMSOL Multiphysics, a powerful finite element analysis software, has been widely used to simulate and analyze various physical phenomena, including heat and mass transfer in humidification processes.

Several studies have investigated the modeling of humidification in wetted wall towers using COMSOL Multiphysics. Kharangate et al. (2015) developed a 2D axisymmetric model of a wetted wall tower using COMSOL to study the heat and mass transfer processes during humidification. They considered the effects of various parameters, such as air velocity, water temperature, and wall wetting conditions, on the humidification performance. The model results were validated against experimental data, showing good agreement.

Bahreini et al. (2017) used COMSOL to simulate a counter-flow wetted wall humidifier. They developed a 3D model considering the coupled heat and mass transfer processes and the influence of the liquid film thickness on the humidification efficiency. The model was used to optimize the design parameters, such as the tower height and the air and water flow rates, to achieve the desired humidification performance.

Ahmadi et al. (2018) investigated the humidification process in a wetted wall column using COMSOL. They developed a comprehensive 3D model that accounted for the heat and mass transfer, fluid flow, and the presence of packing materials. The model was validated against experimental data and used to study the effects of various operating conditions on the humidification efficiency and pressure drop.

Rasouli et al. (2019) used COMSOL to model a novel humidification system consisting of a wetted wall tower integrated with a thermoelectric cooler. They developed a 3D model to simulate the coupled heat and mass transfer processes and the thermoelectric effect. The model was used to optimize the system design and operating conditions for enhanced humidification performance and energy efficiency.

Modeling

The geometry considered in this modeling is a wetted-wall tower with a height of 12 meters, a diameter of 4 cm, an evaporation rate of 1 meter per second, and a relative humidity of 74%. The major equations of this system are:

$$\rho\frac{\partial \mathbf{u}}{\partial t}+\rho(\mathbf{u}.\nabla)\mathbf{u}=\nabla.[-p\mathbf{I}+\mathbf{K}]+\mathbf{F} \quad (1)$$

$$d_z M_v\frac{\partial c_v}{\partial t}+d_z M_v\mathbf{u}.\nabla c_v+\nabla.\mathbf{g}_w=d_z G \quad (2)$$

$$d_z\rho C_p\frac{\partial T}{\partial t}+d_z\rho C_p\mathbf{u}.\nabla T+\nabla.\mathbf{q}=d_z Q+q_0+d_z Q_p+d_z Q_{vd} \quad (3)$$

In these equations, F is the force in Newtons, u is the speed in meters per second, dz is the mass in meters, MV is the molar mass of steam in grams per mole, μ is the viscosity in kilograms per meter per second, K is the permeability in square meters, and l is the height. In meters, ρ is the density in kilograms per cubic meter, CV is the vapor concentration in grams per cubic meter.

Solving these equations has been done using COMSOL software version 6.1. In this software, modules related to physics of mass transfer, heat transfer and laminar flow are used. The conditions are shown in Figure 1.

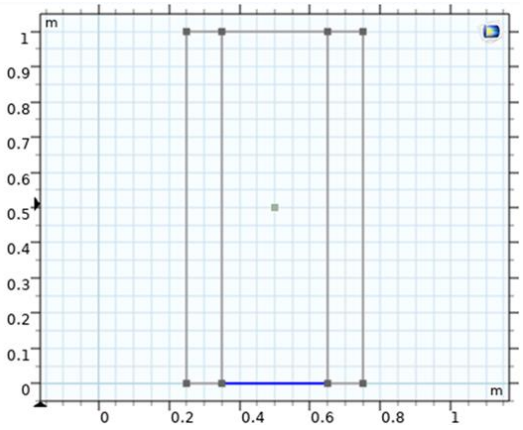


Figure 1. The conditions schematic of the tower in two dimensions

In the add physics section, fluid flow and two-phase flow and then laminar flow are selected for air and water. Then the input and output speeds were determined. Symmetry was chosen for the gas part, because we cut the whole tower in half to make it faster. Inlet velocity and temperature were determined for air and water. Modeling data is shown in Table 1.

Table 1. data input

	Parameter	unit	amount
1	Water inlet temperature	k	293.15
2	Water outlet temperature	k	273.15
3	Air inlet temperature	k	298.15
4	Air outlet temperature	k	280.15
5	diameter	cm	4-8
6	height	m	12-6
7	Water velocity	m/s	1
8	Air velocity	m/s	5
9	Evaporation velocity	m/s	1

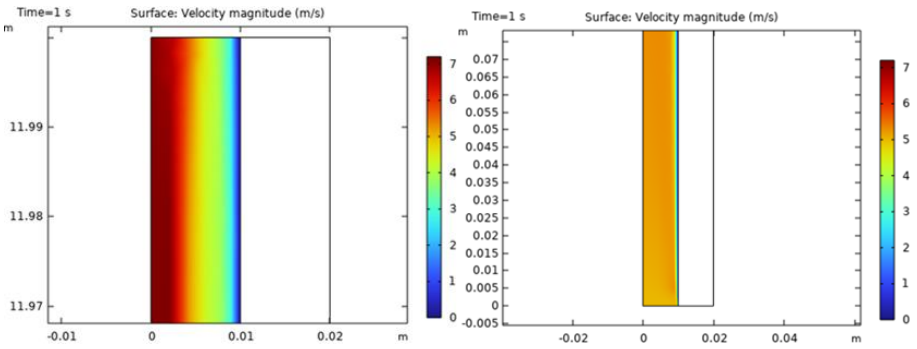
Results and Discussion

Figure 2-a shows the distribution of air speed at the top of the tower and Figure 2-b shows the distribution of air speed at the bottom of the tower.

Figure 3-a shows the water velocity distribution at the top of the tower and Figure 3-b shows the water velocity distribution at the bottom of the tower.

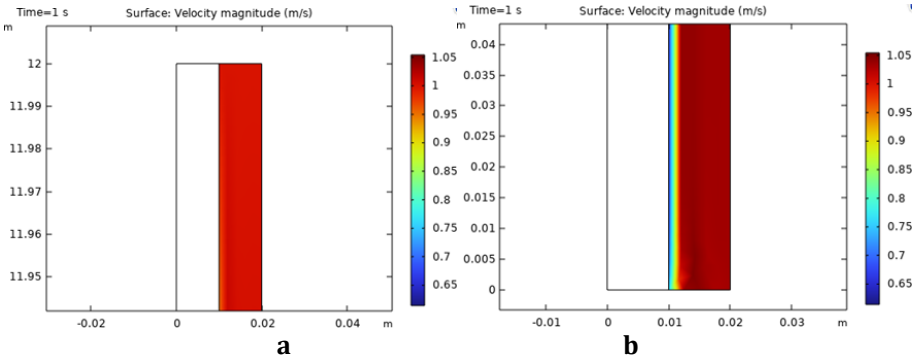
Figure 4-a shows the amount of moisture in the incoming air from the bottom of the tower, and Figure 4-b shows the amount of moisture in the air coming from the top of the tower.

The amount of humidity changes between the inlet and outlet air in this condition is about 80%, which shows that in this condition, desalinated water can be produced by cooling the moist air outlet.



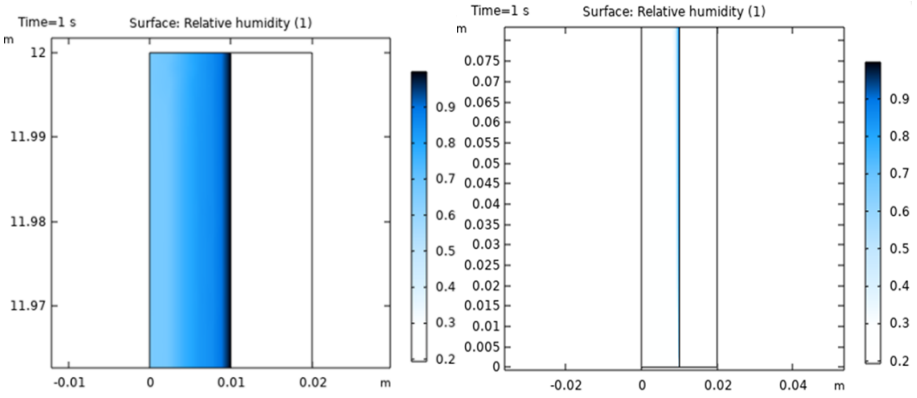
a **b**

Figure 2. air speed, a) Bottom b) Top of the tower



a **b**

Figure 3. water speed, a) Top, b) Bottom



a **b**

Figure 4. Humidity a) air input b) air output

Conclusion

The results showed that the use of a wet wall tower with a height of 12 meters in conditions close to the environment can be used for desalination of salty water and increasing the relative humidity up to about 85% makes it possible to create condensation and produce drinking water.

References

1. Kharangate, C. R., Lee, H., & Mudawar, I. (2015). Computational modeling of turbulent evaporating falling films. International Journal of Heat and Mass Transfer, 81, 52-62.
2. Bahreini, R., Ramiar, A., & Ranjbar, A. A. (2017). Numerical simulation of a counter-flow wet-wall humidifier. Energy Conversion and Management, 150, 236-246.
3. Ahmadi, M., Vahabzadeh, F., & Bonakdarpour, B. (2018). Modeling and optimization of a wetted wall column humidifier using computational fluid dynamics. Chemical Engineering Research and Design, 138, 14-25.
4. Rasouli, E., Naderi, S., & Sheikholeslami, M. (2019). Numerical simulation of a novel humidification system using a wetted wall column and a thermoelectric cooler. Applied Thermal Engineering, 160, 114070.

Advanced Engineering Days

aed.mersin.edu.tr

Ultrasonic reactor modeling and investigation of pressure distribution

Sara Mansouri [1], Kamran Keynejad [*1], Hedayat Azizpour [2], Mohammad Mahdi Heydari [1], Saghar Babaei [1]

[1] *University of Tehran, Fouman Faculty of Engineering, College of Engineering, Iran, saramns1999@Gmail.com, Kamran.Keynejad@ut.ac.ir, M.m.Heydari77@ut.ac.ir, Sagharbabaei98@gmail.com*
[2] *University of Tehran, School of Chemical Engineering, College of Engineering, Iran, h.azizpour@ut.ac.ir*

Cite this study: Mansouri., S., Keynejad, K., Azizpour, H., Heydari, M. M., & Babaei, S. (2024). Ultrasonic reactor modeling and pressure distribution investigation. Advanced Engineering Days, 9, 489-492.

Keywords
Ultrasonic probe
Piezoelectric
Acoustic pressure
Ultrasonic reactor

Abstract

In this research, COMSOL Multiphysics was used as a tool to design and specify an ultrasound probe with a new, multi-branch geometry. The goals of this design are to:1- Overcome the disadvantages of probes with older designs, 2- Increase acoustic pressure by increasing the level of the sound waves. In this simulation, three different physics were designed and coupled together for each part of the ultrasonic system: a) Piezoelectric material model for the transducer. b) Linear elastic material model for radiation. c) Pressure acoustic model for the reactor. According to results, the highest and lowest pressures are in the range of -8000 to 80000 (Pa) and this pressure distribution is observed in the areas near the probe.

Introduction

An ultrasonic reactor is a device that utilizes high-frequency sound waves (ultrasound) to induce various chemical and physical processes, such as sonochemistry, sono-oxidation, and particle synthesis. Modeling and investigating the pressure distribution in ultrasonic reactors is crucial for optimizing their performance, understanding the underlying mechanisms, and enhancing their efficiency in various applications. Here is a literature review on this topic:

Modeling Ultrasonic Reactors: Several mathematical models have been developed to describe the behavior of ultrasonic reactors. One common approach is the acoustic analogy, which relates the pressure fields to the velocity fields using the continuity and momentum equations (e.g., Lighthill's equation). Additionally, finite element analysis (FEA) and computational fluid dynamics (CFD) have been employed to simulate the complex fluid dynamics and acoustic fields inside the reactor [1-2]. These models help in understanding the effects of geometry, ultrasonic frequency, and power input on the reactor's performance.

Pressure Distribution: The pressure distribution within an ultrasonic reactor is influenced by factors such as the transducer design, resonance conditions, and the medium's properties (density, viscosity, and acoustic impedance). Studies like those by Zhang and Zhang [3] and Kim et al [4] have shown that pressure oscillations are non-uniform, with higher pressures near the transducer and lower pressures at the reactor's periphery. These variations can lead to local hotspots and affect the reaction kinetics.

Effects of Pressure Distribution: The pressure distribution plays a critical role in determining the reaction rates and product selectivity. High-pressure zones can cause cavitation, a process where acoustic waves create and collapse tiny bubbles, leading to local temperature and pressure spikes. This phenomenon is responsible for the generation of reactive species and enhances chemical reactions [5]. However, excessive pressure fluctuations can lead to equipment damage or reduced efficiency [6]

Experimental Investigations: To validate the models and understand the pressure dynamics, experimental studies using pressure sensors, particle image velocimetry (PIV), or laser Doppler velocimetry (LDV) have been conducted. For instance, Chen et al. [7] used PIV to measure the acoustic streaming and pressure fields in an ultrasonic reactor, demonstrating the importance of pressure gradients for mass and heat transfer.

Optimization: Researchers have attempted to optimize pressure distribution for enhanced performance. This includes the design of novel transducers, tuning the operating parameters (frequency, power, and duty cycle), and using different reactor geometries [8-9]. These modifications aim to achieve more uniform pressure distribution, improve cavitation, and enhance reaction rates. In conclusion, the modeling and investigation of pressure

distribution in ultrasonic reactors is a multidisciplinary area of research that combines acoustics, fluid mechanics, and chemical engineering. Understanding and optimizing this pressure distribution is essential for the development of more efficient and controllable ultrasonic reactors for various applications, such as waste treatment, nanomaterial synthesis, and chemical reactions.

Material and Method

The geometry considered in this modeling includes a hollow cylinder with a length of 5.2 cm and a width of 3 cm, and the geometry related to the horn (probe) with several branches is considered. This geometry is shown in Figure 1. The governing equations of this system are:

1- The electromechanical behaviors of the isotropic PZT can be expressed by two linearized constitutive equations:

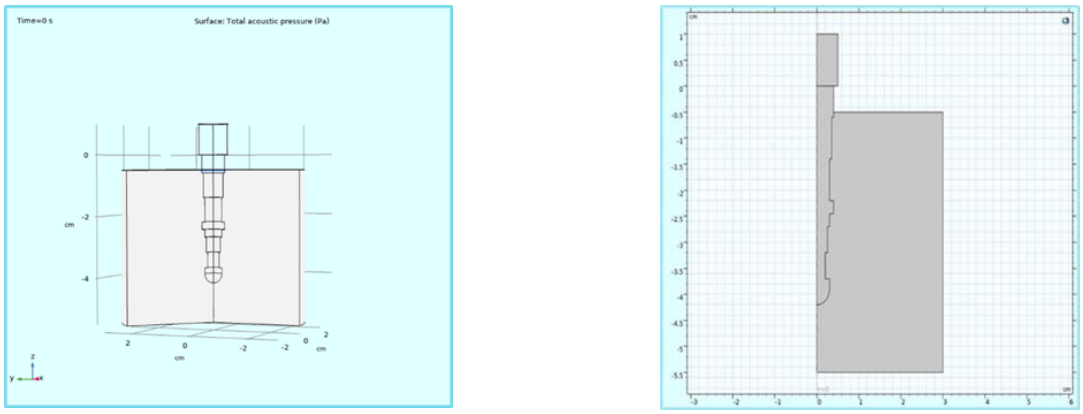


Figure 1. Probe and vessel geometry

$$\text{Stress Charge}\begin{cases} T = c_E S - e^T E \\ D = eS + \varepsilon_s E \end{cases}$$

$$\text{Strain Charge}\begin{cases} S = s_E T + d^T E \\ D = dT + \varepsilon_T E \end{cases}$$

where T (Pa) is the stress vector, S is the strain vector, E (V/m) is the electric field intensity vector, D (C/m^2) is the electric flux density vector, c_E (Pa) is the elastic coefficient matrix at constant electric field strength, e^T (C/m^2) is the piezoelectric coupling matrix, ε_s (F/m) is the dielectric permittivity matrix at constant mechanical strain, sE (1/Pa) is the elastic compliance matrix at constant electric field, d^T (C/N) is the piezoelectric strain constant matrix, and ε_T (F/m) is the dielectric permittivity matrix at constant mechanical stress.

2- Their linear elastic (probe) behavior is governed by Newton's Second Law:

$$\rho\omega^2 u\nabla.\sigma = F_v e^{i\varphi} \quad (1)$$

where u (m) is particle displacement, σ (Pa) is stress, F_v (N/m^3) is force per volume, and $e^{i\varphi}$ indicates the AC.

3- The acoustic wave equation is given as follow:

$$\frac{1}{\rho c^2}\frac{\partial^2 p}{\partial t^2} + \nabla.\left(\frac{1}{\rho}(\nabla_p - q)\right) = Q \quad (2)$$

where p (Pa) is acoustic pressure, ρ (kg/m^3) is density of water, and c (m/s) is speed of ultrasound propagation in the water. The dipole source q (N/m^3) and the monopole source Q (1/s^2) are both optional. The combination ρc^2 is called the adiabatic bulk modulus (Pa).

The boundary conditions after simplification are:

1-A structure-acoustic boundary was set to the interface between irradiator and water:

$$-\mathrm{n}.\left(\frac{1}{\rho_0}(\nabla \mathrm{p} - \mathrm{q})\right) = 0 \quad (3)$$

2- Cylindrical wave radiation boundary condition: This condition allows outgoing waves to leave the modeling domain with minimal reflection:

$$-n.\left(\frac{-1}{\rho c}\nabla p_t - q_d\right) = \left(ik_{eq} + \frac{1}{2r} - \frac{1}{8r(1+ik_{eq})}\frac{(p_i-p)}{\rho_c} + n.\frac{1}{\rho_c}\nabla p_i + \frac{(r\Delta\|pi-r\Delta\|p)}{2(1+ik_{eq}r)\rho_c}\right. \quad (4)$$

3- Ground boundary condition: Ground means that there is a zero potential on the boundary.

$$v = 0 \quad (5)$$

4- Electric Potential boundary condition: It provides an electric potential V0 as a boundary condition

$$v = v_0 \quad (6)$$

The solution of these equations has been done using COMSOL software version 6.0 with meshing (mesh information). In this software, modules related to the physics of Acoustic-Piezoelectric Interaction, Transient Found under Acoustics>Acoustic-Structure, this physics combines acoustic pressure and piezoelectric interfaces to connect and resolve sound pressure changes in fluids with structural deformations in solids and piezoelectric. This physics also includes features from Electrostatics to solve the electric field in piezoelectric materials. This physics includes Pressure Acoustics and Solid Mechanics and Electrostatics.

Table 1. Initial input for modeling

material	Water (Liquid domain)	PZT-5 (Transducer Domain)	(AISI 4340) (Irradiator Domain)
Study		Time Dependent	Frequency Domain
time		Range (0,1.0e-5,0.001)	
Frequency		Range (15000,1000,25000)	
Voltage		110 V	
temperature		293.15 K	

Results

In this modeling, the effect of insulation/voltage on pressure distribution is investigated. the ultrasonic reactor at a frequency of 25,000 Hz Figure 2, the ultrasonic reactor at a time of 0.003 seconds Figure 3.

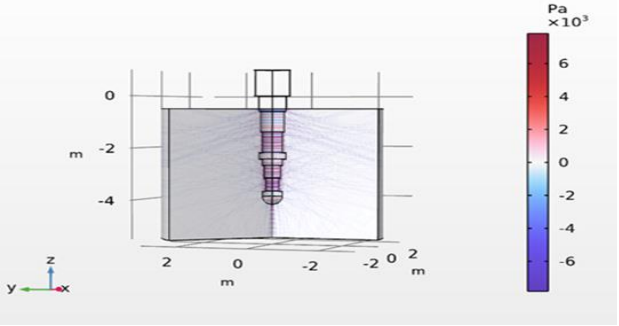


Figure 2. Pressure distribution at 25000 Hz

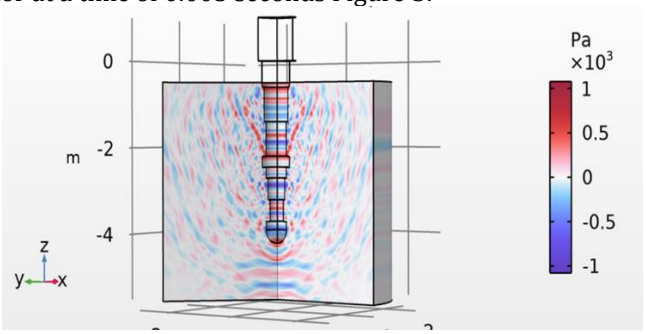


Figure 3. Pressure distribution at 0.003 second

Discussion

According to figures 2 and 3, the highest and lowest pressures are in the range of -8000 to 80000 pascals and this pressure distribution is observed in the areas near the probe. The pressure distribution in the reactor is layered and spread throughout the volume. Whereas in simple probes, the focus of the wave distribution is at the end of the Horn.

Conclusion

In this research, COMSOL was used as a tool to design and specify an ultrasound system with a new geometry (multiple-stepped). The goal was to overcome the disadvantages of old probes, find the most optimal shape for the probe, and control energy loss. In this modeling, three different models were designed and paired together for each part of the ultrasonic system: a piezoelectric model for the transducer, a linear elastic model for radiation, and a pressure acoustic model for the reactor. Using COMSOL, the generation of ultrasound waves in the transducer and their propagation through the probe were modeled. It was found that the reduction of energy loss causes the acoustic pressure to rise. The changes in reactor pressure distribution were in the range of -8000 to 80000 pascals and were layered in the reactor and spread throughout the volume.

References

1. Zhang et al., (2016). Ultrasonic vibration-assisted pelleting of cellulosic biomass for ethanol manufacturing: An investigation on pelleting temperaturesss
2. Liu et al., (2018), Response surface methodology for the optimization of the ultrasonic-assisted rhamnolipid treatment of oily sludge
3. Zhang, W., & Zhang, Y. (2013). Numerical simulation of ultrasonic field in a rectangular horn-type sonochemical reactor. Ultrasonics, 53(8), 1195-1201.
4. Kim, D. H., Jeon, S. H., & Kim, S. J. (2014). Numerical simulation of ultrasonic field in a rectangular sonochemical reactor with a transducer. Ultrasonics, 54(3), 517-522.
5. Stefanopoulou, A. G., Kostoglou, M., & Kostopoulos, V. (2008). Sonochemical synthesis in an ultrasonic bath: Effects of cavitation on the degradation of organic pollutants. Ultrasonics, 46(4), 312-319.
6. Gao, Y., Zhang, X., & Wang, Y. (2019). An experimental study on the influence of ultrasonic power and duty cycle on sonochemical degradation of methylene blue. Ultrasonics Sonochemistry, 56, 104926.
7. Chen, Y., Zhang, Y., & Zhang, W. (2017). Acoustic streaming and pressure fields in an ultrasonic reactor. Ultrasonics, 75, 118-125.
8. Wang, Y., Song, Y., & Wang, Z. (2015). A review of ultrasonic reactors: Design, performance and application. Ultrasonics Sonochemistry, 24, 64-84.
9. Song, Y., Wang, Y., & Wang, Z. (2019). Optimization of a coiled ultrasonic reactor for sonochemical degradation of tetracycline. Ultrasonics Sonochemistry, 53, 231-237.

Advanced Engineering Days

aed.mersin.edu.tr

Optimization of effective parameters on catalytic performance in zone-coated three-way catalyst using Taguchi method

Tal'at Moeini[1], Yousef Zaynali [*2]

[1]*Ayegh Khodro Toos Company, Catalyst Department, Mashhad, talatmoeini@gmail.com*
[2]*University of Mohaghegh Ardabili, Chemical Engineering, Ardabil, y.zaynali@uma.ac.ir*

Cite this study: Moeini, T., & Zaynali, Y. (2014). Optimization of effective parameters on catalytic performance in zone-coated three-way catalyst using Taguchi method. Advanced Engineering Days, 9, 493-495

Keywords
Three-way catalyst
Light-off temperature
Taguchi DOE
Zone-coating
Ceria-Zirconia to Alumina ratio
PGM distribution

Abstract

The optimization of effective parameters over light-off temperature for three way catalysts with zone-coating technology has been studied using the Taguchi method. Taguchi L36 orthogonal array consisting of five design factors listed as proportional length of front zone; referred as architecture of catalyst; CZ/Al ratio, the percentage distribution of Pt, Pd, and Rh at front zone and the response as average of light-off temperature of CO, HC, and NO; were considered in the optimization study. The results of the optimization indicate that a good fresh catalyst with the minimum CO , HC and NOx light-off temperatures can be obtained at catalyst architecture of h/3, CZ/Al ratio of 50/50, the percentage distribution of 90% Pt, 75% Pd and 35% Rh at front zone. The observed optimum condition for aged catalysts operated at catalyst architecture of h/2, CZ/Al ratio of 60/40, the percentage distribution of 70% Pt, 50% Pd and 50% Rh at front zone. In fresh catalysts the Rh concentration used was found to be the most influential parameter of on light off temperature while the catalyst architecture was least influential. On the other hand, it is found that catalyst architecture and CZ/Al ratio have the most and least effect on aged catalysts respectively.

Introduction

In order to meet the standards required by legislations, it is necessary to develop technologies leading to lower exhaust emissions. The Three-way catalyst (TWC) is one of the main components of automobile exhaust gas aftertreatment and well known for catalyzing the reduction of nitrogen oxide (NO) and the oxidation of carbon monoxide (CO) and unburn hydrocarbons (HC) [1-2]. TWC comprises of three main parts: alumina (Al), an oxygen storage component (OSC) such as ceria-zirconia mixed oxide (CZ) and platinum group metals (Pt, Pd, and Rh). Achievement of rapid light-off is important to treat exhaust gases, therefore the proper selection of all three parts can improve light-off performance [3-4].

Recent studies have shown the numerous factors that impact the TWC design. Of those factors are wash coat formulations and catalyst configuration design, e.g. CZ to alumina ration, addition of low amounts of rare earth or alkaline metal promoters; to improve thermal stability; inclusion of zeolites to act as a hydrocarbon or NOx cold trap, and the development of a catalyst with the double -layer and zone-coating technology [5-6].

Another key factor in TWC design is the loading and ratio of PGMs. In recent years, to develop high performance TWCs various technologies including use of bimetallic alloys, spinels, and perovskite structures, layered and zone coated catalyst have been proposed [7-8].

As mentioned above, it is already well known that catalyst architecture, CZ/Al ratio, loading and distribution ratio of Pt/Pd/Rh are of the main parameters that can affect catalytic performance and light-off temperature. Although many studies have investigated the influence of these parameters separately, but combinatorial evaluation of these factors are scarce. The aim of this study was to investigate and optimize these parameters in a two zoned-catalyst by the Taguchi orthogonal array design. The CO, HC, NOx light-off temperature has been chosen as output parameter.

Material and Method

The materials used in the preparation of the desired catalysts include La-Al_2O_3 (3 wt.% La_2O_3) and Ce–Zr mixed oxide which was obtained from Sasol. Nickel nitrate hexahydrate (purity > 99.0 %), zirconium oxynitrate hydrate sourced from Sigma-Aldrich, and barium acetate and lanthanum nitrate hexahydrate (purity > 99.0 %) from Merck were used. PGM in the form of solutions of hexahydroxy-platinate (IV)monoethanolamine (18.85 wt% Pt), $Pd(NO_3)_2$ (20.06 wt.% Pd) and $Rh(NO_3)_3$ (9.73 wt.% Rh) were purchased from Pluaruum Co.

To prepare the catalysts, at first appropriate amounts of La-Al_2O_3, Ce–Zr mixed oxide powders, nickel nitrate, zirconium oxynitrate, barium acetate and lanthanum nitrate were added into mixture of distilled water and acetic acid while stirring. After addition of noble metals solutions, the pH value of the slurry was kept at 4-5. Followed by aging at room temperature for 24 h under continuous stirring, the obtained slurry wash coated onto the ceramic honeycomb monolith of cordierite with a 600 CPSI density. A 1 in. OD×2 in. length monolith is dipped into the wash coat slurry and is cleaned from the excess coating material and blocked channels via an air blow. The coating process is repeated until it reaches the desired weight. The monoliths are then dried at 150 ˚C for 2 hour and consequently calcined at 550˚C for 3 h to obtain the fresh catalysts (labeled as F). To prepare aged samples, the fresh catalysts were hydrothermally treated with gases containing 10vol% H_2O/air at 1000˚C for 8h (labeled as A). All samples are dual-zoned with total PGM loading of 20 g/ft^3 and Pt/Pd/Rh ratio of 13.5/5.7/.08.

Architecture of catalyst; which is proportional length of front zone; CZ/Al ratio, the weight percentage of Pt, Pd and Rh in the front zone have been chosen as affecting parameters and mathematical average of CO, HC and NO_x light-off temperature is measured as output response. "Table 1" displays the input parameters along with their levels in the experimental design. Two parameters in two levels and three parameters in three levels lead to the L36 orthogonal array of the Taguchi design. In this work, the target is to reach low light-off temperature and a smaller signal-to-noise ratio was considered to determine the optimum combination of factors.

Table 1. Factors and their levels

Factors	Level1	Level2	Level3
Architecture of catalyst	h/2	h/3	-
CZ/Al ratio	50/50	60/40	-
Pt (%)	90	70	50
Pd (%)	90	75	50
Rh (%)	27	35	50

Results and discussion

The higher the slope of response of a parameter, the more effective that parameter is. The main effect graph of average response for fresh catalyst is depicted in "Figure 1". As it can be seen, for fresh catalyst, architecture and Pt% has almost no effect, while CZ/Al ratio, Pd% and Rh% shows high impact on the response. Furthermore, Pd% and Rh% show optimum performance at level 2 and CZ/Al can lead to better response at level 1.

Presented by "Figure 2", aged catalysts show different characteristics. In spite of fresh catalyst, architecture has a great impact on the response. The difference can be pointed out for CZ/Al ratio and Rh%, i.e. while these parameters are of great effect at fresh state, they have little impact on the response for aged catalysts. Same thing can be observed for Pt% distribution but in reversed manner. Of all parameters, Pd% shows distinguished and opposite profile between fresh and aged state. Although it has a minumum response at level 2 in the fresh state, but for aged catalysts it shows a maximum response at this level leading to deteriarated performance of aged catalyst at level 2 of Pt%.

Selected parameters at studied levels show different and opposite responses at fresh and aged states of catalyst. Since performance of catalyst deteriorates through aging process, it may be challenging to pass emission regulation standards after aging. So at choosing the optimum level of the parameters, the focus must be on the aged results. Luckily the patterns of responses are in a way that optimum levels can be chosen beneficial for both states. Optimum performance can be attained by Architecture, CZ/Al ratio, Pt%, Pd%, and Rh% at Levels of 1, 1, 2, 1, and 2 accordingly.

Conclusion

Light-off temperature is the main criterion to meet the required emissions standards and assess the level of degradation of the catalyst's performance throughout ageing in TWC. It was demonstrated that using cost-effective Taguchi approach may promote the CO, HC and NOx light-off temperature with efficient and optimum application of the catalyst's design parameters. Consequently; keeping light-off temperature constant; the amount of PGM can be reduced as well which leads to considerable cost saving.

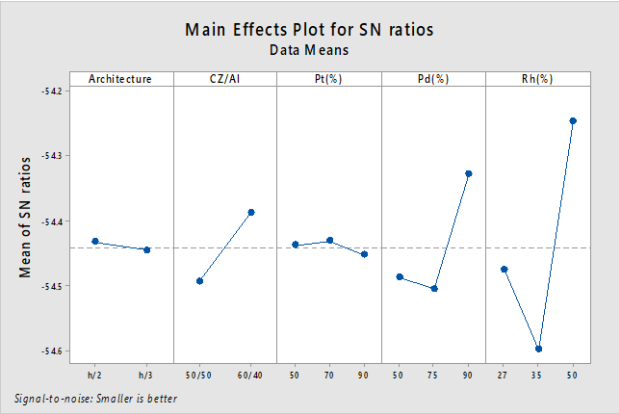


Figure 2. Main effect graphs for the mean of signal-to-noise ratios (F).

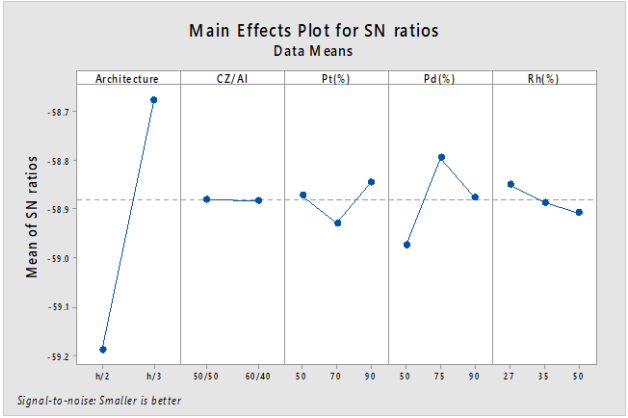


Figure 3. Main effect graphs for the mean of signal-to-noise ratios (A).

The obtained results from "Figures 1 and 2" show that application of optimum quantities of PGM throughout zoned catalysts; in particular applying more Pt and Pd and less Rh at front zone, may result in significant reduction of light-off temperature. This is due to the fact that oxidation reactions happen primarily on the front portion of the catalyst whereas NOx reduction is significant throughout length of catalyst [9]. Furthermore, susceptibility of Rh to poisoning is another factor for higher concentration of it at the rear end of catalyst.

Harsh aging process and thermal sintering caused by it implies for bigger length of front zone [10]. If not so, the degradation caused by aging and small front zone, all together, will lead to the loss of precious materials and performance of the catalyst. So by extending the front zone and distributing PGM along it, performance of catalyst can be maintained after aging.

References

1. Aoki, Y., Sakagami, S., Kawai, M., Takahashi, N., Tanabe, T., & Sunada, T. (2011). Development of Advanced Zone-Coated Three-Way Catalysts. Paper presented at the SAE Technical Paper Series.
2. Choi, B., Jeong, J., Son, G., & Ung, M. J. (2005). Conversion Characteristics of Double-Layer Washcoat Tri-Metal Three-Way Catalyst Using High Cell Density Substrate. *JSME International Journal Series B Fluids and Thermal Engineering, 48*(4), 874-881. doi:10.1299/jsmeb.48.874.
3. Hazlett, M. J., & Epling, W. S. (2018). Heterogeneous catalyst design: Zoned and layered catalysts in diesel vehicle aftertreatment monolith reactors. The Canadian Journal of Chemical Engineering, 97(1), 188-206. doi:10.1002/cjce.23293
4. Yamauchi, T., Kubo, S., Mizukami, T., Sato, N., & Aono, N. (2011). Numerical simulation for optimal design of a multifunctional three-way catalytic converter with detailed chemistry. *R&D Rev. Toyota CRDL, 42*(1), 33.
5. Aoki, Y., Yoshida, T., Tanabe, T., Hatanaka, M., Nagai, Y., Sakagami, S., & Shimizu, M. (2009). *Development of double-layered three-way catalysts* (0148-7191).
6. Fujiwara, T., Takagi, N., Ichinose, H., Yoshioka, M., & Kawai, M. (2009). *Development of High Performance Three-Way-Catalyst Technology to Lower NOx Emission* (0148-7191).
7. Kannepalli, S. (2018). *Mathematical Methods for Design of Zone Structured Catalysts and Optimization of Inlet Trajectories in Selective Catalytic Reduction (SCR) and Three Way Catalyst (TWC).* Dissertation, Karlsruhe, Karlsruher Institut für Technologie (KIT), 2017.
8. Rood, S., Eslava, S., Manigrasso, A., & Bannister, C. (2019). Recent advances in gasoline three-way catalyst formulation: A review. *Proceedings of the Institution of Mechanical Engineers, Part D: Journal of Automobile Engineering, 234*(4), 936-949. doi:10.1177/0954407019859822.
9. Collins, N., Cooper, J., Morris, D., Ravenscroft, A., & Twigg, M. (2005). Advanced three-way catalysts–optimisation by targeted zoning of precious metal. *SAE transactions*, 962-966.
10. Abedi, A., & Epling, W. (2014). Effect of Thermal Degradation on the CO, C3H6, and NO Oxidation Performance of Pt/Al2O3 with a Zoned Distribution of Pt. *Industrial & Engineering Chemistry Research, 53*(14), 5692-5700. doi:10.1021/ie403317w.

Advanced Engineering Days

aed.mersin.edu.tr

Investigating the amount carotenoid extraction using chemical methods from microalgae

Leila Nadaei [1], Hanieh Shokrkar [1*]

[1]Sahand University of Technology, Faculty of Chemical Engineering, Biotechnology-Environment, Tabriz, Iran
leila.nedaiy.76@gmail.com, h_shokrkar@sut.ac.ir

Cite this study: Nadaei, L., & Shokrkar, H. (2024). Investigating the amount carotenoid extraction using chemical methods from microalgae. Advanced Engineering Days, 9, 496-498

Keywords
Carotenoid
Microalgae
Extraction
Solvent

Abstract

Microalgae are very important due to the high production of antioxidants, carotenoids, and some other growth properties. In this research, the production and extraction of chlorophyll and carotenoids from mixed microalgae has been done. According to several researches conducted about the production and extraction carotenoid from pure algae culture, as well as very few studies about mixed algae, mixed algae cultures have been used in this research. The use of pure cultivation leads to costs of sterilization, maintenance, and the cultivation process, and causes investment and operational costs to rise. According to the results obtained from the comparison of the extraction efficiency carotenoid from dry algae to check and select a solvent with high efficiency, a comparison was made be Tween different solvents (acetone, ethanol, methanol, dimethyl ether, and Tween 20% and 85%) in conditions without stirring. became. The results indicate that the highest extraction efficiency carotenoid from dry algae by solvent method, firstly related to 85% Tween on the tenth day, 79.90% respectively, and then Methanol after 10 hours is 62.90%.

1. Introduction

Microalgae are prokaryotic or eukaryotic photosynthetic microorganisms that can grow quickly and live easily in harsh conditions due to their simple unicellular or multicellular structure [1]. Microalgae exist in all ecosystems on the planet, from oceans and fresh waters to hot springs, snow, ice, and even desert sand. Algae do not have roots, stems, and leaves and have chlorophyll as the primary photosynthetic pigment. Under natural growth conditions, algae absorb light from the sun, carbon dioxide from the air, and nutrients from the water habitat [2].

Due to their simple unicellular or multicellular structure, microalgae can survive in harsh conditions [1]. Factors affecting the growth of microalgae include the intensity and amount of light, temperature, salinity, carbon dioxide, and oxygen, controlling the amount of nitrogen, operating conditions such as depth, and stress caused by mixing and harvesting period. Microalgae has many commercial applications in various industries such as agriculture, chemistry, pharmaceuticals, energy, food, paper, glass, and textiles [2]. All kinds of fats, unsaturated fatty acids, oil, natural colors, pigments, all kinds of sugars, antioxidants, biopolymers, proteins, and animal feed are valuable materials that are extracted from this biomass [3]. However, the production of microalgae has disadvantages such as the difficulty of controlling the process, high accumulation of carbon dioxide with low-efficiency pollution problems, and the optimal need for large amounts of salt and solar radiation [4]. Microalgae cultivation is one of the modern branches of biotechnology. The first cultivation of microalgae was carried out in 1890 by Bijrink et al. [5].

Also, the first large-scale cultivation of microalgae was started in Japan in the early 1960s by Nihon et al. with the cultivation of Chlorella [2]. There are approximately more than 50,000 species of microalgae, and since then, large collections of microalgae have been created by researchers in different countries. For example, the largest collection of freshwater microalgae at the University of Coimbra in Portugal has a wide variety of different microalgae that can be used for various applications such as value-added products for medicinal purposes, food products for edible purposes, and also as a source of energy become [3]. Today, microalgae have been considered a valuable source for the production of pigments due to their high growth rate and ability to grow in diverse cultural environments [1]. The pigments are located in the chloroplast of the cell. The extraction carotenoid from microalgae includes several steps, including a selection of microalgae, cultivation of microalgae (light, water,

carbon dioxide, and food), harvesting, drying, breaking the cell wall, and finally extracting chlorophyll and carotenoid. Among the separation methods of these compounds, we can refer to chromatographic methods, solvents, surface absorption, ultrasonic waves, and supercritical fluids. Therefore, the purpose of this study is to compare dry and wet algae, to compare different solvents (acetone, ethanol, methanol, dimethyl ether, and Tween 20% and 85% in conditions without stirring), and to investigate pigment extraction from mixed culture medium with the help of Tween solvent 85% which is studied for the first time in this research.

2. Materials and methods

2. 1 Cultivation of microalgae

First, mixed and indigenous species of microalgae were collected from the water of the El Guli pool in Tabriz City, East Azerbaijan province. Then the first microalgae cultivation operation was carried out in a 500 ml Erlenmeyer flask with stirring. After the growth of microalgae in Erlenmeyer, it was used with a volume of 12 liters and a working volume of 10 liters for the main cultivation of microalgae in a polycarbonate flat plate photobioreactor. Exposure was done with fluorescent lamps with a light intensity of 260 μ mol m^{-2} s^{-1} and a photometer was used to measure the light intensity. The operating conditions of the photobioreactor were aerated at ambient temperature, pH equal to 7, with a flow rate equal to 8 liters per minute per liter with concentrations of 1.25, 0.8, 0.2, 0.1, 0.1, and 0.1 g/l, respectively. The extraction efficiency carotenoid from mixed algae has been investigated using selected organic solvents and in different time intervals. Extraction with solvents can be as efficient as other methods. The main advantage of this type of mining is cost reduction in terms of infrastructure and operational procedures. In this research, it has been tried to use several solvents to extract pigments so that a comparison be Tween solvents can be made to obtain more efficiency. In most studies, ethanol and methanol 90-100% (v/v) have been used. Therefore, in this research, for the extraction of carotenoid, acetone 80%, ethanol 99.9%, methanol 95% and dimethyl ether solvents were used and the tests were carried out over 2 days under conditions without stirring, at ambient temperature and pH equal to 7. Has been studied. Also, in this research, 20% and 85% surfactants have been used in the period of 0 to 10 days for the extraction carotenoid in conditions without stirring, at ambient temperature and pH equal to 7.

3. Discussion and results

The content carotenoid obtained from dry algae using selected solvents in different periods and in conditions without stirring, at ambient temperature, and at neutral pH are presented in the graphs of Figure (1). According to the obtained results, Tween 85% (Figure 1, b) had the highest efficiency. Although pigment production and the effect of Tween on microalgae is slow, after 10 days, the extraction rate of carotenoid from 53.60% has increased to 79.90%. Tween not only plays the role of a carbon source but also enhances the absorption of nutrients into the cell mass. This means that it increases the permeability of the cell membrane. After 85% Tween, the highest amount carotenoid extraction is related to methanol (Figure 1, d), ethanol (Figure 1, c), acetone (Figure 1, e), and dimethyl ether (Figure 1, f), respectively. In all the organic solvents used, small amounts carotenoid extraction are observed in the initial times. But after 10 h, a higher yield has been obtained. For all four selected solvents, after 10 h, the yield reaches a stable state. Of course, placing the tested algae sample in long contact with solvents will lead to the degradation of the extract and decrease the amount carotenoid extraction. The extraction efficiency carotenoid related to methanol, respectively: 67% for ethanol, 52.7% for acetone, and dimethyl ether is 44.5%. Methanol is usually the solvent of choice for carotenoid determination because a very distinct carotenoid absorption peak is obtained when using this solvent. The solvent leads to the destruction of carotenoid. Degradation occurs because at low pH carotenoid may lose magnesium (Mg) ions, leading to the formation of pheophytin and carotenoid allomerization products, which spectrally interfere with carotenoid determination. According to the results of the research of Mace et al. [5], the solvent efficiency of methanol is higher than that of acetone and ethanol in extracting carotenoid. In addition, according to some studies[6], in most brown and green algae, the amount of carotenoid extraction with methanol solvent is higher than with ethanol and acetone solvents, and this efficiency is mostly due to the high polarity of the solvent and the solvent. The results of Jeffrey et al. [2] indicated that the extraction of carotenoid from cholera vulgaris algae using acetone, ethanol, and methanol solvents was more than the pure solvent, and the highest extraction was related to methanol, ethanol, and acetone solvents, respectively. Mace et al., [19] also observed that ethanol is effective and efficient in extracting carotenoid like methanol. Carotenoid are polar molecules due to the presence of hydroxyl groups at the end of the chain. Therefore, they have a greater tendency to dissolve in organic solvents. The different polarity of organic solvents also causes differences in the efficiency carotenoid. According to the results obtained in this research, Tween has a higher efficiency of 85%. As mentioned before, in this research, for the first time, 85% non-ionic surfactant Tween has been used to extract carotenoid from microalgae. Therefore, Tween 85% surfactant can be introduced as a new solvent to extract carotenoid from microalgae.

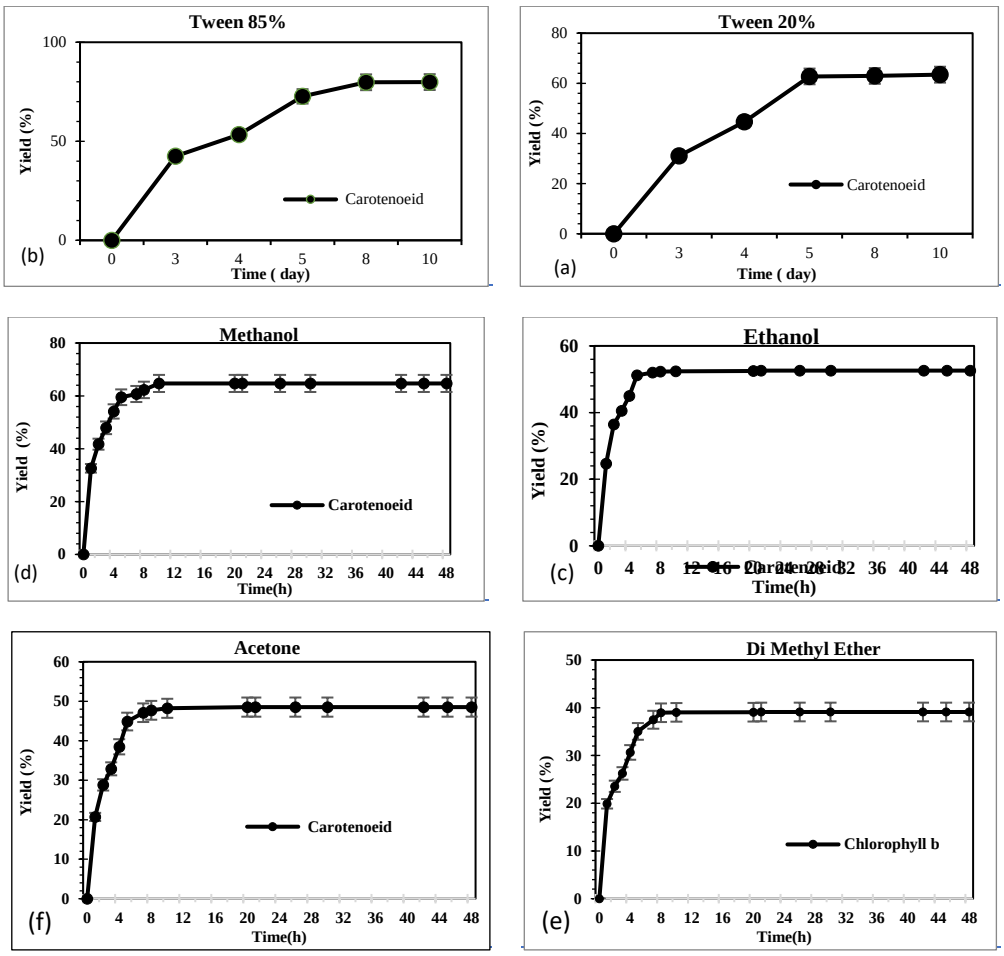


Figure 1. Carotenoid extraction content by a) Tween20%, b) Tween) 85%, c) ethanol, d) methanol, f) dimethyl ether, e) acetone (without stirring, at ambient temperature and pH equal to 7).

4. Conclusion

In this research, to produce and extract carotenoid, mixed species of microalgae were used. After harvesting and drying microalgae, the pigment extraction process from dry microalgae was investigated. The results obtained from the investigation of different solvents show that the highest extraction efficiency carotenoid from dry algae is related to 85% Tween, 79.90%, respectively, and then methanol, respectively 62.90%. Therefore, Tween 85% surfactant can be introduced as a new solvent to extract carotenoid from microalgae.

References

1. Jeffrey, S. W. (1968). Quantitative thin-layer chromatography of chlorophylls and carotenoids from marine algae. *Biochimica et Biophysica Acta (BBA)-Bioenergetics*, *162*(2), 271-285.
2. Nedaei, L., & Shokrkar, H. (2022). A Review on the Extraction of Chlorophyll and Carotenoids from Microalgae. Iranian Chemical Engineering Journal, 21(123), 45-58.
3. Nedaei, L., & Shokrkar, H. (2022). A review of the effects of different stresses on antioxidant production by Dunaliella algae. Iranian Chemical Engineering Journal.
4. Bijrink, G., & Carreon, J. R. (2016). Commercial astaxanthin production derived by green alga Haematococcus pluvialis: A microalgae process model and a techno-economic assessment all through the production line. *Algal research*, *18*, 175-190.
5. Mace, J. P., & Wilson, T. R. S. (2017). The use of thin-layer chromatography for the separation and identification of phytoplankton pigments. *Journal of the Marine Biological Association of the United Kingdom*, *45*(3), 583-591.
6. Shokrkar, H., & Nedaei, L. (2023). Investigating the effect of solvent type on chlorophyll and carotenoid extraction from dry and wet microalgae. Iranian Chemical Engineering Journal.
7. Shokrkar, H., & Nedaei, L. (2023). Chlorophyll and carotenoid extraction from mixed microalgae; experimental and kinetic study. Biomass Conversion and Biorefinery, 1-13.

Advanced Engineering Days

aed.mersin.edu.tr

Using Tween solvent to extract chlorophyll and carotenoids from *Chlorella vulgaris*

Leila Nadaei [1], Hanieh Shokrkar [1*]

[1]Sahand University of Technology, Faculty of Chemical Engineering, Biotechnology-Environment, Tabriz, Iran
leila.nedaiy.76@gmail.com, h_shokrkar@sut.ac.ir

Cite this study: Nadaei, L., & Shokrkar, H. (2024). Using Tween solvent to extract chlorophyll and carotenoids from *Chlorella vulgaris*. Advanced Engineering Days, 9, 499-501

Keywords
Carotenoid
Chlorophyll
Chlorella vulgaris Pigment
Tween

Abstract

Algae are not only a rich source of sugars and proteins, but also a variety of molecules and special compounds that have been isolated from them that have therapeutic effects. Some of these molecules are chlorophyll and carotenoid, which are used as coloring materials in the form of an antioxidant compound in the food, cosmetic, and pharmaceutical industries. In this study, for the first time, 20% and 85% of Tweens have been used to extract chlorophyll and carotenoids from microalgae Chlorella vulgaris. Because Tweens significantly reduce the surface tension of water and lead to easier and more efficient extraction. The obtained results show that the highest efficiency of chlorophyll a, b, and carotenoid extraction with 85% Tween on the tenth day is 91.70%, 87.12%, and 79.90%, respectively.

1. Introduction

Since prehistoric times, humans have been interested in coloring their daily tools using natural pigments of plant, animal, and mineral origin. Humans have always been interested in using these types of colors because of their brightness, relaxation, and non-toxic nature. However, after the discovery of synthetic pigments by William Henry Perkin [1] in 1856, natural colors gradually lost their practical value in many parts of the world. Due to the nature of bio-friendliness and the safety of natural pigments for human health and the environment, people started using them again [2]. Due to their antioxidant properties, non-flammability, non-toxicity, strengthening of the body's immune system, and reducing the risk of diseases such as cancer, heart diseases, cataracts, etc., pigments are used as colors and therapeutic agents in various food, pharmaceutical, and cosmetic industries [3].

In the last few decades, extensive research has been started on the possibility of chlorophyll and carotenoid production from algae, which is easy due to high photosynthetic efficiency, rapid growth, year-round cultivation, and easy downstream processes [4,5]. It has been widely investigated that some microalgae can grow and produce high amounts of pigments in various limitations such as light, salt, and nitrogen [6,7].

According to research [9,10] that was conducted to produce pigment from microalgae Chlorella vulgaris, the cost of using mixed algae cultivation is almost half of the cost of pure algae cultivation. Therefore, this study aims to compare 20% and 85% Tween to extract pigment from algae.

2. Materials and methods

2. 1 Cultivation of microalgae *Chlorella vulgaris*

Microalgae cultivation was done in a 500 ml Erlenmeyer along with stirring. After growing microalgae in Erlenmeyer, it was used in a working volume of 10 L for the main cultivation of microalgae in a polycarbonate flat plate photobioreactor. Exposure was done with fluorescent lamps with a light intensity of 260 µ mol m^{-2} s^{-1} and a photometer was used to measure and record the light intensity. The operating conditions of the photobioreactor were aerated at ambient temperature, pH equal to 7, with a flow rate equal to 8 L per minute with concentrations of 0.8, 1.25, 0.2, 0.1, 0.1, and 0.1 g/l respectively.

2.2 Analysis of pigments

In this research, the total amount of pigments was measured by the spectrophotometric method. To measure the content of chlorophyll a, b, first, a volume of 2 mL was taken from the desired sample and centrifuged for 5

min at 4000 rpm and the supernatant was discarded. Then, after washing twice with distilled water and discarding the supernatant, the sample obtained from the centrifuge was re-vortexed. In the next step, the resulting solution was centrifuged for 5 minutes at 4000 rpm. When the resulting precipitate became white, the absorbance of the supernatant liquid was measured and recorded at two wavelengths of 646 and 663 nm. Since the precipitate is not completely bleached, the volume of solvent should be added until the precipitate is completely white. Tween 85% was used to adjust the spectrophotometer. Finally, the chlorophyll content was calculated from the following equation [11].

$$Chla = 16.72\ A_{663} - 9.16\ A_{646} \quad (1)$$

$$Chlb = 34.09\ A_{646} - 15.28\ A_{663} \quad (2)$$

The measurement of carotenoid content was also done in the same way as above, only the absorbance of the supernatant was recorded at a wavelength of 470 nm and calculated from the following equation [12].

$$Carotenoeid = (1000\ A_{470} - 1.63\ Chl_a - 104.9\ Chl_b) / 221 \quad (3)$$

2.3 Investigating the extraction of pigments from dry algae using Tween

According to the studies and investigations, in this research, it has been tried to use Tween to achieve more efficiency. Therefore, in this study, to extract pigment by chemical methods, 20%, and 85% Tweens have been used in the period of 0 to 10 days in the conditions of pH equal to 7 and ambient temperature.

3. Discussion and results

3.1 The results of extracting pigments from dry algae using Tween

The content of carotenoids and chlorophylls obtained from dry microalgae Chlorella vulgaris using Tween in conditions of neutral pH, ambient temperature, and different time intervals are presented in the graphs of Figure (1).

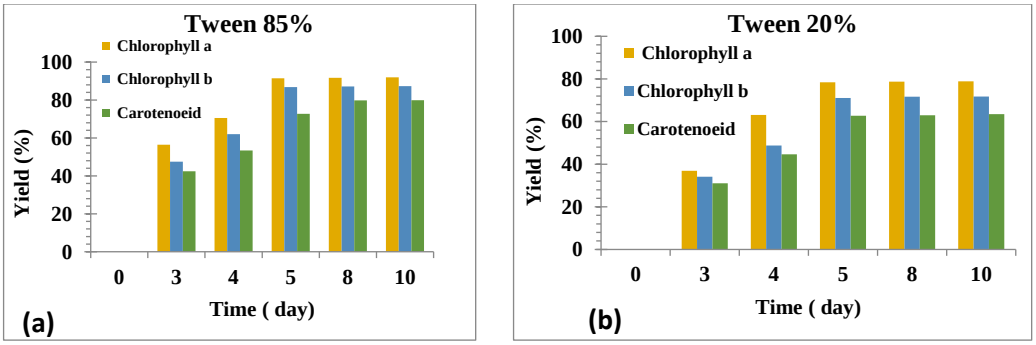


Figure 1. Checking the content of carotenoid and chlorophyll extraction by a) Tween 20% , b) Tween 85% (ambient temperature and pH equal to 7).

The choice of solvent is the most important factor for the effective extraction of pigments from biomaterials because it determines the degree of tendency to the chemical composition of the extracted materials [7]. Solvent extractability potential depends on microalgae cell wall permeability [13,14]. According to the results, Tween 85% (Figure 1, b) has the highest efficiency. Although the extraction of carotenoid and chlorophyll and the effect of Tween on microalgae is slow, after 10 days, the amount of carotenoid extraction by Tween increased from 53.60% to 79.9%, chlorophyll from 56.36% to 91.99%. , chlorophyll b increased from 47.51% to 87.29%. Tween not only plays the role of a carbon source well but also enhances the absorption of nutrients into the cell mass [15]. In the sense that Tween increases the permeability of the cell membrane [16].

4 . Conclusion

Microalgae cells contain valuable pigments such as chlorophylls and carotenoids. In this research, after harvesting and drying microalgae Chlorella vulgaris, the process of extracting pigments from dry microalgae was investigated. The results show that the highest extraction efficiency of chlorophyll a, b, and carotenoid from dry algae corresponding to 85% Tween is 91.70%, 87.12%, and 79.90%, respectively. In this research, for the first

time, Tween 85% has been used to extract carotenoid and chlorophyll from mixed microalgae. Therefore, Tween 85% can be introduced as a new material to extract carotenoid and chlorophyll from microalgae Chlorella vulgaris.

References

1. Aarthi, A., Kumari, S. M. I. T. A., Turkar, P. R. A. C. H. I., & Subramanian, S. A. N. G. E. E. T. H. A. (2018). An insight on algal cell disruption for biodiesel production. *Asian J Pharm Clin Res*, *11*(2), 21-26.
2. Co, D. Y. L., & Schanderl, S. H. (1967). Separation of chlorophylls and related plant pigments by two-dimensional thin-layer chromatography. *Journal of Chromatography A*, *26*, 442-448.
3. Jackson, B. A., Bahri, P. A., & Moheimani, N. R. (2017). Repetitive non-destructive milking of hydrocarbons from Botryococcus braunii. *Renewable and sustainable energy reviews*, *79*, 1229-1240.
4. Jeffrey, S. W. (1968). Quantitative thin-layer chromatography of chlorophylls and carotenoids from marine algae. *Biochimica et Biophysica Acta (BBA)-Bioenergetics*, *162*(2), 271-285.
5. Jiménez, C., Cossío, B. R., Rivard, C. J., Berl, T., & Capasso, J. M. (2007). Cell division in the unicellular microalga Dunaliella viridis depends on phosphorylation of extracellular signal-regulated kinases (ERKs). *Journal of experimental botany*, *58*(5), 1001-1011.
6. Khoo, K. S., Chew, K. W., Ooi, C. W., Ong, H. C., Ling, T. C., & Show, P. L. (2019). Extraction of natural astaxanthin from Haematococcus pluvialis using liquid biphasic flotation system. *Bioresource technology*, *290*, 121794.
7. Mehta, P., Singh, D., Saxena, R., Rani, R., Gupta, R. P., Puri, S. K., & Mathur, A. S. (2018). High-value coproducts from algae—An innovational way to deal with advance algal industry. *Waste to wealth*, 343-363.
8. Nedaei, L., & Shokrkar, H. (2022). A Review on the Extraction of Chlorophyll and Carotenoids from Microalgae. *Iranian Chemical Engineering Journal*, *21*(123), 45-58.
9. Nedaei, L., & Shokrkar, H. (2022). A review on the effects of different stresses on antioxidants production by Dunaliella algae. *Iranian Chemical Engineering Journal*.
10. Nedaei, L., and Shokrkar, H. (2023) The effect of the cultivation environment on the productivity of pigment and algae biomass. The fifth national conference on environmental engineering and management, Qaemshahr.
11. Nedaei, L., and Shokrkar, H. (2023) A review on the effect of different stresses to increase biofuel production from microalgae. 8th clean energy conference, Babol.
12. Nedaei, L., and Shokrkar, H. (2023) Increasing the sustainable growth of algae for biofuel production. 8th clean energy conference, Babol.
13. Panis, G., & Carreon, J. R. (2016). Commercial astaxanthin production derived by green alga Haematococcus pluvialis: A microalgae process model and a techno-economic assessment all through production line. *Algal research*, *18*, 175-190.
14. Riley, J. P., & Wilson, T. R. S. (2017). The use of thin-layer chromatography for the separation and identification of phytoplankton pigments. *Journal of the Marine Biological Association of the United Kingdom*, *45*(3), 583-591.
15. Shokrkar, H., & Nedaei, L. (2023). Investigating the effect of solvent type on chlorophyll and carotenoid extraction from dry and wet microalgae. *Iranian Chemical Engineering Journal*.
16. Shokrkar, H., & Nedaei, L. (2023). Chlorophyll and carotenoid extraction from mixed microalgae; experimental and kinetic study. Biomass Conversion and Biorefinery, 1-13.

Advanced Engineering Days

aed.mersin.edu.tr

A Facile Synthesis Method of Bis (Ethanolammonium) Hexahydroxoplatinum (IV) Solution for Platinum Supported Catalysts

Faezeh Farrokhpey*[1], Yousef Zaynali [2]

[1]*University of Vienna, Chemistry Department, Austria, Faezeh.farrokhpey@univie.ac.at*
[2]*University of Mohaghegh Ardabili, Chemical Engineering Department, Iran, y.zaynali@uma.ac.ir*

Cite this study: Farrokhpey, F., & Zaynali, Y. (2024). A facile synthesis method of Bis (Ethanolammonium) Hexahydroxoplatinum (IV) solution for platinum supported catalysts. Advanced Engineering Days, 9, 502-505

Keywords
Platinum
Ethanolammonium
Platinum nitrate
Three-way catalyst

Abstract

A solution of Bis (Ethanolammonium) Hexahydroxoplatinate(IV) ($(EA)_2Pt(OH)_6$) was prepared with a 97% yield using Platinum bars as the initial material. The synthesis process involved several stages including digestion, hydrolysis, and neutralization dissolution. Key synthesis parameters comprising the molar ratio of Ethanolamine to Platinum, the concentration of the Ethanolamine solution and temperature were meticulously considered and optimized. The thermal decomposition reaction and the crystalline structure of both intermediate and final compounds were analyzed using DTA-TGA and XRD techniques. The chemical structure of the synthesized compounds was confirmed via FT-IR analysis. The resultant compound exhibited a platinum content of 9.27%, with minimal chloride ion content (4.8 mg/kg) and sodium ion content below 220 mg/kg. Furthermore, the morphology and distribution of the platinum compound impregnated on the catalyst support were examined using FESEM and TEM methods. The findings suggest that $(EA)_2Pt(OH)_6$ serves as an appropriate precursor for platinum-supported catalysts.

Introduction

Supported platinum catalysts possess extensive applications, e.g. three-way catalysts which are crucial for mitigating air pollution through converting harmful gases [1]. Despite their widespread use, some platinum compounds have drawbacks such as low thermal stability and corrosiveness leading to decrease in catalyst activity [2-4]. $(EA)_2Pt(OH)_6$) is a promising water-soluble and chlorine-free ligand compound, while most of existing literatures have focused on other platinum compounds like platinum nitrate, neglecting $(EA)_2Pt(OH)_6$ synthesis method[4]. A preparation method of platinum (IV) solution from hexachloroplatinic acid and complexation of Pt(IV) in a nitric acid over time by NMR and Raman spectroscopy was studied [2,3]. In this work, a facile synthesis method to synthesize this precursor is presented and underlying parameters are optimized.

Material and Method

Analytical grade (AR) of Hydrochloric acid (37%), Nitric acid (65%), Sodium hydroxide, Ethanolamine (99.5%), Aceton (99.8%), Methanol (99.9%), and Platinum (99.995% trace metals basis) were purchased from Sigma-Aldrich. Millipore high purity (DI water) was used in this study.

The procedure starts by dissolving 31 gr of platinum pieces in hydrochloric acid (200 ml) and nitric acid (25 ml) in a covered beaker. To make sure of proper dissolution of metallic Pt, additional mixture of nitric acid and hydrochloric was incrementally. After cooling, additional hydrochloric acid (100 ml) was added and boiled until no fumes were observed. This process was repeated until all nitric acid traces were removed. The solution then was concentrated to 50 ml and mildly dried, preventing decomposition of platinum solution into insoluble platinum chlorides. At the next step 2.44 grams of so formed solid of $H_2PtCl_6{\cdot}6H_2O$ (4.7 mmol Pt) was dissolved in 10 ml of DI water, followed by adding 7.0 grams of Sodium hydroxide (175 mmol). The mixture was heated at 100°C for 1 hour, resulting in yellowish solution. Upon cooling, a pale yellow $Na_2Pt(OH)_6$ (Compound I) was precipitated. Further reaction leads to black spots after 2-3 hours, indicating thermodynamic instability. fresh $Na_2Pt(OH)_6$ was converted to $H_2Pt(OH)_6$ (Compound II) by protonation with 2M Nitric acid at 3 pH. Resulting

precipitate was washed with DI water, Methanol, diluted Nitric acid (0.001M), and Acetone respectively, then dried at 50°C for 1 hour. Finally mixing 4.7 ml of 18.5% Ethanolamine solution (equivalent to 14 mmol) and 2.0 gr of $H_2Pt(OH)_6$ powder, conducted for 17 hours at 50°C yields a clear orange solution of $(EA)_2Pt(OH)_6$ with a pH of 10.

Results and discussion

The phase purity and crystallographic nature of $Na_2Pt(OH)_6$, $H_2Pt(OH)_6$ and $(EA)_2Pt(OH)_6$ were shown by using XRD in "Figure 1.a". XRD pattern of $Na_2Pt(OH)_6$ sample indicates single phase and it is compliant with the available XRD for $Na_2Pt(OH)_6$ (JCPDS Card No. 01-070-2238) [5]. Also, as shown in "Figure 1.a", the XRD pattern of $H_2Pt(OH)_6$ completely coincide with the published data for $H_2Pt(OH)_6$ (JCPDS Card No. 00-032-0439) [2,6,7]. The XRD for $(EA)_2Pt(OH)_6$ illustrates that the material is amorphous ("Figure 1.a"). High-temperature XRD (HTXRD) analysis indicated that $H_2Pt(OH)_6$ is unstable above 200°C, as its peaks disappeared at this temperature. As displayed in "Figure 1.b", PtO_2 and Pt phases became more prominent, with their intensity increasing with temperature.

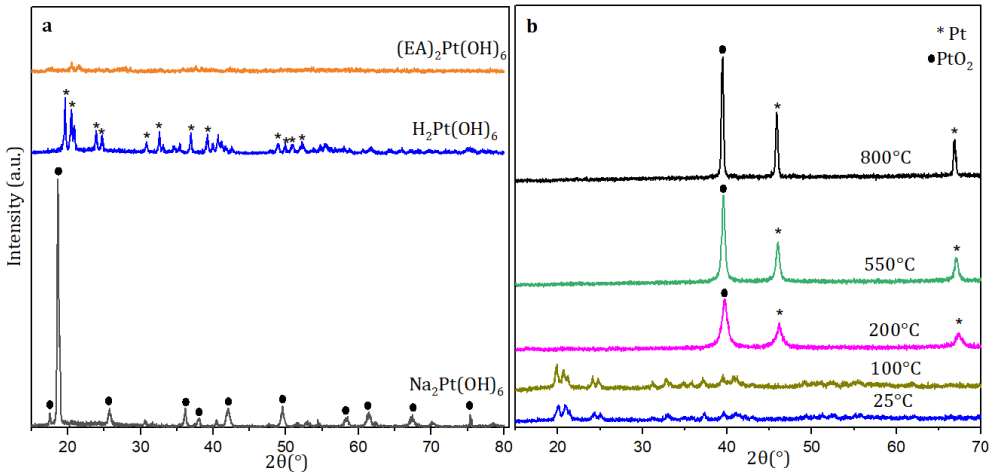


Figure 1. XRD pattern of (a) $Na_2Pt(OH)_6$, $H_2Pt(OH)_6$ and $(EA)_2Pt(OH)_6$. (b) High temperature X-ray diffraction of $H_2Pt(OH)_6$ from 25°C to 800°C.

Thermal decomposition of $Na_2Pt(OH)_6$, $H_2Pt(OH)_6$, and $(EA)_2Pt(OH)_6$ was analyzed via TGA/DTA technique under air up to 1000°C. $Na_2Pt(OH)_6$ showed no weight loss up to 280°C, releasing three water molecules thereafter, forming Na_2PtO_3 ("Figure 2.A"). The thermolysis of $H_2Pt(OH)_6$ is depicted in "Figure 2.B". TGA shows gradual water loss and PtO_2 formation around 520°C, followed by rapid decomposition to Pt metal and O_2 above 580°C [6]. Its thermal decomposition involves three stages: loss of two H_2O molecules below 250°C, again releasing another two H_2O molecules between 250°C and 580°C, then PtO_2 decomposition. TGA profile of $(EA)_2Pt(OH)_6$ ("Figure 2.C") revealed weight loss between 72°C and 160°C, corresponding to the loss of one Ethanolamine group. Another loss occurred between 160°C and 190°C, involving the removal of the second Ethanolamine and $3H_2O$, forming $PtO_2.H_2O$ ($PtO(OH)_2$) [7]. Further heating led to the removal of OH groups and oxygen, leaving metallic platinum.

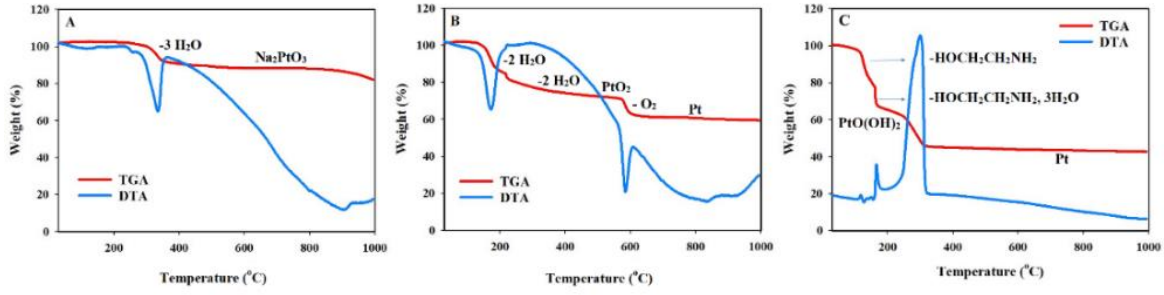


Figure 2. TGA of (A) $Na_2Pt(OH)_6$, (B) H2Pt(OH)6, and (C) $(EA)_2Pt(OH)_6$.

FT-IR spectra of pure ethanolamine and the dried $(EA)_2Pt(OH)_6$ were compared as shown in "Figure 3.A" and "Figure 3.B", both spectra exhibited similar absorption peaks of C-H, C-N, C-C, C-O, N-H, and O-H, confirming the ligand combination of Pt and ethanolamine. Additionally, $(EA)_2Pt(OH)_6$ showed a sharp peak at 500~600 cm^{-1} related to Pt-O vibration [6]. FESEM technique was employed to analyze surface morphology in a catalyst slurry and a calcined catalyst. To prepare TWC a slurry was prepared using γ-Alumina impregnated with Platinum

solution of $(EA)_2Pt(OH)_6$ at pH of 7-8. The platinum slurry was then coated onto a ceramic monolith and calcined at 500°C for 2 hours. FESEM images ("Figure 4") depict spherical Platinum in both slurry and calcined catalyst. The concentrations of Na^+ and Cl^- of the $(EA)_2Pt(OH)_6$ solution were measured 220 mg/kg and 4.8 mg/kg respectively that confirmed appropriate filtration step including the solvents, their quantities used for rinsing the $H_2Pt(OH)_6$ was appropriately applied.

Conclusions

This study presented a facile method for preparing a catalyst precursor, Bis (Ethanolammonium) hexahydroxoplatinum (IV) solution. The underlying synthesis parameters comprising Ethanolamine to Platinum ratio, solution concentration, and temperature were studied. The molar ratio of Ethanolamine to Platinum ranged from 2 to 12, with optimal results between 2 to 4. Ethanolamine solution percentages were considered from 18.5% to 50%, with opacity observed above 20%. Reaction temperature should be maintained in the range of 40 to 60°C. Above 60°C, thermal decomposition occurs, while lower temperatures than 40℃ lead to incomplete reactions.

Crystal phase, thermal decomposition, chemical structure and surface morphology of the prepared precursor were analyzed. The approach offers benefits including ease of control, low chloride and sodium ion content in the Platinum compound, a high yield of 97%, and excellent purity with good water solubility.

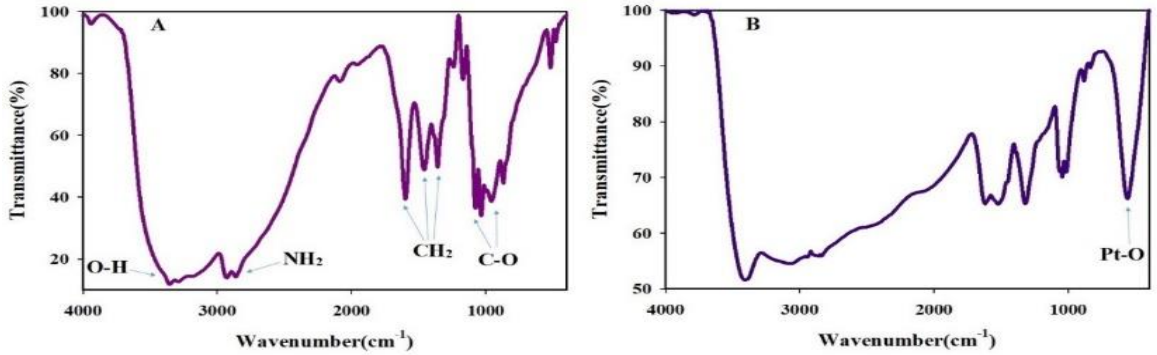


Figure 3. (A) FT-IR spectra of ethanolamine, (B) FT-IR spectra of $(EA)_2Pt(OH)_6$ compound.

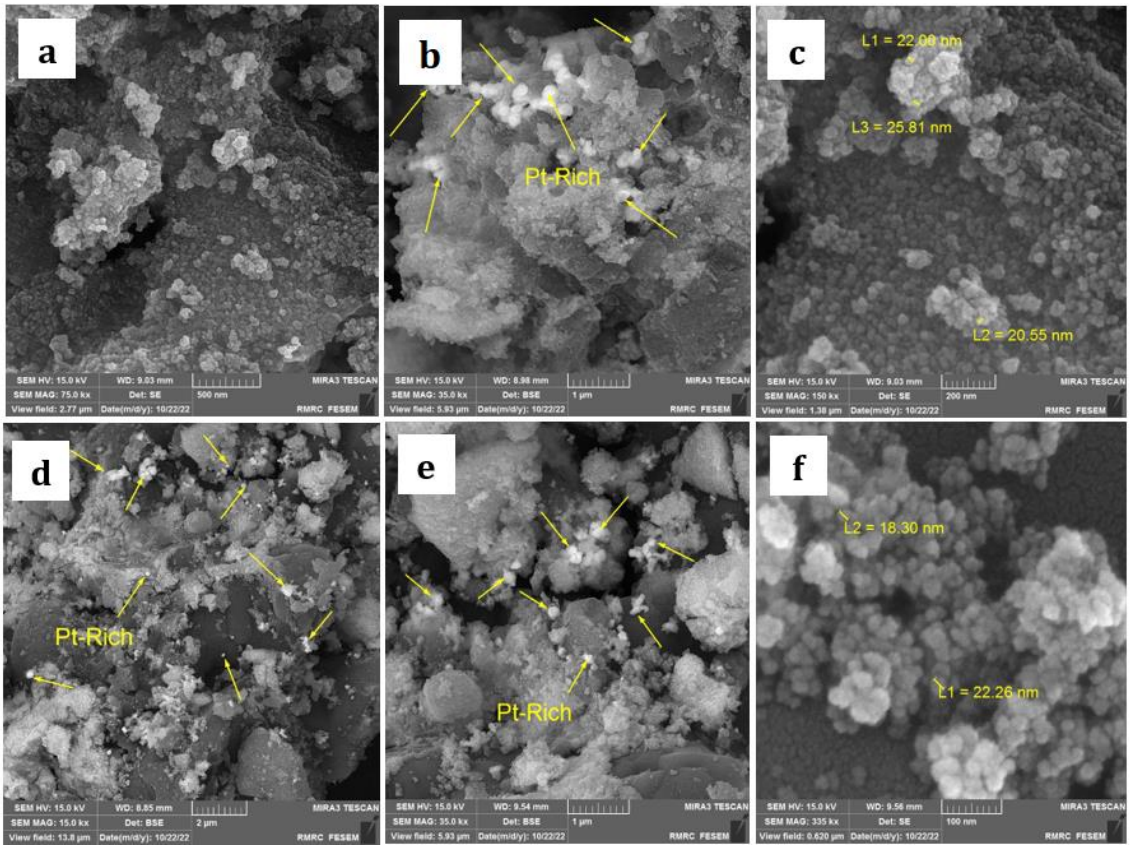


Figure 4. FESEM of the synthesized $(EA)_2Pt(OH)_6$ in the catalyst slurry (a,b,c) and the calcined catalyst (d,e,f).

Reference

1. Van den Tillaart, J. A. A., Leyrer, J., Eckhoff, S., & Lox, E. S. (1996). Effect of support oxide and noble metal precursor on the activity of automotive diesel catalysts. Applied Catalysis B: Environmental, 10(1-3), 53-68.
2. Venediktov, A. B., Korenev, S. V., Vasil'chenko, D. B., Zadesenets, A. V., Filatov, E. Y., Mamonov, S. N. & Semitut, E. Y. (2012). On preparation of platinum (IV) nitrate solutions from hexahydroxoplatinates (IV). Russian Journal of Applied Chemistry, 85(7), 995-1002.
3. Vasilchenko, D., Tkachev, S., Baidina, I., & Korenev, S. (2013). Speciation of platinum (IV) in nitric acid solutions. Inorganic chemistry, 52(18), 10532-10541.
4. Woerner, E., Karch, R., Rivas-Nass, A., Doppiu, A. (2018), Method for producing aqueous preparations of complexes of platinum group metals. U.S. Patent 9,856,280 B2.
5. Bugaris, D. E., Smith, M. D., & zur Loye, H. C. (2013). Hydroflux crystal growth of platinum group metal hydroxides: $Sr_6NaPd_2(OH)_{17}$, $Li_2Pt(OH)_6$, $Na_2Pt(OH)_6$, $Sr_2Pt(OH)_8$, and $Ba_2Pt(OH)_8$. Inorganic chemistry, 52(7), 3836-3844.
6. Dou, D., Liu, D. J., Williamson, W. B., Kharas, K. C., & Robota, H. J. (2001). Structure and chemical properties of Pt nitrate and application in three-way automotive emission catalysts. Applied Catalysis B: Environmental, 30(1-2), 11-24.
7. Giuliano, M., Valsania, M. C., Ticali, P., Sartoretti, E., Morandi, S., Bensaid, S., ... & Sgroi, M. (2021). Characterization of the Evolution of Noble Metal Particles in a Commercial Three-Way Catalyst: Correlation Between Real and Simulated Ageing. *Catalysts*, *11*(2), 247.

Advanced Engineering Days

aed.mersin.edu.tr

Boosting the photocatalytic activity of $ZnCo_2O_4$ spinel via anchoring on graphene nanoplatelets for removing the ciprofloxacin antibiotic

Shadi Ebrahimi [*1], Mohammad Mehdi Heydari [1], Azadeh Ebrahimian Pirbazari [1], Reza Zarghami [2], Fatemeh Esmaeili Khalil Saraei [1]

[1]University of Tehran, College of Engineering, Fouman Faculty of Engineering, Iran, shadi.ebrahimi@ut.ac.ir, M.m.heydari77@ut.ac.ir, aebrahimian@ut.ac.ir, f.esmaeili.kh@ut.ac.ir
[2]University of Tehran, College of Engineering, School of Chemical Engineering, Iran, rzarghami@ut.ac.ir

Cite this study: Ebrahimi, S., Heydari, M. M., Ebrahimian Pirbazari, A., Zarghami, R., & Esmaeili Khalil Saraei, F. (2024). Boosting the photocatalytic activity of $ZnCo_2O_4$ spinel via anchoring on graphene nanoplatelets for removing the ciprofloxacin antibiotic. Advanced Engineering Days, 9, 506-508

Keywords
$ZnCo_2O_4$
Graphene nanoplatelets
Ciprofloxacin
Ammonium persulfate
Photocatalytic degradation

Abstract

Ciprofloxacin (CIP), a threat to the environment, can be effectively removed through heterogeneous photocatalytic degradation using spinel-based photocatalysts. In the present study, $ZnCo_2O_4$ spinel was synthesized via the hydrothermal method and anchored on graphene nanoplatelets ($GO/ZnCo_2O_4$) using the sonochemical/hydrothermal synthesis procedures. PXRD patterns showed the main diffractions of $ZnCo_2O_4$ spinel, and the diffraction of GO was not observable due to its low crystallinity and amount. FESEM micrographs confirmed the anchorage of $ZnCo_2O_4$ on graphene nanoplatelets. The efficiency of the fabricated photocatalysts was examined for the photocatalytic removal of CIP in the presence and absence of ammonium persulfate (APS) under visible and ultraviolet light irradiation. The results showed that the presence of GO as a photosensitizer and electron trap improved the activity of $ZnCo_2O_4$ spinel, 70% and 90% of CIP removed by $GO/ZnCo_2O_4$ in the presence of APS under visible and UV light irradiation, respectively.

Introduction

Ciprofloxacin (CIP) is a commonly used antibiotic for various infectious diseases in humans and animals due to its potent antimicrobial properties [1]. The high concentration of CIP in water sources and pharmaceutical effluents poses significant risks to aquatic organisms and human health [2]. Photocatalytic degradation processes have absorbed much attention due to their high efficiency in removing organic pollutants/antibiotics under room temperature and pressure conditions [3]. Spinel compounds provide higher visible light absorption capacity due to their stability, low surface acidity, high mechanical durability, response to visible light (400-700 nm), and resistance to photocorrosion [4]. Zinc cobalt spinel ($ZnCo_2O_4$) is a p-type semiconductor with a significant band gap energy (E_{bg}=2.0~2.6 eV), making it suitable for various applications [5]. Graphene, a two-dimensional nanostructure of carbon, has a honeycomb-like structure. This unique structure gives graphene distinct physicochemical characteristics such as high surface area, high electron mobility, excellent thermal conductivity, exceptional optical transparency, and mechanical stability. Therefore, these features make graphene a preferred base for significant improvements in the performance of chemical reactors and catalytic processes [6].

In the present study, the aim is to design an ideal photocatalyst in the visible light region. Therefore, we first synthesized spinel $ZnCo_2O_4$ and then anchored it on graphene nanoplatelets to obtain the $GO/ZnCo_2O_4$ nanocomposite. Subsequently, the structural and morphological properties of the synthesized samples were investigated using analytical methods, including PXRD, FESEM, EDS, and elemental mapping. Furthermore, the photocatalytic efficiency of the synthesized photocatalysts was evaluated for the degradation of the ciprofloxacin (CIP) antibiotic in the presence and absence of ammonium persulfate (APS) as a chemical oxidant.

Material and Method

Initially, spinel $ZnCo_2O_4$ was synthesized using the hydrothermal method described in reference [5] with some modifications. Then, the synthesized $ZnCo_2O_4$ was anchored on graphene nanoplatelets using the sonochemical/ hydrothermal methods described in reference [7]. Ciprofloxacin (CIP) hydrochloride was obtained from Exir Pharmaceutical Company, Tehran, Iran, as an organic pollutant model for photocatalytic degradation experiments. Visible light sources (500W OSRAM halogen lamp (ECO)) and UV radiation source (OSRAM krypton lamp (ECO), 230W) were used as irradiation sources. 100 mg of catalyst was added to 100 mL of CIP solution (10 mg/L) and kept in the dark for 30 minutes, then irradiated for 80 minutes for photocatalytic degradation tests. After centrifugation, solution absorption was measured using a UV-Vis spectrophotometer at λ_{max}=275 nm. The percentage of degradation was obtained using equation (1), where A_t and A_0 represent the absorption values at time t and 0, respectively.

$$R\% = 1 - \left(\frac{A_t}{A_0}\right) \quad (1$$

Results and Discussion

Figure 1 shows the PXRD pattern of $ZnCo_2O_4$, displaying intense diffractions indicating a highly crystalline $ZnCo_2O_4$ sample with prominent growth along the (311) plane. All diffractions at 2θ=18.9°, 31.16°, 36.72°, 38.46°, 44.64°, 55.42°, 59.18°, 65.08° and 77.1° matched well with (JCPDS card no.23-1390). In the PXRD pattern of $GO/ZnCo_2O_4$, the diffraction of graphene oxide at 2θ=11.98° is not observable due to low crystallinity and the low amount of graphene, and the diffractions of $ZnCo_2O_4$ remain unchanged. The diffraction intensity in $GO/ZnCo_2O_4$ is higher compared to $ZnCo_2O_4$ due to host-guest interaction (Figure 1).

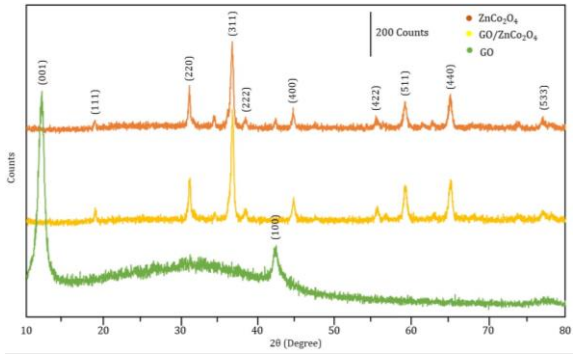


Figure 1. PXRD pattern of the samples

The FESEM micrographs (Figure 2) show the presence of graphene nanoplatelets in $GO/ZnCo_2O_4$. The EDS and elemental mapping confirmed the presence of Zn, Co, O, and C in the samples.

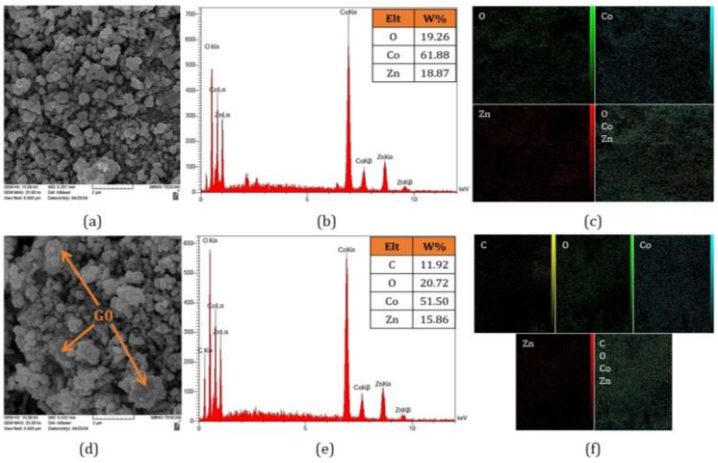


Figure 2. (a, d) FESEM micrographs (b, e) EDS spectra (c, f) elemental mapping images for $ZnCo_2O_4$ and $GO/ZnCo_2O_4$

Figure 3 presents the photocatalytic performance of synthesized samples in the presence and absence of APS for removing CIP under UV and Visible light irradiation. $GO/ZnCo_2O_4$ showed higher performance under UV and visible light irradiation compared to $ZnCo_2O_4$ due to the presence of graphene. Graphene acts as an electron trap, prevents electron-hole recombination, and improves photocatalytic performance. The degradation percent is

higher in the presence of APS (0.0025 mol/L). Persulfate can trap electrons, prevent electron-hole recombination, and increase the formation of radicals on the catalyst surface (Eqs 2-7). Also, under UV irradiation, the degradation percent is higher than visible light due to the higher photon energy of UV radiation [8].

$S_2O_8^{2-} + hv \rightarrow 2SO_4^{\bullet-}$ (2

$S_2O_8^{2-} + e^- \rightarrow SO_4^{2-} + SO_4$ (3

$SO_4^{\bullet-} + e^- \rightarrow SO_4^{2-}$ (4

$SO_4^{2-} + h^+ \rightarrow SO_4^{\bullet-}$ (5

$SO_4^{2-} + OH^{\bullet} \rightarrow SO_4^{\bullet-} + OH^-$ (6

$SO_4^{\bullet-} + H_2O \rightarrow SO_4^{2-} + OH^{\bullet}$ (7

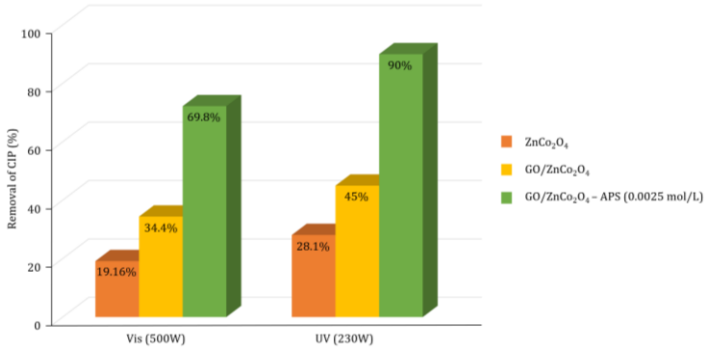


Figure 3. Photocatalytic degradation performance of the prepared samples for ciprofloxacin removal (Volume of CIP: 100mL, CIP concentration: 10 mg/L, Catalyst mass: 100 mg, Irradiation time: 80 min)

Conclusion

This study successfully carried out the anchorage of $ZnCo_2O_4$ spinel on graphene nanoplatelets ($GO/ZnCo_2O_4$). PXRD results confirmed the synthesis of $ZnCo_2O_4$ spinel, and EDS/elemental mapping and FESEM analyses proved the anchorage of $ZnCo_2O_4$ spinel on graphene nanoplatelets. Finally, the photocatalytic performance of the synthesized samples was investigated for ciprofloxacin (CIP) removal at different conditions. The presence of graphene in $GO/ZnCo_2O_4$ as a photosensitizer and electron trap boosted the activity of $ZnCo_2O_4$ spinel. The highest degradation percentage of CIP (90%) was obtained using $GO/ZnCo_2O_4$ in the presence of APS under UV irradiation.

References

1. Selvamani, P. S., Vijaya, J. J., Kennedy, L. J., Mustafa, A., Bououdina, M., Sophia, P. J., & Ramalingam, R. J. (2021). Synergic effect of Cu_2O/MoS_2/rGO for the sonophotocatalytic degradation of tetracycline and ciprofloxacin antibiotics. Ceramics International, 47(3), 4226-4237.
2. Nimshi, R. E., Vijaya, J. J., Kennedy, L. J., Selvamani, P. S., Bououdina, M., & Sophia, P. J. (2023). Effective microwave assisted synthesis of $CoFe_2O_4$@TiO_2@rGO ternary nanocomposites for the synergic sonophotocatalytic degradation of tetracycline and c antibiotics. Ceramics International, 49, 13762-13773.
3. Abdurahman, M. H., Abdullah, A. Z., & Shoparwe, N. F. (2021). A comprehensive review on sonocatalytic, photocatalytic, and sonophotocatalytic processes for the degradation of antibiotics in water: Synergistic mechanism and degradation pathway. Chemical Engineering Journal, 413, 127412.
4. Kirankumar, V. S., & Sumathi, S. (2020). A review on photodegradation of organic pollutants using spinel oxide. Materials Today Chemistry, 18, 100355.
5. Dhanasekar, M., Ratha, S., Rout, Ch. S., & Bhat, S. V. (2022). Self-assembled nanosheets of $ZnCo_2O_4$ as efficient sonophotocatalysts for day light dye degradation. Ceramics International, 48, 29460-29464.
6. Chen, C., Fei, L., Lu, L., Li, B., Raza, S., Shen, L., & Lin, H. (2023). Superwetting graphene-based materials: From wettability regulation to practical applications. Materials Today Chemistry, 29, 101452.
7. Gnanamoorthy, G., Ramar, K., Ali, D., Yadav, V. K., Sureshbabu, K., & Narayanan, V. (2020). A series of $ZnCo_2O_4$/rGO/Pt nanocubes with excellent photocatalytic activity towards visible light. Chemical Physics Letters, 759, 137988.
8. Mokhtari Nesfchi, M., Ebrahimian Pirbazari, A., Esmaeili Khalil Saraei, F., Rojaee, F., Mahdavi, f., & Fa'al Rastegar, S. A. (2021). Fabrication of plasmonic nanoparticles/cobalt doped TiO_2 nanosheets for degradation of tetracycline and modeling the process by artificial intelligence techniques. Materials Science in Semiconductor Processing, 122, 105465.

Advanced Engineering Days

aed.mersin.edu.tr

Study the effect of morphology and structure of CeO_2/TiO_2 and CeO_2/ZrO_2 heterostructures on the degradation efficiency of tetracycline

Mohammad Moradi [1], Mohammad Mehdi Heydari [1], Azadeh Ebrahimian Pirbazari [*1], Fatemeh Esmaeili Khalil Saraei [1]

[1]University of Tehran, College of Engineering, Fouman Faculty of Engineering, Iran, mohammad.moradi75@ut.ac.ir, m.m.heydari77@ut.ac.ir, aebrahimian@ut.ac.ir, f.esmaeili.kh@ut.ac.ir

Cite this study: Moradi, M., Heydari, M. M., Ebrahimian Pirbazari, A., & Esmaeili Khalil Saraei, F. (2024). Study the effect of morphology and structure of CeO_2/TiO_2 and CeO_2/ZrO_2 heterostructures on the degradation efficiency of tetracycline. Advanced Engineering Days, 9, 509-511

Keywords
CeO_2/ZrO_2 nanosheets
CeO_2/TiO_2
Core-shell structure
Photocatalysis

Abstract

The present contribution investigated the effect of structure and morphology on the photocatalytic activity of the hybrid photocatalyst. In this regard, CeO_2/TiO_2 with core-shell structure and CeO_2/ZrO_2 nanosheets were synthesized using the Stöber and co-precipitation methods. The PXRD patterns showed fluorite structure for CeO_2, the anatase phase for TiO_2, and the tetragonal/monoclinic phases for ZrO_2. FESEM analysis confirmed the nanocube morphology for CeO_2, nanosheet morphology for CeO_2/ZrO_2 and core-shell structure for CeO_2/TiO_2. Photocatalytic degradation studies revealed that the CeO_2/TiO_2 core-shell (%removal~50%) had higher photocatalytic activity than CeO_2/ZrO_2 nanosheets (%removal~20%) in the removal of tetracycline (TC) under visible light irradiation. The experimental studies showed that the morphology and structure of coupled photocatalysts have an essential role in the photodegradation activity.

Introduction

Tetracycline (TC) is the secondary most utilized antibiotic to treat illnesses caused by bacteria. During human and animal metabolic processes, approximately 60% and 17–80% of the used TC are excreted in urine and feces to enter soil, surface, and underground waters [1]. Photocatalysis is a wastewater treatment method due to its easy operation, strong oxidation capacity, high mineralization rate, and wide application range, which can effectively remove various organic pollutants [2]. Ceria (CeO_2) is one of the rare earth metal oxides used as a catalyst based on its improved structural and redox properties [3]. In addition, it is considered an effective coupling material with TiO_2 within the field of visible light-driven photocatalysts. The coupling of CeO_2 with TiO_2 positively influences the visible light absorption of TiO_2 and within the facile separation of electron-hole pairs with an increased lifetime of the charge carriers [4]. Zirconia (ZrO_2) has been considered an efficient photocatalyst for the decomposition and mineralization of a wide variety of pollutants due to its generally wide band gap value, high stability, low toxicity, cost-effectiveness, appropriate redox potential and high negative conduction band potential [5]. This study aimed to couple TiO_2 and ZrO_2 with CeO_2 to prepare CeO_2/TiO_2 with core-shell structure and CeO_2/ZrO_2 nanosheets. Photocatalytic activity of the pure and coupled photocatalysts were evaluated for the degradation of tetracycline (TC) as a pollutant model under visible light irradiation. Moreover, structural and morphological characteristics of the synthesized samples were investigated by PXRD and FESEM/EDX analyses.

Material and Method

CeO_2/TiO_2 with core-shell structure was synthesized using a hydrothermal route assisted with the Stöber method [6]. CeO_2/ZrO_2 nanosheets were synthesized using the procedure detailed in the reference [7]. Tetracycline hydrochloride (Batch No.161026) was prepared from Hakim Pharmaceutical Company, Tehran, Iran, as the model of organic pollutant for photocatalytic tests. The OSRAM Halogen (ECO) 500W lamp was a visible light source for illumination tests. Before the illumination, a glass beaker containing 50 mg catalyst and 100 mL artificial TC wastewater (Conc: 30 mg/L) was stirred for 30 min in the dark to achieve adsorption/desorption equilibrium. Afterward, the solution was irradiated for 120 minutes to remove TC. To measure the remaining TC,

5 mL of the solution was taken at fixed intervals and centrifuged. The absorbance of the solution was measured with a Rayleigh UV-2601 UV/Vis spectrophotometer at (λ_{max} = 355 nm).

Results and Discussion

"Figure 1" shows the PXRD pattern of CeO_2 contains eight diffractions at 2θ = 28.5°, 33.0°, 47.3°, 56.3°, 59.1°, 69.3°, 76.8°, and 78.8° are well matched to of fluorite structure (JCPDF #04-0593). The PXRD pattern of TiO_2 nanoparticles shows diffractions at 2θ = 25.28°, 37.80°, 48.05°, 53.89°, 55.06°, 62.69°,70.3° and 75.2° which are proved the formation of anatase phase (JCPDS #21-1272). Diffraction peaks of pure ZrO_2 which appeared at 2θ = 24.2°, 28.2°, 31.4°, 33.9, 38.1, 40.8°, 45.0°, 50.0°, 55.6°, 65.0° and 74.8° are assigned to the monoclinic phase of ZrO_2 (m-ZrO_2, JCPDS #37-1484). While the six peaks at 30.2°, 35.2°, 50.4°, 54.8, 60.0° and 63.2° belong to the tetragonal phase of ZrO_2 (t-ZrO_2, JCPDS #17-0923). In the PXRD pattern of CeO_2/ZrO_2, the number of peaks has decreased, and the intense peaks are mainly related to the tetragonal phase of ZrO_2. In the x-ray diffractogram of CeO_2/TiO_2, the CeO_2 diffractions have a lower intensity than pure CeO_2 due to being surrounded by TiO_2, which confirms the core-shell structure and the diffractions of TiO_2 are not observable due to the low amount of it.

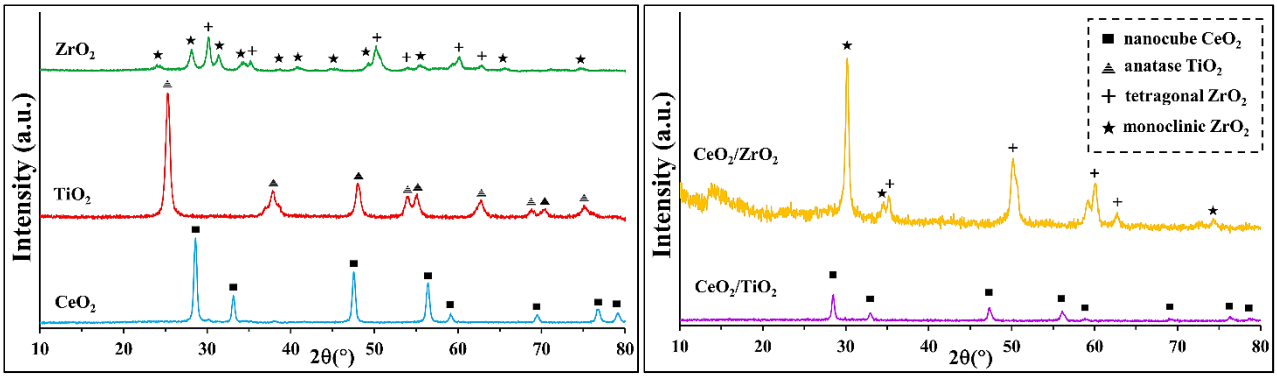


Figure 1. PXRD patterns of the samples

The nanocube morphology for CeO_2, nanoparticle morphology for TiO_2, core-shell structure for CeO_2/TiO_2 and nanosheet morphology for CeO_2/ZrO_2 are observable in the FESEM micrographs (Figure 2). In addition, the weight percent of Ce, O, Zr, and Ti elements was measured using an EDS analysis (Figure 2).

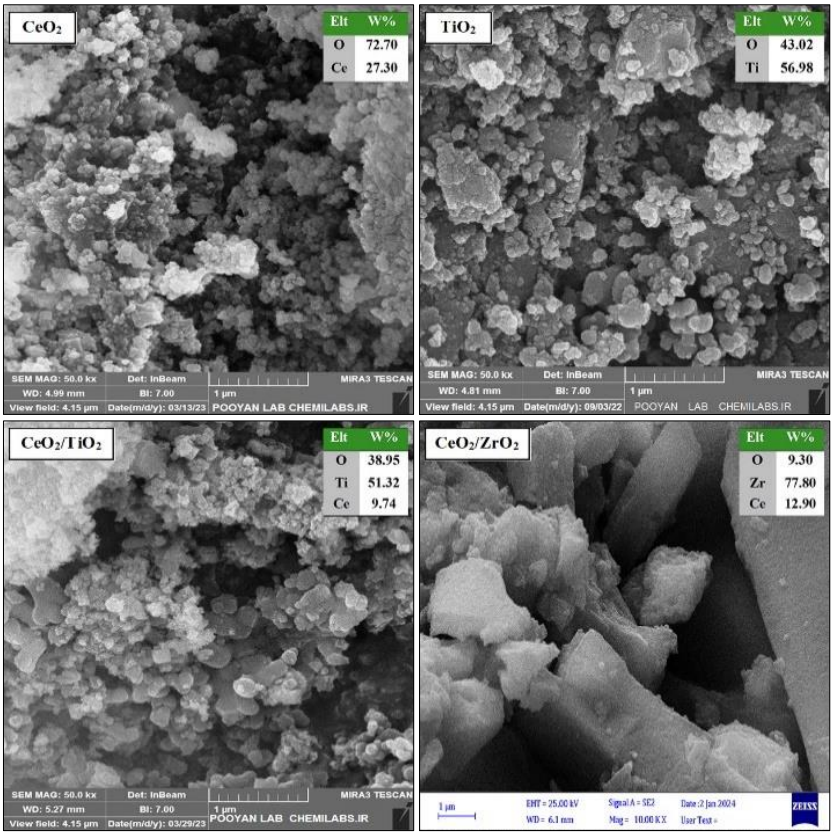


Figure 2. FESEM image of the synthesized samples

"Figure 3" shows the removal percent of TC over the different photocatalysts after 120 minutes of irradiation under visible light. For CeO_2/TiO_2, as the results of FESEM showed, TiO_2 nanoparticles do not entirely cover CeO_2 nanocubes; for this reason, the photocatalytic activity of CeO_2/TiO_2 is closer to pure CeO_2. In other words, CeO_2 has improved the photocatalytic activity of TiO_2. In addition, the results of PXRD and FESEM for CeO_2/ZrO_2 confirmed that ZrO_2 surrounds the surface of CeO_2. Therefore, the photocatalytic activity of CeO_2/ZrO_2 is closer to pure ZrO_2. As a result, the combination of TiO_2 and CeO_2 in the core-shell structure showed better photocatalytic activity in the visible light region than CeO_2/ZrO_2 nanosheets.

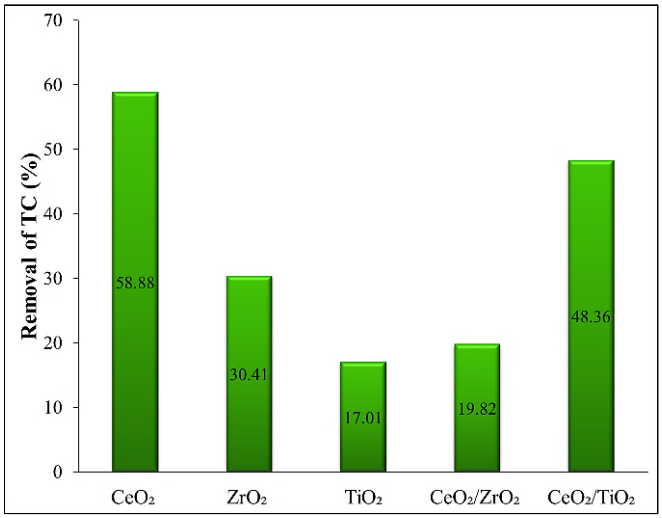


Figure 3. Photocatalytic activity of the samples

Conclusion

This contribution successfully synthesized CeO_2/TiO_2 with core-shell structure and CeO_2/ZrO_2 nanosheets using the Stöber and co-precipitation methods. PXRD analysis verified the formation of fluorite structure for CeO_2, the anatase phase for TiO_2, and the tetragonal/monoclinic phases for ZrO_2. FESEM micrographs confirmed that some parts of CeO_2 nanocubes covered by TiO_2 nanoparticles formed core-shell structures in CeO_2/TiO_2 and nanosheet morphology for CeO_2/ZrO_2. The degradation results showed that CeO_2/TiO_2 with core-shell structure had better photocatalytic activity than CeO_2/ZrO_2 nanosheets for degradation of TC under visible light irradiation. Our findings confirmed that the structure and morphology of nanohybrids is essential for photocatalytic activity.

References

1. Leichtweis, J., Vieira, Y., Welter, N., Silvestri, S., Dotto, G. L., & Carissimi, E. (2022). A review of the occurrence, disposal, determination, toxicity and remediation technologies of the tetracycline antibiotic. Process Safety and Environmental Protection, 160, 25-40.
2. Sun, H., Guo, F., Pan, J., Huang, W., Wang, K., & Shi, W. (2021). One-pot thermal polymerization route to prepare N-deficient modified g-C_3N_4 for the degradation of tetracycline by the synergistic effect of photocatalysis and persulfate-based advanced oxidation process. Chemical Engineering Journal, 406, 126844.
3. Pudukudy, M., Yaakob, Z., Jia, Q., & Takriff, M. S. (2018). Catalytic decomposition of undiluted methane into hydrogen and carbon nanotubes over Pt promoted Ni/CeO_2 catalysts. New Journal of Chemistry, 42(18), 14843-14856.
4. Li, G., Zhang, D., & Jimmy, C. Y. (2009). Thermally stable ordered mesoporous CeO_2/TiO_2 visible-light photocatalysts. Physical Chemistry Chemical Physics, 11(19), 3775-3782.
5. Navío, Hidalgo, Colon, G., Botta, S. G., & Litter, M. I. (2001). Preparation and physicochemical properties of ZrO_2 and Fe/ZrO_2 prepared by a sol–gel technique. Langmuir, 17(1), 202-210.
6. Chen, F., Ho, P., Ran, R., Chen, W., Si, Z., Wu, X., ... & Lee, C. (2017). Synergistic effect of CeO_2 modified TiO_2 photocatalyst on the enhancement of visible light photocatalytic performance. Journal of Alloys and Compounds, 714, 560-566.
7. Usharani, S., & Rajendran, V. (2017). RTFM, RTPL and photocatalytic activity of CeO_2/ZrO_2 nanocomposites. Chinese journal of physics, 55(6), 2588-2596.

Advanced Engineering Days

aed.mersin.edu.tr

Modeling a Recuperator to Investigate Velocity Distribution and Pressure Drop by Varying the Cross-Section Geometry of its Pipes

Erfan Farsijani [1], Kamran Keynejad [*1], Hedayat Azizpour [2], Zahra Nasrollahi [1]

[1]University of Tehran, College of Engineering, Fouman Faculty of Engineering, Iran, erfan.farsijani@ut.ac.ir, kamran.keynejad@ut.ac.ir, z.nasr@ut.ac.ir
[2]University of Tehran, College of Engineering, School of Chemical Engineering, Iran, h.azizpour@ut.ac.ir

Cite this study: Farsijani, E., Keynejad, K., Azizpour, H. & Nasrollahi, Z. (2024). Modeling a Recuperator to investigate velocity distribution and pressure drop by varying the cross-section geometry of its pipes. Advanced Engineering Days, 9, 512-514

Keywords
Recuperator
Heat exchanger
Pressure drop
Velocity distribution

Abstract

In this paper, the distribution of velocity and pressure drop resulting from changes in the geometry of the recuperator pipe cross-sections has been investigated. The modeling results indicate that pipes with a square cross-section exhibit the lowest pressure drop and average velocity, with values of 12.3 kPa and 1.9556 m/s, respectively. Conversely, pipes with a circular cross-section demonstrate the highest pressure drop and average velocity, with values of 16.8 kPa and 1.9619 m/s. Additionally, for pipes with a diamond cross-section, the maximum velocity of the output flow increases by approximately 38% compared to the input flow velocity.

Introduction

Managing wasted energy is crucial for reducing energy consumption and lowering costs across various industries. Heat exchangers can effectively recover wasted energy [1], one of which is a gas-to-gas exchanger [2]. A recuperator is a heat exchanger where two gas fluids are separated by transparent walls [1, 2]. Converting industrial furnaces from non-preheated to preheated mode using a recuperator can improve system energy efficiency by 50 to 60 percent [1].

When designing a heat exchanger, selecting a fluid transfer system to achieve an appropriate pressure level requires careful calculation of the fluid flow through the equipment [2, 3]. Increasing the flow rate enhances the heat exchange process by raising the convective transfer coefficient, which can lower investment costs. However, increased flow velocity also raises fluid flow resistance, necessitating more energy to maintain the appropriate pressure, potentially escalating operational costs. Therefore, it is essential to calculate the fluid's velocity and pressure drop to optimize the converter's size. Calculating fluid flow resistance in the space between pipes is complex. Additionally, ensuring uniform fluid flow in the pipe bundles is critical for maximizing heat transfer and extending pipe lifespan. Improper fluid distribution reduces the overall efficiency of the heat exchanger. Irregular fluid flow distribution can create problematic regions, particularly with high-temperature fluids, which can adversely affect the tubes [3, 4].

Material and Method

The geometry of the model is designed in three dimensions. The geometry of the fluid area includes two cylinders with a diameter of 30 cm and a length of 11.09 cm serving as the fluid inlet and outlet and a rectangular channel measuring 78.55 cm in length, 39.45 cm in width, and 39.88 cm in height, with chamfered corners to reduce flow dead zones. The working fluid passing through the recuperator is air. The geometry of the tubes section consists of prisms arranged in six rows and eight columns. The prisms have circular cross-sections with a diameter of 2.87 cm, square cross-sections with sides of 2.87 cm, and diamond cross-sections with diameters of 2.87 cm. The distance between adjacent tubes is 1.6 cm, while the distance between the first row and the wall is 2.4 cm. All recuperator pipes are made of iron. Figure 1 illustrates the recuperator geometry for the group of tubes with circular cross-sections.

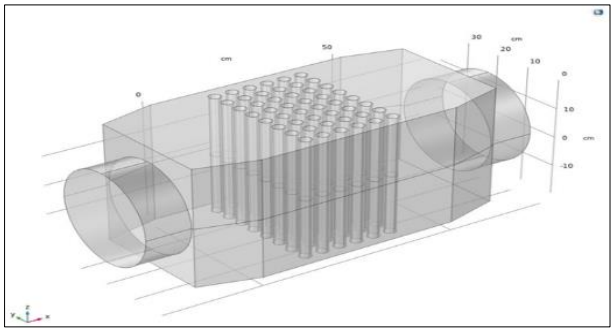


Figure 1. Schematic of the recuperator designed with cylindrical tubes

The governing equations for this system are:

- Continuity equation [6]: $\frac{\partial \rho}{\partial t} + (\nabla, \rho V) = 0$ (1)
- Pressure equation [2]: $\Delta P = 8 \times f \left(\frac{D_s}{d_s}\right) \left(\frac{L}{L_B}\right) (\frac{\rho, V^2}{2})$ (2)
- Equations of motion [6]: $\frac{D(\rho V)}{Dt} = -\nabla p - [\nabla, \tau] + \rho g$ (3)

In these equations, P is the pressure in Pa, ρ is the density in kg/m^3, V is the velocity in m/s, τ is the shear stress in pascals, f is the dimensionless friction coefficient, L is the shell length in m, D_s is the shell diameter in m, d_s is the equivalent diameter in m, and L_B is the characteristic length in m.

After simplification, the boundary conditions are as follows:

- Incoming air enters the converter from the right side at a velocity of 2 m/s.
- Outlet air pressure is assumed to be 0 pascals, indicating direct discharge into the environment.

The equations were solved using COMSOL Multiphysics 6.1 software, with meshing tailored to the physics of the problem detailed in Table 1. The laminar flow physics module within the software was utilized.

Table 1. Information about the meshing of designed geometries

Items	Cross-section of pipes	Average mesh quality	The number of elements	Mesh volume size
1	Circular	0.5772	168340	1.236×10^{-5}cm^3
2	Square	0.496	164820	1.348×10^{-5} cm^3
3	Diamond	0.5188	167463	1.269×10^{-5} cm^3

Results and Discussion

In this three-dimensional model, the two-dimensional distribution of velocity and pressure on the x-y plane for circular, square, and diamond cross-sections has been explored, with results presented in Figure 2 and Figure 3. Figure 2(A) illustrates that within the group of pipes with circular cross-sections, the average outlet velocity of the fluid is 1.9619 m/s, with a maximum velocity of 2.69 m/s. Notably, the maximum fluid velocity within the recuperator occurs in areas between the wall and the first and last rows of pipes, reported at 3.78 m/s. These results were validated against the source modeling results [3]. For the pipe bundles with square cross-sections, as depicted in Figure 2(B), the average outlet velocity is 1.9556 m/s, with a maximum velocity of 2.63 m/s. Similarly, small areas between the wall and the first and last rows of pipes exhibit velocities close to this maximum velocity. Conversely, in the recuperator featuring diamond-shaped tubes (Figure 2(C)), the average outlet velocity is 1.9568 m/s, with a maximum velocity of 2.76 m/s. However, a small region between the tubes and the wall displays a maximum velocity of 3.54 m/s, as depicted in the figure. According to the law of continuity (Equation 1), the average output velocity for all geometries should be the same. Based on our calculations, the maximum relative error in the average output velocity between pipe bundles with square cross-sections and those with circular cross-sections is approximately 0.32%, indicating a low error in the calculations.

Figure 3(A) indicates a pressure drop of 16.8 kPa in the circular cross-section, while Figure 3(B) illustrates a pressure drop of 12.3 kPa for the square cross-section. Additionally, Figure 3(C) displays a pressure drop of 16.5 kPa for the diamond cross-section.

Conclusion

The modeling results indicate that the lowest pressure drop is observed in pipe bundles with a square cross-section, measured at 12.3 kPa. In contrast, the highest pressure drop occurs in cylindrical tubes, with a value of 16.8 kPa, approximately 36.5% higher than the corresponding value in the square tubes.

Furthermore, the results show that the maximum velocity of the output fluid in the pipe bundle with a diamond cross-section is 2.76 m/s, representing about a 38% increase over the initial fluid velocity.

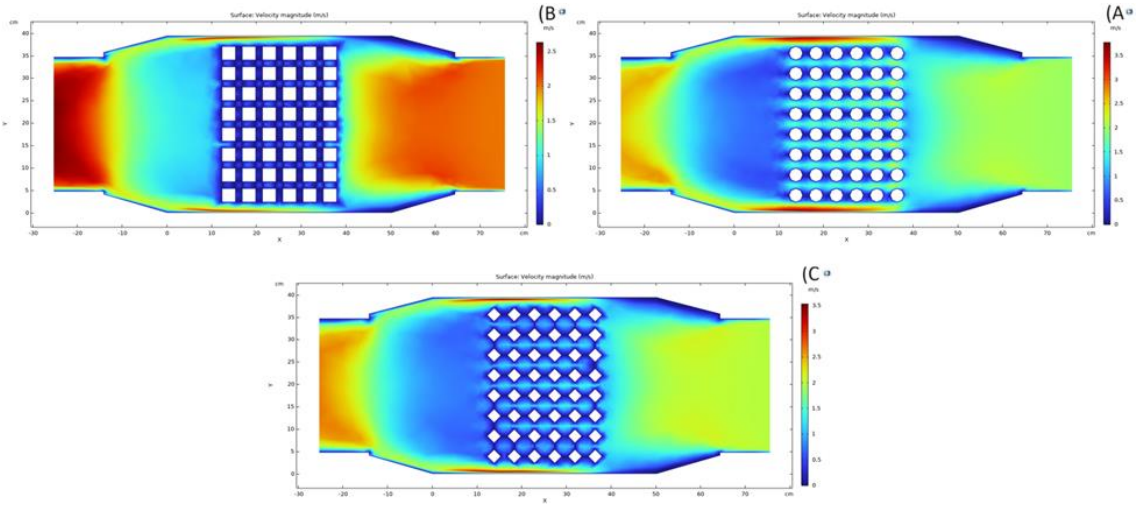


Figure 2. Velocity distribution in a recuperator with a cluster of tubes with cross-sections (A) circular, (B) square, and (C) diamond

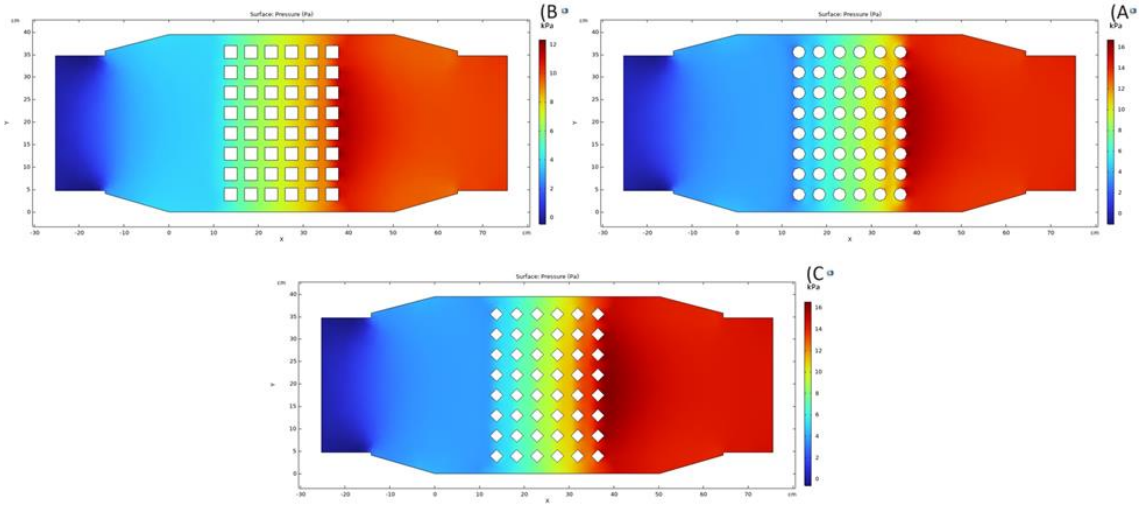


Figure 3. Pressure distribution in the recuperator with a cluster of tubes with cross-sections (A) circular, (B) square, and (C) diamond

References

1. Oyelami, A. T., Adejuyigbe, S. B., & Olusunle, S. O. O. (2021). Thermal Analysis of Recuperator Developed for Waste Heat Recycling in Liquid-Fuel Fired Furnaces. International Journal of Heat and Technology, 39, 121-127.
2. Sekulic, D. P., & Shah, R. K. (2023). Fundamentals of Heat Exchanger Design: Wiley.
3. Ludwig, W., & Zajac, D. (2017). Modification of a recuperator construction with CFD methods. Chemical and Process Engineering, 38. doi:10.1515/cpe-2017-0045
4. Kayabaşı, E. (2023). Technoeconomic Optimization of a Recuperator Considering Pressure Drops and Operating Costs. International Journal of Advances in Engineering and Pure Sciences, 35, 346-358.
5. Bird, R. B., Stewart, W. E., & Lightfoot, E. N. (2006). Transport Phenomena: Wiley.

Advanced Engineering Days

aed.mersin.edu.tr

Removal of hydroquinone from aqueous solution using novel Fe-Mg bimetallic oxide: synthesis, characterization and isotherm modeling

Hesam Malekzadeh*[1], Mohammad Zabihi [1], Morteza Faghihi [2]

[1]*Sahand University of Technology, Chemical Engineering Department, Iran, H.Malekzadeh76@gmail.com, Zabihi@sut.ac.ir*
[2]*Niroo Research Institute, Chemical and Process Research Group, Iran, Mfaghihi@nri.ac.ir*

Cite this study: Malekzadeh, H., Zabihi, M., & Faghihi, M. (2024). Removal of hydroquinone from aqueous solution using novel Fe-Mg bimetallic oxide: synthesis, characterization and isotherm modeling. Advanced Engineering Days, 9, 515-517

Keywords
Adsorption
Hydroquinone
Nanomaterial
Bimetallic oxide

Abstract

Hydroquinone, a major benzene metabolite, is a highly toxic and carcinogenic chemical that can cause cancer in occupational environments. Humans can be exposed to hydroquinone through diet, work, or the environment. Hydroquinone is especially harmful to aquatic organisms, but less so to bacteria and fungi. In this study novel Fe-Mg bimetallic oxide nanomaterial was synthesized via simple co-precipitation method to eliminate aquatic hydroquinone (HQ). The prepared sample was characterized by FT-IR analysis. The adsorption isotherms were also investigated, Both the Langmuir and Freundlich models were employed to describe the adsorption isotherm data. The results indicated the Langmuir isotherm had very high conformity with experimental data. The maximum adsorption capacity of HQ via Langmuir isotherm model is 59.17 mg/g. these results demonstrate the effectiveness of Fe-Mg bimetallic oxide in HQ removal from aqueous solution and it can be a promising candidate for HQ removal from water.

Introduction

Industrial development has led to increased release of pollutants into the environment, which has been linked to human diseases, including immune system disorders. Benzene and its metabolites are notable pollutants that contribute to this public health problems[1]. Hydroquinone which is abbreviated as (HQ) is a benzene metabolite; it is a white crystalline substance which is a chemical that is produced from the breakdown of benzene. Benzene is a known carcinogen, and hydroquinone is also suspected to be carcinogenic[2]. Hydroquinone is a widely used chemical in a variety of products, including photographic developers, dyes, and antioxidants It is important to be aware of the potential health risks associated with hydroquinone exposure and to take steps to minimize exposure. a variety of methods have been developed to remove hydroquinone from water[3], but they often have disadvantages, such as high cost and inefficiency. Adsorption onto adsorbents is a promising method for removing hydroquinone from water because it is relatively simple and effective[4]. The purpose of this study was to synthesize an appropriate, novel and cost-effective adsorbent for the removal of the anionic and pharmaceutical pollutant “hydroquinone”. A bimetallic oxide Fe-Mg was synthesized as an efficient adsorbent using a simple co-precipitation method. Based on the results obtained, the maximum adsorption capacity according to the Langmuir isotherm model for the synthesized adsorbent was 59.17mg/g, which indicates the appropriate adsorption capacity of this adsorbent for the target pollutant. In the present study, in addition to examining the isotherm models, the characterization of the adsorbent was investigated using FT-IR analysis.

Material and Method

Materials: Hydroquinone ($C_6H_6O_2$), Iron (III) nitrate nonahydrate ($FeNO_3.9H_2O$), Magnesium nitrate hexahydrate ($MgNO_3.6H_2O$) and Ammonia (NH_3). Fourier Transform Infrared Spectroscopy (FT-IR) was carried out by spectrophotometer (Tensor II).

Synthesis: Fe-Mg bimetallic oxide was synthesized at room temperature using a simple co-precipitation method. Stoichiometric amounts of iron and magnesium salts were dissolved in double distilled water, and the pH

was raised to 8 with ammonia solution to initiate precipitation. The suspension was stirred for 45 minutes, matured for 24 hours, washed, dried, calcined at 500 °C for 2 hours, and ground to obtain a fine powder[5].

Hydroquinone adsorption experiment: We conducted an experiment to remove HQ from water using 0.05 g of Fe-Mg bimetallic oxide. We kept the experiment's conditions constant, including the initial HQ concentration (50 mg/L), polluted water volume (50 mL), temperature (25°C), and pH (7). We used UV-vis spectroscopy to measure the Final HQ concentration and calculated the RB5 removal efficiency using a specific "equation 1".

$$Re\% = \frac{C_0 - C_e}{C_0} \times 100 \quad (1)$$

Where C_0 and Ce are the initial and the equilibrium concentration of HQ respectively. The final removal efficiency obtained for the specified conditions was 35%.

Results and discussion

FTIR analysis: In the FT-IR graph which presented in "Figure 1" of the Fe-Mg bimetallic oxide, the peak at wavenumber 445 cm^{-1} is indicative of the stretching vibration of Mg-O-Mg bonds, as well as the peaks at wavenumbers 557cm^{-1} and 610 cm^{-1} corresponding to the stretching vibration of Fe-O-Fe bonds. Given the shift of the peak corresponding to the stretching of Fe-O-Fe bonds from a lower frequency to a higher frequency, it can be inferred that the Fe-Mg binary oxide has formed. The peaks corresponding to wavenumbers 1085cm^{-1} and 1163cm^{-1} are caused by the bending vibration of hydroxyl groups on the surface of the adsorbent. Also, the peak at wavenumber 3432cm^{-1} is caused by the presence of water on the surface of the binary oxide nanoparticles[5].

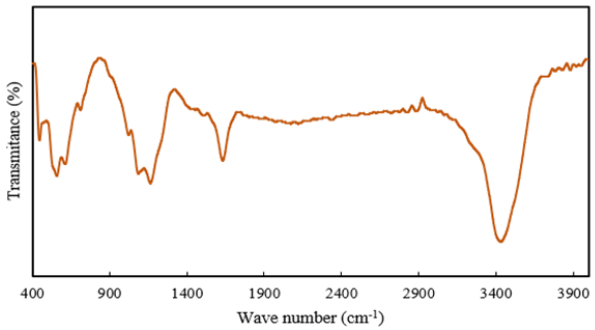


Figure 1. The FT-IR Analysis for Fe-Mg bimetallic oxide

Adsorption isotherm: To investigate the adsorption isotherm of HQ on the Fe-Mg binary oxide, HQ aqueous solutions with a volume of 50 mL and variable concentrations from 10 to 100 ppm were prepared. The dosage of adsorbent used for each sample was 0.01 g. The contact time was 3 hours for each sample, the temperature of the tests was 25 °C, and the pH was 7. The results of the experimental data linearization are shown in "Figure 2", where plot (a) corresponds to the Langmuir isotherm and plot (b) corresponds to the Freundlich isotherm. Based on the correlation coefficient (R^2), it can be concluded that the experimental data obtained has a very good match with the Langmuir isotherm, which in fact suggests that the surface adsorption of hydroquinone, according to the assumptions of the Langmuir isotherm, is monolayer and with a uniform structure, and that every active site that is occupied by hydroquinone molecules does not undergo further adsorption. the maximum adsorption capacity via Langmuir isotherm is 59.17 mg/g. The linear and nonlinear equations of Langmuir and Freundlich isotherms are given in "Table1". Where, C_e is the equilibrium concentration (mg/L), q_e is the amount adsorbed at equilibrium state (mg/g), q_{max} is the maximum adsorption capacity (mg/g) and b is the Langmuir adsorption constant (L/mg) and K_F is the Freundlich adsorption constant (mg/g) and n is the adsorption constant. and the constants and parameters related to the Langmuir and Freundlich isotherms are calculated and presented in "Table2".

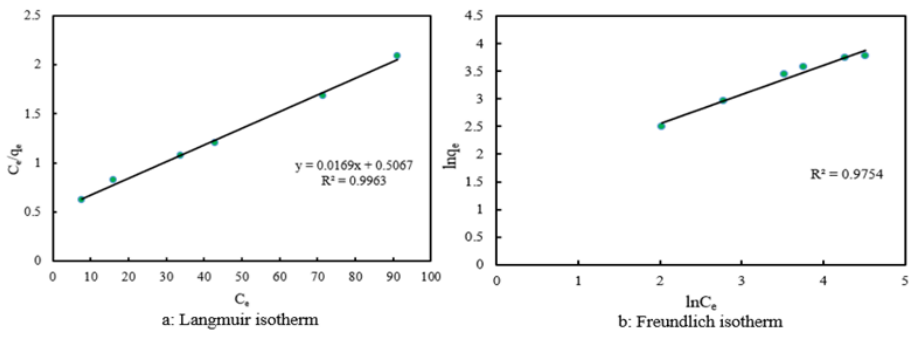


Figure 2. Langmuir and Freundlich isotherms

Table 1. Langmuir and Freundlich linear and nonlinear equations

Nonlinear equation	Linear equation	Isotherm
$q_e = \frac{q_m b C_e}{1 + b C_e}$	$\frac{C_e}{q_e} = \frac{1}{b q_m} + \frac{C_e}{q_m}$	Langmuir
$q_e = K_F C_e^{1/n}$	$\log q_e = \log K_F + \frac{1}{n} \log C_e$	Freundlich

Table2. Langmuir and Freundlich constants

Langmuir			Freundlich		
q_m(mg/g)	b (l/mg)	R^2	n	k_F	R2
59.17	0.033	0.996	1.88	4.43	0.975

Conclusion

In this research, a cost-effective co-precipitation method was used to synthesize Fe-Mg bimetallic oxide, which is a highly effective adsorbent for treating anionic aqueous solutions like HQ. According to FT-IR analysis the presence of OH functional groups on the surface of the adsorbent is considered as one of the important factors in the adsorption of HQ. The synthesized adsorbent is in spherical-shape and the adsorption isotherm experimental data has a very good match with the Langmuir isotherm model.

References

1. Enguita, F.J. and A.L. Leitão (2013), *Hydroquinone: environmental pollution, toxicity, and microbial answers.* BioMed research international.
2. Jang, S.-M. and Y.-S. Kim (2005), *Analysis of hydroquinone and its ether derivatives by using micellar electrokinetic chromatography (MEKC).* Bulletin of the Korean Chemical Society. **26**(5): p. 819-822.
3. McGregor, D. (2007), *Hydroquinone: an evaluation of the human risks from its carcinogenic and mutagenic properties.* Critical reviews in toxicology. **37**(10): p. 887-914.
4. Ding, C., et al. (2018), *Highly selective adsorption of hydroquinone by hydroxyethyl cellulose functionalized with magnetic/ionic liquid.* International journal of biological macromolecules. **107**: p. 957-964.
5. Khan, S.U., et al. (2021), *Evaluation of Fe-Mg binary oxide for As (III) adsorption—synthesis, characterization and kinetic modelling.* Nanomaterials. **11**(3): p. 805.

Advanced Engineering Days

aed.mersin.edu.tr

Study of pH effect on the degradation of naproxen in aqueous solution using MnO_2 photocatalyst

Seyed Taha Hosseini Koohi [1], Zahra Nasrollahi *[1], Kamran Keynejad [1]

[1] *University of Tehran, Fouman Faculty of Engineering, College of Engineering, Iran, seyedtahahosseini@ut.ac.ir, z.nasr@ut.ac.ir, kamran.keynejad@ut.ac.ir*

Cite this study: Hosseini Koohi, S. T., Nasrollahi, Z., & Keynejad, K. (2024). Study of pH effect on the degradation of naproxen in aqueous solution using MnO_2 photocatalys. Advanced Engineering Days, 9, 518-520

Keywords
Photocatalyst
MnO_2
Naproxen
pH

Abstract

In the present study, manganese dioxide (MnO_2) was synthesized to evaluate the degradation of the pharmaceutical pollutant naproxen. Given the band gap of MnO_2, this photocatalyst is activated by the visible light for pollutant degradation. The crystalline structure of MnO_2 was assessed using XRD analytical tools, and the resulting diffractions confirmed the δ-MnO_2 formation. Photocatalytic degradation of naproxen was conducted at three different pH levels (5,7, and 9), with the highest degradation of approximately 33% occurring at pH=7.

Introduction

Water is one of the most vital components for living organisms, especially humans. According to the World Health Organization, only 5% of the water available in the world is suitable for human consumption, as part of this water is too salty, part of it is polluted, and part is inaccessible. Researchers have proposed numerous solutions to each of these problems and obstacles to maximize the water amount accessible in various fields, including drinking water, agriculture, and livestock [1]. In general, water is considered polluted when the dissolved oxygen level in it is less than what is necessary for the life of aquatic organisms. Water pollution ultimately refers to the physical, chemical, and biological changes in water that occur through the dispersion or mixing of foreign substances into the water, which can be harmful to humans and other organisms. Industrial factories, medical facilities, and household sewage are various sources that contribute to water pollution. There are various methods for water purification, among which advanced oxidation processes (AOPs) are one of the most effective, including ozonation, Fenton reaction, photocatalysis, sonocatalysis, and sono-photocatalysis.

Unlike common oxidants such as chlorine gas and ozone, which have dual roles in anti-pollution and disinfection, AOPs prioritize the degradation of organic and inorganic pollutants in water and wastewater. In the advanced oxidation process, hydroxyl radicals attack organic pollutants through four main pathways: radical addition, hydrogen removal, electron transfer, and radical combination [2]. In the photocatalytic process, a semiconductor material is required to act as a catalyst. One of the main characteristics of semiconductor materials is the presence of a band gap energy difference. The mechanism of the photocatalytic process is such that light (ultraviolet or visible) with energy equal to or greater than the band gap energy (E_{BG}) is irradiated onto the catalyst surface, causing the excitation of its molecules. Electrons are transferred from the valence band (VB) to the conduction band (CB), and with the transfer of electrons, positive holes are created in the valence band. In other words, molecular excitation results in the generation of mobile electrons in the conduction band with higher energy (E_{CB}) and positive holes with lower energy (E_{VB}) in the catalyst [3]. Figure 1 illustrates the photocatalytic process. The created holes have a very high oxidation potential, which is sufficient for the production of hydroxyl radicals from water molecules and hydroxide ions adsorbed on the surface of the semiconductor. Additionally, the generated electrons can react with adsorbed oxygen molecules and reduce them to superoxide radicals [4].

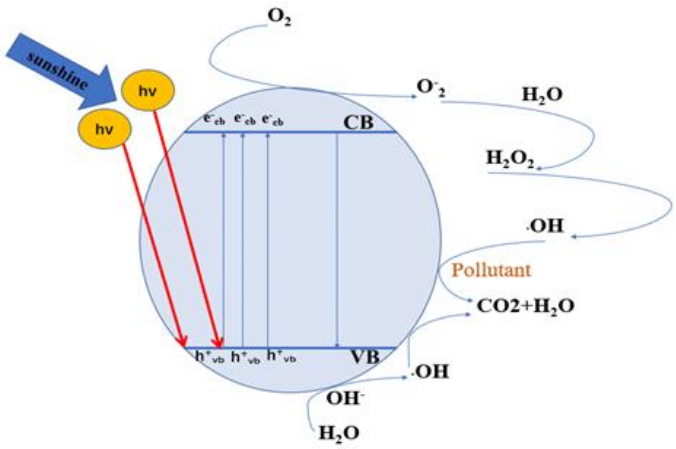


Figure 1. Schematic of Photocatalytic Degradation Process [5]

Manganese dioxide has garnered significant attention due to its environmental compatibility and low production cost. This substance exhibits different band gaps ranging from 1 to 2 eV, depending on its various polymorphs, making it capable of easily absorbing visible light, which is highly desirable for photocatalytic activities. Manganese dioxide is utilized in various fields such as supercapacitors, batteries, sensors, and photocatalytic activities [6]. Naproxen, with the chemical formula $C_{14}H_{14}O_3$, is an anti-inflammatory drug used for conditions such as rheumatoid arthritis and fever. Side effects of this medication may include headaches, dizziness, and drowsiness [7]. In this study, the photocatalytic activity of manganese dioxide was investigated using different pH levels to assess the degradation of the pharmaceutical pollutant naproxen.

Material and Method

Manganese dioxide (MnO_2) was synthesized using manganese sulfate ($MnSO_4 \cdot H_2O$) and potassium permanganate ($KMnO_4$) as precursor materials.

potassium permanganate ($KMnO_4$) was added to the 40 milliliters of distilled water and stirred for four hours at room temperature, and then heat-bathed at 75° C. Afterward, manganese sulfate hydrate ($MnSO_4 \cdot H_2O$) was slowly added to the solution and reacted for three hours. Finally, the mixture was centrifugated, rinsed with DI water three times, and dried at 80° C for six hours [8].

Results

To investigate the formation of the synthesized photocatalyst, XRD analysis was conducted on 0.05 grams of the photocatalyst.

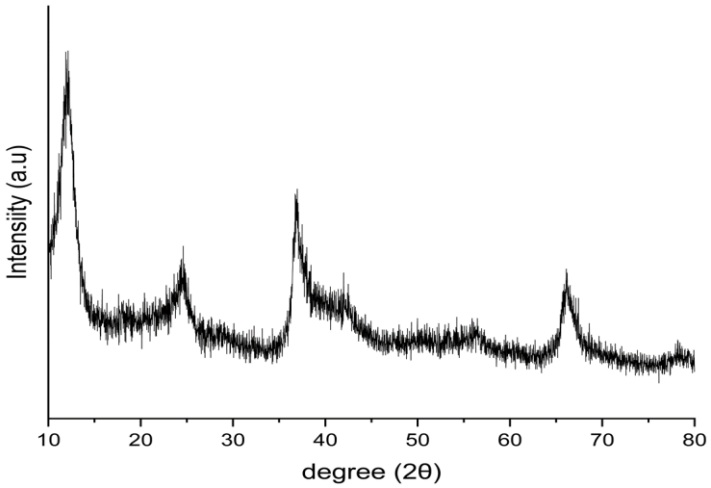


Figure 2. XRD patterns of the MnO_2

Based on Figure 2 and X-ray diffraction (XRD) analysis, diffractions observed at angles of 10, 24, 38, and 65 degrees confirm the formation of manganese dioxide (MnO_2) structure. The synthesized pure sample exhibits six polymorphs, and according to the observed diffractions, it confirms the formation of δ-MnO_2 (JCPDS No. 80-1098) [9].

Discussion

To evaluate the performance of the synthesized photocatalyst in naproxen degradation, a shell and tube reactor was constructed, equipped with a water-cooling system to maintain a constant temperature during the experiment. To conduct the photocatalytic process, a synthetic pollutant solution of naproxen with a concentration of 5 milligrams per liter of distilled water was prepared. Then, to degrade the pollutant, 50 milligrams of the synthesized catalyst was added to 50 milliliters of the wastewater, and the mixture was placed in the reactor. The photocatalytic process was carried out for 90 minutes under visible light irradiation at different pH levels of 5, 7, and 9. In this study, four LED lamps with a power of 12 watts each were used. The temperature measured in the photocatalytic reactor remained constant at 27 degrees Celsius throughout the process.

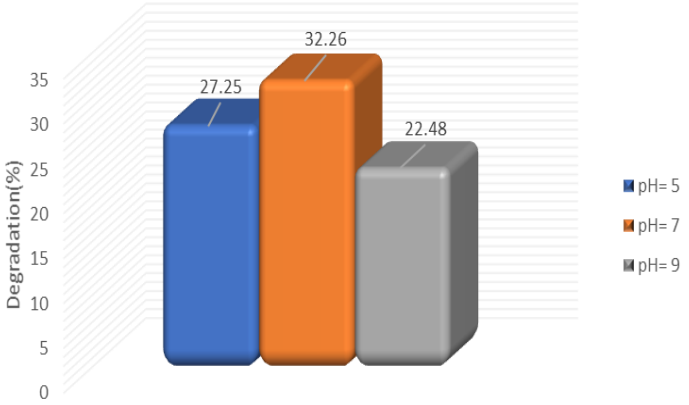


Figure 3. The removal percentage of naproxen solution (5 mg/L) irradiated by Vis light.

Figure 3 shows the degradation of the naproxen pollutant at three different pH levels under equal time conditions. At pH=7, where the solution is neutral, there is greater degradation compared to the basic and acidic states, indicating the formation of more electron-hole pairs under these conditions.

Conclusion

The diffractions obtained from the XRD analytical tool confirm the crystalline structure of δ-MnO_2. Among the different pH levels, pH 7 showed the highest degradation percentage (33%). The low band gap of MnO_2 enables this photocatalyst to be activated in the visible light region, leading to the generation of electron-hole pairs.

References

1. Kordbacheh, F. and G. Heidari, Water Pollutants and Approaches for Their Removal. Materials Chemistry Horizons, 2023. 2(2): p. 139-153.
2. Y. Deng and R. Zhao, Advanced oxidation processes (AOPs) in wastewater treatment, *Curr. Pollut. Reports*, vol. 1, pp. 167‑176, 2015.
3. de Lasa, H., B. Serrano, and M. Salaices, *Photocatalytic Reaction Engineering*. 2006: Springer US
4. Kaspar, T., T. Droubay, and S. Chambers, *Atomic oxygen flux determined by mixed-phase Ag/Ag_2O deposition.* Thin Solid Films, 2010. 519: p. 635–640.
5. Fubao Zhang, Xianming Wang, Haonan Liu, Chunli Liu, Yong Wan, Yunze Long, Recent Advances and Applications of Semiconductor Photocatalytic Technology, *Appl. Sci.* 2019, *9*(12), 2489.
6. Yi-Fan Yao and Gui-Chang Wang, Mechanism Insights into the Aerobic Oxidation of 5-Hydroxymethylfurfural to 2,5-Furandicarboxylic Acid over MnO_2 Catalysts, J. Phys. Chem. C 2021, 125, 3818−3826.
7. Marta Jim´enez-Salcedo, Miguel Monge, María Teresa Tena, The photocatalytic degradation of naproxen with g-C_3N_4 and visible light: Identification of primary by-products and mechanism in tap water and ultrapure water, Journal of Environmental Chemical Engineering 10 (2022) 106964.
8. Xinlu Li, Yonglai Zhang, Qineng Zhong, Tongtao Li, Hongyi Li, Jiamu Huang, Surface decoration with MnO_2 nanoplatelets on graphene/TiO_2 hybrids for rechargeable lithium-ion batteries.
9.] Artem S. Belousov, Evgeny V. Suleimanov, Alina A. Parkhacheva, Diana G. Fukina, Andrey V. Koryagin, Aleksandra V. Koroleva, Evgeny V. Zhizhin, Alexey P. Gorshkov, Regulating of MnO_2 photocatalytic activity in degradation of organic dyes by polymorphic engineering, Solid State Sciences 132 (2022) 1069.

Advanced Engineering Days

aed.mersin.edu.tr

Modeling of fluid flow and heat transfer inside fin and tube heat exchanger with pentagonal cross section of tubes

Reza Ghafuri [1], Zahra Nasrollahi *[1], Hedayat Azizpour [2], Kamran Keynejad [1]

[1] University of Tehran, Fouman Faculty of Engineering, College of Engineering, Iran, reza.ghafuri@ut.ac.ir, *z.nasr@ut.ac.ir, kamran.keynejad@ut.ac.ir*

[2] University of Tehran, School of Chemical Engineering, College of Engineering, Iran, h.azizpour@ut.ac.ir

Cite this study: Ghafuri, R., Nasrollahi, Z., Azizpour, H., Keynejad, K., (2024). Modeling of fluid flow and heat transfer inside fin and tube heat exchanger with pentagonal cross section of tubes .Advanced Engineering Days, 9, 521-524

Keywords
Heat transfer
Fluid flow
Heat exchanger
Pressure drop

Abstract

In this study, we investigated the impact of different inlet air velocities on a fin and tube heat exchanger with a pentagonal cross-section. We analyzed how increasing the speed affected parameters such as pressure drop, friction coefficient, and Colborne coefficient. The Colborne coefficient exhibited a consistent linear behavior and did not change. However, the friction coefficient decreased as the Reynolds number increased, reaching its lowest value at v=2.34 m/s. The pressure drop increased with higher speeds, and the largest temperature change occurred at v=2.13 m/s.

Introduction

Heat exchangers are vital elements in any process plant. Most heat exchangers are of shell and tube type, however, there are several other important types, such as tube and fin, spiral tube, plate and frame, and spiral exchangers. Improving the thermohydraulic performance of heat exchangers can significantly optimize the energy required in various engineering processes. Tube and fin heat exchangers have been increasingly used in recent years, because they offer significant advantages such as a high level of heat transfer compared to conventional heat exchangers. The shape and dimensions of the pipes have a direct effect on the thermal efficiency and pressure drop of this equipment [1,2].

In this study, modeling of fluid flow and heat transfer created in a tube and fin exchanger with a pentagonal cross-section of tubes has been done. The geometry of the designed converter consists of a rectangular plate with a length of 300 mm and a width of 84 mm, which has 30 pentagonal tubes. The depth of the simulated area is 0.5 cm, which is used to calculate the Reynolds number of the flow. The fluid used in this modeling is air, which enters the converter from one side and exits from the other side after passing through the pipes. will be Figure 1 shows the 3D image of the designed heat exchanger.

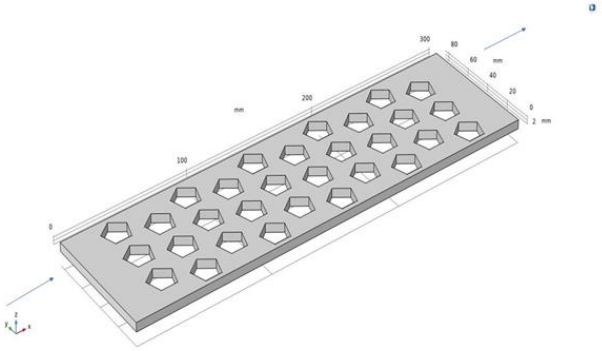


Figure 1. 3D image of the heat exchanger

Materials and Method

Air, as the fluid used in this modeling enters the converter at a temperature of 255 K, and after passing through pipes with a constant wall temperature of 243 K, it leaves the converter. The fluid enters the heat exchanger at 5 different speeds and the pressure drop and outlet temperature parameters are evaluated at these speeds.

The flow inside the converter is turbulent due to the presence of pentagonal tubes and the k-ω turbulent flow model is used to solve the flow equations (Equations 1-4) [3,4].

$$\rho \nabla . \vec{U} = 0 \qquad (1)$$

$$\frac{\partial(\rho k)}{\partial t} + \frac{\partial(\rho u_j k)}{\partial x_j} = \rho P - \beta^* \rho \omega k + \frac{\partial}{\partial x_j}\left[\left(\mu + \sigma_k \frac{\rho k}{\omega}\right)\frac{\partial k}{\partial x_j}\right] \qquad (2)$$

$$P = \tau_{ij}\frac{\partial u_i}{\partial x_j} \qquad (3)$$

$$\frac{\partial(\rho \omega)}{\partial t} + \frac{\partial(\rho u_j \omega)}{\partial x_j} = \frac{\alpha \omega}{k}\rho P - \beta^* \rho \omega^2 + \frac{\partial}{\partial x_j}\left[\left(\mu + \sigma_\omega \frac{\rho k}{\omega}\right)\frac{\partial \omega}{\partial x_j}\right] + \frac{\rho \sigma_d}{\omega}\frac{\partial k}{\partial x_j}\frac{\partial \omega}{\partial x_j} \qquad (4)$$

These equations are gridded and solved using COMSOL 6.1 software. are in the flow. For the side near the wall, due to the fluid passing through the solid surface, layered meshing is used, which gives more accurate results.

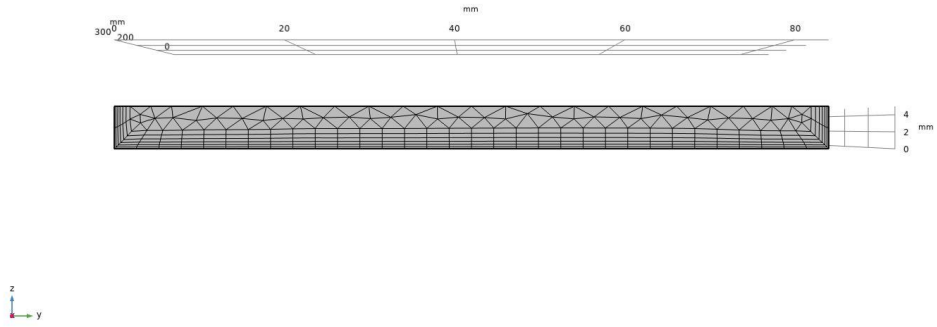


Figure 2. Mesh at the entrance

Table 1. Mesh information

No.	Description
308	Number of vertex elements
4206	Number of edge elements
42246	Number of boundary elements
169721	Number of elements
0.1954	Minimum element quality
308	Number of vertex elements
4230	Number of edge elements
50400	Number of boundary elements
321343	Number of elements
0.03559	Minimum element quality

Results and Discussion

Figure 3 shows the pressure distribution, temperature distribution and speed distribution for the middle speed of 1.93 m/s and the rest of the results are presented in Table 2.

As seen in Figure 3, due to the conservation of mass and energy, by reducing the cross-sectional area of the flow path, the pressure-drop increases and on the other hand, the speed increases. Table 2 shows the values of pressure drop and outlet temperature versus the inlet speed.

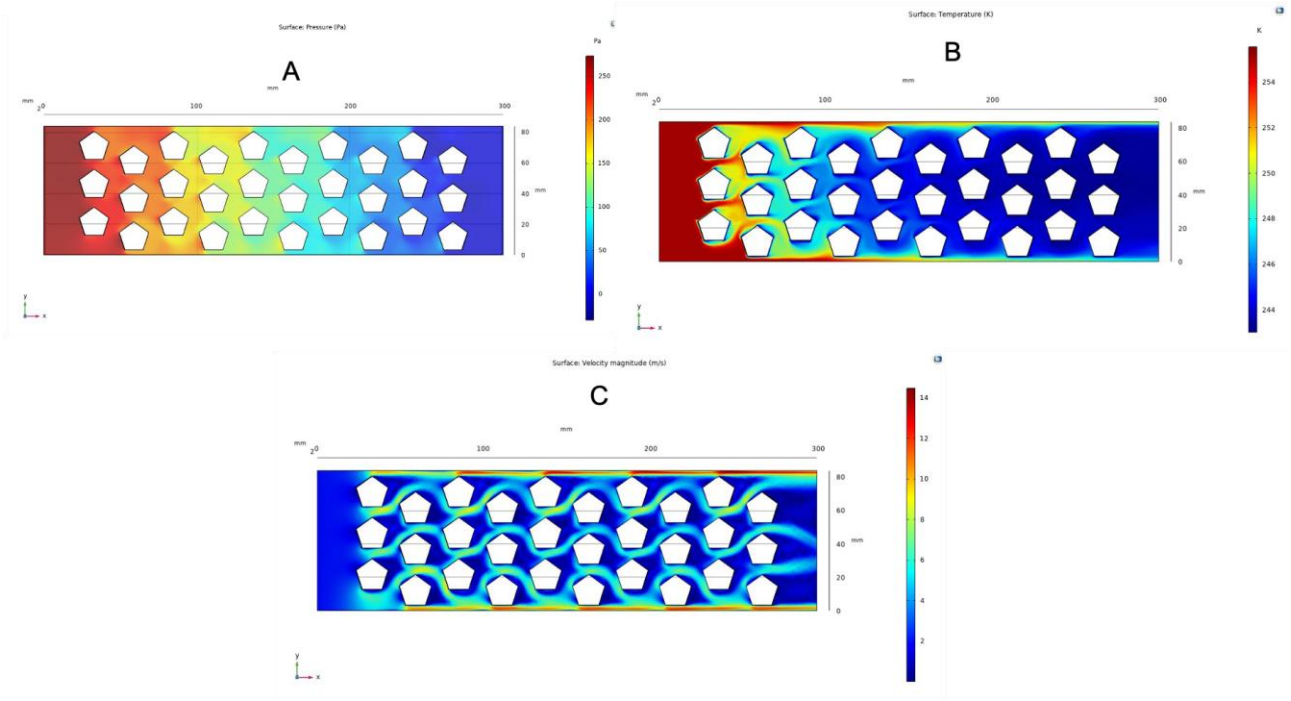


Figure 3. The distribution of pressure, temperature, and velocity for the speed of 1.93 m/s

Table 2. Fluid flow characteristics

Inlet velocity (m/s)	Reynolds number	Output temperature (K)	Pressure Drop (Pa)
1.52	1300	244.0357	172.65
1.72	1475	244.0213	216.69
1.93	1650	244.0114	267.91
2.13	1825	244.0052	321.57
2.34	2000	244.0181	383.22

Also, two parameters of friction coefficient and Colborne coefficient were calculated using equations (5 and 6) and shown in graphs 4 and 5 in terms of Reynolds number.

$$f=\frac{\Delta p\, A_c}{\frac{1}{2}\rho U^2 A_o} \qquad (5)$$

$$j=\frac{Nu}{Re.Pr^{1/3}} \qquad (6)$$

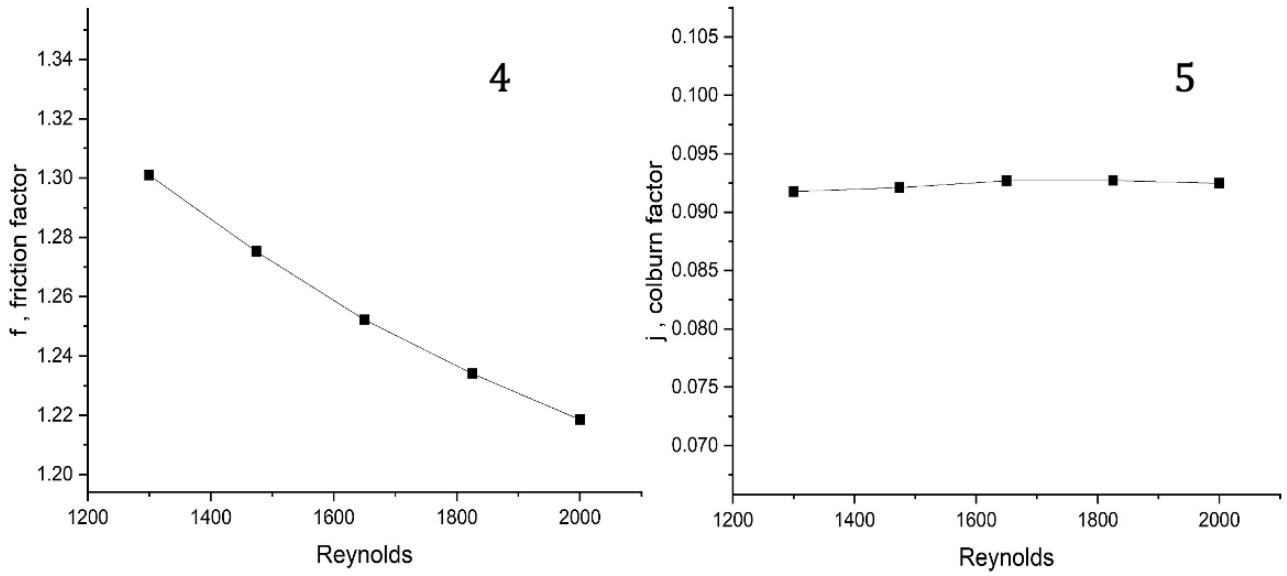


Figure 4 and 5. friction and Colborne coefficients versus Reynolds number

Conclusion

The maximum temperature changes are obtained at the speed of 2.13 m/s and on the other hand, with the increase of the inlet speed, the pressure drop increases linearly. Also, according to the existing relationships for the friction coefficient and the power of two speeds in the denominator, As the speed of the incoming air increases, the friction coefficient decreases and reaches its lowest value (1.218) at a speed of 2.34 m/s, and the Colborne coefficient does not change significantly with changes in speed and shows a linear behavior.

References

1. Dickey, D. S. (2004). Rules of Thumb for Chemical Engineers. *Chemical Engineering*, *111*(5), 10-12.
2. Cao, Y., Salem, M., Elmasry, Y., Galal, A. M., Singh, P. K., Gepreel, K. A., ... & Wae-hayee, M. (2022). Flow and heat transfer in a plain fin-and-hexagonal tube heat exchanger with different side ratios. *Case Studies in Thermal Engineering*, *38*, 102376.
3. Wang, P., Jiang, J., Li, S., Luo, X., Wang, S., & Zhao, W. (2019). An investigation of influence factor including different tube bundles on inclined elliptical fin-tube heat exchanger. *International Journal of Heat and Mass Transfer*, *142*, 118448.
4. Sharma, P., Said, Z., Kumar, A., Nizetic, S., Pandey, A., Hoang, A. T., ... & Tran, V. D. (2022). Recent advances in machine learning research for nanofluid-based heat transfer in renewable energy system. *Energy & Fuels*, *36*(13), 6626-6658.

Advanced Engineering Days

aed.mersin.edu.tr

Complete photocatalytic removal of Ciprofloxacin using $NiAl_2O_4$ spinel grafted on graphene nanosheets

Elnaz Pazdar [*1], Shadi Ebrahimi [1], Mohammad Mehdi Heydari [1], Azadeh Ebrahimian Pirbazari [1], Fatemeh Esmaeili Khalil Saraei [1]

[1] University of Tehran, College of Engineering, Fouman Faculty of Engineering, Iran, elnazpazdar@ut.ac.ir, shadi.ebrahimi@ut.ac.ir, M.m.heydari77@ut.ac.ir, aebrahmian@ut.ac.ir, f.esmaeili.kh@ut.ac.ir

Cite this study: Pazdar, E., Ebrahimi, S., Heydari, M. M., Ebrahimian Pirbazari, A., & Esmaeili Khalil Saraei,F. (2024). Complete photocatalytic removal of Ciprofloxacin using $NiAl_2O_4$ spinel grafted on graphene nanosheets. Advanced Engineering Days, 9, 525-527

Keywords
$NiAl_2O_4$
Graphene nanosheets
Ciprofloxacin
Photocatalysts
Photodegradation

Abstract

Ciprofloxacin (CIP), the second generation of fluoroquinolone antibiotics, has excellent antimicrobial activity and few side effects. CIP pollution in the environmental resources has become a serious issue that requires resolution. In the present study, $NiAl_2O_4$ spinel was synthesized by the sol-gel method and was chemically grafted on graphene oxide (GO). The PXRD diffraction patterns verified the successful synthesis and immobilization of $NiAl_2O_4$ spinel on GO sheets. FESEM micrograph showed the presence of $NiAl_2O_4$ on GO sheets. The CIP photocatalytic degradation results confirmed GO boosted the performance of GO/$NiAl_2O_4$ compared to $NiAl_2O_4$ from 28% to 100% under visible light after 60 min irradiation. It confirmed that GO acts as a photosensitizer and boosts the photoactivity of $NiAl_2O_4$ spinel for CIP removal under visible light.

Introduction

Antibiotics are the most commonly used drugs for treating infectious diseases in humans and animals [1]. Widespread and inadequate use of antibiotics, especially in aquatic ecosystems, leads to the emergence of drug pollutants that harm human health and the environment [2]. Ciprofloxacin (CIP), a second-generation fluoroquinolone antibiotic, has excellent antimicrobial activity and minimal side effects and is prescribed for bacterial infections. With rapid industrial development, pollution of environmental resources has become a serious issue that requires resolution [3]. With the chemical formula AB_2X_4, Spinel is a catalyst that can incorporate various intermediate metal elements and exhibit good catalytic activity [3]. Nickel aluminum spinel ($NiAl_2O_4$) is one of the most essential spinel aluminates, which, due to its high thermal stability and exceptional catalytic properties, can be used in various applications such as pigments, catalysts, magnetic materials, and refractories [4]. In recent years, graphene and various photocatalysts have been widely used to form graphene-based photocatalyst composites. Graphene is a two-dimensional carbon material composed of SP2 hybridized atoms. It has absorbed the researcher's attention due to its unique properties, such as a two-dimensional flat structure, high theoretical specific surface area, superior optical transparency, excellent electronic conductivity, and good chemical stability [5]. This research aims to fabricate an ideal photocatalyst in the visible light region. In this regard, $NiAl_2O_4$ nanoparticles were synthesized first and then immobilized on graphene to obtain the GO/$NiAl_2O_4$ nanocomposite. Subsequently, the morphology and structural characteristics of the synthesized samples were investigated using analytical methods, including XRD, FESEM, and elemental mapping/EDS. The catalytic performance of the synthesized catalysts was evaluated for the photodegradation of ciprofloxacin as a pharmaceutical contaminant model.

Material and Method

Initially, $NiAl_2O_4$ spinel was synthesized using the sol-gel method described in reference [6]. Subsequently, the synthesized $NiAl_2O_4$ was immobilized onto graphene oxide sheets through sonochemical synthesis with modifications in reference [7]. Ciprofloxacin (CIP), obtained from a pharmaceutical company in Tehran, Iran, is used as an organic pollutant for photocatalytic degradation tests. OSRAM (ECO) halogen lamp emitting 500W

visible light and OSRAM (ECO) krypton lamp emitting 240W UV light were used. Then, 0.05 grams of catalyst was mixed with 100 millilitres of artificial wastewater containing ciprofloxacin at a concentration of 10 milligrams per litre for 30 minutes in the dark. Subsequently, it was exposed to UV-Vis light for 60 minutes. The sample was then centrifuged and placed inside the spectrophotometer cell, and the absorption was measured in the range of 230-400nm.

Results and Discussion

The X-ray diffraction pattern of $NiAl_2O_4$ (Figure 1) exhibits sharp peaks, indicating a highly crystalline $NiAl_2O_4$ sample. All peaks (2θ= 31.68°, 37.44°, 45.3°, 55.76°, 60.94° and 66.12°) are in good agreement with JCPDS file No. 10-0339. Additionally, no extra XRD diffraction related to impurities or other phases was observed, indicating the proper formation of phases. The primary X-ray diffraction for graphene oxide can be seen at 2θ=11.4°. The XRD pattern of GO/$NiAl_2O_4$ showed the main diffractions of GO and $NiAl_2O_4$ with low intensity compared to pure samples. It confirmed the spinel nanoparticles are properly immobilized on the graphene oxide nanosheets.

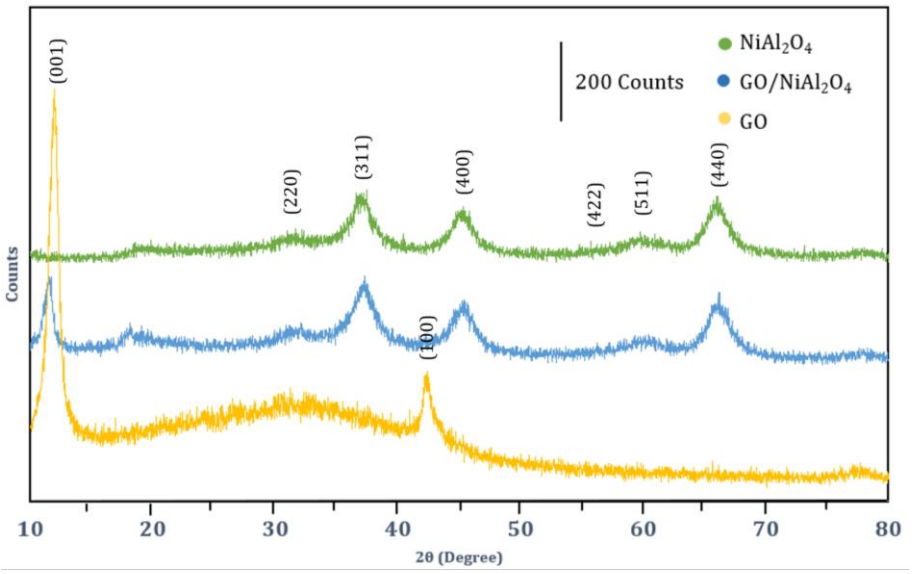


Figure 1. PXRD pattern of the samples

FESEM micrographs (Figure 2) show the presence of graphene nanosheets and spinel nanoparticles in GO/ $NiAl_2O_4$. Also, EDS and elemental mapping confirm the presence of oxygen, carbon, aluminum and nickel elements in the samples.

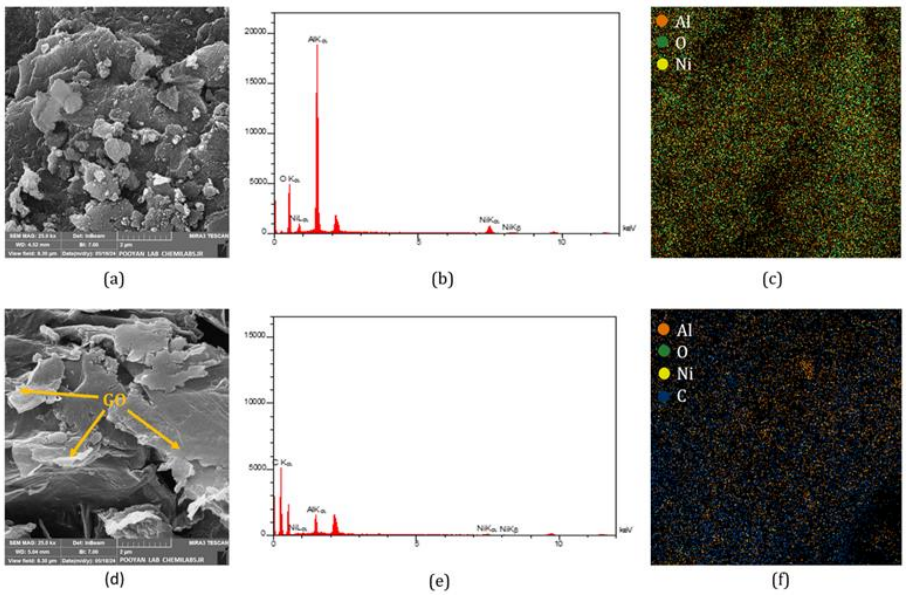


Figure 2. (a, d) FESEM mocrographs (b, e) EDS spectra (c, f) elemental mapping images for $NiAl_2O_4$ and GO/$NiAl_2O_4$

The photocatalytic performance of the synthesized samples was examined for CIP removal during 30 minutes of darkness and 60 minutes under visible light and ultraviolet radiation. GO/$NiAl_2O_4$ shows 100% removal of CIP compared to $NiAl_2O_4$ (28%) (Figure 3) under visible light due to presence of graphene oxide. Graphene acts as a photosensitizer, and electron tarp increases the electron-hole separation and improves the photocatalytic activity of $NiAl_2O_4$ under visible light.

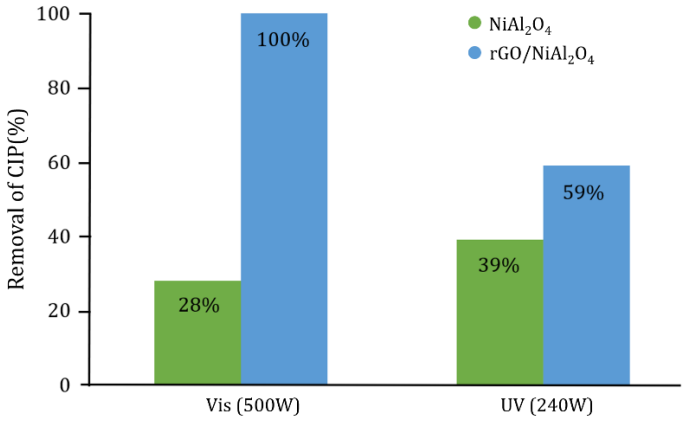


Figure 3. Photocatalytic performance of $NiAl_2O_4$ and GO/$NiAl_2O_4$ catalysts under UV and Vis light.

Conclusion

In this study, the synthesis of $NiAl_2O_4$, GO/$NiAl_2O_4$ photocatalysts was successfully carried out. XRD, EDS/elemental mapping, and FESEM analyses determined the structural and morphological properties of the synthesized nanocomposites. Finally, the performance of the synthesized samples was evaluated for CIP photocatalytic removal under visible light and ultraviolet irradiation. The results showed that graphene can boost the activity of $NiAl_2O_4$ spinel from 28% to 100% under visible light after 60 min irradiation. The synthesized GO/$NiAl_2O_4$ can open new avenues for practical applications of pharmaceutical wastewater treatment.

References

1. Zhang, R., Xu, M., Yu, J., Chen, J., He, J., & Hao, J. (2023). Study on highly efficient p-n heterojunction Bi_2MoO_6/Cu_2O: Synthesis, characterization and visible-light photocatalytic activity toward antibiotics degradation. Journal of SolidState Chemistry, 328, 124330.
2. Ghosh, S., Pourebrahimi, S., Malloum, A., Jacob Ajala, O., Sami AlKafaas, S., Onyeaka, H., Darlington Nnaji, N., Oroke, A., Bornman, Ch., Christian, O., Ahmadi, Sh., & Youns Wani, M. (2023). A review on ciprofloxacin removal from wastewater as a pharmaceutical contaminant: Covering adsorption to advanced oxidation processes to computational studies. Materials Today Communications, 37, 107500.
3. Liu, B., He, Ch., Li, Y., Li, Zh., Wang, W., Lu, Z., Wang, Z., Zhao, Sh., Liu, G., Gao, X. (2024). Quasimetallic high-entropy spinel oxides for full-spectrum solar energy harvesting. Matter 7, 140.
4. Pirsaheb, M., Gholami, T., Seifi, H., Yousif, Q. A., & Salavati-Niasari, M. (2022). Investigate of electrochemical hydrogen storage and coulombic efficiency of $NiAl_2O_4$/NiO, synthesized by cationic, anionic and polymeric, surfactants: Green synthesis and characterization. international journal of hydrogen energy, 47, 34994-35002.
5. Zhang, Y., Li, K., Zang, M., Cheng, Y., & Qi, H. (2023). Graphene-based photocatalysts for degradation of organic pollution. Chemosphere, 341, 140038.
6. Regulska, E., Breczko, J., Basa, A., Szydlowska, B., Kakareko, K., & Rydzewska-Rosołowska, A. (2022). Tomasz Hryszko, Graphene-quantum-dots-decorated $NiAl_2O_4$ nanostructure as supercapacitor and electrocatalyst in biosensing. Materials Today Communications, 33, 104166.
7. Ziarati Saravani, A., Nadimi, M., Aroon, M. A., & Ebrahimi Pirbazari, A. (2019). Magnetic TiO2/NiFe2O4/reduced graphene oxide nanocomposite as a recyclable photocatalyst for photocatalytic removal of methylene blue under visible light. Journal of alloys and compounds, 803, 291-306.

Advanced Engineering Days

aed.mersin.edu.tr

The deposition-precipitation of plasmonic Ag/Ag_3PO_4 nanoparticles on ZnS Micro/nanospheres for photocatalytic treatment of methyl orange and tetracycline artificial effluents

Sogand Rajaei Farid [1], Mohammad Amin Habibi [1], Azadeh Ebrahimian Pirbazari [*1], Fatemeh Esmaeili Khalil Saraei [1]

[1]University of Tehran, Fouman Faculty of Engineering, Iran, rajaei.sogand@ut.ac.ir, m.aminhabibi@ut.ac.ir, aebrahimian@ut.ac.ir, f.esmaeili.kh@ut.ac.ir

Cite this study: Rajaei Farid, S., Habibi, M. A., Ebrahimian Pirbazari, A. & Esmaeili Khalil Saraei, F. (2024). The deposition-precipitation of plasmonic Ag/Ag_3PO_4 nanoparticles on ZnS micro/nanospheres for photocatalytic treatment of methyl orange and tetracycline effluents. Advanced Engineering Days, 9, 528-531

Keywords
ZnS micro/nanospheres
Ag/Ag_3PO_4
Tetracycline
Methyl Orange
Photodegradation

Abstract

This research investigates to fabricate $ZnS/Ag/Ag_3PO_4$ nanocomposites via deposition-precipitation plasmonic Ag/Ag_3PO_4 nanoparticles on ZnS micro/nanospheres (ZMs/A/APs and ZNs/A/APs). Powder X-ray diffraction (PXRD) patterns confirm zinc blende cubic structure for ZnS and body-centered cubic structure for Ag/Ag_3PO_4. Field emission scanning electron microscopy (FESEM) micrographs reveal a sphere-shaped morphology for ZMs and ZNs and an asymmetrical hexagonal-shaped morphology for A/APs. The efficiency of nanohybrids was examined for the photocatalytic treatment of methyl orange (MO) dye and tetracycline (TC) antibiotics artificial effluents. Our findings showed the molecular structure of the pollutant has an essential role in the photocatalytic degradation efficiency, and a higher degradation percentage was obtained for MO (with two rings) compared to TC (with four rings).

Introduction

Freshwater pollution stems primarily from industrialization, population growth, and human activities. Advanced oxidation process (AOPs) is one of the most effective wastewater treatments and includes photocatalysis, sonocatalysis, ozonation, electrochemical oxidation, and Fenton. Among the AOPs, the photocatalytic processes use ultraviolet (UV) or visible light to active catalysts to remove pollutants from water resources at a lower cost [1]. Methyl orange (MO) dye with the $C_{14}H_{14}N_3O_3SNa$ molecular formula is widely used in different industries as a recalcitrant dye and, if disposed of without appropriate treatment, even at very low concentrations in water sources, may cause health and environmental hazards due to cancer, mutagenic properties, and bioaccumulation potential. Therefore, it should be adequately treated before its final release into the environment [2-3]. Tetracycline (TC) with the $C_{22}H_{24}N_2O_8$ molecular formula is one of the primary antibiotic groups, which is widely used for treatment due to its broad activity against bacteria (gram-positive and gram-negative), fungi, and parasites [4]. Zinc sulfide (ZnS) is an n-type semiconductor with essential properties such as a wide band gap (E_{bg}=3.6-3.8 eV), the presence of polar surfaces, excellent transmission properties, good thermal stability, high electrical mobility, non-toxicity, insolubility in water, and low price [5-6]. The use of ZnS as a photocatalyst is limited due to the wide band gap energy and the requirement for ultraviolet radiation to activate the photocatalytic process [7]. The combination of plasmonic silver/silver phosphate (Ag/Ag_3PO_4, p-type semiconductor) nanoparticles (E_{bg}=2.45-2.51 eV) with ZnS is a practical approach to extend the photocatalytic activity of ZnS to the visible light region due to surface plasmon resonance (SPR) [8]. The present study aims to decorate ZnS micro/nanospheres (ZMs and ZNs) with plasmonic Ag/Ag_3PO_4-NPs (A/APs) for photocatalytic elimination of MO as a dye pollutant model and TC as an antibiotic model from artificial wastewater under visible light and UV irradiation. The structural and morphological properties of the synthesized samples were investigated using analytical methods, including PXRD, FESEM, EDS, and elemental mapping.

Material and Method

ZnS microspheres (ZMs) and nanospheres (ZNs) were synthesized by employing a hydrothermal method detailed in references [10] and [11], respectively. Plasmonic A/APs were synthesized on ZMs and ZNs using the procedure detailed in the reference [12]. Methyl orange (MO) was obtained from Certistain dry dye (C.I. 13025), and tetracycline (TC) hydrochloride (Batch No.161026) was purchased from Hakim Pharmaceutical Company, Tehran, Iran, as the organic pollutants for photocatalytic tests. An OSRAM Halogen (ECO) 500W lamp was the visible light source, and an OSRAM krypton lamp (ECO) 240W lamp was the UV radiation source for illumination experiments. Before exposure, a glass beaker containing the 100 mg catalyst and 100 mL artificial wastewater containing methyl orange (Conc: 10 mg/L) or tetracycline (Conc: 30 mg/L) was stirred for 30 min in the dark to achieve adsorption/desorption equilibrium. After, the solution was irradiated for 180 min to remove dye and antibiotic pollutants. After centrifugation, solution absorption was measured using a UV-Vis spectrophotometer at λmax=500 nm for MO and λmax=275 nm for TC. The degradation efficiency of the photocatalysts was calculated using the following formula:

$$\% D = \left(\frac{C_0 - C_t}{C_0}\right) \times 100 \quad (1)$$

where C_0 and C_t represent the initial and time dependent concentrations of MO dye and TC antibiotic.

Results and Discussion

Figure 1 shows the PXRD patterns of ZMs and ZNs with the observed diffractions at 2θ = 28.6° (111), 33.1° (200), 47.6° (220) and 56.4° (311) of the zinc blende cubic structure for ZnS (JCPDS Card No. 05-0566). In the PXRD pattern of A/APs, the main diffractions at 2θ = 21.1° (110), 29.9° (200), 33.5° (210), 36.8° (211), 42.7° (220), 48.0° (310), 52.9° (222), 55.2° (320), 57.5° (321), 61.8° (400), 66.0° (330), 70.1° (420), 72.1° (421), 74.0° (322), which are well matched with significant peaks of the body-centered cubic phase of Ag_3PO_4 (JCPDS No.06–0505). The PXRD of ZMs/A/APs and ZNs/A/APs showed the main diffractions of ZnS and A/APs, which confirmed the simultaneous presence of ZnS and A/APs in the final sample. It is important to note that the intensity of the diffractions in ZMs/A/APs and ZNs/A/APs has decreased compared to the pure samples, which proved again successful synthesis of plasmonic A/APs on ZMs and ZNs.

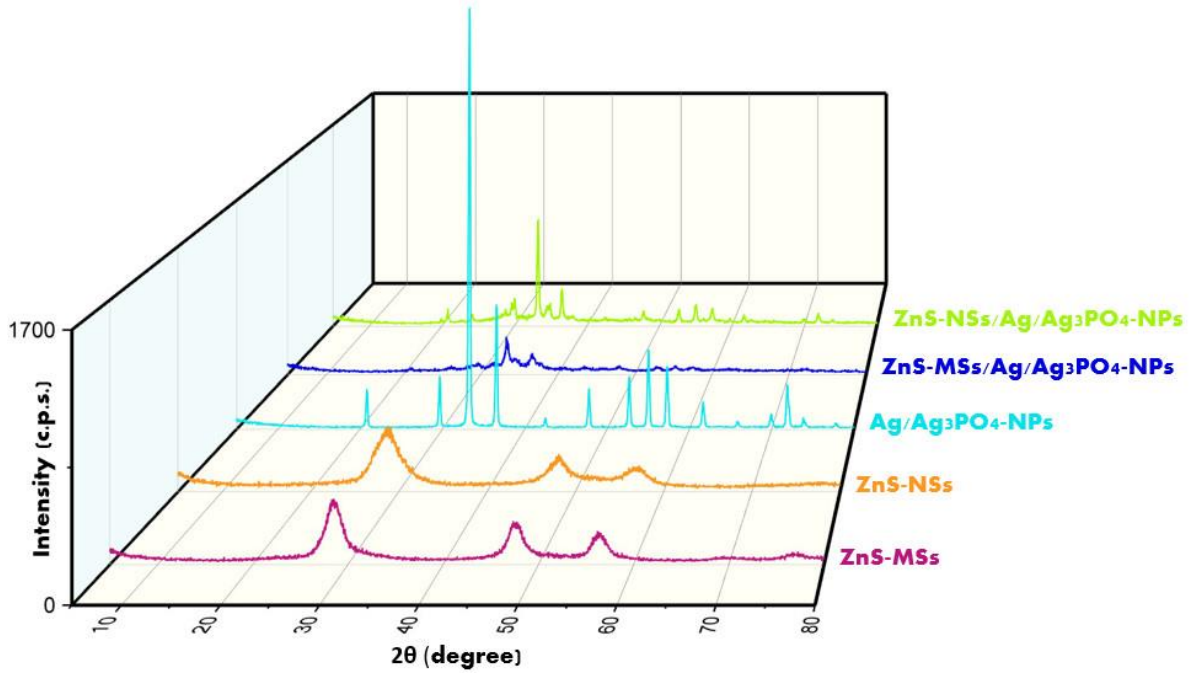


Figure 1. PXRD patterns of the synthesized samples

FESEM micrographs of ZMs and ZNs (Figure 2) revealed a sphere-shaped morphology for ZnS with sizes 2-8 μm and 220-250 nm, respectively. FESEM micrographs of A/APs revealed an asymmetrical hexagonal-shaped morphology with a planer surface for Ag_3PO_4 and a tendency to accumulate. The percentage of Zn, S, Ag, P and O elements in the synthesized samples was measured using EDS analysis, and each element was indicated with different colors in the elemental mapping images.

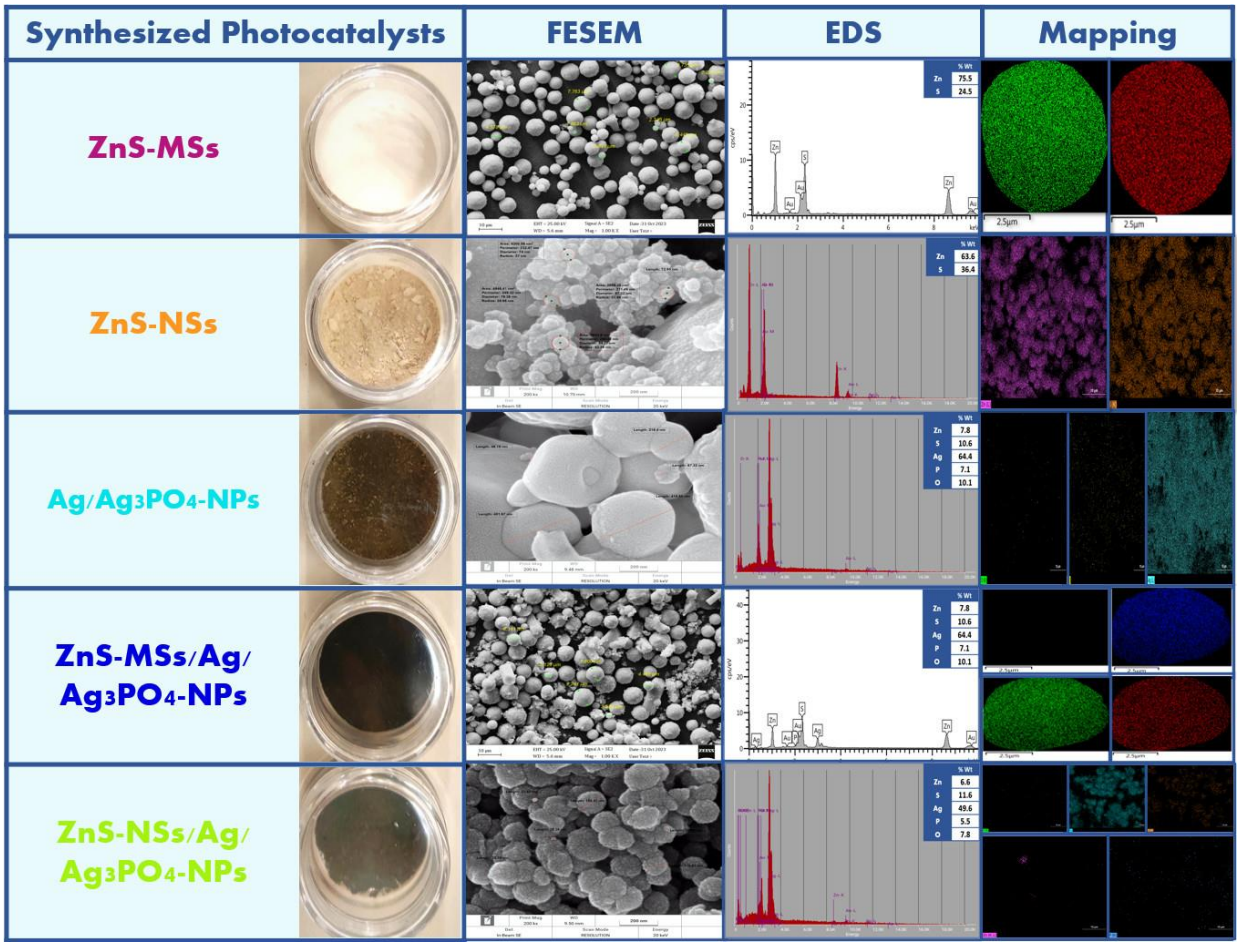


Figure 2. FESEM micrographs, EDS spectra, elemental mapping images of the synthesized samples

Figure 3 illustrates the photocatalytic performance of the synthesized samples for MO dye and TC antibiotic under UV radiation and visible light. Due to the large band gap energy of ZMs and ZNs, they are practically inactive in visible light and showed good performance for MO degradation under UV irradiation because of the higher energy of photons. A/APs presented lower photocatalytic activity for MO under UV irradiation than visible light. It may be related to converting some parts of Ag^{+} to Ag^{0}, and Ag^{0} nanoparticles act as electron traps that reduce photocatalytic activity (Figure 3. a.). Figure 3. b. showed the photocatalytic performance of all catalysts in the photocatalytic degradation of TC was lower than MO. It can be related to the complex molecular structure of TC (with four rings) compared to MO (with two rings).

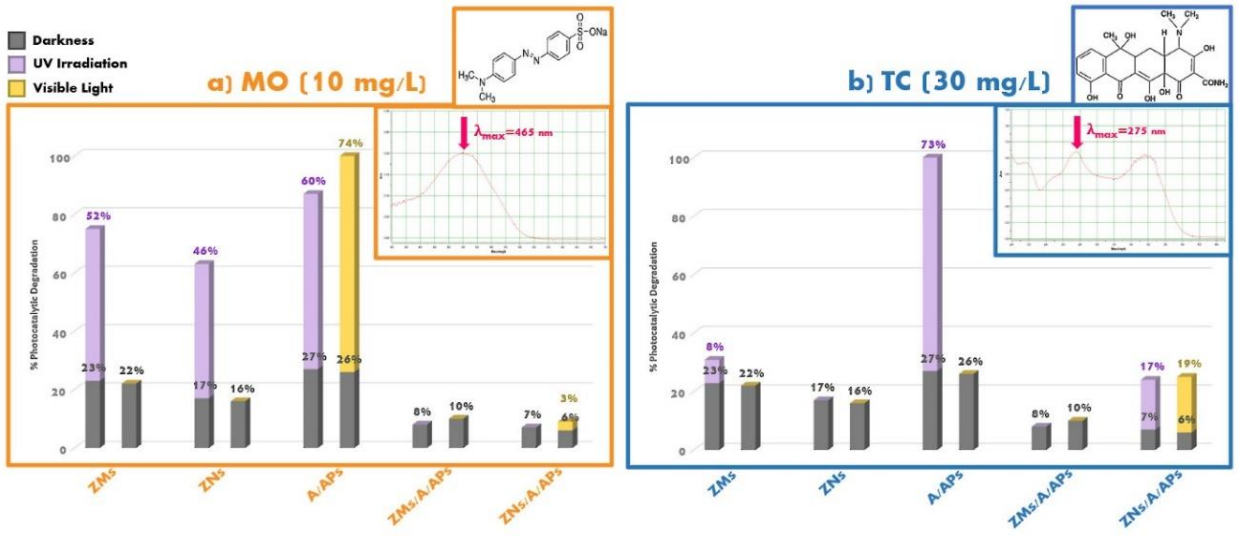


Figure 3. Photocatalytic degradation performance of the synthesized samples for **a)** MO dye **b)** TC antibiotic

Conclusion

The PXRD patterns have confirmed the zinc blende cubic structure for ZMs and ZNs and the body-centered cubic structure for A/APs. The FESEM/EDS analysis presented the sphere-shaped morphology for ZnS micro/nanospheres and an asymmetrical hexagonal-shaped for A/APs. The analysis also detected the presence of Zn, S, Ag, P and O elements, providing a comprehensive understanding of the composition of the samples. The synthesized samples have demonstrated remarkable effectiveness in photodegradation of MO and TC under visible light and UV irradiation. The highest percentage of photocatalytic degradation (100%) was achieved for MO under visible light and (87%) under UV irradiation by A/APs. Similarly, TC's highest photocatalytic degradation percent was obtained (100%) under UV irradiation using A/APs.

References

1. Kadiya, K., vuggili, S., Gaur, U. & Sharma, M. (2021). Comparative photocatalytic dye and drug degradation study using efficient visible light–induced silver phosphate nanoparticles. Environmental Science and Pollution Research, 28, 46390-46403.
2. Hanafi, M. & Sapawe, N. (2020). A review on the water problem associate with organic pollutants derived from phenol, methyl orange, and remazol brilliant blue dyes. Materials Today: Proceedings, 31, 141-150.
3. Kishor, R., Purchase, D., Saratale, G., Ferreia, L., Hussian, Ch., Mulla, S. & Bharagava, R. (2021). Degradation mechanism and toxicity reduction of methyl orange dye by a newly isolated bacterium Pseudomonas aeruginosa MZ520730. Journal of Water Process Engineering, 43, 102300.
4. Gopal, G., Ann Alex, S., Chandrasekaran, N. & Mukherjee, A. (2020). A review on tetracycline removal from aqueous systems by advanced treatment techniques. Royal Society of Chemistry, 10, 27081.
5. Isac, L. & Enesca, A. (2022). Recent Developments in ZnS-Based Nanostructures Photocatalysts for Wastewater Treatment. Molecular Sciences, 318, 8-22.
6. Yu, D., Fang, H., Qiu, P., Meng, F., Liu, H., Wang, S., Lv, P., Cong, X., Niu, Q. & Li, T. (2021). Improving the Performance of ZnS Photocatalyst in Degrading Organic Pollutants by Constructing Composites with Ag2O. Nanoscale Materials in Water Purification, 11, 1451.
7. Chankhanittha, T., Watcharakitti, J., Piyavarakorn, V., Johnson, B., Bushby, R., Chuaicham, C., Sasaki, K., Nijpanich, S., Nakajima, H., Chanlek, N. & Nanan, S. (2023). ZnO/ZnS photocatalyst from thermal treatment of ZnS: Influence of calcination temperature on development of heterojunction structure and photocatalytic performance. Physics and Chemistry of Solids, 179, 111393.
8. Zhuang, H., Chen, X., Xia, J., Lu, K., Huang, W., Liu, X., Yu, C. & Yang, K. (2023). State-of-the-art progress in Ag_3PO_4-based photocatalysts: Rational design, regulation and perspective. Applied Materials Today, 31, 101742.
9. Muruganandham, M., Amutha, R., Repo, E., Sillanpää, M., Kusumoto, Y. & Abdulla-Al-Mamun, Md. (2010). Controlled mesoporous self-assembly of ZnS microsphere for photocatalytic degradation of Methyl Orange dye. Photochemistry and Photobiology A: Chemistry, 216, 133-141.
10. Chanu, T., Samanta, D., Tiwari, A. & Chatterjee, S. (2017). Effect of reaction parameters on photoluminescence and photocatalytic activity of zinc sulfide nanosphere synthesized by hydrothermal route. Applied Surface Science, 391, 548-556.
11. Mokhtari Nesfchi, M., Ebrahimian Pirbazari, A., Esmaeili Khalil Saraei, F., Rojaee, F., Mahdavi, F. & Fa'al Rastegar, SA. (2020). Fabrication of plasmonic nanoparticles / cobalt doped TiO2 nanosheets for degradation of tetracycline and modeling the process by artificial intelligence techniques. Materials Science in Semiconductor Processing, 122, 105-465.

Advanced Engineering Days

aed.mersin.edu.tr

Factors affecting the electrolysis of sodium chloride by a membrane electrochemical cell for the production of sodium hydroxide in an environmentally friendly method

Mohammad Amin Habibi [1], Sogand Rajaei Farid [1], Kamran Keynejad [*1], Hedayat Azizpour [2]

[1]*University of Tehran, Fouman Faculty of Engineering, Iran, m.aminhabibi@ut.ac.ir, rajaei.sogand@ut.ac.ir, kamran.keynejad@ut.ac.ir*
[2]*University of Tehran, School of Engineering, Iran, h.azizpour@ut.ac.ir*

Cite this study: Habibi, M., Rajaei Farid, S., Keynejad, K. & Azizpour, H. (2024). Factors affecting the electrolysis of sodium chloride by a membrane electrochemical cell for the production of sodium hydroxide in an environmentally friendly method. Advanced Engineering Days, 9, 532-534

Keywords
Chlor-Alkali
Sodium hydroxide
Sodium chloride electrolysis
Membrane Cell
Electrolyzer cell parameters

Abstract

The chlor-alkali process is one of the most critical industrial processes for producing alkali metal hydroxides such as sodium hydroxide, potassium hydroxide, lithium hydroxide, and chlorine gas. In this process, the electrolysis of alkali metal chloride solutions, such as sodium chloride and potassium chloride, is carried out. In traditional processes, mercury electrolytic cells and asbestos diaphragm cells were used to produce alkali metal hydroxides. These cells produced high-purity aqueous alkali metal hydroxide solutions with concentrations of about 35 to 50 percent by weight. However, these methods have several disadvantages, including environmental pollution due to mercury and asbestos, high costs of mercury, and process complexity. The modern method of using membrane cells to produce alkali metal hydroxides leverages cation exchange membranes such as Nafion to address the issues of traditional methods. The experiments indicate that the Nafion membrane efficiently facilitates the passage of sodium ions from the anode to the cathode. Time is a critical factor, enhancing production efficiency to 88.7%. Another significant factor is the electric potential difference between the electrodes. An increase of 10 volts in this difference boosts production efficiency by 85%, but prolonged exposure causes membrane swelling. Increased current intensity has a minimal effect on efficiency. Additionally, the anode's average temperature is lower than that of the cathode in these experiments.

Introduction

In traditional processes, alkali metal hydroxide solutions were produced by the electrolytic decomposition of alkali metal halide solutions in mercury electrolytic cells. The product of these cells is typically a highly concentrated aqueous alkali metal hydroxide solution, containing approximately 50% by weight of alkali metal hydroxide and nearly free of the corresponding alkali metal halide [1]. Such a product directly meets the requirements of various industrial applications. However, mercury cells currently have several disadvantages, the most significant of which is the pollution of water streams caused by the effluents from these cells. This discharge leads to mercury contamination in the environment. Although extensive efforts have been made to control mercury pollution from these effluents, eliminating water and soil contamination is nearly impossible. Even if new and advanced methods are developed and introduced to prevent mercury pollution from these cell effluents, and even if environmental regulatory standards can be fully complied with and these cells can still be used in the industry, this process still faces other drawbacks such as the high cost of mercury, the complexity of the process, and the creation of unstable operational conditions. Additionally, operators of these cells are continuously exposed to toxic hazards [2]. Membrane cells have been proposed to overcome the disadvantages of mercury and diaphragm cells for producing alkaline metal hydroxides. The selectively permeable membranes used in these cells are called cationic because they allow the passage of positively charged ions. They are typically made from cation exchange resins, generally, ionic particles embedded or planted in a fibrous matrix or carrier. The main objective

of this paper is to present a method and apparatus for the electrolytic production of high-purity alkaline metal hydroxides and chlorine in a membrane cell. The project's progress has been related to testing sodium and other metals chloride and undergoing laboratory evaluations.

The advantages of this design include the following:

Providing a method and apparatus for the electrolytic production of high-purity alkaline metal hydroxide free from alkaline metal halide and other impurities in a membrane cell with relatively high current efficiency.

Offering a process and apparatus for the economical production of an alkaline metal hydroxide solution with a concentration of approximately 30 to over 55 percent by weight, free from alkaline metal halide and other impurities, without additional purification steps and with minimal cell maintenance requirements [1].

- Producing high-purity alkaline metal hydroxide free from alkaline metal halide and other impurities
- High current efficiency
- High concentration of alkaline metal hydroxide solution with minimal environmental impact
- Low cell maintenance requirements

The aim of this project was to construct a membrane electrochemical setup and observe the effects of various factors on the production of sodium hydroxide from the electrolysis of sodium chloride at ambient temperature. This was done to reduce the costs associated with the energy required to heat the feed entering the cell.

Material and Method

Components:

Anode: In this setup, titanium anodes coated with a particular metal oxide, such as ruthenium oxide, titanium oxide, or iridium oxide, are used [3].

Cathode: 314 stainless steel was selected for this project's cathode material.

Ion exchange membrane: The membrane's chemical and mechanical stability and high permeability to sodium ions are essential criteria. The Nafion membrane with code 117 is used in this project, and the 400 series will also be investigated [4].

Feed solution or electrolyte: The electrolyte is usually an aqueous solution of sodium chloride and other metal halide salts such as lithium and potassium chloride. In this project, a sodium chloride solution is initially used.

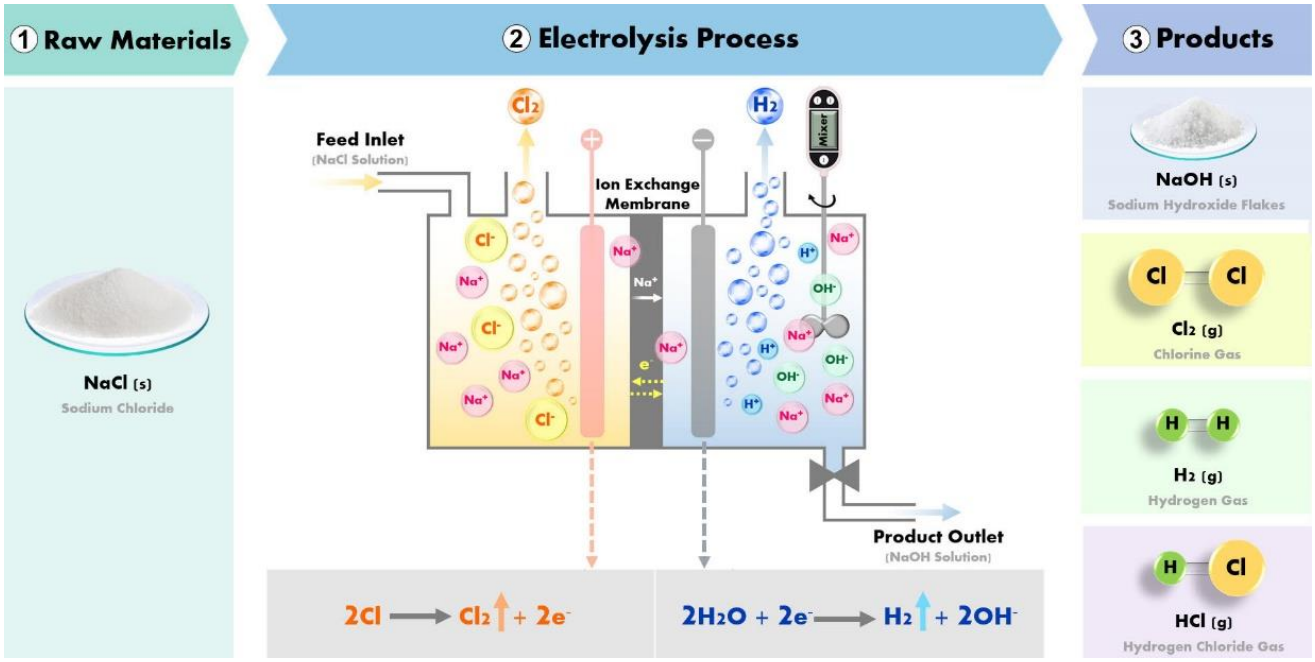


Figure 1. Sodium hydroxide production process through the electrolysis of sodium chloride using a membrane electrochemical cell

Figure 1 shows the process of producing high-purity alkali metal hydroxides in a membrane electrolyzer cell. A cation exchange membrane separates the anolyte and catholyte solutions in a membrane cell. A saturated brine solution of 1 Molar (8.77g/150ml Distilled water) and 2 Molar (17.50g/150ml Distilled water) is fed into the anode chamber, where chlorine gas is released at the anode. The electrical field is then adjusted to 4.15 to 10.00 volts to cause hydrated sodium ions (water-coated) to migrate through the membrane to the cathode. In the cathode chamber, hydrogen is released at the cathode and leaves hydroxide ions, which, along with permeable sodium ions, form caustic soda. The chlorine (Cl_2)

gas in the anode chamber and hydrogen (H_2) gas in the cathode chamber can be separated into two sections. The efficiency of the sodium hydroxide production was calculated using the following formula:

$$\% E = \frac{C_{NaOH}}{C_{NaCl}} \times 100 \quad (1)$$

where C_{NaOH} and C_{NaCl} represent the final concentration of the sodium hydroxide and the initial concentration of the sodium chloride.

Results and Discussion

In this project, factors such as voltage, amperage, stirrer and input feed were investigated in the production of sodium hydroxide (Table 1). Regarding the results obtained in test number 1 and 2, according to the constant consideration of voltage and amperes along with the input to the system, the role of evaluation time and the increase in reaction time in the conditions, in other cases, the increase in product and time have a positive and influential role in efficiency. In the 3rd stage, with increasing the electrolysis time, higher NaOH was determined at a lower voltage than the 1st and 2nd stages and confirmed the essential effect of time. In the case of tests 3 and 4, with increasing voltage at the constant electrolysis time, the efficiency of the cell has increased, which is directly affected by time and voltage. Still, the higher voltage has application limits because it can cause damage to the membrane. In tests 4 and 5, more products were obtained due to the reduction of time and increase in feed concentration. In test number 6, a mixer is used in the cathodic chamber to affect the efficiency by homogenizing the solution in this chamber. Still, the result was better than test 5. In the case of test 7, the highest concentration of NaOH was obtained for a feed concentration of 2 mol/L after 240 min. In test 8, with a dilution of feed, the voltage has increased due to lower amounts of ions. Although the efficiency was high in this run, it may have damaged the membrane.

Table1. Results of sodium hydroxide produced at different conditions

Example Number	Feed brine (mol NaCl/L)	Time (min)	Voltage	Current Density (A)	NaOH Concentration (g/150ml)	Efficiency (%)	Temperature in Chambers (°C)	
							Anode	Cathode
1	1	60	6.70	2.10	1.99	22.70	24.40	26.30
2	1	120	6.61	2.10	4.09	46.73	26.50	28.40
3	1	240	4.15	1.00	5.33	60.87	27.60	30.20
4	1	240	5.19	1.00	7.77	88.70	25.10	28.30
5	2	120	6.70	2.33	9.84	56.24	29.20	30.80
6*	2	120	6.49	2.15	10.0	57.43	28.13	29.58
7	2	240	6.02	1.82	12.58	71.87	25.46	28.36
8	0.5	120	10.00	1.30	3.72	85.00	26.23	27.41

* It means that a mixer was used in test number 6

Conclusion

The results of the experiments show that the Nafion membrane has appropriate efficiency in allowing sodium ions to pass from the anode side to the cathode side. One of the most significant factors influencing this process is time, which has increased production efficiency to 88.7%. The next effective factor is the electric potential difference between the two electrodes. When this voltage difference increases to 10 volts, it results in an 85% increase in production efficiency but causes damages such as swelling in the membrane over extended periods. The increase in electric current intensity has a minimal impact on production efficiency. Additionally, the average temperature of the anode in these experiments is lower than that of the cathode.

References

1. O'Brien, T., Bommaraju, T. V., & Hine, F. (2005). Handbook of Chlor-Alkali Technology.Springer, ISBN-10, 0306486237.
2. Mohamadi, S., & Saeedi, M. (2024). Review and assessment of mercury contamination and risk in sediment and food chain near a Chlor-alkali plant in Northwestern Persian Gulf. Emerging contaminants Journal, 10(4), 100384.
3. Abdel-Aziz, A. B., El-Taib Heakal, F., El Nashar, R. M., & Ghayad, I. M., (2024). Green synthesis and characterization of binary, ternary, and quaternary Ti/MMO anodes for chlorine and oxygen evolution reactions. *Scientific Reports* , 14, 9821.
4. Krol, J. J. (1997) Ion Exchange membrane Principles. Monopolar and Bipolar ion exchange membranes, 1-10.

Advanced Engineering Days

aed.mersin.edu.tr

Adsorption study of methyl orange dye removal from aqueous solutions by using a novel polymeric MOF nanosorbent

Niloofar Razmi [*1], Mohammad Zabihi [1], Sirous Ebrahimi [1]

[1]*Sahand University of Technology, Chemical Engineering, Iran, n_razmi99@sut.ac.ir, zabihi@sut.ac.ir, sirous_eb@yahoo.com*

Cite this study: Razmi, N., & Zabihi, M., & Ebrahimi, S (2024). Adsorption study of methyl orange dye removal from aqueous solutions by using a novel polymeric MOF nanosorbent Advanced Engineering Days, 9, 535-537

Keywords
Methyl orange
Adsorption
Metal-organic framework
Polyacrylamide

Abstract

A significaant category of pollutants is comprised of dyes. When dyes find into the water bodies, they give rise to substantial pollution and their remival presents a formidable chaleenge, because dyes has synthetic nature and molecular structure that makes them more stable and harder to biodegradable. Dyes cause serious problems on the human health and ither animals. Adsorption is commonly employed eco-friendly, cost-effective and high efficiency technology for the removal and sepration of various pollutants from waste water. The purpose of this study is to investigate the efficiency of methyl orange dye removal by metal-organic framework nanosorbent supported on polymer. The supported bimetallic Al/Fe metal-organic frameworks on the polyacrylamide as a substrate was synthesized using a facile solvothermal method. The polymeric MOF was characterized using the Fourier Trasformed Infrared (FTIR). The adsorption isotherm of bimetallic Al/Fe metal-organic framework on the polyacrylamide for methyl orange is in accordance with Langmuir isotrherm model, and the maximum adsorption capasity of Al/Fe@PAA at 298k was 169.4519 mg g^{-1}. Therefor, the results showed this novel polymeric MOF is an effective adsorbent for removing methyl orange from aqueous solutions.

Introduction

Conserving water is imperative for safeguarding our planet and ensuring a secure future for humanity. As our population, society, and advancements in science and technology propel us to new heights, it becomes evident that the price we currently bear or will bear in the near future is bound to be exorbitant[1]. Dyes are fundamentallly chemical compounds capable of bonding to surface or testiles to introduce color. Most dyes consist of intricate organic molecules[2]. Methyl orange (MO) is a frequently employed acidic anionic mono-azo dye, with consistent usage in textiles, laboratory experiments, and various commercial products[3]. Azo dyes are often challenging to remove due to their characteristics. Including water solubility, complex molecular structures and synthetic origins[4]. To eliminate dyes from wastewater, various methods encompassing physical, chemical and biological approaches have been employed. These techniques include adsorption, chlorination, coagulation, ozonation, membrane filtration and photocatalyst degradation. On the contrary, adsorption stands out as a preferable alternative to these methods, thanks to its simplicity, cost-effectiveness, and flexibility in choosing adsorbent materials with a wide range of chemical and physical properties[5]. The aim of this stidy was to synthesize and characterize bimetallic Al/Fe MOF on the polyacrylamide nanosorbent for the removal of methyl orange dye from aqueous solutions. The characterization of the prepared sampale was also studied by using FTIR .

Material and Method

Iron nitrate nonahydrate, Aluminum nitrate nonahydrate, N,N-dimethylforamide (DMF), Ethanol (C_2H_6O), Distilled water, Terphtalic acid (BDC) , Polyacrylamide (PAA) and Methyl orange ($C_{14}H_{14}N_3SO_3Na$) were provided Merk company.

The bimetallic Al/Fe@PAA MOF was prepared via the solvothermal method. To this Aluminum nitrate nonahydrate, Iron nitrate nonahydrate, polyacrylamide and terphtalic acid were dissolved in water, ethanol and DMF, all of them were used as solvents. This prepared solution was Transferred to a Teflon-lined outoclave and then subjected to a hot air oven at 110°C for a 12 hours. Following the process, the resultant solid particles were thoroughly washed and subsequently allowed to dry in an oven.

The adsorption of MO was conducted employing 0.05 g of the supported nanosorbent, while maintaining consistent operational parameters. These parameters encompassed an initial concentration of 50 mg/l, a solution volume of 50 ml, an adsorption temperature of 25°C, and a pH of 6.5. The concentration of MO was determined through UV-vis Spectroscopy, and the removal efficiency was subsequently computed using the provided formula (Eq. 1).

$$RE\% = \frac{(C0 - Ce)}{C0} * 100 \quad (1)$$

Results

FT-IR Spectra: FT-IR serves as a valuable analytical method for confirming the presence of functional groups. Figure 1 illustrates the FT-IR spectra of the Al/Fe@PAA metal-organic framework.The synthesized adsorbent features both 1321.68 cm^{-1} and 1583.54 cm^{-1} asymmetric and symmetric vibrations related O-C-O to the ligands of the ellagic acid. In addition,1401.18 cm^{-1} this band is associated C=C with the bonding and 1662.52 cm^{-1} and 1290.96 cm^{-1} assignment to N-H and CN (7). The strong peaks in range of 1735 to 1750 cm^{-1} are related to the C=O and strong peaks in range of 700 to 950 cm^{-1} are related to CH for polyacrylamide.The appearance of a peak within the wavelength spectrum around 1754 cm^{-1} signifies the emergence of the Al/Fe-O bond. Additionally, various indicative peaks detected at 1450 cm^{-1}, 1476, cm^{-1} and 1593 cm^{-1} are attributed to the stretching vibrations of Al-O bonds.These peaks serves as evidence for the presence of the polyacrylamide in the synthesized polymeric MOF nanosorbent [6].

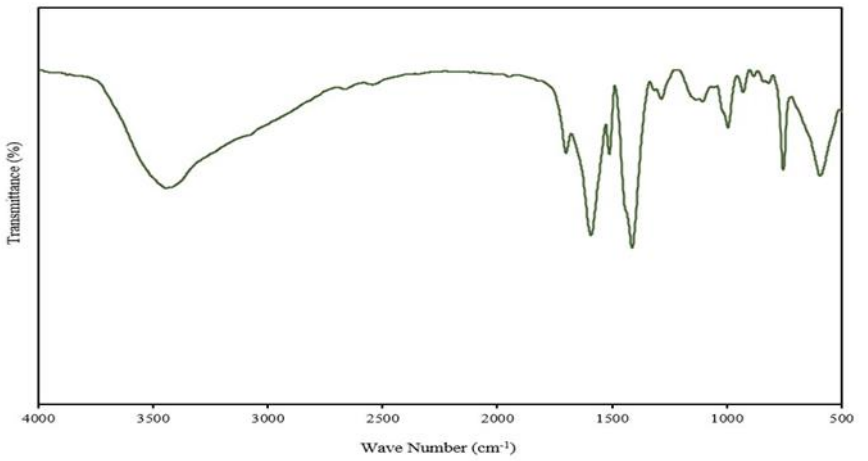


Figure 1. The FT-IR analysis for Al/Fe@PAA MOF

Discussion

Adsorption Isotherm Study: Isotherm models are widely employed to describe and investigate adsorption mechanisms. Equilibrium data of the adsorbent were fitted to Langmuir and Freundlich isotherm models. The linear form of the Langmuir model is expressed as Equation 2:

$$\frac{C_e}{q_e} = \frac{1}{q_{max}K_1} + \frac{C_e}{q_{max}} \quad (2)$$

Where, C_e is the equilibrium concentration (mg/L), q_e is the amount adsorbed at equilibrium (mg/g), q_{max} is the maximum adsorption capacity (mg/g) and K_L is the Langmuir adsorption constant (L/mg). The linear form of the Freundlich isotherm model is represented as Equation 3:

$$Lnq_e = LnK_F + \frac{1}{n} Ln\, C_e \quad (3)$$

Where, K_F is the Freundlich adsorption constant (mg/g) and n is the adsorption constant, if it falls between zero and one, indicates favorable adsorption. The study investigated adsorption isotherms using two models, Langmuir and Freundlich at various concentrations. The results indicate that Langmuir isotherm exhibits a better correlation coefficient R^2>0.999 with the experimental data, and maximum adsorptin capacity obtained from the Langmuir model is 169.4915 (mg/g), as illustrated inthe figure 1. In the table 1 also reports the parameters related to the Lngmuir and Freundlich isotherm models.

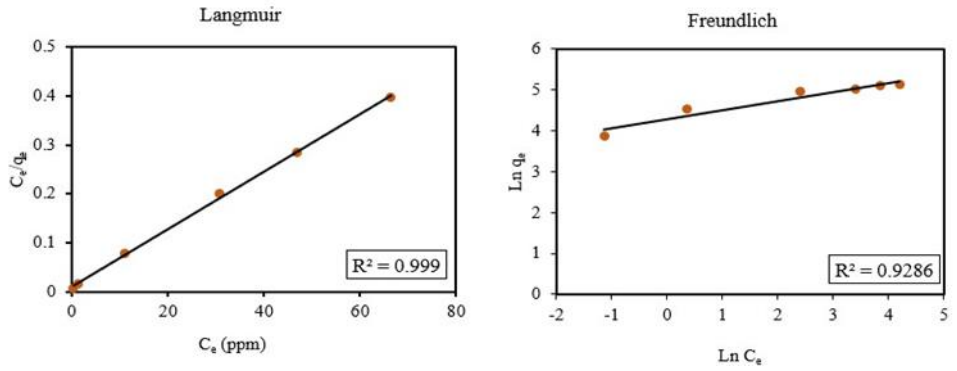


Figure 2. Langmuir and Freundlich isotherm

Table 1. Langmuir and Freundlich constants

Isotherm models	Parameter	Al/Fe@PAA
Langmuir	q_{max} (mg g^{-1})	169.4915
	K_L (L mg^{-1})	0.6413
	R^2	0.999
Freundlich	K_F (mg g^{-1})	73.0029
	n	4.54
	R^2	0.9286

Conclusion

Metal-organic frameworks have proven to be ideal adsorbents due to their high surface area. Nano-adsorbents synthesized via the solvothermal method are suitable for methyl orange adsorption. The synthesized adsorbent was identified through analytical technique FT-IR, confirming the formation of suitable bonds, which is indicative of the correct adsorbent synthesis. Surface adsorption isotherm studies for methyl orange adsorption revealed that the synthesized adsorbent follows the Langmuir isotherm, indicating its effectiveness in methyl orange removal.

References

1. Gupta, V. (2009), *Application of low-cost adsorbents for dye removal–a review.* Journal of environmental management. **90**(8): p. 2313-2342.
2. Yagub, M.T., et al. (2014), *Dye and its removal from aqueous solution by adsorption: a review.* Advances in colloid and interface science. **209**: p. 172-184.
3. Darwish, A., M. Rashad, and H.A. AL-Aoh (2019), *Methyl orange adsorption comparison on nanoparticles: Isotherm, kinetics, and thermodynamic studies.* Dyes and Pigments. **160**: p. 563-571.
4. Kgatle, M., et al. (2021), *Degradation kinetics of methyl orange dye in water using trimetallic Fe/Cu/Ag nanoparticles.* Catalysts. **11**(4): p. 428.
5. Piaskowski, K., R. Świderska-Dąbrowska, and P.K. Zarzycki (2018), *Dye removal from water and wastewater using various physical, chemical, and biological processes.* Journal of AOAC International. **101**(5): p. 1371-1384.
6. Rao, J.P. and K.E. Geckeler (2011), *Polymer nanoparticles: Preparation techniques and size-control parameters.* Progress in polymer science. **36**(7): p. 887-913.

Advanced Engineering Days

aed.mersin.edu.tr

Robust Position Control of AC Servo Motor Using Sliding Mode Control (SMC) Optimized by Grey Wolf Optimization (GWO) Algorithm

Navid Salahshoor*[1], Mahmood Moghadasian [1]

[1] *Shahid Chamran University of Ahvaz, Shohadaye Hoveizeh Campus of Technology, Iran, Navidsalahshor0@gmail.com, m.moghadasian@scu.ac.ir*

Cite this study: Salahshoor, N., & Moghadasian, M. (2024). Robust Position Control of AC Servo Motor Using Sliding Mode Control (SMC) Optimized by Grey Wolf Optimization (GWO) Algorithm. Advanced Engineering Days, 9, 538-541

Keywords
AC Servo Motor
Sliding Mode Control
Grey Wolf Optimization
Robust Control
Position Control
MATLAB Simulation

Abstract

This paper presents a robust position control method for AC servo motors by integrating Sliding Mode Control (SMC) with the Grey Wolf Optimization (GWO) algorithm. The SMC technique is renowned for its robustness against system uncertainties and external disturbances. However, the performance of SMC highly depends on the selection of its control parameters. To address this challenge, the GWO algorithm is employed to optimally tune the SMC parameters, ensuring enhanced control performance. The AC servo motor's dynamic model is used to design the control strategy, where the sliding surface is defined to minimize position errors. The GWO algorithm is applied to find the optimal values for the control gain and sliding surface parameters, minimizing a defined cost function based on the position tracking error. The proposed method is implemented and simulated in MATLAB, demonstrating superior performance in terms of reduced tracking error and improved robustness compared to traditional SMC. The simulation results validate the effectiveness of the proposed GWO-based SMC in achieving precise and reliable position control of AC servo motors, making it a promising solution for industrial applications.

Introduction

AC servo motors are extensively utilized in industrial applications due to their precision and high performance in position control tasks. These motors are essential in fields like automation, robotics, and CNC machinery, where accurate control of angular position and speed is crucial [1]. Sliding Mode Control (SMC) is a prominent control strategy for such applications, known for its robustness against system uncertainties and disturbances. However, the performance of SMC is highly dependent on the proper selection of control parameters, which can be challenging and time-consuming to tune manually.

To address these challenges, optimization algorithms like the Grey Wolf Optimization (GWO) algorithm can be employed. GWO, inspired by the social hierarchy and hunting behavior of grey wolves, is effective in finding optimal solutions in complex search spaces. This paper proposes a novel approach for robust position control of AC servo motors by integrating SMC with GWO. The GWO algorithm optimally tunes the SMC parameters, minimizing a predefined cost function based on position tracking error, thereby enhancing control performance and reducing chattering effects.

The effectiveness of the proposed method is demonstrated through MATLAB simulations, showing improved performance over traditional SMC. This integrated approach not only achieves precise and reliable position control but also offers a practical solution for industrial applications. The remainder of the paper details the dynamic model of the AC servo motor, the design of the SMC, the optimization process using GWO, and the simulation results.

Material and Method

The model of the system consists of a motor coupled to a gear box and an inertia load rigidly fixed to output shaft. The control torque (Tc) for the two phase AC servo motor is described as [2]

$$T_c = K_1 E(t) - K_2 \dot{\theta}(t) \quad (1)$$

Where

T_c = Control torque (Nm)
$\dot{\theta}$ = angular velocity of the AC servo motor (rad/s)
K_1&K_2 = motor constants (Nm/V, Nm/rad/s)
E = rated input voltage (v)

The dynamic equation of the mechanical system is given by

$$T_c = J\ddot{\theta}(t) + B\dot{\theta}(t) + T_L \quad (2)$$

Where

θ = AC servo motor angular position (rad)
$\ddot{\theta}$ = AC servo motor angular acceleration (rad/s2)
B = Friction coefficient
J = Moment of inertia (Kg.cm2)

By equating (1) and (2)

$$J\ddot{\theta}(t) + B\dot{\theta}(t) + T_L = K_1 E(t) - K_2 \dot{\theta}(t) \quad (3)$$

Taking Laplace transform the above equations becomes

$$K_1 E(s) = Js^2\theta(s) + Bs\theta(s) + K_2 s\theta(s) + T_L(s) \quad (4)$$

The transfer function between (s) and E(s) is obtained by putting $T_L(s) = 0$

$$K_1 E(s) = Js^2\theta(s) + Bs\theta(s) + K_2 s\theta(s) \quad (5)$$
$$K_1 E(s) = (Js^2 + Bs + K_2 s)\theta(s) \quad (6)$$
$$\frac{\theta(s)}{E(s)} = \frac{K_1}{Js^2 + K_2 s + Bs} = \frac{K_m}{s(\tau_m s + 1)} \quad (7)$$

Where

K_m = Motor gain constant $= \frac{K_1}{K_2 + B}$
τ_m = Motor time constant $= \frac{J}{K_2 + B}$

The specifications of AC servo system, which has considered for simulation study, are given in below table. By using equation (7) and considering the numerical values in the table (1), the identified transfer function model for the AC servo system is given as:

$$G_P(s) = \frac{0.4}{s(2.7763s + 1)} \quad (8)$$

Table 1. Values of parameters of AC servo motors

Items	value	Items	value
Type	GSM62AE	Moment of inertia (J)	0.052 kg.cm^2
Voltage	230 V	Friction of coefficient	0.01875
Power	100 W	GB ratio	36
Speed	50 rpm	Radius of the output shaft	0.0175 m

The SMC law aims to drive the system's state to a desired equilibrium point. The sliding surface s is defined as:[3]

$$s = e + \lambda \dot{e} \quad (9)$$

where $e = \theta_{desired} - \theta$ is the position error, and λ is a positive constant. The control law u is designed to ensure that $s = 0$ is attractive and invariant:

$$u = \frac{1}{K}\left(J\lambda\ddot{\theta} + b\lambda\dot{e} - k \cdot \text{sign}(s)\right) \quad (10)$$

Here, k is the control gain to be optimized.

The GWO algorithm is employed to optimize the SMC parameters k and λ. The objective function to be minimized is based on the position tracking error:

$$J = \sum_{i=1}^{N} e_i^2 \quad (11)$$

where N is the number of time steps in the simulation.

The GWO algorithm operates by mimicking the leadership hierarchy and hunting mechanism of grey wolves. The steps include initialization of the wolf population, updating positions, and iteratively searching for the optimal solution.

Results

The control system is implemented in Simulink, integrating the AC servo motor model with the Sliding Mode Control (SMC) and Grey Wolf Optimization (GWO) algorithm. The Figure 1 shows simulink block diagram illustrates of the system architecture.

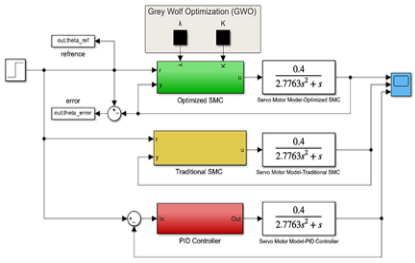


Figure 1. Simulink Diagram System

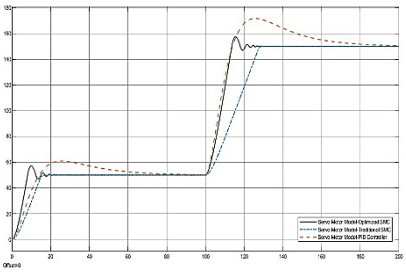


Figure 2. System Response Comparison

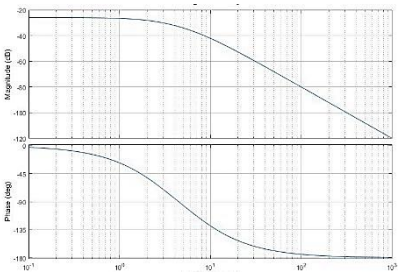


Figure 3. Frequency Response Analysis

The MATLAB code provided earlier contains the implementation of the GWO optimization algorithm. It optimizes the SMC parameters k and λ based on the defined objective function.

Upon running the simulation, we obtained the following results:

1. Position Tracking Performance: The AC servo motor successfully tracks the desired position over time, demonstrating superior performance compared to both traditional models and PID control, as shown in Figure 2.
2. Optimized Control Parameters: The GWO algorithm converged to optimal values for the SMC parameters k and λ, resulting in improved control performance.
3. As shown in the Figure 3, Bode plot analysis evaluates the frequency response, stability, and robustness of the control system. The magnitude plot for the SMC optimized by GWO shows a stable gain profile, suppressing oscillations and maintaining consistent performance. The phase plot indicates the phase shift at various frequencies, with the phase margin representing the system's tolerance to delays. The optimized SMC exhibits an improved phase margin and consistent phase response, especially at higher frequencies, enhancing robustness and overall stability.

Discussion

The results obtained from the integration of Sliding Mode Control (SMC) with Grey Wolf Optimization (GWO) demonstrate significant improvements in the position control of AC servo motors. The simulations conducted in MATLAB highlight the effectiveness of this approach compared to traditional SMC methods and PID control. Specifically, the GWO algorithm optimized the control parameters k and λ, resulting in reduced tracking error and enhanced system robustness.

The Bode plot analysis further validated the performance of the optimized control strategy. The magnitude plot indicated a stable gain profile, effectively suppressing oscillations, while the phase plot showed an improved phase margin, indicating better tolerance to delays and consistent phase response across various frequencies. This stability and robustness are crucial for maintaining reliable performance in practical applications.

Conclusion

The use of Sliding Mode Control (SMC) optimized via the Grey Wolf Optimization (GWO) algorithm offers an effective solution for controlling the position of AC servo motors. MATLAB simulations highlight the significant benefits of this method over traditional SMC, showing notable improvements in precision and stability. Additionally, frequency response analysis with Bode plots was conducted to validate the performance of the control strategy. These plots graphically represent the system's frequency response, displaying its gain and phase shift across various frequencies, which is essential for understanding the control system's dynamic behavior, stability, and robustness. This validation confirms the enhanced performance and reliability of the optimized SMC.

Future research could investigate applying this optimized control strategy to various motor types and more complex systems. Real-time optimization and adaptive control mechanisms could also be advantageous, enabling the control system to adapt dynamically to changing conditions and disturbances. Finally, experimental validation

with physical prototypes would provide deeper insights into the practical feasibility and benefits of the proposed approach.

References

1. Ali, A.W.A., F.A.A. Razak, and N. Hayima, A review on the AC servo motor control systems. ELEKTRIKA-Journal of Electrical Engineering, 2020. 19(2): p. 22-39.
2. Vijayakarthick, M. and P. Bhaba, Position Tracking Performance of AC Servomotor based on New Modified Repetitive Control Strategy. vol, 2012. 10: p. 119-128.
3. Abd El-hamid, A.S. and A.H. Eissa, Position control of AC servomotor using internal model control strategy. International Journal of Engineering Innovation & Research, 2015. 4.

Advanced Engineering Days

aed.mersin.edu.tr

Optimized H-Infinity Controller for Torque Control of PMSM Using Grasshopper Optimization Algorithm (GOA)

Mehran Khalaj Afshar [*1], **Mahmood Moqhadasian** [1]

[1] *Shahid Chamran University of Ahvaz, Shohadaye Hoveize Campus of Technology, Iran, mkhljafshar@gmail.com, m.moghadasian@scu.ac.ir*

Cite this study: Khalaj Afshar, M., & Moqhadasian, M. (2024). Optimized H-Infinity Controller for Torque Control of PMSM Using Grasshopper Optimization Algorithm (GOA). Advanced Engineering Days, 9, 542-545

Keywords
PMSM
Torque Control
H-Infinity Control
GOA
Robust Control
MATLAB/Simulink

Abstract

Permanent Magnet Synchronous Motors (PMSMs) are essential in high-performance applications due to their high efficiency, torque-to-inertia ratio, and low maintenance requirements. However, traditional control methods like Direct Torque Control (DTC) and Field-Oriented Control (FOC) often struggle with sensitivity to parameter variations and external disturbances. This paper presents an optimized H-infinity controller for PMSM torque control, leveraging the Grasshopper Optimization Algorithm (GOA) to enhance controller performance. The H-infinity control method provides robust stability and performance by minimizing the worst-case gain from disturbances to the controlled output. The GOA is employed to optimize the controller parameters, ensuring optimal performance under varying operating conditions. The PMSM model and control strategy are implemented in MATLAB/Simulink r2023b, where the performance of the optimized controller is evaluated through extensive simulations. The results demonstrate significant improvements in torque control accuracy, dynamic response, and robustness compared to conventional methods. This study highlights the potential of combining H-infinity control with GOA for advanced motor control applications, offering a viable solution for enhancing the reliability and efficiency of PMSM-driven systems in industrial settings. Future work will focus on experimental validation and real-time implementation of the proposed control strategy.

Introduction

Permanent Magnet Synchronous Motors (PMSMs) play a critical role in high-performance applications due to their superior efficiency, high torque-to-inertia ratio, and minimal maintenance requirements. These motors are commonly used in industries such as robotics, aerospace, and automotive, where precise control and reliability are paramount. Traditional control techniques like Direct Torque Control (DTC) and Field-Oriented Control (FOC) have been widely implemented for torque management in PMSMs.[1] DTC is appreciated for its quick torque response and simplicity, while FOC offers excellent steady-state performance and decoupled control of torque and flux. However, both methods exhibit limitations, particularly in terms of sensitivity to parameter variations and external disturbances, which can degrade system performance and stability.

To address these challenges, this paper proposes an H-infinity control strategy for torque regulation in PMSMs. The H-infinity control method is designed to enhance system robustness by minimizing the worst-case gain from disturbances to the controlled output, thus improving tolerance to uncertainties and external perturbations. [2] Additionally, the Grasshopper Optimization Algorithm (GOA) is employed to optimize the controller parameters, ensuring optimal performance under varying operating conditions.[3] The proposed approach is implemented and evaluated in the MATLAB/Simulink r2023b environment, demonstrating significant improvements in dynamic response, torque accuracy, and overall robustness compared to conventional methods. This study highlights the potential of integrating advanced control algorithms with optimization techniques to enhance the reliability and efficiency of PMSM-driven systems in demanding industrial applications.

Material and Method

System Model:

Permanent Magnet Synchronous Motors (PMSMs) are modeled using the dq-axis representation in the rotor reference frame. This model captures the dynamic behavior of the motor by describing the relationships between voltages, currents, and flux linkages in the stator and rotor. The voltage equations for a PMSM in the rotor reference frame, are given (1) and The flux linkages are related to the stator currents and the permanent magnet flux linkage (λ_m) by : [4]

$$\begin{cases} v_{qs} = r_s i_{qs} + p\lambda_{qs} + \omega_r \lambda_{ds} \\ v_{ds} = r_s i_{ds} + p\lambda_{ds} - \omega_r \lambda_{qs} \end{cases} \quad (1)$$

$$\begin{cases} \lambda_{qs} = L_q i_{qs} \\ \lambda_{ds} = L_d i_{ds} + \lambda_m \end{cases} \quad (2)$$

Where:

- v_{qs} and v_{ds} are
- the q-axis and d-axis stator voltages.
- i_{qs} and i_{ds} are the q-axis and d-axis stator currents.
- r_s is the stator resistance.
- L_q and L_d are the q-axis and d-axis inductances.
- λ_{qs} andλ_{ds} are the q-axis and d-axis flux linkages.
- ω_r is the rotor electrical angular speed.
- p denotes the derivative operator $\frac{d}{dt}$.
- λ_m is the flux linkage due to the permanent magnets.

The torque T_e generated by the PMSM is given by:

$$T_e = \frac{3}{2} P\left(\lambda_{ds} i_{qs} - \lambda_{qs} i_{ds}\right) \quad (3)$$

Where P is the number of pole pairs.

H-Infinity Control Strategy Optimized With GOA:

H-infinity control aims to design a controller that minimizes the worst-case gain of the transfer function from the disturbance input to the controlled output, thereby achieving robust performance and stability. The design process involves formulating the control problem in the frequency domain and solving a set of matrix inequalities. The state-space representation of the PMSM can be written as:

$$\begin{cases} \dot{x} = Ax + B_u u + B_w w \\ z = C_z x + D_{zu} u + D_{zw} w \\ y = C_y x + D_{yu} u + D_{yw} w \end{cases} \quad (4)$$

- x is the state vector,
- u is the control input,
- w is the disturbance,
- z is the controlled output,
- y is the measured output,
- $A, B_u, B_w, C_z, D_{zu}, D_{zw}, C_y, D_{yu}, D_{yw}$ are matrices of appropriate dimensions.

The goal is to design a controller $K(s)$ that minimizes the H-infinity norm of the closed-loop transfer function from w to z. The H-infinity controller design aims to minimize the worst-case gain from disturbances to the control output. This is achieved by formulating the control problem in the frequency domain and solving a set of matrix inequalities. The Grasshopper Optimization Algorithm (GOA) is employed to optimize the controller parameters, providing an effective solution for achieving robust control.

The simulation is performed in MATLAB/Simulink r2023b, with the following initial parameters : [4]

Table 1. System Initial Parameters

Parameter	Value	Parameter	Value
Stator resistance r_s	0.01 ohms	Permanent magnet flux linkage λ_m	0.1 Wb
d-axis inductance L_d	0.005 H	Number of pole pairs P	4
q-axis inductance L_q	0.005 H	Moment of inertia J	0.01 kg.m2
		Viscous friction coefficient B	0.001 N.m.s

The optimization process and implementation of the H-infinity controller for PMSM torque control are carried out using the Grasshopper Optimization Algorithm (GOA) and MATLAB/Simulink. The objective of the optimization is to minimize the integral of squared error (ISE) between the reference and actual torque values,

thus ensuring optimal performance of the controller. The GOA is configured with a population of 50 agents and runs for 100 iterations to find the best parameters for the H-infinity controller. The model is subjected to various load conditions to evaluate the performance of the optimized controller. During simulation, the controller demonstrates significant improvements in torque control accuracy and system robustness compared to traditional methods. The optimized H-infinity controller achieves a quick response to torque demands and maintains stability across different operating conditions, validating the effectiveness of the proposed optimization approach.

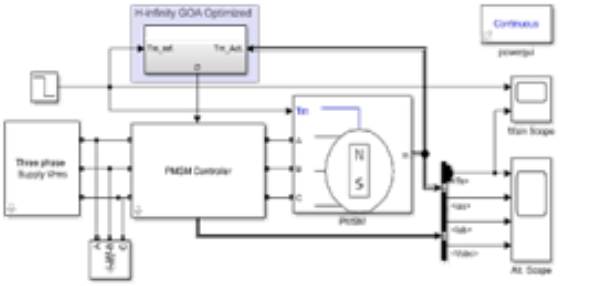


Figure 1. Simulink Diagram System

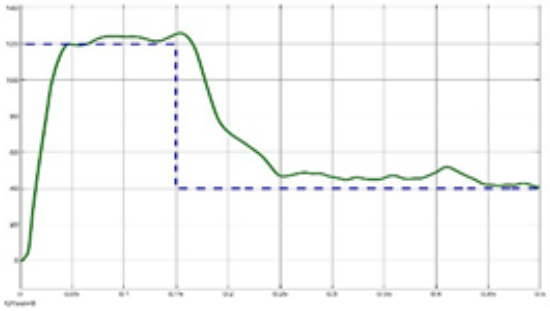


Figure 2. System Step Response

Results

The simulation results confirm the effectiveness of the optimized H-infinity controller for torque control of the Permanent Magnet Synchronous Motor (PMSM). Key findings from the simulations are:

1. *Improved Torque Tracking Accuracy*: The optimized controller demonstrated superior accuracy in tracking the reference torque, maintaining precise control even under varying load conditions and disturbances. The error between the reference and actual torque values was significantly reduced.
2. *Enhanced Dynamic Response*: The system's dynamic response showed considerable improvement. The response to torque demands was quick, with minimal overshoot and reduced settling time, indicating the controller's efficiency in handling rapid changes in torque demand.
3. *Robustness to Disturbances*: The controller maintained stable performance under various operating conditions, including sudden load changes and parameter variations, validating its robustness against external disturbances and internal uncertainties.

These results highlight the potential of combining H-infinity control with the Grasshopper Optimization Algorithm (GOA) for advanced motor control applications. The optimized controller enhances the accuracy, dynamic response, and robustness of the PMSM, making it suitable for high-performance industrial applications. Step Response of the System To visually represent the system's performance, the step response of the PMSM to torque demand changes is shown in Figure 2. The response demonstrates the system's quick adjustment to changes in torque, highlighting the optimized controller's effectiveness in maintaining stability and minimizing overshoot.

Discussion

The simulation results show that the optimized H-infinity controller significantly improves PMSM torque control performance. Compared to traditional methods like Direct Torque Control (DTC), the H-infinity controller provides superior accuracy in tracking reference torque, even under varying load conditions and disturbances. Parameters optimized through the Grasshopper Optimization Algorithm (GOA) enhance the system's dynamic response and robustness. The system demonstrated a quick response to torque changes, maintaining stability and minimizing overshoot and settling time. The integral of squared error (ISE) between reference and actual torque values was significantly reduced, confirming the optimization process's effectiveness. Additionally, the controller's robustness was validated through consistent performance across various operating conditions, including sudden load changes and parameter variations.

Conclusion

This study presents an optimized H-infinity control strategy for torque regulation in Permanent Magnet Synchronous Motors (PMSMs), using the Grasshopper Optimization Algorithm (GOA) for parameter optimization. The combination of H-infinity control and GOA enhances system robustness and dynamic performance, addressing the limitations of traditional methods like Direct Torque Control (DTC). Simulation results demonstrate significant improvements in torque accuracy, response time, and stability under various conditions. These findings suggest that integrating advanced control strategies with metaheuristic algorithms can significantly enhance PMSM-

driven systems' performance in industrial applications. The study offers a robust and efficient solution for more reliable and precise motor drive systems, crucial in sectors demanding high performance and reliability. Future work will focus on experimental validation and real-time implementation to establish the practical applicability of this optimized control strategy.

References

1. Ramesh, P., et al., Development of a PMSM motor field-oriented control algorithm for electrical vehicles. Materials Today: Proceedings, 2022. 65: p. 176-187.
2. Liu, B. Research on h infinity robust tracking controller for permanent magnet synchronous motor servo system. in 2009 International Conference on Information Engineering and Computer Science. 2009. IEEE.
3. Nayak, P.C., R.C. Prusty, and S. Panda, Grasshopper optimization algorithm optimized multistage controller for automatic generation control of a power system with FACTS devices. Protection and Control of Modern Power Systems, 2021. 6(1): p. 1-15.
4. Ramana, P., et al., Direct Torque Control of Inverter Fed PMSM Drive using SVM. 2013, IJAIEM.

Advanced Engineering Days

aed.mersin.edu.tr

Analysis of Different Distribution Configuration for Optimal Photovoltaic Integration: A Case Study

Klajdi Kamberi [*1], Donard Shaliu [1], Marialis Çelo [1], Bajram Leka [2]

[1]*Polytechnic University of Tirana, Electric Power Department, Albania, klajdikamberi98@gmail.com, donard.shaliu@gmail.com, celomarialis@yahoo.com.*

[2] *Polytechnic University of Tirana, Department of Automation, Albania, bajramleka94@gmail.com*

Cite this study: Kamberi, K., Shaliu, D., Çelo, M. & Leka, B. (2024). Analysis of Different Distribution Configuration for Optimal Photovoltaic Integration: A Case Study. Advanced Engineering Days, 9, 546-548

Keywords
Radial feeder
Ring double feeded
Power losses
Overloading
Photovoltaic penetration

Abstract

The transformation of consumers from passive to "prosumers," who produce energy themselves and dispose of the excess, is changing the operation and security of distribution networks (DN). The penetration of photovoltaic (PV) plants linked to the customer in low-voltage (LV) influences the voltage level, element loading and energy losses in the network. This paper compares the effects of varying PV plant penetration levels on the feeder that works in radial operation and in the scenario of double-feed (DF) ring operation. The findings show that for every value of PV penetration from 0% to 100% of the load, there is a significant decrease in line loading and a greater reduction in losses in the case of DF network. Both scenarios resulted in an increased voltage, but when it comes to functioning as DF, the voltage is practically constant and closer to the nominal levels. This research leads us to the conclusion that in order to raise the high long-term values for PV connections in the existing network, the DN's mode of operation should be changed from radial to ring.

Introduction

Supportive schemes from the government to help with the cost of investment in PV plants has increased the interest of consumers connected to LV to invest in this field. PV generation is expected to grow significantly in the upcoming years and as solar generators it becomes more widely used, there will often be benefits and drawbacks for the existing network [1]. The dependence of PV generation on atmospheric conditions may present new challenges for the management of the newly altered network, even though there are many algorithms [2] and techniques available today, to determine an optimal RES project in order to have a lowest negative impact [3]. The generation of PV in LV networks is not only used by household consumers but also by non-residential consumers. [4] and this generation can be increased if control is used for designing maximum power point tracking (MPPT) [5]. This paper is driven by the observation that the network configuration impacts the maintenance of various network parameters and power quality at varying PV penetration levels in LV. We have selected a DN feeder that may function as a radial and ring DF by two distinct substations in this paper to assess the effect of PV plants on power quality parameters, based on the long-term projections for the goals of growing PV generation.

Material and Method

This paper's methodology includes modeling of the network in the neplan software based on the real data collection from the field on the elements and loads of the feeders that can operate as radial and DF. The maximal load regime of operation has been examined using six case studies: the base case, in which no PV plant is added; 100%, 80%, 60%, 40%, and 20% PV plant penetration and an analysis of the voltage magnitude, line loading and power losses in the grid is carried out for every case. PV penetration is on percentage of the total load of DN. Normally, in the ring DF network, the energy supply of consumers is safer [6] than the radial operation, where the voltage is greatly reduced from the beginning of the feeder to its end nodes. Figure 1 shows the schematic design

of the DN under consideration, that belongs to Durres City. By using the switch, we can switch between radial and DF operation.

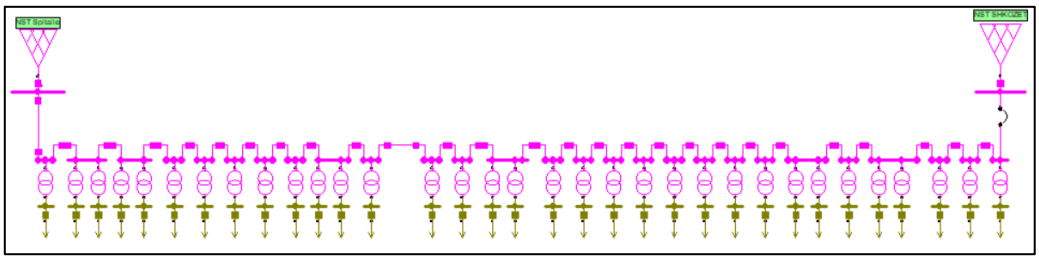


Figure 1. Schematic presentation of the DN

Results

The voltage magnitude changes for each level of PV penetration for the two scenarios under consideration is displayed in Figures 2 and 3. The voltage is more impacted in the radial operation and there is a greater disparity in the voltage change from node 1 to node 27. On the other hand, the voltage in the DF operation is more consistent and nearer the nominal values across the feeder's nodes. When solar plants are the only source of power, the voltage rise is greater in both circumstances, but it always remains within the normalized range. When the network encounters a minimum load and generation from PV is 100%, a voltage increase over the nominal values is expected.

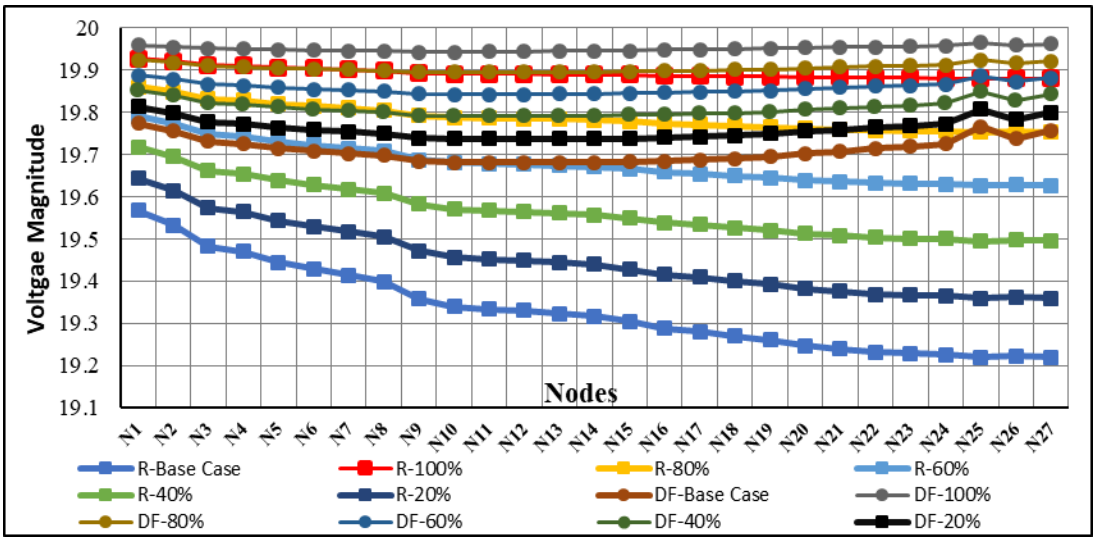


Figure 2. Voltage magnitude at MV nodes for radial and DF configuration

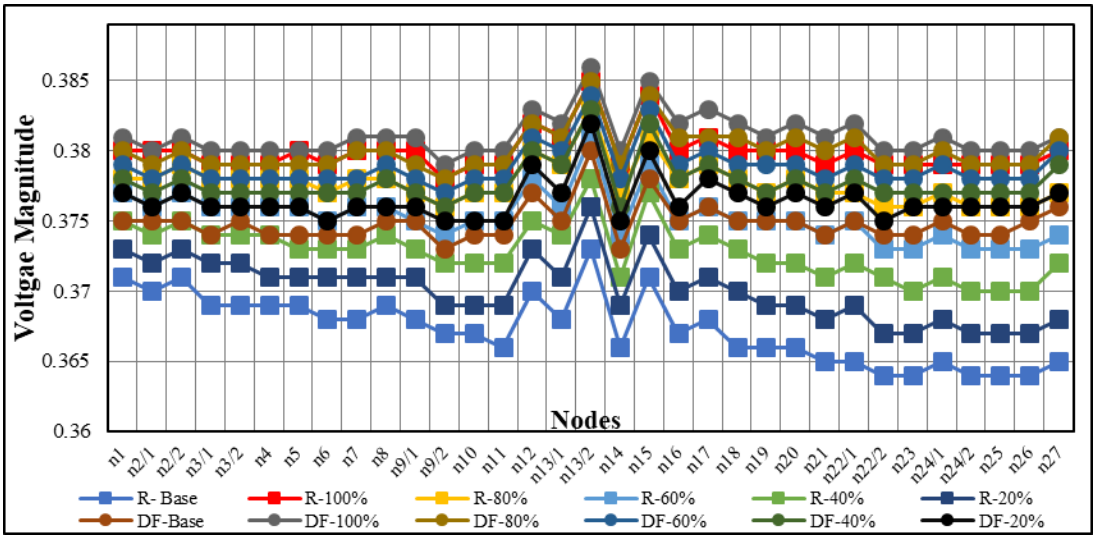


Figure 3. Voltage magnitude at LV nodes for radial and DF configuration

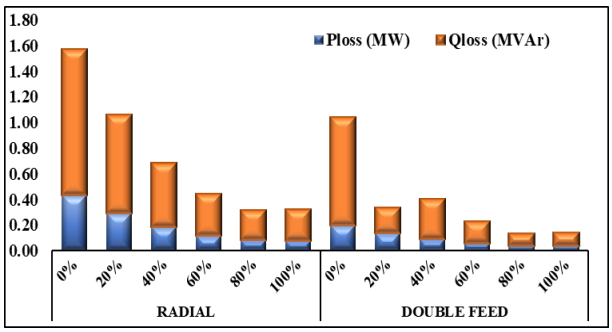


Figure 4. Level of power losess

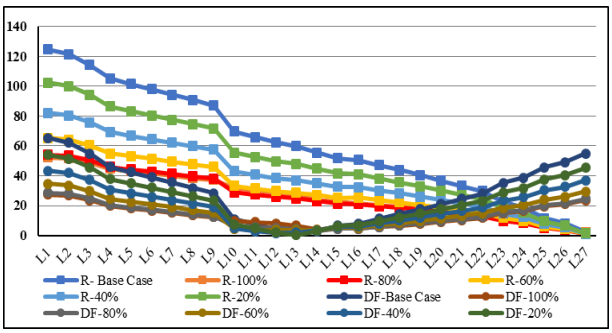


Figure 5. Loading of lines

Figure 4 shows the power losses for the two case studies with different levels of PV penetration. Because photovoltaic integration reduces the amount of power supplied by the network, it appears that the value of the losses is lowered. The scenario with 100% PV penetration in both case studies has the lowest value of losses.

Figure 5 illustrates how the loading decreases toward the end of the feeder and how the first five lines from the substation in the radial operation are overloaded by more than 100%. Following the addition of various PV plant penetration values, the line loading dropped below 100%. When PV penetration is between 100% and 80%, the lines are less burdened in radial operation. Conversely, in the ring DF operation, line loading was less than 60% in the base scenario without PV and line loading dropped below this value with different PV penetration sizes. In this type of configuration, the lines that are lightly loaded are the lines that are located in the middle of the feeder, while the lines that are close to the substations are more loaded compared to the others.

Discussion

The connection of high levels of PV generation in the existing DN has a technical and economic impact, and distribution operators have real challenges in properly planning network connections in order to have a sustainable DN. Changing the way of operation of the existing feeders from radial to ring DF configuration may require large capital investments, but it is a good way for existing DN's to welcome more value from PV penetration. The change in the value of the short-circuit currents and the harmonic distortion brought by the connection of these sources in this paper have not been analyzed.

Conclusion

This article analyzes the case of radial and ring DF topology with solar plants added at varying penetration scales from 0% to 100%. The analysis showed that the impact on the level of voltage, losses and loading of the lines was different for both types and depended a lot on the type of configuration. The conversion of the feeders from radial to DF configuration can be seen as a suitable solution to maintain the proper quality parameters in the network and increase the safety of the energy supply, hence welcoming the high value of the predictions for PV plants in the future.

References

1. Khail, A. A., & Polattaş, Z., "Building integration of solar energy systems in Türkiye and world.," Turkish Journal of Engineering, vol. 8, no. 2, pp. 341-352, 2024.
2. A. Yildiz, "Predicting the energy production of a rooftop pv plant by using differential evolution algorithm," Turkish Journal of Engineering, vol. 3, no. 3, pp. 106-109, 2019.
3. Kantoğlu, B., & Argun, İ. D., "Evaulation of renewable energy source alternatives prioritization," Turkish Journal of Engineering, vol. 7, no. 1, pp. 01-08, 2023.
4. Bayhan, B. Arslan, G., "Applicability of solar and wind energy technologies for a non-residential building," Turkish Journal of Engineering, vol. 2, no. 1, pp. 27-34, 2018.
5. Kececioglu O F, Gani A & Sekkeli M, "Improved HYBRID intelligent controller," Turkish Journal of Engineering, vol. 5, no. 1, pp. 20-28, 2021.
6. Temiz, R., & Tur, M. R. , "Investment technique for ensuring energy supply continuity in ring grids," Turkish Journal of Engineering, vol. 8, no. 2, pp. 186-195, 2024.

Advanced Engineering Days

aed.mersin.edu.tr

Designing PID Controller for Speed Control of Autonomous Vehicle by Utilizing Improved Grey Wolf Optimization Algorithm

Arman Nagizadeh [1], Amir A. Ghavifekr [1], Ayta Mollazadeh [1]

[1]University of Tabriz, Faculty Electrical and Computer Engineering, Iran, armanagizade18@gmail.com, aa.ghavifekr@gmail.com, ayta.mollazadeh@gmail.com

Cite this study: Naghizadeh, A., & Ghavifekr, A. A., & Mollazadeh, A. (2024). Designing PID Controller for Speed Control of Autonomous Vehicle by Utilizing Improved Grey Wolf Optimization Algorithm. Advanced Engineering Days, 9, 549-552

Keywords
Autonomous Vehicle
PID Controller
Grey Wolf Optimization
Speed Control

Abstract

In the field of autonomous vehicles, speed control is an important factor for providing efficient safety, and performance. This paper presents a novel approach to tune parameters of a Proportional-Integral-Derivative (PID) controller for regulation of speed in autonomous vehicles, utilizing the Improved Grey Wolf Optimization (IGWO) algorithm. The conventional Grey Wolf Optimization (GWO) algorithm, inspired by the social hierarchy and hunting strategies of grey wolves, has been improved to enhance convergence speed and optimization accuracy. Numerical results are provided to evaluate the performance of the IGWO-based PID controller against traditional methods. Results indicate noticeable improvements in terms of response time, and robustness under varying operational conditions and disturbances. This paper substantiates the potential of IGWO in advancing autonomous vehicle control systems, providing a reliable and efficient solution for real-time speed regulation.

Introduction

Electric vehicles represent an indispensable leap forward in sustainable transportation, reducing environmental pollution and providing cleaner energy solutions. In addition to their environmental benefits, electric vehicles also offer significantly lower maintenance costs compared to fuel-based vehicles. Safety is a key aspect of electric vehicles, and sensors play a crucial role in ensuring it. These sensors monitor battery conditions and detect collisions, contributing to the overall safety and reliability of electric vehicles [1].

Controllers in the context of electric vehicles are responsible for regulating and managing the behavior of other systems to achieve desired outcomes or maintain specified conditions. Within this array of control methodologies, Proportional-Integral-Derivative (PID) controllers have been widely employed in industrial process control settings and given better consideration due to their straightforward nature and proven effectiveness. For these matters they are commonly integrated into self-driving cars to regulate various aspects such as speed, steering, and braking, ensuring precise and reliable control [2]. They are commonly used in autonomous vehicles [3], DC motors [4], and underwater vehicles [5]. There are numerous tuning methods of PID controllers discussed in [6]. One of these methods is known as evolutionary algorithms (EAs) which are computational methods inspired by natural evolution. EAs have been used in numerous engineering application to provide more optimize results[7-10]. As utilizing PID controller requires a precise tuning and initialization of its parameters, EAs have been used for PIDs accurate tuning purposes[11, 12]. They solve optimization problems by generating and evolving a population of candidate solutions over successive generations, selecting the best ones to produce offspring. In [13] PID controllers have been utilized for Quadruped Robots applying Grey Wolf Optimization algorithm (GWO). The speed control of DC motors is accomplished by designing PID based on Particle Swarm Optimization (PSO) in [14].

In this manuscript, we aim to implement the improved Grey Wolf Optimization algorithm (IGWO) for the purpose of tuning the PID controller to control the speed of autonomous vehicles by minimizing the integral absolute error (IAE), integral square error (ISE), integral time absolute error (ITAE), and integral time-weighted square error (ITSE). We intend to assess and compare GWO with other tuning methods such as Ziegler-Nichols (ZN), Astrom-Hagglund (AH), Cohen-Coon (CC), and Chien-Hrones-Reswick (CHR).

Material and Method

The main difference between electric vehicles (EVs) and traditional fuel-based cars lies in their propulsion systems. The transfer function modeling of an electric vehicle encompasses a second-order system, considering vehicle parameters, and road conditions. The electric vehicle speed transfer function on a concrete road is outlined in [15] and is given by:

$$G(s) = \frac{0.913242}{1.39s^2 + 1.215s + 0.913242}$$

Grey Wolf Optimizer algorithm is an evolutionary algorithm based on how wolves search for prey in group [16]. To emulate the internal leadership hierarchy of wolves, they are categorized into four types: alpha, beta, delta, and omega. In Grey Wolf Optimizer (GWO), the hunting (optimization) process is directed by the alpha, beta, and delta wolves. Essentially, this means the optimization process follows the trajectory of the top three solutions. Additionally, the prey represents the optimal solution of the optimization. The majority of the logic is based on the following equations:

$$D = \left|\vec{C}.\overrightarrow{X_p} - \vec{X}(t)\right| \ , \ \vec{X}(t+1) = \overrightarrow{X_p}(t) - \vec{A}.\vec{D} \quad (1)$$

Where t denotes current iteration, $\vec{A}$ and $\vec{C}$ are coefficients vectors, $\vec{X}_p$ denotes the position vector of the prey, and $\vec{X}$ represents the position of the wolf. Vectors $\vec{A}$ and $\vec{B}$ are defined as:

$$\vec{A} = 2\vec{a}\,.\vec{r}_1 - \vec{a} \ , \ \vec{C} = 2\vec{r}_2 \quad (2)$$

Where components of $\vec{a}$ decrease linearly from 2 to 0 over iterations and $\vec{r}_1$, $\vec{r}_2$ are random vectors with values ranging from [0,1], recalculated for each wolf at each iteration. The vector $\vec{A}$ regulates the balance between exploration and exploitation, while $\vec{C}$ consistently introduces an element of randomness. We record the top three best solutions obtained so far and require the other search agents to update their positions based on the positions of these leading search agents. The following relations are proposed for this purpose:

$$\vec{D}_\alpha = \left|\vec{C}_1\,.\vec{X}_\alpha - \vec{X}\right| \ , \ \vec{D}_\beta = \left|\vec{C}_2\,.\vec{X}_\beta - \vec{X}\right| \ , \ \vec{D}_\delta = \left|\vec{C}_3\,.\vec{X}_\delta - \vec{X}\right| \quad (3)$$

$$\vec{X}_1 = \vec{X}_\alpha - \vec{A}_1.\vec{D}_\alpha \ , \ \vec{X}_2 = \vec{X}_\beta - \vec{A}_2.\vec{D}_\beta \ , \ \vec{X}_3 = \vec{X}_\delta - \vec{A}_3.\vec{D}_\delta \quad (4)$$

$$\vec{X}(t+1) = \frac{\vec{X}_1 + \vec{X}_2 + \vec{X}_3}{3} \quad (5)$$

Where $\vec{X}$ represents the current position of the agent, and $\vec{X}(t+1)$ denotes the updated position. The formula indicates that the wolf's position will be adjusted according to the positions of the top three wolves from the previous iteration [16]. The IGWO incorporates several enhancements to improve the algorithm's balance between exploration and exploitation, as well as its convergence speed. These modifications give IGWO greater adaptability, making it especially suitable for complex optimization problems that demand rapid convergence and effective global search. The updated position of all search agents using IGWO is as follows:

$$\vec{X}(t+1) = \frac{\alpha_{em}\vec{X}_1 + \beta_{em}\vec{X}_2 + \delta_{em}\vec{X}_3}{\alpha_{em} + \beta_{em} + \delta_{em}} \ , \ \alpha_{em} = i^3 \ , \ \beta_{em} = i^2 \ , \ \delta_{em} = i \quad (6)$$

Where $\alpha_{em} > \beta_{em} > \delta_{em}$ are called the emphasis coefficients. Given the significance of the alpha wolf position, our goal is to ensure the influence of the alpha is more than the beta, and the beta has more influence than the sigma. To achieve this, we present a different method than equation (5) where i represents our iteration number and emphasis coefficients are determined according to the equation (6). Notice that the time complexity of the algorithm is dependent on the number of iterations (50), agents (10), and size of the vectors. Pseudo code of the IGWO is shown the table 1.

Table 1. Pseudo code of the IGWO algorithm

Initialize the population of grey wolves randomly within the search space
Initialize an initial value A, C, and a
Calculate the fitness of each search agent
While (t < Max number of iterations) for each search agent
  Select $\boldsymbol{X_\alpha}$ = fittest wolf of the pack , $\boldsymbol{X_\beta}$ = second best wolf , $\boldsymbol{X_\delta}$ = third best wolf
  Update $\boldsymbol{\alpha_{em}}$, $\boldsymbol{\beta_{em}}$ **and** $\boldsymbol{\delta_{em}}$ by equation (6)
  For each search agent
    Update A, C and a
    Update the position of the current search agent by applying improve search strategy by equation (6)
  End for
  Calculate the fitness of all search agents
  t = t + 1
  End while
Update $\boldsymbol{X_\alpha}$, $\boldsymbol{X_\beta}$, $\boldsymbol{X_\delta}$
Return $\boldsymbol{X_\alpha}$

Our results are compared with Ziegler-Nichols (ZN) method [17], the Astrom-Hagglund (AH) method [18], Cohen-Coon (CC) method [19], and Chien-Hrones-Reswick (CHR) [20].

Results and Discussion

In PID controller IGWO optimization gives a better performance in comparison to other tuning methods such as ZN by minimizing IAE, ISE, ITAE and ITSE. These indices are defined as follows:

$$IAE = \int_0^T |e(t)|\,dt \;,\; ISE = \int_0^T |e^2(t)|\,dt \;,\; ITAE = \int_0^T T|e(t)|\,dt \;,\; ITSE = \int_0^T T|e^2(t)|\,dt \quad (7)$$

Table 2 shows specifications and performance indices of electric vehicle servo response using the PID tuning methods (ZN, AH, CC, CHR-1, CHR-2 and IGWO optimization). Different performance index in IGWO-based PID controllers (IGWO-PID) lead to different results, as demonstrated in Table 3.

Table 2. Performance indices using the PID tuning methods

PID tuning	OS%	T_s (sec)	T_r (sec)	IAE	ISE	ITAE	ITSE
IGWO	**0.0**	**0.06**	**0.02**	**0.015**	**0.01**	**0.3 e-3**	**0.23 e-3**
ZN	6.21	7.55	1.69	1.4	0.74	2.62	0.47
AH	15.4	12.1	2.03	2.25	1.17	6.64	1.17
CC	18.1	8.81	1.31	1.61	0.75	3.99	0.6
CHR-1	9.47	8.05	1.83	1.75	0.93	4.1	0.72
CHR-2	8.44	7.5	1.64	1.48	0.77	3.05	0.53

Table 3. PID parameters tuning results

Tuning method	K_p	K_i	K_d
IGWO (IAE)	**86.87**	**65.24**	**99.45**
ZN	0.612	0.587	0.213
AH	2.062	1.381	1.773
CC	2.071	2.792	3.66
CHR-1	3.209	3.557	4.814
CHR-2	3.542	5.304	7.196

Furthermore, Fig. 1 displays an example of how the PID parameters evolve during optimization, showing the convergence of the optimized solution. These parameters are obtained over 50 iterations. Our main goal is to implement IGWO for controlling the speed of electric vehicles by tuning PID controller, so we provide a sperate scheme in Fig. 2 . In Fig. 3 Closed loop servo response of electric vehicle speed control system with PID controller tuned by ZN, AH, CC, CHR-1 and CHR-2 is shown for comparison purposes [21].

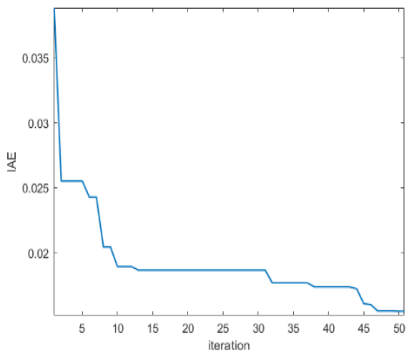


Figure 1. IAE evolution by applying IGWO algorithm

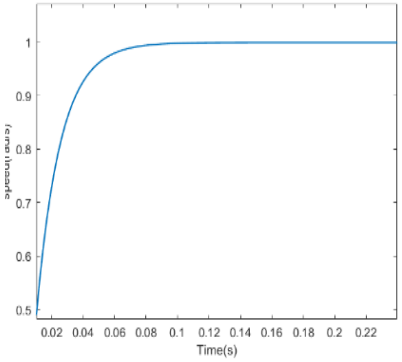


Figure 2. Electric vehicle speed control system with IGWO algorithm

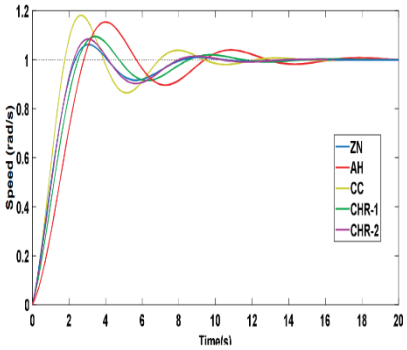


Figure 3. Electric vehicle speed control system with classic PID controller tuning methods [20]

Conclusion

The comparative analysis of our Improved Grey Wolf Optimization (IGWO)-based PID controller with the Ziegler-Nichols (ZN), Astrom-Hagglund (AH), and Cohen-Coon (CC) methods underscores the superiority of the proposed approach in speed control for autonomous vehicles. While the ZN and AH methods are well-regarded for their practical application and effectiveness, our IGWO algorithm demonstrates enhanced performance metrics, including faster response times, greater stability, and superior robustness under varying operational conditions and disturbances. The CC method, known for its simplicity and ease of implementation, remains a viable option for practitioners seeking straightforward solutions. However, despite its practical advantages and capability to

yield effective control system performance, the IGWO algorithm outperforms it by optimizing the PID parameters more precisely, leading to better overall control dynamics. Our findings highlight the potential of the IGWO algorithm to revolutionize PID controller design for autonomous vehicle speed control.

References

1. Hossain, M., et al., *Advancements and future prospects of electric vehicle technologies: a comprehensive review.* Complexity, 2022. 2022(1): p. 3304796.
2. Sahputro, S.D., *Design and implementation of adaptive PID controller for speed control of DC motor*, in *International Symposium on Electrical and Computer Engineering. IEEE, 2017*. 2017.
3. Vartika, V., *A review on intelligent PID controllers in autonomous vehicle.* Advances in Smart Grid Automation and Industry 4.0: Select Proceedings of ICETSGAI4. 0 (2021): 391-399.2021 ,.
4. Kushwah, M., and Ashis Patra, *Tuning PID controller for speed control of DC motor using soft computing techniques-A review.* Advance in Electronic and Electric Engineering 4.2 (2014): 141-148.2014 ,.
5. Sarhadi, P., Abolfazl Ranjbar Noei, and Alireza Khosravi, *Model reference adaptive PID control with anti-windup compensator for an autonomous underwater vehicle.* Robotics and Autonomous Systems 83 (2016): 87-93.2016 ,.
6. Borase, R.P., et al., *A review of PID control, tuning methods and applications.* International Journal of Dynamics and Control, 2021. **9**: p. 818-827.
7. Ghavifekr, A.A., *Application of heuristic techniques and evolutionary algorithms in microgrids optimization problems.* Microgrids: Advances in Operation, Control, and Protection, 2021: p. 219-251.
8. Harati, M., A.A. Ghavifekr, and A.R. Ghiasi. *Model Identification of Single Rotary Inverted Pendulum Using Modified Practical Swarm Optimization Algorithm*. in *2020 28th Iranian Conference on Electrical Engineering (ICEE)*. 2020. IEEE.
9. Abriz, A.F., et al. *Modified Cuckoo Optimization Algorithm for Frequency Regulation of Microgrids*. in *2023 8th International Conference on Technology and Energy Management (ICTEM)*. 2023. IEEE.
10. Tavana, A., et al. *A GOA-Optimized Visible Light Communication System For Indoor High-Precision 3-D Positioning Service*. in *2023 9th International Conference on Control, Decision and Information Technologies (CoDIT)*. 2023. IEEE.
11. Ziamanesh, S., et al., *Optimizing PID Controller Coefficients Using an Improved Biogeography-Based Optimization to Stabilize Movements of Quadcopters*, in *Control, Instrumentation and Mechatronics: Theory and Practice*. 2022, Springer. p. 118-131.
12. Salimi, H., et al. *Modified Grey Wolf Optimization Method for Voltage and Frequency Control of an Islanded Microgrids*. in *2021 11th Smart Grid Conference (SGC)*. 2021. IEEE.
13. ŞEN, M.A., and Mete KALYONCU, *Optimal tuning of PID controller using grey wolf optimizer algorithm for quadruped robot.* Balkan Journal of Electrical and Computer Engineering 6.1 (2018): 29-35, 2018.
14. El-Gammal, A.A., and Adel A. El-Samahy, *A modified design of PID controller for DC motor drives using Particle Swarm Optimization PSO.* 2009 international conference on power engineering, energy and electrical drives. IEEE, 2009.2009 ,.
15. Poorani, S., Kumar, K.U. and Renganarayanan, S, *Design of a fuzzy-based controller for electric vehicles on Indian roads.* Proceedings of the Institution of Mechanical Engineers, Part I: Journal of Systems and control enomeerino. vol. 22..no. 1. 0n.o -14. reb. 2007, 2007.
16. Mirjalili, S., Seyed Mohammad Mirjalili, and Andrew Lewis, *Grey wolf optimizer.* Advances in engineering software 69 (2014): 46-61, 2014.
17. Åström, K.J., and Tore Hägglund, *Revisiting the Ziegler–Nichols step response method for PID control.* Journal of process control 14.6 (2004): 635-650, 2004.
18. Hang, C.C., K. J. Astrom, and Q. G. Wang, *Relay feedback auto-tuning of process controllers—a tutorial review.* Journal of process control 12.1 (2002): 143-162., 2002.
19. Joseph, E.A., and O. O. Olaiya, *Cohen-coon PID tuning method; A better option to Ziegler Nichols-PID tuning method.* ENginerring Research 2.11 (2017): 141-145., 2017.
20. Hambali, N., et al. *Process controllability for flow control system using Ziegler-Nichols (ZN), Cohen-Coon (CC) and Chien-Hrones-Reswick (CHR) tuning methods*. in *2014 IEEE International Conference on Smart Instrumentation, Measurement and Applications (ICSIMA)*. 2014. IEEE.
21. George, M.A. and D.V. Kamath. *Design and tuning of fractional order pid (fopid) controller for speed control of electric vehicle on concrete roads*. in *2020 IEEE International Conference on Power Electronics, Smart Grid and Renewable Energy (PESGRE2020)*. 2020. IEEE.

Advanced Engineering Days

aed.mersin.edu.tr

Enhancing Distribution Network Resilience by Integration Renewable Energy Sources and Energy Storage

Sina Roudnil[1], Kasra Shafiei [1], Saeid Ghassem Zadeh [*1]

[1]University of Tabriz, Faculty of Electrical and Computer Engineering, Iran, sinaroudnil@tabrizu.ac.ir, k.shafiei@tabrizu.ac.ir, g_zadeh@tabrizu.ac.ir

Cite this study: Roudnil, Sina; Shafiei, Kasra; Ghassem Zadeh, Saeid. (2024). Enhancing Distribution Network Resilience By Integration Renewable Energy Sources and Energy Storage. Advanced Engineering Days, 9, 553-556

Keywords
Power system resilience
Energy Storage System (ESS)
Renewable Energy Source (RES)
Power distribution network

Abstract

The increasing number of extreme events has highlighted the need to enhance the resilience of power distribution networks. This paper investigates the integration of Renewable Energy Source (RES) and Energy Storage System (ESS) to enhance the resilience of distribution networks. An integrated system utilizing photovoltaic panels, wind turbines, and batteries within a DC microgrid is simulated over 24 hours, focusing on the agricultural sector's energy demands. The results indicate that the combined use of RES and ESS significantly enhances the resilience metric to 92.13%, ensuring a higher percentage of demand is supplied during disruptions compared to using RES alone. This study underscores the critical role of ESS in mitigating the variability of RES and maintaining power delivery during outages, highlighting the potential for improved power distribution network resilience under critical conditions.

Introduction

In recent years, events such as severe weather, and cyber-physical attacks that cause outages in the power system and affect large numbers of customers have increased significantly [1]. To address this issue, increasing the penetration of Renewable Energy Sources (RESs) can partially compensate lost energy by providing alternative power supplies. However, the weather-dependent variability of these sources escalates uncertainties in the planning and operation of power systems [2]. Therefore, Energy Storage Systems (ESSs) are employed to reduce these uncertainties [3]. Recently, intelligent methods and evolutionary algorithms have been utilized to cover optimization problems in RES and energy storage [4 - 7] . Consequently, integrating RES and ESS in power systems is considered a measure to prepare system against extreme events and improve resilience [8]. In this regard, [9] proposed a resilience-oriented optimization for ESS and RES operations to supply loads, prioritizing economic goals during outages. Furthermore, the combination of Demand Response (DR) programs and ESS is considered for minimizing Distributed Energy Resource (DER) operation costs [10]. In line with these studies, attention has been paid to issues such as electric vehicles to the grid [11], a combination of hydrogen and electrical energy storage systems [12], Fuel Cell model [13], coordinating energy resources [14], New multilevel inverter for high voltage levels [15], and a converter with coupled inductor and low voltage [16] to energy management and improve resilience. However, most of this research focuses on the economic performance of using RES and ESS, which may not be suitable for ensuring system resilience under critical conditions. Thus, an approach for integrating RES and ESS in a distribution network is presented in this paper to enhance distribution network resilience. To validate this approach, a 24-hour simulation is conducted on the DC microgrid model given by [17], as shown in Figure 1. This model consists of RES (photovoltaic panels and wind turbines), ESS (battery), Load (agriculture sector demand), and distribution network.

Material and Method Introduction

The proposed framework begins by integrating the proportions of RESs penetration with generation units. Then, solutions evolve from on common rules of Genetic Algorithm (GA), and the entire process restarts. Optimization stops when function tolerance drops below a certain threshold. The following formula is used to calculate the production of wind farms when wind speed variations are considered [18]:

$$P_{wt}(v)=\begin{cases}0 & if\ v<V_{ci}\\ P_R & if\ V_{ci}<v<V_{co}\\ 0 & if\ V_{co}<v\end{cases} \quad (1)$$

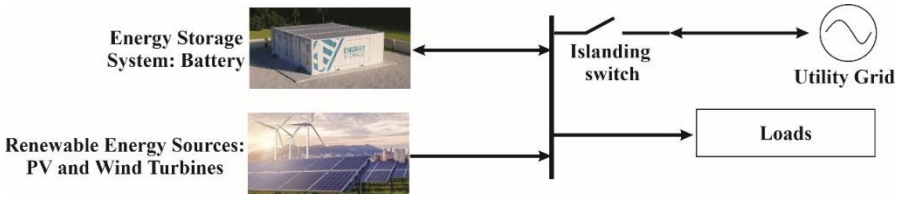


Figure 1 Simulation model power flow

where P_R is the rated capacity of the wind farm; V_{ci}, V_r and V_{co} are cut-in, rated and cut-out wind speed, respectively. The solar radiation intensity and cell temperature determine the photovoltaic array's output power. Eq. (2) describe calculating PV output power using the specified parameters [19].

$$P_{pv}=N_p\times FF\times V_i\times I_i \quad (2)$$

Where Np is number of photovoltaic panels; FF is fill-factor; V_i and I_i are voltage and current of the photovoltaic panels, respectively. This research considers generation units and wind turbine and PV power plants as RES. Furthermore, energy storage is used that can be charged and discharged at different times of the day and night. We present the generation unit function in the section that follows:

$$f_{\text{Total Generation}}=\left\{P_{\text{Traditional Generation}}(1-\alpha)\right\} \quad (3)$$

$$\alpha=\frac{P_{Wind}+P_{Pv}}{P_{Traditional\ Generation}} \quad (4)$$

Eq. (5) defines the generation of energy storage units, electronic power equipment, and network connections, as well as the associated with charging and discharging energy.

$$f_{Battery}=\left\{P_{\text{charge/discharge}}\times t\right\} \quad (5)$$

Each generation unit has a low and high-power generation limit that is determined by Eq. (6) based on its technology and capacity.

$$P_{Gen}^{\min}\le P_{Gen}\le P_{Gen}^{\max} \quad (6)$$

Each unit's generation can only rise or fall for a maximum of two hours in a row. The following equation is used to define this constraint:

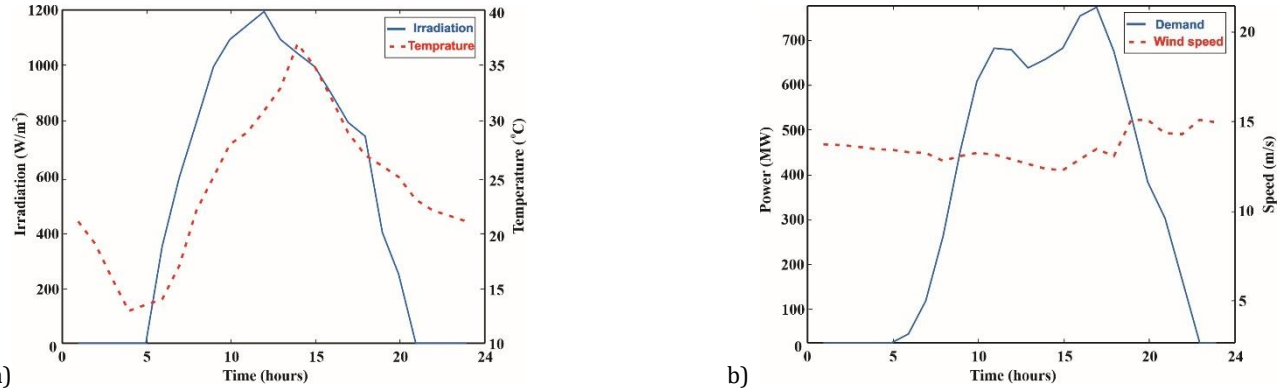
$$\left|P_t-P_{t-1}\right|\le Ramp \quad (7)$$

Results

The proposed method is simulated in the studied microgrid (Figure 1). PV temperature, and irradiation data, demand, and wind speed are shown in Figure 2 according to [19].

In this study, it is assumed that between 9:00 and 15:00, an event in the distribution system interrupts the connection to the upstream network, causing a loss of a part of the power. As a result, part of the demand is unsupplied during this period and in the following hours. Using the proposed energy management method, the microgrid maximizes RES generation, and the resilient performance of the energy storage system makes more energy available. Figure 3 shows the system resilience curve based on the percentage of demand supplied over 24 hours, illustrating the impact of using RES and ESS. Before 9:00, when there is no event in the upstream network, the system operates normally, with the upstream network participating in power flow with maximum capacity and all loads being supplied. During the event between 9:00 and 15:00, the system faces a power shortage due to the unavailability of part of the upstream grid power, resulting in decreased resilience. However, using RES and the resilient performance of ESS ensures a higher percentage of demand is supplied, resulting in a higher resilience

curve. This situation persists in the following hours. After the upstream network reconnects at 16:00, it takes some time to restore the full power supply, and the network returns to its initial function by 23:00.



a) b)

Figure 2. a) Irradiation and Temperature, b) demand and wind speed

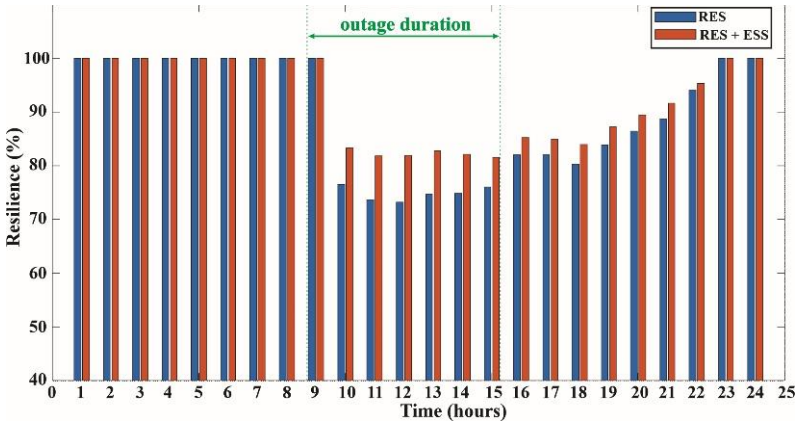


Figure 3. Resilience curve comparing the use of RES and ESS in the distribution network

Discussion

Figure 3 shows that the resilience curve has a higher value when using RES and ESS, this value is 100% in non-event case. The calculated resilience metric which is equal to the area of the curve shows that with the use of RES and ESS, the resilience value for 24 hours is 92.13%., inn contrast, in the conventional case where only RES is used, it is 89.42%. This comparison demonstrates the improvement in resilience when both RES and ESS are utilized.

Conclusion

This study highlights the crucial role of integrating RES and ESS in enhancing the resilience of power distribution networks. A 24-hour simulation of a DC microgrid showed that combining RES and ESS improves resilience metric, ensuring better power supply during outages compared to using RES alone. The findings underscore the need for ESS to mitigate the variability of RES, ensuring a high level of power delivery during critical conditions. Future research should focus on optimizing these systems and exploring their economic impacts and additional technologies.

References

[1] A. B. (2024). Smith, 'U.S. Billion-dollar Weather and Climate Disasters, 1980 - present (NCEI Accession 0209268). [indicate subset used].', *NOAA National Centers for Environmental Information. Dataset.*, 2024.

[2] L. Xu *et al.*, 'Resilience of renewable power systems under climate risks', *Nat. Rev. Electr. Eng.*, vol. 1, no. 1, pp. 53–66, 2024, doi: 10.1038/s44287-023-00003-8.

[3] S. Chen, Z. Li, and W. Li, 'Integrating high share of renewable energy into power system using customer-sited energy storage', *Renew. Sustain. Energy Rev.*, vol. 143, p. 110893, 2021, doi: https://doi.org/10.1016/j.rser.2021.110893.

[4] A. G. Hanizi and A. A. Ghavifekr, 'An Innovative Method for Converting Solar Thermal Energy into Electrical Power', in *2023 13th Smart Grid Conference (SGC)*, 2023, pp. 1–6. doi: 10.1109/SGC61621.2023.10459280.

[5] A. F. Abriz, A. A. Ghavifekr, M. Soltaninejad, A. Tavana, A. Safari, and S. Ziamanesh, 'Modified Cuckoo Optimization Algorithm for Frequency Regulation of Microgrids', in *2023 8th International Conference on Technology and Energy Management (ICTEM)*, 2023, pp. 1–5. doi: 10.1109/ICTEM56862.2023.10083797.
[6] H. Salimi, A. A. Ghavifekr, A. Mohammadzadeh, S. Ziamanesh, A. Tavaana, and S. H. Dizaji, 'Modified Grey Wolf Optimization Method for Voltage and Frequency Control of an Islanded Microgrids', in *2021 11th Smart Grid Conference (SGC)*, 2021, pp. 1–5. doi: 10.1109/SGC54087.2021.9664048.
[7] A. A. Ghavifekr, A. Mohammadzadeh, and J. F. Ardashir, 'Optimal Placement and Sizing of Energy-related Devices in Microgrids Using Grasshopper Optimization Algorithm', in *2021 12th Power Electronics, Drive Systems, and Technologies Conference (PEDSTC)*, 2021, pp. 1–4. doi: 10.1109/PEDSTC52094.2021.9405951.
[8] N. Manoj Kumar, A. Ghosh, and S. S. Chopra, 'Power Resilience Enhancement of a Residential Electricity User Using Photovoltaics and a Battery Energy Storage System under Uncertainty Conditions', *Energies*, vol. 13, no. 16. 2020. doi: 10.3390/en13164193.
[9] J. Tobajas, F. Garcia-Torres, P. Roncero-Sánchez, J. Vázquez, L. Bellatreche, and E. Nieto, 'Resilience-oriented schedule of microgrids with hybrid energy storage system using model predictive control', *Appl. Energy*, vol. 306, no. PB, p. 118092, 2022, doi: 10.1016/j.apenergy.2021.118092.
[10] S. Rahgozar, A. Zare Ghaleh Seyyedi, and P. Siano, 'A resilience-oriented planning of energy hub by considering demand response program and energy storage systems', *J. Energy Storage*, vol. 52, no. PB, p. 104841, 2022, doi: 10.1016/j.est.2022.104841.
[11] L. Mauricette, Z. Dong, L. Zhang, X. Zhang, N. Zhang, and G. Strbac, 'Resilience Enhancement of Urban Energy Systems via Coordinated Vehicle-to-grid Control Strategies', *CSEE J. Power Energy Syst.*, vol. 9, no. 2, pp. 433–443, 2023, doi: 10.17775/CSEEJPES.2022.05270.
[12] S. M. A. Hashemifar, M. Joorabian, and M. S. Javadi, 'Two-layer robust optimization framework for resilience enhancement of microgrids considering hydrogen and electrical energy storage systems', *Int. J. Hydrogen Energy*, vol. 47, no. 79, pp. 33597–33618, 2022, doi: 10.1016/j.ijhydene.2022.07.255.
[13] S. Roudnil; S. Gassemzadeh, 'Real-time Control and Management of a Microgrid, with Dispersed Generation Resources, Utilizing a Integrated Proton Exchange Membrane Fuel Cell Model', *TABRIZ J. Electr. Eng.*, 2024, doi: 10.22034/tjee.2024.58080.4696.
[14] L. Jia, S. Pannala, G. Kandaperumal, and A. Srivastava, 'Coordinating Energy Resources in an Islanded Microgrid for Economic and Resilient Operation', *IEEE Trans. Ind. Appl.*, vol. 58, no. 3, pp. 3054–3063, 2022, doi: 10.1109/TIA.2022.3154337.
[15] A. Seifi, S. H. Hosseini, M. T. Hagh, and M. Hosseinpour, 'New multilevel inverter based on reduced switch basic cell for high voltage levels', *IET Power Electron.*, vol. 17, no. 4, pp. 551–563, 2024, doi: 10.1049/pel2.12673.
[16] A. Nadermohammadi, M. Maalandish, A. Seifi, P. Abolhassani, S. H. Hosseini, and M. Farsadi, 'A non-isolated single-switch ultra-high step-up DC–DC converter with coupled inductor and low-voltage stress on switch', *IET Power Electron.*, vol. 17, no. 2, pp. 251–265, 2024, doi: 10.1049/pel2.12633.
[17] F. S. Al-Ismail, 'DC Microgrid Planning, Operation, and Control: A Comprehensive Review', *IEEE Access*, vol. 9, pp. 36154–36172, 2021, doi: 10.1109/ACCESS.2021.3062840.
[18] K. Shafiei, M. Tarafdar Hagh, and A. Seifi, 'Integration of wind farm, energy storage and demand response for optimum management of generation and carbon emission', *J. Eng.*, vol. 2024, no. 1, pp. 1–8, 2024, doi: 10.1049/tje2.12348.
[19] K. Shafiei, S. G. Zadeh, and M. T. Hagh, 'Planning for a network system with renewable resources and battery energy storage, focused on enhancing resilience', *J. Energy Storage*, vol. 87, p. 111339, 2024, doi: https://doi.org/10.1016/j.est.2024.111339.

Advanced Engineering Days

aed.mersin.edu.tr

sEMG based Hand Gesture Recognition via Simple Feature Extraction and LSTM Model

Ramin Soleimani [1], Saeed Meshgini [1], Mohammad Reza Sayyed Noorani [*2]

[1]*University of Tabriz, Department of Medical Engineering, Iran, r.soleimani@tabrizu.ac.ir, meshgini@tabrizu.ac.ir*
[2]*University of Tabriz, Department of Mechatronics Engineering, Iran, smrs.noorani@tabrizu.ac.ir*

Cite this study: Soleimani, R., Meshgini, S., & Sayyed Noorani, M. R. (2024). sEMG based Hand Gesture Recognition via Simple Feature Extraction and LSTM Model. Advanced Engineering Days, 9, 557-560

Keywords
Pattern Recognition
Electromyography
Feature Extraction
LSTM Model
Hand Gesture

Abstract

The hand gesture recognition based on sEMG (surface electromyography) is practically considered a pattern classification problem in which a supervised model is learned using a large amount of labeled sEMG signals. This model is used to detect the user's intention in performing voluntary movements merely through reflections of muscle activities collected via a Muscle-Computer Interface. Feature extraction and the architecture of the neural network used as the model are two important challenges that have widely been studied. In this context, we propose a novel model in which feature extraction method, done in the frequency domain, possesses a low computational cost yet a high accuracy. Additionally, a LSTM network is utilized as the model employed for the classification of hand gestures by forearm muscle EMG signals. To train and evaluate the proposed model, we exploit from the publicly available CapgMyo dataset. The model has been trained in MATLAB. The results are presented in the form of confusion matrices of train and test. As a superior result we achieved 100% accuracy when all 128 channels of sEMG were used for training. Moreover, even when a much smaller number of channels are used, this model can still provide high accuracy.

Introduction

MCI (Muscle-Computer Interface) has become a bold paradigm in the field of bionic and rehabilitation robotics. Machine Learning (ML) plays a key role in this context, which utilized to establish a map between the sEMG signals, considered as information conveying main features of functional body movements [1-2]. Real-time classification of sEMG signals is one of the obvious nowadays challenges of this area, for example, it has been investigated for controlling a prosthetic hand [3-5].

Surface electromyography is a technique for recording electrical activations of skeletal muscles by means of nonimplanted electrodes placed on the surface of the skin. These electrical activations are resulted of neurophysiological in nature and exhibit obvious individual differences [6]. The EMG signal is a linear combination of several trains of motor unit action potentials (MUAPs), which are produced when a skeletal muscle is contracted. Therefore, we can expect that in performing any specific movement, the sEMG signals of the involved muscles collectively create an almost exclusive pattern of their activations that corresponds to the same movement. Thus, we say that there is a map between the sEMG signals and the body movement. The purpose in the sEMG-based hand gesture recognition is to discover this map between the sEMG signals recorded from the forearm muscles and the hand gestures formed by wrist and finger configurations.

Classification is a major branch of ML in which each input data is assigned to one of a discrete number of classes. From this viewpoint, hand gesture recognition can be considered a classification problem in which sEMG patterns are assigned to classes labeled according to gestures of the hand. There are two essential issues in the classification of EMG signals. First, how many channels are enough to obtain comprehensive information from the responsible muscles contributing to hand gestures? In other words, which are the major muscles from which EMGs must be acquired? Second, EMG signals are, in fact, univariate time series, and algorithms are needed to extract their local and global features, known as feature extraction algorithms, which is a challenging research topic.

Material and Method

Recurrent neural networks (RNN), especially long short-term memory (LSTM) networks, are able to encode the temporal relations from (long) sequential data. Hence, as a superior model they have been applied to analyze sEMG signals for hand movements prediction [7], hand forces estimation [8-9], and hand gestures classification [10-14]. We also exploit a LSTM network to recognize hand gestures, which, after the input layer, is constructed from five layers including *lstm*, *dropout*, *fully connected*, *softmax*, and *output*. This network is, in fact, a multilayer LSTM (set to 100) in which the output is classified with the *softmax*. We utilized the vanilla version for our LSTM structure, which has three gates, a block input, a block output, and a memory cell.

Feature extraction plays the key role in our study. Generally, features of EMG signals are extracted in one of three domains: time, frequency or time-frequency. Hudgin's descriptors, autoregressive (AR) model, and RMS are common features of the time domain that are widely studied in researches. Wavelet analysis is the most common approach for feature extraction in the time-frequency domain. Both of these suffer from computational complexity, which limits their usefulness in real-time applications. On the other hand, Fast Fourier Transform (FFT) algorithm is a low-cost computational method for feature extraction in the frequency domain and has received less attention than time domain methods. Hence, we exploit the FFT algorithm to obtain a set of simple and beneficial features from sEMG signals. Specially, we investigated our proposed method on a publicly available dataset, CapgMyo.

The CapgMyo includes several collections of high-density sEMG signals, from which we used the DB-a dataset. The CapgMyo DB-a has consisted of recordings of 8 finger gestures. Each gesture was held for 3 to 10 seconds, followed by 7 seconds of rest. The set of gestures was recorded 10 times by each subject. The 8 acquisition modules were wrapped around the right forearm and formed an 8 × 16 electrode array. Subjects sat comfortably in an office chair and rested their arms on a desktop. Before donning the devices, the skin of the forearms had been cleaned with alcohol. The imitation stimulus was visual. The subjects were asked to mimic a video of hand gestures shown on the screen with their right hand. The video was then used to generate a label for each sample [15]. The CapgMyo is available at http://zju-capg.org/myo.

In our work, for each subject, we had 80 arrays of 1000×128 corresponding to 8 gestures recorded for 10 trials. In the first stage, for each test in which one gesture had been performed, we calculated the FFT of all 128 leads to obtain early information in the frequency domain. Then, knowing the sampling frequency of 1000 Hz, we divided the whole of frequency spectrum into 9 parts that marked at [0, 20, 40, 60, 80, 100, 200, 300, 400, 500] and by averaging within each interval a 9-value feature is extracted for each lead. In this way, for each test (a gesture as the target of classification) we achieved an array of 128×9 as the features should to be fed to the classifier network. It is, in fact, a two-dimensional input. The whole of the process is illustrated in Fig. 1.

The anatomy of the forearm muscles is very complicated, with layers of muscles crossing in many directions [16]. A high-density sEMG can help capture the details of the forearm muscle activities as much as possible; however, involves redundancy problem and extra calculations. Hence, in the next stage, we examine the effect of eliminating of some leads on the training quality. Thus, the size of the array containing the features which fed as input reduces to N×9, where N indicates the number of selected leads.

Results

We structured and trained this model in MATLAB and ran it on the GPU of an NVIDIA GeForce GTX 1050 Ti 4GB in a Windows-based PC. The ratio of the train-test samples was set at 0.7 and shuffled in each epoch. Four arranges for the selection of leads have been examined including picking all 128 leads, picking in steps of 8 (totally 16 leads), picking in steps of 16 (totally 8 leads), and picking the first 8 leads orderly. In Fig. 2 the accuracy of the classification is evaluated for each arrangement via confusion matrices of the train and test samples. As is obvious, the accuracy of both train and test samples has been 100% when all leads have considered for feature extraction. Furthermore, by reducing the number of leads in steps of 8 and 16 the accuracy is acceptable compared with other researches.

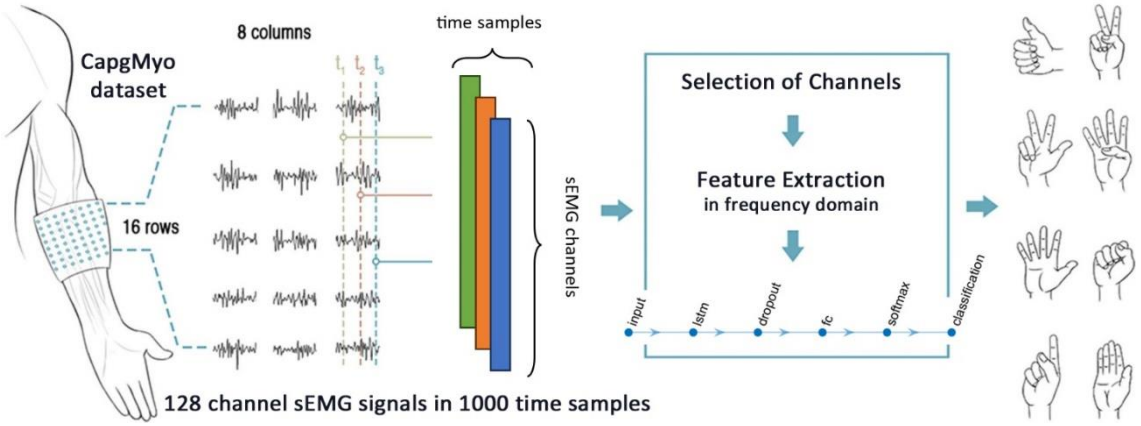


Figure 1. Machine Learning as a tool for mapping the sEMG signals to body movements (e.g. hand gestures) [15].

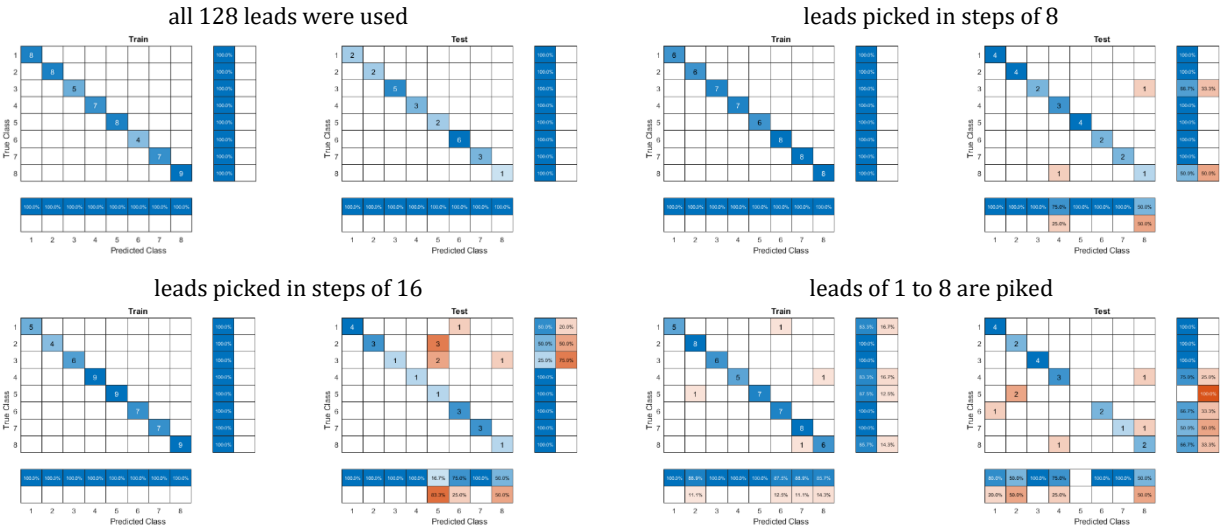


Figure 2. The confusion matrix for the train and test samples

Conclusion

In this paper we addressed to extract features and construct a LSTM network for classifying hand gestures. Our method has been evaluated on the public EMG datasets of CapgMyo DB-a. The feature extraction performed in frequency domain based on a simple process on Fourier transform of channels of the recorded signals in dataset. Our results showed that although the accuracy of 100% may be achieved when all 128 channels of EMG are applied, much smaller number of them can also be sufficient to make an accurate classification. Also, the performance of the proposed LSTM network was superior even when only one type of features is exploited for training. Simplicity and computational efficiency make this method suitable for implementing on onboard processors of prostheses.

References

1. Jia, G., Lam, H. K., Liao, J., & Wang, R. (2020). Classification of electromyographic hand gesture signals using machine learning techniques. *Neurocomputing*, 401, 236-248.
2. Jaramillo-Yánez, A., Benalcázar, M. E., & Mena-Maldonado, E. (2020). Real-time hand gesture recognition using surface electromyography and machine learning: A systematic literature review. *Sensors*, 20(9), 2467.
3. D'Accolti, D., Clemente, F., Mannini, A., Mastinu, E., Ortiz-Catalan, M., & Cipriani, C. (2023). Online classification of transient EMG patterns for the control of the wrist and hand in a transradial prosthesis. *IEEE Robotics and Automation Letters*, 8(2), 1045-1052.
4. Azhiri, R. B., Esmaeili, M., & Nourani, M. (2021, December). Real-time emg signal classification via recurrent neural networks. *In 2021 IEEE International Conference on Bioinformatics and Biomedicine (BIBM)* (pp. 2628-2635). IEEE.
5. Jiralerspong, T., Nakanishi, E., Liu, C., & Ishikawa, J. (2017). Experimental study of real-time classification of 17 voluntary movements for multi-degree myoelectric prosthetic hand. *Applied sciences*, 7(11), 1163.
6. Sun, B., Song, B., Lv, J., Chen, P., Sun, X., Ma, C., & Gao, Z. (2023). A multi-scale feature extraction network based on channel-spatial attention for electromyographic signal classification. *IEEE Transactions on Cognitive and Developmental Systems*, 15(2), 591-601.
7. García-Vellisca, M. A., Matran-Fernandez, A., Poli, R., & Citi, L. (2021, March). Hand-movement prediction from EMG with LSTM-recurrent neural networks. *In 2021 Global Medical Engineering Physics Exchanges/Pan American Health Care Exchanges (GMEPE/PAHCE)* (pp. 1-5). IEEE.
8. Olsson, A. E., Malešević, N., Björkman, A., & Antfolk, C. (2021). End-to-end estimation of hand-and wrist forces from raw intramuscular emg signals using LSTM networks. Frontiers in Neuroscience, 15, 777329.
9. Jabbari, M., Khushaba, R. N., & Nazarpour, K. (2020, July). EMG-based hand gesture classification with long short-term memory deep recurrent neural networks. *In 2020 42nd Annual International Conference of the IEEE Engineering in Medicine & Biology Society (EMBC)* (pp. 3302-3305). IEEE.
10. Karnam, N. K., Dubey, S. R., Turlapaty, A. C., & Gokaraju, B. (2022). EMGHandNet: A hybrid CNN and Bi-LSTM architecture for hand activity classification using surface EMG signals. *Biocybernetics and biomedical engineering*, 42(1), 325-340.
11. Simão, M., Neto, P., & Gibaru, O. (2019). EMG-based online classification of gestures with recurrent neural networks. *Pattern Recognition Letters*, 128, 45-51.

12. Huang, D., & Chen, B. (2019, September). Surface EMG decoding for hand gestures based on spectrogram and CNN-LSTM. *In 2019 2nd China Symposium on Cognitive Computing and Hybrid Intelligence (CCHI)* (pp. 123-126). IEEE.
13. Bittibssi, T. M., Genedy, M. A., & Maged, S. A. (2021). sEMG pattern recognition based on recurrent neural network. *Biomedical Signal Processing and Control*, 70, 103048.
14. Toro-Ossaba, A., Jaramillo-Tigreros, J., Tejada, J. C., Peña, A., López-González, A., & Castanho, R. A. (2022). LSTM recurrent neural network for hand gesture recognition using EMG signals. *Applied Sciences*, 12(19), 9700.
15. Geng, W., Du, Y., Jin, W., Wei, W., Hu, Y., & Li, J. (2016). Gesture recognition by instantaneous surface EMG images. *Scientific reports*, *6*(1), 36571.
16. Sayyed Noorani, M.R., Mortezazadeh, F., Sabbaghi, A. (2024). An Electromyography Recording and On-Line Driving System for a Robotic Wrist. *Transactions on Machine Intelligence*, 7(1), 72-81.

Advanced Engineering Days

aed.mersin.edu.tr

IMU-based Movement Control of Robotic Manipulators – Aided by CoppeliaSim

Alireza Ashrafi Majd [1], Mohammad Reza Sayyed Noorani [*1]

[1]University of Tabriz, Department of Mechatronics Engineering, Iran, ashrafimajd.alireza@gmail.com, smrs.noorani@tabrizu.ac.ir

Cite this study: Ashrafi Majd, A., & Sayyed Noorani, M. R. (2024). IMU-based Movement Control of Robotic Manipulators - Aided by CoppeliaSim. Advanced Engineering Days, 9, 561-564

Keywords
IMU-based Control
Robotic Manipulator
Computer Simulation
CoppeliaSim Software
Trajectory Generation

Abstract

The growing need for advanced robotic systems that have the ability to interact with humans in dynamic and unstructured environments shows the necessity of using strong and reliable control strategies. This paper investigates a movement control strategy for manipulator robots that uses data collected by Inertial Measurement Unit (IMU) sensors. Our setup consists of two parts of hardware and software. An IMU module embedded in an Arduino UNO board provides the movement sensory data that passed to Python through serial communication. The main purpose is that a movement performed by human to be imitated by a robotic manipulator. So, by using Python API in CoppeliaSim, an integrated framework is developed which receives the sensory data from IMU module and processes signals via Kalman Filter, and by solving the inverse kinematics problem, finally, produces the joint trajectories as commands to issue to a simulated robotic arm created in CoppeliaSim software. Experimental validation in the CoppeliaSim simulator environment shows the effectiveness of the proposed control strategy, such that the robot consistently achieves the desired movement paths with minimum error. Our research significantly contributes to the advancement of manipulator robot control, especially in the field of Industry 4.0 applications.

Introduction

From the first dreams in science fiction stories to the fabrication of the first industrial robots, the discussion on security and the way humans and robots interact has always been in the focus of researchers in the field of robotics and automation. Significant advances in the design and construction of robots have created new challenges about human-robot interaction. Entering the era of the industry 4.0, which is founded on smartization, Internet of Things (IoT) and telecommunications, the need to develop smarter, faster and more efficient algorithms to ensure safe and reliable human-robot interaction is felt more than ever [1]. Recognizing the user's intention, specially his/her movement intention, is very essential in human-robot interaction. Several techniques for this purpose including methods based on processing biosignals such as EMG [2] and EEG [3], eye movement tracking [4], physical contact interaction [5], as well as IMU-based movement tracking [6-7], have been developed. Utilizing the IMU sensors for intention detection and movement imitation between human and robot is practically low-cost and high-efficient. Sanchez et.al [8] presented a comparison between RGB-D (as a vision-based) and IMU-based (as a wearable-based) gesture recognition approaches for human-robot interaction. The superiority of IMU based motion tracking is due to its light weight, low cost and less power consumption.

Hence, in this article we investigate the IMU-based movement control of a robotic manipulator evaluated aided by CoppeliaSim robot simulator software. Particularly, we utilize the ABB IRB 4600-40-255 robotic arm model as the manipulator, which imitates the movements experienced by an IMU module moved by the human user's hand. In detail, using an integrated framework developed by Python programming language, the input data are received through serial communication established between an Arduino Uno board, on which the IMU module is embedded, and the host laptop. In addition, the interface between Python and CoppeliaSim is created via corresponding API. Thus, first, by using the Mahoney algorithm to Kalman Filter, estimations of linear and angular movements measured by the IMU are done, and then, according the movement recognized by the IMU and joints information taken from the CoppeliaSim, the motor commands are calculated via solving the inverse kinematic problem.

Material and Method

The material of this research includes two parts of hardware and software that discussed separately as below.

- **Setup of IMU sensor data acquisition**

In this setup, a six-axis MPU6050 sensor is utilized for the purpose of measuring and acquiring data from IMU. This sensor incorporates a 3-axis accelerometer to measure linear accelerations along each of spatial axes, and a 3-axis gyroscope to measure angular velocity about each one. An Arduino UNO board has been employed to facilitate the real-time reading and transmission of sensor data to the host PC through a serial communication established by Python. The sampling frequency was set to 100 Hz. As shown in Fig 1, the setup was fastened on a rigid plate.

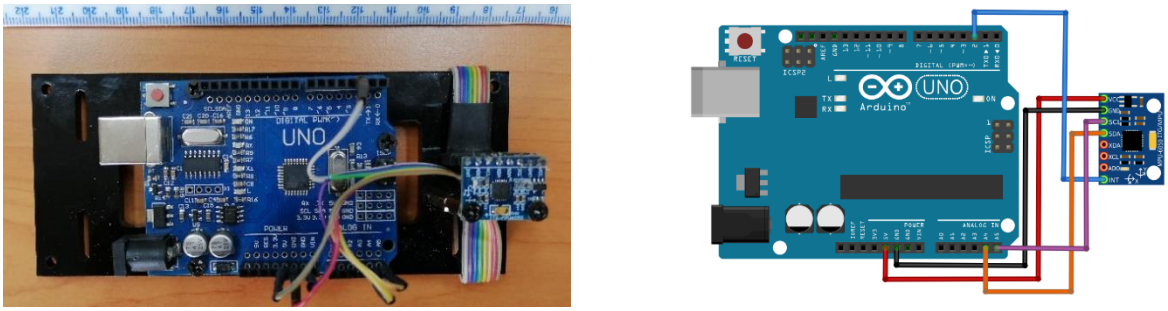


Figure 1. The setup of IMU sensor data acquisition including Arduino Uno board and IMU module

- **Kalman Filter based on Mahony Algorithm for Position Estimation**

By receiving the IMU data in Python, the inertial measurements are utilized to estimate the linear and angular displacements via integrating over time. Thus, these estimates are used as the position and orientation of the robot. In order to integration of IMU measurements according to kinematics relations, it is convenience to exploit from Kalman Filter [9]. In this context, we follow the algorithm developed by Euston et. al [10], commonly referred as Mahony filter, along implementing the Kalman filter. This algorithm utilizes the accelerometer and gyroscope signals provided by the IMU to estimate the Euler angles (i.e. roll, pitch, and yaw). This filter is particularly suitable for real-time applications on robot hardware due to its low computational complexity, high accuracy, and elimination of requirement to the noise covariance matrix.

The Mahony filter calculates the orientation of a moving object in quaternion form denoted $\hat{q}$. According to $\hat{q}_{t-1}$ obtained in previous time step, the rotation matrix describing attitude of inertial reference frame into body frame, denoted ${}^{b}_{i}R$, is calculated; by which we can obtain an estimation of the normalized nominal gravity acceleration within the body frame, denoted $\hat{\boldsymbol{v}}$, calculated as $\hat{\boldsymbol{v}} = {}^{b}_{i}R^{i}\hat{\mathbf{g}} \equiv {}^{b}_{i}R \cdot [0,0,1]'$. By assuming that the actual acceleration of the moving body with respect to the gravity acceleration is neglectable, so it is expected the resultant vector of what measured by IMU accelerometers to be the same nominal acceleration vector described in the body frame, which, after normalization, denoted $\bar{\boldsymbol{v}}$, calculated as $\bar{\boldsymbol{v}} = \frac{\mathbf{acc}}{\|\mathbf{acc}\|}$. Now, if the estimation of the orientation applied to calculate $\hat{\boldsymbol{v}}$ has been correct, then it is expected there is no deviation between the estimated $\hat{\boldsymbol{v}}$ and the one obtained based on measurements, i.e. $\bar{\boldsymbol{v}}$. However, when the ideal condition is not provided, there is an error which obtained via cross product as $e = \bar{v} \times \hat{v}$. The Mahony filter tries to correct its previous estimation of the body orientation in 3 steps: 1- calculation of the innovation δ governed under a proportional-integral (PI) dynamics, 2- calculation of the rate of the quaternion $\dot{q}$, and 3- integrating $\dot{q}$ to achieve a new estimation of $\hat{q}_t$. Therefore, it is [10]:

$$\dot{q} = \tfrac{1}{2}\hat{q} \otimes P(\bar{\Omega} + \delta), \quad \text{where,} \quad \delta = K_p e + K_I \int e dt, \quad \text{and} \quad e = \bar{v} \times \hat{v} \tag{1}$$

where, $\bar{\Omega}$ is the measured angular velocities of the IMU and operator P(.) is defined as a pure quaternion operator so that P(Ω) = (0, Ω). Thus, the true value of angular velocities is considered as $\Omega = \bar{\Omega} + \delta$. It is worth to mention that the error vector e is represented with respect to the components of the estimated quaternion as follows:

$$\hat{v} = [2(\hat{q}_1\hat{q}_3 - \hat{q}_0\hat{q}_2), 2(\hat{q}_2\hat{q}_3 - \hat{q}_0\hat{q}_1), \hat{q}_0^2 - \hat{q}_1^2 - \hat{q}_2^2 + \hat{q}_3^2]' \tag{2}$$

The Kalman filter is exploited in following for position estimation. The procedure is begun by exchanging the description of the measured accelerations from the body frame to inertial frame using the rotation matrix of ${}^{b}_{i}R'$ calculated by the Mahony filter. By subtracting the gravity acceleration, the observations of the Kalman filter are, in fact, the measured accelerations of the body experienced during its movement. Double integration of this signal

predicts the prior estimation of the position which updated by new observation. For more details see [9-10]. Thus, the Kalman filter is employed to estimate displacement along with X, Y, and Z directions, respectively.

- **Inverse Kinematics for Joint Trajectory Generation via Python API in CoppeliaSim**

By using the Python API in CoppeliaSim we complete the simulation of the imitation of human' hand movement which should be performed by the ABB robotic manipulator model. The orientation and position of the body (e.g. human's hand) estimated by Mahony and Kalman filters are considered as the inputs of this stage of the task. Thus, it is desired that the end effector of the robot possesses a configuration associated with the given pose. To this end, we use the *simIK* library and the *damped_least_squares* method which have been developed in the CoppeliaSim API for solving the inverse dynamics problem. In this way, the joint angles of the robot are calculated in each time step, and sent as the commands to the simulation environment, while tracked under a PD low level control.

Results

The described procedure, thoroughly developed in Python, is examined according to an implementing protocol depicted in Fig. 2. In order to avoid the uncontrolled movements, we slide straightly the setup of the IMU sensor along the edge of a ruler towards left/right and up/down directions. As shown in the simulation environment window, the end effector of ABB robotic manipulator follows in real-time a same path, too. Hence, it can be claimed that our objective is earned successfully.

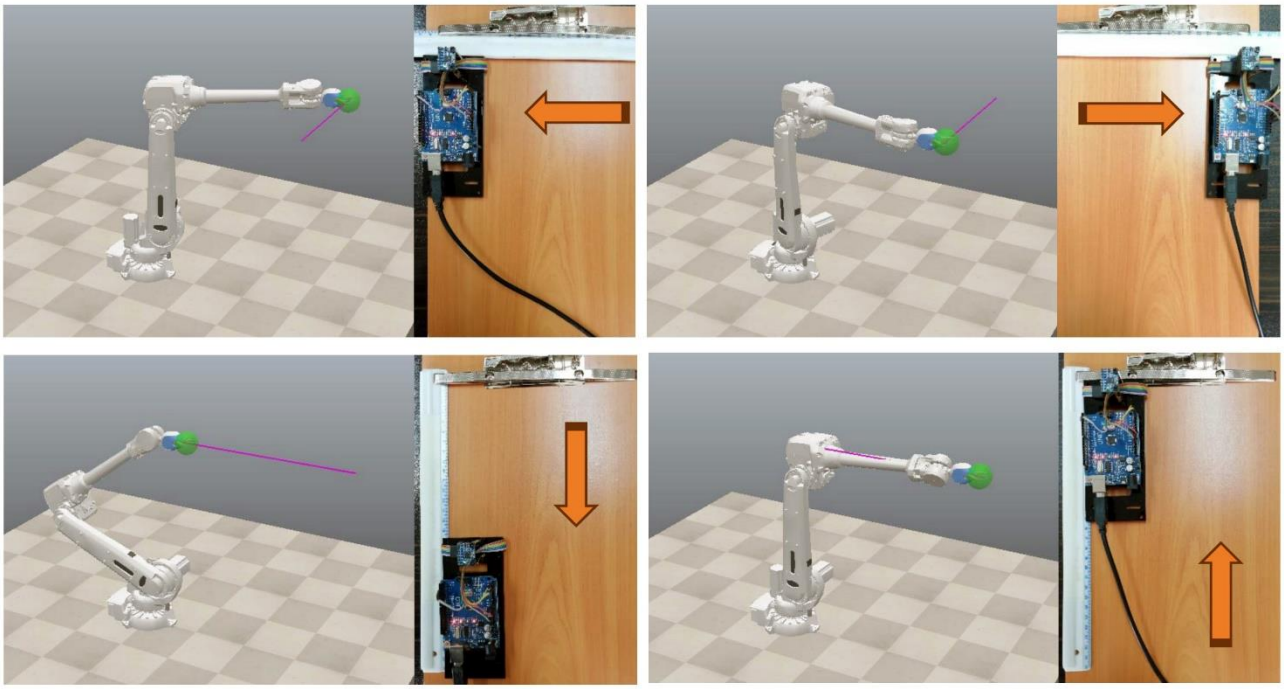


Figure 2. Moving the setup of IMU sensor in four major directions and imitating the corresponding movements by the ABB manipulator simulated in the CoppeliaSim

Conclusion

In this paper we developed an integrated framework for establishing the interface between the IMU sensor as a hardware setup and the CoppeliaSim software as a robotic simulation environment to investigate the future control strategies. This framework was prepared using Python API in CoppeliaSim, in which any required process including receiving sensor signals through serial communication, preprocessing the signals (e.g. low-pass filter), estimating the position and orientation using Kalman/Mahony filters, solving inverse kinematics problem, and low-level PD control for trajectory tracking, is embedded. The proposed framework was examined experimentally and the results showed its success. This framework will be beneficial for virtually examining the control strategies proposed for human-robot interactions before implementing on the real world.

References

1. Patil, S., Vasu, V., & Srinadh, K. V. S. (2023). Advances and perspectives in collaborative robotics: a review of key technologies and emerging trends. *Discover Mechanical Engineering*, *2*(1), 13.

2. Tigrini, A., Pettinari, L. A., Verdini, F., Fioretti, S., & Mengarelli, A. (2021). Shoulder motion intention detection through myoelectric pattern recognition. IEEE Sensors Letters, 5(8), 1-4.
3. Gu, X., Han, J., Yang, G. Z., & Lo, B. (2023). Generalizable Movement Intention Recognition with Multiple Heterogeneous EEG Datasets. In 2023 IEEE International Conference on Robotics and Automation (ICRA) (pp. 9858-9864). IEEE.
4. Scalera, L., Seriani, S., Gallina, P., Lentini, M., & Gasparetto, A. (2021). Human–robot interaction through eye tracking for artistic drawing. Robotics, 10(2), 54.
5. Hogan, N. (2022). Contact and physical interaction. Annual Review of Control, Robotics, and Autonomous Systems, 5, 179.
6. Zhu, L., Wang, Z., Ning, Z., Zhang, Y., Liu, Y., Cao, W., ... & Chen, C. (2020). A novel motion intention recognition approach for soft exoskeleton via IMU. *Electronics*, *9*(12), 2176.
7. Cifuentes, C. A., Frizera, A., Carelli, R., & Bastos, T. (2014). Human–robot interaction based on wearable IMU sensor and laser range finder. Robotics and Autonomous Systems, 62(10), 1425-1439.
8. Roda-Sanchez, L., Garrido-Hidalgo, C., García, A. S., Olivares, T., & Fernández-Caballero, A. (2023). Comparison of RGB-D and IMU-based gesture recognition for human-robot interaction in remanufacturing. The International Journal of Advanced Manufacturing Technology, 124(9), 3099-3111.
9. Sayyed Noorani, M.R., Naiem, S., Aghazadeh, S. (2024). Tremor Suppression in Robot-Assisted Minimally Invasive Surgery using Kalman Filter Adapted by Fuzzy System and Reinforcement Learning. Transactins on Machine Intelligance, 7(2), 72.
10. Euston, M., Coote, P., Mahony, R., Jonghyuk Kim, & Hamel, T. (2008). A complementary filter for attitude estimation of a fixed-wing UAV. 2008 IEEE/RSJ International Conference on Intelligent Robots and Systems, 340–345.

Advanced Engineering Days

aed.mersin.edu.tr

Forecasting Survival Rate from ICU Data Based on LightGBM

Mahmood Seyyedzadeh [1], Alireza Tajdid [1], Ali Firouzi Abriz [1], Kashish Rai [2]

[1] *University of Tabriz, Faculty of Electrical and Computer Engineering, Iran,* mahmoodseyyedzadeh@gmail.com, *alireza.tajdid@yahoo.com, alifirouziabriz@gmail.com*
[2] *SR Institute of Management and Technology, Biotechnology Engineering Department, India, kashishrai@ieee.org*

Cite this study: Seyyedzadeh, M., & Tajdid, A. & Abriz, A. & Rai, K. (2024). Forecasting Survival Rate from ICU Data Based on LightGBM. Advanced Engineering Days, 9, 565-568

Keywords
Intensive care unit
Forecasting
Machine learning
LightGBM

Abstract

This paper investigates the application of the Light Gradient Boosting Machine (LightGBM) for predicting the survival rate of patients in the Intensive Care Unit (ICU). Using a comprehensive dataset which includes clinical and laboratory data from ICU patients admitted for at least 24 hours, we develop a predictive model to estimate mortality rates. Key variables include vital signs, clinical scores, and biochemical test results. The dataset comprises 1087 cases with 50 variables, where 388 patients experienced a change in hospital death status. Our LightGBM model, implemented using scikit-learn, achieved an accuracy of 93.11%, a precision of 82%, a recall of 67%, an F1 score of 0.72, and an AUC score of 0.89. Compared to a previously trained Random Forest algorithm, which achieved an accuracy of 80.28% and an AUC score of 0.85, our LightGBM model demonstrates superior performance in most metrics. These findings underscore the potential of LightGBM in improving predictive accuracy for ICU patient outcomes, highlighting its robustness and efficiency in handling large-scale healthcare data.

Introduction

The intensive care unit (ICU) is a hospital area designed to care for critically ill patients, using a team of specialized professionals and advanced technology to provide the best possible support for those who are usually unstable and at high risk of death. Predicting patient survival rates in the intensive care unit (ICU) is a crucial undertaking that has a substantial influence on clinical decision-making and resource distribution[1, 2]. Hospitals have specialized departments called intensive care units (ICUs) that are devoted to treating patients who have serious or potentially fatal illnesses or injuries. These patients require round-the-clock care and support from a multidisciplinary team that uses cutting-edge medical technology. Considering the significant risks, timely and accurate patient outcome predictions can enhance treatment planning, improve the standard of care, and ultimately save lives[3].

Machine learning has become a very useful tool in the all parts of industry in recent years[4-8]. It can be used to analyze big, complicated datasets and find patterns and predictions that conventional statistical methods might miss. Regarding these merits, the use of machine learning methods in healthcare has increased in recent studies[9-11]. Gradient boosting algorithms[12] are a popular machine learning technique because of their high predictive accuracy and robustness. Among these, Light Gradient Boosting Machine (LightGBM)[13] is a particularly effective and scalable algorithm that can handle the large and complex datasets that are commonly generated in intensive care units. This algorithm has been utilized in several healthcare related studies [14, 15].

This paper presents a comprehensive study on forecasting the survival rate of ICU patients using LightGBM. By leveraging ICU data[16], which includes a variety of clinical parameters and patient information, we aim to develop a predictive model that can accurately estimate survival probabilities. The proposed approach not only highlights the effectiveness of LightGBM in processing and analyzing ICU data but also underscores the potential of advanced machine learning techniques in enhancing patient care and management in critical care environments.

Material and Method

The dataset that plays the central role in this paper, is from the hospital intensive care unit patients who have been admitted for 24 hours in the emergency department. The purpose is to develop a predictive model to gain

the death rate from the dataset. Specifically, the dataset utilized for this prediction task is "WiDS (Women in Data Science) Datathon 2020: ICU Mortality Prediction", which has 2 main points. Firstly, it originates from ICU and emergency department and secondly, it is comprehensive in terms of its coverage.

Attempting to create an understandable predictive model using clinical and laboratory data, variables related to patients' clinical status, such as blood counts, vital signs, clinical scores and biochemical test results, were given priority in the definition of variables of interest. These variables were only removed when ineffective or when they represented the application of formulas rather than measured or scored values, which affected on anthropometric and demographic variables. The only variable in this category that was included is age. Furthermore, the variables of interest did not include variables related to logistical aspects of hospitalization, such as the type and the source of admission and the status of readmission.

In this process, a set which includes 50 variables and 1087 cases was produced, which one of them is predicted variable (outcome variable) and 49 assumed predictive variables. The following numerical variables are : Age, Disease score, Eye opening score on the Glasgow coma scale (GCS, Heart rate, Hematocrit, Mean arterial pressure, Maximum albumin, Maximum bilirubin, Maximum blood urea nitrogen, Maximum calcium, Maximum creatinine, Maximum diastolic blood pressure, Maximum glucose, Maximum HCO3, Maximum hemoglobin, Maximum INR, Maximum lactate, Maximum platelets, Maximum potassium, Maximum sodium, Minimum systolic blood pressure, Maximum saturation of peripheral oxygen (SpO2, Maximum white blood cells (WBC), Minimum albumin, Minimum bilirubin, Maximum blood urea nitrogen, Minimum calcium, Minimum creatinine, Minimum diastolic blood pressure, Minimum glucose, Minimum HCO3, Minimum hemoglobin, Minimum INR, Minimum lactate, Minimum platelets, Minimum potassium, Minimum sodium, Minimum systolic blood pressure, Minimum SpO2, Minimum WBC, Motor response on the GCS, Partial PaO2, Partial pressure of carbonic gas in arterial blood (PaCO2, pH, Respiratory rate, Temperature, and Verbal response on the GCS.

The number of diseases among the following conditions indicated in the disease score: Acquired immunodeficiency syndrome, Cirrhosis, Diabetes, Hepatic failure, Immunosuppression, Leukemia, Lymphoma, and Solid tumor.

Cardiovascular involvement, Gastrointestinal involvement, Genitourinary involvement, Hematological involvement, Metabolic involvement, Musculoskeletal/skin involvement, Neurological involvement, Respiratory involvement, Sepsis, and Trauma were the categories predominant systemic involvement that were taken into assessment.

In this section, we present our model built using the LightGBM framework. LightGBM, short for Light Gradient Boosting Machine, is a gradient boosting framework that uses tree-based learning algorithms. It is designed to be distributed and efficient with the following advantages: faster training speed and higher efficiency, lower memory usage, better accuracy, support of parallel and GPU learning, capable of handling large-scale data.

LightGBM is an improvement framework based on a decision tree algorithm released by Microsoft in 2017. Both LightGBM and Random Forest support parallel arithmetic, but LightGBM stands out as more powerful than the previous Random Forest model. It boasts fast training speed and occupies less memory, which effectively reduces the communication cost of parallel learning. LightGBM's key features include a decision tree algorithm based on gradient-based one-sided sampling (GOSS), exclusive feature bundling (EFB), and a histogram and leaf-wise growth strategy with a depth limit.

For the second part of the analysis, we aim to compare Random forest performance with the predictive model that we utilized in this article.

Results and Discussion

The dataset is separated to 2 parts: training set (80%) and test set (20%). The training set was used to train based on LightGBM which is implemented with scikit-learn, an open source library. The test set was used to evaluate the predictive efficacy of the model using accuracy, precision, recall, F1 score, Area under curve (AUC) score metrics. The methodology adopted is schematically gathered in Figure 1.

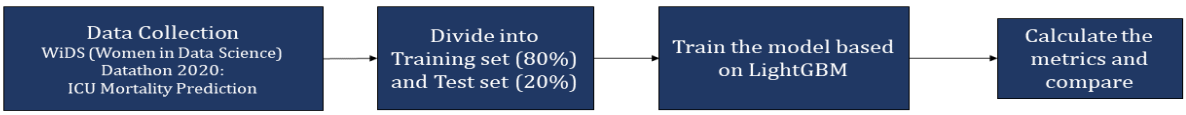


Figure 1. Structure of the algorithm

Following the 1087 ICU patients' data were examined and utilized to create the predictive model, 388 of them experienced a change in hospital death, While the remaining 699 did not. Among the 388 patients who ended up in the hospital, 275 had intubation, 63 did not, and 106 had sepsis as the primary systematic involvement; There were also 18 respiratory involvements, 4 metabolic involvement, 154 cardiovascular involvement, 11 trauma, 16 neurological involvement, 25 gastrointestinal involvement, 2 genitourinary involvement, 1 musculoskeletal/skin

involvement, and 1 hematological involvement. All of the 699 patients that did not die in the hospital, 534 had an intubation and 215 did not; 206 had sepsis as predominant systemic involvement, 107 respiratory involvement, 79 metabolic involvement, 167 cardiovascular involvement, 38 trauma, 49 neurological involvement, 74 gastro-intestinal involvement, 17 genitourinary involvement, 9 musculoskeletal/skin involvement, and 3 hematological involvement.

The model obtained accuracy of 93.11%, precision of 92%, recall of 93%, F1 score of 0.72, and AUC score of 0.89 on the test set, illustrated in Table 1.

Table 1. LightGBM outcome

Metric	Value
Accuracy	93.11%
precision	82%
Recall	67%
F1 Score	0.72
AUC Score	0.89

Elena Caires Silveira et al., in their article where they trained a Random Forest algorithm on the same dataset used in our work, obtained an accuracy of 80.28%, sensitivity of 81.82%, specificity of 79.43%, positive predictive value of 73.26%, negative predictive value of 84.85%, F1 score of 0.74, and an AUC score of 0.85. Comparing these metrics with those calculated using LightGBM, we can see that in some parameters, our method outperforms Random Forest. The robustness of LightGBM is evident in its accuracy, which is 93.11%. The AUC score of our method is 0.89, which is slightly better than that of the Random Forest algorithm. In terms of the F1 score, both methods demonstrate acceptable performance. These results highlight the robustness and effectiveness of the LightGBM model in this context. The metrics from the Random Forest method and LightGBM method are compared in Table 2.

Table 2. Comparison Results

Metric	LightGBM	Random Forest
Accuracy	93.11%	80.28%
F1 Score	0.72	0.74
AUC Score	0.89	0.85

Conclusion

This study demonstrates the effectiveness of using the Light Gradient Boosting Machine (LightGBM) to predict the survival rate of ICU patients based on a comprehensive dataset. By leveraging clinical and laboratory data, our LightGBM model significantly outperforms the Random Forest algorithm, achieving higher accuracy, precision, and AUC scores. The results highlight LightGBM's robustness and efficiency in handling complex, high-dimensional healthcare data, providing valuable insights into patient outcomes. This predictive model can aid healthcare professionals in making informed decisions, optimizing treatment plans, and allocating resources more effectively in critical care settings. Future work could focus on incorporating additional data sources, such as real-time monitoring and longitudinal patient records, to further enhance predictive accuracy.

References

[1] H. R. Darabi, D. Tsinis, K. Zecchini, W. F. Whitcomb, and A. Liss, "Forecasting mortality risk for patients admitted to intensive care units using machine learning," *Procedia Computer Science,* vol. 140, pp. 306-313, 2018.

[2] J. Xie *et al.*, "A review of modeling methods for predicting in-hospital mortality of patients in intensive care unit," *Journal of Emergency and Critical Care Medicine,* vol. 1, no. 8, 2017.

[3] R. Cavallazzi, P. E. Marik, A. Hirani, M. Pachinburavan, T. S. Vasu, and B. E. Leiby, "Association between time of admission to the ICU and mortality: a systematic review and metaanalysis," *Chest,* vol. 138, no. 1, pp. 68-75, 2010.

[4] S. M. Malakouti, A. R. Ghiasi, and A. A. Ghavifekr, "AERO2022-flying danger reduction for quadcopters by using machine learning to estimate current, voltage, and flight area," *e-Prime-Advances in Electrical Engineering, Electronics and Energy,* vol. 2, p. 100084, 2022.

[5] S. M. Malakouti, A. R. Ghiasi, A. A. Ghavifekr, and P. Emami, "Predicting wind power generation using machine learning and CNN-LSTM approaches," *Wind Engineering,* vol. 46, no. 6, pp. 1853-1869, 2022.

[6] P. Emami, A. R. Ghiasi, and A. A. Ghavifekr, "Survey of Multi-Agent Reinforcement Learning to Solve Inverse Kinematic Problems of Redundant Robotic Manipulators," in *2022 8th International Conference on Control, Instrumentation and Automation (ICCIA)*, 2022: IEEE, pp. 1-6.

[7] M. Memar, A. Mokaribolhassan, and A. A. Ghavifekr, "Review on machine learning frameworks in drivers' physiological signal analysis to detect stress," in *2021 7th International Conference on Control, Instrumentation and Automation (ICCIA)*, 2021: IEEE, pp. 1-6.

[8] A. Safari and A. A. Ghavifekr, "Use case of artificial intelligence and neural networks in energy consumption markets and industrial demand response," *Industrial demand response: methods, best practices, case studies, and applications,* vol. 4, p. 379, 2022.

[9] R. Behinfaraz, A. A. Ghavifekr, R. De Fazio, and P. Visconti, "Utilizing Fractional Artificial Neural Networks for Modeling Cancer Cell Behavior," *Electronics,* vol. 12, no. 20, p. 4245, 2023.

[10] H. Habehh and S. Gohel, "Machine learning in healthcare," *Current genomics,* vol. 22, no. 4, p. 291, 2021.

[11] A. Alanazi, "Using machine learning for healthcare challenges and opportunities," *Informatics in Medicine Unlocked,* vol. 30, p. 100924, 2022.

[12] C. Bentéjac, A. Csörgő, and G. Martínez-Muñoz, "A comparative analysis of gradient boosting algorithms," *Artificial Intelligence Review,* vol. 54, pp. 1937-1967, 2021.

[13] J. Fan, X. Ma, L. Wu, F. Zhang, X. Yu, and W. Zeng, "Light Gradient Boosting Machine: An efficient soft computing model for estimating daily reference evapotranspiration with local and external meteorological data," *Agricultural water management,* vol. 225, p. 105758, 2019.

[14] D. D. Rufo, T. G. Debelee, A. Ibenthal, and W. G. Negera, "Diagnosis of diabetes mellitus using gradient boosting machine (LightGBM)," *Diagnostics,* vol. 11, no. 9, p. 1714, 2021.

[15] A. Ghourabi, "A security model based on lightgbm and transformer to protect healthcare systems from cyberattacks," *IEEE Access,* vol. 10, pp. 48890-48903, 2022.

[16] E. C. Silveira, S. M. Pretti, B. A. Santos, C. F. S. Corrêa, L. M. Silva, and F. F. de Melo, "Prediction of hospital mortality in intensive care unit patients from clinical and laboratory data: A machine learning approach," *World Journal of Critical Care Medicine,* vol. 11, no. 5, p. 317, 2022.

Advanced Engineering Days

aed.mersin.edu.tr

Implementation and Optimization of PID Controller Using HHO Algorithm for DC Encoder Motor in Autonomous Guided Vehicles (AGV)

Mohammad Javad Saeidi [*1], **Mahmoud Moqadasian** [1]

[1]*Shahid Chamran University of Ahvaz, Shohadaye Hoveizeh Campus of Technology, Iran, mohammadjavadsaidi74@gmail.com, drmoghadasian@gmail.com*

Cite this study: Saeidi, M., & Moqadasian, M. (2024). Implementation and Optimization of PID Controller Using HHO Algorithm for DC Encoder Motor in Autonomous Guided Vehicles (AGV). Advanced Engineering Days, 9, 569-572

Keywords
PID controller
HHO algorithm
Autonomous guided vehicle
Fuzzy logic
Controller optimization
DC encoder motor
Simulink simulation

Abstract

In this paper, we present the implementation and optimization of a PID controller using the Harris Hawks Optimization (HHO) algorithm for DC encoder motors in autonomous guided vehicles (AGV). The primary focus is on enhancing accuracy and reducing response time in speed and direction control of AGVs. By comparing the fuzzy logic controller with the PID controller, our study demonstrates the effective adjustment of PID parameters using the HHO algorithm, leading to increased system stability and performance. Simulations conducted in the MATLAB Simulink environment reveal significant improvements in AGV performance, showcasing the high precision and efficiency of the system compared to conventional methods. The findings highlight the benefits of using the HHO algorithm for the automatic and optimal tuning of PID controller coefficients, ultimately contributing to the development of more reliable and responsive AGV systems. This research has potential applications in various industries requiring precise and rapid control, such as transportation, industrial automation, and robotics. The innovative approach of combining advanced optimization techniques with control technologies marks a significant step forward in engineering future autonomous vehicles and intelligent systems.

Introduction

Precise speed control in DC motors is crucial for autonomous guided vehicles (AGV). DC motors are preferred in AGVs for their high torque and fast response. Traditional PI controllers often fall short in complex environments due to manual tuning limitations, leading to slow responses and instability.[1] To address these issues, this paper introduces the Harris Hawks Optimization (HHO) algorithm for automatic and optimal tuning of PID controller parameters, enhancing the efficiency and stability of the control system.

The HHO algorithm, inspired by the hunting behavior of Harris hawks, is effective in solving complex optimization problems by balancing exploration and exploitation. This research focuses on improving the performance of PID controllers used in DC encoder motors for AGVs by integrating the HHO algorithm. Simulations in MATLAB Simulink demonstrate significant enhancements in system performance, including reduced response time and increased accuracy, compared to conventional methods such as fuzzy logic controllers.[2]

This innovative approach not only enhances AGV performance but also offers broader applications in fields requiring precise control, such as transportation, industrial automation, and robotics. The combination of advanced optimization techniques with traditional control methods marks a progressive step towards the development of more reliable and responsive autonomous systems.

Material and Method

DC Motor Model:

The DC motor's dynamic behavior is represented using differential equations based on Newton's second law and Kirchhoff's voltage law. The key parameters include: [3]

Motor torque constant (K_a) = 0.04 Nm/Amp
Motor inertia (J) = 0.005 Kg.m^2
Armature inductance (L_a) = 1 Henry
Armature resistance (R_a) = 4 Ω

The transfer function of the DC motor in the Laplace domain, assuming negligible friction, is given by:

$$G(s) = \frac{K_a}{(Js+R_a)(L_a s+1)} \quad (1)$$

Given the parameters of the DC motor the transfer function of the DC motor is derived as follows:

$$G(s) = \frac{\Omega(s)}{V(s)} = \frac{K_a}{L_a J s^2+R_a J s+K_a^2} \quad (2)$$

$$G(s) = \frac{0.04}{1\times 0.005 s^2+4\times 0.005 s+0.04^2} \quad (3)$$

By normalizing the coefficients, the final transfer function of the DC motor is:

$$G(s) = \frac{8}{s^2+4s+0.32} \quad (4)$$

PID Controller Model:

The PID controller aims to minimize the error between the desired and actual motor speed. The transfer function of the PID controller in the Laplace domain is: [4]

$$G_c(s) = K_p + \frac{K_i}{s} + K_d s \quad (5)$$

where K_p, K_i, and K_d are the proportional, integral, and derivative gains, respectively.

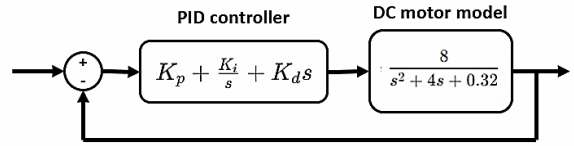


Figure 1. Block diagram of DC motor model with traditional PID controller

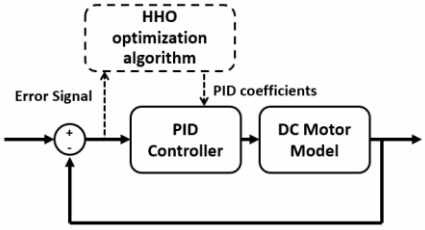


Figure 2. Block diagram of DC motor model with PID controller optimized by the HHO algorithm

Harris Hawks Optimization (HHO) Algorithm:

HHO is an optimization algorithm inspired by the cooperative hunting behavior of Harris hawks. It involves three main phases: [5]

1. *Exploration:* Hawks randomly search the solution space to find potential prey (optimal solutions).
2. *Exploitation:* Once prey is detected, hawks collaborate to encircle and capture it, focusing on fine-tuning the solution.
3. *Socialization:* Hawks update their positions based on the best current solution, refining their approach to converge on the optimal parameters.

System Design:

The primary objective of this study is to improve the performance of PID controllers used in DC encoder motors for AGVs by employing the HHO algorithm for automatic and optimal parameter tuning.

The system comprises the PID controller tuned by the HHO algorithm for optimal performance. The design process involves:

1. *Defining the Objective Function*: The objective function minimizes the error between the reference input and the system output, considering performance metrics such as overshoot, settling time, and stability.
2. *Initializing HHO Parameters*: These include population size, exploration, and exploitation rates, and the number of iterations.
3. *Optimization Process:* Use the HHO algorithm to iteratively adjust the PID controller parameters (K_p, K_i, and K_d) for optimal performance.

Results

In this study, simulations were performed using MATLAB Simulink r2023b to evaluate the performance of the PID controller optimized by the Harris Hawks Optimization (HHO) algorithm for a DC encoder motor in autonomous guided vehicles (AGVs). The simulations were conducted under three scenarios: without any controller, with a fuzzy logic controller, and with the HHO-optimized PID controller.

The Simulink model was designed to incorporate the DC motor's transfer function and the PID controller tuned by the HHO algorithm. The objective was to minimize the system's response time, overshoot, and steady-state error while maintaining stability under varying load conditions.

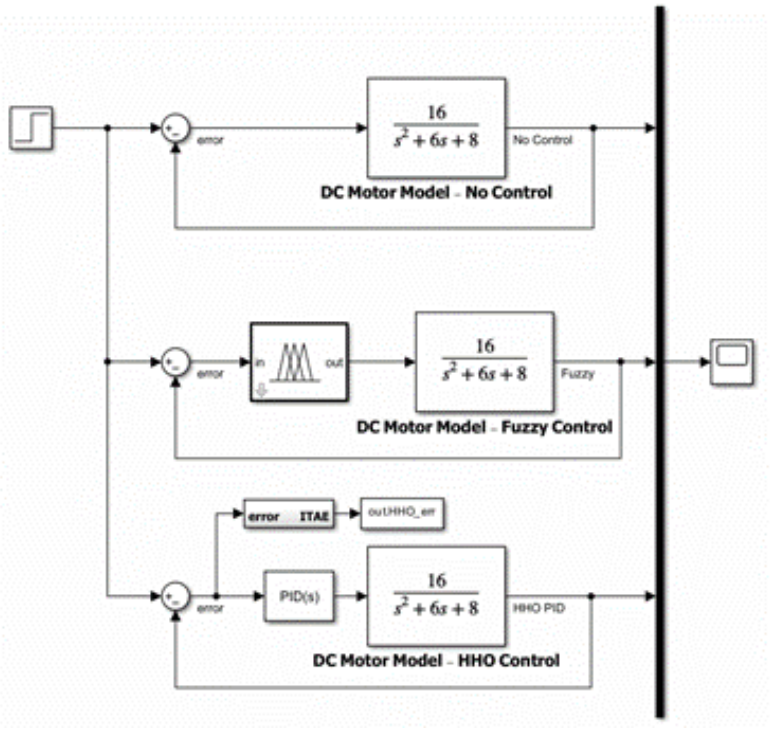


Figure 3. Simulink Diagram System

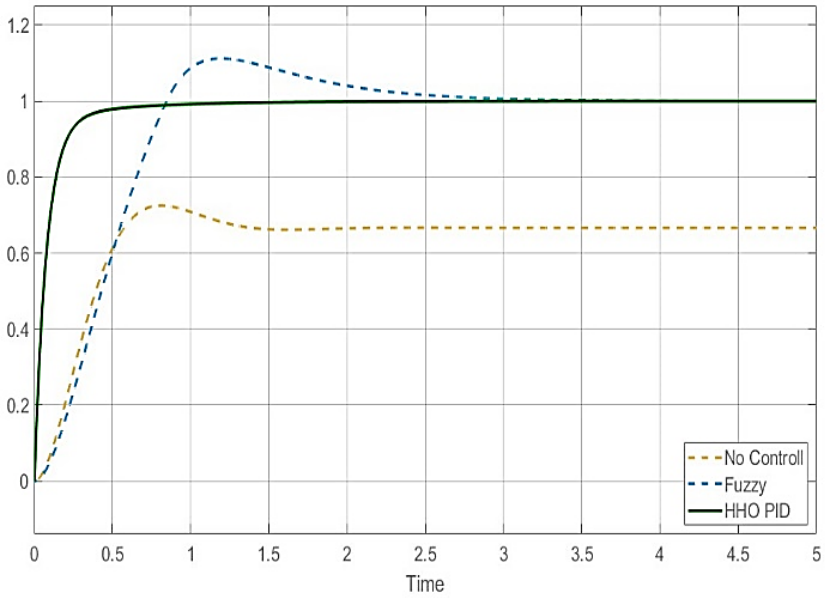


Figure 4. System Response Comparison

Discussion

The simulation results demonstrated significant improvements in the system's performance with the HHO-optimized PID controller compared to the other two scenarios, as shown in Figure 4. Key performance metrics

such as settling time, overshoot, and steady-state error were measured and analyzed. The results are summarized as follows:

1. *Without Controller:* The system exhibited a slow response and failed to reach the desired speed, indicating poor performance and instability.
2. *Fuzzy Logic Controller*: The system showed improved response time and stability compared to no controller but still lagged in achieving optimal performance.
3. *HHO-Optimized PID Controller*: This scenario provided the best performance, with a rapid response, minimal overshoot, and negligible steady-state error, demonstrating the effectiveness of the HHO algorithm in tuning the PID parameters.

Conclusion

This study highlights the successful implementation and optimization of a PID controller for a DC encoder motor in autonomous guided vehicles (AGVs) using the Harris Hawks Optimization (HHO) algorithm. The optimized PID controller significantly improved system performance, demonstrating reduced settling time, overshoot, and steady-state error. Mathematical modeling and simulations in MATLAB Simulink r2023b showed that the HHO-optimized PID controller outperformed both fuzzy logic controllers and systems without controllers. The results indicate enhanced precision, stability, and efficiency, making this approach suitable for high-precision applications in transportation, logistics, and manufacturing. In summary, integrating HHO with traditional PID control offers a robust solution for optimizing motor control in AGVs, paving the way for advancements in autonomous systems and intelligent control technologies. This research underscores the potential of bio-inspired optimization algorithms in enhancing control system performance.

References

1. Parikh, P., R. Vasani, and S. Sheth, Velocity analysis of a dc brushed encoder motor using ziegler-nichols algorithm: a case of an automated guided vehicle. Indian Journal of Science and Technology, 2016.
2. Al Sumarmad, K.A., et al., Energy management and voltage control in microgrids using artificial neural networks, PID, and fuzzy logic controllers. Energies, 2022. 15(1): p. 303.
3. Parikh, P., et al., Implementing fuzzy logic controller and PID controller to a DC encoder motor–"A case of an automated guided vehicle". Procedia Manufacturing, 2018. 20: p. 219-226.
4. Doicin, B., M. Popescu, and C. Patrascioiu. PID Controller optimal tuning. in 2016 8th International Conference on Electronics, Computers and Artificial Intelligence (ECAI). 2016. IEEE.
5. Heidari, A.A., et al., Harris hawks optimization: Algorithm and applications. Future generation computer systems, 2019. 97: p. 849-872.

Advanced Engineering Days

aed.mersin.edu.tr

Optimal Design of 1 MW Grid-Connected Solar Power Plant for increasing Solar Radiation by using PVsyst Software

Amirreza Samadi Bonab [1], Parisa Shirinabadi [1], Kazem Zare [1], Sina Asadian [2], Khadim Moin Siddiqui [3], Neel Kamal [3]

[1] *University of Tabriz, Faculty of Electrical and Computer Engineering, Iran, amirrezasamadibonab@ieee.org, p.shirinabadi@gmail.com, kazem.zare@tabrizu.ac.ir*
[2] *Politecnico di Milano, School of Industrial and information Engineering, Italy, sina.asadiian@gmail.com*
[3] *SR Institute of Management and Technology, EEE Department, India, siddiquikhadim@ieee.org, neelkamal@ieee.org*

Cite this study: Samadi Bonab, A, & Shirinabadi, P., & Zare, K. & Asadian, S. & Moin Siddiqui , K., & Kamal, N. (2024). Optimal Design of 1 MW Grid-Connected Solar Power Plant for increasing Solar Radiation by using PVsyst Software Advanced Engineering Days, 9, 573-576

Keywords
Solar Energy
Photovoltaic System
Grid Connected
Optimization
Pvsyst

Abstract

This paper aims to optimize the design of a 1 MW grid-connected solar power plant in Tabriz, Iran, by using PVsyst software to maximize the use of solar radiation. This study focuses on choosing the most suitable photovoltaic (PV) system configuration, such as panels location, tilt angle, and array layout, to increase energy generation efficiency. Through detailed simulations and analyzes performed at PVsyst, this paper aims to provide insights on optimal design parameters for grid-connected solar power plants in Tabriz, contributing to the advancement of renewable energy deployment in the region.

Introduction

Nowadays , Clean energy production due to the global warming[1] is a challenge that all of the countries are involved. They are trying to use the energies that don't damage the earth . Solar energy is one of the clean energies that countries have focused on using it more .Solar energy is converted into DC electricity by PV, but sometimes we need AC electricity for some purposes, in this case we have to use an inverter to convert DC to AC [2].

The cost of a solar power plant is very high[3], so it is necessary to reduce some costs by using the right equipment and optimal use of the area of the power plant. Also, the way the panel is placed and its slope has a great impact on the efficiency of the system, so that the necessary cost is not wasted, but it is used for maximum efficiency[4] . In fact, the arrangement of PV in a solar system is very important, which can have a great effect on the efficiency of the system [5]. Recently Evolutionally algorithms have been utilized to cover optimization problems in these fields[6-10]. A method for converting solar thermal energy into electrical power is proposed in [11]. A type-2 fuzzy logic system (FLS) based controller is presented for power/voltage control of PV/batery/Fuel system in [12]. Also, , a novel Boost Fifteen-level Flying-Capacitor (BFFC) inverter is suggested in [13].

The higher cost of solar power plants has caused it to be used less. It is necessary to pay attention to what affects the efficiency of a project. In this way it will be easy to create a project with high efficiency. It is better to reduce the cost of solar equipment, so that this issue causes more desire to use solar energy.

Burning fossil fuels produces carbon dioxide gas, which is harmful for the earth. Because of that nowadays solar energy has received much attention from everyone and is known as a clean and sustainable energy [14] . an important issue that it is better to pay attention is solar panel installation location .it should be pay attention to the weather conditions of an area. If there is little sunlight in an area throughout the year, this area will not be a suitable area for installing a solar panel because it will not produce good results [15]. Sunlight is absorbed through solar panels to produce energy. These panels are made of a series of P-N diodes and semiconductor materials [16]. Recently, PVSYST software has attracted the attention of many engineers and researchers. Using this software, you can use a solar project in several places and compare the efficiency of the system in each place [17]. Solar energy can produce about 11 to 16 percent of the energy needed in the world [18].

Material and Method

The PV cell's equivalent circuit model is depicted in Figure (1), consisting of an ideal parallel current source, reverse diode, series resistance, and parallel resistance.

$$I_{out} = I_{ph} - I_r[\exp(\frac{q(V_{in} + i_R)}{CKT}) - 1] - \frac{(V_{in} + iR_s)}{R_{sh}} \quad (1)$$

I_r is the reverse saturation current for PV, which mainly depends on temperature (its value is 10^{-4} A), q is the electric charge ($1/6 \times 10^{-19}$C), T is the temperature of the PV cell, K is Boltzmann's constant ($1/38 \times 10^{-23}$J/K), C is the ideal coefficient. I is the output current of the PV cell, U is the input voltage of the PV cell, R_s and R_{sh} are the equivalent resistances related to temperature.

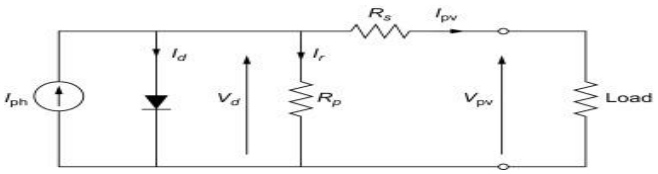


Figure 1. Circuit related to PV

A panel with a larger capacity is used so that it occupies less space and has high efficiency. In fact, when a smaller area is occupied, the cost will be lower. Its details are:

- Mpp voltage : 41.5 v
- Short circuit current : 10.22 A
- Open circuit voltage : 49.7 v
- Max voltage : 1000 v

Also :

$C_{min\text{-}inv} = C_S \times 0.9$ (2)

$C_{min\text{-}inv}$ is Minimum inverter capacity, and C_S is Solar power plant capacity.

The total number of panels for the project is determined as follows:

$$N_{PV} = \frac{P}{P_{Cell}} \quad (3)$$

N_{PV} is number of panels, P is power of Powerhouse and P_{cell} is power of one panel.

In this paper there are some important dates for example panels are in Tabriz with the latitude 38.08 and longitude 46.28 , altitude 1364 m and fixed angle of 33 degrees to the south .When the angle is 38 degrees, the value of GlobHor is 1885.7. Now we change the angle to get the most optimal state. Because at the most optimal angle, we will have the most radiation. Therefore, we change the angle from 38 degrees to 30 degrees. In this case, the value of GlobHor increases to 2050, so the amount of radiation has increased so it will be the optimal model for this system.

Results and Discussion

For 1 MW power plant, inverters of different types can be used. In this paper Kaco new energy inverter is used that is string.

After selecting the panels module and type of inverter, the software automatically detects that it is better to have 19 inverters for this situation. It should be noted that the number of inverters is not selected by the user. The user only selects the type of inverter and its power. The efficiency characteristic curve for the blue planet is displayed in figure 2.

After selecting the panels and inverters, the arrangement of the panels begins. The panels are arranged in a wedge so that there is the least amount of shading. When we place it horizontally, the shading and losses are reduced due to the placement of the bypass diodes in the path, therefore, among the horizontal and vertical placement of the panels, the horizontal mode is the most optimal because the shading is reduced and Therefore, the efficiency increas .Now, after checking the optimal conditions, the results are obtained that the most optimal conditions are created at an angle of 30 degrees, which is the result of the graph below and is related to the amount of electricity production.

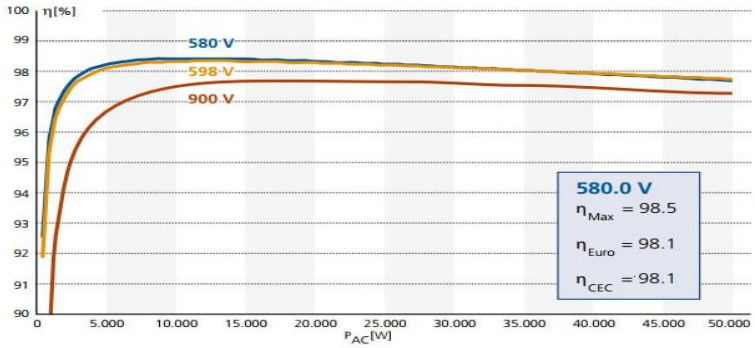


Figure2. The efficiency characteristic curve for the blue planet 50.0 TL3 INT

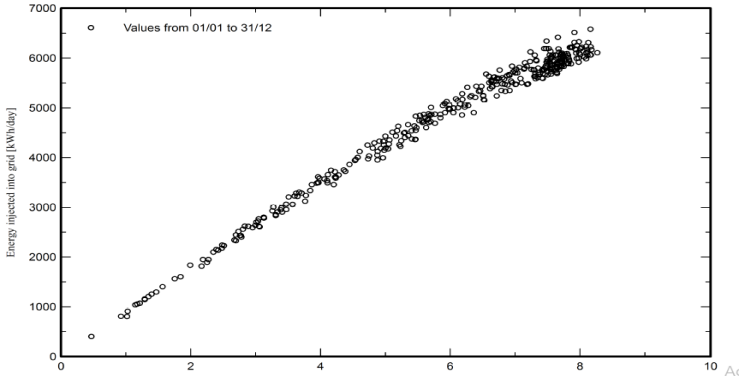


Figure 3. The quantity of power being generated and injected into the network

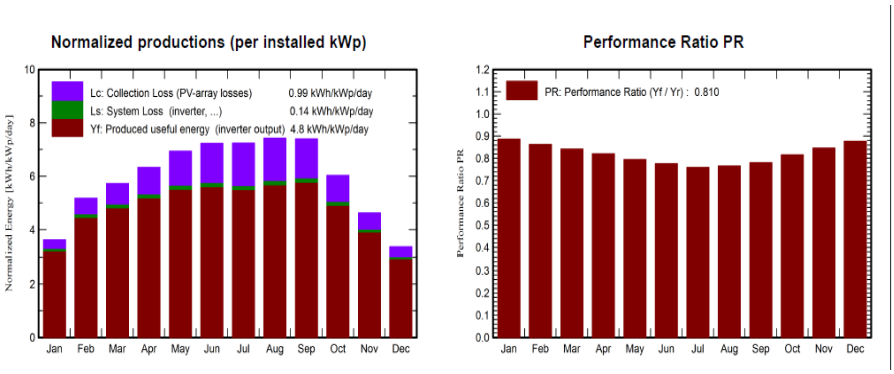


Figure .4. a) A diagram showing the monthly energy losses from equipment and received energy.
b) The power generation of the power plant during various months throughout the year.

Figure (4a) illustrates the average monthly losses per energy produced by PVs at the output of the inverter in this system. These losses are higher during hot months. Figure (4b) displays the performance coefficient of the power plant during one year, . The optimal efficiency range for the power plant is about between 80% and 90%, based on the distribution of energy injected into the grid compared to the amount of energy received by PV.

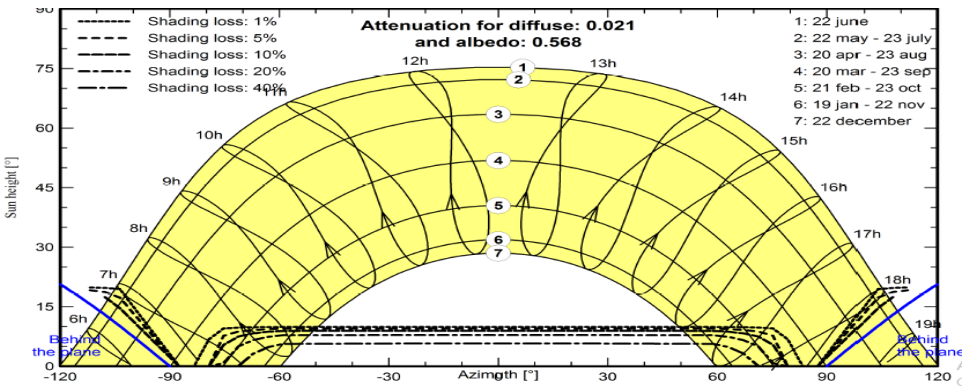


Figure 5. ISO-Shadings diagram for horizontal mode

The diagram illustrating the overall losses of the system, from receiving solar radiation energy to injecting total energy into the network over a year, reveals that the highest loss is 7%. This is primarily due to panel efficiency in standard conditions and ambient temperature. The panel set's energy intake was 2028 (MWh/year) at the power plant complex, but after deducting system losses, it reached 1750 (MWh/year) upon injection into the grid.

Conclusion

In this article, an optimal method was presented to create the most optimal mode by considering the type of panel and inverter and their power. Among the horizontal and vertical modes, the horizontal model was chosen because this mode creates the most optimal mode for us because it reduces shading. Finally, a photovoltaic system was created in 147 strings and 17 series with 2499 panels and the overall efficiency of the system is 56.

References

[1] R. Kumar, C. Rajoria, A. Sharma, and S. Suhag, "Design and simulation of standalone solar PV system using PVsyst Software: A case study," *Materials Today: Proceedings,* vol. 46, pp. 5322-5328, 2021.

[2] C. Kandasamy, P. Prabu, and K. Niruba, "Solar potential assessment using PVSYST software," in *2013 International Conference on Green Computing, Communication and Conservation of Energy (ICGCE)*, 2013: IEEE, pp. 667-672.

[3] B. Belmahdi and A. El Bouardi, "Solar potential assessment using PVsyst software in the northern zone of Morocco," *Procedia Manufacturing,* vol. 46, pp. 738-745, 2020.

[4] R. Tallab and A. Malek, "Predict system efficiency of 1 MWc photovoltaic power plant interconnected to the distribution network using PVSYST software," in *2015 3rd International Renewable and Sustainable Energy Conference (IRSEC)*, 2015: IEEE, pp. 1-4.

[5] S. Jianping, "An optimum layout scheme for photovoltaic cell arrays using PVSYST," in *2011 International Conference on Mechatronic Science, Electric Engineering and Computer (MEC)*, 2011: IEEE, pp. 243-245.

[6] A. A. Ghavifekr, A. Mohammadzadeh, and J. F. Ardashir, "Optimal placement and sizing of energy-related devices in microgrids using grasshopper optimization algorithm," in *2021 12th Power Electronics, Drive Systems, and Technologies Conference (PEDSTC)*, 2021: IEEE, pp. 1-4.

[7] A. F. Abriz, A. A. Ghavifekr, M. Soltaninejad, A. Tavana, A. Safari, and S. Ziamanesh, "Modified cuckoo optimization algorithm for frequency regulation of microgrids," in *2023 8th International Conference on Technology and Energy Management (ICTEM)*, 2023: IEEE, pp. 1-5.

[8] H. Salimi, A. A. Ghavifekr, A. Mohammadzadeh, S. Ziamanesh, A. Tavaana, and S. H. Dizaji, "Modified Grey Wolf Optimization Method for Voltage and Frequency Control of an Islanded Microgrids," in *2021 11th Smart Grid Conference (SGC)*, 2021: IEEE, pp. 1-5.

[9] A. A. Ghavifekr, "Application of heuristic techniques and evolutionary algorithms in microgrids optimization problems," *Microgrids: Advances in Operation, Control, and Protection,* pp. 219-251, 2021.

[10] A. Safari and A. A. Ghavifekr, "Use case of artificial intelligence and neural networks in energy consumption markets and industrial demand response," *Industrial demand response: methods, best practices, case studies, and applications,* vol. 4, p. 379, 2022.

[11] A. G. Hanizi and A. A. Ghavifekr, "An Innovative Method for Converting Solar Thermal Energy into Electrical Power," in *2023 13th Smart Grid Conference (SGC)*, 2023: IEEE, pp. 1-6.

[12] A. Mohammadzadeh and A. A. Ghavifekr, "Converter switching mechanism scheduling by type-2 fuzzy approach for PV/battery/Fuel systems," in *2021 12th Power Electronics, Drive Systems, and Technologies Conference (PEDSTC)*, 2021: IEEE, pp. 1-5.

[13] J. F. Ardashir, B. Rozmeh, M. Gasemi, A. M. Shotorbani, and A. A. Ghavifekr, "A Novel Boost Fifteen-Level Asymmetrical Flying-Capacitor Inverter with Natural Balancing of Capacitor Voltages," in *2021 12th Power Electronics, Drive Systems, and Technologies Conference (PEDSTC)*, 2021: IEEE, pp. 1-5.

[14] M. H. Mahmood, R. H. Mohammed, H. F. Hashim, and A. A. Al-Hilali, "Performance Analysis of 20kW Rooftop Photovoltaic System Installed at MTU University Using PVsyst Software," in *2023 Second International Conference on Electrical, Electronics, Information and Communication Technologies (ICEEICT)*, 2023: IEEE, pp. 01-06.

[15] A. Shrivastava, R. Sharma, M. K. Saxena, V. Shanmugasundaram, and M. L. Rinawa, "Solar energy capacity assessment and performance evaluation of a standalone PV system using PVSYST," *Materials Today: Proceedings,* vol. 80, pp. 3385-3392, 2023.

[16] T. Monu and S. Vadhera, "Optimum Tilt-Pitch Analysis and Design of 25kW Grid Connected Solar PV System using PVSyst Software," in *2023 International Conference for Advancement in Technology (ICONAT)*, 2023: IEEE, pp. 1-4.

[17] T. Rawat, J. Singh, and S. Sharma, "PVsyst Based Comparative Analysis of 1 MW Solar Plant in Jaipur and Dehradun," in *2023 International Conference on Power, Instrumentation, Energy and Control (PIECON)*, 2023: IEEE, pp. 1-5.

[18] M. S. Morshed, S. M. Ankon, M. T. H. Chowdhury, and M. A. Rahman, "Designing of a 2kW stand-alone PV system in Bangladesh using PVsyst, Homer and SolarMAT," in *2015 3rd International Conference on Green Energy and Technology (ICGET)*, 2015: IEEE, pp. 1-6.

Advanced Engineering Days

aed.mersin.edu.tr

EEG-Based Classification of Mental Stress Induced by Arithmetic Task

Morteza Jafari Malali [1], Sepideh Zolfaghari [*1], Aysel Davar [1]

[1]University of Tabriz, Faculty of Electrical and Computer Engineering, Iran, mortezajafarimalali@gmail.com, sepideh.zolfaghari@tabrizu.ac.ir, ayseldavar@gmail.com

Cite this study: Malali, M. J., Zolfaghari, S., & Davar, A. (2024). EEG-Based Classification of Mental Stress Induced by Arithmetic Task. Advanced Engineering Days, 9, 577-580

Keywords
Electroencephalogram
Arithmetic task
Feature extraction
Classification
Stress

Abstract

Exposure to prolonged stress gives rise to various health issues. It is crucial to diagnose stress as early as possible to prevent its detrimental consequences. This study aimed to investigate the Electroencephalography (EEG) signals of 36 subjects to distinguish between the stress from the rest state while engaging in mental arithmetic tasks. These signals were pre-processed and power spectrums of segmented signals were obtained using the Fast Fourier transform (FFT) method. As features, the standard deviation (STD) of power spectrums was calculated in delta, theta, alpha, beta, and gamma frequency bands. Then, important features were selected by Principal component analysis (PCA) and fed into machine learning classifiers. Based on the results, the highest classification accuracy of 93.3% and 86.6% were achieved using a multi-layer perception (MLP) classifier in gamma and beta frequency bands, respectively. Moreover, topographic maps of the brain showed substantial differences in these frequency bands that can be related to stress or concentration.

Introduction

In modern societies, excessive stress has become a prominent concern among individuals. Although stress is a natural response of the body to a particular situation, it can lead to notable problems such as depression, anxiety, sleep disturbances, heart disease, and high blood pressure [1]. Numerous studies have been executed on stressors in real-time or over the long term by considering several conditions and stimuli to observe brain electrical activities. These stress-inducing methods can be broadcasting images in virtual reality [2], the stroop colour test [3], public speaking engagements [4], and mental arithmetic tasks [5]. Mental arithmetic can lead to stress by activating different parts of the brain and affecting the autonomic nervous system [6]. In various studies, electroencephalogram (EEG) signals, which is a non-invasive and cost-effective method, have been analyzed to reveal changes caused by math calculation on brain [7]. Immediate diagnosis of chronic stress using an EEG signal may offer a novel therapeutic intervention for hampering disease progression. Researchers have attempted to discern stress from stress-free states by employing feature extraction and classification methods [8-9]. Extracting features can be implemented in time domain, frequency domain, and time frequency domain. To classify signals into different classes, machine learning algorithms are used.

In this study, several classifiers including Random Forest (RF), K-Nearest Neighbor (KNN), Naive Bayes (NB), multi-layer perception (MLP) and support vector machine (SVM) were used to automatically classify mental arithmetic tasks and resting states in different frequency bands. In addition, a topographic map of the brain was drawn to investigate changes occurring as a result of executing arithmetic tasks.

Material and Method

In this article, five steps were taken to classify the cognitive activity of the individuals while calculating math problems and their rest states through EEG signals. As illustrated in Figure 1, these steps include data acquisition, pre-processing, feature extraction, feature selection, and classification that were simulated in Python 3.8.

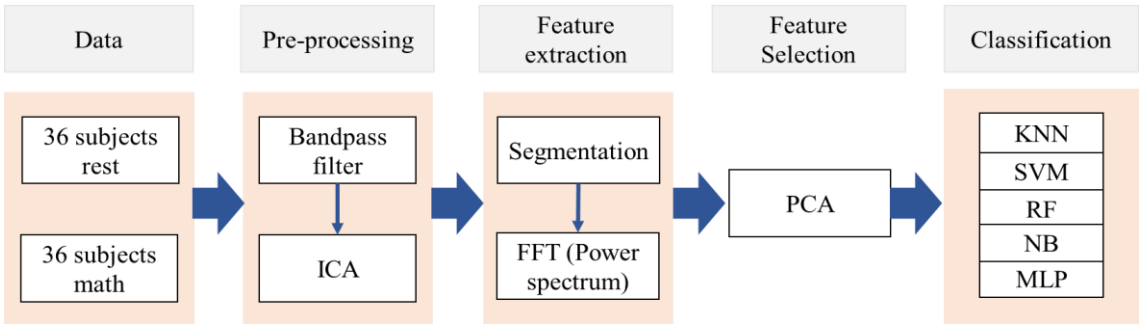


Figure 1. The block diagram of the proposed method

The publically available dataset was used in this work, containing 19 EEG signals of 36 healthy subjects aged between 18 and 26 years old during the performance of arithmetic task (subtraction of two numbers) and resting state [10]. The participants received questions orally and responded by moving their fingers. The EEG signals were preprocessed using a band-pass filter from 0.5 to 45 Hz and Independent component analysis (ICA) to remove artifacts. To extract features, signals with the length of 62 seconds were divided into 62 segments, each consisting of 500 samples. The Fast Fourier transform (FFT) method was applied to these segments for obtaining power spectrums in the theta (4-8 Hz), alpha (8-13 Hz), beta (13-30 Hz), and gamma (30-45 Hz) frequency bands [11]. For each frequency domain, the Standard deviation (STD) of power spectrums were collected to create a feature vector containing 62 features, as shown in Fig 2. Since 19 EEG channels were utilized, the total number of features for a subject became 19×62. Features were standardized and then 22 discriminative features were selected using Principal component analysis (PCA) method [12].

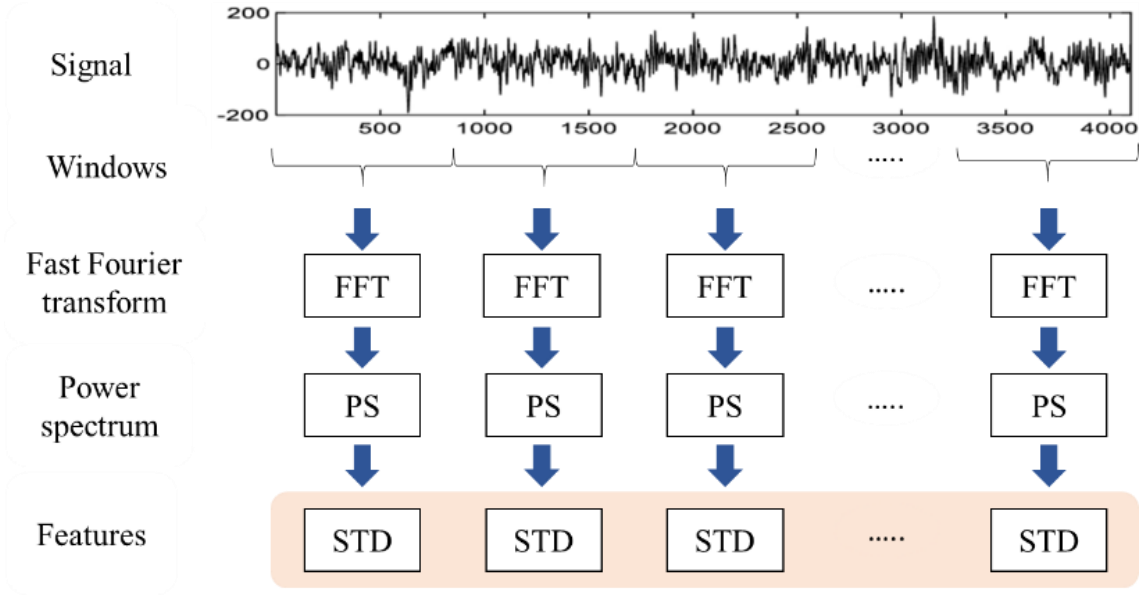


Figure 2. Steps for feature extraction

After labeling features based on rest and math conditions, the data was divided into test and training sets containing 20% (14 subjects) and 80% (58 subjects) of data. In addition, a 5-fold cross-validation was applied. Features of the training set were fed into RF, KNN, MLP, NB, SVM classifiers [13]. These classifiers were tuned using hyper-parameters mentioned in Table 1 to construct appropriate models capable of accurately predicting unseen data. Followed by training these models, their performance was evaluated with the test set.

Table 1. tuning hyper-parameters of classifiers

Classifier	Hyper-parameters
KNN	K=4
SVM	Kernel=RBF, C=5
RF	gini criterion
NB	Bernoulli distribution
MLP	Hidden layer size=(10,10), Learning rate=0.01, Optimizer=SGD, Max_iteration=2000

Results and Discussion

Table 2 presents the classification accuracies in different frequency bands. It is evident that the MLP and SVM classifiers could successfully distinguish between cognitive tasks and rest states, compared to other classifiers. Furthermore, the highest results were related to gamma and beta frequency bands. Regarding the gamma and beta bands, the highest accuracy was achieved by the MLP classifier with 93.3% and 86.6%, respectively. However, the lowest accuracy was reported for the KNN classifier. In the alpha and theta bands, classification accuracy experienced a significant decrease. The results indicate that gamma and beta bands have an important role in concentration and stress.

Table 2. Classification accuracy for different frequency bands

	RF	KNN	MLP	NB	SVM
Gamma	88.3	68.0	93.3	83.0	92.8
Beta	80.7	66.8	86.6	82.2	85.9
Alpha	61.9	63.4	80.0	62.7	68.4
Theta	70.0	66.6	73.3	70.6	68.2

In Figure 3 EEG topographic maps for subject 17 at rest (a) and during the calculation of math subtraction (b) were depicted in five frequency bands. For generating brain maps, the Power spectral density (PSD) method with a rectangular window (length of 500 samples) was used. According to these maps, significant differences can be observed in high-frequency bands.

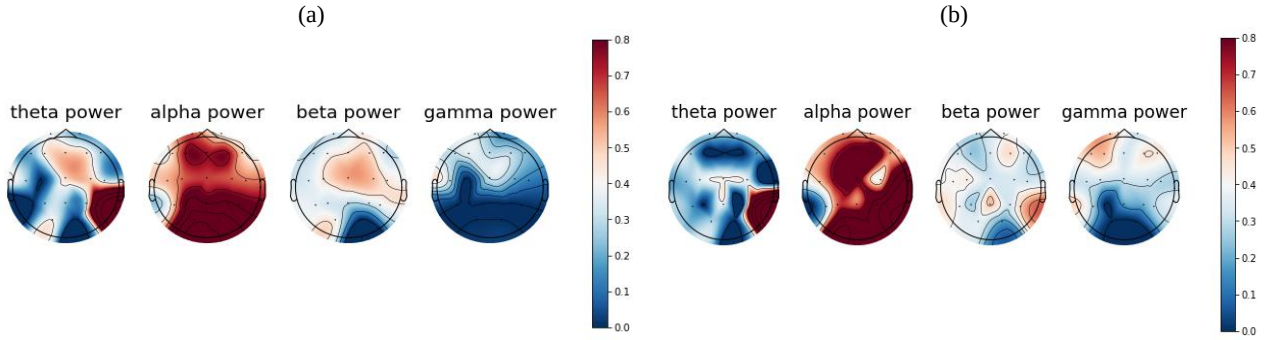


Figure 3. EEG topographic maps in theta, alpha, beta, and gamma bands at rest (a) and calculating math (b)

More complex brain functions, such as concentration and stress, typically manifest at higher frequencies. The significant increase in power in the frontal and temporal regions at gamma frequency suggests that mental arithmetic induces stress in individuals. In the central region of the brain, a decrease in power at beta frequency was observed, which can be attributed to decision-making and finger movement for responses. During mental arithmetic and cognitive tasks, it is common for multiple emotions to be activated in the brain. Among these emotions, stress and concentration are particularly notable during mental calculations.

Conclusion

The study analyzed EEG signals from 36 healthy individuals while they were performing arithmetic tasks and during rest with their eyes closed. By extracting STD features of power spectrums in various frequency bands and using them as inputs to classifiers, a suitable comparison was made between the classifiers. MLP and SVM were identified as the best classifiers with high accuracy rates. The achievement of high accuracy in the beta and gamma bands indicates the influence of mental arithmetic on high-frequency bands.

References

1. Atchley, R., Ellingson, R., Klee, D., Memmott, T., & Oken, B. (2017). A cognitive stressor for event-related potential studies: the Portland arithmetic stress task. Stress, 20(3), 277-284.
2. Johnston, D., Bell, C., Jones, M., Farquharson, B., Allan, J., Schofield, P., ... & Johnston, M. (2016). Stressors, appraisal of stressors, experienced stress and cardiac response: A real-time, real-life investigation of work stress in nurses. Annals of Behavioral Medicine, 50(2), 187-197.
3. Hou, X., Liu, Y., Sourina, O., Tan, Y. R. E., Wang, L., & Mueller-Wittig, W. (2015, October). EEG based stress monitoring. In 2015 IEEE international conference on systems, man, and cybernetics (pp. 3110-3115). IEEE.

4. Davidson, R. J., Marshall, J. R., Tomarken, A. J., & Henriques, J. B. (2000). While a phobic waits: Regional brain electrical and autonomic activity in social phobics during anticipation of public speaking. Biological psychiatry, 47(2), 85-95.
5. Al-Shargie, F. M., Tang, T. B., Badruddin, N., & Kiguchi, M. (2016). Mental stress quantification using EEG signals. In International conference for Innovation in Biomedical Engineering and Life Sciences: ICIBEL2015, 6-8 December 2015, Putrajaya, Malaysia 1 (pp. 15-19). Springer Singapore.
6. Wang, X., Liu, B., Xie, L., Yu, X., Li, M., & Zhang, J. (2016). Cerebral and neural regulation of cardiovascular activity during mental stress. BioMedical Engineering OnLine, 15, 335-347.
7. Jun, G., & Smitha, K. G. (2016, October). EEG based stress level identification. In 2016 IEEE international conference on systems, man, and cybernetics (SMC) (pp. 003270-003274). IEEE.
8. Sulaiman, N., Taib, M. N., Lias, S., Murat, Z. H., Aris, S. A. M., & Hamid, N. H. A. (2011, March). EEG-based stress features using spectral centroids technique and k-nearest neighbor classifier. In 2011 UkSim 13th international conference on computer modelling and simulation (pp. 69-74). IEEE.
9. Memar, M., Mokaribolhassan, A., & Ghavifekr, A. A. (2021, February). Review on machine learning frameworks in drivers' physiological signal analysis to detect stress. In 2021 7th International Conference on Control, Instrumentation and Automation (ICCIA) (pp. 1-6). IEEE.
10. Seleznov, I., Zyma, I., Kiyono, K., Tukaev, S., Popov, A., Chernykh, M., & Shpenkov, O. (2019). Detrended fluctuation, coherence, and spectral power analysis of activation rearrangement in EEG dynamics during cognitive workload. Frontiers in human neuroscience, 13, 270.
11. Cerna, M., & Harvey, A. F. (2000). The fundamentals of FFT-based signal analysis and measurement (pp. 1-20). Application Note 041, National Instruments.
12. Abdi, H., & Williams, L. J. (2010). Principal component analysis. Wiley interdisciplinary reviews: computational statistics, 2(4), 433-459.
13. Zolfaghari, S., Yousefi Rezaii, T., & Meshgini, S. (2024). Applying Common Spatial Pattern and Convolutional Neural Network to Classify Movements via EEG Signals. Clinical EEG and Neuroscience, 15500594241234836.

Advanced Engineering Days

aed.mersin.edu.tr

A Third-Order Quadrature Sinusoidal Oscillator Using Operational Amplifiers

Mohammad Rashtian*[1], Mahdi Shabani [1], Houman Farsadpour [1]

[1]*Civil Aviation Technology College, Department of aviation electronics, Iran, rashtian@catc.ac.ir, mahdi.shabani@ms.catc.ac.ir, houman.farsadpour@ms.catc.ac.ir*

Cite this study: Rashtian, M., Shabani, M., Farsadpour, H. (2024). A Third-Order Quadrature Sinusoidal Oscillator Using Operational Amplifiers. Advanced Engineering Days, 9, 581-583

Keywords
Third-Order Quadrature Sinusoidal Oscillators
Inverse High Pass Filter
Operational Amplifier
Oscillation Condition
Oscillation Frequency

Abstract

This paper proposes a third-order quadrature sinusoidal oscillator (TOQSO) based on the use of a second-order inverse high-pass active filter utilizing OP-07 ICs. In contrast to previous complex methods, this approach employs a simpler design. It combines a second-order inverse high-pass active filter with a standard lossless integrator in a cascaded configuration. This design leverages the lossless integrator to generate quadrature voltage outputs. The paper demonstrates the versatility of this method by showcasing its ability to create various TOQSOs, including a voltage-mode TOQSO built with operational amplifiers (op-amps). The proposed TOQSO has independent control of both the oscillation condition (CO) and the oscillation frequency (FO), is low cost and low sensitive. Finally, the paper validates the theoretical concepts and simulations through experimental results.

Introduction

In communications and instrumentation systems, quadrature oscillators play a critical role due to their inherent ability to generate two sinusoidal waveforms with a 90° phase difference. This unique feature makes them essential in a variety of applications. Quadrature mixers and single-sideband generators in telecommunications use these oscillators. They are also important in instrumentation, such as vector generators and selective voltmeters. As a result, quadrature oscillators have become an indispensable element in a wide range of communications and instrumentation systems [1-3].

Recently, A third-order quadrature sinusoidal oscillator based on inverse high-pass filters was proposed. The paper [4] presented a new, simple method for realizing a quadrature oscillator which consists of a second-order high-pass active filter cascaded by a lossless inverting integrator in a unity feedback loop. The functionality of this approach was validated using current feedback operational amplifiers (CFOAs). Notably, this method offers independent control over both the oscillation condition (CO) and the oscillation frequency (FO). Consequently, this new approach broadens the spectrum of techniques available in the literature for realizing third-order quadrature sinusoidal oscillators (TOQSOs).

This paper proposes a new third-order quadrature sinusoidal oscillator based on [4] method and implemented using operational amplifiers. The proposed circuit configuration generates two sinusoidal outputs with a 90° phase difference. This oscillator leverages third-order characteristic equations, enabling independent control of both the oscillation condition and frequency, similar to the approach presented in [4]. The circuit's reliance on widely available operational amplifiers offers several advantages, including low output impedance, high current drive capability for driving various loads, a simple design, and cost-effectiveness.

Material and Method

For a third-order sinusoidal oscillator, the generalized CE can be expressed as:

$$a_3 s^3 + a_2 s^2 + a_1 s + a_0 = 0 \quad (1)$$

The CE of TOQSO is equal to the following expression:

$$a_3 s^3 = -(a_2 s^2 + a_1 s + a_0) \quad (2)$$

$$1 - \left(\frac{a_2 s^2 + a_1 s + a_0}{s^2}\right)\left(\frac{-1}{a_3 s}\right) = 0 \quad (3)$$

Equation (3) presents an alternative TOQSO design that employs a cascaded non-inverting second-order IHPF and inverting lossless integrator with a unity feedback loop. Figure 1 shows the implementation of the TOQSO based on operational amplifier using the proposed approach.

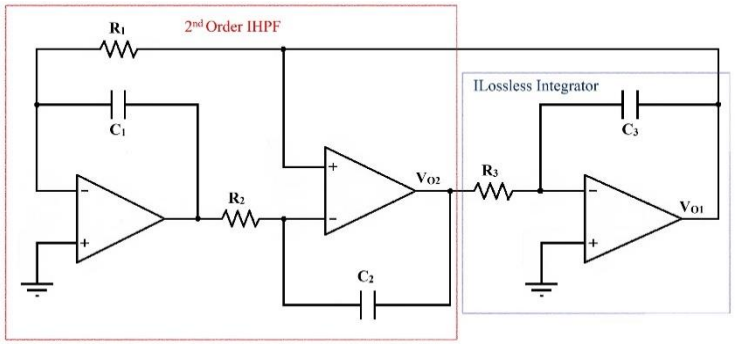


Figure 1. TOQSO implementation based on proposed method using operational amplifiers

The equation that expresses the characteristics of the circuit in Figure 1 is as follows:

$$(C_1 C_2 C_3 R_1 R_2 R_3)s^3 + (C_1 C_2 R_1 R_2)s^2 + (C_1 R_1)s + 1 = 0 \quad (4)$$

Setting s = jω and solving for the real and imaginary parts equal to zero allows us to determine the oscillation condition and the corresponding oscillation frequency in this TOQSO as follows:

$$CO: \quad \frac{R_3}{R_1} = \frac{C_1}{C_3} \quad (5)$$

$$FO: \quad \omega_0 = \frac{1}{\sqrt{C_1 C_2 R_1 R_2}} \quad (6)$$

Equations (5) and (6) show that the oscillation condition and oscillation frequency can be independently controllable.

The resistor R_3 allows for independent adjustment of CO, while R_2 controls FO independently, on the condition that C_1 and C_3 are equal.

The voltage transfer function from V_{O2} to V_{O1} From Figure 1 is:

$$\frac{V_{O1}}{V_{O2}} = \frac{-1}{sC_3R_3} \quad (7)$$

The transfer function shows that the phase difference between V_{O2} and V_{O1} is 90°. It ensures that the voltages are in quadrature.

The equations show that the TOQSO in Figure 1 exhibits low sensitivity to variations in its passive components, obtained as:

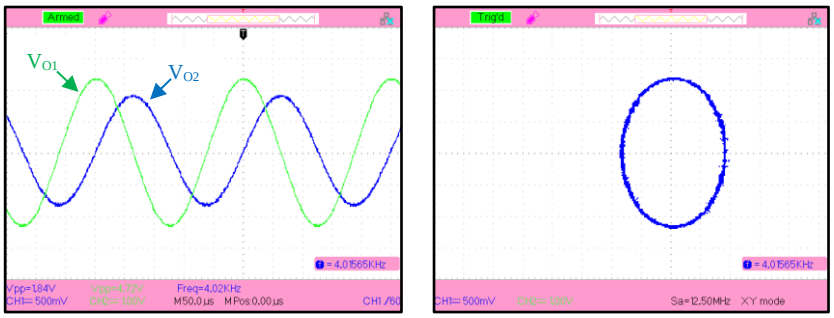
$$S^{\omega_0}_{R_1,R_2,C_1,C_2} = -0.5 \quad (8)$$

Results

The TOQSO in Figure 1 was bread-boarded using OP-07s. Figure 2 (a) represents the experimental quadrature sinusoidal output waveforms of Figure 1 with $C_1 = C_3 = 12$nF, $C_2 = 33$nF, $R_1 = R_3 = 1.2$kΩ, $R_2 = 3.3$k and the power supply ±8V. Figure 2 (b) shows the experimental Lissajous pattern between V_{O1} and V_{O2}. The nominal frequency this circuit is 4.019kHz.

Figure 2 (a) shows that the peak-to-peak output voltages, V_{O1} and V_{O2}, are 4.72V and 1.84V, respectively, with a phase difference of 90.72°. This phase difference indicates a phase error of 0.72°, which is considered favorable. An examination of the Lissajous pattern in Figure 2 (b) demonstrates a perfect match with the results predicted

by simulation. The oscillation frequency is also 4.015 kHz. The results obtained confirm the actual performance of the circuit and validate the simulation results in Pspice.



(a) (b)

Figure 2. The experimental results of TOQSO shown in Figure 1 (a) Quadrature sinusoidal output waveforms of V_{O1} and V_{O2} (b) Lissajous pattern between V_{O1} and V_{O2}

Discussion

The application of the recently proposed approach in [4] for TOQSO design, in conjunction with traditional operational amplifiers (op-amps), represents an intriguing avenue for future investigation. This approach expands the documented TOQSO implementation methods. Additionally, the utilization of novel advanced op-amps could prove advantageous in terms of low power consumption and high speed [5,6], which could be discussed in future explorations.

Conclusion

This paper presents a new third-order quadrature sinusoidal oscillator (TOQSO). The TOQSO is designed using a new, simple approach that utilizes inverse active filters combined with cascaded conventional integrators (both lossy and lossless). The implementation uses a second-order inverse high-pass filter cascaded with an inverting lossless integrator in a unity feedback loop. To verify the experimental results, this TOQSO was designed and tested using operational amplifiers. The measured phase difference between the output voltages was approximately 90.72°, and the simulated total harmonic distortion (THD) in Pspice was found to be as low as 0.19% and 0.69% for V_{O1} and V_{O2}, respectively.

The proposed TOQSO offers several advantages over existing solutions. These include the ability to generate two simultaneous sinusoidal outputs with a 90-degree phase difference, independent control of oscillation condition and frequency, low output impedance and high current drive capability. In addition, they are designed to be simple, cost-effective, and have low sensitivity to component variations.

References

1. Horng, J.W. (2002). Current Differencing Buffered Amplifiers Based Single Resistance Controlled Quadrature Oscillator Employing Grounded Capacitors. IEICE Transactions on Fundamentals of Electronics, Communications and Computer Sciences, E85-A, 1416-1419.
2. Kumngern, M., & Dejhan, K. (2009). DDCC-Based Quadrature Oscillator with Grounded Capacitors and Resistors. Active and Passive Electronic Components, 2009, 1–4.
3. Oliveira, L. B., Fernandes, J. R., Filanovsky, I. M., Verhoeven, C. J., & Silva, M. M. (2008). Analysis and design of quadrature oscillators. Springer eBooks.
4. Raj, A. (2023). New Approach of deriving Third-Order Quadrature Sinusoidal Oscillators. JICS. Journal of Integrated Circuits and Systems, 18(3), 1–5.
5. Rashtian, M. (2021). Adaptive double recycling folded cascode amplifier. Analog Integrated Circuits and Signal Processing, 110(1), 165–174.
6. Rashtian, M., Vafapour, M. (2021). Gain boosted folded cascode Op-Amp with capacitor-coupled auxiliary amplifiers. International Journal of Engineering, 34(5), 1233-1238.

Advanced Engineering Days

aed.mersin.edu.tr

Design and Characterization of a Discrete Curvature-Compensated Bandgap Voltage Reference

Mohammad Rashtian [1], Houman Farsadpour [1], Mahdi Shabani [1], Ali Karimi [1]

[1]*Civil Aviation Technology College, Department of Aviation Electronics, Iran, rashtian@catc.ac.ir, houman.farsadpour@ms.catc.ac.ir, mahdi.shabani@ms.catc.ac.ir, ali.karimi.mehtar@ms.catc.ac.ir*

Cite this study: Rashtian, M., Farsadpour, H., Shabani, M., & Karimi, A. (2024). Design and Characterization of a Discrete Curvature-Compensated Bandgap Voltage Reference. Advanced Engineering Days, 9, 584-586

Keywords
Bandgap voltage reference
Temperature Coefficient
Line Sensitivity
Power Supply Ripple Rejection

Abstract

This paper presents a theoretical and simulation analysis of a Bandgap Voltage Reference circuit without MOSFETs using an Operational Amplifier (OP-Amp) and a Bipolar Junction Transistor (BJT). Manufacturing results are also included. The original proposed circuit and the modified circuit are simulated using LTSpice software. The Temperature Coefficient (TC) of the output voltage is approximately 6.18 ppm/°C over a temperature range of 0°C to 100°C. The Line Sensitivity (LS) of the circuit is 0.00073%/V in the range of 2.3 V to 20 V. The absolute value of the Power Supply Ripple Rejection (PSRR) at an input frequency of 100 Hz is 63.82 dB. With the modified circuit, the Temperature Coefficient of the output voltage is reduced to 3.49 ppm/°C.

Introduction

Voltage and current references with low temperature and low process dependence play a critical role in many analog circuits such as switched capacitor filters, data processing systems, high-precision op-amps, ADC, DAC, etc. [1]. Ideally, this block produces a constant DC voltage of known amplitude that does not vary with temperature or process variation.

BJTs are at the heart of many bandgap circuits. Their base-emitter voltage exhibits a predictable decrease with increasing temperature. This inherent characteristic serves as a temperature-dependent voltage source. They can also be used as a current source. By forcing a constant current through a pair of BJTs with different areas, the proportional to absolute temperature (PTAT) part is created. The op-amp plays a critical role in amplifying and manipulating the PTAT voltage or current from the BJTs. It helps combine this PTAT signal with a complimentary to absolute temperature (CTAT) which is created by VBE to cancel out the overall temperature dependence. The op-amp also provides negative feedback, ensuring that the output voltage remains stable despite variations in process parameters or component tolerances.

Due to the nonlinear behavior of the VBE temperature dependence [2], we have used a curvature compensation method [3], which is provided in the modified design.

Material and Method

As shown in Figure 1 (a), which is the circuit in [4] with a little change and looks similar to [5], due to the presence of the op-amp, the voltages at points X and Y are equal. The voltage across resistor R1 is proportional to the difference between two PN junctions ($V_T \ln n$), producing a PTAT current. The voltage at point X corresponds to the base-emitter voltage, which, in conjunction with resistor R3, produces a CTAT current.

Finally, these two currents are combined and flow through resistor R4.

$$\frac{\partial V_{BE}}{\partial T} = \frac{V_{BE} - (m+4)V_T - \frac{Eg}{q}}{T} = \frac{522mv - 62.5mv - 1120mv}{300^{ok}} = -2.2 \quad (1)$$

Based on the above equation we assume that $\frac{\partial V_{BE}}{\partial T}$ equals to -2.2 mv/°C. We also assume that n equals to 10.

$$V_{BG} = R_4 I_{C3} = \frac{R_4}{R_3} V_{BE} + \frac{R_4}{R_1} V_T \ln n = \frac{R_4}{R_3}\left(\frac{R_3}{R_1} V_T \ln n + V_{BE}\right) \quad (2)$$

Given these assumptions, based on (2) the resistance ratio R3/R1 is determined to be 11.109.

The voltage of a BJT does not change linearly with temperature, so the basic idea is to correct the nonlinear term by a proper combination of the V_{BE} across a junction with a temperature independent currentt and the V_{BE} across a junction with a PTAT current. Figure 1 (b) provides the following equations:

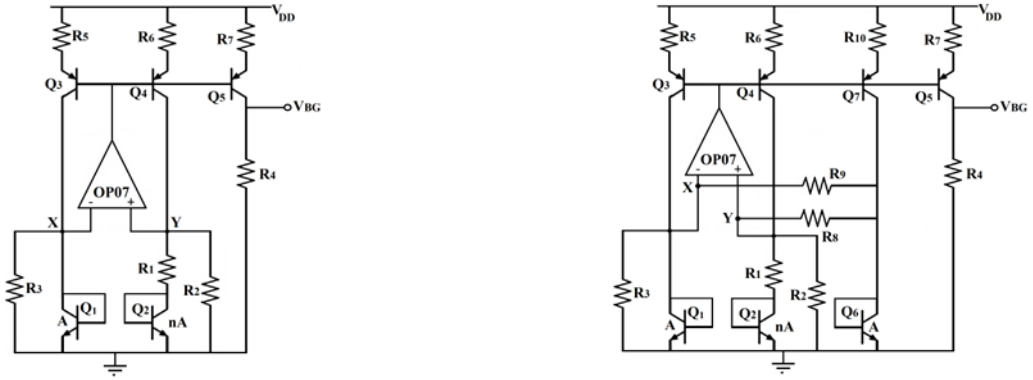
$$V_{BE6} = V_{BG} - (V_{BG} - V_{BE0})\frac{T}{T_0} - \eta V_T \ln\frac{T}{T_0}, V_{BE1,2} = V_{BG} - (V_{BG} - V_{BE0})\frac{T}{T_0} - (\eta - 1)V_T \ln\frac{T}{T_0} \quad (3)$$

$$V_{NL} = V_{BE6} - V_{BE1,2} = V_T \ln\frac{T}{T_0}, V_{BG} = V_T\left(\frac{R_4 \ln n}{R_1}\right) + V_{BE1}\left(\frac{R_4}{R_3}\right) + V_{NL}\left(\frac{R_4}{R_9}\right) \quad (4)$$

$$\frac{\partial V_{BG}}{\partial T}\left(1 + \frac{R_4}{R_3}\left(\frac{T}{T_0} - 1\right)\right) + \frac{R_4}{R_3 T_0} V_{BG} = \left(\frac{R_4}{R_9} - \frac{R_4}{R_3}(\eta - 1)\right)\left(\ln\frac{T}{T_0}\frac{\partial V_T}{\partial T} + \frac{V_T}{T}\right) \quad (5)$$

$$\frac{R_4}{R_9} - \frac{R_4}{R_3}(\eta - 1) = 0 \Rightarrow R_9 = \frac{R_3}{\eta - 1} \quad (6)$$

If we assume that η equals to 1.95 the resistance ratio of R3/R9 equals to 0.95.



(a) (b)

Figure 1. (a)Main Design, (b)Curvature-Compensated Design

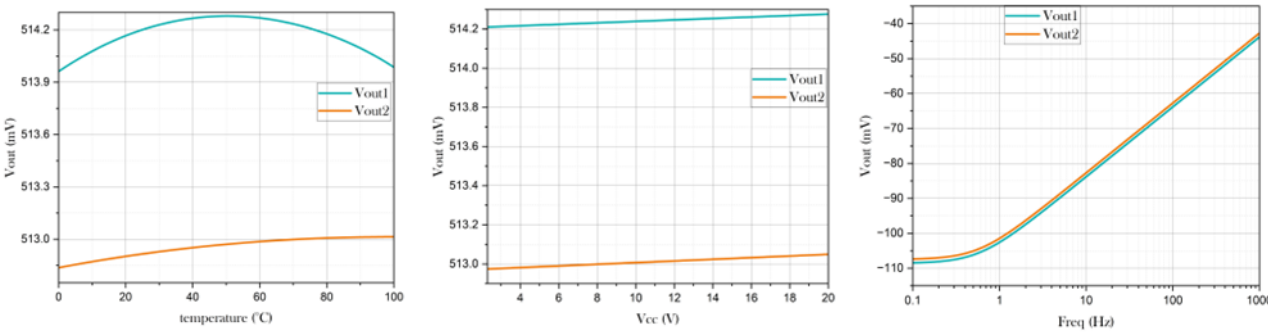
Table 1. Values

Items	Resistor	OP-Amp	Transistor
a*	R_1=10kΩ , $R_{2,3}$=108kΩ , R_4=47.64kΩ , $R_{5,6,7}$=56kΩ	OP07C	PNP:2N2907 , NPN:2N2222
b*	R_1=10kΩ , $R_{2,3}$=106kΩ , R_4=47.64kΩ , $R_{5,6,7}$=56kΩ , $R_{8,9}$=112kΩ	OP07C	PNP:2N2907 , NPN:2N2222

*a=Main Circuit
*b=Modified Circuit

Results

A comparison of the simulation results for the original and modified circuits is shown in Figure 2.



(a) (b) (c)

Figure 2. (a)TC Comparison, (b)LS Comparison, (c)PSRR Comparison

The measured results are as follows:

Table 2. Measured Results

Items	TC	LS	PSRR(100Hz)
a*	41.85 ppm/°C	0.00095 %/V	-63.67dB
b*	27.79 ppm/°C	0.00297 %/V	-63.32dB

*a=Main Circuit
*b=Modified Circuit

The practical circuit uses the OP07 CP operational amplifier. Due to resistor tolerances, discrepancies between experimental and simulation results have been observed. In addition, due to the lack of an oven or suitable alternative heating method for the circuit, the results regarding temperature-induced voltage variations are mere approximations. These limitations are due to the OP07 CP's maximum operating temperature of 70 degrees Celsius. However, the output line sensitivity (LS) has been accurately measured.

Discussion

When considering the design of a voltage reference, the offset of the operational amplifier (op-amp) has the greatest impact on circuit accuracy. However, mismatch errors in current mirrors, resistors, transistors, base-emitter voltage leakage, and resistor tolerances are collectively the primary sources of error in voltage references. In practice, equal-value resistors are used to balance the current mirrors. While the OP07 operational amplifier is a good choice due to its low offset, it's important to note that its operating temperature range is limited to about 70 degrees Celsius. Raising the circuit temperature to 100 degrees Celsius is not practical. In addition, for circuit testing to measure temperature-induced variations in output voltage, the use of an oven and chamber is recommended to ensure uniform temperature changes across all circuit components. To evaluate the power supply ripple rejection (PSRR), a function generator is connected to the circuit along with a 1-ohm resistor or capacitor.

Conclusion

After conducting both experimental and simulation tests, followed by a thorough comparison of the results, it is evident that the modified Curvature-Compensated circuit exhibits superior overall performance compared to the original design.

References

1. Rashtian, M., Hashemipour, O., & Navi, K. (2008). Design of a Low-Voltage High-Speed Switched-Capacitor Filters Using Improved Auto Zeroed Integrator. Journal of Applied Science, VOL.8, Issue 9, 1771-1775
2. Rashtian, M. (2020). Sub 1-V supply voltage-reference based on mutual temperature cancellation of V_T and V_{TH}. Analog Integrated Circuits and Signal Processing, VOL.105, 477-482.
3. Malcovati, P., Maloberti, F., Fiocchi, C., & Pruzzi, M. (2001). Curvature-Compensated BiCMOS Bandgap With 1-V Supply Voltage. IEEE Journal Of Solid State Circuits, VOL.36, NO.7, 1076-1081.
4. Banba, H., Shiga, H., Umezawa, A., Miaba, T., Tanzawa, T., Atsumi, S., & Sakui, K. (1999). A CMOS Bandgap Reference Circuit with Sub_1_V Operation. IEEE Journal Of Solid State Circuits, VOL.34, NO.5, 670-674.
5. Rashtian, M., & Hashemipour, O. (2023). Resistorless sub-bandgap CMOS voltage reference based on lateral BJT. Sādhanā, VOL.48, NO.54.

Advanced Engineering Days

aed.mersin.edu.tr

Transformer-BiGRU: Hybrid Deep Model for Wind Power Prediction

Elman Ghazaei [1], Amir A. Ghavifekr [1], Paolo Visconti [2]

[1] *University of Tabriz, Faculty of Electrical and Computer Engineering, Iran, elmangazayi@gmail.com, aa.ghavifekr@tabrizu.ac.ir*
[2] *University of Salento, Department of Innovation Engineering, Italy, paolo.visconti@unisalento.it*

Cite this study: Ghazaei, E., & Ghavifekr, A. A., & Visconti, P. (2024). Transformer-BiGRU: Hybrid Deep Model for Wind Power Prediction. Advanced Engineering Days, 9, 587-589

Keywords
Transformer-Bidirectional
Windfarm
Deep Learning
Electrical Grid
Power Prediction

Abstract

The integration of renewable energy sources like wind power into the electrical grid paves the way for emerging new generations of AI-based models to improve grid dependability and stability. In this paper, a new hybrid deep model called Transformer-BiGRU is presented to predict wind power. The Transformer Encoder and Bidirectional GRU could obtain many hidden and temporal features from the raw data which can boost the model's eventual performance. The proposed hybrid model can embrace and learn subtle and complex patterns in the data's different attributes (wind speed, direction, pressure, and air temperature) by utilizing its multi-head attention mechanism and bidirectional structure. The Transformer-BiGRU model demonstrates reliable and confident performance in comparison to other conventional Machine Learning-based models.

Introduction

With growing global energy demand and amplified concerns about climate change, the search for appropriate and environmentally responsible energy solutions like wind farms has become vital. In this context, renewable energy sources (RES) can play an important role in avoiding global and local concerns, and they can eradicate other routine and conventional approach problems like fossil fuels toward more eco-friendly alternatives[1].

One of the main components of RES is wind power. Some factors like installation strategic and novel designed to control the kinetic energy make it one of the reliable sources of electrical energy[2].

Deep Learning can gain a novel performance against conventional methods like Decision Trees and SVM, and its results are more reliable and accurate which can be utilized in real-world tasks. Deep models could extract many hidden and subtle features from the raw data since it has the intrinsic capability to decide which data segments can affect our results more[3-6]. In addition, multi-head attention mechanisms can put special weights on some parts of the data that can improve our model's final performance [7].

Different DL architectures have been applied to wind power prediction. For instance, Convolutional Neural Networks (CNNs)[8] operate convolutional operations to extract hidden features, Recurrent Neural Networks (RNNs)[9] to extract sequential features, Long Short-Term Memory networks (LSTMs) [10], or hybrid models like CNN-LSTM[11]. Conventional prediction techniques have shown their limitations in grasping the convoluted temporal and spatial features in wind farm data.

This paper addresses cited issues by presenting a novel method for wind farm power prediction, Transformer-BiGRU. Transformer Encoder as a cutting-edge deep learning model [12] could extract long sequential features by utilizing its Multi-head Attention mechanism. BiGRU has a bidirectional structure that can extract hidden features from both forward and backward [13].

Material and Method

In this paper, the Texas Wind Turbine Dataset [14] is used for training our model. To improve the efficacy of our experiment, the raw dataset has been separated into two distinct parts: The Training dataset and the Evaluating dataset. Moreover, MinMax Scaler is used for converting raw data into between 0 and 1.

The Transformer-BiGRU (Figure1) architecture is a hybrid model that combines the strengths of the Transformer Encoder and Bidirectional Gated Recurrent Unit (BiGRU) networks to enhance sequence modeling tasks. In this architecture, the input sequence is first processed through a Transformer encoder, which employs multi-head self-attention mechanisms to capture global dependencies and contextual relationships between all features in parallel. The output of the Transformer encoder is then fed into a BiGRU layer, which processes the sequence bidirectionally, considering both backward and forward context to capture local dependencies and sequential information effectively. This combination leverages the parallel processing capability and global context understanding of Transformers with the sequential and bidirectional context capturing abilities of BiGRUs.

The final output from the BiGRU layer is passed through the MLP (Multi-layer Perceptron) for regression tasks, to generate the desired output.

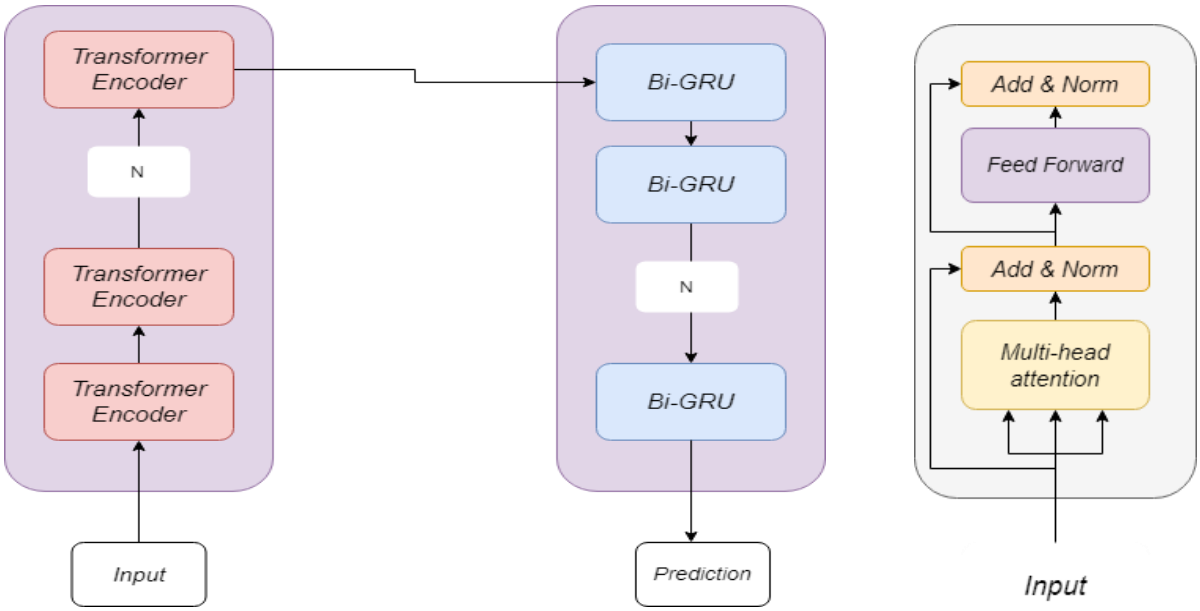


Figure 1. Transformer-BiGRU (right), Transformer Encoder (left)

Results

The results obtained through the evaluation of MSE, RMSE, and MAE contribute to an understanding of the predictive capabilities of the Transformer-BiGRU in the context of wind farm power prediction.

Table 1. Evaluation Results

	RMSE	MSE	MAE
Transformer Encoder	0.061	0.0038	0.038
Random Forest	4.64	21.38	2.56
Transformer-BiGRU	0.053	0.0025	0.027

In this paper, Adam optimizer is utilized for optimization tasks which can decrease the loss by modifying the weights based on gradient computations.

Discussion

As mentioned in the previous part, Transformer-BiGRU can obtain better performance in comparison to other state-of-the-art models like Transformer Encoder and Random Forest. The proposed model gains 0.053 at RMSE which is better than Transformer Encoder and Random Forest which achieves 0.061 and 4.64, respectively.

Conclusion

Renewable energy sources, such as wind power, are recognized as increasingly influential contributors to the energy zone. However, it has many challenges which experts search for solutions via AI-based models. For example, predicting wind power with high accuracy can lead us to use wind in the electrical grid. To accomplish this goal, the Texas wind farm dataset was utilized as a case study. The evaluation of the predictive performance was conducted through accuracy indices, MSE, RMSE, and MAE. Eventually, these metrics show that Transformer-BiGRU (proposed model) reaches reliable results, and it can utilize in real-world matters.

References

1. Halkos, G. E., & Gkampoura, E. C. (2020). Reviewing usage, potentials, and limitations of renewable energy sources. Energies, 13(11), 2906.
2. Roga, S., Bardhan, S., Kumar, Y., & Dubey, S. K. (2022). Recent technology and challenges of wind energy generation: A review. Sustainable Energy Technologies and Assessments, 52, 102239.
3. Ghavifekr, A. A. (2021). Application of heuristic techniques and evolutionary algorithms in microgrids optimization problems. Microgrids: Advances in Operation, Control, and Protection, 219-251.
4. Safari, A., & Ghavifekr, A. A. (2021, December). Quantum neural networks (QNN) application in weather prediction of smart grids. In 2021 11th Smart Grid Conference (SGC) (pp. 1-6). IEEE.
5. Safari, A., & Ghavifekr, A. A. (2022, March). Quantum technology & quantum neural networks in smart grids control: Premier perspectives. In 2022 8th international conference on control, instrumentation and automation (ICCIA) (pp. 1-6). IEEE.
6. Safari, A., & Ghavifekr, A. A. (2022). Use case of artificial intelligence and neural networks in energy consumption markets and industrial demand response. Industrial demand response: methods, best practices, case studies, and applications, 4, 379.
7. Ma, Z., & Mei, G. (2022). A hybrid attention-based deep learning approach for wind power prediction. Applied Energy, 323, 119608.
8. Chen, G., Shan, J., Li, D. Y., Wang, C., Li, C., Zhou, Z., ... & Hao, J. J. (2019). Research on wind power prediction method based on convolutional neural network and genetic algorithm. 2019 IEEE Innovative Smart Grid Technologies-Asia (ISGT Asia), 3573-3578.
9. Huang, B., Liang, Y., & Qiu, X. (2021). Wind power forecasting using attention-based recurrent neural networks: a comparative study. IEEE Access, 9, 40432-40444.
10. Han, L., Jing, H., Zhang, R., & Gao, Z. (2019). Wind power forecast based on improved Long Short Term Memory network. Energy, 189, 116300.
11. Malakouti, S. M., Ghiasi, A. R., Ghavifekr, A. A., & Emami, P. (2022). Predicting wind power generation using machine learning and CNN-LSTM approaches. Wind Engineering, 46(6), 1853-1869.
12. Ashish, V. (2017). Attention is all you need. Advances in neural information processing systems, 30, I.
13. Hameed, Z., & Garcia-Zapirain, B. (2020). Sentiment classification using a single-layered BiLSTM model. Ieee Access, 8, 73992-74001.
14. https://www.kaggle.com/datasets/pravdomirdobrev/texas-wind-turbine-dataset-simulated

Advanced Engineering Days

aed.mersin.edu.tr

GenTradeCast: A Precise Forecasting Predictive Model in Peer-to-Peer Energy Trading Markets–A Dataset Case Study of Germany

Ashkan Safari [1], Amir A. Ghavifekr [1]

[1] *University of Tabriz, Faculty of Electrical and Computer Engineering, Iran, ashkansafari@ieee.org, aa.ghavifekr@tabrizu.ac.ir*

Cite this study: Safari, A., & A. Ghavifekr, A. (2024). GenTradeCast: A Precise Forecasting Predictive Model in Peer-to-Peer Energy Trading Markets–A Dataset Case Study of Germany. Advanced Engineering Days, 9, 590-593

Keywords
Peer-to-Peer Energy Trading
Machine Learning
Optimization

Abstract

In energy markets, the synergy between peer-to-peer (P2P) transactive mechanisms and renewable energy sources has become a focal point of research and technological advancement. This paper presents GenTradeCast, a finely-tuned multi-stacked Random Forest Model tailored for the intricate nuances of the German energy market. Utilizing a comprehensive dataset featuring key parameters such as self-consumption ration (SCR), self suffiency ratio (SSR), demand peak, total load, total PV, imported/exported energy, battery revenue, EPARI, ADMD, and ADME, GenTradeCast adeptly predicts total generation amidst the complex interplay of P2P transactive mechanisms and renewable energy inputs. The model exhibits exceptional accuracy, as evidenced by its remarkably low Mean Absolute Error (MAE) of 0.009, Mean Squared Error (MSE) of 0.00138, Root Mean Square Error (RMSE) of 0.037, an R2 Score of 0.99, Minimal Absolute Percentage Error (MAPE) of 0.002, and Root Mean Square Percentage Error (RMSPE) of 0.009.

Introduction

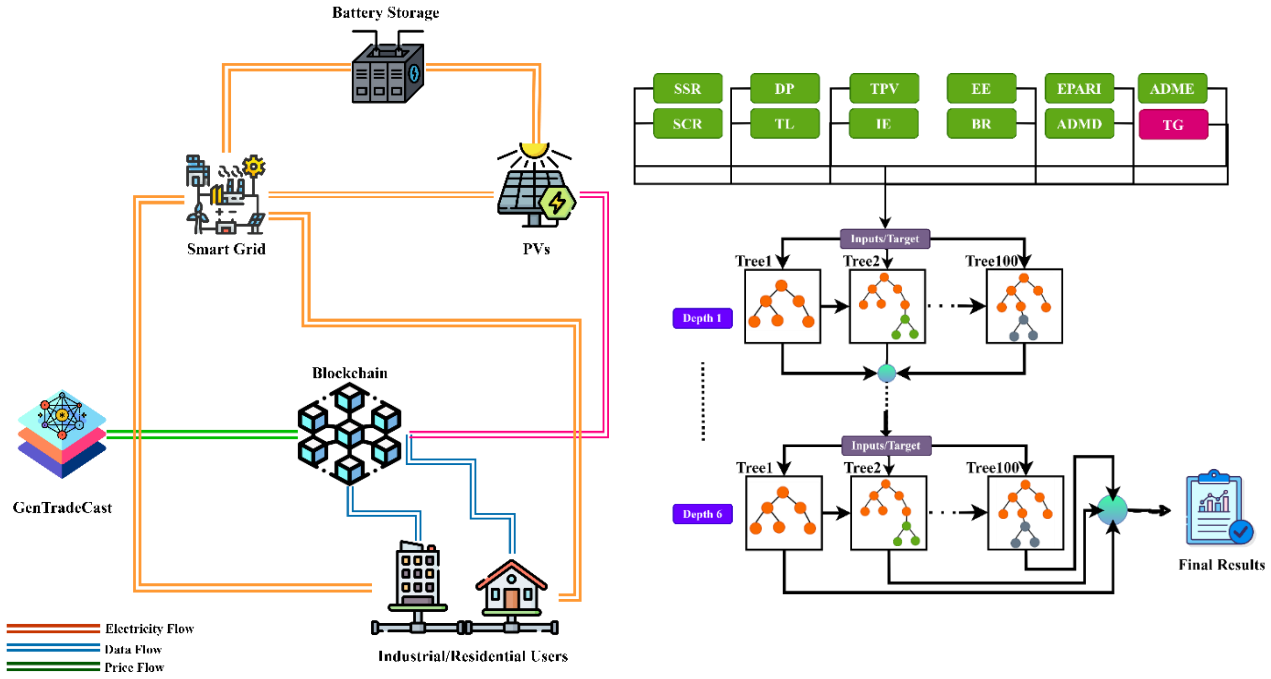
The evolution of energy markets, underscored by the integration of P2P transactive mechanisms and renewable energy sources, has engendered a compelling imperative for precision-driven predictive modeling. By the side of recent advances in the field, [1] introduces a novel distributed controller for voltage and frequency restoration in standalone microgrids (SAMGs), addressing the challenges posed by renewable energy fluctuations. There are numerous studies that have covered application of evolutionary algorithms [2] and machine learning in the filed of smart grids and energy marketing [3-6].

The approach successfully regulates voltage, frequency, and active/reactive power in a SAMG with four inverters. Additionally, the study utilizes machine learning for renewable power forecasting, demonstrating the potential of data-driven methods to enhance power system operation and control. The potential for accurate prediction and management of power system behavior through machine learning and data-driven methods is emphasized in [7]. These methods have gained recent attention due to their capacity to handle substantial data quantities. The paper explores the use of these methods in the context of evolving smart grids and renewable energy systems, facilitated by the Internet of Energy (IoE). It also reviews existing literature, discusses challenges and opportunities, including data quality and availability, and provides recommendations for future research in the predictive analysis of future smart grid-driven power systems powered by the IoE. Residential communities are adopting renewable energy sources to cut energy costs, but the variability of these sources poses reliability challenges. To address uncertainties in power supply, [8] suggests using data-driven methods for cloud-based energy storage management. It develops models to estimate forecasting errors and quantifies net load uncertainties, aiding better decision-making for energy storage system operations. The novelty of GenTradeCast is in this exigency, driven by the pressing need for accurate forecasts for the intricate dynamics of the energy market.

Material and Method

By integrating diverse features like Supply to Consumption Ratio (SCR), Solar Supply Ratio (SSR), Demand Peak, Total Load, TotalPV, Imported Energy, Exported Energy, Battery Revenue, EPARI, ADMD, ADME, and Total Generation, the model captures the multifaceted dynamics of energy production, consumption, and financial

intricacies within communities. P2P energy trading represents a revolutionary concept reshaping the energy industry by enabling direct, decentralized transactions between energy producers and consumers. By providing related technologies, such as blockchain and smart contracts, P2P energy trading facilitates real-time, secure, and transparent exchanges of electricity among prosumers, individuals, or entities producing and consuming energy. Consequently, the overall concept of P2P system, and the applied method are depicted in Figure. 1.



(a) (b)

Figure. 1. (a) The overall concept of a P2P system, and (b) The structure of GenTradeCast

The structure of GenTradeCast is designed using Python and essential machine learning libraries. Initially, the dataset is imported and loaded into a DataFrame. Relevant features including SCR, SSR, Demand_peak, Total_load, TotalPV, Imported, Exported, Batt_revenue, EPARI, ADMD, and ADME are selected, and the target variable Total Generation is defined. The dataset is then split into training and testing sets (80% training and 20% testing). Subsequently, a Random Forest Regressor model with 100 estimators and a specified random state is initialized. The model is trained using the training data, allowing it to learn the underlying patterns within the features and target variable. Once trained, the model makes predictions on the testing set, enabling the evaluation of its performance. The related formulations of P2P market and random forest, utilized in GenTradeCast, are available in [9].

Results

To evaluate the predictive capabilities of GenTradeCast, extensive simulations were conducted utilizing a dataset rich in diverse parameters. The dataset encompassed vital features such as SCR, SSR, Demand Peak, Total Load, Total PV, Imported Energy, Exported Energy, Battery Revenue, EPARI, ADMD, ADME, Real Demand, Total Generation, and Bill. Each feature exhibited distinct statistical properties, with mean values and variances ranging widely across the dataset. The details of the dataset utilized in presented in Table. 1 [10]. As well, the results derived in Fig. 2.

Table 1. This is the example of table formatting

Features	Mean	Variance	TAD	TCD
SCR	50.78395	6.672725	304703.7	6000
SSR	48.97521	2.387178	293851.3	6000
Demand Peak	145.9792	92.04499	875875.2	6000
Total Load	468767.7	1.99E+08	2.81E+09	6000
Total PV	452866.6	5.76E+08	2.72E+09	6000
Imported Energy	239257.8	1.37E+08	1.44E+09	6000
Exported Energy	204526.4	4.57E+08	1.23E+09	6000
Battery Revenue	13260.17	2468969	79561047	6000
EPARI	0.013438	3.71E-07	80.63067	6000
ADMD	0.364948	0.000575	2189.688	6000
ADME	0.596617	0.001818	3579.701	6000
Real Demand	330.194	141.8913	1981164	6000
Total generation	452.8666	576.2005	2717200	6000
Bill	71374.13	98304371	4.28E+08	6000

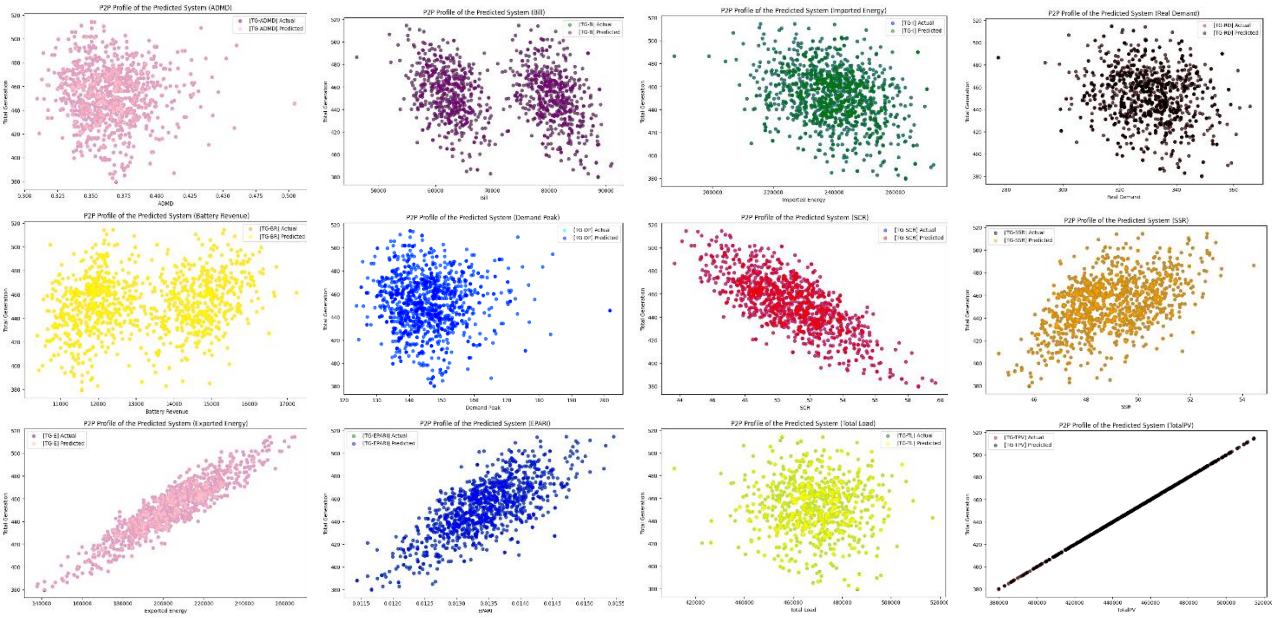


Figure. 2. The scatter property of predicted total generation regrading ADMD, Bill, Battery Revenue, Demand Peak, Exported Energy, EPARI, Imported Energy, Real Demand, SCR, SSR, Total Load, Total PV

Discussion

Evaluation of GenTradeCast's performance is underscored by analysis of several KPI illuminating the model's accuracy in predicting total generation within the energy market context. The exceptionally low MAE of 0.00929 denotes the minimal average deviation between predicted and actual values, exemplifying the model's precision. Further emphasizing its accuracy, the MSE stands impressively low at 0.00138, reflecting minimal variance between predicted and observed data points. The RMSE of 0.03721 signifies the model's effectiveness in capturing the dataset's inherent variability while maintaining low prediction errors. The R^2 Score = 0.999997, nearing unity, indicates the model's capability to explain nearly all the variance in the data, emphasizing its exceptional explanatory power. Moreover, the MAPE and RMSPE values of 0.00214 and 0.00922, respectively.

Conclusion

GenTradeCast, the multi-stacked Random Forest Model, has demonstrated considerable results in predicting total generation within the context of the German energy market characterized by the presence of P2P transactive mechanisms and renewable energy sources. The models remarkable accuracy, as evidenced by its MAE, MSE, RMSE, high R2, MAPE, and RMSPE, illustrates its effectiveness in capturing the intricate relationships among various influencing factors. By providing predictions, GenTradeCast equips stakeholders with valuable insights necessary for informed decision-making in energy trading scenarios

References

1. Ahangar PA, Lone SA, Gupta N. Combining Data-Driven and Model-Driven Approaches for Optimal Distributed Control of Standalone Microgrid. Sustainability. 2023 Aug 11;15(16):12286.
2. Ghavifekr, A. A. (2021). Application of heuristic techniques and evolutionary algorithms in microgrids optimization problems. Microgrids: Advances in Operation, Control, and Protection, 219-251.
3. Safari, A., & Ghavifekr, A. A. (2021, December). Quantum neural networks (QNN) application in weather prediction of smart grids. In 2021 11th Smart Grid Conference (SGC) (pp. 1-6). IEEE.
4. Safari, A., & Ghavifekr, A. A. (2022, March). Quantum technology & quantum neural networks in smart grids control: Premier perspectives. In 2022 8th international conference on control, instrumentation and automation (ICCIA) (pp. 1-6). IEEE.
5. Safari, A., & Ghavifekr, A. A. (2022). Use case of artificial intelligence and neural networks in energy consumption markets and industrial demand response. Industrial demand response: methods, best practices, case studies, and applications, 4, 379.
6. Malakouti, S. M., Ghiasi, A. R., Ghavifekr, A. A., & Emami, P. (2022). Predicting wind power generation using machine learning and CNN-LSTM approaches. Wind Engineering, 46(6), 1853-1869.
7. Strielkowski W, Vlasov A, Selivanov K, Muraviev K, Shakhnov V. Prospects and Challenges of the Machine Learning and Data-Driven Methods for the Predictive Analysis of Power Systems: A Review. Energies. 2023 May 11;16(10):4025.

8. Saini VK, Al-Sumaiti AS, Kumar R. Data driven net load uncertainty quantification for cloud energy storage management in residential microgrid. Electric Power Systems Research. 2024 Jan 1;226:109920.
9. Safari A, Gharehbagh HK, Nazari-Heris M, Oshnoei A. DeepResTrade: A Peer-to-Peer LSTM-Decision Tree-Based Price Prediction and Blockchain-Enhanced Trading System for Renewable Energy Decentralized Markets. Front Energy Res. 2023;11:1275686.
10. Pena-Bello Alejandro, D. Parra, M. Herberz, M. K. Patel, V. Tiefenbeckand U. J. J. Hahnel, "Integration of prosumer peer-to-peer trading decisions into energy community modelling". Zenodo, Feb. 10, 2021. doi: 10.5281/zenodo.5571499.

Advanced Engineering Days

aed.mersin.edu.tr

Application of Quantum Neural Networks for Robotic Motion Control

Ashkan Safari [1], Amir A. Ghavifekr [1], Hossein B. Jond [2], Roberto De Fazio [3] Mina Salim [1], Khadim Moin Siddiqui [4], Neel Kamal [4] , Ajay Kumar [4]

[1] University of Tabriz, Faculty of Electrical and Computer Engineering, Iran, ashkansafari@ieee.org, aa.ghavifekr@tabrizu.ac.ir, m.salim@tabrizu.ac.ir
[2] Czech Technical University in Prague, Faculty of Electrical Engineering, Czech Republic, hossein.barghi.jond@fel.cvut.cz
[3] University of Salento, Department of Innovation Engineering, Italy, roberto.defazio@unisalento.it
[4] SR Institute of Management and Technology, EEE Department, India, siddiquikhadim@ieee.org, neelkamal@ieee.org, ajay262438@ieee.org

Cite this study: Safari, A., Ghavifekr, A. A., Jond, H. B., De Fazio, R., Salim, M., Siddiqui, K. M., Kamal, N., & Kumar, A. (2024). Application of Quantum Neural Networks for Robotic Motion Control. Advanced Engineering Days, 9, 594-597

Keywords
Robotic
Machine Learning
Artificial Intelligence
Motion Control

Abstract

In this paper, application of quantum technology in robotics industry, has been analyzed. When robotics is combined with Artificial Intelligence (AI), and Neural Networks (NN), it will be more efficient. However, using superior field known as "Quantum technology", has superior applications in robotic and motion control. This paper presents motion control systems, their regular techniques, and quantum technology with its use in these systems. Then, it defines the areas of robotics in which quantum technology can make a significant development. Respectively, it compares quantum technology with other regular techniques. Finally, it is concluded that quantum technology has an enormous potential to be combined with other fields and to be processed in a faster, and more accurate way.

Introduction

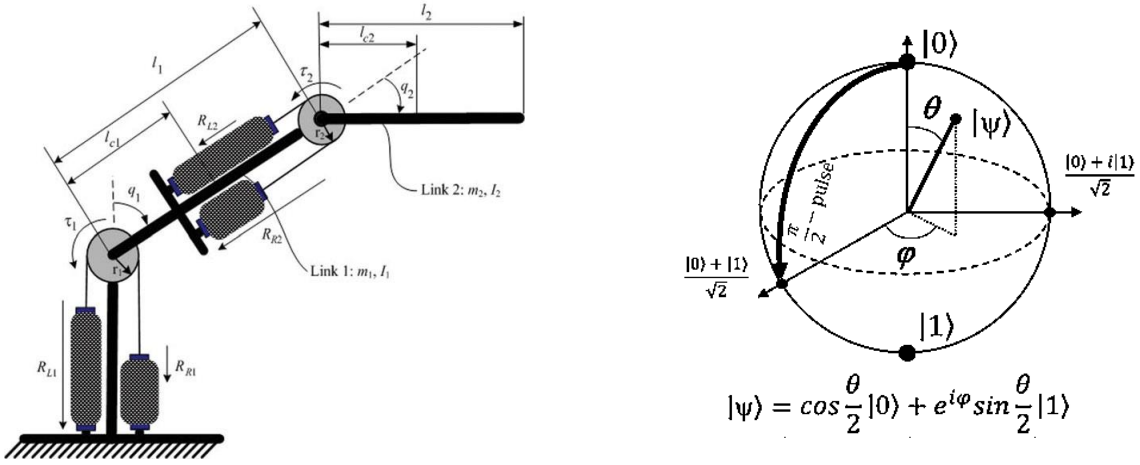
The more industrialization and technology develop, the more, new challenges this field faces. Moreover, the robotics industry has a great potential to be combined with other emerging fields such as Artificial Intelligence (AI). With the upgrading of modern sensors, and microprocessors this field has improved exponentially, and even when combined with AI or Internet of Things (IoT), the robots found much more ability to develop, and enhance their skills [1]. One of the significant areas of robotic is motion control systems such as arm motion control [2-5]. Based on [6] one of the approaches to control arm, and its motion is using the kinematic model. As well, there are other techniques to control the robot motion such as Common filter processing algorithm, Digital filtering methods to perform in low frequency with its sub-methods: Limiting filtering method, and Median filtering method. The same to the digital method in high frequencies, with sub-methods: Arithmetic Average filtering, Moving Average filtering, and Limiting Moving Average filtering method. Also, there is an additional, and important method known as the "PI algorithm" that is used in speed control, and will be fully expressed in the further section of the paper. All of the mentioned methods are combined with AI to perform very well. However, regular, and classical AI has a disadvantage, and it's when the system faces an enormous amount of gathered Big data, it will be inefficient, won't be able to perform the processes, and tasks as well which lead to a higher amount of time, and lack of efficiency. Therefore, they should be combined with a stronger technology to perform the tasks in a much more accurate, and faster way, which this technology is known as "Quantum Technology". As will be expressed, quantum technology is, fundamentally, quantum bits (qubits) which can be in all states between 0, and 1 simultaneously. However, the regular computers are based on bits that can only be 0, or 1. As well, quantum computing is based on the spin of atoms, which makes it process, and execute the data in an enormously fast way. Therefore, this feature causes it to be used in most of the fields in which robotic, and motion control are not an exception. When quantum technology compiles with Neural Networks (NN) technology, the combination leads to Quantum Neural Networks (QNN) which has much more accuracy, with extremely fast processing ability than the regular approaches [7]. This

makes it be used in most of the fields such as the stock market, which needs a high accuracy of prediction [8], and smart Sustainable Cities (SSCs) [9-10]. In this paper, we express the regular robotic motion control techniques, then defined quantum technology, and QNN in robotic fields, and motion control. Therefore, determined some factors, and conducted a brief, and clear review between quantum technology, and the regular ones in the field.

Material and Method

Motion control specifies how a robot should move to perform defined tasks. Robotic arms achieve movement through the rotation and sliding of joints, while mobile robots move via locomotion and steering. Among the various motion control methods, the P-Only controller and the Proportional-Integral (PI) algorithm are notable. The PI algorithm computes and transmits a controller output (CO) signal every sample time (T) to the final control element, such as a variable speed pump. The integral action in PI controllers eliminates offset, a significant limitation of the P-Only controller. In a speed control system, P and I represent the proportional and integral regulators, respectively. The proportional regulator (P) ensures rapid adjustment, while the integral regulator (I) eliminates steady-state error, leading to a fast and stable speed control system. Quantum technology leverages the principles of quantum mechanics and sub-atomic particles, such as quantum entanglement and quantum superposition. This technology is revolutionizing areas like Quantum Sensing and Quantum Computing, the latter providing incredibly fast processing speeds. Quantum Sensing enhances the precision of measurements by exploiting quantum entanglement, leading to advancements in fields such as medical imaging, navigation, and environmental monitoring. Quantum Computing, on the other hand, offers unprecedented computational power, enabling the solution of complex problems in seconds that would take classical computers years to solve.

Incorporating quantum technology into motion control systems could significantly enhance their performance. Quantum algorithms could optimize control processes, reduce latency, and improve accuracy. The integration of Quantum Neural Networks (QNNs) with robotic motion control systems promises to further enhance their capabilities, leading to more efficient and responsive robotic operations. Quantum technology, therefore, not only serves as an alternative to traditional control methods but also opens up new possibilities for innovation and improvement in robotic motion control. A motion control concept, as well as quantum technology computation, known as Bloch sphere, are depicted in Figure. 1.



(a) (b)

Figure. 1. (a) Adaptive tracking control of multi-link robots actuated by pneumatic muscles with additive interferences [11], and (b) Visualization of a qubit known as *"Bloch Sphere"*

Based on Fig. 5, the North, and South poles, respectively, are $|0\rangle$, and $|1\rangle$. In qubits (quantum bits), the state can be across all between, and that's called superposition. Accordingly, particles can be in any states such as position, energy, or speed.

Results

Regarding the results, Fig. 2 represents another application of Deep Quantum Feed-Forward Neural Network (DQFNN)- based master equation solver, and Fisher Information (FI).

The FI is a procedure that is used to measure the amount of information carried by an observable random variable X about an unknown parameter θ of a distribution that models *X*. The FI matrix is used to calculate the covariance matrices blended with maximum-likelihood estimates.



(a) (b)

Figure. 2. (a) A DQFNN- based master equation solver [12], (b) Classical Fisher Information for Gaussian validation [13]

Discussion

This paper presents and analyzes the applications of Quantum Neural Networks (QNNs) in robotic motion control systems. QNNs leverage the unique properties of quantum mechanics, such as superposition and entanglement, to process information in fundamentally new ways. This results in a significant enhancement in computational efficiency and the ability to solve complex problems that are intractable for classical neural networks. Quantum technology demonstrates substantial potential when integrated with related fields such as Artificial Intelligence (AI) and Robotics. The integration of these technologies results in remarkably fast processing speeds and reduced operation times. Quantum-enhanced AI can improve learning algorithms, enabling robots to adapt and respond to their environments more effectively. This synergy between quantum technology and AI paves the way for more sophisticated and autonomous robotic systems. To provide a concise and clear comparison between quantum technology and conventional methods commonly used in robotics, several factors were identified and used as the basis for comparison. These factors include technology level, processing speed, states, particles, and execution time. The comparison highlights the advantages of quantum approaches in handling large datasets and performing parallel computations, which are critical for real-time robotic motion control. The implementation of QNNs in robotic motion control systems offers several benefits. Firstly, the enhanced processing capabilities of quantum systems allow for faster decision-making and more accurate control, which is crucial for applications requiring high precision and responsiveness. Secondly, quantum algorithms can optimize control parameters more efficiently than classical algorithms, leading to improved performance and stability of robotic systems. Moreover, the ability of quantum technology to process information in parallel significantly reduces the time required for complex computations. This is particularly beneficial in dynamic environments where robots need to quickly adapt to changes and make real-time adjustments. The reduced operation times not only enhance the efficiency of robotic systems but also extend their battery life and operational duration. In summary, the integration of Quantum Neural Networks into robotic motion control systems represents a significant advancement in robotics technology. By leveraging the principles of quantum mechanics, QNNs offer superior processing speeds, reduced operation times, and enhanced control capabilities. This paper provides a detailed analysis of these benefits, using identified factors as the basis for comparison, and underscores the transformative potential of quantum technology in the field of robotics. The detailed comparison and results are presented in Table 1 below, illustrating the tangible improvements that quantum technology can bring to robotic motion control. These factors include states, particles, and execution time, though they may vary depending on individual perspectives. The detailed comparison and results are shown in Table 1 below:

TABLE 1. COMPARISON BETWEEN QUANTUM, & THE REGULAR TECHNOLOGIES

Factors	Quantum	Regular ones (Supercomputers)
Level of Technology	Higher	High
Particles	Qubits	Bits
States	0, 1, and all available states at the same time	Only 0, and 1
Processing Speed	Higher	High
Execution Time	Much Less	Less

Conclusion

In the proposed paper robotic motion control systems by using regular AI, and NN-based approaches has been presented and analyzed. Then the challenges of regular approaches have been expressed. Accordingly, it was concluded that another more powerful technology is known as “Quantum Technology”, and “Quantum Neural Networks (QNN)” are required to perform the computation in a much faster, and easier way, with much less execution time. After comparison, because of the potentials of quantum technology, such as enormously fast

processing, and execution speed, and its increasing efficiency, concluded that quantum technology is the future technology that will cover up most of the fields, and robotic industry.

References

1. L. Chen, H. Sun, W. Zhao, and T. Yu, "Robotic arm control system based on AI wearable acceleration sensor," Mathematical Problems in Engineering, vol. 2021, 2021.
2. M. H. Jarrahi, "Artificial intelligence and the future of work: Human-AI symbiosis in organizational decision making," Business Horizons, vol. 61, no. 4, pp. 577-586, 2018.
3. Ghavifekr, A. A., Badamchizadeh, M. A., Alizadeh, G., & Arjmandi, A. (2013, May). Designing inverse dynamic controller with integral action for motion planning of surgical robot in the presence of bounded disturbances. In 2013 21st Iranian Conference on Electrical Engineering (ICEE) (pp. 1-6). IEEE.
4. Ghavifekr, A., Ghaemi, S., & Behinfaraz, R. (2014). A Modified biogeography based optimization (bbo) algorithm for time optimal motion planning of 5 dof pc-based gryphon robot. International Journal of Engineering works.
5. Ghavifekr, A. A., Hassani, R. H., & Calanca, A. (2021). Designing Adaptive Nonlinear Controller for Optimal Tracking of Laparoscopic Robotic Arm with Nonholonomic Constraints. In New Trends in Medical and Service Robotics: MESROB 2020 7 (pp. 97-107). Springer International Publishing.
6. H. Lu, Y. Li, M. Chen, H. Kim, and S. Serikawa, "Brain intelligence: go beyond artificial intelligence," Mobile Networks and Applications, vol. 23, no. 2, pp. 368-375, 2018.
7. R. Eskandarpour, K. J. B. Ghosh, A. Khodaei, A. Paaso, and L. Zhang, "Quantum-enhanced grid of the future: A primer," IEEE Access, vol. 8, pp. 188993-189002, 2020.
8. Safari and A. A. Ghavifekr, "International Stock Index Prediction Using Artificial Neural Network (ANN) and Python Programming," in 2021 7th International Conference on Control, Instrumentation and Automation (ICCIA), 2021: IEEE, pp. 1-7.
9. Safari, A., & Ghavifekr, A. A. (2022, March). Quantum technology & quantum neural networks in smart grids control: Premier perspectives. In 2022 8th international conference on control, instrumentation and automation (ICCIA) (pp. 1-6). IEEE.
10. Safari, A., & Ghavifekr, A. A. (2021, December). Quantum neural networks (QNN) application in weather prediction of smart grids. In 2021 11th Smart Grid Conference (SGC) (pp. 1-6). IEEE.
11. T. Karnjanaparichat and R. Pongvuthithum, "Adaptive tracking control of multi-link robots actuated by pneumatic muscles with additive disturbances," Robotica, vol. 35, no. 11, pp. 2139-2156, 2017.
12. Z. Liu, L.-M. Duan, and D.-L. Deng, "Solving quantum master equations with deep quantum neural networks," arXiv preprint arXiv:2008.05488, 2020.
13. M.-O. Hongler, Y. L. de Meneses, A. Beyeler, and J. Jacot, "The resonant retina: exploiting vibration noise to optimally detect edges in an image," IEEE Transactions on Pattern Analysis and Machine Intelligence, vol. 25, no. 9, pp. 1051-1062, 2003.

Advanced Engineering Days

aed.mersin.edu.tr

New organ design for humans: electrical generating neural network inspired by eel

Arya Gholipoor Hanizi*[1], Sina Asadian [2]

[1]*University of Tabriz, Faculty of Electrical and Computer Engineering, Iran, Arya.Gholipoor@outlook.com*
[2]*Politecnico di Milano, School of Industrial and information Engineering, Italy, sina.asadiian@gmail.com*

Cite this study: Hanizi, A. G., & Asadian, S. (2024). New organ design for humans: electrical generating neural network inspired by eel. Advanced Engineering Days, 9, 598-600

Keywords
Medical implants
Electrical energy
Neurons
3D bioprinting
Caloric intake

Abstract

In the realm of medical implants and prostheses, the challenge of providing reliable energy sources remains paramount. This study explores an innovative approach inspired by electric eel organs to generate electrical energy. By systematically connecting nerve cells, we create a chain reaction of action potentials, yielding clinically usable energy. Our proposed system eliminates reliance on external energy sources, making it applicable to critical areas such as artificial hearts and active prostheses. We exclusively employ neurons, avoiding the disadvantages associated with muscle cells. The engineered structure, constructed using 3D bioprinting and stem cell culture, regulates neuron connections. Modeling these neurons as an electric circuit, we incorporate relays and voltage sources to form a branching network. Investigated in this study is a network comprising approximately 64.5 billion neurons, which exhibits a continuous output power of 9.68 watts, adequately meeting current energy requirements. The dimensions of this neural network are approximately 95 cubic centimeters, and its utilization necessitates an additional caloric intake of approximately 50 calories. The output voltage, resulting from summation across series sources, provides stable and dependable power for medical devices.

Introduction

In the field of medical implants and prostheses, a significant challenge lies in providing energy sources for these devices. This article investigates a novel approach to generating electrical energy by mimicking the electric organs found in eels. By achieving this objective, it can be applied in critical areas such as powering artificial hearts and enabling active hand and foot prostheses. The reliance on an external energy source is eliminated, resulting in stable and dependable energy.

In previous researches, methods for generating electricity from the human body have been presented. Aibing *et al.* made a Wearable Thermoelectric Generators to convert skins thermal energy to electricity[1], Ali *et al.* made a Wearable Piezoelectric Generators to convert human motions to electricity[2].

The proposed system involves systematically and deliberately connecting nerve cells, creating a chain reaction of action potentials that ultimately produces clinically usable energy. Subsequently, we present the methodology for achieving this and simulate the related electrical circuit.

Material and Method

In general, two types of cells in the human body have the inherent ability to generate and conduct action potentials: cardiac SA node muscle cells and neurons. When muscle cells are overused, it may lead to unnecessary contractions and movements and cell proliferation occurs, which moves the structure away from the regular state. In our proposed method, we exclusively use neurons that lack the ability to reproduce cells and do not show the mentioned disadvantages.

In this study, an engineered and regular structure is constructed using methods such as 3D bioprinting and stem cell culture on the engineered scaffold. The goal is to regulate the connections between neurons, thereby controlling the energy production and consumption within the newly formed organ.

Modeling Nerve Cells

To simulate this structure as an electric circuit, we begin by modeling the neurons. In the initial step of modeling, we simplify each neuron to have one input terminal (dendrite) and one output terminal (axon). Additionally, we incorporate a relay and a voltage source.

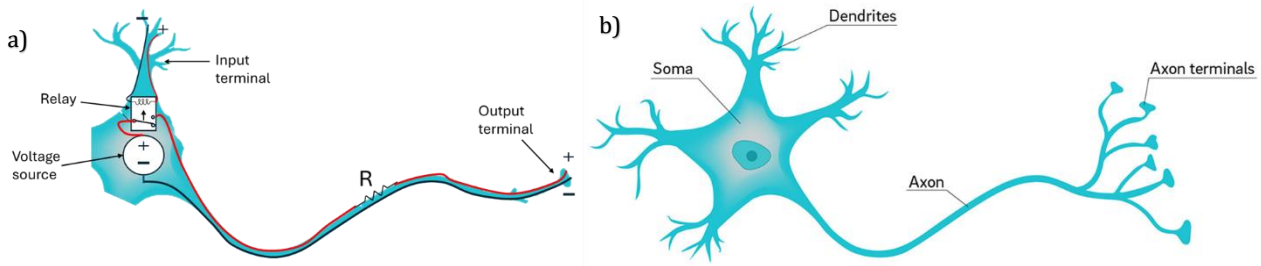


Figure 1. Figure (a) represents a simplified and simulated version of a neuron electrically, and Figure (b) represents a neuron.

Upon arrival of the signal from the dendrite of the preceding neuron, the relay within the control circuit undergoes activation. This transition from an inactive to an active state occurs due to the electric current. Subsequently, the voltage source is introduced into the circuit. It is worth noting that the internal resistance of the neuron (R) plays a minor role in this process. Since ion-mediated current transmission predominates within the neuron, the value of R is negligible and can be safely disregarded in simulations. Average current of nerve cells is approximately equals to 0.15μA [3].

Network Architecture

In the proposed network, an alternating voltage source serves as the pacemaker within our structure. The signal originating from this source propagates through the network, transitioning it into an active phase. The relays are serially connected to prevent current loss. Upon current entry into the relay circuit, the neuron enters a closed circuit state, and an independent voltage source is introduced. Consequently, this circuit can dynamically alter the inactive-to-active state of other neurons. Within this proposed structure, each neuron has the capacity to activate multiple others, forming a branching network. Ultimately, the output voltage results from the summation of voltages across the series sources, providing our desired output energy.

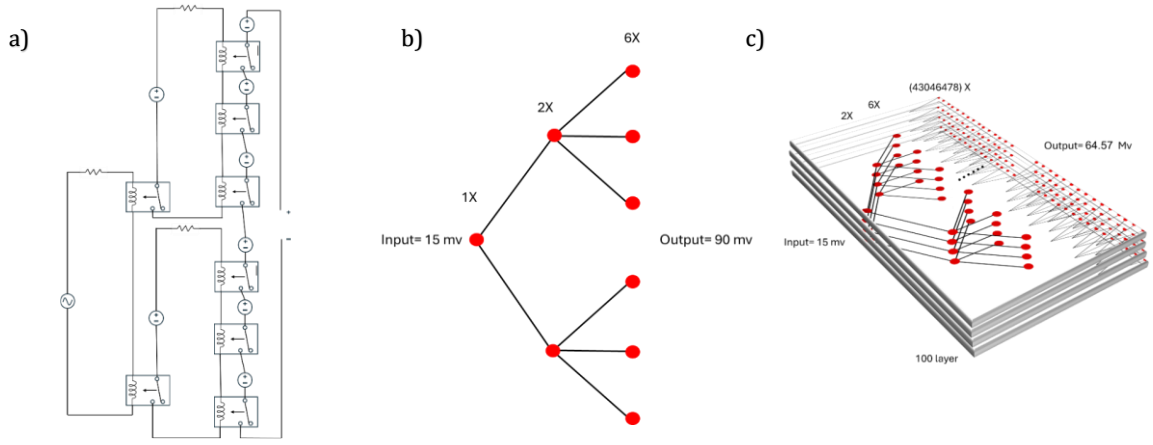


Figure 2. Figure (a) shows the equivalent circuit with six neurons in the terminal branch. Figure (b) shows the circuit in the form of a tree diagram. Figure (c) shows a proposed structure to implement this idea, which includes one hundred layers and 64,569,608 neurons in the terminal branch.

In the modeled network, an alternating voltage source—representing pacing—is powered by a battery. By adjusting the signal period, the final pulse count within the network can be regulated. The minimum pulse duration required for electrical stimulation corresponds to the length of an action potential in the cell, precisely 4 milliseconds.

Upon generating a pulse from the alternating source, the relays within each layer transition to a mode where the voltage source is integrated into the circuit. Each neuron then drives multiple other neurons toward their action potentials. Consequently, a substantial number of neurons in the final layer become stimulated, and their voltages at the output terminal aggregate to form the network's overall output.

For our analysis, we assume that each voltage source in the network maintains a constant value of 15 millivolts—an approximation of the average voltage observed in neurons during action potentials. Additionally, the relays are ideal, characterized by zero resistance and minimal current during switching.

Results

In this study, an innovative method for generating electrical energy inspired by the electric organ of eels was explored. The proposed network comprises approximately 64,569,608 neurons in a single layer, with an additional 43,046,478 neurons in the end branch. The overall structure consists of 100 formed layers, totaling 6.5 billion neurons. When an input signal with an amplitude of 15 millivolts is applied, this network generates a potential difference of 64.57 millivolts at the output.

During an action potential, the average current of 0.15 microamps contributes to an estimated output power of 9.68 watts. This level of energy output is sufficient for various applications. Remarkably, the size of this neural network corresponds to only 7% of the brain, or a maximum of 95.5 cubic centimeters. Due to its systematic structure, it may even be smaller.

To sustain this system, the subject would need to increase their daily calorie intake by 50 calories.

Discussion

The potential implementation of this method would lead to the elimination of artificial heart batteries and the need for periodic surgeries related to battery replacement. Additionally, active prostheses would no longer require charging. The implications extend beyond medical engineering, with possible applications in powering external devices such as mobile phones. However, achieving this goal presents challenges related to cell arrangement optimization, energy requirements, vascular delivery system design, and organ placement within the body.

Conclusion

The proposed plan holds promise as a transformative step in tissue engineering and implant practices, offering ample opportunities for innovation and progress. While this article has only scratched the surface of the comprehensive plan, it underscores the theoretical soundness of the concept.

This proposed network for the structure with about 6.5 billion neurons has a voltage of about 64.57 million volts and a current of 15 microamps, which delivers an instantaneous power of 9.68 watts and has dimensions of about 95 cubic centimeters.

The reported values, albeit obtained through simplified simulations and principles of mechanics and electricity, remain valid. However, it is essential to acknowledge the inherent complexity of this design, which necessitates further research and development.

Compared to similar energy-producing plans involving the human body, this approach offers greater potential for practicality and usefulness. As we continue our journey toward implementation, interdisciplinary collaboration and ongoing refinement will pave the way for a future where self-sustaining medical devices become a reality.

References

1. Zhang, A., Li, G., Wang, B. *et al.* A Theoretical Model for Wearable Thermoelectric Generators Considering the Effect of Human Skin. *J. Electron. Mater.* **50**, 1514–1526 (2021). https://doi.org/10.1007/s11664-020-08695-6
2. Ali, A., Iqbal, S., & Chen, X. (2024). Recent advances in piezoelectric wearable energy harvesting based on human motion: Materials, design, and applications. Energy Strategy Reviews, 53(101422), 101422. doi:10.1016/j.esr.2024.101422
3. Dodge, F. A., & Cooley, J. W. (1973). Action Potential of the Motorneuron. *IBM Journal of Research and Development*, *17*(3), 219–229. doi:10.1147/rd.173.0219

Advanced Engineering Days

aed.mersin.edu.tr

Optimal Sizing of a Grid Connected Microgrid Using Firefly Algorithm

Sina Asadian [1], Ali Firouzi Abriz [2], Arash Faramarzi [3]

[1] *Politecnico di Milano, School of Industrial and information Engineering, Italy, sina.asadiian@gmail.com*
[2] *University of Tabriz, Faculty of Electrical and Computer Engineering, Iran, alifirouziabriz@gmail.com*
[3] *Islamic Azad University, Tabriz Branch, Faculty of Electrical Engineering, Iran, a.faramarzi7298@gmail.com*

Cite this study: Asadian, S, & Firouzi Abriz, A., & Faramarzi, A. (2024). Optimal sizing of a grid connected microgrid using Firefly Algorithm. Advanced Engineering Days, 9, 601-604

Keywords
Microgrid
Sizing optimization
FireFly algorithm
Evolutionary algorithm

Abstract

This paper presents an optimal sizing methodology for a grid-connected microgrid using the Firefly Algorithm (FA). The primary objective functions for the sizing problem are the cost of energy (COE) and the deficiency of power supply probability (DPSP). Optimization of these parameters ensures minimal costs and reliable power supply. COE is calculated by considering the total net present cost (TNPC), which includes replacement, capital, maintenance, and operation costs, normalized by the hourly energy consumption. The capital recovery factor (CRF) is utilized to account for the system life span and interest rates. The Firefly Algorithm is employed to solve this multi-objective optimization problem, demonstrating its efficacy in achieving optimal microgrid sizing by minimizing COE and DPSP, thus ensuring both economic and reliable energy supply.

Introduction

Microgrids have become a viable means of improving the sustainability, dependability, and resilience of energy systems [1]. These small-scale power grids combine traditional generators and energy storage devices with a variety of photovoltaic (PV) panels and wind turbines [2]. They can function independently or in tandem with the larger grid. Microgrid design and operation require intricate decision-making to balance technical and economic performance, particularly in grid-connected configurations where additional complexity arises from interaction with the main grid.

One of the critical aspects of microgrid design is the optimal sizing of its components [3]. Proper sizing ensures that the microgrid can meet the energy demands reliably while minimizing the overall costs [4]. This entails determining the optimal number and capacity of PV panels, wind turbines, batteries, and other components. The objective functions for this optimization problem are typically defined including cost of energy (COE) and the deficiency of power supply probability (DPSP). COE represents the economic aspect by calculating the cost per kilowatt-hour, considering all relevant expenses such as capital, replacement, maintenance, and operational costs. On the other hand, DPSP addresses the reliability aspect, indicating the likelihood of power supply shortages.

The optimization of these parameters presents a multi-objective problem that requires sophisticated techniques to find the best trade-offs between cost and reliability. Traditional optimization methods often fall short due to the nonlinear, non-convex nature of the problem and the presence of multiple conflicting objectives. Therefore, heuristic and metaheuristic algorithms have gained popularity for their ability to efficiently explore large and complex search spaces [5-7]. Also, they have been utilized in wide range of optimization problems of microgrids [8-13]. Among these, the Firefly Algorithm (FA) stands out due to its simplicity, robustness, and effectiveness in handling multi-objective microgrid optimization problems [14].

This paper suggests a Firefly Algorithm-based optimal sizing approach for a grid-connected microgrid. The technique aims to provide a reliable and economically viable power supply by minimizing the COE and DPSP. The total net present cost (TNPC), which is normalized by the hourly energy consumption and comprises all costs related to the microgrid's lifecycle, is used to compute the COE. Interest rates and the system's lifespan are taken into account by the capital recovery factor, or CRF. The DPSP is designed to quantify the microgrid's dependability in supplying energy while accounting for the contributions of diesel generators, PV power, wind turbine power, and battery storage.

The following sections of the paper detail the mathematical formulation of the optimization problem, the implementation of the Firefly Algorithm, and the results of the optimization process. The effectiveness of the proposed approach is validated through a case study, showcasing the benefits of using FA for microgrid design in real-world scenarios.

Material and Method

The objective functions for sizing challenges are generally based on the COE and DPSP. By optimizing these factors, one can achieve both minimal expenses and a reliable energy supply. The COE, quantified in $/kWh, is determined as follows:

$$COE = TNPC / \sum_{t=1}^{8760} P_l(h) \times CRF \tag{1}$$

where TNPC represents the total net present cost, encompassing replacement, capital, maintenance, and operational expenses. $P_l(h)$ signifies the hourly energy consumption, and the capital recovery factor (CRF) is derived from:

$$CRF = r_i(1+r_o)^n / (1+r_i)^n - 1 \tag{2}$$

where r_i and r_o represent the actual and optimal interest rates, and n indicates the system's lifespan. Another modifiable parameter is the DPSP, which can be considered the reliability index of microgrids, indicating the likelihood of power supply shortfall relative to energy demand. It is defined as:

$$DPSP = \sum (P_l - P_{PV} - P_{WT} + P_{SOC} + P_{DG}) / P_l \tag{3}$$

Where $P_l, P_{PV}, P_{WT}, P_{SOC}$ and P_{DG} show energy demand, power for PVs, output power of the wind turbine, minimum battery state of charge and generated power by a DG, respectively.
The constrains are defined as:

$$\begin{aligned} 0 \le N^{PV} \le N^{PV}_{\max} \\ 0 \le N^{WT} \le N^{WT}_{\max} \end{aligned} \tag{4}$$

Where $N^{PV}_{\max}$ and $N^{WT}_{\max}$ show the maximum number of PV and WTs.
The optimization problem is defined as:

$$\begin{aligned} &\min\ U(x) = [u_1(x), u_2(x), \ldots u_k(x)] \\ &\textit{subject to}\ \ c(x) \le 0\ \text{ and }\ g(x) = 0 \end{aligned} \tag{5}$$

Firefly algorithm is utilized to solve this problem. The Firefly Algorithm (FA) is a nature-inspired metaheuristic optimization technique. It is based on the social behavior and flashing patterns of fireflies. The algorithm is particularly effective for solving complex optimization problems due to its simplicity and capability to escape local optima. The primary mechanism of the Firefly Algorithm is the attractiveness of fireflies, which is proportional to their brightness. In the context of optimization, the brightness of a firefly is determined by the objective function value at its current position. Fireflies are attracted to each other based on their brightness; a less bright firefly will move towards a brighter one.

The Firefly Algorithm begins with the initialization phase, where a population of fireflies is placed randomly within the search space, and the objective function to be optimized is defined. During the evaluation phase, each firefly's brightness is calculated based on the objective function value. In the update positions phase, each firefly moves towards brighter ones using an attractiveness formula, combined with a random component to enhance exploration, updating their positions iteratively based on their relative brightness and distance. The convergence check phase involves assessing if the termination criteria, such as reaching a maximum number of iterations or achieving a satisfactory objective function value, have been met. If not, the evaluation and movement steps are repeated. Finally, when the termination criteria are satisfied, the algorithm outputs the best solution found. The Firefly Algorithm (FA) is praised for its ease of use, as it can be applied to a wide range of optimization problems and is easy to understand. Its resilience is demonstrated by its ability to maneuver through intricate environments,

supporting multimodal functions, and skillfully eschewing local optima. FA's adaptability is another of its main advantages; it can be combined with complementary techniques to improve performance and versatility, or it can be easily integrated with other optimization techniques and tailored to particular problem domains. Together, these characteristics highlight FA's attractiveness and efficiency in addressing a broad range of optimization problems in various domains. Fig 1. Shows the related pseudo code for this algorithm.

```
Begin
  1. Initialisation max iteration, α, β_o, γ
  2. Generate initial population
  3. Define the Objective function f(x),
  4. Determine Intensity (I) at cost (x) of each individual determined by f(x_i)
  5. While (t < Iter max)
        For i=1 to n
           For j=1 to n
              if (I_j > I_i)
                 Move firefly i towards j in K dimension
              end if
              Evaluate new solutions and update light intensity
           end for j
        end for i
        Rank the fireflies and find the current best
     end while
  6. Post process results and visualization
End procedure
```

Fig. 1. pseudo code of FA

Results and Discussion

The FA algorithm is utilized to address this optimization challenge and has shown superior performance in comparison to established methods like GA. Similar to its counterparts, it initiates with random particles distributed within the landscape space under specified constraints defined by the user. The number of fireflies in the population is 50. Light Absorption Coefficient (γ) which controls the attractiveness decay with distance is 0.1.

Randomization Parameter (α) which determines the step size of random perturbation and exploration is 0.05. the maximum iteration is selected 1000.

Table 1 details the optimal system sizing and convergence behavior of FA and PSO. Notably, employing FA results in an optimal configuration comprising 27 PV panels and a 4kW wind turbine. Moreover, the cost of energy (COE) is minimized to $0.3668/kWh, which proves lower than that achieved by PSO algorithm.

Table 1. Optimal sizing results

	PSO	FA
DPSP	0	0
Number of WT	7	5
Number of PV	30	27
DG Capacity(kW)	4	4
COE($/kWh)	0.3674	0.3668

The findings indicate that GOA reduces computer memory usage and shortens computation time by converging quickly. Additionally, the CS algorithm outperforms PSO in terms of overall performance.

Conclusion

This paper has explored the optimal sizing of a grid-connected microgrid using the Firefly Algorithm (FA). By focusing on minimizing the cost of energy (COE) and enhancing reliability through the deficiency of power supply probability (DPSP), the FA has demonstrated its effectiveness in achieving a balanced solution. The results from our study highlight FA's capability in determining an optimal configuration of PV panels and wind turbines, leading to a reduced COE of $0.3668/kWh. This performance surpasses other comparative algorithms such as PSO,

underscoring FA's suitability for complex optimization challenges in microgrid design. Moving forward, further research could explore hybrid approaches integrating FA with other metaheuristic methods to enhance robustness and adaptability across diverse microgrid scenarios.

References

1. Abdi, H. (2022). A brief review of microgrid surveys, by focusing on energy management system. *Sustainability*, *15*(1), 284.
2. Muhtadi, A., Pandit, D., Nguyen, N., & Mitra, J. (2021). Distributed energy resources based microgrid: Review of architecture, control, and reliability. *IEEE Transactions on Industry Applications*, *57*(3), 2223-2235.
3. Ouramdane, O., Elbouchikhi, E., Amirat, Y., & Sedgh Gooya, E. (2021). Optimal sizing and energy management of microgrids with vehicle-to-grid technology: A critical review and future trends. *Energies*, *14*(14), 4166.
4. Belboul, Z., Toual, B., Kouzou, A., & Bensalem, A. (2022, March). Optimal sizing of hybrid pv/wind/battery/diesel microgrid system using a multi-objective grasshopper optimization algorithm: A case study in djelfa city algeria. In *2022 3rd International Conference on Smart Grid and Renewable Energy (SGRE)* (pp. 1-7). IEEE.
5. Ziamanesh, S., Salimi, H. S., Tavana, A., & Ghavifekr, A. A. (2022, December). Parameter Tuning of Discontinues Lyapunov Based Controller Based on the Gray Wolf Optimization Algorithm Applied to a Robotic Manipulator. In *2022 8th Iranian Conference on Signal Processing and Intelligent Systems (ICSPIS)* (pp. 1-6). IEEE.
6. Harati, M., Ghavifekr, A. A., & Ghiasi, A. R. (2020, August). Model Identification of Single Rotary Inverted Pendulum Using Modified Practical Swarm Optimization Algorithm. In *2020 28th Iranian Conference on Electrical Engineering (ICEE)* (pp. 1-5). IEEE.
7. Ziamanesh, S., Tavaana, A., Ghavifekr, A. A., Farzamnia, A., & Salimi, H. (2022). Optimizing PID controller coefficients using an improved biogeography-based optimization to stabilize movements of quadcopters. In *Control, Instrumentation and Mechatronics: Theory and Practice* (pp. 118-131). Singapore: Springer Nature Singapore.
8. Salimi, H., Ghavifekr, A. A., Mohammadzadeh, A., Ziamanesh, S., Tavaana, A., & Dizaji, S. H. (2021, December). Modified Grey Wolf Optimization Method for Voltage and Frequency Control of an Islanded Microgrids. In *2021 11th Smart Grid Conference (SGC)* (pp. 1-5). IEEE.
9. Mohammadzadeh, A., & Ghavifekr, A. A. (2021, February). Converter switching mechanism scheduling by type-2 fuzzy approach for PV/battery/Fuel systems. In *2021 12th Power Electronics, Drive Systems, and Technologies Conference (PEDSTC)* (pp. 1-5). IEEE.
10. Safari, A., & Ghavifekr, A. A. (2022). Use case of artificial intelligence and neural networks in energy consumption markets and industrial demand response. *Industrial demand response: methods, best practices, case studies, and applications*, *4*, 379.
11. Abriz, A. F., Ghavifekr, A. A., Soltaninejad, M., Tavana, A., Safari, A., & Ziamanesh, S. (2023, February). Modified cuckoo optimization algorithm for frequency regulation of microgrids. In *2023 8th International Conference on Technology and Energy Management (ICTEM)* (pp. 1-5). IEEE.
12. Ghavifekr, A. A. (2021). Application of heuristic techniques and evolutionary algorithms in microgrids optimization problems. *Microgrids: Advances in Operation, Control, and Protection*, 219-251.
13. Ghavifekr, A. A., Mohammadzadeh, A., & Ardashir, J. F. (2021, February). Optimal placement and sizing of energy-related devices in microgrids using grasshopper optimization algorithm. In *2021 12th Power Electronics, Drive Systems, and Technologies Conference (PEDSTC)* (pp. 1-4). IEEE.
14. Yang, X. S., & Slowik, A. (2020). Firefly algorithm. In *Swarm intelligence algorithms* (pp. 163-174). CRC Press.

Advanced Engineering Days

aed.mersin.edu.tr

Estimation of elbow joint angle based on single channel electromyography signal of selected arm muscle, using machine learning methods

Ayla Ahmadi*[1], Babak Rezaee Afshar [2]

[1]*Islamic Azad University, Tehran East Branch, Technical and Engineering Faculty, Iran, aylaahmadibme@gmail.com*
[2] *Sazegar Industrial Research Center, Iran, babak.rezaee@srbiau.ac.ir*

Cite this study: Ahmadi, A. & Rezaee Afshar, B. (2024). Estimation of elbow joint angle based on single channel electromyography signal of selected arm muscle, using machine learning methods. Advanced Engineering Days, 9, 605-611

Keywords
Electromyography
Angle Estimation
Biceps
ANN
KNN

Abstract

In this study, which was carried out in order to estimate the angle of the elbow joint by biological signals, single-channel surface electromyography (sEMG) was recorded from the biceps brachii muscle area in 71 volunteer females, while performing 20 repetitions of elbow flexion movements. The obtained sEMG signals were normalized in 3-second intervals and divided into 9 ten-degree classes and windowed. A band-pass Butterworth filter and baseline correction were applied. Finally, after extracting four statistical time-domain features from the signal (RMS, STD, Mean, Max), the results were applied to an artificial neural network (ANN) and k-nearest neighbors (KNN) for classification. The artificial neural network classifier was implemented with 10 hidden layers and the average accuracy was 98.73% and the maximum accuracy was 100%. The K-nearest neighbor classifier, with 5 neighbors (K), achieved an average accuracy and a maximum accuracy of 100%. This study can be used in control of robotic hands, exoskeletons, surgical robots, assistive and rehabilitation technology, orthotics and prosthetics, and wearable robots s for support and safety during physical work, and more.

Introduction

Electromyography (EMG) is a bio-signal (biological signal) based on the measurement of the electrical activity of muscles (Chai, Liu, Sun, Wang, & Shi, 2020; Gohel & Mehendale, 2020; Ozdemir, Kisa, Guren, Onan, & Akan, 2020; Triwiyanto, Rahmawati, Yulianto, Mak'ruf, & Nugraha, 2020). The EMG signal is a weak electrical potential generated by active muscle cells, produced 30 to 150 milliseconds before body movement, and it is nonlinear, time-varying, and susceptible to interference(Huang, Chen, Zhang, Wang, & Ota, 2021; Zhang, Liu, Han, Wang, & Zhang, 2019). Muscle signals include muscle contraction and relaxation, which can be detected using biosensors(Irastorza-Landa et al., 2017). Estimating the elbow joint angle and predicting human movement intention, as a result of different muscle contraction levels, can be obtained from the EMG signal, which represents a time-dependent electrical potential(Bi & Guan, 2019; Subasi & Qaisar, 2022).

The two main techniques for recording EMG are: intramuscular and surface. Intramuscular electromyography uses invasive needle-based electrodes, which have a higher signal-to-noise ratio and are suitable for obtaining information from smaller or deeper muscles (Triwiyanto, Pawana, Irianto, Indrato, & Wisana, 2019). Surface electromyography (sEMG) is a non-invasive technique that uses at least one pair of electrodes on the body surface to record the electrical activity of muscles (Suplino, de Melo, Umemura, & Forner-Cordero, 2020). The electromyography signal is used in monitoring medical abnormalities and activation levels, biomechanical analysis of movements, detection of muscle injury, nerve damage, and muscle dysfunction, rehabilitation of limb disabilities caused by stroke, brain injury, and spinal cord injury, medical analysis and improving the condition of athletes, remote surgery with the help of robots, clinical diagnosis, and sports sciences and human-robot collaboration systems (Bi & Guan, 2019; da Silva, Pereira, Leithardt, Seman, & Zeferino, 2020; Gohel & Mehendale, 2020; Li et al., 2020; Liu et al., 2020; Triwiyanto et al., 2019; Zhang et al., 2019).

Decoding the EMG signal can be used for various purposes such as robotic arms, mirror self-rehabilitation training, speech recognition, gait analysis, assistive and rehabilitation technology, orthotics and prosthetics,

ergonomics, exoskeleton control for example for hemiplegic patients, electric wheelchair control, wearable robots for support and safety during physical work, advancing the boundaries of leisure and entertainment, and more (Bi & Guan, 2019; Cai et al., 2019; Chai et al., 2020; da Silva et al., 2020; Desplenter & Trejos, 2018; Gohel & Mehendale, 2020; Hajian & Morin, 2022; Lei, 2019; Leserri, Grimmelsmann, Mechtenberg, Meyer, & Schneider, 2022; Li et al., 2020; Liu et al., 2020; Suplino et al., 2020; Suplino, Sommer, & Forner-Cordero, 2019; Triwiyanto et al., 2019). The application considered in this study is the use of EMG for estimating the kinematics of upper limb movements, which are among the most active parts of the human body and they are vital for daily activities (Bi & Guan, 2019; Hajian & Morin, 2022).

The elbow is a simple joint with one degree of freedom and its angle can be estimated with the help of a few muscles (Suplino et al., 2020). The two main muscles related to elbow flexion and extension movements are the biceps and triceps brachii. The biceps act as the agonist for flexion and the antagonist for extension. Agonists are responsible for accelerating movements, while antagonists, especially in fast movements, reduce speed (Li et al., 2020).

The properties of the electrical signal produced by contraction vary depending on the muscle. Fast-twitch muscles reach maximum tension in one-seventh the time of a slow-twitch muscle. By correctly interpreting electromyography signals, an exoskeleton control system can identify the user's movement intentions (da Silva et al., 2020). Continuous estimation of human joint movements is essential for achieving natural, stable, real-time robotic control with minimal training required for the user (Li et al., 2020; Ma, Lin, Samuel, Xu, & Li, 2020; Suplino et al., 2019; Zhang et al., 2019).

There are various methods for estimating the elbow angle. The main methods for detecting human movement intention are based on human bioelectrical signals and mechanical sensor signals (Li, Zhang, Liu, & Zhang, 2019). For example, computer vision-based methods, methods based on inertial devices, and sEMG-based methods. Due to the placement issue of computer vision and the lack of power information of inertial devices, the focus is mainly on sEMG-based methods (Ma et al., 2020). SEMG, due to its rich information, suitable acquisition technology, and non-invasive nature, is becoming the mainstream in related research (Zhang et al., 2019).

The EMG signal can be accompanied by other equipment such as exoskeletons, goniometers, mechanical force sensors, angle sensors, inertial measurement units, accelerometers, load cells, and pressure sensors to improve modeling performance (Bag, Mandal, Faizyab, & Pandey, 2023; Gohel & Mehendale, 2020; Hajian & Morin, 2022; Li et al., 2019; Liu et al., 2020). Mechanical sensors can be used to collect movement information such as angle, speed, acceleration, and ground reaction force during limb swing, to examine the current movement status. it is necessary to mention that mechanical sensor signals have a significant time delay compared to bioelectrical signals and can affect real-time detection results (Li et al., 2019).

Studies predicting movement intention from the EMG signal have focused on classification models, regression techniques, and physiological (biomechanical) models (Hajian & Morin, 2022; Li et al., 2019; Subasi & Qaisar, 2022). Many studies have focused on identifying, distinguishing, and controlling discrete movements, using a classification-based pattern recognition approach. The use of classifiers enables the identification of movements with an accuracy of over 90% (Li et al., 2020). Regression models focus on estimating continuous upper limb kinematics. The purpose of this method is an EMG-based estimation, during muscle contraction of force/torque, movement intention, velocity, or angular position/displacement (Hajian & Morin, 2022; Triwiyanto et al., 2020). Various regression approaches have been used for estimating continuous upper limb movement. Machine learning (ML) approaches such as linear regression, ANN, SVR, etc., and deep learning (DL) approaches like CNN being more common recently (Hajian & Morin, 2022). Some researchers have used control techniques similar to biomechanics and dynamic models, which model human muscle behavior, as an alternative to artificial intelligence techniques (Li et al., 2020; Triwiyanto et al., 2020).

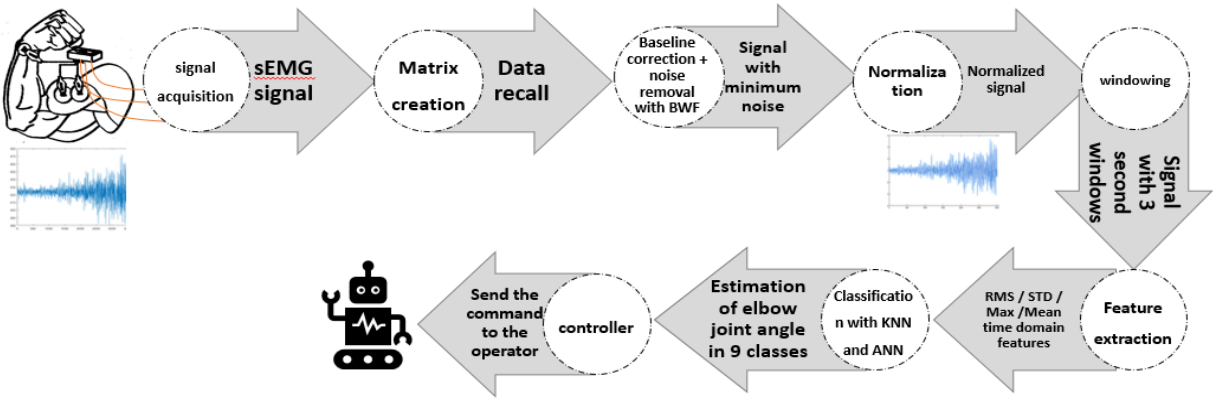


Figure 1. General framework of the sEMG-based control system and elbow angle estimation.

Table1 refers to some examples of previous studies.

Table 1. A Review of Previous Studies in the Field of Hand Movement Classification

Reference	Parameters	Extracted Features	Classific-ation	Result
(Chai et al., 2020)	Angle	-	LSTM	LSTM represents a good sequential time feature and is capable of continuously recording elbow movements.
(Lei, 2019)	Movement and Angle	Time, Frequency, Time-Frequency	BP Neural Network	The angle estimation error was controlled around 5 degrees, ultimately achieving discrete and continuous exoskeleton hand control.
(Hajian & Morin, 2022)	Angle and Speed	-	TS-CNN	Better performance for speed estimation in isokinetic conditions and angle estimation in dynamic conditions was observed. No difference was found between angle and speed estimation in isotonic conditions.
(Suplino et al., 2020)	Movement and Angle	-	NARX	A high correlation between the estimated angular path and the measured path with a maximum RMSE error of 7 degrees was demonstrated.
(Ma et al., 2020)	Angle	-	SCA-LSTM	SCA-LSTM can achieve an estimation accuracy of about 95.7%, which is consistently stable among subjects compared to CNN (86.8%) and MLP (83.4%) models.
(Huang et al., 2021)	Angle and Speed	Time Domain, Time-Frequency	CWT + BPNN	The mean RMSE for estimated angle and speed was 8.78 and 9.59 degrees per second, respectively. The mean RMSE was smaller compared to backpropagation neural networks, higher-order polynomials, and SVR.
(Liu et al., 2020)	Angle	-	AFNN	The speed and accuracy of AFNN for angle estimation is better than BPNN and RBFNN.
(Cai et al., 2019)	Movement Pattern and Angle	Time Domain	SVM	The rehabilitation robot, by detecting the movement of the healthy side, can provide mirror therapy to the affected side and can be used for self-rehabilitation training for stroke patients.
(Leserri et al., 2022)	Movement and Angle	Time Domain, Frequency	FFNN	The IEMG-MNF-ACT feature offers higher accuracy compared to TD features. A specific combination of time and frequency domain features improves the neural network's prediction accuracy compared to the entire set of features.

Material and Method

A total of 71 female subjects, 41 people aged 20±3 and 30 people aged 33±3 voluntarily participated in this study. All participants had similar physical characteristics and weighed approximately 60 to 75 kilograms. The body mass index (BMI) of the individuals ranged from 20 to 24.5 kilograms per square meter, falling within the healthy weight range. Sixteen participants were left-handed, and the remaining were right-handed. Data collection was performed on the dominant hand of all participants. They had no history of neurological or muscular diseases and did not engage in any specific professional sports activities.

In this study we have used a single-channel electromyogram recording system with sampling rate of 1000 Hz per second and bandwidth of 20 to 500 Hz. For better placement of the electrodes on the surface of the skin, three adhesive electrodes of silver/silver chloride have been used with the following conditions:

1. Two round silver/silver chloride electrodes were placed approximately 2 centimeters apart on the biceps brachii muscle to record the sEMG signals. A reference electrode was also placed on the skin of the humeroulnar region of the elbow joint, which has more bone and fewer muscles and EMG signals. The electrode placement was determined according to the Seniam Electrode Placement guidelines.
2. The surface of the skin has been well prepared before electrodes are placed to reduce environmental factors such as skin fat, dead cells and other environmental effects that affect the superficial conductivity of the skin.

The flexion movement of the hand was examined locally at the elbow joint, where the hand starts to bend from an open position (zero degrees) to a flexed position (up to 90 degrees). The participant performed the flexion movement 20 times while observing a video of an arrow moving at a constant speed over a period of 3 seconds, covering 90 degrees (as shown in Figure 2).

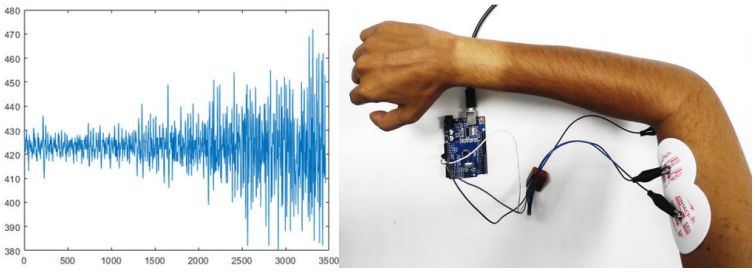


Figure 2. (Right) The connection setup of the signal acquisition device and the hand flexion movement, (Left) Example of the recorded sEMG signal.

Two alligator clip wires, red and black (as shown in Figure 3), were connected to the biceps muscle signal electrodes, and the white alligator clip wire was connected to the reference electrode. The other ends of these wires were connected to the three upper terminals of the Subtle type C module (above the rocket symbol). These three differential cables, responsible for transferring bio-signals from the body to the module, should be as short as possible to prevent noise interference with the main signal. The three lower terminals of the module were connected to the Arduino UNO microprocessor jumper wires. The fourth pin from the top of the module was connected to the Arduino ground (GND), the fifth pin was connected to the A0 analog input on the board, and the last pin of the chipset was connected to the 5V power supply of the Arduino board.

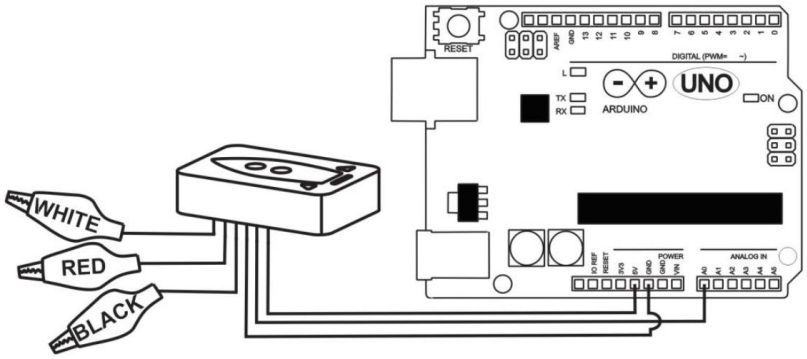


Figure 3. Connection setup of the module to the Arduino board

The Subtle type C module allows for signal reception, amplification with a gain of 880, common mode rejection of 120 dB, filtering of data with minimal noise in the frequency range of 10 to 500 Hz, and finally, sending the pre-processed signals to the microprocessor. The Arduino UNO microprocessor is an analog-to-digital converter with a resolution of 10 bits. It receives analog EMG signal data with a voltage between 0 to 5 volts and converts it to digital levels ranging from 0 to 1023. After converting the analog data to digital using the Arduino, the Serial Oscilloscope program was used to record the data as a standard Excel file with a .csv extension on the computer. This program allowed for simultaneous viewing of graphical images of the EMG signal during data recording.

After the data acquisition and recording of signals, data processing and analysis were performed using MATLAB software, version R2021b. During the software preprocessing, a Butterworth bandpass filter was applied, and baseline correction (bias removal) was performed. The data were then normalized. The filters used in shaping the frequency spectrum of the input signal for minimize noise as much as possible. A bandpass filter is constructed by cascading a low-pass filter and a high-pass filter. Consequently, frequencies higher and lower than the cutoff frequencies of the constituent filters are attenuated. In this study, a Butterworth filter of fourth order was used with cutoff frequencies of 20 Hz and 500 Hz. If we consider a general equation representing a Butterworth filter of order n, then its frequency response according to equation (1) is:

$$H(j\omega) = \frac{1}{\sqrt{1 + \epsilon^2 \left(\frac{\omega}{\omega_p}\right)^{2n}}}$$

In the above equation: n shows the order of the filter, ω represents the angular frequency (ω=2πf), ϵ is equal to the maximum passband gain (A_{max}).

Data collected at different ranges can have undesirable effects on each other and consequently on the algorithm. Therefore, all data must be scaled to a uniform range relative to each other, for example, in the range of 0 to 1. This method is called Min-Max normalization (Phinyomark, 2012), defined by equation (2):

$$normX_i = \frac{X_i - min_i}{max_i - min_i}$$

where X_i is the original value in the signal, $normX_i$ is the normalized value, mini is the minimum value, and maxi is the maximum value in that set, transformed to the range of 0 to 1.

After preprocessing the signals, which were captured in 3-second intervals (3000 samples), they were segmented into windows. Each data set corresponded to 90 degrees of Flexion movement in the elbow joint and was complete. Each of these data sets was divided into 9 windows, each representing 10 degrees of movement (334 samples). These windows were non-overlapping (0% overlap) and placed sequentially next to each other. After concatenating the segmented data of all participants in this study, 4 desirable statistical features in the time domain were extracted from each window for the purpose of classifying the angles related to elbow joint movement.

The mean is one of the measures of central tendency in statistics. In other words, the mean represents the data instead of the entire dataset and is defined by equation (3):

$$\bar{x} = \frac{1}{N}\sum_{i=1}^{N} x_i$$

where x_i is the *i*-th sample in the analysis, among a total of N samples.

The root mean square (RMS) is the measure of the power of sEMG signals related to fatigue-free contractions and other forces affecting muscles. RMS, or the effective value of the signal, is essentially a Gaussian-modulated stochastic process with an amplitude range {Phinyomark, 2012 #27}. Mathematically, this feature can be defined by equation (4):

$$RMS = \sqrt{\frac{1}{N}\sum_{i=1}^{N} {x_i}^2}$$

Where x_i represents the *i*-th sample in the analysis among the total number of samples (N) {Leserri, 2022 #21}{Benazzouz, 2019 #28}.

Standard deviation (STD) is one of the measures of dispersion in statistics. STD indicates on average how far data points are from the mean. Standard deviation is the square root of variance, and its advantage over variance is having the same unit as the original variable. Equation (5) represents STD:

$$\sigma = \sqrt{\frac{1}{N}\sum_{i=1}^{N} (x_i - \bar{x})^2}$$

In this formula, $\bar{x}$ shows the mean of the data, x_i represents the *i*-th sample, and N is the total number of samples {Benazzouz, 2019}. The maximum value (max) of the signal refers to the largest value of the signal under investigation.

After feature extraction, an Artificial Neural Network (ANN) with 10 hidden layers and the K-Nearest Neighbors (KNN) algorithm with 5 neighbors (K) were used for classification and estimation of the elbow joint angle. In general, an Artificial Neural Network (ANN) can be divided into three layers of neurons: input (receives information), hidden (responsible for pattern extraction, performing most internal processing), and output (produces and presents final network outputs). Transfer functions, learning rules, and architecture determine the overall behavior of the neural network. ANN gathers its knowledge by identifying patterns and relationships in data and learning through experience {Shahid, 2019 #30}. K-Nearest Neighbors (KNN) is a simple, understandable, scalable machine learning algorithm with easy interpretation, low computational time, very high predictive power, and effectiveness, especially for very large training datasets. Its mathematical computations are easy to understand and rely on fundamental concepts such as calculating Euclidean distance. KNN groups data into clusters or cohesive subsets and classifies new input data based on its similarity to previously trained data {Taunk, 2019 #32}.

Results

In the feature extraction phase, a table was created showing the maximum, mean, and minimum values of each extracted feature (Table 2).

Table 2. Statistical analysis of 4 extracted features

	Max	Mean	Min
Mean	0.073386	0.015359	-0.01619
RMS	2.143498	0.891539	0.15394
STD	2.146705	0.892656	0.154083
Max	9	5.001904	1

Four features extracted were used as input to the ANN with 10 hidden layers. The dataset was split into 70% for training, 15% for testing, and another 15% for validation. The ANN classifier achieved a maximum accuracy of 100%. Across 20 runs of the ANN, the average accuracy reached 98.73% (figure 4).

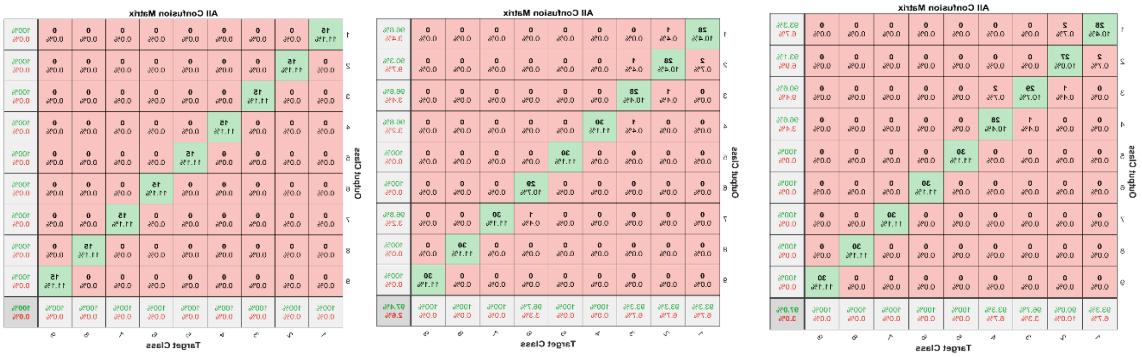


Figure 4. Sample ANN results obtained from 4 participants

For classification using the KNN algorithm with K=5 (neighbors), 80% of the data was used for training and the remaining 20% for testing. The KNN classifier achieved a maximum accuracy of 100% and an average accuracy of 100% in classifying elbow joint angles into 10-degree classes.

Discussion

The results show the effectiveness of both ANN and KNN in accurately classifying and estimating elbow joint angles based on the features extracted from the sEMG signals. Achieving this can result in noise reduction, high signal-to-noise ratio, consideration of interfering factors such as muscle fatigue, elimination of the need for multiple human dynamic and physiological parameter measurements, and adherence to precise instrument requirements.

It is recommended that future studies increase the number of channels, participants, movements, and other auxiliary equipment for multidimensional information fusion, investigate more complex movements and angles of multiple joints such as wrist and shoulder, with greater degrees of freedom and classification of angles less than ten degrees, for more accurate differentiation and a larger number of elbow and other joint movements. The proposed method can be applied to other populations (such as disabled individuals and neuromuscular patients) and complex body conditions, and used for robot control in human-robot interactions.

Conclusion

Based on the obtained results and the classification of ANN with a maximum accuracy rate of 100% and an average accuracy of 98.73%, and the classification with KNN with average and maximum accuracy of 100%, it is possible to classify various angles of the arm joint using single-channel surface electromyography (sEMG). Considering the extracted features and the standard deviation of feature data, the maximum changes had the highest average, while the minimum changes were related to the maximum feature. The results are consistent with findings from {Chai, 2020 #46}{Lei, 2019 #47}{Huang, 2021 #13}{Suplino, 2020 #49}{Ma, 2020 #51} articles. However, this study achieved higher results compared to the mentioned articles by using lighter data, more participants, employing preferred classifiers, and using single-channel electromyography. Based on the obtained results, classification and estimation of elbow joint angles using sEMG can be used for various purposes such as robotic arm construction, mirror therapy, orthotics and prosthetics, ergonomics, external skeleton control for disabled individuals and patients, assistive and rehabilitation technologies, wearable robots to support and be safety during physical activities.

References

Bag, S., Mandal, D., Faizyab, I., & Pandey, R. (2023). Biomechanical Measurement of Muscle Force on Various Degree of Flexion at Elbow Joint.

Bi, L., & Guan, C. (2019). A review on EMG-based motor intention prediction of continuous human upper limb motion for human-robot collaboration. *Biomedical Signal Processing and Control, 51*, 113-127.

Cai, S., Chen, Y., Huang, S., Wu, Y., Zheng, H., Li, X., & Xie, L. (2019). SVM-based classification of sEMG signals for upper-limb self-rehabilitation training. *Frontiers in neurorobotics, 13*, 31.

Chai, Y., Liu, K., Sun, Z., Wang, G., & Shi, T. (2020). *A long short term memory network based on surface electromyography for continuous estimation of elbow joint angle.* Paper presented at the 2020 IEEE 9th Data Driven Control and Learning Systems Conference (DDCLS).

da Silva, L. D., Pereira, T. F., Leithardt, V. R., Seman, L. O., & Zeferino, C. A. (2020). Hybrid impedance-admittance control for upper limb exoskeleton using electromyography. *Applied Sciences, 10*(20), 7146.

Desplenter, T., & Trejos, A. L. (2018). Evaluating muscle activation models for elbow motion estimation. *Sensors, 18*(4), 1004.

Gohel, V., & Mehendale, N. (2020). Review on electromyography signal acquisition and processing. *Biophysical Reviews, 12*(6), 1361-1367.

Hajian, G., & Morin, E. (2022). Deep multi-scale fusion of convolutional neural networks for EMG-based movement estimation. *IEEE Transactions on Neural Systems and Rehabilitation Engineering, 30*, 486-495.

Huang, Y., Chen, K., Zhang, X., Wang, K., & Ota, J. (2021). Motion estimation of elbow joint from sEMG using continuous wavelet transform and back propagation neural networks. *Biomedical Signal Processing and Control, 68*, 102657.

Irastorza-Landa, N., Sarasola-Sanz, A., López-Larraz, E., Bibián, C., Shiman, F., Birbaumer, N., & Ramos-Murguialday, A. (2017). *Design of continuous EMG classification approaches towards the control of a robotic exoskeleton in reaching movements.* Paper presented at the 2017 International Conference on Rehabilitation Robotics (ICORR).

Lei, Z. (2019). An upper limb movement estimation from electromyography by using BP neural network. *Biomedical Signal Processing and Control, 49*, 434-439.

Leserri, D., Grimmelsmann, N., Mechtenberg, M., Meyer, H. G., & Schneider, A. (2022). Evaluation of sEMG Signal Features and Segmentation Parameters for Limb Movement Prediction Using a Feedforward Neural Network. *Mathematics, 10*(6), 932.

Li, K., Zhang, J., Liu, X., & Zhang, M. (2019). Estimation of continuous elbow joint movement based on human physiological structure. *Biomedical engineering online, 18*, 1-15.

Li, K., Zhang, J., Wang, L., Zhang, M., Li, J., & Bao, S. (2020). A review of the key technologies for sEMG-based human-robot interaction systems. *Biomedical Signal Processing and Control, 62*, 102074.

Liu, Y., Li, C., Teng, Z., Liu, K., Wang, G., & Sun, Z. (2020). *Intention recognition of elbow joint based on sEMG using adaptive fuzzy neural network.* Paper presented at the 2020 5th International Conference on Mechanical, Control and Computer Engineering (ICMCCE).

Ma, C., Lin, C., Samuel, O. W., Xu, L., & Li, G. (2020). Continuous estimation of upper limb joint angle from sEMG signals based on SCA-LSTM deep learning approach. *Biomedical Signal Processing and Control, 61*, 102024.

Ozdemir, M. A., Kisa, D. H., Guren, O., Onan, A., & Akan, A. (2020). *EMG based hand gesture recognition using deep learning.* Paper presented at the 2020 Medical Technologies Congress (TIPTEKNO).

Subasi, A., & Qaisar, S. M. (2022). Surface EMG signal classification using TQWT, Bagging and Boosting for hand movement recognition. *Journal of Ambient Intelligence and Humanized Computing, 13*(7), 3539-3554.

Suplino, L. O., de Melo, G. C., Umemura, G. S., & Forner-Cordero, A. (2020). *Elbow movement estimation based on EMG with NARX Neural Networks.* Paper presented at the 2020 42nd Annual International Conference of the IEEE Engineering in Medicine & Biology Society (EMBC).

Suplino, L. O., Sommer, L. F., & Forner-Cordero, A. (2019). *EMG-based control in a test platform for exoskeleton with one degree of freedom.* Paper presented at the 2019 41st Annual International Conference of the IEEE Engineering in Medicine and Biology Society (EMBC).

Triwiyanto, T., Pawana, I. P. A., Irianto, B. G., Indrato, T. B., & Wisana, I. D. G. H. (2019). Embedded system for upper-limb exoskeleton based on electromyography control. *Telkomnika (Telecommunication Computing Electronics and Control), 17*(6), 2992-3002.

Triwiyanto, T., Rahmawati, T., Yulianto, E., Mak'ruf, M. R., & Nugraha, P. C. (2020). Dynamic feature for an effective elbow-joint angle estimation based on electromyography signals. *Indones. J. Electr. Eng. Comput. Sci, 19*(1), 178-187.

Zhang, L., Liu, G., Han, B., Wang, Z., & Zhang, T. (2019). sEMG based human motion intention recognition. *Journal of Robotics, 2019*.

Advanced Engineering Days

aed.mersin.edu.tr

Design of Adaptive PID Controller for Lower Limb Exoskeleton Robot Based on Hybrid Model of Genetic Algorithm and Improved Black Hole Optimization

Amir Ata Nikjoo, Mohanna Arefnezhad

University of Tabriz, Faculty of Electrical and Computer Engineering, Iran, amirata.nikjoo@gmail.com
mohannaarefnejad@gmail.com

Cite this study: Nikjoo, A. A., & Arefnezhad, M. (2024). Design of Adaptive PID Controller for Lower Limb Exoskeleton Robot Based on Hybrid Model of Genetic Algorithm and Improved Black Hole Optimization. Advanced Engineering Days, 9, 612-615

Keywords
Adaptive PID Controller
Lower Limb
Exoskeleton Robot
Black Hole Optimization
Genetic Algorithm

Abstract

In this paper, we present the design and implementation of an adaptive PID controller for a lower limb exoskeleton robot, leveraging a hybrid algorithm that combines Genetic Algorithm (GA) with Improved Black Hole Optimization (IBHO). The primary aim is to enhance the control performance and stability of the exoskeleton, crucial for applications in medical rehabilitation and assistive technologies. The GA-IBHO hybrid algorithm effectively tunes the PID controller parameters, balancing exploration and exploitation to achieve optimal performance. Through extensive simulations, our approach demonstrated superior control accuracy and robustness compared to traditional PID controllers and other optimization methods. The proposed adaptive PID controller significantly improved the dynamic response and stability of the exoskeleton robot. This study highlights the potential of hybrid optimization algorithms in enhancing complex control systems and sets the stage for future research focused on real-world implementation and further algorithmic refinements.

Introduction

In recent years, lower limb exoskeletons have gained significant attention for their roles in human assistance, augmentation, treatment, and protection. These devices, which are worn on the body, work in coordination with the user to perform specific movements. Assistive exoskeletons aid individuals in daily activities impaired by injury, stroke, or age, while rehabilitation exoskeletons aim to restore abilities over time by gradually reducing assistance. Control methods vary depending on the type of exoskeleton [1].

Evolutionary algorithms have been utilized in practical engineering problems widely[2-7]. To design a lower limb exoskeleton (LLE) for walking training, incorporating a controller that minimizes steady-state errors and improves the robot's stability is crucial. Various control strategies for LLEs have been examined in the literature. One approach includes a hybrid PID controller that uses genetic algorithms and particle swarm optimization to fine-tune PID parameters for each joint, thereby enhancing tracking performance and accuracy [8]. Another strategy is a modified adaptive PID controller (MAPID) optimized with Gray Wolf Optimization (GWO), aimed at better control and tracking in lower limb rehabilitation robots [9]. Additionally, a hybrid control method combining a model reference adaptive controller (MRAC) with a PID controller has been suggested for LLEs [10].

A Proportional-Integral-Derivative (PID) controller is a widely utilized control mechanism in various technical systems, renowned for its simplicity and effectiveness. It works by adjusting three parameters: proportional (P), integral (I), and derivative (D), to minimize system error and ensure stability and optimal performance. Proper tuning of these parameters allows the controller to provide precise control and responsiveness, used for determining the optimal settings. Designing an adaptive PID controller for a lower limb exoskeleton robot involves implementing mechanisms that dynamically adjust the controller parameters in real time to adapt to the evolving dynamics and operating conditions of the system. This ensures that the exoskeleton performs optimally and remains stable during various activities while meeting the unique needs of users. Using real-time data, the adaptive mechanism fine-tunes parameters, allowing the robot to maintain balance, provide support, and precisely follow the desired trajectory [11].

Genetic Algorithm (GA) is a population-based stochastic algorithm inspired by Darwinian evolution, involving selection, crossover, and mutation to iteratively improve solutions. It starts with a random population of chromosomes, each representing a potential solution. The selection process favors better solutions based on fitness values, typically using methods like roulette wheel selection. Crossover combines genetic information from two parents to create new offspring, with techniques such as single-point, double-point, and uniform crossover. Mutation introduces random changes to maintain diversity and avoid premature convergence. GA effectively balances exploration and exploitation, making it a robust optimization tool for complex search spaces [12].

The Black Hole Optimization (BHO) algorithm, inspired by black hole's gravitational forces, is a metaheuristic optimization technique for solving complex problems across various domains. It represents potential solutions as stars, with the worst solution acting as a black hole that attracts nearby stars based on fitness. The process involves initializing a set of random solutions, evaluating their fitness, and iteratively applying gravitational attraction and repulsion mechanisms to converge toward an optimal solution. Enhanced through parameter tuning and adaptive strategies, IBHO (Improved Black Hole Optimization) balances exploration and exploitation, handling multimodal and non-linear problems effectively [13].

Material and Method

In this paper, our goal is to improve the performance of the BHO algorithm by presenting an enhanced model of this algorithm. Given that the weights are dynamically updated, we require faster computations. Therefore, we decided to create a hybrid model using the genetic algorithm to accelerate this minimization process. Our proposed hybrid model, named GA-IBHO, first employs the genetic algorithm to generate the initial population and provides the best weights to achieve the minimum cost function value as input to the IBHO algorithm, continuing the optimization process.

The pseudocode for this proposed algorithm is provided below:

Algorithm 1 Hybrid algorithm of GA-IBHO.

```
Start GA-IBHO
Initialize random population with 100 chromosomes
Evaluate initial population
for generation = 1 to 100 do
    Create new generation with crossover and mutation
    Evaluate and sort population
end for
Take best individuals from GA as initial population for IBHO
Initialize N stars with positions from GA output
while generation < 250 do
    Evaluate each star in objective function
    BH = best star
    for each star do
        Update position using BH
    end for
    Normalize fitness and create cumulative probability distribution
    for each star do
        Select new position using roulette wheel
        if star is better than BH then
            swap positions
        if star close to BH then
            Move to random position
    end for
end while
Return best parameters (Kp, Ki, Kd)
End GA-IBHO
```

Results

In this section, we present numerical results for the proposed algorithms. The primary objective of the black hole algorithm in this study is to optimize the parameters of an adaptive PID controller to minimize the control system's output error. This algorithm functions by modeling the control system as a black hole. During each iteration, the PID parameters are adjusted to minimize the objective function, which is the system's output error. The maximum iteration of the algorithms is set 250, and the number of populations is set 100. The attractive force that influences the solutions towards the black hole is set to 0.4, and the acceleration coefficient is set to 0.3.

The optimal parameter values for the adaptive PID controller for the hip and knee joints, obtained using the GA-BHO, IBHO and BHO algorithms are presented in Tables 1 and 2. As shown, GA-BHO significantly outperforms the other two algorithms in achieving more optimal values. Additionally, the proposed approach reaches its

minimum possible value in fewer iterations compared to the other algorithms. This efficiency can be particularly beneficial for robots that require dynamic updates.

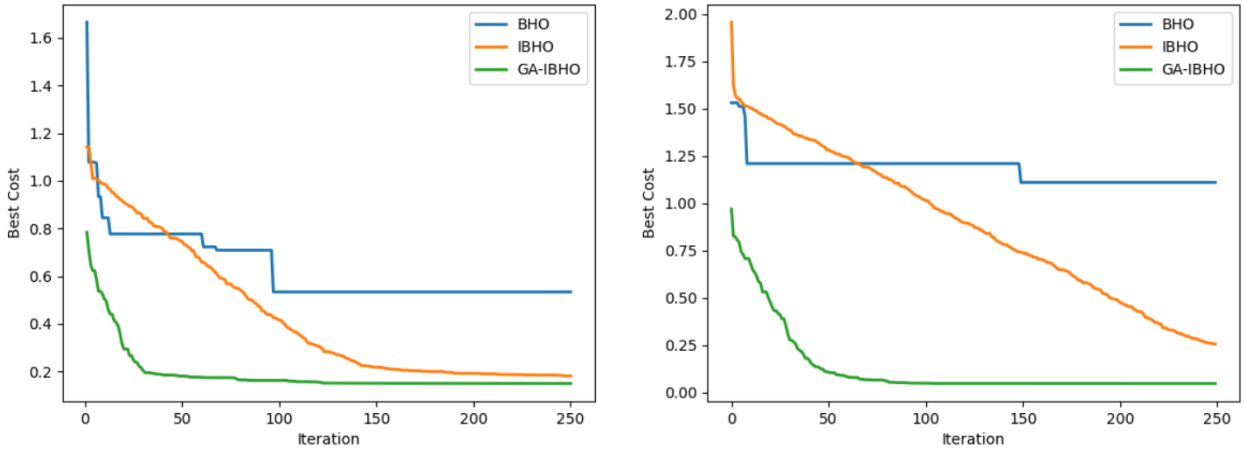
Table 1. Comparison of Adaptive PID controller values for hip

Algorithm	K_p	K_i	K_d	Best Cost
BHO	14.9880	0.1465	7.9328	0.5339
IBHO	15.9790	0.0002	7.4818	0.1816
GA-IBHO	15.9789	0.0002	6.7198	0.1498

Table 2. Comparison of Adaptive PID controller values for knee

Algorithm	K_p	K_i	K_d	Best Cost
BHO	19.8281	0.6334	24.7563	1.0339
IBHO	23.6300	0.0071	20.2943	0.3548
GA-IBHO	23.6591	0.0002	23.8443	0.0474

The best objective function value for the hip and knee joints using the selected optimization algorithm is shown in Figures 1-a and 1-b, respectively. GA-IBHO balances exploration and exploitation through migration and mutation operations and has a very high speed due to the use of the genetic algorithm. BHO requires a considerable amount of time to converge to a local minimum, and IBHO converges relatively quickly, but GA-IBHO not only reaches the minimum and converges at a very high speed, also achieves more optimal values than IBHO, making it very suitable for real-time applications.



(a)Hip (b)Knee

Figure 1. The best objective function value for each joint

Discussion

In this study, we designed an adaptive PID controller for a lower limb exoskeleton robot using a hybrid algorithm combining Genetic Algorithm (GA) and Improved Black Hole Optimization (IBHO). Our results demonstrate significant improvements in control performance compared to traditional PID controllers and other optimization methods. The GA-IBHO hybrid algorithm effectively balances exploration and exploitation, leading to superior tuning of the PID parameters. This enhancement translates to better stability and response of the exoskeleton robot, crucial for practical applications in medical rehabilitation. Despite the promising outcomes, some limitations such as computational complexity and the need for precise parameter tuning remain. Future research should focus on refining these algorithms, conducting real-world tests, and exploring other hybrid approaches to further enhance adaptive control systems for exoskeleton robots.

Conclusion

The proposed method significantly enhanced control performance, indicating its potential to improve the efficiency and safety of exoskeleton robots. The successful combination of GA and IBHO demonstrates the advantages of integrating various optimization techniques to achieve superior results. Future research should focus on further optimizing algorithm parameters, conducting real-world testing, and examining the applicability of this approach to other robotic systems. This research highlights the significance of advanced adaptive control strategies in creating effective and reliable exoskeleton robots for medical use.

References

1. Lee, H., Ferguson, P. W., & Rosen, J. (2020). Lower Limb Exoskeleton Systems—Overview. In Elsevier eBooks (pp. 207–229). doi: 10.1016/b978-0-12-814659-0.00011-4
2. Ziamanesh, S., Salimi, H. S., Tavana, A., & Ghavifekr, A. A. (2022, December). Parameter Tuning of Discontinues Lyapunov Based Controller Based on the Gray Wolf Optimization Algorithm Applied to a Robotic Manipulator. In 2022 8th Iranian Conference on Signal Processing and Intelligent Systems (ICSPIS) (pp. 1-6). IEEE.
3. Salimi, H., Ghavifekr, A. A., Mohammadzadeh, A., Ziamanesh, S., Tavaana, A., & Dizaji, S. H. (2021, December). Modified Grey Wolf Optimization Method for Voltage and Frequency Control of an Islanded Microgrids. In 2021 11th Smart Grid Conference (SGC) (pp. 1-5). IEEE.
4. Tavana, A., Ziamanesh, S., Salimi, H. S., Ghavifekr, A. A., & Visconti, P. (2023, July). A GOA-Optimized Visible Light Communication System For Indoor High-Precision 3-D Positioning Service. In 2023 9th International Conference on Control, Decision and Information Technologies (CoDIT) (pp. 2585-2590). IEEE.
5. Ziamanesh, S., Tavaana, A., Ghavifekr, A. A., Farzamnia, A., & Salimi, H. (2022). Optimizing PID controller coefficients using an improved biogeography-based optimization to stabilize movements of quadcopters. In Control, Instrumentation and Mechatronics: Theory and Practice (pp. 118-131). Singapore: Springer Nature Singapore.
6. Abriz, A. F., Ghavifekr, A. A., Soltaninejad, M., Tavana, A., Safari, A., & Ziamanesh, S. (2023, February). Modified cuckoo optimization algorithm for frequency regulation of microgrids. In 2023 8th International Conference on Technology and Energy Management (ICTEM) (pp. 1-5). IEEE.
7. Harati, M., Ghavifekr, A. A., & Ghiasi, A. R. (2020, August). Model Identification of Single Rotary Inverted Pendulum Using Modified Practical Swarm Optimization Algorithm. In 2020 28th Iranian Conference on Electrical Engineering (ICEE) (pp. 1-5). IEEE.
8. Amiri, M. S., Ramli, R., & Ibrahim, M. F. (2019). Hybrid design of PID controller for four DoF lower limb exoskeleton. Applied Mathematical Modelling, 72, 17–27. doi: 10.1016/j.apm.2019.03.002
9. Sabah, N., Hameed, E., & Al-Huseiny, M. S. (2022). Design of Modified Adaptive PID Controller for Lower Limb Rehabilitation Robot based on Grey Wolf Optimization Algorithm. Webology, 19(1), 295–310. doi: 10.14704/web/v19i1/web19023
10. Aliman, N., Ramli, R., & Haris, S. M. (2021). Hybrid design of model reference adaptive controller and PID controller for lower limb exoskeleton application. In Lecture notes in mechanical engineering (pp. 539–553). doi: 10.1007/978-981-16-0866-7_46
11. Alexandrov, A. G., & Palenov, M. V. (2014). Adaptive PID controllers: State of the art and development prospects. Automation and Remote Control, 75(2), 188–199. doi: 10.1134/s0005117914020027
12. Katoch, S., Chauhan, S. S., & Kumar, V. (2020). A review on genetic algorithm: past, present, and future. Multimedia Tools and Applications, 80(5), 8091–8126. doi: 10.1007/s11042-020-10139-6
13. Nikjoo, A. A., Arefnezhad, M., & Ghavifekr, A. A. (2023). Design of Adaptive PID Controller for Lower Limb Exoskeleton Robot Based on Improved Black Hole Optimization. IEEE. doi: 10.1109/iccia61416.2023.10506373

Advanced Engineering Days

aed.mersin.edu.tr

Neuromusculoskeletal Modeling of Elbow Flexion/Extension – Aided by OpenSim

Mohammad Reza Sayyed Noorani [*1], Farhad Farkhondeh Tale Navi [2], Kimiya Khojand [1]

[1]*University of Tabriz, Department of Mechatronics Engineering, Iran, smrs.noorani@tabrizu.ac.ir, kimiya.kh1401@ms.tabrizu.ac.ir*
[2]*University of Tabriz, Department of Cognitive Neuroscience, Iran, Farkhondeh_F@Tabrizu.ac.ir*

Cite this study: Noorani, M. R. S., Navi, F. F. T., & Khojand, K. (2024). Neuromusculoskeletal Modeling of Elbow Flexion/Extension– Aided by OpenSim. Advanced Engineering Days, 9, 616-619

Keywords
Neuromusculoskeletal
Elbow Movement
Cerebrum
Motor Command
OpenSim software

Abstract

Neuromusculoskeletal (NMSK) models are recently exploited as a non-invasive approach for advanced predictive simulations and subject-specific modeling to enhance clinical applications. A cerebellar model, in addition to a musculoskeletal model, is fundamental to this idea. In this paper, we aim to establish an integrated framework to simulate the role of the cerebellum in producing the motor control commands of flexor/extensor muscles of the elbow. The model of cerebellum is abstracted to a Spiking Neural Network (SNN) that receives sensory information from the musculoskeletal and delivers the motor actions. The Izhikevich model is utilized to capture neuron activity function due to its balance between biological accuracy and computational efficiency. The learning is based on the strategy of Spike Timing-Dependent Plasticity (STDP) modulated by Dopamine (DA). Accordingly, firing of a presynaptic neuron immediately before a postsynaptic neuron results in Long-Term Potentiation (LTP) of synaptic transmission, and the reverse order of firing results in Long-Term Depression (LTD). The trained network provides flexor and extensor command signals to move the elbow for reaching the hand to a target position. By using the OpenSim API in MATLAB, we investigate our neuromusculoskeletal model in a closed-loop procedure in which the elbow muscles in forward dynamics receive the neural excitations and feedback the motion information. This framework highlights the potential of SNN-based cerebellar models in improving motor function rehabilitation through personalized, precise neuromuscular simulations, advancing computational neuroscience, and benefiting both healthy and impaired conditions in clinical settings.

Introduction

Neuromusculoskeletal (NMSK) models are exploited as a computational non-invasive approach for advanced predictive simulations and multi-scale modeling to enhance clinical applications. NMSK models are powerful tools to estimate the complex interactions between neural control, muscle dynamics, and skeletal movement, enabling personalized treatment plans and improved rehabilitation outcomes, for example in human-in-the-loop control of assistive robots [1,2]. These models must be adapted for real-world environments, requiring the integration of high-fidelity simulation data to compensate for lower resolution measurements in settings like fields, gyms, and clinics [1]. Recent research emphasizes the importance of subject-specific modeling and the potential for advanced predictive simulations and multi-scale modeling to enhance clinical applications [3,4].

Neuromusculoskeletal modeling is a complex and interdisciplinary field that has significant implications for both artificial and biological systems. These models are essential for understanding motor control mechanism, designing experiments, and optimizing motor performance. However, current models are not able to fully capture the complexities of the neuromusculoskeletal control system, especially the nonlinear dynamics of skeletal muscle, suggesting a more realistic approach to modeling. Implementation of such models according to brain structures (e.g., the cerebellum) and functions (e.g., spiking activity) could significantly enhance the fidelity of simulations and provide deeper insights into motor control mechanisms [3,4].

The cerebellum plays a crucial role in motor control, prediction, and learning. It processes sensory input and coordinates voluntary movements, ensuring smooth and precise actions. Pathologies affecting the cerebellum can

lead to significant motor impairments. For instance, Geminiani et al. (2018) developed a detailed computational model of the cerebellum embedded in a sensorimotor circuit to study cerebellar pathologies [5]. Moreover, Bruel et al. (2023) addressed to spinal cord (SC) influence on motor learning in the cerebellum to find that dose the SC facilitate or hinder cerebellar motor learning [3].

Research has shown that artificial neural networks (ANNs), particularly spiking neural networks (SNNs), are effective in simulating realistic human body movements, e.g. elbow flexion/extension, for various applications, including assistive technology and rehabilitation systems [1,3,6]. These networks can generate inverse dynamics transformations of arm and hand movements with low torque errors, providing subject-specific parameterization and precise predictions of limb dynamics [7]. They have also been integrated into closed-loop models for human activities of daily living (ADL) movements, accurately predicting angular trajectories during tasks like eating and drinking with high target access rates and minimal error rates.

Recent advancements in spiking neural networks (SNNs) have revolutionized the simulation of biological neural behavior, particularly in motor control tasks like elbow rotational movement. SNNs, inspired by the brain's neural processes, excel in replicating precise spike timing and communication dynamics of biological neurons, offering valuable insights into temporal processing and learning mechanisms [8-9]. Moreover, by incorporating Spike Timing-Dependent Plasticity (STDP), SNNs provide a biologically plausible framework for motor control tasks, making them ideal for controlling robotic systems and modeling biological processes [10]. The utilization of cerebellar-inspired learning rules in SNNs enhances their capability to simulate and control complex movements, such as robotic arm manipulation, showcasing their potential in realistic simulations of motor tasks [11-13].

The objectives of this study are to synthesize current research on SNNs and their application in motor control, elucidate the significance of STDP in learning, and explore the role of cerebellar learning in motor function and pathology. By integrating evidence-based information from neuroscience, robotics, and computational modeling, we aim to provide a comprehensive overview that is accessible to a broad audience, including researchers, engineers, and clinicians.

Material and Method

We utilized the Izhikevich model for its balance between biological accuracy and computational efficiency designing a spiking neural network to simulate cerebellar function in motor control tasks, specifically elbow flexion and extension. The SNN architecture was inspired by previous successful applications, consisting of neurons representing the cerebellar, receiving proprioceptive input and delivering motor commands, see Fig. 1. Spike Timing-Dependent Plasticity (STDP), modulated by dopamine, served as the primary learning mechanism, adjusting synaptic weights based on the temporal correlation of neuronal activity. Structural synaptic plasticity further enhanced network adaptability by allowing the formation and elimination of synaptic connections. Moreover, in a larger time scale, dopamine as the reward of approaching to the target modulates the strength of the synaptic connections. This architecture is, in fact the, inspiration of reinforcement learning in which rewards obtained through interaction of an agent with environment conducts the system towards an optimal policy.

The network underwent a motor babbling phase, generating random motor commands to map sensory inputs to motor commands. The commands serve as activations of the biceps (BIC) and triceps (TRC) muscles to move the musculoskeletal model of the elbow established under OpenSim API in MATLAB [14]. This closed-loop system involved the SNN, as cerebellum model, generating motor commands, applying them to the musculoskeletal model, and receiving proprioceptive feedback. The simulation evaluates the accuracy and efficiency of the control system via performance metrics including target-reaching ability, movement smoothness, and response to perturbations. The Pipeline of the learning algorithm based on STDP and DA modulation is illustrated in Fig. 2.

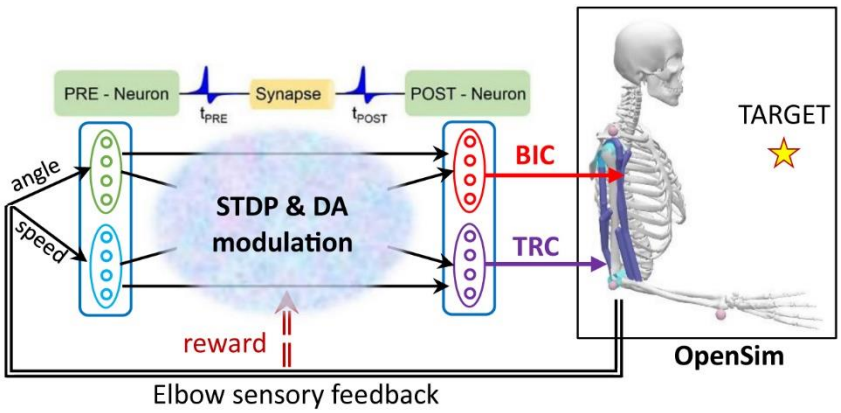


Figure 1. The neuromusculoskeletal model including a SNN architecture trained via STDP & DA modulation.

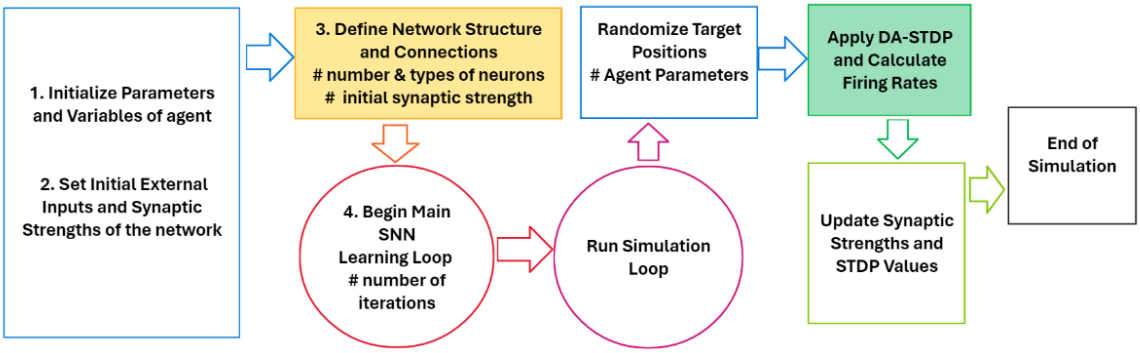


Figure 2. Pipeline and information flow in the neuromusculoskeletal model.

Conclusion

Spiking neural networks, leveraging mechanisms such as STDP and structural plasticity, offer powerful tools for modeling and controlling motor behaviors. The detailed study of cerebellar functions and pathologies through computational models provides valuable insights into the neural basis of motor control and learning. These advancements pave the way for innovative applications in robotics and neuroprosthetics, enhancing the quality of life for individuals with motor impairments. The integration of SNNs with STDP and cerebellar learning models holds promise for developing advanced neuroprosthetics and rehabilitation devices. By mimicking the biological processes underlying motor control, these networks can provide more natural and efficient control mechanisms for robotic limbs and assistive technologies.

Future research should focus on enhancing the scalability and robustness of SNNs, integrating multimodal sensory inputs, and exploring the co-adaptation of neural networks and users in brain-computer interface (BCI) applications. Additionally, further studies on the interplay between different forms of synaptic plasticity and their impact on learning and memory will deepen our understanding of both artificial and biological neural systems.

References

1. Lloyd, David G., Ilse Jonkers, Scott L. Delp, and Luca Modenese. "The history and future of neuromusculoskeletal biomechanics." *Journal of Applied Biomechanics* 39, no. 5 (2023): 273-283.
2. Meattini, Roberto, Davide Chiaravalli, Gianluca Palli, and Claudio Melchiorri. "sEMG-based human-in-the-loop control of elbow assistive robots for physical tasks and muscle strength training." *IEEE Robotics and Automation Letters* 5, no. 4 (2020): 5795-5802.
3. Bruel, Alice, Ignacio Abadía, Thibault Collin, Icare Sakr, Henri Lorach, Niceto R. Luque, Eduardo Ros, and Auke Ijspeert. "The spinal cord facilitates cerebellar upper limb motor learning and control; inputs from neuromusculoskeletal simulation." *PLOS Computational Biology* 20, no. 1 (2024): e1011008.
4. Kainz, Hans, Antoine Falisse, and Claudio Pizzolato. "Neuromusculoskeletal modeling in health and disease." *Brazilian Journal of Motor Behavior* 18 (2024).
5. Geminiani, Alice, Claudia Casellato, Alberto Antonietti, Egidio D'Angelo, and Alessandra Pedrocchi. "A multiple-plasticity spiking neural network embedded in a closed-loop control system to model cerebellar pathologies." *International journal of neural systems* 28, no. 05 (2018): 1750017.
6. Spüler, Martin, Sebastian Nagel, and Wolfgang Rosenstiel. "A spiking neuronal model learning a motor control task by reinforcement learning and structural synaptic plasticity." In *2015 International Joint Conference on Neural Networks (IJCNN)*, pp. 1-8. IEEE, 2015.
7. Manukian, Mykhailo, Serhii Bahdasariants, and Sergiy Yakovenko. "Artificial physics engine for real-time inverse dynamics of arm and hand movement." *Plos one* 18, no. 12 (2023): e0295750.
8. Haşegan, Daniel, Matt Deible, Christopher Earl, David D'Onofrio, Hananel Hazan, Haroon Anwar, and Samuel A. Neymotin. "Training spiking neuronal networks to perform motor control using reinforcement and evolutionary learning." *Frontiers in Computational Neuroscience* 16 (2022): 1017284.
9. Vijayan, Asha, and Shyam Diwakar. "A cerebellum inspired spiking neural network as a multi-model for pattern classification and robotic trajectory prediction." *Frontiers in Neuroscience* 16 (2022): 909146.
10. Izhikevich, Eugene M. "Solving the distal reward problem through linkage of STDP and dopamine signaling." *Cerebral cortex* 17, no. 10 (2007): 2443-2452.
11. Tieck, J. Camilo Vasquez, Pascal Becker, Jacques Kaiser, Igor Peric, Mahmoud Akl, Daniel Reichard, Arne Roennau, and Rüdiger Dillmann. "Learning target reaching motions with a robotic arm using brain-inspired dopamine modulated STDP." *In 2019 IEEE 18th International Conference on* Cognitive Informatics & Cognitive Computing, pp. 54-61. IEEE, 2019.

12. Bouganis, Alexandros, and Murray Shanahan. "Training a spiking neural network to control a 4-dof robotic arm based on spike timing-dependent plasticity." *In The 2010 International Joint Conference on Neural Networks*, pp. 1-8. IEEE, 2010.
13. Azimirad, Vahid, S. Yaser Khodkam, and Amir Bolouri. "A New Hybrid Learning Control System for Robots Based on Spiking Neural Networks." Available at SSRN 4663085.
14. Hassanzadeh Khanmiri, Shaghayegh and Sayyed Noorani, Mohammad-Reza. "Simulation and Control of Human Arm Powered by Exoskeleton using OpenSim - MATLAB Application Programming Interface." *Second International Conference on Motion Analysis*, 2022, https://civilica.com/doc/1476102.

Advanced Engineering Days

aed.mersin.edu.tr

Radar study of mudflow formation mechanisms on the territory of Azerbaijan

Said Safarov[1], Elnur Safarov [1]

[1] Institute of Geography of Ministry of Science & Education, Caspian Sea Hydrometeorology Department, Baku, Azerbaijan, safarov53@mail.ru, elnur.safarov@outlook.com

Cite this study: Safarov, S.H., & Safarov, E.S. (2024). Radar study of mudflow formation mechanisms on the territory of Azerbaijan. Advanced Engineering Days, 9, 620-623

Keywords
Mudflow events
Mudflow forecast
Anomalous processes
River flow
Predictor

Abstract

In the article, using long-term radar data, an assessment of atmospheric precipitation falling in the basins of mudflow-prone rivers was carried out and based on the convective cell structure of thunderstorm processes and the peculiarities of the dynamics of their development, as well as taking into account the geomorphological and hydrological features of river catchments, various mechanisms of formation of mudflows were investigated , and new predictors for their short-term forecast are proposed.

Introduction

On the territory of Azerbaijan dangerous phenomena of precipitation origin, including floods and inundations, are observed mainly in mountainous and foothill areas characterized by complex surface.
The formation of floods occurs more intensively in the mountain systems of the Greater and Lesser Caucasus, which cover about half of the territory of the republic. According to average annual statistical data, the greatest number of floods is observed on the southern slope of the Greater Caucasus and in the highlands of the Nakhchivan MR.

Although many scientific studies have been devoted to the study of geomorphological and hydrological peculiarities of the occurrence and development of floods in Azerbaijan [1-3], in order to study in more detail the influence of meteorological factors on these phenomena, much attention has recently been paid to materials and methods of remote sensing of the Earth (satellite and radar).

In order to determine the factors influencing the formation of flood flows, it is necessary to use remote observation methods and technologies that make it possible to monitor the accumulation of precipitation at river catchments over long distances, at any time and under any weather conditions.

Analysis of long-term data shows that the strongest flood flows on the southern slope of the Greater Caucasus are observed in July-August. At this time, the absence of precipitation for a long time creates conditions for the formation of a sufficient amount of brittle debris necessary for the formation of strong structural floods.Thus, unlike ordinary floods, the most powerful structural floods are mainly caused by intense rainfall after a long period without precipitation.

Material and Method

The data of radar observations (MRL-5) for clouds and precipitation, conducted in 2001-2020, in the radius of 250 km with the use of appropriate software and hardware complexes were used in this work. This system makes it possible to measure the intensity, quantity, and other characteristics of precipitation in real time at any point of space, as well as to provide the most complete data on the presence, location, direction and speed of displacement of storm centers.

Radar measurement of precipitation intensity is based on its dependence on the radar reflectivity value.

In the work by means of radar estimation of precipitation amount, operational analysis of peculiarities of dynamics of development of powerful convective processes, as well as taking into account terrain characteristics, possible mechanisms of debris flow formation are considered. The obtained results were compared with actual ground data.

Results

As already shown in [4] , in most cases, strong flood flows are associated with the state of the velocity vector of the precipitation zone relative to the direction of the flood river flow. It was found that in 2001-2016, structural

flood flows on the southern slope of the Greater Caucasus were observed in most cases when strong precipitation clouds moved in the direction of the mountain range, almost opposite to the river flow (Fig. 1). Intense precipitation creates favorable conditions for the development of flood-forming processes in river floodplains. On the other hand, as a result of movement of the precipitation zone from the bottom to the top of the river basin, intensive precipitation causes strong wetting of soil and rocks in the lower and middle parts of the river basin and weakens their forces, which creates conditions for additional flood feeding due to lowering of valley slopes [5-6].

However, the analysis of the collected radar material shows that in many regions of Azerbaijan, the above-mentioned mechanism of structural flood flow formation is not the only one.

In a number of cases, strong flood flows are formed directly in the floodplains of rivers, actually during the formation of stationary strong rain clouds [7]. At this time, flood formation processes begin as a result of the interaction of intense precipitation with brittle sediment in floodplains, but the continuous flood mass is formed due to the lack of precipitation in the middle and lower parts of the river basin usually hardens quickly, stops moving and forms strong plugs in the river channel.

In the upper part of the river basin, as a result of prolonged rainfall and traffic jams in the riverbed, temporary backwater lakes are formed and severe mudflows and rock floods occur as a result of their collapse. Such floods are usually characterized by sudden onset in the middle and lower reaches of the river and pose a real danger to people and livestock in the river channel at that time. In addition, such floods cause serious damage to the infrastructure of the area and in some cases may be accompanied by human casualties. We can point to the floods caused by this mechanism, which occurred on July 2, 2016 in the Kishchay basin of Sheki district. So. Although no precipitation was recorded on that day at any of the observation stations located in the area, localized precipitation was observed only in the highlands according to satellite data (Figure 1).

It can be assumed that in August 1907, the terrible flood that killed more than 400 people in the Shin River basin of Sheki district was caused by the above-mentioned mechanism. Thus, detection by radar or satellite sensors of low-moving or slow-moving precipitation zones in the upper part of flooded river basins can become an important predictor of the occurrence of flood flows in the next few hours.

As in most hail-prone regions of the world, thunderstorm hail processes observed in the territory of Azerbaijan are mainly of single-cells, multi-cells and super-cells character due to the peculiarities of the core structure and dynamics of development. The characteristic features of this type of processes are described in more detail in [8].

Regular multinuclear processes, in turn, are divided into subtypes: normal and abnormal. In normal processes, due to the formation of a new convective core on the right side of the cloud system, to the right and slightly ahead of the previous core, the bands of individual cell eruptions are located almost parallel to each other [8].

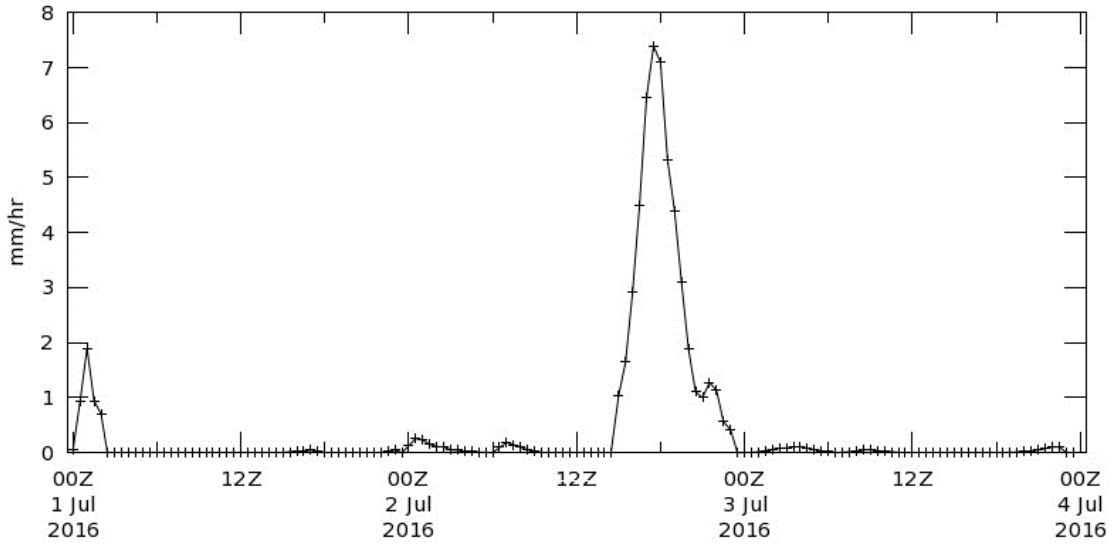


Figure 1. Dynamics of precipitation intensity change in the Upper Kishchay Basin on July 2, 2016 (GMT) from GPM satellite data.

In anomalous subtypes, new convective cells are formed behind the previous cells regardless of the direction of motion (Figure 2). New strong convective cells, periodically appearing behind the previous cells (relative to the direction of motion), move along almost the same trajectories, causing relatively prolonged and intense precipitation, sometimes accompanied by hail. Often the amount of precipitation exceeds 100 mm, causing floods in mountainous areas and dangerous floods in lowlands [7].

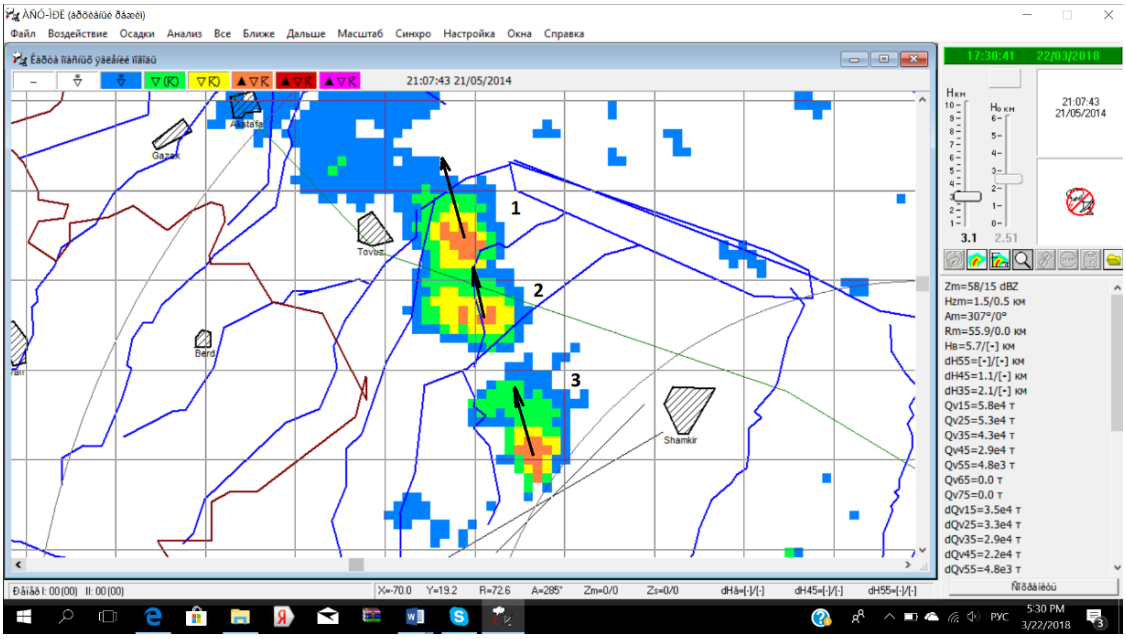


Figure 2. Character of the motion of convective cells in the anomalously organized multicell thunderstorm process observed in the Lesser Caucasus region on May 21, 2014.

→ - direction of motion of convective cells;

1, 2, 3 - serial number of the convection cells;

It should be noted that this type of thunderstorm processes is characteristic mainly for the northern and northeastern parts of the Lesser Caucasus.

Thus, in any part of the territory of Azerbaijan, taking into account the relief features, radar detection of strong anomalous organized multinucell thunderstorm processes can be a predictor of the occurrence of floods, inundations or floods.

Another mechanism for flood formation is the low velocity of a strong thunderstorm cloud moving downstream along the course of a high-water river. At this time, the precipitation cloud stays over the river channel longer, resulting in more intense precipitation there. According to the radar parameters, the stronger the cloud and the longer it stays over the basin, the more dangerous the resulting flooding will be. As an example, a severe flood occurred in Goshgarchai and Ganjachai on May 25, 2023 (Figure 3). Thus, a cloud system consisting of 2 strong convective cells moved from the upper basins towards Ganja city at a low speed (10-12 km/h), causing intense and large amounts of precipitation (more than 40 mm) in the basins of both rivers and, as a consequence, severe flooding. As a result, the infrastructure was seriously damaged and 2 people were killed in Ganjachay.

Thus, according to radar data, a strong thunderstorm cloud moving at low speed in the direction of the flow of flood rivers can be considered a predictor of flood hazard in the channels or basins of these rivers.

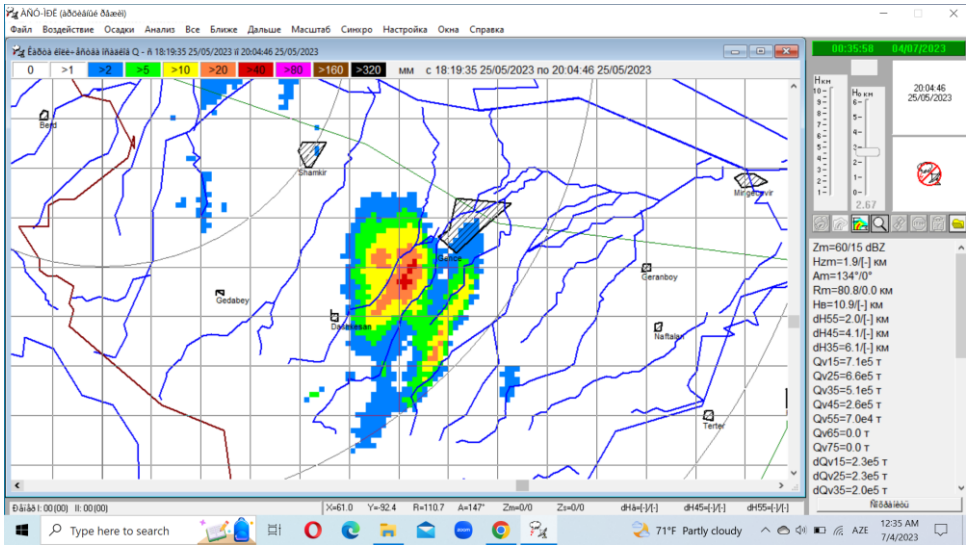


Figure 3: Precipitation distribution in the Ganjachay and Goshgarchay basins on May 25, 2023 according to radar observation

References

1. Rustamov S.G. Flood waters in Azerbaijan // Proc. of the Institute of Geography, 1957. Institute of Geography, 1957, issue 7, pp. 243-277 (in Russian).
2. Budagov B. A. Conditions of formation and flow of structural rivers (by the example of the Kurmukhchay river basin) // Izv. of the Academy of Sciences of Azerbaijan. SSR. Earth Sciences Series, 1965, vol. 5, pp. 117-123 (in Russian)).
3. Eyubov A.D., Guluzade V.A., Nabiyev H.D., Mammedov Ch.H. Lakes of Kish and Shin-Chaylari river basins. Baku: Elm, 1998, 215 p. (in Azerbaijani)
4. Safarov S.H. 2006. Influence of the character of rain clouds movement on mudflow formation. Proceedings of the National Academy of Sciences of Azerbaijan, series Science and Earth, 3, p. 108-113 (in Russian).
5. Budagov B.A., Safarov S.G.. 2008. Flood phenomena on the southern slope of the Greater Caucasus and hydrometeorological factors in their formation. Izvestiya RAN, Geographical Series, 2, pp. 116-121. (in Russian).
6. Safarov S.H., Safarov E.S. 2009. Radar diagnosis of flood situation and forecast of mudflows of storm genesis. Proceedings of geogr. Society of Azerbaijan, volume XIV. Baku. pp. 404-409. (in Russian).
7. Safarov S.H. 2018. Radar studies of different mechanisms of mudflow formation in the territory of Azerbaijan / II All-Russian Scientific Conference / "Modern problems of remote sensing, radar, wave propagation and diffraction". Murom (Russia). pp. 562-566
8. Safarov S.H. Hail and flood phenomena on the territory of Azerbaijan and radar methods of their forecasting / Baku: "Elm", 2012, 292 p. (in Russian)/

Advanced Engineering Days

aed.mersin.edu.tr

Investigating LULC Change Impacts on Surface UHI Using RS Data case study: Kerman City

Amin Raisi Moghadam [1], Khalil Valizadeh Kamran [1]

[1] *Tabriz University, Department of RS and GIS, Tabriz, Iran, raisimoghadama@gmail.com, Valizadeh@tabrizu.ac.ir*

Cite this study: Moghadam, A. R., & Valizadeh Kamran, K. (2024). Investigating LULC Change Impacts on Surface UHI Using RS Data case study: Kerman City. Advanced Engineering Days, 9, 624-627

Keywords
Urban heat island
Land use
Remote sensing
Kerman city

Abstract

The rapid growth of urbanization and industrial activities in metropolises has led to extensive changes in land use, weather and local climate. One of the consequences of these changes is the formation of the urban heat island (UHI) phenomenon, which negatively affects the health and environment of residents. In this research, using satellite images (Landsat 7 and 8) and thermal remote sensing, for land use changes using the OBIA method and for LST using the split window (SW) method, and the effects of land changes on the UHI of Kerman using GIS techniques. has been investigated in the summer season. The results show that between the years 2002 and 2022, the green space of Kerman city decreased from 7743.42 hectares to 3440.61 hectares and the residential land use increased from 4836.33 hectares to 9023.67 hectares, and these changes in land use can be one of the important reasons. Increase the LST in the city.

Introduction

Witnessing an exponential rise in population, the world is experiencing a massive influx of people into cities. As cities expand, they disrupt the natural environment, amplifying the impact of greenhouse gases and driving global warming – a critical challenge of our time (Mathew et al., 2018; Mohammad et al., 2022). Despite their crucial role in regulating urban temperatures (LST), green spaces in cities have undergone a dramatic decline worldwide in recent decades (Choudhury et al., 2019). This decline fosters a cascade of environmental challenges, including land degradation, ecosystem disruption, increased heat waves, urban flash floods, and rising precipitation and temperatures in surrounding areas(Fu and Weng, 2018; Mohammad and Goswami, 2019; Estoque et al., 2017; Malik et al., 2020; Moazzam et al., 2018). Across the globe, a growing trend of urbanization is coming at the expense of vital vegetation(Dilawar et al., 2021; Mumtaz et al., 2020; Singh et al., 2017; Chakraborty and Lee, 2019). Kerman City, the study area, is one of the largest cities in southeastern Iran in terms of size and population. In recent years, population growth has led to spatio-physical changes in Kerman City, and the impact of these changes on the surface temperature of the city is evident. The combination of these factors and research on urban heat islands conducted by domestic and foreign researchers in recent years highlights the importance of this topic for the researcher.

Material and Method

In this study utilized Landsat 7 and 8 satellite imagery from the ETM+ and OLI/TIRS sensors. Three images from the summer seasons of 2002, 2013, and 2022 were selected. Subsequently, LST was extracted using the SW algorithm and LULC was extracted using OBIA techniques. Furthermore, modeling and prediction of LULC changes for the end of the Sixth Development Perspective Document (2026) were performed using CA Marcove. The relationship between LST, LULC, and UHI was then examined. Finally, Google Earth imagery was employed to validate the classified images, and ground-based meteorological station data were used to assess the accuracy of the calculated temperatures.

The study area, depicted in “Figure 1”, is Kerman City, the capital of Kerman Province, located at 50°57'E and 30°17'N. According to the 2016 census, the city's population is 537,718. Kerman is one of Iran's five historical cities, with an area of approximately 13,000 hectares.

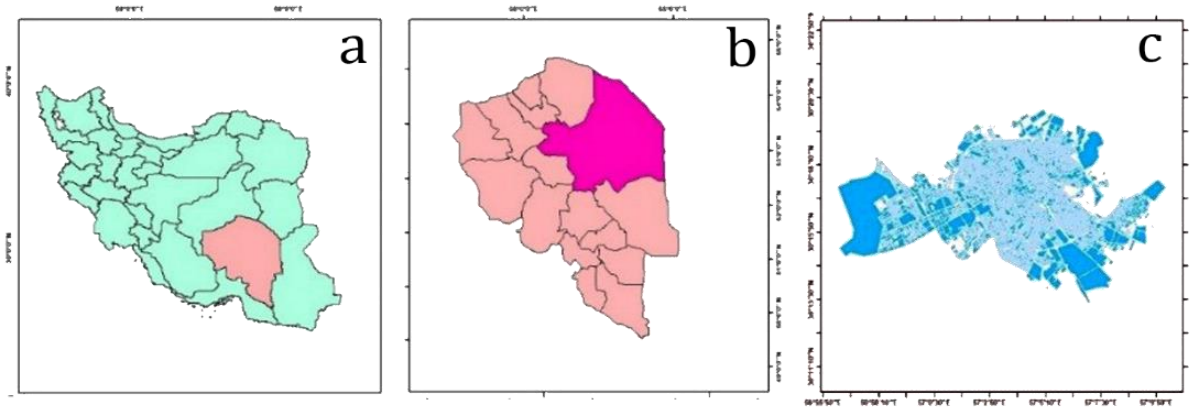


Figure 1. a) Iran country b) Kerman province c) Kerman city

Results

As mentioned in the previous sections, the split window (SW) algorithm, a well-established method for determining land surface temperature (LST), was used to derive LST. Each of these parameters was calculated using mathematical relationships. LST and LULC maps using the methods mentioned above for the years 2002, 2013 and 2022 are presented in "Figure 2".

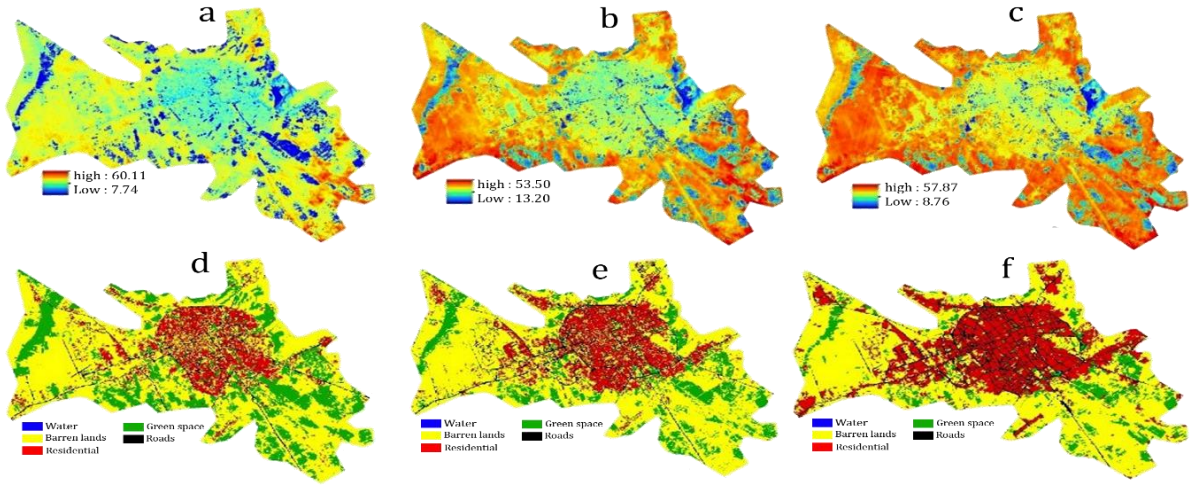


Figure 2. a) LST of 2002, b) LST of 2013 c) LST of 2022 and d) LULC of 2002, e) LULC of 2013, f) LULC of 2022

According to the LST maps for the years under investigation, the minimum and maximum LST values calculated were 7.7°C and 60.11°C for 2002, 13.20°C and 53.50°C for 2013, and 8.76°C and 57.87°C for 2022, respectively. As observed in the LST imagery for 2002, 2013, and 2022, Kerman City has experienced a warmer environment with a reduction in cold patches from 2002 to 2022 Also, green space in Kerman city has had a significant decline from 2002 to 2022, and this decline has been accompanied by an increase in built-up areas and barren lands.

Discussion

The classification accuracy in this research has been measured using two criteria: the overall classification accuracy is 87.0% and the Kappa coefficient is 85.0%. These numbers show the high accuracy of the classification results. More details are given in “Table 1”.

Table 1. This is the example of table formatting

Years	Overall accuracy %	Kappa coefficient %
2002	0.83	0.81
2013	0.86	0.85
2022	0.92	0.90

The CA-Markov algorithm was employed to predict LU in the year 2026. "Figure 3" shows the LULC map predicted for the year 2026 and the relationship between land use and surface temperature in the studied years.

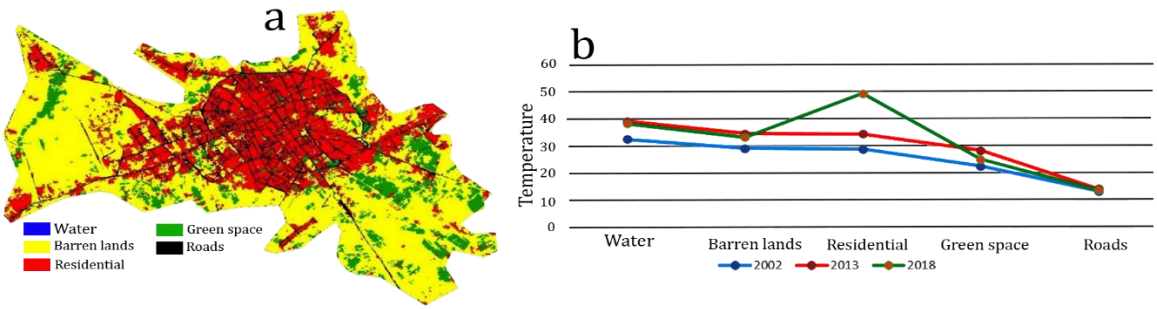


Figure 3. a) CA-Markov prediction map for 2026 and b) relationship between temperature and LULC

This figure illustrates the changes in LU areas in 2026. In order to check the LST according to the type of LULC, the LST for all types of LU was extracted using classified images for all three images of 2002, 2013 and 2022 and their average was calculated. Barren land exhibited the highest LST, attributed to the low heat capacity and thermal conductivity of dry soil. Water bodies and vegetated areas displayed the lowest LST due to evapotranspiration processes. residential areas exhibited intermediate LST values, reflecting the substantial heterogeneity of these areas (asphalt, concrete, vegetation, metals, etc.) and the resulting average properties of various materials within a pixel.

Conclusion

The expansion of UHIs and the concomitant rise in LST in Kerman, are primarily attributed to the conversion of agricultural lands to residential and barren areas, coupled with a decline in inner-city green spaces. Additionally, the surrounding barren lands and the proliferation of roads, which possess a high energy absorption capacity, also contribute significantly to the temperature increase and UHI formation in Kerman. This study revealed that 4363 hectares of agricultural lands and green spaces have been converted to built-up areas. The findings provide a comprehensive understanding of the mechanisms underlying the formation and expansion of UHIs in urban areas.

References

1. Matthews, T., Lo, A. Y., & Byrne, J. A. (2015). Reconceptualizing green infrastructure for climate change adaptation: Barriers to adoption and drivers for uptake by spatial planners. Landscape and urban planning, 138, 155-163.
2. Mohammad, P., Goswami, A., Chauhan, S., & Nayak, S. (2022). Machine learning algorithm based prediction of land use land cover and land surface temperature changes to characterize the surface urban heat island phenomena over Ahmedabad city, India. Urban Climate, 42, 101116.
3. Choudhury, D., Das, K., & Das, A. (2019). Assessment of land use land cover changes and its impact on variations of land surface temperature in Asansol-Durgapur Development Region. The Egyptian Journal of Remote Sensing and Space Science, 22(2), 203-218.
4. Fu, P., & Weng, Q. (2018). Variability in annual temperature cycle in the urban areas of the United States as revealed by MODIS imagery. ISPRS journal of photogrammetry and remote sensing, 146, 65-73.
5. Mohammad, P., & Goswami, A. (2019). Temperature and precipitation trend over 139 major Indian cities: An assessment over a century. Modeling Earth Systems and Environment, 5, 1481-1493.
6. Estoque, R. C., Murayama, Y., & Myint, S. W. (2017). Effects of landscape composition and pattern on land surface temperature: An urban heat island study in the megacities of Southeast Asia. Science of the Total Environment, 577, 349-359.
7. Malik, S., Pal, S. C., Sattar, A., Singh, S. K., Das, B., Chakrabortty, R., & Mohammad, P. (2020). Trend of extreme rainfall events using suitable Global Circulation Model to combat the water logging condition in Kolkata Metropolitan Area. Urban Climate, 32, 100599.
8. MOAZZAM, M. F. U., VANSAROCHANA, A., & RAHMAN, A. U. (2018). Analysis of flood susceptibility and zonation for risk management using frequency ratio model in District Charsadda, Pakistan. International Journal of Environment and Geoinformatics, 5(2), 140-153.
9. Dilawar, A., Chen, B., Trisurat, Y., Tuankrua, V., Arshad, A., Hussain, Y., ... & Sun, S. (2021). Spatiotemporal shifts in thermal climate in responses to urban cover changes: A-case analysis of major cities in Punjab, Pakistan. Geomatics, Natural Hazards and Risk, 12(1), 763-793.
10. Mumtaz, F., Tao, Y., de Leeuw, G., Zhao, L., Fan, C., Elnashar, A., ... & Wang, D. (2020). Modeling spatio-temporal land transformation and its associated impacts on land surface temperature (LST). Remote Sensing, 12(18), 2987.
11. Singh, P., Kikon, N., & Verma, P. (2017). Impact of land use change and urbanization on urban heat island in Lucknow city, Central India. A remote sensing based estimate. Sustainable cities and society, 32, 100-114.

12. Chakraborty, T., & Lee, X. (2019). A simplified urban-extent algorithm to characterize surface urban heat islands on a global scale and examine vegetation control on their spatiotemporal variability. International Journal of Applied Earth Observation and Geoinformation, 74, 269-280.

Advanced Engineering Days

aed.mersin.edu.tr

The role of innovative food packaging in food quality and safety

Samin Adineh[*1]

[1]*Universityof Tabriz, Faculty of Agriculture, Food Science and Engineering Department, Iran, rs.mostajer@yahoo.com*

Cite this study: Adineh, (2024). The role of innovative food packaging in food quality and safety. Advanced Engineering Days, 9, 628-631

Keywords
Food packaging
Food quality
Food safety
Innovative food package
Food security

Abstract

Packaging is an integral part of the food industry, which is related to food quality and safety, including food shelf life and marketing perspective. Traditional food packaging protects food from damage and preserves food products until consumption. Packaging also provides branding and nutritional information and promotes marketing. In past decades, plastic films were used to protect food from heat, moisture, microorganisms, dust and particles. Recent advances have incorporated additional capabilities into barrier films to increase food shelf life, such as active packaging and smart packaging. In addition, consumer perception affects packaging materials and designs. The current trend of consumers looking for environmentally friendly packaging has increased. With the advancement of applied technologies in the food sector, sustainable packaging is emerging in response to consumer preferences and environmental commitments. This article examines the importance of food packaging in relation to food quality and safety. The development and advanced applications of smart, active and intelligent packaging systems, and the properties of an oxygen barrier and the advantages and disadvantages of these packagings are discussed. Consumer perceptions of environmentally friendly packaging that can be used in the food industry are also discussed.

Introduction

Food processing includes a combination of different processes including preparation, formulation, production and packaging, etc. Packaging is an integral part of the food industry, which is related to food quality and safety, including food shelf life and communication from a marketing perspective. After food production and before reaching consumers, food packaging is an important part. The functions of traditional packaging are:
(1) keeping food in packaging for storage, transportation and distribution,
(2) protection against physical damage and chemical and biological deterioration,
(3) Storage of food products until consumption
(4) It also provides branding and nutritional information and promotes marketing (Claudio, 2012).

In recent years, bioactive films and smart techniques have been used in the food sector for packaging. Plastic films have emerged as the most prominent candidates for food packaging applications due to their light weight, ease of processing, and low cost. . In the past decades, plastic films were used as a barrier to preserve food from heat, moisture, microorganisms, dust and dirt particles. Recent advances have introduced additional capabilities in barrier films to increase food shelf life, such as smart packaging, active packaging, and smart packaging. These packaging systems provide a suitable solution to increase the shelf life of food with simplified production processes or food with minimal use of preservatives (Janjaraskol et al., 2017).

Consumers are demanding environmentally friendly packaging. Additionally, verifiable nutrition and health-related information on the front and back of the product can help shoppers make healthier choices. With the advancement of applied technologies in the food sector, sustainable packaging is emerging in response to consumer preferences and environmental commitments (Nakub et al., 2020).

This article reviews the literature published in the last 10 years related to the importance of food packaging in relation to food quality and safety. Packaging applications of polymers (petroleum-based and bio-based); The development and advanced applications of smart, active and intelligent packaging systems, and in addition, the characteristics of an oxygen barrier and consumer perceptions of renewable and environmentally friendly packaging that can be used in the food industry are also discussed in this review.

Food packaging polymers

Polymers are commonly used for packaging because of their easy production, strong molecular networks or cross-links (polymeric matrices, Figure 1), and excellent performance properties (such as strength, barrier to oxygen and moisture, and resistance to attack by food components). Food is used. Polymers are either non-biodegradable or biodegradable. For polymers commonly used in active food packaging, polypropylene (PP), polyethylene (PE), polyethylene co-vinyl acetate (EVA), polyvinyl chloride (PVC), and polyethylene terephthalate (PET) polymers. They are non-biodegradable. Cellulose, chitosan, starch, agar, gelatin, soy protein, and whey protein are natural biodegradable polymers that have advantages over petroleum-based polymers from a consumer and environmental perspective (Dizo et al., 2020).

Biodegradable, stable and abundantly available polymers are categorized into polysaccharide and protein-based polymers. Among polysaccharide-type polymers, cellulose is a polysaccharide consisting of a linear chain of β-1, 4 D-glucose units. Chitosan is a linear polysaccharide composed of random β-1, 4-linked D-glucosamine and N-acetyl-D-glucosamine. Cellulose and chitosan are widely used for food packaging due to their good film and gel forming ability, recyclability and inherent antimicrobial properties. Starch is composed of linear and branched glucose units linked by α-1,4 and α-1,6 glycosidic bonds. It can be used as an adhesive and additive for food packaging. Starch and starch blends available on the market include EcoframTM, SolanylTM, BiocoolTM, BioplastTM and PanticTM. are based on protein. Gelatin has the ability to form a strong film and is commonly used due to its abundance (Hanani et al., 2014). Polylactic acid compound (PLA) is a synthetic thermoplastic polyester. It is an environmentally friendly biodegradable polymer that is commercially available and is combined with antimicrobial agents to form PLA-based films for packaging dry and perishable food products, typically short-life products such as Fruits, vegetables and meat are used (Sarfraz et al., 2021).

Smart Food Packaging System

The rapid growth of packaged food and beverage consumption due to increased product complexity, food globalization, and consumer demand for environmentally friendly packaging has led to innovative packaging systems. As a result, smart packaging, active packaging and innovative packaging have appeared with their applications in the global market (Laun et al., 2016). Intelligent packaging systems are widely used in food and beverages, health care products, personal care and other applications that can control physicochemical effects such as environmental conditions as well as prevent microbiological changes. Active packaging and smart packaging, which are discussed in detail below, are types of innovative packaging (Biji et al., 2015).

Active Packaging System

An active packaging system is an advanced technology that embeds active ingredients (eg, antioxidants) into a polymeric packaging matrix. (Montiano et al., 2019).

The polymer matrix then releases or absorbs substances from the stored food or the surrounding environment to preserve and extend the shelf life of the food. This system acts as a polymer matrix based on the polymerization of polymers or biopolymers and bioactive agents that are naturally released into food or the surrounding environment (Vicuccia et al., 2019).

Active food packaging has great potential in maintaining the quality and safety of food products, especially foods sensitive to oxidation. Active agents for food packaging include antimicrobials, antioxidants, carbon dioxide emitters or absorbers, oxygen absorbers, and ethylene absorbers (Fang et al., 2017).

Antimicrobial

Antimicrobial packaging integrates antimicrobial agents into the polymer film to suppress target microbial activities. Antimicrobial agents such as organic acids (eg, benzoic acid), enzymes (eg, lysozyme), bacteriocins, fungicides, and oxygen scavengers (eg, butylated hydroxytoluene) are widely used in systems. Food packaging has been used to prevent the growth of pathogenic microorganisms in the production, transportation and storage of food products. The advantage of this method is controlled release as the time or slow release of active substances during the assumed period. Antimicrobial packaging is used for food products without preservatives that are likely to have the growth of pathogenic microorganisms, such as bread, cake, cheese, and meat (Rahman et al., 2017).

Antioxidant

Antioxidant agents inhibit unwanted microbiological changes and oxidative reactions to increase the shelf life of food. The use of natural antioxidants in food packaging is a new trend in the food industry in response to increasing consumer demand for natural products (Sanchez et al., 2014).

Plant extracts from stems, roots, leaves and fruit seeds have been effectively used as antioxidant components in food packaging. Plant extracts contain a significant content of polyphenols, flavonoids, alkaloids and terpene substances that have proven antioxidant properties. Plant extracts added to packaging materials are used in the form of films (Vasil et al., 2021).

Oxygen Scavengers

Residual oxygen in food packages causes bacterial spoilage, tastelessness, discoloration, loss of nutrients, and formation of toxic end products. Oxygen absorbers are added to closed packages to remove or reduce the level of oxygen in the package, to prevent the formation of aerobic pathogenic microorganisms and oxidation, and to maintain the quality of foods containing high unsaturated fat. Oxygen absorbers are commonly used for packaged food products and pharmaceutical products (Gaikwad et al., 2018).

Carbon Dioxide Scavengers

The role of carbon dioxide (CO2) used in food packaging is related to the protection of food against oxidation and its antimicrobial effects. Carbon dioxide has the potential to inhibit microbial growth and is highly soluble in food matrices in modified atmosphere packaging. Modified atmosphere packaging (MAP) is a packaging technique that involves active or passive control or modification of the gas composition of the food storage environment to reduce food oxidation and the growth of aerobic spoilage organisms. Passive MAP is achieved when the desired atmosphere is created naturally through inhalation of a food product. Active MAP is achieved by replacing the gases in the package with a mixture of desired gases. Carbon dioxide removal techniques are used in combination with food refrigeration for fresh and fermented food products. The commercial availability of active packaging is still limited due to low industrial scale achievement and low stability of active agents (Hemigoz et al., 2018).

Ethylene Scavenger

Ethylene absorbents are used to preserve fruits and vegetables, because ethylene leads to undesirable color changes and bad taste, which shortens the useful life of fruits and vegetables during postharvest and processes (Firouz et al., 2021).

Intelligent Packaging

An intelligent packaging system indicates and monitors the product's physicochemical conditions (eg, freshness degree), and its environmental effects (eg, temperature, pH level, gas) during transport and storage. The device designed for packaging can sense any internal or external changes and then can inform the consumer about the status of the product by providing audio and visual information (Nesik et al., 2020).

Conclusion

Innovative food packaging offers a useful solution for the food industry in maintaining food quality and safety. Further research will fill the gaps mentioned above to meet large-scale commercial reality, minimize environmental impact, and meet consumer acceptance.

References

1. Biji, K.B.; Ravishankar, C.N.; Mohan, C.O.; Gopal, T.K.S. . 2015, Smart packaging systems for food applications: A review. J. Food Sci. Technol52, 6125–6135.
2. Claudio, L. 2012, Our Food: Packaging & Public Health. Environ. Health Perspect., 120, A232–A237.
3. Díez-Pascual, A.M. 2020, Antimicrobial Polymer-Based Materials for Food Packaging Applications. Polymers 12, 731.
4. Domínguez, R.; Barba, F.J.; Gómez, B.; Putnik, P.; Kovačević, D.B.; Pateiro, M.; Santos, E.M.; Lorenzo, J.M. 2018, Active packaging films with natural antioxidants to be used in meat industry: A review. Food Res. Int. 113, 93–101.
5. Fang, Z.; Zhao, Y.; Warner, R.D.; Johnson, S.K. 2017, Active and intelligent packaging in meat industry. Trends Food Sci. Technol. 61, 60–71.
6. Firouz, M.S.; Mohi-Alden, K.; Omid, M. 2021, A critical review on intelligent and active packaging in the food industry: Research and development. Food Res. Int. 141, 110113.
7. Gaikwad, K.K.; Singh, S.; Lee, Y.S. 2018, Oxygen scavenging films in food packaging. Environ. Chem. Lett. 16, 523–538.

8. Gyawali, R.; Ibrahim, S.A. 2014, Natural products as antimicrobial agents. Food Control 46, 412–429
9. Han, J.-W.; Ruiz-Garcia, L.; Qian, J.-P.; Yang, X.-T. 2018, Food Packaging: A Comprehensive Review and Future Trends. Compr. Rev. Food Sci. Food Saf. 17, 860–877.
10. Hanani, Z.N.; Roos, Y.; Kerry, J. 2014, Use and application of gelatin as potential biodegradable packaging materials for food products. Int. J. Biol. Macromol. 71, 94–102.
11. Irkin, R.; Esmer, O.K. 2015, Novel food packaging systems with natural antimicrobial agents. J. Food Sci. Technol. 52, 6095–6111.
12. Janjarasskul, T.; Suppakul, P. 2017,Active and intelligent packaging: The indication of quality and safety. Crit. Rev. Food Sci. Nutr. 58, 808–831.
13. Kerry, J.P.; O'Grady, M.N.; Hogan, S.A. 2006, Past, current and potential utilisation of active and intelligent packaging systems for meat and muscle-based products: A review. Meat Sci. 74, 113–130.

Advanced Engineering Days

aed.mersin.edu.tr

Numerical Study on the Solidification Process in Conical Shell and Tube Latent Heat Energy Storage Tanks

A. Gholamzadeh [1], A. Shafiei Ghazani [*1]

[1]*Sahand University of Technology, Department of Mechanical Engineering, Iran, gholamzadehamirhossein3@gmail.com, Shafiei.ardalan@sut.ac.ir*

Cite this study: Gholamzadeh, A., & Shafiei Ghazani, A. (2024). Numerical Study on the Solidification Process in Conical Shell and Tube Latent Heat Energy Storage Tanks. Advanced Engineering Days, 9, 632-635

Keywords
Latent Heat
Thermal Energy Storage
Conical Shell and Tube
Phase Change Material
Solidification

Abstract

The latent heat thermal energy storage (LHTES) has emerged as a promising solution to address the intermittency of renewable energy resources. However, the poor thermal conductivity of phase change materials (PCMs) presents a significant challenge, leading to slow charging and discharging rates. Previous research has shown that conical shell and tube configurations improve the charging process compared to cylindrical counterparts due to enhanced natural convection effects. In this study, numerical simulations investigate the impact of conical shell and tube geometry during the discharging or solidification process. Various tilting angles for the shell are considered while keeping PCM volume constant. The simulations are conducted under two conditions: with and without buoyancy effects. Results indicate that increasing the tilting angle prolongs the solidification time. The primary heat transfer mechanism during solidification is conduction, while natural convection plays a minimal role. This conduction mechanism is weakened by the increase in PCM thickness resulting from conical geometry.

Introduction

In today's world, the problems such as population growth, greenhouse gases, global warming, and the limitation of fossil fuels, have led to a rise in energy demand. Renewable and sustainable energies like solar and wind are the best option due to their low cost and cleanliness. Thermal energy storage (TES) falls into three categories: latent heat thermal energy storage (LHTES), sensible heat thermal energy storage (SHTES), and thermochemical energy storage (TCES). Latent heat thermal energy storage has been widely applied in renewable and sustainable energy generation. However, the poor thermal conductivity of phase change materials (PCM) is a significant challenge, leading to slow charging and discharging rates and limiting its application.

To address this deficiency, various techniques have been proposed to intensify the heat transfer rate, such as adding fins [1], embedding PCM into porous matrix [2], using nanoparticles and heat pipes [3]. In addition to these methods, optimal geometric design is also suggested. Seddegh et al. [4] compared the melting and solidification processes in cylindrical and conical shell and tube storage tank. They observed that the melting process could be enhanced in conical shell, while the dominance of conduction heat transfer during solidification was the reason for no noticeable improvement over time. Lu et al. [5] also reported that, the greater the tilting angle, the shorter the charging time and longer the discharging time; however, with an increase of more than 5 degrees, there is no significant effect on charging and discharging time. Mao et al. [6] numerically indicated that by tilting 11.5 degrees, the time of charging and discharging reduced by 32.08% and 21.59%, respectively. Ghazani et at. [7] also numerically investigated the charging performance of the cylindrical and conical shell and nozzle and diffuser tube. Their results showed that conical shell and tube, cylindrical shell and diffuser, and conical shell and diffuser reduces the melting time.

In this study, a series of numerical simulations are conducted to investigate the solidification process in a conical shell-and-tube latent heat storage system with various tilting angles. The focus is on the effects of conduction alone and the combined effects of conduction and natural convection. This research aims to elucidate the dominant mechanisms of heat transfer during the solidification process.

Physical and mathematical model

Fig. 1 shows the physical model of the vertical shell-and-tube LHTES units. The unit with the cylindrical shell is considered the base case, while the units with conical shells are referred to as case A. Different tilting angles are considered for the conical shell units keeping the volume of PCM constant: 1.83°, 3.72°, 5.67°, and 7.70° for cases A1, A2, A3, and A4, respectively. The flow of the heat transfer fluid (HTF) passes from the bottom to the top of the storage tank through a stainless-steel tube. RT35 is employed as the phase change material (PCM). The thermophysical properties of PCM (RT35) and the geometric dimensions are provided in [7]. Due to the axisymmetry of the geometries, the computational domain is considered to be two-dimensional with axisymmetry.

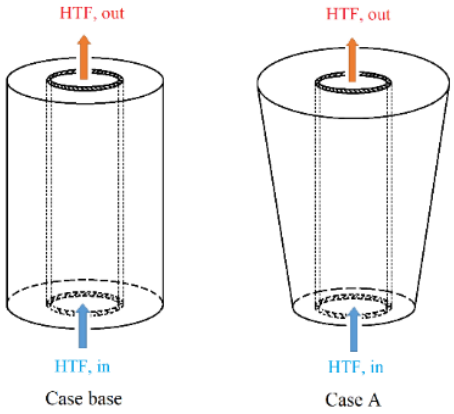


Figure 1. Schematics of cylindrical and conical shell and tube LHTES

The HTF and liquid PCM are assumed to be Newtonian, laminar, unsteady, and incompressible. The change in PCM volume and viscous dissipation are neglected. The enthalpy-porosity method is used to model the melting and solidification processes. The Boussinesq approximation is employed to account for the variation in density due to temperature changes and the resulting buoyancy force. The details of the governing equations, including the continuity, momentum, and energy equations, are provided in Ghazani et al. [7]. The liquid fraction λ for two phase regions is obtained from $\lambda = (T - T_s)/(T_l - T_s)$, Where, T, T_l and T_s represent the cell temperature, liquidus temperature, and solidus temperature of the PCM, respectively. The value of λ is 0 for the solid region and 1 for the liquid region. The initial and inlet temperatures are maintained at 48°C and 20°C, respectively. The flow rate of the HTF is 1.76 ml/s.

Numerical solution

The governing equations were simulated using the ANSYS Fluent 2020 R2 commercial CFD solver software. The SIMPLE and PRESTO schemes were adopted for pressure-velocity coupling and pressure discretization, respectively. The second-order upwind scheme was used for the energy and momentum equations. The convergence criteria were set to 10^{-6} for the continuity and momentum equations, and 10^{-8} for the energy equation. Mesh and time step independency study is performed, indicating that an element number of 9462 and a time step of 0.5 seconds are sufficient to obtain accurate results for all simulations. The validations of temperatures were conducted using experimental data from the literature of Longeon et al. [8]. Fig. 2 illustrates that the numerical results display an acceptable agreement with the experimental data.

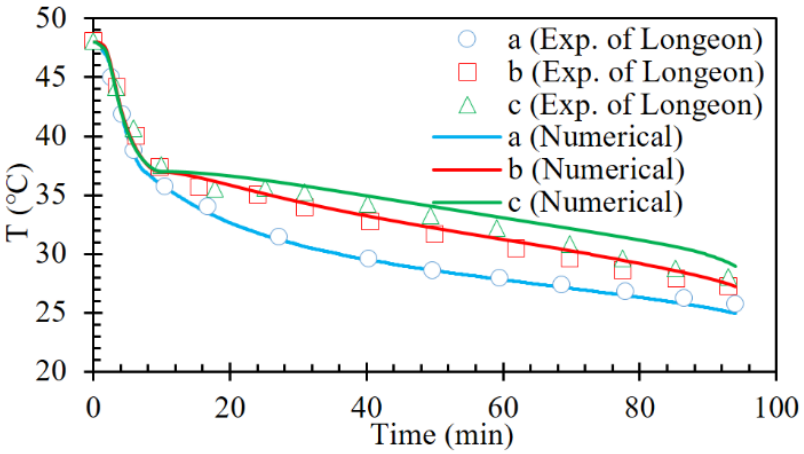


Figure 2. Comparison of the present numerical simulation with experimental data of Longeon et al.[8]

Results and discussion

Fig. 3 depicts the liquid fraction as a function of time for both the base case and case A. It is evident that as the cone angle increases, the solidification time also increases. This contrasts with the melting process, where the melting time decreases with an increase in tilting angle [7]. To delve deeper into the physical rationale behind these contradictory effects of increasing tilting angle during melting and solidification processes, Figure 4 compares the time history of PCM liquid fraction for cases A1 and A4 under two conditions: pure conduction mechanism of heat transfer (PC) and with the addition of gravity (natural convection flow plus conduction mechanism of heat transfer). It is apparent that there is only a marginal difference between pure conduction and cases with the effect of natural convection. This indicates that the dominant mechanism of heat transfer during solidification is conduction, with natural convection playing a minimal role. Therefore, as the tilting angle increases, the thickness of PCM decreases in at the lower part of the annular region filled with PCM, while it increases in the upper half of the tank. Consequently, the thermal conductivity resistance increases in the upper part, leading to weakened conduction heat transfer and longer solidification time.

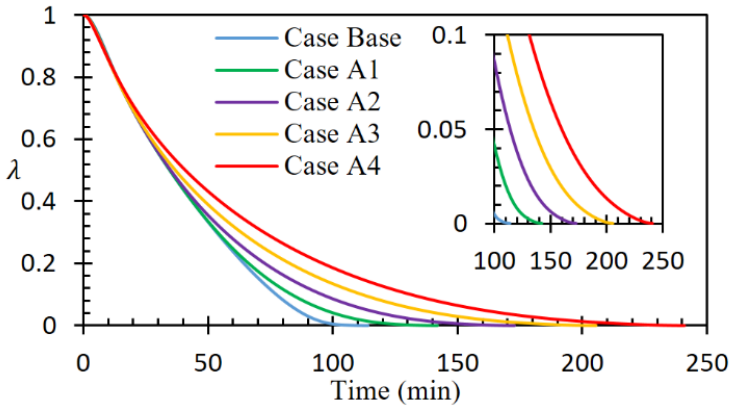


Figure 3. Liquid fraction vs. time for the base case and the conical shell cases with different tilting angles

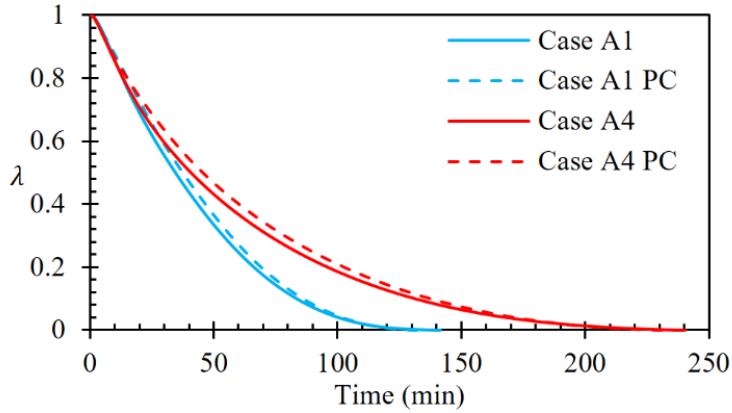


Figure 4. Liquid fraction vs. time for cases A1 and A4 under no gravity (PC) and considering buoyancy effects

Conclusion

Previous studies on the melting of phase change material inside shell and tube systems have demonstrated that the melting time can be reduced by using a conical shell. In this study, numerical simulations were conducted to investigate the effect of a conical shell on the solidification process. Different tilting angles for the shell were considered, and the simulations were conducted under two conditions: accounting for buoyancy effects and neglecting buoyancy effects. It was concluded that the main mechanism of heat transfer during solidification is conduction. Therefore, the conical shell results in non-uniformity of the PCM region thickness, leading to an increase in the maximum thickness, which in turn increases conduction resistance and solidification time.

References

1. He, F., et al., Experimental evaluation of the effect of perforated spiral fins on the thermal performance of latent heat storage units. Journal of Energy Storage, 2023. 58: p. 106359.
2. Zhao, C., et al., Simulations of melting performance enhancement for a PCM embedded in metal periodic structures. International Journal of Heat and Mass Transfer, 2021. 168: p. 120853.

3. Mahdavi, M., S. Tiari, and V. Pawar, A numerical study on the combined effect of dispersed nanoparticles and embedded heat pipes on melting and solidification of a shell and tube latent heat thermal energy storage system. Journal of Energy Storage, 2020. 27: p. 101086.
4. Seddegh, S., et al., Comparison of heat transfer between cylindrical and conical vertical shell-and-tube latent heat thermal energy storage systems. Applied Thermal Engineering, 2018. 130: p. 1349-1362.
5. Lu, B., et al., Enhancement of the charging and discharging performance of a vertical latent heat thermal energy storage unit via conical shell design. International Journal of Heat and Mass Transfer, 2022. 185: p. 122393.
6. Mao, Q., N. Liu, and L. Peng, Numerical investigations on charging/discharging performance of a novel truncated cone thermal energy storage tank on a concentrated solar power system. International Journal of Photoenergy, 2019. 2019.
7. Ghazani, A.S. and A. Gholamzadeh, The effect of conical shell and converging/diverging tube on the charging performance of shell and tube latent heat thermal energy storage system. Journal of Energy Storage, 2023. 65: p. 107262.
8. Longeon, M., et al., Experimental and numerical study of annular PCM storage in the presence of natural convection. Applied energy, 2013. 112: p. 175-184.

Advanced Engineering Days

aed.mersin.edu.tr

A Comparative Study on the Performance of LQG/LTR and Optimized SMIT Controllers in Tracking Control of Flying-Wing UAVs

Sevda Rezazadeh Movahhed*[1], Mohammad Ali Hamed [1]

[1]*University of Tabriz, Department of Mechanical Engineering, Iran, sevda.rezazadeh@tabrizu.ac.ir, ma.hamed@tabrizu.ac.ir*

Cite this study: Movahhed, S. R., & Hamed, M. A. (2024). A Comparative Study on the Performance of LQG/LTR and Optimized SMIT Controllers in Tracking Control of Flying-Wing UAVs. Advanced Engineering Days, 9, 636-638

Keywords
Flight control
SMIT
LQG/LTR
Flying-wing UAV

Abstract

This study presents a comparative analysis of two distinct control methodologies, namely Linear Quadratic Gaussian (LQG/LTR) and Optimized Sliding Mode Integral Tracking (SMIT) controllers, focused on performance in tracking control of flying-wing UAVs. The research investigates their effectiveness in tracking desired trajectories of a specific rudderless flying-wing UAV. Results indicate that while both LTR and SMIT controllers demonstrate promising behavior, the SMIT controller outperforms in terms of tracking behavior, steady state error, settling time, and providing smooth and realizable control signals. The findings provide valuable insights in selecting appropriate control strategies tailored to the requirements of flight control applications.

Introduction

In aerospace science field, the development of robust and efficient control strategies for controlling the Unmanned Aerial Vehicles (UAVs) have garnered significant attention in recent years. In this context, the comparison between two prominent control methodologies, namely the Linear Quadratic Gaussian (LQG/LTR) method and Optimized Sliding Mode Integral Tracking (SMIT) controller is investigated for enhancing the performance of UAV maneuvers considering the reasonable control energy. For this purpose, a challenging design of fixed wing UAVs namely the rudderless flying-wing is selected to perform the evaluation to better demonstrate the effectiveness of the proposed methods. Ali et al. [1] developed a control scheme for lateral mode control in fixed-wing UAVs, but a notable permanent error and slight response delay persist in their results. Anh et al. [2] proposed a sliding mode-based controller for the lateral dynamics of UAVs, demonstrating appropriate tracking behavior. Rezazadeh Movahhed and Hamed [3] introduced a novel method for controlling the longitudinal motion of UAVs, achieving accurate tracking of desired references using a Linear Quadratic Regulator (LQR) optimized sliding mode control with integral action. The LQG/LTR method, rooted in classical control theory, offers a systematic approach to design state feedback controller capable of regulating the aircraft dynamic behavior. It uses the LQG/LTR control method with an output-feedback structure to provide robustness and improved tracking behavior and to retain the good properties of the optimal LQR and Kalman filter control methods simultaneously. Conversely, the SMIT controller represents a modern control technique that integrates sliding mode control principles with integral action, aiming to mitigate chattering effects associated with conventional sliding mode controllers while enhancing tracking accuracy and robustness. Its potential specifically for controlling rudderless flying-wing UAVs lies in its capability to handle challenges inherent in the aircraft dynamics, thereby enabling precise trajectory tracking and disturbance rejection. A comparative study for these control methodologies in the context of tracking control of flying-wing UAVs in longitudinal and lateral motions is investigated in this paper.

Material and Method

The tracking performance of a rudderless flying-wing UAV [4,5] in longitudinal and lateral channels is investigated in this paper comparing LQG/LTR and SMIT control methods performance. For this purpose, the linearized equations of motion are obtained for both longitudinal and lateral channels, in state-space form $\dot{\mathbf{x}} = \mathbf{A}\mathbf{x} + \mathbf{B}\mathbf{u}, \quad \mathbf{y} = \mathbf{C}\mathbf{x}$, by implementing small-disturbance theory [6], where $(\mathbf{A}, \mathbf{B}, \mathbf{C})$ demonstrate system, input, and output matrices respectively. The LQG/LTR methodology presents an advanced strategy that merges the

tracking precision, robustness, and stability attributes of both the LQR controller and Kalman filter. However, a notable challenge is the potential compromise of optimal characteristics in both system gains upon integrating the state feedback regulator and state estimator. Consequently, the Loop Transfer Recovery (LTR) technique is introduced [3,7]. This method initiates by initially formulating a model based on either a Kalman filter or LQR technique, ensuring it possesses desirable features. Subsequently, the LTR procedure proceeds by designing a closed-loop system that combines the LQR regulator and Kalman state estimator so that the closed-loop system gain approximates the optimized loop gain obtained from either the Kalman filter- or LQR-based approach. By proceeding through LQG/LTR design method addressed in [8], the closed-loop controller gain is obtained as follows:

$$\mathbf{u} = \mathbf{K}_{LQ}(S\,\mathbf{I} - \mathbf{A} + \mathbf{B}\mathbf{K}_{LQ} + \mathbf{H}_{KF}\mathbf{C})^{-1}\mathbf{H}_{KF}(\mathbf{r} - \mathbf{y}) \tag{1}$$

$\mathbf{K}_{LQ}, \mathbf{H}_{KF}$ are LQR regulator and Kalman filter gains respectively. Also, $\mathbf{r}, \mathbf{y}$ represent the reference signal and system output vectors, respectively. The control law of the proposed LQR-optimized sliding mode control with integral action [3,9] is defined as follows based on the design procedure discussed in [3]. By augmenting the integral of tracking error with system states, the system equations are rewritten in a transformed state space $(\tilde{\mathbf{A}}, \tilde{\mathbf{B}})$. The sliding surface is defined by $\sigma = \mathbf{S}\tilde{\mathbf{x}} - \mathbf{S}_r\mathbf{r}$ where $\mathbf{S}$ is the sliding hyper-plane matrix optimized by LQR method and $\tilde{\mathbf{x}}$ is the augmented state vector. The control input vector $\mathbf{u}$ is computed using Eq. (2) in which, $\mathbf{\Phi}$, $\mathbf{P}_2$, ρ_c are the stable design matrix, symmetric positive definite matrix, and a design scalar function, respectively. The parameter $\mathbf{S}_r$ is chosen equal to zero and δ_c is smoothing factor. $\mathbf{\Lambda} = \mathbf{SB}$ is a nonsingular diagonal design matrix.

$$\mathbf{u} = -\mathbf{\Lambda}^{-1}(\mathbf{S}\tilde{\mathbf{A}} - \mathbf{\Phi}\mathbf{S})\tilde{\mathbf{x}} - \mathbf{\Lambda}^{-1}(\mathbf{\Phi}\mathbf{S}_r + \mathbf{S}_1\mathbf{B}_r)\mathbf{r} + \mathbf{\Lambda}^{-1}\mathbf{S}_r\dot{\mathbf{r}} - \rho_c\mathbf{\Lambda}^{-1}\frac{\mathbf{P}_2\sigma}{\|\mathbf{P}_2\sigma\| + \delta_c} \tag{2}$$

Results and Discussion

In this section, the results of simulation for the SMIT method are compared with the related results obtained by LQG/LTR approach. The evaluation is based upon tracking behavior and control signal comparison in longitudinal and lateral motion. It may be observed from Figure 2 that the proposed optimized SMIT controller performs more efficiently in comparison to LQG/LTR method and the tracking behavior is significantly improved specially in lateral dynamics. It is also shown that the SMIT controller outperforms the LQG/LTR method in terms of smoothness in control signals. On one hand, it may be inferred from Figure 2a that the steady-state error in longitudinal motion has vanished in optimized SMIT closed loop system. On the other hand, the overshoot and delay due to non-minimum phase nature of lateral dynamics, are considerably decreased in yawing response of SMIT closed-loop system in Figure 2c.

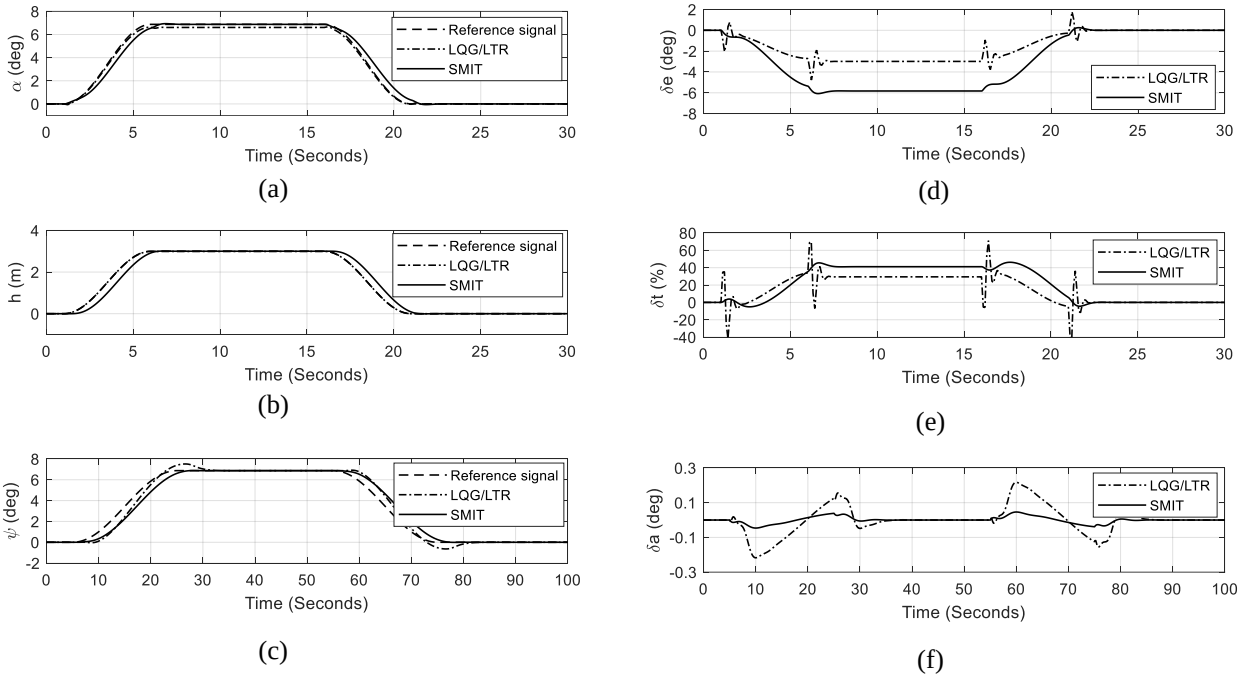


Figure 2. Comparison between tracking performance and control signals of the SMIT and LQG/LTR in longitudinal and lateral motion; a) angle of attack α (deg), b) altitude h (m), c) yaw angle ψ (deg), d) elevator angle δ_e (deg), e) thrust rate δ_t (%), f) aileron angle δ_a (deg)

Conclusion

In this paper a comparative analysis of two control methodologies, namely Loop Transfer Recovery (LQG/LTR) and Optimized Sliding Mode Integral Tracking (SMIT) controllers, focused on tracking performance of rudderless flying-wing UAVs is presented. The simulation results indicate that while both methods demonstrate promising behavior, the optimized SMIT outperforms the LQG/LTR approach and displays superior performance in longitudinal and lateral motions in terms of tracking performance and control signals efficiency. As a main result, the efficiency of LQR-optimization in sliding mode control structure would be highlighted.

References

1. Ali, S. U., Samar, R., Shah, M. Z., Bhatti, A. I., Munawar, K., & Al-Sggaf, U. M. (2016). Lateral guidance and control of UAVs using second-order sliding modes. Aerospace Science and Technology, 49, 88-100.
2. Anh, P. T. P., Vu, N., Lai, P. T., & Vinh, N. Q. (2019). Sliding mode based lateral control of unmanned aerial vehicles. Procedia Computer Science, 150, 78-87.
3. Rezazadeh Movahhed, S., & Hamed, M. A. (2021). Output tracking of a 6-DOF flying wing UAV in longitudinal motion using LQR optimized sliding mode control with integral action. 2021 7th International Conference on Control, Instrumentation and Automation (ICCIA).
4. Bagheri, S. (2014). Modeling, simulation and control system design for civil unmanned aerial vehicle (uav). Umea University,
5. Rezazadeh Movahhed, S., & Hamed, M. A. (2024). Aerodynamic Coefficients Computation for Fixed Wing Aircrafts Using DATCOM Software with Emphasize on Rudderless Flying-Wing UAVs. Journal of Aerospace Science and Technology, 17(1), 60-71.
6. Beard, R. W., & McLain, T. W. (2012). Small unmanned aircraft: Princeton university press.
7. Lewis, F. L., Vrabie, D., & Syrmos, V. L. (2012). Optimal control: John Wiley & Sons.
8. Rezazadeh Movahhed, S., & Hamed, M. A. (2024). Dynamic Modeling and Designing Robust MIMO Controller for Rudderless Flying-Wing UAVs (Accepted). In Emerging Technologies and Trends in Next Generation Transportaions and Unmanned Aircraft Systems: Wiley.
9. Shtessel, Y., Edwards, C., Fridman, L., & Levant, A. (2014). Sliding mode control and observation (Vol. 10): Springer.

Advanced Engineering Days

aed.mersin.edu.tr

Output Feedback Control Using Enhanced SMIT Controller Based on Sliding Mode Observer for Longitudinal Control of Rudderless Flying-Wing UAVs

Sevda Rezazadeh Movahhed*[1], Mohammad Ali Hamed [1]

[1]*University of Tabriz, Department of Mechanical Engineering, Iran, Sevda.rezazadeh@tabrizu.ac.ir, ma.hamed@tabrizu.ac.ir*

Cite this study: Movahhed, S. R.., & Hamed, M. A. (2024). Output Feedback Control Using Enhanced SMIT Controller Based on Sliding Mode Observer for Longitudinal Control of Rudderless Flying-Wing UAVs. Advanced Engineering Days, 9, 639-641

Keywords
Flight control
SMIT
Utkin observer
Longitudinal motion
Rudderless flying-wing

Abstract

This paper presents a novel approach for tracking control of rudderless flying-wing unmanned aerial vehicles (UAVs) in longitudinal motion using an optimized sliding mode integral tracking controller (SMIT) based on sliding mode observer. The study is focused on tracking control of a rudderless flying-wing UAV which suffers from stability and control problems due to its unique design characteristics and reduced control surfaces. The primary objective is to enhance the robustness and accuracy of the considered UAV in maintaining desired flight path in longitudinal motion. The SMIT method combines the advantages of sliding mode control, which is known for its robustness properties, with an integral action to eliminate steady-state errors. The incorporation of the Utkin observer facilitates accurate state estimation, crucial for the effective implementation of the controller. An optimization algorithm is employed to enhance the sliding surface, ensuring optimal performance. Simulation results demonstrate that the proposed SMIT method based on Utkin observer achieves superior tracking precision compared to conventional control methods.

Introduction

Ensuring precise and reliable tracking control of UAVs is a critical task for effective operations, especially for the rudderless flying-wing UAVs with challenging design structure. This unique configuration poses significant challenges for designing robust tracking controllers ensuring system stability. Some studies have been accomplished to design tracking controllers for fixed-wing UAVs, with a few researches focused on rudderless flying-wing UAVs. Hajiev et al. [1] designed a Kalman filter-based LQR controller for UAV altitude tracking control. Bagheri et al. [2] combined LQR and PID control for stability and reference tracking in a small flying-wing UAV. Munoz et al. [3] addressed trajectory tracking using a modified super-twisting sliding mode control with a high order observer. This paper introduces a sliding mode integral tracking controller with optimized sliding surface based on the Utkin observer. This approach leverages the strengths of sliding mode control by introducing an enhanced sliding surface design while integrating integral action to eliminate steady-state errors, thereby enhancing tracking performance. The Utkin observer is incorporated to provide accurate state estimations which are used for further effective construction of the proposed control strategy. The simulation results indicate the efficiency of the proposed controller-observer structure for tracking control of a rudderless flying-wing UAV in longitudinal motion.

Material and Method

The UAV under study is a Freya flying-wing UAV (Figure 1 [4]). The longitudinal dynamic attributes to motion caused by aerodynamic forces and moments in the body plane $x_b - z_b$. The engine thrust rate (δ_t) and the elevator deflection (δ_e) are control inputs. After the linearization of dynamic equations [5-8] by the small disturbance method, the longitudinal equations of motion are expressed in the state space form of Eq. (1).

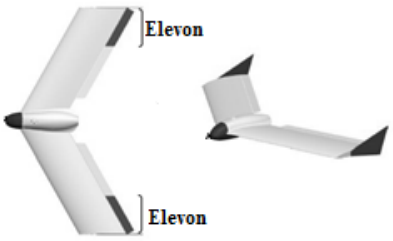


Figure 1. Freya Smartfly UAV

$$\dot{\mathbf{x}} = \mathbf{A}\mathbf{x} + \mathbf{B}\mathbf{u}$$

$$\mathbf{A} = \begin{bmatrix} X_U & X_W V_a \cos\alpha_n & X_Q & -g\cos\theta & 0 \\ Z_U/(V_a\cos\alpha_n) & Z_W & Z_Q/(V_a\cos\alpha_n) & -g\sin\theta/(V_a\cos\alpha_n) & 0 \\ M_U & M_W V_a\cos\alpha_n & M_Q & 0 & 0 \\ 0 & 0 & 1 & 0 & 0 \\ \sin\theta & -\cos\theta V_a\cos\alpha_n & 0 & U\cos\theta + W\sin\theta & 0 \end{bmatrix}, \mathbf{B} = \begin{bmatrix} X_{\delta e} & X_{\delta t} \\ Z_{\delta e}/(V_a\cos\alpha_n) & 0 \\ M_{\delta e} & 0 \\ 0 & 0 \\ 0 & 0 \end{bmatrix} \quad (1)$$

where $\mathbf{x} = [u, \alpha, q, \theta, h]^T$ is the state vector composed of the variation of linear velocity along x_b -axis, angle of attack, pitch rate, pitch angle, and altitude about trim point, respectively. V_a denotes the resultant linear velocity. Also, the terms with indices are stability derivatives [7,9,10]. Now, the control law of the proposed LQR-optimized sliding mode control with integral action [8,11-13] is defined as follows after some transformations to $(\tilde{\mathbf{A}}, \tilde{\mathbf{B}})$ space [11], where $\mathbf{S}$ is the sliding hyper-plane matrix and σ denotes sliding surface. $\mathbf{\Phi}$ is any stable design matrix. The parameter S_r doesn't affect the stability of the closed loop system and usually is chosen equal to zero. $\mathbf{P}_2$ is a symmetric positive definite matrix satisfying $\mathbf{P}_2\mathbf{\Phi} + \mathbf{\Phi}^T\mathbf{P}_2 = -\mathbf{I}$. δ_c is smoothing factor. $\mathbf{\Lambda}$ is a nonsingular diagonal design matrix usually taken as $\mathbf{I}_{m\times m}$. The scalar function ρ_c is also set in the design process.

$$\mathbf{u} = \mathbf{L}\tilde{\mathbf{x}} + \mathbf{L}_r\mathbf{r} + \mathbf{L}_{\dot{r}}\dot{\mathbf{r}} - \rho_c\mathbf{\Lambda}^{-1}\frac{\mathbf{P}_2\sigma}{\|\mathbf{P}_2\sigma\| + \delta_c}, \begin{cases} \mathbf{L} = -\mathbf{\Lambda}^{-1}(\mathbf{S}\tilde{\mathbf{A}} - \mathbf{\Phi}\mathbf{S}) \\ \mathbf{L}_r = -\mathbf{\Lambda}^{-1}(\mathbf{\Phi}\mathbf{S}_r + \mathbf{S}_1\mathbf{B}_r) \\ \mathbf{L}_{\dot{r}} = \mathbf{\Lambda}^{-1}\mathbf{S}_r \end{cases} \quad (2)$$

Also, the Utkin observer structure is defined as follows where ρ_0 is a positive scalar, and $\mathbf{L}$ is designed so that the reduced order motion of error dynamics is stable [11]. The system output $\mathbf{y}_i$ (sensor output) is composed of u, q, h signals, and $\hat{\mathbf{y}}_i$ represents the estimation of system output calculated by observer.

$$\dot{\hat{\mathbf{x}}} = \mathbf{A}\hat{\mathbf{x}} + \mathbf{B}\mathbf{u} + \mathbf{G}_n\upsilon, \qquad \mathbf{G}_n = \begin{bmatrix} \mathbf{L} \\ -\mathbf{I} \end{bmatrix}, \quad \upsilon = \rho_o sign(\hat{\mathbf{y}}_i - \mathbf{y}_i) \quad (3)$$

Results

In this section the simulation results of the proposed approach are presented. Figure 2 depicts angle of angle of attack (α) and altitude (h) tracking performance respectively. In the presumed maneuver, the aircraft pitches up by 7 deg change in angle of attack and ascends up by 3 meters, then maintains this situation for 10 sec and then smoothly returns to level flight.

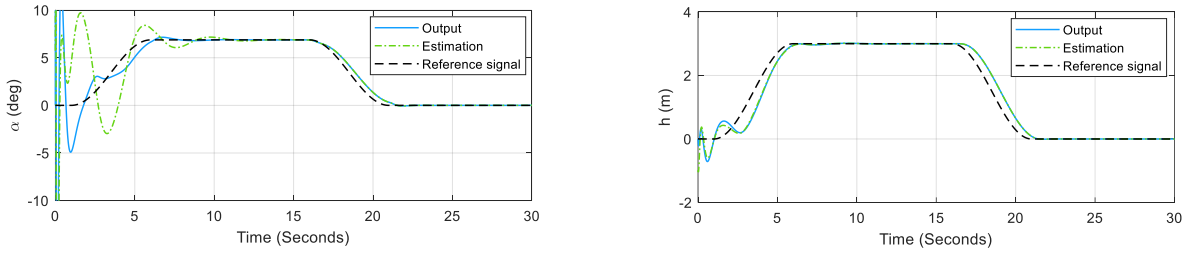


Figure 2. Tracking performance in longitudinal motion; a) angle of attack α (deg), b) altitude h (m)

Discussion

Based on the observations from Figure 2, it can be deduced that the system exhibits effective tracking performance with small discrepancy between the system output and desired values. Additionally, the settle time is minimal; so, there is no significant delay in the system response. Consequently, the tracking performance is accurate and satisfactory, validating the effectiveness of the proposed control methodology in longitudinal motion.

Conclusion

In this paper an optimized sliding mode integral tracking controller based on the Utkin observer is presented for tracking control of rudderless flying-wing UAVs in longitudinal motion. Integrating the robust features of sliding mode control with integral action and taking advantage of the precise state estimation of the Utkin observer, the proposed approach effectively addresses the challenges posed by tracking control of challenging rudderless flying-wing UAVs. Future research may focus on further optimization to enhance the controller-observer performance to implement for tracking purposes in lateral motion and also nonlinear systems.

References

1. Hajiyev, C., & Vural, S. Y. (2013). LQR controller with Kalman estimator applied to UAV longitudinal dynamics. Positioning, 4, 36-41.
2. Bagheri, S., Jafarov, T., Freidovich, L., & Sepehri, N. (2016). Beneficially combining LQR and PID to control longitudinal dynamics of a SmartFly UAV. 7th IEMCON.
3. Muñoz, F., Espinoza, E. S., González-Hernández, I., Salazar, S., & Lozano, R. (2019). Robust trajectory tracking for unmanned aircraft systems using a nonsingular terminal modified super-twisting sliding mode controller. Journal of Intelligent & Robotic Systems, 93(1), 55-72.
4. Bagheri, S. (2014). Modeling, simulation and control system design for civil unmanned aerial vehicle (uav). Umea University,
5. Cook, M. (2013). Flight Dynamics Principles: A Linear Systems Approach to Aircraft Stability and Control: Butterworth-Heinemann.
6. Roskam, J. (1995). Airplane flight dynamics and automatic flight controls: DARcorporation.
7. Beard, R. W., & McLain, T. W. (2012). Small unmanned aircraft: Princeton university press.
8. Rezazadeh Movahhed, S., & Hamed, M. A. (2021). Output tracking of a 6-DOF flying wing UAV in longitudinal motion using LQR optimized sliding mode control with integral action. 7th ICCIA.
9. Nelson, R. C. (1998). Flight stability and automatic control (Vol. 2): WCB/McGraw Hill, New York.
10. Rezazadeh Movahhed, S., & Hamed, M. A. (2024). Aerodynamic Coefficients Computation for Fixed Wing Aircrafts Using DATCOM Software with Emphasize on Rudderless Flying-Wing UAVs. Journal of Aerospace Science and Technology, 17(1), 60-71.
11. Shtessel, Y., Edwards, C., Fridman, L., & Levant, A. (2014). Sliding mode control and observation (Vol. 10): Springer.
12. Sabanovic, A., Fridman, L. M., Spurgeon, S., & Spurgeon, S. K. (2004). Variable structure systems: from principles to implementation (Vol. 66): IET.
13. Edwards, C., & Spurgeon, S. (1998). Sliding mode control: theory and applications: Crc Press.

Advanced Engineering Days

aed.mersin.edu.tr

Engineering an efficient hemostatic fabric by modifying regenerated cellulose

Nastaran Alipour*[1], Roya Salehi [1]

[1] *University of Medical Sciences, Faculty of Advanced Medical Sciences, Drug Applied Research Center and Department of Medical Nanotechnology, Tabriz, Iran nastaranalipoure@gmail.com, roya.salehi@gmail.com*

Cite this study: Alipour, N., & Salehi, R. (2024). Engineering an efficient hemostatic fabric by modifying regenerated cellulose. Advanced Engineering Days, 9, 642-644

Keywords
Biocompatible
Hemostatic fabric
Polydopamine
Cellulose
Antibacterial

Abstract

Effective techniques for managing bleeding are becoming increasingly critical in both medical settings and combat situations. This is because uncontrolled, non-compressible, and large-scale hemorrhaging leads to an alarmingly high rate of mortality. The available hemostatic agents lack the necessary chemical properties to simultaneously activate coagulation factors. As a result, they are unable to effectively control or stop the bleeding. In this work, we have engineered a modified regenerated cellulose fabric using chemical processes such as carboxymethylation, oxidation of regenerated cellulose, and polymerization with dopamine. This modified fabric (PD-OCMRC) is designed to effectively manage non-compressible, severe bleeding properties. The fabric's physicochemical attributes were examined using ATR-FTIR and FESEM analysis. The PD-OCMRC fabric exhibited enhanced blood clotting ability (BCI<5%) and zero hemolysis, which demonstrated the hemostatic capacity and biocompatibility of the prepared fabrics.

Introduction

For minor injuries, the body's natural clotting mechanisms are usually sufficient to stop bleeding. However, severe traumatic injuries that result in uncontrolled bleeding have a high risk of fatality because the normal coagulation process is overwhelmed and unable to stem such significant blood loss. There are only a few minutes of "golden rescue time" for open trauma brought on by accidents [1]. Therefore, achieving rapid hemostasis is essential to preventing further complications during surgery or other emergency medical procedures. Hemostatic materials, which can be derived from natural sources or synthetically produced, function by facilitating blood clotting and coagulation at the wound site. Moreover, severe injuries carry an increased risk of microbial infection, which can impede the body's natural healing mechanisms and potentially result in life-threatening complications.

Conventional cotton gauze has traditionally been utilized as a hemostatic material due to its desirable properties, including safety, flexibility for wound site wrapping, air permeability, hypoallergenic nature, and low cost. However, cotton gauze lacks procoagulant effects and exhibits poor wet adhesion, limited red blood cell and platelet adhesion, and inadequate swelling capacity. As a result, it is ineffective at preventing hemorrhage risk. Furthermore, cotton gauze can adhere to wound tissues, potentially causing re-bleeding complications upon removal [2].

Carboxymethyl cellulose (CMC) is a modified form of cellulose with added carboxymethyl groups, increasing its hydrophilicity, solubility, biocompatibility, and biodegradability. Studies showed that CMC-based wound dressings can absorb significant exudates and maintain a moist environment conducive to wound healing by reducing water loss [3].

Dopamine, derived from mussel mucus, exhibits bioadhesive properties due to its catechol groups. The oxidized catechol facilitates strong adhesion to tissues through covalent and non-covalent bonds. Previous studies show polyphenols like polydopamine have vasoconstrictive abilities, allowing them to constrict blood vessels, reduce bleeding, and adhere to seal wounds via their phenolic hydroxyl groups [4].

In this study, we developed a multifunctional hemostatic fabric device through various chemical modifications (PD-OCMRC). Carboxymethylation enhanced the fabric's absorbency and swelling. Oxidation promoted biodegradability, adhesion, and created active sites. Polymerization with dopamine improved wet tissue adhesion, activated coagulation, and provided antibacterial properties. We propose that the presence of functional groups in the synthesized fabric triggers both the intrinsic and extrinsic blood coagulation pathways.

Material and Method

Regenerated cellulose fabric (RC), Monochloroacetic acid, Sodium hydroxide, sodium periodate, Dopamine hydrochloride, Calcium chloride, Zinc nitrate, 2- propanol, Ethanol, Methanol.

The carboxymethylation process was performed with some modifications from the previous report [2]. briefly, the RC fabric was immersed in solvent containing NaOH, isopropanol and, sodium chloroacetate in bath at 60 ºC for 2 hr. After that, the prepared carboxylate fabric was immersed in a $CaCl_2$ and $ZnCl_2$ solution, washed in ethanol, and dried in a vacuum oven at room temperature, the product was named (CMRC). In second step, NaIO4 solution was slowly added to CMRC in ethanol and reacted for 24 hours at room temperature in the dark. Ethylene glycol was added to stop the reaction (OCMRC). The third step, The OCMRC gauze was soaked in methanol and varying weight percentages of dopamine (1.25%, 2.5%, 5%, 10%, and 20%) at 50°C for 24 hours. the resulting brown-black polydopamine-coated OCMRC (PD-OCMRC) was washed with ethanol and dried at room temperature.

Results

In the current work, the carboxymethylated process enhances water absorption and swelling of regenerated fabric (Figure 1A). The secondary hydroxyl groups at C2-C3 positions in CMRC were oxidized by NaIO4 to dialdehyde groups. This oxidation creates active aldehyde groups for further reactions and causes cellulose degradation into water-soluble fractions. Finally, OCMRC fibers underwent self-polymerization with varying dopamine amounts (1.25%, 2.5%, 5%, and 10% w%) to form the final PD-OCMRC gauze product. The successful preparation of PD-OCMRC in each step was confirmed through ATR-FTIR. In the spectra of CMRC, two new bands at 1594 cm^{-1} and 1416 cm^{-1} are attributed to asymmetrical and symmetrical vibrations for the carboxylate, respectively. During the oxidation process, two new peaks at 1730 cm^{-1} ($\upsilon_{C=O}$) and 700 cm^{-1} (hemiacetal linkage) appeared, which confirmed the aldehyde in OCMRC's structure. Comparing the spectra of RC, CMRC, and OCMRC with PD-OCMRC, there is a noticeable broad absorbance at 1630 (υ_{N-H}) attributed to the indole structure present in polydopamine. This evidently shows PD-OCMRC is successfully prepared (Figure 1B). Also, the color of the fabric, as shown in Figure 1C, changed from white to brown-black, which served as a visible indication of the reaction.

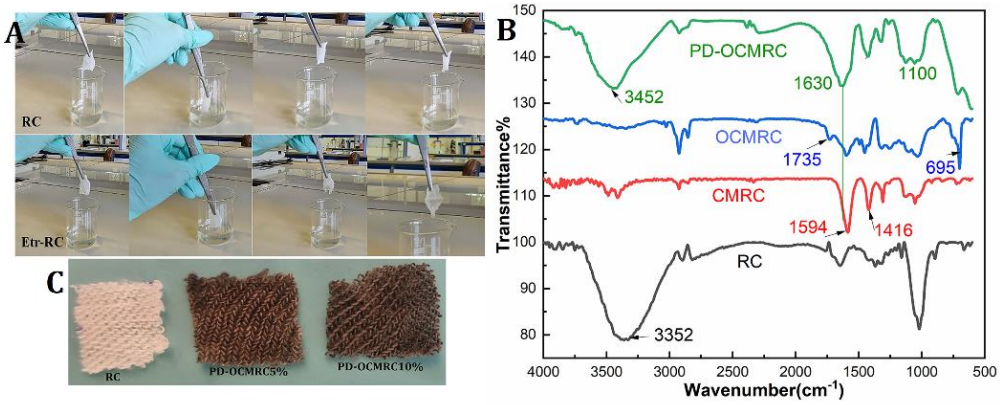


Figure 1. A) Photographs of RC and CMRC and changing their morphology after water absorption, B) ATR-FTIR of RC, CMRC, OCMRC, PD-OCMRC, C) Images of RC, PD-OCMRC 5,10%.

SEM images (Figure 2) showed the unmodified RC fiber had a soft, smooth, capillary structure around 10.2 µm thick. After carboxymethylation to form CMRC fabric, the fiber surface became rougher and thicker with visible protrusions, resulting from the carboxymethylation reaction. Following the polymerization with dopamine, a thin layer of polymer was clearly visible on the surface of the fibers, also the surface roughness on the fibers increased, which is evidence of the successful synthesis of PD-OCMRC.

Biocompatibility is essential for hemostatic materials used at bleeding sites. As shown in Figure 3, the hemolytic potential of CMRC, OCMRC, and PD-OCMRC was evaluated against negative and positive controls (saline, deionized water) and commercial products (ChitoCell®, BloodStop®). Results revealed that increasing dopamine concentrations in PD-OCMRC (1.25%, 2.5%, 5%, 10% w%) progressively reduced erythrocyte hemolysis rates, reaching zero hemolysis at 10% dopamine. The 10% PD-OCMRC supernatant was colorless like the negative control, indicating complete safety as a blood-contacting material. In contrast, ChitoCell® caused 15% hemolysis with a completely red supernatant, indicating that it can damage and rupture blood cells. According to ASTM-F756 standards, materials causing <5% hemolysis are considered safe for blood contact. This demonstrates the excellent biocompatibility of the 10% PD-OCMRC fabric. The blood coagulation index (BCI) evaluates hemostatic capacity in vitro by measuring hemoglobin absorbance released from unclotted red blood cells, with a higher BCI indicating poorer clotting ability. Figure 3 shows that increasing dopamine levels in PD-OCMRC from 1.25% to 5% significantly reduced the BCI, with 5% and 10% dopamine having the lowest BCI values of 4.2% and 5%,

respectively. This demonstrates that polydopamine's catechol groups promote red blood cell capture, aggregation, and clot formation.

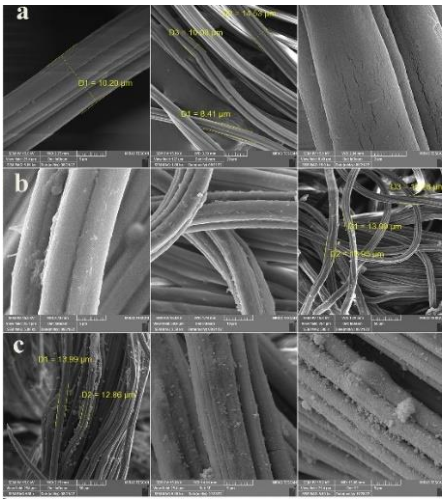


Figure 2. a) SEM image of RC, b) OCMRC, c) PD-OCMRC

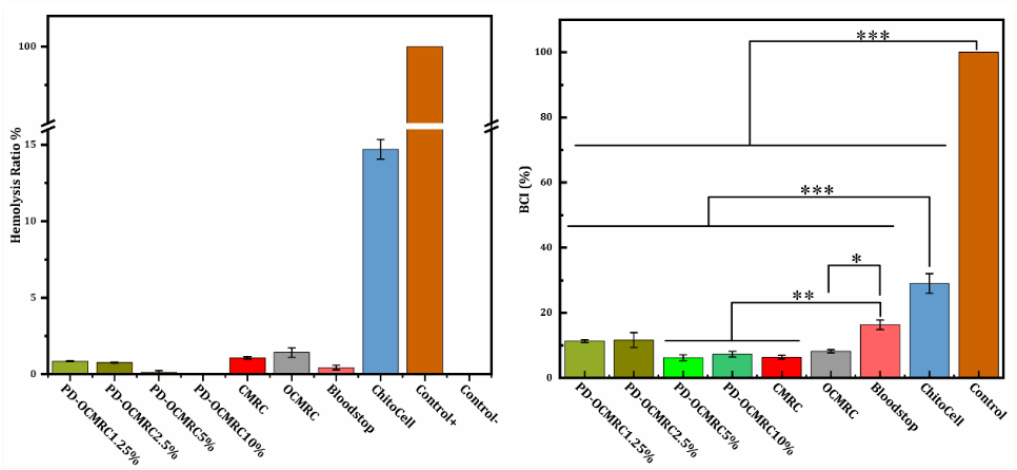


Figure 3. *In vitro* hemolysis ratio and BCI of CMRC, OCMRC, PD-OCMRC, positive and negative controls and commercial products ChitoCell® and BloodStop® (the mean ±SD n=5, ***p < 0.001).

Discussion

The presence of hydrophilic carboxyl groups on CMRC and PD-OCMRC fabrics through the process of etherification leads to a negative charge on their structure. This negative charge can activate blood coagulation factor XII, resulting in a significantly accelerated hemostasis process. Furthermore, the carboxyl and phenolic hydroxyl groups on dopamine have the ability to establish hydrogen bonds with water molecules in the blood.

Conclusion

In this study, a novel hemostatic material based on textile fabric was designed for non-compressible hemorrhage. The step-by-step modification processed was confirmed by FTIR spectroscopic methods. The in vitro tests showed that PD-OCMRC treated groups demonstrated significantly better hemostatic ability.

References

1. Wang, L., Zhong, Y., & Ma, G., (2020). A Natural Polymer-Based Porous Sponge with Capillary-Mimicking Microchannels for Rapid Hemostasis. Acta Biomaterialia Journal ,114, 193-205.
2. Wang, Y., Zhao, Y., & Yang, S., (2021). Cellulose fibers-reinforced self-expanding porous composite with multiple hemostatic efficacy and shape adaptability for uncontrollable massive hemorrhage treatment. Bioactive Materials Journal, 6,2089-2104.
3. Pan, S., Li, Y., & Zhang, Q., (2023). Strongly-adhesive easily-detachable carboxymethyl cellulose aerogel for noncompressible hemorrhage control. Carbohydrate Polymers Journal, 301, 120324.
4. Zheng, Y., Shariati, K., & Annabi, N., (2023). Hemostatic patch with ultra-strengthened mechanical properties for efficient adhesion to wet surfaces. Biomaterials Journal, 301, 122240.

Advanced Engineering Days

aed.mersin.edu.tr

Preparation of mineral distribution map using Hyperion images: A case study of Northwest of Kerman Province

Hossein Fekrat [1], Vahid Kakapor [1], Maryam Sadeghi [1], Khalil Valizadeh Kamran [1], Hassan Emami[1]

[1] University of Tabriz, Faculty of Planning and Environmental Science, Department of Remote Sensing and Geographic Information System, Tabriz, Iran, v.kakapor@gmail.com, Hosseinf7181@gmail.com, sadegi.maryam92@gmail.com, valizadeh@tabrizu.ac.ir, hemamy@gmail.com

Cite this study: Fekrat, H., Kakapor, V., Sadeghi, M., Valizadeh Kamran, K., & Emami, H. (2024). Preparation of mineral distribution map using Hyperion images: A case study of Northwest of Kerman Province. Advanced Engineering Days, 9, 645-648

Keywords
Minerals
Remote sensing
Hyperspectral
Hyperion
Kerman

Abstract

Identifying minerals using hyperspectral remote sensing technologies is one of the effective methods in investigating land resources, which saves time and provides greater accuracy in identifying minerals and mapping compared to traditional methods. . In this research, the distribution of minerals in the north-west of Kerman province (Anar and Babak cities) was investigated by using Hyperion sensor images. For this purpose, FLAASH and Log Residuals methods were used to apply atmospheric and topographical corrections to the hyperspectral image prepared from the study area. Then, by using MF, MTMF, SAM and Unmixing methods, a mineral distribution map was prepared in the studied area. The results of this research led to the discovery of some potential minerals in these areas, such as stearulite, diasphorus, zircon, alunite and quartz. This research shows that in different regions of Iran there is a huge potential for further exploration of minerals using hyperspectral satellite images.

Introduction

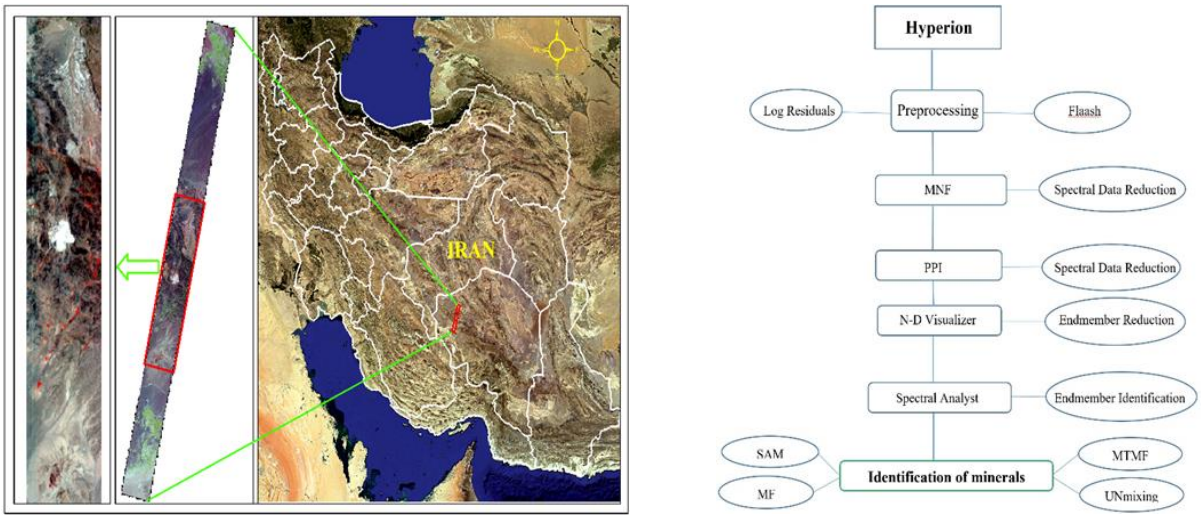
Today, many of the processes of mineral identification and exploration are carried out in old ways and with field work such as speculation, prospecting, drilling, and finally, the preparation of a mineral potential map, which requires a lot of time, money, and manpower. and the removed samples are done discretely and the results are generalized to a continuous space. While some of these valuable minerals appear as veins and may not be sampled [1]. According to the sustainable development goals of the United Nations, the development of the power of mineral resources is considered as a requirement for sustainable economic development for a developing country like Iran. Meanwhile, ultraspectral remote sensing technology can be very useful in identifying minerals. Hyperspectral measurement has made it possible to prepare accurate mineral potential maps, discovery and optimal use of mineral reserves. The hyperspectral images used, due to having features such as band continuity and low bandwidth [2], have the necessary potential to overcome the limitations in the field of access to appropriate information for mineralogical studies [3] Also, these images can be more reliable and efficient by providing a continuous range of objects and more information. On the other hand, it provides the possibility of extracting additional information that the human eye cannot capture with its red, green and blue visual receptors [4].Due to its metal and non-metal mineral resources, Kerman province is one of the richest mineral provinces in the country and is known as "Miner's Paradise". The existence of huge mineral reserves in this province, especially in the northwest, shows the necessity of further investigation and study to discover and identify these valuable resources in this region. In this research, an attempt has been made to determine the spectra of minerals based on the intensity of reflectivity and absorption by using hyperspectral data, and the unknown spectrum obtained from satellite images is compared with reference library spectra and based on its belonging to the mineral collection. Spectral similarity, the possibilities available in the spectral library bank are calculated and the mineral with the most similarity to the unknown mineral is identified.

Material and Method

Study area

The used image of the north-western part of Kerman province includes a part of Anar and Babak cities, which is shown in Figure 1. This area is considered one of the main mineral poles (copper, celsius, turquoise and

construction stones) of Kerman province. In Figure 1, the location of the studied area is shown along with the image used by the Hyperion satellite with false color combination, as well as the research process.



(a) (b)

Figure 1. (a) The scope of the study, (b) the general process of analysis and processing

Materials and Data Analysis

In this research, a Hyperion hyperspectral image with L1R processing level and date 08/09/2004 and row 39 and pass 161 were used. The spatial resolution of the Hyperion meter is 30 meters and the number of bands is 242.

Preprocessing

The image pre-processing stage is done to prepare the data before any processing and analysis, which includes radiometric-atmospheric corrections and geometric corrections [5]. In this research, two atmospheric and topographical correction methods, Flash and Log Residuals, were used.

PPI _ n-D VISUALIZER _ MNF

Pixel Purity Index (PPI): Performs spectral separation and its main goal is to find pure elements and their abundance in mixed pixels. In order to perform spectral separation, the composition of pure elements with related abundances must be modeled [6]. The result of the PPI routine is an image in which the value of each pixel corresponds to the number of times it was detected as a pure pixel in all PPI iterations. These resulting pixels are excellent candidates for endmember selection that can be used in further processing to the n-D imager. The pure and distinct materials that occur in the scene are the final members. Figure 3-a shows the desired result plot from the iteration performed to obtain the best spectral pixels clustered around 6200 pixels, and we checked this data for 20,000 iterations to get a better result (Figure 2-a).

n-D VISUALIZER: The purest pixels are shown in a clustered manner in the next step in N-dimensional space with the n-D VISUALIZER method, which is used for clustering pure pixels [7]. It can be shown in Figure 3-b. The filtered image data obtained from the PPI analysis are displayed by the n-D imager to find endmembers by locating and clustering the purest pixels in the n-dimensional space created by the MNF. In an n-dimensional scatterplot, where n number of bands simply refers to the spectral reflectance values for a given pixel in each band (Figure 2-b).

Minimum Noise Fraction (MNF) transformation: It is a linear transformation that is used to determine the original dimension and volume of the image, to separate noise from other information and to reduce the amount of processing in later stages. In this transformation, at first, the image is divided into noisy and non-noise parts, and then the non-noise part is recognized as the main component and the noise is removed [8]. Figure 5 shows the output of MNF transformation applied to the corrected image with the Flash method, where 48 eigenvectors containing coherent information are determined. (Figure 2-c).

Classification methods

MF _ MTMF _ SAM _ Unmixing

Adaptive Filtering (MF) method: One of the methods used in this study to separate hyperspectral data and prepare a map is Adaptive Filtering (MF) algorithm. In this method, the frequency of each of the end members is calculated separately and the reflection in each pixel is considered as a linear combination of two components [8].

Matched Adaptive Filtering with Mixture (MTMF): It is one of the methods used to prepare the scatter map of predetermined targets. This method inherits the simplicity of the adaptive filtering method and provides the possibility of reducing false alarms, which is not possible with the simple MF method [9]. Spectral Angle Mapper (SAM): This method is widely used in distance measurement, it calculates the angle between the spectral signatures of two vectors and by using the inner multiplication and estimating the spectral angle between the two reference spectral curve vectors and pixels Weir, Determines and calculates the similarity between two vectors. [10].

Unmixing: hyperspectral images makes it possible to examine the Earth's surface in more detail. However, mixed pixels are among the most challenging problems in hyperspectral images, which are caused by various factors, including the low spatial resolution of sensors such as Hyperion [11].

Results

Mineral identification results

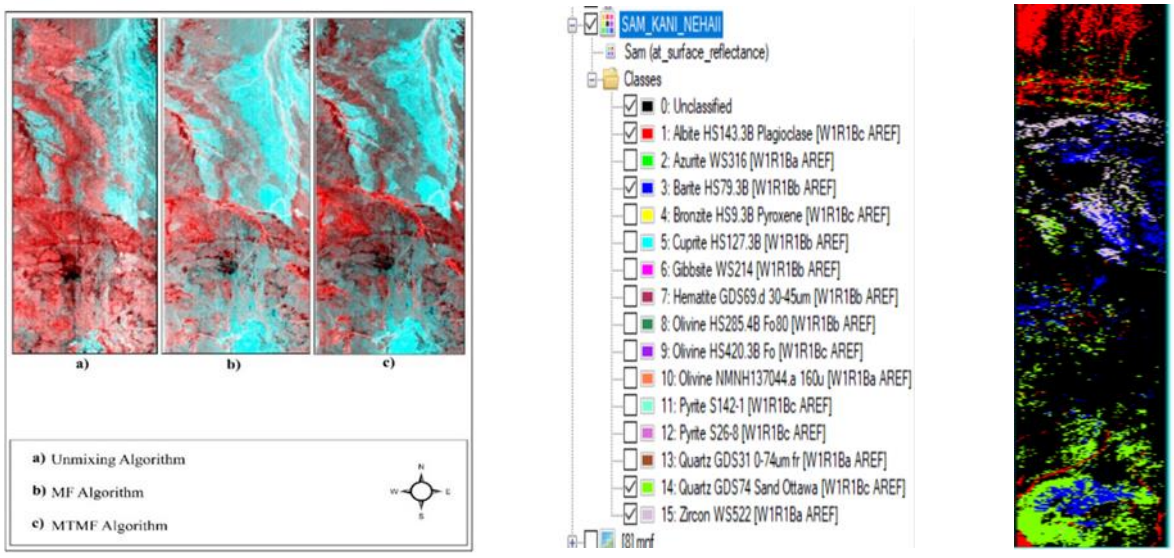
In this study, the spectral signature data of the end member were compared with the spectral data of the USGS mineral library, and the result is presented in Table 1. Spectral Analyst is used to identify materials based on their spectral properties. In this method, the matching of an unknown spectrum with the samples in the spectral library is rated using binary coding techniques, spectral angle mapping and spectral feature fitting. Spectral Analyst generates a ranked or weighted score for each material in the input spectral library. The highest score indicates the closest match and greater confidence in spectral similarity. Similar materials may have relatively high scores, but unrelated materials should have low scores.

Table 1. Comparison table of the spectral signature of the average value of the classes with the USGS spectral library

BE	SCORE	Mineral
0.71	1.909	Quartz
0.70	1.907	Zircon
0.65	1.901	Barite
0.61	1.893	Albite

Discussion

According to the results obtained from the output of mineral identification classification methods including adaptive filtering (MF), adaptive filtering with mixture (MTMF), spectral angle mapping (SAM) and unmixing four minerals, quartz, zircon, bality and orbit were detected, and the output results are shown in figure 3.



(a) (b)

Figure 3. (a) The output of three methods: Unmixing, MF and MTMF, (b) The output of the spectral angle vector mapper (SAM)

Conclusion

This research, on the distribution of minerals in the north-west of Kerman province was investigated using Hyperion sensor images. For this purpose, FLASH and Log Residuals methods were used to apply atmospheric and topographical corrections to the hyper-spectral images prepared from the study area. Due to the comparison table of the spectral signature of the average value of the classes, in the USGS spectral library, Quartz (1.909) highest and Zircon (1.893) obtained the lowest average score. According to the results obtained from the output of mineral identification classification methods, including adaptive filtering (MF), adaptive filtering with mixture (MTMF), spectral angle mapping (SAM) and unmixing four minerals; quartz, zircon, bality and orbit were detected that quartz, and bality has the highest area in the study region.

References

1. Sadeghi, A., Darvishi Boloorani, A., Abdolahi Kakroodi, A., Alaipana, S. K., & Hamzeh, S. (2021). Investigation of the Vegetation Effect on the Surveying and Mineral Exploration Using Hyperspectrsl Data. Iranian Journal of Remote Sensing & GIS, 12(4), 115-131.
2. Bartholomeus, H. (2009). The influence of vegetation cover on the spectroscopic estimation of soil properties. Wageningen University and Research.
3. Cañasveras, J. C., Barrón, V., Del Campillo, M. C., Torrent, J., & Gómez, J. A. (2010). Estimation of aggregate stability indices in Mediterranean soils by diffuse reflectance spectroscopy. Geoderma, 158(1-2), 78-84.
4. Oskouie, M. M., Busch, W. (2008). A Geostatistically Based Preprocessing Algorithm for Hyperspectral Data Analysis. GIScience & Remote Sensing, vol 45, pp. 1–13 [DOI:10.2747/1548-1603.45.3.1].
5. Goetz, A. F. H. (2009). Three decades of hyperspectral remote sensing of the Earth: A personal view. Remote Sensing of Environment,vol 113, pp. 5–16
6. Waldhoff, G., Bubenzer, O., Bolten, A., Koppe, W., & Bareth, G. (2008). Spectral analysis of ASTER, Hyperion, and Quickbird data for geomorphological and geological research in Egypt (Dakhla Oasis, Western Desert). Int. Arch. Photogramm. Remote Sens. Spat. Inf. Sci, 37, 1201-1206.
7. Boardman, J. W. (1998). Leveraging the high dimensionality of AVIRIS data for improved sub-pixel target unmixing and rejection of false positives: mixture tuned matched filtering. In Summaries of the seventh JPL Airborne Geoscience Workshop, JPL Publication, 1998 (Vol. 97, No. 1, pp. 55-56). NASA Jet Propulsion Laboratory.
8. Jin, X., Paswaters, S., & Cline, H. (2009, April). A comparative study of target detection algorithms for hyperspectral imagery. In Algorithms and Technologies for Multispectral, Hyperspectral, and Ultraspectral Imagery XV (Vol. 7334, pp. 682-693). SPIE.
9. Sayedain, S. A., & Maghsoudi, Y. (2013). Exploration of oil seepages using target detection algorithms in hyperspectral images. The International Archives of the Photogrammetry, Remote Sensing and Spatial Information Sciences, 40, 361-363.
10. Boardman, J. W., & Kruse, F. A. (1994). Automated spectral analysis: A geologic example using AVIRIS data, north Grapevine Mountais.
11. Boardman, J. (1998). An average soil erosion rate for Europe: myth or reality?. Journal of Soil and Water Conservation, 53(1), 46-50.

Advanced Engineering Days

aed.mersin.edu.tr

Synthesis and in situ oxidation of copper nanoparticles by glow discharge plasma on liquid

Nazila Mahmoudian*[1], Fatemeh Baharlounezhad [1], Mohammad Ali Mohammadi [1], Mohaddeseh Mousavi [1], Ali Soltani Vala [1]

[1]Tabriz University, Physics, Iran, nazilamahmoudian@gmail.com, f.baharlou@tabrizu.ac.ir, mohammadidorbash@yahoo.com, m.mousavi@tabrizu.ac.ir, asoltani@tabrizu.ac.ir

Cite this study: Mahmoudian, N., Baharlounezhad, F., & Mohammadi, M. A., Mousavi, M., & Soltani Vala, A. (2024). Synthesis and in situ oxidation of copper nanoparticles by glow discharge plasma on liquid. Advanced Engineering Days, 9, 649-651

Keywords
Plasma
Copper oxide
Nanoparticles

Abstract

This article investigates the synthesis and in situ oxidation of copper nanoparticles through the application of glow discharge plasma on the water surface, focusing on the advantages of utilizing low-temperature plasma sources for nanoparticle formation. Results of X-ray diffraction analysis confirmed the successful synthesis of Cu, CuO and Cu_2O nanoparticles with crystallite size (23.36, 11.71 and 16.88), respectively. SEM imaging showed uniform spherical morphology of nanoparticles (10-30 nm). Energy dispersive spectroscopy affirmed purity of synthesized nanoparticles.

Introduction

Plasmas represent one of the four fundamental states of matter, alongside solids, liquids, and gases, playing a significant role in human life and current industrial applications. Plasmas formed through the ionization of neutral gases typically consist of equilibrium between positive ions and negative electrons and occasionally negative ions, alongside neutrals, metastables, excited atoms or molecules, reactive radicals, ultraviolet (UV) radiation, and a strong electric field. Due to the versatile reactivity of species within plasmas, gas-based reactive plasmas find extensive application in various manufacturing sectors, including material [1]. In recent decades, a rapidly advancing field of plasma research known as nanomaterial synthesis through plasma-liquid interactions (PLIs) has emerged, driven largely by the proliferation of novel plasma sources designed to operate at low and atmospheric pressures. In PLIs, plasmas interact either above or within liquids, creating plasma-liquid interfaces conducive to many physical and chemical processes, which can be harnessed to synthesize diverse nanomaterials (NMs). Interestingly, utilizing plasma-liquid interactions for material formation predates the formalization of the term 'plasma,' attributed to Irving Langmuir in 1928 [2]. This idea stretches back even further to 1887 when Gubkin [3] employed a discharge to chemically reduce silver ions (Ag+) within an aqueous solution of $AgNO_3$.

Metal oxide nanoparticles are attractive for extensive applications, including optical, catalytic, mechanical, and electrical [16]. Copper oxide, composed of the elements copper and oxygen, which belong to the block d and block p on the periodic table respectively, exhibits a crystal structure that copper ion is surrounded by four oxygen ions. Copper and copper oxide nanoparticles have significant interest, as copper is a vital component in modern technologies and is abundantly accessible [15]. Recent studies suggest that the CuO and Cu2O phases found in oxidized Cu nanoparticles demonstrate enhanced photocatalytic activity when exposed to visible light. Consequently, the construction of $Cu/CuO/Cu_2O$ heterojunctions presents an appealing strategy for a diverse array of environmental applications.[18]

A discharge in a liquid medium containing oxygen enables the oxidation of metal particles without the need for thermal annealing post-synthesis. This process allows for the precise control of synthesizing monodisperse nanoparticles of oxides, not only limited to copper but potentially for various other metals as well. In this research, copper oxide nanoparticles were synthesized using the plasma method (the interaction of atmospheric pressure direct current oxygen plasma with a water surface). The crystal structure was analyzed by X-ray diffraction (XRD). The morphology of the synthesized copper oxide structures was examined using a scanning

electron microscope (SEM). Weight and atomic percentages of elements were determined by energy dispersive X-ray (EDX).

Material and Method

The plasma reactor designed for producing copper oxide nanoparticles utilized a single-container setup as depicted in "Figure 1". Cylindrical copper rods with an external diameter of 2 mm operated as electrodes, with one electrode positioned at a distance of 2 mm over the water surface. The reactor, with a volume of 200 ml, was filled with distilled water (pH=6.65 and electrical conductivity, EC=2 µs/cm) at room temperature. The voltage difference was created between the cathode electrode and the water surface. Plasma was generated by oxygen gas ionization through a DC power supply at 12 kV. The synthesis was completed in 10 minutes. Oxygen gas was flown with 50 sccm through a glass tube surrounding the plasma generator electrode. The pH value of the water was determined by a desktop pH meter (HI2002 - edge® Dedicated pH Meter). Electrical conductivity was measured using the company's desktop conductivity meter (WTW Cond7310). The crystal structure of the sample was done via X-ray diffraction (TD-3700). Morphology and elemental analysis were performed through field emission scanning electron microscopy (MIRA3 FEG-SEM).

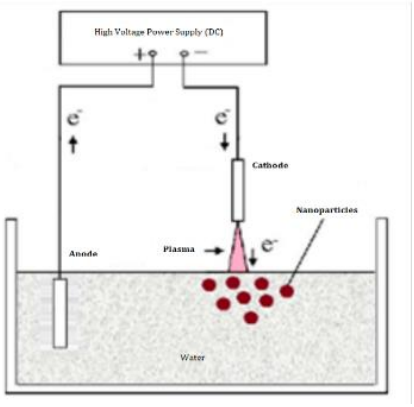


Figure 1. Experimental setup for producing copper oxide nanoparticles.

Results

"Figure 2 (a)" shows a gradual color transition from light brown to dark brown during the synthesis of Copper oxide nanoparticles through a glow discharge on water. The morphology of the synthesized copper oxide nanoparticles was examined using SEM image in "Figure 2 (b)". The average diameter of nanoparticles was estimated to be 10–30 (nm).

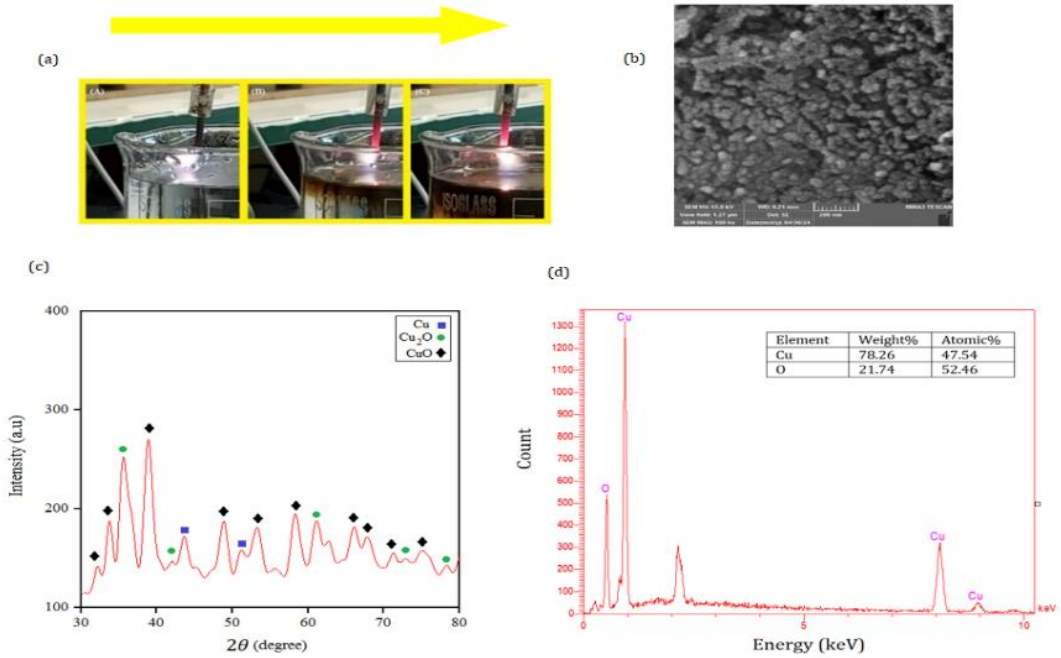


Figure 2. (a) synthesis steps during discharge on water surface, (b) SEM image, (c) XRD pattern, and (d) EDX analysis of copper oxide nanoparticles

The crystal structure and purity of the freshly synthesized copper oxide nanoparticles were analyzed using X-ray diffraction (XRD). "Figure 2 (c)" illustrates the XRD pattern of the copper oxide nanoparticles generated via a glow discharge on the water surface. The analysis revealed low-intensity diffraction peaks characteristic of copper at 43.7°and 50.7° (JCPDS 04-0836), corresponding to the (111) and (200)planes of the face-centered cubic (fcc) structure, respectively [27]. Furthermore, distinct peaks indicative of Cu_2O were observed at 36.37°, 42.26°, 61.36°, 73.664°, and 77.38°, aligning with the (111), (200), (220), (311), and (222) planes of the cubic cuprite phase according to (JCPDS 78-2076) [28]. Crystallographic orientations were identified at 2θ values of 32.6°, 35.5°, 38.6°, 48.8°, 53.5°, 58.2°, 65.9°, 67.82°, 72.17°, and 75.1°, corresponding to the (110), (111), (111), (202), (020), (202), (113), (202), (311), and (004) planes of the CuO monoclinic tenorite phase structure in good agreement with (JCPDS card 48-1548) [29]. The particles average crystallite size for the largest and most symmetrical peak of each sample was evaluated using the Scherrer equation $D=(k\lambda/\beta\cos\theta)$,where D is the average crystallite size, k is the Scherrer constant, λ is the X-ray wavelength, β is the full width at half maximum (FWHM) of the peak, and θ is the diffraction angle [28]. "Table 1" presents the results. The elemental composition of the synthesized nanoparticles was analyzed using energy dispersive spectroscopy (EDS), as depicted in "Figure 2 (d)".

Table 1. The average crystallite size of the samples

Items	Cu	CuO	Cu_2O
D	23.36 nm	11.71 nm	16.88 nm

Discussion

SEM images revealed nanoparticles synthesis with approximately uniform spherical morphology and consistent size. The most intense phase observed in the X-ray diffraction (XRD) analysis of the synthesized copper oxide nanoparticles was CuO tenorite. The EDS results conclusively demonstrated that the synthesized particles consist solely of copper and oxygen Element without any detectable impurities. The utilization of plasma-liquid interactions for nanoparticle synthesis shows significant potential for advancements in various fields, particularly in environmental applications where the photocatalytic properties of $Cu/CuO/Cu_2O$ heterojunctions can be harnessed.

Conclusion

The study demonstrated the successful synthsis of Cu/CuO/Cu2O nanoparticles with a uniform spherical shape and confirmed their purity through detailed structural and compositional analyses. The synthesis of copper oxide nanoparticles via glow discharge plasma on liquid presents a promising and efficient method for producing pure nanoparticles without the need for high-cost equipment or toxic compounds.
Overall, this research contributes to expanding our understanding of complex plasma systems and opens new avenues for exploring innovative approaches to nanomaterial synthesis.

References

1. Lieberman, M. A., & Lichtenberg, A. J. (2005). Principles of plasma discharges and materials processing. Hoboken, NJ: Wiley-Interscience.
2. Langmuir, I. (1928). Physical chemistry of gases. Proceedings of the National Academy of Sciences, 14(4), 627.
3. Gubkin, J. (1887). Eine volumetriiih-thermische Untersuchung iiber das Beziehungen zwischen der Diffusibilat und der Beweglichkeit der Atome. Annalen der Physik und Chemie, 268, 114.
4. Guajardo-Pacheco, M. J., Morales-Sanchez, J. E., González-Hernández, J., & Ruiz, F. (2010). Synthesis of copper nanoparticles using soybeans as a chelating agent. Materials Letters, 64, 1361-1364.
5. Xi, Y., Hu, C., Gao, P., Yang, R., He, X., et al. (2010). Morphology and phase selective synthesis of Cu2O (x = 1, 2) nanostructures and their catalytic degradation activity. Materials Science and Engineering B, 166, 113-117.
6. Elkodous, M. A., Kawamura, G., & Tan, W. K. (2022). Facile one-pot preparation of Cu/CuO/Cu2O heterojunction for photocatalytic applications. Materials Letters, 323, 132606.
7. Betancourt-Galindo, R., Reyes-Rodriguez, P. Y., & Puente-Urbina, B. A. (2014). Synthesis of copper nanoparticles by thermal decomposition and their antimicrobial properties. Journal of Nanomaterials
8. Lam, N. H., Smith, R. P., & Lee, N. (2022). Evaluation of the structural deviation of Cu/Cu_2O nanocomposite using the X-ray diffraction analysis methods. Crystals, 12(4), 566.
9. Welegergs, G. G., Gebretinsae, H. G., & Tsegay, M. G. (2023). Single-layered biosynthesized copper oxide (CuO) nanocoatings as solar selective absorber. Applied Sciences, 13, 1867.

Advanced Engineering Days

aed.mersin.edu.tr

Investigating the physical properties of carbon nanotubes modified by plasma method

Mohaddeseh Mousavi*[1], Fatemeh Baharlounezhad [2], Mohammad Ali Mohammadi [3] Nazila Mahmoudian [4]

[1]University of Tabriz, Department of Physics, Iran, m.mousavi@tabrizu.ac.ir, f.baharlou@tabrizu.ac.ir, mohammadidorbash@yahoo.com, nazilamahmoudian@gmail.com

Cite this study: Mousavi, M., Baharlounezhad, F., Mohammadi, M., & Mahmoudian, N. (2024). Investigating the physical properties of carbon nanotubes modified by plasma method. Advanced Engineering Days, 9, 652-654

Keywords
Carbon Nanotubes
Modify
Plasma
Radio frequency

Abstract

Multi-walled carbon nanotubes tend to accumulate due to their hydrophobic surface. Therefore, they are functionalized with different groups for better dispersion in solutions, which causes their surface to be modified and hydrophilic. In this research, the hydrophobic surface of multi-walled carbon nanotubes became hydrophilic with a certain salt in the presence of oxygen radio frequency plasma. The results of scanning electron microscope, X-ray energy diffraction spectroscopy, and contact angles surface of the modified samples were investigated in an optimal time (6 min). The results of field emission scanning electron microscopy analysis showed a diameter increase after modification. A systematic study by Fourier transform infrared spectroscopy measurement confirmed the attachments of functional groups to the surface of multi-walled carbon nanotubes which decreased the contact angle and led transformation of hydrophobicity property to hydrophilicity property of multi-walled carbon nanotubes surface.

Introduction

After the discovery of carbon nanotubes (CNTs) in 1991, researchers have been trying to better understand their fundamental properties and applications in various fields of science and technology. The main obstacles to investigate the possibility of commercial applications of CNTs are lack of control over chirality, insolubility in almost all solvents, impurities and defects related to growth, formation a mass/package resulting in poor scattering. In order to overcome these disadvantages, researchers have adopted various approaches, such as adjusting the physicochemical properties by covalently attaching chemical groups through wet oxidation, air oxygen, ozone oxidation and plasma oxidation [1] leads to the formation of hydroxyl and carboxyl groups on the nanotubes surface.

Carbon nanotubes are one of the crystalline allotropes of carbon. Carbon nanotubes can be considered as thin sheets of graphene (graphite monolayer), which are in form of tubes with open or closed ends [2]. The application of CNTs faces several challenges, mainly due to the hydrophobic nature of carbon and the formation of long knots stabilized by van der Waals interactions between nanotubes [3]. Many methods including the creation of functional groups on the surface of carbon nanotubes in a covalent and non-covalent way can be used to improve the interaction between nanotubes and the solvent matrix and to facilitate their application.

Chemical modifications, such as oxidation by inorganic acids, covalently apply functional groups to the surface of CNTs [4]. Due to the harsh conditions of wet chemical methods, the structure of nanotubes may be damaged and their length shortened. The thermal conductivity of CNTs depends on the length, and reducing the length affects its conductivity [5]. So, alternative methods with relatively mild conditions such as plasma functionalization can be suggested. Plasma functionalization is known as an attractive technique because of flexible, fast and non-polluting [6]. Functional groups applied to the surface of nanotubes increase their properties such as dispersion in organic and aqueous solutions and polymer matrices. The main purpose of plasma functionalization is to modify the surface properties without changing the bulk properties. In other words, plasma functionalization causes less damage to the structure of nanotubes.

Material and Method

Trifluoroacetic acid with the chemical formula (CF_3COOH), potassium hydroxide (KOH) from Merck, and multi-walled carbon nanotubes (MWCNTs) from US Nanomaterials Research Company were prepared. The amount of 0.1 mol of each trifluoroacetic acid and potassium hydroxide were mixed together in 50 ml of distilled water on a magnetic stirrer at 50 °C to produce intended salt. KOH was gradually added to (CF_3COOH) until pH=9 under ($CF_3COOH+KOH \rightarrow CF_3COOK+H_2O$). The amount of 0.04 gr of MWCNTs with about 20-30 nm outer diameter and about 5-10 nm inner diameter and 0.2 gr salt were placed on a separate microscope slides. "Figure 1" demonstrates the experimental setup of radio frequency (RF) induction discharge by oxygen gas. The slides were placed inside the vacuum chamber of RF plasma reactor. Electric discharge via RF power supply was performed with 50 W, initial pressure of 0.05 Torr, final pressure of 0.06 Torr and oxygen gas for an optimal time 6 min. The structural and physical properties of the MWCNT surface were investigated by scanning electron microscope (SEM) and contact angle after plasma modification. Elemental analysis was done by fourier transform infrared spectroscopy (FTIR).



Figure 1. Experimental setup of RF discharge by oxygen gas

Results

"Figure 2 (a) and (b)" shows the SEM images of before and after modifying MWCNTs by RF oxygen plasma, respectively. "Figure 2" shows SEM images of MWCNTs before and after surface plasma modification. The average diameter of MWCNTs was measured by Digimizer software before (d_{av}=19.774 nm) and after (d_{av}=65.522 nm) surface plasma modification. According to SEM images, the difference in surface morphology between plasma-modified and pure samples was observed. MWCNTs surfaces were smooth and flat before plasma modification. After plasma modification, MWCNTs surfaces became rough, while the integrity of the pattern was maintained.

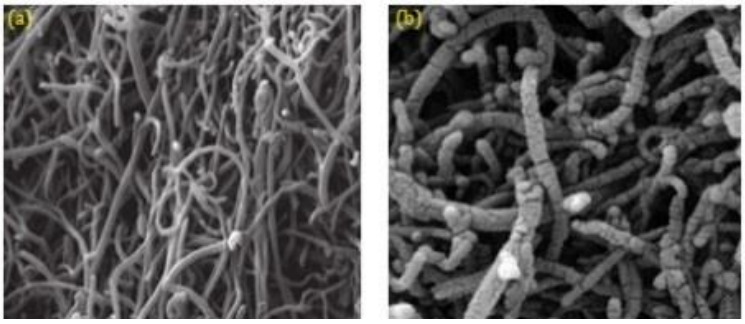


Figure 2. SEM images of MWCNTs (a) before and (b) after surface modification

According to the FTIR results in "Figure 3" and existence of peaks between salt solution and pure nanotubes peaks after RF plasma modification, it was observed that the salt interacted covalently with the surface of multi-walled carbon nanotubes [7].

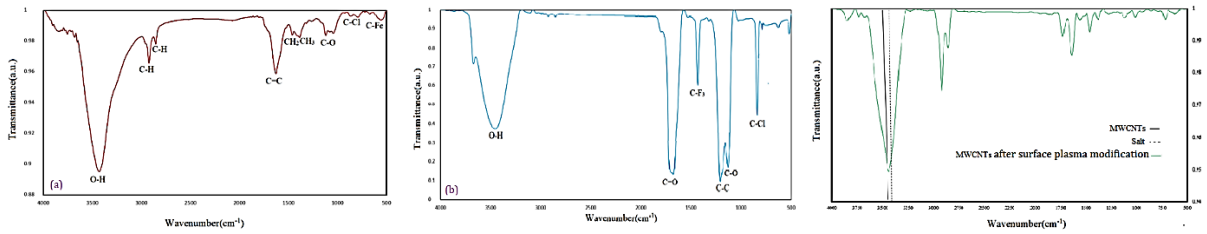


Figure 3. FTIR images of the nanostructure of multi-walled carbon nanotubes (a) pure MWCNTs, (b) salt (c) MWCNTs after surface modification with RF plasma.

"Figure 3" shows that functional groups containing oxygen such as carbonyl and hydroxyl groups were formed during plasma treatment. The process of formation of groups containing oxygen (hydrophilicity factor) on the surfaces of multi-walled carbon nanotubes by RF plasma was in form of O-C=O and C-O-C bonds C≡C, C-F_3 and C=O. It indicated that the salt completely was applied on the surface of carbon nanotubes by RF plasma. The wavelengths of peaks observed in RF oxygen plasma modification are shown in Table 1.

Table 1. Wavelength of peaks observed in pure MWCNTs and MWCNTs after surface modification with RF plasma.

C=O	C-F	C≡ C	C-O-C	O-C=O	Sample
-	-	-	-	-	pure MWCNTs
1802.35	1062.07	2245.91	1166.51	1432.37	MWCNTs after surface modification with RF plasma

Digital microscope images in "Figure 4" showed decreasing the contact angle of CNTs from $\theta_c = 112^\circ$ to $\theta_c = 33.69^\circ$ after oxygen plasma exposing, which indicates an increase in the hydrophilicity of CNTs surface.

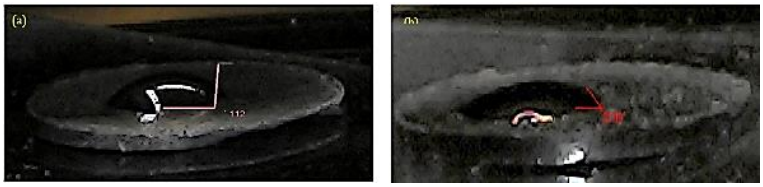


Figure 4. Contact angle images of MWCNTs (a) before and (b) after surface plasma modification

Discussion

According to the analysis, the modified sample with RF oxygen plasma had better results compared to the pure sample. An increase in MWCNTs diameter after plasma modification indicated the thicker surface of carbon nanotubes due to salt elements transfer on the surface of carbon nanotubes. Elemental analysis showed that peaks of hydrophilic groups were observed after surface plasma modification on carbon nanotubes. The results indicate that in the plasma method, the surface of carbon nanotubes has become more active, so it can be concluded that the hydrophilicity of carbon nanotubes was higher in the plasma method, and finally, the surface energy of carbon nanotubes has decreased in the plasma method [8]. Decreasing the contact angle of the CNTs after plasma modification displayed the surface energy decreasing of CNTs and increasing adhesion and wettability of multi-walled carbon nanotubes.

Conclusion

The results of SEM, EDAX, FTIR and contact angle analysises showed that plasma modification of multi-walled carbon nanotubes created hydrophilic functional groups on the surface of CNTs in a short time and without any pollution. In this method, the modification was carried out in only one step simultaneously maintaining the main structure of the multi-walled carbon nanotubes. The oxygen gas flow and used salt had a significant effect on the atomic contents, structural properties and surface modification of carbon nanotubes, which were effective in increasing the hydrophilicity of the MWCNTs surface.

References

1. Byl, O., Liu, J., & Yates, J. T. (2005). Etching of carbon nanotubes by ozone a surface area study. Langmuir, 21(9), 4200-4204.
2. Serp, P., Corrias, M., & Kalck, P. (2003). Carbon nanotubes and nanofibers in catalysis. Applied Catalysis A: General, 253(2), 337-358.
3. Niyogi, S., & et al. (2002). Chemistry of single-walled carbon nanotubes. Accounts of Chemical Research, 35(12), 1105-1113.
4. Marshall, M. W., Popa-Nita, S., & Shapter, J. G. (2006). Measurement of functionalised carbon nanotube carboxylic acid groups using a simple chemical process. Carbon, 44(7), 1137-1141.
5. Datsyuk, & et al. (2008). Chemical oxidation of multiwalled carbon nanotubes. *carbon*, *46*(6), 833-840.
6. Meng, F. Y., Ogata, S., Xu, D. S., Shibutani, Y., & Shi, S. Q. (2007). Thermal conductivity of an ultrathin carbon nanotube with an X-shaped junction. *Physical review B*, 75(20), 205403.
7. Karousis, N., Tagmatarchis, N., & Tasis, D. (2010). Current progress on the chemical modification of carbon nanotubes. *Chemical reviews*, *110*(9), 5366-5397.
8. Mishra, P., & Islam, S. S. (2013). Surface modification of MWCNTs by O_2 plasma treatment and its exposure time dependent analysis by SEM, TEM and vibrational spectroscopy. *Superlattices and Microstructures*, *64*, 399-407.

Advanced Engineering Days

aed.mersin.edu.tr

The plasma synthesis and treatment of tungsten oxide nanoparticles

Fatemeh Baharlounezhad*[1], Mohammad Ali Mohammadi [1]

[1] *University of Tabriz, Faculty of Physics, Tabriz, Iran, f.baharlou@tabrizu.ac.ir, Mohammadidorbash@yahoo.com*

Cite this study: Baharlounezhad, F., & Mohammadi, M. A. (2024). The plasma synthesis and treatment of tungsten oxide nanostructures. Advanced Engineering Days, 9, 655-657

Keywords
Plasma
Nanoparticle
Tungsten trioxide

Abstract

Nanostructured tungsten oxide has attracted considerable attention due to its wide range of technology and applications and notable properties. In this study, tungsten oxide nanoparticles were synthesized by the atmospheric pressure glow discharge and treated by low-pressure radio frequency discharge. The results of X-ray diffraction analysis confirmed the higher crystallinity of treated nanoparticles with smaller crystallite (16.831 nm). SEM imaging showed smaller treated (25-35 nm) nanoparticles than synthesized nanoparticles (30-50 nm). Ultraviolet-visible diffuse reflectance spectroscopy presented higher absorbance of the treated sample in comparison to synthesized nanoparticles resulting in higher semiconducting properties. Energy dispersive X-ray results confirmed the production of $WO_{(3-x)}$ nanoparticles as a result of WO_3 nanoparticles treatment.

Introduction

Nonequilibrium, nonthermal, or cold plasma is generated when electrical energy is applied to a gas, causing a partial ionization of the gas comprising ions, electrons, ultraviolet photons, and reactive neutrals such as radicals, excited and ground-state molecules [1]. Plasma technology has been involved in various applications for a long time, including high-quality nanomaterials manufacture. The plasma-liquid interaction provides two effective methods of producing plasma inside and on the surface of the liquid for the synthesis of nanomaterials [2-3]. In both methods, nanoparticles (NPs) can be obtained in a short process that reduces contaminations. Cold low-pressure plasma treatment is also a useful method without adding an initiator or solvent. It has less pollution, a short time process, easy operation, high efficiency, and safety [4].

Tungsten oxide structures include cubic, triclinic, monoclinic, orthorhombic tetragonal, and hexagonal which have high melting temperature, photo electrochromic, toughness, and mechanical properties. WO_3 is the highest state of tungsten oxide. The ratio of oxygen in WO_3 is usually expressed as WO_{3-x}. Tungsten oxide is a wide band gap semiconductor with excellent conductivity, and high electron hall mobility, which is considered a candidate material for application in optoelectronics, electrochemical, photoelectrochemical, hybrid photocatalysts, electrochemical energy storage, and gas sensors [5].

In this study, tungsten oxide nanoparticles were synthesized via an atmospheric pressure glow discharge interaction with water. WO_3 NPs were treated by low-pressure radio frequency (RF) plasma. The products were analyzed by X-ray diffraction (XRD), field emission scanning electron microscopy (FE-SEM), energy dispersive X-ray (EDX), and ultraviolet-visible diffuse reflectance spectroscopy (UV-Vis-DRS). Elemental analysis was done by fourier transform infrared spectroscopy (FTIR).

Material and Method

In the first step, tungsten oxide nanoparticles were synthesized by interacting air atmospheric pressure DC plasma with the water surface at 9 kV for 10 min. In the second step, the synthesized WO_3 nanoparticles were exposed to Argon RF plasma 13.56 MHz with a power of 50W at 10^{-3} Torr for 14 min. “Figure 1” (a) and (b) show the experimental setup to synthesize and treat nanoparticles. Morphology and elemental analysis were performed through field emission scanning electron microscopy (MIRA3 FEG-SEM). The Band gap was calculated by diffuse reflectance spectroscopy (Evolution 220). The crystal structure of the sample was done via X-ray diffraction (TD-3700).

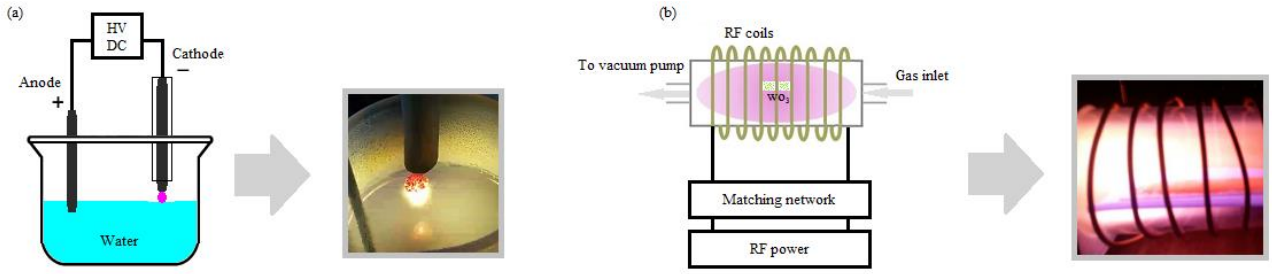


Figure 1. Experimental setup to synthesize and treat nanoparticles

Results

"Figure 2" shows the XRD spectra of the synthesized and treated nanoparticles. Sharp diffraction peaks were at $2\theta = 23.16$, $2\theta = 23.62$, $2\theta = 24.34$, $2\theta = 33.36$ and $2\theta = 34.12$ before RF, assigned to (002), (020), (200), (022), and (202) lattice planes of monoclinic WO_3 respectively [3]. After RF plasma exposing, peaks shifted slightly to 2θ=23.22, 2θ=23.70, 2θ=24.38, 2θ=33.38 and 2θ=34.16. The crystal domain size of WO_3 for the broadening of the prominent peak (200) was estimated using Debye–Scherer's equation, $D=k\lambda/\beta \cos\theta$, where D is the volume average crystallite size of the particles, k is Debye–Scherer constant, λ is the X-ray wavelength, β is (FWHM) of the diffraction peak, and θ is the diffraction angle. D was obtained using the width of the largest and most symmetrical peak for synthesized and treated samples equal to 19.979 nm and 16.831 nm, respectively. The dislocation density of synthesized and treated samples, δ_{np}, was determined by equation $\delta_{np}=1/D^2$ equal to 0.003 nm^{-2} and 0.004 nm^{-2}, respectively.

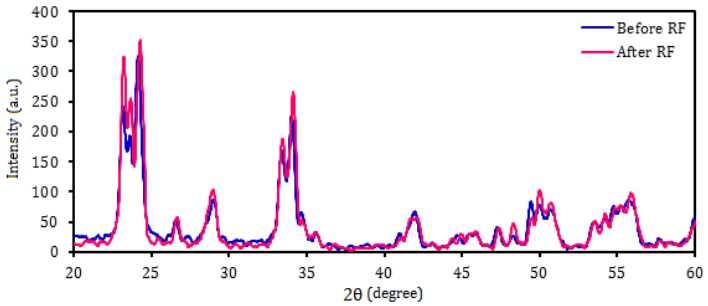


Figure 2. X-ray diffraction spectrum of synthesized and treated WO_3 nanoparticles

"Figure 3" demonstrates DRS spectra of synthesized and treated WO_3 nanoparticles. Absorption in the treated NPs has increased compared to the synthesized NPs, causing the optical band gap enhancement from 2.82 eV to 2.88 eV according to Tauc plot.

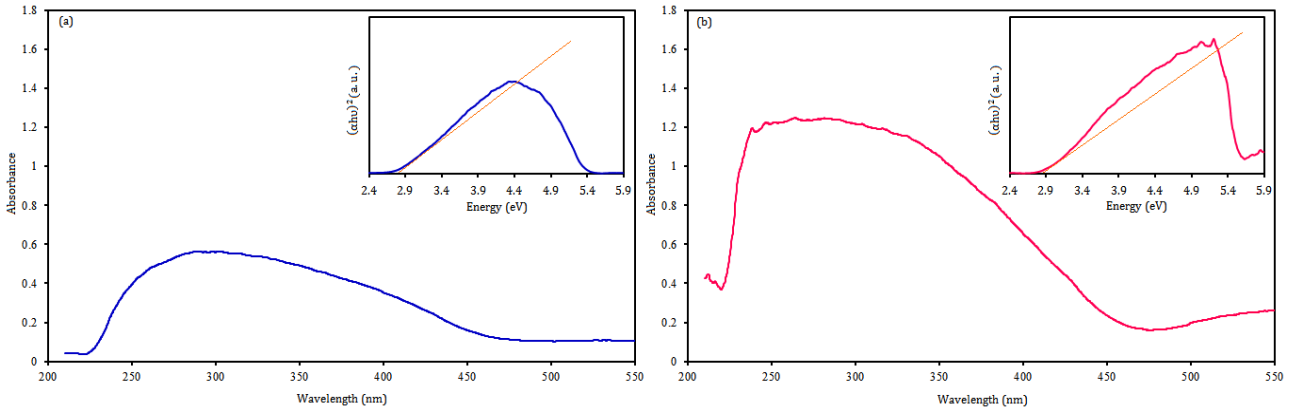


Figure 3. UV-Vis-DRS spectrum and band gap analysis of (a) synthesized and (b) treated WO_3 nanoparticles

"Figure 4" exhibits the images of FESEM/EDX analyses of the synthesized and treated WO_3 spherical nanoparticles. The average diameter of synthesized and treated NPs was estimated at 30–50 nm and 25-35 nm, respectively. The weight and atomic percentages of oxygen and tungsten elements obtained showed a decrease in the atomic ratio of oxygen to tungsten after RF plasma.

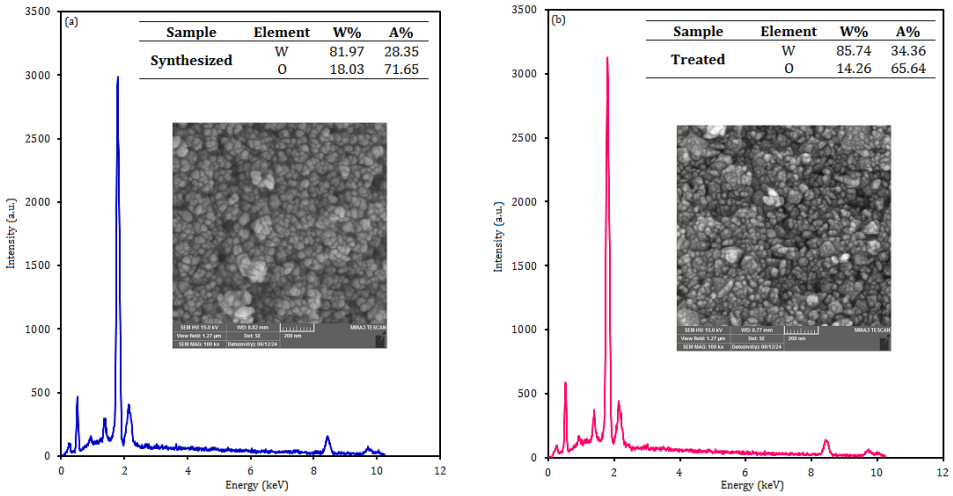


Figure 4. Images of FESEM and EDX analyses of (a) synthesized and (b) treated WO_3 nanoparticles

Discussion

The intensity of the peak is related to the number of atoms in the crystal that can scatter X-rays. The different peak intensities can demonstrate the difference in the material crystallinity. Crystallinity refers to the structural order degree in a solid which also has a large affection on hardness, density, transparency, and diffusion. Higher peak intensity indicates more atoms in the crystal. As a result, the treated samples had a higher crystallinity degree than the synthesized samples [6]. The crystallite size of treated nanoparticles decreased in comparison to the synthesized nanoparticles. Dislocation density presents the degree of crystallinity of the nanoparticle profile. Based on the results, the dislocation density of the nanoparticles obtained in this study was quite small. Small dislocation density indicates a high crystallinity degree. Treated tungsten oxide spherical NPs were smaller in size than synthesized NPs. Reduction of weight and atomic percentages reported WO_{3-x} producing from WO_3.

Conclusion

Although cold plasma has formerly been used very well for nanomaterials synthesis and treatment, more efforts should be made to optimize and expand the role of cold plasma in this field with a comprehensive understanding. In this study, an atmospheric glow discharge technique to synthesize and a low-pressure RF plasma for the treatment of WO_3 NPs were used. The WO_3 spherical nanoparticles were synthesized in the range of 30–50 nm and treated in the range of 25-35 nm. A higher absorption, optical band gap, and semiconducting properties were obtained for treated NPs than synthesized NPs. Smaller crystallite was calculated for treated NPs than synthesized NPs. WO_3 nanoparticles treatment caused WO_{3-x} nanoparticles production.

References

1. Hasirci, V., & Hasirci, N., (2005). 2 - Control of polymeric biomaterial surfaces. Surfaces and Interfaces for Biomaterials. ISBN: 978-1-85573-930-7.
2. Saito G., & Akiyama, T. (2015). Nanomaterial synthesis using plasma generation in liquid, Journal of Nanomaterials. 2015, 23696, 1-21.
3. Baharlounezhad, F., Mohammadi, M. A. & Zakerhamidi, M. S. (2023). Plasma-based one-step synthesis of tungsten oxide nanoparticles in short time. Scientific Reports, 13(1), 7427.
4. Wang, R. M., Zheng, S. R., & Zheng, Y. P., (2011). 4 - Interface of polymer matrix composite. Polymer Matrix Composites and Technology, ISBN: 978-0-85709-221-2.
5. Yao, Y., Sang, D., Zou, L., Wang, Q., & Liu, C., (2021). A review on the properties and applications of WO_3 nanostructure-based optical and electronic devices. Nanomaterials (Basel). 11(8), 2136.
6. Pandurangarao, K., & Kumar, V. R. (2019). Preparation and characterization of nanocrystalline tungsten oxide thin films for electrochromic devices: effect of deposition parameters, Materials Today: Proceeding. 19(6), 2596-2603.

Advanced Engineering Days

aed.mersin.edu.tr

Adapting cities to climate change

Mahmoud Asoude Khyal [*1], **Nasser Mashganbari** [1], **Ali Hamedi** [1] **Hassan Mahmoodzadeh** [1]

[1] *Tabriz University, Department of Urban and Regional Planning, Iran, m.asodeh@yahoo.com, naser.moshghanbari.original@gmail.com, ali1379hamed@gmail.com, hassan.mahmoudzadeh@gmail.com*

Cite this study: Khyal, M. A., Mashganbari, N., Hamedi, A., & Mahmoodzadeh, H. (2024). Adapting cities to climate change. Advanced Engineering Days, 9, 658-660

Keywords
Climate
City
weather

Abstract

As one of the great challenges of the 21st century, climate change has profound effects on cities and communities. Cities, as the main centers of economic, social and cultural activities, are directly affected by climate change, which can have long-term losses on them. This abstract studies and examines different strategies for adapting cities to climate change. In this review, we will examine the economic, social and technical measures at the urban level to reduce the negative effects and increase urban resistance against these changes. Among the actions of this survey, we can mention the development of green infrastructure, improvement of irrigation and sewage systems, creation of urban green spaces, increase of urban flexibility and strengthening of preparedness to face sudden events such as flood and drought. By examining these issues, this abstract shows that adaptation of cities to climate change is not only necessary but can help cities to improve sustainability and quality of life for citizens.

Introduction

Climate change, as one of the big and complex challenges today, has profound effects on cities, communities, and the environment. With the expansion of urbanization and the increase of cities facing natural risks, cities, as the main axes of economic, social and cultural activities, have been directly affected by climate change. These changes include an increase in temperature, a change in precipitation patterns, widespread flooding, multiple droughts, and an increase in the frequency of sudden weather events that have adverse effects on the lives of citizens and urban infrastructure.

In this introduction, the importance and necessity of adaptation of cities to these climate changes is discussed. The concept of adaptation here means the ability of cities to respond to different climatic challenges and increase resistance against these challenges. It includes economic, social, technical and political measures that help cities to manage and control changing and complex climate situations.

Also, this introduction examines the various dimensions of this challenge and shows that adaptation of cities to climate change is not only necessary, but it can facilitate the improvement of urban sustainability, increase flexibility, and create more resilient cities. In this regard, the necessity of adopting appropriate management policies and programs to preserve water resources, optimize energy use, strengthen urban infrastructure structures, and promote environmental and economic cultures has been emphasized.

Material and Method

The research method of the present study is descriptive-analytical, and data collection related to the history of climate change has been prepared from various sources, including meteorological stations, government reports, and scientific articles, which in this regard

Assessing the effects of climate change on urban infrastructure:Investigating the effects of climate change on urban infrastructure, including water and sewer networks, public transportation systems, and residential and commercial buildings.

Examining adaptive solutions: Investigating and evaluating adaptive solutions to deal with the adverse effects of climate change, including the development of water management systems, improving renewable energy, and creating urban green spaces.

Results

According to the research done on the adaptation of cities to climate change, the following results stand out:
1. Climate change analysis:
- Accurate assessment of temperature changes, precipitation pattern, sea level and other climatic parameters in different cities.
2. Effects on urban infrastructure:
- Investigating the effects of climate change on urban infrastructure such as water and sewage networks, transportation systems, buildings and its impact on urban water security and local economy.
3. Adaptive solutions:
- Introduction and assessment of solutions tailored to each city to adapt to climate change, including infrastructure measures, development of water management systems, use of renewable energy, and promotion of urban resilience.
These results show that adaptation of cities to climate change is not only necessary, but can also guarantee the improvement of urban sustainability and the quality of life of citizens. Using these results, it is possible to formulate and implement appropriate policies and programs for better management of these challenges so that cities can resist climate changes and respond to these changes in a good way.

Discussion

In the discussion related to adapting cities to climate change, various factors that should be considered and are important can be as follows:

1. Adaptive solutions:
In this section, different strategies for adapting cities to climate change should be investigated. This includes developing resilient water and wastewater management systems, using renewable energy, developing urban green spaces, improving building energy, and creating food security strategies.
2. Citizen participation and social management:
It should be noted the importance of citizens' participation in the process of adapting cities to climate change, and the role of social management in creating effective measures to deal with climate challenges. This includes education and awareness raising, stimulating local resource productivity, and developing social networks to support the adaptation process.
3. Risk management and continuous monitoring:

Finally, the importance of risk management and continuous monitoring of the effects of climate change on cities and evaluation of the progress and effectiveness of adaptive solutions should be addressed. This assessment allows cities to recover in the long term and choose the best strategies to deal with climate change.

In general, the discussion about the adaptation of cities to climate change requires a broad look at the different dimensions of this challenge, which can help sustainable urban development and improve the quality of life of citizens.

Conclusion

Climate change, as one of the biggest challenges of the contemporary era, has significantly affected cities and their communities. In this study, we examined and evaluated the requirements and solutions that are necessary for cities to adapt to these climate changes.

Among the most important results of this research is the necessity of developing and implementing suitable adaptive strategies to increase urban resistance against climate change. Solutions that include improving water and sewage systems, renewable energy, developing green spaces and creating flexible urban management policies.

Also, this research clearly showed that by increasing awareness and participation of citizens, and facilitating access to new resources and technologies, cities can significantly improve in facing climate change and increase their resilience.

As a conclusion, in order to maintain stability and improve the quality of life in cities, we need to take thoughtful and comprehensive measures to adapt cities to these challenges, considering climate changes. These measures can not only reduce the vulnerability of cities, but also help cities to be recognized as models for sustainability and resistance to climate change and be ready for future developments.

References

1. IPCC Special Report on Cities and Climate Change (2018) - Intergovernmental Panel on Climate Change
2. Climate Change and Cities: First Assessment Report of the Urban Climate Change Research Network (2011) - Cambridge University Press
3. Urban Climate Resilience in Theory and Practice (2016) - Springer
4. The Economics of Climate Resilient Development in Cities: A Conceptual Framework (2012) - The World Bank
5. Climate Change Adaptation in Urban Areas: Best Practices and Lessons Learned (2018) - Routledge

Advanced Engineering Days

aed.mersin.edu.tr

Water resource management and the effects of reducing rainfall in cities

Ali Hamedi [*1], Mahmoud Asoude Khyal [1], Hassan Mahmoodzadeh [1] Reza Mahdinia [1]

[1]Tabriz University, Department of Urban and Regional Planning, Iran, m.asodeh@yahoo.com, ali1379hamed@gmail.com, hassan.mahmoudzadeh@gmail.com, rezamahdinia10@gmail.com

Cite this study: Hamedi, A., Khyal, M. A., Mahmoodzadeh, H., & Mahdinia, R. (2024). Water resource management and the effects of reducing rainfall in cities. Advanced Engineering Days, 9, 661-663

Keywords
Rain
Water resources
City

Abstract

The reduction of precipitation as one of the effects of climate change has created challenges for cities that require the use of new management strategies. This article examines the effects of reduced rainfall on water resources and urban infrastructure and provides solutions for optimal management of these challenges.First, we analyze the direct consequences of reduced precipitation on urban water resources, including reductions in freshwater resource levels, impacts on groundwater quality, and increased risk of water scarcity. Then, we examine how these changes lead to challenges such as reduced water quality, increased water treatment costs, and threats to water supply sustainability.In the following, various management solutions to deal with these challenges are examined. These solutions include modifying urban water consumption patterns, using smart water management technologies, and promoting the use of alternative water sources and documented water management.In general, this article pays attention to the effects and challenges of reducing rainfall on urban water resources and provides solutions for the optimal management of these challenges, which can help the sustainable development of cities and cope with climate change.

Introduction

As one of the major global challenges, climate change has profound effects on the environment and urban infrastructure, especially in the field of water resources and precipitation. The reduction of precipitation in different parts of the world, especially on cities as the main population and economic centers, has had a significant impact, which requires intelligent and integrated management of water resources.

As a vital economic and social center, cities are more dependent on water resources than ever before. Population growth, industrial development, and changes in water consumption patterns are only part of the challenges we face in terms of managing water resources in the context of decreasing rainfall. Also, irregular rainfall fluctuations and losses caused by droughts and floods have gradually caused instability in urban water supply.

This introduction deals with a deeper investigation of the effects of reducing rainfall on urban water resources and raises the basic requirements for formulating appropriate management strategies and solutions. For this purpose, we can mention changing water consumption patterns, optimizing water storage and purification systems, and using new technologies for intelligent water management. The purpose of this research is to provide solutions that will help city managers and decision makers to adopt the best strategies to deal with climate challenges and maintain the sustainability of water resources in cities.

Material and Method

To investigate the management of water resources and the impacts of reduced precipitation in urban areas, a systematic approach was adopted. The study focused on collecting and analyzing relevant data to understand the current water availability and demand dynamics in urban settings under changing precipitation patterns.

Data Collection

Meteorological Data: Historical precipitation records were obtained from local meteorological stations to assess long-term trends and variability in rainfall patterns. Water Supply Data: Information regarding water

sources, reservoir levels, and water distribution networks was gathered from municipal water authorities and relevant agencies.Demographic and Economic Data: Population growth rates, urban development trends, and economic indicators were collected to understand the water demand projections and socio-economic impacts.

Methodology: Statistical Analysis: Statistical methods, including trend analysis and regression modeling, were applied to analyze historical precipitation data and predict future trends.

Hydrological Modeling: Hydrological models such as rainfall-runoff models were used to simulate the impact of reduced precipitation on water availability in urban catchments. Scenario Planning: Different scenarios of future climate change and precipitation patterns were developed to assess their potential impacts on water resources and urban water management strategies. Case Studies: Case studies of selected urban areas were conducted to examine successful water management practices and lessons learned in mitigating the effects of reduced precipitation. Stakeholder Engagement: Consultations with local authorities, community groups, and stakeholders were conducted to incorporate local knowledge and perspectives into the research findings.

Results

The results of rainfall reduction can affect the management of water resources in cities in different ways. Below we examine some of these effects:

1. Reduction of fresh water resources: A decrease in precipitation can lead to a decrease in the supply of fresh water resources, because the lack of water in watersheds and rivers can increase the demand for fresh water in cities.
2. Increased demand for water reuse: In response to the scarcity of fresh water resources, there may be an increased need for more water treatment and water reuse technologies (such as greywater).
3. Social and economic problems: A decrease in rainfall can lead to economic and social problems in cities due to limited water resources, including rising prices and social dissatisfaction.
4. Management of water applications: the need for more accurate and efficient management of the use of water resources, including the distribution of resources and the control of water wastage in irrigation networks and water and sewage networks.
5. Effects on the environment: Lack of water resources can lead to changes in local ecosystems, especially watersheds, which can include reducing biodiversity and increasing environmental stress.
6. The need for crisis management policies: Cities need to develop crisis management policies to apply the best methods to manage the lack of water resources in conditions of reduced rainfall.

As a result, the reduction of precipitation can require the design of water resources management in cities according to the new challenges that arise.

Discussion

Water resource management in cities is one of the main challenges in dealing with climate change and reducing precipitation. Here, we examine some dimensions and impacts of rainfall reduction on water resource management in cities:

1. Decreasing fresh water resources:** The decrease in precipitation leads to the lack of fresh water resources, which is necessary for urban and industrial water supply. This issue requires the optimal use of water purification and reuse technologies, including gray water.
2. Increasing demand for water reuse:** As fresh water resources decrease, the need to develop water reuse systems (such as gray water) and the development of water treatment and reuse technologies increases.
3. Parallel management of water resources:** As precipitation decreases, cities need to develop strategies for parallel management of water resources, including strengthening storage infrastructure, strengthening aquatic ecosystems, and creating sustainable water resource exploitation systems.
4. Crisis Management and Response Strategies:** Cities need to develop crisis management policies and plans to deal with sudden changes in water supply, including developing prevention systems, carefully managing water resources during water shortages, and developing emergency plans for Water supply in critical conditions.
5. Effects on the environment and ecosystems:** Reduced precipitation can lead to negative impacts on local ecosystems, including reduced water flows, reduced biodiversity, and increased environmental stresses.

According to these points, the management of water resources in cities requires an integrated and coordinated approach between economic, social and environmental. The development of sustainable policies to manage water resources and respond to the challenges of reducing rainfall is of great importance in order to reduce the negative effects of this phenomenon and act for a more sustainable future in cities.

Conclusion

The management of water resources in cities in the face of changes caused by the reduction of precipitation is a very basic and complex challenge that requires new approaches and effective policies. This issue has wide effects on urban communities and the environment, which should be examined according to its different dimensions.

With the decrease in rainfall, we first need to carefully check the sources of fresh water in the cities. The lack of fresh water resources can lead to serious problems in providing water for urban consumers. For this purpose, it is necessary to develop and optimize water treatment and reuse technologies, including gray water.

In addition, we need to develop parallel management strategies for water resources. This includes strengthening storage infrastructure, improving the efficiency of irrigation systems and water and sewage networks, and developing systems for sustainable exploitation of water resources.

Due to the limitation of fresh water resources, we need optimal use of new and sustainable technologies for urban and industrial water supply. These measures not only help to improve the quality of life of citizens, but also help to preserve the environment and continue the functioning of water ecosystems.

As a result, it is necessary to adopt inclusive, integrated and sustainable approaches for the effective management of water resources in cities under the conditions of decreasing rainfall. This includes the creation of crisis management policies and programs, strengthening cooperation between different institutions and continuous assessment of the water conditions of the regions in order to be able to respond to future challenges in the best possible way and to provide sustainable infrastructure for managing water resources in cities.

References

1. Gleick, P. H. (ed.) (2018). The World's Water, Volume 9: The Biennial Report on Freshwater Resources. Island Press
2. Bulkeley, H., & Betsill, M. M. (2005). Cities and Climate Change: Urban Sustainability and Global Environmental Governance. Routledge
3. World Bank. (2019). Water Scarce Cities: Thriving in a Finite World. World Bank Group
4. Schreurs, M. A., & Tiberghien, Y. (eds.) (2019). Urban Climate Politics: Agency and Empowerment. Cambridge University Press

Advanced Engineering Days

aed.mersin.edu.tr

The effects of urban management on green space: solutions and challenges: A case study of Tabriz city

Rogayeh Sharafi *[1] , **Mahmoud Asoude Khyal** [2], **Ali Hamedi** [1], **Hassan Mahmoodzadeh** [1]

[1] *University of Tabriz, Department of Urban and Regional Planning, Iran, Sharafirogayeh@gmail.com, m.asodeh@yahoo.com, ali1379hamed@gmail.com, hassan.mahmoudzadeh@gmail.com*

Cite this study: Sharafi, R., Khyal, M. A., Hamedi, A., & Mahmoodzadeh, H. (2024). The effects of urban management on green space: solutions and challenges: A case study of Tabriz city. Advanced Engineering Days, 9, 664-666

Keywords
Urban management
Green space
Citizen participation

Abstract

Urban management, as a fundamental factor in the formation and maintenance of green spaces in cities, has wide-ranging effects on the lives of citizens and the environment. These effects can be positive or negative and can be affected through different solutions and challenges. One of the positive effects of urban management on green space is increasing the quality of life of citizens. which increase mental and physical health, reduce stress and increase social communication. Also, proper management of green space leads to improvement of urban air quality and reduction of air pollution. However, inefficient management can reduce green space, neglect the biological needs of different species, and increase climate change. To solve these challenges, solutions such as: preserving and expanding green spaces, using new technologies to improve the management and sustainable use of natural resources, are necessary. In general, urban management can help improve the quality of life of citizens and preserve the environment. The current research is descriptive and analytical and by using the method of library study and other scientific sources, it deals with the effects of urban management on green spaces: solutions and challenges.

Introduction

Urban management is a very vital thing that affects the sustainable development and improvement of citizens' quality of life. In this regard, the importance of green space as one of the basic environmental and social elements of cities is undeniable. But the optimal management of green space faces its own challenges and solutions. In this introduction, the effects of urban management on green space, as well as solutions and challenges related to it, will be discussed.

Material and Method

The research method of the current research is descriptive-analytical using the method of library study and the review of previous documents and researches. Also, with the help of GIS software, the topic under study has been investigated and in the following sections, more explanation is given in relation to The topic of the research has been discussed.

Results

Urban management, as one of the key factors in the preservation and development of urban green spaces, requires detailed planning, the cooperation of various departments, and the active participation of citizens. By providing appropriate solutions and dealing with existing challenges, urban management can be improved and the quality of green spaces in cities can be increased. According to the current situation and the study of maps of the studied area with the help of GIS software, it is clearly possible to point out the lack of green space compared to the size and population of the metropolis of Tabriz, as well as the northern parts of Tabriz or... Regions like region 6 are in a bad situation in terms of green space per capita. According to the official statistics, green space per capita in Dartbriz is about 17 square meters, which is far away compared to the existing standards, which is

25 square meters. Also, using the calculations and analyzes carried out in the current research, the per capita green space is less than 17 meters. square, which indicates the unfavorable situation in this area. The nature of this research was to provide solutions and challenges related to the green space and gardens of Tabriz metropolis.

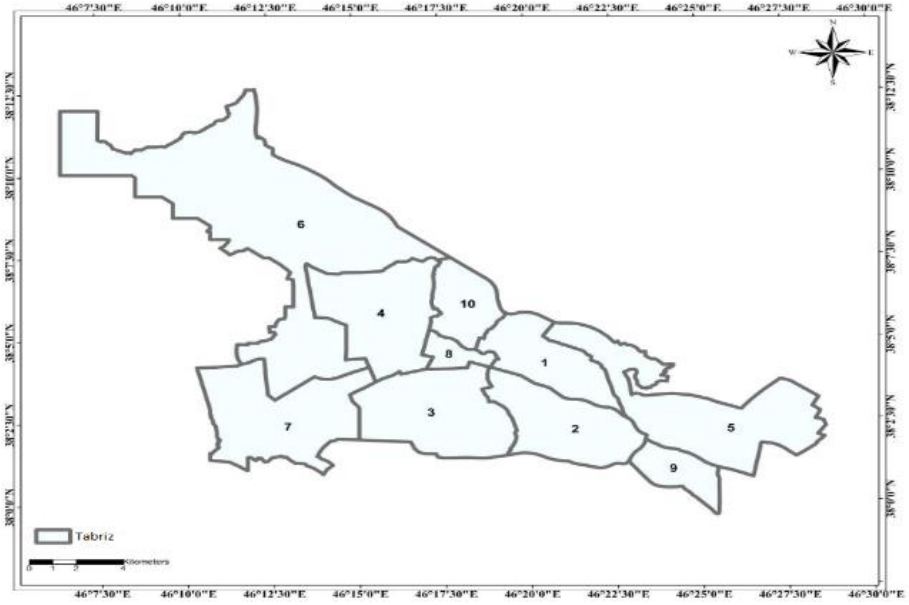


Figure 1.

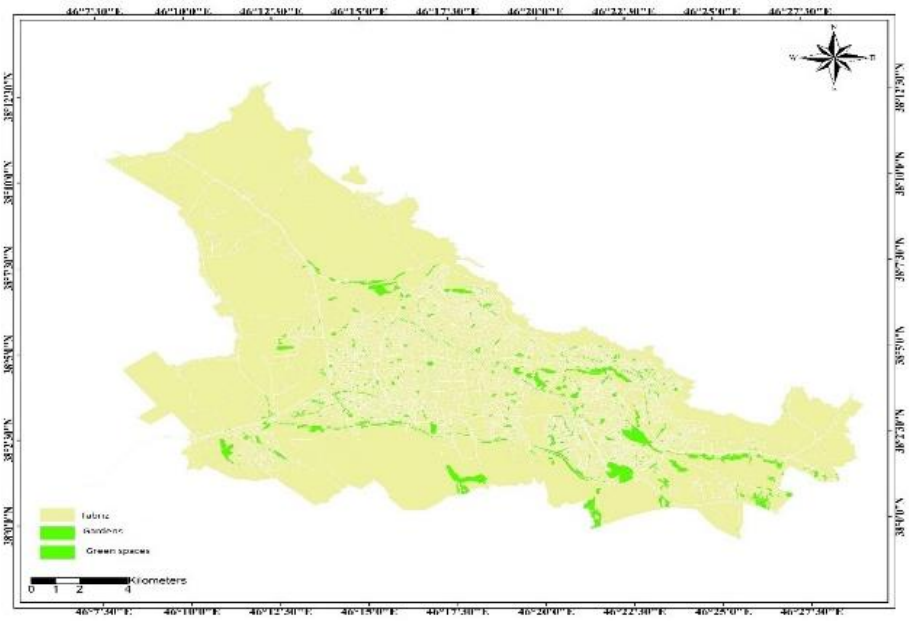


Figure 2.

Discussion

In this part of the research, using the available data and maps, as you can see in Figure 2, by showing the range and amount of green space in Tabriz city, it can be clearly said that based on previous research and analyzes done in this the research pointed out the lack of green space and its lack of proper management. In this regard, there are many challenges and solutions, which can be summarized as solutions such as:

Promoting cooperation between different departments of the municipality: cooperation between different departments of the municipality to implement plans and projects related to green space is one of the effective ways to improve urban management.

Training and knowledge sharing: training mayors and urban experts in the field of green space management and conducting more research in this field will facilitate the improvement of urban management.

Citizen participation:Creating opportunities for citizen participation in the decision-making process and implementation of projects related to green space is one of the ways to increase people's awareness and participation in urban management.

Regarding the challenges, we can also say:

Limitations of financial resources: The limitation of financial resources for the implementation of plans and projects related to green space is one of the main challenges in urban management.

Climate changes: Climate changes and unfavorable weather conditions can lead to the destruction of green space and its quality.

Unbalanced urban development: Unbalanced development and inattention to maintaining green space in the process of urban development can lead to the reduction of green space and the increase of problems related to it.

In general, according to the previous research and the current research, the need to plan and manage green spaces is an important and vital thing that is currently in an unfavorable situation.

Conclusion

In the field of previous studies related to or close to the present research, in terms of method, only the expression and definition of the issue and problem have been discussed and the majority of the solutions and suggestions presented have a repetitive or emphatic aspect, while in the present research, in addition to using Resources and suggestions related to the use of available data and maps. By using GIS software, one can clearly understand the problem of lack of green space compared to the size of Tabriz metropolis, and the only solution is effective planning and management. cannot be suggested in this regard.

References

1. Latinopoulos, D. (2022). "Evaluating the importance of urban green spaces: a spatial analysis of citizens' perceptions in Thessaloniki." Euro-Mediterranean Journal for Environmental Integration 7(2): 299-308.
2. Ilie, D. and S. Cosmulescu (2023). "Spontaneous Plant Diversity in Urban Contexts: A Review of Its Impact and Importance." Diversity 15(2): 277.
3. smarttogether.ir
4. Badiu, D. L., et al. (2019). "From "Red" to Green? A look into the evolution of green spaces in a post-socialist city." Landscape and Urban Planning 187: 156-164.
5. Jabbar, M., et al. (2021). "Assessing the role of urban green spaces for human well-being: A systematic review." GeoJournal: 1-19.

Advanced Engineering Days

aed.mersin.edu.tr

Narrative review of enzymatic oil refining

Afsaneh Ahansaz[*1]

[1]*University of Tabriz, Department of Food Science and Technology, Iran, aahansaz@tabrizu.ac.ir, a.ahansaz@gmail.com*

Cite this study: Ahansaz, A. (2024). Narrative review of enzymatic oil refining. Advanced Engineering Days, 9, 667-669

Keywords
Edible Oil Refining
Enzyme
Degumming
Biorefinery
Refinery

Abstract

Oil refining is operated due to eliminating undesirable compounds in crude oil, reducing loss of oil and suitable compounds and producing high quality oil. With enzymatic biorefinery process, producers can prevent oil loss and make high value-added products with this green method. The aim of this review is to study the trends of novel enzymatic refinery approaches and potential of its application in future.

Introduction

Enzymes, mainly phospholipases, are used to biorefining the extracted crude oil. Using enzyme in oil processing tends to save $1 billion with producing extra refined oil(Marchisio et al., 2023). Enzymatic degumming reduces total oil loss and waste water, running costs and the residue phosphorus (P) to less than 10mG/KG (Jiang, 2019). Environmentally, this technique eliminates damaging organic solvents and reduce wastewaters(Hou et al., 2020). specific enzymes for phospholipids are phospholipases phospholipase A1 (PLA1), A2 (PLA2), B (PLB), C (PLC) and D (PLD). Anti-lipase as protease is used for enzymatic interesterification and deacidification(Jiang, 2019). The aim of this study is to review narrative recombinant enzymes, novel methods of enzymatic refinery and their potential in future of oil industry.

Material and Method

All data about major key-words of refinery process stages, Enzyme, Biorefinery, and related synonyms are searched and screened among Abstract, Title and Keywords of paper from databases which are involved Web of Science, Springer, Science Direct, and Search engine of Google Scholar from 2019 up to 2024. The outline of paper was made. Then, Full texts of most related papers were collected, screened and skimmed to write the sections of this narrative review.

Results

Nowadays some commercial enzymes are used in researches and plants to refining the extracted oil such as Protease of ENZECO Fungal Protease and phospholipases mixture composed of PLA2, PLC, and phosphatidylinositol phospholipase C (PI-PLC)(dos Passos et al., 2022; Jiang, 2019). Novel Recombinant Enzymes are studied to refining oil. recombinant lysophospholipase from *P. abyssi* has high specificity and stability to high temperature. Novel PLC gene from *Thielavia terrestris* CAU709 was cloned and produced within *Pichia pastoris* which is stable against broad pH, elevated temperature and solvent residues(Nazir, Shad, Rashid, Azim, & Sajjad, 2024; Xiang, Wang, Yan, Jiang, & Yang, 2020). The other enzyme is cold-active PLC (AoPC) produced by *Aspergillus oryzae* that is the highest efficiency in oil degumming hence its application tends to save costs and energy(Sharma, Yadav, & Upadhyay, 2019; Wang, Hu, Jiang, Yan, & Yang, 2021).

Some recent novel methods of enzymatic refinery include hydrophobic ceramic membrane-enzyme binding, enzyme-Pickering emulsion catalytic system, ultrasound assisted aqueous enzymatic extraction and refining, moderate process, immobilized Bacillus cereus phospholipase C (PLCBC), magnetic immobilized enzyme (MDSNPCALB)(Dong et al., 2022; Guo, Wan, Huang, Wei, & Xiang, 2021; Hou et al., 2020; Li et al., 2021; T. Wang et al., 2021; Wei et al., 2022; Yu et al., 2022). These methods provide new insights to produce value-added products.

One of value-added products of enzymatic oil refining is rice bran oil (RBO) that contains γ-oryzanol, tocotrienol, and tocopherol; Lower TAG and high mono-(MAG), diglyceride (DAG), and high number of glycolipids

as emulsifier. Lysogums are other by-products of Enzymatic Degumming that refer to Lysophosphatidylcholine (LPC) and Lysophosphatidylethanolamine (LPE). Lecithin also is mentioned as an important value added by-product for biorefinery(Chakrabarti & Jala, 2019).

Limitations of enzymatic refining are: (1) costs of developing refining techniques such as enzymatic, membrane, nano refining; (2)rare studies about industrialization of enzymatic refinery; (3) Clinical ambiguity such as degenerative diseases even for enzymatic refined oils; (4) flux in large production as hindering parameter(Chakrabarti & Jala, 2019; Chew & Nyam, 2020; Fataneh Hashempour-Baltork, Farshi, Alizadeh, Azadmard-Damirchi, & Torbati, 2022; F. Hashempour-Baltork et al., 2023; Jiang, 2019).

Discussion

Enzymatic lipid post-treatment is possible for food products. In recent researches, Catalytic systems with Pickering Emulsions were used for deacidification of oils(T. Wang et al., 2021). In the other hand, Recombinant Enzymes such as TtPLC is a good candidate in oil refining industry(Xiang et al., 2020). The Potential Application of phospholipid refinery by-products in the food and pharmaceutical industries is noticed(Liu et al., 2023). It is feasible that antioxidant enzymes will be used for refined oils as soft degumming. Further Studies for Quality assessment of Cold-pressed oils in compare with enzymatic refined oils can show the level of its quality for safety. Probability of 3-MCPD esters in refined oils is another safety challenge that may be have another form with enzymatic refining. Effect of Enzymatic refinery on health and degenerative diseases and healthy compounds' content in oil such as tocopherols and phytosterols should be researched to compare with previous studies(Azizi-lalabadi, Mousavi, Piravi-vanak, & Azadmard-Damirchi, 2018).

Conclusion

Recombinant Enzymes are confirmed as good candidates for oil refining industry. efficient converting all the gums to their hydratable form is achieved by enzymatic degumming process(T. Wang et al., 2021). The lowest yield loss amongst all degumming methods is about Enzymatic biorefinery. ultrasound-assisted enzymatic refining products are high stable. As lower temperatures by enzymatic refining as higher quality of refined oils. economic feasibility of Enzymatic refined oils with high value-added by-products is probably defined.

References

Azizi-lalabadi, M., Mousavi, M.-M., Piravi-vanak, Z., & Azadmard-Damirchi, S. (2018). MCPD fatty acid esters in vegetable oils: formation, analysis and toxicology. *Journal of Food and Bioprocess Engineering, 1*(1), 71-80. Retrieved from https://jfabe.ut.ac.ir/article_74533.html

Chakrabarti, P. P., & Jala, R. C. R. (2019). Chapter 3 - Processing Technology of Rice Bran Oil. In L.-Z. Cheong & X. Xu (Eds.), *Rice Bran and Rice Bran Oil* (pp. 55-95): AOCS Press.

Chew, S. C., & Nyam, K. L. (2020). Refining of edible oils. In *Lipids and edible oils* (pp. 213-241): Elsevier.

Dong, T., Zhou, X., Dai, Y., Yang, X., Zhang, W., Yu, D., & Liu, T. (2022). Application of magnetic immobilized enzyme of nano dialdehyde starch in deacidification of rice bran oil. *Enzyme and Microbial Technology, 161*, 110116. doi:https://doi.org/10.1016/j.enzmictec.2022.110116

dos Passos, R. M., da Silva, R. M., de Almeida Pontes, P. V., Morgano, M. A., Meirelles, A. J., Stevens, C. V., . . . Sampaio, K. A. (2022). Phospholipase cocktail: A new degumming technique for crude soybean oil. *Lwt, 159*, 113197.

Guo, T., Wan, C., Huang, F., Wei, C., & Xiang, X. (2021). Process optimization and characterization of arachidonic acid oil degumming using ultrasound-assisted enzymatic method. *Ultrasonics Sonochemistry, 78*, 105720.

Hashempour-Baltork, F., Farshi, P., Alizadeh, A. M., Azadmard-Damirchi, S., & Torbati, M. (2022). Nutritional Aspects of Vegetable Oils: Refined or Unrefined? *European Journal of Lipid Science and Technology, 124*(12), 2100149. doi:https://doi.org/10.1002/ejlt.202100149

Hashempour-Baltork, F., Farshi, P., Mirza Alizadeh, A., Eskandarzadeh, S., Abedinzadeh, S., Azadmard-Damirchi, S., & Torbati, M. (2023). Effect of Refined Edible Oils on Neurodegenerative Disorders. *Adv Pharm Bull, 13*(3), 461-468. doi:10.34172/apb.2023.060

Hou, Z., Cao, X., Cao, L., Ling, G., Yu, Z., Pang, M., . . . Jiang, S. (2020). The removal of phospholipid from crude rapeseed oil by enzyme-membrane binding. *Journal of Food Engineering, 280*, 109910. doi:https://doi.org/10.1016/j.jfoodeng.2020.109910

Jiang, Y. (2019). Chapter 4 - Bioprocessing Technology of Rice Bran Oil. In L.-Z. Cheong & X. Xu (Eds.), *Rice Bran and Rice Bran Oil* (pp. 97-123): AOCS Press.

Li, D., Zhang, J., Faiza, M., Shi, L., Wang, W., Liu, N., & Wang, Y. (2021). The enhancement of rice bran oil quality through a novel moderate biorefining process. *Lwt, 151*, 112118. doi:https://doi.org/10.1016/j.lwt.2021.112118

Liu, X., Wang, W., Xu, L., Li, Z., Xu, Q., Yang, B., . . . Wang, Y. (2023). Effects of different degumming processes on the molecular species and microstructures of phospholipids recovered from crude vegetable oils. *Lwt, 185*, 115126.

Marchisio, F., Paoletti, L., Val, D. S., Cerminati, S., Castelli, M. E., & Menzella, H. G. (2023). Chapter 21 - Use of phospholipase enzymes to reduce the environmental impact of traditional chemical processes. In S. Chakraborti (Ed.), *Phospholipases in Physiology and Pathology* (pp. 387-395): Academic Press.

Nazir, A., Shad, M., Rashid, N., Azim, N., & Sajjad, M. (2024). Recombinant production and characterization of a metal ion-independent Lysophospholipase from a hyperthermophilic archaeon Pyrococcus abyssi DSM25543. *International Journal of Biological Macromolecules, 259*, 129345. doi:https://doi.org/10.1016/j.ijbiomac.2024.129345

Sharma, Y. C., Yadav, M., & Upadhyay, S. N. (2019). Latest advances in degumming feedstock oils for large-scale biodiesel production. *Biofuels, Bioproducts and Biorefining, 13*(1), 174-191. doi:https://doi.org/10.1002/bbb.1937

Wang, L., Hu, T., Jiang, Z., Yan, Q., & Yang, S. (2021). Efficient production of a novel alkaline cold-active phospholipase C from Aspergillus oryzae by molecular chaperon co-expression for crude oil degumming. *Food chemistry, 350*, 129212.

Wang, T., Chen, K., Li, Z., Jiang, L., Yu, D., Cheng, J., & Wang, L. (2021). Construction of an enzyme-Pickering emulsion catalytic system and its application in the interfacial catalytic reaction of rice bran oil deacidification. *Lwt, 150*, 111921. doi:https://doi.org/10.1016/j.lwt.2021.111921

Wei, C., Xiao, K., Li, H., Qi, Y., Zou, Z., & Liu, Z. (2022). Optimization of ultrasound assisted aqueous enzymatic extraction of oil from Cinnamomum camphora seeds. *Lwt, 164*, 113689. doi:https://doi.org/10.1016/j.lwt.2022.113689

Xiang, M., Wang, L., Yan, Q., Jiang, Z., & Yang, S. (2020). High-level expression and characterization of a novel phospholipase C from Thielavia terrestris suitable for oil degumming. *International Journal of Biological Macromolecules, 156*, 740-748.

Yu, D., Wang, N., Gong, Y., Wu, Z., Wang, W., Wang, L., . . . Jiang, L. (2022). Screening of active sites and study on immobilization of Bacillus cereus phospholipase C. *Lwt, 159*, 113245. doi:https://doi.org/10.1016/j.lwt.2022.113245

Advanced Engineering Days

aed.mersin.edu.tr

Facile synthesis of Mn-doped carbon aerogel composite cathode for electrochemical oxidation of Cefepim drug waste from contaminated water

Tala Babaei [1], Mahmoud Zarei [*1], Paria Rostamzadeh [1], Hannaneh Mortaghi Ghasemi [1]

[1] University of Tabriz, Faculty of Chemistry, Research Laboratory of Environmental Remediation, Department of Applied Chemistry, Tabriz, Iran, Talababayi@yahoo.com, mzarei@tabrizu.ac.ir, P.Rostamzadeh@tabrizu.ac.ir, hannaneh.m.gh22@gmail.com

Cite this study: Babaei, T., Zarei, M, Rostamzadeh, P, & Mortaghi Ghasemi, H. (2024). Facile synthesis of Mn-doped carbon aerogel composite cathode for electrochemical oxidation of Cefepim drug waste from contaminated water. Advanced Engineering Days, 9, 670-672

Keywords
EF-like process
Carbon Aerogel
Water treatment
Cefepim

Abstract

Strict governmental regulations and sustainable development of the eco-system require more effective water treatment technologies. Antibiotics emerged as a new type of contaminant in recent years with characteristics of low concentrations and complex structures in contaminated waters. Electro-Fenton like (EF-like) process represents an effective strategy to generate strongly oxidative species for the elimination of refractory organic pollutants in water in advanced oxidation processes. In the present study, the EF-like process has been investigated to remove cefepim from an aqueous solution. In the first part of this study, the (carbon aerogel) was synthesized as a 3D cathode electrode. For this purpose, resorcinol-formaldehyde composite containing Mn was prepared by the sol-gel method. Next, the resulting composite was carbonized and the properties were examined by Scaning electron microscopy and Raman analysis. The removal efficiency of cefepim was achieved about 96.78% in 130 min and total organic carbon removal efficiency reached to 83.58% in 300 min over EF-like process.

Introduction

Polluted water resources, particularly those polluted with pharmaceutical, are carcinogenic and hence pose a severe threat to sustainable and longstanding worldwide development. There is a growing interest toward the removal of pharmaceutical-emerging contaminants in water resources because of which there has been a notable increase in their application. As the World Health Organization (WHO) defines, antibiotic resistance can occur naturally and affect anyone and threaten the global health. Cefepim as a member of cephalosporin subgroup in the antibiotic group demonstrates antibacterial performance. By virtue of its persistent structure cefepim has been investigated in this work. A simple, efficient and environmentally friendly EF- like process is highly practical for waste water treatment practical application [1]. this modified EF-like process expands the pH application range and enables the cogeneration and transformation of free radicals, which has broad prospects for application in the effective degradation of organic pollutants for water purification [2].

Main reactions proposed in EF-like process are as follows:

$$Mn^{2+}+H_2O_2+H^+ \longrightarrow Mn^{3+}+H_2O+{}^{\cdot}OH \quad (1)$$

$$Mn^{3+}+e^- \longrightarrow Mn^{2+} \quad (2)$$

Carbon aerogels (CA), have recently attracted attention as a way to circumvent the limit of conventional methods including (sluggish electro generation of H_2O_2 and narrow pH ranges) [3, 4]. the large specific surface areas and macroscopic morphologies enable the uniform immobilization of active materials on the substrates. In addition, the products and by-products are removed easily from the reaction system via high porosity. the remarkable electrical conductivity of CA also contributes to improvement in catalytic performance [4]. The aim of this project is to synthesize Mn-doped carbon aerogel to degrade Cefepim pollutant from contaminated water and characterize the prepared composite with FE-SEM and Raman analysis. furthermore, TOC analysis consequently demonstrate intermediates of cefepim degradation and mineralization of pollutant.

Material and Method

Chemicals

Sodium hydroxide 99%, Sulfuric acid 99%, acetone 99.5%, dichloromethane 99%, sodium sulfate 99%, sodium carbonate 99.5%, and hydrochloric acid 37%, were purchased from Merck (Germany). Resorcinol and Formaldehyde were supplied from Sigma Aldrich (US). Cefepim sulfate with molecular formula of $C_{19}H_{26}N_6O_9S_3$ molecular weight of 578.6 g mol^{-1}, and λ_{max} of 257 nm was provided by Dr. Abidi Pharma Co. All chemicals used in this research were in analytical grade and experimental solutions were also prepared with deionized water.

Experimental procedure

The Cefepim degradation process occurred in a 100 mL one-compartment acrylic cell under a magnetic stirrer with a constant rate of 20 rpm. As-prepared Mn doped CA in test tube shape with dimensions of (2cm×2cm) and pt sheet with dimensions of (2cm × 2cm) were used cathode and anode of process, respectively. The distance between the electrodes was adjusted to approximately 3 cm in all experiments. A DC power supply was implemented to contribute electrolysis in the tests. An air pump was used for the generation of oxygen during EF-like process. Samples were collected during each EF-like degradation process with a 5 mL syringe. The absorbance of each sample in λ_{max} = 578.9 nm for the Cefepim was measured using the spectrophotometric method.

Discussion

Morphology and the formation of microstructures were determined by Field Emission Scanning Electron Microscopy MIRA3 TESCAN SEM instrument. The SEM images of Mn-doped carbon aerogel composite are displayed in Fig. 1. According to the figure the observed pores in carbon-aerogel SEM images confirm the pore fluid exit during the drying process; moreover, the compound consists of relatively uniform and regular particles.

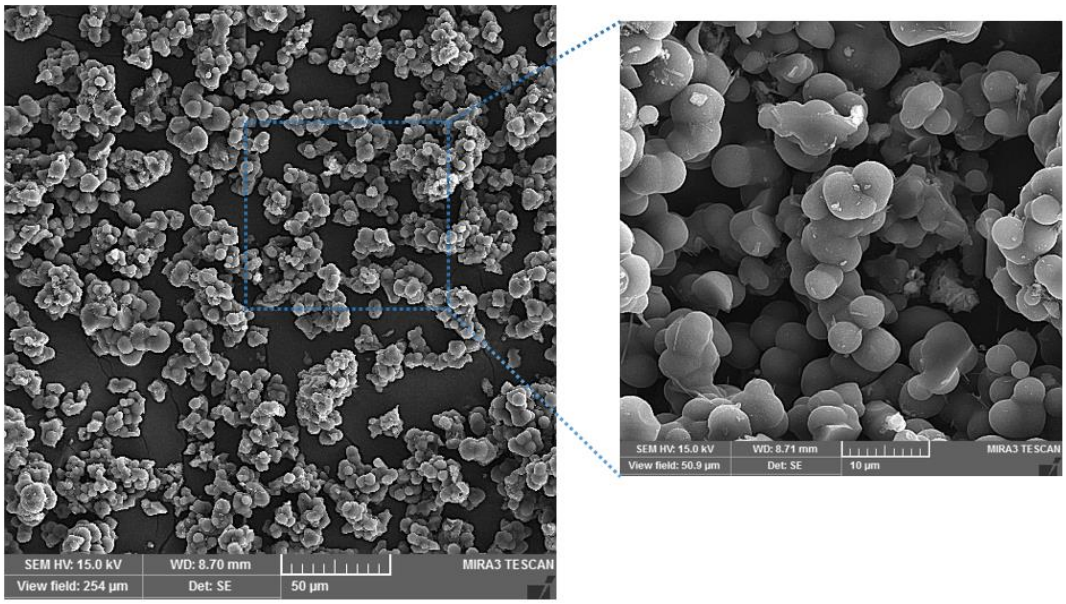


Figure 1. The SEM images of Mn-doped carbon aerogel composite

Raman Spectroscopy

The Raman spectra are shown in Fig. 2. The Mn-doped carbon aerogel composite has only the typical D (disordered) and G (graphitic) peaks of carbon. The utilized temperature and the exothermic nature of the reactions during the deposition caused this value to decrease, meaning that the carbon matrix became more ordered for the composites, Besides the D and G peaks, the presence of the metal oxide peaks in the spectra is apparent.

TOC analysis

In this research, TOC analysis represents mineralization the cefepim pollutant during the EF-like process with Mn-doped carbon aerogel cathode into water and carbon dioxide compounds. In the following, at 110, 240 and 300 minutes respectively, the favorable mineralization percentages of the cefepim are reported to be 32.04, 54.75 and 79.63%.

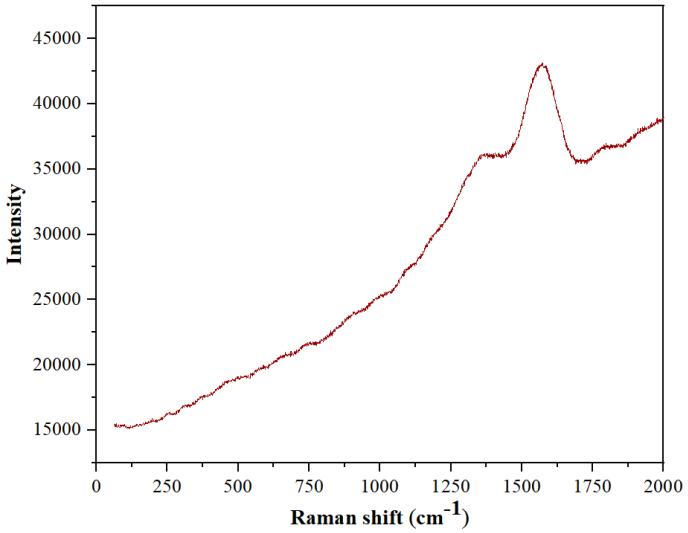


Figure 2. The Raman Spectroscopy of Mn-doped carbon aerogel composite

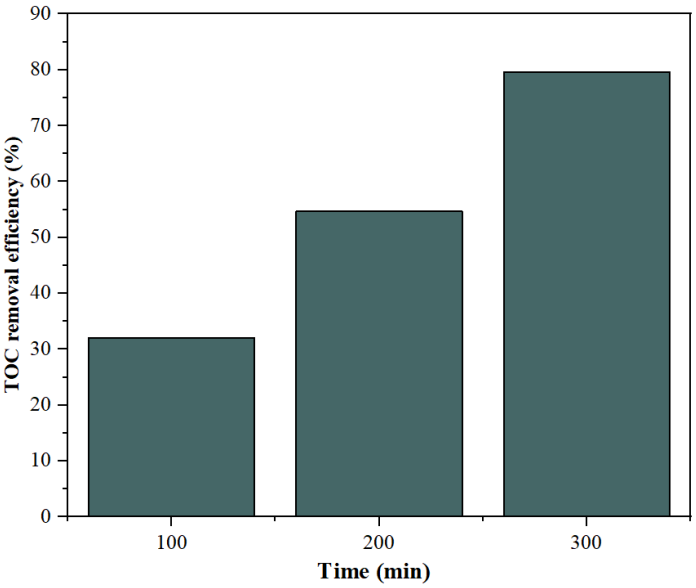


Figure 3. TOC graph for cefepim removal with Mn-doped carbon aerogel composite cathode

Conclusion

A novel Mn-doped carbon aerogel cathode was synthesized through chemical process and evaluated for its electrochemical activity toward degrading Cefepim as an identified emerging water contaminant. To characterize the structural morphology of prepared composite, the FE-SEM analysis was performed. The Raman pattern of sample also confirmed the successful formation of carbon aerogel composite. The degradation efficiency of 96.78 % was achieved in 130 min over EF-like process. The TOC removal efficiency of Cefepim contaminated experimental solution was obtained 79.63 % after 300 min of electrolysis.

References

1.

Advanced Engineering Days

aed.mersin.edu.tr

Thermofluidic analysis of backward facing step Couette-Poiseuille flow with symmetric corrugations and upper moving wall

Hamidreza Toloueinasab [*1], **Ramin Abdollahi** [1], **Ali Rahbar** [1], **Seyed Esmail Razavi** [1]

[1]*University of Tabriz, Department of Mechanical Engineering, Iran, hr_tolouienasab@tabrizu.ac.ir, ra.abdollahi@tabrizu.ac.ir, ali.rahbar98@ms.tabrizu.ac.ir, razavi@tabrizu.ac.ir*

Cite this study: Toloueinasab, H., Abdollahi, R., Rahbar, A., Razavi, S. E. (2024). Thermofluidic analysis of backward facing step Couette-Poiseuille flow with symmetric corrugations and upper moving wall. Advanced Engineering Days, 9, 673-675

Keywords
Backward facing step
Numerical Simulation
Corrugation
Thermofluidic
Couette-Poiseuille

Abstract

Backward Facing Steps have garnered a lot of attention in industrial applications involving fluid dynamics research. The current investigation aims to enhance the heat transfer rate in a backward facing step (BFS) channel flow with an upper moving wall along with corrugated surface for the bottom wall. Numerical analysis is carried out using the finite element method. The governing equations of fluid motion involve the Navier-Stokes equations, continuity, as well as the energy equation within the channel. Effects of corrugation amplitude on the thermofluidic characteristics of the fluid flow are investigated. Numerical results are validated with relevant data from the literature. Findings indicate that as the corrugation amplitude increases, the local Nusselt number dramatically increases. This leads to an enhanced heat transfer rate within the confined channel. Furthermore, it is observed that introducing corrugations on the bottom wall and adding a moving upper wall, significantly influences the fluid flow pattern both hydrodynamically and thermally.

Introduction

The study of fluid dynamics in channels with geometric irregularities has garnered significant interest due to its relevance in both natural and engineered systems. One such configuration is the backward-facing step (BFS) channel, which is a classical benchmark problem in fluid mechanics. The BFS channel is characterized by a sudden expansion, causing flow separation and the subsequent reattachment, phenomena critical to various applications ranging from aerodynamic design to industrial mixing processes.

In recent years, there has been a growing interest in understanding the effects of additional geometric complexities and dynamic boundary conditions within these channels, such as moving walls and corrugations on the channel walls. Introducing a moving upper wall in conjunction with corrugations adds another layer of complexity, influencing the flow behavior in significant ways. The motion of the upper wall can alter the shear layers and affect the reattachment length, turbulence intensity, heat transfer rates, and overall flow stability. Moving boundary condition in any physical geometry is a significant issue in hydrothermal fields as it is widely used in drying, mixing, and coating applications [1]. Another factor contributing to its popularity involves its ability to show principle phenomena such as secondary flows, chaotic motion of particles, eddies, turbulence, instabilities, and transitions [2]. In open literature, various experimental and numerical investigations have been performed on moving walls in channels and cavities under different conditions.

Current study aims to investigate the combined effects of wall corrugations and a moving upper wall in a BFS channel flow. By systematically varying the geometry of the corrugations and the velocity of the moving wall, we aim to elucidate the impact on key flow parameters, including reattachment length, turbulence characteristics, and pressure distribution. Through numerical simulations, we seek to provide a comprehensive understanding of the interplay between the step-induced separation, the corrugation-induced perturbations, and the dynamic boundary conditions imposed by the moving wall.

Material and Method

This study utilizes numerical simulations to investigate the effects of wall corrugations and a moving upper wall in a backward-facing step (BFS) channel flow. The simulations were conducted using a high-fidelity computational fluid dynamics (CFD) approach to capture the complex flow dynamics.

The computational domain represents a two-dimensional BFS channel with the following specifications:

1. Channel dimensions: The channel has a height H and a length L, with a step height h. The expansion ratio is $\frac{H+h}{H}$.
2. Corrugations: The lower wall includes corrugations characterized by an amplitude λ and constant wave length of $a = 10$. The amplitude is systematically varied to study different corrugation patterns.
3. Moving upper wall: The upper wall moves with a constant velocity U_w which is varied to study its impact on the flow characteristics.

The simulations solve the incompressible Navier-Stokes and energy equations given by:

$$\frac{\partial V}{\partial t} + V.\nabla V = -\nabla p + \nu \nabla^2 V \quad (1)$$

$$\nabla . V = 0 \quad (2)$$

$$\frac{\partial T}{\partial t} + V.\nabla T = \alpha \nabla^2 T \quad (3)$$

Where V is the velocity vector, p is the pressure, ν is the kinematic viscosity, T is the temperature, and α is the thermal diffusivity.

The governing equations are discretized using a finite volume method on an unstructured mesh. A second order accurate scheme is employed for both spatial and temporal discretization to ensure high fidelity.

Hydrothermal boundary conditions on the fluid domain are imposed as follows:

1. Inlet: A uniform velocity profile is imposed at the inlet with the inlet flow being considered as the cold fluid.
2. Outlet: A zero-gradient condition is applied at the outlet.
3. Lower Wall: A no-slip boundary condition is used or the stationary corrugated wall along with a constant hot temperature (hot wall).
4. Upper Wall: A moving wall boundary condiion is utilized, where the wall moves with a constant velocity U_w with the wall being thermally insulated.
5. Step Face: A no-slip boundary condition is applied on the step face along with the insulation thermal boundary condition.

Simulation parameters are the Reynolds number ($Re = \frac{U_{in}H}{\nu}$), corrugation parameters (λ, a), and the upper wall velocity (U_w), respectively. The numerical model is validated against benchmark solutions available in the literature for BFS flow without corrugations

Numerical solver is validated using the velocity contours brought forth in the study done by Alhasan et al. [3]. As shown in Figure 1, the velocity contours perfectly match with their corresponding contours in the reference.

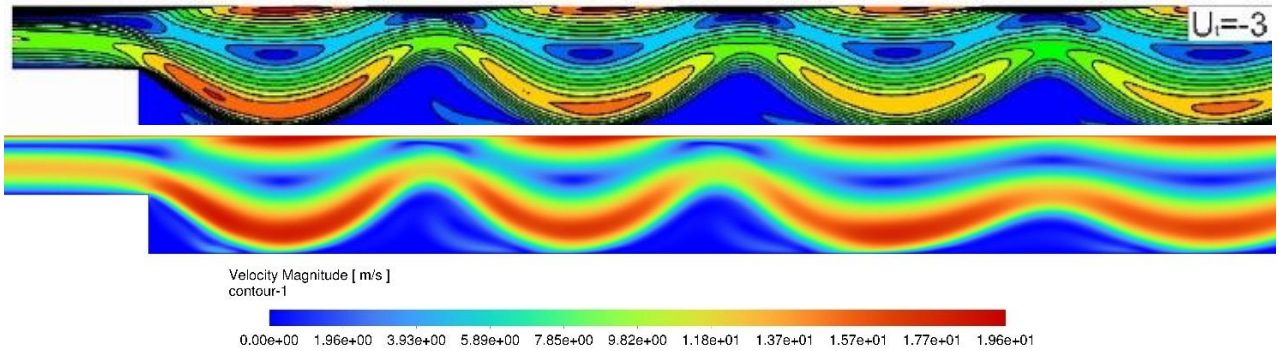


Figure 1. Numerical solver validation (a) Alhasan et al. [1] (b) Current study for Re=400, $U_w = -3$

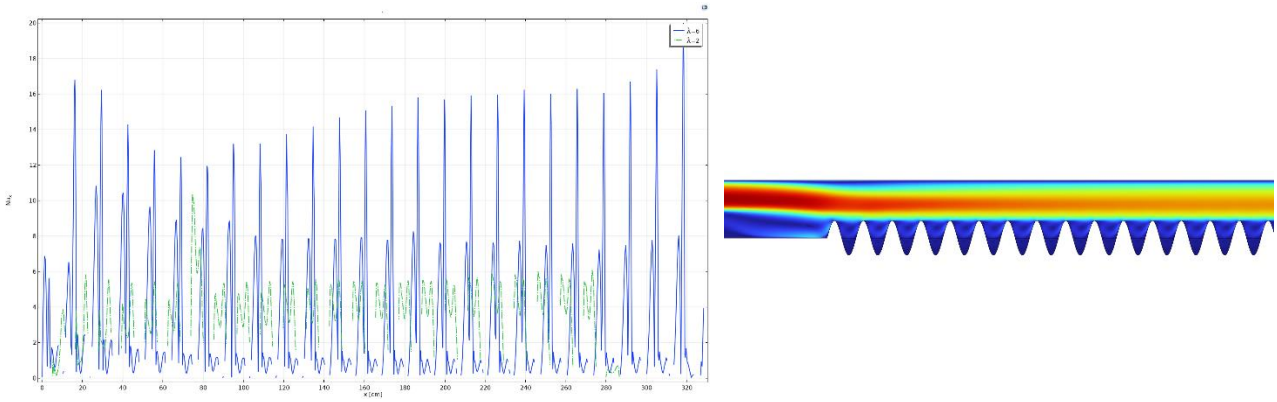
Results

Velocity contours for different corrugation parameters are presented in Figure 2. Furthermore, values of the Nusselt number for different case studies are plotted in Figure 3.

Discussion

Findings show increasing the corrugation amplitude causes the flow to get trapped within the corrugations. As a result, two sets of unsymmetrical vortices begin to form inside the sinusoidal region. This phenomenon enhances the flow mixing and in turn results in an enhanced heat transfer rate. Furthermore, according to the Nusselt number expression, forming vortices causes the convective heat transfer to increase. With the fluid's thermal

conductivity being constant, this proceeding yields in a higher Nusselt number value compared with flat channel case. Another merit of the current design is the utilization of moving wall boundary condition. This greatly effects the fluid flow pattern as it moves downstream of the BFS. Aligned with the ultimate objective of this design, moving upper wall contributes to an even more enhanced Nusselt number within the channel.



(a) (b)

Figure 2. (a) Local Nusselt number and (b) velocity contour for BFS channel flow with corrugations and moving upper wall

Conclusion

Thermofluidic characteristics of the BFS flow with moving upper wall and corrugated bottom wall is investigated numerically using the finite element method. Fluid flow patterns along with the velocity contours and Local Nusselt number variations on the corrugated segment are derived from the simulations. Findings show:

- Enhanced Nusselt number values over corrugated segment with an increase in the corrugation amplitude.
- Double vortices formation within the sinusoidal regions.
- Highly affected reattachment length compared to flat channel BFS flow.
- Enhanced average Nusselt number value within the channel.

References

1. Bhopalam, SR., Perumal, DA., & Yadav, AK. (2021). Computational appraisal of fluid flow behavior in two-sided oscillating lid-driven cavities. International Journal of Mechanical Sciences, 196.
2. Loiseau, J-CH., Bucci, MA., Cherubini, S., & Robinet, J-Ch. (2019). Computational modelling of bifurcations and instabilities in fluid dynamics. Computational modelling of Bifurcations and Instabilities in Fluid Dynamics, 50.
3. Alhasan, M., Hamzah, H. M., Koprulu, A., & Sahin, B. (2024). Couette-Poiseuille flow over a backward-facing step: Investigating hydrothermal performance and irreversibility analysis. Case Studies in Thermal Engineering, 53.

Advanced Engineering Days

aed.mersin.edu.tr

Estimation of control points of the surface model obtained by unmanned aerial vehicle with artificial neural network

Ali Kavak [*1], Halil Kısacıkoğlu [1], Vahdettin Demir [1] Aydın Alptekin [2] Murat Yakar [2]

[1] *KTO Karatay University, Department of Civil Engineering, Konya, Türkiye, alikavak2001@gmail.com, halilozn27@gmail.com, vahdettin.demir@karatay.edu.tr*
[2] *Mersin University, Department of Geological Engineering, Türkiye, aydinalptekin@mersin.edu.tr, myakar@mersin.edu.tr*

Cite this study: Kavak, A., Kısacıkoğlu, H., Demir, V., Alptekin, A., & Yakar, M. (2024). Estimation of control points of the surface model obtained by unmanned aerial vehicle with artificial neural network. Advanced Engineering Days, 9, 676-679

Keywords
Estimation
Unmanned aerial vehicle
Levenberg-Marquardt
Artificial neural networks

Abstract

The aim of this study is to increase the estimation performance of the height points of the area measured by Unmanned Aerial Vehicle (UAV) with artificial neural networks. Data from Anafi Parrot UAV was used in the study. The study area is the pond area located in Kerimler Village, Mersin. The data of seven different control points were estimated using Levenberg-Marquardt, one of the artificial neural network training algorithms. In these estimations, the latitude (X) and longitude (Y) information of the UAV point cloud was prepared as the input data set, and the altitude (Z) information was prepared as the output data set. In the modeling, 100 and 1000 iterations were also tried with hidden layer numbers varying between 1 and 10. The obtained estimates were compared with the altitude data of the control point in the study area. Mean absolute error (MAE), root mean square error (RMSE) and coefficient of determination (R^2) were used in comparisons. When the results were examined, it was seen that the most optimum number of hidden layer cells was 5 and the error criteria were RMSE: 1.1840, MAE: 0.8898, R^2: 0.9701, and the artificial neural network integrated successfully estimated the UAV control points.

Introduction

Measuring the heights of all points in the field is difficult and costly. For this reason, it is an important issue to produce terrain points under the control of closed box models such as artificial neural networks [1, 2].

Measurements-taking or modeling using UAV is a practice included in previous studies in our country [3]. However, training UAV measurements under the control of artificial neural networks is a relatively new application area. By carrying out a pioneering study on this subject, the defense industry, mapping, cadastre, etc. More successful outputs can be achieved in many sectors with more accurate measurement results.

With remote sensing technologies, fast, reliable and low-cost high value-added projects can be developed in the production and management of spatial information. Activities related to remote sensing are carried out with images provided by satellite images, UAV and drone technologies. Remote sensing technologies can be used in agriculture, forestry, environment, water management, defence, intelligence, mining, disaster management, management of underground and surface resources, urban planning and many space-based engineering and research projects [4-6].

UAVs make measurements using photogrammetry technology. Photogrammetry is the science technology of obtaining reliable information about physical objects and the environment through the process of recording, measuring and interpreting photographic images, patterns of electromagnetic radiance and other phenomena [7-8]. Today, precise results are obtained in measurement works carried out using UAV technologies. However, there are still minor errors in the measurements. In this study, it is aimed to estimate control points with the least error using artificial neural networks.

Material and Method

Study Area

The study area is the area between 36.75°-36.78° meridians and 40.90°-40.91° parallels of Kerimler Village of Mersin-Toroslar district. This region has a Mediterranean climate and agriculture, and tourism are the main sources of income. Mersin, which has very productive agricultural lands, has a high rainfall rate in the summer months. Kerimler village has received an average annual rainfall of 972.26 mm in the last 5 years [9]. The biggest reason for choosing this study area is that the data is accessible. In order to fly a UAV The main question of the study is whether the accuracy of a sample UAV data can be increased with ANN without getting involved in the necessary permissions and legal procedures. For this reason, an existing data source and study area were chosen. Figure 1 shows the study area and 7 control points to be used in the test data set.



Figure 1. Image of the work area and 7 control points [3].

Artificial neural networks

ANN is a computing technology inspired by the information processing technique of the human brain. In other words, ANNs provide solutions to problems that normally require a human's natural abilities to think and observe. The main reason why a person can produce solutions to problems that require thinking and observation skills is the ability of the human brain and therefore the human being to learn by experiencing and trying [10]. In this study, Multi-Layer Artificial Neural Networks (MLANN), one of the artificial neural network methods, was used. The model structure of MLANN is shown in Figure 2.

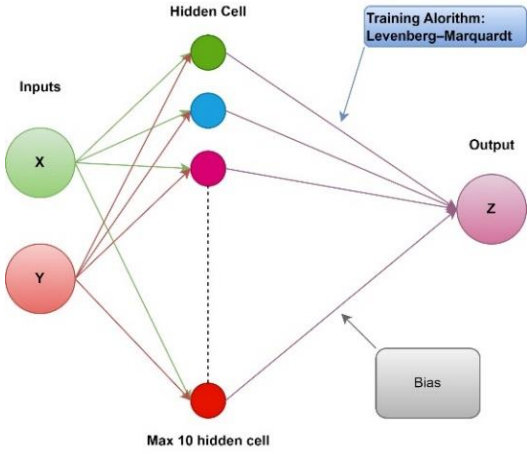


Figure 2. MLANN Structure

In Figure 2, the inputs are X and Y and the output is Z. The number of hidden layers was tried from 1 to 10. Levenberg-Marquardt was used as the training algorithm. For the Levenberg-Marquardt (LM) algorithm, the study of Çavuşlu et all. can be consulted [11].

Result and Discussion

Latitude and longitude information was tried in 3 different combinations to estimate control points. These are: only latitude information (X), only longitude information (Y) and use of both latitude and longitude information (X, Y). As the artificial neural networks training algorithm, the LM algorithm was used inspired by the literature because it gives fast and very accurate results [12]. In addition, the analyzes were tried separately for 100 and 1000 iterations with the number of hidden layer cells ranging from 1 to 10, and comparison criteria were tabulated according to the number of iterations and training-test data sets (Table 1).

Table 1. Comparison criteria for the training and testing phase

Inputs	Iteration	Training			Testing		
		KOKH	OMH	R^2	KOKH	OMH	R^2
X	100	46.4172	35.3619	0.2070	47.4513	36.2441	0.1948
Y		32.9555	24.2504	0.6003	33.1831	24.3725	0.6062
X,Y		1.9088	1.4474	0.9449	1.1840	0.8898	0.9701
X	1000	46.3209	35.2923	0.2103	47.3980	36.2020	0.1967
Y		32.9512	24.2513	0.6004	33.1721	24.3698	0.6065
X,Y		1.9088	1.4474	0.9449	1.1840	0.8898	0.9701

In Table 1, the most successful results were obtained in data sets where 2 inputs were used. The hidden layer cell numbers that give the least error are 3 for X input and X input, and 5 for X and Y inputs. Although increasing the iterations increased the results slightly, it did not change the result of the most successful model. The point chart and scatter plot of the successful results of the two inputs are shown in Figure 3 and Figure 4.

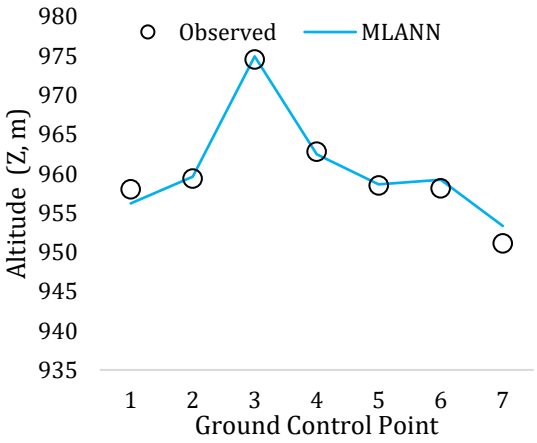


Figure 3. Point Chart

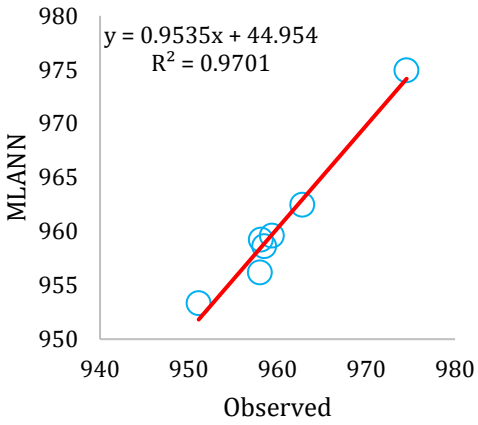


Figure 4. Scatter plot

Conclusion

Creating topography, in other words, determining latitude and longitude coordinates as well as altitude (height) values with appropriate accuracy, are the basic bases needed in most engineering applications. In this study, the height information of 7 different ground control points belonging to a pond area located in Kerimler Village of Mersin-Toroslar district was estimated by artificial neural networks. Three different input sets, the number of hidden layer cells between 1 and 10, and iterations between 100-1000 were tried in the modeling. When the results are examined;

- In modeling; It has been determined that the XY input always gives results with less error than the X, Y and XY inputs.
- The comparison criteria for the most successful training phase result are RMSE: 1.9088, MAE: 1.4474, R^2: 0.9449.
- The comparison criteria for the most successful test phase result are RMSE: 1.1840, MAE: 0.8898, R^2: 0.9701 (Modeling time is 0.29 seconds).

These results show that multilayer artificial neural networks can be used in elevation modeling, which forms the basis of many engineering studies. When looking at 100 iterations and 1000 iterations, it was seen that there was not much difference between them in terms of accuracy, but it was seen that 1000 iterations were one hundred and ten times slower. Therefore, using one hundred iterations is faster.

References

1. Demir V. & Çubukçu E. A. (2021) "Digital Elevation Modeling with Heuristic Regression Techniques Abstract," Eur. J. Sci. Technol., 24, 484–488.
2. Çubukçu E. A., Demir V., & Sevimli M. F. (2021) "Digital Elevation Modeling Using Generalized - Radial Based – Multi Layered Artificial Neural Networks," Turkish J. Eng., 6 (3), 199–205.
3. Alptekin, A., & Yakar, M. (2022). Modelling a landslide site using UAV photogrammetry in Değirmençay village, Mersin. Intercontinental Geoinformation Days, 4, 196-198.
4. Karataş, L., Alptekin, A., Karabacak, A., & Yakar, M. (2022). Detection and documentation of stone material deterioration in historical masonry buildings using UAV photogrammetry: A case study of Mersin Sarisih Inn. Mersin Photogrammetry Journal, 4(2), 53-61.
5. Kanun, E., Alptekin, A., Karataş, L., & Yakar, M. (2022). The use of UAV photogrammetry in modeling ancient structures: A case study of "Kanytellis". Advanced UAV, 2(2), 41-50.
6. Alptekin, A., & Yakar, M. (2020). Heyelan bölgesinin İHA kullanarak modellenmesi. Türkiye İnsansız Hava Araçları Dergisi, 2(1), 17-21.
7. Şasi, A., & Yakar, M. (2017). Photogrammetric modelling of sakahane masjid using an unmanned aerial vehicle. Turkish Journal of Engineering, 1(2), 82-87.
8. Yakar, M., & Dogan, Y. (2019). 3D Reconstruction of Residential Areas with SfM Photogrammetry. In Advances in Remote Sensing and Geo Informatics Applications: Proceedings of the 1st Springer Conference of the Arabian Journal of Geosciences (CAJG-1), Tunisia 2018 (pp. 73-75). Springer International Publishing.
9. Alptekin A. & Yakar M. (2020) "Determination of pond volume with using an unmanned aerial vehicle," Mersin Photogramm. J.,2 (2),59–63.
10. Hassan O., Elnazeer E., & Zomrawi N. (2015) "Application of Artificial Neural Network for Height Modelling," Int. J. Recent Innov. Trends Comput. Commun. 3 (3), 1374–1377.
11. Çavuşlu M. A., Becerikli Y., & Karakuzu C. (2012) "Hardware Implementation of Neural Network Training with Levenberg-Marquardt Algorithm," Turkish Informatics Foundation Information Science and Engineering Journal., 5 (5), 1–7.
12. Çubukçu E. A., Demir V., & Sevimli M. F. (2022) "Estimating Streamflow Data with Machine Learning Techniques," Gazi J. Eng. Sci., vol. 8, no. 2, pp. 257–272, 2022, doi: 10.30855/gmbd.0705009.

Advanced Engineering Days

aed.mersin.edu.tr

The importance of determining value-based land shares: Business center application

Muhammed Emin Işık[1], Nuri Erdem*[2]

[1]*Osmaniye Korkut Ata University Graduate School of Natural and Applied Sciences Civil Engineering, Osmaniye, Türkiye*
[2]*Osmaniye Korkut Ata University, Faculty of Engineering, Department of Geomatic, Osmaniye, Türkiye*

Cite this study: Işık, M. E., & Erdem, N. (2024). The importance of determining value-based land shares: Business center application. Advanced Engineering Days, 9, 680-682

Keywords
Land share
Valuation
Floor easement
Separate Section

Abstract

In this study; The importance of the value-based approach in determining land shares has been investigated. Although current practices determine the land shares of Separate sections based on square meters, this practice has errors and shortcomings. In addition, urban transformation, expropriation, earthquake, flood, etc. In the reconstruction of buildings destroyed as a result of natural disasters or expropriation by paying their financial value, their value is based on the land share, and this becomes the subject of some unfair practices or lawsuits that will last for many years. For this reason, when determining land shares at the floor easement establishment stage and creating management plans, it will be more fair to determine the land share along with the goodwill share, not only on m2 basis , but also on criteria such as the floor of the Separate section, facade, view, visibility and rental income. In this way, any negativities that may occur in the future can be prevented.

Introduction

Since the concept of value is a concept used by many disciplines and handled in different contexts, it is known that there is no single generally accepted definition of value. The meaning of the word value is an abstract measure that helps determine the importance of something, the equivalent of something that can be measured in money; It means value, price [1]. The main reason why there are different definitions of the concept of value is that it varies from person to person as a result of objective or subjective evaluations. In addition, many different disciplines have defined the concept of value differently according to their own needs [2, 3]. Reflecting the evaluation of real estate in taxes is one of the most important economic approaches of modern societies [3].

In accordance with the Law No. 6306 on the Transformation of Areas Under Disaster Risk dated 16/5/2012 [4], the concept of land share is the main criterion in decisions to be made about the main real estate that is the subject of the urban transformation project. Because in the absolute majority decision-making rule, the quorum is measured by land share. As clearly stated in the article of the law, very important decisions can be made according to the land share ratio regarding the real estate to be included within the scope of urban transformation. While determining the land share, while creating the management plan during the establishment of floor easement or direct condominium ownership, the land share should be given to the Separate sections of the parcel where the main building or multiple buildings are located, in proportion to their market values.

However, it is known that municipalities and land registry offices do not show the necessary sensitivity in sharing the land share in accordance with the law and within the framework of equity. As a result, many cooperatives and contractors who are not familiar with the subject distribute land shares equally to the number of Separate sections in the building [2]. In addition, it is known that the land shares are not equal even on the m2 basis, and that the land shares of some Separate sections are given more and some are given less. This is an unfair and very wrong practice. Misapplications in determining the land share may result from incomplete information or, unfortunately, self-interested approaches. As a result of the natural disasters experienced in recent years, the importance of determining the land share correctly increases even more.

Land shares have a significant impact on many criteria. These can be listed as follows;

- *Situation vis-à-vis Common Places*
- *Obligation to Participate in Some Common Expenses*

- *Insurance Expenses and Insurance Cost Sharing*
- *Meeting and Decision Quorum*
- *Making Innovations and Additions to Common Areas*
- *In Terms of General Provisions*

Land Share Determination Criteria

The elements that should be taken into consideration in determining the land share ratio of each separate section are;

- Square meter, floor, facade, sunlight exposure, rental income,
- Privacy; Whether the inside of the house can be seen from the outside or from the stairs, in front of the elevator or from other apartments,
- Determining the goodwill of the Separate division is also one of the important elements. The concept of goodwill may differ in each project. For this reason, as soon as the floor easement is established, on-site inspections must be made and the value of each Separate section must be determined.

Incorrect Determination of Land Share

The main reasons for incorrect land share calculations are; Not having enough information about the subject or speeding up official procedures. In addition, there are also practices carried out by contractors with malicious intent. However, with the acceleration of urban transformation efforts in recent years, the importance of the concept of land share has increased. For this reason, many lawsuits have been filed in the civil courts of peace to correct incorrect land calculations. Nowadays, it seems that even most large construction companies do not give enough importance to the concept of land share. In case of incorrect determination of land shares;

- Urban transformation applications,
- Controlled demolition as a result of destruction or damage under the influence of a disaster,
- Expropriation-expropriation,

Disagreements and injustices arise in studies such as these, and time and financial losses are experienced in resolving them.

Material and Method

The land share errors and miscalculations made in the application were examined with the data of 1 housing project and 1 Business Center project among the completed application projects in Osmaniye city center. Figures 1 and 2 show screenshots of the drawing program of the architectural application project for the business center examined.

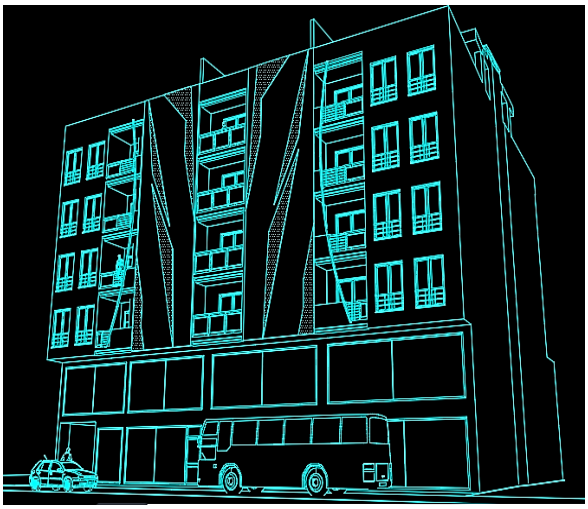


Figure 1. Business Center Angled View from the Front.

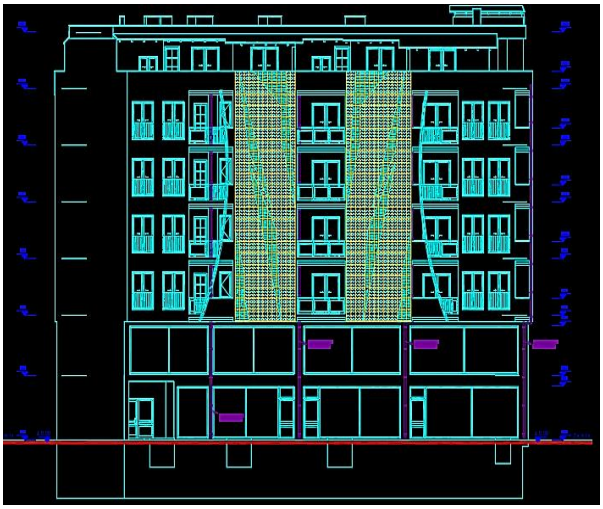


Figure 2. View from the Main Road Front

Business Center (861 m2):
Separate Section No. 29 : 228 m ^{2} , land share: 88.8 m ^{2}
Separate Section No. 30 : 116 m ^{2} , land share: 79 m ^{2}
Separate Section No. 31 : 232 m ^{2} , land share: 87.7 m ^{2}
Separate Section No. 22 : 145 m ^{2} , land share: 26 m ^{2}

Separate Section No. 27 : 115 m ^{2} , land share: 26 m ^{2}
Separate Section No. 28 : 79 m ^{2} , land share: 26 m ^{2}

As in the business center example, although the square meters of the Separate sections are different, the land shares are distributed close to each other or in a meaningless way. The square meters of the Separate section and the floor it is located on, rental income, etc. Considering the factors, more equitable and value-indexed land shares should be determined. The final distribution of business center land shares is given in Figure 3.

Bulunduğu Bağımsız Arsa

Bulunduğu Kat No	Bağımsız Bölüm No	Arsa Payı	Niteliği	Maliki	Hissesi
Birinci Kat	01	1063407/35724832	İŞYERİ	[redacted]	Tam
Birinci Kat	02	810000/35724832	İŞYERİ	[redacted]	Tam
Birinci Kat	03	810000/35724832	İŞYERİ	[redacted]	Tam
Birinci Kat	04	810000/35724832	İŞYERİ	[redacted]	Tam
Birinci Kat	05	810000/35724832	İŞYERİ	[redacted]	Tam
Birinci Kat	06	920000/35724832	İŞYERİ	[redacted]	Tam
Birinci Kat	07	620416/35724832	İŞYERİ	[redacted]	Tam
İkinci Kat	08	1080000/35724832	İŞYERİ	[redacted]	Tam
İkinci Kat	09	810000/35724832	İŞYERİ	[redacted]	Tam
İkinci Kat	10	810000/35724832	İŞYERİ	[redacted]	Tam
İkinci Kat	11	810000/35724832	İŞYERİ	[redacted]	Tam
İkinci Kat	12	810000/35724832	İŞYERİ	[redacted]	Tam
İkinci Kat	13	920000/35724832	İŞYERİ	[redacted]	Tam
İkinci Kat	14	620000/35724832	İŞYERİ	[redacted]	Tam
Üçüncü Kat	15	1080000/35724832	İŞYERİ	[redacted]	Tam

Figure 3. Distribution of Business Center Land Shares

Housing Project (985 m2):
Separate Sections No. 1-2-3-4-5-6: 86 m ^{2} , land share: 111 m ^{2}
No. 7-8 : 86 m ^{2} , land share: 101 m ^{2}
Separate Section No. 9 : 104 m ^{2} , land share: 86.6 m ^{2}
Separate Section No. 10 : 28 m ^{2} , land share: 28.8 m ^{2}

Conclusion

In current practices, it is possible to determine accurate and fair land share rates by making some changes to the existing land share determination system. With these changes, not only fair land shares will be obtained, but also a database of the usage areas of each Separate section in the main building will be created based on the market value on the date the floor easement was established.

References

1. Akpınar, B. (2019). Concept, Importance and Calculation of Land Share in Real Estate Valuation, Marmara University / Institute of Social Sciences / Department of Business Administration / Real Estate Valuation and Finance, Master's Thesis.
2. Turkish Language Association Current Turkish Dictionary, “Value”. https://sozluk.gov.tr/, (April 27, 2024)
3. Önal, YB, & Tezcan, K. (2008). Real Estate Valuation and Its Importance: An Evaluation from a Tax Perspective, Overview of Accounting and Auditing (24), 15-36.
4. Law on Transformation of Areas Under Disaster Risk, http://www.mevzuat.gov.tr (27 April 2024).

Advanced Engineering Days

aed.mersin.edu.tr

Development of Porous Asphalt Pavement using Recycled Surface Dressed Pavement Materials (RSM)

Ibrahim Sheikh Ibrahim[1], Hassan Shuaibu Abdulrahman[2]

[1]Federal University of Technology, Department of Civil Engineering, Minna, Niger State, Nigeria, Ibrahim.m1700204@st.futminna.edu.ng, abdul.hassan@futminna.edu.ng

Cite this study: Ibrahim, I. S., & Abdulrahman, H. S. (2024). Development of Porous Asphalt Pavement using Recycled Surface Dressed Pavement Materials (RSM). Advanced Engineering Days, 9, 683-685

Keywords
Porous
Asphalt
Pavement
Recycled
Surface Dressed

Abstract

The study aims to create sustainable porous asphalt by integrating recycled surface-dressed pavement materials (RSM) instead of traditional dense asphalt mixes. Experiments show RSM meets eco-friendly pavement construction standards, with mixtures ranging from 0% to 80% RSM. Physical properties like Aggregate Impact Value (AIV), elongation, flakiness, 6water absorption, and specific gravity differ between virgin aggregates (VA) and RSM. Despite flow and stability issues, the Marshal quotient meets industry standards. Permeability studies reveal a link between RSM percentage and porous asphalt permeability, highlighting the need for material optimization. The research emphasizes the cost-effectiveness and performance of recycled materials in porous asphalt, offering a practical solution for managing runoff water and promoting sustainable infrastructure. Utilizing RSM in porous asphalt provides sustainability and cost benefits.

Introduction

It is crucial to use sustainable paving materials while building and maintaining roads, highways, and other transportation systems in order to minimize the environmental effects of infrastructure development. Utilizing resource- and environmentally-conscious materials that encourage long-term sustainability and reduce environmental harm is central to the idea of sustainable pavement materials.

Reclaimed and recycled asphalt from previous or current asphalt pavements is referred to as "Recycled surface dressed pavement material," or RSM. Old asphalt is milled or removed during road or pavement rehabilitation or repair, and the recovered material is then gathered and processed for use in new pavement construction. [1] Laboratory testing on virgin mixes and mixes with 20% RSM revealed that adding RSM enhances all the bituminous mixes' properties, suggesting that mixes with 20% RSM would function better than the virgin mixes in comparable circumstances.

The performance and longevity of asphalt pavements are largely dependent on bitumen, an essential component of asphalt mixes. The impact of bitumen content on several mechanical, rheological, and environmental aspects of asphalt mixes is examined in the literature.
[2], The ideal amount of bitumen in the mixture is defined as such that the porosity and water saturation are outside of the GOST 9128–97 requirements while the strength of the asphalt concrete is at its highest. The excessive amount of bitumen in the mixture lowers the asphalt concrete's strength, shear stability, and fluidity, which causes shears to form in hot weather. Excessive bitumen in asphalt concrete is indicated by a low water saturation value. The strength and frost and corrosion resistance of asphalt concrete are diminished when bitumen is absent.

A special kind of pavement known as permeable or porous pavement serves as a structural surface for cars and pedestrians as well as a tool for managing storm water runoff and lowering surface runoff. Although there are many unique choices and associated technologies available, the most popular permeable pavements include plastic grid-stabilized systems, porous asphalt pavement (PAP), pervious concrete (PC), and permeable interlocking concrete pavement (PICP). PAPs have a number of positive environmental and sustainable effects, including as lowering storm runoff volumes, replenishing groundwater, enhancing water quality, and improving driving quality and safety by lowering noise levels and hydroplaning tendencies, [3].

Material and Method

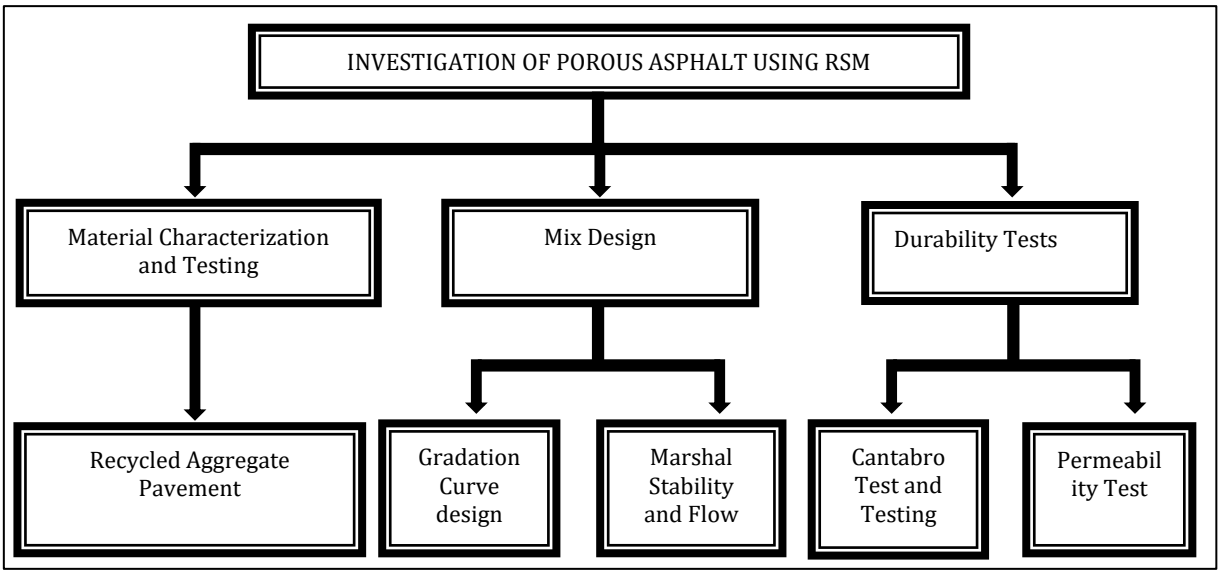


Figure 1. Investigation of porous asphalt containing RSM

The kinds of materials consider are as follows:

1. Aggregates
   i. Recycled surface dressed pavement material (RSM)
   ii. Virgin aggregates
2. Bitumen 60/70

Results

Table 1. Physical properties of Virgin aggregates and RSM

Test	Virgin Aggregates	Recycled surface dressed pavement material
Specific gravity	2.64	2.45
Water Absorption	5.03	4.30
Aggregate Impact Value	8.77	14.10
Flakiness	10	5
Elongation	44	15

Table 2. Percentage passing of Virgin and RSM aggregates

Sieve	100% RSM	100% VA	80% VA & 20% RSM	60% VA & 40% RSM	40% VA & 60% RSM	20% VA & 80% RSM
Pan	0.00	0.00	0.00	0.00	0.00	0.00
5.00mm	9.33	34.83	19.70	18.67	23.78	17.59
6.30mm	13.14	40.23	24.80	21.78	27.66	21.23
10mm	26.58	53.67	40.99	34.96	39.45	34.63
14mm	54.16	70.77	71.44	57.19	57.36	60.04
20mm	86.96	81.67	81.93	79.26	82.34	84.80

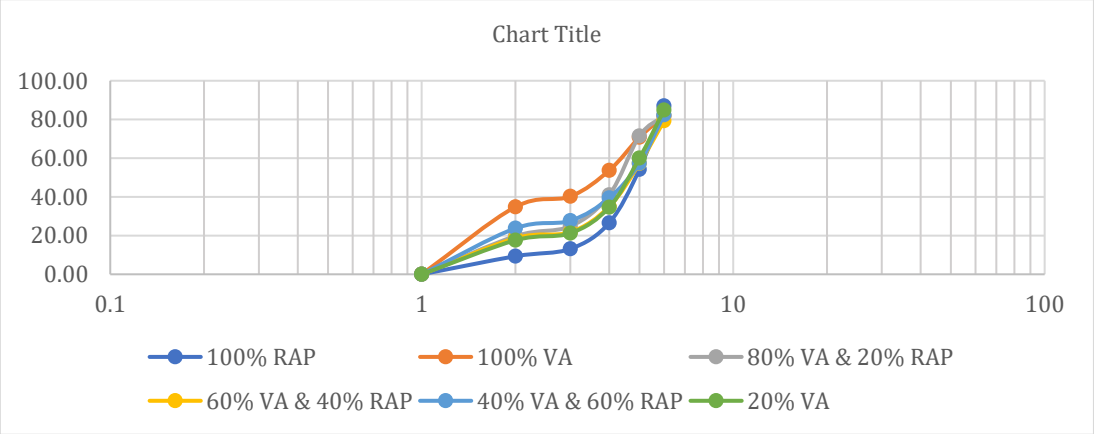


Figure 2. Percentage passing of Virgin and RSM aggregates

Table 3. Porous Asphalt properties

SN	Stability (kg)	Flow (mm)	Permeability (mL/s)	Drain down (%)	Cantabro (%)	RSM (%)	VA (%)	BC (%)	MQ
1	650	9.3	449	0	6.94	0	100	5	69.9
2	370	7.3	413	0.8	8.14	20	80	5	50.7
3	360	7.6	278	5.5	11.42	40	60	5	47.4
4	290	9.9	275	9.4	14.52	60	40	5	29.3
5	285	9.6	222	28.9	14.7	80	20	5	29.7

Discussion

Models were developed from the experimental data to show the relationships between measured responses and variables, and among measured responses. Excel package was used for this purpose and only one parameter was considered at this stage model. Some of the relationships were linear and nonlinear models such as polynomial equations with higher degrees were used. This is to allow validation of the models through statistical analysis since the excel package can only perform linear regression. The regression was done at 95% confidence interval.

Conclusion

The experimental results from the porous asphalt gradation show that the creation of Porous Asphalt Pavement using Recycled surface dressed pavement material (RSM) has been a promising undertaking. The project's aggregates have proven to follow the recognized guidelines for porous asphalt pavement, highlighting the practicality of using recycled resources in building.

The utilized Recycled Aggregates Pavement (RSM) has desirable characteristics, including a specific gravity of 2.45, a water absorption of 4.3, and an Aggregate Impact Value (AIV) of 14.1.

References

1. Papavasiliou, V. Loizos, A. Field performance and fatigue characteristics of recycled pavement materials treated with foamed asphalt. Constr. Build. Mater. 2013, 48, 677–684.
2. Otakulov, Bakhromjon Adhamovich, Kodirov, Bekzod Xomidjonovich, & Solijonov, Hojiakbar Solijon O'G'Li. (2021). Selecting the optimal bitumen content. *Scientific progress, 2*(8), 415-420.
3. Kevern, Kun Zhang and John. (2021). Review of porous asphalt pavements in cold regions: the state of practice and casestudy repository in design, construction,and maintenance. *Journal of Infrastructure Preservation and Resilience*, 17. doi: 10.1186/s43065-021-00017-2

Advanced Engineering Days

aed.mersin.edu.tr

Statistical evaluation of theoretical and nonparametric approaches to Standardized Precipitation Index

Ahmad Abu Arra[*1, 2], **Eyüp Şişman** [1, 3]

[1]*Yildiz Technical University, Department of Civil Engineering, Istanbul, Türkiye, ahmad.arra@std.yildiz.edu.tr; esisman@yildiz.edu.tr*
[2]*An-Najah National University, Department of Civil Engineering, Nablus, Palestine, s11419527@stu.najah.edu*
[3]*Istanbul Medipol University, School of Engineering and Natural Sciences, Department of Civil Engineering, Istanbul, Türkiye, esisman@medipol.edu.tr*

Cite this study: Abu Arra, A., & Şişman, E. (2024). Statistical evaluation of theoretical and nonparametric approaches to Standardized Precipitation Index. Advanced Engineering Days, 9, 686-689

Keywords
Nonparametric
Temporal evaluation
SPI
SDAT
Probability Distribution Functions

Abstract

Accurate drought evaluation is critical for effective water resource management and mitigation strategies. This research aims to compare the nonparametric precipitation drought index using the Standardized Drought Analysis Toolbox (SDAT) tool with the conventional Standardized Precipitation Index (SPI) using different probability distribution functions (CDFs). The comparison employs various statistical metrics, including coefficient of determination (R^2), correlation coefficient (CC), mean squared error (MSE), root mean squared error (RMSE), mean absolute error (MAE) and mean bias error (MBE). The Oxford station, with monthly precipitation data spanning from 1767 to 2023, was selected to calculate SPI1 and SPI12. The results highlight the importance of selecting an accurate function for drought analysis. Both theoretical and empirical distributions yielded very similar outcomes; for example, the GEV distribution almost perfectly fit the empirical data (R^2 = 0.999, CC = 0.999). However, using the SDAT tool offers the advantage of achieving results without error, contributing significantly to the academic field and water resource management.

Introduction

Natural disasters, including droughts, have become more frequent, with more and more records in the last years [1]. Droughts involve serious contractions in precipitation, which is important for the hydrological cycle and other important sectors such as agriculture [2]. For drought evaluation and monitoring, different drought indices have been introduced, such as the Standardized Precipitation Index (SPI) [3] and the Standardized Precipitation Evapotranspiration Index (SPEI) [4]. According to the World Meteorological Organization [5], the SPI is one of the most universally used indices. SPI is used for meteorological drought assessment at different time scales, including short, medium, and long scales. Also, for effective water resources management and drought mitigation strategies, accurate and reliable drought assessment is a crucial step [6].

Standardized drought indices (SDIs), such as SPI, rely on fitting the original datasets for each drought index into an appropriate theoretical probability distribution function (PDF) [3, 7]. These functions can be the Gamma, Weibull, and any function based on the data and the goodness-of-fit tests. This function is then transformed probabilistically into a normal. On the other hand, the Standardized Drought Analysis Toolbox (SDAT) developed by Farahmand and AghaKouchak [8] offers a comprehensive framework for deriving nonparametric standardized indices.

This research aims to compare different probability distribution functions and the Standardized Drought Analysis Toolbox (SDAT) for the SPI over long-term data spanning more than two centuries at various time scales. Using precipitation data from the Oxford station in the UK, covering the period from 1767 to 2023, the study employs temporal drought evaluation and various statistical metrics for this comparison. This research contributes significantly to the academic field and water resources management by providing insights into the most effective methods for assessing and monitoring droughts over extended periods.

Material and Method

Study area

Oxford station, located in Oxford, England, has been meticulously recording monthly precipitation data from 1767 to 2023, providing a valuable dataset spanning over 250 years. This extensive period, with an annual average precipitation of 641.4 mm and a standard deviation of 31.2 mm, is crucial for understanding long-term climatic patterns and variability in terms of drought evaluation. Oxford's climate is classified as temperate maritime, characterized by relatively mild winters and cool summers, with precipitation distributed fairly evenly throughout the year. Such a comprehensive record is rare and provides a unique opportunity to improve the accuracy of drought prediction models and to develop effective water management strategies to mitigate the effects of droughts. This station was selected for application due to its extensive and long-standing data collection.

Standardized Precipitation Index (SPI):

The Standardized Precipitation Index (SPI), developed by McKee et al. [3], evaluates meteorological drought across various timescales using monthly precipitation data. These precipitation records are initially fitted to an appropriate probability density function (PDF). The suitability of a PDF is determined by performing goodness-of-fit tests, such as the Chi-Square and Kolmogorov-Smirnov tests, on the precipitation data [9]. The next step involves calculating probabilities based on the monthly precipitation records, which are then standardized to a normal PDF with a mean of zero and a standard deviation of one. This research considers the Weibull, GEV, and Gamma distribution functions.

Standardized Drought Analysis Toolbox (SDAT):

The Standardized Drought Analysis Toolbox (SDAT) is a sophisticated tool designed for the nonparametric assessment of drought conditions. Unlike traditional drought indices that rely on fitting precipitation data to specific probability distributions, SDAT utilizes Gringorten plotting position [10] to standardize drought metrics. SDAT is particularly valuable for regions with complex or highly variable precipitation patterns, providing a robust and adaptable means for drought analysis and decision-making.

Statistical metrics:

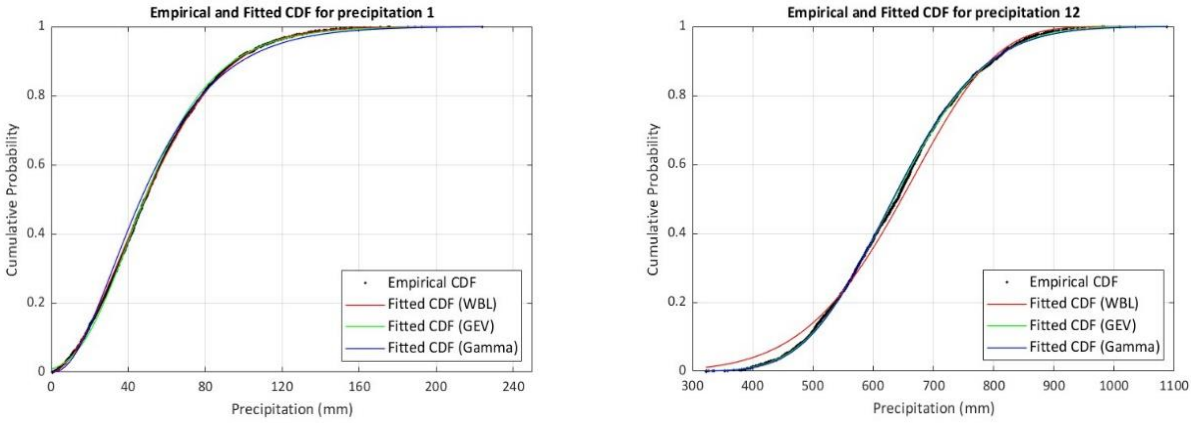
This research comprehensively evaluates the SDAT by comparing it with various theoretical cumulative distribution functions (CDFs) for the SPI-1 and SPI-12. To ensure a rigorous comparison, several statistical metrics are employed: the coefficient of determination (R^2), Pearson's Correlation Coefficient (CC), Mean Squared Error (MSE), Root Mean Squared Error (RMSE), Mean Absolute Error (MAE), and Mean Bias Error (MBE). These metrics provide a multifaceted assessment of the accuracy and reliability of different theoretical CDFs in representing drought conditions, enabling a clear comparison with the SDAT used for SPI calculations.

Results

The cumulative probabilities for the 1-month and 12-month time scales for the precipitation dataset at the Oxford station, spanning from 1767 to 2023, reveal significant insights when analyzed using empirical CDF, Weibull, GEV, and Gamma distributions. For the 1-month time scale (Figure 1.a), the empirical CDF aligns closely with the Weibull, GEV, and Gamma distributions, indicating a strong fit across these methods. Among these, the Weibull distribution shows the closest alignment with the empirical data, followed by GEV and Gamma. This close fit suggests that the Weibull distribution is particularly effective in capturing the variability of short-term precipitation patterns at this station. For the 12-month time scale (Figure 1.b), a similar pattern of agreement is observed, with the GEV distribution providing an almost perfect fit to the empirical data. While still a good fit, the Weibull distribution shows slightly larger deviations compared to Gamma and GEV, indicating that it may be less effective in modeling long-term precipitation patterns than the other distributions.

The results of the SPI using different statistical metrics, as presented in Table 1, further elucidate the performance of these distributions. For the 1-month time scale, the highest R^2 and CC are observed in the comparison between ECDF and Weibull, indicating the best fit. The error metrics, including MSE, RMSE, and MAE, are the lowest for the Weibull distribution, reinforcing its superior fit. The GEV and Gamma distributions also perform well but show slightly higher error metrics. In contrast, for the 12-month time scale, the GEV distribution demonstrates exceptional agreement with the empirical data, evidenced by R^2 and CC values of 0.999 and minimal error metrics. While the Weibull distribution also performs well, it shows slightly higher errors compared to GEV and Gamma. Although highly correlated with the empirical data, the Gamma distribution exhibits larger deviations, particularly in the longer time scale analysis. These findings highlight the strong performance of the Weibull and

GEV distributions in modeling both short-term and long-term precipitation variability, with the GEV distribution showing exceptional fit for the 12-month scale.



a) b)

Figure 1. Cumulative probabilities for the 1-month and 12-month time scales for precipitation data at Oxford station (1767-2023), comparing empirical CDF with Weibull, GEV, and Gamma distributions.

Table 1. Statistical metrics comparing the empirical CDF with Weibull, GEV, and Gamma distributions for the at 1-month and 12-month time scales at Oxford station.

SPI - 1	R^2	CC	MSE	RMSE	MAE	MBE
ECDF vs Weibul	0.981	0.99	0.019	0.138	0.022	-0.00293
ECDF vs GEV	0.98	0.99	0.02	0.141	0.04	-0.0049
ECDF vs Gamma	0.975	0.987	0.025	0.159	0.077	-0.00779
SPI - 12	**R^2**	**CC**	**MSE**	**RMSE**	**MAE**	**MBE**
ECDF vs Weibul	0.979	0.99	0.021	0.146	0.098	-0.00951
ECDF vs GEV	0.999	0.999	0.001	0.034	0.02	0.00001
ECDF vs Gamma	0.998	0.999	0.002	0.048	0.033	-0.00012

Discussion

Despite the critical importance of selecting an appropriate theoretical CDF for accurate drought evaluation, the use of the SDAT tool, particularly its empirical CDF (ECDF), demonstrates a robust capacity to represent original data without error, especially for long-term datasets. This result agrees with the result obtained by Farahmand and AghaKouchak [8]. Also, this effectiveness is notably evident in the context of the Oxford station data, spanning over 250 years, contributing to the analyzed data's stability and reliability. The high performance of the Weibull, GEV, and Gamma distributions, as shown in our statistical metrics, underscores the benefit of long-term data, which enhances the statistical robustness and reduces variability. The ECDF method via the SDAT tool shows exceptional alignment with these distributions, achieving high R^2 and CC, particularly for the GEV distribution in the 12-month scale, which demonstrates almost perfect agreement (R^2 = 0.999, CC = 0.999). This indicates that the inherent stability provided by extensive historical data, coupled with the accuracy of the SDAT tool, provides a powerful approach to precipitation analysis, ensuring minimal errors and high efficiency in representing drought. The statistical metrics further support this, with low MSE and MAE, particularly in long-term data modeling, highlighting the superior performance of the empirical methods facilitated by SDAT.

Conclusion

In conclusion, this research aims to compare the SDAT tool and different CDFs in terms of drought analysis using SPI1 and SPI12. The results showed that the performance of both methods is similar, making the SDAT tool preferable to minimize any error.

References

1. Dabanli, I., Şişman, E., Güçlü, Y. S., Birpınar, M. E., & Şen, Z. (2021). Climate change impacts on sea surface temperature (SST) trend around Turkey seashores. Acta Geophysica, 69, 295-305.
2. Şen, Z. (2020). Water structures and climate change impact: a review. Water Resources Management, 34(13), 4197-4216.

3. McKee, T. B., Doesken, N. J., & Kleist, J. (1993, January). The relationship of drought frequency and duration to time scales. In Proceedings of the 8th Conference on Applied Climatology (Vol. 17, No. 22, pp. 179-183).
4. Vicente-Serrano, S. M., Beguería, S., & López-Moreno, J. I. (2010). A multiscalar drought index sensitive to global warming: the standardized precipitation evapotranspiration index. Journal of climate, 23(7), 1696-1718.
5. WMO, World Meteorological Organization. (2012). Standardized precipitation index user guide. M Svoboda, M Hayes and D Wood.
6. Abu Arra, A., & Şişman, E. (2023). Characteristics of hydrological and meteorological drought based on intensity-duration-frequency (IDF) curves. Water, 15(17), 3142.
7. Abu Arra, A., & Şişman, E. (2024). Innovative Drought Classification Matrix and Acceptable Time Period for Temporal Drought Evaluation. Water Resources Management, 1-23.
8. Farahmand, A., & AghaKouchak, A. (2015). A generalized framework for deriving nonparametric standardized drought indicators. Advances in Water Resources, 76, 140-145.
9. Stephens, M. A. (1970). Use of the Kolmogorov–Smirnov, Cramer–Von Mises and related statistics without extensive tables. Journal of the Royal Statistical Society Series B: Statistical Methodology, 32(1), 115-122.
10. Gringorten, I. I. (1963). A plotting rule for extreme probability paper. Journal of Geophysical Research, 68(3), 813-814.

Advanced Engineering Days

aed.mersin.edu.tr

Suspended sediment dynamics in the semiarid Mediterranean environment: A case study of the Ksob basin, Algeria

Fouad Sakhraoui [1*], Ahmad Abu Arra [*2, 3], Mahmoud Hasbaia [1, 4], Eyüp Şişman [2, 5]

[1]*University of Bejaia, Research Laboratory of Applied Hydraulics and Environment (LRHAE), Faculty of Technology, Bejaia, Algeria, fouad.sakhraoui@univ-bejaia.dz*
[2]*Yildiz Technical University, Department of Civil Engineering, Istanbul, Türkiye, ahmad.arra@std.yildiz.edu.tr; esisman@yildiz.edu.tr*
[3]*An-Najah National University, Department of Civil Engineering, Nablus, Palestine, s11419527@stu.najah.edu*
[4]*University of M'sila, CEHSD Laboratory,* M'Sila 28000, Algeria, mahmoud.hasbaia@univ-msila.dz
[5]*Istanbul Medipol University, School of Engineering and Natural Sciences, Department of Civil Engineering, Istanbul, Türkiye, esisman@medipol.edu.tr*

Cite this study: Sakhraoui, F., Abu Arra, A., Hasbaia, M., & Şişman, E. (2024). Suspended sediment dynamics in the semiarid Mediterranean environment: A case study of the Ksob basin, Algeria. Advanced Engineering Days, 9, 690-693

Keywords
Sediment transport
Suspended sediment
Semiarid
Algeria
Rainfall
SRC

Abstract

Understanding suspended sediment dynamics is crucial for effective water resource management and environmental preservation, particularly in semiarid regions where flood events significantly influence sediment transport. This research evaluates the dynamics of suspended sediments during flood events in the semiarid Mediterranean environment of the Ksob basin, Algeria. Analyzing data from major floods recorded over 18 years (1974-1991), the study compares suspended and water sediment yields from flood events to annual yields. The sediment rating curve (SRC) approach was employed to simulate suspended sediment concentration and water discharge. The key findings indicate total water sediment yields of 214.48 million m^3 and 6.22 million tons during floods. This accounted for 19.27% of the total water load and 29.90% of the total suspended sediment load. Flood events between 1974 and 1991 transported approximately 41.33 million m^3 of water and 1.86 million tons of suspended sediments. The SRCexplained over 92% of the variance in sediment transport for significant floods, highlighting the predominance of annual floods in sediment dynamics. The regression relationship between SRC parameters at the flood events (R^2 = 0.80) suggests consistent suspended sediment processes during floods, providing essential insights for calculating river sediment loads and understanding sediment transport behavior in semiarid regions.

Introduction

Determining suspended sediment transport in Wadis environments is essential for several reasons: assessing sediment dynamics, estimating erosion and soil loss rates, and predicting reservoir siltation. The rates of erosion are influenced by geology, land use, and climatic conditions [1], and understanding their spatial distribution is crucial for soil conservation in watersheds. Soil degradation is a significant global environmental issue, especially in the Mediterranean region, where accelerated erosion is common due to specific geological and climatic conditions as well as human land use [2].

The North Africa region, characterized by a Mediterranean climate, faces significant erosive dynamics, evident in high water erosion rates, loss of fertile soil, substantial suspended sediment transport, and dam siltation. Sedimentation in North African dams, particularly in Algeria, is notably high compared to international standards [2]. Soil erosion rates in Algeria vary across watersheds, with the northwest being the most affected, accounting for 47% of the country's total area and experiencing a dam siltation rate of about 15%. The deposited suspended sediment along the Mediterranean coast of Algeria is estimated at 47 million tons.

This research aims to evaluate, examine, and discuss suspended sediment dynamics during floods in the Ksob basin, Algeria. Major floods documented during the 18 years between 1974 and 1991 were identified, and the suspended and water yields from such events were analyzed and compared to annual yields. The sediment rating curve approach was used to simulate water discharge and suspended sediment concentration (C).

Material and Method

The study area and data collection

The Ksob basin in central Algeria is a sub-basin of the larger Hodna basin (26000 km²). The Ksob basin covers an area of 1418 km², with a broad plateau in the center and very steep terrain in the mountains, ranging in altitude from 595 m to 1903 m (Figure 1). It lies between 35° 48′ and 36° 09′ north latitude and 4° 28′ and 5° 09′ east longitude. The Gravelius compactness coefficient of the watershed is 1.59, and its perimeter measures 214 km. It experiences an average rainfall of 303 mm, which is intense and erratic in space and time.

Suspended sediment and discharge data were provided by the Algerian National Agency for Hydraulic Resources (NAHR). One gauging station, Medjez, is responsible for the Ksob basin. It is located at the outlet point in the basin (X = 673.35 km, Y = 289.65 km, and Z = 636 m). The data measurements cover a period of 18 years, spanning from 1974 to 1991.

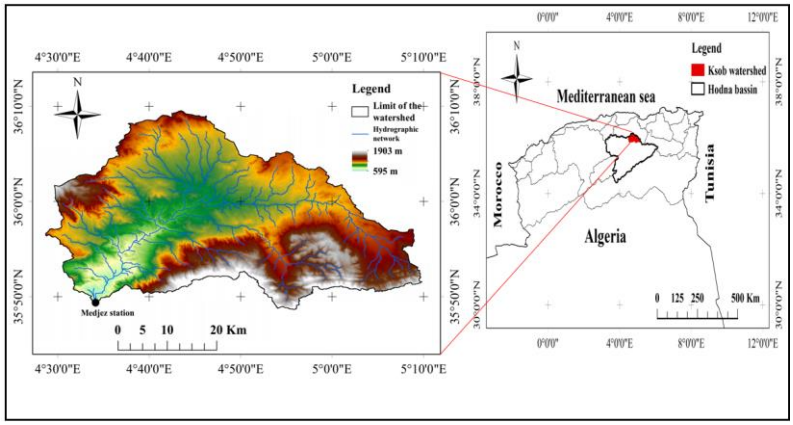


Figure 1. Location of the Ksob basin.

Sediment rating curve model

The linear regression methodology between streamflow discharge Q_L and C is used to identify the variations and trends in river sediment concentrations. The sediment rating curve (SRC) is one of the most widely used models to quantify suspended sediment loads over time. The empirical correlations, according to Campbell and Bauder [3], and Crawford [4], are:

$$C = a\, Q_L^{b-1} \quad (1)$$

$$Q_S = a\, Q_L^{b} \quad (2)$$

Where:
Q_L: water flow discharge in (m^3/s); Q_S: sediment discharge in (kg/s); and C: suspended sediment concentration in (g/l).

Suspended sediment yield

The following formula is used to determine the suspended sediment load over a given period:

$$S_Y = \sum_1^n \frac{[(Q_{i+1} C_{i+1}) + (Q_i C_i)]}{2} (t_{i+1} - t_i) \quad (3)$$

Where:
Q_{Li}, Q_{Li+1}, C_i, and C_{i+1} are measured at t_i and t_{i+1};
Q_{Li} and Q_{Li+1} at any time in m^3/s: water flow discharges in m^3/s;
C_i and C_{i+1}: suspended sediment concentrations in g/l;
S_Y: Suspended sediment load (tons/year).

Water yield calculation:

$$W_Y = \sum_1^n \frac{[(Q_{Li+1}) + (Q_{Li})]}{2} (t_{i+1} - t_i) \quad (4)$$

Where:
W_Y: water yield (m^3/year).

Results and discussion

The total measured water and sediment yields are 214.48 million m^3 and 6.22 million tons during flood. These results show that 19.27% of the total water volume (load) and 29.90% of the total suspended sediment volume (load). This result is consistent with the research in Algeria [5, 6]. The Ksob basin transported approximately 41.33 million m^3 of water yield and 1.86 million tons of suspended sediment loads during the floods (1974 – 1991). According to Table 1, more than 92%, 94%, 95%, 96%, and 98% of the variance in sediment transport for the May 1982, January 1979, June 1975, September 1989, and September 1990 floods, respectively, is explained by the sediment rating curve for each flood. This result makes sense in semiarid regions because of the predominance of annual flood runoff. Regarding sediment transport in hydrological studies, the rainfall event is the most appropriate temporal unit. Many river systems have shown variations in the parameters of the SRC model, a and b, over a specific period. It is generally assumed that these changes result from changes in the sediment supply and/or erodibility in the basin. A stronger regressive relationship (power) is established between a and b coefficients at the flood events scale (R^2 = 0.80) (Figure 2), suggesting that suspended sediment processes for a wadi exhibit the same behavior at the flood events scale.

These results are very important because they allow the calculation of river sediment loads. Also, this analysis has shown that a and b are correlated, such as in global research.

Table 1. Characteristics of the Ksob water yields and suspended sediment loads during the flood period (1974 - 1991).

Floods (Month – Year)	P Monthly (mm)	Wy Annual (Mm^3)	Sy Annual (Mt)	Wy Flood (Mm^3)	Sy Flood (Mt)	Wy Flood (%)	Sy Flood (%)	Erosion (ton/km^2)	R^2	a	b
06-1975	36	5.79	0.33	2.96	0.08	51.12	24.24	256.41	0.95	17.33	1.13
01-1979	44	12.79	0.48	2.28	0.09	17.82	18.75	377.60	0.94	2.31	1.69
09-1979	108	14.50	0.76	3.51	0.26	24.21	34.21	599.33	0.74	4.34	1.62
10 -1981	38.2	33.20	1.07	4.80	0.20	14.46	18.69	839.60	0.87	10.35	1.30
05-1982	69.2	33.20	1.07	13.15	0.38	39.61	35.51	839.60	0.92	5.15	1.33
10-1985	61	25.81	0.79	3.05	0.13	11.82	16.46	385.66	0.85	8.26	1.36
09 -1989	49.5	19.42	0.78	9.66	0.58	49.74	74.36	610.86	0.96	19.01	1.21
09 - 1990	38.5	9.17	0.23	1.92	0.14	20.94	60.87	181.55	0.98	7.88	1.506

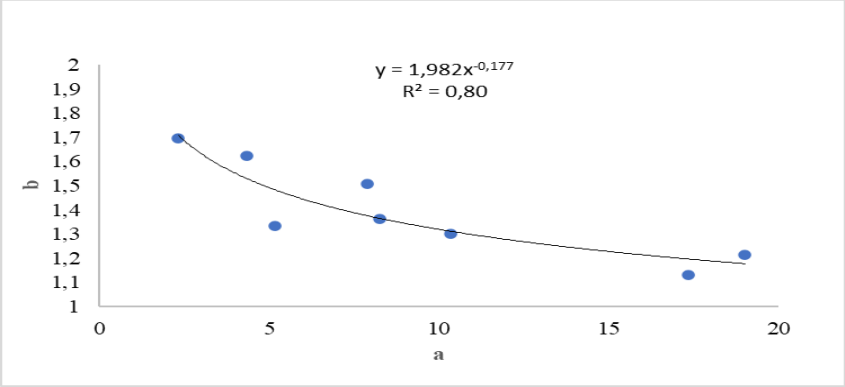


Figure 2. The power function of SRC parameters (a, b) at the scale of flood events.

Conclusion

Suspended sediment transport is critical for developing countries, especially in semiarid climates. In this investigation, during floods, the Ksob basin moves 1.86 million tons of silt and about 41.33 million m^3 of water. Additionally, at the flood scale for the Ksob watershed, there is a stronger inverse relationship (power) between a and b coefficients (R^2 = 0.80). The Sediment Rating Curve (SRC) models have been extensively validated on different time scales in numerous basins in Algeria. While there is no universal physical explanation for the SRC coefficients, specific relationships can be used to explain them. At the flood scale, these parameters also show a good power relationship.

References

1. Giaccone, E., Vergari, F., Del Monte, M., & Fratianni, S. (2015). L'impact du climat sur les dynamiques morphologiques en Toscane (Italie centrale). Proceedings of the "XXVIIIe Colloque de l'Association Internationale de Climatologie", Liège 2015.

2. Hallouz, F., Meddi, M., Mahé, G., Toumi, S., & Rahmani, A. S. E. (2018). Erosion, suspended sediment transport and sedimentation on the Wadi Mina at the Sidi M'Hamed Ben Aouda Dam, Algeria. Water, 10, 895. doi: 10.3390/w10070895.
3. Campbell, F. B., & Bauder, H. A. (1940). A rating curve method for determining silt discharge of streams. American Geophysical Union, 21, 603-607. doi: 10.1029/TR021i002p00603.
4. Crawford, C. G. (1991). Estimation of suspended-sediment rating curves and mean suspended-sediment loads.
5. Benselama, O., Hasbaia, M., & Djoukbala, O. (2021). Suspended sedimentary dynamics under Mediterranean semiarid environment of Wadi El Maleh watershed, Algeria. Modeling Earth Systems and Environment, 8, 1013–1023. https://doi.org/10.1007/s40808-021-01133-4.
6. Djoukbala, O., Mazour, M., Hasbaia, M., & Benselama, O. (2018). Estimating of water erosion in semiarid regions using RUSLE equation under GIS environment. Environmental Earth Sciences, 77, 1–13. https://doi.org/10.1007/s12665-018-7532-1

Advanced Engineering Days

aed.mersin.edu.tr

Assessment of drought using a probabilistic standardized index

Burak, Kızılöz*[1], Gizem Aylin Şahin [2]

[1]*Kocaeli Metropolitan Municipality Water and Sewerage Administration, Kocaeli, Türkiye, bkiziloz@isu.gov.tr*
[2]*Gebze Technical University, Environmental Engineering, Kocaeli, Türkiye, gsahin2020@gtu.edu.tr*

Cite this study: Kızılöz, B., & Şahin, G. A. (2024). Assessment of drought using a probabilistic standardized index. Advanced Engineering Days, 9, 694-696

Keywords
Drought
SPI
PSI
Probabilistic
Kocaeli

Abstract

Global climate change has an increasing impact throughout the world. Researchers use various hydrological, meteorological, and agricultural drought indexes suggested by the World Meteorological Organization (WMO) to analyze and evaluate the impacts of global climate change. In this study, the drought assessment was made through the Probabilistic Standardization Index (PSI) approach for a 3-month-time-scale in Kocaeli province. Gamma, Weibull, Generalized Extreme Value, Rayleigh, Gumbel, Logistic, and Normal distributions were preferred to obtain the best distribution for precipitations. Also, the best distribution was determined as Weibull with the help of the Taylor Diagram (TD). According to PSI-3, it is clear that dry months are 6% higher than wet months. Therefore, it is required to make risk management and action plans for water resources in the region. In future studies, making comparisons with different indices and time scales may be useful in terms of the assessment of drought severity.

Introduction

In recent years, scientists have discussed sensitively extreme events such as drought arising out of global warming and climate change. In particular, the increasing trend of drought results in environmental, agricultural, and economic crises in arid and humid climates [1]. Drought-induced natural disasters cause a significant economic loss, about 8 billion dollars every year throughout the world [2]. On the other hand, the Intergovernmental Panel on Climate Change's Fifth Assessment Report (IPCC) indicates that the global temperature increased by 0.85°C (1880-2012) and, in case the increase of global greenhouse gas emissions at the current rate until 2100, the mean temperature will increase between 1.1 and 4.6°C [3]. Changes in rainfall patterns and a potential increase in the frequency of droughts can be taken into account as the main consequences of climate changes resulting from global warming.

To evaluate meteorological, hydrological, and agricultural droughts, various drought indices and indicators have been suggested by the World Meteorological Organization [4]. Among these drought indices, the Standardized Precipitation Index (SPI) is used most commonly in researches. The SPI, proposed by [5] uses the Gamma and Standard Normal PDF to classify drought. The SPI calculation consists of two steps; in the first step, the best cumulative distribution function (CDF) is identified for a specific hydro-meteorological time series data, and in the second step, the data are converted into a Gaussian (standard normal) PDF with standard deviation 1 and mean 0. This is called the Probabilistic Standardized Index (PSI) [6]. In the literature, certain manuscripts with the correct SPI implementations are available [7], [8], and [9]. These manuscripts were published in different journals. In this study, a 3-month time scale employing 742 monthly rainfall data (1956-2022) of Kocaeli province obtained from the General Directorate of State Meteorology was analyzed through the PSI approach suggested by [6].

Material and Method

Probabilistic standardized index (PSI)

SPI (Standardized Precipitation Index) was recommended by [5] to monitor and analyze meteorological drought in different areas and on different month-time scales. The Standardized Precipitation Index is based on the PSI. In this study, firstly, the best cumulative distribution function (CDF) that is compatible with long-term

precipitation time series data was obtained. Secondly, the probability values corresponding to each original precipitation data were identified through the CDF. Finally, the data transformation was made by determining the values of each probability value in the standard normal PDF. Each statistical Z-score value obtained from the data transformation represents the actual PSI (SPI) value (Figure 1).

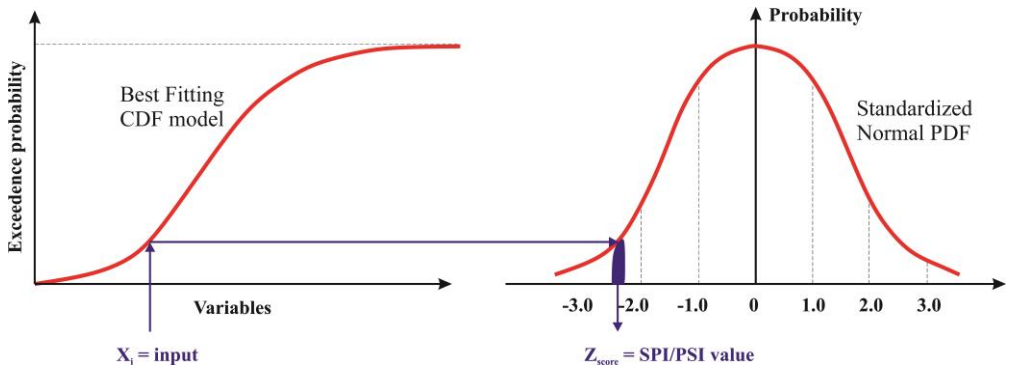


Figure 1. PSI procedure

Taylor Diagram (TD)

The spatial consistency between target variables and model output can be evaluated quantitatively with TD [10]. This one is widely preferred to compare the model performances statistically. It also includes certain metrics such as correlation coefficient (R), standard deviation (SD), root mean square error (RMSE).

Results and Discussion

In this study, 742 monthly precipitation data (1961-2022) belonging to Kocaeli precipitation station no.17066, obtained from the General Directorate of State Meteorology was analyzed. CDFs were drawn through the Python program to identify the fit of the original precipitation data with Gamma, Weibull, Generalized Extreme Value, Rayleigh, Gumbel, Logistic, and Normal distributions. It is seen in the below figure that the original precipitation data of the Generalized Extreme Value, Rayleigh, and Normal distributions are not compatible with the CDFs distributions (Figure 2).

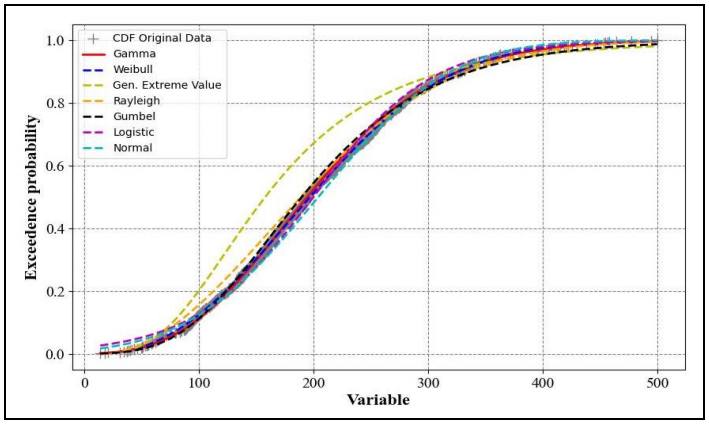


Figure 2. Selecting the best CDF

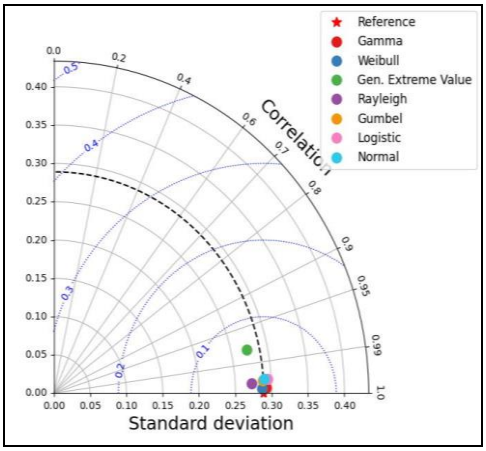


Figure 3. TD diagram

TD was used to statistically identify the optimal CDF that is compatible with the original data. Figure 3 indicates that the most statistically compatible distribution is the Weibull distribution. The correlation coefficient value of this distribution was calculated as 0.99979, and its standard deviation is 0.287.

The PSI-3 values for the 3-month-time-scale obtained through the Weibull distribution are available below (Figure 4). According to Figure 4, 380 months are dry, and 360 months are wet. Extremely dry months account for 4% of all dry months, and normal dry months for 42%. Also, the maximum extreme dry (-3.37) was recorded in September 1969. Similarly, extremely wet months account for 6% of all wet months and normal wet months for 35%. The maximum extreme wet (2.89) was recorded in December 1973.

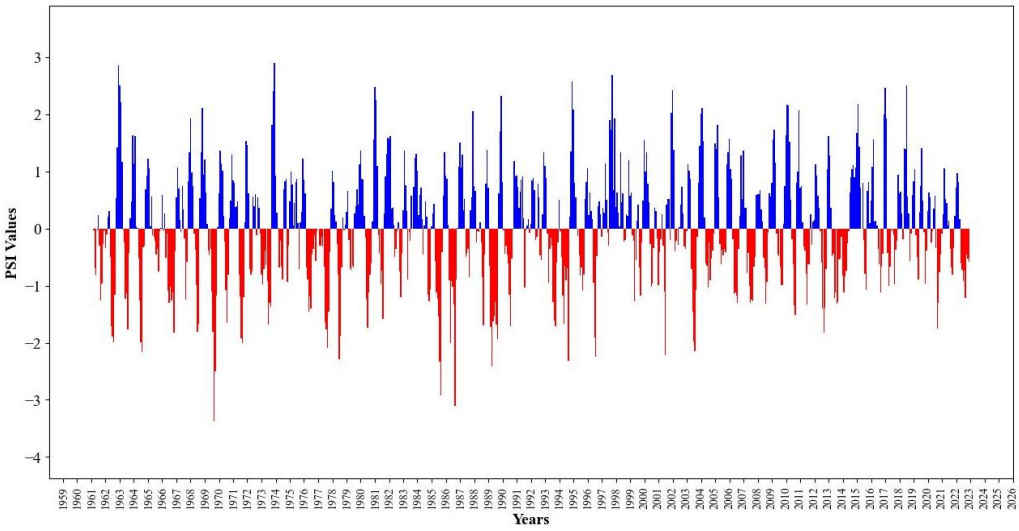


Figure 4. PSI-3 values

Conclusion

According to the PSI-3 analysis made in Kocaeli province, the drought has an impact on the region. Therefore, protecting water resources, preventing water losses in drinking water supply networks, and using recycled water are required to prevent drought. In future studies, considering different month-time scales such as 3, 6, 9, and 12 months and analyzing different indices may be useful in terms of drought assessment.

References

1. Li, B., Su, H., Chen, F., Wu, J., & Qi, J. (2013). The changing characteristics of drought in China from 1982 to 2005. Natural Hazards, 68(2), 723–743. https://doi.org/10.1007/s11069-013-0649-3
2. Liu, Q., Huo, A., Zhao, Z., Zhao, X., Rebouh, N.Y., Luo, C. (2024). Spatial differentiation and influencing factors analysis of drought characteristics based on the standardized precipitation index: a case study of the yellow river basin. Water, 16(10), 1337. https://doi.org/10.3390/w16101337
3. IPCC 2013 Summary for policymakers. In Climate Change 2013: The Physical Science Basis, Contribution of Working Group I to the Fifth Assessment Report of the Intergovernmental Panel on Climate Change.
4. WMO (2016). Handbook of Drought Indicators and Indices. Geneva, Switzerland: Meteorological Organization WMO-No. 1173.
5. Mckee T. B., Doesken, N. Y., & Kleist, Y. (1993) The relationship of drought frequency and duration to time scales. In: Proceedings of the 8th Conference on Applied Climatology, Anaheim, CA, USA, 17(22), 179–184.
6. Şen, Z., & Şişman, E. (2024). Probabilistic standardization index adjustment for standardized precipitation index (SPI). Theoretical and Applied Climatology, 155(4), 2747–2756. https://doi.org/10.1007/s00704-023-04784-8
7. Bouaziz, M., Medhioub, E., & Csaplovisc, E. (2021). A machine learning model for drought tracking and forecasting using remote precipitation data and a standardized precipitation index from arid regions. Journal of Arid Environments, Academic Press. https://doi.org/10.1016/j.jaridenv.2021.104478
8. Abu Arra, A., & Şişman, E. (2023). Characteristics of hydrological and meteorological drought based on intensity-duration-frequency (idf) curves. Water (Switzerland), 15(17). https://doi.org/10.3390/w15173142
9. Şen, Z. (2024). Fuzzy standardized precipitation index (FSPI) for drought early warning procedure. Theoretical and Applied Climatology, 155(2), 1281–1287. https://doi.org/10.1007/s00704-023-04691-y
10. Taylor, K. E. (2001). Summarizing multiple aspects of model performance in a single diagram. Journal of Geophysical Research Atmospheres, 106(D7), 7183–7192. https://doi.org/10.1029/2000JD900719

Advanced Engineering Days

aed.mersin.edu.tr

Environmental sustainability in line with urban infrastructure development with focus on sustainable development

Mahdi Jalili Marand *[1], **Sheyda Sarikhan Kheljan** [2]

[1] *University of Tabriz, Civil Engineering Department, Iran, mahdi.jalilimarand@gmail.com*
[2] *University of Tabriz, Landscape Engineering Department, Iran, sheydasarikhan77@gmail.com*

Cite this study: Jalili Marand, M., & Sarikhan Kheljan, S. (2024). Environmental sustainability in line with urban infrastructure development with focus on sustainable development. Advanced Engineering Days, 9, 697-699

Keywords
Environment
Infrastructure
Sustainability
Development
Urban

Abstract

A human-made site consists of its components interaction, especially infrastructure and environment. The issue of sustainability in today's modern era has been so much considered that by ignoring, any conversation about the environment and urban infrastructure development is incomplete. Adapting the infrastructure of cities with environmental sustainability is one of the best ways to prevent the influence of inappropriate climate parameters and global warming on urban lifestyle. the environmental sustainability of urban infrastructure is an efficient and productive that takes steps to preserve human values according to the needs of future and guide cities towards sustainable regional and national development and ecological preparations.

Introduction

The issue of sustainability in today's modern era has been so much considered that by ignoring, any conversation about the environment and urban infrastructure development is incomplete. It can be said that sustainability expresses the continuity of current and future and it focuses on all the environmental, social, cultural and economic aspects of infrastructure to supply human needs considering the ability of future generation to receive the requirements. In other words, urban infrastructure and human activities should be carried out without reducing and degrading the surrounding natural environment and coordinate the use of resources, development and investment's guidance, technologies and innovations, changes and etc. to support generations demand in all dimensions of time. We must mention; It is necessary to pay attention to topics of construction facilities, operational methods and management practices to promote artificial and natural infrastructure based on sustainable development and environment.

Material and Method

Adapting the infrastructure of cities with environmental sustainability is one of the best ways to prevent the influence of inappropriate climate parameters and global warming on urban lifestyle. nowadays the infrastructures have inappropriate patterns such as incorrect and inefficient location of city applications, traditional transportation patterns, predominance of personal motor vehicles, destruction and deterioration of natural areas with frequent construction activities, utilization of materials with weak thermal properties, use of new urban development models without considering the theoretical foundations of atmosphere and etc. have significant effects in slowing down the process of sustainable development.
It can be said that following 4 infrastructures are the main foundations of sustainable and ecological city development:

A. Green infrastructure: including green natural areas.

B. Blue infrastructure: including hydraulic management and conservation system of water and sewage.

C. Gray infrastructure: including sewage collection equipment, waterways and roads.

D. Red infrastructure: including artificial and man-made areas, buildings and open spaces.

Results

Cities are the engines of economic growth and innovation, providing a wealth of opportunities for people to live, work, and play. However, rapid urbanization and industrialization have resulted in a plethora of environmental and social issues that are detrimental to human health and well-being. These include poor air quality, traffic congestion, and the urban heat island effect. Sustainable urban infrastructure is essential for creating livable, healthy cities that meet the needs of their residents while protecting the environment. Infrastructures are a group of interconnected structural factors that create the urban structure. The topic of development in urban planning is an evolving process with the aim of improving the existing situation in human societies, respecting environmental laws and increasing human welfare and comfort. It can be said that activities such as refraining from tree and dense vegetation planting in narrow passages, paying attention to fresh air corridors, greening city facades and roofs with plants, shrubs and trees (green roofs and walls), focusing on urban agriculture and horticulture, construction of open spaces and urban parks in central city context, paying attention to climatic and resistance characteristics of plants, planting deciduous vegetation (provide summer shade and winter light), planting coniferous plants (wind protection), planting hedges in Heavy traffic roads, avoiding vegetation plant that emits hydrocarbons (sycamore and fir), using building materials with high reflection (white and green color), using solar cells, wooden materials utilization (atmospheric carbon absorption), reducing steel and concrete usage, creating lightweight structures with good insulation (salt and paraffin), making trombe walls, increasing the slope of roofs, clear and appropriate geometrical orientation of buildings, paying attention to the structures protection from effects of wind channel, installation of wind channel turbines, traffic reduction, creation of premium public transportation, developing east-west blocks (facing south), constructing wind towers, biophilic (bio-friendly) design, creating vertical forests (green buildings), passive solar architecture (cooling and heating), passive wind architecture (ventilation), qualitative attention to water bodies, ponds and lakes, preservating natural urban landscapes, refraining from Building commercial applications in the outer limits of city, giving priority to the distribution of commercial applications over their concentration in one place, city promotion with relative density, preventing the city from expanding excessively, avoiding new city and industrial applications construction near the coasts, separating cities with high-speed railway lines and etc. are among the topics that play an effective role in increasing human well-being, relationship between man and nature and maintaining the livability of cities.

The benefits of sustainable urban infrastructure are many and varied. Perhaps the most significant benefit is the reduction of air pollution and greenhouse gas emissions. The transportation sector is a significant contributor to air pollution in cities. Sustainable transportation infrastructure, such as bike lanes and public transit systems, can reduce emissions and improve air quality. According to the American Public Transportation Association, the use of public transit reduces greenhouse gas emissions by 37 million metric tons annually. 6 fields of green mobility, waste management (production, recycling and safe disposal), air pollution (removal of polluting particles with dry sediment), energy consumption, urban biodiversity, and water management are among the important links of the practical programs. It should be mentioned that environmental sustainability has been examined with qualitative criteria and factors such as preserving the quality of natural resources and the landscape of geographical space, compatibility with climate and geography, biological vitality, developing organic and ecologic construction, considering flexibility, connecting open spaces, providing basic infrastructure (electricity, energy, water and sewage), Paying attention to the energy consumption efficiency, reducing and stabilizing the consumption of non-renewable resources (mineral and fossil resources, underground water and plants), using renewable energy, decreasing and maintaining the limit of pollutant production in local and global capacity (greenhouse gases, chemicals and toxic waste), climatic comfort attention, sounds and smells attention, preservating of ecosystem and nature, reducing production and increasing waste recycling, hazardous waste management and etc. have a significant role in its improvement.

Examples of sustainable urban infrastructure are many and varied. Green roofs and walls are a popular form of sustainable infrastructure that can reduce the urban heat island effect, improve air quality, and provide habitat for wildlife. Green roofs are vegetated surfaces on rooftops that can absorb and store rainwater, reducing the amount of storm water runoff that enters the sewer system. They can also insulate buildings, reducing the energy needed for heating and cooling. Green walls are vertical gardens that can be installed on the exterior or interior of buildings, providing a range of benefits such as improving air quality, reducing noise pollution, and enhancing the aesthetic appeal of buildings. Roadside and urban infrastructures such as street furniture are prone to damage and deterioration. As infrastructure deteriorates, it requires either replacement or enhancement. Existing public funding sources are inadequate to meet these needs. Self-healing technology could protect surrounding paving and foundations from damage when items of infrastructure are impacted, which can reduce maintenance and improve the sustainability of urban developments. Self-healing developments result in zero waste and zero-landfill from maintenance on items of urban infrastructure for the life of the development. technology is key factor in the implementation of renewable energy sources, which not only improve energy efficiency, but also the electricity demand of communication networks and the self-sufficiency of a city in the instance of disaster. Projects that involve zero-energy buildings, reduced cooling and heating demand, and greater understanding of occupant behavior achieve a greater holistic perspective of wasteful energy sourcing.

Discussion

The environmental sustainability of urban infrastructure is an efficient and productive that takes steps to preserve human values according to the needs of future and guide cities towards sustainable regional and national development and ecological preparations. In other words, preventing the aimless and heterogeneous development of cities and related problems such as pollution, physical and mental illnesses, continuous improvement of the life's quality, inspiration from natural environment, provision of renewable resources and energy by applying minimal changes to the earth's surface and having achievements are the most general and important results of sustainable cities. Sustainable urban infrastructure also promotes public health by reducing exposure to pollutants and encouraging physical activity. Air pollution is linked to a range of health problems, including respiratory and cardiovascular diseases. Sustainable transportation infrastructure can encourage active modes of transportation, such as walking and cycling, which are associated with better health outcomes.

The position of infrastructure elements in urban sustainability:

A. habitation

B. Transportation system

C. Municipal facilities and equipment

C1. Places and service centers (Superstructure facilities and equipment):

Educational/ Sports/ Green and open spaces/ Health care/ Cultural - religious/ Administrative/ Commercial/ Military/ Industrial – manufacturing/ Cemetery

C2. Urban infrastructures (Infrastructure facilities and equipment):

water supply/ Remote communication/ Electrification/ Wastewater and Surface water disposal/ Collection and disposal of waste/ Refueling and energies supply/ Food distribution and storage/ Maintenance and keeping facilities

Conclusion

A human-made site consists of its components interaction, especially infrastructure and environment. On the other hand, perhaps the biggest challenge of humanity and most prominent threat to cities around the world is climate change. Therefore, the coherent redefinition of urban and environmental platform's interactive model, study of effective structure's scientific foundations, examination of infrastructure levels, presentation of construction guidelines to reduce the negative effects of environmental challenges and the link with principles of sustainable urbanism are among the most important achievements of the article. Sustainable urban infrastructure expands on the concept of urban infrastructure by adding the sustainability element with the expectation of improved and more resilient urban development. In the construction and physical and organizational structures that enable cities to function, sustainability also aims to meet the needs of the present generation without compromising the capabilities of the future generations.

References

1. Akbari, H., Menon, S., & Rosenfeld, A. (2009). Global cooling: increasing world-wide urban albedos to offset CO2. Climatic change, 94(3), 275-286.
2. Besir, A. B., & Cuce, E. (2018). Green roofs and facades: A comprehensive review. Renewable and Sustainable Energy Reviews, 82, 915-939.
3. Bohrani, K., & Akbari, M. (2016). Urban planning and climate change. National Congress of Modern Urban Planning and Management, Tehran.
4. Buffi, A., & Angelini, G. M. (2019). Adaptive timber towers. An evolutionary prototype for the 21st century skyscraper. Digital Wood Design: Innovative Techniques of Representation in Architectural Design, 971-987.
5. Fallmann, J., Emeis, S., & Suppan, P. (2013). Mitigation of urban heat stress–a modelling case study for the area of Stuttgart. DIE ERDE–Journal of the Geographical Society of Berlin, 144(3-4), 202-216.
6. Hasani, A., & Mofidi Shamirani, M. (2019). The interaction of urban design and climate change based on theories. Geography (Regional Planning) Journal, 11(1), 461-472.

Advanced Engineering Days

aed.mersin.edu.tr

Effect of groundwater level change on retaining wall design

İhsan Yaman [1], Abdülkadir Özcan [1], Esra Uray [*2]

[1]*KTO Karatay University, Institute of Postgraduate Education, Department of Civil Engineering, Türkiye, 211300192@ogrenci.karatay.edu.tr, kadirozcan42@hotmail.com*
[2]*KTO Karatay University, Department of Civil Engineering, Türkiye, esra.urayækaratay.edu.tr*

Cite this study: Yaman, İ., Özcan, A., Uray, E. (2024). Effect of groundwater level change on reinforcement wall design. Advanced Engineering Days, 9, 700-702

Keywords
Retaining wall
Groundwater level
Stability of retaining wall
Failure scenario

Abstract

Retaining structures are critical structures for the effective and efficient use of land. Especially on lands with high slopes, they are often used to ensure effective use. It can be seen that the use of retaining structures has increased in today's crowded cities. In areas where the height levels vary, it is a frequently used solution in crowded residential areas due to the congestion and in cut areas of intercity highways. Therefore, the design and construction of retaining structures are essential in terms of human and environmental safety. In our country, the water pressure that occurs when the water flow on the ground cannot be drained from the ground environment due to increasing rainfall also causes stability problems in the retaining walls. In the design of the retaining wall, the effect of the groundwater level as well as the horizontal ground pressure occurring between two different ground levels must be taken into account. In this study, the importance of the effect of change in groundwater level on the stability of the retaining wall is given together with literature studies.

Introduction

A retaining wall is a support structure built to hold the volume of soil behind it. It is commonly used in stabilizing slopes, deep excavations, and addressing height differences in terrain. Methods of construction include the use of rubble stone, concrete, or reinforced concrete. However, in recent years, we are all aware of the risk of retaining walls collapsing, leading to loss of life and property. The first question that needs to be asked in such cases is why a retaining wall collapses years after its construction. In areas where groundwater is close to the surface, it is important to take the necessary precautions by performing stability analyses for different water levels during the design phase of the retaining wall. The design of retaining walls in geotechnical engineering is a complex engineering problem with many unknowns, limitations, and limitations due to parameters such as variable soil properties, stratification, special conditions of the construction area, and groundwater status. Instead of using traditional methods for obtaining appropriate structural designs that take into account all parameters affecting the behavior of the system, the utilizing of metaheuristic optimization algorithms based on mathematical formulas of traditional design methods possible to obtain optimum designs in terms of cost [1,2]. Taking into account the effect of changing water height in retaining wall designs, using this kind of algorithm to find the most suitable design is important to obtain the critical water height at which the stability of the wall deteriorates. Since the stabilization checks for sliding overturning, and slope stability vary depending on the changing wall dimensions in the retaining wall design, obtaining of safe and optimum design among many wall design combinations is an alternative and fast way via optimization algorithms [3]. It is an important criterion for the design to complete the retaining wall design, which provides stability verifications determined by taking into account the soil properties obtained from the field and laboratory, as well as the loading and land conditions, as soon as possible. It can be seen that the retaining wall stability problem shown in Figure 1 is caused by the effect of precipitation and changes in the groundwater level. This article aims to contribute to the design of widely used reinforced concrete retaining walls.



Ankara, 2022 [4]



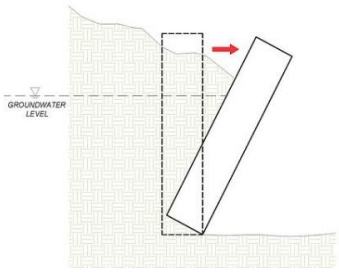
Elazığ, 2023 [5]



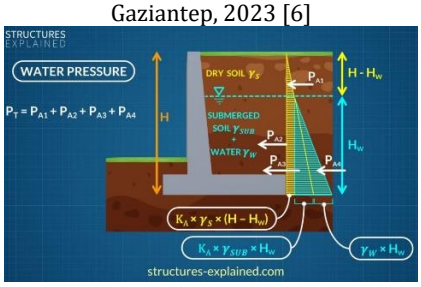
Gaziantep, 2023 [6]



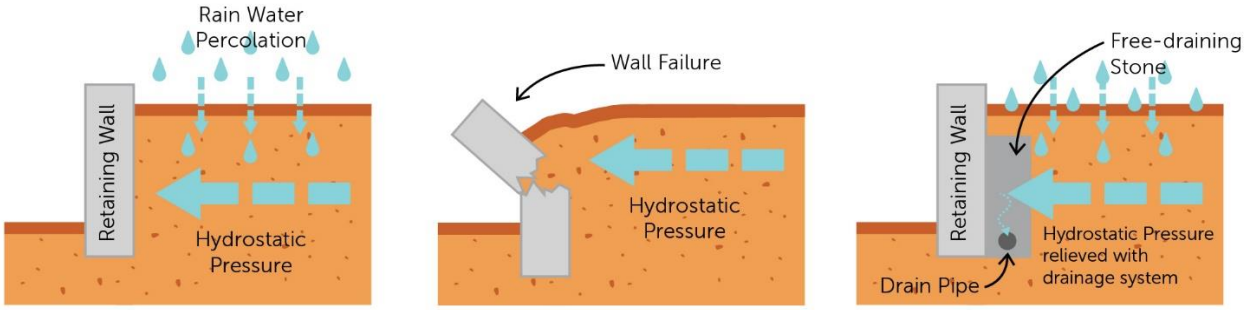
İstanbul, 2024 [7]



Retaining wall overturning [8]



Groundwater level effect on the wall [9]



Draine system behind the wall [10]

Figure 1. Groundwater level effect behind retaining wall and failure cases

Discussion Based on Literature Review

The retaining wall, which occurs after heavy rains, loses its stability and causes loss of life and property. Excessive and intense precipitation caused by climate change, one of the most important global problems of today, has increased flood risks and loss of life and property in many parts of the world such as Ethiopia [11], Egypt [12], Europe [13], and Brazil [14]. Not taking into account the effect of increasing intense and excessive rainfall in the design of the retaining wall and not being able to drain the rising water behind the wall due to blockage in the drainage channels are the most important factors affecting the stability of the retaining wall. Köktan et al. [15] examined the behavior of the retaining wall under the influence of seismic loads in the case of different groundwater levels. Similarly, the loss of stability caused by the change in groundwater level in slope stability was investigated by installing geotechnical analysis software. [16]. Fluctuations in groundwater levels can impact lateral pressure, influencing the design of retaining wall constructions. Since changes in groundwater level cause changes in pore water pressure in the ground, a statistical method was used to evaluate this effect [17]. Groundwater level changes are crucial in the design of reinforcement walls. Proper drainage design, including dewatering pipes and drainage bodies, can reduce pressure on retaining walls [18].

Conclusion

In the literature review, there were not many studies examining the stability effect of groundwater level on retaining walls. According to the studies examined, it was seen that the increasing groundwater level caused stability problems in the retaining wall. It may be the case that the design of the retaining wall did not take into account the impact of water at all. In addition, seasonal normal precipitation was taken into account in the design of the retaining wall, and another consideration may be that increased precipitation intensity was not foreseen.

Appropriate drainage measures must be taken to discharge the groundwater rising behind the retaining wall, and necessary maintenance and repair must be carried out to prevent clogging of the drainage pipes throughout the service life of the wall. Another important thing to consider is the use of permeable fill ground material behind the retaining wall. The use of cohesive soil as a backfill behind the wall may cause negative situations due to the increased amount of water. However, when the retaining wall is constructed using gabion baskets, it does not

require drainage measures due to its permeable and void structure. The possible critical water level that will be created by precipitation that increases in severity and intensity based on today's changing climate conditions must be taken into account in the design.

References

1. Gandomi, A. H., Kashani, A. R., Roke, D. A., & Mousavi, M. (2015). Optimization of retaining wall design using recent swarm intelligence techniques. *Engineering Structures*, *103*, 72–84.
2. Kalemci, E. N., İkizler, S. B., Dede, T., & Angın, Z. (2020). Design of reinforced concrete cantilever retaining wall using Grey wolf optimization algorithm. *Structures*, *23*, 245–253. https://doi.org/10.1016/j.istruc.2019.09.013
3. Uray, E., Tan, Ö., Çarbaş, S., & Erkan, H. (2021). Metaheuristics-based pre-design guide for cantilever retaining walls. *Teknik Dergi*, *32*(4). https://doi.org/10.18400/tekderg.561956
4. Ankara. (2022). *News 1, Query: Retaining wall collapsed after rain, Data Accessed: 10.06.2024*. https://www.dha.com.tr/yerel-haberler/ankara/ankarada-istinat-duvari-yikildi-4-apartman-1-2082787
5. Elazığ. (2023). *News 2, Query: Retaining wall collapsed after rain, Data Accessed: 10.06.2024*. https://www.iha.com.tr/elazig-haberleri/elazigda-istinat-duvari-kismen-coktu-binalar-ucurumun-esiginde-46696392
6. Gaziantep. (2023). *News 3, Query: Retaining wall collapsed after rain, Data Accessed: 10.06.2024*. https://www.ntv.com.tr/galeri/turkiye/yogun-yagis-sonrasi-istinat-duvari-coktu-araclar-altindakaldi,N7F9P8LLekuuWx88YX6EaQ/fXivHMX8REyjqOFzSDuHXQ
7. İstanbul. (2024). *News 4, Query: Retaining wall collapsed after rain, Data Accessed: 10.06.2024*. https://www.yirmidort.tv/gundem/pendikte-asiri-yagis-nedeniyle-istinat-duvari-coktu-146381
8. Engineer Mike. (2024). *Ways Retaining Walls Fail*. https://www.sitedamage.com/retaining-walls
9. Structures Explained. (2021). *Retaining Walls Explained, Types, Forces, Failure and Reinforcement*. https://structures-explained.com/retaining-wall-types-failure-reinforcement/
10. MH Site Construction. (n.d.). *Drainage*. https://mhsiteconstruction.com/retaining-walls/
11. Gebreigziabher, E. T. (2020). Analysis Rainfall Intensity-Duration-Frequencyrelationships Under Climate Change for Mekele City, Ethiopia. *International Journal of Technical Research & Science*, *5*(2), 1–11. https://doi.org/10.30780/IJTRS.V05.I02.001
12. Mahgoob, Y. (2023). Impact of Climate and Environment Changes on the Sustainability of the Coastal Areas The Case of Ain Sukhna, Red Sea, Egypt. *International Journal of Multidisciplinary Studies in Architecture and Cultural Heritage*, *6*(1), 98–116. https://doi.org/10.21608/IJMSAC.2023.193634.1020
13. Frei, C., Schöll, R., Fukutome, S., Schmidli, J., & Vidale, P. L. (2006). Future change of precipitation extremes in Europe: Intercomparison of scenarios from regional climate models. *Journal of Geophysical Research: Atmospheres*, *111*(D6). https://doi.org/10.1029/2005JD005965
14. Marengo, J. A., Ambrizzi, T., Alves, L. M., Barreto, N. J. C., Simões Reboita, M., & Ramos, A. M. (2020). Changing Trends in Rainfall Extremes in the Metropolitan Area of São Paulo: Causes and Impacts. *Frontiers in Climate*, *2*, 557121. https://doi.org/10.3389/FCLIM.2020.00003/BIBTEX
15. Makalesi, A., Research, /, Konsol, A. B., Duvarının, İ., Davranışına, S., Su, Y., Değişimlerin, S., İncelenmesi, E., Köktan, U., Demir, G., & Kerem, M. (2019). Bir Konsol İstinat Duvarının Sismik Davranışına Yeraltı Su Seviyesindeki Değişimlerin Etkisinin İncelenmesi. *Gümüşhane Üniversitesi Fen Bilimleri Dergisi*, *9*(2), 307–317. https://doi.org/10.17714/GUMUSFENBIL.398875
16. Tutuk, T. (2004). *Zemin tabakalanması ve yer altı su seviyesi değişiminin şev stabilitesi üzerine etkisi (The effect of groundwater level and soil layers on slope)*. Yüksek Lisans Tezi (Master Thesis), Anadolu Üniversitesi, Fen Bilimleri Enstitüsü, İnşaat Mühendisliği.
17. Molina-Gómez, F., Bulla-Cruz, L. A., Moreno-Anselmi, L. Á., Ruge, J. C., & Arévalo-Daza, C. (2019). Assessment of groundwater level variations using multivariate statistical methods. *Ingeniería e Investigación*, *39*(1), 36–42. https://doi.org/10.15446/ing.investig.v39n1.71670
18. Lu, H., Yin, Y., & Liu, Y. (2021). Force analysis and design of backfill retaining wall in large complex Goaf. *IOP Conference Series: Earth and Environmental Science*, *768*(1), 012094. https://doi.org/10.1088/1755-1315/768/1/012094

Advanced Engineering Days

aed.mersin.edu.tr

Literature Review of Artificial Intelligence and Geostatistical Analyses in Geotechnical Engineering

Hatice Beyza Urgancı [1], Burak Bilir [1], Esra Uray *[2], Vahdettin Demir [2]

[1]KTO Karatay University, Institute of Postgraduate Education, Department of Civil Engineering, Türkiye, 211300053@ogrenci.karatay.edu.tr, 221300475@ogrenci.karatay.edu.tr
[2]KTO Karatay University, Department of Civil Engineering, Türkiye, esra.uray@karatay.edu.tr, vahdettin.demir@karatay.edu.tr,

Cite this study: Urgancı, H. B., Bilir, B. Uray, E., Demir, V. (2024). Literature Review of Artificial Intelligence and Geostatistical Analyses in Geotechnical Engineering. Advanced Engineering Days, 9, 703-705

Keywords
Artificial intelligence
Geostatistical analyses
Geotechnical engineering
Soil properties
Standard penetration test

Abstract

Artificial intelligence has managed to make a name for itself in every field with the development of technology in recent years. With the development of technology, the use of artificial intelligence methods in geotechnical engineering is becoming widespread. In this study, artificial intelligence studies in the field of geotechnical engineering were examined. Another subject that is emphasized is some relations between Standard Penetration Test (SPT)-N and the engineering parameters of the soil. The success of the method used was compared according to the success or failure rates achieved. When the studies are evaluated, the results of the concept of artificial intelligence in geotechnical engineering are quite promising. Another important method examined in this study is geostatistical analysis utilized in solving some real-world engineering problems in geotechnical engineering. These analyses, which are based on Inverse Distances Weighted (IDW), Kriging Interpolation, and Radial Based Function (RBF) methods conducted via ArcGIS software, allow forming of visualized maps based on real landscape or soil properties values from field tests or observations. Especially using results of the standard penetration test, which is used commonly to obtain soil characteristics in the field, provides to obtain maps like bearing capacity and settlements of the soil. These kinds of maps may be used to have rapid and effective knowledge of areas that cover huge sites.

Introduction

Artificial intelligence is the modeling of complex and real-world problems and solving them by using appropriate algorithms. With the developing technology, the use of artificial intelligence algorithms in various fields of science is increasing day by day. Today, the concept of artificial intelligence has spread to a very wide area and has reached a level that can produce practical solutions in many fields [1]. In geotechnical engineering, artificial intelligence is frequently used in the design of complex soil models. Various artificial intelligence methods have been adopted for geotechnical engineering applications such as tunneling construction, slope displacement prediction, landslide susceptibility assessment, and pile-bearing capacity assessment [2–4]. Thanks to these methods, it can be an alternative method where artificial intelligence algorithms can be applied more easily than accepted methods in geotechnical engineering. Thanks to these methods, it can be an alternative method where artificial intelligence algorithms can be applied more easily than accepted methods in geotechnical engineering. Estimation of many soil-related parameters using standard penetration test results from a field experiment and solution of many geotechnical problems such as slope stability and liquefaction analysis are possible by using high-accuracy AI models.

Geostatistical analyses are essential tools for mapping soil geotechnical properties and providing valuable information for construction projects, agricultural practices, and environmental assessments [5,6]. By leveraging geostatistical techniques and GIS integration, researchers can effectively characterize the spatial variability of soil attributes. Furthermore, geostatistical analyses including Ordinary Kriging (OK) interpolation, semi-variogram

modeling, and inverse distance weighting are essential in mapping soil geotechnical properties, providing insights into the spatial variability of soil characteristics [7,8]. Geostatistical approaches have been employed in geotechnical engineering to model the spatial variability of soil properties crucial for construction projects. By integrating Geographic Information Systems (GIS) with geostatistical analyses, researchers have developed accurate soil maps and predicted ground suitability for various engineering endeavors [9]. Geostatistical techniques like kriging have been effective in predicting soil variables based on regression models, providing valuable information for soil management and land-use planning [10]. The SPT is an old field test widely used in geotechnical engineering [11]. It is used to determine the strength parameters inside the borehole. The equipment used is simple, durable, and inexpensive, which is one of the important reasons why it is preferred. This test can be applied to various soil types ranging from soft clays and loose sands to very stiff clays and tight sands. One of the important situations in geotechnical engineering is the need for prediction due to the scarcity of experimental results. These predictions to determine the properties of the soil are cheap, fast, and provide very close predictions. The most common field test used in soil estimation is SPT. SPT-N values determined by SPT are used to estimate various engineering parameters of soils [8,12].

Artificial Intelligence Analyses

Artificial neural networks are computer systems developed to realize abilities such as creating and discovering new information by using the learning path. The most basic task of artificial neural networks is to determine an output that can correspond to an input shown to it [13]. Machine learning, one of the sub-branches of artificial intelligence, is to enable computers to learn what to do instead of giving them the necessary steps to solve the problem in advance. The machine learning method aims to obtain results that are difficult to obtain with algorithmic methods from complex data with this developed model. This developed model will take a certain set of data as input data and produce results for a certain purpose as output [4]. Although there are some important differences between deep learning and machine learning, they mean the same thing. Deep learning is a subcategory of machine learning. Although it gave good results with machine learning techniques in the early days, it has not been able to provide sufficient developments as the data set sizes have increased in recent years. In general, deep learning and machine learning are similar to each other. Feature extraction in machine learning is determined by the user, which limits the feature view. To avoid this limitation, the feature maps in the data set are found by the network with a deep learning structure and made predictions in this direction [14]. Fuzzy Logic is widely used in scientific fields. While classical logic only has definitive evaluations such as true-false, and yes-no, fuzzy logic can have intermediate evaluations. Mathematically, in fuzzy logic, a variable can belong to multiple clusters simultaneously, with its membership characterized by values known as membership degrees. The degree of membership is quantified through a generalized function referred to as the membership function [13].

Geostatistical Analyses

Youden [15], and Matheron [16] are credited with advancing the field of geostatistics. Many areas, including soil mapping, meteorology, ecology, oceanography, geochemistry, epidemiology, human geography, and geomorphometry, have effectively used geostatistical techniques [17]. Geostatistics addresses the requirement to forecast sampled properties (maps) in unsampled places using limited, often expensive data [18]. GIS systems are successfully used in visualizing geostatistical analyses. Thus, analysis results can gain different meanings through visualization as well as forecasts. In solving the Geotechnical Engineering problems examined in this study; " IDW, Kriging, and RBF" methods based on weights, distances, and functions can be successfully applied in the GIS environment and the results can be compared and contributed to the literature. In the study conducted by Selim et al. [19], a correlation map was created with the kriging approach using corrected SPT values.

Conclusion

In this study, different artificial intelligence methods in the field of geotechnical engineering in the literature are discussed and the studies conducted in this field are compiled. According to the results of the studies, the suitability of the method used was determined. Some of the studies conducted were examined and their achievements were discussed. Considering the results obtained from this study, it is observed that engineering problems that are difficult and costly to solve with artificial intelligence methods can be solved more quickly and effortlessly. Determining the right one between IDW, Kriging, and RBF methods for ground mapping depends on the data structure, amount of data, and precision required. While IDW is preferred when a fast and simple method is sought or the density of data points is homogeneous, Kriging is used in cases where high accuracy is required and spatial correlation between data points is important. RBF is used especially when complex surfaces need to be modeled and high-quality interpolation results are desired. These methods must be applied carefully with appropriate parameters and methods to obtain accurate results in ground mapping projects.

References

1. Goodfellow, I., Bengio, Y., & Courville, A. (2016). *Deep Learning*. The MIT Press.
2. Zhang, W., Li, H., Li, Y., Liu, H., Chen, Y., & Ding, X. (2021). Application of deep learning algorithms in geotechnical engineering: a short critical review. *Artificial Intelligence Review*, *54*(8), 5633–5673. https://doi.org/10.1007/S10462-021-09967-1/TABLES/2
3. Uray, E., Demir, V., Keskin, A. Ü., & Tan, Ö. (2019). Use of Artificial Neural Networks in Stability Control of Cantilever Retaining Walls. *International Civil Engineering and Architecture Conference*, 469–478.
4. Demir, V., Uray, E., & Carbas, S. (2023). *Modeling Civil Engineering Problems via Hybrid Versions of Machine Learning and Metaheuristic Optimization Algorithms* (S. M. Bekdaş, G., Nigdeli (ed.); pp. 199–233). Springer, Cham. https://doi.org/10.1007/978-3-031-34728-3_11
5. John, K., Afu, S. M., Isong, I. A., Aki, E. E., Kebonye, N. M., Ayito, E. O., Chapman, P. A., Eyong, M. O., & Penížek, V. (2021). Mapping soil properties with soil-environmental covariates using geostatistics and multivariate statistics. *International Journal of Environmental Science and Technology*, *18*(11), 3327–3342. https://doi.org/10.1007/S13762-020-03089-X/METRICS
6. Söylemez, M. (2022). Zemin Taşıma Gücü Haritalarının Oluşturulması: Altınşehir (Adıyaman) Örneği. *Cukurova University Journal of the Faculty of Engineering*, *37*(2), 411–418. https://doi.org/10.21605/CUKUROVAUMFD.1146118
7. Sarı, H. (2019). Geostatistical Assessments for Characteristics of Soils Around Naip Dam. *International Journal of Scientific Research and Management*, *7*(02), 213–219. https://doi.org/10.18535/IJSRM/V7I2.AH01
8. Sanad, H., Moussadek, R., Mouhir, L., Lhaj, M. O., Dakak, H., Azhari, H. El, Yachou, H., Ghanimi, A., & Zouahri, A. (2024). Assessment of Soil Spatial Variability in Agricultural Ecosystems Using Multivariate Analysis, Soil Quality Index (SQI), and Geostatistical Approach: A Case Study of the Mnasra Region, Gharb Plain, Morocco. *Agronomy 2024, Vol. 14, Page 1112*, *14*(6), 1112. https://doi.org/10.3390/AGRONOMY14061112
9. Kim, H. S., Sun, C. G., Kim, M., Cho, H. I., & Lee, M. G. (2020). GIS-Based Optimum Geospatial Characterization for Seismic Site Effect Assessment in an Inland Urban Area, South Korea. *Applied Sciences 2020, Vol. 10, Page 7443*, *10*(21), 7443. https://doi.org/10.3390/APP10217443
10. Hengl, T., Heuvelink, G. B. M., & Stein, A. (2004). A generic framework for spatial prediction of soil variables based on regression-kriging. *Geoderma*, *120*(1–2), 75–93. https://doi.org/10.1016/J.GEODERMA.2003.08.018
11. Sivrikaya, O., & TOĞROL, E. (2010). İnce daneli zeminlerde SPT sonuçlarının düzeltilmesi üzerine bir çalışma. *İTÜDERGİSİ/D*, *2*(6). http://160.75.25.161/index.php/itudergisi_d/article/view/803
12. Baghbani, A., Choudhury, T., Costa, S., & Reiner, J. (2022). Application of artificial intelligence in geotechnical engineering: A state-of-the-art review. *Earth-Science Reviews*, *228*, 103991. https://doi.org/10.1016/J.EARSCIREV.2022.103991
13. Zou, J., Han, Y., & So, S. S. (2008). Overview of Artificial Neural Networks. *Methods in Molecular Biology*, *458*, 14–22. https://doi.org/10.1007/978-1-60327-101-1_2
14. Döş, M. E., & Uysal, M. (2019). Uzaktan algılama verilerinin derin öğrenme algoritmaları ile sınıflandırılması. *Turkish Journal of Remote Sensing*, *1*(1), 28–34. https://dergipark.org.tr/en/pub/tuzal/issue/50531/648988
15. Youden, W. J. (1951). *Statistical Methods for Chemists*. John Wiley & Sons. https://www.amazon.com/Statistical-Methods-Chemists-W-J-Youden/dp/0471979112
16. Matheron, G., & Armstrong, M. (1987). *Geostatistical Case Studies (Quantitative Geology and Geostatistics*. Springer.
17. Hengl, T., Minasny, B., & Gould, M. (2009). A geostatistical analysis of geostatistics. *Scientometrics*, *80*(2), 491–514. https://doi.org/10.1007/S11192-009-0073-3/METRICS
18. Burrough, P. A. (2001). GIS and geostatistics: Essential partners for spatial analysis. *Environmental and Ecological Statistics*, *8*(4), 361–377. https://doi.org/10.1023/A:1012734519752/METRICS
19. Altun, S., Göktepe, A. B., & Sezer, A. (2013). Geostatistical interpolation for modelling SPT data in northern Izmir. *Sadhana - Academy Proceedings in Engineering Sciences*, *38*(6), 1451–1468. https://doi.org/10.1007/S12046-013-0183-8/METRICS

Advanced Engineering Days

aed.mersin.edu.tr

Improvement Effect of Artificial Pozzolan Waste Material and Cement Additive on Crushed Stone Ground and Taguchi Method

Mehmet Hilmi Tutumlu[1], Esra Uray *[2]

[1]*KTO Karatay University, Institute of Postgraduate Education, Department of Civil Engineering, Türkiye, 211300190@ogrenci.karatay.edu.tr*
[2]*KTO Karatay University, Department of Civil Engineering, Türkiye, esra.uray@karatay.edu.tr*

Cite this study: Tutumlu, M. H., & Uray, E. (2024). Improvement Effect of Artificial Puzolan Waste Material and Cement Additive on Crushed Stone Ground and Taguchi Method. Advanced Engineering Days, 9, 706-708

Keywords
Cement ground improvement
Silica fume
Ground blast furnace slag
Fly ash
Taguchi Method

Abstract

Improving weak ground properties is also achieved in issues such as road pavement performance, service life, maintenance cost, and cost. With the addition of cement to weak natural soil or crushed stone soil that is removed and replaced, the soil properties are greatly improved and a sub-base or foundation structure that will not pose a problem in terms of stability can be formed. In this scope, the optimum mixture of crushed stone improved by cement and pozzolan material like blast furnace slag, fly ash, and silica fume with the parametric effect on strength comes into prominence. Based on literature studies, this study aims to present the parametric effects and optimal mixture components of blast furnace slag, fly ash, and silica fume pozzolans on cement-improved crushed stone using statistical experimental design methods. Thus, the importance of using statistical methods to examine the parametric effect and obtain optimum design with less experiment is emphasized by economic and environmental benefits. In addition, using pozzolan materials instead of cement in the mixture diminishes the negative effect on the environment and enables the recycling of industrial waste pozzolans. Designing and constructing with optimal elements can significantly reduce carbon dioxide emissions, thereby minimizing environmental harm. Consequently, this study prioritizes reducing environmental damage using mixtures that require less cement derived from industrial waste and the necessity of utilizing statistical experimental methods to reduce investigation costs and research time in soil improvement experimental studies.

Introduction

Today, the increasing population and developing technology have increased the use of concrete, which is the most used building material in infrastructure and housing construction. Cement, which causes high carbon dioxide emissions during its production, is one of the main components of concrete. For this reason, artificial pozzolana materials, which are produced as industrial waste, are widely used to reduce the use of cement in the concrete mixture [1,2]. The improvement effect in concrete production using a cementitious mixture with the Pozzolan additive can be seen from studies in the literature [2–5]. The optimum amount of cement used in ground improvement works is important in terms of causing less harm to the environment and reducing construction costs. In addition, the use of artificial posing materials, which arise as industrial waste, in improvement works instead of a certain amount of reduced cement is an important, effective, and sustainable outcome in terms of both the recycling of waste material and the improvement contribution it provides to the mixture.

In case of poor-quality soil in the foundation or sub-base layers of highways and railways, ground improvement is carried out. In ground improvement works, a qualified layer with increased bearing capacity is obtained by mixing different soils with cement. Nowadays, many methods of soil improvement can be applied by removing the poor quality soil and compacting it by laying suitable stabilized material or improving the poor soil on-site [6–8]. Especially when the clay foundation soil, which has a diameter of less than 0.002 mm and a very large specific surface area, is exposed to water, behaviors such as swelling or shrinkage occur in the soil [9].

Artificial Puzolan Waste Material and Cement Additive on Crushed Stone Ground

In geotechnical engineering, to safely transfer building loads to the ground, the ground must have good properties such as bearing capacity, settlement amount, shear strength, swelling potential, and permeability. Poor-quality soils can be transformed into a safe supporting environment by improving or changing them. Cement, lime, or pozzolana-added ground improvement methods are widely used in highway and railway subbase layers, and these methods improve the performance, service life, maintenance cost, and cost of the road pavement.

Studies on cement stabilization have shown its applicability in different types of soil. Bell [10] and Uddin et al. [11] studied the stabilization of clayey soils. Kök et al. [12] investigated the effect of cement stabilization on the cost of flexible pavement, Gürsoy et al. [13] examined the improvement of sediment soils in Izmir Bay, and Uray et al. [7] presented improvement studies made with cement on natural ground. It is important to determine the water and binder ratios in improvement works.

When cement combines with water, CSH gels with binding properties are produced as a product, and lime ($Ca(OH)_2$) is formed as an alkaline material. This released lime negatively affects the strength properties as it melts when it comes into contact with water. Therefore, the free lime released as a result of the hydration of cement must be removed from the environment. Pozzolan materials, which normally have little or no binding properties on their own, react with free lime to form CSH gels with binding properties, resulting in a more durable structure that increases in strength over time. Pozzolans are materials of silica (SiO2) and alumina (Al2O3) origin, and the use of these materials in history dates back thousands of years. Artificial pozzolans appear as fly ash, silica fume, blast furnace slag, and rice husk ash obtained as waste materials as a result of production in industrial buildings. Fly ash, silica fume, and blast furnace slag, which are waste materials, can be used as chemical additives instead of the improvement using cement, providing a more durable structure [14,15]. Silica fume (SD) is a material obtained by rapid cooling and condensation of the gas formed during the production of silicon metal or silicon metal alloys. This by-product, with a specific surface area of 14400 cm^2/g and a density of 2.2 g/cm^3, consists of spherical glass silica (SiO_2) particles [16]. Fly ash (LF) is the material obtained by separating the ash from the chimney, which is generally formed as a result of burning coal in thermal power plants that produce electricity. Fly ash, which contains Si, Al, Ca, and S in its chemical structure, and compounds containing SiO_2, Fe_2O_3, and MgO, consists of dark gray and very small spherical grains. Its density is between 2.2-2.7 g/cm^3 and its specific surface area is between 2800-3800 cm^2/g [17]. Ground blast furnace slag (GRFC) is a by-product of the combustion of iron ore, limestone, and coke in blast furnaces producing iron and steel. This material, which has a density of 2.08 g/cm^3 and a specific surface area of 2750 cm^2/g, is ground into very fine grains and has binding properties. Its main component is SiO_2 and it contains components such as CaO and Al_2O_3. The grinding state and vitreous structure affect the binding properties [18].

Taguchi Method

Taguchi method [19] is a statistical design method used in quality control and quality improvement processes. This method, developed by Genichi Taguchi, aims to optimize product and process design by focusing on the variables and factors in the production process. The Taguchi method is used to analyze the influence of continuous and discrete factors, increase sensitivity to fluctuations in the production process, and improve product performance. By using the orthogonal arrays suggested by Taguchi given in Table 4, the variance and optimum values of the parameters affecting the target value can be obtained with fewer experiments. The general representation of orthogonal arrays created by Taguchi, which allows parameter levels to be changed simultaneously with a small number of tests, is Ld(a)k or Ld. Here, d is the total number of experiments, a is the number of levels of parameters, k is the number of parameters and L is the orthogonal array. The number of combinations formed by five design parameters, each with four levels, corresponds to 4^5 = 1024 different situations, and by using L16 orthogonal array tables, it is possible to obtain the effect of the design parameters on the target value with only 16 trials, without making 1024 trials [20].

Conclusion

No comprehensive study has been found in the literature in which the experimental studies of cementitious ground improvement with the contribution of pozzolans are applied together with Taguchi statistical test design methods for cement-bonded granular base layer ground improvement. According to the literature research, improvement studies have generally been carried out with soils containing clay and sand, with or without the addition of Pozzolan. Unlike the literature studies, the use of crushed stone stabilized material in the improvement works will contribute to the literature. Determining the optimum component values of the cementitious mixture prepared with the addition of silica fume, ground blast furnace slag, and fly ash pozzolan materials will contribute to the literature by obtaining the effects of the components on the target test values parametrically by statistical-based methods. Since there is no similar study in which the improvement of the road infrastructure for crushed

stone ground is investigated using the statistical-based Taguchi method along with the target values of compressive strength, it is anticipated that the results obtained will bring innovation to the literature.

References

1. Hınıslıoğlu, S., & Bayrak, O. Ü. (2007). Optimization of early flexural strength of pavement concrete with silica fume and fly ash by the Taguchi method. Civil Engineering and Environmental Systems, 21(2), 79–90. https://doi.org/https://doi.org/10.1080/10286600410001684562
2. Kate, G. K., Nayak, C. B., & Thakare, S. B. (2021). Optimization of sustainable high-strength–high-volume fly ash concrete with and without steel fiber using Taguchi method and multi-regression analysis. Innovative Infrastructure Solutions, 6(2), 1–18. https://doi.org/10.1007/S41062-021-00472-6/TABLES/24
3. Uysal, M. (2012). Taguchi and Anova approach for optimisation of design parameters on the compressive strength of HSC. Magazine of Concrete Research, 64(8), 727–735. https://doi.org/10.1680/MACR.11.00156
4. Akçaözoğlu, K., Emre GÜLDÜR, Ş., Ömer Halisdemir Üniversitesi, N., Fakültesi, M., & Mühendisliği Bölümü, İ. (2017). Mikronize Kalsit ve Uçucu Kül Katkısının Beton Özelliklerine Etkisinin Araştırılması. Afyon Kocatepe Üniversitesi Fen Ve Mühendislik Bilimleri Dergisi, 17(2), 658–668. https://doi.org/10.5578/fmbd.58620
5. Uysal, M. (2011). Mineral katkılı betonların donmaçözülme etkisi altındaki davranışının incelenmesi. THBB Kongresi.
6. Makusa, G. P. (2012). Soil stabilization methods and materials in engineering practice : State of the art review. Division of Mining and Geotechnical Engineering. http://urn.kb.se/resolve?urn=urn:nbn:se:ltu:diva-24093
7. Uray, E., Erkan, İ. H., Özçelik, M., & Tan, Ö. (2017, May). An Example of Cement Stabilization Application in Railway Systems (Aladdin-Adliye Tramway). International Conference on Civil and Environmental Engineering (ICOCEE). https://acikerisim.karatay.edu.tr/handle/20.500.12498/1503
8. Uray, E., Sancıoğlu, S., Çubukçu, E. A., & Doğukan, E. M. (2016). Çimento İle Stabilizasyonda Optimum Çimento Oranının Belirlenmesi. Ulusal Genç Geoteknik Mühendisleri Sempozyumu, 12.
9. Emarah, D. A., & Seleem, S. A. (2018). Swelling soils treatment using lime and sea water for roads construction. Alexandria Engineering Journal, 57(4), 2357–2365. https://doi.org/10.1016/J.AEJ.2017.08.009
10. Bell, F. G. (1995). Cement Stabilization and Clay Soils, with Examples. Environmental & Engineering Geoscience, I(2), 139–151. https://doi.org/10.2113/GSEEGEOSCI.I.2.139
11. Uddin, K., Balasubramaniam, A. S., & Bergado, D. T. (1997). Engineering behavior of cement-treated Bangkok soft clay. Geotechnical Engineering, 28, 89–119. https://www.academia.edu/download/43983854/37_-_Engineering_behavior_of_cement-treated_Bangkok_soft_clay.pdf
12. Kök, B. V., Yilmaz, M., & Geçkil, A. (2012). Çimento Stabilizasyonlu Zeminin Esnek Üstyapı Maliyetine Etkisi. Pamukkale Üniversitesi Mühendislik Bilimleri Dergisi, 18(3), 165–172. https://doi.org/10.5505/PAJES.2012.39974
13. Gürsoy, Z. (2015, November). Körfez Bölgesi Çökelmiş Zeminlerin Kireç ve Çimento ile Islahı. 6. Geoteknik Sempozyumu. https://doi.org/10.5505/2015GEOTEKNIK.S066
14. Tan, O., Gungormus, G., & Zaimoglu, A. S. (2014). Effect of Bentonite, Fly Ash and Silica Fume cement injections on uniaxial compressive strength of granular bases. KSCE Journal of Civil Engineering, 18(6), 1650–1654. https://doi.org/10.1007/S12205-014-0227-6/METRICS
15. Zaimoglu, A. S. (2015). Optimization of unconfined compressive strength of fine-grained soils modified with polypropylene fibers and additive materials. KSCE Journal of Civil Engineering, 19(3), 578–582. https://doi.org/10.1007/S12205-015-1425-6/METRICS
16. Tohumcu, İ., & Bingöl, A. F. (2013). Silis dumanı ve uçucu kül katkılı kendiliğinden yerleşen betonların taze beton özellikleri ve basınç dayanımları. Dokuz Eylül Üniversitesi Mühendislik Fakültesi Fen ve Mühendislik Dergisi, 15(43), 31–44. https://dergipark.org.tr/en/pub/deumffmd/issue/40819/492497
17. Güler, G., Güler, E., İpekoğlu, Ü., & Mordoğan, H. (2005). Uçucu Küllerin Özellikleri ve Kullanım Alanları. Uluslararası Madencilik Kongresi ve Fuarı, IMCET2Q05, 09-12 Haziran 2005, 9–12.
18. Yüksel, İ., Özkan, Ö., Bilir, T., Karaelmas Üniversitesi, Z., Fakültesi, M., Mühendisliği Bölümü, İ., Meslek Yüksek Okulu, A., Prog Böl, T., Üniversitesi, O., & Fakültesi, M.-M. (2007). Yüksek fırın cürufu ikameli parke ve bordür üretim. Pamukkale University Journal of Engineering Sciences, 13(2), 289–296. https://dergipark.org.tr/en/pub/pajes/issue/20517/218463
19. Taguchi, G. (1986). Introduction to quality engineering: designing quality into products and processes. The Organization.
20. Uray, E., Carbas, S., Geem, Z. W., & Kim, S. (2022). Parameters Optimization of Taguchi Method Integrated Hybrid Harmony Search Algorithm for Engineering Design Problems. Mathematics 2022, Vol. 10, Page 327, 10(3), 327. https://doi.org/10.3390/MATH10030327

Advanced Engineering Days

aed.mersin.edu.tr

An analysis on the distributional justice of medical centers in the 2nd district of Tabriz metropolis

Rogayeh Sharafi [*1], Mahmoud Asoude Khyal [1], Ali Hamedi [1], Hassan Mahmoodzadeh [1]

[1] University of Tabriz, Department of Urban and Regional Planning, Iran, Sharafirogayeh@gmail.com, m.asodeh@yahoo.com, ali1379hamed@gmail.com, hassan.mahmoudzadeh@gmail.com

Cite this study: Sharafi, R., Khyal, M. A., Hamedi, A., & Mahmoodzadeh, H. (2024). An analysis on the distributional justice of medical centers in the 2nd district of Tabriz metropolis. Advanced Engineering Days, 9, 709-711

Keywords
Health centers
Region 2
Tabriz metropolis

Abstract

Considering the necessity and importance of people's health in this era and the necessity of planning and management in this direction in order to examine the way of distribution of welfare facilities around these centers, the present research shows and reviews the characteristics and the way of placement and distribution of welfare services around the medical centers. In the 2nd region of Tabriz, it has investigated and presented the results and suggestions to improve the current situation, the study and investigation of medical centers in the 2nd region of Tabriz city shows that the unbalanced distribution of centers, the quality of medical services, and the liquidity of doctors are among the basic issues that need to be improved to improve the situation. It is suggested that measures such as balanced distribution of centers, recruitment of quality doctors, improvement of center technology and educational programs should be carried out to improve the health status. These measures will lead to improving citizens' access to medical services and improving the quality of services in the 2nd region of Tabriz. The research method of the current research is descriptive-analytical and using library sources and studies and field surveys through Gis software to investigate the subject under study Paid(Marmot, M.2019).

Introduction

Equitable distribution of health and medical services is the most basic priority of any health organization. The (Lancet.2020) But studies show that in many regions, this distribution is done unevenly and unfairly. Problems in the distribution of medical centers and medical services in urban areas can lead to the creation of unstable social and economic justice. Therefore, a detailed study and analysis on the equitable distribution of medical centers in the 2nd district of Tabriz is essential. This study can lead to a better understanding of the weaknesses and strengths in the distribution of medical services and offer suggestions to improve the situation. Therefore, in this research, we will investigate and analyze the justice distribution of medical centers in the 2nd district of Tabriz and try to provide appropriate solutions to improve the situation (De et al.,2019).

Material and Method

Any research or research to go through the process and reach the desired result must have a method appropriate to the subject. To analyze the raw data through GIS, the topic is investigated. The scope of study in this article is focused on the areas of Tabriz. This area includes all medical centers and health centers (hospitals, clinics, clinics, neighborhood health centers, etc.). From these centers, we have only visited hospitals, which include 6 civilian hospitals of Imam Reza (AS), Shahada, Razi, Waliasr International, 29 Bahman.

Results

Among the 6 medical centers located in the 2nd district of Tabriz, in terms of fair distribution of services, all medical centers are in almost the same conditions and access to welfare and social facilities is easy, but among these 6 centers, Waliasr International Hospital is in terms of providing services. And the expertise of doctors and Dara is in a better condition than other centers without a relatively healthy and healthy environment, but the costs of this center are not affordable for ordinary people compared to other centers.

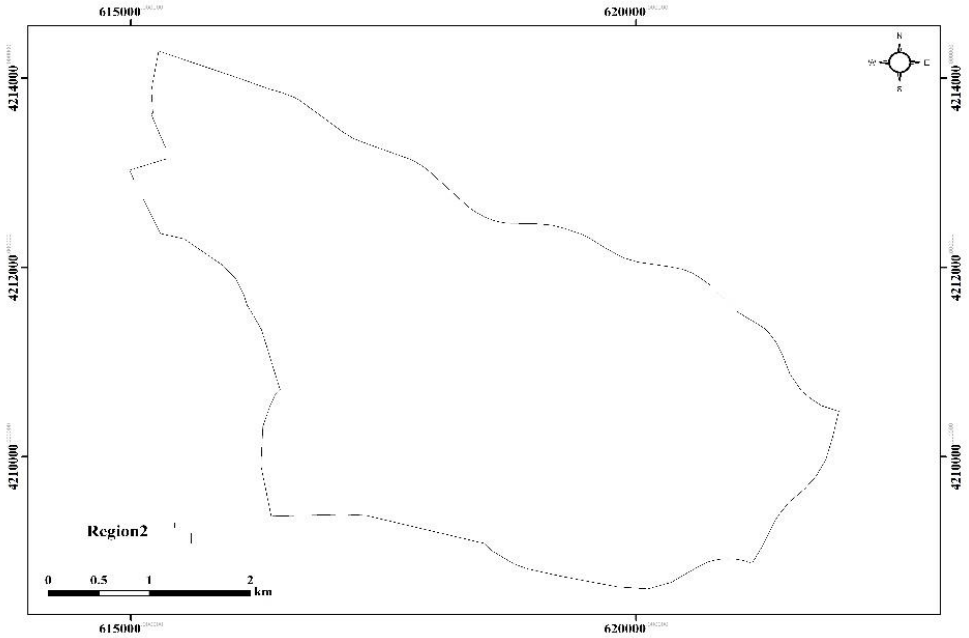


Figure 1.

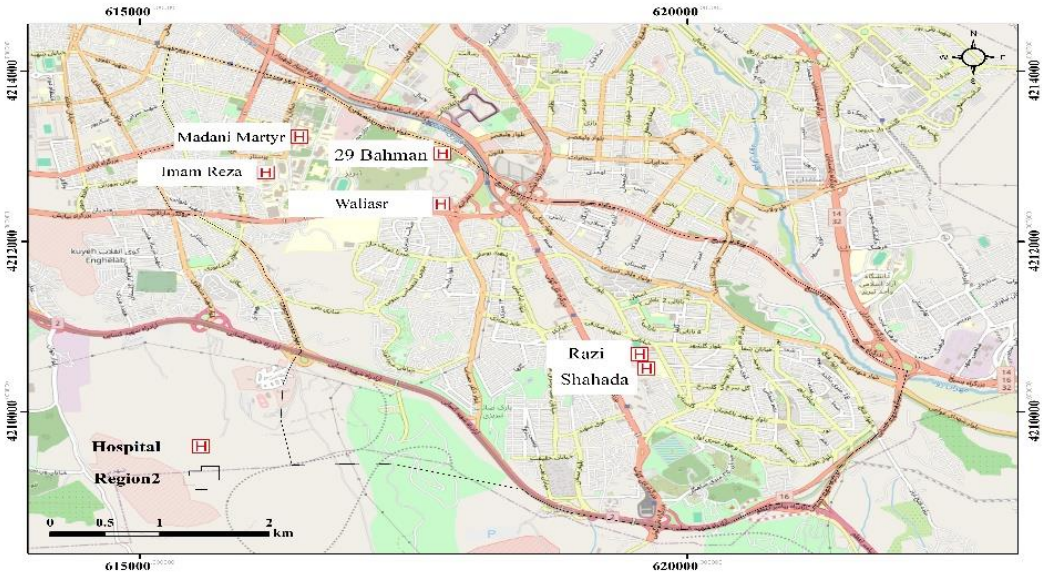


Figure 2.

Discussion

The issue of distributive justice in healthcare facilities in Region 2 of Tabriz is a critical topic that requires thoughtful analysis and consideration. Distributive justice refers to the fair and equitable distribution of resources, services, and opportunities among individuals or groups within a society. In the context of healthcare, it is vital to ensure that all residents in Region 2 of Tabriz have equal access to quality healthcare services regardless of their socioeconomic status, ethnicity, or other factors. One of the key challenges in achieving distributive justice in healthcare facilities in Region 2 of Tabriz is the unequal distribution of resources and services. Disparities in healthcare infrastructure, equipment, medical staff, and funding can result in some areas having better access to healthcare services than others. This can lead to increased health inequalities and preventable health disparities among the residents of Region 2.

Another important aspect to consider in the discussion on distributive justice in healthcare facilities in Region 2 of Tabriz is the role of government policies and regulations. It is essential for the government to implement policies that promote equitable access to healthcare services and address the underlying factors contributing to healthcare disparities. This may include investing in health infrastructure, improving healthcare financing mechanisms, and ensuring that healthcare facilities are distributed in a way that meets the needs of all residents in Region 2.Furthermore, community engagement and participation are crucial in addressing issues of distributive

justice in healthcare facilities. Involving local communities, healthcare providers, and policymakers in decision-making processes can help identify and address the unique healthcare needs of different populations in Region 2 of Tabriz. Collaboration and dialogue among stakeholders can lead to more effective and sustainable solutions to improve the overall distribution of healthcare services. In conclusion, the discussion on distributive justice in healthcare facilities in Region 2 of Tabriz underscores the importance of ensuring equal access to quality healthcare services for all residents. By addressing disparities in healthcare resources, policies, and community engagement, we can work towards achieving greater equity in healthcare delivery and promoting better health outcomes for the entire population in Region 2.

Conclusion

According to the results of this study, it is clear that the distribution of medical centers in region 2 does not meet the needs of the society and there is a need for correction and improvement in this area. These results show that the most benefits and medical services are provided to those who are economically and socially superior. Therefore, it is necessary to distribute medical resources and services in such a way that everyone has equal and fair access to healthcare services.

References

1. De Maio, G., & García-Remesal, M. (2019). Equity in access to health care services: The case of Spain. International Journal for Equity in Health, 18(1), 1-11.
2. Marmot, M. (2019). Social justice, epidemiology and health inequalities. European Journal of Epidemiology, 34(4), 381-387.
3. Ridde, V. (2017). Equity and health policy in Africa: Using concept mapping in Moore (Burkina Faso). BMC Health Services Research, 17(1), 263.
4. World Health Organization. (2016). Monitoring equity in access to AIDS treatment programs: A review of concepts, models, methods and developments. World Health Organization.
5. The Lancet. (2020). Achieving health equity for all through primary care. The Lancet, 396(10256), 537.

Advanced Engineering Days

aed.mersin.edu.tr

Hydroclimatic Trend Analysis of Gorgan Coastal Region, Iran

Vahid Azimi*[1], Hirsa Taherimashhadi [2]

[1]*Shahid Beheshti University, Civil, Water and Environmental Engineering Faculty, Tehran, Iran, azimiwater@gmail.com*
[2]*University of Tehran, Alborz Campus, Faculty of Environment, Iran, Hirsa.taheri@ut.ac.ir*

Cite this study: Azimi, V., Taherimashhadi, H. (2024). Hydroclimatic Trend Analysis of Gorgan Coastal Region, Iran. Advanced Engineering Days, 9, 712-716

Keywords
Coastal Region
Trend
Rainfall
Sen Slope
Mann-Kendall

Abstract

Climate change on coastal regions have become critical for water resources management. The trends of hydroclimatic parameters such as temperature, relative humidity, and rainfall were examined during 1986-2020 in the Gorgan coastal region, Iran. The findings of the research suggest that the area experiences fluctuations, a reduction in rainfall, and an increase in temperature and relative humidity. When examining the statistical results of the Mann–Kendall and Sen's slope test on the total annual rainfall, a P-value of -0.7 was obtained, suggesting the absence of a discernible trend in the dataset or variability in rainfall, with a decreasing tendency observed. These outcomes could potentially aid policymakers and water resource managers in implementing more sustainable approaches and techniques for water resource management.

Introduction

Climate change as one of the most severe global challenges is influenced by environmental and socioeconomic factors (Feyissa et al., 2023). The diverse climatic patterns have become a global concern due to their adverse impacts on the environment mainly caused by human activities such as deforestation, alteration of land use, and urban development as well as the emission of greenhouse gases (Adler et al., 2017; Qureshi et al., 2023). Rainfall prediction is a major issue that is important to both government and scientific research to protect human lives and resources (Praveena et al., 2023; Vijayalakshmi et al., 2022). It helps to manage water resources, produce hydroelectricity, early warning of floods and droughts, and maintain urban sewer systems (Vivas et al., 2023; Wei & You, 2022).

Research on rainfall patterns worldwide (Ahmad et al., 2015; Sun et al., 2021; Tommaso Caloiero et al., 2011; Treppiedi et al., 2023) and in Iran (Ghaedi & Shojaian, 2020; Lornezhad et al., 2023; Shobeiri et al., 2021) has been conducted in the past several years. Most studies used various statistical tests to detect rainfall trends, such as Simple linear trend (Guo et al., 2020), Mann–Kendall test (Alifujiang et al., 2020; Guo et al., 2020; Patakamuri et al., 2020), Sen's slope (Yetik et al., 2024), and Spearman's rho tests (Patakamuri et al., 2020). Combining Mann–Kendall test with Sen's Slope estimator (MAKESENS) technique is the most effective for trend detection. The current study utilized Mann–Kendall test and Sen's slope estimator technique to identify rainfall trend.

Iran has experienced changes in climate extremes, with rising temperatures leading to more frequent heatwaves and longer warm seasons. Precipitation patterns have become more variable, with some regions experiencing increased droughts and others facing more intense rainfall events. Gorgan, situated in the province of Golestan, posed an unprecedented flooding in March-April 2019, primarily related to climate change. This geographical region was selected as the case study area to analyze trend precipitation. While studies have shown trends in rainfall patterns in regions like Khorasan Razavi province, there is a lack of detailed analysis on the precipitation trends in the north of Iran, especially Gorgan, using Mann-Kendall test and Sen's slope estimator. Therefore, the goal of the current study was to evaluate the prevalence of climate change through trend identification in Gorgan utilizing extreme precipitation and temperature data from 1966 to 2015. Trend analysis in various time series enhances trend recognition and determination. The forecasting of precipitation patterns is essential for a range of fields, including agriculture, water resource management, and preparedness for disasters. To give policymakers and decision-makers more reliable information, this study focuses on the rainfall and temperature anomalies that occurred over the statistical period as well as the trends of severe precipitation and

temperature. Sen's slope estimator was utilized to calculate the gradient of the trend line, and the Mann-Kendall test was employed to ascertain the trend.

Material and Method

Study area

Gorgan Bay is a partially enclosed basin situated in the southeastern part of the Caspian Sea in Iran, covering an approximate area of 715 km2. The bay is about 60 km long and is approximately 12 km wide. It exhibits relatively shallow characteristics, boasting a maximum depth of 5 m and an average depth of 1.8 m. The northern segment of the bay displays greater depths compared to its southern counterpart (Fig. 1). This bay is predominantly isolated from the primary Caspian water mass by a lengthy barrier formation known as the Miankaleh Peninsula. An opening, approximately 3 km wide, in the northeastern section serves as the link between Gorgan Bay and the Caspian Sea (Bastami et al., 2012).

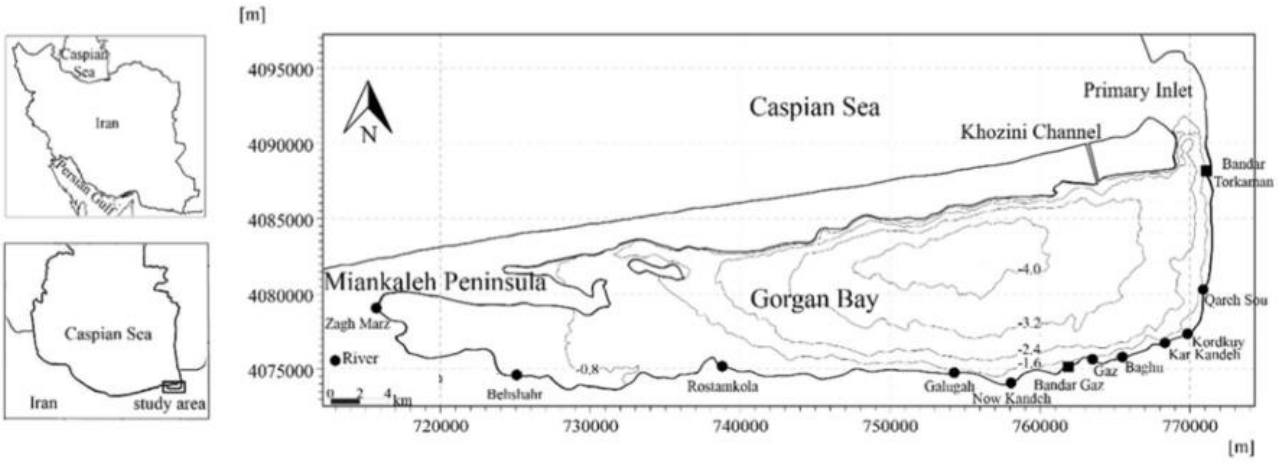


Figure 1. Gorgan bay, located in north of Iran.

Mann-Kendall Test

The MK test is utilized for the detection of statistically significant decreasing or increasing trends within long-term temporal datasets (Mallick et al. 2021). Derived from two distinct hypotheses, the MK trend test consists of a null (H0) hypothesis and an alternative (H1) hypothesis (Gadedjisso-Tossou et al. 2021). While H0 posits the absence of any trend, H1 indicates a notable ascent or descent in precipitation data (Agbo et al. 2021). Under a 5% significance level, acceptance of the alternative hypothesis occurs when the p-value is <0.05, signifying the presence of a trend; conversely, acceptance of H0, denoting no trend, takes place if the p-value exceeds 0.05 (Baig et al. 2021). The equation representing the formula is as follows:

$$S = \sum_{i=1}^{n-1} \sum_{j=i+1}^{n} \text{sign}(X_j - X_i) \tag{1}$$

the n represents the number of data points, where Xj and Xi denote the yearly values in years j and i, respectively, with j being greater than 1. The function Sign (Xj – Xi) is determined by applying the specified equation:

$$\text{Sign}(X_j - X_i) = \begin{cases} -1 \text{ for } (X_j - X_i) < 0 \\ 0 \text{ for } (X_j - X_i) = 0 \\ +1 \text{ for } (X_j - X_i) > 0 \end{cases} \tag{2}$$

Sen's slope estimator

The examination was originally devised by Sen to assess statistical linear relationships (Agarwal et al. 2021). Its primary purpose is to determine the extent of trends within long-term temporal data (Agarwal et al. 2021). Sen's method is preferred for identifying linear relationships due to its resilience to outliers within the dataset (Ray et al. 2021). In this investigation, Sen's approach is implemented to evaluate the trend magnitude in temperature and precipitation data. The subsequent formula is utilized for computing each specific slope (Qi):

$$Q_i = \frac{Y_j - Y_i}{j - 1} \tag{3}$$

where i = 1 to n − 1, j = 2 to n, Yj and Yi represent the data values at time j and i (j > i), respectively. If there are n values of Yj within the time series, the number of slope estimates will be N = n(n − 2)/2. The Sen's slope is:

$$Q_{ij} = \begin{cases} \dfrac{Y_j - Y_i}{j-1} & \text{if } n \text{ is odd} \\ \dfrac{1}{2}\left(Q\dfrac{N}{2} + Q\left[\dfrac{N+2}{2}\right]\right) & \text{if } n \text{ is even} \end{cases} \quad (4)$$

The positive Qi denotes a rising trajectory, whereas the negative Qi values signify a declining trend in the temporal dataset. The Sen's slope (Qi) is measured in units of slope magnitude per annum.

Results

The results of Mann–Kendall and Sen's slope test for the total maximum annual rainfall show a P-value of -0.7 which means there is no trend in the series or variability of rainfall and the negative Qi values (−1.262) show that there is a decrease in the rainfall data (Table 1). The slope of rainfall trend analysis shows that the rainfall graph for Gorgan station has a negative trend. For the mean annual temperature (Tmin, Tmax, Tmean), the P-value is 2.33, 4.33 and 3.04 respectively, which means there is a trend in the series or the temperature will continue increasing and the positive Qi values (0.040, 0.062, 0.044) indicate an increasing trend (Table 1). For the mean annual relative humidity (RHmin, RHmax, RHmean), the P-value is -0.6, -4.55 and -3.89 respectively, which means there is a trend in the series or the relative humidity will continue decreasing and the negative Qi values (-0.017, -0.197, -0.104) indicate an decreasing trend (Table 1). Figure 2 shows sen slope graphs for significance hydroclimatic parameters.

Table 1. Mann-Kendall and Sen's slope estimate parameters

Time series	Test Z	Q	Significance
Tmin	2.33	0.040	*
Tmax	4.10	0.062	***
Tmean	3.04	0.044	**
RHmin	-0.60	-0.017	
RHmax	-4.55	-0.197	***
RHmean	-3.89	-0.104	***
Rainfall	-0.70	-1.262	

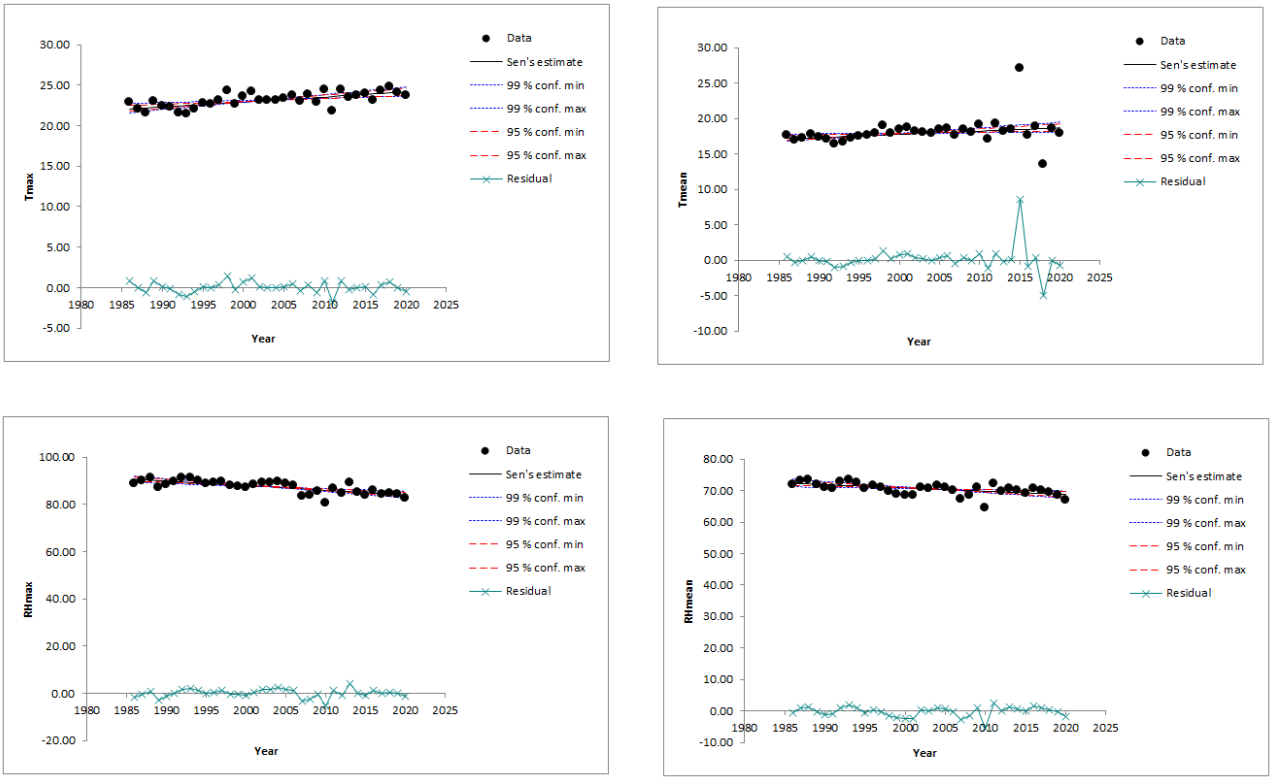


Figure 2. Tmax, Tmean, RHmax and RHmean trends during statistical period

Discussion

Trend identification is a crucial aspect of research in conservation agriculture adoption and climate change, as highlighted in numerous previous studies. Our study's results validate past research findings, demonstrating that adopting conservation agriculture is a more dependable approach to enhancing agricultural productivity, thereby upholding sustainability objectives. Conversely, the planning and execution of strategies for adaptation and mitigation in response to changes in water resources due to climate change and the occurrence of water scarcity events necessitate increased investments of both time and financial resources.

Conclusion

The mitigation of risks linked to the impact of climate change on land cover could be achieved through the implementation of improved conservation agriculture practices. The findings imply that the decline in land productivity within the area is a result of fluctuations, reduced rainfall, as well as heightened temperatures and relative humidity levels. This indicates a decreasing utilization of conservation agriculture methods. Nonetheless, effective planning and management of agricultural practices could significantly mitigate these risks. In times of water scarcity, conservation agriculture should prioritize the efficient utilization and collection of water resources.

References

Adler, R., Gu, G., Sapiano, M., Wang, J.-J., & Huffman, G. (2017). Global Precipitation: Means, Variations and Trends During the Satellite Era (1979–2014). *Surveys in Geophysics*, *38*, 1–21. https://doi.org/10.1007/s10712-017-9416-4

Agarwal S., Suchithra A. & Singh S. P. (2021). Analysis and interpretation of rainfall trend using Mann-Kendall's and Sen's slope method. Indian Journal of Ecology 48 (2), 453–457.

Agbo E. P., Ekpo C. M. & Edet C. O. (2021). Analysis of the effects of meteorological parameters on radio refractivity, equivalent potential temperature and field strength via Mann-Kendall test. Theoretical and Applied Climatology 143, 1437–1456.

Ahmad, I., Tang, D., Wang, T., Wang, M., & Wagan, B. (2015). Precipitation trends over time using Mann-Kendall and spearman's Rho tests in swat river basin, Pakistan. *Advances in Meteorology*, *2015*. https://doi.org/10.1155/2015/431860

Alifujiang, Y., Abuduwaili, J., Maihemuti, B., Emin, B., & Groll, M. (2020). Innovative trend analysis of precipitation in the Lake Issyk-Kul Basin, Kyrgyzstan. *Atmosphere*, *11*(4), 1–16. https://doi.org/10.3390/atmos11040332

Bastami, K., Bagheri, H., Haghparast, S., Soltani, F., Hamzehpoor, A., & Bastami, M. (2012). Geochemical and geo-statistical assessment of selected heavy metals in the surface sediments of the Gorgan Bay, Iran. *Marine Pollution Bulletin*, 64, 2877–2884.

Feyissa, T. A., Demissie, T. A., Saathoff, F., & Gebissa, A. (2023). Evaluation of General Circulation Models CMIP6 Performance and Future Climate Change over the Omo River Basin, Ethiopia. *Sustainability (Switzerland)*, *15*(8). https://doi.org/10.3390/su15086507

Gadedjisso-Tossou A., Adjegan K. I. & Kablan A. K. M. (2021). Rainfall and temperature trend analysis by Mann–Kendall test and significance for Rainfed Cereal Yields in Northern Togo. Science 3 (1), 17.

Ghaedi, S., & Shojaian, A. (2020). Spatial and Temporal Variability of Precipitation Concentration in Iran. *Geographica Pannonica*, *24*(4), 244–251. https://doi.org/10.5937/GP24-27361

Guo, B., Zhang, J., Meng, X., Xu, T., & Song, Y. (2020). Long-term spatio-temporal precipitation variations in China with precipitation surface interpolated by ANUSPLIN. *Scientific Reports*, *10*(1), 81. https://doi.org/10.1038/s41598-019-57078-3

Lornezhad, E., Ebrahimi, H., & Rabieifar, H. R. (2023). Analysis of precipitation and drought trends by a modified Mann-Kendall method: a case study of Lorestan province, Iran. *Water Supply*, *23*(4), 1557–1570. https://doi.org/10.2166/WS.2023.068

Mallick J., Talukdar S., Alsubih M., Salam R., Ahmed M., Kahla N. B. & Shamimuzzaman M. (2021). Analysing the trend of rainfall in Asir region of Saudi Arabia using the family of Mann-Kendall tests, innovative trend analysis, and detrended fluctuation analysis. Theoretical and Applied Climatology 143, 823–841.

Patakamuri, S. K., Muthiah, K., & Sridhar, V. (2020). Long-Term homogeneity, trend, and change-point analysis of rainfall in the arid district of ananthapuramu, Andhra Pradesh State, India. *Water (Switzerland)*, *12*(1). https://doi.org/10.3390/w12010211

Praveena, R., Babu, T. R. G., Birunda, M., Sudha, G., Sukumar, P., & Gnanasoundharam, J. (2023). Prediction of Rainfall Analysis Using Logistic Regression and Support Vector Machine. *Journal of Physics: Conference Series*, *2466*, 12032. https://doi.org/10.1088/1742-6596/2466/1/012032

Qureshi, H. U., Shah, S. M. H., & Teo, F. Y. (2023). Trend assessment of changing climate patterns over the major agro-climatic zones of Sindh and Punjab. *Frontiers in Water*, *5*. https://doi.org/10.3389/frwa.2023.1194540

Ray S., Das S. S., Mishra P. & Al Khatib A. M. G. (2021). Time series SARIMA modelling and forecasting of monthly

rainfall and temperature in the south Asian countries. Earth Systems and Environment 5, 531–546.

Shobeiri, S., Sharafati, A., & Neshat, A. (2021). Evaluation of different gridded precipitation products in trend analysis of precipitation features over Iran. *Acta Geophysica*, *69*(3), 959–974. https://doi.org/10.1007/s11600-021-00595-5

Sun, Q., Zhang, X., Zwiers, F., Westra, S., & Alexander, L. V. (2021). A global, continental, and regional analysis of changes in extreme precipitation. *Journal of Climate*, *34*(1), 243–258. https://doi.org/10.1175/JCLI-D-19-0892.1

Tommaso Caloiero, Coscarelli, R., Ferraric, E., & Mancini, M. (2011). Trend detection of annual and seasonal rainfall in Calabria (Southern Italy). *INTERNATIONAL JOURNAL OF CLIMATOLOGY*, *31*, 44–56. https://doi.org/10.1002/joc.2055

Treppiedi, D., Cipolla, G., Francipane, A., Cannarozzo, M., & Noto, L. V. (2023). Investigating the Reliability of Stationary Design Rainfall in a Mediterranean Region under a Changing Climate. *Water (Switzerland)*, *15*(12). https://doi.org/10.3390/w15122245

Vijayalakshmi, C., Sangeeth, K., Josphineleela, R., Shalini, R., Sangeetha, K., & Jenifer, D. (2022). Rainfall Prediction using ARIMA and Linear Regression. *2022 International Conference on Computer, Power and Communications (ICCPC)*, 366–370. https://doi.org/10.1109/ICCPC55978.2022.10072125

Vivas, E., de Guenni, L. B., Allende-Cid, H., & Salas, R. (2023). Deep Lagged-Wavelet for monthly rainfall forecasting in a tropical region. *Stochastic Environmental Research and Risk Assessment*, *37*(3), 831–848. https://doi.org/10.1007/s00477-022-02323-x

Wei, M., & You, X. (2022). Monthly rainfall forecasting by a hybrid neural network of discrete wavelet transformation and deep learning. *Water Resources Management*, *36*(11), 4003–4018. https://doi.org/10.1007/s11269-022-03218-w

Yetik, A. K., Arslan, B., & Şen, B. (2024). Trends and variability in precipitation across Turkey: a multimethod statistical analysis. *Theoretical and Applied Climatology*, *155*(1), 473–488. https://doi.org/10.1007/s00704-023-04645-4

Advanced Engineering Days

aed.mersin.edu.tr

Hydrodynamic Analysis of Lake Urmia: Effects of Causeway and Water Levels on Flow Patterns

Mehran Dadashzadeh*[1], Alireza Mojtahedi [1], Javad Parsa [2]

[1]*University of Tabriz, Faculty of Civil Engineering, Iran, mehrandadashzadeh@tabrizu.ac.ir, a.mojtahed@tabrizu.ac.ir*
[2]*University of Tabriz, Faculty of Agriculture, Iran, jparsa@tabrizu.ac.ir*

Cite this study: Dadashzadeh, M., Mojtahedi, A. & Parsa, J. (2024). Hydrodynamic Analysis of Lake Urmia: Effects of Causeway and Water Levels on Flow Patterns. Advanced Engineering Days, 9, 717-720

Keywords
Hydrodynamic Analysis
Flow Simulation
Low-water conditions
Causeway
Lake Urmia

Abstract

Lake Urmia, one of the largest saline lakes in the world, has faced significant environmental challenges in recent decades, including drastic reductions in water levels, increased salinity, and ecosystem degradation. These issues have been exacerbated by climate change, upstream water diversion, and reduced precipitation. The construction of a causeway dividing the lake into northern and southern parts has further altered its natural hydrodynamic conditions. This study focuses on assessing the hydrodynamic conditions of Lake Urmia through advanced flow simulations. Numerical modeling was utilized to analyze various factors affecting the lake currents, including wind patterns, river inflows, precipitation, and evaporation. The MIKE model was employed for this purpose. Sensitivity analysis was conducted to identify critical parameters for model calibration. The results were validated against measured data, and different scenarios were simulated and analyzed, considering varying water levels and the presence or absence of the causeway. The findings indicate that the simulations accurately reflect the hydrodynamic conditions of Lake Urmia under various scenarios.

Introduction

Lake Urmia, located in the northwestern region of Iran, is one of the largest saline lakes in the world. This endorheic basin has historically been a crucial ecological and economic resource, supporting diverse biological habitats and local livelihoods. The lake's unique hydrology and high salinity levels make it an important subject of scientific study [1]. Over the past few decades, Lake Urmia has faced significant environmental challenges, including drastic reductions in water levels, increased salinity, and ecosystem degradation. These changes have been attributed to various factors, such as climate change, upstream water diversion for agriculture, and reduced precipitation. The resulting environmental crisis has severely affected local biodiversity, agriculture, and socio-economic conditions [2-4].

On the other hand, the construction of the causeway has divided the lake into two parts: the northern part (38%) and the southern part (62%), with the only connection between these two parts being a passage approximately 1250 meters long. Undoubtedly, the construction of this causeway has significantly impacted the lake's natural hydrodynamic conditions [5]. Given the economic, connectivity, and environmental significance of Lake Urmia and the constructed causeway, a detailed investigation of the hydrodynamic conditions and flow patterns of the lake is essential. Safaie and Jamaat extended a three-dimensional FVCOM to investigate hydrodynamics and salinity transport processes in Lake Urmia [6]. Dadashzadeh et al. conducted simulations to investigate wave dynamics in Lake Urmia, aiming to explore its hydrodynamic conditions [7]. This study aims to analyze Lake Urmia's hydrodynamic conditions under various scenarios, focusing on the impact of the causeway and the implications of low-water conditions on the lake's overall health and sustainability.

Material and Method

Model description

In this study, the MIKE flow model from the Danish Hydraulic Institute (DHI) software package was employed. This software is recognized for its reliability and widespread use in the field of marine and coastal hydrodynamics.

The three-dimensional model is specifically designed for simulations of oceans, coastal areas, and estuaries. It is capable of modeling transient flows while accounting for bed changes, density variations, and tidal fluctuations.. For this study, an irregular horizontal grid was utilized, while the vertical layering was a combination of sigma and z levels. The numerical method applied to solve the equations was the finite volume method.

Model Setup

In the modeling process, the flow simulation encompasses all hydrodynamic conditions of the area, and the governing forces in the hydrodynamic equations include wind, atmospheric pressure, waves, river inflows, and the Coriolis force. This model incorporates the effects of wetting and drying along the shoreline. Additionally, in the flow model, horizontal viscosity was calculated based on the Smagorinsky formula, and vertical viscosity was calculated using k-ε relationships. The wind field and atmospheric pressure inputs for the model were derived from the outputs of the WRF meteorological model. Additionally, river discharge data were incorporated based on daily discharge records from the Iran Water Resources Management Company. Precipitation and evaporation data were sourced from the Urmia Synoptic Meteorological Station, provided by the National Meteorological Organization.

Results and Discussion

To assess flow conditions under different lake levels, scenarios were defined based on the lake's water level and the presence or absence of the causeway, and corresponding models were executed. Historical analysis of lake water level changes (data spanning 1965 to 2014, recorded by the Iran Water Resources and Power Development Company) indicates an average annual range from approximately 1278 meters to 1270 meters. Given the current lake conditions and its critical importance, this study investigates the minimum annual water level. Additionally, the presence or absence of the causeway can significantly impact lake flow patterns, necessitating simulations for both scenarios.

Models were executed over a long-term period (at least one year) to first determine the frequency of various storm events throughout the year and secondly, to assess the long-term impacts of these storms. Evaluation of wind patterns across different years on the lake reveals minimal variability in wind regimes. Figure 1 illustrates the comparison of wind roses derived from the WRF wind field for three different years at a specific location within the lake. As depicted, wind regimes show consistent patterns across these years. Hence, it is inferred that running models for a one-year period will encompass diverse wind regimes. Consequently, the year 2002 was selected as the reference year for running various scenarios, and subsequent simulation results for this year are presented.

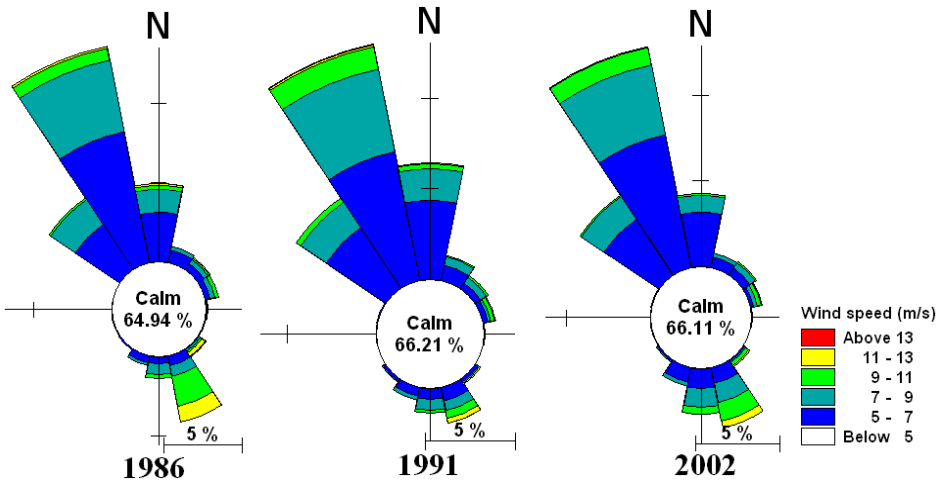


Figure 1. Comparison of wind roses derived from the WRF wind field for three different years at a point within the lake

To evaluate the flow patterns across the lake's surface, flow roses derived from simulations were analyzed at various locations under low-water conditions (at a 1270-meter elevation), considering scenarios with and without the causeway. Figure 2 depicts these flow roses for different lake points, illustrating averaged flows at specific depths. The predominant flow directions across different lake points vary with wind alignment and the asymmetric lakebed topography, transitioning from northeast-southwest in the northern areas to north-south in the central and northwest-southeast at the causeway opening. Flow patterns in the northern areas show minimal variation between scenarios with and without the causeway, except for significantly increased flow velocities at the causeway inlet due to channel constriction. The maximum flow velocities recorded at this level were 1.05 and 0.4 meters per second for scenarios with and without the causeway, respectively. Southern regions under low-water conditions are nearly devoid of significant flow.

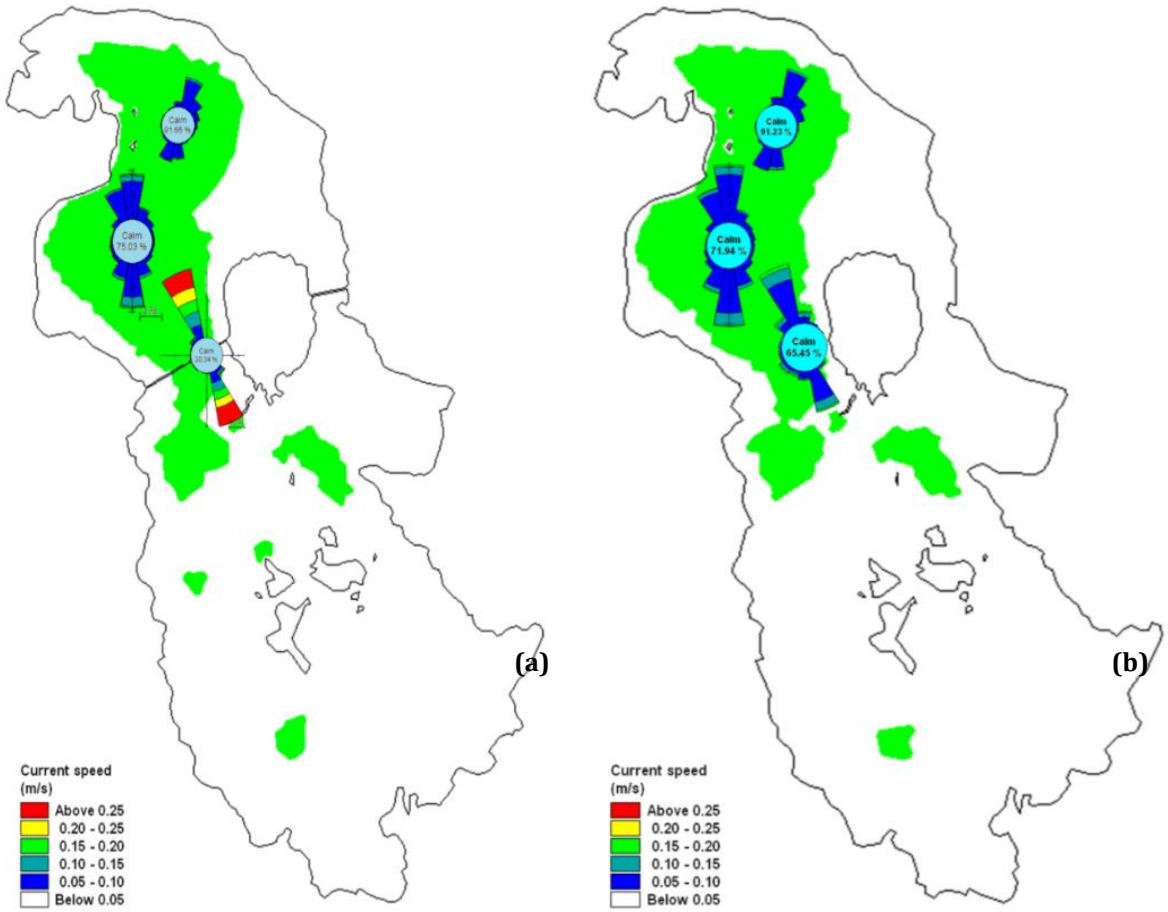


Figure 2. Flow roses derived from simulations at different locations within the lake under low-water conditions for scenarios (a) with and (b) without the causeway

Conclusion

To evaluate flow conditions at various lake levels, scenarios were established based on the lake's water level and the existence of the causeway, with corresponding models executed for each scenario. Considering the current state of the lake and its critical importance, this study focuses on the low-water conditions.

The analysis of simulated flow conditions reveals that under low-water conditions, substantial portions of the lake's southern areas dry up and are thus excluded from the simulations. In these scenarios, flow patterns in the northern regions of the lake closely follow wind variations, leading to the formation of vortices in different areas as wind speeds increase. Due to the extensive drying in the southern regions and their exclusion from the computational domain, the presence or absence of the causeway has minimal impact on the flow patterns and water levels in the northern regions.

The findings underscore the importance of maintaining sufficient water levels to preserve the lake's overall hydrodynamic balance and ecological health. Future management and restoration efforts should prioritize strategies that prevent the southern regions from drying up to ensure the lake's sustainable recovery and functionality.

References

1. Mojtahedi, A., Dadashzadeh, M., Azizkhani, M., & Others. (2022). Assessing climate and human activity effects on lake characteristics using spatio-temporal satellite data and an emotional neural network. Environmental Earth Sciences, 81(61).
2. AghaKouchak, A., Norouzi, H., Madani, K., Mirchi, A., Azarderakhsh, M., Nazemi, A., Nasrollahi, N., Farahmand, A., Mehran, A., & Hasanzadeh, E. (2015). Aral Sea syndrome desiccates Lake Urmia: Call for action. Journal of Great Lakes Research, 41(1), 307-311.
3. Alizadeh-Choobari, O., Ahmadi-Givi, F., Mirzaei, N., & Owlad, E. (2016). Climate change and anthropogenic impacts on the rapid shrinkage of Lake Urmia. Environmental Research Letters, 36(13), 4276-4286.
4. Dadashzadeh, M., Parsa, J., & Mojtahedi, A. (2020). Spatiotemporal evaluation of water temperature distribution in north-south parts of Lake Urmia using meteorological information and MIKE3 hydrodynamic model. Iranian Water Researches Journal, 14(3), 133-144.

5. Dadashzadeh, M., Mojtahedi, A., & Parsa, J. (2021). Evaluation the impacts of causeway remedial actions on Urmia Lake ecosystem using computational fluid dynamics and spatial analysis method. Journal of Civil and Environmental Engineering, 51(3), 41-53.
6. Safaie, A., & Jamaat, A. (2024). Numerical study of hydrodynamics and salinity transport processes in a hypersaline lake: A case study of Lake Urmia. Advances in Water Resources, 185, 104632.
7. Dadashzadeh, M., Parsa, J., & Mojtahedi, A. (2020). Investigation over the interaction of Lake Urmia wave pattern and causeway using meteorological models and computational fluid dynamics. Journal of Oceanography, 11(41), 49-61.

Advanced Engineering Days

aed.mersin.edu.tr

Investigation of damping properties on the wavelet-based damage detection in steel beam under noise effect: A numerical study

Farhad Jedari Zare Zadeh [*1], **Mehran Dadashzadeh** [1]

[1]*University of Tabriz, Faculty of Civil Engineering, Iran, farhadjedari@tabrizu.ac.ir, mehrandadashzadeh@tabrizu.ac.ir*

Cite this study: Jedari Zare Zadeh, F., & Dadashzadeh, M. (2024). Investigation of damping properties on wavelet-based damage detection in blast loaded steel beam: A numerical study. Advanced Engineering Days, 9, 721-723

Keywords
Damage detection
Wavelet Transform
Damping properties
Noise effect
Steel beams

Abstract

The existence of damage in the structures is an inevitable event that can intensify if preventive operations are not performed. The Continuous Wavelet Transform (CWT) is an efficient tool that is often used to detect and localize damage in structural members. Various factors can affect the wavelet-based damage detection approach. In this paper, the effect of damping properties is investigated in a numerical steel beam model under white Gaussian noise. Therefore, the stiffness was reduced in two possible locations along the beam to simulate the damage effect and the dynamic displacement response was extracted under impulse excitation with and without considering the damping properties of the beam. Then, the white Gaussian noise with a level of 5 percent was added to the extracted response. A CWT analysis was applied to the noisy response and the wavelet coefficients were obtained. It was shown that the maximum values of wavelet coefficients along the beam were highly correlated to the damage location. The results indicate that the wavelet transform estimated the damage location efficiently with and without damping properties under noise effect.

Introduction

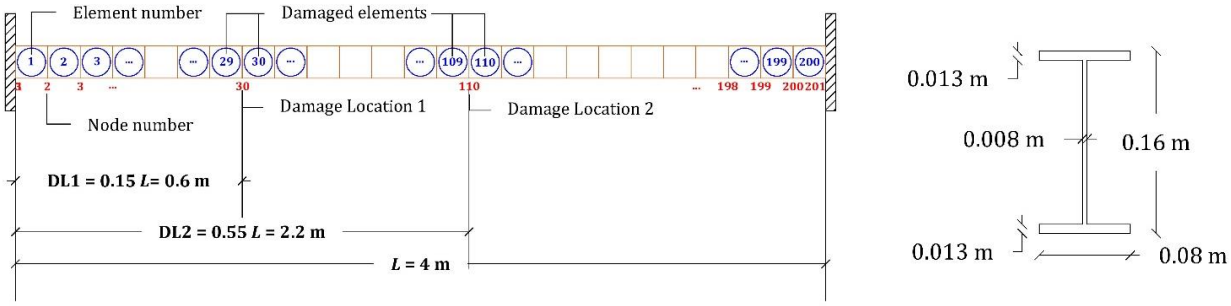
Structural Health Monitoring (SHM) is an important system to protect civil infrastructures from natural or manmade hazards. Monitoring the structural components like beams, columns, and braces is a vital role that has developed according to various approaches. In recent years, wavelet-based damage detection methods are often used in various studies. Liu et al. used the wavelet threshold method to denoise the response signal of a steel beam. Then, a proposed index of wavelet total energy change (WTEC) is applied to the new decomposed signals to localize damages [1]. In an experimental study, Janeliukstis et al. used 78 wavelet functions to localize the damage location with the structural response of aluminum beams [2]. The Continuous Wavelet Transform (CWT) analysis has shown a meaningful effect on incremental damage. Based on a numerical study, the sensitivity of the wavelet coefficients to crack propagation in concrete beams was appraised by Jedari et al. [3].

The wavelets are the functions with finite lengths that cause the large coefficients at both extremities of the input signal. This issue is called the edge effect. To prevent masking damage by edge effects, Jedari et al. proposed to extrapolate the input signal at extremities to reduce edge effects [4]. According to an experimental study, Kumar and Singh investigated the crack detection method near the end of a beam. The deflection of the beam was measured by image processing tools and analyzed by CWT to localize the damage [5].

The effect of noise on the experimental data is an inevitable factor. The source of noise depends on various factors such as environmental conditions. Su et al. and Abdulkareem et al. studied the noise effect on the performance of wavelet-based damage detection methods in composite and steel plates, respectively [6-7]. In some cases, machine learning methods were used as a noise reducer. For instance, Principal Component Analysis (PCA) is used to reduce the noise effect for damage detection aims by Jedari et al. [8].

In this paper, the effect of damping properties on the wavelet-based damage detection method was studied in a numerical steel beam model under noise effect. Therefore, the dynamic response of the beam was extracted under the impulse excitation, while the stiffness of the beam was reduced in two possible locations along the beam.

A CWT analysis was applied to the noisy response of the beam and the location of the damage was evaluated by the value of the wavelet coefficients.



(a) **(b)**

Figure 1. Geometric details of the steel beam and considered damage locations, (b) Cross-section of the beam

Material and Method

According to Figure 1(a), a steel beam (L = 4 m) with fixed support conditions was simulated in ABAQUS 2023 software. The cross-section of the beam is illustrated in Figure 1(b). The Mass density, Elastic modulus, and Poisson ratio of the steel were defined as 7.85×10^{-9} gr/m^3, 210 MPa, and 0.3 respectively. The damping properties of the beam were set based on Rayleigh damping which is proportional to a linear combination of mass and stiffness (α =50 and β = 0). In finite element modeling of the beam, the mesh size was defined as 0.005L = 0.02 m (201 nodes and 200 Elements), and the damage locations were considered at 0.15L = 0.6 m (Node 30) and 0.55L = 2.2 m (Node 110) from the left support of the beam. To simulate the damage scenario in each location, the elastic modulus of the beam was reduced by 10 percent. The dynamic displacement response of the beam was extracted under the impulse excitation.

In this study, wavelet transform was used as an efficient approach for damage detection and localization. The extracted response of the beam was considered an input signal for CWT analysis. The wavelet coefficients were obtained from convolution integral as equation (1)

$$C(s,u)=\frac{1}{\sqrt{s}}\int_{-\infty}^{\infty} f(x).\psi^{*}\left(\frac{x-u}{s}\right)dx \quad (1)$$

where f, ψ, s, and u are the input signal, the wavelet mother function, the scale factor, and the shifting parameter [9]. To investigate the effect of noise on the damage detection results, white Gaussian noise was added to the response of the beam. The Signal to Noise Ratio (SNR) was obtained by equation (2) and the noise was added to the main signal by equation (3) in MATLAB software.

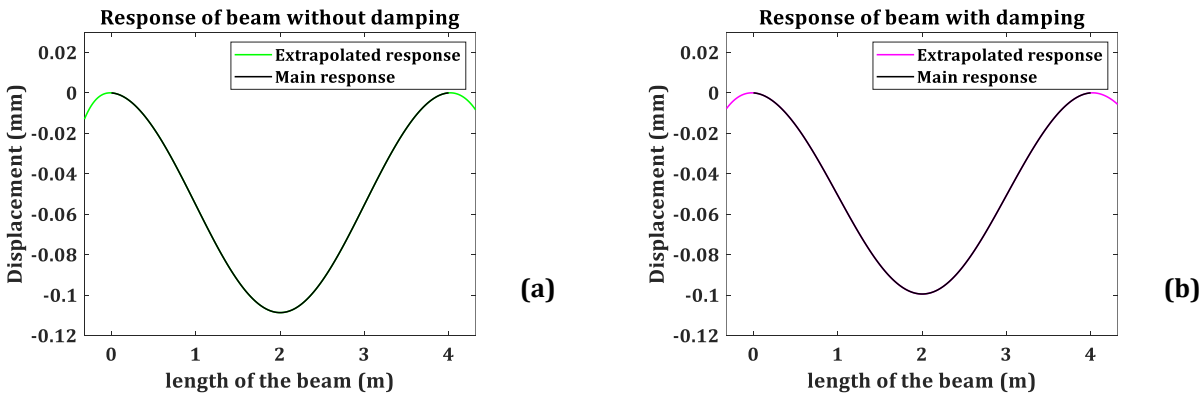
$$SNR=20\log_{10}^{(\frac{1}{n})} \quad (2)$$

$$S_n = \text{awgn}\,(x, SNR) \quad (3)$$

where n, S_n, and x are noise level (as a percentage), noisy signal, and noise-free signal [7].

Results

To extract the dynamic displacement response of the beam, the impulse excitation with the intensity of 500 N



(a) **(b)**

Figure 2. The noisy main and extrapolated response of the beam with the cubic spline method (a) without damping, (b) with damping

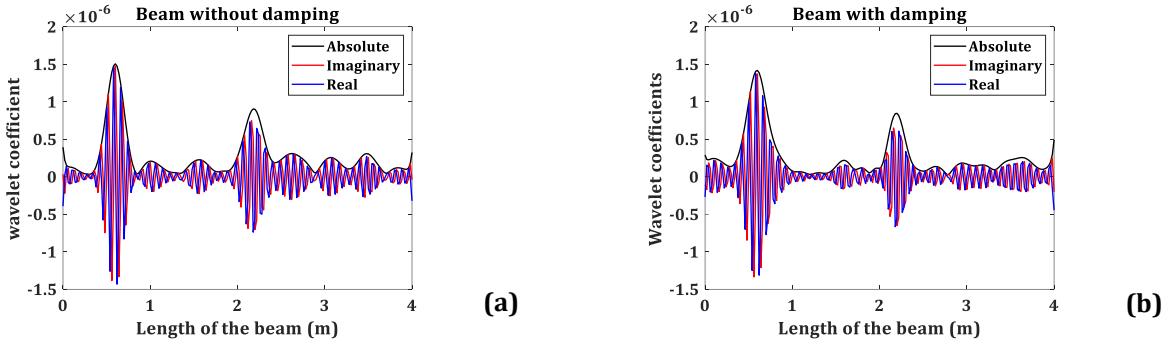


Figure 3. The absolute, imaginary, and real values of wavelet coefficients along the beam (a) without damping, (b) with damping in scale 9

was applied in the middle of the beam span. Then, the white Gaussian noise with a level of 5 percent was added to the response of the beam. To reduce the edge effect of the CWT analysis at the extremities of the beam, cubic spline extrapolation was used to extrapolate the response in 16 nodes at each end of it. Figure 2 illustrates the maximum noisy response and the extrapolation of it. A CWT analysis was applied to the noisy extrapolated response with the Morlet mother wavelet function. The absolute, imaginary, and real values of wavelet coefficients are shown in Figure 3 along the beam with and without the damping properties. The results show that the wavelet coefficients estimated the damaged locations with the desired accuracy under noise effect. In addition, even though the stiffness was reduced by the same percentage at both locations along the beam, the value of the wavelet coefficient in damage location 1 is greater than in damage location 2. By comparing the value of the wavelet coefficient in damaged locations, it is shown that the damping properties caused about a 15 percent reduction at each location.

Conclusion

A numerical study was performed on the finite element model of a steel beam to investigate the effect of damping properties on a wavelet-based damage detection approach under the white Gaussian noise. A damage scenario was applied by reducing the stiffness at two possible locations along the beam. Then, the dynamic displacement response of the beam under impulse excitation was extracted and the noise was added. A CWT analysis was applied to the noisy response and the wavelet coefficients were obtained. The results showed that damaged locations were estimated with good accuracy with damping properties under the noise effect.

References

1. Liu, J.L., Wang, S.F., Li, Y.Z., & Yu, A.H. (2024). Time-varying damage detection in beam structures using variational mode decomposition and continuous wavelet transform. Construction and Building Materials, 411, 134416.
2. Janeliukstis, R., Rucevskis, S., Wesolowski, M., & Chate, A. (2017). Experimental structural damage localization in beam structure using spatial continuous wavelet transform and mode shape curvature methods. Measurement, 102, 253-270.
3. Jedari Zare Zadeh, F., Farzam, M., & Dadashzadeh, M. (2024). Localization and investigation of damage extension in reinforced concrete beams using signal processing and machine learning. Journal of Structural and Construction Engineering, 11(2).
4. Jedari Zare Zadeh, F., Farzam, M., & Bagheri, S. (2024). Wavelet transform with reduced edge effects for damage identification in the beams under incremental damage. Civil Infrastructure Researches.
5. Kumar, R., Singh, S. K. (2021). Crack detection near the ends of a beam using wavelet transform and high-resolution beam deflection measurement. European Journal of Mechanics / A Solids, 88, 104259.
6. Su, C., Jiang, M, Liang, J., Tian, A., Sun, L., Zhang L., Zhang, F., & Sui, Q. (2020). Damage assessments of composite under the environment with strong noise based on synchrosqueezing wavelet transform and stack autoencoder algorithm. Measurement, 156, 107578.
7. Abdulkareem M., Bakhary, N., Vafaei M., Noor M. N., Mohamed R. N. (2019). Application of two-dimensional wavelet transform to detect damage in steel plate structures. Measurement, 146, 912-923.
8. Jedari Zare Zadeh, F., Farzam, M., & Dadashzadeh, M. (2022). Wavelet-based analysis of dynamic response for damage localization in reinforced concrete beams using machine learning. International Conference on Structural Engineering, 6, 1-13.
9. Nourani, V., Dadashzadeh, M., & Eslamian, S. (2022). Flood Handbook: Analysis and Modeling: Application of Integral Transforms in Flood Studies. CRC Press, Taylor & Francis Group. ISBN: 9780429463938.

Advanced Engineering Days

aed.mersin.edu.tr

Unraveling topological features of complex networks

Leyla Naghipour *[1], Khalil Valizadeh Kamran [1], Mohammad Taghi Aalami [2], Vahid Nourani [3]

[1] University of Tabriz, Faculty of Planning and Environmental Sciences, Department of Remote Sensing and GIS, East-Azerbaijan, Iran
[2] University of Tabriz, Faculty of Civil Engineering, Department of Water Resources Engineering, Tabriz, East-Azerbaijan, Iran
[3] Center of Excellence in Hydroinformatics and Faculty of Civil Engineering, University of Tabriz, 29 Bahman Blvd., Tabriz East-Azerbaijan, Iran

Cite this study: Naghipour, L., Valizadeh Kamran, K., Aalami, M. T., & Nourani, N. (2024). Unraveling topological features of complex networks. Advanced Engineering Days, 9, 724-726

Keywords
Collective dynamics
Complex systems
Network reconstruction

Abstract

Network reconstruction is a widely applied technique for enhancing the fundemental understanding of real-world systems, allowing for the realization of physical interactions within complex dynamical systems and the elucidation of collective dynamics behavior. Advanced approaches, including network reconstruction and the analysis of functional connectivity, are essential tools, providing detailed characterizations that reveal the intricate patterns and the underlying interactions governing complex networks. Various methods have been employed in this context. These methods were applied to both linear and nonlinear collective dynamics. The dynamics of interconnected units were simulated across different complex topologies commonly observed in empirical systems. By considering widely used network models, we simulate different collective dynamics and show that the interplay between structure and dynamics hinders accurate reconstructions. Nevertheless, the underlying connectivity is more reliable when inference is based on phase-space reconstruction from the observed dynamics. Unraveling the underlying topological features of complex networks is pivotal for understanding their structural and functional properties. By analyzing these features, researchers can gain insights into the organization, dynamics, and robustness of various natural and artificial systems across numerous disciplines, including biological, social, information, engineering, and physical sciences.

Introduction

Complex networks are extensively employed across numerous disciplines, including biological, social, information, engineering, and physical sciences, to enhance our understanding of the collective dynamics and functionality of complex natural and artificial systems as they evolve over time [1-3]. Determining the interconnections between elements in real-world complex systems is essential for understanding the nature of ongoing interactions. Therefore, the intrinsic connectivity between components must be characterized, often by mapping physical connections onto a network. The effects of this connectivity are frequently explored using the concept of complex networks.

The extensive applicability and success of networks in providing insights into the structure and function of both natural and human-made systems have generated considerable excitement across various scientific fields. Examples include transportation networks, such as airline routes and road and rail networks [4-6]; disease containment strategies based on cellular network data [7]; characterizing interactions in online social networks [8]; inferring migration patterns [9]; organization and functioning of the human brain [10]; detailed descriptions of protein-genetic interactions [11]; modeling of complex climate systems [12-13]

The quantitative study of networks is fundamental for characterizing complex systems. Notably, machine learning techniques are common across a diverse array of fields [14-15]. In this study, we propose a novel statistical approach to overcome existing challenges and enhance the understanding and predictability of the complex systems.

Material and Method

Here, we outline our approach, focusing on two widely used linear correlation statistics: Cross-Correlation (CC) and Spectral Coherence (SpeCoh); two prevalent information-theoretic measures: Mutual Information (MI) and

Transfer Entropy (TE); and one non-parametric similarity measure: Spearman's rank Correlation (SC). In the next step, we will discuss a method centered on reconstructing the underlying phase space, specifically Convergent Cross-Mapping (CCM). CCM is extensively utilized for inferring causal relationships between observed dynamics, providing insights into the underlying mechanisms driving system behavior.

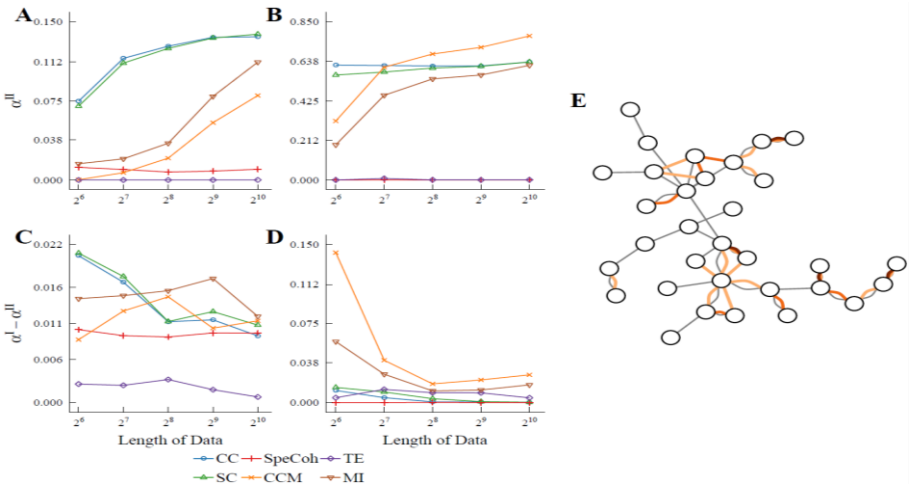


Figure 1. Type-I error for the reconstruction of undirected networks

Results

We provide an overview of the statistical methods commonly employed for reconstructing network structures from observations of collective dynamics. While these methods vary in the type of correlation, similarity, or causality they estimate between two stochastic processes, X(t) and Y(t).

This work also serves as a comprehensive study for the application of the convergent cross-mapping (CCM) method and the evaluation of commonly used methods. Our approach integrates dynamical systems techniques with statistical analysis. Finally, we demonstrate how surrogate models can partially reproduce nonlinear dynamics.

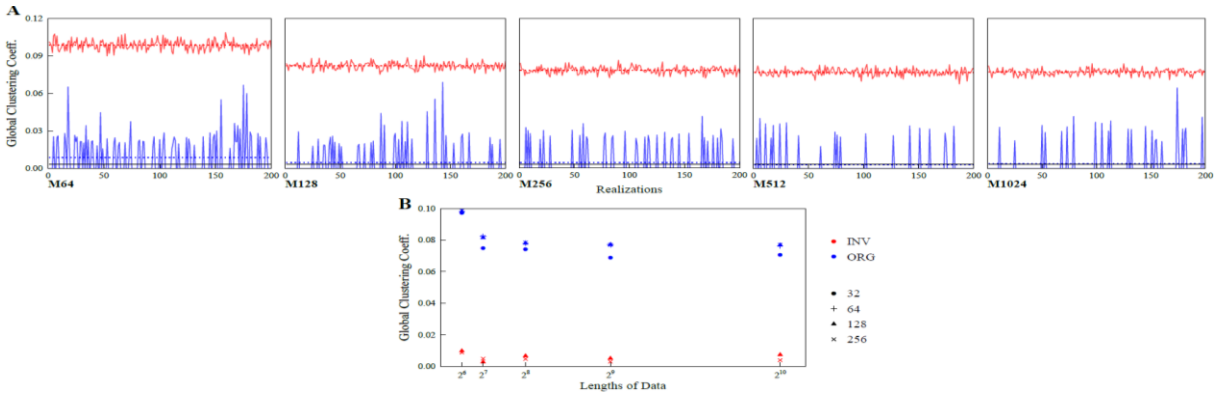


Figure 2. GCC of RNs in one and multi-layer networks reconstructed by CCM method with changing topological structures and length of observations

Global clustering coefficient (GCC) for the random network is presented in Figure 3 with N=256 nodes showing how the GCC is influenced by changing length of the generated data. Dashed lines are average of the obtained GCC between 200 realizations and black solid line is the expected GCC. Figure 2 (B) presents variation of the average of the GCC with changing number of nodes and length of generated data on the networks.

Discussion

Constructing the structure of a complex climate network based on observations of its dynamical units poses a significant challenge in understanding coupling patterns and physical interactions within the complex system. Quantifying pairwise statistical dependencies is a widely adopted approach, but it may encounter several limitations. While statistical analysis effectively maps the functional connectivity of complex systems, it is crucial to note that understanding how units within the system, which are not directly connected, exchange information or participate in specific functions is often pivotal for gaining new insights.

Conclusion

The analysis of collective dynamics is usually used to reconstruct the network backbone of many complex systems, from the human brain to climate. However, this functional reconstruction is too often used to make assessments about the underlying structure.

By considering widely used network models, we simulate different collective dynamics and show that the interplay between structure and dynamics hinders accurate reconstructions. Nevertheless, the underlying connectivity is more reliable when inference is based on phase-space reconstruction from the observed dynamics. This is statistically more robust than the state-of-the-art and mitigates many undesired effects of pairwise statistical inference.

Acknowledgement

This study is supported by the research grant of the University of Tabriz (Number 718).

References

1. Albert, R., & Barabási, A. L. (2002). Statistical mechanics of complex networks. Reviews of Modern Physics, 74(1), 47.
2. Boccaletti, S., Latora, V., Moreno, Y., Chavez, M., & Hwang, D. U. (2006). Complex networks: Structure and dynamics. Physics Reports, 424(4-5), 175-308.
3. Naghipour, L., Aalami, M. T., & Nourani, V. (2023). Collective dynamics analysis based on the multiplex network method to unravel the backbone of fluctuations in groundwater level data. Computers & Geosciences, 172, 105310.
4. Sen, P., Dasgupta, S., Chatterjee, A., Sreeram, P. A., Mukherjee, G., & Manna, S. S. (2003). Small-world properties of the Indian railway network. Physical Review E, 67(3), 036106.
5. Gastner, M. T., & Newman, M. E. (2004). Diffusion-based method for producing density-equalizing maps. Proceedings of the National Academy of Sciences, 101(20), 7499-7504.
6. Li, D., Fu, B., Wang, Y., Lu, G., Berezin, Y., Stanley, H. E., & Havlin, S. (2015). Percolation transition in dynamical traffic network with evolving critical bottlenecks. Proceedings of the National Academy of Sciences, 112(3), 669-672.
7. Lima, A., De Domenico, M., Pejovic, V., & Musolesi, M. (2015). Disease containment strategies based on mobility and information dissemination. Scientific Reports, 5(1), 10650.
8. Omodei, E., De Domenico, M., & Arenas, A. (2015). Characterizing interactions in online social networks during exceptional events. Frontiers in Physics, 3, 59.
9. Matamalas, J. T., De Domenico, M., & Arenas, A. (2016). Assessing reliable human mobility patterns from higher order memory in mobile communications. Journal of The Royal Society Interface, 13(121), 20160203.
10. Reis, S. D., Hu, Y., Babino, A., Andrade Jr, J. S., Canals, S., Sigman, M., & Makse, H. A. (2014). Avoiding catastrophic failure in correlated networks of networks. Nature Physics, 10(10), 762-767.
11. Jeong, H., Mason, S. P., Barabási, A. L., & Oltvai, Z. N. (2001). Lethality and centrality in protein networks. Nature, 411(6833), 41-42.
12. Naghipour, L., Aalami, M. T., & Nourani, V. (2021). Reconstruction of network connectivity by the interplay between complex structure and dynamics to discover climate networks. Theoretical and Applied Climatology, 143, 969-987.
13. Naghipour, L., Aalami, M. T., & Nourani, V. (2022). Unravelling the backbone of climate networks from the analysis of collective dynamics and time reversal. International Journal of Climatology, 42(11), 5535-5553.
14. Khatibi, R., Naghipour, L., Ghorbani, M.A., Smith, M.S., Karimi, V., Farhoudi, R., Delafrouz, H., & Arvanaghi H., (2013) Developing a predictive tropospheric ozone model for Tabriz. Atmospheric Environment 68, 286-294.
15. Khatibi, R., Ghorbani, M.A., Naghipour, L., Jothiprakash, V., Fathima, T.A., & Fazelifard M.H., (2014) Inter-comparison of time series models of lake levels predicted by several modeling strategies. Journal of Hydrology 511, 530-545.

Advanced Engineering Days

aed.mersin.edu.tr

Forecasting of Beyşehir Lake Levels with Artificial Neural Networks and Levenberg Training Algorithm

Beyza Değişli [1], Vahdettin Demir [2]

[1] KTO Karatay University, Engineering and Natural Sciences Faculty, Department of Civil Engineering, Konya, Türkiye
beyza.degisli@ogrenci.karatay.edu.tr, vahdettin.demir@karatay.edu.tr

Cite this study: Değişli, B., & Demir, V. (2024). Forecasting of Beyşehir Lake Levels with Artificial Neural Networks and Levenberg Training Algorithm. Advanced Engineering Days, 9, 727-731

Keywords
Forecast
Lake Level
Artificial Neural Networks
Levenberg Marquart
Beyşehir Lake

Abstract

Forecasting of lake water level is a fundamental requirement for irrigation and drinking water supply management and many other engineering and socio-economic activities such as fishing, tourism, wildlife conservation and others. In this study, the data of the lake observation station numbered D16G175, located on the Beyşehir lake in the Konya Closed Basin, was estimated using Artificial Neural Networks (ANN). In the study, 12-month past lake levels from time "T" were divided into 75% Training and 25% test, and lake levels at "T" moment were estimated. Comparison values were obtained by using the Levenberg Marquart (LM) algorithm and 100 iterations as the training algorithm in ANN. Root Mean Square Error (RMSE), Mean Absolute Error (MAE) and coefficient of determination (R^2) were used as comparison criteria in the study, and when the results were examined, the most successful result was obtained in the 12 inputs and 10 hidden layers.

Introduction

Significant changes are observed in lake levels due to factors such as climate change and human-induced water use. The use of water resources to provide more water than normal due to both agricultural water needs and water needs in cities causes the capacity of water reserves such as lakes to decrease or disappear [1]. For these reasons, monitoring and effective use of lake levels are among the topics of increasing importance in the literature.

Recently, a number of neural network models have demonstrated a remarkable ability to model lake, river system, and streamflow water levels. Research has used artificial neural networks [2], support vector machines [3], adaptive neuro fuzzy inference systems [4], generalized regression neural networks [5], hybrid MLP-FFA model [6], and fuzzy logic models [7].

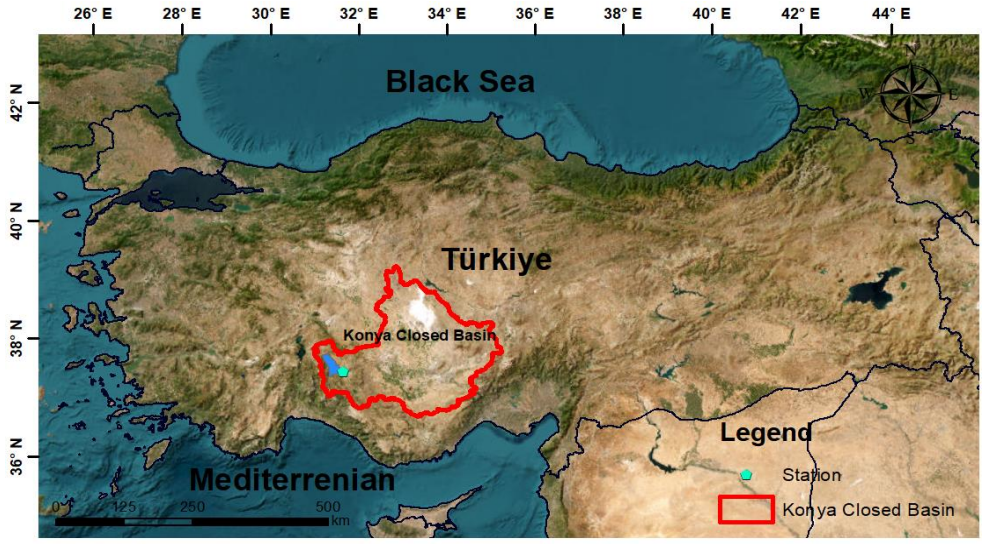
In this study, the lake water levels of Beyşehir Lake, located in the Konya closed basin, were modeled using the Levenberg Marquardt training algorithm and MANN and compared according to various input numbers.

Material and Method

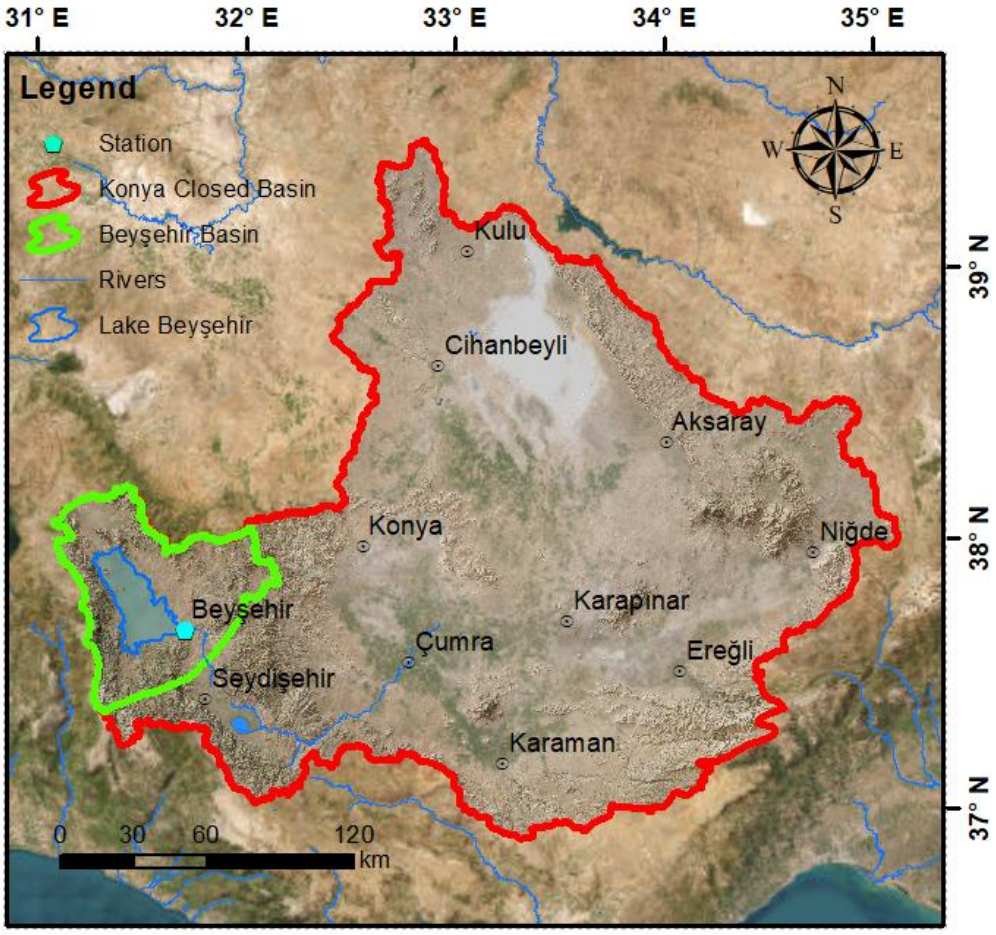
Study area and Data

Beyşehir lake, located within the borders of Konya and Isparta provinces, is between 37°47′0″N and 31°33′0″E. Although Beyşehir Lake is surrounded by mountains, it is in a tectonic pit. There are Taurus Mountains in the west and south of Beyşehir Lake, Erenler Mountain in the east, and Sultan and Amanas Mountains in the northwest and southeast respectively [8]. The visual of the study area is shown in Figure 1.

The monthly average data (m) used in the study was obtained from the 4th Regional General Directorate of State Hydraulic Works (DSİ) and covers the years 1950-2022.



(a)



(b)

Figure 1. KCB location in Turkey (a) Study area and Beyşehir Lake Observation Station (b)

Multilayer Artificial Neural Networks (MANN)

Artificial neural networks, inspired by the human brain, consist of layers of parallel processing elements called neurons. Each layer in MANN is connected to the advancing layer by interconnection weights. During the training phase, randomly assigned initial weight values are corrected iteratively. Among many algorithms for arranging the weights, the LM algorithm was used because it gives faster and more accurate results than others [9]. The model structure of multilayer artificial neural networks is shown in Figure 2.

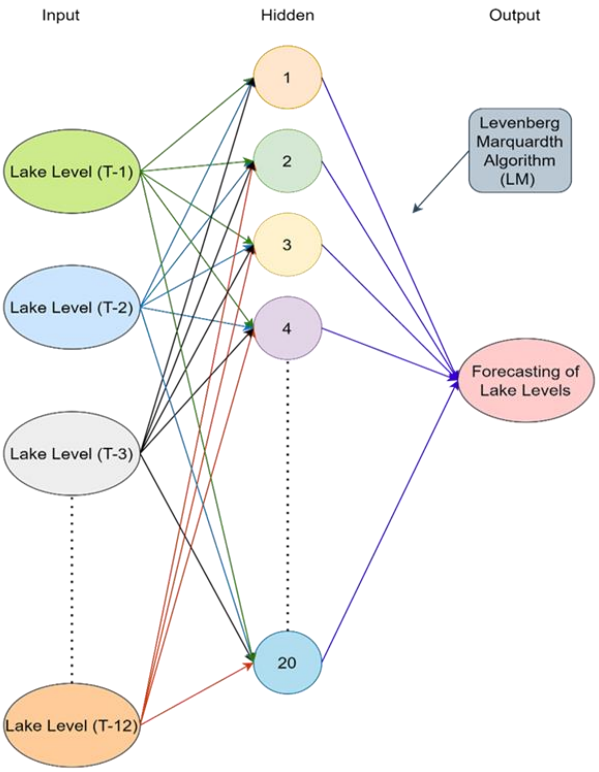


Figure 2. ANN structure used in the study

Comparison (Error) Criteria

RMSE, MAE and R^2 were used as comparison criteria in the study. For details of the comparison criteria used, the following reference can be examined [10]. Having minimum error values and R^2 values close to 1 determines the success of the model. The workflow diagram of the study is shown in Figure 3.

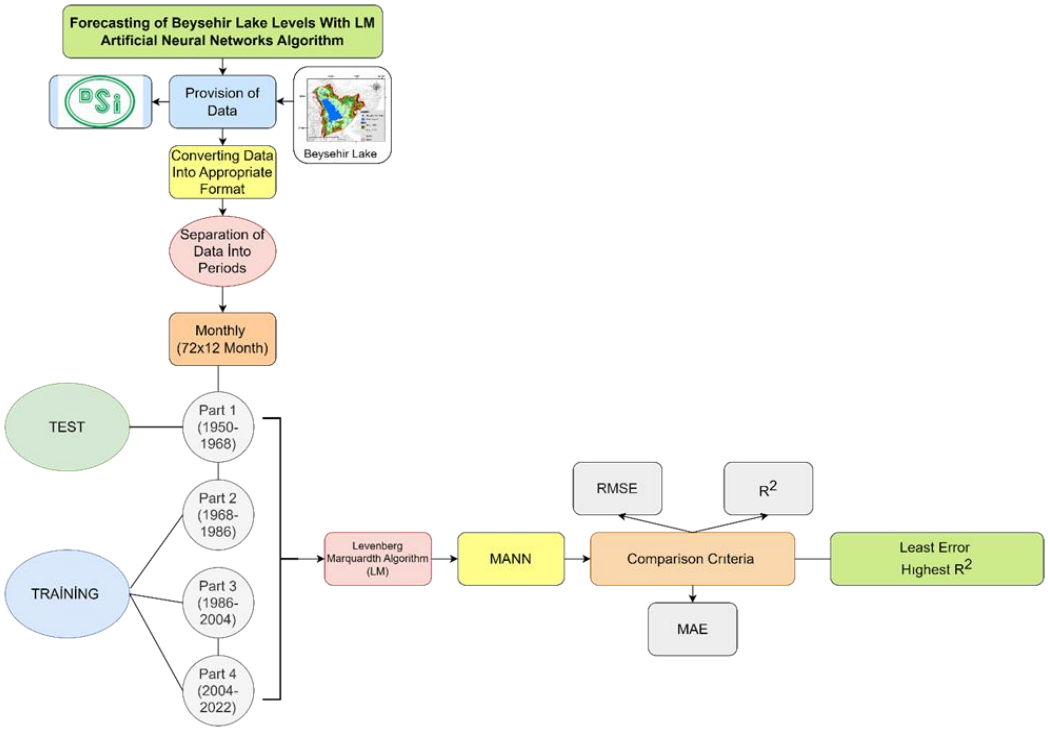


Figure 3. Study workflow diagram

Results

The study was carried out with codes written in the MATLAB software, and modeling was carried out in the MANN model structure with 12 inputs (Lag-time), 100 iterations, the number of hidden layer cells varying up to 20, and normalization of the data between 0.2 and 0.8 with the LM training algorithm. The model results are shown in Figure 4, according to the number of inputs.

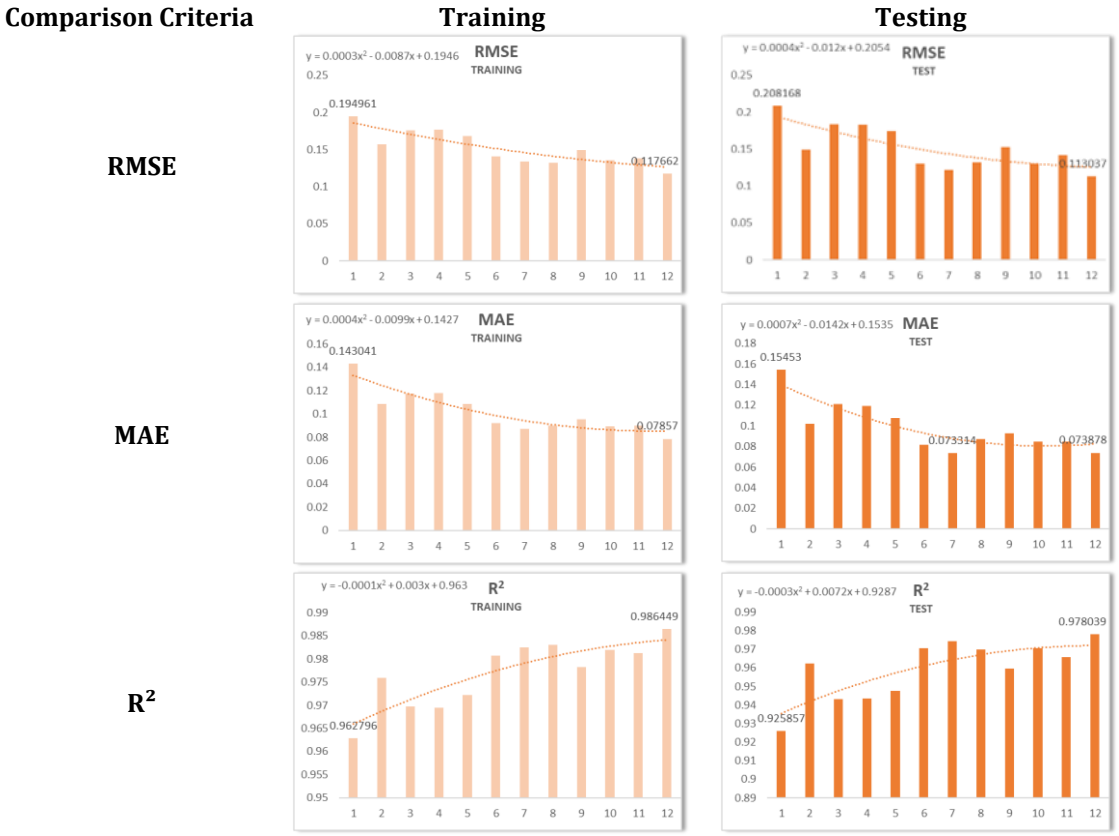


Figure 4. Change chart of the comparison criteria of the Training and Testing phase according to the number of inputs

Figure 4 shows the change of the criteria of the inputs used according to the error. Errors in these sections are obtained according to the hidden layer cell, ranging from 1 to 20. Figure 3 shows RMSE values between 0.208-0.113, MAE between 0.154-0.078 and R^2 values between 0.92-0.98 in the training and test data sets. Completion of the training phase was achieved with the 12th input data set and 10 hidden layer cell forms according to the highest determination coefficient (RMSE = 0.117, MAE = 0.078 and R^2 = 0.986). Test phase results were obtained with the 12th input data set and 10 hidden layer cell forms (RMSE = 0.114, MAE = 0.047 and R^2 = 0.978).

Discussion

The artificial neural networks are widely used for hydrological level modeling and detection. It comes to the fore in many studies in terms of ease of application and accuracy. In their study, Keskin and Demir (2021), performed multi-layered artificial neural networks and regression analyzes in the modeling of the Mert River basin with artificial neural networks. They found the most successful result with MANN in modeling the Mert River basin with a methodology similar to our study (R^2=0.948) [11]. Yarar and Onuçyıldız (2009), used artificial neural networks to determine Beyşehir Lake level changes. It is similar to our study in terms of method and research area. The best result with artificial neural networks was obtained as 0.056285 in the Matched Gradient model with 1 hidden layer and 7 hidden nodes [12]. Çubukçu et al. (2021), estimated the monthly average lake levels of Lake Michigan with 3 different artificial neural networks. Radial-based artificial neural networks (RBANN), generalized regression artificial neural networks (GRANN) and multilayer artificial neural networks (MANN) were used. In the study, MANN (R^2 = 0.9906) gave the most accurate result for the test phase [13].

Conclusion

In this study, the forecasting of Beyşehir Lake levels was conducted using MANN. Monthly average data from the D16G175 lake observation station, covering the years 1950 to 2022, were utilized. Comparison criteria values were calculated for the last 25% of the data set based on the input data from the previous month. Upon examining the results;

- As the number of inputs increases, the error values generally decrease, and the determination coefficient increases. Therefore, lag time modeling is a parameter that enhances model performance.
- The most successful results in both the training and test phases were obtained using the input data sets up to the 12th input, which includes data from one year prior. This is believed to be due to the high correlation and annual fluctuations observed in the lakes over the previous years.
- In the training phase, the highest determination coefficient was achieved with the 12th data set and 10 hidden layer cells (RMSE = 0.117, MAE = 0.078). In the test phase, using the same data set and cell configuration, the RMSE was 0.114 and the MAE was 0.047.

In future studies, the remaining 25% of the data sets will be explored using other training algorithms and different iterations commonly used in the literature.

Acknowledgments

This study is supported by the 2209-A (University Students Research Projects Support Program) within the scope of the 2023-1 period with the application number 1919B012308506 and the KTO Karatay University Scientific Research Projects (BAP number: 10062412) program. Additionally, the authors would like to thank the Konya State Hydraulic Works 4th Regional Directorate and its employees for their support in providing the data.

References

1. Albek, E. A., Albek, M. & Göncü, S. (2017). Trend Analysis of Burdur, Eğirdir, Sapanca and Tuz Lake Water Levels Using Nonparametric Statistical Methods. Afyon Kocatepe University Journal of Sciences and Engineering, 17(2), 555–570.
2. Buyukyildiz M, Tezel G, Yilmaz V (2014) Estimation of the change in lake water level by artificial intelligence methods. Water Resour Manag 28:4747–4763
3. Hipni A et al (2013) Daily forecasting of dam water levels: comparing a support vector machine (SVM) model with adaptive neuro fuzzy inference system (ANFIS) Water. Resour Manag 27:3803–3823
4. Yarar A, Onucyıldız M, Copty NK (2009) Modelling level change in lakes using neuro-fuzzy and artificial neural networks. J Hydrol 365:329–334
5. Vaheddoost B, Aksoy H, Abghari H (2016) Prediction of water level using monthly lagged data in Lake Urmia, Iran. Water Resour Manag 30:4951–4967
6. Altunkaynak A, Şen Z (2007) Fuzzy logic model of lake water level fluctuations in Lake Van, Turkey. Theor Appl Climatol 90:227–233
7. Ghorbani, M.A., Deo, R.C., Karimi, V. et al. Implementation of a hybrid MLP-FFA model for water level prediction of Lake Egirdir, Turkey. Stoch Environ Res Risk Assess 32, 1683–1697 (2018). https://doi.org/10.1007/s00477-017-1474-0
8. Soyaslan, İ. İ., & Hepdeniz, K. (2018). Beyşehir Gölü havzasının yeraltısuyu akım modellemesi esaslı hidrojeolojik özelliklerinin değerlendirilmesi. Mehmet Akif Ersoy Üniversitesi Fen Bilimleri Enstitüsü Dergisi, 9(1), 63-74.
9. Marquardt D. W. , "An algorithm for leastsquares estimation of nonlinear parameters," J. Soc. Indust. Appl. Math., vol. 11, no. 2, pp. 431– 441, June 1963. Doi:10.1137/0111030
10. Yıldız, M. F., & Demir, V. (2023). Forecasting of Water Levels by Artificial Neural Networks Technique in Lake Michigan-Huron. Advanced Geomatics, 3(2), 63-71.
11. Demir, V., & Keskin, A. Ü. (2020). Yapay Sinir Ağları Yardımıyla Yükseklik Modellemesi (Samsun-Mert Irmağı Havzası Örneği). Gazi Mühendislik Bilimleri Dergisi, 6(1), 54-61.
12. Yarar, A., & Onüçyıldız, M. (2009). Yapay sinir ağlari ile beyşehir gölü su seviyesi değişimlerinin belirlenmesi. Selçuk Üniversitesi Mühendislik, Bilim Ve Teknoloji Dergisi, 24(2), 21-30
13. Çubukçu, E. A., Yılmaz, C. B., Demir, V., & Sevimli, M. F. (2021). Forecasting of monthly average lake levels of Lake Michigan with artificial neural networks. Advanced Engineering Days (AED), 1, 4-7.

Advanced Engineering Days

aed.mersin.edu.tr

Evaluating the Effect of Monopile Diameter on the Static Deformation Response Using Finite Element Method

Özgür Lütfi Ertuğrul [*1], **Fatma Dülger Canoğulları** [2]

[1]*Mersin University, Department of Civil Engineering, Mersin, Türkiye, ertugrul@mersin.edu.tr*
[2]*Toros University, Department of Civil Engineering, Mersin, Türkiye, fatma.dulger@mersin.edu.tr*

Cite this study: Ertugrul, O. L., & Canogullari, F. D. (2024). Evaluating the Effect of Monopile Diameter on the Static Deformation Response Using Finite Element Method. Advanced Engineering Days, 9, 732-734

Keywords
Monopile
Finite element method
Lateral displacement

Abstract

Over the past twenty years, there has been significant development in the offshore wind and wave energy sectors with the aim of providing sustainable energy. The majority of offshore energy structures utilized in current projects are monopiles located in shallow water. This choice is mostly due to the simplicity of their design, installation, and control. In this study, monopile foundations with diameters of 4 meters, 6 meters, and 8 meters were modeled using Plaxis 3D software, and the effect of pile diameter on horizontal deformation was investigated. The analysis results indicate that increasing the diameter of monopile foundations significantly reduces lateral displacement.

Introduction

Offshore technology has experienced rapid growth since the installation of the first offshore wind turbine "Vindeby" in Denmark in 1991. Numerous advantages support this growth. Some of these advantages are as follows [1]:

- Wind intensity increases as you move away from the shore, significantly boosting energy production per unit;
- There are no size limitations for offshore wind turbines, as components can be more easily transported by sea;
- The visual and noise impacts of wind turbines can be mitigated if they are installed at a sufficient distance from the shore;
- Large continuous areas are available, so installations will not occupy or interfere with land use.

The steel profile, known as a monopile, is the most often used support structure for wind turbines. It is constructed on the seabed and is popular for its simplicity, ease of application, and cost-effectiveness Although previously it was believed that piles were not financially viable beyond 25 meters below the seabed, it is now possible to use single pile-supported turbines to depths of up to 40 meters. A monopile foundation is currently one of the most commonly used transporter for wind turbine foundations.

Monopiles are a prevalent foundation solution for offshore wind turbines and other marine structures due to their simplicity and cost-effectiveness. The diameter of a monopile plays a critical role in determining its performance under various loading conditions, including static and dynamic loads. Understanding the impact of pile diameter on the structural and dynamic behavior of monopiles is essential for optimizing their design and ensuring their longevity and stability.

Material and Method

The continuous rise in population, urbanization, and industrialization leads to a corresponding increase in home and industrial energy needs. Wind power is a renewable and sustainable energy source that could satisfy the need for electricity in an ecologically beneficial way. It is a great alternative to traditional methods of electricity generation that rely on fossil fuels like coal, oil, and natural gas. The most efficient and easily transportable type of energy is obtained with the use of wind turbines, which became popular in the late twentieth century [2].

This study included conducting static analyses at various monopile diameters using the Plaxis 3D [3] software. An evaluation was conducted to compare the results of the analyses.

The properties of the soil and pile used in the analyses are shown in Table 1. The pile has an embedded length of 10 meters, a length above the ground of 5 meters, and a wall thickness of 0.01 meters. The diameter of monopile has been modeled as 4 meters, 6 meters, and 8 meters, respectively.

A lateral load is applied at the corner of the pile and the applied horizontal load in all three analyses is 720 kN.

Table 1. Properties of the soil and monopile

	Unit weight (kN/m^3)	Modulus of elasticity (kN/m^2)	Poisson's Ratio	Angle of internal friction (°)
Soil	16,6	$8x10^3$	0,2	38
Monopile	78	$210x10^6$	0,3	-

Results and Discussion

Lateral displacement refers to the horizontal movement of the monopile under various loads such as wind, waves, and currents. Understanding this effect is crucial for the design and stability of offshore structures. The deformation contours of the soil surface for a lateral horizontal load of 720 kN are shown in Figure 1.

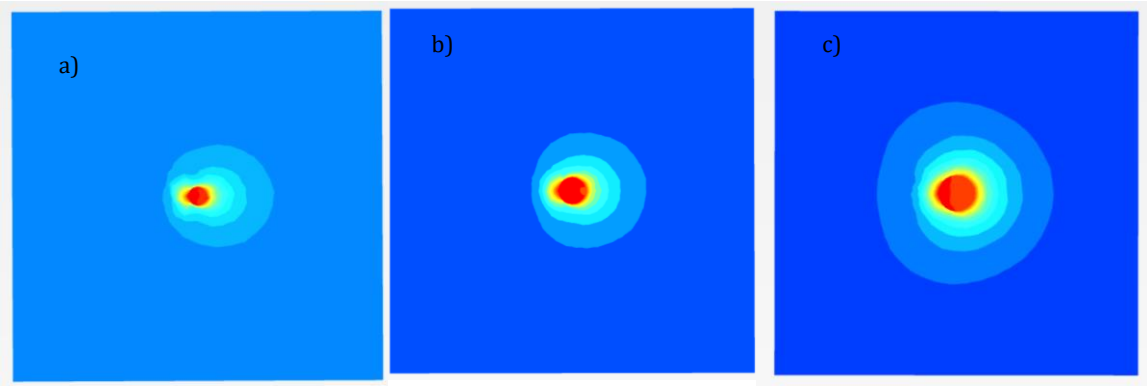


Figure 1. The deformation contours of the soil surface at different diameters of monopile a) 4 m b)6 m c) 8 m

After reviewing the results of the analysis the maximum deformation values at the ground surface for monopile foundations with diameters of 4 meters, 6 meters, and 8 meters were found to be 0,04 m, 0,02 m, and 0,01 m, respectively. Additionally, as a result of the analyses conducted, a curve depicting the horizontal deformations along the pile was plotted. The curve, plotted for pile diameters of 4 meters, 6 meters, and 8 meters, is shown in Figure 2.

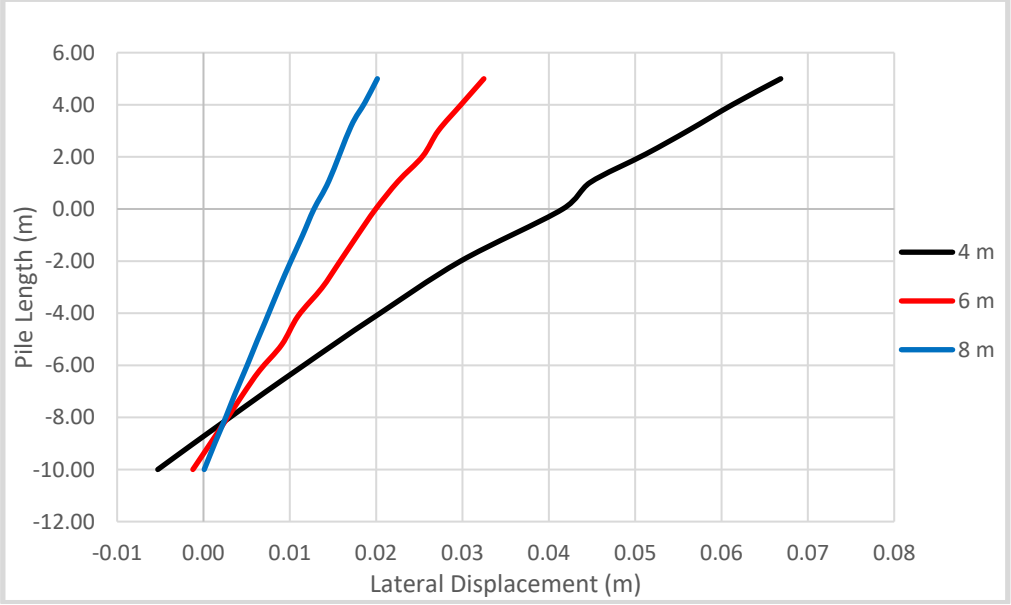


Figure 2. Pile length – lateral displacement curve for different monopile diameters

As the diameter of the monopile increases from 4 m to 8 m, the lateral displacement at any given length decreases. This confirms that larger diameter monopiles are stiffer and can resist lateral loads more effectively.

Conclusion

Over the past twenty years, there has been significant development in the offshore wind and wave energy sectors with the aim of providing sustainable energy. The majority of offshore energy structures utilized in current projects are mono-piles located in shallow water. This choice is mostly due to the simplicity of their design, installation, and control. In this study, monopile foundations with diameters of 4 meters, 6 meters, and 8 meters were modeled using Plaxis 3D software, and the effect of pile diameter on horizontal deformation was investigated. In the analysis results, increasing the diameter of monopile foundations significantly reduces lateral displacement. This reduction is due to increased stiffness, improved soil-structure interaction, higher flexural rigidity and greater critical buckling loads. These factors are essential for the effective and reliable design of offshore wind turbine foundations, ensuring structural stability and operational efficiency.

References

1. Leite O. B. (2015). Review of Design Procedures for Monopile Offshore Wind Structure, University of Porto.
2. Sarak, S. (2022) Soil-Pile Interaction for Offshore Wind Turbine Foundations in Liquefiable Soils. Dokuz Eylül Üniversitesi, İzmir.
3. Plaxis 3D, User Manual (2020). Bentley Systems.

Advanced Engineering Days

aed.mersin.edu.tr

Investigation of Loading Frequency Effects on the Dynamic Lateral Load- Displacement Curves of Monopiles

Özgür Lütfi Ertuğrul*[1], Fatma Dülger Canoğulları [2]

[1]*Mersin University, Department of Civil Engineering, Mersin, Türkiye, ertugrul@mersin.edu.tr*
[2]*Toros University, Department of Civil Engineering, Mersin, Türkiye, fatma.dulger@toros.edu.tr*

Cite this study: Ertugrul, O. L., & Canogullari, F. D. (2024). Investigation of Loading Frequency Effects on the Dynamic Lateral Load- Displacement Curves of Monopiles. Advanced Engineering Days, 9, 735-737

Keywords
Monopile
Load frequency
Dynamic analysis

Abstract

Monopiles are commonly used as foundational structures in offshore wind farms, where they must endure dynamic forces generated by waves, wind, and operating vibrations. It is crucial to determine how these structures react to horizontal stresses at various frequencies in order to ensure their stability and durability. This study examines the behavior of monopiles under horizontal loads of different frequencies using Plaxis 3D software. The results of this study offer important knowledge on the specific design requirements for maximizing the efficiency of monopile foundations in offshore conditions. The lateral load- deflection curves resulting from dynamic analyses were compared.

Introduction

Most offshore wind turbines are constructed on monopile foundations, which are single pile foundations consisted of large diameter steel profiles. Monopile foundations are exposed to cyclic and complex horizontal loads, which are distinct continuously based on the surrounding circumstances and the working state of the turbine. When utilizing complex dynamic modeling for wind turbine design, it is crucial to accurately forecast cyclic behavior. Under cyclic stress, the individual pile may experience cumulative horizontal displacement and/or pile rotation, resulting in varying shapes of the hysteresis cycle. Both of these behaviors are crucial to take into account when designing a single-pile foundation [1].

Material and Method

Offshore wind turbine systems utilize single pile foundations that are situated in a complex marine environment and are subjected to different cyclic stresses, including wind, waves, and current. Upon researching the scientific literature, it becomes evident that several small-scale studies have been conducted to investigate the response of single piles to lateral cyclic pressures. Nevertheless, analyzing the results of small-scale tests for cyclic loading at the prototype scale is complicated. It is obvious that the loading conditions in the 1g model studies, commonly referenced in literature, do not precisely replicate the stresses experienced by a full-scale prototype. Upon reviewing the literature, it was observed that numerical analyses were employed to investigate the behavior of individual piles under real-life situations [2].

This study included conducting dynamic analyses at various loading frequencies using the Plaxis 3D [3] software. A comparison was made between the outcomes of the analyses.

The properties of the soil and pile used in the analyses are shown in Table 1. Furthermore, the pile has a diameter of 6 meters, an embedded length of 10 meters, a length above the ground of 5 meters, and a wall thickness of 0.01 meters.

Table 1. Properties of the soil and monopile

	Unit weight (kN/m^3)	Modulus of elasticity (kN/m^2)	Poisson's Ratio	Angle of internal friction (°)
Soil	16,6	8x10^3	0,2	38
Monopile	78	210x10^6	0,3	-

The model geometry used in all three analyses is given in Figure 1. A Lateral load is applied at the corner of the pile and the applied horizontal dynamic load in all three analyses is 1000 kN.

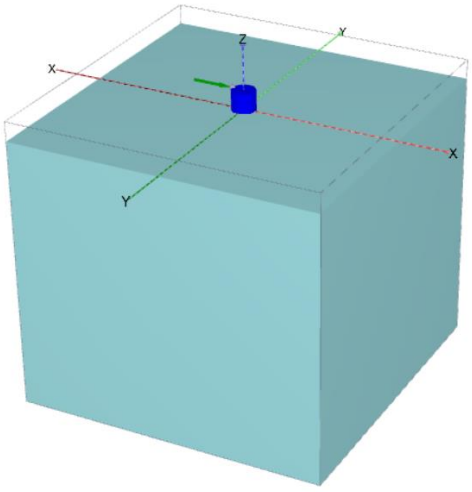


Figure 1. Example finite element model geometry

Dynamic analyses were carried out at load frequencies of 0.5, 1, and 2 Hz. Horizontal-load deformation curves were compared for a single cycle in each analysis. A lateral load occurs at the corner of the pile, and the magnitude of the applied horizontal dynamic load is 1000 kN in all three analyses.

Results and Discussion

Lateral load-lateral displacement curves are important in geotechnical and structural engineering to explain the behavior of structures, specifically piles, when under lateral loads. The curves show the correlation between the lateral load and the related lateral displacement noticed at the pile head. The behavior of these curves is affected by other factors, such as the frequency of the applied loads.

The horizontal deformation contours generated along the monopile for a lateral dynamic load of 1000 kN are shown in Figure 2.

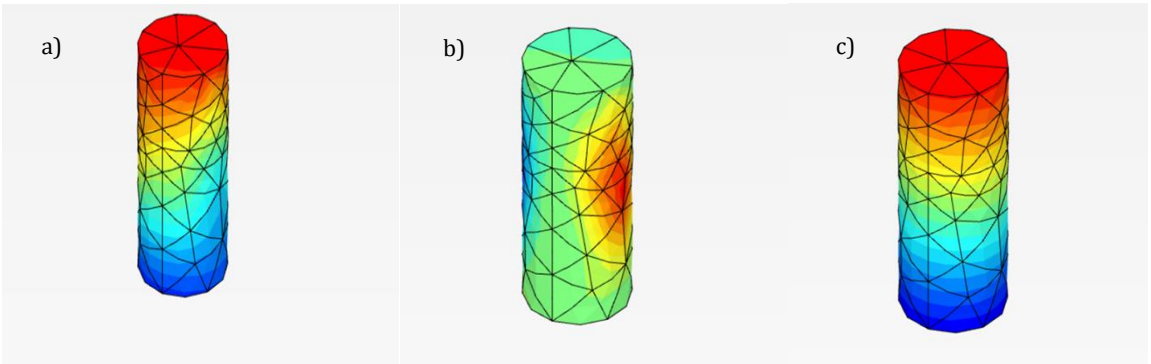


Figure 2. Monopile deformation contours for a) 0.5 Hz b)1 Hz c) 2 Hz loading frequencies

Analysis results show that the deformation values at 1000 kN are 0.059, 0.051 and 0.028 meters for frequencies of 0.5, 1 and 2 Hz, respectively. According to the results shown in Figure 3, it can be said that the deformation values related to the maximum load decrease as the frequency increases.

The increase in frequency value has led to a narrower and more elliptical curve, a greater increase in stiffness and a more linear behavior.

Conclusion

Monopiles, commonly used as foundations for offshore wind turbines and other marine structures, are subjected to various dynamic loads, including those from wind, waves, and operational forces. The analysis of hysteresis curves at different loading frequencies (0.5 Hz, 1 Hz, and 2 Hz) provides significant insights into the behavior of monopiles under dynamic conditions.

Hysteresis loops are useful to evaluate the dynamic performance and durability of the structural system under various loading rates. The observed variations in stiffness and energy dissipation properties are essential for understanding the response of materials and structures under repeated loading, particularly in the context of seismic or wind-induced vibrations.

In this study, the limiting of the loops as the frequency increases from 0.5 Hz to 2 Hz suggests an increase in stiffness or a reduction in flexibility. Energy dissipation is inversely correlated to frequency, meaning that higher frequencies result in lower energy dissipation per cycle. The decreasing area within the hysteresis loops clearly depicts the reduction in energy dissipation at higher frequencies.

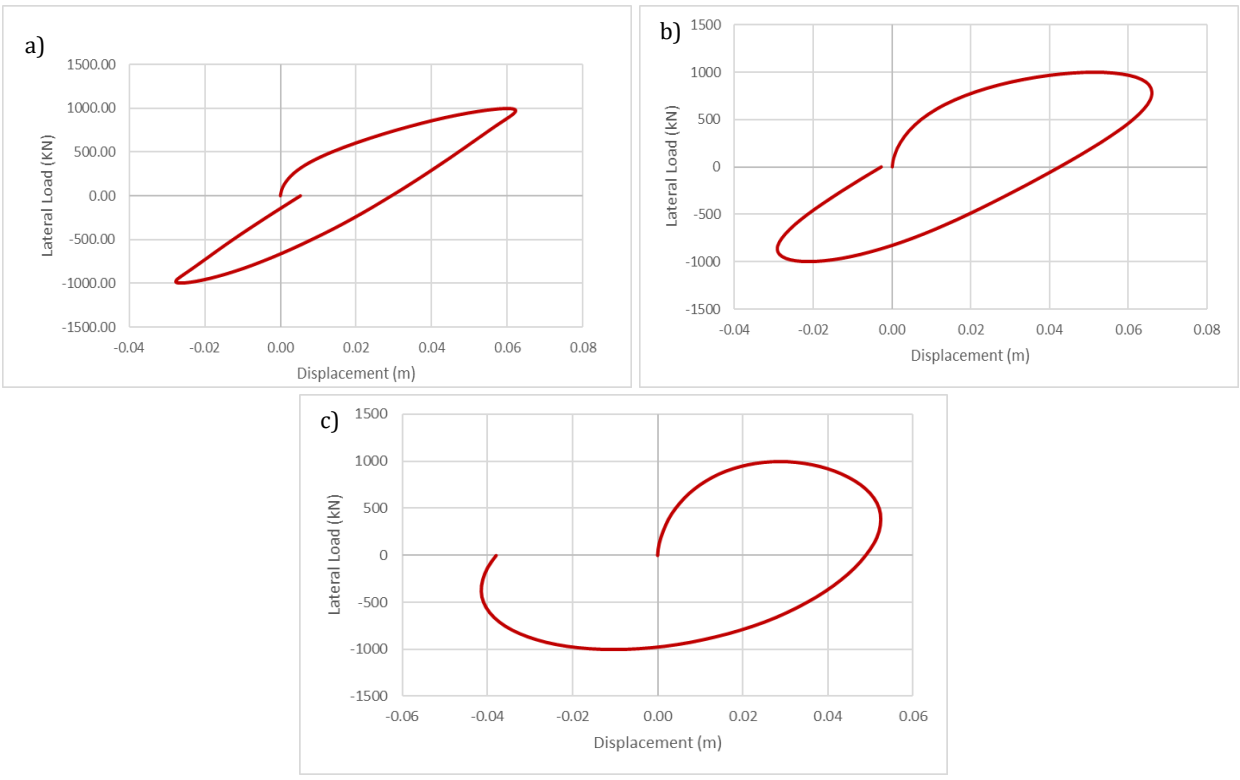


Figure 3. Lateral load – displacement curves for a) 0.5 Hz b)1 Hz c) 2 Hz loading frequencies

References

1. Richards, I. A. (2019). Monopile foundations under complex cyclic lateral loading. Trinity: University of Oxford.
2. Leblanc, C., Houlsby , G., & Byrne, B. (2010). Response of stiff piles in sand to long-term cyclic lateral loading. Géotechnique, 60(2), 79-90.
3. Plaxis 3D, User Manual (2020). Bentley Systems.

Advanced Engineering Days

aed.mersin.edu.tr

Evaluation of GPM and TRMM Precipitation Data versus Observational data in Lake Urmia Basin

Fatemeh Hosseinpour Asl*[1], Saeed Jahanbakhsh Asl [2], Hashem Rostamzadeh [3]

[1] *University of Tabriz, Department of Climatology, Iran, f.hosseinpour1402@ms.tabrizu.ac.ir, s_jahan@tabrizu.ac.ir, h_rostamzadeh@tabrizu.ac.ir*

Cite this study: Hosseinpour Asl, F., Jahanbakhsh Asl, S., & Rostamzadeh, H. (2024). Evaluation of GPM and TRMM Precipitation Data versus Observational data in Lake Urmia Basin. Advanced Engineering Days, 9, 738-741

Keywords
Ground station
GPM satellite
TRMM satellite

Abstract

Precipitation with many temporal and spatial changes plays an important role in the hydrological cycle and is an important factor in agricultural studies, water resources and ecosystems. One of the most important problems for researchers in atmospheric and hydrological studies is the lack of up-to-date and long-term data with proper accuracy. Therefore, using the precipitation data recorded by satellites can be a good supplement to address the shortage of this type of data. The aim of this study is to evaluate the accuracy of satellite data versus observational data. In this study, the monthly rainfall images recorded by the GPM sensor with a resolution of 1/0 × 1/0 degrees and the TRMM sensor with a resolution of 25/0 × 25/0 degrees in the Lake Urmia basin were evaluated between June 1, 2000 and December 31, 2023. To this end, the monthly precipitation data of 5 synoptic stations has been used as observational data and to evaluate data from statistical indicators R2, MSE, RMSE, BIAS. Bias, MSE, RMSE values confirmed that the IMERG product, at the Bonab station, had the lowest error rate with observational data. In general, GPM is highly accurate due to its superior technology and is a good tool for hydrological predictions.

Introduction

Precipitation is one of the important parameters in the hydrological cycle, where the time and spatial changes of this parameter, as well as its high impact on the natural and human environment, cause a lot of attention to this parameter in various climatic, meteorological, hydrological, environmental and environmental studies (Montaigne, 2002). On the other hand, the direct impact of this atmospheric element on the availability of fresh water, as well as the consequences of its intensity such as storms, storms, floods, droughts and landslides, has increased the importance of this phenomenon (Futrel & Coauthors, 2005). However, one of the most important problems is the lack of up-to-date and long-term data with proper accuracy. Because in many different regions of the world, precipitation is typically measured by ground-level stations with a lack of uniform distribution, and in some regions by radars with multiple problems. In less developed countries, desert and mountainous areas where the measurement of precipitation characteristics is of great importance, existing synoptic and barometric stations are not well distributed at appropriate distances, and their distances do not follow a certain rule. Various sensors are active in this field, including TRMM and GPM, which is the new generation of GPM meteorological satellites designed to measure light rain and snowfall, which also monitors heavy tropical rainfall well (Sharifi et al., 2016).

Calibration of rain gauge and radar data is very expensive and not cost-effective for determining global rainfall distribution. Therefore, efforts have been made to use infrared and visible waves to estimate rainfall. The TRMMsatellite is the first satellite to examine rainfall in different dimensions. The satellite's measurement system includes a precipitation radar, a multi-frequency microwave radiometer, and a visible infrared riometers, and is the product of a TRMM satellite with a spatial resolution of 25/0 × 25/0 degrees (KUMMEROW et al., 1998).

in this study, we have assessed two GPM and TRMM satellite rainfall products at 5 stations in the Lake Urmia Basin and examining the accuracy of monthly rainfall using two products over a period of about 20 years (June 1, 2000 to December 31, 2023).

The results, on a monthly scale, show a high correlation of GPM satellite precipitation data and station observation data; also, RMSE and MSE, on a monthly scale, show GPM satellite accuracy in rainfall forecasting, greater than TRMM satellite accuracy.

Material and Method

Area of study

Lake Urmia Basin is located in the provinces of East and West Azerbaijan and Kurdistan. Its western border is the Iran-Turkey border heights. The highest elevations of the basin include Sablan and Sahand and the lowest point of the basin is Lake Urmia at an average altitude of 1.280 m. The average rainfall of the basin is 550 mm, and its main origin is the Mediterranean air masses. In this study, 5 synoptic stations of the Lake Urmia basin include the cities of Bonab, Shabster, Ajabshir, Sarab and Bostan-Abad, which is shown in Figure 1.

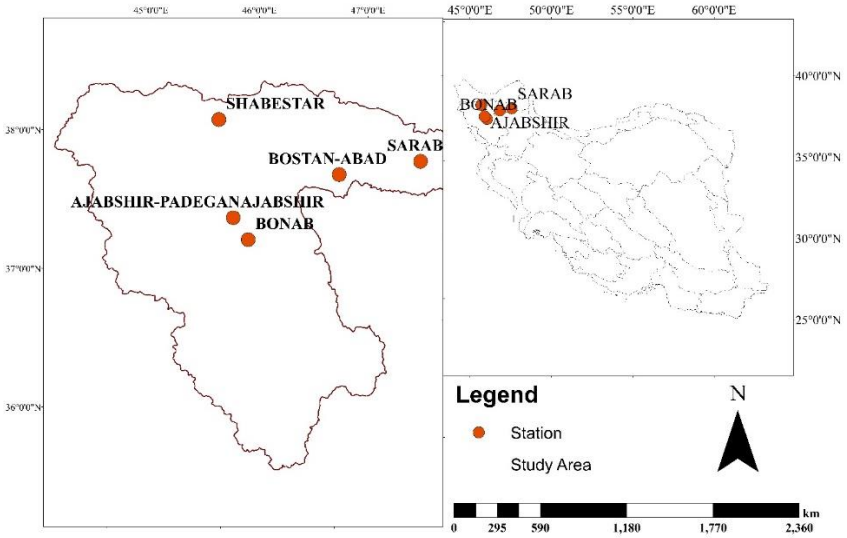


Figure 1. Geographical location of the Lake Urmia Basin.

The data from June 1, 2000 to December 31, 2023, were used to compare on a monthly scale with the data were of the GPM satellite with and 3IMERGM V06 and the TRMM satellite with the product 3b43 V7. The monthly rainfall data from the stations were received from the National Weather Service, and the daily data from satellite sensors were downloaded from NASA and converted into numerical data Arc GIS software. The following were compared with estimated and observational data.

Data validation

Statistical indices such as the mean root of the error squares (RMSE)(1), the mean error source (MSE)(2), the relative deviation (Bias)(3), and the correlation coefficient (R)(4) were used to assess the accuracy of precipitation information. The statistical criterion of the correlation coefficient was used to determine the correlation between the actual and estimated values, and the mean root of the error squares and the mean error source (both in millimeters) and the relative deviation, to determine the estimated error values.

$$\text{RMSE}=\sqrt{\frac{\sum_{j}^{n}=1(\widehat{yi}-yi)^2}{n}} \quad (1)$$

$$\text{MSE}=\sum_{j}^{n}=1\frac{(\widehat{yi}-yi)2}{n} \quad (2)$$

$$\text{Bias}=\frac{\sum_{j}^{n}=1^{yi}}{\sum_{j}^{n}=1^{y}} \quad (3)$$

$$\text{R}=\frac{\sum(yi-\overline{yi})\,(y-\overline{y})}{\sqrt{\sum(yi-\overline{yi})^2\sum(y-\overline{y})^2}} \quad (4)$$

In equations (1) to (4), (Yi) is the estimated precipitation with the satellite, (y) is the observational precipitation and the low error values clearly indicate high accuracy of estimation versus observational values.

Discussion

Figure 2 and 3 show the values of the statistics used to assess the accuracy of the monthly precipitation data of the GPM and TRMM gauge versus the observational data in the Lake Urmia Basin.

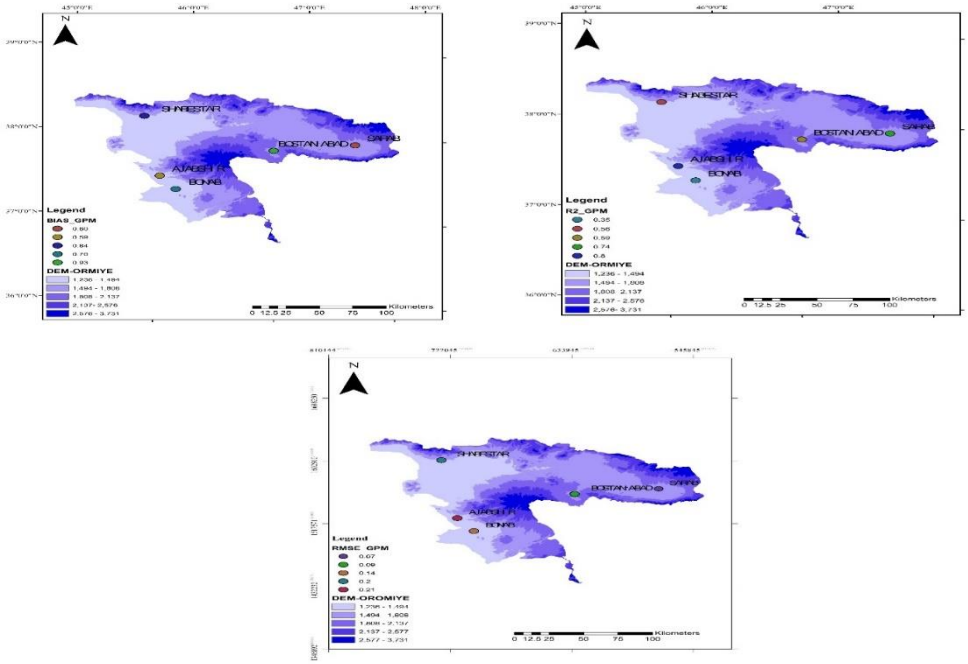


Figure 2. Comparison of GPM monthly precipitation data with actual monthly precipitation of synoptic stations using statistical indicators, determination coefficient, square error mean component, beveled index.

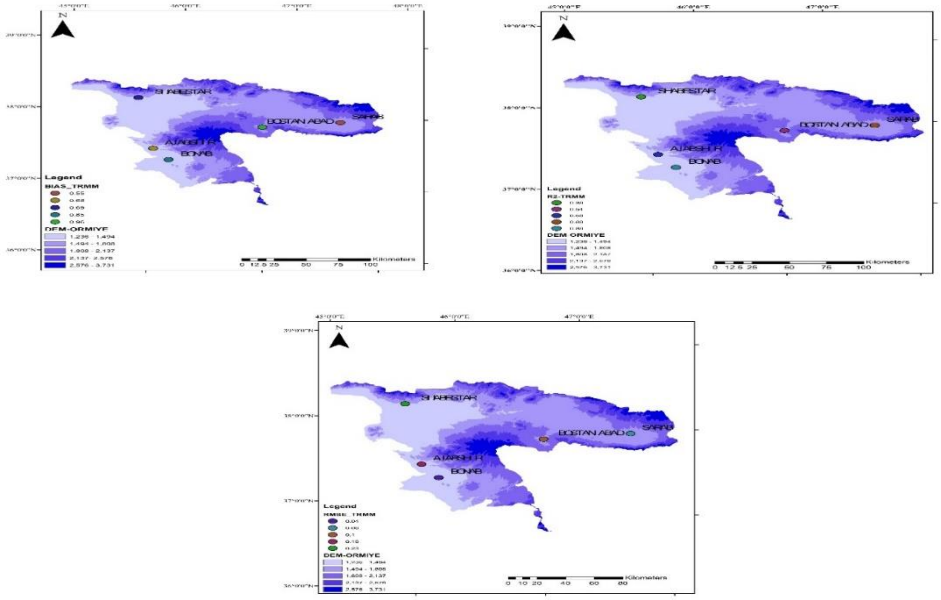


Figure 3. Comparison of TRMM monthly precipitation data with actual monthly precipitation of synoptic stations using statistical indicators, determination coefficient, square error mean component, beveled index.

Conclusion

The aim of the present study was to assess the accuracy of the daily precipitation data of two TRMM and GPM instruments versus the monthly data of 5 synoptic stations during the period 2000-2023.

The rate of deviation, the mean of the error squares and the mean of the error indicates the minimum difference between the ground precipitation data and the IMERG product forecast, and according to these values, the results are consistent. IMERG showed higher accuracy due to the new and accurate sensors installed on the GPM and the

high frequency of this product to observe precipitation throughout the planet (half an hour), as well as the size of smaller pixels (1/0 degree). Finally, based on the results, IMERG's performance is greater than the product's

The 3B43 V7 is accepted and the IMERG product estimate is very close to the observational data in monthly rainfall. In the future, it can be used for application projects, long-term forecasts, meteorological studies and more. Based on extensive studies on the evaluation of precipitation satellite products, conducted around the world, and the results of this research, it can be concluded that satellite precipitation products have different accuracy in different weather conditions and altitudes and latitudes. Their study requires separate research in each climate diversity. Therefore, based on the detailed studies and the time spent on the present research, as well as past studies, many of which have evaluated precipitation satellite products only in a specific region, the evaluation of various climatic regions within the country can be proposed in the form of an opportunity for future research and compared with the results obtained from this study.

References

1. Futrel, J. H., & Coauthors. (2005). Water: Challenges at the intersection of human and natural systems, NSF/DOE tech, rep, PNWD – 3597, 50 PP, DOI: 10.2172/1046481.
2. Montaigne, F. (2002). National Geographic Magazine, Vol. 202 (3), International Publishing, 2 – 33.
3. Sharifi, E., Reinhold, S., Saghafian, B. (2016). Assessment of GPM – IMERG and other Precipitation Products against Gauge Data under Different Topographic and Climatic Conditionsin Iran, Remote Sens, 8, 15; Doi: 10.3390/ Rs8020135.

Advanced Engineering Days

aed.mersin.edu.tr

Pollution Study of Hajilar Chai Basin in East Azerbaijan Province, Iran

Ali Mohammad Khorshiddoust [*1], Ali Asghar Azad [2], Azadeh Mirzaahmadi [3]

[1] *University of Tabriz, Department of Climatology, Iran, khorshid@tabrizu.ac.ir*
[2] *Department of Environment, East Azerbaijan Province, Iran, azad.a1346@gmail.com*
[3] *University of Tabriz, the Department of Chemistry, Iran, a.mirzaahmadi@tabrizu.ac.ir*

Cite this study: Mohammad Khorshiddoust, A., Azad, A. A., & Mirzaahmadi, A. (2024). The Study of Environmental Pathology of Hajilar Chai Catchment in East Azerbaijan Province, Iran. Advanced Engineering Days, 9, 742-747

Keywords
Environment
Pollution
Pathology
Catchment
Abatement, Iran

Abstract

Hajilar Chai River has an area of 1155 Km^2 and along the route from the source to Varzegan region; it is flat and slightly mountainous. This river has two dams. In recent years, with the increasing development of human activities along this river and the discharge of industrial, urban and agricultural wastewater and effluents into the river, the possibility of changes in the ecosystem of this river has made problems in terms of environmental concerns**.** The presence of heavy metals in excess of the standards defined in the environment causes environmental problems and affects the inhabitants of this area and the ecosystem. Our aim in this research was to update the basic water resources studies in the area, and to determine the share of each of the actual and potential pollution centers in environmental changes of the basin, and to investigate the trend of changes in physical and chemical factors of the Hajilar Chai River in order to determine the actual and potential effects of contaminants entering the catchment. We used various field sampling and laboratory analyses for determining the pollution sources and pathology of the basin. Results indicated various polluted areas by heavy metals in the area under study.

Introduction

Industry is the main source of pollutants in various areas including water ways (Moore, 1991). About 69% of the world's water consumption is used for agriculture and irrigation in general, and 23% is used for industry, and household consumption accounts for only about 8%. The vast majority of industrial wastewater production units containing heavy metals lack treatment systems and discharge large amounts of industrial wastewater into the environment or municipal wastewater network on a daily basis, polluting water resources. On the other hand, in developed countries, agriculture and industry have the highest water consumption and play the highest role in water pollution (World Health Org., 2023). However, in areas where industrial development is lower than in agriculture, the major pollutants are agricultural fertilizers containing heavy metals (cadmium, lead, zinc, nickel and copper) and the use of fungicides and herbicides (copper compounds) on farms. It is fish farming (Spencer and Green, 1891). Copper, zinc, nickel and chromium metals are considered as representatives of heavy metals in determining water quality indicators and on the other hand, the amount of organic matter in the natural aquatic environment is usually the balance between biomass productions (organisms determine the decomposition of organic matter, which ultimately lead to the mineralization process). The effect of organic compounds in nutrient-rich waters or water contaminated by humans is very important in the rate of toxicity and accumulation of heavy metals in living organisms (Leather land and Woo, 1998). Heavy metals, unlike organic waste, are persistent contaminants that are not normally degraded by bacteria. Even if decomposed, it is so slow that it can be considered as a sustainable additive to the aquatic environment.

Heavy metals as one of the environmental pollutants have various effects such as growth retardation, behavior change, genetic changes and mortality in aquatic animals (Mance, 1987). Therefore, toxic metals cause fish death in various ways. Most metal compounds or their ions accumulate in body tissues, especially liver, gills, heart, spleen and bone (Jalali Jafari and Aghazadeh Meshgi, 2007). Because the Hajilar Chai River has a variety of uses, any pollution in it will quickly adversely affect the biodiversity of the river ecosystem and human communities. The diversion of water from the surface currents of the Hajilar Chai River is done using empty

dams. About 15 years ago, at a distance of about 4 km north of Hajilar village, a diversion dam and a 24 km long transmission canal were built by the Jihad Sazandegi. The purpose of constructing this dam was to provide safe water intake from Hajilar Chai River to irrigate one thousand ha of rain fed lands of Lilab village, but at present, due to landslides, the canal cannot be used.

Its basin is located in the western part of Varzegan and it may expose to potential of water resources contamination due to placement of Zarrin Dagh Astarkan gold extraction factory in this area. In order to monitor the water sources of the Hajilar chai basin, water samples were collected and analyzed. The results showed that the concentration of some elements is higher than permissible limit of Iranian water standards in some places. The aim of this study is to evaluate the hydro-chemical characteristics and source of contamination of water sources using laboratory and field techniques for analysis.

Materials and methods

- Supervised classification methods on satellite images (maximum probability algorithm) to determine the land use map of the region
-Using a variety of geostatistical interpolation methods (kriging) for qualitative zoning of catchments based on pollution centers and the share of pollution based on conventional pollution indicators.
-Use of topographic maps of the study area at a scale of 1: 25000 and 1: 50000
-Geological maps at a scale of 1: 100000
-Use of climatic data based on stations in the study area.
- Field methods including direct sampling to study the issues.
- Preparing the land use map of the study area, the map prepared by the Natural Resources Organization and Google Earth.

The geographical situation of the area under study

Hajilar Chai catchment area with an area of 1160 Km^2 and an area of 190 Km^2 with an irregular geometric shape in 46 to 50 eastern longitudes and 35 46 to 38 27 to 38 52 northern latitudes in the northern part of East Azerbaijan province in the section Kharvana is located in the city of Varzegan and also includes part of the Siah Rud section of the city of Jolfa and the central part of Marand. This basin is one of the sub-tributaries of Aras river which receives branches such as Goy Chai, Astmal Chai, Marzabad Chai, Joshin Chai and Hizeh Jan Chai and after a route with a south-north trend of approximately 61.9 Km in the area between the villages of Kordasht and Duzal flow from the functions of the Siah Rud section to the Aras River.

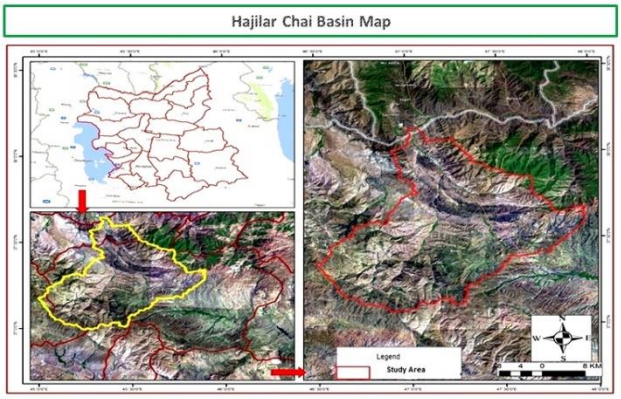


Figure 1. Map of the geographical location of the study area (Source: Research Findings)

Those studies that examine the physical characteristics and morphology of a basin are called physiography. Knowledge of the physiological characteristics of a basin along with information about the climatic conditions of the region can provide us with a relatively accurate picture of the quantitative and qualitative functioning of the hydrological system of that basin. In order to study a catchment better and more accurately, it is divided into smaller hydrological units called sub-basins so that each of them can be analyzed separately. Some physiographic and topographic features such as altitude and slope can intensify or modify many climatic factors such as temperature and fluctuations, type and amount of annual rainfall, evapotranspiration and in general can be said to cause emergence of local or regional climates. Among the most important physical characteristics of a basin are area, environment, shape, height, and slope and drainage density. Physiographic studies play an essential role in the identification, planning and management of watersheds. Because other studies such as erosion and sediment, hydrology, meteorology, etc. depend on it, and most of the parameters obtained in the

physiographic knowledge of the basin are used in formulas and experimental relationships. Therefore, physiographic study of the basin has been performed using the latest capabilities of ArcGIS software.

Materials and methods of analysis

Sampling was done in May 2020 in ten river basins. From the desired parameters, the concentrations of copper, zinc, lead and cadmium were measured by atomic absorption method in the Faculty of Chemistry, University of Tabriz and the concentrations of arsenic, mercury, aluminum and cyanide anion by ICPMass in *Radin* Laboratory (Tabriz). Other parameters (such as pH, EC, TDS, TSS, turbidity and concentration of anions and base cations including sulfate, chloride, bromide, fluoride, bicarbonate, carbonate, sodium, potassium, calcium, magnesium) as well as concentration of nitrate anions and nitrite were measured and analyzed in the central laboratory of the University of Tabriz. In sampling and transfer of samples to laboratories, factors affecting the accuracy of samples, equipment contamination, sample size, observing the time interval between collections, and transfer to the laboratory were also considered. During the sampling, interfering factors in the amount of total cyanide and other effective parameters were identified and the samples were protected by standard methods.

Selected monitoring stations include the following ten points. In this report, first the condition of the tributaries is discussed and then the main river is discussed.

1- First station (HJ1): Hajilar Chai entrance
2- Second station (HJ2): Hajilar Chai output
3- Third station (HJ3): Arzil output
4- Fourth station (HJ4): Arzil entrance and exit of Akhor
5- Fifth station (HJ5): entrance to the manger
6- Sixth station (HJ6): Hajilar Chai before Andarian (continuation of Arzil exit)
7- Seventh Station: (HJ7): Downstream of Andarian
8- Eighth station: (HJ8): Blue dome
9- Ninth station: (HJ9): Varzegan three-way station
10- Tenth Station: (HJ10): Downstream of Shadi Farm

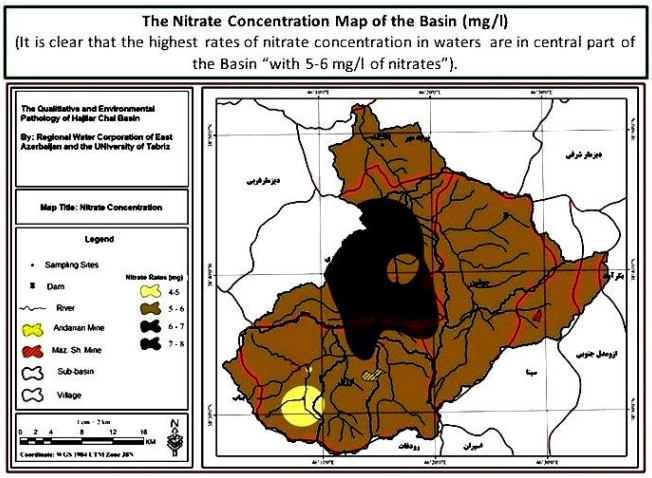


Figure 2: Map of nitrate emission in the whole Hajilar Chai basin and its sub-basins (mg/l), (Source: Research Findings)

According to Figure (2), the highest area of nitrate emission in sub-basin 1 in the 142-1740 class is equal to 161 Km^2 and the minimum in sub-basin 5 in 6534-8131 is equal to 5 Km^2.

Heavy metals

Concentrations of heavy metals such as lead, arsenic, cadmium, mercury, zinc, copper and aluminum as well as cyanide anion have been measured in Hajilar Chai basins.

1. Nitrate and TDS parameters have been investigated to check the contamination load in Hajilar Chai. Examination of the results of laboratory analysis of water samples prepared from different monitoring stations shows that the highest load of nitrate contamination (with the amount of 8145 Kg/day) and TDS (with the amount of 144461 Kg/day) is from Gonbad Kaboud station. Examination of the pollution load in

Hajilar Chai catchment shows that the nitrate pollution load in the downstream branch of Shadi Farm and the TDS pollution load in the Tarzam Chai inlet branch are the lowest.

Discussion

Examination of water quality in terms of nitrate and nitrite anions shows that the concentration of these anions in different basins of Hajilar Chai plantations is lower than the allowable drinking limit and show good quality. The results of metals show that cadmium, copper and mercury metals are not observed in the monitored catchments of Hajilar Chai and their concentrations are zero and the concentrations of aluminum, zinc and even arsenic (except in the inlet basin of Arzil and Flower manger output) has not limited the quality of water for drinking and agricultural use and their concentration is below the allowable limit. Among the monitored elements, the concentration of cyanide anion in most basins is close to the permissible level (70 ppb) and in this regard is at risk and the causes of contamination caused by this anion should be investigated. Also, the concentration of lead toxic metal in all basins has exceeded the drinking standard (equivalent to 10 ppb) compared to the amount reported in 2009 (13 ppb). The amount of this metal has increased more than ten times. According to the results, further explanations about the possible contamination caused by the three cases seem necessary. Due to heavy rainfall during the winter of 2018 and early spring of 2019 in the study area, the statistics show an increase of at least 40% of rainfall compared to the long-term average rainfall of the basin. This causes the accumulation of rainwater with high oxygen content in surface and subcortical layers have caused the leakage of heavy metal elements as well as heavy metal effluents used in the mines of the region and the complexes of these elements have been spread in the study area. There is also a gold mining mine in the study basin in which the process of extracting gold from the ore after crushing is done by leaching operation using sodium cyanide solution and the tailings ponds of these mines contain some cyanide compounds.

External threats

H- Competition over the use and allocation of water resources in the Aras Basin (Hajilar Chai River catchment) Increasing development of water resources in agriculture, industry and urbanization increases competition for water and reduces the water allocated to the Aras River.

2- Water pollution Increased discharge of pollutants from mining and industrial industries in the Aras River catchment area

3- Reducing incoming water flow Operation of river flow through dams and irrigation networks and development of industrial uses and increasing temperature and evaporation reduces the share of environmental flow to Aras catchment.

4- Increasing sediments entering the Aras River Agricultural development, land use change, destruction of natural pastures and development of metal mines

5- Vulnerability and disruption of wildlife corridors Nagorno-Karabakh conflict between the Republic of Azerbaijan and Armenia and infliction of casualties on wildlife in minefields.

Threats Explained

H- Land use change and development of mines Development of agricultural lands along the Hajilar Chai River, construction of water structures including Astmal Dam and Gonbad Kaboud

Development of metallic and non-metallic mines including Andarian gold mine and Shadi farm and Avansar and Alefabad copper mines

2- Decreased water quality Increased eutrophication in storage behind dams

Return of irrigation streams into Hajilar Chai River

Drainage of human and animal wastewater

Introduction of polluting streams from mines and active industries in Hajilar Chai catchment

3- Increasing pressure on water resources Excessive use of agricultural irrigation in hot seasons and non-nutritional water resources

Development of orchards and planting of water tree species regardless of the capacity of the water resources of the basin

Therefore, a strategy with an ecosystem approach for the comprehensive management of water resources in the Hajilar Chai catchment area in a way that can ensure the balance, protection and sustainable use of water resources in this basin is proposed as follows:

H- Forming a working group to develop a management plan

The purpose of forming a working group to develop a quantitative and qualitative management plan for the Hajilar Chai catchment is to operationalize the process of participatory development of a management plan and to formulate a way to implement it in order to achieve achievements such as the following:

The main stakeholders in the future of Hajilar Chai catchment should be identified and their representatives should agree to form a management team.

Identify the information available and required for the preparation of the management plan and the roadmap and facilities required.

The Steering Committee should consider the requests of various departments and agencies regarding the Hajilar Chai catchment and the current laws and regulations regarding this catchment.

Public awareness opportunities for stakeholders should be explored and next steps designed.

Define metrics to measure the success of a management program.

Identify the process of progress and move forward with time targets and estimated budgets.

2- Road map

According to the experiences in the field of compiling comprehensive management plans, in a participatory manner and based on the existing instructions, the Hajilar Chai catchment management plan should be developed with the participation of all stakeholders and based on management principles that emphasize the participation of stakeholders and wisdom. Collectively, the following steps should be implemented to develop the program:

A) Development of long-term vision of the catchment

B) Collecting available information and trying to supplement basic information deficiencies

C) Review and prioritization of values and functions of Hajilar Chai catchment

D) Review and prioritize the issues and threats ahead

E) Defining a long-term goal to achieve the vision

F) Defining short-term goals based on pre-identified values and threats

G) Develop an action plan to achieve the goals

H) Develop a monitoring and evaluation program to implement the program

After passing these steps and formulating a management plan, this plan will be approved by the competent authorities in the province for implementation. These steps are somewhat interchangeable according to the characteristics of the catchment and temporal and spatial conditions, as well as the possibility of increasing or decreasing other activities according to the decisions of the working group, the schematic algorithm of which is as follows.

International rules and regulations of Border Rivers

Iran shares Border Rivers and water resources with all its neighbors, and this vastness of transboundary water basins highlights the importance of studying the subject. Using international documents and information, the existing international laws in the field of transboundary waters as well as existing water treaties between countries and the approaches used to resolve disputes have been reviewed. The results of the studies show that in the process of sharing transboundary water resources, there are laws and regulations at the international level, the most valid of which is Convention number 1. According to the provisions of this convention, every state located in the common river basin has the right to use the water flow of the transboundary watershed fairly and reasonably in its territory, without requiring serious harm to other common countries. Have. This right is determined by considering the natural factors of the catchment, existing and potential uses, social and economic needs of the watershed countries and the effects of exploitation on other watershed countries, but the factors presented for this purpose are general. And has different technical and legal interpretations in each of the transboundary water basins, which makes their use difficult. For this purpose, new approaches to resolving water disputes in transboundary basins have been defined, which are mainly based on meeting the needs of basin countries or relying on economic approaches including efficient use of water, sharing the benefits of different uses of border water instead of division. Water and the creation of a portfolio of interests (blue and non-blue) and it seems that these approaches can help resolve water disputes between countries and be considered by policymakers.

However, after the presentation of the Convention in 1996 and before its implementation, the general and important rules of the Convention were used as customary law by arbitral tribunals and international organizations, for example, four months after the presentation of the Convention in The United Nations (in the same year 1997), the International Court of Justice in its judgment in the kovo-Nagymarosi Gabc project, relied on it and in its judgment of three of its requirements, including fair and reasonable use, no serious harm and information previous media used planned actions, as customary international law. In the provisions of this convention, fair and reasonable use in the international waterway is supported and indicators to determine and distinguish fair and reasonable use in terms of principle; Obligation not to cause serious injury; It is presented to other countries in the basin, which should all be considered as a whole, and none of these indicators has priority over the other. Since there is no universally accepted method for the equitable distribution of transboundary water resources, and international water law, including Convention because of its general and comprehensive

provisions and in terms of all the conditions of the world's border basins, researchers and theorists "Practitioners, as well as some politicians, have tended to use a need-based approach instead of a legal one."

Therefore, considering the location of Hajilar Chai river basin in relation to Aras transboundary river and threats of internal and external factors of Aras catchment, it is expected that the beneficiary countries in proportion to the common share, interests and interests to maintain sustainable water resources and ecological potential of the catchment. Commit to common interpretations of international law governing transboundary rivers.

References

- Jalali Jafari, B., & Aghazadeh Meshgi, M. Fish poisoning due to heavy metals in water and its importance in public health, Tehran: Book Publishing. 134 pages. In Persian.
- Leatherland, J.F., and Woo, P.T.K. (1998), Fish diseases and disorders: Volume 1, Infectious disorders, CABI Publishing, London.
- Mance G (1987). Pollution threat of heavy metals in aquatic environment. Elsevier, London, 363 pp.
- Moore, G. A. (1991). Crossing the Chasm: Marketing and Selling High-Tech Goods to Mainstream Customers. New York: Harper Business.
- Spencer, H. (1891). The development hypothesis. In H. Spencer (Ed.), Essays: Scientific, political and speculative (Vol. 1, pp. 1–7). London: Williams & Norgate. Originally published in 1852.
- World Health Organization (2023). Drinking Water: Key Facts, September Report.

Advanced Engineering Days

aed.mersin.edu.tr

Investigating the texture of region 5 of Tabriz city with emphasis on earthquake vulnerability

Shiva Sattarzadeh Salehi *[1], **Firouz Jafari** [1]

[1]*University of Tabriz, Urban and Regional Planning, Iran, sattarzadeh423@gmail.com, F-jafari@tabrizu.ac.ir*

Cite this study: Sattarzadeh Salehi, S., & Jafari, F. (2024). Investigating the texture of area 5 of Tabriz city with emphasis on earthquake vulnerability. Advanced Engineering Days, 9, 748-751

Keywords
GIS
Earthquake
Tabriz
Vulnerability
AHP

Abstract

Urban damage against natural events such as earthquakes is a function of human behavior that indicates the degree of influence or ability of economic, social units, and urban physical assets against natural hazards. The current research aims to evaluate the vulnerability of the five cities of Tabriz due to earthquakes. The research method is applied in terms of purpose and descriptive-analytical in terms of method. The research indicators include physical and natural factors and the distance of the nearest access to the effective uses. Library and field methods were used to collect information, and the hierarchical analysis method was used in ArcGIS 10.8 software to extract vulnerability status. The results show that the distribution of the study area with high vulnerability can be seen in most parts of the range, which has the largest area. Most of these spaces are places with open spaces and newly built buildings, but most of the buildings in the region are in the high-vulnerability category, so the distribution of high-vulnerability places in the north, west, and south of the region is determined.

Introduction

One of the most important and general phenomena in the world today is the increase in urban areas and the intense and increasing physical development of cities, which is the result of the intensity of the urbanization process and the use of the facilities and facilities of life in these environments (1). These issues are generally caused by the most extensive measured human interventions in natural environments, including indiscriminate construction in the area of faults, the absence or disregard of construction rules and standards, and many other factors that have exacerbated the crises resulting from natural disasters (2). In the meantime, issues such as the general weakness of the city's body and lack of proper planning in this regard, inappropriate roads, high population and construction density, inappropriate way of population distribution, and in general, lack of attention to crisis management in planning cause an increase in human and financial losses (3). Also, throughout history, cities have never been safe from the damage of natural disasters, in such a way that since the past, one of the basic ways to prepare for dangers is to know the degree of vulnerability of the city in case of such an occurrence. All of them have increased the vulnerability of cities to the point where 90% of the country's cities have become vulnerable to a 5.5 Richter earthquake (4,5). Undoubtedly, one of the effective factors in reducing the vulnerability of cities, especially damages caused by earthquakes, is the shape and structure that cities have, and it is possible to reduce the vulnerability of cities by using basic urban planning and design and attention to crisis management. effective harvest Reducing the vulnerability of urban communities against earthquakes will occur when safety against earthquakes is considered at all levels of planning (6). Therefore, the present study investigated the texture of the 5th district of Tabriz city with an emphasis on the vulnerability caused by earthquakes.

Material and Method

The current research is applied in terms of purpose and descriptive-analytical method, and library and field researches were used to collect the required information. By adapting the indicators for the studied area, the vulnerability of the area is assessed “Table 1” .

Table 1. The indicators investigated in the research in the evaluation of vulnerability due to earthquakes

factors	Index
Physical	Building quality, building age, type of materials, number of floors
access	Access to open spaces, access to road network, access to medical centers, access to firefighting centers
Natural	Distance from the fault

Several methods have been used to assess the vulnerability of cities and regions against earthquakes. Analytical Hierarchy Process (AHP) has been used to assess vulnerability; In order to assess the degree of vulnerability to earthquake risk, it is necessary to first prepare the data and layers required for each criterion in the ArcGIS software for the study area, and then the necessary information is classified according to each criterion. In this model, the work method consists of three main steps: a) creation of a two-by-two comparison matrix, b) calculation of criteria weight, c) estimation of durability or compatibility ratio (7).

Therefore, in order to create a matrix, two-by-two comparisons have been made. At this stage, the relative priority of one criterion over another can be placed in a basic scale from 9 to 1, and then by calculating the geometric mean of each row and dividing it into the total. The geometric mean of the rows, the final weight of each criterion is obtained. This method connects personal judgments and values in a logical way. This process forms a hierarchical structure using people's imagination, knowledge and experience, and leads to favorable judgments using inspiration, experience and logic.

Study Area

Tabriz is a city in the Central District of Tabriz County, in the East Azerbaijan province of northwestern Iran. It is the sixth-most-populous city in Iran (8,9). Region 5 of Tabriz municipality, with an area of 3230 hectares, is included in about 14.6% of the total area of Tabriz city. Region 5 in the east and northeast of Tabriz, is adjacent to areas 1, 2, and 9. This urban area has about 3297.7 hectares, and about 126124 people live there (10). The gross population density of this area is 68 and 29 people per hectare in the dense urban context. The area of residential use in this area is 269 hectares and the net population density is equal to 345 people per hectare “Figure 1”.

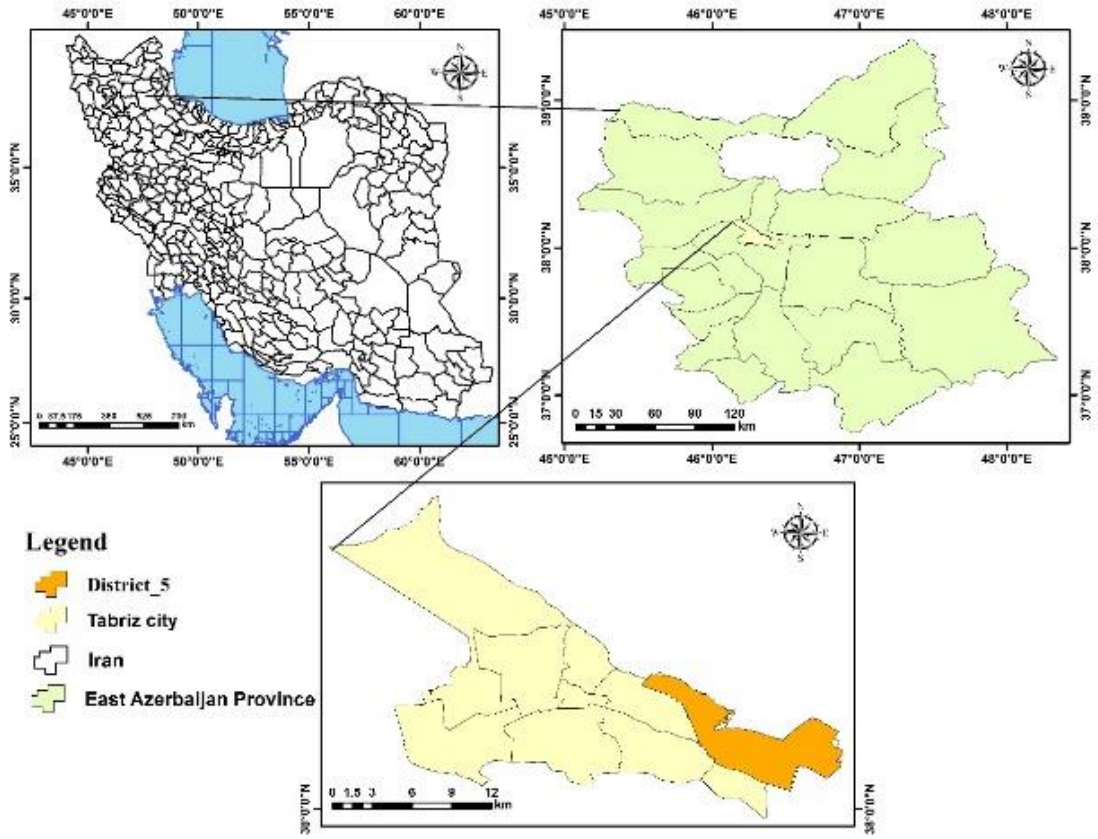


Figure 1. Location of the study area

Results

The great fault north of Tabriz is the largest and most prominent tectonic phenomenon known. So far, the boundaries of the North Tabriz fault and its connection with other faults have not been determined in the available studies and reports; This fault is a type of vertical fault with a dextral component, and it starts from the Misho mountains with a general direction of 115 degrees and continues after passing through Tabriz to the vicinity of the middle. Its length is more than 150 kilometers, and in terms of tectonics, the area behind this fault is considered to be the continuation of the Anatolian fault system that runs across the northern part of Turkey (11). The excessive proximity of this area to the great fault in the north of Tabriz, as well as having a combination of all kinds of urban tissues (especially with a major part of worn-out and marginalized tissues) and unbalanced communication networks are among the vulnerabilities of this region. In the conducted studies, the distances from the fault are divided into 5 classes (0 to 450 meters, 450 to 900 meters, 900 to 1400 km, 1400 to 2000 km, 2030 to 3100 km). The quality of the building in terms of vulnerability is also in four categories (new construction, restoration, maintainable, demolition), which has the highest amount of new construction and maintainable. The more we move from one-story and two-story units to units with a higher number of floors, the greater the intensity and effect of the earthquake will be felt.

The vulnerability map of the region is divided into five classes (very low vulnerability, low vulnerability, moderate vulnerability, high vulnerability, and very high vulnerability) The northern, western, and southern parts of the region, which are closer to the number one, have a high level of vulnerability. In general, the results show that there is little or no vulnerability in the unbuilt part of the city, but in the built part of the city, the vulnerability includes moderate vulnerability that includes Vali-e-Asr 2, Fereshteh and Azad University neighborhoods, and high vulnerability includes more parts of the city and very high vulnerability in the central parts and the worn-out and historical texture of the area. It can be said that there is a relatively low-risk zone in this area to a small extent, and this indicates a high risk of earthquakes in this city “Figure 2”.

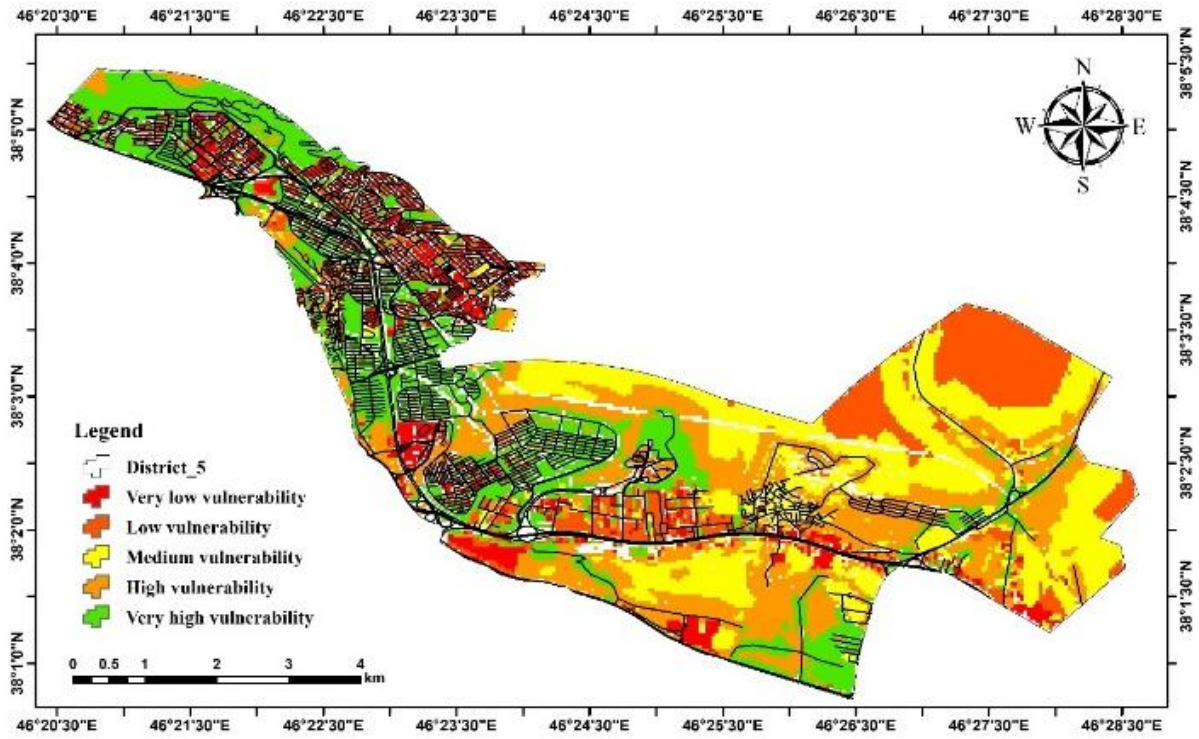


Figure 2. The final vulnerability map of the 5th region of Tabriz

Discussion

The city of Tabriz has had about 9 devastating earthquakes with an average of 6 on the Richter scale. These earthquakes occurred in connection with the North Tabriz fault, therefore; Paying attention to the matter of knowing the level of vulnerability in the area of Tabriz city becomes doubly important because in the event of an earthquake due to the existence of informal settlements, it will experience a higher level of damage, destruction, and casualties.

Conclusion

The low-risk area occupies about 40% of the area of the region, which according to the land use map of this zone is within the boundaries of the region, but mainly includes barren lands, without buildings and gardens of the city and the neighborhoods of Rushdieh and Elahiyeh. On the other hand, in high-risk and very high-risk areas, there are vital service uses such as educational, medical, administrative, and other residential and commercial areas of the region, which will face serious problems in the critical situation of controlling the area. Among the criteria, the importance of the fault distance criterion is more important than other factors because the gap and acceleration caused by the displacement of faults in a possible earthquake have a significant effect on soil runoff and slope stability. Among the criteria of physical factors, the importance of the criteria of the type of materials and the age of the building, in general, the rate of wear and tear of the texture is more than all the criteria. These criteria are more effective in destroying buildings and thus causing financial and human damages. Accessibility factors such as proximity to open spaces, proximity to fire stations, and distance from medical centers are all important, especially since these three criteria are more effective in reducing human casualties after an earthquake.

References

1. Asgari Azad, M. (2012). Taken from the book of theoretical views of passive defense, p. 11.
2. Azmoudeh Ardalan, A., Forotan, A. and Agha Mohammadi, H. (2006). Spatial modeling to reduce earthquake damage. Proceedings of the first conference on dealing with natural disasters, scientific pole of mapping engineering, technical campus of Tehran University.
3. Rezaei, M. (2011). Application of spatial models and network analysis in urban crisis management using GIS (Study case: Isfahan's three cities region). Taken from the master's thesis under the guidance of Dr. Ali Zangibadi, Faculty of Geographical Sciences and Planning, Isfahan University.
4. Kazeminia, A (2017). Locating the location of the construction of emergency shelter in Kerman using GIS. Crisis Management, 8(2), 47-59.
5. Akashe, b (2004). On the day of Rudbar, yesterday, Bam, tomorrow..., abstracts of the articles of the sustainable development perspective neighborhood development conference, Tehran Municipality.
6. Habibi, K (2008). Determining the effective factors in the vulnerability of the ancient urban fabric of Zanjan using the fuzzy method and geographic information system, Fine Arts, University of Tehran, 33.
7. Ibrahim, I. M., & Alreshaid, K. (2005). Decision support system for selecting the proper project delivery method using analytical hierarchy process (AHP). International journal of project management, 23(7), 564-572.
8. Salehi, S. S., & Jafari, F. (2024). Evaluation of the worn texture of the region 4 in Tabriz, Iran, with an emphasis on increasing populatability. Advanced Engineering Science, 4, 25-34.
9. Salehi, S. S., & Jafari, F. (2023). Increasing the efficiency of worn-out urban fabric areas with an emphasis on the segmentation of buildings in the 4th district of Tabriz in Iran. Advanced Engineering Days (AED), 8, 121-124.
10. Hosseinzadeh Delir, K., Rasulzadeh, Z. and Mohammad Khanali, H. (2020). Measuring the level of satisfaction with the quality of the urban environment from the citizens' point of view (case study: District 5 of Tabriz Metropolitan Municipality). Perspective of urban and rural studies, 1(1), 1-15.
11. Khayyam, M. (1995). Attitude towards the geomorphological bottlenecks of the development of Tabriz city, Journal of Faculty of Humanities and Social Sciences, Tabriz University, 519-519.

Advanced Engineering Days

aed.mersin.edu.tr

Analysis of Urban Planning policies in earthquake-affected areas and lessons from the cities of Kahramanmaraş and Hatay in Türkiye

Fereidoun Babaei Aghdam [*1], Shiva Sattarzadeh Salehi [1], Murat Yakar [2], Aydin Alptekin [2]

[1]*University of Tabriz, Urban and regional planning, Iran, F.babayi.ag@gmail.com, Sattarzadeh423@gmail.com*
[2]*University of Mersin, Engineering, Turkiye, myakar@mersin.edu.tr, aydinalptekin@mersin.edu.tr*

Cite this study: Babaei Aghdam, F., Salehi, S. S., Yakar, M., Alptekin, A. (2024). Analysis of Urban Planning policies in earthquake-affected areas and lessons from the cities of Kahramanmaraş and Hatay in Türkiye. Advanced Engineering Days, 9, 752-756

Keywords
Urban planning
Turkiye
Earthquake
Kahramanmaraş
Hatay

Abstract

Turkiye has been struck by several powerful earthquakes during the last decades. The 1999 earthquake was the most recent and devastating before the last one happened in 2023. Therefore, the current research intends to examine the effects of the Turkiye recent earthquake in evaluating the amount of destruction of buildings and the political role of urban planning applied in the earthquake-affected areas. For collecting the required information has been used from library research and documents and other past studies related to Hatay and Kahramanmaraş earthquakes. According to the surveys, the total number of buildings in Hatay is 357,467 in the residential sector, 33511 in the Workplace sector, and 10382 in the public sector, as well as in Kahramanmaraş, the residential sector is 219351, the workplace is 12358, and the public sector is 6879. it was determined that the main determining factors in the destruction of buildings were the severity of ground motion, the low bearing capacity of the soils where buildings' foundations were laid, and the deficiencies in the quality of buildings in terms of design and construction.

Introduction

Earthquake is considered the biggest potential source of damage and injuries from a natural hazard and experts in various fields have faced it as a global problem [1,2]. Turkiye is located in a seismic zone known as the Anatolian Seismic Zone. Because of these issues, this country has a history of experiencing devastating earthquakes, with 269 recorded between 1900 and 2023, resulting in significant loss of lives and economic damage (3). Türkiye's first disaster management system was published in response to these devastating earthquakes after the 1939 Erzincan Earthquake. It is also significant to note that Türkiye's Sendai Mid-term Report in 2022 very recently highlighted that national-level risk reduction plan and local risk reduction plans, which were completed in 2022, have identified actions to be taken, alongside the responsible actors in various sectors before any event occurs (4).

On 6 February 2023, two devastating earthquakes, measuring 7.7 and 7.6 on the Richter Scale, struck the Kahramanmaraş region in Türkiye. In the days after the initial earthquakes, thousands of aftershocks followed (5). The provinces of Hatay, Kahramanmaraş, Adıyaman, Malatya and Gaziantep (Islahiye and Nurdağı districts) were reportedly hardest hit. These earthquakes are the largest experienced in Türkiye in the last century, and the most significant to strike the country's southeast region in hundreds of years (6).

The recent earthquakes of this country have highlighted the shortcomings of its infrastructure and construction standards in the field of seismic activity. Nearly 98% of collapsed structures were constructed before 2000, a significant year for Turkish construction regulations because it followed the devastating 1999 earthquake in Izmit. Rebuilding the affected areas will require a significant number of resources, time, and further fundamental changes to construction permit laws. These catastrophes have emphasized the urgent need for disaster preparedness and response in Turkiye and highlighted the importance of safe and earthquake-resistant housing. Therefore, the current research intends to evaluate the political role of urban planning in the earthquake-affected cities of Hatay and Kahramanmaraş, crisis management, and urban reconstruction rules before and after the earthquake.

Material and Method

The current research is of applied purpose type and descriptive method. For collecting the required information has been used from library research and documents and other past studies related to Hatay and Kahramanmaraş earthquakes. Therefore, the current research intends to examine the effects of the Turkiye recent earthquake in evaluating the amount of destruction of buildings and the political role of urban planning applied in the earthquake-affected areas of Kahramanmaraş and Hatay.

Study Area

Kahramanmaraş is the name of a city in Türkiye. This city is located at the foot of the Taurus Mountains and its population in 2022 was 1,177,436 people. 7.7 and 7.6 magnitude earthquakes on February 6, 2023 in Turkiye, which have killed about 48,000 people in southern Turkiye in addition to many casualties. It also caused heavy financial losses to the country's economy (7). The city of Hatay in the Mediterranean region of south-central Turkiye is a depression in Syrian territory under Turkish rule, with a population of 1,686,043 in 2022. It is also one of the oldest parts of Turkiye and has several important cities (8). Its most important city is Antakya, the capital of the province and the biggest city of this province is Iskenderun "Figure 1".

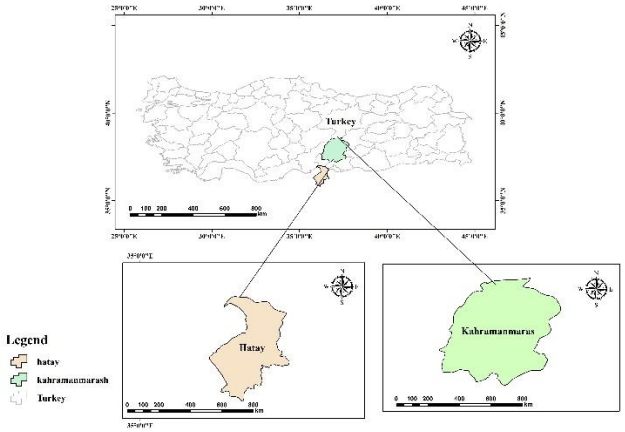


Figure 1. Map of the geographical location of the study area

Results

In 2022, the population of the 11 earthquake-affected provinces accounted for 16.4% of Turkiye 's population, and more than 47,000 people died in these earthquakes. There are 3,029,422 households in the earthquake-affected region, with an average household size of 3.5 persons. Given that the average household size in Türkiye is 3.2 persons in the same period, the number of individuals in a household in an earthquake-affected region is above the average value for Türkiye (9). approximately 280,000 buildings collapsed or sustained severe damage, and significant material losses were suffered in 11 provinces located on and around the North Anatolian Fault Line. The total number of buildings in Hatay is 357,467 in the residential sector, 33511 in the Workplace sector, and 10382 in the public sector, and in Kahramanmaraş, the residential sector is 219351, the workplace is 12358, and the public sector is 6879 "Table 1". Of these buildings, approximately 90% are residential, 3% are public buildings, and 6% are workplaces, and the number of residential units in the 11 earthquake-affected provinces in 2022 is 5.6 million units, which is a 14.05% share of the total housing stock across Turkiye.

Table 1. Number of Total Buildings in study area

Province	Resident	Workplace	Public	Other	Overall Total
Kahramanmaraş	219351	12358	6879	4565	243153
Hatay	357467	33511	10382	5489	406849

Although such measures as ensuring quality in building construction, evaluating and reinforcing the building stock for resistance to earthquakes, and establishing principles and standards for disaster-sensitive development plans have been taken, the settlement problems, particularly on unlicensed constructions, could not be solved at the level desired. Article 8 of the Regulation on Making Spatial Plans states that "For settlements or built urban environment where disaster and other urban risks are high, urban risk analyses or avoidance planning studies are conducted if deemed necessary. Risk mitigation measures for disasters and other urban risks shall be taken as basis in the plans." This regulation includes the concepts of "risk mitigation" and "avoidance measures" in spatial plans. Clarification of the criteria according to which risk mitigation measures will be taken as basis in plans and

how the result data of geoscientific studies will be transferred to spatial plans in the legislation in question will facilitate monitoring and supervision of the conditions related to the measures in the following stages. Looking at the urban regeneration works that were carried out for the purpose of regeneration or renewal of disaster-prone areas and structures in our country, these works could not reach the desired speed in cities, particularly in the areas with old buildings, due to financing, ownership problems and so on (9,6). In the earthquake-affected areas, the total number of high-risk areas in Hatay (9612) and the number of destroyed units (250 units) and the number of high-risk and destroyed areas in Kehrman maras are equal to (5584) and (1149), respectively "Table 2".

Table 2. Distribution of Risky Areas and Buildings in Earthquake-Affected area

Province	Number of risky Buildings	Number of areas	Number of Demolished Units	Number of Detached Units
Kahramanmaraş	5584	3	1149	3994
Hatay	9612	2	250	6215

Within the scope of urban transformation efforts, the renewal of risky buildings was carried out in a partially in areas whose financing was based on precedent increases. This has led to the creation of new residential areas with high building density. To ensure the construction of resistant buildings, the Regulation on Earthquake Resilience of Buildings was updated twice, in 2007 and 2018, in line with the new findings and needs determined after the earthquakes. The final version of the Regulation on Earthquake Resilience of Buildings entered into force in 2019 after being published in the Official newspaper of 18 March 2018 issue. 30364-bis, and stipulates the necessary rules and minimum requirements for the design and construction of the whole or parts of public and private buildings and building-type structures that are to be reconstructed, renovated, or extended as of 2019, and for the evaluation of the resistance performance of existing buildings to earthquakes and reinforcing them, if required. The Regulation is of critical importance since it stipulates the minimum requirements for the earthquake-resistant design and construction of structures by taking into account the earthquake-related risks of the region and ground properties in terms of construction, engineering-architecture, technical consulting, and contracting services. The Türkiye Earthquake Hazard Map was renewed in accordance with Decree No. 2018/11275 of the Council of Ministers on the Türkiye Earthquake Hazard Map and Parameter Values, which was published in the same Official newspaper (9).

Actions Done During Disaster Response Process in Earthquake-affected areas

In the first stage, 350 tent cities were established to provide temporary shelter for people affected by the disaster, 1 million tents were shipped to the region and 2.5 million people were provided with shelter. Work was carried out to meet the needs of earthquake victims such as food and shelter in the administrative buildings and social facilities of public institutions organizations and universities in the region (10). 478 thousand people were placed in the dormitories of the Credit and Dormitories Institution, and 710 thousand people were placed in various hotels and guesthouses. 3,549,443 people were evacuated from the region and the travel expenses of 1,543,499 people were covered "Figure 2".



Figure 2. An example of tents created in earthquake-affected areas (4)

Investments and Activities of Housing After the Earthquake

To carry out damage assessment studies more efficiently, the relevant process is carried out in a digital environment and a single transaction through the damage assessment software created by the Ministry of Environment, Urbanization and Climate Change, General Directorate of Construction Works. By making damage assessments in the digital environment, the damage status of the building, the information about the building, and the coordinates and photographs of the building are instantly transferred to the central system of the Ministry, and the damage assessment works are followed. As a result of the studies carried out in the area affected by the

disaster by the technical committees assigned within the framework of the relevant legislation under the coordination of the Ministry, the damage caused by the earthquake to the building is evaluated observationally. In line with the plans prepared at the national and local level, damage assessment teams consisting of civil engineers and architects formed in 81 provinces conduct post-disaster inspections and classify the buildings at the level of undamaged, slightly damaged, moderately damaged, severely damaged, or demolished urgently/demolished (4).

After an earthquake, the building should not be destroyed from the outside, or if there is no damage to many carrier elements, the structuralist of the damage to the carrier system of the building is checked by taking into account the most damaged floor. In addition, unmanned aerial vehicles such as UAVs and drones take images of the structures in the areas affected by the disaster, and the dangerous parts of the elements such as roof covers, chimneys, and roof intermediate walls are detected and precautions are taken.

In Hatay, 81,006 out of a total of 116,994 beneficiaries will participate in the draw. A total of 37,988 beneficiaries who applied for on-site conversion/reserve areas were not included in the draw. The number of houses to be drawn is 7,275 and in Kahramanmaraş, 27,635 of the total 59,166 beneficiaries will participate in the draw. 31,531 beneficiaries who applied for on-site conversion/reserve area were not included in the draw. The number of houses to be drawn is 9,289. Among the 387,776 beneficiaries, there are those whose applications for both on-site transformation and permanent disaster housing were accepted in all provinces and districts, including those with moderately damaged buildings. Due to the ongoing process regarding the status of beneficiaries in moderately damaged buildings, approximately 63 thousand beneficiaries were not included in the draw. On the other hand, the number of beneficiaries to be drawn has been determined as 207,586 due to reasons such as some of the beneficiaries choosing on-site conversion, those in rural areas not being included in the draw in some provinces, and the drawing stage not yet being reached in some districts (10).

Türkiye's Construction Urbanization Policies After the Earthquake

The earthquake also significantly affected the construction industry. The earthquakes have revealed the importance of the project implementation process, ground capacity, professional competence, use of quality building materials, building inspection and safe construction, Disruptions have occurred in the process of granting building permits by the administrations regarding this issue. In this process, the risk of unlicensed construction has emerged by citizens trying to meet their urgent shelter needs. The judicial process has begun for contractors, project designers, and building inspection organizations, and while contractors and project designers have been punished, the Ministry of Environment, Urbanization and Climate Change, and other relevant institutions have faced compensation.

Healing the wounds of the earthquake, which had such a great impact on every area, and the reconstruction process requires a long-term effort. In the Twelfth Development Plan, covering the period 2024-2028, the policy framework for reconstruction and rehabilitation works in the earthquake zone was put forward with a holistic development approach. In this regard, resilience to disasters is considered one of the five main axes in the Plan (9). The Development Plan aims to rebuild the cities affected by earthquakes with an urbanism approach that is climate-friendly, disaster-resistant, and increases the quality of life, taking into account their historical, social, and cultural textures. In the Development Plan, measures to be taken in many sectors such as industry, services, transportation, and agriculture were determined to normalize the economic and social life in the earthquake region. With this perspective, policies and measures have been determined for rapid, effective, and holistic planning of all stages of disaster management, including pre-disaster, disaster, and post-disaster. In particular, policies regarding housing, urbanization, and urban transformation have been planned in detail in terms of their dimensions to prevent disaster risk. The Development Plan also aims to increase resilience against disaster risks in the allocation of public investments (10).

Discussion

It is seen that the percentage of steel construction structures, which are generally recognized to be earthquake-resistant even though they have a high cost, is very low. The fact that the majority of the building stock in the earthquake-affected region is made of reinforced concrete can only be interpreted if detailed information is obtained about the load-bearing systems of damaged buildings. Besides, it is also required to collect data on buildings without a building permit. Such buildings pose a higher risk since they have not been subjected to controls or inspections during the design and construction phases.

Conclusion

According to the analyses carried out by various institutions, including ITU and METU, it was found that the main determining factors in the destruction of buildings are the intensity of ground movement, proximity to the fault line, and the low bearing capacity of the foundations of the buildings (residential areas that Agricultural lands were settled on alluvial soils and have suffered the most damage, while buildings built on bedrock have more resistance, which is the hero of Marash, the quality of the buildings in terms of design and construction, the age of

the buildings. , the non-compliance of the construction of the buildings with the laws and regulations, and the difference in the height levels of the floors of the adjacent buildings.

The percentage of masonry structures, the most problematic category in terms of earthquake resistance, is very low. On the other hand, it is seen that the percentage of steel construction structures, which are generally recognized to be earthquake-resistant even though they have a high cost, is very low. The fact that the majority of the building stock in the earthquake-affected region is made of reinforced concrete can only be interpreted if detailed information is obtained about the load-bearing systems of damaged buildings. Besides, it is also required to collect data on buildings without a building permit. Such buildings pose a higher risk since they have not been subjected to any controls or inspections during the design and construction phases.

References

1. Ebrahimzadeh, E., Kashefi, D., & Hosseini, A (2014). Assessing the vulnerability of urban neighborhoods against earthquakes (case example: Piranshahr city), Scientific-Research Journal of Spatial Planning (Geography),1(16),26.
2. Karimzadeh, S. and Ghasemi, M. (2023). Damage assessment of buildings after the Maras earthquake in Turkiye) using radar images with multi-temporal artificial aperture and deep learning, Tabriz International Conference on Investment Opportunities.
3. Strategy and Budget Office of the Presidency of the Republic of Türkiye (2023) Türkiye earthquakes recovery and reconstruction assessment. https:// www. sbb. gov. tr/ wp- conte nt/ uploa ds/ 2023/ 03/ Turki ye-Recovery- and- Recon struc tion- Asses sment. Pdf.
4. AFAD (2022b) Türkiye's voluntary national report for the midterm review of the implementation of the Sendai framework for disaster risk reduction 2015–2030 (MTR SF). September 2022. Retrieved 6 Nov 2023 from https://sendaiframework-mtr.undrr.org/media/84534/download?startDownload=true.
5. AFAD (2022c) Provincial Disaster Risk Reduction Plans for 81 provinces. Retrieved 6 Nov 2023 from https:// www. afad.gov. tr/ il- planl ari
6. Un women(2023). The impact of earthquakes in Turkiye: Barries to access to justice after the earthquakes-field research findings on womens legal priorities, Union of Turkish Bar Associations.
7. Lestrange, G. (2013). Historical geography of Eastern Caliphate lands. Scientific and cultural. 138.
8. http://turkeymehr.com.
9. President's Strategy and Budget Presidency (2023), Kahramanmaraş and Hatay report.20-26.
10. President's Strategy and Budget Presidency(2024), Kahramanmaraş and Hatay earthquake, reconstruction and development report, Ankara.

Advanced Engineering Days

aed.mersin.edu.tr

Engineering analysis of multidimensional vulnerability due to earthquake occurrence

Peyman Yariyan*[1], Abolfazl Ghanbari [1], Mohammadreza Karami [2]

[1]*University of Tabriz, Department of Remote sensing and GIS, Iran, p.yariyan@tabrizu.ac.ir, A_ghanbari@tabrizu.ac.ir*
[2] *University of Payame Noor, Department of Social Sciences, Iran, karami_mohammadreza@ymail.com*

Cite this study: Yariyan, P., Ghanbari, A., & Karami, M. (2024). Engineering analysis of multidimensional vulnerability due to earthquake occurrence. Advanced Engineering Days, 9, 757-760

Keywords
Seismic vulnerability
Spatial analysis
Machine learning
GIS
Iran

Abstract

The main goal of this study is to identify areas with high seismic risk in order to reduce vulnerability in Kermanshah. To achieve this goal, a total of 14 factors affecting vulnerability, a training dataset and two machine learning models were used. The results show that different areas of the studied area show different reactions to earthquakes and their vulnerability percentages are different. The combined Fuzzy-ANN model had a better performance for preparing the seismic prediction map. Vulnerability of over 30% in the entire region suggests the necessity of planning based on crisis management principles.

Introduction

Based on the growth rate of population in cities, it is predicted that the possible risks of earthquakes will increase by two times by the year 2050 [1]. Meanwhile, in the 21st century, more than 1000 devastating earthquakes occurred in the whole world, as a result of which more than 1,500,000 people died [2]. Hence, earthquakes as one of the natural events can have many destructive social and economic effects on the body of cities [3]. Although, the vulnerability of cities and residential areas caused by earthquakes has a direct and significant relationship with the urban management system and the necessary preparation against such events [2].

Therefore, with the aim of reducing the amount of damage and human casualties caused by earthquakes, accurate and locational studies are needed to identify high-risk areas [4]. In this regard, many researchers have been anxiously conducting research to identify areas at risk of earthquakes. Some studies evaluated seismic vulnerability through GIS data [5-9]. However, the approach of these studies is one-dimensional and only physical factors such as the age of the building, building density, strength of the building, etc. have been considered as factors that drive and intensify vulnerability in cities.

Hence, with the aim of eliminating the shortcomings and limitations of previous studies, such as a one-dimensional look at the factors affecting vulnerability caused by earthquakes, using models containing uncertainty and the lack of final validation of the results; the present study was compiled with an innovation regarding the vulnerability assessment of urban areas of Kermanshah. So that, 14 factors affecting earthquake vulnerability (environmental, social, physical) and two machine learning models, Artificial Neural Network (ANN) and Support Vector Machine (SVM) have been used.

Material and Method

Study area

Kermanshah city is located in the center of Kermanshah province at 34◦ 19’ north latitude and 47◦ 7’ east longitude (Figure 1). This city with high seismic potential has a height of 1200 meters above sea level, an area of 956816 hectares and a population of 946651 people.

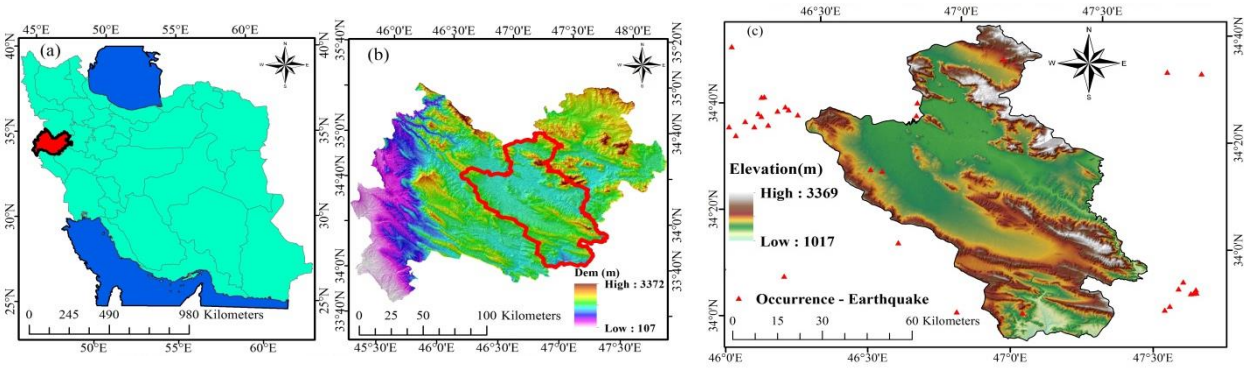


Figure 1. Location of the study area (a: Iran, b: Kermanshah province, c: Kermanshah city).

It is almost impossible to prevent the occurrence of an earthquake; however, there are factors that affect the severity or reduction of the vulnerability caused by it [10]. In this regard, the number of 14 factors affecting seismic vulnerability, i.e. physical factors (power tower, gas line, railway line, distance to road, distance to city, Distance to Village, Distance to Medical Emergency), environmental factors (Distance to river, Slope, Elevation, Geology, Land use, Distance to fault) and social factors (Population density) have been used in this study (Figure 2).

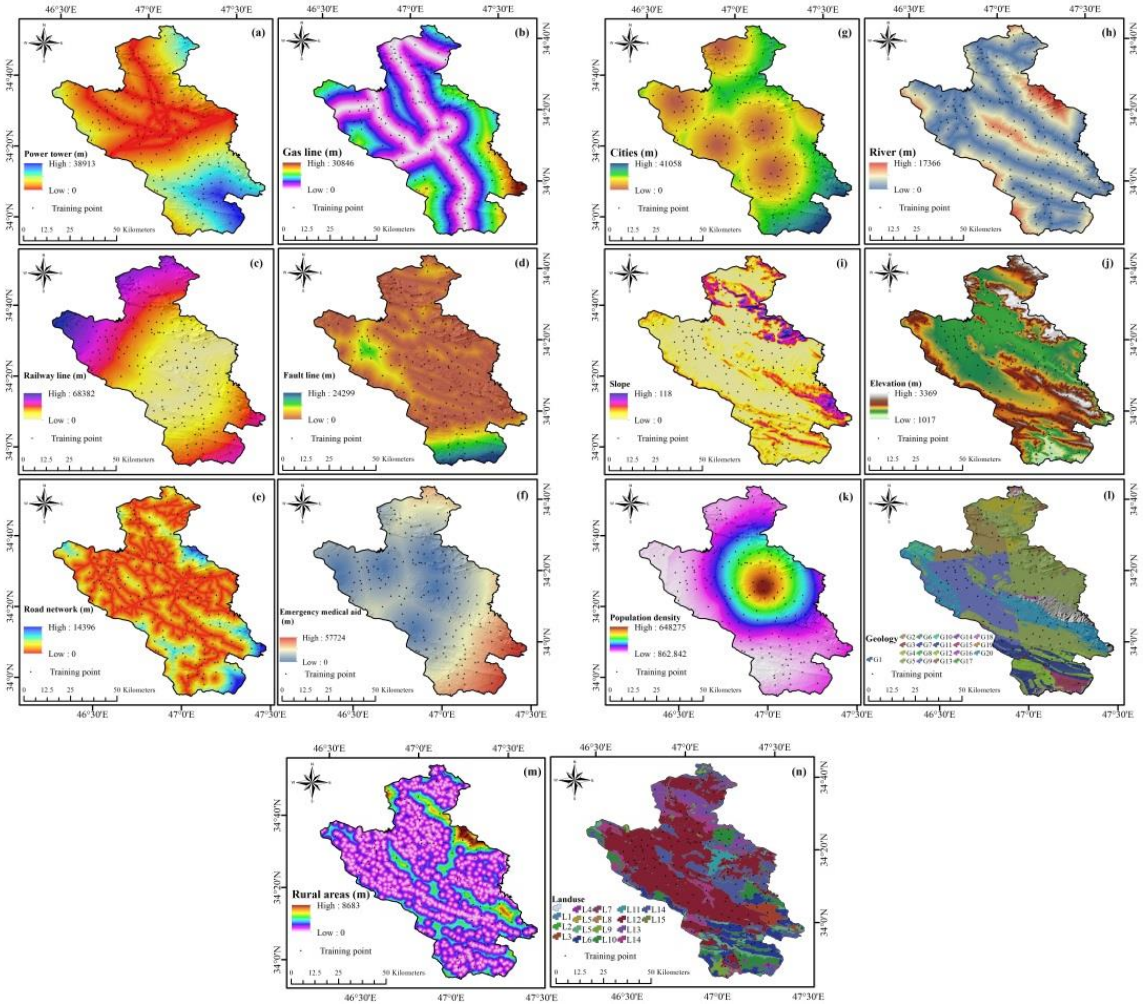


Figure 2. Effective factors of seismic vulnerability.

2.2 Methodology

This study includes four stages (Figure 3). In the first stage, based on the opinion of experts from the Department of Remote Sensing and Geographical Information Systems of Tabriz University, 14 factors were selected as effective factors in urban seismic vulnerability. In the second stage, the factors were edited and

standardized using different functions in ArcGIS 10.8 software. In the third stage, based on the earthquake inventory map, i.e., the locations of previous earthquakes, compiled by the Institute of Geophysics of Tehran University, according to the higher magnitude of the earthquake, training data was prepared for the implementation of two machine learning models (ANN and SVM). In the last step, the map prepared by each model was validated.

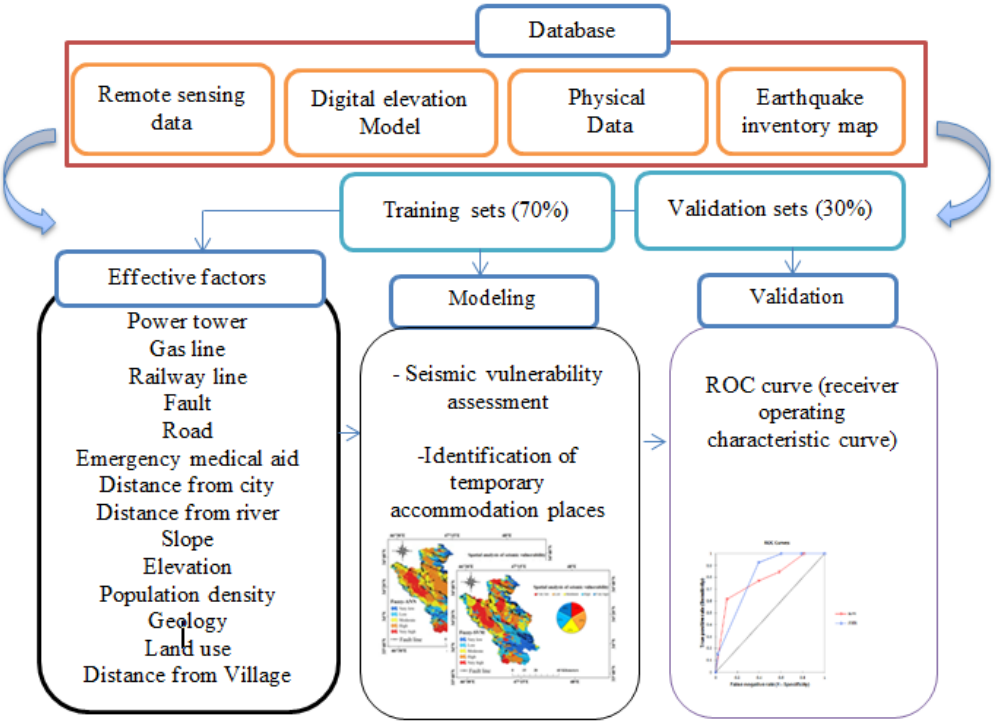


Figure 3. Methodological diagram of the study.

3. Results

"Figure 4" shows the map prepared for each of the machine learning models regarding the seismic vulnerability assessment in Kermanshah city. These maps are the result of combining the maps of each factor in a fuzzy manner with earthquake occurrence points by two ANN and SVM models. In this way, each map is classified into five vulnerability sensitivity classes: very low, low, moderate, high and very high. In the ANN model, 34% of high and very high risk areas, 27% moderate risk areas, and 39% low and very low risk areas are classified. Also, in the SVM model, the percentages with not much difference, 40%, 21% and 39%, respectively, indicated the high potential of vulnerability in the western and southern regions of Kermanshah.

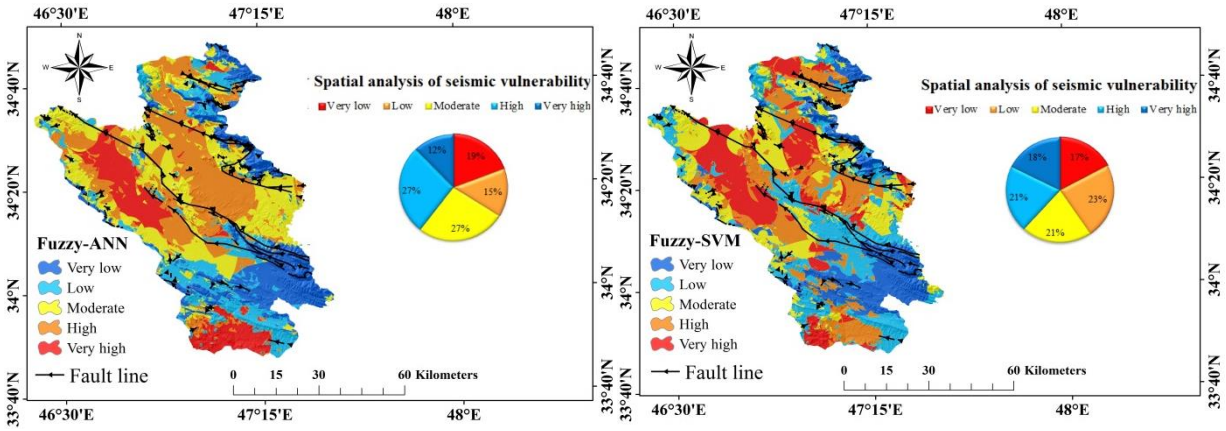


Figure 4. Earthquake vulnerability maps.

3.1 Performance assessment of models

Validation of seismic vulnerability maps was done by An ROC curve (receiver operating characteristic curve). According to this, the ANN model with AUC= 0.8 has a better performance than the SVM model with AUC= 0.78 for the evaluation of seismic vulnerability in Kermanshah city (Figure 5).

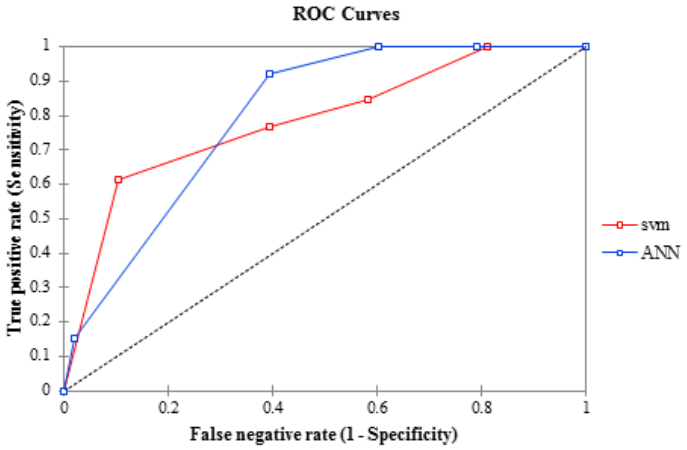


Figure 5. Evaluating the predictive performance of machine learning models.

4. Discussion and Conclusion

Kermanshah city, as the capital of Kermanshah province, has a high potential for seismic vulnerability due to its high population density, proximity to active faults, lack of compliance with engineering principles in construction, etc. As mentioned in the introduction, despite conducting numerous studies around the world in order to assess seismic vulnerability, they are often criticized due to the one-dimensional view of the factors and the use of models containing uncertainty. The current study with a new approach and the combination of many effective variables and using the potential ability of machine learning models aimed to solve the shortcomings of previous studies. Validation of forecasting models indicated the better performance of Fuzzy-ANN hybrid model for predicting damages caused by earthquakes. Although, the Fuzzy-SVM hybrid model also had a favorable performance. Forecast maps show high vulnerability for the western regions, parts of the city center and the south. This level of vulnerability in both models has predicted a percentage above 30. So that, areas with high vulnerability potential overlap significantly with proximity to gas lines, power tower, faults, cities, low elevation and flat lands and areas with high population density.

Hence, the most important practical suggestion based on the results of this study is to prevent construction in the area close to faults, to comply with construction strength regulations and to prevent high population density and marginalization. Also, the forecast maps prepared in this study can be a road map for planning to reduce vulnerability and crisis management.

References

1. Sauti, N.S., et al., *GIS spatial modelling for seismic risk assessment based on exposure, resilience, and capacity indicators to seismic hazard: A case study of Pahang, Malaysia.* Geomatics, Natural Hazards and Risk, 2021. 12(1): p. 1948-1972.
2. Yariyan, P., et al., *GIS-based seismic vulnerability mapping: a comparison of artificial neural networks hybrid models.* Geocarto International, 2022. 37(15): p. 4312-4335.
3. Avcil, F., et al., *Effects of the February 6, 2023, Kahramanmaraş earthquake on structures in Kahramanmaraş city.* Natural Hazards, 2024. 120(3): p. 2953-2991.
4. Shafapourtehrany, M., et al., *Evaluating the application of K-mean clustering in Earthquake vulnerability mapping of Istanbul, Turkey.* International Journal of Disaster Risk Reduction, 2022. 79: p. 103154.
5. Leggieri, V., G. Mastrodonato, and G. Uva, *GIS multisource data for the seismic vulnerability assessment of buildings at the urban scale.* Buildings, 2022. 12(5): p. 523.
6. Ramírez Eudave, R., et al., *Implementing open-source information systems for assessing and managing the seismic vulnerability of historical constructions.* Buildings, 2023. 13(2): p. 540.
7. Maky, A.M., M. AlHamaydeh, and M. Saleh, *GIS-Based Regional Seismic Risk Assessment for Dubai, UAE, Using NHERI SimCenter R2D Application.* Buildings, 2024. 14(5): p. 1277.
8. Aydın, M.C., et al., *Earthquake Risk Assessment Using GIS-Based Analytical Hierarchy Process (AHP): The Case of Bitlis Province (Türkiye).* International Journal of Environment and Geoinformatics, 2024. 11(1): p. 1-9.
9. Demir, M. and N. ALTAŞ, *Determination of areas with earthquake damage risk potential in Kars city based on GISbased AHP analysis.* GEOMATIK, 2024(1).
10. Alizadeh, M., et al., *Social vulnerability assessment using artificial neural network (ANN) model for earthquake hazard in Tabriz city, Iran.* Sustainability, 2018. 10(10): p. 3376.

Advanced Engineering Days

aed.mersin.edu.tr

Accuracy assessment of captured land-covered maps in urban fringes, (cases from Tabriz, Iran and Mersin, Turkiye)

Fereidoun Babaei Aghdam [*1], Shiva Sattarzadeh Salehi [1], Murat Yakar [2], Khalil Valizadeh Kamran [3]

[1]*University of Tabriz, Urban and Regional Planning, Iran, F.babayi.ag@gmail.com, sattarzadeh423@gmail.com*
[2] *University of Mersin, Department of Geomatics Engineering, Turkiye, myakar@mersin.edu.tr*
[3] *University of Tabriz, Remote Sensing and GIS, Iran, valizadeh@tabrizu.ac.ir*

Cite this study: Babaei Aghdam, F., Salehi, S. S., Yakar, M., Kamran, K. V. (2024). Accuracy assessment of captured land-covered maps in urban fringes, (cases from Tabriz, Iran and Mersin, Turkiye). Advanced Engineering Days, 9, 761-765

Keywords
Land use
Land-cover
Accuracy
Urban fringes
Kappa

Abstract

Land use refers to how land is utilized by humans (e.g., agriculture, urban development) while land cover describes the physical material at the earth's surface (e.g., forests, crops). These concepts are fundamental in understanding human activities' interaction with the environment. Therefore, the current research intends to evaluate the accuracy of land cover maps extracted from Esri in order to evaluate its accuracy and error for use in the city. First, the classification of land cover images was done, and then the Kappa coefficient of agreement method was used to evaluate the quality result of the extracted classes to check the accuracy and detect errors. According to the coefficient of agreement, the Kappa of Ciflik Koy is (30%) and the Kappa of Konduri is also (15%). The results show that the land cover maps produced by Esri software have low accuracy and different land cover classes were not classified correctly. Therefore, the results obtained from these land cover maps should be used with caution and it is preferable to use land cover maps with higher accuracy prepared by reliable organizations.

Introduction

One of the most important natural resources on the planet is land, which is also a basis for sustaining life and supporting development (1). “Land use” describes the economic or social functions related to a particular land area. On the other hand, the types of features on the land's surface are related to the land cover (2). The spatial details of this data are also critical for environmental protection and spatial planning. Land use classification is also vital because it gives data that can be used as input for modeling, especially the one dealing with the environment, for instance, models deal with climate change and policy developments (3). Hence, the combined LULC provides a comprehensive understanding of geo-biophysical and socioeconomic system behaviors and interactions (4). To provide more useful information on land cover, Remote Sensing is often paired with Geographic Information System (GIS) technique. Remote sensing plays a crucial role as the primary source of various thematic data essential for GIS analyses, such as land use and land cover characteristics. Aerial and Landsat satellite images are commonly utilized to assess land cover distribution and update geospatial features. The significance of remote sensing in Geospatial Information Systems (GIS) has greatly increased with the advent of remote sensing systems and image processing software (5). The increased utilization of remote sensing data and techniques has enhanced the speed and capability of geospatial processing, but it has also introduced greater complexity, leading to a higher potential for errors (6). Previously, accuracy assessment was not a priority in image classification studies. However, because of the accelerated chances for error presented by digital imagery, accuracy assessment has become a very vital process (7). in the meantime, Esri is a company that provides geographic information systems (GIS) software and geodatabase management applications. Their software, such as ArcGIS, is widely used for mapping, spatial analytics, and managing geographic information. However, Esri's satellite images are of moderate accuracy and are only sufficient for some general applications. However, for urban design and planning, especially in dense urban areas, they may not have the necessary accuracy. In these cases, the use of aerial images with higher resolution is recommended. Therefore, the current research intends to evaluate the accuracy of the land cover map in some areas of Tabriz and Mersin to obtain the number of existing errors.

Material and Method

The descriptive and analytical research method was used to collect information from Google Earth and Esri Land cover for the year 2022. The purpose of this research is to evaluate the accuracy and error detection of land cover maps of Esri company in the cities of Iran (Konduri in the Fringes of Tabriz City) and Turkiye (Ciflik Koy of Mersin city). First, the land cover image classification is done and then to evaluate the quality result of the extracted classes, the Kappa coefficient of agreement method is used to check the accuracy and error detection. This validation method is done by comparing the classified samples with the correct ones (reference) obtained from Google Earth (or a superior reference). It should be noted that due to the large scale of the cities studied in the research, several parcels from each city were selected on a case-by-case basis.

Results

Accuracy assessment is an important part of any classification project. It compares the classified image to another data source that is considered to be accurate or ground truth data. Ground truth can be collected in the field; however, this is time consuming and expensive. Ground truth data can also be derived from interpreting high-resolution imagery, existing classified imagery, or GIS data layers. So, to ensure accurate accuracy assessment in image classification, the values of your reference dataset need to match the schema used in the classification process. The most common way to assess the accuracy of a classified map is to create a set of random points from the ground truth data and compare that to the classified data in a confusion matrix. Although this is a two-step process, you may need to compare the results of different classification methods or training sites, or you may not have ground truth data and are relying on the same imagery that you used to create the classification. To accommodate these other workflows, this process uses three geoprocessing tools: Create Accuracy Assessment Points, Update Accuracy Assessment Points, and Compute Confusion Matrix.

The Kappa coefficient of agreement (Kappa) method used in the present research can easily evaluate the performance of multi-class algorithms. This criterion can consider the number of samples in an unbalanced data set and express the quality of the algorithm according to the number of samples. Therefore, this criterion can be used for problems with different classes and also for problems with unbalanced data. For this purpose, we have first classified the current situation of captured images of Mersin (2022) and Konduri in the Fringes of Tabriz City (2023) “Figure 1”.

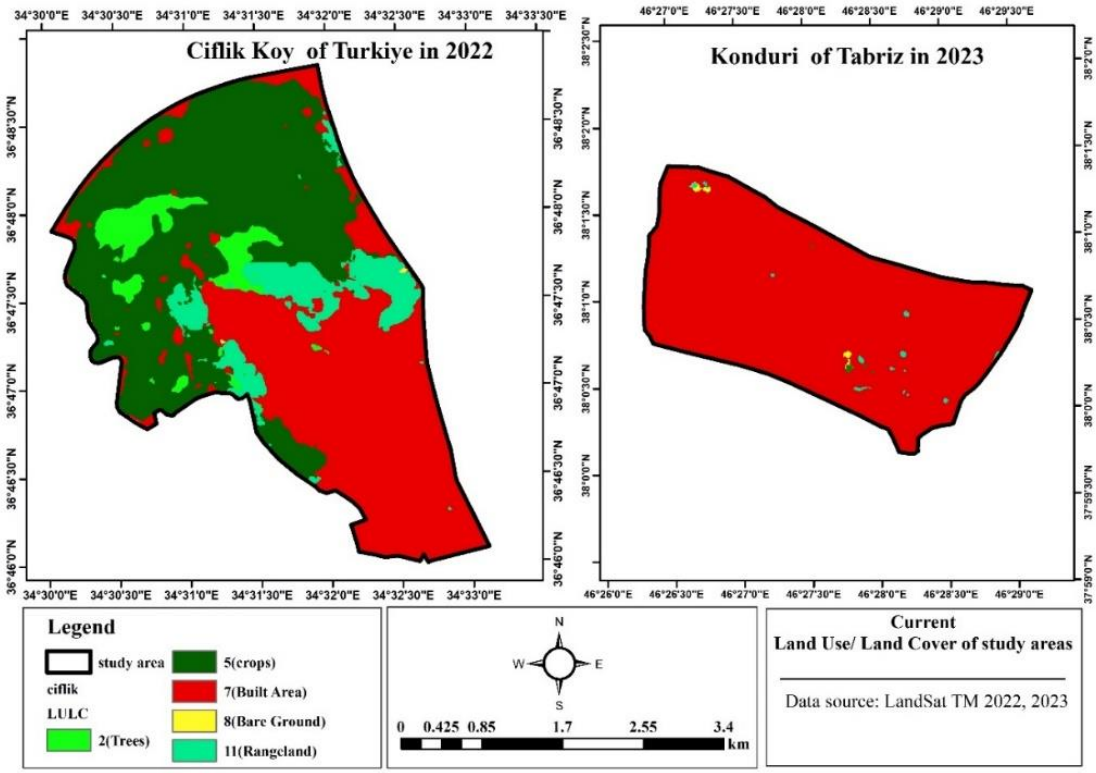


Figure 1. Current LULC of study areas

We randomly took 23 points from Ciflik Koy of Mersin and 21 points from Konduri of Tabriz, representing our classified land classes “Figure 2”. Then, we used Google Earth as a reference source to check the points. Then we will check whether these user values are correct or wrong and number the producer value.

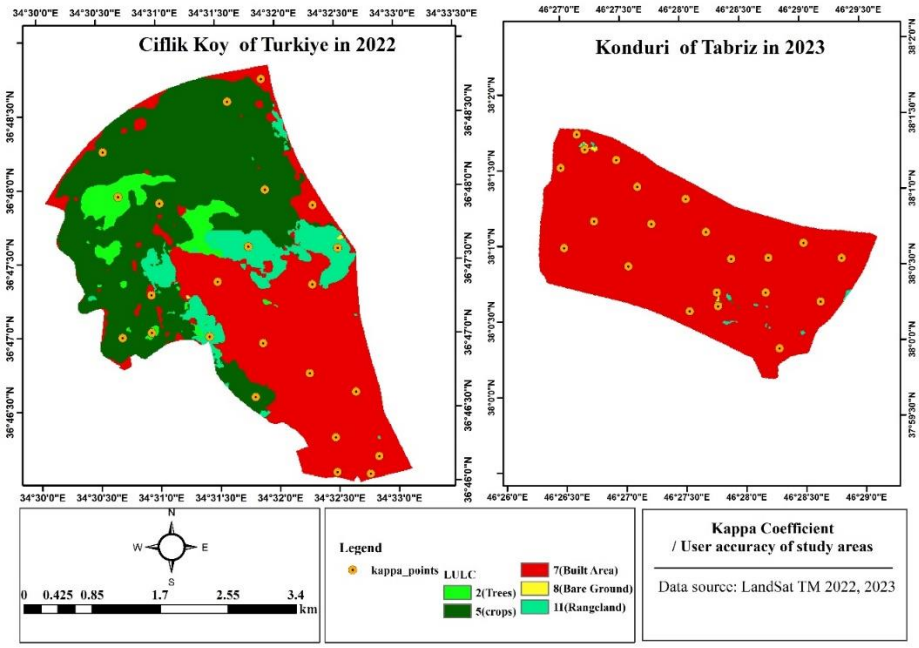


Figure 2. Kappa Coefficient/ user accuracy of study areas

Table for accuracy assessment is valuable for evaluating the accuracy of land cover classification or other spatial data analysis conducted for a specific area. This table usually consists of rows representing reference data (ground truth from Google Earth) and columns representing the classified data. "Table 1 & 2".

It shows the number of pixels or samples that were correctly classified (along the diagonal) and those that were misclassified (off-diagonal elements). Various accuracy metrics can be calculated from this information, such as:

-Overall Accuracy: The percentage of correctly classified pixels or samples out of the total number of samples.

-User's Accuracy (Reliability): The probability that a pixel classified on the map represents that category on the ground.

-Producer's Accuracy (Omission Error): The probability that a pixel on the ground is correctly classified on the map.

-Kappa Coefficient: A statistical measure that considers the agreement occurring by chance, providing a more robust assessment of classification accuracy.

Table 1. Accuracy Assessment Table of Ciflik Koy

	Trees	Crops	Built Area	Bare Ground	Rangeland	Total (User)
Trees	1	1	0	0	0	2
Crops	0	4	0	1	1	6
Built Area	3	2	3	2	2	12
Bare Ground	0	0	0	0	0	0
Rangeland	0	1	0	0	2	3
Total (producer)	4	8	3	3	5	23

Table 2. Accuracy Assessment Table of Konduri

	Trees	Crops	Built Area	Bare Ground	Rangeland	Total (User)
Trees	0	0	0	0	0	0
Crops	0	0	0	1	1	2
Built Area	0	6	4	3	1	14
Bare Ground	0	0	0	1	1	2
Rangeland	0	1	0	0	2	3
Total (producer)	0	7	4	5	5	21

Through a thorough examination of the accuracy assessment table, researchers and decision-makers can identify specific classes or regions with higher or lower accuracy. This information can then be used to guide further analysis, on-site verification, or enhancements to the classification process. Accuracy assessment is a vital component of quality assurance and validation in remote sensing and GIS projects, ensuring the reliability and

applicability of spatial data for various purposes, including land use planning, environmental monitoring, and resource management.

$$Overall\ accuracy = \frac{Total\ number\ of\ correctly\ classified\ pixels\ (Diagonal)}{Total\ number\ of\ reference\ pixels} \times 100$$

$$users\ accuracy = \frac{number\ of\ correctly\ classified\ pixels\ in\ each\ category}{Total\ number\ of\ classified\ pixels\ in\ that\ category(the\ row\ total)} \times 100$$

$$producer\ accuracy = \frac{number\ of\ correctly\ classified\ pixels\ in\ each\ category}{Total\ number\ of\ reference\ pixels\ in\ that\ category(the\ column\ total)} \times 100$$

$$Kappa\ Coefficient\ (T) = \frac{(TS \times TCS) - \sum(column\ total \times row\ total)}{TS^2 - \sum(column\ total - row\ total)} \times 100$$

According to the analyses of overall accuracy carried out according to the above formula, 43.48% of Ciflik Koy and 33.33% of Konduri were obtained. Then, based on the formulas of user and Producer, we can obtain each neighborhood (Ciflik Koy and Konduri). User accuracy analysis for Ciflik Koy including trees (50 %), crops (67 %), built areas (25%) and Rangeland (67%) was obtained, and for Konduri crops equal to (0), built areas (8%), Bare Ground (50%) and Rangeland (67%) and the producer accuracy analysis for Ciflik Koy including trees (25 %), crops (50 %), built areas (100%) and bare ground (0) was obtained, and for Konduri crops equal to (0), built areas (86%), Bare Ground (20%) and Rangeland (40%). Based on the agreement coefficient, Ciflik Koy's kappa is (30%) and Konduri's kappa is also (15%).

Discussion

Land cover planning is an important part of natural resource assessment and land management. Land cover maps are prepared from remote sensing data such as satellite images, where the image pixels are classified into different land cover classes such as forest, pasture, agriculture, etc. based on their spectral characteristics. Classification of remote sensing images can be done in two supervised and unsupervised ways. Kappa statistic is an important statistical index used in assessing accuracy, which is used in many remote sensing image processing software such as Esri. According to the analysis, land cover maps produced by Esri software have low accuracy and different land cover classes are not classified correctly. This may be due to the lack of proper performance of the classification algorithms used in this software, the lack of proper data preprocessing functions, or the lack of sufficient and quality training data to train the classification algorithm.

Conclusion

t's crucial to understand that land use and land cover are closely linked. Alterations in land use frequently led to changes in land cover, and vice versa. For example, transforming a forest (land cover) into agricultural land (land use) requires clearing the trees and changing the land cover to cropland. It is essential to understand the difference between land use and land cover for a wide range of purposes, including urban planning, environmental monitoring, natural resource management, and studies on climate change. Precise mapping and analysis of land use and land cover patterns can offer a valuable understanding of human activities, environmental changes, and the sustainable management of our natural resources. The purpose of this research is to evaluate the accuracy and error detection of land cover maps of Esri company in the cities of Iran (Konduri in the Fringes of Tabriz City) and Turkiye (Ciflik Koy of Mersin City). First, the land cover image classification is done, and then to evaluate the quality result of the extracted classes, the Kappa coefficient of agreement method was used to check the accuracy and error detection. Based on the agreement coefficient, Ciflik Koy's kappa is (30%) and Konduri's kappa is also (15%).

According to the analysis, land cover maps produced by Esri software have low accuracy, and different land cover classes are not classified correctly. This may be due to the lack of proper performance of the classification algorithms used in this software, the lack of proper data preprocessing functions, or the lack of sufficient and quality training data to train the classification algorithm. Therefore, the results obtained from these land cover maps should be used with caution and it is preferable to use land cover maps with higher accuracy prepared by reliable organizations.

References

1. Hundu, W.T., Anule, P.T., Kwanga, G.M. and Dam, D.P. (2021) Assessment of Land Use and Land Cover Change Using GIS and Remote Sensing Techniques in Katsina-Ala Local Government Area of Benue State, Nigeria. Journal of Research in Forestry, Wildlife & Environment, 13, 195-204.
2. Chaikaew, P. (2019) Land Use Change Monitoring and Modelling Using GIS and Remote Sensing Data for Watershed Scale in Thailand. In: Loures, L.C., Ed., Land Use—Assessing the Past, Envisioning the Future, IntechOpen, London.
3. Disperati, L., Gonario S. and Virdis, P. (2015) Assessment of Land-Use and Land-Cover Changes from 1965 to 2014 in Tam Giang-Cau Hai Lagoon, Central Vietnam. Applied Geography, 58, 48-64.
4. Moran, E. F., Skole, D.L. and Turner, B.L. (2004) The Development of the International Land-Use and Land-Cover Change (LUCC) Research Program and Its Links to NASA's Landcover and Land-Use Change (LCLUC) Initiatives. Kluwer Academic Publication, Netherlands.
5. Merchant, J.W. and Narumalani, S. (2009) Integrating Remote Sensing and Geographic Information Systems. Papers in Natural Resources, Paper 216.
6. Murty, P.S. and Tiwari, H. (2015) Accuracy Assessment of Land Use Classification —A Case Study of Ken Basin. Journal of Civil Engineering and Architecture Research, 2, 1199-1206.
7. Congalton, R.G. (1991) A Review of Assessing the Accuracy of Classifications of Remotely Sensed Data. Remote Sensing of Environment, 37, 35-46.
8. https://en.wikipedia.org/wiki/Mersin#
9. Salehi, S. S., & Jafari, F. (2024). Evaluation of the worn texture of the region 4 in Tabriz, Iran, with an emphasis on increasing populatability. Advanced Engineering Science, 4, 25-34.
10. Salehi, S. S., & Jafari, F. (2023). Increasing the efficiency of worn-out urban fabric areas with an emphasis on the segmentation of buildings in the 4th district of Tabriz in Iran. Advanced Engineering Days (AED), 8, 121-124.

Advanced Engineering Days

aed.mersin.edu.tr

A review of GIS application in urban green landscapes

Mohammad Khezrollah [1], Zanyar Samadi Todar [*2], Khalil Valizadeh Kamran [1]

[1]*University of Tabriz, Department of Remote sensing and GIS, Iran, xzrollam@gmail.com, Valizadeh@tabrizu.ac.ir*
[2] *University of Tabriz, Department of Landscape Architecture, Iran, Zanyar.samadi51@gmail.com*

Cite this study: Khezrollah, M., Samadi Todar, Z., Valizadeh Kamran, K. (2024). A review of GIS application in urban green landscapes. Advanced Engineering Days, 9, 766-771

Keywords
Urban green space
GIS
NDVI
Urban

Abstract

Urban green spaces are one of the most important indicators of the mental and physical health of people in cities. In addition, it is one of the city's most pressing needs in the ecological catchment area and an essential component of a healthy urban environment, the use and development of which, according to research, can also contribute to the ecosystem in this catchment area and reduce deaths due to pollution. Geomatics or GIS_RS for analyzing spatial data using various sensors and OPTIC-SAR images have made significant progress in all scientific areas. The urban green space has not left this progress behind either. GIS has become one of the most important tools in urban green space in relation to various ecological and ecological aspects and locations as well as maintaining food security in the city. For example, the use of indices, especially the NDVI index, one of the most commonly used vegetation value indices among other indices, identifies the vegetation by calculating the difference between the red band and the near red band.

Introduction

The urbanization process has caused a number of negative impacts on urban spatial planning [1], including the ecological destruction of forest areas [2], the management of urban areas [3,4], a water resource crisis [5] and the decline in the happiness index of residents. In urban construction and management, more attention needs to be paid not only to the protection and restoration of natural ecology, but also to the desire of urban residents for the natural environment, which makes humanities and urban development the most important topics in urban planning [6], which the countries prompted to rethink the relationship between urban residents and the environment [7], with the aim of planning a just and sustainable city [8–10]. In order to further improve the urban ecological environment, maintain high-quality urban development, realize the value of ecological services and optimize the living environment of residents, the construction of green spaces has become an important measure of urban planning and construction of urban green spaces The Spaces network has become a necessary path for sustainable urban development.

Urban green spaces are an essential part of the urban ecosystem, which is closely related to the urban ecological environment [11], biodiversity [12], human physical and mental health [13], quality of life of residents [14] and social situation Security [15]. With the rapid development of urbanization, urban construction areas are encroaching on a variety of urban green spaces [16,17,18]. This leads to greater fragmentation of green spaces [19,20] and deterioration of the urban ecological environment. In order to better represent the “green concept” and create a “livable city” with a suitable living environment and a harmonious society, the first requirement is rapid and efficient monitoring of the condition of urban green spaces.

Urban Green Space (UGS)

Urban green spaces include parks, open fields, trees, agricultural land, roadside plants [21,22], and areas covered with green infrastructure [23,24] within the city. Green spaces are an essential part of a healthy environment. It is called the lungs of the city because it promotes both physical and mental health and improves social relationships among people [25,30] green spaces also help reduce environmental impacts, help regulate microclimate and make an excellent contribution to ecological integrity [31-34]. According to UNEP, a city in

developing areas must consist of healthy green spaces [35]. Attention as its importance is recognized (36) and it has become a topic of interest in research, business and urban planning [34,37].

In the initial phase, the focus is on functions in the design of green spaces [38], which is primarily manifested in the planning of urban open spaces [39], the construction of city parks [40] and the expansion of urban green spaces. Little emphasis is placed on the quality of grassland [41]. In the later phase, the focus gradually shifts to the urban suburbs, as high priority is given to nature conservation and the construction of green and open spaces [42]. The design of the green space network is also appreciated. Furthermore, as the relationship between urban green spaces and cities becomes more evident, urban public spaces need to be repaired and improved [43,44] and regional green spaces need to be protected and enhanced [45].

Green spaces promote the balance between carbon and oxygen and help keep the air clean. It also serves to reduce ozone levels [46]. A study in Ankara showed that improving green spaces provides citizens with more facilities and social interactions [22]. According to Wolch, green spaces promote public health and also provide ecosystem services [30]. A study in Belgium showed that residences with more green plants had lower mortality from respiratory diseases [29]. Green spaces also promote the maintenance of carbon sequencing and environmental quality measurement [47].

Geographic Information Systems (GIS)

Geographic information systems (GIS) and remote sensing are often used for geospatial data analysis. Since remote sensing satellite data are freely available, it is easier for developing countries to conduct analyzes using these data [48]. Several studies have used GIS and remote sensing methods to analyze green spaces [21,49-53].

Theoretical, scientific and technological advances have also led to significant advances in green space research methods, with geographic information systems (GIS) and remote sensing (RS) predominating. With the continuous segmentation of research areas and purposes, people's needs and environmental protection have attracted increasing attention [54]. In the 1960s, Roger Tomlinson first proposed the term GIS [55]. Since the 1990s, GIS has been gradually introduced into the study of ecological planning of urban green spaces, such as the current situation of landscape analysis [56] and spatial development prediction [57]. In the construction of urban green spaces, GIS is used in various aspects, such as source identification [58]. When identifying ecological sources, some scientists use remote sensing images to identify large forests, bodies of water [59,60], scenic areas and nature reserves to define ecological sources [61,62]. Some scholars have used GIS to analyze the sensitivity [63] and suitability [64] according to the characteristics of the study area and city, and constructed a comprehensive evaluation index system for patch selection. Taking into account the service function of ecosystem areas, the water balance equation [65,66], food supply, water production, soil protection, habitat protection and aquatic recreation [67], as well as factors such as the value of biodiversity conservation, security of water resources, etc. Soil protection [68] were integrated into the ecological area assessment indicators by GIS. Previous literature has extensively considered factors such as spatial structure [69] and landscape connectivity [70].

GIS in UGS

Urban greenspaces are widely associated with positive effects on human health and well-being. Depending on the discipline, pathway, and context, they are typically examined using one of three types of data sources [71-74]. First, data collected through large-scale questionnaires that reflect individual people’s perceptions of greenspace, for example of their residential neighborhood, are typical of environmental psychology research [75,76]. Second, vegetation indices derived from satellite imagery, such as the Normalized Difference Vegetation Index (NDVI), are commonly employed in epidemiological studies to study the abundance of vegetation around people’s homes (76-79). Finally, Land Use / Land Cover (LULC) maps that describe the land surface in distinct categories, such as OpenStreetMap (OSM), are frequently used in city planning or policy assessment to quantify the availability, accessibility, or size of formal greenspaces (78, 80-83).

While environmental perceptions from questionnaires are critical in the study of human activities (81,84), such data are difficult to scale due to time, cost, geographic coverage, and spatial extent limitations. NDVI and LULC maps such as OSM, on the other hand, are freely available worldwide and are regularly updated over time, making them valuable for assessing the availability or accessibility of green spaces on a large scale or prioritizing sites for interventions [84,85,86]. Although LULC maps often only represent formal green spaces such as parks and urban forests, it has been shown that informal and small-scale green spaces or green streets also benefit people (73-74-75-78-86-87). Furthermore, while both NDVI and LULC maps are essential for green space studies, they may not reflect subjective human perception (29-75-88-89-90). Although, to the best of our knowledge, recent work has attempted to incorporate the human perspective into large-scale green space studies using street-level images (73-75-76-91). Computer vision techniques such as automated object recognition and scene recognition were primarily used, which do not take into account the subjectivity of human perception.

Among all vegetation indices derived from satellite images, the Normalized Difference Vegetation Index (NDVI) is the most widely used (78). NDVI is an objective remote sensing index that detects vegetation by calculating the difference between red and near-infrared light reflected from the land surface. NDVI maps are often obtained from Landsat or Sentinel satellite missions. Both missions regularly provide global open data, with the European Sentinel-2 mission providing data at a high resolution of 10 m (92,93). Alternatives to the NDVI are the Green Ratio Vegetation Index (GVRI) (75), the Soil Adjusted Vegetation Index (SAVI) (73) and the Enhanced Vegetation Index (EVI) (75). Indices such as the NDVI are particularly relevant for studying the presence or availability of green spaces, for example near homes or along their chosen routes, as captured in GPS tracks (94-75-95-96).

Conclusion

The use of geographic information systems (GIS) and remote sensing (RS) plays a very important role in the management and development of urban green spaces. These technologies can help urban planners and managers make better decisions in the design, maintenance and optimization of green spaces by creating accurate maps of existing green spaces and identifying and analyzing the spatial distribution of urban green spaces for planning and development. Also identify areas that lack urban green space. By using indicators such as NDVI to monitor vegetation changes and the health of green spaces, you can monitor the health of trees and plants, prevent diseases and pests, and provide the public with up-to-date information about urban green spaces and their impact on use VGI (Citizen-Oriented GIS) enabled citizens to participate in the protection and maintenance of green spaces. The use of GIS and RS can lead to greater efficiency and lower costs in the management of urban green spaces. and at the same time, it can improve the quality of life of citizens.

References

1. Li, Y. 2005, Thinking of developing urban planning theory. Urban Plan., 5, 34–38. 2.
2. Shahtahmassebi, A.R.; Li, C.; Fan, Y.; Wu, Y.; Gan, M.; Wang, K.; Malik, A.; Blackburn, G.A. 2021, Remote sensing of urban green spaces: A review. Urban For. Urban Green., 57, 126946.
3. Shafique, M.; Xiaowei, L.; Jian, Z. 2020, Photovoltaic-green roofs: A review of benefits, limitations, and trends. J. Sol. Energy, 202, 485–497.
4. Puttinaovarat, S.; Horkaew, P.A. 2022, Geospatial platform for crowdsourcing green space area management using GIS and deep learning classification. ISPRS Int. J. Geo-Inf., 11, 208.
5. Shafique, M.; Reeho, K. 2018, Recent progress in low-impact development in South Korea: Water-management policies, challenges and opportunities. Water, 10, 435.
6. Luo, P.P.; Mu, Y.; Wang, S.T.; Zhu, W.; Binaya, K.M.; Huo, A.D.; Zhou, M.M.; Lyu, J.Q.; Hu, M.C.; Duan, W.L.; et al. 2021, Exploring sustainable solutions for the water environment in Chinese and Southeast Asian cities. Ambio., 51, 1199–1218.
7. Narain, V. 2017, Taken for a ride? Mainstreaming periurban transport with urban expansion policies. Land Use Policy, 64, 145–152.
8. Riechers, M.; Barkmann, J.; Tscharntke, T. 2018, Diverging perceptions by social groups on cultural ecosystem services provided by urban green. Landsc. Urban Plan. 175, 161–168.
9. Wei, X.D.; Wang, N.; Luo, P.P.; Yang, J.; Zhang, J.; Lin, K. 2021, Spatiotemporal assessment of land marketization and its driving forces for sustainable urban–rural development in Shaanxi Province in China. Sustainability. 13, 7755.
10. Zha, X.B.; Luo, P.P.; Zhu, W.; Wang, S.T.; Lyu, J.Q.; Zhou, M.M.; Huo, A.H.; Wang, Z.H. 2021, A bibliometric analysis of the research on Sponge City: Current situation and future development direction. Ecohydrology. 14, e2328.
11. Yang, J.; McBride, J.; Zhou, J.; Sun, Z. 2005, The urban forest in Beijing and its role in air pollution reduction. Urban For. Urban Green. 3, 65–78.
12. Dwivedi, P.; Rathore, C.S.; Dubey, Y. 2009Ecological benefits of urban forestry: The case of Kerwa Forest Area (KFA), Bhopal, India. Appl. Geogr., 29, 194–200.
13. Thompson, C.W.; Roe, J.; Aspinall, P.; Mitchell, R.; Clow, A.; Miller, D. 2012, More green space is linked to less stress in deprived communities: Evidence from salivary cortisol patterns. Landsc. Urban Plan., 105, 221–229.
14. Xiao, R.; Zhou, Z.; Wang, P.; Ye, Z.; Guo, E.; Ji, G. 2004, Application of 3S technologies in urban green space ecology. Chin. J. Ecol., 23, 71–76.
15. Groenewegen, P.P.; Van den Berg, A.E.; De Vries, S.; Verheij, R.A. Vitamin, G. 2006, Effects of green space on health, well-being, and social safety. BMC Public Health 6, 149.
16. Seto, K.C.; Woodcock, C.; Song, C.; Huang, X.; Lu, J.; Kaufmann, R. 2002, Monitoring land-use change in the Pearl River Delta using Landsat TM. Int. J. Remote Sens. 23, 1985–2004.
17. Yuan, F.; Sawaya, K.E.; Loeffelholz, B.C.; Bauer, M.E. 2005, Land cover classification and change analysis of the Twin Cities (Minnesota) Metropolitan Area by multitemporal Landsat remote sensing. Remote Sens. Environ. 98, 317–328.

18. Portillo-Quintero, C.; Sanchez, A.; Valbuena, C.; Gonzalez, Y.; Larreal, J. 2012Forest cover and deforestation patterns in the Northern Andes (Lake Maracaibo Basin): A synoptic assessment using MODIS and Landsat imagery. Appl. Geogr., 35, 152–163.
19. Hurd, J.D.; Wilson, E.H.; Lammey, S.G.; Civco, D.L. 2001, Characterization of forest fragmentation and urban sprawl using time sequential Landsat imagery. In Proceedings of the ASPRS Annual Convention; Citeseer: St. Louis, MO, USA, V., 21.
20. Miller, M.D. 2012, The impacts of Atlanta's urban sprawl on forest cover and fragmentation. Appl. Geogr. 34, 171–179.
21. Davies, R., Barbosa, O., Fuller, R., Tratalos, J., Burke, N., Lewis, D., Warren, P.H., Gaston, K.J, 2008. City-wide relationships between green spaces, urban land use and topography. Urban Ecosyst. 11 (3), 269–287
22. Byomkesh, T., Nakagoshi, N., Dewan, A., 2012. Urbanization and green space dynamics in Greater Dhaka, Bangladesh. Landsc. Ecol. Eng. 8 (1), 45–58.
23. Kong, F., Nakagoshi, N., 2006. Spatial-temporal gradient analysis of urban green spaces in Jinan, China. Landsc. Urban Plan. 78 (3), 147–164.
24. Uy, P., Nakagoshi, N., 2007. Analyzing urban green space pattern and eco-network in Hanoi, Vietnam. Landsc. Ecol. Eng. 3 (2), 143–157.
25. McPherson, E.G., 1992. Accounting for benefits and costs of urban greenspace. Landsc. Urban Plan. 22 (1), 41–51.
26. Luo, Y., Xe, J., Yue, W., 2005. A model for the evaluation of urban green spaces' system using RS and GIS methods Seoul. In: Proceedings of the IEEE International Geoscience and Remote Sensing Symposium, pp. 1456–1459.
27. Lee, A., Maheswaran, R., 2010. The health benefits of urban green spaces: a review of the evidence. J. Public Health 33 (2), 212–222.
28. Zhou, X., Rana, M.P., 2012. Social benefits of urban green space. Manag. Environ. Qual. Int. J. 23 (2), 173–189.
29. Wolch, J.R., Byrne, J., Newell, J.P., 2014. Urban green space, public health, and environmental justice: the challenge of making cities 'just green enough'. Landsc. Urban Plan. 125, 234–244.
30. Cay, R.D., Asilioglu, F., 2014. Benefits of urban green spaces for citizens: Ankara case study, ecology of urban areas. In: Proceedings of the IV International Conference: "Ecology of Urban Areas 2014".
31. Cetin, M., 2015. Using GIS analysis to assess urban green space in terms of accessibility: case study in Kutahya. Int. J. Sustain. Dev. World Ecol. 1–5.
32. De Ridder, K., Adamec, V., Bañuelos, A., Bruse, M., Bürger, M., Damsgaard, O., Dufek, J., Hirsch, J., Lefebre, F., Perez-Lacorzana, J.M., Thierry, A., Weber, C., 2004. An integrated methodology to assess the benefits of urban green space. Sci. Total Environ. 334-335, 489–497.
33. Nowak, D.J., Crane, D.E., Stevens, J.C., 2006. Air pollution removal by urban trees and shrubs in the United States. Urban For. Urban Green. 4 (3–4), 115–123.
34. Heidt, V., Neef, M., 2008. Benefits of urban green space for improving urban climate ecology. Plan. Manag. Urban For. 84–96.
35. Sevik, H., cetin, M., 2015. Effects of water stress on seed germination for select landscape plants. Pol. J. Environ. Stud. 24.
36. Shuvo, F.K., Hakim, S.S., 2013. A proposed framework for regenerating urban green in Dhaka city. J. Bangladesh Inst. Plan. 6, 13–22 ISSN 2075-9363 Vol.December 2013.
37. Yang, J., Li, C., Li, Y., Xi, J., Ge, Q., Li, X., 2015. Urban green space, uneven development and accessibility: a case of Dalian's Xigang District. Chin. Geogr. Sci. 25 (5), 644–656.
38. Morris, K.I., Chan, A., M.C, Ooi, Oozeer, M., Abakr, Y.A., Morris, K.J.K, 2016. Effect of vegetation and waterbody on the garden city concept: an evaluation study using a newly developed city, Putrajaya, Malaysia. Comput. Environ. Urban Syst. 58, 39–51.
39. Sponge City: Current situation and future development direction. Ecohydrology 2021, 14, e2328.
40. Regional Plan Association. Shaping the Region; Regional Plan Association: New York, NY, USA, 2015.
41. Turner, T. 1992, Open space planning in London: From standards per 1000 to green strategy. Town Plan. Rev. 63, 365.
42. Tang, Y. Central Park New York City USA. Chin. Landsc. Archit. 1994, 4, 38–41. 14. Bullock, C.H. Valuing urban green space: Hypothetical alternatives and the status quo. J. Environ. Plan. Manag. 2008, 51, 15–35.
43. Thompson, C.W. 2002, Urban open space in the 21st century. Landsc. Urban Plan. 60, 59–72.
44. Mensah, C.A. Urban green spaces in Africa: Nature and challenges. Int. J. Ecosyst. 2014, 4, 1–11.
45. Peschardt, K.K.; Schipperijn, J.; Stigsdotter, U.K. 2012, Use of small public urban green spaces (SPUGS). Urban For. Urban Green. 11, 235–244.
46. James, P.; Tzoulas, K.; Adams, M.D.; Barber, A.; Box, J.; Breuste, J.; Elmqvist, T.; Frith, M.; Gordon, C.; Greening, K.L.; et al. 2009, Towards an integrated understanding of green space in the European built environment. Urban For. Urban Green. 8, 65–75.
47. Bauwelinck, M., Casas, L., Nawrot, T.S., Nemery, B., Trabelsi, S., Thomas, I., Aerts, R., Lefebvre, W., Vanpoucke, C., van Nieuwenhuyse, A., Deboosere, P., Vandenheede, H., 2021. Residing in urban areas with higher green space

is associated with lower mortality risk: a census-based cohort study with ten years of follow-up. Environ. Int. 148, 106365.
48. Senanayake, I., Welivitiya, W., Nadeeka, P., 2013. Urban green spaces analysis for development planning in Colombo, Sri Lanka, utilizing THEOS satellite imagery – a remote sensing and GIS approach. Urban For. Urban Green. 12 (3), 307–314.
49. Dong, Y., Forster, B., Ticehurst, C., 1997. Radar backscatter analysis for urban environments. Int. J. Remote Sens. 18 (6), 1351–1364
50. Zhou, X., Wang, Y.C., 2011. Spatial–temporal dynamics of urban green space in response to rapid urbanization and greening policies. Landsc. Urban Plan. 100 (3), 268–277.
51. Esbah, H., Cook, E.A., Ewan, J., 2009. Effects of increasing urbanization on the ecological integrity of open space preserves. Environ. Manag. 43 (5), 846–862.
52. Fan, P., Xu, L., Yue, W., Chen, J., 2017. Accessibility of public urban green space in an urban periphery: the case of Shanghai. Landsc. Urban Plan. 165, 177–192.
53. Abebe, M.T, Megento, T.L, 2017. Urban green space development using GIS-based multi-criteria analysis in Addis Ababa metropolis. Appl. Geomat. 9 (4), 247–261.
54. Ahmed, B., Kamruzzaman, M., Zhu, X., Rahman, M.S, Choi, K., 2013. Simulating land cover changes and their impacts on land surface temperature in Dhaka, Bangladesh. Remote Sens. 5 (11), 5969–5998.
55. Toledo-Pereyra, L.H. Raul Romero-Torres. 2006, Surgeon, teacher, and pioneer (1928–2005). J. Investig. Surg. 19, 331.
56. Apan, A.A.; Raine, S.R.; Paterson, M.S. Mapping and analysis of changes in the riparian landscape structure of the Lockyer Valley catchment, Queensland, Australia. Landsc. Urban Plan. 2002, 59, 43–57.
57. Tomlinson, R. 2007, Thinking about GIS; Esri Press: California, CA, USA, p. 6.
58. Wolf, W.J. 2000, Maryland's green infrastructure—Using landscape assessment tools to identify a regional conservation strategy. Environ. Monit. Assess. 63, 265–277.
59. Barton, C.M.; Bernabeu, J.; Aura, J.E.; Garcia, O.; La Roca, N. 2010, Dynamic landscapes, artifact taphonomy, and land use modeling in the Western Mediterranean. Geoarchaeol. Int. J. 17, 155–190.
60. Bunn, A.G.; Urban, D.L.; Keitt, T.H2000, Landscape connectivity: A conservation application of graph theory. J. Environ. Manag. 59, 265–278.
61. Wang, X.X.; Peng, L.; Su, C.J.; Xu, D.D.; Chen, T.T. 2016, Development and utilization of low-slope hilly land resources based on a landscape security pattern theory: A case study in Luxian County, Sichuan Province. Acta Ecol. Sin. 36, 3646–3654.
62. Wang, M.Y.; Li, J.L.; Zheng, Z.N.; Jiang, W.D.; Xu, L.H.; Yang, L.; Yuan, Q.X.; Lu, X.Z.; Xiao, W. 2015, Landscape pattern optimizationbased on intensity of ecological function of mud flat reclamation: A case study of Dongtai County of Jiangsu Province. Chin. J. Ecol. 34, 1943–1949.
63. Li, H.; Yi, N.; Yao, W.J.; Wang, S.Q.; Li, Z.Y.; Yang, S.H. 2011, Shangri-La county ecological land use planning based on landscape security pattern. Acta Ecol. Sin. 31, 5928–5936.
64. Li, J.F.; Li, L.; Guo, L.; Du, S.H. 2016, Assessment on the ecological suitability in Zhuhai City, Guangdong, China, based on minimum cumulative resistance model. Chin. J. Appl. Ecol. 27, 225–232.
65. Yang, T.R.; Kuang, W.H.; Liu, W.D.; Liu, A.L.; Pan, T. 2017, Optimizing the layout of eco-spatial structure in Guanzhong urban agglomeration based on the ecological security pattern. Geogr. Res., 36, 441–452.
66. Liu, X.F.; Shu, J.M.; Zhang, L.B. 2010, Research on applying minimal cumulative resistance model in urban land ecological suitability assessment: As an example of Xiamen City. Acta Ecol. Sin. 30, 421–428.
67. Shao, M.; Li, F.Z.; Li, X. 2021, Evaluation of supply and demand of green space ecosystem service function in Chengdu-Chongqing Urban agglomeration based on multi-source data. Landsc. Archit. 28, 60–66.
68. Mu, D.; Luo, P.P.; Lyu, J.; Zhou, M.; Huo, A.; Duan, W.; Nover, D.; He, B.; Zhao, X. 2020, Impact of temporal rainfall patterns on flash floods in Hue City, Vietnam. J. Flood Risk Manag. 14, e12668.
69. Peng, J.; Li, H.L.; Liu, Y.X.; Hu, Y.N.; Yang, Y. 2020, Identification and optimization of ecological security pattern in Xiong'an New Area. Acta Geogr. Sin. 73, 701–710.
70. Wang, Y.Y.; Jin, X.B.; Shen, C.Z.; Bao, G.Y.; Liu, J.; Zhou, Y.K. 2019, Establishment of an ecological security pattern in the eastern-developed regions: A case study of the Sunan District. Acta Ecol. Sin. 39, 2298–2310.
71. Zhu, J.; Su, J.; Yin, H.W.; Kong, F.H. 2020, Construction of Xuzhou ecological network based on comprehensive sources identification and multi-scale nesting. J. Nat. Resour. 35, 1986–2001.
72. Wu, M.Q.; Hu, M.M.; Wang, T.; Fan, C.; Xia, B.C. 2019, Recognition of urban ecological source area based on ecological security pattern and multi-scale landscape connectivity. Acta Ecol. Sin. 39, 4720–4731.
73. Labib, S. M., Lindley, S., & Huck, J. J. 2020. Spatial dimensions of the influence of urban green-blue spaces on human health: A systematic review. Environmental Research, 180, Article 108869.
74. Nieuwenhuijsen, M. J., Khreis, H., Triguero-Mas, M., Gascon, M., & Dadvand, P. 2017. Fifty shades of green: Pathway to healthy urban living. Epidemiology, 28(1), 63–71.
75. Markevych, I., Schoierer, J., Hartig, T., Chudnovsky, A., Hystad, P., Dzhambov, A. M., de Vries, S., Triguero-Mas, M., Brauer, M., Nieuwenhuijsen, M. J., Lupp, G., Richardson, E. A., Astell-Burt, T., Dimitrova, D., Feng, X., Sadeh,

M., Standl, M., Heinrich, J., & Fuertes, E. 2017. Exploring pathways linking greenspace to health: Theoretical and methodological guidance. Environ Res, 158, 301–317.
76. Zhang, L., Tan, P. Y., & Richards, D. 2021. Relative importance of quantitative and qualitative aspects of urban green spaces in promoting health. Landscape and Urban Planning, 213.
77. Kruize, H., Van Kamp, I., Van den Berg, M., Van Kempen, E., Wendel-Vos, W., Ruijsbroek, A., Swart, W., Maas, J., Gidlow, C., Smith, G., Ellis, N., Hurst, G., Masterson, D., Triguero-Mas, M., Cirach, M., Grazuleviciene, R., Van den Hazel, P., & Nieuwenhuijsen, M. 2020. Exploring mechanisms underlying the relationship between the natural outdoor environment and health and well-being - results from the phenotype project. Environment International, 134, Article 105173.
78. Larkin, A., & Hystad, P. 2019. Evaluating street view exposure measures of visible green space for health research. J Expo Sci Environ Epidemiol, 29(4), 447–456.
79. Helbich, M., Yao, Y., Liu, Y., Zhang, J., Liu, P., & Wang, R. 2019. Using deep learning to examine street view green and blue spaces and their associations with geriatric depression in beijing, china. Environ Int, 126, 107–117.
80. Roberts, H. V. 2017. Using Twitter data in urban green space research: A case study and critical evaluation. Applied Geography, 81, 13–20.
81. Dadvand, P., Nieuwenhuijsen, M. J., Esnaola, M., Forns, J., Basagana, X., Alvarez Pedrerol, M., Rivas, I., Lopez-Vicente, M., De Castro Pascual, M., Su, J., Jerrett, M., Querol, X., & Sunyer, J. 2015. Green spaces and cognitive development in primary schoolchildren. Proceedings of the National Academy of Sciences of the United States of America, 112(26), 7937–7942.
82. Kabisch, N., & Haase, D. 2014. Green justice or just green? provision of urban green spaces in berlin, germany. Landscape and Urban Planning, 122, 129–139.
83. Wood, L., Hooper, P., Foster, S., & Bull, F. 2017. Public green spaces and positive mental health - investigating the relationship between access, quantity and types of parks and mental wellbeing. Health & Place, 48, 63–71.
84. Taubenbock, ¨ H., Reiter, M., Dosch, F., Leichtle, T., Weigand, M., & Wurm, M. 2021. Which city is the greenest? a multi-dimensional deconstruction of city rankings (p. 89). Environment and Urban Systems: Computers.
85. Flowers, E. P., Freeman, P., & Gladwell, V. F. 2016. A cross-sectional study examining predictors of visit frequency to local green space and the impact this has on physical activity levels. BMC Public Health, 16, 420.
86. Fongar, C., Aamodt, G., Randrup, T. B., & Solfjeld, I. 2019. Does perceived green space quality matter? linking norwegian adult perspectives on perceived quality to motivation and frequency of visits. Int J Environ Res Public Health, 16(13).
87. Luo, S., & Patuano, A. 2023. Multiple ecosystem services of informal green spaces: A literature review. Urban Forestry & Urban Greening, 81.
88. Rao, M., Prasad, S., Adshead, F., & Tissera, H. 2007. The built environment and health. The Lancet, 370(9593), 1111–1113.
89. Leslie, E., Sugiyama, T., Ierodiaconou, D., & Kremer, P. 2010. Perceived and objectively measured greenness of neighbourhoods: Are they measuring the same thing? Landscape and Urban Planning, 95(1–2), 28–33.
90. Kothencz, G., & Blaschke, T. 2017. Urban parks: Visitors' perceptions versus spatial indicators. Land Use Policy, 64, 233–244.
91. Rzotkiewicz, A., Pearson, A. L., Dougherty, B. V., Shortridge, A., & Wilson, N. 2018. Systematic review of the use of google street view in health research: Major themes, strengths, weaknesses and possibilities for future research. Health & Place, 52, 240–246.
92. Biljecki, F., & Ito, K. 2021. Street view imagery in urban analytics and gis: A review. Landscape and Urban Planning, 215.
93. Lu, Y. 2019. Using google street view to investigate the association between street greenery and physical activity. Landscape and Urban Planning, 191.
94. Sripada, R. P., Heiniger, R. W., White, J. G., & Meijer, A. D. 2006. Aerial color infrared photography for determining early in-season nitrogen requirements in corn. Agronomy Journal, 98(4), 968–977.
95. Huete, A., Didan, K., Miura, T., Rodriguez, E. P., Gao, X., & Ferreira, L. G. 2002. Overview of the radiometric and biophysical performance of the MODIS vegetation indices. Remote Sensing of Environment, 83, 195–213.
96. Robinson, O., Tamayo, I., de Castro, M., Valentin, A., Giorgis-Allemand, L., Hjertager Krog, N., Marit Aasvang, G., Ambros, A., Ballester, F., Bird, P., Chatzi, L., Cirach, M., Dedele, A., Donaire-Gonzalez, D., Grazuleviciene, R., Iakovidis, M., Ibarluzea, J., Kampouri, M., Lepeule, J., Maitre, L., McEachan, R., Oftedal, B., Siroux, V., Slama, R., Stephanou, E. G., Sunyer, J., Urquiza, J., Vegard Weyde, K., Wright, J., Vrijheid, M., Nieuwenhuijsen, M., & Basagana, X. 2018. The urban exposome during pregnancy and its socioeconomic determinants. Environ Health Perspect, 126 (7), Article 077005.
97. Spotswood, E. N., Benjamin, M., Stoneburner, L., Wheeler, M. M., Beller, E. E., Balk, D., McPhearson, T., Kuo, M., & McDonald, R. I. 2021. Nature inequity and higher covid-19 case rates in less-green neighbourhoods in the United States. Nature Sustainability.
98. Roberts, H., & Helbich, M. 2021. Multiple environmental exposures along daily mobility paths and depressive symptoms: A smartphonebased tracking study. Environment International, 156, Article 106635.

Advanced Engineering Days

aed.mersin.edu.tr

Evaluating the performance of remote sensing to monitor the severity of drought through the comparison of three drought severity indicators (NDDI, NDWI and NDVI) in the Karkheh basin

Vahid Kakapor [1], Hossein Fekrat *[1], Maryam Sadeghi [1], Khalil Valizadeh Kamran [1], Maryam Bayati Khatibi [1]

[1] University Tabriz, Faculty of Planning and environmental science, Department of Remote sensing and geographic information system, Tabriz, Iran. v.kakapor@gmail.com, Hosseinf7181@gmail.com, sadegi.maryam92@gmail.com, valizadeh@tabrizu.ac.ir, m_bayati@tabrizu.ac.ir

Cite this study: Kakapor, V., Fekrat, H., Sadeghi, M., Valizadeh Kamran, K., & Bayati Khatibi, M. (2024). Evaluating the performance of remote sensing to monitor the severity of drought through the comparison of three drought severity indicators (NDDI, NDWI and NDVI) in the Karkheh basin. Advanced Engineering Days, 9, 772-777

Keywords
Drought monitoring
Remote sensing
NDDI
NDVI
NDWI
Karkheh basin

Abstract

Droughts are the most complex, slow-onset, and devastating natural disasters that affect more people than ever before. Recently, remote sensing has played a role in providing a large amount of data for drought risk monitoring at large spatial and temporal scales. This study was conducted with the aim of monitoring the severity of drought in Karkheh basin based on the results of calculating the Normalized Difference Drought Index (NDDI) in the years 2013, 2016, 2019 and 2021. The method used to obtain NDDI was by subtracting the Normalized Difference Index of Vegetation (NDVI) by the Normalized Difference Index of Water (NDWI) and then dividing by NDVI plus NDWI. The results were shown in five drought severity classes: very low, low, medium, high and very high. The year 2019 had the highest amount of drought severity and the areas classified as high and very severe have an area of 238 km2and 6205 km2, respectively. These results show that many areas have the potential to experience drought in Karkheh basin. The results of this analysis can be an input to carry out mitigation measures such as building reservoirs and infiltration wells, maintaining the karst area and increasing vegetation against drought disasters in the future.

Introduction

In recent years, global warming, increased water consumption, decreased rainfall, and lack of attention to smart agricultural techniques have affected the water resources crisis. The above factors lead to the occurrence of different types of drought [1, 2]. Drought also affects climate change, soil conditions, human activities (land use), overgrazing and other factors in different parts of the world: hydrological, meteorological, agricultural, and socio-economic [3]. The effects of drought on geographical scales and climate regimes are evident all over the world. For example, from 1980 to 2013, the United States experienced more than 18 droughts that caused more than $250 billion in damage [3, 4, 5]. In sub-Saharan Africa, several droughts have occurred, including the droughts of 1982–1983 and 1991–1992, which were reported to be the most severe meteorological droughts of the 20th century [6, 7]. Also, drought is one of the most critical environmental stresses that reduces crop productivity [8]. However, drought stress may increase in different regions [9], information and maps from remote sensing can be used as an indicator to assess the level of disease or drought effects [10].Vegetation indices are the most used criteria for satellite remote sensing calculations. These indices are used to estimate vegetation cover, investigate different types of vegetation cover, and also analyze vegetation cover in an area over time [11]. Choosing suitable indicators for meteorological, agricultural and hydrological droughts has become a challenge. Selecting appropriate drought indicators is a critical step in the development of integrated drought monitoring systems that can enable effective drought risk monitoring and management and help implementation [12]. Drought is an important problem for most dry countries, and Iran is one of these countries [13]. Iran is located in the dry and semi-arid belt, where

about 65% of the country has a dry and semi-arid climate. Its average rainfall is about 250 mm, which is almost a third of the average rainfall of the world's dry areas [13, 14]. According to the country's comprehensive water plan studies, atmospheric precipitation is the main source of Iran's water resources. Of this amount, about 71% of it is removed as evaporation and only a part of it is harvested for the use of agriculture, industry, mining and drinking. The decrease of rainfall on one hand and its inappropriate spatial distribution on the other hand have caused many parts of Iran to be in the dry climate zone. In addition, the frequent droughts in recent years have made water supply in the country one of the most important challenges. Karkheh watershed is also one of the places affected by the drought problem [15]. This basin, which is considered one of the four large basins of the country, is located in the west of the country and in the central and southwestern regions of the Zagros mountains. Due to the fact that the Karkheh basin is located in several provinces, including Hamedan, Kermanshah, Kurdistan, Ilam, Merkazi, Lorestan and Khuzestan provinces, and the Karkheh river is considered the third largest river in Iran after the Karun and Dez rivers in terms of watershed and from This direction plays an important role in providing the needed water for a large part of the country, for this reason, continuous droughts in this basin can cause many challenges in the economic sector and ultimately environmental, economic and social crises in a large part of the country. Which depend on the water of this basin. Therefore, the current research tries to investigate and evaluate the agricultural drought in Karkheh watershed by using NDVI, NDWI and NDDI indices. Therefore, the results of this research can determine the ability of these profiles to identify agricultural droughts and the possibility of using them for drought monitoring in the region.

Material and Method

Study area

The Karkheh River Basin (KRB) is located in the southwest of Iran, between 30◦ 580 to 34◦ 560 N latitude and 46◦ 060 to 49◦ 100 E longitude. The area is about 47732 km2, with considerable variation in elevation, from a minimum of -69 m in the south to a maximum of 3623 m in the Karin Mountains in the north (Figure 1). The climate of the basin is semi-arid to arid. Most of the agricultural area in the upper KRB is rained and a large part of the region's agricultural livelihoods is based on dry land farming systems.

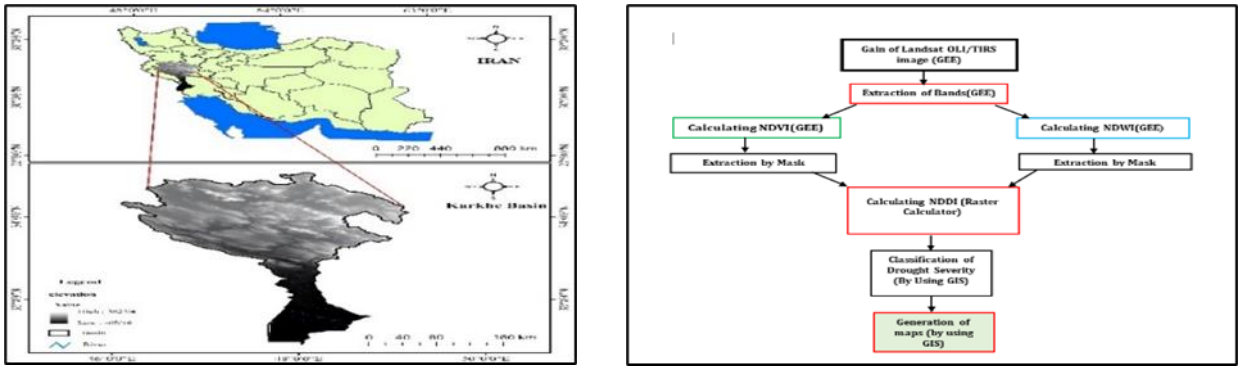


Figure 1. Figure to the left of the study area and the left -hand -to -right area of the work process.

Materials and Data Analysis

The tools used in this research were Google Earth Engine and ArcGIS. The materials needed were Landsat 8 OLI/TIRS satellite imagery that has been radio metrically corrected (Top of Atmosphere/ToA Reflectance) for the four years (2013_2016_2019_2021) in the Karkheh basin from the United States Geological Survey (USGS) and the Earth Engine Data Catalog that has been carried out.

NDVI: Drought Severity can be evaluated using remote sensing as the crop plants' reflectance features vary due to physiological and morphological changes resulting from water stress in plants and soil [16]. The NDVI is the normalized reflectance difference between the two spectral bands, i.e., near-infrared (NIR) and visible red bands [17, 18]. Is used mainly for monitoring vegetation of earth's surface [19, 20]. The concept of NDVI was given by Deering [21] and Tucker [66], and the ratio is expressed in Eq. (1): NIR and RED represent reflectance in the near-infrared and red bands, respectively [22, 23]. The temporal change in NDVI-based drought indices were obtained using satellite images and a GIS tool which was further used for assessing drought severity for the study area.

$$\text{NDVI} = \rho NIR - \rho\text{RED} / \rho NIR + \rho\text{RED} \quad (1)$$

NDWI: The NDWI index was used to identify the presence of open water features by remote sensing using NIR and green (G) bands [11], or NIR and short-wave infrared (SWIR) bands. The NDWI calculation formula (2). The

range of NDWI values is -1 to 1. If the NDWI value is above 0, it is an area with a water surface. Meanwhile, if the value is below 0, it is not water area [24].

$$NDWI = \rho NIR - \rho RED / \rho NIR + \rho RED \quad (2)$$

Normalized Difference Drought Index (NDDI): Normalized Difference Drought Index (NDDI) is used for drought monitoring. This index is the combination of the above two NDVI and NDWI indices [80]. The method used to obtain NDDI was by subtracting the Normalized Difference Vegetation Index (NDVI) by the Normalized Difference Water Index (NDWI) and then dividing by the NDVI plus the NDWI. The equation to get NDDI [3] is:

$$NDDI = NDVI - NDWI / NDVI + NDWI \quad (3)$$

The drought severity based on the NDDI value is divided into five classes, namely very low, low, medium, high, and very high, presented in Table 1.

Table 1. Drought severity by NDDI value

Classes	NDDI Value	Drought Severity Class
1	<-2	Very low
2	-2-0/7	Low
3	0/7-1/25	Moderate
4	1/25-3	High
5	>3	Very high

Results

Based on the analysis of the results for the years2013, 2016،2019 and 2021 the highest coefficient of variation in the NDVI is related to 2013, so that the value of this index is between 0.52-0.79. Also, the highest value of NDVI coefficient was related to 2013 and the lowest value was related to 2019 with values of 0.79 and -0.649, respectively. If the normalized difference vegetation index values are high in one place and then this index decreases the same place, this means that the vegetation cover is related to health stress or a decrease in the amount of vegetation cover or a change in land use. NDVI distribution map in Karkheh basin is presented in Figure (2). The NDWI value also varied spatially. The analysis of the NDWI for the years 2013, 2016،2019 shows that the most changes in the NDWI are related to the year 2019 with the coefficient of variation -0.74_0.79. Also, the highest NDWI value was in 2019 and the lowest NDWI value in 2016 were 0.79 and -0.65, respectively. Areas with a high value NDWI are a dense vegetation or areas with high humidity content or rivers and water bodies. In the Karkheh basin, the highest amount of moisture is related to the karst formations with high vegetation in the north of the basin and the water bodies in the south of the basin, such as the Karun Dam. As well as areas with a low value NDWI indicate a lack of humidity in the desired location these results follow the findings of previous studies [25]. NDWI distribution map in Karkheh basin is presented in Figure 3.

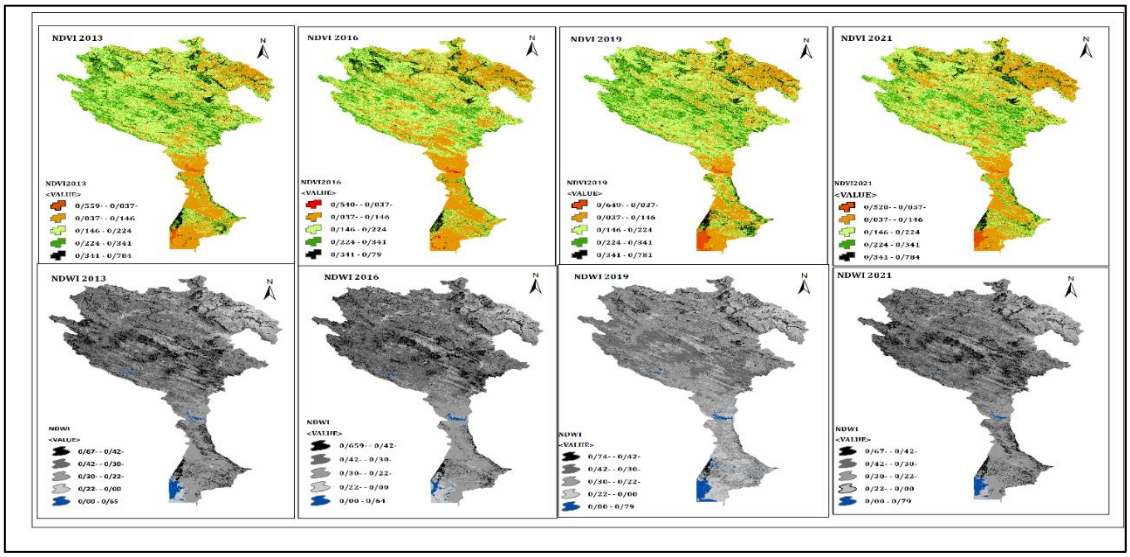


Figure 2. Map of NDVI distribution in Karkheh basin

Figure3. Map of NDWI distribution in Karkheh basin

After the results of the NDVI and NDWI calculations were obtained, the NDDI calculation was carried out to determine the drought severity in Karkheh basin by subtracting the NDVI by the NDWI and then dividing it by the NDVI plus the NDWI. The NDDI calculation in Karkheh basin resulted in 5 drought severity classes: very low, low, medium, high, and very high. Most areas of the Karkheh basin have low drought severity for four years, but some places have high to very high drought severity. A map of the distribution of drought severity based on NDDI calculations is presented in Figure 4.

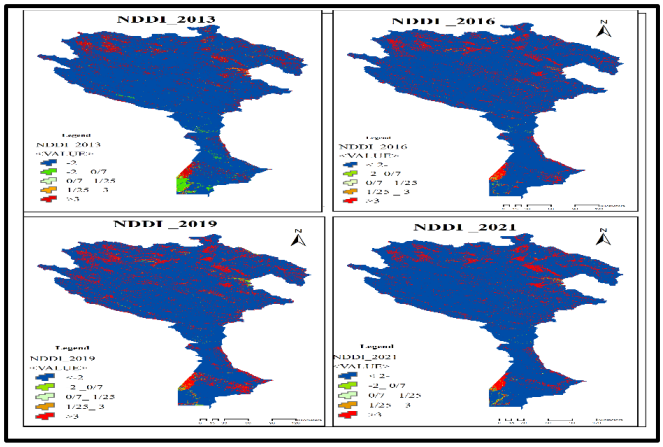
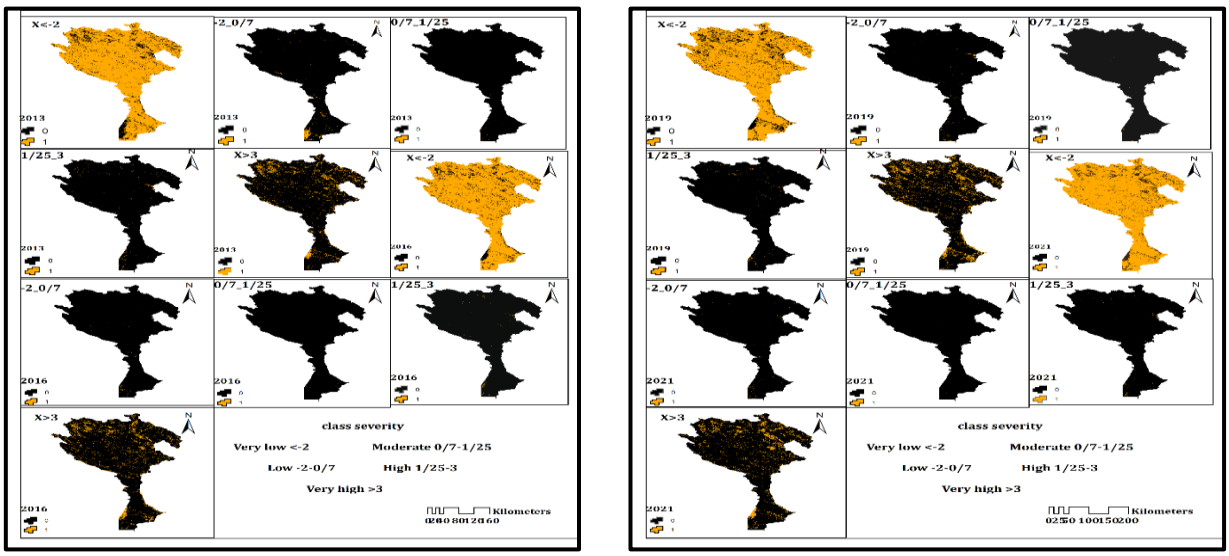


Figure 4. Map of the distribution NDDI

The area with very low drought severity with an NDDI value of less than -2 for the years 2013, 2016, 2019 and 2021 were 42290, 42720,40677 and 42815 km2 respectively, that Most of this area was located in the north of the basin in Kermanshah and Hamedan provinces and the south of the basin in Khuzestan province. Areas with low severity and moderate severity they did not have a large area, so that the largest area of the two classes corresponds to the year 2019 and 2016, respectively. The high severity level with NDDI values of 1.25 to 3 mostly located in the northern and South regions Meanwhile, the very high intensity level with NDDI values above 3 in 2019 with an area of 6205 km2 is the highest. The distribution of each drought severity level in the Karkheh basin can be seen in Figure 5. The area and 4. Percentage of each class are presented in Table 2.

Table 2. Area and percentage of each drought severity class

NO	Drought Severity Classes	A (Km^2) 2013	A (Km^2) 2016	A (Km^2) 2019	A (Km^2) 2021	P (%) 2013	P (%) 2016	P (%) 2019	P (%) 2021
1	VLS	42290	42720	40677	42815	88/67	89/58	85/2	89/7
2	LS	66	47	205	95	1/41	0/189	0/437	0/279
3	MS	25	43	21	18	0/086	0/029	0/043	0/043
4	HS	29	138	238	10	0/0601	0/29	0/568	0/243
5	VHS	4391	4678	**6205**	4630	9/22	9/890	**13/68**	9/73



Figur5. Distribution map of each drought severity class

Discussion

Drought is a slow-onset phenomenon; thus, its effects are not immediate. For this reason, quantifying its intensity and describing its behavior is a complex task compared to other natural phenomena. In this work, we conclude that the NDDI calculated with Landsat OLI images for monitoring and quantifying drought in the Karkheh basin. The average rainfall of the basin in 2019 was lower than in 2013, 2016 and 2021, and this decrease in the average amount of rainfall had an effect on the amount of soil moisture, vegetation covers and water reserves of the reservoirs. Therefore, the severity of the drought for 2019 in two classes VHS and HS was higher than in 2013, 2016 and 2021 years.

References

1. Shi, S., Yu, J., Wang, F., Wang, P., Zhang, Y., & Jin, K. (2021). Quantitative contributions of climate change and human activities to vegetation changes over multiple time scales on the Loess Plateau. Science of the Total Environment, 755, 142419.
2. Orimoloye, I. R., Belle, J. A., Olusola, A. O., Busayo, E. T., & Ololade, O. O. (2021). Spatial assessment of drought disasters, vulnerability, severity and water shortages: a potential drought disaster mitigation strategy. Natural Hazards, 105, 2735-2754.
3. Masih, I., Maskey, S., Mussá, F. E. F., & Trambauer, P. (2014). A review of droughts on the African continent: a geospatial and long-term perspective. Hydrology and earth system sciences, 18(9), 3635-3649.
4. Svoboda, M. D., Fuchs, B. A., Poulsen, C. C., & Nothwehr, J. R. (2015). The drought risk atlas: enhancing decision support for drought risk management in the United States. Journal of Hydrology, 526, 274-286.
5. Svoboda, M.; Fuchs, B.A. Handbook of Drought Indicators and Indices Integrated Drought Management Programme (IDMP), Integrated Drought Management Tools and Guidelines Series 2; World Meteorological Organization (WMO): Geneva, Switzerland; Global Water Partnership (GWP): Stockholm, Sweden, 2016.
6. Monnik, K. Role of Drought Early Warning Systems in South Africa's Evolving Drought Policy. 2000. Available online: https://www.researchgate.net/publication/253446727 (accessed on 1 May 2021).
7. West, H.; Quinn, N.; Horswell, M. Remote Sensing for Drought Monitoring & Impact Assessment: Progress, Past Challenges and Future Opportunities. Remote Sens. Environ. 2019, 232, 111291.
8. Azmat, A., Yasmin, H., Hassan, M. N., Nosheen, A., Naz, R., Sajjad, M., ... & Akhtar, M. N. (2020). Co-application of bio-fertilizer and salicylic acid improves growth, photosynthetic pigments and stress tolerance in wheat under drought stress. PeerJ, 8, e9960.
9. Skendžić, S., Zovko, M., Lešić, V., Pajač Živković, I., & Lemić, D. (2023). Detection and evaluation of environmental stress in winter wheat using remote and proximal sensing methods and vegetation indices—a review. Diversity, 15(4), 481.
10. Andaryani S, Trolle D, Asl AM. 2019. Application of hyperion data for investigating agriculture field stress to drought conditions. 2516-2314.EasyChair.
11. Asokan, A., & Anitha, J. (2019). Change detection techniques for remote sensing applications: a survey. Earth Science Informatics, 12(2), 143–160. doi:10.1007/s12145-019-00380-5
12. Mukhawana, M. B., Kanyerere, T., & Kahler, D. (2023). Review of in-Situ and remote sensing-based indices and their Applicability for integrated drought monitoring in South Africa. Water, 15(2), 240.
13. Sabzevari,A. (2015).analysis of the Effect of Drought Z Normal of Rainfall in Geographic Information Systems Systems in Kashan Region. Physical Geography Quarterly.105_124.
14. Khosravi,H., Eskandari Dameneh, H., Eskandari Dameneh, H., Borji, M., Nakhaee Nejadfard, S. (2018). Drought Trend Assessment in Riverheads of Karkheh and Dez Basins based on Streamflow Drought Index (SDI). Desert Ecosystem Engineering Journal. DEEJ, 7 (2) 45-54
15. Neisi, M., Bijani, M., Abbasi, E., Mahmoudi, H., & Azadi, H. (2020). Analyzing farmers' drought risk management behavior: Evidence from Iran. Journal of Hydrology, 590, 125243.
16. Patil, P. P., Jagtap, M. P., Khatri, N., Madan, H., Vadduri, A. A., & Patodia, T. (2024). Exploration and advancement of NDDI leveraging NDVI and NDWI in Indian semi-arid regions: A remote sensing-based study. Case Studies in Chemical and Environmental Engineering, 9, 100573.
17. Rouse Jr, J. W., Haas, R. H., Deering, D. W., Schell, J. A., & Harlan, J. C. (1974). Monitoring the vernal advancement and retrogradation (green wave effect) of natural vegetation (No. E75-10354).
18. Tucker, C. J. (1979). Red and photographic infrared linear combinations for monitoring vegetation. Remote sensing of Environment, 8(2), 127-150.
19. Kulkarni, S. S., Wardlow, B. D., Bayissa, Y. A., Tadesse, T., Svoboda, M. D., & Gedam, S. S. (2020). Developing a remote sensing-based combined drought indicator approach for agricultural drought monitoring over Marathwada, India. Remote Sensing, 12(13), 2091.
20. Halder, B., Tiyasha, T., Shahid, S., & Yaseen, Z. M. (2022). Delineation of urban expansion and drought-prone areas using vegetation conditions and other geospatial indices. Theoretical and Applied Climatology, 149(3), 1277-1295.

21. Deering, D. W. (1978). RANGELAND REFLECTANCE CHARACTERISTICS MEASURED BY AIRCRAFT AND SPACECRAFTSENSORS. Texas A&M University.
22. Gu, Y., Brown, J. F., Verdin, J. P., & Wardlow, B. (2007). A five-year analysis of MODIS NDVI and NDWI for grassland drought assessment over the central Great Plains of the United States. Geophysical research letters, 34(6).
23. Chandrasekar, K., & Sesha Sai, M. V. R. (2015). Monitoring of late-season agricultural drought in cotton-growing districts of Andhra Pradesh state, India, using vegetation, water and soil moisture indices. Natural Hazards, 75, 1023-1046.
24. Jiang, T., Su, X., Singh, V. P., & Zhang, G. (2022). Spatio-temporal pattern of ecological droughts and their impacts on health of vegetation in Northwestern China. Journal of Environmental Management, 305, 114356.
25. Salehnia, N., Zare, H., Kolsoumi, S., & Bannayan, M. (2018). Predictive value of Keetch-Byram Drought Index for cereal yields in a semi-arid environment. Theoretical and Applied Climatology, 134(3), 1005-1014.

Advanced Engineering Days

aed.mersin.edu.tr

Comparing the efficiency of Object-Based fuzzy operators in extraction of urban built-up area of Tabriz metropolis

Mostafa Mousapour*[1], Bakhtiar Feizizadeh [2]

[1] *University of Tabriz, Department of Remote Sensing and Geographical Information System, Iran, mostafa427@gmail.com, bakhtiar.feizizadeh@gmail.com*

Cite this study: Feizizadeh, B., & Mousapour, M. (2024). Comparing the efficiency of Object-Based fuzzy operators in extraction of urban built-up area of Tabriz metropolis. Advanced Engineering Days, 9, 778-781

Keywords
Object-Based
Fuzzy
Urban Built-Up
Sentinel-2
Tabriz

Abstract

Urban growth results from complex interactions between humans and the physical and natural environment. satellite image processing has been proposed as an efficient tool for identifying and extracting land cover maps and identifying changes over time. The aim of this research is Comparing the efficiency of Object-Based fuzzy operators in extraction of urban built-up area of Tabriz metropolis. In this research, a multi-spectral image with a spatial resolution of 10 meters from the Sentinel 2 satellite of Tabriz metropolis was used. eCognition software was used for segmentation and classification based on object-Based fuzzy operators. At this stage, segmentation was carried out based on different scales, shape factor and compactness factor in order to reach the optimal scale, shape factor and compactness factor. After reaching the optimal segmentation state, training points were identified and the classification process was performed using fuzzy operators, including AND, OR, MGE, MAR, MGWE and ALP. The most appropriate segmentation included the scale of 80 and the shape factor of 0.3 and the compactness factor of 0.7. According to the results of the research, among all the methods used in this research, the fuzzy operator AND with an overall accuracy of 96.07% and a kappa coefficient of 0.9616.

Introduction

The growth of the global population has been raising surging demand in expanding urban areas. It has been estimated that urban areas have expanded by about 0.25 million km^2 in the past two decades, with a further 0.6 million km^2 expansion up until 2050 (Dong et al., 2024). Urban growth results from complex interactions between humans and the physical and natural environment. The physical characteristics of the natural environment are consistently utilized and altered by human settlements in time and space. The geographical distribution of human settlements at local and regional scales and its changing trends from the past to the present are essential spatial information for land use planning, as well as transportation, environmental planning, and other uses. The information will support long-term planning and policy decisions for the mitigation of the negative environmental and socioeconomic effects of urban growth (Kim et al., 2024). Although cities occupy 3% of the Earth's land surface, they are responsible for 60%–80% of energy usage and 70% of greenhouse gas emissions. The frequent city renewal and rapid urban growth lead to substantial changes within cities. These alterations can have adverse repercussions on the environment and ecology, e.g., urban heat island, the greenhouse effect, and resource depletion (Li et al., 2024). In recent years, satellite image processing has been proposed as an efficient tool for identifying and extracting land cover maps and identifying changes over time. Land cover classification using satellite images can be carried out using pixel-based or object-based methods. In pixel-based processing of images, single-pixel information is the basis and criterion of classification. In object-based processing, spectral and spatial values and other existing information in a similar set of pixels, called an object or phenomenon, are the basis of processing. In addition to spectral information, other information such as context, shape, size and direction, is also used in classification by object-based processing. Due to problems with pixel-based classification, object-based classification has been increasingly used by many researchers over the past two decades (Arabi Aliabad et al., 2022). In terms of classification methods, with the improvement of remote sensing image resolution, the advantages of Object-Based classification have gradually showed up. Not only does it avoid the 'salt and pepper

phenomenon' of traditional pixel-based classification methods, but also, compared with traditional pixel-based classification methods that can only use pixel spectral information for classification, Object-Based classification can integrate texture information, geometry, and contextual relationships for classification; consequently, it finds effective application in target extraction and land classification (Zhao et al., 2024). A rich volume of research has attempted to detect urban growth (Byun & Kim, 2022; Kim et al., 2022; Lu, Mausel, Brondizio, & Moran, 2004; Naik, Kominers, Raskarb, Glaesere, & Hidalgo, 2017; Reba & Seto, 2019; Viana et al., 2019; Zhan, Ma, & Zhang, 2019; Zhang et al., 2018). The aim of this research is Comparing the efficiency of Object-Based fuzzy operators in extraction of urban built-up area of Tabriz metropolis.

Material and Method

Case study

The metropolis of Tabriz with an area of about 2,455,913 hectares is the largest metropolis in northwest Iran, which is located at the geographical coordinates of 46 degrees 17 minutes east and 38 degrees 05 minutes north of the Greenwich meridian. This city is located in the northeastern part of Lake Urmia and 150 kilometers south of Jolfa, located on the border of Iran and the Republic of Azerbaijan. The metropolis of Tabriz is bounded from the south by the solitary and always snow-filled Sahand mountain range and from the northeast by the Eynali mountain range. Aji Chai River (Talkhe rood) passes through the north and northeast part of Tabriz and after passing a significant distance in the plain of Tabriz, it flows into Lake Urmia. The metropolis of Tabriz is located in a wide plain and on the soft bed of Mehran River and Aji Chai Valley, which covers an area of about 300 square kilometers. Figure 1 shows the location of Tabriz metropolis in Iran and East Azarbaijan province.

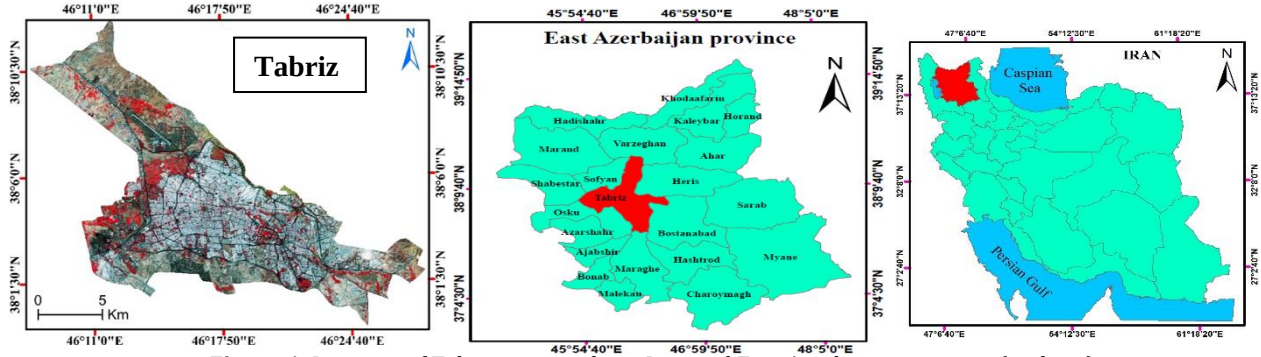


Figure 1. Location of Tabriz metropolis in Iran and East Azarbaijan province (authors)

Methodology

In this research, a multi-spectral image with a spatial resolution of 10 meters from the Sentinel 2 satellite including bands 2 (blue), 3 (green), 4 (red) and 8 (near infrared) of Tabriz metropolis was used on April 27, 2024. The image used is related to the processing level 2 of the European Space Agency. After downloading the image from the archive of the European Space Organization, in the SNAP software environment, which is special for the processing of Sentinel satellite images, using the MTD_MSIL2A.xml file in the relevant image folder, the desired image is called and multi-spectral bands with spatial resolution 10 meters of the image, including bands 2, 3, 4 and 8, were selected and cut using the shape file of the studied area, and the output image was saved in TIFF format. Considering that the satellite image used is related to the level 2 processing data of the Sentinel 2 satellite, there was no need to perform pre-processing operations because these data are provided to the users in a corrected form. eCognition software was used for segmentation and classification based on object-Based fuzzy operators. At this stage, segmentation was carried out based on different scales, shape factor and compactness factor in order to reach the optimal scale, shape factor and compactness factor. After reaching the optimal segmentation state, training points were identified and the classification process was performed using fuzzy operators, including AND, OR, MGE, MAR, MGWE and ALP. Then, using ground truth sample points, accuracy assessment was done for all production maps. In the post-processing stage, using the majority filter with dimensions of 3 x 3 pixels, individual pixels that caused noise in the classification process were removed. Finally, based on production maps, the fuzzy operator with the highest classification accuracy was identified.

Results

In order to perform the image classification process based on Object-Based fuzzy operators, the satellite image of the study area in 2024, which was saved in TIFF format, was called in the eCognition software environment and saved as a project. In order to create and produce visual objects, segmentation operations were carried out in different scales, compactness coefficients and shape coefficients to achieve optimal segmentation. In this step, the

multiresolution segmentation method was used to segment the image. The most appropriate segmentation included the scale of 80 and the shape factor of 0.3 and the compactness factor of 0.7. Because in scales higher than 80, the construction of visual objects was not done correctly, so that several distinct complications were placed in one piece, and in scales less than 80, in some cases, one complication was placed in several pieces. took Figures 2 to 5 show segmentation in different scales, including 120, 100, 70 scales, as well as the average image objects resulting from optimal segmentation.



Figure 2. Sentinel-2 Satellite Image

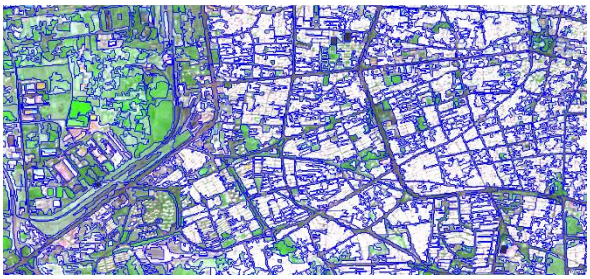


Figure 3. Segmentation with a scale of 120

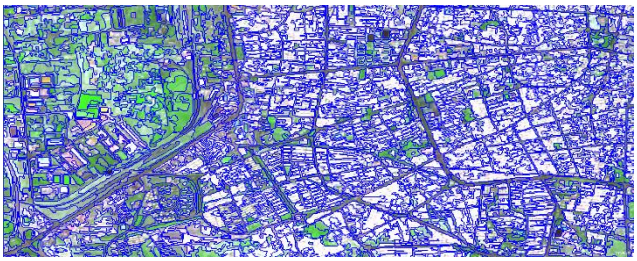


Figure 4. Segmentation with a scale of 100

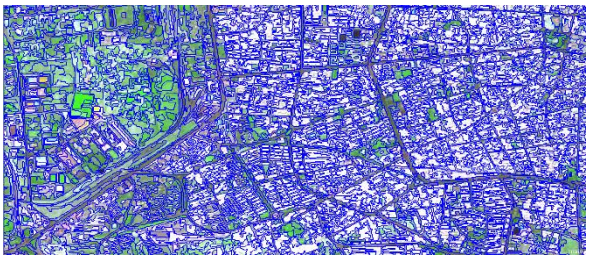


Figure 5. Segmentation with a scale of 80

After the segmentation operation, two classes of urban built-up land and unbuilt-up land were defined, and a number of points from the built-up objects in the segmentation stage were selected as training samples and a number of points were selected as ground truth samples. Figure 6 shows a number of selected points of ground truth samples.



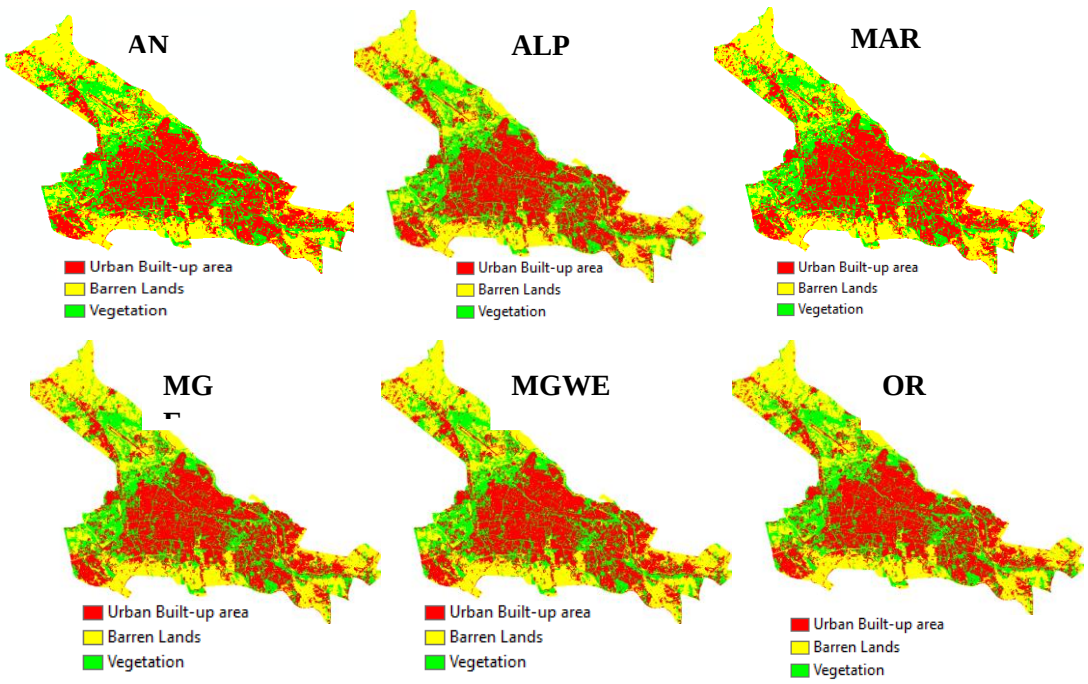
Figure 6. Selected training samples for the classes

In order to fuzzily the produced image objects, the fuzzy operators AND, OR, MGE, MAR, MGWE and ALP were defined separately and after applying each fuzzy operator, the classification operation was performed. In this step, the classification was done based on the nearest neighbor method and by selecting the mean, standard deviation, skewness and texture parameters for each band. Figures 7 to 12 show the maps produced by the Object-Based method.

After preparing a map of urban built-up lands through Object-Based fuzzy operators, the classification accuracy of each of the used operators was calculated. In order to calculate the classification accuracy of the Object-Based model through eCognition software, using selected ground Truth control points, the overall accuracy and kappa coefficient for the Object-Based model were calculated. Table 1. shows the overall accuracy and kappa coefficient obtained in this research.

Table 1. Overall accuracy and kappa coefficient

overall accuracy	kappa coefficient	fuzzy operator
96.07	*0.*9616	AND
94.22	0.9481	OR
95.07	0.9537	MGE
95.23	0.9601	MAR
95.03	0.9577	MGWE
95.52	0.9557	ALP



Discussion and Conclusion

In this research, the effectiveness of Object-Based fuzzy operators including AND, OR, MGE, MAR, MGWE and ALP was compared in the production of urban land in Tabriz. For this purpose, bands with spatial resolution of 10 meters of Sentinel 2 satellite were used. Based on the results of this research, using multi-spectral images with 10 meters resolution of Sentinel 2 satellite, it is possible to map the built-up areas of Tabriz using object-oriented model with acceptable accuracy. According to the results of the research, among all the methods used in this research, the fuzzy operator and logical sharing expression contains the lowest value of the fuzzy values with an overall accuracy of 96.07% and a kappa coefficient of 0.9616. Showed more accuracy. Therefore, according to the accuracy of the object-oriented fuzzy operators in this research, it can be said that the object-oriented processing methods of satellite images in the classification of digital satellite images, because they are mostly based on the information produced from Information to be done. Related to shape texture, position, content and geometrical features are also used in the classification process and make it possible to achieve higher accuracy. One of the most important reasons for achieving higher accuracy in object-oriented methods is checking the degree of fuzzy membership in the classification and using the points that have the highest degree of membership. In this regard, due to the heterogeneity of the environment and the presence of complexity in the urban environment, it causes confusion in pixel-based methods, but it is possible in object-oriented methods.

References

Arabi Aliabad, F., Malamiri, H. R. G., Shojaei, S., Sarsangi, A., Ferreira, C. S. S., & Kalantari, Z. (2022). Investigating the Ability to Identify New Constructions in Urban Areas Using Images from Unmanned Aerial Vehicles, Google Earth, and Sentinel-2. *Remote Sensing*, *14*(13), 3227. https://www.mdpi.com/2072-4292/14/13/3227

Dong, B., Zheng, Q., Lin, Y., Chen, B., Ye, Z., Huang, C., Tong, C., Li, S., Deng, J., & Wang, K. (2024). Integrating physical model-based features and spatial contextual information to estimate building height in complex urban areas. *International Journal of Applied Earth Observation and Geoinformation*, *126*. https://doi.org/10.1016/j.jag.2023.103625

Kim, J.-h., Kim, D., Jun, H.-J., & Heo, J.-P. (2024). The detection of residential developments in urban areas: Exploring the potentials of deep-learning algorithms. *Computers, Environment and Urban Systems*, *107*. https://doi.org/10.1016/j.compenvurbsys.2023.102053

Li, Q., Mou, L., Sun, Y., Hua, Y., Shi, Y., & Zhu, X. X. (2024). A Review of Building Extraction From Remote Sensing Imagery: Geometrical Structures and Semantic Attributes. *IEEE Transactions on Geoscience and Remote Sensing*, *62*, 1-15. https://doi.org/10.1109/TGRS.2024.3369723

Zhao, X., Jing, L., Zhang, G., Zhu, Z., Liu, H., & Ren, S. (2024). Object-Oriented Convolutional Neural Network for Forest Stand Classification Based on Multi-Source Data Collaboration. *Forests*, *15*(3). https://doi.org/10.3390/f15030529

Advanced Engineering Days

aed.mersin.edu.tr

Identification of Sunflowers (*Helianthus annuus* L.) from Multi-Temporal UAV Orthomosaics Using Deep Learning Models

Esra Yildirim*[1], Ismail Colkesen [1], Umut Gunes Sefercik[1]

[1]*Gebze Technical University, Engineering Faculty, Department of Geomatics Engineering, Turkey, esrayildirim@gtu.edu.tr*

Cite this study: Yildirim, E., Colkesen, I., & Sefercik, U. G. (2024). Identification of Sunflowers (*Helianthus annuus* L.) from Multi-Temporal UAV Orthomosaics Using Deep Learning Models. Advanced Engineering Days, 9, 782-785

Keywords
Deep Learning
UAV Remote Sensing
Sunflower Crop
DeepLab V3
U-Net

Abstract

Unmanned aerial vehicle (UAV) technology is capable of delivering high spatial, spectral, and temporal resolution data that facilitate the monitoring of crops over time and provide crucial timely and quantifiable information about the yield, growth, and health of crops. Accurate identification of sunflower crops from UAV orthomosaics is essential for achieving high yields and ensuring sustainable production. In this study, the performance of deep learning-based U-Net and DeepLab V3 architectures in identifying sunflowers from multi-temporal UAV data was investigated. To this end, DJI Phantom 4 Pro V2 RGB camera-equipped UAV was used to collect high-resolution aerial photos of the study site Arifiye, Sakarya and sunflowers were manually delineated in generated UAV orthomosaics. Three different datasets were created for three different phenological stages of sunflowers and were used for the training and validation of the models. The results revealed that sunflowers were identified by both U-Net and DeepLab V3 with the highest accuracy in the 29 August dataset and with the lowest accuracy in the 19 July dataset. Moreover, the U-Net outperformed DeepLab V3 on the 19 July and 29 August datasets with an F-Score of 82.517% and 88.206%, respectively.

Introduction

Sunflower (*Helianthus annuus* L.) is an important agricultural crop with high nutritional, medicinal, and economic values. In addition to being a widely cultivated product in different regions of the world, it is one of the most crucial oilseed resources for some countries such as Turkey [1]. As an oilseed crop, it has various applications in food and industry, including the production of edible oil, animal feed, biofuels, and soap manufacturing [2]. Identifying the sunflowers at different phenological stages is crucial to achieving high yields and ensuring sustainable production. However, traditional crop monitoring methods, relying on manual investigations and field observations, are time-consuming and labor-intensive. Unmanned aerial vehicle (UAV), providing periodic and high-resolution data, is an effective technology for mapping crops, monitoring crop growth stages, detecting diseases, and assessing the quality of crops [3-5]. In recent years, the combination of UAV imagery and deep learning models has shown superior performance in automated crop identification and monitoring. For instance, Yang et al. (2020) employed a convolutional neural network (CNN) architecture to identify the principal growth stages of rice from UAV imagery. The deep network demonstrated superior performance in estimating rice phenological stages, with results closely agreeing with ground observations, achieving an 83.9% top-1 accuracy rate [6]. In another study by Song et al. (2023), the growth stages of sunflower crops were identified using deep semantic segmentation networks and multispectral UAV images. The results revealed that the PSPNet combined with the weighted loss function obtained a higher recognition accuracy of 89.01% [3].

The main aim of this study is to investigate the performance of deep semantic segmentation networks, namely U-Net and DeepLab V3, in identifying sunflowers at different phenological stages from high-resolution multi-temporal UAV orthomosaics. To meet the objective of the study, UAV orthomosaics were generated on three different phenological stages of sunflowers over the study area, and three different datasets were created from these images by manually labeling sunflower crops for the training and validation of deep learning models. Afterward, the U-Net and DeepLab V3 models were trained, and their detection performances were quantitatively and qualitatively compared according to the phenological stages.

Study Area and Dataset

The study area is located within the fields managed by the Sakarya Maize Research Institute in the Arifiye district of Sakarya province, northwestern Türkiye (Figure 1). The primary dataset used in this study consists of three orthomosaics produced from the aerial photos of DJI Phantom 4 Pro V2 UAV, which has a Sony Exmor 20 MP RGB camera with 8.8 mm focal length (f). The aerial photos were collected with ~1.4 cm average ground sampling distance (GSD) from 50 m altitude by applying nadir-view polygonal flights during the Reproductive (R) stage of sunflower growth (i.e., 19 July, 26 July, and August 2023). To achieve more realistic description performance in the orthomosaics, front and side overlaps were applied as 80% and 60%, respectively, in the flights.

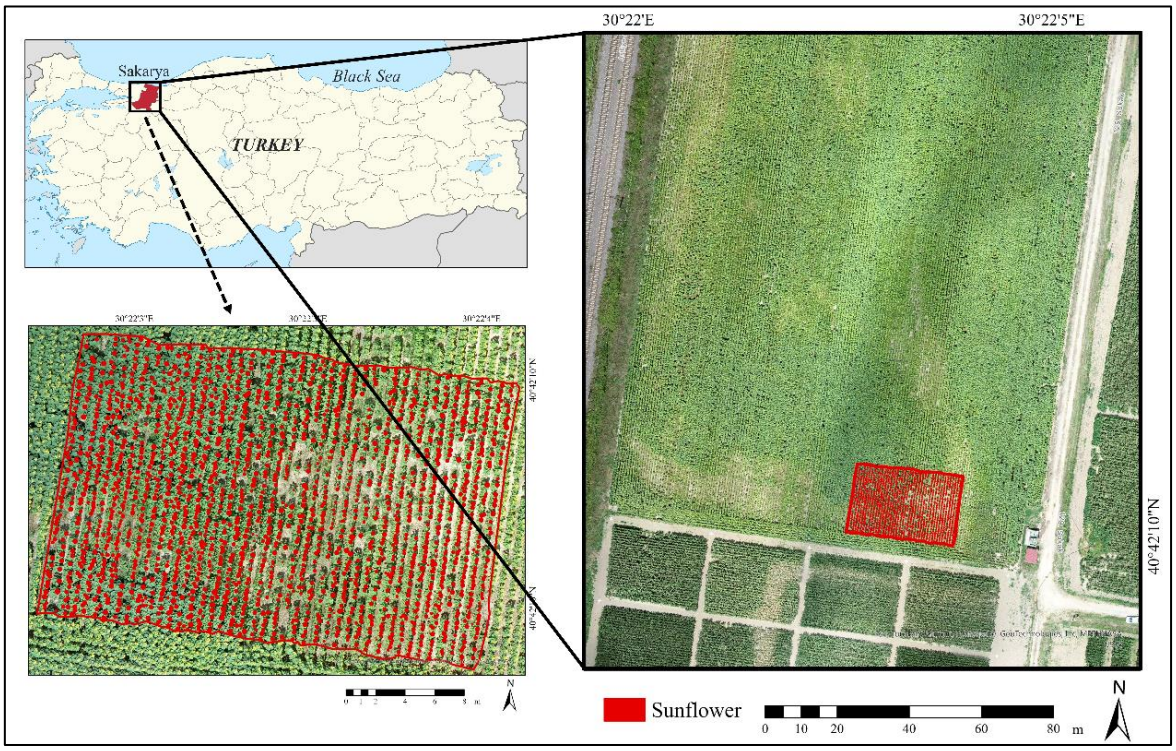


Figure 1. The UAV orthomosaic obtained on 26 July 2022, showing the location of the study area.

Methodology

First, the orthomosaics were produced from UAV data by applying photogrammetric processing steps in the Structure from Motion (SfM)-based Agisoft Metashape Professional software. Afterwards, the sunflower boundaries were manually delineated utilizing ArcGIS Pro 3.03 software on each three orthomosaics. The orthomosaics were split into 256×256 pixel-sized image tiles with a 50% overlap (128×128 pixels). Additionally, the training datasets were augmented by rotating 90^0, 180^0, and 270^0 to increase the number of image samples. As a result, three different datasets, each containing about 500 images, were created in this study to train the deep learning models. Moreover, the 19 July, 26 July, and 29 August datasets included 10,148, 24,696, and 24,912 features, respectively.

In the study, U-Net and DeepLab V3 deep semantic segmentation networks were employed to identify sunflowers using multi-temporal UAV orthomosaics. The U-Net [7] architecture, initially developed for semantic segmentation in biomedical imaging, is a popular fully convolutional network model used in studies for classifying remotely sensed data. This symmetric CNN framework includes an encoder to capture input image context, a bottleneck, and a decoder to map and restore contextual information to its original resolution. On the other hand, DeepLab v3 [8] utilizes multiscale atrous convolutions to address the challenges of multiscale objects in image segmentation. Unlike traditional convolutions, these atrous convolutions enlarge the field of view of filters without increasing the parameter numbers or the computational burden [9].

The created three datasets were used to train the U-Net and DeepLab V3 models. Both models were implemented using pre-trained ResNet-34 architecture for transfer learning to boost the speed and accuracy of the model training. For each model, 90% of the datasets were used for training, and 10% was used for validation. In the experiments, both models were trained for 50 epochs and with a batch size of 8. The same training configuration was employed for three distinct sunflower datasets and six experiments were conducted. A laptop with an Intel® Core™ i-5-10200H CPU, 8 GB RAM memory, and an NVIDIA GeForce RTX 1650 Ti graphics card was utilized for the training process.

Results

After the training and validation, the performances of the models were evaluated using Precision, Recall, and F-Score accuracy metrics. Accuracy assessments showed that both U-Net and DeepLab V3 models performed better on the 29 August dataset, followed by the 26 July and 19 July datasets (Table 1). These results revealed that the models better identified sunflower crops at higher growing stages. The models demonstrated higher accuracy in identifying sunflower heads at the later Reproductive (R) stage (R5.9) captured in August 2023, compared to earlier stages, likely due to more distinct and developed features at this advanced growth stage. On the other hand, the U-Net model outperformed DeepLab V3 on the 19 July and 29 August datasets. To be more specific, it obtained an F-Score of 82.517% and 88.206% for the 19 July and 29 August datasets, respectively. However, the DeepLab V3 surpassed the U-Net on the 26 July dataset regarding F-Score by approximately 1%.

Table 1. Performance comparison of U-Net and DeepLab V3 for three different sunflower growth stages

	19 July		26 July		29 August	
Metrics	**U-Net**	**DeepLab V3**	**U-Net**	**DeepLab V3**	**U-Net**	**DeepLab V3**
Precision (%)	86.879	83.772	88.299	87.169	89.834	88.194
Recall (%)	78.573	81.024	82.463	84.871	86.636	85.099
F-Score (%)	82.517	82.375	85.281	86.004	88.206	86.619

With the intention of visual evaluation of the identification performances, the sunflower prediction results of the models on the validation dataset were quantitatively analyzed (Figure 2). In general, it was clear that both models could detect sunflowers at three different phenological stages. However, some issues, such as masks not accurately matching the ground truth in tiny crops and false negatives, were observed in the DeepLab V3 model (red rectangles in Figure 2b).

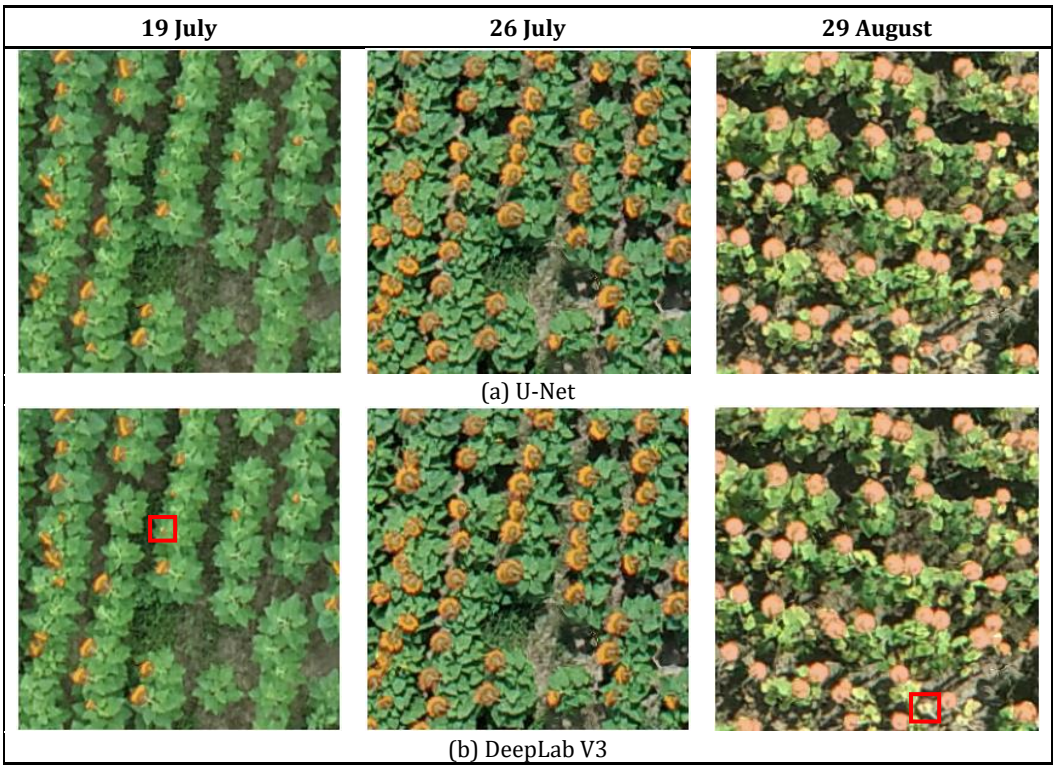


Figure 2. Comparison of prediction results of U-Net and DeepLab V3 on the validation dataset

Conclusion

Deep learning models have demonstrated significant potential in numerous smart agriculture applications, such as crop mapping and weed or pesticide detection from UAV data. In this study, the performances of the U-Net and DeepLab V3 models in identifying sunflowers at different phenological stages from multi-temporal UAV orthomosaics were investigated. Experimental results revealed that both models could identify sunflowers with highest accuracy in 29 August dataset, and with the lowest accuracy in 19 July dataset. The U-Net performed better than DeepLab V3 both for the 19 July and 29 August datasets. Both deep learning models obtained satisfactory results for each dataset and achieved an F-Score of above 80%. These results highlight that deep semantic segmentation models could be reasonable tools for identifying sunflowers at different phenological stages.

References

1. Kurtulmuş, F. (2021). Identification of sunflower seeds with deep convolutional neural networks. Journal of Food Measurement and Characterization, 15(2), 1024–1033. https://doi.org/10.1007/s11694-020-00707-7
2. Gulzar, Y., Ünal, Z., Aktaş, H., & Mir, M. S. (2023). Harnessing the power of transfer learning in sunflower disease detection: A comparative study. Agriculture, 13(8), 1479. https://doi.org/10.3390/agriculture13081479
3. Song, Z., Wang, P., Zhang, Z., Yang, S., & Ning, J. (2023). Recognition of sunflower growth period based on deep learning from UAV remote sensing images. Precision Agriculture, 24(4), 1417–1438. https://doi.org/10.1007/s11119-023-09996-6
4. Pádua, L., Marques, P., Hruška, J., Adão, T., Peres, E., Morais, R., & Sousa, J. J. (2018). Multi-temporal vineyard monitoring through UAV-based RGB imagery. Remote Sensing, 10(12), 1907. https://doi.org/10.3390/rs10121907
5. Aeberli, A., Johansen, K., Robson, A., Lamb, D. W., & Phinn, S. (2021). Detection of banana plants using multi-temporal multispectral UAV imagery. Remote Sensing, 13(11), 2123. https://doi.org/10.3390/rs13112123
6. Yang, Q., Shi, L., Han, J., Yu, J., & Huang, K. (2020). A near real-time deep learning approach for detecting rice phenology based on UAV images. Agricultural and Forest Meteorology, 287, 107938. https://doi.org/10.1016/j.agrformet.2020.107938
7. Ronneberger, O., Fischer, P., & Brox, T. (2015). U-Net: Convolutional networks for biomedical image segmentation. In Medical Image Computing and Computer–Assisted Intervention–MICCAI 2015: 18th International Conference, Munich, Germany, October 5–9, 2015, Proceedings, Part III 18 (pp. 234–241). Springer International Publishing. https://doi.org/10.1007/978-3-319-24574-4_28
8. Chen, L. C., Papandreou, G., Schroff, F., & Adam, H. (2017). Rethinking atrous convolution for semantic image segmentation. arXiv preprint arXiv:1706.05587. https://doi.org/10.48550/arXiv.1706.05587
9. Chen, L. C., Papandreou, G., Kokkinos, I., Murphy, K., & Yuille, A. L. (2017). DeepLab: Semantic image segmentation with deep convolutional nets, atrous convolution, and fully connected CRFs. IEEE Transactions on Pattern Analysis and Machine Intelligence, 40(4), 834–848. https://doi.org/10.1109/TPAMI.2017.2699184

Advanced Engineering Days

aed.mersin.edu.tr

Assessment of Urban Green Space Using UAV-Based Green Leaf Index: A Case Study of Harran University Osmanbey Campus

Nizar Polat[1], Seyma Akca *[1]

[1]*Harran University, Department of Geomatics Engineering, Türkiye, nizarpolat@harran.edu.tr, seymakca@harran.edu.tr*

Cite this study: Polat, N., & Akca, S. (2024). Assessment of Urban Green Space Using UAV-Based Green Leaf Index: A Case Study of Harran University Osmanbey Campus. Advanced Engineering Days, 9, 786-789

Keywords
Urban
UAV
GLI
Green Space

Abstract

This study assesses the urban green spaces of Harran University Osmanbey Campus using UAV and GLI. SfM photogrammetry was used to create a detailed orthophoto of the campus, while GLI was used to identify and quantify green areas. The Total Green Space Area was determined to be 8.8 ha out of a Total Urban Area of 46.4 ha, resulting in a GSR of 18.97%. This GSR value indicates that approximately 19% of the urban area is covered by green spaces, reflecting a moderate but significant vegetation cover that contributes to the environmental quality and well-being of the campus community. The study highlights the importance of integrating UAV-based indices into urban green space assessments and suggests that increasing the GSR to near or above 20% could further enhance ecological and social benefits.

Introduction

Urban green spaces play a critical role in enhancing the quality of life in cities by providing ecological, social, and health benefits. These spaces include parks, gardens, green roofs, and other vegetated areas that contribute to urban biodiversity, mitigate the urban heat island effect, and offer recreational opportunities for residents. Assessing and managing urban green spaces effectively is therefore essential for sustainable urban development [1]. Recent advancements in remote sensing technologies, particularly the use of Unmanned Aerial Vehicles (UAVs), have revolutionized the way urban green spaces are monitored and analyzed. UAVs equipped with high-resolution cameras and sensors can capture detailed images and data, enabling precise assessment of vegetation health and distribution. One of the key indices used in such assessments is the Green Leaf Index (GLI), which provides a measure of vegetation greenness based on the visible spectrum [2]. The use of the GLI is particularly advantageous for urban green space assessments due to its simplicity and the widespread availability of RGB imagery. Unlike other indices that require specialized sensors, GLI can be derived from standard RGB cameras, making it cost-effective and accessible. This simplicity does not undermine its effectiveness; on the contrary, it makes GLI a practical tool for urban planners and environmental managers [3]. In recent years, several studies have demonstrated the effectiveness of UAV-based indices in urban green space assessments. For instance, a study conducted by Liu et al. (2020) utilized UAV imagery to evaluate the spatial distribution of urban green spaces in Shanghai. The study highlighted the benefits of high-resolution UAV data in capturing detailed vegetation patterns and suggested that such data could significantly enhance urban planning and management efforts [4]. Similarly, Xie and Weng (2017) employed UAVs to monitor urban vegetation in Indianapolis, showcasing the potential of UAVs in providing timely and accurate information on urban green spaces [5]. This study aims to assess the urban green spaces of Harran University Osmanbey Campus using UAV-based remote sensing techniques. By capturing high-resolution RGB imagery with UAVs, we will evaluate the greenness and health of the campus's vegetation using the GLI. The specific objectives of this study are to map the spatial distribution of green spaces and analyze the vegetation health across different areas of the campus. Effective management and enhancement of these green spaces can contribute to the well-being of the campus community and support the university's sustainability goals [6]. The methodology involves conducting UAV flights over the campus to collect RGB imagery, processing the images to calculate the GLI, and performing spatial analysis.

Material and Method

Structure from Motion (SfM) Photogrammetry

To create a detailed 3D model of the Harran University Osmanbey Campus, we utilized Structure from Motion (SfM) photogrammetry. This technique involves capturing overlapping aerial photographs using a UAV equipped with a standard RGB camera. SfM photogrammetry processes these images to identify common features and reconstruct the camera positions, creating a 3D point cloud and subsequent 3D model of the terrain and vegetation [7]. This method has been widely used in various fields for its accuracy and efficiency in generating high-resolution 3D models from 2D images [8, 9].

Green Leaf Index (GLI)

The GLI is a vegetation index used to estimate the greenness and health of vegetation. It is calculated using the visible spectrum bands (red, green, and blue) from RGB imagery.

GLI is particularly advantageous because it relies on standard RGB imagery, making it accessible and cost-effective. Unlike indices that require near-infrared (NIR) data, GLI can be derived from any RGB camera, including those mounted on UAVs. GLI is sensitive to chlorophyll content in the vegetation, which correlates with plant health and vigor. Higher GLI values generally indicate healthier vegetation with more chlorophyll content, while lower values may indicate stress or poor health [2].

The formula for GLI is:

$$GLI = \frac{2\times G - R - B}{2\times G + R + B} \qquad \textbf{Eq. 1}$$

where (R), (G), and (B) represent the red, green, and blue bands of the image, respectively. This formula was implemented using the Band Math tool in ENVI software.

Green Space Ratio

The Green Space Ratio (GSR) is a critical metric for evaluating the proportion of green spaces within urban areas. It is calculated as the ratio of the total green space area to the total urban area, providing a quantitative measure of urban greenness. This ratio is important for urban planning and sustainability as it directly relates to environmental quality, biodiversity, and residents' well-being. Higher GSR values indicate a greater presence of green spaces, which are associated with numerous benefits such as improved air quality, temperature regulation, and recreational opportunities for city dwellers [1]. Research has shown that urban green spaces contribute significantly to mitigating the urban heat island effect, enhancing stormwater management, and providing habitat for urban wildlife. Furthermore, green spaces are linked to various social and health benefits, including stress reduction, increased physical activity, and enhanced social cohesion among urban residents. In urban planning, the GSR is often used to set targets for green space provision and to monitor the progress of urban greening initiatives. The formula for GSR is:

$$GSR = \left(\frac{Total\ Green\ Space\ Area}{Total\ Urban\ Area}\right) \times 100 \qquad \textbf{Eq. 2}$$

Where; "Total Green Space Area" is the sum of all areas designated as green spaces within the urban boundary. This includes parks, gardens, green rooftops, and other vegetated areas and "Total Urban Area" is the sum of all land uses within the defined urban boundary, including buildings, roads, pavements, parking sites, sports facilities, and other developed or undeveloped areas.

Results

Within the scope of the study, only the faculties, dormitories, and lodgings area of the campus, which covers more than 600 hectares, were considered. The rest of the campus, with no human activity, was excluded. Consequently, an orthophoto of approximately 47 hectares was analyzed. In the study area, three artificial water pools were masked because they interfere with the vegetation index (Figure 1).

The GLI index was calculated according to Equation 1 by using the masked orthophoto given in figure 1. The index values range between -1 and 1. All healthy and unhealthy vegetation have a GLI value greater than zero. A threshold value was used to delineate these vegetation areas (Figure 2).



Figure 1. Orthophoto with masked water areas: Osmanbey campus.

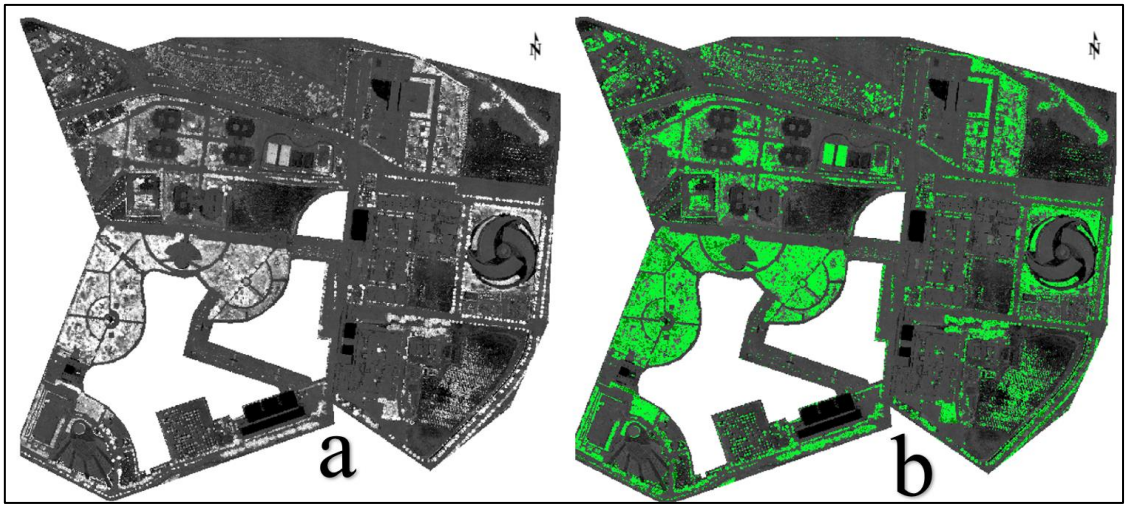


Figure 2. GLI Index: (a) Raw GLI index and (b) GLI index with vegetation highlighted.

When the GLI index is analyzed together with the orthophoto in Figure 1, it is evident that the index is very successful in identifying green areas. For the rest of the study, the "Total Green Space Area" and "Total Urban Area" are needed to calculate the GSR. In this context, the "Total Urban Area" refers to the entire study area of 46.4 hectares. The "Total Green Space Area" was calculated to be 8.8 hectares using the GLI index, which highlights the vegetations as shown in Figure 2.

Discussion

The European Environment Agency (EEA) suggests that cities should aim for at least 20-25% of their area to be dedicated to green spaces to promote environmental sustainability and quality of life [11]. The GSR value was calculated according to formula 2 and was found to be 18.97. This calculated GSR of 18.97% indicates that approximately 19% of the studied urban area is covered by green spaces. This percentage is significant within the context of an academic campus, as it highlights the extent of green areas that contribute to environmental quality and the well-being of students and staff. A GSR value of 18.97% reflects a healthy proportion of green space, aligning with urban sustainability goals that advocate for increased green coverage to mitigate urban heat islands, improve air quality, and provide recreational areas.

The calculated GSR value of 18.97% for the Harran University Osmanbey Campus falls within the moderate range, indicating a reasonable provision of green spaces that contribute to the environmental quality and well-being of the campus community. However, striving for a higher GSR, closer to or above 20%, could further enhance the ecological and social benefits provided by green spaces.

Conclusion

The application of the GLI and *SfM* photogrammetry in this study successfully identified and quantified green spaces within the Harran University Osmanbey Campus. The calculated GSR of 18.97% indicates a significant proportion of the campus is dedicated to green areas, which is vital for maintaining environmental quality and enhancing the well-being of students and staff. This study highlights the efficacy of using UAV-based remote sensing techniques for urban green space assessment and supports the implementation of similar methodologies in other urban environments to promote sustainability and ecological health.

References

1. Kabisch, N., & Haase, D. (2013). Green spaces of European cities revisited for 1990-2006. Landscape and Urban Planning, 110, 113-122.
2. Hunt, E. R., Cavigelli, M., Daughtry, C. S. T., McMurtrey, J. E., & Walthall, C. L. (2005). Evaluation of Digital Photography from Model Aircraft for Remote Sensing of Crop Biomass and Nitrogen Status. Precision Agriculture, 6, 359–378.
3. Ritchie, G. L., Rosas-Anderson, P., Schwartz, B. M., & Mako, A. A. (2010). Using RGB and NIR images to classify crop residue in agricultural fields. Computers and Electronics in Agriculture, 70(2), 176-181.
4. Liu, Y., Guo, L., & Huang, J. (2020). UAV-based high-resolution remote sensing for urban green space mapping and evaluation. Remote Sensing, 12(5), 798.
5. Xie, J., & Weng, Q. (2017). Spatiotemporal variations of urban vegetation in Indianapolis with remotely sensed imagery. Remote Sensing, 9(10), 1054.
6. Kaya, E., Demir, N., & Karaca, F. (2021). Photogrammetric Applications in Various Fields. Mersin Photogrammetry Journal, 2(2), 64-75.
7. Remondino, F., & El-Hakim, S. (2006). Image-based 3D Modelling: A Review. The Photogrammetric Record, 21(115), 269-291.
8. Westoby, M. J., Brasington, J., Glasser, N. F., Hambrey, M. J., & Reynolds, J. M. (2012). 'Structure-from-Motion' photogrammetry: A low-cost, effective tool for geoscience applications. Geomorphology, 179, 300-314.
9. Gruen, A. (2012). Development and Status of Image Matching in Photogrammetry. The Photogrammetric Record, 27(137), 36-57.
10. European Environment Agency (EEA). (2011). Green infrastructure and territorial cohesion: The concept of green infrastructure and its integration into policies using monitoring systems**.**

Advanced Engineering Days

aed.mersin.edu.tr

Ensuring information security in teaching students

Asrorov Oybek Asror ogli

University of Economics and Pedagogy, Computer systems, Uzbekistan, asrorovoybek@gmail.com

Cite this study: Asrorov, O. (2024). Ensuring information security in teaching students. Advanced Engineering Days, 9, 790-791

Keywords
Information
Security
Antivirus
Network
Firewall

Abstract

In this article, professors and teachers working in higher education highlight the necessary guidelines for ensuring information security in teaching subjects to students, as well as for implementing information security. In addition, the main concepts of information technology are discussed in detail. In particular, the most popular software tools against viruses that can damage information are discussed. Important indicators of firewalls are also mentioned to protect against various malicious attacks coming from computer networks. Particular attention is paid to the advantages and disadvantages of the currently widely used information systems in higher education, including platforms such as HEMIS, Moodle, and LMS. Special importance is given to the programmatic and theoretical stages of information protection. In particular, basic information such as measures to ensure that information is transmitted, received, and processed through the network, is fully processed in the network without damage, and measures to ensure that external unauthorized actions do not occur.

Introduction

Today, information and communication technologies (ICT) are developing rapidly, because they allow the introduction of ICT in all areas, ease of work and freedom from excessive paperwork.

Effective and safe use of ICT by Internet users has always been a topical issue. At the same time, it is important to use the Internet in compliance with information security.

Material and Method

Information security is the practice of preventing unauthorized access, use, disclosure, destruction, alteration, inspection, recording, or destruction of information. This universal concept applies equally to all data regardless of its form (e.g. electronic or physical). The main goal of information security is to protect the confidentiality, integrity and availability of data in a balanced way. This is achieved primarily through a multi-step risk management process that identifies tangible and intangible assets, threat sources, vulnerabilities, potential exposures and risk management opportunities.

Protected information is information that must be protected in accordance with the requirements of regulatory legal documents or the requirements set by the owner of the information [2].

The owner of information is a person who has independently created information or has received the right to allow or restrict access to information determined by any criteria based on law or contract.

The organization of information protection is a set of actions aimed at identifying threats to information security, planning and implementing information protection measures, and monitoring the state of information protection [2].

Hardware and software of the information security system [3] means of protection against unauthorized access, systems of analysis and modeling of information flows (CASE systems), network monitoring systems, analysis protocols, antivirus programs, firewalls, cryptographic tools, backup systems, continuous including power systems, authentication systems, tamper and anti-theft devices, access control devices, security systems analysis.

The hardware and software of the information security system includes anti-virus programs based on the analysis tools of protection systems. These programs are the main means of ensuring information security.

Antivirus software is a special program for detecting computer viruses, as well as incoming (perceived malicious) programs and restoring files damaged (modified) by such programs and preventing infection (modification) of files or the operating system with malicious code [4].

Results

Currently, systems such as Higher Education Management Information System (HEMIS), free and open source educational management system (Moodle) are used in the field of education. Systems like these aim to provide a learning management system that protects the privacy and security of student and staff information. Security is an ongoing process in the development of systems such as these. Any errors in these systems are quickly detected and corrected, reducing the impact of vulnerabilities and security breaches.

In addition, it is necessary to pay special attention to the safety of computer equipment when conducting the educational process through ICT. The reason is that computers have access to the global network, and this requires the installation of firewalls to ensure data security, in addition, it is advisable to use special antivirus programs to prevent threats from any device that connects to computer devices externally. will be

Discussion

Examples of currently widely used antivirus programs include Norton, TotalAV, McAfee, Avast, Nod32, and Kaspersky.

Every teacher uses ICT in teaching subjects to students, and thus takes and analyzes science-related information from the Internet, and uses it in various scientific works, literature, and training manuals during his career. In this case, it is necessary to comply with the rules of using the Internet, and it is advisable to use protection against unauthorized access, firewalls and antivirus programs to ensure the security of information in ICT equipment itself.

Conclusion

It would be appropriate to introduce these programs to the staff working in the field of education and to the equipment in the computer rooms of higher education institutions, and to teach students about these programs and information security when teaching subjects related to information technologies.

References

1. Asrorov O.A, Saidov E.R. (2024). TA'LIMGA VEB PLATFORMALARNI JORIY ETISHNI TAHLIL QILISH., Golden brain., 1, 92-97.
2. Asrorov O.A. (2024). Talabalarda GPON texnologiyasi asosida axborot kompetentligini rivojlantirish., Pedagogika Ilmiy-nazariy va metodik jurnal.,2, 294-297.
3. Домарев В. В. (2013). Безопасность информационных технологий. Системный подход., К.: ООО ТИД Диа Софт., 3, 992.
4. Язов Ю. К., Соловьев С. В. (2015). Защита информации в информационных системах от несанкционированного доступа. Пособие. — Воронеж: Кварта., 4, 440.

Advanced Engineering Days

aed.mersin.edu.tr

The effectiveness of hybrid automobiles and the reduction of urban pollution: A case study

Ledia Bozo [*1], Asllan Hajderi [2], Rrezart Bozo [3]

[1] *University of Tirana, Faculty of Natural Sciences, Department of Informatics, Tirana, Albania; lediabozo@gmail.com*
[2] *Albanian University, Department of Engineering, Tirana, Albania; ashajderi@yahoo.com*
[3] *Polytechnic University of Tirana, Institute of Geosciences, Tirana, Albania; rrezart.bozo@gmail.com*

Cite this study: Bozo, L., Hajderi, A., & Bozo, R. (2024). The effectiveness of hybrid automobiles and the reduction of urban pollution. A case study. Advanced Engineering Days 9, 792-795

Keywords
Hybrid/electric vehicle
Pollution from cars
Reducing environmental pollution

Abstract

In this paper, a classification of hybrid automobiles that are produced today in the world is given, in order to analyze their construction and effectiveness. On this basis, the benefits have been analyzed in order to make it known and to choose the most effective type, resulting in plug-in hybrid electric vehicles (PHEV), which can achieve zero pollution and production of carbon dioxide in urban areas. In order to reduce the pollution from vehicles, it is proposed that plug-in hybrid and electric cars be added to the circulation in the amount of half of the cars that are imported in a year. For an urban intersection in the city of Tirana, we have calculated the amount of pollution from vehicles, for the existing and the proposed structure with 15,000 PHEV additional. The results show that the level of pollution at the intersection for the current structure of vehicles is high. For the proposed structure with cars PHEV and EV, the level of pollution at the intersection can be reduced up to 23 % and carbon dioxide up to 16%.

Introduction

Economic growth is linked to the individual mobility of people, which is a basic need, which is carried out by personal vehicles. The use of conventional vehicles has been increasing a lot in the world, reaching over 1 billion in 2012 and it is expected that in 2050 will exceed 2 billion [1,2]. In the US over 30.7% of energy is consumed in the transportation sector and 82% of this is consumed by vehicles. [10]. Meanwhile, it is the problem of pollution from the gases that vehicles release into the atmosphere, which are CO, NOx, HC, CO_2, and PM particles, which affect human health and create the greenhouse effect in disrupting the balance of the planet. Therefore, the challenge today is to reduce energy consumption and CO_2 emissions in the conditions of the increase in the number of cars until 2050].

Solving this problem requires finding cars with low fuel consumption and pollution. For this problem, as early as 1993, the International Energy Agency (IEA) set the task of increasing the efficiency of fuel use.For this purpose, the production of hybrid cars was experimented (1993-2001)[5]. So, in 2015, from 80 million cars per year, 1.2 million are hybrid vehicles, mainly in the USA and Japan [2]. Recently, production has increased and production costs have decreased. A hybrid car not only saves fuel, but also produces less CO_2 emissions and other pollution [7,9].

The lack of knowledge about hybrid/electric cars has created doubts among citizens about the possibility, that these vehicles replace conventional vehicles. *This is also the object of this paper, to increase citizens' interest in the use of hybrid/electric cars, with the aim of reducing the degree of pollution in urban areas and improving human life*.

Material and Method

For the effectiveness of HEV, theoretical analysis will be used on the classification of HEV, that are produced today in the world and the analysis of their effectiveness in urban areas. In order to reduce pollution in urban areas, it is proposed that efficient cars be put into circulation, where the number of these imported should be half of the cars, that are imported in a year. The method for determining pollution in urban areas will be that of calculating pollutant emissions by vehicles at a city intersection in accordance with the CE standards.

Hybrid/electric vehicle types and benefits

HEV vehicles produced from factery are in many varieties. They aim to improve fuel efficiency. The new generation of hybrid/electric vehicles can be divided into three categories [2,5,9]:

a) Hybrid Electric Vehicles (HEV) These use the energy of an engine (ICE) and an electric motor. The power provided by the electric motor allows for a smaller conventional engine, resulting in better fuel economy and less pollution. The battery is charged by the conventional engine and regenerative braking, which captures energy lost during braking.

b) Plug-in Hybrid Electric Vehicles (PHEV) These use energy from an engine ICE and electricity from the grid, reducing fuel consumption and pollutant emissions. These have larger battery packs, than HEV and make it possible to drive the vehicle on electric power alone. The batteries can be charged from the engine (ICE), from the electric power grid and from regenerative braking. These are more environmentally friendly.

c) Electric Vehicles (EV) These use only electricity from the grid, which costs less, to charge the batteries. Although the production of electricity can contribute to air pollution, the Environmental Protection Agency (EPA) considers these to have zero pollutant emissions, because they do not use fuel. These are more environmentally friendly than the two types above.

The main advantages of a hybrid car are [9]:

1. It is ecologically friendly, because it has the lowest pollution rate

2 It has a regenerative braking system, which captures braking energy and charges the battery.

3. They have high resale values, they are the most wanted after and they are the future.

4. There are financial benefits, because hybrid cars are supported by incentives set by the state.

While the main disadvantages of hybrid cars are:

-They are more expensive than conventional cars and can cost $5,000-$10,000 more. However, this surcharge can be offset by the lower cost of driving and tax exemptions.

-They have higher maintenance costs, because they are more complicated. It is also difficult to find an experienced mechanic for these cars.

- They work with high voltage, which in case of an accident, can be deadly for the user.

Besides these, there is a popular myth that they are not powerful and are for driving in the city and are not for high speed and acceleration. This is not true, because combined with the battery, hybrid cars have as much power as conventional cars and have no problem with traction on mountain roads.

From the analysis of effectiveness, it result that PHEV and EV are with interest to be used in our country. So, we propose to put PHEV into circulation, because they save up to 5 times fuel, which reduces up to 5 times the production of CO_2 and other emission [9].

The analysis of the benefits of hybrid/electric cars, in relation to fuel economy, emission reduction and driving cost is given in the constructed graph [9,10] (fig 1):

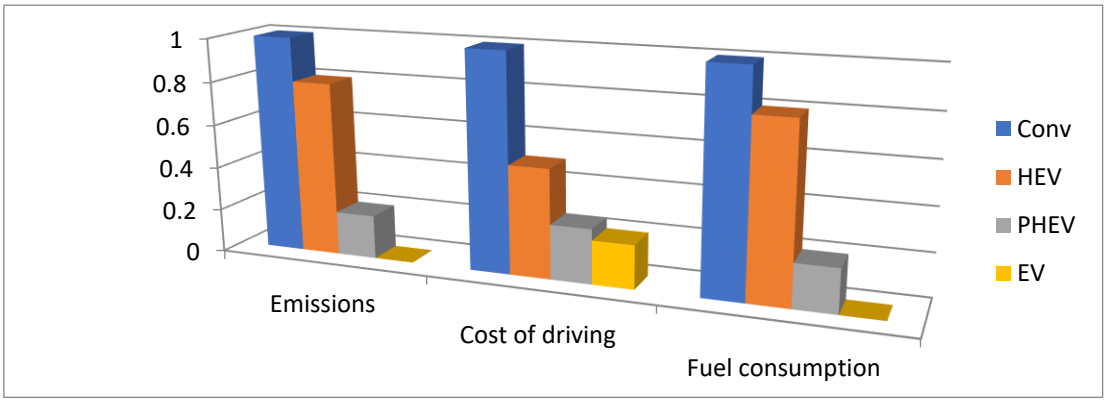


Figure 1. Comparative analysis of HEV

Determining the amount of pollution at the intersection from vehicles

The number of vehicles in circulation in our country has increased a lot, reaching at the end of 2023 to 598,766 in total for the whole country, and the vehicles structure according to the years of production can be grouped in tab 1. [3]. The number of imported vehicles is about 30,000 per year, which can renew old vehicles, that are out of circulation. According to the agreement of the IEA [8], Albania should have put into circulation more than 25,000 hybrid cars by 2020, we propose to import about 15,000 PHEV every year, which replace vehicles produced before 2000.

Table 1. Number of vehicles in circulation in Albania, according to years of production

Euros and Years	Euro 1 1985-1995	Euro 2 1996-1999	Euro3 2000-2005	Euro 4 2006-2009	Euro 5 2010-2014	Euro 6 (7) 2015-2023
No. of vehicles	144600	112300	121100	106400	65600	48500

Since the number of vehicles at this intersection in 2023 is slightly different from that of 2022, therefore, with the data obtained by accepting only cars with diesel engines, we have calculated the amount of pollution at this intersection [11].

Results and discussions

The amounts of pollution in kg/h for the main pollutants CO, NOx+HC and PM, calculated for the current structure of vehicles in circulation and for the proposed structure, with PHEV, are shown in figure 2. While the amount of CO_2 gas for the existing situation is 24 tons/hour, while for the proposed structure 20 tons/h.

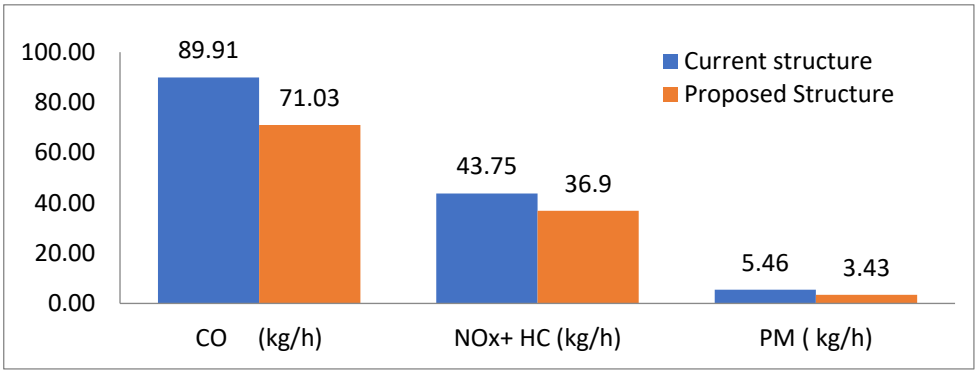


Figure 2 Pollution values in kg/h for the current and the proposed structure at the intersection

From the comparison of the pollution values of Euro 5 with Euro 3, it results that for vehicles manufactured after 2009 compared to those manufactured before 2005, we will have a reduction in pollution for CO, 1.3 times, for (NOx+HC), 2 times and for PM 10 times, with a total reduction of the pollution level about 4.5 times.
The results show that for the proposed structure with the introduction into circulation of 15,000 (2.5%) PHEV, we have a reduction of pollution, from CO 18kg/h, from (NOx+HC) 8kg/h and PM around 2kg/h, or we have a total reduction of 23%. While the benefit for carbon dioxide is about 4 tons/h, or 16%.

Conclusion

The greatest interest to be purchased by users, in the first phase, when the infrastructure and services are not complete, are PHEV (plug-in hybrid electric vehicle) , because they have high performance, the cost of driving is **5 times** lower and they reduce pollution over 80% in urban areas.

High environmental pollution from vehicles in urban areas is caused by vehicles manufactured before 2000, which have a pollution rate of about 4.5 times higher than those manufactured after 2009 and which prevail in circulation over 4 times in our country.

The proposed structure with the introduction of 2.5% of PHEV in circulation, ensure a reduction of environmental pollution in urban intersections up to 23% and a reduction of CO_2 up to 16%.

References

1. Car Exhaust, Air Pollution, Combustion Engines, (February,2020) http://www.nutra.med.com/environment/carsepa.htm
2. Hybrid and Electric Vehicles. (2015) Implementing Agreement for Co-operation on Hybrid and Electric Vehicle Technologies and Programmes International Energy Agency; April 2015. www.ieahev.org
3. European Environment Agency,EEA (2020) Monitoring CO2 emissions from passenger cars and vans in 2018, ISBN 978-92-9480-222-4
4. International Energy Agency (2013), Hybrid and Electric Vehicles, www.ieahev.org
5. Halderman D. J. (2012) "Automotive technology principles, diagnosis and service" p. 918-945,
6. Hajderi A. (2010) "On the reduction of environmental pollution caused by automobile emissions"; Jurnal of studies on economics & society Vol.2 No 2 p 113-124

7. Hajderi A., Lumi D., etc (2012) . **"***Case Study on Reduction of Environmental Pollution from usage of Vehicles in Albania"* International conference on energy, environmental and sustainable development, Venice, April 11-12, 2012; World Academy of Science, Engineering and Technology (WASET)
8. Hajderi A., Bozo L., Basholli F. (2024) "The impact of alternative fuel on diesel in reducing pollution from vehicles" Engineering Applications" V 3 (Issue), p. 15-24
9. Hajderi A., Paco S. (2017); " Hybrid vehicles and their impact on pollution reduction in urban areas Interdisciplinary Journal of Research and Development (IJRD) ISSN 2313-058X. Vol 2, no. 2/2017; p. 35-42;
10. Haideri A. Bozo L. Basholli F. (2023). The impact of HEV in reducing pollution from vehicles. Advanced Engineering Days, AED. 5, p. 60-63.
11. Hajderi A. Bozo L. (2014) "*Air pollution from vehicles and their effect on human health in urban areas"* :

(IJESIT) Vol. 3, Issue 3, May 2014 p.41-47.

Advanced Engineering Days

aed.mersin.edu.tr

Mapping potential risk factors of cultural monument sites at the middle and upper part of River Vjosa in the accelerated climate change circumstances

Laura Shumka

Faculty of Applied Sciences and Creative Industries, Barleti University, Tirana, Albania, l.shumka@umb.edu.al, shumkalaura@gmail.com

Cite this study: Shumka, L. (2024). Mapping potential risk factors of cultural monument sites at the middle and upper part of River Vjosa in the accelerated climate change circumstances. Advanced Engineering Days, 9, 796-798

Keywords
Threat
Monuments
Heritage
Climate change
River basin

ABSTRACT

There are numerous cultural monuments within upper and middle part of River Vjosa that in the new period of proclaimed National Park plays a crucial role for the integrity of the protected area. Cultural heritage buildings, structures, and places as old bridges deteriorate over time due to a variety of local weather- and climate-related causes. A portion of these factors are impacted by climate change and a portion of these changes show up as acceleration in the pace of degradation. This paper aims to review the current situation with particular reference to the different threatening factors that considers monuments as an integral part of the landscape, both nature and man-made components A preliminary threat analyses of the impacted components and structures important to cultural heritage is attempted, along with a suggested methodological approaches.

Introduction

Even though there are a lot of unanswered questions regarding management in the future, climate change is increasingly acknowledged as one of the greatest risks to natural values and cultural heritage, which heritage practitioners need to actively combat [1,2,3). Attaining this is difficult since site managers currently don't understand the hydrology of the site, the soil moisture regimes, or the potential effects that visitors may be having on the soils and buried archeological sites [4]. Human well-being and biodiversity are linked, and biodiversity is a crucial component of human survival and growth. The creation of protected areas (PAs) is a practical means of conserving biodiversity while preserving the many roles that ecosystem services play [5,6). Two pressing worldwide environmental challenges are addressing climate change and biodiversity protection. To overcome the current environmental catastrophe, strengthening synergies between biodiversity protection and climate change adaptation is essential [8,9]. PAs are specific spatial areas whose primary purpose is to protect ecosystems. They are crucial for conserving biodiversity, preserving ecosystem stability, enhancing the quality of the ecological environment, and ensuring national ecological security [1). Cultural heritage assets include historical structures, archeological sites, monuments, as well as their collections, contents, and intangible qualities. These remnants of the past give the local populace a sense of place, identity, and aesthetic well-being [1]. These historical resources have always been subject to changes brought about by interactions with their surroundings, often known as weathering processes. Another possible concern is climate change, which can accelerate the projected rates of decay and/or lead to the emergence of new decay phenomena [9]. After [9] the change in climate patterns and perturbations of the geophysical equilibrium is reflected through consequences of increasing atmospheric temperatures ('global warming'), additional changes in geophysical features is expected, as follows: (i) Change of precipitation patterns; (ii) Change of the frequency, intensity and seasonality of extreme events such as droughts, fires, heavy precipitations, floods, storms, tropical cyclones; (iii) Rise in sea level (caused by glacier retreat, ice melt and thermal expansion of sea water in response to higher temperatures) with serious implications for low-lying coastal areas and islands; (iv) Increase of carbon dioxide levels in the atmosphere and dissolved in the oceans causing increased marine acidification.

Material and Methods

The threat assessment carried out in this paper is based on the guidelines provided by both the International Union for Conservation of Nature (IUCN) and the Global International Waters Assessment (GIWA). The IUCN threat classification scheme was used, which is primarily designed to assess key threats to species. They involve past, ongoing and future threats, using a time frame of three generations or ten years, whichever is the longer (not exceeding 100 years in the future) as required by the Red List Criteria (IUCN,2001). Environmental impacts were assessed using the scoring scheme provided by GIWA, which is more ecosystem oriented. Four impact scores ranging from 0 (impact unknown) through 1 (slight impact), 2 (moderate impact) to 3 (severe impact) were used to quantify the importance of each key issue. Details on determining impact scores can be found in the GIWA Methodology handbook for scaling and scoping (GIWA, 2001). Average scores were calculated for each threat class and maximum values are given. The level of knowledge regarding these threats was subjectively estimated.

Results and Discussions

In more close and detailed analyses it seems that the fragmentation of habitat into small patches due to human activities as mining (in case of Vjosa mining and river mining considered as well) and logging is the major threat for terrestrial biodiversity and ecosystems integrity within this corridor. Apparently, the fragmentation directly inhibit dispersal, reduces gene flow and decrease food availability, in both terrestrial and aquatic part of the Vjosa wide basin. As the climate changes, many species will need to move to new habitats in the landscape and fragmentation will impede range shifts in those that have trouble crossing gaps between patches. So, Landscape fragmentation and human-induced land-cover changes are two of the main current threats to nature conservation. Other *challenge include*: (i) Land tract management type usually is defined by different objectives and uses (e.g., resource extraction, fishing, mining, grazing, recreation, and conservation), mandates (e.g., preservation, multiple use), political hierarchy (e.g., central/municipality), and intensity. (ii) An increase in the number of management types cause corridors to arise even faster or be more distinct than an increase in the number of management units alone. (iii)The human and financial capacities of PA management structures (at the national and regional levels) are limited, in both the numbers of staff and in their competencies. The lack of experts for nature conservation, rangers, education, interpretation, and tourism is evident; (iv) Lack of efficient monitoring of the use of resources in PAs; (v) Weak law enforcement in the field of nature conservation which has resulted in illegal logging and hunting in PAs and in other areas despite the Moratoriums; (vi) Activities such as education and knowledge sharing are not sufficiently developed or supported in PAs.

References

[1] Sesana, E., Gagnon, A.S., Cinatelli, C., Cassar, J. (2021). Climate change impacts on cultural heritage: A literature vrvew. WIREs Climate Change. 12:e710. wires.wiley.com/climate change 1 of 29. https://doi.org/10.1002/wcc.710

[2] Shumka, L, Papastefani, A., Shumka, S., Mali, S. (2023a): The Potentials for the Ecological Management of Landscape Connectivity Including Aquatic Ecosystems in Northeast Albania. Hydrobiology, 2, 44–54. https://doi.org/10.3390/hydrobiology2010004

[3] Shumka, S., Nagahama, Y., Hoxha, S., Asano, K. (2023b). Overfishing and recent risk for collapse of fishery in coastal Mediterranean lagoon ecosystem (Karavasta lagoon, southeastern Adriatic sea). Fishery and Aquatic Science, 26(4):294-303 https://doi.org/10.47853/FAS.2023.e25

[4] Shumka, S. Sanda, R. Dhora, Dh., Grapci-Kotori, L. (2024). Fish Resources of Inland Waters and Fisheries in Albania. In: Management, Sustanability, and Conservation. Ecological Sustainability of Fish Resources of Inland Waters of the Western Balkans (By Vladica Simic (Editor), Snezana Simic (Editor), Vladimir Pesic (Editor). Springer, p. 220-261. https://doi.org/10.1007/978-3-031-36926-1_7

[6] Shumka, L., Peri, L., Lato, E. (2020). The Needs for Determining Degradation Risks from Temperature and Relative Humidity of Post-Byzantine Church Indoor Environment, Journal of Environmental Management and Tourism (JEMT), Vol. 11, No. 3,601-606,

[7] [Shumka, L. (2019). Comparison of Indoor Climate Features Following Different Climate Guidelines in Conservation Examples of Selected Churches in Albania International Journal of Conservation Science (IJCS), Volume 10, Issue 4: 623-630.

[8] Shumka, L. (2018). Considering Landscape and Water in the Dumrea Region: Challenges for Integrated Planning and Sustainability. The Journal: Thalassia Salentina, Italy Volume 40 supplement 1, e-ISSN: 1591-0725 [154-147] https://doi.org/10.1285/i15910725v40sup2p147

[9] UNESCO World Heritage Centre (2007). Climate Change and World Heritage Report on predicting and managing the impacts of climate change on World Heritage and Strategy to assist States Parties to implement appropriate management responses

[10] GIWA (2001). Methodology Handbook. Scaling and Scoping. www.unep.org/dewa/giwa/methodology

Table 1. Summary chart of IUCN threat classification scheme, key threats, current impact and expected future (mid-term) importance in the Vjosa basin. Four scores ranging from 0 (no know impact) through 1 (slight impact), 2 (moderate impact) to 3 (severe impact) were used to assess the current impact according to the scoring scheme provided by GIWA (2001). Average scores were calculated for each threat class and maximum values are also given.

Threat class	Key threat	Level of knowledge	Impact	Average impact	Maximum impact
1. Residential & commercial development	1.1. Housing & urban areas	well-known	3	2	3
	1.2. Commercial & industrial areas	well-known	1		
	1.3. Tourism & recreation areas	well-known	2		
2. Agriculture & aquaculture	2.1 Annual & perennial non-timber crops	less known	2	1(1.25)	2
	2.2 Wood & other plantations	less known	1		
	2.3 Livestock farming & ranching	less known	2		
	2.4 Marine & freshwater aquaculture	–	0		
3. Energy production & Mining &river ming	3.1 Oil & gas drilling	well-known	1	2 (1.75)	3
	3.2 Mining & quarrying	well-known	3		
	3.3 Renewable energy	moderately-known	1		
4. Transportation & service corridors	4.1 Roads & railroads	less known	2	1(0.5)	2
	4.2 Utility & service lines	–	0		
	4.3 Shipping lanes	–	0		
	4.4 Flight paths	–	0		
5. Biological resource use	5.1 Hunting & trapping terrestrial animals	less known	1	1(0.5)	1
	5.2 Gathering terrestrial plants	–	0		
	5.3 Logging & wood harvesting	–	0		
	5.4 Fishing & harvesting aquatic resources	less known	1		
6. Human intrusions & disturbance	6.1 Recreational activities	less known	3	1(1.33)	3
	6.2 War, civil unrest & military exercises	–	0		
	6.3 Work & other activities	less known	1		
7. Natural system modifications	7.1 Fire & fire suppression	less known	2	2(2.33)	3
	7.2 Dams & water management/use	well-known	2		
	7.3 Other ecosystem modifications	less known	3		
8. Invasive & other problematic species & genes	8.1 Invasive non-native/alien species	moderately known	2	1(1.33)	2
	8.2 Problematic native species	–	0		
	8.3 Introduced genetic material	less known	2		
9 .Pollution	9.1 Domestic & urban waste water	well-known	3	2	3
	9.2 Industrial & military effluents	moderately-known	3		
	9.3 Agricultural & forestry effluents	moderately-known	2		
	9.4 Garbage & solid waste	well-known	3		
	9.5 Air-borne pollutants	less known	1		
	9.6 Excess energy	–	0		
10 Geological events	10.1 Volcanoes	–	0	0	0
	10.2 Earthquakes/tsunamis	–	0		
	10.3 Avalanches/landslides	–	0		
11. Climate change & severe weather	11.1 Habitat shifting & alteration	well-known	3	2	3
	11.2 Droughts	moderately-known	3		
	11.3 Temperature extremes	less known	3		
	11.4 Storms & flooding	less known	1		
	11.5 Other impacts	–	0		

Advanced Engineering Days

aed.mersin.edu.tr

Skin Imaging methodology to improve analysis of geometric deviation

Elnaz Ghanbary [*1], Mehran Mahboubkhah [1], Ahmad Barari [2]

[1]*University of Tabriz, Department of Mechanical Engineering, Iran, Elghanbaryk@gmail.com, Mahboobkhah@tabrizu.ac.ir*
[2]*University of Ontario Institute of Technology, Department of Mechanical and Manufacturing Engineering, Canada, Ahmad.barari@uoit.ca*

Cite this study: Ghanbary, E., Mahboubkhah, M., & Barari, A. (2024). Skin Imaging methodology to improve analysis of geometric deviation. Advanced Engineering Days, 9, 799-801

Keywords
Geometric Deviation
Skin Model Shapes
Digital Twin
Machine Vision Inspection
Point Cloud

Abstract

Geometric variation are inherent in manufactured surfaces due to manufacturing error and measurement uncertainty. The nominal surface model defined by the designer is ideal geometry. The need for non-ideal geometry is addressed by the Geometric Product Specification (GPS) standard, which introduces the concept of Skin Model to detail the geometric deviations of the surface. Despite its importance, few methodologies exist for skin model generation. A skin model is a continuous surface that consists of an infinite set of points. Coordinate Metrology provides real information about the surface geometry in the form of a finite set of discrete data points. 'Skin Imaging' methodology, as a new approach of skin model, provides an enriched continuous two-dimensional (2D) representation of the geometric deviation of three-dimensional (3D) surface, processed from discrete data points. Skin Image illustrates the actual geometric deviation of the manufactured surface from the ideal geometry via intensity variation of its pixels. This paper examines geometric deviations in three planar case studies using Skin Imaging, showcasing this methodology's effectiveness in providing a detailed model of the actual manufactured surface and aiding in the smart assessment of geometric deviations.

Introduction

Detailed Deviation Zone Evaluation (DZE) is the pinnacle of Coordinate Metrology, providing a model of the actual manufactured surface from a discrete, unorganized point cloud, enabling estimation of deviations at non-measured locations. This model is particularly required for establishing a closed-loop of manufacturing and inspection processes, an online manufacturing error detection and correction cycle [1-3] , and the precise assessment of design tolerances and assembly accuracy [4-6].

The most important approach to generate DZE of the surface is introduced in GPS standard (ISO 22432) [7] as Skin Model. Skin Model is non-ideal geometrical model of the surface which can be generated at the early stage of the product lifecycle, or during the manufacturing process based on the results of Coordinate Metrology [8]. Anwer et al. [9] investigated the fundamentals of the skin model at a conceptual, geometric and computational level. Schleich et al. [10] declared that the skin model can be used in various applications of manufacturing and inspection. The finite element method was used by Lalehpour and Barari [11] to generate the Skin Model.

The concept of *Skin Imaging* methodology has been recently introduced in [12], presenting a novel approach of skin model. It was thoroughly discussed on planar and non-planar surfaces such as Non-Uniform Rational B-Spline (NURBS). While Skin Model is a detailed, continuous 3D digital twin of the surface, Skin Image is 2D digital twin that captures the *actual* geometric deviation of surface through its pixels' intensity variations. Its fundamentals are further discussed in [2] with its extension to cylindrical and spherical industrial case studies. Skin Imaging efficiently converts unorganized, discrete 3D PC into grayscale 2D image, simplifying neighbor searches and enabling the use of image processing for the smart inspection of geometric deviations. In the current paper, Skin Imaging is employed to evaluate and analyze the geometric deviation of three planar case studies.

Material and Method

PCs deviation calculation - Acquiring PCs of the inspected planar surface, the ideal surface is fitted to PC by Principal Coordinate Analysis (PCA) [12]. X_{PCA} and Y_{PCA} in "Figure 1" are the coordinates of the image-point on the fitted plane, and Z_{PCA} is the deviation of the measured point from the fitted plane.

Skin Image generation - The $(X\text{-}Y)_{PCA}$ plane is divided to obtain the cells of the image's matrix. Deviation of the measured points are used to define the value of each cell such that if a cell contains an image-point (black points in "Figure 1"), its Z_{PCA} is considered as the value of that cell. Cell values without image-points (red cell in "Figure 1") are interpolated from the surrounding points P'_1, P'_2 and P'_3. The variations of cells' values represent the geometric variation of the surface. Matrix values are mapped to the 0-255 integer range to display the Skin Image.

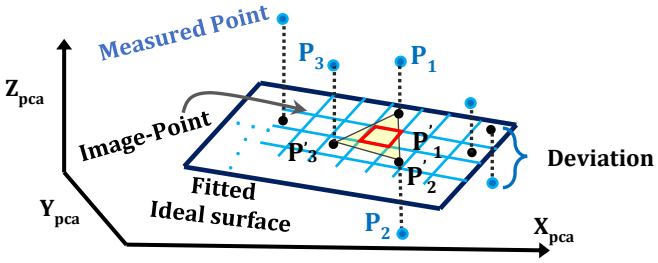


Figure 1. Skin Image generation procedure

Results

Case study 1- flat surface: "Figure 2" shows a ground aluminum workpiece. This is a flat surface with low deviation and all its PC have similar deviations (average deviation is 0.005mm). Therefore, its skin image shows low intensity variation and as illustrated by the image histogram all its pixels have dark intensity.

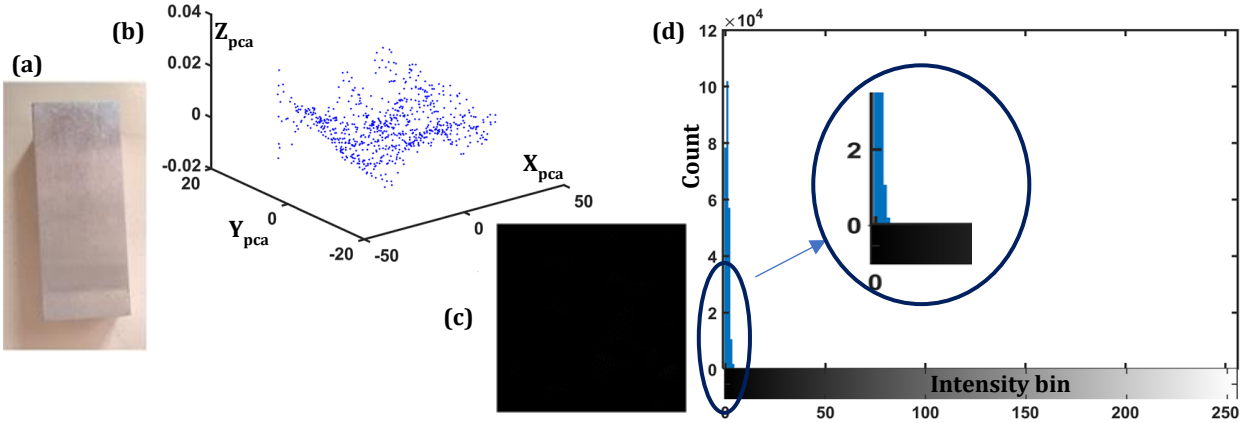


Figure 2. Case study 1(a) Flat surface, (b) PC, (c) Skin Image, (d) Histogram of the Skin Image

Case study 2 - surface with general defect: "Figure 3" shows a curved surface that most of its measured PC have considerable deviation. This will result in bright corresponding pixels for them in skin image. As illustrated in the histogram, the image includes most of the intensity bins in considerable counts, since the fact that general defect occurs continuously on the surface from a maximum deviation to minimum deviation and/or vice versa.

Case study 3 - "Figure 4" displays a ground surface with local defects. The defects appeared in bright intensity in the image due to the high deviation of their PC. The more deviated the defect is, the brighter the corresponding pixels are. Since the deviations of the points are almost similar and just the defected parts have considerable deviations, the number of the histogram's bin with considerable counts is lower compared with the case study 2.

Discussion

Analyzing the Skin Image, deviation zone evaluation can be done with full-grown image processing techniques. According to Table 1. and histograms of the skin images, the inspected surface is flat if the maximum intensity in the image is considerably low (such as for the first case study is 5); this means that the pixels are almost in a similar value and the PCs are in a similar deviation from the ideal surface. The average intensity is low, as well. The histogram of the skin image with a wide shape represents the surface with general defect, while the compressed histogram shows that there are some local anomalies. Besides, the average intensity of the image belonging to case study 2, as the general defected surface, is considerably higher than case study 3, as the locally defected surface.

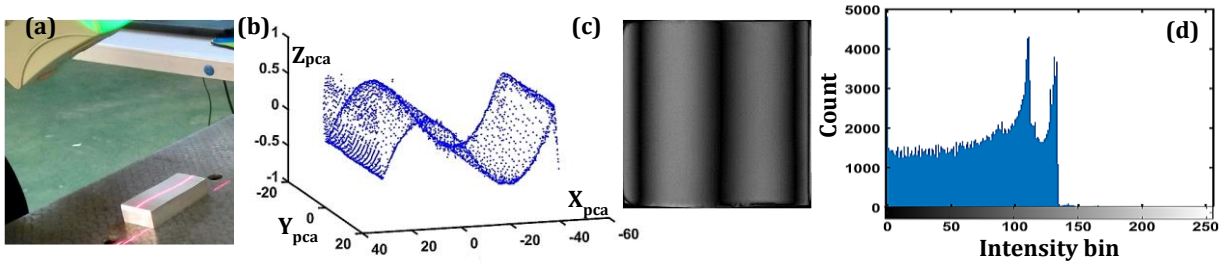


Figure 3. Case study 2; (a) surface with general defect, (b) PC, (c) Skin Image, (d) Histogram of the Skin Image

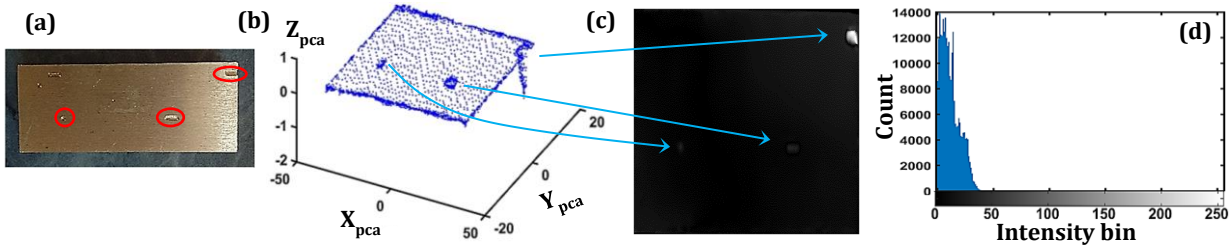


Figure 4. Case study 3; (a) surface with local defects, (b) PC, (c) Skin Image, (d) Histogram of the Skin Image

Table 1. Skin Image information for the case studies

Case Studies	Number of PC	Average deviation of PC	Image Maximum intensity	Image Average intensity
1	2029	0.005	5	1.024
2	3947	0.303	253	75
3	2451	0.084	255	11.88

Conclusion

Skin image, as the new paradigm of the Skin Model, is a 2D digital twin of the inspected surface, such that intensity variation of its pixels is proportional to geometric deviation of the surface. The efficiency of this method was demonstrated by analyzing DZE of three planar case studies.

References

1. Berry, C., & Barari, A. (2019). Cyber-Physical System Utilizing Work-Piece Memory in Digital Manufacturing. IFAC-PapersOnLine, 52(10), 201-206.
2. Ghanbary Kalajahi, E., Mahboubkhah, M., & Barari, A. (2023). Skin Imaging: A Digital Twin for Geometric Deviations on Manufactured Surfaces. Applied Sciences, 13(23), 12971.
3. Barari, A., & Pop-Iliev, R. (2009). Reducing rigidity by implementing closed-loop engineering in adaptable design and manufacturing systems. Journal of Manufacturing Systems, 28(2-3), 47-54.
4. Shen, T.-H., & Lu, C. (2023). Assembly accuracy analysis of cylindrical parts based on skin model shapes considering form deviations and local surface deformations. Precision Engineering, 80, 256-273.
5. Shen, T., & Lu, C. (2023). An Approach of Assembly Deviation Analysis based on Jacobian Model and Skin Model Shapes. 1557-1562.
6. Zhao, G., Li, J., Zhang, B., Zhang, P., Wang, H., & Xiao, W. (2022). An Aero-Engine Assembly Deviation Analysis Method Based on Skin Model Shapes. 78-89.
7. STANDARD, I. I. (2011). Geometrical product specifications (GPS) — General concepts - Part 1: Model for geometrical specification and verification (ISO 22432:2011(E)) General concepts —Part 1: Model for geometrical specification and verification.
8. Zhang, M., Anwer, N., Stockinger, A., Mathieu, L., & Wartzack, S. (2013). Discrete shape modeling for skin model representation. Proceedings of the Institution of Mechanical Engineers, Part B: Journal of Engineering Manufacture, 227(5), 672-680.
9. Anwer, N., Schleich, B., Mathieu, L., & Wartzack, S. (2014). From solid modelling to skin model shapes: Shifting paradigms in computer-aided tolerancing. CIRP Annals, 63(1), 137-140.
10. Schleich, B., Anwer, N., Mathieu, L., & Wartzack, S. (2014). Skin Model Shapes: A new paradigm shift for geometric variations modelling in mechanical engineering. Computer-Aided Design, 50, 1-15.
11. Lalehpour, A., & Barari, A. (2017). Developing skin model in coordinate metrology using a finite element method. Measurement, 109, 149-159.
12. Ghanbary Kalajahi, E., Mahboubkhah, M., & Barari, A. (2023). On detailed deviation zone evaluation of scanned surfaces for automatic detection of defected regions. Measurement, 221, 113462.

Advanced Engineering Days

aed.mersin.edu.tr

A case survey of dietary intake for assessing diet diversity score among vulnerable groups of society

Estela Pinderi *[1] Joana Vogli [1] Marinela Leka [1]

[1]Agricultural University of Tirana, FBF, Department of BFS, Tirana, Albania, pinderiestela1@gmail.com, voglij1@gmail.com, marinelaleka7@gmail.com

Cite this study: Pinderi, E., Vogli, J., & Leka, M. (2024). A case study of dietary intake for assessing diet diversity score among vulnerable groups of society. Advanced Engineering Days, 9, 802-804

Keywords
Diets
Dietary index
Diversity
Food
Nutrients

Abstract

Dietary diversity is a qualitative measure of food consumption that reflects household access to a variety of foods, and is also a proxy for nutrient adequacy of the diet of individuals. The Food and Agriculture Organization (FAO) was developing the "Guidelines for measuring household and individual dietary diversity". So, our survey has been conducted in the period of October-December 2023 following standard questionnaire that represents a rapid, user-friendly and easily administered low-cost assessment tool. The 442 respondents were adult female and children's from the region of Tirana. The results analyses revealed a dietary diversity index value for the adult female oscillating from 0.3 to 0.7, while in case of children's it was showing values in between 0.42 to 0.85. The survey is in line with different individual dietary diversity scores assessment that aims to reflect nutrient adequacy. Studies indifferent age groups have shown that an increase in individual dietary diversity score is related to increased nutrient adequacy of the diet. It is worth to mention that these data are preliminary one, and in the following period the team will dedicate time to find out the relationship among nutrient adequacy of the diet with food borne dieses.

Introduction

Since the 1990s, the supply of many food groups in Albania has increased, particularly for dairy products and eggs, and fruit and vegetables. Consequently, the diet has become more diversified, especially in urban areas [1]. Presently, at national level, the dietary energy supply is largely sufficient to meet the population's energy requirements. Overall, the prevalence of undernourishment is low. However, Albania is increasingly dependent on imports of cereals. Besides the nature resources and diversity [2, 3, 4], the food commodities are secured on both locally and abroad. Feeding habits for infants and young children are insufficient. Even though the vast majority of babies are nursed, exclusive breastfeeding is rarely used and nursing is started later than expected after birth. Preschoolers' poor nutritional condition, which seems to have gotten worse in recent years, is a result of these insufficient practices, poverty, and limited access to appropriate health treatments. Roughly one in ten children under five were wasted and about a third were stunted in 2000. At the same time, the population is going through a nutritional shift, and adults in Tirana, the capital, are more likely to be overweight or obese.

This approach is based on expressing diet diversity indicators such as the diet diversity score (DDS) or food variety score as a reflection for dietary quality and measure the diversity of unique food groups and food items consumed, respectively.

Material and Methods

The used approach was based on a questionnaires conducted during the year 2024 and the DDS for women was a count of the total number of food groups consumed from a list of 10: (i) grains, white roots and tubers, and plantains; (ii) pulses; (iii) nuts and seeds; (iv) dairy; (v) meat, poultry, and fish; (vi) eggs; (vii) dark-green leafy vegetables; (viii) other vitamin A-rich vegetables and fruits; (ix) other vegetables; and (x) other fruits. For children, a seven food-group classification was used, including the following: (i) grains, white roots and tubers, and plantains; (ii) legumes, nuts, and seeds; (iii) dairy; (iv) meat, poultry, and fish; (v) eggs; (vi) vitamin A-rich fruits and vegetables; and (vii) other fruits and vegetables. Following references a 15-g minimum quantity consumed was considered as a cutoff for species inclusion in the DDS for women but not for children. The questionnaire considered 242 adult woman and 242 children. The Minimum Dietary Diversity (MDD) was used

as a cutoff for higher nutrient adequacy and refers to a minimum of five and four food groups for women and children, respectively. Due to the fact that the study assessed the level of food biodiversity in the diet, intake of breast milk was not considered in the calculation of biodiversity indicators, as recommended by [5]. The consumption of different parts of particular plant or animal species was counted once, with no minimum quantity. No minimum quantity consumed was applied to include a species in the biodiversity indicators.

Results and Discussions

The current method, as described in the introduction section, sought to suggest a cross-cutting indicator that assesses the diversification of foods in human diets and aids in directing activities that simultaneously promote environmental and human health. A similar method was used by [6], who assessed the relationship between three ecological biodiversity indicators and nutrient adequacy by applying them to dietary intake data of women and children in seven low- and middle-income countries.

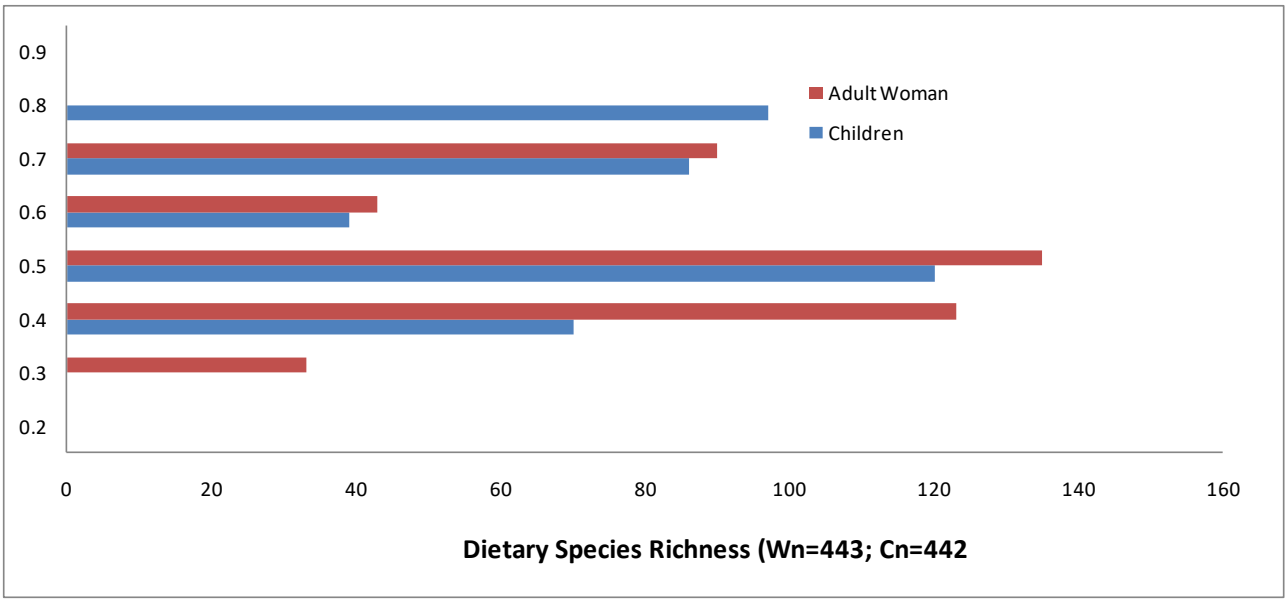


Figure 1. Dietary Species richness (Woman-n=442 and Children n=442)

The study evaluated the relationships among food biodiversity, diet diversity, and nutrient adequacy as three complementing aspects of diet quality and that is in line with FAO recommendations [7]. It is important to note that throughout the past three decades, Albania has seen significant changes. A significant portion of the population has moved from highland to lowland areas, and traditional cuisines and foods have been replaced by western ones.

In addition, we evaluated and compared the minimal food biodiversity cutoff with the current minimum diet diversity cutoff in order to determine which diets are more nutrient-adequate. As can be seen from the data in Figures 1 and 2, the analysis of the samples reveals that the average value of dietary species richness was somewhat greater (0.52) for children than for adult women, with over 40% of adult women having values lower than 0.5.

Conclusions

Evaluating a species' contribution to the diet allows one to pinpoint the species that have the most potential to enhance diets in various geographical contexts. It also offers further information on how important food diversity is to maintaining the quality of diets. Additional correlations between the data and the health status of the analyzed social groupings are possible. The current study offers data regarding the contribution of various food commodities to the energy and micronutrient intakes of the rural population as well as those living in these areas. Food consumption at the species level allows for the addition of data that benefits sustainable food system strategies as well as conservation.

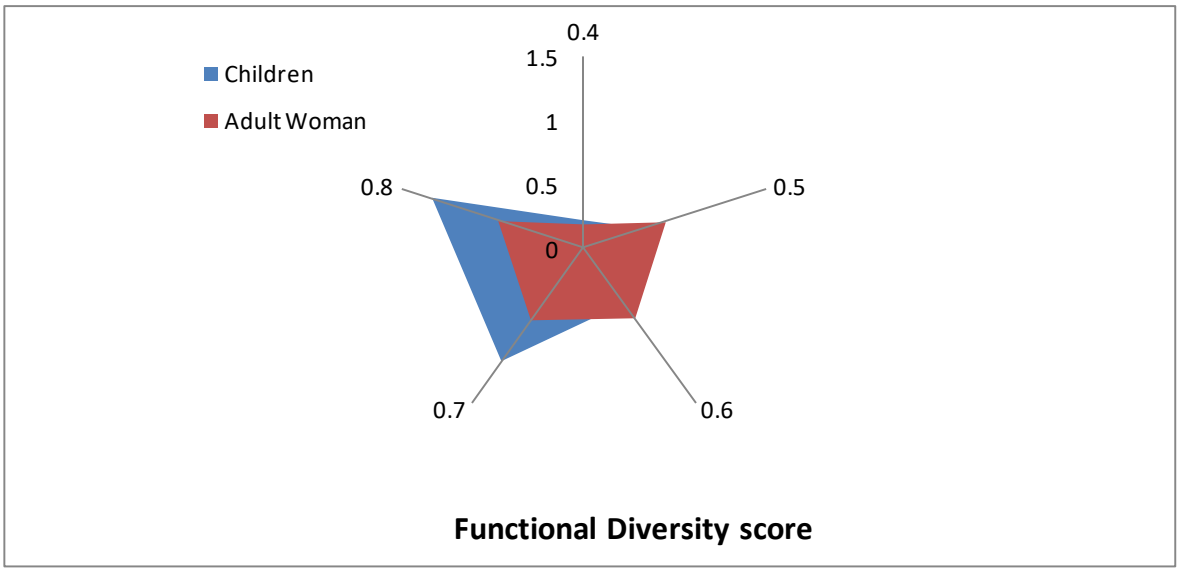


Figure 2. Functional Diversity score (Woman-n=442 and Children n=442)

References

[1] FAO, 2010. Albanian Nutrition profile-the basic indicators overview and assessements. Rome. 33 pp
[2] Shumka S, Lalaj S, Šanda R, Shumka L**,** Meulenbroek P, 2023. Recent data on the distribution of freshwater ichthyofauna in Albania. Croatian Journal of Fisheries, 2023, 81, 33-44. http://.doi.org/10.2478/cjf-2023-0004
[3] Shumka, S., Mucollari, N. 2023. A review of fish diversity and management of the Vjosa basin: the first free flow river protected area in the Balkans. Innovare Journal of Agri. Sci, vol 11, issue 6, 2023, 32-3633. https://doi.org/10.22159/ijags.v11i6.49107
[4]Shumka, S., Berberi, E., Kulici, M. Mucaj, S., Vladi, F. 2022. Assessing the relationship between biodiversity conservation and slow food culture in selected protected areas in Albania. BIODIVERSITAS, 2022: 1319-1326. https://doi.org/10.13057/biodiv/d230316
[5] Khourya., C, Bjorkmanc., A, Dempewolfd., H, Ramirez-Villegasa., J, Guarinof., L, Jarvisa., G, Riesebergd., L, Struik, P. (2014). Increasing homogeneity in global food supplies and the implications for food security. PNAS, 111: 4001-4006
[6] Khourya., C, Bjorkmanc., A, Dempewolfd., H, Ramirez-Villegasa., J, Guarinof., L, Jarvisa., G, Riesebergd., L, Struik, P. (2014). Increasing homogeneity in global food supplies and the implications for food security. PNAS, 111: 4001-4006
[7] FAO, (2018). Sustainable food systems - Concept and framework. CA2079EN/1/10.18

Advanced Engineering Days

aed.mersin.edu.tr

The impact of the magnetic field on the reduction of pollution from vehicles: A case study

Asllan Hajderi [*1], **Ledia Bozo** [2]

[1] *Albanian University, Department of Engineering, Tirana, Albania; ashajderi@yahoo.com*
[2] *University of Tirana, Faculty of Natural Sciences, Department of Informatics, Tirana, Albania; lediabozo@gmail.com*

Cite this study: Hajderi, A., & Bozo, L. (2024). The impact of the magnetic field on the reduction of pollution from used vehicles: A case study. Advanced Engineering Days 9, 805-808

Keywords
Diesel engines
Reducing pollution from vehicles
Engine performance
Use of vehicles

Abstract

This study analyzes the problem of vehicle performance change and their pollution degree during their use. In the study the causes of the decrease of engine performance and the increase of the pollution level of vehicles and ways to increase them were analyzed. For this, three diesel vehicles were studied, in which they are put constant magnetic with different magnetic field. The impact of the magnetic field on the performance of the vehicles is seen in relation to the changes of engine revolutions, to the reduction of pollution and the period of work, when the change of the performance of the engine by the magnetic field occurs. The results of the study showed that the influence of the magnetic field increases the effectiveness of the fuel, making a faster and more complete combustion, ensuring the recovery of the initial performance. The increase in performance goes up to 15% and the pollution reduction up to 4 times, but the effect of the action and the working period depends on the carbon deposits that have been created. The use of magnets shows that it serves us for their maintenance all the time

Introduction

In today's world, the number of vehicles that use the thermal energy released by burning fuels has increased greatly. The fuels that remain massive are the fossil hydrocarbons, which have C and H on their composition. Thus, for a pure fuel, typical combustion in automobile engines can be expressed [1, 2, 3].

Fuel + Air => Hydrocarbons + Carbon Monoxide + Carbon Dioxide + Nitrogen Oxides + Water Vapor

Hydrocarbons are parts of fuel molecules, partially burned, due to the type of fuel and the short mixing time.

Carbon monoxide is a product of incomplete combustion of fuel. It is produced when there is a lack of air for fuel combustion Carbon dioxide is a product of perfect combustion.

Nitrogen oxides are formed from nitrogen and oxygen atoms under conditions of high pressure and temperature in the engine (at high loads). Nitrogen oxides, as well as hydrocarbons, are ancestor to ozone formation and contribute to acid rain.[3, 4]. In order to ensure the level of pollution during the use of vehicles, the CE has issued directives to strengthen the technical control in terms of regular maintenance of vehicles, as stated in directive 2009/40/EU dt. 06.05.2009.

In order to maintain the performance of the engines during their use, the use of additives for the fuel system is recommended, but it is not recommended for common rail system [3]. Meanwhile, another method, that is recommended is using permanent magnets in the treatment of fuel before combustion. For this purpose, certified devices are marketed, produced in the USA and also marketed in Europe [5], in which the advantages are: increase of engine power, fuel economy, reduction of environment and increase of engine life. However, they are few, because they often do not give a positive result. While there are technical journals that dispute the advantages shown above. Thus, from the experiments carried out for 3 types of magnets taken from the market in Italy, it has resulted that the increase in engine performance and the reduction of environmental pollution have been negligible [6]. From these, there is doubt about for the influence of these magnets in the combustion process on the performance of the vehicle engine.

Material and Method

For the realization of the study, the theoretical analysis of the performance and pollution rate of the vehicle engine and the possibility of experimental measurement of the performance and the pollution rate of the vehicle is used.

Vehicle performance analysis

Useful period of the use of vehicle, based on vehicle usage practice [6,7], can be divided into 2 phases:

- The first stage is the period when the engine is still new and develops the performance given by the factory, staying at the given torque and number of revolutions. During this time the combustion chamber, valves, sprayers, etc. are clean from soot.

- The second stage is the period when the performance of the engine drops and it does not provide the torque and revolutions, according to the given characteristic. The beginning of this phase for a given engine depends on the conditions of use and the quality of the fuel used and fluctuates between 70,000 and 100,000 km [3]. During this phase, the normal working conditions of the engine deteriorate and we have an additional fuel consumption of 10 - 15%. At this stage, due to the complete non-burning of hydrocarbons, soot particles settle in the nozzle of the sprayer and in the parts of the combustion chamber (engine head, piston, valves, etc.) breaking its calculated shape and worsening the spraying and the mixture of fuel with air and the combustion process. During this it is noticed that the engine does not get the maximum revolutions of the factory [8-10].

Experimental determination of performance and pollution rates of vehicle

In Albania, the automobiles with diesel engine are mainly used, so for experimentation we have chosen:

a. Three vehicles included with a diesel engine, which are:

- *Mercedes Benz car C 250*; year of production -1998, Fuel system with linear high pressure pump. (State 269,500 km)

- *Mercedes Benz car A170CDI* ; year of production -2001, Fuel system with Commun Rail. (State 230,000 km)

- *Ford car Fiesta* GAJA 1.8, year of production -1997, Fuel system with Lucas pump. (State 276,000 km)

b. " E*xtra super fuel max*" magnetic device with 1100 Gauss [5] and "Powrmag XP2" with 600 Gauss. It consists of 2 Neodium magnets in 2 plastic slots, which must be placed on the plastic fuel supply pipe, after the diesel filter, before entering the high pressure line

c. Automotive emission analyzer Trademaster MAHA T800, for measuring of gases pollution, that use to measure the level of pollutant gases during the vehicle technical inspection by SGS Automotive Albania, [11]. According to CE directive 40/2009/ , for the degree of pollution for engines, service the measurement of the opacity coefficient, as an adequate information about gas emissions. Its measurement is performed when the vehicle engine is in normal working condition, then the data of the vehicle to be tested (engine type, fuel type, cylinder capacity, year of production) are entered into the odometer computer and the data receiver is placed in the exhaust pipe. According to the standard test, the green field of revolutions (over 2500 rpm) appears on the monitor, which must be tested, and the device outputs the average value of the opacity coefficient.

-*Methodology of performing tests*

1. At first, measurements of the opacity coefficient are performed for 3 vehicles given (without magnetic device) and the values of the number of minimum and maximum revolutions are fixed . All 3 vehicles used same diesel
2. Then, the magnetic devices are placed in the vehicle engines. They are placed in the fuel supply line after the fuel filter (fig. 1).
3. The vehicles are put to work and the change in engine performance for the same rotations is monitored. This is visible in the first gear when the engine gets maximum revolutions. The number of km is fixed.
4. The opacity coefficient measurements are made for 3 given vehicles, after the magnetic effect and the number of minimum and maximum revolutions are recorde

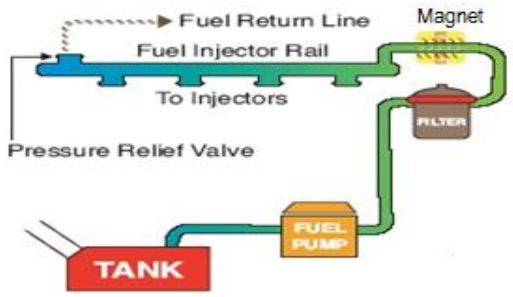


Figure 1. Schema of the fuel system



Figure 2 Magnet placed in the engine of Benz A170 CDI

Results and discussions

According to the given methodology, the opacity measurements are made for the 3 vehicles before the placement of the magnets, which are given in table 1 and the minimum and maximum numbers of engine revolutions, which are given in table 2.

Then the magnets were placed. In the vehicles with 1.7 and 1.8 liters, a magnet with 1100 gauss is placed, while in the vehicle with 2.5 liters, 2 magnets (2200G) were placed. The placement of the magnet (yellow) in the Benz A170 CDI vehicle, shows in fig. 2. After installation, the number of km was fixed. During use, the moment when performance changes occurred were kept under surveillance. At this point it was noticed that the engine has a reduction in noise and minimum revolutions and the engine reacts better.. According to the given methodology, the opacity measurements were made for the 3 vehicles after the placement of the magnet, which are given in table 1 and the minimum and maximum of revolutions are given in table 2.

Table 1. Opacity coefficients according to the standard technical control test

Without the magnetic device			**With the magnetic device**		
Benz C250D	Benz A170CDI	Ford Fiesta GAJA 1.8	Benz C250D	Benz A170CDI	Ford Fiesta GAJA 1.8
6.2	9.9	3.8	1.8	1.9	1.9

Table 2. Opacity coefficients according to the standard technical control test

Engine RPM	**Without the magnetic device**			**With the magnetic device**		
	Benz C250D	Benz A170CDI	Ford Fiesta GAJA 1.8	Benz C250D	Benz A170CDI	Ford Fiesta GAJA 1.8
Min	750	900	900	650	750	800
Max	3200	3100	3300	4500	4200	4500

From the experiments, it seems that the value of opacity in used vehicles (over 100,000 km) reaches high values (9.6-9.9 m-1), which exceed about 4 times the allowed value (k=2.5).

The results show that the action of the magnetic field on the fuel treatment before combustion has a great impact on reducing the opacity up to 4 times

The above analysis can be explained by the fact that the magnetic field acts on the fuel molecules creating vibrations of the fuel molecules with high frequency (10^{11}-10^{12}), close to infrared rays (10^{12}-10^{14}) [12]. This magnetic field not only changes the direction or rotates the molecules, but also gives it energy, which helps burn the fuel faster and better, not creating soot, but also burning carbon deposits.

So, the strong magnetic field (>1100Gaus) affects more in the better combustion of the fuel, making it faster and more complete, protecting the combustion chamber from soot. For new vehicles (< 100,000 km) the performance and pollution level given by the factory is maintained, therefore the influence of the magnetic field is imperceptible, which is consistent with the measurements made for new trucks [6]

Conclusion

The magnetic field in the fuel system affects in the better and faster burning of fuel in the engine. It helps maintain vehicles during use, to maintain engine performance and reduce pollution. This influence depends on the strength of the magnetic field and the quality of the used fuel.

In vehicles used with more than 100,000 km, the use of the magnetic field affects in the cleaning of carbon deposits in the combustion chamber, leading to increased performance and fuel savings up to 15% and reduction of pollution up to 4 times. The effect of the action depends on the strength of the field and the period of work that has created carbon deposits.

References

1. Hillier V.A.W. & Peter Coombes (2005) "Hillier's Fundamentals of Motor Vehicle Technology" 5 th edition Book 1
2. Pulkrabek W W (1999). Engineering Fundamentals of the Internal Combustion Engine. University of Wisconsin- p 283-289
3. Stone R. & Ball K.J., (2004). Automotive Engineering Fundamentals, USA
4. Hajderi A. (2010) "On the reduction of environmental pollution caused by automobile emissions"; Jurnal of studies on economics & society Vol.2 No 2 p 113-124
5. Burn out catalog 2011, p. 4; p. 165; www.fuelsaver.gr ;
6. Tre "economizzatori" alla prova(2007); Quattroruote, nr.618, Italia 2007 p. 80-84; www.quattroruote.it
7. Halderman D. J. (2012) Automotive technology principles, diagnosis and service; p. 918-945

8. Hajderi A., Lumi D., etc (2012) . **"**Case Study on Reduction of Environmental Pollution from usage of Vehicles in Albania" International conference on energy, environmental and sustainable development, Venice, April 11-12, 2012; World Academy of Science, Engineering and Technology (WASET)
9. Hajderi A., Sefa S. (2015); "The impact of alternative fuels in vehicles to reduce the global warming" Interdisiplinary Journal of Research and Development (IJRD) ISSN 2313-058X. Vol 2, nr.2/2015; p. 35-42
10. Hajderi A., Bozo L., Basholli F. (2024). "The impact of alternative fuel on diesel in reducing of pollution from vehicles " Engineering Applications" V 3 (Issue), p. 15-24
11. SGS Automotive Albania shpk; www.sgs.com
12. Ball P. (2001) "Stories of the invisible- A guide Tour of Molecules" Oxford Univ. Press 2001

Advanced Engineering Days

aed.mersin.edu.tr

Acoustic pollution in industrial environments

Fatmir Basholli [*1], **Aydın Alptekin** [2]

[1]*Albanian University, Department of Engineering, Tirana, Albania, fatmir.basholli@albanianuniversity.edu.al*
[2] *Mersin University, Department of Geomatics engineering, Türkiye, aydinalptekin@mersin.edu.tr*

Cite this study: Basholli, F., & Alptekin, A. (2024). Acoustic pollution in industrial environments. Advanced Engineering Days, 9, 809-811

Keywords
Acoustic noise
Sound
Industrial environments
Monitoring
Exposure to noise

Abstract

The research carried out an acoustic noise analysis in a non-alcoholic soft drink manufacturing plant. The study aims to identify the sources of noise in this environment, to examine its levels and characteristics, as well as to analyze the possible impact on workers, the internal environment and the external environment. For this purpose, noise measurement tools were used to record and evaluate the noise levels in the different spaces of the factory. Through a detailed analysis, the main sources of noise are identified such as production machines, material transport and other industrial activities that accompany production. In conclusion, the study recommends some corrective and preventive measures to improve the quality of the working environment and reduce the impact of noise on the external environment in the studied factory.

Introduction

The impact of acoustic noise in industrial environments is an important problem for the health and well-being of workers, as well as for the external environment. In this context, we conducted a scientific study to investigate the levels and effects of noise in a non-alcoholic soft drink manufacturing plant [1-2].

Breweries often involve various industrial processes that cause significant noise, which can have adverse impacts on the health and performance of workers, as well as outsiders in the local community.

In this study, we aimed to identify the main sources of noise in our brewery, determine its levels and characteristics, and analyze the possible impact on the work environment and the external environment. Using specialized noise measurement tools, we collected and analyzed data on noise levels in the various factory spaces [3-4].

This study aims to contribute to the further understanding of acoustic noise in industrial environments and to offer recommendations for its reduction.

Material and Methods

Measurements were performed using the CIRRUS 161 B instrument (Class I), equipped with a calibrator model CR:515 (Class I). The noise level measurement instrument was calibrated before the measurements at each point selected for monitoring. Noise level measurements were made by placing the instrument at a height of 1.5-1.7 m above ground level. The measurements were carried out for a period of 60 minutes, with the aim of evaluating the level of noise created by the subject during work and in his external environment during the normal regime of activity. The measurements were of an integral character, with a short time, as reflected in graph No. 1.

Selection of monitoring points

The monitoring of the noise level in the work environment is carried out to understand if the noise level exceeds the limit values determined by the standards and the relevant legislation, thus becoming a concern for the employees. For this reason, 8 points were selected in different installation environments, the coordinates and layout of which are presented (Figure 2) below:

The following auxiliary lines and plants are installed in the silo:

0.25L glass returnable bottle filling line, 222ml jug filling line, PET plastic bottle filling line 0.5L, 0.90L, 1.5L, 2L, PET bottle blowing line

Auxiliary facilities include: Water treatment plant, Production line washing room, Syrup preparation room, Sugar warehouse, Refrigerated room (for concentrate storage), Freezer room (for concentrate storage), Raw material warehouses, Boilers, Offices - mechanical, electrical, control laboratory, production office, meeting room, maintenance and repair (service) environment ALL [5-6].



Figure 1. CIRRUS 161 B device



Figure 2. Location plan of noise monitoring points

In the outer space there are: Wells, Undressing area for workers, mints, Meeting rooms, First aid, Hygienic services

The wastewater treatment plant consists of: Compressors, Generator, Cooling system for lines, Oil distributor, CO2 storage plant, Water tanks

Requirements of the national and international legal framework

The monitoring of the noise level of the activity in the factory was carried out based on:

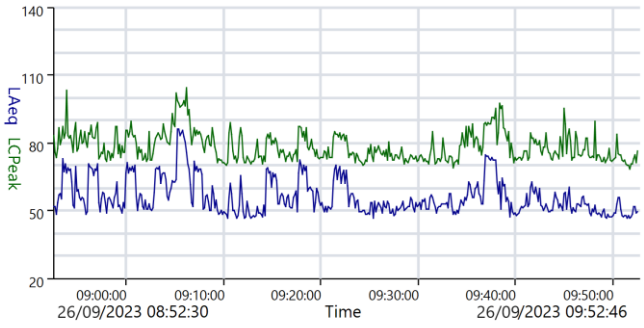
Directive 2003/10/EC of the European Parliament and of the Council of February 6, 2003, on the minimum health and safety requirements regarding the exposure of workers to the risks arising from physical agents (noise), constitutes the current European legislation that regulates the protection of workers from the risk of noise in the work environment. Based on the ISO 1999 standard, the Directive defines the exposure limits depending on the equivalent noise level for an 8-hour working day and obliges the employer to take appropriate steps if the limits are exceeded. The regulation on noise at work recommends three levels of action for professional environments [7-10]:

- the first (low) action level set at LEX,8h = 80 dBA;
- the second (upper) action level set at LEX,8h = 85 dBA; and,
- maximum exposure limits set in LEX,8h = 87 dBA.

Limits should be converted using a time-intensity shift of 3 dB increments per time halving. For example, exposure to noise at 97 dBA for 30 minutes per day would equate to the second action level (85 dBA for 8 hours), assuming long-term exposure.

3. Results and Discussions

Below are the results for one of the 8 points where the noise level in the subject was monitored (Chart 1, Figure 4).



.

Graph 1. Noise level at point 1



Figure 4. Photo during noise level monitoring at Point 1

Interpretation of the results of point 1:
The results obtained in connection with monitoring the level of exposure to noise, measured at Point 1, where the subject's activity takes place, show that:
- The maximum value of the noise level LAmax was 92.8 dB, this value is lower than the limit value of 110 dBA
- The equivalent noise level, measured in scale A (LAeqT day) was 67.2 dB, this value is lower than the allowed value (70 dBA).

In conclusion, we can say that the level of exposure to noise as a result of the activity in the Factory at Point 1 is within the allowed norms, in accordance with the National Legal Framework [11-14].

4. Conclusions

At first, identifying the main sources of noise in the factory allows us to understand the nature and scale of the problem. Production processes, material transport and other industrial activities are the main contributors to high noise levels in the workplace.

Furthermore, we have observed that acoustic noise has a significant impact on the health and well-being of workers. High noise levels can cause stress, increased fatigue, hearing damage and other health problems.

To address these issues, we propose a number of corrective and preventive measures. These include the use of advanced technology to reduce noise at the source,

the use of acoustic insulation materials, and the implementation of safety policies and the protection of the work environment in accordance with the European and Comet legal framework.

References

1. Peng-Li, D.; Mathiesen, S.L.; Chan, R.C.K.; Byrne, D.V.; Wang, Q.J. Sounds Healthy: Modelling sound-evoked consumer food choice through visual attention. Appetite 2021, 164, 105264. [CrossRef] [PubMed]
2. European Environment Agency report No 22/2019, Environmental noise in Europe — 2020, European Environment Agency, 2020, ISBN 978-92-9480-209-5, ISSN 1977-8449, doi:https://doi.org/10.2800/686249,Retrieved from https://www.eea.europa.eu/publications/environmental-noise-in- europe
3. Sohrabvandi, S.; Mousavi, S.M.; Razavi, S.H.; Mortazavian, A.M.; Rezaei, K. Alcohol-free Beer: Methods of Production, Sensorial Defects, and Healthful Effects. Food Rev. Int. 2010, 26, 335–352. [CrossRef]
4. Basholli, F., Mema, B., Hyka, D., Basholli, A., & Daberdini, A. (2023). Analysis of security challenges in SCADA systems, a technical review on automated real-time systems. Advanced Engineering Days, 8, 18-22
5. Spence, C.; Wang, Q. Sensory expectations elicited by the sounds of opening the packaging and pouring a beverage. Flavour 2015, 4, 35. [CrossRef]
6. Komatsuzaki, T.; Han, J.; Uchida, H. Approach for combining physical properties and sensibility for pleasant beverage canopening sound. Appl. Acoust. 2016, 103, 64–70. [CrossRef]
7. Ringler, C.; Sirianni, N.J.; Christenson, B. The Power of Consequential Product Sounds. J. Retail. 2021, 97, 288–300. [CrossRef]
8. Velasco, C.; Salgado-Montejo, A.; Marmolejo-Ramos, F.; Spence, C. Predictive packaging design: Tasting shapes typefaces, names, and sounds. Food Qual. Prefer. 2014, 34, 88–95. [CrossRef]
9. Basholli, F., Minga, J., & Grepcka, A. (2024). Protection of buildings on a university campus from lightning strikes. Advanced Engineering Days, 8, 35-38
10. Simner, J.; Cuskley, C.; Kirby, S. What Sound Does That Taste? Cross-Modal Mappings across Gustation and Audition. Perception 2010, 39, 553–569. [CrossRef]
11. Roque, J.; Lafraire, J.; Auvray, M. Audiovisual Crossmodal Correspondence between Bubbles' Size and Pouring Sounds' Pitch in Carbonated Beverages. Foods 2020, 9, 966. [CrossRef] [PubMed]
12. Wang, Q.J.; Spence, C. The Role of Pitch and Tempo in Sound-Temperature Crossmodal Correspondences. Multisens. Res. 2017, 30, 307–320. [CrossRef]
13. World Health Organization, (2018), Environmental Noise Guidelines for the European Region, ISBN 978 92 890 5356 3
14. Mendonça KT, Leite JC, Evaluation of acoustics in the built en-vironment, mapping and estimation of noise in the stamping sector of a metallurgical industry, Int J Adv Eng Res Sci 6, 2 2019, https://doi.org/10.22161/ijaers.6.2.34

Advanced Engineering Days

aed.mersin.edu.tr

Simulation based on historical data and expectations for tsunamis in the Adriatic and Ionian seas

Fatmir Basholli*[1], Adisa Daberdini [2], Rrapo Ormeni [3]

[1] *Albanian University, Department of Engineering, Tirana, Albania, fatmir.basholli@albanianuniversity.edu.al*
[2] *Aleksander Xhuvani University, Elbasan, Albania, adisa.daberdini@gmail.com*
[3] *Institute of Geosciences, Energy, Water and Environment, Tirana, Albania, rrapo55@yahoo.com*

Cite this study: Basholli, F., Daberdini, A., & Ormeni, R. (2024). Simulation based on historical data and expectations for tsunamis in the Adriatic and Ionian seas. Advanced Engineering Days, 9, 812-814

Keywords
Adriatic Sea
Ionian Sea
Tsunami risk
Seismic source
Sea waves

Abstract

In this study, we have presented the methods by which we can analyze the tsunami data in the Adriatic and Ionian Sea basins. These have been reconstructed on the basis of historical data that have been presented in various publications. The applications and their support are made with direct simulations on the geographical maps that are in google maps. In the construction of the structure of the sea basin, map data were obtained from the Military Geographical Institute. The calculations have been developed taking into account the various earthquake events that have occurred in our country, those with epicenters in the Adriatic and Ionian seas and seismic events in neighboring countries that have caused a tsunami, which are presented in the data published in various studies. At the end of this study, we have presented an analysis of the risk levels that tsunamis may have in our coastal area.

Introduction

In this study, we will deal with a physical phenomenon of the earth, which is one of the geological phenomena that clearly demonstrates the dynamics of the planet in which we live. Given that Albania and the entire Mediterranean basin is one of the areas with a very large seismic activity and in our country earthquake events with different magnitudes occur all the time, where we will consider the impact of marine earthquakes in the generation of tsunamis. In the last two decades, studies of tsunami deposits have grown rapidly [1-3]. This research has been fueled by increasing estimates of tsunami deposits in its risk assessment. Tsunami deposits are evidence that a tsunami can overturn an area. In this study, we will present a simple simulation model on the effects of the tsunami on the Albanian coast [4-7].

Material and Methods

We presented several scenarios and analyzed all the results we obtained from the calculations and simulations made. We have taken scenarios for risk assessment in both our seas and we have also given the effects they will have on the ecology of coastal areas and underwater ecology. Despite the fact that most of the seismic tsunamis are generated in the oceans as well as in the basins of in small seas such as the Adriatic and the Ionian, these phenomena can occur [8-13].

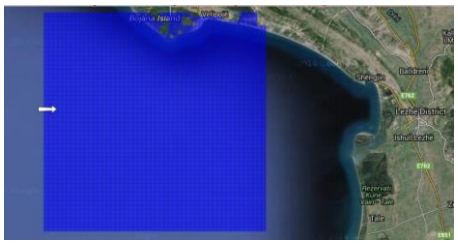
Google Tsunami Mapper program for tsunami assessment in the Adriatic and Ionian seas

Tsunami mapper is a google maps application that uses the elevation service to show areas that are likely to be affected by tsunamis. After the tsunami map is built, we can zoom in on it and see how far the wave will go and what percentage of the land can be flooded, and if any inhabited areas appear flooded on the map, etc [14-16].

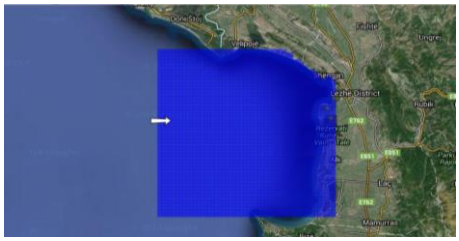
EMS scales (European Macroseismic Scale) of tsunami Intensity and simulations on the Albanian coast

Map of the expectation of tsunamis in our territory, starting from the two highest levels that can occur in the territory of Albania [17-19] (Figure 1, a, b and Figure 2):

For the V degree of the tsunami:



(a)



(b)

Figure 1, a, b. The spread of the V-level tsunami with a wave height of 1 m in Ulcinj (a) and Velipoje (b).

This tsunami occurring near the mouth of the Drin (Figure 1, a, b.) would cause a wave that would start from one meter and near the ground it could be even more. It would cause the flooding of Bojana Island and the areas near the coast of Velipoja.
For the VI degree of the tsunami:



Figure 2. Spread of the 6th degree tsunami with a wave height of 2m in Vlora.

This tsunami (Figure 2) will have a much greater impact than the magnitude five tsunami we saw above. It would enter near the Novosela area and up to Orikum.

3. Results and Discussions

The result of this study shows how to build an approximate model for the effects of a tsunami according to the structure that the Albanian coast has and that can be subjected to a seismic activity, in which in some cases tsunamis can develop in marine dimensions. Physical structure can be damaged by wave force itself, physical attraction of fauna and flora and increased sediment load can affect species sensitive to sedimentation and inhibit the development of coastal life [20-21].

The numerical analysis obtained from the numerical modeling is given by means of a simple numerical method and we have considered the construction of a scenario for the initial amplitude that we would have for the tsunami at sea and the amplitude that the wave would have on the coast along different profiles [22].

4. Conclusions

The Ionian-Adriatic region has economic and tourism growth with an increase in coastal population, making them future targets of a large-scale disaster even if the tsunami wave height is moderate.

Large tsunami events require the presence of a thick layer of water that can only be found in oceanic areas, but they can also occur in small basins such as the Ionian and Adriatic seas, in which many tsunamis have been reported during historical periods.

References

1. Triantafyllou, I. (2021). Impact of earthquakes in Greece from the antiquity up to now: Database development and space-time distribution with GIS tools. PhD Thesis, National & Kapodistrian University of Athens, p. 210.
2. Papadopoulos, G. A., Imamura, F., Nosov, M., & Charalampakis, M. (2020). Tsunami magnitude scales, 1st ed. In M. Engel, J. Pilarczyk, S. M. May, D. Brill, & E. Garrett (Eds.), Geological records of tsunamis and other

extreme waves (pp. 33–45).
3. Adisa Daberdini, Rrapo Ormeni (2013) "Generation of tsunami wave by earthquake in Adriatic Sea" Alb-Shkenca International Conference, Tirana,.
4. Papadopoulos, G.A. (2002). "Tsunamis in the East Mediterranean: A Catalogue for the Area of Greece and Adjacent Seas", Proceedings of the International Workshop on Tsunami Risk Assessment beyond 2000: Theory, Practice and Plans, Moscow, Russia, pp. 34-42.
5. Papadopoulos, G.A. and Plessa, A. (2001). "Historical Earthquakes and Tsunamis of the South Ionian Sea Occurring from 1591 to 1837", Bulletin of the Geological Society of Greece, Vol. XXXIV, No. 4, pp. 1547-1554.
6. Tinti, S. and Maramai, A. (1996). "Catalogue of Tsunamis Generated in Italy and in Côte d' Azur, France: A Step towards a Unified Catalogue of Tsunamis in Europe", Annali di Geofisica, Vol. 39, pp. 1253-1299.
7. Tinti, S., Maramai, A. and Graziani, L. (2004). "The New Catalogue of Italian Tsunamis", Natural Hazards, Vol. 33, No. 3, pp. 439-465.
8. Ambraseys, N.N. (2002). "Seismic Sea-Waves in the Marmara Sea Region during the Last 20 Centuries", Journal of Seismology, Vol. 6, No. 4, pp. 571-578.
9. Davies, G., Griffin, J., Løvholt, F., et al. (2017). A global probabilistic tsunami hazard assessment from earthquake sources. In E. M. Scourse, et al. (Eds.), Tsunamis: Geology, Hazards and Risks (p. 456). Geological Society London, Special Publications.
10. Grezio, A., Babeyko, A. Y., Baptista, A. M., et al. (2017). Probabilistic Tsunami Hazard Analysis (PTHA): Multiple sources and global applications. Reviews of Geophysics, 55, 1158–1198.
11. Alongi, D.M. (2008). Mangrove forests: Resilience, protection from tsunamis, and responses to global climate change. *Estuarine, Coastal and Shelf Science* 76: 1-13.
12. Ormeni Rrapo, Dushi Edmond, Shatro Astrit, Adisa Daberdini,Basholli Fatmir (2013). "Resent seismic activity of the Lezha-Ulqini seismogenic zone and its associated hazard". International Balkans Conferance on Challenges of Civil
13. Papadopoulos, G. A. (2016). Tsunamis in the European-Mediterranean Region: From Historical Record to Risk Mitigation (p. 271).
14. Papazachos BC, Dimitriu PP, (1991) Tsunamis in and near Greece and their relation to the earthquake focal mechanisms, *Nat. Hazards*, **4**, 161-170.
15. Soloviev, S.L., Solovieva, O.N., Go, C.N., Kim, K.S. and Shchetnikov, N.A. (2000). "Tsunamis in the Mediterranean Sea 2000 B.C.-2000 A.D.", Kluwer Academic Publishers, Dordrecht, The Netherlands.
16. Basholli, F., Mema, B., Hyka, D., Basholli, A., & Daberdini, A. (2023). Analysis of security challenges in SCADA systems, a technical review on automated real-time systems. Advanced Engineering Days, 8, 18-22
17. Taymaz T, Jackson, JA, Westway R, (1990) Earthquake mechanisms in the Hellenic Trench near Crete, *Geophys. J. Int.*, 102, 695-732.
18. Zaytsev, A. I., Babeyko, AYu., Kurkina, A. A., Yalciner, A. C., & Pelinovsky, E. N. (2019). Tsunami hazard assessment on the Egyptian Coast of the Mediterranean, Izvestiya. Atmospheric and Oceanic Physics, 55, 462–469.
19. Basholli, F., Minga, J., & Grepcka, A. (2024). Protection of buildings on a university campus from lightning strikes. Advanced Engineering Days, 8, 35-38
20. Yavuz, A. (2021). Overestimation of displacement due to misinterpretation of earthquake rupture parameters. Journal of Scientific Reports-A, 47, 39–46
21. Daberdini, A., Basholli, F. & Metaj, N. (2022). Simulation with the Mirone application for the construction of marine mechanical waves generated by possible seismic events in the territory of the Adriatic and Ionian seas. 5th Advanced Engineering Days, 84-87
22. Daberdini, A., Basholli, F., & Metaj, N. (2023). Simulation with the Mirone application for the construction of marine mechanical waves generated by possible seismic events in the territory of the Adriatic and Ionian seas. Advanced Engineering Science, 3, 46-54

Advanced Engineering Days

aed.mersin.edu.tr

Reconstruction of the historical building based on archaeological excavations and studies

Khojiakbar Egamberdiyev [*1], Noila Xidirova [*1], Asilbek Shukurov [*2], Jakhongir Davronov [*2], Jonibek Xolmurodov [*2]

[1] *Economical and Pedagogical University, Computer systems, Uzbekistan, kh.egamberdiev1984@gmail.com, noilaxidirova1989@gmail.com*
[2] *Karshi branch of TUIT, Programming Engineering, Uzbekistan, bombardearsnake@gmail.com, nzonik731@gmail.com, jonik705a@gmail.com*

Cite this study: Egamberdiyev, K., Xidirova, N., Shukurov A., Davronov, J., & Xolmurodov, J. (2024). Reconstruction of the historical building based on archaeological excavations and studies. Advanced Engineering Days, 9, 815-817

Keywords
Nakhshab, Yerkurgan
Curtius Rufus
3D models
Rectangular towers
Camera views
2D editor
Unreal Engine 4
3D reconstruction

Abstract

The city of Karshi, located in the southern region of Uzbekistan, is a city with several hundred years of history. Its antiquity can be seen in the example of the city of Yerkurgan, which is 9 km away from the city of Karshi, and has become a ruin today. Due to various battles, invasions and various natural conditions, today only the remains of this city can be seen. Through the remains of these ruins, archeological excavations and historical inscriptions, we can visualize the city. Other interested non-specialists, such as tourists, students, and the like, will find it easy to visit and observe these places. Therefore, it is an urgent task to restore the historical city through archeological excavations, studies and historical correspondence in laboratory conditions, on the basis of 3D modeling added to computer graphics, and to bring it to the interested public.

Introduction

For the first time, the materials of archaeological long-term research of Nakhshab, in particular the results of excavations of the Yerkurgan settlement, are summarized in the monograph by R.H. Suleymanov "Ancient Nakhshab" Problems of the civilization of Uzbekistan of the 7th century. BC. – VII century AD released in 2000. Later in 2004, R.H. Suleymanov published a brochure analyzing the finds of Yerkurgan entitled "Nakhshab - the secrets of a forgotten civilization." A paragraph is dedicated to Yerkurgan in M.S. Bulatov's book "Space and Architecture", where the author makes a preliminary archaeoastronomical analysis of the site, although, as the researcher admits, the situational plans and architectural measurements had not yet been published. E.V. Rtveladze first identified the city of Branchidae with a specific place in the 1980s and this was the site of Talashkantepa. But in recent years, E.V. Rtveladze, recognizing this identification as erroneous, based on the messages of Curtius Rufus and Arrian, proposed a new localization of the city of the Branchids - Yerkurgan. This idea is most widely presented in the monograph: "Alexander the Great in Transoxiana: Campaigns, Historical Geography" 2019 [1].

Material and Method

History of ancient city Yerkurgan

Yerkurgan, the ancient city ruin, was the first urban capital of the city of Karshi, which existed from the 9th-8th centuries BC to the 6th centuries AD. It is located 9 km north of the modern city of Karshi. In historical sources, Bolo is mentioned as Nakhshab. The ruin of Yerkurgan consists of outer and inner fortress walls. The outer fortress wall is 150 hectares, the inner fortress wall (Shahristan) is pentagonal up to 8 meters high and occupies an area of approximately 40 hectares. It includes buildings such as the governor's palace, a temple, a potter's neighborhood, and residences.

In the area of the city's outer walls, a tomb, a mausoleum, and a blacksmith's quarter were discovered and studied by archaeologists.

During the archeological excavations conducted in Yerkurgan, various types of ceramic vessels (khum, khumcha, bowls, pots, bowls, cups, etc.), objects used in religious ceremonies, ceramic figurines of goddesses, Nakhshab coin, water Specimens of 'd writing, a copy of a seal were found.

Through many years of research at the unique settlement, archaeologists have discovered a typological diversity of buildings - these are temple complexes, a palace, a mausoleum, a citadel of the 3rd century. AD, Dakhma III-II centuries. BC, craft quarters and others. The structure of the city of Yerkurgan can be described as a conglomerate of continuous carpet buildings, over which monumental buildings for religious and administrative purposes rise. The architectural center of Yerkurgan is the temple complex, consisting of two buildings: the central temple (little studied) and the sanctuary. In front of the sanctuary there is a vast space - the central city square. It is noteworthy that monumental buildings are mainly concentrated in the northern part of the city.

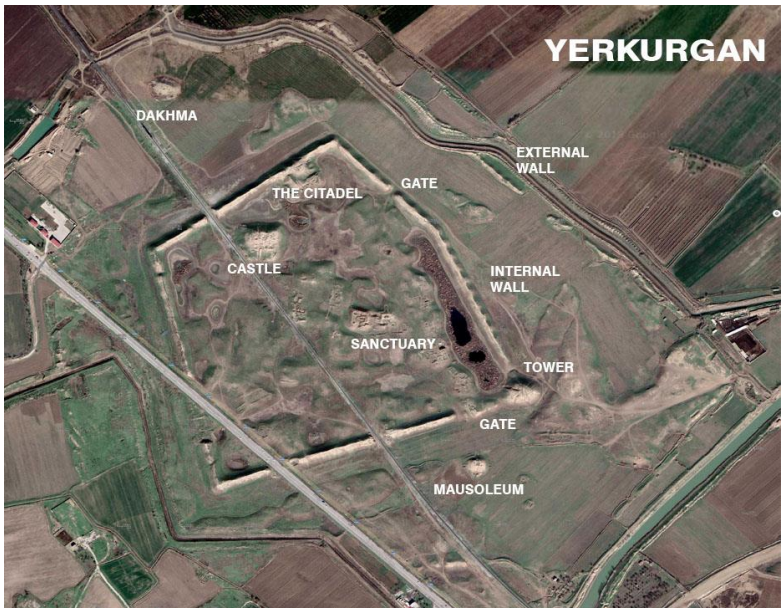


Figure 1. https://www.google.com/maps/place/38%C2%B056'56.5%22N+65%C2%B042'50.5%22E/@38.9497622,65.7141066,15z/data=!3m1!1e3?hl=ru-KG

In the microrelief here around the palace, near the citadel and behind the sanctuary, vast spaces free from buildings are noticeable. Taking into account the hypothesis that Yerkurgan is a city of the Branchidae, here we locate the sacred groves described by Curtius Rufus.

Results

Source base of the study

Sources in this work are divided into text and graphic. It was planned to record the current state of the complex using photogrammetry technologies in the form of a point cloud, but such a step is not possible, since work is underway on the territory of the Yerkurgan complex; only traces of the wall, temple, palace and other objects remain at the complex. For this reason, recording the current state of the object was transferred to digital photography from the ground.

The textual sources mainly consist of data from a restoration project in the 1970s. They contain historical information, the state of the complex at the time of drawing up the project, extracts from archival files and earlier literature, as well as the restoration project itself. In addition to textual materials, archival files contain a small number of photographs taken both during reconnaissance work and before it was carried out, and measurement drawings of buildings. For three-dimensional reconstruction, the presence of such a corpus of sources provides invaluable assistance, since the availability of accurate data on objects significantly speeds up the reconstruction process, and photographs make it possible to determine the dynamics of the destruction of the Yerkurgan complex and highlight features of buildings that are not reflected in the drawings. Most of the information in archival files is devoted to the inner cities of Yerkurgan, since the features of its decor and style allow it to be classified as a cultural heritage site, at least of regional significance. There are approximate photographs of the gates of the complex, temple, palace and other special buildings that formed the features of the landscape. Today, the structure

of the Yerkurgan complex has been largely lost, and therefore these photographs are also important in restoring the area. For this reason, the sample was drawn from their surviving portion.

All 3D editor programs have a common base:

1. A similar interface, including the following elements and functions: ready-made "primitives" that are used when constructing any 3D model (cube, cylinder, triangle, cone, sometimes ball, etc.), copy, paste, mirror functions object, object lighting functions, etc.

2. A similar system for constructing 3D models: polygonal modeling, which includes Editable mesh (editable surface) and Editable poly (editable polygon). Modeling methods can be combined with each other. Modeling based on standard objects, as a rule, is the main method and serves as a starting point for creating objects of complex structure, which is associated with the use of primitives in combination with each other as elementary parts of composite objects.

We list the main three-dimensional editor programs: Autodesk 3D Max, Autodesk Maya, Zbrush, AutoCAD, ArhiCAD, Catia, Hexagon, MoI, Nevercenter Silo, 3DWorldStudio, Argile, Google SketchUp, Blender, Wings 3D, Cartography Shop. The last four programs are free software.

We list the main programs for three-dimensional converters of 3D models: Deep Exploration CAD, 3D Photo Browser, 3D Object Converter, etc.

3) 3D engines – computer programs necessary for building virtual "interactive worlds" into which three-dimensional models are placed. The most common three-dimensional engines used to develop virtual historical reconstructions are the following programs: Cry Engine 3, Unreal Tournament UDK, Unity 3DQuest 3D, 3DVia Studio (Virtual Tools), Torque Game Engine, Nebula Device, ShiVa 3D game engine, Unigine, 3D Game Studio, etc.

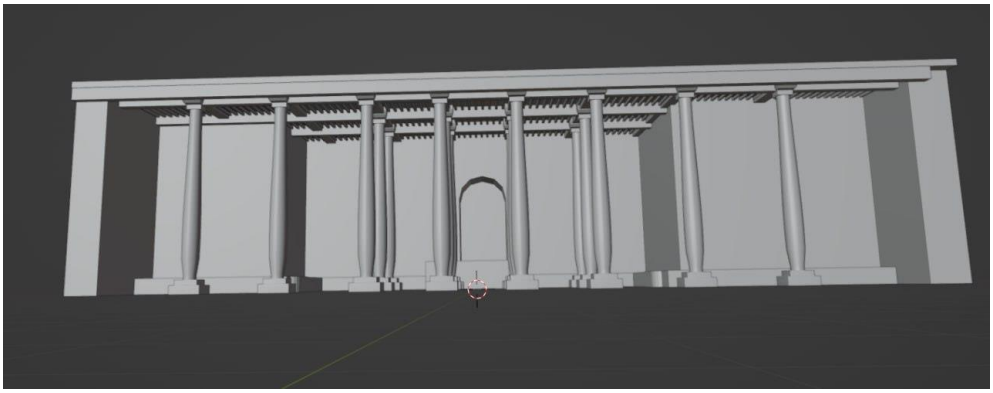


Figure 2. Geometry modeling on Blender

Conclusion

The result of the virtual 3D reconstruction of the historical city of Yerkurgan is both image renderings of the external and internal premises of the building, and a ready-made virtual environment for those interested in history. The historical heritage in this case provides great scope for the use of virtual 3D reconstruction methods. This work allows not only to reproduce and preserve images and processes of the past, but also to draw attention to the problem of preserving historical heritage, which is often forgotten, finding ancient buildings less interesting and worthy of attention. Currently, further work is underway to apply virtual 3D reconstruction methods and virtual reality technologies to various objects in the city of Yerkurgan.

References

1. Nurulin T.S. (2022), 3D reconstruction of the Yerkurgan settlement // Architecture and construction of Uzbekistan. – Tashkent. - No. 2-3. – pp. 27-38.
2. Hasanov, A. (2022), Technologies of 3 d-modeling in problems of virtual reconstruction of industrial heritage (using the example of the Trehgorny brewery in Moscow). The importance of digital technologies in the study of the history of Uzbekistan, 1(01), 186–193. https://doi.org/10.47689/.v1i01.13369
3. Suleymanov R.Kh. (2000), Ancient Nakhshab. Problems of civilization of Uzbekistan in the 7th century. BC-VII century AD – Samarkand-Tashkent: "FAN". – 312 p.
4. Rtveladze E.V. (2019). Alexander the Great in Transoxiana: Campaigns, historical geography. St. Petersburg: Eurasia. – 368 p.
5. Litvinsky B.A., Pichikyan I.R. Hellenistic temple of Oxus in Bactria (Southern Tajikistan). T. 1. Excavations. Architecture. Religious life. – M.: Publishing company "Oriental Literature" RAS, 2000. -503 p.: ил.

Advanced Engineering Days

aed.mersin.edu.tr

Methodology for teaching computer science using information and communication technologies

Madina Makhkamova*[1], Noila Xidirova*[2], Sadokat Kamolova*[3]

[1] *Chirchik State Pedagogical University, Methods of Teaching Computer Science, Uzbekistan, mmahkamova857@gmail.com*
[2] *Economical and Pedagogical University, Computer systems, Uzbekistan, noilaxidirova1989@gmail.com*
[3] *Karshi branch of TUIT, Computer Systems, Uzbekistan, kamolovasadoqat16@gmail.com*

Cite this study: Makhkamova, M., Xidirova, N., & Kamolova, S. (2024). Methodology for teaching computer science using information and communication technologies. Advanced Engineering Days, 9, 818-820

Keywords
Game methods
Project -based learning
e-learning
m-learning
Blended learning
LMS

Abstract

This article discusses modern methods of teaching computer science based on the use of information and communication technologies (ICT). The advantages and disadvantages of ICT in the educational process are analyzed, and recommendations are offered for their effective implementation in the educational process.

Introduction

Modern society is characterized by the rapid development of information technology, which requires educational institutions to adapt curricula and teaching methods. Teaching computer science using ICT is becoming an integral part of the educational process, helping to improve the quality of education and prepare students for the demands of the digital age.

Computer science, as an academic discipline, occupies an important place in school and university education. This article examines various computer science teaching methods, including traditional and modern approaches, to identify the most effective strategies.

Material and Method

The research used methods of literature analysis, surveys of teachers and students, as well as the experimental implementation of various methods in the educational process. The data was collected from scientific articles, educational portals and the results of pedagogical experiments. The main attention was paid to a comparative analysis of the effectiveness of various teaching methods.

Results

Traditional teaching methods

Traditional methods include lectures, laboratory work and seminars. These methods are time-tested and have a number of advantages:

- **Lectures**: allow you to convey a large amount of theoretical information.
- **Laboratory work**: contribute to the practical development of the material.
- **Workshops**: Develop critical thinking and problem solving skills.

Modern teaching methods

Modern approaches include the use of digital technologies and interactive methods:

- **Online courses and MOOCs**: Platforms such as Coursera and edX provide access to courses from top universities.
- **Gaming methods**: Using educational games and gamification to increase student motivation.

- **Project-Based Learning**: Emphasis on completing projects that develop practical skills and teamwork.

Comparative analysis

A comparison of traditional and modern methods has shown that a combination of different approaches gives the best results. For example, integrating lectures with online courses and project-based learning significantly increases student learning and satisfaction with the learning process.

Table 1. Comparison of traditional and modern methods of teaching computer science

Method	Advantages	Flaws
Lectures	Transfer of theoretical information	Limited interactivity
Laboratory works	Practical mastery of the material	Requires equipment
Online courses	Access to a variety of resources	The need for self-organization
Game methods	Increased motivation	Possibility of distraction from the main goal
Project-based learning	Development of practical skills	Difficulty in assessment

Methodology

Basic approaches

The use of ICT in computer science teaching includes various techniques, such as:

1. **Electronic learning (e- learning)**: includes the use of online courses, virtual classrooms and electronic textbooks.
2. **Mobile learning (m- learning)**: using mobile devices to access learning materials and interact with teachers.
3. **Blended learning**: a combination of traditional teaching methods and ICT, which allows you to maximize the effectiveness of the educational process.

Tools and technologies

1. **Learning Management Systems (LMS)**: Platforms such as Moodle and Blackboard allow you to organize learning experiences, manage materials, and track student progress.
2. **Virtual Labs and Simulators**: Provide hands-on learning and experimentation in a virtual environment.
3. **Interactive multimedia resources**: video lessons, interactive presentations and animations help make learning more visual and fun.

Benefits of ICT in Computer Science Education

1. **Accessibility and flexibility**: Students can study anytime and anywhere, which is especially important for correspondence and distance learning.
2. **Interactivity and Engagement**: Interactive elements encourage active student participation in the learning process.
3. **Personalization of learning**: ICT allows learning materials to be tailored to the individual needs of each student.
4. **Accelerate information sharing**: Instant access to up-to-date training materials and resources.

Disadvantages and challenges

1. **Technical problems**: Internet access problems and equipment incompatibility can make using ICT difficult.
2. **Need for teacher training**: Teachers must have appropriate skills to effectively use ICT in teaching.
3. **Information security risks**: protecting students' personal data and educational materials is an important task.

Recommendations for the implementation of ICT in computer science education

1. **Teacher training**: conducting trainings and advanced training courses for teachers on the use of ICT.

2. **Infrastructure**: providing educational institutions with the necessary equipment and access to the Internet.
3. **Curriculum adaptation**: Integrating ICT into curriculum and creating interactive learning materials.
4. **Monitoring and evaluation**: regularly assess the effectiveness of the use of ICT in teaching and make necessary adjustments.

Discussion

The use of modern technologies in computer science teaching opens up new opportunities, but also requires appropriate training of teachers and the availability of the necessary resources. It is important to take into account the individual characteristics of students and adapt methods to their needs. In addition, attention should be paid to the ethical aspects of using digital technologies in education.

Conclusion

Effective teaching of computer science requires a combination of traditional and modern techniques. Integration of various approaches makes it possible to create a more flexible and adaptive educational environment that meets the requirements of modern society. Further research should be aimed at optimizing these techniques and adapting them to changing conditions.

The use of information and communication technologies in computer science teaching opens up new opportunities for improving the quality of education. However, for the successful implementation of ICT, it is necessary to take into account both the advantages and disadvantages of these technologies, as well as the readiness of teachers and students to use them. The introduction of ICT into the educational process requires a systematic approach and constant monitoring to achieve the best results.

References

1. Bocharova E.V. (2020). Use of ICT in the educational process. Bulletin of Education, 3, 45-56.
2. Ivanova N.A., & Petrov, S.B. (2019). E-learning: modern technologies and prospects. Education and Science, 12, 78-89.
3. Sidorov V.P. (2018). Interactive teaching methods in higher education. Pedagogy, 5, 23-34.
4. Egamberdiev Kh. Eyes and Lenses: A Comparison and Differences// Journal of Multimedia and Information System VOL. 3, NO. 2, June 2016 (pp. 43-46): ISSN 2383-7632 http://dx.doi.org/10.9717/JMIS.2016.3.2.43
5. Egamberdiev Kh., Nurimov P. The art of immersion: the history and development of panorama. // "Information and communication technologies in education and science" Collection of materials of the V International Scientific and Practical Conference (April 25 - 28, 2016) p. 168
6. Egamberdiev Kh., Nurimov P. Chan Koh. The differences between camera lens and the human eye. // 2016 년도춘계학술발표대회 논문집Korea multimedia societe http://www.kmms.or.kr/ 131-134 pages

Advanced Engineering Days

aed.mersin.edu.tr

Modeling the stability indicator taking into account the bending deformation of the freight car body

Anzhelika Shvets [1], Leontii Muradian [1], Angela Shvets [*2]

[1]*Ukrainian State University of Science and Technologies, Wagons and Wagon Facilities, Ukraine, angtiger.am@gmail.com, leontymuradian@gmail.com*

[2]*Ukrainian State University of Science and Technologies, Engineering and Design Specialized Department «Microprocessor-Based Control Systems and Safety in the Railway Transport» (EDSD MBCSS), Ukraine, angela_shvets@ua.fm*

Cite this study: Shvets, A., Muradian, L., & Shvets, A. (2024). Modeling the stability indicator taking into account the bending deformation of the freight car body. Advanced Engineering Days, 9, 821-823

Keywords
Shift of the cargo
Railway
Gondola cars
Body elasticity
Mathematical modeling

Abstract

The influence of flexural deformation of the freight car body on the stability indicator is studied. A theoretical study was carried out using a model of spatial vibrations of a freight car as part of a homogeneous train. When carrying out calculations, the car body was considered as an absolutely rigid body and as a discrete multi-mass system with elastic connections between the masses. When choosing a design scheme, it was assumed that the car body is a deformable body and, when bending, has finite rigidity in the vertical and horizontal planes. As a result of the research, the dependence of the wheel stability indicator from derailment on the flexural deformation of the body and the speed of movement was obtained. The presented study makes it possible to estimate the permissible speed of movement of the car based on the elastic characteristics of the body in the vertical and horizontal plane, the displacement of the center of mass of the cargo in the car, and also to take into account the longitudinal quasi-static forces arising under operating conditions.

Introduction

The largest number of cars in the freight fleet of railways are gondola cars, as the most versatile and popular type of rolling stock. The design of the gondola car allows extensive use of mechanization during loading and unloading. Imperfect technology for loading cars very often leads to significant damage during loading and unloading operations. Therefore, research into the reliability, strength and stability of rolling stock during operation is an urgent scientific and technical task [1-5].

A preliminary assessment of the dynamic characteristics of the car can be achieved using mathematical modeling. Modeling makes it possible to determine the dynamic characteristics of cars as they move along straight and curved sections of the railway track. Software systems allow modeling with real irregularities in the vertical and horizontal planes, as well as taking into account the real rolling surfaces of the wheel and rail head profile [6-8].

Material and Method

When studying the spatial vibrations of gondola cars, the following assumptions were made: it is assumed that the cars consist of 12 solid bodies (cargo, body, two bolsters, four side frames and four wheelsets). The bogie frame design is assumed to be articulated. The elastic-viscous and inertial properties of the track base in the vertical and horizontal planes are taken into account [8-10].

A mathematical model of spatial oscillations of a freight car in the form of a nonlinear mechanical system with 54 degrees of freedom is presented in [9]. The center of mass of the car body is placed at the origin of the coordinate system, and the center of mass of the cargo is shifted by the values A_x in the longitudinal direction and A_y in the transverse direction. Taking into account the equations of relations, the differential equations of the

oscillations of the car were compiled using the d'Alembert principle. In this study, the car body and cargo were considered as absolutely rigid bodies.

It was noted in [11, 12] that in order to obtain the full spectrum of natural vibration frequencies of the bolster structure of a gondola car, the body should be considered as a deformable body (Fig. 1).

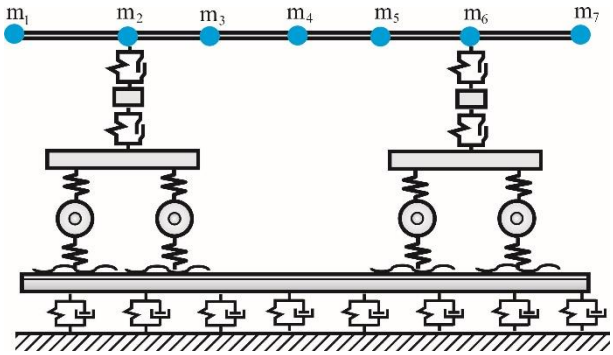


Figure 1. Calculation scheme of a 4-axle freight car

The car body is considered as a deformable body. That is, when bending, it has finite rigidity in the vertical and horizontal planes. Wheelsets and bogie sides are still considered to be rigid bodies. The car body (Fig. 1) is considered in the form of a weightless elastic beam of constant rigidity with seven concentrated masses. When considering the vibrations of an empty car, the inertial coefficients will be equal to the masses of the corresponding parts of the body structure. In the case of a loaded car, the mass of the cargo must be added to these masses.

The longitudinal force acting on the first and the last car of the coupling from the side of the thrown away parts of the train at any moment is determined from the solution of the problem of the longitudinal dynamics of the train (LTD). The forces occurring in the draft gears of the coupling cars are determined in accordance with the works [13, 14].

Results

The study was carried out using a model of spatial vibrations of homogeneous train cars. The running gear of the car, wheel tread and rail head profile were examined in normal technical condition. During the modeling process, the car body was considered as an absolutely rigid and elastic body (Fig. 1).

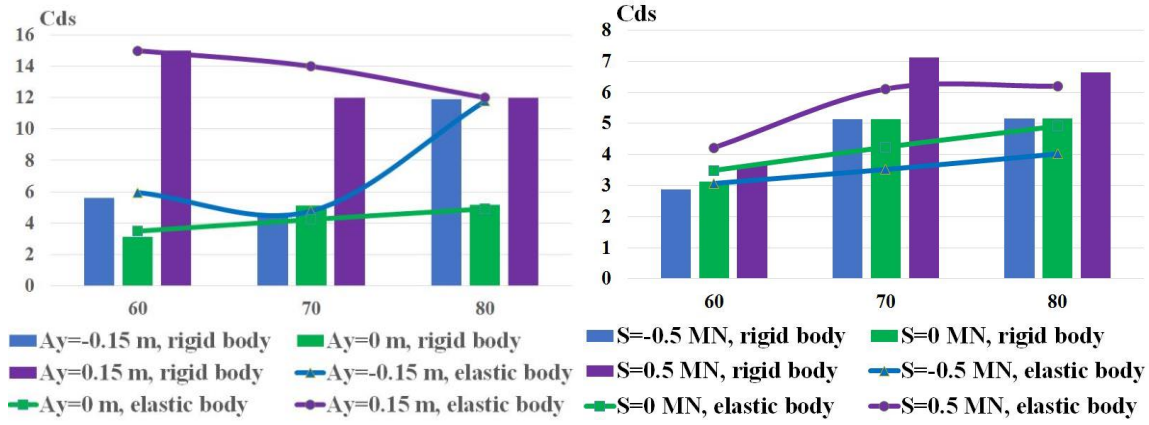


Figure 2. Dependencies of wheel derailment safety coefficient: a) the load shift in the lateral direction; b) the longitudinal quasi-static forces

The shift of the center of mass along the axes is considered within a range from 0 and 0.15 m. Fig. 2 (a) shows the graphs of the dependence of the wheel derailment safety coefficients on the value of the load centre shift in the lateral direction for the value of the longitudinal shift of 0 m.

Simulation of the process of interaction of the rolling stock with the rails in the presence of the lateral load center shift of the car shows (Fig. 2, a) the absence of influence of the characteristics of the body as an absolutely rigid and elastic body on the wheel derailment safety coefficient.

When modeling, the influence of longitudinal quasi-static tensile and compressive forces was considered depending on the change in speed in the range from 60 to 80 km/h with a change in the value of the force from

the tension of 0.5 MN; 0 and before compression of 0.5 MN. Graphs of the change in the wheel derailment safety coefficient during the movement of loaded wagons along the straight section of the track are shown in Fig. 2 (b).

The wheel derailment stability coefficient significantly exceeds the minimum allowable value [C_{ds}]=1.3. On the basis of the theoretical studies carried out, it can be concluded that the longitudinal quasi-static forces arising in the operational modes of motion also do not have a significant effect on the derailment of the wheels. [10].

Conclusion

The body of a freight car was considered as an absolutely rigid body and as a discrete multi-mass system with elastic connections between the masses. Analytical simulation was used to study the influence of the displacement of the center of mass of the load and operational longitudinal forces on the indicator of wheel stability from derailment when moving along a straight section of track with uneven surfaces.

Analyzing the results of theoretical studies, we can conclude that over the entire speed range when a loaded car moves along a straight section of track, both with reinforced concrete and wooden sleepers, the flexural deformation of the body does not have a noticeable effect on the indicator of wheel stability from derailment.

The presented study shows the need for further theoretical and experimental studies of bending vibrations of the car body as an elastic beam.

References

1. Muradian. L., Pitsenko, I., Shaposhnyk, V., Shvets, A., & Shvets, A. (2022). Predictive model of risks in railroad transport when diagnosing axle boxes of freight wagons. Proceedings of the Institution of Mechanical Engineers, Part F: Journal of Rail and Rapid Transit, 1-5. doi:10.1177 /09544097221 122043.
2. Shvets, A., Shvets, A., & Kasianchuk, V. (2020). Research of strength characteristics of element of the unit rolling stock. Railroad car fleet, 1(157), 7-12.
3. Shvets, Angela O., Bolotov, O. M., Saparova, L. S., & Shvets, Angelika O. (2019). Wear wheels and rails at the uneven loading of gondola cars. Bulletin of Certification of Railway Transport, 1(53), 4-17.
4. Shatunov, O. V., Shvets, A. O., Kirilchuk, O. A., & Shvets, A. O. (2019). Research of wheel-rail wear due to non-symmetrical loading of a flat car. Science and Transport Progress, 4(82), 102-117. doi:10.15802/stp2019/177457.
5. Shvets, A. O., Zhelieznov, K. I., Akulov, A. S., Zabolotnyi, O. M., & Chabaniuk, Y. V. (2015). Determination of the issue concerning the lift resistance factor of lightweight car. Science and Transport Progress, 6(60), 134-148. doi:10.15802/stp2015/57098.
6. Myamlin, S., Neduzha, L., & Shvets, A. (2014). Determination of friction performance influence in the system "body–bogie" on the freight car dynamics. Science and Transport Progress, 2 (50), 152-163. doi: 10.15802/stp2014/23792.
7. Shvets, A. O. (2018). Specifics of determining the moments of inertia a freight wagons bodies. Bulletin of Certification of Railway Transport, 5(51), 20-34.
8. Shvets, A., Muradıan, L., & Shvets, A. (2023). Investigation of wear of wheels and rails when the center of mass of cargo in gondola cars shifts. Advanced Engineering Days, 7, 109-112.
9. Muradian, L., Shvets, A., & Shvets, A. (2023). Some dynamic processes at longitudinally-transverse shift of the cargo. Scientific Journal of Silesian University of Technology. Series Transport, 120, 187-204. doi:10.20858/sjsutst.2023.120.12.
10. Shvets, A. (2023). Multibody model of freight railcars interaction in a train. In: Sharma, S.K., Upadhyay, R.K., Kumar, V., Valera, H. (eds) Transportation Energy and Dynamics. Energy, Environment, and Sustainability, 217-241. Singapore: Springer. doi:10.1007/978-981-99-2150-8_10.
11. Lazaryan, V. A. (1985). Vehicle Dynamics: Selected Works. Kiev: Publisher “Naukova dumka”.
12. Ushkalov, V. F. (1965). Investigation of flexural vibrations of freight car bodies. Dnepropetrovsk: Dnepropetrovsk Institute of Transport Engineers.
13. Blokhin, Y. P., & Manashkin, L. A. (1982). Train dynamics (unsteady longitudinal oscillations). Moscow: Transport.
14. Blokhin, Y. P., Manashkin, L. A., & Stambler, Y. L. (1986). Calculations and tests of heavy trains. Moscow: Transport.

Advanced Engineering Days

aed.mersin.edu.tr

Length-weight relationships of the Twait shad - *Alosa falax* (Lacepède, 1803) from the South western Adriatic coast of Albania

Nertila Muçollari [1] **Spase Shumka** [1]

[1]Agricultural University of Tirana, FBF, Department of BFS, Tirana, Albania, nertilamucollari@gmail.com, sprespa@gmail.com

Cite this study: Mucollari, N., & Shumka, S. (2024). Length-weight relationships of the Twait shad - *Alosa falax* (Lacepède, 1803) from the South western Adriatic coast of Albania. Advanced Engineering Days, 9, 824-826

Keywords
Anadromous
River Vjosa
Conservation
Adriatic Sea
Specimens

Abstract

Twaite shad, *Alosa fallax* (Lacépède, 1803) is one of the anadromous fish species that is close related to the Allis shad, *Alosa alosa* (Linnaeus, 1758) and a congeneric Clupeidae species, i.e., closely related, even hybridising with each other, which makes it very difficult to differentiate between them. The marine phase represents the major part of the life cycle of these species, yet there are still large gaps in the knowledge of the biology, ecology and distribution during this phase. In this article there are provided recent data on Twaite shad, length-weight relationship of 121 specimens. The results reveals a value of R^2 0.965, also emphasizing the needs for habitat conservation and advancement following the species ecology and its life patterns.

Introduction

River Vosa with a catchment of 6700 km^2 has a mean annual discharge of 204 m^3/s. While the discharge during dry periods (Summer) drops down to levels of 40-50 m^3/s, annual flood events show a magnitude of >1000 m^3/s. This river shows a very active sediment regime with an estimated transport at the Pocem bridge of 5 million tons per year. The sediments mainly consisted of the substrate classes psammal, akal and mikrolithal [1,2].he very recent research and literature data focused to the freshwater of Albania and River Vjosa have confirmed that the current fish fauna consists of 34 species from 10 orders and 14 families [3,4,5,6,7]. (Markova et al., 2010; Meulenbroek; Shumka et al., 2023). Among them 29 species are native to the River Vjosa basin: with 12 species, *Cyprinidae* are by far the most specious family, followed by *Mugilidae* (five). *Salmonidae* and *Acipenseridae* are represented by 2 species each. The remaining ten families are represented by a single species. At least five species (*Pseudorasbora parva*, *Oncorhynchus mykiss*, *Carassius gibelio, Chtenopharyngodon idella* and *Gambusia holbrooki)* were introduced into the Vjosa basin. The lower river reach is populated by other species as: European eel (*Anguilla anguilla*), species of Family*Mugilidae* (*Mugil cephalus, Chelon ramada, Chelon salienes* and *Chelon labrosus*), Seabream (*Sparus aurata),* Seabass *(Dincentrarchus labrax)*, Flatfish (*Platichthys flesus,* Common sole (*Solea* spp.) etc*,* while the resident species associated with saline water incluce, are numerically prevalent with the two species *Atherina boyeri* and *Aphanius fasciatus* showing presence and significance. The remaining four alien species, all introduced over the past 100 years as a consequence of human activity or unintentional one [8,9,10,11]. Following [12] the twaite shad *Alosa fallax* (Lacépède, 1803) occurs along the Atlantic coast from Morocco to Ireland and Scotland, in the North Sea to Bergen, including the southern Baltic Sea, in the northern Mediterranean, and occasionally in the northern Black Sea reaching Crimea.

Material and Methods

The specimens of Twait shad *(Alosa falax)* were collected between July 2023 and April 2024 at the River Vjosa two estuary localities (40°39'6.37"N/ 19°19'48.97"E and 40°39'55.76"N / 19°21'1.02"E), south-western Adriatic coast of Albania. A total of 121 specimens were captured by gill net and special locally designed lifting net close to the village of Pisha. After capture, all the fishes were immediately processed. Total length (TL), fork length (FL) and standard length (SL) of each fish obtained specimen was measured to the nearest cm and total weight (W) to the nearest 0.05 g. The length weight relationship was analyzed and the R^2 was showed after a simple excel analyses. Full specimens were transferred at the Laboratory of Hydrobiology at the Agricultural University of Tirana for further analyses.

Results and Discussions

Of the 121 specimens ranging from 11.5 to 47.0 cm TL, 65 were males and 56 were females. Length-frequency indicated that the 17-21 and 35-45 cm length classes had the highest number of specimens (Figure 1,2). The sample size, size range (cm, TL), mean TL, total weight range (g, W), mean W, the estimated parameters of relationship base don analyses of 121 specimens resulted r^2 of 0.965.

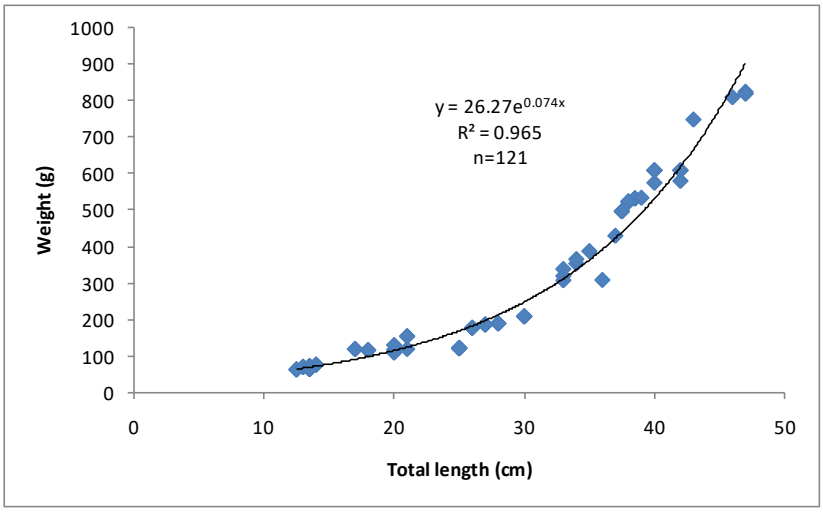


Figure 1. Length–weight relationships for Twait shad species from River Vjosa estuary

Among fishes 29 species are native to the River Vjosa basin: with 12 species, *Cyprinidae* are by far the most specious family, followed by *Mugilidae* (five). *Salmonidae* and *Acipenseridae* are represented by 2 species each. The remaining ten families are represented by a single species. At least five species (*Pseudorasbora parva*, *Oncorhynchus mykiss*, *Carassius gibelio, Chtenopharyngodon idella* and *Gambusia holbrooki)* were introduced into the Vjosa basin. The lower river reach is populated by other species as: European eel (*Anguilla anguilla*), species of Family*Mugilidae* (*Mugil cephalus, Chelon ramada, Chelon salienes* and *Chelon labrosus*), Seabream (*Sparus aurata),* Seabass *(Dincentrarchus labrax)*, Flatfish (*Platichthys flesus,* Common sole (*Solea* spp.) etc*,* while the resident species associated with saline water incluce, are numerically prevalent with the two species *Atherina boyeri* and *Aphanius fasciatus* showing presence and significance. The remaining four alien species, all introduced over the past 100 years as a consequence of human activity or unintentional one. According to the Albanian red list (MoE, 2013), three species are endangered (*Acipenser naccarii, Acipenser sturio,* and *Asphanius fasciatus)* and two vulnerable *(Petromyzon marinus* and *Platychthis flesus).* IUCN considers three species to be critically endangered *(Acipenser naccarii, Acipenser sturio* and *Anguilla Anguilla)* and additionally *Gobio skadarensis* is categorized as endangered. The Bern convention lists three species in Annex II (strictly protected fauna species) (*Acipenser naccarii, Acipenser sturio* and *Asphanius fasciatus*) and two as in Annex III (*Alburnoides aff. prespensis, Chondrostoma vardarense, Pachychlion pictum* and *Petromyzon marinus*) [13, 14, 15, 16]. There is a severe lack of knowledge concerning these systems compared to other systems in Europe, resulting in limited available data information about these species and their population status. This means that more species than previously thought could be severely threatened.



Figure 2. Twait shad *(Alosa falax)*

The results found and presented here are similar to those reported by [13, 14]. The free-flowing Vjosa Rivre is home to rich fish diversity, while basin itself is shelter for numerous flora and fauna species. It is as typical dynamic systems create a distinct longitudinal sequence of steep gradient headwaters, braided and meandering channel types and deltaic areas. This enables existence of rich fish diversity and large migration corridor [11]. The conservation actions for habitats integrity is a precondition also for securing fish species including Twait shad preservation.

Acknowledgement: The results of this article are part of the activities implemented under the Project: "Environmental assessment of the Vjosa riverscape as the basis for an integrated water management and sustainable catchment development" that is supported by APPEAR Academic Partnership, 2022-2026.

References

[1] Hauer, C., 2019. Measuring of sediment transport and morphodynamics at the Vjosa river / Albania. Wien.
[2] Hammerschmied, U. 2019. Fish species composition, diversity and abundanceof the lower river Vjosa, Albania. Master Theses, Department of Water, Atmosphere and Environment (WAU); Institute of Hydrobiology and Aquatic Ecosystem Management (IHG), Vienna, p. 99
[3] Marková, S., Šanda, R., Crivelli, A., Shumka, S., Wilson, I. F., Vukić, J., Berrebi, P. & Kotlík, P. 2010. Nuclear and mitochondrial DNA sequence data reveal the evolutionary history of *Barbus* (Cyprinidae) in the ancient lake systems of the Balkans. *Molecular Phylogenetics and Evolution* **55**, 488–500. doi:10.1016/j.ympev.2010.01.030
[4] Meulenbroek P, Shumka S, Schiemer F, 2018. First reconnaissance of habitat partitioning and fish diversity in the alluvial zone of the river Vjosa, Albania. *Acta ZooBot Austria, früher Verhandlungen der Zoologisch-Botanischen Gesellschaft in* Österreich *Band* 155, 177–186.
[5] Shumka S, Lalaj S, Šanda R, Shumka L**,** Meulenbroek P, 2023. Recent data on the distribution of freshwater ichthyofauna in Albania. Croatian Journal of Fisheries, 2023, 81, 33-44. http://.doi.org/10.2478/cjf-2023-0004
[6] Shumka S, Meulenbroek P, Schiemer F, Sanda R, 2018. Fishes of the River Vjosa – an annotated Checklist. *Acta ZooBot Austria, früher Verhandlungen der Zoologisch-Botanischen Gesellschaft in* Österreich *Band* 155/1, 163–176. [7] Meulenbroek P, Hammerschmied U, Schmutz S, Weiss S, Schabuss M, Zornig H, Shumka S, Schiemer F, 2020. Conservation Requirements of European Eel (Anquilla anquilla) in a Balkan Catchment. Sustainability 12, 8535. https://doi.org/10.3390/su12208535
[8] Šanda, R., Vukić, J., Choleva, L., Křížek, J., Šedivá, A., Shumka, S. & Wilson, I. F. 2008. Distribution of loach fishes (Cobitidae, Nemacheilidae) in Albania, with genetic analysis of populations of *Cobitis ohridana*. *Folia Zoologica* **57**(1–2), 42–50.
[9] Snoj, A., Marić, S., Berrebi, P., Crivelli, A. J., Shumka, S. & Sušnik, S. 2009. Genetic architecture of trout from Albania as revealed by mtDNA control region variation. *Genetics Selection Evolution* **41**, 22: 1–11. doi:10.1186/1297-9686-41-22
[10] Stierandová, S., Vukić, J., Vasileva, E., Zogaris., S., Shumka, S., Halačka, K., Vetešník, L., Švátora., M., Nowak, M., Stefanov, T., Koščo, J., Mendel, J.2016. A multilocus assessment of nuclear and mitochondrial sequence data elucidates phylogenetic relationships among European spirlins (*Alburnoides*), Molecular Phylogenetics and Evolution, 94 (B): 479-491
[11] Shumka, S., Mucollari, N. 2023. A review of fish diversity and management of the Vjosa basin: the first free flow river protected area in the Balkans. Innovare Journal of Agri. Sci, vol 11, issue 6, 2023, 32-3633. https://doi.org/10.22159/ijags.v11i6.49107
[12] Kottelat M., Freyhof J., 2007, *Handbook of European Freshwater Fishes*, Kottelat, Cornol, Switzerland and Freyhof, Berlin, Germany, pp. 646
[13] Dulcic J, Glamuzina B (2006). Length-weight relationships for selected fish species from three eastern Adriatic estuarine systems (Croatia). J. Appl. Ichthyol. 22: 254-256.
[14] Erguden, D., Turan, C., Gurlek, M., Turan, F., Erguden, S. 2011. Length-weight and length-length relationships of the Mediterranean shad *Alosa agone* (Scopoli, 1786) from the Northeastern Mediterranean coast of Turkey African Journal of Biotechnology Vol. 10(33), pp. 6332-6336, 6 July, 2011

Advanced Engineering Days

aed.mersin.edu.tr

Energy production and income of 5 kW solar power plant in Boukan, Iran

Khadijeh Mirza[*1]

[1]*Soran University, Chemical Engineering Department, Iraq, khadijeh.mirza@cheme.soran.edu.iq*

Cite this study: Khadijeh, M. (2024). Energy production and income of 5 kW solar power plant in Boukan, Iran. Advanced Engineering Days, 9, 827-829

Keywords
Solar power
Clean energy
Electricity
Income
Energy production

Abstract

In today's life, energy supply sources are one of the concerns of societies. Excessive consumption of non-renewable resources, including fossil fuels and environmental pollution, leads people to use renewable and clean energy sources. Considering that solar energy is one of the available and clean sources of energy, in this study we examined the income from the electricity produced by a 5 kW solar power plant in Iran. The highest efficiency of the power plant was obtained in June and July and the lowest efficiency was obtained in December and January. In this article, two effective factors including adjustment rate and government policies on power plant income have been investigated. The adjustment rate increases monthly depending on the inflation rate, and as a result, the income of the solar power plant increases. However, due to economic problems in Iran, the government has reduced the power plant's income by reducing the price of electricity by 14.42% and this decision has a negative impact on investment in using solar energy.

Introduction

Energy supply and greenhouse gas emissions caused by excessive use of energy sources, including fossil fuels, have become a global concern [1, 2]. According to the reports of the International Energy Agency (IEA) and the Intergovernmental Panel on Climate Change (IPCC) estimates that 67% of energy consumption and 70% of greenhouse gas emissions occur in cities [1, 3, 4]. The increase in greenhouse gases resulting from human activities has caused the phenomenon of global warming and climate change. On the other hand, with the excessive increase in population, non-renewable energy sources are decreasing [5]. Therefore, the best solution is replacing non-renewable sources with renewable sources, such as solar energy. Solar energy reaches the Earth directly from the sun and is considered an accessible energy source. The use of solar energy not only removes the concern of reducing non-renewable energy sources but also solves the problem of air pollution caused by the emission of greenhouse gases [6].

The highest yield of solar energy is achieved in areas with sunny days and cool weather. Because hot weather reduces the lifespan of solar panels. The northwest of Iran are suitable area for setting up a solar power plant [7]. Therefore, we set up a 5 kW solar power plant in the city of Boukan in West Azerbaijan province, Iran. One of the problems in setting up a solar power plant in Iran is that there is no accurate estimate of the amount of energy produced, income, and how to calculate the power plant's income. This paper aims to check the amount of energy produced and the income of the power plant in one year.

Power plant description

The solar power plant was established on a land of 50 square meters with 1,190,000,000 Rials as a start-up cost in 2022. The required devices include thirteen 390-watt monocrystalline panels, an inverter, a structure, and a protection device. According to a 20-year contract, the electricity produced by the power plant is sold to the Renewable Energy and Energy Efficiency Organization at the base price of 14,560 Rials per kilowatt. The income of the power plant is paid 45 days after the reading of the electricity meter every two months. The generated electricity income is calculated from the following formula:

$$P = E \times [\beta \times b \times \alpha \times (1 + i) + t] \quad (1)$$

Where,
P: incomes / two months

E: Electricity produced / two months
β: Annual coefficient
b: Base price
i: Internal manufacturing factor
α: Adjustment rate
t: Transfer service price

The energy production capacity of the solar power plant will decrease with the passage of time and this will reduce the income and also, according to the contract, the power plant's income will be reduced by 60% in the eighth, twelfth, and sixteenth years. Therefore, the operation of the solar power plant will not be economical. For this reason, in the calculation of the income from the produced electricity, the adjustment rate (α) is applied, which is the effect of the increase in inflation rate and currency on the price of produced electricity. By increasing a, the power plant's income increases.

Results and discussion

The income from the power plant is affected by factors such as the amount of solar energy received by the panels, adjustment rate, government policies, and the efficiency of devices. In this article, the effect of the adjustment rate and government policies on the income of the solar power plant is examined.

As shown in Figure 1. The amount of income is the highest in June and July because of the long and sunny days of spring and summer and the lowest income is in December and January due to the short and cloudy days of autumn and winter.

By comparing two curves with adjustment rate and without adjustment rate, it can be seen that applying adjustment rate has increased the income. The amount of adjustment rate has increased from 2% to 12% from the beginning of the year to the end of the year.

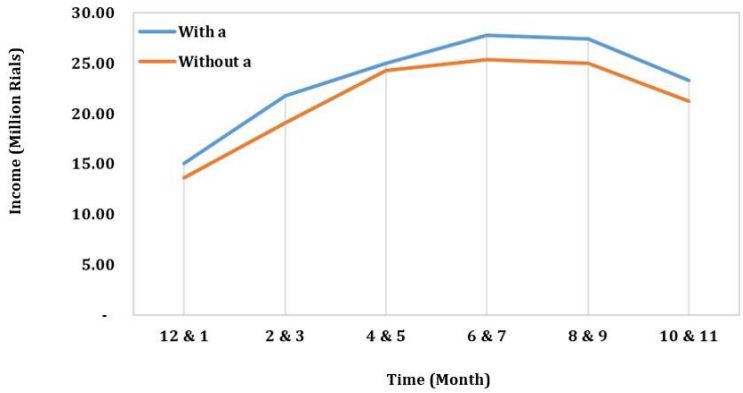


Figure 1. Effect of adjustment rate on the income.

According to the announcement of the Central Bank of Iran, the adjustment rate has increased by 19.29% from April to May 2013, but due to economic problems in Iran, the Renewable Energy Organization has taken a new decision and increased the base price from 14,560 to 17,500 Rials and the adjustment rate has decreased from 1.40304 to 1. As mentioned in Table 1, the price change has caused a 14.42% decrease in revenue. Considering the contract period (20 years) of the solar power plant, this price reduction is not economical. Unfortunately, this decision will reduce investment in the solar power plant.

Table 1. Calculation of solar power plant income with old and new prices.

a) Income with old price.				
Month No.	**Electricity produced**	**Adjustment rate**	**Base price (Rials)**	**Income (Rials)** $P = E \times [\beta \times b \times \alpha \times (1 + i) + t]$
4 & 5	1647 Kw	1.40304	14560	1647 × [1560 × 1.40304 × 1 +140]
6 & 7	1711 Kw	1.48098	14560	1711 × [1560 × 1.48098 × 1 +140]
			Total income:	71,009,878 Rials
b) Income with new price.				
4 & 5	1647 Kw	1	17500	1647 × [1560 × 1 × 1 + 140]
6 & 7	1711 Kw	1.05555	17500	1711 × [1560 × 1.05555× 1 +140]
			Total income:	60,898,425 Rials

Reducing in income % = (71,009,878 - 60,898,425) / 71,009,878 = 14.24 %

Conclusion

In this study, the method of calculating the income for a 5 kW solar power plant in Iran has been studied. The adjustment rate and government policies have a significant impact on the power plant's income. Due to the reduction of the efficiency of the equipment with time, the adjustment rate increases monthly, and as a result, the income of the power plant increases despite the decrease in the efficiency of the equipment. However, the government's policies, such as a 14.42% reduction in the total price, have worried the owners of solar power plants. Because the reduction of 14.42% in 20 years of the contract is not economical.

References

1. Kraaijvanger, C.W., et al., Does the sun shine for all? Revealing socio-spatial inequalities in the transition to solar energy in The Hague, The Netherlands. Energy Research & Social Science, 2023. 104: p. 103245.
2. Bilgen, S., Structure and environmental impact of global energy consumption. Renewable and Sustainable Energy Reviews, 2014. 38: p. 890-902.
3. Agency, I.E., Empowering Cities for a Net Zero Future: Unlocking Resilient, Smart, Sustainable Urban Energy Systems. 2021: OECD Publishing.
4. Pörtner, H.-O., et al., IPCC, 2022: Summary for policymakers. 2022.
5. Child, M., et al., Sustainability guardrails for energy scenarios of the global energy transition. Renewable and Sustainable Energy Reviews, 2018. 91: p. 321-334.
6. Dinçer, H., et al., Analysis of solar module alternatives for efficiency-based energy investments with hybrid 2-tuple IVIF modeling. Energy Reports, 2023. 10: p. 61-71.
7. Salehi, S., The role of developers in accepting solar energy in Iran: A case study in Golestan province. Solar Energy, 2023. 264: p. 111967.

Advanced Engineering Days

aed.mersin.edu.tr

Study of the influence of different car types on the wear indicators of the "wheel-rail" couple

Angela Shvets[*1]

[1]*Ukrainian State University of Science and Technologies, Department of Engineering and Design Specialized Department «Microprocessor-Based Control Systems and Safety in the Railway Transport» (EDSD MBCSS), Ukraine, angela_shvets@ua.fm*

Cite this study: Shvets, A. (2024). Study of the influence of different car types on the wear indicators of the "wheel-rail" couple. Advanced Engineering Days, 9, 830-832

Keywords
Freight cars
Railway
Wear of wheels and rails
Mathematical modeling
Wear indicators

Abstract

The technical level of railway rolling stock directly affects the economic performance of the transport industry and the country's economy as a whole. This leads to the need to improve control and quantify the dynamic load of rolling stock to maintain safe and reliable communication on the railways. The purpose of this work is to study the influence of different types of cars on the work of friction forces on the rolling surface and wheel flange. The study is based on the method of mathematical and computer modeling of the dynamic load of freight rolling stock. The paper presents an analysis of theoretical studies of wear indicators using the example of gondola cars, flat cars and hoppers. The work investigated the influence of loading modes of freight cars on the wear of the "wheel-rail" couple in order to solve the problem of improving the technical and economic performance of railway transport.

Introduction

Processes of integration into the international economic area lead to an increase in the need for transportation, including by rail. To satisfy the growing demand, as well as to increase the attractiveness of the created transport corridors, including transit ones, it is necessary to increase the productivity of the transportation process along the railway network using highly efficient methods while taking into account the required level of the economy of the industry as a whole [1-4].

The operation of obsolete rolling stock with low dynamic properties is one of the reasons for the insufficient level of train safety and high operating costs. This leads to increased costs for repair work and increased energy consumption for the traction of trains. In turn, new requirements are being imposed, leading to an increase in the level of forces of dynamic interaction between the rolling stock and the track, which is unacceptable in conditions of significant wear of the undercarriage of the rolling stock of the previous generation [5-8].

In addition, in railway transport, there is a very acute problem of intensive wear of the lateral rolling surface and wheel flanges. It is obvious that these and other tasks can be achieved only on the basis of innovative technical solutions, technologies, and scientific research [2-4].

The purpose of this work is to study the influence of various types of rolling stock, taking into account the loading mode and the movement speed on the work of friction forces on the rolling surface and wheel flange.

Material and Method

To study the work of the friction forces of the "wheel-rail" couple, mathematical modeling of forced spatial oscillations of the "car–rail track" systems was used when moving in the curves of a freight car on standard three-piece bogies [9, 10].

Theoretical studies have been carried out under the condition of movement of several types of freight cars: gondola car (model 12-532), hopper car for coal transportation (model 12-4034), and flat car with a long cargo (model 13-401) along the curves with radii 350 and 600 m, with superelevation 130 and 120 mm, correspondingly [11-13].

The complement of the mathematical models of spatial oscillations by the initial data with the specified inertial characteristics of the car and cargo elements makes it possible to approximate the results of calculations

to the real state of objects and thereby increase the objectivity of mathematical and computer simulation. It was for solving this problem that the "Software complex for determining the moments of inertia of car bodies" was created. Preparatory calculations the weight of the cars, the inertia moments of the body I_x, I_y, I_z and the height of the mass center of the body h_c above the level of rail heads (LRH), which are given in Table 1 [14].

Table 1. Inertia and geometric characteristics of cars at different loading modes

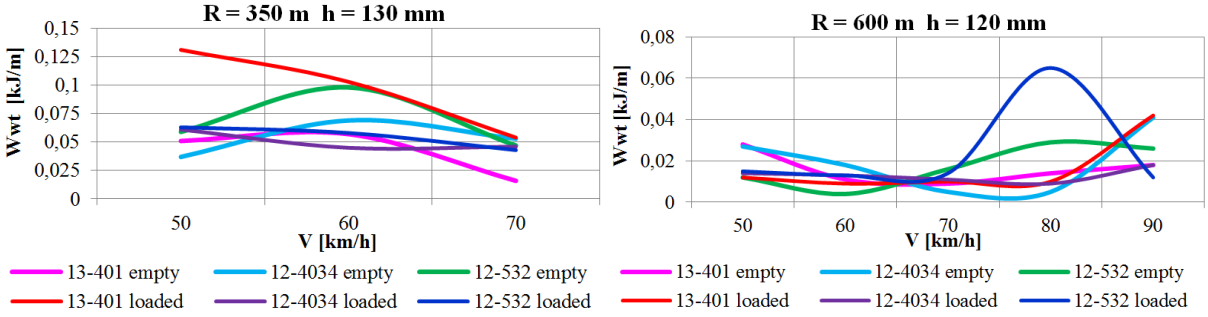
Parameters	Designations	Name of cars		
		Gondola car of the model 12-532	**Hopper car for coal 12-4034**	**Flat car of the model 13-401**
Car base	$2L$, m	8.66	7.84	9.72
Car weight	M_o, t	76.5 (13.3)*	88.34 (18.72)	63.6 (13.6)
Inertia moments	I_x, t m^2	75 (20)	160 (33.6)	22 (13.5)
	I_y, t m^2	1050 (300)	1190 (300)	1194 (240)
	I_z, t m^2	1100 (300)	1245 (307)	1223 (260)
Mass center height above the LRH	h_c, m	1.843 (1.6)	2.7 (1.77)	2.1 (1.1)

* – in brackets the values of cars` parameters in the empty mode are specified

Mathematical modeling makes it possible to determine the wear indicators of the “wheel-rail” couple, which represent the average work of friction forces (pseudo-slip) upon contact between the wheel flange and the side face of the rail head. Wear indicators are determined when they move along a railway track with real irregularities in the vertical and horizontal planes, taking into account the actual rolling surface of the wheel and the profile of the rail head [3-5].

Results

The work of friction forces in the contact of the “wheel-rail” couple is an indicator that reflects the physical phenomena that occur when the wheel flange slides along the side edge of the rail. This indicator is convenient for comparing rolling stock when assessing the wear rate of wheels and rails when they move in curves of different radii. Figure 1 shows graphs of the dependence of wear indicators on the rolling surface of the wheel W_{wt} on the loading mode while driving along the corresponding curve.



a *b*

Figure 1. The influence of car loading on wear indicators W_{wt}: *a* – R=350 m; *b* – R=600 m

In the curve R=350 m at a speed of 50-60 km/h, the W_{wt} of a loaded flat car increases significantly (Figure 1, *a*). At a speed of 80 km/h, wear indicators on the rolling surface of the wheel increase significantly for a gondola car in the curve R=600 m. There is also an increase in W_{wt} at a speed of 90 km/h in the curve R=600 m for an empty hopper car and loaded flat cars (Figure 1, *b*).

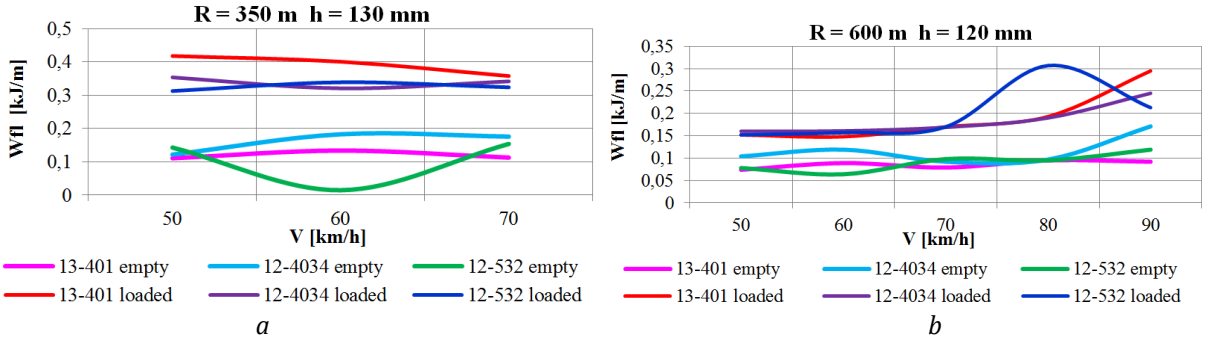
Graphs of the dependence of wear indicators on the wheel flange W_{fl} on the loading mode while driving along the corresponding curve are presented in Figure 2.

The wear indicators on the wheel flange W_{fl} significantly exceed the similar values for assessing wear on the wheel rolling surface W_{wt}. The average values of the work of the friction forces of the “wheel-rail” couple on the wheel flange have a noticeable dependence on the loading mode of the car. An empty gondola car at a speed of 60 km/h in the curve R=350 m has the lowest W_{fl} value (Figure 2, *a*).

Conclusion

Wear of the wheel flange and the side face of the rail head has a great impact on traffic safety since the outlines of the wheel and rail profiles change. In addition, strong friction of the wheel flange on the side surface of the rail head increases the resistance to train movement. Several types of freight cars are considered: gondola car (model 12-532), hopper car for coal transportation (model 12-4034), and flat car with a long cargo (model 13-401) on typical bogies 18-100 under different loading conditions. The practical significance of theoretical

studies of the influence of freight rolling stock of various types under different load conditions on the dynamic interaction with the track lies in determining the wear indicators of the wheel-rail couple.



a *b*

Figure 2. The influence of car loading on wear indicators W_{fl}: *a* – R=350 m; *b* – R=600 m

References

1. Muradian. L., Pitsenko, I., Shaposhnyk, V., Shvets, A., & Shvets, A. (2022). Predictive model of risks in railroad transport when diagnosing axle boxes of freight wagons. Proceedings of the Institution of Mechanical Engineers, Part F: Journal of Rail and Rapid Transit, 1-5. doi:10.1177 /09544097221 122043.
2. Shvets, A., Muradıan, L., & Shvets, A. (2023). Investigation of wear of wheels and rails when the center of mass of cargo in gondola cars shifts. Advanced Engineering Days, 7, 109-112.
3. Fomin, O. V., Shvets, A. O., Bolotov, O. M., & Saparova, L. S. (2020). Definition of indicators wear in an uneven load freight rolling stock. Bulletin of Certification of Railway Transport, 1, 19-29.
4. Shvets, Angela O., Bolotov, O. M., Saparova, L. S., & Shvets, Angelika O. (2019). Wear wheels and rails at the uneven loading of gondola cars. Bulletin of Certification of Railway Transport, 1(53), 4-17.
5. Myamlin, S., Neduzha, L., & Shvets, A. (2014). Determination of friction performance influence in the system "body–bogie" on the freight car dynamics. Science and Transport Progress, 2(50), 152-163. doi:10.15802/stp2014/23792.
6. Shvets, A. O. (2023). Influence of the instability form on the traffic safety of freight rolling stock. Advanced Engineering Days, 6, 111-113.
7. Shvets, A. O., Zhelieznov, K. I., Akulov, A. S., Zabolotnyi, O. M., & Chabaniuk, Y. V. (2015). Determination of the issue concerning the lift resistance factor of lightweight car. Science and Transport Progress, 6(60), 134-148. doi: 10.15802/stp2015/57098.
8. Myamlin, S., Neduzha, L., & Shvets, A. (2013). Research of friction indices influence on the freight car dynamics. Teka. Commission of motorization and energetics in agriculture, 13(4), 159-166.
9. Muradian, L., Shvets, A., & Shvets, A. (2023). Some dynamic processes at longitudinally-transverse shift of the cargo. Scientific Journal of Silesian University of Technology. Series Transport, 120, 187-204. doi:10.20858/sjsutst.2023.120.12.
10. Shvets, A. (2023). Multibody model of freight railcars interaction in a train. In: Sharma, S.K., Upadhyay, R.K., Kumar, V., Valera, H. (eds) Transportation Energy and Dynamics. Energy, Environment, and Sustainability, 217–241. Singapore: Springer. doi:10.1007/978-981-99-2150-8_10.
11. Shvets, A. O. (2021). Dynamic indicators influencing design solution for modernization of the freight rolling stock. FME Transactions, 49(3), 673-683. doi:10.5937/fme2103673S.
12. Shvets, A. O. (2020). Interaction dynamics of some types of freight cars with a railway track. Science and Transport Progress, 5(89), 142-159. doi:10.15802/stp2020/217649.
13. Shvets, A. O., Bolotov, O. M., Percevoj, A. K., Ghlukhov, V. V., Bolotov, O. O., & Saparova, L. S. (2020). Research of dynamic indicators and influence of different types of rolling stock on railway track. IOP Conference Series: Materials Science and Engineering, 1-10. doi:10.1088/1757-899X/985/1/012014.
14. Shvets, A. O. (2018). Specifics of determining the moments of inertia a freight wagons bodies. Bulletin of Certification of Railway Transport, 5(51), 20-34.

Advanced Engineering Days

aed.mersin.edu.tr

Energy piles design parameters optimization by using fuzzy logic

Çetin Önder İncekara[*1]

[1]*BOTAŞ, Assoc. Prof. Dr., Transit Pipeline Manager, BOTAŞ Genel Müdürlüğü, Bilkent, Ankara, Türkiye, cetinincekara@gmail.com*

Cite this study: İncekara, Ç. Ö. (2024). Energy piles design parameters optimization by using fuzzy logic. Advanced Engineering Days, 9, 833-836

Keywords
Energy piles
Design Parameters
Efficiency
Soil Energy
Geothermal
GSHP
NZEB
Fuzzy Logic
FMCDM

Abstract

Energy pile uses environmental-friendly technology, i.e. low carbon footprint and greenhouse gas (GHG) emissions, and cost-effective. The use of energy piles have been increasingly grown due to the combination of their transferring load from structure into the bearing layer and exchanging of heat with the soil, i.e. environmental benefits. Energy Piles are used renewable energy designed to utilize the relative constant temperature of the soil (soil energy: geothermal) that surrounds the energy piles for heating and cooling of buildings by the use of ground source heat pump (GSHP). Energy piles have been harvesting energy from the soil that surrounds the piles by using buried pipe networks which aims to reduce their carbon footprint and to increase the energy efficiency of the building, i.e. to have energy-efficient building. In the study the design parameters of energy piles (diameter/size/length of pile and type of foundation, length/diameter/thickness/location of pipe pattern inside energy piles, dimensions & the arrangement/pattern of energy piles and pipes, type of concrete, and fluid characteristics inside pipes, power & location of GSHP, diameter & length of energy piles, soil thermal properties & soil temperature, groundwater level, depth to bedrock, type of concrete, type of GSHP, type of fluid inside pipes, pipe configuration inside energy piles…, i.e. all related design parameters) that affect their design of energy pile and related pipes are evaluated by using fuzzy logic. The thermal efficiency of energy piles improves significantly by increasing the number & configuration of pipes inside the energy piles and by adding thermally conductive materials to the concrete within acceptable limits. By using Fuzzy method; the calculated criteria weights for energy piles design parameters' weights are as follows: the most important evaluation dimension/main-criteria is "Soil thermal properties & Soil temperature", the second important evaluation dimension is "Pipe configuration inside Energy Piles" and the third important evaluation dimension is "Diameter & length of energy piles". By using energy piles buildings will have minimum carbon footprint and will be environmental-friendly green buildings.

Introduction

Energy consumption of buildings has become a relevant international issue, and various design strategies have been developed to enhance energy saving in many countries. Today, Buildings' responsibility for approximately 40% of total energy consumption and over 30% of greenhouse gas emissions has shifted global interest toward the so-called "Nearly zero energy buildings" (NZEB). The design of an NZEB has the purpose of constructing buildings with less energy consumption and low carbon emission. The development of energy geo-structures contributes to this goal as applying shallow geothermal energy in geo-structures for space cooling and heating of buildings. This environmentally friendly technology can be applied to all types of soil-embedded structures such as the diaphragm walls, tunnels, shallow foundations, and piles.

Piles are structural foundation components that are relatively long and usually slender and transport loads from superstructures to deep layers of soil. Due to the enormous amounts of energy used for different purposes nowadays, the significance of energy conservation is being emphasized more and more. The building industry consumes a significant portion of energy (more than 30%) globally. Deep foundations/piles have underutilized geothermal mass, which can absorb and store soil's temperature/energy better than many other materials. For little additional construction cost, the energy loops of a heat exchange system/pipes (energy pipes) are buried in the concrete piles.

Energy piles are new technology that consist of pile foundations combined with closed-loop ground sourced heat pump (GSHP) systems by using energy pipes. Their purpose is to provide support to the building, as well as

acting as a heat source and a heat sink. In effect, the thermal mass of the ground enables the building to store unwanted heat from cooling systems and allows heat pumps to warm the building in winter.

Material and Method

In the study; an integrated Fuzzy AHP- Fuzzy TOPSIS- Fuzzy VIKOR approaches are used to assess/evaluate energy piles design parameters optimization factors. In literature Fuzzy Multi Criteria Decision Making Methods (FMCDM) are used in different fields by many researchers [1-27] by using MATLAB program.

Fuzzy multi criteria decision making methods (FMCDM)

In literature, Fuzzy Multi Criteria Decision Making Methods (FMCDM) are used in different fields by many researchers and Fuzzy AHP & Fuzzy TOPSIS are also used in many sectors, i.e. evaluation of energy piles' design parameters. The evaluation of energy piles design parameters optimization, to evaluate parameters, to evaluate the criteria for human resource for science and technology, for analyzing customer preferences, to evaluate risk analysis in green supply chain, and to select machine tools.

Table 1. Linguistic Variables for the Alternatives

Linguistic Terms-Abbreviation	Linguistic Variables	Triangular Fuzzy Numbers
SDA	Strongly Disagree	(0, 0, 0.15)
DA	Disagree	(0.15, 0.15, 0.15)
LDA	Little Disagree	(0.30, 0.15, 0.20)
NC	No Comment	(0.50, 0.20, 0.15)
LA	Little Agree	(0.65, 0.15, 0.15)
A	Agree	(0.80, 0.15, 0.20)
SA	Strongly Agree	(1, 0.20, 0)

Selection of Energy Piles' Design Parameters Optimization Criteria: Dimensions and Evaluation Model

In the study 8 main criteria, i.e. Diameter & length of energy piles (C1), Soil thermal properties & Soil temperature (C2), Groundwater level (C3), Depth to bedrock (C4), Type of Concrete (C5), Type of Ground Sourced Heat Pump (C6), Type of Fluid inside pipes (C7), Pipe configuration inside Energy Piles (C8) and 41 related subcriteria are evaluated/assessed by each expert/DM. For the case of prioritization of the criteria, after the aggregation process performed with the answers of the 32 experts, the comparison matrix was obtained. The pairwise comparison matrices for subcriteria and alternatives are calculated.

Results

After acquiring the fuzzy comparison matrices, importance weights of energy piles design parameters' dimensions; evaluation criteria is calculated by using Fuzzy method. According to the calculated criteria weights for energy piles design parameters' weights; the most important evaluation dimension/main-criteria is "Soil thermal properties & Soil temperature", the second important evaluation dimension is "Pipe configuration inside Energy Piles" and the third important evaluation dimension is "Diameter & length of energy piles".

Conclusion

Energy piles use environmental-friendly and climate-friendly technology, they are clean, cost-effective, space-efficient and quiet systems therefore they are very popular. They can be installed all type of foundations in the World. Only efficiency of them changes since it depends on the location of energy piles. The factor that affect the design and efficiency of energy piles are; thermal conductivity of soil types, humidity, depth below the ground surface, groundwater level, soil temperature, heat capacity of soil, depth to bedrock, thickness of the soil layer, soil temperature that changes with seasonal, i.e. mean earth temperature, thermal diffusivity of the soil, density of soil, rainfall and wind speed that leads to a reduction of the ground surface temperature. The soil temperature profiles that provide an indication of frost depth which can have an impact on spring snowmelt runoff rates is considered in the design of energy piles. Each rock type has a different thermal conductivity, which is a measure of the ability of a material to conduct heat. Rocks that are rich in quartz, like sandstone, have a high thermal conductivity and rocks that are rich in clay or organic material, like shale and coal, have low thermal conductivity, meaning that heat passes less readily through these layers. The other factors that affect the design of energy piles. Heat flow, which is affected from the items related with soil parameters that are listed above, is calculated by multiplying the geothermal gradient and the thermal conductivity.

By using energy piles, we can save energy cost up to 55%. If energy pile's locations are near geothermal area/locations, we can save energy cost of up to 70%. By using energy piles, we can reduce our building's operating costs, energy costs and CO2 emissions compared with conventional heating systems. By using structural piles as energy piles, the piles under the building have dual functionality, i.e. structural and energy source.

References

1. Chan F. T. S., & Kumar N. (2007). Global Supplier Development Considering Risk Factors Using Fuzzy Extended AHP-based Approach. Omega International Journal of Management Science, 35, 417-431.
2. İncekara, Ç. Ö., & Oğulata, S. N. (2011). Enerji darboğazında ülkemizin alternatif enerji kaynakları. Sosyal ve Beşeri Bilimler Dergisi, 3(1).
3. İncekara, C. O. & Oğulata, S. N. (2012). EU and Turkey's Energy Strategies. International Journal of Economics and Finance Studies, 4(2), 35-43.
4. İncekara, Ç. Ö., & Oğulata, S. N. (2017). Turkey's energy planning considering global environmental concerns. Ecological Engineering. Elsevier, A.B.D., 589-595.
5. Incekara, C. O. (2018). Ülkemizdeki Enerji Santral Yatırımlarının AHP Yöntemi ile Değerlendirilmesi. Çukurova Üniversitesi Mühendislik Fakültesi Dergisi, 33 (4), 185-196.
6. Incekara, C. O. (2019a). Use of an Optimization Model for Optimization of Turkey's Energy Management by inclusion of Renewable Energy Sources. International Journal of Environmental Science and Technology, Springer, 121-133.
7. İncekara, Ç. Ö. (2019b). Türkiye ve AB'nin Enerji Stratejileri ve Politikaları. Journal of Turkish Operations Management, 3(2), 298-313.
8. Incekara, C. O. (2019c). Turkey's Energy Management Plan by Using Fuzzy Modeling Approach. Scholars' Press, ISBN-10: 6138829697, Book, 38-52.
9. Incekara, C. O. (2020a). Türkiye' nin Elektrik Üretiminde Doğalgaz Talep Tahminleri. Journal of Turkish Operations Management, 3(2), 298-313.
10. İncekara, Ç. Ö. (2020b). Evaluation of Turkey's International Energy Projects by Using Fuzzy Multi-Criteria Decision Making Methods. Euroasia Journal of Mathematics, Engineering, Natural & Medical Sciences, Cilt 7, Sayı 9 (2020), 206-217. (https://doi.org/10.38065/euroasiaorg.143)
11. İncekara, Ç. Ö. (2020c). Turkey's natural gas demand projections. EJONS Internatıonal Journal, Vol. 4,No. 15 (2020): EJONS Journal, 489-505. (https://doi.org/10.38063/ejons.269)
12. Incekara, C. O. (2020d). Bulanık Mantık ile Sanayii Sektöründe ISO 50001 Enerji Yönetim Sistemi Uygulaması. Afyon Kocatepe Üniversitesi Fen ve Mühendislik Bilimleri Dergisi, 20(6), 991-1013.
13. İncekara, Ç. Ö. (2020e). Enerji Sektöründe Faaliyet Gösteren Bir İşletmede İş Sağlığı ve Güvenliği Yönetim Sistemi. Mehmet Akif Ersoy Üniversitesi Uygulamalı Bilimler Dergisi, 4(1), 152-177.
14. İncekara, Ç. Ö. (2021a). Bulanık TOPSIS ve Bulanık VIKOR yöntemleriyle bir enerji şirketinde kurumsal hafızanın oluşturulması. Euroasia Journal of Mathematics, Engineering, Natural & Medical Sciences, Cilt 8, Sayı 17, (2021), 1-20. (https://doi.org/10.38065/euroasiaorg.589)
15. Incekara, C. O. (2021b). Post-COVID-19 Ergonomic School Furniture Design under Fuzzy Logic. Work, 69, 1197–1208.
16. İncekara, Ç. Ö. (2021c). Dünyanın ve Türkiye' nin Doğal Gaz Talep Senaryosu. Euroasia Journal of Mathematics, Engineering, Natural & Medical Sciences, Cilt 8, Sayı 17 (2021), 44-57. (https://doi.org/10.38065/euroasiaorg.610)
17. İncekara, Ç. Ö. (2021d). Global Natural Gas Demand Projections under Fuzzy Logic. EJONS Internatıonal Journal, Vol. 5, No. 18 (2021): EJONS Journal, 367-385. (https://doi.org/10.38063/ejons.430)
18. Incekara, C. O. (2022a). Designing Ergonomic Post-Covid-19 School Furniture. South African Journal of Industrial Engineering, 33(2), 211–224.
19. İncekara, Ç. Ö. (2022b). Sigorta Eksperlerinin Dask Sigortası Değerlendirmelerinin Bulanık Mantık Altında İncelenmesi. Euroasia Journal of Mathematics, Engineering, Natural & Medical Sciences, Cilt 9, Sayı 21 (2022), 14-41. (https://doi.org/10.38065/euroasiaorg.952)
20. Incekara, Ç. Ö. & Lala, S. (2022c). Enerji projelerinde arazi edinim faaliyetleri ve arazi değerlemesi. Geomatik, 8(1), 61-71.
21. Kumar Sahu A., Datta S., & Mahapatra S.S. (2016). Evaluation and selection of resilient suppliers in fuzzy environment. Benchmarking: An International Journal, 23(3), 651-673.
22. Satrovic, E. (2018). The Human Development Relies on Renewable Energy: Evidence from Turkey. 3rd International Energy & Engineering Congress, 19-27.
23. Shukla A. K (2014). Interpretability Assessment in Fuzzy Rule Based Systems. International Journal of Scientific & engineering Research, Volume 5, Issue 7, 506-509.
24. Wang, C. (2015). A Study Of Membership Functions On Mamdani-Type Fuzzy Inference System For Industrial Decision-Making. PhD Theses And Dissertations. Lehigh University, (Paper:1665).

25. İncekara, Ç. Ö. (2023). Industrial internet of things (IIoT) in energy sector. Advanced Engineering Days (AED), 5, 181-184.
26. İncekara, Ç. Ö. (2023). Internet of Things (IoT) in GIS. Advanced Engineering Days (AED), 6, 53-57.
27. İncekara, Ç. Ö. (2023). Intelligent digital twin for energy industry in AIoT networks. Advanced Engineering Days (AED), 7, 36-40.

Advanced Engineering Days

aed.mersin.edu.tr

Aluminum Forging Technology, Applications and Analysis

Sait Gül, Esat Erdinç Önel, Hüseyin Tat

[1]*ÇİMSATAŞ Çukurova Construction Machinery IND. TRADE. A.S. Mersin, Türkiye, foundry@cimsatas.com*

Cite this study: Gül, S. & Önal, E. E. & Tat, H. (2024). Aluminum Forging Technology, Applications and Analysis. Advanced Engineering Days, 9, 837-840

Keywords
Aluminum
Aluminum Forging
Aluminum Design
Parameter
FEA method
Die deformation

Abstract

The aim of this study, indicate of Aluminum forging applications, analysis and the observation of problems in production. Aluminum forging products has been increasingly used in automotive and aerospace industry due to their lightness and strength. Part and dies are designed in CATIA-V5. The proposed process has been simulated by using the Finite Element Method and the required forging force, the temperature distribution and the effective stress distribution in the parts have been obtained. During forging of aluminum part sticks to the die under temperature and pressure. In order to avoid this problem, it was solved by changing the radiuses in the design of the pre-shaped molds, changing the design of the ejector in the dies, adjusting the timing of the ejectors in the presses and adequate lubrication.

Introduction

In the aerospace and automotive industries, the use of forgings is widely preferred. These parts offer the advantages of high productivity, low cost and good performance. Aluminum alloys play an important role, especially in high-strength structural applications. Aluminum alloys formed by forging are used in many industries such as aerospace, automotive and defense industries. Forging is a process in which a piece of material is placed on a fixed lower die and shaped by applying pressure by a moving upper die. However, due to complex deformations, some forming defects can occur in the forging process. One of these defects, folding, is caused by disturbances in the material flow and can have adverse effects on the surface quality, mechanical properties and functionality of the part. Factors such as inhomogeneity of material flow during the forging process, low deformation temperature and improper adjustment of forging parameters can contribute to the occurrence of folding defects. This defect depends on the geometry of the product, the shape of the raw material, friction and forging temperature. are the most preferred alloys in the industry due to their light weight. However, high geometrical accuracy, good surface finish and targeted microstructural properties must be achieved during the forging process to ensure good assembly and service performance [1-4].

Malleability is very sensitive to changes in the temperature of raw materials. If the deformation temperature is low, recrystallization does not take place completely and undesirable microstructural dispersion can occur. In addition, large grains with inhomogeneous structures can lead to poor mechanical properties in the forging. In particular, the change in the deformation rate during forging also increases the strength of the forgings. In the study, forging simulations were made by designing dies. Then, improvements were made in the pre-form dies and ejector designs in order to solve the problem of the part sticking to the die caused by the 1st forging process. In the forging press, the timing of the ejector was adjusted to remove the aluminum from the burr line and the part was easily removed from the burr line without sticking [4-6].

Material and Method

In this study, EN AW 6082 T6 aluminum raw material was obtained from the aluminum production company. Dies were prepared in CATIA V5 and forging operation was simulated with deform simulation program. When it was applied in the forging process, the problem of adhesion was encountered. Because of this problem, improvements works were carried out on the dies. First of all, dies radii were enlarged due to the stick to the dies,

ejector was added to the dies and ejector times was adjusted on the press. And the amount of lubrication in the dies was increased to prevent the part from sticking.

Experiments were carried out with 430-460°C for forging temperature. With the results of the experiment, the structure, hardness and mechanical strength of the raw material were observed.



Figure 1. Raw material experiments

Design And Simulation Applications

Preform, finish dies and part design was done in Catia V5 program.

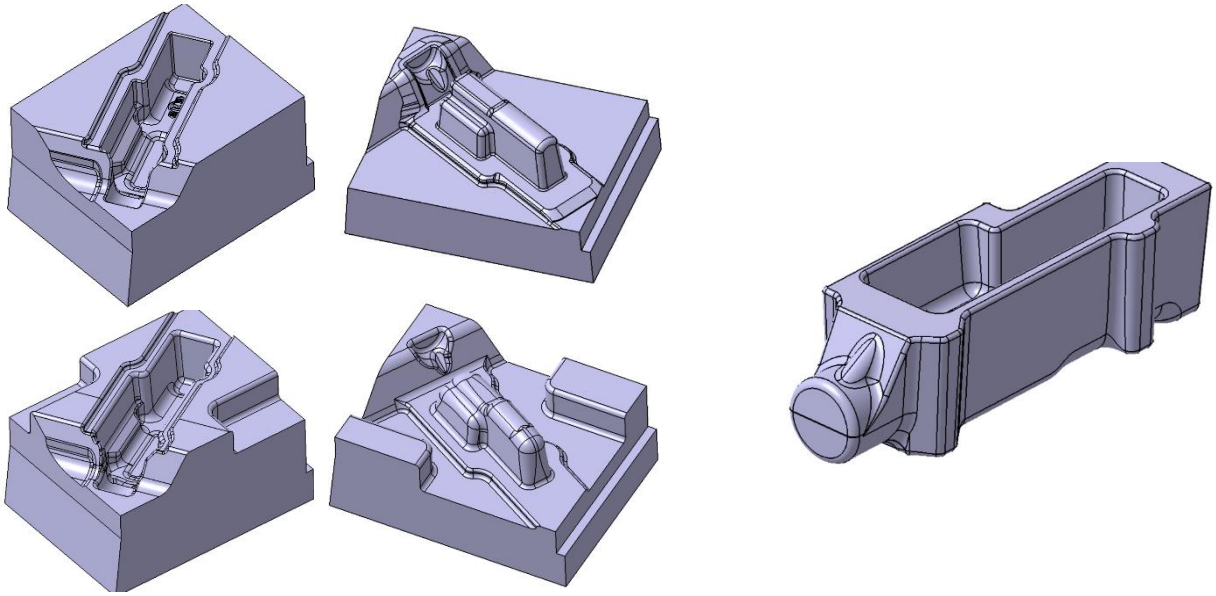


Figure 2. Design of the dies and part

Simulation was done with Deform Program.

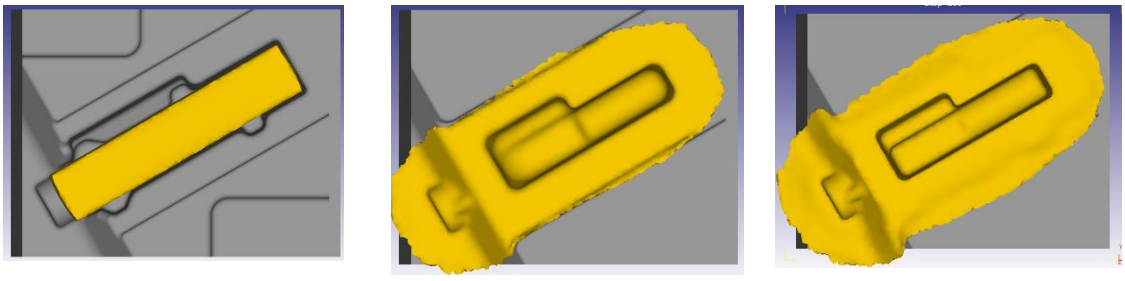


Figure 3. Simulation of the part

1st Method

In this method, the part was heated in an induction furnace at 430°C and the initial temperatures of the preform and finish molds varied between 140-170°C. Adhesion of the parts to the molds was observed.



Figure 4. Pre form and finish dies without ejector

2nd Method

In this method, the part was heated in an induction furnace at 460°C. As a result of forging, cracks were observed at the bottom radius of the molds. Sticking to the mold continued. Modeled bottom radii were enlarged due to adhesions and mold breakage.



Figure 5. Cracking in the dies

3rd Method

In this method, the part was heated in an induction furnace at 460°C. Due to the sticking problem in the previous forging process, ejectors were designed for the molds. The ejectors were designed from the burr line and since the part was hot, the ejector pierced the burr and was not a solution.

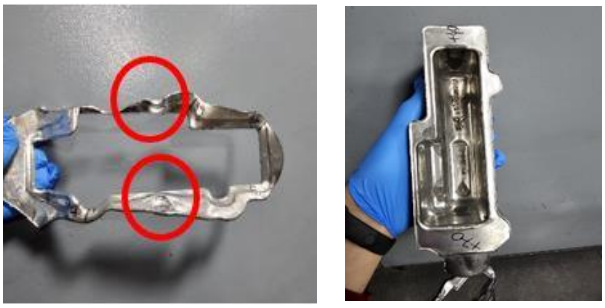


Figure 6. Burr line of the part



Figure 7. Dies with ejector

4rd Method

In this method, the part was heated in an induction furnace at 460°C. In addition to the design of the ejector, a burr limiter was made in the dies due to non-filling in the part. Also, the ejector timing was adjusted to allow the burr to cool down. In this way, the burr was less affected by the deformation caused by the ejector and reflected the demolding force to the part. As a result of these application, Sticking of the part and unfilling problems have been solved.



Figure 8. Burr limiter on the dies

References

1. A. Samancı, H. Coşkun, G. Atay, *Design Development and Simulation to Improve the Folding Defect in the Forging of 2024 Aluminum Alloy,* 2024, p 70-78.
2. M. W. Fu and M. W. Fu, *Flow-Induced Defects in Multiscaled Plastic Deformation, Des. Dev. Met.-Form. Process. Prod. Aided Finite Elem.* Simul., 2017, p. 131–180,
3. M. Sedighi and S. Tokmechi, *A new approach to preform design in forging process of complex parts*, J. Mater. Process. Technol., 2008, vol. 197, no. 1–3, p. 314–324.
4. X. Ge, Y. Yu, H. Yu, and G. Wang, *Study on Folding Defect Elimination Method of Track Link Forging Based on Preforming Design*, Int. J. Precis. Eng. Manuf., 2023, vol. 24, no. 1, p. 61– 71.
5. S. Cecchel, D. Ferrario, G. Cornacchia*, Heat treatments of EN AW 6082 aluminum forging alloy: effect on microstructure and mechanical properties,* 2020, p. 6-13.
6. Öztürk, H. *, Analysıs And Desıgn For Alumınum Forgıng Process,* 2008, p.26-33.

Advanced Engineering Days

aed.mersin.edu.tr

Modeling of fluid flow and heat transfer inside fin and tube heat exchanger with pentagonal cross section of tubes

Reza Ghafuri [1], Zahra Nasrollahi *[1], Hedayat Azizpour [2], Kamran Keynejad [1]

[1]*Fouman Faculty of Engineering, College of Engineering, University of Tehran, Iran, reza.ghafuri@ut.ac.ir, z.nasr@ut.ac.ir kamran.keynejad@ut.ac.ir*
[2]*School of Chemical Engineering, College of Engineering, University of Tehran, Iran, h.azizpour@ut.ac.ir*

Cite this study: Ghafuri, R., Nasrollahi, Z., Azizpour, H., & Keynejad, K. (2024). Modeling of fluid flow and heat transfer inside fin and tube heat exchanger with pentagonal cross section of tubes .Advanced Engineering Days, 9, 841-844

Keywords
Heat transfer
Fluid flow
Heat exchanger
Pressure drop

Abstract

In this study, we investigated the impact of different inlet air velocities on a fin and tube heat exchanger with a pentagonal cross-section. We analyzed how increasing the speed affected parameters such as pressure drop, friction coefficient, and Colborne coefficient. The Colborne coefficient exhibited a consistent linear behavior and did not change. However, the friction coefficient decreased as the Reynolds number increased, reaching its lowest value at v=2.34 m/s. The pressure drop increased with higher speeds, and the largest temperature change occurred at v=2.13 m/s.

Introduction

Heat exchangers are vital elements in any process plant. Most heat exchangers are of shell and tube type, however, there are several other important types, such as tube and fin, spiral tube, plate and frame, and spiral exchangers. Improving the thermohydraulic performance of heat exchangers can significantly optimize the energy required in various engineering processes. Tube and fin heat exchangers have been increasingly used in recent years, because they offer significant advantages such as a high level of heat transfer compared to conventional heat exchangers. The shape and dimensions of the pipes have a direct effect on the thermal efficiency and pressure drop of this equipment [1,2].

In this study, modeling of fluid flow and heat transfer created in a tube and fin exchanger with a pentagonal cross-section of tubes has been done. The geometry of the designed converter consists of a rectangular plate with a length of 300 mm and a width of 84 mm, which has 30 pentagonal tubes. The depth of the simulated area is 0.5 cm, which is used to calculate the Reynolds number of the flow. The fluid used in this modeling is air, which enters the converter from one side and exits from the other side after passing through the pipes. will be Figure 1 shows the 3D image of the designed heat exchanger.

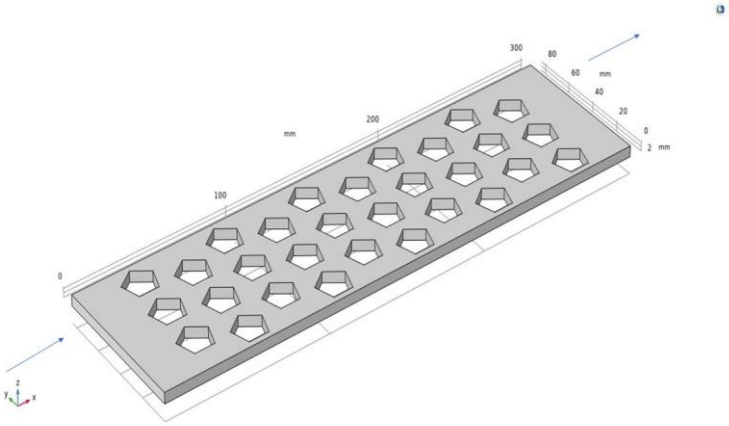


Figure 1. 3D image of the heat exchanger

Materials and Method

Air, as the fluid used in this modeling enters the converter at a temperature of 255 K, and after passing through pipes with a constant wall temperature of 243 K, it leaves the converter. The fluid enters the heat exchanger at 5 different speeds and the pressure drop and outlet temperature parameters are evaluated at these speeds.

The flow inside the converter is turbulent due to the presence of pentagonal tubes and the k-ω turbulent flow model is used to solve the flow equations (Equations 1-4) [3,4].

$$\rho\nabla.\vec{U} = 0 \qquad (1)$$

$$\frac{\partial(\rho k)}{\partial t} + \frac{\partial(\rho u_j k)}{\partial x_j} = \rho P - \beta^* \rho\omega k + \frac{\partial}{\partial x_j}\left[\left(\mu + \sigma_k \frac{\rho k}{\omega}\right)\frac{\partial k}{\partial x_j}\right] \qquad (2)$$

$$P = \tau_{ij}\frac{\partial u_i}{\partial x_j} \qquad (3)$$

$$\frac{\partial(\rho\omega)}{\partial t} + \frac{\partial(\rho u_j \omega)}{\partial x_j} = \frac{\alpha\omega}{k}\rho P - \beta^* \rho\omega^2 + \frac{\partial}{\partial x_j}\left[\left(\mu + \sigma_\omega \frac{\rho k}{\omega}\right)\frac{\partial\omega}{\partial x_j}\right] + \frac{\rho\sigma_d}{\omega}\frac{\partial k}{\partial x_j}\frac{\partial\omega}{\partial x_j} \qquad (4)$$

These equations are gridded and solved using COMSOL 6.1 software. are in the flow. For the side near the wall, due to the fluid passing through the solid surface, layered meshing is used, which gives more accurate results.

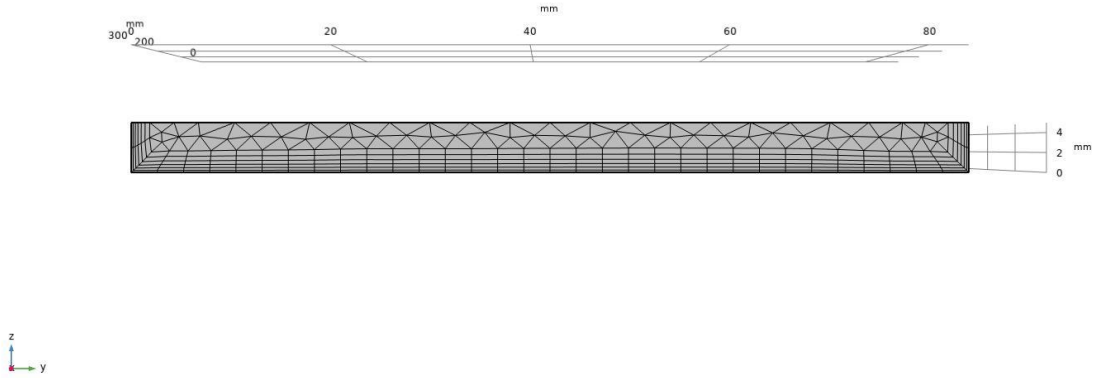


Figure 2. Mesh at the entrance

Table 1. Mesh information

No.	description
308	Number of vertex elements
4206	Number of edge elements
42246	Number of boundary elements
169721	Number of elements
0.1954	Minimum element quality
308	Number of vertex elements
4230	Number of edge elements
50400	Number of boundary elements
321343	Number of elements
0.03559	Minimum element quality

Results and Discussion

Figure 3 shows the pressure distribution, temperature distribution and speed distribution for the middle speed of 1.93 m/s and the rest of the results are presented in Table 2.

As seen in Figure 3, due to the conservation of mass and energy, by reducing the cross-sectional area of the flow path, the pressure-drop increases and on the other hand, the speed increases. Table 2 shows the values of pressure drop and outlet temperature versus the inlet speed.

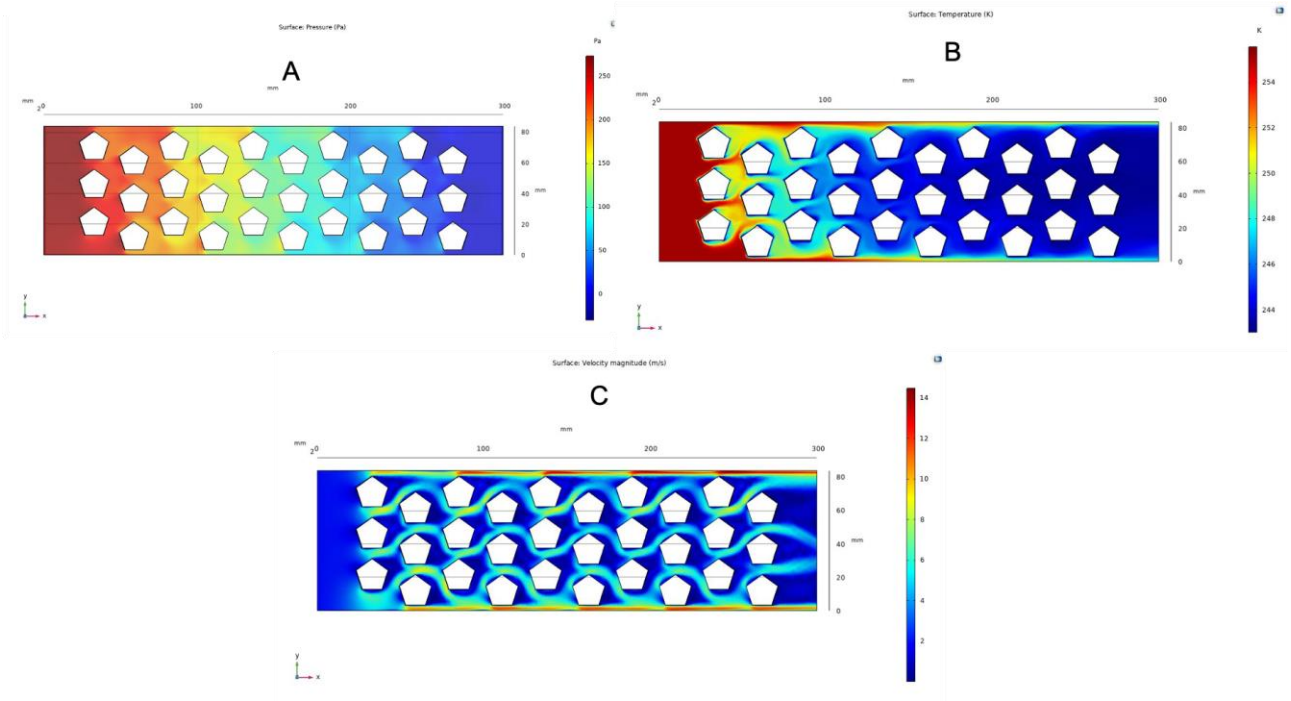


Figure 3. The distribution of pressure, temperature, and velocity for the speed of 1.93 m/s

Table 2. Fluid flow characteristics

Inlet velocity (m/s)	Reynolds number	Output temperature (K)	Pressure Drop (Pa)
1.52	1300	244.0357	172.65
1.72	1475	244.0213	216.69
1.93	1650	244.0114	267.91
2.13	1825	244.0052	321.57
2.34	2000	244.0181	383.22

Also, two parameters of friction coefficient and Colborne coefficient were calculated using equations (5 and 6) and shown in graphs 4 and 5 in terms of Reynolds number.

$$f=\frac{\Delta p\, A_c}{\frac{1}{2}\rho U^2 A_o} \qquad (5)$$

$$j=\frac{Nu}{Re.Pr^{1/3}} \qquad (6)$$

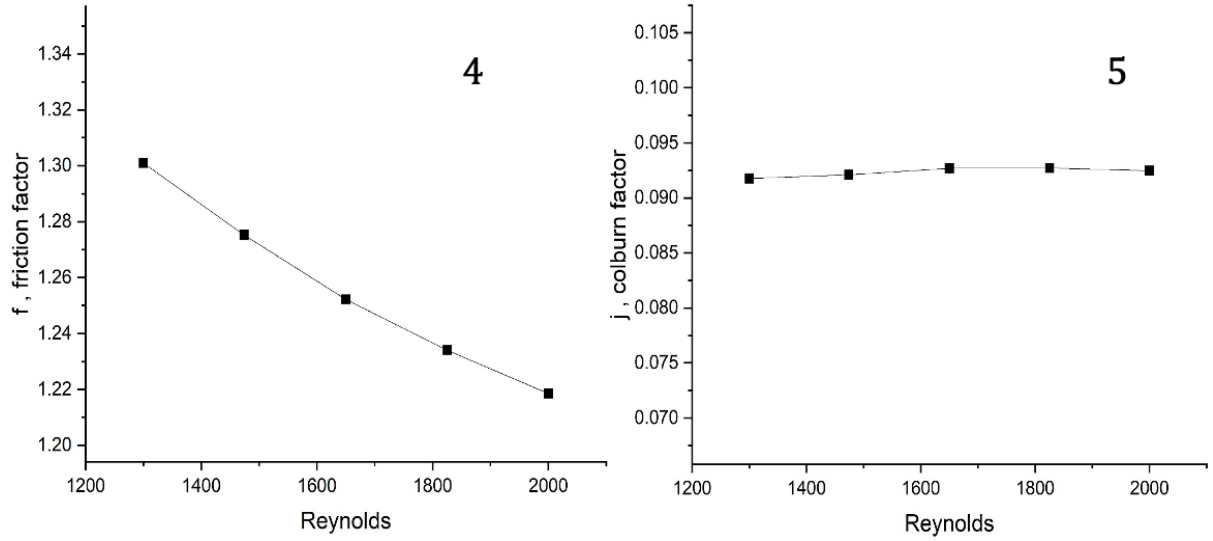


Figure 4 and 5. friction and Colborne coefficients versus Reynolds number

Conclusion

The maximum temperature changes are obtained at the speed of 2.13 m/s and on the other hand, with the increase of the inlet speed, the pressure drop increases linearly. Also, according to the existing relationships for the friction coefficient and the power of two speeds in the denominator, As the speed of the incoming air increases, the friction coefficient decreases and reaches its lowest value (1.218) at a speed of 2.34 m/s, and the Colborne coefficient does not change significantly with changes in speed and shows a linear behavior.

References

1. Dickey, D. S. (2004). Rules of Thumb for Chemical Engineers. *Chemical Engineering*, *111*(5), 10-12.
2. Cao, Y., Salem, M., Elmasry, Y., Galal, A. M., Singh, P. K., Gepreel, K. A., ... & Wae-hayee, M. (2022). Flow and heat transfer in a plain fin-and-hexagonal tube heat exchanger with different side ratios. *Case Studies in Thermal Engineering*, *38*, 102376.
3. Wang, P., Jiang, J., Li, S., Luo, X., Wang, S., & Zhao, W. (2019). An investigation of influence factor including different tube bundles on inclined elliptical fin-tube heat exchanger. *International Journal of Heat and Mass Transfer*, *142*, 118448.
4. Sharma, P., Said, Z., Kumar, A., Nizetic, S., Pandey, A., Hoang, A. T., ... & Tran, V. D. (2022). Recent advances in machine learning research for nanofluid-based heat transfer in renewable energy system. *Energy & Fuels*, *36*(13), 6626-6658.

Advanced Engineering Days

aed.mersin.edu.tr

Innovative intelligent methods in integer programming

Javad Nematian [*1], Khadijeh Daneshfar [1], Neda Shah Mohammadi [1]

[1] *University of Tabriz, Department of Industrial Engineering, Iran, Jnematian@tabrizu.ac.ir, lizadaneshfar97@gmail.com, Shahmohammadineda1985@gmail.com*

Cite this study: Nematian, J., Daneshfar, K., & Mohammadi, N. S. (2024). Innovative intelligent methods in integer programming. Advanced Engineering Days, 9, 845-847

Keywords
Integer programming
Genetic algorithms
Reinforcement learning
Deep neural networks
Hybrid algorithms

Abstract

This paper examines novel intelligent methods for solving integer programming problems. It begins by introducing the significance of integer programming and the challenges associated with solving these problems. A review of traditional and intelligent methods, including genetic algorithms, reinforcement learning, and deep neural networks, is presented. The advantages and limitations of each method are discussed, followed by a case study comparing the performance and solution quality of these methods in solving a production scheduling problem in a factory. The results show that the combined genetic-branch and bound method reduces solution time and improves solution quality. Finally, suggestions for research and development in improving hybrid algorithms, applying deep learning in optimization, automatic parameter tuning, applications in new problems, and utilizing quantum computing are provided. This paper helps readers familiarize themselves with novel intelligent methods in integer programming and understand their practical applications.

Introduction

Integer programming is one of the key branches of mathematical optimization, which is used in many industrial problems and complex systems. From transportation issues and supply chain management to telecommunication network design and resource allocation, integer programming is considered as one of the key tools in solving optimization problems(Schrijver, 1998). These problems in particular involve variables that can only take integer values, which increases the complexity and difficulty of solving them.

In recent years, significant improvements have been made in algorithms and methods for solving integer programming problems. Especially with the introduction of smart techniques such as machine learning algorithms and methods based on artificial intelligence, the performance and efficiency of these methods have increased significantly. Traditional methods such as branch and bound algorithms and cutting plane algorithms are still widely used (Schrijver, 1998; Sutton & Barto, 2018), but these methods face challenges such as time-consuming and high memory requirements. For example, the branch-and-bound algorithm, which is one of the most widely used methods for solving integer programming problems, needs a lot of time to reach the optimal solution in large problems.

Therefore, the need for new smart methods that can solve these challenges is strongly felt. Modern intelligent methods, using machine learning techniques and genetic algorithms, try to reduce the limitations of traditional methods and solve larger and more complex problems with higher efficiency.

One of the most important recent innovations is the use of genetic algorithms and hybrid methods, such as genetic-branch-and-bound hybrid algorithms, which have been able to significantly improve the solution time and the quality of answers. Genetic algorithms, inspired by the process of natural evolution, generate and improve a population of solutions using operators such as selection, crossover, and mutation to approach the optimal solution. These algorithms can be effectively used especially in large and complex problems that have a large search space.

In addition, reinforcement learning techniques and deep neural networks have also recently been introduced as effective methods for solving integer programming problems. Reinforcement learning, which is based on learning from interaction with the environment and optimizing policies based on received rewards, can be used to solve dynamic and complex optimization problems. Deep neural networks, with their high ability to model

complex relationships and learn important features from data, play a significant role in improving the performance of integer programming algorithms.

However, the use of these new methods requires a deep understanding of the theoretical foundations and the ability to implement them in practice. For example, one of the main challenges in using genetic algorithms is the adjustment of algorithm parameters such as population size, crossover rate, and mutation rate, which have a great impact on the final performance of the algorithm. Also, reinforcement learning and deep neural networks require a large amount of data and high computing power, which may cause limitations in some applications.

In this article, we review and introduce new smart methods in integer programming and compare the performance of these methods with traditional methods. For this purpose, we will first explain the theoretical foundations and traditional methods in integer programming. Then, we will investigate machine learning algorithms, genetic algorithms and other intelligent methods and present their experimental and comparative results.

In the following, we analyze the advantages and disadvantages of each of these methods and examine the role of each in solving various integer programming problems. Also, we present the limitations of the current research and suggestions for future research.

The main goal of this article is to present a comprehensive and comparative view of modern intelligent methods in integer programming and analyze their performance in facing the existing challenges. It is hoped that this research can contribute to a better understanding and further development of these methods and facilitate the improvement of performance and efficiency in solving integer programming problems..

Material and Method

The following methods and algorithms are used in this article:

1- Genetic Algorithms(河内正浩 & 安東宣善, 1992)
2- Reinforcement Learning(Sutton & Barto, 2018)
3- Deep Neural Networks(Goodfellow, Bengio, & Courville, 2016)
4- Hybrid Algorithms(Bertsimas & Dunn, 2019)

Implementation and improvement of algorithms

One of the most important aspects of using these new methods is the implementation and adjustment of algorithm parameters. For example, in genetic algorithms, setting parameters such as population size, crossover rate, and mutation rate has a great impact on the final performance of the algorithm (Sutton & Barto, 2018). Also, in reinforcement learning and deep neural networks, setting the learning values and choosing the appropriate neural network architecture plays an important role in the success of the algorithm (Scheuerer, 2008).

Performance Comparison

To compare the performance of these methods, criteria such as solution time, quality of answers and convergence rate are used. Comparison charts and tables can show the performance of each method well. For example, comparing the solution time, the combined genetic-branch-and-bound method takes less time than branch-and-bound and genetic algorithms, while providing a higher answer quality. The Convergence rate of different algorithms is shown in Table 1.

Table 1. Convergence rate of different algorithms

Iteration	Branch and Bound	Genetic Algorithm	Hybrid Genetic-Branch and Bound
1	0.1	0.2	0.3
10	0.3	0.5	0.6
20	0.5	0.7	0.8
30	0.7	0.8	0.9
40	0.8	0.85	0.95
50	0.9	0.9	0.98

Experimental results

For this purpose, several benchmark problems have been solved using different methods and the performance of each of these methods has been compared in terms of solution time, response quality, and convergence rate.

Benchmark Problems

To evaluate the performance of different methods, a set of benchmark problems has been selected from reliable sources. These problems include transportation problems, resource allocation, and scheduling problems, which have been widely used in previous research (Hooker & van Hoeve, 2018; Silver et al., 2016).

Implementation and test settings

Algorithms are implemented using widely used programming languages such as Python and standard optimization libraries. To ensure the accuracy of the results, each experiment was repeated several times and the average results were reported in Table 2. Algorithm parameters are also determined based on default values and optimal settings (Sutton & Barto, 2018; 河内正浩 & 安東宣善, 1992) The results of the implementation of the algorithms on benchmark problems in Table 2.

Table 2. The results of the implementation of the algorithms on benchmark problems

Convergence rate	Response quality	Solving time (seconds)	algorithm	problem
0.9	0.90	120	branch and border	Transportation
0.7	0.85	45	Genetic algorithm	Transportation
0.95	0.95	30	branch and border-Hybrid genetics	Transportation
0.85	0.88	150	branch and border	resource allocation
0.75	0.83	60	Genetic algorithm	resource allocation
0.9	0.92	40	branch and border-genetic combination	resource allocation
0.88	0.89	180	branch and border	timing
0.78	0.84	70	Genetic algorithm	timing
0.92	0.93	50	branch and border-Hybrid genetics	timing

Analysis of the results

The results show that the combined genetic-branch-and-bound method generally performs better than the other two methods. This method has less solution time and provides better quality answers. Also, the convergence rate of this method is higher than the genetic algorithm, which indicates its stability and efficiency in various problems(Sutton & Barto, 2018).

Results

This research investigated and analyzed new intelligent methods in solving integer programming problems. The obtained results showed that the combined and intelligent methods have better performance than the traditional methods. Among the advantages of these methods, we can mention higher efficiency in solving time, better quality of answers and more flexibility. In particular, the combined genetic-branch-and-bound method was able to reduce the solution time and improve the quality of the answers. These findings show the high capability of intelligent methods in solving complex problems and optimization (Karlof, 2005).

Suggestions for future research

To improve and expand research in this field, the following suggestions are made:

Development of new hybrid algorithms: Development of new hybrid algorithms that can exploit the advantages of different methods can help improve the efficiency and quality of answers.

Optimization of parameters: using automatic methods to adjust parameters of algorithms can help improve their performance.

References

1. Bertsimas, D., & Dunn, J. (2019). *Machine learning under a modern optimization lens*: Dynamic Ideas LLC Charlestown, MA.
2. Goodfellow, I., Bengio, Y., & Courville, A. (2016). *Deep learning*: MIT press.
3. Hooker, J. N., & van Hoeve, W.-J. (2018). Constraint programming and operations research. *Constraints, 23*, 172-195 .
4. Karlof, J. K. (2005). *Integer programming: theory and practice*: CRC Press.
5. Scheuerer, S. (2008). Metaheuristics: Heuristic Techniques for Combinatorial Optimization Problems. In *Encyclopedia of Decision Making and Decision Support Technologies* (pp. 604-611): IGI Global.
6. Schrijver, A. (1998). *Theory of linear and integer programming*: John Wiley & Sons.
7. Silver, D., Huang, A., Maddison, C. J., Guez, A., Sifre, L., Van Den Driessche, G., . . . Lanctot, M. (2016). Mastering the game of Go with deep neural networks and tree search. *nature, 529*(7587), 484-489 .
8. Sutton, R. S., & Barto, A. G. (2018). *Reinforcement learning: An introduction*: MIT press.
9. 河内正浩, & 安東宣善. (1992). Goldberg, DE: Genetic Algorithms in Search, Optimization & Machine Learning, 401pp., Addison-Wesley (1989). *人工知能, 7*(1), 168-168 .

Advanced Engineering Days

aed.mersin.edu.tr

Designing a Flexible Interface Mechanism to Convert an Industrial Gripper into a System Suitable for Medical Applications

Leila Effati Aghdam [*1], Hamidreza Arefi [1], Seyed Mohammadreza Akrami[1], Reza Abdollahi [1]

[1] *University of Tabriz, Department of Mechatronics Engineering, Iran, Leila.effati73@gmail.com, hamidray76@gmail.com, mr.akrami@tabrizu.ac.ir, r.abdollahi98@ms.tabrizu.ac.ir*

Cite this study: Aghdam, L. E., Arefi, H., Akrami, S. M., & Abdollahi, R. (2024). Designing a Flexible Interface Mechanism to Convert an Industrial Gripper into a System Suitable for Medical Applications. Advanced Engineering Days, 9, 848-855

Keywords
Gripper
Robotics
ARM robot
Mechanism
Gripper surgery

Abstract

Nowadays, the use of grippers to make changes in the surgical department in the hospital has become popular. Grippers are able to move objects or apply desired operations by grabbing other tools. In this research, we intend to design a mechanism that can be easily attached to linear grippers to turn an industrial robot into a surgical robot. This structure will be able to analyze the amount of displacement of the output of the system to control it if the force is more than required by the system. Soft materials are used to design the desired system, which is one of the methods of designing flexible systems. We use electronic elements to calculate the movements and force applied to the captured object. In this way, it is obtained when changing to gripper and calculating displacement in mechanical elements. In this regard, we use the flexible part to detect collisions with the body so that the robot can get the definite position of the body and then perform the surgery using its cutting tool. We should consider that the designed system is inspired by CMM and industrial grippers.

Introduction

A robotic arm is a mechanical system that is controlled using electronic circuits. The last part of the movement chain of the mechanical arm is called the end effector. Grippers, which are considered to be one of the final effective types, can move objects or perform desired operations by grabbing other tools.

In this research, we intend to design a mechanism that can be easily attached to linear grips to turn an industrial robot into a surgical robot. This structure will be able to analyze the amount of displacement of the system output to control it in case of entering more force than the system needs. Calculating direct or inverse kinematics for joint control is not among the goals of this research, and only the interface gripper design section is addressed. The grippers designed in the past researches are not able to be connected to the current grippers and must be connected to the robotic systems directly, and they also use very expensive elements in calculating the hardness of the captured object.

In 1998, Caffaz and his colleagues designed and developed a special DIST-hand gripper. DIST-hand is a four-finger device that is moved by a tendon and has 6 degrees of freedom, which is designed to perform experiments in the field of reach control and telemanipulation [1].

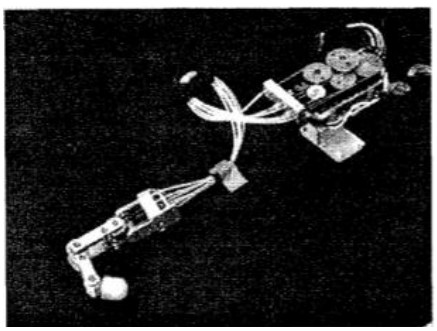


Figure 1. The mechanical structure of the finger and its stimulating system

In 2014, Song Soko and Mateen City addressed the issue of adhesion characteristics of fibrillar adhesives on soft deformable membranes. A soft-clamp with a swelling membrane covered by elastomeric mushroom-shaped microfibers has a superior combination with non-planar 3D part geometry, enabling the printing of different parts in series or parallel.[2] In 2015, Ariangela Manti et al presented a paper on the development of a gripper for general information with simple control and maintenance capabilities through a control scheme. Using a combination of soft materials shows how a bio-inspired design can be turned into soft devices that have grasping capabilities with a simple actuation and control system.[3][4] In 2109, Cheng and his colleagues conducted a study on the softness-based pneumatic sensor for bending angle and contact force detection. This paper presents the design and development of a smoothness-based pneumatic sensor for measuring external bending angle and compressive contact forces.[5]

According to the past studies and reviews, our general goal is to design and build a set to apply to the robot to perform necessary surgeries.

Material and Method

Finite element analysis method (FEM) is a powerful and modern calculation tool. This method is the most widely used method for solving engineering and mathematical problems and models. The main idea in the finite element method is to divide the structure, object or area under analysis into a large number of finite elements or, more simply, elements. The next step is to select the appropriate displacement function (field variable). In the following, the extraction of the elemental stiffness matrix and the elemental force vector, the assembly of the elemental equations and the application of boundary conditions to calculate the unknown field variable and also the calculation of the elemental stresses and strains are discussed. In the following, all the things required for the practical implementation of the article, including the review of the characteristics of the required materials, the design of the spring and the special shape of the designed spring, the design of the surgical tool unit to hold the surgical blade, the design of the clip part to hold the tool by the robot, etc.

1- FEM finite element method materials

The finite element analysis method is a powerful and modern computational tool. The finite element method is a special numerical method for solving partial differential equations in two or three spatial variables. This is achieved by discretizing a specific space in space dimensions.

2- Simulation and simulation of solidwork and stress analysis

Analysis and simulation of components or finite element is used for static and dynamic loading of mechanical equipment and structures. The main purpose of carrying out simulation is loading simulation, static analysis and stress analysis in the desired part and equipment. By stress simulation and analysis, it is possible to determine the critical points of a structure or equipment and calculate the reliability factor in the part or chassis.

3- Springs

Any object that has elastic properties is called a spring. The spring changes its shape in response to an external force and returns to its original state when the force is removed.

4- The elastic part of the spring

In this article, the general goal is to design a mechanical assembly so that we can use this assembly to produce an electrical signal related to the collision, so that in this structure, the robot can first determine the position of the object by using the sensor part that includes the sensor and mechanical circuits. or find the body. In this way, the robot first moves the assembly towards the body and when it reaches the body, the two conductors on the spring collide due to the high flexibility of the spring, and the robot realizes that it has hit an object or body. For this purpose, we designed a special spring to be an elastic object and to show a physical reaction to the collisions and not to harm the patient, and also to stick the key together in case of collision between two open conductors. Therefore, we used different types of designs for the spring, and in the end, the one that answered all the needs of this project was the following structure.

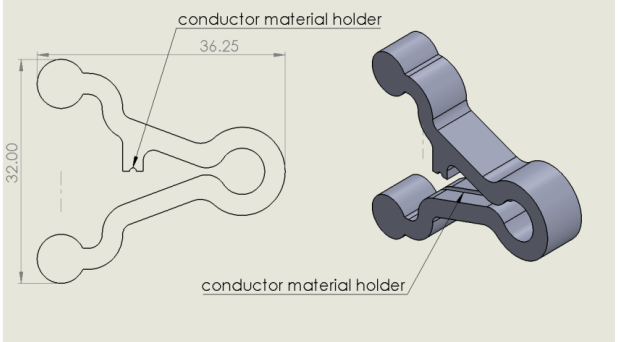


Figure 2. Resilient spring design

This section was analyzed under a force of 1075 N using materials similar to polyethylene PE and was used as the elastic and spring section of the system.

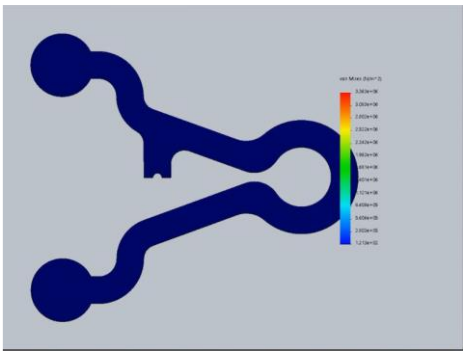


Figure 3. The designed spring in the open state

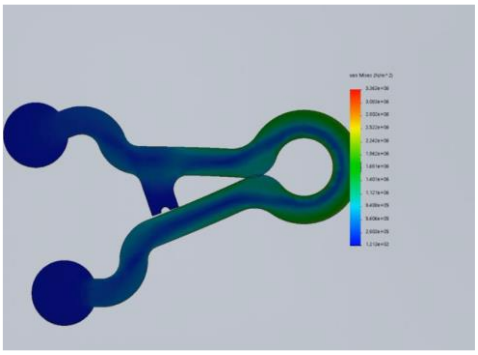


Figure 4. The designed spring in closed state

5- Solid body

A solid body is a body that contains a large number of fixed particles whose distance from each other is always constant. This distance remains constant even if a force is applied to the object or it moves.

6- Bistouri blade

It is a type of surgical blade that is very successful and is used for body surgery, autopsy and sometimes in handicrafts. Scalpels may be disposable or permanent.

In the following, experiments are presented to design and select the appropriate material, and a discussion has been held about the obtained results.

A) How to print parts

For the printing of parts, the need to check the way of printing and checking their difference was discussed in the way that the amount of tensile tolerance is important in different cases, and testing has been done in this regard. To do this important thing, two sample pieces were made, which were printed horizontally and vertically. These two samples were given to the laboratory for the tensile stress test and the answers of the samples are given below, and in the examination of these cases, the results were obtained that the samples that were printed horizontally had more bearing capacity.

ReportNo	Width	Thickness	Area	Speed	Max Load	ISO 527	Tensile Strength	Elongation at Break
		mm	mm²	mm/min	N	MPa	MPa	%
1	13.000	3.300	42.900	5.000	1963.057	631.047	45.759	2.750

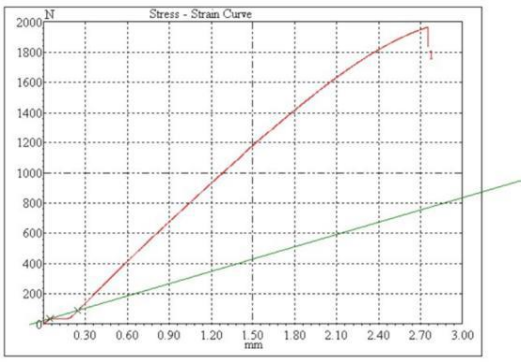


Figure 5. The amount of tolerance in horizontal print 1

Table 1. The amount of tolerance in horizontal print 1

Time:sec	Load:kgf	Stroke:mm	Spare1	Spare2
0.00500	0.032	0.00050	0.00000	0.00000
0.01000	0.047	0.00088	0.00000	0.00000
0.01500	0.063	0.00129	0.00000	0.00000
0.02000	0.102	0.00225	0.00000	0.00000
0.03000	0.158	0.00308	0.00000	0.00000
0.21000	1.426	0.01908	0.00000	0.00000
0.21500	1.477	0.01938	0.00000	0.00000
38.12000	186.946	2.74977	0.00000	0.00000
38.13500	186.926	2.74977	0.00000	0.00000
38.14000	186.918	2.74977	0.00000	0.00000
38.15500	186.898	2.74977	0.00000	0.00000
38.16000	186.891	2.74977	0.00000	0.00000
38.16500	186.885	2.74977	0.00000	0.00000

ReportNo	Width	Thickness	Area	Speed	Max Load	ISO 527	Tensile Strength	Elongation at Break
		mm	mm²	mm/min	N	MPa	MPa	%
2	13.000	3.300	42.900	5.000	1966.891	10.770	45.848	2.563

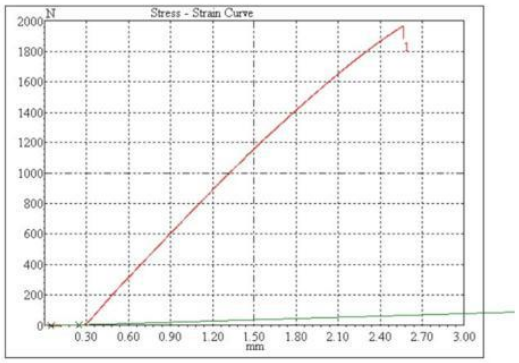


Figure 6. The amount of tolerance in horizontal print 2

Table 2. The amount of tolerance in horizontal print 2

Time:sec	Load:kgf	Stroke:mm	Spare1	Spare2
0.00500	0.018	0.00050	0.00000	0.00000
0.01000	0.025	0.00100	0.00000	0.00000
0.01500	0.033	0.00146	0.00000	0.00000
0.02000	0.047	0.00246	0.00000	0.00000
0.03000	0.059	0.00333	0.00000	0.00000
37.67500	191.962	2.56319	0.00000	0.00000
37.69000	191.952	2.56319	0.00000	0.00000
37.69500	191.948	2.56319	0.00000	0.00000
37.70500	191.939	2.56319	0.00000	0.00000
37.71000	191.936	2.56319	0.00000	0.00000
37.73000	191.930	2.56319	0.00000	0.00000

ReportNo	Width	Thickness mm	Area mm²	Speed mm/min	Max Load N	ISO 527 MPa	Tensile Strength MPa	Elongation at Break %
1	12.700	3.300	41.910	0.500	581.793	2426.087	13.882	0.626

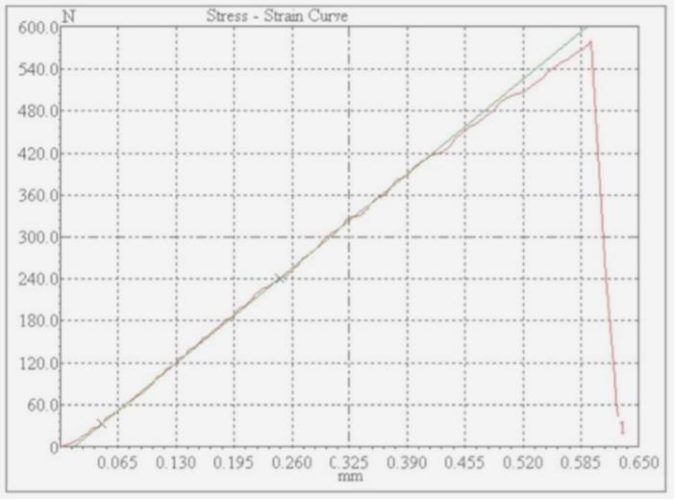


Figure 7. The amount of tolerance in vertical print 1

Table 3. The amount of tolerance in vertical print 1

Time:sec	Load:kgf	Stroke:mm	Spare1	Spare2
0.00000	0.111	0.00000	0.00000	0.00000
0.00500	0.135	0.00250	0.00000	0.00000
0.01000	0.271	0.00596	0.00000	0.00000
0.01500	0.435	0.00950	0.00000	0.00000
0.02000	0.602	0.01308	0.00000	0.00000
0.02500	1.086	0.01679	0.00000	0.00000
0.03000	1.147	0.02054	0.00000	0.00000
0.72500	59.187	0.59642	0.00000	0.00000
0.73000	59.327	0.60050	0.00000	0.00000
0.73500	45.664	0.60213	0.00000	0.00000
0.74000	32.292	0.60855	0.00000	0.00000
0.74500	24.717	0.61280	0.00000	0.00000
0.75000	12.165	0.61763	0.00000	0.00000
0.75500	10.068	0.62246	0.00000	0.00000

ReportNo	Width	Thickness mm	Area mm²	Speed mm/min	Max Load N	ISO 527 MPa	Tensile Strength MPa	Elongation at Break %
2	12.700	3.300	41.910	0.500	474.338	2271.912	11.318	0.536

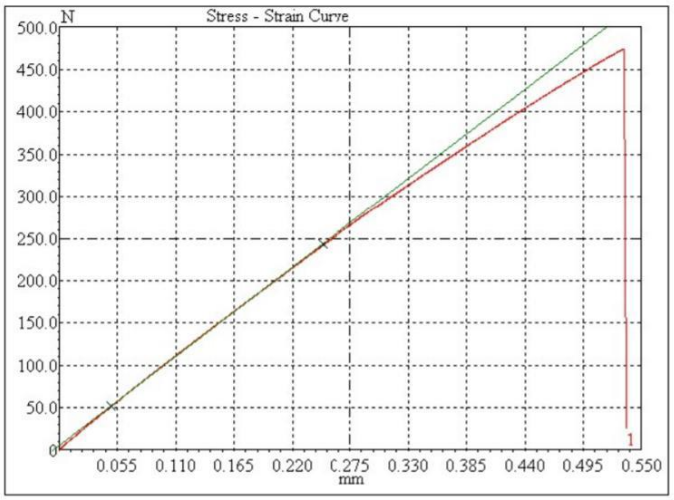


Figure 8. The amount of tolerance in vertical print 2

Table 4. The amount of tolerance in vertical print 2

Time:sec	Load:kgf	Stroke:mm	Spare1	Spare2
0.00500	0.022	0.00021	0.00000	0.00000
0.01000	0.031	0.00033	0.00000	0.00000
0.01500	0.039	0.00042	0.00000	0.00000
0.02000	0.049	0.00054	0.00000	0.00000
0.02500	0.069	0.00063	0.00000	0.00000
0.03000	0.079	0.00083	0.00000	0.00000
31.95500	48.361	0.53305	0.00000	0.00000
31.96000	48.364	0.53313	0.00000	0.00000
31.97000	48.366	0.53330	0.00000	0.00000
31.98000	48.367	0.53342	0.00000	0.00000
31.99000	48.369	0.53355	0.00000	0.00000
31.99500	48.368	0.53363	0.00000	0.00000
32.01000	15.982	0.53484	0.00000	0.00000
32.01500	5.208	0.53571	0.00000	0.00000

b) Material selection

To have flexible samples, we must choose materials that have high strain and high breaking point. Therefore, among different materials, TPU types have this feature. The only problem with this type of material is that due to multiple movement and loading in the direction of the printed layers, it causes separation. To solve this problem, we used the result that we got in the previous part about how to print the parts to design the part in this way. that loading is not aligned with the printed layers.

PLA and ABS materials were available for printing rigid parts.

The parts printed with ABS materials did not achieve good results in terms of the elasticity of the layers, and all the parts were separated and had very little resistance. But PLA parts have a high adhesive ability, so they better tolerate the resistance in the direction of the layers and are obtained according to homogeneous parts. So all hard parts were designed and made from PLA.

c) Material selection steps

After designing, all the parts were made using a printer and finally connected and assembled.

To form a regular set of robot parts, we investigated the adaptation methods and required tolerances of the parts. The arrangement of parts next to each other is shown in Figure 9.

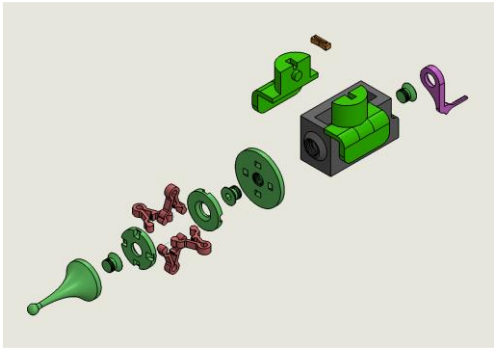


Figure 9. The layout of the robot parts

By arranging these parts next to each other and inside each other, the final arrangement of the robot will be like Figure 10.

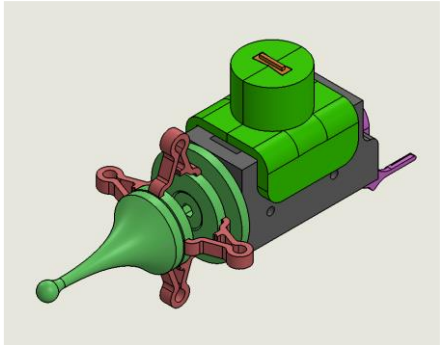


Figure 10. Final positioning of the robot

To be able to use a surgical knife, we need to make a knife handle for the robot as a special tool for using a razor, the design of the special tool is shown in Figure 11.

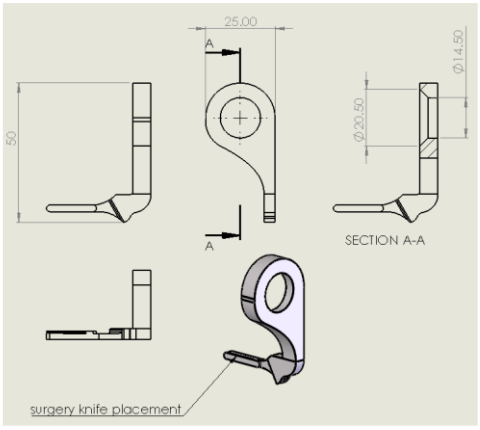


Figure 11. Positioning of surgical instruments

To be able to grab the piece using the desired robot, we must design the tool in such a way that it fits in the structure of the robot's clamp, therefore, the set shown in figure 12 is designed for holding.

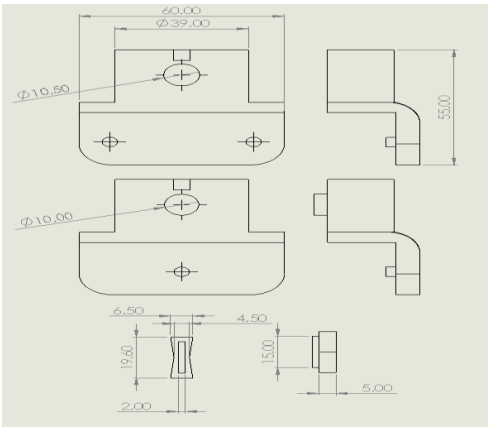


Figure 12. Design set for keeping parts

To place the wiring and the designed circuit on the robot, a base is needed in a way that can hold the tools and sensors. The designed base is shown in Figure 13.

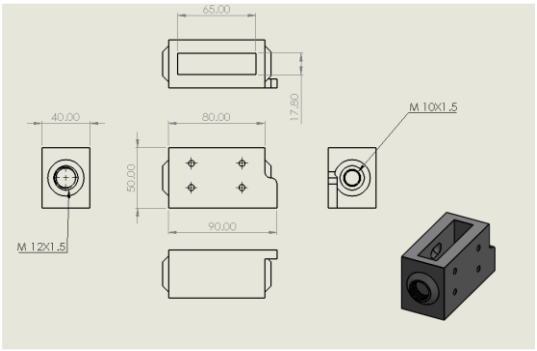


Figure 13. General design basis

In the center of the base, there is a place for the required wiring. The solid body in this part is designed with the aim of fully delivering energy and force to the spring sensor. In this design, the issue of access to all points should be taken into consideration, therefore, the design is made in the form of a cone, which is shown in Figure 14.

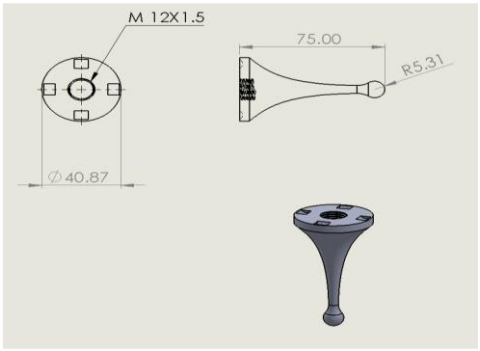


Figure 14. Designed rigid body

Results

An example of the final design of the parts is shown in Figure 15 and 16. As mentioned before, all the parts are designed and built and installed on the main robot.

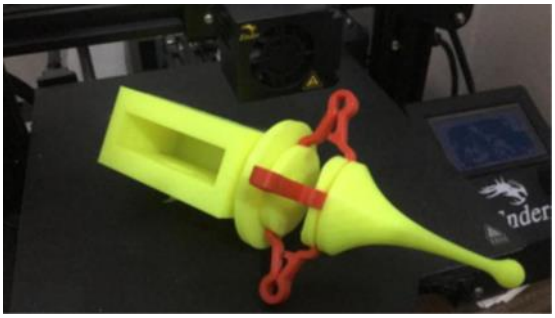


Figure 15. Overview of the fabricated parts

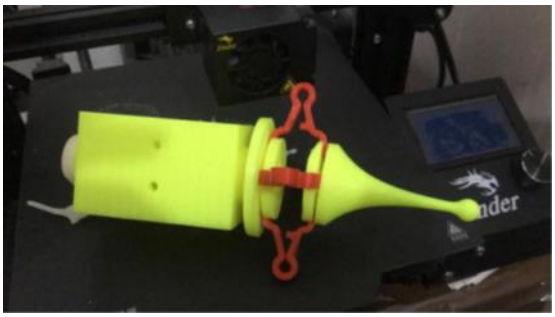


Figure 16. The designed and built robot from another view

Discussion

As it turned out, this system will be able to be taken by pneumatic grippers and perform the necessary operations using the tool connected to it.

Conclusion

As it turned out, this system will be able to be taken by pneumatic grippers and perform the necessary operations using the tool connected to it.

References

1. Caffaz, A., & Cannata, G. (1998, May). The design and development of the DIST-Hand dextrous gripper. In *Proceedings. 1998 IEEE International Conference on Robotics and Automation (Cat. No. 98CH36146)* (Vol. 3, pp. 2075-2080). IEEE.
2. Song, S., & Sitti, M. (2014). Soft grippers using micro-fibrillar adhesives for transfer printing. *Advanced materials (Deerfield Beach, Fla.)*, *26*(28), 4901-4906.
3. Manti, M., Hassan, T., Passetti, G., D'Elia, N., Laschi, C., & Cianchetti, M. (2015). A bioinspired soft robotic gripper for adaptable and effective grasping. *Soft Robotics*, *2*(3), 107-116.
4. Arefi, H., Dadashzadeh, B., Allahverdizade, A., & Abdollahi, R. (2023, December). Design, modeling and control of a soft gripper with TCP actuator using image processing. In *2023 11th RSI International Conference on Robotics and Mechatronics (ICRoM)* (pp. 626-632). IEEE.
5. Cheng, N., Low, J. H., Ang, B. W., Goh, A. J., & Yeow, C. H. (2018). Soft fabric-based pneumatic sensor for bending angles and contact force detection. *IEEE Sensors Journal*, *19*(4), 1269-1279.

Advanced Engineering Days

aed.mersin.edu.tr

Simulation, trajectory design and motion control of robotic hand with sensing force control

Ali Korehpaz Saeid [*1], Reza Abdollahi [1], Seyed Mohammadreza Akrami [1] Melika Fahmi [1]

[1] *University of Tabriz, Department of Mechatronics Engineering Tabriz, Iran, alikoorehpaz72@gmail.com, r.abdollahi98@ms.tabrizu.ac.ir, mrakrami@tabrizu.ac.ir, melika1998fahmi@gmail.com*

Cite this study: Saeid, A. K., Abdollahi, R., Akrami, S. M., & Fahmi, M. (2024). Simulation, trajectory design and motion control of robotic hand with sensing force control. Advanced Engineering Days, 9, 856-865

Keywords
Trajectory design
Motion control
Robotic hand
Control
Sensing force

Abstract

Designing the function of actuators such as a controlled robot hand for use in various work or industrial environments requires the design of a controlled robot hand such as ideal motion control similar to a robot hand. The purpose of this article is to present a sample of a robotic hand and design an optimal movement path based on the control of the forces applied by the fingers of the robotic hand to grasp hard and soft objects.The movement principles are based on the control algorithm design of the touch sensor data in each of the robotic fingers in the tangential force controller. The data of the touch sensors in each of the fingers of the robotic hand is measured and then by optimizing the applied force data, the optimized movement range of the fingers of the robotic hand is obtained in the designed controller. Kinematic simulation is done with Solid Works software, and the control that is on the hand in the simulation part of Matlab software is designed according to the purpose of the controller; The first part is related to controlling the position of the fingers until they come in contact with the desired object, and the second part is related to controlling the force in the desired range of motion, which creates a sensitivity of 0.01N, of the order of 0.001N, and does not cause the desired object to slip; Therefore, the sensitivity of the force sensor can be ignored and is desirable.

Introduction

Design of robotic hand and drives

Since the robotic hand is supposed to perform the same tasks as the human hand, it must have the same capabilities and characteristics as the human hand. In the design of robotic hand components, it is necessary to know the principles of kinematic movement of the hand to model the robotic hand and also to implement the optimal movement algorithm of the hand based on the allowed range of movement created by the data received from the sensors.

needed for a skilled hand. The fourth and fifth fingers are generally added to increase the skill and stability of the hand and make the robotic hand more similar to the human hand [1] The most common types of drives in robotic hands are electric motors. Especially with the progress in making electric motors with high efficiency and high compression, these drives have found the ability to be placed in the hand itself, which reduces the volume of the hand and also simplifies its structure. Another common type of actuator are pneumatic actuators that were used and have a function very similar to the human hand. One of the problems of pneumatic actuators is their location. Since these drivers are relatively large, all of them are placed in the forearm; For this reason, these hands cannot be installed on any arbitrary robotic arm [2] [3] [4].

Power transmission system and control of the robotic hand

According to the type of actuator and the location of the actuators, as well as different power transmission systems are used in robotic hands. One of the power transmission systems in robotic hands, especially human-like hands, is the tendon, which is modeled after the power transmission system in the human hand. Many

robotic hands use this system for power transmission [5], [4]pointed out. The second category of power transmission systems is gears. These systems have less error than tendons and friction is more in these systems. [6], [3] In general, the following four-step general strategy can be presented for holding objects by hand:

- Identifying the shape of the object by sight
- Getting the fingers closer to the object by controlling the position and force
- Optimizing the force and place of contact with the body
- Controlling the grip force of the object

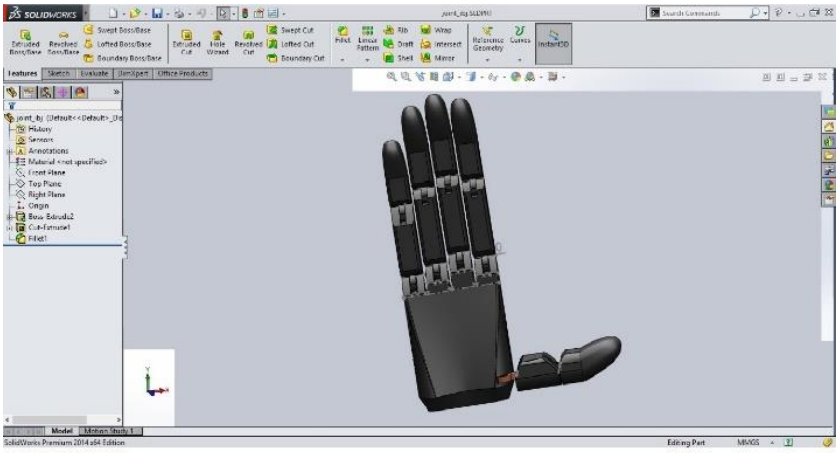


Figure 1. Robotic hand design in SolidWorks environment

Optimal modeling of the robotic hand

The robotic hand designed to work in the range of motion must have at least 9 degrees of freedom, that is, three fingers with three joints, which increases the ability of the robotic hand by increasing the number of fingers and degrees of freedom. However, the increase in fingers and degrees of freedom causes more complexity in controlling the robotic hand. Therefore, by presenting the optimized controller in the kinematics of the hand proposed in the article, which includes only 3 three fingers similar to a finger and a thumb with two bands and an additional degree of freedom in the palm, which behaves like a hand, by adding inputs in the controller Optimized, the number of fingers can be increased.

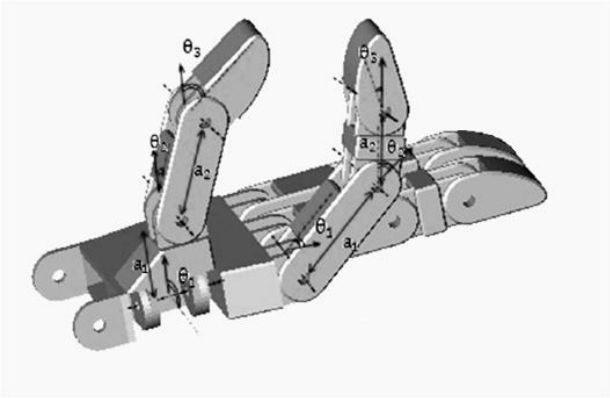


Figure 2. Modeled robotic hand and its parameters

Denavit-Hartenberg values for finger (three similar fingers) and thumb in the designed hand are presented in Tables 1 and 2.

Table 1. Denavit Hartenberg parameters of the robotic thumb

i	α_i	$\mathbf{a_i}$	d_i	θ_i
1	0	45mm	0	θ_1
2	0	30mm	0	θ_2
3	0	29mm	0	θ_3

Table 2. Parameters of Denavit Hartenberg robotic index finger

i	α_i	a_i	d_i	θ_i
1	$\pi/2$	33mm	0	θ_1
2	0	40mm	0	θ_2
3	0	13mm	0	θ_3

Kinematics of modeled robotic fingers

According to the dimensions and design of the hand and its degrees of freedom, the kinematic relationships of the index finger and thumb are considered as follows:

For index finger if in general mode $x = \begin{bmatrix} x \\ y \end{bmatrix}$ Consider the coordinates of the center of mass of the knuckle relative to the primary joint (horizontal x coordinates and y height relative to the palm and in the working space of the index finger are located in one plane), the location of the center of mass of each joint is calculated as follows: (Here x1, x2 and x3 are the coordinates of the center of mass of the first, middle and last fingers respectively)

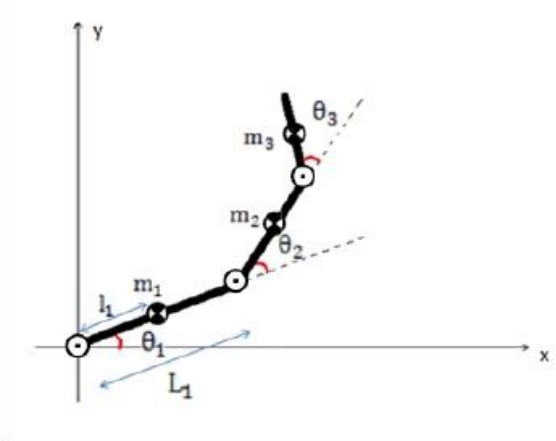


Figure 3: Schematic of the robotic index finger

(1) $$\begin{bmatrix} x_1 \\ y_1 \end{bmatrix} = \begin{bmatrix} l_1 \cos\theta_1 \\ l_1 \sin\theta_1 \end{bmatrix} = x_1$$

(2) $$\begin{bmatrix} x_2 \\ y_2 \end{bmatrix} = \begin{bmatrix} L_1 \cos\theta_1 + l_2 \cos(\theta_1 + \theta_2) \\ L_1 \sin\theta_1 + l_2 \sin(\theta_1 + \theta_2) \end{bmatrix} = x_2$$

(3) $$\begin{bmatrix} x_3 \\ y_3 \end{bmatrix} = \begin{bmatrix} L_1 \cos\theta_1 + L_2 \cos(\theta_1 + \theta_2) + l_3 \cos(\theta_1 + \theta_2 + \theta_3 \\ L_1 \sin\theta_1 + L_2 \sin(\theta_1 + \theta_2) + l_3 \sin(\theta_1 + \theta_2 + \theta_3 \end{bmatrix} = x_3$$

Given that $V = \dot{X}$ and $\dot{\theta} = \left[\dot{\theta}_1 \dot{\theta}_2 \dot{\theta}_3\right]^T$:

(4) $$v_1 = J_1 \dot{\theta} = \begin{bmatrix} -l_1 \sin\theta_1 00 \\ l_1 \cos\theta_1 00 \end{bmatrix} \begin{bmatrix} \dot{\theta}_1 \\ \dot{\theta}_2 \\ \dot{\theta}_3 \end{bmatrix}$$

(5) $$v_2 = j_2\dot{\theta} = \begin{bmatrix} -L_1\sin\theta_1 - l_2\sin(\theta_1+\theta_2) - l_2\sin(\theta_1+\theta_2)0 \\ -L_1\cos\theta_1 - l_2\cos(\theta_1+\theta_2) - l_2\cos(\theta_1+\theta_2)0 \end{bmatrix}\begin{bmatrix} \dot{\theta}_1 \\ \dot{\theta}_2 \\ \dot{\theta}_3 \end{bmatrix}$$

(6) $$v_3 = j_3\dot{\theta} =$$

$$\begin{bmatrix} -L_1 sin\theta_1 - L_2\sin(\theta_1+\theta_2) - l_3\sin(\theta_1+\theta_2+\theta_3) - L_2 sin(\theta_1+\theta_2) - l_3\sin(\theta_1+\theta_2+\theta_3) l_3\sin(\theta_1+\theta_2+\theta_3) * \\ -L_1 cos\theta_1 - L_2\cos(\theta_1+\theta_2) - l_3\cos(\theta_1+\theta_2+\theta_3) - L_2 cos(\theta_1+\theta_2) - l_3\cos(\theta_1+\theta_2+\theta_3) l_3\cos(\theta_1+\theta_2+\theta_3) \end{bmatrix}\begin{bmatrix} \dot{\theta}_1 \\ \dot{\theta}_2 \\ \dot{\theta}_3 \end{bmatrix}$$

In high relations j1 , j2 and j3 According to the Jacobian, they are related to the center of mass of the primary,middle, and end of the index finger.

The dynamics of modeled robotic fingers

According to the Euler-Lagrange equations of motion, we have:

(7) $$\frac{d}{dt}\frac{\partial\varsigma}{\partial\theta} - \frac{\partial\varsigma}{\partial\theta} = \tau$$

The kinetic energy of the finger can be written in such a way that k_t represents the translational kinetic energy and k_r represents the rotational kinetic energy.

(8) $$k(\theta) = k_r + k_t$$

The rotational kinetic energy can be calculated from the following equation:

(9) $$k_r = \frac{1}{2}\omega_1^T I_1\omega_1 + \frac{1}{2}\omega_2^T I_2\omega_2 + \frac{1}{2}\omega_3^T I_3\omega_3 = \frac{1}{2}\dot{\theta}^T I\dot{\theta}$$

For the thumb, the three angular velocity vectors are:

(10) $$\omega_1 = \dot{\theta}_1 e_1$$

(11) $$\omega_2 = \dot{\theta}_1\sin\theta_2 e_1 + \dot{\theta}_1\cos\theta_2 e_2 + \dot{\theta}_2 e_3$$

(12) $$\omega_3 = \dot{\theta}_1\sin(\theta_2+\theta_3)e_1 + \dot{\theta}_1\cos(\theta_2+\theta_3)e_2 + (\dot{\theta}_2+\dot{\theta}_3)e_3$$

Also, the transferable kinetic energy of the system in route design can be calculated from the TSK fuzzy method:

(13) $$k_t = \frac{1}{2}\dot{\theta}^T (J_1^T m_1 J_1 + J_2^T m_2 J_2 + J_3^T m_3 J_3)\dot{\theta}$$

It should be kept in mind that since the reference coordinate is located on the palm, the direction of the earth's gravity will change concerning the reference coordinate. Therefore, to calculate the potential energy in the general state, considering g as a vector with the size of $9.8005 m/s^2$ and arbitrary direction relative to the palm as a reference, the following relationship has been used:

(14) $$V(\theta) = -m_1\vec{x}_1.\vec{g} - m_2\vec{x}_2.\vec{g} - m_3\vec{x}_3.\vec{g}$$

With Placement x1 , x2, and x3 With the vectors for the index finger and thumb, the potential energy for each finger can be calculated. For the index finger:

(15) $$V(\theta) = -m_3\Big(g_y(L_2\,sin(\theta_1+\theta_2)+L_1\,sin\,\theta_1+l_3\,sin(\theta_1+\theta_2+\theta_3))+g_x(L_2\,cos(\theta_1+\theta_2)+L_1\,cos\,\theta_1+l_3\,cos(\theta_1+\theta_2+\theta_3))\Big)-m_2\big(g_x l_2\,cos(\theta_1+\theta_2)+L_1 g_x\,cos\,\theta_1+g_y l_2\,sin(\theta_1+\theta_2)+L_1 g_y\,sin\,\theta_1\big)-l_1 m_1(g_x\,cos\,\theta_1+g_y\,sin\,\theta_1)$$

For the thumb, by placing the potential energy relations in the general state, the following relation will be obtained:

(16) $$V(\theta) = -m_2\Big(g_x l_2 sin\theta_2+g_y cos\theta_1(L_1+l_2 cos\theta_2)\Big)+g_y sin\theta_1(L_1+l_2 cos\theta_2)-m_3\big(g_x l_3\sin(\theta_2+\theta_3)+L_2 g_x sin\theta_2+2L_1 g_y sin\theta_1+g_y l_3\cos(\theta_2+\theta_3)\,cos\theta_1+g_y l_3\cos(\theta_2+\theta_3)\,sin\theta_1+2L_2 g_y cos\theta_2 sin\theta_1\big)-g_y l_1 m_1(cos\theta_1+sin\theta_1)$$

By placing the equations in the Euler-Lagrange equation as well as the numerical values related to each of the fingers in the above relationships, the input torque vector can be obtained as a function of $\theta, \dot{\theta}, \ddot{\theta}$ and, in the general state of this relationship, it can be expressed as follows:

(17) $$\tau = M(\theta)\ddot{\theta}+v(\theta,\dot{\theta})+G(\theta)$$

In this case, M is called the mass matrix and its components are a combination of the mass of the connections and their length, the center of mass of each knuckle, and their inertia tensor. V is the movement speed matrix of the joints of the fingers, taking into account the centrifugal and criollos forces related to this part of the equation. G is related to the force due to gravity. In MATLAB software, based on Hartenberg kinematics principles, each of the fingers has been obtained to determine the dynamic parameters for solving the controller equations designed in the Simulink part of MATLAB software in the simulation of the adaptive fuzzy controller of the force applied to the body. Also, the correctness of the outputs obtained by simulating and quantifying the kinematic parameters of the angles of the robotic fingers to design the path in artificial intelligence proposed in the robotic hand controller in the state of holding the object or applying manual control to control the degree of the joints of the robotic fingers in the static state is confirmed.

Touch sensor modeling

In this simulation, from the set of sensors available in the SolidWorks software, the mass sensor is used according to the role of the controller, and the modeling of this desired sensor element is provided by a spring model. Also, according to the proposed sensor, the range of the relevant parameters should not exceed a certain value during the deformation of the sensor element, or the applied stress should not exceed the specified force limit that is consistent with the settings of the SolidWorks software. To simplify the selection of the desired touch element type on the end band of each of the robotic fingers, it is necessary to design the optimal dynamic range of the physical properties of the touch sensor used, which is between 0.01N-10N (1:1000) [7-8]. Since in the simulated experiments, grasping of objects with fingertips is investigated and the object is in contact only with the end strap of the fingers, the touch sensor is also placed on the end strap, and for the simplicity of the model, the end of the spring is exactly at the center of mass of the strap. The end is connected. The external surface of the touch sensor is also a disc with a diameter of 0.4 mm and a radius of 6.25 mm.

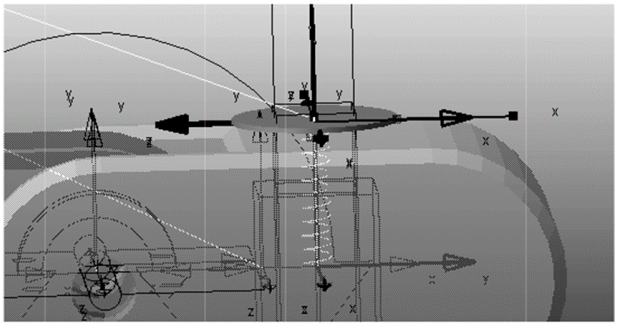


Figure 4. Force sensor applied on the last joint of the robotic finger

According to the kinematic characteristics of the robotic hand for the sensor located on the end of the index finger, we have:

(18)

$$F = \begin{bmatrix} F_x \\ F_y \end{bmatrix}$$
$$= \begin{bmatrix} \cos\theta_1 - \sin\theta_1 \\ \sin\theta_1 \cos\theta_1 \end{bmatrix} \begin{bmatrix} \cos\theta_2 - \sin\theta_2 \\ \sin\theta_2 \cos\theta_2 \end{bmatrix} \begin{bmatrix} \cos\theta_3 - \sin\theta_3 \\ \sin\theta_3 \cos\theta_3 \end{bmatrix} \begin{bmatrix} F_x \\ F_y \end{bmatrix}$$
$$= \begin{bmatrix} \cos(\theta_1 + \theta_2 + \theta_3) - \sin(\theta_1 + \theta_2 + \theta_3) \\ \sin(\theta_1 + \theta_2 + \theta_3) \cos(\theta_1 + \theta_2 + \theta_3) \end{bmatrix} \begin{bmatrix} f_x \\ f_y \end{bmatrix}$$

Because the index finger of the hand in question does not have the ability to move in the z direction. The components related to this axis have been removed from the relevant calculations. The rotation matrix related to the thumb sensor is also calculated according to its kinematics from this relationship:
(19)

$$F = \begin{bmatrix} F_x \\ F_y \\ F_z \end{bmatrix}$$
$$= \begin{bmatrix} 1 & 0 & 0 \\ 0 & cos\theta_1 & -sin\theta_1 \\ 0 & sin\theta_1 & cos\theta_1 \end{bmatrix} \begin{bmatrix} cos\theta_2 & -sin\theta_2 & 0 \\ sin\theta_2 & cos\theta_2 & 0 \\ 0 & 0 & 1 \end{bmatrix} \begin{bmatrix} cos\theta_3 & -sin\theta_3 & 0 \\ sin\theta_3 & cos\theta_3 & 0 \\ 0 & 0 & 1 \end{bmatrix} \begin{bmatrix} f_x \\ f_y \end{bmatrix}$$
$$= \begin{bmatrix} cos(\theta_2 + \theta_3) & -sin(\theta_2 + \theta_3) & 0 \\ sin(\theta_2 + \theta_3)cos\theta_1 & cos(\theta_2 + \theta_3)cos\theta_1 & -sin\theta_1 \\ sin(\theta_2 + \theta_3)sin\theta_1 & cos(\theta_2 + \theta_3)sin\theta_1 & cos\theta_1 \end{bmatrix} \begin{bmatrix} f_x \\ f_y \\ f_z \end{bmatrix}$$

Controller design

The control algorithm required for grasping objects by a robotic hand can be divided into three general parts:

- Determining the initial position of the fingers
- Control the location of fingers
- Collision detection
- Force control

In the first part of the research, the problem of location control is based on the TSK fuzzy method, which is the same type of decision-making to take objects, in the design of control theory intelligence, based on the parameters of the ANFIS neural network; Therefore, the general form of grasping is predetermined, and initial angles have already been determined for grasping each object. The condition of using feedback linearization in the controller design of a system of system state equations is as follows:

(20) $$\dot{x} = Ax + B\gamma(x)\left[u - \alpha(x)\right]$$

where in $\alpha(x)$ and $\gamma(x)$ Sentences are non-linear. The control diagram for controlling the angle of each of the robotic knuckles is as follows:

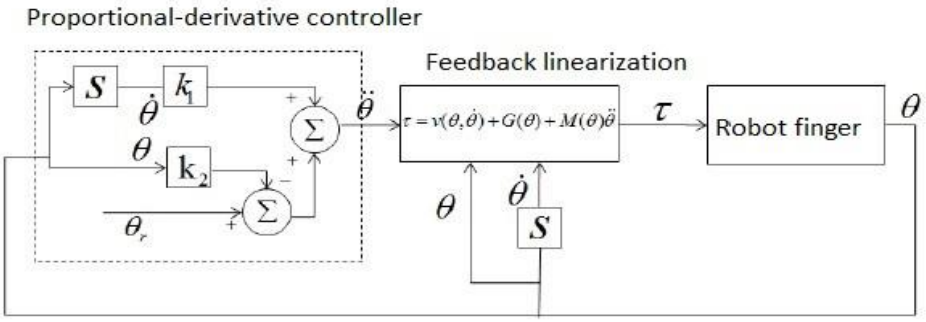


Figure 5. Location controller diagram

The presented control algorithm was applied on the robotic index fingers and thumbs in the SolidWorks environment and the results are shown in the following diagrams. The final destination of each section was 15 degrees for the beginning section, 30 degrees for the middle section, and 60 degrees for the last section. Also, during the simulation, the direction of gravity is in the direction of the vector perpendicular to the palm, and its value is considered equal to $9.80665 m / S^2$.

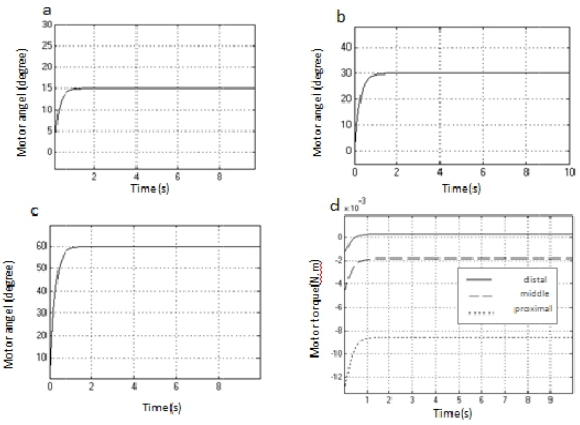


Figure 6: a- diagram related to the location of the primary joint, b- related to the location of the middle joint, c- location of the final joint, and d- diagram of the torque applied to each joint of the robotic index finger.

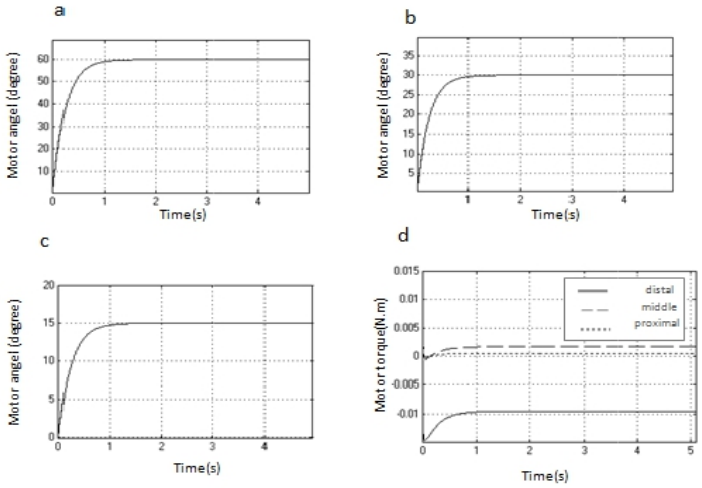


Figure 7: a- diagram related to the location of the primary joint, b- related to the location of the middle joint, c- location of the final joint, and d- diagram of the torque applied to each joint of the robotic thumb.

In Figure 6, the system has reached the final value without oscillation and overshoot, and according to the values of K_1 and K_2, the time to reach the final value is about 1 second, and also in Figure 7, the time to reach the final value for the robotic thumb is approximately 1.5 seconds and The provided controller moved the knuckles to the desired position without error.

Force control

To introduce force F by the robotic finger, the torque τ obtained by using the following relationship should be applied to the joints [9]:

(21) $$\tau = J^T(\theta)F$$

The final output of the controller is the torque required to create the desired force.

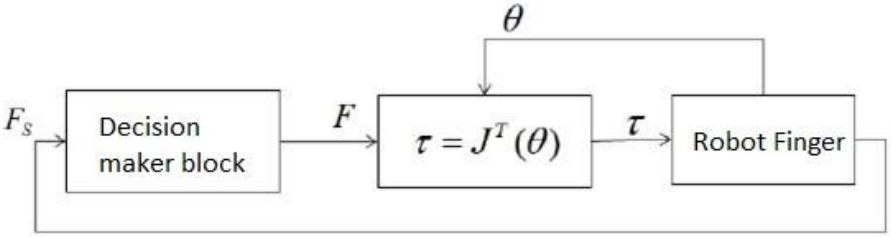


Figure 8: force control diagram

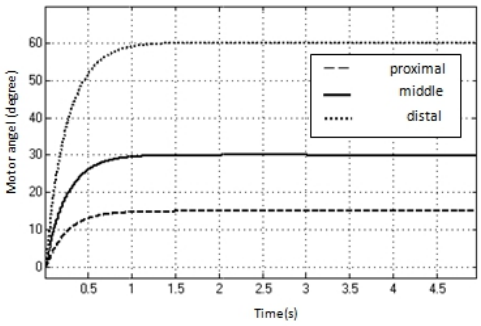


Figure 9: Diagram of the position of the angles of the joints of the robotic index fingers after applying force

It can be seen that despite applying force to the robotic index finger, the connection angles have not changed and the force controller was able to follow and neutralize the applied force well and almost without delay.

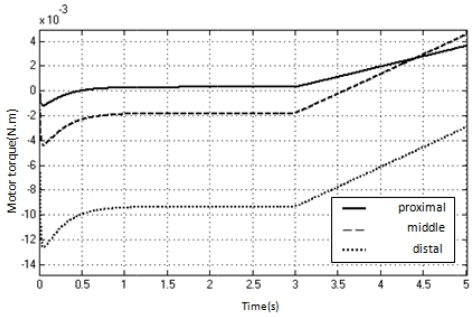


Figure 10: The diagram of changes in the torque of the actuators after applying the force

Figure 10 shows that the changes in torque after applying force are proportional to the changes in applied force.

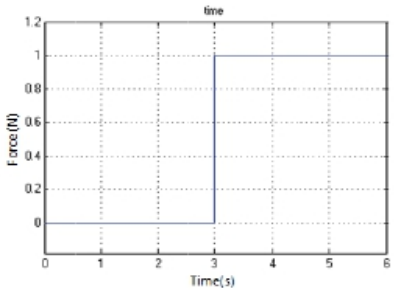


Figure 11: Diagram of the force applied to the moving robotic index finger

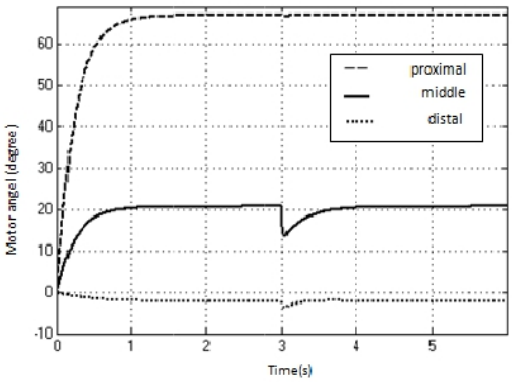


Figure 12: Diagram of changes in connection angles when force is applied

In Figure 12, it can be seen that despite applying force to the robotic index finger at time t=3s, the connection angles changed at the first moment and the force controller could not follow and neutralize the

applied force well and almost without delay; For this reason, the robotic index finger is slightly out of its original position. After this moment, the force applied by the force controller is neutralized and the position of the robotic index finger is returned to its original state by the location controller; In other words, the delay created after t=3s has become ineffective.

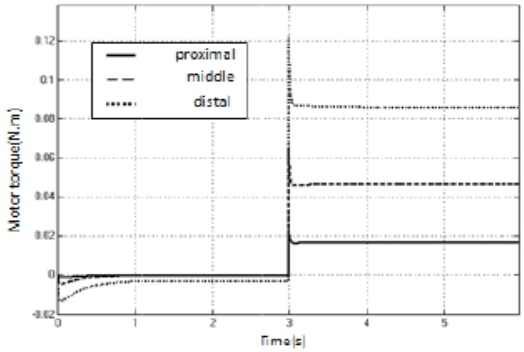


Figure 13. diagram of torque applied to each connection

It is shown in Figure 13 that at time t=3s, the sudden changes in force at the first moment were not neutralized by the force controller, and because of this, the robotic index finger is slightly out of its initial position. After this moment, the force applied by the force controller is neutralized and the position of the robotic index finger is returned to the initial state by the location controller. Also, at time t=3s, the strong changes in the force applied to the sensor caused the strong response of the force controller and overshoot.

The simulation results of catching objects based on route design

Sim-mechanics was first used to simulate the grasping of objects by a robotic hand, but in this type of simulation, by default, the effects of friction and other effective factors are ignored, and the simulation of collisions between objects requires the definition of functions and conditions. There are many for the simulator and the results of the simulation are not very real, the simulation results with sim-mechanics were only used to check the location controllers. Finally, the simulations performed with the designed robotic hand will be simultaneously simulated in the working environments of SolidWorks and MATLAB software, the control of the robotic hand will be implemented by MATLAB software, And the Controls Solid plugin has been used to import controllers and simulate simultaneously. In the simulations, according to the instructions for using the Controls Solid plugin, the Simulink execution code of the ode15 (stiff/NDF) type and with variable steps is considered; Also, the relative tolerance in Simulink is set as 0.001.

Conclusions

By designing a robotic hand and applying appropriate control algorithms, the path design is presented based on a method for capturing objects. Then, by simulating the neural network for grasping objects by this robotic hand, its efficiency has been investigated. Since the force controller in this research is made using a linearizer, the change in the position of the robotic fingers when applying force in the design of the created path due to the existence of the adaptive neural network does not hurt the performance of the controller, and also the force controller against increasing the applied force. It works well up to 5N. It was also observed during the simulation that if the speed and gain related to the speed control stage of the robotic fingers in the tolerance of the touch sensor for the incoming force of the order of 10^{-3} is small enough, not only capturing the objects by the adaptive fuzzy method in the stage The collision of the robotic index finger with the object under the force of 5N will be safe; Rather, we will get the advantage of touch sensors based on the 0.1N sensitivity of the force sensor. When the thumb of the robotic hand hits the object, it will change its position under the influence of the position and shape of the captured object.

References

[1] F. Lotti, P. Tiezzi, G. Vassura, L. Biagiotti, G. Palli, and C. Melchiorri,"Development of UB Hand 3: Early Results," Proc. 2005 IEEE Int. Conf. Robot. Autom., pp. 4488–4493.

[2] G. A. Bekey, R. Tomovic, and I. Zeljkovic, "Control architecture for theBelgrade/USC hand," in in Dextrous robo t hands, Springer, 1990, pp. 136–149.

[3] C. S. Lovchik and M. a. Diftler, "The Robonaut hand: a dexterous robothand for space," Proc. 1999 IEEE Int. Co nf. Robot. Autom. (Cat. No.99CH36288C),vol. 2, no. May, pp. 907–912, 1999.

[4] S. Jacobsen and E. Iversen,Design of the Utah/MIT dextroushand," Robot, vol. 3, pp. 1520–1532, 1986.

[5] R. Walker, "Shadow dextrous hand technical specification," Shad. Robot Co., 2005.

[6] J. Ueda, M. Kondo, and T. Ogasawara, "The multifingered NAIST handsystem for robot inhand manipulation," Mech. Mach. Theory, vol. 45, no. 2, pp.224–238, Feb. 2010.

[7] R. S. Dahiya, G. Metta, M. Valle, and G. Sandini, "Tactile SensingFrom Humans to Humanoids," IEEE Trans. Rob ot., vol. 26, no. 1, pp. 1–20, Feb.2010.

[8] B. L. Gery and S. N. Gottschlich, "A tactile sensing system fordexterous manipulation," Intell. Robot. Syst. 94, v ol. 2, pp. 13841390, 1994

Advanced Engineering Days

aed.mersin.edu.tr

Influence of new advanced split injection strategy on emissions and performance of a dual-fuel RCCI engine

Seyed Ali Sadri Jahanshahi [*1], **Amirreza Javaherian** [1], **Mortaza Yari** [1]

[1]*University of Tabriz, Department of Mechanical Engineering, Iran, a.jahanshahi@tabrizu.ac.ir, a_javaherian@tabrizu.ac.ir, myari@tabrizu.ac.ir*

Cite this study: Jahanshahi, S. A. S, Javaherian, A., Yari, M. (2024). Influence of new advanced split injection strategy on emissions and performance of a dual-fuel RCCI engine. Advanced Engineering Days, 9, 866-868

Keywords
RCCI engine
Split injection strategy
Emission control
Injection timing
Dual-fuel combustion

Abstract

In this study, the effect of using biogas fuel with replacement ratios of 20% and 40%, besides the effect of timing and optimal strategy of diesel fuel injection on the performance and emissions of a controlled reactivity compression ignition engine is investigated. In all cases, input energy, pressure, profile, and total time of fuel injection, engine speed, and the overall equivalence ratio are kept constant. The results obtained from the simulations show that the addition of biogas fuel as a fuel with low reactivity leads to a decrease in the temperature of the combustion chamber gases and an increase in the pressure of the chamber. The biggest power loss is due to biogas fuel with a replacement ratio of 40% and 9.18%. By increasing the biogas fuel replacement ratio, the emissions of unburned hydrocarbons increase. While nitrogen oxide emissions decrease. Using the optimal strategy of fuel injections of 1% and 2%, while reducing the ignition time delay, prevents knocking. The optimal strategy of fuel injection, especially in the amount of 1%, leads to an optimal reduction of emissions and a small compensation of the power loss in the RCCI engine compared with the diesel engine.

Introduction

Utilization of biogas fuel in compression ignition engines leads to a reduction in emissions despite the possibility of a reduction in output power. The use of alternative fuels with low reactivity alongside fossil fuels offers significant potential to address some environmental challenges such as pollutant emissions through the invention of more efficient technologies such as the Reactivity Controlled Compression Ignition (RCCI) engine [1].

Mahmoudi et al. [2] evaluated the effects of modified biogas fraction on RCCI engine characteristics numerically, which showed the reduction of emissions of nitrogen oxide, soot, and unburned hydrocarbons. Li et al. [3] reported that the RCCI engine shows lower exergy destruction than diesel engine under the same load conditions. Also, the exergy destruction was related to the homogeneity and equivalence ratio.

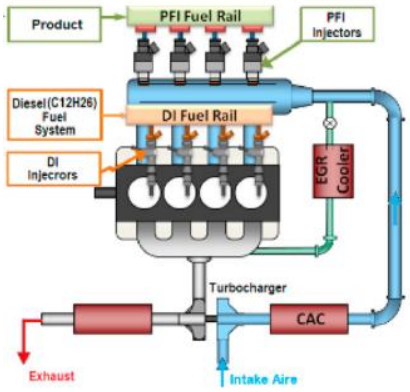
The fuel injection timing is one of the parameters that directly determines the quality of the engine combustion process. A delay in the injection time can reduce the volume of fuel in the rapid ignition period and can lead to a reduction in the combustion speed and prevent knocking [4]. Simultaneously, the delay in the injection time can reduce the peak temperature of gases in the cylinder and the high temperature area and thus, prevent the production of nitrogen oxides. However, late fuel injection causes insufficient engine power output [5]. In this research, the effect of using biogas fuel with replacement ratios of 20% and 40%, besides the effect of timing and optimal strategy of diesel fuel injection on the performance and emissions of a RCCI engine is investigated.

Material and Method

In Figure 1, the schematic of the set-up studied in the present research is represented.

The proposed engine of the current research is Caterpillar 3401. The cylinder diameter, cylinder stroke, connecting rod length, compression ratio, and cylinder displacement are, respectively, 137.2 mm, 165.1 mm, 261.6 mm, 16.1:1, and 2.44 liters [6].

Figure 1. Schematic of the set-up studied in the present research [2]



The chemical composition of biogas fuel on molar basis used as fuel with low reactivity is as CH_4: 74.66%, O_2: 0.03%, H_2: 0.01% H_2O: 0.04%, CO_2: 25.24%, and N_2: 0.02%. The conservation equations of mass, momentum and energy governing the simulation of current engine processes are stated below.

$$\frac{\partial \rho}{\partial t} + \frac{\partial \rho u_i}{\partial x_i} = S \tag{1}$$

$$\frac{\partial \rho u_i}{\partial t} + \frac{\partial \rho u_i u_j}{\partial x_j} = -\frac{\partial P}{\partial x_i} + \frac{\partial \sigma_{ij}}{\partial x_j} + \rho g_i + S_i \tag{2}$$

$$\frac{\partial \rho e}{\partial t} + \frac{\partial u_j \rho e}{\partial x_j} = -P\frac{\partial u_j}{\partial x_j} + \sigma_{ij}\frac{\partial u_i}{\partial x_j} + \frac{\partial}{\partial x_j}(K\frac{\partial T}{\partial x_j}) + \frac{\partial}{\partial x_j}(\rho D \sum_m h_m \frac{\partial Y_m}{\partial x_j}) + S_i \tag{3}$$

Results

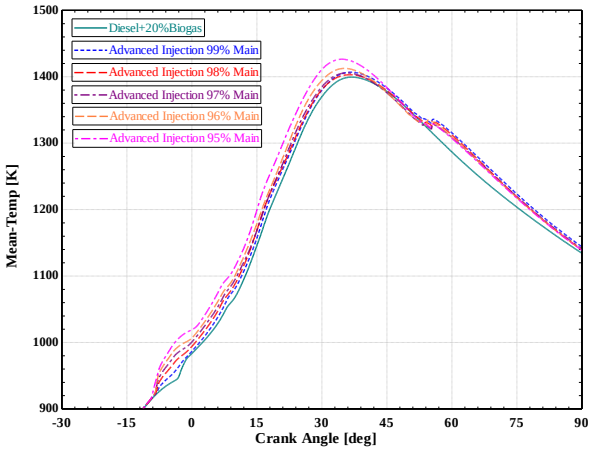


Figure 2. The effect of different pre-injections on the average temperature inside the cylinder of RCCI engine and biogas fuel with a ratio of 20%

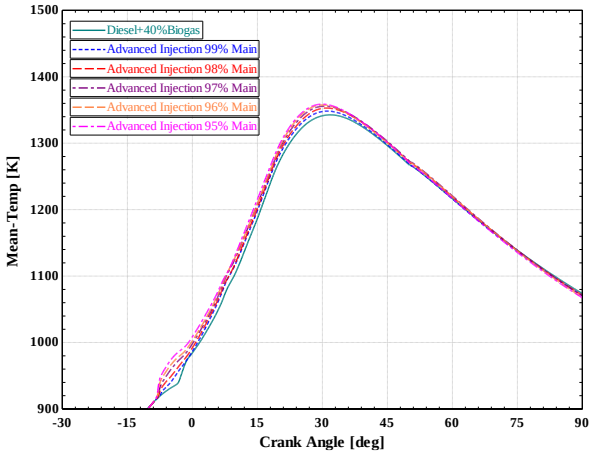


Figure 3. The effect of different pre-injections on the average temperature inside the cylinder of RCCI engine and biogas fuel with a ratio of 40%

In Table 1, The effect of different pre-injections on the emissions of the engine are shown.

Table 1. The effect of different pre-injections on the emissions of the engine

	Emission	100	99	98	97	96	95
20%	Soot	0.13459	0.12496	0.12599	0.12769	0.12726	0.1228
	HC	8.4948	6.5174	6.7003	6.75378	6.6624	6.32608
	Nox	2.74352	2.43282	2.36384	2.4473	2.59186	2.78549
	CO	3.7409	3.6186	3.67512	3.60675	3.68413	3.54254
40%	Soot	0.24976	0.22093	0.22256	0.22339	0.22667	0.22581
	HC	21.02693	18.49767	18.20597	18.05294	18.31314	18.22113
	Nox	2.9582	2.61457	2.64145	2.70269	2.77635	2.86174
	CO	6.75032	5.95566	6.14617	6.16595	6.18049	6.2809

Discussion

The average temperature inside the cylinder and the maximum value of this parameter in all pre-injections increases. For the replacement ratio of 20% and the pre-injection of 5%, the temperature increases by 26.93 ℃. Also, for the replacement ratio of 40% and the pre-injection of 5%, the temperature increases by 16.13 ℃.

By increasing the pressure, especially the mean effective pressure, as well as the increase of temperature inside the combustion chamber, the carbon-containing fuels mostly react and the amount of soot pollutant decreases. Therefore, the observed decreasing trend is as expected. The 5% pre-injection strategy has the highest pressure inside the cylinder and also has a higher temperature than the initial case, so the emission has the largest reduction and reaches 0.1228 g/kWh. But by applying restrictions to prevent knocking, strategies with low pre-injection percentage are suitable, among which the amount of pollutant in pre-injection of 1% is optimal and its amount is 0.12496 g/kWh, which requires the use of post-refining systems to reach the current standards.

Conclusion

In this study, the effect of using biogas fuel with replacement ratios of 20% and 40%, besides the effect of timing and optimal strategy of diesel fuel injection on the performance and emissions of a RCCI engine was investigated. The addition of 20% and 40% biogas replacement ratios caused the temperature of the gases inside the combustion chamber to decrease and the pressure inside the cylinder to increase. The highest temperature decrease was related to the replacement ratio of 40% to the value of 36.20 K and the highest pressure increase also belonged to the replacement ratio of 40% and to the amount of 0.3378 MPa.

With the increase in the biogas fuel replacement ratio, the emission of unburned hydrocarbons increased due to the emergence of a thicker wall, while nitrogen oxide emissions decreased.

Using the optimal strategy of fuel injection in amounts of 1% and 2%, while reducing the ignition time delay, prevented knocking and compensated for some decrease in the RCCI engine power compared to diesel engine.

References

1. Cardona, C. A., & Amell, A. A. (2013). Laminar burning velocity and interchangeability analysis of biogas/C3H8/H2 with normal and oxygen-enriched air. *International Journal of Hydrogen Energy*, *38*(19), 7994-8001.
2. Mahmoodi, R., Yari, M., Ghafouri, J., & Poorghasemi, K. (2021). Effect of reformed biogas as a low reactivity fuel on performance and emissions of a RCCI engine with reformed biogas/diesel dual-fuel combustion. *International Journal of Hydrogen Energy*, *46*(30), 16494-16512.
3. Li, Y., Jia, M., Chang, Y., Kokjohn, S. L., & Reitz, R. D. (2016). Thermodynamic energy and exergy analysis of three different engine combustion regimes. *Applied Energy*, *180*, 849-858.
4. Hamzehloo, A., & Aleiferis, P. (2014). *Numerical modelling of mixture formation and combustion in DISI hydrogen engines with various injection strategies* (No. 2014-01-2577). SAE Technical Paper.
5. Li, Y., Bai, X. S., Tunér, M., Im, H. G., & Johansson, B. (2019). Investigation on a high-stratified direct injection spark ignition (DISI) engine fueled with methanol under a high compression ratio. *Applied Thermal Engineering*, *148*, 352-362.
6. Chuahy, F. D., & Kokjohn, S. L. (2017). High efficiency dual-fuel combustion through thermochemical recovery and diesel reforming. *Applied energy*, *195*, 503-522.

Advanced Engineering Days

aed.mersin.edu.tr

Smooth Path Planning for Autonomous Mobile Robots: Integration of Improved A-Star with Artificial Potential Field Method

Amir Amjadi [*1], Samira Kharratian [1], Seyed Mohammadreza Akrami [1], Yousef Seyfari [2]

[1]*University of Tabriz, Department of Mechatronics Engineering, Iran, amiramjadi105@gmail.com, skharratian99@ms.tabrizu.ac.ir, mr.akrami@tabrizu.ac.ir*
[2]*University of Maragheh, Department of Computer Science, Iran, Seyfari@tabrizu.ac.ir*

Cite this study: Amjadi, A., Kharratian, S., Akrami, S. M., & Seyfari, Y. (2024). Smooth Path Planning for Autonomous Mobile Robots: Integration of Improved A-Star with Artificial Potential Field Method. Advanced Engineering Days, 9, 869-872

Keywords
Path Planning
Smooth Trajectories
Autonomous robots
A-Star
Artificial Potential Field

Abstract

Path planning is a critical component of autonomous mobile robots, enabling efficient and safe navigation across diverse environments. Achieving optimal path planning is essential for ensuring both smooth trajectories and computational efficiency. The A-star (A*) algorithm is extensively utilized for path optimization due to its effectiveness in identifying the shortest path. However, it frequently generates non-smooth paths, particularly in low-resolution environments, which can adversely affect robot performance and safety. To address this limitation, this paper integrates the A* algorithm with cubic B-spline interpolation. Cubic B-splines enhance path smoothness by increasing the number of reference points and generating more continuous trajectories. While the improved A* method excels in static environments, dynamic obstacle avoidance is managed through the Artificial Potential Field method (APF). Our hybrid approach preserves the strengths of A* while significantly improving path smoothness and dynamic obstacle handling. Simulation results indicate that this combined method produces smoother trajectories without extending path length or increasing computational complexity, thereby augmenting the navigation capabilities of autonomous robots.

Introduction

Autonomous Mobile Robots (AMRs) exhibit increased efficiency by independently navigating through various applications such as transportation, manufacturing, healthcare, and agriculture [1]. An essential aspect of AMRs autonomy involves efficient path planning, enabling optimal route navigation while avoiding obstacles. Smoothness in path trajectories is essential for enhancing AMRs' capabilities, ensuring stable and efficient movement in dynamic environments.

Path planning techniques can be classified into two primary categories: global and local methods, based on the utilization of environmental information. Global path planning algorithms provide the robot with complete environmental information before movement begins. This allows the AMR to calculate an optimal route from the starting point to the destination while considering obstacles along the way [2]. One of the efficient and commonly used global methods for finding the low cost path is the A* algorithm [3]. However, a significant limitation of A* is its tendency to produce paths with sharp turns and non-smooth trajectories in low-resolution environment [4]. To address this challenge, an improved version of the A* algorithm is suggested. This enhanced algorithm aims to mitigate the shortcomings of traditional A* by incorporating additional techniques for path smoothing and obstacle avoidance [3], [4]. Furthermore, while the enhanced A* algorithm effective in static environments, it may encounter difficulties in navigating through dynamic environments with moving obstacles. To overcome this challenge, we introduce a hybrid approach that combines the improved A* algorithm with the Artificial Potential Field (APF) method for real-time obstacle avoidance. The APF method is a widely used approach for dynamic obstacle avoidance in robotics [5].

In this paper, we combine A*, cubic B-spline, and APF algorithms to improve path planning. The integration, enhances global responsiveness and computational speed, while also avoiding local optima. The resulting approach ensures optimal length and smoothness, providing appropriate direction in dynamic environments.

Material and Method

The A* algorithm is a widely used pathfinding and graph traversal algorithm. The A* algorithm uses an evaluation function $f(n)$, which combines the actual cost g(n) to reach node n and the heuristic cost $h(n)$ to reach the goal from n [3]:

$$\boldsymbol{f(n) = g(n) + h(n)} \tag{1}$$

where actual cost is the actual cost from the start node to the current node n and is calculated as:

$$\boldsymbol{g(n) = g(n') + c_{n,n'}} \tag{2}$$

Here, g(n') is the cost-so-far to reach node n, and $c_{n,n'}$ is the cost of traversing from n' to n.
h(n) is the heuristic estimate of the cost from n to the goal node, often computed using the Euclidean distance:

$$\boldsymbol{h(n) = \sqrt{(x_n - x_{goal})^2 + (y_n - y_{goal})^2}} \tag{3}$$

where (x_n, y_n) is the position of the current node and (x_{goal}, y_{goal}) is the position of the goal node.

Cubic B-spline interpolation uses piecewise cubic polynomials to create a continuous and smooth path. Each segment of the path between two consecutive points is defined by a cubic polynomial, ensuring that the entire path is smooth and continuous up to the second derivative. This continuity is important for maintaining smooth trajectories that are physically feasible for the robot to follow.

The cubic (3-ordered) B-spline function $S(t)$ for a segment between control points *Pi* and *Pi*+1 is defined as [6]:

$$\boldsymbol{F_s(t) = \sum_{i=0}^{3} P_i \; B_{i,3}(t), \qquad t \in [0,1]} \tag{4}$$

Where $B_{i,3}(t)$ for i=0,..,3 is the basis function of B-spline that define by :

$$\boldsymbol{B_{i,3}(t) = \frac{1}{6}\begin{cases} (1-t)^3 \\ 3t^3 - 6t^2 + 4 \\ -3t^3 + 3t^2 + 3t + 1 \\ t^3 \end{cases}} \tag{5}$$

The output of the cubic B-spline algorithm is without any sharp angles along the path. A measure to increase the smoothness value was presented by:

$$\boldsymbol{S = \alpha\left(1 - \frac{DA_l}{N_f - 1}\right) + \beta\left(1 - \frac{S_{min}}{N_f}\right)} \tag{6}$$

where α and β are weight coefficients. DA_l is the number of deviation angles greater than the desired variable, N_f is the total number of track segments, and S_{min} is the least number of segments in the path.

It is based on the concept of simulating artificial forces that guide the robot towards its goal while repelling it from obstacles. Here's a detailed explanation of how APF works and its integration with the improved A* algorithm for dynamic obstacle avoidance.

APF method is a widely used technique for real-time dynamic obstacle avoidance in robotics. In the APF method, the environment is modeled using two potential fields: the Attractive Potential Field U_{att} (Eq.7.), which pulls the robot towards the goal, and the Repulsive Potential Field U_{rep} (Eq.8.), which pushes the robot away from obstacles as shown in figure 1 [7].

$$\boldsymbol{U_{att} = \frac{1}{2}\,k_{att}\|q - q_{tar}\|^2} \tag{7}$$

$$\boldsymbol{U_{rep}(q) = \begin{cases} \frac{1}{2}\,K_{rep}\left(\frac{1}{\rho(q)} - \frac{1}{p}\right)^2, & \text{if } \rho(q) \le \rho_0 \\ 0, & \text{if } \rho(q) > \rho_0 \end{cases}} \tag{8}$$

where q and q_{tar} are the current position and target position of the robot respectively, and k_{att} is a positive constant. Where ρ(q) is the distance from the robot to the nearest obstacle, ρ_0 is the influence distance of the obstacle, and K_{rep} is a positive constant.

The total potential U(q) is the sum of the attractive and repulsive potentials. The robot moves in the direction of the negative gradient of the total potential field ($F\ (q) = -\nabla U\ (q)$).

$$\boldsymbol{U}\ (\boldsymbol{q}) = \boldsymbol{U_{att}}(\boldsymbol{q}) + \boldsymbol{U_{rep}}(\boldsymbol{q}) \tag{9}$$

Results and Discussion

Figure 2.a. illustrates the path generated by the A* algorithm with a designated number of reference points. This route demonstrates sharp turns, which could pose safety risks for AMR involved in cargo transportation. To address this issue, the next phase involves integrating the cubic spline method into the basic path planning approach, as shown in Fig. 2.b. This integration aims to smooth the path and enhance safety. Table 1 presents the characteristics of the primary planned path by A* and the optimized path by cubic B-spline. α and β are both set to 1, and S_{min} is 4. The smoothness coefficient (S) increases using the cubic B-spline method. Fig. 1.c. illustrates an exploration of the issue concerning robots becoming trapped in local minima, conducted through the real-time artificial potential field algorithm. This approach is designed to enable the robot to navigate around dynamically placed obstacles along its path to the target, ensuring it can overcome these obstacles efficiently without being slowed down excessively.

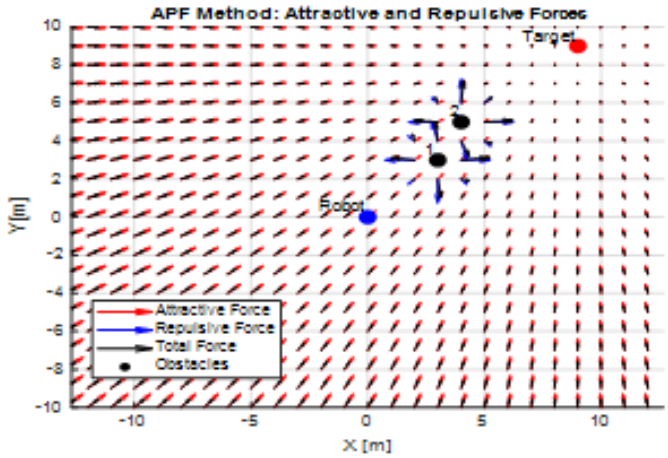
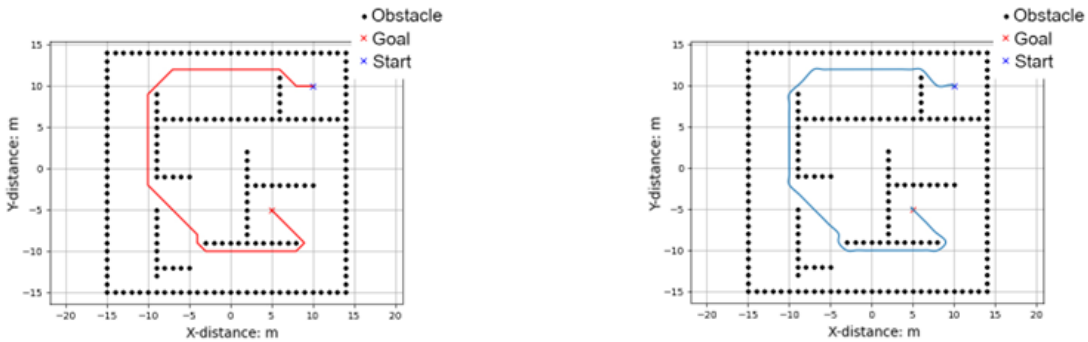


Figure 1. Artificial Potential Field method

Table 1. Characteristics of the primary and optimized Path

Method	NRP	D_{Al}	N_f	S
Planned path	57	8	56	1.7831
Optimized path	5700	1	5699	1.9991



(a) (b)

Figure 2. Path planning optimization. a. A-star method b. cubic B-spline method
*NRP= Number of reference point

Conclusion

In summary, this paper introduces a novel method for smooth path planning in autonomous mobile robots by integrating A-star (A*) with cubic spline interpolation and Artificial Potential Field (APF) methods. The hybrid approach addresses A*'s limitations in generating non-smooth paths and enhances dynamic obstacle avoidance. Simulation results validate improved path smoothness and obstacle handling without compromising computational efficiency. This approach holds promise for advancing autonomous robot navigation in various environments, with potential for further optimization and real-world implementation.

References

[1] A. Loganathan and N. S. Ahmad, "A systematic review on recent advances in autonomous mobile robot navigation," *Eng. Sci. Technol. an Int. J.*, vol. 40, p. 101343, Apr. 2023, doi: 10.1016/j.jestch.2023.101343.

[2] H. Zhang, W. Lin, and A. Chen, "Path Planning for the Mobile Robot: A Review," *Symmetry (Basel).*, vol. 10, no. 10, p. 450, Oct. 2018, doi: 10.3390/sym10100450.

[3] P. Hart, N. Nilsson, and B. Raphael, "A Formal Basis for the Heuristic Determination of Minimum Cost Paths," *IEEE Trans. Syst. Sci. Cybern.*, vol. 4, no. 2, pp. 100–107, 1968, doi: 10.1109/TSSC.1968.300136.

[4] G. Tang, C. Tang, C. Claramunt, X. Hu, and P. Zhou, "Geometric A-Star Algorithm: An Improved A-Star Algorithm for AGV Path Planning in a Port Environment," *IEEE Access*, vol. 9, pp. 59196–59210, 2021, doi: 10.1109/ACCESS.2021.3070054.

[5] O. Khatib, "Real-time obstacle avoidance for manipulators and mobile robots," in *Proceedings. 1985 IEEE International Conference on Robotics and Automation*, Institute of Electrical and Electronics Engineers, pp. 500–505. doi: 10.1109/ROBOT.1985.1087247.

[6] M. Munguia, *Cubic B-spline: Derivation with two applications*. The University of Texas-Pan American, 2014.

[7] F. A. Raheem, M. M. Badr, and others, "Development of Modified path planning algorithm using artificial potential field (APF) based on PSO for factors optimization," *Am. Sci. Res. J. Eng. Technol. Sci.*, vol. 37, no. 1, pp. 316–328, 2017.

Advanced Engineering Days

aed.mersin.edu.tr

Neuromusculoskeletal Modeling of Elbow Flexion/Extension – Aided by OpenSim

Mohammad Reza Sayyed Noorani [*1], Farhad Farkhondeh Tale Navi [2], Kimiya Khojand [1]

[1]*University of Tabriz, Department of Mechatronics Engineering, Iran, smrs.noorani@tabrizu.ac.ir, kimiya.kh1401@ms.tabrizu.ac.ir*
[2]*University of Tabriz, Department of Cognitive Neuroscience, Iran, Farkhondeh_F@Tabrizu.ac.ir*

Cite this study: Sayyed Noorani, M. R., Farkhondeh Tale Navi, F., & Khojand, K. (2024). Neuromusculoskeletal Modeling of Elbow Flexion/Extension– Aided by OpenSim. Advanced Engineering Days, 9, 873-876

Keywords
Neuromusculoskeletal
Elbow Movement
Cerebrum
Motor Command
OpenSim software

Abstract

Neuromusculoskeletal (NMSK) models are recently exploited as a non-invasive approach for advanced predictive simulations and subject-specific modeling to enhance clinical applications. A cerebellar model, in addition to a musculoskeletal model, is fundamental to this idea. In this paper, we aim to establish an integrated framework to simulate the role of the cerebellum in producing the motor control commands of flexor/extensor muscles of the elbow. The model of cerebellum is abstracted to a Spiking Neural Network (SNN) that receives sensory information from the musculoskeletal and delivers the motor actions. The Izhikevich model is utilized to capture neuron activity function due to its balance between biological accuracy and computational efficiency. The learning is based on the strategy of Spike Timing-Dependent Plasticity (STDP) modulated by Dopamine (DA). Accordingly, firing of a presynaptic neuron immediately before a postsynaptic neuron results in Long-Term Potentiation (LTP) of synaptic transmission, and the reverse order of firing results in Long-Term Depression (LTD). The trained network provides flexor and extensor command signals to move the elbow for reaching the hand to a target position. By using the OpenSim API in MATLAB, we investigate our neuromusculoskeletal model in a closed-loop procedure in which the elbow muscles in forward dynamics receive the neural excitations and feedback the motion information. This framework highlights the potential of SNN-based cerebellar models in improving motor function rehabilitation through personalized, precise neuromuscular simulations, advancing computational neuroscience, and benefiting both healthy and impaired conditions in clinical settings.

Introduction

Neuromusculoskeletal (NMSK) models are exploited as a computational non-invasive approach for advanced predictive simulations and multi-scale modeling to enhance clinical applications. NMSK models are powerful tools to estimate the complex interactions between neural control, muscle dynamics, and skeletal movement, enabling personalized treatment plans and improved rehabilitation outcomes, for example in human-in-the-loop control of assistive robots [1,2]. These models must be adapted for real-world environments, requiring the integration of high-fidelity simulation data to compensate for lower resolution measurements in settings like fields, gyms, and clinics [1]. Recent research emphasizes the importance of subject-specific modeling and the potential for advanced predictive simulations and multi-scale modeling to enhance clinical applications [3,4].

Neuromusculoskeletal modeling is a complex and interdisciplinary field that has significant implications for both artificial and biological systems. These models are essential for understanding motor control mechanism, designing experiments, and optimizing motor performance. However, current models are not able to fully capture the complexities of the neuromusculoskeletal control system, especially the nonlinear dynamics of skeletal muscle, suggesting a more realistic approach to modeling. Implementation of such models according to brain structures (e.g., the cerebellum) and functions (e.g., spiking activity) could significantly enhance the fidelity of simulations and provide deeper insights into motor control mechanisms [3,4].

The cerebellum plays a crucial role in motor control, prediction, and learning. It processes sensory input and coordinates voluntary movements, ensuring smooth and precise actions. Pathologies affecting the cerebellum can lead to significant motor impairments. For instance, Geminiani et al. (2018) developed a detailed computational

model of the cerebellum embedded in a sensorimotor circuit to study cerebellar pathologies [5]. Moreover, Bruel et al. (2023) addressed to spinal cord (SC) influence on motor learning in the cerebellum to find that dose the SC facilitate or hinder cerebellar motor learning [3].

Research has shown that artificial neural networks (ANNs), particularly spiking neural networks (SNNs), are effective in simulating realistic human body movements, e.g. elbow flexion/extension, for various applications, including assistive technology and rehabilitation systems [1,3,6]. These networks can generate inverse dynamics transformations of arm and hand movements with low torque errors, providing subject-specific parameterization and precise predictions of limb dynamics [7]. They have also been integrated into closed-loop models for human activities of daily living (ADL) movements, accurately predicting angular trajectories during tasks like eating and drinking with high target access rates and minimal error rates.

Recent advancements in spiking neural networks (SNNs) have revolutionized the simulation of biological neural behavior, particularly in motor control tasks like elbow rotational movement. SNNs, inspired by the brain's neural processes, excel in replicating precise spike timing and communication dynamics of biological neurons, offering valuable insights into temporal processing and learning mechanisms [8-9]. Moreover, by incorporating Spike Timing-Dependent Plasticity (STDP), SNNs provide a biologically plausible framework for motor control tasks, making them ideal for controlling robotic systems and modeling biological processes [10]. The utilization of cerebellar-inspired learning rules in SNNs enhances their capability to simulate and control complex movements, such as robotic arm manipulation, showcasing their potential in realistic simulations of motor tasks [11-13].

The objectives of this study are to synthesize current research on SNNs and their application in motor control, elucidate the significance of STDP in learning, and explore the role of cerebellar learning in motor function and pathology. By integrating evidence-based information from neuroscience, robotics, and computational modeling, we aim to provide a comprehensive overview that is accessible to a broad audience, including researchers, engineers, and clinicians.

Material and Method

We utilized the Izhikevich model for its balance between biological accuracy and computational efficiency designing a spiking neural network to simulate cerebellar function in motor control tasks, specifically elbow flexion and extension. The SNN architecture was inspired by previous successful applications, consisting of neurons representing the cerebellar, receiving proprioceptive input and delivering motor commands, see Fig. 1. Spike Timing-Dependent Plasticity (STDP), modulated by dopamine, served as the primary learning mechanism, adjusting synaptic weights based on the temporal correlation of neuronal activity. Structural synaptic plasticity further enhanced network adaptability by allowing the formation and elimination of synaptic connections. Moreover, in a larger time scale, dopamine as the reward of approaching to the target modulates the strength of the synaptic connections. This architecture is, in fact the, inspiration of reinforcement learning in which rewards obtained through interaction of an agent with environment conducts the system towards an optimal policy.

The network underwent a motor babbling phase, generating random motor commands to map sensory inputs to motor commands. The commands serve as activations of the biceps (BIC) and triceps (TRC) muscles to move the musculoskeletal model of the elbow established under OpenSim API in MATLAB [14]. This closed-loop system involved the SNN, as cerebellum model, generating motor commands, applying them to the musculoskeletal model, and receiving proprioceptive feedback. The simulation evaluates the accuracy and efficiency of the control system via performance metrics including target-reaching ability, movement smoothness, and response to perturbations. The Pipeline of the learning algorithm based on STDP and DA modulation is illustrated in Fig. 2.

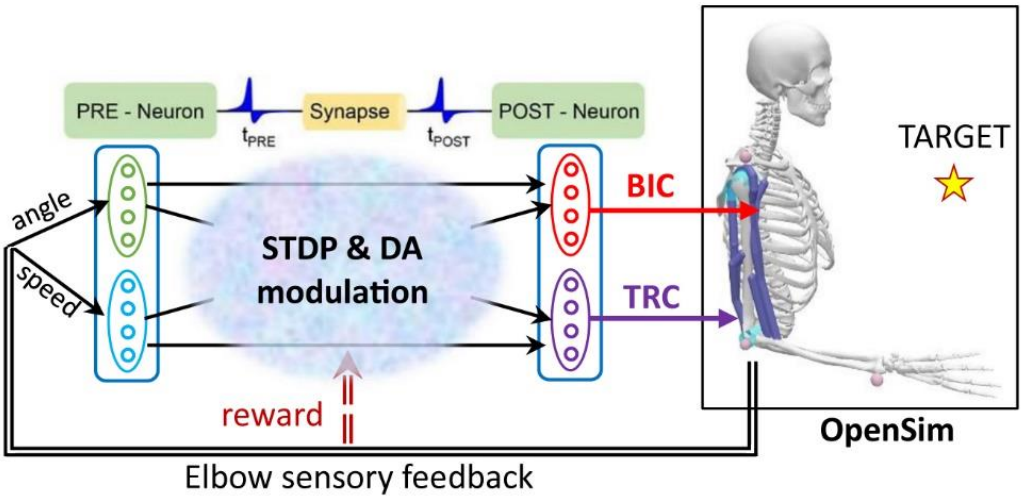


Figure 1. The neuromusculoskeletal model including a SNN architecture trained via STDP & DA modulation.

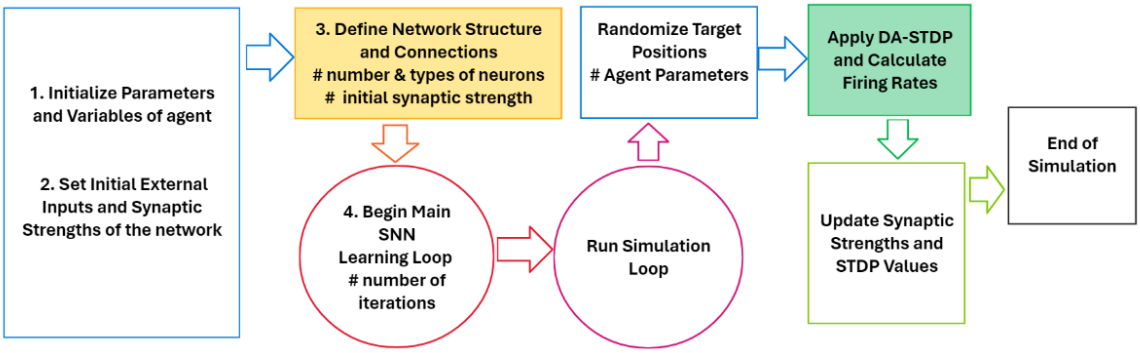


Figure 2. Pipeline and information flow in the neuromusculoskeletal model.

Conclusion

Spiking neural networks, leveraging mechanisms such as STDP and structural plasticity, offer powerful tools for modeling and controlling motor behaviors. The detailed study of cerebellar functions and pathologies through computational models provides valuable insights into the neural basis of motor control and learning. These advancements pave the way for innovative applications in robotics and neuroprosthetics, enhancing the quality of life for individuals with motor impairments. The integration of SNNs with STDP and cerebellar learning models holds promise for developing advanced neuroprosthetics and rehabilitation devices. By mimicking the biological processes underlying motor control, these networks can provide more natural and efficient control mechanisms for robotic limbs and assistive technologies.

Future research should focus on enhancing the scalability and robustness of SNNs, integrating multimodal sensory inputs, and exploring the co-adaptation of neural networks and users in brain-computer interface (BCI) applications. Additionally, further studies on the interplay between different forms of synaptic plasticity and their impact on learning and memory will deepen our understanding of both artificial and biological neural systems.

References

1. Lloyd, David G., Ilse Jonkers, Scott L. Delp, and Luca Modenese. "The history and future of neuromusculoskeletal biomechanics." *Journal of Applied Biomechanics* 39, no. 5 (2023): 273-283.
2. Meattini, Roberto, Davide Chiaravalli, Gianluca Palli, and Claudio Melchiorri. "sEMG-based human-in-the-loop control of elbow assistive robots for physical tasks and muscle strength training." *IEEE Robotics and Automation Letters* 5, no. 4 (2020): 5795-5802.
3. Bruel, Alice, Ignacio Abadía, Thibault Collin, Icare Sakr, Henri Lorach, Niceto R. Luque, Eduardo Ros, and Auke Ijspeert. "The spinal cord facilitates cerebellar upper limb motor learning and control; inputs from neuromusculoskeletal simulation." *PLOS Computational Biology* 20, no. 1 (2024): e1011008.
4. Kainz, Hans, Antoine Falisse, and Claudio Pizzolato. "Neuromusculoskeletal modeling in health and disease." *Brazilian Journal of Motor Behavior* 18 (2024).
5. Geminiani, Alice, Claudia Casellato, Alberto Antonietti, Egidio D'Angelo, and Alessandra Pedrocchi. "A multiple-plasticity spiking neural network embedded in a closed-loop control system to model cerebellar pathologies." *International journal of neural systems* 28, no. 05 (2018): 1750017.
6. Spüler, Martin, Sebastian Nagel, and Wolfgang Rosenstiel. "A spiking neuronal model learning a motor control task by reinforcement learning and structural synaptic plasticity." In *2015 International Joint Conference on Neural Networks (IJCNN)*, pp. 1-8. IEEE, 2015.
7. Manukian, Mykhailo, Serhii Bahdasariants, and Sergiy Yakovenko. "Artificial physics engine for real-time inverse dynamics of arm and hand movement." *Plos one* 18, no. 12 (2023): e0295750.
8. Haşegan, Daniel, Matt Deible, Christopher Earl, David D'Onofrio, Hananel Hazan, Haroon Anwar, and Samuel A. Neymotin. "Training spiking neuronal networks to perform motor control using reinforcement and evolutionary learning." *Frontiers in Computational Neuroscience* 16 (2022): 1017284.
9. Vijayan, Asha, and Shyam Diwakar. "A cerebellum inspired spiking neural network as a multi-model for pattern classification and robotic trajectory prediction." *Frontiers in Neuroscience* 16 (2022): 909146.
10. Izhikevich, Eugene M. "Solving the distal reward problem through linkage of STDP and dopamine signaling." *Cerebral cortex* 17, no. 10 (2007): 2443-2452.
11. Tieck, J. Camilo Vasquez, Pascal Becker, Jacques Kaiser, Igor Peric, Mahmoud Akl, Daniel Reichard, Arne Roennau, and Rüdiger Dillmann. "Learning target reaching motions with a robotic arm using brain-inspired dopamine modulated STDP." *In 2019 IEEE 18th International Conference on* Cognitive Informatics & Cognitive Computing, pp. 54-61. IEEE, 2019.

12. Bouganis, Alexandros, and Murray Shanahan. "Training a spiking neural network to control a 4-dof robotic arm based on spike timing-dependent plasticity." *In The 2010 International Joint Conference on Neural Networks*, pp. 1-8. IEEE, 2010.
13. Azimirad, Vahid, S. Yaser Khodkam, and Amir Bolouri. "A New Hybrid Learning Control System for Robots Based on Spiking Neural Networks." Available at SSRN 4663085.
14. Hassanzadeh Khanmiri, Shaghayegh and Sayyed Noorani, Mohammad-Reza. "Simulation and Control of Human Arm Powered by Exoskeleton using OpenSim - MATLAB Application Programming Interface." *Second International Conference on Motion Analysis*, 2022, https://civilica.com/doc/1476102.

Advanced Engineering Days

aed.mersin.edu.tr

Separation of active zones of electromyographic signals

Kudratjon Zohirov [1], Sardor Boykobilov [2], Mamadiyor Sattorov [3]

[1]Karshi branch of the Tashkent University of Information Technologies named after Mahammad al-Khwarizmi, Computer systems, Uzbekistan, qzohirov@gmail.com
[2]Karshi branch of the Tashkent University of Information Technologies named after Mahammad al-Khwarizmi, Software of Information Technologies, Uzbekistan, sardorboyqobilov9997@gmail.com
[3]Karshi branch of the Tashkent University of Information Technologies named after Mahammad al-Khwarizmi, Natural sciences, Uzbekistan, mamadiyorsattorov29@gmail.com

Cite this study: Zohirov, K., & Boykobilov, S., Sattorov, M. (2024). Separation of active zones of electromyographic signals. Advanced Engineering Days, 9, 877-879

Keywords
EMG signal
Electrode
Bluetooth
BITalino
software

Abstract

Nowadays, the creation and implementation of devices based on biosignals is one of the current scientific directions. Because it is possible to achieve efficiency by using such devices in rehabilitation in the military field and in sports. An important process for devices based on biosignals is the identification of the active and passive zones of the biosignal. In this paper, an algorithm for identifying the active zone of the electromyography (EMG) signal obtained by the BITalino device, which is an innovative single-channel, portable, do-it-yourself (DIY) device in real time, is proposed. The average error of this algorithm is 1.54% on average. and the deviation was 2.56. The obtained results may be the basis for creating devices that are controlled based on biosignals in real time in the future.

Introduction

Electromyography (EMG) is the measurement of muscle activity through electrical signals and is widely used in medicine, sports science and robotics. EMG can be used to understand how muscles work, diagnose diseases or injuries and create artificial limbs. The main purpose of using EMG signals is to more effectively manage and analyze muscle work by clearly distinguishing active and passive zones. This process is important not only in medical diagnostics, but also in technological applications such as sports training and artificial limbs [1-4].

Material and Method

A number of important hardware tools are used in EMG signal recording and processing. These tools are designed to accurately and efficiently record, filter and analyze the EMG signal. One of these hardware tools is the BITalino device [7-8]. The EMG signal can be recorded using the BITalino device. BITalino is designed for recording biomedical signals a portable, inexpensive and easy-to-use device. It is a biometric signal recording all necessary components (electrodes, amplifiers, A/D converters and the ability to transmit data via Bluetooth). Recording the EMG signal through the BITalino device and then the process of obtaining the data in .txt the format is carried out as follows:

1. Installation of the device;

- First, the necessary software to install the BITalino device is downloaded and installed. This can be OpenSignals (r)evolution or other compatible software.
- EMG electrodes are placed on the muscle. Usually, for EMG two electrodes are used [5-6].

2. Signal recording;

- BITalino device is connected to the computer via Bluetooth.
- The installed software is run.

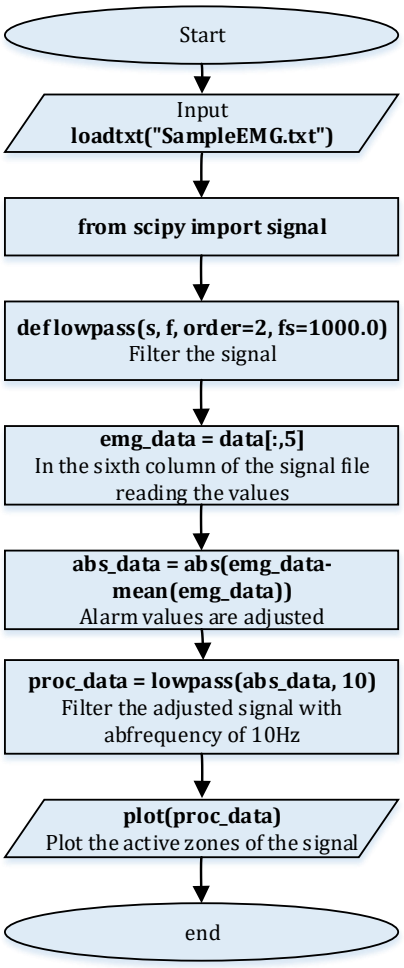
- The EMG channel is activated and the necessary settings (e.g. sample rate, level of amplification) are entered.
- Press the "Start" button to begin recording the signal. In this, the electrical impulses received through the electrodes are amplified, digitized and displayed on the computer screen [9].

3. Data storage and export

- After finishing the recording, click the "Stop" button.
- The data recorded through the software can be viewed. The export option is selected to save the data in .txt format.
- In the Export data window, select ".txt" as the file format and enter the required settings (e.g. delimiters, time stamps) the file.
- Can be saved with a name and then analyzed with a text editor or data analysis.

4. Analysis

The received data in .txt format is analyzed using the Python programming language.



#Upload data from "SampleEMG.txt" file recorded from BITalino;

#Call a special library for processing biosignals;

#Pass the 1kHz frequency signal through a second-order lowpass filter;

Read the 6th column of data from the file (index starts from 0 in Python).

#Discard negative values by adjusting signal amounts;

#Process absolute values by low-pass filtering, there the filter threshold is 10 Hz.

#Draw a graph of the active areas of the processed (filtered) EMG signal.

Figure 1. Algorithm block scheme for extracting active zones of EMG signals.

Results

In order to process the EMG signal in real-time or offline mode, it is necessary to identify the active zones. Active zones corresponded to the period when the muscle was active. When the muscle contracts, active zones are formed, but when the muscles relax, the signal values do not change. Determining the activation zones of the EMG signal is important in the development of various applications and devices.

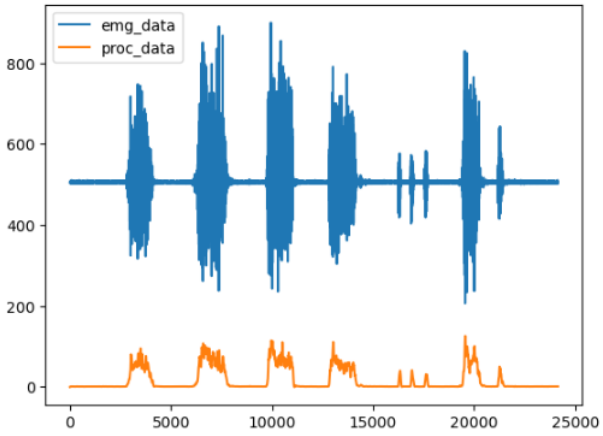


Figure 2. Filtered and unfiltered view of the EMG signal

Discussion and Conclusion

Determining the zone of muscle activation is considered as the duration of the start and end of EMG activity. Activation onset (onset) is defined as the onset of muscle contraction or expansion, while activation termination (offset) is defined as the end of muscle contraction and expansion. A simple way to determine the muscle activation zone is visual inspection. However, visual inspection leads to various difficulties and errors. Therefore, it is advisable to use automatic methods and algorithms to determine activation zones. This paper proposes to detect active zone using a single-threshold algorithm. The average error of this algorithm is 1.54% on average. and the deviation was 2.56.

References

1. Zohirov Q.R. “Elektromiografiya signalining faol potensial chegarasini aniqlashda yangicha yondashuv” .“Digital transformation and artificial intelligence” Ilmiy jurnali. № 1(3), 2023. Toshkent. - B.1-6
2. Merletti, R., & Parker, P. A. (2004). Electromyography: Physiology, Engineering, and Non-Invasive Applications. John Wiley & Sons.
3. De Luca, C. J. (1997). The Use of Surface Electromyography in Biomechanics. Journal of Applied Biomechanics, 13(2), 135-163.
4. Hermens, H. J., Freriks, B., Disselhorst-Klug, C., & Rau, G. (2000). Development of recommendations for SEMG sensors and sensor placement procedures. Journal of Electromyography and Kinesiology, 10(5), 361-374.
5. Farina, D., Leclerc, F., Arendt-Nielsen, L., Buttelli, O., & Madeleine, P. (2008). The change in spatial distribution of upper trapezius muscle activity is correlated to contraction duration. Journal of Electromyography and Kinesiology, 18(1), 16-25.
6. Basmajian, J. V., & De Luca, C. J. (1985). Muscles Alive: Their Functions Revealed by Electromyography. Williams & Wilkins.
7. Zohirov, K., Boyqobilov, S., & Madatov, Q. (2024). Sport biomexanikasida ishlatiluvchi portativ o‘lchov qurilmalari va ularning tahlili. Digital transformation and artificial intelligence Ilmiy jurnali, 2(1), 131–142.
8. Zohirov Q.R., Boyqobilov S.X., Sattorov M.E., “Biosignallarni qayta ishlash va tasniflash usullari tahlili” O‘zbekiston milliy axborot agentligi – O‘zA ilm-fan bo’limi (elektron jurnal) №3 (53):204-214.Toshkent 2024.
9. Zohirov Q.R., Boyqobilov S.X., Meyliyeva Sh. “Inson harakatlarini kinematik va kinetik tahlil qilish” “Raqamli texnologiyalarning iqtisodiyot va ta’limdagi o‘rni” mavzusidagi xalqaro ilmiy-amaliy anjumani ma’ruzalar to‘plami 2024. Samarqand. -B.250-253.

Advanced Engineering Days

aed.mersin.edu.tr

Comparative Analysis of Machine Learning and Deep Learning Models for Multilingual Multitarget Stance Detection

Muhammad Ebrahim Ahmadi [1], Monireh Hosseini [*2]

[1] IT Department, Faculty of Industrial Engineering, K. N. Toosi University of Technologyline Tehran, Iran, me.ahmadi@email.kntu.ac.ir

[2] IT Department, Faculty of Industrial Engineering, K. N. Toosi University of Technologyline Tehran, Iran, hosseini@kntu.ac.ir

Cite this study: Ahmadi, M., & Hosseini, M. (2024). Comparative Analysis of Machine Learning and Deep Learning Models for Multilingual Multitarget Stance Detection. Advanced Engineering Days, 9, 880-887

Keywords
Social Networks
Stance Detection
Machine Learning

Abstract

Social Network Analysis (SNA) is an approach where nodes represent individuals, and the relationships between them are depicted using edges. In today's digital landscape, social networks play a pivotal role in facilitating communication, information sharing, and relationship-building among individuals, communities, and organizations. The field of stance detection is essential for understanding human behavior and interactions across various domains. By analyzing individuals' stances on specific topics, valuable insights can be gained into their opinions, positions, and beliefs. This information has broad applications, including the analysis of social phenomena, customer opinions, and political dynamics. Stance detection, the task of identifying a speaker's attitude or viewpoint toward a particular topic, is a critical component of many natural language processing (NLP) applications such as sentiment analysis, opinion mining, and fake news detection. However, multilingual stance detection is challenging due to the complexity and diversity of language use. In this study, we investigate various models in the literature for multilingual stance detection. This paper examines the performance of several deep learning and machine learning models on a multi-language, multi-target dataset for stance detection. This dataset is a complex set consisting of 3 languages and 150 targets, which has not been comprehensively studied before. Specifically, we analyze 15 machine learning and deep learning models under the multilingual data set. We conduct this study based on a two-class classification. Additionally, we analyze the models and highlight their strengths and weaknesses. The analysis reveals that machine learning models outperform deep learning models in terms of performance. The main conclusion of our analysis is that despite the numerous machine learning and deep learning models, they still lack high accuracy and require stronger models.

Introduction

With the emergence of Web 2.0, numerous online platforms have been created for user-generated content, such as social media and discussion websites. This content typically includes images, videos, reviews, blog posts, and discussions. Currently, social media platforms serve as a common medium for communication and expression of opinions in our daily lives. Consequently, the available data is growing rapidly. However, this data lacks structure and is often in textual form. As the volume of user-generated content increases, there is a noticeable demand for automated processing of this content. Machine learning techniques, particularly deep learning, can be employed to extract valuable information from textual data.

Stance detection is an automated task that predicts the stance of authors toward a specific topic of interest. This task involves examining textual content and sometimes social activities of users on discussion platforms (such as social media). Various definitions of stance dection exist. In the following sections, we will present different perspectives on the concept. From a sociolinguistic standpoint, the paper [1] defines stance as "an action performed by an individual or social group within the context of discourse, where evaluation of objects, individuals' positions, and agreements with others regarding important social and cultural aspects are presented." The work in [2] characterizes it as an expression of judgment by an individual toward a proposal, thereby aligning

themselves with others. Different definitions of stance detection (also known as stance classification) exist within the field of linguistics. The primary concern in stance detection is inferring the embedded viewpoint from the authors' text. A study on stance detection identifies the following factors associated with stance: linguistic features (such as tense, vocabulary, topic, and subject), personal identity, and social activity [3]. Stance significantly shapes the tone of authors' messages and the words they choose.

In the domain of machine learning, the term "stance classification" refers to the task of categorization. The input in this task is typically a text and a target, and the output is one of the following categories: agree, disagree, or neither. Some researchers also introduce a category labeled as "neutral," representing an author's neutral stance toward the target [4]. However, true neutrality is rare, as people usually position themselves either in favor of or against a proposal. Additionally, in the literature, there is a reasonable consensus that if a text's stance toward a target is neither supportive nor opposing, the appropriate stance category is "none" rather than "neutral," as no information about the text's stance is obtained. Therefore, the "none" category typically encompasses all cases except for agree and disagree.

In summary, stance detection, as observed in the literature, involves determining authors' stances toward a target by examining the text they write or their social activities on social media platforms (such as communication and preferences). Furthermore, stance detection is related to sentiment analysis (or opinion mining). Sentiment analysis focuses on the polarity of emotions explicitly expressed in the text. The primary emotional polarities considered by some researchers are positive, negative, and neutral. In contrast, stance detection deals with classifying the stance of a text toward a target, whether explicitly or implicitly mentioned in the text. Two subtasks within sentiment analysis are more closely related to stance detection: (1) target-dependent sentiment analysis and (2) aspect-based sentiment analysis. Both tasks involve identifying sentiments related to a specific target (e.g., iPhone vs. Galaxy) or different aspects of a target (e.g., iPhone's display and battery life). Some studies in social networks analysis have highlighted ambiguities between the definitions of stance detection and general sentiment analysis [5]. Below, we list the key differences between these two concepts.

1. General sentiment analysis deals with emotional sentiment without a specific purpose. At the same time, in stance detection, a specific goal must be determined to evaluate the stance relative to this goal.

2. Stance may not match feeling. In other words, a text can contain a positive sentiment, while its stance is against the goal of confrontation, and vice versa. For example, the sentence: "I'm so glad that Trump lost the election" has a positive taste, but its position is against Trump.

Due to the importance of the multilingual stance detection field in areas such as fake news detection and sentiment analysis, we conduct comprehensive work to measure the performance of different models for stance detection. The subsequent sections of this paper are organized as follows: Section Related work provides an overview of related works, Section Methods elucidates the methodologies employed in this study, Section Experimental results presents the analysis of experimental results, and finally, Section Conclusion offers concluding remarks.

Related work

Supervised learning is a machine learning technique where an algorithm learns from labeled data to make predictions or decisions. In this approach, a model is trained on a dataset that includes input features and corresponding output labels. The goal is for the model to learn patterns and hidden relationships in the data, so it can accurately predict output labels for new or future input data. Deep learning is a subset of machine learning that focuses on training artificial neural networks with multiple layers to learn from large datasets and make predictions. Its primary objective is to simulate the human brain's ability to process and understand data by creating complex models. Essentially, deep learning leverages deep neural networks to learn for specific tasks, ranging from simple classification to complex reasoning [6].

In the previous works, efforts have been made to detect stance, which we will refer to. Hashemian and colleagues in their article [7] stated that sentiment analysis on social networks is still a challenging research topic. In recent years, various methods and techniques have been proposed to address this issue. They also highlighted that the main challenge in stance detection is that content does not directly indicate the sentiment, and most research has used auxiliary information such as user interactions, target phrases, and external knowledge to enhance the performance of their methods. For the reasons mentioned, they proposed a diachronic perspective on stance detection, considering that users' stance changes over time. The two critical challenges in diachronic sentiment analysis include evolution extraction and model adaptability. In the proposed method, they considered extracting users' stance evolution using auxiliary information and adapting to the evolution. Specifically, the proposed method is a two-phase approach. In the first phase, using inherent conflict detection, they determine the times when each user had inactive sentiment towards the target. In the second phase, they extract the impact of active stance evolution by creating a coherent state. Their proposed method utilizes user tweets and interest lists as auxiliary information for detecting evolution. Their experiments with a diachronic-based model, which was first introduced, on the SemEval-2016 Task 6A dataset showed good performance compared to the examined models.

Zero-shot stance detection aims to classify stances on previously unseen topic data. This is done to ensure that the learned model can generalize across real-world topics. In a recent paper by [8], a novel zero-shot stance detection framework is proposed. By reducing information from seen data in the encoder and focusing on improving sentiment classification ability in zero-shot conditions, the proposed framework effectively extends sentiment identification. The proposed framework includes two learning stages: zero-shot text encoder learning and zero-shot fine-tuning. The framework achieved significant improvements on three datasets.

Jiang and colleagues [9] highlighted a critical challenge in stance detection: the lack of sufficient textual information about targets. Current approaches often focus on introducing external knowledge to supplement target information, but the linking process becomes problematic due to noise in the data, affecting their performance. The authors propose a simple yet effective multi-purpose adversarial learning framework for stance detection. Their framework leverages both labeled and unlabeled data. To achieve this, they design target-oriented adversarial learning and label-oriented adversarial learning, resulting in a more comprehensive representation of targets and improved discriminative features for sentiment. Extensive experiments on three datasets—SemEval-2016, WT-WT, and VAST—demonstrate the superiority of their method.

Most stance detection studies do not delve into understanding the rationale behind a solution. Gomez and colleagues [10] propose a two-phase classification system for stance detection in tweets based on topic modeling features. Their approach significantly differs from previous solutions because it extracts stance label explanations through highly relevant terms within tweet topics. Consequently, their method is flexible, adjusting vocabulary based on topic information. Additionally, they construct a set of features for specific tweet content, including sentiment indicators, mental cues, target features, phrase distribution, and word embeddings. The obtained Results indicate the superiority of their approach over deep learning models, emphasizing the potential of topic-based modeling to enhance classification outcomes.

In the presented work by [11] , a novel method for identifying stance on Twitter is proposed. This method involves a three-phase process comprising preprocessing, feature generation, and classification. Lai and colleagues [12] explore multilingual sentiment detection in political discussions on social media platforms. Their research involves collecting multilingual data from various social media platforms and utilizing machine learning algorithms to detect user sentiment toward different political discussions. Models fine-tuned with large domain-specific data have emerged as a new superior approach in various natural language processing tasks, including stance detection. Furthermore, Kawintiranon and Singh [13] propose a re-finetuning method based on BERT [14]. Table 1 illustrates the recent works for stance detection.

Table 1. The recent works for stance detection

Stance detection methods	**Year**
diachronic perspective	2023
Meta-learning with topic-agnostic representations	2023
multi-perspective contrastive learning with unlabeled data	2023
A topic modeling approach supporting explainability	2023
fusing ranked lists and sentiments	2021
Multilingual stance detection in social media political debate	2020
Knowledge enhanced masked language model	2021

Table 2 illustrates the previous works for stance detection under the popular datasets.

Comparing the performance of deep learning and machine learning models for multilingual stance detection is crucial due to the inherent complexity of processing multiple languages. This evaluation helps identify models that can effectively handle diverse linguistic structures and nuances, ensuring robust generalization across languages without sacrificing accuracy.

While deep learning models often demand substantial computational resources and training time, traditional machine learning models may offer faster inference times with varying levels of accuracy. By systematically comparing these models for multilingual stance detection, researchers can make informed decisions about the most suitable techniques for real-world applications. This study contributes to the development of efficient multilingual stance detection systems, advancing natural language processing and its practical applications.

Furthermore, this study investigates the efficacy of various deep learning and machine learning models on a multi-language, multi-target dataset designed for sentiment analysis. The dataset comprises three distinct languages and 150 diverse targets, a configuration that has not been extensively explored in previous research. The findings presented in this paper have potential implications for future investigations in this domain.

Experimental results

In this section, we describe the data and the experimental results.

Dataset: In this paper, we will utilize the dataset provided in the presented work by Vamvas and Sennrich [28] for all experiments. This dataset refers to a large-scale stance detection dataset of written opinions about election candidates in Switzerland. It includes texts in German, French, and Italian, enabling cross-lingual stance detection

evaluation. The dataset comprises 67,000 opinions related to over 150 political issues in German, French, and Italian languages. Unlike other datasets, this one contains diverse topics. Each sample in this dataset consists of a question, an opinion, and a topic, aiming to investigate whether agreement or disagreement with the given content (question, opinion, and topic) exists. Therefore, we are dealing with a binary classification task to examine the stance (favorable or unfavorable) toward the provided question.

	Table 2: the recent works for stance detection				
Paper	**language**	**features**	Model	**dataset**	F1 **Best score**
Sobhani et al. [15]	English	N-gram SE Sentiment words	SVM	SE16-T6	59.21
Ebrahimi et al. [16]	English	N-gram Sentiment subject	Maximum entropy	SE16-T6	61.04
Chen et al. [17]	English	SE	Voting CNN	SE16-T6	67.33
Pamungkas et al. [18]	English	N-gram , POS, ,vocabulary, feelings	LibSVM	SE16-T6	77.11
Xuan et al. [19]	English	N-gram , POS, ,vocabulary, feelings SE	SVM	SE16-T6	70.30
Dey et al. [20]	English	N-gram ,text ,words, emotions the syntactical structure of	SVM	SE16-T6	74.44
Zhu et al. [21]	English	SE modeling objective	BiGRU CNN	SE16-T6	67.40
Siddiqua et al. [22]	English ,	, POS, tree, syntactic structural ,	tree kernel SVM counted a majority of the votes	SE16-T6	70.03
Sun et al. [23]	English	SE ,vocabulary, feelings , ,dependency parser	for LSTM attention	SE16-T6	61
[24]Wei et al.	English	SE modeling goal	BiGRU attention network architecture	SE[12]16-T6	71.04
Al-Ghadir et al. [11]	English	TF-IDF Sentiment words	Weighted KNN	SE16-T6	76.45
Ahmed et al. [25]	English ,	SE , POS, structural statistical ,	random forest MLP CNN	SE16-T6	70.46
Chen et al. [26]	English	N-gram ,vocabulary feelings structural SE	DNRFAF DSRFE DECCV	SE16-T6	71.24
Du et al. [27]	English Chinese	SE modeling objective	RNN for LSTM attention	SE16-T6	68.79
Lai et al. [12]	English French , Italian , Spanish	N-gram , BOW, structural vocabulary of feelings	SVM , LR, CNN for LSTM BiLSTM	SE16-T6 IberEval2017	64.51

Evaluation metrics: To evaluate all models, we will employ standard metrics in equations 1 through 6. In the following formulas, TP represents the true positive count, TN represents the true negative count, FP represents the false positive count, and FN represents the false negative count. TP and FN correspond to the number of

correctly identified positive instances. Similarly, TN and FP represent the number of correctly identified negative instances. Recall measures the proportion of positive instances correctly classified, while Precision focuses on the percentage of correct predictions for each class. F1 score represents the weighted harmonic mean of Precision and Recall. Accuracy calculates the ratio of correct predictions to the total number of predictions.

The formulas are as follows:

Formula 1

$$Precision\ (False) = \frac{\#TP}{\#TP + \#FP}$$

Formula 2

$$Recall\ (False) = \frac{TP}{\#TP + \#FN}$$

Formula 3

$$Precision\ (True) = \frac{TP}{\#TP + \#FP}$$

Formula 4

$$Recall\ (True) = \frac{\#TP}{\#TP + \#FN}$$

Formula 5

$$F1\ = 2 \times \frac{Precision \times Recall}{Precision + Recall}$$

Formula 6

$$Accuracy = \frac{\#TP + \#TN}{\#TP + \#TN + \#FP + \#FN}$$

Experimental results: The results in Table 3 compare various machine learning models for multilingual stance detection across several metrics: Precision, Recall, F1 score for two classes (Class 0 and Class 1), and overall Accuracy. Random Forest, Support Vector Machine (SVM), and Logistic Regression models exhibit superior performance, whereas ensemble methods and Stochastic Gradient Descent achieve a balanced level of effectiveness. Bayesian models and AdaBoost demonstrate moderate performance, while K-Nearest Neighbors (KNN) and Decision Trees exhibit lower performance. Based on their balanced and high performance across all metrics, Random Forest, SVM, and Logistic Regression emerge as the optimal models for stance detection. In the following, we will describe the obtained results:

Random Forest: Random Forest performs well overall with a balanced performance between precision and recall, leading to high F1 scores for both classes and the highest accuracy among the models.

Support Vector Machine (SVM): SVM shows similar performance to Random Forest but with slightly lower F1 scores and accuracy. It still maintains a good balance between precision and recall.

K-Nearest Neighbors (KNN): KNN's performance is lower compared to Random Forest and SVM, with balanced but generally lower scores in all metrics.

Bayesian: The Bayesian model shows moderate performance, with decent precision and recall but lower F1 scores and accuracy compared to the top-performing models.

SGD (Stochastic Gradient Descent): Stochastic Gradient Descent provides balanced performance between the two classes with consistent F1 scores and accuracy.

Logistic Regression: Logistic Regression shows strong and balanced performance for both classes, with high F1 scores and accuracy, making it one of the top-performing models.

AdaBoost: AdaBoost shows high performance for Class 0 but struggles with Class 1, leading to lower F1 scores and overall accuracy.

Decision Tree: The Decision Tree model shows balanced but relatively low performance in all metrics.

Ensemble: The Ensemble model combines multiple algorithms and shows high performance, with high precision and recall for Class 0, decent metrics for Class 1, and solid overall accuracy.

Table 3: Comparison of studied machine learning models for multilingual stance detection

	Class 0			Class 1			
Model	Precision	Recall	F1	Precision	Recall	F1	Accuracy
Random Forest	68.13	75.14	71.46	72.28	64.83	68.35	69.99
SVM	67.94	74.56	71.09	71.79	64.80	68.11	69.68
KNN	64.29	63	63.61	63.68	64.92	64.28	63.96
Bayesian	65.20	70.43	67.71	67.82	62.38	64.98	66.40

Stochastic Gradient Descent	66.95	67.21	67.03	67.17	66.80	66.93	67
Logistic regression	69.32	68.87	69.09	69.05	69.49	69.26	69.18
AdaBoost	63.31	70.74	66.78	66.90	58.96	62.62	64.85
Decision tree	64.24	63.93	64.07	64.10	64.40	64.23	64.16
Ensemble	66.71	72.27	69.38	69.73	63.92	66.70	68.1

The analysis presented in Table 4 evaluates several deep learning models for multilingual stance detection, considering key performance metrics such as precision, recall, F1 score (for both Class 0 and Class 1), and overall accuracy. RCNN and CNN stand out as the top-performing models because they exhibit high precision and recall for both classes (Class 0 and Class 1), striking a good balance. Their F1 scores are competitive, and overall accuracy is good. Graph Neural Network (GNN) achieves moderate results. While its precision and recall are reasonable, the F1 scores are not as high as the best models. LSTM falls into this category, with a trade-off between precision and recall. Multi-head Transformer performs reasonably well, maintaining a balanced trade-off between precision and recall. RNN has the poorest performance its low precision and recall for both classes result in the lowest F1 score and accuracy. In the subsequent, we describe obtained results from this comparative study.

RCNN: RCNN achieves relatively high precision for both classes (Class 0 and Class 1), indicating that it correctly identifies instances of each stance. However, the recall for Class 0 is slightly lower, suggesting that it may miss some instances of this class. The F1 score balances precision and recall. Overall accuracy is 67.84%.

CNN: CNN performs similarly to RCNN in terms of precision and recall. It maintains a good balance between precision and recall for both classes. The accuracy of 66.72% is consistent with RCNN.

Graph Neural Network (GNN): GNN shows moderate performance. While its precision and recall are reasonable, the F1 scores are not as high as RCNN and CNN. Accuracy stands at 65.13%.

LSTM: LSTM has a higher recall for Class 1, suggesting it captures more instances of this class. However, its precision for Class 0 is lower. The overall accuracy is 66.06%.

RNN: RNN's performance is suboptimal. Both precision and recall are low for both classes, resulting in a low F1 score. Accuracy is the lowest at 52.09%.

Multi-head Transformer: Multi-head Transformer performs reasonably well. Its precision and recall are balanced, leading to a decent F1 score. Accuracy is 59.67%.

Table 4: Comparison of studied deep learning models for multilingual stance detection

	Class 0			Class 1			
Model	Precision	Recall	F1	Precision	Recall	F1	Accuracy
RCNN	69.05	65.75	67.17	67.05	69.94	68.30	67.84
CNN	67.60	65.27	66.12	66.40	68.17	67.03	66.72
Graph neural network	65.31	64.94	64.88	65.41	65.32	65.13	65.13
LSTM	67.08	63.59	65.14	65.35	68.53	66.80	66.06
RNN	52.20	52.23	51.94	52.09	51.95	51.70	52.09
Multi-head Transformer	59.76	63.24	61.21	60.58	56.28	58.28	59.67

Conclusion

Stance detection, the task of automatically determining an individual's stance or viewpoint on a given topic, has emerged as a critical area of research in natural language. With the proliferation of online discussions, social media platforms, and user-generated content, the ability to accurately discern the stance expressed in textual data has become increasingly crucial for a wide range of applications. Effective stance detection can provide valuable insights into public opinion, facilitate the identification of polarization, and enable the development of more nuanced and targeted interventions in areas such as political discourse, societal debates, and policy-making. Moreover, the accurate classification of stance can enhance the understanding of user behavior, inform content moderation strategies, and support the design of more inclusive and balanced recommendation systems. In light of the growing importance of stance detection, this paper aims to conduct a comprehensive evaluation of the comparative performance of various machine learning and deep learning models for this task. This paper evaluates the performance of deep learning and machine learning models on a unique multi-language, multi-target dataset for stance detection. This dataset features 3 languages and 150 targets, which has not been extensively studied

before. The results of this research could have significant implications for future studies in this field. By rigorously assessing the models across multiple evaluation metrics, the investigation seeks to provide valuable insights that can guide the selection of optimal techniques for real-world stance detection applications. In the realm of machine learning, the Random Forest, Support Vector Machine (SVM), and Logistic Regression models emerged as the top-performing approaches, exhibiting a well-balanced and high-level of performance across all the evaluated metrics. This finding underscores the suitability of these models for stance detection tasks, as they demonstrate the ability to effectively capture the nuanced textual and contextual cues that are crucial for accurate classification. The ensemble model, which combined the strengths of multiple machine learning algorithms, also showcased the potential benefits of leveraging ensemble learning techniques in this domain. For the deep learning models, the Recurrent Convolutional Neural Network (RCNN) and Convolutional Neural Network (CNN) models demonstrated their dominance, maintaining high precision and recall for both class labels and consequently achieving competitive F1-scores and overall accuracy. These results highlight the capacity of these deep learning architectures to effectively learn and extract relevant features from the input data, enabling robust stance detection. The Graph Neural Network (GNN) and Long Short-Term Memory (LSTM) models also exhibited moderate performance, suggesting their potential applicability in certain stance detection scenarios. In contrast, the comparatively lower performance of models such as K-Nearest Neighbors (KNN), Decision Trees, AdaBoost, Bayesian, Stochastic Gradient Descent (SGD), Recurrent Neural Network (RNN), and Multi-head Transformer indicates the need for further optimization and improvement of these techniques for the task at hand. Nevertheless, the balanced effectiveness exhibited by some of these models, like SGD and the Ensemble, suggests that they may hold promise with additional refinement and fine-tuning. The findings of this study contribute to the growing body of literature on stance detection, providing a comprehensive comparative analysis of a diverse set of machine learning and deep learning models in multilingual stances. The superior performance of Random Forest, SVM, Logistic Regression, RCNN, and CNN highlights their suitability for real-world applications that require accurate and reliable stance detection. These insights can guide researchers and practitioners in selecting the most appropriate models for their specific use cases, and inspire further investigations into the enhancement and adaptation of these techniques for enhanced stance detection capabilities.

References

[1] J. W. Du Bois, "The stance triangle," *Stancetaking in discourse: Subjectivity, evaluation, interaction,* vol. 164, no. 3, pp. 139-182, 2007.

[2] P. Kockelman, "Stance and subjectivity," *Journal of Linguistic Anthropology,* vol. 14, no. 2, pp. 127-150, 2004.

[3] A. Jaffe, "In monolingual contexts, speakers take stances by using a variety of linguistic forms, some of which are sociolinguistically salient. In bilingual contexts, speakers have an added stance resource: language choice. The significance of language choice is, of course, related to the specifics of the sociolinguistic context, including the political economy in which the two languages circulate as well as ideologies about language," *Stance: Sociolinguistic Perspectives,* p. 119, 2009.

[4] L. Grimminger and R. Klinger, "Hate towards the political opponent: A Twitter corpus study of the 2020 US elections on the basis of offensive speech and stance detection," *arXiv preprint arXiv:2103.01664,* 2021.

[5] A. AlDayel and W. Magdy, "Stance detection on social media: State of the art and trends," *Information Processing & Management,* vol. 58, no. 4, p. 102597, 2021.

[6] T. Hastie, R. Tibshirani, J. H. Friedman, and J. H. Friedman, *The elements of statistical learning: data mining, inference, and prediction*. Springer, 2009.

[7] M. Hashemian, S. K. Rahimi, and A. B. Dastjerdi, "An influences-adapted two-phase approach to stance detection in the diachronic perspective," *Expert Systems with Applications,* vol. 231, p. 120773, 2023.

[8] K. Choi and Y. Ko, "Meta-learning with topic-agnostic representations for zero-shot stance detection," *Pattern Recognition Letters,* vol. 171, pp. 15-20, 2023.

[9] Y. Jiang, J. Gao, H. Shen, and X. Cheng, "Zero-shot stance detection via multi-perspective contrastive learning with unlabeled data," *Information Processing & Management,* vol. 60, no. 4, p. 103361, 2023.

[10] M. Gómez-Suta, J. Echeverry-Correa, and J. A. Soto-Mejía, "Stance detection in tweets: A topic modeling approach supporting explainability," *Expert Systems with Applications,* vol. 214, p. 119046, 2023.

[11] A. I. Al-Ghadir, A. M. Azmi, and A. Hussain, "A novel approach to stance detection in social media tweets by fusing ranked lists and sentiments," *Information Fusion,* vol. 67, pp. 29-40, 2021.

[12] M. Lai, A. T. Cignarella, D. I. H. Farías, C. Bosco, V. Patti, and P. Rosso, "Multilingual stance detection in social media political debates," *Computer Speech & Language,* vol. 63, p. 101075, 2020.

[13] K. Kawintiranon and L. Singh, "Knowledge enhanced masked language model for stance detection," in *Proceedings of the 2021 conference of the north american chapter of the association for computational linguistics: human language technologies*, 2021, pp. 4725-4735.

[14] J. Devlin, M.-W. Chang, K. Lee, and K. Toutanova, "Bert: Pre-training of deep bidirectional transformers for language understanding," *arXiv preprint arXiv:1810.04805,* 2018.

[15] P. Sobhani, S. Mohammad, and S. Kiritchenko, "Detecting stance in tweets and analyzing its interaction with sentiment," in *Proceedings of the fifth joint conference on lexical and computational semantics*, 2016, pp. 159-169.

[16] J. Ebrahimi, D. Dou, and D. Lowd, "A joint sentiment-target-stance model for stance classification in tweets," in *Proceedings of COLING 2016, the 26th international conference on computational linguistics: Technical papers*, 2016, pp. 2656-2665.

[17] W.-F. Chen and L.-W. Ku, "Utcnn: a deep learning model of stance classificationon on social media text," *arXiv preprint arXiv:1611.03599,* 2016.

[18] E. W. Pamungkas, V. Basile, and V. Patti, "Stance classification for rumour analysis in twitter: Exploiting affective information and conversation structure," *arXiv preprint arXiv:1901.01911,* 2019.

[19] K. Xuan and R. Xia, "Rumor stance classification via machine learning with text, user and propagation features," in *2019 International Conference on Data Mining Workshops (ICDMW)*, 2019: IEEE, pp. 560-566.

[20] K. Dey, R. Shrivastava, and S. Kaushik, "Twitter stance detection—A subjectivity and sentiment polarity inspired two-phase approach," in *2017 IEEE international conference on data mining workshops (ICDMW)*, 2017: IEEE, pp. 365-372.

[21] L. Zhu, Y. He, and D. Zhou, "Neural opinion dynamics model for the prediction of user-level stance dynamics," *Information Processing & Management,* vol. 57, no. 2, p. 102031, 2020.

[22] U. A. Siddiqua, A. N. Chy, and M. Aono, "Stance detection on microblog focusing on syntactic tree representation," in *Data Mining and Big Data: Third International Conference, DMBD 2018, Shanghai, China, June 17–22, 2018, Proceedings 3*, 2018: Springer, pp. 478-490.

[23] Q. Sun, Z. Wang, Q. Zhu, and G. Zhou, "Stance detection with hierarchical attention network," in *Proceedings of the 27th international conference on computational linguistics*, 2018, pp. 2399-2409.

[24] P. Wei, W. Mao, and D. Zeng, "A target-guided neural memory model for stance detection in twitter," in *2018 International Joint Conference on Neural Networks (IJCNN)*, 2018: IEEE, pp. 1-8.

[25] M. Ahmed, A. N. Chy, and N. K. Chowdhury, "Incorporating hand-crafted features in a neural network model for stance detection on microblog," in *Proceedings of the 6th International Conference on Communication and Information Processing*, 2020, pp. 57-64.

[26] P. Chen, K. Ye, and X. Cui, "Integrating n-gram features into pre-trained model: a novel ensemble model for multi-target stance detection," in *International conference on artificial neural networks*, 2021: Springer, pp. 269-279.

[27] J. Du, R. Xu, Y. He, and L. Gui, "Stance classification with target-specific neural attention networks," in *26th International Joint Conference on Artificial Intelligence, IJCAI 2017*, 2017: International Joint Conferences on Artificial Intelligence, pp. 3988-3994.

[28] J. Vamvas and R. Sennrich, "X-stance: A multilingual multi-target dataset for stance detection," *arXiv preprint arXiv:2003.08385,* 2020.

Advanced Engineering Days

aed.mersin.edu.tr

Offensive Context detection in social network using graph neural net

Minou Kouh Soltani*[1]

[1]*University of Tabriz, Mianeh Technical and Engineering Faculty, Iran, kouhsoltani@tabrizu.ac.ir*

Cite this study: Kouh Soltani, M. (2024). Offensive context detection in social network using graph neural net. Advanced Engineering Days, 9, 888-890

Keywords
Text classification
Graph neural network
Convolutional neural net
Hate speech
Offensive context

Abstract

With the rapid growth of social media, there are many people with different cultures which may use offensive words in their messages against others. The offensive word recognition is very helpful for vulnerable people such as young girls. In this research we used Graph Neural Network (GNN) for offensive content recognition with indexing words. We compared the introduced recognizer with LSTM and CNN, and fusion of these recognizers. In this research the HASOC dataset was used. The results show that with GNN the higher accuracy has been achieved.

Introduction

Social networks (SNs) are expanding rapidly and this has caused more people to connect and exchange information between each other [1]. Despite the very positive effects of SNs on people's lives, the exchange of offensive words has unwanted negative effects on people's emotions, private lives, and social beliefs [2]. The existence of offensive language and deliberate destruction of people especially the well-known personalities highlight the need to detect offensive contents [3].

Current studies investigate the complexity of detecting offensive content owing to the exorbitant subtleties in languages as well as contextual dependencies of the online contents [4]. In addition, the dynamics of language, personal, social and cultural factors add to its complexity [5]. These issues have resulted in numerous research works in the field of offensive content detection, which endeavors to accurately detect and mitigate hateful language. These endeavors are in languages with variable research resources including a variety of strategies from traditional methods to machine learning to deep learning techniques [6].

Classical techniques, as first attempts to abusive content detection, rely on explicit lexicon separation and implementation of rules in the text [7]. These strategies are based on cutting out offensive words, phrases and profanities. However, these methods are highly ineffective in implementing in intricate language structures, sarcasm or conceptually offensive content, which results in high error rates [8].

Relying on lexical features and ignoring the content and structural aspects of the language in classical techniques highlight the limitations of this approach. In addition, the static mode of word filtering requires updating and frequently becomes outdated over time due to changes in the language used in SNs and might be discarded [9].

Machine learning has led content detection models towards more accurate and adaptable approaches [10]. Supervised learning methods in machine learning, for instance Support Vector Machines (SVMs), have been applied to classify texts based on a set of additional features. Higher accuracy than those of traditional strategies has been obtained by regarding semantic and syntactic features. In spite of the advances, the machine learning techniques are limited by the factors of comprehensiveness and quality of feature sets, necessitating extraction of extra features and knowledge of the field. Furthermore, when a content is covered with apparently non-offensive expressions, these models try to find the meanings of the text that is mixed with the offensive text [11-12].

Deep learning, as an efficient approach, has emerged offering simultaneous learning and feature extraction capabilities. Convolutional Neural Network (CNN) has been represented to achieve promising results in offensive content detection and text analysis due to its inherent capability in text feature extraction [13]. Long Short-Term Memory (LSTM) network, as an advanced variant of Recurrent Neural Network (RNN), has achieved great successes in understanding sequential data and handling text analysis [14]. Nevertheless, when these techniques are applied separately, bring their own limitations, which in CNN is focusing on feature extraction and in LSTM is the ability of detecting sequential contents [15].

Graph analyzing techniques have been demonstrated to be efficient for resolving these challenges [16], where the SN data is represented to have graph structure [17]. This study proposes Graph Neural Network (GNN) for offensive language detection in SN. This is for the compensation of the limitations of employing the CNN and LSTM models separately, resulting in more accurate and nuanced detection network. The dataset that we used is based on SPAM and twitter datasets. We applied these datasets in the developed network and compared the results with other research works and methods.

Material and Method

In this research we implemented a Graph Neural Net (GNN). The training steps are represented in Figure 1. According to this figure, the sentences of dataset were read. Then, GNN's word matrix was generated. Every input sentence was converted to a 2D matrix where that number of separate words was the size of matrix.

The GNN Preprocessing was as bellows:

1. Remove unnecessary words (for, "." , the , a , an).
2. Assign an index for each word.
3. Make 2D matrix based on graph of sentences (undirected).
4. Train GNN.

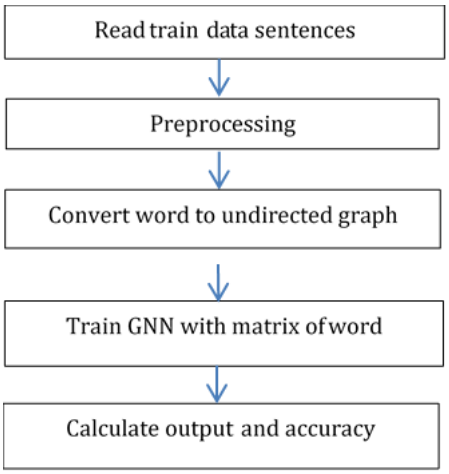


Figure 1. GNN training steps.

In this research, Python programming language was used. The OGB and torch library were applied for GNN training. We used two datasets to evaluate our work. K-Fold 10 was implemented for calculating accuracy and F-Score. Adam algorithm was applied for training data. The system incorporated for training is core-i9 intel 11900K with 128GB Ram and 1650 NVIDIA with 896 CUDA cores graphic card.

Results

We implemented this work on two datasets. The first dataset is SPAM and the other is HASOC, offensive content of twitter dataset. The SPAM dataset consists of email messages that are normal or spam. The HASOC dataset consists of twitters' messages which are labeled with offensiveness degree.

In Table 1, the result of this research is presented. This table includes accuracy and precision for SMSSPAM dataset. According to this table, GNN has higher accuracy than other research works. In Table 2, the results of our work applied to HASOC dataset, are presented. This table consists of different twitter datasets. The results demonstrate the superiority of our proposed work.

Conclusion

In this research, we implemented GNN as well as CNN to increase the accuracy of offensive context detection in SNs. According to the results, GNN has higher accuracy than CNN, LSTM and their fusion. The results of current research work can be widely applied to SN applications such as Facebook, Instagram and twitter. For future, more research works can be performed on word embedding.

Table 1. Results for SMSSPAM dataset

Comment	F-Score	Accuracy	Author
CNN		98.19%	Ghourabi et al [15]
LSTM		98.13%	Ghourabi et al [15]
CNN-LSTM		98.37%	Ghourabi et al [15]
CNN	96.03%	98.98%	This work
LSTM	15.29%	97.04%	This work
GNN	96.34%	**99.04%**	This work

Table 2. Results for twitter datasets

Comment	F-Score	Accuracy	Dataset	Author
CNN	77.52%	77.96%	ETHOS	Rajput et al [19]
Bert Embedding Bi-LSTM	79.71%	80.15%	ETHOS	Rajput et al [19]
Word Embedding	63.66%	85.27%	HASOC	Kovács et al [18]
CNN	54.16%	78.11%	HASOC	This work
LSTM	58.03%	88.66%	HASOC	This work
GNN	74.63%	**89.11%**	HASOC	This work

References

1. Heidemann, J., Klier, M., & Probst, F. (2012). Online social networks: A survey of a global phenomenon. Computer networks, *56*(18), 3866-3878.
2. Rao, B. N., & Kalyani, V. (2022). A study on positive and negative effects of social media on society. Journal of Science & Technology (JST), *7*(10), 46-54.
3. Tucker, J. A., Guess, A., Barberá, P., Vaccari, C., Siegel, A., Sanovich, S., ... & Nyhan, B. (2018). Social media, political polarization, and political disinformation: A review of the scientific literature. *Political polarization, and political disinformation: a review of the scientific literature (March 19, 2018)*.
4. Miran, A. Z., & Abdulazeez, A. M. (2023). Detection of Hate-Speech Tweets Based on Deep Learning: A Review. Jurnal Informatika dan Sains (JISA), *6*(2), 174-188.
5. Tuarob, S., Satravisut, M., Sangtunchai, P., Nunthavanich, S., & Noraset, T. (2023). FALCoN: Detecting and classifying abusive language in social networks using context features and unlabeled data. Information Processing & Management, 60(4), 103381.
6. Mullah, N. S., & Zainon, W. M. N. W. (2021). Advances in machine learning algorithms for hate speech detection in social media: a review. IEEE Access, 9, 88364-88376.
7. Chen, H., McKeever, S., & Delany, S. J. (2018). A comparison of classical versus deep learning techniques for abusive content detection on social media sites. In Social Informatics: 10th International Conference, September 25-28, Part I 10, 117-133.
8. Alrashidi, B., Jamal, A., Khan, I., & Alkhathlan, A. (2022). A review on abusive content automatic detection: approaches, challenges and opportunities. PeerJ Computer Science, 8, e1142.
9. Zdziarski, J. A. (2005). Ending spam: Bayesian content filtering and the art of statistical language classification. No starch press.
10. Dikshitha Vani, V., & Bharathi, B. (2022). Hate speech and offensive content identification in multiple languages using machine learning algorithms. Proceedings of FIRE.
11. Ratan, S., Sinha, S., & Singh, S. (2021). SVM for Hate Speech and Offensive Content Detection. In FIRE, 459-466.
12. Liu, H., & Lang, B. (2019). Machine learning and deep learning methods for intrusion detection systems: A survey. applied sciences, 9(20), 4396.
13. Sultan, D., Omarov, B., Kozhamkulova, Z., ... & Abdrakhmanov, R. (2023). A Review of Machine Learning Techniques in Cyberbullying Detection. Computers, Materials & Continua, 74(3).
14. Hamza, M. A., Alshahrani, H. J., Tarmissi, K., … & Yaseen, I. (2023). Improved Attentive Recurrent Network for Applied Linguistics-Based Offensive Speech Detection. Computer Systems Science & Engineering, 47(2).
15. Ghourabi, A., Mahmood, M. A., & Alzubi, Q. M. (2020). A hybrid CNN-LSTM model for SMS spam detection in arabic and english messages. Future Internet, 12(9), 156.
16. Xu, K., Hu, W., Leskovec, J., & Jegelka, S. (2018). How powerful are graph neural networks?. *arXiv:1810.00826*.
17. Campbell, W. M., Dagli, C. K., & Weinstein, C. J. (2013). Social network analysis with content and graphs. *Lincoln Laboratory Journal*, *20*(1), 61-81.
18. Kovács, G., Alonso, P., & Saini, R. (2021). Challenges of hate speech detection in social media: Data scarcity, and leveraging external resources. SN Computer Science, 2(2), 95.
19. Rajput, G., Punn, N. S., Sonbhadra, S. K., & Agarwal, S. (2021). Hate speech detection using static bert embeddings. In Big Data Analytics: 9th International Conference, December 15-18, *9*, 67-77.

Advanced Engineering Days

aed.mersin.edu.tr

Enhancing VM Migration in Clouds with Heuristic-based Granular Computing

Seyyed Meysam Rozehkhani [1], Farnaz Mahan [*1]

[1] *Faculty of Mathematics, Statistics and Computer Science, University of Tabriz, Tabriz, Iran, m.roozekhanii@tabrizu.ac.ir, mahan@tabrizu.ac.ir*

Cite this study: Rozehkhani, S. M., & Mahan, F. (2024). Enhancing VM Migration in Clouds with Heuristic-based Granular Computing. Advanced Engineering Days, 9, 891-893

Keywords
VM Migration
Cloud Computing
Granular Computing
Resource Utilization
Information Granules

Abstract

Cloud computing is a fast-growing and ever-expanding field of the business world. This development has attracted more attention from businesses wishing to tap into its potential. As cloud computing resource management evolves rapidly and is increasingly demanded, new challenges arise. In cloud computing, an effective virtual machine (VM) migration is significant for optimal resource utilization and meeting service-level agreements (SLAs). Subtle decision-making factors are often overlooked in traditional approaches. Therefore, a Heuristics-based Granular Computing (HGC) approach for VM migration is proposed in this paper, which improves migration efficiency by analyzing cloud environments at finer levels of granularity. In this way, our method allows the formation of informational granules based on the characteristics of VMs and availability of resources enabling informed selection of VMs and hosts thus enhancing resource allocation. The paper discusses the benefits of this approach and outlines future research directions.

Introduction

In the dynamic environment that cloud computing provides, virtual machine migration is essential to ensuring efficient resource allocation and high application performance. When making migration decisions, traditional approaches sometimes ignore the finer points of the cloud architecture, such as workload patterns and VM migration sensitivity, in favor of simple indicators like CPU utilization. This method may result in performance bottlenecks, inefficient resource allocation, and needless migration downtime [1-2].

This paper proposes a Heuristics-based Granular Computing approach for VM migration. Granular computing provides a framework for analyzing information at multiple levels of detail, allowing us to capture the complex relationships between VMs, hosts, and their resource requirements [2-3]. We define information granules based on VM characteristics (e.g., CPU usage, memory consumption, migration sensitivity) and resource availability on potential destination hosts. This enables more informed decision-making during the VM migration process.

Granular Computing (GrC) is an interdisciplinary field that is becoming more and more popular because of its capacity to resolve challenging issues across a wide range of domains. GrC's primary goal is to represent and work with data as sets of objects known as granules, which have similar characteristics [4-5].

Material and Method

We develop two sets of heuristics based on information granules:

1. VM Selection Heuristics:
   Resource Usage Granule: VMs are grouped based on their current resource consumption patterns. For example, a granule might encompass VMs with high CPU usage (e.g., above 80%). Heuristics can prioritize migrating VMs from high-usage granules to free resources on destination hosts, alleviating performance bottlenecks on the source host.
   Migration Sensitivity Granule: VMs are grouped based on their sensitivity to migration downtime. For instance, a granule might include VMs running latency-critical applications that cannot tolerate even

brief interruptions. Heuristics can avoid migrating highly sensitive VMs unless necessary, minimizing application downtime.

2. Destination Selection Heuristics:

Resource Availability Granule: Potential destination hosts are grouped based on their available resources. A granule might include hosts with sufficient CPU and memory capacity to accommodate the migrating VM. Heuristics can select hosts within resource availability granules that best match the migrating VM's requirements, ensuring successful migration without overwhelming the destination host.

Workload Granule: Hosts are grouped based on their current workload patterns. For example, a granule might include hosts running CPU-intensive workloads. Heuristics can prioritize migrating VMs to hosts with workloads that complement the migrating VM (e.g., memory-intensive VM to a host with high memory availability). This helps minimize the performance impact on co-located VMs on the destination host.

The HGC framework operates as follows:

1. Information Granule Formation:
The system continuously monitors VMs and hosts, collecting data on resource usage, workload patterns, and migration sensitivity. This data is used to dynamically create information granules for VMs and hosts.
2. Heuristics Evaluation:
Based on the current state of information granules, the system applies the VM selection and destination selection heuristics. Scores are assigned to each VM-host pair based on the heuristic evaluations.
3. Optimal Migration Selection:
The VM-host pair with the highest combined score is chosen for migration. This ensures the selected VM benefits from migration while minimizing disruption to the target host.

In Figure 1, the flowchart illustrates the sequential steps involved in the decision-making process for VM migration. Starting from the initial step of information granule formation, the flow progresses through heuristics-based VM and destination selection, followed by granules assessing resource usage, migration sensitivity, resource availability, and workload. Subsequently, heuristics are evaluated to determine the optimal migration strategy, concluding with the end of the process.

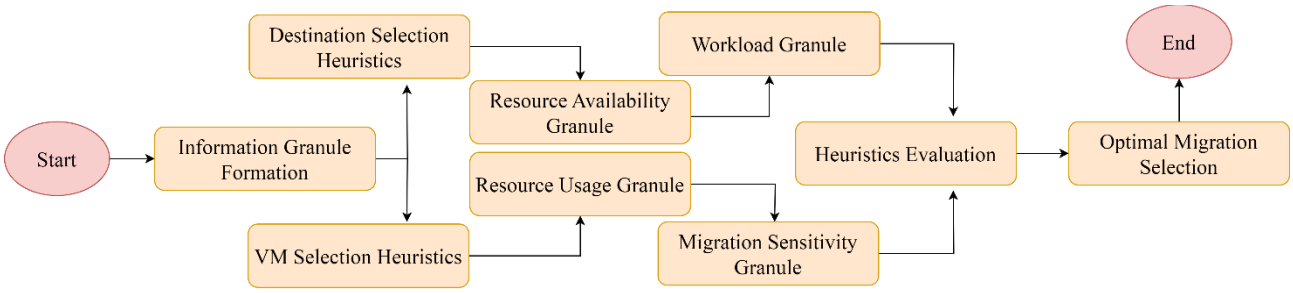


Figure 1. Flowchart depicting the process of VM migration decision-making.

Benefits of HGC-based VM Migration

- **Enhanced Decision-Making:** By considering multiple factors through information granules, HGC leads to more informed VM selection and destination selection.
- **Improved Resource Utilization:** By focusing on migrating high-usage VMs and placing them on suitable hosts, HGC optimizes overall resource allocation in the cloud.
- **Reduced Downtime:** The selection of less migration-sensitive VMs minimizes downtime during the migration process.

Results

This section presents a comparative analysis of traditional virtual machine (VM) migration techniques against the proposed Hierarchical Granular Clustering (HGC) approach. The comparison focuses on key decision-making factors, information granularity, VM and destination selection criteria, resource utilization, downtime implications, decision-making processes, and implementation complexity. The HGC approach demonstrates significant advancements over traditional methods by offering multi-faceted decision-making capabilities that consider resource usage, migration sensitivity, and workload patterns. It enhances resource allocation efficiency, minimizes downtime, and adapts dynamically to varying cloud conditions through adaptive heuristics. However,

these benefits come with increased processing overhead and complexity in implementation, necessitating careful heuristic design and tuning.

Table 1 illustrates a comprehensive comparison between traditional VM migration techniques and the innovative HGC approach proposed in this study.

Table 1. Comparison of Traditional vs. HGC-based VM Migration Techniques

Feature	Traditional Approach	HGC-based Approach
Decision-Making Factors	Limited (e.g., CPU utilization)	Multi-faceted (resource usage, migration sensitivity, workload patterns)
Information Granularity	No	Yes (groups VMs and hosts based on specific characteristics)
VM Selection	Basic prioritization (e.g., high CPU usage)	Considers resource usage and migration sensitivity
Destination Selection	Focuses on raw resource availability	Prioritizes hosts with sufficient resources and workload complementarity
Resource Utilization	Potentially suboptimal	Aims for improved allocation by migrating high-usage VMs and placing them on suitable hosts
Downtime	Risk of migrating sensitive VMs	Minimizes downtime by avoiding migration of highly migration-sensitive VMs unless necessary
Decision-Making Process	Static rules or thresholds	Dynamic and adaptable based on current cloud state
Complexity	Simpler to implement	More complex due to information granule formation and heuristic evaluation

Conclusion

This paper introduced a HGC approach for VM migration in cloud environments. By leveraging information granules and tailored heuristics, HGC enables a more nuanced and efficient approach to VM migration, leading to improved resource utilization and reduced downtime.

HGC uses special rules to analyze this information intelligently. This allows the system to decide when and how to move VMs in the best way possible. By analyzing information in detail, HGC ensures that VMs are migrated with minimal disruption and that the cloud system runs better overall. HGC can also handle how cloud environments change all the time, so it can adapt to new conditions and workloads as they happen

Future research can explore:

- Implementing the HGC framework in a cloud management platform for real-world evaluation.
- Developing adaptive heuristics that can adjust based on dynamic cloud conditions.
- Integrating HGC with machine learning models for more sophisticated decision-making.

References

1. Rozehkhani, S. M., Mahan, F., & Pedrycz, W. (2024). Efficient cloud data center: An adaptive framework for dynamic Virtual Machine Consolidation. *Journal of Network and Computer Applications*, *226*, 103885.
2. Rozehkhani, S. M., & Mahan, F. (2022). VM consolidation improvement approach using heuristics granular rules in cloud computing environment. *Information Sciences*, *596*, 15-29.
3. Mahan, F., Rozehkhani, S. M., & Pedrycz, W. (2021). A novel resource productivity based on granular neural network in cloud computing. *Complexity*, *2021*(1), 5556378.
4. Rozehkhani, S. M., & Mohammadzad, M. (2022). Rule Extraction for Screening of COVID-19 Disease Using Granular Computing Approach. *Computational and Mathematical Methods in Medicine*, *2022*(1), 8729749.

Advanced Engineering Days

aed.mersin.edu.tr

Honeypot-Based Detection of Advanced Persistent Threats: A New Methodology

Maryam Mohammadzad*[1], Jaber Karimpour [1]

[1]*University of Tabriz, Computer Science, Iran, m.mohammadzad@tabrizu.ac.ir, karimpour@tabrizu.ac.ir*

Cite this study: Mohammadzad, M., & Karimpour, J. (2024). Honeypot-Based Detection of Advanced Persistent Threats: A New Methodology. Advanced Engineering Days, 9, 894-896

Keywords
Honeypots
Advanced Persistent Threats
Cyber security
Threat Detection
Intrusion Detection Systems

Abstract

Advanced Persistent Threats (APTs) pose a significant hurdle for modern cybersecurity. Traditional defenses often struggle to identify and counteract these complex attacks. This research proposes a novel method for APT detection utilizing honeypot systems. We strategically deploy custom-built honeypots to lure malicious actors and gain in-depth understanding of their tactics, techniques, and procedures (TTPs). Our approach incorporates real-time data analysis alongside advanced machine learning algorithms to bolster honeypots' ability to effectively detect and respond to threats. Rigorous testing across various network environments confirms that this honeypot-driven approach significantly improves the capability to identify and mitigate APTs. These results underscore the potential of adaptable honeypot systems in fortifying cybersecurity defenses against persistent and evolving threats.

Introduction

The evolving cybersecurity landscape faces a major challenge from APTs. These threats are known for their stealth, persistence, and use of multi-stage intrusions to maintain long-term access [1, 2, 3]. Traditional defenses like firewalls and signature-based IDS often fall short against these advanced attackers who can bypass them [4]. Honeypots, decoy systems designed to deceive and study attackers, have become valuable tools. These systems act as bait, attracting attackers without risking critical assets, allowing security professionals to gather intelligence on malicious activities [5, 6]. However, their effectiveness against APTs remains limited due to the complexity and adaptability of these threats [7]. This paper proposes a new method to improve APT detection using honeypots. By combining advanced machine learning with adaptable honeypot deployment strategies, we aim to create a dynamic defense that identifies and mitigates APTs in real-time. Our approach involves deploying honeypots in diverse network environments, capturing extensive attacker behavior data, and using this data to refine threat detection and response. By advancing honeypot technology and refining their use against APTs, this research seeks to significantly contribute to cybersecurity. This will provide practitioners with stronger tools to defend against some of the most dangerous digital threats.

Material and Method

Our honeypot system uses a combination of low-interaction (LI) and high-interaction (HI) honeypots to capture a broad spectrum of attacker behaviors. LI honeypots mimic common services and operating systems, offering minimal interaction to attract automated attacks and basic scans. HI honeypots, in contrast, are fully functional systems designed to engage attackers for extended periods, allowing observation of their advanced Tactics, Techniques, and Procedures (TTPs). Honeypots were strategically deployed across diverse network environments including corporate networks, cloud infrastructures, and internet-facing positions. This varied deployment aims to attract a wider range of attack vectors and attacker profiles. Each deployment included monitoring tools to capture network traffic, system logs, and user interactions. The Honeypot systems logged all interactions in detail, including network traffic (captured using tools like Wireshark and tcpdump), system logs (via syslog and custom scripts), and user activity (using tools like TTY recording and scripting). This comprehensive logging ensured we collected in-depth information on attacker behaviors and methodologies.

Collected data underwent pre-processing to remove unnecessary information. This involved filtering out harmless traffic and automated scans that didn't exhibit APT characteristics. Data normalization techniques were applied to standardize log formats for easier analysis.

Key features were extracted from the pre-processed data for machine learning algorithms. These features included network packet characteristics, command sequences, file access patterns, and system call traces. Feature selection techniques, such as Principal Component Analysis (PCA) and Recursive Feature Elimination (RFE), were used to identify the most relevant features for APT detection.

Several machine learning algorithms were evaluated for their effectiveness in detecting APT activities. This included Support Vector Machines (SVM), Random Forests (RF), Gradient Boosting Machines (GBM), and Deep Learning models like Recurrent Neural Networks (RNN) and Convolutional Neural Networks (CNN). The models were trained using a labeled dataset containing both benign and malicious activities, with a focus on identifying patterns indicative of APTs. The performance of the trained models was evaluated using standard metrics. These included accuracy, precision, recall, F1-score, and the Area Under the Receiver Operating Characteristic Curve (AUC-ROC). Cross-validation techniques were applied to ensure the models' robustness and generalizability. Additionally, the models were tested in live honeypot environments to assess their real-world applicability.

A testbed was set up to simulate a realistic network environment with a mix of Honeypot types and monitoring tools. The network included various services and applications to mimic a typical corporate IT infrastructure. This setup allowed us to validate our methodology under conditions that closely resemble real-world scenarios.

To evaluate the effectiveness of our Honeypot-based detection system, we simulated APT attacks using known TTPs from publicly available APT reports and threat intelligence feeds. These simulated attacks were designed to mimic the behavior of actual APT groups, providing a robust test of our system's capabilities. All experiments were conducted ethically and with control, ensuring no harm to external systems or unauthorized data access. The Honeypot systems were isolated from production environments to prevent accidental exposure of sensitive data. Furthermore, data collection and analysis were performed in compliance with relevant privacy and data protection regulations.

Results

During deployment, our honeypots captured a significant volume of interactions, exceeding 1 million events. LI Honeypots attracted a large number of automated scans and basic attacks, while HI Honeypots engaged attackers in more intricate and extended interactions.

Analysis of the data revealed distinct behavioral patterns. Automated tools and scripts primarily targeted LI Honeypots, attempting common exploits and vulnerability scans. HI Honeypots, however, encountered more advanced attacks, such as manual command execution, attempts at lateral movement within the network, and data exfiltration activities.

Feature selection techniques identified key indicators of APT activities. These included unusual network traffic patterns, atypical command sequences, and anomalies in how attackers accessed files. These features were crucial for differentiating between benign and malicious activity. The machine learning models achieved high accuracy in detecting activities linked to APTs (as shown in Table 1).

Table 1. Performance Metrics of Machine Learning Models for APT Detection

Method	Accuracy (%)	Precision (%)	Recall (%)	F1-Score (%)	AUC-ROC
SVM	94.5	92.3	91.8	92	0.96
RF	95.2	93.7	92.9	93.3	0.97
GBM	96	94.5	93.8	94.1	0.98
RNN	96.5	95.2	94.6	94.9	0.99
CNN	97	95.7	95.1	95.4	0.99

In real-world honeypot deployments, the models maintained their effectiveness, accurately identifying and flagging activities linked to APTs with minimal false positives. This integration of machine learning with honeypots enabled real-time detection and response, significantly improving overall security posture.

Compared to traditional IDS, our Honeypot system demonstrated a substantial improvement in APT detection. Traditional systems suffered from higher false negative rates, often missing subtle signs of APT activity. Our honeypot approach reduced false negatives by over 30%, providing a more reliable and comprehensive threat detection mechanism.

Adaptive honeypots, which dynamically adjusted their configurations based on attacker behavior, proved particularly effective. These systems were adept at attracting more sophisticated attackers and capturing detailed information on advanced techniques, furthering our understanding of APT methodologies.

Discussion

This study highlights the significant benefits of combining honeypot systems with machine learning for Advanced Persistent Threat (APT) detection and mitigation. The strategic deployment of both LI and HI Honeypots effectively captured a broad spectrum of attacker behaviors, providing valuable insights into their tactics, techniques, and procedures (TTPs). Machine learning models, especially deep learning architectures like Recurrent Neural Networks (RNNs) and Convolutional Neural Networks (CNNs), achieved high accuracy in identifying subtle patterns indicative of APT activity. This led to a reduction in false negatives and an overall improvement in detection capabilities. Adaptive honeypots, which dynamically adjust their configurations based on real-time attacker behavior, further enhanced engagement and captured detailed information on advanced attack techniques. Compared to traditional IDS, our approach demonstrated a substantial improvement in detecting APTs, particularly those employing stealthy, low-and-slow methodologies. These findings emphasize the potential of advanced honeypot systems to strengthen cybersecurity defenses against sophisticated and evolving threats.

Conclusion

In conclusion, our research underscores the effectiveness of honeypot-based systems augmented with machine learning in detecting and mitigating Advanced Persistent Threats (APTs). By leveraging both low- and high-interaction honeypots, we successfully captured a diverse range of attacker behaviors and gained valuable insights into their strategies. The integration of machine learning algorithms, such as Recurrent Neural Networks (RNN) and Convolutional Neural Networks (CNN), significantly enhanced our ability to identify subtle indicators of APT activities, thereby improving detection accuracy and reducing false negatives. Adaptive honeypots, capable of dynamically adjusting to evolving attack tactics, proved instrumental in engaging sophisticated adversaries and gathering detailed threat intelligence. Our findings highlight the limitations of traditional security measures and emphasize the importance of adopting advanced, proactive defense mechanisms in today's cybersecurity landscape. Moving forward, the continued development and deployment of honeypot-based solutions offer promising avenues for bolstering organizational resilience against persistent and emerging cyber threats.

References

1. Yue, H., Li, T., Wu, D., Zhang, R., & Yang, Z. (2024). Detecting APT attacks using an attack intent-driven and sequence-based learning approach. Computers & Security, 140, 103748.
2. Mohammadzad, M., Karimpour, J., & Mahan, F. (2024). Cyber attacker's next action prediction on dynamic real-time behavior model. Computers and Electrical Engineering, 113, 109031.
3. Do Xuan, C., & Cuong, N. H. (2024). A novel approach for APT attack detection based on feature intelligent extraction and representation learning. PloS one, 19(6), e0305618.
4. Lee, K., Lee, J., & Yim, K. (2023). Classification and analysis of malicious code detection techniques based on the APT attack. Applied Sciences, 13(5), 2894.
5. Mohammadzad, M., & Karimpour, J. (2023). Using rootkits hiding techniques to conceal honeypot functionality. Journal of Network and Computer Applications, 214, 103606.
6. Mohammadzad, M., Karimpour, J., & Mahan, F. (2023). MAGD: Minimal attack graph generation dynamically in cyber security. Computer Networks, 236, 110004.
7. Lee, K., Lee, J., & Yim, K. (2023). Classification and analysis of malicious code detection techniques based on the APT attack. Applied Sciences, 13(5), 2894.

Advanced Engineering Days

aed.mersin.edu.tr

Face Mask Detection System by Transformer Learning Model

Salar Mokhtari Laleh*[1], Seyed Mahdi Abdi Oskouei[2], Mohammad Sarhangzadeh[3]

[1]University of Tabriz, Electronics and Computer Engineering, Iran, salarmokhtari0@gmail.com, mahdi.abdi.oskuie@gmail.com m.sarhangnote@gmail.com

Cite this study: Laleh, S. M., Oskouei, S. M., & Sarhangzadeh, M. (2024). Face Mask Detection System by Transformer Learning Model. Advanced Engineering Days, 9, 897-900

Keywords
Face Mask Detection
Convolutional Neural Network
Image Classification
Public Health

Abstract

This paper introduces a novel approach utilizing Convolutional Neural Networks (CNNs) for the automated detection of face masks in images. The significance of face masks in preventing the transmission of infectious diseases has amplified the need for effective monitoring tools. Our model leverages the VGG16 architecture, adapted through fine-tuning for binary classification to discern between faces with masks and without masks. Extensive preprocessing techniques, including image augmentation and normalization, were applied to enhance the model's generalization capabilities. Training incorporated strategic methodologies such as early stopping and learning rate scheduling to optimize performance. The findings illustrate high accuracy, underscoring the potential of CNNs in applications related to public health monitoring. This approach is poised for integration into surveillance systems to enforce mask mandates and support public health initiatives.

Introduction

The global COVID-19 pandemic has underscored the critical role of face masks in curbing virus transmission. Consequently, the demand for automated systems capable of detecting face masks in public spaces has surged. This study aims to develop a reliable face mask detection model using Convolutional Neural Networks (CNNs) [7]. We employed a pre-trained VGG16 [2] model, fine-tuned specifically for the binary classification task of distinguishing between masked and unmasked faces. Our methodology involved rigorous data preprocessing and augmentation [6] to ensure robustness and scalability. This approach holds promise for deployment in diverse public health monitoring applications to ensure compliance with face mask mandates and bolster public health efforts. By harnessing advanced deep learning techniques, our objective is to establish an efficient tool for real-time face mask detection.

Recent advancements in computer vision and deep learning have made it feasible to develop sophisticated image recognition systems with high accuracy. Face mask detection, as a specific application of these technologies, benefits greatly from the robustness and adaptability of CNNs. By utilizing the VGG16 [2] architecture, which is renowned for its deep layers and extensive feature extraction capabilities, our approach ensures a high level of precision in differentiating between masked and unmasked faces. Additionally, the integration of comprehensive data augmentation [6] techniques helps to mitigate the challenges posed by varied real-world conditions, such as differences in lighting, facial orientations, and mask types. This study not only addresses an immediate public health need but also lays the groundwork for future innovations in automated health monitoring systems, contributing to a safer and more resilient society.

Material and Method

The dataset utilized for this study was sourced from publicly available repositories containing images of individuals wearing and not wearing face masks. These images were categorized into two distinct classes: "with mask" and "without mask," and organized into separate directories for streamlined preprocessing. Key preprocessing steps included:

Conversion of each image to RGB format and resizing to 224x224 pixels to align with the input requirements of the VGG16 model.

Normalization of pixel values to a scale of 0 to 1 by dividing by 255.0.

Stratified splitting of data into training and testing sets with an 80-20 ratio to maintain class balance. The face mask detection model was constructed using the VGG16 [2] architecture renowned for its efficacy in image classification tasks. The VGG16 [2] base model was customized by removing its top layers and incorporating additional layers tailored for binary classification:

A global average pooling layer to condense feature maps from the VGG16 base, summarizing feature presence effectively.

Integration of a fully connected layer comprising 256 neurons with ReLU activation for introducing non-linearity.

Application of a 50% dropout rate to mitigate overfitting during training by randomly zeroing half of input values.

Inclusion of batch normalization to stabilize training by normalizing outputs from previous layers.

A single neuron utilizing a sigmoid activation function for binary classification purposes. The training phase encompassed data augmentation techniques aimed at enhancing model generalization. Techniques such as rotation, shifting, shearing, zooming, and horizontal flipping were employed. The model was optimized using the Adam optimizer [5] and trained with a binary cross-entropy loss function [9], with accuracy serving as the primary performance metric. Early stopping mechanisms were implemented to cease training if validation loss stagnated for 10 consecutive epochs, thus preventing overfitting. Additionally, a learning rate scheduler was employed to progressively reduce the learning rate during training, ensuring optimal model convergence.

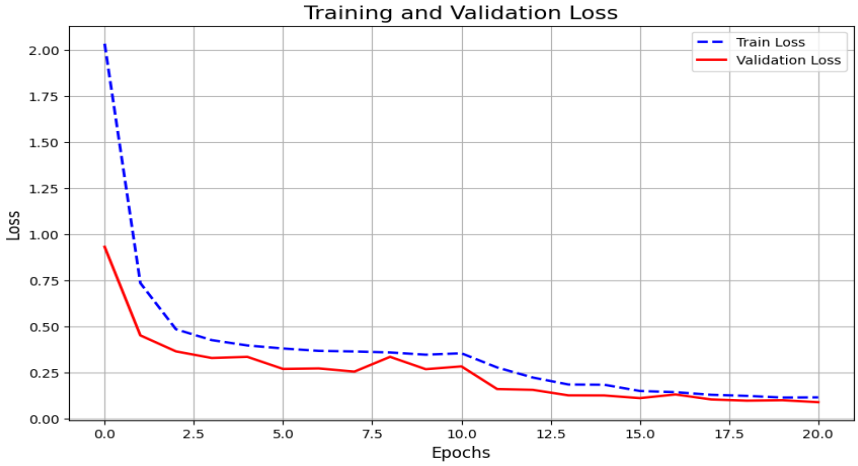


Figure 1. Training and Validation Loss

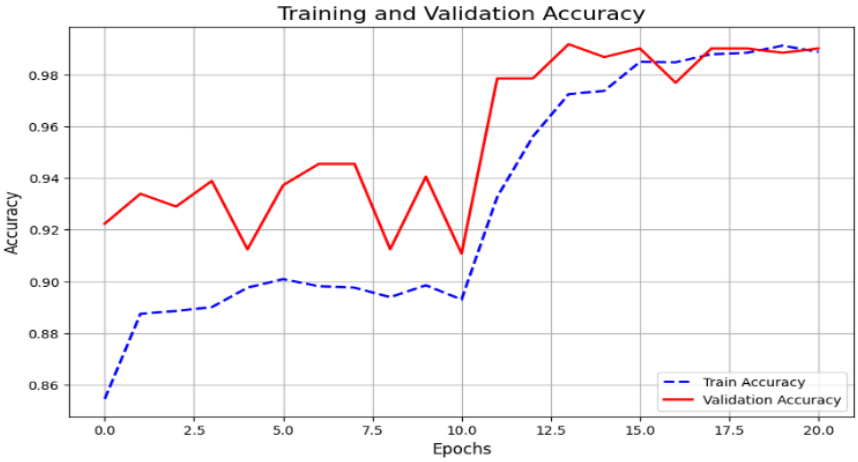


Figure 2. Training and Validation Accuracy

Results

The trained model demonstrated exceptional accuracy, validating its efficacy in distinguishing between masked and unmasked faces. The datasets were divided such that 70% of the data was used for training, 10% for validation, and 20% for testing. The evaluation included the following accuracies: **Training Accuracy:** 99.50%, **Test Accuracy:** 99.01%, Validation Accuracy: 98.84%

Table 1. VGG16 Model Summary

Layer (type)	Output Shape	Param #
vgg16 (Functional)	(None, 4, 4, 512)	14,714,688
global_average_pooling2d_1	(None, 512)	0
dense_3 (Dense)	(None, 256)	131,328
batch_normalization_2	(None, 256)	1,024
dropout_2 (Dropout)	(None, 256)	0
dense_4 (Dense)	(None, 128)	32,896
batch_normalization_3	(None, 128)	512
dropout_3 (Dropout)	(None, 128)	0
dense_5 (Dense)	(None, 1)	129
Total params		14,880,577
Trainable params		165,121
Non-trainable params		14,715,456

The table describes the layer architecture of the CNN model used for face mask detection. The VGG16 [2] model, pre-trained on the ImageNet dataset, is utilized as the base for feature extraction. The global_average_pooling2d layer reduces each feature map to a single value, summarizing the presence of features in each map. The dense_3 layer is a fully connected layer with 256 neurons, introducing non-linearity and learning complex patterns. batch_normalization_2 normalizes the output of the previous layer to stabilize and accelerate training, while dropout_2 is a regularization technique that randomly sets a fraction of input units to 0 during training to prevent overfitting. The dense_4 layer further abstracts learned features with 128 neurons, followed by batch_normalization_3 and dropout_3 for additional normalization and regularization. The final dense_5 layer has a single neuron with a sigmoid activation function, designed for binary classification between masked and unmasked faces. The table also shows the total number of parameters in the model, including the trainable and non-trainable parameters, which are inherited from the pre-trained VGG16 [2] model.

Discussion

The outcomes highlight the efficacy of our CNN-based approach in face mask detection. Leveraging the VGG16 [2] architecture, coupled with extensive preprocessing and normalization, significantly enhanced model performance. This methodology holds promise for deployment in various public health applications aimed at enforcing face mask mandates. Future research endeavors may focus on real-time deployment integration with video surveillance systems and exploration of alternative architectures to further refine detection capabilities.

Conclusion

This study successfully developed and evaluated a CNN-based model utilizing the VGG16 [2] architecture for face mask detection. The model exhibited robust performance through rigorous preprocessing, including comprehensive image augmentation and normalization. This approach represents a significant advancement in automating the monitoring of mask compliance across diverse settings, thereby bolstering public health measures. Future investigations could explore real-time deployment scenarios and alternative architectural enhancements [1, 3, 4, 7] to further optimize detection capabilities.

References

1. He, K., Zhang, X., Ren, S., & Sun, J. (2016). Deep residual learning for image recognition. In Proceedings of the IEEE conference on computer vision and pattern recognition (pp. 770-778).
2. Simonyan, K., & Zisserman, A. (2014). Very deep convolutional networks for large-scale image recognition. arXiv preprint arXiv:1409.1556.
3. Howard, A. G., Zhu, M., Chen, B., Kalenichenko, D., Wang, W., Weyand, T., ... & Adam, H. (2017). Mobilenets: Efficient convolutional neural networks for mobile vision applications. arXiv preprint arXiv:1704.04861.

4. Chollet, F. (2017). Xception: Deep learning with depthwise separable convolutions. In Proceedings of the IEEE conference on computer vision and pattern recognition (pp. 1251-1258).
5. Kingma, D. P., & Ba, J. (2014). Adam: A method for stochastic optimization. arXiv preprint arXiv:1412.6980.
6. Plompen, A. J., Cabellos, O., De Saint Jean, C., Fleming, M., Algora, A., Angelone, M., ... & Žerovnik, G. (2020). The joint evaluated fission and fusion nuclear data library, JEFF-3.3. The European Physical Journal A, 56, 1-108.
7. Zhao, Z. Q., Zheng, P., Xu, S. T., & Wu, X. (2019). Object detection with deep learning: A review. IEEE transactions on neural networks and learning systems, 30(11), 3212-3232.
8. Huang, G., Liu, Z., Van Der Maaten, L., & Weinberger, K. Q. (2017). Densely connected convolutional networks. In Proceedings of the IEEE conference on computer vision and pattern recognition (pp. 4700-4708)
9. Zhang, Z., & Sabuncu, M. (2018). Generalized cross entropy loss for training deep neural networks with noisy labels. Advances in neural information processing systems, 31.

Advanced Engineering Days

aed.mersin.edu.tr

Strategic Monitoring and Proactive Measures for Mitigating Network-Level Threats and Malware in Albania

Klorenta Pashaj*[1], Eralda Gjika, Vilma Tomco [3]

[1]*National Authority for Cyber Security, Albania, klorenta.pashaj@gmail.com*
[2] *University of Tirana, Department of Applied Mathematics, Albania, eralda.dhamo@fshn.edu.al*
[3] *State Authority for Geospatial Information, Albania, vilma.tomco@asig.gov.al*

Cite this study: Pashaj, K., Gjika, E. & Tomco, V. (2024). Strategic Monitoring and Proactive Measures for Mitigating Network-Level Threats and Malware in Albania. Advanced Engineering Days, 9, 901-903

Keywords
Cybersecurity
ISP Monitoring
Malware Prevention
Time Series Analysis
Cluster Analysis

Abstract

Monitoring and notification on prevention and reduction of threats and malware at the network level is crucial for maintaining cybersecurity. This study emphasizes forecasting these indicators, focusing on monthly data from Internet Service Providers (ISPs) in Albania over 2021 and 2022, including 7 ISPs. The goal is to understand seasonal trends and take proactive measures for future years. We analyze the impact of measures implemented from the beginning to the end of the data recording period, assessing their effectiveness in reducing threats and malware. Time series models and cluster analysis are employed to understand patterns in the data. Time series models forecast upcoming values for each ISP, while cluster analysis identifies groups of ISPs and months with similar behaviors. Our observations revealed three distinct periods with similar patterns. Cluster analysis helps identify ISPs experiencing similar fluctuations in demand or traffic during specific months, such as higher demand during holidays or lower usage in summer. These methods aim to enhance forecasting accuracy by tailoring models to each cluster's behavior. This methodology can help stakeholders improve forecasts, resource allocation, capacity planning, and marketing strategies. The study highlights the crucial role of ISPs in monitoring and reporting, emphasizing real-time communication to improve end-user security and collaboration with regulatory institutions.

Introduction

In today's geopolitical climate, cybersecurity has emerged as a critical area of concern, particularly as cyberwarfare is now acknowledged as the fifth domain of warfare [1]. The rapid digitization of public services and the pervasive use of the internet have vastly improved the efficiency of daily life for both citizens and businesses. However, these advancements have simultaneously created new vulnerabilities, providing fertile ground for cybercriminals, hackers, and hacktivists to exploit.

In Albania, the imperative to protect digital infrastructures and systems is more pronounced than ever. The National Cyber Security Authority of Albania (NCSA) is leading efforts to bolster network and information system security nationwide. Internet Service Providers (ISPs) are essential in identifying and managing malware threats.

This study focuses on examining malware-related information collected from seven ISPs in Albania across two distinct periods: May to December 2021 and January to December 2022 [3]. The goal is to identify seasonal trends in malware incidents and to assess the efficacy of actions taken by ISPs in reducing or controlling these threats. By using advanced analytical techniques such as time series models and cluster analysis, we seek to gain a detailed understanding of malware behaviour and its impact on network security.

The methodological framework of this research combines the predictive power of time series models for forecasting malware occurrences, alongside cluster analysis to identify groups of ISPs exhibiting similar behaviours. This combined approach not only refines the accuracy of our predictive models but also offers critical insights of intervention strategies and measure optimization.

The insights gleaned from this study are intended to assist stakeholders in enhancing their cybersecurity practices. By recognizing seasonal trends and assessing the impact of specific measures, stakeholders can make more informed decisions regarding resource allocation, capacity planning, and strategic interventions. This

research underscores the necessity of ongoing monitoring, real-time communication, and close collaboration between ISPs and regulatory bodies to fortify Albania's overall cybersecurity framework.

Material and Method

Data for this study were collected from seven different Internet Service Providers (ISPs) over a period from May 2021 to July 2022 [2]. The dataset contains monthly malware detection counts for each ISP. All data values were complete and did not require any preprocessing. Descriptive statistics were calculated to summarize the data, including means, standard deviations (SD), minimum (Min), and maximum (Max) values for each ISP.

Table 1. Descriptive Statistics

ISP	Mean	SD	Min	Max
ISP 1	15742.1	3521.5	7448.0	21526.0
ISP 2	37903.9	30625.9	5223.0	89745.0
ISP 3	5269.7	4800.3	51.0	15494.0
ISP 4	20559.3	22237.1	114.0	73210.0
ISP 5	7447.3	7506.1	3.0	17508.0
ISP 6	9630.2	4257.9	3442.0	15024.0
ISP 7	7243.2	6579.6	263.0	15551.0

From the descriptive statistics, several key observations were made:

- ISP 2 exhibited the highest variability in malware detection counts with a mean of 37,903.9 and a standard deviation of 30,625.9. This indicates significant fluctuations in malware detections over the observed period.
- ISP 4 had a high mean malware detection count of 20,559.3, but also showed considerable variability with a standard deviation of 22,237.1, and a range from a minimum of 114 to a maximum of 73,210.
- ISP 3 and ISP 5 had relatively low mean counts of 5,269.7 and 7,447.3 respectively, but ISP 3 showed a notable minimum detection count of just 51, highlighting periods of very low malware activity.
- ISP 1 had a consistent detection pattern with a mean of 15,742.1 and a standard deviation of 3,521.5.
- ISP 7 had the lowest mean of 7,243.2 among the ISPs, with a relatively high standard deviation of 6,579.6, indicating some months with very low counts and others with significantly higher counts.

Results

The time series analysis was conducted to identify patterns in the number of malware detections over time. We observed three distinct patterns in the data:

- *Pattern 1:* Months 1 to 3 (May 2021 to July 2021)
- *Pattern 2:* Months 4 to 9 (August 2021 to January 2022)
- *Pattern 3:* Months 10 to 15 (February 2022 to July 2022)

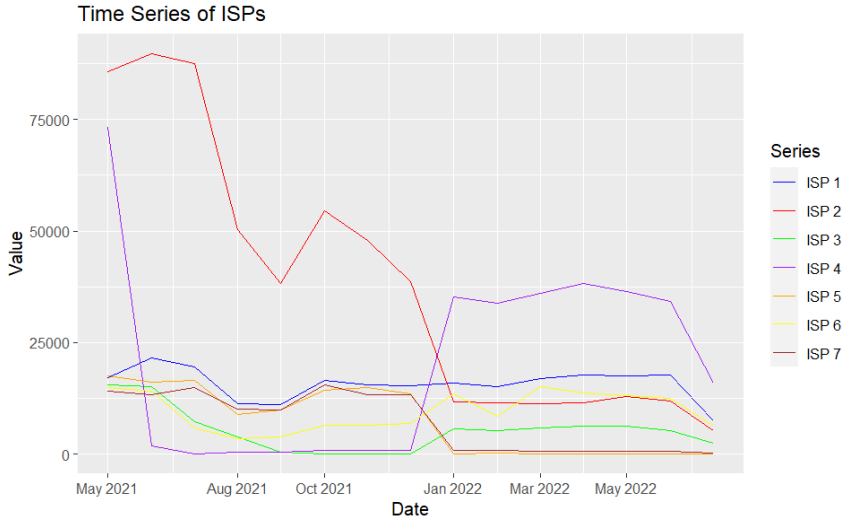


Figure 1. Time series of ISPs

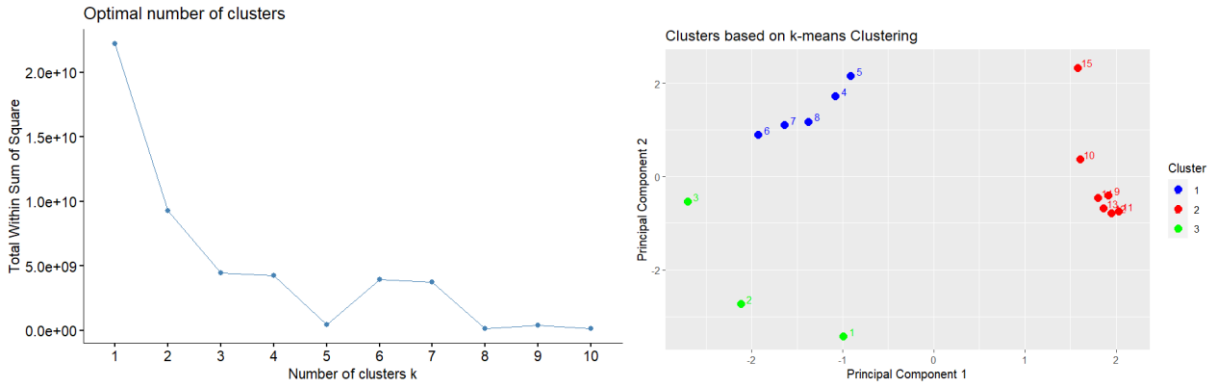


Figure 2. (a) Optimal number of clusters (b) K-means cluster analysis (of months)

In support of this observation, we also performed a cluster analysis using the K-means algorithm (R was used as a statistical tool). The clustering analysis revealed three main periods where the behavior of the ISPs was similar or closely aligned in terms of the number of malwares detected. We observed a clear separation of clusters indicating distinct groups in the data. For the first cluster (months of observations 1, 2, 3) we may see a slight distance between the individuals (months) which may be related to the precautions taken after these observations which show to be high in the first month in some of the ISPs.

Discussion

The time series analysis highlighted three distinct patterns in the malware detection counts across the 15-month period considered:

Pattern 1 (Months 1-3: May 2021 to July 2021): This period showed the highest variability and counts for several ISPs, particularly ISP 2 and ISP 4, indicating a peak in malware activity during the early months.

Pattern 2 (Months 4-9: August 2021 to January 2022): This period saw a relative stabilization in malware detection counts, with a noticeable decline in variability for most ISPs. The counts were generally lower compared to the previous months.

Pattern 3 (Months 10-15: February 2022 to July 2022): This period exhibited a further reduction in detection counts and variability for most ISPs, with some ISPs like ISP 3 and ISP 5 showing consistently low counts.

The K-means clustering analysis revealed on the other hand three main clusters that correspond to the identified patterns in the time series analysis:

Cluster 1: High malware detection counts and high variability, primarily corresponding to the initial months (May 2021 to July 2021).

Cluster 2: Moderate detection counts with reduced variability, corresponding to the middle months (August 2021 to January 2022).

Cluster 3: Low detection counts and low variability, corresponding to the final months (February 2022 to July 2022).

Conclusion

Analyzing this data reveals patterns in malware activities, highlighting the effectiveness of countermeasures over time. By identifying high, stable, and low activity periods, we can develop strategies for future detection and prevention. Our findings indicate periods of increased activity, stable detection, and sustained control, suggesting varying levels of threat and response effectiveness.

References

1. Dinu, M.-Ş. (2017). THE 5 TH OPERATIONAL DOMAIN AND THE EVOLUTION OF NATO'S CYBER DEFENCE CONCEPT. Retrieved from https://www.aos.ro/wp-content/anale/MTVol9Nr2Art.8.pdf
2. NCSA. (2022, March). Raport Vjetor 2022. Retrieved May 28, 2024, from NCSA website: https://cesk.gov.al/raport-vjetor-2022/
3. Tomco, V., Harizaj, M. & Prendi, A. (2022). A simple mechanism for controlling and reducing malwares at network level, preventing possible cyber incidents. 5th Advanced Engineering Days, 57-59

Advanced Engineering Days

aed.mersin.edu.tr

Person Identification in Healthcare Applications Using Binary Chimp Optimization-based EEG Channel Selection

Shabnam Oskouei [*1], **Saeed Meshgini** [1], **Hadi S. Aghdasi** [1]

[1]*University of Tabriz, Faculty of Electrical and Computer Engineering, Iran, oskouei@tabrizu.ac.ir, meshgini@tabrizu.ac.ir, aghdasi@tabrizu.ac.ir*

Cite this study: Oskouei, Sh., Meshgini, S. & Aghdasi, H. S. (2024). Person Identification in Healthcare Applications Using Binary Chimp Optimization-based EEG Channel Selection. Advanced Engineering Days, 9, 904-907

Keywords
EEG signals
Person identification
Binary chimp optimization
Channel selection
High accuracy

Abstract

Recently, person identification based on electroencephalogram (EEG) signals has been proposed as a novel technique in healthcare applications. Many studies have shown that EEG provides unique and universal features, as well as specific resilience against spoofing attacks. EEG signals measured by electrodes on the scalp (channels) and achieving high accuracy with the minimum number of channels is the researchers' main goal for realizing healthcare applications. In this paper, we model binary chimp optimization algorithm (BChOA) for the EEG channel selection besides KNN as a classifier (BChOA-KNN) to solve the person identification problem. We use a standard EEG motor imagery dataset to prove the efficiency of the proposed method. The simulation results show that BChOA-KNN outperforms state-of-the-art algorithms by achieving 94.45% accuracy with selecting only 23 EEG channels.

Introduction

Recently, biometrics such as facial features, fingerprints, voices, and brain EEG signals have received much attention in identification systems as an alternative to other identification methods, such as passwords or cards, which can be easily stolen or forgotten [1, 2]. EEG signals seem like a great alternative because several studies have shown that such information is exclusive, universal, and naturally robust to spoofing attacks when designing new biometric systems and realizing healthcare applications [1, 2]. A review of existing works found that recent studies in person identification for healthcare application systems used EEG signals to increase accuracy and considered reducing number of selected channels [3, 4]. In [3], authors used a multi-objective binary cuckoo search algorithm besides the KNN classifier (MOBCS-KNN) to select the optimal EEG channels, capture relevant information, and increase accuracy. With only 24 channels, MOBCS-KNN achieved 93.86% accuracy. A binary version of the Grey Wolf Optimizer and SVM classifier (BGWO-SVM) has been presented in [4] to optimize channel selection and maximize accuracy for person identification problem. By using only 23 selected channels out of 64 ones BGWO-SVM achieved 94.13% accuracy.

In this paper, we exploit the characteristics of the recently published binary chimp optimization algorithm (BChOA) [5] to solve the person identification problem with EEG signals. Our main goal is to achieve high accuracy with minimum selected channels as much as possible. The proposed method named BChOA-KNN, models BChOA to EEG channel selection and then applies KNN classifier for person identification problem. Simulation results on standard EEG motor imagery dataset [6], show that BChOA-KNN has a good performance in comparison with MOBCS-KNN and BGWO-SVM. The proposed method reaches an accuracy of 94.45% by 23 selected EEG channels.

Material and Method

Dataset

We use the standard EEG motor imagery dataset [6] to show the efficiency of the proposed method. The brain signals of this dataset are collected from 109 subjects from 64 channels when they open and close their eyes.

Filtering and Feature Extraction

First, we apply a low-pass filter to keep only frequencies from 0.1 to 30 Hz. The Frequencies above 30 Hz are related to gamma information, and this frequency shows its effect when the brain is highly active not in the rest mode. After, filtering the data, the features should be extracted. Before feature extraction, the information every 60 seconds in both eyes opened and eyes closed scenarios are divided into 10 same parts for each channel. In other words, we have obtained one feature vector for every 6 seconds, so will have 20 feature vectors for each person. Each feature vector also contains 10 features obtained from the following metrics:

- Auto Regressive Model: Extract 5 features
- Kurtosis: Extract 1 feature
- Skewness: Extract 1 feature
- Tsallis Entropy: Extract 1 feature
- Mean Curve Length: Extract 1 feature
- Shannon Entropy: Extract 1 feature

Proposed Method

In this section we introduce Binary Chimp Optimization Algorithm with KNN classifier (BChOA-KNN) as our proposed method for EEG channel selection in person identification problem. We exploit the characteristics of Binary Chimp Optimization Algorithm (BChOA) [5] and model it to EEG channel selection. BChOA-KNN considers accuracy as its fitness function and uses KNN as classifier. In the following ChOA [7], BChOA [5], and the considered fitness function will be explained.

Chimp Optimization Algorithm

Chimp Optimization Algorithm (ChOA) [7], exploits chimpanzee hunting behavior influenced by their intelligence and sexual motivation. ChOA is easier to implement, more stable, and is not constrained by many initial parameters. In the ChOA, chimp groups in a search space rely on their best-performing chimps to guide other chimps toward optimal areas. During the continuous iterative search process, four chimps (attacker, barrier, chaser, and driver) predict the possible location of the captured object, guiding the search process to find a globally optimal solution. In summary, a chimp chasing prey can be mathematically modeled as follows:

$$X_{Chimp}(t+1) = X_{Prey}(t) - a.\left|C.X_{Prey}(t) - m.X_{chimp}(t)\right| \quad (1)$$

where X_{prey} is the position vector of the prey, X_{Chimp} is the position vector of the current individual chimp, t is the number of current iteration, and a, C, m are the coefficient vectors calculated as follows:

$$a = 2.fr_1 - f \quad (2)$$
$$C = 2.r_2 \quad (3)$$
$$m = chaotic_value \quad (4)$$
$$f = 2 - \frac{2.t}{T} \quad (5)$$

where f is the convergence factor whose value decreases non-linearly from *2* to *0* as the number of iterations increases, r_1 and r_2 denoted random number between [0,1]. T is the maximum number of iterations, a is a random vector that determines the distance between the chimp and the prey, m is the chaotic vector generated by the chaotic mapping, C is the control coefficient for the Chimp expulsion and prey chasing, and its value is a random number between [0, 2].

$$d_{attracker} = |c_1 . X_{attracker} - m_1 . X(t)| \quad (6)$$
$$d_{barrier} = |c_1 . X_{barrier} - m_2 . X(t)| \quad (7)$$
$$d_{chaser} = |c_1 . X_{chaser} - m_3 . X(t)| \quad (8)$$
$$d_{driver} = |c_1 . X_{driver} - m_4 . X(t)| \quad (9)$$

The mathematical model of a chimp attacking its prey is as follows:

$$X_{1=}X_{attracker} - a_1 \ . d_{attracker} \quad (10)$$
$$X_{2=}X_{barrier} - a_2 \ . d_{barrier} \quad (11)$$
$$X_{3=}X_{chaser} - a_3 \ . d_{chaser} \quad (12)$$
$$X_{4=}X_{driver} - a_4 \ . d_{driver} \quad (13)$$
$$X_{chimp}(t+1) = \frac{(X_1 + X_2 + X_3 + X_4)}{4} \quad (14)$$

Based on Eqs. (10 to 14), $X_{chimp}(t+1)$ is the updated chimp's position, $X(t)$ represents the current Chimp's position, $X_{attacker}$ is the attacker position, the position of barriers shown with $X_{barriers}$, X_{chaser} is the chaser's position vector, and X_{driver} is the driver's position.

Binary Chimp Optimization Algorithm

EEG channel selection problem needs encoding each solution to binary where 1 means the channel will be selected and 0 the opposite situation. We use the transfer function for converting continuous values of chimps to binary ones defined in [5]:

$$X_{Chimp}(t+1) = \begin{cases} 1 \; if s\left(\dfrac{(X_1 + X_2 + X_3 + X_4)}{4}\right) \geq 0.5 \\ 0 \; , else \end{cases} \quad (15)$$

It is worth mentioning that, Eq. 15 will be used for calculating $X_{Chimp}(t+1)$ in the algorithm. Also, $s(x)$ is the sigmoid function calculated as Eq. 16:

$$s(x) = 1/1 + \exp(-10(x - 0.5)) \quad (16)$$

Problem Model and Fitness Function

In this paper, first, we randomly initialize the matrix of the population $X(N*D)$ (N=number of chimps, D=maximum channel number) by *1* or *0* (*1*=channel selected and *0*=channel not selected). Second, we calculate the fitness of each chimp with Eq. 17 and using KNN classifier.

$$Accuracy = (True\ positives + True\ Negatives)/(True\ positives + True\ negatives + False\ positives + False\ negatives) \quad (17)$$

Results and Discussion

Our simulations run on a PC equipped with an Intel Core i7 11800H 8Cores-2.3GHz, 32G RAM, and Microsoft Windows 11 Enterprise by utilizing Matlab 2022b. We compare BChOA-KNN with two of the best algorithms in this field named BGWO-SVM [4] and MOBCS-KNN [3] and consider T=100, N=30 for all algorithms. Each algorithm run 25 times and reports the average accuracy. Table 1 represents the achieved results.

Table 1. Average results of running metaheuristic algorithms

Metrics	BChOA-KNN	BGWO-SVM	MOBCS-KNN
Accuracy	94.45	94.13	93.86
Number of selected Channels	23	23	24

The outcomes of simulation results in Table 1 show the efficiency of the BChOA-KNN in comparison with BGWO-SVM and MOBCS-KNN. Compared with BGWO-SVM, our method reaches a high accuracy with the same channel number. In addition, BChOA-KNN outperforms MOBCS-KNN in both evaluation metrics.

Conclusion

In this paper, a BChOA-KNN was proposed to identify the person with high accuracy using the minimum number of EEG channels. Simulation results have shown that the proposed method reached an accuracy of 94.45% with 23 EEG channels out of 64. BChOA-KNN outperformed state-of-the-art algorithms in this field named BGWO-SVM and MOBCS-KNN. In the future, we will use deep learning methods as classifiers besides optimization methods for EEG channel selection in person identification systems.

References

1. Unar, J. A., Seng, W. C., & Abbasi, A. (2014). A review of biometric technology along with trends and prospects. Pattern recognition, 47(8), 2673-2688.
2. Alyasseri, Z. A. A., Khader, A. T., Al-Betar, M. A., & Alomari, O. A. (2020). Person identification using EEG channel selection with hybrid flower pollination algorithm. Pattern Recognition, 105, 107393.
3. Abdi Alkareem Alyasseri, Z., Alomari, O. A., ... & Rho, S. (2022). EEG channel selection using multiobjective cuckoo search for person identification as protection system in healthcare applications. Computational Intelligence and Neuroscience, 2022(1), 5974634.
4. Alyasseri, Z. A. A., Alomari, O. A., Makhadmeh, S. N., Mirjalili, S., Al-Betar, M. A., Abdullah, S., ... & Abasi, A. K. (2022). EEG channel selection for person identification using binary grey wolf optimizer. Ieee Access, 10, 10500-10513.

5. Ayeche, F., & Alti, A. (2023). Efficient Feature Selection in High Dimensional Data Based on Enhanced Binary Chimp Optimization Algorithms and Machine Learning. *Human-Centric Intelligent Systems*, *3*(4), 558-587.
6. Goldberger, A. L., Amaral, L. A., & Stanley, H. E. (2000). PhysioBank, PhysioToolkit, and PhysioNet: components of a new research resource for complex physiologic signals. circulation, 101(23), e215-e220.
7. Khishe, M., & Mosavi, M. R. (2020). Chimp optimization algorithm. Expert systems with applications, 149, 113338.

Advanced Engineering Days

aed.mersin.edu.tr

Investigation of Stone Deterioration in Gaziantep Yüzükçü Inn

İlhami Ay [*1], Murat Dal[2], Şefika Ergin[3]

[1]*Hakkari University, Çölemerik Vocational School, Hakkari, Türkiye, ilhamiay@hakkari.edu.tr*
[2]*Munzur University, Faculty of Fine Arts, Design and Architecture, Tunceli, Türkiye muratdal1122@gmail.com*
[3]*Dicle University, Institute of Science and Technology, Diyarbakır, Türkiye, sefika@dicle.edu.tr*

Cite this study: Ay, İ., Dal, M. & Ergin, Ş. (2024). Investigation of Stone Deterioration in Gaziantep Yüzükçü Inn. Advanced Engineering Days, 9, 908-911

Keywords
Stone Deterioration
Gaziantep
Yüzükçü Inn
Type of Deterioration

Abstract

The high strength value and durability of stone in traditional stone structures are important in terms of transferring traditional structures to future generations. It is important for the structures to determine the deterioration of the stone surfaces exposed to climatic and external factors and to determine the causes and to offer solutions. In this study, the deterioration of the Yüzükçü Inn in Gaziantep is discussed. In this context, the deterioration was visually examined, classified and analysed as physical, chemical, biological and anthropogenic. It is aimed that the data obtained from the study will form the basis for the conservation projects to be carried out in the coming years.

Introduction

The protection of historical stone structures, which are cultural heritage, and taking precautions against stone deterioration are important for the structures to survive for a longer period of time. Natural stones, which are the main construction material of traditional stone buildings, were used in historical buildings until 1800s. Stone materials cause deterioration on stone surfaces against natural climatic conditions and external factors. If appropriate measures are not taken against these deterioration and solutions are not offered, the buildings will face extinction. Correct detection of deterioration and damages occurring in the structures is important for the survival of the structures [1–3]. Correct diagnosis, correct analysis, correct restoration, periodic maintenance and sustainable protection are required for the transfer of stone structures to future generations [4–6].

Material and Method

In this study, the stone deterioration observed in the Yüzükçü Inn in Şahinbey District of Gaziantep was analysed. According to the analysis, the deteriorations were visually analysed and recorded by photographs. The deterioration on the courtyard façade and exterior walls of the Yüzükçü Inn was analysed, identified and classified [7, 8]. According to the classification, deterioration is examined in four groups as physical, chemical, biological and anthropogenic [9, 10].

Results

The deterioration that occurs on the surfaces of historical stone structures, which are cultural heritage, causes deterioration in the physical and petrographic properties of the stone. In some cases, these deteriorations also prepare the environment for another deterioration [11–13]. It is important to determine the degradation of natural stones, to investigate the causes, to develop solution proposals and to take measures against degradation in order to transfer the structures to future generations [14–16]. In this context, in this study, stone deterioration

in Gaziantep Yüzükçü Inn was examined, classified and analysed. The deterioration was classified and analysed as physical, chemical, biological and anthropogenic deterioration.

Surface losses that occur on stone surfaces as a result of changes in the mechanical properties of stone due to climatic factors are called physical deterioration. Fractures, cracks, abrasion and joint losses on stone surfaces are examples of physical deterioration. The physical deterioration observed in the Yüzükçü Inn is shown in Figure 1.



Figure 1. Physical deteriorations in Yüzükçü Inn

The type of deterioration that occurs on the stone surface depending on the climatic characteristics, temperature and humidity factors of the region is called chemical deterioration. Effects such as colour changes, salting and foliation on stone surfaces are examples of chemical deterioration [17, 18]. The chemical deterioration that occurred in Gaziantep Yüzükçü Inn is shown in Figure 2.



Figure 2. Chemical deteriorations in Yüzükçü Inn

The degradation that occurs on the surfaces of traditional stone structures as a result of the reaction of biological substances on the stone surface is called biological degradation. Moss and algae formation, plant formations and accumulations on stone surfaces are examples of biological degradation [19, 20]. The biological degradation in Gaziantep Yüzükçü Inn is shown in Figure 3.



Figure 3. Biological deteriorations in Yüzükçü Inn

Anthropogenic deterioration is a type of deterioration that occurs as a result of conscious or unconscious damage to traditional stone structures by humans [21, 22]. Misuse, neglect, wear and tear and inappropriate

restoration practices are examples of anthropogenic deterioration. The anthropogenic deterioration that occurred in Yüzükçü Inn is shown in Figure 4.

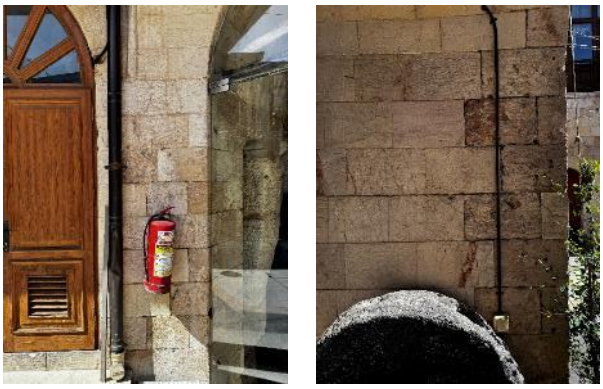


Figure 4. Anthropogenic deteriorations in Yüzükçü Inn

Conclusion

This study focuses on the deterioration observed in Gaziantep Yüzükçü Inn. The deterioration was detected by visual analysis and categorised and analysed. Physical, chemical, biological and anthropogenic deterioration were observed.

The data obtained in the study is intended to form the basis for both academic studies and future restoration projects. In addition, this study is also important in terms of taking the necessary measures to ensure that traditional stone structures survive for a longer period of time.

References

1. Ay, İ., Ergin, Ş., & Dal, M. (2023). Geleneksel Taş Yapılarda Meydana Gelen Taş Alterasyonları: Gaziantep Hamam Müzesi Örneği (pp. 515–523). IKSAD Yayınevi.
2. Ay, İ., Ergin, Ş., & Dal, M. (2023). Geleneksel Taş Yapılarda Meydana Gelen Taş Alterasyonları: Gaziantep Millet Hanı Örneği. In *UMTEB - XIII International Scientific Research Congress* (pp. 507–514). IKSAD Yayınevi.
3. Ay, İ., Dal, M., & Ergin, Ş. (2023). Investigation of stone deterioration in Gaziantep Kumandan Fountain. *Advanced Engineering Days (AED)*, *8*, 56–59.
4. Biçen Çelik, A., Ergin, Ş., Dal, M., & Ay, İ. (2023). Analysis of Stone Deterioration on the Facades of Hatuniye Madrasah. *Journal of Architectural Sciences and Applications*, *8*(1), 355–369. https://doi.org/10.30785/mbud.1302007
5. Tokmak, M., & Dal, M. (2020). Classification of Physical, Chemical and Biological Deteriorations Observed in Ankara Stone Monuments. *International Journal of Pure and Applied Sciences*, *6*(1), 8–16. https://doi.org/10.29132/ijpas.718466
6. Biçen Çelik, A., Ay, İ., Ergin, Ş., & Dal, M. (2024). Stone deterioratins in Mardin Madrasas: The case of Şehidiye and Kasımiye Madrasas. *Cultural Heritage and Science*, *5*(1), 38–51. https://doi.org/10.58598/cuhes.1441372
7. Dal, M. (2021). The Deterioration Problems Observed in the Natural Building Blocks of Saint George Church in Diyarbakır Province. *Online Journal of Art and Design*, *9*(1), 254–262.
8. Ay, İ., Dal, M., & Ergin, Ş. (2023). Investigation of stone deterioration in Gaziantep Historical Gümrük Inn. *Advanced Engineering Days (AED)*, *8*, 52–55.
9. Öcal, A. D., & Dal, M. (2012). *Doğal Taşlardaki Bozunmalar* (Müka Matba.). İstanbul: Mimarlık Vakfı İktisadi İşletmesi.
10. Biçen Çelik, A., Ergin, Ş., Dal, M., & Ay, İ. (2023). Analyzes of Stone Deterioration on the Facades of the Şehidiye Madrasah in the Central District of Mardin Province. *Uluslararası Doğu Anadolu Fen Mühendislik ve Tasarım Dergisi*, 248–271. https://doi.org/10.47898/ijeased.1342472
11. Ergin, Ş., Dal, M., & Biçen Çelik, A. (2020). Şeyh Çabuk Camii Cephelerinde Görülen Taş Bozunma Sorunlarının İrdelenmesi ve Kimyasal Analizlerinin Karşılaştırılması. In *Mimarlık Üzerine-1* (pp. 103–124). Ankara: IKSAD Yayınevi.
12. Ergin, Ş., Gökdemir, B., Yardımlı, S., & Dal, M. (2022). Deterioration On The Stone Surfaces Of The Diyarbakır Nebi Mosque. *International Refereed Journal of Design And Architecture*, (27), 1–32. https://doi.org/10.17365/TMD.2022.TURKEY.27.01
13. Ay, İ., & Ergin, Ş. (2023). Geleneksel Taş Yapılardaki Alterasyoınlar: Gaziantep Kürkçü Hanı Örneği. In H. Demir Kayan (Ed.), *Mekan/Çevre/Kültür* (pp. 164–178). Ankara: Atlas Akademik.
14. Dal, M., Ergin, Ş., Çelik, A. B., & Ay, İ. (2023). Stone Alterations in Hatuniye Madrasah. In *Advanced Engineering Days (AED)* (Vol. 7, pp. 77–80).

https://publish.mersin.edu.tr/index.php/aed/article/view/1124
15. Dal, M., & Yardımlı, S. (2021). Taş Duvarlarda Yüzey Bozunmaları. *Kent Akademisi*, *14*(2), 428–451. https://doi.org/10.35674/kent.922313
16. Ay, İ., & Ergin, Ş. (2023). Geleneksel Taş Yapılarda Meydana Gelen Bozunmalar: Hakkari Meydan Medresesi Örneği. In A. Biçen (Ed.), *Mimari İncelemeler ve Güncel Yaklaşımlar* (pp. 151–168). Ankara: Atlas Akademik.
17. Çelik, A. B., Ay, İ., Dal, M., & Ergin, Ş. (2023). Stone Alterations in Zinciriye Madrasah. In *Advanced Engineering Days (AED)* (Vol. 7, pp. 89–91). https://publish.mersin.edu.tr/index.php/aed/article/view/1127
18. Ay, İ., Dal, M., Ergin, Ş., & Çelik, A. B. (2023). Stone Alterations in Kasımiye Madrasah. In *Advanced Engineering Days (AED)* (Vol. 7, pp. 81–84). https://publish.mersin.edu.tr/index.php/aed/article/view/1125
19. Dolar, A., & Yardımlı, S. (2017). Tarihi Yapı Taşarlındaki Alg ve Bakteri Alterasyonları. In *Uluslararası Katılımlı 6. Tarihi Yapıların Korunması ve Güçlendirilmesi Sempozyumu* (pp. 143–152).
20. Dal, M., Zülfikar, H. C., & Dolar, A. (2020). Mimari Taş Yapılarda Görülen Biyolojik Bozunmalar. In *Geleneksel ve Çağdaş Mimari Yapılar Üzerine Akademik Çalışmalar* (pp. 29–62). Ankara: İksad Yayınevi.
21. Ergin, Ş., Çelik, A. B., Ay, İ., & Dal, M. (2023). Stone Alterations in Şehidiye Madrasah. In *Advanced Engineering Days (AED)* (Vol. 7, pp. 85–88). https://publish.mersin.edu.tr/index.php/aed/article/view/1126
22. Biçen Çelik, A., Ay, İ., Ergin, Ş., & Dal, M. (2023). Mardin Medreselerinde Görülen Taş Alterasyonları: Şehidiye ve Hatuniye Medreseleri Örneği. *Kültürel Miras Araştırmaları*, *4*(2), 79–90. https://doi.org/10.59127/kulmira.1381600

Advanced Engineering Days

aed.mersin.edu.tr

Investigation of Stone Deterioration in Gaziantep Lala Mustafa Pasha Inn

İlhami Ay [*1], Murat Dal [2], Şefika Ergin [3]

[1]*Hakkari University, Çölemerik Vocational School, Hakkari, Türkiye, ilhamiay@hakkari.edu.tr*
[2]*Munzur University, Faculty of Fine Arts, Design and Architecture, Tunceli, Türkiye muratdal1122@gmail.com*
[3]*Dicle University, Institute of Science and Technology, Diyarbakır, Türkiye, sefika@dicle.edu.tr*

Cite this study: Ay, İ., Dal, M. & Ergin, Ş. (2024). Investigation of Stone Deterioration in Gaziantep Lala Mustafa Pasha Inn. Advanced Engineering Days, 9, 912-915

Keywords
Stone Deterioration
Gaziantep
Lala Mustafa Pasha Inn
Type of Deterioration

Abstract

The high strength value and durability of stone in traditional stone structures are important in terms of transferring traditional structures to future generations. It is important for the structures to determine the deterioration of the stone surfaces exposed to climatic and external factors and to determine the causes and to offer solutions. In this study, the deterioration of the Lala Mustafa Pasha Inn in Gaziantep is discussed. In this context, the deterioration was visually examined, classified and analysed as physical, chemical, biological and anthropogenic. It is aimed that the data obtained from the study will form the basis for the conservation projects to be carried out in the coming years.

Introduction

The protection of traditional stone structures, which are cultural heritage, and taking measures against stone degradation are important in terms of transferring the structures to future years. Natural stones used in traditional stone buildings were used as the main building material of historical buildings until 1800s. When stone materials are exposed to natural climatic conditions and external factors, deterioration occurs on stone surfaces. If appropriate measures are not taken against these deteriorations and solutions are not offered, the structures will face extinction. Accurate detection of deterioration and damages occurring in the structures is important for the survival of the structures [1–3]. Correct diagnosis, correct analysis, correct restoration, periodic maintenance and sustainable protection are required for the transfer of stone structures to future generations [4–6].

Material and Method

In this study, the stone deterioration observed in the Lala Mustafa Pasha Inn located in Gaziantep Şahinbey District was analysed. The deterioration was visually analysed and photographed and recorded. The deterioration on the walls of the Lala Mustaaf Pasha Inn, which was completely demolished and survived as a result of later restorations, was analysed, identified and classified [7, 8]. According to the classification, deterioration is analysed in four groups: physical, chemical, biological and anthropogenic [9, 10].

Results

The deterioration that occurs on the surfaces of historical stone structures, which are cultural heritage, causes deterioration in the physical and petrographic properties of the stone. In some cases, these deteriorations also prepare the environment for another deterioration [11–13]. It is important to determine the degradation of natural stones, to investigate the causes, to develop solution proposals and to take measures against degradation

in order to transfer the structures to future generations [14–16]. In this context, in this study, stone deterioration in Gaziantep Lala Mustafa Pasha Inn was examined, classified and analysed. The deterioration was classified and analysed as physical, chemical, biological and anthropogenic deterioration.

Changes occur in the properties of stone as a result of internal and external factors. Surface losses that occur on stone surfaces as a result of these changes are called physical deterioration. Fractures, cracks, abrasion and joint losses on stone surfaces are examples of physical deterioration. The physical deterioration observed in Lala Mustafa Pasha Inn is shown in Figure 1.

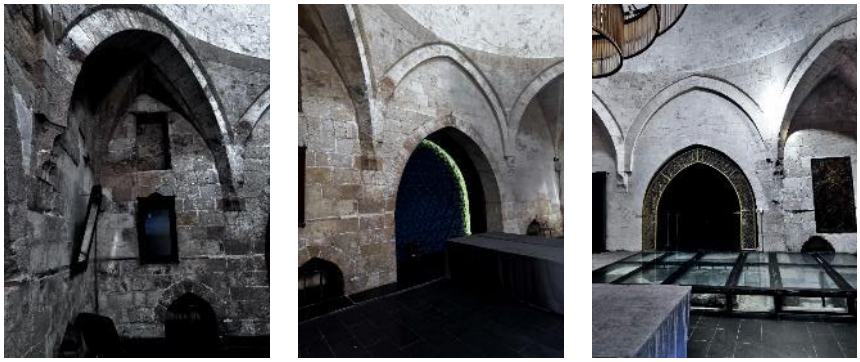


Figure 1. Physical deteriorations in Lala Mustafa Pasha Inn

The degradation that occurs on the stone surface due to the climate, temperature and humidity factors of the region is called chemical degradation. Effects such as colour changes, salting and foliation on stone surfaces are examples of chemical deterioration [17, 18]. The chemical deterioration that occurred in Gaziantep Lala Mustafa Pasha Inn is shown in Figure 2.



Figure 2. Chemical deteriorations in Lala Mustafa Pasha Inn

The degradation that occurs on the stone surfaces of traditional stone structures as a result of the reactions of biological substances on the stone surface is called biological degradation. Algae and moss formation, plant formations and accumulations on stone surfaces are examples of biological degradation [19, 20]. Biological degradation in Gaziantep Lala Mustafa Pasha Inn is shown in Figure 3.



Figure 3. Biological deteriorations in Lala Mustafa Pasha Inn

Anthropogenic deterioration is a type of deterioration that occurs as a result of conscious or unconscious damage to traditional stone structures by humans [21, 22]. Misuse, neglect, wear and tear and inappropriate

restoration practices are examples of anthropogenic deterioration. The anthropogenic deterioration that occurred in Lala Mustafa Pasha Inn is shown in Figure 4.



Figure 4. Anthropogenic deteriorations in Lala Mustafa Pasha Inn

Conclusion

This study focuses on the deterioration observed in Gaziantep Lala Mustafa Pasha Inn. The deterioration was detected by visual analysis and categorised and analysed. Physical, chemical, biological and anthropogenic deterioration were observed.

The data obtained in the study is intended to form the basis for both academic studies and future restoration projects. In addition, this study is also important in terms of taking the necessary measures to ensure that traditional stone structures survive for a longer period of time.

References

1. Ay, İ., Ergin, Ş., & Dal, M. (2023). Geleneksel Taş Yapılarda Meydana Gelen Taş Alterasyonları: Gaziantep Hamam Müzesi Örneği (pp. 515–523). IKSAD Yayınevi.
2. Ay, İ., Ergin, Ş., & Dal, M. (2023). Geleneksel Taş Yapılarda Meydana Gelen Taş Alterasyonları: Gaziantep Millet Hanı Örneği. In *UMTEB - XIII International Scientific Research Congress* (pp. 507–514). IKSAD Yayınevi.
3. Ay, İ., Dal, M., & Ergin, Ş. (2023). Investigation of stone deterioration in Gaziantep Kumandan Fountain. *Advanced Engineering Days (AED)*, *8*, 56–59.
4. Biçen Çelik, A., Ergin, Ş., Dal, M., & Ay, İ. (2023). Analysis of Stone Deterioration on the Facades of Hatuniye Madrasah. *Journal of Architectural Sciences and Applications*, *8*(1), 355–369. https://doi.org/10.30785/mbud.1302007
5. Tokmak, M., & Dal, M. (2020). Classification of Physical, Chemical and Biological Deteriorations Observed in Ankara Stone Monuments. *International Journal of Pure and Applied Sciences*, *6*(1). https://doi.org/10.29132/ijpas.718466
6. Biçen Çelik, A., Ay, İ., Ergin, Ş., & Dal, M. (2024). Stone deterioratins in Mardin Madrasas: The case of Şehidiye and Kasımiye Madrasas. *Cultural Heritage and Science*, *5*(1), 38–51. https://doi.org/10.58598/cuhes.1441372
7. Dal, M. (2021). The Deterioration Problems Observed in the Natural Building Blocks of Saint George Church in Diyarbakır Province. *Online Journal of Art and Design*, *9*(1), 254–262.
8. Ay, İ., Dal, M., & Ergin, Ş. (2023). Investigation of stone deterioration in Gaziantep Historical Gümrük Inn. *Advanced Engineering Days (AED)*, *8*, 52–55.
9. Öcal, A. D., & Dal, M. (2012). *Doğal Taşlardaki Bozunmalar* (Müka Matba.). İstanbul: Mimarlık Vakfı İktisadi İşletmesi.
10. Biçen Çelik, A., Ergin, Ş., Dal, M., & Ay, İ. (2023). Analyzes of Stone Deterioration on the Facades of the Şehidiye Madrasah in the Central District of Mardin Province. *Uluslararası Doğu Anadolu Fen Mühendislik ve Tasarım Dergisi*, 248–271. https://doi.org/10.47898/ijeased.1342472
11. Ergin, Ş., Dal, M., & Biçen Çelik, A. (2020). Şeyh Çabuk Camii Cephelerinde Görülen Taş Bozunma Sorunlarının İrdelenmesi ve Kimyasal Analizlerinin Karşılaştırılması. In *Mimarlık Üzerine-1* (pp. 103–124). Ankara: IKSAD Yayınevi.
12. Ergin, Ş., Gökdemir, B., Yardımlı, S., & Dal, M. (2022). Deterioration On The Stone Surfaces Of The Diyarbakır Nebi Mosque. *International Refereed Journal of Design And Architecture*, (27), 1–32. https://doi.org/10.17365/TMD.2022.TURKEY.27.01
13. Ay, İ., & Ergin, Ş. (2023). Geleneksel Taş Yapılardaki Alterasyoınlar: Gaziantep Kürkçü Hanı Örneği. In H. Demir Kayan (Ed.), *Mekan/Çevre/Kültür* (pp. 164–178). Ankara: Atlas Akademik.
14. Dal, M., Ergin, Ş., Çelik, A. B., & Ay, İ. (2023). Stone Alterations in Hatuniye Madrasah. In *Advanced Engineering Days (AED)* (Vol. 7, pp. 77–80). https://publish.mersin.edu.tr/index.php/aed/article/view/1124

15. Dal, M., & Yardımlı, S. (2021). Taş Duvarlarda Yüzey Bozunmaları. *Kent Akademisi*, *14*(2), 428–451. https://doi.org/10.35674/kent.922313
16. Ay, İ., & Ergin, Ş. (2023). Geleneksel Taş Yapılarda Meydana Gelen Bozunmalar: Hakkari Meydan Medresesi Örneği. In A. Biçen (Ed.), *Mimari İncelemeler ve Güncel Yaklaşımlar* (pp. 151–168). Ankara: Atlas Akademik.
17. Çelik, A. B., Ay, İ., Dal, M., & Ergin, Ş. (2023). Stone Alterations in Zinciriye Madrasah. In *Advanced Engineering Days (AED)* (Vol. 7, pp. 89–91). https://publish.mersin.edu.tr/index.php/aed/article/view/1127
18. Ay, İ., Dal, M., Ergin, Ş., & Çelik, A. B. (2023). Stone Alterations in Kasımiye Madrasah. In *Advanced Engineering Days (AED)* (Vol. 7, pp. 81–84). https://publish.mersin.edu.tr/index.php/aed/article/view/1125
19. Dolar, A., & Yardımlı, S. (2017). Tarihi Yapı Taşarlındaki Alg ve Bakteri Alterasyonları. In *Uluslararası Katılımlı 6. Tarihi Yapıların Korunması ve Güçlendirilmesi Sempozyumu* (pp. 143–152).
20. Dal, M., Zülfikar, H. C., & Dolar, A. (2020). Mimari Taş Yapılarda Görülen Biyolojik Bozunmalar. In *Geleneksel ve Çağdaş Mimari Yapılar Üzerine Akademik Çalışmalar* (pp. 29–62). Ankara: İksad Yayınevi.
21. Ergin, Ş., Çelik, A. B., Ay, İ., & Dal, M. (2023). Stone Alterations in Şehidiye Madrasah. In *Advanced Engineering Days (AED)* (Vol. 7, pp. 85–88). https://publish.mersin.edu.tr/index.php/aed/article/view/1126
22. Biçen Çelik, A., Ay, İ., Ergin, Ş., & Dal, M. (2023). Mardin Medreselerinde Görülen Taş Alterasyonları: Şehidiye ve Hatuniye Medreseleri Örneği. *Kültürel Miras Araştırmaları*, *4*(2), 79–90. https://doi.org/10.59127/kulmira.1381600

Advanced Engineering Days

aed.mersin.edu.tr

Investigation of Stone Deterioration in Gaziantep Tabakhane Bridge

İlhami Ay [*1], Şefika Ergin[2], Murat Dal[3]

[1]*Hakkari University, Çölemerik Vocational School, Hakkari, Türkiye, ilhamiay@hakkari.edu.tr*
[2]*Dicle University, Institute of Science and Technology, Diyarbakır, Türkiye, sefika@dicle.edu.tr*
[3]*Munzur University, Faculty of Fine Arts, Design and Architecture, Tunceli, Türkiye muratdal1122@gmail.com*

Cite this study: Ay, İ., Ergin, Ş. & Dal, M. (2024). Investigation of Stone Deterioration in Gaziantep Tabakhane Bridge. Advanced Engineering Days, 9, 916-918

Keywords
Stone Deterioration
Gaziantep
Tabakhane Bridge
Type of Deterioration

Abstract

In traditional stone structures, the strength value and durability of the stone are important in terms of transferring the structure to future generations. It is important for the structures to determine the deterioration and causes of the deterioration on the surface of the stone as a result of climatic and external factors and to offer solutions. In this study, the deterioration of the Tabakhane Bridge in Gaziantep is discussed. In this context, the deterioration was visually examined, classified and analyzed as physical, chemical, biological and anthropogenic. It is aimed that the data obtained from the study will be the basis for the conservation projects to be carried out in the coming years.

Introduction

The protection of traditional stone structures, which are cultural heritage, and taking measures against degradation are important in terms of transferring the structures to future years. Natural stones used in traditional buildings were used as the main construction material until 1800s. When stone materials are exposed to natural climatic conditions and external factors, degradation occurs on stone surfaces. If appropriate measures are not taken and solutions are not offered for these deteriorations, the buildings will face extinction. Accurate detection of deterioration and damage to the structures is important for the survival of the structures [1-2]. Correct diagnosis, correct analysis, correct restoration, periodic maintenance and sustainable protection are required for the transfer of stone structures to future generations [3-4].

Material and Method

In this study, the stone deterioration of the Tabakhane Bridge located in Çakmak Neighborhood of Gaziantep Şahinbey District was examined. The deterioration was visually analyzed and recorded by photography. The stone bridge, which has a single span with pointed arches, was built entirely with cut stone. Concrete was poured on the upper part and a road was built for pedestrians to walk. There is no additional ornamentation on the bridge. The deterioration on the walls of the Tabakhane Bridge was analyzed, identified and classified [5]. According to the classification, deterioration is analyzed in four groups: physical, chemical, biological and anthropogenic [6].

Results

The degradation on the surfaces of stone structures, which are cultural heritage, causes deterioration in the physical and petrographic properties of the stone. In some cases, these degradations also prepare the environment for another degradation [7-8]. Determining the degradation of natural stones, developing solution

proposals and taking measures against degradation are important for the transfer of structures to future generations [9-10]. In this context, in this study, the deterioration of Gaziantep Tabakhane Bridge was examined, classified and analyzed. The deterioration was analyzed by classifying them as physical, chemical, biological and anthropogenic deterioration.

Surface losses on stone surfaces as a result of changes in the petrographic and mechanical properties of the stone as a result of internal and external factors are called physical degradation. Deterioration such as fractures, cracks, abrasion and joint losses on stone surfaces are examples of physical deterioration types [11]. The physical deterioration observed at Tabakhane Bridge is shown in Figure 1.



Figure 1. Physical deteriorations in Tabakhane Bridge

The degradation on the stone surface due to climatic factors, temperature and humidity is called chemical degradation. Effects such as color changes, salinization and foliation on stone surfaces are examples of chemical degradation types [12]. Chemical deterioration in Gaziantep Tabakhane Bridge is shown in Figure 2.



Figure 2. Chemical deteriorations in Tabakhane Bridge

The degradation that occurs on the stone surface as a result of the reactions of biological substances on the stone surfaces in traditional buildings is called biological degradation. The formation of algae and mosses on stone surfaces, plant formations and accumulations are examples of biological degradation types [13-14]. The biological degradation at Tabakhane Bridge is shown in Figure 3.



Figure 3. Biological deteriorations in Tabakhane Bridge

Anthropogenic degradation is the degradation that occurs as a result of conscious or unconscious damage to traditional stone structures by humans [15]. Misuse, neglect, wear and tear and improper restoration practices

are examples of anthropogenic deterioration. Anthropogenic deterioration of Tabakhane Bridge is shown in Figure 4.



Figure 4. Anthropogenic deteriorations in Tabakhane Bridge

Conclusion

This study focuses on the deterioration observed on the Gaziantep Tabakhane Bridge. The deterioration was identified by visual analysis and categorized and analyzed. Physical, chemical, biological and anthropogenic deterioration were observed.

The data obtained in the study is intended to form a basis for both academic studies and future restoration projects. In addition, this study is important in terms of taking the necessary measures to ensure the survival of traditional stone buildings for a longer period of time.

References

1. Ay, İ., Ergin, Ş., & Dal, M. (2023a). *Geleneksel Taş Yapılarda Meydana Gelen Taş Alterasyonları: Gaziantep Hamam Müzesi Örneği*. UMTEB - XIII International Scientific Research Congress, 515–523.
2. Ay, İ., Ergin, Ş., & Dal, M. (2023b). *Geleneksel Taş Yapılarda Meydana Gelen taş Alterasyonları: Gaziantep Millet Hanı Örneği*. UMTEB - XIII International Scientific Research Congress, 507–514.
3. Biçen Çelik, A., Ergin, Ş., Dal, M., & Ay, İ. (2023). Analysis of Stone Deterioration on the Facades of Hatuniye Madrasah. *Journal of Architectural Sciences and Applications*, *8*(1), Article 1. https://doi.org/10.30785/mbud.1302007
4. Tokmak, M., & Dal, M. (2020). Classification of Physical, Chemical and Biological Deteriorations Observed in Ankara Stone Monuments. *International Journal of Pure and Applied Sciences*, *6*(1), 8–16. https://doi.org/10.29132/ijpas.718466
5. Dal, M. (2021). The Deterioration Problems Observed in the Natural Building Blocks of Saint George Church in Diyarbakır Province. *Online Journal of Art and Design*, *9*(1), 254–262.
6. Öcal, A. D., & Dal, M. (2012). *Doğal Taşlardaki Bozunmalar* (Müka Matbaası). Mimarlık Vakfı İktisadi İşletmesi.
7. Ergin, Ş., Dal, M., & Çelik, A. (2020). Şeyh Çabuk Camii Cephelerinde Görülen Taş Bozunma Sorunlarının İrdelenmesi ve Kimyasal Analizlerinin Karşılaştırılması. In *Mimarlık Üzerine-1* (pp. 103–124). IKSAD Yayınevi.
8. Ergin, Ş., Gökdemir, B., Yardımlı, S., & Dal, M. (2022). Deterioration On The Stone Surfaces Of The Diyarbakır Nebi Mosque. *International Refereed Journal of Design And Architecture*, *27*, 1–32. https://doi.org/10.17365/TMD.2022.TURKEY.27.01
9. Dal, M., Ergin, Ş., Çelik, A. B., & Ay, İ. (2023). Stone Alterations in Hatuniye Madrasah. *Advanced Engineering Days (AED)*, *7*, 77–80.
10. Dal, M., & Yardımlı, S. (2021). Taş Duvarlarda Yüzey Bozunmaları. *Kent Akademisi*, *14*(2), 428–451. https://doi.org/10.35674/kent.922313
11. Ay, İ., Dal, M., Ergin, Ş., & Çelik, A. B. (2023). Stone Alterations in Kasımiye Madrasah. *Advanced Engineering Days (AED)*, *7*, 81–84.
12. Çelik, A. B., Ay, İ., Dal, M., & Ergin, Ş. (2023). Stone Alterations in Zinciriye Madrasah. *Advanced Engineering Days (AED)*, *7*, 89–91.
13. Dal, M., Zülfikar, H. C., & Dolar, A. (2020). Mimari Taş Yapılarda Görülen Biyolojik Bozunmalar. In *Geleneksel ve Çağdaş Mimari Yapılar Üzerine Akademik Çalışmalar* (pp. 29–62). İksad Yayınevi.
14. Dolar, A., & Yardımlı, S. (2017). Tarihi Yapı Taşarlındaki Alg ve Bakteri Alterasyonları. *Uluslararası Katılımlı 6. Tarihi Yapıların Korunması ve Güçlendirilmesi Sempozyumu*, 143–152.
15. Ergin, Ş., Çelik, A. B., Ay, İ., & Dal, M. (2023). Stone Alterations in Şehidiye Madrasah. *Advanced Engineering Days (AED)*, *7*, 85–88.

Advanced Engineering Days

aed.mersin.edu.tr

Investigation of Stone Deterioration in Gaziantep Balıklı Masjid

İlhami Ay [*1], Şefika Ergin[2], Murat Dal[3]

[1]*Hakkari University, Çölemerik Vocational School, Hakkari, Türkiye, ilhamiay@hakkari.edu.tr*
[2]*Dicle University, Institute of Science and Technology, Diyarbakır, Türkiye, sefika@dicle.edu.tr*
[3]*Munzur University, Faculty of Fine Arts, Design and Architecture, Tunceli, Türkiye muratdal1122@gmail.com*

Cite this study: Ay, İ., Ergin, Ş. & Dal, M. (2024). Investigation of Stone Deterioration in Gaziantep Balıklı Masjid. Advanced Engineering Days, 9, 919-922

Keywords
Stone Deterioration
Gaziantep
Balıklı Masjid
Type of Deterioration

Abstract

In traditional stone structures, the strength value and durability of the stone are important in terms of transferring the structure to future generations. It is important for the structures to determine the deterioration and causes of the deterioration on the surface of the stone as a result of climatic and external factors and to offer solutions. In this study, the deterioration of the Balıklı Masjid in Gaziantep is discussed. In this context, the deterioration was visually examined, classified and analyzed as physical, chemical, biological and anthropogenic. It is aimed that the data obtained from the study will be the basis for the conservation projects to be carried out in the coming years.

Introduction

Natural stones used in traditional stone structures are one of the main construction materials that have been used in architectural structures for many years and are effective in making the structures permanent. When we look at the usage areas of natural stones, it is also used in the fields of decorative art besides building materials [1-2]. Natural stones, especially depending on climate and time, degradation occurs on stone surfaces. Due to these degradations, the durability of the stones decreases [3-4]. Detecting these deteriorations in the structures and taking the correct measures is important for the permanence of the structures [5-6]. It is important to diagnose and analyze the deterioration correctly for the permanence of cultural heritage historical buildings and for the buildings to survive longer [7-8].

Material and Method

In this study, the stone deterioration of Balıklı Masjid in Çukur Neighborhood of Gaziantep Şahinbey district was examined. The deterioration was analyzed by visual analysis method and recorded by photography method. The upper part of the masjid structure, which has a rectangular plan close to the square, is covered with a dome. The transitions to the dome are provided with pandandif. There is not much ornamentation in the building. The ornament is only on the mihrab. The deterioration on the walls of Balıklı Masjid, which was built with white cut stone, was examined, identified and classified [9]. According to the classification, deterioration is analyzed in four groups: physical, chemical, biological and anthropogenic [3, 10].

Results

As a result of the deterioration of the stone surfaces of traditional historical buildings, changes occur in the physical and petrographic properties of the stone. These deteriorations on the surfaces may also prepare the environment for another deterioration [11-12]. In this study, the deterioration that occurred in Balıklı Masjid

was determined and analyzed by classifying the deterioration in order to take measures against deterioration. The degradation of the structure was analyzed by classifying them as physical, chemical, biological and anthropogenic degradation.

The disintegration or crumbling of natural stones as a result of the weakening of the bonds between them without any change in the minerals that make up the natural stones is called physical degradation [13-14]. Physical deterioration is observed more as a result of high temperature difference, salt, ice and root cracking. Deterioration such as fractures, cracks, abrasion and joint losses on stone surfaces are examples of physical deterioration types. The physical deterioration observed at Balıklı Masjid is shown in Figure 1.



Figure 1. Physical deteriorations in Balıklı Masjid

The degradation that occurs on the surface of the stone as a result of the minerals that make up the natural stone entering into chemical reactions with different substances is called chemical degradation. As a result of the chemical reaction of the stones, the stone loses its strength. Effects such as color changes, salinization and foliation on stone surfaces are examples of chemical deterioration [15]. Chemical deterioration in Gaziantep Balıklı Masjid is shown in Figure 2.



Figure 2. Chemical deteriorations in Balıklı Masjid

The degradation that occurs on the stone surface as a result of the reactions of biological substances on the stone surfaces in traditional buildings is called biological degradation. The formation of algae and mosses on stone surfaces, plant formations and accumulations are examples of biological degradation types [16-17]. The biological degradation at Balıklı Masjid is shown in Figure 3.



Figure 3. Biological deteriorations in Balıklı Masjid

Anthropogenic deterioration is the type of deterioration that occurs in traditional stone structures as a result of human damage to the structure. Misuse, neglect, wear and tear and inappropriate restoration practices are examples of anthropogenic deterioration. Anthropogenic deterioration in Balıklı Masjid is shown in Figure 4.



Figure 4. Anthropogenic deteriorations in Balıklı Masjid

Conclusion

This study focuses on the deterioration observed on the Gaziantep Balıklı Masjid. The deterioration was identified by visual analysis and categorized and analyzed. Physical, chemical, biological and anthropogenic deterioration were observed.

The data obtained in the study is intended to form a basis for both academic studies and future restoration projects. In addition, this study is important in terms of taking the necessary measures to ensure the survival of traditional stone buildings for a longer period of time.

References

1. Ergin, Ş., Karahan, B., & Dal, M. (2021). Sultan Hamza-i Kebir Camii'nde Görülen Taş Bozunmaları. *Kent Akademisi*, *14*(2), 414–427. https://doi.org/10.35674/kent.931428
2. Hasbay, U., & Hattap, S. (2017). Doğal Taşlardaki Bozunma (Ayrışma) Türleri ve Nedenleri. *Bilim ve Gençlik Dergisi*, *5*(1), 23–45.
3. Öcal, A. D., & Dal, M. (2012). *Doğal Taşlardaki Bozunmalar* (Müka Matbaası). Mimarlık Vakfı İktisadi İşletmesi.
4. Kuloğlu Yüksel, F. Ş., & Güven, N. (2020). Şanlıurfa'da Bulunan Harran Kalesi'nin Taşlarında Meydana Gelen Bozunmaların Tespiti. *Harran Üniversitesi Mühendislik Dergisi*, *5*(3), 247–259.
5. Biçen Çelik, A., Ergin, Ş., Dal, M., & Ay, İ. (2023). Analysis of Stone Deterioration on the Facades of Hatuniye Madrasah. *Journal of Architectural Sciences and Applications*, *8*(1), Article 1. https://doi.org/10.30785/mbud.1302007
6. Dal, M., Ergin, Ş., Çelik, A. B., & Ay, İ. (2023). Stone Alterations in Hatuniye Madrasah. *Advanced Engineering Days (AED)*, *7*, 77–80.
7. Ay, İ., Dal, M., Ergin, Ş., & Çelik, A. B. (2023). Stone Alterations in Kasımiye Madrasah. *Advanced Engineering Days (AED)*, *7*, 81–84.
8. Ay, İ., Ergin, Ş., & Dal, M. (2023). Geleneksel Taş Yapılarda Meydana Gelen Taş Alterasyonları: Gaziantep Hamam Müzesi Örneği. *UMTEB - XIII International Scientific Research Congress*, 515–523.
9. Dal, M. (2021). The Deterioration Problems Observed in the Natural Building Blocks of Saint George Church in Diyarbakır Province. *Online Journal of Art and Design*, *9*(1), 254–262.
10. Çelik, A. B., Ay, İ., Dal, M., & Ergin, Ş. (2023). Stone Alterations in Zinciriye Madrasah. *Advanced Engineering Days (AED)*, *7*, 89–91.
11. Ergin, Ş., Dal, M., & Çelik, A. (2020). Şeyh Çabuk Camii Cephelerinde Görülen Taş Bozunma Sorunlarının İrdelenmesi ve Kimyasal Analizlerinin Karşılaştırılması. In *Mimarlık Üzerine-1* (pp. 103–124). IKSAD Yayınevi.
12. Ergin, Ş., Gökdemir, B., Yardımlı, S., & Dal, M. (2022). Deterioration On The Stone Surfaces Of The Diyarbakır Nebi Mosque. *International Refereed Journal of Design And Architecture*, *27*, 1–32. https://doi.org/10.17365/TMD.2022.TURKEY.27.01
13. Dal, M., Yalçin, M., & Öcal, A. D. (2016). Gazimağusa Kaleiçindeki Tarihi Taş Yapılarda Görülen Bozunmalar. *Çukurova Üniversitesi Mühendislik-Mimarlık Fakültesi Dergisi*, *31*(2), 355–364. https://doi.org/10.21605/cukurovaummfd.310316
14. Ergin, Ş., Çelik, A. B., Ay, İ., & Dal, M. (2023). Stone Alterations in Şehidiye Madrasah. *Advanced Engineering Days (AED)*, *7*, 85–88.
15. Ay, İ., Ergin, Ş., & Dal, M. (2023). Geleneksel Taş Yapılarda Meydana Gelen Taş Alterasyonları: Gaziantep Millet Hanı Örneği. *UMTEB - XIII International Scientific Research Congress*, 507–514.

16. Dal, M., Zülfikar, H. C., & Dolar, A. (2020). Mimari Taş Yapılarda Görülen Biyolojik Bozunmalar. In *Geleneksel ve Çağdaş Mimari Yapılar Üzerine Akademik Çalışmalar* (pp. 29–62). İksad Yayınevi.
17. Dolar, A., & Yardımlı, S. (2017). Tarihi Yapı Taşarlındaki Alg ve Bakteri Alterasyonları. *Uluslararası Katılımlı 6. Tarihi Yapıların Korunması ve Güçlendirilmesi Sempozyumu*, 143–152.

Advanced Engineering Days

aed.mersin.edu.tr

Investigation of Stone Deterioration in Gaziantep Köseç Ahmet Ağa Fountain

İlhami Ay *[1], **Şefika Ergin**[2], **Murat Dal**[3]

[1]*Hakkari University, Çölemerik Vocational School, Hakkari, Türkiye, ilhamiay@hakkari.edu.tr*
[2]*Dicle University, Institute of Science and Technology, Diyarbakır, Türkiye, sefika@dicle.edu.tr*
[3]*Munzur University, Faculty of Fine Arts, Design and Architecture, Tunceli, Türkiye muratdal1122@gmail.com*

Cite this study: Ay, İ., Ergin, Ş. & Dal, M. (2024). Investigation of Stone Deterioration in Gaziantep Köseç Ahmet Ağa Fountain. Advanced Engineering Days, 9, 923-926

Keywords
Stone Deterioration
Gaziantep
Köseç Ahmet Ağa Fountain
Type of Deterioration

Abstract

In traditional stone structures, the strength value and durability of the stone are important in terms of transferring the structure to future generations. It is important for the structures to determine the deterioration and causes of the deterioration on the surface of the stone as a result of climatic and external factors and to offer solutions. In this study, the deterioration of the Köseç Ahmet Ağa Fountain in Gaziantep is discussed. In this context, the deterioration was visually examined, classified and analyzed as physical, chemical, biological and anthropogenic. It is aimed that the data obtained from the study will be the basis for the conservation projects to be carried out in the coming years.

Introduction

Natural stones used in stone structures, which are cultural heritage, have been used in buildings for many years and are one of the main construction materials that are effective in making the structures permanent. Natural stones are preferred in ornamental areas other than columns, flooring and facade elements [1-2]. Natural stones, depending on climate and time, degradation occurs on stone surfaces and these degradations cause the durability of the stone to decrease [3-4]. Correctly detecting the deterioration of the structures and taking precautions is important for the permanence of the structures [5-6].It is important to analyze the deterioration correctly in order for the structures to survive longer [7-8].

Material and Method

In this study, the stone deterioration of Köseç Ahmet Ağa Fountain located in İsmetpaşa Neighborhood of Gaziantep Şahinbey district was examined. The deteriorations were visually analyzed and documented by photographs. The ornamentation in the building is provided by the stones used on the facade. The deterioration on the walls of Köseç Ahmet Ağa Fountain, which was built with black and white cut stone, was analyzed, identified and classified [9]. According to the classification, deterioration is analyzed in four groups: physical, chemical, biological and anthropogenic [3, 10].

Results

The deterioration that occurs on the stone surfaces of stone structures, which are cultural heritage, changes the properties of the stone, as well as preparing the environment for different degradation and increasing the degradation process [11-13]. In this study, the deterioration of Köseç Ahmet Ağa Fountain in Gaziantep was

examined, classified and analyzed. As a result of the examination, the deterioration in the structure was analyzed by dividing into groups as physical, chemical, biological and anthropogenic deterioration.

Physical degradation is the degradation that occurs in natural stones as a result of the weakening of the bonds between the stones as a result of fragmentation, breaking or crumbling of the stones [14-15]. Physical degradation in natural stones is mostly caused by high temperature difference, salt, ice and root cracking. Degradation such as fracture, cracking, abrasion, joint discharges are examples of physical degradation. The physical deterioration observed at Köseç Ahmet Ağa Fountain is shown in Figure 1.



Figure 1. Physical deteriorations in Köseç Ahmet Ağa Fountain

The degradation that occurs on stone surfaces as a result of the reaction of the minerals that make up natural stones with the substances in the stone is called chemical degradation. Effects such as color changes, salinization and foliation on stone surfaces are examples of chemical deterioration [16]. The chemical deterioration in Gaziantep Köseç Ahmet Ağa Fountain is shown in Figure 2.



Figure 2. Chemical deteriorations in Köseç Ahmet Ağa Fountain

The degradation of the stone surface as a result of the reactions of biological substances on the surfaces of traditional stone structures is called biological degradation. Algae and moss formation, plant growth and accumulation on stone surfaces are examples of biodegradation [16-17]. The biological degradation at Köseç Ahmet Ağa Fountain is shown in Figure 3.



Figure 3. Biological deteriorations in Köseç Ahmet Ağa Fountain

Anthropogenic deterioration is the type of deterioration that occurs in traditional stone structures as a result of human damage to the structure. Misuse, neglect, wear and tear and inappropriate restoration practices are examples of anthropogenic deterioration. Anthropogenic deterioration in Köseç Ahmet Ağa Fountain is shown in Figure 4.



Figure 4. Anthropogenic deteriorations in Köseç Ahmet Ağa Fountain

Conclusion

This study focuses on the deterioration observed on the Gaziantep Köseç Ahmet Ağa Fountain. The deterioration was identified by visual analysis and categorized and analyzed. Physical, chemical, biological and anthropogenic deterioration were observed.

The data obtained in the study is intended to form a basis for both academic studies and future restoration projects. In addition, this study is important in terms of taking the necessary measures to ensure the survival of traditional stone buildings for a longer period of time.

References

1. Ergin, Ş., Karahan, B., & Dal, M. (2021). Sultan Hamza-i Kebir Camii'nde Görülen Taş Bozunmaları. *Kent Akademisi*, *14*(2), 414–427. https://doi.org/10.35674/kent.931428
2. Hasbay, U., & Hattap, S. (2017). Doğal Taşlardaki Bozunma (Ayrışma) Türleri ve Nedenleri. *Bilim ve Gençlik Dergisi*, *5*(1), 23–45.
3. Öcal, A. D., & Dal, M. (2012). *Doğal Taşlardaki Bozunmalar* (Müka Matbaası). Mimarlık Vakfı İktisadi İşletmesi.
4. Kuloğlu Yüksel, F. Ş., & Güven, N. (2020). Şanlıurfa'da Bulunan Harran Kalesi'nin Taşlarında Meydana Gelen Bozunmaların Tespiti. *Harran Üniversitesi Mühendislik Dergisi*, *5*(3), 247–259.
5. Biçen Çelik, A., Ergin, Ş., Dal, M., & Ay, İ. (2023). Analysis of Stone Deterioration on the Facades of Hatuniye Madrasah. *Journal of Architectural Sciences and Applications*, *8*(1), Article 1. https://doi.org/10.30785/mbud.1302007
6. Dal, M., Ergin, Ş., Çelik, A. B., & Ay, İ. (2023). Stone Alterations in Hatuniye Madrasah. *Advanced Engineering Days (AED)*, *7*, 77–80.
7. Ay, İ., Dal, M., Ergin, Ş., & Çelik, A. B. (2023). Stone Alterations in Kasımiye Madrasah. *Advanced Engineering Days (AED)*, *7*, 81–84.
8. Ay, İ., Ergin, Ş., & Dal, M. (2023). Geleneksel Taş Yapılarda Meydana Gelen Taş Alterasyonları: Gaziantep Hamam Müzesi Örneği. *UMTEB - XIII International Scientific Research Congress*, 515–523.
9. Dal, M. (2021). The Deterioration Problems Observed in the Natural Building Blocks of Saint George Church in Diyarbakır Province. *Online Journal of Art and Design*, *9*(1), 254–262.
10. Çelik, A. B., Ay, İ., Dal, M., & Ergin, Ş. (2023). Stone Alterations in Zinciriye Madrasah. *Advanced Engineering Days (AED)*, *7*, 89–91.
11. Dal, M., & Yardımlı, S. (2021). Taş Duvarlarda Yüzey Bozunmaları. *Kent Akademisi*, *14*(2), 428–451. https://doi.org/10.35674/kent.922313
12. Ergin, Ş., Dal, M., & Çelik, A. (2020). Şeyh Çabuk Camii Cephelerinde Görülen Taş Bozunma Sorunlarının İrdelenmesi ve Kimyasal Analizlerinin Karşılaştırılması. In *Mimarlık Üzerine-1* (pp. 103–124). IKSAD Yayınevi.
13. Ergin, Ş., Gökdemir, B., Yardımlı, S., & Dal, M. (2022). Deterioration On The Stone Surfaces Of The Diyarbakır Nebi Mosque. *International Refereed Journal of Design And Architecture*, *27*, 1–32. https://doi.org/10.17365/TMD.2022.TURKEY.27.01
14. Dal, M., Yalçin, M., & Öcal, A. D. (2016). Gazimağusa Kaleiçindeki Tarihi Taş Yapılarda Görülen Bozunmalar. *Çukurova Üniversitesi Mühendislik-Mimarlık Fakültesi Dergisi*, *31*(2), 355–364. https://doi.org/10.21605/cukurovaummfd.310316

15. Ergin, Ş., Çelik, A. B., Ay, İ., & Dal, M. (2023). Stone Alterations in Şehidiye Madrasah. *Advanced Engineering Days (AED)*, *7*, 85–88.
16. Ay, İ., Ergin, Ş., & Dal, M. (2023). Geleneksel Taş Yapılarda Meydana Gelen Taş Alterasyonları: Gaziantep Millet Hanı Örneği. *UMTEB - XIII International Scientific Research Congress*, 507–514.
17. Dal, M., Zülfikar, H. C., & Dolar, A. (2020). Mimari Taş Yapılarda Görülen Biyolojik Bozunmalar. In *Geleneksel ve Çağdaş Mimari Yapılar Üzerine Akademik Çalışmalar* (pp. 29–62). İksad Yayınevi.
18. Dolar, A., & Yardımlı, S. (2017). Tarihi Yapı Taşarlındaki Alg ve Bakteri Alterasyonları. *Uluslararası Katılımlı 6. Tarihi Yapıların Korunması ve Güçlendirilmesi Sempozyumu*, 143–152.

Advanced Engineering Days

aed.mersin.edu.tr

Data-driven Energy Management of H-MGs using Fuzzy Reinforcement Learning

Azam Salari [1], Mahdi Zeinali [*2], Mousa Marzband [3]

[1] *Sahand University of Technology, Electrical Engineering, Iran, Salari.azam90@gmail.com*
[2] *Sahand University of Technology, Electrical Engineering, Iran, zeinali@sut.ac.ir*
[3] *Islamic Azad University of Lahijan, Electrical Engineering, Iran, mousa.marzband@gamil.com*

Cite this study: Salari, A., Zeinali, M., & Marzband, M. (2024). Data-driven Energy Management of H-MGs using Fuzzy Reinforcement Learning. Advanced Engineering Days, 9, 927-929

Keywords
Reinforcement Learning
PEV Management
Renewable Energy Source
Electricity Market Pricing
Real Time EMS

Abstract

The increasing popularity of plug-in electric vehicles and the growing use of renewable energy sources have paved the way for advanced energy management systems (EMSs) that optimize energy use and distribution in home microgrids (H-MGs). This study focuses on energy management in H-MGs using an EMS and analyzes its impact on electric power grids. The results show that an efficient EMS can increase the overall efficiency of H-MGs by intelligently scheduling combined heat and power and gas boiler, maximizing the use of locally generated renewable energy, and utilizing plug-in electric vehicle energy during peak hours. In this research, it is shown that a cooperative multi-agent EMS system managed by a continuous and real-time fuzzy Q-learning method can decrease the utilization of neutral gas and electricity by 17% and 21%, and the consumption of electrical loads by 0.9% and thermal loads by 24%, Compared to the fuzzy logic control method. The electricity market price can be reduced by 18%.

Introduction

Central energy management means energy management at the central level of an organization or system. This approach requires the coordination of different parts of the organization and advanced technologies in energy management [1]. Distributed energy management means energy control and management at a local and more detailed level instead of centralized management. This method enables end users and distributed energy resources in electric energy distribution systems to independently manage energy consumption and interact with the energy distribution network. Decentralized energy management systems are highly flexible and can contribute to the profitability of energy systems, i.e. Distributed energy management allows consumers to maintain their privacy and manage their energy consumption data [2]. Multi-agent energy management refers to the management of distributed energy resources and energy consumption by several independent agents in a system. These systems are made up of different agents, each of which makes independent decisions regarding energy consumption and generation. This method takes into account the interaction between energy production and demand, and different agents can make joint decisions for energy supply at different times and places, allowing operators to use more renewable and clean energy sources and reduce greenhouse gas emissions. Through the interaction between different agents, multi-agent energy management systems can help to better manage the risks associated with energy production and distribution, as well as energy security [3].

Model-free multi-agent energy management is based on data analysis. A real-time learning-based energy management using machine learning algorithms helps to improve energy efficiency, reduce costs and achieve greater efficiency in energy consumption and distribution. This approach requires access to real-time data and expertise in data analytics and machine learning. However, in this type of approach, most of the data is analyzed discretely, which reduces the accuracy of the method.

Continuous-time energy management uses systems and methods to manage and optimize energy consumption and distribution over time. In fuzzy Q-learning (FQL) approach, energy consumption and distribution are monitored continuously and decisions are made based on time changes and immediate conditions. Continuous-time energy management by focusing on real-time energy consumption changes helps energy users optimize energy resources, improve energy efficiency, and reduce costs over time [4].

Material and Method

Figure 1 shows the structure of H-MG, with electricity and natural gas, two different external energy sources, as inputs. H-MG can use its own internal energy sources such as combined heat and power (CHP), gas boilers (GBs) and photo voltaic (PV) panels to supply the energy it needs, or connect to external energy sources such as the electricity distribution grid, which provides the opportunity to sell the surplus electrical energy generated by H-MG.

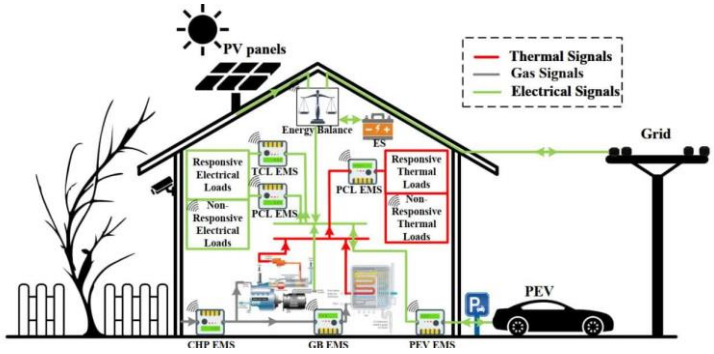


Figure 1. H-MG structure

Plug-in electric vehicles (PEVs), which use batteries for energy storage, are another type of electrical energy source. When the PEV transfers energy from the grid to the vehicle (G2V), i.e. when it is charging, it is considered a consumer of electricity. However, with the right model, the PEV can also be used as an energy source to feed energy into the H-MG in vehicle to grid (V2G) mode when the battery is discharged. Thermal and electrical loads are the two main categories of loads for H-MGs, and they are also divided into two groups: responsive loads and non-responsive loads. Non-responsive loads are uncontrollable and depend on predetermined energy standards, while responsive loads allow control over quantity and timing. There are two types of responsive loads, time control loads (TCL) and power control loads (PCL). H-MG has the option to purchase electricity from the electricity distribution grid or sell it to the electricity distribution grid, provided that its total internal electricity generation, which includes generation from CHP, PEV battery chargers and PV panels, is sufficient. To meet the power requirement of this H-MG, it is important to note that thermal loads must always be met by CHP and GB output. In order to effectively manage energy in an H-MG, it is necessary to establish an objective function. The main objective of this study is to minimize the costs related to energy consumption. To achieve this goal, the optimization of the objective function specified in equation (1) is followed and the output variables related to the problem are identified.

$$\text{Objective Function} = \sum_{t=1}^{24}(\lambda(t)_e)(E(t)_{in} + (\lambda(t)_g)(G(t)_{in}) - (\lambda(t)_{tr})(E(t)_{ic}) \quad (1)$$

where the variable t represents time. The amount of electricity required to be purchased is denoted by $E(t)_{in}$, while its price is denoted by $\lambda(t)_e$. Similarly, the amount of gas required to be purchased is denoted by $G(t)_{in}$ and its price is denoted by $\lambda(t)_g$. Furthermore, $E(t)_{ic}$ represents the electricity that H-MG sells to the grid, and its price is denoted by $\lambda(t)_{tr}$.

Results

In this section, numerical results of implementation of multifactorial fuzzy reinforcement learning method in multifactor H-MG are presented. Six factors are identified in this H-MG which are TCL electric charge, PCL electric charge, thermal charge PCL, PEV, CHP and GB, respectively. Although these factors are collaborative, each agent creates its own management function and optimizes the value of the agent at the moment. The simulation parameters are shown in Table 2.

Table 2. Properties of agents in H-MG

Operation parameters	Loads	CHP	GB	$PEV_{ch/dch}$
η_e	0.99	0.3	-	0.88
η_h	0.95	0.4	0.8	-
α	0.1	0.1	0.1	0.1
γ	0.9	0.9	0.9	0.9

With the amendments made in the consumption of loads, peak demand periods in the middle hours of the day have been announced.

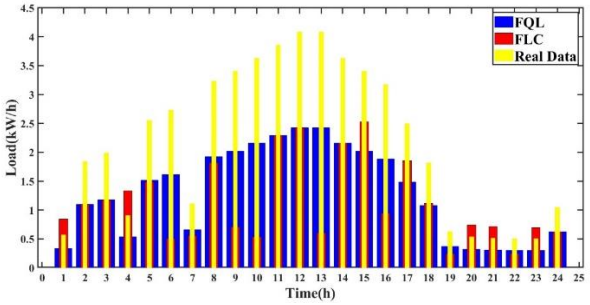


Figure 2. Comparison of electric loads in real data and fuzzy methods

In Figure 3, electric energy in two types of FQL and FLC methods are compared. The proposed energy management system reduces the average purchase of electrical energy from the grid by 21%.

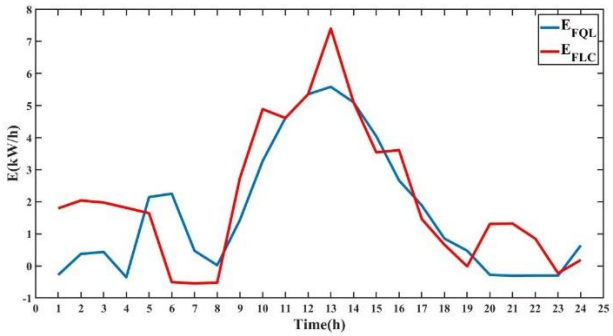


Figure 2. Purchase of electric energy

where, the negative value means the purchase of electricity from the power grid, and the positive value indicates the purchase of electricity from the power grid.

Discussion

The aim of this optimization is to make optimal use of available energy sources, reduce peak demand loads, and reduce reliance on external energy sources. The average managed price is reduced by 18%. According to the outputs, it can be emphasized that the implementation of an effective EMS for a multi-energy H-MG can significantly increase energy efficiency, reduce operating costs, and provide greater stability and flexibility.

Conclusion

Fuzzy Q-Learning within a H-MG entails the execution of a managerial strategy aimed at enhancing the efficiency of the energy resources within the H-MG through the utilization of the learning methodology. The primary objective of this strategy is to identify optimal continuous time actions for overseeing energy generation, consumption, and storage. Within this multi agent H-MG system, various sources of energy are present, including PV panels, PEV, as well as grid connections like natural gas and electricity. The EMS operates intelligently to allocate energy among these sources and electrical/thermal loads in a manner that maximizes electric loads efficiency by 0.9% and thermal loads efficiency by 24%, minimizes costs by 18%, and has the potential to decrease reliance on external energy gas sources by 17% and electricity by 21%.

References

1. A.S. Daramola, S. E. Ahmadi, M. Marzband, A. Ikpehai, A cost-effective and ecological stochastic optimization for integration of distributed energy resources in energy networks considering vehicle-to-grid and combined heat and power technologies, Journal of Energy Storage 57 (2023) 106203.
2. K. Kumar, S. Bae, Two-layer energy management strategy for renewable power-to-gas system-based microgrids, Journal of Energy Storage 61 (2023) 106723.
3. Y. Zou, Y. Xu, C. Zhang, A risk-averse adaptive stochastic optimization method for transactive energy management of a multi-energy microgrid, IEEE Transactions on Sustainable Energy 14 (3) (2023) 1599–1611.
4. Azam Salari and Seyed Ehsan Ahmadi and Mousa Marzband and Mahdi Zeinali, Fuzzy Q-learning-based approach for real-time energy management of home microgrids using cooperative multiagent system, Sustainable Cities and Society 95 (2023) 104528.

Advanced Engineering Days

aed.mersin.edu.tr

Wind Energy Potential of Türkiye

Seçkin Tekin [*1], Emine Banu Burkut [2], Murat Dal [3]

[1]*Munzur University, School of Graduate Studies, Department of Culture and Arts Administration, Türkiye, tez.seckintekin@gmail.com*
[2] *Konya Technical University, Faculty of Architecture, Department of Architecture, Türkiye, burkutbanu@gmail.com*
[3]*Munzur University, Faculty of Fine Arts, Design and Architecture, Department of Architecture, Türkiye, muratdal@munzur.edu.tr*

Cite this study: Tekin, S., & Burkut, E. A., & Dal, M (2024). Wind Energy Potential of Türkiye. Advanced Engineering Days, 9, 930-933

Keywords
Wind Energy
Energy
Ecology
Sustainability
Renewable Energy

Abstract

With its large geographical area and coastlines, Turkey has a high wind energy potential. As an environmentally friendly and sustainable resource, wind energy plays an important role in meeting energy needs and combating climate change. This study aims to identify potential locations for new wind power plants (WPPs) in Turkey by analyzing the increased rates and location distribution of WPPs in Turkey over the years. The efficiency and effectiveness of wind energy in power generation are continuously growing with technological advances and increased investments, which leads us to expect wind energy to play a greater role in future energy production.

Introduction

The significance of renewable energy sources is growing in the modern world due to rising energy consumption and environmental issues [1]. The developing world's growing population and industrialization have made energy a vital necessity. As a result, the globe has shifted away from finite energy resources and toward limitless natural resources. Renewable energy sources are very advantageous because of their longevity and environmental friendliness, even if environmental contamination is a result of the processes involved in the production, transportation, and consumption of energy [2]. Wind energy is particularly noteworthy in this regard as a clean and sustainable energy source [3]. Since they don't produce harmful emissions, clean and sustainable renewable energy sources are crucial to reducing the negative effects of climate change. Wind power plants are an essential renewable energy source that is both environmentally friendly and technologically efficient. Wind power plants are becoming more common both onshore and offshore as a clean, dependable, and limitless source of electricity [4]. The efficiency of wind energy is an important component in determining how effective this resource is in energy generation. This study will examine the growth rates and possibilities of wind power plants (WPPs) in Turkey throughout time. The study's goal is to assess wind energy efficiency and potential in Turkey.

What is Wind Energy?

Wind energy is a renewable energy source produced by the movement of air (wind) induced by atmospheric pressure differentials. The sun's energy heats both the earth and the atmosphere, resulting in pressure variations. Wind is created as air masses move from high to low-pressure regions. Wind energy is a type of energy that produces no emissions, does not deplete natural resources, does not contribute to global warming, does not produce acid rain, and is environmentally sensitive. As an indirect form of solar energy, it is produced by the interplay of various degrees of warmth and pressure centers on Earth. Wind, which is abundant and free in the environment, is a steady, dependable, safe, and continuous source of energy that also transports kinetic energy. Wind turbines use the kinetic energy of the wind to generate electricity [5].

Advantages of Wind Energy

- Wind energy protects the environment by reducing greenhouse gas emissions and air pollution.
- The wind energy industry requires labor, especially during the maintenance and operation phases, and encourages local employment.
- Wind energy reduces dependence on energy imports and increases energy diversity.
- The development of renewable energy technologies stimulates the economy and increases technical capacity [6].

Challenges with Wind Energy

- Wind turbines can only convert a fraction of the wind's kinetic energy into electricity.
- Wind power generation depends on the presence and strength of the wind, which can lead to a discontinuity in energy supply.
- Wind power plants generally have a lower capacity factor compared to fossil fuel power plants.
- Wind power plants are costly to build and operate, especially in terms of capital costs [6].

Material and Method

The method used in this study is the "survey model." The survey model is "a research approach that aims to describe a past or present situation as it exists. At the same time, in this model, "the individual or object that is the subject of the research is tried to be defined in its conditions and as it is," and "no effort is made to change or affect the variables in any way" [7].

Results

Turkey has a large land surface and a high wind energy potential. There are coastlines suitable for wind power generation in various parts of the country, and wind speeds are generally above 3 m/s. In addition, the abundant sunlight and high wind speeds provide an ideal climate for wind and solar energy investments [8]. To understand the wind energy potential in Turkey and the areas where the wind is strong, it will be useful to evaluate the "Turkey Wind Atlas" (9) map published by the General Directorate of Meteorology in Figure 1. According to the map, the regions with the highest wind are shown in dark blue, and the regions with the lowest wind are shown in light blue.

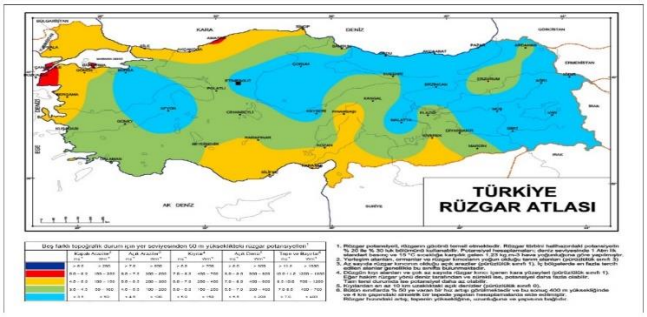


Figure 1 - Turkey Wind Atlas (General Directorate of Meterology)

According to the Turkish National Energy Plan [10], which was released by the Turkish Ministry of Energy and Natural Resources in 2022, Turkey expects to generate 29.6 GW of wind energy by 2035, with 24.6 GW on land and 5 GW offshore. According to the "Turkey Wind Energy Statistics Report" [11] of the Turkish Wind Energy Association for the year 2022, the development of wind power plants has increased from 2010 to 2022, as shown in Figure 2. in Figure 3, wind power plants account for 10.72% of total electricity output in Turkey in July 2022.

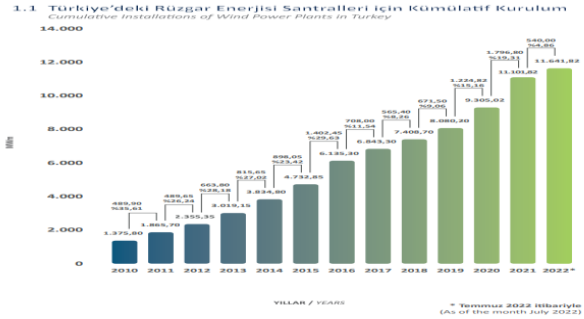


Figure 2 - Development of Wind Energy Investments in Turkey

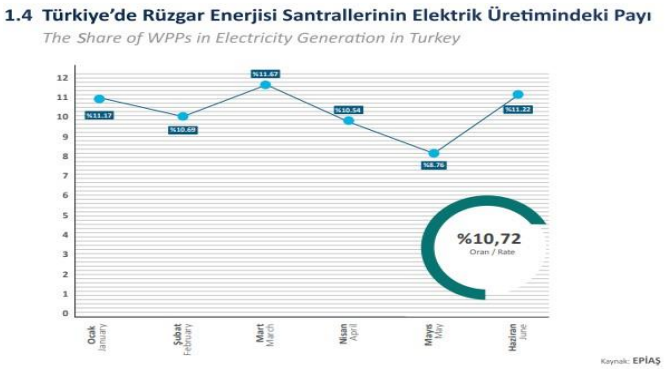


Figure 3 - Share of Wind Power Plants in Electricity Generation in Turkey

Discussion

Wind energy is one of the fastest-growing renewable energy sources, and it is predicted to play an increasingly important part in power generation in the future. Wind energy efficiency is constantly improving because of technological advancements and increased investment. Furthermore, the value of wind energy in terms of environmental sustainability and energy security is growing. "Our country is ranked 12th in the world after Italy, with 11,396 MW of installed capacity as of 2022. In addition to increasing wind energy applications, lowering and localizing turbine installation costs is critical. In this situation, the first issue that must be addressed is the development of a household generator.

To develop domestic energy solutions in Turkey, a 100% domestic wind turbine project is planned to be located in Alaçatı as of 2024 in partnership with ASELSAN and EÜAŞ. In addition, the YEKA and MilRES Projects, which aim to encourage domestic production, can be characterized as works that have been realized and provide added value" [12].

Conclusion

As a result, studying the efficiency of wind energy contributes to the more effective and widespread use of this clean energy source [13]. Wind energy will play a critical role in meeting the energy needs of the future with its low carbon emissions and renewable features. Updates can be made to the Renewable Energy Law to increase renewable energy incentives in Turkey and make it attractive for clean energy investments. These updates should include tax reductions to speed up procurement processes and expanding credit opportunities in cooperation with banks to encourage production. Awareness should be raised to popularize wind energy applications, and energy topics should be included in school curricula to instill an awareness of energy conservation and the importance of renewable energy at an early age. This will encourage children to pursue these professions in the future and expand their employment opportunities. In addition, wind energy should receive more media coverage, and investment incentives should be increased by improving technical infrastructure and conditions.

References

1. Öymen, G. (2020). Yenilenebilir Enerjinin Sürdürülebilirlik Üzerindeki Rolü. İstanbul Ticaret Üniversitesi Sosyal Bilimler Dergisi, 19(39), 1069-1087. https://doi.org/10.46928/iticusbe.769022
2. Bekar, G. (2020). Türkiye'de Rüzgar Enerjisi Sistemleri Yatırımlarının Ekonomik Analizi [Yüksek lisans tezi, Manisa Celal Bayar Üniversitesi]. Manisa Celal Bayar Üniversitesi Fen Bilimleri Enstitüsü.
3. Oskay, C. (2014). Sürdürülebilir kalkınma çerçevesinde rüzgâr enerjisinin önemi ve Türkiye'de rüzgâr enerjisi yatırımlarına yönelik teşvikler. Niğde Üniversitesi İktisadi ve İdari Bilimler Fakültesi Dergisi, 7(1), 76.
4. Tanrıverdi, H., Karakuş, G., & Ulukan, A. (2023). Wind turbine inspection with drone: Advantages and disadvantages. Journal of Energy Systems, 7(1), 57-66.
5. Berkmen, U. (2015) Avrupa Birliği'nde Rüzgar Enerjisi Politikaları ve Türkiye Karşılaştırması1. Yüksek Lisans Tezi, Ege Üniversitesi, Fen Bilimleri Enstitüsü.
6. Maradin, D. (2021). Advantages and disadvantages of renewable energy sources utilization. International Journal of Energy Economics and Policy, 11(3), 176-183.
7. Karasar, N. (2012). Bilimsel araştırma yöntemleri (24. baskı). Ankara: Nobel Yayınevi
8. İmrahor, S. (2020). Bir Model Yapının Elektrik Sarfiyatının Güneş ve Rüzgâr Enerjisi ile Karşılaştırılmasının İncelenmesi. İstanbul Arel Üniversitesi Lisansüstü Eğitim Enstitüsü, İstanbul.

9. Meteoroloji Genel Müdürlüğü. (2024). Türkiye Rüzgar Atlası. https://mgm.gov.tr/genel/ruzgar-atlasi.aspx
10. Enerji ve Tabii Kaynaklar Bakanlığı. (2022). Türkiye Ulusal Enerji Planı. Enerji ve Tabii Kaynaklar Bakanlığı. https://enerji.gov.tr/eigm-raporlari
11. Türkiye Rüzgar Enerjisi Birliği. (2022, Temmuz). Türkiye Rüzgar Enerjisi İstatistik Raporu. https://tureb.com.tr//yayin/turkiye-ruzgar-enerjisi-istatistik-raporu-temmuz-2022/149
12. Aslan, Y. (2023). Türkiye rüzgar enerjisinden yararlanma analizi: Yenilenebilir enerji kaynaklarının enerji ihtiyacını karşılamadaki payının artırılması kapsamında (Yüksek Lisans Tezi). Akdeniz Üniversitesi Fen Bilimleri Enstitüsü, Makine Mühendisliği Anabilim Dalı, Antalya.
13. Amal, E., Yılmaz, K., & Özdemir, E. (2022). Rüzgar Enerji Santrallerinin Elektrik Şebekesine Etkilerinin İncelenmesi. Kocaeli Üniversitesi Fen Bilimleri Dergisi, 5(2), 50-65. https://doi.org/10.53410/koufbd.1096254

Advanced Engineering Days

aed.mersin.edu.tr

Focus on solar energy in architecture and design

Emine Banu Burkut*[1], Murat Dal [2], Seçkin Tekin [3]

[1]*Konya Technical University, Department of Architecture, Türkiye, burkutbanu@gmail.com*
[2]*Munzur University, Faculty of Fine Arts, Design and Architecture, Department of Architecture, Türkiye, muratdal@munzur.edu.tr*
[3]*Munzur University, School of Graduate Studies, Department of Culture and Arts Administration, Türkiye, tez.seckintekin@gmail.com*

Cite this study: Burkut, E. B., & Tekin, S., & Dal M. (2024). Focus on solar energy in architecture and design. Advanced Engineering Days, 9, 934-936

Keywords
Architectural Design
Ecology
Energy
Solar Energy
Sustainability

Abstract

The importance of building energy-efficient buildings in architecture is increasing day by day. Many factors, such as global warming, increased temperatures in cities, drought, and climate change, aim to increase energy-efficient buildings and lower energy consumption levels in new construction. In new residential construction, it is expected to include photovoltaic systems large enough to meet the annual electricity consumption of the building. The importance of benefiting from the clean and efficient energy provided by the sun in modern architectural designs will continue to increase in the coming years. This research contributes to the field of science by considering the potential contributions of solar energy to building design. In addition, the use of solar energy in modern designs, its contribution to design, and its sustainable, ecological, and economic aspects are revealed. With existing examples, ideas will be given about the use of solar energy in architectural designs.

Introduction

Global energy consumption is expanding year after year, and fossil resources such as coal, natural gas, and oil are being exploited. The combustion of fossil fuels to create electricity wastes a considerable amount of energy as heat while also emitting particulate matter, global warming gasses, and a variety of other toxic compounds into the atmosphere. Due to population increase, global warming, and climate change, the need of low energy consumption and efficient energy use in buildings is rising. Renewable energy sources include solar, wind, geothermal, hydrogen, and water-based energy [1]. This research aims to give examples of the use of solar energy in architecture and design and to give ideas for increasing the use of solar energy in buildings in the future. Solar energy is the most effective type of renewable energy used in buildings, such as day and night lighting, water purification, swimming water heating, heat, and electricity production, by integrating into active heating and air conditioning systems and providing heat and electricity-based energy in architectural structures. Solar architecture is a building design that aims to get the most efficiency from solar energy. It aims to benefit from the heat and light of the sun in the longest and most intense way. In line with this goal, large windows are placed on the sunny facades of the buildings, thus creating natural heat and light from solar energy inside the building.

Some countries in the United States, Europe and Asia have enacted laws to encourage the application of solar energy in new residential construction, which can meet the annual electricity loads of the building [2]. According to the Türkiye Solar Energy Potential Map (SEM) prepared by the Ministry of Energy and Natural Resources; Average annual sunshine duration = 2766.5 hours / year, average daily total sunshine duration = 7.58 hours / day, average annual radiation intensity = 1527.1 kWh / m2-year and average daily radiation intensity was calculated as = 4.18 kWh / m2-day [3].

Turkey's largest solar power facility is in the Karapınar neighborhood of Konya. The competition was held for a solar power plant with sustainable and renewable energy potential in Karapınar, a desert shadow [4]. The most obvious drivers in the design of the building are solar panels. The solar panels, positioned on a flat area of 20 square kilometers and at a height of 150cm from the ground, have virtually created a new ground level for the entire region. While the facade design ensures meticulous use of the energy of the building, it also serves as an important part of the building's identity. The facade, which consists of two walls, is designed to minimize the radiation falling on the main facade. The following figures show examples of competition projects [5].



Figure 1 Solar power plant architectural project [5]

Material and Method

In this study, the survey model was used as the method. The survey model is a research approach that aims to describe a past or present situation as it exists [6-7]. In this method, the research subject is defined as it is current situation is presented as it exists without any effort to change or influence the variables.

Literature Review of Solar Energy and Architecture

In the literature review on the use of solar energy in architecture, examples of solar energy use and aesthetic solutions in the field of landscaping and solar energy architecture [8-12], urban planning [13, 14, 15], advantages and disadvantages [16-17], building integrated solar energy and the case of Sweden [18-19], solar architecture [20], New designs of building integrated solar energy systems [21], criteria and guidelines [22], geometrical and architectural characteristics [23], Achieving solar energy in architecture [24], sustainable architecture and solar energy [25], building design a guide for architects and builders [26], and green architecture and energy efficiency, innovative design and construction techniques [27].

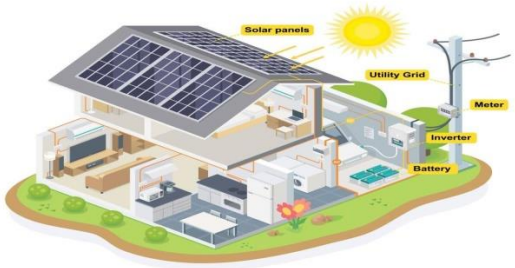


Figure 2 Integration of Solar Energy Systems into Building Design [26]

Conclusion

The importance of benefiting from the clean and renewable energy provided by the sun will continue to increase in the coming years. Installing solar energy systems on the facade or roof systems of existing buildings and many structural elements integrated with solar energy in newly constructed buildings will benefit the user [27]. It is aimed at considering the potential contributions of solar energy to building design. In addition, those who want to use solar energy systems in the project and implementation processes of architectural designs will give ideas and set an example. In this research, studies on the use of solar energy, urban architecture, and design are presented with a general evaluation and overview. The research sheds light on current research. However, as a suggestion, research can be developed by evaluating the use of solar energy in architecture by a certain period, region, city, or nationality. How solar energy is handled in architectural design studios, how it is included in projects, or its place in the architectural education curriculum can be addressed as a research topic or by a designer. Additionally, how solar energy is handled in architectural design studios, how it is included in projects, or its place in the architectural education curriculum can be addressed as a research topic.

References

1. Hestnes, A. G. (1999). Building integration of solar energy systems. Solar energy, 67(4-6), 181-187.
2. Kılıç, U., & Kekezoğlu, B. (2022). A review of solar photovoltaic incentives and Policy: Selected countries and Turkey. Ain Shams Engineering Journal, 13(5), 101669.
3. https://enerji.gov.tr/bilgi-merkezi-enerji-gunes-en
4. https://www.arkitera.com/proje/kalyon-karapinar-1-350-mwp-ges-merkezi-kontrol-binasi/
5. Karasar, N. (2012).Bilimsel Araştırma Yöntemleri. Ankara. Nobel Yayınevi
6. Büyüköztürk, Ş., Akgün Ö., E. Karadeniz, Ş., Demirel, F., & Kılıç, E. (2013). Bilimsel Araştırma Yöntemleri. Pegem Akademi, Ankara.
7. Özek, E., (2009). Peyzaj mimarisi uygulamalaında güneş enerjsi kullanımını değerlendirilmesine yöneik bir araştırma, İTÜ
8. Cengizoğlu Başaran, F. P., & Yildirim, M. T. (2022). Mimari Formların Enerji Etkin Tasarım Bağlamında Güneş Enerjisi Kazanım Analizleri. Online Journal of Art & Design, 10(2).
9. Kanters, J., & Horvat, M. (2012). Solar energy as a design parameter in urban planning. Energy Procedia, 30, 1143-1152.
10. Kanters, J., Horvat, M., & Dubois, M. C. (2014). Tools and methods used by architects for solar design. Energy and Buildings, 68, 721-731.
11. Demircan, R. K., & Gültekin, A. B. (2017). Binalarda pasif ve aktif güneş sistemlerinin incelenmesi. TÜBAV Bilim Dergisi, 10(1), 36-51.
12. Danacı, H. M., & Gültekin, R. E. (2009). Yapılaşmada güneş enerjisi kullanımı ve estetik çözümler. V. Yenilenebilir Enerji Kaynakları Sempozyumu, Diyarbakır.
13. Littlefair, P. (1998). Passive solar urban design: ensuring the penetration of solar energy into the city. Renewable and Sustainable Energy Reviews, 2(3), 303-326.
14. Mohajeri, N., Upadhyay, G., Gudmundsson, A., Assouline, D., Kämpf, J., & Scartezzini, J. L. (2016). Effects of urban compactness on solar energy potential. Renewable Energy, 93, 469-482.
15. Lobaccaro, G., Croce, S., Lindkvist, C., Probst, M. M., Scognamiglio, A., Dahlberg, J., ... & Wall, M. (2019). A cross-country perspective on solar energy in urban planning: Lessons learned from international case studies. Renewable and Sustainable Energy Reviews, 108, 209-237.
16. Ugli, T. J. T. (2019). The importance of alternative solar energy sources and the advantages and disadvantages of using solar panels in this process.
17. Stevanović, S., Stevanović, S., & Živković, R. (2022). Advantages and disadvantages of solar energy production and use. Journal of Agricultural, Food and Environmental Sciences, JAFES, 76(4), 65-70.
18. https://www.tandfonline.com/doi/full/10.1080/24751448.2019.1571846?scroll=top&needAccess=true
19. Kanters, J., Dubois, M. C., & Wall, M. (2013). Architects' design process in solar-integrated architecture in Sweden. Architectural Science Review, 56(2), 141-151.
20. Schittich, C. (2003). Solar architecture. Trick Hauser, Basel, 9.
21. Tripanagnostopoulos, Y. (2014). New designs of building integrated solar energy systems. Energy Procedia, 57, 2186-2194.
22. Munari Probst, M. C., Roecker, C., Frontini, F., Scognamiglio, A., Farkas, K., Maturi, L., & Zanetti, I. (2013). Solar Energy Systems in Architecture-integration criteria and guidelines. Report T.41.A.2: IEA SHC Task 41 Solar energy and Architecture.
23. Vassiliades, C., Agathokleous, R., Barone, G., Forzano, C., Giuzio, G. F., Palombo, A., ... & Kalogirou, S. (2022). Building integration of active solar energy systems: A review of geometrical and architectural characteristics. Renewable and Sustainable Energy Reviews, 164, 112482.
24. Wall, M., Probst, M. C. M., Roecker, C., Dubois, M. C., Horvat, M., Jørgensen, O. B., & Kappel, K. (2012). Achieving solar energy in architecture-IEA SHC Task 41. Energy Procedia, 30, 1250-1260.
25. Afshari Basir, N., & Reza Afshari Basir, M. (2012). Using Solar Energy in Building from the Viewpoint of Sustainable Architecture. Applied Mechanics and Materials, 110, 2081-2086.
26. https://arka360.com/ros/integrating-solar-energy-with-building-design-a-guide-for-architects-and-builders/
27. Umoh, A. A., Adefemi, A., Ibewe, K. I., Etukudoh, E. A., Ilojianya, V. I., & Nwokediegwu, Z. Q. S. (2024). Green architecture and energy efficiency: a review of innovative design and construction techniques. Engineering Science & Technology Journal, 5(1), 185-200.

Advanced Engineering Days

aed.mersin.edu.tr

Impact of industrial use on nitrogen dioxide air pollutant distribution (case example: Tabriz, Iran)

Paria Ali Mohammadi *[1], **Iraj Teymuri** [2]

[1] *Tabriz University, Faculty of planning and Environmental Science, Iran, pariaa.mohammadi@gmail.com*
[2] *Tabriz University, Faculty of planning and Environmental Science, Iran, iraj-teymuri@tabrizu.ac.ir*

Cite this study: Ali Mohammadi, P., & Teymouri, I. (2024). impact of industrial use on nitrogen dioxide air pollutant distribution (case example: Tabriz, Iran). Advanced Engineering Days, 9, 937-940

Keywords
Air pollution
Nitrogen dioxide
Industrial zones

Abstract

Nitrogen Oxides (NOx) is One of major primary pollutant which is expelled from high temperature combustion, and are also produced naturally during thunderstorms by electric discharge. This research investigates the distribution of pollutant (NO2) levels within the time frame of December 22, 2022, to March 22, 2023. Based on studies conducted, pollutants (2NO) are mostly concentrated in the western and southwestern parts of Tabriz city. This corresponds to the fact that most industrial activities are concentrated in this area. As previously mentioned, the predominant wind direction carries pollutants from industrial activities and suspended particles towards the center of Tabriz city. This leads to the concentration of air pollution in the urban area of Tabriz, especially during the cold seasons. Given that the accumulation of air pollutants, particularly NO2, has harmful and sometimes lethal effects on the lives of animals and the environment, it is necessary to consider the location of pollutant sources and utilize natural and artificial purifiers such as plants, air filters, and the like. These measures help improve air quality and reduce the detrimental effects of pollutants on the lives of animals and the environment.

Introduction

Environmental pollutions and related security risks have become major threats to human health (Mofrad, Hamzeh, Moradi, & Bahari, 2022).

Air pollution is contamination of the indoor or outdoor environment by any chemical, physical or biological agent that modifies the natural characteristics of the atmosphere (World health organization, 2024). Air pollution is a problem as old as history itself and cause harm or discomfort to humans or other living organisms, or cause damage to the natural environment or built environment (Hutton, 2011).

Air pollutant is known as a substance in the air which can cause harm to humans and the environment and can be in the form of solid particles, liquid droplets, or gases. Besides, they may be natural or man-made and can also be classified as either primary or secondary pollutants. Primary air pollutants are substances directly emitted from a process and are present in the atmosphere with the same composition as they are emitted, such as ash from a volcanic eruption, the Carbon monoxide gas from vehicular emissions or Sulphur dioxide released from industries. Secondary pollutants are not emitted directly into atmosphere but when primary pollutants react or interact, they form or transform into another compound in the atmosphere like ground-level ozone and photochemical smog. (Bhargav, Bhargava, Singhal, & Twinkle, 2020).

Exposure to fine particle outdoor air pollution is the largest environmental risk factor for premature death globally. Air pollution exposure contributes to a number of key illnesses globally but its contribution is not borne equally across the world. For example, air pollution is linked to 20 percent of ischemic heart disease deaths globally but over 30 percent in the Middle East and North Africa regions. Children are particularly vulnerable to the damaging health effects of air pollution due to their unique susceptibility and exposure. 20 percent of newborn deaths globally are attributed to air pollution exposure (UNEP, 2023).

Nitrogen Oxides (NOx) is One of major primary pollutant. Especially nitrogen dioxide is expelled from high temperature combustion, and are also produced naturally during thunderstorms by electric discharge. Can be seen as the brown haze dome above or plume downwind of cities. Nitrogen dioxide is the chemical compound with the

formula NO2. It is one of the several nitrogen oxides. This reddish-brown toxic gas has a characteristic sharp, biting odor. NO2 is one of the most prominent air pollutants (Choudhary & Garg, 2013).

Table 1. Environmental effects of air pollution

Acid rain	is precipitation containing harmful amounts of nitric and sulfuric acids. These acids are formed primarily by nitrogen oxides and sulfur oxides released into the atmosphere when fossil fuels are burned. These acids fall to the Earth either as wet precipitation (rain, snow, or fog) or dry precipitation (gas and particulates) Some are carried by the wind, sometimes hundreds of miles. In the environment, acid rain damages trees and causes soils and water bodies to acidify, making the water unsuitable for some fish and other wildlife. It also speeds the decay of buildings, statues, and sculptures that are part of our national heritage.
Eutrophication	is a condition in a water body where high concentrations of nutrients (such as nitrogen) stimulate blooms of algae, which in turn can cause fish kills and loss of plant and animal diversity. Although eutrophication is a natural process in the aging of lakes and some estuaries, human activities can greatly accelerate eutrophication by increasing the rate at which nutrients enter aquatic ecosystems. Air emissions of nitrogen oxides from power plants, cars, trucks, and other sources contribute to the amount of nitrogen entering aquatic ecosystems.
Haze	is caused when sunlight encounters tiny pollution particles in the air. Haze obscures the clarity, color, texture, and form of what we see. Some haze-causing pollutants (mostly fine particles) are directly emitted to the atmosphere by sources such as power plants, industrial facilities, trucks and automobiles, and construction activities. Others are formed when gases emitted to the air (such as sulfur dioxide and nitrogen oxides) form particles as they are carried downwind
Ozone	affects human health, forests, grasslands, crops and contributes to corrosion of materials. ICP Vegetation has shown that ozone pollution may partly suppress the terrestrial carbon sink via its adverse effects on plant growth, poses a threat to food security by reducing yield and quality and can also make vegetation less able to withstand periods of drought.

(Patrick, Murray, Sullivan JR., & Kimmell, 2024), (Bak, et al., 2012)

Material and Method

This research investigates the distribution of pollutant (NO2) levels within the time frame of December 22, 2022, to March 22, 2023. The necessary data were obtained from Sentinel-5P OFFL NO2 satellite images. Subsequently, using GIS software, the raster files were converted to vector format, and then the distribution of these pollutants at the level of Tabriz city was shown using the optimized hotspot command.

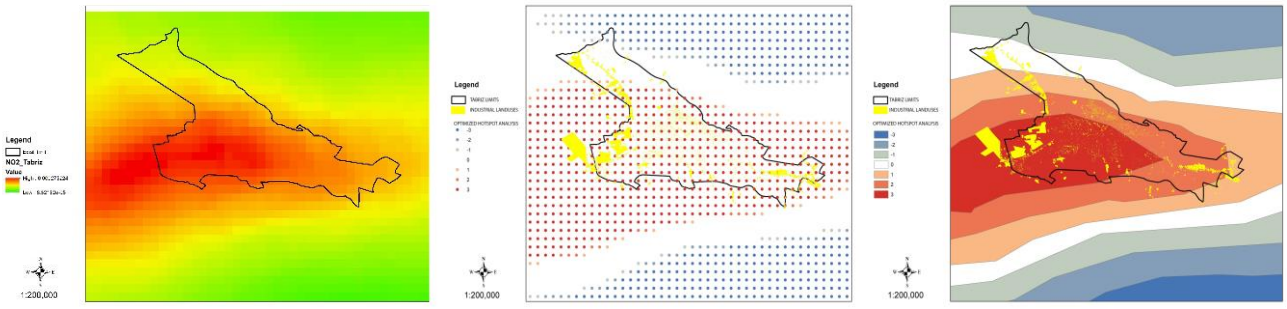


Figure 1. NO_2 distribution in Tabriz city, Hotspot analysis

Results

Nitric oxide (NO) is a key molecule that plays a significant role in various physiological processes within the human body. However, when present in excess amounts in the atmosphere, it can have detrimental effects on both human health and urban environments.

In terms of health, elevated levels of nitrogen dioxide (NO_2), a major component of air pollution formed through the oxidation of NO, can lead to respiratory issues such as asthma, bronchitis, and other respiratory infections. Long-term exposure to high concentrations of NO2 has been linked to decreased lung function and increased susceptibility to respiratory diseases, particularly in vulnerable populations such as children, the elderly, and individuals with pre-existing respiratory conditions. In addition to its health impacts, nitrogen oxides (NO_x), which include NO and NO_2, contribute to the formation of acid rain when they react with atmospheric moisture. Acid rain can damage vegetation, aquatic ecosystems, buildings, and infrastructure, thereby posing environmental challenges for urban areas.

Moreover, nitrogen oxide emissions from vehicles, industrial processes, and power plants also contribute to the formation of fine particulate matter (PM2.5), which can penetrate deep into the lungs and bloodstream, causing a range of adverse health effects including respiratory and cardiovascular diseases.

Therefore, mitigating the emissions of nitrogen oxides is crucial for safeguarding both human health and urban environments. Strategies such as implementing stricter emission standards for vehicles and industrial sources, promoting the use of cleaner energy sources, investing in public transportation, and enhancing green spaces can all help reduce nitrogen oxide pollution and its associated health and environmental impacts. By taking concerted action to address nitrogen oxide emissions, we can strive towards healthier, more sustainable cities for present and future generations

According to climate data for the region, during the autumn and winter seasons, the temperature is moderate, with low precipitation, humidity, and wind speed. In the winter and spring seasons, the air temperature is cool, accompanied by strong winds and heavy precipitation. In the summer season, dry and hot conditions prevail, with low precipitation and strong winds. During the winter-spring seasons, the levels of suspended particles and pollution are higher. The predominant wind direction is southwest to northeast with a speed of 7 meters per second. It is a prevailing circulation direction originating from Saudi Arabia and Iraq, transporting dust and sandstorms from Iraq and Saudi Arabia towards southwest Iran and the study area. Moreover, most of the major industries in the city, such as thermal power plants, petrochemical complexes, refineries, machinery manufacturing, tractor manufacturing, and dozens of brick kilns, are located in the western part of the city. Tabriz is surrounded by walls of unevenness and is situated in a valley, preventing pollutants from easily dispersing to the surroundings and sometimes causing them to accumulate above the region. Wind from the west carries suspended particles onto the city, and the Ain Al and Zin Al mountains in the northeast of the city act as barriers against the wind flow, causing suspended particles carried by the wind to settle over the city. The temporary nature of suspended particle pollution confirms the temporary factor, namely wind. Therefore, there is a direct relationship between the increase in air suspended particles and the wind blowing from the southwest of Tabriz city. Urban construction and activities, intra-city activities, and agricultural activities are also considered sources of particle emissions that affect air quality (Analyzing Tabriz wheater tips and air pollutions, 2020).

Discussion

This study, using Sentinel 5 data, examined the air pollution levels caused by the copper smelting factory in Khatounabad, Kerman, and determined its radius of influence. The results obtained from the classification of images related to nitrogen dioxide gas show that the concentration of nitrogen dioxide around the factory exceeds normal levels. Considering the minimum and maximum concentrations of this gas in the study area, it is observed that during warm months, the concentration of nitrogen dioxide gas is higher compared to cold months. Due to the rapid dispersion of nitrogen dioxide gas in the atmosphere by the wind, it is inferred that images obtained from two-week to one-month intervals provide better information about the concentration of nitrogen dioxide around the factory. Based on this, it is concluded that during two-week to one-month intervals in cold months, this gas is present around the factory. However, in warm months, due to its high dynamics and wind blowing, the gas moves away from the factory and is observed at farther distances (Hasan Zadeh, Hasan Zadeh, Hoseinjani Zadeh, & Honarmand, 2023) .

Factors influencing the increase in nitrogen dioxide, as identified in the study on air pollution in Isfahan based on nitrogen dioxide pollutant, include urbanization, population growth, and the indiscriminate use of fossil fuels and vehicles. Among these, topography and temperature inversion, as well as low wind speed, do not have a significant impact on the increase of this pollutant (Shah Mohammadi, Bayat, & Mashhadi Zadeh, 2020)

Many studies have shown that air pollution, particularly nitrogen dioxide, is significantly higher in industrial areas. The main reason for this is twofold: industrial and manufacturing activities originating from human sources and the lack of effective land distribution in these areas. The high density of industries, the use of fossil fuels, and high consumption of fossil fuels in these areas contribute to the increase in pollutant gases. Additionally, wind patterns play a crucial role in the transport of pollutants from industrial areas to other regions. Winds blowing from industrial areas towards urban and residential areas carry air pollutants with them, exacerbating air pollution in those areas.

Generally , examining and managing air pollutants in industrial areas is essential to minimize the effects of air pollution and preserve the air quality in residential areas. This requires collaboration between research centers, industry, and government to implement policies and utilize clean-up technologies to reduce pollutants.

Conclusion

Based on studies conducted, pollutants (2NO) are mostly concentrated in the western and southwestern parts of Tabriz city. This corresponds to the fact that most industrial activities are concentrated in this area. As previously mentioned, the predominant wind direction carries pollutants from industrial activities and suspended particles towards the center of Tabriz city. This leads to the concentration of air pollution in the urban area of Tabriz, especially during the cold seasons.

Given that the accumulation of air pollutants, particularly NO2, has harmful and sometimes lethal effects on the lives of animals and the environment, it is necessary to consider the location of pollutant sources and utilize natural and artificial purifiers such as plants, air filters, and the like. These measures help improve air quality and reduce the detrimental effects of pollutants on the lives of animals and the environment.

References

1. Analyzing Tabriz wheater tips and air pollutions. (2020). National geography, 52(3), 375-394.
2. Bak, J., Doytchinov, S., Fisher, R., Forsius, M., Grennfelt, P., Harmens, H., . . . Wright, R. (2012). Impacts of air pollution on ecosystems, human health and material under different Gothenburg protocol scenarios. UNECE.
3. Bhargav, A., Bhargava, S., Singhal, R., & Twinkle, A. (2020). Air pollution - sources and classification. Open access journal of biogeneric science and research, 1(4), 1-4.
4. Choudhary, M. P., & Garg, V. (2013). Causes, consequences and control of air pollution. All India seminar on methodologies for air pollution control (pp. 1-11). Jaipur, Rajashtan, India: Malviya national institute of technology.
5. Hasan Zadeh, N., Hasan Zadeh, R., Hoseinjani Zadeh, M., & Honarmand, M. (2023). Investigation of the variation in concentrations of Sulfur Dioxide and Nitrogen Dioxide gases in the air of industrial areas using Remote Sensing and GIS: a case study of the copper smelting factory in Khatounabad, Kerman province. Geographical information, 32(125), 7-27.
6. Hutton, G. (2011). Air pollution global damage costs of air pollution from 1900 to 2050. Copenhagen consensus on human challenges, 1-39.
7. Mofrad, A. a., Hamzeh, F., Moradi, O., & Bahari, N. (2022). Designing a model to reduce air pollution in order to increase the scurity of metropolitan areas with the approach of nanotechnology (case study: Tehran). Regional planning, 12(45), 229-244.
8. Patrick, D. L., Murray, T. P., Sullivan JR., R. K., & Kimmell, K. L. (2024, 01 16). Massachusetts department of environmental protection. Retrieved from Mass.gov: https://www.mass.gov/air-pollutants-toxics
9. Shah Mohammadi, A., Bayat, A., & Mashhadi Zadeh, S. (2020). An Assessment of air pollution in the city of Isfahan based on measured nitrogen dioxide pollutant using an OMI sensor. Applied research of geographic sciences, 22(67), 41-55.
10. World health organization. (2024, 01 16). Retrieved from https://www.who.int/health-topics/air-pollution#tab=tab_1

Advanced Engineering Days

aed.mersin.edu.tr

Statistical Analysis and Machine Learning Applications of radiolarite-hosted manganese mineralization in Taşdemir (Kahramanmaraş, Türkiye)

Cihan Yalçın*[1], Yusuf Uras [2], Tekin Akkütük [3]

[1] *Ministry of Industry and Technology, World Bank Project Implementation Unit, Ankara, cihan.yalcin@sanayi.gov.tr*
[2] *Kahramanmaraş Sütçü İmam University, Department of Geological Engineering, Kahramanmaraş, yuras@ksu.edu.tr*
[3] *Kahramanmaraş Sütçü İmam University, Geological Engineering, Kahramanmaraş, Turkey, mtekinakkutuk@gmail.com*

Cite this study: Yalçın, C., Uras, Y., & Akkütük, T. (2024). Statistical Analysis and Machine Learning Applications of radiolarite-hosted manganese mineralization in Taşdemir (Kahramanmaraş, Türkiye). Advanced Engineering Days, 9, 941-943

Keywords
Manganese
Geochemical analysis
Statistical
Machine learning
Mineralization
Taşdemir Village

Abstract

Manganese (Mn), an essential metal with significant strategic value, is indispensable in several sectors because of its distinct chemical and physical characteristics. This research analyzes the geochemical data of manganese mineralization in Taşdemir Village, situated in the Kahramanmaraş area. The study used statistical and machine learning approaches to investigate the data. Manganese deposits, which are created via subsurface hydrothermal, hydrogenetic, and sedimentary processes, are crucial for the manufacturing of steel and lithium-ion batteries. The research utilizes data processing and visualization technologies like Python, pandas, numpy, scikit-learn, seaborn, and matplotlib. Additionally, Microsoft Excel is used for data organizing. The study starts by presenting summary statistics and a correlation matrix, which emphasize noteworthy associations among various aspects. The linear regression analysis shows a significant negative connection between the concentrations of MnO and SiO_2, with an R-squared value of 0.951. This indicates that changes in SiO_2 may account for 95.1% of the fluctuations in MnO concentration. The p-value for SiO_2 is 0.000, indicating its statistically significant influence on MnO levels. The K-Means cluster analysis classifies the samples into three main clusters based on their SiO_2 and MnO concentrations, which helps identify regions with unique mineral compositions. The findings of this research provide significant understanding into the processes involved in the creation and deposition of manganese ore. Applying machine learning methods is efficient in evaluating intricate geochemical information and finding prospective new deposits. This study serves as a fundamental reference for future Mn exploration endeavors, showcasing the effectiveness of machine learning techniques in mineral resource assessments.

Introduction

Manganese, a key element in the production of steel and batteries, is created by geological and hydrothermal mechanisms, which account for its extensive use across several sectors.

Manganese (Mn) is a very valuable metal of strategic importance, mostly owing to its exceptional chemical and physical qualities. It is extensively used in the manufacture of steel to effectively eliminate oxygen and remove sulphur. Additionally, Mn is crucial in the manufacturing of high-strength low-alloy steels, stainless steels, and many specialized alloys. Additionally, it is much sought after globally since it functions as an electrode material in lithium-ion batteries.

Manganese deposits may originate from sub-marine hydrothermal, hydrogenetic, and sedimentary processes [1-2]. Research has shown that hydrogenetic deposits often exhibit a Fe/Mn ratio of around 1, while sub-marine hydrothermal deposits exhibit much lower ratios. Previous research has concentrated on the processes of how Mn deposits are formed, the chemical characteristics of these deposits, and the distribution of trace elements within

them [3]. Choi and Hariya's study [4] revealed elevated concentrations of nickel (Ni) and zinc (Zn) in hydrothermal deposits, as well as cobalt (Co) in hydrogenetic deposits.

Machine learning theory has become a crucial tool for analyzing extensive datasets and investigating mineral resources. Machine learning techniques are used to analyze geochemical data and develop mineralization models. In their study, Hastie et al. [5] demonstrated the successful use of machine learning algorithms in classifying and interpreting geological data sets. Kohavi and Provost [6] highlighted the significant advantages of using machine learning approaches for investigating mineral resources, particularly in the examination of intricate data sets. Machine learning techniques are crucial in this scenario for identifying and assessing possible mineral resources based on geochemical data.

This work seeks to assess the geochemical data of manganese mineralization in Taşdemir Village [7], located in the Kahramanmaraş area, using the use of statistical and machine learning analytic techniques. To fully comprehend the source of manganese deposits linked to radiolarites in the Upper Cretaceous Koçali formation and to assess the efficiency of machine learning methods in identifying possible new deposits, it is crucial to consider this background.

Material and Method

The data acquired from geochemical studies were examined using a variety of statistical and machine learning techniques. Python was used for data processing and visualization. The libraries used are pandas, numpy, scikit-learn, seaborn, and matplotlib. Additionally, Microsoft Excel was used for the pre-processing and organization of the data.

Statistical Analysis and Machine Learning Applications

The analytical findings are evaluated using summary statistics and a correlation matrix (Figure 1). The correlation matrix displays the presence of robust positive or negative associations among certain items. For instance, there exists an inverse relationship between the levels of MnO and SiO_2, suggesting that when one element is present in large quantities, the other element is likely to be found in lower quantities.

The linear regression analysis investigating the correlation between MnO concentration and SiO_2 concentration is shown in Figure 2. The R-squared value of 0.951 indicates that 95.1% of the fluctuations in MnO concentration can be accounted for by changes in SiO_2. The coefficient of SiO_2 is -0.9322, indicating that for every unit increase in SiO_2 concentration, there is a predicted drop of 0.9322 units in MnO concentration. The p-value for SiO_2 is 0.000. The data suggests that SiO_2 has a statistically significant impact on MnO.

Subsequently, K-Means cluster analysis, Elbow technique, and linear regression studies were used. These strategies facilitated comprehension of the concentrations of diverse components and the interconnections among them.

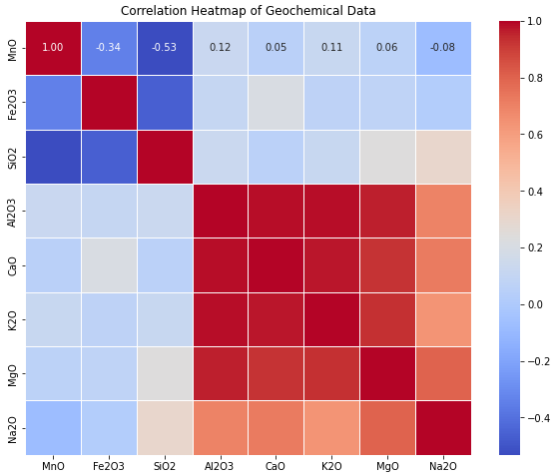


Figure 1. The correlation matrix of the major oxides

Simultaneously, the samples were categorized into three primary clusters by K-Means cluster analysis, as seen in Figure 2. The graph above displays the clusters based on their SiO_2 and MnO concentrations. Each sample was allocated to a distinct cluster, with these clusters including samples that had comparable mineral compositions.

The outcomes of cluster analysis may assist in the identification of areas exhibiting distinct mineral compositions. The regression analysis indicates a significant negative correlation between SiO_2 and MnO. These discoveries may provide crucial insights into the processes involved in the generation and mineralization of manganese ore.

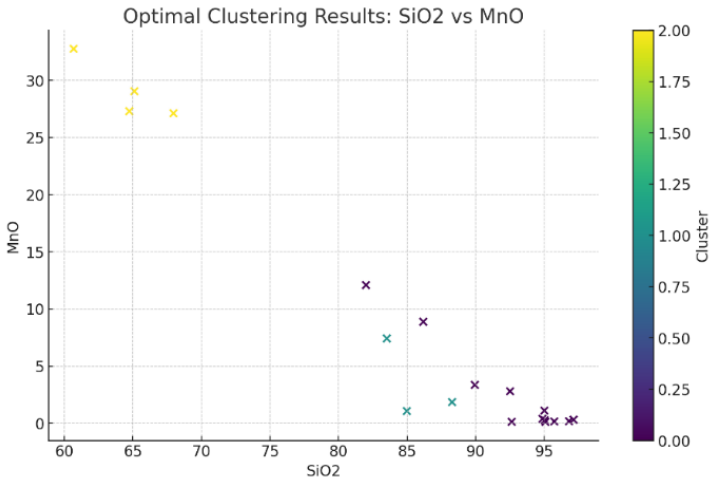


Figure 2. Optimal clustering results versus SiO_2-MnO

Discussion

The outcomes of cluster analysis may assist in the identification of areas exhibiting distinct mineral compositions. The regression analysis findings indicate a significant inverse relationship between SiO_2 and MnO. These results may provide crucial insights into the processes of formation and mechanisms of mineralization of manganese ore.

The K-means clustering technique reveals that geochemical data may be categorized into distinct groups based on certain main oxide concentrations. For instance, one cluster may have elevated levels of MnO and SiO_2, while another cluster may display lower quantities. Analyses of this kind are crucial in assessing geological formations and the potential for minerals [8].

Conclusion

This research conducted a statistical and machine learning analysis to examine the geochemical data of manganese mineralization near Taşdemir village in the Kahramanmaraş province. The collected findings serve as a crucial foundation for future investigations on Mn exploration. Specifically, the usage of machine learning methods in this research shows its efficacy in analyzing intricate geochemical datasets and categorizing mineralization kinds.

References

1. Bonatti, E., Kraemer, T., & Rydell, H., (1972). Classification and genesis of submarine iron-manganese deposits. In: Ferromanganese deposits on the Ocean Floor, 149–161.
2. Bonatti, E., Zerbi, M., Kay, R., & Ryddell, H., (1976). Metalliferous deposits from the Apennine ophiolites: Mesozoic equivalents of the modern deposits from oceanic spreading centers. Geol. Soc. Am. Bull. 87, 83–94.
3. Rona, P. (1978). Hydrothermal Mineralization at Sea Floor Spreading Centers. Earth-Science Reviews, 14(1), 1-19.
4. Choi, S., & Hariya, Y. (1992). Geochemistry of Hydrothermal Manganese Ores from the East Pacific Rise. Marine Geology, 107(3-4), 207-220.
5. Hastie, T., Tibshirani, R., & Friedman, J. (2009). The Elements of Statistical Learning: Data Mining, Inference, and Prediction. Springer.
6. Kohavi, R., & Provost, F. (1998). Glossary of terms. Machine Learning, 30(2-3), 271-274.
7. Yalçın, C., Akkütük, M. T., & Uras, Y. (2022). Mineralogy and Geochemical signatures of the Mn mineralization in Taşdemir (Pazarcık, Kahramanmaraş, Turkey). Advanced Engineering Science, Volume 2, 147-153.
8. MacQueen, J. (1967). Some methods for classification and analysis of multivariate observations. In *Proceedings of the fifth Berkeley symposium on mathematical statistics and probability* (Vol. 1, No. 14, pp. 281-297).

Advanced Engineering Days

aed.mersin.edu.tr

Utilizing International Experiences in the Revitalization of Lake Urmia

Seyyed Asadullah Hijazi [1], saye habibzadeh

[1] Department of Geography, University of Tabriz, Tabriz, Iran, s.hejazi@tabrizu.ac.ir
[2] Department of Geography, Tabriz University, Tabriz, Iran, spatialplanningtabriz@gmail.com

Cite this study: Hijazi, A., & Hbibzadeh, S. (2024). Utilizing International Experiences in the Revitalization of Lake Urmia. Advanced Engineering Days, 9, 944-947

Keywords
Lake Urmia
International Experiences
Aral Sea

Abstract

Lake Urmia is the largest inland lake in Iran, the second largest saltwater lake in the world, and the twentieth largest lake in the world. This ecosystem is considered the most important habitat for Artemia and serves as a climate regulator for the region. Starting in the 1950s with the construction of dams, population growth, industrialization, and agriculture, and from the late 1960s to the early 1970s, the reduction in water inflow from rivers to Lake Urmia, along with increased temperatures and decreased rainfall, has had a significant impact on the reduction in the volume of water in this lake and the expansion of its salt flats. This has had significant health and environmental consequences for the residents of the region and poses a threat to neighboring provinces, including the abandonment of villages to the east of the lake. This research aims to draw on international experiences in other parts of the world, such as the Aral Sea, Lake Chad, Lake Baikal, and Lake Aiding, in order to meet the environmental requirements for the sustainable preservation and revitalization of Lake Urmia.

Introduction

Research conducted on the drying of Lake Urmia has focused more on the environmental, economic, health, and sustainable development aspects, and so far, little attention has been paid to international experiences in the direction of the requirements of sustainable environmental protection and restoration of Lake Urmia. Lake Urmia is the largest internal lake in the country and the second saltiest lake in the world, with high importance in various economic, social, and environmental aspects in the country and the region. The Lake Urmia basin covers about 3.15% of the country's surface area and holds about 7% of the country's total surface water resources. In recent years, due to drought and climate change on one hand, and the construction of water facilities, implementation of development projects, and excessive water extraction from rivers in the basin on the other hand, the water level of this lake has severely decreased, to the extent that nearly half of the lake's area has turned into salt marshes. The current situation of Lake Urmia is a suitable indicator to delve into the depths of the water crisis and the consequences of inefficient and irresponsible water resource management and excessive extraction in this limited water resource area of Iran. Currently, a significant portion of the 5000 square kilometer area of this lake has dried up, and over 30 billion cubic meters of water have been lost compared to previous periods of high water levels, leaving the lake with a shortage of over 12 billion cubic meters.

Material and Method

Study area

The vast catchment area of Lake Urmia, with an area of 51,876 square kilometers, covers areas of the three provinces of East Azarbaijan, West Azarbaijan and Kurdistan located in the south. The geographical coordinates of this vast area are 35 degrees 30 minutes, 38 degrees 30 minutes north latitude and 44 degrees 15 minutes east longitude. West Azarbaijan Province is 47.7%, East Azarbaijan Province is 4.4% and Kurdistan Province is 8.9% of the watershed coverage in each province. The catchment area of Lake Urmia is generally a mountainous area that includes two famous Iranian volcanic peaks, Sahand with a height of 3707 meters and Sablan with a height of 4810 meters, and vast areas of fertile lands in the valleys and around the lake. Most parts of the basin are located at an

altitude of more than 1280 meters above sea level. The changes in the water level of the lake are between 1271 and 1278 meters above sea level.

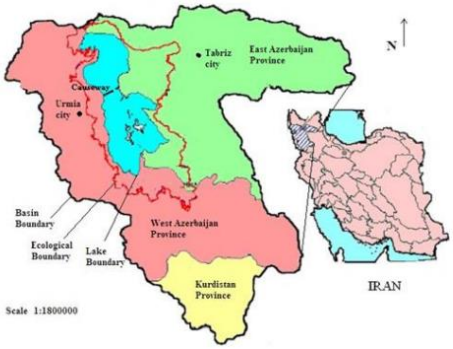


Fig. 1- Geographic levels of the Lake Urmia

Changes in Lake Urmia: Recent studies have examined the harsh conditions of Lake Urmia and the irreversible changes in its water level due to hydrological and climatic changes. Various theories have been proposed regarding the influx of water into Lake Urmia, with the need for further research. The water level of Lake Urmia has shown a decreasing trend from 1374 to 1384. The seriousness of the water balance problem in Lake Urmia in recent years is evident. The ecological water level of this lake has been proposed to be 274.1 meters, but reports suggest a lower level of 5.1 cubic meters in 1385. Reports from UNEP in 2012 indicate that the water level of Lake Urmia was at its highest in 1995 over the past 40 years.

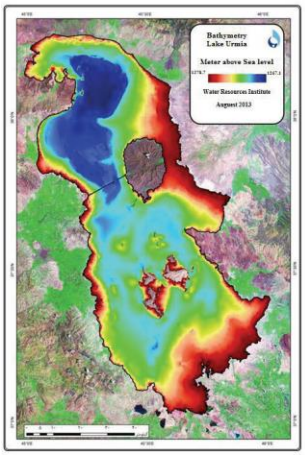


Fig 2- Bathymetry of Lake Urmia showing flat bottom, conversion of the lake to playa

Table 1 Please replace with your table caption.

Year	Area (Km2)	Dried Area compared to earlier period (Km2)
1976	5266	-
1989	5423	-157
1998	5650	-227
2000	4610	+1040
2003	4241	+369
2005	4049	+142
2007	3841	+258
2009	3106	+734
2010	2005	+1102
2013	953	+1051

Discussion and findings

Similar cases of Lake Urmia in other parts of the world:

Aral Lake

Dr. Kaveh Madani, a specialist in water issues from Imperial University of London, draws attention to Lake Urmia in Iran and notes similarities with Central Asia. "What we are witnessing in Lake Urmia is the Aral Lake syndrome, and Lake Urmia is not the only example. We see this syndrome occurring in many places. Madani notes that this syndrome is a product of mismanagement and not climate change. "The Aral Lake is perhaps a classic example of mismanagement and human-made disasters that we witness everywhere. The problem lies in developing countries. Perhaps we have not yet understood the depth of the disaster. Studies are currently being conducted in some Asian countries that are affected by these crises. But most of these studies have been done recently. Even without comprehensive information, the evidence indicates a dire situation and there is no immediate solution. The population of Central Asia was 6 to 8 million people at the beginning of the 20th century, but this figure has increased to 66 million people today. One of the main causes of the dryness of the Aral Lake was the irrigation of Central Asian regions, especially the former Soviet Union's decision to cultivate cotton in Moscow. After the decline of the water on the shores of the Aral Lake, plans such as the transfer of water from the rivers of southern Siberia and Russia to the Aral Lake or the plan to transfer water from the Ob watersheds to the lake were proposed by the Soviet government; But these plans either failed or were abandoned due to excessive costs.

Eiding Cool Lake:

This lake is located in China, 35 km south of Turian city, because of the presence of a layer of white salt along the lake and creating a bright appearance, it is known as Moonlight Lake. The lake is about 40 km long from east to west, and its width is The direction from north to south is about 8 km, the size of the lake is about 27 square kilometers, and it was created during the formation of the Himalayas. The water in the lake is primarily supplied by the melting of snow, after the Dead Foot, in the place of the second lowest point on the planet, at an altitude of 155 meters. Compared to the level of open water, due to the use of lake water in agriculture and evaporation, its level has been lower in summer and higher in winter due to the development of agriculture and the use of lake water for drinking water purposes and under the influence of climate change in 1958. It reaches 22 square kilometers. In 2000, only parts of the south-west of the lake remained and the rest became Koirenmak. Today, the location of the lake has turned into a white alum mine and the raw material for chemical products is rock salt and gypsum. The amount of salt in the lake is not estimated to be more than 300 million tons.

Bega Lake:

Lake Bega is located next to a city called Victoria, Australia. Also, this lake is located 325 km northwest of Melbourne. As a result of drought and water shortage in the region between 2007 and 2009, the water volume of the lake decreased to zero. Flooding was very useful and valuable for local communities from an economic and environmental point of view, but after it dried up, the negative effects of this environmental crisis were felt on the economic, environmental and health conditions of the society. Dust storms, air pollution caused by the smell of corruption and the decomposition of aquatic animals (including fish), the reduction of the quality of life, in addition to causing physical diseases, have also had a significant impact on the society in terms of mental and emotional health, and he pointed out that it also has a significant impact on the society due to the increase in unemployment, the increase in migrations, and the decrease in value. As a result of the economic isolation of the community and the lack of tourists and the loss of recreational facilities: swimming, water skiing and sailing, there have been significant negative effects, although the main cause of the drying up of the lake water cannot be attributed to climate changes alone, but there is hope to return the lake water again. It is an important factor in keeping the populations that have not yet migrated.

Salt Lake:

In America, Salt Lake in Utah and Ones in California have conditions similar to Lake Urmia. Americans did a lot of research and activities to revive this lake. Dr. Bijan Kushan, a geologist and environmental expert, says: "They transfer the water of Ounce Lake to the city of Los Angeles, and the government invests 2 billion dollars there to be able to use this water. They established 4 salt factories to use the salts economically. We can use this experience in Iran so that the region has economic growth and job creation and the lake is revived." Using the experiences of the experts of this lake and similar lakes, taking into account the climatic, cultural, economic and social differences, can be very fruitful.

Conclusion and solution presentation:

According to the public relations report of Urmia Lake Restoration Headquarters, Masoud Tajrishi mentioned 27 solutions to solve the Urmia Lake crisis, the first of which is to control and save water consumption in the agricultural sector. In this way, it is necessary to achieve the goal of saving 40% in agricultural, drinking and industrial water consumption during a five-year program under the management of the Ministry of Energy and the Ministry of Agricultural Jihad. This goal will be realized mainly through the formulation and implementation of programs to increase the productivity of 60% of water consumption of agricultural production by the Ministry of Agricultural Jihad. The next solutions are to prohibit any increase in the withdrawal of water resources from the Urmia basin and also to prevent new uses, with a special focus on management. It is agricultural production. Also, it is necessary to suspend all dam construction projects except Shahid Madani and Chirag Weiss, and manage downstream water supply and irrigation networks throughout the catchment area of Lake Urmia. Systematic monitoring and management of underground water wells throughout the catchment area of Lake Urmia with The use of smart measurement technology is one of the other solutions that was emphasized by this faculty member of Sharif University of Technology.

References

-Hassanzadeh, Youssef. (2013). study of the hydrodynamic behavior of Lake Urmia and its effects on the nearby coasts, National Conference on Climate Change and its Impact on Agriculture and the Environment of Tabriz, pp. 3-5..

-Delavar, M, Murid, S, Shafifar, M. (2017). Simulation, sensitivity and uncertainty analysis of changes in the water level of Lake Urmia in relation to its water balance components, Hydraulic Journal, 3(1), 45/55.

-Akbarzadeh, M. (2015). geopolitical consequences of the drying up of Lake Urmia, pp. 59, 99.

-Reports of Urmia Lake Restoration Headquarters 2016.

- Khushrovan, H, Farshchi, P. (2014). Acquaintance with the hydromorphological and environmental characteristics of Urmia Lake, its mysteries.

Advanced Engineering Days

aed.mersin.edu.tr

Identification and classification of karst landforms based on Cvijic, Waltham, Fookes, Komatina and Herak models (Case study: Travertine springs of Badab Soort)

Shahram Roostaei*[1], Bahareh Akbari [2]

[1]University of tabriz, Geomorphology, Iran, roostaei@tabrizu.ac.ir
[2]University of tabriz, Geomorphology, Iran, Bahareh.akbari93@yahoo.com

Cite this study: Roostaei, Sh., & Akbari, B. (2024). Identification and classification of karst landforms based on Cvijic,Waltham, Fookes, Komatina and Herak models (Case study: Travertine springs of Badab Soort). Advanced Engineering Days, 9, 948-950

Keywords
Karst Landforms
Travertine
Karst
Badab soort spring

Abstract

Karst landforms are mainly formed in areas with soluble carbonate bedrock by chemical dissolution of water with low acidity. Travertine is mainly young carbonate sediments that are formed in a dry environment and from the seepage of fresh water springs with hydrothermal. The travertine springs of Badab Soort in oroost region of Mazandaran province are an example of these springs which create various forms of karst by creating sediments and travertine deposits. This research is carried out with the aim of Identification and classification of karst landforms in the area of Badab Soort spring. Research tools include topographical and geological maps of Kiyasar, satellite images, DEM, ARC GIS. The model and method of identifying karst landforms are the classification methods of cvijik, Waltham, Fookes, Komatina and Herak. The study of the karst landforms of the Badab Soort spring determined that, based on the classification of cvijik, these landforms are in the transitional karst category, Based on the classification of Waltham and Fookes in the category of young karsts, based on the classification of Komatina in the category of flat or platform karsts, and based on Herak's classification, it is placed in the row of orogenic karsts.

Introduction

Karst geomorphology studies the specific morphological and hydrological features of dissolvable rocks (mostly carbonates). Karst forms are the product of climatic phenomena and elements and geological conditions in limestone areas (Zanganeh Asadi and et al., 2002).These forms are mainly formed in areas with soluble carbonate bedrock by chemical dissolution of water with low acidity(Palmer,2007). Travertine is mainly young carbonate sediments that are formed in a dry environment and from the seepage of fresh water springs with hydrothermal (Rahmani and et al., 2011). Due to the release of waters containing calcium and other iron, manganese, copper, silicon and some other elements from the earth, the conditions for the release of carbon dioxide are provided and due to the evaporation of water rich in calcium compounds, it gradually leaves calcium in the form of calcium carbonate. This composition is based on the type of impurity that they have get colors including yellow, red, beige, white, green, brown, etc. On the other hand, with the change of season and stopping, reducing and increasing the speed, the sedimentation process is done in layers and finally, over thousands of years, a travertine area is formed. Badab Soort springs is also a spring with relatively warm water and rich in solutes which has left travertine stones over time. (Saffari and et al., 2018).

Wide areas of non-glacial arid and semi-arid lands of the planet Earth are covered with karst-prone carbonate formations and approximately 20 to 25 percent of the world's population depends mostly or entirely on karst resources (Ford and William, 2007). About 20% of the world's lands are covered by karst rocks (Milanovich, 1981). Due to the high importance of these areas, karst in the world and Iran has been investigated by various researchers including: From the eighties onwards, the study of karst regions gained momentum and more researches were conducted in most regions of the world Among the most important of them, we can mention the classification of karst forms by cvijik (1925), Waltham and Fookes (2003), Komatina (1973) and Herak (1977).

In Iran, we can refer to researchers such as Eshghi and Servati in 2000, Maleki Shohani and Alaei Taleghani in 2008, Behniafar et al. in 2009, Velayati and Khanalizadeh in 2011, Khanlari and Momeni in 2012, Khoshrafter and et al in 2016, khezri and et al. in 2017, and Rezaei Arefi and colleagues in 2019 mentioned who they worked in this field.

Material and Method

In this research, in order to classify the karst forms in the area of Badab Soort spring, first, by using library studies, the required information and data have been collected. Then, using a topographic map with a scale of 1:50,000, a geological map with a scale of 1:100,000 by Kiysar and Google Earth satellite images, the study area has been defined and demarcated. Also, the types of formations and types of faults and their roles in karst forms were identified using the geological map of Kiyasar.

Finally, by using cvijic, Waltham, Fookes, Herak classification methods, the landforms were identified and classified. The classification of karst forms is done in order to study them better and it plays an important role in their separation and identification (Rezae Arefi et al., 2018). At the end, with observations and field visits, images of karst geomorphological forms were prepared and matched with the obtained results (Figure 1).

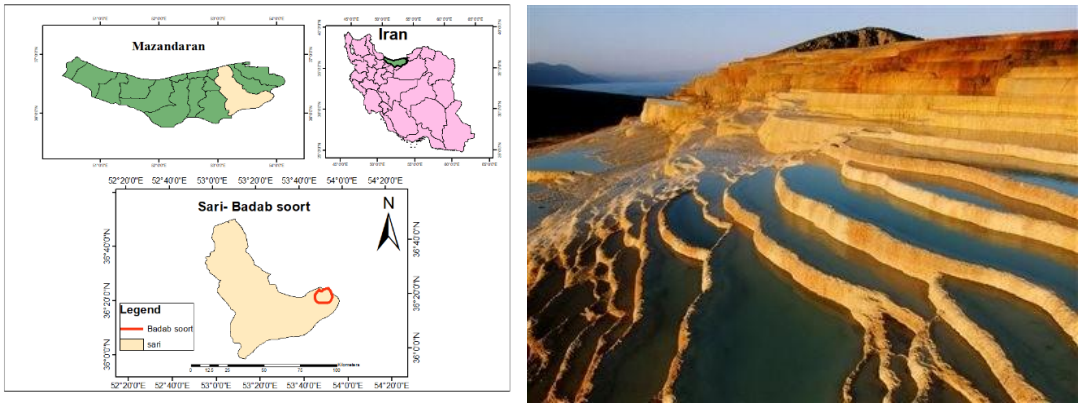


Figure 1. map of the study area

Badab Soort springs are located at 53º 51' 14" to 53º51'28" east longitude and 36º 21' 02" to 36º 21' 20" north latitude, in Sari city, Kiyasar city, Chahar Dange district, Dehistan Pushtkoh is located in the village of Soort, between the villages of Oroost and Malkhast. These springs were formed at the same time as the last folding of Alborz in Pleistocene and Pliocene (Bagheri et al, 2012).

Results & Discussion

The requirement for the classification of karst forms is their identification, which is done using field methods and techniques, aerial photos, satellite images and geological maps. In identifying and classifying the karst forms of the studied area, we tried to use methods that are compatible with its geomorphology. Therefore, the karst forms of the region were identified and classified based on the classifications of cvijik (1925), Waltham and Fuchs (2003), Komatina (1973) and Harak (1977):

1. cvijic classification model: The basis of this classification is based on geomorphological and geological conditions. n this classification, karst forms are divided into three categories: complete, incomplete and transitional karst (Table 1).

Table 1. Classification of karst forms based on cvijik classification

karst type	type of stone	stone face	Karst landforms	Karst development
Complete karst (Holokarst)	High dissolution limestones	Completely rocky and without vegetation	Surface and deep karst phenomena	very high
Incomplete karst (Merokarst)	non-limestone rocks, low purity lime	Vegetation - non-limestone soils	Incomplete karst forms, lack of macrokarst	very little
Transitional karst	A combination of limestone layers between thin layers of formations non-limestone	A combination of limestone and other formations - sparse vegetation	Underground karst,microkarst, incomplete dolines, lack of pulleys	The expansion of underground forms, the formation of slow karens and the lack of expansion of pulleys

2**. Waltham and Fookes model:** The basis of that classification has been considered the maturity level and karst development rate. According to this classification, the karst forms created in carbonate rocks can range from the young stage to the full old stage or the most developed stage.

It is widely used in road construction, construction, urban development and land preparation activities and is based on the type and presence of dolines in a region.

3**. Komatina model:** The classification of Komatina is based on the main geological characteristics and most importantly, lithological and structural, topographical and hydrological characteristics. The type of karst is determined by considering the geological characteristics of the basin. In this classification, karsts are divided into the following two categories (Komatina, 1975):

A- flat karst or platform B- Synclinal Karst (Milanovich, 1981).

4. **Herak model:** In the classification of Herak, the influence of tectonic activities plays an important role in the classification of karsts.

Based on this, karsts are divided into two groups: inter-orogenic karsts (before orogeny) or epierogeny (including sheet or columnar, folded, basin and deep karsts) and epigenetic (including lenticular, folded, crushed karsts). and cumulative or collapsed and debris) are divided (Herak, 1977).

Badab Soort travertine spring area in Kiasar, Mazandaran of geology, most of its formations are limestone and in terms of weather conditions, its weather is semi-arid. The area of Badab Soort spring in cvjik classification considering that in terms of rock type, among the limestone layers, there are non-limestone impurity layers and other additional compounds such as iron, manganese and copper. And in terms of the face of stone and earth, it is a combination of lime with other formations and there is sparse vegetation and in terms of karst forms, they include microkarst, incomplete dolines and karns, except for transitional karst.

In the classification method of Waltham and Fookes, since the environment of the Badab Soort spring in the city of Kiasar is classified as temperate and mountainous, and this spring is located in the highlands and in terms of karst and geomorphic shapes, seams, cracks and small dolines can be seen and it lacks evolved forms of karst, it is placed in the young karst class or young stage. In the classification model of karst forms, Komatina Badab Soort spring is placed in the category of flat or platform karst.

And in the classification of Herak, which is based on the state of tectogenesis, according to the investigations of the geological map and landslide faults in the region and the earthquakes that occurred in recent years, the tectonics of the region is active and it is considered as part of karst orogeny.

Conclusion

According to the field surveys, geological and tectonic maps and the structure and lithology of the region and the identification of karst forms, based on the classification of cvijik, the karsts of this region are in the category of transitional karsts, based on the classification of Waltham and Fookes, in the category of the young karst, according to the classification of Komatina, was placed in the row of flat karsts and according to the classification of Harak, it was placed in the row of folded orogenic karsts. This classification revealed that the karst forms of the basin are often young and undeveloped, and the most important factor that accelerates them is the geological and lithological conditions.

References

1. Bagheri, M., Elandani, M. & Bagheri, S (2012). Development of therapeutic tourism in the area of Badab Soort mineral spring, National Conference on Tourism, National Capitals and Future Prospects, Isfahan.
2. Rahmani, S., Khodabakhsh, S., Mohseni, M. & Ghaemi, . (2011). The geotourism importance of limestone springs and travertine sediments, (northeast of Qorveh), The 5th specialized geology conference, Abhar.
3. Zanganeh Asadi, M., Ghayor, H., Ramesht, M., & Velayati, S. (2002). Karst perspectives of Akhlmad and its environmental management. Tehran, Journal of Geographical Research, No. 42, pp. 101-87.
4. Cvijic, J., (1925). Type's morphologiques des terrains calcaires. Comptes Rendus, Académie des Sciences (Paris), 180, 592–594
5. Ford, D., & Williams, P. D. (2007). Karst hydrogeology and geomorphology. West Sussex, England: John Wiley & Sons.
6. Herak, M. (1977). Tecto-genetic approach to the classification of karst terrains. Carsus Iugoslaviae, 9(4), 227-238.
7. Komatina, M. (1973). Development conditions and regionalization of karst In A. Burger & L. Dubertret (Eds.), Hydrogeology of karstic terrains: Case histories(pp. 21-29). Paris, France: IAH
8. Milanovic, P. J. (1981). Karst hydrogeology. Colorado, CO: Water - Resources ublications.
9. Palmer, A. N., (2007). Cave Geology: Dayton, Ohio, Cave Books, p. 454.
10. Waltham, A.C. & Fookes, P.G. (2003). Engineering classification of karst ground conditions.Quaterly Journal of Engineering Geology and Hydrogeology, 36, 101–18.

Advanced Engineering Days

aed.mersin.edu.tr

Investigation of land use change effects on water quality of Tabriz plain

Zahra Sedghi*[1], Ata Allah Nadiri [2]

University of Tabriz, Department of Natural Sciences, sedghizahra@tabrizu.ac.ir
University of Tabriz, Department of Natural Sciences, Nadiri@tabrizu.ac.ir

Cite this study: Sedghi, Z, & Nadiri, A.A. (2024). Investigation of land use change effects on water quality of Tabriz plain**.** Advanced Engineering Days, 9, 951-953

Keywords
Land use
Remote Sensing
Groundwater
Quality Index
Tabriz Plain

Abstract

Population growth and increased land use changes, coupled with excessive groundwater exploitation, have severely degraded groundwater resources in the Tabriz Plain. This study investigates how these land use changes impact groundwater quality, utilizing various parameters and applying the Groundwater Quality Index (GWQI) for effective drinking water management. Using Landsat satellite images with TM and OLI sensors and geographic information systems, the study analyzed land use changes in the Tabriz Plain from 2013 to 2023. Over this period, the residential area expanded from 7.91% to 13.57%, a +6.66% change, while the farmland area increased from 16.58% to 23.55%, reflecting a +6.97% change. These substantial expansions in residential and farmland areas have significantly contributed to the deterioration of drinking water quality in the Tabriz Plain, as confirmed by the GWQI calculations.

Introduction

Groundwater offers advantages over surface water, such as better quality and lower contamination levels. However, factors like population growth, land use changes, and increased exploitation have deteriorated groundwater quality, leading to issues like salinization. Monitoring groundwater resources is crucial for regional development, and creating maps of land use changes and groundwater quality variations is vital for sustainable resource management and informed decision-making. Remote sensing and GIS methods are effective in this context, as demonstrated in studies from Punjab, India, and the Guishui River Basin, China, which used satellite images and groundwater data to assess the impacts of land use changes on groundwater resources. These studies found that increased urban land use and decreased grassland areas reduced annual groundwater recharge [1-2]. Building on these insights, the current study examines the relationship between land use changes and groundwater quality over a 10-year period in the Tabriz Plain. Using remote sensing technology and the Maximum Likelihood Classification method in ENVI 5.3 software, land use maps for 2013 and 2023 will be generated to detect changes and assess their impact on drinking water quality in the Tabriz Plain.

Material and Method

The Tabriz Plain, spanning approximately 700 square kilometers in northwest Iran, is part of the Urmia Lake drainage basin. It is surrounded by mountain ranges, the city of Tabriz, and the salt marshlands of Urmia Lake [3]. This study examines land use changes and groundwater quality in the Tabriz Plain from 2013 to 2023. Data include 60 annually measured groundwater samples with on-site pH and electrical conductivity (EC) measurements, and laboratory analyses of cations and anions following American Public Health Association methods [4]. Landsat 8 OLI sensor images from 2013 and 2023, corrected for geometric and atmospheric accuracy, were used. Land cover maps were prepared using the Maximum Likelihood Classification method in ENVI 5.3 software. The study combines groundwater quality data with land use maps derived from remote

sensing imagery to analyze the relationship between land use changes and groundwater quality over the 10-year period. The results show an increase in urban land use and a decline in groundwater quality due to these changes.

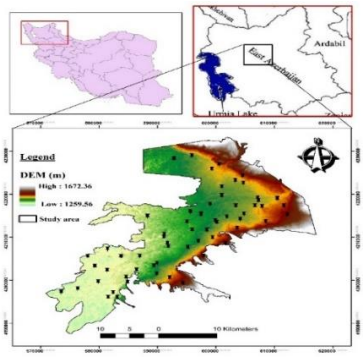


Figure 1. Location of the study area

Results

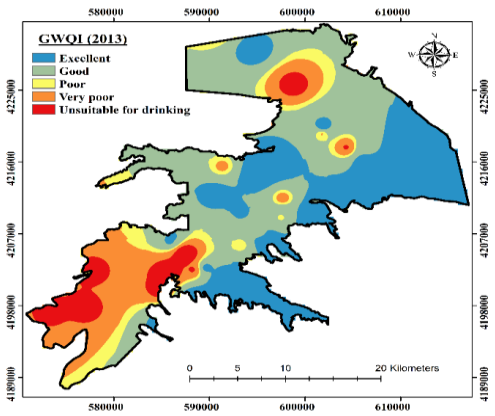
This study utilized a groundwater quality index based on Geographic Information System (GIS), incorporating water quality data for various parameters to present the information clearly. Landsat satellite images from 2013 and 2023, along with field visit data, were analyzed to examine land use changes in the Tabriz plain. Figure 2 illustrates the land use map and groundwater quality changes for these periods, while Table 1 details the area of each land use type. The results indicate that changes in urban and agricultural land use have led to a decline in groundwater quality. The kappa coefficient and overall accuracy of the classification method, evaluated using the error matrix, are reported in Table 2. The 2023 LULC maps are significantly more accurate than those from 2013, attributed to improved sensor detector lifespan, sensitivity, signal-to-noise ratios, and sensor characteristics.

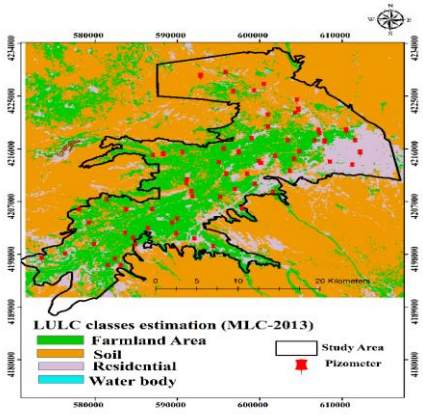
Table1. LULC classes estimation (percentage) for the years 2013 and 2023.

CLASS	2013	2023	TOTAL CHANGE (2013-2023)
FARMLAND AREA	16.58	23.55	+6.97
RESIDENTIAL	7.91	13.57	+6.47
SOIL	75.46	62.75	-12/71
WATER BODY	0.05	013	+0.07

Table 2. Overall accuracy (%) of the LULC maps for the years 2013 and 2023

	2013	2023
OVERALL ACCURACY (%)	97.26	98.93
KAPPA COEFFICIENT	0.98	0.99





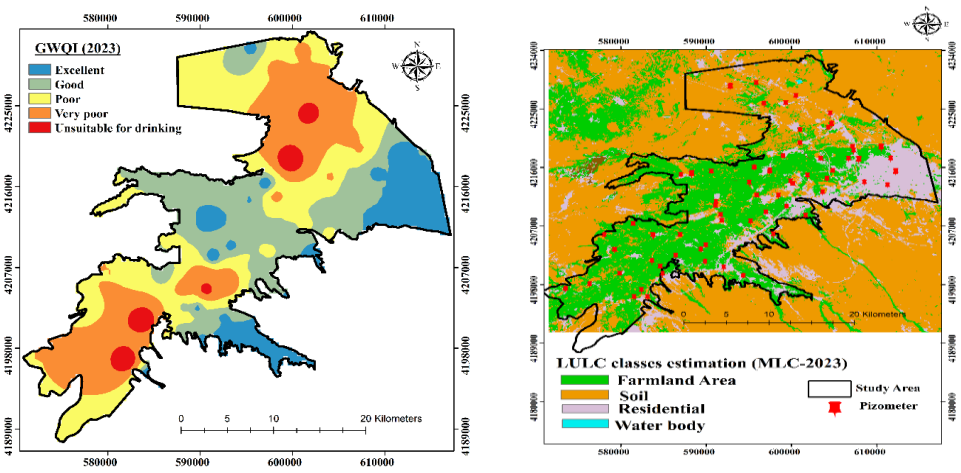


Figure 2. Results of the Maximum Likelihood Classification method and the groundwater quality changes map

Conclusion

There is an urgent need for legislation to regulate water usage and control rapid changes in Land Use and Land Cover (LULC), as these changes threaten the hydrological resources of the Tabriz plain. This study examines the degradation of groundwater quality (GWQI) in the Tabriz Plain due to land use changes and increased groundwater exploitation. Using Landsat satellite images from the OLI (2013-2023) sensor analyzed with the Maximum Likelihood Method, the study assessed groundwater quality through cations and anions. The results show that the drinking water quality index has increased over time, indicating a deterioration in groundwater quality, especially in the north, south, and southwest regions. Human activities and land use changes significantly contribute to this degradation, leading to increased groundwater pollution. This underscores the need for sustainable land and water management practices to prevent further deterioration. The study's findings offer valuable insights for land-use planners and water resource managers. LULC and hydrological maps can reveal new spatial relationships between rapid LULC changes and land subsidence. Further investigation into the impact of groundwater level depletion and land subsidence is recommended to better understand the environmental and geotechnical implications of spatiotemporal variations in groundwater level and quality.

References

1. Singh, S., Singh, C., & Mukherjee, S. (2010). Impact of land-use and land-cover change on groundwater quality in the Lower Shiwalik hills: a remote sensing and GIS based approach. *Open geosciences*, *2*(2), 124-131.
2. Pan, Y., Gong, H., ZHou, D., Li, X., & Nakagoshi, N. (2011). Impact of land use change on groundwater recharge in Guishui River Basin, China. *Chinese Geographical Science*, *21*, 734-743.
3. Berberian, M. (1976). *Contribution to the seismotectonics of Iran (part II-III): In commemoration of the 50th anniversary of the Pahlavi dynasty* (No. 40). Ministry of Industry and Mines, Geological Survey of Iran, Tectonic and Seismotectonic Section.
4. APHA (2005) Standard methods for the examination of water and wastewater. American Public Health Association, Washington.

Advanced Engineering Days

aed.mersin.edu.tr

Monitoring the impacts of investment in the tourism sector on land use changes in the Hir City using the Change Detection Technique

Mohsen Aghayari Hir*[1], Sahar Ahmadzadeh Naghadeh [1], Milad Manzelati [1]

[1] *University of Tabriz, Faculty of Planning and Environmental Sciences, Iran, aghayarihir@gmail.com, ahmadzade603@gmail.com, miladmanzalati@yahoo.com*

Cite this study: Aghayari Hir, M., Naghadeh, S. A., & Manzelati, M. (2024). Monitoring the impacts of investment in the tourism sector on land use changes in Hir City using the Change Detection Technique, 9th Advanced Engineering Days, 9, 954-964

Keywords
investment
tourism
land use changes
Hir City

Abstract

Tourism, as a significant economic activity, is one of the key investment sectors worldwide. This activity is one of the sectors that can play a role in spatial expansion, both directly and indirectly; in other words, one of the important consequences of this activity is land use change. The present research is applied in terms of purpose and descriptive-analytical in terms of nature and method. For analyzing, Change Detection Technique were used. One of the key aspects of the tourism industry is the dynamic land use, especially changes in land use. In the current research, this dynamic was investigated in the boundary of Hir City, Ardabil County. Wherever, with investment by the private sector with the participation of Hir Municipality, for the construction of the Hir Glass Bridge since 2020, has promoted tourism and also caused significant changes in the area of land use. These changes can be observed in the expansion and development of the built-up lands in the around of Hir City in the 10-year period (2013-2023). In contrast to these changes, farm and horticultural lands have decreased significantly. So, agricultural land use near to the invested part (Hir Glass Bridge) have been converted to different tourism uses (including residential, entertainmentand, ...). Considering the trend of land use changes that have occurred, it is necessary to make appropriate planning and decisions in the field of the management of land use changes after investment in the tourism sector.

Introduction

Investment is any kind of sacrifice of value now in the hope of obtaining any value in the future. In other words, the investor sacrifices a specific value in the present in order to obtain a particular value of interest in the future (1). Accordingly, the investment is vital for the growth of the general economy and especially the tourism sector (2); also, this industry is an economic activity dependent on capital process and market economy (3). However, it has significant potential in generating income and employment; so, investing in the development of this sector is necessary to reap from its benefits (2). Moreover, the conventional view of investment in the tourism sector is that it can be a driver for economic growth and development, especially in developing countries, tourism can be a major source of income in rural areas and help reduce inequalities between urban and rural regions (4).

Today, tourism is considered as the largest and most diverse industry in the world (5). Because, the World Tourism Organization predicts that by 2030, the number of tourist trips world will increase to 1/8 billion per year. At the same time, with such an increase, a significant increase in investment sector in order to provide services such as accommodations, transportation, catering facilities, entertainment and attractions, and other tourism-related services and the necessary infrastructure to meet the expected demand, a simultaneous increase in economic, social and environmental results is expected (6,7). Accordingly, various theories about tourism have been explained, which can be examined in Figure 1 (8).

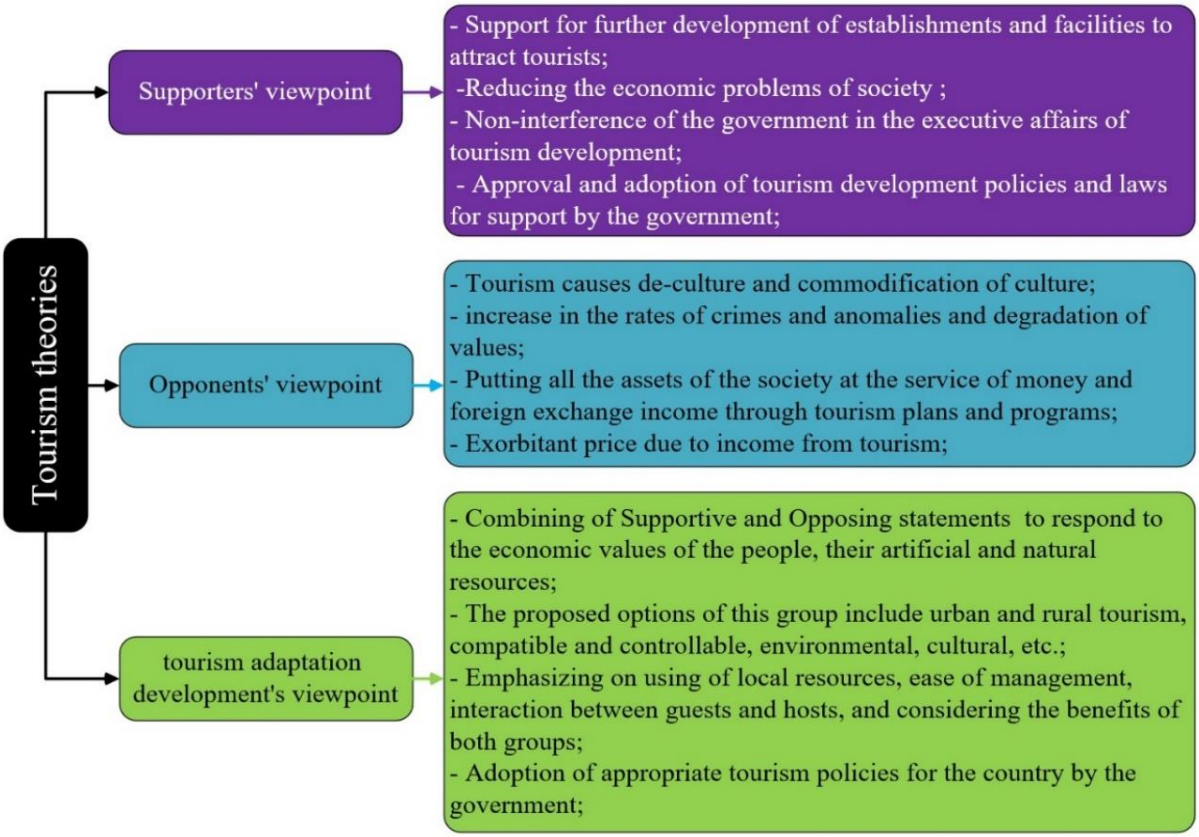


Figure 1. Tourism Theories

Economic benefits are more pronounced in the initial stages of tourism development, but in the massive and uncontrolled scale of tourism development and its inappropriate development, they will be followed negative effects and social and environmental costs in the later stages (9). The most common effect of tourism that all tourism workers, from planners to investors and local people, strive to achieve, is the economic factor and earning more profit, this factor leads to the creation of different effects in the physical condition of the region (10). In the development of tourism, the logic of land use is to gain as much profit from the land as possible, which make activities such as farm and horticulture uneconomical, and most of the land is allocated for the development of the tourism sector, and it disrupts the balance of the land use system and leads the instability of the development (11). Therefore, the issue of land use in tourism destinations is considered one of the key issues, because tourism activities are basically dependent on resources, i.e., they are included in the category of basic resource activities and the life and prosperity of the destination largely depend on the quality of its resources. Attracting a lot of tourists to the destination and the demand pressure resulting from it causes tourism resources to be sensitive and vulnerable to changes (12).

Also, the experiences of many tourist destinations in the world have shown, that the lack of proper management of the construction of tourism structures can have environmental, social and even economic consequences. Encroachment on the privacy of natural resources, construction and overloading of capacity in limited and ecologically sensitive lands, distribution pollutants in the environment, removing and destroying natural resources and landscapes, will be among these instances (12). In other words, land use change is one of the most important negative effects of tourism. If the development of tourism is not in accordance with the principles of land physical planning, it can create problems in the region (13). In addition, such a form of tourism greatly changes the livelihood of local residents and it may lead to a large change in the land use from agricultural to residential. In other words, the expansion of this type of tourism in many regions in the not-so-distant future will lead to decrease in agricultural land and a sharp drop in agricultural production (13). The necessary conditions for the progress and success of tourism host communities include maintaining traditions, relationships and culture, that action to preserve agricultural land use in terms of quantity and quality, while tourism is happening in it (14).

For this purpose, in the study area of the research, which is the tourist areas under the influence of Hir Glass Suspension Bridge, land use changes have been investigated with the origin of time before the establishment of Hir Glass Suspension Bridge and after it, by recognizing the changes in land use that have taken place as a result of the construction of this structure that attracts tourism after 2020 in the studied area, for more appropriate planning measures for this area should be suggested.

In this part of the research, various internal and external sources have been investigated (Table 1).

Table 1. Check internal and external sources

No	Author(s) (year)	title	result
1	Atik et al., (2010)	Land use changes in relation to coastal tourism developments in Turkish Mediterranean	The results of the research showed that 816 hectares of agricultural land and 457 hectares of natural coastal forests have been converted into tourism infrastructure such as hotels, service buildings and residences. The destruction of coastal forests was more at the beginning of tourism development, but this trend has been proven, while continuous changes in agricultural land are expected to continue in the coming years. So, it is essential that tourism development programs are accompanied by a set of ecological, social and economic systems for tourism livelihood and exploitation of the region.
2	Zaheri et al., (2012)	A research on second houses and their role in rural area land use changes (case study: Heravi villages, Haj Abdal and Dizaj Leili Khani located in East Azerbaijan Lighvan Valley)	The results of this research show that the changes have occurred mainly in recent years and the construction of second houses, while imposing major changes on the land use of these villages, have caused a significant part of the agricultural function of these villages to become a recreational-leisure function.
3	Karimi Rastgar (2015)	The effects of land use change due to tourism development on rural areas, case study: the central part of Tonekabon County	The results obtained showed that there is an inverse relationship between the two variables of tourism development and various effects of use changes in the study area. This means that the negative effects have more growth than positive effects by the growth of tourism. And this negative consequence is also higher than the other aspects to the environmental dimension; there is also a significant difference between the impressible different aspects of social, economic and environmental.
4	Bakhtiari (2017)	Investigating the role of tourism in land use change in coastal villages, case study: Mahmoodabad Villages	The results of the present research show that there is significant relationship between tourism and land use change in the coastal villages of Mahmoud Abad City at the level of 99%. Also, there is a significant relationship between the performance of managers and responsible trustees in controlling land use change at the level of 99%.
5	Safi Samaghabadi (2017)	Investigating and analyzing the effects of rural tourism on the land use pattern in the rural area of Taleghan case study: Kenar Roud Rural District	The results indicate that the lands of the villages of Hasanjun and Seyyed Abad located in the village of Kenarrud Taleghan, they are subject to changing land use patterns. That is the way in recent years with the increase of the arrival of rural tourists to the region as well as significant increased tourism second homes, land uses of crops, garden and pastures have converted to recreational- leisure, service, tourism and residential land use.
6	Sojasi Qeidari., & Sadrossadat (2019)	Analyzing the effects of tourism development on land use changes of Binaloud County's Rural Areas	Results indicated that there is a significant correlation between the presence of tourists and four components of: physical changes, incentives for more land use changes, structural and communication changes and economic changes in rural areas. The regression results revealed that a considerable part of the dependent variable (land use change) is explained by the independent variable (the tourists). Also, the results of the ranking of the studied villages in terms of the impact of land use changes on tourism indicated that three villages namely: MayanOlia, Mayansofla and Mayanvosta have experienced more land use changes than the others.
7	Li et al., (2020)	Impacts of rural tourism-driven land use change on ecosystems services provision in Erhai Lake Basin, China	The results show that the built-up area in Erhai Lake Basin (ELB), especially in the lakeside area, increased from 2000 to 2015 due to the tourism boom (in which tourism income increased 12 times), at the cost of agricultural land, grassland and forest. With these land changes, ecosystem services also changed greatly, to the detriment of ELB as a whole and especially the lakeside zone. By 2015, soil retention had decreased and nitrogen and soil export had increased, compared with the levels in 2000, while there was only a slight fluctuation in carbon storage and water yield. The nitrogen and soil exports are impairing water quality in Erhai Lake and causing severe environmental problems. This study provides empirical evidence of the important impact of tourism-driven land use change on provision of multiple ecosystem services. For environmentally friendly tourism in ELB and beyond, a form of sustainable tourism should be established.
8	Pandya et al., (2022)	Rendering land touristifiable:(eco) tourism and land use change	Empirical research reveals that while this initial boom of outsiders buying land has waned, land owning villagers are now setting up tourism enterprises on their own land, thereby diversifying land use from agriculture to tourism. Critical agrarian research has shown that material

No	Author(s) (year)	title	result
			and symbolic factors influence farmers' decision-making regarding land use change. An agrarian studies perspective thus facilitates a nuanced understanding of tourism-related land use diversification and change. By bringing agrarian and ecotourism studies approaches together here, we contribute to both by emphasising the importance of (eco)tourism in agrarian change and of attention to land use change in ecotourism studies to understand how rural people negotiate and navigate (eco)tourism in relation to land use.
9	Husnaini (2023)	The effect of the existence of Pangsan Tourism Village on changes in land use, economic, and social communities	These results indicate that the presence of Pangsan Tourism Village affects changes in land use where forests and rice fields are used as tourist attractions to support tourism activities. The existence of the tourism village also has an effect on the economy, especially the expansion of job opportunities and increased revenues. The developments of a tourism village with many tourists who come also affect social conditions that are reflected in the patterns of behavior and attitude of people skills. As for the distribution of increased community skills gained from training for manage the tourism village. The results of the research are expected to be a guideline for stakeholders to develop Pangsan Tourism Village.
10	Wang & Shariff (2023)	Response of ecosystem and eco-economic system to the land use structure change in tourism typical town: a case study in Yanyang Town of Guangdong Province, China	Rural tourism is more conducive to the coordination development of rural ecosystem and economy than traditional agricultural production. However, in the process of tourism development, it is very important to reduce the interference to land use, protect ecological land, maintain the continuity and complexity of land use, enhance the Ecosystem Services Value (ESV) of land use, and pay attention to the excavation of ecosystem value and cultural connotation.
11	Tonolli et al., (2024)	From grapes to getaways: unraveling the residential tourism impact on land use change and soil erosion processes in Menfi District	The results allow us to conclude that the decrease in the area with vineyards results in a reduction in soil erosion. The main drivers of the change in land use are socioeconomic factors, including the aging of farmers, the shift of subsequent generations to alternative activities, and the overall decrease in agricultural income. In addition, the expansion of tourist infrastructure was accentuated in the new land with olive orchard groves in south-faced, medium-altitude, and lower slope areas, which together provide landscape value and contribute to the reduction of soil erosion.
12	Meng et al., (2024)	Exploring the relationship between regional tourism development and land use efficiency: a case study of Guangxi Zhuang Autonomous Region, China	The results show that Guangxi has a good level of tourism development and a high land use efficiency. Also, there is a reciprocal causation relationship between the regional tourism development level and land use efficiency in Guangxi, with significant levels of 0/005 and 0/034 respectively, indicating high credibility. This indicates that there is a mutual promotion and interaction between the two, which rely on and drive each other, promoting the joint sustainability of tourism development and land use efficiency. In addition, the tourism development level is greatly influenced by itself, with impact values all above 0/99. At the same time, land use also has a significant self-impact, with impact values all above 0/87. Their internal optimization system is solid and endogenous impetus is robust, which can drive their development. Establishing an effective strategy for developing and protecting land use is beneficial to promote the long-term effectiveness of sustainable tourism development, enhancing high-quality development of the tourism economy and improving people's living standards and quality.

Material and Method

Hir City is one of the cities in the southeast side of Ardabil County, which is located at an average height of 1557 meters above sea level (Figure 2). This city is located in terms of longitude and latitude in the coordinates of 48/50589933 and 38/08051233 respectively. According to the last census conducted in 2016, Hir City has 681 households and 2080 people, of which 1054 are men and 1026 are women, so the sex ratio is 102/73. According to the data of Ardabil Meteorological Station in 2021, the average annual temperature is 11/19 degrees celsius, the average annual rainfall is 203/2 mm, the average relative humidity is 67/5%, the number of frosty days is 102 days, and the average maximum wind speed is 17/25 meters per second (27). Also, it can be to mention the various tourist attractions located in Hir City, including the Hir Glass Bridge, horticultural land and the surrounding natural environment such as Darband, Khulli, Qiz Aghaji, Vero, Babaketil, Buyukmil, Sharaf Gozehsi and etc. The glass bridge is built on the Hir Historical Castle and Varo Area, and it is the biggest investment made in connection with the tourism sector of this city, which is located in the eastern side of Hir City.

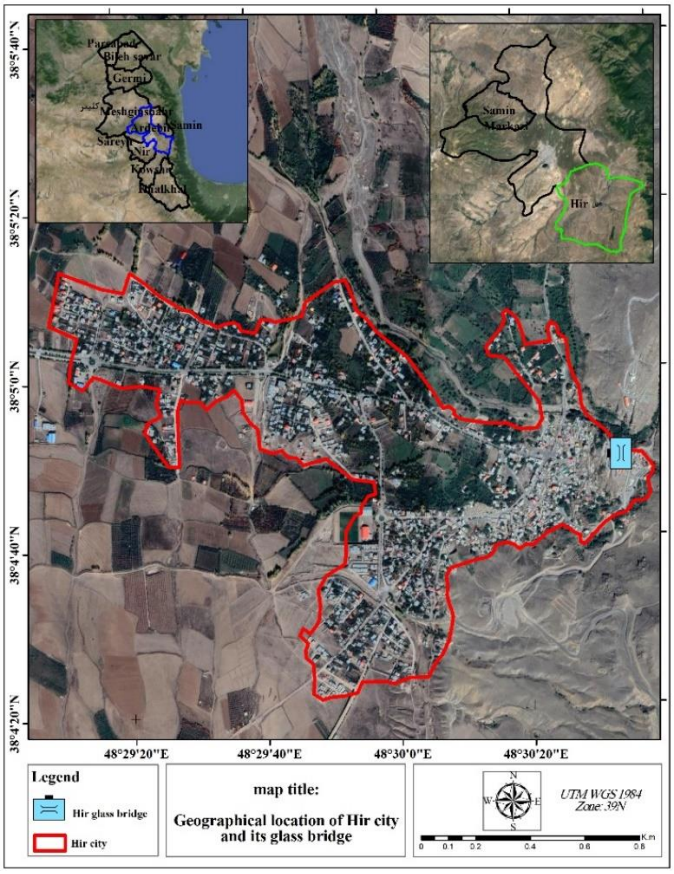


Figure 2. Hir City (Study Area)

The dataset used in this study was obtained from secondary sources. First, to classify land use from ENVI 5.1 software, to control ground and assessment accuracy from ArcGIS 10.8.2, Google Earth Pro, Portable Base map Server and Excel 2019 software (28) and finally used for the corrections of classified land use and case evaluations. ArcGIS 10.8.2 software was used.

In this part, data from OLI-TIR sensors of Landsat satellite were used to prepare land use maps. Images from USGS site with 30m spatial resolution downloaded from USGS website (https://earthexplorer.usgs.gov/)(29). The relevant data includes Landsat satellite images with row 34 and path 167, which includes OLI-TIRS Landsat 8 and 9 sensor images in 2013 and 2023, which can be seen in Table 2.

Table 2. The data of the satellites used in the research

Satellite	Sensor_ID	Path	Row	Data				Format	Resolution (m)	Layers
				Year	Month	Day	Time			
Landsat 8 OLI/TIS	LC81670342013168LGN01	167	034	2013	09	12	07:28:12	GeoTiff	30*30	11
Landsat 9 OLI/TIS	LC91670342023188LGN00	167	034	2023	07	07	07:25:48	GeoTiff	30*30	11

For the proper use of satellite images and the possibility of extracting correct and desired information, before any use of these images, an operation called image processing should be performed on these data so that, in addition to correcting existing errors, these images are prepared for classification. In general, this process of digital processing of satellite images is divided into 3 stages: pre-processing (atmospheric, geometric errors and radiometric correction), processing (classification) and post-processing (correcting and completing data, merging classes, removing useless and partial data and filtering to prepare classification results that in order to get close to desired final form and increasing the quality and accuracy of classification) (30).

In this research, supervised classification is used. This classification is based on training examples defined by the user to the software. In addition, the satellite image classifier software does each class based on the similarity of the training data (31). One of the most common supervised classification methods is the maximum likelihood classification method, which has been used in this research because this method has many advantages. In addition, this method has considered not only the average values in assigning classification, but also the variability of brightness values in each class (32).

One of the most important final steps in the classification process is the accuracy assessment (33). Therefore, users of land use/land cover (LULC) maps should know the accuracy of the map so that it can be used more

effectively and correctly. Therefore, overall accuracy, producer accuracy, user's accuracy and kappa coefficient were used to evaluate the accuracy of figures and these terms have been explained in detail in many studies. Relationships 1 to 4 show how to evaluate them (34).

(1) $$\text{User's accuracy} = \frac{\text{Number of Correctly Classified Pixels in each Category}}{\text{Total Number of Reference Pixels in that Category (The Row Total)}} * 100$$

(2) $$\textit{Producer accuracy} = \frac{\text{Number of Correctly Classified Pixels in each Category}}{\text{Total Number of Reference Pixels in that Category (The Column Total)}} * 100$$

(3) $$\textit{Total (overall) accuracy} = \frac{\text{Total Number of Correctly Classified Pixels (Diagonal)}}{\text{Total Number of Reference Pixels}} * 100$$

(4) $$\textit{Kappa Cofficient } (T) = \frac{(\text{TSxTCS}) - \sum(\text{Column Total x Row Total})}{TS2 - \sum(\text{Column Total} - \text{Row Total})}$$

According to Table 3, kappa coefficient is divided into 6 categories (34).

Table 3. Rating criteria of kappa statistics

0/81- 1/00	0/61- 0/80	0/41- 0/60	0/21- 0/40	0/00- 0/20	0>
Almost perfect	Substantial	Moderate	Fair	Slight	Poor

The land use data set for the two periods of 2013 and 2023 was prepared for the area of Hir City. In the current research, land use is divided into 5 classes (farm land, horticultural land, grass land, built-up land and rocky outcrops). As can be seen in Figure 3, the largest area of land use in the years 2013 and 2023 was related to the grass and then farm land. The most built-up, rocky outcrops and horticultural uses are located in the western, eastern and northeastern sides of the range, respectively. According to the under Figure, it can be admitted that the most changes have been made in the area of Hir City and the most direction of land use growth is towards the glass bridge built in the boundary of Hir City. In addition, on the central and northern side, the development area of built-up lands has been expanding towards Hir City. Most of the horticultural and farm lands in the around of Hir City have been destroyed or reduced dramatically in a period of 10 years.

Considering the investment made by the private sector with the participation of Hir Municipality in the tourism sector and visiting high number of tourists to this area, the land use changes have caused to occur completely upward and high speed, and the built-up lands have replaced farm, horticultural and grass lands in that boundary. In addition, the existing glass bridge in the city has affected the villages and other areas close to Hir City and caused many negative land use changes in the boundary.

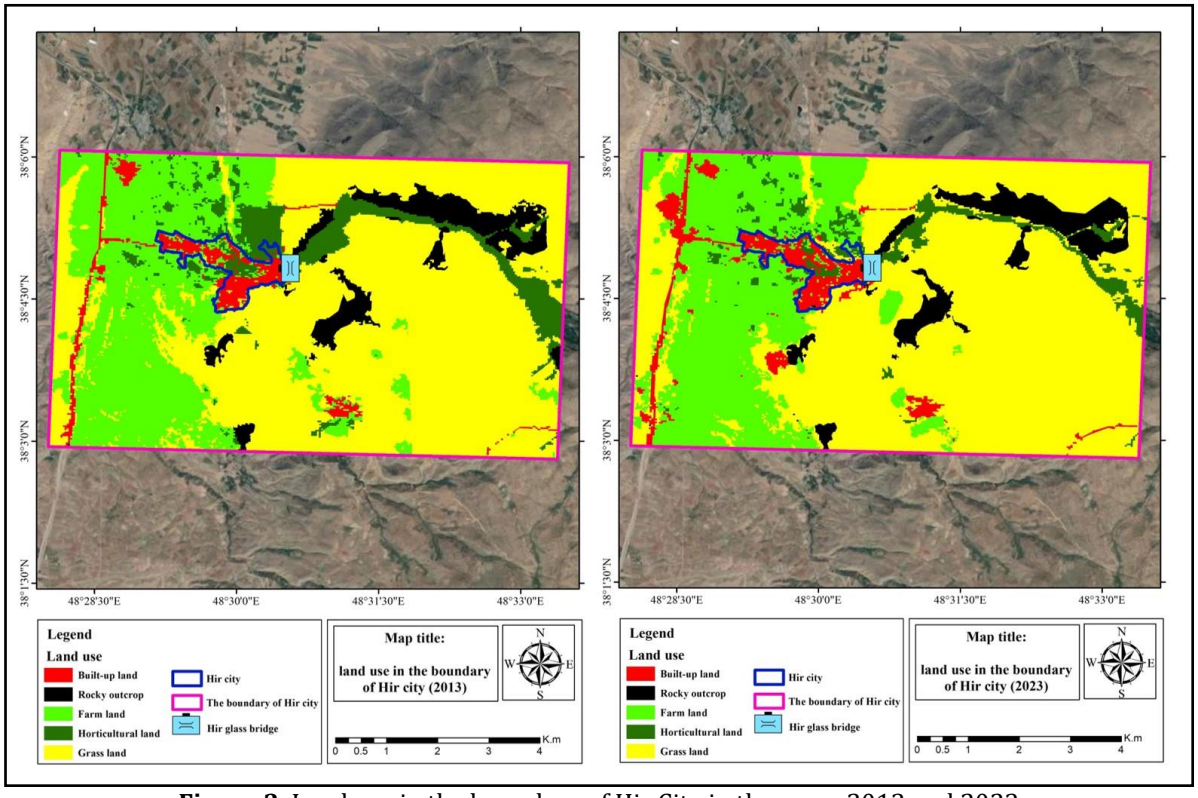


Figure 3. Land use in the boundary of Hir City in the years 2013 and 2023

According to Figure 4, the most changes in land use during the two periods of 2013 and 2023 were related to the increase of built-up lands and the decrease of farm and horticultural lands in Hir city. As can be seen in the figure, the communication roads connected to Hir City and residential uses have been developed in the boundary, and for increasing the level of this use, farm and horticultural lands within the privacy and boundaries of Hir City have been destroyed.

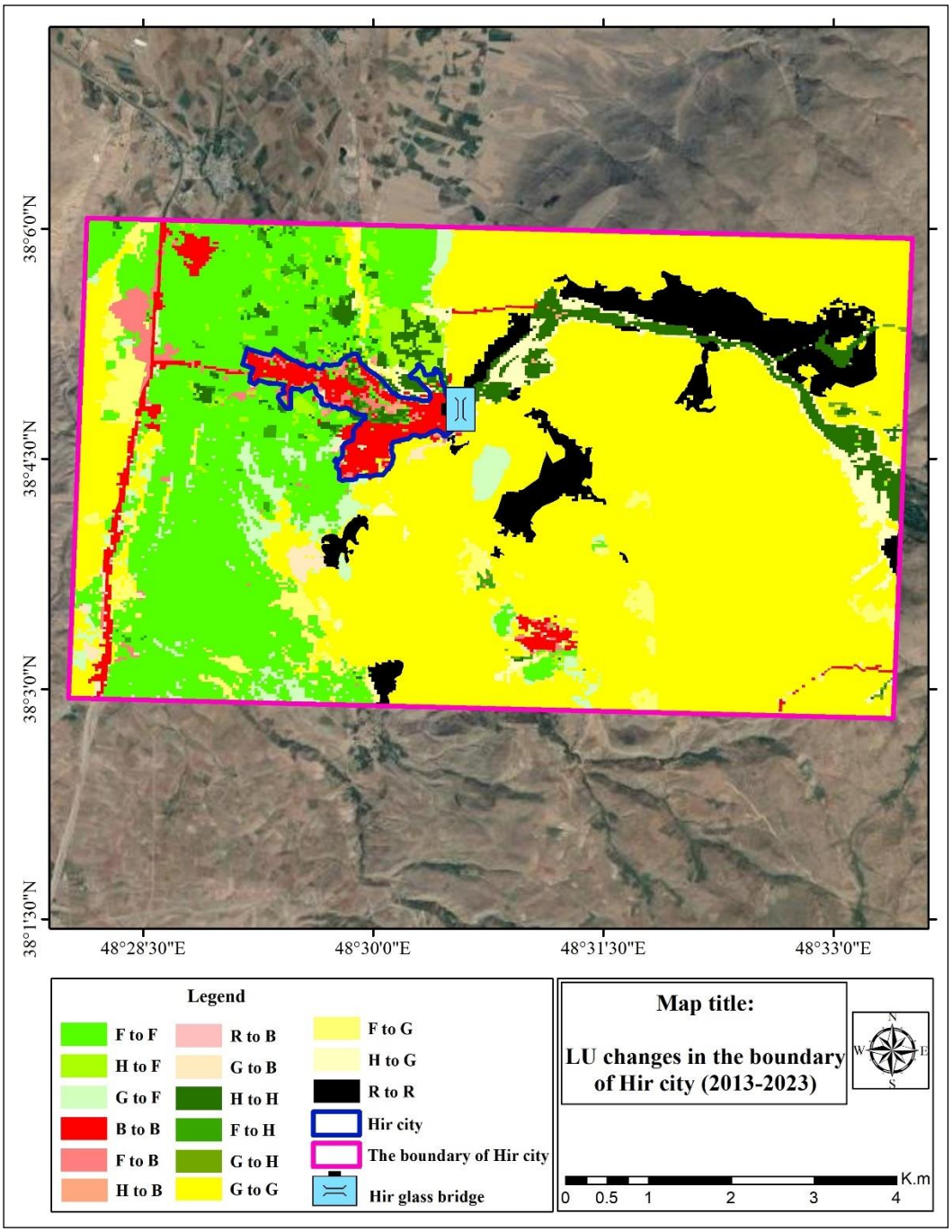


Figure 4. Changes in land use between 2013 and 2023[1]

Using Table 4, it can be stated that the most land use changes in the ten-year period are related to built-up land use, which accounts for approximately more than one quarter changes to itself is assigned. But most of the lost or changed lands are related to horticultural land use, which this use includes more than one-third of the changes. Also, the results of the table show that almost 10% of the farm lands have been lost, and this percentage of the mentioned change of use means that more than 38 hectares of farm lands have been lost.

[1] Built-up land= B
Rocky outcrop= R
Farm land= F
Horticultural land= H
Grass land= G

Table 4. LU/LC (2013, 2023) and its changes

LU Class	Area 2013 (Ha)	Area 2023 (Ha)	Change LU (2013-2023) (Ha)	Change LU (2013-2023) (%)
Built-up land	155/96	254/57	98/61	26/04
Rocky outcrop	265/75	265/45	-0/30	0/08
Farm land	1212/88	1174/55	-38/33	10/12
horticultural land	330/83	180/12	-150/71	39/80
Grass land	2594/83	2685/57	90/74	23/96
Total	4560/26	4560/26	371/83	100/00

As can be seen in Table 5, nearly 60 hectares of farm land, 32 hectares of grass land and 7 hectares of horticultural land have been changed to built-up land use. Also, 54 hectares of horticultural lands have been converted into farm lands and 96 hectares of farm lands have been changed to grass lands. These land use changes indicate the loss of horticultural and farm lands of valuable food and environmental.

Table 5. Matrix of LU/LC changes (2013-2023) (Ha)

LU Class	Built-up land	Rocky outcrop	Farm land	Garden land	Grass land	Total (2013)
Built-up land	155/96	0/00	0/00	0/00	0/00	**155/96**
Rocky outcrop	0/30	265/45	0/00	0/00	0/00	**265/75**
Farm land	59/81	0/00	964/46	28/65	159/79	**1212/88**
Garden land	6/96	0/00	77/33	146/93	99/60	**330/83**
Grass land	31/54	0/00	132/58	4/53	2426/18	**2594/83**
Total (2023)	**254/57**	**265/45**	**1174/55**	**180/12**	**2685/57**	**4560/26**

Figure 5 obtained from satellite images and information from previous tables and figures, it can see that the built-up land has increased dramatically and they have been replaced farm and horticultural lands, and these lands have had a significant decrease in the period of 10 years (2013 to 2023).

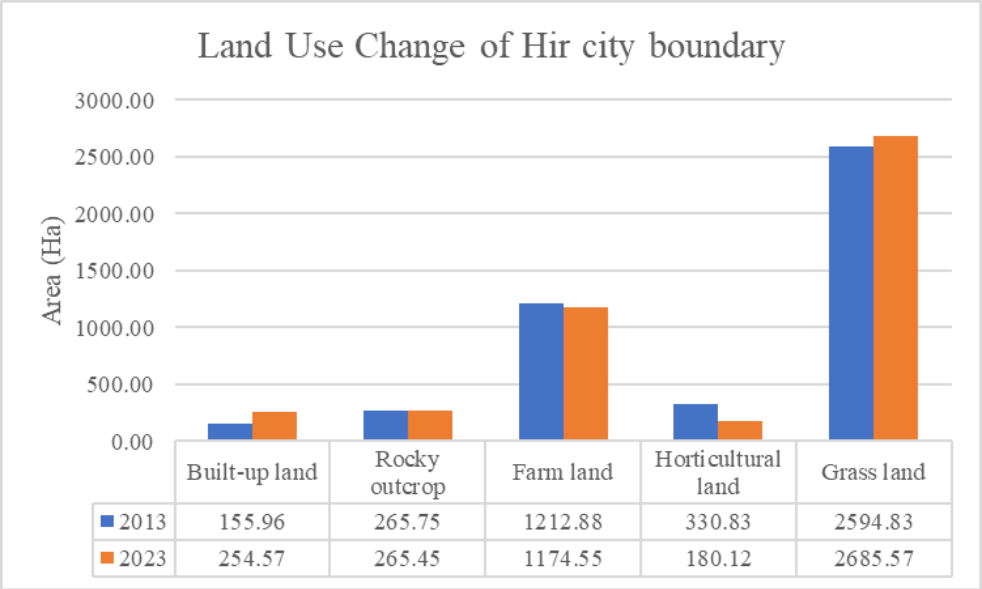


Figure 5. Land use change of Hir City boundary for the year 2013-2023 (Ha)

To evaluate the accuracy of the land use figures of the studied area, from kappa coefficients and overall accuracy were used. The results obtained show that the kappa coefficient in 2013 and 2023 is 0/83 and 0/94, respectively, and the overall accuracy is 86/67 and 95/24%, respectively. Finally, the kappa coefficient and the overall accuracy have scored above 0/8 and 80% in both periods, and so the classified land use have relatively high accuracy.

To check the level of further accuracy of land use figures, the accuracy of user and producer has also been calculated for both periods. According to the obtained data, the lowest user accuracy in 2013 and 2023 is related to built-up land use and grass land, respectively. Also, the lowest producer accuracy in 2013 and 2023 is related to grass land and farm use, respectively. By looking at Table 6, it can be seen that the accuracy of the user and the producer in most of the studied uses have obtained high points.

Tabel 6. Users and Producer accuracy assessment (2013-2023)

LU Class	User′s accuracy (2013)	User′s accuracy (2023)	Producer accuracy (2013)	Producer accuracy (2023)
Built-up land	71/34	100/00	100/00	100/00
Rocky outcrop	100/00	100/00	100/00	100/00
Farm land	75/00	81/82	100/00	83/33
horticultural land	90/00	90/00	100/00	100/00
Grass land	100/00	72/73	80/00	100/00

As it was checked in the previous two tables, it can be observed in Figure 6 that the classification accuracy rate is high and it has less error rate. In 2013, among 45 randomly selected points; Only 6 points were not correctly identified and in 2023, out of 42 random points, only 2 wrong points have been identified.

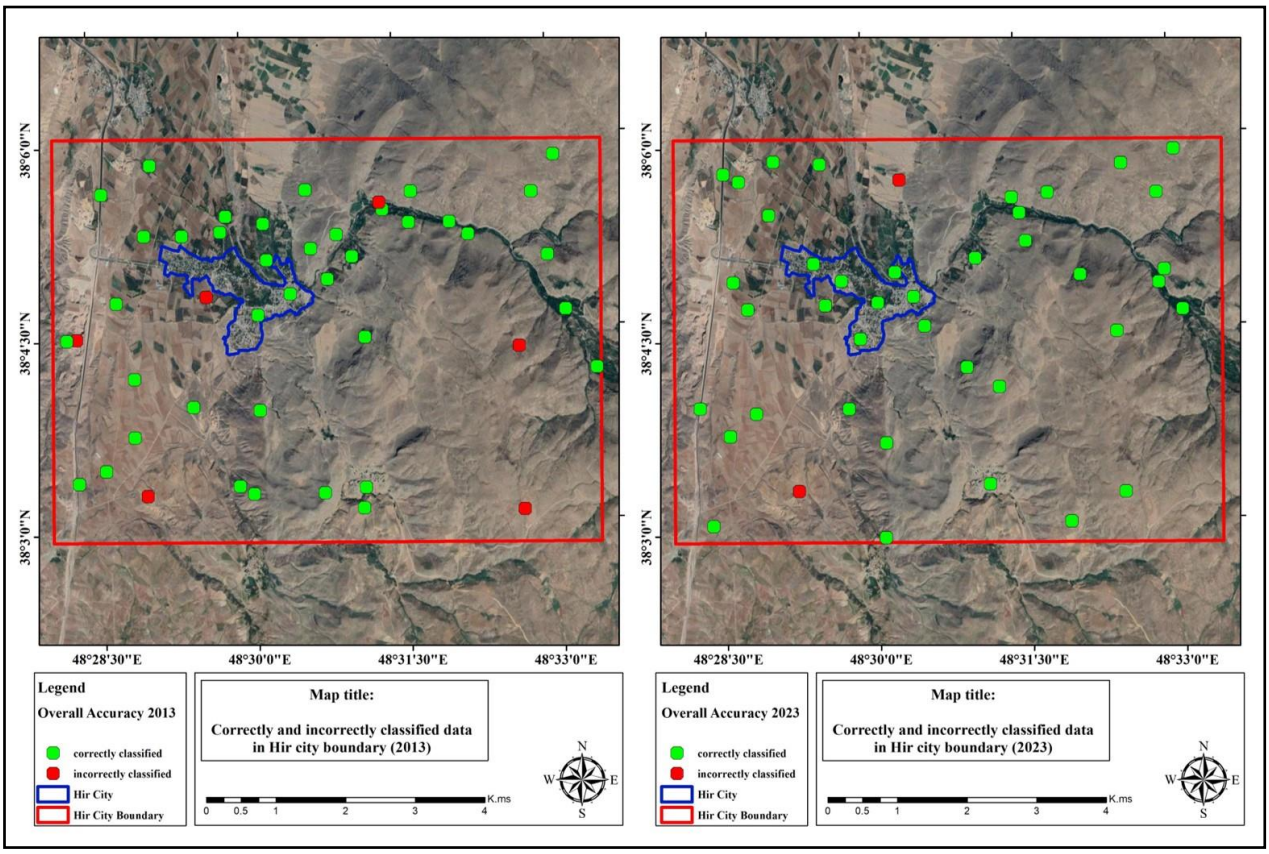


Figure 6. Correctly and incorrectly classified data

Discussion

The results obtained from the research of Sojasi Qeidari, & Sadrossadat (2019) indicate that there is a significant relationship between the presence of tourists and physical changes, the desire to change use, and structural-communicational evolutions (19). Furthermore, the results of the present research are aligned with the results obtained in the research of Gadami et al. (2010) (12), like this, the investment made in the tourism sector has caused extensive changes in the land uses of agricultural, garden and forest lands and has also caused the destruction of natural resources in the past decades.

Conclusion

According to the land use changes in the area of Hir City during two periods (2013-2023), almost more than one quarter of the changes are related to built-up lands. For creating these constructions, nearly 50% of farm and horticultural lands have been destroyed. In other words, in a period of 10 years, grass and built-up lands have increased by 90 and 98 hectares, respectively, and farm and horticultural lands have decreased by 38 and 150 hectares, respectively. The land use changes have occurred, based on amount of the kappa coefficient and the overall accuracy obtained for both periods, have almost perfect accuracy. Such changes indicate that there is a lack of systematic and proper management and planning in the studied area.

Furthermore, the results obtained from the processing of satellite images in a period of 10 years (2013-2023) show increasing in the level of land use built-up in Hir City and the villages and areas connect to Hir City and its communication road and in contrast, farm and horticultural lands in the city boundary, especially the lands around

of the glass bridge created in the city, have decreased significantly. In 2013, a large part of Hir City of privacy was farm and horticultural lands; While in 2023, the most farm and horticultural lands have been converted into residential lands due to the constructions. One of the main reasons for this development and expansion of built-up lands is the investment made for the construction of the Glass Bridge in Hir City. Because since the construction of this bridge (in 2020), many tourists have visited this area. Local people to respond to the accommodation needs of tourists, as well as the expansion of villa construction, have started new constructions in the city and its surrounding areas, and in order to do this, the land use change has intensified in this area.

According to the results obtained from land use changes due to investments made in the tourism sector, following recommendations are proposed to prevent negative environmental impacts:

- Continuous monitoring of land use changes and directing it towards 3rd and 4th grade farm lands;
- Prohibition of change of land use in 1st and 2nd grade farm lands;
- strict implementation of laws related to land use change;
- Informing residents about the importance of farm land and preventing its destruction;
- Formation of NGOs communities and organizations in connection with environmental considerations;

References

1. Ziyaee, M., Ebrahimi, M., & hajigholam, E. (2013). Prioritizing the factors affecting community investment in rural tourism development. Journal of Tourism Planning and Development, Vol. 2, Issue. 4, Serial Number. 4, pp. 29-42.
2. Nawaz, Muhammad. A., & Hassan, Sallahuddin. (2016). Investment and Tourism: Insights from the literature. International Journal of Economic Perspectives. Vol. 10, Issue. 4, pp. 581-590.
3. Goodarzi, M. (2024). Compiling and Prioritizing Investment Development Strategies in Tourism of Khuzestan Province. Journal of Tourism and Development, doi: 10.22034/jtd.2024.426027.2855.
4. Banerjee, Onil., Cicowiez, Martin., & Gachot, Sebastien. (2015). A quantitative framework for assessing public investment in tourism–An application to Haiti. Tourism Management. Vol. 51, Issue. C. pp. 157-173.
5. Mirza Ali, Mohammad., & Abedi, Mohammad Reza. (2017). Rural tourism and its effects on architecture. Journal of new researches of geographical sciences. Architecture and Urbanism. Vol, 2. No, 15. pp. 49-72.
6. Zarębski, Patrycjusz., Kwiatkowski, Grzegorz., Malchrowicz-Mośko, Ewa., & Oklevik, Ove. (2019). Tourism investment gaps in Poland. Sustainability. Vol. 11, Issue. 22, pp. 1-19.
7. Rahmani, Fatemeh., Khaksar, Hamideh., Barati, Javad., Rafiei, Hadi., Thabet Teymouri, Mozhgan., Sakhdari, Javad., Rahnama, Ali and Zarei, Afsaneh. (2017). Identifying and prioritizing investment opportunities in the tourism of Mashhad. Intra-university research project. Tourism Institute of Khorasan Razavi University Jihad.
8. Rezaei, Fahime., Khajeh Shahkoohi, Alireza., & Sahne, Bahman. (2022). The Role of Tourism Development in the Physical Changes of Rural Settlements (Case Study: Ziarat Village, Gorgan City). Journal of Geography and Regional Development, Vol. 20, Issue. 3, Serial Number. 40, pp. 256-227. doi: 10.22067/jgrd.2023.76229.1140.
9. Dadvar- khani, Fazileh., & Mohamadzadeh Larijani, Fatemeh. (2013). The assessment of Environmental subsequence of second homes tourism on rural areas in Babol township. Journal of Geography and Regional Development, Vol. 11, Issue. 1, Serial Number. 20, pp. 109-131, doi: 10.22067/geography.v11i20.30709.
10. Ghadirimasoom, Mojtaba., Motiei langeroodi, Seyed. Hasan., & Mehrpouya, Hasan. (2013). Explain the Impact of Tourism on Rural Areas Case Study: The East District of Klardasht. Journal of Tourism Planning and Development, Vol. 2, Issue. 5, Serial Number. 5, pp. 33-49.
11. ashornejad, G., heydari, Z., & Matinfar, H. (2013). An analysis on relation and environmental results of tourism development and land use changes in Ramsar City by using TM Landsat images. Journal of Tourism Planning and Development, Vol. 2, Issue. 4, Serial Number. 4, pp. 123-144.
12. Gadami, Mustafa., Aliqlizadeh Firouzjaei, Nasser., & Bardi Anamradanjad, Rahim. (2010). Investigating the role of tourism in land use changes of the destination (case study: central part of Nowshahr county). Journal of urban and regional studies and researches. Vol 1. No, 3. pp. 21-42.
13. Lotfinia, Mohammad. Taghi., & amar, Teymour. (2019). Analysis of the role of second homes tourism in the environmental changes of Target tourism villages of East of Guilan province in the last decade. Geography (Regional Planning), Vol. 9, Issue. 36, pp. 179-193.
14. jafari, Hamid., & shakhali, Mihadeseh. (2016). Tourism's Role in the Physical and Functional Revolutionize of Rural Settlements (Case Study: Villages in the Central Subarea County of Lahijan). Regional Planning, Vol. 6, Issue. 23, Serial Number. 23, pp. 191-200.
15. Zaheri, Mohammad., Kargar, Nahid., & Rahimipour, Bahareh. (2012). A Research on Second Houses and their Role in Rural Area Land Use Changes (Case Study: Heravi villages, Haj Abdal and Dizaj Leili Khani Located in East Azerbaijan Lighvan Valley). Journal of Geography and Planning, Vol. 17, Issue. 43, Serial Number. 43, pp. 123-144.

16. Karimi Rastgar, Mansoureh. (2015). The effects of land use change due to tourism development on rural areas, case study: the central part of Tonekabon county. Master's thesis. Department of Geography and Ecotourism. Faculty of Humanities and Social Sciences. Mazandaran University.
17. Bakhtiari, Samia. (2017). Investigating the role of tourism in land use change in coastal villages, case study: Mahmoodabad villages. Master's thesis. Department of Geography and Rural Planning. Faculty of Humanities. Golestan University.
18. Safi Samaghabadi, Mahsa. (2017). Investigating and analyzing the effects of rural tourism on the land use pattern in the rural area of Taleghan case study: Kenar Roud Rural District. Master's thesis. Regional Development Planning Group. Faculty of Social Sciences. Allameh Tabatabai University.
19. Sojasi Qeidari, Hamdollah., & Sadrossadat, Aida. (2019). Analyzing the Effects of Tourism Development on Land Use Changes of Binaloud County's Rural Areas. Physical Social Planning, Vol. 6, Issue. 3, Serial Number. 15, pp. 11-30. doi: 10.30473/psp.2019.6387.
20. Atik, Meryem., Altan, Türker., & Artar, Mustafa. (2010). Land use changes in relation to coastal tourism developments in Turkish Mediterranean. Polish Journal of Environmental Studies. Vol. 19, No. 1, pp. 21-33.
21. Li, Jinghui., Bai, Yang., & Alatalo, Juha. M. (2020). Impacts of rural tourism-driven land use change on ecosystems services provision in Erhai Lake Basin, China. Ecosyst Services. Vol. 42, Issue. C, pp. 1-10.
22. Pandya, Revati., Dev, Hari. Shankar., Rai, Nitin. D. Rai., & Fletcher, Robert. (2022). Rendering land touristifiable:(eco) tourism and land use change. Tourism Geographies. Vol. 25, Issue. 4, pp. 1068- 1084.
23. Husnaini, Adi. (2023). The Effect of The Existence of Pangsan Tourism Village on Changes in Land Use, Economic, and Social Communities. International Journal of Sustainable Competitiveness on Tourism. Vol. 2, No. 2, pp. 96-103.
24. Wang, Zhiming., & Shariff, Nurhazani Mohd. (2023). Response of Ecosystem and Eco-Economic System to the Land use Structure Change in Tourism Typical Town: A Case Study in Yanyang Town of Guangdong Province, China. International Journal of Professional Business Review: Int. J. Prof. Bus. Rev., Vol. 9, No. 12, pp. 1-26.
25. Tonolli, Alejandro., Pisciotta, Antonino., Scalenghe, Riccardo., & Gristina, Luciano. (2024). From grapes to getaways: Unraveling the residential tourism impact on land use change and soil erosion processes in Menfi district. Land Use Policy. Vol. 137, Issue. C, pp. 1-9.
26. Meng, Qiuli., Pi, Hongwen., Xu, Tao., & Li, Lihua. (2024). Exploring the relationship between regional tourism development and land use efficiency: A case study of Guangxi Zhuang Autonomous Region, China. Plos one, Vol. 19, Issue. 1, pp. 1- 16.
27. Publication of Iran Statistics Center. (2021). Statistical yearbook of Ardabil province.
28. Pertiwi, Titis. Chris. Monika., & Saputra, Aditya. (2024). Landuse Change Prediction on Super-Priority Tourism Destination in Labuan Bajo, Indonesia. In E3S Web of Conferences. Vol. 500, NO. 03043, pp. 1-11. EDP Sciences.
29. Govindaraj, Vellaiyan., and Dr. Lakshumana. Chokkalngam. (2022). Identification of Susceptible Zones through Temporal Landuse/ Landcover Changes in Gomukhi Watershed, Tamil Nadu, India. Indian Journal of Spatial Science. Issue.12(2), pp.97- 102.
30. Ahmadzadeh Naghdeh, Sahar. (2021). The effects of land use change on the ecosystem services of rural areas during the years 1989 and 2019 (case study: villages of Tabriz county). Master's thesis. Department of Geography and Rural Planning. Faculty of Planning and Environmental Sciences. Tabriz University.
31. Asokan, Anju., Anitha, J., Ciobanu, Monica., Gabor, Anderi., Naaji, Antoanela., & Hemanth, Jude D. (2020). Image processing techniques for analysis of satellite images for historical maps classification—an overview. Applied Sciences. Vol. 10. Issue. 12, pp. 1- 21.
32. Zhang, Fei., Kung, Hsiang. Te., & Johnson, Verner. Carl. (2017). Assessment of land-cover/land-use change and landscape patterns in the two national nature reserves of Ebinur Lake Watershed, Xinjiang, China. Sustainability. Vol.9, Issue. 5, pp. 1-22.
33. Rwanga, Sophia. S., & Ndambuki, J. M. (2017). Accuracy assessment of land use/land cover classification using remote sensing and GIS. International Journal of Geosciences. Vol. 8, No. 4, pp. 611- 622.
34. Islami, F. A., Tarigan, S. D., Wahjunie, E. D., & Dasanto, B. D. (2022). Accuracy assessment of land use change analysis using Google Earth in Sadar watershed mojokerto regency. In IOP Conference Series: Earth and Environmental Science. Vol. 950, No. 1, pp. 1-8. 012091. IOP Publishing.

Advanced Engineering Days

aed.mersin.edu.tr

Integrated Assessment of Forest Fire Vulnerability: A Multi-dimensional Approach

Elnaz Nejatiyanpour [1,3], Omid Ghorbanzadeh *[2], Josef Strobl [3], Khalil Gholamnia[4], Rasoul Yousefpour[5] Mahmoud Daneshvar Kakhki [1], Hamid Amirnejad[6], Mahmoud Sabouhi Sabouni[*1]

[1]Ferdowsi university of Mashhad, Faculty of Agriculture, Department of Agricultural Economics, Mashhad, Iran.nejatianpour84@mail.um.ac.ir; daneshvar@um.ac.ir; sabouhi@um.ac.ir.
[2] University of Natural Resources and Life Sciences, Institute of Geomatics Peter-Jordan-Straße 82, 1190 Vienna, Austria. omid.ghorbanzadeh@boku.ac.at.
[3] University of Salzburg, Department of Geoinformatics—Z_GIS, 5020 Salzburg, Austria. Josef.Strobl@sbg.ac.at.
[4] Charles University, Department of Applied Geoinformatics and Cartography, Albertov 6, 128 43 Prague 2, Czech Republic. gholamnk@natur.cuni.cz.
[5] University of Toronto, John H. Daniels Faculty of Architecture, Landscape, and Design, Toronto, Canada. r.yousefpour@daniels.utoronto.ca.
[6] Sari Agricultural Sciences and Natural Resources University, Faculty of Agricultural Engineering, Department of Agricultural Economics, Sari, Iran. h.amirnejad@sanru.ac.ir

Cite this study: Nejatiyanpour, E., Ghorbanzadeh, O., Strobl, J., Gholamnia., K., Yousefpour, R., Daneshvar Kakhki, M., Amirnejad, H., & Sabouhi Sabouni, M. (2024). Integrated Assessment of Forest Fire Vulnerability: A Multi-dimensional Approach. Advanced Engineering Days, 9, 965-967

Keywords
Susceptibility map
GIS
Random Forest
Hyrcanian forests

Abstract

The study addresses the escalating threat of forest fires, exacerbated by climate change and human activities, particularly in fire-sensitive ecosystems. Focused on forestry cities of Golestan Province, Iran, it utilizes the IPCC framework to analyze forest fire susceptibility through remote sensing and random forest analysis. Thirty risk indicators were identified, integrating biophysical, environmental, and socio-economic factors into risk maps. The research underscores the critical need for targeted interventions and strategic planning to mitigate fire impacts, emphasizing key indicators pivotal in assessing Hyrcanian forest fire risks.

Introduction

Forest fires are sudden natural hazards with significant impacts on ecosystems and societies. They are sparked by both natural occurrences, like lightning (4% globally), and human activities, intentional and unintentional (1).



Figure 1. The concept of Forest fire vulnerability

The consequences are extensive, ranging from biodiversity loss and greenhouse gas emissions to socio-economic repercussions such as infrastructure damage and health risks (2). Economically, Europe alone faced EUR 54 billion in losses from 2000 to 2017, averaging EUR 3 billion annually (3). Forest fires also challenge urban areas, agriculture, and tourism, particularly in regions like the Western US and Florida during peak tourist seasons.

Understanding the socio-economic impacts is critical for effective fire risk assessment and policy development. Vulnerability, encompassing susceptibility and the ability to cope, is key to addressing ecosystem and community-specific risks (4). Our study advances this by developing a Forest Fire Vulnerability Index integrating exposure, sensitivity, and adaptive capacity across social, economic, and environmental dimensions. This framework aids in identifying high-risk areas and shaping targeted mitigation strategies. The novelty of the present study lies in developing a comprehensive Forest Fire Vulnerability, which incorporates three main components: exposure, sensitivity, and adaptive capacity, using a comprehensive set of social, economic, and environmental indicators (see Figure 1). This approach will facilitate the identification of high-risk areas and the formulation of effective mitigation and management strategies.

Material and Method

Golestan Province stretches across latitudes from 36° 30′ to 38° 8′ north and longitudes from 53° 57′ to 56° 22′ east, situated in the northeastern region of Iran. Covering an area of approximately 2,037,809 hectares and comprising 14 cities, it constitutes about 1.33% of Iran's total landmass. Forest fire vulnerability is a critical concept that assesses the susceptibility of forested areas to the devastating impacts of wildfires, which can lead to significant consequences. This assessment typically integrates three primary components: exposure, sensitivity, and adaptive capacity, as defined by the Intergovernmental Panel on Climate Change (5).

Forest fire exposure is influenced by a combination of biophysical and socio-economic factors. Climate impacts fire behavior through its effects on temperature and precipitation, which affect fuel dryness and moisture levels (6). The terrain and wind conditions further shape fire dynamics, with factors such as elevation, slope, and wind speed playing crucial roles in fire spread and intensity (7). Human activities are responsible for the majority of forest fires (8). Forest fire sensitivity evaluates sensitivity across environmental, social, and economic dimensions. Forest fires severely damage ecosystems by destroying plants, disrupting reproductive cycles, and promoting invasive species, thereby threatening plant survival and conservation areas. Forest fire adaptive capacity is the ability of forests and their surrounding communities to withstand, recover from, and prepare for wildfires. This capacity includes environmental factors that enhance resilience by increasing vegetation cover and biodiversity (9).

Forest fire vulnerability mapping using Random Forest (RF)

In this study, the RF algorithm was utilized to assess biophysical, environmental and socio-economic indicators influencing forest fire exposure. Training options included 1000 trees, 25 variables per split, and an out-of-the-bag (OOB) sample statistic for model evaluation. Feature importance was gauged using the Mean Decrease Impurity method, leveraging MODIS fire-event data from 2013 to 2023 to map fire-prone regions.

Results and discussion

The findings reveal that a significant portion of these cities exhibits very high levels of vulnerability, as visually represented in Figure 2, which categorizes forest fire vulnerability. A detailed analysis highlights specific indicators that are prominent in each area. The results show that significant factors in each aspect play a critical role. Environmental factors, such as precipitation, elevation, the presence of rare and endangered plants, forest reserves, animal habitats, reforestation efforts, and post-fire rehabilitation, underscore the ecological importance of these regions. Economic factors, including recreation areas, timber and non-timber forest products, infrastructure investments, farmers' insurance, and unemployment rates, illuminate the economic aspects contributing to the regions' vulnerabilities. Social factors, particularly the dependence on forests for livelihoods, emphasize the interaction between human communities and the environment, and the consequent impact on local populations. The forest fire vulnerability is assembled into five classes, and Table 1 represents the obtained areas in hectares for each class.

Table 1. Area of each class of the resulting integrated forest fire vulnerability map.

No	Class	Area (ha)
0	Very low	25817209
1	Low	183799.5
2	Moderate	263885
3	High	233979.8
4	Very high	163203.7

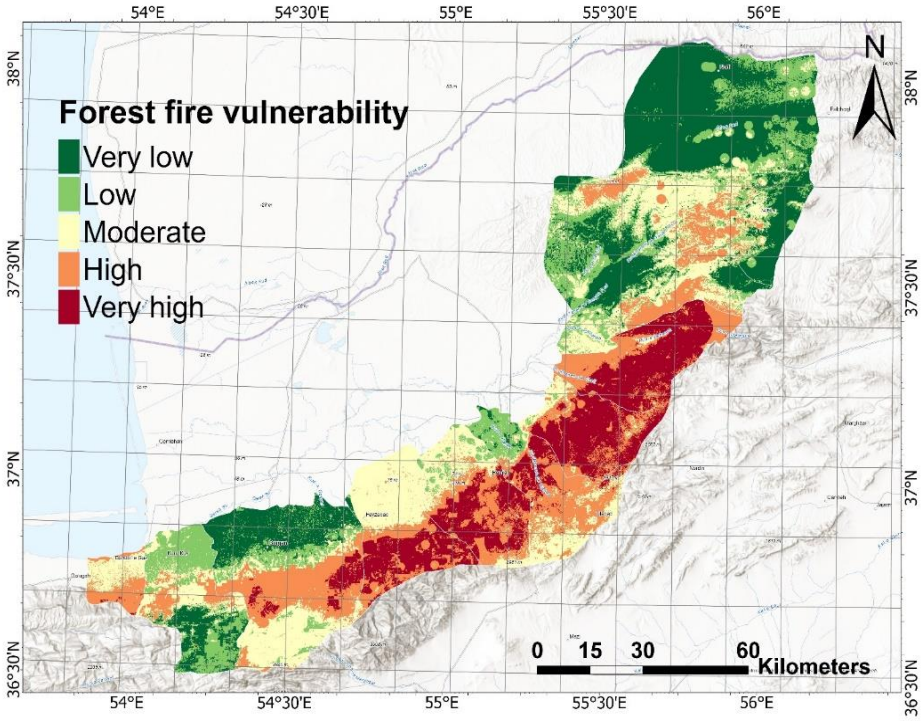


Figure2. The integrated forest fire vulnerability map for forestry cities in Golestan Province, Iran.

Conclusion

The study concludes that forest fires are influenced by a complex mix of socioeconomic factors, going beyond the usual environmental and biophysical considerations. It highlights the importance of factors such as land use for recreation, housing density, road layouts, livestock practices, population movements, and income levels in determining fire frequency and severity. The research also reveals differences in how communities are affected by forest fires, based on population size, economic reliance on forests, use of forest products, forestry output, healthcare access, education levels, investment in fire prevention and response, insurance coverage, unemployment, and the presence of protected areas.

References

1. Bowman, D. M. J. S., Williamson, G. J., Abatzoglou, J. T., Kolden, C. A., Cochrane, M. A., & Smith, A. M. S. (2017). Human exposure and sensitivity to globally extreme wildfire events. Nature Ecology and Evolution, 1(3). https://doi.org/10.1038/s41559-016-0058.
2. Eskandari, S., Pourghasemi, H. R., & Tiefenbacher, J. P. (2021). Fire-susceptibility mapping in the natural areas of Iran using new and ensemble data-mining models. Environmental Science and Pollution Research, 28(34), 47395–47406. https://doi.org/10.1007/s11356-021-13881-y.
3. Viccaro, M., & Caniani, D. (2019). Forest, Agriculture, and Environmental Protection as Path to Sustainable Development. In Natural Resources Research (Vol. 28). https://doi.org/10.1007/s11053-019-09497-2.
4. Grigorescu, I., Mocanu, I., Mitrică, B., Dumitraşcu, M., Dumitrică, C., & Dragotă, C. S. (2021). Socio-economic and environmental vulnerability to heat-related phenomena in Bucharest metropolitan area. Environmental Research, 192. https://doi.org/10.1016/j.envres.2020.110268.
5. IPCC. (2014). IPCC Fifth Assessment Synthesis Report-Climate Change 2014 Synthesis Report. IPCC Fifth Assessment Synthesis Report-Climate Change 2014 Synthesis Report.
6. Xu, R., Yu, P., Abramson, M. J., Johnston, F. H., Samet, J. M., Bell, M. L., Haines, A., Ebi, K. L., Li, S., & Guo, Y. (2020). Wildfires, Global Climate Change, and Human Health. New England Journal of Medicine, 383(22). https://doi.org/10.1056/nejmsr2028985
7. Piralilou, S. T., Einali, G., Ghorbanzadeh, O., Nachappa, T. G., Gholamnia, K., Blaschke, T., & Ghamisi, P. (2022). A Google Earth Engine Approach for Wildfire Susceptibility Prediction Fusion with Remote Sensing Data of Different Spatial Resolutions. Remote Sensing, 14(3). https://doi.org/10.3390/rs14030672.
8. Zhao, P., Zhang, F., Lin, H., & Xu, S. (2021). Gis-based forest fire risk model: A case study in laoshan national forest park, nanjing. Remote Sensing, 13(18). https://doi.org/10.3390/rs13183704.
9. Souza-Alonso, P., Saiz, G., García, R. A., Pauchard, A., Ferreira, A., & Merino, A. (2022). Post-fire ecological restoration in Latin American forest ecosystems: Insights and lessons from the last two decades. In Forest Ecology and Management (Vol. 509). https://doi.org/10.1016/j.foreco.2022.120083.

Advanced Engineering Days

aed.mersin.edu.tr

Ground deformation monitoring in Hatay Airport using GACOS-corrected StaMPS PSI

Mahmut Gorken*[1], Umut Gunes Sefercik [2], Mertcan Nazar [2]

[1]*Yozgat Bozok University, Architecture and Urban Planning, Land Registry and Cadastre Program, Şefaatli Vocational School, Türkiye, mahmut.gorken@bozok.edu.tr*
[2]*Gebze Technical University, Department of Geomatics Engineering, Türkiye, sefercik@gtu.edu.tr, mnazar@gtu.edu.tr*

Cite this study: Gorken, M., Sefercik, U. G., & Nazar, M. (2024). Ground deformation monitoring in Hatay Airport using GACOS-corrected StaMPS PSI. Advanced Engineering Days, 9, 968-971

Keywords
Hatay Airport
Reclamation area
StaMPS PSI
MT-InSAR
Deformation monitoring

Abstract

In order to meet the demands of rapid population growth and economic development, coastal cities are undertaking land reclamation projects with the objective of constructing new airport areas. Nevertheless, it is important to note that subsidence can occur as a result of this process. Therefore, monitoring ground deformation in reclaimed airports is a crucial task. In this study, a dataset of 151 Sentinel-1A single-look complex (SLC) images between 2 December 2017 and 29 January 2023 was utilized in the application of the Stanford Method for Persistent Scatterers (StaMPS) for persistent scatterer interferometry (PSI) based ground deformation monitoring in the Hatay Airport area. Furthermore, phase delay errors resulting from atmospheric contributions were corrected using Generic Atmospheric Correction Online Service for InSAR (GACOS) data. The results indicate that the average line-of-sight (LOS) deformation velocity across the area was between -6.25 mm/year and 9.02 mm/year, with variations observed in different locations. The deformation trend exhibited contrasting behaviors on the northern and southern sides. It can be observed that certain areas exhibit a deficiency in PS points in comparison to the remainder, which can be attributed to the presence of low-coherence regions. Overall, the application of StaMPS PSI for ground deformation monitoring demonstrated sub-centimeter accuracy in a reclaimed airport area.

Introduction

Cities along the coastline worldwide are engaged in engineering initiatives to reclaim land to accommodate rapid population growth and economic development. The process of reclaiming buildable land from too moist agricultural areas, oceans, seas, riverbeds, and lakebeds involves the alteration of the ground morphology [1]. Nevertheless, subsidence and cracking may occur during the process of land reclamation due to a number of factors, which can present a significant risk to structures and the safety of people [2]. In particular, airports constructed on reclaimed land require the monitoring of ground deformation in a timely manner to prevent disasters and ensure the continued safety of operations [3].

Conventional terrestrial ground deformation monitoring techniques offer high precision, but they require a significant investment of labor, are often time-consuming, and have low resolution for identifying surface deformation at high resolution [4]. Interferometric synthetic aperture radar (InSAR) is a highly effective tool that has been employed for several decades to generate 3D solid models of the Earth and to monitor surface deformation with sub-centimeter accuracy by interpreting phase differences between successive SAR images [5-8]. In addition, the differential InSAR (DInSAR) technique utilizes the InSAR technology to obtain surface deformations in the radar line-of-sight (LOS) direction by examining the phase difference between SAR data acquired during distinct periods and varying orbits [9]. To overcome the limitations of the DInSAR technique, including decorrelation, sensitivity to atmospheric variations, and shifts in orbital trajectories, the multi-temporal InSAR (MT-InSAR) approach was proposed for monitoring ground deformation in different time series [10-12].

An innovative MT-InSAR method known as persistent scatterer interferometry (PSI) was developed to monitor ground displacements with millimetric precision by utilizing highly coherent targets, commonly referred to as persistent scatterers (PS) [13-14]. To enhance the detection capability of PSI for low-amplitude observation points, the Stanford Method for Persistent Scatterers (StaMPS) technique was developed [15]. Furthermore, several approaches have been proposed to address the issue of atmospheric phase delay error. One example is the recently proposed Generic Atmospheric Correction Online Service for InSAR (GACOS), which utilizes an iterative tropospheric decomposition (ITD) model [16-18].

In this study, the StaMPS PSI technique was employed for ground deformation monitoring at Hatay Airport, utilizing 151 Sentinel-1A single look complex (SLC) SAR images obtained between 2 December 2017 and 29 January 2023. Furthermore, atmospheric phase delay correction was conducted using GACOS data.

Study Area and Dataset

The airport is located northeast of Antakya, Hatay province, Türkiye at 36°21'46.0"N and 36°16'56.0"E. The airport is equipped with a single concrete runway, with dimensions of 3000 x 45 m. The airport was constructed on the site of the now-drained Lake Amik basin, occupying an area of approximately 2.70 km^2.

As part of this study, a Sentinel-1A SLC dataset was acquired in descending orbit in interferometric wide swath (IW) mode over the Hatay Airport area between 2 December 2017 and 29 January 2023. The SAR images used were in vertical polarization (VV) and were downloaded from the Alaska Satellite Facility's (ASF) Vertex Platform.

Methodology

The methodology of this study was carried out in two steps, including pre-processing of the Sentinel-1A dataset and StaMPS PSI processing. Atmospheric phase delay correction was performed using the GACOS products during StaMPS PSI processing. The preprocessing for StaMPS PSI was conducted using the Sentinel Application Platform (SNAP) 9.0.0 toolbox for Sentinel-1A, developed by the European Space Agency (ESA).

The selection of an optimal master is a crucial step in the generation of interferograms, as all slave images will be processed in connection with the selected master. This process was conducted in accordance with the stipulation of maintaining a minimum level of geometrical and temporal decorrelation [19-20]. In accordance with the aforementioned criteria, the master image was selected as the one acquired on 29 September 2020. The remaining processes were completed by the SNAP Graph Builder operator, thereby enabling the construction of chains of processing commands or graphs that can be applied in batch through the Graph Processing Tool (GPT). The aforementioned processes encompass sub-swath and burst selection, orbital correction, coregistration, which is achieved through the utilization of the Shuttle Radar Topography Mission (SRTM) 3 arc-sec (~90 m) digital elevation model (DEM), deburst operation, interferogram generation, which entails the removal of flat-earth phase and topographic phase, and finally, StaMPS export.

The PSI processing was conducted using StaMPS 4.1b, which is available from the GitHub repository (https://github.com/dbekaert/StaMPS). The StaMPS PSI processing steps were executed in MATLAB R2022b, which was installed on an Ubuntu 18.04.6 LTS virtual machine. The point selection process for the PS candidate was conducted by applying a default threshold of 0.4 for pixel amplitude dispersion values [11]. Following the initial selection of PS candidates, the StaMPS processing steps from 1 to 7, as detailed in the StaMPS/MTI manual (Version 4.1b) [21], were carried out. Instead of step 8, the atmospheric phase delay correction was conducted within the Toolbox for Reducing Atmospheric InSAR Noise (TRAIN), an atmospheric phase correction toolbox module compatible with StaMPS developed by the University of Leeds [22-23]. The GACOS products were imported into TRAIN (Version 3beta), which is accessible from the GitHub repository (https://github.com/dbekaert/TRAIN) for this purpose.

Results and Discussion

The map displaying the average deformation velocity in the LOS direction was generated using the StaMPS PSI processing with GACOS correction of the Sentinel-1A SLC dataset acquired between 2 December 2017 and 29 January 2023 (Figure 1). Figure 1 illustrates that the average LOS deformation trend exhibited a clear differentiation across the airport area, with velocities in the LOS direction exhibiting a range of -6.25 mm/year to 9.02 mm/year. The average LOS deformation movement observed on the northern side of the airport area was closer to the satellite, while on the opposite southern side, it was further away. Furthermore, the density of points observed in the flat runway and terminal area was found to be lower than in other areas. The phenomenon may be attributed to the presence of planted lawns within the confines of the flat runway and taxiway movement areas, a factor that can contribute to a reduction in coherence, particularly in the context of reclaimed airport areas, thus resulting in a lack of identifiable scattering targets [24].

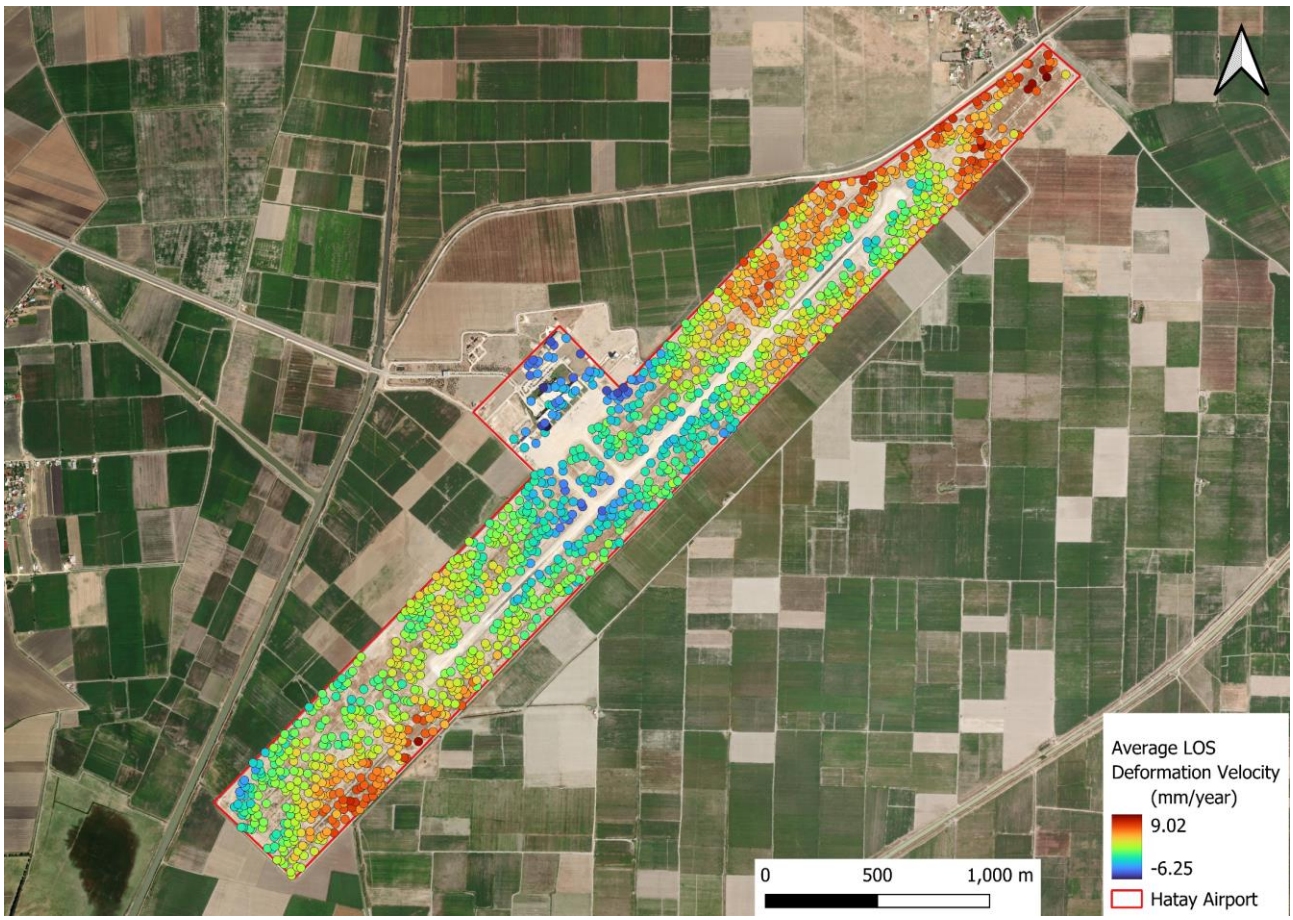


Figure 1. The average LOS deformation velocity map generated by the GACOS-corrected StaMPS PSI processing of the Sentinel-1A dataset

Conclusion

In conclusion, ground deformation monitoring of Hatay Airport was conducted using the StaMPS PSI application with GACOS correction on a Sentinel-1A dataset comprising 151 images acquired between 2 December 2017 and 29 January 2023. The results indicated that the average LOS deformation movement was observed in different directions on opposite sides of the airport area, with velocities ranging from -6.25 mm/year to 9.02 mm/year. The implementation of MT-InSAR techniques to monitor deformation with sub-centimeter accuracy in airport areas represents an effective tool for airport management systems, with the potential to prevent the occurrence of risks.

References

1. Martín-Antón, M., Negro, V., del Campo, J. M., López-Gutiérrez, J. S., & Esteban, M. D. (2016). Review of coastal land reclamation situation in the world. Journal of Coastal Research, 75, 667-671.
2. Shi, X., Zhong, J., Yin, Y., Chen, Y., Zhou, H., Wang, M., & Dai, K. (2023). Integrating SBAS-InSAR and LSTM for subsidence monitoring and prediction at Hong Kong international airport. Ore and Energy Resource Geology, 15, 100032.
3. Bao, X., Zhang, R., Shama, A., Li, S., Xie, L., Lv, J., Fu, Y., Wu, G., & Liu, G. (2022). Ground deformation pattern analysis and evolution prediction of Shanghai Pudong International Airport based on PSI long time series observations. Remote Sensing, 14(3), 610.
4. Buzzanga, B., Bekaert, D. P., Hamlington, B. D., & Sangha, S. S. (2020). Toward sustained monitoring of subsidence at the coast using InSAR and GPS: An application in Hampton Roads, Virginia. Geophysical Research Letters, 47(18), e2020GL090013.
5. Lu, Z., Kwoun, O., & Rykhus, R. (2007). Interferometric synthetic aperture radar (InSAR): its past, present and future. Photogrammetric engineering and remote sensing, 73(3), 217.
6. Sefercik, U. G. (2013). Productivity of TerraSAR-X 3D data in urban areas: A case study in Trento. European Journal of Remote Sensing, 46, 597-612.
7. Biggs, J., & Wright, T. J. (2020). How satellite InSAR has grown from opportunistic science to routine monitoring over the last decade. Nature Communications, 11(1), 3863.

8. Sefercik, U. G., Buyuksalih, G., & Atalay, C. (2020). DSM generation with bistatic TanDEM-X InSAR pairs and quality validation in inclined topographies and various land cover classes. Arabian Journal of Geosciences, 13, 560.
9. Pepe, A., Solaro, G., Calo, F., & Dema, C. (2016). A minimum acceleration approach for the retrieval of multiplatform InSAR deformation time series. IEEE Journal of Selected Topics in Applied Earth Observations and Remote Sensing, 9(8), 3883-3898.
10. Massonnet, D., & Feigl, K. L. (1998). Radar interferometry and its application to changes in the Earth's surface. Reviews of geophysics, 36(4), 441-500.
11. Hooper, A. (2008). A multi-temporal InSAR method incorporating both persistent scatterer and small baseline approaches. Geophysical Research Letters, 35(16).
12. Cigna, F., Del Ventisette, C., Liguori, V., & Casagli, N. (2011). Advanced radar-interpretation of InSAR time series for mapping and characterization of geological processes. Natural Hazards and Earth System Sciences, 11(3), 865-881.
13. Ferretti, A., Prati, C., & Rocca, F. (2001). Permanent scatterers in SAR interferometry. IEEE Transactions on geoscience and remote sensing, 39(1), 8-20.
14. Ferretti, A., Prati, C., & Rocca, F. (2000). Nonlinear subsidence rate estimation using permanent scatterers in differential SAR interferometry. IEEE Transactions on geoscience and remote sensing, 38(5), 2202-2212.
15. Hooper, A., Zebker, H., Segall, P., & Kampes, B. (2004). A new method for measuring deformation on volcanoes and other natural terrains using InSAR persistent scatterers. Geophysical research letters, 31(23).
16. Yu, C., Penna, N. T., & Li, Z. (2017). Generation of real-time mode high-resolution water vapor fields from GPS observations. Journal of Geophysical Research: Atmospheres, 122(3), 2008-2025.
17. Yu, C., Li, Z., & Penna, N. T. (2018a). Interferometric synthetic aperture radar atmospheric correction using a GPS-based iterative tropospheric decomposition model. Remote Sensing of Environment, 204, 109-121.
18. Yu, C., Li, Z., Penna, N. T., & Crippa, P. (2018b). Generic atmospheric correction model for interferometric synthetic aperture radar observations. Journal of Geophysical Research: Solid Earth, 123(10), 9202-9222.
19. Ferretti, A., Prati, C., & Rocca, F. (2000). Nonlinear subsidence rate estimation using permanent scatterers in differential SAR interferometry. IEEE Transactions on geoscience and remote sensing, 38(5), 2202-2212.
20. Rucci, A., Ferretti, A., Guarnieri, A. M., & Rocca, F. (2012). Sentinel 1 SAR interferometry applications: The outlook for sub millimeter measurements. Remote Sensing of Environment, 120, 156-163.
21. Hooper, A., Bekaert, D., Hussain, E., & Spaans, K. (2018). StaMPS/MTI Manual (Version 4.1b). University of Leeds, UK, Available online: https://homepages.see.leeds.ac.uk/~earahoo/stamps/StaMPS_Manual_v4.1b1.pdf (accessed on 1 July 2024).
22. Bekaert, D. P. S., Walters, R. J., Wright, T. J., Hooper, A. J., & Parker, D. J. (2015a). Statistical comparison of InSAR tropospheric correction techniques. Remote Sensing of Environment, 170, 40-47.
23. Bekaert, D. P. S., Hooper, A., & Wright, T. J. (2015b). A spatially variable power law tropospheric correction technique for InSAR data. Journal of Geophysical Research: Solid Earth, 120(2), 1345-1356.
24. Jiang, Y., Liao, M., Wang, H., Zhang, L., & Balz, T. (2016). Deformation monitoring and analysis of the geological environment of Pudong international airport with persistent scatterer SAR interferometry. Remote Sensing, 8(12), 1021.

Advanced Engineering Days

aed.mersin.edu.tr

Türkiye cracked the code in topographic earth representation

Arif Oguz Altunel[1], Samet Doğan[2]

[1]*Kastamonu University, Faculty of Forestry, Forest Engineering, Kastamonu, Türkiye, aoaltunel@kastamonu.edu.tr*
[2]*Kastamonu University, Ihsangazi Vocational School, Mapping and Cadaster, Kastamonu, Türkiye, sametdogan@kastamonu.edu.tr*

Cite this study: Altunel, A. O. & Doğan, S. (2024). Türkiye cracked the code in topographic earth representation. Advanced Engineering Days, 9, 972-974

Keywords
Topography
Aerial Photogrammetry
DEM
Resolution
GNSS

Abstract

DEM generation since the turn of 21th century, predominantly relied upon space-borne imagery captured with active or passive sensors. However, Türkiye recently managed just that utilizing stereo captured air photography. Considerably high resolution national Digital Elevation Model, 5 m spatial, was the resampled version of the originally built 0.30 m baseline DEM which is custom tailored to national 1:25000 topographic map grid. Mosaicked Kastamonu study area spanning 119 piece such topographic map frames, was subjected to previously recorded GNSS readings. Educational/cadastral and dam-reservoir measurement related CORS records collected since 2014, were used to assess to see how this new national DEM behaved, vertically. Overall results showed that both Root Mean Square Error and Mean Absolute Error were less than 2.5 m overall.

Introduction

Globally generated digital elevation model concept started with the release of Global 30 arc-second elevation (GTOPO30) in 1996. 30 arc-second (~1 km) spatial resolution was rather coarse compared to today's datasets (1). Then came Global multi-resolution terrain elevation data 2010 (GMTED2010) with variable resolutions of 30, 15 and 7.5 arc-second in 2011. Boasting a tenfold higher global RMSE assurance of 6 m was rather competitive when compared to that of GTOPO30, (66 m) based on the same set of National Geospatial-Intelligence Agency (NGA) control points (2). As GTOPO30 was the only globally achievable elevation dataset, a joint endeavor between NASA and NGA put the space shuttle Endeavour into orbit for 11 days in February, 2000. Two radar instruments, C-band SAR by NASA and X-band SAR by German/Italian Space Agencies as tried and tested in the earlier missions in 1994, collected extensive data to later produce the acclaimed Shuttle Radar Topography Mission (SRTM) DEMs. In 2009, Japan with help from NASA also entered into DEM making, utilizing space borne stereo image capture, releasing the first ever ASTER GDEM. It and the subsequent newer versions were extensively used in the SRTM void filling (3). Other noteworthy inclusions into the global DEM making e. g. ALOS-PALSAR, AW3D30, showcased their claim in improving the elevations until the original TanDEM-X 12 m data were released in September 2016. It paved the way for other products such as World DEM, Copernicus DEM, FABDEM and Diluvium DEM. The latter two also showed us how new algorithms can further improve the earlier examples (4, 5). Amidst all these advancements, Türkiye, thanks to its 70+ years of air-photography capture capacity and know-how, released a 5 m national DEM generated with stereo air-photo auto correlation technique (6, 7). In the scope of this study, direct GNSS point to corresponding DEM cell elevation matching and comparison were made over Kastamonu provincial study area.

Material and Method

Turkish national DEM as produced and supplied by the General Directorate of Mapping, was used in a single raster file subsetted to Kastamonu administrative border in UTM-WGS84 projection and horizontal datum combination (Figure 1). GNSS records collected over the course of 10+ years for educational and administrative purposes were used as reference. Both the DEM and GNSS receivers provided the elevation records as calculated over WGS84 ellipsoid. Although the DEM was delivered as orthometric, GNSS records were always kept in ellipsoidal state, so TG-20 Turkish GEOID was used to turn them into orthometric state, so both the validation and the comparison elevation records were in sync with one another.

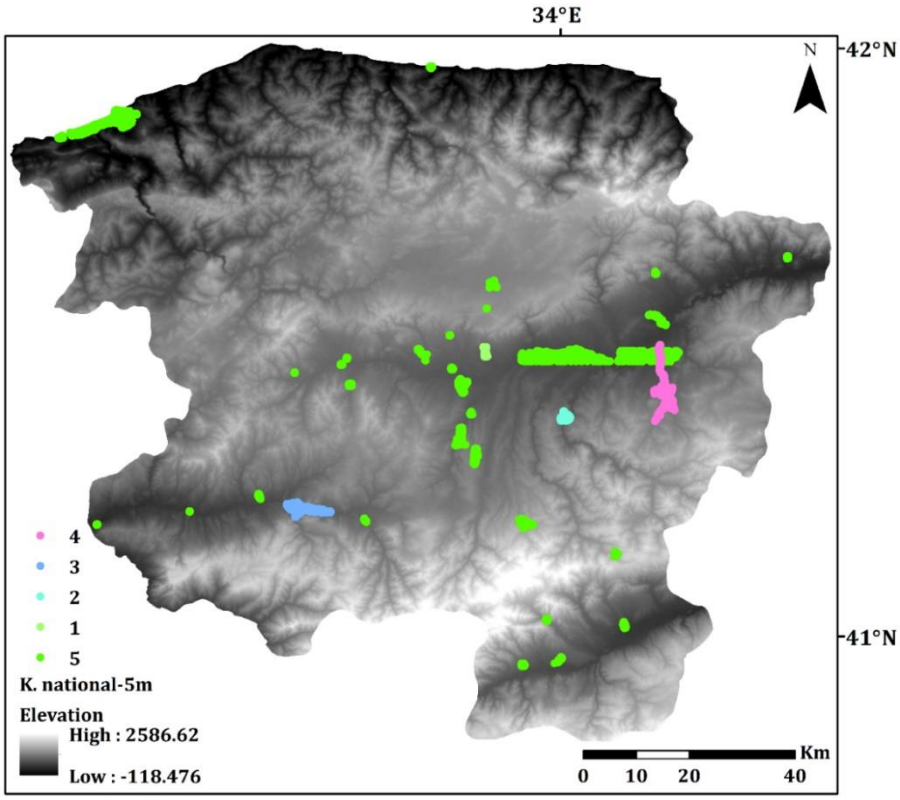


Figure 1. Kastamonu provincial study area

1 through 4 in "Figure 1" were dam reservoir areas measured using GNSS receivers for engineering purposes, 5 was aggregated for educational and administrative purposes. Root Mean Square Error (RMSE) (1) and Mean Absolute Error (MAE) (2), Standard Error (STDE) (3) and Line error 90% (LE90) (4) were calculated.

$$RMSE = \sqrt{\frac{1}{n}\sum_{1}^{n}\left(\Delta {H_i}^2\right)} \quad (1)$$

$$MAE = \frac{\sum_{1}^{n}(|\Delta H|)}{n} \quad (2)$$

$$STDE = \sqrt{\frac{\sum_{1}^{n}(X-Xi)^2}{n-1}} \quad (3)$$

$$LE90 = STDE\ x\ 1.6449 \quad (4)$$

, where X was the GNSS record, and Xi was the arithmetic mean of the 5 m DEM extracted elevation record.

The Mean Absolute Error (MAE) and Root Mean Square Error (RMSE) are commonly employed as standard statistical measures to evaluate model performance in many research investigations. However, there is a lack of agreement on which metric is the best suitable (8). One drawback of the RMSE is its inability to differentiate between different types of errors, such as random, systematic, or blunders. Thus, additional error measures were concurrently adopted for this study. Although (9; 10) stated that the errors in a DEM may not necessarily conform to a normal distribution, we assumed that the vertical errors were normally distributed (11).

Results

Table 1. Comparison settings of the 5 m DEM and the summary of statistics

Error Metric / Site	# of GNSS points	Elevation range (m)	*RMSE*	*MAE*	*STDE*	*LE90*
1 (Dam reservoir)	**10791**	**760 - 860**	***1.83***	***1.62***	***0.25***	***0.41***
2 (Dam reservoir)	**24192**	**714 - 927**	***3.84***	***3.25***	***0.3***	***0.5***
3 (Dem reservoir)	**58643**	**665 - 812**	***1.53***	***2.33***	***0.13***	***0.22***
4 (Dem reservoir)	**33964**	**585 - 1024**	***1.31***	***0.92***	***0.59***	***0.97***
5 (Educational/Cadastral)	**311014**	**0 - 1446**	***1.88***	***1.42***	***0.67***	***1.1***
Overall	**438604**	**0 - 1446**	***2.35***	***2.31***	***0.53***	***0.87***

GNSS records were initially categorized in 5 different settings, and only in site 2 were both MSE and MAE above 3 m, obviously raising the overall results above 2 m for both error metrics (Table 1). Although elevation range was

greater in site 4, the reason that site 2 scored the highest in error metrics was because of the distribution of those records to the terrain (Figure 1). Smaller site created more topographical distortions, so the resulting facades in the corresponding part of the raster DEM produced more error.

Discussion and Conclusion

First SRTM, then TanDEM-X have become ubiquitous topographic earth representations all over the World. SRTM has been subjected to very many studies throughout the years and bounded by the ± 16 m absolute vertical accuracy (90% confidence level) (12; 13). Germany, on the other hand, immensely capitalized on the experience gained during the SRTM's X-band data collection and finally came up with an extremely good DEM with an absolute vertical accuracy of < 10 m (LE90 based) and ~4 m (>20% slope) (14). The precision in elevation records is a matter of sensor spatial resolution and the ability of the operators to employ the right algorithm to approximate. This pretty much summarizes the leap forward attained in today's DEMs. No matter what type of platform is used, apparent from the Turkish example, DEMs can be produced in so many ways. Smaller the final product's spatial resolution, better the outcome in theory. Türkiye obviously proved that theory by releasing this national DEM. Although this particular study was a direct comparison between GNSS records and DEM extracted elevation values, shear number of GNSS points was enough assurance that many topographic derivatives had surely been included during the points' recording, and the overall mean absolute accuracy of the new Turkish DEM was found less than 2.5 m in Kastamonu study area. Additional studies from other parts of the country will further solidify that there is possibly no other DEM in the production to depict Turkish topography better.

Acknowledgment

We thank both the General Directorate of Mapping for providing the new Turkish national DEM for scientific purposes and our institution for providing the essential means to produce sound works.

References

1. URL-1. (2024). USGS EROS Archive - Digital Elevation - Global 30 Arc-Second Elevation (GTOPO30). Available through https://www.usgs.gov/centers/eros/science/usgs-eros-archive-digital-elevation-global-30-arc-second-elevation-gtopo30?qt-science_center_objects=0#overview, last accessed on 03/07/2024.
2. URL-2. (2024). Global Multi-resolution Terrain Elevation Data 2010 (GMTED2010). Available through https://pubs.usgs.gov/of/2011/1073/pdf/of2011-1073.pdf, last accessed on 03/07/2024.
3. Robinson, N., Regetz, J., & Guralnick, R. P. (2014). EarthEnv-DEM90: A nearly-global, void-free, multi-scale smoothed, 90m digital elevation model from fused ASTER and SRTM data. ISPRS Journal of Photogrammetry and Remote Sensing, 87, 57-67.
4. Dusseau, D., Zobel, Z., & Schwalm, C. R. (2023). DiluviumDEM: Enhanced accuracy in global coastal digital elevation models. Remote Sensing of Environment, 298, 113812.
5. Hawker, L., Uhe, P., Paulo, L., Sosa, J., Savage, J., Sampson, C., & Neal, J. (2022). A 30 m global map of elevation with forests and buildings removed. Environmental Research Letters, 17(2), 024016.
6. Ozturk, E., & Kocak, E., (2007). Farklı kaynalardan değişik yöntem ve ölçeklerde üretilen sayısal yükseklik modellerinin doğruluk araştırması (in Turkish). Harita Dergisi, 73(137), 25-41.
7. Yilmaz, A., & Erdogan, M., (2018). Designing high resolution countrywide DEM for Turkey. International Journal of Engineering and Geosciences, 3(3), 98-107.
8. Hodson, T. O. (2022). Root mean square error (RMSE) or mean absolute error (MAE): When to use them or not. Geoscientific Model Development Discussions, 2022, 1-10.
9. Höhle, J., & M. Höhle. (2009). "Accuracy Assessment of Digital Elevation Models by Means of Robust Statistical Methods." ISPRS Journal of Photogrammetry and Remote Sensing 64 (4): 398–406.
10. Carrera-Hernández, J. J. (2021). "Not All DEMs are Equal: An Evaluation of Six Globally Available 30 M Resolution DEMs with Geodetic Benchmarks and LiDar in Mexico." Remote Sensing of Environment 261:112474.
11. Grohmann, C. H. (2018). Evaluation of TanDEM-X DEMs on selected Brazilian sites: Comparison with SRTM, ASTER GDEM and ALOS AW3D30. Remote Sensing of Environment, 212, 121-133.
12. Miliaresis, G. C., & Paraschou, C. V. (2005). Vertical accuracy of the SRTM DTED level 1 of Crete. International Journal of Applied Earth Observation and Geoinformation, 7(1), 49-59.
13. Uuemaa, E., Ahi, S., Montibeller, B., Muru, M., & Kmoch, A. (2020). Vertical accuracy of freely available global digital elevation models (ASTER, AW3D30, MERIT, TanDEM-X, SRTM, and NASADEM). Remote Sensing, 12(21), 3482.
14. Rizzoli, P., Martone, M., Gonzalez, C., Wecklich, C., Tridon, D. B., Bräutigam, B., ... & Moreira, A. (2017). Generation and performance assessment of the global TanDEM-X digital elevation model. ISPRS Journal of Photogrammetry and Remote Sensing, 132, 119-139.

Advanced Engineering Days

aed.mersin.edu.tr

Mapping Wetlands Using Sentinel-2 Satellite Imagery and Auxiliary Data with Google Earth Engine

Zelalem Getachew Ayalke [*1], **Aziz Şişman** [1]

[1]*Ondokuz Mayis University, Department of Geomatics Engineering, Türkiye, 19211596@stu.omu.edu.tr, asisman@omu.edu.tr*

Cite this study: Ayalke, Z. G., & Şişman, A. (2024). Mapping Wetlands Using Sentinel-2 Satellite Imagery and Auxiliary Data with Google Earth Engine. Advanced Engineering Days, 9, 975-978

Keywords
Wetlands
Sentinel image
Google earth engine
Random forest
Supervised classification

Abstract

To effectively manage and conserve wetlands, accurate mapping is essential. This study used Sentinel-2 remote sensing imagery to map wetlands in the Ramsar area of Samsun using Google Earth Engine (GEE). Random Forest (RF) algorithm was applied for supervised classification of wetlands. To enhance the extraction of wetlands, the Normalized Difference Vegetation Index (NDVI) and the Normalized Difference Water Index (NDWI) were used. The classification accuracy was evaluated using overall accuracy (OA) and Kappa coefficient (K). According to the results mapping and monitoring of wetlands in Ramsar areas could be greatly improved by integrating Sentinel-2 imagery approach with spectral indices in GEE using RF algorithm, which would result in more precise conservation and management of wetlands.

Introduction

Wetlands are diverse ecosystems, covering 6% of the earth's total land surface [1], permanently or temporarily flooded, providing habitats for diverse species, contribute to agricultural production, and perform essential functions like flood prevention and water quality protection. Preserving and protecting wetlands is crucial for a sustainable future[2]. Accurate mapping of wetlands involves systematically identifying and delineating these complex ecosystems to provide foundational data essential for monitoring changes in wetland extent, composition, and health over time [3].

Remote sensing (RS) has emerged as a crucial tool for wetland mapping, offering cost-effective, timely, and wide-area coverage. Different RS approaches, including aerial, multispectral, and synthetic aperture radar (SAR) have been utilized. Sentinel imagery, particularly from the Sentinel-1 and Sentinel-2 satellites, has proven to be highly effective for wetland mapping. Sentinel-2's multispectral optical sensors, with their high spatial and temporal resolution, enable detailed analysis of vegetation and water bodies in wetlands [4, 5].

Google Earth Engine (GEE) is a crucial tool for wetland mapping due to its efficient processing of large-scale satellite data. It allows researchers to analyze time-series data from sources like Landsat, Sentinel, and MODIS, improving map accuracy and resolution [6].

The objective of this study is to produce wetlands map using Sentinel-2 satellite data and derived indices with RF machine learning algorithm in the GEE environment.

Study area

The study focused on the 19 Mayis district in Samsun, Turkiye (Figure 1) which is a designated Cultural and Natural Asset and Permanent Wildlife Reserve and is part of the Kızılırmak Delta. The area has a variety of habitats, including wooded areas beaches seasonal marshes shallow lakes and dunes. Seasonally flooded forests and vast reedbeds make up the dominant vegetation[7].

Material and Method

In this study, RF based wetlands classification was conducted in the GEE environment within the 19 Mayis district as a case study. The method we used is illustrated in Figure 2. The wetlands Mapping process followed these steps: (1) pre-processing the sentinel 2 image; (2) computing NDVI and NDWI from selected bands; (3) normalization to ensure data is within the same scale range (0–1); (4) collecting training and test data; (5) training algorithms; (6) model evaluation based on criteria like Kappa value, overall accuracy, and producers' and users' accuracy.

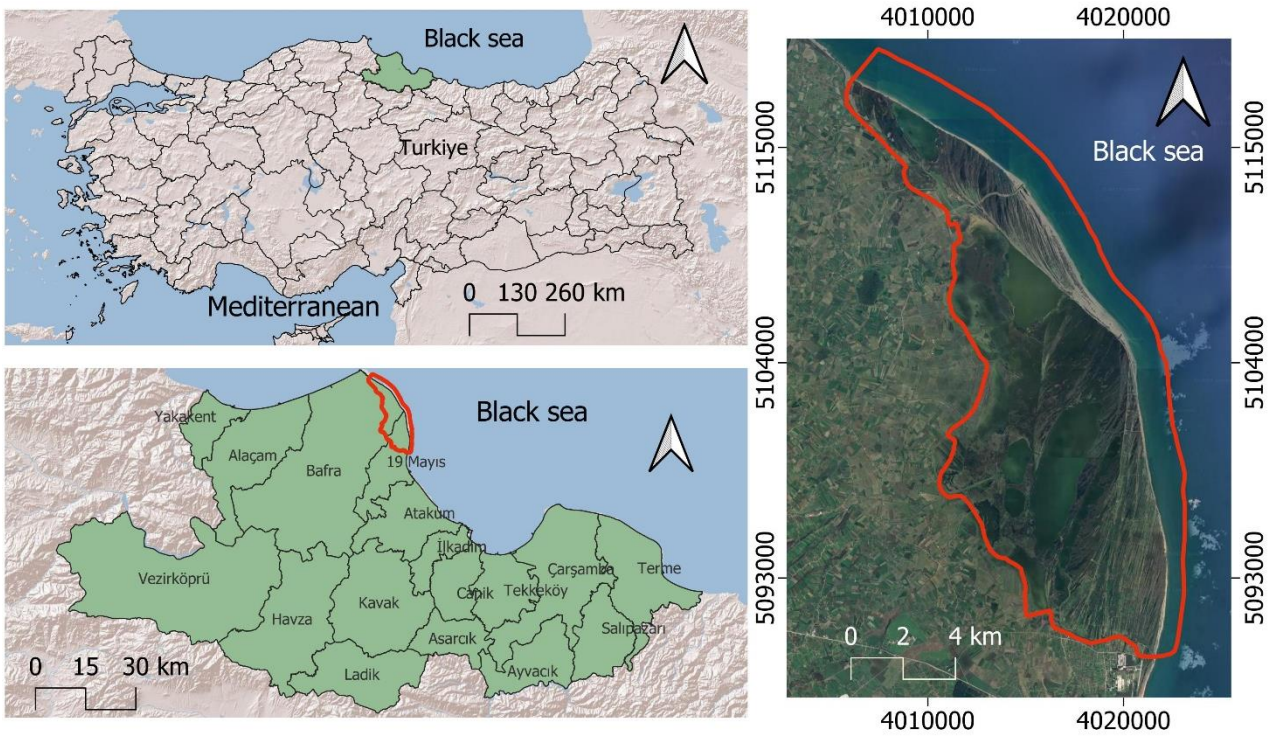


Figure 1. map of study area

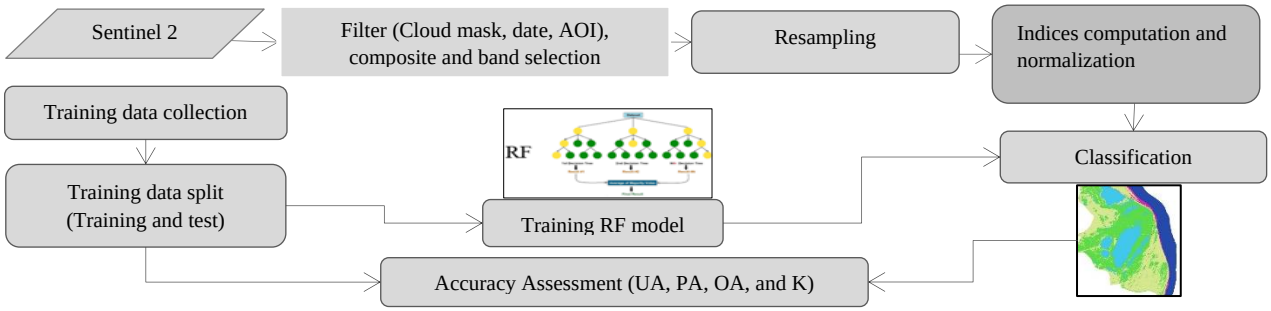


Figure 2. Workflow of the study

The Sentinel-2 Harmonized Image Collection was filtered to include only images with less than 10% cloud cover, captured between May 1, 2023, and June 1, 2023. The images were provided by the European Space Agency (ESA) through the Copernicus Open Access Hub at https://scihub.copernicus.eu. Sentinel-2 sensor provides images at spatial resolution of 10, 20, and 60 m, with a revisit period of 5 days. The image was geometrically corrected, and bands with 10 m resolution (B2, B3, B4, B8) and 20 m resolution (B11 and B12) were selected and resampled.

In this study, the NDVI and NDWI were extracted from the selected spectral bands to provide additional information, enabling the model to better differentiate land classes [8]. Table 1 illustrates the spectral indices used to enhance the accuracy of classification.

Table 1. Spectral indices used in to enhance classification accuracy

Indices	Formula	Description
NDVI	$\frac{(NIR - Red)}{(NIR + Red)}$	Detects vegetation utilizing red and near-infrared spectrum. The values range from -1 to +1, with higher values representing better vegetation.
NDWI	$\frac{(Green - NIR)}{(Green + NIR)}$	Analyses water bodies using Green and Near-Infrared bands. Effective for highlighting water.

After pre-processing and extracting the required spectral bands and spectral indices the input features were normalized. In this study, sufficient sample points were collected in GEE environment for training and test process. We collected 17742 sample points, with 14785 used for model training and 2957 for model test. Random Forest (RF)

algorithm, is a multipurpose machine learning classifier consisting of numerous decision trees, was utilized. Each tree votes in classifying an input, and their combined output enhances classification accuracy [9, 10].

Results and Discussion

The wetlands were classified into six categories: settlements, sea, lake, barren land, marshes and farm land. The contribution of each feature is illustrated in Figure 3. Standard confusion matrices were employed to calculate classification accuracies. The predicted Kappa coefficient and overall accuracy of the RF classifiers from Figure 4 are presented in Table 2.

Table 2. Confusion matrices and computed User's Accuracy (UA), Producer's Accuracy (PA), Overall Accuracy (OA), and Kappa coefficient (K)

Classes		Test									
		Settlements	Sea	Lake	Barren land	Marshes	Vegetation	UA	PA	OA	K
Classification	Settlements	67	0	0	0	1	3	0.944	0.848	0.964	0.955
	Sea	0	721	2	0	0	0	0.997	0.996		
	Lake	0	1	524	0	1	1	0.994	0.953		
	Barren land	2	2	0	243	0	2	0.976	0.949		
	Marshes	0	0	18	0	734	27	0.942	0.975		
	Vegetation	10	0	6	13	17	562	0.924	0.945		

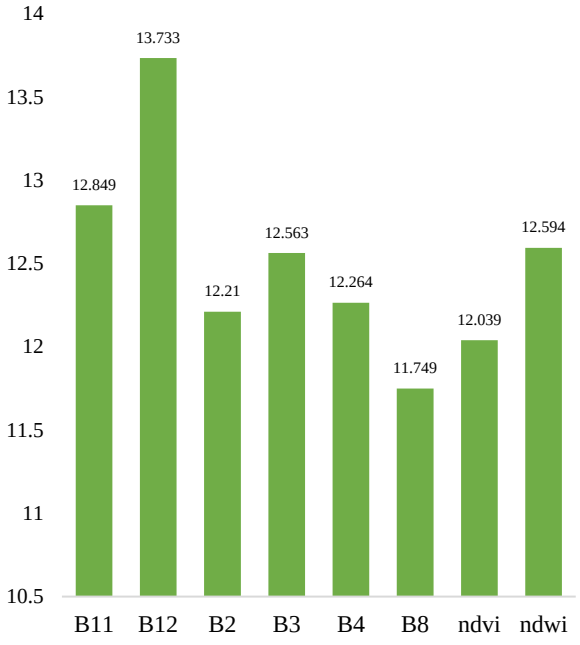


Figure 3. Importance of features computed by RF

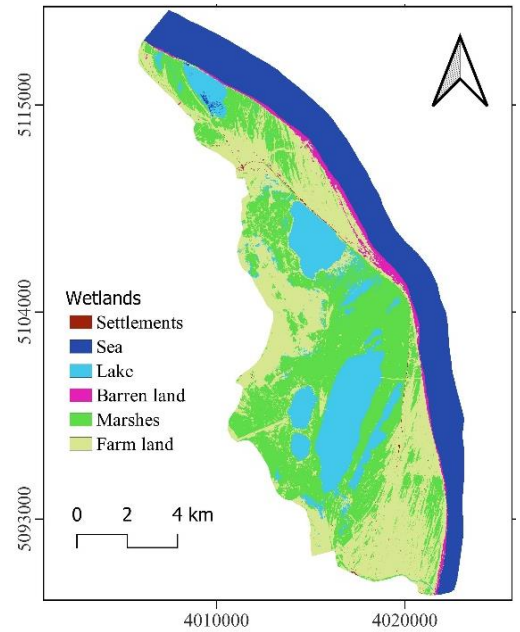


Figure 4. Wetlands classified map using RF

The wetland classification using the RF algorithm shows high accuracy, with an OA of 0.964 and K of 0.955 indicating a substantial agreement between the classified results and the test data.

Conclusion

In conclusion, the synergy between Sentinel-2 satellite imagery, machine learning techniques like Random Forest, and Google Earth Engine represents a paradigm shift in how we study and manage wetland ecosystems. These technologies offer unprecedented opportunities to enhance our understanding of wetland dynamics, assess anthropogenic impacts, and implement effective conservation strategies to protect these vital ecosystems for future generations.

References

[1] World Wetlands Day 2023 – Geneva Environment Network (2023). Available at: https://www.genevaenvironmentnetwork.org/events/world-wetlands-day-2023/ (accessed 1 July 2024).
[2] Igwe V, Salehi B and Mahdianpari M (2023) Rapid Large-Scale Wetland Inventory Update Using Multi-Source Remote Sensing. Remote Sensing 15(20). Multidisciplinary Digital Publishing Institute (MDPI).
[3] Gemechu GF, Rui X and Lu H (2022) Wetland Change Mapping Using Machine Learning Algorithms, and Their

Link with Climate Variation and Economic Growth: A Case Study of Guangling County, China. Sustainability (Switzerland) 14(1). MDPI.
[4] Mahdavi S, Salehi B, Granger J, et al. (2018) Remote sensing for wetland classification: a comprehensive review. GIScience and Remote Sensing. Taylor and Francis Inc.
[5] Hu B, Brown G, Stirling C, et al. (2024) Land Cover Classification of Subarctic Wetlands Using Multisource Remotely Sensed Data. IEEE Journal of Selected Topics in Applied Earth Observations and Remote Sensing 17. Institute of Electrical and Electronics Engineers Inc.: 5073–5092.
[6] Jafarzadeh H, Mahdianpari M, Gill EW, et al. (2024) Enhancing Wetland Mapping: Integrating Sentinel-1/2, GEDI Data, and Google Earth Engine. Sensors 24(5). Multidisciplinary Digital Publishing Institute (MDPI).
[7] Kizilirmak Delta | Ramsar Sites Information Service (1998). Available at: https://rsis.ramsar.org/ris/942 (accessed 1 July 2024).
[8] Sinha S, Sharma LK and Nathawat MS (2015) Improved Land-use/Land-cover classification of semi-arid deciduous forest landscape using thermal remote sensing. Egyptian Journal of Remote Sensing and Space Science 18(2). Elsevier B.V.: 217–233.
[9] Breiman L (2001) Random forests. Statistics Department University of California Berkeley. Epub ahead of print 2001.
[10] Tumer K and Ghosht J (1996) Analysis of Decision Boundaries in Linearly Combined Neural Classifiers. Pattern Recognition.

Advanced Engineering Days

aed.mersin.edu.tr

Enhancement of Zirconium Oxide-Based Graphite Electrode through Mechanochemical Methods for Electrochemical Applications

Mary Gojeh*[1], Ishaya Sugbeh Alhassan [2], Manasseh Tachia Bwankwot [3], Jonah Rebeccah Aji [4], Habiba Kakangi Dalhatu [5], Solomon Ogobuto [6]

[1] *Kaduna State University, Department of Pure & Applied Chemistry, Nigeria, gojehm@gmail.com*
[2] *Naval Headquarters, Naval Engineering Branch, Nigeria, alhassanishaya@gmail.com*
[3] *Kaduna State University, Department of Pure & Applied Chemistry, Nigeria, tbwankwot@gmail.com*
[4] *Kaduna State College of Education, Department of Chemistry, Nigeria, beckysnech@gmail.com*
[5] *Kaduna State University, Department of Pure & Applied Chemistry, Nigeria, habibadalhatkkg@gmail.com*
[6] *Kaduna State University, Department of Pure & Applied Chemistry, Nigeria, solomonogobuto@gmail.com*

Cite this study: Gojeh, M., Alhassan, S. I., Bwankwot, M. T, Aji, J. R., Dalhatu, H. K., & Ogobuto, S. (2024). Enhancement of Zirconium Oxide-Based Graphite Electrode through Mechanochemical Methods for Electrochemical Applications. Advanced Engineering Days, 9, 979-981

Keywords
Mechanochemical
Electrochemical
Enhancement,
Zirconium Oxide
Graphite Electrode

Abstract

Zirconium oxide-based graphite electrodes have gained significant attention in electrochemical applications due to their excellent conductivity and stability. This study focuses on the enhancement of zirconium oxide-based graphite electrodes through mechanochemical methods for improved performance in electrochemical applications. Mechanochemical methods involve the use of mechanical energy to induce chemical reactions, leading to modifications in the structure and properties of materials. By utilizing mechanochemical techniques such as ball milling, high-energy milling, and attrition milling, zirconium oxide-based graphite electrodes can be tailored to exhibit enhanced electrochemical properties such as increased surface area, improved conductivity, and enhanced stability. The preparation process involves the synthesis of zirconium oxide nanoparticles and their incorporation into the graphite matrix using mechanochemical techniques. Characterization techniques such as X-ray diffraction, scanning electron microscopy, and energy-dispersive X-ray spectroscopy are employed to analyze the structural and morphological properties of the enhanced electrode material. The resulting electrodes show great potential for applications in various fields including energy storage devices, sensors, catalysis, and electrochemical analysis. The application of the enhanced electrode is demonstrated through cyclic voltammetry studies on ferricyanide anodic responses, showcasing its superior electrochemical performance compared to traditional electrodes. This study highlights the potential of mechanochemically enhanced zirconium oxide-based graphite electrodes and emphasizes the importance of sustainable materials and processes in achieving a more environmentally friendly approach to electrochemical applications.

Introduction

Zirconium oxide-based graphite electrodes have garnered significant attention in the field of electrochemical applications due to their excellent properties such as high thermal stability, chemical inertness, and good electrical conductivity. However, there is a growing interest in enhancing the performance of these electrodes through mechanochemical methods. Mechanochemical methods involve the use of mechanical energy to induce chemical reactions or structural changes in materials, leading to improved properties. This approach offers a promising avenue for tailoring the structure and properties of zirconium oxide-based graphite electrodes to meet the specific requirements of various electrochemical applications [1].

The enhancement of zirconium oxide-based graphite electrodes through mechanochemical methods involves processes such as ball milling, attrition milling, and high-energy mechanical milling. These techniques facilitate the uniform dispersion of zirconium oxide nanoparticles within the graphite matrix, resulting in enhanced electrochemical performance. The mechanochemical treatment also promotes the formation of a stable interface between zirconium oxide and graphite, leading to improved charge transfer kinetics and overall electrode stability [2].

This research aims to explore the recent advancements in the enhancement of zirconium oxide-based graphite electrodes through mechanochemical methods for electrochemical applications. By delving into these approaches' underlying principles, methodologies, and outcomes, this review seeks to provide insights into the potential benefits and challenges associated with utilizing mechanochemical methods for electrode modification.

Material and Method

All the chemicals and reagents used for this research were of Analytical grade. Mechanochemical synthesis of Graphite/Zr-oxide was achieved by weighing (0.2 g) of oxide and 0.8 g of graphite and mixing in a mortar & pestle with paraffin oil (0.1 ml) and dichloromethane (2.0 ml) and compacted into the syringe). Mechanical energy generated by the grinding balls leads to the breaking of chemical bonds and promotes solid-state reactions between the zirconium oxide and graphite particles as reported by [3] with little modification. The final zirconium oxide-based graphite electrode material is characterized using XRD, SEM, and FTIR techniques to analyze its structural and chemical properties.

Results

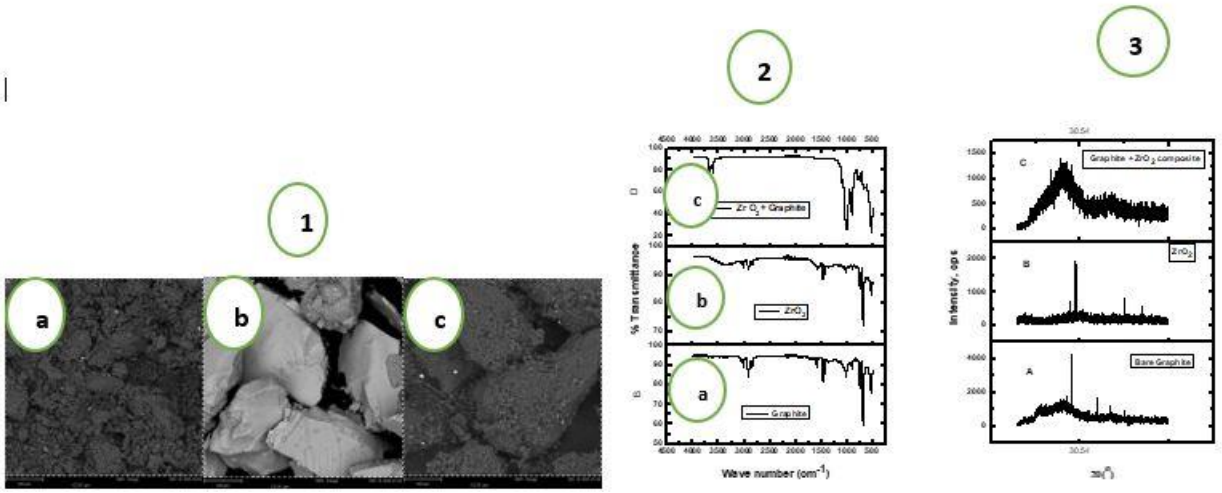


Figure 1: SEM image for (a) Graphite (b) ZrO_2 (c) Graphite/ZrO_2, **Figure 2**: FTIR Pattern for (a) Graphite (b) ZrO_2 (c) Graphite/ZrO_2, **Figure 3**: XRD Pattern for (a) Graphite (b) ZrO_2 (c) Graphite/ZrO_2

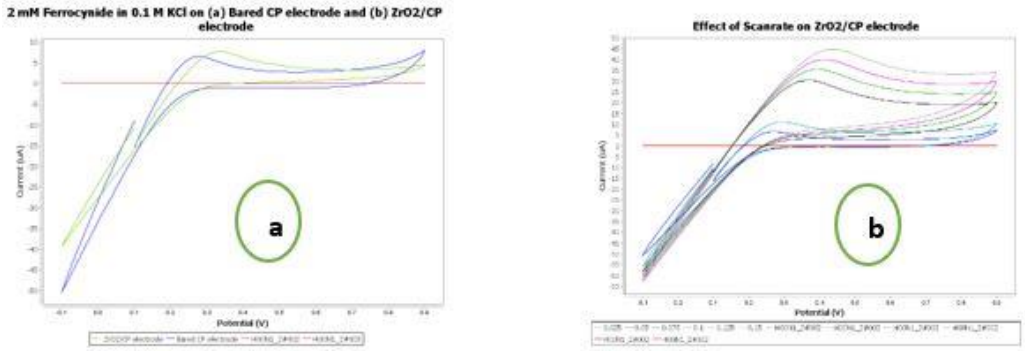


Figure 4: Cyclic Voltammogram of (a) Anodic peak current response Graphite (blue) and Graphite/ZrO_2 (green), (b) Increasing anodic scan rate (25, 50, 75, 100, 125 and 150 mVs^{-1}) of 2 mM Ferricyanide in 0.5 M KCl electrolyte at Graphite/ZrO_2

Discussion

Characterization

Research results indicate that enhancing zirconium oxide-based graphite electrodes through mechanochemical methods shows promising potential for electrochemical applications. X-ray diffraction (XRD) analysis reveals changes in the crystal structure of the composite material, indicating the successful incorporation of zirconium oxide as reported in the literature [4]. Fourier-transform infrared spectroscopy (FTIR) analysis confirms the

chemical bonding between zirconium oxide and graphite, while scanning electron microscopy (SEM) analysis demonstrates a more uniform distribution of zirconium oxide particles on the graphite surface, leading to improved electrochemical performance (Figures 1, 2 and 3). These findings suggest that mechanochemical methods can effectively enhance the properties of zirconium oxide-based graphite electrodes for various electrochemical applications as reported in [5].

Cyclic Voltammograms of ferricyanide Anodic responses

Mechanochemical methods such as ball milling improve the properties of zirconium oxide-based graphite electrodes by promoting homogeneity, increasing surface area, and enhancing conductivity. These improvements lead to a more pronounced anodic peak response in cyclic voltammetry, indicating better electrochemical performance (Figure 4a) for various applications such as sensors, energy storage devices, and catalysis. The anodic peak current typically increases with increasing scan rate due to enhanced mass transport and faster kinetics at higher scan rates (Figure 4b) which are to the reported literature [6].

Conclusion

In conclusion, enhancing zirconium oxide-based graphite electrodes through mechanochemical methods for electrochemical applications has shown promising results. The use of X-ray diffraction (XRD), Fourier-transform infrared spectroscopy (FTIR), and scanning electron microscopy (SEM) analysis techniques have provided valuable insights into the structural and morphological changes induced by these methods. The mechanochemical approach has proven effective in improving the conductivity and stability of zirconium oxide-based graphite electrodes, making them suitable for various electrochemical applications.

References

1. Gogotsi, Y. (2001). Mechanochemistry. In Encyclopedia of Materials: Science and Technology (Second Edition).
2. Chen, X. (2019). Ball-Milling-Assisted Synthesis of ZrO_2-Graphite Composite Electrodes for Supercapacitor Applications." Journal of Solid-State Electrochemistry 23, 2147-2156.
3. Gojeh. M., Tesfaye R., Onwumere M., Titus Y. M., Wyasu G., (2016). Electrocatalysis of Insitu polyaniline for speed up of redox reaction at electrode surface, IOSR Journal of Applied Chemistry (IOSR-JAC), e-ISSN: 2278-5736. 9(3), 23-27.
4. Wang, Gu. (2017). Mechanochemical Synthesis of Zirconia Nanoparticles. Journal of Materials Chemistry A 5, 22241-22247.
5. Li, M. (2019). Mechanically Activated Synthesis and Characterization of ZrO_2-Graphite Composites for Electrochemical Applications. Journal of Alloys and Compounds 789 234-241.
6. Zhang, X. (2018). Enhanced Electrochemical Performance of Zirconia-Graphite Composite Electrodes Prepared by High-Energy Mechanical Milling. Journal of Power Sources 396, 123-130.

Advanced Engineering Days

aed.mersin.edu.tr

Photogrammetric recording of epigraphic documentation

Cengiz Alyılmaz[*1]

[1] *Bursa Uludağ Üniversitesi, Fen-Edebiyat Fakültesi, Türkiye, calyilmaz@gmail.com*

Cite this study; Alyılmaz, C. (2024). Yazıtların epigrafik ve fotogrametrik belgelemeleri yapılırken dikkate alınması gereken hususlar. Advanced Engineering Days, 9, 982-984

Keywords
Inscription
Inscription science
Photogrammetry
Old Turkic inscriptions

Abstrract

Writing emerged from the human need to document emotions, thoughts, social, cultural, and commercial relations and agreements, to embody knowledge, store it, and pass it on to future generations. The field of epigraphy is a scientific discipline dedicated to the study and analysis of inscriptions on various subjects, types, and objects, along with other graphic language elements. It maintains close connections with numerous other branches of science. This paper explores the relationship between photogrammetry and epigraphy, emphasizing how an interdisciplinary approach can extend beyond traditional methods in inscription research to achieve accurate reading and interpretation. It examines the contributions of photogrammetry to academic studies—including articles, papers, and projects—focused on ancient Turkish inscriptions. Additionally, the paper provides examples of how photogrammetry can facilitate future research efforts on ancient Turkish inscriptions.

Introduction

Writing is the only solution that mankind, who cannot eliminate death in any way, can find against death. Writing is the photograph of intelligence. It surpasses all history by passing from age to age, from hand to hand. It contains the lights of the eyes that roam over every leaf of human life, and the shadows of the thinking mind (Yücel, 1937). Writing arose from the need for mankind to document their feelings and thoughts, their social, cultural, commercial etc. relations / agreements with each other, to concretize, store and transfer their knowledge to future generations. In order to express the concept of inscription, the words “bitig”, “bengü taş”, “yazıt” and “anıt” in Turkish were used in different periods of the Turkish language; and in Arabic, the concept signs such as “kitabe (kitābe)” and “abide (ābide)” etc. were used. Inscription is a form of engraving, embossing, painting etc. on standing stones, rocks, statues, stone fathers, coins, seals, ornamental and utility objects. Epigraphy (epigraphy / épigraphie / epigrafi / epigrafya): Epigraphy is a branch of science that conducts research and examination on inscriptions and other graphic language elements (petroglyphs, stamps, etc.) written / processed on different subjects, different types and objects (rocks, stones, trees, papers, sculptures, balbals, walls, architectural works, ornamental and usable objects), and has close relations with many branches of science (history, art history, geography, linguistics, paleography, paleontology, archaeology, anthropology, ethnology, numismatics, photogrammetry, geodesy, etc.) (Alyılmaz, 2010, pp. 313-314).

Methods and Techniques Used in Inscription Science

Many methods and techniques are used while performing epigraphic documentation of inscriptions. The main ones are as follows:

- ✓ Documenting inscribed surfaces in their natural environment without using any tools.
- ✓ Documenting inscribed surfaces using a magnifying glass or reflective devices.
- ✓ Documenting inscribed surfaces by tactile inspection with the fingers.
- ✓ Documenting inscribed surfaces through the application of estampage techniques.
- ✓ Documenting inscribed surfaces by hand-drawing (or rendering) onto paper.
- ✓ Documenting inscribed surfaces by filling in the inscriptions.

- ✓ Documenting inscribed surfaces by making them more distinct using tools such as chisels or punches.
- ✓ Documenting inscribed surfaces using transparent materials.
- ✓ Documenting inscribed surfaces by applying moisture.
- ✓ Documenting inscribed surfaces through shading or darkening techniques.
- ✓ Documenting inscribed surfaces by ensuring adequate illumination.
- ✓ Performing epigraphic documentation using images obtained from manual cameras.
- ✓ Documenting inscribed surfaces using video recordings.
- ✓ Performing epigraphic documentation based on molds or copies of the inscriptions.
- ✓ Performing epigraphic documentation using digital photogrammetry techniques (Alyılmaz, 2007, s. 78-79).

- **Photogrammetry**

Photogrammetry, in its general and widely accepted definition, is a technology, art, and science that involves the recording, measurement, and interpretation of photographic images and patterns obtained from sensing systems to derive reliable and metric information about physical objects and the environment (Yıldız, Yakar vd. 2001, s. 371).

- **Relationship Between Photogrammetry and Epigraphy:**

Photogrammetry, which has rapidly evolved alongside technological advancements and developed numerous sub-disciplines, is increasingly intertwined with fields such as architecture, art history, archaeology, and epigraphy, contributing significantly to them. Indeed, researchers closely following developments in photogrammetry—including architects, art historians, archaeologists, and epigraphists—are now making extensive use of digital photogrammetry for various applications. These include the identification of historical and archaeological sites, architectural surveys and façade documentation, epigraphic recording, scaled and detailed drawings and modeling of historical artifacts and inscriptions, conservation, maintenance, and restoration of cultural heritage, shape and structure studies, and the creation of models, busts, and industrial prototypes. Consequently, photogrammetry, particularly digital photogrammetry, has become one of the most relevant fields for the science of epigraphy in recent years.

- **Importance and benefits of digital photogrammetry technique in terms of epigraphic documentation faydaları:**

The importance and benefits of digital photogrammetry in the context of epigraphy and epigraphic documentation can be summarized as follows:

- ✓ The effective execution of epigraphic documentation using digital photogrammetry depends primarily on suitable environmental conditions and the absence of objects obstructing the acquisition of images and coordinates in front of, behind, or around the inscription.
- ✓ For accurate drawing and modeling of the inscription, it is essential to carefully and thoroughly photograph all its facades. Without this, it is not possible to produce scientific-quality drawings and models of the inscriptions.
- ✓ Images captured with digital cameras:
- ✓ Should be reviewed using the camera's LCD screens during shooting; however, it should be noted that LCD screens can sometimes lead to inaccuracies.
- ✓ The images should be transferred to a computer and reviewed before leaving the field to ensure correct exposure of the inscription.
- ✓ Archiving the captured images/photos is as important as the actual capture. Photos should be saved to memory devices (hard drives) with minimal risk of deterioration, and indispensable images should be printed from the memory cards.
- ✓ For the publication, cataloging, and preparation of albums of inscriptions documented through digital photogrammetry, the following additional considerations should be observed:
- ✓ Digital photogrammetry provides the capability for multi-dimensional imaging and high-quality, metric drawings of inscriptions.
- ✓ Images and metric measurements obtained through digital photogrammetry enable the creation of molds and copies/modeling of inscriptions without causing any damage to the inscriptions.
- ✓ Restoration and conservation of inscriptions, as well as the surveying of monumental tomb complexes, can be carried out using images/photos obtained through digital photogrammetry.
- ✓ Digital photogrammetry greatly facilitates the preparation of maps of the locations/regions where the inscriptions are found.

Conclusion

The application of photogrammetric methods and techniques has made significant contributions to the field of epigraphy and has introduced a new area of study within photogrammetry itself. Today, it has become essential for researchers involved in epigraphy to collaborate with experts in photogrammetry. Consequently, it is important for epigraphers to familiarize themselves with the fundamental resources, methods, and techniques of photogrammetry, while photogrammetrists should gain an understanding of the core principles and techniques of epigraphy. To foster collaboration, professionals in both fields should organize joint workshops and symposiums, share their expertise and knowledge, undertake collaborative projects, and publish multilingual books related to their respective fields.

References

1. Alyılmaz, C. (2001). *Bilge Tonyukuk yazıtları üzerine birkaç düz*eltme*. TDAY Belleten 2000*, 11-18.
2. Alyılmaz, C. (2003). Epigrafik belgelemeler ve yüzey araştırmaları / epigraphic documantation and surface researches. *Moğolistan'daki Türk Anıtları Projesi 2001 Yılı Çalışmaları / Work for The Project Turkish Monuments in Mongolia in Year 2001*, 329-379.
3. Alyılmaz, C. (2003). Moğolistan'da eski Türk kültür ve medeniyetine ait bazı eserler ve bulundukları yerler*. Atatürk Üniversitesi Türkiyat Araştırmaları Enstitüsü Dergisi*, 21, 181-199.
4. Alyılmaz, C. (2005). *Orhun Yazıtları'nın bugünkü durumu*. Ankara: Kurmay Yay.
5. Alyılmaz, C. (2007). *(Kök)türk harfli yazıtların izinde*. Ankara: KaramM Yay.
6. Alyılmaz, C. (2015). *İpek yolu kavşağının ölümsüzlük eserleri*. Ankara: Atatürk Üniversitesi Yay.
7. Alyılmaz, C. (2016). *"Gobu"stan'ın gizemi ("Kıpçaklar"a giden yol).* Ankara: Bitlis Eren Üniversitesi Yay.
8. Alyılmaz, C. (2016). Kosova ve Makedonya'daki Osmanlı Dönemi mezar taşlarının bugünkü durumu. *Uluslararası Türkçe Edebiyat Kültür Eğitim Dergisi*, *5*(1), 56-93.
9. Alyılmaz, C. (2018). Yazıt bilimci kimdir? *Türk Dünyası Dil ve Edebiyat Dergisi*, 42, 117-126.
10. Alyılmaz, C. (2021). *Bilge Tonyukuk yazıtları.* Ankara: TDK Yay.
11. Yakar, M., & Yılmaz, H. M. (2008). Kültürel miraslardan tarihi Horozluhan'in fotogrametrik rölöve çalişmasi ve 3 boyutlu modellenmesi. *Selçuk Üniversitesi Mühendislik, Bilim ve Teknoloji Dergisi*, *23*(2), 25-33.
12. Gürbüz, H. (1982). *Fotogrametriye giriş.* Konya: Konya Devlet Mimarlık ve Mühendislik Akademisi Yay.
13. Turan, M. H. (2004). Mimarî fotogrametri alanındaki çağdaş gelişmelerin değerlendirilmesi, *Gazi Ünii Müh.-Mim. Fak. Dergisi, 19*(1), 43-50.
14. Tüdeş, T. (1986). *Yersel fotogrametri.* KTÜ Mühendislik-Mimarlık Fakültesi Yay.
15. Yakar, M, Yıldız & Yılmaz, H. M. (2005). Tarihi ve kültürel mirasların belgelenmesinde jeodezi fotogrametri mühendislerinin rolü. *TMMOB Harita ve Kadastro Mühendisleri Odası 10. Türkiye Harita Bilimsel ve Teknik Kurultayı 28 Mart - 1 Nisan 2005 Ankara, 1-5.*
16. Mohammed, O., &Yakar M.. "Yersel fotogrametrik yöntem ile ibadethanelerin modellenmesi." Selcuk University Journal of Engineering Sciences 15.2 (2016): 85-95.
17. Unal, M., Yakar, M., & Yildiz, F. (2004, July). Discontinuity surface roughness measurement techniques and the evaluation of digital photogrammetric method. In Proceedings of the 20th international congress for photogrammetry and remote sensing, ISPRS (Vol. 1103, p. 1108).
18. Yakar, M., & Doğan, Y. (2017). Mersin Silifke Mezgit Kale Anıt Mezarı fotogrametrik rölöve alımı ve üç boyutlu modelleme çalışması. Geomatik, 2(1), 11-17.
19. Pulat, Fatih, & Murat Yakar, "Comparison of photogrammetric software using the terrestrial photogrammetric method: The case of Hüsrev Paşa Mosque." Intercontinental Geoinformation Days 4 (2022): 192-195.
20. Kanun, Engin, Aydın Alptekin, and Murat Yakar. "Cultural heritage modelling using UAV photogrammetric methods: a case study of Kanlıdivane archeological site." Advanced UAV 1.1 (2021): 24-33.
21. Alyılmaz, C., Yakar, M., & Yılmaz, H. M. (2010). Drawing of petroglyphs in Mongolia by close range photogrammetry.
22. Alyilmaz, C., Alyilmaz, S., & Yakar, M. (2010). Measurement of petroglyhps (rock of arts) of Qobustan with close range photogrammetry. International Archives of Photogrammetry, Remote Sensing and Spatial Information Sciences, 38(5), 29-32.

Advanced Engineering Days

aed.mersin.edu.tr

The importance of academic field work in social sciences

Semra Alyılmaz*[1], Cengiz Alyılmaz [2]

[1] *Bursa Uludağ Üniversitesi, Eğitim Fakültesi, Türkiye, semraalyilmaz@uludag.edu.tr*
[2] *Bursa Uludağ Üniversitesi, Fen-Edebiyat Fakültesi, Türkiye, calyilmaz@gmail.com*

Cite this study: Alyılmaz, S., & Alyılmaz, C. (2024). Bilim insanlarının alan araştırmaları sırasında karşılaştıkları sorunlar ve çözüm önerileri. Advanced Engineering Days, 9, 985-987

Keywords
Field
Scientist
Problem
Solution

Abstract

Academic studies in the field in the social sciences are critical to understanding the relationship between theory and practice and to delving deeper into social dynamics and human behavior. Every profession that focuses on human well-being and aims to ensure a healthy, peaceful, and happy life has its own challenges and rewards. Those aspiring to become scientists often find themselves in a world far more intense and complex than they anticipated when they first embarked on their graduate studies. It is well-known that scientists, particularly those working in disciplines requiring fieldwork, encounter significant difficulties both during and after their graduate education.This study draws on the experiences of the authors, who have pursued academic careers involving extensive fieldwork in the social sciences. It provides a detailed account of these experiences to guide others who may wish to follow a similar academic path. The study highlights how various factors—such as one's social and cultural background, upbringing, belief systems, education, knowledge, experience, mental and physical health, and economic situation—directly influence the success one can achieve in fieldwork.

Introduction

If people were asked, "How many types of professions are there in the world?" various opinions would likely be put forward; at best, the answer might be something like "No more than around 1,000." However, research has shown that there are approximately 42,000 professions worldwide, with around 1,000 of these present in Turkey. If the question were posed, "Which of these professions are the most difficult?" undoubtedly many would classify their own profession among the most challenging. The truth is that every profession, which fundamentally centers on and aims to improve human life, has its difficult and easy aspects. Nearly everyone agrees on the difficulty and sensitivity of professions related to health, education, law, security, and other fields that concern everyone.

The multifaceted education process, which extends from family-based education to preschool, and from preschool to higher education (university), is truly challenging at every stage for everyone involved. This is because each stage of the education process demands effort and dedication. These processes are just as difficult for families and students as they are for those who bear the true responsibility of this work—those referred to as "teachers," "instructors," "scientists," and "academics."

Given that our topic focuses on certain challenges faced by scientists at universities, we'll set aside discussions of other educational levels and concentrate on the issues encountered by scientists after completing undergraduate education. As is well known, the path to becoming an academic—another term for "scientist"—at universities involves successfully passing certain exams and then pursuing graduate education (master's and doctoral programs).

Then aspiring scientists begin their graduate education, they often find themselves in a completely different world and level of intensity, far beyond what they initially anticipated or imagined. While taking graduate courses to enhance their knowledge and expertise, they are also required to contribute to the academic operations of their departments by teaching classes. This dual responsibility, often experienced during what is referred to as the "assistantship" or "research assistantship" period, can become overwhelming. Many scientists who have gone through these stages are well aware of these challenges, as they have experienced similar situations to varying degrees. However, this reality is often accepted as "normal" and "natural" over time, leading to a reluctance to

challenge it. Even when objections are raised, there is a widespread belief that little will change, which forces everyone within the system to gradually accept and adapt to the status quo.

In addition to the challenges faced during graduate education, working in the field is often a necessity in certain scientific disciplines. It is well-known that scientists working in these field-intensive disciplines encounter significant difficulties both during and after their graduate studies.

Some of the challenges and problems scientists face are undoubtedly personal and individual. A person's social and cultural environment, the setting in which they were raised, their belief system, the education and training they received, their knowledge and experience, mental and physical health, and economic situation all directly impact the success they will achieve in the field.

Researchers who are required to work in the field for short or extended periods face not only issues originating from themselves but also challenges arising from the people, institutions, organizations, systems, laws, and environments they interact with. Depending on the conditions of the working environments, some of these issues are local, regional, or national, while others are international in scope and nature.

Based on the knowledge, experience, and insights gained from our extensive national and international work in the field, we can outline the main challenges faced by researchers working in the Social Sciences—particularly in fields such as linguistics, epigraphy, folklore, history, art history, archaeology, geography, and cultural studies—and potential solutions to these challenges as follows:

Results

- ✓ Problems arising from the inability to obtain work permits, visas, etc.
- ✓ Issues related to the working environments.
- ✓ Problems resulting from inadequate planning or the absence of alternative plans.
- ✓ Challenges related to time and scheduling.
- ✓ Issues arising from different languages, religions, ethnicities, and cultural values.
- ✓ Problems related to nutrition, accommodation, health, and safety.
- ✓ Issues arising from different scientific/academic perspectives.
- ✓ Problems stemming from academic competition and jealousy.
- ✓ Problems caused by psychological violence such as "bullying" or "mobbing."
- ✓ Issues originating from administrators and project managers.
- ✓ Problems arising from conflicts and disagreements between female and male researchers within the research/project team.
- ✓ Issues resulting from the lack of interdisciplinary relations.
- ✓ Problems related to assistants such as guides, translators, drivers, etc.
- ✓ Challenges related to transportation and communication tools.
- ✓ Issues stemming from a lack of materials and the use of electronic devices.
- ✓ Problems arising from the absence or insufficiency of reference sources, guidebooks, maps, and geographic information system data.,

Conclusion

Difficulties and issues encountered in field research are often attributed to a lack of professional knowledge, experience, and qualified personnel. These problems have various causes, including "individual," "social," "cultural," "administrative," and "economic" factors, and can occur at local, regional, national, and international levels.

In the stages of graduate education and training, providing courses focused on professional training and field research, nurturing and supporting scientists who will work in the field, emphasizing field research, ensuring interdisciplinary collaboration in field research, preparing theses related to field research, prioritizing the publication of works resulting from field research in multiple languages, establishing national and international research centers and institutes related to the subject, and sharing obtained information, findings, and documents with the scientific community and stakeholders... will enhance the quality of the work conducted and ensure its acceptance on an international level.

References

1. Alyılmaz, C. (2004). İpek yolu ve Orhun yazıtları. *Atatürk Üniversitesi Türkiyat Araştırmaları Enstitüsü Dergisi*, 24, 181-192.
2. Alyılmaz, C. (2005). *Orhun yazıtlarının bugünkü durumu.* Ankara: Kurmay Yay..
3. Alyılmaz, C. (2007). *(Kök)türk harfli yazıtların izinde.* Ankara: KaraM Yay.
4. Alyılmaz, C. (2010). Yazıt bilimi ve eski Türk yazıt bilimi. *I. Uluslararası Uzak Asya'dan Ön Asya'ya Eski Türkçe Bilgi Şöleni, 18-20 Kasım 2009*, Afyonkarahisar, 313-314.
5. Alyılmaz, C. (2015). *İpek Yolu kavşağının ölümsüzlük eserleri*. Ankara: Atatürk Üniversitesi Yay.

6. Alyılmaz, C. (2018). (Kök)türk harfli yazıtlara ilgili sorunlar. *Türk Moğol Tarihi: Bozkırın Avazı,* 303-324, (ed. K. Yıldırım), İstanbul: Yeditepe Yay.
7. Alyılmaz, C. (2018). Yazıt bilimci kimdir*? Türk Dünyası Dil ve Edebiyat Dergi*si, 42, 117-126.
8. Alyılmaz, C. (2020). "Türk", "Türkçe" ve "Türk Dili" kavram işaretleri üzerine. *Türkçe Eğitiminin Güncel Sorunları,* 1-44, (ed. C. ALYILMAZ, O. ER ve İ. ÇOBAN), Ankara: Eğiten Yay.
9. Alyılmaz, C. (2022). Moğolistan'daki eski Türk eserleriyle ilgili bazı sorunlar ve çözüm önerileri. *Ötüken'den Anadolu'ya Türk-Moğol Tarihinde Yeni Araştırmalar,* 29-49, (Ed. K. Yıldırım), İstanbul: Bilgeoğuz Yay.
10. Orkun, H. N. (1940). *Eski Türk yazıtları III*. TDK Yay.
11. Sertkaya, O. F., Alyılmaz, C. ve Battulga, Ts. (2001). *Moğolistan'daki Türk anıtları projesi albümü.* Ankara: TİKA Yay.
12. Tekin, T. (2003). *Orhon yazıtları Kül Tigin Bilge Kağan Tunyukuk.* Yıldız Yay.
13. Useev, N. (2011). *Yenisey cazma estelikteri I: leksikası cana tekstter.* Bişkek: Kırgız Millî Bilimler Akademisi ve Kırgızistan-Türkiye Üniversitesi Yay.

Advanced Engineering Days

aed.mersin.edu.tr

Building interior modeling with wearable mobile LIDAR

Atilla Karabacak *[1], Murat Yakar [2]

[1] *Mersin University, Vocational School of Technical Sciences, Mersin, Türkiye, atilakarabacak@mersin.edu.tr*
[2] *Mersin University, Department of Geomatics Engineering, Mersin, Türkiye, myakar@mersin.edu.tr*

Cite this study: Karabacak, A., & Yakar, M. (2024). Building interior modeling with wearable mobile LIDAR. Advanced Engineering Days, 9, 988-991

Keywords
Remote sensing
Wearable Mobile Lidar
Photogrammetry
Laser Scanning
3D

Abstract

The 3D model and orthophoto were created within the error limits with the Wearable Mobile LIDAR (GML) of the Mapping and Cadastre laboratory located in the Çiftlikköy campus of Mersin University. In the study, 5 Ground Control Points (GCP) were placed on the walking line in the field and the laser scanning was completed in 7 minutes and 17 seconds with a closed route. It has been shown that the system can be used for building measurements, but it should be used with caution in narrow and undetailed places within the structure.

Introduction

Mersin University Vocational School of Technical Sciences Survey and Cadastre laboratory and garden were chosen as the study area. The building is reinforced concrete and single-storey. To measure the laboratory building, a GCP was created around the building. Walking time with GML took approximately 7 minutes. With this study, the laboratory building and garden were modeled in 3D.

Material and Method

The WML Gexcel Heron Wearable 3D Mobile Mapping System that we use in measuring the mapping laboratory. The system has a history of 9 years. The system calculates the location while moving with the SLAM algorithm and can be used in areas where people can walk. The system can be preferred to measure visible artificial and natural objects. The system produces 3D point cloud data.

In the study, 5 YKN distributed along the walking route were placed with a tatalstation device, no dots were placed inside the structure. In the study, local coordinates were given to the polygons.

The device we use in laboratory building measurement is the Heron wearable Lidar device produced by Mobile laser scanner Gexcel. The system works with infrared light and its wavelength is 903 nm. While it covers 360 degrees horizontally, it covers a vertical angle of 30 degrees, with 15 degrees from the foot end of the Lidar head and 15 degrees from the head end. Its effective range is 100 m and a manufacturer-specified accuracy of 3 cm can be achieved. [1-7]. Spatial applications such as simulation, animation, modeling and field imaging of the real world can only be done with three-dimensional studies [8]. Light Detection and Ranging (LIDAR) technology allows us to reveal the 3D model of the object without touching it. [9-10]. In other words, Terrestrial laser scanning (YLT) technology is widely used in many professions. [11]. Technically, a laser beam is sent to the object within minutes with a laser scanner, and distance measurement is made with the beams hitting the object and returning. [12-20].

Mersin University Map and Cadastre Laboratory 3D Modeling Studies

The laboratory building where the study was carried out and the moment of measurement with GML are visible (Figure 1).

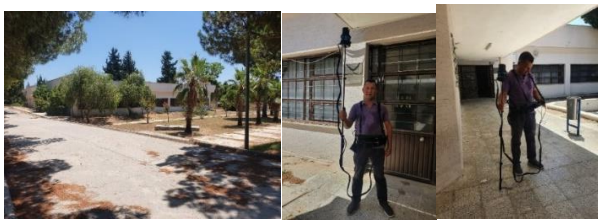
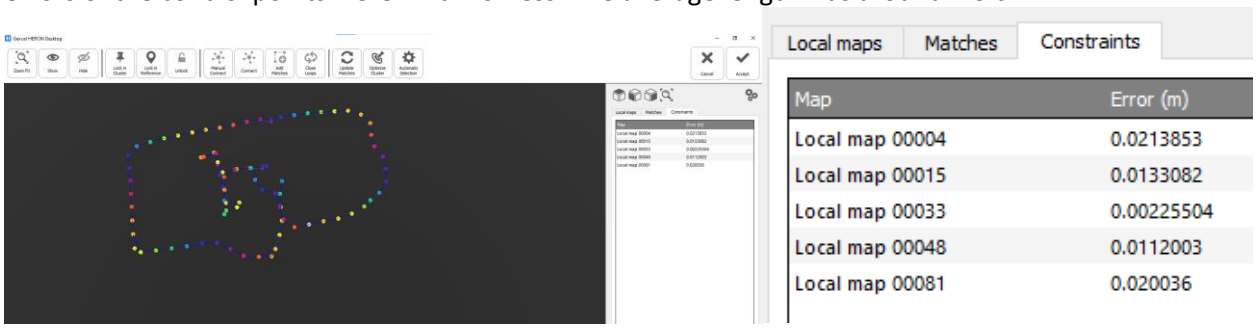


Figure 1. Mersin University Mapping and Cadastre Laboratory and GML measurement.

Figure 2 shows the route and ties used in laboratory measurement. As a result of the adjustment, the errors of the control points were 2.1cm or less. The average length was around 1.3 cm.

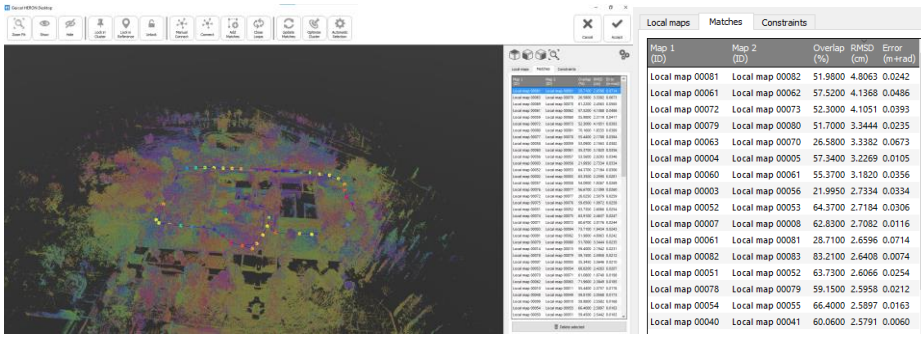


Local maps | Matches | Constraints

Map	Error (m)
Local map 00004	0.0213853
Local map 00015	0.0133082
Local map 00033	0.00225504
Local map 00048	0.0112003
Local map 00081	0.020036

Şekil 2. Dengeleme sonucu kontrol noktalarına isabet eden hata miktarı.

The largest error in the ties was 7 cm at only one point. The average error of all ties is around 1.0 cm. The largest RMSD was 4.8 cm and the mean was 2 cm. The points where errors increase are the points where turns are made in narrow spaces inside the building (Figure 3).



Local maps | Matches | Constraints

Map 1 (ID)	Map 2 (ID)	Overlap (%)	RMSD (cm)	Error (m·rad)
Local map 00081	Local map 00082	51.9800	4.8063	0.0242
Local map 00061	Local map 00062	57.5200	4.1368	0.0486
Local map 00072	Local map 00073	52.3000	4.1051	0.0393
Local map 00079	Local map 00080	51.7000	3.3444	0.0235
Local map 00063	Local map 00070	26.5800	3.3382	0.0673
Local map 00004	Local map 00005	57.3400	3.2269	0.0105
Local map 00060	Local map 00061	55.3700	3.1820	0.0356
Local map 00003	Local map 00056	21.9950	2.7334	0.0334
Local map 00052	Local map 00053	64.3700	2.7184	0.0306
Local map 00007	Local map 00008	62.8300	2.7082	0.0116
Local map 00061	Local map 00081	28.7100	2.6596	0.0714
Local map 00082	Local map 00083	83.2100	2.6408	0.0074
Local map 00051	Local map 00052	63.7300	2.6066	0.0254
Local map 00078	Local map 00079	59.1500	2.5958	0.0212
Local map 00054	Local map 00055	66.4000	2.5897	0.0163
Local map 00040	Local map 00041	60.0600	2.5791	0.0060

Figure 3. Error and RMSD in ties.

An orthophoto of the laboratory is given below (Figure 4).

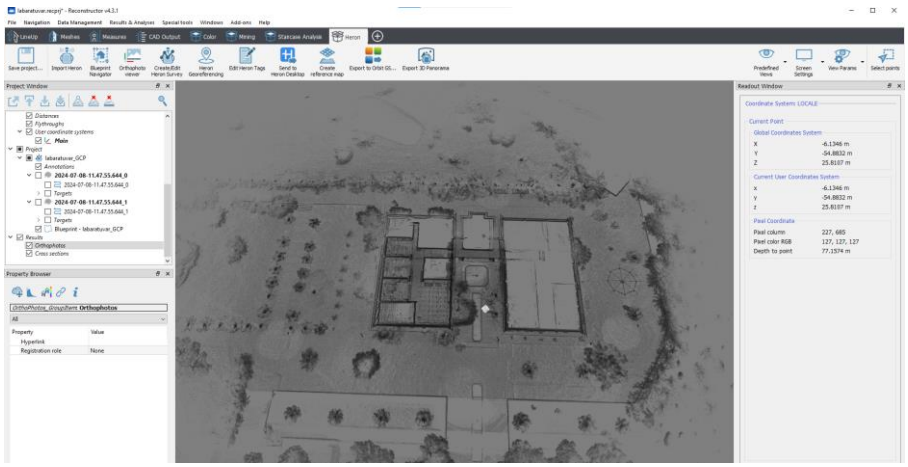


Figure 4. Orthophoto of labrotory

The 3D model of the laboratory from different angles is given below (Figure 5).

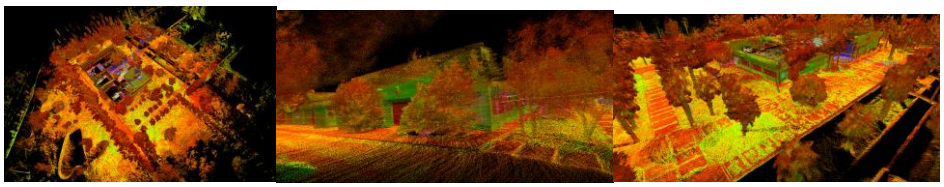


Figure 5. 3D model of the laboratory

Results

In the 3D modeling study of the laboratory building, the largest error in the ties was 7 cm, within the error limits expected from the system.

Discussion

Since no GCP point was placed inside the building in the study, and there were no narrow and detailed corridors and wide turning areas that were not suitable for GML, the error rate in the building increased to 7 cm. A closed route and GCP in the work area prevented the amount of errors from increasing further.

Conclusion

It has been shown in this study that the feasibility of building measurements with WML and, as a result, the error rate increases in the measurement of structures with GML if there are narrow and non-detailed routes within the structure.

References

1. Karabacak, A., & Yakar, M. (2023). 3D modeling of Mersin Akyar Cliffs with wearable mobile LIDAR. *Advanced Engineering Days (AED)*, *6*, 86-89.
2. Yakar, M., & Karabacak, A. (2023). Giyilebilir Mobil Lidar ve Uygulamaları. *Mersin Üniversitesi Harita Mühendisliği Kitapları*.
3. Karabacak, A., & Yakar, M. (2022). Giyilebilir Mobil LİDAR Kullanım Alanları ve Cambazlı Kilisesinin 3B Modellemesi. *Türkiye Lidar Dergisi*, *4*(2), 37-52.
4. Karabacak, A., & Yakar, M. (2023). 3D Modeling of Mufti Abdullah Sıddık Mosque using Wearable Mobile LiDAR. *Advanced LiDAR*, *3*(1), 01-09.
5. Karabacak, A., & Yakar, M. (2023). 3D modeling of Mersin Sarisih Caravanserai with wearable mobile LIDAR. *Advanced Engineering Days (AED)*, *6*, 90-93.
6. Karabacak, A., & Yakar, M. (2023). Giyilebilir Mobil LiDAR'ın Kadastroda Kullanılabilirliği. *Türkiye Lidar Dergisi*, *5*(2), 52-60.
7. Karabacak, A., & Yakar, M. (2023). Incorrect use of wearable mobile LiDAR: Example of Mersin Soli Beach and Ankara National Library Underpass. *Intercontinental Geoinformation Days*, *7*, 234-237.
8. Karabacak, A., & Yakar, M. (2022). Giyilebilir Mobil LİDAR Kullanım Alanları ve Cambazlı Kilisesinin 3B Modellemesi. *Türkiye Lidar Dergisi*, *4*(2), 37-52.
9. Karabacak, A., & Yakar, M. (2023). 3D Modeling of Mufti Abdullah Sıddık Mosque using Wearable Mobile LiDAR. *Advanced LiDAR*, *3*(1), 01-09.
10. Karabacak, A., & Yakar, M. (2023). 3D modeling of Mersin Sarisih Caravanserai with wearable mobile LIDAR. *Advanced Engineering Days (AED)*, *6*, 90-93.
11. Karabacak, A., & Yakar, M. (2023). Giyilebilir Mobil LiDAR'ın Kadastroda Kullanılabilirliği. *Türkiye Lidar Dergisi*, *5*(2), 52-60.
12. Karabacak, A., & Yakar, M. (2023). Incorrect use of wearable mobile LiDAR: Example of Mersin Soli Beach and Ankara National Library Underpass. *Intercontinental Geoinformation Days*, *7*, 234-237.
13. Alptekin A & Yakar M (2020). Mersin Akyar Falezi'nin 3B modeli. Türkiye Lidar Dergisi, 2(1), 05-09
14. Alptekin A & Yakar M (2020). Kaya Bloklarının 3B nokta bulutunun yersel lazer tarayıcı kullanarak elde edilmesi. Türkiye Lidar Dergisi, 2(1), 01-04
15. Nazari, S. W., Akarsu, V., & Yakar, M. (2023). Analysis of 3D Laser Scanning Data of Farabi Mosque Using Various Softwaren . Advanced LiDAR, 3(1), 22–34
16. Yakar, M., Yilmaz, H. M., & Mutluoglu, O. (2009). Comparative Evaluation of Excavation Volume by Terrestrial Laser Scanner and Total Topographic Station Based Methods. *Lasers in Engineering*, *19*(5), 331.
17. Yılmaz, H. M., & Yakar, M. (2006). Lidar (Light Detection And Ranging) Tarama Sistemi. Yapı Teknolojileri Elektronik Dergisi, 2(2), 23-33.

18. Nazari, S. W., Akarsu, V., & Yakar, M. (2023). Analysis of 3D Laser Scanning Data of Farabi Mosque Using Various Softwaren. *Advanced LiDAR*, *3*(1), 22-34.
19. Alptekin, A., & Yakar, M. (2020). Mersin Akyar Falezi'nin 3B modeli. *Türkiye Lidar Dergisi*, *2*(1), 5-9.
20. Yakar, M., Yilmaz, H. M., & Mutluoglu, O. (2014). Performance of photogrammetric and terrestrial laser scanning methods in volume computing of excavtion and filling areas. *Arabian Journal for Science and Engineering*, *39*, 387-394.

Advanced Engineering Days

aed.mersin.edu.tr

3D Modeling with Wearable Mobile LIDAR and Mezitli Stone Bridge example

Atilla Karabacak*[1], Murat Yakar [2]

[1] *Mersin University, Vocational School of Technical Sciences, Mersin, Türkiye, atilakarabacak@mersin.edu.tr*
[2] *Mersin University, Depaartment of Geomatics Engineering, Mersin, Türkiye, myakar@mersin.edu.tr*

Cite this study: Karabacak, A., & Yakar, M. (2024). 3D Modeling with Wearable Mobile LIDAR and Mezitli Stone Bridge example. Advanced Engineering Days, 9, 992-994

Keywords
Remote sensing
Wearable Mobile Lidar
Photogrammetry
Laser Scanning
3D

Abstract

The 3D model and orthophoto of the Ottoman heritage Mezitli Stone Bridge, located in the Mezitli district of Mersin city, were created within error limits with Wearable Mobile LIDAR (GML). In the study, 5 Ground Control Points (GCP) were created and laser scanning was completed in 6 minutes with a closed route. It has been shown that the system can be used for stone bridge measurements.

Introduction

Mersin is a distinguished city of Turkey with cultural heritage. Mezitli stone bridge, built in the 19th century in Mersin Mezitli district, is an important structure in terms of the recent history of the city. The structure is a stone bridge that is strengthened by a single vertical arch made of cut stones. The building has been restored and brought to good condition and serves pedestrian traffic. A GCP was created to increase the accuracy of the study. Field work with GML was completed in approximately 6 minutes. In this study, the stone bridge was modeled in 3D with GML.

Material and Method

Simultaneous Localization and Mapping (SLAM) technology is developing rapidly today and is now used in various fields. Working on SLAM-based technology, the device can determine its location on the map and create a virtual environment of the surrounding area. Calculates an optimal estimate of its actual location. Location data is collected every few seconds, features are matched, and the prediction is constantly improved.One of the main advantages of SLAM is that it can work in places where GPS cannot. As it is known, GPS is ineffective in places where it cannot receive a signal, such as underground. However, SLAM works by interacting directly with its environment, capturing details of the environment and preserving the path traveled. Thus, it overcomes the limitations faced by GPS.

In the study, 5 GCPs distributed along the walking route were measured with a total station device. In the study, location coordinates were given to the polygons. The device we use in stone bridge measurement is the Heron wearable Lidar device produced by Mobile laser scanner Gexcel. It emits infrared laser beams at a wavelength of 903 nm and provides 300,000 dots/second in single rotation mode from 360o horizontal vision and 30o vertical vision. Its range is 100 m. According to the manufacturer's specifications, the system provides a local accuracy of 3 cm and a final global accuracy of 5 cm. The SLAM algorithm can be affected by the presence of system loops and occlusions, as well as the characteristics of the scanned environment, and the accuracy can decrease to 20-50 cm [1-7]. Spatial applications such as simulation, animation, modeling and field imaging of the real world can only be done with three-dimensional studies [8]. Light Detection and Ranging (LIDAR) technology allows us to reveal the 3D model of the object without touching it. [9-10]. In other words, Terrestrial laser scanning (YLT) technology is widely used in many professions. [11]. During measurement with a laser scanner, the laser beam sent from the sensor and the rays that hit the object and return are recorded and distance measurement can be made [12-20].

Mezitli stone Bridge 3D Modeling Studies

The Mezitli Taş bridge, where the work was carried out, can be seen (Figure 1).



Figure1. Mezitli Stone Bridge

The route and ties used in bridge measurement are shown below. As a result of the balancing, the errors of the control points were 1.4 cm or less. It was around 1 cm on average (Figure 2).

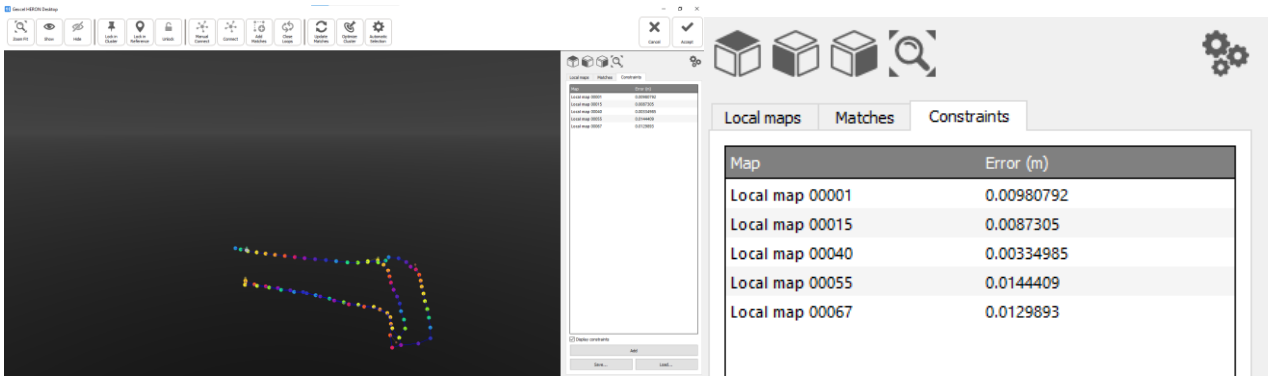


Figure 2. Amount of error hitting control points as a result of adjustment

The largest RMSD and the largest error in the ties were 3.3 cm. The average error of all ties is around 2 cm. An orthophoto of the bridge is given below (Figure 3).

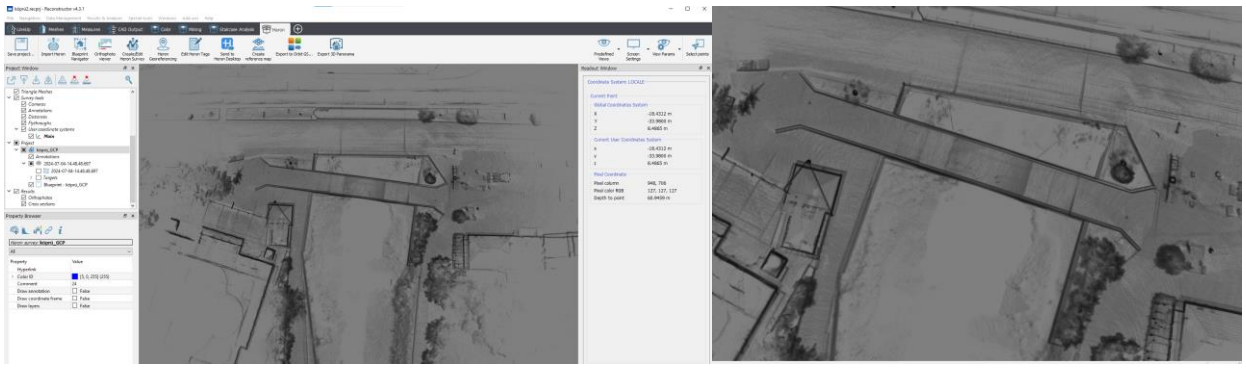


Figure 3. Orthophoto of bridge

The 3D model of the bridge from different angles is given below (Figure 6).

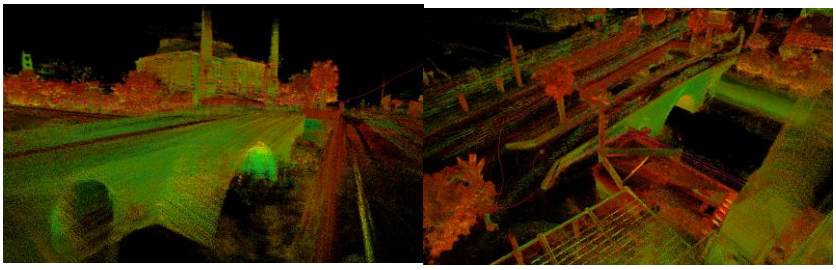


Figure 6. 3D model of the bridge.

Results

In the 3D modeling study of the stone bridge, the largest error in the ties was 3.3 cm, within the error limits expected from the system.

Discussion

Since the GCP point was used in the study, the errors that may occur in the proper distribution of GCP points on the route were small. Creating a route in advance for the route followed for GML and creating the route in a closed way also reduced the error values and made the study successful.

Conclusion

This study has shown that 3D modeling of our cultural heritage can be done with GML and as a result, 3D models and orthophotos can be created with GML within error limits in bridge-shaped structures.

References

1. Karabacak, A., & Yakar, M. (2023). 3D modeling of Mersin Akyar Cliffs with wearable mobile LIDAR. *Advanced Engineering Days (AED)*, *6*, 86-89.
2. Yakar, M., & Karabacak, A. (2023). Giyilebilir Mobil Lidar ve Uygulamaları. *Mersin Üniversitesi Harita Mühendisliği Kitapları*.
3. Karabacak, A., & Yakar, M. (2022). Giyilebilir Mobil LİDAR Kullanım Alanları ve Cambazlı Kilisesinin 3B Modellemesi. *Türkiye Lidar Dergisi*, *4*(2), 37-52.
4. Karabacak, A., & Yakar, M. (2023). 3D Modeling of Mufti Abdullah Sıddık Mosque using Wearable Mobile LiDAR. *Advanced LiDAR*, *3*(1), 01-09.
5. Karabacak, A., & Yakar, M. (2023). 3D modeling of Mersin Sarisih Caravanserai with wearable mobile LIDAR. *Advanced Engineering Days (AED)*, *6*, 90-93.
6. Karabacak, A., & Yakar, M. (2023). Giyilebilir Mobil LiDAR'ın Kadastroda Kullanılabilirliği. *Türkiye Lidar Dergisi*, *5*(2), 52-60.
7. Karabacak, A., & Yakar, M. (2023). Incorrect use of wearable mobile LiDAR: Example of Mersin Soli Beach and Ankara National Library Underpass. *Intercontinental Geoinformation Days*, *7*, 234-237.
8. Yılmaz, H., & Yakar, M. (2016). Lıdar (Lıght Detectıon and Rangıng) Tarama Sistemi. Yapı Teknolojileri Elektronik Dergisi, 2(2), 23-33.
9. Alptekin, A., & Yakar, M. (2020). Mersin Akyar Falezi'nin 3B modeli. Türkiye Lidar Dergisi, 2(1), 5-9.
10. Karataş, L., Alptekin, A., & Yakar, M. (2022). Determination of Stone Material Deteriorations on the Facades with the Combination of Terrestrial Laser Scanning and Photogrammetric Methods: Case Study of Historical Burdur Station Premises. Advanced Geomatics, 2(2), 65–72
11. Kanun, E., Metin, A., & Yakar, M. (2021). Yersel Lazer Tarama Tekniği Kullanarak Ağzıkara Han'ın 3 Boyutlu Nokta Bulutunun Elde Edilmesi. Türkiye Lidar Dergisi, 3(2), 58-64. https://doi.org/10.51946/melid.1025856
12. Alptekin, A., & Yakar, M. (2020). Kaya Bloklarının 3B Nokta Bulutunun Yersel Lazer Tarayıcı Kullanarak Elde Edilmesi. Türkiye Lidar Dergisi, 2(1), 1-4
13. Alptekin A & Yakar M (2020). Mersin Akyar Falezi'nin 3B modeli. Türkiye Lidar Dergisi, 2(1), 05-09
14. Alptekin A & Yakar M (2020). Kaya Bloklarının 3B nokta bulutunun yersel lazer tarayıcı kullanarak elde edilmesi. Türkiye Lidar Dergisi, 2(1), 01-04
15. Nazari, S. W., Akarsu, V., & Yakar, M. (2023). Analysis of 3D Laser Scanning Data of Farabi Mosque Using Various Softwaren . Advanced LiDAR, 3(1), 22–34
16. Yakar, M., Yilmaz, H. M., & Mutluoglu, O. (2009). Comparative Evaluation of Excavation Volume by Terrestrial Laser Scanner and Total Topographic Station Based Methods. Lasers in Engineering, 19(5), 331
17. Yılmaz, H. M., & Yakar, M. (2006). Lidar (Light Detection and Ranging) Tarama Sistemi. *Yapı Teknolojileri Elektronik Dergisi*, *2*(2), 23-33.
18. Nazari, S. W., Akarsu, V., & Yakar, M. (2023). Analysis of 3D Laser Scanning Data of Farabi Mosque Using Various Softwaren. *Advanced LiDAR*, *3*(1), 22-34.
19. Alptekin, A., & Yakar, M. (2020). Mersin Akyar Falezi'nin 3B modeli. *Türkiye Lidar Dergisi*, *2*(1), 5-9.
20. Yakar, M., Yilmaz, H. M., & Mutluoglu, O. (2014). Performance of photogrammetric and terrestrial laser scanning methods in volume computing of excavtion and filling areas. *Arabian Journal for Science and Engineering*, *39*, 387-394.

Advanced Engineering Days

aed.mersin.edu.tr

3D Modeling of Mersin University Vocational School of Technical Sciences with Wearable Mobile LIDAR

Atilla Karabacak [1], Murat Yakar [2]

[1] *Mersin University, Vocational School of Technical Sciences, Mersin, Türkiye, atilakarabacak@mersin.edu.tr*
[2] *Mersin University, Department of Geomatics Engineering, Mersin, Türkiye, myakar@mersin.edu.tr*

Cite this study: Karabacak, A., & Yakar, M. (2024). 3D Modeling of Mersin University Vocational School of Technical Sciences with Wearable Mobile LIDAR. Advanced Engineering Days, 9, 995-998

Keywords
Remote sensing
Wearable Mobile Lidar
Photogrammetry
Laser Scanning
3D

Abstract

In this study, a study was carried out for error limits by producing a 3D model and orthophoto map with Wearable Mobile LIDAR (GML). Vocational School of Technical Sciences located on the Çiftlikköy campus of Mersin University was chosen as the study area. In the study, 6 Ground Control Points (GCP) were established along the walking line in the field and laser scanning was completed in 11 minutes and 31 seconds with a closed route.

Introduction

Spatial applications such as simulation, animation, modeling and field imaging of the real world can only be done with three-dimensional studies [1]. Light Detection and Ranging (LIDAR) technology allows us to reveal the 3D model of the object without touching it. [2-3]. In other words, Terrestrial laser scanning (YLT) technology is widely used in many professions. [4]. Technically, millions of point shots are made on the object within minutes with a laser scanner, and the points that hit the object and return are recorded. [5]. Mobile lidar consists of a system carried on the back or on the vehicle. Handheld or backpack models of human-carryable mobile LIDAR are available on the market. Since the system is carried on a person's back, it can be easily moved and worked in narrow and complex structures, and these systems are called Wearable Mobile Laser Systems (GML) [6-8].

Material and Method

A wearable lidar device was used in the study and 6 GCPs distributed along the walking route were measured with a total station device. In the study, the first two floors of the building were modeled by visiting only the classroom corridors.The system emits infrared light and its wavelength is 903 nm. While it covers 360 degrees horizontally, it covers a vertical angle of 30 degrees, with 15 degrees towards the foot end of the Lidar head and 15 degrees towards the head end. Its effective range is 100 m and an accuracy of 3 cm given by the manufacturer can be achieved. In cases where the SLAM algorithm is not suitable, the error can be up to 50 cm depending on the closure, route and object characteristics. [9-19].

Mersin University Vocational School of Technical Sciences 3D Modeling Studies

In the study carried out within the scope of the project, the measurement moment in the Technical Sciences Vocational School building is shown in Figure 1.



Figure 1. Mersin University Technical Sciences Vocational School measurement moment

Figure 2 shows the route and ties used in measuring the study area. As a result of the balancing, the errors hitting the control points were 0.8 cm.

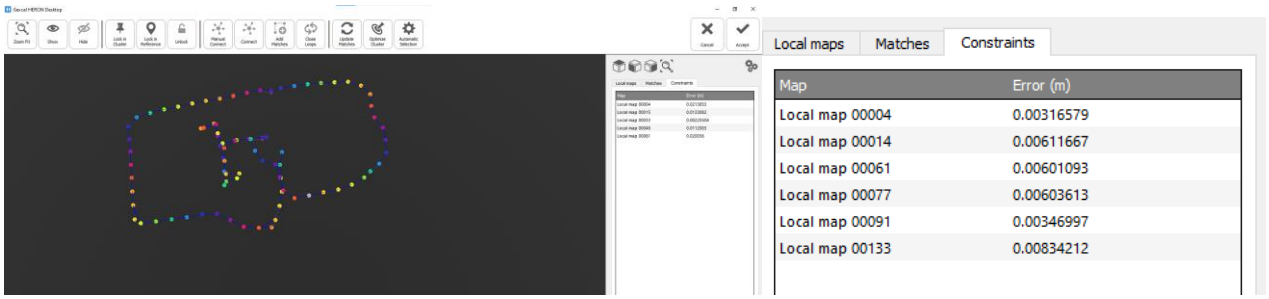


Figure 2. Error amount of control points as a result of adjustment

As a result of balancing, the largest error in the ties was found to be 10 cm. The largest RMSD was 4.8 cm and the mean was 2.5 cm. The points where errors grow are the corridor areas inside the building. The fact that the corridors are long and flat areas with no details increases the amount of error (Figure 3).

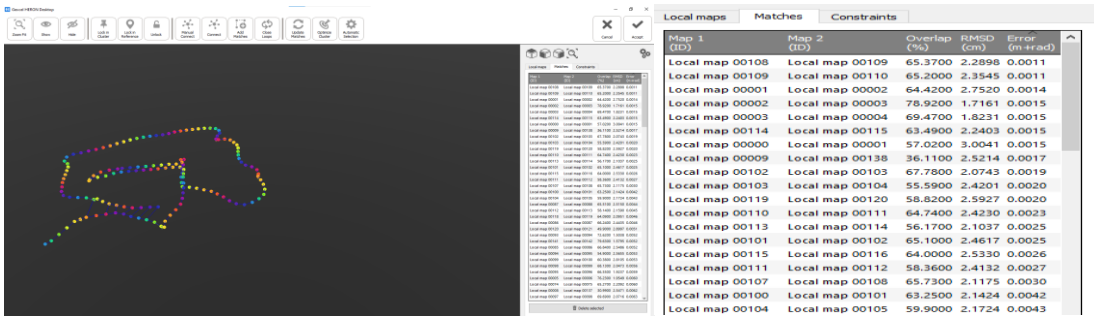


Figure 3. Error amount of control points as a result of adjustment

While traveling on the route during the odemeter stage (Figure 4 left), the route gets disrupted at the staircase section (Figure 4 right). This situation can be resolved with different parameters.

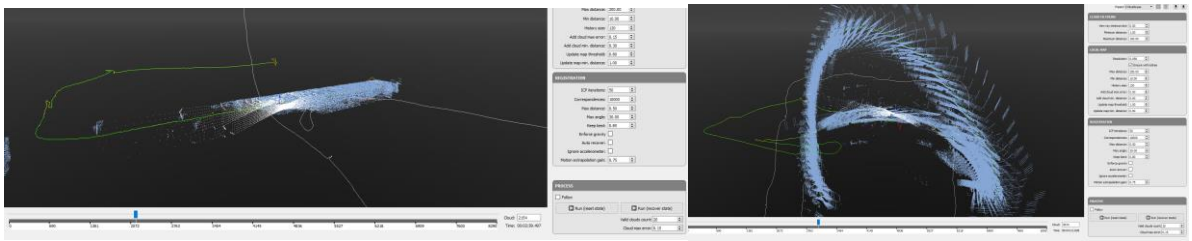


Figure 4. A problematic area in the Adjustment Odometer stage.

The orthophoto data obtained from the school building can be seen in Figure 5.

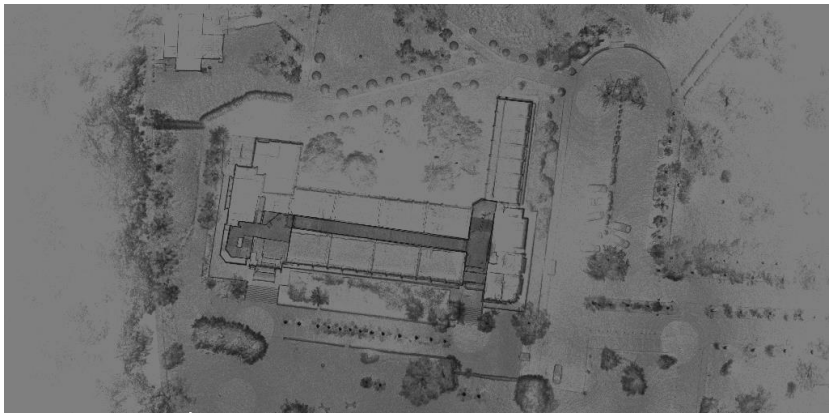


Figure 5. Orthophoto of the study area

Vocational School of Technical Sciences 3D model is shown below from different angles (Figure 6).

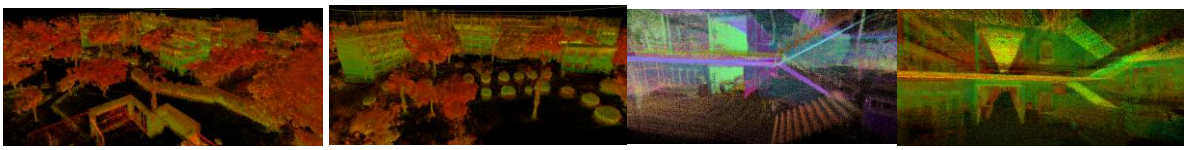


Figure 6. 3D model of Vocational School of Technical Sciences

Results

In the 3D modeling study of the laboratory building, the largest error in the ties was 10 cm, within the error limits expected from the system. It has been shown that the system can be used for indoor measurements, but the amount of error increases in long and undetailed corridors within the building.

Conclusion

In this study, the building is reinforced concrete and has 4 floors. To measure the laboratory building, a ground control point was established around the building. Walking time with GML took approximately 11.5 minutes. Since no GCP point was placed inside the building in the study, and there was a 42 m long corridor without details, which was not suitable for GML, this resulted in an error of up to 10 cm inside the building.

It has been demonstrated that building measurements can be made with GML, and as a result, it has been shown in this study that when measuring structures with GML, the error rate increases if there are no details in the structure and long routes.

References

1. Yılmaz, H., & Yakar, M. (2016). Lıdar (Lıght Detectıon And Rangıng) Tarama Sistemi. Yapı Teknolojileri Elektronik Dergisi, 2(2), 23-33.
2. Alptekin, A., & Yakar, M. (2020). Mersin Akyar Falezi'nin 3B modeli. Türkiye Lidar Dergisi, 2(1), 5-9.
3. Karataş, L., Alptekin, A., & Yakar, M. (2022). Determination of Stone Material Deteriorations on the Facades with the Combination of Terrestrial Laser Scanning and Photogrammetric Methods: Case Study of Historical Burdur Station Premises. Advanced Geomatics, 2(2), 65–72
4. Kanun, E., Metin, A., & Yakar, M. (2021). Yersel Lazer Tarama Tekniği Kullanarak Ağzıkara Han'ın 3 Boyutlu Nokta Bulutunun Elde Edilmesi. Türkiye Lidar Dergisi, 3(2), 58-64. https://doi.org/10.51946/melid.1025856
5. Alptekin, A., & Yakar, M. (2020). Kaya Bloklarının 3B Nokta Bulutunun Yersel Lazer Tarayıcı Kullanarak Elde Edilmesi. Türkiye Lidar Dergisi, 2(1), 1-4.
6. Karabacak, A., & Yakar, M. (2023). 3D modeling of Mersin Akyar Cliffs with wearable mobile LIDAR. *Advanced Engineering Days (AED)*, *6*, 86-89.
7. Yakar, M., & Karabacak, A. (2023). Giyilebilir Mobil Lidar ve Uygulamaları. *Mersin Üniversitesi Harita Mühendisliği Kitapları*.
8. Karabacak, A., & Yakar, M. (2022). Giyilebilir Mobil LİDAR Kullanım Alanları ve Cambazlı Kilisesinin 3B Modellemesi. *Türkiye Lidar Dergisi*, *4*(2), 37-52.
9. Karabacak, A., & Yakar, M. (2023). 3D Modeling of Mufti Abdullah Sıddık Mosque using Wearable Mobile LiDAR. *Advanced LiDAR*, *3*(1), 01-09.
10. Karabacak, A., & Yakar, M. (2023). 3D Modeling of Mersin Sarisih Caravanserai with wearable mobile LIDAR. *Advanced Engineering Days (AED)*, *6*, 90-93.
11. Karabacak, A., & Yakar, M. (2023). Giyilebilir Mobil LiDAR'ın Kadastroda Kullanılabilirliği. *Türkiye Lidar Dergisi*, *5*(2), 52-60.
12. Karabacak, A., & Yakar, M. (2023). Incorrect use of wearable mobile LiDAR: Example of Mersin Soli Beach and Ankara National Library Underpass. *Intercontinental Geoinformation Days*, *7*, 234-237.
13. Alptekin A & Yakar M (2020). Mersin Akyar Falezi'nin 3B modeli. Türkiye Lidar Dergisi, 2(1), 05-09
14. Alptekin A & Yakar M (2020). Kaya Bloklarının 3B nokta bulutunun yersel lazer tarayıcı kullanarak elde edilmesi. Türkiye Lidar Dergisi, 2(1), 01-04
15. Nazari, S. W., Akarsu, V., & Yakar, M. (2023). Analysis of 3D Laser Scanning Data of Farabi Mosque Using Various Softwaren . Advanced LiDAR, 3(1), 22–34

16. Yakar, M., Yilmaz, H. M., & Mutluoglu, O. (2009). Comparative Evaluation of Excavation Volume by Terrestrial Laser Scanner and Total Topographic Station Based Methods. Lasers in Engineering, 19(5), 331
17. Yılmaz, H. M., & Yakar, M. (2006). Lidar (Light Detection and Ranging) Tarama Sistemi. *Yapı Teknolojileri Elektronik Dergisi*, *2*(2), 23-33.
18. Nazari, S. W., Akarsu, V., & Yakar, M. (2023). Analysis of 3D Laser Scanning Data of Farabi Mosque Using Various Softwaren. *Advanced LiDAR*, *3*(1), 22-34.
19. Alptekin, A., & Yakar, M. (2020). Mersin Akyar Falezi'nin 3B modeli. *Türkiye Lidar Dergisi*, *2*(1), 5-9.

Advanced Engineering Days

aed.mersin.edu.tr

Investigation of natural factors affecting landslide formation

Aydın Alptekin*[1], Murat Yakar [1]

[1] *Mersin University, Department of Geomatics Engineering, Türkiye, aydinalptekin@mersin.edu.tr, myakar@mersin.edu.tr*

Cite this study: Alptekin, A., & Yakar, M. (2024). Investigation of natural factors affecting landslide formation. Advanced Engineering Days, 9, 999-1001

Keywords
Landslide
Natural factors
Soil stability

Abstract

Landslides are common natural hazards that can result in significant loss of life and property. This study investigates natural factors influencing landslide occurrence, including rivers, rainfall, aspect, slope, elevation, tectonic structure, vegetation, and clayey materials. These factors contribute to the reduction of soil stability and facilitate slope failures. Multiple factors typically combine to trigger landslides.

Introduction

Landslide is defined as the movement of a mass of rock or unconsolidated material down a slope under the influence of gravity. The soil mass is under equilibrium state by the forces acting on it. These forces are the triggering and resisting forces of the slide. When the triggering forces are stronger, a landslide will occur in the soil.

Landslides are geological events caused by the movement of materials on the earth's surface downward along a slope under the influence of gravity. They cause the reshaping of the earth's surface.

Results

River

Within a basin, characteristics such as stream length, frequency, density, and catchment area affect fluvial processes and cause failures due to toe erosion [1]. Streams alter the slope angle by eroding the toe slope and saturating the material below the slope. This destabilizes the slope and causes landslides.

Rainfall

Intense rainfall and snowmelt increase the hydrostatic pressure, disturbing the balance of soil masses. Water facilitates soil slippage, reduces cohesion and the coefficient of friction, and increases the plasticity limit, thus causing landslides [2]. The duration, amount and intensity of rainfall that triggers landslides must be known in landslide investigations.

Aspect

While not a direct causal factor in slope failure formation, exposure to sunlight, a key meteorological variable, aspect is significant due to its correlation with precipitation and wind events [3]. In the Northern Hemisphere, north-facing slopes exhibit higher humidity levels and prolonged snow cover periods relative to south-facing slopes owing to reduced solar insolation [1].

Slope

Steeper slopes are more prone to landslides compared to gentler slopes [4]. As the slope increases, the shear stress on the materials on the slope also increases. When this stress exceeds the strength of the material, a landslide occurs.

Steep slopes commonly cause landslide types such as rockfalls and debris flows, which are typically rapid and destructive. Moderate slopes provide conditions for a variety of landslide types, including both rapid and slow-moving movements. Gentle slopes are usually associated with slower-moving landslides like earth creep.

Elevation

Although elevation is not a direct factor, its importance increases when combined with other factors. Higher altitudes lead to increased precipitation, which increases the amount of water in the soil and thus the risk of landslides. As altitude increases, temperature decreases. This condition increases the frequency of freeze-thaw cycles in rocks, accelerating physical weathering and increasing the risk of landslides.

Tectonic structure

Seismic movements cause the movement of ground masses. Seismic waves can cause ground and rock masses to displace and move in the direction of the slope.

Vegetation

Vegetation is closely related to soil and plays a significant role in the occurrence and impacts of landslides. It has both positive and negative effects. Vegetation significantly reduces landslide risk by strengthening soil structure, retaining water, and preventing erosion. However, in some special cases, vegetation can also increase landslide risk. Therefore, the impact of vegetation should also be considered when assessing landslide risk. Landslides are less frequent in areas without vegetation compared to forested areas. This is because plant roots penetrate deep into the slope, adding weight to the slope and reducing stability [1].

Argillaceous material

Clayey materials trigger a series of mechanisms that initiate landslides due to their fine-grained structure and changing properties when interacting with water. Clay minerals have the ability to absorb water molecules. This causes the clay layer to become saturated with water and swell. The swollen clay layer increases the pore water pressure within the soil, reducing the soil strength, and increasing the landslide potential.

Moreover, the voids between clay minerals allow water to move easily. Water that enters the soil during rainy periods or as a result of irrigation activities moves downward through the clay layers. This movement causes the clay layer to become slippery and the ground stability to deteriorate. Especially on sloping terrains, the soil mass on clay layers begins to move downward under the influence of gravity, resulting in landslides.

As a result, the significance of clayey materials in landslide formation cannot be overlooked. Therefore, the presence and properties of clayey materials must be considered in landslide risk assessment studies. By determining the engineering properties of clayey soils through geotechnical investigations, measures can be taken to reduce landslide risk. These measures may include the installation of drainage systems, stabilization of slopes, and relocation of settlements to suitable areas.

Clays have a high water retention capacity. This leads to an increase in volume in the soil, reducing friction and shear strength. For this reason, landslides are frequently observed in formations with high clay content, while they are less common in formations with low clay content.

Conclusion

To take the necessary precautions against landslides, it is necessary to periodically monitor the areas at risk of landslides. This can be achieved by conducting field observations and periodically preparing digital surface models (DSM) and orthophotos of the region. Landslide occurrence is a complex process resulting from the interaction of multiple factors rather than a single factor.

Acknowledgement

This study is supported by Mersin University Scientific Research Projects coordination Unit. Project Number: 2023-1-TP3-4846

References

1. Cihangir, M. E. (2018). Kelkit Çayi vadisinde (Umurca-Koyulhisar arasi) heyelan riskinin belirlenmesi. [Doktora Tezi, İstanbul Üniversitesi]. İstanbul, Türkiye
2. Sür, Ö. (1972). Heyelan Olaylarına sebep olan faktörler ve bunların Türkiye'de etkili bulunduğu alanlar. Coğrafya Araştırmaları Dergisi, (1-2), 215-223.
3. Kaçka, N. (2019). Karamürsel (Kocaeli) güneyi ve güneybatısındaki heyelanların sismik deformasyon analizi. [Doktora Tezi, Ankara Üniversitesi]. Ankara, Türkiye
4. Biçer, Ç. T. (2017). Heyelan risk haritalamasi üzerine yari sayısal bir değerlendirme. [Doktora Tezi, Hacettepe Üniversitesi]. Ankara, Türkiye